REPORT DOCUMENTATION PAGE

Form Approved OMB NO. 0704-0188

The public reporting burden for this collection of information is estimated to average 1 hour per response, including the time for reviewing instructions, searching existing data sources, gathering and maintaining the data needed, and completing and reviewing the collection of information. Send comments regarding this burden estimate or any other aspect of this collection of information, including suggesstions for reducing this burden, to Washington Headquarters Services, Directorate for Information Operations and Reports, 1215 Jefferson Davis Highway, Suite 1204, Arlington VA, 22202-4302. Respondents should be aware that notwithstanding any other provision of law, no person shall be subject to any oenalty for failing to comply with a collection of information if it does not display a currently valid OMB control number.
PLEASE DO NOT RETURN YOUR FORM TO THE ABOVE ADDRESS.

1. REPORT DATE (DD-MM-YYYY)	2. REPORT TYPE	3. DATES COVERED (From - To)
28-04-2014	Final Report	1-Apr-2010 - 30-Jun-2010

4. TITLE AND SUBTITLE
Final Report for Support for 2010 Symposium on the Application of Geophysics to Engineering and Environmental Problems (SAGEEP)

5a. CONTRACT NUMBER
W911NF-10-1-0080

5b. GRANT NUMBER

5c. PROGRAM ELEMENT NUMBER
611102

6. AUTHORS
Vic Labson

5d. PROJECT NUMBER

5e. TASK NUMBER

5f. WORK UNIT NUMBER

7. PERFORMING ORGANIZATION NAMES AND ADDRESSES
Environmental and Engineering Geophysica
1720 S. Bellaire St., Ste. 110

Denver, CO 80222 -4303

8. PERFORMING ORGANIZATION REPORT NUMBER

9. SPONSORING/MONITORING AGENCY NAME(S) AND ADDRESS (ES)
U.S. Army Research Office
P.O. Box 12211
Research Triangle Park, NC 27709-2211

10. SPONSOR/MONITOR'S ACRONYM(S)
ARO

11. SPONSOR/MONITOR'S REPORT NUMBER(S)
57970-EV-CF.1

12. DISTRIBUTION AVAILIBILITY STATEMENT
Approved for Public Release; Distribution Unlimited

13. SUPPLEMENTARY NOTES
The views, opinions and/or findings contained in this report are those of the author(s) and should not contrued as an official Department of the Army position, policy or decision, unless so designated by other documentation.

14. ABSTRACT
A wide variety of engineering geophysical presentations on topics that reflect the diverse nature of our applied science. Jim LoCoco, Technical Program Chair, and the local organizing committee have been successful in building a program of interesting sessions on timely issues. In addition to traditional topics,
some non-traditional sessions have been assembled, including a new session on
Geophysics in Intelligent Geoconstruction. As always, technical presentations will provide the year's best look at the work going on today in our field.

15. SUBJECT TERMS
Geophysics, Engineering, Environment

16. SECURITY CLASSIFICATION OF:			17. LIMITATION OF ABSTRACT	15. NUMBER OF PAGES	19a. NAME OF RESPONSIBLE PERSON
a. REPORT	b. ABSTRACT	c. THIS PAGE			William Doll
UU	UU	UU	UU		19b. TELEPHONE NUMBER 865-483-2548

Report Title

Final Report for Support for 2010 Symposium on the Application of Geophysics to Engineering and Environmental Problems (SAGEEP)

ABSTRACT

A wide variety of engineering geophysical presentations on topics that reflect the diverse nature of our applied science. Jim LoCoco, Technical Program Chair, and the local organizing committee have been successful in building a program of interesting sessions on timely issues. In addition to traditional topics,
some non-traditional sessions have been assembled, including a new session on
Geophysics in Intelligent Geoconstruction. As always, technical presentations will provide the year's best look at the work going on today in our field.

Enter List of papers submitted or published that acknowledge ARO support from the start of the project to the date of this printing. List the papers, including journal references, in the following categories:

(a) Papers published in peer-reviewed journals (N/A for none)

Received Paper

TOTAL:

Number of Papers published in peer-reviewed journals:

(b) Papers published in non-peer-reviewed journals (N/A for none)

Received Paper

TOTAL:

Number of Papers published in non peer-reviewed journals:

(c) Presentations

Number of Presentations:

Non Peer-Reviewed Conference Proceeding publications (other than abstracts):

Received Paper

TOTAL:

Number of Non Peer-Reviewed Conference Proceeding publications (other than abstracts):

Peer-Reviewed Conference Proceeding publications (other than abstracts):

Received Paper

TOTAL:

Number of Peer-Reviewed Conference Proceeding publications (other than abstracts):

(d) Manuscripts

Received Paper

TOTAL:

Number of Manuscripts:

Books

Received Paper

TOTAL:

Patents Submitted

Patents Awarded

Awards

Graduate Students

NAME	PERCENT_SUPPORTED

FTE Equivalent:
Total Number:

Names of Post Doctorates

NAME	PERCENT_SUPPORTED

FTE Equivalent:
Total Number:

Names of Faculty Supported

NAME	PERCENT_SUPPORTED

FTE Equivalent:
Total Number:

Names of Under Graduate students supported

NAME	PERCENT_SUPPORTED

FTE Equivalent:
Total Number:

Student Metrics

This section only applies to graduating undergraduates supported by this agreement in this reporting period

The number of undergraduates funded by this agreement who graduated during this period: .....

The number of undergraduates funded by this agreement who graduated during this period with a degree in science, mathematics, engineering, or technology fields:.....

The number of undergraduates funded by your agreement who graduated during this period and will continue to pursue a graduate or Ph.D. degree in science, mathematics, engineering, or technology fields:.....

Number of graduating undergraduates who achieved a 3.5 GPA to 4.0 (4.0 max scale):.....

Number of graduating undergraduates funded by a DoD funded Center of Excellence grant for Education, Research and Engineering:.....

The number of undergraduates funded by your agreement who graduated during this period and intend to work for the Department of Defense .....

The number of undergraduates funded by your agreement who graduated during this period and will receive scholarships or fellowships for further studies in science, mathematics, engineering or technology fields: .....

Names of Personnel receiving masters degrees

NAME

Total Number:

Names of personnel receiving PHDs

NAME

Total Number:

Names of other research staff

NAME PERCENT_SUPPORTED

FTE Equivalent:
Total Number:

Sub Contractors (DD882)

Inventions (DD882)

Scientific Progress

23rd Annual Symposium on the Application of Geophysics to Engineering and Environmental Problems (SAGEEP).

Technology Transfer

Home
EEGS Information
GOVT Sponsors
Table of Contents
Author Index
Disclaimer
Search Proceedings
CD-ROM Support
Copyright

Dear Colleagues

Welcome to Keystone, Colorado for our 23rd Annual Symposium on the Application of Geophysics to Engineering and Environmental Problems (SAGEEP). The conference also serves as the annual meeting of the Environmental and Engineering Geophysical Society (EEGS). This year's theme is "Building New Markets for Geophysics".

By now, you are probably aware of the many mountain recreational activities there are to choose from in Summit County as you decide how to spend your free time. Ski, snowshoe, or hike at lower elevations – or stop by the registration area to ask about other options. Keystone operates a local shuttle free for guests. Summit County operates a free bus service from Keystone to Arapahoe Basin ski area and other nearby communities including Frisco, Silverthorne, Breckenridge and Copper Mountain. April weather can be cool, and walking can be sloppy, so before heading out for the day, check conditions and plan accordingly.

The conference begins late afternoon Sunday with the annual Ice Breaker. Be sure to attend – this is a good time to reconnect with friends, make new acquaintances, relax, and make plans for the conference week. Please take a moment to review the technical program and the wide variety of engineering geophysical presentations on topics that reflect the diverse nature of our applied science. Jim LoCoco, Technical Program Chair, and the local organizing committee have been successful in building a program of interesting sessions on timely issues. In addition to traditional topics, some non-traditional sessions have been assembled, including a new session on Geophysics in Intelligent Geoconstruction. As always, technical presentations will provide the year's best look at the work going on today in our field.

Monday morning's Keynote Speaker will be Dr. Robert Grimm of the Southwest Research Institute in Boulder, Colorado, who will present his talk "Extraterrestrial Near-Surface Geophysics", review work done during the Apollo Moon landings, discuss an array of possible robotic explorers, and point to future human exploration of the Moon, Mars, and asteroids. On Tuesday, we're pleased to offer the EEGS Luncheon featuring the EEGS/Geonics Early Career Award winner, Dr. Niklas Linde, who will speak on "Joint Inversion in Hydrogeophysics" after a short awards ceremony.

New this year to the SAGEEP program is the SAGEEP Café in the Longs Peak Foyer area of the Conference Center on Monday and Wednesday, offering an alternative for lunch as well as the Hot Topics poster session featuring posters on late breaking discoveries, observations, and results too fresh to have been submitted to the Technical Program and the Proceedings CD. If you haven't gotten tickets for the SAGEEP Café, check with registration for availability.

Tuesday evening you will want to enjoy a comfortable social time of cocktails and a fine dinner with wine at Keystone Ranch, highly regarded for its excellent cuisine and warm, mountain resort ambiance.

On both Monday and Wednesday, exhibitors will be sponsoring happy hours after the technical talks in the Exhibit Hall (Colorado Rockies Ballroom).

And, finally, and if you haven't already, consider the Short Course and Workshop line up and register for an expanded version of last year's popular course on Principles and Applications of Seismic Refraction Tomography, 2) a course on the Implementation and Interpretation of Time-Domain Electromagnetic Data presented by David Fitterman, and 3) a course on the Geophysical Investigations of Dams and Levees. Additionally, a Workshop will be offered on Environmental Applications for new Time-Domain Airborne Electromagnetic Systems. Geophysical experts, novices, and interested professionals in other fields can all benefit from the opportunities to

learn more at Keystone this year. We're pleased you could join us.

Welcome,

Vic Labson
SAGEEP 2010 General Chair

Copyright 2010 Environmental and Engineering Geophysical Society

Produced by X-CD Technologies Inc.

Home
EEGS Information
GOVT Sponsors
Table of Contents
Author Index
Disclaimer
Search Proceedings
CD-ROM Support
Copyright

Environmental and Engineering Geophysical Society (EEGS)

Your professional society is proud to present the Symposium on the Application of Geophysics to Engineering and Environmental Problems (SAGEEP) 2010 Proceedings

Click here to see the SAGEEP Committee members

EEGS invites you to visit its website at www.eegs.org to learn more about the society's programs and products including:

Membership

Journal of Environmental and Engineering Geophysics

FastTIMES Newsletter

Publications

Additional SAGEEP Proceedings

Future SAGEEP Programs and much more!

EEGS is the premier society championing the development and appropriate use of environmental and engineering geophysics.

Copyright 2010 Environmental and Engineering Geophysical Society

Produced by X-CD Technologies Inc.

Home
EEGS Information
GOVT Sponsors
Table of Contents
Author Index
Disclaimer
Search Proceedings
CD-ROM Support
Copyright

Government Sponsorship of SAGEEP 2010

EEGS is grateful to the following government agencies that have agreed to sponsor SAGEEP 2010, and the individuals within these organizations (cited below) who helped to secure the commitment. Their financial support ensures that SAGEEP will continue to maintain a high standard of quality and ultimately makes EEGS a stronger organization.

US GEOLOGICAL SURVEY

The US Geological Survey is the science agency of the Department of the Interior. Created by an act of Congress in 1879, the USGS serves the Nation as an independent fact-finding agency that collects, monitors, analyzes, and provides scientific understanding about natural resource conditions, issues, and problems. The value of the USGS to the Nation rests on its ability to carry out studies on a national scale and to sustain longterm monitoring and assessment of natural resources. Because it has no regulatory or management mandate, the USGS provides impartial science that serves the needs of our changing world. The diversity of scientific expertise enables the USGS to carry out large-scale, multi-disciplinary investigations that build the base of knowledge about the Earth.

Web site: www.usgs.gov

SERDP/ESTCP

The Environmental Security Technology Certification Program (ESTCP) is a corporate Department of Defense (DoD) program that promotes innovative, cost-effective environmental technologies through demonstration and validation at DoD sites. The Strategic Environmental Research and Development Program (SERDP) identifies, develops, and transitions environmental technologies that relate directly to defense mission accomplishment.

Web sites: www.estcp.org and www.serdp.org
Contact: Dr. Jeffrey Marqusee
Ph: 703-696-2120
email: Jeffrey.Marqusee@osd.mil

ARMY RESEARCH OFFICE

The primary mission of the ARL Army Research Office is to serve as the Army's premier extramural basic research agency, funding basic research at universities in the engineering, physical, information and life sciences; developing and exploiting innovative advances to insure the Nation's technological superiority.

Web site: www.aro.army.mil

U.S. DEPARTMENT OF TRANSPORTATION
FEDERAL HIGHWAY ADMINISTRATION
CENTRAL FEDERAL LANDS HIGHWAY DIVISION

The Federal Highway Administration (FHWA) is responsible for ensuring the safety, efficiency, and economy of the Nation's highway transportation system. The Federal Highway Administration oversees all phases of highway policy, planning, research, design, operations, construction, and maintenance. The Federal Aid Highway Program offices, in cooperation

with the State Departments of Transportation, administer the nation's comprehensive highway system. The Federal Lands Highway Program offices in cooperation with Federal land managing agencies provide transportation-engineering services for planning, design, construction, and rehabilitation of the highways and bridges providing access to federally owned lands. The Federal Lands Highway organization also provides training, technology, deployment, engineering services, and products to other customers.

Web sites: www.cflhd.gov www.fhwa.dot.gov/flh
Contact: Mr. Khamis Haramy
Ph: 303-716-2192
email: khamis.haramy@fhwa.dot.gov

Copyright 2010 Environmental and Engineering Geophysical Society

Produced by X-CD Technologies Inc.

Home
EEGS Information
GOVT Sponsors
Table of Contents
Author Index
Disclaimer
Search Proceedings
CD-ROM Support
Copyright

Table of Contents

Advances in GPR Modeling, Imaging, and Inversion
Best of Near-Surface 2009 - EAGE Dublin
Borehole Geophysics
Dam, Levee and Reservoir
Electromagnetic Induction: Methods and Concepts
Geophysics in Agriculture
Geophysics in Hydrogeology
Geophysics in Intelligent Geoconstruction
Geotechnical & Geological Mapping
High-Resolution Potential Field Methods
Karst Geophysics
Near-Surface Seismic Methods #1
Near-Surface Seismic Methods #2
Non-Destructive Evaluation of Infrastructure
Poster Session
Resistivity & IP Imaging
Urban and Archaeological Geophysics
UXO/MEC

Copyright 2010 Environmental and Engineering Geophysical Society

Produced by X-CD Technologies Inc.

NOT SUCH AN EASY TARGET: A STUDENT CASE STUDY USING GROUND PENETRATING RADAR TO LOCATE BURIED MORTARS AT WEST POINT

Anton V. Faustmann, U.S. Army, Fort Stewart, GA
Katelin R. Abraham,U.S. Army, Lakewood, WA
Mindy A. Kimball,U.S. Army, Silver Spring, MD
Benjamin M. Wallen,U.S. Army, Round Rock, TX

Abstract

One, or possibly two, of the 12-inch coastal artillery mortars used for cadet artillery instruction between 1902 and 1931 remain buried roughly two to six meters below the surface of the northern edge of the Plain at the United States Military Academy at West Point, New York. This survey used a Sensors and Software PulseEKKO 1000 Ground Penetrating Radar (GPR), 225 MHz antennae, together with geo-referenced imagery to attempt to locate these mortars. The intrinsic value of 132 tons of buried iron, the historic value of the mortars, and sheer curiosity provided the impetus for this study. Geo-referenced aerial photography of Battery Byrne provided a starting point for the search, and we developed a data collection grid to estimate the most likely location.

We collected data in conjunction with independent study classes from September 2007 through April 2008, collecting a total of 7,690 GPR traces. After processing initial data with EkkoView and EkkoMapper, we found a distinct hyperbola at Trace 386 of Line 16. We then constructed a tighter grid to characterize our point in higher resolution, but the reflection we identified may be too shallow to be the first mortar. For the second mortar, we focused on a location identified from a 2002 GPR survey, which indicated a mortar near the corner of a gravel pit on the grass of the Plain. The data indicated a small hyperbola shape in the East-West transect of Line 12, so we designed a second tighter grid to further investigate. Again, the results were not as conclusive as we had hoped. Additional research with another ground-truthing method, such as a magnetic or a gravity survey, could validate our findings.

This survey has opened the way for future work. More GPR data with a different frequency would be beneficial, preferably 110 MHz to achieve greater penetration. Alternate methods of near surface geophysics would be very valuable, such as magnetic, gravity, or even seismic refraction. Additionally, a partnership with the Department of Civil Engineering could determine the costs, benefits, and feasibility of an excavation project. The West Point Historian may eventually want to erect a plaque describing the historical importance of Battery Byrne for the artillery instruction of cadets. Finally, locating these mortars would provide an interesting geophysics laboratory exercise for future West Point cadets in science and engineering classes.

Background

In 1929, the two massive seacoast mortars from Battery Byrne discharged their final volleys. The century-long existence of the West Point Artillery School had, in effect, ended. The huge mortars and the remnants of Battery Byrne were eventually buried in place in 1931, but very few records remain describing their location and condition.

Figure 1: Photographs from the early 20th century show the breach-loaded mortars at Battery Byrne, operated by 12-cadet teams, poised at their firing angles (USMA Library, 1915-1929).

Battery Bryne was constructed in the early 1900s inside a kettle lake known as Execution Hollow. The natural depression gained its nick-name during the late 1800s when criminals and traitors were put to death during the Revolutionary War. In 1910, portions of the kettle lake were filled with earth from a nearby excavation (possibly soil, granitic gneiss, and glacial till) in order to expand the parade field known as the Plain and to construct a coastal firing battery for cadet artillery practice (Schwabe, 1987). In 1911, two 15-ton model M1890 mortar tubes (Figure 1) were mounted in Battery Byrne on 48-ton model M1896 carriages, which rotated on a 52-ton traversing base (U.S. Ordnance Office, 1925).

In 1931, the entire Battery Byrne was filled in to completely level off the Plain, bury the obsolete coastal artillery mortars, and expand the parade field. Firsthand accounts from the burial of the mortars indicate that the guns were in good condition and were coated in cosmoline (a protectant used on artillery pieces to prevent corrosion), possibly to be recovered at a later date for their metallic content (Nock, 1987). Other accounts indicate that several salvage attempts were made through 1968, and that the Ordnance Department brought either one or both of the guns to the surface before the Battery was completely filled in an attempt to torch cut the tubes for use as scrap metal (Nock, 1987). The welding equipment available at the time was not sufficient to cut the tubes and attempts to auction the tubes met little interest because the highly tempered nature of the steel prevented it from being "reduced" (Hercz, 1987).

In 2002, Brigadier General (retired) King conducted a geophysical survey using GPR and magnetic investigations to locate the buried mortar tubes. He concluded the location of one mortar, at a depth of approximately 2.5 m, but the software used by the GPR was optimized for locating utility pipes and may have falsely adjusted the depth and size of the possible mortar as if it were a pipe (King, 2002). We chose this site for further investigation due to the attractive nature and likelihood of finding 130,000 pounds of metal in the shallow subsurface of a parade field. Our department owned the GPR equipment, and we had easy access to the site location nearly every day. We thought it to be an easy target.

Data Collection and Processing

We collected 57 lines of data using a Sensors & Software PulseEKKO 1000 GPR, 225 MHz antennae, 0.1 m step size, 200 ns time window, and 64 stacks, using a hand-held configuration (Figure 2). We estimated a depth of penetration of about 4 m through the field, which was comprised of landscaped grass, topsoil, graded fill, and glacial till. We considered using 110 MHz antennae to

achieve greater resolution and deeper depths, but the physical size of the antennae were too large to fit beneath two sets of permanently-mounted metal bleachers directly at the suspected location of the mortars.

Figure 2: PulseEKKO 1000, 225 MHz GPR configuration during data collection. Notice the graded gravel pad beneath the permanently-mounted bleachers in left photo. View of Hudson River and Battle Monument in right photo (same monument as seen in early 1900s photo at Figure 1).

Several cultural features presented obstacles for our survey. The grass on the parade field is highly manicured, watered regularly, and fertilized often. The water and chemical content of the soil likely caused noise in the GPR data. Furthermore, there were two concrete sidewalks running through the site location, one short concrete wall, sprinkler pipes, and permanently-mounted aluminum bleachers on a graded gravel base. Despite these cultural features, we were confident that our large 15-ton mortars would be easy to detect with GPR.

We set up a coarse grid, with lines spaced two to three meters apart for initial investigation. After collecting the coarse grid, we then designed finer grids to characterize specific locations with greater resolution. For the coarse grid, we started out with a grid of nine East-West lines and 19 North-South lines. After identifying two separate areas of interest, we designed a fine grid for each and named them the Faustmann grid and the King grid. The King grid was named for the location that corresponded with the 2002 King survey, and the Faustmann grid was named for the newly identified area of interest. Figure 3 illustrates the data collected to date on the site.

We collected the GPS coordinates of the start and end points on each line so that the results of our study could be geo-referenced for future studies (our GPR was not fitted with an integrated GPS). We also recreated a cartography project to geo-reference historic imagery of the site; 1922 aerial photography showing Battery Byrne with the mortar tubes mounted, and 2006 imagery as the site exists now.

We used the Sensors & Software EKKO_View program to view individual lines and identify point targets or stratigraphic targets. After our two fine grids were collected, we used a trial version of the Sensors & Software EKKO_Mapper program to compute depth slices.

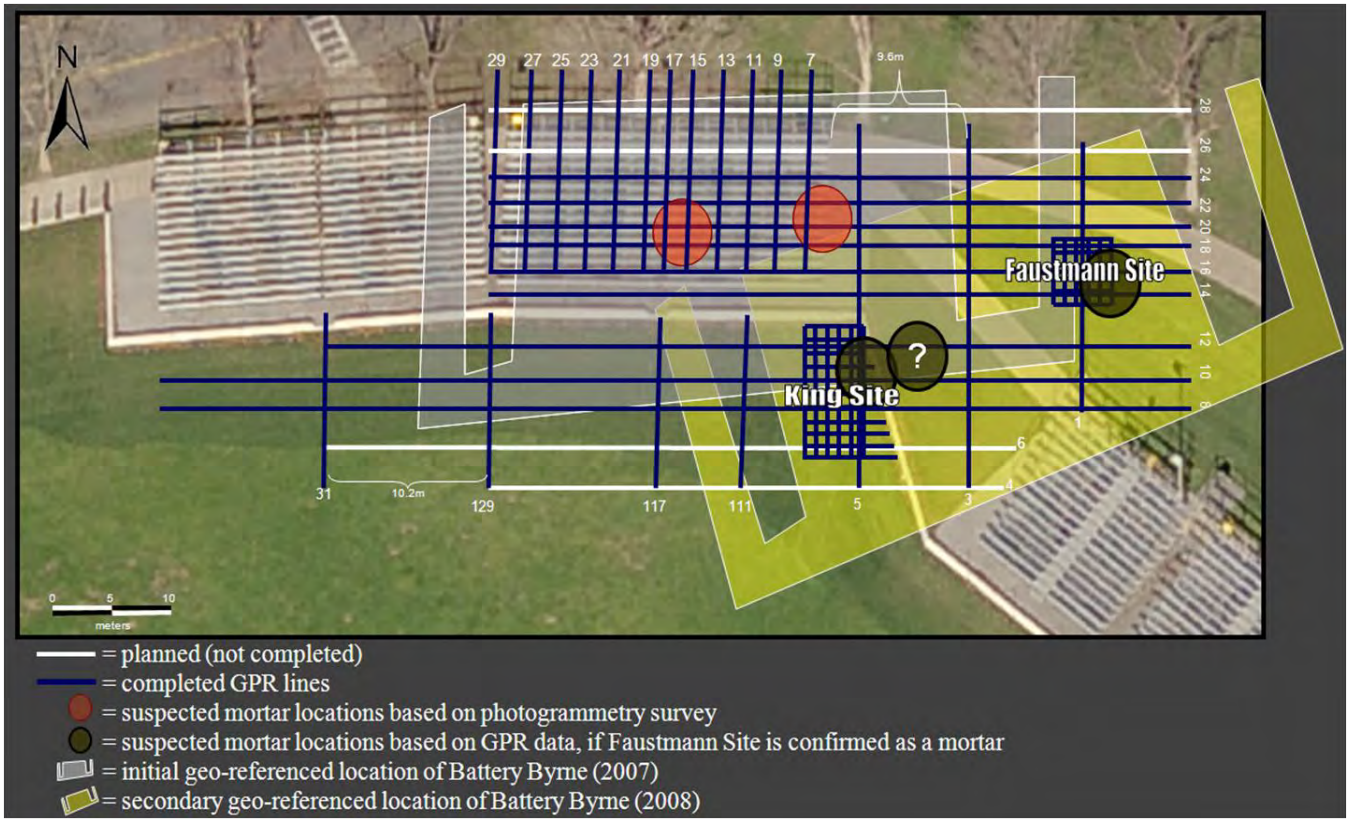

Figure 3: Data collection grids depicted on 2006 imagery. The grey and yellow shapes depict two possible locations for the buried battery structure.

Results

In four of the coarse East-West lines, we detected a sloping discontinuity, possibly the gentle sloping walls of the kettle lake known as Execution Hollow. We did not attempt to process the coarse grid data with the EKKO_Mapper software due to the wide spacing between the lines. We used initial data from the course grid to hone our further data collection towards a reflection on the northeast corner of our site (Figure 4, the Faustmann grid), and another reflection on the south side of our site (Figure 5, the King grid).

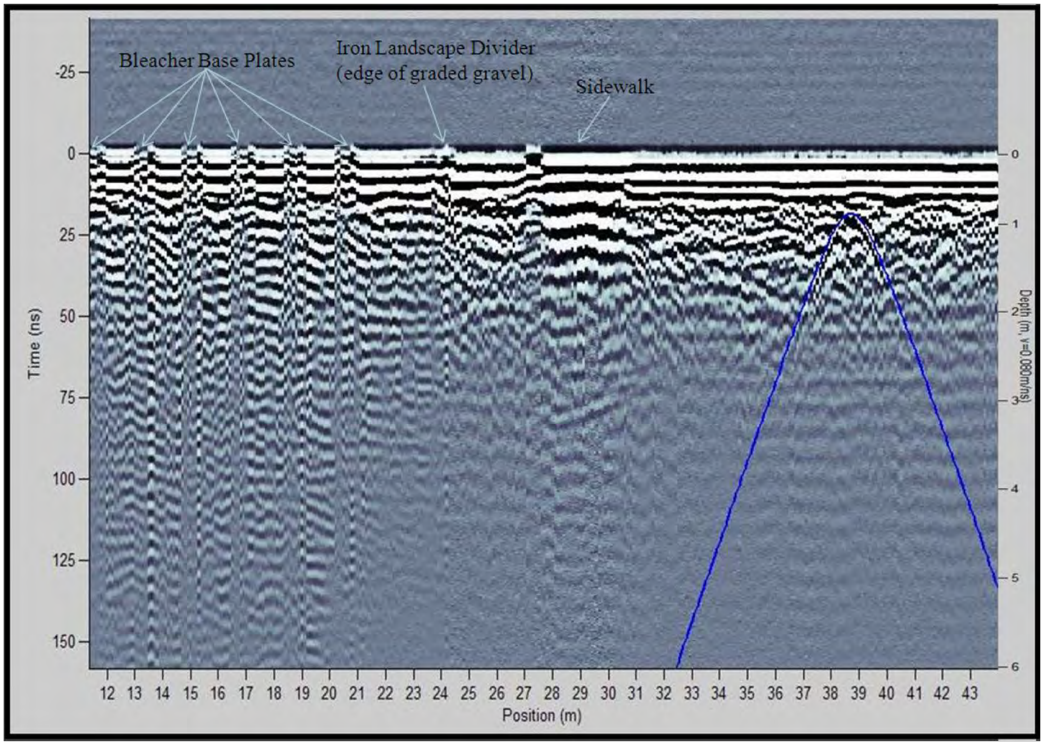

Figure 4: Line 16 from the coarse grid, with hyperbola highlighted in blue at 38.6 m and approximately 25 ns. The hyperbola is located at the center of our finer grid, the Faustmann grid.

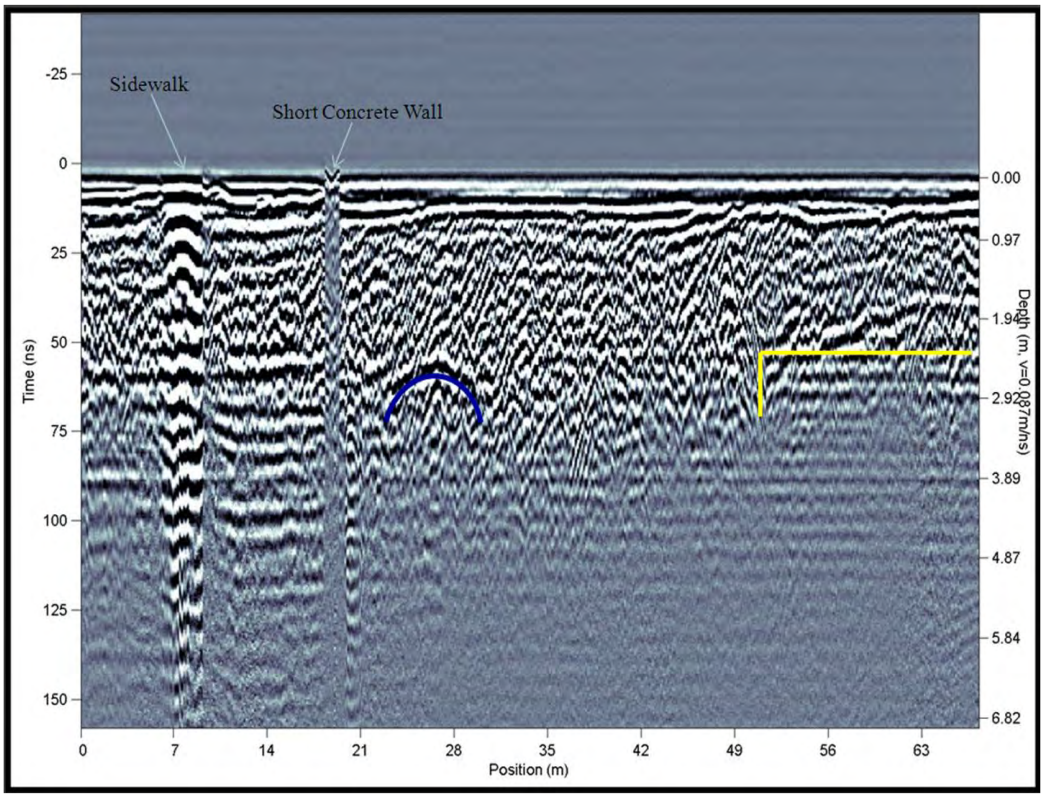

Figure 5: Line 10 from the coarse grid shows both a hyperbola near 27 m (highlighted in blue) and a possible wall corner near 49 m (highlighted in yellow). The hyperbola matches roughly with the location of the King grid.

In the Faustmann fine grid, we determined that an oblong reflection lay in the southeastern corner of the grid, from depths of 2.1 m to 2.5 m. The best single line of data from the Faustmann fine grid is Line 1008 (Figure 6), which indicates a strong reflector at a shallow 1 m depth. Other lines in the grid indicated weak reflectors, but at slightly deeper depths. After using the trial version of the EKKO_Mapper software to process all 12 lines in the fine grid, there were four depth slices that indicated a reflector in the shape of a mortar at just deeper than 2 m depth. The depths correspond to the historic data regarding the burial of the mortars. The processed data does not indicate any discontinuities greater than 2.5 m deep, but that is the limit of penetration of our GPR antennae.

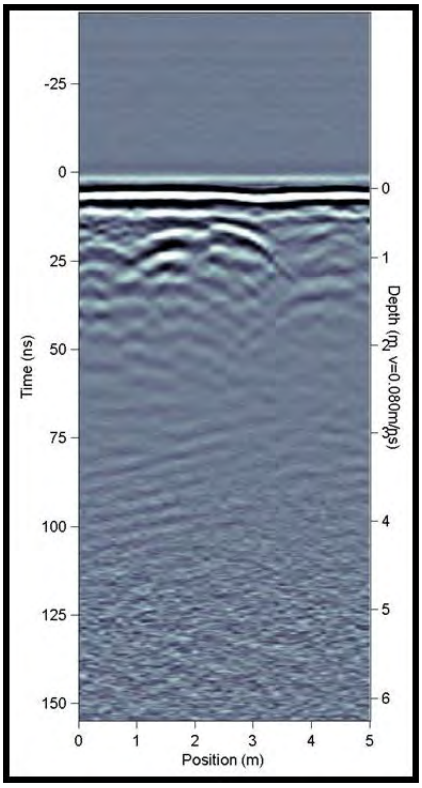

Figure 6: Line 1008 from the Faustmann grid (an east-west line in the center of the fine grid) indicates a strong reflector at approximately 1 m depth.

In the King fine grid, we detected a reflection at approximately 2.3 m depth, that stretched for approximately 3.5 m length (the actual mortars were 3.6 m in length). The best single line of data from the King grid is Line 2005 (Figure 7), which indicates a strong reflector at fairly shallow depth. Again, we used the trial version of EKKO_Mapper software to process all 17 lines in the fine grid, and were able to correlate reflections from adjacent lines that indicated the length of the strong reflection. There are two possible conclusions to be made from this data. The 2002 survey records are not very well documented as to their precise geolocation, and if the records are slightly inaccurate then this reflector in the King grid may be the same one detected back in 2002. Secondly, we initially dismissed the idea that this reflector was the mortar because of its shallow depth. Upon further investigation of the historic documents, it is possible that one or both of the mortars was raised to a more shallow depth in an attempt to salvage the metal and then subsequently buried again but not at the original depth of the floor of Battery Byrne.

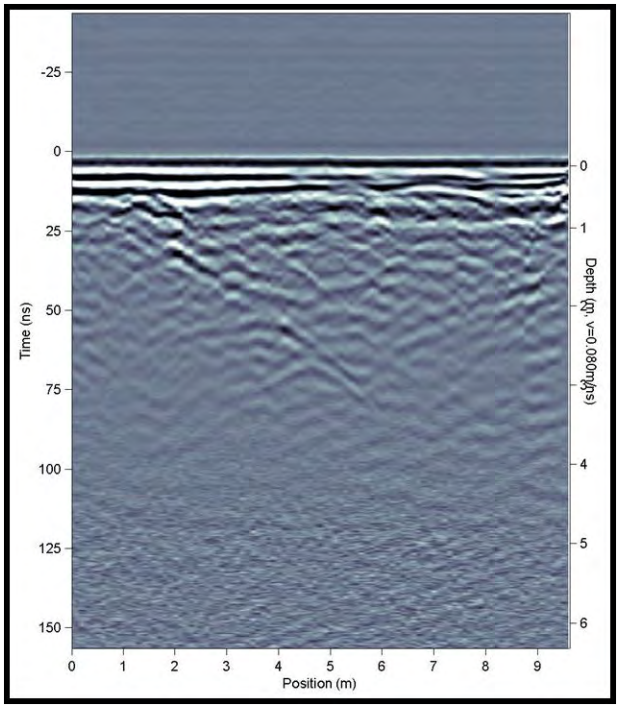

Figure 7: Line 2005 from the King grid (a north-south line in the center of the fine grid) indicates several weak reflectors between 0.5 m and 3 m depth, the strongest of which is at about 2 m (position) and approximately 30 ns (time).

A crude re-creation of a 2007 cartography study indicates that the easternmost mortar's carriage corresponds directly with the location where the 2002 survey located a mortar. If there is indeed a mortar at the King grid, then the object at the Faustmann grid may be the staircase leading out of Battery Byrne. It is also possible that one of the mortars was abandoned and/or buried at the staircase location after failed salvage attempts in the early to mid-1900s. If the cartography study is inaccurate due to the accuracy or distortion of the 1922 aerial photography, then the reflection at the Faustmann grid may very well correspond with the easternmost mortar in Battery Byrne.

Conclusions

As with all forms of geophysical studies, our results must be paired with ground-truthing methods to confirm or reject our results. We think that we may have possibly found two mortars buried on the Plain at West Point, one at 2.1-2.5 m depth at the Faustmann grid, and one at 2.3 m depth at the King grid. Furthermore, we may have detected the natural slope of the kettle lake known as Execution Hollow.

Unfortunately, our selection of 225 MHz antennae may have not given us enough depth penetration to do justice to the GPR survey. A 110 MHz system could provide the necessary depth, but the physical limitations of the site may prevent that data from being collected unless a different GPR system is used. Ultimately the site requires more investigation for definite conclusions to be made. The location is ideal for undergraduate student projects, and with further development could provide an excellent location for short-duration, high-payoff geophysics lab projects.

Future Work

More GPR work should be done at the site, together with alternate forms of near-surface geophysical investigation. The location lends itself well to gravity, magnetics, and seismic refraction. Borehole and other invasive methods will not likely be permitted due to the historic nature of the site and the continual use of the field for official ceremonies and cadet parades.

We also propose that several academic departments assemble an interdisciplinary team of cadets (students) who are interested in an independent study. Preferably, cadets with backgrounds in Civil and Mechanical Engineering would work on the excavation phases, Engineering Management to plan the whole operation, Geology or Physics for further geophysical studies, and Military History to assemble enough historical interest in the excavation of these massive mortar tubes. First, the cadet team would need to verify the results of this study with other data methods. The second phase would be to provide a cost-benefit analysis to determine if the mortars are worth excavation. The third phase would be to develop a specific excavation plan. The fourth and fifth phases (occurring simultaneously with the first three phases) would be to obtain approval through the appropriate federal, state, and installation-level authorities to excavate these mortars, and to raise the money required to excavate, restore, and display them. Throughout the project, the cadet historian on the team would educate others about the historical significance of this project, thereby generating public support. These large mortars are now over 100 years old and can classify for protection under the Archaeological Resources Protection Act of 1979 (Saini).

Until, or unless, the site is excavated, we recommend the development of this site for a geophysics lab. The academic materials could be developed to direct students to the location of a small geophysical survey, and the mortars could be easily detected with little data processing. The lab could be tailored to a host of different goals, such as survey design, data collection, or data processing. Having historic data to establish the background situation provides the interest factor and the illusion of the easy target.

References

Hercz, A.R., 1987, Memorandum to Directorate of Operations, Plans, and Security, West Point, NY, 1.

King, C., 2002, Unpublished Geophysical Survey and GPR data, West Point, NY.

Nock, W. J., 1987, Personal Correspondence to Michael E. Moss, West Point Museum, NY. 2.

Pictometry International, 2006, Image File NYUSMA005013NeighObliq6094N_061204, US Military Academy Geographic Science Lab.

Saini, M. K., 1986, Memorandum to Deputy Engineer, E&EMD, West Point, NY. 2.

US Military Academy Library, 1915-1929, West Point Special Collections Photographs.

US Ordnance Office, 1925, Data Sheet: Mortar Data & Information, US War Department. 346-355.

Disclaimer

Any use of trade names is for descriptive purposes only and does not imply endorsement by the U.S. Government, the U.S. Army, or the U.S. Military Academy at West Point.

GROUND PENETRATING RADAR: UTILITY/REBAR/CABLE DETECTION AND CONCRETE/SUBGRADE DEBONDING

Neil L. Anderson, Missouri University of Science & Technology, Rolla, MO
Evgeniy Torgashov, Missouri University of Science & Technology, Rolla, MO
Oleg Kovin, Missouri University of Science & Technology, Rolla, MO

Abstract

Ground penetrating radar (GPR) profiles acquired during seven separate field investigations are presented. The intent is simply to illustrate that GPR can be used to detect rebar, pre-tensioned tendons, deteriorated and/or detached concrete/fill, buried utilities, underground storage tanks, and buried foundations. The objective of each investigation is summarized, accompanied by brief descriptions of the nature of the target of interest. The application of GPR to the investigations described in this paper is not new. However, the presentation and illustration of multiple applications of this imaging technology in a single manuscript is somewhat unique.

Introduction

The ground penetrating radar tool is routinely used to determine the pattern, placement and density of rebar and pre-tensioned tendons in concrete (http://www.geomodel.com/; He et. al., 2009; http://www.gp-radar.com/posttension.htm), to detect deteriorated and/or detached concrete/fill (http://www.penetradar.com/Bridge_Deck_Inspection.htm; http://utc.mst.edu/documents/i44.pdf; http://utc.mst.edu/documents/grpen_ralls.pdf) and to locate buried utilities, under-ground storage tanks and buried foundations (http://www.enviroscan.com/html/ust_detection.html; http://www.global-gpr.com/services/locate-tank.html; Roberts et.al., 2009; Pringle et. al., 2009; Conyers and Osburn, 2006). Authors generally report that GPR is an excellent tool for mapping rebar and post-tension cables embedded in concrete except where the depth to the rebar/tendons exceeds the capability of the antenna required to image these small diameter targets. Similarly, authors typically report that GPR is an excellent tool for locating buried metal-based utilities, underground metal storage tanks, and buried concrete foundations with embedded rebar, unless the targets are below the depth range of the antenna employed or sealed in clayey soil. Non-metal bearing targets are normally more difficult to image; air-filled voids beneath detached concrete are also problematic.

Case Study 1: Pattern, Placement and Density of Rebar

Ground penetrating radar data were acquired along multiple traverses in four separate areas on the roof of a single storey High School so that the bearing strength of the roof could be determined prior to the construction of a second level (Figure 1). The objectives of the GPR survey were to: 1) estimate the thickness of the concrete; 2) determine the spacing of rebar along the designated traverses; and 3) identify locations where the concrete could be chipped (so that the rebar could be exposed and its size visually determined). The concrete roof was covered by tar paper and asphalt shingles.

Figure 1: Photograph of High School showing GPR Areas 1, 2, 3 and 4.

To illustrate the effectiveness of GPR as a rebar detection tool, data acquired along radial traverse P1 (GPR Area 1; Figures 1 and 2) are presented (Figure 3). As shown in Figure 3 (and confirmed by core control), the concrete roof of the school is 2.5 inches thick. Rebar spacing along radial traverse P1 is nominally 12 inches; spacing along axial traverse P4 is nominally 8 inches. Comparable results were obtained on the other radial and axial GPR profiles. Chipping at designated locations exposed #4 rebar (0.5 in diameter).

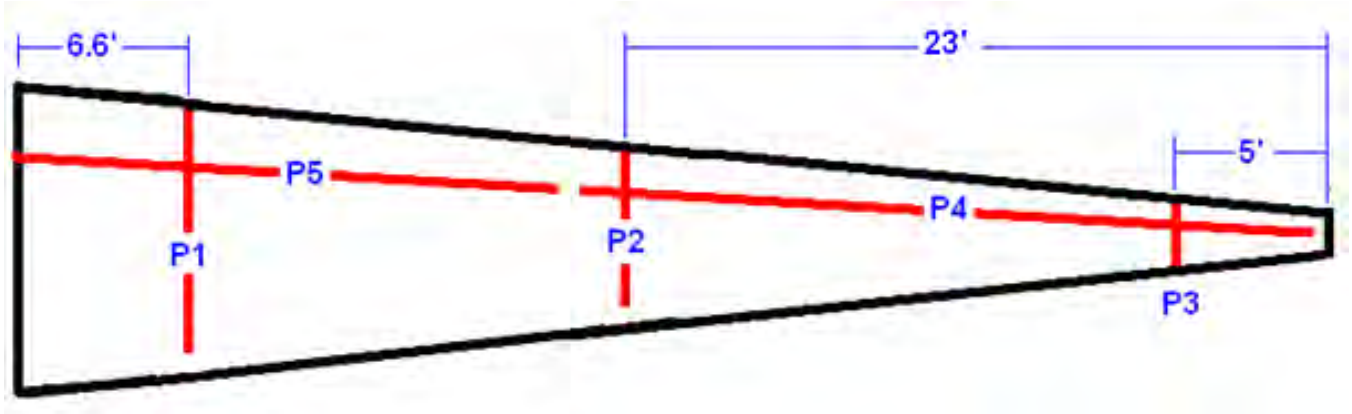

Figure 2: Schematic of GPR Area 1 (Figure 1) showing locations of radial traverses P1-P3 and axial profiles P4-P5.

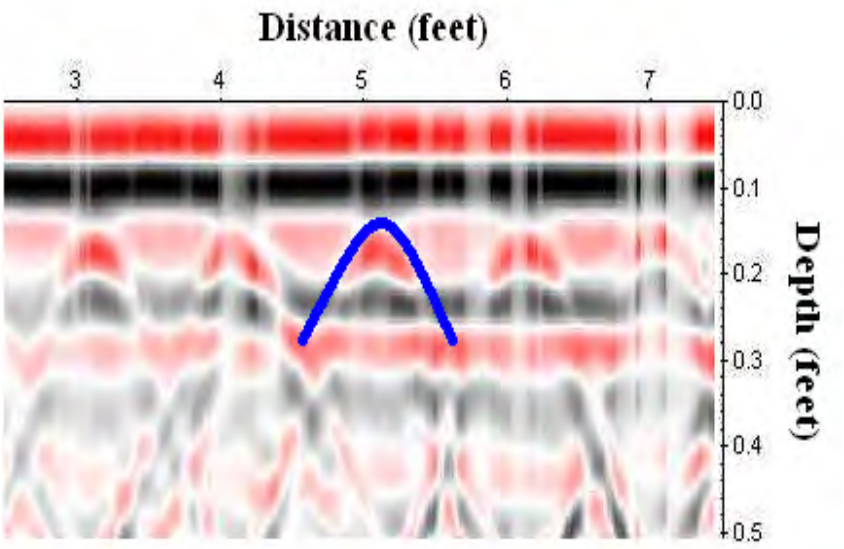

Figure 3: Segment of GPR profile P1 (Figure 2) acquired using a GSSI 1500 MHz antenna. Hyperbolas (one highlighted in blue) generated from five rebar, are observed on profile P1. The depth to the top of the rebar is 1.5 inches; the spacing between rebar is 12 inches.

Case Study 2: Locating Pre-tensioned Tendons

Ground penetrating radar data were acquired along traverses on multiple floors of an apartment complex. The objective was to locate pre-tensioned tendons in the concrete floor prior to coring and the installation of upgraded utilities (Figure 4). The GPR survey was authorized after a worker accidentally severed a pre-tensioned tendon during coring, necessitating the removal and replacement of an entire slab of pre-tensioned flooring, at a cost that was multiple times that of the entire GPR survey.

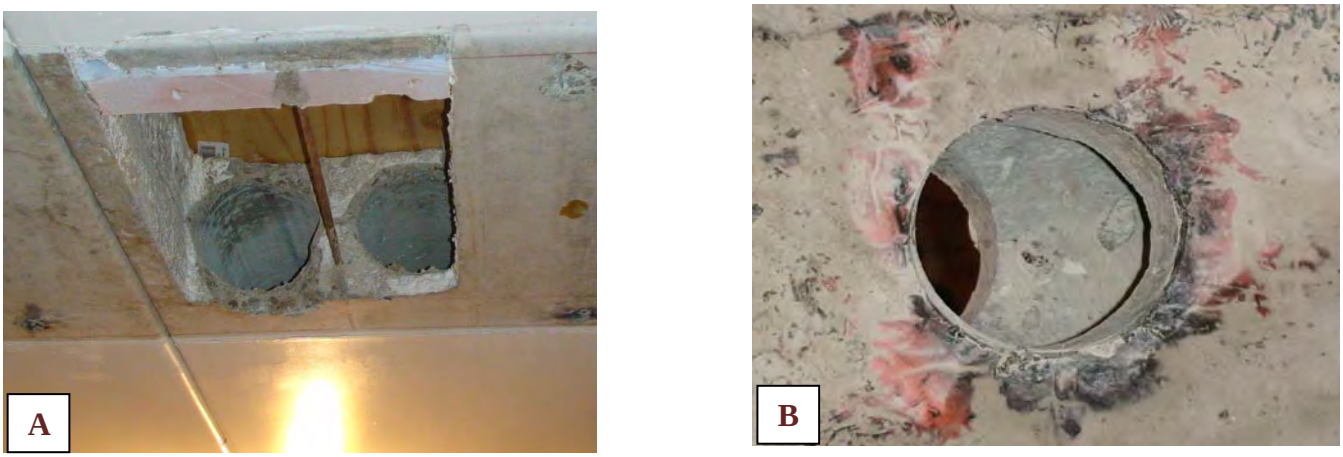

Figure 4: Two air-filled cylindrical voids and a pre-tensioned tendon are exposed in photo A. A cored utility line (intersected cylindrical void; missed adjacent tendons) is shown in photo B. Superposed red lines denote locations of pre-tension tendons as determined using GPR.

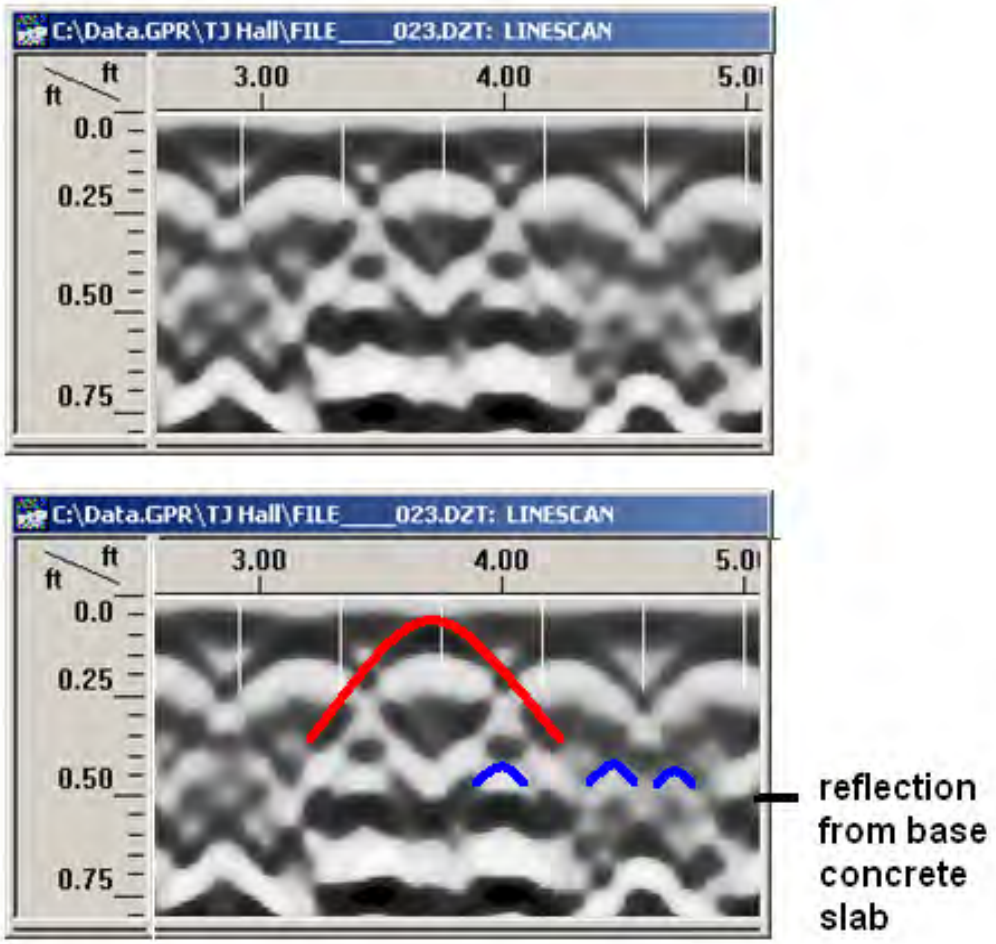

Figure 5: Segment of GPR profile acquired using a GSSI 1500 MHz antenna. The tops of the 5 in diameter cylindrical voids are characterized by prominent hyperbolic reflections/ diffractions (red); tendons are characterized by less prominent reverse polarity diffraction hyperbola (blue). One tendon is between each cylindrical void except where adjacent slabs abut. The cylindrical voids in adjacent slabs are separated by two tendons.

To illustrate the effectiveness of GPR as a tool for mapping pre-tensioned tendons, a segment of an acquired profile is presented as Figure 5. The vertical depth scale on this GPR profile was generated using a dielectric permittivity of 4.5 (suitable for dry concrete). The use of this dielectric permittivity value results in unreliable depth estimates because the slabs are not comprised entirely of dry concrete. More specifically, the reflection from the base of the 7.5 in thick floor slab is seen to be at a depth of ~6 in at the 5 ft mark (immediately beneath center of air-filled cylinder; Figure 5) and at a depth of ~7 in beneath the contact between adjacent slabs (4.6 ft mark; Figure 5).

The most prominent features on the GPR profile are the hyperbolic reflections/diffractions generated by the tops of the cylindrical voids. The diffraction hyperbolas generated by the tendons are reverse-polarity and much less prominent. Note that two adjacent tendons are imaged on (either side of the contact between adjacent slabs) near the 2.8 ft and 4.6 ft marks.

Case Study 3: Locating Buried Utilities

Ground penetrating radar data were acquired along parallel traverses in several areas on the ground floor of a hospital complex (Figure 6). The objective was to locate buried utilities prior to the saw-cutting of the concrete floor. The GPR survey was authorized after a worker accidentally severed a buried electric cable during the refurbishing process.

To illustrate the effectiveness of GPR as a tool for mapping buried utilities, a segment of an acquired profile is presented as Figure 7. As illustrated, the most prominent feature on the GPR profile is the diffraction hyperbola generated by the buried metal utility. Note also that the in-filled utility trench is readily identified on the GPR profiles. These trenches also housed small diameter non-metal utilities (which could not be confidently mapped using the 1500 MHz antenna) and were identified as areas of extreme concern prior to saw cutting.

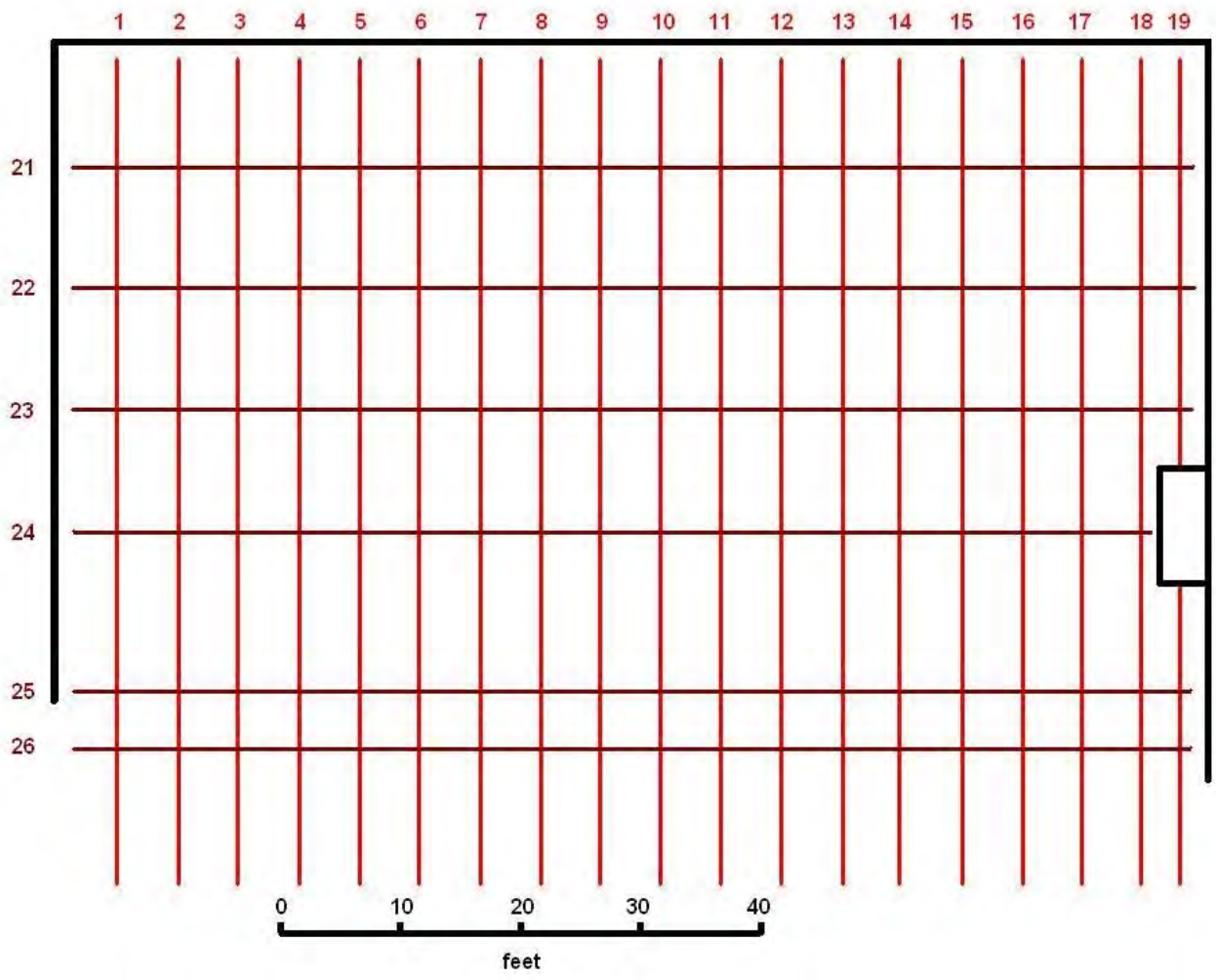

Figure 6: Map showing locations of GPR traverses in one surveyed area of the hospital

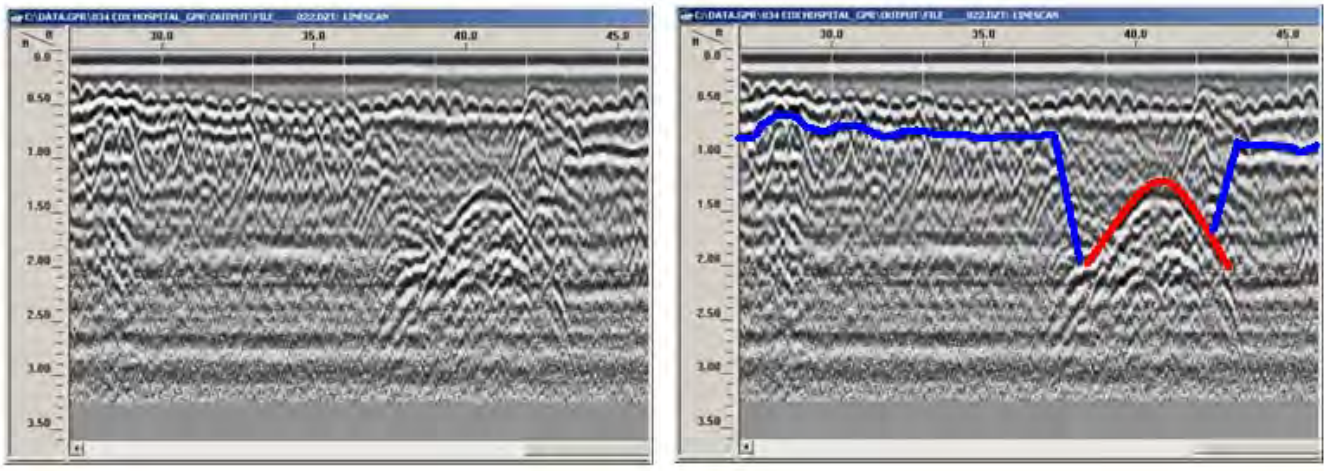

Figure 7: Segment of GPR profile 24 (Figure 6; acquired using GSSI 1500 MHz antenna). Metal utility is characterized by a prominent hyperbola (red); in-filled trench (blue line is top of subgrade) housed small diameter non-metal utilities that could not be imaged using a 1500 MHz antenna.

Case Study 4: Locating Underground Storage Tanks

Ground penetrating radar and metal detector data were acquired along parallel traverses in the parking lot of an abandoned gas station (Figures 8, 9 and 10) prior to a pending sale to determine whether the metal underground gasoline storage tanks had been removed.

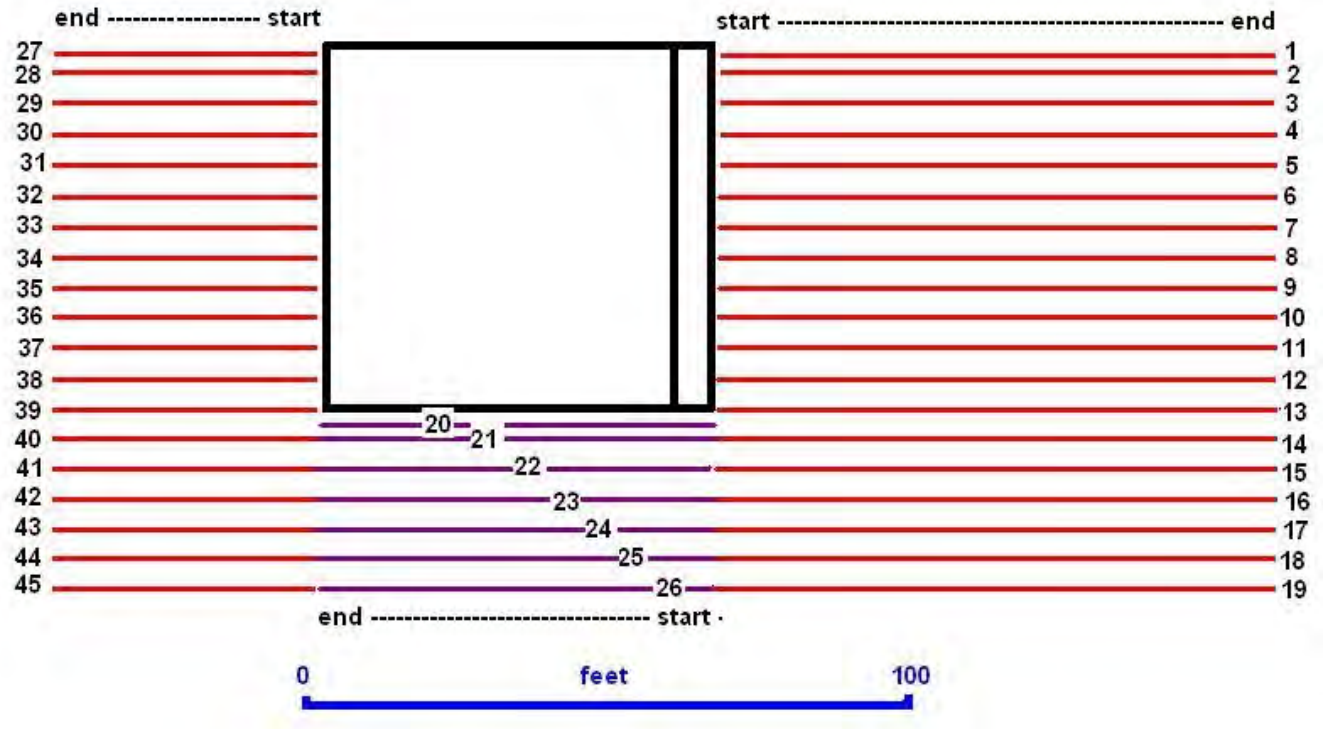

Figure 8: Map showing locations of geophysical traverses

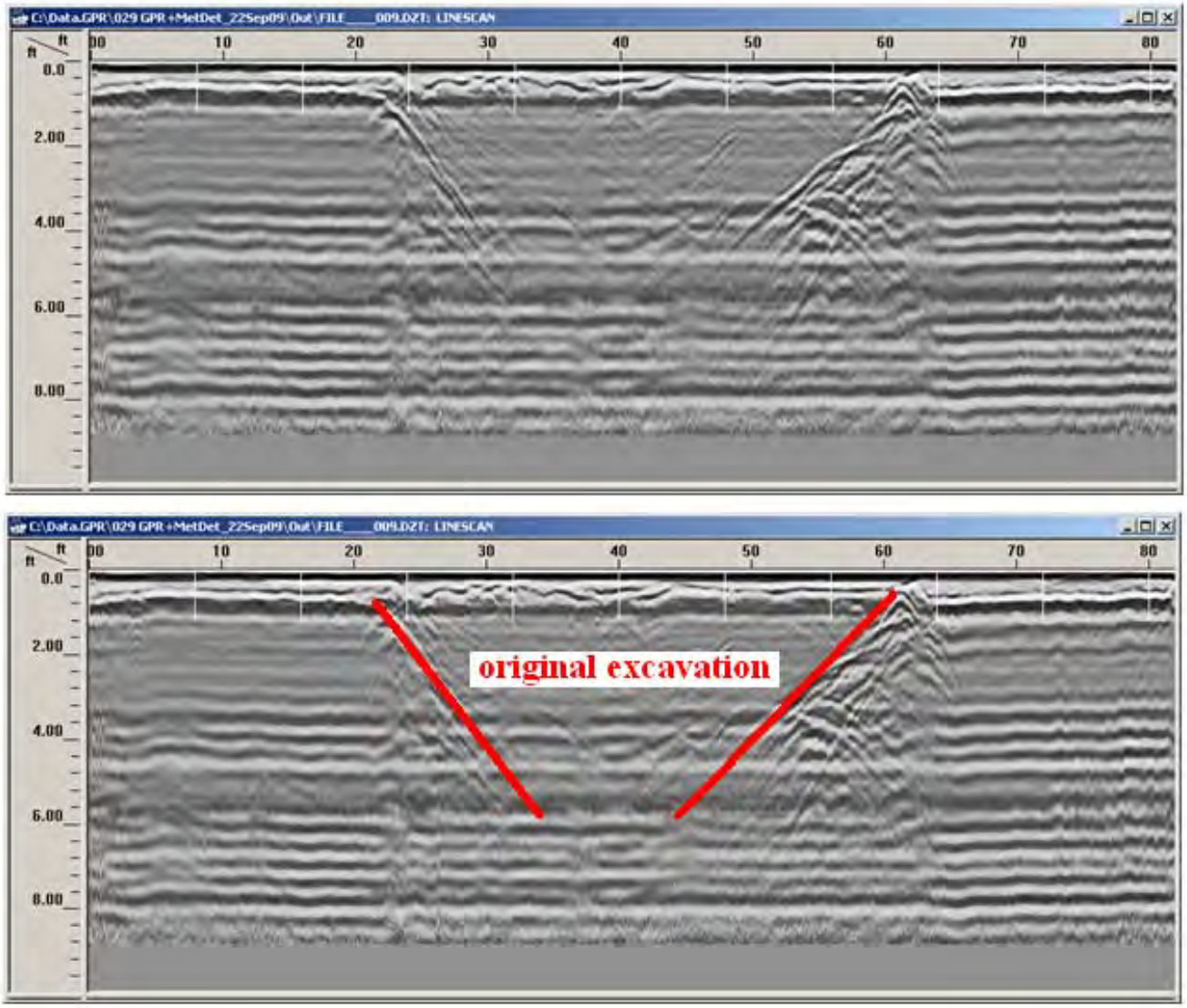

Figure 9: Uninterpreted and interpreted versions of GPR profile 9 (Figure 8; acquired using 400 MHz GSSI antenna) showing original excavation into which tank(s) were placed. Metal storage tanks are not imaged on the GPR data, indicating they have been removed.

To illustrate the effectiveness of the GPR tool for locating buried metal underground storage tanks, un-interpreted and interpreted versions of GPR profile 9 are presented (Figure 9). Metal tanks are not imaged on GPR profile 9. However the back-filled excavation into which the tanks were originally placed is clearly imaged. Metal detection data acquired on-site (Figure 10) validates the interpretation of the GPR data and the conclusion that the metal storage tanks have been removed. The concrete slab identified on Figure 10 was also imaged on the GPR data set, verifying the associated metal detector anomaly is attributable to presence of embedded rebar.

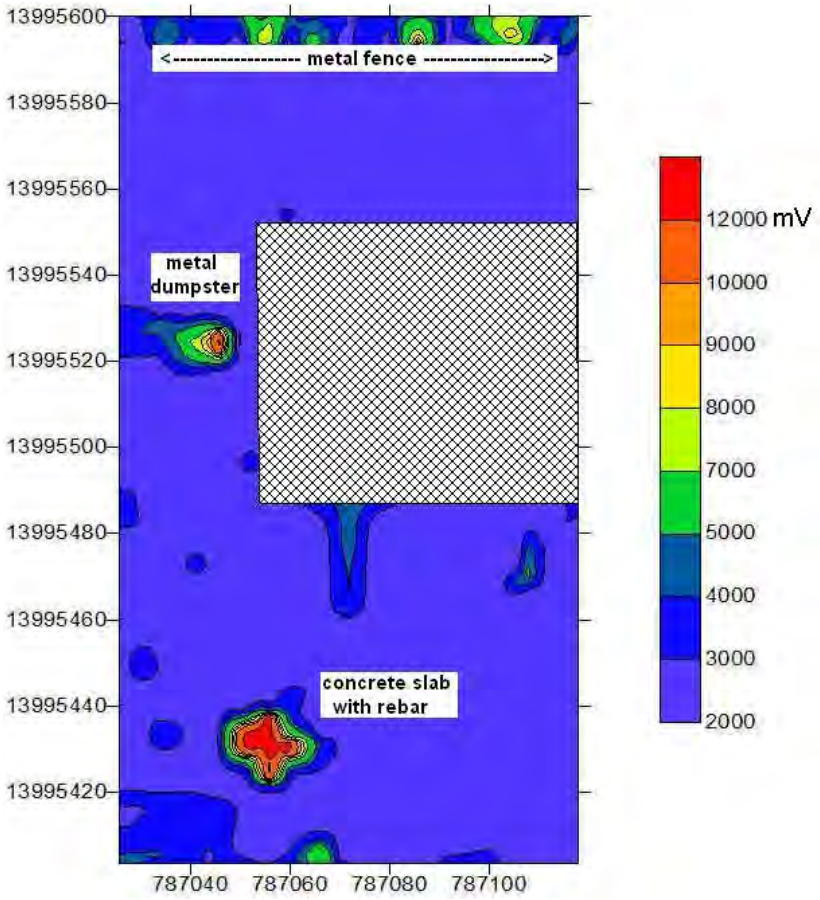

Figure 10: Metal detection data (Figure 8; acquired using a Geonics EM61-MK2). The origins of the most prominent anomalies are identified. The absence of anomalies in areas identified on GPR profiles as excavated validates the interpretation of the GPR data and the conclusion that the metal storage tanks have been removed.

Case Study 5: Locating Buried Foundations

Ground penetrating radar and metal detector data were acquired along parallel traverses in the parking lot of a school (Figures 11 and 12) in an effort to locate the foundation of an old structure that had been demolished from the ground level up (around 1940) and covered with backfill and asphalt. Expectations were that the old foundation did not contain rebar. However, metal detector data were acquired in case this supposition proved incorrect and with a view to locating proximal water and sewer utility lines.

To illustrate the effectiveness of the GPR tool for locating buried foundations, un-interpreted and interpreted versions of GPR profile 6 are presented as Figure 12. The GPR tool proved capable of imaging the remnant vertical concrete walls of the demolished structure. The absence of corresponding metal detector anomalies indicated the concrete did not contain reinforcing steel. The concrete floor which was encountered by follow-up borings at a depth of 4 ft could not be confidently identified on the GPR data, probably because the foundations were covered with clayey fill.

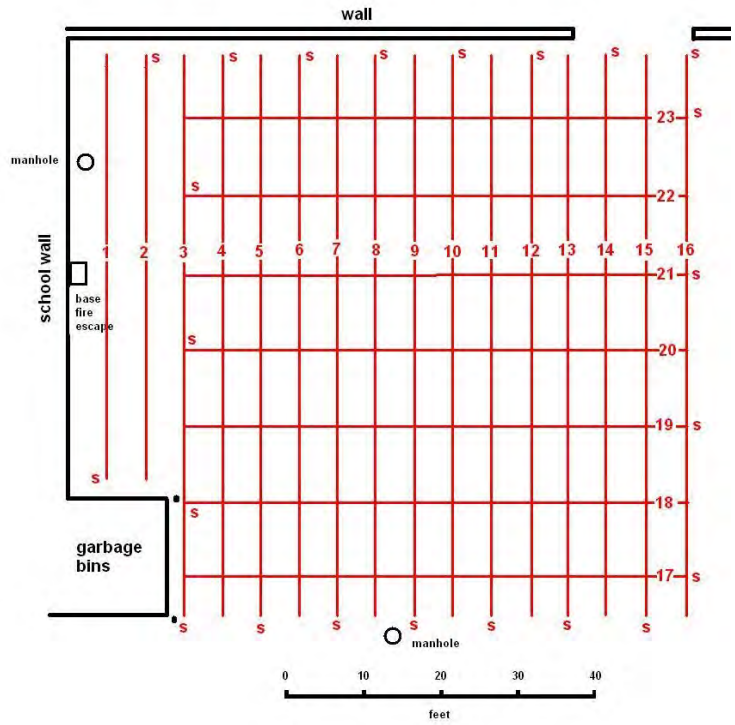

Figure 11: Map showing locations of geophysical traverses.

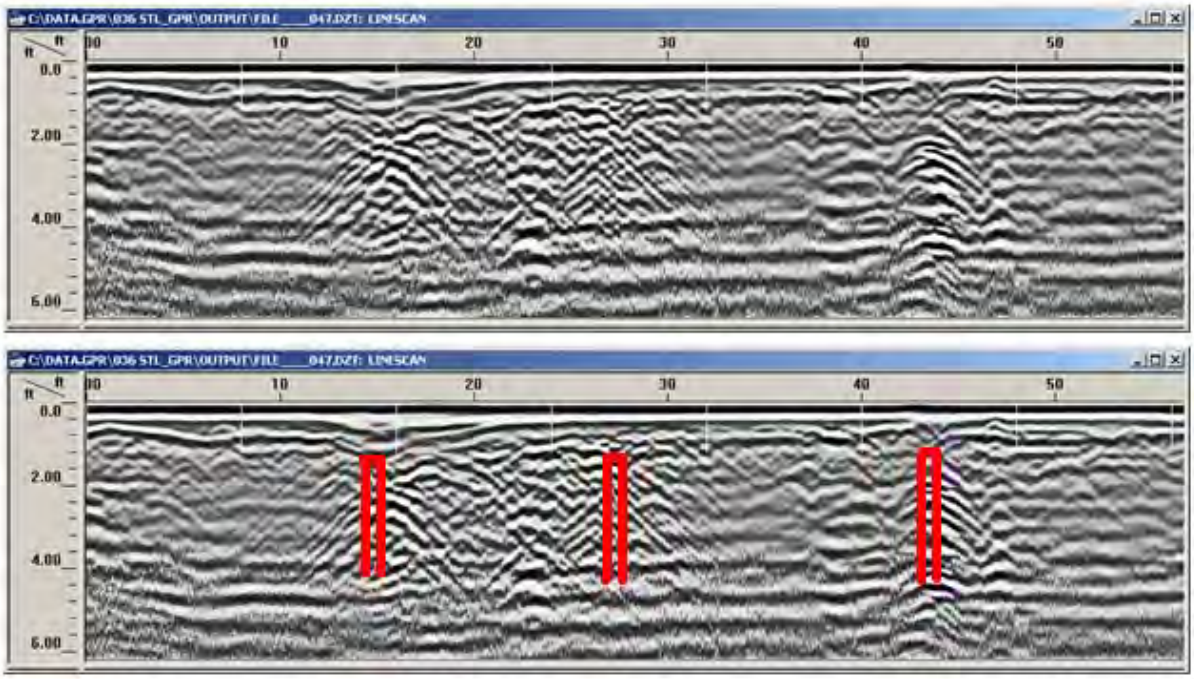

Figure 12: GPR profile 6 (Figure 11; acquired using a GSSI 400 MHz antenna). The prominent diffractions are generated by the buried remnants of vertical concrete walls and can be correlated across multiple GPR profiles.

Case Study 6: Locating Deteriorated Concrete

Ground penetrating radar profiles were acquired along parallel traverses on the concrete floor of a waste water treatment tank (Figure 13) in an effort to identify areas where the concrete was deteriorated. The GPR tool proved capable of identifying areas where significant deterioration had occurred. Such areas were characterized by: 1) anomalously high apparent depths to the top of the embedded rebar; 2) anomalously high apparent depths to the top of the subgrade; and 3) a visually identifiable decrease in the magnitude of the reflections from the base of the concrete slab and the top of the subgrade (Figure 13). Areas identified as deteriorated on the GPR dataset, were subsequently tested acoustic-tested using a hammer and cored. The areas identified as deteriorated sounded "hollow" when struck by a metal hammer. Concrete core samples were noticeably deteriorated.

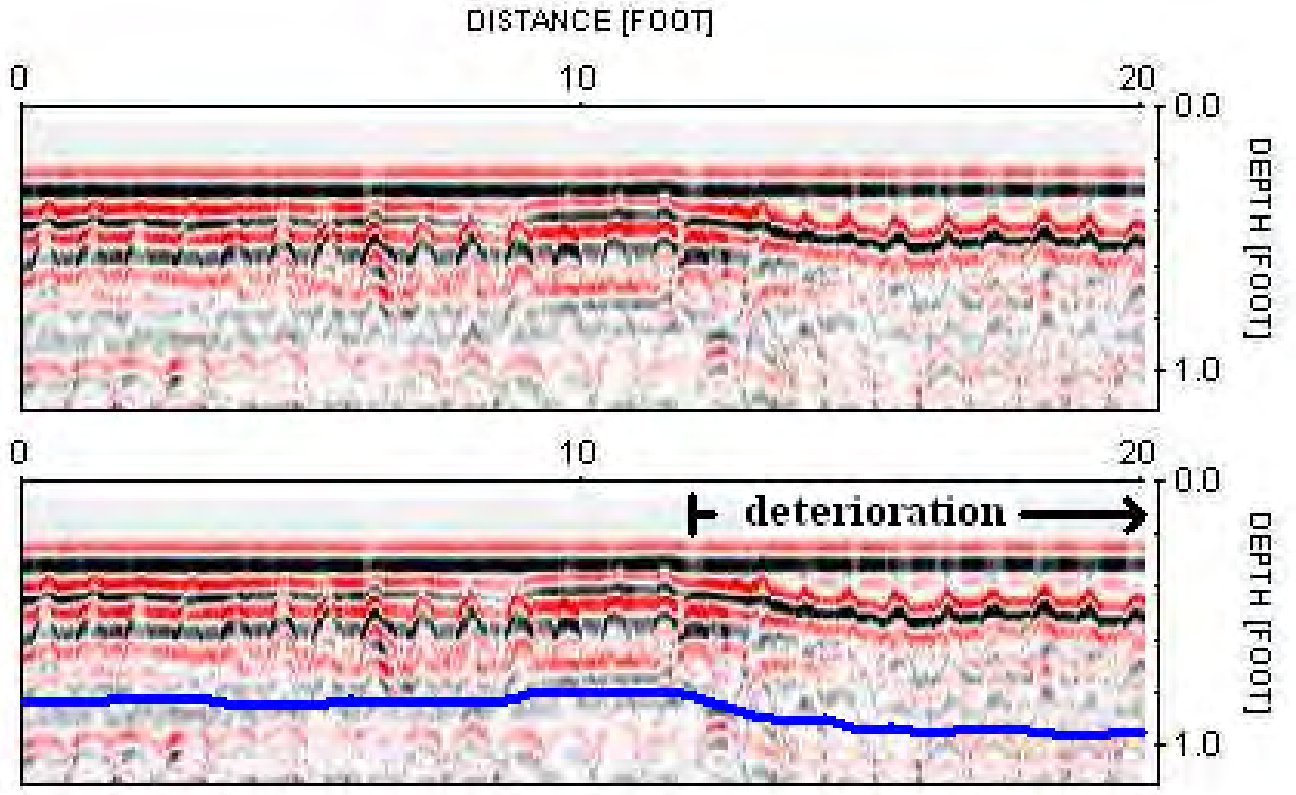

Figure 13: Segment of example GPR profile. Areas of deteriorated concrete are characterized by: 1) anomalously high apparent depths to the top of the embedded rebar; 2) anomalously high apparent depths to the top of the subgrade; and diminishment of the magnitude of the reflections from the base of the concrete slab and the top of the subgrade (blue line).

Case Study 7: Locating Voids beneath Concrete

Ground penetrating radar profiles were acquired along multiple traverses on the concrete floor of an office complex (Figure 14) in an effort to evaluate the effectiveness of remediation efforts (injection of grout) following the rupture of a high-volume underground water line. The primary objective was to identify areas (if any) where the concrete was not effectively coupled to the original underlying fill or

the injected grout. To illustrate the effectiveness of the GPR tool for locating areas where the base of concrete is not effectively coupled to injected grout or original fill, a segment of GPR profile 3 is presented (Figure 15).

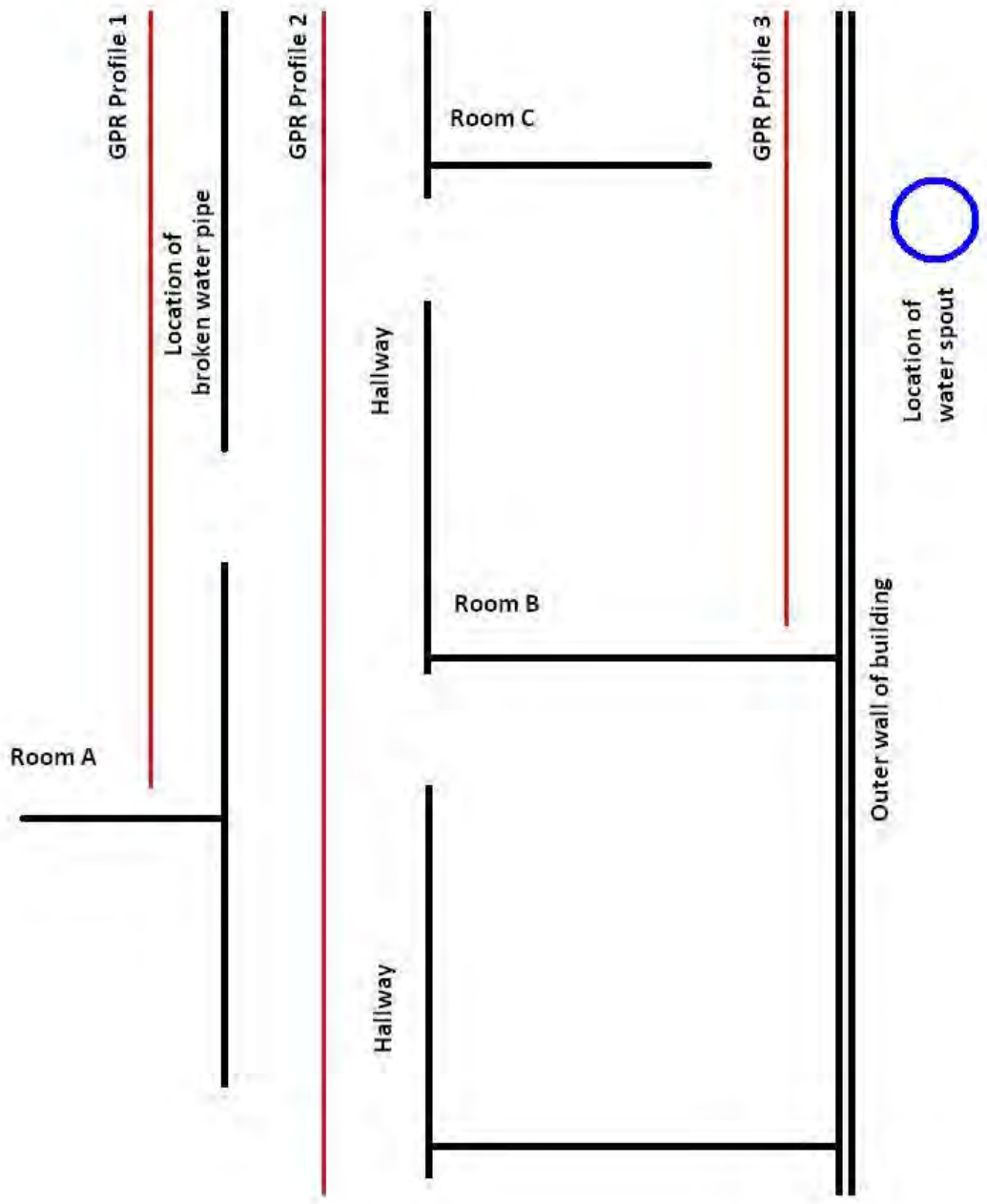

Figure 14: Map showing the locations of several geophysical traverses. The ruptured underground water pipe was located in Room A. The pressurized water lifted the concrete floor before scouring a channel and exiting the building as a high-volume spout (blue circle). For mitigation purposes, pressurized grout was injected into the channel. GPR data were acquired after the grout set in an effort to determine if the concrete floor was effectively coupled to the injected grout and/or original fill.

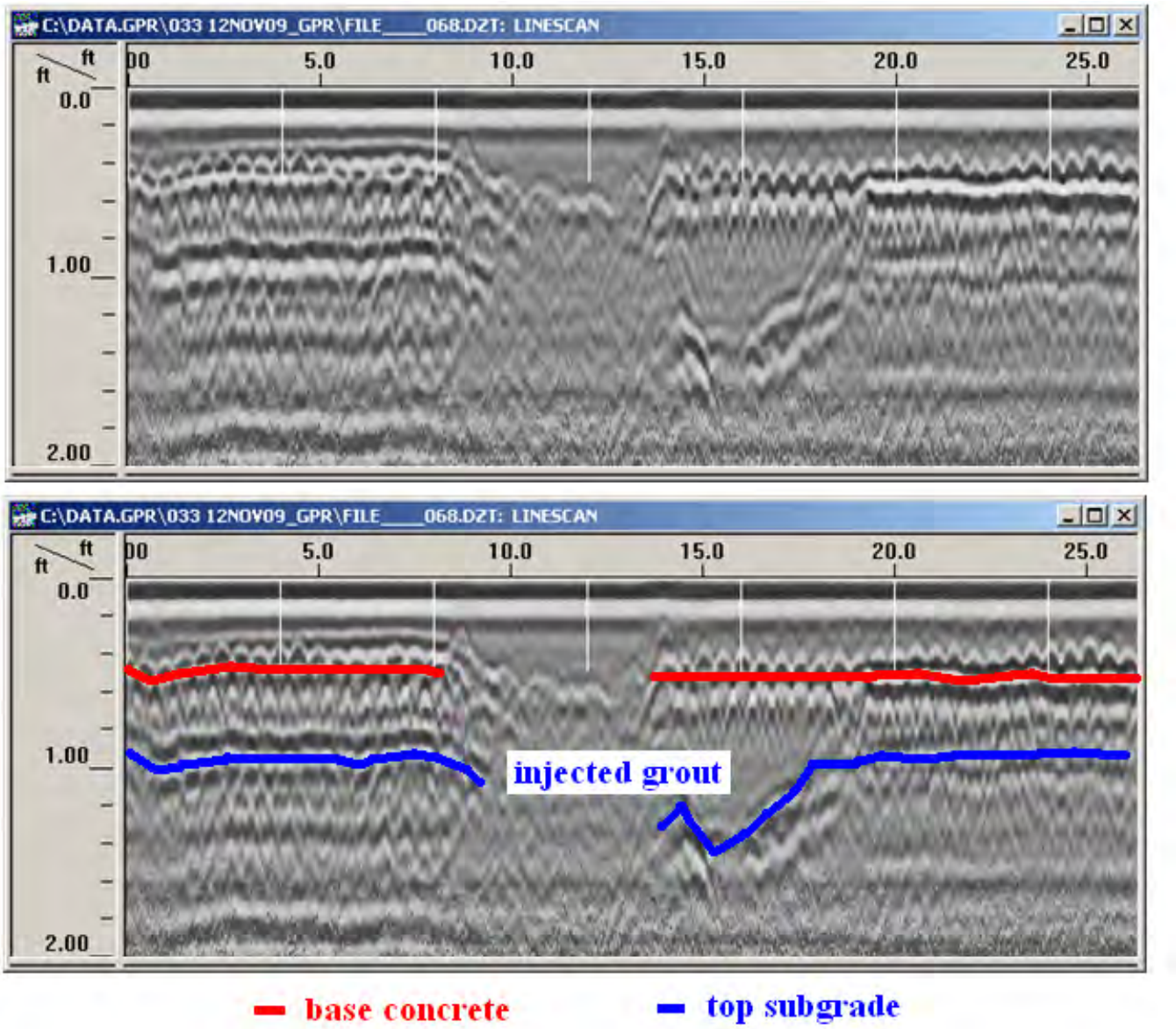

Figure 15: Segment of GPR profile 3 (Figure 14). The scoured channel extends from the 8 ft mark to the 18 ft mark, and appears to have incised the fill/subgrade to a depth of at least 1.5 ft. The original concrete floor (8 ft to 13 ft) was removed immediately prior to grouting, and replaced (without rebar).

The incised scour channel is clearly visible on Figure 15. The concrete patch (8 ft to 13 ft) is characterized by the absence of reinforcing steel. In areas where the concrete is effectively coupled to the grout and/or fill (0 ft to 19 ft), the reflection from the base of the concrete is relatively low amplitude, because the concrete, grout and fill have similar dielectric properties. In areas where the concrete was determined to be decoupled from either the injected grout and/or original fill (manifested as horizontal air space; 19 ft to 27 ft), the reflection from the base of the concrete is higher amplitude and reverse polarity. This sheet-like void (as mapped using GPR) formed where those sections of the uplifted concrete floor did not properly resettle and/or because fill was removed in places by flowing water.

Conclusion

Ground penetrating radar is routinely used to determine the pattern, placement and density of rebar and pre-tensioned tendons in concrete, to detect deteriorated and/or detached concrete/fill and to locate buried utilities, underground storage tanks and buried foundations. The GPR examples presented herein reaffirm what the authors of related investigations generally report. GPR is an excellent tool for mapping rebar and post-tension cables embedded in concrete except where the depth to the rebar/ tendons exceeds the capability of the antenna required to image these small diameter targets. GPR is also an excellent tool for locating buried metal-based utilities, underground metal storage tanks, and buried reinforced concrete foundations, unless the targets are below the depth range of the antenna employed or sealed in clayey soil. Non-metal bearing targets are normally more difficult to image; air-filled voids beneath detached concrete are also problematic.

References

Conyers, L. B., and Osburn, T., 2006, Test Anthropological Hypotheses: A Study from Comb Wash, Utah, American Southwest; 11th International Conference on Ground Penetrating Radar, June 19-22, 2006, Columbus Ohio, USA)

He, X., Zhu, Z., Liu, Q., and Lu, G., 2009, Review of GPR Rebar Detection: PIERS Proceedings, 804-813.

Roberts, R., Cist, D., and Kathage, A., 2009, Full-Resolution GPR Imaging Applied to Utility Surveying: Insights from Multi-Polarization Data Obtained over a Test Pit: http://www.geophysical. com/Documentation/WhitePapers/IWAGPR2009-Robertsetal.pdf

Pringle, J.K., Lenham, J.W. and Reynolds, J.M., 2009, GPR investigations to characterize Medieval and Roman foundations under existing shop premises: a case study from Chester, Cheshire, UK: Near surface Geophysics, Vol 7, No. 2, April 2009, pp. 93-100

Wamweya, A., Torgashov, E., Anderson, N., 2009, Bridge Deck Assessment Using Ground Penetrating Radar (GPR). Missouri Science and Technology University. Symposium on the Application of Geophysics to Engineering & Environmental Problems, 2009. Volume 22.

GROUND PENETRATING RADAR AS A SENTINEL DEVICE

Peter J. Hutchinson, The Hutchinson Group, Ltd., Murrysville, PA
Bryan J. Teschke, The Hutchinson Group, Ltd., Murrysville, PA

Abstract

Geophysical methods provide a non-destructive non-intrusive method of subsurface investigation. Oftentimes, however, the target is difficult to "see" due to lack of contrast between the target and background. This lack of contrast can be rectified through the use of a sentinel device. A series of sentinel devices were used in downtown Pittsburgh, Pennsylvania to determine potential subsidence beneath a building plaza. This sentinel strategy was performed to predict future deformation of the sidewalk and to prevent foot-traffic hazards.

The building was installed in 1983 and the building footprint was over-excavated to provide for the construction of the basement. Soldier piles were installed to keep the loose sand, clay and gravel deposits from collapsing into the construction area. Prior to the installation of the perimeter sidewalk, 0.15 meter compacted lifts of fine- to medium-grained sand were placed in the annular space between the soldier piles and the native soil. A 0.3 meter (1 ft.) thick grout and 0.3 meter (1 ft.) thick concrete pad were placed on the fine- to medium-grained sand and overlain with a 4-inch sand sub-base prior to the installation of the decorative granite pavers (Figure 1).

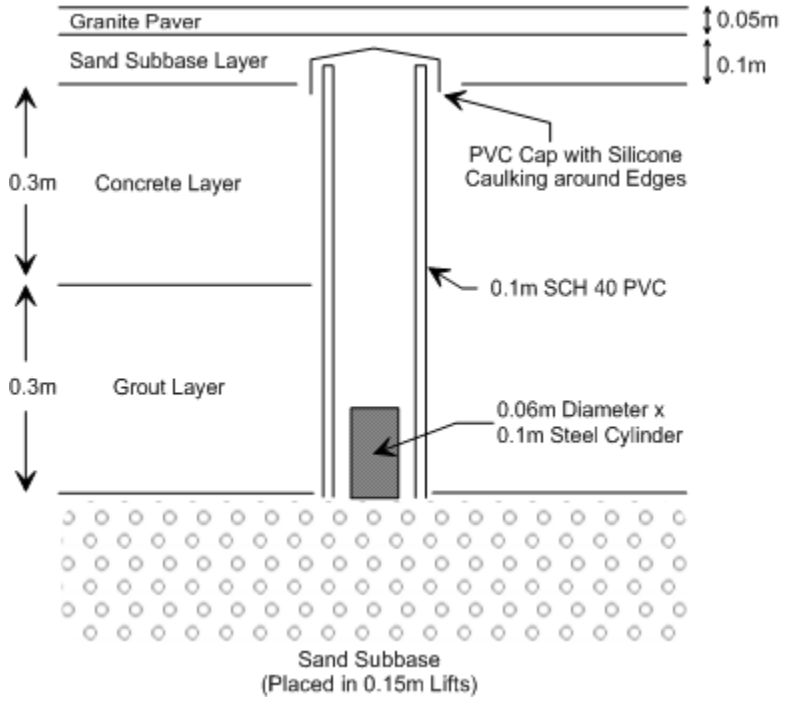

Figure 1: Profile of the plaza and underlying materials, showing the sentinel device for GPR detection.

Unfortunately, 15 years later the sand, cement/grout layer and pavers have subsided in many areas (Figure 2). The cost of the removal of the pavers and/or replacement of the pavers coupled with the cost of rehabilitating the subsurface was costing over $100,000 each event. Building management was keen

to find a solution that would fit into a manageable budget since broken 1.2 meter by 1.5 meter granite pavers cost $4,000 to replace and the risk of injuries to pedestrian traffic was unacceptable.

Figure 2: Subsidence of the fill material around the building has left voids beneath the granite pavers.

The solution to the subsidence of the granite pavers also had to be non-destructive and not detract from the ambiance of the building and landscape. Geophysical solutions were addressed since they are non-destructive and non-intrusive investigative methods (Reynolds, 1997). Ground penetrating radar (GPR) was selected due to its ease of deployment, high-resolution subsurface imaging capabilities and ability to image through reinforced concrete (Daniels, 1996).

Ground Penetrating Radar

Ground penetrating radar is used to image shallow regions of the subsurface primarily for geology, engineering, environmental science, and archeological exploration (Daniels, 1996). This survey utilized a 250 MHz GPR antenna array to image to a depth of approximately 1.8 meters below grade by transmitting radar waves (microwave band) downward from a transmitting antenna and collects the reflected energy at the receiving antenna (Figure 3). Variations in the dielectric properties of the subsurface materials are used to identify the presence of structures, voids, and changes in composition.

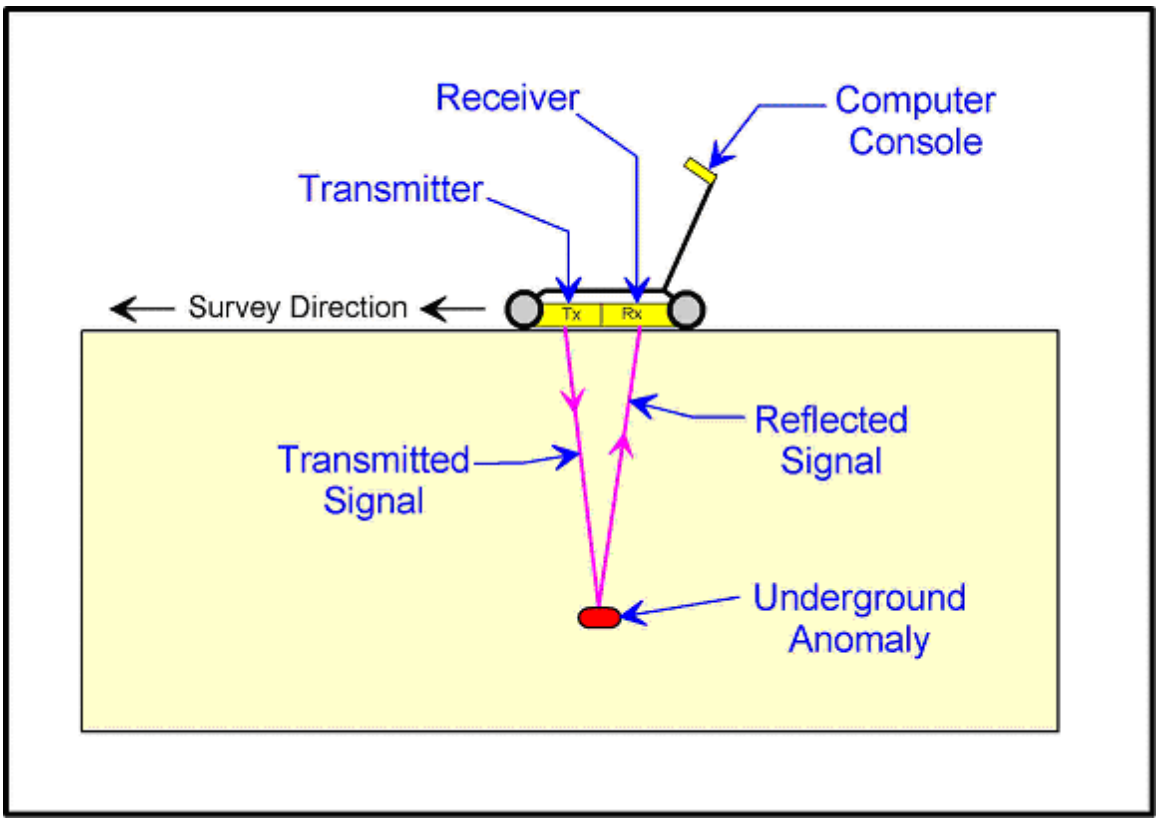

FIGURE 3: Schematic diagram of the ground penetrating radar system.

The dielectric properties of the subsurface determine the radar wave travel time. Materials with greater amounts of moisture increase the radar wave travel times. Consequently, dry soils and rock produce lower travel times:

$$V_m = \frac{c}{\sqrt{\varepsilon_r}}$$

Depth of the buried object or change in composition can be obtained from the velocity:

$$D = \frac{cT}{2\sqrt{\varepsilon_r}} = \frac{V_m T}{2}$$

Where, V_m is the velocity of the material; **c** is the velocity of light, ε_r is the relative dielectric constant; and **T** is the two-way travel time in nanoseconds (ns; 1 ns = 1 x 10^{-9}) (Hutchinson, 2002). Attenuation of the radio waves occurs as survey depth increases and also depends on the dielectric properties of the subsurface material. Therefore, signal attenuation will occur as the conductivity of the media increases.

Velocity and time were used in order to accurately monitor the depth to the steel cylinder between measurement dates.

Sentinel Installation

An investigation was conducted using a three-dimensional time-depth GPR mapping strategy to determine areas of potential subsidence. Fifteen areas were identified as having voids at depths associated with the loss of sand subgrade and collapse of the grout/concrete layer into the void (Figure 2). The loss of the sand subgrade may be related to poor placement of the sand or flushing of the sand from between the soldier piles and the outer wall of the former excavation. Nevertheless, these 15 areas in question were rehabilitated at great expense and building management required a sentinel strategy to minimize future cost and prevent injuries related to subsidence.

A 0.1 meter hole was cored through the cement/grout beds and a 0.1 meter Sch. 40 PVC pipe was grouted in place. The open-ended PVC pipe rests on the sand sub-grade and a 0.06 meter diameter by 0.1 meter long stainless steel bar was placed in the pipe. The depth to the top of the stainless steel bar resting on the on the sand subbase was measured. The bar then acts as a sentinel device; when the sand shifts the stainless steel bar will settle with it and GPR will be able to determine depth to the top of the bar. The pipe was capped and covered with 0.1 meters of the sand sub-base layer and the pavers were laid on top of the sand sub-base (Figure 1).

After completion of the installation of 44 sentinel devices in the 15 rehabilitated areas and 29 other areas along 305 meters of sidewalk, ground penetrating radar images were collected over the sentinels (Figure 4). The time-depth to the top of each bar was noted on the 2-way time profile from the GPR image. The velocity was determined using the measured placement depth to the top of bar and the 2-way time to the top of the bar. The velocity was recorded and will be used for each sentinel event to determine the depth to the top of each bar. An increase in the depth to the top of the bar is considered to be evidence of continued subsidence.

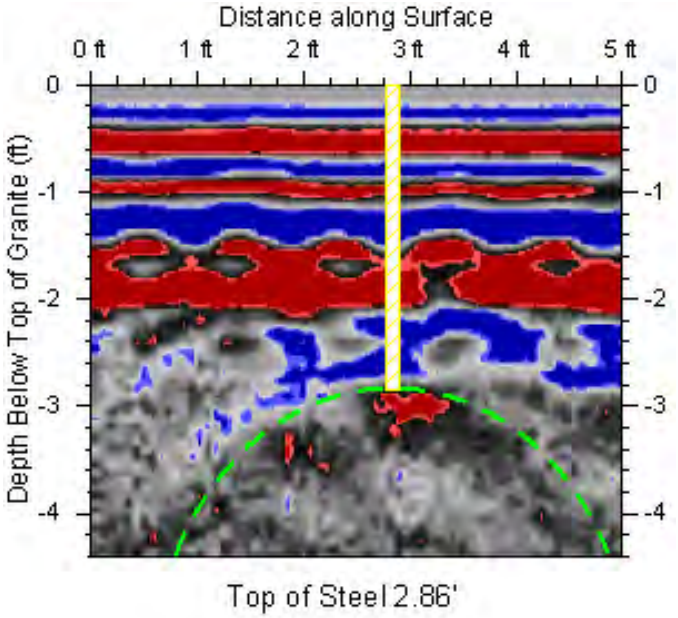

FIGURE 4: Ground penetrating profile image showing the diffraction pattern from the top of the solid steel cylinder.

Conclusions

Two years of biannual monitoring show that there have been only slight increases in the depth to the top of the bars in a few of the sentinel devices. These slight increases are assumed to be minor adjustments and not the development of a subsidence event. Nevertheless, these areas will be closely monitored in future monitoring events.

References

Daniels, D. J. (1996). Surface-Penetrating Radar. IEE Radar, Sonar, Navigation and Avionics Series, V. 6. London, England.

Hutchinson, P. J., L. Barta, and S. Young. (2002). *Subsurface Imaging Using Non-intrusive Ground Penetrating Radar:* **American Cemetery.** v. 74(6). p. 22, 24, 56.

Reynolds, J. M. (1997). An Introduction to Applied and Environmental Geophysics. New York, NY, Wiley.

Introduction

The absence of geologic materials associated with subsurface anomalies such as voids creates an abrupt and distinct change in material properties. These voids can be challenging to image directly using geophysical techniques, but their effect on surrounding materials may produce physical property variations that are detectable. This has been described as the "halo" effect, where changes in density, stress, fracturing, etc. may produce a geophysical anomaly larger than the actual target. The removal of geologic material causes an increase in effective stress as the load previously borne by the removed material is transferred to the sidewalls and roof of the void. Shear-wave velocity (V_s) is directly related to stress and it is not unreasonable to suggest that localized changes in stress will result in V_s variations. Examples from seismic surface wave and reflection studies showing detectable increases in V_s coincident with zones of expected stress build up are presented.

Shear-wave velocities are calculated from material responses to stress and strain. Since failure of consolidated rock is related more to the matrix than the pore conditions, monitoring changes in V_s should represent a highly sensitive method of detecting load-related changes in stress. Changes in V_s for a particular rock are related to differential stress and associated non-linearity in the stress-strain curve (Dvorkin et al., 1996).

Shear-wave velocity can be expressed as:

$$V_s = \sqrt{\frac{\mu}{\rho}},$$

where μ represents the shear modulus and ρ is the bulk density. Assuming that density remains relatively constant and there is negligible change in pore fluids, V_s is controlled by the shear modulus, which is the change in force across a unit area (stress) divided by the lateral change in cross-section for a given length (strain), expressed as:

$$\mu = \frac{\sigma}{\gamma} = \frac{\Delta F / A}{\Delta L / L}.$$

For a given material, the shear modulus is considered constant under static pressures and within the elastic deformation portion of the stress-strain curve. V_s is reduced when mechanical damage occurs in the rock as a result of stress-induced plastic deformation (Winkler, 2005). Conversely, localized increases in V_s are observable as effective stress associated with the tension dome surrounding subsurface cavities (Davies, 1951) increases due to the increased load on the void walls (Figure 1).

Laboratory measurements of compressional and shear-wave velocities show marked, non-linear increases with increased confining stress (Eberhart-Phillips et al., 1989; Khaksar et al., 1999; Siggins, 2006) with V_s increases upwards of 25% using ultrasonic measurements of shale and sandstone samples. Stress build up in both coal pillars and mine roofs associated with the room-and-pillar coal-mining method have also exhibited increased velocities (Snodgrass, 1990). These measured changes in velocity suggest variations in effective stress, like variations that would be present above a void or a reservoir under production pressures could cause significant changes in velocity of the affected rocks.

Analogous observations have been made in oil and gas reservoirs as the production of hydrocarbons leads to changes in the stress field of the reservoir and surrounding rocks (Sayers, 2004). Stress-sensitive discontinuities within the rock, such as grain boundaries, microcracks, and fractures, cause changes in elastic wave velocities as effective stress changes. Vertical V_s is sensitive to horizontal and vertical changes in stress, which are observable in seismic data. Time-lapse variations in seismic data occur in and around the reservoir due to production-induced changes (Herwanger and Horne, 2005). As pore pressure is reduced through production and bears less load, stress is transferred to the rock matrix. The increased load on the rock matrix leads to compaction and increased velocity within the reservoir and decreased velocity in the overburden and surrounding rock due to stress relief and relaxation. An opposite, but very similar process is occurring as a subsurface void evolves. As material is removed from the subsurface its load-bearing potential is eliminated

and the stress is transferred to the surrounding rock, including the side walls and void roof (Figure 1). The increased load carried by the surrounding material, and subsequent increased stress, translates into higher localized shear-wave velocities.

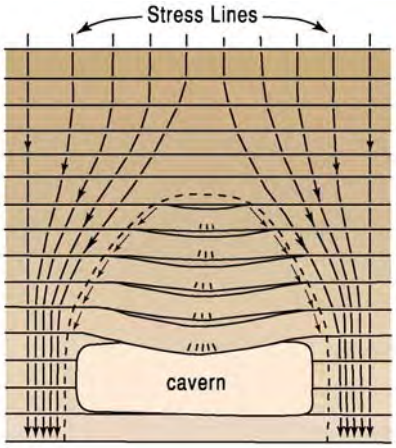

Figure 1. Tensional dome and distribution of stress lines around a cavern opening in horizontal strata (modified from Davies, 1951).

The strength of individual rock layers can be qualitatively described in terms of stiffness or rigidity and empirically estimated from measurements of V_s. Shear-wave velocity is directly proportional to stress and inversely related to strain. Since the V_s of earth materials changes when the stress on those materials becomes relatively large, it is reasonable to suggest that load-bearing roof rock above voids may experience elevated shear-wave velocities due to loading between load-bearing side walls. This localized increase in V_s is not related to increased strength, but is instead caused by increased load.

Examples

Shear-wave reflection methods were used at a salt-dissolution mine field located in central Kansas, USA, to test their use as a technique to discriminate locations with increased potential for roof failure based on documented subsurface conditions. Dissolution mining, where fresh water is injected into a salt deposit and brine is pumped back to the surface, often leaves subsurface voids that can potentially lead to sinkhole formation if too much salt is removed and cap rock is reached. The condition of many of these voids is unknown and poses a threat to public safety. When the lateral extent of the unsupported roof rock becomes greater than its strength to support overburden, failure occurs and the void may potentially migrate through overlying rock layers. Relatively higher V_s measurements may serve as an indicator of increased stress on the load-bearing walls and roof rock and corresponding failure potential.

Figure 2a shows common-midpoint shear-wave reflection data acquired over an area representative of native conditions with no known voids. The seismic line in figure 2b was collected over an area where known voids are present in the subsurface and vertical migration has progressed upward through the overlying shale. Both the presence and extent of the voids would be expected to cause a relative increase in the effective stress manifested as changes in the V_s of the overlying materials. Figure 2c shows a plot of NMO velocities for reflections from bedrock and a dolomite layer along the lines. Of particular interest is the discrepancy between the NMO velocities from the dolomite reflection, representing a change upwards of 20%. The velocity of the unconsolidated overburden remains relatively constant between the two lines, suggesting the change in velocity is related only to changes in the shale layer overlying the dolomite with no influence from overlying unconsolidated sediments.

At least one void is known to have migrated into the shale cap rock along the line in figure 2b. Several other wells are also located adjacent to the seismic line that are of the same

construction and vintage, shown with overlays of the void geometries. The dashed lines indicate that geometry and size is approximately based on tonnage removed and historical borehole data while solid lines are derived from sonar, geophysical logs, tonnage, and historical borehole data. Void geometries were not interpreted from seismic data. The elevated velocity along the entire line suggests that more than one void may be influencing the velocity measurements. Additional lines also show elevated velocities coincident with known voids, as well as velocity decreases in areas where subsidence has already occurred.

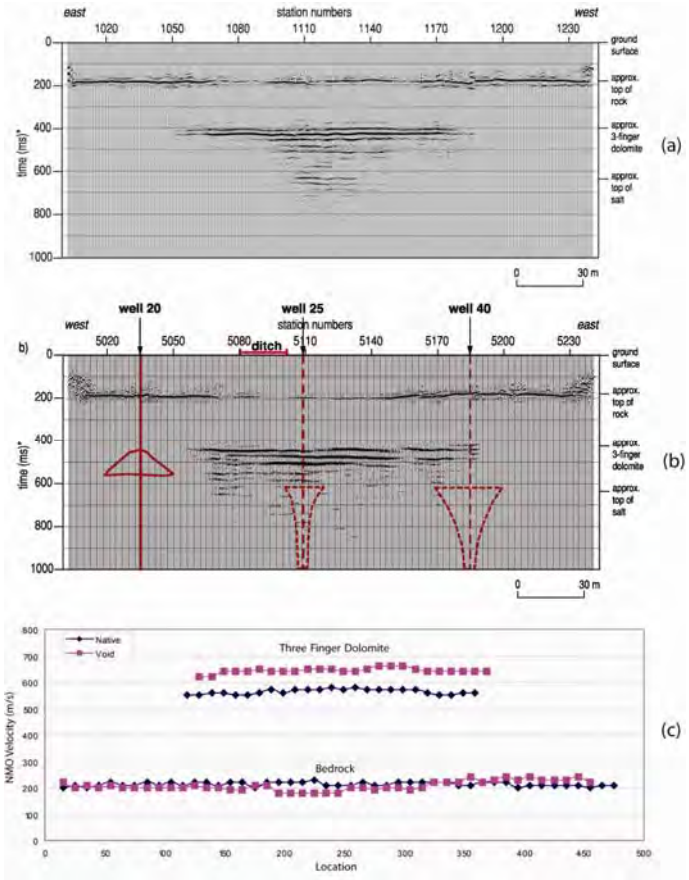

Figure 2. Stacked reflection sections acquired over native subsurface conditions (a) and a void that has migrated into the overlying shale caprock (b), with void geometries overlain. The graph (c) shows a plot of shear-wave NMO velocities for the Three-Finger Dolomite and bedrock reflections for lines acquired over native conditions (blue) and known voids (pink).

Figure 3 shows a V_s profile inverted from surface wave data acquired using the Multichannel Analysis of Surface Waves (MASW) method acquired over an area of a suspected void. The anomaly highlighted by the red-dashed circle shows a low-velocity feature with a high-velocity closure above it. The area marked by lower relative velocity is interpreted to be a void with a high-velocity halo immediately above it likely induced by the increased stress on the supporting walls and roof. Previous surface wave studies over mine workings and dissolution features have observed similar velocity patterns over suspected voids (Miller et al., 1999; Miller et al., 2000). Surface wave backscatter and diffractions were also observed at the same location. Diffraction moveout velocities and apex times are in agreement with the depth interpreted on the MASW data.

Conclusions

Lateral V_s variability can theoretically be linked to changes in the stress field as defined by principles governing the elastic moduli in rocks. Reflection data shown here are

the first known to provide empirical evidence relating the changes in stress associated with the tensional dome concept of Davies (1951) to non-invasively measured shear-wave seismic velocities. Variations in V_s correlate to areas of known or suspected voids and these changes are likely diagnostic of changes in rock properties or layer geometry related to voids. These techniques may be a valuable tool for identifying void-induced changes in the localized stress field, especially in conjunction with other proven methods. For shear-wave seismic reflection to be a viable method to characterize the degree of change in stress associated with a single void, resolution must be improved and velocity discrimination techniques must be developed that can isolate changes in velocity to sub-optimum offset distances.

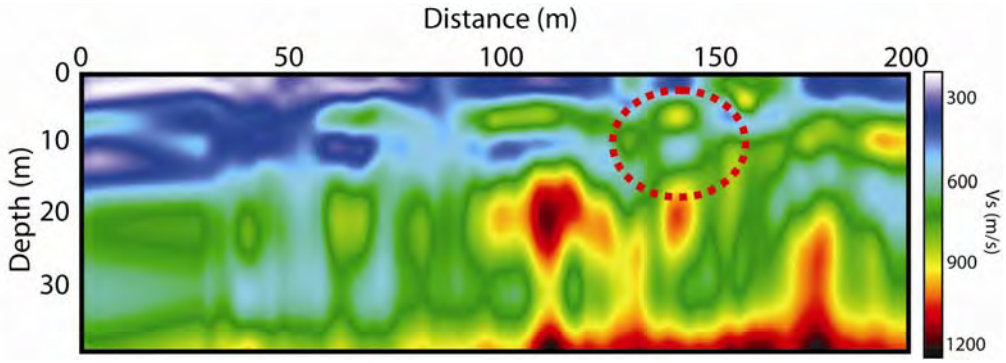

Figure 3. Shear-wave velocity profile from inverted surface wave data. The red-dashed circle indicates the location of a suspected void, marked by the high-velocity closure directly above a low-velocity anomaly.

References

Davies, W. E. [1951] Mechanics of cavern breakdown. *National Speleological Society*, **13**, 6–43.

Dvorkin, J., Nur, A., and Chaika, C. [1996] Stress sensitivity of sandstones. *Geophysics*, **61**, 444–455.

Eberhart-Phillips, D., Han, D-H., and Zoback, M. D. [1989] Empirical relationships among seismic velocity, effective pressure, porosity, and clay content in sandstone. *Geophysics*, **54**, 82–89.

Herwanger, J., and Horne, S. [2005] Predicting time-lapse stress effects in seismic data. *The Leading Edge*, **24**, 1234–1242.

Khaksar, A., Griffiths, C. M., and McCann, C. [1999] Compressional- and shear-wave velocities as a function of confining stress in dry sandstones. *Geophysical Prospecting*, **47**, 487–508.

Miller, R. D., and Xia, J. [1999] Seismic Surveys at Alabama Electric Cooperative's Proposed Damascus, Alabama Site. Open-File Report No. 99-12, Kansas Geological Survey.

Miller, R. D., Xia, J., Park, C. B., Ivanov, J., Laflen, D., and Anderson, J. M. [2000] Detecting fracture related voids and abandoned lead/zinc mines and appraising the subsidence potential near Baxter Springs, Kansas. Open-File Report No. 2000-75, Kansas Geological Survey.

Sayers, C. M. [2004] Monitoring production-induced stress changes using seismic waves. *74th Annual Meeting, Expanded Abstracts, SEG*, 2287–2290.

Snodgrass, J. J. [1990] Sonic full-waveform applications to stress evaluation in coal mines. Proceedings of the Third International Symposium on Borehole Geophysics, MGLS, **2**, 731-745.

Siggins, A. F. [2006] Velocity-effective stress response of C02-saturated sandstones. *Exploration Geophysics*, **37**, 98–103.

Winkler, K.W. [2005] Borehole damage indicator from stress-induced velocity variations. *Geophysics*, **70**, F11-F16.

Introduction

The urban development of the city of Trondheim in the last century has extended onto the near-shore areas (Figure 1). In the last 15 years, land reclamation has been intensified for construction work and building activity. Historical landslides are known to have occurred along the shore (e.g., L'Heureux et al., 2007). Damages to coastal infrastructures and loss of life resulted from these events. In one case (1888) a devastating tsunami wave struck the shoreline (Figure 1). The combination of historical landslides and urbanization has increased the concerns about the stability of the near-shore slopes. Therefore, numerous geological, geophysical and geotechnical investigations were carried out in recent years to explore in detail the stratigraphy of the fjord-valley fill and to investigate the stability both on land and in the fjord. One of the purposes of this paper is to show the ability of the shear-wave seismic method to study fjord-valley sediments from paved areas. In addition, we demonstrate the exceptionial potential for correlation between land-seismic and shallow-marine seismic data sets.

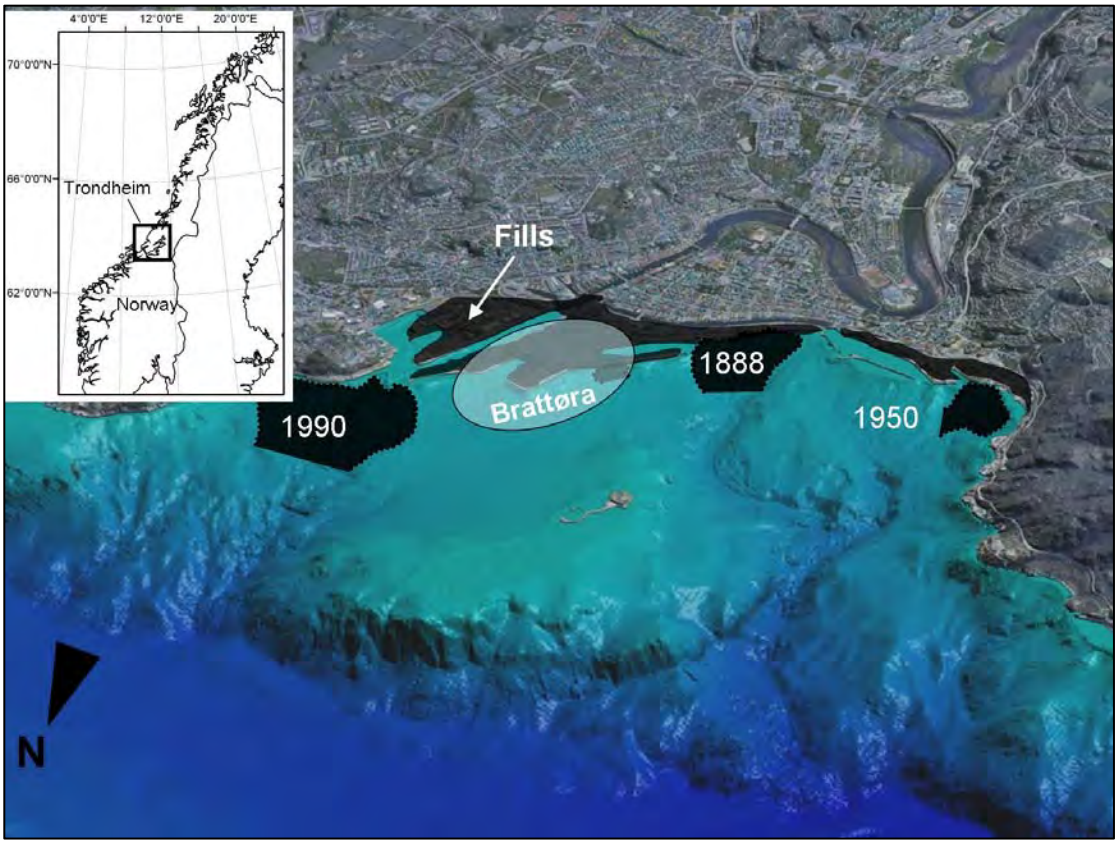

Figure 1: Overview over Trondheim, Mid-Norway, and location of the study area (encircled). Historic landslide scars (year in white) and land reclamation areas are indicated.

Methods

In the fjord, shallow high-resolution marine-seismic methods were applied using a) a shallow water streamer and ventilated sleeve airgun, and b) the TOPAS PS 40 parametric sub-bottom profiling sonar system. Sonar profiling gave excellent and high resolution results in the range of decimeters (L'Heureux et al., 2007; L'Heureux et al., 2009). Unfortunately, these methods tend to fail towards the shore line due to relatively coarse-grained sediments at the seabed.

Onshore, a land streamer system for SH-polarized shear-wave reflection seismics on paved roads was applied experimentally for the seismic imaging of the fjord-valley fill down to the

bedrock (Polom et al., 2009). Besides the stratigraphic information, the derived shear-wave velocity, in combination with shallow geotechnical investigations, provides an indicator of the stiffness of the sediments. The initial tests were carried out in the Brattøra area (Figure 1).

The high-resolution shear-wave seismic operations were carried out using a shear-wave land streamer of 120 SH-wave receivers configured to geophone intervals of 1 m and a newly developed, buggy-mounted shear wave vibrator source of 30 kN peak force operating in SH-configuration also (Figure 2). This technique is comparable to that used by, e.g., Inazaki et al. (2004) and Pugin et al. (2004), but here, the field configuration was especially adapted for the application on paved surfaces with underlying unconsolidated sediments of more than 100 m in thickness.

Figure 2: SH-wave land streamer system and LIAG shear wave vibrator buggy (30 kN peak force) during data acquisition close to the water side in the Brattøra harbour area of Trondheim. The arrow indicates the orientation of the SH-wave particle motion of source and receivers.

The seismic data was recorded by a Geometrics GEODE instrument installed in the recording van in front of the land streamer unit. Data storage was done uncorrelated to enable subsequent data improvement by, e.g., specialized deconvolution techniques. Parallel to the recording, quality control of each data record was carried out using the display-only correlation mode of the GEODE system. The recording parameters were initially optimised on site to meet the requirements of the field procedure. The sweep parameters were configured to 25-100 Hz range, 10 s duration, and using 14 s recording time sampled by 1 ms interval. The peak force was reduced to 60% to prevent slipping of the ground-coupling unit.

Seismic operations were carried out at night in time slots from midnight to 5 am to minimize the ambient vibration noise from surrounding heavy traffic of trains, trucks and other heavy equipment, and for safety reasons. Road closures also helped to minimize the noise from heavy traffic.

Results

The low ambient noise level during the night and the road closure enabled a high productivity rate with less down time due to passing traffic. Based on these experimental results, the initial profiling grid designed for the experiment stage was expanded considerably for a subsequent data production stage covering most of the harbour area at Brattøra. The land-based shear-wave data showed a resolution of 1 m vertically, clear detection of the bedrock, and probably also structures within the bedrock. The FD depth migration process gives excellent results, imaging fluviatile and marine sedimentary sequences overlying an undulating bedrock surface, and focussing bow-ties and diffractions in the bedrock zone (Figure 3). Due to the clear and continuous reflection events, shear-wave velocity could be calculated down to the bedrock to indicate the dynamic stiffness of the sediment layers, as superimposed in Figure 3. The bedrock surface may be easily correlated with marine seismic data (air-gun; Figure 4). Due to missing reference velocities for the marine seismic data (no offset), depth correlations

have been estimated. Another correlation between land and high-resolution marine seismic data is presented in Figure 5 (sub-bottom profiling). In this figure, several seismic events can be followed in the unconsolidated sediments, from land and into the fjord.

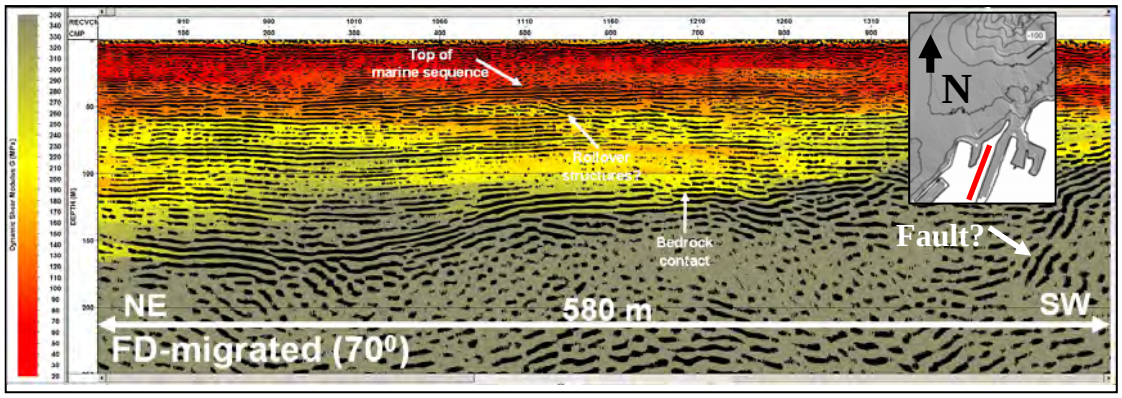

Figure 3: FD-migrated depth section (colour coding for dynamic shear modulus G0).

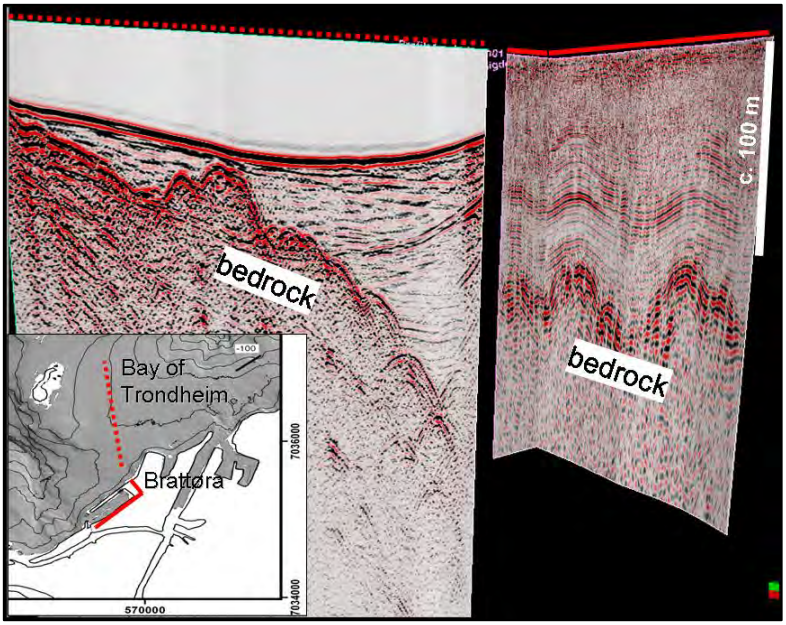

Figure 4: Correlation of marine air-gun seismic data (left) and shear-wave land seismics (right) from the bay of Trondheim and at Brattøra, respectively.

Figure 5: Correlation of marine sonar profiling (right) and shear-wave land seismic (left) from the bay of Trondheim and at Brattøra, respectively. The correlated stratigraphic divisions (colour and text) correspond to those proposed by L'Heureux et al. (2009).

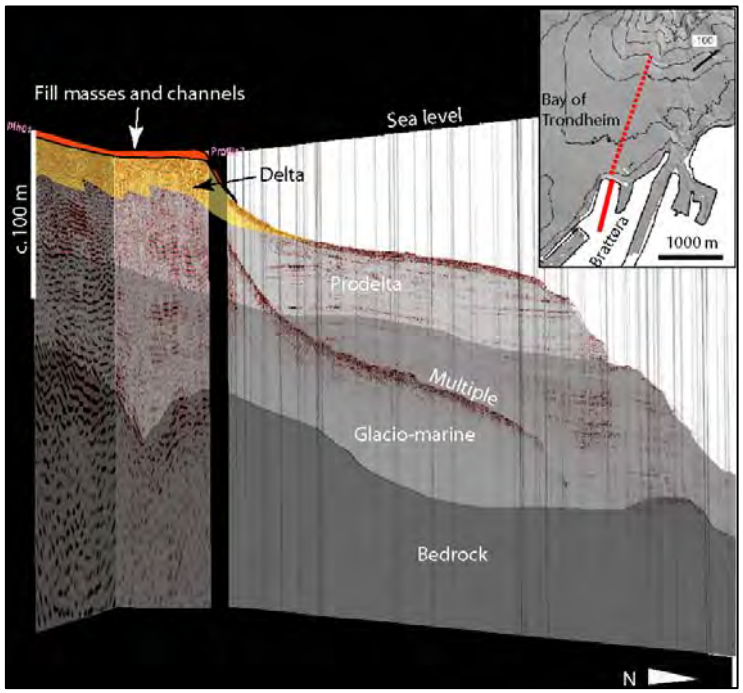

Conclusions and Outlook

The 2.5D profiling results achieved in 2008 show the excellent practicability of the SH-wave reflection seismic method on paved areas in Brattøra by combining a vibratory source and a SH-wave land streamer. Shifting of field work operations into the late night hours combined with closing of the traffic in the neighborhood of the field work activities led to excellent data quality due to the low ambient noise level. During the seismic data processing, application of FD time migration was an important process to image correctly the structures near the bedrock. The migration behavior of diffractions and bow-tie structures could be used additionally to improve the shear-wave velocity field used for the final depth conversion.

Results show that bedrock surface and several seismic events within the fjord valley fill can be followed from land into the fjord. The combined onshore-offshore seismic profile grid provides a basis for further structural and geotechnical interpretation. The derived shear-wave velocities should be combined with cone penetrometer testing and borehole results to achieve a spatial overview of fjord-valley fill geotechnical properties.

The future aim of this combined effort is the planning of a well at Brattøra, preferentially down to the bedrock, for further geological and geophysical analysis, and validation of the seismic results.

Acknowledgements

The authors gratefully acknowledge the Trondheim harbour authorities and the local companies for their permitting and the support during the field campaign. The high-resolution shear-wave reflection seismic survey (June 2008) was kindly sponsored by StatoilHydro. The authors thank also Maarten Vanneste (ICG/NGI) and Shyam Chand (ICG/NGU) for their support during this project and master-student Karl Magnus Nielsen (Univ. of Oslo) for his help during the preliminary noise-evaluation campaign carried out in Brattøra end of 2007. This is contribution # 259 of the International Centre for Geohazards (ICG).

References

Inazaki, T. [2004] High resolution reflection surveying at paved areas using S-wave type land streamer. *Exploration Geophysics, 35, 1-6.*

L´Heureux, J.-S., Longva, O., Hansen, L. and Vingerhagen, G. [2007] The 1990 submarine slide outside the Nidelv river mouth, Trondheim, Norway. In: *Submarine Mass Movements and Their Consequences*, edited by V. Lykousis, D. Sakellariou and J. Locat, pp. 259-267, Springer.

L'Heureux, J.-S., Hansen, L. and Longva, O. [2009] Development of the submarine channel at the mouth of the Nidelva River, Trondheimsfjorden, Norway, *Marine Geology*, 260, 30-44.

Polom, U., Hansen, L., L'Heureux, J.-S., Longva, O., Lecomte, I. and Krawczyk, C.M. [2009] High-resolution shear wave reflection seismic in the harbour area of Trondheim, Norway, *71st EAGE Conference & Exhibition*, Extended Abstracts, Amsterdam.

Pugin, A.J.M., Larson, T.H., Sargent, S.L., McBride, J.H. and Bexfield, C.E. [2004] Near-surface mapping using SH-wave and P-wave seismic land-streamer data acquisition in Illinois, U.S. *The Leading Edge (Tulsa, OK), 23(7), 677-682.*

Summary
A radiomagnetotelluric (RMT) survey is carried out to solve geomorphological studies concerning the evolutionary history of the terraces of the river Rhine in the Lower Rhine Bay next to Cologne, Germany.
Geomorphological studies concern e.g. the evolutionary history of the valleys and the classic geomorphologic approach is to take drilling samples to examine the spreading of the covering sediments. The geophysical task is to map continiously the two boundaries between tertiary sands, fuvial gravel and loess.
The measurements were realized using the new tensor RMT-device developed recently. Horizontal components of the magnetic and electric fields were observed in the frequency range from 10 kHz to 1MHz. Military and civilian radiostations broadcasting in this frequency range were used as transmitters. Transfer functions (e.g. apparent resistivities and phases) are determined by spectral analysis using a newly developed processing software. The observed apparent resistivities and phases were reliable and they showed a smooth frequency dependence.
The data was inverted for 2D conductivity models and compared with two-dimensional inversion results of DC measurements and with existing boreholes. The good comparability indicates that radiomagnetotellurics can be optimally applied to this kind of geomorphological questions.

Measurement device and data processing
The Radiomagnetotelluric device is a four channel device which records time-series of all four horizontal field components (Hx, Hy, Ex, Ey) simultaneously [cp. Tezkan and Saraev, 2008]. The system consists of a receiver unit, an electrical antenna to observe the horizontal electric field components and magnetic coils to observe the horizontal magnetic field components (cp. Fig.1). The magnetic measurements are performed with a magnetic coil of about 30cm length and a multisection coil. The electric antenna is represented by a symmetrical dipole with two arms. In the presented study the electrical line was ungrounded with a length of 20m.
Time series of the electrical and the magnetic fields are recorded, saved in the receiver unit and later transferred to a field PC. The time series contain all the frequencies from 10kHz to 1MHz radio stations, which were used as transmitters. They were recorded in two different bands:
1. 10-100 kHz, sampling frequency: 312.5 kHz and
2. 100 kHz - 1 MHz, sampling frequency: 2.5 MHz.
The processing software calculates auto and cross spectra out of the time series. Radio transmitters can be easily identified in the power spectra as strong signals over narrow frequency intervals and are chosen via a certain coherency level (Fig. 2 top)

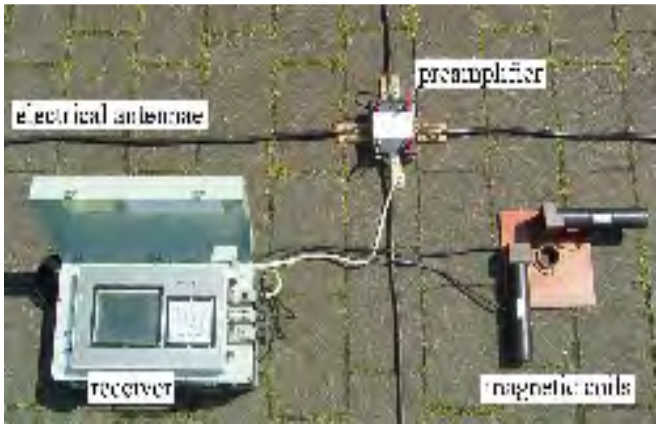

Figure 1: RMT system: digital receiver, electric antennae, magnetic Coils, preamplifier for the electric field

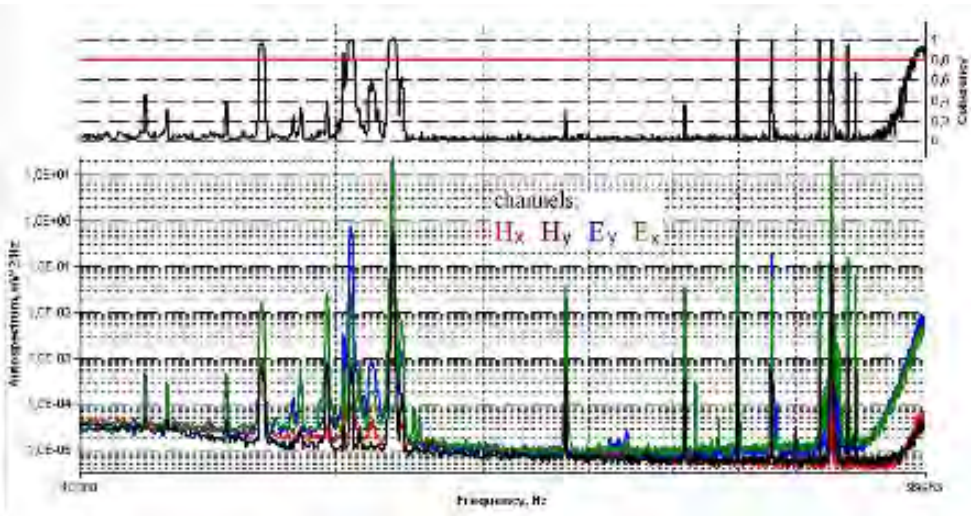

Figure 2: Auto spectra calculated from time series for one station on profile 1 (Fig. 3). Only the frequency band from 10-100 kHz is presented. The existing transmitters can easily be seen in the spectra as dominant lines. On top the coherency of the channels Hx and Ey is presented.

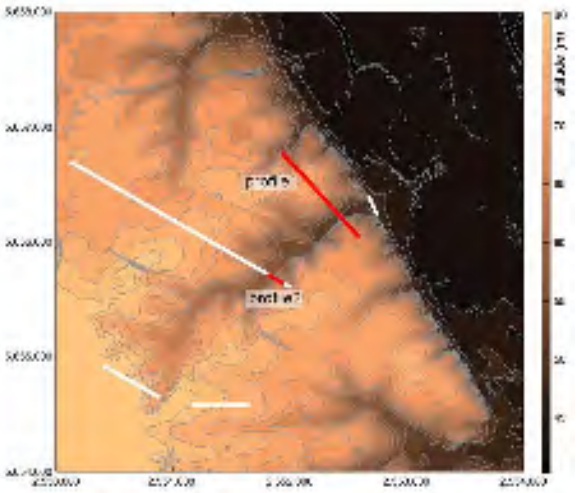

Figure 3: Map of the survey area. The two presented profiles are marked. The profile numbers correspond to the geomorphological questions presented below

Figure 4: Schematic scetch of the studied geomorphologic questions. Shown is the covering of tertiary sands with fluvial sediments. A and B deal with the evolutionary history of a valley. C is about today's wrong shape of original tertiary terrace.

Geology of the survey area and geomorphologic questions

The survey area is part of the terraces of the river Rhine, which are arranged in steps. More precisely, the area is characterized by the transition from the lowest terrace to the middle terrace, which is covered with loess. The geophysical task is now to map the two boundaries between tertiary sands, fluvial gravel and loess.

The main geomorphologic question concerns the spreading of the quarternary sediments. The tertiary topography is not traceable from today's topography.

In detail, the two geomorphologic questions examined with RMT are:

1. The evolutionary history of a valley: Did a tertiary valley exist before the covering with sediments (Fig. 4A) or did the valley emerged later, after the sedimentation (Fig. 4B)?

2. Fluvial gravel and Loess cover the tertiary sands and pretend a wrong shape of the original terraces (Fig.4C): The fact that today's top ground surface is not at the same place as the tertiary top ground surface can be seen in figure. 4C: the edge is shifted to the left.

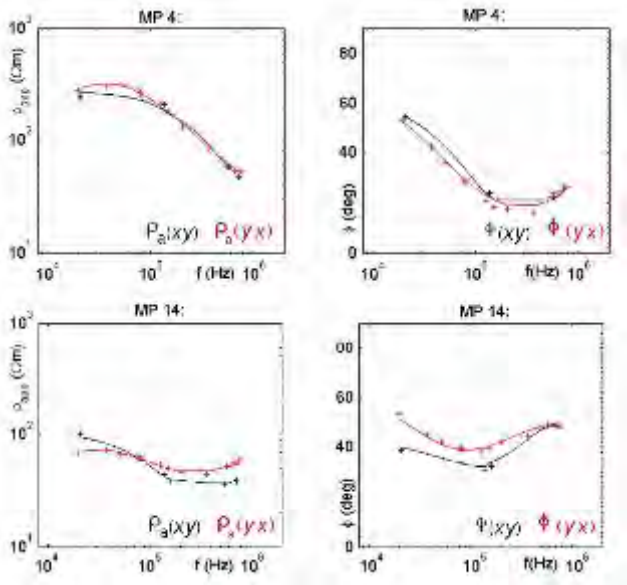

Figure 5: Data of two stations (Fig. 6). Cross: measured data, line: calculated data. The transfer functions a smooth dependence of frequency.

RMT data and Inversion results

For the inversion of the RMT data the 2D-inversioncode by Mackie & Rodi [2001] was used. It uses a nonlinear-conjugate-gradient algorithm with Tikhonov-regularization and a finite differences forward calculation. As a quality control for the results normalised sensitivity values are calculated for every cell. A comparison with the maximal depth of investigation according to Spies [1989] shows that both methods of quality control give similar depths for reliable results.

As an example in figure 5 the transfer functions of two stations from profile 1 (Fig.3) are shown. Their locations are marked in figure 6. The solid lines are the results from the inversion, which fit the measured data well.

As one can see in the inversion-results (Fig.6 and 7b) the boundary between the two resistive layers tertiary sands and gravel from the terrace is not very well reproduced: the boundary blurs to a region with lateral increasing ρ values. Whereas the two layers resistive gravel and covering conductive sediments are well separated. This fact was also observed in synthetical modeling with typical transmitter frequencies and resistivities situated in the survey area. Typical resitivity values come from a laboratory geoelectric measurements at drilling samples from the survey area (not presented). The RMT inversion results were compared with inversion results of geoelectric data. Both methods produce comparable images of the subsurface (Fig. 7).

Also in figure 7, one can compare the drilling results done in this area (Fischer [2003]). Not every pedologic result can be reproduced by this geophysical methods, but the main features, like tertiary sands and covering sediments are principally solved.

Geomorphologic questions answered with RMT

By mapping the upper border of the resistive tertiary sands, RMT can answer the asked geomorphologic questions:

1. The evolutionary history of a valley can be revealed. In the RMT section presented in figure 6 one can see that in this case the valley existed before the covering with sediments: one can see the original valley carved in the resistive tertiary sands. Furthermore one can see the asymmetric shape of today's valley, which differs from the tertiary valley. This asymmetric shape is typical for valleys emerged in glazial times.

2. The tertiary shape of the terraces can be mapped, although covered with sediments. An example therefore is the profile in Fig. 7, where today's top ground surface doesn't correspond to the tertiary one.

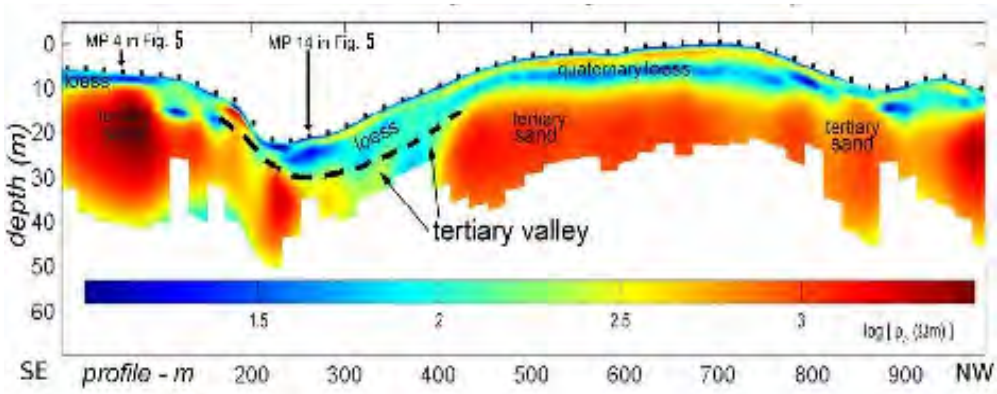

Figure 6: Profile 1: RMT joint-inversion of both modes. For localizations (Fig. 3). RMS=1.81 %. Areas below the maximal depth of investigation (Spies[1989]) are whitened. The tertiary valley is accentuated: it existed before the covering with loess (Fig. 4A).

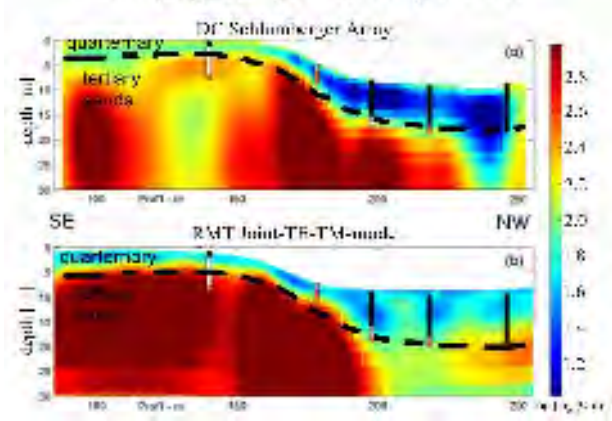

Figure 7: Profile 2 (Fig. 3): Comparison of DC and RMT inversion results: (a) DC, Schlumberger array and (b) RMT. Today's topography doesn't respond to the tertiary topography. Tertiary sands are presented in red in the drilling core, the covering sediments are black (Loess) and white (Kolluvium)

Conclusion

The geophysical method RMT can be applied for some geo-morphological issues. Concerning the mapping of the terraces, the results are comparable to drilling results. Of course, RMT can not substitute percussion drilling together with pedological laboratory studies. But RMT gives an adequate geological overview and can perfectly assist the choice of new drilling spots. The advantage is the measuring speed, the nondestructive measurement and continious subsurface information.

References

Fischer, P. [2003]: *Pleistozäne und holozäne Relief- und Bodenentwicklung in der mittleren Niederrheinischen Bucht am Beispiel des Vinkenpützer Grundes nordwestlich von Köln*., diplom-thesis, University of Cologne.

Lippert, K. [2007]: *Anwendung Geophysikalischer Methoden auf Geomorphologische Fragestellungen*., diploma-thesis, University of Cologne.

Mackie, R. L. and Rodi, W. [2001]: *Nonlinear conjugate gradients algorithm for 2-d magnetotelluric inversion.*, Geophysics, 66.

Spies, B. R. [1989]: *Depth of investigation in em sounding methods*, Geophysics , 54.

Tezkan, B. and Saraev, A. [2008]: *A new broadband radiomagnetotelluric instrument: applications to near surface investigations*. Near Surface Geophysics, 6. 243-250

ADVANCED INVERSION STRATEGIES USING A NEW GEOPHYSICAL INVERSION AND MODELLING LIBRARY

Thomas Günther, Leibniz Institute for Applied Geophysics, Hannover (Germany)
Carsten Rücker, Institute for Geophysics and Geology, University of Leipzig (Germany)

Abstract

Geophysical inverse problems often suffer ambiguity and yield fuzzy subsurface images. Often satisfactory results can only be obtained if additional information is incorporated in the inversion. The latter can be structural information about known boundaries or information about the parameters or their limits. However, this is rarely done by the available inversion software packages.

We present an extremely versatile inversion and modeling framework for solving inverse problems on arbitrary geometries. Irregular meshes are used to incorporate known discontinuities. The generalized minimization scheme allows for controlling every model cell and every cell boundary individually. Moreover the subsurface can be subdivided into regions that represent different geological units or different physical properties. For each region the model transformation function can be set, e.g. for incorporating petrophysical relations, logarithmic barriers or a combination of it. The constraint type, e.g. smoothness, and the strength and characteristics can easily by varied in the course of iterations. Different joint inversion schemes are easily derived from that.

By hand of a synthetic ERT study we show how the approach can be used to imagine small contrasts within a contrasted environment and to monitor small changes with time-lapse inversion.

Introduction

Most geophysical techniques lead to the solution of inverse problems. The inherited ambiguity of results can often only be coped by simplifications or assumptions such as smoothness constraints. By the latter we are able to see the main structures as a more or less fuzzy image but often artifacts are produced.

In many cases, additional information is available in form of

- structural information about existing boundaries from boreholes or reflection data
- parametric information about values and valid parameter ranges from borehole or lab data

They are often compared to verify the results but rarely incorporated in the inversion. Structural information helps to yield clearer images by allowed boundaries (Günther and Rücker, 2006). Parametric information can drastically reduce the ambiguity as well. However, the individual units in the model may require different regularization schemes. Since the algorithms are identical for all methods the solution is a versatile framework software.

The inversion framework

As an inversion method-independent framework we created the open-source C++ class library GIMLi – Geophysical Inversion and Modeling Library. It holds algorithms for different tasks and is

structured into four layers (Fig. 1) that are based on each other:

The basic layer holds fundamental algebraic methods and mesh containers for model parametrization

The modeling&region layer administrates the modeling classes that are based on a basis class and the connection to constraints and transform functions

The inversion layer is a template class for minimization with different methods, inverse solvers, line search, λ optimization and resolution analysis

In Inversion frameworks sophisticated techniques are formulated, e.g. time-lapse strategies, roll-along inversion or different kinds of joint inversion

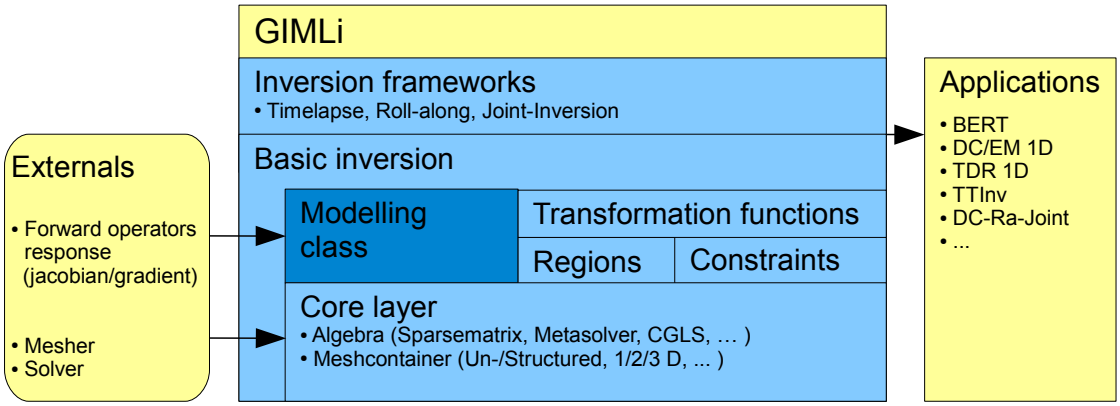

Figure 1: Scheme of the GIMLi library, applications and externals

Note that the library itself is purely mathematical. Physics is involved by applications that apply specific forward operators. After defining the forward operator, the inversion consists only of 1 line of code.

We use a generalized minimization scheme after Günther and Rücker (2006)

$$||\mathbf{D}(\mathbf{d}-\mathbf{f}(\mathbf{m}))||_2^2 + \lambda||\mathbf{W}^{\mathrm{b}}\mathbf{C}\mathbf{W}^{\mathrm{m}}(\mathbf{m}-\mathbf{m}_0)||_2^2 \rightarrow \min \quad (1)$$

$\mathbf{d}$ is the data vector, $\mathbf{m}$ the model vector and $\mathbf{f}$ the forward operator. $\mathbf{D} = \mathrm{diag}(1/\varepsilon_j)$ is the inverse data covariance matrix and $\mathbf{C}$ is the constraint matrix, which can either be a discrete derivative (smoothness constraints) or the identity (minimum length). $\mathbf{m}_0$ is a reference model for keeping the gradients (smoothness) or the model itself (min. length) close to it. The matrix $\mathbf{W}^{\mathrm{b}} = \mathrm{diag}(\mathbf{w}_j^{\mathrm{b}})$ is used to weight the individual cell boundaries (boundary control) allowing structural constraints. On the contrary, $\mathbf{W}^{\mathrm{m}} = \mathrm{diag}(\mathbf{w}_j^{\mathrm{m}})$ contains the weights for the individual model cells (model control) allowing parameter control.

Equation (1) is minimized by any method such as NLCG or Gauss-Newton. A forward operator must provide a response function and can overload the automatic generation of the sensitivity matrix or the gradient vector by appropriate methods. Instead of the original data and model parameters arbitrary functions of it can be used as $\mathbf{m}$ and $\mathbf{d}$ (Günther et al., 2008). One motivation can be to ensure positivity or

limit the model parameters in a range by logarithmic functions. Another idea is to incorporate petrophysical relations, both can be combined. Finally the ambiguity is decreased by problem-dependent model/data functions. Different data are easily combined since they are weighted by their variances and they can have different transformations. For example, a logarithmized amplitude and a linearized phase are combined for MT inversion.

The Jacobian matrix of the transformed parameters is not calculated explicitly. Instead, a specialized variant of the CGLS inverse solver (Günther et al., 2006) incorporates the transformations, such that it can be changed flexibly.

Parameterization and the region technique

A parameterization defines how the neighboring relations of the model cells are. Possible dimensions can be 0d (independent parameters), 1/2/3 spatial dimensions (regular or irregular) or 4d (for different times or frequencies). The model is a set of so-called regions, each region is independent and has it's own inversion properties such as the transform function (including bounds), starting values, constraint type and model/boundary control. Regions can be different geological units of one parameter or different parameters. Examples for regions are:

- Resistivity and Thickness in a Block 1d DC/EM inversion, both are 0d meshes
- Water content and Resistivity in a smooth MRS inversion, each is a 1d or 2d region
- Velocity distribution and a trigger offset for each shot in refraction tomography

A hydrogeophysical ERT example

We demonstrate the region technique by a synthetic hydrogeophysical investigation. Figure 2a shows a regularly parameterized synthetic model comprising three main zones:

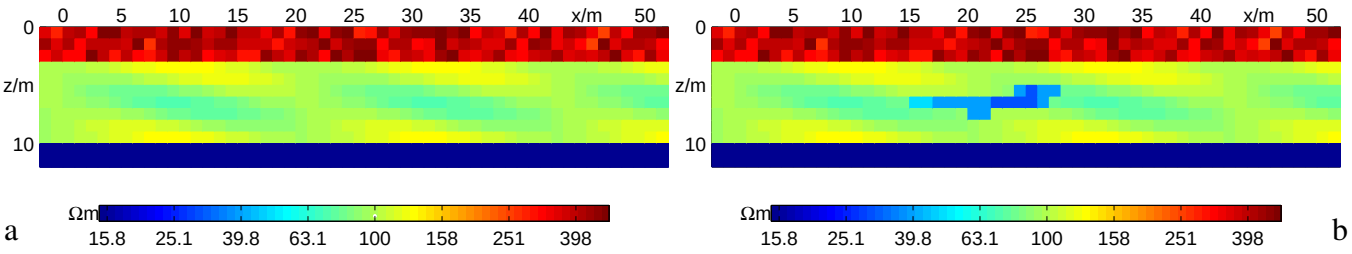

Figure 2: Synthetic model before (a) and after (b) tracer injection in the well at 15m, white dots denote electrodes

1. the unsaturated zone with resistivities of about 500 Ωm is characterized by statistical heterogeneities that are typical for the surface layer
2. the aquifer from 3 to 10m has moderate resistivities around 100 Ωm and shows more or less layered characteristics with relatively small contrasts

3. the aquiclude has a unique resistivity of 15 Ωm as typical for a clay layer

Aim of the study is to image structures within the aquifer and to monitor tracer injection using time-lapse inversion. However, both the surface heterogeneities and the large contrasts between the main units make this almost impossible. In Figure 2b the assumed resistivity distribution after tracer injection is shown. The tracer moves almost horizontally.

Synthetic data are generated by an FD forward operator (Günther, 2004). A surface profile of 50 electrodes with 1 m spacing applies combined dipole-dipole and Schlumberger data with successively increasing dipole lengths. In the borehole at x=15 m electrodes are installed and used to simulate Pole-dipole data between hole and surface. The synthetic data are contaminated by Gaussian noise of 3%+50μV(I=100mA) standard deviation. The inversions are done with the BERT algorithm (Günther et al., 2006), always such that the data are fitted within noise ($\chi^2 = 1$). Figure 3a shows an inversion result by slightly enhancing vertical variations over horizontal ones. We clearly see the three main units and heterogeneities in the first layer. However the boundaries are smooth and structures inside the aquifer cannot be observed.

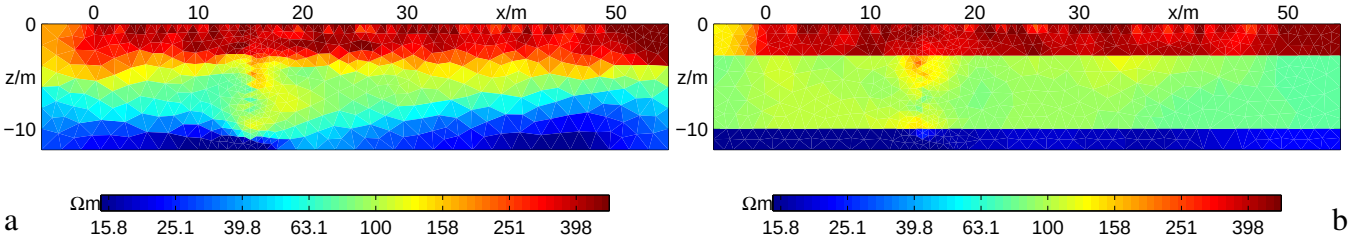

Figure 3: Result of smoothness-constrained inversion (a) and with structural information (b)

Assume we know the layer boundaries from the borehole, GPR or seismic data. We introduce the layers as polygonal constraints in the mesh generation and set the individual constraint weights to zero (Günther and Rücker, 2006). The result is displayed in Figure 3b. The unit boundaries are accepted and thus the clay resistivity comes close to the synthetic one. However, it is not possible to detect the synthetic aquifer structures. Instead, artifacts are shown at the borehole and at the left-hand side.

We now define the units between the boundaries as independent regions with individual inversion properties. The unsaturated region obtains minimum length constraints but a relatively high model control. The aquiclude can either be defined as a single region with unknown resistivity or a fixed parameter region. The aquifer region keeps smoothness constraints but with weaker model control. By the double-logarithmic model function $m_i = \log(\rho_u - \rho_i) - \log(\rho_i - \rho_l)$ the resistivity can be limited to lie within the lower and upper bounds $\rho_l = 50\,\Omega$m and $\rho_u = 200\,\Omega$m. The result (Figure 4a) shows more similarities with the synthetic model and a constant clay layer.

Finally, inversion of the synthetic tracer injection data are inverted. There are several strategies for time-lapse inversion: independent inversion, linearized projection, ratio inversion and reference inversion with the single-state result as reference model. We choose the latter but change the model properties of the regions. Since changes are expected to appear only in the aquifer, we fix the unsaturated zone and the aquifer by using minimum length constraints and very large model control. For the aquifer, minimum length constraints are chosen in order to avoid artifacts, but with much lower model control. The ratio of the two time steps is displayed in Figure 4b and illustrates that changes are restricted to the aquifer.

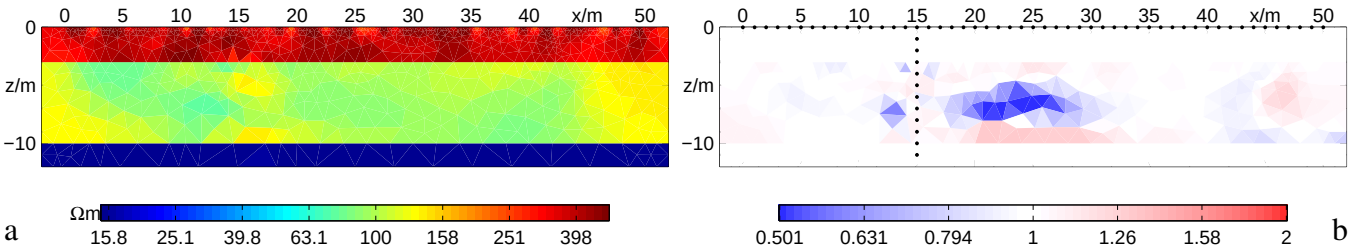

Figure 4: Result using region control parameters for single-state inversion (a) and ratio between time-lapse and single-state result (b)

Joint inversion strategies

Joint inversion of different methods is a popular way to decrease ambiguity. Different types can be distinguished:

- An inversion of different data for one parameter is easily applied by combined forward operator (see above).
- A structural inversion can be done by using the gradient of one model as model control for the other (Günther and Rücker, 2006). This can be restricted to specified regions (e.g. the aquifer).
- The model transformations open the way to a petrophysical joint inversion for combined parameters. Figure 5 shows how GPR and ERT can be jointly inverted for water content or porosity. Even the parameters of the relations can be inverted for.

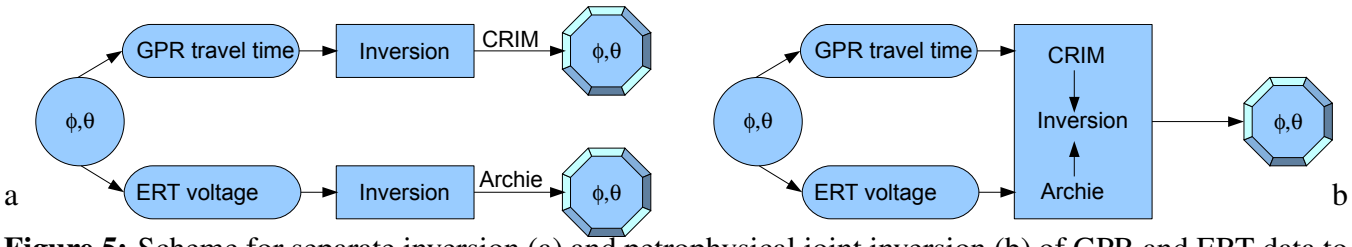

Figure 5: Scheme for separate inversion (a) and petrophysical joint inversion (b) of GPR and ERT data to obtain an image of porosity or water content

Conclusions

We presented a method-independent library for solving inverse problems in geophysics. Main components are a generalized minimization approach and arbitrary transformation functions, which allow for introducing structural and parametric information. A region technique has been presented that allows for treating different parameters or different geological units individually.

Using a synthetic ERT study we demonstrated the applicability to improve problems with limited resolution and time-lapse inversion by defining regions with different properties. Furthermore the presented techniques open the way for various joint inversion approaches.

References

Günther, T., 2004, Inversion Methods and Resolution Analysis for the 2D/3D Reconstruction of Resistivity Structures from DC Measurements, Ph.D. thesis, University of Mining and Technology Freiberg, available at `http://fridolin.tu-freiberg.de`.

Günther, T., Müller-Petke, M., Hertrich, M., and Rücker, C., 2008, The role of transformation functions in geophysical inversion, in Ext. Abstract, EAGE Near Surface Geophysics Workshop. 15.-17.9.08, Krakow (Poland).

Günther, T. and Rücker, C., 2006, A general approach for introducing information into inversion and examples from dc resistivity inversion, in Ext. Abstract, EAGE Near Surface Geophysics Workshop. 4.-6.9.06, Helsinki(Finland).

Günther, T., Rücker, C., and Spitzer, K., 2006, 3-d modeling and inversion of DC resistivity data incorporating topography - Part II: Inversion, Geophys. J. Int., 166, 2, 506–517, doi:10.1111/j.1365-246X.2006.03011.x.

BOREHOLE FLOWS, HYDRAULIC HEADS, AND FRACTURE-ZONE CONNECTION IN THE POTSDAM SANDSTONE AT THE ALTONA FLAT ROCK RESEARCH SITE IN NORTHERN NEW YORK

John H. Williams, U. S. Geological Survey, Troy, New York
Frederick L. Paillet, University of Arkansas, Fayetteville, Arkansas
David A Franzi and Edwin A Romanowicz, Plattsburgh State University, Plattsburgh, New York

Numerous borehole-geophysical methods are available for the characterization of fractures penetrated by boreholes but relatively few of these methods help to characterize the connections between fractures in the rock surrounding boreholes. Unfortunately, most studies in fracture-rock hydrology conclude that the characteristics of connections between locally transmissive fractures have a greater influence over aquifer-scale permeability than the local aperture of individual fractures (Long and others, 1996; LeBorgne and others, 1996; Shapiro and others, 2007). The study described here focused on the application of borehole-flow methods in the characterization of possible hydraulic connections between fracture zones penetrated by open bedrock boreholes.

The Potsdam sandstone of Cambrian age forms an extensive fractured-rock aquifer in northern New York. The hydraulics of three interconnected boreholes that penetrated multiple fracture zones in the Potsdam sandstone aquifer were studied at the Plattsburgh State University Flat Rock research site near Altona, New York. Televiewer and natural-gamma logs were used to correlate fracture zones penetrated by two shallow boreholes and a deep borehole at the Flat Rock site. Vertical flows in the multi-zone boreholes were measured with heat-pulse or electromagnetic flowmeters under quasi-steady-state ambient and pumped conditions. Flows also were measured under transient cross-borehole pumped or injection and recovery conditions. Composite hydraulic heads, which reflect the transmissivity-weighted average of the fracture-zone heads, were measured daily in the deep and one of the shallow boreholes in 2002-2003. The transmissivity, hydraulic head, and connection geometry of the penetrated fracture zones were determined through single- and cross-borehole flow-modeling methods described by Paillet (1998 and 2000).

In 2000, shallow boreholes 500A (USGS Cl-215) and 500B (USGS Cl-216) were drilled 20 ft apart and penetrated the Potsdam sandstone from 680 to 550 ft above sea level. In 2002, deep borehole 102 (USGS Cl-214) was drilled 400 ft northeast of boreholes 500A and 500B and penetrated the Potsdam sandstone from 670 to 535 ft above sea level. The lower part of borehole 102 penetrated Altona shale and siltstone and Precambrian crystalline bedrock. The composite hydraulic head in borehole 500B dropped more than 10 ft during air-hammer drilling of borehole 102 (fig. 1). Following drilling, the head in borehole 500B recovered for 3 days to within 3 ft of the pre-drilling trend before continuing on the seasonal recession. The composite hydraulics heads in boreholes 500B and 102 showed very similar seasonal fluctuations in their timing and magnitude during 2002-2003.

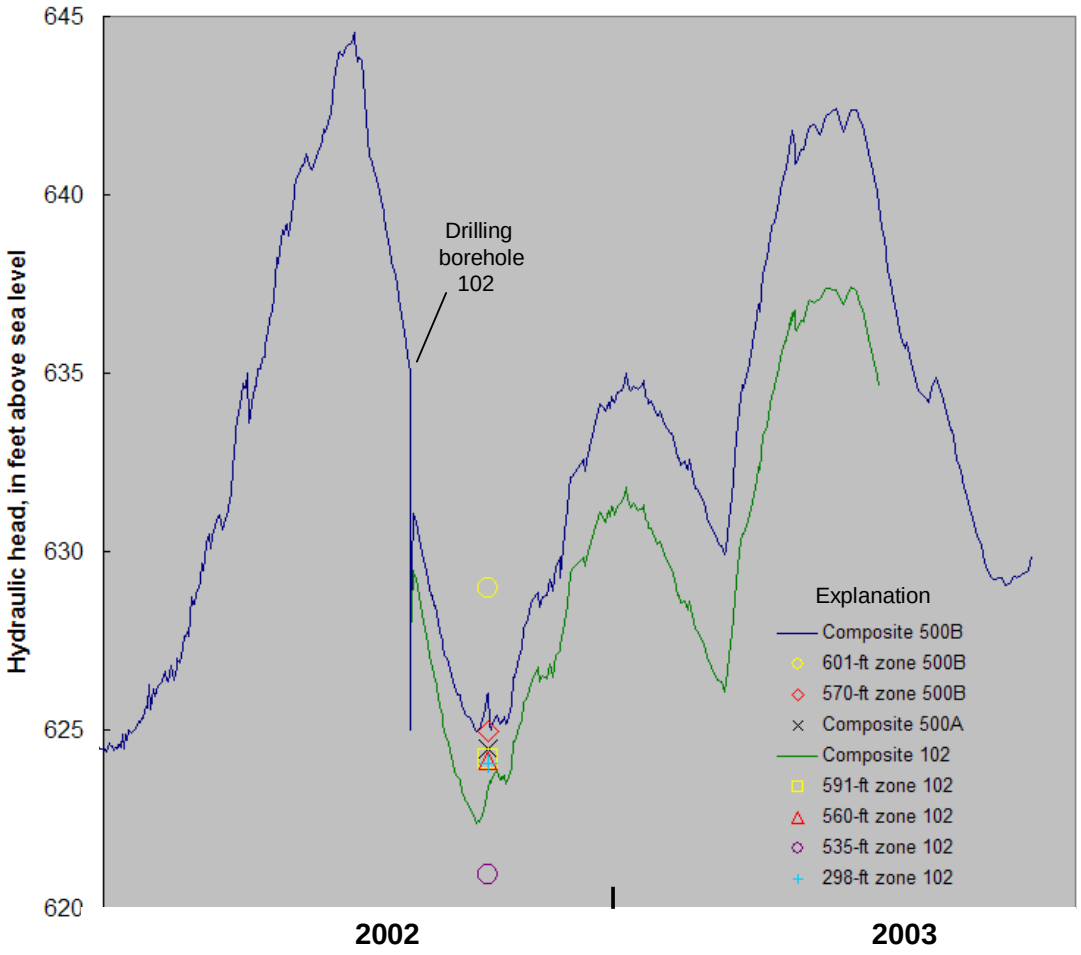

Figure 1. Daily measured composite hydraulics heads for 2002-2003 and estimated fracture-zone hydraulic heads for Fall 2002 in boreholes 500B and 102, Altona Flat Rock research site, northern New York

Boreholes 500A and 500B penetrated subhorizontal bedding-related fracture zones at 601 and 570 ft above sea level. The transmissivity of the upper and lower zones in borehole 500B estimated from the single borehole-flow model was 80 and 230 ft^2/d, respectively. The estimated transmissivity of the lower zone in borehole 500A was 1,100 ft^2/d. No transmissivity was detected at the upper fracture zone in borehole 500A. This dramatic change in permeability over a short distance indicates the presence of flow channeling within the fracture zone. In Fall 2002, ambient flow in borehole 500B was downward at more than 1 gal/min from the upper to the lower zone. The hydraulic heads estimated from the borehole-flow model were 629 and 625 ft above sea level for the upper and lower zones, respectively, which corresponds to a 4-ft head difference of between the zones (fig.1). Pumping of 3 gal/min from borehole 500A in Fall 2002 increased the outflow to the lower zone in borehole 500B indicating that this zone provided the hydraulic connection between the boreholes. Measured transient cross-borehole flows were best simulated by modeling a single isolated connection (fig.2).

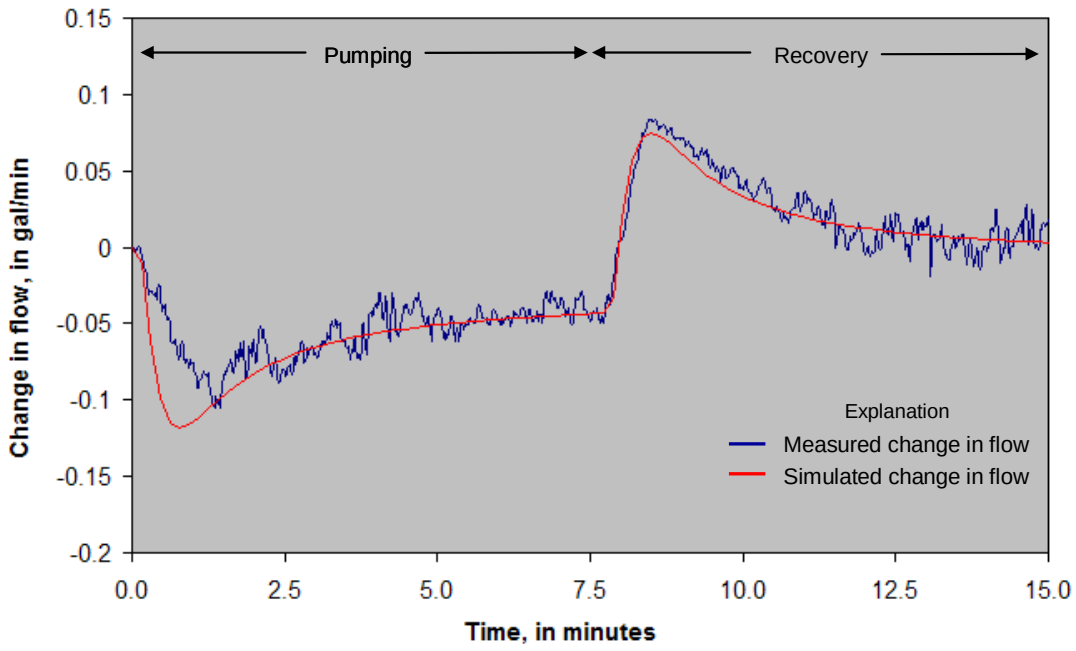

Figure 2. Measured and simulated transient change in flow between the 601- and 570-ft fracture zones in borehole 500B during pumping and recovery in borehole 500A, Altona Flat Rock research site, northern New York

Borehole 102 penetrated subhorizontal bedding-related fracture zones at 591, 560, 535, and 298 ft above sea level (fig.3). Estimated transmissivity of the zones from shallowest to deepest were 50, 1300, 340, and 200 ft^2/d. A near vertical fracture was observed on the televiewer log of the borehole just above the 535-ft fracture zone. The fracture zones at 591 and 560 ft above sea level appeared on the televiewer and gamma logs to be the same zones penetrated by boreholes 500A and 500B. The 535-ft zone projects to about 5 ft below the drilled depth of boreholes 500A and 500B. In Fall 2002, ambient flow in borehole 102 was downward from the 591- and 560-ft zones and upward from the 298-ft zone with both flows exiting at the 535-ft zone. The hydraulic heads estimated from the borehole-flow model were 624 ft above sea level for the 591-, 560-, and 298-ft zones and 621 ft above sea level for the 535-ft zone, which corresponds to a 3-ft head difference between the zones (fig.1). This head distribution indicates that the 535-ft zone is the bottom drain of the groundwater flow system. Injection of 30 gal/min into borehole 500A in Fall 2007 caused inflow from the 560-ft zone in borehole 102 indicating that this fracture zone provided the most direct connection between the boreholes. The injection also caused a small inflow from the 535-ft zone, which suggests that there is a connection of this zone to the main bedding-related zone connection, most likely through vertical fractures. Measured transient cross-borehole flows were best simulated by modeling a primary connection at the 560-ft zone and a secondary connection at the 535-ft zone.

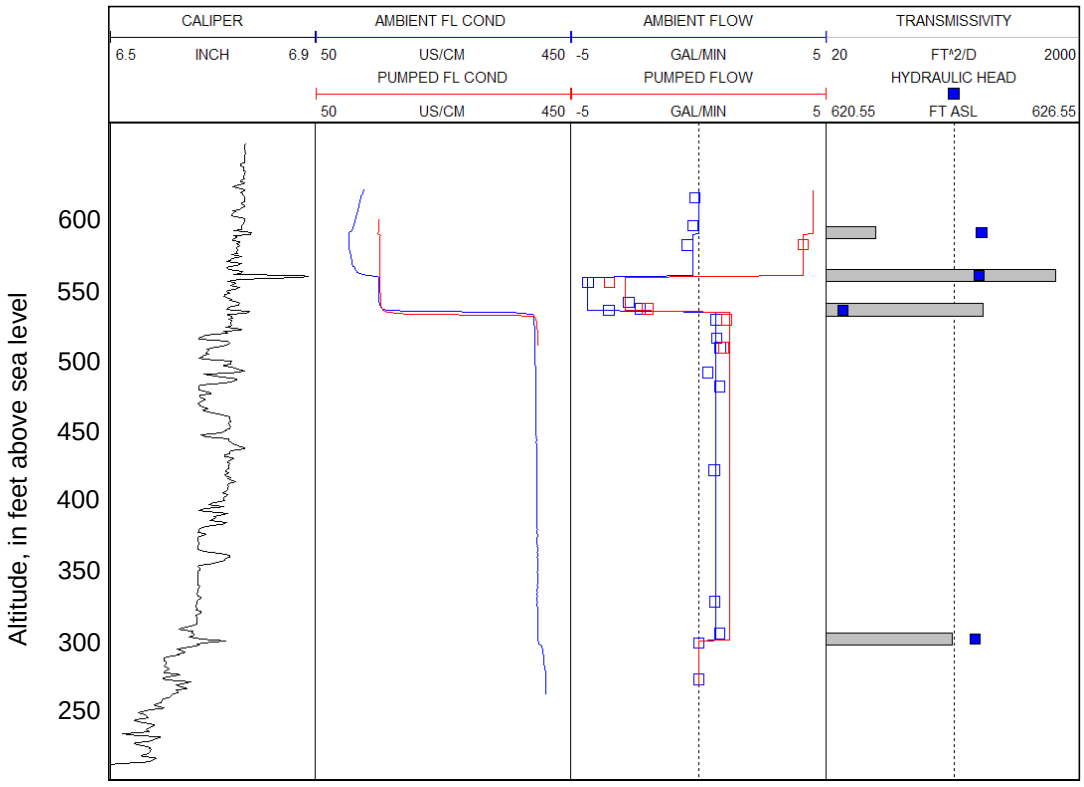

Figure 3. Caliper, ambient and pumped fluid conductivity and flow, and fracture-zone transmissivity and hydraulic-head difference in borehole 102, Altona Flat Rock research site, northern New York

Results of this fractured-rock site study suggest that flow-logging methods can be used to help characterize hydraulic connections between fracture zones penetrated by open boreholes. The study demonstrated the lateral continuity of subhorizontal bedding-related fracture zones between boreholes as well as the presence of flow channels within and vertical connections between individual zones.

References

Paillet, F.L., 1998, Flow modeling and permeability estimation using borehole flow logs in heterogeneous fractured formations, Water Resources Research, 34, 997-1010.

Paillet, F.L., 2000, A field technique for estimating aquifer parameters using flow log data: Ground Water, v. 38, no. 4, p. 510-521.

Shapiro, A.M., Hsieh, P.A., Burton, W.C., and Walsh, G.J., 2007, Integrated multi-scale characterization of ground water flow and chemical transport in fractured crystalline rock at Mirror Lake, New Hampshire, p 201-225 in American Geophysical

Union, Geophysical Monograph Series 171, Subsurface Hydrology – Data Integration for Properties and Processes.

Le Borgne, Tanguy, Paillet, F. L., Bour, Olivier, and Caudal, Jean-Pierre, 2006, Using a borehole flowmeter to measure transient hydraulic head in multiple-aquifer boreholes, Ground Water, v. 44 no. 3, p 244-252.

Long, J.C.S., Remer, J. S., Wilson, C. R., and Witherspoon, P. A., 1996, Rock fractures and fluid flow--Contemporary understanding and applications: Washington, D.C., National Academy Press, 551 p.

COMPARISON OF BOREHOLE FLOW MEASUREMENTS OBTAINED BY HEAT PULSE FLOWMETER AND DILUTION LOGGING IN A FRACTURED BEDROCK AQUIFER

Frederick Paillet
Dept of Geosciences
University of Arkansas, Fayetteville, AR

John Williams
U. S. Geological Survey
Troy, NY

Edwin Romanowicz
Center for Earth and Environmental Science
Plattsburgh State University, Plattsburgh, NY

EEGS' Annual Meeting
Keystone, Colorado
April 11-15, 2010

Abstract

We compare flow measurements made under ambient and pumping conditions in a bedrock borehole using high-resolution flow (heat pulse flowmeter) and fluid column dilution (repeat conductivity profiles after brine emplacement) methods. A second round of brine emplacement was avoided by using the fluid column conditions at the end of the ambient part of the dilution experiment as the initial condition for the pumping part of the dilution experiment. The estimates of flow by both methods yielded results that were in close agreement. The dilution method yielded direct estimates of flow based on the movement of interfaces, but logistics would have required the experiment to be repeated at two different pumping rates for most accurate results. The flowmeter yielded interval-averaged estimates of flow that agreed with the dilution results, but there was scatter of as much as 100% among the individual flow measurements. The flowmeter also required measurements under more than one pumping rate, and this was logistically much easier to accomplish than for the dilution experiment. We conclude that the methods are largely equivalent, with offsetting advantages and disadvantages for each method such that best results would be obtained using both methods in the same borehole.

Introduction

Borehole flow measurements are regularly used in hydrogeology to investigate the location and hydraulic properties of water-producing zones in boreholes (Molz et al, 1994; Paillet, 2004; James et al, 2006). High-resolution flow measurements are especially useful because they can be conducted under low-flow conditions at low pumping rates so that drawdown is relatively small, water level stabilizes soon after the start of pumping, and the quantity of contaminated water produced for disposal is kept small. There are two general classes of such flow

measurements: 1) flow measured in a cylindrical tube suspended in the center of the borehole where flow is forced through the measurement section by flexible diverters sealing the annulus between measurement section and borehole wall; and 2) dilution techniques based on following the evolution of the fluid column under the influence of natural inflow and water movement after the column has been replaced by a water column of distinctly different electrical conductivity from that of the natural ground water. Scientists use both of these techniques in the research mode, and both are offered as services by geophysical contractors. However there are almost no existing case studies where the two methods are applied to the same borehole at the same time so that a direct comparison can be made.

This study was designed to provide a side-by-side comparison of both methods in the same borehole under exactly the same hydraulic conditions. The intent was to first indicate how the trade-offs of the strengths and disadvantages of each technique play out in a typical practical field study. High-resolution flowmeters provide precise measurements of the flow passing through the measurement section, but the variable efficiency of the diverter seal at each measuring point often introduces significant scatter in the data (Hess, 1986; Molz et al, 1994). Dilution methods give a direct and unambiguous measurement of the movement of fluid column interfaces along the borehole, but also require rather elaborate plumbing to insure that the initial fluid column condition is set up by either "staining" the column with a uniform distribution of solute, or replacing the column with distilled water (Tsang et al, 1970; Pitrak et al, 2005; James et al, 2006; Paillet and Pedler, 1996).

A second objective was to assess the performance of each method in a situation where there are water-producing zones with large variations in transmissivity, and where the zones are communicating with each other under ambient conditions. The advantage of both flowmeter and dilution methods is that they provide hydraulic data from open boreholes without using packers. The disadvantage is that the response of weaker zones has to be recognized within the generally larger responses of the strongest producing zones – a problem that is avoided by straddle-packer isolation (Paillet, 2004). Therefore, an important part of the comparison of flowmeter and dilution methods is evaluating how well each deals with the detection of low transmissivity zones in the presence of flow induced from other high-transmissivity zones in the same borehole.

A third objective was to determine if there was an inherent advantage in using both methods on the same study. In theory, each alone is capable of measuring the vertical flow distribution in a borehole under ambient and steady pumping conditions. In practice, both methods have complications. We wanted to see if there were off-setting characteristic that could make the simultaneous use of both methods a real advantage in any given study.

Borehole 1-02 at Altona

We selected borehole 1-02 at the Altona Flat Rock site, a glacially scoured sandstone plateau in northeastern New York, as the location for the test (Franzi and Adams, 1999; Franzi et al, 2007). This borehole has been previously logged and the general character of the producing zones already known (figure 1). The borehole contains zones that differ in transmissivity by between one and two orders of magnitude, which is known to be near the limit of resolution for high-resolution flow logging (table 1). Although we have obtained several HP and EM flowmeter profiles in this borehole in the past, the flow regime is known to change significantly with the water season and the depth of the local water table. We expected conditions to be different from those of previous logging, which were generally much later in the yearly hydraulic

cycle, so that this would be effectively a new logging experiment for both flowmeter and dilution applications.

Dilution Model

We modeled the effects of inflow and outflow to borehole 1-02 using a simple mass-balance model. In this approach, the column is divided into a series of cells of specified length. The length is equal to or larger than the borehole diameter so that the assignment of a single conductivity value to each depth point can be made. The cells are mixed at regular intervals according to specified inflow at various points, where the inflowing water has a known electrical conductivity. In this calculation, the cell size effectively represents the longitudinal dispersion length scale. In more complex models, dispersion length is shown to vary with flow rate, which is rarely constant along the entire borehole. However, repeated passage of the borehole probe in logging is assumed to provide a minimum scale for longitudinal dispersal. Our code is designed for situations where inflow occurs at discrete points within the column. In most situations we would model the movement of conductivity interfaces in the vicinity of each such zone individually. The flow rate in each of these zones would be constant. Thus, the dispersion scale for each such sub-zone could be fixed. Significant variations in flow rates along the borehole can thus be accounted for by using different dispersion length scales in different intervals.

Experimental Procedure

Heat-pulse flowmeter profiles were made under ambient and pumping conditions in borehole 1-02 the day before the dilution experiment, as required to have the data needed to solve for both transmissivity and hydraulic head in each producing zone (Paillet, 1998). Pumping measurements were made under several different pumping rates in an attempt to characterize inflow from the deeper, low transmissivity zones listed in table 1. These rates were generally different from the 3 liter per minute rate used for the pumping phase of the dilution experiment. The flow inferred from each different pumping rate was normalized using the assumption that flow rates were proportional to the drawdown at each given pumping rate (figure 2). HP flowmeter data for pumping flow measurements were normalized to correspond to a 3 liter per minute flow rate whenever compared to flow rates inferred from the dilution model analysis under pumping conditions

Initial conditions for the dilution experiment were established by suspending 65 m of approximately 2-cm diameter hose in borehole 1-02 (West and Odling, 2006). Brine was mixed by adding 0.35 kg of table salt to12 liters of water. This mixture was poured into the hose to displace the hose volume, with an extra amount added to generate a plug of brine below the bottom of the hose. The plug was created as a way to mark the upward movement of water from the deep 115-m inflow zone. The hose was then withdrawn from the borehole leaving a “thread” of brine to mix with the rest of the column, with an estimated dilution of about 60 to 1. Subsequent fluid column logging showed that the plug at the bottom of the hose had an initial conductivity of 3500 µS/cm and the mixing in the column above the plug produced an initial conductivity of 800 µS/cm.

The experiment was begun by monitoring the evolution of the fluid column under the influence of ambient flow in borehole 1-02. Eight logging runs were made over a 126-minute period after brine emplacement. A conventional fluid column probe was run at a rate of about 6 meters per minute, requiring about 11 minutes per run over 70 m of column. In most dilution experiments, the pumping phase of the experiment is accomplished as a separate experiment requiring re-establishment of the initial conditions. This imposes a significant logistical penalty, and may allow residual brine from the first experiment to influence the second. In this experiment we decided to use the end of the ambient phase as the initial condition for the pumping phase. After 126 minutes of ambient experiment, a pump was inserted into the borehole and steady pumping started at a rate of 3 liters per minute. This rate was used to insure a measurable change from ambient flow, but was low enough that borehole storage effects would be minimal to allow comparison with a dilution flow model based on a steady flow rate established at the start of the pumping. Five subsequent fluid column profiles were obtained over the 126-206 minute interval. In each case, the nominal run time was given as the mid-point between recorded times for the start and end of the run, rounded off to the nearest minute.

Analysis and Results

The flowmeter data set showed ambient downflow to 41 m and upflow from below that depth. The downflow was reversed to upflow under pumping conditions. The data set is characterized by substantial scatter among the various measurements even in intervals where previous analysis had shown that flow rates would be constant. This scatter (here as much as 100%) is typical of both HP and EM flowmeter measurements and is attributed to the variable amount of flow leaking around the diverter used to force flow through the probe's measurement section (Paillet, 2004). The measurements are further complicated by flow magnitudes that are close to or even slightly below the nominal resolution of the HP flowmeter (0.1 lpm). We suspect that these values are not very accurate, and this suspicion is confirmed by the fact that measured flow rates below 41 m were greater under ambient than under pumping conditions. This result, if taken at face value, would mean that a drawdown increasing the head difference driving flow into the borehole from the 115-m zone decreases the inflow rate. Such a condition would imply negative transmissivity according to the definition of that parameter, which we consider to be physically impossible. We were unable to increase these flow rates into a consistently measurable range by increasing the pumping rate to the full capacity of our submersible pump. This is attributed to the large mismatch in transmissivity among the four zones. Increases in pumping rate were mostly accommodated by the very productive zone at 34 m, so that we could not effectively increase the head difference driving inflow from the deeper zones. For this reason we simply present the interval-averaged flow rates in table 1 and use the transmissivity values derived from previous logging when flow rates were more consistently measurable. Note that the ambient flow profile is otherwise consistent with previous logging, where the lowest hydraulic head was always associated with the 41-m zone (Williams et al, 2010). The measurements indicate downflow to this depth and upflow from below, but the magnitude of the values was just not reliable under prevailing hydraulic conditions to be used to infer transmissivity and hydraulic head for the zones below 34 m in depth.

The ambient dilution experiment (figure 3) showed inflow at the 24-m zone, and indicated inflow from below 65 m by upward movement of the top of the brine plug at the bottom of the brine column. No response was indicated for the 34 and 41 m zones, but no response would be

expected for outflow into these zones as indicated by the ambient flowmeter profile. Model fitting to estimate the flows associated with interface movement (figure 4) yielded values in close agreement with the average of the flowmeter values in the 24-34-m and 41-115 m intervals (table 1). Although both flowmeter and dilution model data sets agree, the latter has the additional advantage of avoiding the substantial measurement scatter associated with the flowmeter.

Although we expected the pumping phase of the dilution experiment to indicate inflow at the 34 and 41-m zones as well as at the 24 and 115 -m zones, no such inflow was apparent (figure 5). We conclude that the amount of inflow was not enough to be recognized in the presence of the inhomogeneities induced by the brine emplacement and the mixing produced by the passage of the logging probe. We had used a relatively low pumping rate (3 lpm) so that the assumption of constant flow at the start of the experiment would not be violated by a prolonged time to achieve quasi-steady flow. A recognizable flow from the two inactive zones might have been attained at a greater pumping rate. We tested this by modeling flow for larger pumping rates (for example, 12 lpm in figure 6A), with borehole flow predicted using the transmissivity values in table 1. The modeled inflow at 34 and 41 meters is large enough to generate significant spikes of reduced fluid electrical conductivity. The magnitude of these spikes would probably have been large enough to recognize in the data. However, the logistics of reproducing the entire dilution experiment at this greater flow rate (12 lpm) would have been formidable. Figure 6 also demonstrates that the increased flow rates would have made it impossible to estimate the flow above the 34-m zone because the greater flow rates sweep all of the brine from the upper column before the first logging run can be completed. We thus conclude that the mismatch in transmissivity values among several inflow zones introduces the same complications that are found for HP and EM flowmeter profiling. The only recourse is to repeat the experiment at two or more different rates. This is easily done with the flowmeter, but imposes a significant logistical penalty on dilution logging.

The results of this experiment show that the flow values given by the HP flowmeter and model fitting of the dilution profiles are in close agreement for the intervals (three of the four flow zones) where model data could be given for the dilution profiles (figure 7). The direct comparison of the two flow measurement methods was the primary objective of this study, but the dilution experiment in borehole 1-02 also yielded some insight into the practical aspects of dilution logging using brine emplacement and a conventional fluid column logging probe. A simple mass balance model appears to capture the propagation of the inflowing electrical conductivity contrasts very effectively. We found that a single dispersion scale could be used for each inflow zone even if different values were needed to accommodate large differences in flow rates. Mixing of the column by passage of the probe probably influenced the ability to detect small inflows. We also found that modeling of the brine plug required significantly different mixing lengths for the top and bottom of the plug. This is attributed to the directional bias imposed by the density of the brine. Downward motion of the probe in the presence of the density bias induced an effective mixing length on the bottom of the plug that was about five times greater than the mixing length on the upper edge of the plug. This difference did not prevent effective modeling of the upward movement of the top of the brine plug under the influence of steady upflow from the 122-m zone, where the weak ambient upflow and the small increase in upflow associated with pumping could be identified. The finite time required to complete each logging run did not seem to have much of an effect on the ability to fit the data profiles to a model based on a profile computed for a specific elapsed time. The short time

required to establish steady flow under pumping conditions had a relatively minor effect on the interpretation. The reversal of ambient downflow and the build-up of upflow cause the first model run in figure 5 to leap ahead of the first data profile, but the two are in approximate agreement by the second profile.

The use of brine emplacement in the design of this experiment was influenced by two factors: 1) the ease of installing the initial condition instead of replacing the column with distilled water, 2) the use of a conventional fluid column logging probe with a low conductivity measurement limit of about 10 μS/cm. A significant increase in sensitivity to small inflow rates might be achieved by using a specially designed fluid column probe capable of measuring very low fluid conductivity and with a slim probe shape designed to minimize disturbance to the column. This would allow plotting of data resistivity units, significantly enhancing the signature of weak inflow against a very large resistivity background. However, the plotting of fluid column profiles in resistivity units at the relatively low resistivity values in this experiment do not improve the resolution of inflow zones as illustrated in figure 6B.

Conclusions

Although the results for the ambient phase of the experiment showed HP flowmeter and dilution model results in close agreement, the HP data contained a relatively large degree of scatter about the unambiguous and precise downflow of 0.87 lpm for the upper part of the borehole given by dilution, and of the 0.04 lpm upflow for the lower part of the borehole. A similar agreement for flow in these two zones was obtained for the pumping phase of the experiment. The actual interval-averaged flowmeter measurements are in close agreement and both values lie well within the flowmeter data scatter. In contrast, the dilution analysis could not characterize flow zones where ambient outflow occurred because this produced no salinity interface in the column. No inflow was indicated by either method under various pumping rates for some known inflow zones producing weak inflow under the prevailing hydraulic conditions. We expected the dilution method to be more sensitive, but that method was also affected by flow produced by more productive zones above and below. The dilution experiment might have been able to characterize both low and high productivity zones, but only by running the experiment under two or more different pumping conditions. We conclude that the two methods are roughly equivalent for flow logging under low flow regimes, but that the unique advantages of each method may indicate that best characterization results when both methods are used in the same study.

Table 1 – Flow zones and transmissivity estimates for borehole 1-02, showing flow rates under ambient and pumping conditions given by the flowmeter and dilution experiments.

Zone Depth (m)	Zone Trans-missivity[1] (m^2/day)	Ambient flowmeter[2] (lpm)	Pumped Flowmeter[2,4] (lpm)	Ambient dilution flow[3] (lpm)	Pumped dilution flow[3] (lpm)
24	10	0.00	3.00	0.00	2.86
34	110	-0.79	1.70	-0.87	1.66
41	10	-0.06	0.02	Not determined	Not determined
115	10	0.06	0.017	0.04	0.08

1. Zone transmissivity as determined in previous studies.

2. Interval averages of normalized HP flowmeter measurements obtained in the interval just above the zone during this experiment.
3. Flow values used to produce model fit in the interval above the zone to column profiles obtained during the dilution experiment.
4. Flowmeter measurements were normalized to 3.0 lpm to correspond with the measured pumping rate.

References

Franzi, D.A., and Adams, K.B., 1999, Origin and fate of the sandstone pavement pine barrens in northeastern New York, in Wright, S., ed., New England Intercollegiate Geological Conference Guidebook No. 91: p.201–212.

Franzi, D.A., Rayburn, J.A., Knuepfer, P.L.K., and Cronin, T.M., 2007, Late Quaternary history of northeastern New York and adjacent parts of Vermont and Quebec: 70th Reunion of the Northeast Friends of the Pleistocene, Plattsburgh, New York, 73p.

Hess, A. E, 1986, Identifying hydraulically conductive fractures with a slow velocity borehole flowmeter, Canadian Journal of Earth Sciences, v. 23, p. 69-78.

James, S. C., R. A. Jepson, R. L. Beauheim, W. H. Pedler, and W. A. Mandell, 2006, Simulation to verify horizontal flow measurements from a borehole flowmeter, Ground Water, v. 44, no. 3, p. 394-405.

Molz, F. J., G.K. Bowman, S.C. Young, and W.R. Waldrop, 1994, Borehole flowmeters – field application and data analysis, Journal of Hydrology, v 163, p. 347-371.

Paillet, F.L., 1998, Flow modeling and permeability estimation using borehole flow logs in heterogeneous fractured formations, Water Resources Research*, 34*, 997-1010.

Paillet, F. L., 2004, Borehole flowmeter applications in irregular and large-diameter boreholes, Journal of Applied Geophysics, v. 55, no. 1, p. 39-59.

Paillet, F.L, and W.H. Pedler, 1996, Integrated borehole logging methods for wellhead protection applications: Engineering Geology, v. 42, p. 155-165.

Pitrak, M., S. Mares, and M. Kobr, 2007, A simple borehole dilution technique in measuring horizontal ground water flow, Ground Water, v. 45, no. 1, p. 89-92.

Tsang, C.-F., P. Hufschmied, and H.V. Frank, 1990, Determination of fracture inflow parameters from a borehole fluid conductivity method, Water Resources Research, v. 26, no. 6, 561-578.

West, L. J., and N. E. Odling, 2006, Characterization of a multi-layer aquifer using open well dilution tests, Ground Water, v. 44, no. 1, p. 74-84.

Williams, J. H., Paillet, F. L., Franzi, D. A., and Romanowicz, E. A., 2010, Borehole flows, hydraulic heads, and fracture-zone connection in the Potsdam sandstone at the Altona Flat Rock research site in northern New York, , *in* Proceedings of the Symposium on the Application of Geophysics to Engineering and Environmental Problems, April 11-15, 2010, Keystone, Colorado: Denver, Colorado, Environmental and Engineering Geophysical Society.

Acknowledgements

This work was supported in part by Golder Associates

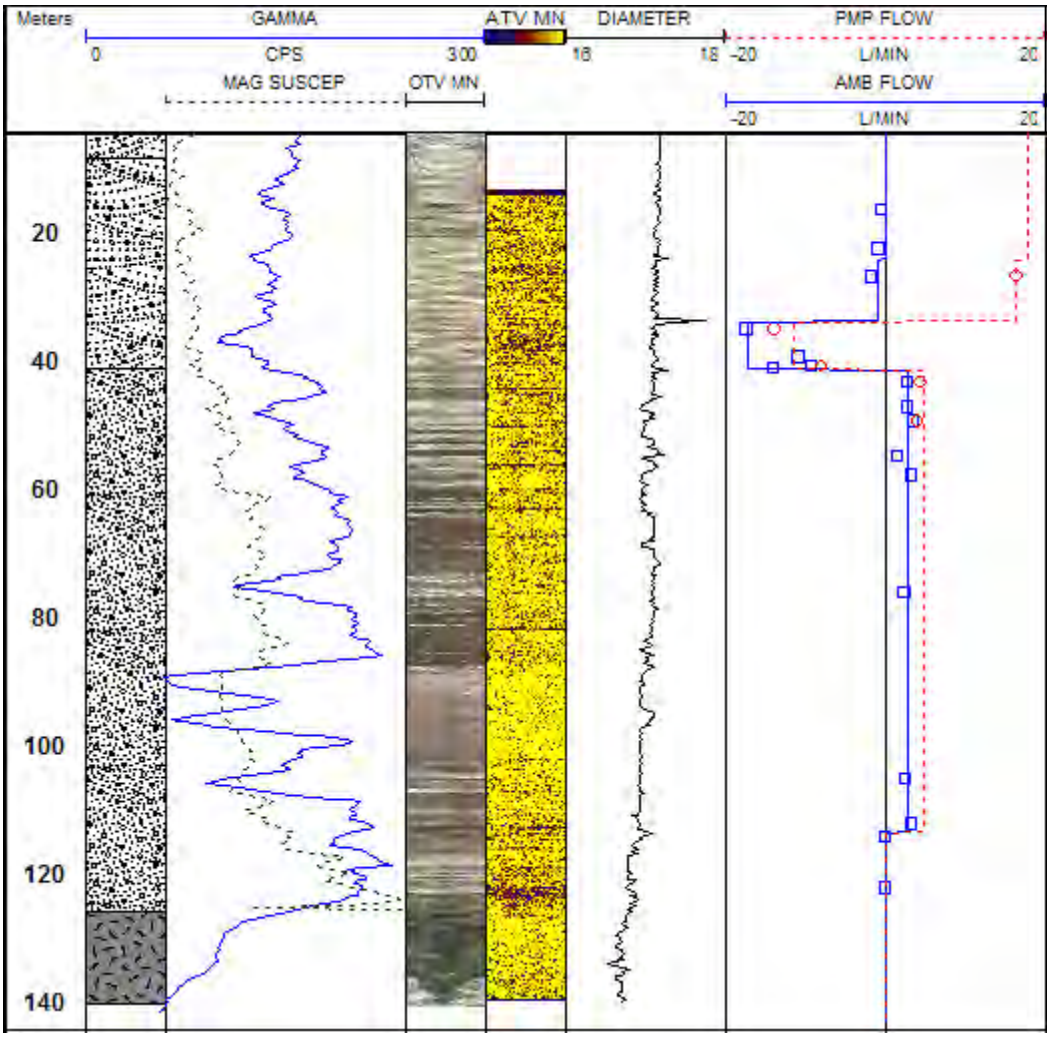

Figure 1 – Log composite (gamma, magnetic susceptibility, televiewer, caliper, and flowmeter) for borehole 1-02

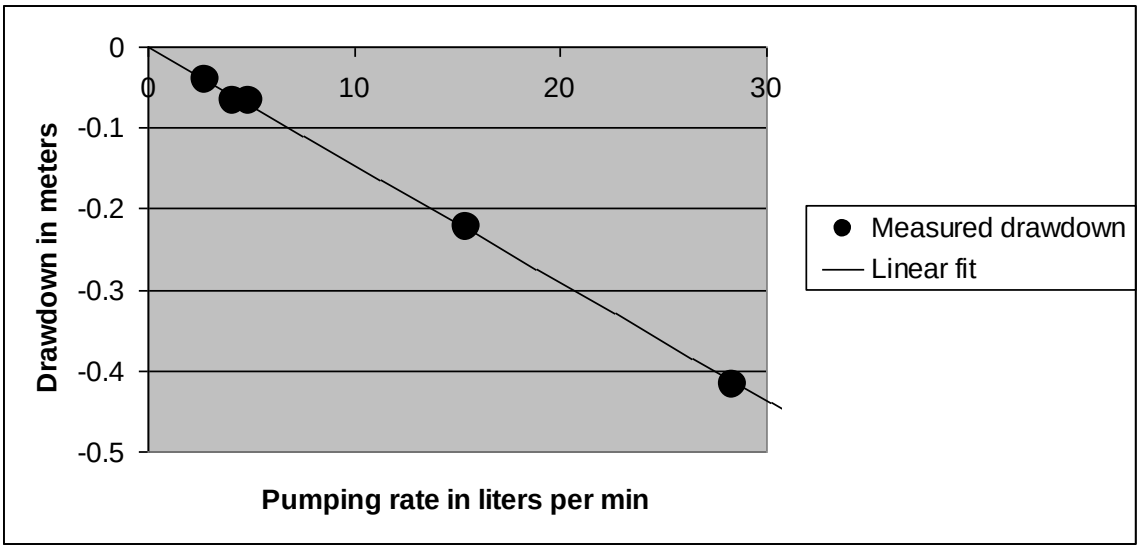

Figure 2 – Drawdown at various pumping rates demonstrating a linear relationship between discharge and drawdown for pumping rates less than 30 lpm.

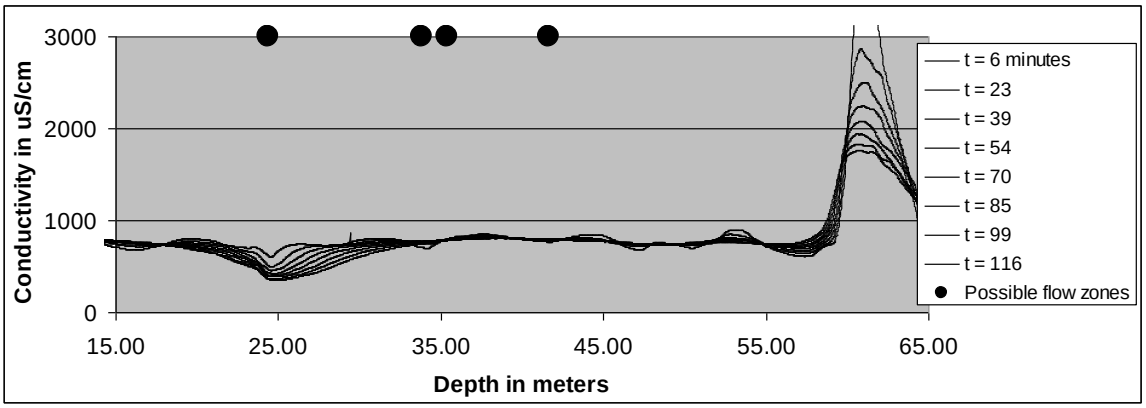

Figure 3 - Profiles of fluid electrical conductivity obtained under ambient conditions.

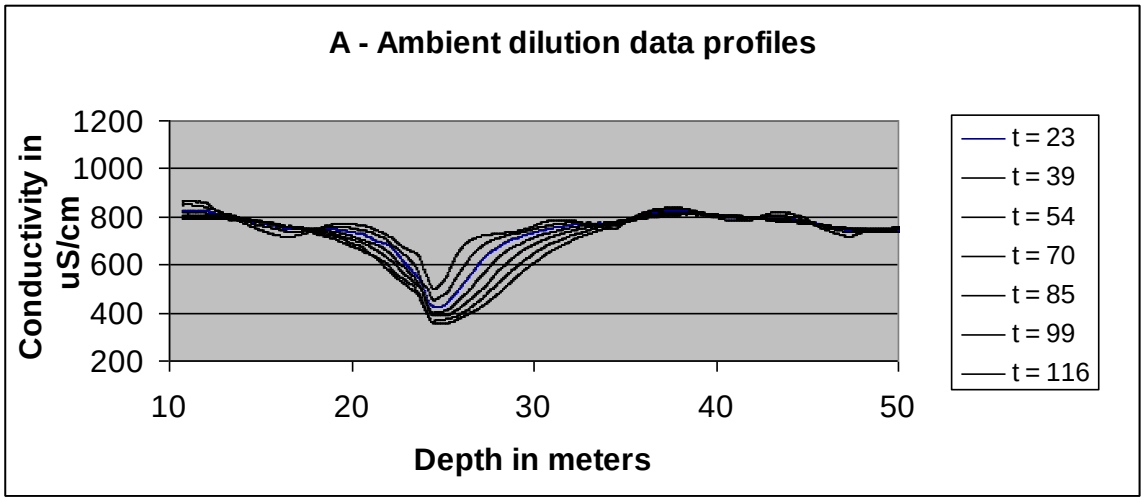

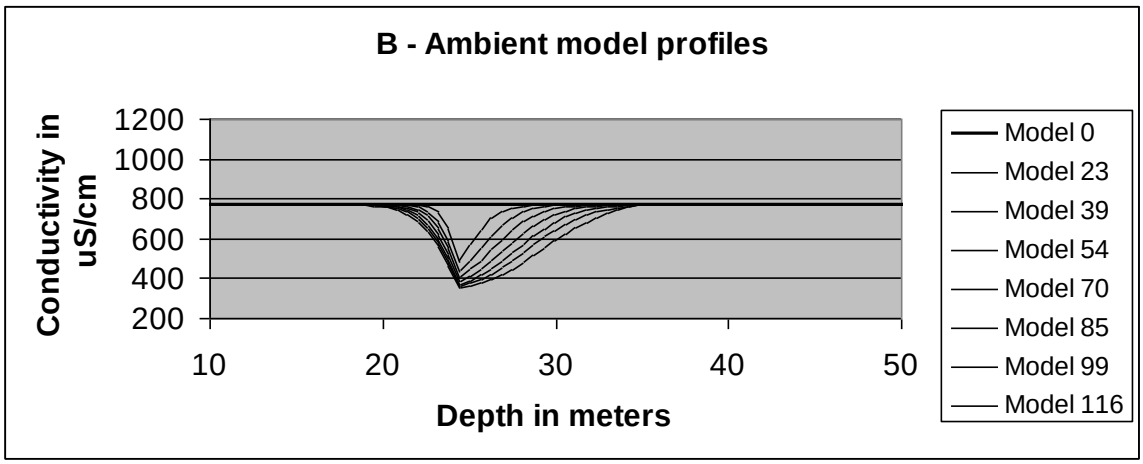

Figure 4 – Model fit to ambient dilution data for the 24-m zone showing model prediction of solute interface movement under the influence of ambient downflow; data profile times correspond to the midpoint in minutes between the starting and stopping times for the logging run.

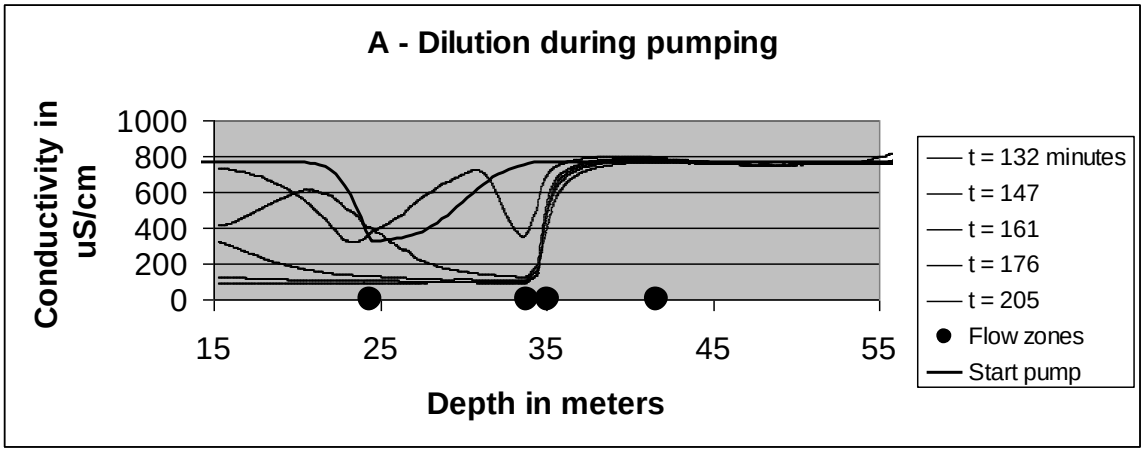

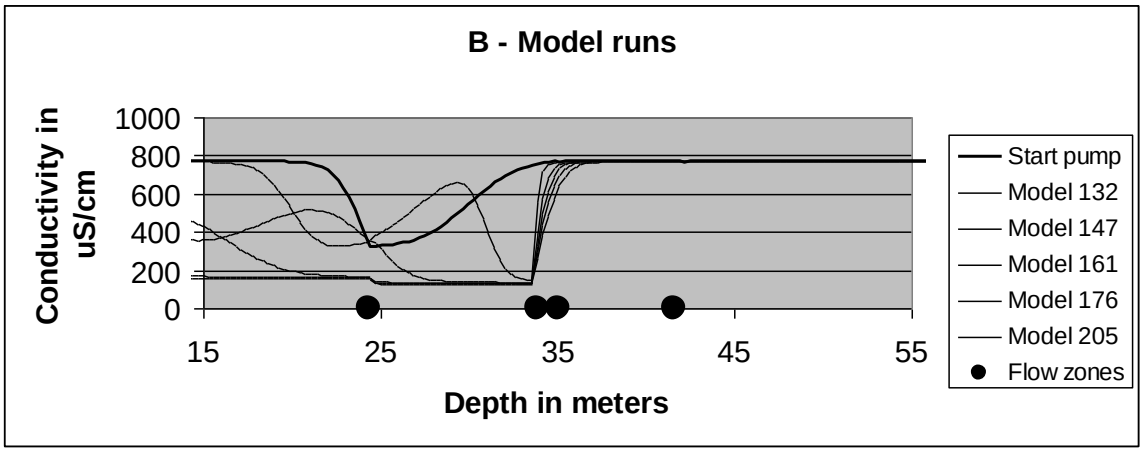

Figure 5 - Model fit to profiles obtained during pumping phase of the dilution experiment

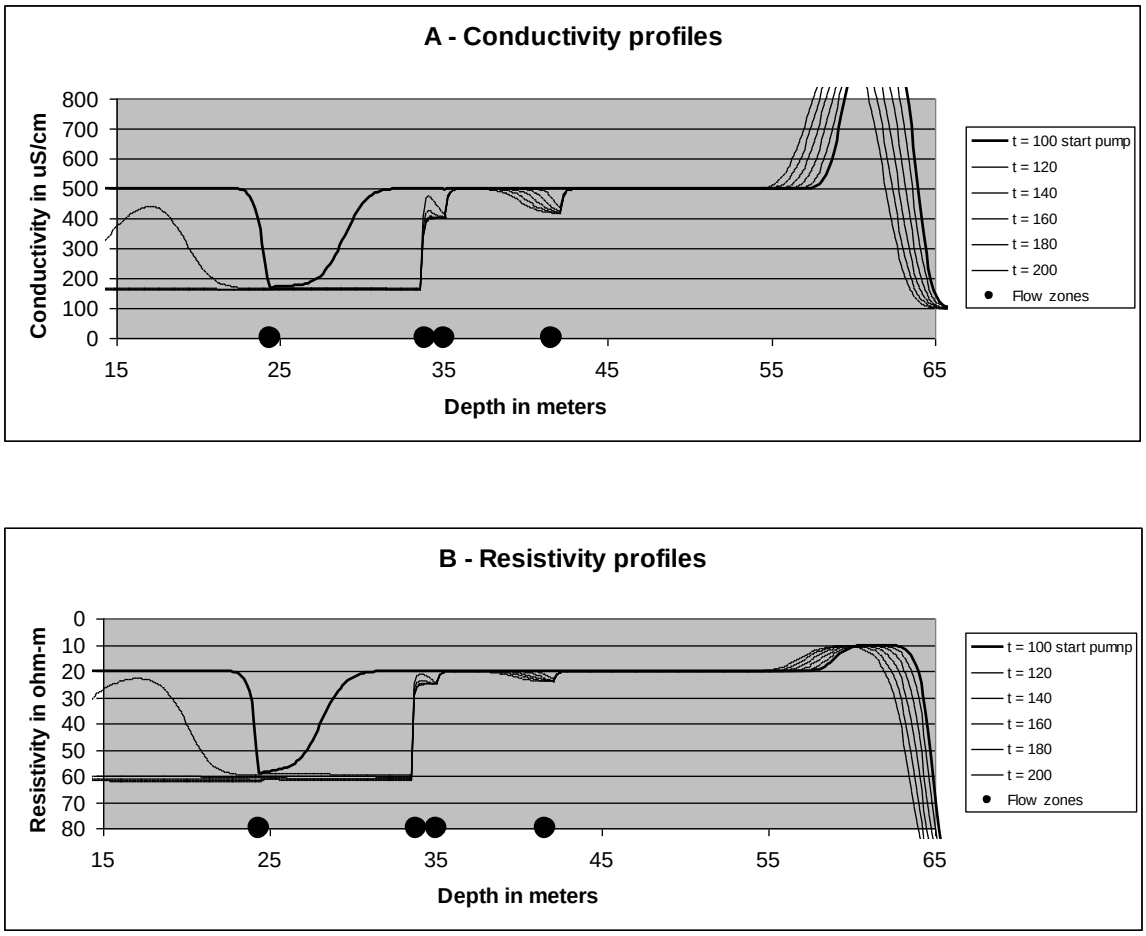

Figure 6 – Model predictions for fluid column profiles if the pumping phase of the dilution experiment were repeated at 12 lpm; profiles corresponding to runs at 20-minute intervals after 100 minutes of ambient flow; with profiles plotted in units of: A) conductivity, and B) resistivity.

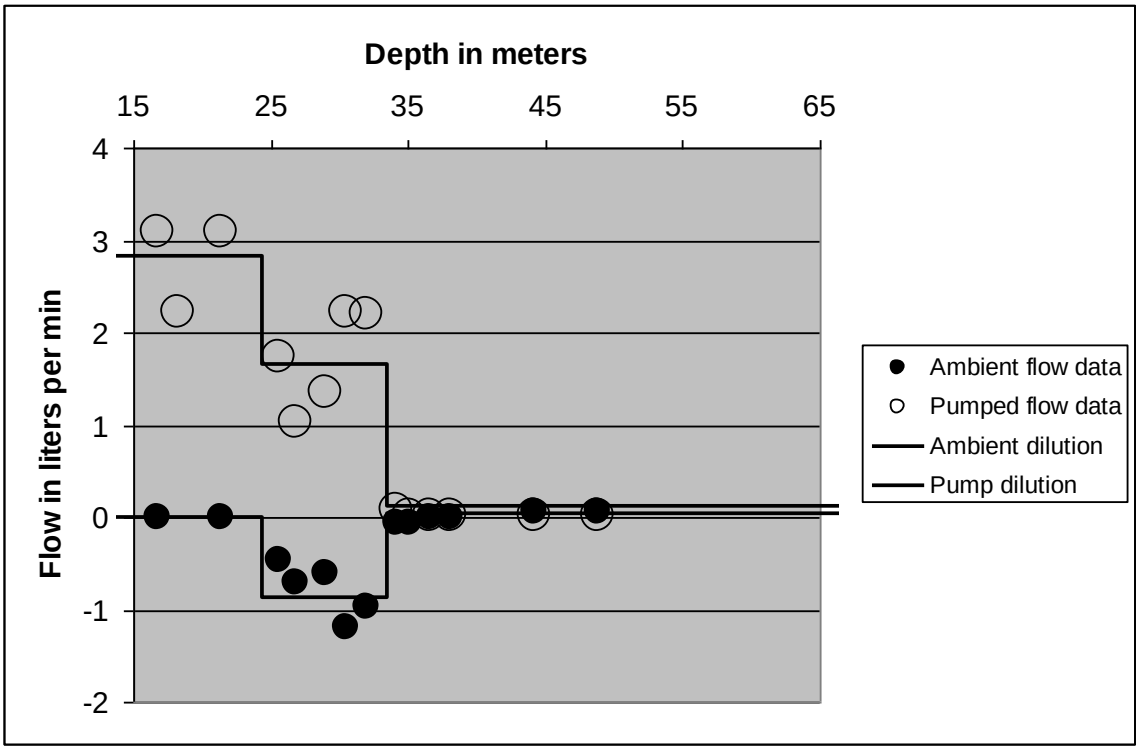

Figure 7 – Comparison of heat-pulse flowmeter data and dilution model estimates of flow for ambient and pumping conditions; all flowmeter data normalized to a pumping rate of 3 lpm and dilution flow profiles do not account for any inflow at the 41-m flow zone.

BOREHOLE GEOPHYSICAL INVESTIGATION: SEMINOE DAM, WY CHARACTERIZATION OF INTERNAL FRACTURING AND DYNAMIC MODULI REDUCTION OF MASS CONCRETE UNDERGOING AAR

S. Kristen Swaim, United States Bureau of Reclamation, Denver, CO

Abstract

Alkali aggregate reaction (AAR) is the general term for a slowly occurring chemical reaction in which highly alkali cement paste reacts with concrete aggregate. AAR is a common problem in concrete poured prior to the 1950's. The reaction leads to the formation of an alkali silicate gel at the interface of the aggregate and cement. This gel product is less dense than the reactants, causing expansion. The gel product also increases in volume with water.

During July of 2009, five six-inch diameter boreholes with varying depths were drilled into Seminoe Dam. Down hole optical and acoustic imaging tools were utilized to locate and characterize fractures within the concrete surrounding the borehole. Data collected from sonic and density logging tools were used to calculate the in-situ dynamic modulus values of the concrete surrounding the borehole wall.

Imaging data was analyzed for fracture dip, orientation and frequency. Sonic data was analyzed for the concrete's compression and shear wave velocities. Concrete density was computed from gamma ray logging data. In-situ shear, bulk and Young's modulus values were determined throughout the depth of the boreholes. Characterization of the fractures and in-situ dynamic modulus values of the concrete are used in comparison with past investigations of Seminoe Dam to gauge the progression and effects of AAR throughout the structure.

Location and background information

Seminoe Dam is a mass concrete arch dam consisting 160,556 m^3 of mass concrete, poured in 1938. Seminoe is the first dam downstream of the head waters of the North Platte River. Its foundation is in a narrow granite gorge. Table 1 summarizes some of Seminoe Dam's important structural and hydrological information. Figure 1 shows locations of the 5 boreholes in plan-view of the dam's crest. Early signs of AAR were first documented at Seminoe Dam in 1951; at that time it was not considered a concern (USBR, 2000). The Bureau of Reclamation has been periodically monitoring the progression of the reaction since, with the first major investigation conducted in 1975, indicating a high degree of deterioration in the top five feet with signs of minor AAR to a depth of 25 feet (USBR, 2000). Seminoe is constructed of mass concrete, which further enhances the AAR affects by providing a larger surface area for the reaction. Volumetric expansion due to AAR within a concrete structure can lead to fracturing and loss of material strength. The dam is also located in a region where it frequently experiences freeze thaw conditions; compounding the deteriorating effect of AAR (Acres International, 2000).

Table 1: Summary of Seminoe Dam's Important Structural and Hydrological Information

Structural Height	295 ft
Crest Elevation	6361.0 ft
Crest Length	530 ft
Crest Width	15 ft
Base Width	85 ft
Radius of Upstream Face	290 ft
Volume of Dam Construction Materials	210,000 cubic yards
Total Water Storage Capacity	1,017,279 acre-ft
Average (median) Reservoir Elevation (since 1970)	6340 feet

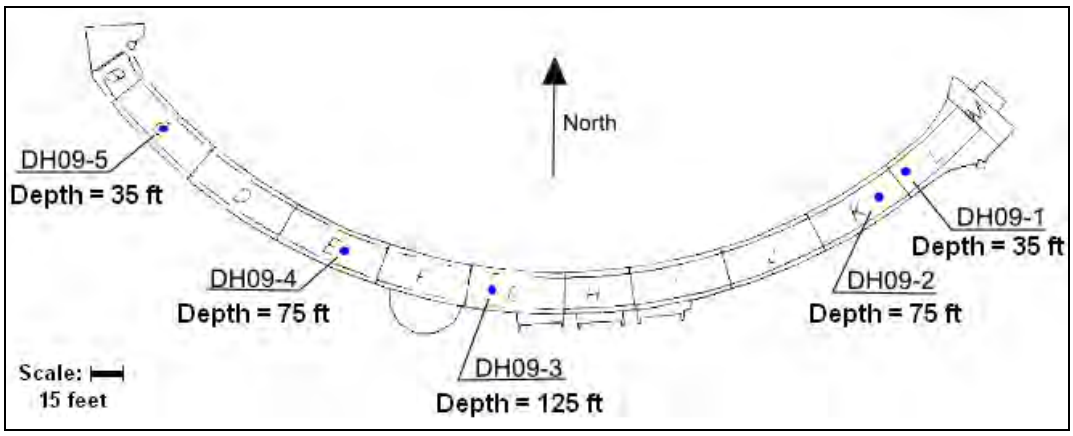

Figure 1: Plan view of the crest of Seminoe Dam. For the purpose of indicating drill hole locations, naming scheme and depths.

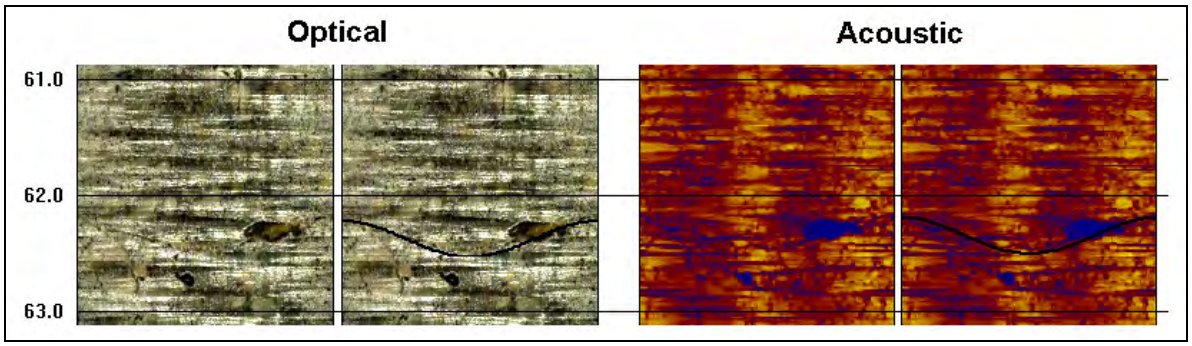

Figure 2: Two foot interval of optical and acoustic amplitude borehole images from DH09-4. Left side is raw data, while the right side shows a fracture pick overlain on top of the image.

Geophysical data collection, processing and data reduction

Optical and acoustic logging data were visually inspected for the entire depth of each borehole to locate fractures. Figure 2 is a two foot interval of both optical and acoustic amplitude data from borehole DH09-4. The figure includes both the raw data and data with a fracture pick overlaid. The oblong darker shape on the right side of each borehole image is indicative of a piece of missing aggregate. The white semi-horizontal stripes on the optical images were caused by scoring of the borehole wall by the drill bit. The imaging tools also record the tools orientation while data is collected so that once a fracture has been picked, both the fracture's dip and orientation can be determined. Polar plots of the fractures for each borehole were created. These plots are included in figure 3.

A four receiver sonic logging tool was used to determine compression and shear wave velocities for the in-situ concrete in the vicinity of each borehole. A dual spaced gamma ray density tool was also used to determine in-situ concrete density. Young's, bulk and shear dynamic moduli were calculated using the density along with the P and S wave velocities. Due to the fundamental differences in testing procedures, static and dynamic moduli values are not equal (Mockovciakova, et al. 2002). Dynamic moduli values tend to be greater than static moduli values (Zimmer, 2005). For this paper, percent reduction of dynamic modulus will be considered, as opposed to the calculated moduli values. Through inspection of the dynamic modulus values and fracture locations, an area in borehole DH09-3 (from depth 75 to 90 feet) contained little variation of the moduli values, suggesting that this portion of the dam has been relatively unaffected by AAR. The moduli values in this zone were arithmetically averaged to find an average unaffected modulus value (AUDMV). The AUDMV was used to calculate the in-situ dynamic modulus reduction. Table 2 lists the AUDMV used for each dynamic modulus. The percent of modulus reduction was plotted versus depth, to illustrate the decrease in modulus values near the crest of the dam. Figure 4 contains these plots.

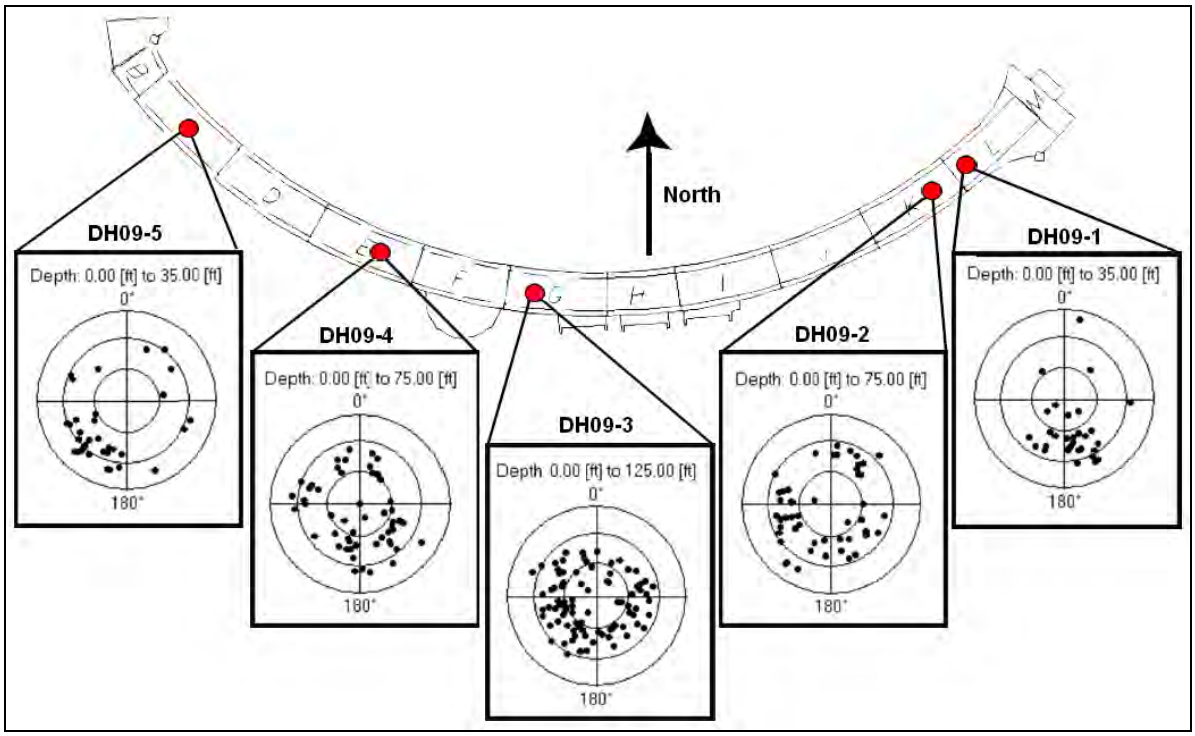

Figure 3: Schmidt [equal area, southern hemisphere] polar projection plot of fractures within the borehole wall, corrected to true north. The radial location of a pole indicates the fracture's angle of dip [center = 0º], the pole's azimuthal location indicates the up gradient direction of the fracture plane.

Table 2: Average unaffected dynamic modulus values (AUDMV) used to calculate dynamic modulus percent reductions in all 5 bore holes.

Dynamic Modulus	Average Unaffected Dynamic Modulus Value		Standard Deviation	
	GPa	Mpsi	GPa	Mpsi
Shear Modulus	18.3	2.66	0.7	0.10
Bulk Modulus	25.4	3.69	0.9	0.14
Young's Modulus	44.3	6.43	1.5	0.22

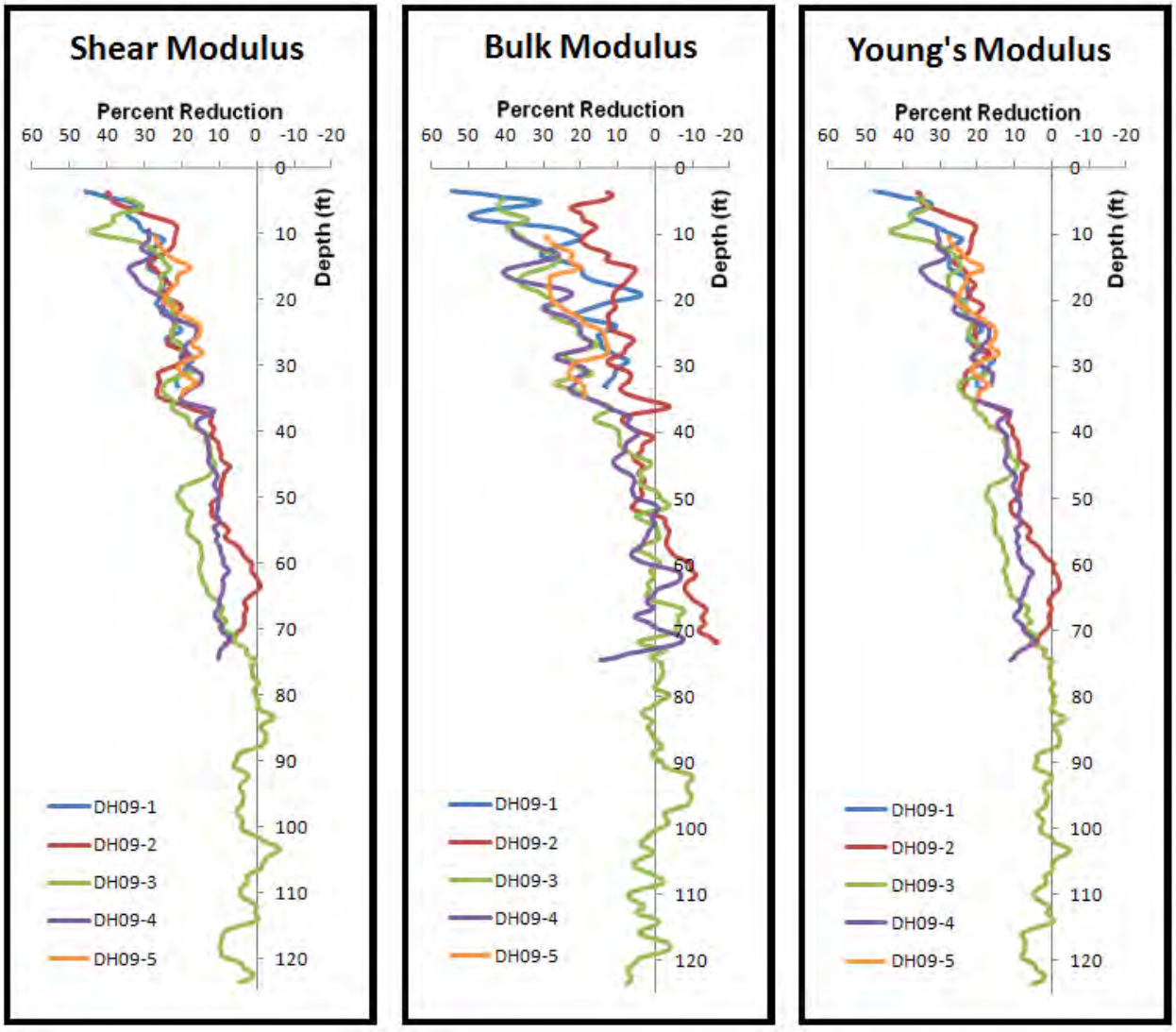

Figure 4: Plots of the percent reduction of bulk, shear and Young's modulus values within each bore hole. Dynamic modulus values were computed from in-situ measurements, percent reductions are derived from AUDMV.

Conclusions

The fracture analysis has revealed that fracture frequency decreases with depth. The fractures tend to dip more steeply towards the dam's abutments. This correlates with the visual inspections at the dam. Figure 5.a is a photograph of the right abutment that was taken in the field during data collection; 5.b highlights the fractures that can be seen on the downstream face of the dam. Fractures near the abutments also have a preferential orientation towards the downstream side of the dam, see figure 3. This trend in fracture orientation was previously unknown and could not be determined without data from within the structure.

Figures 5.a and 5.b: Photographs taken during data collection of the downstream face of the dam, viewing the right abutment. 4.b highlights some obvious fractures, with steeper fractures highlighted in blue and horizontal fractures in green.

Seminoe Dam is experiencing a decrease in all dynamic modulus values, with greater decreases seen at the crest of the dam and leveling to a stable value with less variation at depth, see figure 4. The concrete at the top of the structure is more compressible, as indicated by a lower bulk modulus. The concrete is also becoming more flexible and less rigid, as indicated by the decrease in Young's and shear modulus values, see figure 4. The results from this investigation indicate that the upper 40 feet of the dam is experiencing concrete deterioration associated with freeze thaw and AAR. This is a progression from the previously determined upper 35 foot zone, (Acres International, 2004). Analysis of the data also indicates the effect of AAR extending to a depth of at least 75 feet.

References

Acres International, January 2001, Preliminary structural analysis study for Seminoe Dam

Acres International, April 2004, Seminoe Dam: finite element stress analysis of concrete growth

Mockovciakova, A., Pandula, B., April 2002, Study of the Relation Between the Static and Dynamic Moduli of Rocks

Schimschal, U, USBR Technical Services Center, October 1998, Borehole geophysical investigations Seminoe Dam, Kendrick Project, Wyoming, Technical Memorandum No. D8330-98-036

USBR Technical Services Center, May 2000, Seminoe Dam ASR concrete deterioration issue evaluation data package

Zimmer, M.A., 2005, Comparison of Static and Dynamic Bulk Moduli in Unconsolidated Sands, American Geophysical Union, abstract #NS41B-04

FORMAT SUMMARY FOR SAGEEP EXTENDED ABSTRACTS

Use this as your primary reference when formatting your extended abstract. Note that it is formatted for brevity and not for SAGEEP publication. Final files must be in PDF format with all fonts embedded and the header visible (use this document as your template and the header will be visible in your final paper).

Initial Setup (For 8½" x 11" paper)

Please set up your word processor to these initial settings. Your paper should follow these formatting styles listed below.

Base Font:	12pt Times (or Times New Roman)
Justification:	Full
Line Height:	Auto
Line Space:	Single spaced
Margins:	0.75" sides, 1" top and bottom
Tab Settings:	Every 0.5" (Additional tabs/indents may be set for tables or other items.)

Paper Title

Maximum of three lines for your title.

Font Size:	14pt
Attribute:	Bold and All Caps
Justification:	Center
Position:	Top margin
Spacing:	Single spaced, one blank line after last line of title.

Author/Byline Information

Please type author's full name, affiliation, city and state abbreviation. Try to abbreviate affiliations when possible. Do NOT include street address, titles, departments, etc.

Font Size:	12pt
Attribute:	Italicized and Initial Caps
Justification:	Center
Spacing:	Single spaced, two blank lines after last author line

Headings

Headings should include Abstract, Conclusions and References at a minimum.

Font Size:	14pt
Attribute:	Bold and Initial Caps
Justification:	Center
Spacing:	Blank line before and after

Subheadings

Break out subsections of major headings as appropriate.

Font Size:	12pt
Attributes:	Bold, Italicized and Initial Caps
Justification:	Left
Spacing:	Single spaced, one blank line before all new subheads. No blank line before paragraph text.

Body or Paragraph Text

Indent the first line of each new paragraph 0.5". Please do NOT use spaces to indent. Use full justification, letting the text wrap – no hard returns except when starting a new paragraph. Use the base font already indicated (12pt). Do NOT double space between paragraphs. However, double space before starting a new heading or subheading.

Font Size:	12pt
Attributes:	Regular
Justification:	Full, initial indent
Spacing:	Single spaced, no blank line between paragraphs. One blank line before all new subheads.

Figures and Tables

Figures and tables should be labeled with a bold number reference followed by regular text (e.g. **Figure 1:** Plot of data Y vs. X.), using the standard font. Figures should be labeled below the graphic and tables above. Borders or boxes around figures are optional. Scales and units are required for all data graphs, plots and maps.

Font Size:	12pt
Attribute:	Bold reference, regular text
Justification:	Left
Spacing:	Single spaced

Page Numbering

Leave space for numbers using margins, but do not number your pages. Numbers will be inserted consecutively throughout the CD volume.

CHARACTERIZATION OF A SLIM-HOLE GAMMA-RAY SONDE FOR POTASH EXPLORATION APPLICATIONS IN A SIMPLE TEST PIT ENVIRONMENT

Stefani D. Whittaker; The Discovery Group; Denver, CO
Ryan Sharma; The Discovery Group; Denver, CO
Daniel Hallau; The Discovery Group; Denver, CO
James P. Lewis; Intrepid Potash; Denver, CO
Robert M. Cluff; The Discovery Group; Denver, CO

Abstract

Prior studies of gamma-ray tools have all been focused around instruments that typically evaluate sandstone, shale, and limestone formations that are encountered in oilfield logging. For this study, a set of experiments were conducted to characterize the lateral and vertical response functions for a slim-hole gamma-ray sonde used in the mining industry to locate potash mineral deposits.

The experiments were conducted in an indoor warehouse environment utilizing a set of large plastic tanks that were filled with light evaporite minerals (granular halite and sylvite) in differing arrangements to simulate various possible formation configurations. Measurements were taken while using a centralized slim-hole gamma ray tool in an air filled 4.5 inch plastic borehole.

Sequential tests were run to establish the linearity of tool response, the radial depth of investigation, the vertical response function, and the repeatability of the measurement. Radial depth of investigation was measured using concentric radioactive rings of increasing diameter with two possible intermediary substances, air and halite. To test vertical response a column structure was built using halite as the bottom "bed" and a sylvite layer was systematically added in known quantities to acquire a response function of increasing thicknesses. Repeatability of the measurements was verified by logging several points with multiple tools of the same model for all the various experimental setups.

Results were corrected for background radiation to predict the response in solid subsurface conditions without incident surface radiation seen in the experiments. The findings were also corrected for the differences between low porosity subsurface conditions and the unconsolidated granular products that were used in the simulated formation.

The experimental results were surprisingly close to theoretical tool response for an oil field sonde, as well as to published specifications of major oilfield logging vendor's tools. Consequently, gamma-ray logs collected with a slim-hole tool in shallow mineral core holes should be directly comparable to oilfield gamma-ray tools run in open-hole wellbores, once corrections for borehole size and fluid content using best practices are applied.

Introduction

Gamma-ray logging has been applied to mineral exploration problems for many years, including uranium exploration (e.g. Dodd, 1966; Hawkins & Gearhart, 1968) and the evaluation of potash deposits (Alger & Crain, 1965; Crain & Anderson, 1966; Tixier & Alger, 1967). In the context of the latter the most useful tool has proven to be the gamma-ray log, because it responds directly to the potassium content of the formation.

While the underlying physics of these methods are straightforward, all applications of geophysical logging suffer from certain common problems including characterizing the volume of investigation or resolution of the measurements; motion of the logging tools as the data are captured; calibration of the tools; and a variety of environmental effects related to the presence of a borehole, its size and shape, the properties of fluids filling the borehole, presence of any steel casing and cement sheath between the borehole and the formation of interest, etc. This study was instigated to better understand the vertical and horizontal resolution of a typical mineral industry gamma-ray logging tool Once the basic tool response is established, other effects such as tool motion and the borehole can be incorporated into a quantitative model.

Gamma-ray logging is based on the decay of naturally occurring radioisotopes. The most common radioactive isotopes in the Earths' crust that contribute to natural gamma radiation are potassium-40 (K^{40}), uranium-238 (U^{238}), and thorium-232 (Th^{232}). Other radioactive isotopes, such as U^{235}, naturally occur but only in minute amounts. Both U^{238} and Th^{232} decay through a series of 10 or more intermediate products to stable lead, with gamma radiation emissions of different energies at each step (Bassiouni, 1994). K^{40}, which constitutes about 0.01% of all potassium, decays by both beta decay and electron capture. The latter decay process constitutes about 11% of all decays and yields Ar^{40} plus a 1.46 MeV gamma-ray. The natural gamma radiation is detected using a sodium iodide crystal within a scintillation device, where a sensitive photomultiplier mechanism attached to one end of the crystal records the individual light flashes that result when a gamma-ray photon interacts with an atom of the crystal. These are amplified, counted, and the resultant count rate is directly proportional to the gamma-ray flux through the crystal. The absolute count rate is a function of detector size, efficiency and the shielding provided by the surrounding tool body; consequently the counts must be calibrated to a source of known radioactivity to use the data in a quantitative manner. This is accomplished by logging a test pit with blocks of some standard material. The primary logging reference pit for gamma-ray logging is located in Houston, Texas (Belknap et al, 1959), and several secondary standard pits have subsequently been established around the U.S. Modern gamma-ray detectors of the type used in this study are extremely sensitive and detect nearly all of the gamma photon interactions with the NaI crystal. In a total gamma-ray tool all counts from gamma-rays of any energy are summed together; in a spectral gamma-ray tool the counts are separated into bins based on the intensity of the light flashes which are proportional to the energy of the incident gamma photons. This study utilized a total gamma-ray tool.

We conducted a series of laboratory tests in a warehouse environment using a slim-hole gamma-ray tool and granular potash product (both sylvite and langbeinite) in air background and shielded by granular halite (NaCl), Tests were designed initially to obtain an approximate volume of investigation in air so as to determine tank size and amount of product required for subsequent tests; followed by a simple test to verify the response of the tool varies linearly with the amount of surrounding radioactive material. We then conducted several experiments in large plastic tanks with a plastic pipe borehole, using spacers made of thin sheet plastic to make confined horizontal layers and radial nested cylinders. Details of the test arrangements and apparatus are given below.

Methods

Intrepid Potash purchased a 2PGA-1000 gamma-ray probe from Mt Sopris Instruments[1]. The probe is a slim hole tool 1.63 inches in diameter, weighing 7 lbs, with a 3 inch x 0.875 inch NaI crystal detector similar to those used in standard oilfield gamma-ray logging tools. Because the tool diameter and housing materials are different than tools that have been characterized in the literature, and because the detector is not precisely the same, we expected the tool response to be similar, but not identical, to a typical oilfield tool. The tool output was recorded in counts/sec, and has been calibrated to equivalent API units using the Houston, TX test pits to be 1 CPS = 1.19 API units as shown in Figure 1. Two additional tools of identical design and manufacture were rented and used to assess the repeatability of the measurements and variation between tools.

The materials used for tests were provided by Intrepid Potash as 50 lb. bags of unconsolidated halite, sylvite, and langbeinite. All materials were from single plant runs so the variation of materials between sacks is thought to be minimal. Each bag of potash was individually weighed prior to use to verify the exact amounts of radioactive material used. Because these products are granular, all the materials include some unknown amount of air filled voids. The bulk density for each loose material, without tamping or otherwise packing, was therefore determined by weighing a known volume of material. By comparison to the known grain density of the mineral phase, we estimate the porosity of the granular products we used to be 33% in sylvite, 39% in halite, and 43% in langbeinite. The variations in porosity between materials result from differing grain size and shapes of the crushed commercial product.

All tests were conducted in a warehouse located in central Denver, about 3 miles NE of the downtown area. The surficial deposits are thin Pleistocene eolian deposits overlying bedrock Paleocene and Upper Cretaceous Denver Formation shales (Trimble & Machette, 1979; Moore et al 2001). The background radioactivity in the area is relatively high, averaging ~82 cps as determined by a tool hung in air 4 ft above the concrete floor of the building. The background radiation increased to ~93 cps when the tool was adjacent to the floor. These are equivalent to air readings on the order of 95-110 API units.

Three sets of tests were conducted. Initially, the tool response hanging in air was measured using 50 lb. bags of sylvite (referred to as "product") arranged radially around the tool, where the number of bags of product and diameter of the ring of bags from the tool was varied (Figure 2). All readings were taken with a stationary tool for a period up to 1200 seconds. These "bag tests" were used to 1) determine the time required to get a statistically stable reading; 2) verify linear response of the tool with the amount of radioactive product; and 3) determine the approximate volume of investigation to aid in the design of a test tank for the subsequent experiments.

The second set of tests were designed to determine the radial depth of investigation of the tool in air and when shielded by a volume of halite surrounding the tool. These are referred to as the "radial tests". A constant volume of sylvite (14.73 cu ft; or ~23 sacks = 1150 lbs) was used for all tests so the amount of radioactive source material was held constant. These tests were conducted in a 7 ft diameter x 3 ft tall plastic tank (Figure 3A). An air filled borehole was constructed by securing a 4.5 inch O.D. length of PVC pipe to the floor of the tank with a plastic pipe flange. The tool was centered in the plastic borehole using Styrofoam standoffs (Figure 3B), and a 12.5 inch tall Styrofoam block was placed in the bottom of the tube so that the NaI detector was centered in the tank, 18 inches off bottom. Concentric rings of Plas-Tex, a thin and flexible waterproof plastic wall paneling material, were used to confine the granular sylvite in a ring surrounding the tool and the plastic borehole. Because the material is weak, plywood forms were used at the top and bottom to hold the cylinder in place when filled with product (Figure 4). The number of different rings and the largest

[1] Mt Sopris Instrument Co, 4975 E 41st Ave, Denver, CO 80216; http://www.mountsopris.com/

outer diameter was limited by the amount of material available to fill the ring with sylvite and the inner cylinder with halite. A total of five rings were constructed (*Table 1*), beginning with sylvite immediately surrounding and in contact with the borehole up to a midpoint of the ring radius of 3 ft. The width of the ring had to be varied so as to accommodate a constant volume of radioactive material.

The third experiment was designed to determine the vertical resolution of the tool. Only a single bed contact is required to characterize this response, so a 6 ft. tall x 2.5 ft radius test tank was constructed and filled with halite to a depth of 3 ft (Figure 5). The tool was then logged across this surface in a series of 25 station measurements 3 inches apart (6 ft total tool movement). Sylvite product was then added on top of the halite layer in initially 1 inch increments and then 2 inch increments until a total sylvite layer of 32 inches was achieved. The entire 6 ft. vertical hole was logged again after each incremental increase in the thickness of the radioactive material.

All measurements were collected with a stationary tool in "time mode" for a period of 30 seconds and do not mimic the response of a moving tool. Gamma-ray counts from the detector were summed for a period of 1 second, written to file as counts/sec, the buffer flushed and measurement cycle repeated to yield a stream of 30 data points or more per station measurement. In an actual logging job data would be collected in "depth mode", where the tool would be in motion and after each selected depth increment (e.g. 0.5 ft) the summed counts would be divided by the elapsed time for that increment, the value written to file as counts/sec, and the next measurement cycle started. For a typical oilfield logging speed of 1800 ft/hr, the tool would move approximately 0.5 ft per second.

Results

Initial air tests ("bag tests")

The bag tests were used to assess how long the tool needed to be held on station to achieve a statistically stable answer. This is shown in Figure 6 for one test, where the X axis is the time on station, *t*, for one experiment, and the Y axis shows the standard deviation of the average from 0 to *t* in counts/sec. The tool exhibits significant instability in the readings for several seconds, then settles to a value near the long running average of 75.5 cps after about 50 seconds. The initial 5-10 seconds instability appears related to cold starting the data collection process and is not a factor once the tool has begun acquiring data. From this experiment we determined a minimum run of 30 seconds on station, and better 60 seconds, was required to get an accurate reading.

A second test was run as a simple verification of the linear response of the tool to the amount of radioactive material surrounding the tool. This was accomplished by laying 7 bags of product in a 1 foot radius circle surrounding the tool hanging in air. After measuring the response for 400 seconds, a second layer of 7 bags was added and the measurement repeated, and so forth until the stack was 5 bags tall (35 bags total, or approximately 1750 lbs of KCl. The response was absolutely linear with an R^2 of 0.998 (Figure 7), projecting back to an air background of 72 cps.

Other tests were run to determine the approximate volume of investigation in air and when the tool was surrounded by salt in order to design a suitable test tank for the subsequent experiments. These experiments were not evaluated quantitatively.

Radial (horizontal) response tests

The radial response function of the tool was determined by a series of measurements of a constant weight/volume of KCl in five concentric rings. Because the volume of radioactive material was held constant, the only variables in the test were the radius of the successive rings and the material occupying the void space between the ring and the borehole. One set of measurements were made with air in the inner cylinder, and a second set with halite in the inner cylinder.

The results of these two experiments are show in Figure 8. The uppermost set of points are the data collected with an empty inner cylinder; while the points just below them are the same readings with background radiation contribution subtracted out. The background correction varies with the radius of the ring because the sylvite ring itself acts as shielding to radiation coming from outside the ring. Therefore as the ring gets smaller a greater amount of background radiation was shielded by the geometry of the experiment relative to a large ring where significant radiation comes up through the floor of the inner cylinder; the larger the inner air filled ring, the larger the background counts received. The bottom two sets of points represent the raw readings with the inner ring filled with salt, and those readings that were background corrected. In this case the background corrections are small because most radiation was shielded by the salt and sylvite surrounding the tool. We estimated an average of 10 cps results from radiation coming directly up the axis of the borehole from the floor, plus a small amount of ambient radiation passes through the salt when the ring is small. Only three readings were taken with salt in the inner cylinder due to a limited volume of halite available for the experiment.

The generalized relationship for attenuation of gamma-rays in a medium is given by:

$$N = N_0 e^{-\mu\rho x} \qquad [1]$$

where N is the gamma-ray flux at the detector, N_0 is the total gamma-ray flux, μ is the mass adsorption coefficient of the medium, ρ is the material bulk density, and x is the distance over which gamma-rays are being attenuated (Ellis, 1987). In this experiment, the gamma-ray flux was measured; the bulk density of the medium and the attenuation distance are known; and the total gamma-ray flux (N_0), while unknown, was held constant by using a fixed quantity of radioactive material (sylvite). The mass adsorption coefficients of the medium are thus the only unknowns. By regression analysis of the raw data we are able to determine the quantity $\mu\rho$ for the two experiments (inner cylinder air; inner cylinder of halite), then correcting for the measured porosity of the granular medium and the density of solid salt, we compute the radial geometrical factor for three cases: air, salt with 39% air filled porosity, and solid salt. The J functions are shown in Figure 9. In the present experiment, with a centered slim tool in a 4.5" borehole, 90% of the response in dense salt (density 2.16 g/c3) is at 31 cm (12.2 inches) and the 50% point is at 11.5 cm (4.5 inches). The mass adsorption coefficient for halite estimated from these data is 0.039 cm2/g.

Our measured tool response is similar to, but not identical, to the published J function for 1.46 MeV K^{40} gamma-rays obtained by Monte Carlo modeling (Wahl, 1983), where the 50% cumulative response is shown to be 15 cm (5.9 inches) from the center of an 8 inch borehole, and the 90^{th} percentile is at 27 cm (10.6 inches). This is shown by the heavy solid line in Figure 9. Wahl modeled a formation density of 2.2 g/c3, a liquid filled borehole, with a borehole eccentered tool. Although he did not state the mass adsorption coefficient, we determined it is ~0.047 cm2/g based on our curve fit to the published illustration and assuming the lithology was porous limestone. For comparison, we show an additional curve computed using a solid quartz sandstone density of 2.65 g/c3 (0% porosity) and assuming the mass adsorption coefficient for quartz is similar to that determined for salt. This is a reasonable approximation for matter composed of light elements. The 50% response point for sandstone is at 9.5 cm (3.7 inches) and the 90% point at 25 cm (9.8 inches). Note that our sandstone curve and the Wahl curve converge at approximately 28 cm (11.0 inches).

The curve offsets <28 cm apparently result from the difference in borehole size, tool positioning, and borehole liquid. Also our curve is empirically determined, whereas the Wahl curve is a model assuming some hypothetical tool/detector configuration. Our prediction for sandstone with 27% porosity, with a bulk density of 2.2 g/c3, is very close to the solid salt line shown on Figure 9.

Vertical resolution tests

The vertical resolution of a logging tool can be determined by logging a sharp interface between two materials. Logging a second interface, for example across a thick bed, is unnecessary because the upper interface is just a mirror image of the response across the lower interface.

For this experiment, we filled a plastic tank as described previously with 3 ft of granular halite. An initial logging run to determine the baseline response without any radioactive layer was run and is shown as the heavy dashed line on Figure 10. The minimum reading of ~16 cps was attained when the sensor was 23.5 inches off bottom. Readings closer to the floor are higher, and the response slowly increases towards the salt-air interface at 36 inches then increases to an air background of 77 cps when the tool is 5 ft off bottom.

These data were interpreted as gamma radiation from the earth beneath the tank is largely shielded by the salt in the tank, but some radiation comes directly vertically through the air filled borehole and is counted by the sensor. When the tool was positioned at the midpoint of the salt, it had the maximum shielding from ambient radiation, and as it logged out the top of the salt section it received increasing radiation reflected off the building and the air coming down the top of the borehole. The maximum reading of 77 cps reflects an air reading with the ground below partly shielded by the salt filled tank.

Accordingly, these background readings were subtracted from the subsequent experiments to attain a background corrected log. These are shown by the solid lines in Figure 10. The data were collected as a series of 30-second station measurements at 3 inch increments from tool on tank bottom (where the sensor is located 5.5 inches above tool measure point) to 6 ft off bottom, for a total of 25 stations. Initially sylvite was added in 1 inch increments, with a "logging run" between each additional buildup of the radioactive layer. After 6 inches, material was added in 2 inch increments up to a total of 32 inches. For graphical clarity only selected curves are shown on Figure 10.

The 1 inch KCl curve on Figure 10 illustrates the response to a very thin radioactive layer after baseline correction. The bottom and top part of the log show a base-lined response near 0 cps, and the peak reading was 56 cps at the 38.5 inch station immediately above the KCl layer. This remains true up to a layer thickness of 6 inches, after which the peak reading starts to migrate slowly higher with increasing KCl layer thickness until a 26 inch layer is attained, at which point the peak readings stabilize at 46.5-49.5 inches above tank bottom. The peak reading of 700 cps is constant in the subsequent experiments up to a layer thickness of 32 inches, at which point the readings had clearly reached a flat plateau. This clearly defines a thick bed for this tool.

Above 40 to 50 inches off bottom, depending on the layer thickness, the readings drift back to lower values up to the top of the log at 75.5 inches off bottom. The position of the inflection point is related to the thickness of the KCl layer, and the readings start to drop back when the sensor is close to or above the KCl-air interface. The readings never dropped back entirely to the zero baseline because the tool sees an air response to the thick radioactive layer below when it is raised above the KCl layer.

Figure 11 shows the tool response to the 28 inch thick KCl layer with the top and base of the sylvite layer marked. The log is slightly asymmetric because it is salt below and air above this layer, with the upper half space tailing off more slowly than the lower half space into salt. Overall this curve shows full response at the midpoint of the 28" bed. The vertical resolution of the tool is estimated at 68 cm (27 inches), and the shoulders on either side of a bed boundary are located 13.5 inches above and below the bed boundary respectively. At the midpoint of the bed, the tool reads the peak reading of 700 cps and thicker beds do not

increase this value. All of these numbers are based on granular material with 33-39% air filled porosity, as described previously. Based on the results of the horizontal depth of investigation tests, we expect the bed resolution in solid material will be slightly sharper due to the greater attenuation of non-porous materials. The estimated bed resolution in solid halite is 49 cm (19 inches), using the mass adsorption coefficient for halite determined previously.

Linear response test for mixtures of potash and salt

A simple test in a small tank was conducted to verify the linearity of tool response to various mixtures of halite and sylvite. Five readings were taken in a very large plastic garbage can with a 4.5 inch borehole in the middle. The annular volume was filled with mixtures consisting of 100% halite; 75% halite/25% sylvite; 50% halite/50% sylvite; 25% halite/75% sylvite; and 100% sylvite. All mixtures were based on weights, and the granular product was well mixed prior to filling the tank. A single station measurement with the tool sensor centered in the test tank was used to determine the counts. The tank used was sufficiently large to include the 90% depth of investigation based on the prior radial testing.

The results of this experiment are shown in Figure 12. Like the simple bag test to verify linearity of response with amount of radioactive material, this test reveals a highly linear response function ($R^2 = 0.998$) and projects to a background reading in salt of 62 cps, or 65% of the reading in air. From this test we conclude sylvite and halite have essentially identical mass adsorption coefficients, and $\%K_2O$ content of a mixed sylvite-halite ore body can be determined with high precision without correction for different gamma-ray adsorption characteristics of the two components.

Tool repeatability test

Three different gamma-ray sondes, all of the same tool manufacture and model, were available to us during the testing phase of this project, although not all at the same time. Several tests were run with a tool hung in air around an array of bags of product to assess the variability in readings between tools. These included background radiation readings with various amounts of halite surrounding the tool as shielding; and product tests with variable amounts of KCl arrayed around the tools hung in air. The results of this are shown in Figure 13. The tool response was remarkably similar, with all tools reading within +/- 3 cps of the same value for each experiment. Repeatability of a single tool to measurements under the same conditions were similarly precise. For a typical peak reading of 700 cps in a thick sylvite layer, the precision and repeatability exceeds 0.5%. Accuracy, of course, is a function of the tool calibration, the model used to convert tool counts to $\%\ K_2O$, and the thickness of the layer compared to the vertical resolution shown in Figure 11. For a typical measurement in a thick (>28 inch) sylvite layer, with a stationary or slowly moving tool so the average count time per station exceeds 1 second[2], the precision of the counts should be better than 1% and the corresponding %K2O determination within 0.18%.

[2] The tool should not be logging any faster than 0.5 fps or 30 ft/min in order to count for 1 sec over each 0.5 ft increment, assuming standard oil field logging resolution. For high resolution logging to resolve thin ore zones (e.g. 0.2 ft sampling rate) we recommend not more than 12 ft/min = 720 ft/hr. Obviously, only the section of interest needs to be logged at a reduced rate for high resolution data and the remainder of the section can be pulled at normal logging speeds.

Discussion

Comparisons to published oilfield tool responses

Table 2 summarizes the characteristics of the mineral logging sonde used in this study alongside the published specifications for several modern oilfield logging tools. This list was compiled from company brochures and websites and is not comprehensive. Also shown are the specifications taken from the computer modeling approach taken by Wahl (1983). We suspect many of the published tool specifications were actually estimated by modeling rather than measured as was done in this study. Figure 14 is an example log that shows the gamma ray response of the Mount Sopris tool (solid green line track 3 converted to API units) overlaid by the total K2O results from the mineral assay analysis (lime green bars in track 3) .

From this, we conclude the Mt. Sopris logging sonde is quite similar in response to typical oilfield tools deployed by the major service vendors. Although borehole size, borehole fluid, positioning of the tool in the borehole, etc. will vary between the test environment used here and actual field logging conditions and for that matter from well to well, the overall response functions should be very close. We find no fundamental or theoretical barriers to cross-calibrating the mineral logging data, which is commonly tied to core analyses, to oilfield tool responses collected in either open-holes or cased-holes. Borehole environment corrections and normalization will be required to reconcile the data from well to well, these procedures are well established in the log interpretation community and are routine. Constructing a simple test pit with a large borehole for oilfield sonde testing would greatly facilitate the direct comparisons of these data sets.

Conclusions

Based on the experiments described above, we found:

1. A typical slim-hole, minerals logging gamma-ray sonde has similar (but not identical) response characteristics to a standard oilfield gamma-ray tool.
2. The depth of investigation in pure, solid salt is 11.5 cm (4.5 inches), defined as the 50% cumulative response. The 90% cumulative response is at 31 cm (12.2 inches).
3. The vertical bed resolution is 68 cm (27 inches) in granular product and was estimated to be 49 cm (19 inches) in solid salt. Vertical resolution is defined as the minimum bed thickness required to measure a full peak response (for the radioactivity of the surrounding source) at the midpoint of the bed.
4. The gamma-ray tool response is absolutely linear with respect to the amount of radioactive material within the volume of investigation, to a high degree of precision. This was verified by both varying the total amount of radioactive material in the volume of investigation, and by determining the gamma-ray counts for varying mixtures of radioactive and non-radioactive evaporate.
5. The mass adsorption coefficients of sylvite (KCL) and halite (NaCl) are nearly identical, and are very close to sandstone (SiO_4). In the absence of significant heavy elements, differences in mineralogy can likely be ignored for potash ore grade determination.
6. The tool response experimentally determined in this study is in agreement with published modeling studies of gamma-ray logs.
7. There are no fundamental limitations or barriers to the application of gamma-ray logs to determine the potassium content of potash and langbeinite ores.

References

Alger, R.P. and E.R. Crain, 1965, Defining evaporite deposits with electrical well logs: Trans. Northern Ohio Geol. Society 2nd Symposium on Salt, 15 p.

Bassiouni, Z., 1994, Theory, measurement and interpretation of well logs: Society of Petroleum Engineers, Textbook Series v. 4, 372 p.

Belknap, W.B., J.T. Dewan, C.V. Kirkpatrick, W.E. Mott, A.J. Pearson, and W.R. Rabson, 1959, API calibration facility for nuclear logs: American Petroleum Institute, Drilling and Production Practice, p. 289-317 (summary of RP33; reprinted in SPWLA Reprint Volume on Gamma Ray, Neutron, and Density Logging, Mar. 1978).

Crain, E.R. & W.B. Anderson, 1966, Quantitative log evaluation of the Prairie Evaporite Formation in Saskatechewan: Petroleum Society of CIM 17th Ann. Technical Meeting, 8 p.

Dodd, P.H., 1966, Quantitative logging and interpretation systems to evaluate Uranium deposits: Trans. SPWLA 7th Ann. Logging Symposium, Paper P, 21 p.

Ellis, D., 1987, Well logging for earth scientists: Elsevier, New York, 532 p.

Hawkins, W.K. & M. Gearhart, 1968, Use of logging in Uranium prospecting: Trans. SPWLA 9th Ann. Logging Symposium, Paper T, 13 p.

Moore, David W., Arthur W. Straub, Margaret E. Berry, Michael L. Baker, and Theodore R. Brandt, 2001, Generalized surficial geologic map of the Denver 1° x 2° quadrangle, Colorado: U.S. Geological Survey Miscellaneous Field Studies Map MF-2347, 1 sheet 1:250,000, available online at http://pubs.usgs.gov/mf/2001/mf-2347/.

Tixier, M.P., and R.P. Alger, 1967, Log evaluation of non-metallic mineral deposits: Trans. SPWLA 8th Ann. Logging Symposium, Paper R, 22 p.

Trimble, Donale E., and Michael N. Machette, 1979, Geologic map of the greater Denver area, Front Range urban corridor, Colorado: U.S. Geological Survey Miscellaneous Investigations Map I-856-H, 1 sheet 1:100,000, available online at http://pubs.usgs.gov/imap/i-856-h/.

Wahl, J.S., 1983, Gamma-ray logging: Geophysics, v 48, n 11, p 1536-1550.

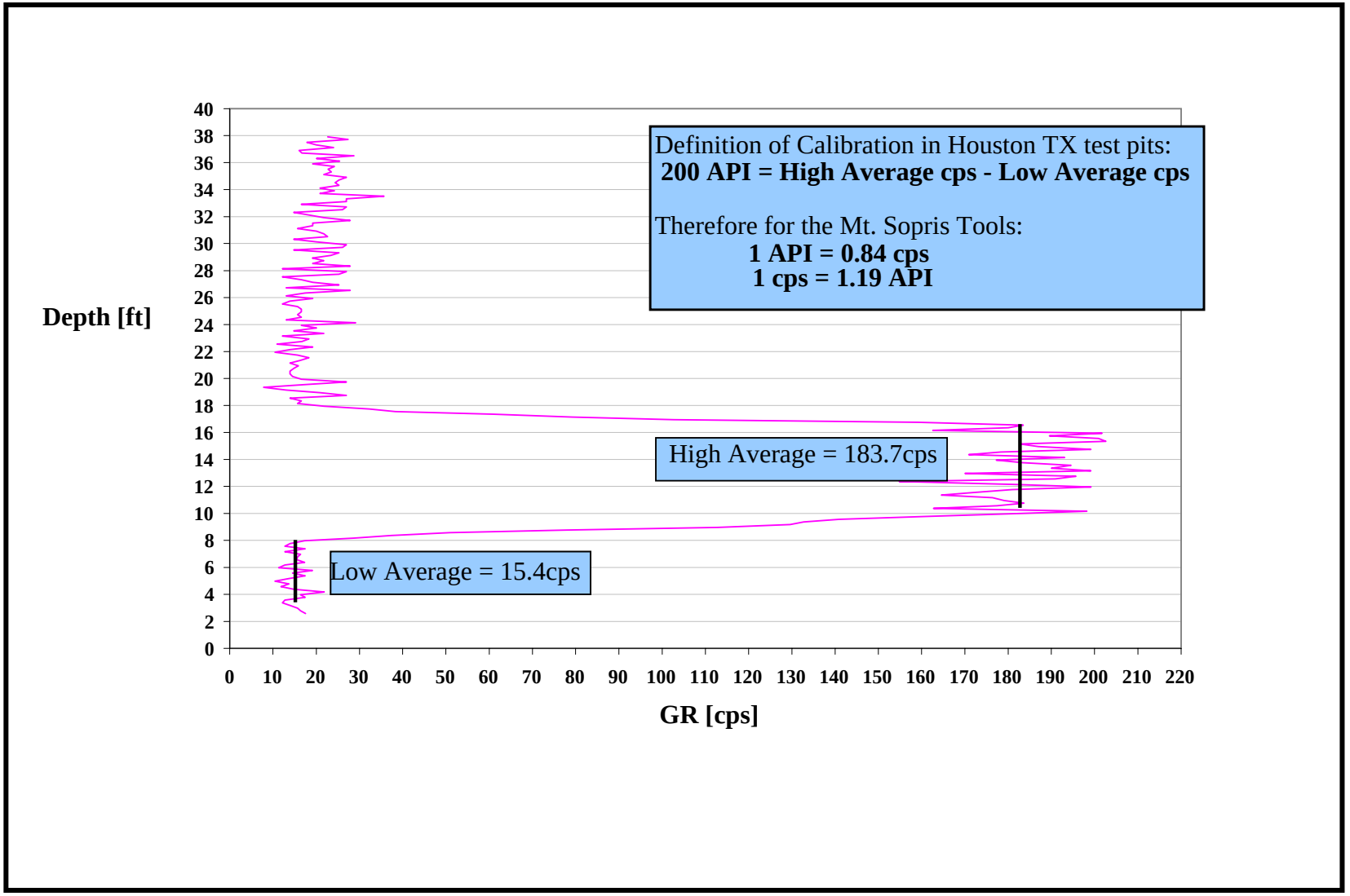

Figure #1: API Calibration Test Pit in Houston, TX

Figure #2: Photos of the initial "bag tests"

Figure #3A: Empty test tank with 4.5” borehole

#3B: Gamma-ray sonde with Styrofoam centralizers

Figure #4A: Test tank set up for radial depth of investigation tests showing plywood forms and nested cylinders, prior to filling with product.

Figure #4B: Radial tank set up after filling with product.

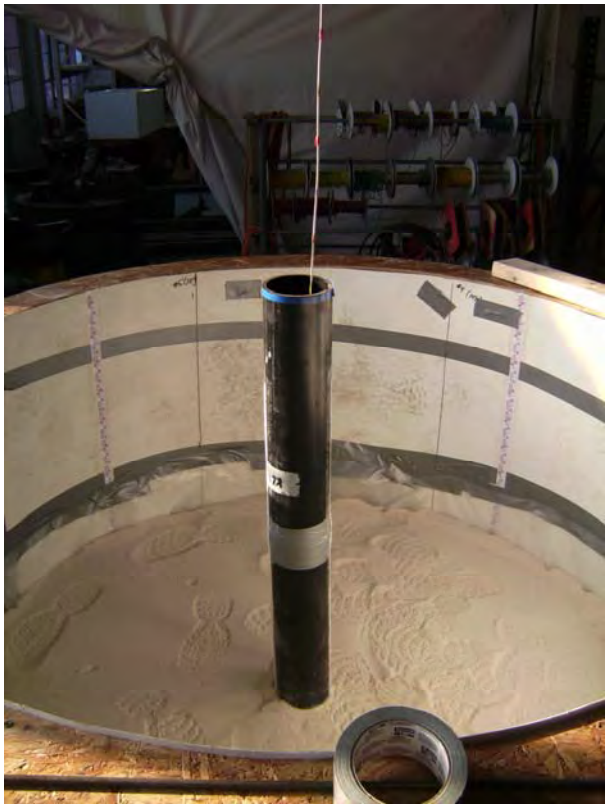

Figure #5: Test tank set up for vertical resolution experiments.

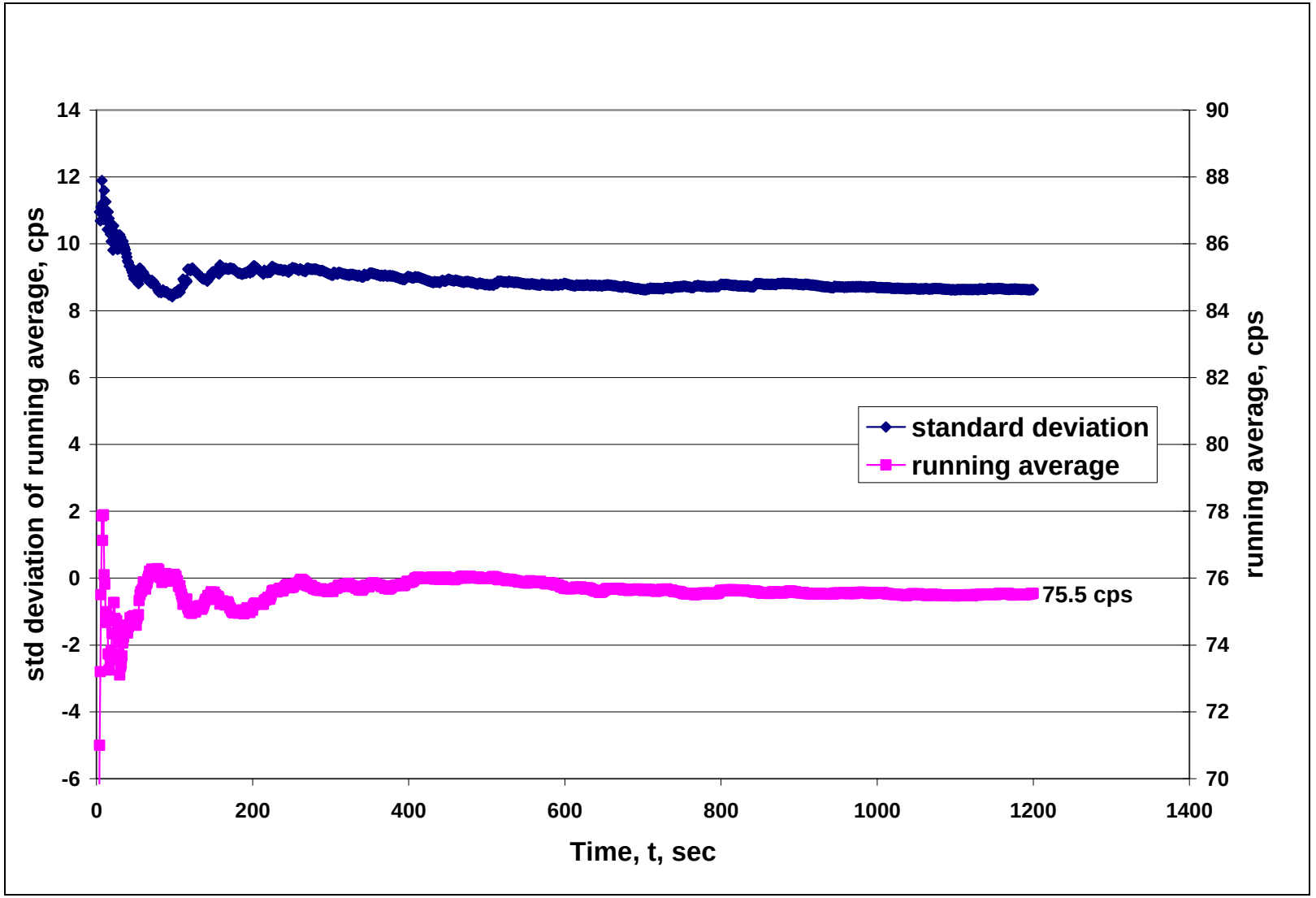

Figure #6: Bag test showing raw data for a 20-minute single station measurement.

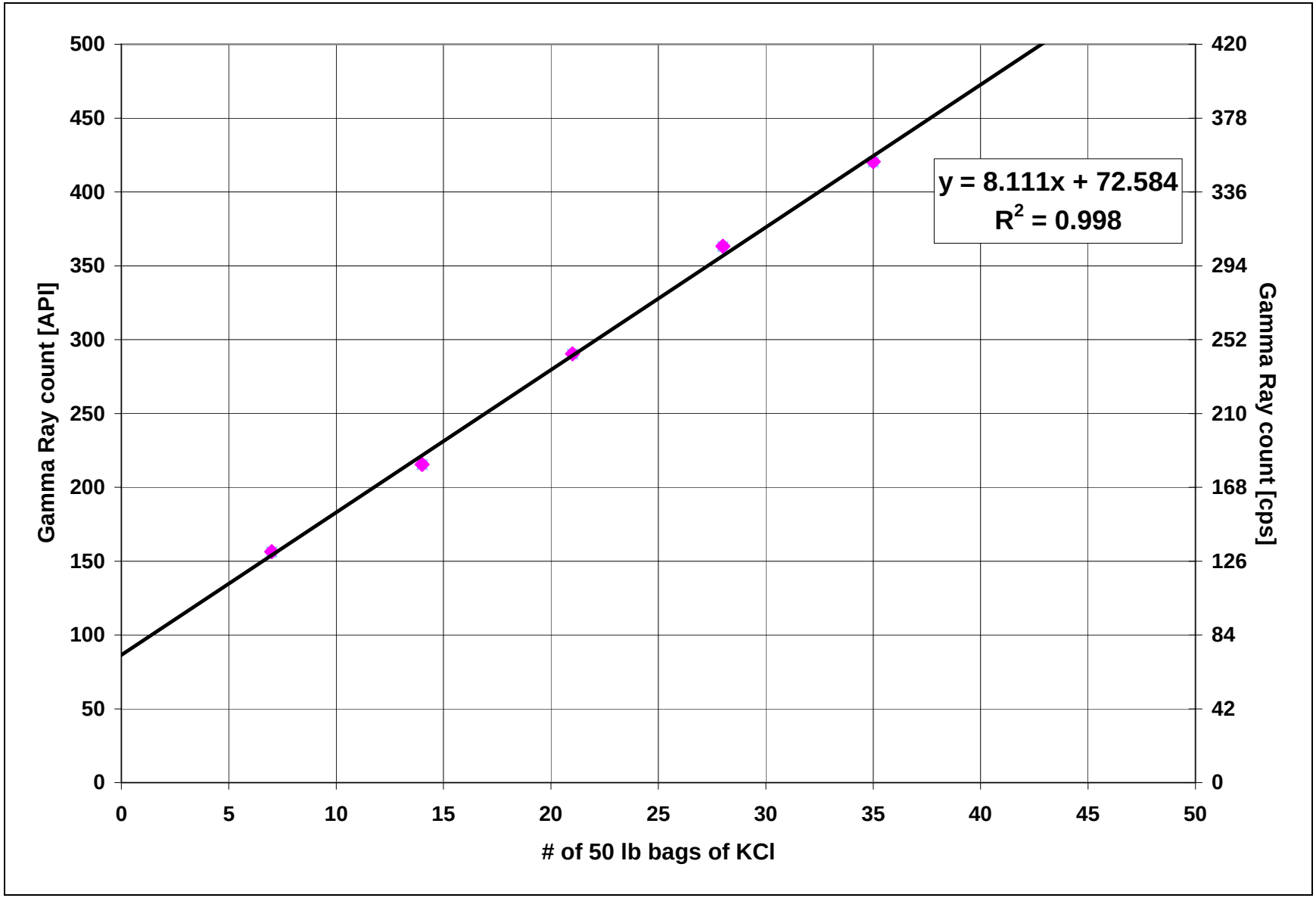

Figure #7: Response linearity test using 7 to 35 bags of product in a 1 ft radius array around tool hung in air.

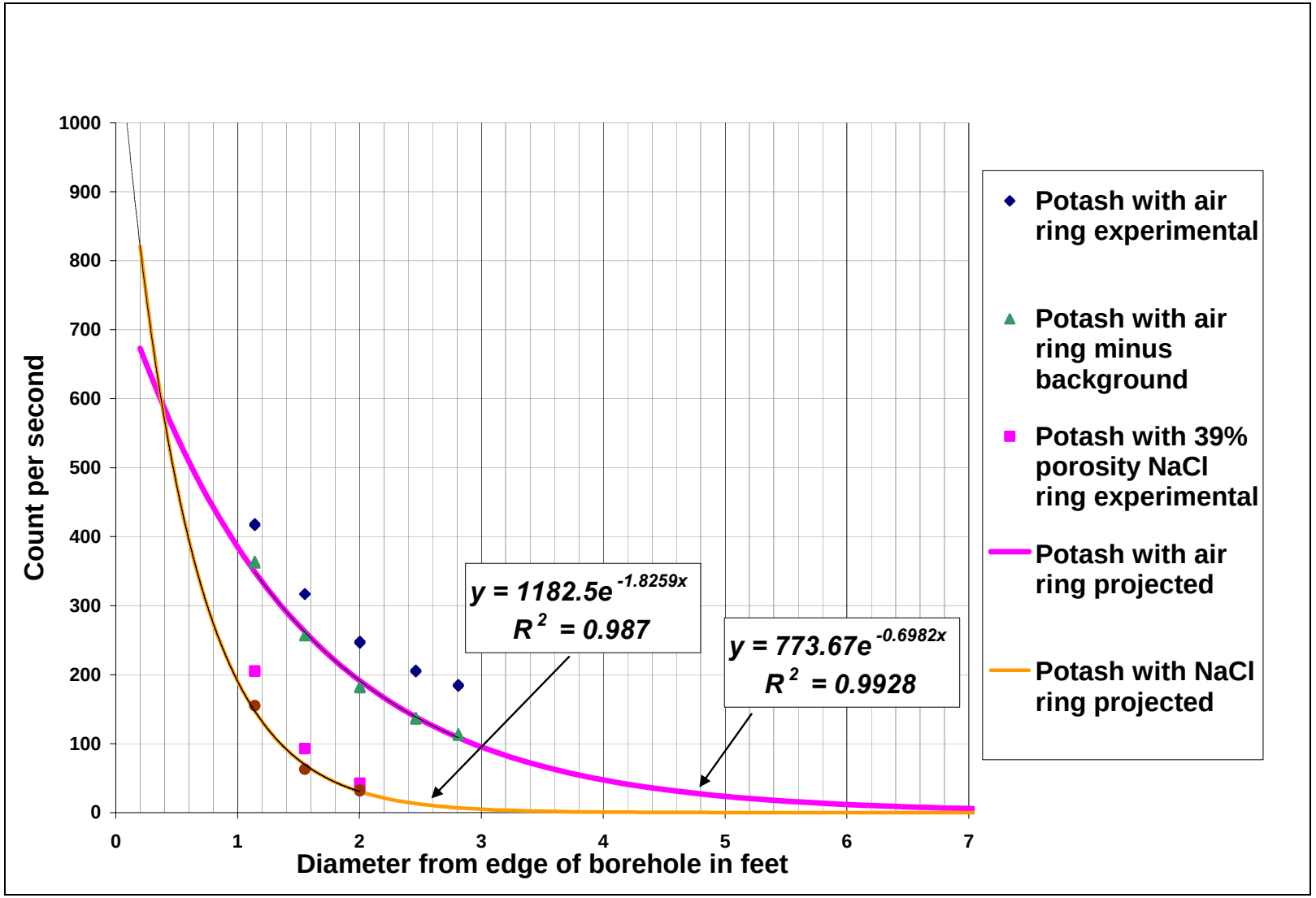

Figure #8: Radial response tests raw and background corrected data.

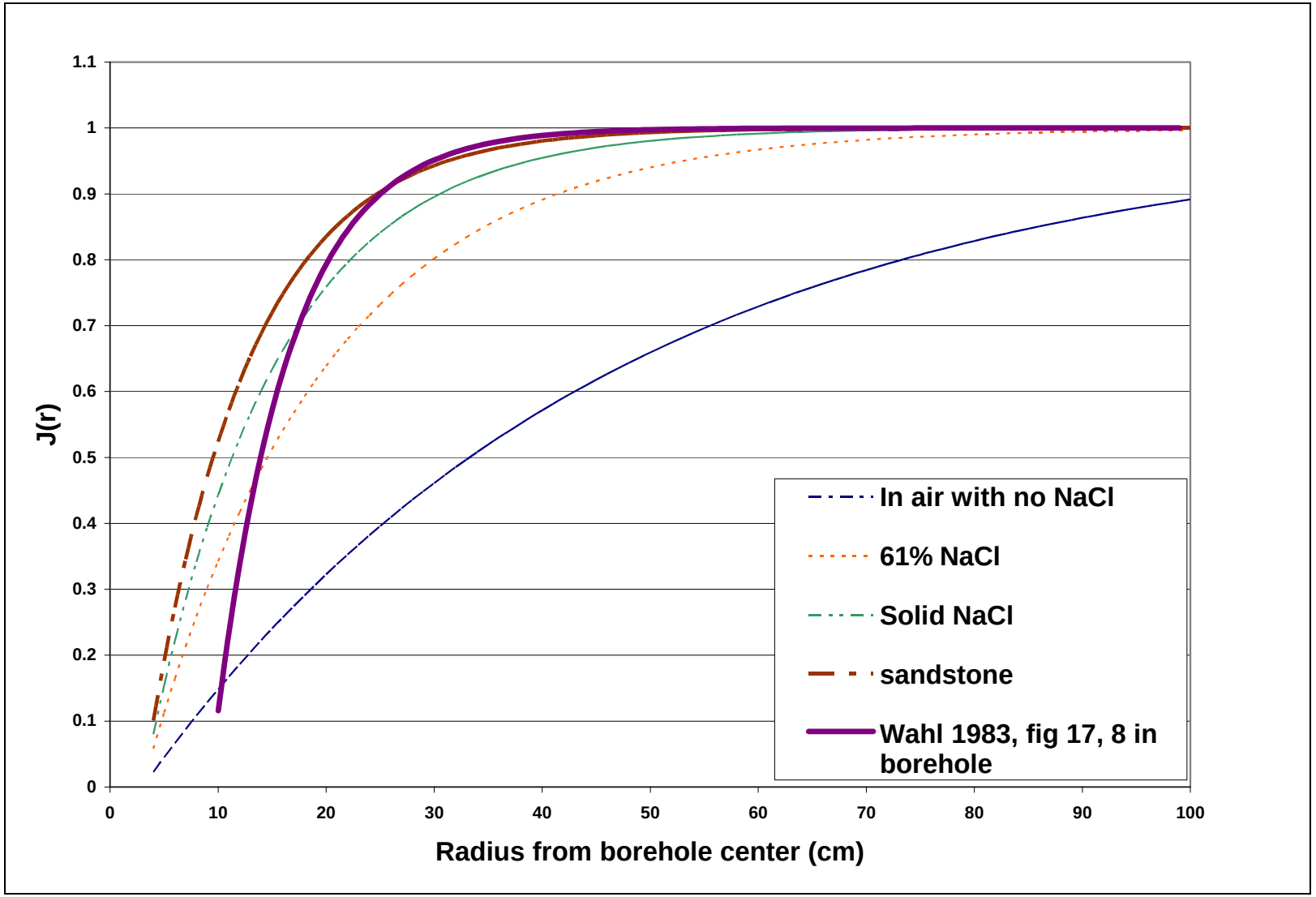

Figure #9: Radial depth of investigation (J function).

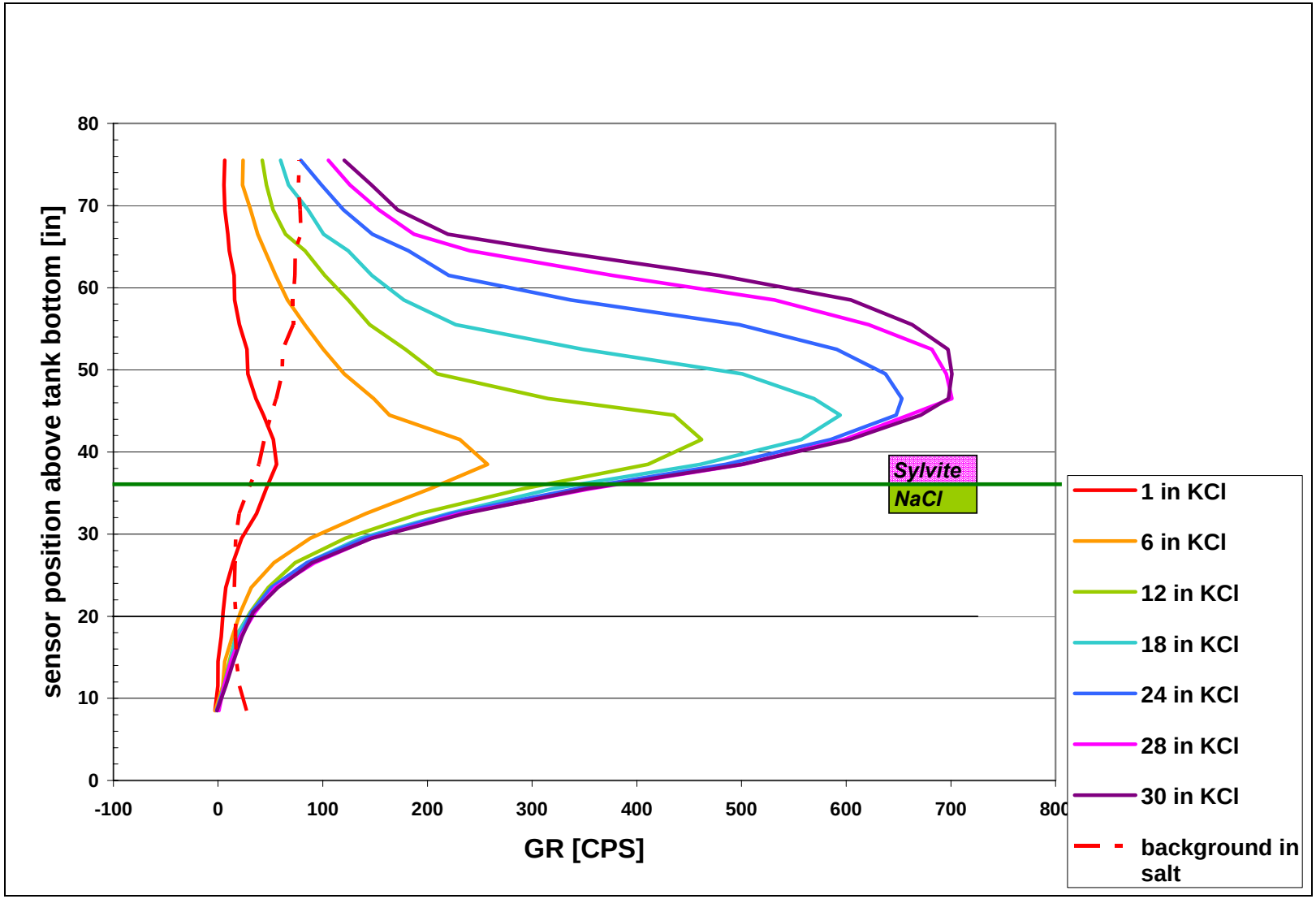

Figure #10: Vertical resolution tests (background corrected) for 1-32 inches of KCl on a 36 inch salt base.

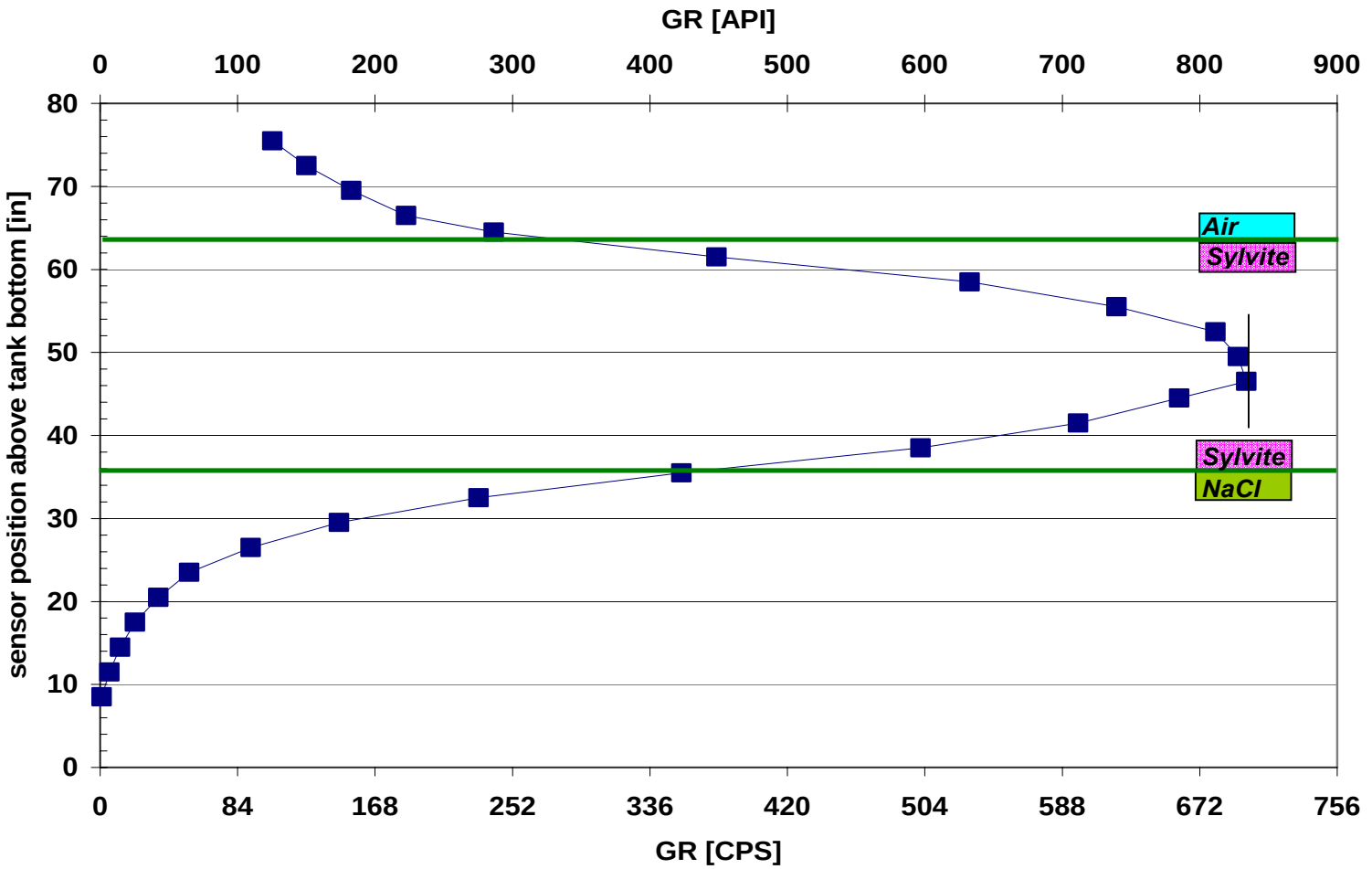

Figure #11: Baselined vertical response function for 28 inch layer of granular KCl. This is essentially a vertical J function for this tool in a porous evaporite media.

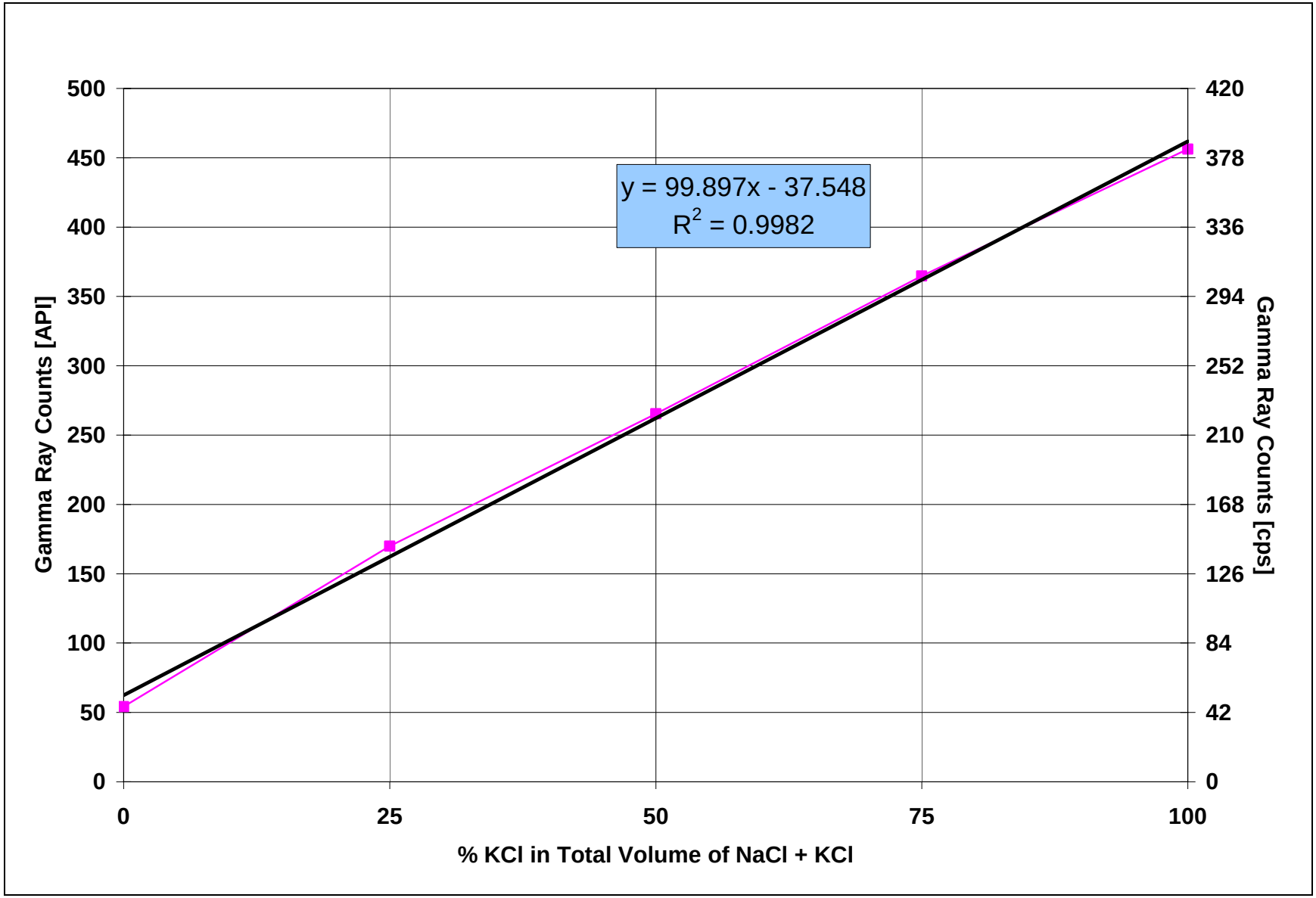

Figure #12: Linear response test for several mixtures of potash and salt.

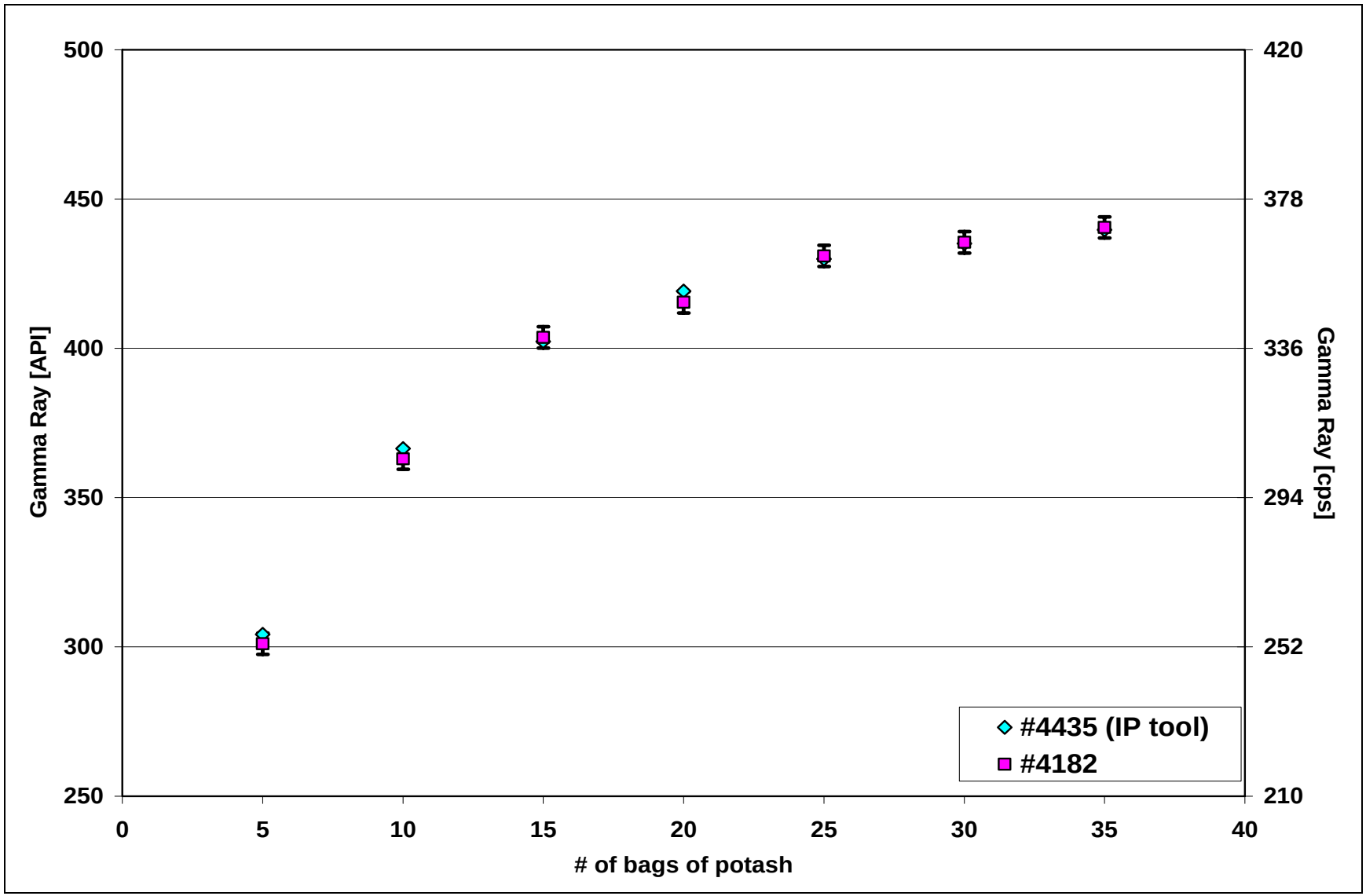

Figure #13A: Variation between different logging tools - "Bag test" with sylvite directly around bucket

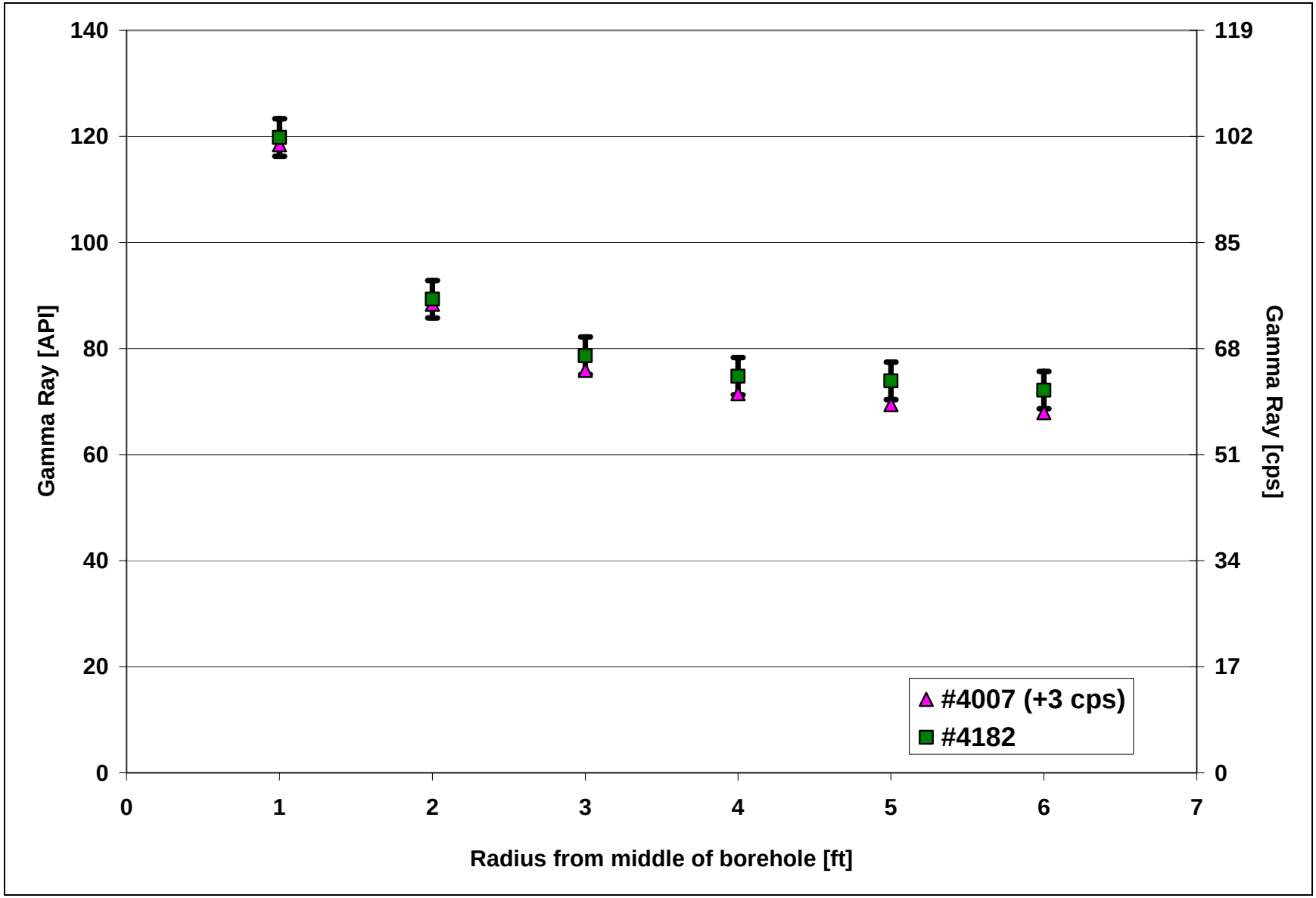

#13B: Variation between different logging tools - 6 bags of KCl vs. radius from tool. (Tool #4007 was normalized by +3 cps)

Table #1: Table of radial ring dimensions

Substance Filling Inner Ring	Inner Radius	Outer Radius	Mid Radius
Air	2.875’	3.13’	3’
Air	2.5’	2.80’	2.65’
Air and NaCl	2’	2.36’	2.19’
Air and NaCl	1.5’	1.95’	1.74’
Air and NaCl	1’	1.60’	1.33’
Sylvite directly around borehole	0.1875’	1.26’	0.90’

Table #2: Table of Published Gamma Ray Specifications

	Mt. Sopris Instruments	Schlumberger	Halliburton	Baker	Weatherford	Wahl Tool Model
Measurement Range	0-100,000 CPS gamma	N/A	N/A	N/A	0 - no practical limit	theoretical response
Depth of Investigation	4.5 in (50%); 12 in (90%) in 2.16 g/c3 salt	9 ~ 15 in.	4 in (50%); 11 in (90%)	12" for 8" hole with 20% φ	N/A	4 in (50%) and 10 in (90%) in 2.20 g/c3 formation
Vertical Resolution	19 in in salt	24 in.	18 in	N/A	N/A	~30-35 cm
Precision / Resolution	0.02% of full scale	N/A	At 30 ft/min ±5% or ±5 API, whichever is greater At 60 ft/min ±7% or ±7 API, whichever is greater	N/A	0.7 API	N/A
Accuracy	±1% of full scale	±7 GAPI at 1800 ft/hr	±5 API	±2.6 p.u. in shale	N/A	N/A

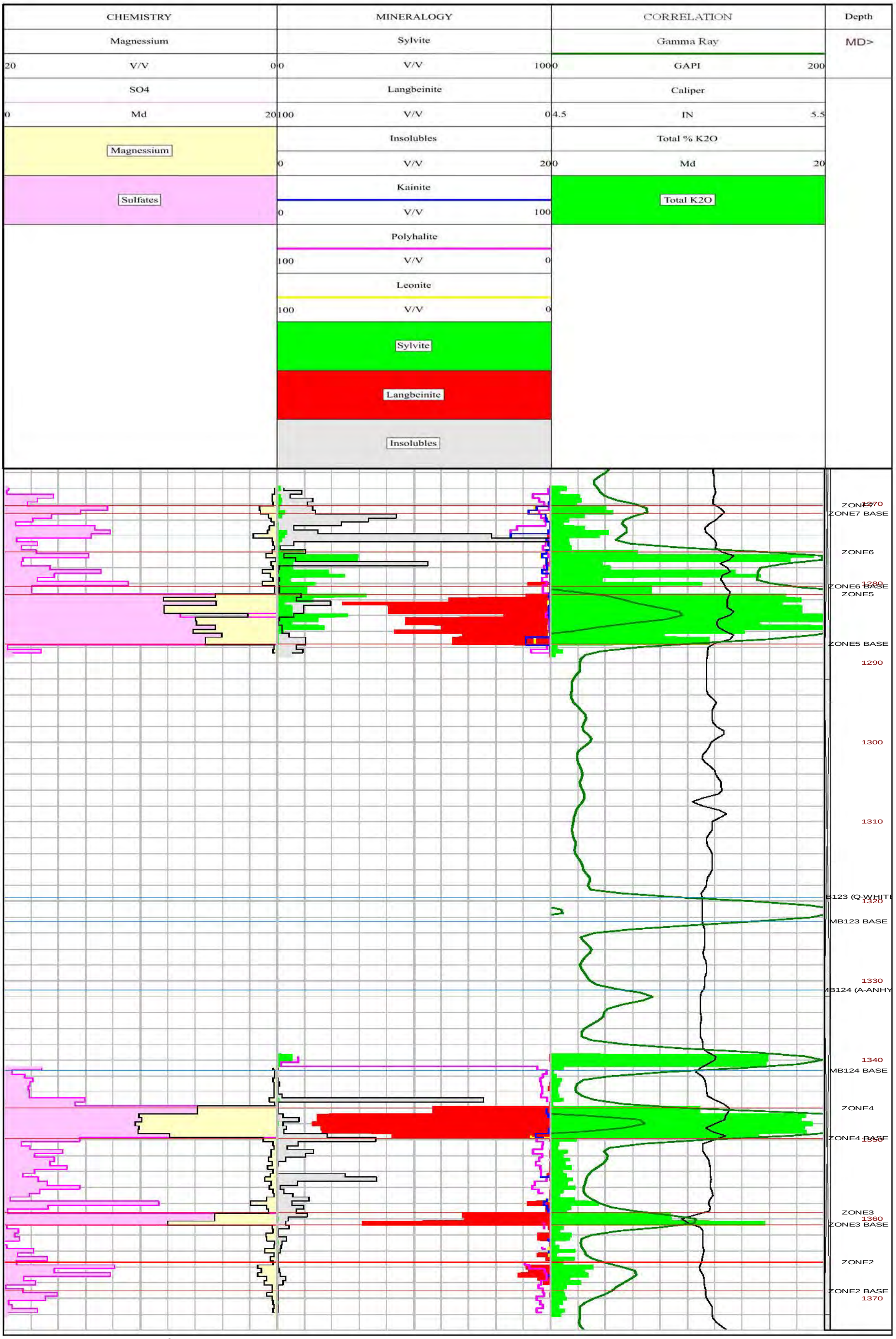

Figure 14: Example log of Gamma Ray Response in API to mineral assay data

PRACTICAL FOCUSING OF SURFACE-WAVE INVERSION TO IMAGE LEVEES IN SOUTHERN NEW MEXICO

Julian Ivanov, Kansas Geological Survey, Lawrence, KS
Richard D. Miller, Kansas Geological Survey, Lawrence, KS
Shelby Peterie, Kansas Geological Survey, Lawrence, KS
Joseph B. Dunbar, Engineer Research and Development Center, Vicksburg, MS

Abstract

Existing algorithms for inversion of dispersion-curves estimated from analyzing the seismic surface-wave data provide a reasonable representation of the overall shear-wave velocity structure. However, in some cases these results may not meet the resolution requirement of the survey objectives targeting the upper portion of the subsurface section. Near-surface geophysical surveys often look for greater detail in the very near surface, such as the case for levees, while still being interested in the overall velocity structure at greater depth. The proposed method for applying surface-wave inversion revolves around applying a greater degree of focusing on the very near-surface component of the inversion model through the practical use of existing algorithms. Specifically by eliminating the low frequency portion of the dispersion-curve data and using a shallower model. The proposed inversion technique is demonstrated using the multi-channel analysis of surface waves (MASW) inversion algorithm. As a result of using this near-surface focusing approach, surface-wave velocity estimates of the levees possess greater detail and resolution. Results presented here demonstrate the potential of the proposed approach to more accurately image the very shallow subsurface top portion of other near surface MASW sites.

Introduction

This work represents a continuation of an applied research project designed to evaluate the feasibility and applicability of several seismic techniques with the potential to identify, delineate, and estimate changes in physical characteristics or properties within levees during a simulated flood event. Several surface seismic measurements were taken using state-of-the-art equipment and analyzed using well-established and new research methods (Ivanov et al., 2006). These methods included P- and S-wave refraction tomography, surface-wave propagation, surface-wave dwell, and surface-wave (Rayleigh wave and Love wave) dispersion curve analysis (MASW).

Seismic investigations were conducted at a levee site located along Rio Grande river in the La Mesa Quadrangle, New Mexico, USA (Figure 1).

Multichannel surface-wave inversion techniques have proven capable of revealing anomalous shear-wave velocity zones within and below fill materials (Miller et al., 1999). Surface-wave analysis provided the greatest reliability in shear-wave velocity determination in the levee.

The MASW method involves the following steps. A single seismic-data record is acquired by a set

Figure 1. Survey site near Las Cruces, New Mexico.

of low-frequency (e.g., 4.5 Hz) geophones evenly spaced along a line. The seismic data from each shot record is transformed into a phase-velocity – frequency image, which allows the evaluation of the dispersion-curve trend of the fundamental-mode of the Rayleigh wave. The estimated dispersion curve is then inverted to produce a 1-D shear-wave velocity (V_s) model and assigned to the middle of the geophone spread. A 2-D V_s model can be obtained by assembling numerous 1-D V_s models derived from consecutively recorded seismic shot records along a seismic line,.

A popular approach for surface-wave inversion is to use a constant number of layers for each of which a V_s value is estimated. The actual number of layers used is a trade off between the vertical resolution and inversion instability. The latter can be observed as extreme high- and low-velocity V_s estimates from the inversion results. Such instabilities can be resolved by smoothing (i.e., regularization; Meju, 1994) or by reducing the number of layers (which can be regarded as a form of local smoothing as well). Both of these approaches can lead to a reduced vertical resolution and loss of desired detail. The conventional approach uses the optimum number of layers (e.g., 5 to 10) that provide sufficient resolution and requires minimum regularization.

In our work we demonstrate a practical approach for increasing the vertical resolution of the shallowest part of the existing section without increasing the number of layers and thereby increase the risk of instability in the inversion results. We typically select the optimal number of layers at levee sites necessary to allow a relatively deep overall estimation of V_s with depth and simultaneously focus on the top several meters of the levees by using only the high-frequency portion only of dispersion-curve data and a relevant shallow depth model that uses the same number of layers (e.g., 10). Using this approach we obtained more detailed results at these levee sites that are consistent with the local geologic understanding and drill data.

Data Acquisition

A compressional-wave geophone survey line was deployed along the riverside edge of the levee road (parallel to the river and levee). The levee crest was approximately 6 m wide, while the levee itself was 3 m high with a uniform 1-to-3 slope on each side (Figure 2). Single 10 Hz compressional-wave geophones were placed every 0.6 m for a total spread length of 72 m and 120 channel records. Sources tested included various sized sledgehammers and a mechanical weight drop, each impacting appropriate sized striker plates. Source spacing was 2.4 m with source points extending off-end out to a distance equivalent to the maximum depth of investigation.

Figure 2. Field site, crew working, and semi parked on levee.

Results

To establish a general understanding of energy partitioning and model distribution we analyzed several representative complete shot records. At this stage most of the processing effort was focused on identifying the fundamental mode of the surface wave and separating it from higher modes and noise.

Next, an optimum trace-offset range was determined that would best image the target critical fundamental-mode energy (Ivanov et al., 2008), while maintaining as narrow a spread as possible for better horizontal resolution of the final 2-D V_s section.

The quality of fundamental-mode energy was appraised for six spread ranges starting with the closest (2-20 m), (fundamental mode and higher modes were blurred together), and concluding with the longest offset range 2-37 m (Ivanov et al., 2008). The 2-33 m offset range was estimated to be optimal for imaging and picking the fundamental-mode surface waves (Figure 3). Greater offsets were discarded to optimize the lateral resolution of the MASW survey 2-D V_s section.

Based on dispersion curve analysis the levee was principally interrogated by energy with frequencies above 25 Hz. The wavelength for 25 Hz Rayleigh Wave energy was roughly estimated to be 150(m/s)/25(Hz) = 6 m, which is a wavelength proposed to represent materials in the upper 3 m (using half-wavelength assumption; Song et al., 1989).

Furthermore, at 60 Hz the fundamental mode is at 120(m/s)/60(Hz) = 2 m wavelength = 1 m depth. Therefore, frequencies above 60 Hz would primarily provide information for the upper 1 m of the levee. Guided by previous observations the optimum spread selected for analysis was focused on fundamental-mode energy around and above 25 Hz.

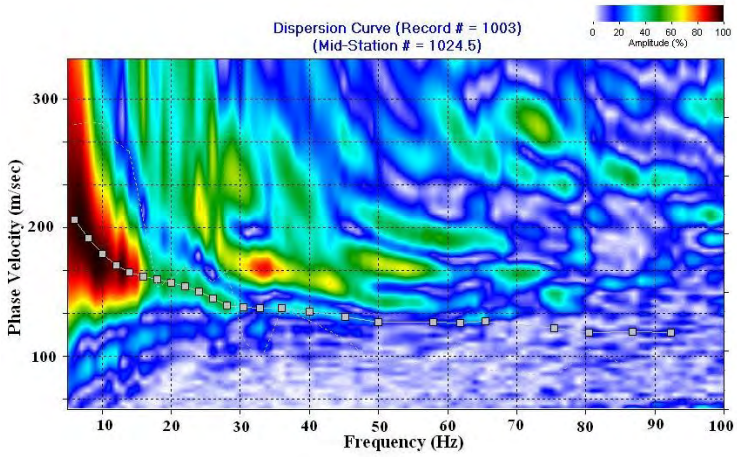

Figure 3. Dispersion curve estimated from a 2-33 m offset trace range.

Traditional MASW Processing

It was possible to estimate the fundamental-mode dispersion curve within a wide frequency range (Figure 3). Initially the dispersion curves were interpreted for all observed frequencies (6 to 80 Hz; Figure 3). Conventional inversion results provided a 2-D Vs image for depths down to 18 m (Figure 4).

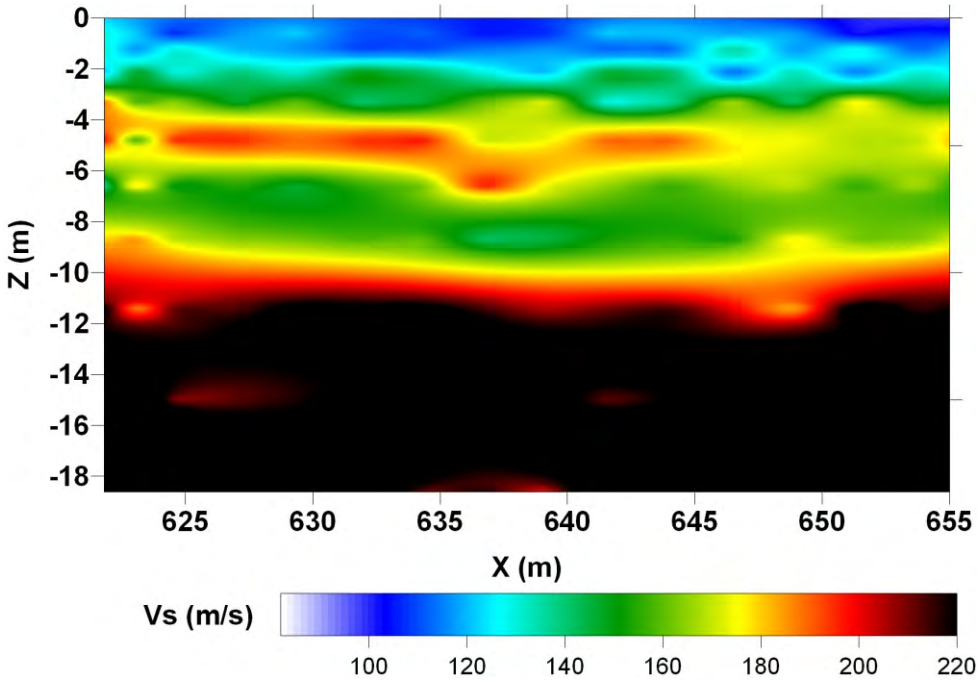

Figure 4. MASW Vs estimates using a deep 10-layer depth model.

These results provided important guidance and information about the overall structure and characteristics of the sediments within the levee, foundation, and the majority of the unconsolidated sediments above bedrock. However, resolution of the upper 3 m or so, which represented the levees did not meet the objectives of the survey.

Levee focused MASW Processing

To better focus and control the MASW method on the levees themselves we tested various inversion parameters using different models. We were specifically looking for parameters that resulted in the optimum and realistic image of the levee. Using a shallower depth model consisting of the same number of layers as the deep model (i.e., 10), but half space constrained at 7 m depth, provided more details for the upper 3 m (Figure 5).

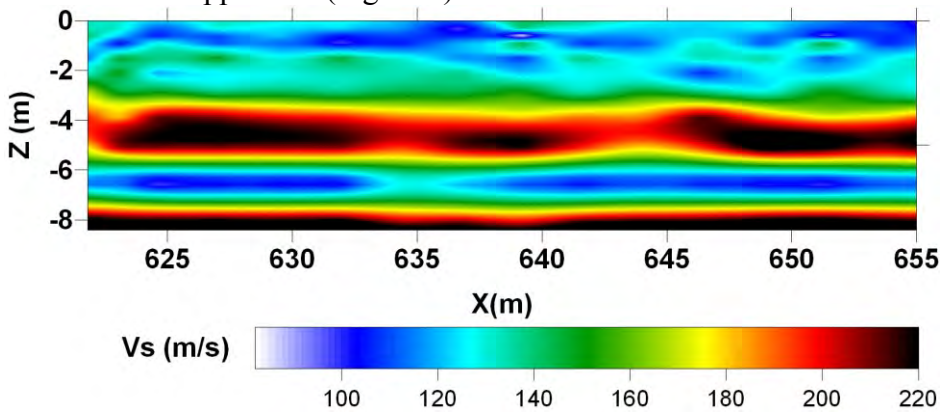

Figure 5. MASW Vs estimates using a shallow 10-layer depth model.

However, the inversion model did not provide deep enough layers that would match the low frequency range (7 – 10 Hz) of the observed dispersion curves. This lack of deeper layers caused instability (extreme high and low values at 4.5 and 6.5 m) compared to inversions using a deep model that matched the frequency range (Figure 4). In search of a more reliable solution, the high-velocity gradient of the dispersion curves for frequencies below 11 Hz was removed, Frequencies this low are likely influenced by the high-velocity (> 210 m/s) part of the section below 9 m (Figure 4). Without these low frequency estimates the new dispersion-curve frequency range matched the shallow inversion model with a half space at 7 m. With this more depth-constrained approach the inversion model focused on the shallower portion of the line and provided a much better image of the internal characteristics of the levee (Figure 6) in comparison with inversion result using a deep model (Figure 2).

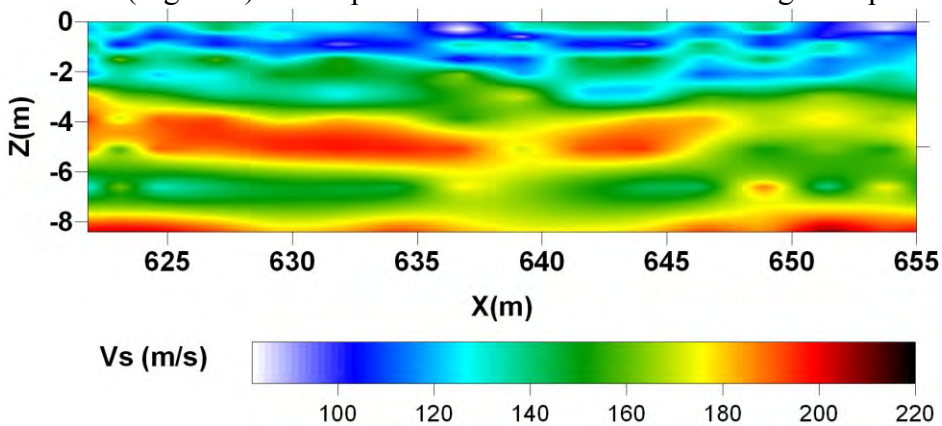

Figure 6. MASW Vs estimates using a shallow 10-layer depth model.

As well, in comparison with inversion results from using the same shallow model and dispersion curves containing lower (6-10 Hz) frequencies (Figure 5) the shallow-focused inversion (Figure 6) provided a better image of the levee core and lacked the extreme values. The levee body can be observed as a high V_s anomaly in the depth range 0-3 m on the 2D V_s images. The base of the levee is also well imaged.

Conclusions

The MASW method proved to be a useful tool for assessment of levees after tuning the inversion through the use of a shallower depth model and avoiding low-frequency dispersion-curve estimates and therefore a deeper model. The main value to be extracted from our work is the demonstration of a practical approach to improving shallow focusing and resolution without increasing the number model parameters (number layers), which could represent risk for inversion instabilities.

The improved shallow image and the image from traditional processing can be used to integrate for a combined final image. Similar results could probably be achieved by using a greater number of layers and specific type and weight of regularization. However, finding appropriate regularization parameters can be a difficult and time-consuming task from practical perspective. Thus, this suggested technique is an efficient practical approach for improving the resolution of the top half or third of the MASW 2D V_s section.

This approach provided useful results at all levee sites, identifying anomalous zones either within the levee or beneath the levee consistent with ground truth. Therefore, the MASW survey achieved the goals of identifying zones with structural deficiencies and failure potential.

Acknowledgments

Support and assistance from the U.S. Section of the International Boundary and Water Commission is greatly appreciated and without which this research would not have been possible. Permission to publish this paper was granted by the Commissioner, U.S. Section of the International Boundary and Water Commission, and by the Director, Geotechnical and Structures Laboratory, Engineer Research and Development Center.

References

Ivanov, J., R.D. Miller, G. Tsoflias, 2008, Some practical aspects of MASW analysis and processing: Symposium on the Application of Geophysics to Engineering and Environmental Problems (SAGEEP 2008), Philadelphia, Pennsylvania, April 6-10, 21, No. 1, 1186-1198.

Ivanov, J., Miller, R.D., Stimac N., Ballard R.F., Dunbar, J.B., and Smullen, S., 2006, Time-lapse seismic study of levees in southern New Mexico: 76th Annual International Meeting, SEG, Expanded Abstracts, 3255-3258.

Meju, M. A., 1994, Biased estimation: a simple framework for inversion and uncertainty analysis with prior information: Geophysical Journal International, 119, 521-528.

Miller, R. D., Xia, J., Park, C. B., and Ivanov, J.M., 1999a, Multichannel analysis of surfaces waves to map bedrock: Leading Edge, 18, 1392-1396.

Song, Y.Y., J.P. Castagna, R.A. Black, and R.W. Knapp, (1989), Sensitivity of near-surface shear-wave velocity determination from Rayleigh and Love waves, Technical Program with Biographies, SEG, 59th Annual Meeting, Dallas, Texas. 509-512.

GEOPHYSICAL SURVEYS, LEVEE CERTIFICATION GEOPHYSICAL INVESTIGATIONS, DC RESISTIVITY

Daniel J. Liechty, US Department of the Interior, Bureau of Reclamation, Denver, CO

Abstract

The Yuma Area Levee system, running along the northern boundary of the city of Yuma (Arizona), trends parallel to sections of the Gila and Colorado Rivers. These Levees constructed from the surrounding earth, are composed of an assortment of sands, silts, clays, and quarried rock (which armors the river side of each levee structure). Sections of the levee system, and portions of the levee system near Walker's Ranch have been chosen for investigation to determine structural integrity and areas susceptible to slope failure or internal erosion in the event of flooding.

By using direct current resistivity (DCR), an assessment of the subsurface levee structure can be made, identifying material properties within the levee itself that indicate the presence of sands, clays, or anomalous void spaces if present. This data is used to help determine locations for levee remediation.

This report discusses results from the DCR surveys performed at various locations along the levees. In general, areas of high electrical resistivity can represent locations of clean sands and gravels which may be prone to internal erosion at flood stage river levels. Areas of localized very low resistivity can indicate the presence of steel or other metallic materials such as culverts.

This report provides a table of all direct current resistivity soundings and their quality of processed data. A few of the soundings revealed very high root mean square (RMS) error. These soundings will be disregarded. Direct current resistivity soundings with lower RMS error more accurately reveal areas of high resistivity sands and gravels within the levee structure. Only soundings classified as Good Data and Very Good Data will be used in evaluating the subsurface conditions when considering possible levee remediation locations.

Direct Current Resistivity

Summary

Using a multi-electrode direct current (DC) resistivity system, DC resistivity Wenner surveys were performed at 14 locations along the Levees north of Yuma, AZ. These surveys were interpreted through multiple inversions using the Earth Imager 2D software package (Advanced Geosciences, Inc.).

Background

Areas of high resistivity may indicate areas containing sands, gravels, other openwork coarse grained materials, or void space within the structure (although large void spaces are unlikely). Structures including culverts and steel pipes may appear as low resistivity (high conductivity) areas. However, because these structures have limited diameters, DCR measurements may not be sensitive to influence of their material properties. Areas of lower resistivity usually indicate higher clay content or a relative increase of water saturation.

Embankment sections composed of very high sand content may create weaker areas within the levee, more susceptible to slope failure or internal erosion.

Field Coordinates and Data Acquisition

The DC resistivity profile displayed below in Figure 1 (and in all other DC resistivity profiles shown throughout this report) is displayed with low coordinate numbers (feet) on the left side of the profile and high numbers on the right side of the profile. By convention the low coordinate numbers are always downstream along the levee, and the higher coordinate numbers are always upstream.

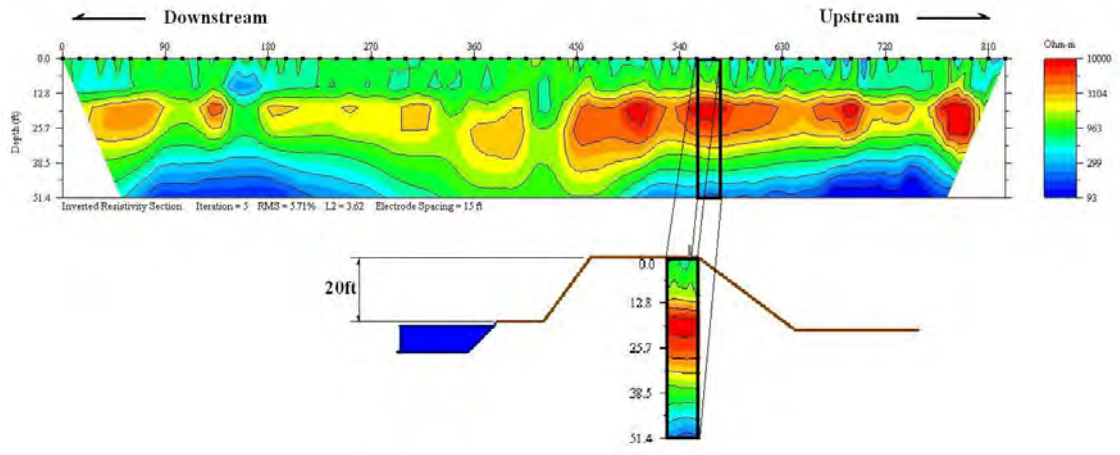

Figure 1: 0 feet – downstream, 825 feet – upstream

DC resistivity surveys were performed at 14 different locations along the levee systems bordering the Gila and Colorado Rivers. A handheld global positioning system (GPS) unit was used to record the locations of the surveys. Most of the surveys were 825 feet long (with the exception of 7-9one, 7-9two, and 7-9three performed at locations 1, 2, and 3). The locations of the 27 DC resistivity surveys at 14 different locations are shown in Figure 2, Figure 3, and Figure 4 on the next two pages.

Two surveys were performed at each location; a forward survey and reverse survey (with the exception of locations 1, 2, and 3). The forward survey simply means the measurements progressed from left to right along the survey line, and the reverse survey made resistivity measurements progressing from right to left along the survey line. This was done as a check for reproducibility of measurement data.

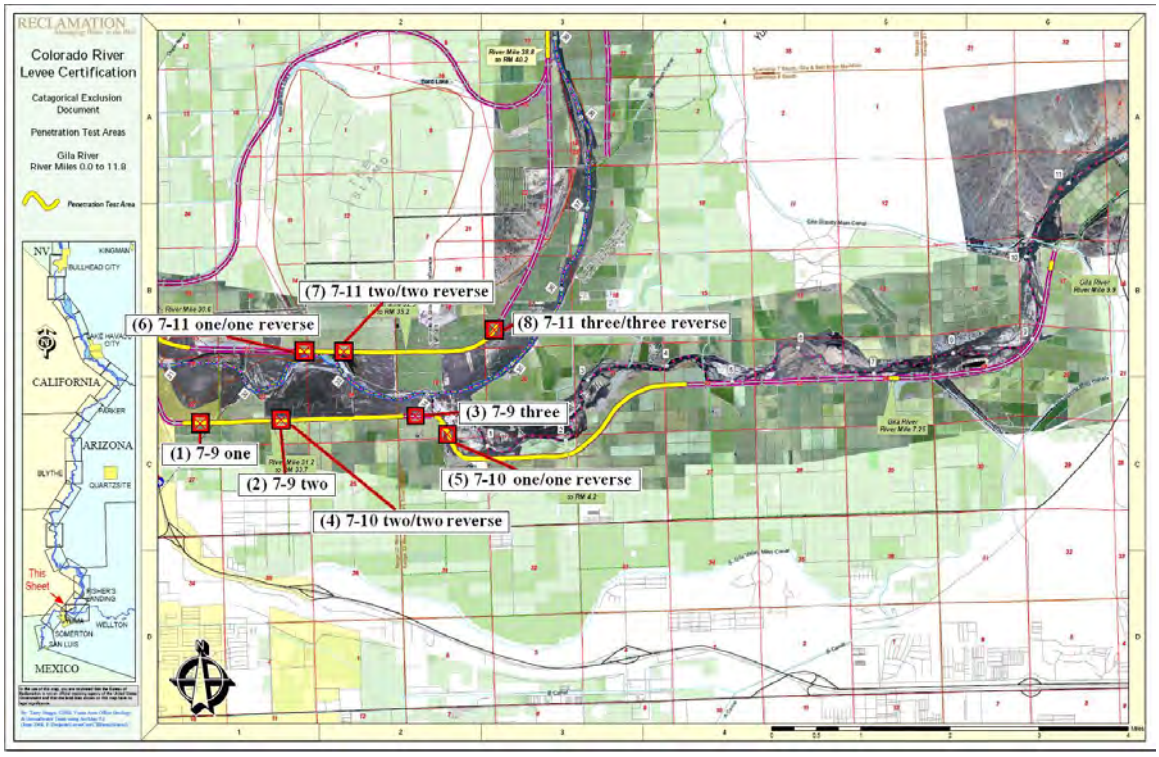

Figure 2: Survey Locations 1-8 Directly North of Yuma, AZ

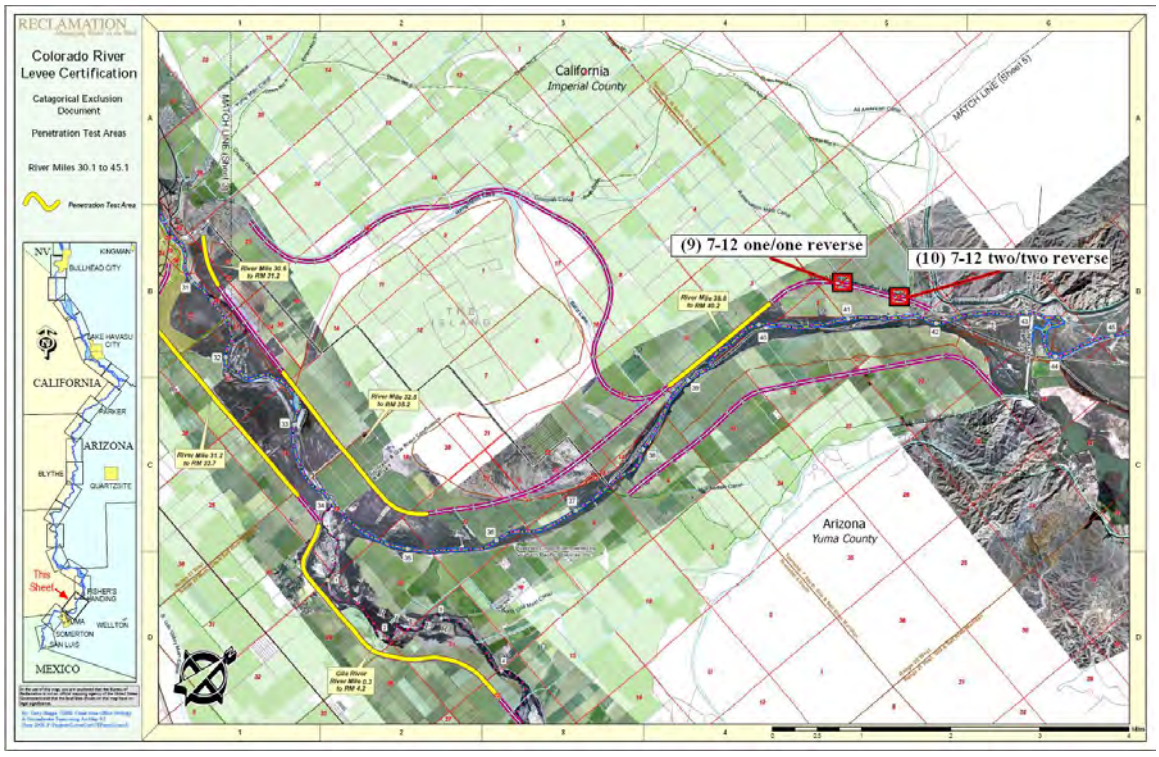

Figure 3: Survey Locations 9 & 10

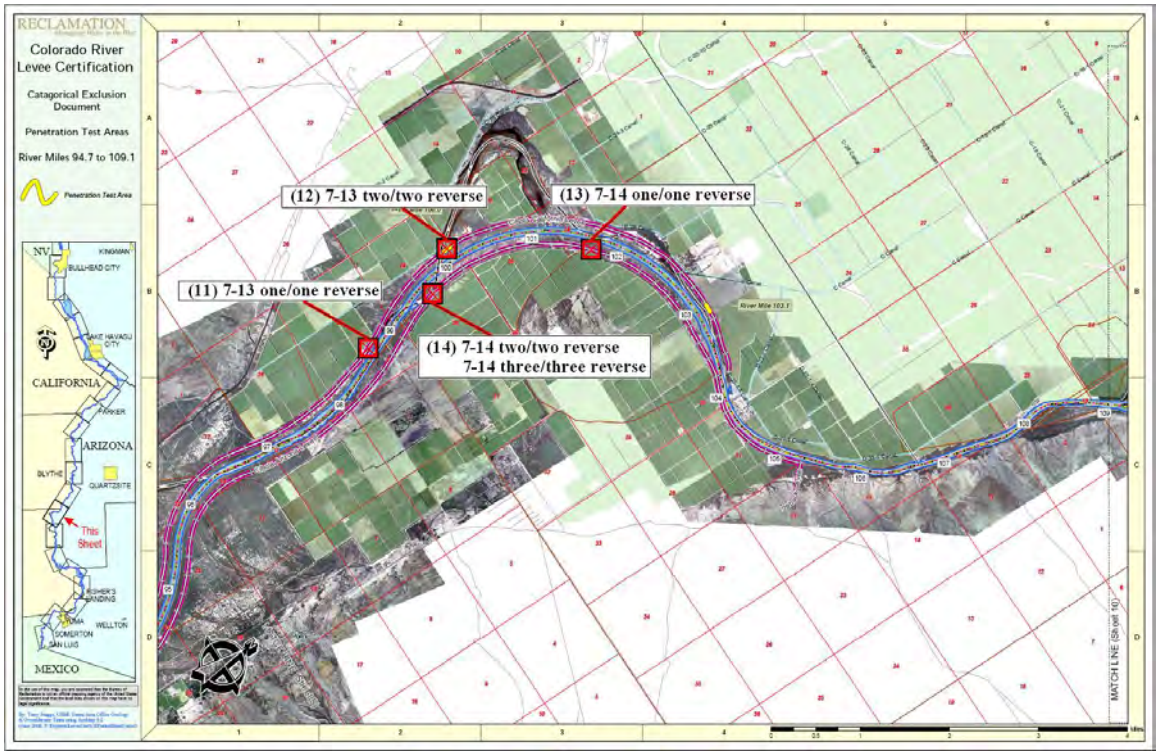

Figure 4: Survey Locations 11-14

Depth Approximation

Each surveyed line consists of hundreds of different measurements of resistivity. The array of electrodes systematically activates various electrodes, creating a canvas of measurements seen in Figure 5 below. Effectively the active current and voltage electrodes are spaced at several different increasing distances in order to investigate various depths. The further the electrode or pin spacing, the deeper the survey investigates the material properties of apparent resistivity, seen in Figure 6 on the next page. The vertical axis is labeled in ES (electrode spacing). Electrode spacing is the distance between immediately adjacent electrodes in the field. In general, depending upon the actual resistivity values, the length of electrode spacing is approximately equal to the depth of investigation. [Note: depending on the conductivity of the subsurface environment, depth of investigation can be a smaller fraction of the length of electrode spacing]

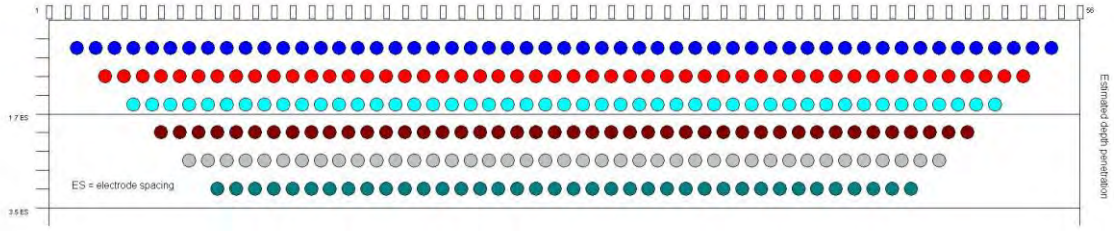

Figure 5: Subsurface Measurement Array

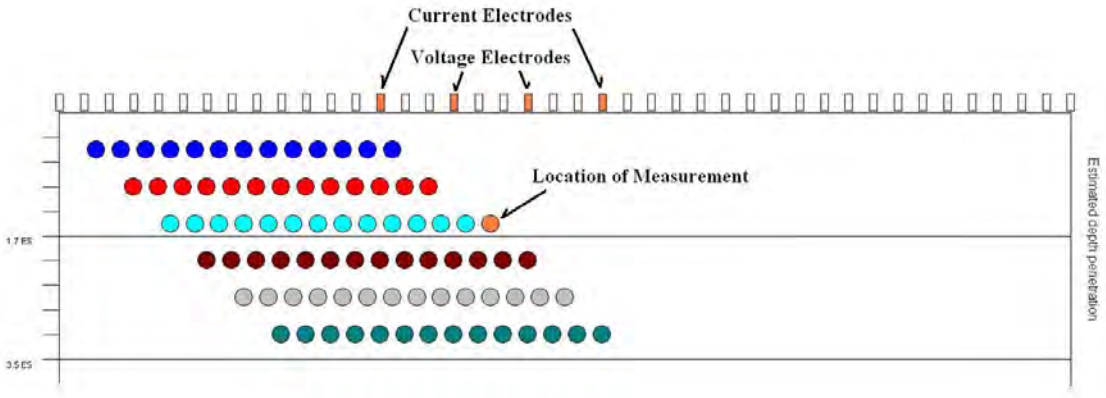

Figure 6: Depth of Investigation Based on Electrode Spacing

Inversion Interpretation

The resistivity unit computer collects all the resistivity data into a file that is transferred to the processing software, in this case Earth Imager 2D (publ. by Advanced Geosciences, Austin, TX). This software package performs multiple inversions of the measured apparent resistivity data along the survey profile (also providing a cross section of measured apparent resistivities), processing the measured data into an inverted resistivity profile section as seen in the sample profile from Figure 7 below.

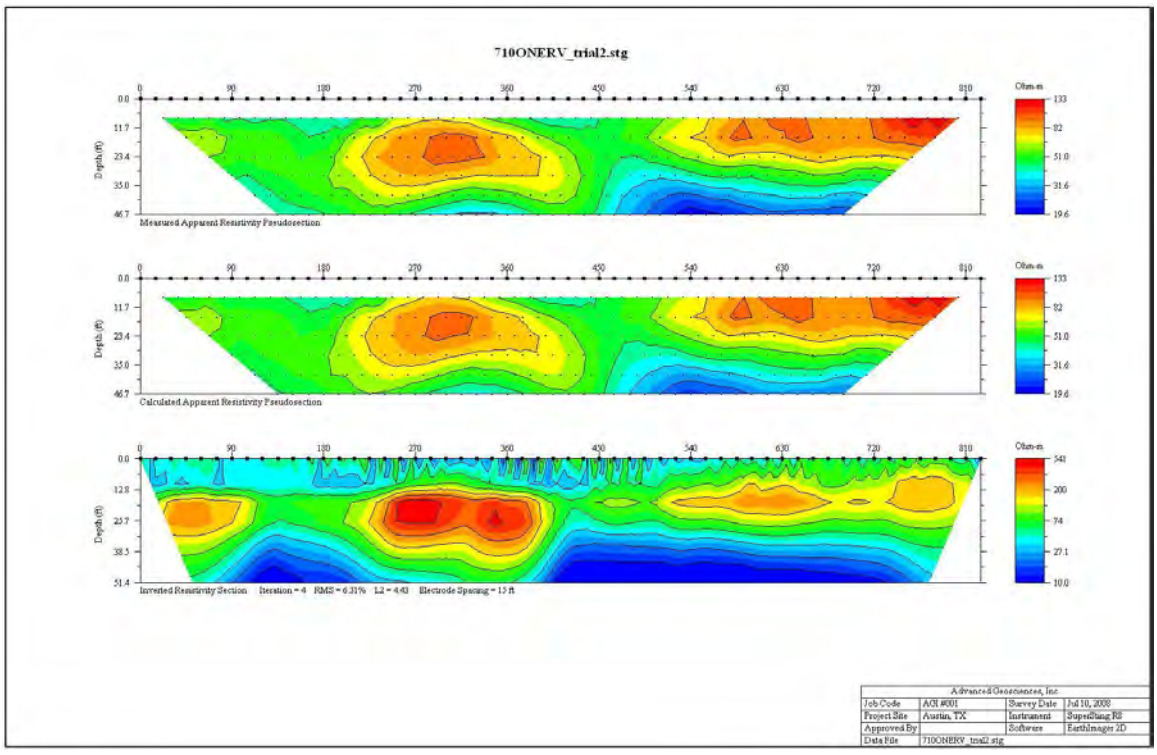

Figure 7: Resistivity Profile with Measured, Calculated, and Inverted Resistivities

It is important to note that the models used in the processing software assume half-space geometry as the subsurface. Half-space geometry assumes perfectly flat ground spanning in all directions from the location of the survey electrodes, (or no change in topography or relief); earth below and free air above. When electric current is introduced into the subsurface, it flows in all directions filling the half-space below the source electrode and eventually flowing into the sink electrode spaced at a different location. When calculating the apparent resistivities based on resistance measurements, the computer uses half-space geometry to convert resistance into resistivity.

In the case of these surveys, the electrodes were placed on the levee crests, effectively creating "empty space" on either side of the levees where the electric current could not flow. This condition created a half-space with small areas of high resistance running parallel to the direction of the survey line, not shown in a cross section profile, which slightly biases the values of the measured and inverted apparent resistivities towards more conductive values.
Figure 8 below extracts a sampled location from the survey profile and displays it in a perpendicularly aligned cross section of the levee. This reveals the scale of the levee structure with respect to the depth of the Wenner survey and shows the geometry of the levee itself with "empty space" or free air to the sides of the levee structure. This cross section also shows the location of the electrode placement on the levee embankment crest. The electrodes were always located, running along the crest of the levee on the "dry" side of the crest (not the river side). This placement was chosen both to reduce the effect of the imperfect half-space (the non-river side of the levee had a more gradual slope, or more earth adjacent to the survey) and because the river side of the crest was armored with large boulders making insertion of the electrodes problematic, creating poor electric coupling to the ground.

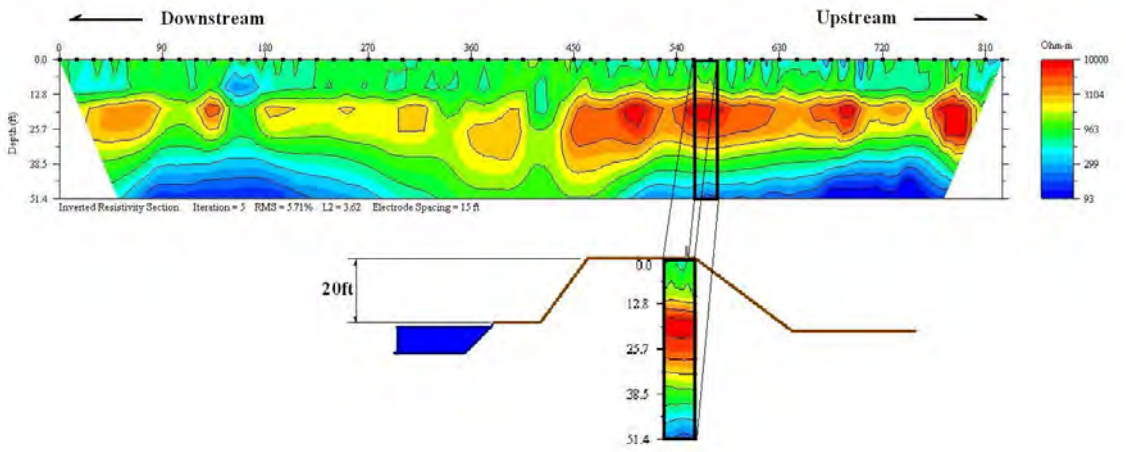

Figure 8: Sampled Cross Section of Levee (perpendicular to survey cross section**)**

Conclusions

Figure 9 on the next page is a resistivity cross section from the Wenner sounding acquired at location #4 (seen on the map in Figure 2). This resistivity cross section reveals a large area of relatively high-resistivity material (200 ohm-m to 500 ohm-m) located from about 225 ft to 405 ft along the profile and at a depth from about 10 ft to 30 ft. Smaller anomalies of

high resistivity material concentrations are also evident, centered below the lateral coordinates: 45 ft, 615 ft, and 765 ft.

The large resistive anomaly in this particular inversion correlates to a visible ridge of sand from a dried out stream bed which cuts through the base of the levee at the same location as the coordinates of the anomaly. In general, resistivity values below about 150 ohm-m suggest the presence of clays, silts, sandy silts, or a mixture of these (moisture dependent). The same resistivity values might indicate a higher saturation of water (most cross sections reveal much lower resistivities at greater depths of about 35 ft and deeper). Resistivity values of 150 ohm-m and greater suggest a higher concentration of sands and gravels. High resistivities close to the surface can also be a result of very dry desert conditions in the region. This sounding in particular correlates well with visual surface structures at the site and offers a low root mean square (RMS) value of 6.31%, suggesting low error in the inversion process.

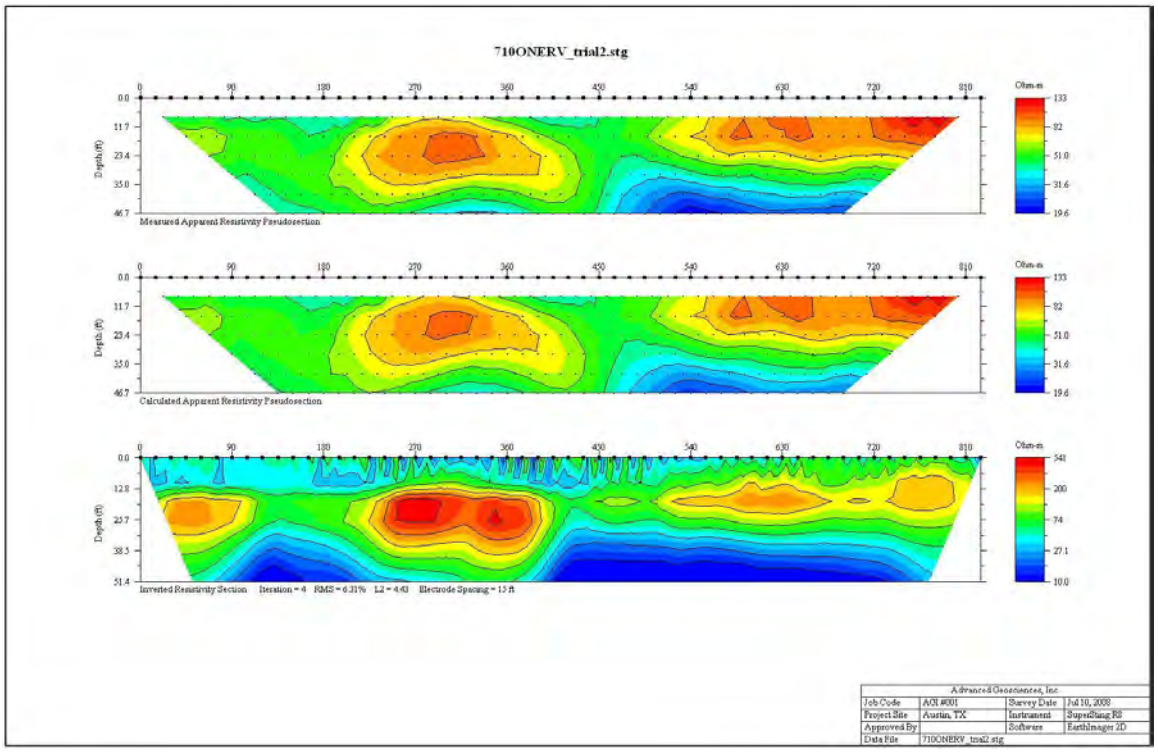

Figure 9: 7-10 one reverse

References

Liechty, D.J., May 2009, Geophysical Surveys Electrical Resistivity Electromagnetic Conductivity Yuma Area Levee Certification Support Lower Colorado Region Arizona/California, pg. 1-13.

TIME-LAPSE MONITORING OF THE SLOPE FAILURE PROCESS OF A MODEL LEVEE

Tomio INAZAKI, Public Works Research Institute, Tsukuba, Japan
Makoto INOUE, Global Infotec Inc., Urawa, Japan
Yukiko SAITO, Public Works Research Institute, Tsukuba, Japan
Satoshi ARAKANE, Public Works Research Institute, Tsukuba, Japan
and Naoto YOSHIDA, Public Works Research Institute, Tsukuba, Japan

Abstract

A half-shaped model levee 3 m high and 20 m long with a 3.5-m wide crest was time-lapse monitored over a period of four days. The purpose of the monitoring was to clarify the behavior of water migration in the levee during the deformation process. The time-lapse data included the height of the water table in the levee body measured using a water gauge array, apparent resistivity along a line set on the slope shoulder, surface temperature, and slope surface topography scanned by means of a 3D laser imaging system. Data were acquired basically at 1-hour intervals. Groundwater conditions in the levee body were controlled by infiltration from a perforated tank set at the rear side and supplemental surface watering. Surface deformation was recognized 5 hours after the surface watering, and it took another 2 hours until small slope failure occurred. Resistivity data strongly indicated that infiltration of surface water through the vadose zone and its connection with the water table in the body triggered the surface slope failure.

Introduction

Recent severe floods occurring worldwide have highlighted the importance of vulnerability assessment of existing levee systems. It is reasonable to assume that non-homogeneous levee structures and groundwater behavior greatly affect the failure potential of levee bodies when attacked by flooding. Except for large acceleration by earthquakes, most levee failures result from surface erosion by overtopping, seepage and piping through or under the body. Breaches of levee systems may occur even when water heights are lower than flood level conditions triggered by seepage and piping. Thus, these conditions are seen as precursory phenomena observed on slope surfaces or around the feet of levees. Indeed, seepage and piping caused about half of the levee failures and associated damage in Japan over the past 50 years. In addition, recent safety assessments conducted nationwide on the major levee systems exposed that one-third of the existing levees were at risk of failure due to seepage flow. The safety assessments, however, were based on conventional static slope stability analysis assuming circular slip surfaces and transient seepage flow analysis that does not take into consideration the behavior of the vapor phase in the vadose zone. To accomplish more reliable analysis for the safety assessment of levee systems, it is requested to take into account the behavior of not only pore water but also of vapor phase in vadose zone.

Geophysical investigation methods might come to play an important role in the assessment of levees, and have already provided useful information on the internal inhomogeneity of levee systems (Inazaki, 2007). Moreover, geophysical investigations are expected to reveal groundwater flow patterns in levee bodies. Since groundwater behavior varies with time, it needs to be monitored repeatedly. Furthermore, water in the vadose zone shows complex, nonlinear behavior controlled by gravity and

capillary flow in mutual interaction with vapor in the levee body materials. Therefore, time-lapse monitoring is needful to clarify the hydrological response of levee bodies during floods. Time-lapse geophysical monitoring techniques have advanced rapidly over the last two decades in reservoir production technology (Lumley, 2001). The technique has also been utilized in the near-surface geophysics field including vadose zone investigation (Deiana *et al.*, 2007) and aquifer hydrology (Harry, 2006). However, it has rarely been applied to field monitoring of levee failure because the target failure phenomena were inherently unpredictable both in time and space. Time-lapse geophysical techniques are quite effective when applied to such controllable measurements as laboratory core tests and small-scale model tests. For example, Lei and Xue (2009) precisely monitored changes in ultrasonic velocity and attenuation during CO_2 injection into porous sandstone, and clearly mapped CO_2 migration in the tested specimen. Inoue *et al*. (2006) demonstrated the usefulness of resistivity monitoring of the near-surface zone during groundwater recharge and revealed that recharge zones that developed under recharge conditions formed specifically on impervious layers. Inazaki (2005) observed 20% decreases in near-surface S-wave velocity using surface watering.

Based on these previous works, we conducted time-lapse geophysical monitoring of a seepage failure experiment on an earthen levee model. The time-lapse monitoring data collected strongly indicated that infiltration of surface water through the vadose zone and its connection with the water table in the levee body triggered surface slope failure.

Model Levee and Seepage Failure Experiment

Model Levee

The model levee, on which we conducted time-lapse monitoring, had been mounded in 2006 in a 3-m deep open test pit, located on the ground of the PWRI Tsukuba Central institute, Ibaraki Prefecture, Japan (**Fig. 1**). Construction of the model levee was originally purposed to test durability performance of buried-type sensors to measure groundwater level in the levee body. The durability test was ended in 2008 and the sensors were to be retrieved from the model levee. Seepage failure experiment was then implemented as the last event and to easily recover sensors from the body.

The cross-section and surface views of the model levee, along with the configuration of installed water gauges and geophysical sensors are shown in **Fig. 2** ***(a)*** and ***(b)***, respectively. The model levee was half-shaped, 3 m high, 20 m long and 3.5 m wide at its crest. The slope gradient was 1:2. During construction, a 0.5-m thick impervious layer was embanked using tephric loess material to serve as the levee substratum. The levee body was stacked and roller compacted in 20-cm lifts with water gauges embedded at specified positions and depths. Compaction ranged from 80 to 91%. Permeability was about 2×10^{-3} to 2×10^{-4} cm/s, estimated from infiltration tests. The slope surface was covered with lawn and the crest was paved with 5-cm thick asphalt. A total of 38 wells were sunk in the model levee body to accommodate various gauges. Only 4 of the active holes used for the experiment are shown in **Fig. 2**.

Figure 1. Model levee used for time-lapse geophysical monitoring. It had been built in a 3-m deep open test pit.

Seepage Failure Experiment

The seepage failure experiment was carried out in July 2008. To generate seepage failure, water was made to infiltrate into the levee body from a perforated tank located at the rear of the model levee (**Fig. 2 (a)**). We also sprinkled supplementary water onto the central portion (8 m in width) of the model to simulate rainfall. The intensity of precipitation was estimated to be about 60 mm/hour, obtained from the capacity of the pump and the effective sprinkled area. The water level over time in the perforated tank is shown in **Fig. 3**. First, we raised the water level to 2.3 m above the body/substratum boundary over a 2-hour period starting at 18:00, July 22, 2008 (*Day 0*). The water level was kept at 2.3 m for 36 hours until 08:00, July 23, 2008 (*Day 1*), and then raised 20 cm to 2.5 m, the maximum level. The maximum water level was maintained until the end of the experiment (*Day 3*, 15:00). Water was sprinkled on the slope shoulder starting at 14:00 on July 24 and continuing until 09:00 July 25 (*Day 3*). Incidentally, there was no natural precipitation during the course of the experiment. Hereafter, time is reported using two different starting points. One uses July 22, 2008 as *Day 0*, and the other counts 20:00 July 22 as *0h*.

As a result of continuous infiltration from the rear side of the half-shaped model levee, a small amount of seepage occurred low in the central section of the slope at about *25h* (*Day 1*, 21:00). Almost a day later, heaving occurred around the seepage point at *47h*, 5 hours after the start of surface watering. The heaving was followed by generation of a

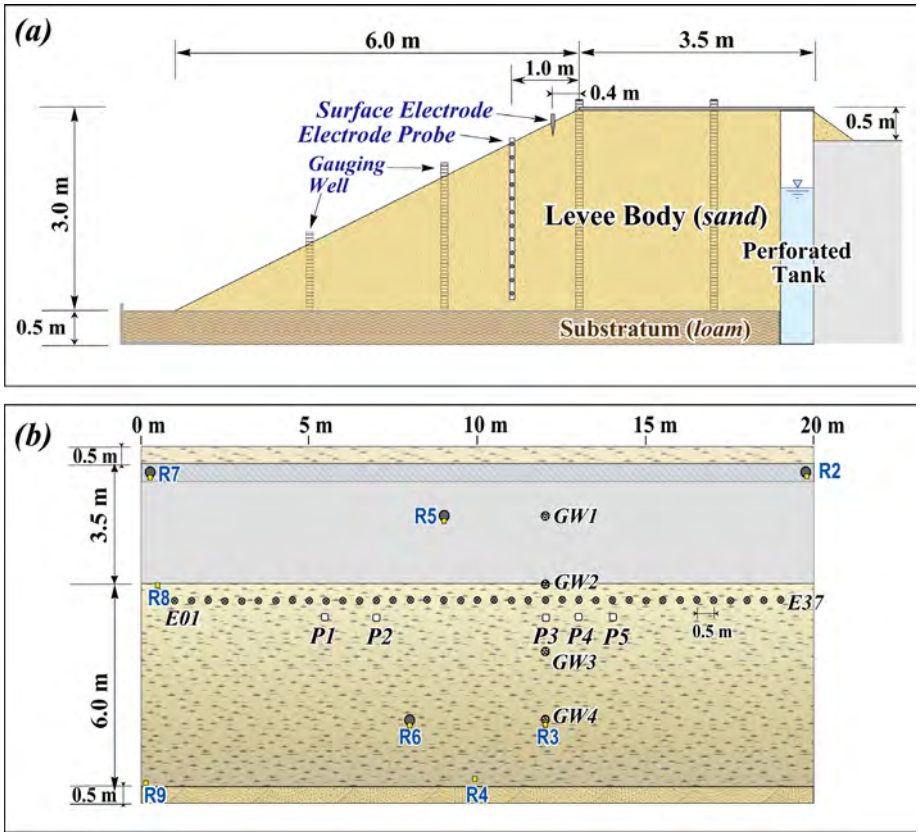

Figure 2. Structure of the model levee and configuration of gauges and sensors. ***(a)***: section view; ***(b)***: surface view. ***GW1-GW4****: Gauging well;* ***E01-E37****: Surface electrode;* ***P1-P5****: Electrode probe;* R1-R9*: Reflection marker point for laser scanning*

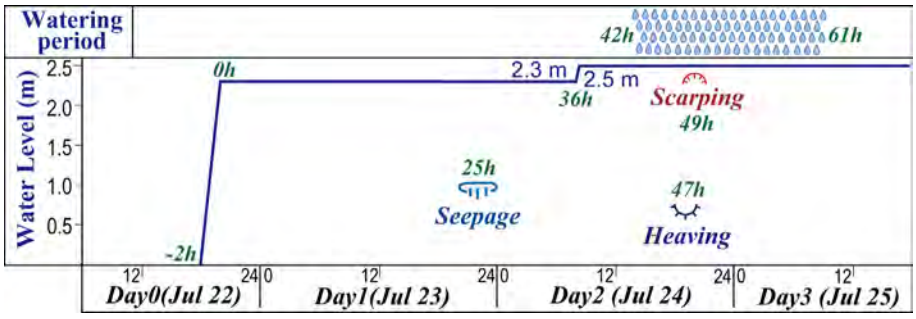

Figure 3. Timetable showing the perforated tank water level set for the infiltration, and period of surface watering. Major surface events were also plotted at times of occurrence.

4-m long scarp at the slope shoulder in the sprinkled zone at about *49h*. The scarp spread and soon connected with the heaved portion to form a thin slide block about 4 × 6 m as shown in **Fig. 4**.

The water level changes observed at gauging wells within the model levee, resulting from infiltration from the perforated tank are shown in **Fig. 5**. Values on the water level curves denote the elapsed times beginning from 20:00 July 22 when the water table in the tank was set to 2.3 m. Data in the figure indicate that the water level in well 1 (*GW1)* rose immediately in response to the 20-cm rise in the tank water level. Water levels in wells 2 and 3 (GW2 and GW3) rose characteristically just after surface watering started at *42h*. Water levels in the slope decreased slightly after *48h* or *Day 2*, 20:00 when surface failure had become obvious.

Figure 4. Surface failure caused by combined seepage and surface watering loadings.

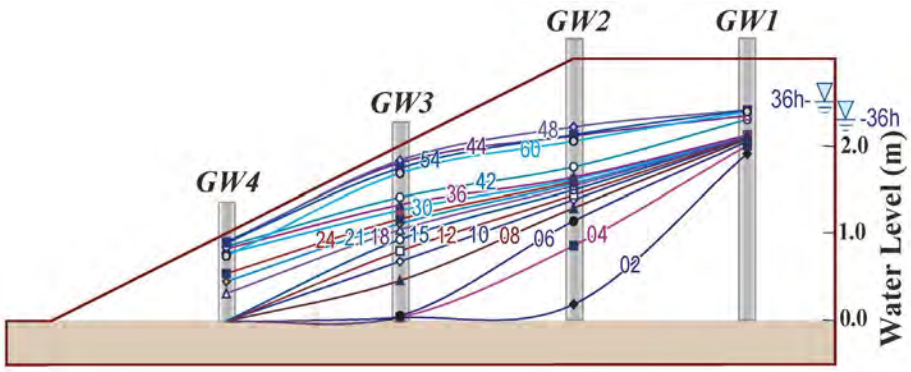

Figure 5. Water level changes in the levee body during the experiment. Values on the levels denote elapsed time beginning from 20:00 July 22.

Time-lapse Geophysical Monitoring

Outline

Besides pressure gauges set in the gauging wells, water levels were measured by means of manometers embedded at the bottom of the model. The water levels measured by manometers agreed with those measured using pressure gauges. Measurements were taken at 1-hour intervals, for a total of 70 readings. Time-lapse measurements of surface resistivity along a line set on the slope shoulder; resistivity tomography between vertical arrays inserted in the model levee; surface topography scanned by means of a 3D laser scanner; and surface temperatures measured by infrared thermography were also gathered. Measurement parameters and total measurements for each of these are listed in **Table 1**.

Surface Resistivity Imaging

Time-lapse surface resistivity imaging was conducted along a line set at the slope shoulder, 0.4 m from the crest margin (**Fig. 2**). Thirty-seven steel stakes were planted along the line at 50-cm intervals to form the electrode array. We used an automated electrical scanner (AES light) which could control up to 64 channel electrodes with 220 VDC maximum applied voltage, and 100 mA maximum transmitting current. It took about 17 minutes to finish a total of 170 measurements down to 2.5 m, and the elapsed time was set to 1-hour intervals.

Table 1. Monitored variables and measurement parameters.

Variable	Equipment	Measured Points	Number of Measurements
Water Level	Pressure Gauge	4	70
	Manometer	24	51
Resistivity	Surface Electrode	37	66
	Array Probe	61	66
Deformation	Laser Scanner	600 x 300	71
Temperature	IR Thermograph	160 x 120	140

Figure 6 compares inverted resistivity profiles (left) obtained before and during the surface watering, and maps (right) showing change rate of resistivities obtained by comparing each profile with data from its original state measured at *Day 0*, 18:00. A roughly flat pattern in the resistivity profile with larger decreases in the lower part of the variation map for *Day 2*, 12:00 indicates uniform infiltration over the model levee. Note that resistivity at the surface decreased caused by the surface watering in the central section. The decreases in resistivity caused by watering are more clearly visible in the change rate maps. In particular, after the beginning of surface watering (*Day 2*, 14:00), resistivity changes became more significant in the central section as elapsed time advanced. It seems that tongues of low surface resistivity extended downward, finally isolating relatively high resistivity areas in the middle by connecting to the low resistivity body at the bottom.

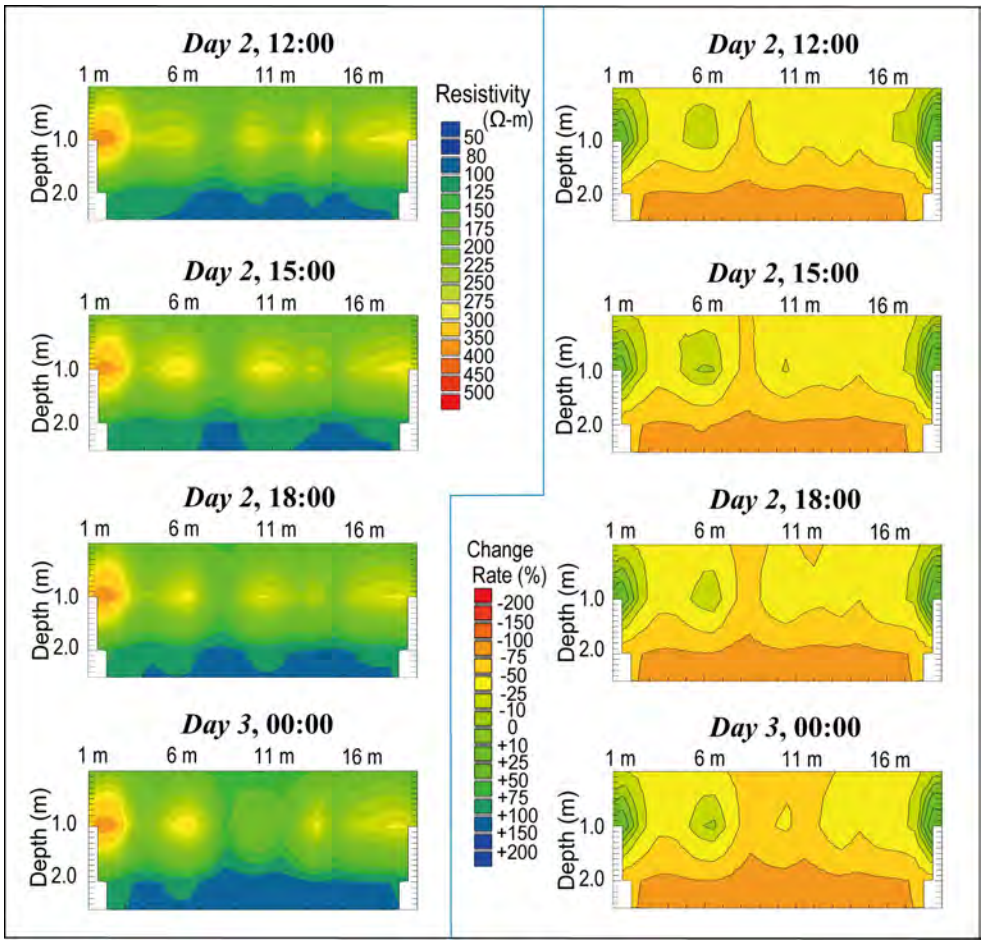

Figure 6. Inverted resistivity profiles (left) and resistivity change rates (right).

Tomographic Resistivity Imaging

We conducted time-lapse electric resistivity tomography measurements using 5 electric probes inserted in the model levee. First, slim holes were opened manually using a dynamic cone penetrometer. Next, we inserted dry-hole type electrode array probes. The probe was a 2 × 2 cm flexible rod on which button-type electrodes were plugged at 10-cm intervals. Owing to the flexibility of the probe, button electrodes properly coupled with the wall materials. Therefore, the probe was suitable for measuring resistivity even in the vadose zone. Taking the geometry of the holes (**Fig. 2**) into consideration, tomographic measurement was applied to 3 pairs of probes, P1-P2, P3-P4, and P4-P5. It took about 34 minutes to acquire data for a total of 337 electrode pairs.

The time-lapse changes in apparent resistivity measured between two holes, P3 and P4, are shown in **Fig. 7**. These two holes were located on the slope, 1 m from the shoulder to depths of 2.4 and 2.2 m respectively. The holes were 1 m apart, located in the zone that received supplemental surface watering. Data plotted in **Fig. 7** are from pairs of electrodes that were at nearly the same depth. For example, the curve labeled "3P24_4P22" displays data from an electrode pair, one 2.4 m deep in hole P3, and the other at 2.2 m in hole P4. The depths of the electrodes in hole P3 are also labeled at the beginning of the curves for convenience. The curves clearly show that the shallower electrode pairs had higher initial resistivity. This indicates that the model levee body had a water potential gradient before the infiltration began. In addition, most curves show obvious resistivity decrease over time. The trend is more distinct for the shallow electrodes. In contrast, resistivity deep in the profile decreases slightly from low initial values. These characteristic trends in resistivity strongly suggest an increase in the height of the water table in the body due to infiltration from the rear tank, but also an increase in water potential in the vadose zone.

Significant changes caused by the surface watering are also recognizable on the curves. First, a remarkable decrease occurred simultaneously with the beginning of the surface watering (*Day 2*, 14:00), followed by a slight increase, especially for shallow pairs of electrodes. Some curves also showed sudden, large rises coincident with the surface rupture event that became evident after *Day 2*, 21:00. Because no anomaly was recorded in electrode coupling resistance data at that time, the surge event was interpreted as indicative of mass movement in the body.

Squeezing of pore water in the levee body, volumetric increases in the vapor phase, or appearance of a slide zone are regarded as possible mechanisms that could explain the increase in resistivity. However, it is reasonable to assume that a compression field did not occur in our seepage failure experiment. As shown in **Fig. 6**, bodied with high resistivity remained under the watered zone. Therefore, it is possible to speculate that vapor had been trapped in the vadose zone by the surface watering, then moved upward and finally leaked out at the surface rupture event.

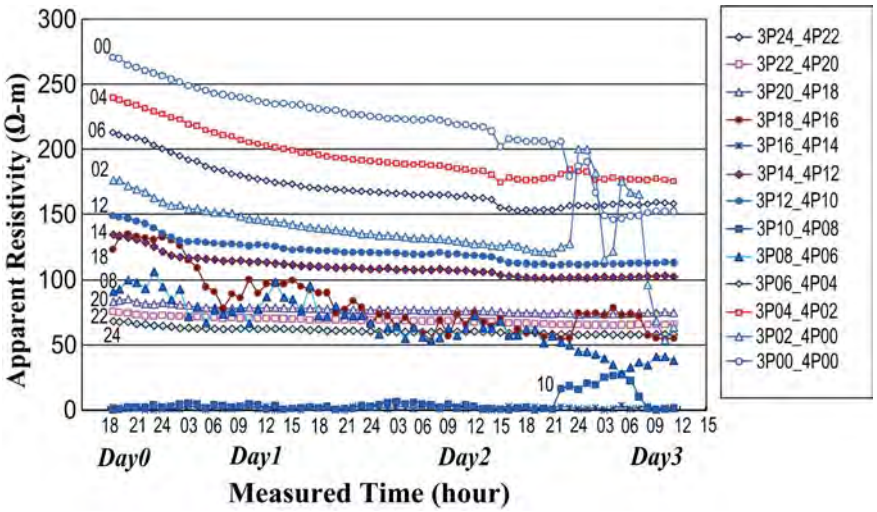

Figure 7. Time-lapse changes in apparent resistivity measured between two holes, P3 and P4. Values at the left of each curve denote the electrode depth in hole P3.

3D Laser Scanner Imaging

A 3D laser scanner (RIEGL's LMS-Z210) was used to conduct time-lapse surface topography scanning. We set the scanner 20 m in front of the model levee, and gathered 600 line by 300 pixel data covering the entire model levee slope, which took less than 2 minutes. A total of 71 datasets were obtained during the experiment. The data, originally written in polar coordinates, was converted to CSV files with Cartesian coordinates. These files were used to produce Digital Elevation Model (DEM) on a 10 × 10 cm grid for the slope surface of the model levee.

Fence sections at the central part of the slope are shown in **Fig. 8** ***(a)***: just before the surface rupture and ***(b)***: at the end of the surface rupture phase. Figures beside the fences correspond to coordinates defined in **Fig. 2** ***(b)***. The surface deformation associated with the slope rupture is shown in **Fig. 8**. The shoulder of the slope dropped more than 20 cm while, conversely, the lower part of the slope heaved more than 30 cm. The entire DEM of the entire model levee ***(c)*** demonstrates that the surface rupture occurred in the central part of the slope.

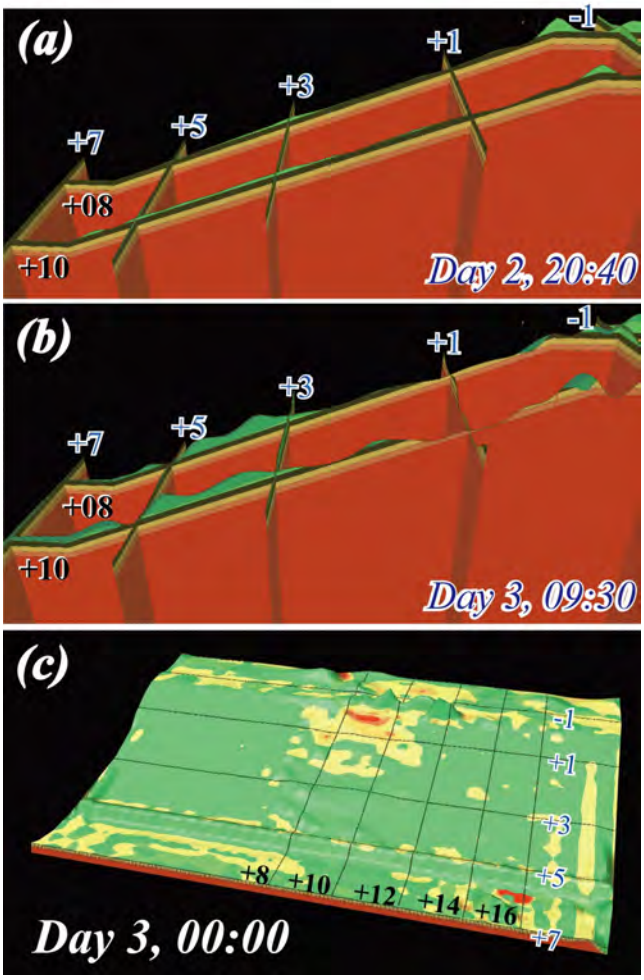

Figure 8. 3D laser scanner image just before ***(a)*** and at the end ***(b)*** of the surface rupture. Entire DEM ***(c)*** shows a scarp and depression colored red and yellow.

Infrared Thermography Imaging

Time-lapse surface temperature measurements were also conducted using infrared thermography with 160 × 120-pixel resolution. Because the test pit where the model levee had been built was open, the temperature of the levee's surface varied with sunshine, but relative changes over time or physical anomalies were detectable using thermal imaging. In fact, the leakage from the slope surface was clearly visible, as shown in **Fig. 9**. The thermal image also showed that the toe of the slope had relatively low temperatures (green). As mentioned, the surface of the slope was grassed with lawn, not covered with tall grasses. Therefore, use of thermal imaging for actual levee systems should be limited to appropriate seasons, but thermal time-lapse monitoring has the capability to detect anomalies on levees when carried out appropriately.

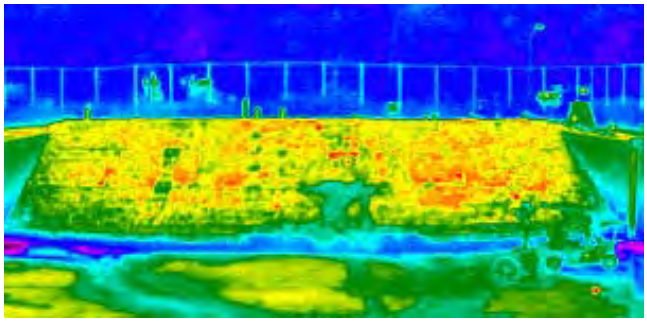

Figure 9. Infrared thermography image clearly mapping seepage low on the slope (cool colors).

Conclusions

We conducted time-lapse geophysical monitoring on a half-shaped model levee during a 4-day seepage failure experiment. As a result, resistivity changes were clearly mapped in response to an increase in water level caused by infiltration into the model levee body. Images were also captured showing specific resistivity fluctuations in the vadose zone, caused by surface watering, that were synchronized with surface rupture. In contrast, water pressure gauges did not detect any precursors or events that were simultaneous with the surface failure. The time-lapse resistivity data strongly suggested that the interaction of rising water levels caused by infiltration and gravitational flow of surface water into the levee body caused levee failure through the destabilization of the vadose zone. This emphasizes that it is essential to take into account the behavior of not only pore water but also of the vapor phase in the vadose zone for more reliable assessment of levee systems. Recently, a deformation analysis method which simultaneously considers deformation and unsaturated seepage flow has been proposed for safety assessment of levee systems. However, few field measurements were done to clarify the dynamic response of both the vapor and the fluid phase in levee bodies under high-water attack. Time-lapse resistivity monitoring, as demonstrated here, is expected to provide information useful in the development of accurate assessment methods. However, shortening the monitoring time cycle to allow measurement of more rapid fluctuations is necessary.

Acknowledgements

The authors thank Mr. Sadao Katano and Isao Takeda, of Toyo Survey and Research Inc., Tsukuba, who supported the seepage failure experiment including manual readings of manometer levels at 1-hour intervals throughout the 4-day experiment.

References

Deiana, R., Cassiani, G., Kemna, A., Villa, A., Bruno, V., and Bagliani, A., 2007, An experiment of non-invasive characterization of the vadose zone via water injection and cross-hole time-lapse geophysical monitoring, *Near Surface Geophysics*, vol. 5, 183-194.

Harry, D. L., and Koster, J. W., 2006, Time-lapse resistivity imaging of a fluvial aquifer in Columbus, Mississippi: Effects of water saturation, *Annual Symposium of Environmental Engineering Geophysical Society (SAGEEP2006) Expanded Abstracts*, CD-ROM, 9p.

Inazaki, T., 2005, Measurement of change in S-wave velocity of near-surface ground using a small seismic cone array, *Proceedings of Society of Exploration Geophysicist 112th Meeting*, 153-156. (*in Japanese with English abstract*).

Inazaki, T., 2007, Integrated geophysical investigation for the vulnerability assessment of earthen levee, *Annual Symposium of Environmental Engineering Geophysical Society (SAGEEP2007) Expanded Abstracts*, CD-ROM, 8p.

Inoue, K., Nakazato, H., Kubota, T., Nakanishi, N., and Takeuchi, M., 2006, Resistivity monitoring for groundwater recharge test in Shirasu plateau, *Proceedings of Society of Exploration Geophysicist 114th Meeting*, 117-118. (*in Japanese*).

Lei, X., and Xue, Z., 2009, Ultrasonic velocity and attenuation during CO_2 injection into water-saturated porous sandstone: Measurements using difference seismic tomography, *Physics of the Earth and Planetary Interiors*, vol. 176, 224-234.

Lumley, D. E., 2001, Time-lapse seismic reservoir monitoring, *Geophysics*, vol. 66, 50-53.

A CASE STUDY OF SELF-POTENTIAL DETECTION OF SEEPAGE AT THE JUNCTION OF TWO EMBANKMENT DAMS

Linda Armelle Nzumotcha Tchoumkam, Ecole Polytechnique, Montreal, Canada
Michel Chouteau, Ecole Polytechnique, Montreal, Canada
Bernard Giroux, INRS, Quebec, Canada
Patrice Rivard, Université de Sherbrooke, Sherbrooke, Canada
Kaveh Saleh, Hydro-Quebec, Varennes, Canada
Alain Côté, Hydro-Quebec, Varennes, Canada

Abstract

This paper deals with a case study of the self-potential (S.P.) method applied to the detection of seepage occurring at the junction of two embankment dams. We took advantage of the controlled progressive emptying of the upstream reservoir to monitor changes of S.P. together with changes in water level. Seepage flow rate was also monitored. DC resistivity tomography was used to control changes in electrical resistivity. Repeated measurements in time with dual non-polarizable electrodes before the outset of the experiment showed that the repeatability of the measurements is better than 3 mV. The mapping of the electric potential showed an upstream low and a downstream high as expected. We have computed the effective electrokinetic coupling coefficient from the variation of potential with water level and flow rate. Horizontal gradients of potential were computed to display directions of preferential flow through the dam.

Introduction

Amongst the mechanisms that causing the presence of self-potential in the ground, the electrokinetic or electrofiltration effect (also called streaming potential) could be the foundation of the most promising tool to detect water flow in the environment. The self-potential (S.P) method is based on the measurement of the natural electric potential occurring within the subsurface. In the electrokinetic (EK) mechanism, an electrical current is generated in the presence of a hydraulic gradient that causes water flow in the ground. This process is expressed by the classical equation of Helmholtz-Smoluchowski that relates the electrical potential gradient (ΔV) to the pressure gradient (ΔP) by a cross-coupling coefficient, namely the cross-coupling EK coefficient (C). The latter depends on the microstructure of the ground.

$$\Delta V = -C.\Delta P$$

The EK potential has been recently used into a method to investigate leakage in embankment dams. Revil and Jardani (2009) give a thorough overview of the recent applications. Bolève *et al*. (2009) used S.P. to detect water infiltration and seepage in an embankment dam. They were able to model quite convincingly the potential data. Limitations are illustrated in cases presented by Salmon and Johansson (2003). They show that S.P. is not applicable with the presence of highly conductive water that leads to subsurface ground soil conductivities larger than 2.5×10^{-2} S/m.

The interpretation of S.P. data measured on dams is often obfuscated because of partial knowledge of the dam construction, material heterogeneity, unknown cross-coupling coefficient for each material (cross-coupling coefficient variability) and poorly understood leakage morphology (like piping). To validate the self-potential method as a technique to determinate seepage position and its importance in embankment dams, the technique was tested in the case of a complex dam structure,

consisting in two dams built at different times and two reservoirs. The seepage has been monitored for some time; its approximate position and flow rate are known. The information about its approximate position and depth were updated when injection tests were carried out to seal the leakage. However the construction of the dam is little known and does not comply with actual construction design of embankment dam. As S.P. anomalies present at the site can be generated by other mechanisms than EK, only the ones caused by EK would change with changes in water pressure gradients. A strategy was used to take advantage of the emptying of the dam reservoir to monitor S.P. variations.

Site description

Dam A and dam B are two embankment dams located along a channel of Saint Laurent River upstream near the Montreal area (Canada). Built respectively in 1914 and 1971, the two dams were joined by a watertight grout curtain (Smith, *et al.*, 2009). The grouting material consisted in a mixture of cement and sand. The execution of the junction between the two dams was complex and the materials used for the junction are poorly known.

Seepage flow measurements were taken downstream of dam B, east of E2 (Figure 1). The flow rate values were around 3 l/s in 1972 and increased up to 200 l/s in spring 2009. Seepage flows have been yet observed when the reservoir B is empty. The flows measured during emptying and impounding of reservoir B showed the same trend. Throughout the emptying of reservoir B, the flow rate decreased almost linearly with decrease in water level for the first two meters. Then, it tended to remain constant whatever the water level until it reached the shallowest water level of the reservoir.

Figure 1: Survey location: junction of dam B/dam A with the position of DC resistivity profiling (S1, S2, S3, A1, and A2), location of electrodes E1 to E18 and visible seepages (in blue) during the emptying and the filling of the dam B reservoir. S.P. data for electrodes E7 and E11 are shown in Figure 4.

Test Methodology and results

To display the EK effect at the junction of the two dams, S.P. measurements have been conducted during the controlled emptying of reservoir B, over four successive days. They have been complemented with two electrical resistance tomography (ERT) profiles (A1 and A2) taken during the same period of time (Figure 1).

The acquisition of the S.P. data was carried out at ground surface between roving electrodes and a reference electrode (namely E1 in Figure 1). Eighteen non-polarizable electrodes (PMS 9000 from SDEC France) were carefully installed to insure a good coupling with the ground. The electrodes were installed into holes with smooth bottoms, stabilized with sand and covered with a plastic cap at the top of the hole to prevent possible effects caused by showers, wind gusts or small animals. Tests were made to check that the measured voltages resulted from self-potential phenomenon and not from electrode wear, desaturation, poor coupling or high telluric noise. Electrodes were checked first by installing all of them on a small area at one site before and after the surveys, and measuring their potential differences. Measurements of S.P. were also performed with two parallel electrodes at every electrode site before beginning our survey. The potential data were referred to electrode (E1). At each electrode location, five S.P. values were measured using a SAS1000 Terrameter (ABEM) by integrating potential in windows of 20 milliseconds for 4 seconds total.

For each electrode, the five readings showed standard deviations from 1 mV to 3 mV. Recording at three different time of the day showed that the data was repeatable within 4 mV (Figure 2). It was noticed that between two parallel electrodes the potential is not identical at a same location. Between parallel electrodes voltage values differed by 4 to 10 mV.

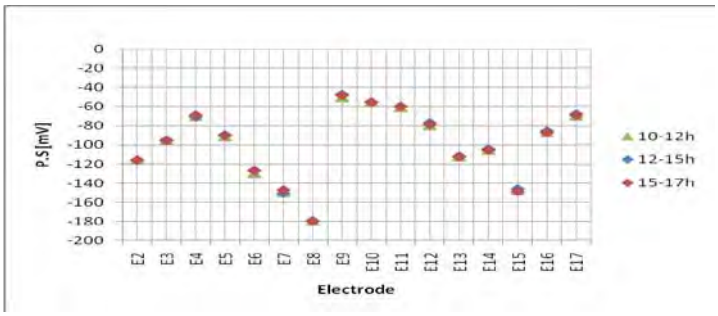

Figure 2: Repeatability of S.P. measurements observed before emptying dam B reservoir. At each electrode site S.P. data was recorded at three different times of the day. S.P. values are repeatable within 4 mV.

The potential at the junction was negative and varied between -65 mV and -165 mV depending on the water level. Its distribution pointed out an increase from the Southeast to Northwest and from Southwest to Northeast (Figure 3). In addition, the potential decreased with the water level in the reservoir, and kept a similar spatial distribution over the four successive days. A feasibility S.P. test carried out in 2008 showed similar potential distribution.

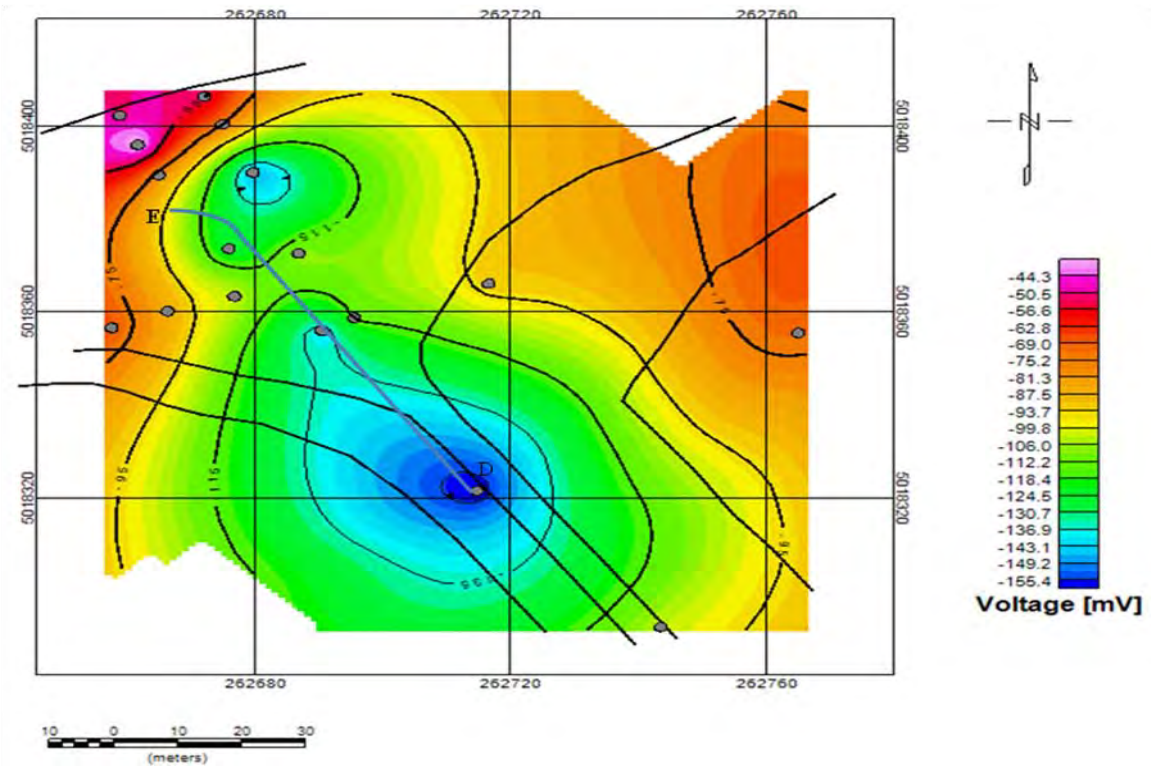

Figure 3: S.P. voltage at the junction of dams A and B for day 3 (water level~ 33.91 m). ERT profile A2 is shown (blue line D E).

S.P. variations recorded with decrease of water level in the reservoir B for the first two meters showed the same trend as the distribution of the seepage flow rate during the emptying of the reservoir. In Figure 4 (top), the flow rate measured at downstream dam B is plotted against water level for three different time periods (one impounding, spring 2009, and two emptying, fall 2008 and 2009). In the first part of the flow rate curve (level above 33.5 m), a linear relationship is found between the flow rate and the decreased water head in the reservoir, in accordance with Darcy's Law. Below 33.5 m, the flow rate became independent of the water level. The later seems to point at a constant seepage of about 22 l/s coming from elsewhere. It also indicates that the main seepage in dam B comes from a vertical location corresponding to level 33.5 m. Figure 4 (bottom) shows the S.P. data for two electrodes plotted against water level. The two electrodes E7 and E11 were in the vicinity of the junction between the two dams. It appears that the S.P. data and the water level at each electrode are linearly related above 33.5 m. At these electrode positions, an effective cross-coupling coefficient relating S.P. and water head is estimated to be 13.62 mV/m for electrode E7 and 4.83 mV/m for electrode E11.

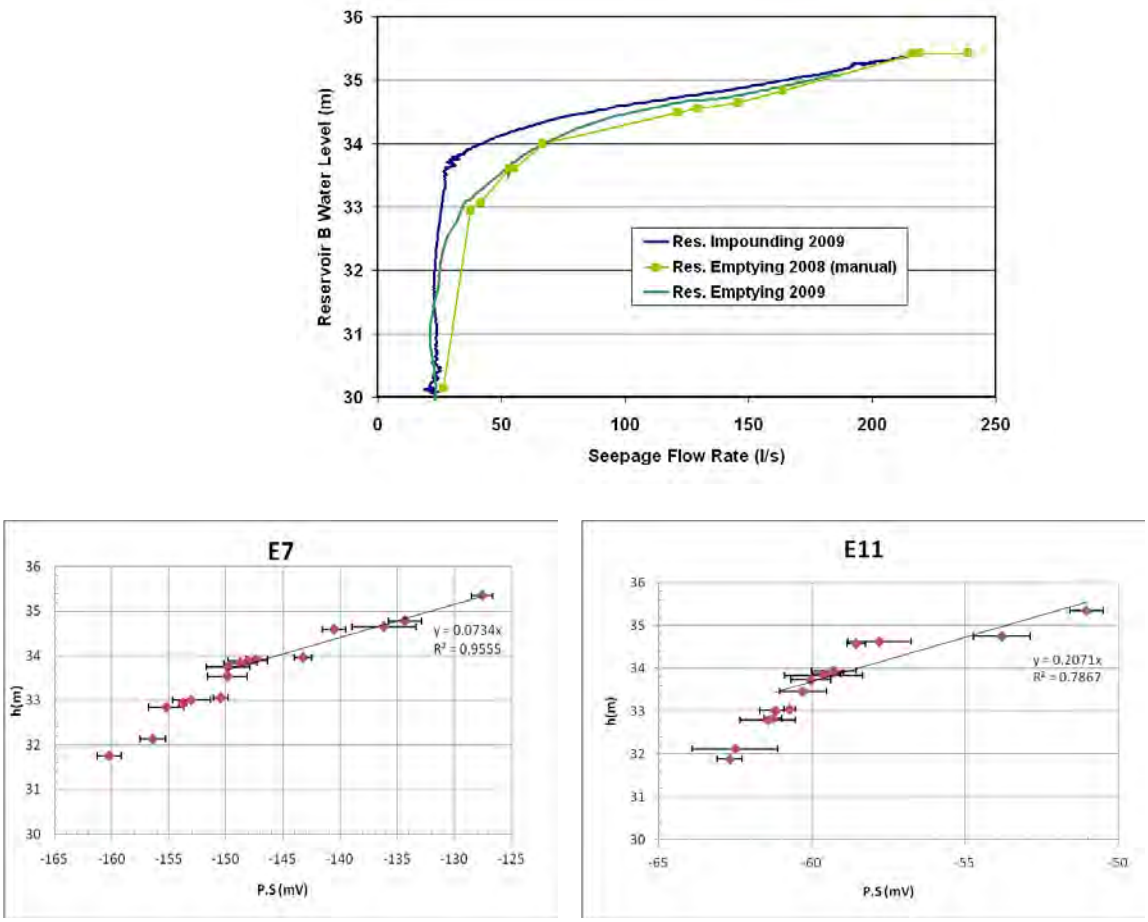

Figure 4: top) seepage flow-rate recorded at dam junction (Côté *et al.*, 2009) for three different time periods; (bottom) S.P. data observed for electrodes E7 and E17 against reservoir water level; error bars show ± one standard deviation.

The electrical resistance tomography (ERT) profiles were carried out using dipole-dipole and Wenner arrays, with spacing varying from two to four meters between the electrodes. Measurements were taken once each day. The purpose for collecting the ERT data was to map the resistivity distribution within the dam and detect structures possibly related with the seepage. Also the resistivities could be used to model the S.P. data caused by EK (see Bolève *et al.*, 2009). The data were inverted using Res2DINV. Time-lapse inversion was also performed between the first ERT data (water level ~ 34.65 m) and the latest (water level ~ 31.97 m). It indicates a variation of the resistivity in some places (Figure 5). Of particular interest is the resistive anomaly found at location x ~ -32: it is at the approximate water level 33.7 m, the level for which the main seepage appears to stop. The x location is coincident with the known upstream seepage location (see Figure 1).

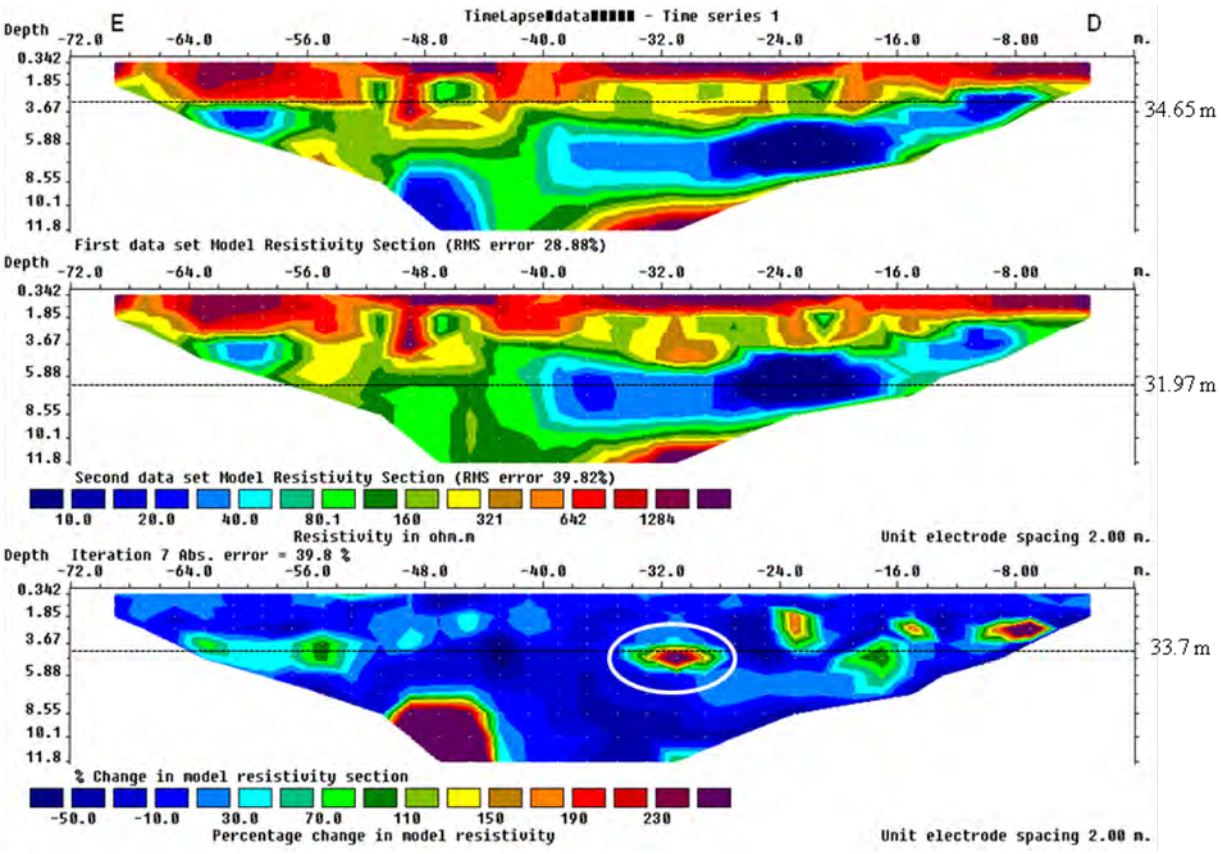

Figure 5: ERT sections for day 1 and day 4 (top and center) and time-lapse section (bottom) for profile A2 (Line DE in Figure 3). The horizontal lines show the water level at 34.65m for the first data, 31.97 m for the fourth data (middle), and the level 33.7 m on the time-lapse. On the latter, a resistive anomaly (>230% resistivity change) occurs at x ~ -32 m at a known seepage location.

In addition to the S.P. variation with water level, the lateral variations of the S.P. field show interesting features. The lateral variation is defined in terms of horizontal gradients. The horizontal gradients are calculated in two orthogonal directions (NE and SE, parallel to the directions of dams A and B). Oasis Montaj (Geosoft) was used to grid the S.P. data at 0.5 m spacing, and compute the gradient maps. Maps were computed for five different water levels in reservoir B. They show preferential directions of seepage for each measurement point. In the maps shown in Figure 6, horizontal gradients are positive in the direction of dam A (about 1.2 mV/m) and are negative in the direction of dam B (around -1 mV/m up to 33.35m, and -0.3 mV/m below). This result suggests: a) a seepage pathway downstream of dam B and b) a change in the flow rate.

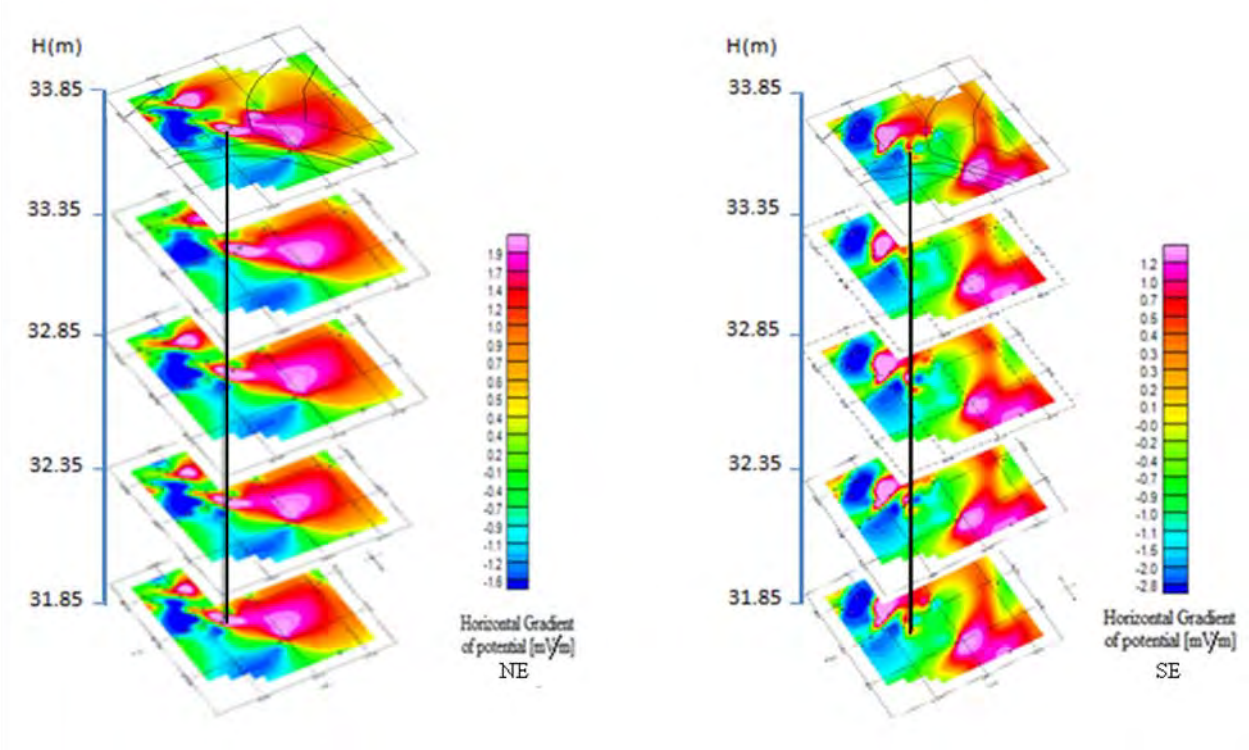

Figure 6: Horizontal gradients computed in NE and SE directions respectively (directions of dams A and B respectively). Gradient maps are shown for various water levels in reservoir B.

Discussion

The S.P. data collected before the emptying of reservoir B showed anomalies consistent with seepage with upstream inlet located between electrodes E7 and E8 (see Figure 1). We must be very careful to jump to conclusions since S.P. anomalies on the dam can be caused by other sources. Only anomalies caused by EK would be flow pressure dependant. Therefore, noting changes of S.P. anomalies with changes in water level is a definitive way to display seepage. As the water level decreases, pressure and seepage flow rate should decrease accordingly and potential differences between seepage inlet and outlet should also decrease. Maximum horizontal gradients of S.P. data delineate water flow direction. Care must be taken however as heterogeneities in material (and consequently in the EK coupling coefficient) may mask the real seepage path. Accurate computation of horizontal gradients necessitates a denser sampling on a larger area that was made available in this survey. We anticipate carrying out a S.P. survey using a larger number of non-polarizable electrodes next spring during impounding of reservoir B. Results will be compared with present survey.

Effective coupling coefficients measured on the dam (4 - 14 mV/m) appear somewhat larger than the one noted by Suski *et al.* (2004) for sand (2.8-3.8 mV/m). However, the coupling coefficients depend on the dam material as well as on the water conductivity and temperature. At the time of the survey the water temperature was 8°C and its conductivity 1.94×10^{-2} S/m. Material from various depths was collected during the drilling program performed for injection in the seepage zone. Their EK coupling coefficients will be measured in the laboratory with a system very similar to the one described in Suski *et al.* (2004). Those coupling coefficients will be used to compute the S.P. response of the known seepage in the dam and its variations with water level changes using a code similar to the one presented by Bolève *et al.* (2009).

Figure 4 (top) shows that the seepage flow rate is linearly dependant on the water level down to about 33.5 m. Below this level, the flow rate is more or less constant to 20 l/s. We believe that they are two sources for this seepage. The main one is mapped by the S.P. anomaly and is located between electrodes E7 and E8 on the upstream side; the secondary source for the 20 l/s flow rate could be either a seepage running NE along dam A and then south-east, or a permanent small seepage through dam B at its foot, or drainage (in the ditch where the flow rate is measured) of the land located downstream just below dam B.

Conclusion

Time-lapse S.P. measurements during emptying of the dam reservoir allowed mapping the main seepage location. Effective EK coupling coefficients were estimated and could be used to predict S.P. anomaly. Seepage seems to be caused by two sources: a main one in the vicinity of electrodes E7 and E8 and a secondary one which exact origin has to be investigated. The use of horizontal gradients computed from S.P. data is promising. However it needs a well-sampled S.P. data over the zone of interest.

Future work is underway to estimate the EK cross-coupling coefficient and to model the S.P. data in order to confirm the proposed interpretation.

References

Bolève, A., Révil, A., Janod, F., Mattiuzzo, J., & Fry, J.-J. (2009). Preferential fluid flow pathways in embankment dams in imaged by self-potential tomography. *Near Surface Geophysics , 7* (5-6), 447-462.

Côté, A., Smith, M., & Saleh, K. (2009). *Localisation of seepage in dams.* Montreal « In French : *Localisation des infiltrations d'eau dans les barrages - LIBAR.* Montréal».

Révil, A., & Jardani, A. (2009). The self-potential method: Did the Ugly Duckling of Environmental Geophysics Turn into a Beautiful Swan? *SAGEEP* (22), 795-800.

Salmon, G., & Johansson, S. (2003). Research on geophysical methods of detecting seepage and piping in embankment dams with case studies of geophysical measurements at two swedish tailings dams. *Procs. International Symposium on Major Challenges in Tailings Dams 71st Annual Meeting of the International Commission on Large Dams (ICOLD), 15 June 2003*, Montreal, Canada, 275-289.

Smith, M., Côté, A., Noel, P., & Babin, D. (2009). Characterizing seepage at the junction of two embankment dams. *Annual Conference of the Canadian Dam Association*, Whistler.

Suski, B., Rizzo, E., and Révil, A. (2004). A sandbox experiment of self-potential signals associated with a pumping test. *Vadose Zone Journal*, 3, 1193-1199.

Suski, B., Révil, A., Titov, K., Konosavsky, P., Dagès, C., Voltz, M., et al. (2006). Monitoring infiltration experiment using the self-potential method. *Water Resources Research* (42) W08418.

Acknowledgements

We would like to thank Hydro-Quebec for funding this project on seepage detection and modeling, and for giving us the authorization to present the preliminary results at the SAGEEP meeting. We would like to extend our thanks also to Danick Charbonneau (University of Sherbrooke) for managing field logistics and participating in the geophysical survey.

AIRBORNE ELECTROMAGNETIC SURVEYS BY THE U. S. GEOLOGICAL SURVEY OVER CONCEALED GLACIAL AQUIFERS, CENTRAL UNITED STATES

Bruce D. Smith, U.S. Geological Survey, Denver, CO
Jared D. Abraham, U.S. Geological Survey, Denver, CO,
Scott C. Lundstrom, U.S. Geological Survey, Denver, CO

Abstract

The U.S. Geological Survey (USGS) over the last decade has performed several airborne electrical resistivity (helicopter electromagnetic, HEM) surveys over buried glacial features that constitute major aquifers in different regions of the central United States (Figure 1). These surveys have been conducted to map geology, contaminants, and hydrogeology for groundwater studies. Glacial deposits also can contain significant aggregate resources in the United States (Langer, 2002). This paper summarizes the USGS HEM applications in three different glacial terrains. The HEM systems applied in the surveys described here used frequency domain methods that, in electrically conductive areas may be limited to mapping depths less than 60 m. The frequency range typically is from about 100,000 Hz to 400 Hz.

Discussion

The major focus of interest in concealed glacial aquifers is buried or tunnel valleys (Lundstrom, 2009; Hooke and Jennings, 2006) and how they control groundwater resources. Other glacial geomorphic features such as outwash deltas, eskers, and moraines may also constitute important local aquifers. Figure 2 illustrates the general geomorphic aspects of glacial features that can be important aquifers. One classification scheme, shown in Figure 3, for buried glacial valleys given by Russell et al. (2006) is useful to compare and contrast the three study areas. A comprehensive geophysical study of buried glacial valleys was carried out in Europe with several cooperating institutions in different countries (Burval, 2007; Weiderhold, 2009; http://www.burval.org/). This study discussed a number of study areas considered typical of buried valleys. The purpose of the BurVal project was to improve understanding of the structural and hydrological properties of deeper groundwater resources found in buried glacial valleys. The North American and European studies suggest a methodology that could lead to the development of spatial planning strategies that take these glacial groundwater reservoirs into account.

The first helicopter survey in Berrien County, Michigan (box 1, Figure 1), conducted by the USGS in 2001 (Duval et al., 2002) consisted of electromagnetic (EM), total field magnetics, and radiometric measurements. The objective of this study was to geologically map the sequences and characteristics of glacial deposits (Stone, 2001). The glacial features here consist mostly of moraines, and deltaic, and glacial lake sediments. The general geology consists of Holocene deposits some of which are younger Lake Chicago deposits covering deltaic deposits. The glacial material overlays electrically conductive Paleozoic shale. EM measurements from this survey had high electrical and system noise that precluded computing resistivity depth sections along the flight lines. However, the

apparent resistivity maps were used to refine the geological map of the glacial stratigraphy. The new mapping was based on the correlation of low-resistivity anomalies associated with silts and clays and higher resistivity anomalies associated with sands and gravels. A second helicopter EM (HEM) survey was flown in 2002 using a system that was less susceptible to powerline noise. That instrumentation had less system noise but the power line noise still interfered with measurements in some areas. The data from the 2002 survey were suitable for inversion, and depth sections were calculated that allowed 3D interpretations of the geology. Figure 4 shows the elevation of conductive bedrock units, which are Paleozoic shales that are also an aquitard. The higher elevations are bedrock ridges where glacial deposits are thin and which may be barriers to local groundwater flow. Figure 5 shows the geologic map superimposed on the digital elevation (top panel). The blue colors are lake sediments and darker colors are deltaic deposits. The bottom panel shows a 3D model of the resistivity constructed from resistivity depth sections along the flight lines. The coarser-grained sediment packages (sands and gravels) are the more resistive red areas. Note that their subsurface distribution trends across and under the surficial glacial lake sediments. This glacial system has poorly defined tunnel valleys such as the one shown in the outwash area in Figure 2.

An HEM survey (Figure 6) was conducted in 2004 of part of the Poplar Oil field on the Ft. Peck Indian Reservation (box 2 on Figure 1) to map subsurface saline groundwater contaminants associated with energy production (Smith et al. , 2006). Pioneer Natural Resources has undertaken an extensive remediation for one saline water plume, termed the Biere Plume (Jacobs et al., 2008). Although the objective of this HEM survey was focused on contaminants, the interpretation of glacial features was important in design of the remediation efforts. There are about 30-50 m of glacial sediments overlying the Cretaceous Bear Paw Shale. The margin of the continental glacier is marked by the Poplar River through the middle of the survey area and the Missouri River south of the study area. The HEM apparent resistivity (Figure 6) maps very conductive glacial lake sediments, silty sand units that have moderate conductivities, and cleaner sands that have higher resistivities. The conductivity depth sections shown in Figure 6 define the conductive Biere plume (feature B in Figure 6), which has a much higher conductivity than the glacial sediments. Since the plume occupies a buried glacial channel, it acts like a tracer to map the channel location in the conductivity depth sections (Figure 7). The glacial gravels mapped by this survey are like the type 3 buried glacial valleys in Figure 3. Using brine plumes as groundwater flow tracers has also been the subject of ground electrical surveys used in a USGS study of brine contamination to prairie potholes from energy development in the Williston Basin (Smith et al., 2009; http://steppe.cr.usgs.gov/). These brine plumes also can be used to interpret groundwater flow in shallow glacial features that characterize the Prairie Pot Hole region of the Williston Basin.

HEM surveys were flown in the glacial terrain of eastern Nebraska in 2007 and 2009 primarily in support of groundwater resource studies (Smith et al., 2008a and 2008b; Divine et al., 2009). Since the groundwater resources in this area are integrally tied to glacial features, the airborne geophysical surveys also demonstrate applications to subsurface geologic mapping. Four areas have been flown that represent different glacial terrains. The Oakland area, not shown here, is typical of shallow glacial sands within a thick, electrically conductive till. Buried glacial valleys and pre-glacial channels that are incised into the bedrock (type 2 in Figure 3) are beneath the depth of HEM mapping. The Ashland area, also not shown here, contains a partially exposed ancestral Platte River valley (called Todd Valley) and glacial gravel deposits west of the present Platte River. Todd Valley has a complex geometry of sandy silts and gravels. Groundwater resources in the third area, Swedburg, are isolated sand bodies successfully mapped by the HEM survey and are typical of glacial outwash plains. The shallow geology of the fourth area, Firth, is a buried glacial valley complex defined in-part from interpreted transmissivity (Divine et al., 2009). The glacial features compose the Crete-Princeton Aquifer which has recently been described

by Druliner and Mason (2001). The HEM survey done in 2007 was extended in 2009 to better define the westward extension of the aquifer. Figure 8 shows the 8,200 Hz apparent resistivity map for the Firth area (Divine et al., 2009). The high resistivities correspond to sands and gravels of the aquifer and buried glacial features. The HEM data have been used to construct resistivity depth images along each flight line. The resistivity depth interpretation along each flight line has then been used to construct a three-dimensional voxel model of the eastern part of the Firth area. The glacial feature in the northern part of the block is associated with high electrical resistivities that have the geometry of a sand/gravel filled paleovalley. The additional data flow in 2009 indicates that this channel becomes more dispersed to the west. This geometry could be indicative of an outwash feature; however more geologic investigations are needed to evaluate this hypothesis.

Conclusions

Helicopter electromagnetic electrical resistivity surveys have been conducted by the USGS in different mid-continent glacial terrains for geologic mapping, contaminant mapping, and groundwater studies. The studies have demonstrated that concealed glacial feature such as buried glacial valleys, outwash sediments, and alluvial fans can be mapped using airborne resistivity methods. In areas where glacial sediments are clay rich and electrically conductive, the depth of mapping may be limited to 60 m or less using the methods in the current studies. Recently developed airborne resistivity systems (time domain EM) offer deeper penetration to 100 m or more. In addition, advances in processing and computation of resistivity depth sections may improve future applications to understanding the hydrogeologic framework of concealed glacial deposits and aquifers. These studies suggest a methodology that includes systematic airborne geophysical surveys as a tool to aid in formulating spatial planning strategies that take these glacial features into account for groundwater resources.

References

BurVal Working Group, 2007, Groundwater Resources in Buried Valleys - a Challenge for Geosciences; *http://www.burval.org/*, 308 p.

Divine, D., Steele, G.V., Smith, B.D., Ehrman, R.L., and Korus, J.T., 2009, Preliminary Results from Helicopter Electromagnetic Surveys over a Paleovalley Aquifer in Eastern Nebraska, Geological Society of America Abstracts with Programs, Vol. 41, No. 7, p. 286.

Druliner, A.D. and Mason, J.P., 2001, Hydrogeology and Water Quality of Five Principal Aquifers in the Lower Platte South Natural Resources District, Eastern Nebraska, 1994: U.S. Geological Survey Water-Resources Investigations Report 00–4155, 36 p.

Duval, J.S., Pierce, H.A., Daniels, D.L., Mars, J.C., Webring, M.W., and Hildenbrand, T.G., 2002, Aerial Magnetic, Electromagnetic, and Gamma-ray Survey, Berrien County, Michigan, U.S. Geological Open-File Report 2002-117.

Hooke R.L., Jennings C.E., 2006, Formation of the tunnel valleys of the southern Laurentide ice sheet. – Quaternary Science Reviews 25:1364–1372.

Jacobs, M., Tyrell, C., Smith, B.D., 2008, Case Study of Site Characterization and Remedial Plans for Removal of Contamination from Oilfield Produced Waters, East Poplar Oil Field, Fort Peck Indian Reservation, Roosevelt County, Montana: American Association of Petroleum Geologists, International Conference, Cape Town South Africa, Proceedings, 1 p.

Langer, W.H., 2002, An overview of aggregate resources in the United States, in Scott, P.W., and Bristow, C.M., eds., Industrial minerals and extractive geology: The Geological Survey, London, p. 17-42.

Lundstrom, S., 2009, Tunnel Valley Morphology And Sedimentary Characteristics: Constraints On Development Of Hypotheses Concerning Subglacial Geomorphic Processes: Geological Society of America Abstracts with Programs, Vol. 41, No. 7, p. 213

Russell, H.A.J., Hinton, M.J., van der Kamp, G., and Sharpe, D.R., 2006, An Overview Of The Architecture, Sedimentology And Hydrogeology Of Buried-Valley Aquifers In Canada: 57TH Canadian Geotechnical Conference, p. 26-33.

Smith, B.D., Thamke, J.N, and Tyrrell, C., 2006, Geophysical and Hydrologic Studies of Shallow Aquifer Contamination, East Poplar Oil Field Area, Northeastern Montana: Proceedings Symposium on Engineering and Environmental Geophysics Seattle WA, 16 p.

Smith, B.D., Abraham, J.A., Cannia, J.C., Steele, G.V., and Peterson, S.M., 2008a, Helicopter Electromagnetic Surveys for Hydrological Framework Studies in Nebraska: American Geophysical Union Annual Meeting, San Francisco, 1 p.

Smith, B.D.; Abraham, J.D.; Cannia, J.C.; Steele, G.V.; Hill, P.L., 2008b, Helicopter Electromagnetic and Magnetic Geophysical Survey Data, Oakland, Ashland, and Firth Study Areas, Eastern Nebraska, March 2007: U.S. Geological Survey Open-File-Report 2008-1018, 38 p, 1 plate.

Smith, B.D., Sodja, R.S., Gleason, R.A., Thamke, J.N., Preston, T., and Reiten, J., 2009, Brine Contamination To Prairie Potholes From Energy Development In The Williston Basin: A Developing Integrated Science Project: Geological Society of America Abstracts with Programs, Vol. 41, No. 7, p. 651.

Stone, B.D., 2001, Surficial Geologic Map of Berrien County, Michigan, U.S. Geological Survey Open File Report 2001 -156, 1 plate.

Wiederhold, H, and BURVAL Working Group, 2009, Geophysical Mapping Of Buried Valley Aquifer Systems: Geological Society of America Abstracts with Programs, Vol. 41, No. 7, p. 214

Figure 1. Location of airborne resistivity surveys over concealed glacial aquifers contracted by the U.S. Geological Survey. Colored areas define regional watersheds such as the Missouri River Basin shown in blue. Number boxes are areas investigated with airborne electrical resistivity surveys and are discussed in text: 1) Berrien County, Michigan, 2) Ft. Peck Indian Reservation, Montana, 3) eastern Nebraska groundwater studies.

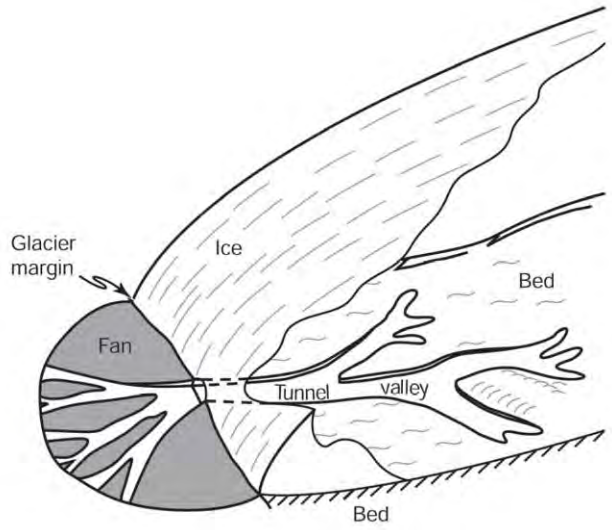

Figure 2. Generalized 3D diagram of a tunnel valley and geomorphic features that can be associated with glaciers (Hooke and Jennings, 2006).

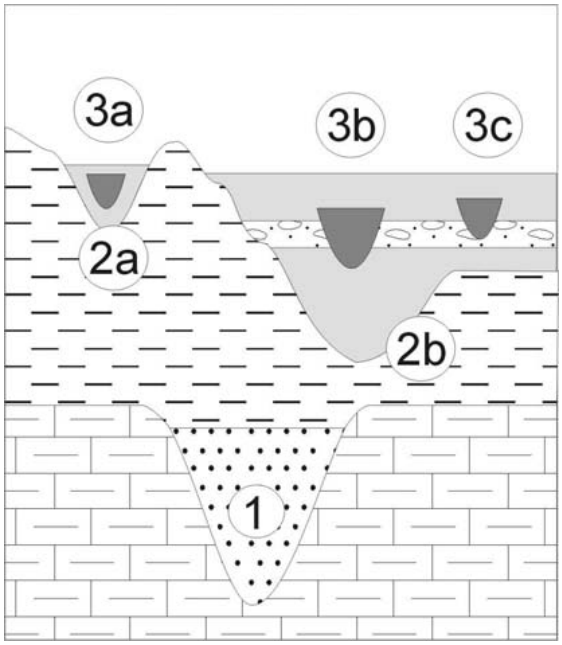

Figure 3. Schematic illustration of valley type: 1, bedrock; 2a, partially filled bedrock incised valley; 2b, buried bedrock incised valley; 3a, Quaternary sediment buried valley nested in a partially infilled bedrock valley; 3b, Quaternary sediment valley breaching regional aquitard; 3c Quaternary sediment valley that only partially erodes the aquitard (Russell et al., 2006).

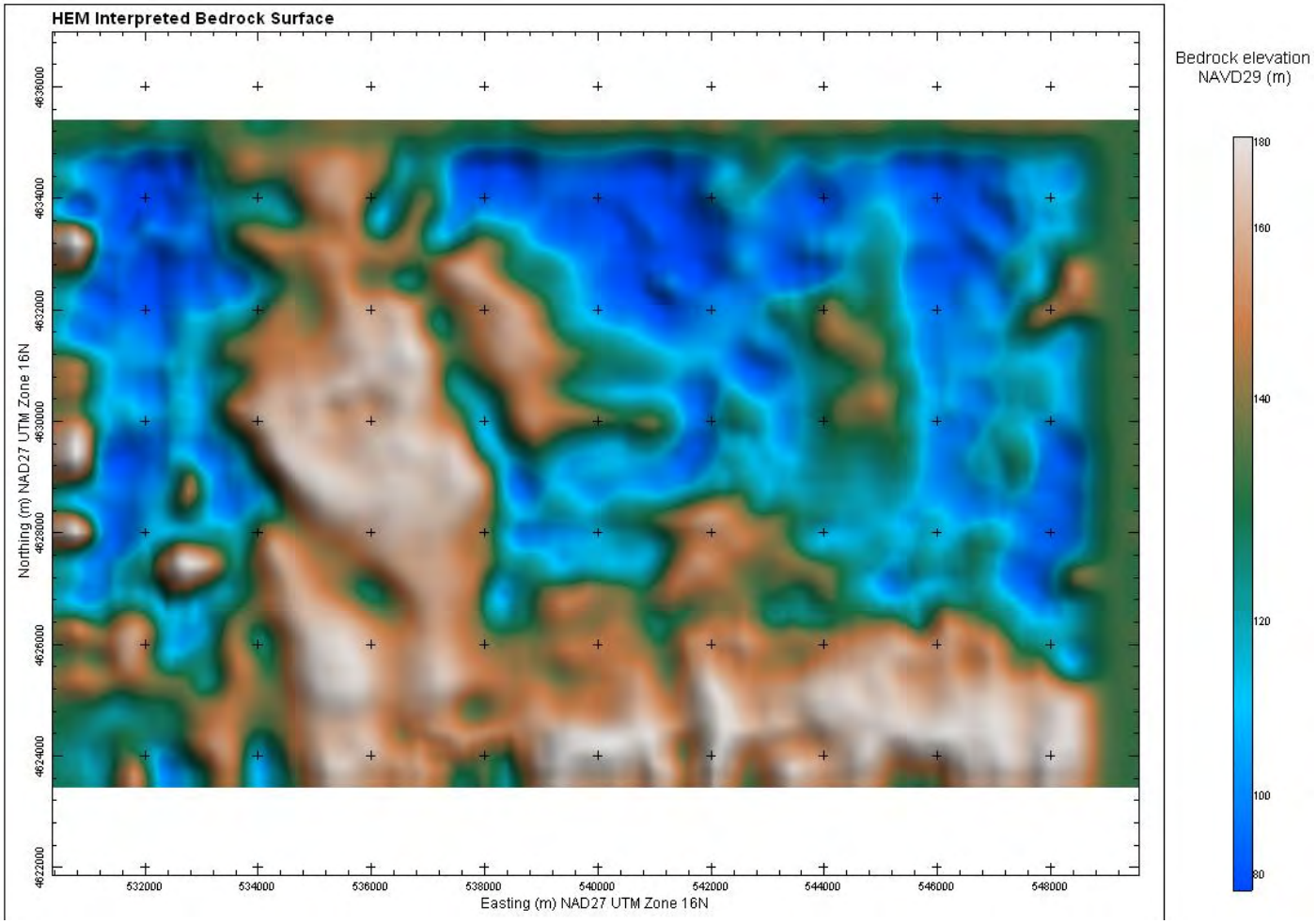

Figure 4. Bedrock elevation map where cooler colors indicate thicker glacial deposits. The elevation has been estimated from the depth of conductive bedrock determined from resistivity depth sections along flight lines. See also Figure 5.

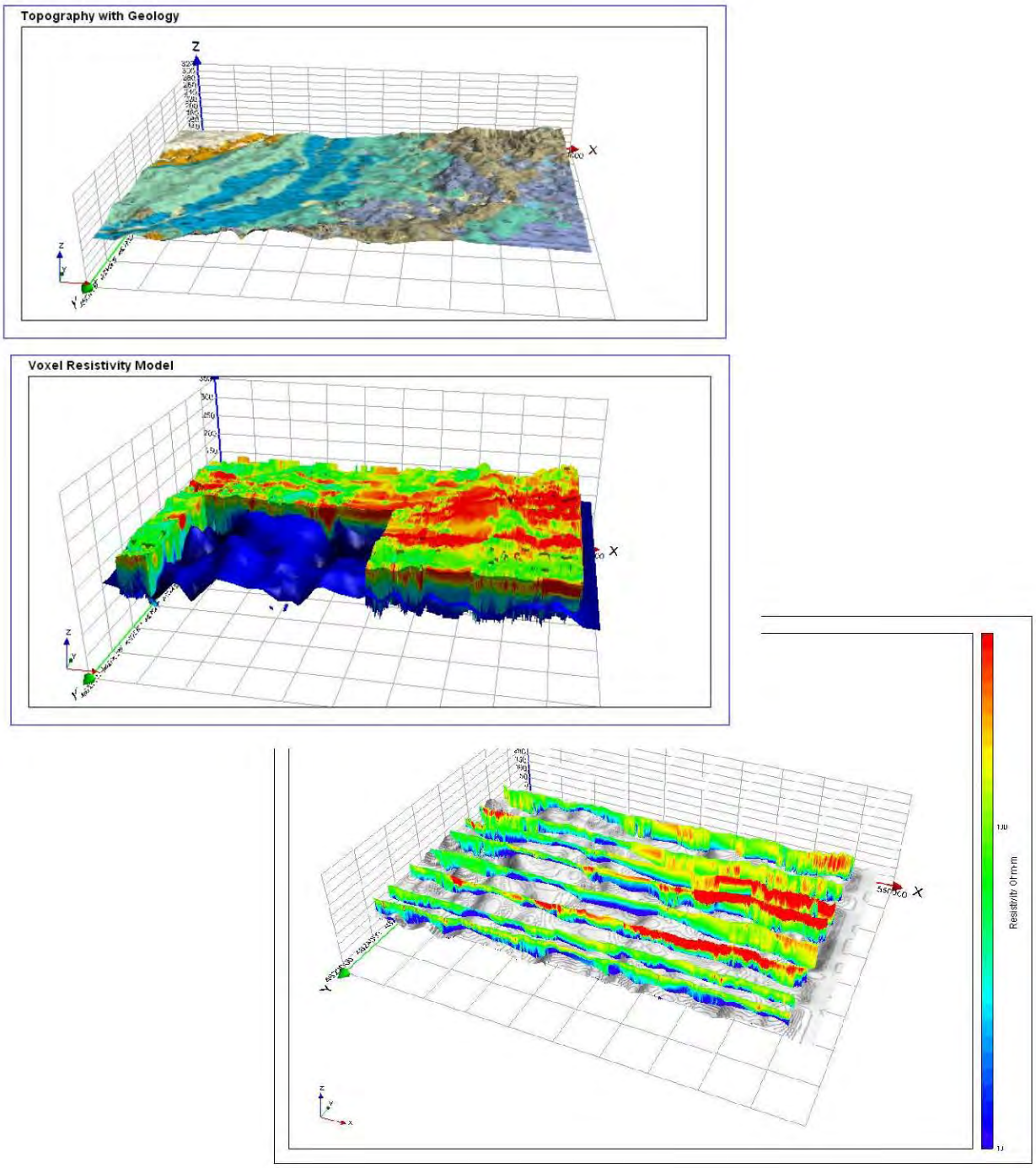

Figure 5. Resistivity depth section interpretation along flight lines: a) geology superimposed on digital elevation, b) 3D voxel model from flight-line resistivity depth sections (shown in c) where the deep blue color is the electrically conductive basement for the glacial sediments, and c) resistivity depth sections along flight lines.

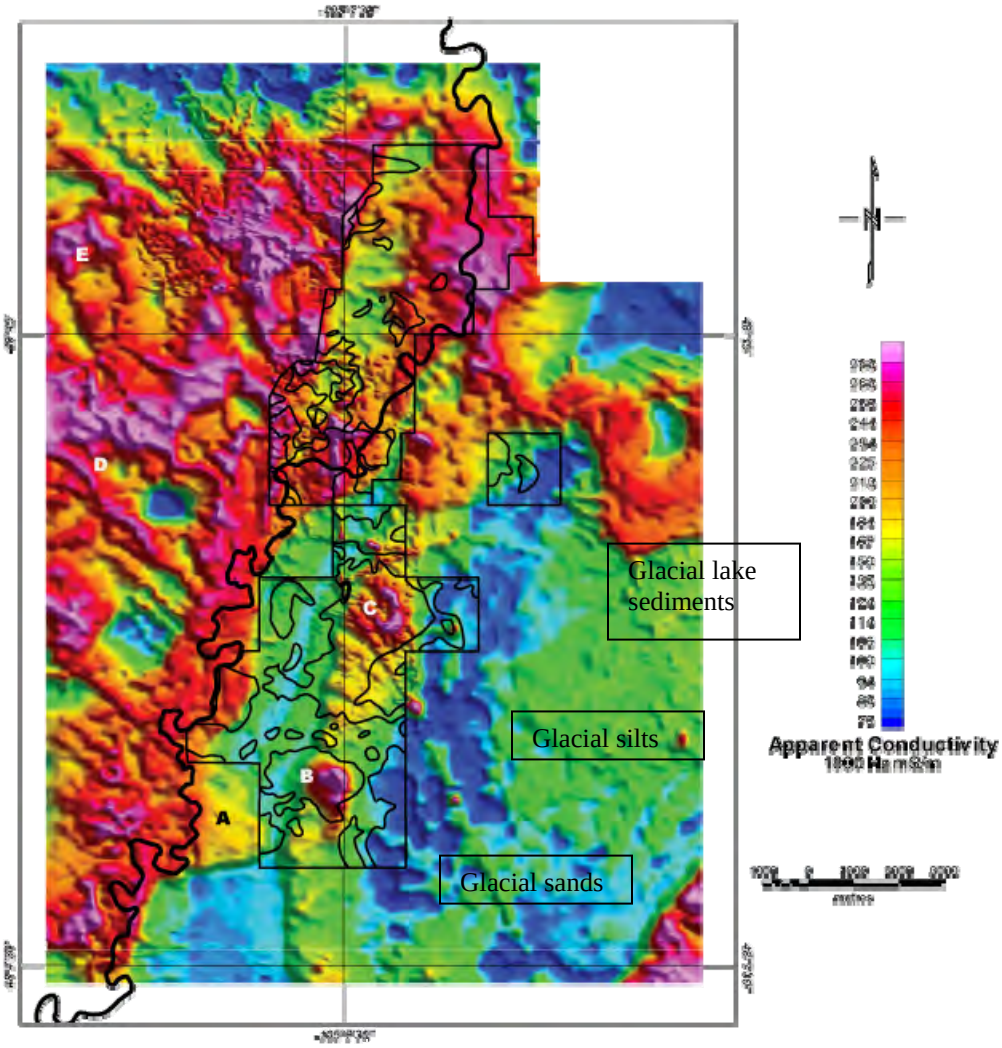

Figure 6. Apparent conductivity (mS/m) for 1,800 Hz. Note that conductivity scale is inverse of resistivity color scale so conductive areas appear red. Heavy black line is the Poplar River. Light black lines outline features identified as probable oil field contamination. Area A is a paleo-stream meander, B is the Biere produced water plume conductive area, C is a pipeline, D is an incised drainage exposing Bearpaw Shale, and E is an area of salinization. Glacial tills occur east of the Poplar River. Glacial sands are resistive blues in this color scale.

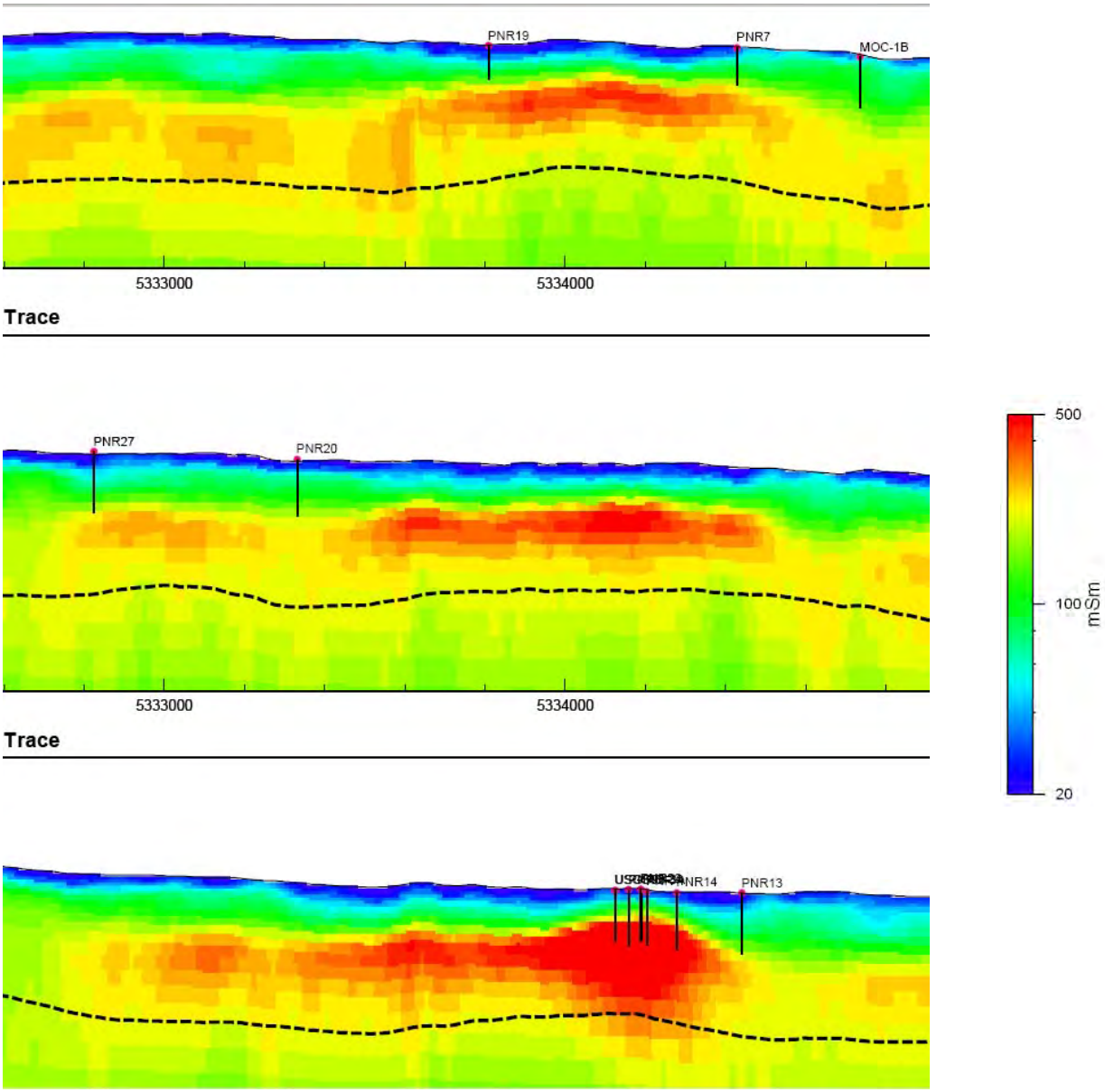

Figure 7. Conductivity depth sections through the Biere Plume with locations of drill holes shown by vertical black lines and with the estimated depth of mapping shown by the dashed line. The depth of the sections is 60 m. The bottom profile is through the center of the conductive plume (anomaly B in Figure 6). The profiles above this are successive flight lines 200 m apart going west. The east-to-west change in position of the plume follows a gravel channel suggested from drilling.

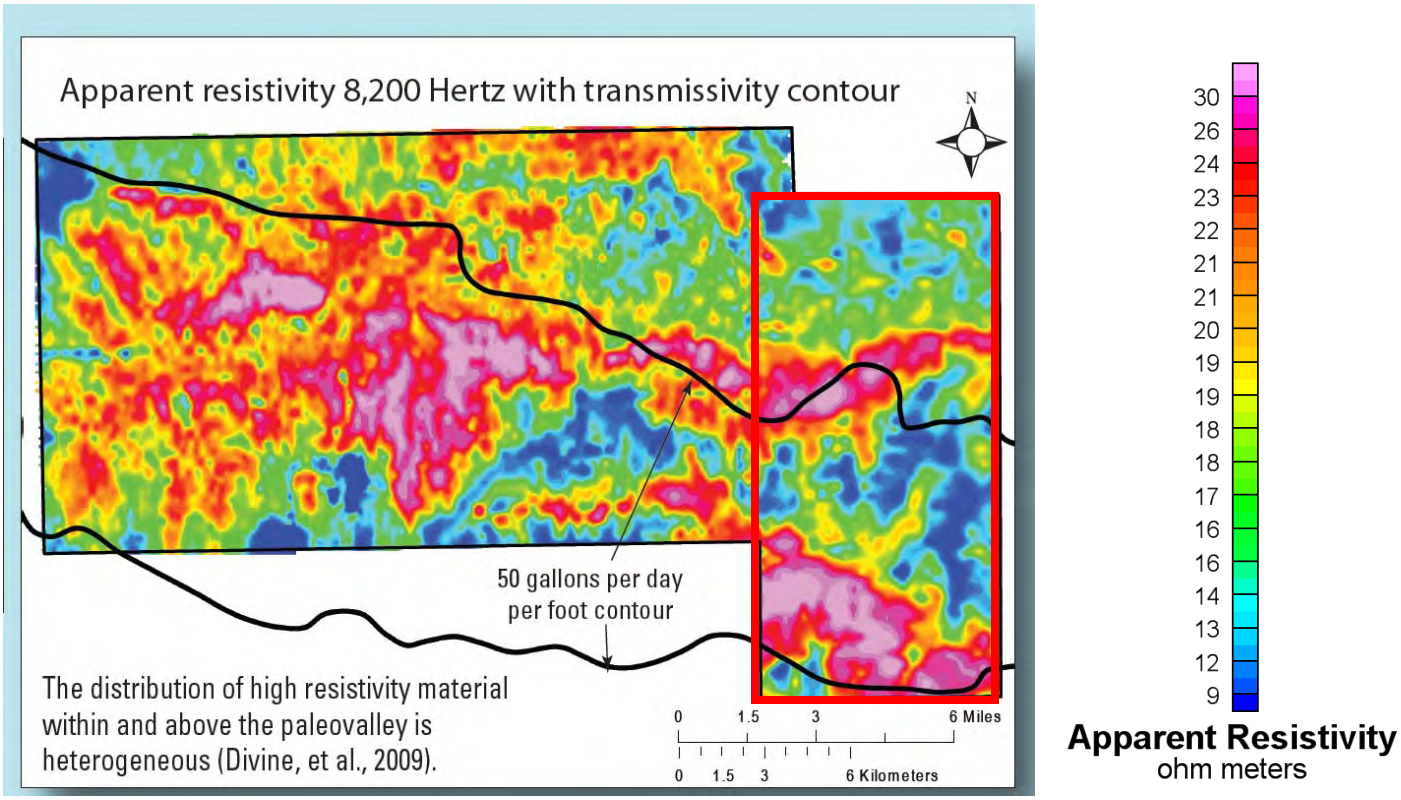

Figure 8. Apparent resistivity map for 8,200 Hz for the Firth area. The red box is area flown in 2007 and the area to the west was flown in 2009. The transmissivity contour is taken from water well data.

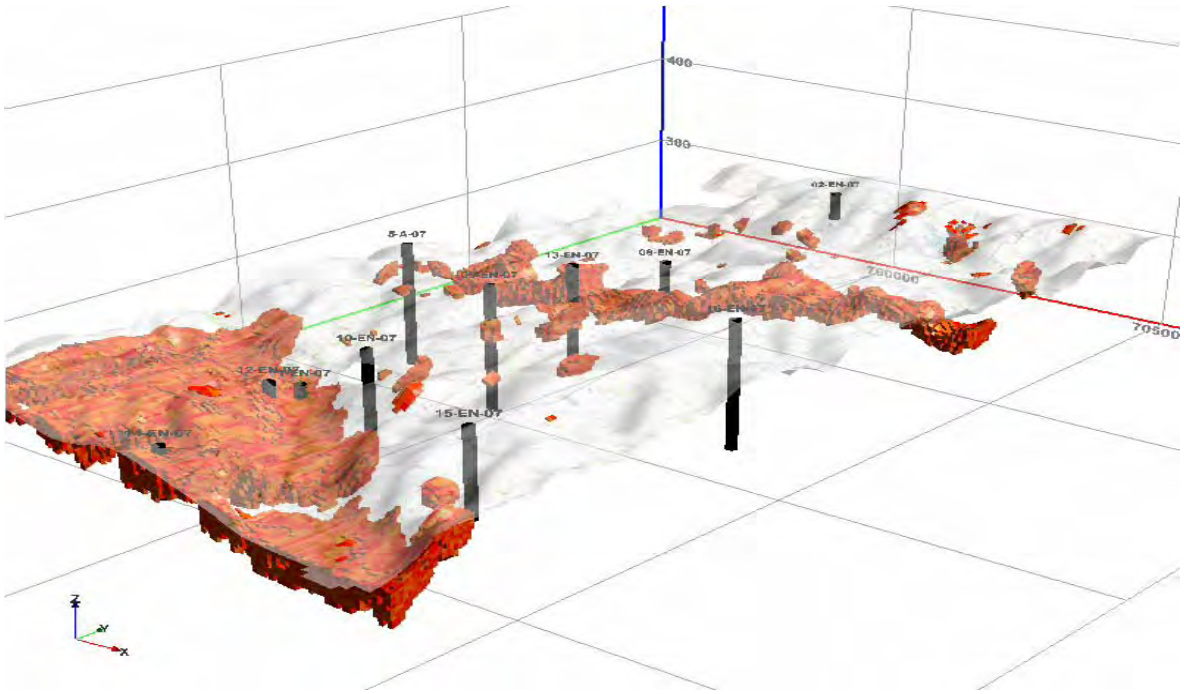

Figure 9. Three-dimensional voxel model for the eastern part of the Firth area (red box in Figure 8) showing resistivities higher than 25 ohm meters. The model has been constructed from inversion of HEM data along flight lines to resistivity depth sections. Black vertical lines are water resource study wells drilled before the airborne survey.

AIRBORNE ELECTROMAGNETIC SYSTEMS AND THEIR ENGINEERING AND ENVIRONMENTAL APPLICATIONS

Dima Amine, Fugro Airborne Surveys, Mississauga, Ontario
Greg Hodges, Fugro Airborne Surveys, Mississauga, Ontario

Abstract

Airborne geophysical surveys have been used in the mining industry for over 50 years as a standard part of exploration programs (Fountain, 1998). Only recently have airborne geophysics surveys been used to help solve engineering and environmental problems.

Introduction

All electromagnetic (EM) airborne systems work using the same basic principles. A primary field is transmitted which induces electrical currents in conductive material. These currents are shifted in time from the primary field, and generate a secondary EM field which is detected at the receiver. These measurements are generally divided into in-phase (the component in phase with the primary field), and quadrature (the component out-of-phase to the primary). EM systems must also deal with the very strong primary field at the receiver.

Most of the induced electrical currents concentrate in conductive layers in the ground, making them distinguishable. Resistive layers are harder to detect since the induced currents will flow around, above and below the layer. Unless the layer has significant thickness the change in current distribution can be hard to detect. Thickness of layer and contrast to surrounding rock also play an important role in distinguishing layers. Electrical current measurements are then calculated into conductivity values which can be associated with different material types, (Figure 1).

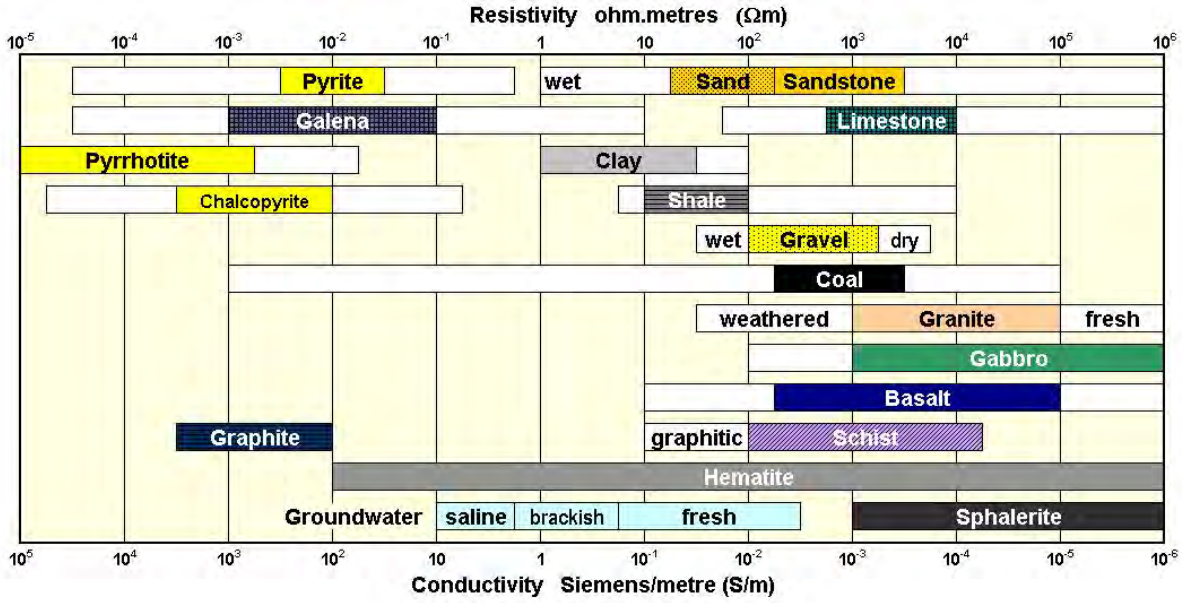

Figure 1. Conductivity / resistivity of common rocks and minerals (modified from Palacky, 1987).

Airborne Electromagnetic Systems

Within the airborne electromagnetic industry there are a variety of systems by different providers, all of which can be classified as either helicopter or fixed wing and frequency or time domain. Fugro Airborne Surveys provides frequency-domain electromagnetic (FDEM) systems on helicopter platforms and time-domain electromagnetic (TDEM) systems on both helicopter and fixed wing platforms. Offering this variety of EM systems allows for a full range of sensitivity to different targets at a wider range of depths of exploration.

Most of the electromagnetic theory for geophysical application was developed in the frequency domain, but in recent years time domain systems have become increasingly important. Table 1 below shows most of the industry AEM systems.

Table 1: Commercially available airborne electromagnetic systems.

Platform	**Frequency Domain Electromagnetics**	**Time Domain Electromagnetics**
Helicopter	DIGHEM, RESOLVE, Hummingbird, IMPULSE/GEM	HeliGEOTEM, VTEM, AEROTEM, SkyTEM,THEM
Fixed Wing	GTK, Hawk	MEGATEM, GEOTEM, TEMPEST, GENESIS

The depth of exploration of a system is a complex determination, dependent on target, frequency, system power and noise, and geological noise. A rough approximation for standard data processing (not including inversions) for a layered earth is about 3/4 skin depths. Under ideal conditions, with inversions, the depth of exploration can extend to 2 skin depths. The skin depth is defined as the depth at which an EM field is reduced to 1/e of the surface value, and is calculated from:

$SK = 503 (\rho / f)^{1/2}$ *where* ρ *is the resistivity, f is the frequency.*

Standard helicopter electromagnetic (HEM) systems used for mineral exploration have both CX (coaxial- horizontal dipole) and CP (coplanar - vertical dipole) transmitters and receivers. These are designed to complement each other in providing geometric information and maximum sensitivity to a variety of geometric shapes. This combination of coil pairs is possible with frequency domain systems because of the high sensitivity to the discrete frequencies, and subsequent small size of the transmitter coils. Time domain EM systems require much larger transmitter coils, and it is extremely difficult to drag such a coil through the air with the plane of the coil vertical (dipole horizontal). For detection of conductive mineralization, the dual coplanar and coaxial (horizontal dipole) configuration provides the best measure of the conductive target geometry. The coaxial coils have a much narrower anomaly over moderate-to-steep dipping dike-like conductors and line-source conductors, providing better discrimination and interpretation of multiple targets. The lower sensitivity of coaxial coil pairs to near-surface horizontal (overburden type) conductors gives the coaxial coil pair a significantly greater depth of exploration in areas with a complex variety of overburden and bedrock conductors.

Frequency Domain Electromagnetic

Frequency domain electromagnetic (FDEM) transmit a continuous harmonic EM signal (the primary field) and the response of the earth is seen as modification in strength and phase of the field as well as by directional distortions as a result of a secondary field. Frequency-domain EM systems measure the secondary in the presence of the primary field by electronically or digitally removing or "bucking" the primary signal at the receiver. The conductivity (resistivity) of the ground is measured by the change in amplitude and phase of the secondary field. As the ground becomes progressively more resistive, the phase angle increases (more quadrature) and the amplitude decreases.

Fugro's RESOLVE and DIGHEM systems offer a frequency of 390 Hz – 137,000 Hz with a depth of exploration to 150 meters in ideal resistive environments. The RESOLVE system has five coplanar frequencies and one coaxial making it ideal for mapping horizontal layers. The DIGHEM systems, however, have 3 coplanar and 2 coaxial coils, making it sensitive to geometry and ideal for mapping vertical conductors.

Time Domain Electromagnetic

With the time-domain (TDEM) system, the primary field is transmitted as a series of pulses of various shapes. The same time-shift of the secondary field described in frequency domain EM can be observed as transients, or decaying fields, during the off-time between primary field pulses. Measurement during the off-time only avoids the problem (described for frequency domain systems) of measuring the weak secondary field in the presence of the strong primary field. This limits measurements to only the quadrature component of the secondary field, and reduces the sensitivity to very highly conductive targets.

Measuring the earth response during the primary field on-time is possible if the receiver can be placed such that the primary is reduced by null-coupling the receiver from the primary field, or by placing the receiver sufficiently distant (to reduce the primary strength) that both the primary and secondary fields can be measured together. Measurement of the secondary field in the on-time extends the sensitivity of the system to both weak and strong conductors. In any case, the strength of the primary is still too strong, and too variable, to allow measurement of the in-phase component of the response.

The time domain approach is better in areas of high surface conductivity such as many parts of Australia. Finite time windows can be used to evaluate the response of the host rock, the overburden and the target.

Fugro's TDEM HeliGEOTEM system uses a half-sine waveform, measures on-time, and has a multi-coil receiver with X, Y, and Z components. With a peak dipole moment of 1.2 million Am^2 it has a depth of exploration of 500 meters in ideal resistive environments. Fugro's array of fixed wing airborne systems have a range of dipole moments from 55,800 Am^2 up to 1.57 million Am^2. These utilize a variety of waveform frequencies and pulse widths.

Engineering and Environmental Examples

Resolution is a function of flight altitude and system footprint. The smaller footprint of the RESOLVE and DIGHEM HFEM systems and low level flying altitude provides better near surface resolution. The GEOTEM, TEMPEST and MEGATEM fixed wing electromagnetic systems provide fast coverage of larger areas and deeper depth of penetration. Conductivity variations in the soil can be linked to different soil types or water content. Saline water will have a higher conductivity then fresh water and these changes can be mapped from the air. Soil types may also be distinguished in areas of

interest. The following will briefly discuss some examples of AEM systems being used to provide complete subsurface mapping for a variety of applications.

Groundwater study using time domain data

In 2002 a TEMPEST time domain fixed wing survey was flown over 160 km^2 in the United Arab Emirates. The goal of the survey was to find freshwater for irrigation. Figure 2 below is a plan view of the near surface 9 ohm-m resistive zone as interpreted to contain fresh water based on higher resistivity. The extent of the aquifer was outlined with a solid line, and the dashed lines highlight the stronger, thicker zones. Figure 3 is a water quality contour map supplied by the client showing the total dissolved salts obtained by analyzing groundwater samples from boreholes. The shape of this resistive zone is generally in good correlation with the 3,000 ppm salinity contour in the central and southern part of the area as shown in Figure 3. Overlaying the aquifer outline from Figure 2 on Figure 3 shows good correlation with the two lobes of the identified aquifer.

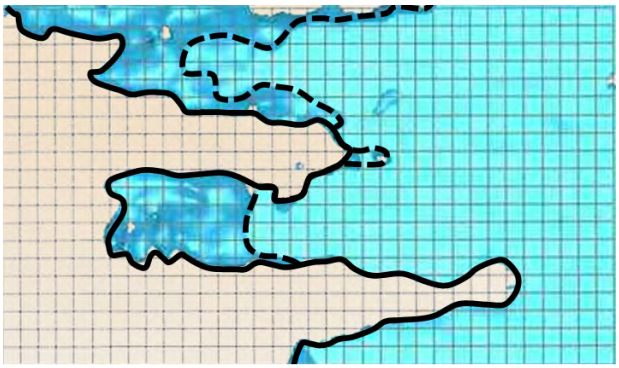

Figure 2. Conductivity data showing interpreted Freshwater

Figure 3. Aquifer outline overlain on Hydrogeological data.

In the north, however, there is an extensive resistive zone, extending from east to west across the area which shows a lack of correlation with the northern lobe of the hydrogeological map. This area has noticeably fewer boreholes and the contour values on the salinity map have largely been interpolated. This suggests that greater confidence should be placed on the resistive zone as mapped by TEMPEST, rather than the contours depicting salinity values derived from sparse borehole data. Although the AEM provided reliable and continuous coverage more drilling at this stage would be advisable to further confirm the northern extent of the aquifer.

Mapping contamination pathways and fracture systems

In 2000, Fugro was contracted by the U.S. department of Energy (DOE) and the U.S. Environmental Protection Agency (EPA) to conduct an airborne DIGHEM electromagnetic survey at the Sulphur Bank Mine in Lake County, California. This abandoned mercury mine was the source of contamination into Clear Lake, which was surrounded by homes. It was assumed that the mine was leaking conductive, contaminated water into a small lake, which was leaking into the larger lake through unknown pathways. A 2.5 million dollar drill program which was conducted missed all the contaminant pathways, one by less than 3 meters. Airborne and ground geophysical data were used to improve their knowledge of mine drainage, contaminant sources and contaminant pathways through fracture systems. The path could be assumed, but was uncertain. The DIGHEM airborne survey mapped geological

structure on land and below the lake as well as lithology and geological structure. This was used to identify natural conduits for the movement of groundwater.

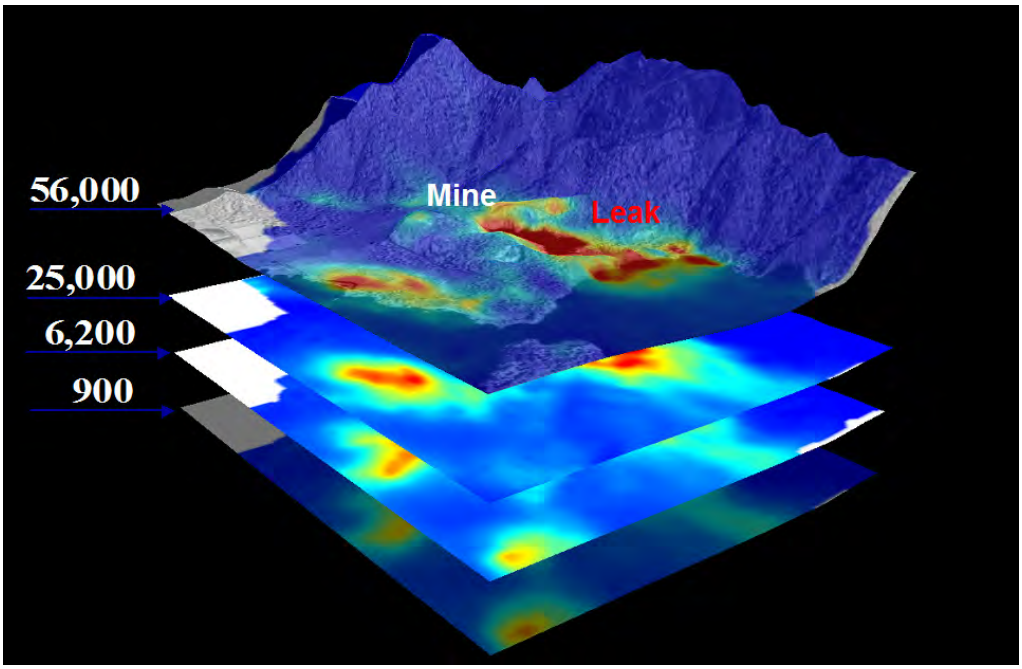

Figure 4. Apparent conductivity draped on topography (Hammack, 2002).

The data overlain on topography in Figure 4 show the location of the mine. As shown, the HEM survey mapped the plume at surface, and indicated the pathway into Clear Lake. However, what was not expected was that the survey also mapped a plume deep under the lake, where contaminated water was interpreted to be following geological fractures into the lake. The data showed that acidic water and mercury from the mine were contaminating the lake. In this case the AEM data provided useful and continuous data over the area.

Sand and Gravel Aggregate deposit mapping

A test area approximately 3 km by 5 km was flown for the Saskatchewan Department of Highways and Transportation. This area was covered by inter-layered sand and glacial till. There were 6 drilled areas before the survey was conducted. The HEM RESOLVE survey detected all of the previously known gravel deposits as well as some that were not previously detected. One of the previously known deposits appeared as a strong anomaly of 30 ohm-m indicating that it was thick and large. The AEM showed that the strongest part of this anomaly and hence the best part of the deposit was located between two groups of drill holes in this test area. The drilled holes covered most of the anomalous zone, but did not offer the full coverage of the area nor did they extend deep enough indicating the depths of the deposits. The drill results for this deposit show an average depth to the top of 1.5 m to 2 m. A few holes in the centre of the deposit that were drilled beyond 4 m showed a depth of 10m or more to the bottom. Shown in Figure 5 is a rough estimate of the depth of the deposits along one of the lines, based on the airborne EM and the few deep drill holes.

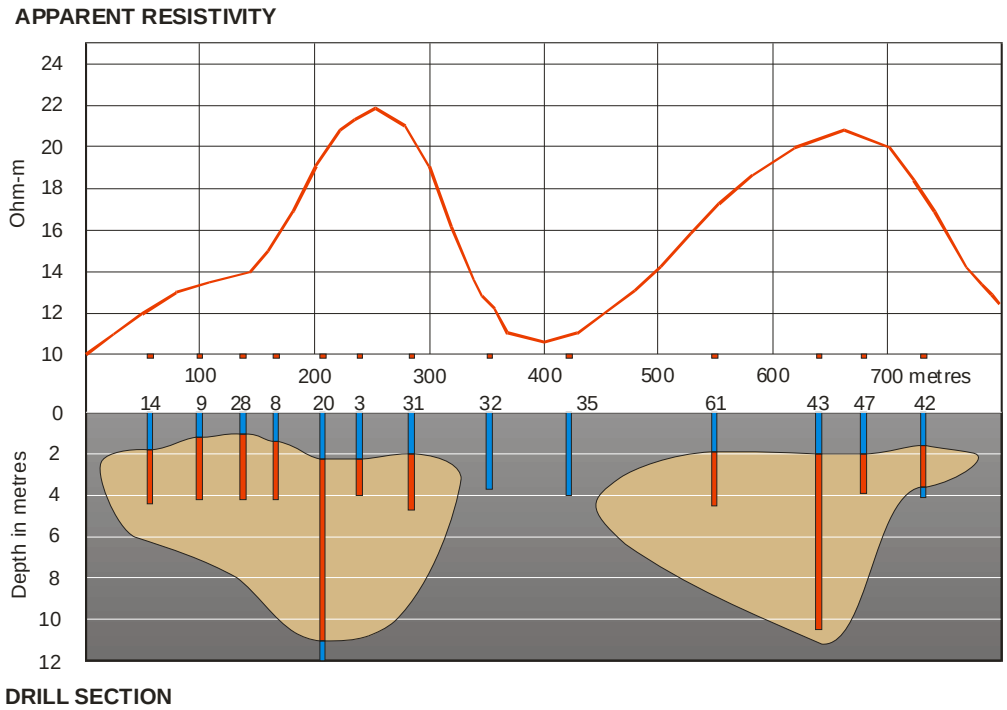

Figure 5. Resistivity and borehole data comparison (Hodges, 1999)

In Figure 5. the brown areas represent sand and gravel deposits while the gray areas represent glacial till and clay deposits. The apparent resistivity values obtained by the HEM survey are presented in profile format at the top of the image. The bottom of the image is a vertical cross-section for a selected line in the Saskatchewan Test Area as determined by drilling results. The results from the AEM and drill data show the areas of high resistivity correlate with the presence and the thickness of the sand and gravel deposits. The survey also detected a previously unknown aggregate deposit existing within the test area boundary. As a result of this successful test survey, the Saskatchewan government went on to fly two more surveys over much larger areas to successfully define aggregate resources for highway construction projects.

Conclusions

Mapping the conductivity / resistivity of the subsurface using airborne electromagnetic data can be applied to several engineering and environmental problems. Applications include: pipeline route mapping, contamination mapping, salt and fresh water mapping, aggregate and sand etc. Airborne Electromagnetic data can be used in conjunction with ground data to help constrain the parameters used for any modeling. With customized service to engineering and environmental clients Fugro has catered its suite of services and products to help deliver solutions to engineering and environmental problems.

References

Fountain, D.K., (1998), Airborne electromagnetic systems – 50 years of development, Exploration Geophysics. Volume 29, 1-11.

Hammack RW, Veloski GA, Sams JI, Mabie JS (2002) The use of airborne EM conductivity to locate contaminant flow paths at the Sulphur Bank Mercury Mine Superfund Site. Proc, Application of Geophysics to Engineering and Environmental Problems (SAGEEP, Feb 11-13, 2001), Las Vegas, NV.

Hodges, Greg; and Latoski, Michael, (1999), The application of airborne electromagnetics and ground geophysics to the detection of buried gravel deposits, in Johnson, K. S. (ed.), Proceedings of the 34th forum on the geology of industrial minerals, 1998: Oklahoma Geological Survey Circular 102, p. 313-318.

Palacky, G.J., (1987). Clay mapping using electromagnetic methods. First Break 5, 295–306.

.

AEM DATA FOR ASSESSING IRRIGATION CHANNEL LEAKAGE – A MERITORIOUS APPROACH IN AN AUSTRALIAN SETTING?

Tim Munday, CSIRO, Perth, Australia
Mike Hatch, University of Adelaide, Adelaide, Australia
Andrew Fitzpatrick, CSIRO, Perth, Australia
David Allen, Groundwater Imaging Pty Ltd, NSW, Australia

Abstract

Geophysical technologies, and in particular electrical and electromagnetic methods, have the potential to provide a rapid and relatively inexpensive approach to determining the location and extent of seepage along irrigation canals or channels. Although showing potential, the application of airborne electromagnetic (AEM) systems for these purposes has been very limited, in part because of the fine scale information required and also the costs associated with acquisition. However, recent developments in AEM system technologies have contributed to substantial improvements in the definition of conductivity at *shallow* depths and we believe these trends have made these systems a more relevant technology for the systematic mapping and detection of variations associated with irrigation infrastructure. In this paper we examine that potential through the analysis of high resolution HEM data for an irrigation system located in Victoria, Australia. Inverted data from a RESOLVE FDHEM survey along an irrigation channel were compared with an inverted ground resistivity array data set. Results demonstrated that the spatial patterns and magnitude of conductivity variations are generally comparable. The ground geophysical technique benefitted from being able to map variations at finer scales. However, there may be merit in considering the deployment of airborne mapping methods if large surveys are considered and a rapid turn-around of information is required.

Introduction

Geophysical technologies, and in particular electrical and electromagnetic methods, have the potential to provide a rapid and relatively inexpensive approach to determining the location and extent of seepage along irrigation canals or channels (see, for example, ANCID 2000a,b, Allen 2007, and Ball et al. 2006). They also offer the means for spatially contiguous measurements and can be employed along and adjacent to channels, without disrupting their use. Although they can be applied at a range of scales, their deployment becomes more cost effective with large surveys and where the data generated can be linked to ground investigations that offer the opportunity for meaningful verification.

Electrical or electromagnetic methods applied to seepage measurement depend primarily on being able to detect a contrast in terrain conductivity (or resistivity) in the sub-surface profile along and adjacent to the irrigation channel (ANCID 2000a). In this way they can be used to:

1. *Directly measure the conductivity of the ground, and identify the conductivity contrast of the subsurface sediments saturated in fresher channel water as it seeps into and dilutes saltier native groundwater (where present). Decreasing the salinity of the groundwater will cause a decrease in electrical conductivity (or an increase in its inverse, resistivity).*
2. *Identify conductivity contrasts in surface material properties and infer the likelihood of seepage through more permeable materials in the unsaturated zone. Formations more likely to allow*

seepage, such as sands, are naturally lower in conductivity (higher in resistivity) due to lower porosity and lower cation exchange capacity than clay, or silty-clay dominated formations. In addition the higher permeability of sandy sediments can lead to better drainage and lower salt content, further reducing conductivity. The magnitude of seepage is assumed to be related to unsaturated zone soil/sediment properties beneath or adjacent to the channel.

To-date, most applications of geophysical technology in assessing channel seepage have been confined to "ground-based" approaches with devices mounted in boats, or towed behind a craft of some kind (see for example, Bell et al. 2006, Allen 2007, and Allen and Merrick 2003). The application of airborne electromagnetic (AEM) systems for these purposes has been very limited, in part because of the fine scale information required and also the costs associated with acquisition. However, their potential for mapping irrigation leakage has been flagged by Smith et al (2009).

Compared with ground-based systems, Airborne EM technologies are capable of the relatively rapid and systematic coverage of large areas at a relatively low cost, without causing ground disturbance. Recent developments in AEM systems (see Thompson *et al.* 2007, Macnae 2007) with the better definition of system geometry and greater attention to calibration, have contributed to substantial improvements in conductivity definition at *shallow* depths. We believe these trends, coupled with our ability to better process, image and display AEM data, have made these systems a more relevant technology for the systematic mapping and detection of variations associated with irrigation infrastructure. In this paper we examine that potential through the analysis of high resolution HEM data for an irrigation system located in Australia with the specific goals of determining:

1. *Whether a helicopter EM system was capable of effectively tracking along irrigation infrastructure in the manner presented schematically in Figure 1,*
2. *Whether the system had the resolution to detect variability that might be associated with irrigation channel leakage through appropriate modelling, and*
3. *Whether the measured conductivity response could be processed and displayed in a way to highlight areas of potential seepage.*

At this stage the project has been concerned with a demonstration of concept rather than a full validation, and as an aid to understanding the capability of the HEM data for mapping leakage, we also undertook a ground survey using a more conventional, and widely accepted approach to irrigation channel surveys, specifically a towed resistivity array.

Study Area

This study was undertaken along the 6/7 Irrigation Channel located north of the Tutchewop Lakes in Victoria, Australia (Figure 2). This is one of the main trunk systems that form part of a complex of irrigation canals exceeding some 3000km in length. The 6/7Channel is underlain by Late-Cainozoic fluvio-lacustrine sediments (Brown and Stephenson 1991), approximately 200m thick. The water table is within a few metres of the ground surface in the area surrounding the Lakes and 6/7 Channel.

Irrigation Channel 6/7 Geophysical Surveys

AEM System and Survey Parameters

The 6/7 irrigation channel AEM survey comprised three parallel lines flown 250m apart from Lake Tutchewop to the Little Murray River. The survey was orientated with one line down the centre of the 6/7 irrigation channel, with the other two lines flown on either side in the manner presented

schematically in Figure 1, and also shown in Figure 3. The survey was undertaken in May 2007. We used the RESOLVE frequency domain helicopter EM (FDHEM) system for this survey, given the need for high spatial resolution information, near surface conductivity data and a requirement to fly along a channel with sharply changing orientations. The helicopter flew at an average airspeed of 30m/sec with an EM sensor height of approximately 30m above the ground. While the potential to fly lower with this technology (with a sensor height of 10m above the ground), has been demonstrated in previous surveys (see Fitzpatrick et al. 2007), we chose to demonstrate a technological capability in the first instance with acquisition parameters at more usual survey heights.

The RESOLVE FDHEM system contains five horizontal coplanar coils, and in the Tutchewop survey measured an EM response at the nominal frequencies of 400Hz, 1800Hz, 8200Hz, 40,000Hz and 140,000Hz. It also had one coaxial coil pair which measured a response at 3300Hz.

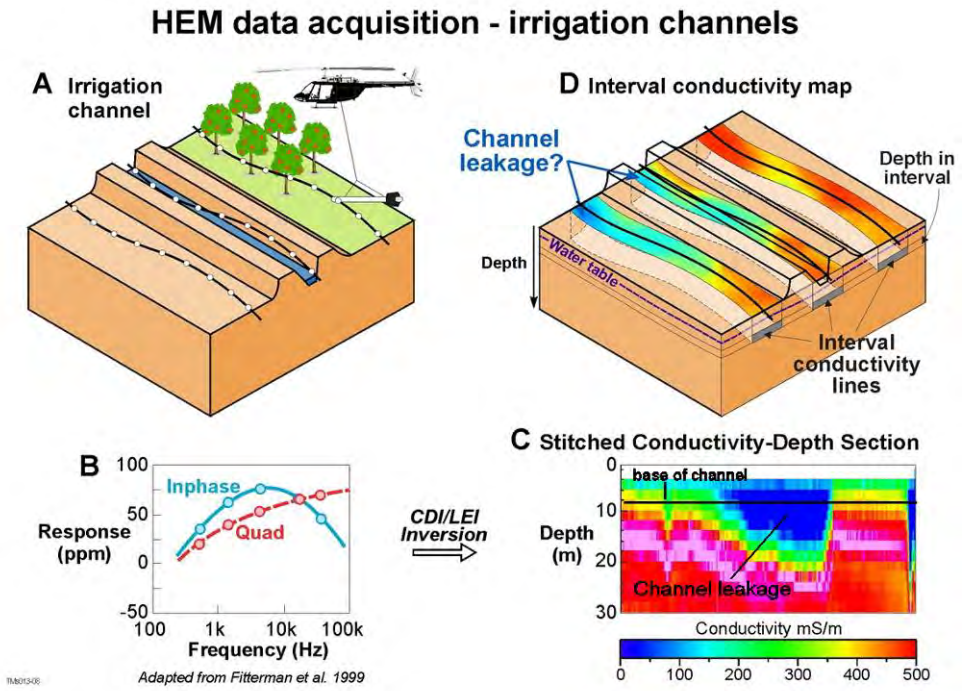

Figure 1: Schematic representation of helicopter frequency domain EM data acquisition and interpretation strategy employed for mapping seepage along and adjacent to an irrigation canal/channel. A) Data are acquired along parallel flight lines, one centred on the irrigation canal, and one on either side, with measurements made every ~10-15m along each flight line; B) The EM receiver located in the "Bird", which is towed beneath the helicopter, measures the combined primary and secondary responses and derives two parameters, the in phase response and out of phase (quadrature) response for each transmitted frequency.; C) The measured ground response is used to determine the conductivity-depth function by transformation or inversion; D) Conductivity-depth values can be calculated for each observation and then stitched together into conductivity-depth sections to provide a representation of the 2D variation of conductivity. Conductivity depth profiles can be combined into a 3D gridded volume from which arbitrary sections, horizontal depth slices (or interval conductivity images) and isosurfaces can be derived showing the spatial distribution of conductivity as it varies with depth. Conductivity-depth sections can be interpreted as indicated in C, with leakage identified as zones of low conductivity (or resistive zones) extending beneath the channel base. The lateral extension of possible seepage may be picked up in lines flown adjacent to the channel, again as resistive zones (see D).

Figure 2 Location of the Lake Tutchewop study area in Victoria

Submerged Resistivity Array

A submerged resistivity system developed by Groundwater Imaging Pty Ltd was used to acquire resistivity data along the 6/7 channel for comparison with the HEM data. This system is a 42 m long staggered centre galvanic DC Resistivity array, which is towed along the canal bottom behind a small boat (Allen and Merrick, 2003). This array is set up in an inverse Schlumberger configuration, with two transmitting electrodes set near the centre of the array (3.75 m apart, towed approximately 22 m behind the boat), and eight receiving electrodes arranged in offset pairs asymmetrically around the transmitting pair. In this configuration the spacings for the seven receiving electrode pairs ranged from 4.95 m to 34m. Data were collected every 8 to 10 seconds at approximately 10 m intervals along the canal. GPS locations and water depth data were collected at the same time.

Inversion

Both the submerged DC resistivity array and the RESOLVE HEM data sets acquired for this study were inverted using EM1DINV (Auken, 2008). EM1DINV is a flexible routine that may be implemented as a "smooth-model", "minimum-structure" type of inversion, or as a "blocky", "discrete layer" type of inversion. For both types of data inverted for this study, a number of different inversion strategies were tested.

RESOLVE HEM Data Inversion

For the HEM RESOLVE data we used a simple starting model when inverting the three lines of data. The best results were obtained with a starting conductivity of 300 mS/m (3.3 ohm-m). From prior experience with the RESOLVE system in similar environments it was deemed reasonable to expect that the depth of investigation would exceed 30m across most of the survey area. Therefore a total depth for all stations was fixed at 60m. Layer thicknesses were based on the number of layers defined for a particular iteration of the inversion (i.e. 3, 4, 5 layer blocky or 12 layer smooth). They were also set to

increase logarithmically with depth (i.e. layers near the surface were thinner than deeper, less resolved layers).

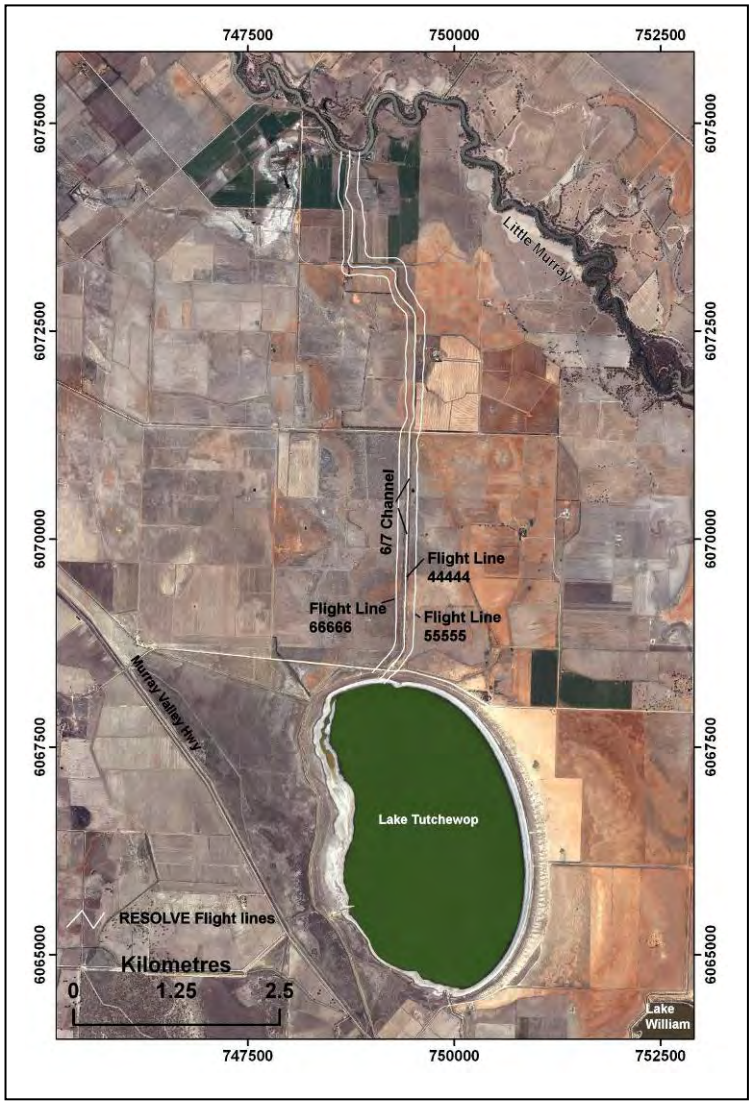

Figure 3: Location of the three HEM flight lines paralleling the 6/7 Channel north of Lake Tutchewop. Data from the submerged resistivity array were collected along the 6/7 channel, near coincident with the central survey line shown.

Submerged DC Resistvity Array data inversion

For the 6/7 channel submerged DC resistivity array data set, the starting model resistivity assigned to each station was based on standard apparent resistivity calculations made for each dipole. These were averaged and this average used as the starting value for all layers. Starting model total depths were based on depth sensitivity studies (Roy and Apparao, 1971; Allen and Merrick, 2007) that mostly depend on the electrode spacing to calculate depth. Layer thicknesses were based on the number of layers used in a given run of the inversion (i.e. 3, 4, 5 layer blocky or 12 layer smooth). As with the RESOLVE inversion, layer thicknesses were set to increase logarithmically with depth (i.e. layers near the surface were thinner than deeper, less resolved layers).

As the array for this study was towed on the bottom of the irrigation channel and the position of each electrode in the array is important to the apparent resistivity calculation and therefore to the inversion results, it was necessary to make a few simplifying assumptions to allow each electrode

position to be calculated. At the time of the survey a GPS unit logged the boat position at set time intervals along the channel. A boat bearing based on the average of a number of adjacent GPS readings was calculated. These averaged bearings were used to estimate individual electrode positions (there were 8 receiver and 2 transmitter electrodes to position for each data sounding). We believe these estimated positions were reasonable for situations when the array is towed in a straight line, but are less accurate as the boat and the array are towed around sharp bends. The 6/7 channel had a number of near right angle turns along its length, where calculated electrode positions were assumed to be incorrect. Similarly, the depth of the canal is measured at each GPS position, and also reflects the depth of the canal at the GPS receiver position. Electrode depth estimation was simplified by assuming that all electrodes at each sounding were at the same depth as the GPS receiver. This is a reasonable assumption as the depth of the canal generally varied smoothly from approximately 0.3 m to 1.6 m.

Results

Results from a smooth model (12 layer) inversion for data acquired by both the submerged resistivity array and the RESOLVE HEM systems are shown in Figure 4.

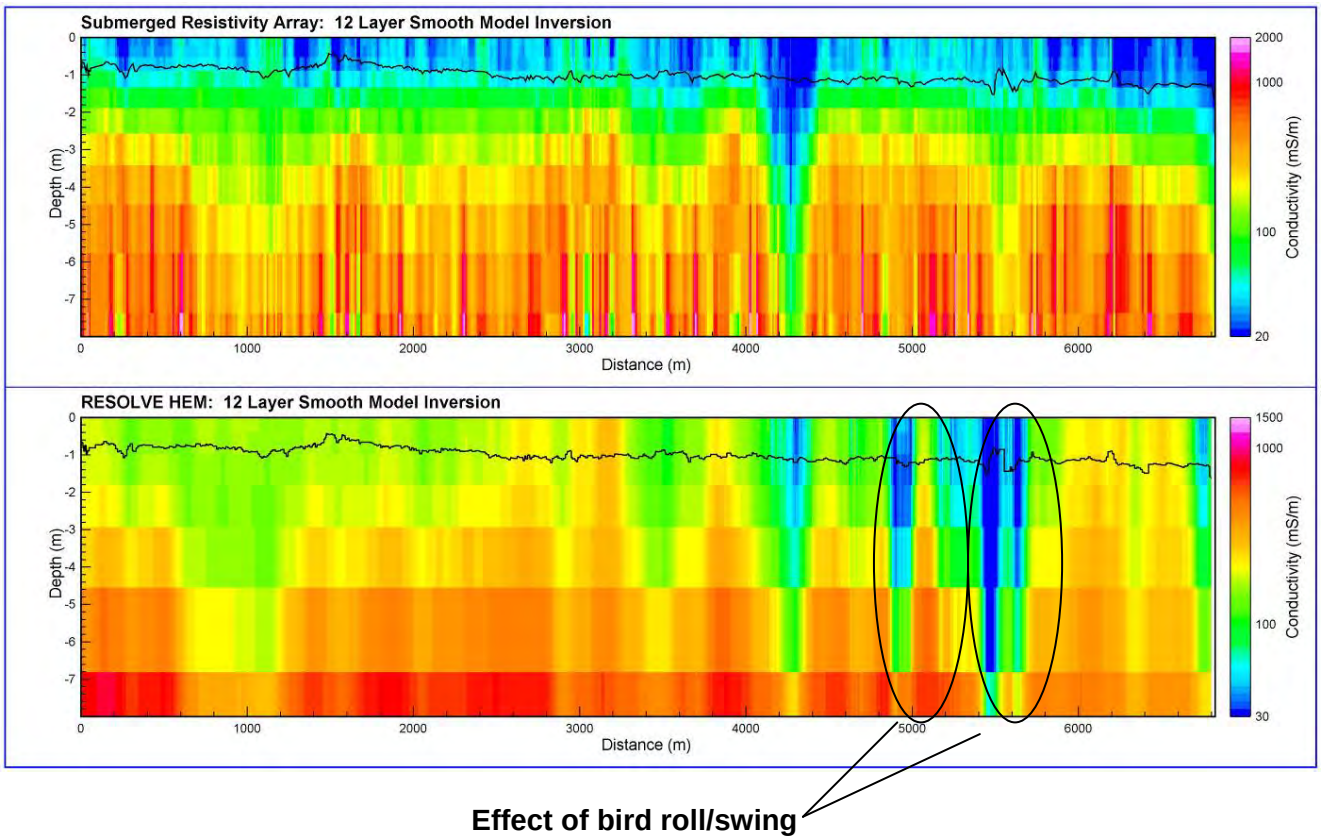

Figure 4: Comparison between conductivity-depth sections for a smooth model inversion of the submerged resistivity array (top) and the RESOLVE FDHEM data sets (bottom). The data are from the 6/7 irrigation channel surveyed line. The black sub-horizontal line in the section is the depth of the channel defined in the ground survey.

Overall the spatial patterns of conductivity match reasonably well, although ground system, not surprisingly, maps more detail. This is to be expected given the resolution and sampling rate of the two

systems. The base of the channel appears relatively resistive which may suggest that it leaks slowly along its full length. However there are several places, for example around the 1km, 3.5 km, and 4.3km marks, where both data sets suggest leakage may be more pronounced. Both data sets map an underlying saline substrate. In the RESOLVE inversion results, at about the 4.9km and 5.5 km markers, several resistive zones are identified and on scrutiny of the survey data, bird roll at these locations is in excess of 40 degrees. These areas are also coincident with marked changes in the channel orientation (~90˚). In a normal survey mode helicopter tracks the channel relatively well, but sharp changes in flight orientation lead to significant changes in the orientation and roll of the towed bird. Whilst incorporation of attitude and altitude in the inversion can compensate for these effects, correcting for roll is particularly problematic and we believe that survey data acquired for similar purposes elsewhere should be interpreted with these effects in mind.

Both the RESOLVE and submerged resistivity array data sets can be presented in a spatial sense, and a map of ground conductivity for a depth interval located immediately beneath the channel is shown in Figure 5 for a subset of the 6/7 Channel survey line. The two data sets are directly comparable in this example. Both identify the same regions along the irrigation canal that may be subject to leakage, but further ground work is required to confirm these observations.

Summary and Conclusions

Results from the 6/7 irrigation channel survey using the RESOLVE FDHEM system have demonstrated that the spatial patterns and magnitude of conductivity variations are generally comparable with results obtained from a more conventional ground geophysical technique used for mapping potential zones of channel leakage. The observed spatial patterns along and adjacent to the 6/7 channel are consistent with there being seepage beneath and away from this irrigation system, but this requires on-ground investigation for the purposes of validation. Further, quantification of the results, particularly in terms of seepage rates, requires the integration of these geophysical observations with other techniques for their calibration.

Spatial resolution may be an issue to consider in the context of such studies. Helicopter EM technologies have a large footprint (~30-50m) and potentially only the larger areas of seepage may be detected along any given channel section. Results from the 6/7 channel study indicate that some of the zones potentially linked to seepage are relatively large, and in these situations an airborne system works particularly effectively. We accept that airborne surveying techniques tend to provide a coarser resolution data set when compared with ground systems, but we believe, that this may be offset somewhat by flying at lower than nominal survey heights (i.e. 10m vs 30m). Another issue to consider is bird geometry during acquisition. Failure to account for these parameters may lead to the erroneous interpretation of the resulting data set, including the identification of “leakage zones” that don’t exist. Care given to the rate (i.e. speed of the helicopter) of data acquisition may help alleviate this, along with the incorporation of attitude and altitude effects in the subsequent inversion.

Whilst the costs for airborne data acquisition are high, the survey of large irrigation systems may be warranted particularly where costs can be defrayed against fast data acquisition and information turn-around compared with ground surveying methods. Potentially the cost of a ground survey over large areas could be of a similar magnitude to that of an airborne survey. In these circumstances or where the costs of airborne acquisition can be shared with adjacent surveys, there may be some merit in considering their application and use.

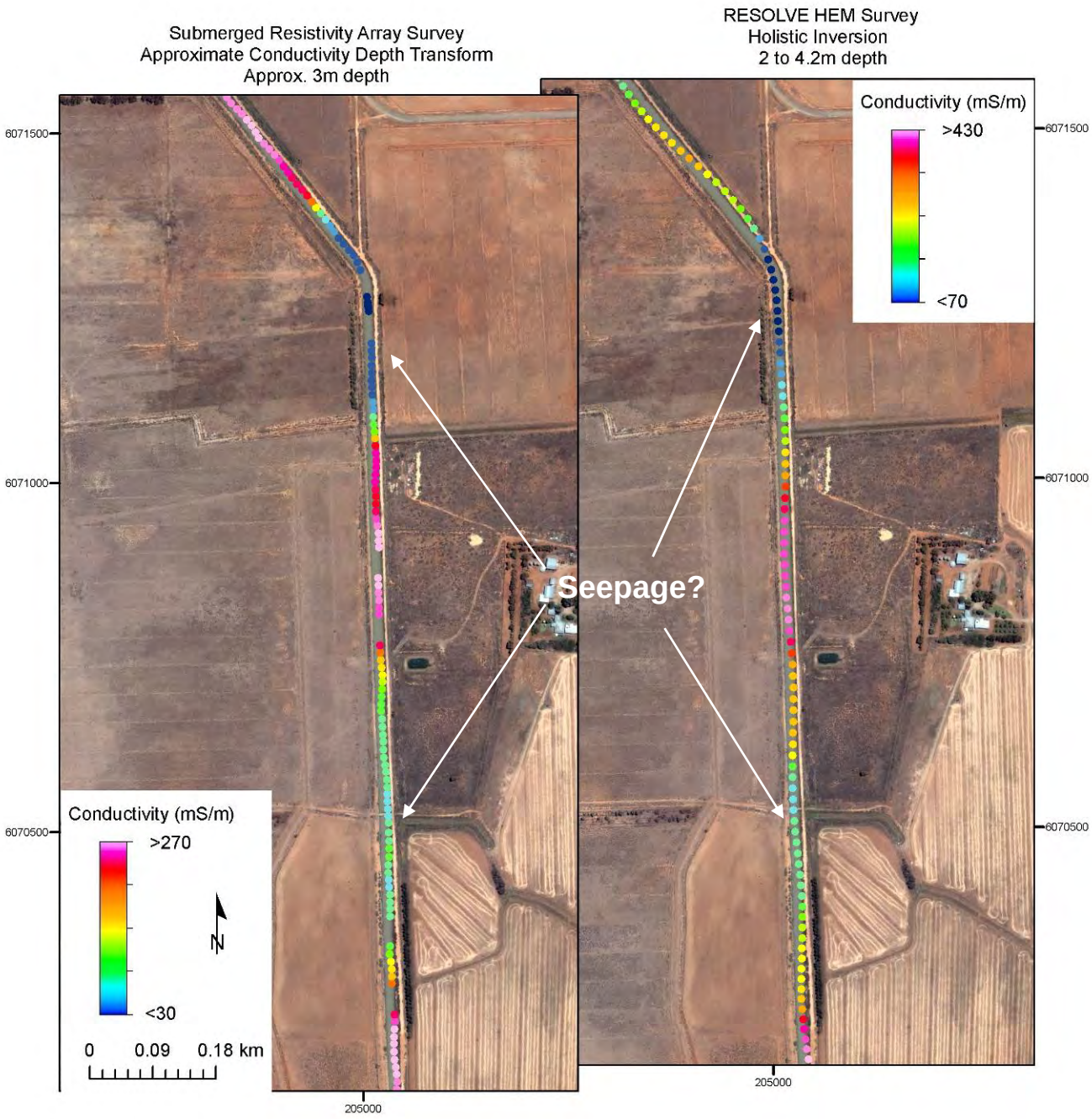

Figure 5: Interval conductivity image for ~ 3m depth interval for a subset of the data acquired by the submerged resistivity array (left) and the RESOLVE HEM system (right) along the 6/7 irrigation canal. The depicted spatial patterns in conductivity are of a similar extent and magnitude.

References

Allen, D. A. and Merrick, N.P., (2003). A floating electrode array for continuous geoelectrical imaging. ASEG 16th Geophysical Conference and Exhibition, Adelaide, SA, Australia, ASEG.

Allen, D. A. and Merrick N.P., (2007), Robust 1D inversion of large towed geo-electric array datasets used for hydrogeological studies: Exploration Geophysics, 10, 50-59.

Allen, D.A., (2007) Irrigation Insights No. 7. Geophysics for the Irrigation Industry. Land and Water Australia, 180pp.

Australian National Committee on Irrigation, Drainage (ANCID), (2000a). Open Channel Seepage and Control, Vol. 1.2. Current Knowledge of Channel Seepage Issues and Measurement in the Australian Rural Water Industry. ANCID/Sinclair Knight Merz: Armadale, Australia.

Australian National Committee on Irrigation and Drainage (ANCID), (2000b): Open Channel Seepage and Control, Vol 1.4. Best practice guidelines for Channel Seepage identification and Measurement. Prepared by Sinclair Knight Merz, January 2003. 114 pp.

Ball, L.B., Kress, W.K., Steele, G.V., Cannia, J.C., Andersen, M.J., (2006), Determination of canal leakage potential using continuous resistivity profiling techniques, Interstate and Tri-State Canals, western Nebraska and eastern Wyoming, 2004: U.S. Geological Survey Scientific Investigations Report 2006-5032.

Fitzpatrick A.D., Munday T.J., Berens V., Hatch M.A. & Telfer A.L., (2007), Mapping Salt-Loads of the Murray River, Australia, Using Airborne and In-River Electromagnetic Methods Near Surface 3-5 September 2007, European Association of Geoscientists and Engineers, Istanbul, Turkey. Extended Abstract 4pp.

Macnae J.C (2007). Developments in Broadband Airborne Electromagnetics in the Past Decade In Proceedings of Exploration 07: Fifth Decennial International Conference on Mineral Exploration, CD of Conference Proceedings. Toronto, Canada Sept 9 to 12, 2007 (Ed B Milkereit), pp. 387-398. Prospectors and Developers Association of Canada, Toronto, Canada

Roy, A. and. Apparao, A., (1971), Depth of investigation in direct current methods: Geophysics, 36, 610-625.

Thompson S, Fountain D and Watts T (2007). Airborne Geophysics – Evolution and Revolution. In Proceedings of Exploration 07: Fifth Decennial International Conference on Mineral Exploration. CD of Conference Proceedings. Toronto, Canada Sept 9 to 12, 2007 (Ed B Milkereit) pp. 19-37, Prospectors and Developers Association of Canada, Toronto, Canada

Smith, B.D., Abraham, J., Cannia, J.C., and Hill, P.L., (2009), Helicopter electromagnetic and magnetic geophysical survey data for portions of the North Platte River and Lodgepole Creek, Nebraska, April 2008: U.S. Geological Survey Open-File Report 2009-1110, 34 p

TRANSIENT ELECTROMAGNETIC MAPPING OF CLAY UNITS IN THE SAN LUIS VALLEY, COLORADO

David V. Fitterman, U.S. Geological Survey (retired), Denver, CO
V.J.S. Grauch, U.S. Geological Survey, Denver, CO

Abstract

Transient electromagnetic soundings were used to obtain information needed to refine hydrologic models of the San Luis Valley, Colorado. The soundings were able to map an aquitard called the blue clay that separates an unconfined surface aquifer from a deeper confined aquifer. The blue clay forms a conductor with an average resistivity of 6.9 ohm-m. Above the conductor are found a mixture of gray clay and sand. The gray clay has an average resistivity of 21 ohm-m, while the sand has a resistivity of greater than 100 ohm-m. The large difference in resistivity of these units makes mapping them with a surface geophysical method relatively easy. The blue clay was deposited at the bottom of Lake Alamosa which filled most of the San Luis Valley during the Pleistocene. The geometry of the blue clay is influenced by a graben on the eastern side of the valley. The depth to the blue clay is greater over the graben. Along the eastern edge of valley the blue clay appears to be truncated by faults.

Introduction

The San Luis Valley located in south-central Colorado is an area of many uses including agriculture, ranching, and recreation, all of which are tied together through the need for water. As in many parts of the western U.S., water is a limited resource that requires well-informed management to meet the needs of all users. In recent years the water supply has been severely impacted by regional drought conditions.

Great Sand Dunes National Park and Preserve (GRSA), which is located on the eastern edge of the San Luis Valley (Figure 1), was involved in a legal action to establish an in-place water right for the GRSA. In support of the National Park Service's (NPS) effort and as part of internal U.S. Geological Survey (USGS) projects, several studies of the San Luis Valley have been undertaken to better understand the geological history of the area and its impact on the hydrology. This paper describes one effort to geophysically map a regional clay unit called the blue clay which separates the unconfined surface aquifer from the deeper, artesian confined aquifer.

Geology and Hydrology

The San Luis Valley overlies a structural basin related to the formation of the Rio Grande rift (Tweto, 1979a). The valley is bounded by volcanic rocks of the San Juan Mountains on its western side and by Precambrian crystalline and Paleozoic sedimentary rocks of the Sangre de Cristo Mountains on its eastern side (Tweto, 1979b). The structural basin, which is divided into two parts by the northerly trending Alamosa horst (Burroughs, 1981), is filled with Quaternary- and Tertiary-age sediments known as the Santa Fe Group, which are derived from the eastern and western bounding mountain ranges (Leonard and Watts, 1989; Ingersoll et al., 1990; Brister and Gries, 1994).

Limited outcrops and well logs in the valley reveal that the Santa Fe Group consists of conglomerate, sand, gravel, clay, interbedded basalt, and volcaniclastic deposits (Powell, 1958, Brister

and Gries, 1994). The upper Santa Fe Group contains unconsolidated gravel, sand, silt, and clay, and underlies large portions of the valley (Powell, 1958), including the vicinity of the GRSA (Madole et al., 2008). Clays range in color from brown to green to bluish-gray and are often interfingered with the sands and gravels.

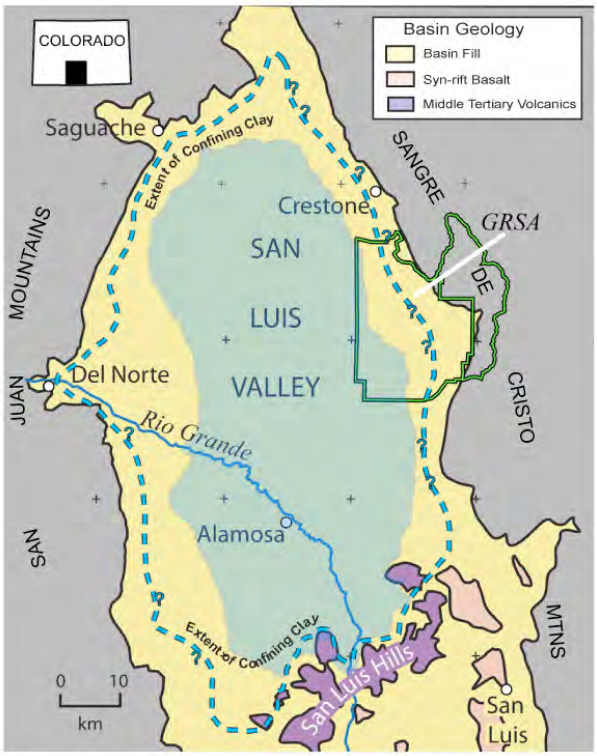

Figure 1: Location of the Great Sand Dunes National Park and Preserve (GRSA), and the San Luis Valley, Colorado. Also shown is the generalized geology, the extent of the Pleistocene lake at its most recent high stand (blue-green shade) from Machette et al. (2007), and the limit of the related confining clay at depth delineated by well data (blue dashed line; from E. Harmon, written communication, 2004).

The existence of a large lake that filled the San Luis Valley during the Pleistocene was hypothesized by Siebenthal (1910), who named the sediments deposited in the lake the Alamosa Formation. Machette et al. (2007) provided further evidence of the lake, which they call Lake Alamosa. According to these authors, the lake experienced transgressions and regressions over a period of about 3 million years, until it overtopped a barrier of volcanic rocks in the San Luis Hills (Figure 1) at about 440 ka. Knowledge of the extent and history of the lake is critically important to understanding the hydrology of the San Luis Valley as it influenced the deposition of the aquitard which separates the unconfined and confined aquifers.

Most water in the San Luis Valley comes from wells (Siebenthal, 1910; Powell, 1958; Harmon, 1987; Schenk and Harmon, 1999). Schenk and Harmon (1999) discuss the relationship of the hydrology to the various geologic units, which are controlled by structural and stratigraphic factors. The aquifers from surface to depth are: (1) the unconfined aquifer, (2) a confined aquifer which produces large quantities of water, and (3) a deeper, less productive confined aquifer. Clay deposited in deeper parts of the lake during high stands of Lake Alamosa forms an aquitard between the unconfined and upper confined aquifers and is known colloquially as the “blue clay.” Machette et al. (2007) recognized that 95 percent of the artesian wells in the valley fall within the high-water level of Lake Alamosa. More

importantly, Machette et al. (2007) point out that most groundwater models of the valley do not incorporate lateral and vertical discontinuities in the blue clay caused by interfingering of lacustrine and alluvial deposits at the margins of Lake Alamosa as it increased and decreased in size over time.

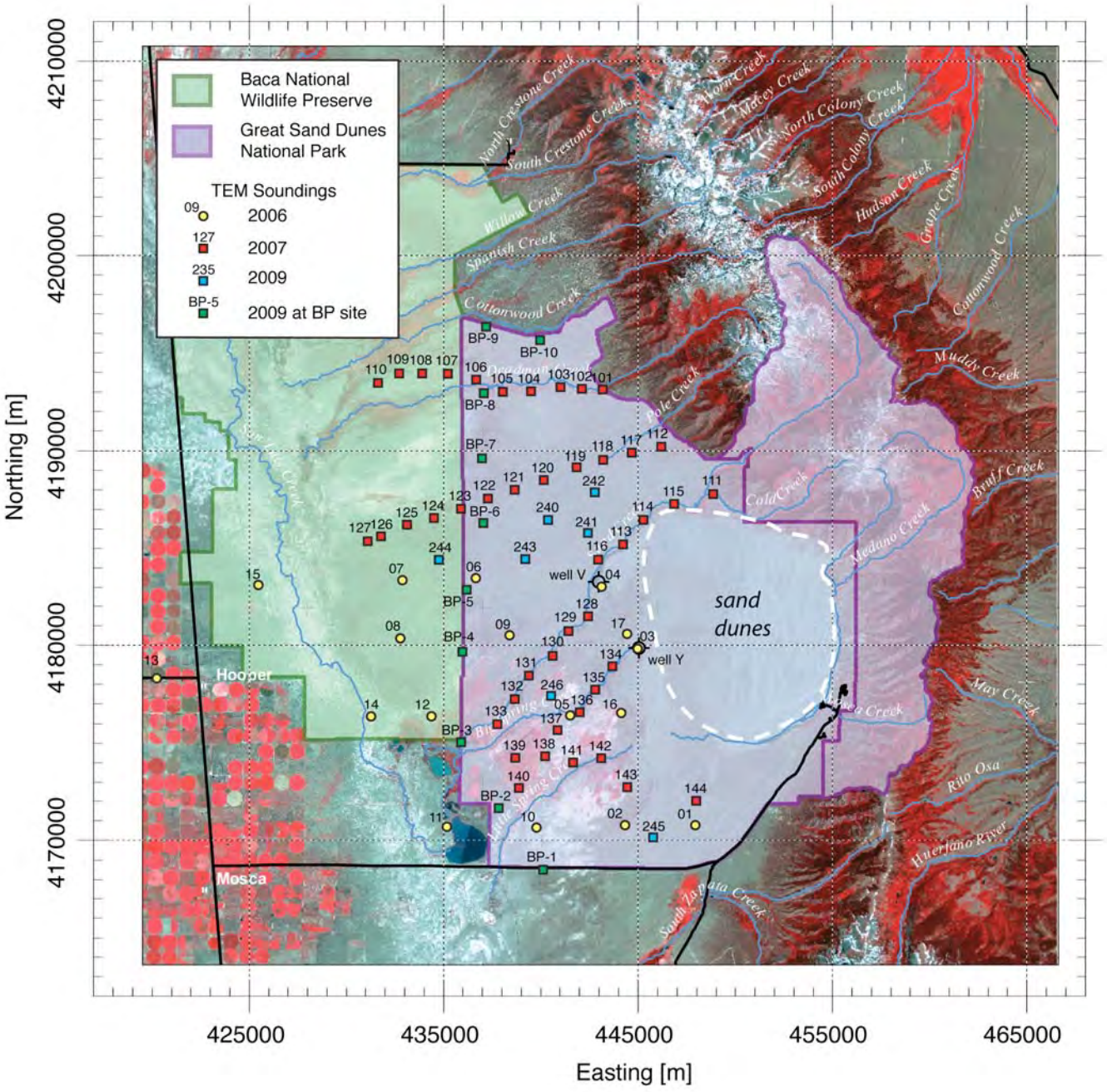

Figure 2: Location of TEM soundings. The soundings prefixed with BP are located at boundary piezometers installed for the GRSA. The location of two deep wells (well V and well Y) with lithology and geophysical logs are shown (HRS Water Consultants, 1999).

Transient Electromagnetic Survey

Transient electromagnetic (TEM) soundings were made in the San Luis Valley starting in 2006 to assess the utility of the method to map the blue clay (Fitterman and de Sozua Filho, 2009). This initial survey determined that TEM soundings could map the blue clay. Subsequent field work was conducted in 2007 and 2009 (Figure 2). Soundings were made with a Geonics PROTEM[1] system using a central induction loop geometry with a 40 m by 40 m transmitter loop and a battery powered EM-47 transmitter. Data were measured in the time range of 6.81 μs to 6.987 ms after transmitter turn off. Data were typically too noisy to use for inversion at times greater than 2 ms. Ten sets of transients were averaged to estimate measurement uncertainty. Data points with more than 10 percent uncertainty in apparent resistivity were usually unusable. Data were inverted with a layered model using the fewest layers necessary to obtain a good fit to the data with reasonable model parameter uncertainty.

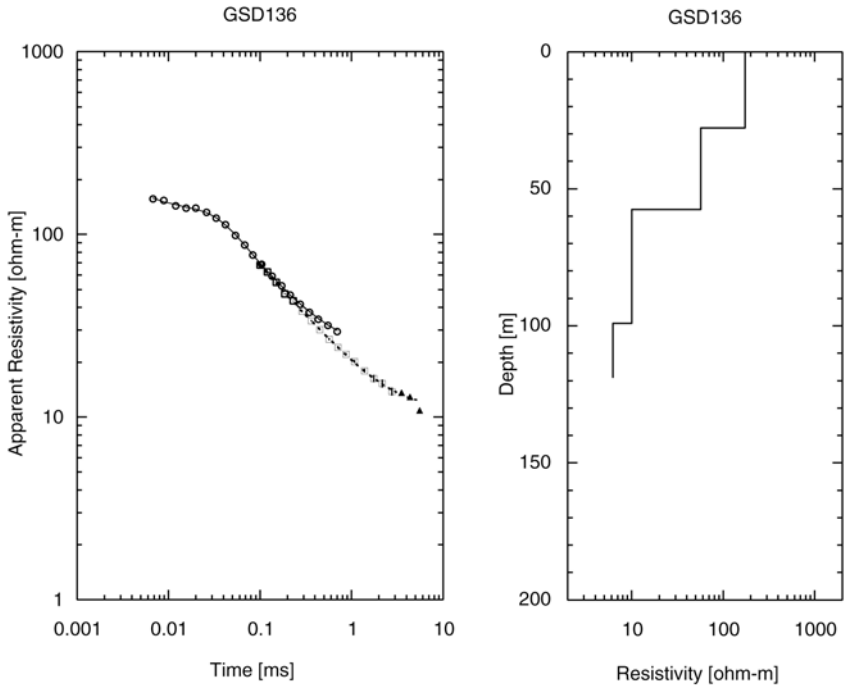

Figure 3: Typical San Luis Valley TEM sounding and interpretation. Measured apparent resistivities (left) are shown as open symbols, and the model response is shown as solid and dashed lines. The two sets of symbols and responses correspond to ultra high and high measurement times of the PROTEM receiver. Vertical lines through the data points are the measurement uncertainty, most of which are smaller than the data symbols and can not be seen. Masked points, which were not used in the data inversion, are shown as solid triangles. The interpreted resistivity-depth that best fits the data is shown to the right.

A typical TEM sounding and interpretation is shown in Figure 3. The apparent resistivity decreases with time, and the interpreted layer resistivity decreases with depth. The best fit was obtained with a four-layer model. The first layer resistivity is about 175 ohm-m indicative of dry sand. The

[1] Any use of trade, product, or firm names is for descriptive purposes only and does not constitute endorsement by the U.S. Government.

resistivity drops to a value of 10 ohm-m at a depth of 58 m. A resistivity this low is probably due to clay or a clay and sand mixture. At a depth of 99 m the interpreted resistivity drops even further to a value of 6.3 ohm-m attributable to clay.

Well Information

Wells can provide lithologic and geophysical logs of use in geologically interpreting the TEM soundings, however, the number of wells with the required logs in the study area is limited. The National Park Service has drilled wells near Indian Springs (well Y) and Sand Creek (well V) in the GRSA for hydrologic purposes that are ideal for interpreting the TEM soundings (HRS Water Consultants, 1999). The well locations are shown in Figure 2. These wells were drilled and logged to depths of 351 ft (107 m) and 394 ft (120 m) respectively. The induction logs are shown in Figure 4. The resistivity log for well V gradually decreases from a high of 670 ohm-m at a depth of 16 m to about 23 ohm-m at a depth of 76 m. A marked decrease starts at 83 m and continues to a relative low of 9.7 ohm-m at a depth of 100 m. At the bottom of the log the resistivity has decreased to 5.7 ohm-m. Well Y behaves somewhat similarly. There is a significant decrease in resistivity from a high of 1000 ohm-m at a depth of 72 m to a low of 6.0 ohm-m at a depth of 80 m. The resistivity decreases further to a value of 3.8 ohm-m near the end of the log.

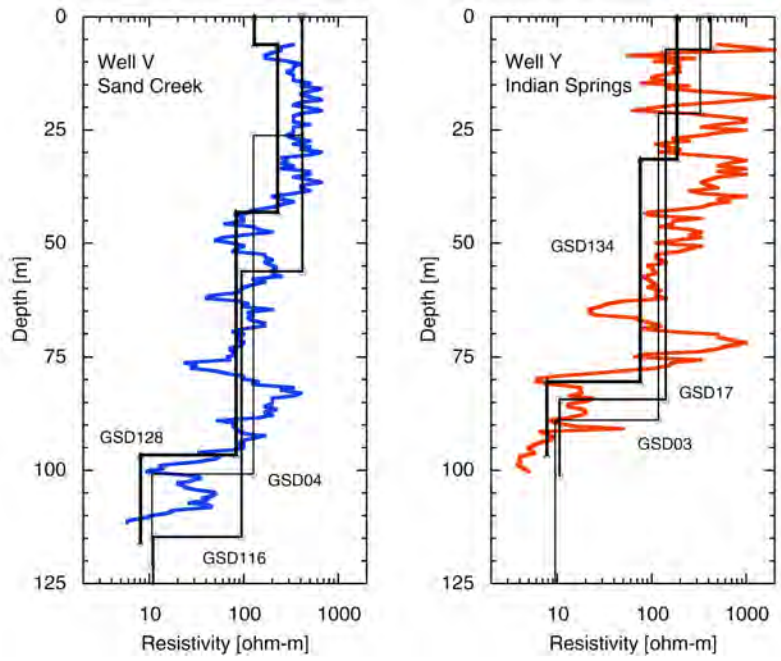

Figure 4: Induction logs from wells V and Y, and interpreted resistivity-depth functions from nearby TEM soundings. See Figure 2 for locations.

The interpreted resistivity-depth functions of the TEM soundings nearest the wells are plotted over the well logs in Figure 4. The general agreement between the induction logs and the TEM soundings is quite good. In particular, the final decrease in the induction logs corresponds to a decrease in interpreted layer resistivity.

Using the lithologic logs as a key, the induction log values for the wells were sorted into categories of sand, gray clay, and blue clay. Histograms of well-log resistivities for these categories are

shown in Figure 5 along with their geometric mean. The average resistivities of the lithologies are: sand 177 ohm-m, gray clay 21.4 ohm-m, and blue clay 6.9 ohm-m. The large separation between these three categories is significant and allows the resistivity values to be used to predict lithology.

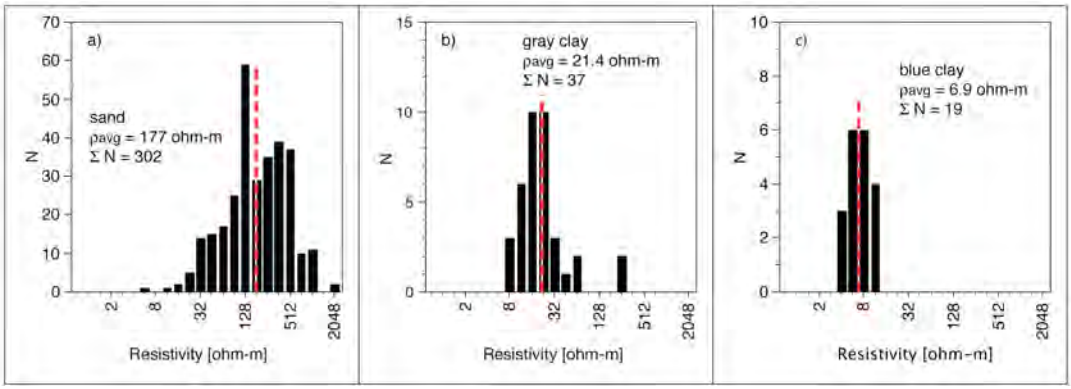

Figure 5: Induction log histograms from wells V and Y sorted by lithology. The geometric mean of the resistivity values is shown as a dashed red bar.

Interpretation

Three cross sections were constructed from the TEM soundings; their locations are shown in Figure 6 in relation to gravity data, which reflects the depth of the structural basin underlying the San Luis Valley. The cross sections (see Figure 7) show the boundaries and resistivity values from the 1-D TEM interpretations. Based on the well-log analysis, parts of the cross sections were color coded. These include a resistive, near-surface zone with resistivities of greater than 100 ohm-m, a deep conductive (low resistivity) zone with resistivities less than 10 ohm-m, and a zone with intermediate resistivities (10-100 ohm-m). The cutoff resistivities were chosen based on the histograms in Figure 5. Also shown in the cross sections are the highest shoreline level (2335 m) of Lake Alamosa mapped by Machette et al. (2007), and the range of water table levels in the area in 1980 (Crouch, 1985).

The Antelope Springs cross section (A-A') is located north of the sand dunes. The near-surface, resistive unit is interpreted to be a sand unit about 100 m thick (color coded tan). This unit is represented in the geophysical model by two layers. The sand unit thins near sounding 124 to 10 m or less and consists of only one layer in the geophysical model. The second layer to the west of sounding 124 has resistivities in the range of 67 to 88 ohm-m. We interpret this to be a mixture of sand and clay with a small amount of clay. The TEM measurements are not able to resolve thin layers; interbedded sand and clay will appear as a single layer with a resistivity that is an average of its constituents. The third layer from sounding 117 to the west ranges in resistivity from 18 to 60 ohm-m. Based on the well-log analysis this is a mixture of sand and clay. The deepest unit westward of sounding 118 has resistivities of 6.6 to 11 ohm-m indicative of the blue clay. The eastward extent of the blue clay is around sounding 118. Sounding 112 on the east end of the profile has a high basement resistivity suggesting that the surface sand unit is underlain by crystalline bedrock of the Sangre de Cristo Mountains.

The Sand Creek cross section (B-B') has a near-surface resistive zone which is interpreted to be a sand layer. The sand has a thickness of almost 200 m on the east end of the section. The sand gradually thins to the west becoming about 20 m thick near sounding 133. The deep conductor, which is interpreted to be blue clay, goes from the west end of the line to sounding 116. Further eastward the basement resistivity is twice as resistive indicating that the blue clay is not present or is mixed with sand, possibly through interfingering of the deposits. On the east end of the section the basement has a

resistivity of 1100 ohm-m suggesting that the surface sand rests directly on crystalline bedrock. Between soundings BP03 on the west and 128 on the east, there is an intermediate resistivity zone that is probably a mix of sand (or gravel) and clay.

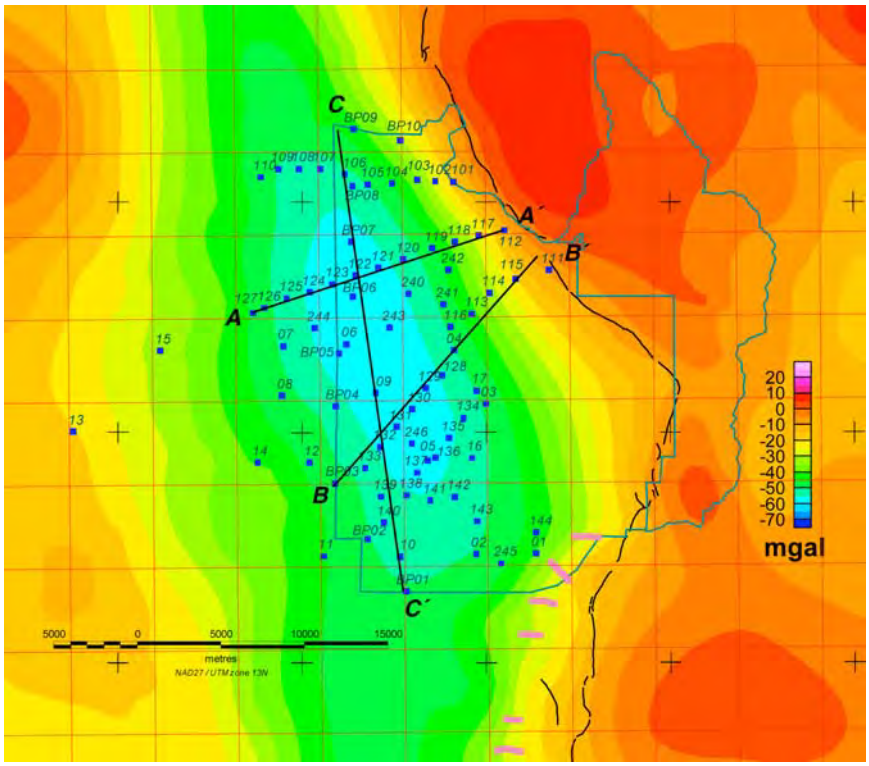

Figure 6: The isostatic residual gravity map shows a low over the western part of the GRSA that corresponds to a deep basin of the Rio Grande rift (gravity data courtesy of B. Drenth, USGS). TEM sounding locations are shown as blue squares. The bold black lines are the locations of cross sections shown in Figure 7. The curving black lines represent the mapped range front faults (U.S. Geological Survey and Colorado Geological Survey, 2006). Additional TEM soundings (marked in magenta) are part of a separate study investigating faults parallel to the range front (Grauch et al., 2010).

The north-south cross section (C-C') has a resistive surface layer that is 40 m thick at the north end of the line (sounding BP09). This unit thickens to the south with a maximum thickness of 125 m at sounding BP07 and then thins to a thickness of 21 m at sounding 139. The deep conductor starts at a depth of 107 m at sounding BP09 reaching its maximum depth of 194 m at sounding 122. To the south the conductor continues to rise toward the surface, which falls away to the south. At the south end of the line (sounding BP01) the conductor is only 51 m deep. A zone of intermediate resistivities (18 to 91 ohm-m) separates these surface and basement units. Most of the soundings are best fit with four-layer models with a few soundings best modeled with three-layers.

The geometry of the deep conductor, which is interpreted to be the blue clay, is interesting and resembles the isostatic residual gravity anomaly (see Figure 6). As the conductor deepens along the north-south cross section the gravity anomaly becomes more negative. Farther south, as the clay becomes shallower, the gravity anomaly becomes more positive. The maximum depth and lowest elevation of the conductor in the Antelope Springs cross section (sounding 122) occurs near the minimum of the gravity anomaly. Similarly for the Sand Creek cross section, the maximum conductor

depth between soundings 130 and 133 corresponds to the most negative gravity anomaly. The correspondence between the depth to the top of the conductor and the shape of the gravity anomaly suggests that the top of the blue clay mimics the shape of the structural basin. This implies that 1) the basin subsided after the clay was deposited, 2) the depth of the clay can be estimated throughout the area of the structural basin by extrapolating the TEM results using the gravity data, and 3) a large volume of sand and interbedded sand and clay was deposited on top of the blue clay within the area of the structural basin. With the addition of age dates on the clay, the first implication provides a timeline for understanding the history of the lake, the basin, and fault activity at the range front that may have implications for seismic hazards today. The second implication presents an intelligent way for regional groundwater modelers to extrapolate information to a larger area. The third implication suggests that the unconfined aquifer above the conductor is thickest over a large area that coincides with the structural basin. This large thickness of sand and interbedded sand and clay had been observed earlier in isolated wells, but its lateral extensiveness had not been anticipated. Questions then arise about the depositional environment and processes that were involved in the accumulation of such a large volume of sediment: Were these processes climatically or tectonically driven?

Also of note is the 60 m decrease in the conductor depth between the Antelope Springs and Sand Creek cross sections. Between the Sand Creek cross section and a line along Big Spring Creek to the south going through soundings 134 and 140 (not shown) there is an additional 50 m decrease in the conductor depth. High-resolution aeromagnetic data (not shown here) over the eastern edge of the San Luis Valley shows a possible fault or drainage near the present location of Sand Creek (Grauch et al., 2010) that could be responsible for this moderately abrupt change of conductor elevation. These examples represent only small fault offsets on the top of the extensive, massive blue clay.

The cross-sections also suggest that the blue clay layer persists to within 5 km or less of the range front, suggesting that it is present under much of the area of the sand dunes. Proximity to the range front is also observed in the TEM sounding profiles to the southeast (Grauch et al., 2010), where the clay terminates against sand at inferred faults that parallel the range front. Deep-water deposition in the lake this close to the range front raises questions about the role of faults in guiding mountain-front recharge into the confined aquifer and about the geologic development of the uplifted mountain front. In contrast, the interbedded sand and clay layers interpreted to lie above the deep conductor (the white layer in the models of Figure 7) appear to vary in resistivity both vertically and laterally and do not extend as far east as the deep conductor. These relations are consistent with the heterogeneity of lithologies that would be expected for sediment deposited at a lake margin that was regressing and transgressing over time and interfingering with alluvium shed from the developing mountain front.

Conclusions

Transient electromagnetic soundings were able to map the location of a ubiquitous conductor in the eastern portion of the San Luis Valley near Great Sand Dunes National Park and Preserve. Using geological and geophysical data obtained from a few deep wells in the study area, the conductor was shown to be caused by an aquitard called the blue clay. The geometry of the conductor resembles the isostatic residual gravity anomaly suggesting that the blue clay conforms to the basin structure. There are indications that faulting may have occurred during deposition of the clay. Away from the high water level of Lake Alamosa the faulting did not disrupt the clay deposition, while closer to the edge of the lake faulting appears to have terminated deposition. A very resistive, near-surface unit corresponds to thick sand deposits, which become thinner at greater distances from the dunes and the mountain front, was also mapped using the TEM soundings. Between this surface unit and the blue clay lies a large

volume of sediments, which thickens over the structural basin. The addition of geologic age data to our results will provide a better history of the relationship between Lake Alamosa, the basin, and fault activity.

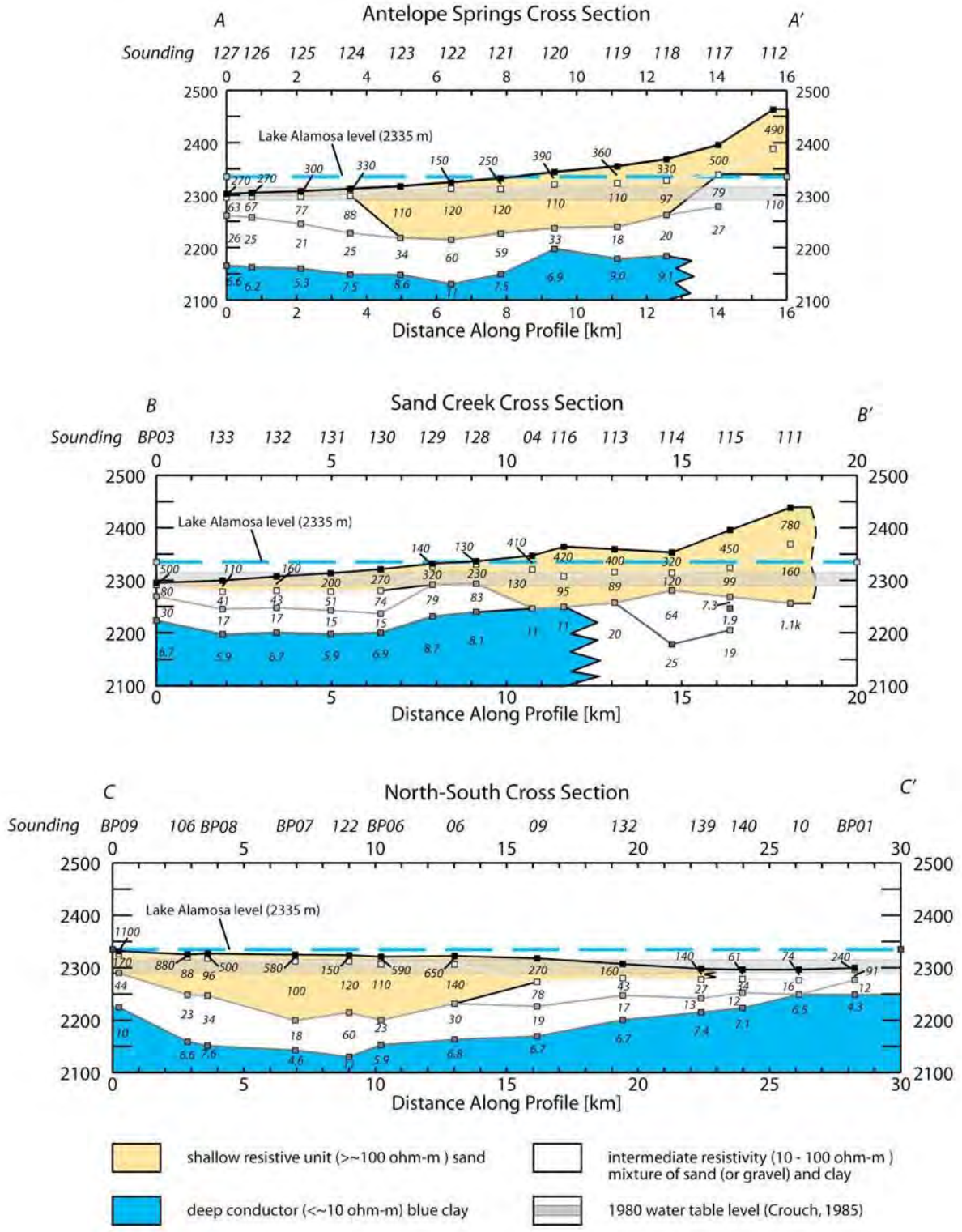

Figure 7: TEM cross sections. Numbers in the cross sections are the interpreted layer resistivities.

References

Brister, B.S., and Gries, R.R., 1994, Tertiary stratigraphy and tectonic development of the Alamosa basin (northern San Luis Basin), Rio Grande rift, south-central Colorado, *in* Keller, G.R., and Cather, S.M., eds., Basins of the Rio Grande Rift: Structure, Stratigraphy, and Tectonic Setting: Special Paper 291: Boulder, Geological Society of America, p. 39-58.

Burroughs, R.L., 1981, A summary of the geology of the San Luis Basin, Colorado-New Mexico with emphasis on the geothermal potential for the Monte Vista graben: Colorado Geological Survey Special Publication 17, 30 p.

Crouch, T.M., 1985, Potentiometric Surface, 1980, and Water-Level Changes, 1969-80, in the Unconfined Valley-Fill Aquifers of the San Luis Basin, Colorado and New Mexico: U.S. Geological Survey Hydrologic Investigations Atlas HA-683, 2 sheets.

Fitterman, D.V., and de Sozua Filho, O.A., 2009, Transient electromagnetic soundings near Great Sand Dunes National Park and Preserve, San Luis Valley (2006 Field Season), Colorado: U.S. Geological Survey Open-File Report 2009-1051, 63 p.

Grauch, V.J.S., Fitterman, D.V., and Drenth, B.J., 2010, Finding faults using high-resolution aeromagnetic data in Great Sand Dunes National Park and vicinity, San Luis Valley, Colorado: Proceedings of the Symposium on the Application of Geophysics to Engineering and Environmental Problems SAGEEP 2010, Keystone Colorado, Environmental and Engineering Geophysical Society.

Harmon, E., 1987, San Luis Valley confined aquifer study, Phase 1, Final report—Prepared for Colorado Water Resources and Power Development Authority: HRS Water Consultants, 138 p.

HRS Water Consultants, 1999, Hydrogeologic investigations Sand Creek and Indian Springs area, Great Sand Dunes National Monument, Colorado: Report to National Park Service 92021–04, 40 p.

Ingersoll, R.V., Cavazza, W., Baldridge, W.S., and Shafiqullah, M., 1990, Cenozoic sedimentation and paleotectonics of north-central New Mexico: Implications for initiation and evolution of the Rio Grande rift: Geological Society of America Bulletin, v. 102, p. 1280-1296.

Leonard, G.J., and Watts, K.R., 1989, Hydrogeology and simulated effects of ground-water development on an unconfined aquifer in the Closed Basin Division, San Luis Valley, Colorado: U.S. Geological Survey Water-Resources Investigations Report 87-4284, 41 p.

Machette, M.N., Marchetti, D.W., and Thompson, R.A., 2007, Ancient Lake Alamosa and the Pliocene to middle Pleistocene evolution of the Rio Grande (Chapter G), *in* M.N. Machette, M-M. Coates, and M.L. Johnson, 2007 Rocky Mountain Section Friends of the Pleistocene Field Trip—Quaternary geology of the San Luis Basin of Colorado and New Mexico, September 7–9, 2007: U. S. Geological Survey Open-File Report, pp. 157-167.

Madole, R.F., Romig, J.H., Aleinikoff, J.N., VanSistine, D.P., and Yacob, E.Y., 2008, On the origin and age of the Great Sand Dunes, Colorado: Geomorphology, v. 99, p. 99-119.

Powell, W.J., 1958, Ground-Water Resources of the San Luis Valley, Colorado: U.S. Geological Survey Water-Supply Paper 1379, 284 p.

Schenk, A.J., and Harmon, E.J., 1999, Hydrogeology of the San Luis Valley, Colorado, *in* Schenk, C.J., ed., Proceedings of National Park Service Research Symposium No. 1, Hydrologic, Geologic, and Biologic Research at Great Sand Dunes National Monument, Colorado, National Park Service, p. 74-90.

Siebenthal, C.E., 1910, Geology and Water Resources of the San Luis Valley, Colorado: U.S. Geological Survey Water-Supply Paper 240, 128 p.

Tweto, O., 1979a, The Rio Grande rift system in Colorado, *in* Riecker, R.E., ed., Rio Grande Rift: Tectonics and Magmatism: Washington, D. C., American Geophysical Union, p. 33-56.

Tweto, O., 1979b, The Geologic Map of Colorado: Special Publication, U.S. Geological Survey, Reston, Virginia.

Upson, J.E., 1938, Physiographic subdivisions of the San Luis Valley, southern Colorado: Journal of Geology, v. 47, p. 721-736.

U.S. Geological Survey and Colorado Geological Survey, 2006, Quaternary fault and fold database for the United States, accessed 29 March 2007, from USGS web site: http//earthquakes.usgs.gov/regional/qfaults/

DIRECT AND INVERSE TDEM METHOD FOR NEAR SUBSURFACE RESISTIVITY IMAGING

I. Merhasin, RAFAEL, Israel

Abstract

We investigate the applicability of TDEM technology for near subsurface mapping. In the direct method, we use time domain response of a multi-layered earth to a dipole excitation based on Fréchet derivatives. Expected sensitivity of detection of a low-conducting layer is analyzed for various ground conductivities and layer depth. Our inversion method is based on Marquard technique and gives 1-D conductivity depth profile for each time sequence measurement.

Introduction

Time-domain electromagnetic (TDEM) technology is widely used by geophysicists for underground layers mapping for depth up to 500 m (Hoekstra and Blohm 1990; Kaufman and Keller 1983). The lateral and vertical resolution of this technique is often better than other EM techniques. But still, in geophysical mappings the aim of the measurements is to recover ground layers structure for depth up to 200-500 m with resolution of tens of meters in the best case. Is it possible to use TDEM technology in archeological or constructional mappings of underground in order to discover details which size is of 1 m in size and depth is of 20-40 m? In this short article we are trying to answer this question.

Time domain response of layered earth to excitation caused by vertical magnetic dipole step change

Frequency-domain response of layered earth to excitation caused by vertical magnetic dipole placed at height h above surface can be expressed as (see Ward and Hohmann, 1987)

$$H_z(\omega) = \frac{m}{4\pi}\int_0^\infty \left[e^{-u_0\cdot(z+h)} + r_{TE}\cdot e^{u_0\cdot(z-h)}\right]\frac{\lambda^3}{u_0}J_0(\lambda\cdot r)\,d\lambda \qquad (1)$$

where m is vertical magnetic dipole moment, r_{TE} is reflection coefficient, $u_n = \sqrt{\lambda^2 - k_n^2}$, $k_n^2 = \omega^2\mu_n\varepsilon_n - i\omega\mu_n\sigma_n$, $\mu_n, \varepsilon_n, \sigma_n$ are layers (1 to n, 0 is for air) magnetic permeability, dielectric permittivity and electric conductivity. Reflection coefficient is given by

$$
\begin{aligned}
r_{TE} &= \frac{1-\hat{u}_1}{1+\hat{u}_1}, \\
\hat{u}_1 &= u_1 \frac{\hat{u}_2 + u_1 \tanh(u_1 h_1)}{u_1 + \hat{u}_2 \tanh(u_1 h_1)}, \\
&\ldots, \\
\hat{u}_n &= u_n
\end{aligned}
\qquad (2)
$$

here h_n are layers width. Transient (or step) response may be obtained by inverse Fourier or inverse Laplace transformation of equation (1). General form of such solution for a layered earth is not known, but for a homogeneous ground it can be cast in the following form (Kaufman and Keller, 1983):

$$
\begin{aligned}
h_z(t) &= \frac{m}{4\pi r^3}\left[\frac{9}{2\theta^2 r^2}\operatorname{erf}(\theta r) - \operatorname{erf}(\theta r) - \frac{1}{\sqrt{\pi}}\left(\frac{9}{\theta r} + 4\theta r\right)e^{-\theta^2 r^2}\right] \\
h_z(t)' &= \frac{m}{2\pi m_0 \sigma r^5}\left[9\operatorname{erf}(\theta r) - \frac{2\theta r}{\sqrt{\pi}}\left(9 + 6\theta^2 r^2 + 4\theta^4 r^4\right)e^{-\theta^2 r^2}\right]
\end{aligned}
\qquad (3)
$$

here $h_z(t)$, $h_z(t)'$ are vertical magnetic field and its time derivative after magnetic dipole termination, $\theta = \sqrt{\frac{\mu_0 \sigma}{4t}}$, and r is horizontal distance from the dipole. The following figure presents homogeneous ground of conductivity 50 mS/m response to unit value magnetic dipole which terminated abruptly:

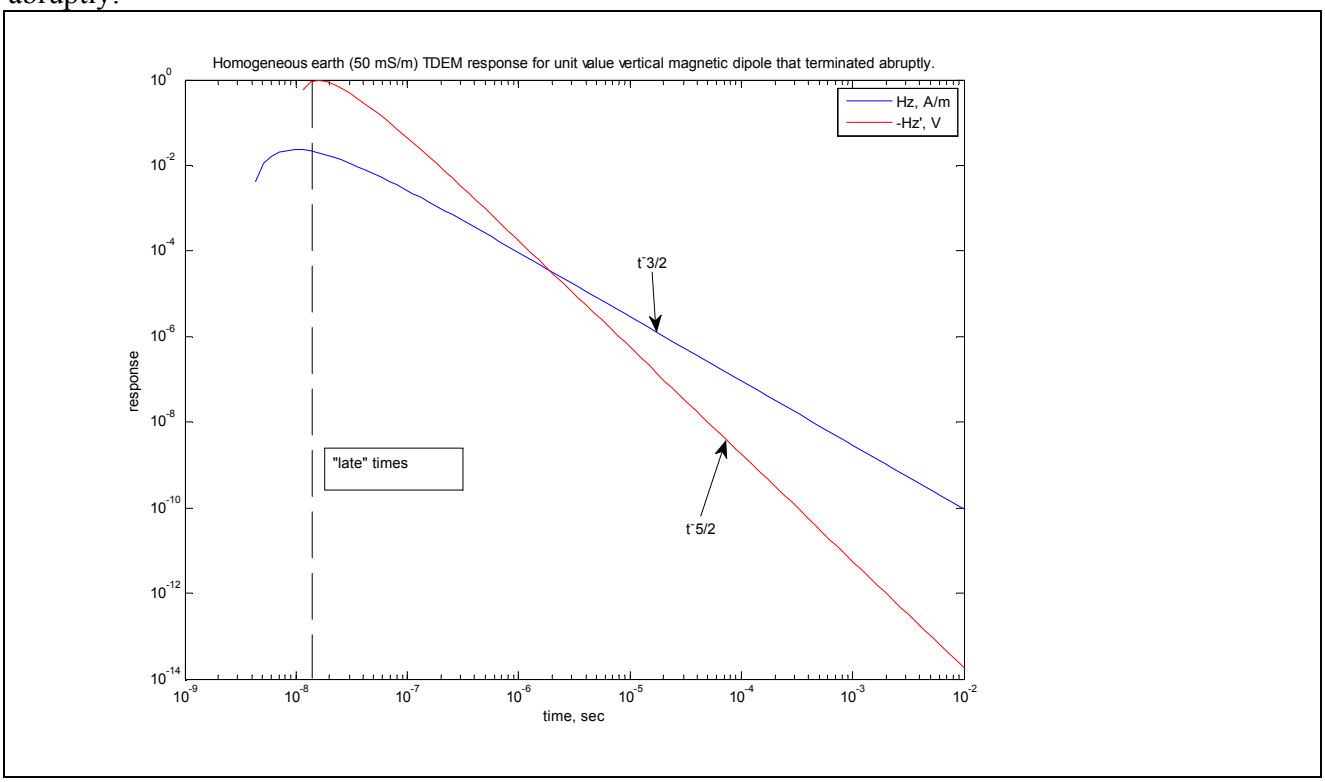

Figure 1: Homogeneous 50 mS/m ground response to vertical magnetic dipole which terminated abruptly.

"Late" time may be defined as a time when both curves change monotonically, i.e. $\mathsf{J}_{\max} = \sqrt{\frac{\mu_0 \sigma}{4 t_{\max}}} = 1$. For late times an asymptotic expression for both fields $h_z(t)$, $h_z(t)'$ can be obtained:

$$h_z(t) = \frac{m}{30}\left(\frac{\sigma\mu_0}{\pi}\right)^{3/2} t^{-3/2}$$
$$h_z(t)' = -\frac{m}{20}\left(\frac{\sigma\mu_0}{\pi}\right)^{3/2} t^{-5/2} \qquad (4)$$

As mentioned before, it is not simple to obtain an analytical expression for an n-layered earth time response for a vertical magnetic dipole. But, fortunately, in recent studies a simple approximate method has been found (see the works of Christensen, 1995, 1996). It is called method of Fréchet derivatives. Layered earth time response is looked for in the following form:

$$h_z(t) = h_z^{(0)}(t) + \int_0^\infty F(\sigma_0, t, z)\cdot(\sigma(z) - \sigma_0)dz$$
$$h_z(t)' = h_z^{(0)}(t)' + \int_0^\infty F(\sigma_0, t, z)_t'\cdot(\sigma(z) - \sigma_0)dz \qquad (5)$$

where $h_z^{(0)}(t) = \frac{m}{30}\left(\frac{\sigma_0\mu_0}{\pi t}\right)^{3/2}$ and $h_z^{(0)}(t)' = -\frac{m}{20}\left(\frac{\sigma_0\mu_0}{\pi}\right)^{3/2} t^{-5/2}$ are homogeneous ground of conductivity σ_0 responses, and analytical form of Fréchet kernel is known:

$$F(\sigma, t, z) = \frac{m}{4\pi\sigma}\mathsf{J}^4\left\{\frac{2u}{\sqrt{\pi}}(2u^2+1)e^{-u^2} - (4u^4+4u^2-1)\operatorname{erfc}(u)\right\},$$
$$\mathsf{J} = \sqrt{\frac{\mu_0\sigma}{4t}}, u = \mathsf{J}z \qquad (6)$$

It is interesting to note, that last expression gives us estimation of expected time delay t in response to structure detail found at depth d in a homogeneous ground:

$$u = \mathsf{J}d = \sqrt{\frac{\mu_0\sigma}{4t}}d \approx 2.5 \qquad (7)$$

Table 1: Time delay in response to structure details in a homogeneous ground

Structure detail depth, m	**10**	**20**	**40**
Time delay, sec	0.2e-6	0.7e-6	2.8e-6

Most existing TDEM systems will have a problem with depth 10 m and time-delay of 0.2 micro sec, but a larger depth should be feasible.

Expression (5) may be recast in the following way:

$$h_z(t_i) = \int_0^\infty F(\sigma_0, t_i, z) \cdot \sigma(z) dz = \sum_j \sigma_j \int_{z_j}^{z_{j+1}} F(\sigma_0, t_i, z) dz$$
$$h_z'(t_i) = \int_0^\infty F'(\sigma_0, t_i, z) \cdot \sigma(z) dz = \sum_j \sigma_j \int_{z_j}^{z_{j+1}} F'(\sigma_0, t_i, z) dz \quad (8)$$

here σ_j are layer conductivities. The last equation gives us a way to calculate time-dependent step response for a point vertical magnetic dipole over layered ground.

Inversion of time domain response of layered earth to excitation caused by vertical magnetic dipole step change for finding ground layers

An inversion problem for TDEM exploration can be formulated in a following way: given time-domain response for magnetic dipole excitation find ground layers structure. From a mathematical point of view we have a problem of solving linear equations system. Indeed, time-dependent response can be written in the form:

$$h_z(t_i) - h^{(0)}(t_i) = \sum_j \widetilde{F_{ij}} (\sigma_j - \sigma_j^{(0)}) \quad (9)$$

where $\widetilde{F_{ij}} = \int_{z_j}^{z_{j+1}} F(\sigma_0, t_i, z) dz$ are Fréchet derivatives forming system matrix, $h_z(t_i), h^{(0)}(t_i)$ are measured and expected response, $\sigma_j, \sigma_j^{(0)}$ are actual and estimated layers conductivities. It seems that a solution of (9) can be obtained simply by inversion of matrix $\widetilde{F_{ij}}$:

$$\sigma_i - \sigma_i^{(0)} = \sum_j \widetilde{invF_{ij}} (h_j - h_j^{(0)}) \quad (10)$$

But, this method does not give a stable and valid solution due to a singularity of matrix $\widetilde{F_{ij}}$. Here we will use a method called Marquardt's method presented in the work of Haoping Huang, 2003.

Let's look for an SVD decomposition of matrix $\widetilde{F_{ij}}$:

$$\tilde{F} = U \Lambda V^T \quad (11)$$

here U and V are eigenvector matrices and Λ is a diagonal matrix whose elements are singular values. So let's look for a solution of (9) in the following form:

$$d\sigma_i = \sigma_i - \sigma_i^{(0)} = \sum_j \widetilde{pinvF_{ij}} (h_j - h_j^{(0)}),$$
$$\widetilde{pinvF} = V \Lambda (\Lambda^2 + e^2 I)^{-1} U^T \quad (12)$$

here I is a unit matrix and e is a damping parameter defined as a certain percent of a largest singular value l_1. So, at every step of iteration we will update values of layers conductivities: $\sigma_i = \sigma_i^{(0)} + d\sigma_i$.

Simulation results

We start simulation using direct response model (8) in order to find sensitivities expected at structure details detection experiment for various detail depth and various grounds. Let us use 3-layer model: ground followed by 1 m width low-conducting layer at different depth and then ground again. Ground conductivity will be set at 5 and 50 mS/m. Simulation results are presented at Fig. 2.

One can conclude from Fig. 2 that low-conducting layer detection sensitivity depends on the apparent ground conductivity and low-conducting layer depth. For small depth (less than 5-8 m) there is a technical problem to observe a valuable change by TDEM system, especially for less conductive ground because of very short response time (less or equal to 1 micro-sec). Otherwise, for a deeper laying layer (15-25 m) and for a more conductive ground (50 mS/m) it is expected to get a valuable change in response (as compared to a homogeneous ground) at time-delay around 0.1 msec.

In an inverse problem simulation we have tried our algorithm on a synthetic data obtained by a direct simulation for a 5-layer ground including 1m width low-conducting layer at 20 m depth. Simulation results compared with "actual" data are presented at Fig. 3. One can see that inversion results are in good agreement with "actual" data.

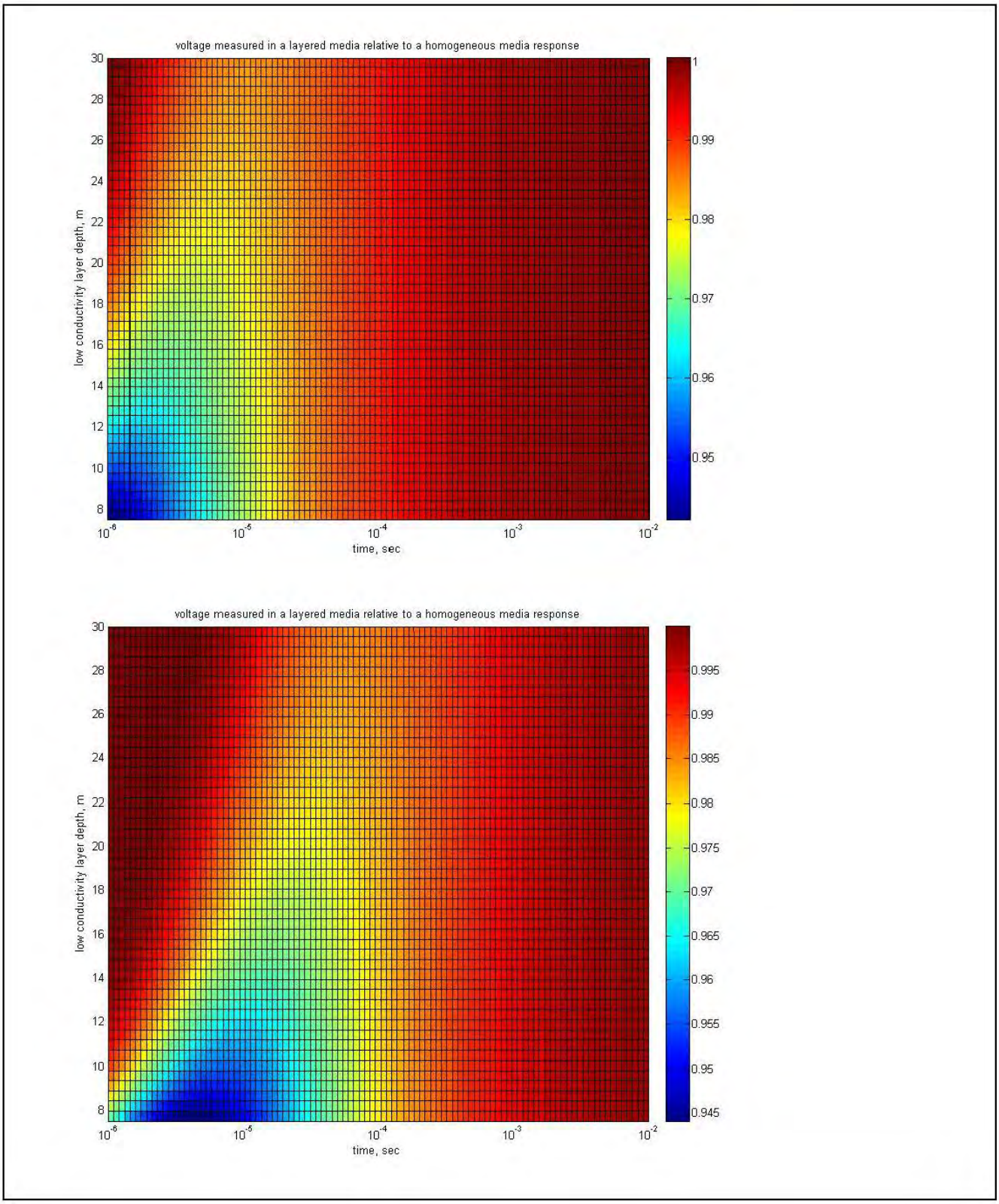

Figure 2: Voltage response of TDEM system (relative to a homogeneous ground) for detection of 1 m width low-conductivity layer. Top panel: ground conductivity is 5 mS/m, bottom panel: 50 mS/m.

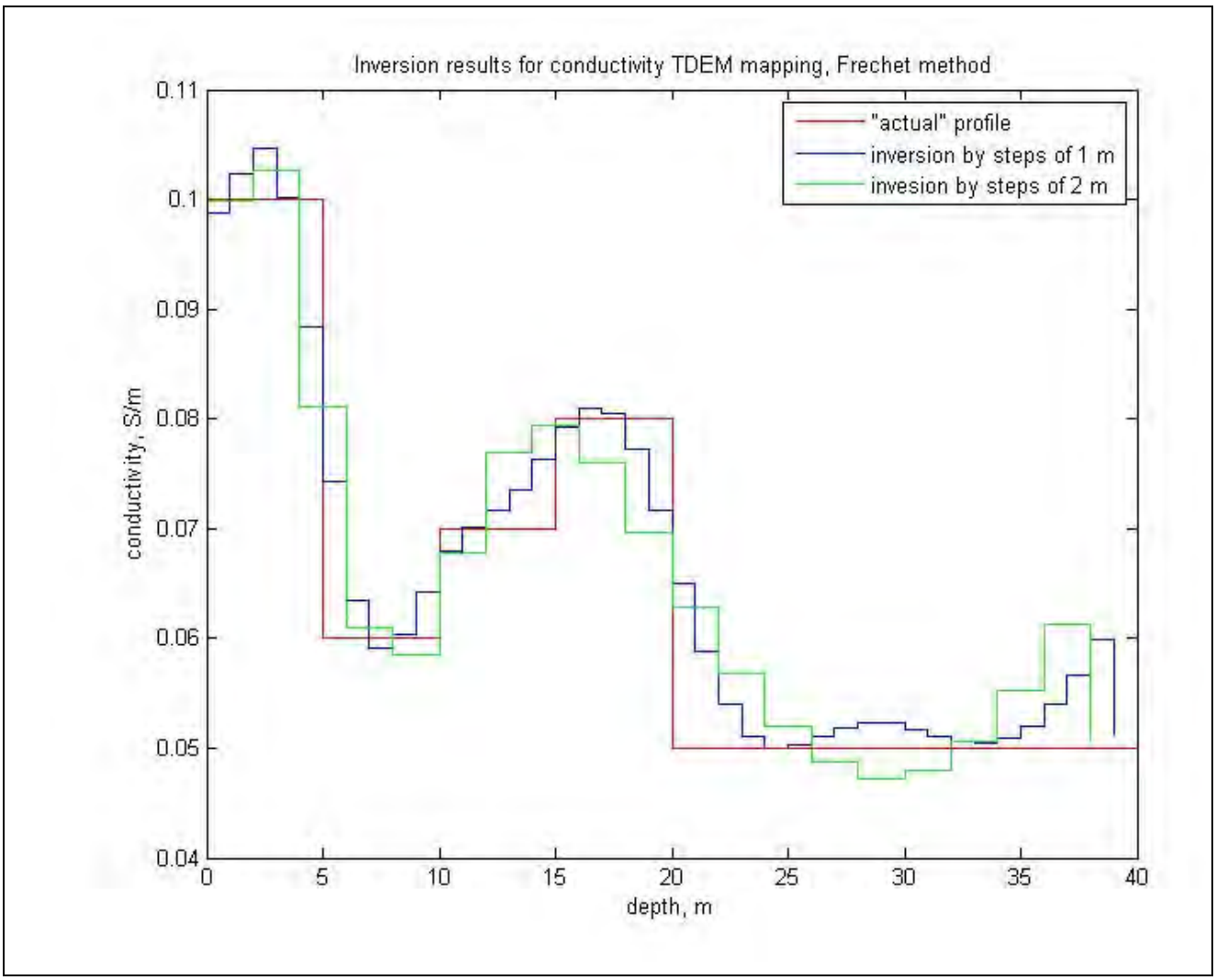

Figure 3: Inversion simulation results for conductivity versus depth mapping

Conclusions

We have presented direct and inverse methods for processing results of TDEM measurements of time-domain response of a layered ground to vertical magnetic dipole. Direct method is based on analytical form of Fréchet kernel and subsequent integration on layers width. Expected sensitivity of detection is analyzed for various ground conductivities and layer depth.

Our inversion method based on Marquard technique and gives 1-D conductivity depth profile for each time sequence measurement. Simulation results were in good agreement with "actual" data obtained from direct simulations and this may serve a basis for using TDEM technology for near subsurface mapping.

References

Christensen, N.B., 1995, Imaging of central loop transient electromagnetic soundings, *Journal of Environmental and Engineering Geophysics*, **0**(1), 53–66.

Christensen, N.B., 1996, Imaging of transient electromagnetic soundings using a scaled Fréchet derivative, in B.H. Jacobsen, K. Mosegaard, and P. Sibani (ed.), *Inverse Methods. Interdisciplinary Elements of Methodology, Computation and Applications*, Lecture Notes in Earth Sciences, vol. 63, Springer-Verlag, Berlin-Heidelberg, ISSN 0930-0317, ISBN 3-540 - 61693-4.

Haoping Huang and Douglas C. Fraser, 2003. Inversion of helicopter electromagnetic data to a magnetic conductive layered earth**,** *GEOPHYSICS*, VOL. 68, NO. 4 (JULY-AUGUST 2003); P. 1211–1223

Hoekstra, P and M. W. Blohm, 1990. Case histories of time domain electromagnetic soundings in environmental geophysics. In Geotechnical and Environmental Geophysics, Vol II, Stanley H. Ward, ed. Society of Exploration Geophysics, Tulsa, Oklahoma, pp. 1-15.

Kaufman, A.A and G. V. Keller. 1983. Frequency and Transient Soundings. Elsevier Publ., New York, pp. 315-340

EQUIVALENCE ANALYSIS OF DC AND EM DATA FOR LAYERED MODELS USING THE RESOLUTION MATRIX

Charles H Stoyer, Interpex Limited, Golden, CO

Abstract

Ridge-regression inversion (Inman, 1975) is used to formulate and carry out the inversion of DC resistivity and Electromagnetic (EM) data. A by-product of this process is the resolution matrix, which is symmetric and defines the linear combinations of the parameters which have been resolved in the inversion process. Subtracting the resolution matrix from the identity matrix yields the linear combinations of the parameters which are *not* resolved. The implication is that the model can be varied indefinitely in these directions without affecting the fitting error. In practice, there can be a limit to the extent to which the model can be varied in these unconstrained directions.

After obtaining a best fit and the resolution matrix, the model is varied in the unconstrained directions to find the point where the fitting error exceeds the best fit error by a specified amount or until the parameter variation exceeds a specified limit. Variation is done in both increasing and decreasing directions for each original parameter. For m parameters, the resulting collection of 2m+1 models and synthetic curves shows the range of models which satisfactorily fit the data and their corresponding synthetic curves. The results concur with known equivalence principles for thin surface and buried layers and the method provides a convenient means of illustrating the equivalence status of any inversion result.

Introduction

The principle of equivalence states that a model which fits the data may not be the only possible model which will fit the data. In a perfect world, where a resistivity curve is sampled continuously over spacings from zero to infinity with no measurement errors, the layered model which perfectly fits these data would be unique. However, resistivity soundings are not sampled continuously, they are sampled over a limited range, and they are subject to both measurement errors and geologic noise. Electromagnetic methods do not respond well to resistive layers, and this adds an additional complication for those measurements. In particular, finite sampling range of any data set can limit the resolution of the near-surface and deep parts of the section and introduce additional equivalence there.

Equivalence analysis attempts to illustrate the degree to which the model can vary from the best fit model and still provide almost the same fit to the data. It assumes linearity and does not show the complete range of possible models; it is intended only to illustrate the constraints on parameter resolution.

The resolution matrix is a by-product of the inversion process. This matrix shows the linear combinations of the parameters which are resolved. This matrix is used as a guide in the equivalence analysis process in order to dictate which directions the model can (should be able to) be adjusted without affecting the fitting error. In the examples shown here, the adjustments are performed incrementally until the fitting error reaches 1.2 times the best fit error. This determines the range for this equivalent parameter. The test is carried out by both increasing and decreasing the parameter, so that for m parameters, 2m equivalent models are generated.

Parameters which are varied by a factor of 100 from their initial values are considered widely

variable (not at all constrained) and the process is stopped at this point.

Fixed parameters are not used in the equivalence analysis.

Forward Problem for DC Resistivity (VES)

The ridge regression method of inversion is basically a method of least squares fitting of nonlinear data. This is to say that the relationship of the (synthetic) data to the model parameters is nonlinear. We start by defining $\boldsymbol{o}$ as the vector of observed values, $\boldsymbol{c}$ as the corresponding vector of synthetic values and $\boldsymbol{p}$ as the vector of model parameters. For the DC resistivity problem and a given model $\boldsymbol{p}$, the synthetic values, $\boldsymbol{c}$, are calculated by

$$c_i(\boldsymbol{p}) = \int_0^\infty RHO(g)\, J_1(g \cdot AB_i/2)\, dg \qquad (1)$$

where $\boldsymbol{p}$ is the parameter vector ($\rho_1, \rho_2, \rho_3, \ldots, r_n, h_1, h_2, h_3, \ldots, h_{n-1}$), with r denoting layer resistivity and h denoting layer thickness. The value c_i is the apparent resistivity for $AB_i/2$ (i=1,m), RHO(g) is the apparent resistivity in the Hankel Wavenumber domain (determined by recursion relations from the layer parameters, J_1 is the Bessel function of order 1 and g is the Hankel wavenumber. RHO(g) is determined by starting with eq. (2a), recursively solving eq. (2b) and (2c) and obtaining the final result using (2c):

$$k_n = \rho_n \qquad (2a)$$

$$r_1 = (\rho_1 - k_{i-1})/(\rho_i + k_{i-1}) \qquad (2b)$$

$$k_i = (1 \exp(-2\, g h_i))/(1 + \rho_i \exp(-2\, g h_i)) \qquad (2c)$$

$$RHO(g) = \rho_1\, k_1 \qquad (2d)$$

This problem is clearly nonlinear. Having the model parameters, $\boldsymbol{p}$ and using linear digital filters like those developed by Anderson (1989), we can easily calculate the synthetic data, $\boldsymbol{c}$, but having the data, there is no way to calculate the parameters. Equation (1) is called the "forward problem" and obtaining the parameters, $\boldsymbol{p}$, from the observed data, $\boldsymbol{o}$, is called the "inverse problem".

Linearization of the Forward Problem

A forward problem such as is shown above in eq. (1) through (2d) is nonlinear and must be linearized in order to solve the inverse problem. Linearization is carried out by expanding the forward problem in terms of a Taylor series and retaining only the first two terms. In order to do this, we need a starting or seed model, $\boldsymbol{p_o}$. We then expand the forward solution around this seed model using a (small) incremental model, $\Delta\boldsymbol{p}$.

$$c(\boldsymbol{p_o}+\Delta\boldsymbol{p})_i = c(\boldsymbol{p_o})_i + \Sigma(\Delta p_j\, \partial c(\boldsymbol{p_o})_i/\partial p_j), \qquad (3)$$

With the sum being carried out over j-1,n_p, n_p being the total number of parameters. In matrix notation, with $\boldsymbol{A}$ being the Jacobian matrix of partial derivatives, $\partial c(\boldsymbol{p_0})_i/\partial p_j$, this becomes

$$\boldsymbol{c}(\boldsymbol{p_0}+\Delta\boldsymbol{p}) = \boldsymbol{c}(\boldsymbol{p_0}) + \boldsymbol{A}\,\Delta\boldsymbol{p} \qquad (4)$$

Now, we wish to have the model $\boldsymbol{p_0}+\Delta\boldsymbol{p}$ match the observations, $\boldsymbol{o}$. So we write

$$\boldsymbol{O} = \boldsymbol{c}(\boldsymbol{p_0}) + \boldsymbol{A}\,\Delta\boldsymbol{p} \qquad (5)$$

or

$$\boldsymbol{d} = \boldsymbol{o} - \boldsymbol{c}(\boldsymbol{p_0}) = \boldsymbol{A}\,\Delta\boldsymbol{p} \qquad (6)$$

where $\boldsymbol{d}$ is the difference vector between the present synthetic values and the observed data. The problem is now in linear form and we can solve it iteratively by taking sufficiently small steps in the model correction, $\Delta\boldsymbol{p}$, so that we do not violate the linear assumption and the fact that, even though in most cases there are far more observations than model parameters, the problem is underdetermined. We can address both of these concerns by using "damping" or "regularization".

Now this is solved by calculating the squared error and setting its derivative to zero:

$$E_{sq} = (\boldsymbol{d}. - \boldsymbol{A}\,\Delta\boldsymbol{p})^t\,(\boldsymbol{d} - \boldsymbol{A}\,\Delta\boldsymbol{p}) \qquad (7)$$

Now, the system can be stabilized by adding a term proportional to the magnitude of the parameter correction, $\Delta\boldsymbol{p}$:

$$(\boldsymbol{d}. - \boldsymbol{A}\,\Delta\boldsymbol{p})^t\,(\boldsymbol{d} - \boldsymbol{A}\,\Delta\boldsymbol{p}) + k^2\,\Delta\boldsymbol{p}^t\Delta\boldsymbol{p} \qquad (8)$$

Where k^2 is a Lagrange multiplier, damping factor, trade-off parameter or ridge parameter. For large values of k, the parameter correction will be small and for small values it can be large, depending on the size of the difference, $\boldsymbol{d}$. Taking the derivative of the quantity in eq. 8 with respect to each model parameter and setting it to zero, we get the equation which we need to solve to find the model correction $\Delta\boldsymbol{p}$:

$$\boldsymbol{A}^t\,\boldsymbol{d} = (\boldsymbol{A}^t\,\boldsymbol{A} + k^2\,\boldsymbol{I})\,\Delta\boldsymbol{p} \qquad (9)$$

The optimum value for k is found by trial and error at each iteration. Several values are tried; the model correction is added, a forward calculation is carried out, and the RMS error is found. The value of k which gives the best improvement (lowest error) is then used to make the model correction for this iteration.

Figure 1 shows a cartoon illustrating the behaviour of the RMS error after model correction using variable k values (this is called the "ridge trace"). Generally, the system becomes more linear (and therefore stable) as convergence is reached. After convergence is reached, no further improvement is possible and making k too small will only increase the error.

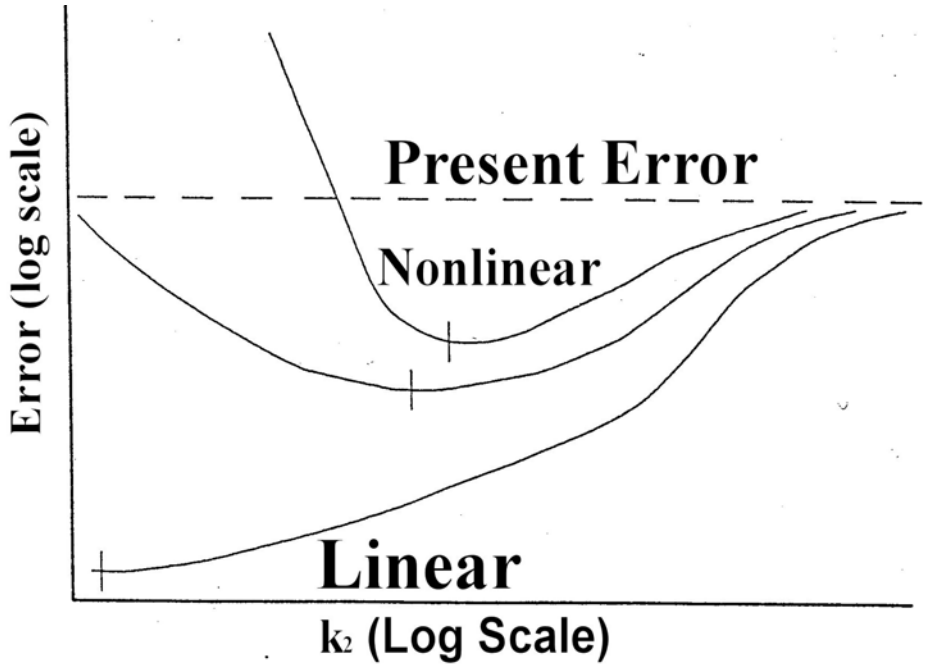

Figure 1. Behavior of RMS error after model correction vs. damping (ridge trace) for varying linearity conditions**.**

Resolution of Parameters

Once a solution to the inverse problem is obtained, it is desirable to assess the meaning of the results. Most inverse solutions contain a degree of nonuniqueness, so that many different models will fit the data equally well. Most often, there is an interconnection among the different parameters; so that changing one of the parameters and adjusting the remaining parameters will preserve the best fit condition. Provided we do not stray too far from the linearity condition, the resolution matrix shows us how to make those adjustments.

The condition of convergence is stated by

$$\Delta \boldsymbol{p} = 0 = (\boldsymbol{A}^t \boldsymbol{A} + k^2 \boldsymbol{I})^{-1} \boldsymbol{A}^t \boldsymbol{d}. \qquad (10)$$

Where k is the smallest value that does not increase the fitting error and the term multiplying $\boldsymbol{d}$ can be thought of as the inverse of $\boldsymbol{A}$ or "$\boldsymbol{A}^{-1}$". Substituting for $\boldsymbol{d}$ from eq. (6) gives

$$(\boldsymbol{A}^t \boldsymbol{A} + k^2 \boldsymbol{I})^{-1} \boldsymbol{A}^t \boldsymbol{A} \Delta \boldsymbol{p} = \boldsymbol{R} \Delta \boldsymbol{p} = \Delta \boldsymbol{p} = 0 \qquad (11)$$

where $\boldsymbol{R}$ (= $(\boldsymbol{A}^t \boldsymbol{A} + k^2 \boldsymbol{I})^{-1} \boldsymbol{A}^t \boldsymbol{A}$) is called the parameter resolution matrix. This matrix equation implies that there are n linear averages of $\Delta \boldsymbol{p}$ which are known. This also implies that there are n linear combinations of $\boldsymbol{p}$ which are *not* known, since any large variation in $\Delta \boldsymbol{p}$ will result in a corresponding variation in $\boldsymbol{p}$ (Glenn, et al, 1973). If the resolution matrix is the identity matrix, then the linear averages are the individual parameters themselves and we have perfect resolution. If it is not, then the parameters themselves are not resolved, but certain combinations of them are resolved.

In practice, the parameters ρ_j and h_j are *not* actually used, but the *logarithms* of the values are used. This is because resistivity curves behave in a logarithmic fashion and using the logarithms of the parameters instead of the parameters themselves solves two problems. First it makes the system more linear and second it removes the issue of parameters with large values dominating the system. We must keep this in mind when we view the resolution matrix because this makes the linear combinations products and quotients of the real parameters, rather than sums and differences.

We can take, for example, a three layer DC resistivity problem. If all layers are thick with respect to the depth of burial and if the long and short spacing asymptotes of the sounding curve are defined, we can expect good resolution, and $\boldsymbol{R}$ should be nearly equal to $\boldsymbol{I}$. If this is not the case, $\boldsymbol{R}$ will be different from $\boldsymbol{I}$, and the difference will depend on the nature of the ambiguity in the model. For instance, in the case of a thin intermediate resistive layer, we would expect the transverse resistance to be resolved, and the longitudinal conductance to be unresolved. Remembering that we are using logarithms of resistivity and thickness (as described above), we would expect $\boldsymbol{R}$ to look like that shown in Table 1.

Table 1. Resolution matrix for thin resistive second layer in 3-layer model.

	ρ_1	ρ_2	ρ_3	h_1	h_2
ρ_1	1	0	0	0	0
ρ_2	0	0.50	0	0	0.50
ρ_3	0	0	1	0	0
h_1	0	0	0	1	0
h_2	0	0.50	0	0	0.5

Note that $\boldsymbol{R}$ is symmetric, so only the lower triangular part need be shown. Since we are dealing with logarithms, we see that this resolution matrix shows the following:

1. resistivity 1 is resolved (ρ_1 = constant).
2. transverse resistance 2 is resolved ($\rho_2^{1/2}\, h_2^{1/2}$ = constant).
3. resistivity 3 is resolved (ρ_3 = constant).
4. thickness 1 is resolved (h_1 = constant).
5. transverse resistance 2 is resolved ($\rho_2^{1/2}\, h_2^{1/2}$ = constant) - (same as #2).

Note that there is *not* a line in the matrix which shows that the longitudinal conductance of layer 2 is resolved, so it is apparently unresolved as expected.

Generally, the resolution matrix will be far more complicated than this simple example. For instance, layers will rarely be truly thick or thin. Thus, adjustments in a buried layer will require adjustments in the layers above and below, both in resistivity and thickness, in order to maintain a good fit. So inspection of the resolution matrix reveals something about the nonuniqueness in the model, but it does not display it in a transparent (or "user friendly") fashion. It also does not respond to the nonlin-

earity of the real problem, but shows only the resolution of the linearized problem. We must therefore look to other methods to display the information and to account for nonlinearity.

Semi-linear Equivalence Analysis

Semi-linear equivalence analysis allows us to represent the information present in the parameter resolution matrix and display the range of equivalent models predicted. The full nonlinear forward problem is used to constrain the limits of these variations to lie within a certain specified error. This is one step beyond the display of the resolution matrix, and is better because it gives a more transparent picture and allows the limits to be defined by the nonlinear theory.

If the resolution matrix shows us the known linear combinations of parameters, then [**I** - **R**] shows us the unknown linear combinations of parameters. This means that, according to the linearized theory, we can vary the model as much as we like in the direction given by any row (column) of [**I** - **R**], without increasing the fitting error. This is because, according to the linear theory, these combinations of parameters have not been resolved. Of course, the problem is nonlinear, so this will work only over a limited range. We can use the real forward problem to determine the range over which this is valid.

The procedure is to first perform an inversion to obtain a satisfactory result. The resolution matrix is a by-product of this inversion. There will be one row in the resolution matrix for each original parameter. Each row is a re-parameterized parameter which is resolved. Subtract this matrix from the identity matrix to obtain a matrix which shows the parameters that are not resolved. Now, for each row in the matrix, the diagonal element refers to the i^{th} original parameter. Vary this parameter slightly and adjust the other parameters in the row accordingly. Perform a forward calculation and compare to the data. For both increasing and decreasing values, find the point where the RMS error is increased to some preset level (in this case 1.2 times the original best-fit RMS error). This defines the limit of allowed variation of this re-parameterized parameter.

Numerical Example

The first example is a synthetic Schlumberger (VES) curve with 5% random noise added. The model, synthetic data from the model and the synthetic data with noise are shown in Figure 2.The synthetic data are indicated by the line and the synthetic data with noise are indicated by the boxes on the graph.

We perform an inversion using the true model as the starting model. Then, we perform an equivalence analysis using the resolution matrix as described above. The final inverted model and equivalent models are shown in Figure 3. The best fit model is shown by the red line in the model graph and the dashed green lines are the equivalent models, two for each parameter. The corresponding resolution matrix is shown in Table 2. The RMS fitting error is 3.89%, which is consistent with 5% noise having been added to the data but does show that we are fitting the noise to some degree.

Keeping in mind that the parameters used in the inversion were the logarithms of the resistivities and thicknesses, we must read the rows of the resolution matrix as powers rather than as multiplicative factors. For instance, the second row of the resolution matrix would say that

$$\rho_1^{-0.03} \bullet \rho_2^{0.52} \cdot h_1^{-0.07} \cdot h_2^{0.48} = \text{constant} \cdot (1 \pm 0.01 \cdot \text{RMS fit})$$

The resolution matrix in Table 2 shows that the third layer resistivity is resolved since the third row (or column) shows no linear dependence on any of the other parameters. The first row (or column)

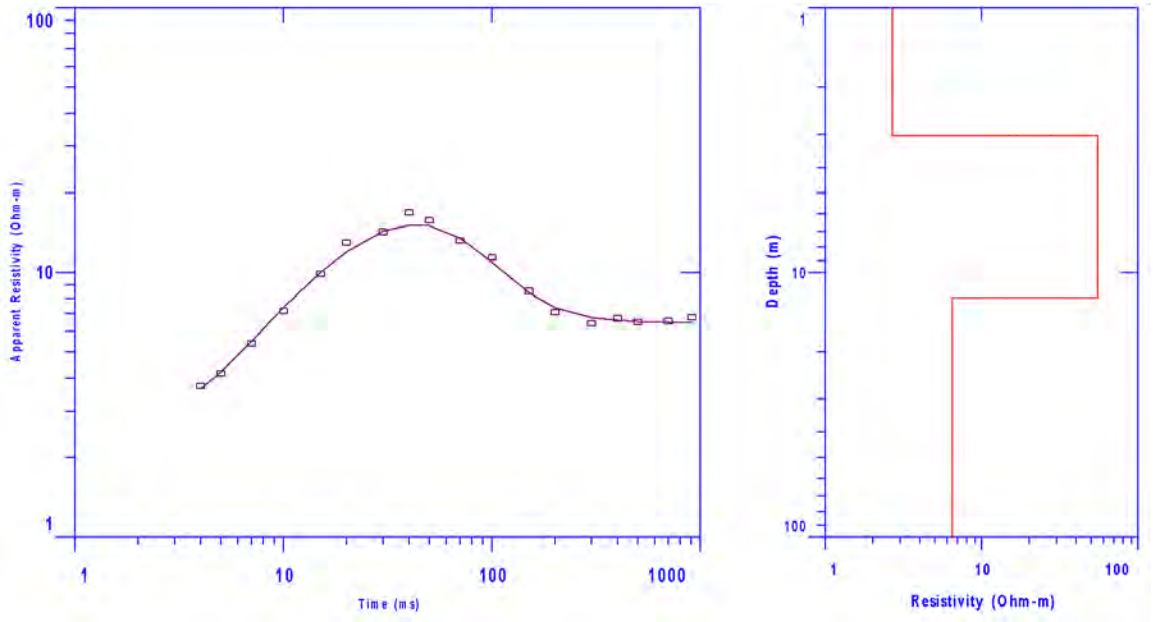

Figure 2. Synthetic Schlumberger data for numerical example.

shows that the surface resistivity is fairly well resolved as the linear dependence on the other parameters is small. Note that the first layer thickness has the strongest interdependence. This makes sense because the layer is thin compared with the shortest spacings so the asymptote is not reached. The fourth row (or column) shows that the first layer thickness is also fairly well resolved and that the strongest interdependence is with the first layer resistivity. The second and fifth rows (or columns) show that the second layer is not well resolved and has minor interdependence with the parameters of the other layers.

The results of the equivalence analysis are shown graphically in Figure 3 with a numerical summary in Table 3. These results were obtained by varying the model in the directions shown to be unconstrained by the matrix ($\boldsymbol{I} - \boldsymbol{R}$) until the RMS error increased to 1.2 of the best fit value. The variation was both increasing and decreasing so we have two equivalent models for each parameter.

Table 2. Resolution matrix for the inversion result shown in Figure 2

	ρ_1	ρ_2	ρ_3	h_1	h_2
ρ_1	**0.91**	**0.03**	**0**	**0.11**	**0.02**
ρ_2	**0.03**	**0.52**	**0**	**0.07**	**0.48**
ρ_3	**0**	**0**	**1**	**0**	**0**
h_1	**0.11**	**0.07**	**0**	**0.87**	**0.06**
h_2	**0.02**	**0.48**	**0**	**0.06**	**0.50**

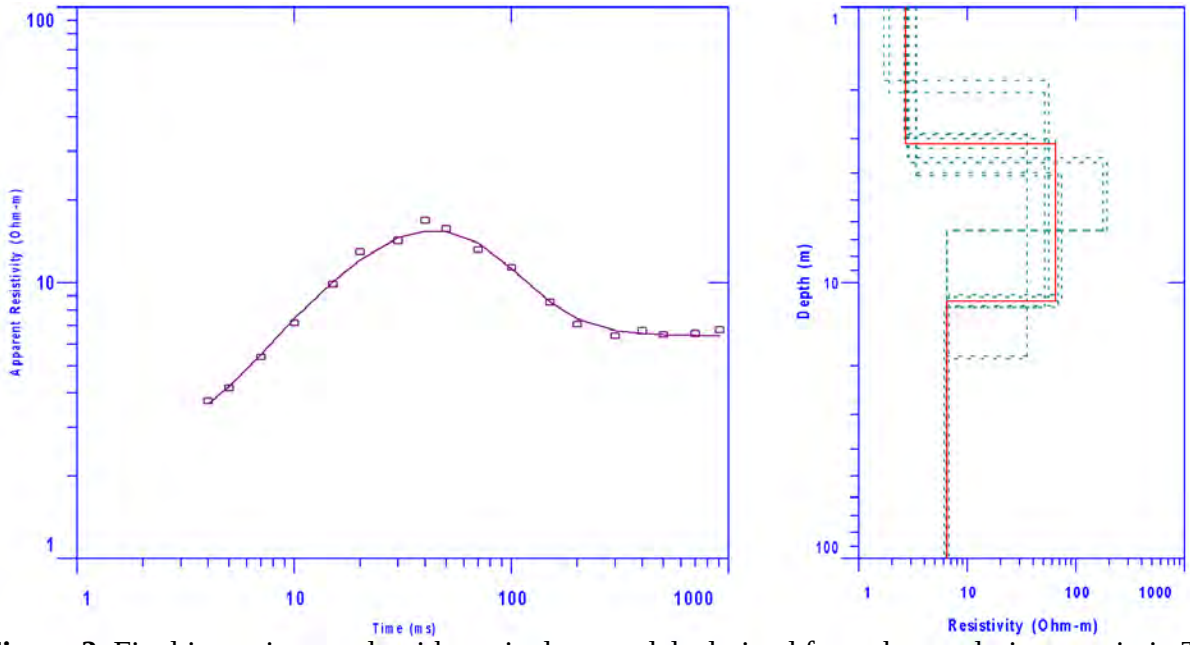

Figure 3. Final inversion result with equivalent models derived from the resolution matrix in Table 2.

Table 3. Summary of equivalence analysis results displayed in Figure 3**.**

Parameter	Min	Best	Max	+/- %
ρ_1	1.70	2.70	3.36	31%
ρ_2	35.2	64.1	193	123%
ρ_3	6.12	6.41	6.71	5%
h_1	1.84	3.12	4.07	36%
h_2	2.79	8.52	15.97	77%

We see that the resistivity of the third layer, shown by the resolution matrix to be well resolved, varies only slightly in Figure 3 and in Table 3 we see it is consistent with perfect resolution and 5% noise. The parameters of the first layer, known to be fairly well resolved but interdependent, have considerably more variation but not nearly as much as the parameters of the second layer, which show a fairly high degree of equivalence. Note that when the second layer is resistive it is thin and when it is more conductive it is thicker. This is consistent with T-equivalence (transverse resistance is resolved but longitudinal conductance is not).

Field Data Example

The second example is a TEM field curve taken with Geonics equipment as shown in Figure 4. There are three sweeps taken with three different transmitter frequencies. The synthetic data from the best fit model are indicated by the line and the field data are indicated by the boxes on the graph. Each

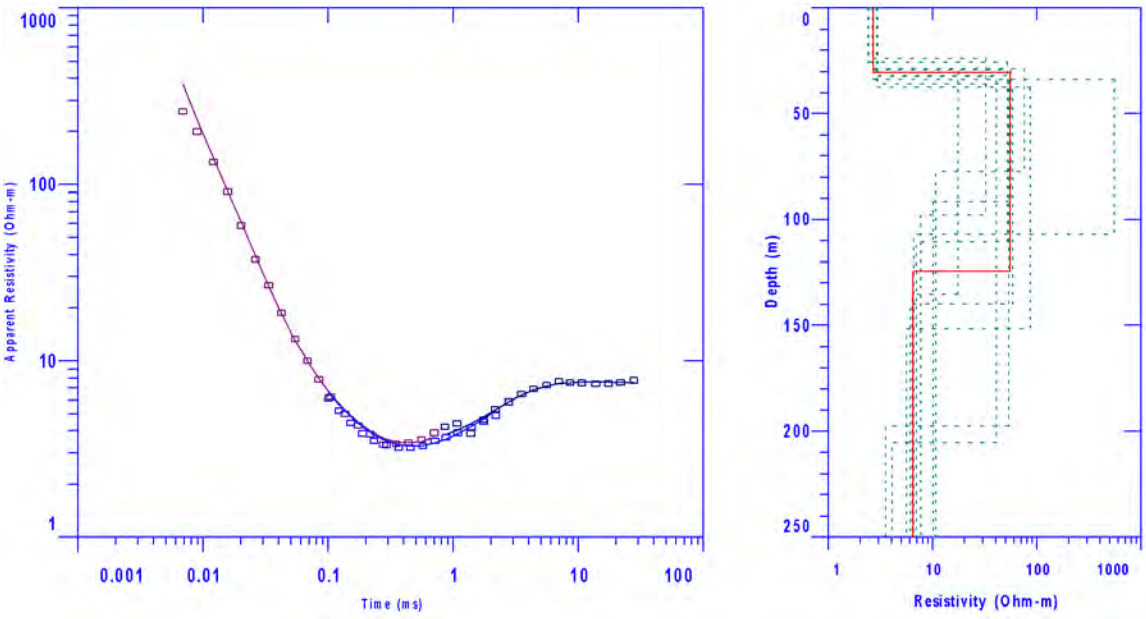

Figure 4. Final inversion result for TEM field curve example with equivalent models derived from the resolution matrix in Table 4.

Table 4. Resolution matrix for the inversion result shown in Figure 4.

	ρ_1	ρ_2	ρ_3	h_1	h_2
ρ_1	0.99	0	0	-0.01	0
ρ_2	0	0.03	-0.01	-0.04	0.11
ρ_3	0	-0.01	0.82	0.01	0.17
h_1	-0.01	-0.04	0.01	0.98	-0.02
h_2	0	0.11	0.17	-0.02	0.78

Table 5. Summary of equivalence analysis results displayed in Figure 4.

Parameter	Min	Best	Max	+/- %
ρ_1	2.39	2.66	2.96	11%
ρ_2	17.4	55.0	550	484%
ρ_3	3.52	6.45	10.67	55%
h_1	23.7	30.5	37.5	23%
h_2	45.6	93.8	173	68%

sweep is shown in a different color for clarity. The RMS fitting error to a three-layer model is 11.27%.The resolution matrix is shown in Table 4 and the summary of the equivalence analysis is shown in Table 5.

Aside from the first two points, the beginning of the curve is fairly consistent, indicating the first layer should be well resolved. The late time asymptote is also fairly well defined, indicating the basement should also be well resolved. There is some noise in the data which will likely introduce some uncertainty in the definition of the middle conductive layer, which is not thin, but it is not thick either.

Table 4 shows the resolution matrix for the TEM field example displayed in Figure 4. The first row shows that the first layer resistivity is well resolved. The third row shows that the third layer resistivity is well resolved. The fourth row shows that the first layer thickness is fairly well resolved and the fifth row shows the second layer thickness is fairly well resolved but there is a considerable degree of equivalence among the second layer thickness and resistivity and the third layer resistivity. The second row shows little resolution and indicates a degree of equivalence in the second layer parameters not shown in other rows.

The equivalence analysis shown numerically in Table 5 and graphically in Figure 4 indicates good resolution for the first layer resistivity and thickness and a fair resolution for the third layer resistivity and second layer thickness. The second layer resistivity is not so well resolved, which would be expected since it is resistive. What is not so obvious from Table 5 but very apparent in Figure 4 is that the position of (depth to) the base of the second layer is widely variable, from about 75 to 205 m. Thus, the interplay among the parameters serves to produce different picture than might be conjured up from looking at the variation in the individual parameters themselves.

Conclusions

Ridge regression inversion of electrical and EM data produce a resolution matrix as a by-product of the inversion procedure. This resolution matrix illustrates the interdependence of the inversion parameters in a numerical way. Using the rows of the resolution matrix in conjunction with repeated forward calculations allows this interdependence to be shown in a graphical way with a numerical summary. The combination of these two illustrates the degree of equivalence present in the resulting inverted model.

The results are consistent with what is known about T– and S equivalence for thin layers and for the thickness equivalence in the case of electromagnetic data. Although semi-linear equivalence analysis does not show the complete extent of the range of models which would satisfy the data, it gives a good and easy to read indication of what parameters are resolved and to what degree the other parameters are not resolved.

References

Anderson, W. L., 1989, A hybrid fast Hankel transform algorithm for electromagnetic modeling : Geophysics, **54,** 263-266.

Glenn, W. E., Jisoo Ryu , S. H. Ward , W. J. Peeples and R. J. Phillips, 1973, The inversion of vertical magnetic dipole sounding data: Geophysics, 38 , **6**, 1109-1129.

Inman, J. R., 1975, Resistivity inversion with ridge regression: Geophysics, **40**, pp. 798-817.

CALIBRATION AND FILTERING STRATEGIES FOR FREQUENCY DOMAIN ELECTROMAGNETIC DATA

Burke J. Minsley, U.S. Geological Survey, Denver, Colorado
Bruce D. Smith, U.S. Geological Survey, Denver, Colorado
Richard Hammack, National Energy Technology Laboratory, Pittsburgh, Pennsylvania
James I. Sams, National Energy Technology Laboratory, Pittsburgh, Pennsylvania
Garret Veloski, National Energy Technology Laboratory, Pittsburgh, Pennsylvania

Abstract

Techniques for processing frequency-domain electromagnetic (FDEM) data that address systematic instrument errors and random noise are presented, improving the ability to invert these data for meaningful earth models that can be quantitatively interpreted. A least-squares calibration method, originally developed for airborne electromagnetic datasets, is implemented for a ground-based survey in order to address systematic instrument errors, and new insights are provided into the importance of calibration for preserving spectral relationships within the data that lead to more reliable inversions. An alternative filtering strategy based on principal component analysis, which takes advantage of the strong correlation observed in FDEM data, is introduced to help address random noise in the data without imposing somewhat arbitrary spatial smoothing.

Introduction

Multi-frequency electromagnetic (EM) data are commonly acquired from airborne and ground-based systems in order to provide spatially continuous information about subsurface electrical resistivity variability, with widespread applications related to mineral deposits, groundwater, agriculture, and environmental remediation (e.g., Auken et al., 2006, and references therein). The EM data are most frequently presented as maps of apparent resistivity (or conductivity) in order to highlight anomalous features of interest. Information about changes with depth can be obtained by plotting data from different frequencies, where lower frequencies are generally sensitive to greater depths. In order to provide quantitative information about subsurface resistivity structures, however, the EM data must be inverted to recover the true distribution of resistivity values with depth in the subsurface. In many cases, estimates of soil properties such as salinity or moisture content are estimated from the inverted resistivity profiles using petrophysical or site-specific empirical relations.

Data errors, both random and systematic, can strongly impact the inverse problem and must be accounted for in order to recover accurate resistivity models that can be interpreted in a quantitative fashion. Random errors from cultural or instrument noise are somewhat easier to deal with and are typically reduced by applying a spatial low-pass filter to the data. Systematic errors can have numerous sources, including incorrect instrument calibration, drift, and improper data leveling. These systematic errors are more difficult to account for, and can have a much greater impact on the inversion results. Abraham *et al.* (2006) collected repeat measurements at a fixed reference location periodically throughout a ground-based survey to account for instrument bias and drift. Deszcz-Pan *et al.* (1998) and Fitterman and Deszcz-Pan (1998) calculated instrument calibration and bias correction factors for airborne data by utilizing several “known” earth models derived from well logs or other ground-based soundings. Brodie and Sambridge (2006) built on the work of Deszcz-Pan *et al.* (1998) by computing

correction factors that also incorporate known earth models, but primarily rely on requiring lateral continuity between one-dimensional (1D) soundings in a large three-dimensional (3D) survey.

In this current study, we account for systematic errors by calibrating ground-based multi-frequency GEM-2[1] data using the method described by Deszcz-Pan *et al.* (1998), where the known resistivity model is derived from a two-dimensional (2D) direct current (DC) resistivity survey. Additionally, we present a new filtering strategy for frequency-domain electromagnetic (FDEM) data that addresses random noise and has important benefits over traditional filtering methods. In both cases, we provide insights into the importance of spectral relationships within the data that must be preserved in order to produce good inversion results. To illustrate these processing techniques, we utilize field data collected at an agricultural site in the Powder River Basin (PRB). Ongoing work at the PRB site involves the use of repeat geophysical measurements to track changes in soil properties associated with subsurface drip irrigation systems which utilize water that is co-produced with coal bed methane (Sams et al., 2008).

Calibration

The calibration method developed by Deszcz-Pan *et al.* (1998) for airborne datasets corrects for errors in instrument gain, phase, and bias. This method results in both multiplicative and additive calibration terms, shown in equation (1), where each term is implicitly a function of frequency.

$$d^I_{obs} + jd^Q_{obs} = Ge^{j\phi}\left(d^I_{cal} + jd^Q_{cal} + B^I + jB^Q\right) \quad (1)$$

The observed data, d^I_{obs} and d^Q_{obs}, are the in-phase and quadrature response in ppm, and $j = \sqrt{-1}$. d^I_{cal} and d^Q_{cal} represent the theoretical in-phase and quadrature response predicted for a known earth model (which we also call the calibration model) that is spatially coincident with the observed FDEM data, and are computed using the forward modeling algorithm em1dfmfwd (Farquharson *et al.*, 2003). For each frequency, the calibration parameters include a gain factor (G), a phase (ϕ), and in-phase and quadrature bias terms (B^I and B^Q), which are determined using a nonlinear least-squares algorithm that minimizes the difference between the left and right sides of equation (1).

Figure 1A shows a 2D resistivity model that results from the inversion of a DC resistivity profile collected on an agricultural field in the PRB, and is used as the known earth model in this study. Individual 1D resistivity profiles are extracted from this calibration model, and the FDEM forward response is computed for the same instrument height above the ground and seven logarithmically spaced frequencies (1.5 kHz to 48 kHz) that are used in a GEM-2 survey along the same transect. Figure 2A and Figure 2B shows that there is a good qualitative agreement between the data predicted by the DC resistivity profile (black curves) and the measured GEM-2 data (green curves) for both the in-phase (A) and quadrature (B) components of the data (only 13,590 Hz is shown for brevity).

Inversion of the GEM-2 data results in the model shown in Figure 1B, which has substantial errors in the distribution and magnitude of resistivity values. More importantly, unreasonably high data misfit values are found during the inversion, which suggests that there are no valid earth models that can fit the measured data. Further evidence for this problem is shown in Figure 2C, which shows the phase-amplitude relationship for the DC resistivity-predicted data (solid dots) and the measured GEM-2 data (x) for three different frequencies (colors). Here, it is apparent that gain and phase calibration errors result in a distortion of the expected spectral response which, in turn, leads to the high data misfit values.

[1] Any use of trade, product, or firm names is for descriptive purposes only and does not imply endorsement by the U.S. Government

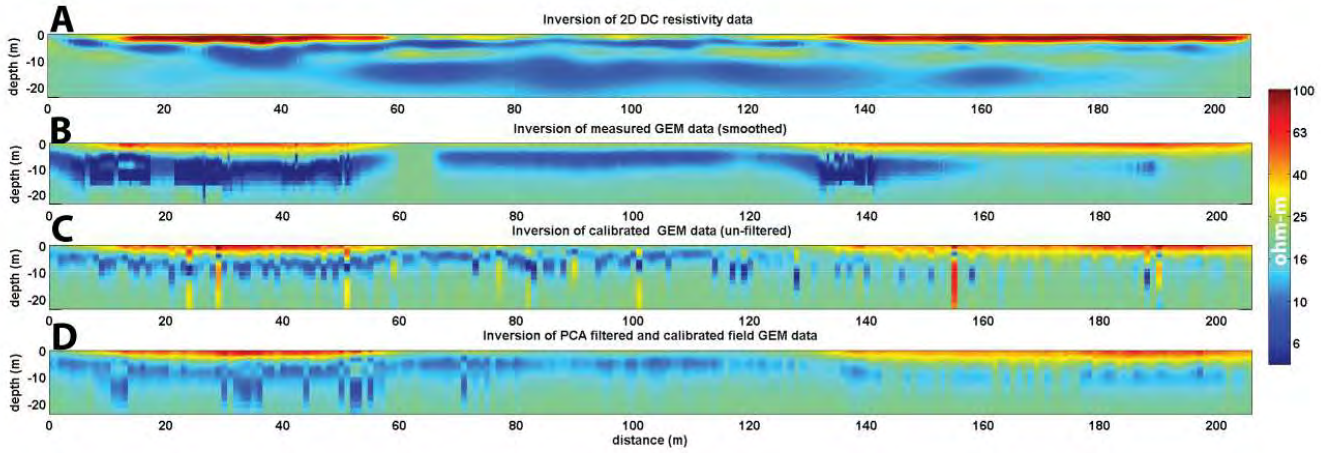

Figure 1. (A) 2D inversion of a dipole-dipole DC resistivity dataset. (B) Inversion of the measured GEM-2 data that have been smoothed with a low-pass filter. (C) Inversion of calibrated, but unfiltered GEM-2 data. (D) Inversion of PCA-filtered and calibrated GEM-2 data.

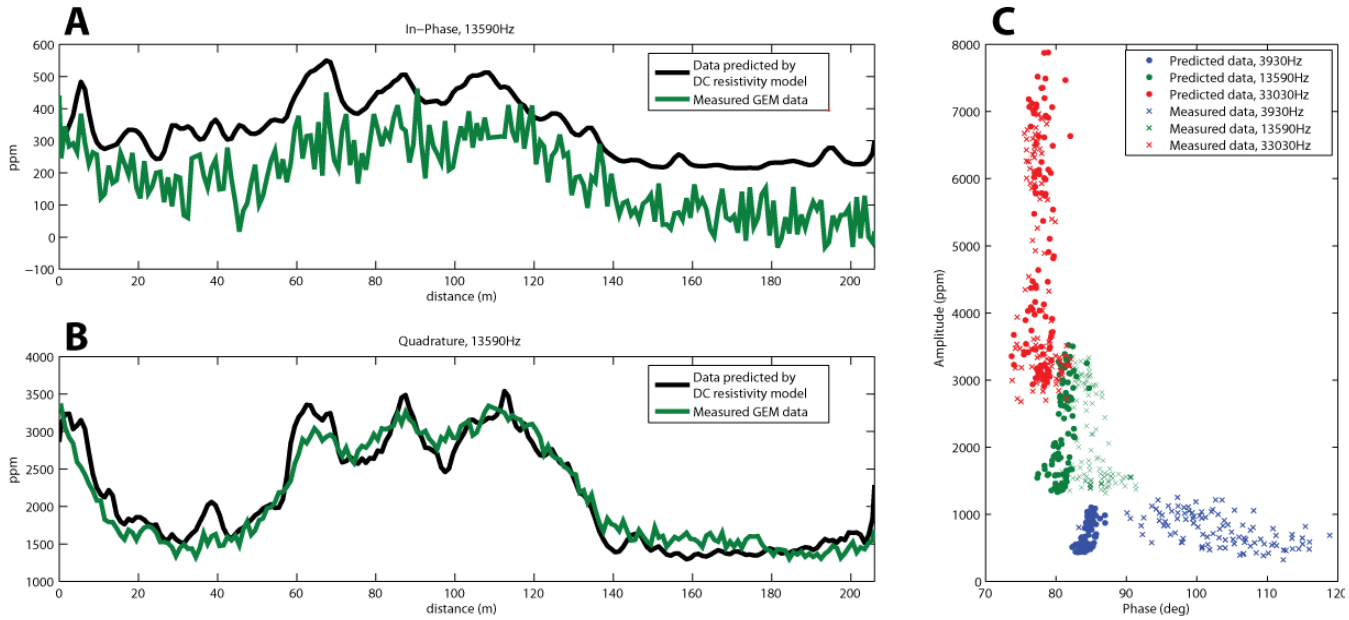

Figure 2. (A) In-phase and (B) quadrature data predicted for the DC resistivity model (black) and measured by the GEM-2 (green) at 13,590 Hz along the entire profile. (C) Phase-amplitude relationship for the entire profile of data at three different frequencies (colors). Solid dots show the data predicted by the DC resistivity model, measured GEM-2 data are shown with 'x'.

The measured GEM-2 data are next calibrated to the DC resistivity model by computing calibration factors according to equation (1). This process ensures that inversion of the calibrated data will result in models that have characteristics similar to the calibration model. Although this significantly improves the ability to invert the data for realistic earth models, it also means that errors in the calibration model are propagated into the calibrated data and care should be taken to use reliable models. Calibration parameters are computed for each frequency using equation (1) along the entire profile. For each frequency, a single best-fitting value of G, ϕ, B^I, and B^Q are computed. This creates an over-determined system of equations that is solved in a least-squares sense, as the number of data points

for each frequency is equal to twice the number of soundings, but there are only four unknown parameters. Technically, two soundings are needed to provide a just-determined system of equations.

Inversion of the calibrated dataset is shown in Figure 1C. These results appear somewhat noisy because the calibration was applied to the raw, unfiltered data, which is addressed in the following section. The effect of calibration is illustrated in Figure 3, which shows the phase-amplitude relationship for a single frequency (3,930 Hz) along the entire profile. Here, the black dots represent the data predicted by the calibration model, and the red dots show the measured GEM-2 data. Similar to the data in Figure 2C, the predicted and measured data are not aligned. The blue dots in Figure 3 represent the calibrated data, which are now properly centered on the data predicted by the calibration model. By properly correcting the phase-amplitude relationship for each frequency, physically realistic models that are consistent with the calibration model can be recovered, and the inversion data misfit values are substantially improved. The magenta dots in Figure 3 result from filtering the calibrated data, and are discussed in the following section.

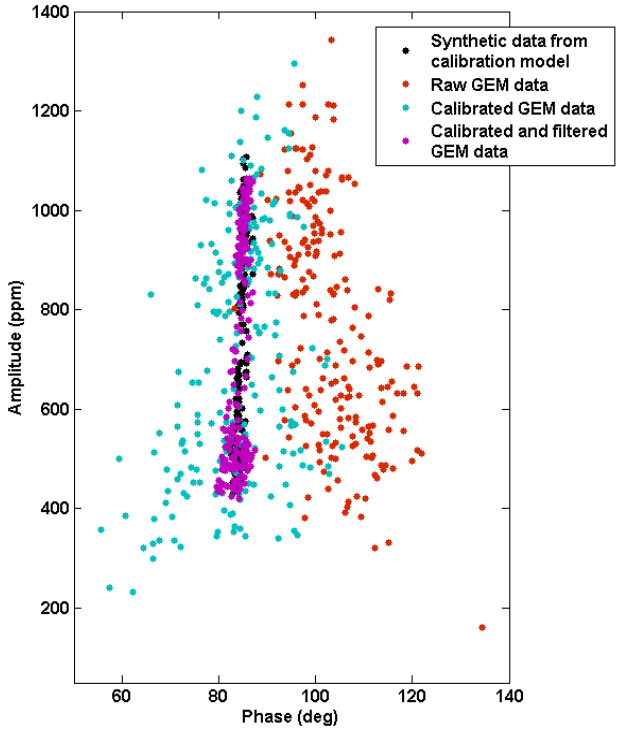

Figure 3. Phase-amplitude relationship for the 3,930 Hz data predicted by the calibration model (black), measured GEM data (red), calibrated GEM data (blue), and calibrated and PCA-filtered GEM data (magenta).

Filtering

Traditional filtering strategies for FDEM data typically involve some form of spatial low-pass filter that is applied to the data, often separately for each frequency and in-phase/quadrature profile. Spatial filtering is a relatively simple and useful way to attenuate random noise within the data, but can also be somewhat arbitrary given that the user must choose an appropriate filter length that attenuates noise but not real structure within the data. We propose a new approach to filtering FDEM data that has a similar effect of reducing random noise in the data, but also has several important properties: (1) it is based on the fact that the data at different frequencies are strongly correlated (which previously has been

viewed primarily as a drawback to this kind of data), (2) it operates on all of the data simultaneously, thereby preserving important spectral relationships within the data, and (3) it does not involve the imposition of an arbitrary filter smoothing length.

Our approach utilizes principal component analysis (PCA) filtering of the data, which, by definition, preserves the component of the data that is most highly correlated across frequencies. Because highly correlated data are expected from the physics of the FDEM method, this is an effective way to isolate geologically meaningful components of the data from uncorrelated noise. One obvious limitation, however, includes the case where noise is also highly correlated, such as when there are errors in survey elevation.

The PCA filter is based on the singular value decomposition (SVD) of the data matrix, **D**, which contains all of the data for a single survey line. **D** has *nf* (number of frequency) rows, and *ns* (number of soundings) columns, and each element in the matrix is a complex number composed of the in-phase and quadrature components of the data as expressed on the left side of equation (1). Before computing the SVD, defined in equation (2), the mean value for each frequency is subtracted from **D** so that the rows have zero mean.

$$\mathbf{D} = \mathbf{U}\mathbf{S}\mathbf{V}^T \tag{2}$$

U and **V** contain columns of orthonormal singular vectors that span the frequency-space and sounding-space, respectively. **U** therefore has dimensions of *nf* x *ns*, while **V** is *ns* x *ns*, and it is assumed that *nf* is less than *ns*. **S** is a diagonal (*ns* x *ns*) matrix that contains the singular values, but only *nf* of these are non-zero. Filtering is accomplished by reconstructing **D** from only *k* of the singular values and singular vectors, where $k < nf$, which is equivalent to operating on the original data matrix with a filter constructed from *k* frequency-space singular vectors, as shown in equation (3).

$$\mathbf{D}_{filt} = \mathbf{U}_k\mathbf{S}_k\mathbf{V}_k^T = \mathbf{U}_k\mathbf{U}_k^T\mathbf{D} \tag{3}$$

The mean value for each frequency that was removed prior to the SVD calculation is added back to the filtered data. The component of the data matrix that has the greatest degree of correlation is contained in the singular vectors associated with the largest singular value, and correlation decreases proportionally with decreasing singular values. By filtering the data using a limited number of singular vectors, the correlated portion of the data is preserved, which is an expected property of FDEM data.

The PCA filtering approach is compared with a more traditional spatial averaging filter in Figure 4. Figure 4A shows the strong correlation between the noise-free data predicted for the calibration model in Figure 1A at two different frequencies (23,070 Hz and 47,970 Hz). The data phase is displayed for the purpose of combining in-phase and quadrature information, where $\text{phase} = \tan^{-1}\left(d^Q/d^I\right)$. Figure 4B shows the same relationship for the calibrated, but otherwise unfiltered, GEM data. Random noise is clearly evident as a substantial amount of scatter that reduces the apparent correlation between the two frequencies. In Figure 4C, the data in Figure 4B have been filtered using an 11-point averaging filter. This traditional filtering approach has reduced the degree of noise, but also removes the extreme phase values due to spatial averaging. Figure 4D shows the result of the PCA filter applied to the data in Figure 4B, using only the first singular vector information. The PCA filter preserves the high correlation expected in the data, but does not impose excessive smoothing.

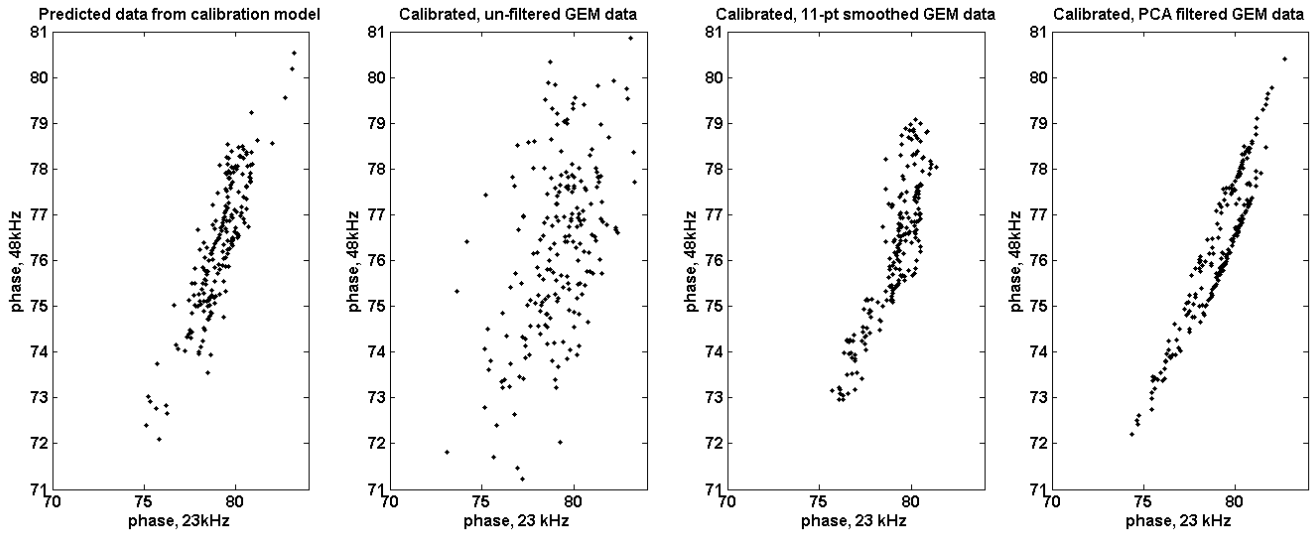

Figure 4. Correlation of phase values between 23,070 Hz and 47,970 Hz for (A) data predicted by the calibration model, (B) calibrated, un-filtered GEM data, (C) calibrated GEM data that are smoothed with an 11-point averaging filter, and (D) calibrated GEM data that are filtered using the PCA technique.

Figure 1D shows the result of inverting the calibrated and PCA-filtered GEM dataset, resulting in a model that is the most consistent with the calibration model, but limited in resolution due to noise in the measured GEM-2 data. Finally, the magenta points in Figure 3 show good agreement between the data predicted by the calibration model and the fully calibrated and filtered GEM data.

Summary

Proper calibration and filtering is a critical step towards being able to invert FDEM data for meaningful subsurface resistivity models that can be interpreted quantitatively. This work has implemented existing calibration techniques developed for airborne FDEM data with ground-based GEM data, and has provided new insight into the importance of preserving specific spectral relationships within the data. We have also introduced an alternative PCA filtering strategy that takes advantage of the fact that the FDEM data are highly correlated across frequencies, and avoids the selection of arbitrary spatial low-pass filters.

References

Abraham, J.D., Deszcz-Pan, M., Fitterman, D.V. and Burton, B.L., 2006. Use of a handheld broadband EM induction system for deriving resistivity depth images. Symposium on the Application of Geophysics to Engineering and Environmental Problems, 19(1): 1782-1799.

Auken, E., Pellerin, L., Christensen, N.B. and Sørensen, K., 2006. A survey of current trends in near-surface electrical and electromagnetic methods. Geophysics, 71(5): G249-G260.

Brodie, R. and Sambridge, M., 2006. A holistic approach to inversion of frequency-domain airborne EM data. Geophysics, 71(6): G301-G312.

Deszcz-Pan, M., Fitterman, D.V. and Labson, V.F., 1998. Reduction of inversion errors in helicopter EM data using auxiliary information. Exploration Geophysics, 29: 142-146.

Farquharson, C.G., Oldenburg, D.W. and Routh, P.S., 2003. Simultaneous 1D inversion of loop--loop electromagnetic data for magnetic susceptibility and electrical conductivity. Geophysics, 68(6): 1857-1869.

Fitterman, D.V. and Deszcz-Pan, M., 1998. Helicopter EM mapping of saltwater intrusion in Everglades National Park, Florida. Exploration Geophysics, 29: 240-243.

Sams, J.I., Lipinski, B.A. and Veloski, G., 2008. Using ground based geophysics to evaluate hydrogeologic effects of subsurface drip irrigation systems used to manage produced water in the Powder River Basin, Wyoming. Symposium on the Application of Geophysics to Engineering and Environmental Problems, 21(1): 916-925.

AGRICULTURAL GEOPHYSICS: PAST, PRESENT, AND FUTURE

Barry J. Allred, USDA/ARS – Soil Drainage Research Unit, Columbus, OH.
Robert S. Freeland, Biosystems Eng. and Soil Science Dept., Univ. of Tennessee, Knoxville, TN.
Hamid J. Farahani, Dept. of Agric. and Biol. Eng., Clemson Univ., Blackville, SC.
Mary E. Collins, Soil and Water Science Dept., Univ. of Florida, Gainesville, FL.

Abstract

Geophysical methods are becoming an increasingly valuable tool for agricultural applications. Agricultural geophysics investigations are commonly (although certainly not always) focused on delineating small- and/or large-scale objects/features within the soil profile (~ 0 to 2 m depth) over very large areas. The three geophysical methods predominantly employed for agricultural applications, both past and present, are resistivity, electromagnetic induction (EMI), and ground penetrating radar (GPR). Some of the more important past developments for agricultural geophysics include: soil water content monitoring using resistivity methods beginning in the 1930s and 1940s; soil salinity assessment with resistivity and EMI methods beginning in the 1960s and 1970s; updates and improvements in U.S. national program soil survey mapping using GPR beginning in the late 1970s and on into the 1980s; and for precision farming purposes, the delineation of spatial variations in soil properties with resistivity and EMI methods beginning in the 1990s. There has been significant recent advancements in agricultural geophysics, with resistivity, EMI, GPR, and other geophysical methods presently being used or evaluated for applications ranging from soil hydrologic characterization, determination of clay-pan depth, soil nutrient monitoring at confined animal feeding operation sites, crop/tree root biomass surveying, subsurface drainage system infrastructure detection, identification of subsurface flow pathways, soil compaction evaluation, etc. However, before agricultural geophysics can reach its full potential, new developments are needed, such as: expanding possible agricultural applications for resistivity, EMI, and GPR methods; greater employment of geophysical methods that have not traditionally been applied to agriculture; construction of multi-sensor geophysical equipment platforms, perhaps integrated with agricultural machinery; development of agricultural geophysics expert system computer software; etc. Achieving these future advancements in agricultural geophysics will require close collaboration between those in both the agricultural and environmental/engineering geophysics communities.

Introduction

The scale for geophysics applications to agriculture is extremely small compared to the scale of geophysical investigation in the petroleum and mining industries. The geophysical investigation depth for agricultural applications is also typically smaller than geophysical investigation depths needed for many environmental or engineering site evaluations. The scale of agricultural geophysics applications can in fact sometimes be only a few centimeters in magnitude, one example being the geophysical imaging of interior portions of a tree trunk (al Hagrey, 2007). For the most part, geophysical methods have been used in agriculture principally for some manner of soil investigation. Consequently, agricultural geophysics tends to be largely focused on depths from the ground surface down to 2 m, which is the interval generally containing the soil profile, including the entire crop root zone (Allred et al., 2008). With respect to agricultural geophysics applications, this extremely shallow 2 m depth of

interest is certainly an advantage, since most geophysical methods presently available have investigation depth capabilities that far exceed 2 m.

However, there are complexities associated with agriculture geophysics not always encountered with the application of geophysical methods to other industries or disciplines. One such complexity involves the transient nature of certain soil conditions and properties that affect geophysical measurements. For instance, apparent soil electrical conductivity (EC_a) measured using resistivity and electromagnetic induction methods, is significantly influenced by temperature and moisture conditions, and these temperature and moisture conditions can change appreciably over a period of days or even hours, in turn significantly altering the measured EC_a over the same timeframe. Moisture conditions also govern the soil relative dielectric permittivity (or dielectric content); thereby impacting ground penetrating radar results obtained within agricultural settings. Measured EC_a is additionally affected by soil nutrient levels and salinity that sometimes exhibit little variation over long periods, but will then change rapidly with an irrigation or fertilizer application event. Other soil properties affecting EC_a, if they vary temporally at all, do so at a much slower rate, and in this category are properties including pH, organic matter content, amount and type of clay minerals present, cation exchange capacity, specific surface, etc.

Another complexity regarding agricultural geophysics is that the soil conditions and properties impacting geophysical measurements vary not only temporally, but also spatially, often exhibiting substantial variability over very short horizontal and vertical distances. For soils without salinity or nutrient build-up concerns, it has been noted that although average EC_a values for an agricultural field may vary with changes in soil temperature and moisture, the EC_a spatial pattern itself within an agricultural field tends to remain relatively consistent over time, regardless of the transient temperature and shallow hydrologic conditions, thus indicating that EC_a spatial patterns were governed predominantly by the spatial variations in the more stable soil properties (Banton et al., 1997; Lund et al., 1999; Farahani and Buchleiter, 2004; Farahani et al., 2005; Allred et al., 2005a; Allred et al., 2006). In many cases, EC_a is a quantitative proxy for a single soil property such as for salinity within some irrigated agricultural areas within California (Rhoades and Ingvalson, 1971; Lesch et al., 1992); but conversely, there are also agricultural areas in which a complex relationship exists between EC_a and several soil properties (Johnson et al., 2001; Allred et al., 2005a; Carroll and Oliver, 2005; Allred et al., 2009).

The three geophysical methods predominantly used for agricultural purposes are resistivity, electromagnetic induction (EMI), and ground penetrating radar (GPR). An extensive discussion on the use of these three geophysical methods for agriculture can be found in Allred et al. (2008). Continuous measurement galvanic contact resistivity systems integrated with Global Positioning System (GPS) receivers have been developed specifically for agriculture. Steel coulters (disks) that cut through the soil surface are utilized as current or potential electrodes. These resistivity systems can have more than one four-electrode array providing shallow investigations depths of 0.3 to 2 m, with short time periods (~ 1 per second) or distance intervals between the continuously collected discrete EC_a measurements. The location for each EC_a measurement is determined accurately by GPS. Consequently, these resistivity systems, with their fast EC_a measurement rates and integrated GPS receivers, are capable of surveying large agricultural fields in a relatively short period of time. Figure 1 shows two examples of continuous measurement galvanic contact resistivity systems that are currently employed for agricultural applications. It should be noted that capacitively-coupled resistivity systems integrated with GPS receivers also have potential for agricultural use, but these systems have not as yet been extensively evaluated for this purpose.

Figure 1. Examples of continuous measurement galvanic contact resistivity systems. (**a**) Veris 3100 Soil EC Mapping System (Veris Technologies, Salina, Kansas, U.S.A.). (**b**) Close-up of steel coulters used for current and potential electrodes by the Veris 3100 Soil EC Mapping System. (**c**) Automatic Resistivity Profiling (ARP) – 03 device (Geocarta SA, Paris, France). (**d**) Close-up of steel coulters used for current and potential electrodes by the ARP – 03 device.

Some EMI ground conductivity meters have been developed, which are quite well suited for agricultural applications. The ground conductivity meters typically employed for obtaining agricultural EC_a measurements have intercoil spacings of around 1 m; and as a consequence, effective investigations depths of 1.5 m or less when positioned near the ground surface, based on McNeill (1980). Vertical, horizontal, and perpendicular dipole orientations of the ground conductivity meter transmitter and receiver coils can provide different EC_a investigation depths within an agricultural setting. Most of these EMI ground conductivity meters can easily be integrated with GPS receivers to provide accurate locations of continuously collected discrete EC_a measurements. As with the previously described resistivity systems, the proper EMI ground conductivity meter integrated with a GPS receiver is capable of relatively quick EC_a mapping over large agricultural fields. Although primarily used to map EC_a, ground conductivity meters can also be used to measure magnetic susceptibility, a property that has been demonstrated useful for delineating hydric soils (Grimley and Vepraskas, 2000; Grimley et al., 2008;

Wang et al., 2008). Two examples of ground conductivity meters commonly used for agricultural applications are shown in Figure 2.

Figure 2. Examples of ground conductivity meters used in agricultural settings. (**a**) DUALEM-1S (Dualem Inc., Milton, Ontario, Canada). (**b**) EM38-MK2 (Geonics Limited, Mississauga, Ontario, Canada).

The GPR systems utilized for agricultural purposes typically employ antennas with center frequencies in the range of 100 MHz to 1.5 GHz. This antenna frequency range covers many agricultural scenarios where the goal is to image small, shallow buried features/objects within 2 m of the surface. The anticipated depth and size of the subsurface feature/object of interest will provide guidance on the antenna frequency to use. For example, 250 MHz antennas are appropriate for locating a 20 cm diameter subsurface drainage system pipe main at 1.5 m depth in a silt loam soil, while 1.5 GHz antennas might be a good choice for imaging 0.5 cm tree roots at depths up to 0.5 m in a well-drained, sandy soil. Again, as with the resistivity and EMI systems, most GPR systems can be integrated with GPS receivers to provide accurate locations for GPR measurements; and because of fast GPR measurement rates, GPR systems integrated with GPS receivers are capable of surveying large agricultural fields in a relatively short amount of time. Finally, although resistivity, EMI, and GPR are by far the dominant geophysical methods currently employed, other geophysical methods such as magnetometry, self-potential, and seismic are now beginning to be evaluated for various agricultural purposes.

Past Developments in Agricultural Geophysics

Some of the earliest agricultural geophysics research activity occurred in the 1930s and 1940s, and this work focused on soil water monitoring through EC_a measurement with resistivity methods (McCorkle, 1931; Edlefson and Anderson, 1941; Kirkham and Taylor, 1949). Soil water monitoring

using the resistivity method, and now EMI and GPR methods, can provide useful insight for scheduling irrigation and controlled drainage operations within an agricultural field. The application of geophysical methods to agriculture did not substantially gain momentum until the 1960s, and to a greater extent the 1970s, with the use of resistivity methods for soil salinity assessment (Shea and Luthin, 1961; Roades and Ingvalson, 1971; Halvorson and Rhodes, 1974; Rhoades et al., 1976). Through the use of resistivity methods, and now EMI methods, geophysical EC_a measurements are successfully employed to gauge salinity levels in soil, so that field operations, such as soil profile water flushing, can be initiated well before salinity build-up causes crop damage. Starting in the late 1970s and on into the 1980s, another important development in agricultural geophysics was the use of GPR for updating and improving U.S. national program soil survey mapping (Collins et al., 1986; Collins and Doolittle, 1987; Doolittle, 1987; Schellentrager et al., 1988). In this regard, GPR has proved extremely valuable with respect to decreasing soil survey mapping time, providing more accurate delineation of map unit boundaries, and isolating representative pedons for soil sampling.

In the 1990s, EC_a mapping with resistivity and EMI methods became an increasingly important precision farming tool. Precision farming is a growing agricultural trend that combines geospatial datasets, state-of-the-art farm equipment technology, geographic information systems (GIS), and GPS to support spatially variable field application of fertilizer, soil amendments, pesticides, and even tillage effort (National Research Council, 1997; Morgan and Ess, 1997). The benefits to farmers are maximized crop yields and/or reduced input costs. Better protection of the environment is an additional benefit. Since precision farming operations result in just the right amounts of fertilizer, soil amendments, pesticides, and tillage being applied on different parts of the field, there are less agrochemicals and sediment released offsite via subsurface drainage and surface runoff. With less offsite release of these chemical and sediment contaminants, adverse environmental impacts on adjacent waterways are in turn reduced. So in essence, precision farming techniques allow an agricultural field to be divided into different management zones for the overall purpose of optimizing economic benefits and environmental protection. Horizontal spatial variations in EC_a have commonly been found to correlate relatively well with horizontal spatial variations in both crop yield (Jaynes et al., 1995a; Lund et al., 1999) and soil properties (Banton et al., 1997; Lund et al., 1999; Carroll and Oliver, 2005). As a consequence, EC_a mapping with resistivity and EMI geophysical methods can often be used to delineate the horizontal spatial patterns in soil properties that strongly influence within field variations in crop yield. These EC_a maps can in turn be used to partition an agricultural field into different management zones so that precision farming techniques (variable rate application of agrochemicals and tillage) can be employed to maximize economic benefits and environmental protection.

Present Agricultural Geophysics Research

Recently, within the past 15 years, there has been a rapid expansion of research related to potential agricultural geophysics applications. Most of these research activities are again focused on resistivity, EMI, and GPR methods; however, research is now also being conducted on possible agricultural uses for other geophysical methods, such as magnetometry, self-potential, and seismic. Besides soil water monitoring, salinity assessment, soil survey mapping, and precision farming; geophysical methods are presently being employed or evaluated in a wide range of additional agricultural topic areas including forestry, high value crops, animal waste management, soil hydrologic characterizations, buried infrastructure location/assessment, etc. Table 1 highlights some of the more recent research related to agricultural applications of geophysical methods which have not already been mentioned previously.

Table 1. Recent Agricultural Geophysics Research

Geophysical Method	Agricultural Application	Literature Source
Resistivity	Soil Drainage Class Mapping	Kravchenko et al., 2002
Resistivity	Small-Scale Soil Crack Imaging	Samouëlian et al., 2003
Electromagnetic Induction (EMI)	Determining Clay-Pan Depth	Doolittle et al., 1994
EMI	Estimation of Herbicide Partition Coefficients in Soil	Jaynes et al., 1995b
EMI	Mapping Flood Deposited Sand Depths on Farmland Near River	Kitchen et al., 1996
EMI	Soil Nutrient Monitoring from Manure Applications	Eigenberg and Nienaber, 1998 Eigenberg et al., 2002
EMI	Soil Salinity Assessment	Doolittle et al., 2001 Kaffka et al., 2005
Ground Penetrating Radar (GPR)	Indicator for Perched Water Table in Soil Profile	Freeland et al., 1998
GPR	GPR Soil Suitability Maps	Doolittle et al., 2003
GPR	Tree/Crop Root Biomass Surveying	Butnor et al., 2001 Butnor et al., 2003 Barton and Montagu, 2004 Konstantinovic et al., 2007 Konstantinovic et al., 2008
GPR	Identification of Subsurface Flow Pathways	Gish et al., 2002 Freeland et al., 2006
Seismic	Soil Water Potential	Lu and Sabatier, 2009
Seismic	Soil Compaction	Lu et al., 2004
Resistivity and EMI	Sand Blow Location in Alluvial Soils	Doolittle, et al., 2002
Resistivity and Seismic	Tree Trunk Imaging	al Hagrey, 2007
Resistivity, Electrical Resistance Tomography, EMI, GPR, Seismic, and Self-Potential	Soil Water Content Determination and Soil Water Flow Monitoring	Zhou et al., 2001 Grote at al., 2003 Huisman et al., 2003 Blum et al., 2004 Maineult et al., 2004 Lunt et al., 2005 Lambot et al., 2006 Weihermüller et al., 2006 Tromp-van Meerveld and McDonnell, 2009
GPR and Magnetometry	Agricultural Field and Golf Course Drainage Pipe Detection	Boniak et al., 2002 Allred et al., 2005b Allred et al., 2005c Rogers et al., 2005 Rogers et al., 2006

Future Trends in Agricultural Geophysics

Agricultural geophysics has in the past been a rapidly evolving discipline, which is still true at present, and therefore in the future, there is every expectation of continued development of new/innovative methods, equipment, and field procedures. In this regard, based primarily on Allred et al. (2008) and discussions held at the Soil Science Society of America – "Bouyoucos Conference on

Agricultural Geophysics" (September 8-10, 2009, Albuquerque, New Mexico), the following list was produced which summarizes probable future trends in agricultural geophysics.

1) New applications will continue to be discovered for the geophysical methods already used in agriculture (resistivity, EMI, and GPR).
2) Geophysical methods not traditionally employed in the past for agricultural purposes will find more significant use in the future. The geophysical methods likely to make inroads into agriculture include, magnetometry, self-potential, and seismic. Agricultural opportunities for other geophysical methods, such as nuclear magnetic resonance, induced polarization, seismoelectric, airborne EMI/magnetometry, etc., may also exist.
3) The incorporation of Global Positioning System (GPS) receivers will become the norm, especially with regard to real-time kinematic (RTK) GPS, which will allow geophysical measurement positions to be determined with horizontal and vertical accuracies of a few centimeters or less. Guidance devices, video display tracking systems, or even simple on-the-go guesstimates of the spacing distance between transects, when integrated with an accurate GPS, can provide the capability of efficiently conducting geophysical surveys over large agricultural field areas without the need to mark out a well-defined grid at the ground surface. For some geophysical methods, the computer processing procedures used for horizontal mapping of measurements may require some modification for input of data collected along a set of transects with somewhat irregular orientations and spacing distances.
4) Geophysical surveying with more than one sensor will become a standard approach, because of the variety of field information required to make correct agricultural management decisions. Multi-sensor systems based on a single geophysical method have already been produced, and these systems are certainly beneficial to agriculture. Examples include EMI or GPR systems having more than one set of transmitter/receiver coils or antennas, and continuously-pulled resistivity electrode arrangements containing more than one four-electrode array. However, multi-sensor systems based on more than one geophysical method still need to be developed for agricultural purposes, something likely to happen in the near future. These multi-sensor systems might even be directly integrated with farm machinery to allow on-the-go decisions regarding precision farming operations.
5) Multiple geophysical datasets integrated and analyzed together along with other geospatial information can provide agricultural insight not available when analyzing each geophysical dataset separately. Geostatistical analysis techniques can be especially useful in this regard. Geographic information systems (GIS) are particularly well adapted for integration and geostatistical analysis of multiple geophysical and non-geophysical spatial datasets. Consequently, GIS will play a greater and greater role in the analysis of geophysical data collected in agricultural settings. Furthermore, as the practice of precision farming continues to grow, there is expected to be an increasing need to input geophysical data into the GIS used to make proper management decisions in regard to different areas of an agricultural field.
6) Expert system computer software will be developed for specific agricultural applications, so as to automatically analyze and interpret geophysical data.
7) There is likely to be a substantial increase beyond present levels in the use of inverse modeling and enhanced data visualization computer software to analyze agricultural geophysics data.
8) Tomographic procedures will be employed in certain circumstances to obtain geophysical data in agricultural settings. It is usually not possible to conduct geophysical surveys in an agricultural field during the growing season, once the crop emerges and begins to develop. Tomographic data collection and analysis procedures are a potential solution to this field access problem,

allowing the within field horizontal spatial pattern of a physical property(s) to be determined from information obtained by geophysical sensors placed along the field periphery instead of inside the field itself. Tomographic data collection and analysis procedures can also provide valuable geophysical information for smaller-scale scenarios and even for circumstances when field access is not a problem.

9) Outreach efforts provided by those with an agricultural geophysics background will accelerate as there becomes a greater need to educate the general agricultural community not only on the many possible applications of agriculture geophysics but also on the strengths and limitations of the various geophysical methods employed for agricultural purposes.

Summary and Conclusions

Geophysical methods can be an important tool for agricultural applications. Past developments in agricultural geophysics have included the use of resistivity, EMI, and GPR methods for soil water monitoring, soil salinity assessment, soil survey mapping, and precision farming. At present, the agricultural applications of resistivity, EMI, and GPR geophysical methods continue to increase rapidly, and in addition, other geophysical methods, such as magnetometry, self-potential, and seismic are now just beginning to find agricultural use. Future advancements in agricultural geophysics are likely to include: (1) further expansion in potential agricultural applications for resistivity, EMI, and GPR methods; (2) greater employment of geophysical methods that have not traditionally been applied to agriculture; (3) integration of geophysical equipment with RTK-GPS receivers; (4) construction of multi-sensor geophysical equipment platforms; (5) more utilization of GIS for enhanced agricultural interpretations based on combined analysis of multiple geophysical and non-geophysical spatial datasets; (6) development of agricultural geophysics expert system computer software; (7) increased use of inverse modeling and enhanced data visualization computer software to evaluate agricultural geophysics data; (8) employment of tomographic procedures; and (9) accelerated outreach efforts to the agricultural community in general. These future advancements in agricultural geophysics will not be possible unless there is close collaboration between those in both the agricultural and environmental/engineering geophysics communities. More information regarding agricultural geophysics can be found at www.ag-geophysic.org.

References

al Hagrey, S. A. 2007. Geophysical imaging of root-zone, trunk, and moisture heterogeneity. *J. Exper. Botany*. v. 58, pp. 839-854.

Allred, B. J., M. R. Ehsani, and D. Saraswat. 2005a. The Impact of temperature and shallow hydrologic conditions versus soil properties on near-surface electromagnetic induction based electrical conductivity measurements. *Trans. A*SAE. v. 48, pp. 2123-2135.

Allred, B. J., J. J. Daniels, N. R. Fausey, C. Chen, L. Peters, Jr., and H. Youn. 2005b. Important considerations for locating buried agricultural drainage pipe using ground penetrating radar. *Applied Eng. Agric.* v. 21, pp. 71-87.

Allred, B. J., D. Redman, E. L. McCoy, and R. S. Taylor. 2005c. Golf course applications of near-surface geophysical methods: A case study. *J. Environ. Eng. Geophys.* v. 10, pp. 1-19.

Allred, B. J., M. R. Ehsani, and D. Saraswat. 2006. Comparison of electromagnetic induction, capacitively coupled resistivity, and galvanic contact resistivity methods for soil electrical conductivity measurement. *Applied Eng. Agric.* v. 22, pp. 215-230.

Allred, B. J., M. R. Ehsani, J. J. Daniels. 2008. Chapter 1 – General considerations for geophysical methods applied to agriculture. in *Handbook of Agricultural Geophysics*. edited by B. J. Allred, J. J. Daniels, and M. R. Ehsani. CRC Press LLC. Boca Raton, Florida. pp. 3-16.

Allred, B., B. Clevenger, and D. Saraswat. 2009. Application of GPS and near-surface geophysical methods to evaluate agricultural test plot differences. *FastTIMES*. v. 14, pp. 15-24.

Banton, O., M. K. Seguin, and M. A. Cimon. 1997. Mapping field-scale physical properties of soil with electrical resistivity. *Soil Sci. Soc. Am. J.* v. 61, pp. 540-548.

Barton, C. V. M, and K. D. Montagu. 2004. Detection of tree roots and determination of root diameters by ground penetrating radar under optimal conditions. *Tree Physiology*. v. 24. pp. 1323-1331.

Blum, A., I. Flammer, T. Friedli, and P. Germann. 2004. Acoustic tomography applied to water flow in unsaturated soils. *Vadose Zone J.* v. 3, pp. 288-299.

Boniak, R., Chong, S. K., Indorante, S. J., and J. A. Doolittle. 2002. Mapping golf course green drainage systems and subsurface features using ground penetrating radar. in *Proceedings of SPIE, Vol. 4758, Ninth International Conference on Ground Penetrating Radar*. edited by S. K. Koppenjan and H. Lee. April 29 – May 2, 2002. Santa Barbara, CA. SPIE. Bellingham, WA. pp. 477-481.

Butnor, J. R., J. A. Doolittle, L. Kress, S. Cohen, and K. H. Johnsen. 2001. Use of ground-penetrating radar to study tree roots in the southeastern United States. *Tree Physiology*. v. 21, pp. 1269-1278.

Butnor, J. R., J. A. Doolittle, K. H. Johnson, L. Samuelson, T. Stokes, and L. Kress. 2003. Utility of ground-penetrating radar as a root biomass survey tool in forest systems. *Soil Sci. Soc. Am. J.* v. 67, pp. 1607-1615.

Doolittle, J. A. 1987. Using ground-penetrating radar to increase the quality and efficiency of soil surveys. in *Soil Survey Techniques*. edited by W. U. Reybold and G. W. Petersen. *SSSA Special Publication Number 20*. Soil Science Society of America. Madison, WI. pp. 11-32.

Doolittle, J. A., K. A. Sudduth, N. R. Kitchen, and S. J. Indorante. 1994. Estimating depths to claypans using electromagnetic induction methods. *J. Soil and Water Cons.* v. 49, pp. 572-575.

Doolittle, J., M. Petersen, and T. Wheeler. 2001. Comparison of two electromagnetic induction tools in salinity appraisals. *J. Soil and Water Cons.* v. 56, pp. 257-262.

Doolittle, J. A., F. E. Minzenmayer, S. W. Waltman, and E. C. Benham. 2003. Ground penetrating radar soil suitability maps. *J. Environ. Eng. Geophys.* v. 8, pp. 49-56.

Collins, M. E., G. W. Schellentrager, J. A. Doolittle, and S. F. Shih. 1986. Using ground-penetrating radar to study changes in soil map unit composition in selected Histosols. *Soil Sci. Soc. Am. J.* v. 50, pp. 408-412.

Collins, M. E. and J. A. Doolittle. 1987. Using ground-penetrating radar to study soil microvariability. *Soil Sci. Soc. Am. J.* v. 51, pp. 491-493.

Edlefson, N. E. and A. B. C. Anderson. 1941. The four-electrode resistance method for measuring soil-moisture content under field conditions. *Soil Sci.* v. 51, pp. 367-376.

Eigenberg, R. A. and J. A. Nienaber. 1998. Electromagnetic survey of cornfield with repeated manure applications. *J. Eniviron. Qual.* v. 27, pp. 1511-1515.

Eigenberg, R. A., J. W. Doran, J. A. Nienaber, R. B. Ferguson, B. L. Woodbury. 2002. Electrical conductivity monitoring of soil condition and available N with animal manure and a cover crop. *Agric. Ecosys. Environ.* v. 88, pp. 183-193.

Farahani, H. J. and G. W. Buchleiter. 2004. Temporal stability of soil electrical conductivity in irrigated sandy fields in Colorado. *Trans. ASABE*. v. 47, pp. 79-90.

Farahani, H. J., G. W. Buchleiter, and M. K. Brodahl. 2005. Characterization of apparent soil electrical conductivity variability in irrigated sandy and non-saline fields in Colorado. *Trans. ASAE*. v. 48, pp. 155-168.

Freeland, R. S., J. C. Reagan, R. t. Burnes, and J. T. Ammons. 1998. Sensing perched water using ground-penetrating radar- A critical methodology examination. *Applied Eng. Agric.* v. 14, pp. 675-681.

Freeland, R. S., L. O. Odhiambo, J. S. Tyner, J. T. Ammons, and W. C. Wright. 2006. Nonintrusive mapping of near-surface preferential flow. *Appl. Eng. Agric.* v. 22, pp. 315-319.

Gish, T. J., W. P. Dulaney, K.-J. S. Kung, C. S. T. Daughtry, J. A. Doolittle, and P. T. Miller. 2002. Evaluating use of ground-penetrating radar for identifying subsurface flow Pathways. *Soil Sci. Soc. Am. J.* v. 66, pp. 1620-1629.

Grimley, D. A. and M. J. Vepraskas. 2000. Magnetic susceptibility for use in delineating hydric soils. *Soil Sci. Soc. Am. J.* v. 64, pp. 2174-2180.

Grimley, D. A., J. Wang, D. A. Liebert, and J. O. Dawson. 2008. Soil magnetic susceptibility: A quantitative proxy of soil drainage for use in ecological restoration. *Restoration Ecology*. v. 16, pp. 657-667.

Grote, K., S. Hubbard, and Y. Rubin. 2003. Field-scale estimation of volumetric water content using ground-penetrating radar ground wave techniques. *Water Resources Research*. v. 39, pp. 1321-1333.

Halvorson, A. D. and J. D. Rhoades. 1974. Assessing soil salinity and identifying potential saline-seep areas with field soil resistance measurements. *Soil Sci. Soc. Am. Proc.* v. 38, pp. 576-581.

Huisman, J. A., S. S. Hubbard, J. D. Redman, and A. P. Annan. 2003. Measuring soil water content with ground penetrating radar: A review. *Vadose Zone J.* v. 2, pp. 476-490.

Jaynes, D. B., T. S. Colvin, and J. Ambuel. 1995a. Yield mapping by electromagnetic induction. in *Proceedings of Site-Specific Management for Agricultural Systems: Second International Conference*. edited by P. C. Robert, R. H. Rust, and W. E. Larson. March 27-30, 1994. St. Paul, MN. ASA, CSSA, and SSSA. Madison, WI. pp. 383-394.

Jaynes, D. B., J. M. Novak, T. B. Moorman, and C. A. Cambardella. 1995b. Estimating herbicide partition coefficients from electromagnetic induction measurements. *J. Environ. Qual.* v. 24, pp. 36-41.

Johnson, C. K., J. W. Doran, H. R. Duke, B. J. Wienhold, K. M. Eskridge, and J. F. Shanahan. 2001. Field-scale electrical conductivity mapping for delineating soil condition. *Soil Sci. Soc. Am. J.* v. 65, pp. 1829-1837.

Kaffka, S. R., S. M. Lesch, K. M. Bali, and D. L. Corwin. 2005. Site-specific management in salt-affected sugar beet fields using electromagnetic induction. *Computers and Electronics Agric.* v. 46, pp. 329-350.

Kirkham, D. and G. S. Taylor. 1949. Some tests of a four-electrode probe for soil moisture measurement. *Soil Sci. Soc. Am. Proc.* v. 14, pp. 42-46.

Kitchen, N. R., K. A. Sudduth, and S. T. Drummond. 1996. Mapping of sand deposition from 1993 Midwest floods with electromagnetic induction measurements. *J. Soil and Water Cons.* v. 51, pp. 336-340.

Kravchenko, A. N., G. A. Bollero, R. A. Omonode, and D. G. Bullock. 2002. Quantitative mapping of soil drainage classes using topographical data and soil electrical conductivity. *Soil Sci. Soc. Am. J.* v. 66, pp. 235-243.

Konstantinovic, M., S. Wöckel, P. Schulze Lammers, J. Sachs, and M. Martinov. 2007. Detection of root biomass using ultra wideband radar – An approach to potato nest positioning. *Agr. Eng. Intl.* v. 9, Manuscript IT 06 003.

Konstantinovic, M., S. Wöckel, P. Schulze Lammers, and J. Sachs. 2008. UWB radar system for yield monitoring of sugar beet. *Trans. ASABE.* v. 51, pp. 753-761.

Lambot, S., Weihermüller, L., Huisman, J.A., Vereecken, H., Vanclooster, M. and Slob, E.C., 2006. Analysis of air-launched ground-penetrating radar techniques to measure the soil surface water content. *Water Resources Research*, v. 42. W11403, doi:10.1029/2006WR005097.

Lesch, S. M., J. D. Rhoades, L. J. Lund, and D. L. Corwin. 1992. Mapping soil salinity using calibrated electromagnetic measurements. *Soil Sci. Soc. Am. J.* v. 56, pp. 54-60.

Lu, Z., C. J. Hickey, and J. M. Sabatier. 2004. Effects of compaction on the acoustic velocity in soils. *Soil Sci. Soc. Am. J.* v. 68, pp. 7-16.

Lu, Z. and J. M. Sabatier. 2009. Effects of soil water potential and moisture content on sound speed. *Soil Sci. Soc. Am. J.* v. 73, pp. 1614-1625.

Lund, E. D., P. E. Colin, D. Christy, and P. E. Drummond. 1999. Applying soil electrical conductivity technology to precision agriculture. in *Proceedings 4th Int. Conf. Precision Agric.* edited by P. C. Robert, R. H. Rust, and W. E. Larson, editors. July 19-22, 1998. St. Paul, MN. ASA, CSSA, and SSSA. Madison, WI. pp. 1089–1100.

Lunt, I. A., S. S. Hubbard, and Y. Rubin. 2005. Soil moisture content estimation using ground-penetrating radar reflection data. *J. Hydrology*. v. 307, pp. 254-269.

Maineult, A., Y. Bernabé, and P. Ackerer. Electrical response of flow, diffusion, and advection in a laboratory sand box. *Vadose Zone J*. v. 3, pp. 1180-1192.

McCorkle, W. H. 1931. Determination of soil moisture by the method of multiple electrodes. *Texas Agricultural Experiment Station Bulletin 426*. Texas A & M University. College Station, TX. 20 pages.

McNeill, J. D. 1980. Electromagnetic terrain conductivity measurement at low induction numbers. *Technical Note TN-6*. Mississauga, Ontario, Canada: Geonics Ltd. 15 pages.

Morgan, M. and D. Ess. 1997. *The Precision-Farming Guide for Agriculturists*. John Deere Publishing. Moline, IL. 124 pages.

National Research Council. 1997. *Precision Agriculture in the 21st Century*. National Academy Press. Washington, D.C. 149 pages.

Rhoades, J. D. and R. D. Ingvalson. 1971. Determining salinity in field soils with soil resistance measurements. *Soil Sci. Soc. Am. Proc.* v. 35, pp. 54-60.

Rhoades, J. D., P. A. C. Raats, and R. J. Prather. 1976. Effects of liquid-phase electrical conductivity, water content, and surface conductivity on bulk soil electrical conductivity. *Soil Sci. Soc. Am. J.* v. 40, pp. 651-655.

Rogers, M. B., J. R. Cassidy, and M. I. Dragila. 2005. Ground-based magnetic surveys as a new technique to locate subsurface drainage pipes: A case study. *App. Eng. Agric.* v. 21, pp. 421-426.

Rogers, M. B., J. E. Baham, and M. I. Dragila. 2006. Soil iron content effects on the ability of magnetometer surveying to locate buried agricultural drainage pipes. *App. Eng. Agric.* v. 22, pp. 701-704.

Samouëlian, A., I. Cousin, G. Richard, A. Tabbagh, and A. Bruand. 2003. Electrical resistivity imaging for detecting soil cracking at the centimeter scale. *Soil Sci. Soc. Am. J.* v. 67, pp. 1319-1326.

Schellentrager, G. W., J. A. Doolittle, T. E. Calhoun, and C. A. Wettstein. 1988. Using ground-pentrating radar to update soil survey information. *Soil Sci. Soc. Am. J.* v. 52, pp. 746-752.

Shea, P. F. and J. N. Luthin. 1961. An investigation of the use of the four-electrode probe for measuring soil salinity in situ. *Soil Sci.* v. 92, pp. 331-339.

Tromp-van Meerveld, H. J. and J. J. McDonnell. 2009. assessment of multi-frequency electromagnetic induction for determining soil moisture patterns at the hillslope scale. *J. Hydrology*. v. 368, pp. 56-67.

Wang, J., D. A. Grimley, C. Xu, and J. O. Dawson. 2008. Soil magnetic susceptibility reflects soil moisture regimes and the adaptability of tree species to these regimes. *Forest Ecology and Management*. v. 255, pp. 1664-1673.

Weihermüller, L., J. A. Huisman, S. Lambot, M. Herbst, and H. Vereecken. 2006. Mapping the spatial variation of soil water content at the field scale with different ground penetrating radar techniques. *J. Hydrology*. v. 340, pp. 205-216.

Zhou, Q. Y., J. Shimada, and A. Sato. 2001. Three-dimensional spatial and temporal monitoring of soil water content using electrical resistivity tomography. *Water Resources Research*. v. 37, pp 273-285.

THIRD YEAR OF SUBSURFACE DRIP IRRIGATION MONITORING USING GEM2 ELECTROMAGNETIC SURVEYS, POWDER RIVER BASIN, WYOMING

James I. Sams, National Energy Technology Laboratory, Pittsburgh, PA
Bruce D. Smith, U.S. Geological Survey, Denver, CO
Garret Veloski, National Energy Technology Laboratory, Pittsburgh, PA
Burke J. Minsley, U.S. Geological Survey, Denver, CO
Mark A. Engle, U.S. Geological Survey, Reston, VA
Richard Hammack, National Energy Technology Laboratory, Pittsburgh, PA
John Zupancic, BeneTerra LLC, Sheridan, WY

Abstract

The National Energy Technology Laboratory and the U.S. Geological Survey are collaborating with BeneTerra LLC to comprehensively monitor a sub-surface drip irrigation (SDI) system at a site in the Powder River Basin (PRB) of Wyoming. Irrigation water for the SDI system is coalbed natural gas (CBNG) co-produced water. The study is being conducted at the Headgate Draw area, located approximately 17 km south of Arvada, Wyoming at the confluence of Crazy Woman Creek and the Powder River. The study site encompasses six fields and covers an approximate area of 1.2 km^2 (Figure 1). The project is an integration of geophysical, geochemical, and soil science studies. The third year of a five year geophysical monitoring study is reported here.

Discussion

Subsurface drip irrigation (SDI) is an emerging technology being applied in the PRB basin for the beneficial use of CBNG co-produced water (DOE, 2003; BLM, 2003). The pre-treated CBNG waters are applied to the root zones of agricultural land to aid in irrigation. CBNG water is filtered and then transported to field valves which release the water to multiple underground laterals. The laterals are placed two to three feet underground about at a 40-60 inch distance between each lateral. Water drains from the perforated laterals at a rate of 0.75 to 1.5 gallons per day. This style of irrigation is capable of applying two to three times more water on a particular site than traditional surface irrigation (Engle and others 2009a and b). A subsurface system may be operated year round, rather than just during the 6- to 7-month growing season of the PRB. The method is deigned to minimize environmental impacts by parking potentially detrimental salts in the vadose zone. This research project investigates the transport and fate of the water and salts from the injected CBNG produced waters at the SDI site, adjacent to the Powder River.

Ground, borehole, and helicopter electromagnetic conductivity surveys were conducted at the site prior to the installation of the SDI system (Sams and others 2008a and b; Smith and others, 2009). After the installation of the subsurface drip irrigation system, ground and borehole electromagnetic conductivity surveys have been performed quarterly (weather permitting). We summarize geophysical survey results from the first 3 years of a planned 5-year study of the SDI system. Findings from this project provide a critical understanding of water and salt dynamics associated with SDI systems using

CBM produced water. The information obtained can be used to improve SDI and other CBM produced water use/disposal technologies in order to optimize the productive use of produced waters.

In order to optimize an SDI system, knowledge of soil properties and subsurface geology is important. The location of saturated soils, accumulated salts, clay pans and clay lenses, are essential for properly locating subsurface laterals. A comprehensive site assessment before, during, and after application of CBNG produced water is critical to track salt movements and possible alterations in soil properties. These data are necessary to evaluate soil quality and plant productivity during the operation of the system.

A preconstruction ground-based geophysical survey of the proposed 1.2 km^2 SDI site was completed in several fields in June 2007. The survey served as a baseline for subsequent surveys designed to monitor the EM response resulting from CBNG water discharged through the SDI system. The completed survey generated in approximately 55 line km of data. Quality assurance measures included drift checks, duplicate line surveys, and repeat field surveys (Sams and others, 2008a).

The multifrequency electrical conductivity surveys were completed using a Geophex GEM2[1] instrument mounted on a sled constructed of PVC pipe. The sled was towed behind a utility vehicle using a differential GPS navigation system to aid in guidance. Five frequencies were programmed into the instrument (1530 Hz, 8250 Hz, 23070 Hz, 33030 Hz, and 47970 Hz). Data were collected at a sampling rate of 10 Hz with 25 m line spacing. The inphase/quadrature responses were filtered using a 10 point along-line median filter and converted into apparent conductivity (mS/m) values. A minimum curvature method was used to create a surface grid with a 5 m cell size. Since 2007, several geophysical surveys have been performed at the Headgate Draw site in order to evaluate the capability of these methods in monitoring the subsurface hydrogeologic changes produced by the SDI system over time (Sams and others 2008a and b).

GEM2 EM surveys consisting of 30 line kilometers was completed in October 2008, March and August 2009 to monitor any changes in conductivity resulting from operation of the SDI system (Figure 2 and 3). By August of 2009 the SDI system was full implemented, though the amount of water used in the irrigation was less than anticipated due to lower natural gas production. Figure 3 shows the fields where the SDI system had been installed and used. Comparison of data from field 9, not developed for SDI, shows that there were no major changes in apparent conductivity over the survey period. The lack of change suggests that the leveling procedures used (Abraham et al., 2006) accounted for instrumental changes.

Field 6 is the highest terrace above the Powder River and has the lowest background conductivity from the pre-development survey and also from the pre-development airborne conductivity survey. Figure 4 shows an enlargement of the surveys for field 6 at the same conductivity color scale. The average apparent conductivity in the 48 kHz frequency (near surface) values in Field 6 have nearly doubled between March and August of this year. By comparison, there has been no obvious increase in specific conductivity in groundwater measured from well 09MW, located on the down-gradient edge of the field. These results suggest that the response in EM conductivity may due to dissolution of salts in the vadose zone (Engle et al., 2009a and 2009b, 2010). Patterns in the change in conductivity in the central part of the field follow the trend of the subsurface drip lines suggesting that their application of water is different in different irrigation sections. The SDI system is laid out in blocks as indicated in Figure 4. The most dramatic increase in conductivity is in the southwest part of the field (Figure 4). This is the lowest part of the field and is where water may accumulate. Figure 5 shows the change in the quadrature component of the GEM2 along one line in Field 6. The quadrature component is displayed since calibration of apparent conductivities is under investigation (Minsley et al., 2010). The overall

increase in conductivity is obvious as well as the dramatic increase in the southwest part of the field. Adjustments are being made in the SDI operation to optimize operation in this field.

Apparent conductivity values for field 5 are shown (Figure 6) for October 2008 and August 2009. March surveys were not done due to excessive mud during spring thaw. Not the entire field was developed for SDI as indicated by the red boxes in Figure 6. The areas which have not been developed show the least change in the low conductivity areas in apparent conductivity maps between surveys. The higher conductivity areas generally correspond to areas with higher groundwater and/or soil water (Engle et al., 2009a and b, 2010). Note the northwest corner of field 5 was not developed because the water sampling and the ground geophysics both indicated salinity. The areas which have been developed in field 5 generally show an increase in apparent conductivity from the maps in Figure 6. There are some patterns in the change in conductivity that may relate to the how water is being applied from the SDI system since changes follow the trends of the SDI installation. Figure 7 shows changes in GEM2 quadrature at 47,790 kHz along line 8. The quadrature has been used since calibration procedures are being developed for the conductivity measurements. The largest changes are in the north end of the line where the SDI development has been. In the south end of the line there are also changes where the background resistivity is high. Mechanisms that can produce these changes are under study but areas of high conductivity here are due to high salinity in the shallow water. Consequently changes in salinity may be seasonal or related to precipitation.

Conclusion

Subsurface drip irrigation (SDI) has recently been considered as an alternative means of managing produced water in an environmentally responsible and beneficial manner. This style of irrigation is capable of applying of 2 to 3 times more water on a particular site than traditional surface irrigation because water is introduced near the bottom of the root zone. Furthermore, a major advantage of this practice over surface application is the requirement that this subsurface system be operated year round, rather than just during the 6- to 7-month growing season in the Powder River Basin of Wyoming.

The results of this investigation indicate that ground based geophysical instruments, such as the GEM2, provide a method for characterizing near surface electromagnetic properties. These types of EM surveys provide useful data to optimize the design of SDI systems. The potential for identifying subsurface soil and geologic conditions, such as the location of clay pans and clay lenses, is useful in locating and spacing subsurface SDI emitters. Comprehensive integrated hydrogeophysical methods are useful for site assessment before, during, and after application of CBNG produced water. Ground GEM2 surveys are promising for tracking salt movements and possible alterations in soil properties.

Acknowledgements

The Wyoming Department of Environmental Quality encouraged the study and provided logistical support. In addition to DOE program funding, the USGS Energy program provided funding for these studies.

[1]Any use of trade, product, or firm names is for descriptive purposes only and does not imply endorsement by the U.S. Government.

References

Abraham, J.D., Deszcz-Pan, M., Fitterman, D.V., and Burton, B.L., 2006, Use of a handheld broadband EM induction system for deriving resistivity depth images: Symposium on the Application of Geophysics to Engineering and Environmental Problems (19)1, p. 1782-1799.

BLM, 2003a, Final environmental impact statement and proposed plan amendment for the Powder River Basin oil and gas project: Bureau of Land Management Environmental Impact Statement WY-070-02-065.

—, 2003b, Final statewide oil and gas environmental impact statement and proposed plan amendment for the Powder River Basin and Billings resource management plans: Bureau of Land Management Environmental Impact Statement BLM/MT/PL-03/005.

DOE, 2003, Coal Bed Methane Primer: New source of natural gas - environmental implications: National Energy Technology Laboratory National Petroleum Technology Office

Engle, M.A, Bern, C.R., Healy, R.W., Sams, J., Zupancic, J., and Schroeder, K, 2009a, Subsurface Drip Irrigation As A Method To Beneficially Use Coalbed Methane Produced; Water: Initial Impacts To Groundwater, Soil Water, And Surface Water; Geological Society of America Abstracts with Programs, Vol. 41, No. 7, p. 548.

Engle, M.A, Bern, C.R., Healy, R.W., Sams, J., Zupancic, J., and Schroeder, K, 2009b, Initial Results for a Hydrogeochemical Investigation of Coalbed Natural Gas Produced Water Application via Subsurface Drip Irrigation, Powder River Basin, Wyoming; Proceedings AAPG Annual Convention and Exhibition, Denver, Colorado, June 7-10, 2009.

Engle, M.A., Sams, J.I., Veloski, G., Smith, B.D., Zupancic, J.W., Bern, C.R., Schroeder, R.W., and Healy, R.W., 2010, Subsurface Drip Irrigation as a Method to Beneficially Use Coalbed Methane Produced Water in the Powder River Basin: Geochemical and Geophysical Responses during the First Year of Operation, National Ground Water Monitoring Conference, Denver CO., Proceedings, 1p.

Minsley, B.J., B.D. Smith, R. Hammack, J.I. Sams, and G. Veloski, 2010, Calibration and filtering strategies for frequency domain electromagnetic data: Symposium on the Application of Geophysics to Engineering and Environmental Problems, this proceeding.

Sams, J.I., Lipinski, B.A. and Veloski, G., 2008a, Using Ground Based Geophysics to Evaluate Hydrogeologic Effects of Subsurface Drip Irrigation Systems Used to Manage Produced Water in the Powder River Basin, Wyoming. Symposium on the Application of Geophysics to Engineering and Environmental Problems, 21(1): 916-925.

Sams, J.I., Smith, B.D., Veloski, G., Hammack, R., and Zupancic, J., 2008b, Integration of Airborne, Ground, and Borehole Geophysical Surveys to Characterize Shallow Hydrogeology in an Area of Coal Bed Natural Gas Production in the Powder River Basin, Wyoming: Integrated Petroleum Environmental Conference, Albuquerque NM, 1p.

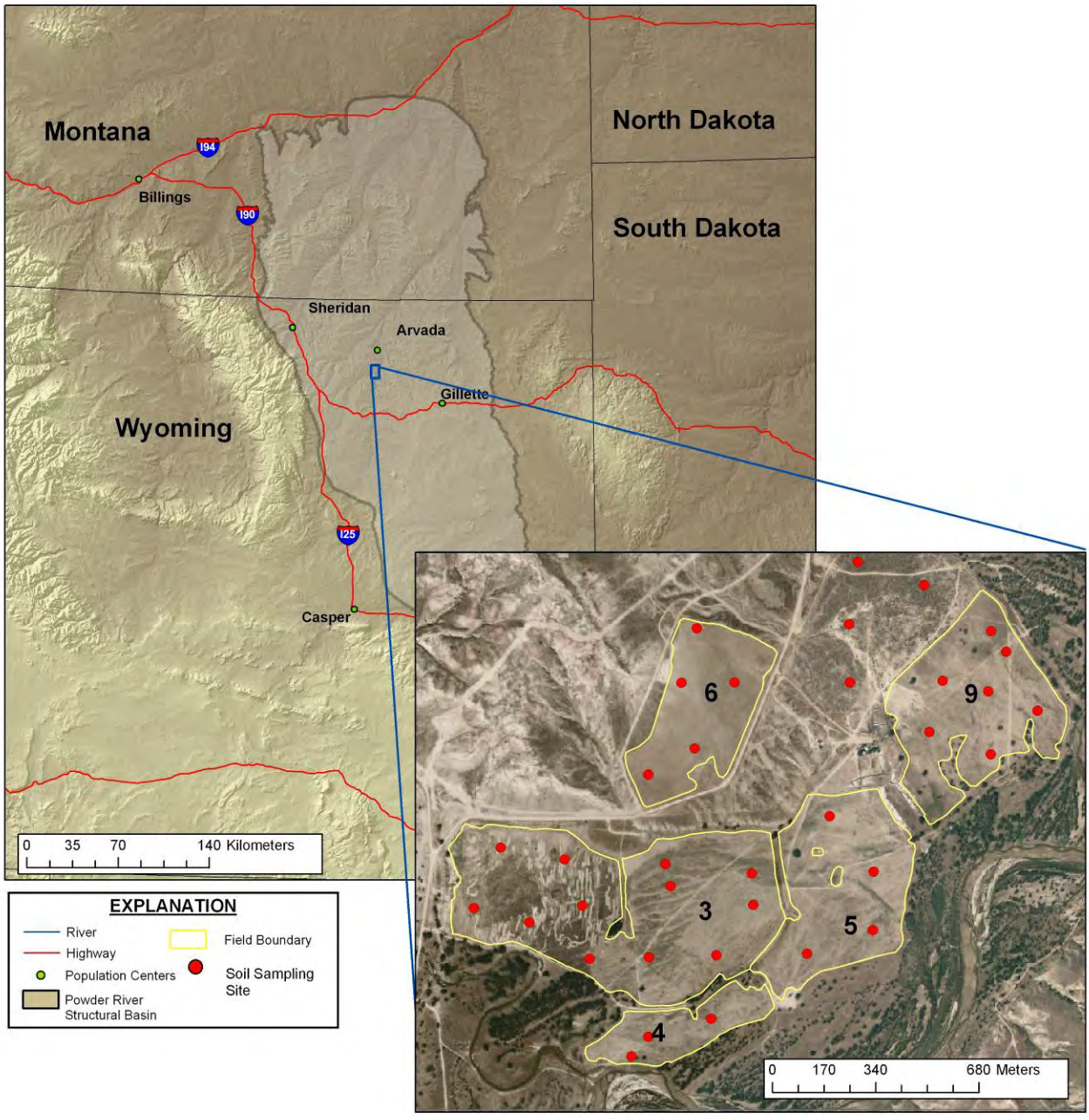

Figure 1. Location of Headgate Draw project study area, Powder River basin, Wyoming. Field numbers are shown in black. Not all of the yellow outlined area has been developed for subsurface drip irrigation.

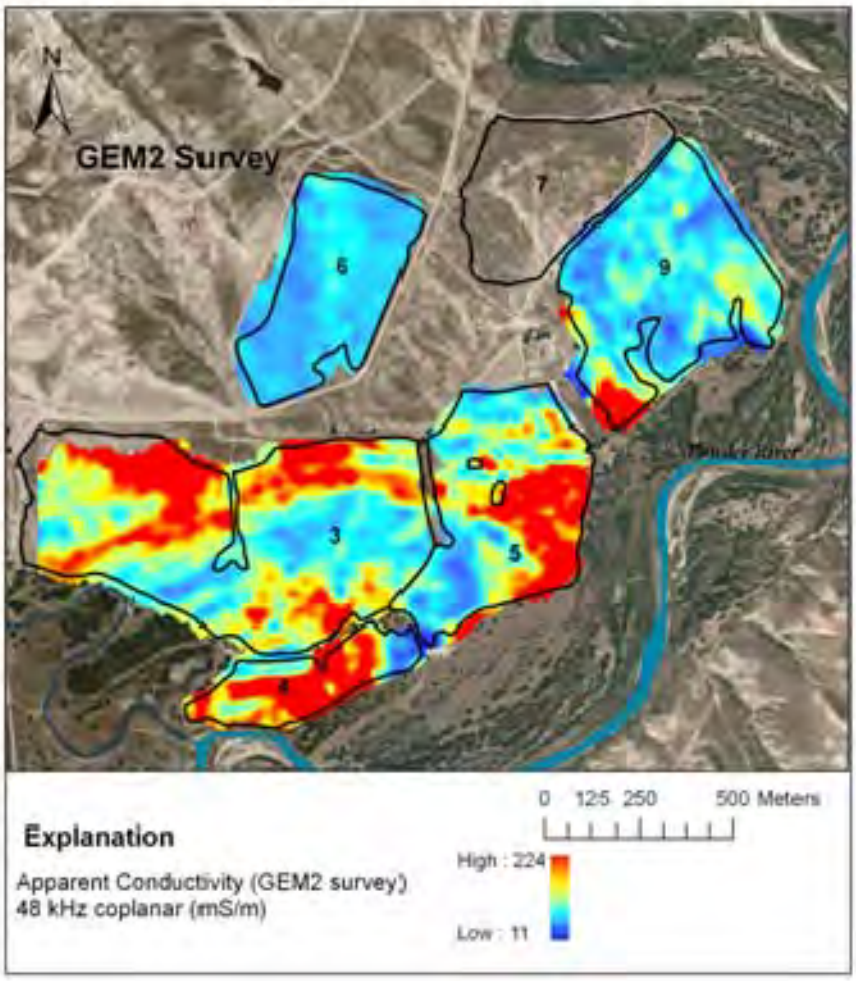

Figure 2. Apparent conductivity map created using the 47,750 Hz data for all 5 fields from 2008 GEM2 survey of the Headgate site.

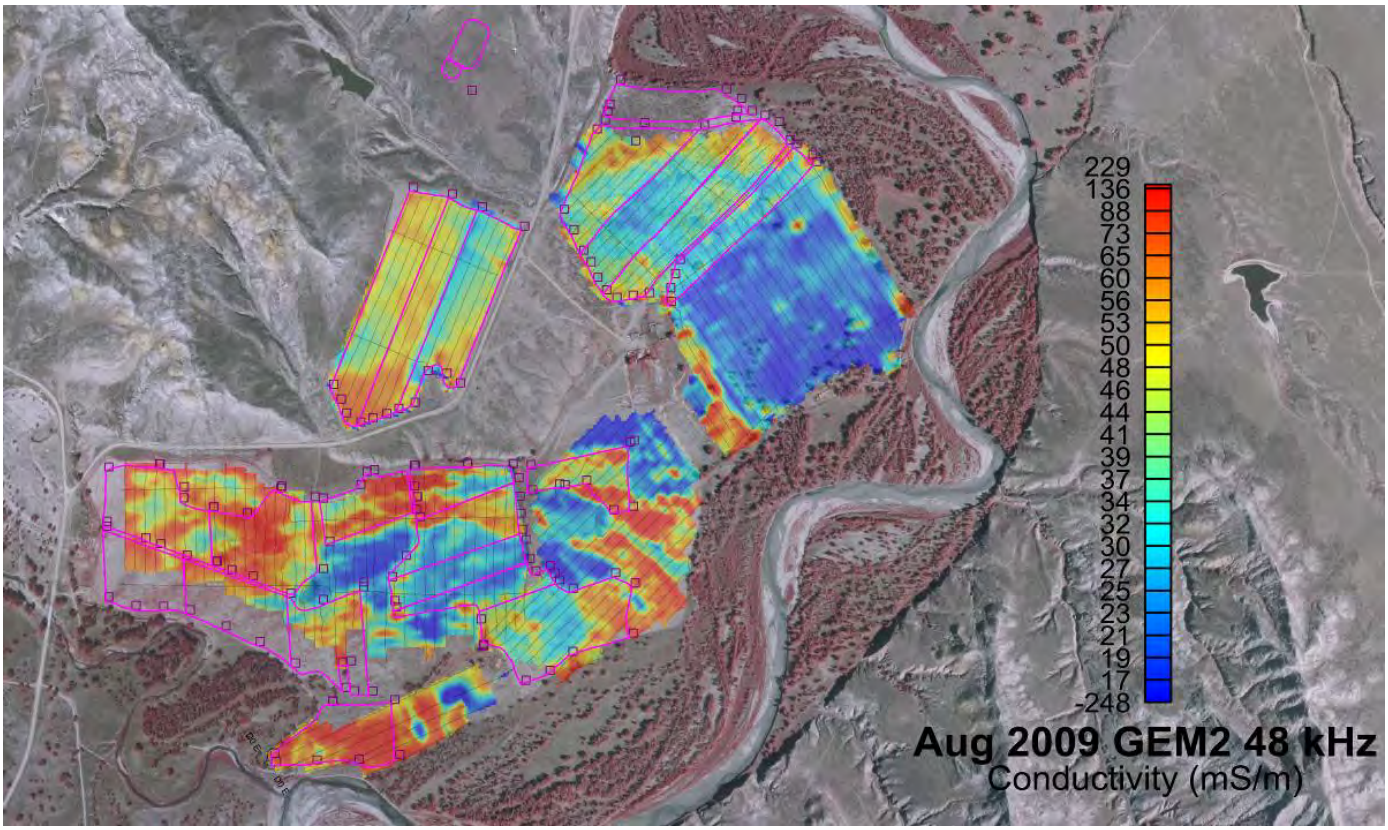

Figure 3. Apparent conductivity map created using the 48 kHz data for all 5 fields GEM2 survey of the Headgate site August 2009. Black lines are GEM2 survey tracks. Red outlines active subsurface drip irrigation fields.

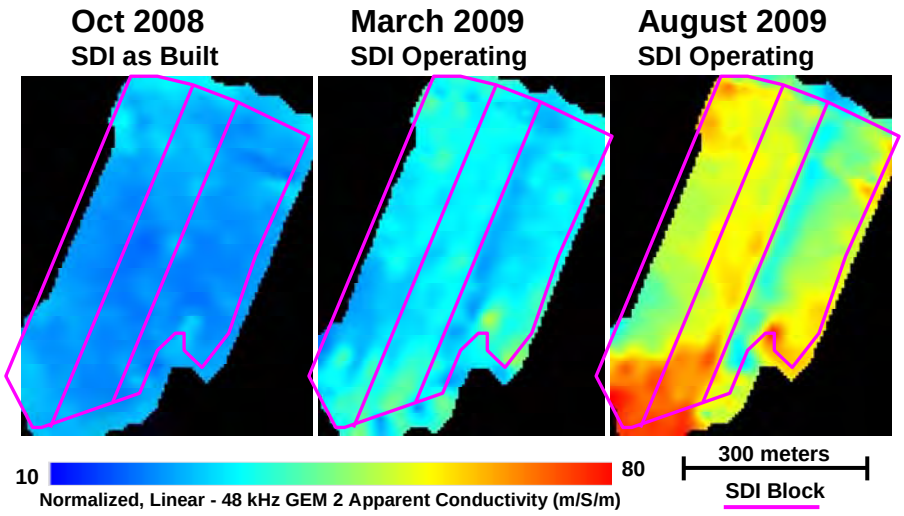

.

Figure 4 Temporal changes in apparent conductivity at 48 kHz for the Headgate Draw site, field 6, subsurface drip irrigation system. The red lines indicate blocks of the SDI system where the drip lines are laid out parallel to the long axis

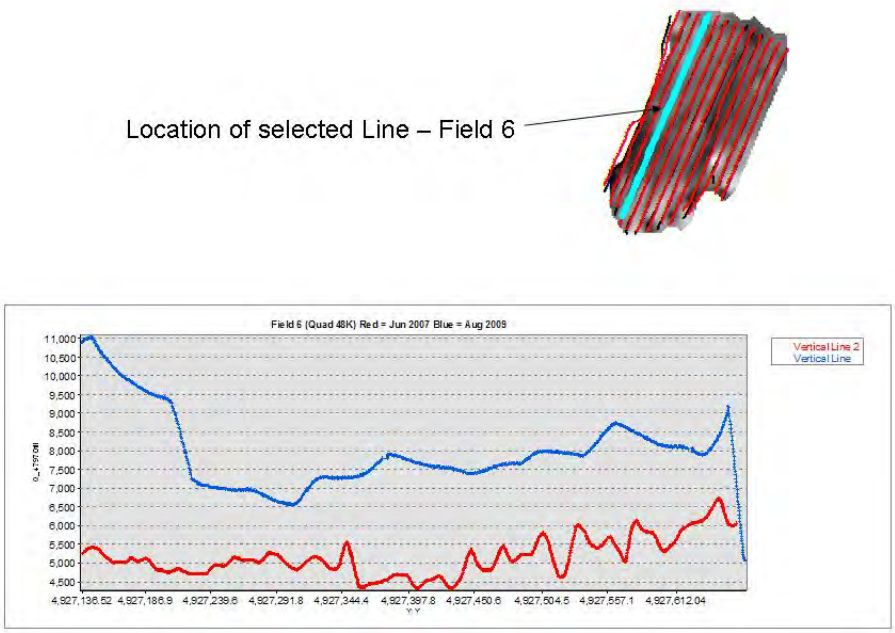

Figure 5. Comparison of GEM2 quadrature values for survey line field 6 (June 2007 and August 2009).

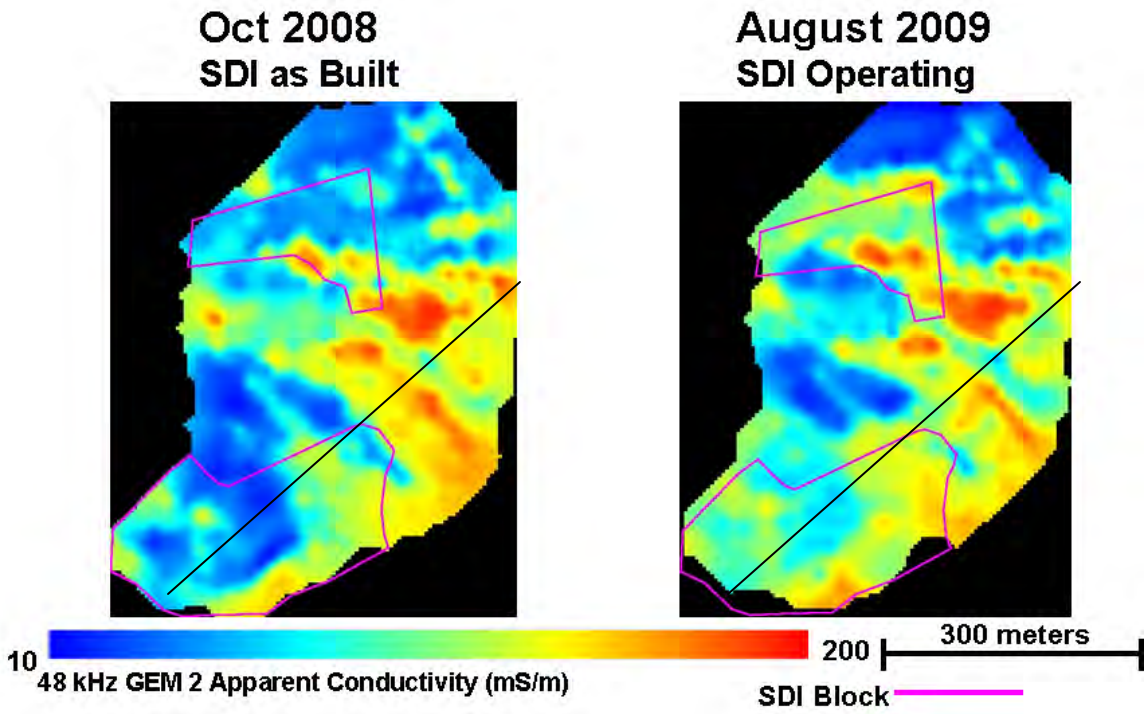

Figure 6. Temporal change in apparent conductivity at Headgate Draw, field 5. SDI blocks are indicated by the red lines. Black shows line 8 plotted in profile in Figure 7 below.

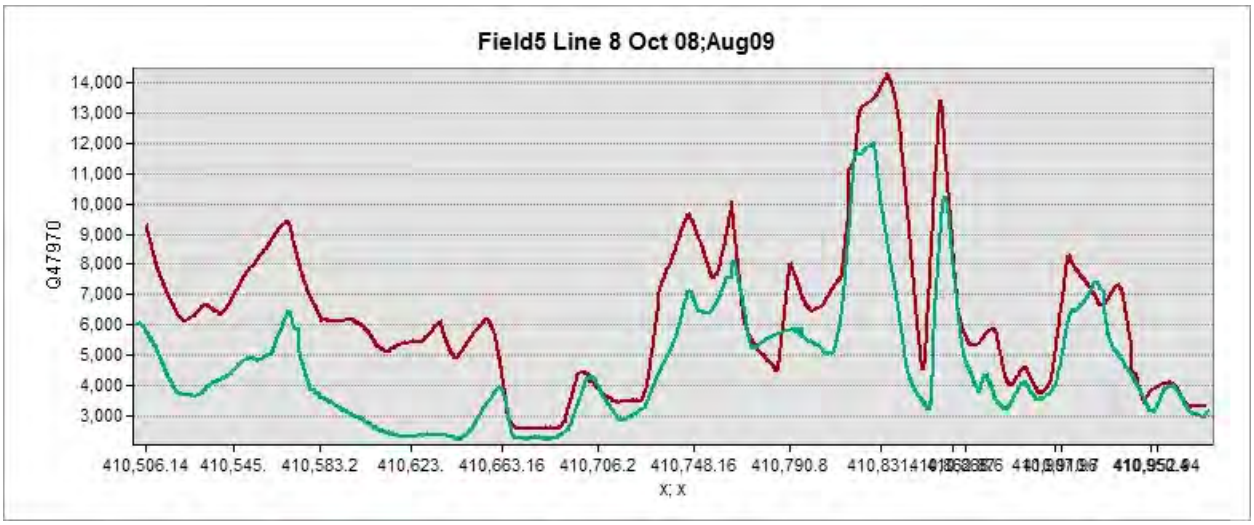

Figure 7. Comparison of quadrature values for survey line field 5 (October 2008 and August 2009

APPLICATIONS OF SELF-POTENTIAL METHOD IN AGRICULTURE

Larisa Golovko, Landviser, LLC, Houston, TX
Anatoly I. Pozdnyakov, Moscow State University, Moscow, Russia

Abstract

Electrical geophysical methods are classified as methods measuring natural electrical potentials of the ground without introducing additional electrical field and methods utilizing artificial electrical or electromagnetic fields to measure soil electrical parameters. Method of self-potential (SP) measures the naturally existing electrical potentials in soils and "bio-potentials" in plant, which are important in agriculture. Despite growing popularity of electrical resistivity/conductivity methods in precision agriculture, method of self-potential is rarely used. The SP method is based on measuring the natural potential differences, which generally exist between any two points in the soil or plant. Electrical potential in Soil-Plant system is a combination of the natural electrical potential differences on the interfaces inside soil (between soil horizons or peds), on the interfaces inside growing plant (between different plant tissues), as well as between soil and plant. The largest electrical potential differences were observed inside soils between soil horizons drastically different in physical and chemical properties. In most soils topsoil has higher electrical potentials than subsoil. The highest potential difference between soil horizons reported for Spodosols (40-60 mV), decreasing to 20-40 mV in Alfisoils and to ~20 mV in Mollisols, and even lower in Aridisols. Maps of electrical potentials in topsoil help to reveal the micro-environments for plant growth and correspond to plant biomes in natural ecosystems. Electrical resistivity (ER) or conductivity (EC) maps are generally similar to the maps of self-potentials, but using combination of those methods brings more information about infiltration and subsurface water fluxes and aid in search for clogged drainage pipes and reclamation planning. Recent advances in geophysical equipment, such as LandMapper ERM-02 also allow non-invasively measure natural electrical potentials between soils and plants, which are very small (μV magnitude), but nevertheless can be used to study plant water and nutrient stresses and manipulated to facilitate plant growth.

Introduction

Many kinds of electrical fields and potentials are often simultaneously observed in natural soil; thus, it is difficult to know what mechanism is responsible for their formation. Stationary electrical fields originated in deep geological formations can be observed in soils together with electrical fields of a various nature, arising directly in soil profiles (Semenov, 1980). The potentials originated in soil profiles were classified into diffusion-adsorption potentials, electrode potentials, and potentials of "varying in time fields" (Semenov, 1980). The "geological" potentials are limited to certain natural conditions, such as sharp change of oxidation-reduction conditions above an ore deposit or perched mineralized groundwater. The natural "soil" electrical potentials, on the contrary, can form under any soil condition.

All the natural electrical fields can be classified by mechanisms and nature of their occurrence in two large groups: electrical fields of stationary processes, existing on the contacts of various media and non-stationary, transient, electrical fields, arising in saturated and unsaturated soils due to movement of

soil solutions. The most widespread electrical fields in soils are attributable to diffusion-adsorption potentials, in which sorption typically contributes more than diffusion. The natural electrical fields are measured together with electrode potentials, which can be considered as artificially created potentials on the contacts of electrodes with soil.

Natural electrical fields and their potentials were studied in some soils in Russia (Borovinskaya, 1970; Vadunina, 1979; Pozdnyakov et al., 1996). Vadunina (1979) indicated that potentials measured on the soil surface could be used to estimate different soil properties in the whole soil profile. The measurements of natural potentials on the surface of some Aridisols (including Natrargids) and Alfisols (Pozdnyakov et al., 1996) show that such estimation is possible only when the surface soil horizons are genetically related to the other horizons in the soil profile.

We consider soil electrical potentials as diffusion-adsorption potentials on the contacts of different soil structures, such as soil aggregates, horizons, and pedons in topographic sequences. This concept, based on Poisson's and Maxwell's laws of electromagnetism and Boltzmann's distribution law of statistical thermodynamics, was used to explain relationships among various soil properties, mobile electrical charges, and electrical parameters. The theory considers soil cover as a huge "source" generating natural electrical fields and allows constructing models of electrical profiles in various soils.

History of self-potential method in geophysical prospecting

The SP method was used by Fox as early as 1830 on sulphide veins in a Cornish mine, but the systematic use of the SP and electrical resistivity methods in conventional geophysics dates from about 1920 (Parasnis, 1997). The SP method is based on measuring the natural potential differences, which generally exist between any two points on the ground. These potentials are associated with electrical currents in the soil. Large potentials are generally observed over sulphide and graphite ore bodies, graphitic shale, magnetite, galena, and other electronically highly conducting minerals (usually negative). However, SP anomalies are greatly affected by local geological and topographical conditions. These effects are considered in exploration geophysics as "noise". The electrical potential anomalies over the highly conducting rock are usually overcome these environmental "noise", thus, the natural electrical potentials existing in soils are usually not considered in conventional geophysics.

Perspective of self-potential method in environmental, agricultural and engineering applications

In soil studies researchers are especially interested in the measurement of such "noise" electrical potentials created in soils due to soil-forming process and water/ion movements. The electrical potentials in soils, clays, marls, and other water-saturated and unsaturated sediments can be explained by such phenomena as ionic layers, electro-filtration, pH differences, and electro-osmosis. Soil-forming processes can create electrically variable horizons in soil profiles, thus electrical potential differences measured between soil horizons can be used to study soil forming processes and soil genesis.

Another possible environmental and engineering application of self-potential method is to study subsurface water movement. Measurements of electro-filtration potentials or streaming potentials have been used in Russia to detect water leakage spots on the submerged slopes of earth dams (Semenov, 1980). Method of self-potential in addition to EC mapping and vertical electrical sounding/ imaging (VES) can aid in archaeological and civil engineering projects (Pozdnyakova et al., 2001).

Materials and Methods

Potentials generated by subsurface environmental sources are lower than those induced by mineral and geothermal anomalies and often associated with high noise polarization level (Corwin, 1990). Therefore, the usage of non-polarizing electrodes is mandatory when the SP method is applied in soil and environmental studies. The non-polarizing electrode consists of a metal element immersed in a solution of salt of the same metal with a porous membrane between the solution and the soil (Corwin and Butler, 1989). Because of easy breakage of the membrane and leakage of the electrode solution we adopted firm non-polarizing electrodes (carbon cores from the exhausted electrical cells) to develop non-polarizing electrodes for soil studies (Pozdnyakov, 2001). In addition, low-polarizable and non-polarizable electrodes used in medical studies (available from In-Vivo Metrics, CA) were successfully used on soils/plants in the field and lab conditions. For soils with high potential differences between horizons gold-plated electrodes can be used. For seasonal monitoring in plant physiology we recommend high quality solid sintered Ag-AgCl sensor electrodes (Figure 1). Those silver-silver chloride electrodes are very stable and performance is exceptionally reproducible. Should the electrode surface become damaged or contaminated, a new surface can be exposed with sandpaper to restore the electrode's original performance.

Figure 1: Solid-state Ag-AgCl non-polarizing electrodes manufactured by In-Vivo Metrics, CA.

Figure 2: LandMapper ERM-02, hand-held device for measuring electrical resistivity, conductivity and self-potential, manufactured by Landviser, LLC.

To measure small electrical potential differences in soils accurately, in addition to non-polarizing electrodes, the measuring device should be modified and as such should have isolated connectors and high internal impedance. Most leading geophysical resistivity instruments, such as ABEM SAS, Syskal, and Sting provide such connections, but coupling electrodes are bulky, leaky and generally not useable in plant/soil studies. We developed LandMapper ERM-02 with self-potential measuring capability and easy coupling with medical-grade non-polarizing electrodes. LandMapper ERM-02, in addition to electrical conductivity and resistivity measurements also allows non-invasively measure natural electrical potentials in soils and plants when two special non- polarizing electrodes are connected to MN terminals (Figure 2). Table 1 lists technical characteristics of LandMapper ERM-02, portable device that measures three basic electrical parameters in field soils, plants, animals and liquid and solid samples in the laboratory.

Table 1. Technical Specifications of LandMapper ERM-02

Range of measurements……ER= 0.1-1*10^6 Ohm m
…… EC= 1*10^{-6} – 10 Sm^{-1}
…….……EP= -1 to +1 V (Δ0.01 mV)
User-selectable ER/EC/EP modes of measurement. Automatically adjusts electrical resistivity/conductivity/potential ranges to provide best measurement accuracy. Error of measurements is typically less than 1%.
User-defined K (geometrical coefficient)……..…….…….……...0.1 up to 99.9
Quantity of changeable K-coefficients..……....9
Quantity of data storage locations…….……..……999
Range of operation temperatures……...from - 10 up to + 40 C^0 or 14 to 100 F
Air humidity, no more than……..…….……85 %
Weight of the device, no more…….…….…….…….. 250 g or 8 oz
Current of consumption, no more……..…….……..7.0 mA
Output voltage, no more……..…….……5 V
Measurements comparable with DC methods, frequency…..……1.25 Hz
Computer connection…….……serial port

Measuring electrical potential with LandMapper ERM-02

1. Connect non-polarizing electrodes to MN socket on the front panel of the device.
2. Choose the reference electrode and put it in the presumable area of low electrical potential, usually wettest and clay-rich areas. For example, for measuring electrical potential difference in soil pits, put reference electrode in the lowest layer of subsoil. When measuring potential difference between soils and plants, it is advised to put reference electrode on soil surface and the measuring electrodes on the leaves or trunk of growing plants (Fig. 3).
3. The actual value of electrical potential between the electrodes is shown in mV. The device automatically takes a reading every second, takes 10 readings and outputs average value every 10 sec (natural potentials will fluctuate). This data cannot be saved in the RAM of Landmapper during field measurements if device is used as stand-alone (without PC). However, if Landmapper is connected to PC during measurements, the values of potentials are displayed on the PC screen and can be saved on PC directly. Software to automatically direct measurements from computer is under development by Landviser, LLC, but PC connect protocol in C++ is provided to customers upon request. You can manually record as many readings at the same location as you like.

Figure 3: Correct placement of electrodes when measuring electrical potential difference between soils and plants.

Case Studies

Electrical potential differences between soil horizons

The largest electrical potential differences were observed between soil horizons drastically different in physical and chemical properties. In most soils topsoil has higher electrical potentials than subsoil. The highest potential difference between soil horizons reported for Spodosols (40-60 mV), decreasing to 20-40 mV in Alfisoils and to ~20 mV in Mollisols, and even lower in Aridisols (Figs. 4 and 5). Probably, the higher potential difference in Spodosols and Alfisols profiles guides growth of woody plants with well developed root system spreading deep into the subsoil. Natural electrical potential differences between soil horizons facilitate root growth. Those differences also form in uniform soil profiles under consistent vertical or horizontal water fluxes. Lysimeter studies on uniform soil column confirm that negative potential gradient forms downwards after intensive infiltration.

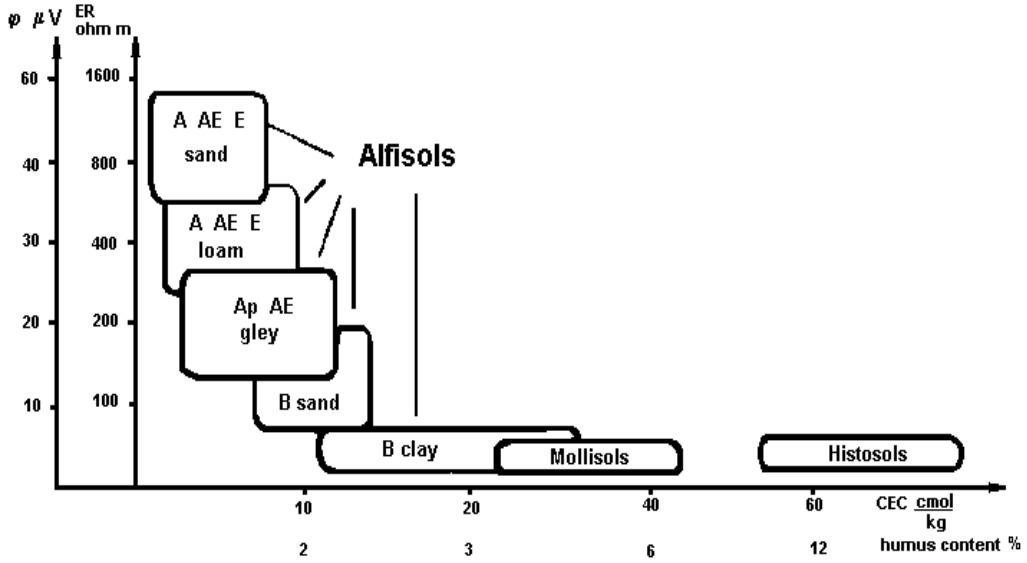

Figure 4: Schematic relationship between electrical parameters and soil properties showing approximate distribution of data for soils in humid areas.

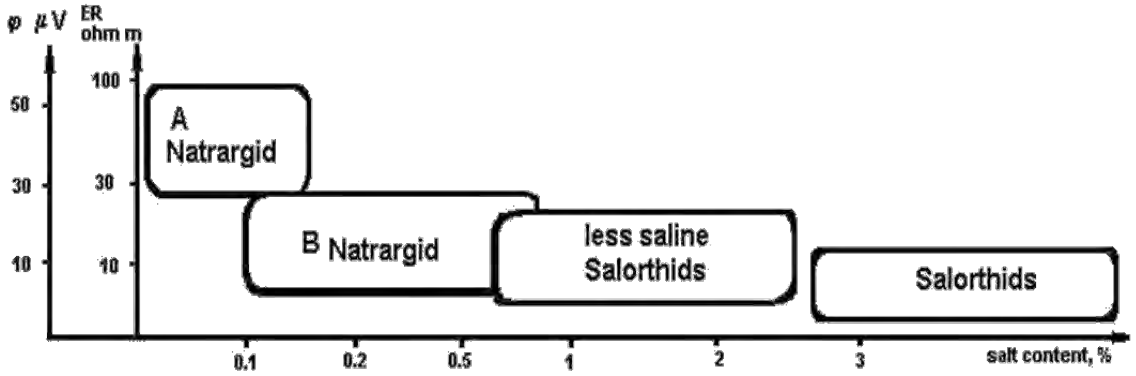

Figure 5: Schematic relationship between electrical parameters and soil properties in arid soils.

Electrical potential differences in topsoil

Maps of electrical potentials in topsoil help to reveal the micro-environments for plant growth and correspond to plant biomes in natural ecosystems (Pozdnyakov, 2008). Electrical resistivity (ER) or conductivity (EC) maps are generally similar to the maps of self-potentials, but using combination of those methods brings more information about infiltration and subsurface water fluxes and aid in search for clogged drainage pipes and reclamation planning.

Electrical potential differences between plants and topsoil

Many soil properties influencing plant growth and yield can be identified and mapped with electrical geophysical methods, which explains recent advances in electrical conductivity method application in precision agriculture. Moreover, our recent studies have shown that soil electrical potentials influence plant growth directly and electrical geophysical methods can be used to monitor plant health (Fedotov and Pozdnyakov, 2001). The biopotentials or micro electrical potentials of the plant tissues and their effect on plant growth have been studied by plant physiologists for quite some time. However, practically no research has been conducted on natural electrical potentials between soil and a growing plant, or "macro-potentials" of the plants.

Earth is an "electrical" planet in nature. All the processes in biosphere occur in ever-changing electrical fields, which arise due to changes in solar activity, magnetic field of the Earth, and electrical processes in atmosphere. These global and local fluctuations in electrical fields create electro-tropism at all levels of biosphere, including the Soil-Plant system. Electro-tropism in Soil-Plant system is a combination of the natural electrical potential differences on the interfaces inside soil (between soil horizons or peds), on the interfaces inside growing plant (between different plant tissues), as well as between soil and plant. The largest electrical potential differences were observed inside soils. The natural electrical potentials (stationary and fluctuating) in soils were studied by our group for last 40 years and the results were summarized and presented on 17th World Congress of Soil Science in 2002 (Pozdnyakov and Pozdnyakova, 2002).

Recently, we advanced to measure and research the natural electrical potentials between soil and growing plants (Pozdnyakov et al., 2006). Natural electrical potentials between soils of major genetic types and more than 100 species of native and cultural plants of Ukraine, Russia, and Philippines in different growing conditions have been studied in 2003-2005 (Pozdnyakov, et al., 2005).

The electrical potential difference between soil and a plant was always negative. This difference was highest during spring and for young plants in summer, and decreased in the fall when plants in Russia are ready for dormancy. Tropical plants showed higher potential differences than plants of temperate climate. The potentials for all plants decreased in a row flower-leaf-stem. Electrical potential of herbaceous plants is directly related with the leaf area and the highest potentials were observed for burdock, cow-parsnip, and young banana palms. The research is underway for establishing relationships between natural electrical potentials/resistivity of plants/soils and plant's water stress (Terehova et al., 2007).

Conclusions

The SP method is based on measuring the natural potential differences, which generally exist between any two points in the soil or plant. The electrical potentials in soils, clays, marls, and other water-saturated and unsaturated sediments can be explained by such phenomena as ionic layers, electro-filtration, pH differences, and electro-osmosis. Soil-forming processes can create electrically variable horizons in soil profiles. Self-potential method can be used in agriculture to study soil-forming processes altering distribution of mobile electrical charges, i.e. subsurface water movement, search for clogged drain pipes, mapping preferential water flow paths.

Electrical potential in Soil-Plant system is a combination of the natural electrical potential differences on the interfaces inside soil (between soil horizons or peds), on the interfaces inside growing plant (between different plant tissues), as well as between soil and a plant. Electrical potential differences within plants are of μV-mV magnitude, but can be used to study plant water and nutrient stresses and manipulated to facilitate plant growth. Soil-plant electrical potential difference was negative for all plants and decreased in a row flower-leaf-stem. Electrical potential of herbaceous plants was directly related to the leaf area. This potential difference shown seasonal dynamics and was lowest in the fall. Electrical potentials between topsoil and growing plants can be used to monitor plant growth and health continuously and non-destructively.

References

Borovinskaya, L.B. 1970. *Application of self-potential method to study filtration in soils and grounds*. (In Russian.) Rus. Soil Sci. 11:113-121.

Corwin, R.F. 1990. *The self-potential method for environmental and engineering applications*. *In:* S.H. Ward (ed). Geotechnical and environmental geophysics. Vol. I: Review and tutorial. Soc. of Exploration Geophysics. P.O. Box 702740/Tulsa, OH 74170-2740.

Corwin, R.F., and D.K. Butler. 1989. *Geotechnical applications of the self-potential method; Rept 3: Development of self-potential interpretation techniques for seepage detection*: Tech. Rep. REMR-GT-6, U.S. Army Corps of Engineers, Washington DC.

Fedotov, G. N. and Pozdnyakov, A. I., 2001. "Электрическая активность почв и ее влияние на рост растений. (*Electrical soil activity as is influences plant growth*)." J. Actual Problems of Modern Science, Series: Soil Science, Russia 2, 15-24.

Parasnis, D.S. 1997. *Principles of applied geophysics*. Chapman & Hall, 2-6 Boundary Row, London SE1 8HN, UK.

Pozdnyakov A.I. 2008. *Electrical Parameters of Soils and Pedogenesis*. Eurasian Soil Science, 2008, Vol. 41, No. 10, pp. 1050–1058.

Pozdnyakov, A. and Pozdnyakova, L., 2002. *Electrical fields and soil properties.* in "17 World Congress of Soil Science," Bangkok, Thailand.

Pozdnyakov, A., Mikus, A., Fedotov, G. and Pozdnyakova, L., 2005. *Electrical potentials in system "Soil-Plant".* in ASA-CSSA-SSSA International Annual Meetings," Salt Lake City, UT, USA.

Pozdnyakov, A., L. Pozdnyakova, L. and G. Fedotov. 2006. *Electro-tropism in "Soil-Plant" System*. in 18th World Congress of Soil Science, Philadelphia, PA, USA.

Pozdnyakov, A.I, L.A. Pozdnyakova, and A.D. Pozdnyakova. 1996. *Stationary electrical fields in soils* (in Russian with English summary). KMK Scientific Press, Moscow, Russia. 1-358

Pozdnyakova, L., A. Pozdnyakov, and R. Zhang. 2001. *Application of geophysical methods to evaluate hydrology and soil properties in urban areas*. London, UK, Urban Water 3:205-216.

Semenov, A.S. 1980. *Electroexploration with the method of natural electrical field (self-potential)*. (In Russian.). Nedra. Leningrad. Russia.

Terehova, N. V., Fedotov, G. N. and Pozdnyakov, A. I. 2007. *Develop method of estimating plant health by measuring electrical parameters in system Soil-Plant.* In Russian. in "International conference "Spatial-temporal organization of soil cover: theory and applications" (Материалы международной научной конференции "Пространственно-временная организация почвенного покрова: теоретические и прикладные аспекты)," St. Petersburg State University, St. Petersburg.

Vadunina, A.F. 1979. *Electroreclamation of saline soils*. (In Russian). Moscow Univ. Press. Moscow.

DEVELOPMENT OF METHODS FOR DETERMINING THE SUITABILITY OF EPHEMERAL STREAMS FOR PRODUCED WATER DISCHARGES

Garret A. Veloski, U.S. Department of Energy, National Energy Technology Laboratory, Pittsburgh, PA
Bruce D. Smith, U.S. Geological Survey, Denver Federal Center, Denver, CO
James S. Sams, U.S. Department of Energy, National Energy Technology Laboratory, Pittsburgh, PA
Richard W. Hammack, U.S. Department of Energy, National Energy Technology Laboratory, Pittsburgh, PA
Burke J. Minsley, U.S. Geological Survey, Denver Federal Center, Denver, CO

Abstract

Wyoming's Agricultural Use Protection Policy allows discharge of produced water from coal bed natural gas operations to ephemeral streams with irrigated lands, on the basis of water quality implied from root zone soil salinity measurements. Critics of the policy argue that the soil and water quality sampling methods used to set quality limits for produced water discharges do not accurately represent existing soil conditions or indicate the potential for soil damage that can result from contact with the sodic, brackish produced water. To improve the understanding of interactions between soil and the discharges of sodic, brackish water from CBNG production, the National Energy Technology Laboratory conducted airborne, ground, and borehole electrical conductivity surveys and optical remote sensing surveys over the Beaver Creek Watershed in the central Powder River Basin of Wyoming. The airborne electrical conductivity data were found to quickly map possible areas of high soil salinity (EC_e) for the extensive sub-irrigated areas that provide forage for livestock. Hyperspectral remote sensing data can help identify surface soil minerals and vegetation susceptible to the influence of CBNG produced water and identifies evidence of other possible impacts along waterways. The combined methods are potentially useful in land and water management decisions related to salinization.

Introduction

The Power River Basin (PRB) is an area of extensive coal bed natural gas (CBNG) resources with over 80,000 wells. Gas production involves reducing the hydraulic head in the coal/water aquifer allowing desorption of gas from the coal. The water thus produced varies considerably throughout the basin in terms of salinity. A major concern over CBNG produced water disposal is its potential impact on soils. When exposed to a high sodium ion concentration, the soils are susceptible to swelling and dispersion of the clay mineral particles that may result in a decrease in water infiltration rates by altering the hydraulic conductivity. PRB soils are also generally high in swelling clay (exchangeable sodium) content and thus highly susceptible to irrigation water high in sodium and low in calcium and magnesium. Compromised soils reduce available water and air to the root systems of crops. Discharge of produced water into stream drainages with an existing irrigation use is subject to Wyoming water quality regulation Section 20. Under Section 20, the predicted degradation to soils resulting from CBNG produced water discharge must not adversely impact the most vulnerable plant species or cause a decline in agricultural production, due to water quality. A proxy for predicting degradation that has been used by the Wyoming Department of Environmental Quality (WDEQ) for existing water quality or agricultural use is EC measured from soil/water extracts from irrigated soils in the vicinity of discharge locations employing soil coring and saturated paste extraction methods (WDEQ, 2007).

The WDEQ proposed making the Section 20 policy a rule and employed two independent consultants to examine the scientific basis for the proposed rule (Hendrickx and Buchanan, 2009). The consultants found the proposed rule "to **not** be reasonable or scientifically valid." WDEQ subsequently withdrew the proposed rule. However, WDEQ will continue to use the Agricultural Use Protection Policy to permit new produced water discharges although more groundwater monitoring may be required to assure non-degradation of downstream agricultural use (http://deq.state.wy.us/wqd/wypdes_permitting/; accessed, January 2010).

Soil Chemistry

The sodium absorption ratio (SAR), an empirically-derived index is used to determine the relative impact of saline water on clayey soils having a high percentage of exchangeable sodium, is based upon the ratio of sodium to divalent cations according to the relationship:

$$SAR = \frac{[Na^+]}{\sqrt{\frac{1}{2}([Ca^{2+}]+[Mg^{2+}])}}$$

SAR can be used to access the risk of irrigation waters to plants. The relationship between salinity (EC) and SAR was described by Hanson (1999) where calcium and magnesium moderate the effects of salinity on soil. The relationship between SAR and EC can be expressed by the equation SAR< 7.10 x EC - 2.48. This equation represents a line on the Hanson Graph that separates a domain of EC and SAR values that corresponds to no reduction in water infiltration from a domain that has a moderate reduction in infiltration. Bulk soil apparent electrical conductivity (EC_a) measurements have been routinely used (Lesch, Strauss, and Rhodes, 1995a and b) to estimate soil salinity (EC_e). Deterministic regression models have been developed for predicting soil salinity from electromagnetic (EM) induction measurements as input from EM38 and EM31 instruments along with secondary soil properties (Corwin Lesch, Rhodes, 2000). .

Electromagnetic Data

Helicopter electromagnetic (HEM) data were collected in the Beaver Creek area from a helicopter platform employing the Fugro Resolve® frequency domain system in 2004 and 2008. The calibrated electromagnetic instrument simultaneously acquires in phase and quadrature data at six frequencies while being flown at 35 m above ground level. The 2004 survey used 100 m line spacing flown north-south in the Burger Draw area near the confluence of Beaver Creek and the Powder River (Sams and others, 2004). The 2008 survey used 50 m line spacing flown in blocks parallel to the direction of the drainage in Beaver Creek The frequencies employed in the two surveys were similar using high frequencies of about 140,000 and 115,000 Hz. Figure 2 shows an example of how HEM can delineate ephemeral streams and sub-irrigated areas surrounding Beaver Creek exhibiting higher apparent conductivity as a result of salinity and moisture.

In the current study, helicopter electromagnetic (HEM) and remote sensing data were collected over the Beaver Creek Watershed in the PRB of Wyoming (Figure 1). The HEM data were collected over sub-irrigated areas of the watershed parallel to the direction of the drainage in Beaver Creek. The

optical remote sensing data were acquired from a fixed-wing aircraft at an altitude of 5500' above the ground and over the entire 295 km^2 Beaver Creek Watershed

Ground EM, resistivity, and borehole data was collected in the Burger Draw area in 2004 (Lipinski and others, 2004). The ground EM data was collected with a wide-band GEM2 hand held system. These data have been used to map saline waters generated from an infiltration pond and to map shallow soluble salts and high natural salinity.

Airborne Hyperspectral Data

Airborne hyperspectral data has been used extensively for land classification, vegetative stress, species identification, material mapping, change detection and a number of other purposes. The high-resolution (1 m^2), 72-band visible-near infrared (VNIR, 380-1050 nm) compact airborne spectral imager (CASI) hyperspectral and 15 cm color digital aerial camera system (DACS), multispectral imagery These optical remote sensing data sets were ortho-rectified using LiDAR (3-4 postings/m^2) that was acquired simultaneously. In addition, 128 band, (4 m^2 pixels) VNIR and shortwave infrared (SWIR, 430-2500 nm) Probe-1 hyperspectral flight lines were obtained from a survey conducted by the US Geological Survey in 2005. The data was converted to surface reflectance using Atmospheric CORrection Now (ACORN) software to remove atmospheric effects.. The 100 km^2 Probe-1 data set overlaps with portions of the area imaged with CASI and was evaluated for the purpose of materials mapping.

Material mapping algorithms employing library spectra can be used to identify mineral species from the signature of their reflectance spectra at characteristic wavelengths. Afforded the benefit of spectral angle mapping (SAM) tools such as those found in popular image processing software, the complexity of identifying and mapping relative abundances of minerals has been greatly simplified. SAM tools provide a means of identifying the quality of match between the sample and library reflectance spectra. SAM processing generates a classified image map for a given input material where an estimate of the percentage of the material of interest in each pixel is related to the DN value.

SAM analysis was performed on a subset of the Probe-1 hyperspectral data to explore the possibility of mapping the relative risk to soils from the application of CBNG produced water. Areas having soils at higher risk of developing sodicity from the application of irrigation water from CBNG generally have high smectitic clay content (KC Harvey Report, 2007). A scene was selected from the imagery surrounding a center pivot irrigation system used to dispose CBNG produced water and the material mapping tool in ERDAS Imagine was used to generate a classified image that employed the library spectrum for a Wyoming montmorillonite as input (Figure 3). Ground truth verification for swelling clay content of soils obtained on the basis of SAM processed hyperspectral imagery will require field sampling and analysis.

Discussion and Conclusions

HEM EC measurements have been shown to be able to map saline soils and clays on local and regional scales in the management of groundwater in arid agricultural areas of Australia (Munday and others, 2003). Lipinski and others (2008) have demonstrated that airborne EC surveys in the upper Powder River Basin can be used to map salinity variations. Indeed HEM apparent conductivity measurements in some geoelectrical settings can produce better conductivity estimates than ground measurements (Figure 4) particularly in areas of high cultural noise and limited accessability.

Measurements made with three types of EM conductivity systems in a salinity survey in Australia (Munday and others, 2003) are shown in Figure 5, and are consistent with the trends shown in Figure 4..

Electrical conductivity in sediments is controlled primarily by pore water conductivity, amount of water, and amount of conductive clay minerals. The process of calibration of EC for a particular site involves sampling the sediments in the first two feet and measuring the properties of the water and mineral extracts (Lesch and others, 2000). The calibration is greatly aided if there are ancillary measurements such as the multispectral data that can determine the clay content in the near surface.

Airborne and ground electromagnetic and multispectral geophysical surveys have the capability to make measurements that characterize near surface soil and rock properties rapidly over large areas. In this context they may be a viable means for assessing the possible impacts on drainages of direct discharge of CBM produced waters. One step in this characterization is to relate airborne and ground electrical conductivity to soil salinity. This step has been studied over several years by the Department of Agriculture and has resulted in a software package termed ESAP-95 that estimates field scale ground EM conductivity measurements to soil salinity (Lesch, Rhoades, and Corwin, 2000). An essential step in using this software to estimate soil salinity is to adequately calibrate the EM measurements with field soil sample analyses (Lesch and others, 1995a and b).

Remotely acquired data would be advantageous for addressing permitting issues requiring accurate estimates of soil salinity. Using airborne EM data it may be possible to predict soil salinity along drainages and also provide more representative data than soil core conductivity measurements alone over a larger areal extent. Similarly, apparent conductivity maps obtained from airborne EM data have been used to develop GIS-based models for siting surface water infiltration impoundments elsewhere in the PRB (Sams, 2008).

We conclude from the present data sets that an integrated interpretation of salinity in drainages is possible with airborne and ground geophysical methods. The recommended way to implement this interpretation would be to integrate geophysical measurements with sediment sampling. Improvements in calibration of ground EM measurements such as described by Minsley and others (2010, these proceedings) provides an important step in quantitatively relating geophysical measurements to soil salinity. Additional work on analysis of the HEM data for resolution of near surface EC could, perhaps improve prediction of near surface salinity.

Acknowledgements

The Wyoming Department of Environmental Quality provided data from Beaver Creek Watershed and encouraged the study. The U.S. Department of Energy appreciates the cooperation of the USGS Rocky Mountain Mapping Center for their contribution of the Probe-1 hyperspectral dataset. Any use of trade, product, or firm names is for descriptive purposes only and does not imply endorsement by the U.S. Government.

References

Hanson, B., Gratta, S.R. and Fulton, A.F. 1999. Agricultural Salinity and Drainage. Division of Agriculture and Natural Resources Publication 3375. University of California Irrigation Program. University of California, Davis CA.

Hendrickx, J.M.H., B. Baerends, Z.I. Raza, M. Sadiq, and M.A. Chaudhry. 1992. Soil salinity assessment by electromagnetic induction on irrigated land. Soil Sci. Soc. Am. J. 56:1933-1941.

Hendrickx, J.M.H. and Buchanan, B.A., 2009, Expert Scientific Opinion On The Tier-2 Methodolgy, Report to the Wyoming Environmental Quality Council (unpublished), 27p.

K C Harvey Incorporated, 2007.Section 20 Tier 2 Compliance Analysis for Proposed Discharges to Beaver Creek in a report prepared for the Bill Barrett Corporation, Denver CO. July 26, 2007.

Lesch, S.M.,D.J. Strauss, and J.D. Rhoades. 1995a. Spatial prediction of soil salinity using electromagnetic induction techniques: 1. Statistical prediction models: A comparison of multiple linear regression and cokriging; Water Resources Research vol. 31, p. 373-386.

Lesch, S.M., Strauss, D.J., and Rhoades, J.D., 1995b. Spatial prediction of soil salinity using electromagnetic induction techniques: 2. An efficient spatial sampling algorithm suitable for multiple linear regression model identification and estimation; Water Resources Research vol. 31, p. 3387-398.

Lesch, S.M., Rhodes, JD., and Corwin, D.L., 2000, ESAP-95 Version 2.01R User Manual and Tutorial Guide. Research Report No. 146. , USDA-ARS, George E. Brown, Jr., Salinity Laboratory, Riverside, California, 87p.

Lipinski, B A, Harbert, W., Hammack, R., Sams, J., Veloski, G., and Smith, B.D., 2004, : Using Airborne and Ground Electromagnetic Surveys and DC Resistivity Surveys to Delineate a Plume of Conductive Water at an In-Channel Coalbed Methane Produced Water Impoundment Near the Powder River, Wyoming, American Geophysical Union Annual Meeting, San Francisco, 1p.

Lipinski, B.A., Sams, J.I., Smith, B.D., and Harbert, W., 2008, Using HEM surveys to evaluate disposal of by-product water from CBNG development in the Powder River Basin, Wyoming: Geophysics, vol. 73, no. 3, p. 77-84.

Minsley, B.J., B.D. Smith, R. Hammack, J.I. Sams, and G. Veloski, 2010, Calibration and filtering strategies for frequency domain electromagnetic data: Symposium on the Application of Geophysics to Engineering and Environmental Problems, this proceeding.

Munday, T., Brodie, R., Green, A., Lane, R., Sattel, D, Cook, P., Barnett, S., and Walker, G. 2003, Developing recharge reduction strategies in the Riverland of South Australia using airborne electromagnetic data – a case study in tailoring airborne geophysics given a particular target and a desired set of outcomes, Extended Abstracts ASEG 16th Geophysical Conference and Exhibition, February 2003, Adelaide, 6p.

Sams, J.I., Smith, B.D., Lipinski, B., and Harbert, W., 2006, Applications of Airborne Electromagnetic Surveys to Improve Management of Produced Water in the Powder River Basin: Symposium on Environmental and Engineering Geophysics, Seattle WA. 2006 Annual Meeting Proceedings, 7p.

Sams, J.I., Lipinski, B.A. and Veloski, G., 2008. Using Ground Based Geophysics to Evaluate Hydrogeologic Effects of Subsurface Drip Irrigation Systems Used to Manage Produced Water in the Powder River Basin, Wyoming. Symposium on the Application of Geophysics to Engineering and Environmental Problems, 21(1): 916-925.

Wyoming Department of Environmental Quality (WYDEQ). March, 2007. Wyoming Water Quality Rules and Regulations, Chapter 1. Wyoming Surface Water Quality Standards. Proposed Rules. EQC Draft, 31 p.

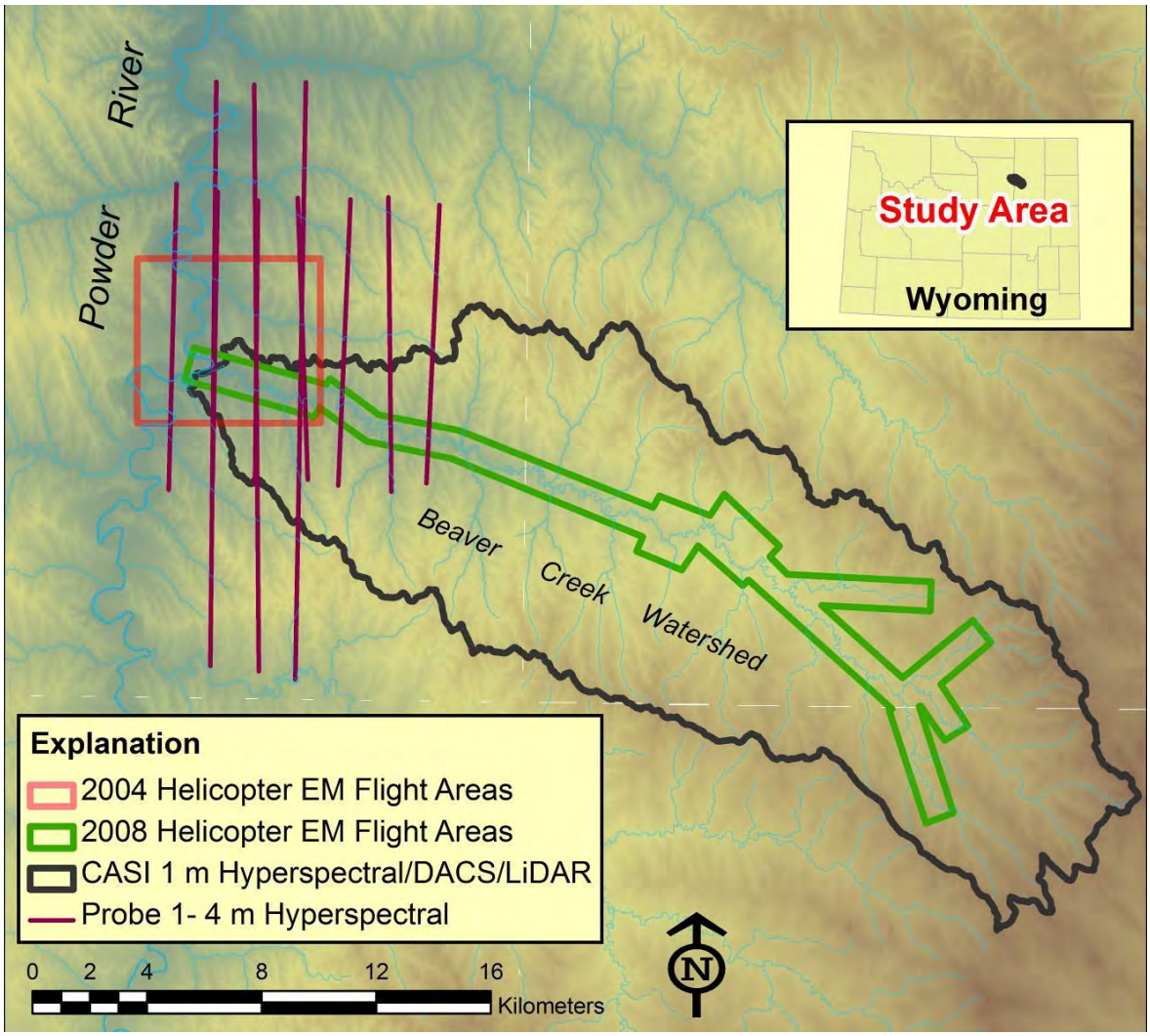

Figure 1: Location map of the Beaver Creek watershed study area. Helicopter EM surveys were conducted in 2008 along the main stem of Beaver Creek and previously in 2004 in the Burger Draw area (rectangular area outlined in red). Digital aerial camera system (DACS) imagery and 1 m2 VNIR hyperspectral were collected over the entire watershed. The Probe 1, 4 m VNIR/SWIR hyperspectral data was collected only along the N-S lines in northeast portion of the watershed.

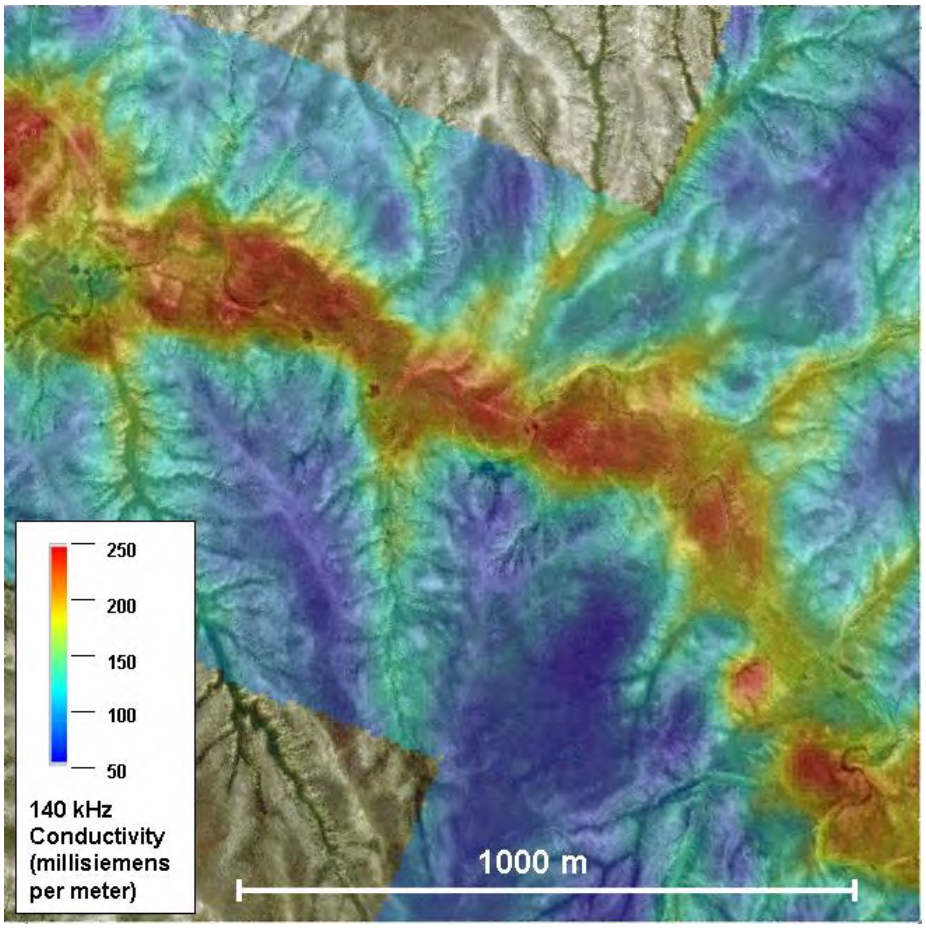

Figure 2: Gridded 140,000 Hz helicopter EM data subset draped over 15 cm DACS imagery. The ephemeral streams and sub-irrigated areas surrounding Beaver Creek exhibit generally higher apparent conductivity than outlying areas as a result of high salinity and moisture.

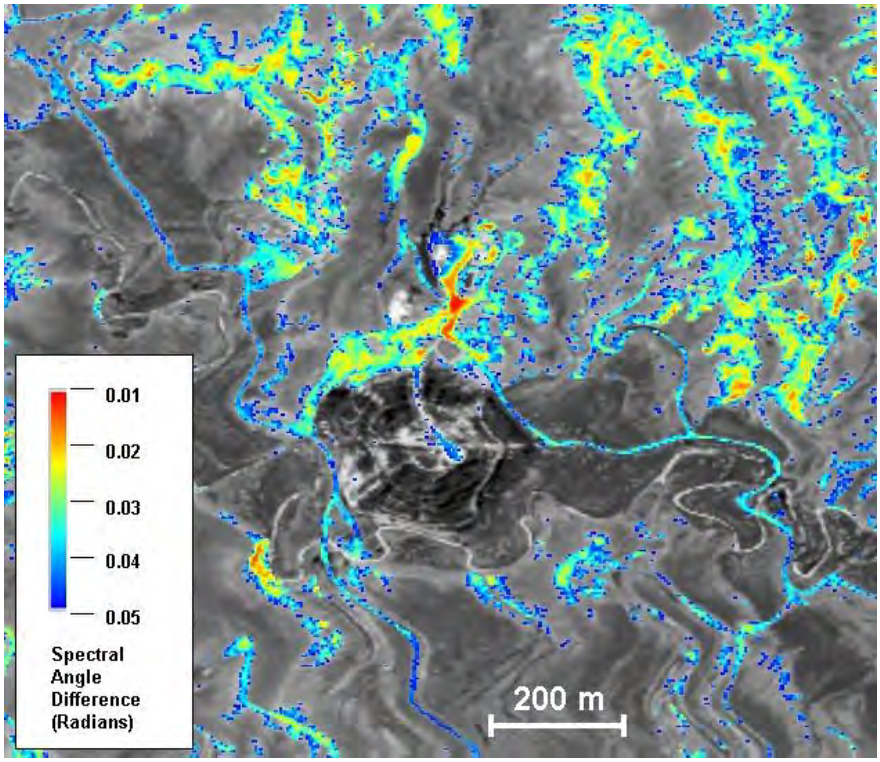

Figure 3: Warmer colors in this classified, SAM processed, Probe-1 hyperspectral scene, indicate a higher quality of match for the reference spectrum of montmorillonite. The center pivot irrigation system is visible at center. The imagery has not been geometrically corrected

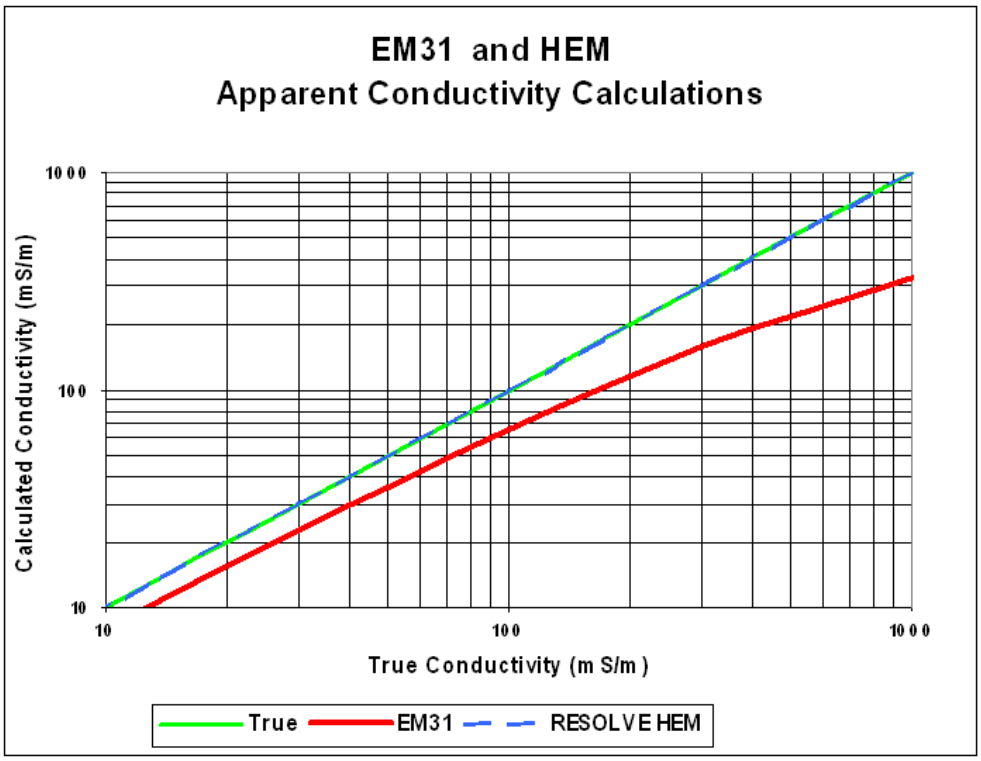

Figure 4: Low induction number comparison of helicopter EM conductivity and ground EM31 conductivity estimates (graph from Hodges, pers. Comm., 2009).

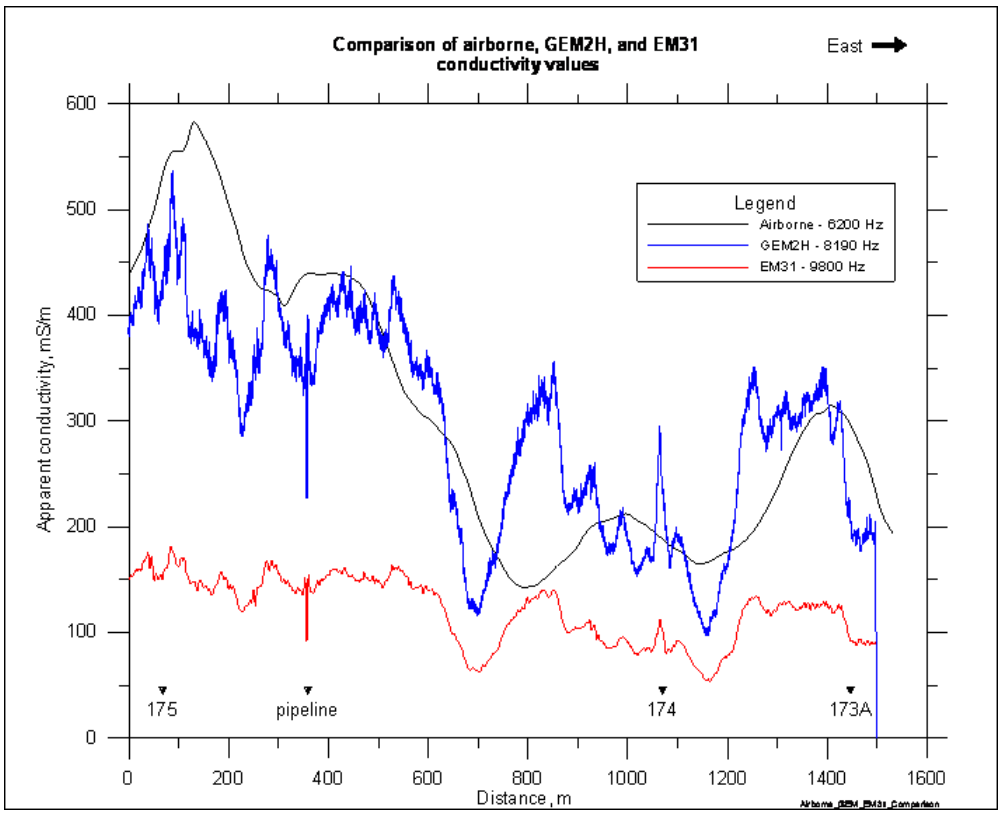

Figure 5: Comparison of ground and airborne apparent conductivity measurements along a coincident line (Munday and others, 2003)

CASE HISTORY: SITING SHALLOW GROUNDWATER WELLS WITH THE AID OF GEOPHYSICS

Norman R. Carlson, Zonge Engineering & Research Organization, Inc., Tucson, AZ
Paul G. Ivancie, AMEC Earth and Environmental, Inc., Lakewood, CO
Phil C. Sirles, Zonge Geosciences, Inc., Lakewood, CO

Abstract

Although the Colorado Division of Wildlife's Bellvue Fish Hatchery site is relatively small, covering approximately 30 acres, groundwater drilling results across the site are variable and unpredictable; the site includes both productive, artesian wells as well as dry wells. The site is underlain primarily by the Lykins Formation, which includes interbedded siltstones, limestones, claystones, and evaporites. In preparation for new wells, geophysical surveys were done in an attempt to better understand the subsurface with respect to groundwater production. Both transient electromagnetic (TEM) and galvanic dipole-dipole resistivity lines were run, and substantial variations in resistivity within the Lykins are evident (as might be expected from the prior drilling results). The first test well after the geophysical survey was sited to test a locally conductive zone; the well was successful and flowed artesian. Similarly, a second test in a conductive zone also flowed artesian, while a third hole, not based on the geophysical survey (but sited primarily on the basis of permits and logistical considerations) was unproductive. The geophysical data confirm the heterogeneous nature of the Lykins at this site, agrees well with downhole logging, and has been clearly useful in successfully siting groundwater production wells.

Introduction

The Bellvue Fish Hatchery is an interesting site geologically and geophysically. It is roughly triangular in shape, covering only 30 acres. The Lykins formation is at the surface across the entire site, and extends beyond the depth of interest (approximately the upper 200 feet) over the entire site with the exception only of the westernmost lines, where the deeper Lyons sandstone and Satanka shale are evident. The Lykins is far from a homogeneous subsurface, however, and is comprised of interbedded siltstones, limestones, claystones, and evaporites dipping approximately 25 degrees to the east. Just a few miles to the south, the Lykins underlies the Horsetooth Reservoir, where it is considered a geologic hazard due to the sinkholes that occasionally develop. The heterogeneous nature is manifested at Bellvue as variable production from groundwater wells; dry wells and production wells can be separated by only hundreds of feet. The site is surrounded by fences, and includes active power lines, operating electric pumps, pipelines, cased wells, and other cultural features that can contaminate geophysical measurements. As a result, two different methods were proposed at Bellvue: TEM and galvanic resistivity. After two short test lines, 10 lines of resistivity data were acquired in the dipole-dipole array, and 275 TEM soundings were made. The locations and orientations of lines were determined primarily by the location and orientation of the cultural features. Figure 1 is an aerial photograph, showing the locations of the survey lines and soundings. Cultural effects were evident in much of the data, but since cultural effects vary based on the type of survey and survey parameters (dipole size, orientation, etc.), it was possible to develop a good electrical understanding of the subsurface from the combined data sets.

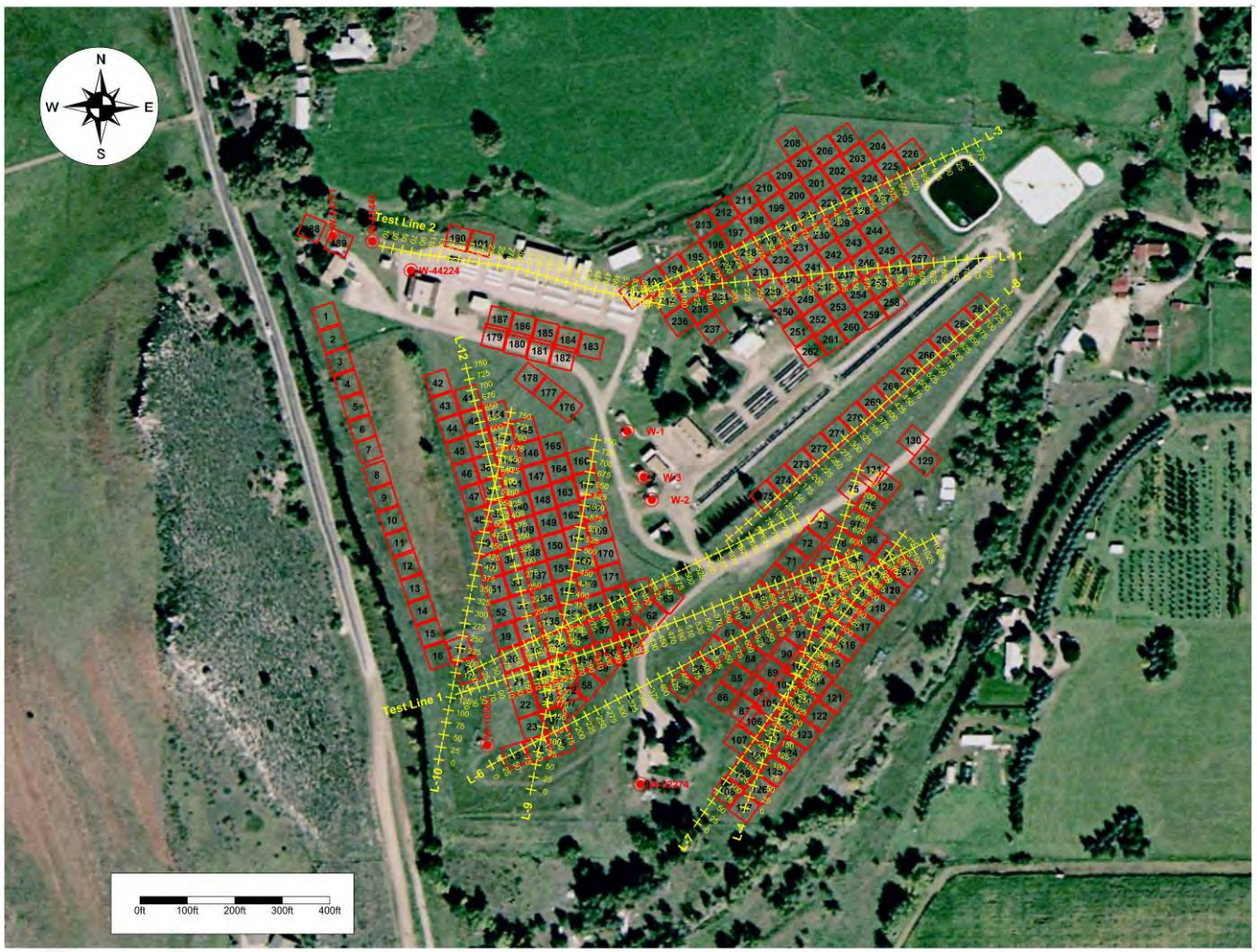

Figure 1: Locations of the dipole-dipole lines (shown in yellow) and the TEM soundings (shown as red squares) at the Bellvue Fish Hatchery.

Survey Results

Figure 2 shows the results of a typical dipole-dipole survey line on this project. Measured apparent resistivities are generally moderately low, usually ranging only from around 20 ohm-meters to 100 ohm-meters in the depth range of interest, and 2D smooth-model inversion results usually showed very good fits between the observed (raw) resistivities and the calculated model resistivities. Good correlation of features between survey lines was seen; broad low resistivity zones labeled “C” and “D” on Figure 2 were evident on other lines, and the line-to-line correlations of these features established a north-northwest trend, in good agreement with the mapped geologic strike of contacts and faults in this area. In addition to broad zones of low resistivity, several narrow zones of sharp resistivity contrasts (also oriented north-northwest) were identified, and may represent fault or fracture zones within the Lykins.

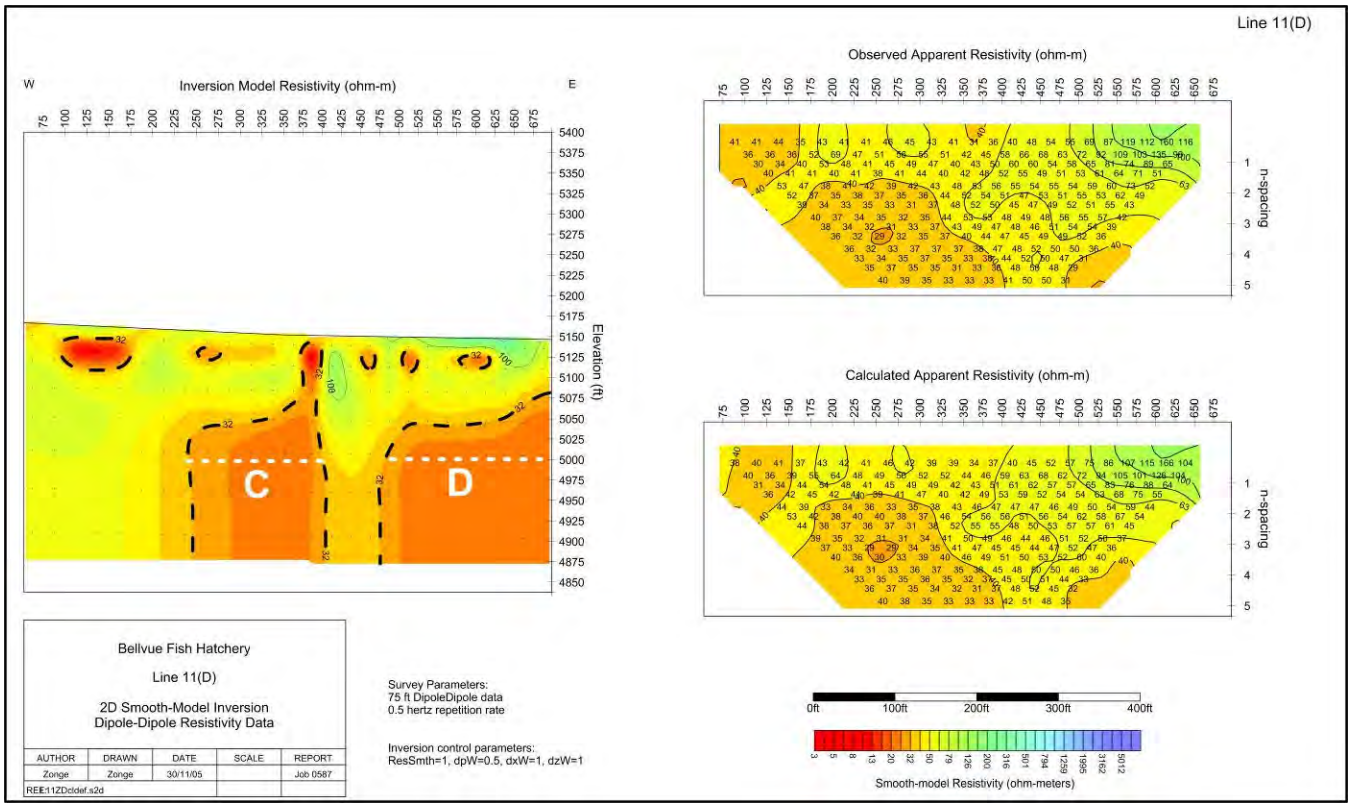

Figure 2: Typical dipole-dipole results on the Bellvue project, showing raw (Observed) resistivity and calculated model resistivity pseudosections (right) and 2D smooth model inversion results (left). The areas labeled C and D are low resistivity zones correlatable from line-to-line.

The combined interpretation of the survey results is shown in plan view in Figure 3. Broad conductive zones A, B, C, and D are outlined in orange dashed lines, and narrow, sharp changes in resistivity contrast are shown as blue dashed lines. The conductive zones could represent increased amounts of groundwater, but might also represent increased clay content, which can be problematic for groundwater production. Similarly, the sharp contrasts identified could indicate increased groundwater production from fractures, but may also represent flow barriers. After considering the known hydrology and geology of the area, the decision was made to site the first of two test holes (called the JRE #1) in conductive zone B. This well flowed artesian, and the results were good enough that the second well was also sited on a conductive zone, rather than to test one of the narrow zones of sharp contrasts. The JRE #2 was sited to the north in conductive zone C, and also flowed artesian. Subsequently, a third well was drilled, although the site selection was based entirely on well permits and logistical considerations. The location was near the west end of Test Line 2, in the northwest corner of the project site, and no interpretation of that specific location was possible from the geophysics. This third well did not produce water, but because it was drilled very near the end of a line, in an area complicated by cultural features, it is not known whether the location is in one of the low resistivity zones, in one of the narrow features, or simply in the geophysical “background” for this site.

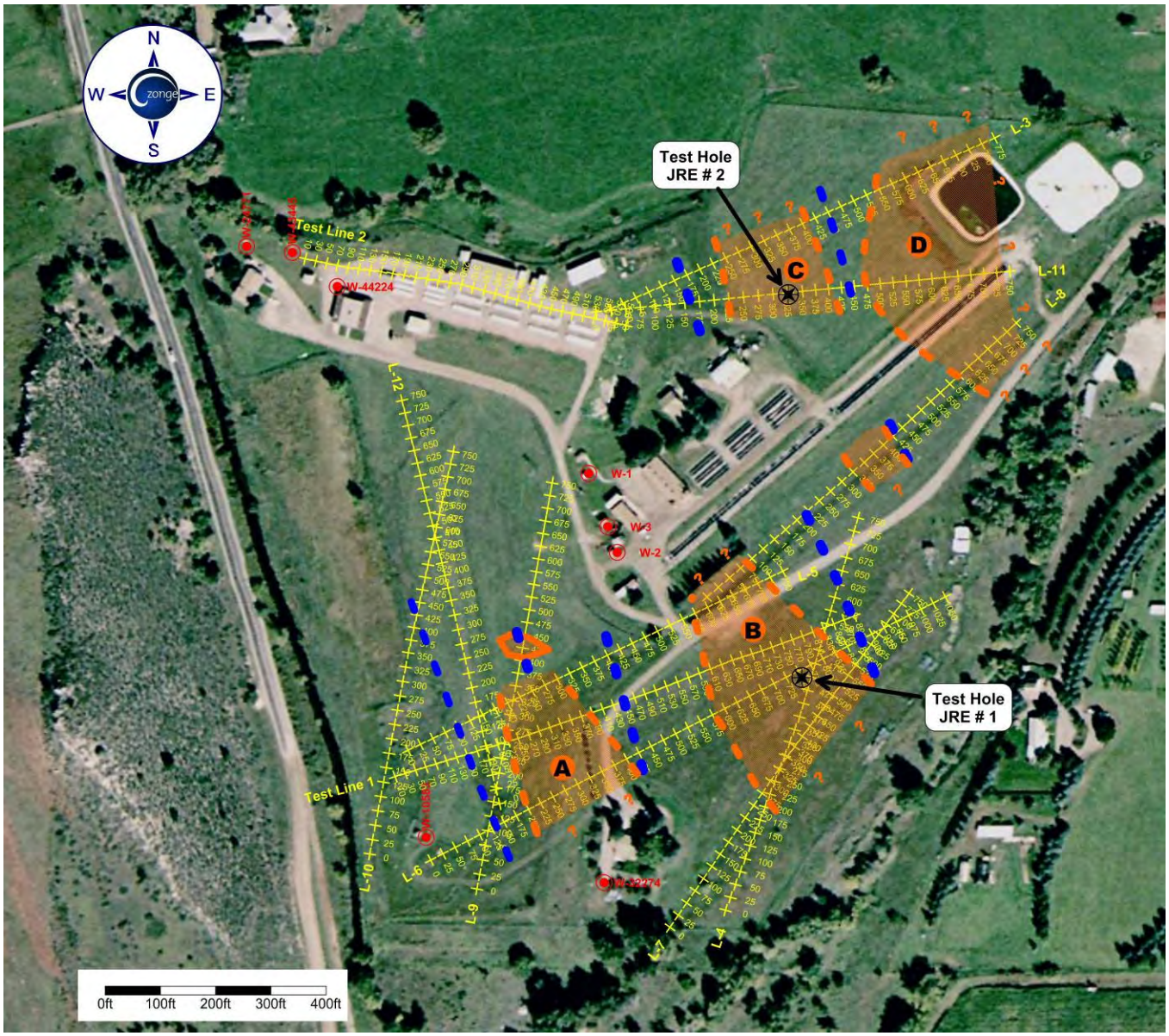

Figure 3: Plan view of the interpretation of the survey results, showing broad conductive zones A, B, C, and D (outlined in orange), with the locations of the two test wells JRE #1 and JRE #2.

Conclusions and Caveats

Although the interpretation was complicated by cultural effects, the survey results showed good correlation to the known and suspected geology at this site, good line-to-line correlation, and most importantly, two test holes drilled on the basis of the geophysics resulted in good groundwater wells. The significance of the narrow zones of sharp resistivity contrasts remains unknown at this time however, and it has not yet been determined how groundwater production in the low resistivity zones compares to production from "background" areas. As more drilling is completed, and down hole lithology and well logs can be added to the interpretation, geophysical surveys in this area should not

only be able to direct successful drilling, but may lead to a better understanding of the local groundwater recharge of this sensitive site.

Figure 4: The JRE #1 test hole.

References

US Bureau of Reclamation, 2007, Resource management plan/environmental assessment: Horsetooth Reservoir, Carter Lake, Pinewood Reservoir, Flatiron Reservoir, RMP dated June 29, 2007.

Pearson, R.M. and Hurcomb, D.R., 2002, Gypsum karst of the Lykins formation and effects for the Colorado Front Range water projects; Horsetooth and Carter Lake reservoirs, Paper 93-10, presented at the 2002 Denver Annual Meeting, Geological Society of America, October 2002.

EVALUATING CHLORIDE CONTAMINATION IN SAND AND GRAVEL AQUIFERS AND BEDROCK FRACTURES USING TERRAIN CONDUCTIVITY AND VERY LOW FREQUENCY GEOPHYSICS

Bradley W. Tirone, M.S., Hillier & Associates, Inc., Augusta, ME
Christopher L. Covel, C.G., P.G, Hillier & Associates, Inc., Augusta, ME
James E. Hillier, C.G., C.P.G., Hillier & Associates, Inc., Augusta, ME

Abstract

In April 2009, dissolved chloride concentrations at a public school water supply in south-central Maine were found to exceed 400 milligrams per liter (mg/L). The Maine Maximum Contaminant Level (MCL) and Federal Drinking Water Standard for chloride (250 mg/L) had been exceeded, rendering the School's water supply non-potable. Contaminated well water was blamed for: health risks for some of the students and employees; corrosion of pipes, pumps, plumbing fixtures, and school kitchen equipment; and other potential negative impacts to School infrastructure and associated property.

School officials believed the problem originated with road salt stored at a Town facility located approximately six hundred feet from the school's drinking water supply well. However, some Town officials blamed remnant salt-water intrusion that followed sea-level rise during the Pleistocene Era, or road salting performed by the State Department of Transportation. Therefore, an impartial and scientific investigation was needed to both solve the water supply problem and, correctly assign liability.

The situation required developing and interpreting a substantial amount of geologic data, as well as safely locating and installing a new 20,000 gallons per day potable water supply before the fall School session commenced in early September. This would involve mapping and interpreting key characteristics of surficial and multiple bedrock aquifers in order to isolate the existing chloride plume from a target bedrock aquifer. We elected to design a site-specific investigation employing both shallow electro-magnetic terrain conductivity (TC), and deep geophysical Very Low Frequency (VLF) investigations to achieve these goals.

After geologic review and initial reconnaissance, we hypothesized that the Town road salt storage area was the source of chloride contamination. Surficial mapping in the site vicinity differed slightly from the literature and identified a fine-to-medium sand layer that locally increased the hydraulic conductivity in the overburden. Aerial photograph/lineament analysis confirmed the primary fracture pattern in the Waterville Formation was more or less north-south in the 'X/Y' plane. On-site bedrock mapping confirmed a moderate east-dipping fracture pattern. Close observation found one of the major lineaments trended beneath the road salt storage area. We also confirmed the Devonian granite intrusion through the Waterville Formation was on Town property and resulted in an east-dipping fracture pattern in the 'Z' plane. Bedrock mapping confirmed the north-south trending lineament was in fact a bedrock fracture with an east dip in the 'Z' plane.

TC surveys were conducted to identify and delineate surface and subsurface areas that may have been impacted by the road salt storage area. TC surveys totaling 1,933 meters in length were conducted along eight (8) lines. Anomalous data collected in the vicinity of the road salt storage area indicated that the subsurface zone adjacent to the road salt storage area had been impacted by stored road salt. Sandy fill that lay beneath the storage area facilitated the infiltration of chloride-contaminated water into the overburden then the bedrock fractures.

Water chemistry analyses for chloride found the School, Town office and fire department water supply wells exhibited elevated chloride concentrations. It appeared that chloride contamination had entered the School water supply well under linear anisotropic pumping conditions via the east dipping bedrock fractures.

VLF geophysical survey lines were laid out in the field in an east-west pattern to cross the two north-south trending fractures observed in aerial photographs. Both potable and contaminated ground water signatures were observed in the VLF data at this site. VLF data showed strong in-phase and strong out-of-phase geophysical signatures indicative of chloride contamination in the plume area of the eastern most north-south striking fracture. It was believed this fracture was directly connected to the chloride-contaminated wells. These data linked the chloride-contaminated wells to the road salt storage area via fractured bedrock linear flow under anisotropic pumping conditions. This was the final confirmation necessary to conclude that the road salt storage area was in fact the source of chloride contamination of both the School and Town water supplies.

The remaining task involved finding a drill target at the School property that would yield potable water for the School. Fortunately, the locally deformed bedrock structure provided a portion of the fractured rock aquifer that was distinctly separate from the water bearing fractures, which conducted the chloride-contaminated water to the original School well. VLF was again used to identify a safe drill target for the new water supply well. Placement of the new well was achieved within the allotted time and was facilitated by the use of fracture trace/lineament analysis, bedrock mapping, and VLF geophysics. The VLF geophysical survey identified bedrock fractures that were not contaminated with chloride. Knowing the bedrock fracture was free of chloride contamination before drilling provided a significant cost savings to the school district. The new well was drilled to 500-feet below ground surface and air lifted 7.5-gallons per minute. Chloride ion was measured in the field during well drilling via titration methods at 16 mg/L, a concentration well below the MCL.

A pumping test was performed on the replacement well, during which water levels in the contaminated school water supply well were monitored to evaluate the potential influence of aquifer stress under pumping conditions on the chloride-impacted aquifer. Little or no influence was observed during the 48-hour pump test. The new water supply well was given final approval and licensed by the Maine Drinking Water Program, Maine Department of Health and Human Services. The new water supply was online and approved in time for the start of classes in September 2009, and is now successfully serving the water supply needs of the School.

Introduction and Purpose

Maine is a predominantly rural state where drilled ground water wells serve the majority of the residential and public water supply needs. Residential and municipal land uses are frequently clustered together in village style settings, where the school is the center of the community. Winter snowfalls are frequent and Town roads are plowed and salted using Town equipment to ensure safe travel. The Maine Department of Transportation is responsible for plowing and salting the larger State roads. Accordingly, Maine towns typically maintain their own plowing and salting equipment on a local Public Works or "Town garage" property.

This was the case in the Town of West Gardiner Maine (Figure 1), the location of the Helen Thompson School, where this study occurred. In early summer 2009 review of available School drinking water chemistry records dating from 2001 to 2009 indicated that chloride concentrations had steadily increased from 45 mg/L to 400 mg/L over that period. School administrators believed that the

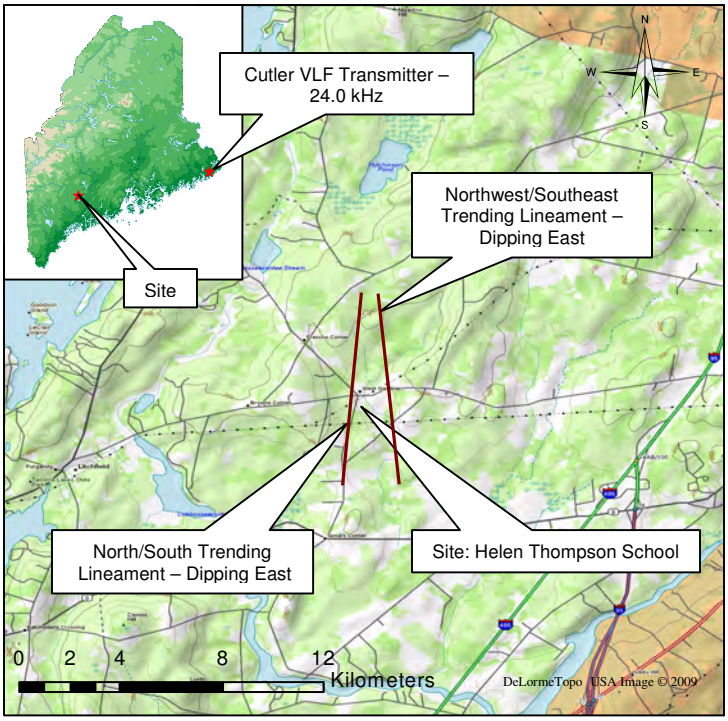

Figure 1: Topographic and fracture trace lineament location map - West Gardiner, Maine.

increase was a direct result of the road salt storage facility and its proximity to the School public water supply well.

To meet the goal of providing potable drinking water to the School by September 2009, as mandated by State and Federal drinking water rules and regulations, a geophysical and hydrogeologic investigation was immediately initiated. After an initial site visit, discussions with Town personnel, and evaluation of existing topographic maps, aerial photographs, and geologic maps, a scientific investigation was developed to meet the goal of obtaining potable water and identifying the source of chloride contamination prior to the opening of school in September 2009. This paper is a case study of the integrated methodologies used to collect geophysical and other geologic data; the interpretation and use of these data; and the equitable and cost effective result of providing a safe and plentiful drinking water supply.

Site Description

The school, which is sited on approximately a 6-acre parcel, was built in 1996. Two main rural roads abut the school property; Spears Corner Road on the West and High Street on the North. Wooded areas buffer the school on the north, east, and south. A Town-owned parcel consisting of the Town office, fire department, Town garage, and an associated road salt storage pile is located northwest of the School property and across Spears Corner Road (Figure 2). In 1988 a road salt storage shed was constructed at the Town garage site to cover and protect the road salt storage pile.

Individual drinking water supplies for these Town facilities are drilled bedrock wells, with the exception the Town office, which utilizes a drilled overburden well that is reportedly 50-feet in depth. This well is estimated to have been drilled circa 1950. The School well, drilled in 1995, is approximately 52 meters deep. The fire department and the Town garage share a bedrock well that was drilled in 2007 to depth of 70 meters below ground surface (bgs). This well encountered bedrock at 9.8 meters bgs, has 13.7 meters of casing and, according to well driller documentation, initially yielded over 60-gallons per minute. Neither the fire department nor the Town garage utilizes this well as a potable water source because it is was reported to be “salty”.

The surficial aquifer gradient in the area is from the north-northwest to the south-southeast toward an unnamed stream. This unnamed stream flows adjacent to school property on its eastern boundary (Figure 2).

Surficial and Bedrock Geology

Surficial geologic deposits found in the project area are mapped by the Maine Geological Survey (MGS), as predominantly glacio-marine sediments referred to as the Presumpscot Formation. This overburden, which formed during the Pleistocene Era, consists of ocean-bottom sediments including silt; clay and local sandy beds derived from proximal and distal glacial outwash deposits. Of particular note was a local soil unit identified by MGS as artificial fill. This fill area is located both near and beneath the road salt storage area. Other than the covered road salt storage shed, the fill was exposed to the elements.

Bedrock geology in the vicinity of the site is mapped by the MGS as the Waterville Formation of Ordovician age. This rock type is a metamorphic limestone that exhibits dominant north-south trending lineaments as its primary fracture pattern. Bedrock geology at the site is complicated by a granite intrusion of Devonian age (younger) that locally uplifted the Waterville Formation, resulting in an eastward dip to the deformed beds. The associated bedrock fracture pattern, as observed near the road salt storage area, appeared to support anisotropic ground water flow trending from the north to the south toward the School property on the eastern side of the site.

Review of the bedrock geology map titled Purgatory Quadrangle, Maine published by the MGS identified bedrock at the site as the Waterville Formation, and the intrusive Litchfieldite and syenite of the Litchfield pluton. The Waterville Formation is mapped as stratified rocks of Silurian age. The Litchfieldite and syenite of the Litchfield pluton are mapped as Permian-Devonian (?) in age. This pluton is mapped as being located in the west and southwest portion of the site. No bedrock outcrops were observed at the site or in the immediate site vicinity. Bedrock mapping at an outcrop northwest of the site identified the primary fracture pattern to be striking approximately N 7° E and dipping approximately 62° East. A second fracture pattern was mapped as approximately N 87° W and dipping approximately 84° North. The dominant north-south strike is consistent with the fracture trace/lineament analysis work done by the authors.

Review of the United States Geological Survey (USGS) Purgatory Quadrangle topographic map and commercially available aerial photographs identified two primary lineaments trending more or less north-south. This lineament trend is consistent with the strike of bedrock outcrops observed in the field, which dip moderately to the east.

Shallow Terrain Conductivity Investigation

We selected the Geonics Limited (Mississaugua, Ontario Canada) EM-31 as an efficient and reliable instrument and methodology with which to perform the shallow terrain conductivity investigation. The elevated conductivity of ground water impacted by road salt provided a contamination characteristic that was readily identified and delineated using this method. Shallow Terrain Conductivity Surveys totaling 1,933-meters were conducted along eight (8) survey lines strategically located on the School property and adjacent properties (Figure 2). The purpose of the surveys was to measure background and potentially anomalous terrain conductivity in areas up gradient, down gradient, and directly adjacent to the road salt storage facility. Figure 2 consists of a map exhibiting TC geophysical lines and plume geometry. The surveys determined that background terrain conductivity along the eight survey lines ranged from approximately 1.0 millisiemens per meter (mS/m) up to 10.0 mS/m. This is considered to be background data and represents “typical” electrical conductivity of surficial deposits in the site vicinity. Interpretation of TC data determined anomalous

conductivity ranged from 11.0 mS/m to 119.0 mS/m in the vicinity of and down gradient of the salt storage facility.

The TC surveys identified surficial and shallow subsurface areas adjacent to the road salt storage facility that had been impacted by storage and use of road salt. The TC surveys measured anomalous elevated terrain conductivity in the range of 11.0 mS/m to 119.0 mS/m in the vicinity of the road salt storage facility. Elevated terrain conductivity associated with storage and use of road salt is particularly notable in Shallow Terrain Conductivity Survey Lines 4, 5, 6, 7, and 8 (Figure 2).

Very Low Frequency Geophysical Investigation

Historically, VLF geophysics has been used to identify and delineate contaminated bedrock fracture zones (Covel and Robinette, 1994 and Covel et al., 1996). VLF geophysics is a proven scientific technology used in locating a drill target for bedrock water supply wells at a site by identifying potential specific water bearing fractures before the actual drilling is performed. This is possible, as water bearing bedrock fractures will have different geophysical signatures from contaminated water bearing bedrock fractures. Collection of VLF geophysical data enables the geophysicist to identify contaminated bedrock fractures without a costly and potentially liable drilling program.

The VLF instrument used in this project was the WADI™, manufactured by ABEM Instrument, AB, Sundbyberg, Sweden. The WADI™ utilizes the electromagnetic components of VLF waves produced by VLF transmitters around the world. VLF transmitters are primarily located near oceans and inland seas and are used by military personnel around the world to communicate with submarines. The frequency of the VLF wave emitted from these transmitters ranges from 15 to 30 Kilohertz (KHz). VLF waves can propagate many thousands of kilometers and can penetrate below the oceans and earth's surface.

The VLF transmitter selected for this investigation was Rugby, Great Britain, 22.6 KHz. Rugby was selected because the orientations of the fractures at the site were northeast southwest. Cutler, Maine, 24.0 KHz is often used in New England for northeast-southwest fractures. However, due to the site location (Figure 1), it was determined that Cutler was too far east of the site for proper orientation to geophysical lines in the field (Figure 3).

As discussed, the advantage of performing VLF geophysics at a chloride-contaminated site is that a contaminated bedrock fracture will have a geophysical signature that exhibits a high current density signature in both the in-phase and out-of-phase components. This geophysical profile can be interpreted as a contaminated bedrock fracture. Further, VLF geophysics can also identify non-contaminated water-bearing bedrock fractures. After review of surficial and bedrock geology, fracture trace/lineament analysis, and results of the shallow terrain conductivity surveys, we chose the VLF geophysical method to identify the pathway of chloride from the road salt storage pile to the School water supply well via the bedrock fractures. In addition, VLF was also used to identify a drill target that was not hydraulically connected to the School well or chloride plume via the bedrock fracture system.

Three VLF geophysical lines were laid out at the site more-or-less perpendicular to the north-south trending lineaments (Figure 3). The purpose of this VLF orientation was to confirm that the lineaments observed in the field were in fact dipping east as mapped in the bedrock outcrop. All three lines were laid out at a bearing 110°/290° Magnetic and totaled 2,700-meters (Figure 3). All VLF geophysical lines were replicated three times to ensure accuracy and repeatability of geophysical data. As documented during bedrock mapping, data collected on VLF geophysical lines confirmed that both the eastern and western lineaments (both north-south trending) were bedrock fractures, both dipping moderately east.

After field data collection, data was downloaded from the WADI™ to the desktop computer with the use of RAMAG™ VLF software, a computer program that produces a current density profile for the location measured. These data are interpreted to identify potential water bearing zones in the bedrock.

Results of the VLF investigation revealed two distinct bedrock fractures at the site and site vicinity. After review and interpretation of VLF geophysical data, one fracture, a north-south trending lineament on the western portion of the site vicinity was interpreted as containing chloride-contaminated water. The second north-south trending lineament located on the eastern portion of the School property, also dipping east, was interpreted by the VLF survey as containing potable, non-chloride contaminated water (Figure 4a and Figure 4b). Figure 4a is a VLF geophysical profile of data from the School forensic geophysical line (6809N). Figure 4b is the VLF geophysical profile of the southern most VLF line (7449N). The filtered VLF geophysical data collected on this line (6809N) contains a chloride-contaminated water-bearing signature (Figure 5a). The filtered VLF geophysical data collected on this line (7449N) contains a non-contaminated water-bearing signature (Figure 5b). Line 7449N (Figure 3, Figure 4b, and Figure 5b) indicates a non-contaminated geophysical signature that we later used as the drill target for the School new water supply well. Review of geophysical data from Line 6809N and Line 7449N indicated the bedrock fractures did not appear to be hydraulically connected to the proposed new well location (Figure 4a and Figure 4b).

Conclusions

A new potable water supply drilling target was staked on what was interpreted to be a non-contaminated water bearing fracture identified as VLF Line 7449N at 0+79W (Figure 3 and Figure 4b). We were contracted to supervise drilling and logging of the new well.

The new well was advanced through 5.5 meters of glacial till overburden to competent bedrock. Once bedrock was encountered the driller was instructed to rollerbit an additional 6.1 meters into competent bedrock and then grout the driveshoe at the bedrock socket-driveshoe interface. To ensure no pathways existed for migration of the contaminated surficial aquifer into the borehole, grouting was performed from the driveshoe-bedrock interface to the ground surface. This grout mixture was then allowed to cure for a minimum of 48 hours prior to further drilling into bedrock.

As anticipated after interpretation of the VLF data, the well intercepted two water bearing fractures, one at approximately 57 to 58 meters bgs, and a second water bearing fracture at approximately 86 meters bgs. The total airlift yield of these fractures was 7.5 gallons per minute. A pumping test was performed on the replacement well, during which water levels in the contaminated school water supply well were monitored to evaluate the potential influence of aquifer stress on the chloride-impacted aquifer. Little or no influence was observed during the 48-hour pump test. The new water supply well was given final approval and licensed by the Maine Drinking Water Program, Maine Department of Health and Human Services. The new water supply was online in time for the start of classes in September 2009, and is now successfully serving the water supply needs of the School at a sustained pumping rate of 20,000-gallons per day.

References

ABEM 1987, 1992 ABEM Instruments AB Alle'n AB, S-172 66 Sundbyberg, Sweden. Simple State of the Art Water Prospecting Instrument Technical Specifications: WADI™

Covel, C.L. P.G., D.T Kaymen, I.M. Phillips, L.S.P., and J.C. Harrison, (VLF) Very Low Frequency Geophysics: A Case Study on Locating Bedrock Wells in Water Bearing Fracture Zones for use in Contaminant Migration Interception. Environmental and Engineering Geophysical Society Proceedings SAGEEP 1996 Annual Conference pgs. 61-79.

Covel, C.L. P.G. and Robinette, M.S. 1994, Predicting Contaminant Migration in Bedrock with VLF Geophysical Techniques, Annual Symposium, March 12,1994, Burlington, Massachusetts, Association of Engineering Geologists, New England Section.

DeLorme Topo USA, Software Version 4.0, 2002

Geonics Limited, 1745 Meyerside Dr. Unit 8, Mississauga, Ontario, Canada L5T 1C6; EM-31 Terrain Conductivity Instrument

Google Earth; Europa Technologies, U.S. Dept. of State Geographer, 2010 Tele Atlas. Data S10, NOAA, U.S. Navy, NGA, GEBCO

Hildreth, C.T. et. al. Purgatory Quadrangle, Maine, Surficial Geology, Open-File No. 05-46; 2005 Maine Geological Survey. www.maine.gov/doc/nrimc.htm

Osberg, P.H. et. al. 1985, 1:500,000 Bedrock Geologic Map of Maine

United States Geologic Survey, United States Department of Interior, Purgatory Quadrangle, Maine 1:24,000; 1980

Walen, P., RAMAG VLF Software 2003, 633 Quail Gardens Lane, Encinitas, California, 92024

West, David P. et. al., 1980, Purgatory Quadrangle, Maine, Bedrock Geology, Open-File 08-35; 2008 Maine Geological Survey. http://www.maine.gov/doc/nrimc.htm

Acknowledgements

The authors would like to acknowledge several people critical to the production and editing of this paper. Their diligence, perseverance, long hours and expert work product allowed for a fine polish to this document. Ms. Amy D. Fitzherbert of Hillier & Associates was indispensable in the production of the Figures with excellent editing and thoughtful input regarding both the Figures and text. Ms. Fitzherbert is also acknowledged for her contribution during the data collection during less than optimum field conditions. We would like to thank Ms. Darryn Kaymen-Covel for her editorial suggestion and recommendations, which honed the document and added an outside perspective allowing for a well-balanced paper. Finally we would like to thank the staff of the Helen Thompson School, Selectman of the Town of West Gardiner, Maine and Town of West Gardiner, Maine Public Works Department, all who were cooperative and forth coming with invaluable historical information during the entire investigation allowing for full access to files, property, buildings etc. Their cooperation facilitated the speed at which we were able to complete the investigation and reach tangible conclusions.

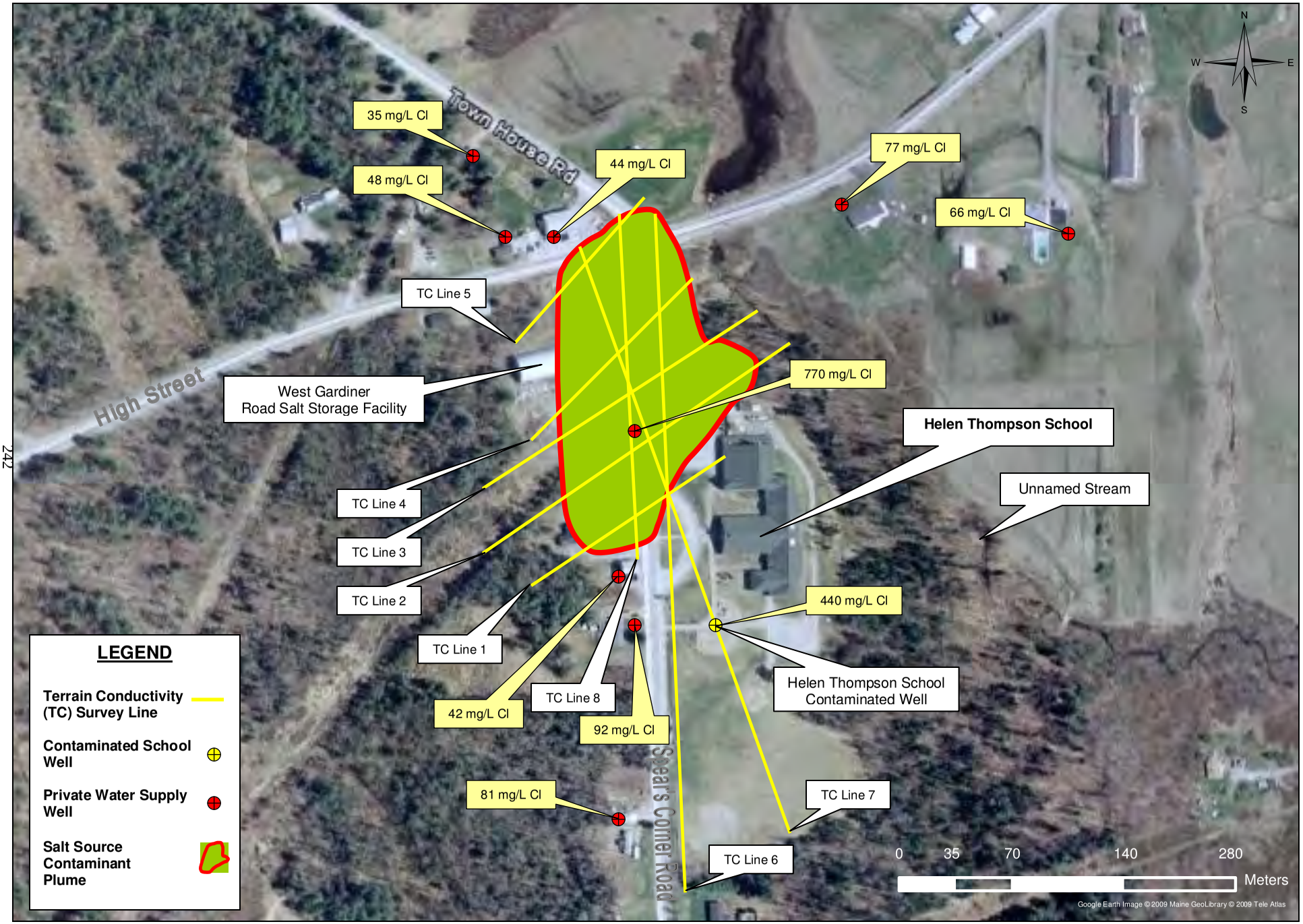

Figure 2: Terrain conductivity survey line and chloride plume locations.

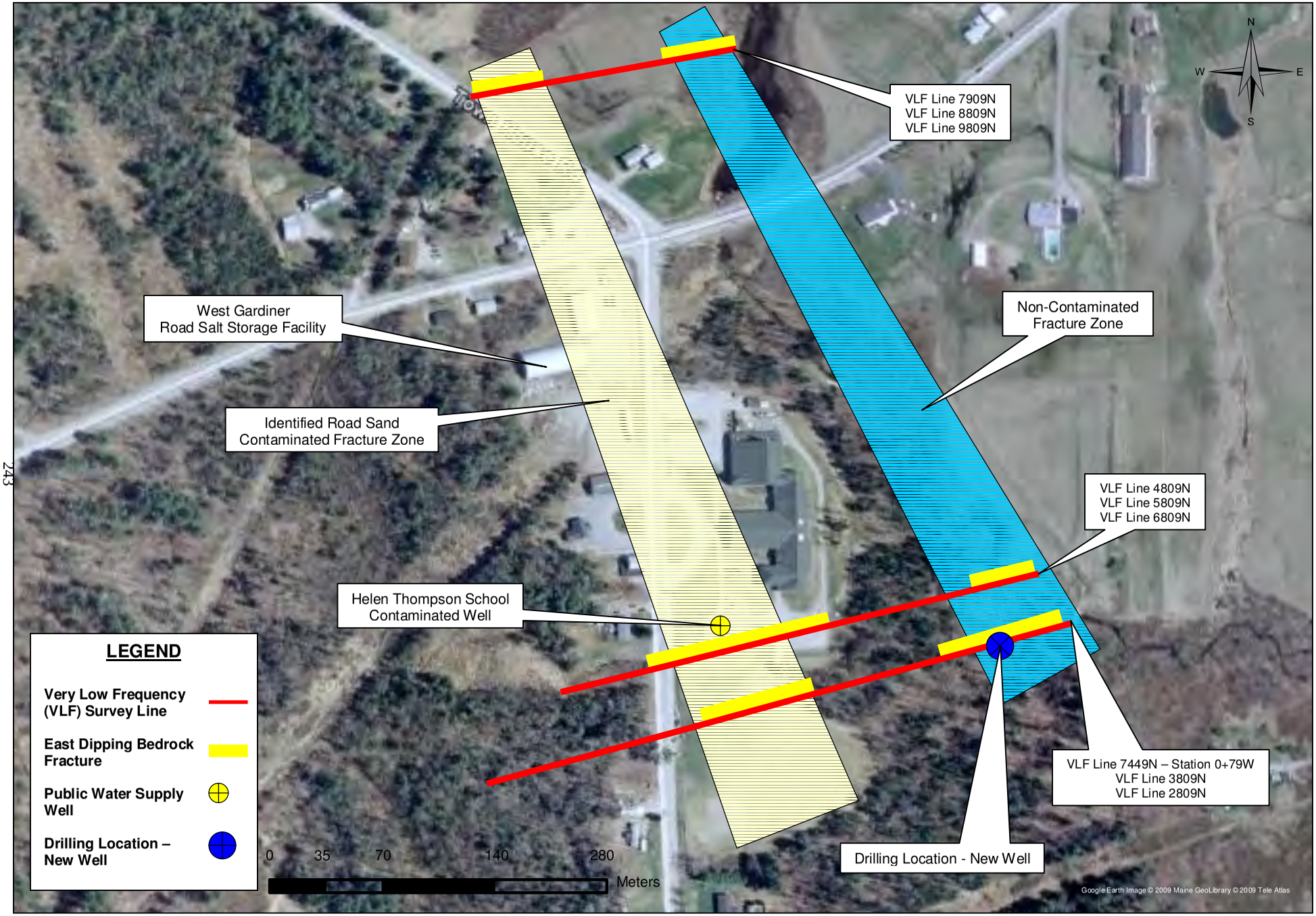

Figure 3: VLF (Very Low Frequency) geophysical survey line location summary and new well location.

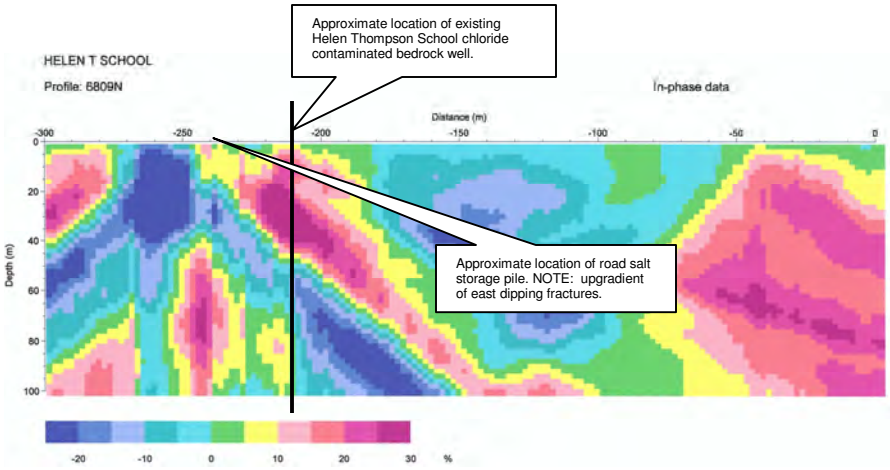

Figure 4a: Color cross-section of chloride contaminated well showing east dipping fracture.

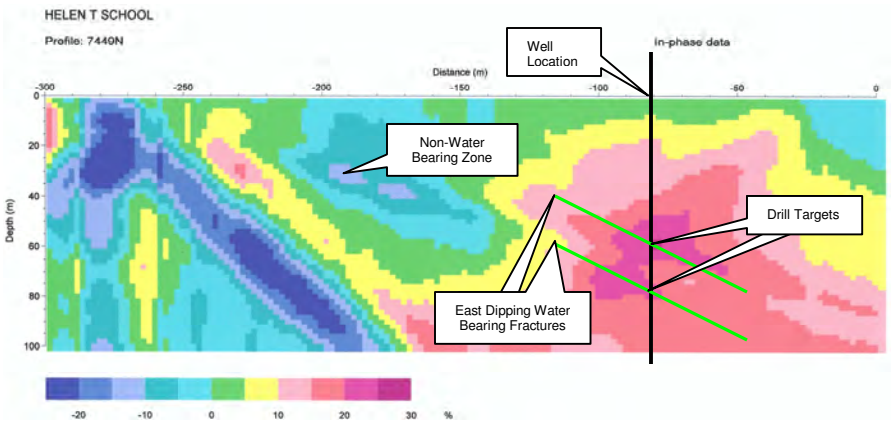

Figure 4b: Color cross-section of School potable water supply well.

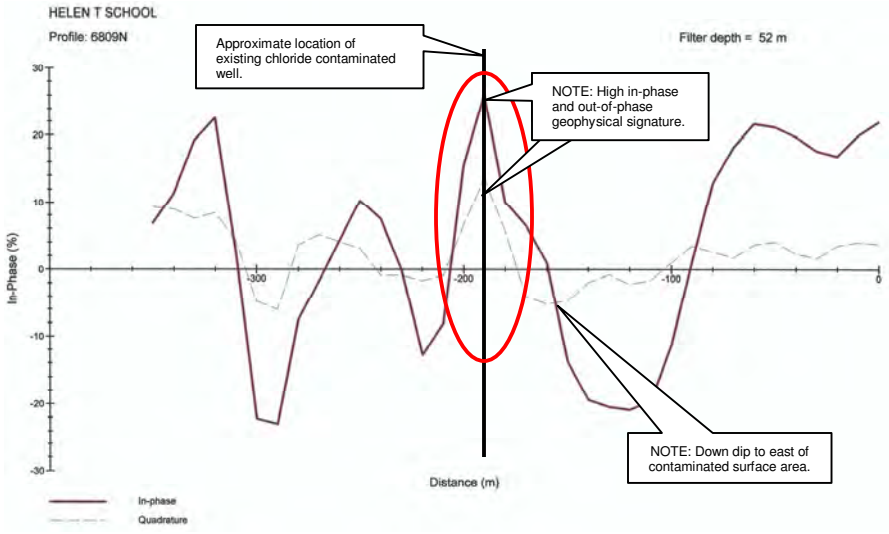

Figure 5a: Forensic chloride contaminated VLF geophysical signature at a filtered depth of 52 meters below ground surface.

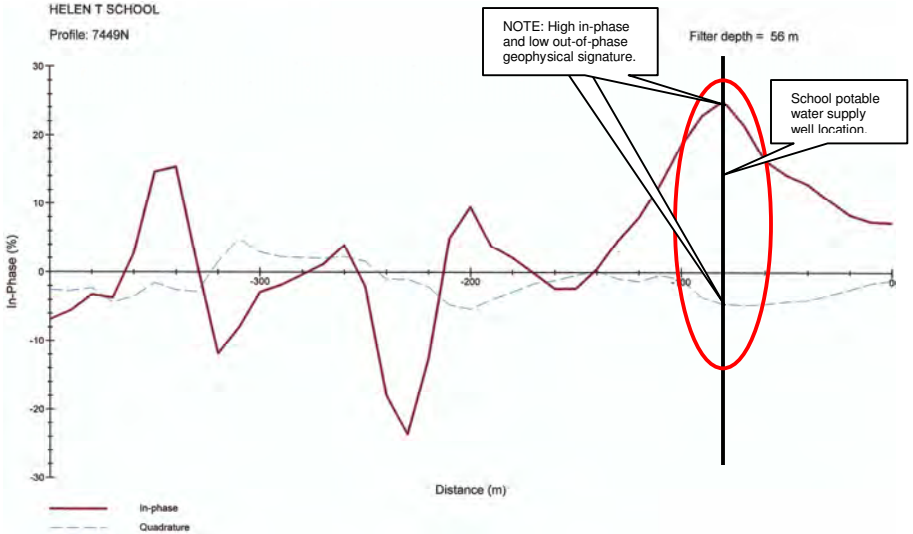

Figure 5b: Water bearing VLF geophysical signature at a filtered depth of 56 meters below ground surface.

AN INTEGRATED GROUNDWATER STUDY: CHASNIGUA, HONDURAS

Catherine Skokan, Colorado School of Mines, Golden, CO
David Munoz, Colorado School of Mines, Golden, CO

Abstract

A group from the Humanitarian Engineering Program at the Colorado School of Mines has employed a suite of geophysical tools to characterize subsurface water for the village of Chasnigua, Honduras. The village is small, with approximately 50 families (200 people) that rely on trucking their water to their homes. They have asked for assistance in developing water well, storage and distribtution systems. Honduras is economically one of the poorest countries in the western hemisphere, with about half the population below the poverty line. Consequently, the people do what they can to subsist on the land. This location is one with economic hardships and complex geology and hydrology. Because of the complex nature of the site and because of a lack of previous geophysical information, a suite of measurements was used. These included Magnetic and Magnetic Gradient Measurements, DC Resistivity, and Frequency Domain Electromagnetic Studies. Soil and water sampling and testing, as well as topographic mapping, augmented the geophysical data. These geophysical surveys have aided in the determination of a location for a water well in the volcanic/limestone terrain. Along with the geophysical data, an interdisciplinary team of senior level engineering students, working through the Humanitarian Engineering Program at Colorado School of Mines, cooperated with the people of Chasnigua and developed a design for the water treatment, storage and distribution system.

Location

The village of Chasnigua, Honduras, is located in the mountains near the borders of the Cortez and Santa Barbara Departments. Figures 1 shows the location of the village. The village is small, with approximately 50 families (200 people) that rely on trucking their water to their homes. They have asked for assistance in developing a water well, as well as water storage and distribtution systems. Honduras is economically one of the poorest countries in the western hemisphere, with about half the population below the poverty line. Consequently, the people do what they can to subsist on the land. In many small rural villages basic infrastructure is lacking and the nearby municipalities do not have the resources to provide the infrastructure. This is a new project and is funded by the Society of Exploration Geophysicisits Geoscientists Without Borders program. However, it is near a large water project that the Humanitarian Engineering Program (Humanitarian Engineering, 2010) of the Colorado School of Mines worked on for Colinas de Suiza, located within the same municipality. The Colinas de Suiza (Skokan and Munoz) project used dipole-dipole resistivity methods to map the groundwater extent in the valley. Therefore, success with one geophysical tool has been established in a nearby location, as well as a substatial contact base has already been developed with local government and non-governmental organizations.

Figure 1: Map of northern Central America, highlighting Honduras with a circle showing field site (Google maps, 2009).

The CSM Humanitarian Engineering teams have been working in Honduras since 2004. The village of Colinas de Suiza was established in 1998 after hurricane Mitch devastated Honduras and parts of Guatemala and Nicaragua, killing at least nine thousand people and leaving a similar number of people missing. The people of Colinas de Suiza were given a small piece of land to settle on but no services. They have been forced to purchase water delivered by truck since them. This has been a collaborative project between local and US-based Non-governmental agencies, Plastic Pipe and Fitting Association, the Municipality of Villanueva and the Patronato (elected village leadership) and people of Colinas de Suiza (Savage, et al. 2008). To date, a water system design has been completed, 44 km of plastic pipe have been donated (by the PPFA) and delivered (by the NGOs) and buried in the ground (by the people of the village and the Water and Sanitation Department within the Municipality), a 140 m deep well has been developed and a pump purchased (by the Municipality). The people of Colinas de Suiza selected a local contractor and are paying for a 250,000 gallon water tank. Sustainability requirements dictate that the people have significant ownership through physical, mental and financial participation (Kandachar and Halme, 2008). It is hoped that similar success can be achieved at Chasnigua.

Geophysical Approach and Field Program

The village of Chasnigua in Honduras is located in volcanic/carbonate terrain. A geologic map of Honduras (Figure 2) shows an area of Tertiary Volcanism with nearby outcrops of carbonates. Therefore, the geology and hydrology are complicated and and the hydrology is complex and possibily fracture - or structure - controlled. An airborne magnetic survey (Mann, 2007) illustrates general structural trends in Honduras (see Figure 3) . Previous work by Colorado School of Mines at Colinas de Suiza mapped water table using Dipole-Dipole Resistivity measurements (Skokan and Munoz, 2006). This tool proved helpful as well in this more mountainous area. However, the more complex structure was better mapped with different tools, or a combination of devices: electromagnetic, magnetics and magnetic gradiometry, and DC resistivity. Soil and water samples were also taken to analyze the physical properties of the near-surface and assist in the interpretation process. The results were also used in the larger-scale project of water distribution. The results from these studies have helped to determine the best location for the citing of a water well for the community.

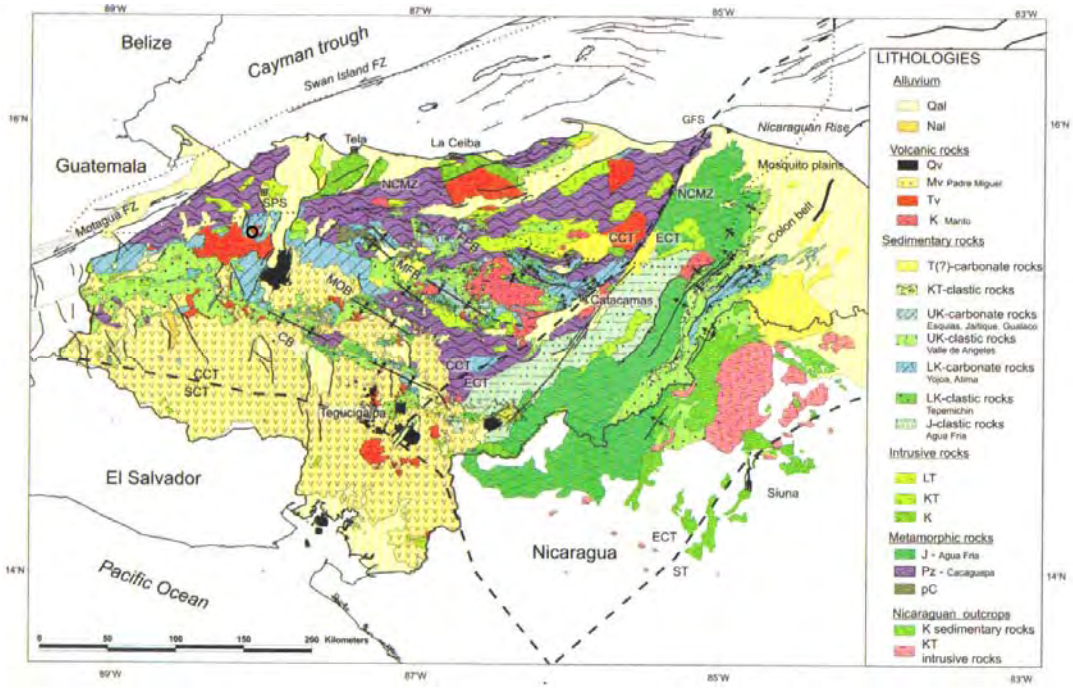

Figure 2: Geologic map of Honduras with a circle showing the field site (Bundschuh and Alvarado, 2007).

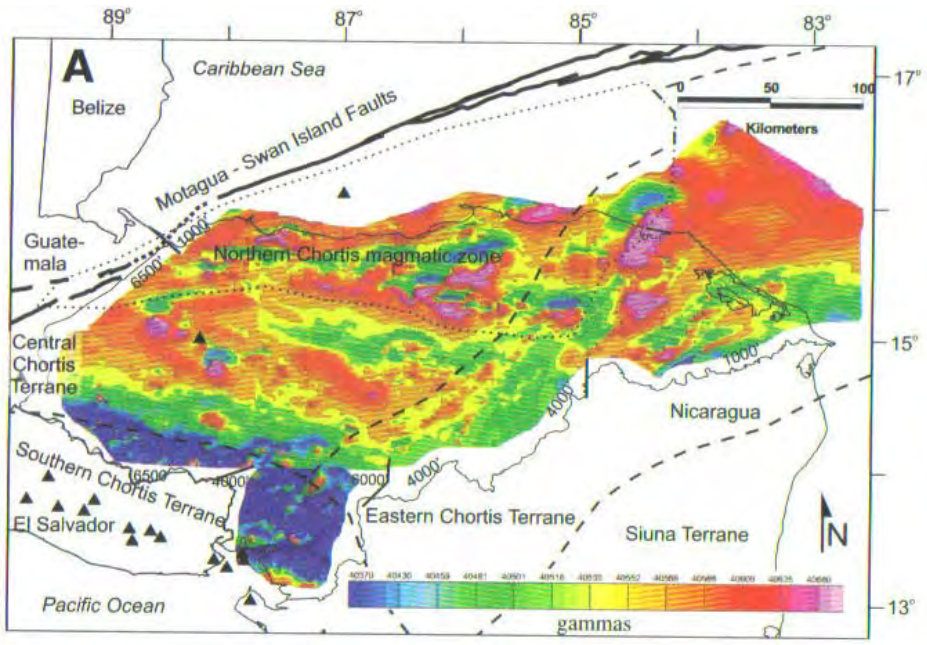

Figure 3: Airborne magnetic and structural map of Honduras (Mann 2007).

Two trips to Chasnigua were made to collect data. The first trip field schedule included a total-field magnetics survey, a magnetic gradiometer survey, and EM-31 and EM-34 mapping. A grid was established in an 80 by 100 meter area with ten meter spacings. The Trimble Pro-XRS GPS units were used for station location determinations. Magnetic and both veritcal and horizontal magnetic gradient measurements were first surveyed. Then EM-31 and EM-34 (Figure 5) measurements were made at the same locations as the magnetic survey stations. For the EM-34 measurements, 10 – 20- and 40 meter spacings were recorded. Also, soil and water were sampled, and a topographic map was created with use of a GPS system (Figure 4). The EM 31 and EM43 data were consistant with the magnetic and magnetic gradient measurements and helped to delineate the local structure. A structural trend striking NW-SE appeared along with a set of more complex structures to the south. In the second visit, DC resistivity surveys using the dipole-dipole configuration were undertakenwith a Supersting Resistivity Meter. The location of the first line was situated perpendicular to the overall structural trend. N-spacings of 5, 10, and 20 meters were used. A second survey line was located perpendicular survey line to the first dipole-dipole line (see Figure 6). The lines extended beyond the original 80 by 100 meter survey area where the magnetic and electromagnetic data were collected.

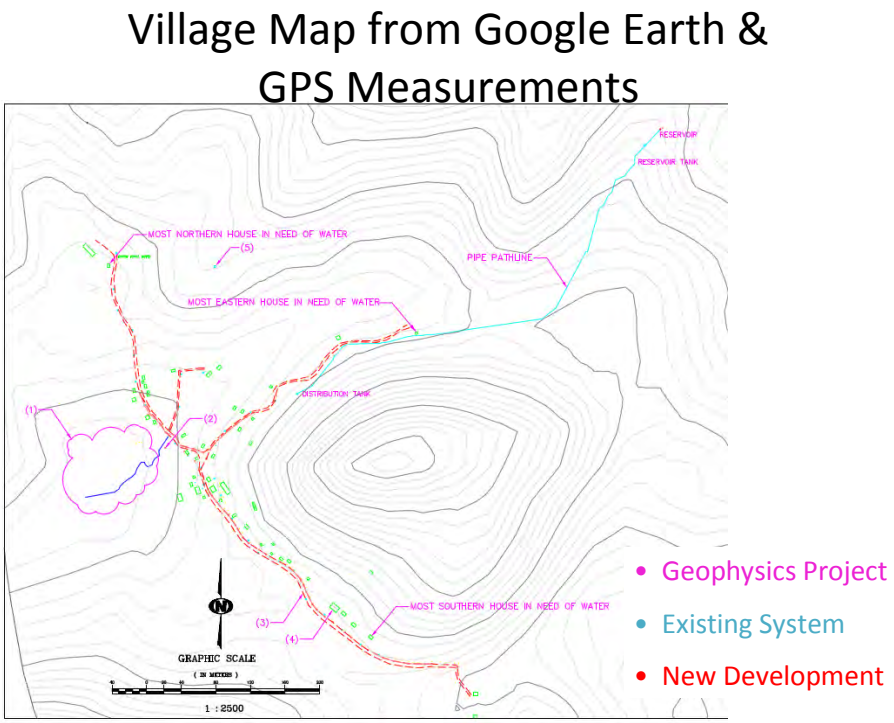

Figure 4: Map of the Village of Chasnigua showing the location of the detailed geophysical surveys along with measurements made for present and future water distribution systems.

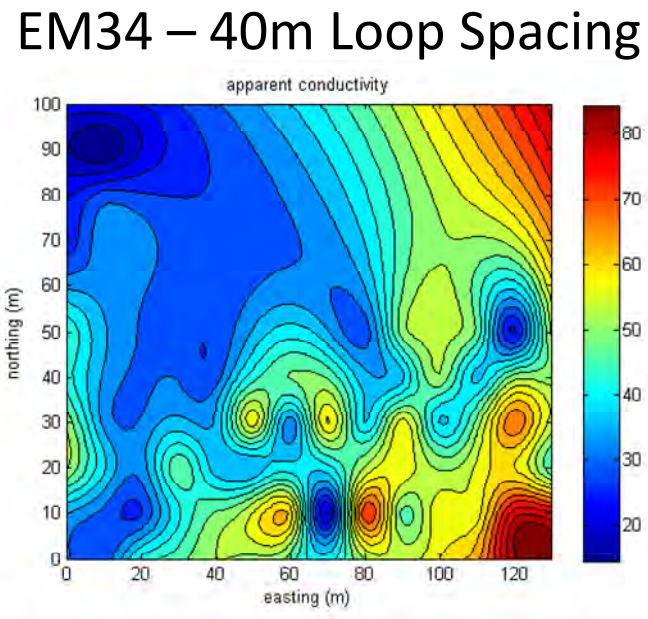

Figure 5: EM-34 measurements using a 40 meter loop spacing.

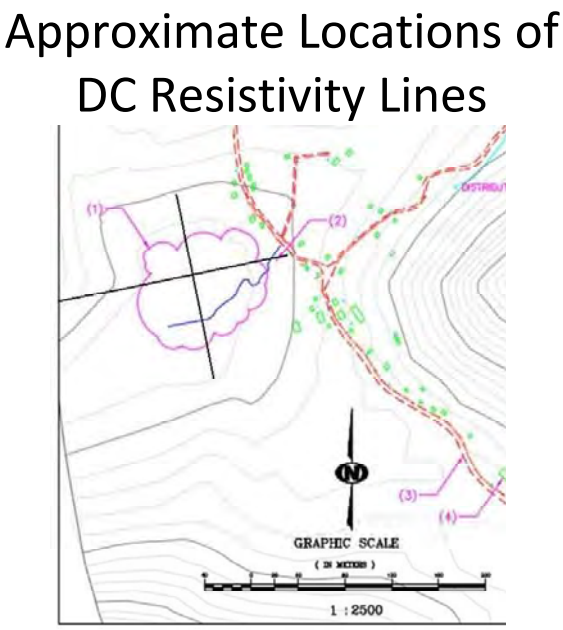

Figure 6: Location of the DC Resistivity lines showing the extension beyond the purple survey area where magnetic and electromagnetic data were taken.

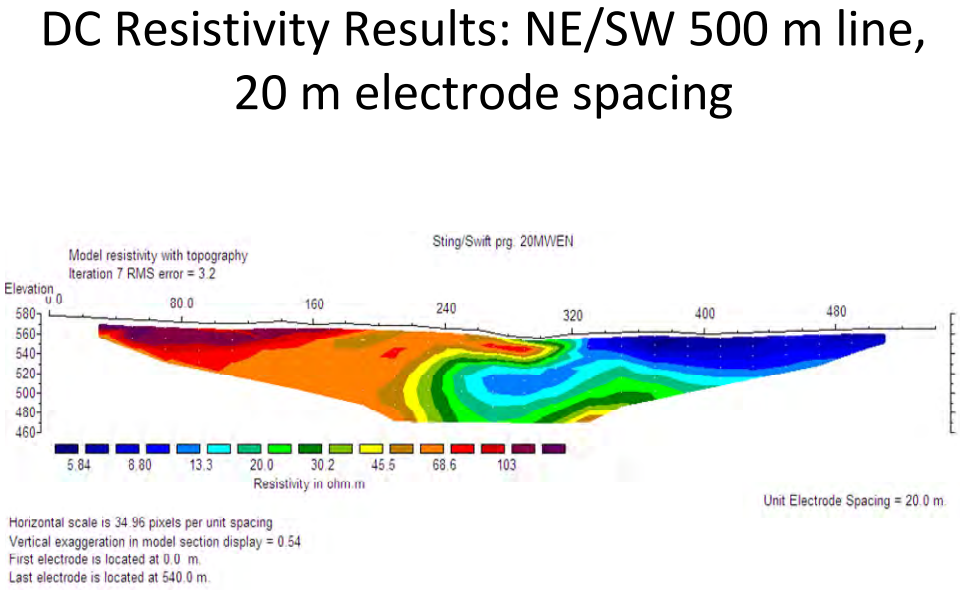

Figure 7: Results of Dipole-Dipole inversion of data from a NE/SW 500 meter line using electrode spacings of 20 meters.

Interpretation and Conclusion

The initial survey tools, magnetics and electromagnetics, confirmed the complex nature of the geology of the area. However, a structural trend northwest-southeast was recognized. Overlaying the regional trend were more complex signatures. Based upon the general structural trend, the dipole-dipole soundings were located. These perpendicular surveys with multiple n-spacings showed a highly resistive region to the northwest where there were numerous volcanic outcroppings. Toward the middle of the profiles, a more conductive zone appeared on all of the inverted cross sections. This could be a good location for a water well for the Chasnigua community.

Additionally a team of engineering students mapped the area with the GPS units to yield sufficient information to design a water distribution system, locating the water storage tank to provide sufficient pressure for gravity feed to each home. Water samples were extracted from the source flows and at various home storage tanks (called “pilas”). Laboratory testing results indicate nonfecal coliform levels well above World Health Organization (WHO) standards and acceptable metal concentrations. To mitigate the bacterial water quality issues, a system including a novel self cleaning rough filter, followed by a slow sand filter, were designed and included in a final report that was translated into Spanish and shared with the villagers.

Acknowledgements

The authors wish to thank the Society of Exploration Geophysicists Foundation Geoscientists without Borders Program that supplied funding for travel, shipping of equipment, laboratory analysis, and other field expenses. We also thank the William and Flora Hewlett Foundation sponsored Humanitarian Engineering at Colorado School of Mines for support of the senior design students and their broader project.

References

Bundschuh, J. and Alvarado, G.E., 2007, Central America geology resources hazards: vol. 1, Taylor & Francis Group plc, London, UK, p. 70 – 90.

Google Maps, 2008, http://maps.google.com, accessed 11/08

Humanitarian Engineering, 2010, http://humanitarian.mines.edu/; Video:http://www.youtube.com/watch?v=m4hwhj_Zc, accessed 1/10

Kandachar, P. and Halme, M. (Editors), 2008, Sustainability Challenges and the Solutions at the Base of the Pyramid; Business, Technology and the Poor, Greenleaf Publishing Ltd., Sheffield, UK.

Mann, P., 2007, Geologic and tectonic development of the Caribbean Plate boundary in northern Central America: Special Paper 428, The Geological Society of America, p.65-88.

Savage, J., Muñoz, D. and Godel-Gengenbach, K., 2008, In Search of Sustainable Community Development through Practice; Application: Colinas de Suiza, Honduras, ICEE, Hungary.

Skokan, C., and Munoz, D., 2006, A Groundwater Study in Colinas de Suiza, Villanueva, Honduras: SAGEEP 2006, Denver, CO.

INTEGRATED USE OF SURFACE GEOPHYSICAL METHODS FOR SITE CHARACTERIZATION -- A CASE STUDY IN NORTH KINGSTOWN, RHODE ISLAND

Carole D. Johnson, U.S. Geological Survey, Storrs, CT
John W. Lane, Jr., U.S. Geological Survey, Storrs, CT
William C. Brandon, U.S. Environmental Protection Agency, Boston, MA
Christine A.P. Williams, U.S. Environmental Protection Agency, Boston, MA
Eric A. White, U.S. Geological Survey, Storrs, CT

Abstract

A suite of complementary, non-invasive surface geophysical methods was used to assess their utility for site characterization in a pilot investigation at a former defense site in North Kingstown, Rhode Island. The methods included frequency-domain electromagnetics (FDEM), ground-penetrating radar (GPR), electrical resistivity tomography (ERT), and multi-channel analysis of surface-wave (MASW) seismic. The results of each method were compared to each other and to drive-point data from the site.

FDEM was used as a reconnaissance method to assess buried utilities and anthropogenic structures; to identify near-surface changes in water chemistry related to conductive leachate from road-salt storage; and to investigate a resistive signature possibly caused by groundwater discharge. Shallow anomalies observed in the GPR and ERT data were caused by near-surface infrastructure and were consistent with anomalies observed in the FDEM data. Several parabolic reflectors were observed in the upper part of the GPR profiles, and a fairly continuous reflector that was interpreted as bedrock could be traced across the lower part of the profiles. MASW seismic data showed a sharp break in shear wave velocity at depth, which was interpreted as the overburden/bedrock interface. The MASW profile indicates the presence of a trough in the bedrock surface in the same location where the ERT data indicate lateral variations in resistivity. Depths to bedrock interpreted from the ERT, MASW, and GPR profiles were similar and consistent with the depths of refusal identified in the direct-push wells.

The interpretations of data collected using the individual methods yielded non-unique solutions with considerable uncertainty. Integrated interpretation of the electrical, electromagnetic, and seismic geophysical profiles produced a more consistent and unique estimation of depth to bedrock that is consistent with ground-truth data at the site. This test case shows that using complementary techniques that measure different properties can be more effective for site characterization than a single-method investigation.

Introduction

Characterization of unconsolidated materials and determination of the underlying bedrock surface is critically important for investigations of contaminant migration because heterogeneity of the sediments and the bedrock surface can impart geologic control on the distribution of contamination. Although exploratory drilling and boreholes provide the best subsurface information, drilling is expensive and represents a limited sampling of the subsurface. Drilling data represents only a one-

dimensional (1D) point on a three-dimensional (3D) surface and can provide only limited information in a highly heterogeneous setting. Thus, it is critical to optimally locate boreholes to provide the best possible site characterization information. Surface geophysical methods are non-invasive, rapid, and spatially continuous, and can provide high-resolution representations of the subsurface that can be used to help optimize drilling locations. The objective of this work was to evaluate the complementary use of multiple surface geophysical methods to map the bedrock surface, improve the confidence in interpretation of bedrock surface, and characterize the overlying materials.

Field Study

In 2009, the U.S. Geological Survey (USGS), in cooperation with the United States Environmental Protection Agency (USEPA), conducted surface geophysical investigations at the former Davisville Naval Construction Battalion Center (NCBC), on the Narragansett Bay in North Kingstown, Rhode Island. The U.S. Army Corps of Engineers and the U.S. Navy have been investigating multiple sites on the former naval center for site remediation and base closure. Site characterization studies are ongoing adjacent to the study area for three known contaminant sources that are located to the northeast (Site 3), the northwest (NIKE Missile site), and the southeast (Site 16). The chemicals of concern are generally chlorinated hydrocarbons; however each site has detailed investigations that identify specific chemicals constituents (EA Engineering, Science, and Technology, 1988a, 1988b, 1988c). The current area of investigation can be described as the land between these formally named sites, and includes the undeveloped field northeast of the North Kingstown Department of Public Works (DPW); the automobile transfer lot located between Davisville, Jones, and Marine Roads; and Davol Pond to the south (Figure 1). This case study presents the results of geophysical surveys collected in the field northeast of the DPW.

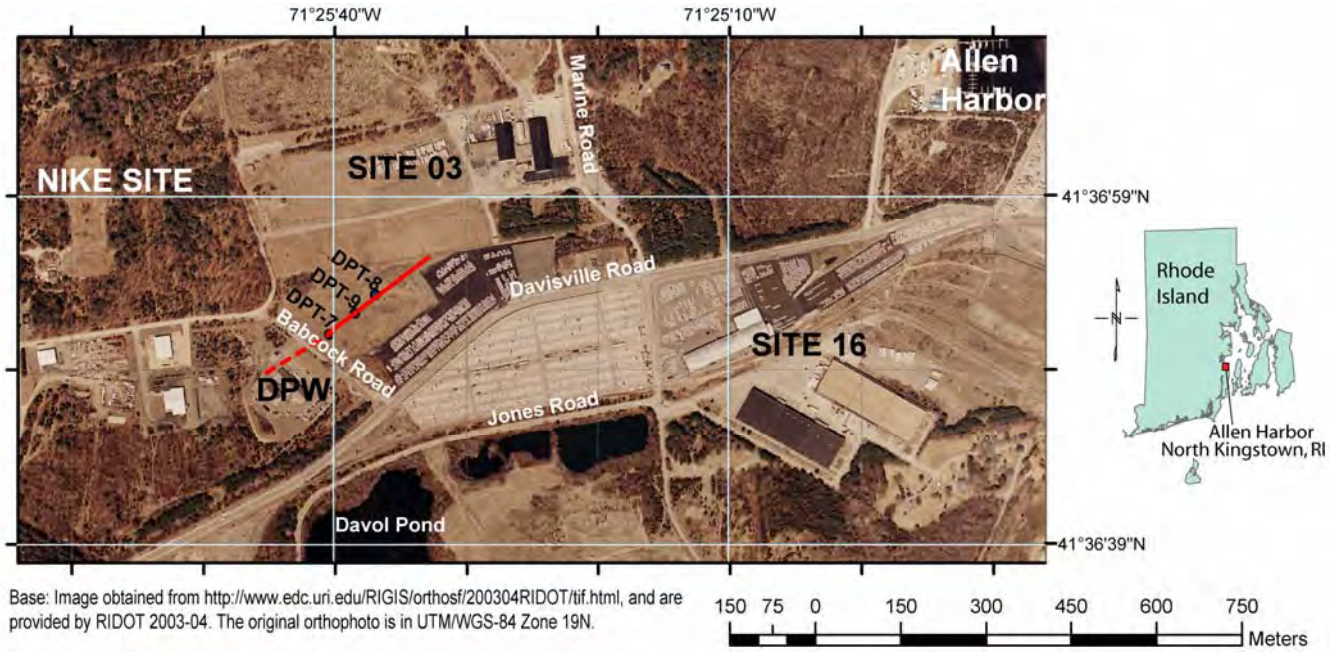

Figure 1. Study area and field site, North Kingstown Rhode Island

Geophysical surveys were used to image the subsurface and help identify possible subsurface controls on contaminant distribution. The USEPA installed a line of direct-push (DPT) points to refusal in the field across from the North Kingstown DPW Facility (Figure 1). Adjacent to the direct-push points, a suite of surface geophysical data were collected (Figure 1; red line) using electrical, electromagnetic, and seismic methods to assess their usefulness for improving the subsurface characterization. There is a possibility that the refusal depths from the DPT points may be - in some cases – at higher elevations than the true top-of-bedrock surface. DPT points hit refusal on cobbles, till, fractured bedrock, or solid bedrock. Without detailed core and/or borehole geophysical logs, the actual refusal surface is unknown. However, the DPT points provide at least a minimum depth of the overburden that can be used for comparison with the interpreted geophysical profiles. At this site, the magnitude of the discrepancy can be 3 meters (m) or more, but typically, refusal depths are within 1.5 m of the bedrock surface.

Site Setting, Topography and Surficial Geology

The site is located in an area of low relief. Ground surface elevations reach a local maximum of just over 9.1 m above mean sea level (amsl) near the former NIKE site; the local topographic low is Davol Pond, approximately 5.5 m amsl (USGS, 1995). Allen Harbor is approximately 1 km to the east of the site, and the Narragansett Bay shoreline is approximately 1 km to the southeast of Davol Pond. Much of the original land surface at the NCBC has been reworked, leveled, and/or paved due to the site's history as a training ground for military heavy equipment operators. However, relict morphological features from Pleistocene glaciation are still evident in some locations of the site. In the subsurface, the natural overburden deposits are glacial in origin, and consist of outwash sediments and water-laid ice-contact deposits that were deposited over metasedimentary metamorphic bedrock. The total thickness of glacial deposits at the site ranges from less than 1 m in the vicinity of the NIKE site to over 30 m to the south and east across the site. Schafer (1961) provides a detailed map and discussion of surficial geology of the area. Soil borings from environmental investigations (EA EST, 1988; EA EST 1998a; EA EST, 1998b) identified a wide range of deposits ranging from lenses of silty clay to sand and fine gravel. Subsurface borings commonly penetrate discontinuous deposits of ground moraine (till) at depth. These deposits, where present, are typically 1 to 3 m in thickness. In many areas, the boundary between tills and weathered bedrock is quasi-gradational. The nature of this contact is important to groundwater and contaminant flow at the site. The bedrock underlying the site is mapped as undifferentiated Rhode Island Formation of Pennsylvanian age, which includes light to dark gray meta-sandstones, conglomerates, and mica-schists (Williams, 1964).

Methods

Frequency domain electromagnetics (FDEM) methods were used to image the shallow subsurface for changes in electrical conductivity with depth and location. Changes in apparent conductivity can be caused by changes in the soil, overburden, saturation, or water quality, and/or by the presence of shallow buried infrastructure. A modified GEM-2[1] multi-frequency electromagnetic induction tool with a 1.6-m long antenna was used in the vertical- and horizontal-dipole modes (Geophex Ltd., 2009) to collect the FDEM data. Methods of calibration and data analysis are described by Abraham and others (2006). Data were collected in stepped-frequency mode at 15 user-selected frequencies ranging from 6 to 54 kHz, which is almost the full range of the equipment. Lower

[1] Any use of trade, product, or firm names is for descriptive purposes only and does not imply endorsement by the U.S. Government.

frequencies penetrate to deeper depths, but the data are an average over a larger volume, while higher frequencies penetrate only to shallow depths but provide a smaller volume-averaged measurement. A cart was used to keep the antenna at a fixed distance of 1.0 m above land surface to minimize noise induced by variation in tool position. Profiling data were collected at walking speeds of 3 km/hr, with a full suite of 15 frequencies measured every 0.5 s, which translates to a complete measurement suite about every 0.4 m along the profile. All measurements were located with a global positioning system (GPS). The data were corrected for drift and were plotted to identify possible sources of contamination, interference, or unknown buried structures to avoid with the other methods.

Ground-penetrating radar (GPR) was used in the DPW field to image the subsurface structure. Although a shielded antenna is usually better than an unshielded antenna in places with infrastructure and possible interference, a 25- MHz rough-terrain antenna (RTA) (Malå Geoscience, 2010) was chosen because of its ease of use and because its low frequency would achieve greater penetration than a 100-MHz shielded antenna. The antenna was mounted in a streamer to maintain good contact with the land and provide good coupling of the signal into the subsurface. The velocity of the radar in the subsurface was determined to be 70.7 m/μs using a common midpoint analysis. The radar data were interpreted using the software Ground Vision (Malå Geoscience), and were processed for direct-current removal, time-zero adjustments, background removal, and a band pass filter to minimize high-frequency noise. The characteristics of the radar record, including attenuation and reflector type (such as planar, parallel, chaotic, etc.) were identified and were used to interpret the stratigraphy of the subsurface as described by Beres and Haeni (1991).

Two dimensional electrical resistivity (2DRes) surveys were conducted to image the subsurface materials, identify the depth to water, and determine the bedrock surface. 2DRes surveys were collected with an Advanced Geoscience Instrument SuperSting R8 (Advanced Geosciences Incorporated, 2009) with a 56-electrode array with 4-m separation between electrodes. Wenner and dipole-dipole survey geometries were used in a west-east profile coincident with the GPR and MASW profiles. Reciprocal errors were collected for the dipole-dipole survey and measurement errors were collected for the Wenner array to evaluate the quality of the measurements. RES2DINV was used for the inversion of the profiles (Loke, 2004). A joint inversion, which included both the Wenner and dipole-dipole surveys, was used to capitalize on the strengths of both survey geometries. The dipole-dipole survey is more sensitive to lateral changes in resistivity, but at the cost of depth of penetration. The Wenner array can image deeper than the dipole-dipole method and is effective in identifying changes in resistivity with depth (Sharma, 1997). The resultant profile represents an image of the subsurface to a depth of about 30 m below land surface.

The multi-channel analysis of surface waves (MASW) seismic method was used to delineate the bedrock surface. Surface waves travel through the shallow layers of the earth, primarily controlled by the shear-wave velocity (*Vs*) and layer geometry (Xia and others, 1999). MASW seismic measures the surface wave (ground roll) generated from a compressional source as it propagates from source to receivers. Surface waves are dispersive—different frequencies of the surface wave propagate at different phase velocities. Higher frequency surface waves have lower velocities, while lower frequency surface waves have higher velocities. By plotting the frequency content and the travel time to each geophone, a dispersion curve can be generated for each shot point. Dispersion curves relate frequency and phase velocity and can be inverted to estimate *Vs* as a function of depth. For each shot location, a surface-wave dispersion curve was generated and inverted using SurfSeis (Kansas Geological Survey, 2007) to produce a 1D-*Vs* profile. The profiles were stitched together to produce a smooth, contoured model that represents the 2D-*Vs* section. Variations in the model section are interpreted as changes in the

subsurface earth material. Methods of data collection and analysis are described in the SurfSeis Manual (Kansas Geological Survey, 2007) and by Ivanov and others (2008).

A MASW profile was collected in the DPW field from east to west (Figure 1; red line) using a 48-channel Geometrics seismograph and a towed seismic land streamer. The streamer has 24 stations spaced 1.25 m apart. Two vertical-displacement geophones were located at each station, 4.5 and 28 Hz, and were mounted on metal plates that are pressure-coupled to the earth, eliminating the need for planting geophones. The seismic source was a 40-kg accelerated weight-drop source and a metal strike plate. The seismic source was mounted on the back of the lead vehicle and the streamer was advanced by a second vehicle. Data were collected at 5-m intervals; at each shot point, five shots were stacked in the field. Dispersion curves were generated for the 4.5- and 28-Hz data in stacked overtone images, and the fundamental modes were picked. Within SurfSeis, a trial-and-error process was used to pick the best modeling approach, and ultimately a 10-layer model was used for all 1D inversions.

Integrated results and evaluation of geophysical methods

To evaluate the use of the different surface geophysical methods, data were collected on one line in the DPW field about 15 m north of the DPT points using FDEM, GPR, 2DRes, and MASW methods (Figure 1, red line). Additional FDEM data were collected to the southwest across Babcock Road (Figure 1, red dashed line).

The FDEM method was effective for identifying shallow (less than 5 m) changes in electrical conductivity. The apparent conductivity data were plotted in log scale (Figure 2a) and in high-contrast display to highlight conductive anomalies (Figure 2b). At the southwest end of the plots, the FDEM data show an increase in electrical conductivity due to road-salt storage. Additional low conductivity anomalies are observed in the middle of the DPW field. A line (black arrows in Figure 2b) can be traced from one survey line to the next, suggesting the presence of a linear feature, such as a buried pipeline or other type of infrastructure.

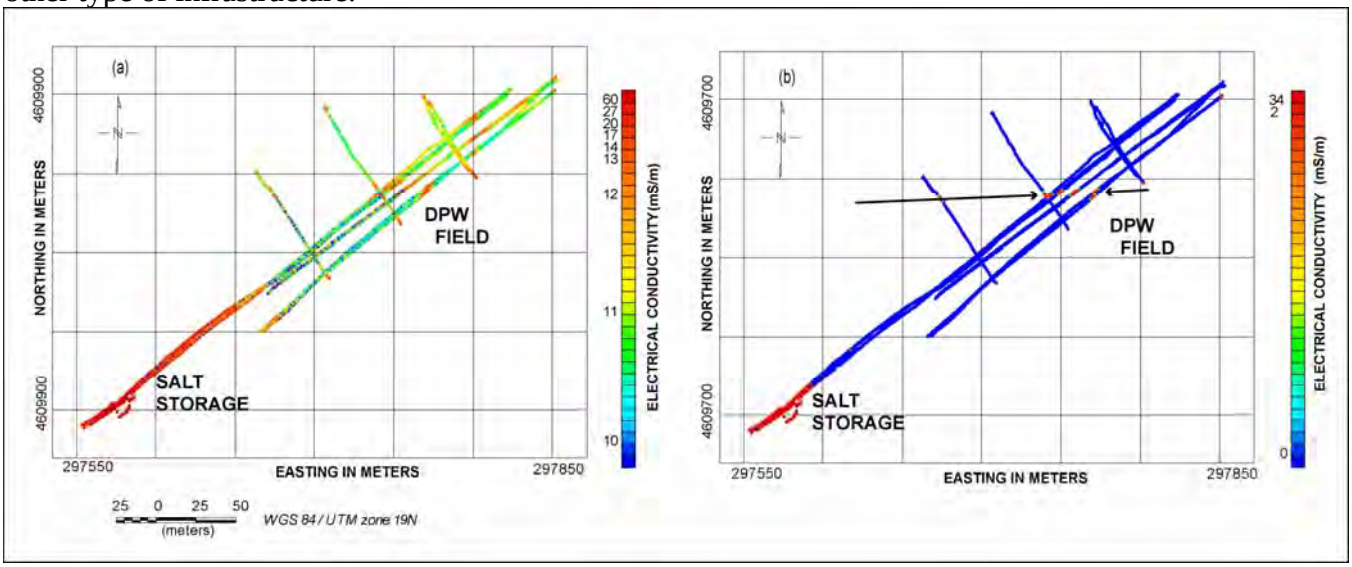

Figure 2. Frequency domain electromagnetic GEM2 plots of apparent electrical conductivity from the North Kingstown Department of Public Works field in Rhode Island. (a) Apparent conductivity in log scale, (b) apparent conductivity in high contrast display to highlight anomalies.

Data for the FDEM line along the red profile in Figure 1 were plotted as a scatterplot of the total electrical conductivity (EC) along the profile (Figure 3a). The high-conductivity zone that is interpreted as infrastructure is centered at 100 m along the profile. The GPR record (Figures 3b and 4b) shows a point reflector centered between 95 and 100 m. In addition, the GPR identified multiple point reflectors at shallow depths that could be boulders or other buried debris or infrastructure. A fairly continuous reflector could be traced across most of the profile at a depth of about 15 to 20 m below land surface (Figures 3b and 4b). This continuous reflector shown as a solid red line (Figure 4b) was interpreted as the bedrock surface because of its sub-planar shape and continuity. On the western side of the plot from 0 to 75 m, the reflector is broken up and discontinuous. Two sub-parallel reflectors can be traced through this zone, one at a depth of about 15 m and the other at about 20 m below land surface. These reflectors are indicated by dashed lines in Figure 4b. The multiple point reflectors (shown in blue, Figure 4b) and somewhat chaotic nature of the planar reflectors may indicate the presence of coarse material, such as till, broken up rock, or possibly buried ice-contact deposits in this section of the profile.

The 2DRes results are shown in Figure 3c with the interpretations in Figure 4c. The highly resistive layer near the surface (red and orange) is interpreted as an unsaturated zone. Below this layer, the resistivity decreases with depth. The shallow decrease in resistivity near 100 m along the profile indicates the presence of infrastructure, consistent with the high conductivity anomaly observed in the FDEM data. The water table appears to be 5 to 7 m below the land surface. The bedrock, which is more conductive than the overburden, is interpreted to start at the 500-ohm-m contour at depths of about 17 to 27 m below land surface (dashed line in Figure 4c). The apparent doming of the bedrock surface in the middle of the profile is an inversion artifact caused by the shallow bulls-eye anomaly, which is interpreted as near-surface infrastructure as identified in the FDEM data. Consequently, the bedrock surface is interpreted to remain fairly flat as indicated by the dashed line interpreting the depth to bedrock.

Comparison of the GPR and 2DRes profiles shows zones of high attenuation in the radar profile and low resistivity (high electrical conductivity) in the resistivity profile at depths of about 7 to 17 m below land surface (Figure 3b and 3c from 85-115 m along the profile). In addition, the GPR record shows zones of high attenuation from 0 to 15 and 170 to 200 m along the profile. Possible causes for these zones of attenuation and low resistivity could be changes in the stratigraphy or an increase in the fluid electrical conductivity. These zones coincide with increases in the total electrical conductivity in the FDEM data plot (Figures 3a and 4a). Only the feature at about 100 m along the profile is interpreted as a pipe or infrastructure, because of the presence of the point reflector in the GPR data, and the apparent continuity of the high conductivity feature from one FDEM line to the other (Figure 4b).

The plot of *Vs* for the MASW profile in the DPW field is shown in Figure 3d, and appears to be consistent with the other geophysical methods. The 1D inversions of the seismic record indicate the lower layer, which is interpreted as bedrock, has *Vs* of 500 m/s, and is shown in black on the sections. Only minor variations in unconsolidated deposits in the upper part of the plot were observed, and the contrast in *Vs* between the slower *Vs* materials (overburden) and the faster *Vs* materials (which was interpreted as bedrock) was clear (in the 1D inversion models). The MASW results show a fairly uniform depth to bedrock of 15 to 20 m over most of the profile. On the west end of the profile (from 45 to 75 m along the profile), a deepened trough (depth to bedrock greater than 20-m deep) is present. This is the same area where the GPR data (Figures 3b and 4b) show multiple point reflectors and discontinuous planar reflectors. This zone may represent a zone where the bedrock surface is eroded, weathered, or fractured, which would cause the lower *Vs* to extend deeper in that part of the MASW profile. The total depth of penetration for the MASW method was about 25 m below land surface.

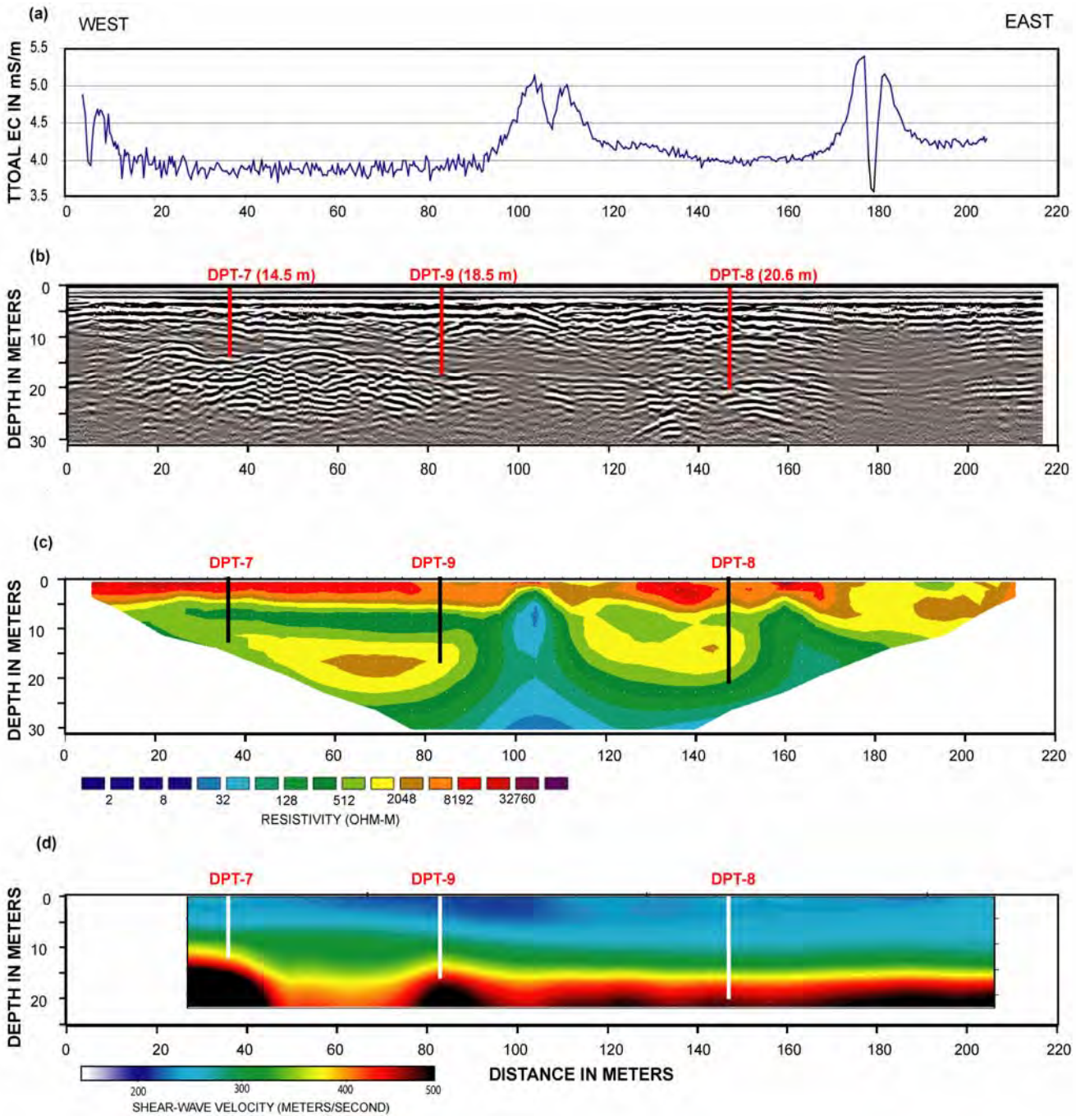

Figure 3. Composite of geophysical data from the field across from the Department of Public Works in North Kingstown, Rhode Island: (a) frequency domain electromagnetic induction showing total electrical conductivity (EC) in millisiemens per meter (mS/m) with distance along the profile, (b) ground-penetrating radar, (b) resistivity profile showing the inverted section of the combined Wenner and dipole-dipole surveys, and (c) multi-channel analysis of surface-wave seismic smooth approximation section of shear-wave velocity. Location and depth to refusal in meters are show for the direct-push profile points (DPT) on each profile. The DPTs were located approximately 15 meters south of the profiles.

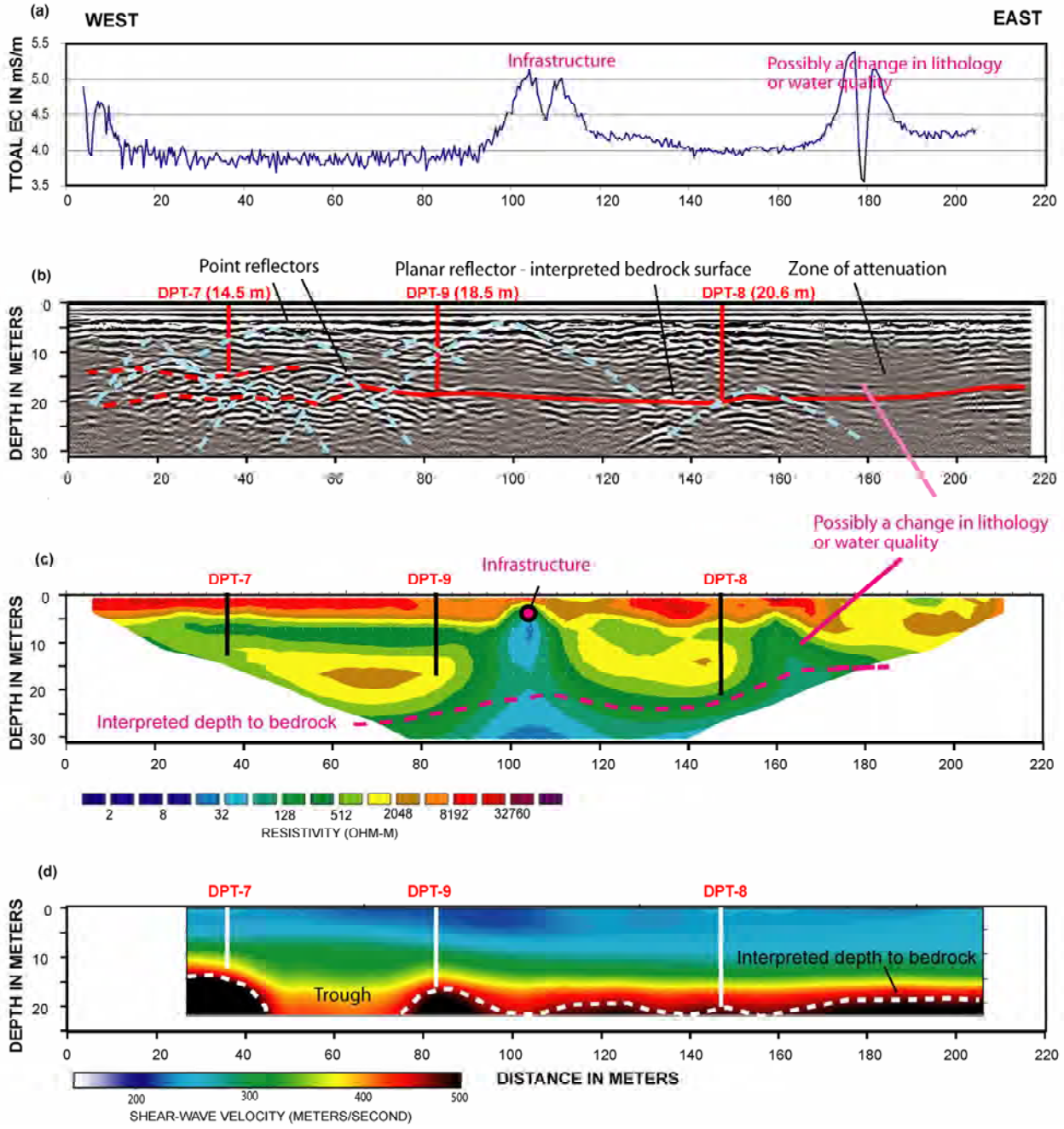

Figure 4. Composite of geophysical data from the field across from the Department of Public Works in North Kingstown, Rhode Island, annotated with interpretation: (a) frequency domain electromagnetic induction showing total electrical conductivity (EC) in millisiemens per meter (mS/m) with distance along the profile, (b) ground-penetrating radar, (c) resistivity profile showing the inverted section of the combined Wenner and dipole-dipole surveys, and (d) multi-channel analysis of surface-wave seismic smooth approximation section of shear-wave velocity. Location and depth to refusal in meters are shown for the direct-push profile points (DPT) on each profile. The DPTs were located approximately 15 meters south of the profiles.

A comparison of the results indicates the interpretations of depth to bedrock surface were similar for the MASW, 2DRes, and GPR methods (Figure 4). These interpretations were consistent with direct push profiling conducted across the field and adjacent to the profiles (Figures 1, 3, and 4). The results indicate that the MASW and GPR methods were useful for estimating the depth to bedrock. The sharp contrast in the MASW *Vs* suggests the contact between the overburden and a deeper layer, which we interpret as bedrock. In the GPR record, we identify a fairly continuous reflector through the middle and eastern side of the profile that is continuous and fairly smooth. This reflector is interpreted as bedrock, but it may represent another layer above the bedrock surface. On the western side the record is characterized by multiple point-reflectors and two discontinuous, sub-parallel, uneven reflectors that can be traced in the record. These reflectors may characterize cobble layers, till, broken-up rock, or possibly buried ice-contact deposits. The 2DRes profile shows the least resolution of the bedrock surface; the added information about the potential water quality and the possible indication of fractures in the bedrock surface, however, make this method valuable. The GPR and FDEM data also added information about potential changes in water quality, stratigraphy, and presence of infrastructure.

Conclusions

The depth to the bedrock surface is important in the investigation of contaminant distribution at the former NCBC site. Possible channels or knobs in the bedrock surface can affect groundwater flow and possible contaminant migration. Thus, determining the depth and shape of the bedrock may provide valuable information to complement ongoing investigations of contaminant migration and to inform the selection and design of a remedy. As the results of this study indicate, the best practices are to combine more than one geophysical method, preferably using methods that measure different properties of the subsurface.

This investigation used four methods including the MASW seismic method to measure mechanical properties, GPR and FDEM methods to measure electromagnetic properties, and resistivity to measure electrical properties of the subsurface. Data were collected along the same line using the four methods, and were evaluated to characterize the subsurface and test the effectiveness of the tools. FDEM was used as a reconnaissance method and was effective for identifying shallow changes in electrical conductivity. Shallow anomalies observed in the GPR and ERT data were consistent with anomalies observed in the FDEM data. Depths to bedrock interpreted from the ERT, MASW, and GPR profiles were similar, about 14 to 25 m below land surface, and were consistent with the depths of refusal identified in the direct-push wells. While all three methods gave similar interpreted depths to bedrock along this test line, the GPR data had many parabolic reflectors, which hindered interpretation, and the 2DRes profile showed the least resolution of the bedrock surface. This test case shows that complementary techniques that measure different properties can be more effective for site characterization than a single-method investigation.

The overall agreement of interpreted results from seismic, resistivity, radar, and electromagnetic methods with ground-truth data shows that these tools can be used effectively to identify infrastructure, which can be a possible source of interference, and to determine subsurface features such as changes in sediments, saturation, water chemistry, and/or the bedrock surface. The estimate of the bedrock surface from these methods can be used to site observations wells, which can be used to validate these interpretations of the bedrock surface or to improve the interpretation. If the observation wells validate

the interpretation, the results of the surface geophysical surveys can be used to refine subsurface images and to serve as a tool for optimizing the locations of additional wells.

References

Abraham, J.D., Deszcz-Pan, M., Fitterman, D.V., and Burton, B.L., 2006, Use of a handheld broadband EM induction system for deriving resistivity depth images, in Gamey, J., ed., 19th Annual Symposium on the Application of Geophysics to Engineering and Environmental Problems, Seattle, Washington, April 2 - 6, 2006, 18 p.

Advanced Geosciences, Incorporated, 2009, SuperSting R8 IP 8 channel Memory Earth Resistivity and IP Meter accessed January, 2009 at http://www.agiusa.com/supersting.shtml

Beres, Milan, Jr. and Haeni, F. P., 1991, Application of Ground-Penetrating-Radar Methods in Hydrogeologic Studies, Ground Water, vol. 29, no.3, pp 375-386.

EA Engineering, Science, and Technology (EA EST), 1988a, Final Interim Report of Site 03/NIKE Source Area Characterization and Offsite Investigation, Naval Construction Battalion Center, Davisville, Rhode Island, Prepared for Department of the Navy.

EA Engineering, Science, and Technology, 1998b, Phase III Comprehensive Remedial Investigation, Study Areas 01 and 04 and IR Program Sites 02 and 03, Naval Construction Battalion Center, Davisville, Rhode Island, Revised Draft Final, Volume I: Technical Report and Appendix A, Prepared for Department of the Navy.

EA Engineering, Science, and Technology, 1998c, Revised Draft Final, Study Areas 01 and 04 and IR Program Sites 02 and 03, Phase III Comprehensive Remedial Investigation, Volume II: Appendices B Through J, Naval Construction Battalion Center, Davisville, Rhode Island, Prepared for Department of the Navy.

Geophex, Ltd. 2009, GEM-2 Broadband EMI sensor: accessed January, 2009 at http://www.geophex.com/GEM-2/GEM-2%20home.htm

Ivanov, J., Miller, R.D., and Tsoflias, G., 2008, Some practical aspects of MASW analysis and processing: *in* Symposium on the Application of Geophysics to Engineering and Environmental Problems, April 6-10, 2008, Philadelphia, Pennsylvania, Proceedings: Denver, Colorado, Environmental and Engineering Geophysical Society, 13 p.

Kansas Geological Survey, 2007, SurfSeis Manual: accessed January, 2009 at http://www.kgs.ku.edu/software/surfseis/s2intro.html

Loke, M.H., 2004, Tutorial: 2-D and 3-D electrical imaging surveys, accessed 9 January 2010, at http://www.geoelectrical.com.

Mala Geoscience USA Inc., 2010, Application Note – No. 2887 accessed January, 2010, at http://www.malags.com/getattachment/f054ef7b-2e97-450d-be8f-6732852cda2e/Using-the-MALA-RTA.aspx

Sharma, P. V., 1997, Environmental and Engineering Geophysics: Cambridge University Press, Cambridge, 475 p.

Schafer, J.P., 1961, Surficial Geology of the Wickford Quadrangle, Rhode Island. U. S. Geological Survey Quadrangle Map GQ-136, Scale 1:24,000.).

U.S. Geological Survey, 1995, Wickford, RI Quadrangle, 7.5 - minute series (topographic), NIMA 6767 III SW Series V-815

Williams, R.B., 1964, Bedrock Geology of the Wickford quadrangle, Rhode Island. U.S. Geological Survey Bulletin 1158-C, 15.

Xia, J., Miller, R.D., Park, C.B., Hunter, J. A. and Harris, J.B., 1999, Estimation of near-surface velocity by inversion of Rayleigh waves: Geophysics, v. 64, p. 691-700.

Acknowledgements

This work was conducted in cooperation with the U.S. Environmental Protection Agency under IAG ID: DW-14-94029401-5 agreement. The authors appreciate the cooperation of the land owners and managers for providing access to private and municipal property. Also we would like to acknowledge field support and assistance of Troy Brosten, Rory Henderson, Peter Joesten, and Emily Voytek of the USGS. Finally we are grateful to Cian Dawson, Jason Sorenson, and Sandra Cooper of the USGS for their technical reviews of this work.

ESTIMATING GROUNDWATER STORAGE CHANGES IN THE WESTERN KANSAS USING GRACE DATA

Bo Chen, Institute of Geophysics & Geomatics, China University of Geosciences, Wuhan, China
Jianghai Xia, Kansas Geological Survey, The University of Kansas, Lawrence, Kansas
Qiuge Wang, Institute of Geophysics & Geomatics, China University of Geosciences, Wuhan, China
Chao Chen, Institute of Geophysics & Geomatics, China University of Geosciences, Wuhan, China
Richard D. Miller, Kansas Geological Survey, The University of Kansas, Lawrence, Kansas
Qing Liang, Institute of Geophysics & Geomatics, China University of Geosciences, Wuhan, China

Abstract

The Gravity Recovery and Climate Experiment (GRACE) delivers monthly gravity fields since it was launched in March 2002, which provides a new way to monitor the groundwater storage variations for large regions. In this study, we attempt to apply the GRACE data combined with estimated soil moisture based on the water balance approach to estimate monthly groundwater changes in the western Kansas of approximately 100,000 km^2. The comparison of different Gaussian smoothing radiuses indicated that a smaller filter radius (150 km) is more appropriate for this size of the study area to get more effective gravity signals. The results are compared with in situ yearly measurements of groundwater levels and show a prominent seasonal cycle. The groundwater storage changes estimated from GRACE data agree well with the measured groundwater levels during 2003 and 2008. Both of them show a decline trend. Such observation results from GRACE data will provide regional fundamental information for water resource management.

Introduction

Groundwater is an important component of water resources, which is used as primary source of drinking water, agricultural irrigation and industrial activities. Around the world, groundwater resources are under increasing pressure caused by human activities and climate changes. To better assess and manage groundwater supplies, monitor groundwater changing become more and more important. However, the traditional well network monitoring is labor intensive and expensive. Additionally, this only can operate at local scales. Thus, satellite observations are now playing an increasingly important role in global groundwater resources assessment. Especially, satellite observations of Earth's time-variable gravity field from the Gravity Recovery and Climate Experiment (GRACE) mission represent a new opportunity to monitor groundwater storage changes from space (Rodell and Famiglietti, 2002). GRACE data have been used in a number of studies to estimate water storage variability in continents (Tapley et al., 2004, Schmidt et al., 2006). Combined with auxiliary data, some studies also show the potential for using GRACE data to estimate the seasonal or monthly groundwater variability in some large river basins (Rodell et al., 2007, Rodell et al., 2009) or large aquifers (Strassberg et al., 2009).

We apply the GRACE data basing on the water balance approach to estimate groundwater variations in the western Kansas in this study. The climate of the region is semiarid, receiving average annual precipitation about 400 mm. In general, groundwater is the primary source in the western Kansas, where irrigation dominated, especially in summer. Most of this region relies on groundwater from the High Plains (HP) Aquifer for irrigation. The HP Aquifer is a vast yet shallow underground water table aquifer located beneath the Great Plains in the United States, which is one of the world's largest aquifers. In Kansas, the HP aquifer is made up of several smaller sub-regional aquifers (Figure 1), the Ogallala, Great Bend Prairie and Equus Beds (Sophocleous, 1998). The Great Bend Prairie and Equus Beds aquifers are generally closer to the land surface and are more responsive to recharge. They are managed as sustainable systems, while the Ogallala is generally deeper and, with less annual precipitation, has little natural recharge. The Ogallala Formation of Miocene age and overlying hydraulically connected Quaternary deposits are the principal geologic units in the aquifers and consist of unconsolidated materials (gravel, sand and silt) deposited by streams. Because of the large-scale and intensive ground water pumping for irrigation purposes and several years of below normal precipitation, groundwater levels in the western Kansas have declined significantly. The monitoring well network shows that water levels in the HP aquifer in parts of the southwestern Kansas had declined more than 30 m by 1980 (McGuire, 2007).

Strassberg et al. (2007, 2009) validated the potential for using GRACE data with in situ measurements of soil moisture to estimate groundwater storage variability in the HP Aquifer. In this study, a time series of spatially averaged groundwater storage changes are evaluated by using GRACE data and simulated soil moisture over this area approximately 100,000 km^2 (See Figure 1), which are compared with in situ measurement of groundwater levels in consecutive seven years ranged from 2003 to 2009. Together with the available soil moisture and groundwater data, we try to assess the applicability of GRACE data for monitoring groundwater storage changes over such a small area.

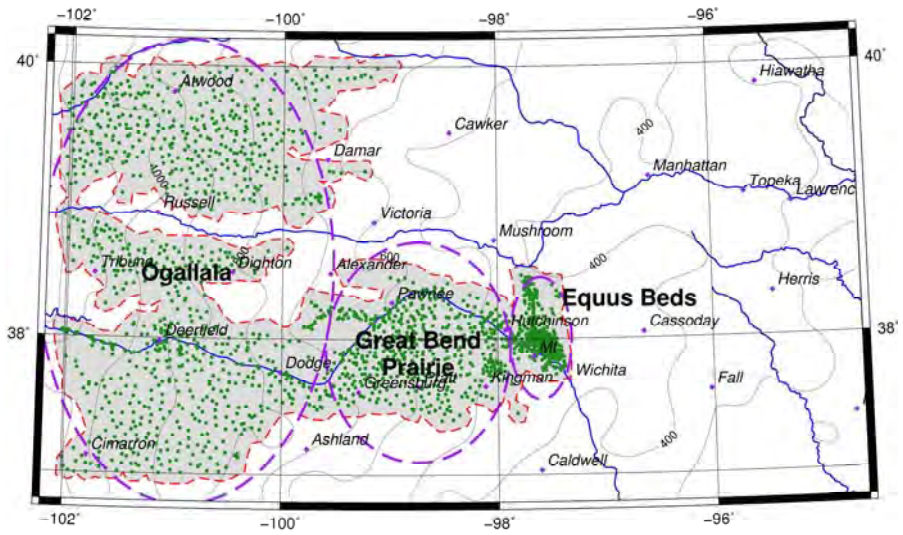

Figure 1. Aquifer Systems of Kansas, U.S. showing locations of observation wells by green dots. The thin red dash line shows the study area where is filled with grey color. Contours with the interval 100 m give the levels of topography. The three areas rounded by thick dash line are the subregional aquifer systems in the western Kansas.

Gravity Signals Caused by Groundwater

Time-variable gravity changes are caused by a combination of mass redistribution within the Earth (e.g. postglacial rebound) and on or above its surface, such as atmospheric fluctuation, the water, and snow and ice redistribution on land and in the ocean. Wahr et al. (1998) discussed the methodology for converting time-variable gravity field coefficients to estimate water storage changes.

The Earth' global gravity field is commonly described in terms of the shape of geoid. Suppose there is a time-dependent change in the geoid ΔN. It is usual to expand the geoid shape ΔN as a sum of spherical harmonics:

$$\Delta N(\theta,\phi) = a\sum_{l=0}^{\infty}\sum_{m=0}^{l}\overline{P}_{lm}(\cos\theta)(\Delta C_{lm}\cos(m\phi) + \Delta S_{lm}\sin(m\phi)) \tag{1}$$

where a is the radius of the Earth, θ and ϕ are co-latitude and east longitude, respectively, l and m are the degree and order of the spherical coefficients, respectively, ΔC_{lm} and ΔS_{lm} are coefficient changes, and $\overline{P}_{lm}(\cos\theta)$ is normalized associated Legendre function.

Let $\Delta\rho(r,\theta,\phi)$ be the density redistribution causing this geoid change. It can be shown that

$$\begin{Bmatrix}\Delta C_{lm}\\ \Delta S_{lm}\end{Bmatrix} = \frac{3}{4\pi a\rho_{ave}(2l+1)}\int\Delta\rho(r,\theta,\phi)\overline{P}_{lm}(\cos\theta)\left(\frac{r}{a}\right)^{l+2}\begin{Bmatrix}\cos(m\phi)\\ \sin(m\phi)\end{Bmatrix}\sin\theta d\theta d\phi dr \tag{2}$$

where ρ_{ave}=5515 kg/m^3 is the average density of the Earth. Suppose $\Delta\rho(r,\theta,\phi)$ is concentrated in a thin layer of thickness *H*, which include those portions of the atmosphere, oceans, ice caps, and belowground water storage with significant mass fluctuation. Suppose *H* is thin enough that $(l_{\max}+2)H/a << 1$, then $r \approx a$, and $\Delta\rho(r,\theta,\phi)$ can be replaced by surface density $\Delta\sigma(\theta,\phi)$ through the radial integral of the layer:

$$\Delta\sigma(\theta,\phi) = \int\Delta\rho(r,\theta,\phi)dr \tag{3}$$

The gravitational attraction of the surface mass distribution to the geoid can be shown as

$$\begin{Bmatrix}\Delta C_{lm}\\ \Delta S_{lm}\end{Bmatrix}_{SurfMass} = \frac{3}{4\pi a\rho_{ave}(2l+1)}\int\Delta\sigma(\theta,\phi)\overline{P}_{lm}(\cos\theta)\begin{Bmatrix}\cos(m\phi)\\ \sin(m\phi)\end{Bmatrix}\sin\theta d\theta d\phi \tag{4}$$

The surface mass also loads and deforms the underlying solid Earth, which causes an additional geoid contribution:

$$\begin{Bmatrix}\Delta C_{lm}\\ \Delta S_{lm}\end{Bmatrix}_{SolildEarth} = \frac{3k_l}{4\pi a\rho_{ave}(2l+1)}\int\Delta\sigma(\theta,\phi)\overline{P}_{lm}(\cos\theta)\begin{Bmatrix}\cos(m\phi)\\ \sin(m\phi)\end{Bmatrix}\sin\theta d\theta d\phi \tag{5}$$

where k_l is load Love number of the degree l. The total geoid change is the sum of (4) and (5). The surface density $\Delta\sigma$ also can expand as a sum of spherical harmonics:

$$\Delta\sigma(\theta,\phi) = a\rho_{wat}\sum_{l=0}^{\infty}\sum_{m=0}^{l}\overline{P}_{lm}(\cos\theta)(\Delta\hat{C}_{lm}\cos(m\phi) + \Delta\hat{S}_{lm}\sin(m\phi)) \tag{6}$$

where ρ_{wat} is the density of water. $\Delta\hat{C}_{lm}$ and $\Delta\hat{S}_{lm}$ can be expressed as:

$$\begin{Bmatrix}\Delta\hat{C}_{lm}\\ \Delta\hat{S}_{lm}\end{Bmatrix} = \frac{1}{4\pi a\rho_{wat}}\int \Delta\sigma(\theta,\phi)\overline{P}_{lm}(\cos\theta)\begin{Bmatrix}\cos(m\phi)\\ \sin(m\phi)\end{Bmatrix}\sin\theta d\theta d\phi \tag{7}$$

By using equations (4), (5) and (7), the simple relation between $\Delta\hat{C}_{lm}$ ($\Delta\hat{S}_{lm}$) and ΔC_{lm}, (ΔS_{lm}) is

$$\begin{Bmatrix}\Delta\hat{C}_{lm}\\ \Delta\hat{S}_{lm}\end{Bmatrix} = \frac{\rho_{ave}}{3\rho_{wat}}\frac{2l+1}{1+k_l}\begin{Bmatrix}\Delta C_{lm}\\ \Delta S_{lm}\end{Bmatrix} \tag{8}$$

Therefore, the change in surface mass density can be represented using the change coefficients in the geoid. Note that $\Delta\sigma/\rho_{wat}$ is the change in the surface mass expressed in equivalent water thickness $\Delta h(\theta,\lambda)$. Using equation (8), it is expressed as:

$$\Delta h(\theta,\phi) = \frac{a\rho_{ave}}{3\rho_{wat}}\sum_{l=0}^{\infty}\sum_{m=0}^{l}\overline{P}_{lm}(\cos\theta)\frac{2l+1}{1+k_l}(\Delta C_{lm}\cos(m\phi)+\Delta S_{lm}\sin(m\phi)) \tag{9}$$

which can be used to estimate the variability in groundwater from change coefficients ΔC_{lm} and ΔS_{lm}.

Data

Gravity Recovery and Climate Experiment (GRACE), launched in March 2002, consists of two satellites that are separated along track by 220 km and co-orbiting at near polar inclinations at 300-500 km altitude. Monthly gravity field are obtained with a spatial resolution range from 400 to 40000 km (Tapley et al., 2004) and can be used to estimate the terrestrial water storage (TWS) changes such as the equivalent water thickness given in equation (9). TWS changes derived from GRACE observations represent a vertically integrated measure of water storage changes based on equation (9), which contains all the water components such as groundwater, soil moisture, surface water, snow and biomass. Thus, to gain the component of groundwater storage (GWS), changes in snow, surface water and soil moisture (SM) must be removed from GRACE-derived TWS (Rodell and Famiglietti, 2002). Strassberg et al. (2007) considered that soil moisture and groundwater are dominant components in TWS variations in the High Plains. To estimate groundwater storage changes in the western Kansas, the gravitational component of soil moisture has to be considered.

In this study, the time series of monthly TWS, SM or GWS changes relative to the values in January 2003 are obtained to compare the water level measurements in the western Kansas.

TWS derived from GRACE data

Monthly TWS in the equivalent water thickness are calculated using data during the period from January 2003 to September 2009, which are produced by the Center for Space Research (CSR), The University of Texas at Austin. Data are released in the form of pairs of spherical harmonic (Stokes) coefficient. These Stokes coefficients are made in maximal degree and order 60 and have been removed atmospheric and oceanic contributions. The $C_{2,0}$ term is replaced by zero because the error level of $C_{2,0}$ is high due to a limited number of GRACE data available to determine it.

Figure 2 shows relative TWS derived from GRACE data in Kansas from 2004 to 2009, relative to that in January 2003. Data have been processed using a quadratic polynomial correlation-error filter in a moving window of width 9 (spherical harmonic coefficients used in the filter are selected from a moving window that contains 9 spherical harmonic coefficients) and a 300-km radius Gaussian-smoothing factor that will be discussed in the next section. The distributions of relative TWS in different years have similar features regionally. The maximal amplitude of variation is around 200 mm.

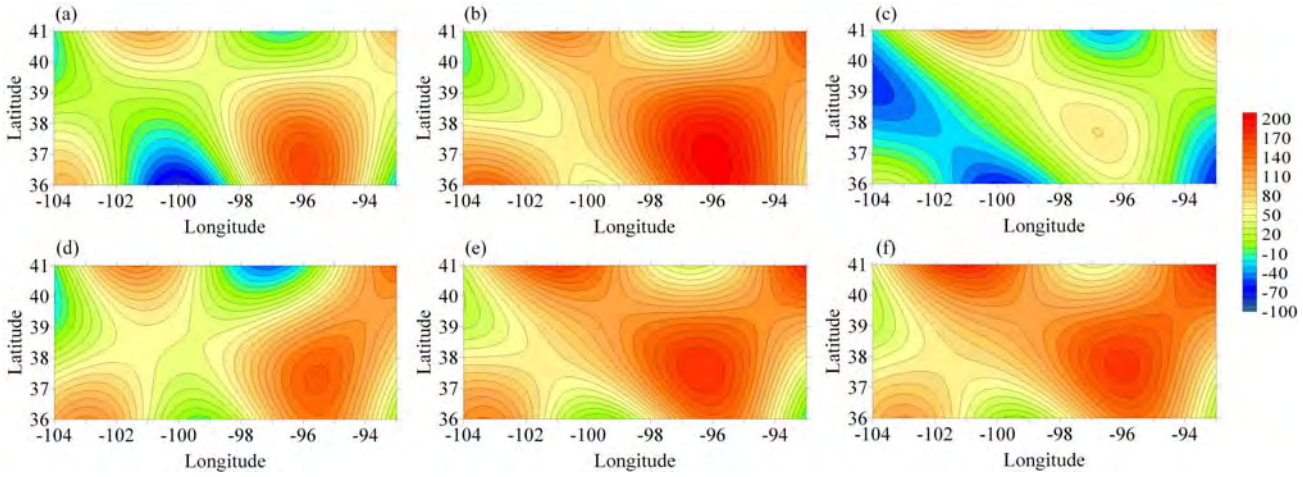

Figure 2. Yearly relative TWS in January from 2004 to 2009 relative to that in January 2003 over the Kansas (36°N~41°N, -104°E~-93°E); (a) Jan. 2004, (b) Jan. 2005, (c) Jan. 2006, (d) Jan. 2007, (e) Jan. 2008, (f) Jan. 2009. (Unit in mm, accounted based on the data from http://www.csr.utexas.edu/grace/)

Soil moisture (SM) data

Change of soil moisture plays an important role in TWS variations. The mass of SM in a unite area can be transformed to the equivalent water level per unit area using a hydrological model such as a one-layer hydrological model (Fan et al., 2004). Monthly SM data in this study are estimated using this kind of model based on the precipitation, temperature and evaporation in the region and released by Climate Prediction Center (CPC), NOAA with spatial resolution of about 0.5°, which is called as CPC SM model. SM data relative to that in January 2003 are used to determine GWS from GRACE data.

Although relative SM yearly changes during 2004-2009 in Kansas do not show an obvious trend during the period (Figure 3), monthly changes of the averaged soil moisture in the western Kansas relative to January 2003 (Figure 4) reveal features of seasonal and annual cycles. They are impacted on obviously by the regional precipitation, especially, about 75 percent of the state's annual precipitation occurs from April to September. The annual precipitation varies greatly from year to year in Kansas in past decades (Sophocleous, 1998). Nevertheless, a certain pattern of relative SM changes can be found, of which higher levels occur during summer and fall and lower levels occur during winter and early spring. The variations of relative SM through 6 years range from -20 mm to 180 mm. The expected SM dropping in the period from December 2006 to March 2007 does not happen.

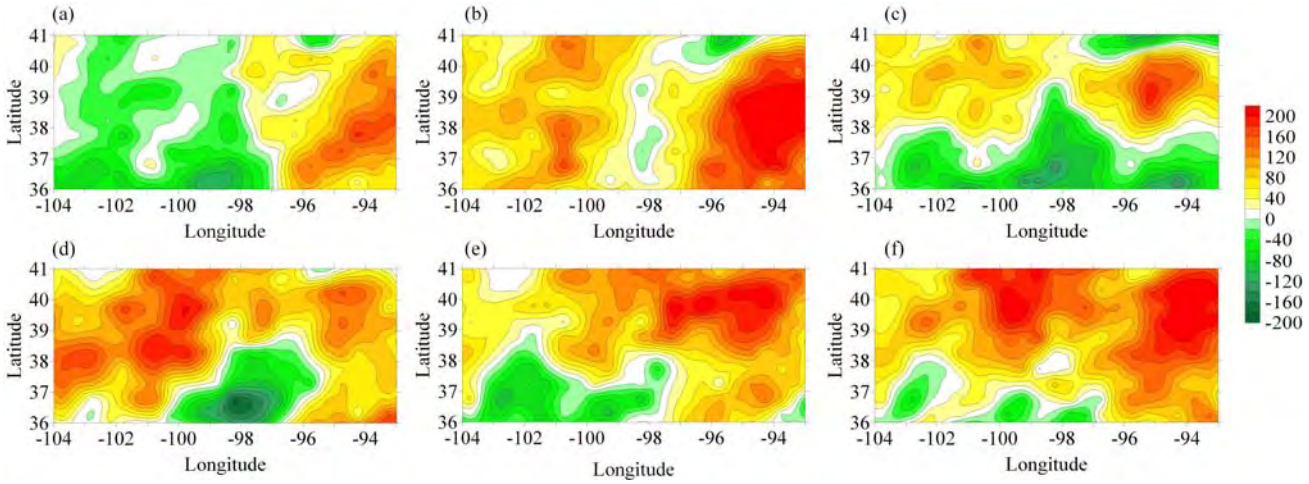

Figure 3. Yearly soil moisture changes in January relative to January 2003 in Kansas. (a) Jan. 2004, (b) Jan. 2005, (c) Jan. 2006, (d) Jan. 2007, (e) Jan. 2008, (f) Jan. 2009. (Unit in mm, The data are derived from http://www.cpc.ncep.noaa.gov/soilmst/leaky_glb.htm)

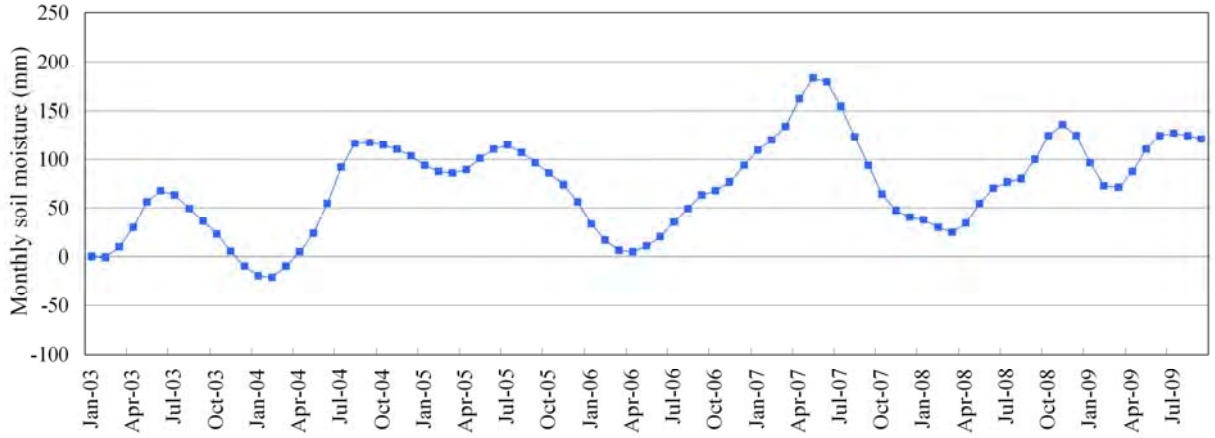

Figure 4. Monthly averaged relative SM changes in the western Kansas.

Groundwater storage (GWS) from measured water level

Groundwater storage in a large area can be estimated using a simple approach, which only depends on ground water table level (WTL) and drainable porosities of rocks (Special Yield, SY) in situ. The change of water volume is considered as WTL rising or dropping in a certain area. A previous research shows an attempting using WTL data to modeling the variation of gravity on the surface from time-laps gravity survey (Gehman, et al, 2009). The relationship of GWS with WTL and SY is given in GWS = WTL*SY.

In this study, groundwater level data from nearly 2500 wells in the western Kansas are provided by the Kansas Geological Survey. The data were measured in the winter of every year, generally in

December, January and February. The measuring scheme has an advantage of aquifers having a chance to be recharged from the more transient and localized effects of pumping for irrigation. Most of wells are located within the saturated extent of the High Plain aquifers (Figure 1). Figure 5 shows WTL's changes from 2004 to 2009 relative to 2003. The appearance of WTL in the Ogallala declined consecutively during winters of 2004 to 2009. Variations from the Great Bend Prairie and the Equus Beds kept in balance during 2004 and 2007, and had an increase trend in 2008 and 2009.

Data measured from 2003 to 2009 are selected to calculate the GWS. The distribution of SY is generally determined by properties of rocks and geologic formation in situ. The averaged value of 0.1 is assigned to SY for calculation of GWS.

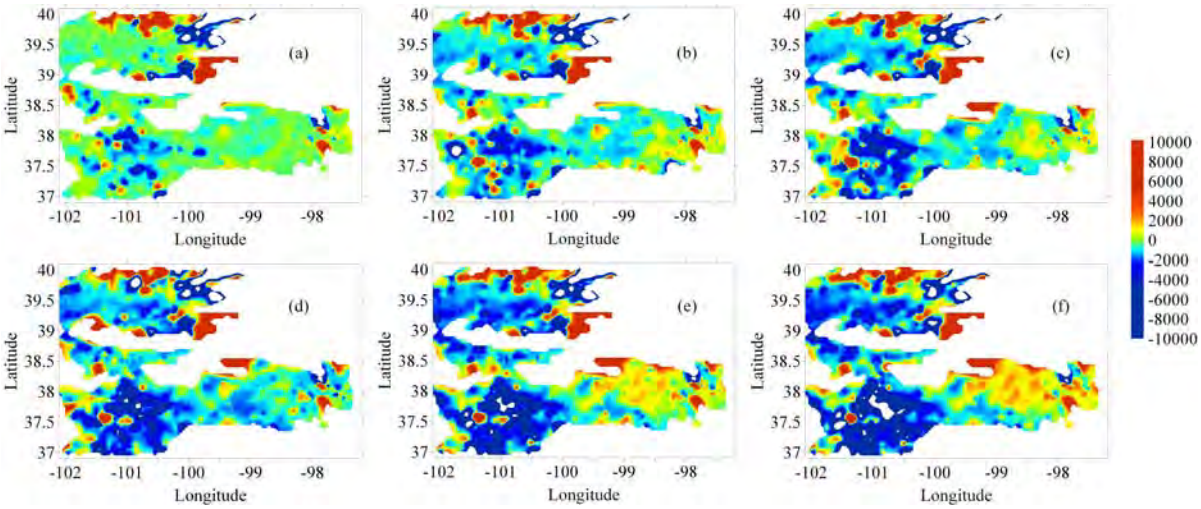

Figure 5. The water level changes relative to January 2003 in the western Kansas. There are some extreme differences in the area. (a) Jan. 2004; (b) Jan. 2005; (c) Jan. 2006; (d) Jan. 2007; (e) Jan. 2008; (f) Jan. 2009. (Unit in mm)

GRACE Data Filtering

The analyses of GRACE monthly gravity field are accomplished using Stokes coefficient sets. They are complete to some limited degree and order 60 or 120, although the higher degrees and orders within these ranges are expected to be nosier and therefore require some kinds of filtering. Figure 6a shows relative TWS determined by unsmoothed GRACE data. The results are seriously disturbed by noise. It is necessary to reduce this noise using some filtering methods, such as isotropic Gaussian filter (Wahr et al., 1998), anisotropic filter (Han et al., 2005), correlated-error filter (Swenson & Wahr, 2006) and/or statistical filter (Davis et al., 2008). Figures 6b, 6c, and 6d show the filtering results using different smoothing approaches.

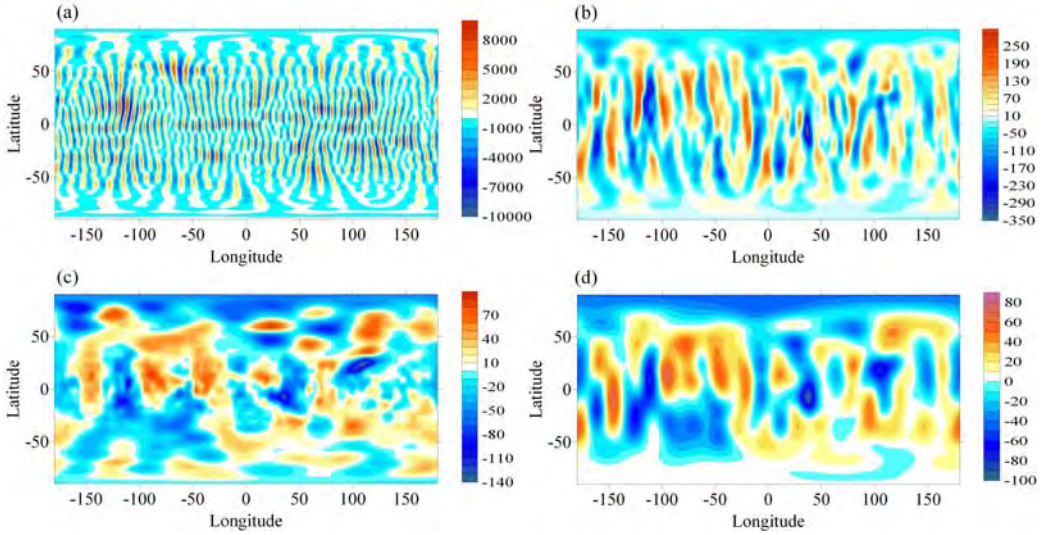

Figure 6. Relative TWS changes derived from GRACE in January 2004. (a) Unfiltered, no smoothing; (b) Smoothed with Gaussian filter 500 km; (c) Filtered with correlated-error filter and smoothed with 500 km Gaussian; (d) Smoothed with Gaussian filter 800 km. (Unit in mm)

To suppress the errors derived from the higher degree coefficients, the Gaussian-type filter (Wahr et al., 1998) combined with correlated-error filter (Swenson and Wahr, 2006) is applied in this study. The Gaussian average function can be given as

$$W(\theta,\phi,\theta',\phi') = W(\gamma) = \frac{b}{2\pi}\frac{\exp[-b(1-\cos\gamma)]}{1-e^{-2b}} \tag{10}$$

where $b = \dfrac{\ln 2}{(1-\cos(r/a))}$, r is the average radius, $W(\theta,\phi,\theta',\phi')$ depends only on the angle γ between the points (θ,ϕ) and (θ',ϕ'). Jekeli (1981) found the recursion relations to compute the coefficients with weights W_l:

$$\left.\begin{aligned} W_0 &= \frac{1}{2\pi} \\ W_1 &= \frac{1}{2\pi}\left[\frac{1+e^{-2b}}{1-e^{-2b}} - \frac{1}{b}\right] \\ W_{l+1} &= -\frac{2l+1}{b}W_l + W_{l-1} \end{aligned}\right\} \tag{11}$$

The resulting relative weight as a function of the Stokes coefficient degree is shown in Figure 7 with

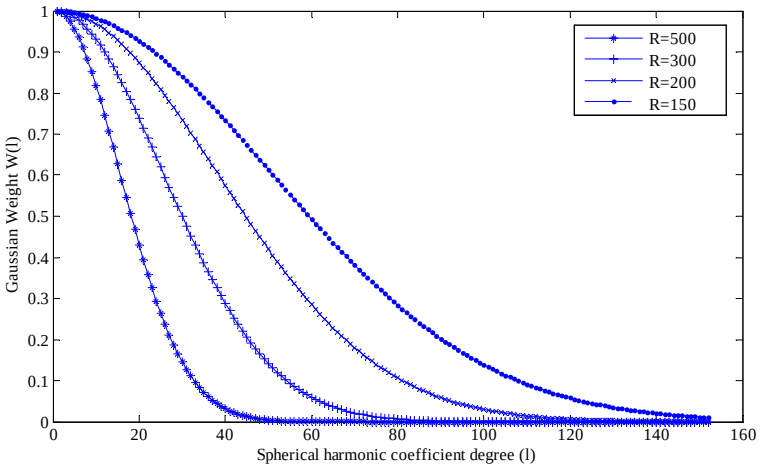

Figure 7. Gaussian averaging weights as function of spherical harmonic coefficients for different averaging radiuses.

different averaging radiuses. Gaussian filter can largely smooth the strips in the monthly anomaly and make maps clearer. However, filters with the large radius degrade the geophysical signals of interest. Swenson and Wahr (2006) found that the presence of stripes indicates a high degree of spatial correlation in the GRACE errors, which comes from the correlations between odd and even degree spherical harmonic coefficients. They applied the correlated-error filter to isolate and remove the correlated errors, and followed by the Gaussian filter that can obviously enhance the precision in latitude direction (Figure 6c).

With the current level of precision, the TWS from GRACE data were processed with a quadratic polynomial correlation-error filter in a moving window of width 9, and a 300-km radius Gaussian-smoothing factor to remove spurious north-south trending bands. However, this longer smoothing radius suppresses more of the shorter wavelength features, thereby minimizing the overall amplitude of the features in the study area (Figure 8a, R = 300 km). Thus, to get more information from the short wavelength, shorter smoothing radius (200 km and 150 km) of Gaussian filters are tried because groundwater level data in the study area can be used to verify the filtered results.

The time series of TWS (Figure 8a) shows this smoothing processing with small radii, which enhanced the amplitude of the monthly signals. However, it also causes some jagged or dramatic changes occurring in some months, such as that in October 2004. Thereby, a moving averaging over a 3-month time window is also applied to improve the temporal gravity signals in the monthly GRACE estimates (Figure 8b). Furthermore, comparing the results reveals that the different Gaussian filter radius (150 km and 200 km) can affect the amplitude of TWS changes with standard deviation of the residuals about 17 mm. Figure 8b shows that the TWS changes present a prominent seasonal trend with peaking around spring (March/April) and reaching a minimum near September/October in fall. The amplitudes of the averaged GRACE TWS changes range from about -100 mm to100 mm relative to the beginning of 2003.

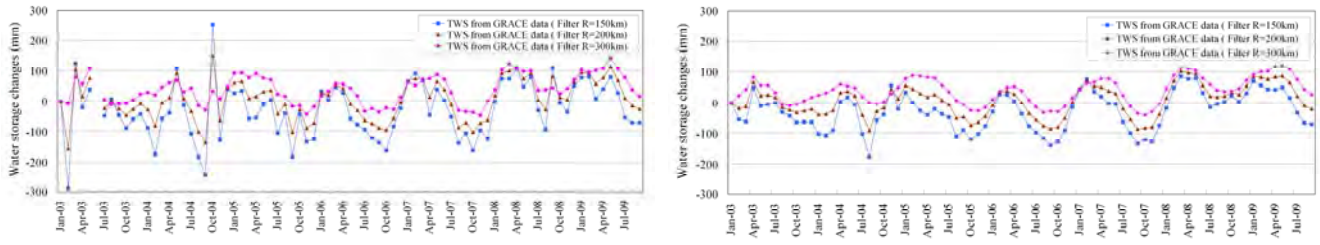

(a) (b)

Figure 8. Monthly GRACE TWS changes over the western Kansas. R = 300 km, 200 km, and 150 km represent the smoothing Gaussian filter radiuses are 300 km, 200 km, and 150 km, respectively. (a) Before temporal averaging, (b) after temporal three-month moving averaging.

Results and Discussion

By subtracting the soil moisture from the TWS determined by GRACE data, we obtain a residual time series describing regional monthly changes of the GRACE-derived GWS during January 2003 to

September 2009. Yearly changes from January 2004 to January 2009 (Figure 9) illustrate that the GRACE-derived GWS almost decline consecutively in the southwestern of the study area, which is consistent with the GWS changes from in situ measurements (Figure 5). The time series of monthly GRACE GWS changes (Figure 10) are compared with the in situ measurements GWS changes. The amplitudes of the GRACE time series range from about -200 to 80 mm and show a strong seasonal cycle with the maximum storage in winter spring, and the minimum storage in summer and fall. Although the measured groundwater storages from well data are only available for winter period (in January), they are still compared well with GWS from GRACE, except for some of the prominent differences occurring in January 2009.

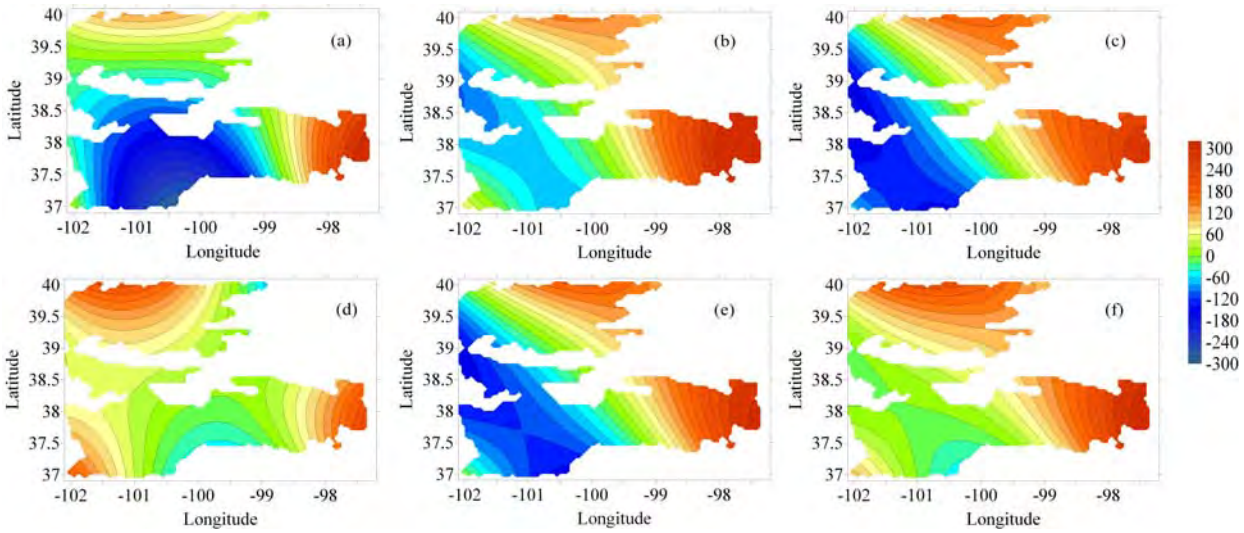

Figure 9. Yearly GRACE-derived GWS changes from January 2004 to January 2009 relative to January 2003. (a) Jan. 2004; (b) Jan. 2005; (c) Jan. 2006; (d) Jan. 2007; (e) Jan. 2008; (f) Jan. 2009. (Unit in mm)

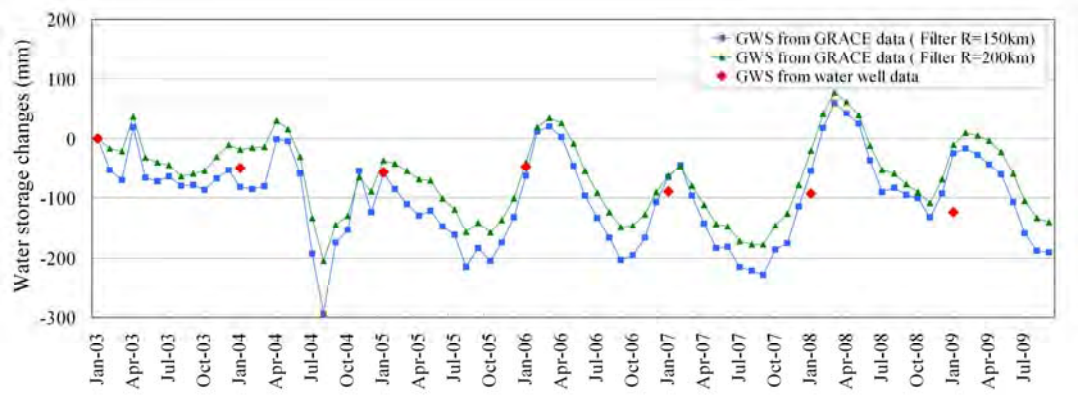

Figure 10. Changes in GWS from GRACE compared with GWS changes from in situ measurements of GW levels.

The USGS (McGuire, 2007, 2009) also published the annual GWS changes of the High Plain Aquifer in the western Kansas from 2003 to 2007. GWS total volume changes from USGS are transformed to GWS changes per unit area by dividing the area (100,000 km^2) relative to that in 2003 (Table 1). In situ measurement GWS were obtained from measured water table level (described in section Data). Compared the results among USGS estimates, in situ measurements, and deriving from GRACE, the groundwater changes mainly decline over this area from 2003 to 2007 (Table 1). However, some differences between in situ measurements and GRACE GWS occur in 2008 and 2009. The in situ measured GWS continued to decline in the two years, but GWS derived from GRACE shows an increase compared with prior year. It is possible that the wells were still recovering from recent pumping at the time of measurement. In addition, groundwater levels in the western Kansas are closely related to snowfall in winter. The groundwater level in the study area did not fully recharge due to the snowfall declined obviously in the winter of 2008.

Table 1. Groundwater changes in winter in the western Kansas.

Year	GWS Changes (mm)			
	USGS	**Measurement**	**GRACE (R=200)**	**GRACE (R=150)**
2004	-33.3	-49.5	-18.6	-82.1
2005	-40.7	-57.0	-36.6	-59.7
2006	-56.7	-48.0	-40.6	-62,7
2007	-91.2	-89.0	-62.9	-65.1
2008	--	-92.5	-20.9	-55.0
2009	--	-123.3	-11.4	-25.4

Summary

This study presents the comparison of monthly changes in terrestrial water storage minus soil moisture with groundwater storage from in situ measurement well data in seven year over the western Kansas approximately 100,000 km^2. The terrestrial water storage changes are evaluated from GRACE by using different Gaussian filter radiuses combined with quadratic polynomial correlation-error filter to reduce the error in GRACE gravity field. Different Gaussian smoothing radiuses are used in this analysis to smooth the gravity error, and try to get more useful signals from groundwater. Furthermore, the time series of monthly TWS, SM and GWS changes (relative to the value in January 2003) are obtained by regional spatial average to enhance the GRACE detectability.

Although this area is not as large as studies in Mississippi River basin (900,000 km^2, Rodell et al., 2007), in High Plains aquifer (450,000 km^2, Strassberg et al., 2007) or in Illinois (280,000 km^2, Swenson et al., 2008), results show that GRACE still have the ability to detect the GWS seasonal changes in this region with maximum storage in winter and spring, minimum storage in summer and fall. The estimated GWS agree well with in situ measurement groundwater levels in winter during 2003 to 2007, both of which show a prominent decline trend in the western Kansas. This may mainly owe to intensive ground water pumping for irrigation. Nevertheless, they do not agree well in the year 2008 and 2009. In fact, it

is not necessary to expect the GWS derived from GRACE can agree very well with in situ measurement for all year under the inherent spatial and temporal resolution of GRACE at present in this small area. This also indicates many other factors also should be considered using GRACE gravity data to estimate GWS in such a small area, such as the leakage around the region, the filter method, the resolution and reliability of soil moisture and other gravity changes except the groundwater and soil moisture.

Acknowledgements

Chao Chen and Jianghai Xia are grateful for the Merriam Research Award. The authors wish to thank Brownie Wilson of the Kansas Geological Survey for providing the measurements of groundwater levels. We also thank Climate Prediction Center for providing the simulated soil moisture data.

References

Davis J., Tamisiea M., Elosegui P., et al, 2008. A statistical filtering approach for Gravity Recovery and Climate Experiment (GRACE) gravity data. *J. Geophys. Res.*, *113*, D10102, doi:10.1029/2007JB005043.

Fan Y. & van den Dool H., 2004. Climate Prediction Center global monthly soil moisture data set at 0.5 resolution for 1948 to present. *J. Geophys. Res.*, *109*, D10102, doi:10.1029/2003JD004345.

Gehman, C. L., et al., 2009, Estimating specific yield and storage change in an unconfined aquifer using temporal gravity surveys, *Water Resour. Res.*, 45, W00D21, doi:10.1029/2007WR006096.

Han S., Shum C., Jekeli C., et al., 2005. Non-isotropic filtering of GRACE temporal gravity for geophysical signal enhancement. *Geophys. J. Int.*, *163*, 18–25, doi:10.1111/j.1365-246X.2005.02756.

Jekeli C., 1981. Alternative methods to smooth the Earth's gravity field. *Reports of Department of Geodetic Science and Surveying*, Ohio State Univ., Columbus, Report 327.

McGuire V., 2007. Water-level changes in the High Plains aquifer, predevelopment to 2005 and 2003 to 2005: U.S. Geological Survey Scientific Investigations Report 2006-5324, 7 p.

McGuire V., 2009. Water-level changes in the High Plains aquifer, predevelopment to 2007, 2005–06, and 2006–07: U.S. Geological Survey Scientific Investigations Report 2009–5019, 9 p., available at: http://pubs.usgs.gov/sir/2009/5019/.

Rodell M., & Famiglietti J., 2002. The potential for satellite-based monitoring of groundwater storage changes using GRACE: the High Plains aquifer, Central US. *Journal of Hydrology*, *263*, 245–256.

Rodell M., Chen J., Kato H., et al., 2007. Estimating ground water storage changes in the Mississippi River basin (USA) using GRACE. *Hydrogeology. J.*, *15*, doi:10.1007/s10040-006-0103-7.

Rodell M., Velicogna I., & Famiglietti J., 2009. Satellite-based estimates of groundwater depletion in India. *Nature*, *263*, doi:10.1038/nature08238.

Schmidt R., Schwintzera P., Flechtner F., et al., 2006. GRACE observations of changes in continental water storage. *Global and Planetary Change*, *50*, 112–126.

Sophocleous M., 1998. Water Resources of Kansas: A Comprehensive Outline. In: Sophocleous, M. (ed.). Perspectives on Sustainable Development of Water Resources in Kansas. Kansas Geological Survey, Bulletin 239, p. 22.

Swenson S, Wahr J., 2006. Post-processing removal of correlated errors in GRACE data. *Geophys. Res. Lett.*, *33*, L08402, doi:10.1029/2005GL025285.

Swenson S., Famiglietti J., Basara J., et al. 2008. Estimating profile soil moisture and groundwater variations using GRACE and Oklahoma Mesonet soil moisture data. *Water Resources Research*, *44*, W01413, doi:10.1029/2007WR006057.

Strassberg G., Scanlon B., & Rodell M., 2007. Comparison of seasonal terrestrial water storage variations from GRACE with groundwater-level measurements from the High Plains Aquifer (USA). *Geophys. Res. Lett.*, *34*, L14402, doi:10.1029/2007GL030139.

Strassberg G., Scanlon B., & Chambers D., 2009. Evaluation of groundwater storage monitoring with the GRACE satellite: Case study of the High Plains aquifer, central United States. *Water Resources Research*, *45*, W05410, doi:10.1029/2008WR006892.

Tapley B. D, Bettadpur S, Ries J, et al., 2004. GRACE measurements of mass variability in the Earth system. *Science*, *305*, 503–505.

Wahr J., Molenaar M., & Bryan F., 1998. Time-Variability of the Earth's Gravity Field: Hydrological and Oceanic Effects and Their Possible Detection using GRACE. *J. Geophys. Res.*, *103*, 30205–30229.

SPATIO-TEMPORAL MONITORING WITH AIRBORNE EM DATA – STILL WISHFUL THINKING, OR A REALISTIC PROPOSITION?

Tim Munday, CSIRO, Perth, Australia
Andrew Fitzpatrick, CSIRO, Perth, Australia
Volmer Berens, DWLBC, Adelaide, Australia
Andrea Viezzoli, Aarhus Geophysics, Aarhus, Denmark
Kevin Cahill, CSIRO, Perth, Australia

Abstract

Although the notion of spatio-temporal monitoring of natural landscapes and phenomena using multi-date airborne electromagnetic (AEM) surveys has been around for some time, examples are very limited in scope, particularly when defining vertical and lateral changes with time. We demonstrate an effective procedure for defining spatio-temporal variations in ground conductivity across a salinised floodplain in South Australia, using multi-date FDHEM data. Lateral *and* vertical changes in the conductivity of the floodplain have been resolved. We believe the advent of improved calibration procedures, geometry correction, calibrated broad band AEM systems and advanced inversion procedures that obviate the necessity of system calibration – recalibration, such as the holistic inversion, provide for the realistic proposition of using AEM data for the semi-quantitative and quantitative monitoring of landscape change in the subsurface. However, we emphasize the need for caution when considering observed spatial variations, stressing the importance of accounting for system investigation depth and the potential for artifacts that might be introduced from noise, system geometry and/or data interpretation procedures, when comparing data and derived conductivity models from different dates.

Introduction

Although the notion of spatio-temporal (spatial and time-related) monitoring of natural landscapes and phenomena using multi-date airborne electromagnetic (AEM) surveys has been around for some time, it could be argued that the realities associated with survey cost, with technology limits (linked to system calibration, noise etc), and the limited availability of robust inversion procedures have combined to hinder consideration and take-up for these purposes.

Included among the very few examples that have been mentioned in the open literature is the work described by Fitterman et al. (1995) and Fitterman and Deszcz-Pan (1998), and that reported by Beamish and Mattsson (2003). In the former, the use of multi-date frequency domain helicopter EM data for mapping saltwater intrusion in the Everglades National Park in Florida, USA is explored. Two surveys of substantially the same area; one flown in the rainy season and another that was flown in the dry season were compared, although the results have not been published. The flights were in April 1994 and December 1994. Comparison was made by ratioing the apparent resistivity maps for different frequencies for the different dates, and two things showed up: 1) there appeared to be a seaward movement of the saltwater front on some of the maps, and 2) a small bay which is hypersaline in the dry season showed a marked decrease in apparent resistivity in the wet season flight (D. Fitterman *pers comm*. May 2009). Repeat AEM surveys were flagged as a means of assessing long term changes in the aquifer system resulting from changes in water management policies aimed at restoring the South Florida ecosystem (Fitterman and Deszcz-Pan 1998).

In the second study described by Beamish and Mattsson (2003), the aim was to examine the performance that might be expected of AEM methods in relation to the long-term monitoring of large, active, contain and seal landfills. They considered repeat AEM survey data obtained from a fixed-wing frequency domain airborne electromagnetic system across a landfill structure located near Helsinki, Finland. The time interval between the surveys was 4 years. They studied single frequency (3.1 kHz) data obtained at a similar flight line spacing (100 m) over the 4 year span to ascertain whether detectable effects associated with mass (leachate) transport behaviour could be defined. The single frequency data were inverted to yield half-space conductivity models with the resulting data expected to have a mean depth of investigation of about 15 m within the landfill. Conductivities within the landfill are observed to be three orders of magnitude above background. In the initial survey data, a specific distribution of high conductivity material was identified in three of the landfill cells, and four years later, a considerable redistribution of material was observed in the results obtained across two of the three cells. They subtracted the two time-lapse conductivity models to define the dynamic components of the conductivity distribution (expressed as an increase in time) to be mapped within individual landfill cells.

However, among the significant issues identified in these early studies were problems of calibration and the difficulty of being able examine variability as a function of changing depth, that is changes associated with vertical conductivity structure, given that comparisons were made between inversions of single frequencies. We believe relatively advent of digital broadband airborne EM systems, combined with the development of procedures for their calibration (eg. Deszcz-Pan et al 1998, Brodie et al. 2004, Lane et al. 2004, Ley-Cooper et al. 2006, Davis and Macnae 2007) and correcting for system geometry (eg. Fitterman and Yin 2004, Yin and Fraser 2004, Davis et al 2006), along with more robust and flexible inversion procedures (eg. Brodie and Sambridge 2006), now provides the basis for realizing the potential of AEM in the spatio-temporal monitoring of dynamic landscapes. We see value in employing these techniques particularly those where lateral and vertical changes in subsurface character are critical to an understanding of surface water- groundwater processes and in monitoring the consequences of particular management actions.

In this paper we describe a methodology, employing multi-date AEM data sets, for defining spatio-temporal variations in ground conductivity that represent the consequence of naturally induced changes and/or those arising from specific management practices. Results from a case study which was aimed at mapping relatively fine-scale spatio-temporal changes in ground conductivity occurring across a salinised floodplain system in the Lower Murray Basin in South Australia are discussed.

Environmental Issues and Rationale for Geophysical Data

Salinisation is a major economic and environmental concern in Australia affecting Australia's most significant river, the Murray River and the sectors of agriculture, industry and recreation that it supports. It is estimated that some 40,000ha (40%) of floodplain vegetation on the lower River Murray in South Australia is now dead, dying or stressed. This severe dieback in native floodplain vegetation is largely due to floodplain salinisation, a result of saline regional groundwater discharge, decreased natural flood frequencies, permanently held weir (river) levels and a severe current drought (Overton and Jolly 2004). . In order to manage the problem and to protect the ecology and biodiversity along the river, a range of management strategies are being employed including the development of salt interception schemes (SIS), the management of environmental flows and improved land management practices. However, whilst a range of tools are being deployed for management purposes, there is an accompanying need to acquire biophysical data that permit these tools and their outputs to be calibrated and validated. Geophysical, particularly electrical, methods have the potential to provide detailed spatio-

temporal information on the distribution of salinity in soils and groundwater, thereby indicating spatial patterns of groundwater evapotranspiration and baseflow across salinising floodplains that characterize the lower River Murray. Therefore they have considerable potential to inform management and its consequences.

Study Area

This trial study was focused on a small floodplain - the Bookpurnong floodplain located adjacent to the Bookpurnong Irrigation District on the Murray River in the Riverland region of South Australia (Figure. 1). This floodplain represents a suitable study site for pilot investigations from which outcomes will feed into the management and planning of larger stretches of the Murray River floodplains. It is conveniently located and has existing power, and a currently operational groundwater salt interception scheme.

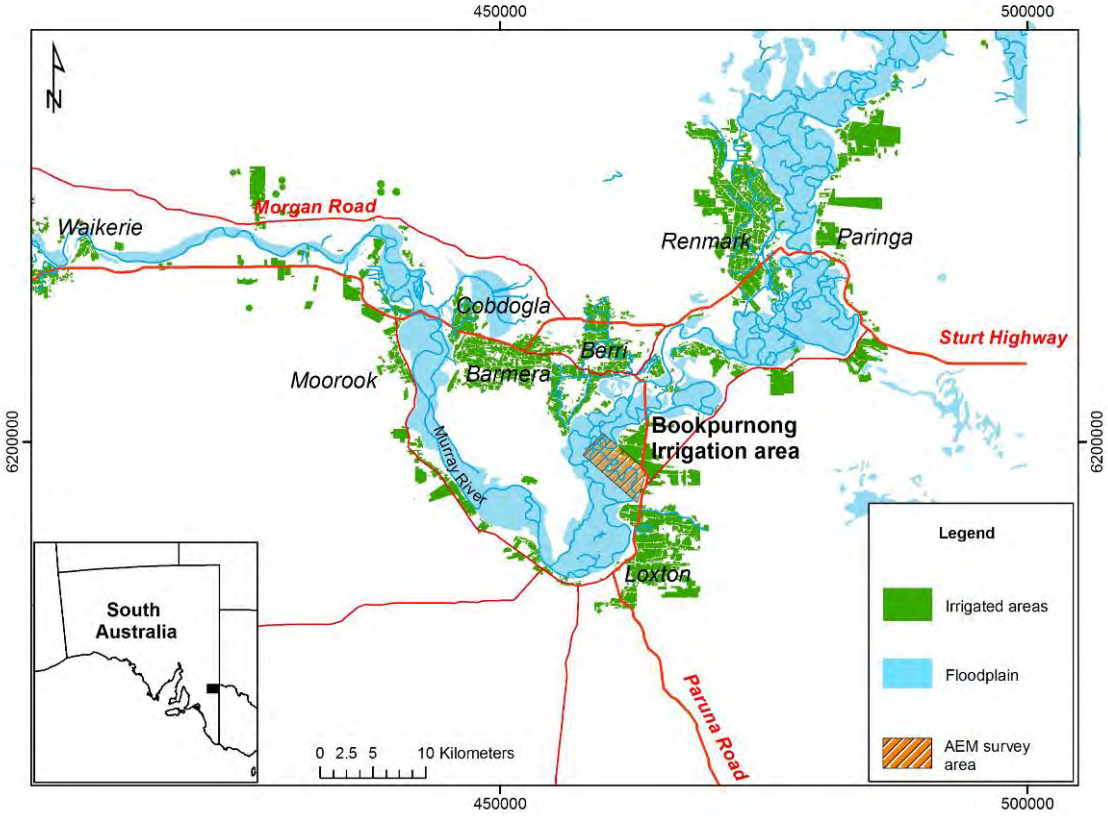

Figure 1: Bookpurnong floodplain trail study area in the Riverland of South Australia

Bookpurnong floodplain area and hydrogeology

The study area has a hydrogeology characteristic of the eastern part of the lower Murray River (see Figure 2). Floodplain sediments consist of a clay (the Coonambidgal Clay) ranging from 3 to 7 m thick, overlying a sand (the Monoman Formation) which is approximately 7-10m thick in this area. These sediments occupy the Murray Trench which cuts into a sequence of Pliocene sands (the Loxton-Parilla Sands) up to 35m thick

These sands outcrop in the adjacent cliffs, and are covered by a layer of Woorinen Sands over Blanchetown Clay, each approximately 2 m thick (Figure 2). The whole area is underlain by the Bookpurnong Beds, which act as an aquitard basement to the shallow aquifer that encompasses the Monoman Formation and Loxton Sands. Regional groundwater salinity in the Loxton Sands and

Monoman Formation ranges between 30 and 40 000 mg/L, with the high salinities commonly found on the floodplain resulting from evaporative concentration. Irrigation recharge salinity is typically 1 000-3 000 mg/L. Excess recharge from the Bookpurnong Irrigation District has led to the formation of a groundwater mound, which displaces saline groundwater towards the floodplain and has led to increased waterlogging and salinisation on the floodplain, and groundwater seepage at the break of slope adjacent to the cliffs. Black box (Eucalyptus largiflorens) and red gum (E. camaldulensis) tree communities have been most affected by the salinisation of the floodplain. There is considerable variation of evapotranspiration and seepage depending on distribution of soils, vegetation type, floodplain elevation and geometry.

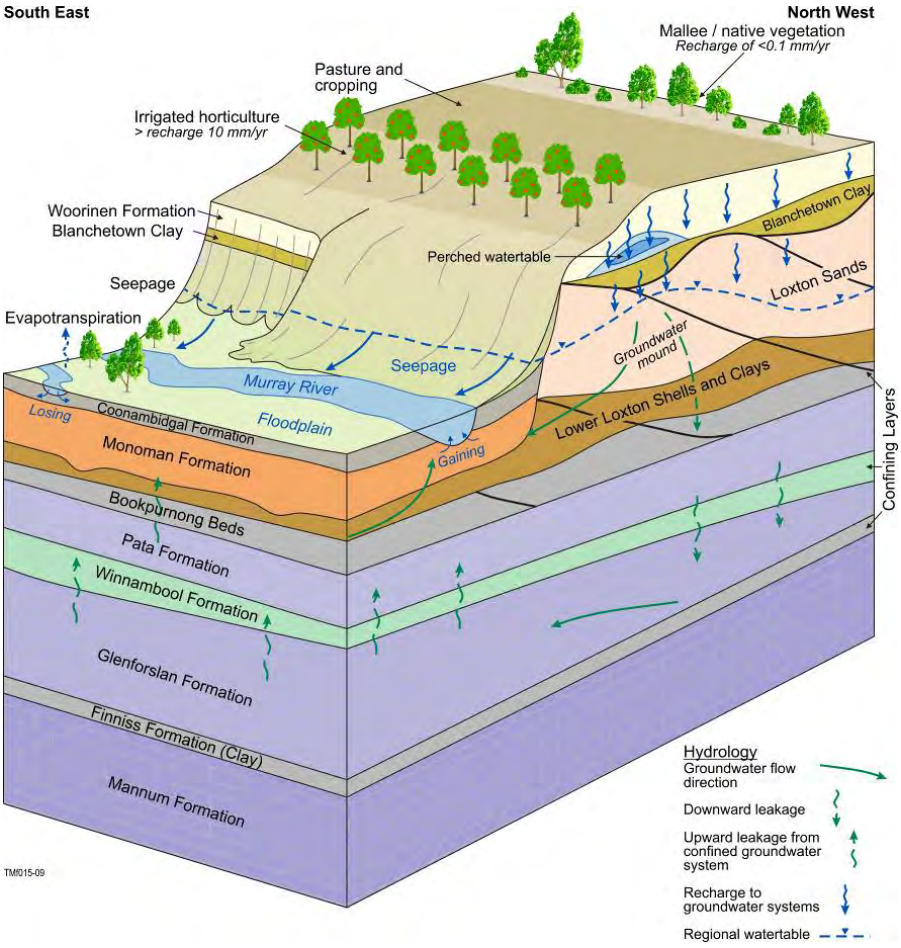

Figure 2: Schematic hydrogeological model of the Bookpurnong floodplain and adjacent highland areas. High recharge from irrigation on the highlands adjacent to the floodplain results in the development of localized perching and the formation of a groundwater mound in the Loxton-Parilla sands. The mound increases the hydraulic gradient towards the floodplain causing a rise in water levels in the floodplain sediments. Groundwater seepage at the break of slope adjacent to the cliffs occurs locally. High water levels coupled with high rates of evapotranspiration, concentrates salt in the near surface across the floodplain. Elevated water levels also promote the discharge of saline groundwater into the Murray River, along "gaining" stretches of the river system.

Geophysical Methods

AEM system

This study involved a comparison of data acquired on two dates using the RESOLVE frequency domain helicopter electromagnetic (HEM) system, operated by Fugro Airborne Surveys. The RESOLVE is a six frequency EM system that makes use of transmitter and receiver coils housed in a torpedo-shaped tube made of Kevlar called a "Bird" that is towed beneath a helicopter. The bird is approximately

9 m long and is slung 30 m below the helicopter. During surveying, the bird is flown ~30 m above the land surface. Using six different frequency-coil-pair combinations, the electromagnetic response is measured as a function of frequency. Data are acquired about every 3 - 5m along flight lines.

Details of the RESOLVE HEM system frequencies used in the Bookpurnong surveys are summarised in Table 1. The very high frequencies arguably help detect very near surface conductors as might be represented by the clay-rich near-surface materials found in floodplains. The lower frequencies increase the depth of investigation and will provide information on the groundwater quality. The RESOLVE is a fully digital frequency domain EM system with internal calibration coils for automatic phase and gain calibration in the air (Garrie, 2005).

Table 2. Summary of RESOLVE coil sets and nominal frequencies used in the Bookpurnong surveys

Nominal Frequency (Hz) 2005 Survey	Nominal Frequency (Hz) 2008 Survey	Separation (m)	Orientation
390	382	7.91	HCP
1798	1,822	7.91	HCP
3242	3,258	8.99	VCX
8177	7,970	7.91	HCP
39470	35,920	7.91	HCP
132700	130,100	7.91	HCP

Note: HCP = Horizontal coplanar; VCX = Vertical coaxial

AEM data acquisition

Bookpurnong area was surveyed fist in July 2005 and then again in August 2008 with the Fugro RESOLVE frequency domain helicopter EM system. The 26 and 24 lines of data, orientated NW-SE, were acquired in July 2005 and August 2008 respectively, with a line spacing of ~100m (Figure 3).

Calibration of the AEM data

At the time of the Bookpurnong surveys in 2005 and 2008, RESOLVE surveys were being undertaken over other parts of the floodplain in the Riverland. Inductive conductivity data from boreholes located in these adjacent areas were used to calibrate the RESOLVE data for the Bookpurnong flights. The calibration procedure followed the methodology described by Brodie et al. (2004). Specifically, the down-hole conductivity information was averaged over 1m intervals and the resulting layered earth model was used, with the observed bird altitude, as input to an EM forward modelling procedure to estimate the expected airborne response.

The forward models were calculated using a layered earth forward modelling routine based on the formulation of Wait (1982) for the frequency domain response of vertical and horizontal magnetic dipole sources over a horizontally layered medium. Evaluation of the Hankel transforms was achieved via the filter coefficients derived by Guptasarma and Singh (1997). Deszcz-Pan *et al*. (1988) discuss methods for calibrating FDHEM data. They suggest that the observed data is the result of multiple gain and offset distortions of the true data represented by the response predicted by the forward modelling. For the observed In-phase and Quadrature data, X_i and X_q with complex representation $X= X_i + jX_q$ and modelled data $M= M_i + jM_q$ then

$$X = Ge^{j\phi}(M + B)$$

Here $Ge^{j\phi}$ (the amplitude scaling factor) is a complex gain and phase correction and $B= B_i + jB_q$ is a complex bias correction. In their formulation ϕ, B_i *and* B_q change on a per-flight basis while G is constant for the whole survey. In this work we only attempted to correct for the amplitude-scaling factor.

Further correction on a flight-by-flight basis was deemed both unnecessary and difficult to achieve. Forward models from the borehole conductivity data, deemed "truth" for the purposes of this exercise, were compared to the observed HEM responses for surveys in areas adjacent to Bookpurnong. The response for each frequency was examined in order to calculate appropriate scaling coefficients, and these were then applied to the two Bookpurnong data sets. These coefficients are summarized in Table 2. The subsequent scaled data were used as input into the inversion modeling.

.

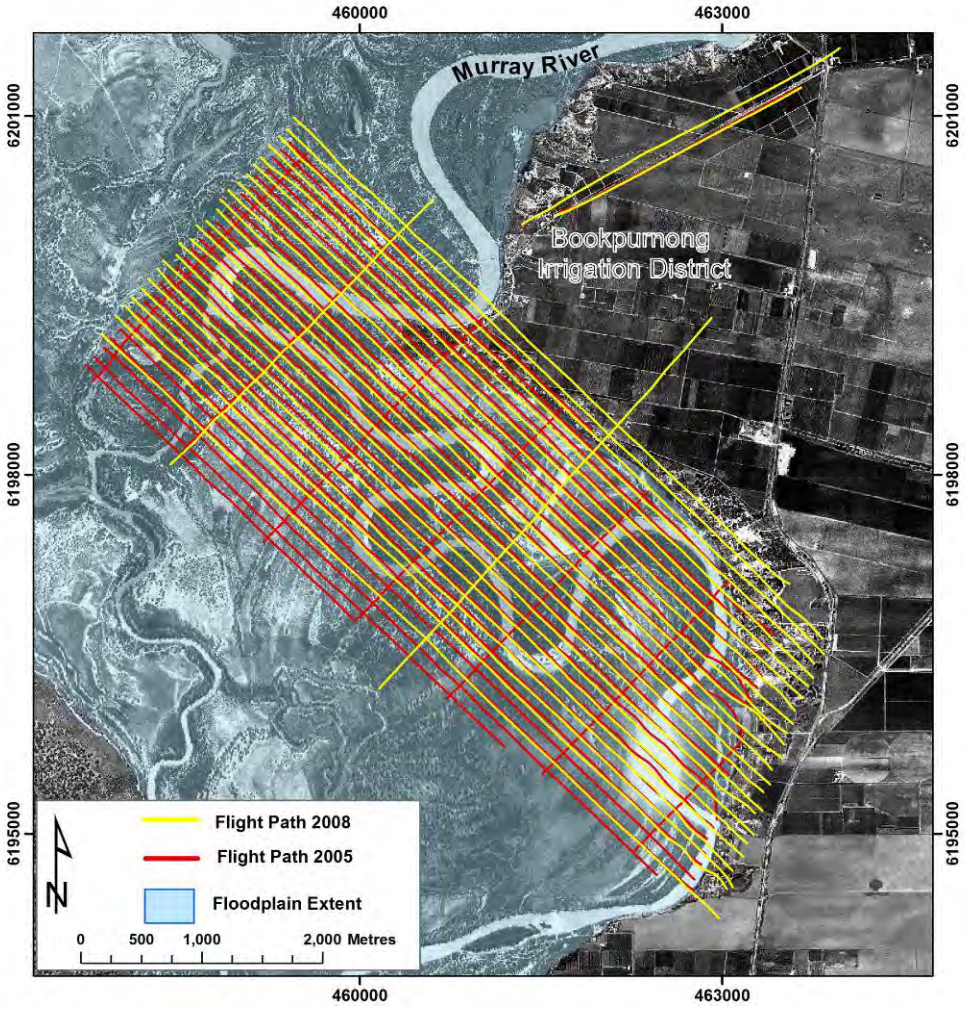

Figure 3: Detail of the Bookpurnong loodplain study site in the South Australian Riverland of the Lower Murray Basin. The surveyed lines for two RESOLVE FDHEM surveys (2005 in red and 2008 in yellow) are shown. The survey area covers most of the Bookpurning floodplain and some parts of the adjacent highlands where irrigated agriculture has been developed.

Table 2: Scaling coefficients applied to the 2005 and 2008 FDHEM data for Bookpurnong.

	2005 Survey		2008 Survey	
Nominal Frequency	**Gain**	**Phase**	**Gain**	**Phase**
390	1.05	-2.47	1.06	-8.52
1800	1.07	-0.42	1.11	-2.36
3300	0.97	1.13	1.16	-0.53
8200	1.06	-0.62	1.35	-0.32
40K	1.12	-1.38	1.35	-0.56
140K	1.11	-1.46	1.22	-0.46

Inversion Procedure

The conductivity models generated from the RESOLVE data for the two surveys employed the holistic inversion algorithm developed by Brodie and Sambridge (2006, 2009). This method simultaneously calibrates, processes, and inverts frequency-domain airborne electromagnetic data, permitting the recovery of a spline-based, 3D, layered conductivity model covering the complete survey area. The holistic inversion formulation includes a mathematical model to account for systematic calibration errors such as incorrect gain and zero level drift. Previous studies have demonstrated that the holistic inversion method yields accurate estimates of ground conductivity often superior to the output of more conventional 1D LEI inversion of final processed data (Brodie and Sambridge 2006). The holistic model consisted of 18 layers with a starting conductivity of 500 mS/m. An example of the interval conductivity for one layer, for both dates, is shown in Figure 4.

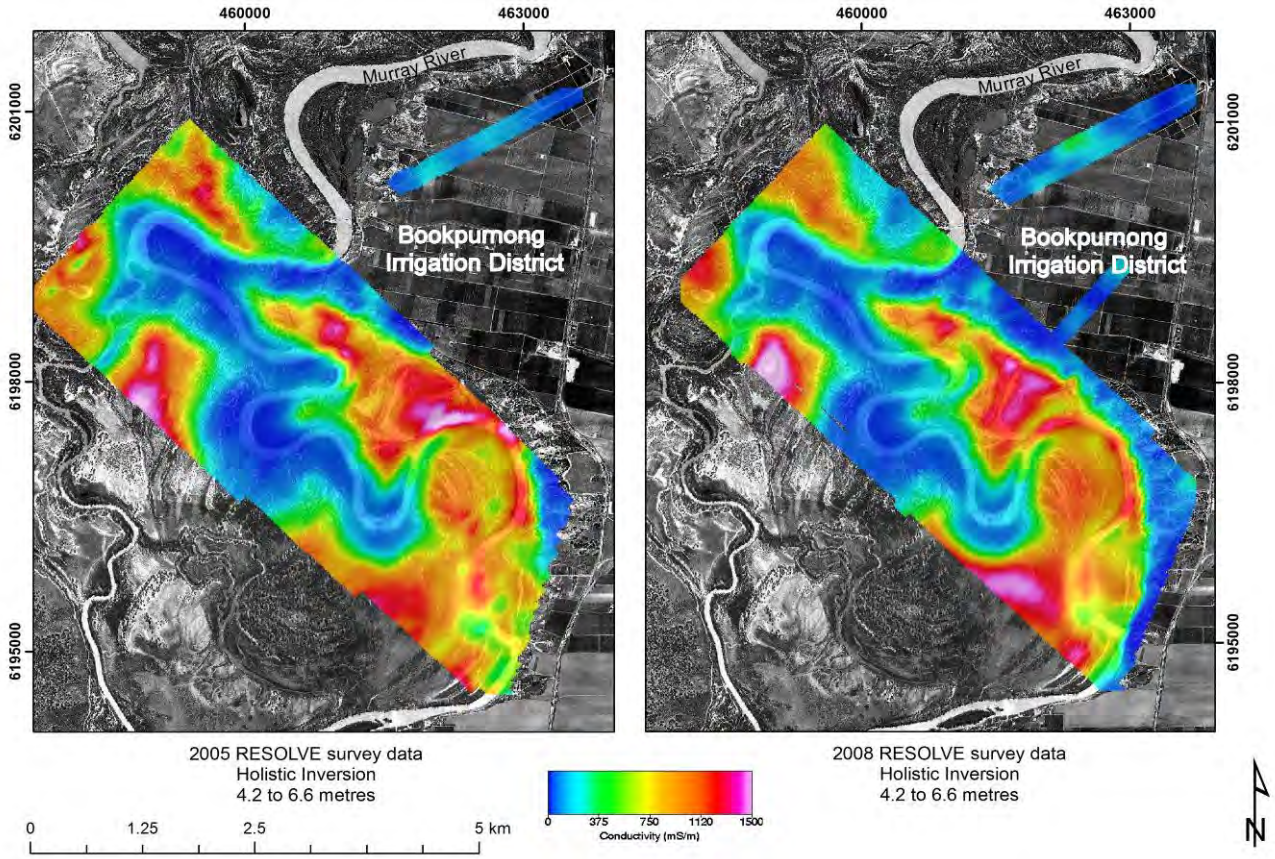

Figure 4: Conductivity for 4.2 – 6.6m depth interval for the 2005 and 2008 surveys derived from a Holistic inversion

Investigation depth

Key to a comparison of multi-date AEM data and derived information at depth is to ensure that the observed variations in measured conductivity reflect changing ground conditions (ie the data) rather than model driven changes arising from artefacts of the inversion process, specifically the *a priori* constraints used in the parameterisation of the inversion model. This issue has been addressed by Oldenburg and Li (1999) in the context of DC resistivity and IP inversion by performing two inversions with different reference or *a priori* values for each model parameter. They defined a depth-of-investigation (DOI) parameter as the ratio of the difference in each model parameter to the difference in

the reference values for that parameter between the two inversions. Lane et al (2004) developed this concept further with AEM data and defined a "percent data influence" (PDI) parameter based on results for two closely related inversions. In this study, PDI solutions proved problematic with the RESOLVE data sets over Bookpurnong, which we attributed to the high spatial variability and magnitude of conductivity. As an alternative we adopted a simpler approach and assumed that the total conductance limit of the RESOLVE was a conservative 3 Siemens. This was based on observations made with several test lines flown over the ocean. We then calculated where this depth occurred in the conductivity model for both dates. This allowed us to generate a crude estimate of the depth of investigation for the two survey dates and provide a basis for comparing the results of changes in ground conductivity between the dates both laterally and spatially, for what we term *the common investigation volume* (defined as the same subsurface area observed in both dates below the 3 Siemens limit). The average depth of investigation over the highly saline floodplains was limited to around 5m, whereas over the river it was significantly greater (see Figure 5).

Results

We present differences in the ground conductivity between the two dates, as maps of changes for a given depth below the ground surface in Figure 6. Two depth intervals are defined in this example, with the spatial differences or changes in ground conductivity for these depths represented as either reds (gains or increases in conductivity) or blues (a decrease, or reduction in conductivity). Areas of no change are represented as white. These differences can also be defined in 3D (not shown). Spatially coherent patterns associated with an increase in ground conductivity are apparent on the floodplains adjacent to the river. However there are also parts of the landscape where noticeable reductions in ground conductivity are apparent. Further work is required to determine the causal mechanisms for these observed differences, but in some areas they may reflect the influence of the Salt Interception Scheme operating on the floodplain adjacent to the Bookpurnong Irrigation District. We have also shown the influence of the depth of investigation on each depth interval by decreasing the intensity (by 70%) of the colour displayed. This gives the interpreter greater confidence in ascribing observed changes to real changes or those that might be linked to artifacts relating to system geometry, poor calibration, or data interpretation methods.

Conclusions

We have demonstrated an effective procedure for defining spatio-temporal variations in ground conductivity across a salinized floodplain using FDHEM data. Lateral *and* vertical changes in the conductivity of the floodplain have been resolved. We believe the advent of improved calibration procedures, geometry correction, calibrated broad-band AEM systems and advanced inversion methods that obviate the necessity of system calibration – recalibration, provide for the realistic proposition of using AEM data in the semi-quantitative and quantitative monitoring of landscape change.

These changes can be mapped in the subsurface, whether naturally induced or arising as a consequence of a particular management strategy. Nevertheless, we emphasize the need for caution when considering the observed spatial variations, stressing the importance of understanding and accounting for system investigation depth and the potential for artifacts that might be introduced from noise, system geometry and/or data interpretation procedures. These issues should always be borne in mind when comparing data and derived conductivity models from different dates.

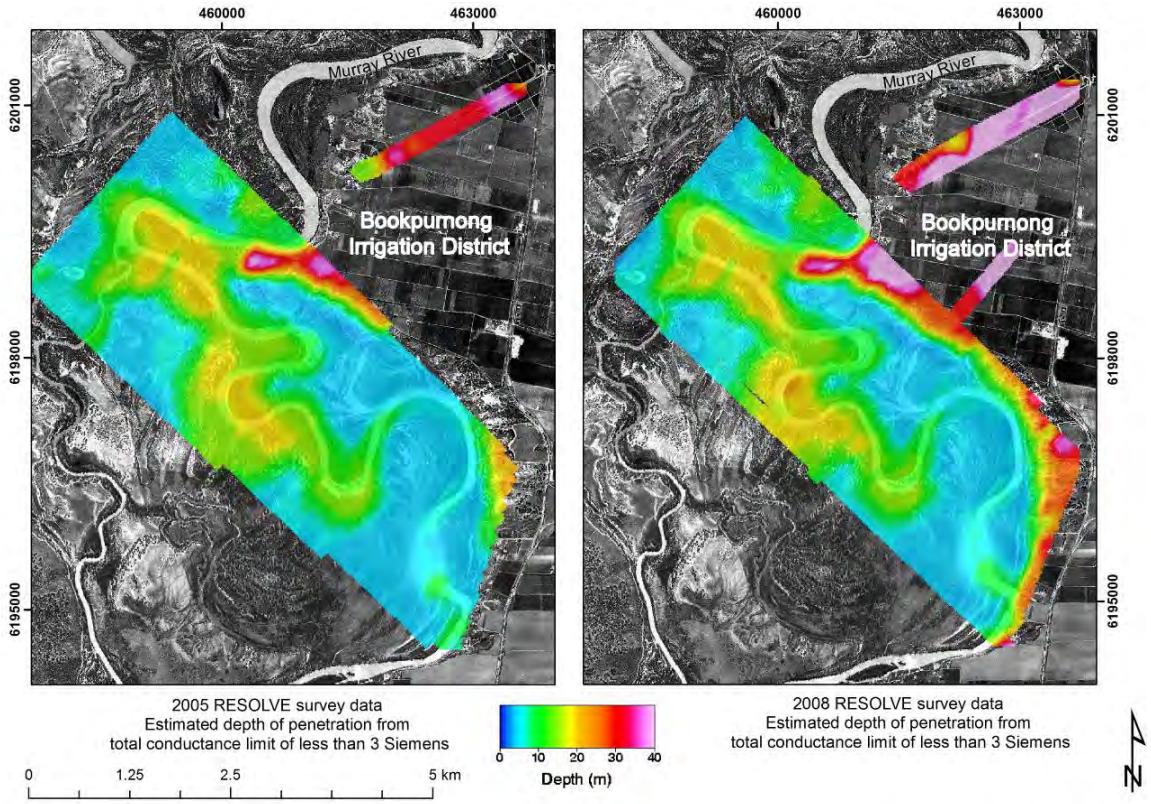

Figure 5: Estimated depth of penetration for the 2005 (left) and 2008 (right) surveys.

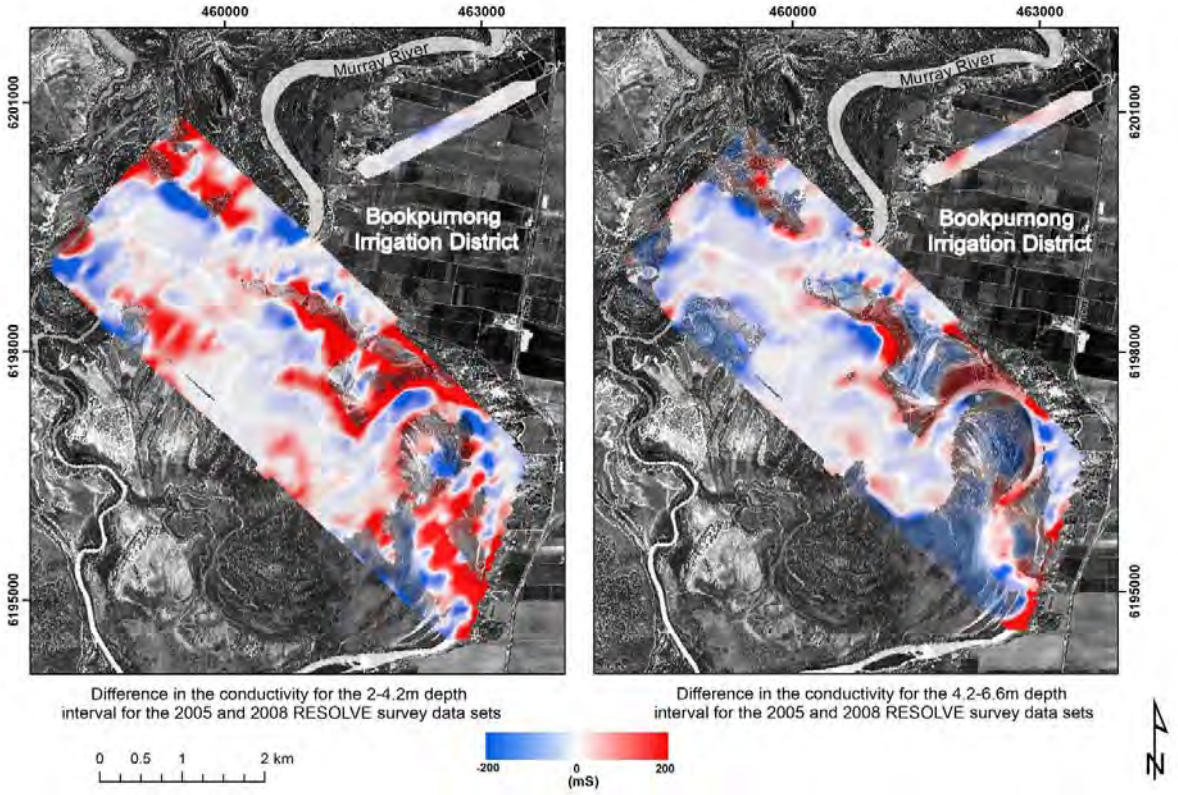

Figure 6: Differences in ground conductivity observed between 2005 and 2008 RESOLVE FDHEM surveys as a function of depth.

References

Brodie, R.C., Green, A.A., and Munday, T.J., (2004), Calibration of RESOLVE airborne electromagnetic data – Riverland and East Tintinara, South Australia: Cooperative Research Centre for Landscapes, Environment and Mineral Exploration, Open file report 173.

Brodie, R.C., and Sambridge, M., (2006), A holistic approach to inversion of frequency-domain airborne EM data, Geophysics, v. 71(6), 301-312

Brodie, R.C. and Sambridge, M., (2009), Holistic inversion of frequency-domain airborne electromagnetic data with minimal prior information. Exploration Geophysics, 2009, 40, 8–16

Beamish, D. and Mattsson, A., (2003), Time-lapse airborne EM Surveys across a municipal landfill. JEEG, 8(3), 157-165.

Davis, A.C., Macnae, J and Robb, T, (2006), Pendulum motion in airborne HEM systems, Exploration Geophysics (2006) 37, 355-362

Davis, A.C., and J. Macnae, (2007), Calibration of time domain AEM systems using aground loop: Extended Abstract, ASEG 2007, Perth, Australia.

Deszcz-Pan, M., Fitterman, D.V., and Labson, V.F., (1998), Reduction of inversion errors in helicopter EM data using auxiliary information, Exploration Geophysics, v. 29, p. 142-146.

Fitterman, D.V. and Deszcz-Pan, M.,(1998), Helicopter EM mapping of saltwater intrusion in Everglades National Park, Florida, Exploration Geophysics, 29, 240-243.

Fitterman, D.V., and Yin, C., (2004), Effect of bird manoeuvre on frequency-domain helicopter EM response: Geophysics, 69, 1203-1215.

Fitterman, D.V., Fennema, R.J., Fraser, D.C. and Labson, V.F., (1995), Airborne electromagnetic resistivity mapping in the Everglades National park, Florida: SAGEEP'95, Florida, 657-670.

Garrie, D., (2005), RESOLVE Survey for CSIRO Exploration and Mining, Southern Australia. Fugro Airborne Surveys Report No. 05050.

Guptasarma, D., and Singh, B., (1997), New digital linear filters for Hankel J0 and J1 transforms, Geophysical Prospecting, 45, 745-762.

Ley-Cooper, Y., Macnae, J., Robb, T., and Vrbancich, J., (2006), Identification of calibration errors in helicopter electromagnetic (HEM) data through transform to the altitude-corrected phase-amplitude domain: Geophysics, 71, G27-G34.

Lane, R., Brodie, R.C. and Fitzpatrick, A. (2004), Constrained inversion of AEM data from the Lower Balonne area, Southern Queensland, Australia. CRC LEME Open File Report 163, 140pp.

Oldenburg, D.W., and Li, Y., (1999), Estimating depth of investigation in DC resistivity and IP surveys: Geophysics, 64, 403-416.

Overton, I., and Jolly, I., (2004), Integrated studies of floodplain vegetation health, saline groundwater & flooding on the Chowilla floodplain South Australia. CSIRO L&W Tech. Rept: 20/04, 169pp.

Yin, C., and Fraser, D.C., (2004), Attitude corrections of helicopter EM data using a superposed dipole model: Geophysics, 69, 431-439.

Wait, J.R. (1982), Geo-Electromagnetism. Academic Press, New York.

REDEFINING THE GROUNDWATER RESOURCE OF THE EYRE PENINSULA, SOUTH AUSTRALIA USING AEM DATA

Andrew Fitzpatrick, CSIRO, Perth, Australia
Tim Munday, CSIRO, Perth, Australia
Kevin Cahill, CSIRO, Perth, Australia
Volmer Berens, DWLBC, Adelaide, Australia

Abstract

The groundwater aquifer lens systems of the lower Eyre Peninsula are an important water supply source for Eyre Peninsula. Demand from the aquifers is near the current extraction limits and there is a need to undertake further modelling of the groundwater systems to ensure confidence in the limits determined. This paper describes the use of airborne electromagnetics to map important elements of the Quaternary and Tertiary aquifer systems in the area. TEMPEST time domain EM data were acquired over the known extent of groundwater lens systems. These data were inverted using both constrained and unconstrained techniques to define the conductivity structure in three dimensions. Hydrogeologically significant bounding surfaces were then defined, through the use of a line-by-line interpretation procedure to link borehole data with the observed ground conductivity structure.

Introduction

Groundwater in the Eyre Peninsula of South Australia is scarce with potable resources limited to the western coastal margin and the southern tip of the peninsula as a consequence of slightly elevated rainfall and a suitable host rock (a Quaternary limestone) which can recharge rapidly (Evans, 2002). These groundwater resources are often referred to as lenses and are defined by the 1000mg/L isohaline contour within the saturated zone of the unconfined Quaternary limestone aquifer.

In the last 30 years, the Uley South and Coffin Bay A lenses (Figure 1) have assumed particular significance as sources of reticulated public water supply. Consequently an understanding of their extent has become particularly important. Whilst it is known that the Coffin Bay A lens extends under the Coffin Bay National Park, land access for drilling has been limited. While an application to drill several test holes has been lodged with the National Parks and Wildlife Service a decision was also made to investigate the use of airborne geophysics as a non-intrusive method of assessing aquifer extent. This followed some encouraging results from a series of ground electromagnetic surveys which suggested that important elements of the Quaternary and Tertiary aquifer systems could be resolved by electrical methods (see Clarke et al. 2003), thereby suggesting that airborne electromagnetics (AEM) might have value in doing the same.

In September 2006, an airborne EM survey was undertaken with the TEMPEST AEM system across the Coffin Bay and Uley South areas in the lower Eyre Peninsula. Preliminary results from an initial analysis and interpretation of these data were reported by Fitzpatrick and Munday (2007). They recommended integration with available bore data, regional airborne magnetics and ground observations to better define the geometry of specific bounding surfaces of hydrogeological relevance. Although airborne geophysical data have the potential to assist in delivering hydrogeological information, they

usually require careful constrained interpretation, particularly to deliver targeted information on aquifer bounds and characteristics.

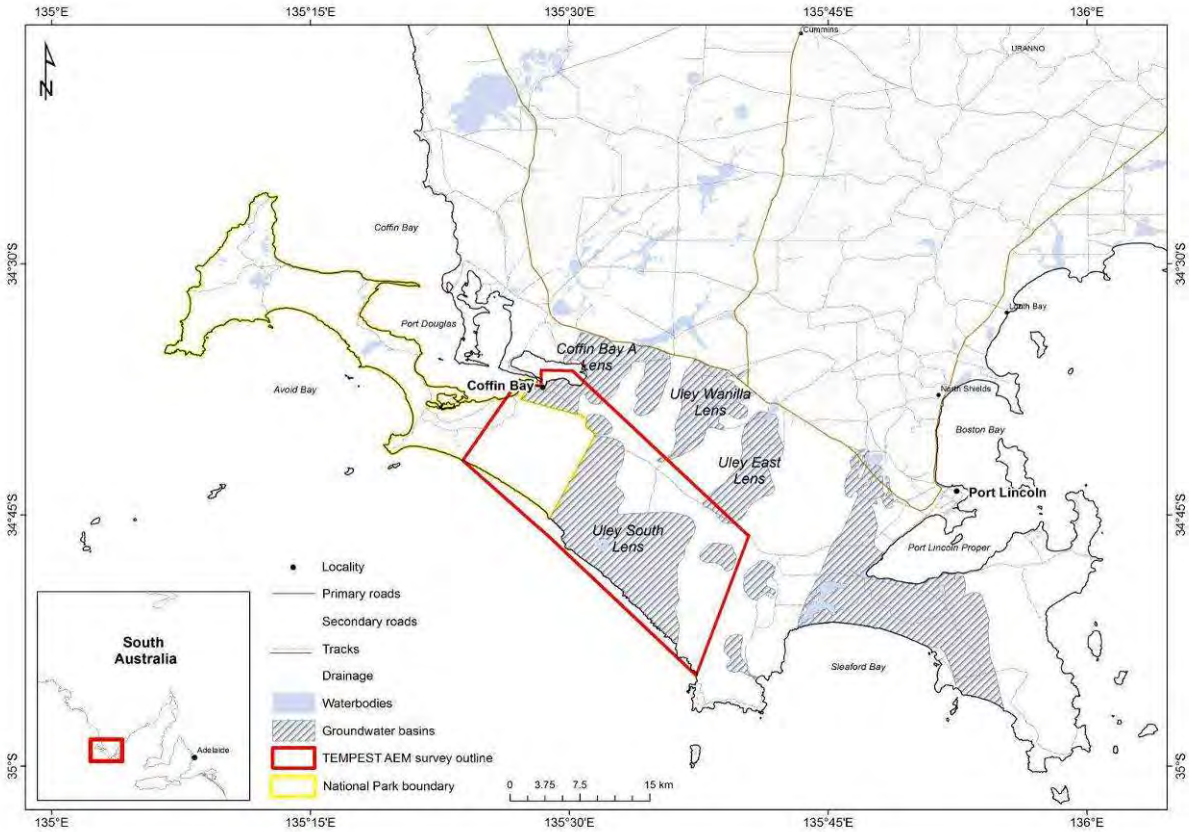

Figure 1: Map showing the location of the study area, and the known extent of the groundwater lens systems of the Southern Basins on the Eyre Peninsula. The area surveyed by the TEMPEST AEM system is also defined. (Data courtesy of SA Water and DWLBC).

Geology

The groundwater resources in the Southern Eyre Peninsula occur predominantly within three different aquifer systems (Figure 2), namely the Quaternary Bridgewater Formation- a limestone unit, the underlying Tertiary sand aquifers (Uley and Wanilla Formations) and a fractured, locally weathered, basement aquifer in volcano-sedimentary rocks (Evans 2002). The main groundwater resource lies within the limestone of the Bridgewater Formation. The basement forms a topographically undulating surface, featuring a series of north-south trending ridges and troughs that reflect differences in lithotype. In the regional airborne magnetics these differences are manifest as marked changes in magnetic intensity orientated in a north-south direction.

Available borehole data indicates that the Quaternary formation and the underlying Tertiary sediments thin over the basement highs and thicken in the adjacent troughs or basins. The consequence is a marked litho-structural control on the distribution and thickness of the important Quaternary limestone aquifer (Evans 2002). There are three main groundwater "lenses" associated with this aquifer, which are characterised by high yields and low salinity (<1000mg/L). They occur in a series of sub-

basins known as the Coffin Bay, Uley and Lincoln Basins, and are separated by local topographic highs coincident with basement highs.

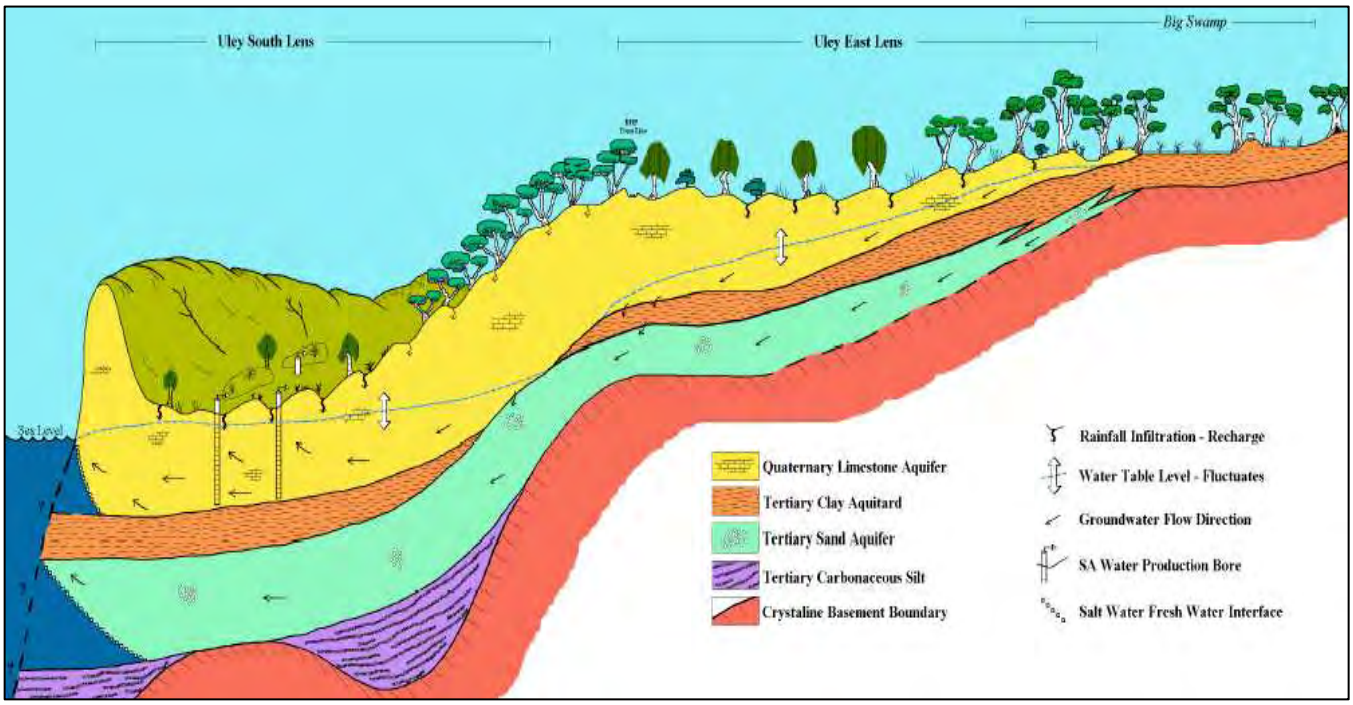

Figure 2: Schematic geological cross section of the Uley Basin (Source Evans 2002).

Methodology

The Coffin Bay airborne electromagnetic survey was conducted with the TEMPEST fixed-wing, towed-bird time domain electromagnetic system. A total of 1016 line km of data were acquired on 11 flights across the area. Lines were orientated 140 – 320 degrees true, with line spacing of 400 metres (Figure 8). Sampling was at 0.2 seconds, equating to an along-line spacing of 15 metres.

A number of conductivity models were generated using a 1D Layered Earth constrained inversion algorithm (for descriptions of methodology, see Lane et al., 2004) that solves for ground conductivity and variable geometry of the system by jointly inverting both X and Z component data. The constrained inversion uses a priori information (i.e. constraints) about the conductivity-depth distribution and by solving for the geometry of the AEM system allows a solution to converge when inverting both X- and Z-component data simultaneously. By solving for the geometry in the inversion, more accurate conductivity predictions in the near surface are obtained (Lane et al., 2004).

Two types of conductivity modelling were tested on the Coffin Bay data, a smooth multi-layer model and a blocky model. An examination of the available borehole conductivity data suggested that the Coffin Bay data set could be modelled using a 3-4 blocky-layer model, with layer 1 representing the Quaternary Bridgewater Formation, layer 2 representing Tertiary Uley and Wanilla Formations , layer 3, the weathering zone (i.e. weathered basement) and layer 4 representing resistive basement. A 3-layer model was also tested, which assumed that Tertiary layers and weathering layer were the same (i.e. the

layers were combined). Unfortunately as the conductivity properties for the different aquifers were not distinct from one another the blocky models failed to adequately define aquifer bounds across the whole survey area. Several iterations were tested but there were large differences between the models, providing limited confidence in the results and interpreted hydrogeological bounding surfaces. In some places the blocky-layer model boundaries matched particular aquifer bounds defined from drilling, but the results weren't consistent across the whole survey area.

We therefore adopted a different approach to the interpretation of the AEM data, which incorporated results from the smooth-layer conductivity model and a detailed line-by-line (section-by-section) analysis of the conductivity data against the available borehole stratigraphy and geophysics. This strategy permitted a more considered interpolation of hydrostratigraphic boundaries and a better definition of the extent of saline groundwater zones through the area.

Interpretation

The interpretation of a derived conductivity model is commonly performed by examining plan or section form images, and in some cases in 3D using visualisation software. Usually it is based on associating conductivity patterns with particular geological features. Given that the conductivity of sediments is largely driven by conduction through pore water, it follows that conductivity is primarily controlled by a combination of the rock porosity and the properties of the groundwater (i.e. water quality). Commonly, the only other significant contributor to conductivity is related to the abundance of clay minerals. In the Coffin Bay area, it was expected that the saturated Quaternary and Tertiary sediments would be more conductive than the resistive basement. Weathered basement was also expected to be more conductive than crystalline basement due to an increase in porosity and development of weathering clays, but as stated previously this "in situ" regolith may not be differentiable from the overlying Quaternary and Tertiary sediments. Areas of saline groundwater (i.e. seawater salinity) are relatively easy to identify as they are highly conductive. However in these areas differentiating hydrostratigraphic boundaries within these highly conductivity areas were extremely difficult and were simply non-defined. Where the observed conductivity structure was complex and/or potentially ambiguous, we used the available borehole hydrostratigraphic logs to reduce that ambiguity. This gave confidence to the derived interpretation particularly where bore density was high. The relationships between conductivity and hydrostratigraphy, as defined in these areas, were extrapolated to other areas where bore density was limited.

Analysis of the conductivity model in 3D provided the basis for better understanding the geometry of the aquifer systems against the inferred bounds of the groundwater lens systems, and mapped groundwater levels. It also provides a basis for examining the AEM derived aquifer bounds against available bore data. A 3D image of the surface topography is shown in (Figure 3) to provide an overview of the contemporary landscape. The interpreted base of the Quaternary limestone aquifer (Bridgewater Formation) derived from the AEM data set is presented in Figure 4. The base of the Quaternary aquifer shows a predominant low within the current groundwater extraction bore network of the Uley South Lens as expected. However another depression is located to the northeast underneath the National Park which appears to be connected to the southern lens (through a gap in a basement ridge). The interpreted base of the Tertiary aquifer derived from the AEM data set is presented in Figure 5. The base of the Tertiary aquifer features a series of north-south trending ridges and troughs. These features

are coincident with features observed in the regional airborne magnetic datasets reflecting the magnetic basement immediately underlying the Tertiary sequence. By using a combination of the DEM, and interpreted geological surfaces, the thickness of the Quaternary and Tertiary sequences can be calculated. These products can be incorporated into future groundwater models of the area.

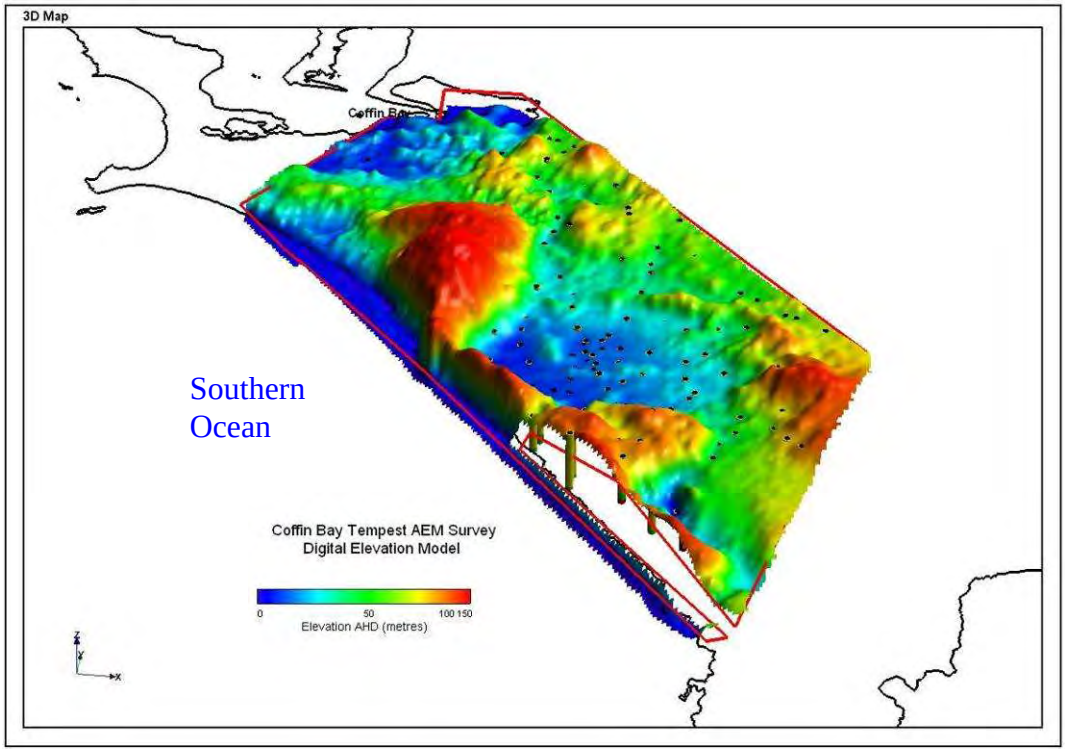

Figure 3: 3D perspective representation of the digital elevation model for the Coffin Bay AEM survey area. Black circles indicate groundwater monitoring bore network. View is approximately looking north.

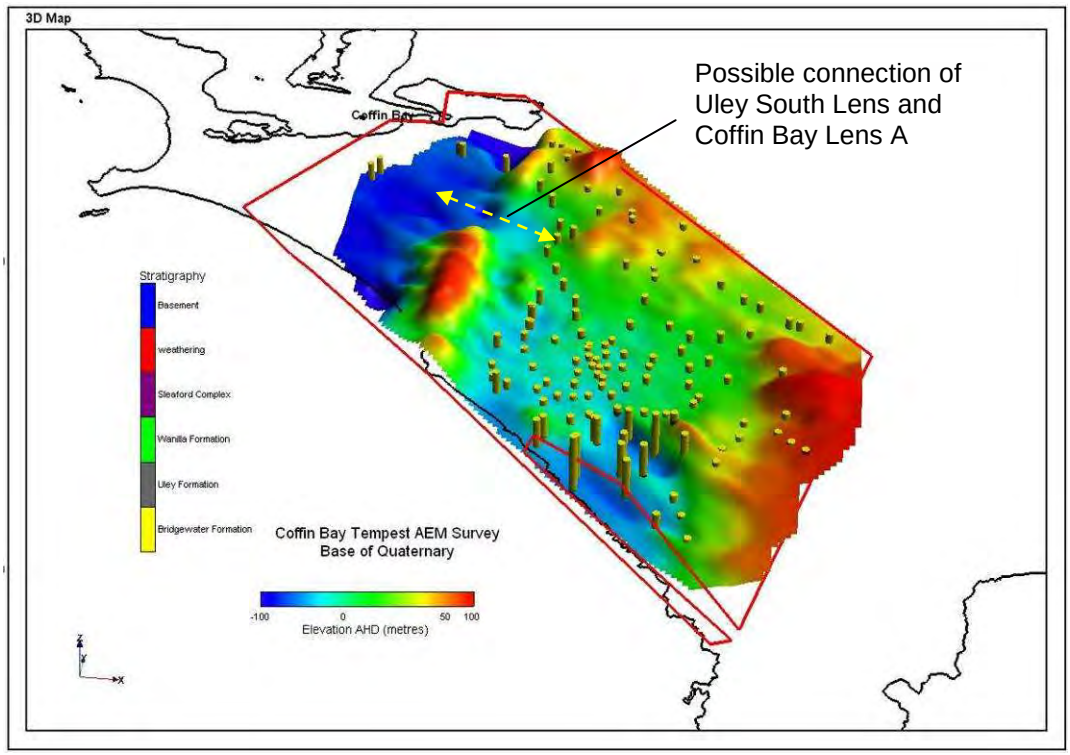

Figure 4: 3D perspective representation of elevation of the base of the Quaternary Bridgewater Formation. Vertical cylinders show the logged hydrostratigraphy for existing boreholes. View is approximately looking north.

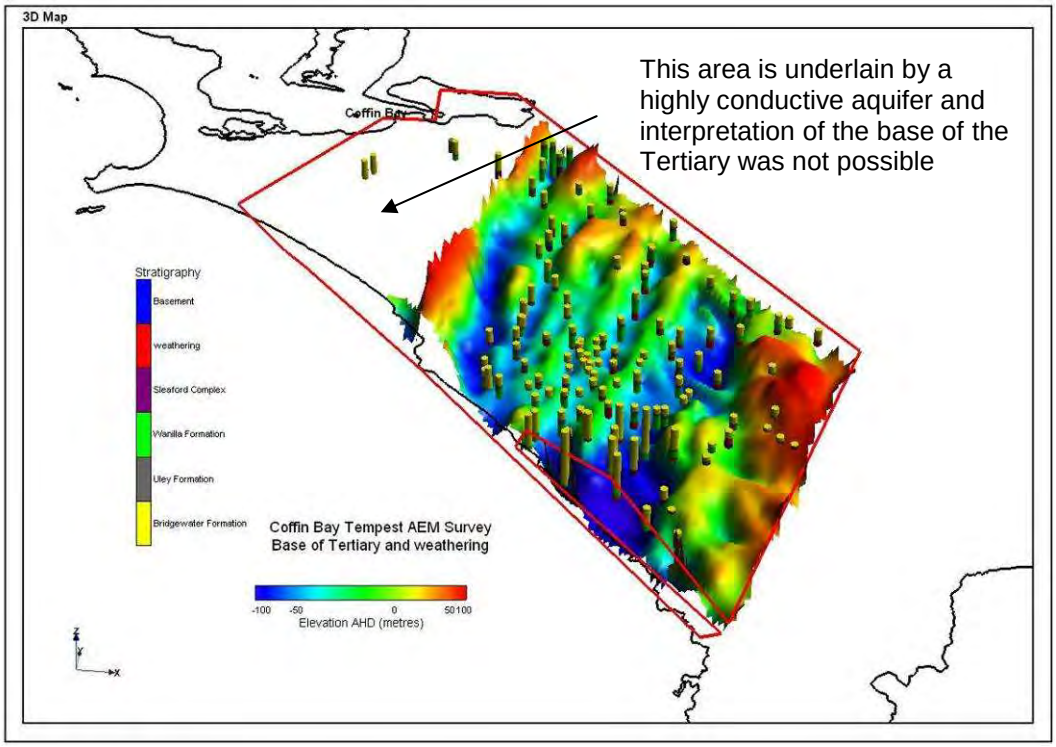

Figure 5: 3D Perspective view of the base of the Tertiary/weathering layer. Vertical cylinders indicated the logged hydrostratigraphy of boreholes. View is approximately looking north.

Conclusions

A low resolution TEMPEST fixed wing time domain airborne electromagnetic survey was undertaken over the Eyre Peninsula region of South Australia to provide additional information on aquifer geometry and characteristics in the area. The resulting data have been inverted using a constrained inversion approach to generate an enhanced ground electrical conductivity model for the area. The modelled conductivity was assessed against available borehole conductivity data.

The resulting conductivity model mapped important elements of the Quaternary and Tertiary aquifer systems in the area. Hydrogeologically significant bounding surfaces were defined, specifically:

1. Elevation of the base of the Quaternary limestone aquifer (Bridgewater Formation).
2. Elevation of the base of the Tertiary aquifer (combined with the in situ regolith layer).
3. Thickness of the Tertiary aquifer.
4. Thickness of the Quaternary and thickness of saturated Quaternary.

The resulting aquifer bounds compare well with those generated from the borehole data alone and give confidence in the extrapolation of those surfaces into areas where bore data is absent or extremely limited. A comparison of these surfaces against known groundwater levels in the unconfined Bridgewater Formation aquifer, which hosts the groundwater lens systems in this area, suggests that the Uley-South groundwater lens is connected (through a gap in a basement ridge) with a freshwater lens system that underlies the National Park and is itself connected to the Coffin Bay A lens system. These products provide a sound basis for the enhanced constraint of groundwater models, particularly where bore data is absent or limited.

Acknowledgements

We thank Glyn Ashman of SA Water for his support for this project. We thank Jonathan Cark of the Eyre Peninsula Natural Resources Management Board in providing information on the hydrogeology of the Eyre Peninsula. We thank Ross Brodie of Geoscience Australia and the Australian National University in providing access to his constrained inversion algorithm. We thank the iVEC centre for access to its supercomputing facilities. iVEC is a joint venture between CSIRO, Curtin University of Technology, Edith Cowan University, Murdoch University and the University of Western Australia and is supported by the Western Australia Government. This work was undertaken as part of the Groundwater Characterisation and Management Project in The CSIRO-led Flagship Water for a Healthy Country.

References

Clarke, D.S., Berens, V., Dennis, K.J., 2003, Uley South-Coffin Bay Observation Well Network Review. South Australia. Department of Water, Land and Biodiversity Conservation Report DWLBC 2003/04.

Evans, S.L, 2002. Southern Basins Prescribed Wells Area groundwater monitoring status report 2002, South Australia. Department of Water, Land and Biodiversity Conservation Report DWLBC 2002/13.

Fitzpatrick, A., and Munday, T.J., 2005, Forward Modelling Airborne Electromagnetic Data for Application in Mapping the Coffin Bay Groundwater Lens. CRCLEME 224R/CSIRO E&M Report P2005/347.

Lane, R., Brodie R. & Fitzpatrick A., 2004 Constrained inversion of AEM data from St George, Queensland, Australia, CRCLEME Open File Report 163.

GROUNDWATER PURVEYING USING VERY LOW FREQUENCY FRACTURE DELINEATION METHODS

Peter J. Hutchinson, The Hutchinson Group, Ltd., Murrysville, PA
Maggie H. Beird, The Hutchinson Group, Ltd., Murrysville, PA
Matthew Mitchell, Moody & Associates, Washington, PA

Abstract

Random drilling for commercially-productive groundwater wells is a haphazard method within the Pennsylvanian-aged rocks of the Appalachian Plateau Region of southwestern Pennsylvania. These rocks have low permeability and porosity and the average production well produces only enough yield for homeowner use. Often these wells are installed as an open hole to 300 feet to insure an adequate water supply for the homeowner since the well bore acts as a storage reservoir during recovery and drawdown.

Three sites mapped with Very Low Frequency (VLF) methods delineated fractures with the potential to maximize bedrock production through increased fracture-induced permeability. A boring was advanced from a location at each of the three sites selected through VLF mapping. The borings penetrated fractures at the anticipated depths of between 10 and 20 meters below grade. Pump tests indicate that these three borings can produce between over 1,000l/min with little drawdown. Each of the three wells is a commercial success.

Introduction

Commercially quantities of groundwater are rarely discovered in southwestern Pennsylvania. Most wells average 75 liters per minute (L/m) or less (Piper, 1933). Often, deep open-hole borings (>100 m) substitute as groundwater storage within these tight rocks. Random drilling, often for homeowners, invariably exacerbates the notion of low production potential within these Pennsylvanian-aged rocks. Curiously, fracture-induced permeability is available but rarely exploited.

Southwestern Pennsylvanian-aged rocks are classic examples of cyclothemic sediments. These deposits consist of shale, claystone, siltstone, sandstone, coal and minor amounts of limestone. Due to the high concentration of very fine-grained sediments, these rocks have very low permeabilities and low porosities. Consequently, secondary porosity and permeability are necessary to achieve groundwater yields of greater than 400 L/m. Areas of localized fracturing are ideal for the production of commercial quantities of groundwater.

Most streams within southwestern Pennsylvania were created by fracture-mediated weathering and erosion following Pleistocene glacial retreat and eustatic uplift. Unfortunately, fracture-controlled streams do not have high specific yields unless a fracture cuts the stream channel (Olson, Hutchinson, Woods, 2002). The intersection of 2 fractures maximizes the potential for elevated production (ABEM, 2001),

Very Low Frequency (VLF) surveying is an effective method for detecting long, straight, electrical conductors and has been used to locate fractures, to image subsurface voids, to map landfill margins and to delineate buried conductive utilities (Hutchinson and Barta, 2002). High-powered military transmitters operating in the 15 to 30 kHz range propagate far-field planar electromagnetic

waves that can induce secondary eddy currents in electrically conductive linear and planar targets. VLF meters record responses to the induced current and through filtering can accurately locate linear and steeply-dipping planar subsurface anomalies.

Although VLF surveying is simple and quick to use, geophysicists have been reticent to employ this method. This apparent oversight is difficult to explain; however, it is probably borne from lack of source control (i.e., transmitter is operated by the military, and subject to their control), and partial knowledge of the tool's capabilities and limitations. The hand-held VLF meter records the transmitted signal derived from any one of 42 global ground military communication transmitters that operate in the very low frequency radio range (15 to 30 kHz) (ABEM, 2001). Paterson and Ronka (1971) reported that the first commercial ground VLF meter was available in 1964. Currently, there are several commercial instruments that can measure the VLF signal and through microprocessors collect both the in-phase (real or tilt angle) and out-of-phase (imaginary, ellipticity or quadrature) components of the signal's response to a subsurface conductor (Reynolds, 1997).

VLF surveying has many advantages, including ease of use, rapid deployment, simple processing, and low cost. Limitations of this method include lack of control of the transmitter operation, sensitivity to ferrous and non-ferrous cultural noise, single-point data collection, and relatively shallow depth of investigation. Transmitter operation is dependent on the military; therefore, the transmitter may be turned off during a data collection event. Dependence upon a military transmitter can be obviated by the use of commercial transmitter, which decreases the rapid deployment of the tool. Further, the tool's depth of the investigation (probably no more than 100 meters) is shallow but still within the depth window of groundwater purveyors. Nevertheless, the tool can provide an inexpensive alternative to random drilling or other intrusive investigations.

Theory

VLF surveying falls into the far-field system of electromagnetic data collection. The VLF transmitter is a military-based communications antenna that emits a very powerful electromagnetic wave, which when detected tens of kilometers from the source, behaves as a horizontally propagated plane wave (Nabighian and Macnae, 1991).

The propagating signal has horizontal and linearly polarized magnetic and electrical components of the radiowave field in the absence of a subsurface conductor. However, eddy currents are generated when the radiowave field passes through a buried conductor, creating a secondary electromagnetic field (Figure 1). The increase in the flow of induced currents causes the magnetic field to tilt in the vicinity of conducting structures (McNeil, 1988). Since this causes a phase shift with respect to the homogeneous primary field, the total field is elliptically polarized and tilts with respect to the horizontal axis. Consequently, tilt-angle variations follow a response across the anomaly and thus the cross-over point coincides with the center of the anomaly (Figure 2).

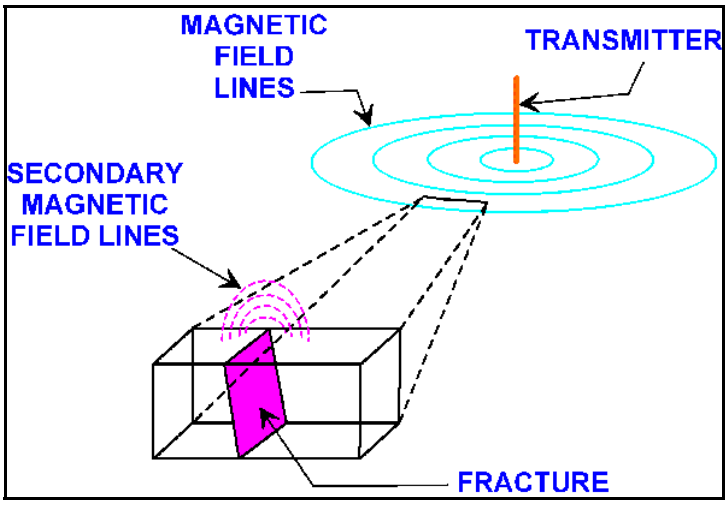

Figure 1: Schematic diagram of very low frequency radiowave with enlargement of secondary magnetic field. Note the horizontal orientation of the electrical and magnetic components of the radiowave field.

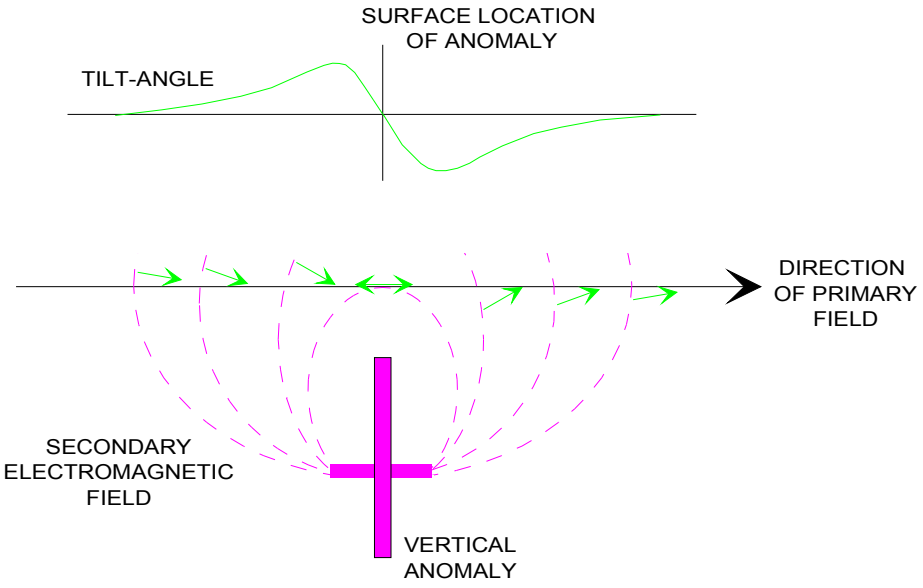

Figure 2: Schematic diagram of the tilt-angle profile over a vertical anomaly.

Many commercial instruments measure the changes in the different parameters of the total field. For example, some instruments measure the dip of the major axis and the ellipticity of the polarization ellipse; whereas other instruments measure the vertical and horizontal field components. These components of the anomalous field can be converted into ratios of the vertical anomalous field to the horizontal primary field for tilt angle analysis. Further, a current density can be calculated with respect to depth from the measured magnetic field.

For example, a buried sheet conductor in a resistive medium in a horizontal primary magnetic

field will induce changes in the amplitude and direction of the primary field in proximity to the target (Figure 2). Consequently, on one side of the target, the angle between the vectors of the primary and secondary components of the radiowave field will reach a maximum near an object and change to a minimum upon passing a buried target. The point at which the tilt angle passes through zero, the "crossover" point lies immediately above the target (Babu, Ram and Sundararajan, 2007). If the target dips, then the tilt-angle measurements on one side of the anomaly are accentuated at the expense of the tilt-angle measurements on the other side of the target.

The tilt angle and current density derived from the anomalous magnetic field can be used in subsequent statistical analyses to locate and to image the subsurface target.

Linear filtering

Linear filtering of the tilt-angle measurements can aid in locating the position of a buried target. Fraser (1969) proposed a simple linear statistical filter of tilt-angle data that converts tilt-angle crossovers into peaks for ease of analysis. Fraser-filtering consists of averaging the tilt-angle measurement produced by a subsurface conductor. In a linear sequence of tilt-angle data M_1, M_2, M_3,..., M_n measured at a regular interval, the Fraser filter $\mathbf{F}_i$ is:

$$F_1 = (M_3 + M_4) - (M_1 - M_2) \quad (1)$$

The first value $\mathbf{F_1}$ is plotted half way between positions $\mathbf{M_2}$ and $\mathbf{M_3}$; the second value is plotted halfway between $\mathbf{M_3}$ and $\mathbf{M_4}$.

Current Density Filtering

Many instruments can calculate a current density from the magnitude of the measured magnetic field (Reynolds 1987). Karous and Hjelt (1983) developed a statistical linear filter, based upon Fraser (1969) and linear field theory of Bendat and Piersol (1968). This filter provides an apparent depth profile from the current density (H_0) which is derived from the magnitude of the vertical component of the magnetic field at a specific location (Figure 3). The depth profile can be calculated from:

$$I_a(0) = \frac{2\pi(-0.102H_{-3} + 0.059H_{-2} - 0.561H_{-1} + 0.561H_1 - 0.059H_2 + 0.102H_3)}{z} \quad (2)$$

Where, the equivalent current density $\mathbf{I_a}$ at a specified horizontal position and depth $\mathbf{z}$ is based upon a symmetrical filter of the measured current (from the measured magnetic component of the anomalous field).

VLF surveys are conducted to locate fractures that can be exploited for groundwater production. Several surveys were performed using the ABEM Wadi and a 23.9-kHz signal from the transmitter located in Cutler, Maine. A sub-meter-accurate Global Positioning System (GPS) was used for exact spatial positioning of collected data. The tilt-angle data were collected every 10 meters parallel to a portion of the stream bed. Fraser (1969) filtering of the tilt-angle data was performed to locate any targets.

Three types of anomalies were located and represent small-, medium- and large-sized fractures or

fractured zones. Discrete, low tilt-angle readings are interpreted to represent shallow fractures or poorly developed fractures. Many small-sized fractures were identified throughout the survey area. Medium-sized anomalies are interpreted to be well-developed deep-seated (greater than 20 meters deep) fractures with a regional extent. These fractures are normally sealed and thus provide limited opportunity for commercial production of groundwater. Large-sized fractures represent regional deformation and integrate a large area and many fractures, thus have a much greater potential for production than smaller shallow fractures. The working hypothesis for these investigations consisted of mapping fractures that may cross creek beds and increase the potential for fracture production of groundwater. Most creeks within southwestern Pennsylvania are created through fracture-mediated erosion and weathering (Olson, Hutchinson, and Wood, 2002).

Case Studies

Case 1

A commercial venture required a continuous source of water of at least 1,000 L/min in the southwestern portion of Pennsylvania. Two VLF profiles were collected adjacent to an unnamed creek, presumed to be fracture induced.

The boring TW-1 was advanced to 32.8 meters below grade and encountered water-bearing fractures at 9.31 m and 17.0 m below grade. Water level stabilized at 8.29 m below grade.

The boring was cased to 6.1 m below grade and completed as an open hole. A pump test conducted for 19 hours indicated a production rate of 1,150 l/min. After 19 hours drawdown was only 2.9 m indicating that commercial quantities of groundwater were available.

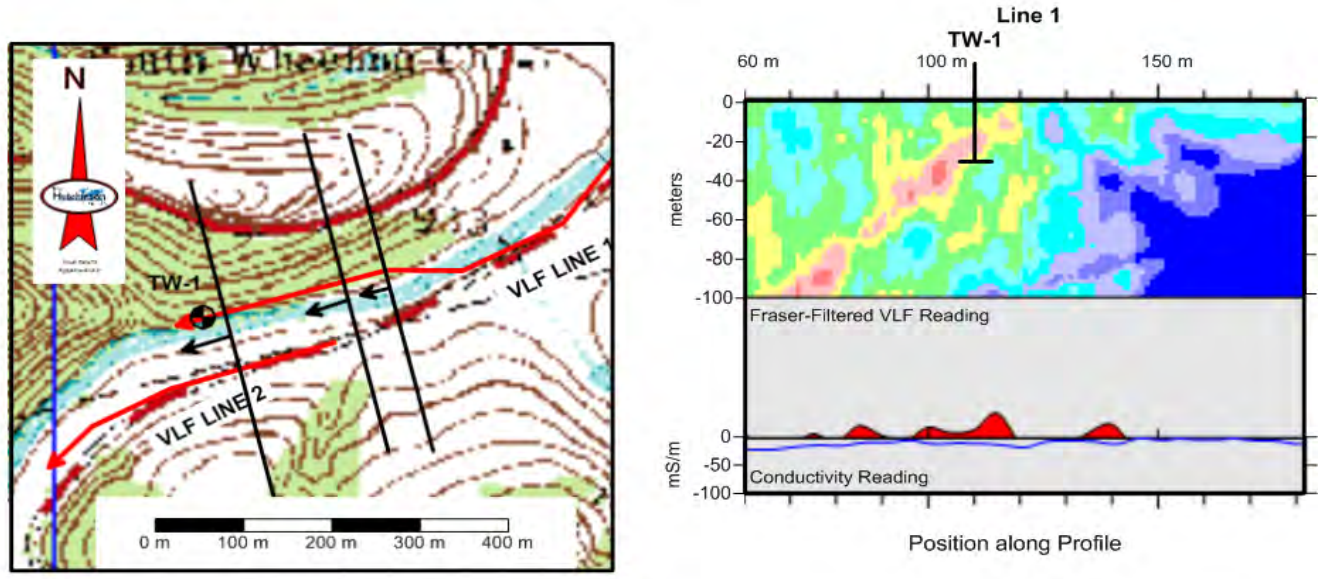

Figure 3: The left figure is a plan map of the Case 1 study area. The right figure shows the processed data in the form of 3 graphs; the upper graph is a representation for the fracture profile derived from the inphase component of the signal (RAMAG program; Walden, 2004) where reds represent a fracture and blues non-fractured rock; the middle graph is the presentation of the Fraser-filtered inphase signal (arbitrary scale); and the bottom graph is the quadrature phase converted linearly to terrain conductivity.

Case 2

Another commercial venture required a continuous source of water of at least 500 l/min in the southwestern portion of Pennsylvania. One VLF profile was collected adjacent to Crafts Creek. Again the creek is assumed to be created by fracturing parallel to the creek bed.

Boring TW-2 was advanced to 54.9 meters below grade and encountered water-bearing fractures at 8.5 m and 15.2 m below grade. The boring was cased to 5.8 m below grade and completed as an open hole. Water level stabilized at 0.9 m below grade after completion of the well.

A pump test was conducted for 13.6 hours at a production rate of 1,325 l/min. After 13.6 hours of production, drawdown was only 5.4 m below grade indicating that this well met the design basis for the commercial user.

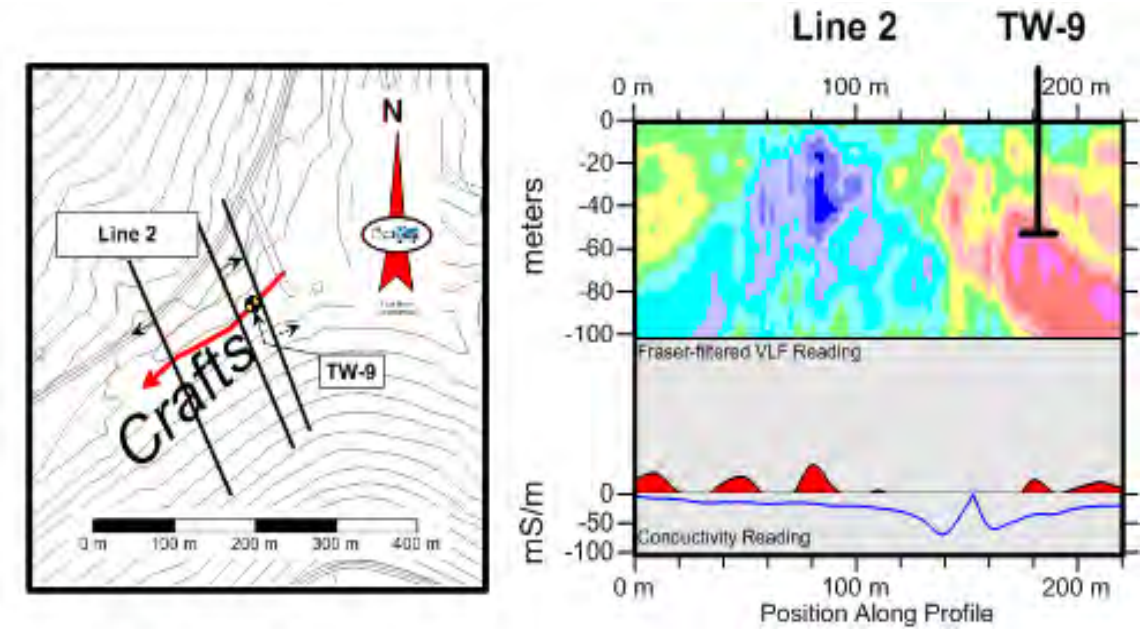

Figure 4: The left figure is a plan map of the Case 2 study area. The right figure shows the processed data in the form of 3 graphs; the upper graph is a representation for the fracture profile derived from the inphase component of the signal (RAMAG program; Walden, 2004) where reds represent a fracture and blues non-fractured rock; the middle graph is the presentation of the Fraser-filtered inphase signal; and the bottom graph is the quadrature phase converted linearly to terrain conductivity.

Case 3

The third commercial venture required a continuous source of water of at least 400 L/min in the southwestern portion of Pennsylvania. Several VLF profiles were collected adjacent to Templeton Creek, a creek assumed to be created by fracturing parallel to the creek bed (Figure 5).

Boring TW-3 was advanced to 18.3 meters below grade and encountered water-bearing fractures at 8.5 m below grade. Water level stabilized at 4.9 m below grade.

The boring was cased to 6.1 m below grade and completed as an open hole. A pump test was conducted for 24 hours at a production rate of 475 L/min. After 24 hours, drawdown was only 2.2 m indicating that this well met the client's needs.

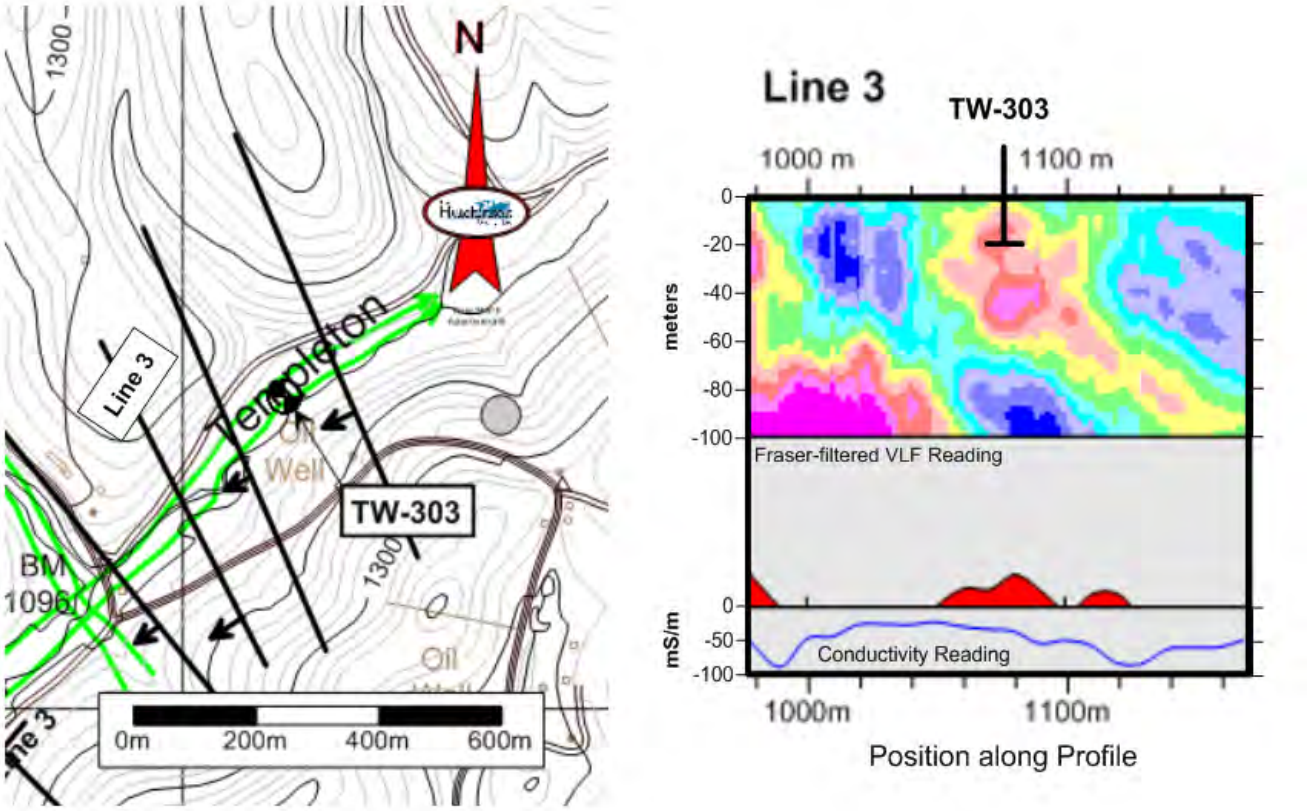

Figure 5: The left figure is a plan map of the Case 3 study area. The right figure shows the processed data in the form of 3 graphs; the upper graph is a representation for the fracture profile derived from the inphase component of the signal (RAMAG program; Walden, 2004) where reds represent a fracture and blues non-fractured rock; the middle graph is the presentation of the Fraser-filtered inphase signal; and the bottom graph is the quadrature phase converted linearly to terrain conductivity.

Conclusion

VLF mapping has been deployed for decades as a useful tool in detecting steeply dipping water-filled fractures and is a useful tool to delimit fractures for commercial water production.

Applying structural geology and VLF mapping to a groundwater production investigation increases the prospect for finding wells that have significant yields. Three prospective areas delineated by VLF mapping were drilled. All three wells intercepted productive fractures and their sustainable yields are well above the required design basis.

References

ABEM, (2001). WADI VLF International Frequency List. ABEM AB printed matter No. 93062. ABEM AB, Bromma, Sweden.

Bendat, J.S. and Piersol, A.G. (1968). Measurement and Analysis of Random Data. Wiley, New York.

Fraser, D.C. (1969). Contouring of VLF-EM data. Geophysics, V. 34(6): 958-967.

Hutchinson, P. J., and L. Barta. (2002). VLF Surveying to Delineate Longwall Mine-induced Fractures: The Leading Edge. v. 21(5). p. 491-493.

Karous, M. and Hjelt, S. E. (1983) Linear filtering of VLF dip-angle measurements: Geophysical Prospecting, v. 31, p. 782-794.

McNeill, J.D. (1988). Electromagnetics. In "Proceedings on the Application of Geophysics to Engineering and Environmental Problems, Pp. 251-348.

Nabighian, M.N. and Macnae, J. C. (1991). Time domain electromagnetic prospecting methods. In: Nabighian, M.N. (ed.), Electromagnetic Methods in Applied Geophysics. Vol. 2: Applications, Part B. Tulsa: Society of Exploration Geophysicists, 427-520.

Olson, D. N., P. J. Hutchinson, R. M. Wood, (1992). Hydrogeologic characterization and groundwater monitoring in the Appalachian Plateau region of western Pennsylvania. Proceedings of the FOCUS Conference on Eastern Regional Ground Water Issues, Newton, Massachusetts, National Ground Water Association, Pp. 589-602.

Paterson, N.R. and Rönkä, V. (1971). Five years of surveying with the very low frequency electromagnetic method. Geoexploration, Vol. 9: 7-26.

Piper, A. M. (1933). Ground Water in Southwestern Pennsylvania, Pennsylvania Topographic and Geologic Survey: Bulletin W-1, Pp. 406.

Reynolds, J.M. (1997). An Introduction to Applied and Environmental Geophysics. Wiley, New York: 796p.

V. Ramesh Babu, Subhash Ram, and N. Sundararajan. (2007). Modeling and inversion of magnetic and VLF-EM data with an application to basement fractures: A case study from Raigarh, India; Geophysics **72**, B133.

AQUIFER CHARACTERIZATION USING COUPLED INVERSION OF DC/IP AND MRS DATA ON A HYDROGEOPHYSICAL TEST-SITE

Thomas Günther, Raphael Dlugosch, Raphael Holland & Ugur Yaramanci
Leibniz Institute for Applied Geophysics, Hannover (Germany)

Abstract

Among hydrogeophysical methods, Magnetic Resonance Sounding (MRS) and Direct Current resistivity / Induced Polarization (DC/IP) measurements can be particularly interesting and useful, since the underlying parameters are related to hydraulic properties. We present a combined investigation of a well-known test site with two aquifers. The inversions for MRS and DC/IP data are combined using a structural coupling and yield improved models due to common but free boundaries. A further combination is achieved by cluster analysis of the obtained resistivity, phase and water content distribution. The approach of the coupled inversion is applied to data of the test site Schillerslage (Hannover, Germany). The simple model obtained agrees with ground truth from boreholes and laboratory as well as with other geophysical measurements.

Introduction

Hydrogeophysical methods can provide unique and cost-efficient information about aquifers as well as their storage and transport properties. Among them, direct current (DC) resistivity, induced polarization (IP) and magnetic resonance soundings (MRS), also called Surface Nuclear Magnetic Resonance (SNMR), are suited since they are directly (MRS water content) or indirectly (Archie's law and T_2^* or IP phase dependency on inner surface) related to hydraulic parameters such as porosity, water content/saturation and hydraulic conductivity. However, very often they suffer from ambiguity due to the limited resolution properties and the equivalence of different geologic units. Therefore, a combination of different methods and the incorporation of a-priori information promises reduced ambiguity (Hertrich and Yaramanci, 2002).

Our study area is a well-known test-site with two main aquifers separated by till layers. An MRS and a DC/IP sounding is combined using a structurally coupled inversion according to (Günther and Rücker, 2006). The gradient of one model is used to control the degree of smoothness for the other to enforce common structures. In order to avoid the usual smooth models and to build more instructive models, cluster analysis can provide an integrative view (Paasche et al., 2006). We present measurements and their interpretation compared to a close-by borehole. Ground-truth is obtained by laboratory measurements on core samples of the investigated and derived parameters.

Test-site, data acquisition and processing

The new LIAG test site Schillerslage consists of two quaternary aquifers divided by a till layer (12-16 m) over Cretaceous marl (Fig. 1). The upper aquifer (0-12 m) shows up medium sand with interbed peat layers over coarse sand and a very shallow (≈0.5-1 m) groundwater table. The lower aquifer (16-22 m)

consists of medium sand again.

The MRS sounding was done with the new GMR device (Walsh, 2008) using a 50 m diameter loop with two turns as both transmitter and receiver. Approximately logarithmically-spaced pulse-moments between 8 and 0.07 As have been injected. Signals were processed using a 200 Hz band-pass filter and show a good data quality with a noise level of about 20 nV. The covariances of the fitted initial amplitudes (E_0) were used as data variances in inversion. The subsurface was equally discretized using 0.5 m spacing down to a maximum depth of 50 m. A cotangent transform was used to restrict the water content to lie between 0 and 40 %. Starting model was a homogeneous half-space of 20% water. Smoothness constraints of first order were used for regularization. The degree of smoothness was chosen such that the data were fitted within error bounds ($\chi^2 = 1$). Figure 1 shows inversion result and data fit. The water content distribution can clearly distinguish the two main aquifers from the surrounding water-free layers at their correct depths. However, particularly in the lower part the model is smoothed, which leaves uncertainties for layer boundaries and water content of the lower aquifer.

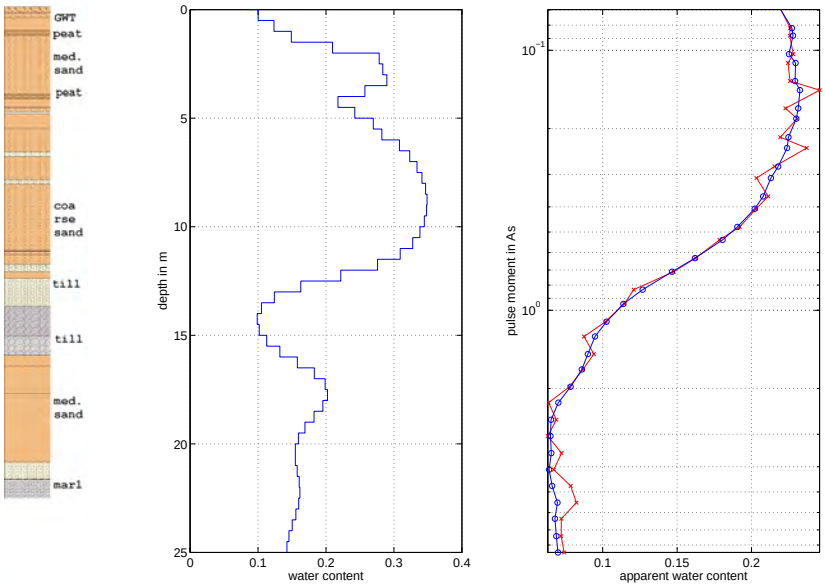

Figure 1: Borehole description (left). MRS inversion result for water content (center). Measured (red) and modelled (blue) data as apparent water content (right).

The DC/IP resistivity data consists of a Schlumberger sounding with AB/2 spacing reaching from 1.5 to 125 m. Different frequencies between 366 mHz and 1000 Hz were measured using the SIP Fuchs (`www.radic-research.de`) instrument. However, only single-frequency data using the lowest value are presented, since they were least affected by electromagnetic disturbances. For reasons of comparison, the identical fixed layering as applied for MRS was used. We are aware of the fact that neither smooth inversion is typical for resistivity nor the use of an equidistant discretization. Model parameter were the logarithms of the resistivities to ensure positive values. Again, smoothness-constraints were applied and optimized such that data were fitted within the assumed error level of 2 %. Figure 2 shows the resistivity model (a) and the fit of the sounding curve (b). Since the latter steadily decreases the inverse problem is severely ill-posed. Nevertheless, the resistivity model shows the expected behaviour with high values at the surface, medium values in the aquifer and low values at the till and marl layers. However, the lower

layers are far too deep and furthermore the model is so smooth that a site assessment would not be possible from resistivity alone.

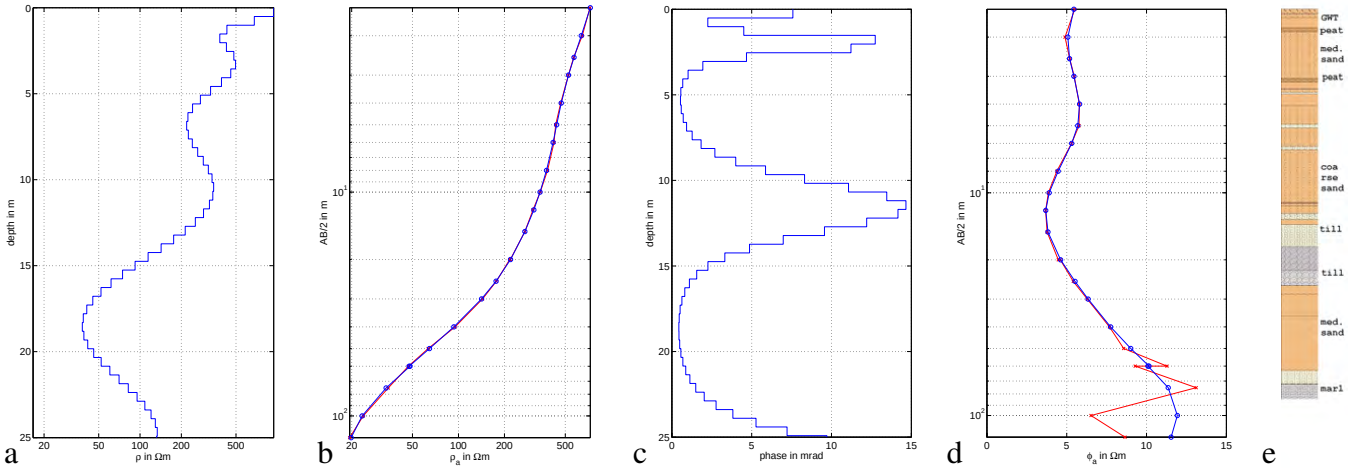

Figure 2: DC/IP inversion results: resistivity model (a), measured (red) and modelled (blue) data (b), phase model (c), measured (red) and modelled (blue) apparent phases (d). Borehole description (e).

Based on the resistivity model the induced polarization data are inverted. The measured apparent phases are transferred to imaginary apparent resistivities ρ_a''. Those are related to the subsurface imaginary resistivities ρ'' via the sensitivity function, which is real-valued for small phases and thus known from amplitude inversion. Similarly, a logarithmic transformation is used to ensure positive ρ''. The sounding curve (Fig. 2d) shows high phases on the very top, at shallow depths and for large spacings. The latter can be associated to the till/marl layers. However, data quality is significantly reduced for higher spacings as a result of electromagnetic coupling and noise. The phase model obtained from the inverted ρ'' (Fig. 2c) clearly depicts the till layer with phases up to 20 mrad. The layer appears too thin and a little too shallow. Furthermore there are two high-phase anomalies at the surface that are associated with humus and peat horizons. The marl layer shows up with high phases, but only at dephts below 30 m.

Structurally coupled inversion

All of the single methods are able to image the present layers qualitatively. However, the models represent equivalent solutions within the accuracy of the data and show systematic shifts of layer boundaries. Consequently, the inverted properties are systematically distorted and affected by the smoothness constraints. Hence, a quantitative analysis is very limited. An improvement can be achieved by a robust re-weighting of the model constraints according to the L1 distribution of the roughness (Claerbout and Muir, 1973), which results in more contrasted models. However, the equivalence of solutions remains.

In order to reduce ambiguity and to obtain more reliable parameters and layer boundaries, a combined data analysis is required. One solution could be a block inversion with common layer thicknesses, since the geologic units determine the parameter changes (Hertrich and Yaramanci, 2002). We follow a different approach (Günther and Rücker, 2006) that is based on the ideas of robust modelling, i.e. in all inversions each layer boundary obtains a weighting factor for the smoothness contribution, which is determined by the roughness of the other method(s).

After our experience, an L1 scheme as used in (Günther and Rücker, 2006) is enforcing mainly the biggest contrast leading to few improvements at the other. Therefore we chose an alternative function for the weights w_i that is independent on the distribution, i.e.

$$w_i = \left(\frac{\alpha}{|r_i| + \alpha} + \alpha \right)^c \quad , \tag{1}$$

where r_i is the model gradient $m_{i+1} - m_i$ of the other method and α is a small quantity (e.g. 0.1) to keep the weight w_i between about 0 (large gradient) and 1 (small gradient). With the parameter c the strength of the coupling can be controlled, in our example we used $c = 1$. The first iterations of the individual inversions are independent on each other. After this, gradients in one model parameter lead to reduced constraint weights for the other and vice versa. Hence, common gradients between different parameters can establish and lead to high-contrasted models. Among all models fitting the data equivalently, the one is preferred that structurally agrees with the other.

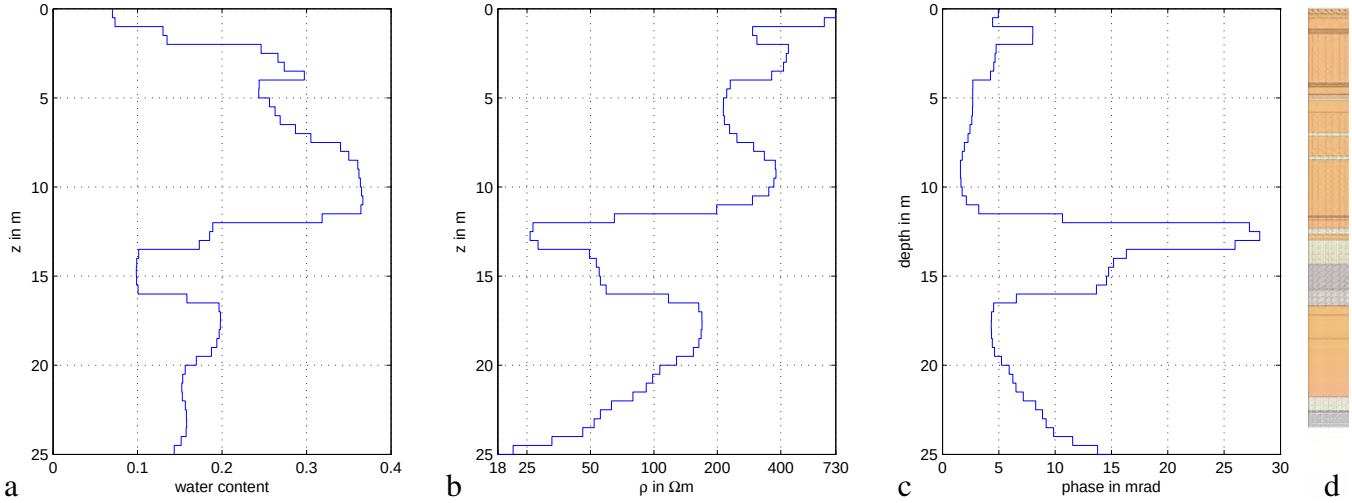

Figure 3: Result from structurally coupled joint inversion of MRS (a), DC resistivity (b) and phase (c) data together with borehole description (d).

Figure 3a/b shows the result of the coupled MRS/DC inversion. Many sharp transitions are observable in both parameters and can be associated to known geologic boundaries, i.e. at 0.5 m (groundwater level), 3 m (lower end of peat horizons), 8 m (medium-to-coarse sand), 12 m and 16 m (till aquiclude). Within these boundaries, the parameters are much more constant and can be used quantitatively. The upper aquifer is known to contain medium sands with some peat and clay components over coarse sand, which is reflected by higher water content and resistivity.

Based on theses results, the IP inversion is carried out with the structural constraints from both water content and resistivity distribution. A coupling of the two weights into one can be obtained by the mean or the product of both. Whereas by the first only common boundaries are enhanced, the second will also account for changes of only one parameter, e.g. between water-free units of different clay content.

Figure 3c shows the resulting phase model. It has reasonable phases on the first 3 m, within the till, and also at the lower model boundary (marl). Both upper and lower boundary of the till are very distinct since IP shows up the strongest contrast. The layer itself seems to be divided into two parts which is supported by the borehole cores showing a gravel&clay-rich upper and a carbonate-rich lower part.

An integrative model

The results of geophysical inversion need to be demonstrated in a rather simple way for decision-making, in terms of geological units and without smooth transitions. Cluster analysis can be used to automatically combine different parameters by minimizing the distance of the points to the cluster centres, which represent mean values. Fuzzy c-means is a variant that additionally yields a membership function f_m for each cluster (Paasche et al., 2006), from which a reliability factor $f_r = (f_m - 1)/(n_c - 1)$ is computed (n_c is the number of clusters).

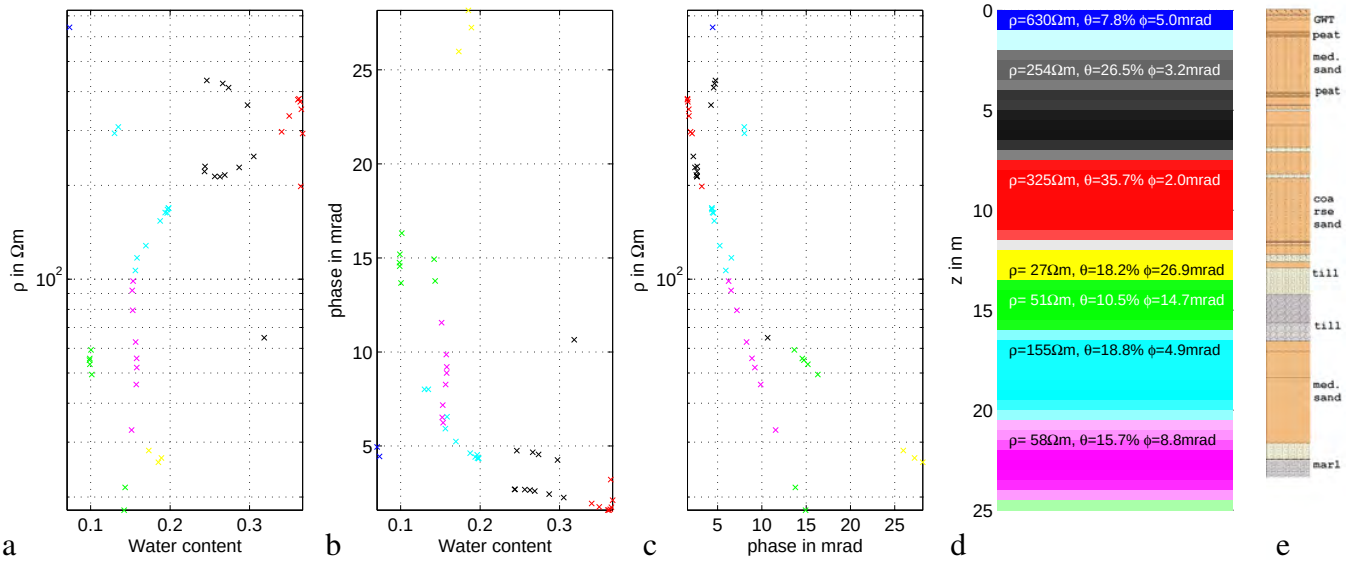

Figure 4: Cross-plots of the three investigated parameters: ρ vs. θ (a), ϕ vs. θ (b), ρ vs. ϕ (c). Final subsurface model with cluster centers and reliability measure (d) and borehole description (e).

Figure 4 shows the distribution of the three parameters as three cluster plots. Furthermore, the resulting cluster number is shown in Fig. 4d using f_r for alpha shading in order to characterize how well the clusters can be distinguished from each other. Whereas resistivity mainly divides the unsaturated zone and the upper aquifer from the rest, water content shows a split of the upper aquifer and separates the lower aquifer from the surroundings. The phase values distinguish peat, till and clay from sandy layers. As in the single results, a split-up of the till layer (gravelly over carboniferous till) is hinted. The layering coincides well with the borehole description (Fig. 4e).

Whereas the cluster centers of the upper aquifer seem to be plausible, the lower aquifer (cyan) obtains remarkably low resistivity and water content. We presume that in regions of low resolution smoothness still dominates and leads to erroneous values that are affected by the two neighbouring aquicludes. First laboratory measurements do not fully comply with the resistivity with values of 40-60 Ωm but agree with phases between 2 and 6 mrad. Other laboratory data yield results comparable to the cluster centers but are not finished yet. Further measurements will assess the ability to derive hydraulic conductivities from the field-scale parameters in comparison to pumping tests, grain size analyses and laboratory k_f measurements. Valuable information lies in the spectral behaviour of MRS and IP relaxation times, which is not considered yet.

Conclusions & Outlook

Both MRS and DC/IP methods are able to provide hydrologically relevant information from aquifers. Using a structurally coupled inversion of all three data sets, the limitations from smoothness constraints can be overcome yielding less ambiguous results. Furthermore clustering algorithms are able to yield a combined subsurface model. The finally resulting parameters are more significant for quantitative analysis, which should be proved using resolution analysis methods. The approach is not restricted to 1d subsurface, but can also be applied to 2d or 3d models (Günther and Rücker, 2006) and different methods.

In order to fully exploit the data, the spectral content of MRS and SIP, i.e. in terms of decay times, should also be used by appropriate inversions. As a result, pore-size distributions could be derived that lead to reliable estimates of hydraulic conductivity in the field scale with minimum prior knowledge. In the presented 1d case, a block inversion with common layers (Hertrich and Yaramanci, 2002) could be obtained similarly reliable parameters. However, for the presented case a very accurate starting model would be needed that is not known beforehand. Going beyond classical inversion into application, only approaches that incorporate the petrophysical relations and the whole in the inversion can yield a hydrological model from geophysical data.

References

Claerbout, J. F. and Muir, F., 1973, Robust modeling with erratic data, Geophysics, 38, 1, 826–844.

Günther, T. and Rücker, C., 2006, A new joint inversion approach applied to the combined tomography of dc resistivity and seismic refraction data., in Ext. Abstr., 19th EEGS annual meeting (SAGEEP), April, 2-6, 2006; Seattle, WA.

Hertrich, M. and Yaramanci, U., 2002, Joint inversion of Surface Nuclear Magnetic Resonance and Vertical Electrical Sounding, Journal of Applied Geophysics, 50, 1-2, 179–191.

Paasche, H., Tronicke, J., Holliger, K., Green, A. G., and Maurer, H., 2006, Integration of diverse physical-property models: Subsurface zonation and petrophysical parameter estimation based on fuzzy c-means cluster analyses, Geophysics, 71, 3, H33–H44.

Walsh, D., 2008, Multi-channel surface NMR instrumentation and software for 1D/2D groundwater investigations, Journal of Applied Geophysics, 66, 3-4, 140–150.

COMPARISON OF 2D AND 3D ELECTRICAL RESISTIVITY IMAGING METHODS TO TARGET HIGH-YIELD WATER-BEARING VERTICAL FRACTURE ZONES

Brent B. Waters, Golder Associates, Richmond, VA
Robert (Kim) Davis, Golder Associates, Decatur, Alabama
Mac G. Morrow, Golder Associates, Richmond, VA
Colin D. Langford, Golder Associates, Richmond, VA

Abstract

In bedrock terrain, groundwater predominantly flows through discrete fracture zones within a low permeability bedrock matrix. Fracture zones are typically long, linear, near-vertical zones of increased fracture density found in most geologic settings. These zones are typically very narrow and are often expressed as natural topographic depressions such as straight stream valley segments, swales and sags in the land surface, or as linear tonal or vegetative alignments often referred to as lineaments or fracture traces. Often, however, fracture zones do not have surface expressions. In such cases, finding and intersecting fracture zones with a well is like finding the proverbial needle in the haystack.

Electrical resistivity imaging (ERI), however, is changing all of this. ERI can be used to map the lateral and vertical variations in the electrical resistivity of the subsurface in a two-dimensional (2D) profile beneath a survey line, or as a three-dimensional (3D) image of the subsurface. Fracture zones are easily identified in ERI profiles because of the large contrast in electrical properties between porous fractured rock saturated with water (low resistivity) and surrounding dry unfractured rock (high resistivity). The use of electrical resistivity imaging by groundwater scientists has resulted in the development of many high yielding wells in areas typically characterized by low well yields. These successes are favorably changing our concept on the viability of using groundwater to meet future water supply needs of many local communities.

Multiple 2D and 3D ERI surveys were completed over a known location of a bedrock fracture zone where a high yield well was successfully drilled. Although the well was originally located on the basis of one 2D ERI survey line, the completion of shallow and deep 3D ERI surveys offered significant additional detail and resolution on the nature (i.e., strike, dip, width) of this bedrock fracture zone. The 3D survey provided more accurate characterization of subsurface geology. The 2D profiles showed the vertical bedrock fracture zone but were also complicated by false anomalies projected into the profiles from areas off the survey line. The 3D ERI surveys are not limited to 2D representation and therefore represent more accurate images of the subsurface geology. 2D and 3D ERI results were compared and analyzed to develop a conceptual model of the bedrock fractures zone. This information was useful in analyzing aquifer test data and developing a 3D numerical groundwater flow model data for the site.

USING AIRBORNE GEOPHYSICAL SURVEYS TO IMPROVE GROUNDWATER RESOURCE MANAGEMENT MODELS

Jared D. Abraham, US Geological Survey, Denver, CO
James C. Cannia, US Geological Survey, Lincoln, NE
Steven M. Peterson, US Geological Survey, Lincoln, NE
Bruce D. Smith, US Geological Survey, Denver, CO
Burke J. Minsley, US Geological Survey, Denver, CO
Paul A. Bedrosian, US Geological Survey, Denver, CO

Abstract

Increasingly, groundwater management requires more accurate hydrogeologic frameworks for groundwater models. These complex issues have created the demand for innovative approaches to data collection. In complicated terrains, groundwater modelers benefit from continuous high-resolution geologic maps and their related hydrogeologic-parameter estimates. The USGS and its partners have collaborated to use airborne geophysical surveys for near-continuous coverage of areas of the North Platte River valley in western Nebraska. The survey objectives were to map the aquifers and bedrock topography of the area to help improve the understanding of groundwater–surface-water relationships, leading to improved water management decisions. Frequency-domain heliborne electromagnetic surveys were completed, using a unique survey design to collect resistivity data that can be related to lithologic information to refine groundwater model inputs. To render the geophysical data useful to multidimensional groundwater models, numerical inversion is necessary to convert the measured data into a depth-dependent subsurface resistivity model. This inverted model, in conjunction with sensitivity analysis, geological ground truth (boreholes and surface geology maps), and geological interpretation, is used to characterize hydrogeologic features. Interpreted two- and three-dimensional data coverage provides the groundwater modeler with a high-resolution hydrogeologic framework and a quantitative estimate of framework uncertainty. This method of creating hydrogeologic frameworks improved the understanding of flow path orientation by redefining the location of the paleochannels and associated bedrock highs. The improved models reflect actual hydrogeology at a level of accuracy not achievable using previous data sets.

Introduction

The North Platte River valley is critical to the management of endangered species management along the Platte River corridor. The Platte River Recovery and Implementation Program is a partnership between the U.S. Department of Interior, Wyoming, Colorado, and Nebraska. The majority of the surface water which fills Lake McConaughy comes through the North Platte River. In turn some of this water is distributed downstream to the critical reaches of the Platte. Understanding the complex groundwater–surface-water relationships of the North Platte River allows managers to better control the limited supplies of water for all uses including endangered species.

Managing endangered species is not the only concern for water management along the North Platte River. Major groundwater–surface-water management issues related to water availability and water quality for humans and wildlife exist both locally and downstream. The North Platte River provides surface water to ~350,000 acres for irrigation. There are ~200,000 acres of groundwater

irrigation within the valley. Much of the water provided for irrigation is used and reused many time along its course downstream. Irrigation is the dominant water use, and much of the irrigation water is from dual sources (surface and groundwater). The use of dual-source water creates a complex relationship between its source and fate, making management difficult. Water quality also is impacted by anthropogenic activities through these multiple uses.

Data from the helicopter electromagnetic (HEM) surveys will be used in the USGS High Plains Groundwater Water Availability Study, Cooperative Hydrology Study (COHYST) (Cannia and others, 2006), and are actively being incorporated within the North Platte River Basin Optimization groundwater models. It will also be used in the Greater Platte River Basin climate study.

Airborne Geophysical Data Collection, Inversion, and Interpretation

A Fugro RESOLVE frequency-domain HEM system was selected for data collection in the North Platte Valley. The selection was based on the electrical conductivity-versus-depth information that was required for the groundwater model and the previous knowledge of the geological materials within the study area. From the understanding gained from boreholes and the COHYST model depth to the base of aquifer, the Tertiary White River Group Brule Formation and, in limited areas, undifferentiated Cretaceous rocks were typically within 100 meters of the land surface. The typical materials mapped included Hydrostratigraphic Unit (HU) 2 (Quaternary Alluvial/Valley Fill Deposits) above HU 8, 9, and 10, generally Tertiary White River Group Brule Formation Siltstones (Figure 1). Borehole geophysical logs acquired by the University of Nebraska Lincoln Conservation and Survey Division (CSD) indicated that the alluvial/valley fill deposits are electrically resistive (40 to 400 ohm-m) and the underlying siltstones are relatively electrically conductive (10 to 20 ohm-m). This provides a good detectable electrical contrast between the aquifer material and the confining unit. Due to the extent of the area of the groundwater model (~100 square miles) and the limited resources to gather additional information, an innovative approach to data collection HEM was implemented in the North Platte Valley. Combining information from a subset of the ~400 CSD boreholes and the ~2,600 registered irrigation wells, and surface geologic maps, the COHYST HU's were complied. This information was combined with preliminary groundwater model results indicating areas where model performance was poor. These areas were selected to be mapped with the HEM in two distinct manners (Figure 2). One flight plan configuration was to fly the blocks in a typical fashion, with lines trending a specific direction with evenly spaced lines from 220 to 400 m separation. The second configuration used widely spaced lines oriented in the direction that would provide the widest areal coverage possible for delineating the confining unit. These widely spaced lines were termed reconnaissance lines and are used to provide a detailed look into the subsurface in areas where the groundwater model was poorly constrained.

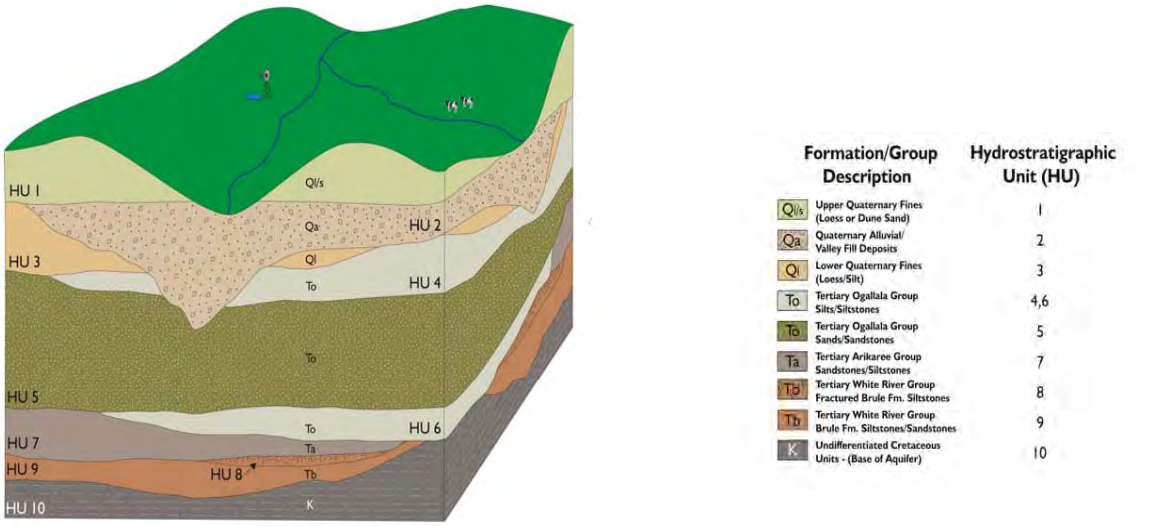

Figure 1: COHYST Model Hydrostratigraphic units. HU 2, 8, and 9 are present within the study area. Hydrostratigraphic units were developed for the COHYST Model by combining stratigraphic units with known hydrologic properties.

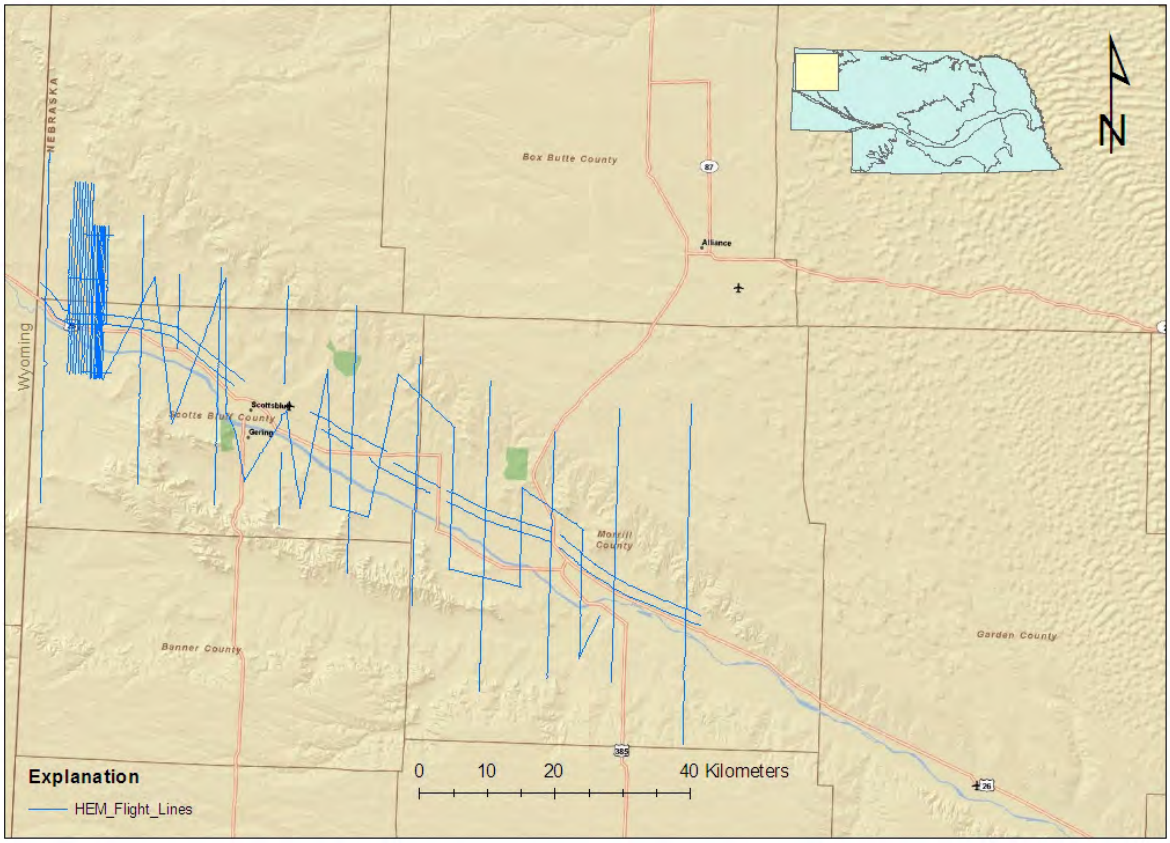

Figure 2: Location of the study area in western Nebraska. Blue lines denote the position of HEM data collection, and indicate both block flights and reconnaissance lines.

The Fugro RESOLVE system was configured to collect in-phase and quadrature data at six frequencies: 140,000, 40,000, 8,200, 3,300, 1,800, and 400 Hertz. Details on the survey specifications can be found in Smith and others, 2009. After processing and leveling by Fugro, the data were inverted using the University of British Columbia Inversions Facilities program EM1DFM (Farquharson and others, 2003). After the data inversion, an approach based on Oldenburg and Li, 1999, was applied, for which a depth of investigation (DOI) metric was calculated. This approach combines multiple inversions from different starting models to define areas where the models are no longer sensitive to the data, that is, where the model resistivity values tend toward the background starting model. This DOI allows the plotting of the data with a cutoff value to eliminate the regions below the DOI (Figure 3). The DOI provides the geophysicist and geologist with a level of confidence in interpreting resistivity values related to the feature being mapped. An interpretation for the location of the confining unit was completed in a Graphical Information System (GIS) that provided X, Y, and Z coordinates. Each of the interpreted locations or picks of the top of the aquifer were run through a comparison with the DOI value for that HEM sounding, and a confidence for each interpretation was calculated from 1 to -1, with 1 being the highest confidence (picked horizon is well within the depth of investigation). Using existing borehole information, irrigation wells, surface outcrops, and the new HEM-derived interpretations, a new base of aquifer map was produced.

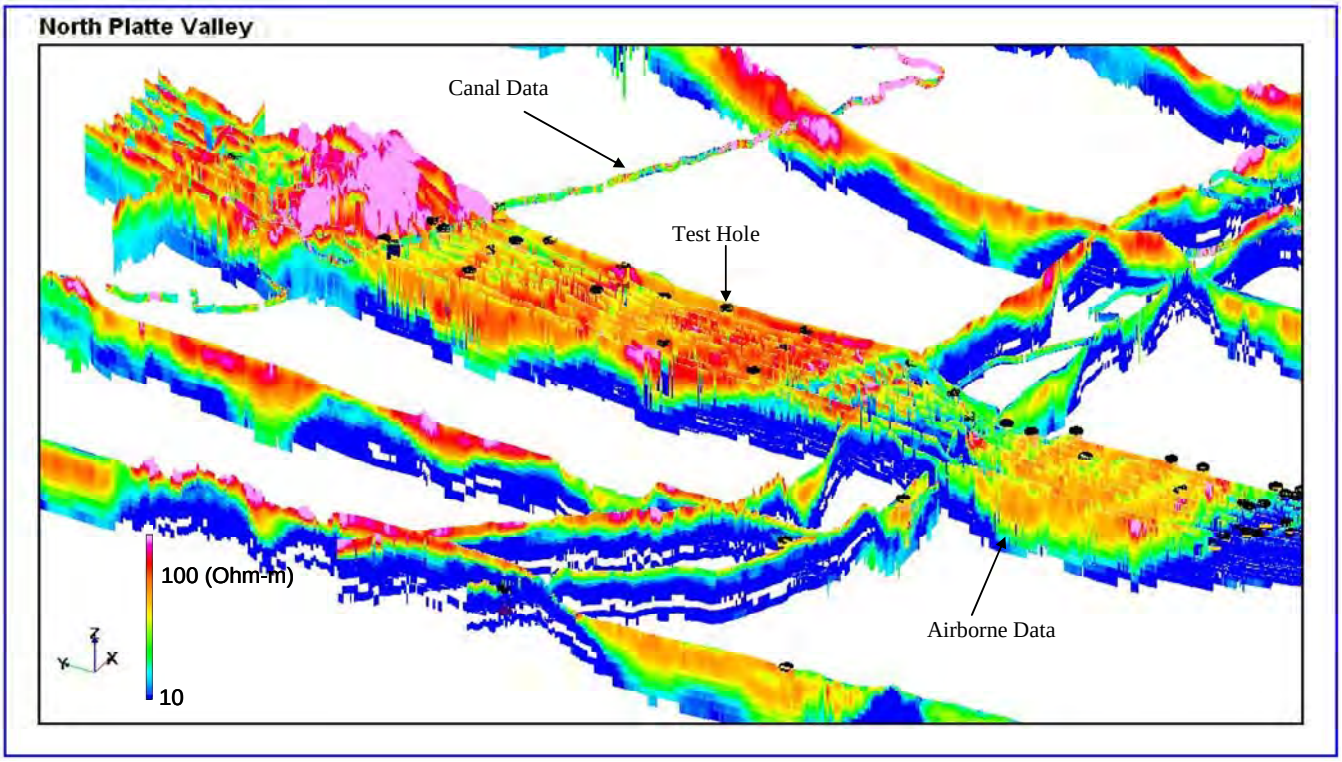

Figure 3: 3-D plot of the HEM inversions displayed with a resistivity color scale from 10 to 200 ohm-m of a portion of the study area around Morrill, NE. Also shown are the locations of CSD test holes (black dots) and canal resistivity data collected by Ball and others, 2006. The block of data is approximately 25 km wide and the vertical exaggeration is 1:15.

Groundwater Model Improvements

Currently, three active groundwater modeling projects cover the North Platte River Valley. These are the COHYST model, the US Geological Survey Northern High Plains Groundwater Availability model, and the North Platte Valley Optimization model. The most detailed of these models is the North Platte River Basin Optimization model. It was the first of these models to use the new HEM-derived interpretations of the hydrogeologic framework. Initial results from the model indicate the following: the creation of the refined hydrogeologic framework resulted in a redistribution of flow path orientation (redefining the location of paleochannels), and the improved groundwater models represent actual hydrogeology at a level of accuracy not achievable using previous data sets. Figure 4 shows the magnitude and location of these changes.

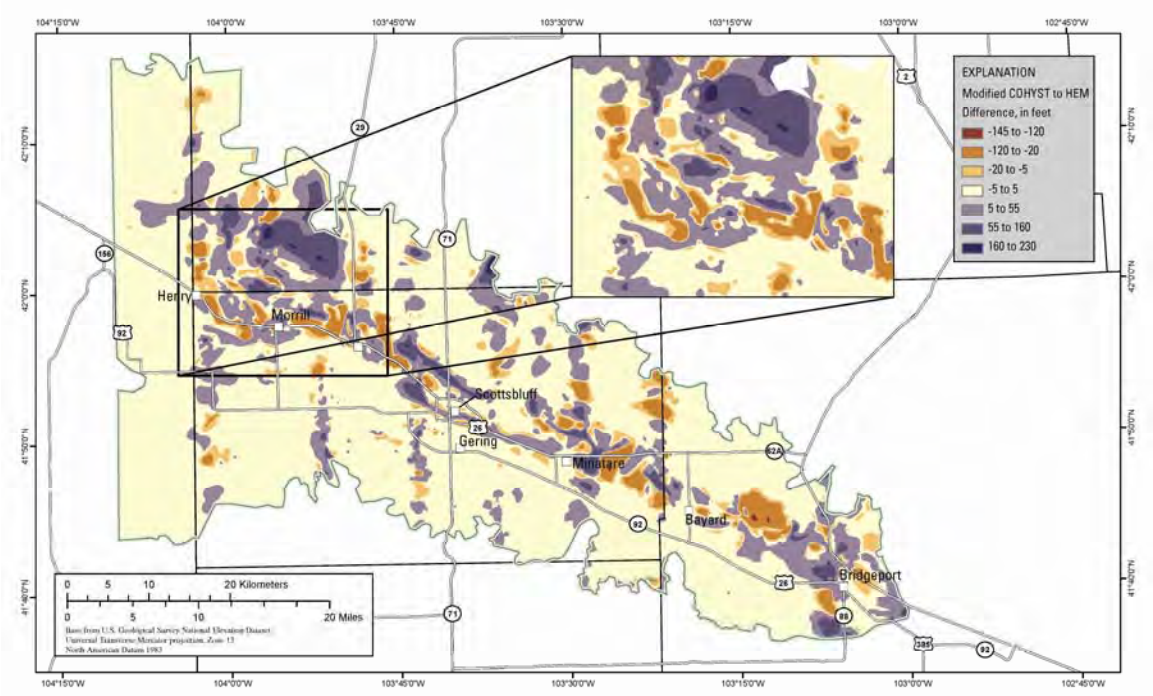

Figure 4: Difference between the original and post-HEM base of aquifer within the study area.

Conclusions

The HEM survey provided considerable improvement to the understanding of the hydrogeologic framework of the North Platte River Valley, which was used to improve groundwater models of the area. Understanding the complex groundwater–surface-water relationships of the North Platte River allows managers to better control the limited supplies of water for all uses including endangered species. The North Platte Valley Optimization model is being built specifically to test a range of management scenarios aimed at balancing agricultural water supply and demand as well as surface and groundwater interactions, inflows, and outflows. Data from the HEM surveys will be used in the U.S. Geological Survey High Plains Groundwater Availability Study, COHYST, North Platte River Basin Optimization groundwater models, and the Greater Platte River Basin climate study.

This study illustrates the manner in which a geophysical survey is driven by the need for a refined hydrogeological framework for a groundwater model. The improved HEM-derived framework represents the actual hydrogeology at a level of accuracy not achievable using previous data sets.

References

Ball, L.B., Kress, W.H., Steele, G.V., Cannia, J.C., Andersen, M.J., 2006, Determination of canal leakage potential using continuous resistivity profiling techniques, Interstate and Tri-State Canals, western Nebraska and eastern Wyoming, 2004, U.S. Geological Survey Scientific-Investigations Report 2006-5032, 53 p.

Cannia, J.C., Woodward, D., and Cast, L.C., 2006, Cooperative hydrology study COHYST hydrostratigraphic units and aquifer characterization report, Cooperative Hydrology Study, http://cohyst.dnr.ne.gov/, 96 p.

Farquharson, C.G., Oldenberg, D.W., and Routh, P.S., 2003, Simultaneous one-dimensional inversion of loop-loop electromagnetic data for magnetic susceptibility and electrical conductivity, Geophysics, v. 68, p. 1857-1869.

Oldenberg, D.W., Li, Y., 1999, Estimating depth of investigation in DC resistivity and IP surveys, Geophysics, v. 64, p. 403-416.

Smith, B.D., Abraham, J.D., Cannia, J.C., and Hill, P., 2009, Helicopter electromagnetic and magnetic geophysical survey data for portions of the North Platte River and Lodgepole Creek, Nebraska, June 2008, U.S. Geological Survey Open-File Report 2009-1110, 27 p.

Acknowledgements

The authors would like to thank the following sponsors of this project: Nebraska Environmental Trust, North Platte Natural Resources District, U.S. Geological Survey Cooperative Hydrology Program, South Platte Natural Resources District, and the University of Nebraska, Lincoln, School of Natural Resources, Conservation and Survey Division. A special thank you to Steven Sibray, Conservation and Survey Division School of Natural Resources, University of Nebraska, Lincoln, Panhandle Research and Extension Center, for his geological knowledge. The authors would also like to acknowledge the many U.S. Geological Survey staff from the Crustal Imaging Science Center in Denver, CO, The Nebraska Water Science Center in Lincoln, NE, and the Texas Water Science Center in Austin, TX, including: Maria Deszcz-Pan, Lyndsay Ball, Jonah Sullivan, Bethany Burton, Erika Curry-Elrod, Pat Hill, Derek Ryter, Jennifer Stanton, Amanda Flynn, Christopher Hobza, Ryan Tompkins, Brian Imig, Andy Teeple, Wade Kress, Jason Payne, and Michaela Johnson.

.

GROUNDWATER EVALUATION USING VTEM HELICOPTER ELECTRO-MAGNETICS IN THE SOUTH PLATTE NRD, SIDNEY, NEBRASKA

Jean M Legault, and Paolo Berardelli, Geotech Ltd., Aurora, Canada
Jared Abraham, USGS, Denver, CO, and James Cannia, USGS, Mitchell, NE
Kerim Martinez, COWI A/S, Lyngby, Denmark

Abstract

A VTEM time domain helicopter-borne electromagnetic survey was undertaken for groundwater evaluation in western Nebraska with the objective to map the extent of deep freshwater aquifers. The VTEM system combines near surface high resolution resistivity imaging and deep penetration making it a low cost, rapid reconnaissance mapping tool in areas with thick, conductive terrain. The survey was preceded by a synthetic computer modeling study that proved its resolution and penetration capability below 200m depth. The test survey that followed used a new X-Z component system and caesium magnetometer that covered a 165 square km region of the South Platte NRD in two short survey days. Data analysis using a variety of 1D (layered-earth) inversion and conductivity-depth imaging (CDI) tools indicate that, in spite of significant presence of man-made culture (powerlines and metallic structures), the moderately conductive Ogallala Group aquifer was successfully mapped to a known depth of 160m above the conductive White River Group Brule Formation bedrock aquitard. Simulated penetration depths in excess of 200m appear to have been easily reached, suggesting the use of VTEM to be extended into deeper, more conductive aquifers within the Natural Resource Districts of Nebraska.

Introduction

Groundwater in the Lodgepole Creek area around Sidney, western Nebraska is sometimes insufficient and alternate water sources are limited in extent. The U.S. Geological Survey (USGS) and the South Platte Natural Resources District (NRD) recently began a cooperative study to evaluate the ground water near Sidney (Steele et al., 2007). One of the initiatives was to fly the region using helicopter electromagnetic (HEM) surveys to determine the extent of sand and gravel aquifers in the area. Frequency domain EM systems have been used successfully in the region but lack the penetration necessary to map the base of the deeper and more conductive aquifers in the region (Smith et al, 2009).

In March, 2009, the USGS contacted Geotech Ltd. (Aurora, Ontario, Canada) to undertake 1D layered-earth forward modeling as a proof of concept in the use of its VTEM (versatile time-domain electromagnetic) helicopter system for mapping the base of deep aquifers in Nebraska. A VTEM test survey soon followed in April, 2009 over a survey block located near the town of Sidney in Cheyenne County in the South Platte NRD of Nebraska (Figure 1). The survey objectives were to map the base of the Tertiary Ogallala Group aquifers that extends from near surface to below 130m (400ft) depth above the Tertiary White River Group Brule Formation bedrock. Subsequent 1D layered earth inversion and conductivity depth imaging were performed to map the extent of the Ogallala aquifer, with the final report (Bournas et al., 2009) submitted in early June, 2009. This paper presents a case history detailing the forward model simulation, the eventual EM survey and the results of the inversion modeling study.

Survey Location and Description

The center of the Sidney Block (41° 21.745'N, 103° 1.143'W) is located approximately 25 kilometres north of the town of Sidney, Nebraska. The 40.4 km long NS survey block extends from Cheyenne County into southern Morrill County (Figure 1).

Topographically, the Sidney Block exhibits moderate relief; with an elevation ranging from 1151 to 1328 metres above sea level over an area of 165 square kilometres (see Figure 1). The survey area consists primarily of irrigated farmlands with many small drainages running throughout that covers a network of rural roads (generally on every side of each square mile), highways and railway lines. Other more notable cultural features running through the survey block include two major northwest-southeast electrical transmission lines and NW-SE pipeline that cross-cut the survey block (see Figure 7).

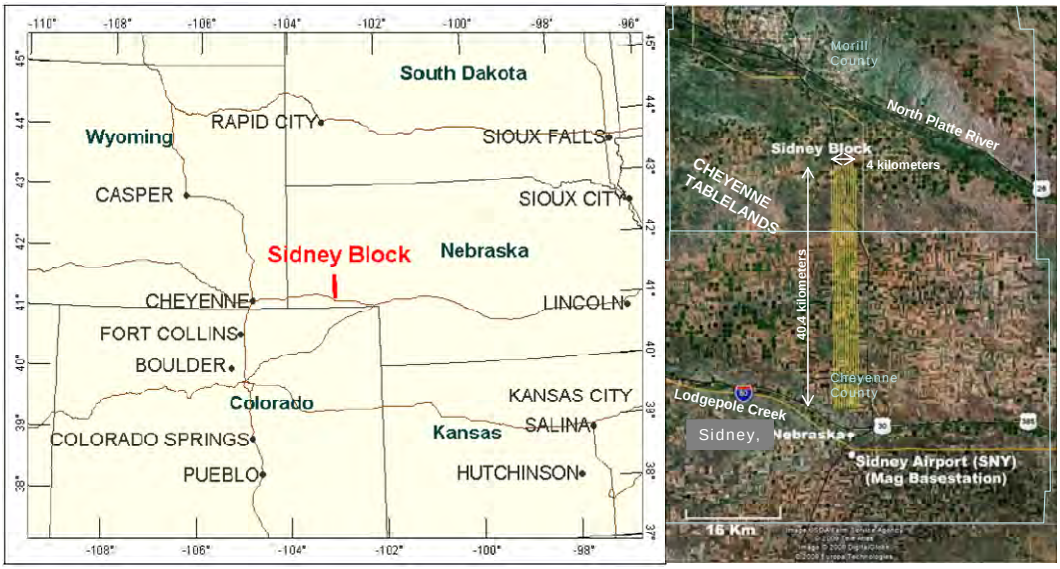

Figure 1: Sidney Block general property location in southwest Nebraska (left) and VTEM survey flight line planning for region north of Sidney, NE, showing agricultural land use, in Google Earth (right).

Geology and Geophysical Properties

The geologic stratigraphy of the Sidney survey area consists of Quaternary alluvium overlying the Tertiary Ogallala Group which contains a mixture sand, gravel and sandstone aquifers and Tertiary White River Group bedrock (Figure 2). The Holocene and Pleistocene age Quaternary alluvium is mainly found in the Lodgepole valley and consists of unconsolidated silt, sand and gravel boulders, up to 10 metres in thickness, with a resistivity of 30 to 70 ohm-metres. The Tertiary (Miocene) Ogallala Group is mainly composed of interbedded layers of clay, silt, fine to coarse-grained sand, gravel, conglomerate, calcareous sandstone and volcanic ash, with a thickness up to 120 metres, and resistivity of 50 to 100 ohm-metres. The bedrock layer (Tertiary, Lower Oligocene) consists of White River Group, Brule Formation brown siltstone and mudstone, which are rich in volcanic glass shards. The thickness of this layer is over 180m with a resistivity of 8 to 18 ohm-m (Steele et al., 2007; Cannia et al., 2006).

Hydrogeology

Lodgepole Creek is the predominant watercourse in the South Platte NRD and it is intensively used for irrigation with wells open to aquifers in the fractured Brule Formation and the overlying alluvial aquifer (Figure 2a). In contrast, irrigation wells in the Cheyenne tablelands that lie in the VTEM

survey area are developed in the Ogallala Group and to a lesser extent in deep wells into sand and gravel channel deposits (Brule Sands) in the Brule Formation (Figure 2b). The Brule Formation, composed mainly of siltstones, otherwise does not yield substantial quantities of water unless fractured. The Ogallala, because it contains individual beds of unconsolidated sand and gravel up to 20 metres or more, is an important aquifer north of Lodgepole Creek in the tablelands. The water table of the tablelands generally trends northeast towards the North Platte River. In the project area the water table can be up to 60m (200ft) deep. Specific conductance of the water is generally not a factor in the electrical signature. A median conductivity of 405 µ S/cm has been reported for water from the Ogallala Group. Quaternary alluvium deposits are relatively thin and are not regarded as a source of water (Steele et al., 2007).

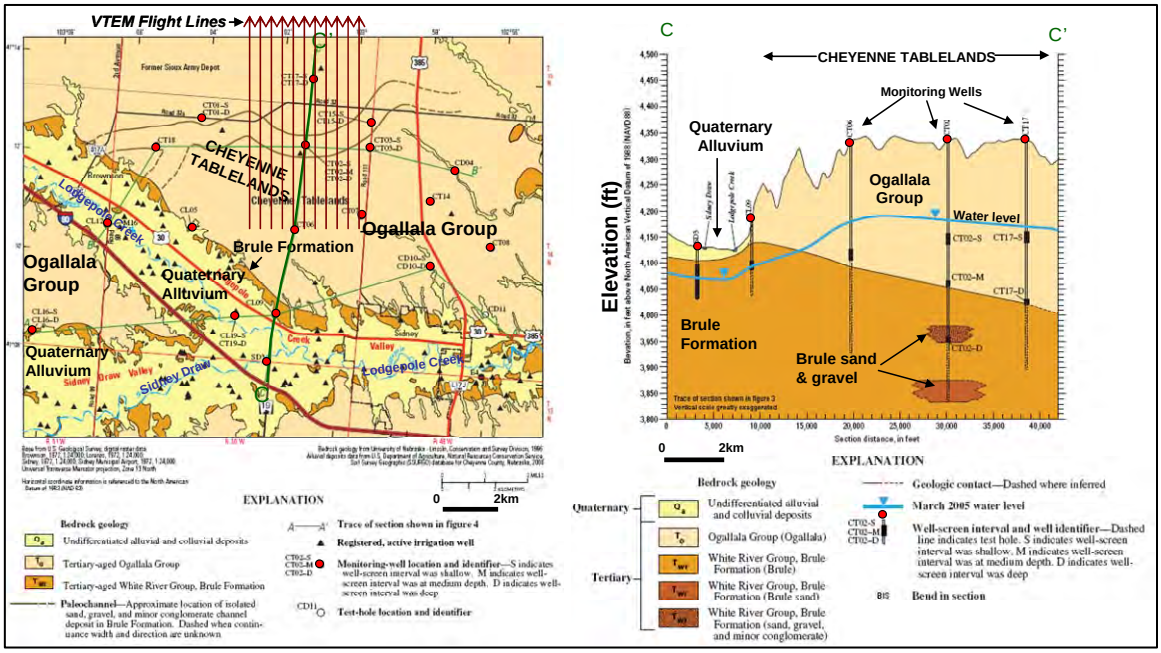

Figure 2: (Left) Generalized bedrock geology plan in Sidney region showing monitoring wells and approximate locations of VTEM survey lines; (Right) Geologic cross-section in southern VTEM survey area (both modified after Steele et al., 2007).

VTEM System

The VTEM system (Witherly et al., 2004) has a 26 metre diameter, vertical axis, 4 turn transmitter coil and can produce over 500,000 NIA of dipole-moment, giving it its deep penetration capability. The VTEM system configuration consists of a 2-axis (Z-vertical & X-horizontal) induction type (dB/dt) EM receiver coils deployed in the middle of the transmitter coil and optically pumped caesium magnetometer suspended above it (Figure 3). The horizontal in-loop transmitter-receiver geometry (coincident-coplanar) produces a symmetric response is well suited for sounding applications. During the Sidney Block survey the helicopter was maintained at a mean height of 76 metres above the ground with a nominal survey speed of 80 km/hour. This allowed for a nominal EM sensor terrain clearance of 41 metres and a magnetic sensor clearance of 63 metres.

The VTEM transmitter is digitally controlled and can easily operate in a variety of base frequencies, using different pulse widths and shapes. The pulse shape is trapezoidal and elongated to approxi-

mate a step response that is optimal for layered-earth response modeling. At Sidney Block, a 7.2 millisecond pulse width (43% duty cycle) was utilized. The digital acquisition system at the receiver utilizes 24 bit A/D sampling at 2500Hz. The data recording rates at output are 0.1 second for electromagnetics, magnetometer and 0.2 second for altimeter and GPS. This translates to a geophysical reading about every 2 metres along flight track. Navigation is assisted by a CDGPS receiver and data acquisition system, which reports GPS co-ordinates as latitude/longitude and directs the pilot over a pre-programmed survey grid. The EM dB/dt and calculated B-field decays are derived using twenty-four (24) time measurement gates centered 120 to 6578 μ sec after the end of the pulse (Figure 3).

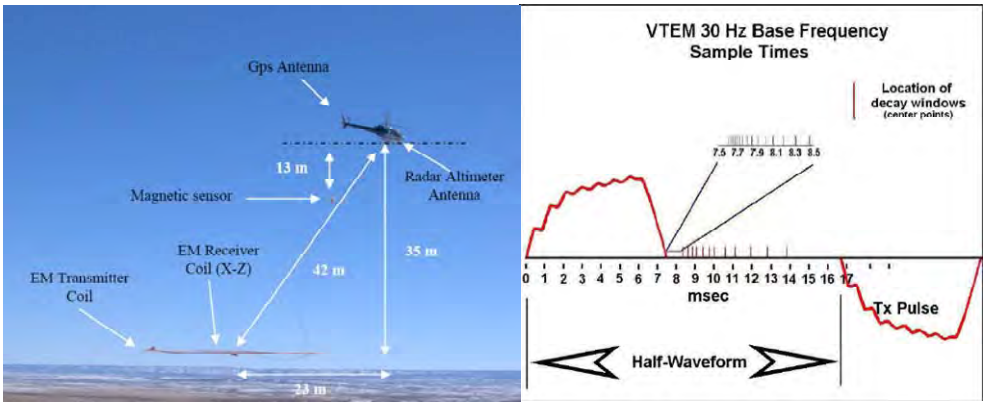

Figure 3: VTEM helicopter system, showing time-domain EM system and magnetic sensor configuration in flight (left) and VTEM transmitter current waveform and off-time receiver time-gate positioning in off-time (right).

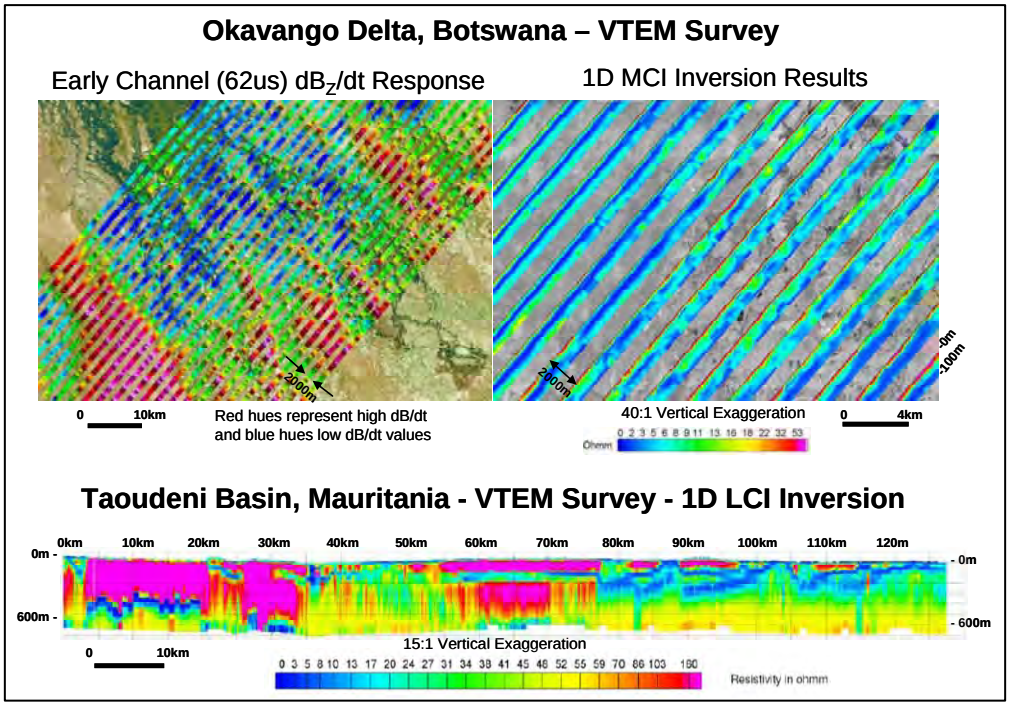

Figure 4: VTEM ground water examples from: a) Okavango Delta, Botswana, showing VTEM dBz/dt EM decay strength as grid contours (top left) and Stacked mutually-constrained (MCI) 1d inversions as stacked 2D resistivity sections in plan (top right); b) 1D laterally-constrained inversions (LCI) from Taoudeni Basin, Mauritania (bottom) as a 2D resistivity section (modified after Martinez, et al. (2008).

The VTEM system has been designed for mineral exploration with a wide conductivity aperture optimized to detect and resolve poor to good sulphide conductors, ranging from zinc-rich(0.1 S/m) to nickel sulphides (>1000 S/m). The low base frequency, long pulse width, and the derived B-field are techniques used to better detect and resolve high conductivity targets.

The interest for water resources airborne electromagnetic surveys include high-resolution mapping of resistivities both at the near-surface as well as at great depth. Near-surface imaging requires an early time acquisition capability not normally needed in mineral surveys but obtainable with VTEM. Depth penetration is required to give water resource managers a new look into more complex deep-lying hydrogeology targets of interest. With a proven depth-detection capability for conductive bodies below 300-600m (Witherly and Irvine, 2006), the VTEM system is ideally suited for deep conductive aquifer mapping. Examples of successful applications of VTEM for water resource objectives include the Okavango Delta region of Botswana and in the Taoudeni Basin of Mauritania (Figure 4), both complex and conductive brackish-freshwater environments (Martinez et al., 2008).

1D Forward Modeling

As a proof of concept, the applicability of VTEM system to map the Sidney Block hydrogeology was evaluated using synthetic Layered Earth model testing. VTEM responses (Z component of dB/dt) were calculated synthetically for a variety of layered-earth models chosen by USGS and were then inverse-modeled to derive the expected responses. The proposed models for the study consisted of 2 and 3 layers with resistivities and thicknesses that were appropriate for Sidney groundwater resource objectives. Particular emphasis was to resolve the base of the Ogallala aquifer to 200 metres (Figure 5).

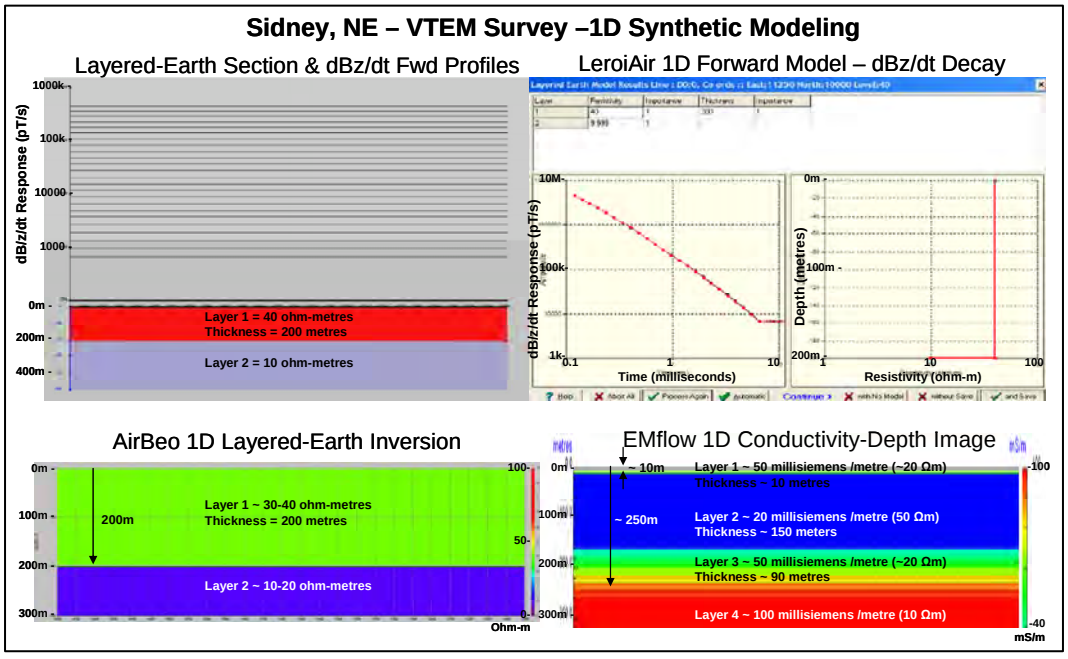

Figure 5: 1D Layered-earth model simulation of VTEM for Sidney hydrogeological model: a) Synthetic 1D forward model VTEM data calculated using LeroiAir for 200m thick Ogallala aquifer above Brule basement (above); b) Predicted 1D layered-earth model for forward model VTEM data using Airbeo 1D LE inversion (bottom-left) and EMflow CDI conductivity-depth image (bottom-right).

The forward modeling was carried out with Leroi Air algorithm (CSIRO, North Ryde, NSW, Australia) that is integrated into the Maxwell software platform (EMIT Technology Pty, Midland, WA, Australia). 1D Inversions of the synthetic forward model data were performed for the VTEM system configuration and waveform using two different tools: 1) Conductivity depth imaging (CDI) using the EMflow software (Pitney-Bowes/Encom Technology Pty., Sidney, NSW, Australia) and 2) 1D discrete-layer inversion using Airbeo (CSIRO). Modeling and inversion results of one of the proposed synthetic models, a thick Ogallala Group 30 ohm-metre aquifer extended to 200m below surface above the conductive (10 ohm-m) Brule Formation basement, is illustrated in Figures 5. The results indicate that the VTEM system would be successful in detecting and resolving aquifer thicknesses below 200m depths.

The study showed that the theoretical VTEM decay responses for all models proposed were above the noise levels (~500 pT/s). 1D inversion results obtained with Airbeo were able to satisfactorily replicate/reproduce the initial forward model parameters. Similarly, conductivity-depth images obtained using EMflow showed a good agreement with the initial models, but generally demonstrated poor resolving power, in comparison with 1D inversion, particularly in the case of weaker resistivity contrast between adjacent layers. Inversion artifacts, such as apparent thin near-surface conductive layers and transitional resistivity layering above the basement units, were also observed (see Figure 5b)

VTEM Survey Results

Following the successful synthetic modeling study, a VTEM test survey was commissioned in April, 2009, over a 4 x 40km block in the Cheyenne tablelands north of Sidney, Nebraska (Figures 1 and 2). The survey extends from the South Platte NRD of Cheyenne County into the North Platte NRD of Morill County where Ogallala Group thicknesses were expected to exceed 160m depths, based on well-hole data (Figure 6). The Sidney Block was flown in a north to south (N 358° E) direction along eleven (11) 40.4 kilometre length survey lines, totaling 444km (165km^2) at a line spacing of 400 metres.

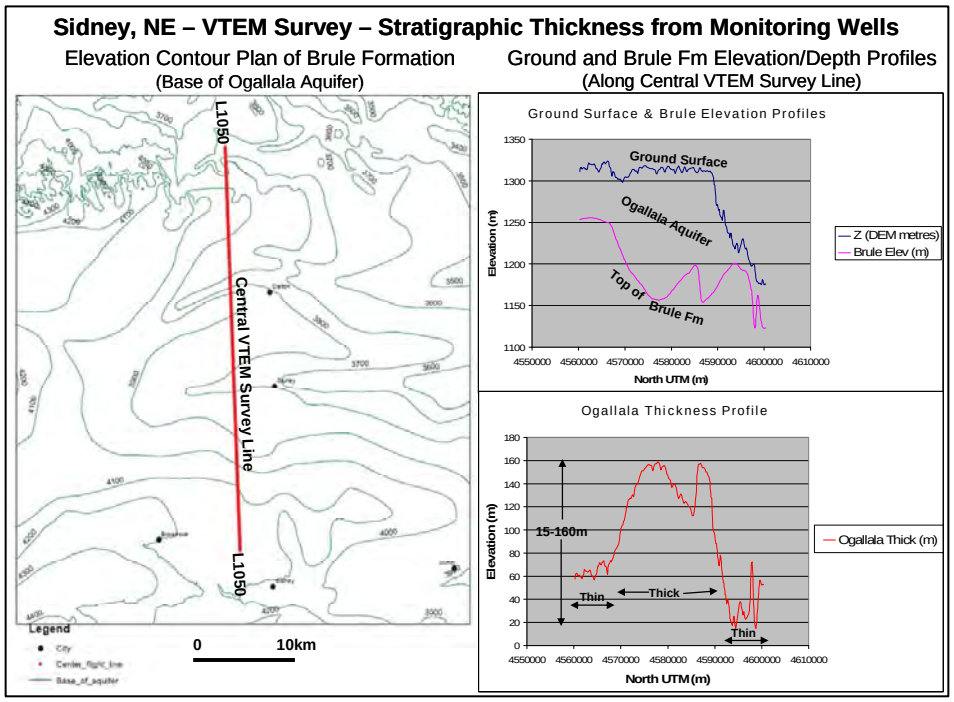

Figure 6: Stratigraphic elevations & thickness from wells along central VTEM line (Cannia et al, 2006).

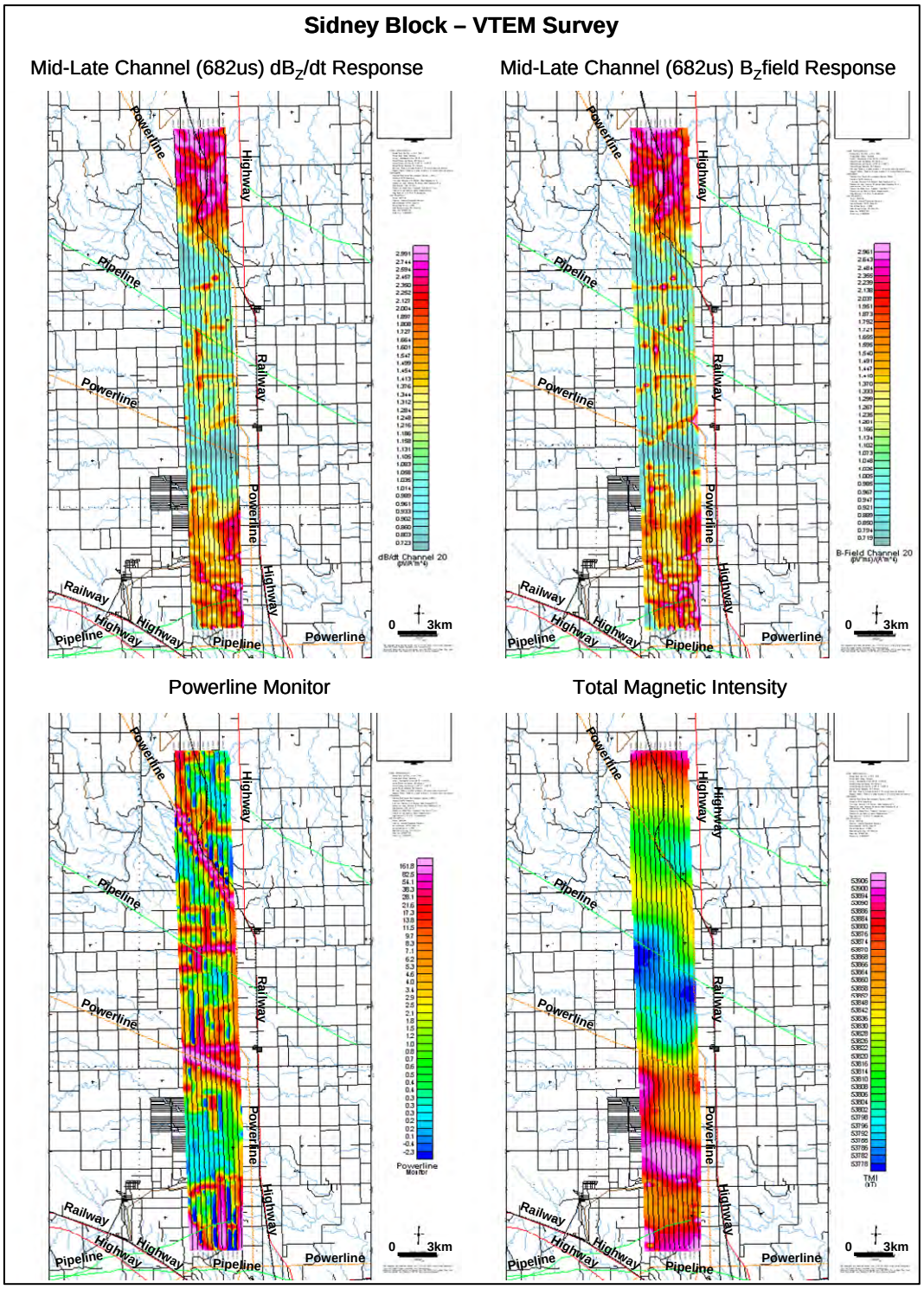

Figure 7: VTEM survey results shown in plan for Sidney Block: a) Middle to late channel (ch20 = 682 μ sec delay) vertical component (dBz/dt) EM signal strength (above left), showing conductive response highs in red, resistive low responses in blue; b) Identical channel/gate EM signal for vertical calculated B-field (Bz) response (above right); c) Powerline monitor (below left) signal strength, showing cultural noise sources in red; d) Total magnetic intensity (below right), showing magnetic susceptibility highs in red and magnetic lows in blue.

The VTEM survey results over Sidney Block are presented as plan view contours in Figure 7. The dB/dt EM response and calculated B-field are shown for a mid-late time decay channel (ch20 = 682 μ seconds) in the upper panel, and powerline monitor and total magnetic intensity (TMI) in the lower panel. The overall response pattern indicates more conductive bedrock to the north and south; which is consistent with the known depth-to-top of the more conductive Brule Formation basement rocks, as illustrated in Figure 6. The more resistive rocks in the central survey area correspond to regions of thicker, more resistive Ogallala Group aquifer in the central Cheyenne tablelands. Numerous thin conductive lineaments that overprint the VTEM response are evidence of pervasive man-made metallic and powerline cultural features that cross-cut the area, some of which are confirmed by their similarity to the powerline monitor, while others are non-60Hz (Figure 8) and likely correspond to grounded fences or buried metallic infrastructure. In spite of the abundance of man-made culture, the VTEM results are characterized by their high data quality that is required for accurate 1D layered earth imaging and inversion to great depth.

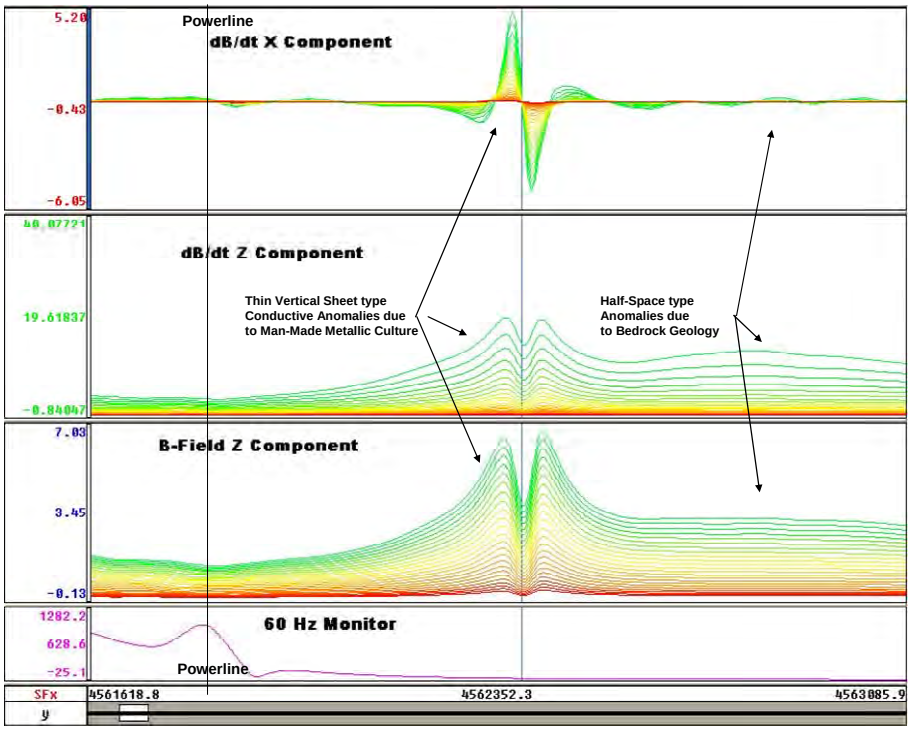

Figure 8: VTEM profile data from Sidney block showing powerline effect with minimal noise, man-made metallic culture (highly conductive, thin vertical plate type responses) and bedrock (weakly conductive, wide-prism/half-space type) signatures.

1D Inversion Modeling

Conductivity depth imaging (CDI) and 1D layered-earth (LE) EM Inversions were performed on all lines at the Sidney Block (11 lines) using the EMflow and Airbeo platforms, identical to those used in the earlier synthetic forward modeling study. The VTEM electromagnetic data were also inverse-modeled for comparison purposes using the pseudo 2D laterally-constrained inversion (2D LCI) based on Auken and Christensen (2004) and employed by COWI A/S (Lyngby, Denmark) that was previously used in the Okavango Delta and Taoudeni Basin VTEM groundwater studies, described in Martinez et al. (2006).

A comparison of the various inversion and imaging results is presented in Figure 9, for L1050, the central profile in the Sidney Block VTEM survey. A 3 layer model was used to fit the data in the Airbeo 1D LE inversion model (Figure 9-top) which matches the thin conductive Quaternary alluvium at the top, the more resistive Ogallala sediment aquifer in the middle and conductive Brule Tertiary bedrock at bottom. The Airbeo resistivity cross-section displays significant variability that appears to coincide with cultural distortion of the VTEM data, based on the powerline monitor. For points away from obvious culture, the depth to basement estimates range from approximately 60 to 160 metres, which is close to the 15-160m range indicated in the well data (Figure 6). The Brule basement resistivity ranges between 8-20 ohm-metres. Airbeo 1D LE inversion depth-to-basement and basement resistivity results for all lines have been combined as plan view grid contours in Figure 10.

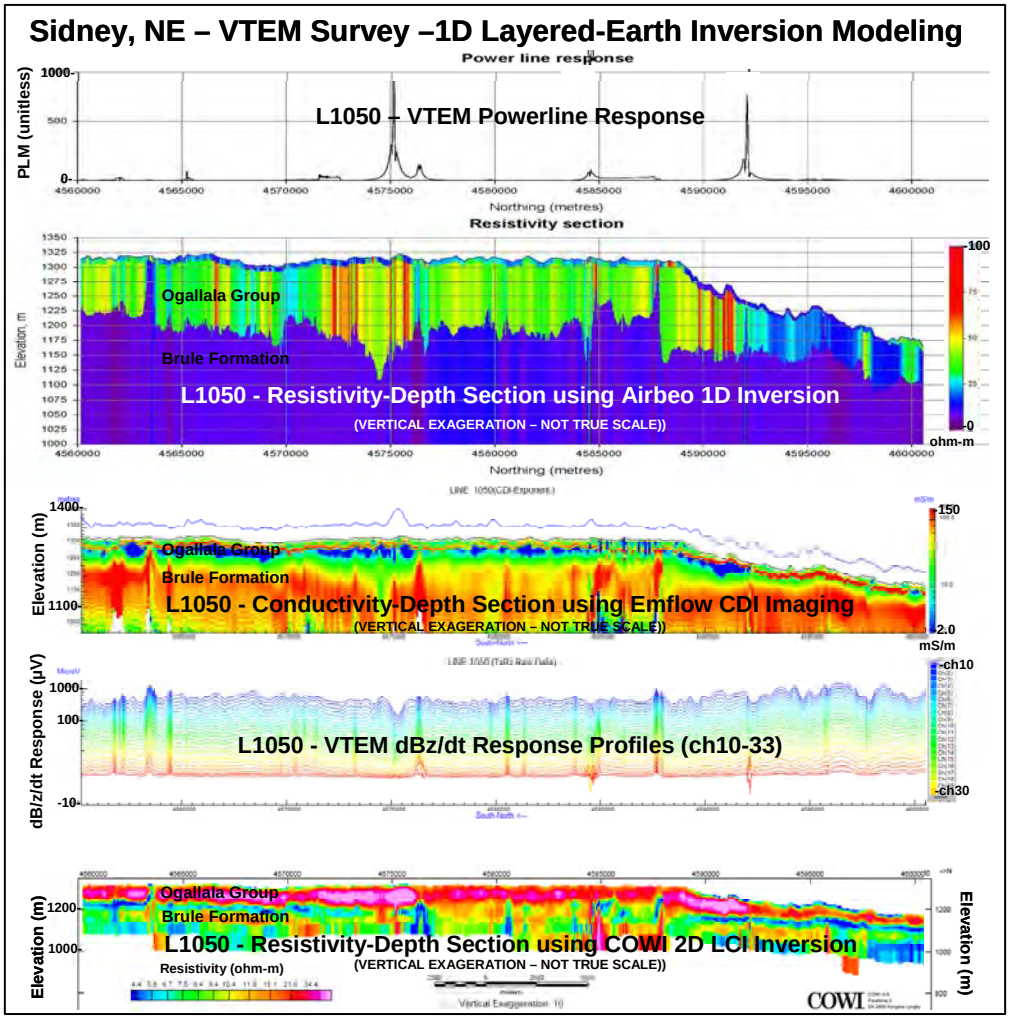

Figure 9: 1D Layered earth inversion modeling results for VTEM central line (L1050) in Sidney Block: a) Powerline monitor profile (top), showing peak responses that coincide with anomalous VTEM data and disrupted 1D layered-earth behaviour; b) Resistivity-depth section from Airbeo 1D LE inversion (2ND from top), showing discrete 3-layer model results; c) Conductivity-depth from EMflow CDI imaging (middle), showing smooth-model (multi-layer) representation; d) VTEM dBz/dt profiles (2ND from bottom) showing alternating peak responses that correspond to metallic and powerline culture, and laterally smooth responses over bedrock geology; e) Resistivity-depth section from COWI 2D LCI inversion (bottom) showing laterally continuous model (19-layer), with sharper layer boundaries than CDI.

The EMflow CDI section for L1050 (Figure 9-middle) is surprisingly similar to that obtained from the Airbeo 1D LE inversion; However the CDI voltage transformation lacks the accuracy, appearing to underestimate the depth-to-basement, and also containing spurious near-surface layering that suggest inversion artifacts. The pseudo 2D LCI smooth inversion (Figure 9-bottom) used a 19 layer model as a simplified starting model not based on any geological or hydrological parameters. The 2D LCI displays more lateral continuity along section than the 1D LE results and sharper layer boundaries relative to the CDI. Similar LCI results along adjacent lines indicate data continuity. The L1050 2D LCI shows a distinct boundary between a higher and lower resistivity layer at 50-125 m depth along the line, which is slightly underestimated relative to the Airbeo 1D LE results and known geology based on well data.

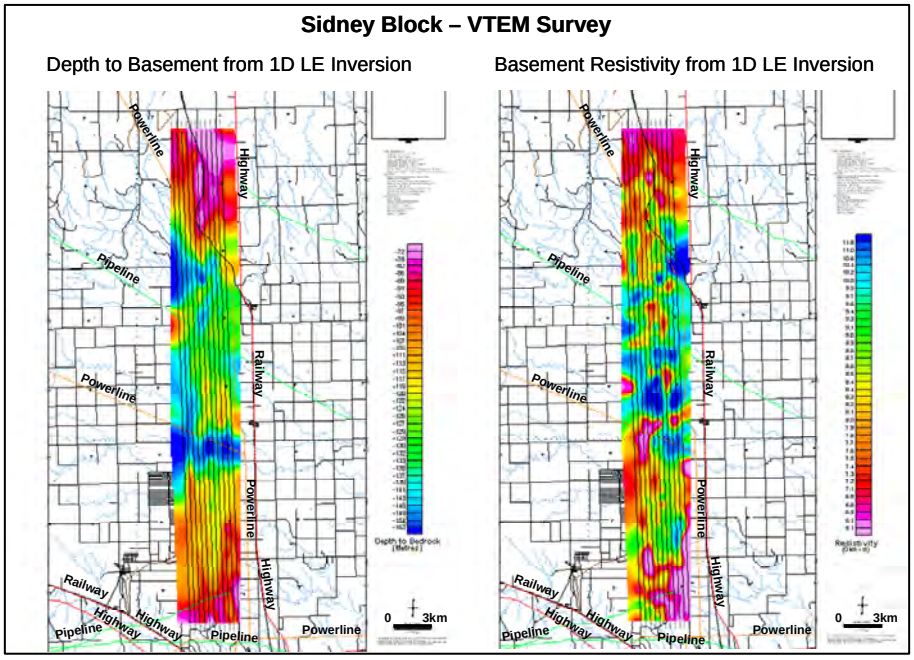

Figure 10: 1D LE Layered earth inversion modeling results for Sidney Block VTEM data shown in plan: a) Depth to basement (left) showing 55-185m thickness variation in Ogallala+Quaternary across survey area; b) Basement Resistivity (right), showing 2-14 ohm-metre variation in Brule Formation.

Conclusions

In the South Platte NRD region of Cheyenne County, in western Nebraska, standard frequency domain helicopter EM systems lack sufficient penetration to adequately map deep aquifers that extend below 160m depths in the Cheyenne Plateau north of Sidney, NE. Synthetic layered-earth model testing showed that the VTEM helicopter time-domain EM system would be capable of mapping the base of the Ogallala Group sand and gravel units above the White River Group Brule Formation siltstone basement rocks to depths below 200 metres. VTEM time-domain EM data were collected from a 4x40km test block where well logs place the base of the Ogallala at 160m depth. In spite of abundant man-made metallic culture that distorts the VTEM data locally, good quality data were obtained. The VTEM data were analyzed using layered-earth (LE & LCI) 1D inversions and conductivity-depth imaging (CDI). Inversion results indicate that the conductive basement at the base of the Ogallala aquifer was successfully mapped to depths estimated at 60 to 160 metres above the Brule basement rocks, which are consistent with the well log data. Based on simulated penetration depths in excess of 200m, VTEM could be extended into deeper, more conductive aquifers in other natural water resource districts of Nebraska.

References

Auken, E., and Christensen, A.V., 2004, Layered and laterally constrained 2D inversion of resistivity data, Geophysics, **69**, 752-761.

Bournas, N., Legault, J.M, and Steffler, E., 2009, Report on helicopter-borne versatile time-domain electromagnetic (VTEM) geophysical survey, Sidney Block, Nebraska, for United States Geological Survey, internal report (9148) by Geotech Ltd., June, 2009, 67 p.

Cannia, J.C., Woodward, D., and Cast, L.C., 2006, Cooperative hydrology study COHYST hydrostratigraphic units and aquifer characterization report, Cooperative Hydrology Study, http://cohyst.dnr.ne.gov/, 96 p.

Martinez, K., Lo, B., Ploug, C., Pitcher, D. and Tishin, P., 2008, Water resources applications with the VTEM system, Expanded abstract, AEM2008: 5TH International Conference on Airborne Electromagnetics, Haikko, Finland, 6 p.

Smith, B. D., Abraham, J.D., Cannia, J.C., and Hill, P., 2009, Helicopter electromagnetic and magnetic geophysical survey data for portions of the North Platte River and Lodgepole Creek, Nebraska, June 2008, US Geological Survey Open-File Report 2009-1110, 27 p.

Steele, G.V., Sibray, S.S., and Quandt, K.A., 2007, Evaluation of ground water near Sidney, Western Nebraska, 2004-05, Scientific Investigations Report 2007-5086, U.S. Department of the Interior and U.S. Geological Survey, 64 p.

Witherly, K., and Irvine, R, 2006, The VTEM airborne electromagnetic system – benchmarking continuous improvement via repeat surveys over time, SEG Expanded Abstracts, **25**, 1273-1277.

Witherly, K., Irvine, R., and Morrison, E.B., 2004, The Geotech VTEM time domain helicopter EM system, SEG Expanded Abstracts, **23**, 1217-1221.

Acknowledgements

The authors thank Geotech Ltd., COWI A/S and the United States Geological survey for allowing the presentation of the survey and study results.

ADVANCES IN THE EVALUATION OF PILE AND SHAFT QUALITY

Frank Rausche, GRL Engineers, Inc., Cleveland, OH
Brent Robinson, North Carolina State University, Raleigh, NC

Abstract

For the past half century, great efforts have been made and progress has been achieved in developing a variety of electronic testing methods for the quality control and quality assurance of deep foundations. These developments took advantage of major advances in ever more accurate and sensitive sensor manufacturing and faster and more powerful computers. The dynamic pile testing methods were the primary beneficiaries of these R&D efforts and its application has been expanded from bearing capacity assessment of driven piles to drilled shafts, micro piles and even penetrometers. In addition to soil resistance, results from construction monitoring now provide information about stresses along the pile, pile integrity and occasionally soil vibrations. Dynamic pile testing methods also include non-destructive techniques involving sonic and ultra sonic signals. Much of the recent developments involved not only ruggedizing hardware and preparation of more user friendly software, but also deriving reliable calculation procedures and presenting results in a way which is easy for the report recipient to understand. Additionally, experiences from construction sites showed that an immediate assessment of the foundation characteristics is imperative. This requirement lead to the need for easily used simulation software and workshops. Today such training events are frequently performed over the internet. This presentation summarizes several recent hardware and software developments and shows a few typical results.

Introduction

Four different types of deep foundation quality evaluations will be examined. They include:

(a) Construction monitoring,
(b) Post construction evaluation of the pile or shaft bearing capacity,
(c) Post construction evaluation of the pile or shaft structural integrity,
(d) Length and quality evaluation of foundations under existing structures.

Main emphasis in this paper will be placed on driven pile monitoring. Monitoring of driven piles by the Pile Driving Analyze® (PDA) and the related Dynamic Pile Load Testing (DLT) with analysis by CAPWAP® (Likins et al., 2008), Pulse Echo Testing (or Pile Integrity Testing, PIT) and Cross Hole Sonic Logging (CSL) are generally referred to as "Dynamic Pile Testing Methods". They rely on motion measurements to determine wave speeds and/or the response of the deep foundation to an impact. Except for the Cross Hole Method, dynamic testing methods also require or make use of force measurements. Most convenient is, of course, that measurements are taken at the pile top, however, embedded sensors have also are occasionally employed as another means of determining concrete quality or pile toe response.

The fourth task, evaluating foundation type and length under existing structures, often is completed by PIT, however, parallel borehole methods are also available. For concrete piles a stress wave is introduced in the pile and sensed in the borehole and for steel piles, an inductive device senses the proximity of a conductor. These methods have been described elsewhere (Rausche, 2004) and will not be further discussed in this presentation.

Additional background information on these methods will be included in the following summary. A few examples will demonstrate those methods which are of primary interest to the geophysicist with an emphasis on recently improved or developed technologies.

Description of Methods

1. Pile Driving Monitoring

This is the most important and most frequently used dynamic pile testing method. Strain (or force) and acceleration measurements of an impact driven pile during installation are the basis for the calculations. Typical strain and acceleration ranges are between 100 and 2000 με and 50 to 2000 g's, respectively. The method has been standardized in ASTM D4945-08. Analysis is done in closed form by the so-called Case Method which solves the one-dimensional wave equation and which has been programmed in a PDA. Taking advantage of the fact that force and velocity at a point can be transformed into the force and velocity components of the upward and downward traveling wave, bearing capacity, pile stresses and pile integrity can be calculated from the upward traveling wave (Likins et al., 2008). Additionally, hammer performance can be evaluated as energy transferred to the pile top together with calculated hammer stroke for open end diesel hammers.

To satisfy the LRFD requirements now demanded by several codes (e.g., AASHTO, 2009), 2 to 5% of the piles on a site are often monitored by the PDA. For reasons of safety, testing speed and convenience, the sensors are now sending signals wirelessly to the PDA. An even greater time and money savings can be achieved by remote monitoring, which allows the experienced test engineers to view the data in real time on their office computer while field personnel installs the sensors and connects the PDA to the internet via broadband devices. The advantage of this method is the ease of test scheduling for the contractor and the reduced travel time and travel cost expense.

Vibrations near a pile driving operation may be considered destructive or at best annoying and certain limits of ground motions have been published (Woods, 1997). More and more frequently it is therefore required to measure surface vibrations in the neighborhood of a pile driving operation. Using commercially available geophones or accelerometers, the PDA accepts, saves and evaluates up to six ground motion signals. This makes possible, direct correlation with energy transferred from the hammer to the pile, pile velocities, or resistances on a blow by blow basis. Furthermore, because the pile impact measurement provides for a distinct trigger signal, accurate timing of the arrival of the compressive wave at the geophone allows for soil wave speed measurements as a function of pile tip penetration (Figure 1). A PDA record of pile top velocity, obtained when a 3 Mg (3.3 ton) ram impacted the 450 mm (18 inch) diameter, augered cast-in-place pile is shown in Figure 2. The pile was 9 m (30 ft) in total length and had a penetration of 8.1 m into the silty, clay soils. Figure 2 also shows vertical particle velocities of the ground surface at a horizontal distance of 6 m (20 ft) and 12 m (40 ft) away from the pile. In this case the compressive wave speeds in the partially saturated soil with slightly frozen top surface was between 975 m/s (3200 ft/s) and 1070 m/s (3500 ft/s). In the future, additional measurements can and should include the horizontal motion components for an assessment of the total, geometric peak particle velocity (PPV).

Combining assessment of ground surface PPV values with pile measurements also can lead to interesting relationships. Figure 3 shows for the site of Figures 1 and 2, the energy transferred to the pile top and the PPV values measured at a 6 m (20 ft) distance from the pile. The transferred energy, calculated as the time integral of the product of pile top force and velocity, was variable because the 3.3 ton ram was dropped from heights between 0.3 (1 ft) and 1.2 m (4 ft).

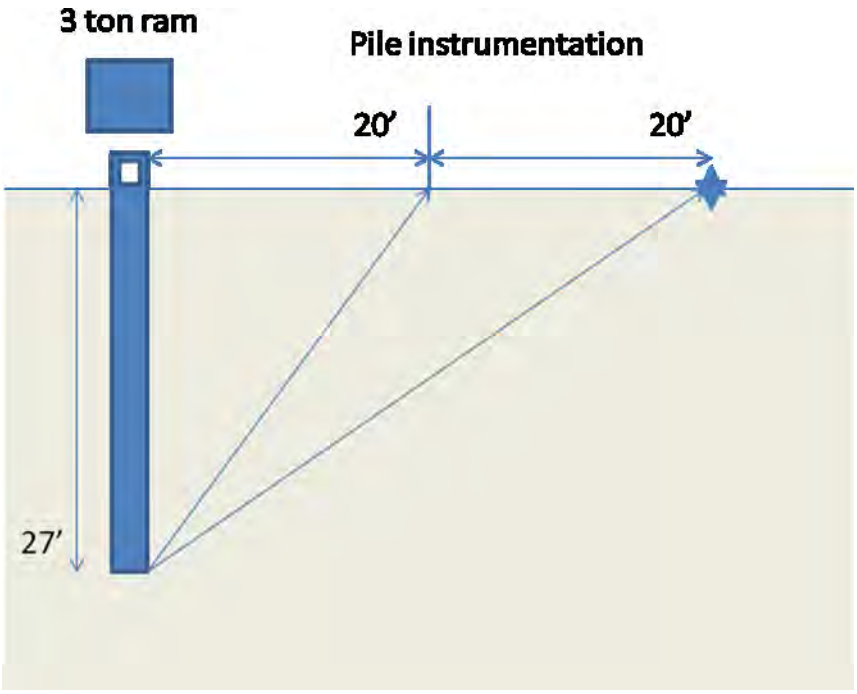

Figure 1: PDA test setup with ground surface velocity measurements.

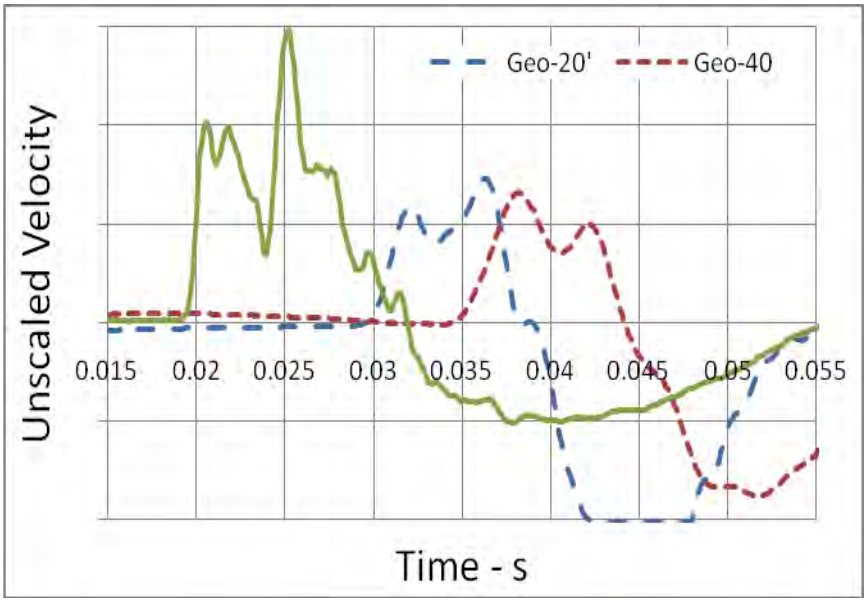

Figure 2: Results from PDA measurements of ground surface and pile top velocity

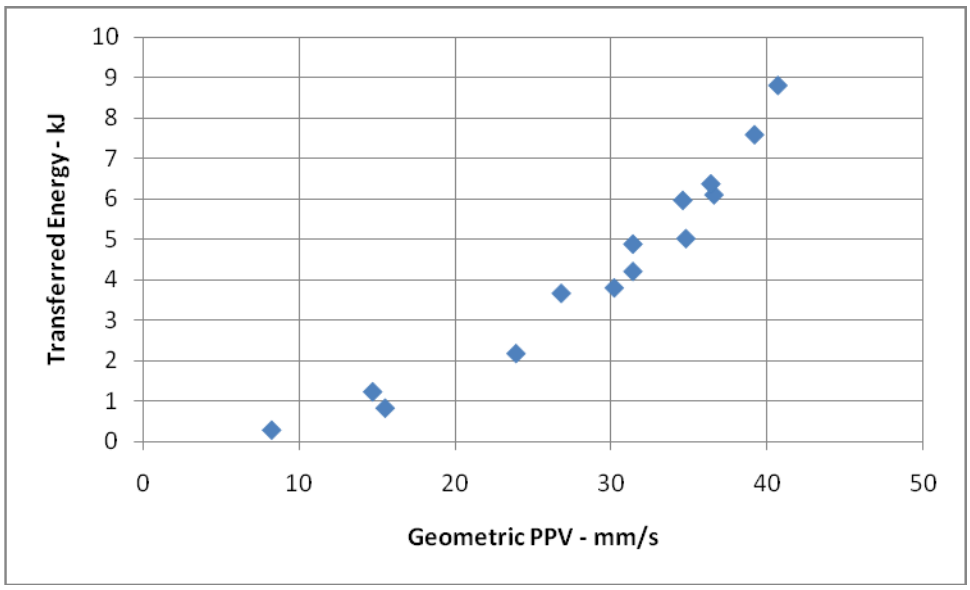

Figure 3: Transferred energy in pile and ground surface PPV at a distance of 6 m (20 ft) from pile

A more extensive study was performed by Robinson, 2006. As shown in Figure 4, he combined ground motion measurements of peak particle velocities (PPV) for consecutive hammer impacts measured at a large construction site in Wisconsin with PDA pile velocity measurements. The PDA monitoring was primarily utilized to determine bearing capacity of the 300 mm (12 inch) to 400 mm (16 inch) diameter, closed ended pipe piles, both at the end of driving and during restrike testing. Using these measurement results, Robinson showed that this information can also be used to develop a wave equation based prediction of PPV at some distance from the pile driving site, based on the GRLWEAP (Pile Dynamics, 2005) hammer-pile-soil model and wave propagation theory.

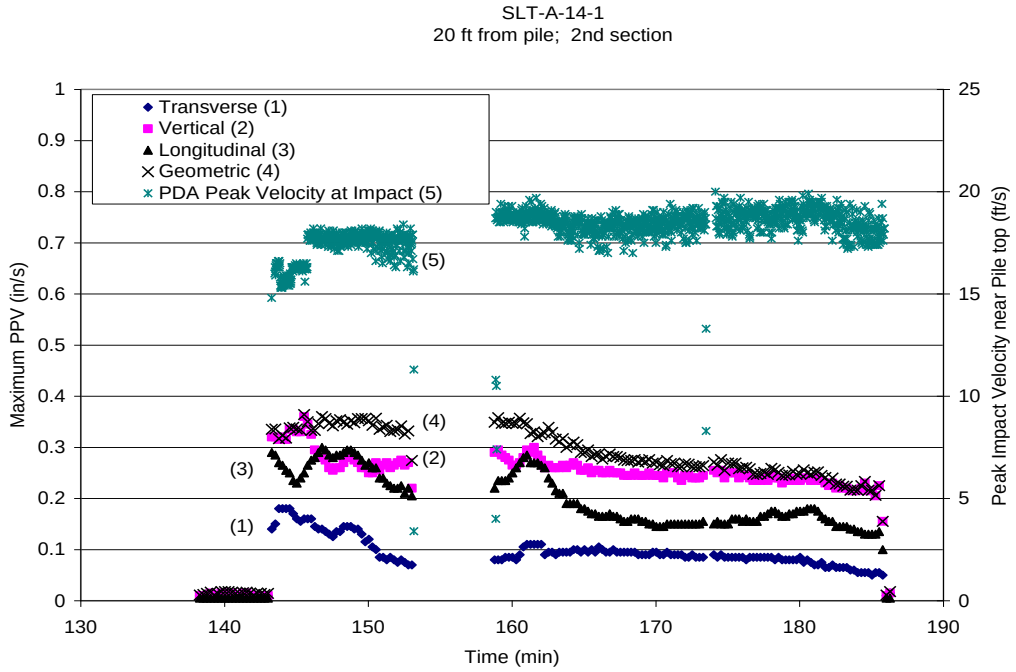

Figure 4: pile top and ground surface PPV values (Robinson 2006)

2. *Dynamic Pile Load Testing*

Performing strain and acceleration measurements at the pile top under a high strain impact according to ASTM D4945-08 yields the necessary measurements for a Dynamic Load Test. The data is analyzed with the numerical CAPWAP approach yielding the load-set curve of a very quick load test. This method is a natural extension of the pile driving monitoring but it has been expanded to very large drilled shafts and to smaller micro piles or ACIP piles (Hussein, et al., 2008; Gomez et al., 2004). In many instances, even for driven piles, a special impact device has to be brought to the site. The so-called APPLE system allows for the measurement of the ram deceleration and, therefore, a pile strain independent determination of pile top force. A pile top transducer is an additional recent development.

Rausche et al., (2007), have described dynamic load test results and their most recent recommendation for the selection of the appropriate record. This is not necessarily trivial, since normally a number of impacts are applied in a dynamic load test and both hammer energy and soil resistance parameters change from blow to blow. Results from a test obtained with a 54 Mg (60 ton) ram on a 1.8 m (6 ft) diameter pile can be seen in Figure 5. In this case, four consecutive hammer blows were evaluated by the CAPWAP program and their simulated load-set curves plotted versus accumulated penetrations.

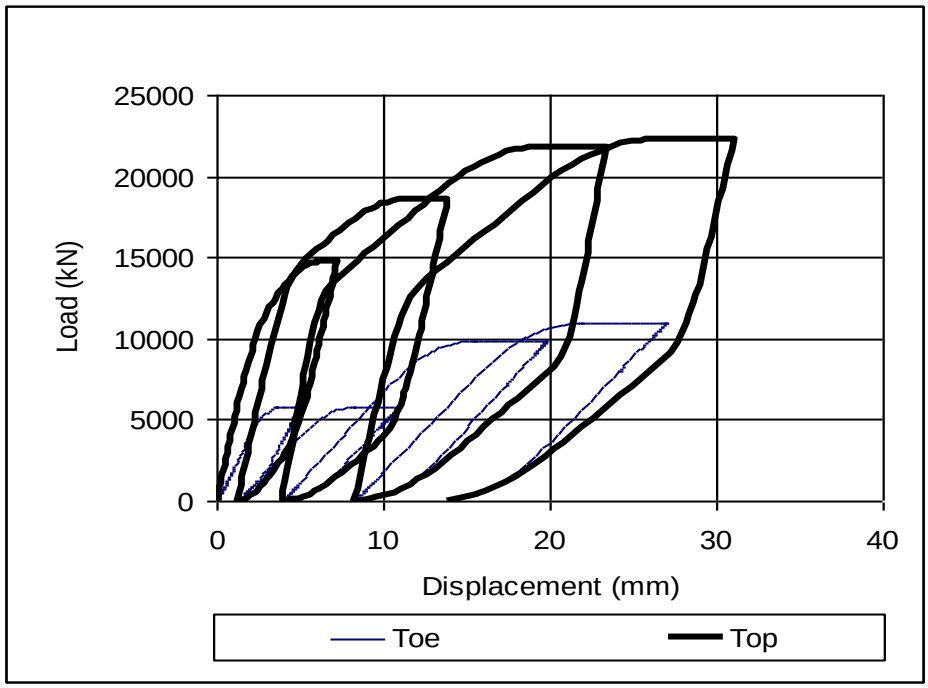

Figure 5: CAPWAP calculated load cycles for 1.8 m diameter drilled shaft (Rausche et al., 2007)

The dynamic load test requires a ram weight between 1 and 2% of the test load. However, it can also take the form of a Rapid Load Test. In this case a very heavy ram, typically 5 to 10% of the required test load, impacts the pile top on a rather soft cushioning. This produces a longer force pulse than the dynamic load test and potentially reduced tension stresses. A recent development, the Hybridnamic device, has a ram weight of up to 80 Mg or 88 tons.

3. *Automatic Blow Count and Hammer Energy Monitoring*

Another, less thorough monitoring of hammer and pile has become necessary because of the variety of pile driving hammers which are being developed and implemented. These hammers offer

different features and performance characteristics. For example, open end diesel hammers are now being built with ram weights of up to 25 Mg (28 tons), while hydraulic hammers offer even higher ram weights and associated driving energies. The working and rating principles of these hammer types differ substantially and require occasional monitoring for energy performance verification. Kinetic energy measurements (that is the energy which the ram has immediately prior to impact) can now be made with the E-Saximeter™. Essentially, the measurements determine ram position and timing information for each hammer blow and these results can be converted to ram impact velocity and therefore the hammer's kinetic energy. For diesel hammers the hammer stroke can also be calculated together with stroke. The relative position between hammer and leads (and thus the pile penetration and blow count) can additionally be measured by digital encoder on a cable fastened to hammer and leads, or by laser, radar or other devices. The measured data can be transmitted to a data collector either wirelessly or through cables. This method of pile installation monitoring can be fully automated and, therefore, can be applied to every pile on a site yielding an electronic pile driving log which can be downloaded to a computer spread sheet..

4. Pulse Echo Integrity Testing

The Pulse Echo Method, embodied in the PIT equipment, requires a low strain (less than 10 με) impact with a hand held hammer (Rausche, 2004). The method is standardized by ASTM 5882-07. Instrumentation includes one or two accelerometers and, optionally, an instrumented hammer. The latest developments do that with wireless equipment and a very low weight, high resolution monitoring equipment (Figure 6).

Evaluation of the records is normally done in the time domain and takes advantage of the fact that the force pulse is a simple half sine pulse which is short compared to the wave travel time. The velocity has a proportional impact pulse but then displays the upward traveling wave which provides information about pile and soil characteristics. The analysis can also be done in the form of mobility vs frequency which additionally yields a dynamic stiffness value. A Pile Profile provides an easily understood visual result. Admittedly, this result is somewhat subjective and relies for its accuracy on (a) knowledge of the concrete volume, (b) the actual pile top diameter and (c) a clear reflection from the pile toe.

Figure 7 shows both a pile top force-velocity-time record (time downward positive) and a calculated profile from a Pulse Echo Test measurement taken on a 610 mm (24 inches) diameter pile. Calculation of this profile involves first the definition of a reference line which accounts for the soil resistance effects on the pile top velocity and secondly, an integration over time of the difference between velocity and reference curves. In the present example, the record indicates a reduction of size of concrete quality between approximately 7 (23 ft) and 9 m (30 ft) depth.

Further analysis provides the response of the pile top in the frequency domain. For the example of Figure 7, the force, velocity and mobility (velocity divided by force) curves are shown in Figure 8. The linear increase of mobility at the origin can be interpreted as a characteristic pile stiffness. Frequency intervals between peak mobility peaks indicate pile length and depth to defect. However, these distance values are easier evaluated in the time domain. Similarly, distinguishing between bulges and necks are also more easily determined in the time plots. The reason is that bulges produce a leading negative signal followed by a positive one while necks have the opposite phase information. Because of the missing phase information in the frequency response plot, such timing information is not apparent.

It should be mentioned that it is very instructive to perform a so-called PIT-S simulation of a Pulse Echo Test. The software is freely available on www.pile.com for initial inspection and tryout. It allows for the variation of hammer impact point, measurement location, soil strength and distribution

and pile configuration. This software is very versatile and aids in the preparation and interpretation of a PIT test.

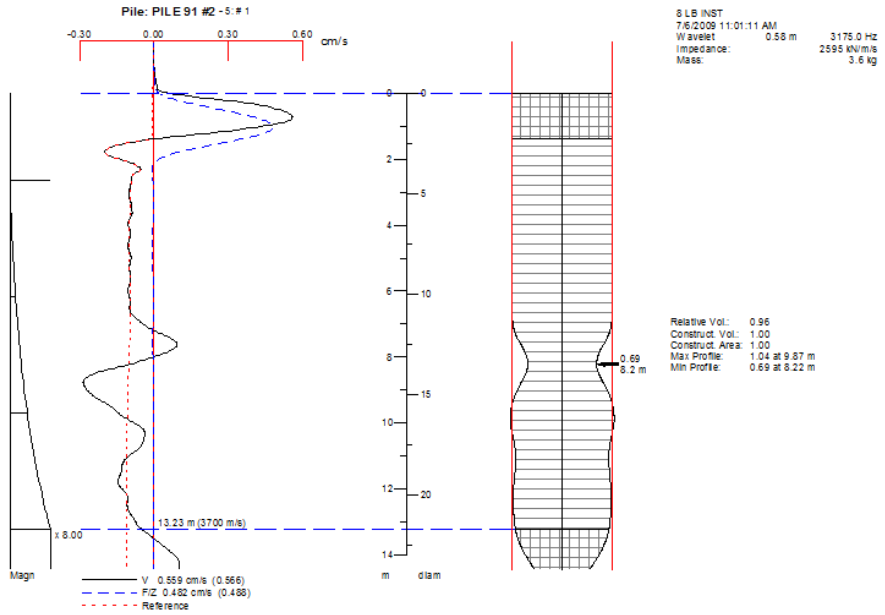

Figure 7: Pile Profile calculated from PIT records for a 610 mm diameter drilled shaft

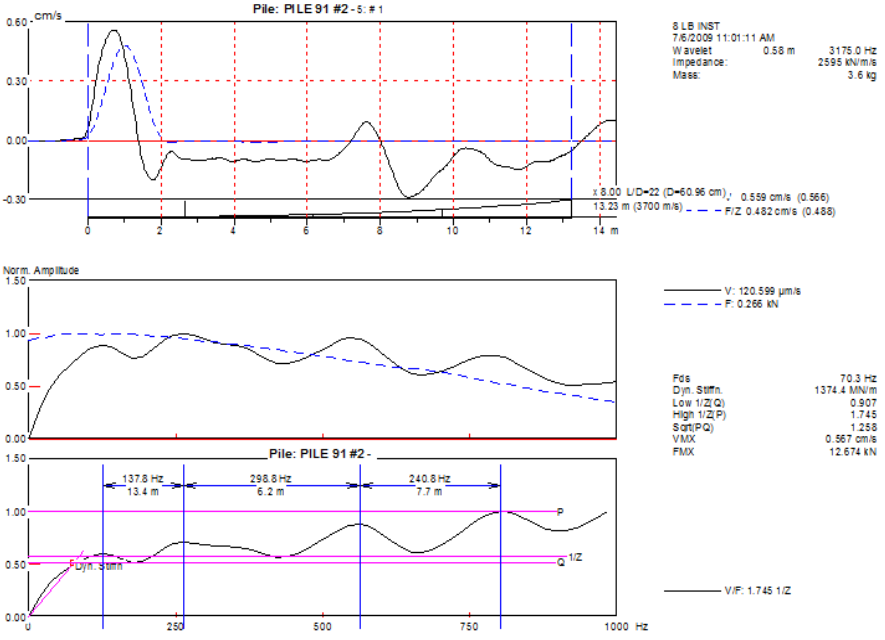

Figure 8: Frequency response of the Figure 7 example

5. Cross Hole Sonic Logging

Cross-Hole Sonic Logging is another dynamic pile testing method which is based on the traveling wave concept. As described by Rausche 2005, the method uses ultra-sonic pulses transmitted horizontally from one vertical inspection tube to another one. Measuring the wave travel time between the inspection tubes yields a detailed concrete quality assessment. The method is standardized by ASTM 6760-08. Recent improvements have been made in the area of sensor sensitivity allowing clear signal arrival detection for distances in excess of 3m (10ft). Also, the work can now be greatly simplified by means of motorized cable drums. The method allows for quality assessments of large piles and/or barrettes. A related method, Single Hole Logging, of either ultrasonic pulses or back scattered gamma radiation, helps identify defects in the concrete cover zone of a drilled shaft. Interpretation is not always simple and further study is warranted.

After a defect has been detected in a shaft by CSL, further quantification is usually desired. This can be achieved with a Tomography analysis which is closely related to geophysical data presentations. The relatively limited information from a CSL test is subjected to an inverse analysis which finds the most likely wave speed distribution in a shaft element grid from the wave speeds measured between inspection tubes. An example is show in Figure 9. This is the image obtained for a 1.5 m diameter shaft of 12 m (40 ft) length with known defects. Measurements were taken between 8 inspection tubes. Zones with concrete wave speeds less than 2100 m/s (7000 ft/s) have been depicted with dark colors as those of potential defects. In the present case these defects were either sheets of Styrofoam or sand filled buckets.

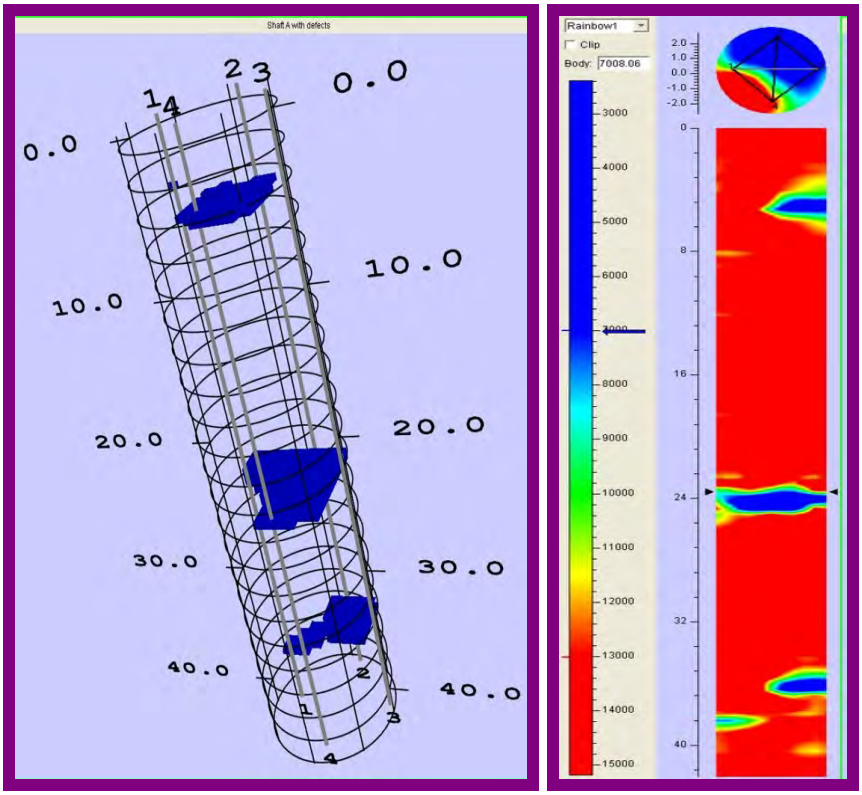

Figure 9: Tomography of a shaft with planned defects.

Summary

Today's deep foundation QA/QC methods take advantage of a number of different dynamic testing methods which are based on motion and force measurements and whose interpretation is based on wave propagation theory. The more powerful methods involve not only motion but also force measurements and provide results of pile capacity, stresses and soil stiffness. Recent developments allow for simultaneous measurements of soil surface motion. In addition, the methods provide for pile material wave speed results which can be interpreted regarding material quality and strength. Advances have been made in the quantity and quality of measurements and in the interpretation techniques. In addition wireless and remote testing technologies help reduce the cost of QA/QC.

References

Gomez, J., Cadden, A., and Webster, O.C., 2004. Static and dynamic testing variability. *Proc. of the 5th Int. Conf. on Case Histories in Geot. Eng.* New York, NY. (CD-ROM).

Hussein, M., Bullock, P., Rausche, F., and McGillivray, R., 2008. Large-scale dynamic high-strain load testing of a bridge pier foundations; *Proc. of the 8th Int. Conf. on the Application of Stress Wave Theory to Piles*, Lisbon, Portugal.

Likins, G., Piscsalko, G., and Rausche, F., 2008a. PDA Testing, 2008 State of the Art , *Proc. of the 8th Int. Conf. on the Application of Stress Wave Theory to Piles*, Lisbon, Portugal.

Pile Dynamics,Inc., 2005. GRLWEAP Background Report, www.pile.com.

Rausche, F., 2004. Non-Destructive Evaluation of Deep Foundations. *Proc. of the 5th Int. Conf.on Case Histories in Geot. Eng.*: New York, NY. (CD-ROM)

Likins, G. E., Piscsalko, G., Roppel, S., Rausche, F., September, 2008. PDA Testing: 2008 State of the Art. *Proc. of the 8th Int. Conf. on the Application of Stress Wave Theory to Piles*, Lisbon, Portugal, pp 395-402.

Rausche, F., Likins, G., and Hussein, M., 2008. Analysis of Post-Installation Dynamic Load Test Data for Capacity Evaluation of Deep Foundations; *ASCE, GSP 180: From Research to Practice in Geotechnical Engineering*, J.E. Laier, D.K. Crapps and M. Hussein, editors; pp 312-330.

Robinson, B., 2006. "Models for Prediction of Surface Vibrations from Pile Driving Records" *Master's Thesis, North Carolina State University*. Accessed January 12, 2010. http://www.lib.ncsu.edu/theses/available/etd-08172006-085403/

Woods, Richard D. (1997). "Dynamic Effects of Pile Installations on Adjacent Structures." *Synthesis of Highway Practice 253.* National Cooperative Highway Research Program.

QUALITY MANAGEMENT OF STABILIZED SOIL CONSTRUCTION USING LAB AND FIELD SEISMIC TESTING

Nathan M. Toohey, Colorado School of Mines, Golden, CO
Michael A. Mooney, Colorado School of Mines, Golden, CO
Nils Ryden, Lund University, Lund, Sweden

Abstract

Current pavement design practice for stabilized soils specifies a 28-day modulus and stiffness value. There is a need to evaluate performance after 5 to 7 days to ensure efficient constructability. There is a large disconnect between quality management programs not only for design and construction, but between lab and field evaluations during construction. The difference in design and measured parameters, lab and field, for performance evaluation does not permit a direct comparison. Current quality management techniques do not permit assessment of the true performance of the pavement construction. Seismic wave based testing offers considerable potential for quality assessment of stabilized soils. Surface wave analysis can be used to assess low-strain or seismic modulus of stabilized soils in the field while travel-time analysis and free-free resonance testing can be used to estimate seismic modulus of laboratory specimens. Lab and field seismic moduli are directly related, thus permitting seismic analysis to bridge the gaps encountered by current quality management techniques. This paper presents lab and field seismic testing protocol and results which indicate its effectiveness as a combined quality management technique.

Introduction

Stabilization of roadway subgrade soils is commonly used to increase subgrade stiffness and strength. The stabilized soil (SS) layer is considered a structural component of the pavement system whereby strength and modulus are important performance-related design parameters (e.g., MEPDG 2007). Figure 1 presents an instance of field application of lime and in-situ processing of soil for stabilization.

Figure 1: Field application and processing of lime for soil stabilization

As the pavement geotechnics community moves towards improved quality assessment, including measurement of performance related parameters, the assessment of SS presents a number of challenges. Strength and stiffness development in SS stems from chemical reactions that continue over months (e.g., Boardman et al. 2001), and design is typically predicated on 28-day modulus and strength. However, efficient construction often requires the evaluation of acceptance after 5-7 days.

Current field practice typically evaluates performance with respect to in-situ moisture and density measurements. This does not effectively indicate values of strength or modulus, establishing as a great disconnect from design parameters for performance evaluation. Laboratory evaluation involves unconfined compressive strength (q_u) testing on field-cored or remolded cylinders. A resilient modulus is determined for cylinders following 28-days of curing, prior to q_u testing. While there are established correlations between resilient modulus and Young's modulus, the specific relationship has been shown to vary. Regardless, resilient modulus is not a design parameter. The disconnect between lab and field parameter measurements for performance evaluation does not permit a direct comparison or provide measurement of the pavement construction's true performance.

There is a need to effectively measure design strength and modulus in both laboratory and field environments. Seismic wave based testing offers considerable potential for quality assessment of SS. Surface wave analysis has been used to assess low-strain or seismic modulus of cement-stabilized soils in the field (Ryden et al. 2006) while travel-time analysis and free-free resonance (FFR) testing has been used to estimate seismic modulus of laboratory specimens (Nazarian et al. 2002, Ryden et al. 2006, Åhnberg 2008, Hillbrich et al. 2007). Lab and field seismic moduli are directly related (Nazarian et al. 2002, Ryden et al. 2006). Seismic testing is nondestructive and can be applied during early field and lab curing. Ryden et al. (2006) and Åhnberg and Holmen (2008) explored FFR-based modulus characterization of cement-treated and lime-treated soils. This paper presents seismic testing protocol and results which indicate its effectiveness as a combined quality management technique.

Conceptual Overview

Seismic analysis can be effectively performed in both lab and field environments to measure a low-strain (seismic) modulus. While the conceptual background and data analysis techniques are similar for lab and field application, the basic equipment and testing procedures do vary. Laboratory testing employs the FFR test. Field testing uses a multi-analysis surface wave (MASW) technique. Test setups for both lab and field applications are shown in Figure 2. This section describes the individual testing protocols and the conceptual fashion in which these analyses can be used in tandem to accurately and efficiently assess construction performance.

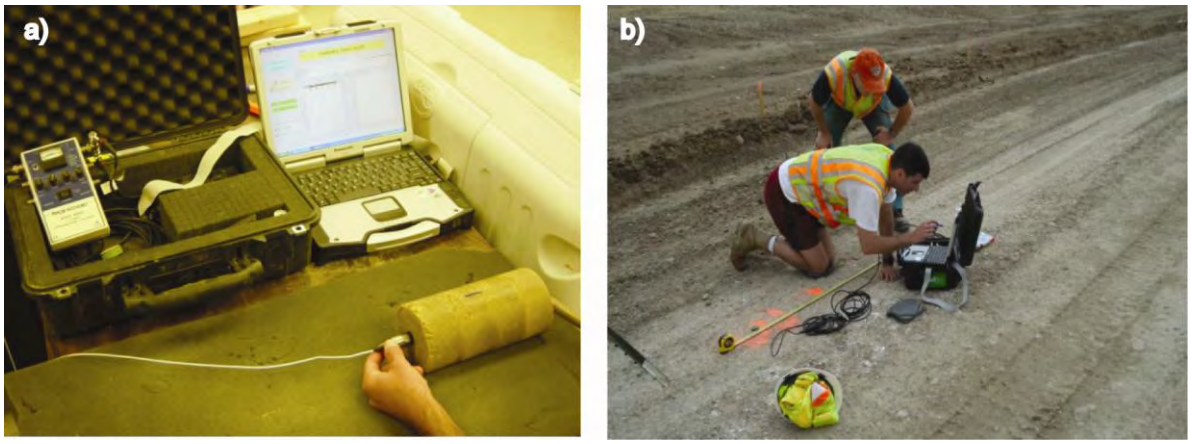

Figure 2: Seismic test setups for lab (a) and field (b) applications

In the lab, FFR testing is performed with the stabilized soil cylinders lying horizontally on a sheet of foam. On a daily basis, specimens are subject to longitudinal excitation, to measure resonant frequencies associated with compressive wave propagation. To ensure accurate and representative results, each test consists of impacting the specimen 5 times. A fast-Fourier transform (FFT) is performed on each vibration time-history response and the average resonant frequency is determined from the 5 records.

FFR testing involves the measurement of a specimen's natural frequency of free vibration. Knowing the specimen's mass density (ρ) and length (L) permits the calculation of a low-strain (seismic) Young's (E) modulus from the resonant frequencies measured during longitudinal (f_{rp}) excitation. For specimens having length-to-diameter ratios of 2 or more, E can be determined using Equation 1 (Nazarian 1999), where V_p is the wave velocities.

$$E = \rho(2 f_{rp} L)^2 = \rho(V_p)^2 \qquad (1)$$

In the field, non-destructive surface wave testing can be performed to estimate the seismic Young's modulus (E) of the stabilized soil. Surface wave testing of the thickness and stiffness of the top layer is especially robust and accurate since it does not require the full inversion of deeper embedded layers (Nazarain et al. 1999). If the shear wave velocity (V_S) is estimated using surface waves the corresponding seismic E-modulus can be calculated using Equation 2, where ν is Poisson's ratio.

$$E = 2\rho(V_S)^2(1+\nu) \qquad (2)$$

If the stabilized soil layer is significantly stiffer than the underlying unsaturated soil, an even simpler alternative is to evaluate the direct P-wave velocity propagating along the surface. Assuming Lamb wave type of wave propagation within the stabilized layer, the seismic E-modulus can then be calculated by Equation 3, where ν is taking the 2D boundary conditions into account.

$$E = \rho(V_p)^2(1-\nu^2) \qquad (3)$$

A schematic of a typical seismic field test set-up is shown in Figure 3. The system is comprised of a portable computer for data acquisition, a fixed accelerometer acting as the receiver, and a hammer serving as the impact source. The hammer provides an impact source at variable distances from the fixed accelerometer. Surface seismic waves measured from multiple source locations are used in the MASW technique to determine a seismic *E*-modulus.

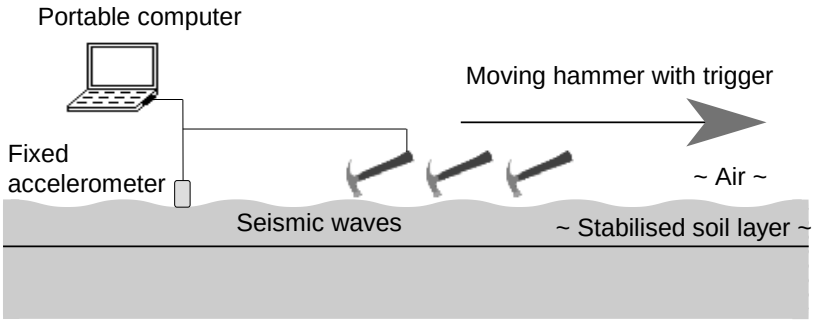

Figure 3: Schematic field set-up using one receiver and one source to record a MASW data set.

Since both techniques measure the same low-strain seismic modulus, their results are directly comparable. A direct comparison enables lab and field testing to be used in tandem for an accurate and efficient construction management technique. Prior to construction, daily FFR lab testing permits the establishment of a soil-specific modulus growth curve for the entire 28 day curing duration (Figure 4).

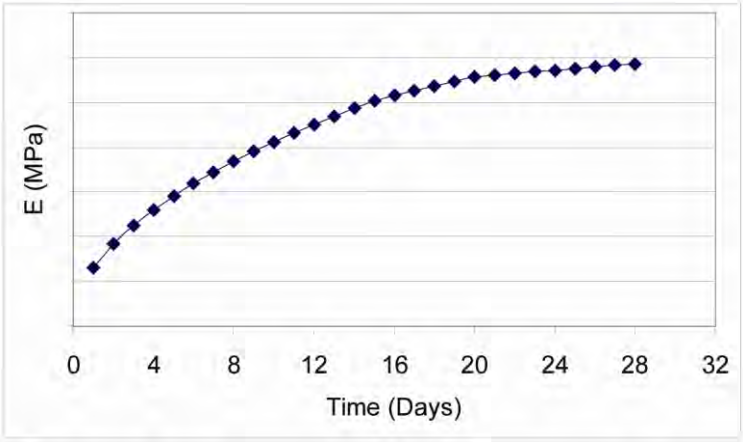

Figure 4: Hypothetical modulus growth curve determined from FFR testing prior to construction

Field testing with MASW a few days following construction completion can be directly compared to the modulus growth curve established in the lab (Figure 5). As shown in Figure 5, acceptance can be determined based upon comparison of the pre-determined lab modulus value and the in-situ field value measured for a given day. Field measurements are indicated in Figure 5 by open circles. Acceptance requires that field measurements lie above the pre-determined modulus growth curve including an appropriate safety factor. Measurements falling below the curve indicate performance failure.

Figure 5: Comparison of field measure modulus to pre-determined lab modulus growth curve.

Sample Results

Extensive research has been performed regarding the effectiveness of both lab and field seismic testing and analysis (Toohey 2009, Ryden et al. 2006). As previously mentioned, data analysis and processing for both lab and field seismic analysis are similar. The following section presents results of the research performed by Toohey (2009) and Ryden et al. (2006) for stabilized soils in the lab and field, respectively.

Lab FFR testing was employed on a near daily basis to monitor the growth in soil modulus resulting from time-dependent pozzolanic reactions. The growth in seismic modulus during curing of five specimens from two lime-stabilized soils (LSS) is presented in Figure 6. Day 1 to 28 modulus gain was significant for both soils 1 and 2, nominally 350%, and 250%, respectively, as measured from day 1 modulus. It should be noted that Figure 6 demonstrates some variability in growth curves between specimens for a given soil. This is largely due to the heterogeneous nature of soil. A more detailed discussion of factors influencing testing variability is presented by Toohey (2009).

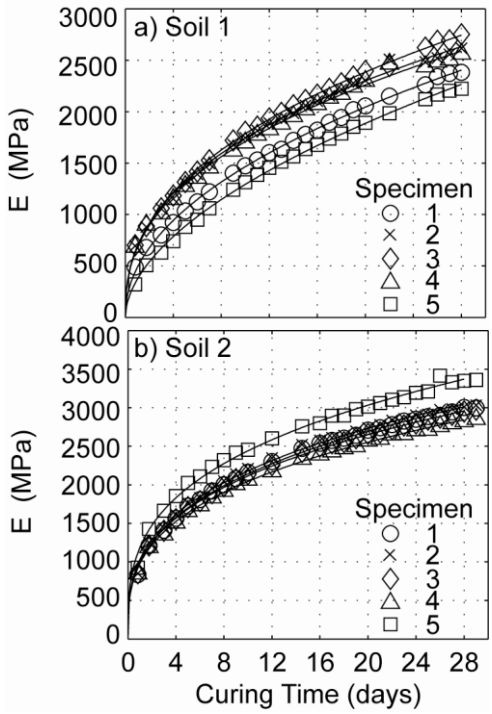

Figure 6: Modulus growth with curing time for two lime-stabilized soils

In addition to modulus, unconfined compressive strength q_u also serves as a performance-based parameter for LSS pavement layers. Both 28-day and 7-day q_u values are of interest for long term performance assessment and short term constructability, e.g., construction trafficability. The direct assessment of q_u traditionally requires compression testing of LSS specimens either remolded from field-mixed soil and cured or directly cored from the constructed layer. Similar to modulus, there is a need to predict 28-day q_u from early curing data.

The observed relationship between E and q_u for both soils is shown in Figure 7. For the two soils, unconfined compression testing was performed (per ASTM D5102) on the 100 mm diameter by 200 mm tall specimens following 3, 6, 7, and 14 day curing (3 specimens each day) and 28 day curing (5 specimens). The data in Figure 7 reflects the averages of the 3 or 5 specimens accordingly. The data in Figure 7 indicates that the proportionality of E and q_u does not change during curing, at least beyond the initial 3 days. Each soil exhibits relatively linear E and q_u relationships with curing time. The proportionality of E and q_u is somewhat soil dependent, i.e., see the regression-estimated slopes in Figure 7. However, when plotted together, one regression equation provides a reasonable estimate for each of the soils. These results suggest that E provides an acceptable predictor for q_u. And because the proportionality of E and q_u is constant with curing time, early day E data would provide a reasonable estimate of 28-day q_u.

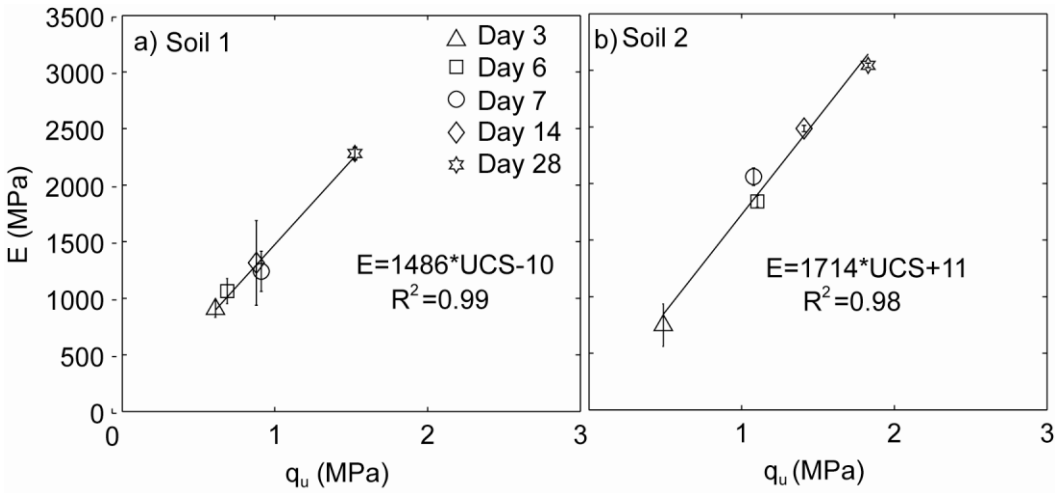

Figure 7: Relationship between E and q_u for each soil. Each point reflects the mean of 3 or 5 specimens; error bars reflect 1 σ uncertainty

Figure 8 shows an example of a typical MASW data set recorded on top of a 0.25-0.30 m thick stabilized soil layer. Data was collected using only one receiver (accelerometer) and multiple hammer impacts from distances of 0.10 to 3.0 m at 0.10 m increments along the surface. The recorded data is presented as a multi-channel record in Figure 8a. The P-wave velocity, 1698 m/s, is evaluated from the first arrivals in the time domain and indicated as a red dotted line in Figure 8a. For good quality seismic data with a high signal-to-noise ratio, this simple evaluation of the direct P-wave is all that is needed to estimate the seismic E-modulus of a stabilized soil layer resting on a softer unsaturated soil (Equation 3).

Surface wave analysis can also be performed on the same data set and is usually more robust for estimating a mean E-modulus of the stabilized layer. Figure 8b shows the same data in phase velocity-frequency domain using the MASW transformation technique (Park et al. 1999). The matching dotted red curve plotted on top of the measured data is a fundamental anti-symmetric (A0) Lamb wave dispersion curve. This theoretical dispersion curve is a function of both the shear wave velocity (V_S) and the thickness of the top layer, making it possible to estimate both these parameters. The seismic E-modulus can then be calculated using Equation 2 and the compressive strength estimated from the correlation presented in Figure 7.

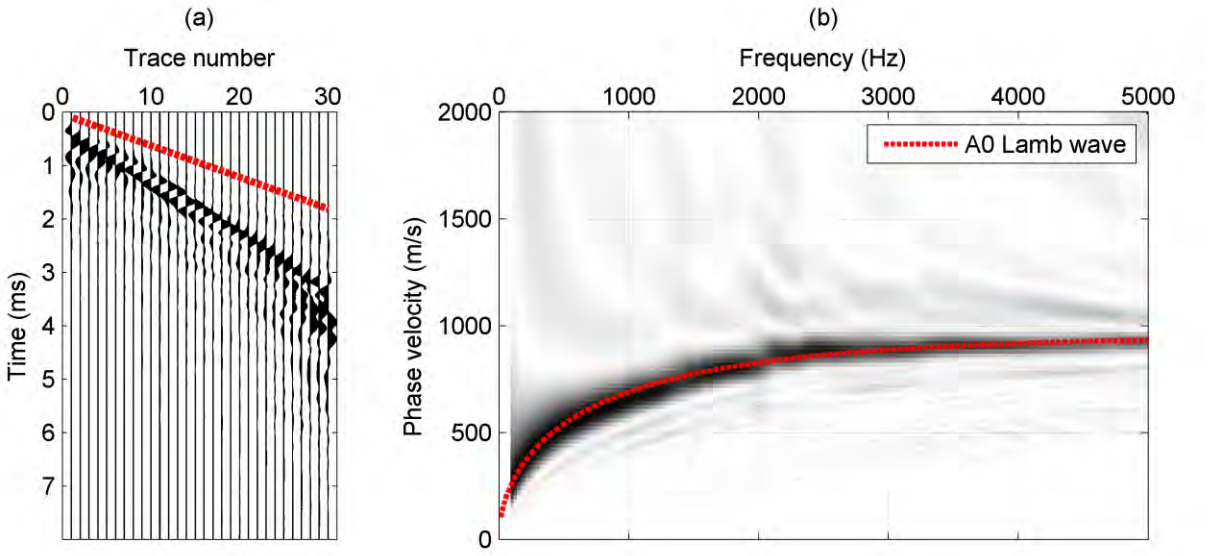

Figure 8: Typical MASW data set from a stabilized soil layer in (a) distance-time domain and (b) phase velocity-frequency domain. The first arrival P-wave velocity is indicated by a red dotted line in (a) and the matching A0 Lamb wave dispersion curve is plotted with a red dotted line in (b).

Conclusions

Current pavement design practice for stabilized soils specifies a 28-day modulus and stiffness value. There is a need to evaluate performance after 5 to 7 days to ensure efficient constructability. There is a large disconnect between quality management programs not only for design and construction, but between lab and field evaluations during construction. The true performance of the pavement construction is not being assessed with respect to design parameters. Lab and field performance assessments are based on different parameters and thus do not permit a direct comparison. Seismic testing can measure the same low-strain (seismic) Young's modulus in both lab and field environments. There is evidence to suggest a strong correlation between seismic modulus and unconfined compressive strength, indicating that seismic analysis can be used to predict q_u. Seismic analysis has the potential to bridge the gaps encountered in current quality management programs for stabilized soils.

REFERENCES

Åhnberg, H. and Holmen, M., 2008, "Laboratory determination of small-strain moduli in stabilized soils," Swedish Geotechnical Institute, Sweden.

ASTM D 5102, 2004, "Standard Test Method for Unconfined Compressive Strength of Compacted Soil-Lime," ASTM International, West Conshohoken, PA.

Boardman, D.I., Glendinning, S., and Rogers, C.D.F., 2001, "Development of stabilisation and solidification in lime-clay mixtures," *Geotechnique*, Vol. 50, No. 6, pp 533-543.

Hilbrich, S.L. and Scullion, T., 2007, "Rapid Alternative for Laboratory Determination of Resilient Modulus Input Values on Stabilized Materials for AASHTO Mehanistic-Empirical Guide," *Transportation Research Record* 2026, Journal of Transportation Research Board, TRB, National Research Council, Washington D.C., pp.62-69.

Mechanistic-Empirical Pavement Design Guide (MEPDG), 2007, www.trb.org/mepdg/.

Nazarian, S., Yuan, D., and Arellano, M., 2002, "Quality Management of Base and Subgrade Materials with Seismic Methods," *Transportation Research Record* 1786, Journal of Transportation Research Board, TRB, National Research Council, Washington D.C., pp.3-10.

Nazarian, S., Yuan, D., and Tandon,V., 1999, "Structural Field Testing of Flexible Pavement Layers with Seismic Methods for Quality Control," *Transportation Research Record* 1654, Transportation Research Board, Washington D.C., pp. 50-60.

Park, C.B., Miller, R.D., and Xia, J., (1999) "Multichannel analysis of surface waves", *Geophysics*, Vol. 64, pp.800-808.

Ryden, N., Park, C. B., Ulriksen, P. and Miller, R. D., 2004, "Multimodal approach to seismic pavement testing", *Journal of Geotechnical and Geoenvironmental Engineering*, ASCE, Vol. 130, No. 6, pp. 636-645.

Ryden, N., Ekdahl, U., and Lindh, P., 2006, "Quality Control of Cement Stabilised Soils using Non-Destructive Seismic Tests," Advanced testing of fresh cementitious materials, Lecture 34, August 3-4, 2006. Stuttgart, Germany.

Toohey, N.M., 2009, "Determination of Strength and Modulus Gain for Lime-Stabilized Soils," Master's Thesis, Colorado School of Mines, Golden, CO.

INTEGRATED THREE DIMENSIONAL GPR AND EM STUDY OF THREE LARGE WATER SUPPLY PIPES

Steven P. DiBenedetto, Underground Imaging Technologies, Inc.
Heron R. Mochny, Malcolm Pirnie, Inc.

Abstract

A new 16-inch municipal water supply line is to be installed between two siphon chambers in the right-of-way (ROW) of three very large diameter (9+ft) steel water supply conduits in the northeastern United States. While excellent as-built records of the conduits were available, given the age of the infrastructure, exact surveyed locations of the large water supply pipes were unknown within the ROW, and were required during the design phase of the project in order to safely perform geotechnical borings and facilitate the routing of the installation trench for the 16-inch line. Additionally, the mapping of any underground utilities within the ROW and adjacent to an existing pump station was required for design in advance of excavation and construction activities relating to the expansion of the pump station.

A geophysical survey was performed by Underground Imaging Technologies, Inc. (UIT), acting as a subcontractor to Malcolm Pirnie along the ROW in order to determine the precise location of the large water supply pipes and also the locations of any underground utilities or other subterranean features that may interfere or otherwise impact the installation of the new waterline. Multi-channel Ground Penetrating Radar (GPR), multi-sensor Time Domain Electromagnetic Induction (TDEMI) and a Ground Conductivity Electromagnetic (GCEM) survey was performed to obtain the requisite data. The geophysical survey was performed between May 19th and 22nd, 2009 and over 182,000 square feet were surveyed. The results of the geophysical survey were able to accurately determine the horizontal positions and depths of the water supply pipes throughout the investigation area, in addition to mapping the positions of utilities in the vicinity of future construction for a pump station upgrade. Several geological anomalies were detected that warrant consideration in any excavation or construction activities.

Depth below ground surface of the pipes obtained via GPR was converted to elevation by subtracting from USGS 10m DEM ground surface elevation. This allowed for the construction of a fully georeferenced, elevation-based, three-dimensional digital model of the pipes within the investigation area in AutoCAD.

Geophysical Approach and Tools

A multi-instrument geophysical approach was selected for this project in order to ensure the highest chances of success in locating the water supply pipes and any other utilities present within the survey area. Three separate, complimentary geophysical technologies were utilized to accomplish the goals. These technologies included Ground Penetrating Radar, Time Domain Electromagnetic Induction (TDEMI), and Frequency Domain Electromagnetic Induction. Each technique has its specific advantages and potential drawbacks, but when all devices are combined the resulting integrated survey has a much greater likelihood of detecting buried features and being able to provide depth estimations.

Ground penetrating radar was the primary component of the work performed on this project and two frequencies and deployment strategies were utilized. A major benefit of GPR is that it can provide a more refined depth estimate of any detected features if soil conditions are known and it is also is able to

detect non-metallic utilities and features. The main drawback for GPR is that its penetration depth can be limited by clay rich, moist, or otherwise conductive soil conditions that attenuate the radar signal.

TDEMI is essentially a sensitive metal detector that allows for the precise discernment of the conductivity of the ground beneath the instrument. The signal response can be used, in some cases, as a proxy for depth to a metallic feature. However, this instrument is generally only able to detect highly conductive (i.e., metallic) features. Also it is susceptible to interference from above-ground metallic objects in the vicinity of the device, and external EM fields produced by power lines.

Ground Conductivity EM is a frequency domain ground conductivity measurement technique, that is similar to Time Domain EM, but the configuration of the device allows for a much deeper depth of investigation. The DualEM-4 device utilized on this project has a transmitter-coil spacing that provides investigation depths up to approximately 20 feet depth. However the sensitivity of the device also makes it susceptible to interference from any metallic objects within an approximately 20 foot radius.

Multi-Channel GPR System

The TerraVision II^{TM} multi channel Ground Penetrating Radar (GPR) system used by UIT is a 14-channel, cart-based unit that is typically towed behind a vehicle during survey operations, as shown in Figure 1. The GPR system consists of two banks of seven (7) antennas each arranged in a herringbone pattern with a fixed spacing between each antenna module of 4 in (12 cm). Data are acquired by each of the 14 channels at a spacing of 0.08 ft (1 in. / 2.5 cm) in the direction of travel, i.e., 12 measurements per foot. The complete 14 channel system is capable of imaging a 5.12 ft wide data swath in a single pass and multiple adjacent survey passes are typically performed to create a three dimensional (3-D) data set covering the entire project area. The central frequency of each GPR antenna element is nominally 400 MHz.

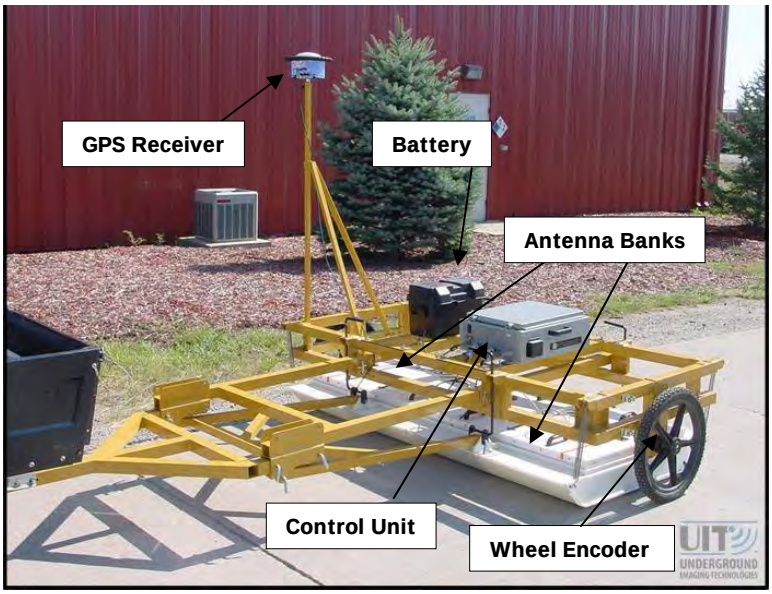

Figure 1: Multi-Channel GPR system and its components.

The system can acquire data at speeds of 2 to 3 miles per hour across the ground surface with acquisition timing controlled by a wheel encoder whose secondary function is to measure survey line length. Positioning information is logged with a differential global positioning system (DGPS) receiver and robotic total station. Data recorded via each antenna bank are stored in separate computers housed

in the system control unit and are later downloaded to the primary acquisition computer. The GPR data sets are processed using standard GPR algorithms and merged with the appropriate GPS and total station positioning data files. The multiple survey swaths, georeferenced to the desired coordinate system, are assembled into composite three-dimensional (3-D) data blocks of the project area from which existing buried utilities and other subsurface features may be interpreted. The interpreter uses special proprietary three dimensional geophysical interpretation software that allows for the import of multiple formats of geophysical, and cadastral and survey data including orthorectified aerial photos, CAD as-built and survey plans, 3D GPR data, and EMI data. This specialized "geophysical GIS" software is used to interpret the varied datasets in layers and record the detected target locations, depths, and orientations such that the information may be documented and/or transferred to standard CAD/GIS software for presentation.

A 200MHz single channel GPR antenna was also used to collect data in multiple transects perpendicular to the water pipes. This was the main dataset utilized to plot the positions and depths of the large pipes, while the multi-channel GPR data was used to search for unknown utilities, confirm the locations of known utilities on as-built maps, and investigate geologic conditions throughout the ROW and adjacent to the pump station.

Multiple Sensor TDEMI System

The multi-sensor time domain electromagnetic induction (TDEMI) system consists of three Geonics EM61-MK2 coil systems configured and synchronized to operate simultaneously as a single array along a survey swath. The TDEMI coils are mounted on an electrically non-conductive deployment cart (Figure 2) that is towed behind a survey vehicle. The complete system is able to cover a five (5) foot wide swath in a single pass at survey speeds up to 5 miles per hour. The TDEMI system is calibrated in an area free of conductive objects prior to any surveying in order to maximize the response to any buried metallic features.

The individual TDEMI coil systems are time domain based metal detectors which detect both ferrous and non-ferrous metallic objects. Each system consists of a transmitter coil which generates a pulsed primary electromagnetic field using a unipolar, rectangular current. This primary field induces secondary currents in any buried metallic objects or other subsurface, electrically conductive targets. Two receiver coils measure the decay of the secondary EM field response using four time windows or gates after shut-off of the primary field. The four time gates are centered at 256, 406, 706, and 1306 microseconds (μsec) after the transmitter coil is turned off and the measured secondary response is recorded in terms of millivolts (mV). The four time gates are referred to as Channels 1, 2, 3, and 4, respectively. Using this TDEMI system array, the response for an isolated metallic target is a typically a single peak which can be easily identified and located in profile or contour plots of the data..

The TDEMI data acquisition software can trigger the transmitter coils based on distance with a wheel encoder or based on time at 0.5 or 1.0 second intervals. A 0.2m distance interval was utilized for this project. Position information is acquired simultaneously using a global positioning system and robotic total station survey which is then merged with the TDEMI data acquired from the four data channels of each of the three coils. Converting the geographic positioning information to the desired coordinate system, the data response from each of the three coils' four time gates are plotted in two-dimensional (2-D) contour plots in order to determine the location of any buried, electrically conductive targets. In certain instances, the depth to a target may be estimated from data inversion algorithms.

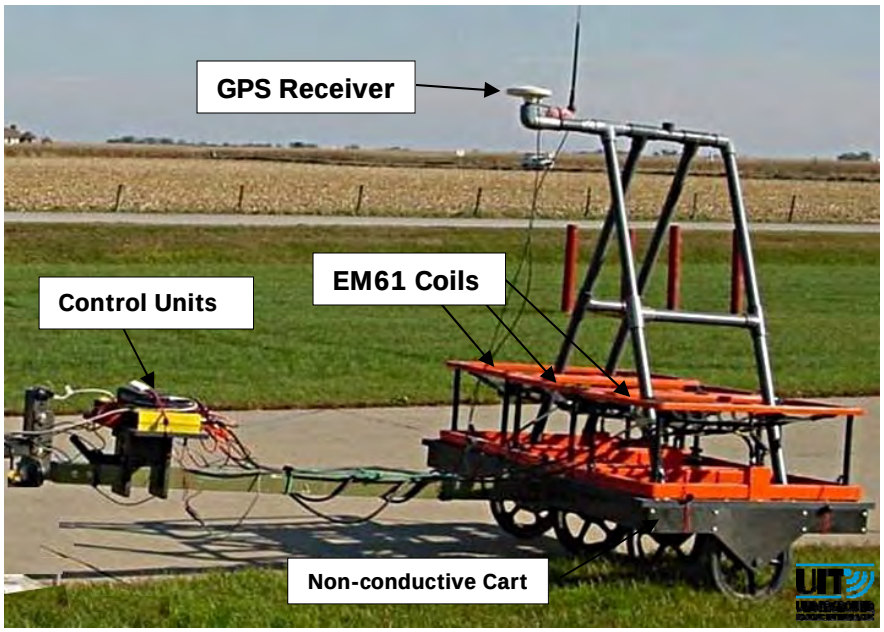

Figure 2: Multiple sensor TDEMI cart and its components.

Ground Conductivity System

While the multi-sensor TDEMI system above is typically used as a large metal detector to locate buried utilities, a frequency domain EM device was utilized in this project in order to measure overall conductivity of the subsurface and potentially detect deeper conductive targets. The geo-conductivity electromagnetic (GCEM) sensor used for this study was the DUALEM-4 terrain conductivity system. This GCEM system incorporates a dual-geometry consisting of a horizontal transmitter coil and two receiver coils oriented horizontally and vertically. The transmitter coil generates a time-varying electromagnetic field using an alternating current. This primary field induces secondary currents within the subsurface in any buried metallic objects or other buried electrically conductive targets. The receiver coils sense these secondary electromagnetic fields and measure both in-phase and quadrature phase components. The system uses the ratio between the measured secondary quadrature response and the primary quadrature to determine the apparent terrain conductivity. The apparent conductivity is measured in terms of milliSiemens/meter (mS/m). Metallic features yield complex EM characteristics which may be delineated using the in-phase response measurements from each transmitter-receiver coil pair. These measurements are recorded in terms of 'parts-per-thousand' or ppt of the secondary field as compared to the primary field. The ability of the GCEM instrument to measure both in-phase and quadrature of two coil orientations enhances its capability to detect pertinent features of the site by allowing separation of shallow average response (HCP) from deeper average response (PRP).

The sensitivity of the device and the 4 meter (13 ft.) transmitter-receiver coil spacing results in a large area over which the instrument is responsive to metallic objects. In an urban environment it is susceptible to stray electromagnetic field responses produced by passing vehicles, overhead power and telephone lines, signs, fences, parking meters, manhole covers, and other metallic items. In this case, there were high-tension high-voltage electrical transmission lines present directly above the majority of the northern portion of the investigation area and the water supply pipes themselves were large metallic features over 9 feet in diameter. These conditions overwhelmed the instrument with response amplitude, impacted the character of the data, and hindered the ability to isolate the subtle departures in conductivity values from the background level produced by the targeted buried metallic utilities. The

GCEM data was not reliable enough to be included in the analysis and was not used in the interpretation; however, TDEMI data was more than sufficient to map the location of the water supply pipes (Figure 3).

Geophysical Survey Results

The project investigation area was broken down into three areas, Eastern, Central, and Pump Station. Over the course of the four days of data collection, over 24,300 linear feet of multi-channel data swaths were collected, equivalent to over 64 miles of "single channel" GPR data, in addition to over 4 acres of multi-sensor TDEMI data. The following is a brief discussion of the results of the geophysical survey within each individual area.

Figure 3: Aerial photo of individual investigation areas.

Eastern Area

This was a small ~10,000 square foot area triangular shaped area located between two roads. Geotechnical borings collected soon after geophysical data collection indicated groundwater was likely above the large water pipes at the time of data collection preventing their detection with GPR. However, a subtle anomaly along the projected trend of the large pipes from their location further to the west was present within the TDEMI data confirming their location in this area. Multichannel GPR and EM data in this eastern area was able to confirm and map the presence of numerous shallower utilities associated with an adjacent pumping station (Figure 4). Figure 4 shows the correlation between interpreted GPR data (red lines) and as-built position of waterline (blue line with "W") especially through center where a "kink" is present in the waterline. Also, the reddish anomaly in the inset image of the EM data corresponds to the position of this shallower service waterline and an associated manhole. Several other utility features were located and mapped within the data as well.

Central Area

This was the largest of the study areas, and consisted of an open grassy field sloping upwards towards the west. Figure 5 shows the results obtained through this area. These results indicate the correlation between the plotted water supply pipe position (solid blue lines) obtained from 200MHz single channel GPR and the linear trending EM anomalies produced by the pipes. The intensity of the color and relative response is also a proxy for pipe depths; i.e., those areas with higher responses (reds, blues & greens) correspond to those areas where pipe depth is shallowest. Note how shallow the central and northern pipes are through the area of cross section X-X' and how the deepest southern (left) pipe does not have a corresponding EM anomaly in the upper image.

This is excellent confirmation of the pipe position obtained through data fusion. The greens and blues of mid amplitude response along the northern portion are caused by interference from the overhead high-tension power lines (Figure 6). The pipe is still discernable in regions areas within this area of interference, especially where it is shallow. This is a fine example of the strengths of data fusion, where two complimentary technologies (GPR & TDEMI) independently combine to give a more

robust understanding of the subsurface locations and conditions of target features, and act as a built-in confirmation technique on locations of anomalies.

In general, GPR data quality increased westward, away from a stream and generally lower elevations present at the eastern end of the survey area with improved clarity and better resolution of the pipes possible in the drier soils. Geotechnical soil boring data obtained after the geophysical survey confirmed that clay layers and shallow groundwater hindered the ability to resolve the top of pipes in the easternmost portions of this area. A silt and clay layer near the stream was found at approximately 7 feet, which is above the crowns of the pipes measured at 8+ feet deep in GPR data further to the west (Figure 4). In the central areas of the study, there were no clay layers noted in the boring logs.

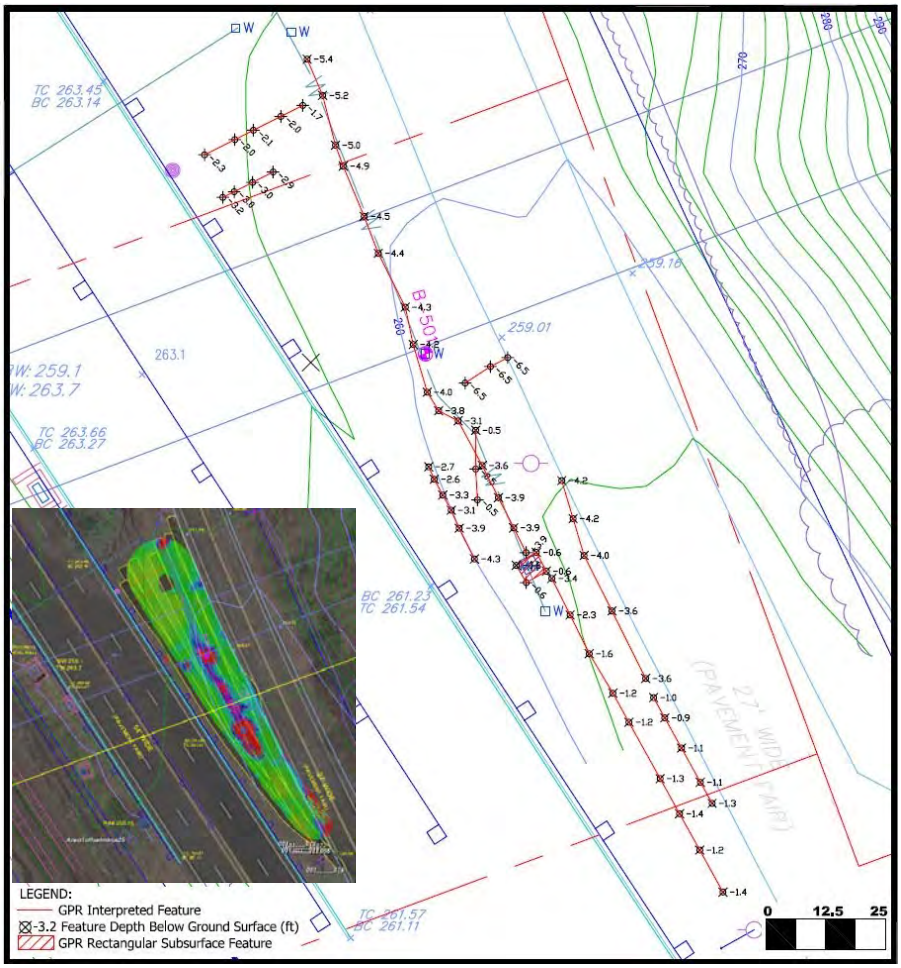

Figure 4: Interpreted multi-channel GPR results in eastern study area overlain onto CAD survey basemap. Inset image in lower left is TDEMI data overlain onto aerial photograph. Individual multi-channel GPR swaths are also shown as the black swaths with yellow outlines beneath the EM data

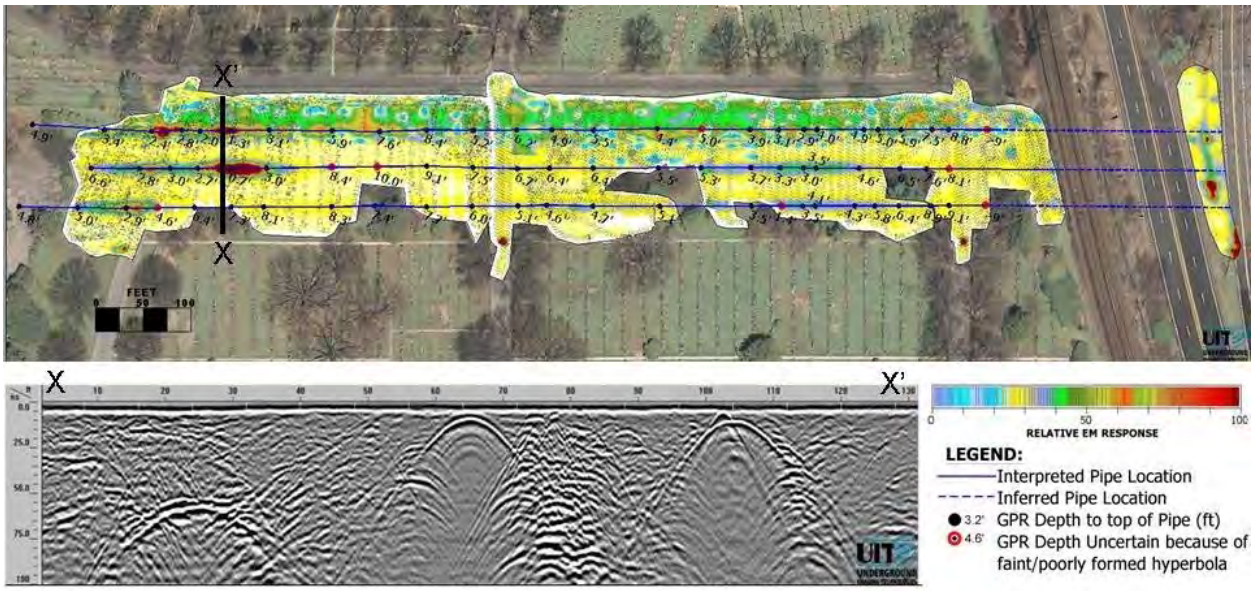

Figure 5: TDEMI Survey results and 200MHz GPR cross section through area of shallow pipe placement. EM response is relative because raw mV data were non-linearly scaled to enhance visualization. Horizontal scale on GPR cross section is in feet, vertical is two way travel time in nanoseconds. Green signal response at north side of EM data represents interference from overhead high-tension lines, but northern pipe is still visible within data.

Figure 6: Photo looking west showing relation of power lines to northern pipe. Total station is setup just to south (left) of crest of northern pipe. The GCEM data collection cart can be seen in the midground of the photo.

Pump Station

This area was the smallest of the study areas and the most complex in physical layout and density of utilities. Encouraging results were obtained in this investigation area, notably several utilities were mapped that were not present on as-built plans (Figure 7). Additionally, there was determined to be a departure of several of the mapped utilities from the presumed layout of the utilities as shown on existing design plans for the area. The plans showed two parallel utilities to be present underneath an access road, with a third crossing utility present. The geophysical mapping, however, revealed that the

utilities were in fact not parallel and crossed in a configuration differing from what was shown on the plans (Figure 7). Relative depths of these utilities were also able to be determined from the GPR data, allowing for precise mapping of the cross-cutting relationships to be determined, i.e., which pipe was above the other. The determination of any such departures away from existing plans and details of pipe configurations is important in avoiding conflicts during design and construction.

An interesting observation was also made in the GPR data that transected several utilities of varying diameter. The lower right portion of Figure 7 presents a cross –section through a 16", 10" and 8" utility lines that shows the relative amplitude response and size of the corresponding hyperbolas. While it is generally accepted that GPR data can not be used to determine the absolute diameter of pipes, this data shows that the larger pipe had a stronger and larger hyperbola associated.

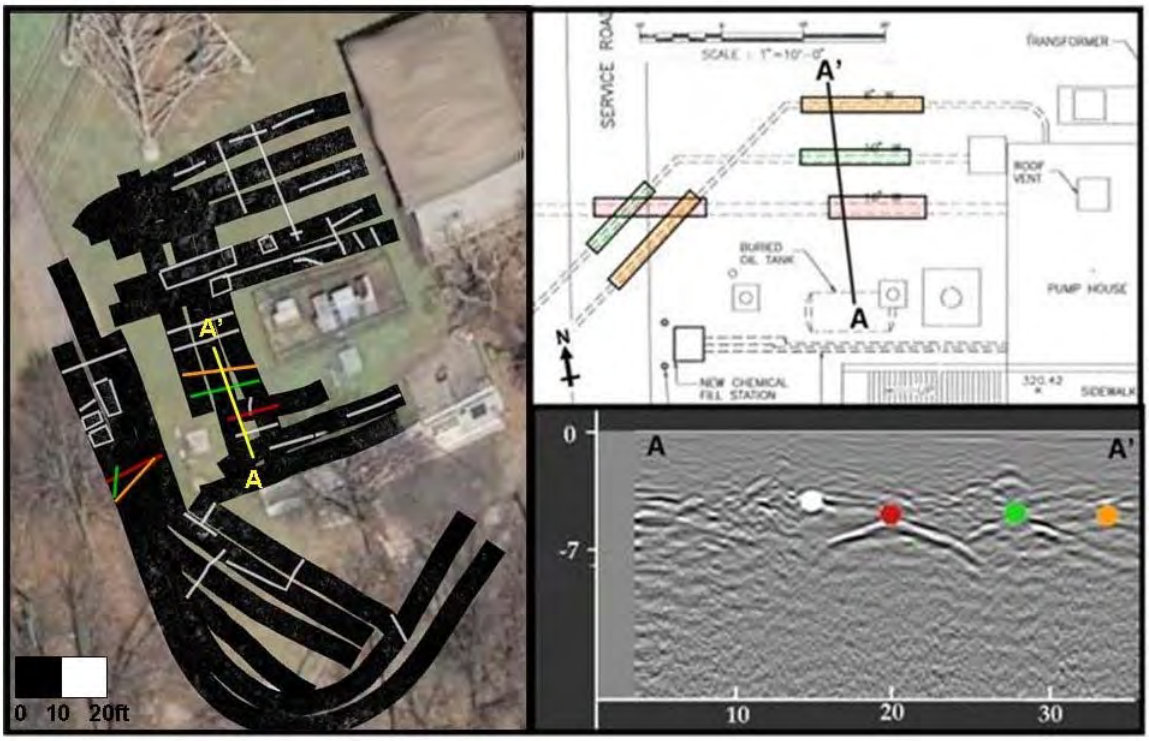

Figure 7: Correlation between as-built plans and GPR data in pump station vicinity. Left pane shows interpreted utility features in white overlain onto an aerial with multi-channel GPR swaths in black. White, red, green and orange features are interpreted to be the 16", 10", and 8" lines respectively as shown in the plans in the upper right. Lower right panel is cross section A-A', colored dots represent peaks of hyperbolas interpreted to be above mentioned lines.

Three Dimensional Site Model

A georeferenced three-dimensional site model was created in AutoCAD Civil3D in order to provide for enhanced visualization of site conditions, pipe depths and location (Figure 8). This model was constructed by draping a site aerial photo onto a modeled ground surface constructed from USGS 10m Digital Elevation Model (DEM) data. Images of the 200MHz GPR cross sections were imported into their respective locations and the pipe depths obtained from GPR were subtracted from the surface elevation to calculate elevation of top of the pipes. Such a 3D site model can assist engineers in the project design phase by providing engineers with a means to visualize the optimal route for any new installations while being able to see potential conflicts in true scale.

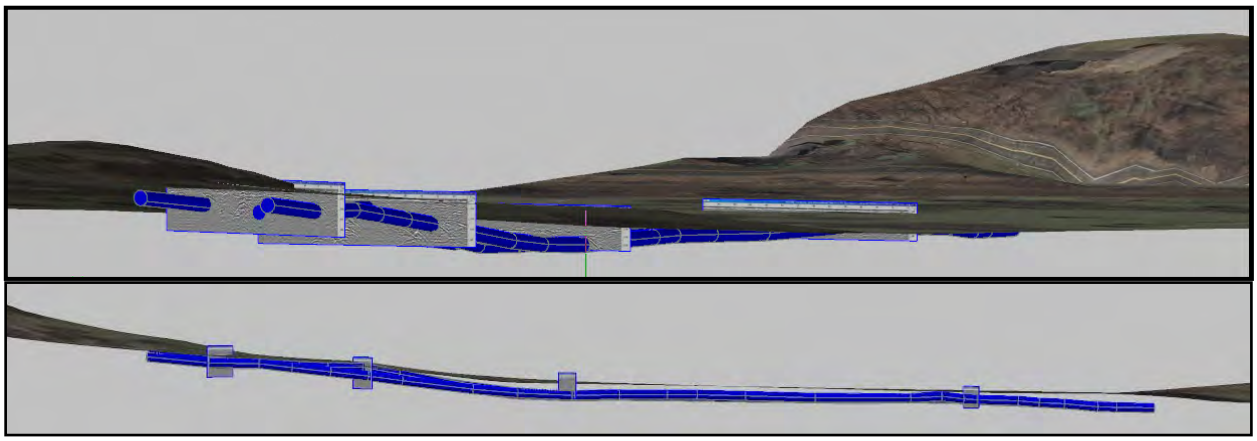

Figure 8: Perspective (top) and profile (lower) views of three-dimensional site model, based on draping an aerial photograph over a USGS 10m DEM and subtracting depth to top of pipes from ground surface elevation. GPR cross sections have also been inserted into their respective locations in the model and are visible as the grey features above.

Conclusions

Overall, the integrated geophysical survey of single and multi-channel GPR and TDEMI was very successful in determining the precise position of the three large water conveyance pipes throughout the investigation area. Additionally, multi-channel GPR data was also very effective in mapping a number of other utilities in the eastern and pump station areas of the survey. Within these areas, complex subsurface utility configurations would have proved challenging to more traditional single channel GPR mapping. Data fusion of the GPR and EM was a powerful technique used to confirm mapping results between differing geophysical technologies, and led to a high degree of confidence for the pipe position.

CONTINUOUS EXPLORATION AHEAD OF THE TUNNEL FACE BY TSWD - TUNNEL SEISMIC WHILE DRILLING

EEGS' Annual Meeting
Keystone, Colorado
April 11-15, 2010

Ewald Brückl, Vienna University of Technology, Vienna, Austria
Werner Chwatal, Vienna University of Technology, Vienna, Austria
Stefan Mertl, Vienna University of Technology, Vienna, Austria
Alexander Radinger, Pöyry Infra GmbH, Salzburg, Austria

Abstract

Seismic measurements using the VSP principle have been carried out for over 20 years to investigate the rock ahead of a tunnel face and made a contribution to reduce the risks during construction for conventional tunnelling, as well as for tunnelling with a **T**unnel **B**oring **M**achine (TBM). However, reflecting horizons intersecting the tunnel axis obliquely cannot be imaged at their intersection with the tunnel. This circumstance imposes a major uncertainty on the prediction of the geological situation ahead of the tunnel face. A possibility to image all reflecting horizons, regardless of their orientation, at least near to their intersection with the tunnel axis is offered by continuous monitoring with the drilling head of a TBM as the seismic source (**T**unnel **S**eismic **W**hile **D**rilling - TSWD). In this study we present continuous TSWD data from a gallery drilled in limestone and dolomite of the Northern Calcareous Alps, Austria. This gallery intersects a deeply incised valley, filled with sediments. The two main goals for the processing were the derivation of high signal to noise seismograms from the pilot and receiver signals and the removal of the first arrivals from the data in order to uncover reflected phases, even from reflectors very near to the TBM drilling head. Both goals were achieved satisfactorily and the main geological structure was well resolved. Geophysical issues which need further investigation are addressed. The results of our study suggest that substantial risk reduction could be achieved by continuous TSWD. However, the high production rate of modern TBMs imposes a major challenge on real time monitoring, processing and prediction.

Introduction

Deeply incised valleys, karst cavities, fault zones and other unexpected degradations of rock quality can substantially affect safety and efficiency of tunnel construction. While conventional tunnel construction is relatively flexible towards deteriorations of rock quality, similar circumstances can lead to persistent interruptions and expensive remedial measures during tunnelling with a **T**unnel **B**oring **M**achine (TBM) (e.g. Pircher, 1987). Seismic measurements using the **V**ertical **S**eismic **P**rofiling (VSP) principle have been carried out for over 20 years to investigate the rock ahead of a tunnel face and made a contribution to reduce the risk of construction for conventional tunnelling, as well as for tunnelling with a TBM (e.g. Brückl et al, 2001; Dickmann, 2008). However, only reflecting horizons which intersect a straight tunnel axis orthogonally are imaged at their true intersection with the tunnel axis. This circumstance imposes a major uncertainty on the prediction of the geological situation ahead of the tunnel face (Brückl et al., 2008).

Walk-away VSP could be used to image reflecting horizons at their true intersection with the tunnel axis even if their orientation is not orthogonal to the tunnel. While it is no problem to deploy a wide spread of source locations at the surface around boreholes in walk-away VSP surveys, it would require a major effort to place the receivers in deep boreholes drilled radially to the tunnel axis in order to realize a walk-away VSP geometry in a tunnel. Only in rare cases such expenditure would be reasonable.

A more effective method to image all reflecting horizons at least near to their intersection with the tunnel axis is continuous monitoring with either the source, or the receiver, or both located at the current position of the drilling head. Construction with a TBM allows the drilling head of the TBM to be employed as a seismic source (Petronio and Poletto, 2002). This method is based on experience from **SWD** - **S**eismic **W**hile **D**rilling (e.g., Poletto and Miranda, 2004) and has been called **TSWD** - **T**unnel **S**eismic **W**hile **D**rilling (Petronio et al., 2003). In this study we describe a continuous data acquisition by TSWD and investigate the potential of this method to image reflecting horizons close to their intersection with the tunnel axis. First results were already presented at the 57th Geomechanics Colloquium in Salzburg, Austria, October 2008 (Brückl et al., 2008).

TSWD data acquisition in the Hieflau gallery

The Hieflau gallery with a total length of 5.6 km is situated in limestone and dolomite of the Northern Calcareous Alps in Austria (**Fig. 1**). It is part of the enlargement of an existing hydropower plant. The TBM was of the type Robbins DS-TBM 194-272-2 with a diameter of 6.2 m.

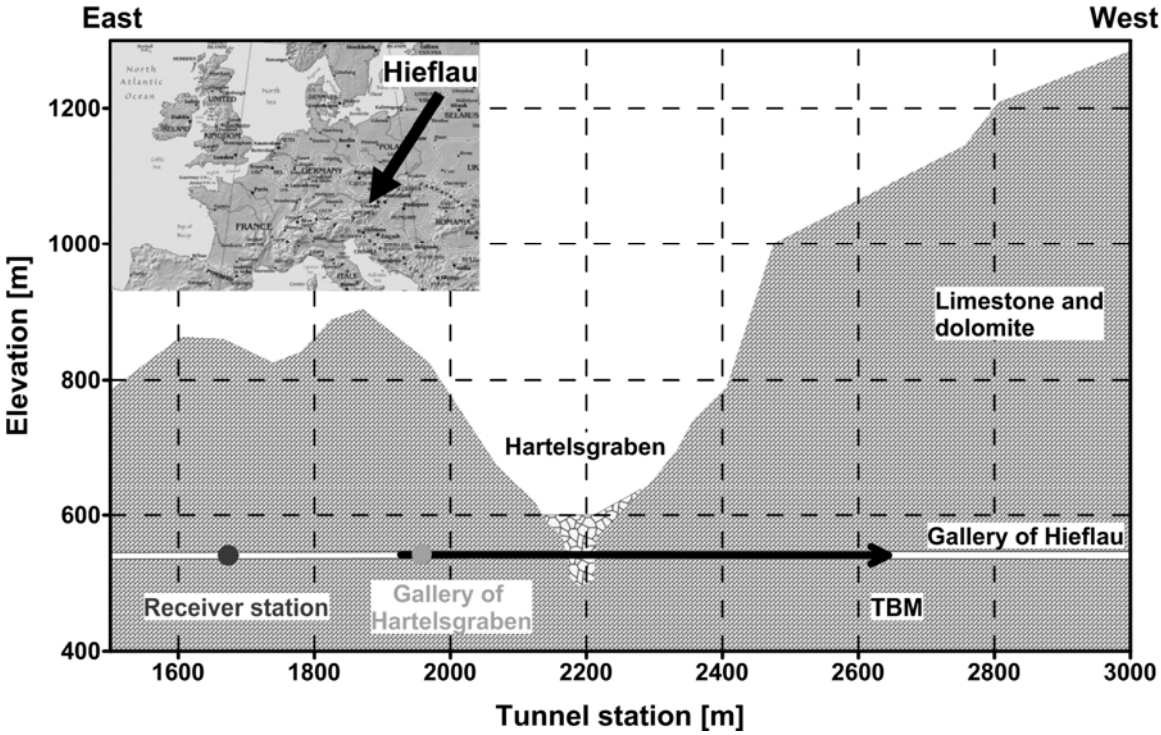

Figure 1: Longitudinal section of the geological and geometrical settings for the gallery of Hieflau; position of receiver and transverse gallery Hartelsgraben, as well as source locations (cutting head of the TBM with pilot sensor) are shown; inset shows the location of Hieflau in Austria on small scale.

A most essential part of the TSWD data acquisition system is the sensor for recording the vibrations of the TBM´s cutting head during drilling. We will name this sensor “pilot sensor” within the

scope of this paper. We assume that this signal propagates from the drilling head to the shaft of the main bearing. Therefore we fixed two 3C accelerometers on the non-rotating part of the main bearing to record this pilot signal. The recording unit for the pilot signal was placed in a special casing about 10m behind the cutting head at the TBM control station.

The receiver sensors (two 3C borehole geophones) with 15 Hz natural frequency were installed in 5 and 10m deep boreholes at the right and left side wall of the gallery at tunnel station 1673 (**Fig. 1**). The three components of the geophones were axial, tangential and radial to the tunnel axis.

From May to October 2008 nearly continuous monitoring of the pilot and receiver signals generated by the TBM drilling head was carried out between tunnel stations 1927-2644. In this region, at tunnel stations 2176-2208 the tunnel construction intersects a geological feature of special interest, the buried gorge Hartelsgraben, which is filled with fluvial and/or glacial sediments. Furthermore, the main gallery goes through the transverse gallery of Hartelsgraben at tunnel station 1953 (**Fig. 1**).

Seismic data were recorded by REFTEK 130 units. The sampling rate for the pilot and receiver signals was 1000 Hz and the data storage capacity was 8 Gigabyte. Data were retrieved from the acquisition units on a weekly basis, but because of technical problems some data gaps occurred. Due to logistical reasons the recording units could not be synchronized with GPS time, which causes undefined seismic velocities. We assume a P-wave velocity of 6000 m/s for the limestone and dolomite. The lack of exact information on the P-wave velocity of the rock does not pose a fundamental obstacle in testing the potential of the method to image all reflecting horizons very close to the tunnel axis.

Processing

Figure 2 shows a data sample of the TBM signal and the simultaneous record of the axial component (direction of the tunnel axis) of the 3C borehole geophone. One can see that the envelopes of the pilot- and receiver signals correlate well. The frequency content of the pilot signal is limited by the sampling rate and the corresponding anti-aliasing filter. The major energy of the receiver signal is found in a frequency range below 200Hz.

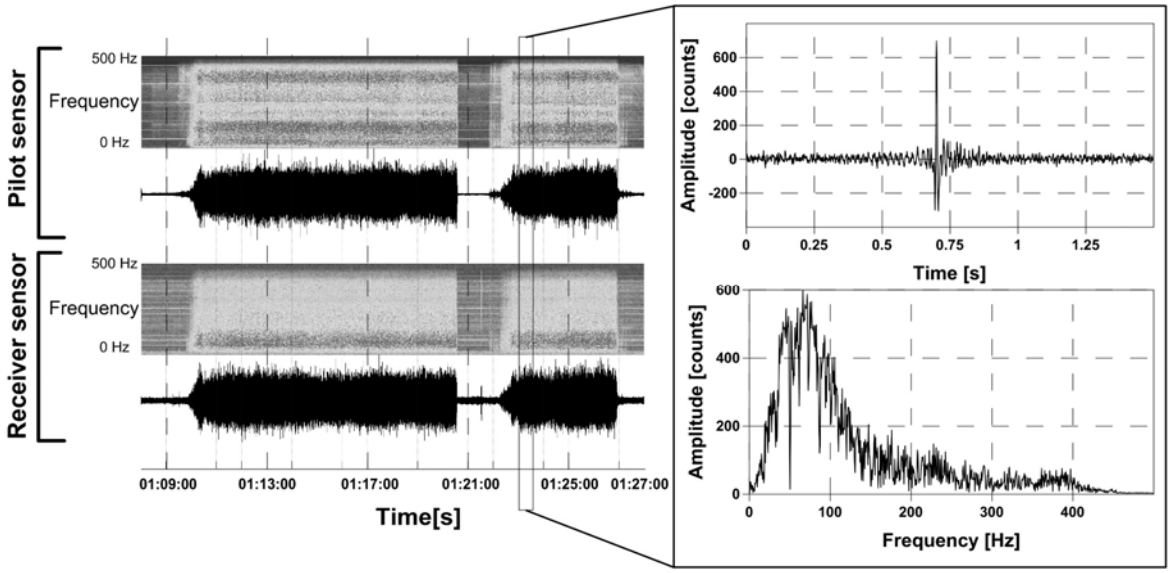

Figure 2: Raw data recorded by the TBM sensor (above) and the receiver sensor (below) at tunnel station 2000; 18 min recording together with spectrogram; 50 Hz notch filter and equalization of the amplitudes in the frequency range was applied; right side shows a seismogram and its frequency spectrum generated from 30 s of continuous recording.

The standard method to derive interpretable seismograms from this data is the correlation between the pilot- and the receiver signal (e.g., Poletto and Miranda, 2004). We applied an alternative method, which is based on the assumption that the pilot signal is a source wavelet convolved with a random sequence of spikes. Equal time windows with a length of 30 seconds are cut out of the pilot and the receiver data. We calculate the minimum delay transform of the pilot signal and apply this filter to the receiver record (Brückl et al, 2008). In order to remove a possible mixed delay character of the source wavelet we applied a delayed spike deconvolution preceding the minimum delay transform of the pilot signal. Power line contamination (50 Hz) is suppressed by predictive deconvolution. Thereafter, each trace can be interpreted as generated by a shot or an impulse source at the tunnel face and recorded by the receivers.

The production of seismic traces for time steps of 30 seconds corresponds to source distances in the range of a few centimetres. To have the seismic traces in well-defined intervals, the traces are stacked to a bin size of 1m, which again improves the signal to noise ratio. Prior to this step, seismic traces with a low signal to noise ratio are eliminated.

Figure 3a shows the seismic traces between the tunnel stations 1925-2750 calculated by this method for the axial component of the borehole geophone in the left borehole at 10 m depth. The maximum amplitude of the direct P-wave is positive and we pick the first arrival travel time at this maximum. Thereafter these travel times are used to align the first arrivals at time zero. The first arrivals show very continuous wavelets. At stations around the Hartelsgraben these wavelets are slightly disturbed. A second, less strong arrival may be an S wave, but more probably a Rayleigh wave (Bohlen et al, 2007). In case we assume Vp = 6000m/s, the velocity of the R-wave would be Vr = 3100 m/s.

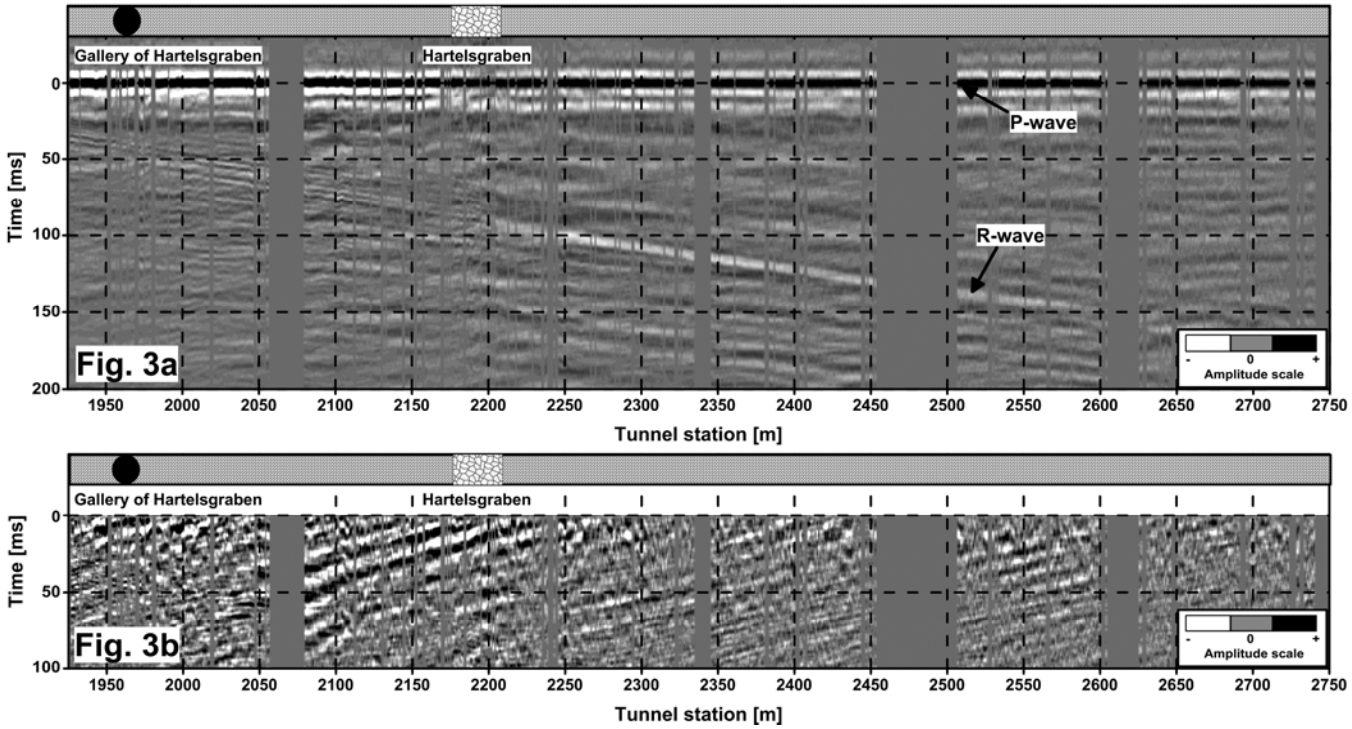

Figure 3: a) P-wave aligned seismic traces for the axial component of the left receiver with a source interval of 1m between the tunnel stations 1925-2750; P- and R-wave arrivals are marked by arrows b) Reflecting wave field for the same receiver and component; alignment to the arrival time of the P-wave was performed.

A crucial processing step is the removal of the first arrivals as well as the R-wave (at short source-receiver distances) in order to extract the reflected signals. This is done by aligning the wave type to be eliminated and then subtracting an average wavelet, which is generated by mixing 51 traces. The preceding application of an amplitude normalisation with the amplitude of the first arrival for each trace is essential for this procedure. After the suppression of the first arrivals, reflected signals become clearly visible, almost to the arrival times of the direct P-wave, or to zero time in the presentation given by **Figure 3b**.

We detected further strong signals at times larger than the R-wave arrivals, which were recorded by the tangential and radial components of the receivers. These signals indicate phases, which travel from the TBM to the reflecting horizons as P- or S-waves, and are reflected as P- or S-waves, and finally converted to an R-wave at the tunnel face (Bohlen et al., 2007; Lüth et al., 2008). **Figure 4** shows these phases after the alignment of the traces to the R-wave arrivals. In this study we do not analyze the potential of these phases for exploration ahead of the tunnel face.

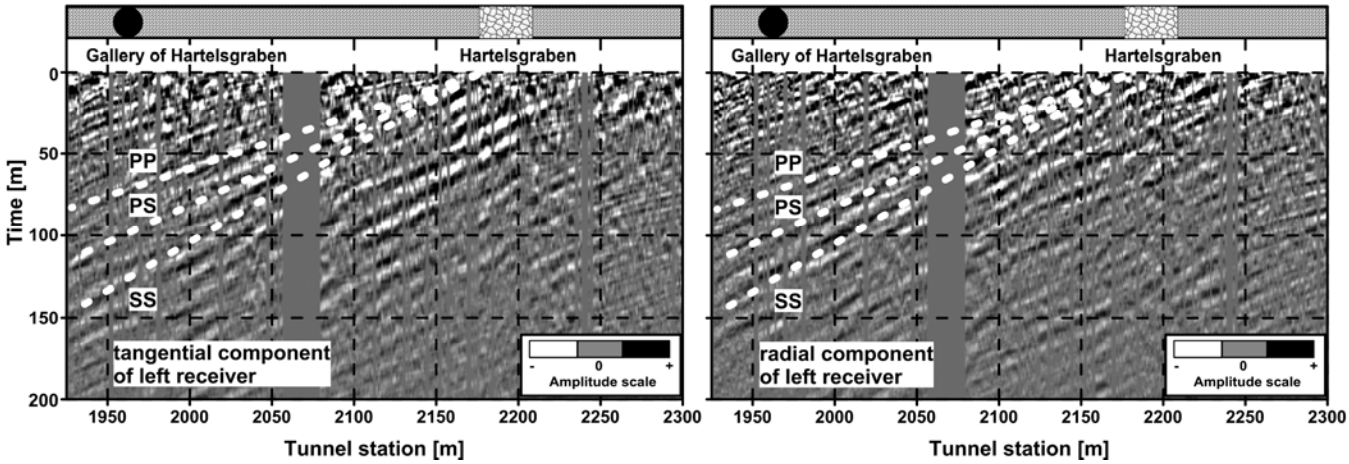

Figure 4: Reflected wave field of the R-wave: aligned tangential and radial component of the left receiver for the tunnel stations 1925-2300; possible TWTs of reflections of the beginning of the buried gorge Hartelsgraben are marked with the wave type PP, PS and SS making the assumption that this interface is perpendicular to the tunnel axis

Interpretation

The data shown in **Fig. 3b** represents the basis for a prediction of geological boundaries and fault zones ahead of the current tunnel face. We perform a mapping of this data from the original space (tunnel station, time) to (tunnel station + prediction distance, prediction distance = velocity*time/2). This transformation manages that signals from interfaces crossing the tunnel axis perpendicularly are mapped at constant tunnel stations, presuming the velocity has been estimated correctly (**Fig.5**).

The most prominent signal in **Figure 5** correlates with the Hartelsgraben, the only geologic structure, which represented a severe construction risk. We assume that the TBM drilling head, like a drill-bit, represents a single force source which generates compression P-waves in forward and dilation P-waves in backward direction of the tunnel (Poletto and Miranda, 2004). The boundary from the compact rock to the Hartelsgraben represents a decrease of the acoustic impedance and therefore the incident compression P-wave is reflected as a dilation P-wave, having the same polarity as the direct P-wave at the receiver location. Reflections from Hartelsgraben gallery can also be identified and correlated at the very beginning of our data (tunnel stations < 2000 m). Correlation of the reflected wave field with the wavelet of the first arrival supports exact location of the discontinuities (**Fig. 6**). From this

data we estimate the location accuracy of significant discontinuities crossing the tunnel axis to be about +/- 5 m.

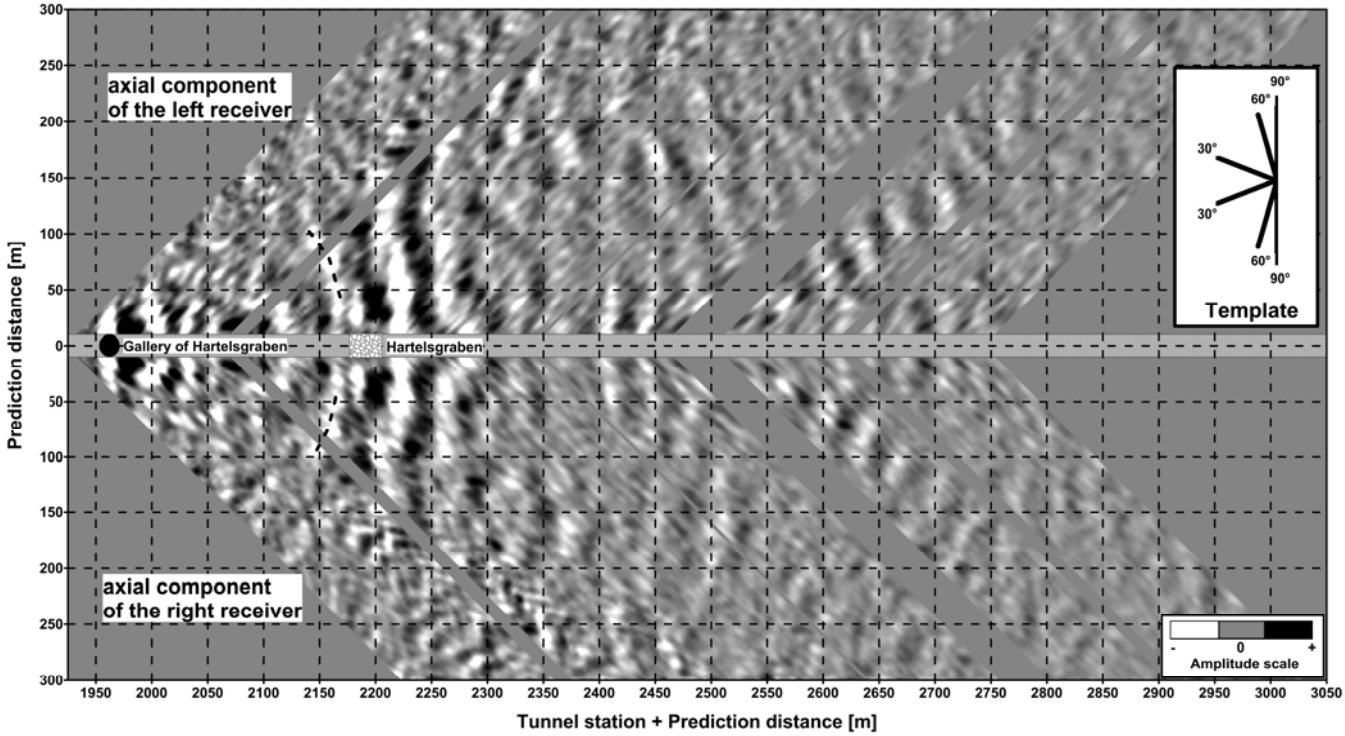

Figure 5: Mapping of reflected wave field of the axial component for the left and right receiver for the tunnel stations 1925-2750; the interpretation of the reflections at the beginning of the buried gorge Hartelsgraben and the template of expected dip of this reflection oriented 30° , 60° and 90° to tunnel axis is inserted.

The reflection band correlating with the Hartelsgraben is not exactly orthogonal to the tunnel axis in **Figure 5**, indicating an oblique intersection of the boundary to the Hartelsgraben with the tunnel axis. A template (inset in **Figure 5**) shows the expected slopes of the reflection band for different angles of intersection. By the use of this template we estimate an intersection angle of 60° or even higher. In order to determine the orientation of the boundary to the Hartelsgraben unequivocally, the particle motion recorded by the 3C borehole geophones could be used. These studies are currently in progress.

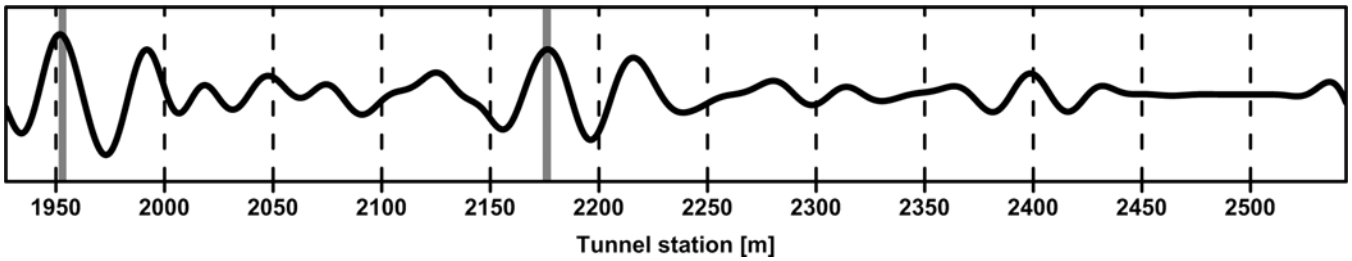

Figure 6: Correlation of a stacked trace (prediction distances 20 - 30 m, left and right receivers) with the first arrival wavelet; maxima correlate with the Hartelsgraben gallery and the beginning of the Hartelsgraben (grey bars at tunnel stations 1953 m and 2176 m).

Conclusions

Seismic data were nearly continuously acquired by the TSWD method in the Hieflau gallery, covering a section of about 700 m length. The pilot signal was taken from the main bearing of the TBM drilling head, the receivers were situated in 5 – 10 m deep boreholes in a cross section about 250 m behind the first TBM drilling head station (tunnel station 1927). An alternative method to conventional correlation was successfully applied to convert 30 seconds long recordings of the pilot and the receiver signals to standard seismograms. The compressed seismograms contain signals with frequencies up to 170 Hz and the signal to noise ratio was excellent up to the maximum source-receiver distance of about 1 km. The wavelet of the first arrival has a nearly constant shape regardless of the source-receiver distance and it was not influenced by the very different geologic conditions. Because of this favourable circumstance, the first arrivals could be removed almost completely from the data and reflected signals could be traced from about 200 m to less than 10 m ahead of the TBM drilling head. This new achievement implies a significant reduction in prediction uncertainty.

The Hartelsgraben is a deeply incised valley which intersects the gallery otherwise running through compact limestone. It can be clearly identified in the reflected wave field (**Fig. 5**). Another, known reflector is the Hartelsgraben gallery which crosses the Hieflau gallery nearly orthogonally at the very beginning of our monitoring section. It can also be seen clearly in the reflected wave field. These two discontinuities, representing a significant reduction of the acoustic impedance, were located with an error of about +/-5 m by correlation with the first arrival wavelet (**Fig. 6**).

The data presentation used for **Figure 5** offers an easy way to decide if a discontinuity recognized in the reflected wave field intersects the tunnel axis nearly orthogonally or obliquely. The detection of the particle motion recorded by the 3C borehole geophones could help to unequivocally estimate the orientation of such a discontinuity.

In the future, continuous applications of the TSWD method require the problem of timing to be solved, either by relative timing between the pilot sensor and the receivers, or by absolute timing (e.g. GPS). Our study did not intend to supply prediction in time. Modern TBMs can drill about 50 m per day under favourable geologic conditions. This imposes a major challenge on real time monitoring, processing, and prediction. However, the problems which need to be solved to achieve this goal have more of a data transmission and logistic character and are beyond the scope of this study.

References

Bohlen, T.; Lorang, U., Rabbel, W., Müller, C., Giese, R., Lüth, S., Jetschny, S., 2007, Rayleigh-to-shear wave conversion at the tunnel face - From 3D-FD modeling to ahead-of-drill exploration, Geophysics, 72, 6, p. T67-T79

Brückl, E., Chwatal, W., Dölzlmüller, J., Jöbstl, W., 2001, A study of the application of VSP to exploration ahead of a tunnel, Int. Journal of Rock Mechanics and Mining Sciences, 38 , p. 833-841

Brückl, E., Chwatal, W., Mertl, S., Radinger, A., 2008, Exploration Ahead of a Tunnel Face by TSWD-Tunnel Seismic While Drilling, Geomechanics and Tunnelling, Volume 1, Issue 5, p. 460-465

Dickmann, T, 2008, Theoretical and applied case studies of seismic imaging in tunnelling, Geomechanics and Tunnelling, Volume 1, Issue 5, p. 436-441

Lüth, S.; Giese, R.; Otto, P.; Krüger, K.; Mielitz, S.; Bohlen, T.; Dickmann, T., 2008, Seismic investigations of the Piora Basin using S-wave conversions at the tunnel face of the Piora adit

(Gotthard Base Tunnel), International Journal of Rock Mechanics and Mining Sciences, 45, 1, p. 86-93

Poletto, F. and Miranda, F., 2004, Seismic while drilling: Fundamentals of drillbit seismic for exploration, Handbook of geophysical exploration, Seismic exploration series, Vol. 35, Elsevier, Amsterdam

Petronio, L. and Poletto, F., 2002, Seismic-while-drilling by using tunnel-boring-machine noise, Geophysics, 67, p. 1798-1809

Petronio, L., Poletto, F., Schleifer, A., Morino, A., 2003, Geology prediction ahead of the excavation front by Tunnel-Seismic-While-Drilling (TSWD) method, Society of Exploration Geophysicists, 73rd Annual International Meeting, Expanded Abstracts

Pircher, W., 1987, Die Überwindung von Störzonen beim Fräsvortrieb des 22 km langen Druckstollens Strassen-Amlach (Surmounting of fault zones at the TBM-drive of the 22 km long pressure tunnel Strassen-Amlach), Tunnel, 1987, p.73-78

Acknowledgements

We want to thank the VERBUND - Austrian Hydro Power AG and ARGE Erweiterung KW Hieflau (Jäger - Strabag - Frutiger) for the permission to carry out the seismic measurements and also for logistic support during preparation and data acquisition. Furthermore, we thank Dipl.-Ing. Andreas Bilak for geologic information and his valuable support of seismic data transfer.

GEOELECTRICAL IMAGING FOR DETECTION OF WATER MIGRATION IN A BIOREACTOR LANDFILL

Håkan Rosqvist
Department of Research and Environment, NSR AB, Helsingborg, Sweden
Torleif Dahlin
Engineering Geology, Lund University, Lund, Sweden

Abstract

In this paper we describe field investigations of leachate recirculation at a bioreactor landfill using geoelectrical imagining technique (i.e., electrical resistivity) combined with a tracer test. The use of geoelectrical imagining techniques is an established practice for environmental investigations and monitoring of various landfill processes and in recent years also the bioreactor landfill concept has been emphasised. In the study, the electrical resistivity technique was evaluated and the possibility to detect water and gas migration in the waste mass was investigated. Results showing moisture migration through the bioreactor landfill, during leachate flushing and during a tracer test, are presented. Also results indicating the resistivity technique being useful for biogas detection are shown.

Introduction

The bioreactor concept was developed to reduce and control the environmental impact of landfills and to utilise the energy potential of the waste, and in recent years the interest for bioreactor landfill techniques have been at a high level (Barlaz and Reinhart, 2004). The main principle of the bioreactor concept is to enhance waste biodegradation by recirculation of leachate in the waste mass, and consequently, the potential long-term risks will be reduced, and post operation costs will be decreased. Moreover, the enhanced waste biodegradation leads to an increase of biogas production for energy utilisation. Spatial distribution of moisture content is recognised to be of great importance to the biodegradation and methane production in a bioreactor. The overall objective of the project was therefore to investigate the spatial distribution of water flow within a bioreactor landfill with leachate recirculation.

The use of geoelectrical imaging techniques is an established practice for environmental investigations and monitoring of various landfill processes (e.g., Bernstone and Dahlin, 1997, Rosqvist et al, 2003, Cardelli and Di Filippo, 2004), and in recent years also the bioreactor landfill concept has been emphasised (Guerin et al, 2004, Moreau, et al., 2004, Rosqvist et al, 2005). In the study, the electrical resistivity technique was evaluated and the increase in moisture content as a result of the start of leachate recirculation was investigated. In this paper we describe field investigations of water recirculation at a bioreactor landfill using a geoelectrical imaging technique (i.e., resistivity) combined with a tracer test.

Materials and methods

The Bioreactor landfill

The field campaign was carried out at a bioreactor landfill at the Filborna landfill site, Helsingborg, Sweden, which was 120 by 60 meter, with a depth of approximately 16 meter. The bioreactor landfill was isolated from the surroundings by the use of low permeable clay as a bottom liner. During the construction of the bioreactor landfill it was built up in 5 meter layers, each layer covered with an intermediate cover of compost. Horizontal pipes for leachate recirculation were placed in trenches filled with wooden chips, together with gas collection pipes. The pipes for leachate recirculation were installed at the bottom of the trenches and the gas collection pipes in the upper part. Altogether 7 trenches for leachate recirculation and biogas collection pipes were installed with a 20-meter distance between the trenches (see Figure 1). At the bottom of the bioreactor landfill, a leachate collection system was installed and in the interior horizontal pipes for gas collection was installed.

The geoelectrical-imaging techniques

Geoelectrical imaging techniques are envisaged to have three major applications in connection with ground and groundwater contamination around landfills: mapping for identification and delineation of contaminants, quality control of soil stabilisation/contaminant immobilisation, and long term monitoring. Leakage from municipal and mining waste deposits is generally associated with high ion concentrations and hence very low resistivities. This makes geoelectrical imaging techniques particularly interesting for leachate migration inside, and around, landfills. In the study presented here the use of geoelectrical imaging techniques for bioreactor landfill process monitoring have been addressed. The electrical resistivity is suitable for monitoring of water fluxes in landfills since it links with moisture content and ionic content in the water, as pointed out in Guérin et al., (2004).

The geoelectrical imaging method is based on measurement of the potential distribution arising when electric current is transmitted to the underground via electrodes. The data acquisition was done as two-dimensional (2D) resistivity imaging, using the ABEM Lund Imaging System. The system is computer controlled and consists of a resistivity-IP instrument, a relay-switching unit, four electrode cables, connectors and steel electrodes. The 2D imaging layouts used comprises around 80 electrodes, and measurement lines can be expanded via a roll-along technique. A multiple gradient array electrode configuration was used in order to get good resolution and fast data acquisition. The measured data was processed with inverse numerical modelling (inversion) to produce model cross-sections of the resistivity and chargeability distribution of the ground using the software Res2dinv.

The experimental set up

A 2-D resistivity and IP survey was performed in which three parallel lines, each 160 m long, were measured perpendicular to the leachate distribution pipes (Figure 1). The electrode distance was 2 m and multiple current source gradient array was used. A number of resistivity and IP-surveys were carried out with the cable layout in fixed positions. In this paper only the resistivity measurements are shown.

A flushing experiment started in March 2006 and continued for 85 days. To get a picture of the bulk resistivity of the waste material in the bioreactor the fieldwork started with a set of background measurements. The irrigation system was started after the background measurements had been carried out, and seven further measurements were carried out during the experimental period. During the

experiment, in all 922 m3 of water was introduced to the bioreactor landfill, corresponding to less than 2 mm/day.

Once the flushing experiment a tracer test was started. The irrigation system was turned off and a one cubic meter Lithium Bromide tracer pulse was introduced to one of the leachate circulation pipes. Once the tracer pulse had been introduced to the waste mass, all leachate circulation pipes were put back in normal use. The tracer pulse was diluted in the leachate recirculation system before it reached the distribution pipe and consequently, the tracer concentration in the pulse entering the waste mass was not known.

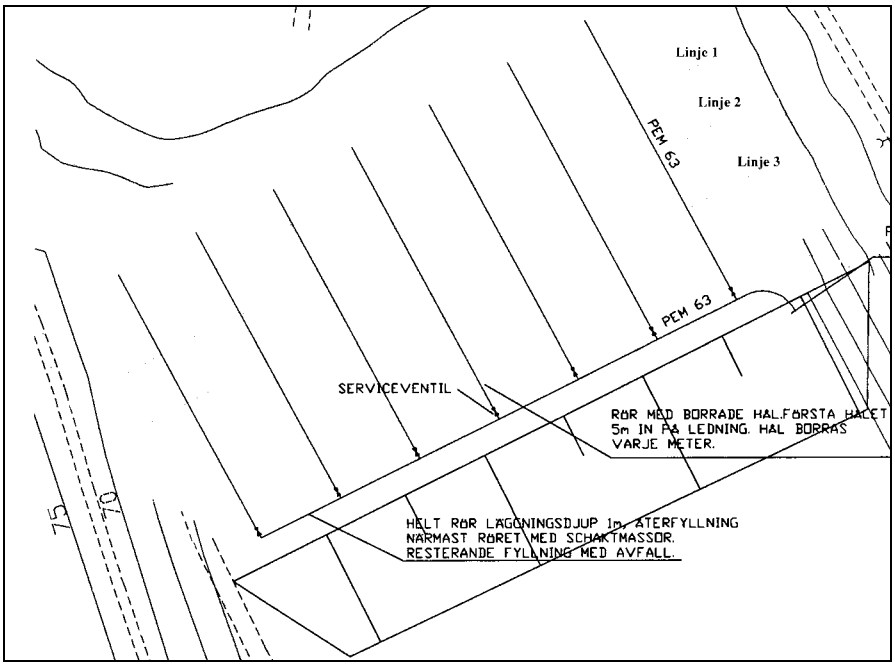

Figure 1: Plan of the bioreactor landfill showing the distribution pipes for leachate and the lines for resistivity measurements (Line 1 – 3).

Results

Flushing test

In Figure 2 the resistivity measurements at line 1 from day no 8 to 85 are presented as the relative difference between the measurements at day one and the current day. The scale in Figure 2 is –0.1 to 0,1 which stands for a 10% increase and decrease in resistivity, respectively. In Figure 2 also the input of water to the bioreactor landfill are shown. In all, 922 m3 of water was introduced to the bioreactor landfill during the experimental period.

In Figure 2 the moisture migration in the waste is shown as a decrease in resistivity. It is shown that after 8 days the migrating water results in a scattered pattern of lowering of the resistivity (blue/dark) zones near the surface. These zones are interperted as a non-uniform water flow through the upper layer

of the waste. As the water input continued, the zones with decreased resistivity showed a more uniform pattern, which is interpreted as higher moisture content. At the end of the experimental period (day 85), the low resistivity zone showed a relatively homogenous pattern reaching to a depth of almost 10 meter. In Figure 2 also an increase in resistivity has been recorded in irregular zones at various locations during the experimental period. The appearance of high resistivity zones could not be experimentally evaluated. However, the most probable explanation for the irregular pattern of high resistivity zones is migration of gas in the bioreactor landfill.

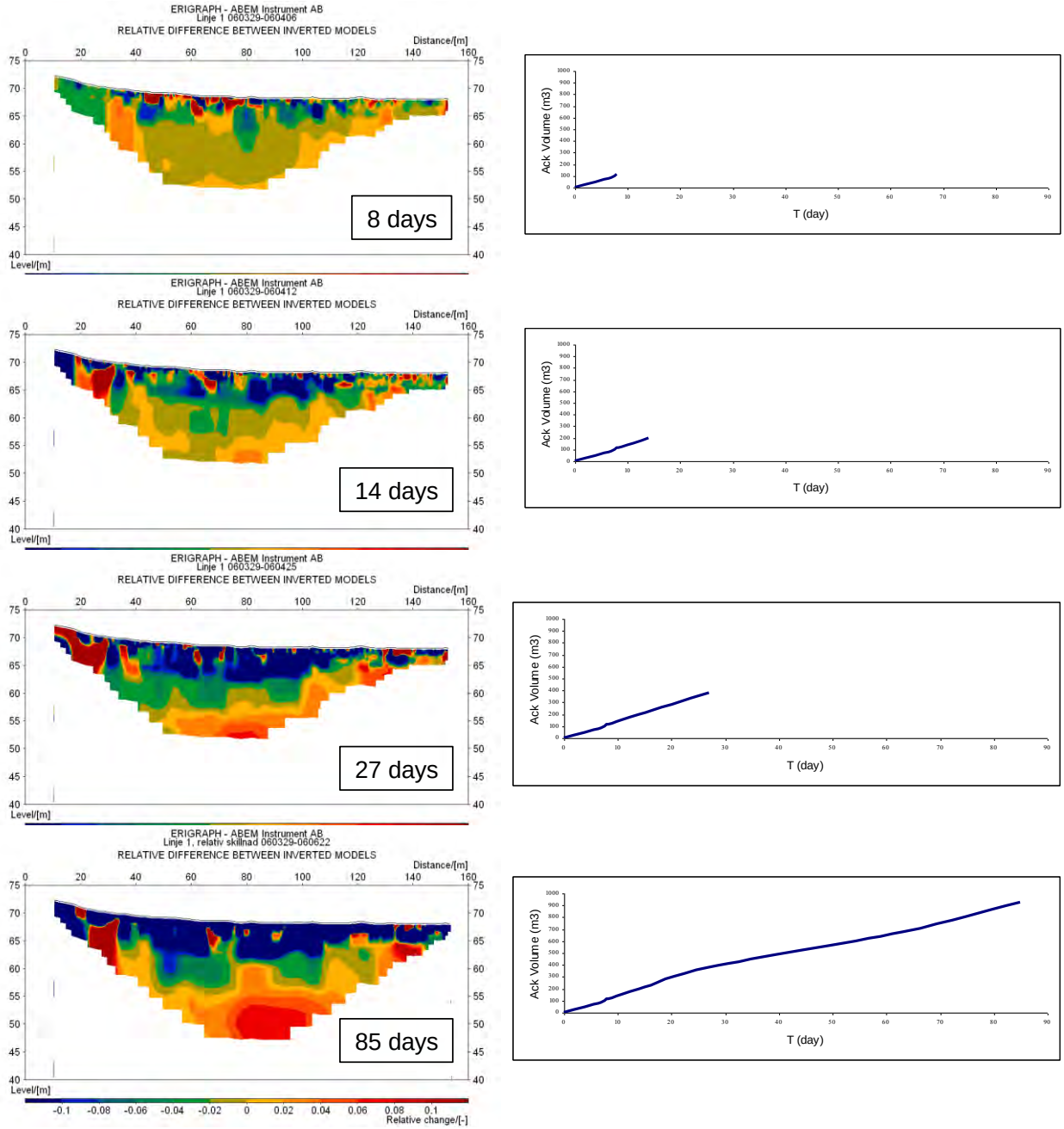

Figure 2: Inverted resistivity sections for line 1 presented as relative change from day no 8 to 85, and the accumulated input of water to the bioreactor landfill.

Tracer test

In Figure 3 the resistivity measurements at line 3 during the tracer test are shown. The figure shows the relative differences in resistivity from the start of the experiment and the current day. The relative differences are presented in two scales of relative differences, +/- 10 and 50 percent, respectively. To the left in Figure 3 the +/- 50 percent scale, and to the right the +/- 10 percent scale, are shown.

As described above, the tracer pulse was introduced through a leachate recirculation pipe at the distance of approximately 88 meter (see sections in Figure 3). As shown in all six sections in Figure 3, the tracer pulse appears at the 88-meter point as a clear decrease in resistivity (dark blue) in a zone propagating down from the surface. After one day only, the low resistivity zone reached to a depth of approximately 2 to 3 meter, and after seven days no significant changes in the depth of the low resistivity zone could be observed. However, in Figure 3, the +/- 50 percent shows that the relative changes in resistivity had decreased from over 50 percent (day 4, blue) to approximately 30-40 percent (dark green) after 7 days. It was thus indicated that the tracer pulse was diluted from day 4 to 7.

In Figure 3 an increase in resistivity has also been recorded in irregular zones at various locations during the experimental period. In particular in the interval between approximately 45 and 80 meters irregular zones are appearing, most clearly in the sections showing +/- 10 percent change. These zones are showing large changes in resistivity with time, resulting in a graduall chang in positions. The appearance of high resistivity zones could not be experimentally evaluated.

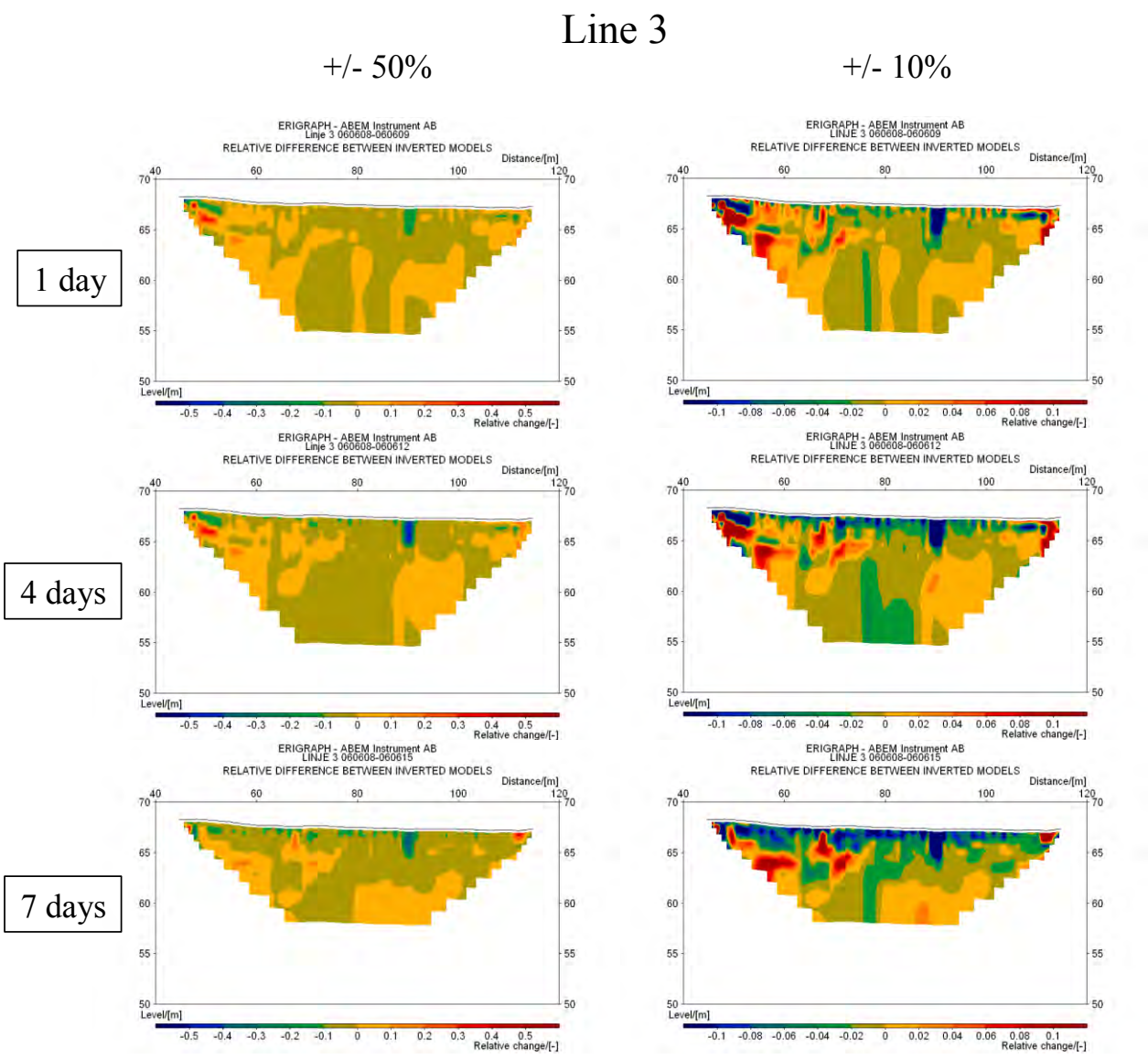

Figure 3: Inverted resistivity sections for line 3, presented as relative change during the tracer test.

Conclusions

The fieldwork was performed under good conditions resulting in high quality field data showing a fairly consistent picture of the waste mass in the bioreactor landfill. In the bioreactor the resistivity of the relatively wet waste mass at depth was measured to be in the range of 3 to 30 Ωm, which is in the same range (Guérin et al., 2004) or somewhat lower (Bernstone and Dahlin, 1997), than results presented elsewhere. High water content and ionic content, and high organic content in the bioreactor can partly explain the relatively low resistivity. Also the temperature may influence the outcome of the measurements (Guérin et al., 2004).

The main objective with the study was to investigate the spatial distribution of recirculated leachate in a bioreactor landfill at field scale. It was concluded that the experiment could successfully detect the

distribution of recirculated leachate through the waste mass by comparing interpretations of resistivity measurements at different time steps (i.e., relative differences) in 2-D resistivity sections.

After 8 days of irrigation non-uniform water flow through the upper layer of the waste was indicated by the resistivity measurements. As the water input continued zones with decreased resistivity showed a more uniform moisture flow pattern and after 85 days a uniform low resistivity zone indicated increase in moisture content. It is concluded that the use of different plotting scales for the inverted resistivity sections or relative difference sections is beneficial for the interpretation, since different information can be extracted at different plot intervals. In our study +/- 10 and +/- 50 percent variation was shown to be the most appropriate levels.

The results of the combination of a tracer test and resistivity measurements clearly suggest this technique to have potential for detecting and quantifying subsurface moisture movement in landfills. Further research is however required for optimisation of the approach and a more comprehensive understanding of the results. It is suggested that future experiments combining resistivity measurements with tracer tests should facilitate for water sampling in order to detect the migration of the tracer pulse. The results suggest the tracer pulse to migrate to a depth of 2-3 meter in less than one day, indicating the water migration to occur as a fast vertical flow. The occurrence of fast vertical flow have been reported in previous studies to be due to non-uniform flow in the physically heterogeneous waste mass e.g., Rosqvist and Destouni (2000).

In recent years a study addressing gas migration in landfills has been reported (Moreau, et al., 2004). In Moreau, et al., (2004) variation in electrical resistivity indicated biogas migration and an interpretation of leachate recirculation effects on biogas migration were proposed. An increase in resistivity was recorded in irregular zones at various locations in the waste mass during the experimental period. The appearance of high resistivity zones could not be experimentally evaluated. However, the most probable explanation for the irregular pattern of high resistivity zones is migration of gas in the bioreactor landfill. Therefore it is concluded that that the resistivity measurement could be a viable method for detection of gas migration in landfills. It is therefore suggested that the use of resistivity should be further investigated in order to develop systems for landfill gas monitoring.

Based on the results of the geo-electrical measurements, it is suggested that the technique provide an interesting possibility for development of bioreactor and MSW landfill monitoring and process control. For future R&D, it is suggested that moisture and gas migration through the waste mass should be investigated and clarified. For a better understanding experiments in laboratory and pilot-scale landfills are suggested. For example, in an experiment combining a tracer test with resistivity measurements in lab-scale, experimental conditions such as, moisture content, temperature, and tracer concentrations, can be kept under control.

References

Barlaz, M.A., and Reinhart, D. 2004. Bioreactor landfills: progress continues. Editorial, Waste management, 24, 859 – 860.

Bernstone, C., and Dahlin, T. 1997. DC resistivity mapping of old landfills: two case studies. European Journal of Environmental and Engineering Geophysics 2, 121-136.

Cardelli, E., and Di Filippo, G. 2004 Integrated geophysical surveys on waste dumps: evaluation of physical parameters to characterise an urban waste dump (four case studis in Italy). Waste Manage Res. 2004: 22: 390-402.

Guérin, R., Munoz, M.L., Aran, C., Laperrelle, C., Hidra, M., Drouart, E., and Grellier, S. 2004.

Leachate recirculation: moisture content assessment by means of a geophysical technique. Waste Man, 24, 785 – 794.

Moreau, S., Bouyè, J-M., Duquennoi, C., Barina, G., and Oberti, O. 2004. Electrical resistivity survey to investigate biogas migration under leachate recirculation events. Waste 2004; Integrated waste management and pollution control policy and pracyice, research and solutions, Stratford-upon-Avon, September, 2004.

Rosqvist H., and Destouni G., 2000. Solute transport through preferential pathways in municipal solid waste. J. Cont Hydrol. 46, 39-60.

Rosqvist, H., Dahlin, T., Fourie, A., Rohrs, L., Bengtsson, A., and Larsson, M. 2003. Mapping of leachate plumes at two landfill sites in South Africa using geoelectrical imaging techniques. Proc. Ninth International Waste management and landfill symposium, Cagliari, Sardinia, Italy.

Rosqvist, H., Dahlin, T., and Lindhé, C (2005). Investigation of water flow in a bioreactor landfill using geoelectrical imagining techniques. Proceedings Sardinia-05, Tenth International Waste Management and Landfill Symposium, Cagliari, Sardinia, Italy.

AN EVALUATION OF THE POTENTIAL OF THE GEOELECTRICAL RESISTIVITY METHOD FOR MAPPING GAS MIGRATION IN LANDFILLS

Håkan Rosqvist, NSR AB, Helsingborg, Sweden
Virginie Leroux, Lund University, Sweden
Torleif Dahlin, Lund University, Sweden
Sara Johansson, Tyréns AB, Sweden
Mats Svensson, Tyréns AB, Sweden

Abstract

Methane is a powerful greenhouse gas and growing concern regarding global climate changes over the last years has pointed out the need to quantify and control the leaking of methane into the atmosphere. Landfill gas is regarded as one of the major sources for methane migration to the atmosphere. In this study we present research work with the objective to evaluate the use of geoelectrical resistivity to detect gas migration in landfills. Extensive field experiments were conducted at the Filborna landfill site in Helsingborg, Sweden, in August 2008. In general, the resistivity measurements showed results corresponding to results reported from previous investigations in waste. However, also large variations in resistivity were indicated. Relatively high variability and high mean resistivity in the surface-near layers clearly indicate influence on the resistivity in the upper zone of the landfill. The variability and high resistivity may partly be explained by appearance and migration of landfill gas.

Introduction

Methane is a powerful greenhouse gas and growing concern regarding global climate changes over the last years has pointed out the need to quantify and control the leaking of methane into the atmosphere. Landfills are one important anthropogenic methane source among others, such as rice paddies, biomass burning and domestic animals (Chapin et al. 2002). There are two major advantages in collecting landfill gas, the environmental benefit of reducing the amounts of methane emissions to the atmosphere, and the economical considerations, i.e., when the energy in the landfill gas is used. In that respect landfill gas is regarded as being a renewable energy source.

Landfills are highly heterogeneous formations in which the migration of landfill gas can be expected to be highly non-uniform. Subsurface accumulation of gas causes the gas pressure to rise, which results in pressure differences throughout the landfill. The gas migrates from high pressure to low pressure zones under the soil surface (Crawford & Smith 1985). Gas flow follows the paths of highest permeability until the gas eventually finds its way into the atmosphere, generally through fissures and cracks. Theoretically, landfill gas is transported mainly horizontally due to the compaction of waste in layers. The rate of emission depends on several factors, but the most important is the soil moisture in the

upper soil, since high soil moisture content in soil pores can more or less constrain gas from diffusing to the atmosphere. (Boeckx et al 1996).

To recover the energy potential and to mitigate the environmental impact from methane, effective techniques for landfill gas collection are crucial. The location of wells for landfill gas collection is important, and there is therefore a need for development of techniques to detect and locate the presence and migration of gas in landfills.

It has been pointed out that the electrical resistivity technique is suitable for monitoring of water fluxes in landfills since it links with moisture content and ionic content in the water (e.g., Guérin et al., 2004). In recent years resistivity has been used at landfills for various applications like mapping landfill cover (e.g. Leroux et al., 2007), detecting and mapping pollution plumes (e.g. Rosqvist et al. 2003), and for studies of moisture migration processes during leachate recirculation at bioreactor landfills (e.g. Marcoux, et al., 2007, Rosqvist et al, 2005, and Rosqvist et al, 2007). In those experiments growing resistive anomalies were observed at the same time as the moisture spread. Moisture movement explained low resistivity zones, whereas the presence and accumulation of gas was one plausible explanation for the irregular high resistivity zones. In the experiments it was concluded that resistivity could be used for detecting and localizing landfill gas.

As a consequence of the expected sequential nature of the release of landfill gas to the atmosphere, it is expected that the zones with landfill gas migration will signal themselves by large variations in resistivity. It is, however, also expected that the variations in resistivity will be related to soil temperature and moisture resulting in a complex situation for data analysis. Gas accumulations are expected to be visible as high resistivity zones in the data.

In this study we present research work with the objective to evaluate the use of geoelectrical resistivity to detect zones in municipal solid waste landfills where gas migration occurs.

Materials and methods

The field site

The field measurements were performed at the Filborna landfill site, managed by NSR AB in Helsingborg, Sweden. The measurements were conducted for three weeks in August 2008, with a main focus on the initial 5 days. In Figure 1 and 2, the experimental site is shown. The red and yellow plastic tape in Figure 1 shows the position of the lines where the resistivity was measured.

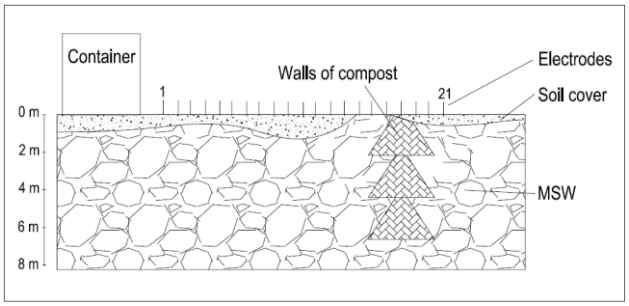

Figure 1: Photo showing the experimental site at the Filborna landfill.
Figure 2: Section of the experimental site at the Filborna landfill (sketch)

The experimental site was located in a sloping hill (Figure 1). As shown in Figure 2, an intermittent soil cover of an irregular thickness around 0 – 0.5 meter covered the waste layer. MSW and industrial waste had been deposited in the landfill from autumn 2005 until summer 2007 resulting in high gas recovery from the gas extraction system at the site. Field investigation concluded that the groundwater table was at depth greater than 16 meter.

In addition to the general heterogeneous structure of the waste in the landfill, a subsurface body of compost material was situated along the experimental site as shown in Figure 2. The compost body consisted of soil and wood chips and was assumed to have a relatively high porosity and it was thus assumed to have high gas permeability.

Resistivity measurements

Geoelectrical imaging techniques are envisaged to have several applications in connection with monitoring of landfill sites including groundwater investigations around landfills, for example, mapping for identification and delineation of contaminants, quality control of soil stabilisation/contaminant immobilisation, and long-term monitoring. Leakage from municipal and mining waste deposits is generally associated with high ion concentrations and hence very low resistivities. This makes geoelectrical-imaging techniques particularly interesting for leachate migration inside and around landfills.

Resistivity is a geoelectrical imaging method that is based on the measurement of the potential distribution arising when electric current is transmitted to the underground via electrodes. In our experiments resistivity monitoring was carried out along nine parallel lines with the ABEM Lund Imaging System multi-electrode system (Dahlin and Zhou, 2004). The lines were separated by 2 meter and with an electrode spacing of 0,5 meter, resulting in a 16 by 20 meter experimental site. The system is computer controlled and consists of a resistivity instrument, a relay-switching unit, four electrode cables, connectors and steel electrodes. The resistivity measurements were monitored using a remote controlled system and designed for 3D-measurements and 3D-interpretation. All data for each complete set of measurements were inverted using Res3Dinv, and a true 3D-model was computed for each measurement.

Gas emission measurements

A hand-held Siemens AG, CT PS 8 laser system, developed for field-based remote detection of emission of natural gas, was used for methane detection at the landfill surface (see also Ljungberg et al., 2009). The laser system operates with an infrared laser and is a backscatter system. The laser beam is transmitted and records the concentration of methane gas along a beam length, where the laser beam is reflected from a background surface, and the laser gives a mean concentration along the relevant measurement distance from the laser to the backscatter surface. The laser system is designed with a laser for detecting natural gas, i.e. gas with a methane content of 96-98 per cent as opposed to a methane content of 40-60 per cent for landfill gas. The lower methane content of landfill gas makes it less detectable compared with natural gas.

Additionally, methane emissions were measured with the static chamber method. Air samples were collected from the chambers with syringes, and analyzed in a laboratory through separation by gas chromatography (GC, Shimadzu 17A) and detection by flame ionization detection (FID).

Pore pressure measurements

Pore pressure was measured with BAT MKIII Vadose sensors, installed at depths of 1,5m below the soil surface. Since the ground water level was at several meters depth at the experimental site,

presence of gas in the soil was assumed to be indicated by high pore pressure values. The positions of the sensors were based on early resistivity data. Sensor F1 was located in a zone where resistivity values were high at 1,5m depth, while F2 was placed in a zone with low resistivity values (see figure 3).

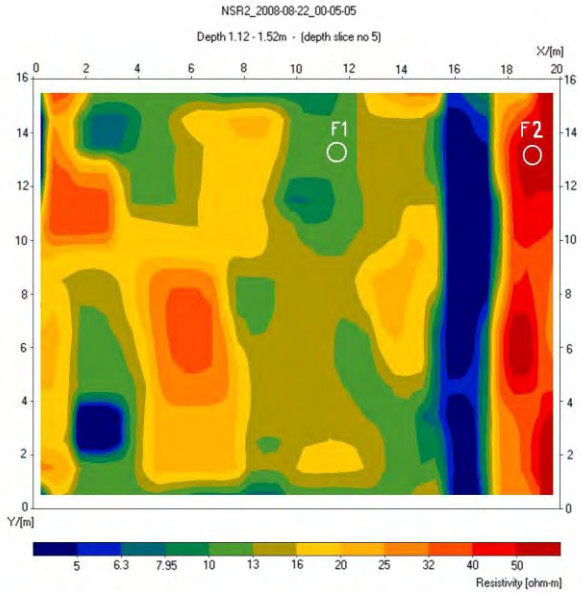

Figure 3: Positions of the pore pressure sensors at 1.12-1.52m depth on a resistivity profile.

Results and discussion

Resistivity

Figure 4 shows a 3D-modell of the resistivity measurements at the Filborna landfill, conducted on August 18, 2008. The inverted resistivity data varied from very low (under 3 Ωm) to relatively high (over 500 Ωm) resistivity values. However, most of the resistivity data were in the same range as previous investigations on MSW has shown, varying between very low resistivity and up to approximately 50 Ωm. At the surface, the positions of the electrodes are visible as red dots in Figure 3. This is an artifact arising during the inverse modelling procedure, which most likely could be reduced by an optimization of the software settings or of the software code.

Three main areas of difference in resistivity were observed. One area with low resistivity (below 10 Ωm), that agrees well with the position of the subsurface compost wall (green area to the right in Figure 3). The second area, to the left of the subsurface compost wall, shows resistivity values in a range up to approximately 50 Ωm. The third area, characterized by high resistivity values, appears at a zone near the surface above the subsurface compost wall. In this area resistivity values over 500 Ωm were registered. This area is particularly interesting since the high resistivity values may indicate gas migration near the subsurface compost wall.

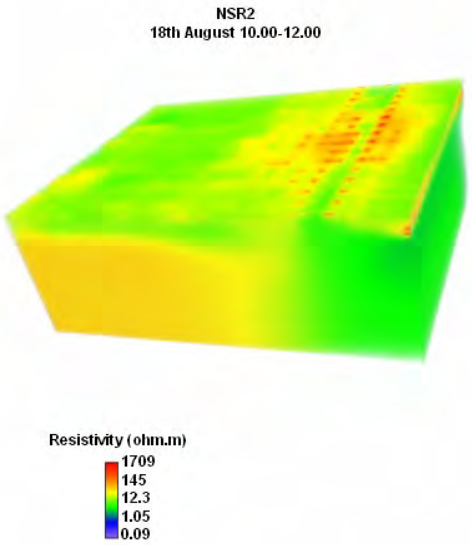

Figure 4: 3D-modell of the resistivity measurements at the Filborna landfill, conducted on August 18, 2008.

In Figure 5 the mean resistivity and coefficient of variation at different depths at the Filborna landfill during measurements in August 11 to 18, 2008 are shown in 17 layers, representing different depths from 0,1 to 13,6 meter. The resistivity values were relatively high at the surface (50 Ωm) with a rapid decrease down to approximately 20 Ωm at one-meter depth. At depths below two meters the mean resistivity stabilizes at 25 Ωm. The inert soil cover probably influences the relatively high resistivity values at the surface layers.

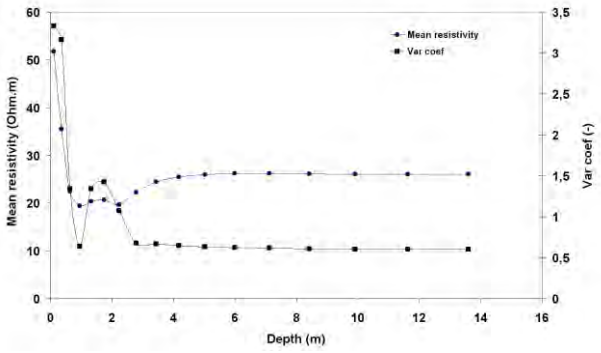

Figure 5: Mean resistivity and coefficient of variation at different depths at the Filborna landfill during measurements in August 18 to 22, 2008.

The coefficients of variation show a similar pattern as the mean resistivity with high coefficient of variation at the surface (over 3) and low and stable coefficient of variation at depths below 2 meters (0,7 to 0,6). Moreover, at the layers between 1 and 2 meter a local peak is shown with coefficient of variation rising from approximately 1 to 1.5.

The main focus in the study was on the temporal and spatial variability in the resistivity data, as it was assumed that large variability in the data could indicate gas migration in the waste mass. Figure 6 shows a 3D-plot of the coefficient of variation for the inverted resistivity data at the Filborna landfill site for the measurements conducted during August 18 to 22, 2008. The coefficient of variation varies from very low values, below 0.01 (blue and green areas in Figure 6) to higher values (yellow and red areas in Figure 5). The high variability in the data in the uppermost layers and a decrease in variability with depth, which is shown in Figure 5, is also indicated in Figure 5.

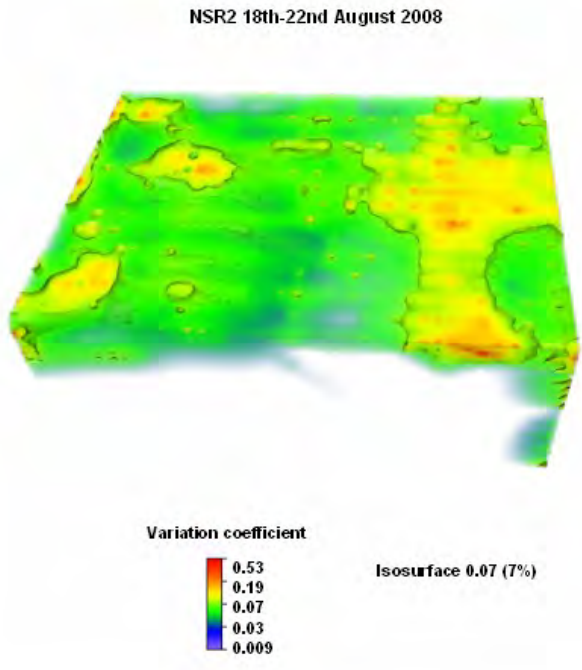

Figure 6: A model of the coefficient of variation for the resistivity measurements at the Filborna landfill during August 18 to 22, 2008.

The temporal variation in resistivity for a limited area of the upper soil is shown in figure 7. The correlation between the variations in resistivity and soil temperature suggests that the gas in the soil pores is affected by the variations in temperature. A possible explanation is that the pore gas pressure increases with increasing soil temperature, resulting in higher resistivity values.

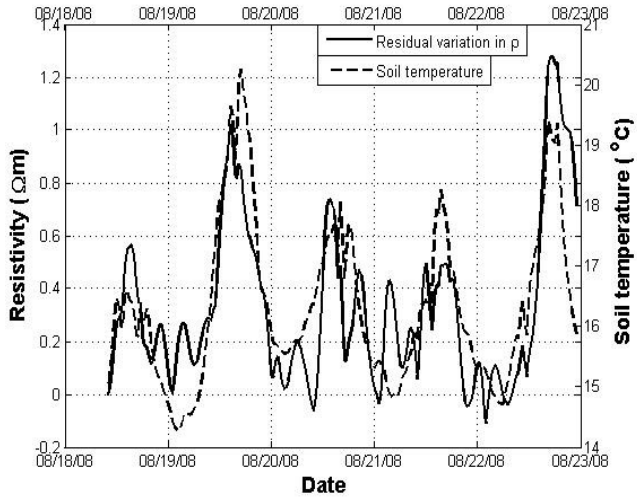

Figure 7. Example of temporal variations in resistivity and soil temperature.

Gas emission measurements at the surface of the landfill

In Figure 8, laser-scanning results show high levels of methane gas concentrations at the surface along the subsurface compost wall (200 – 600 ppm; red area). Also an area of concentrations at lower levels was measured at the test area (70 – 100 ppm; green area). The high levels of methane gas concentrations along the subsurface compost wall are particularly interesting since they correspond well with the resistivity measurements showing high resistivity (Figure 4), and high variability in resistivity data in the same area (Figure 6).

The positions of the static chamber measurements are also seen in figure 8. The results showed that the average methane emission from the two chambers furthest to the right in figure 6 was 322mg/m^2/s. Average methane emission from the other four chambers was -3mg/m^2/s. Negative methane emissions indicate that the gas emitted into the chamber consists of mostly carbon dioxide.

Thus, when measurements at the surface (Laser system and static chamber) were compared with the subsurface measurements (resistivity) the same pattern of methane migration was observed.

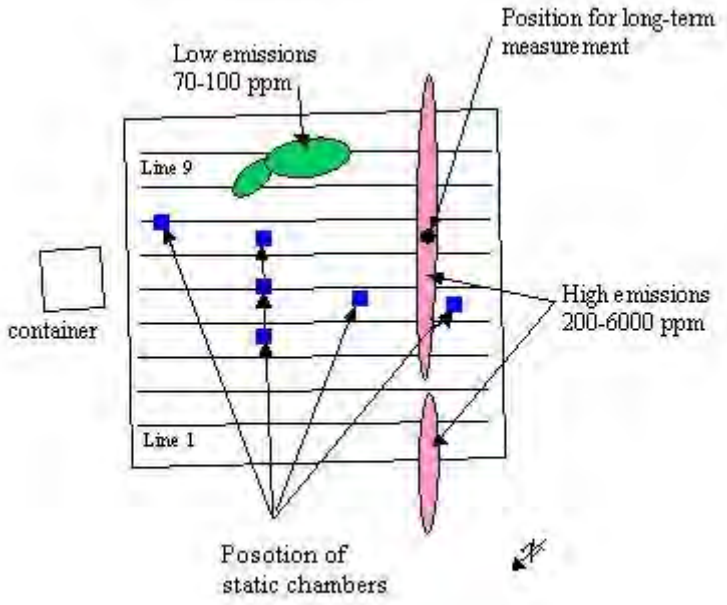

Figure 8: Laser-scanning results and static chamber position at the Filborna landfill site

Pore pressure measurements

Figure 9 shows the results of the pore pressure measurements. An initial overpressure of 7 mH_2O was measured at sensor F1, where after the pore pressure gradually declined to 3,5 mH_2O. This can be an indication of gas presence in the high resistivity zone where sensor F1 was installed. Possible reasons for the decline in pore pressure could be gas migration to other parts of the landfill, or leakage through the bentonite sealing surrounding the BAT sensor. The pore pressure measured at sensor F2 was relatively stable at around 0 mH_2O throughout the measurement period. The results support the assumption that high resistivity values can indicate gas.

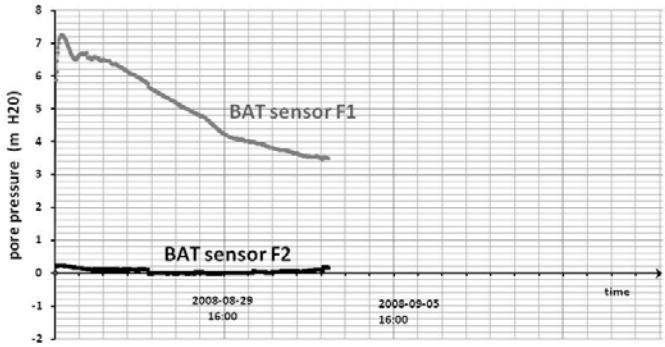

Figure 9: Pore pressure results from sensor F1 (high resistivity) and sensor F2 (low resistivity).

Conclusions

In this study we present research work with the objective of evaluating the use of geoelectrical resistivity technique to detect landfill gas migration. Extensive field experiments were conducted at the Filborna landfill site in Helsingborg, Sweden, in August 2008.

In general, the resistivity measurements showed results corresponding to results reported from previous investigations in waste. However, large variations in resistivity values were also indicated. Relatively high variability and high mean resistivity in the surface-near layers clearly indicate influence on the resistivity in the upper zone of the landfill. The variability and high resistivity may partly be explained by the presence and migration of landfill gas. However, other factors such as temperature, soil moisture and organic content in the waste may influence the resistivity and variability in the data.

The pore pressure results support the assumption of a link between gas presence and high resistivity values. When methane measurements at the surface (Laser system and static chamber) were compared with the subsurface measurements (resistivity measurements) the same pattern of possible landfill gas migration was observed. It is therefore concluded that the resistivity technique has a potential for mapping of landfill gas migration. The relationship is however complex and site-dependent, but given a good combination of information from different field data, it appears to be possible to image the migration of gas inside a landfill.

It is suggested that future R&D work should aim at a better understanding of the potential in geo-electrical methods for detecting landfill gas migration. In particular, gas migration at greater depth and at larger surface areas should be addressed. Also other processes such as, temperature and moisture content should be addressed. The R&D should also further investigate the interaction between subsurface processes and the landfill gas migration through soil cover of landfills.

References

Boeckx, P., Van Cleemput, O., Villaralvo, I. (1996). CH4 emission from a landfill and the CH4 oxidizing capacity of its covering soil. In: Soil. Biochem. Vol. 28, No. 10/11. 1397-1405.

Chapin III, F.S, P.A. Matson and H.A. Mooney, (2002). Principles of Terrestrial Ecosystem Ecology. New York, NY, USA.

Crawford, J.F. & P.G. Smith. (1985). Landfill technology. London, UK.

Dahlin, T and Zhou, B. (2004) A Numerical Comparison of 2D Resistivity Imaging with Ten Electrode Arrays, Geophysical Prospecting, 52, 379-398.

Dahlin T., Leroux V., Rosqvist H., Svensson M., Lindsjö M., Månsson C.-H., Johansson S. (2008). Potential of geoelectrical imaging techniques for detecting subsurface gas migration in landfills – an experiment, Procs. 14th European meeting of environmental and engineering geophysics, Near Surface Conference, Krakow, 15-17 September.

Guérin, R., Munoz, M.L., Aran, C., Laperrelle, C., Hidra, M., Drouart, E., and Grellier, S. (2004). Leachate recirculation: moisture content assessment by means of a geophysical technique. Waste Man, 24, 785 – 794.

Johansson, S. (2009) Electrical resistivity as a tool for analysing soil gas movements & gas emissions from landfill soils. Master of science thesis, Department of Physics, Lund, University, Sölvegatan 14C, S-22362 Lund.

Leroux, V., Dahlin, T. and Svensson, M. (2007). Dense resistivity and IP profiling for a landfill restoration project at Härlöv, Southern Sweden, Waste Management & Research, 25(1), 49-60.

Ljungberg, S-Å., Meijer, J-E., Rosqvist, H., and Mårtensson, S-G. (2009). Detection and quantification of methane leakage from landfills. SGC Rapport 204.

Marcoux, M.A., Adib, R., Lagier, T., and Gourc, J-P. (2007). Monitoring of leachate recirculation in a bioreactor landfill: Comparison of lysimeter and resistivity measurements. Proceedings Sardinia-07, Eleventh International Waste Management and Landfill Symposium, Italy

O'Leary, P. & Walsh, P. (2002). Landfill gas movement, control and energy recovery. Waste age; Mar 2002; 33,3: ABI/INFORM Global.

Rosqvist, H., Dahlin, T., Fourie, A., Rohrs, L., Bengtsson, A., and Larsson, M. (2003). Mapping of leachate plumes at two landfill sites in South Africa using geoelectrical imaging techniques. Proceedings Ninth International Waste management and landfill symposium, Cagliari, Sardinia, Italy.

Rosqvist, H., Dahlin, T., and Lindhé, C. (2005). Investigation of water flow in a bioreactor landfill using geoelectrical imagining techniques. Proceedings Sardinia-05, Tenth International Waste Management and Landfill Symposium, Italy.

Rosqvist, H., Dahlin, T., Linders F., and Meijer J-E. (2007). Detection of water and gas migration in a bioreactor landfill using geoelectrical imaging and a tracer test. Proceedings Sardinia-07, Eleventh International Waste Management and Landfill Symposium, Italy.

Acknowledgements

The Swedish Waste Management, the Swedish Gas Centre, Tyréns Stiftelse, NSR AB, NÅRAB and VAFAB are acknowledged for financial support of the study.

CASE HISTORY: MONITORING RESIN INJECTIONS WITH THE AID OF 4D GEOPHYSICS

Justin B. Rittgers, Zonge Geosciences, Inc., Lakewood, CO
Phil Sirles, Zonge Geosciences, Inc. Lakewood, CO
Gianfranco Morelli, Geostudi Astier s.r.l., Livorno, Italy
Marco Occhi, Geosec s.r.l., Livorno, Italy

Abstract

Ground improvement is an important practice in areas where the combined presence of expansive soils and fluctuating moisture content often result in differential heaving and settling soils and variable confining forces exerted on foundations. In fall of 2009, three-dimensional (3D) seismic pressure wave (p-wave) refraction and 3D electrical resistivity tomography (ERT) surveys were performed to determine the effectiveness of seismic refraction tomography in imaging the permeation of resin injected during ground improvement efforts within problematic soils. A test site near Piacenza, Italy was selected for this undertaking: Data were collected around the perimeter of an existing house suffering damage due to differential ground settlement. Three independent yet identical surveys were conducted using both methods, producing 3D images of the spatial distribution and variations in subsurface material properties before, during and after resin injection. The site is underlain primarily by a two to three meter thick layer of silt and clay with some sand lenses over an alluvial silty sand base layer. Prior to resin injection, substantial variations in both electrical resistivity and p-wave velocity are evident beneath the particular corner of the structure that exhibits the highest extent of damage (e.g., cracking and settling). During and after resin injections and curing, resistivities and velocities can be seen to change in the surrounding vicinity of injection points, and the magnitude of change in both data sets appears to be related to the amount of resin injected at each point. Geophysical measurements confirm the heterogeneous nature of the near-surface soil at this site, results from both methods correlate well with each other and additional field data (i.e., CPT data), and resultant 3D models are clearly useful in siting injection points as well as time-lapse monitoring the extent of resin permeation.

Introduction

Polymer resin injections can displace existing moisture within problematic soils and help to stabilize moisture content by semi-permanently filling pore spaces and compartmentalizing volumes of expansive soils. However, effective injections ultimately depend on a resin's ability to sufficiently infiltrate and seal inter-granular pore spaces and fractures, displacing and minimizing fluctuations in soil moisture. The extent of injection permeation can be influenced by factors such as resin injection amounts, injection pressures and injection rates. The specific polymer resin injected at the Italy survey site by Geosec s.r.l. expands as it cures, and as a result, the resin exhibits an increasingly low bulk density and much higher electrical resistivity relative to the hosting soils allotting geophysical imaging as a promising approach to evaluating and monitoring the extent of resin permeation. The site is shown in Figure 1 and is referred to as the House-Site herein.

In evaluating the ability of 3D seismic refraction tomography to image injected resins, seismic data were compared with ERT results. ERT surveys have been successfully applied by GeoStudi Astier s.r.l., an Italy-based geophysical services company, for the past 5 years as a monitoring technique to

evaluate efficiency and accuracy of resin injection treatments in building restoration tasks (Fischanger et al., 2007). Innovative electrodes geometries have been developed for 3D ERT surveys in urban contexts: electrodes are set free to arrange around the walls of the investigated buildings and specific quadrupolar sequences are generated. The following schemes of geometries for electrodes can be identified: L-shaped arrangements, loops of electrodes (LAB array – Loop Around Building arrangements), and C-shaped arrangements as used for this House-Site survey. The 3D models of electrical resistivity distributions are used preliminary to injection treatments in order to detect conditions within the soils that are subject to displacements (voids, fresh groundwater volumes, clays, etc.). These data are then integrated with other a-priori information gathered by conventional soil exploration methods and added to structural data, like a map of existing fractures in load-bearing walls, the state of settlements and the structural slots. This allows for on-site design of an effective injection treatment. During the injection treatment, intermediate ERT measurements are carried out, and real-time feedback is derived from the resistivity models and the percentile variations of resistivity distribution in the subsoil. A similar ERT approach was utilized in this study to help evaluate the applicability of 3D seismic refraction tomography in resin injection monitoring.

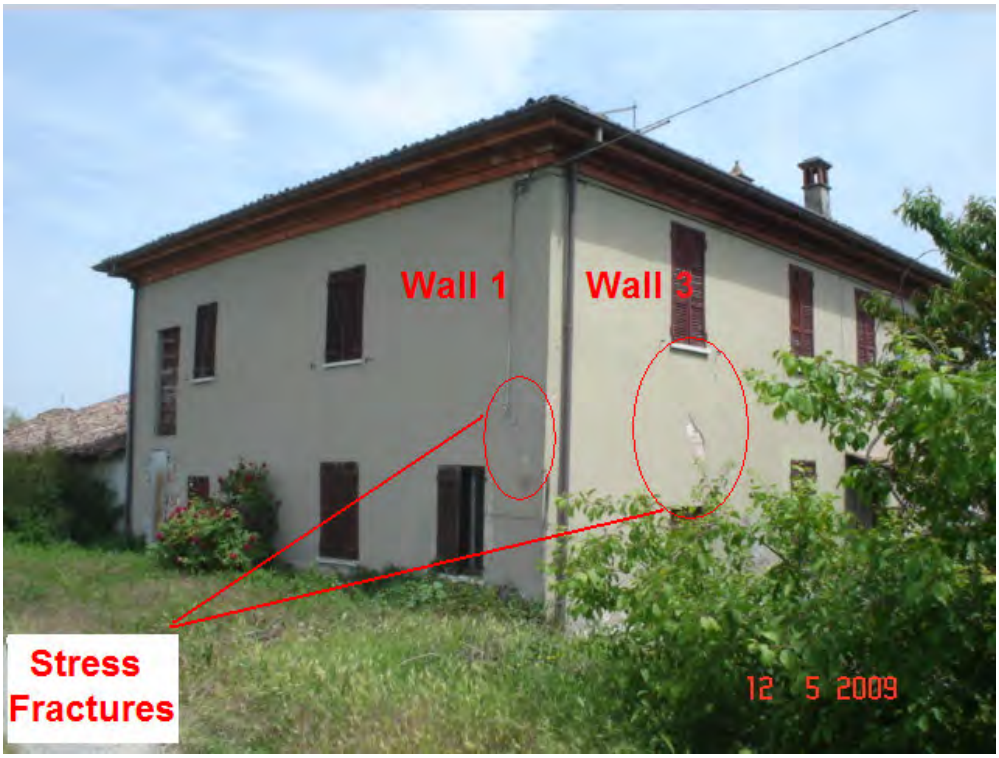

Figure 1: Photograph of the existing structure at the Italy House-Site. Stress fractures can be observed on wall #1 and wall #3 adjacent to closest corner shown in the photo. Wall #2 is an interior load-bearing wall parallel to wall #1 (not seen here).

At the House-Site, 3D seismic p-wave refraction data were collected utilizing a 48 channel seismograph, 4.5Hz vertical component geophones placed in a 'C-shape' array configuration at 1-meter intervals around the house perimeter (see Figure 2). A 16-pound sledge hammer and plate were used as the seismic source. Data were acquired using identical survey geometry and acquisition parameters before, during (prior to curing or additional injections), and after resin injections were completed,

allowing for quantitative comparison of spatial distributions of seismic velocity. These comparisons equate to a 4D or time-difference survey, where significant spatiotemporal changes between a given pair of 3D models should only be due to the increased amount of resin present or the related displacement of interstitial water. Ambient conditions varied over the course of each survey (e.g., rain or wind), but data quality was generally good to excellent with few sources of noise for either method.

First arrivals from each seismic survey were initially auto-picked, and picks for each shot record were then visually verified and manually corrected where necessary and all outliers were removed. Finally, all first arrival times and associated source and receiver geometry information were input into GAP SIT modeling software, a 3D seismic refraction tomography inversion program developed by Alan Rock of Summit Peak Technologies (Sirles, et. al., 2006, and Sirles, 2006). The GAP software performs a type of tomography which utilizes the discrete element method and particle flow code (DEM-PFC). Several inversions were performed on each data set using various initial velocity models to avoid local minima in the inversion fit-errors and to ensure validity of the results. 3D p-wave velocity models were generated for each survey, plotted with the ERT models, and these results were eventually integrated with resin injection data and cone-penetration test (CPT) results for interpretation. It is important to note that all seismic data processing was completed prior to knowledge of injection point locations, CPT results, and resistivity results.

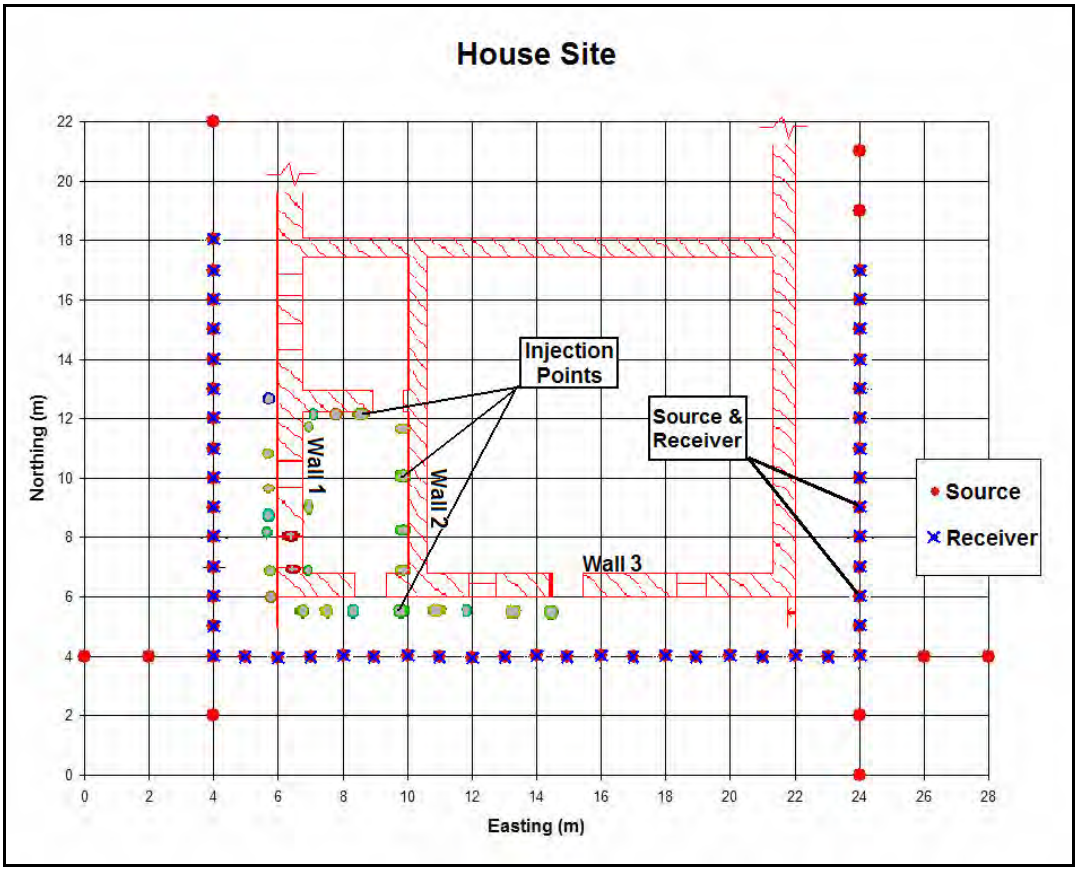

Figure 2: Geophone and seismic source point location plot for the Italy House-Site. The house foundation walls, labels and injection points have been annotated on the plot.

Survey Results

3D p-wave velocity model results are presented here as 2D depth-slices, 2D cross-sections and 3D perspective plots of p-wave velocity (m/s) and percent change. 3D ERT models are also presented here as 2D depth-slices, 2D cross-sections and 3D perspective plots of electrical resistivity (ohm-m) and percent change of resistivity for comparison to resultant seismic models.

Figure 3 exemplifies the strong correlation between CPT results and the model of post-injection seismic velocities along wall 1, offering confidence in the accuracy of 3D seismic models. Figure 4 shows the plan-view results of the pre- intermediate- and post-injection resistivity surveys at various depth slices for comparison. Measured apparent resistivities are generally moderately low, usually ranging only from around 5 ohm-meters to 100 ohm-meters in the depth range of interest. Figure 5 compares 2D cross-sectional views of intermediate and final percent changes in p-wave velocity, and it is apparent that the final injections and curing/expansion of resin caused the majority of changes seen in velocity distributions throughout the site. Similarly, Figure 6 shows 2D plan-view depth-slices of final percent change in p-wave velocities. The 3D volume image presented in Figure 7 shows significant increases in resistivity values in the immediate vicinity of injection points. In areas surrounding these resistivity increases, Figure 8 shows 3D volumes exhibiting significant final p-wave velocity increases. Finally, Figure 9 compares 3D results from both methods, and clearly shows significant changes in both resistivity and velocity distributions in the vicinity of injection points.

Electrical resistivity increases are primarily seen in regions directly surrounding and above injection points, suggesting that pore pressures direct infiltrating resin outwards and upwards. The 3D seismic models indicate that velocities increased in regions just outside of volumes of increased resistivity, suggesting that velocities increased in regions ahead of the suspected resin plumes. It is believed that soil compaction and soil saturation has occurred in these surrounding volumes as a result of resin expansion and displacement of water. Minor p-wave velocity decreases occurred primarily within the immediate vicinity of resin injection points and along discontinuities identified in the pre-injection models.

Conclusions and Caveats

3D seismic models generally compliment the CPT and 3D resistivity results at the House-Site, offering confidence in the final seismic models presented herein. While Figure 9 shows some small scattered volumes of change in both resistivity and velocity that are unaccounted for, the majority of change observed between 3D models appears to be related to resin injections. Consistently, there are large velocity increases in regions surrounding resin injection points. While further testing and development of refraction survey geometries is warranted, results of this investigation suggest that 3D seismic tomography can be successfully applied to help evaluate and monitor resin injections. This approach to 3D and 4D imaging could likely be extended successfully to other areas including the evaluation of grout injections, surface subsidence and collapse propagation subsequent to underground mining activities or dissolution, ground water table fluctuations within soft sediments, permafrost boundary fluctuations and soil improvement efforts.

References

Fischanger F., Morelli G., LaBrecque D.J., Occhi, M., 2007. Monitoring resins injection with 3D Electrical Resistivity Tomography (ERT) using surface and multi-borehole electrode arrays. *In Proceedings of SAGEEP 20th Annual meeting, Denver, CO., April 1-5, 2007.*

Sirles, P., A. Rock, and K. Haramy, 2006, Advancements in Subsurface Imaging Using 3D Seismic Refraction, *in Proceedings for SAGEEP, Philadelphia, PA.*, April 2005

Sirles, P., 2006, Advancements in 3D Subsurface Modeling using Seismic Refraction Data – A New Perspective, *in Proceedings for GEOPHYSICS 2006, the 3rd International Conference on Applied Geophysics, St. Louis, MO, December 2006.*

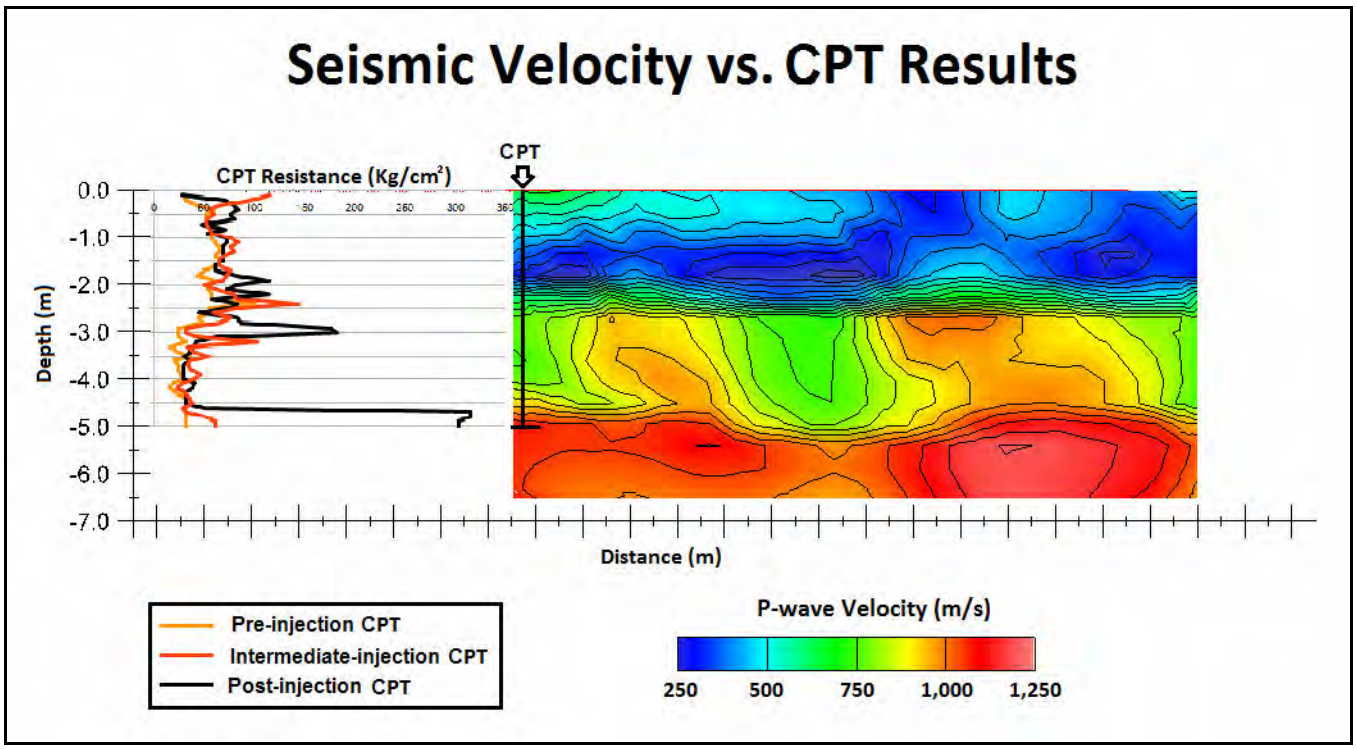

Figure 3: 2D cross-sectional view showing correlation between post-injection p-wave velocities along wall 1 and CPT results.

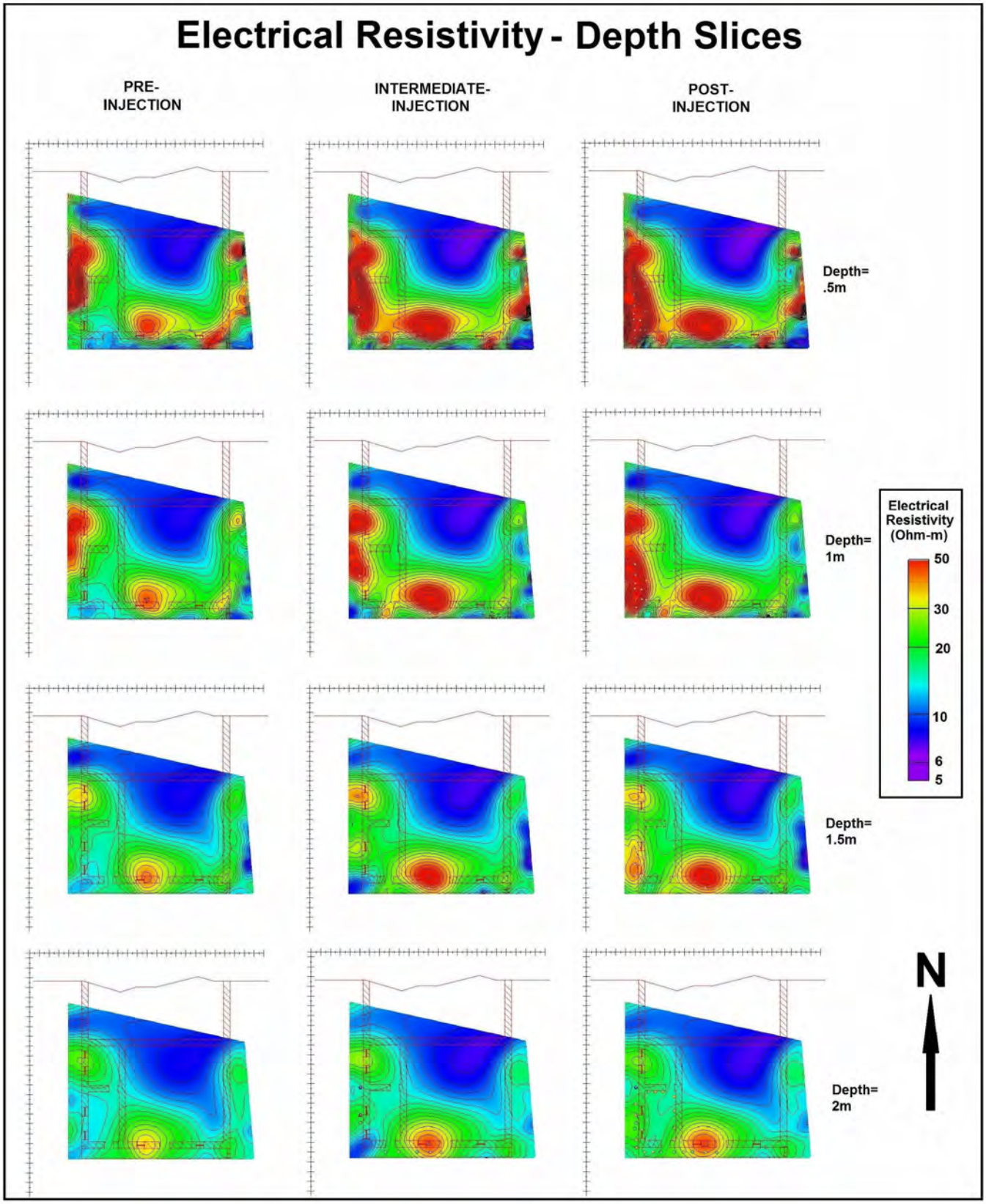

Figure 4: Plan view comparison of pre- intermediate- and post-injection 3D ERT models at various depths. Injections were generally located 1.8 meters deep and in the southwest quadrant of the models.

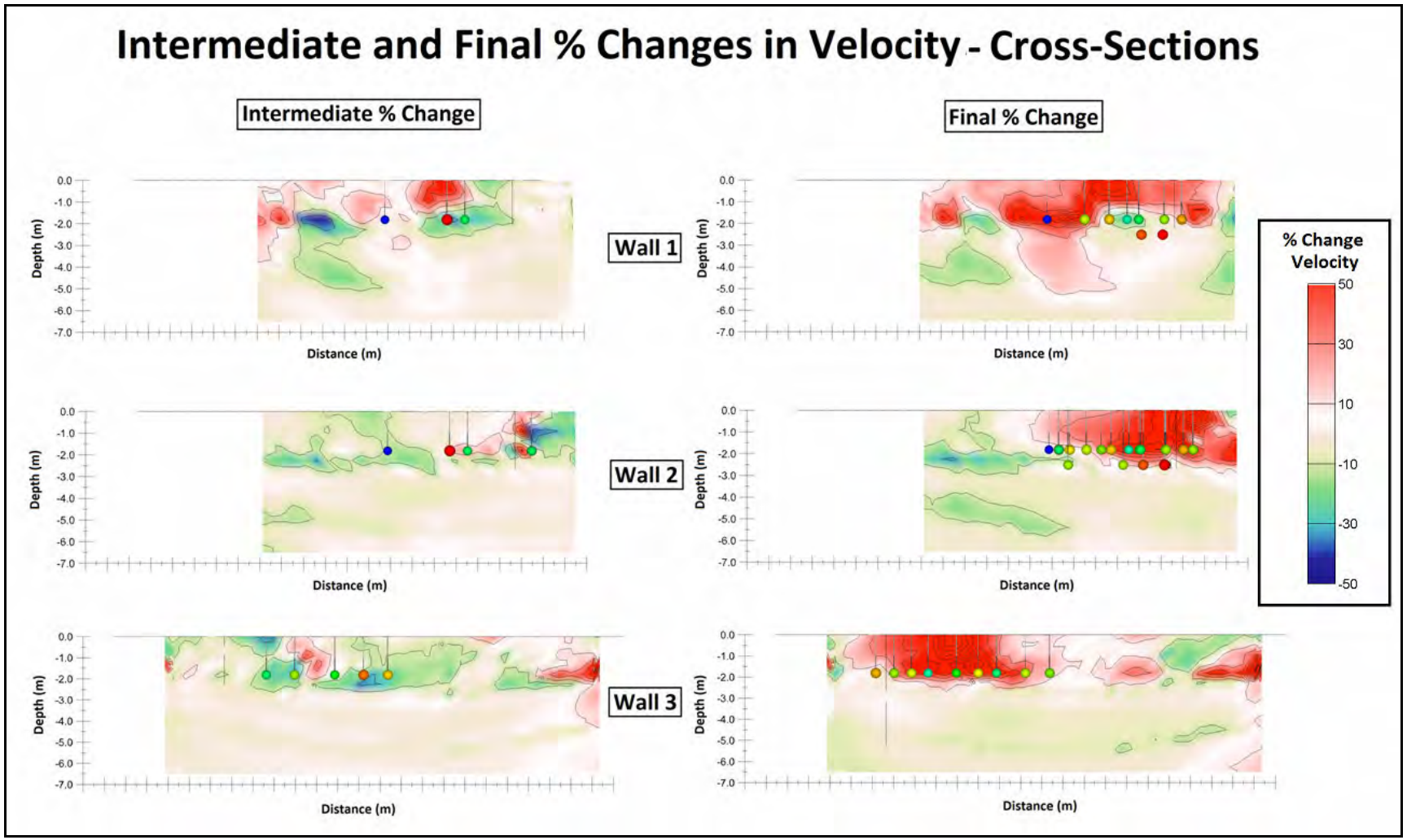

Figure 5: 2D cross-sections derived from 3D seismic models comparing intermediate and final percent changes in p-wave velocities along walls 1, 2 and 3. Injection points were generally located 1.8 meters deep and are indicated by the colored spheres. The colors of the spheres represent relative amounts of resin injected, where green is less and red is more.

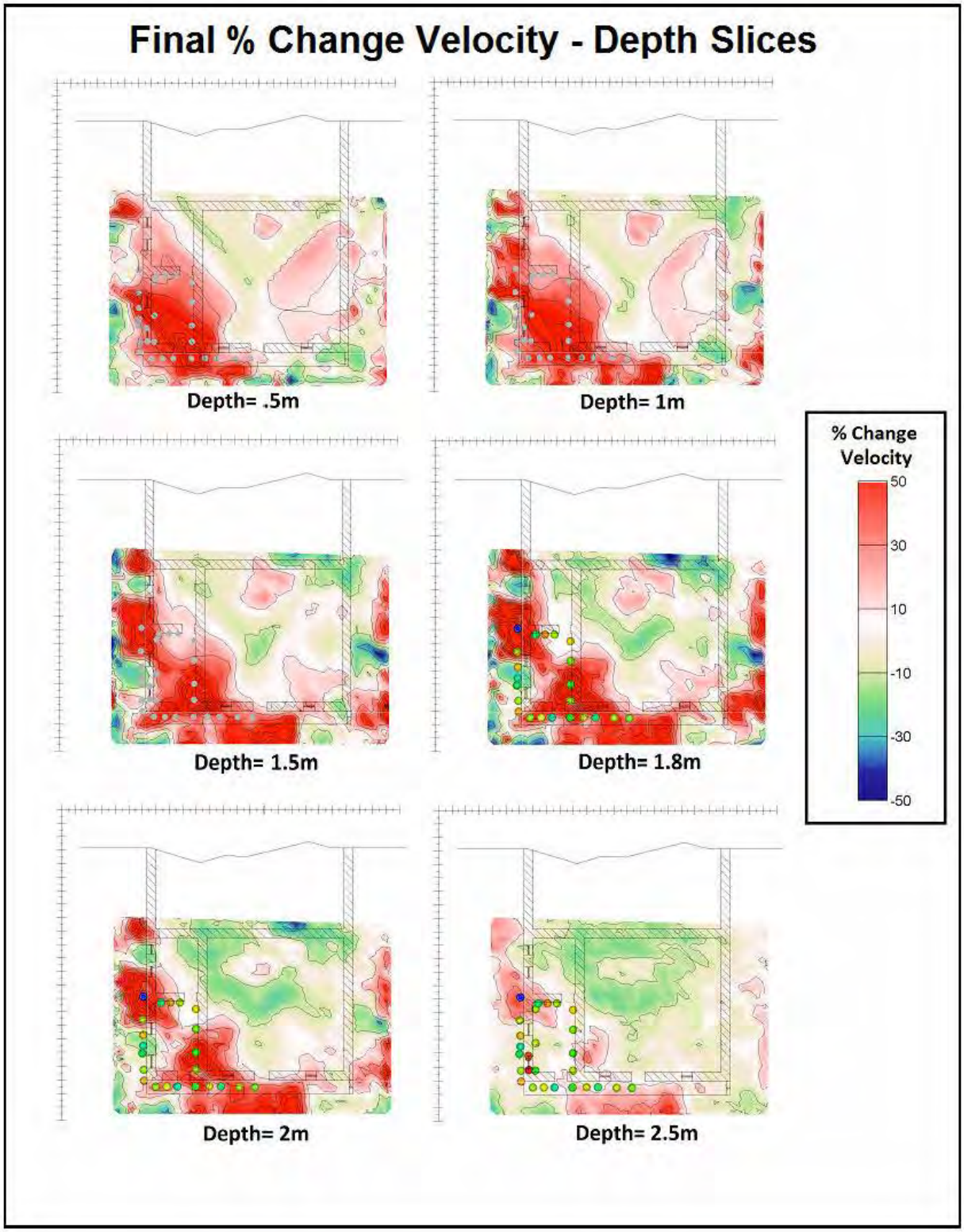

Figure 6: 2D depth-slices derived from 3D seismic models showing final percent changes in p-wave velocities after completing injections and resin curing has taken place. Injection points were generally located 1.8 meters deep and are indicated by the colored spheres. The colors of the spheres represent relative amounts of resin injected, where green is less and red is more.

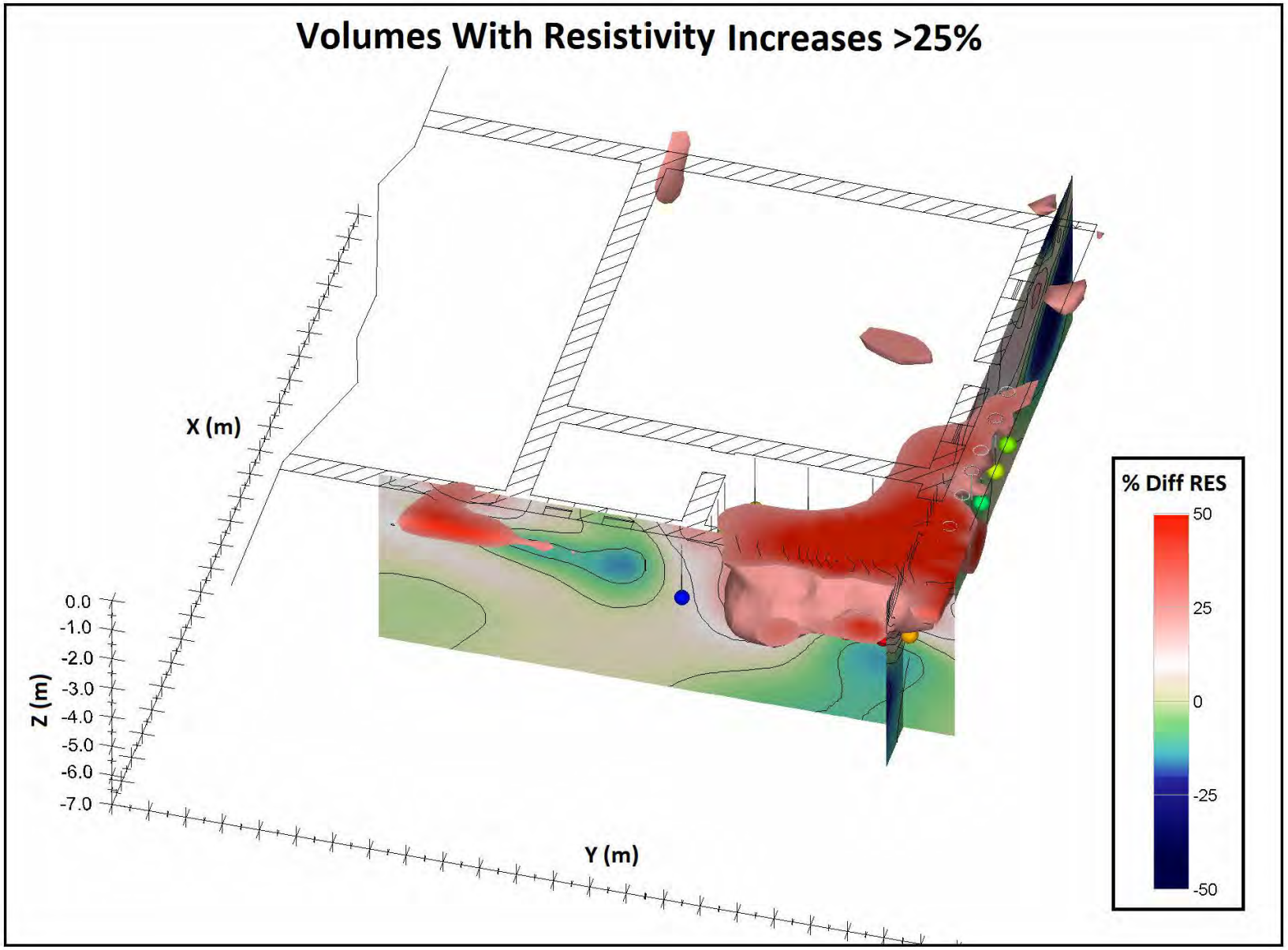

Figure 7: Combined 2D cross-sections and 3D volumes showing final percent changes in resistivity. Here, 3D model thresholds were applied to show only volumes exhibiting increases in resistivity of 25 percent or more.

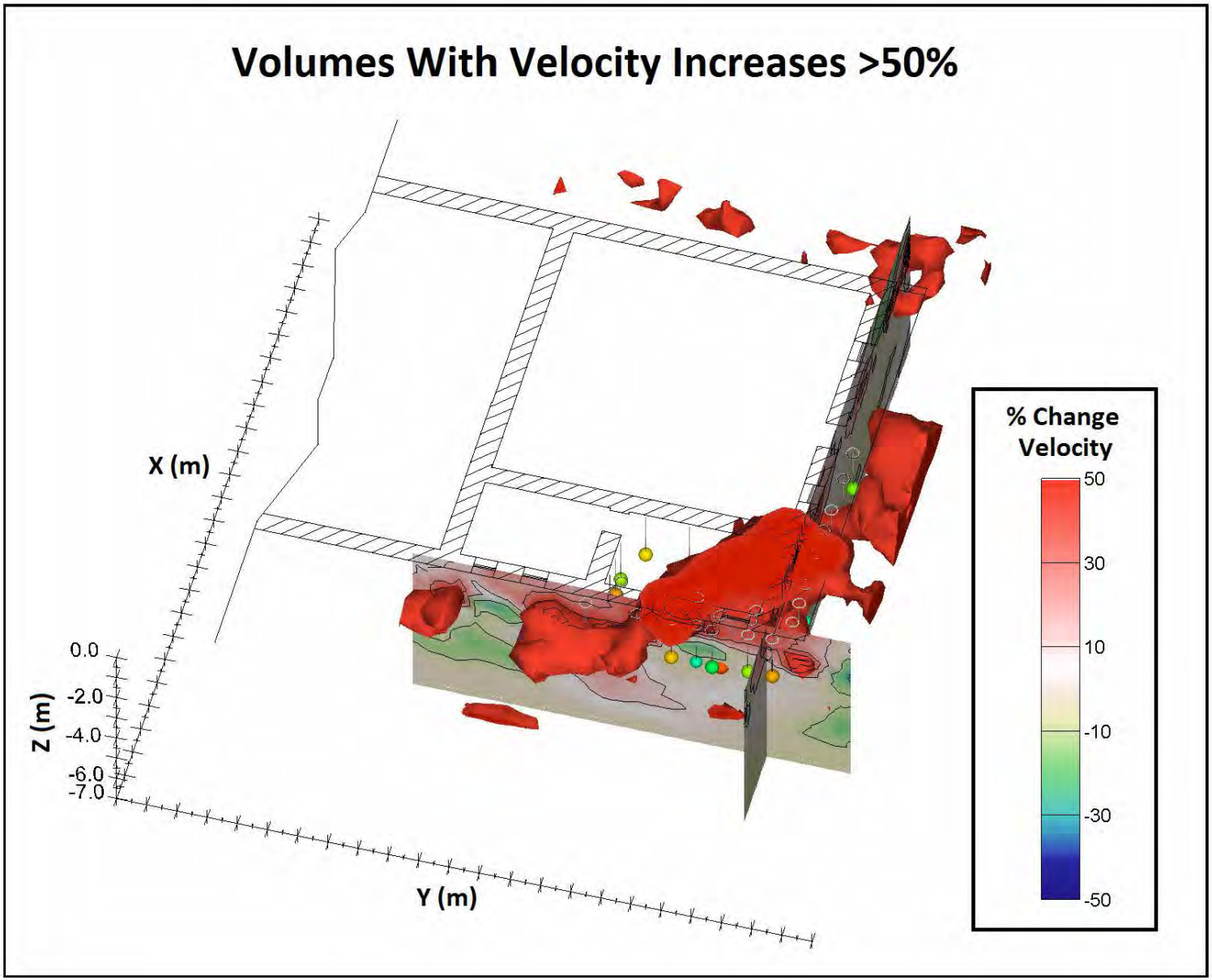

Figure 8: Combined 2D cross-sections and 3D volumes showing final percent changes in p-wave velocity. Here, 3D model thresholds were applied to show only volumes exhibiting increases in seismic p-wave velocity of 50 percent or more.

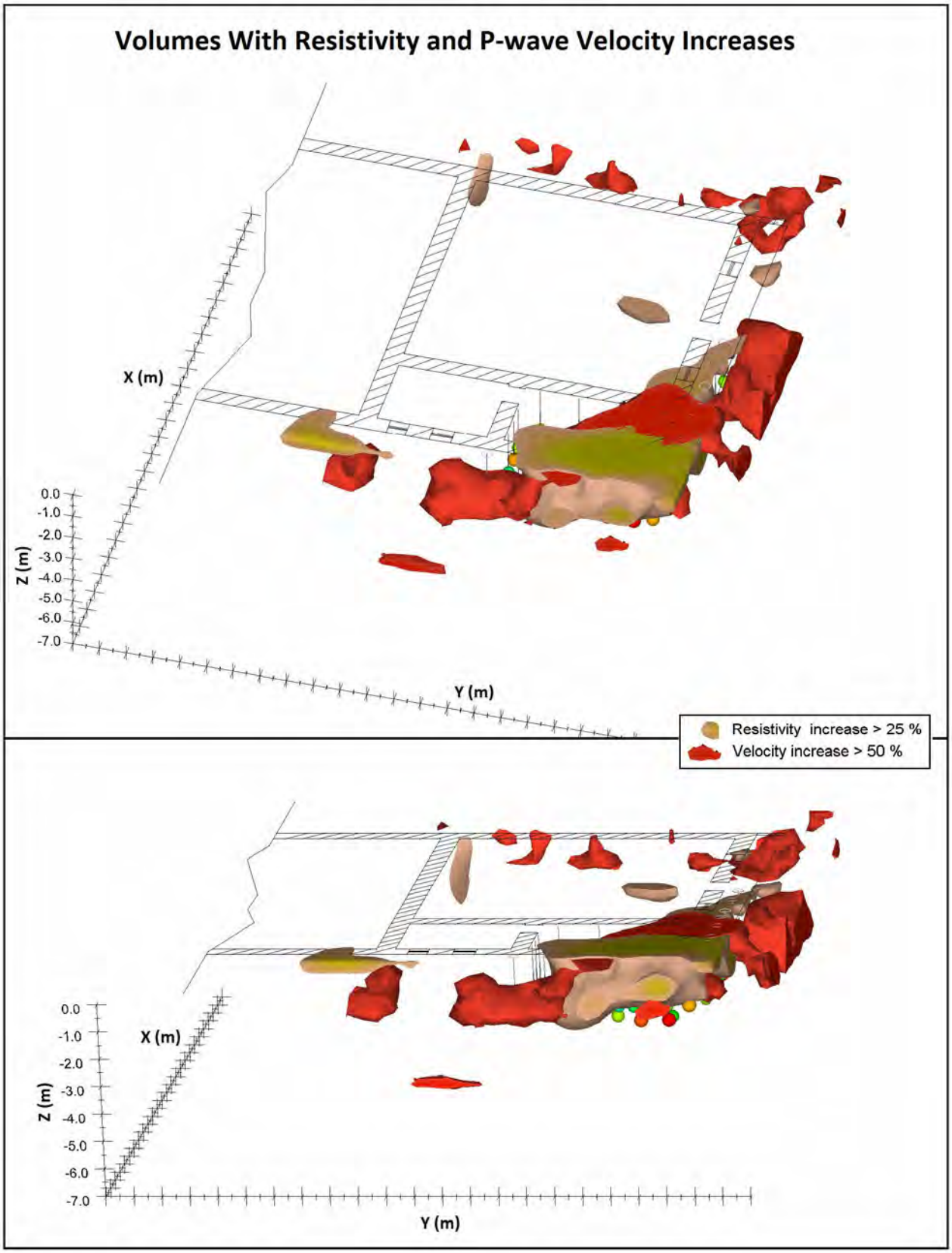

Figure 9: 3D comparison of volumes with final increases in p-wave velocities greater than 50% and of volumes with final increases in electrical resistivity greater than 25%

IDENTIFICATION OF THE POLARIS FAULT USING LIDAR AND SHALLOW GEOPHYSICAL METHODS

Lewis E. Hunter, U.S. Army Corps of Engineers, Sacramento, California 95814
Michael H. Powers, U.S. Geological Survey, Denver, Colorado 80225
Bethany L. Burton, U.S. Geological Survey, Denver, Colorado 80225

Abstract

As part of the U.S. Army Corps of Engineers' (USACE) Dam Safety Assurance Program, Martis Creek Dam near Truckee, CA, is under evaluation for earthquake and seepage hazards. The investigations to date have included LiDAR (Light Detection and Ranging) and a wide range of geophysical surveys. The LiDAR data led to the discovery of an important and previously unknown fault tracing very near and possibly under Martis Creek Dam. The geophysical surveys of the dam foundation area confirm evidence of the fault in the area.

Introduction

The work described in this paper supports the USACE evaluation of Martis Creek Dam. The dam is located approximately three miles east of Truckee, California on Martis Creek, a tributary to the Truckee River (Figure 1). Recent studies of the dam are addressing deficiencies related to seepage, spillway inadequacy, and stability issues in the event of an earthquake. USACE internal studies of dam breach scenarios indicate significant consequences to downstream areas including the inundation of portions of the Reno-Sparks metropolitan area. As a result, the recent screening process by the USACE gave a rating of Dam Safety Action Class One (DSAC-I) to Martis Creek Dam that requires "urgent and compelling" action to mediate hazards it imposes downstream.

LiDAR Fault Detection

The DSAC-I classification has resulted in a series of studies to evaluate the dam and its foundation. In support of these studies, the USACE purchased nine square miles of airborne LiDAR (Light Detection and Ranging) data collected for the Truckee-Donner Public Utility District to provide high-resolution topographic data of the Martis Creek dam property, from which a two-feet contour map could be produced. Initial review of the bare earth topographic data (Hunter et al., 2009a) revealed lineaments southeast of the Martis Creek reservoir on the east Martis Creek fan (Figure 2). This was surprising after a 2008 seismic hazard assessment (Wong et al., 2008) indicated no tectonic geomorphic features suggestive of Quaternary faulting on the fan. However, the recommendations of the seismic hazard report indicated that LiDAR data would be useful for evaluating faulting because of its ability to penetrate thick vegetation and allow for digital modeling of the Earth's surface (e.g., Harding and Berghoff, 2000; Sherrod et al., 2004). In response to the discovery of the lineaments, the USACE purchased the remaining LiDAR data available for the Truckee Basin and discovered lineaments extending across the area of coverage in a general north to south orientation. Additional LiDAR data extending from Sierra Valley in the north to Tahoe City along the north shore of Lake Tahoe were then acquired to define the extent of these features (Figure 1). Hunter et al. (2009a & 2010) show that these data exhibit tectonic geomorphic features indicative of a largely unmapped fault zone that extends for

more than 20 miles, and includes a subtle surface expression between Martis Creek Dam and its spillway (Figure 3).

Investigation of the dam site has included field observations, boreholes, paleoseismic trenching, and geophysical surveys. Geomorphic features indicative of faulting observed in the field and LiDAR imagery include a series of tectonic benches, linear swales, offset terrace risers, shunted bedrock ridges, mole tracks (series of topographic highs and lows that fall along the fault trace) and bedrock scarps and valley walls. Interpretation of the fault has helped explain vertical offsets in geologic contacts noted in adjacent boreholes, and one borehole placed along the interpreted fault trace encountered fault related disturbance. Two paleoseismic trenches on the East Martis Creek Fan mapped by a Kleinfelder-Geomatrix joint venture documented multiple rupture events in both trenches (Kleinfelder-Geomatrix, 2009; Hunter et al., 2009b).

Geophysical Investigations

A large geophysical study conducted concomitant to the other studies was designed to provide insight into the stratigraphic relationships that impact seepage as well as to aid in the geotechnical characterization of the foundation. Methods applied to date include compressional (P) and shear (S) wave seismic reflection and refraction, direct current (DC) resistivity, magnetotellurics (MT), magnetics, self potential and time-domain electromagnetics. Field work has been conducted in three phases. Phase I focused on the upstream region of the dam and was used to evaluate the responses of the various methods. Phase II focused on the downstream toe region with some lines re-located to investigate the fault. Based on preliminary results of Phases I and II, Phase III concentrated on the acquisition of a large-coverage grid of two-dimensional DC resistivity profiles. P-wave seismic reflection profiles from Phases I and II indicated faulting within the foundation of the dam (Figure 4). The broad coverage of DC resistivity data has led to a valuable interpretation of the base of the unconfined aquifer (base of glacial outwash deposit) in the reservoir basin, and a visualization of two buried channels that were previously unknown (Figure 5). The location of these channels helps explain several of the seepage issues that have been documented over the past 30 years of operation. An integrated analysis of these data further demonstrated that much of the “buried topography” observed in the DC resistivity models at the interpreted top of the Prosser Creek Formation appears to be fault related. Several features originally described as “M-structures” (topographical high-low-high sequence over short lateral distance noted on the boundary between overlying electrically resistive and underlying electrically conductive boundary) corresponded to the location of the inferred fault trace from the LiDAR data and were used to further deduce that multiple fault strands were present in the subsurface (Figure 6). When fault traces interpreted from the seismic reflection data are superimposed onto the DC resistivity models, significant portions of the DC variability can be explained as fault related.

Summary

This study describes the detection of the Polaris Fault (Hunter et al. 2009a) using airborne LiDAR imagery and how geophysical surveys have aided in further characterizing the fault and subsurface stratigraphy near the foundation of Martis Creek Dam. DC resistivity and seismic methods have proven to be especially informative in evaluating conditions at the dam. Simultaneously visualizing these data in a 3-D visualization package has been especially useful in defining the features of the dam foundation and reservoir basin geology.

References

Harding, D.J., and Berghoff, G.S., 2000, Fault scarp detection beneath dense vegetation cover: Airborne lidar mapping of the Seattle fault zone, Bainbridge Island, Washington State: Proceedings of the American Society of Photogrammetry and Remote Sensing Annual Conference, Washington, D.C., May, 2000, 9 p., http://duff.geology.washington.edu/data/raster/lidar/ harding.pdf (March 2003).

Hunter, L.E, Howle, J.F, Rose, R.S., Bawden, G.W., 2009a. The "Polaris Fault": A Previously Unmapped Fault Discovered Using LiDAR near Martis Creek Dam, Truckee, CA. Seismol. Res. Let., v. 80, no. 2, p. 305.

Hunter, Rose, R.S., Howle, J.F., Brown, V.W. Powers, M.H., Hilton, B., and Hubbard, E., 2009b. Geotechnical and Paleoseismic Investigations of the Martis Creek Dam, Truckee, California, AEG 2009 Field Trip Guide Book, September, 2009.

Hunter, L.E, Howle, J.F, Rose, R.S., Bawden, G.W., 2010. LiDAR Assisted Identification of an Active Fault near Truckee, California, Bulletin of the Seismological Society of America (in revision).

Kleinfelder-Geomatrix, 2009, Martis Creek DSAP Fault Trenching Interim Report, Nevada County, California. Sacramento, California. Kleinfelder-Geomatrix Joint-Venture, Report Prepared for Sacramento District, U.S. Army Corps of Engineers under Contract No. W91238-08-D-0015, Task Order 0009. July 2009.

Sherrod, B.L., Brocher, T.M., Weaver, C.S., Bucknam, R.C., Blakely, R.J., Kelsey, H.M., Nelson, A.N., and Haugerud, R., 2004. Holocene fault scarps near Tacoma, Washington, USA. Geology, v. 32, no. 1, 9-12.

Wong, I., Dawson, T., Thomas, P., Olig, S., Dober, M. and Terra, F., 2008, Seismic Hazard Analyses and Development of Design Ground Motions for Martis Creek Dam, California. Oakland, California, URS Corporation, Report prepared for U.S. Army Corps of Engineers.

Acknowledgements

USGS Water Resources office in Carnelian Bay, CA has been a valued partner in the interpretation of the LiDAR imagery and evaluation of the tectonic geomorphology. Funding for the work has been provided through the Dam Safety Assurance Program under Ronn Rose while project management has been provided by Veronica Petrovsky and Adam Riley. Verne Brown, USACE, has overseen all geotechnical investigations.

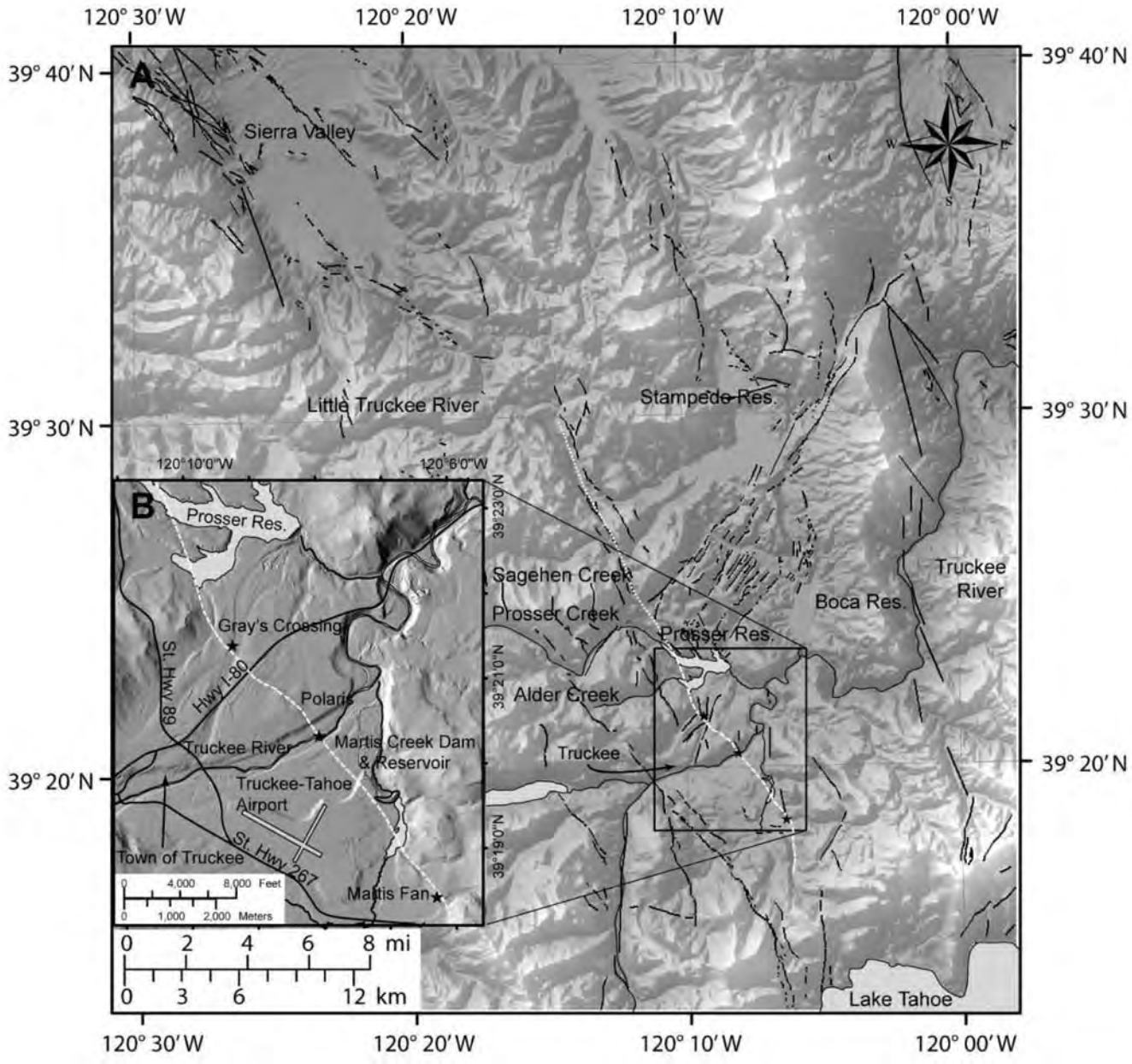

Figure 1. Plan view location of Martis Creek Dam near Lake Tahoe, CA. (from Hunter et al., 2009b). White dashed line denotes the approximate trace location of the newly discovered Polaris fault.

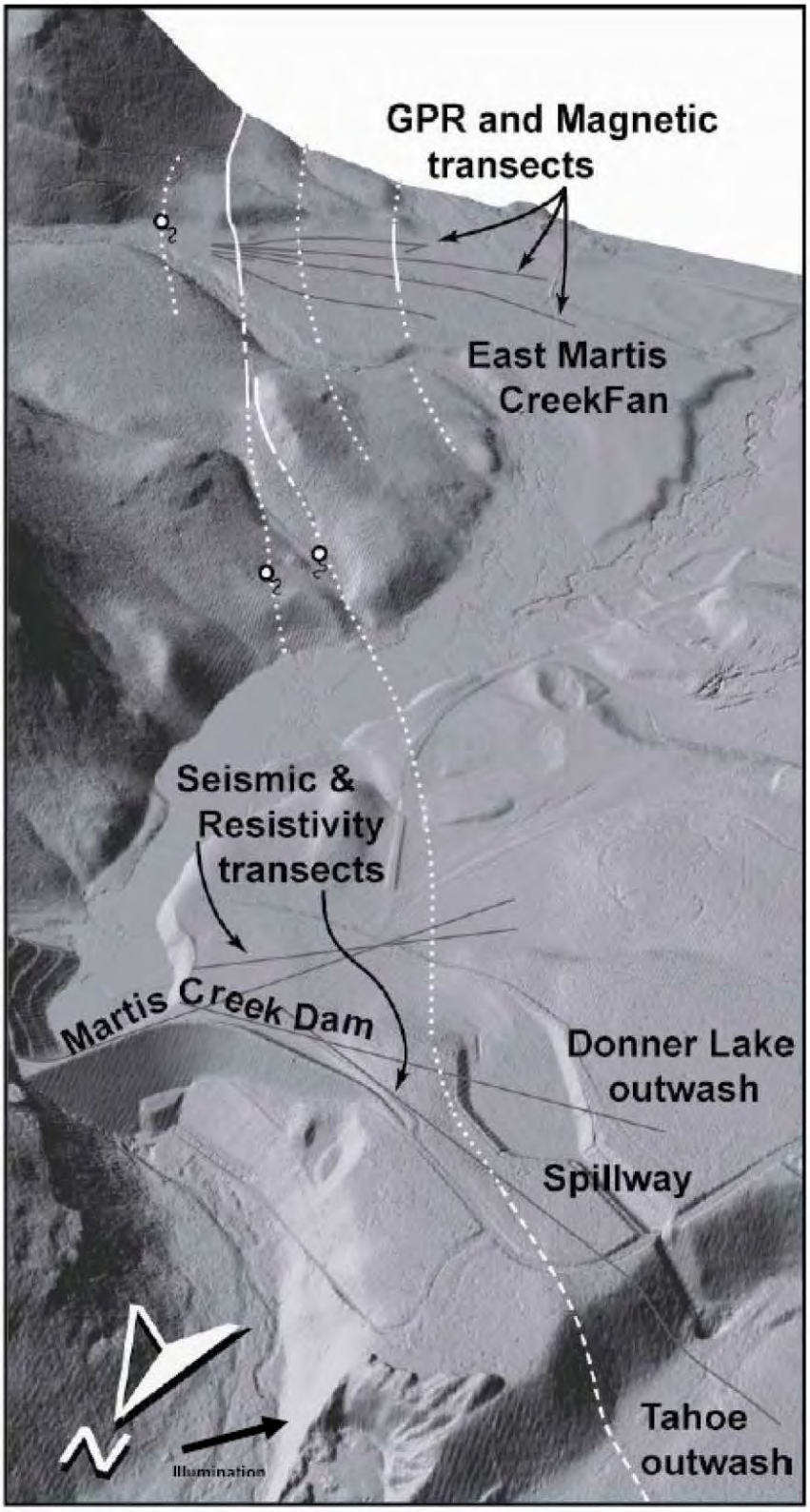

Figure 2. Oblique view of the Martis Creek Dam property showing strands of the newly discovered Polaris Fault identified in the airborne LiDAR imagery (From Hunter et al., 2009b).

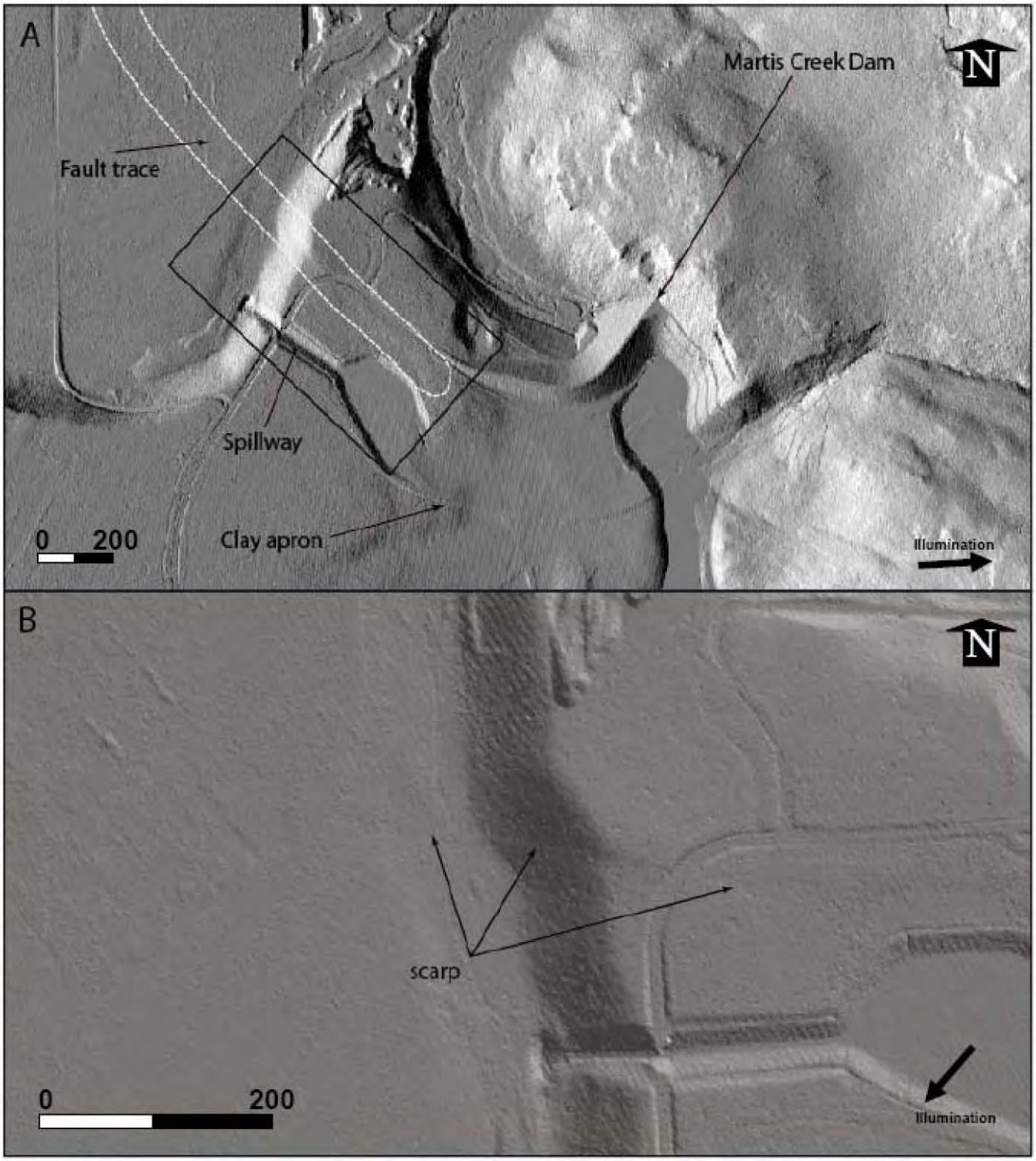

Figure 3. Imagery showing fault trace between left abutment and spillway of Martis Creek Dam. A) General location relative to select features and highlighting the fault lineament. Black box indicates focused area shown in B) where fault lineament is shown where it crosses the terrace riser and projects to the north side of the spillway (From Hunter et al., 2009b).

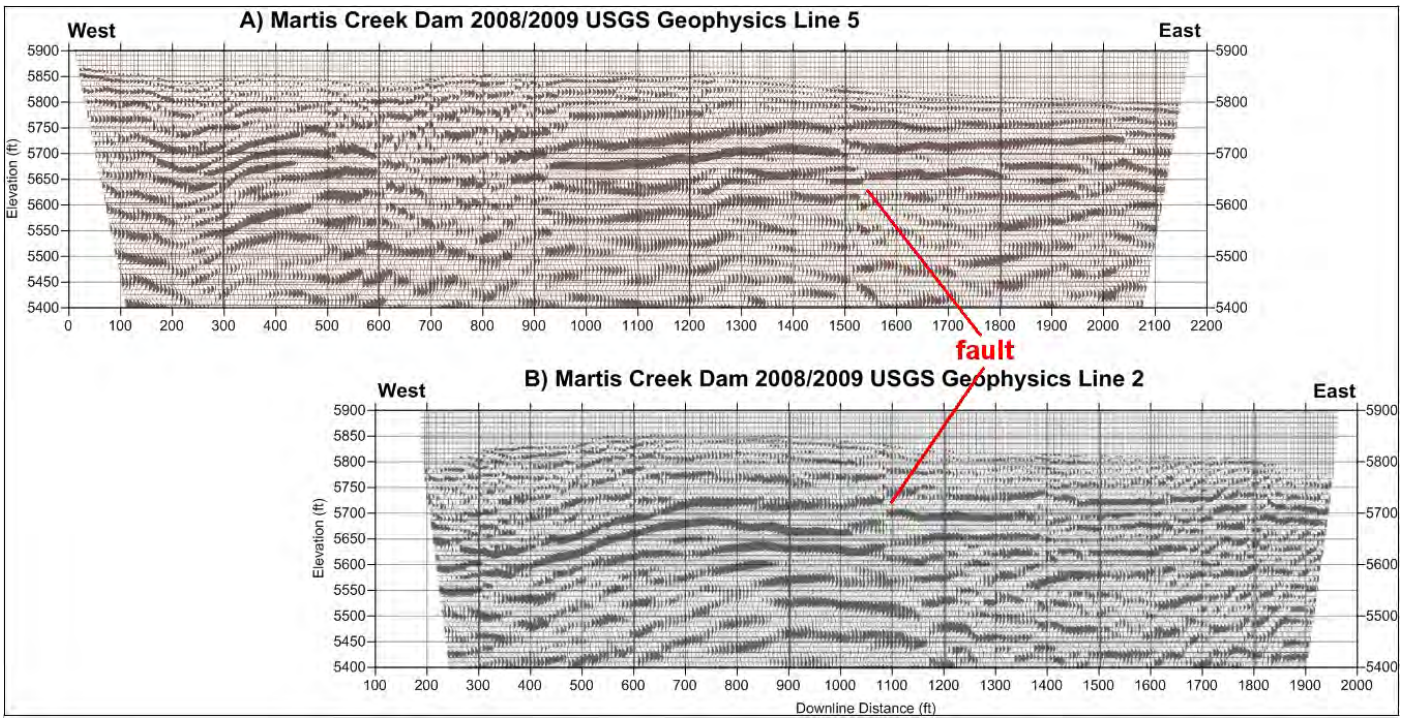

Figure 4. P-wave seismic reflection lines 2 and 5 on the upstream and downstream toes of the left side of the dam show evidence of faulting in the dam foundation materials.

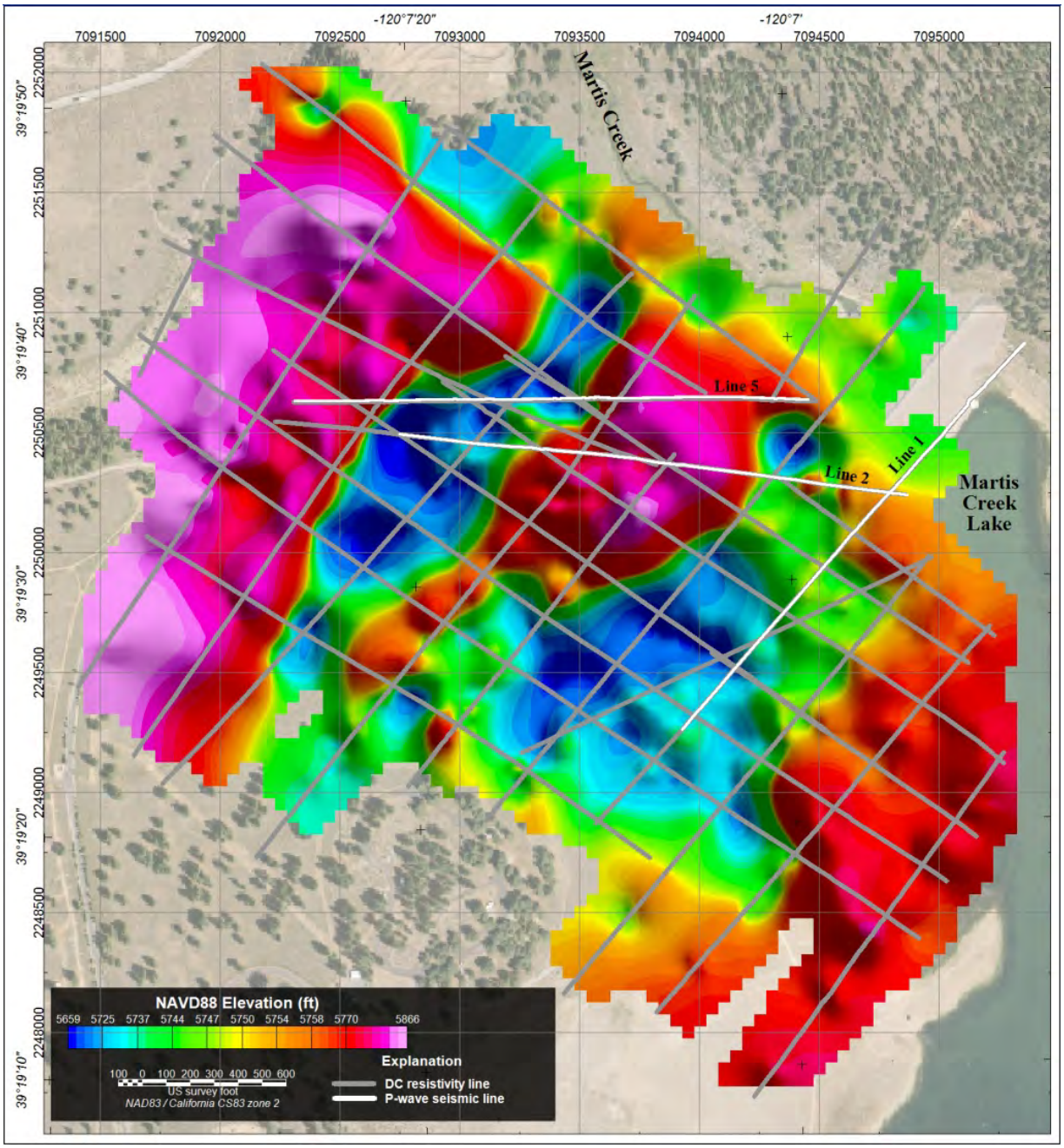

Figure 5. Geophysical DC resistivity and seismic lines are shown on a plan view map of the dam area. The color overlay represents the elevation of the top of relatively impervious Prosser formation under surface deposits of relatively pervious glacial outwash. Two evident channels exist on this paleosurface trending NNE under the left side of the dam where seepage concerns have been concentrated.

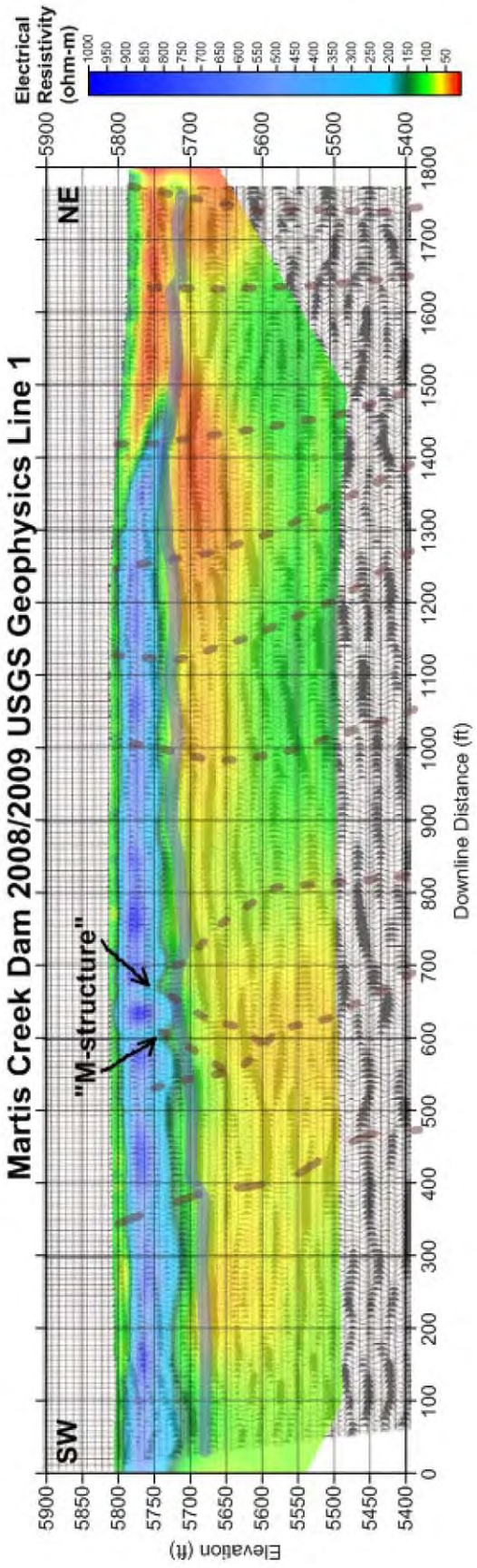

Figure 6. The DC resistivity model for line 1 overlain on the seismic reflection profile shows an “M-structure” on the top of Prosser formation. The independent fault interpretations from the seismic profile match the location of the “M-structure”.

INTERNAL STRUCTURE OF AN ILMENITE MINE WASTE ROCK PILE MODELLED FROM IP IMAGING AND LABORATORY MEASUREMENTS

Michel Chouteau, École Polytechnique de Montréal, Canada
Rachid Intissar, École Polytechnique de Montréal, Canada
Michel Aubertin, École Polytechnique de Montréal, Canada

Abstract

Nickel concentrations occasionally above the allowed norm have been measured in water samples in the vicinity of the Petitpas waste rock pile at the Tio mine, Québec, Canada. In order to understand the chemical and hydrodynamic mechanisms responsible for the nickel dissolution and release in the environment a large hydrogeological/geotechnical/geophysical study was undertaken on the very large rock pile (600 m x 300 m x 150 m). Geotechnical and physical properties were measured in the laboratory on samples of waste with various moisture content and salinity. Induced polarization allowed the determination of electrical resistivities and chargeabilities that were to be used to interpret time-domain IP tomography surveys carried out on the waste rock pile. IP survey data were inverted in 2-D. The resistivity models for all survey lines show common features. From surface to 25-30 m depth, the subsurface is resistive and show lateral changes which suggests large grain size heterogeneities and low water content; below and up to 50 m, a quasi uniform layer with resistivities in the range 50-250 ohm.m suggests fine-grained material with increased saturation. Finally below a depth of 50 m, the subsurface becomes very resistive again, indicative of coarse low-moisture content material. The chargeability model shows no structural correlation with the resistivity model. In general, chargeabilities are very large (up to 100 mV/V) and show no layering. From the laboratory and the survey results, we interpret the resistivity to be sensitive to water content and salinity while chargeability is sensitive to the metal concentration. The geoelectrical model and the interpreted hydro-geotechnical model will be useful for modeling water flow and reactive transport through the waste rock pile.

Introduction

Waste rock piles are non-economic rocks mined out and stored at ground surface. These piles are sometimes a source of Acid Mine Drainage (AMD) (e.g Aubertin et al, 2002) or Contaminated Neutral Drainage (CND) (Nicholson, 2004). These two types of mine leachate are typically the result of water flowing through mining wastes (i.e. waste rock pile or tailings impoundment) containing sulphide minerals such as pyrite. AMD waters are usually characterized by a low pH, a high acidity and a high concentration of sulphate and heavy metals. Many metals, such as nickel, zinc, selenium, cobalt and arsenic, are also soluble at a pH near neutrality (Bussière et al, 2008). These can be a source of contamination of the effluents without the presence of acidic conditions (Pepin, 2009). The present study was performed on waste rocks from the Lac Tio mine, which is the largest Canadian ilmenite deposit. The mine, located near Havre-Saint-Pierre, Québec, Canada, is operated as an open pit by QIT Inc., a division of Rio Tinto. This waste rock pile faces a CND problem of contaminated neutral drainage (Bussière et al, 2008) due to a relatively high concentration of nickel in its effluents.

The internal structure of a pile has a significant influence on the flow of water and air inside the waste rocks (e.g. Aubertin et al, 2002). This leads to the need to determine the hydro-geotechnical units

that make up the pile and to assess the physical properties of the materials in each of these units (as the construction history of old piles is usually unknown). This characterization is required to predict, using numerical simulations, the fluxes within existing piles. The numerical models can also be used to investigate new ways of building piles in order to minimize infiltration of water and air flow inside a reactive waste rock pile. Drilling and trenching are sometimes considered the most credible approach to determine internal structure of a pile and to assess the geochemical and physical properties of recovered wastes. However, such approach is costly and difficult to implement because of the coarse, heterogeneous nature of waste rocks and the poor recovery rate in drilling.

Under these conditions, geophysical methods offer an attractive alternative for characterizing the internal structure of waste rock piles (e.g. Poisson et al, 2008; Anterrieu et al, 2010). The advantages of these methods include being non-destructive, ease of implementation and relatively low cost compared to drilling and trenching. However, geophysical methods also have limitations in terms of resolution, depth of investigation, and the nature and significance of the gathered information and interpretation.

Previous work has shown that electrical methods based mainly on mapping resistivity and chargeability seem to be the best suited geophysical techniques for imaging waste rock piles under unsaturated conditions (e.g. Poisson et al, 2008; Anterrieu et al, 2010). These methods were used at Lac Tio mine. The work presented here consisted of two parts. The first part focused on the laboratory measurement of electrical properties of waste rocks sampled from the pile. These measurements showed that the resistivity varies significantly with the electrical conductivity of the interstitial fluid and the degree of saturation. Also, the observed chargeability is fairly high (over 100 mV/V), indicating a strong dissemination of ore in the wastes. The chargeability also varies with the electrical conductivity of the interstitial fluid and the degree of saturation. The second part of this study was dedicated to electrical measurements performed on the largest waste rock pile at the Lac Tio mine (QIT – Rio Tinto). The in situ measurements indicate that the pile includes complex features, such as thick layers of contrasting resistivity. Also, the field data indicate the presence of a large concentration of metallic particles in the waste rock.

Laboratory Measurements

The purpose of the laboratory measurements was to study the electrical properties of waste rocks as a function of the degree of saturation and conductivity of the interstitial fluid. In turn, the results would help with the interpretation of field measurements, in terms of grain size and water content. A cylindrical Acrylic column with a diameter of 0.3 m and a height of 1 m was used. Stainless steel electrodes were inserted into holes through the wall of the column and sealed with silicone. Electrodes were also installed along the central axis (on a rigid plastic tube) to increase sensitivity of the system. A total of 9 levels of electrodes, with 8 cm spacing, were installed in the column. The particle size analysis for the waste rock, truncated at 10 mm, showed that D_{10} = 0.012 cm and D_{60} = 0.36 cm, which gives a coefficient of uniformity C_U ($C_U = D_{60}/D_{10}$) of about 30. This ratio reflects the widely graded distribution of the material tested in the laboratory (Bowles, 1984; McCarthy, 2002). A mineralogical analysis by X-ray diffraction was carried out (at UQAT) on a sample of waste rock for grains with a diameter less than 5 mm; the main results are presented in Table 1.

Table 1: DRX mineralogical analysis for a sample of mine wastes fraction < 5 mm. (data obtained from UQAT, 2009).

Mineral	Chemical Formula	Weight %
Ilmenite	FeTiO3	53.66
Labradorite	$(Ca,Na)(Si,Al)_4O_8$	18.14
Hematite	Fe_2O_3	18.06
Pyrite	FeS_2	2.57
Gehlenite	Ca2 Al (Si,Al) O7	1.78
Muscovite	$KAl_2 (Si_3Al)O_{10}(OH,F)_2$	1.36
Pyrrhotite 3T	Fe1-x S (x=0 … 0.17)	1.35
Augite	(Ca,Na)(Mg,Fe,Al,Ti)(Si,Al)2 O6	0.77
Chlorite	$(Mg,Fe,Al)_6(Si,Al)_4O_{10}(OH)_8$	0.67
Hercynite	Fe+2 Al2 O4	0.63
Quartz	S_io_2	0.30
Calcite	$CaCO_3$	0.26
Chalcopyrite	$CuFeS_2$	0.25
Akermanite	Ca2 Mg Si2 O7	0.13
Iron alpha		0.08

Table 1 shows a large contribution of iron oxides (with the most conductive being, ilmenite and hematite) at about 72%. It may suggest a possible electronic conduction through the metal particles in contact, which would act in parallel with the electrolytic conduction through the interstitial fluid.

Before the column test was set up, the waste rocks were moistened with deionised water to reach a water content w (mass water/ mass solid, %) close to 4%. Filling of the column was done one layer (of about 4 cm thick) at a time; each layer was compacted to the pre-set level before adding the next layer. The average porosity (volume of voids/total volume, %) in the column after complete filling, was about 24 %. The resistivity of the distilled water used for saturating the material was 2257 Ωm. Twenty (20) days after assembling and saturating the column with distilled water, a first series of measurements was conducted using the Syscal Junior system (Iris Instrument, V11.5 ++) in standard mode. Figure 1a shows a section of 3D resistivity of the column obtained by 3D inversion of the collected data using the BERT software (Günther et al, 2009). This software considers the geometry (closed cylinder) and the location of each electrode as well as combinations of individual measurements with their respective errors. The volume is then meshed using a non-uniform grid made of tetrahedrons. A finer grid is generated near the electrodes where potentials vary rapidly. A model with a homogeneous average resistivity is considered for the starting model. The model is iteratively updated to reduce the difference between the measured and the modelled response. When the χ^2 value between observed and computed response does not significantly decrease, inversion stops and the RMS value (indicative of the data fit) is displayed.

Resistivity of the material varies between 30 Ω.m and 90 Ωm and it tends to increase from the top to the bottom of the column. This increase toward the base could be attributed to settlement that makes the bottom layers denser (with a lower porosity) than layers near the top of the column. The measured chargeability ranges between 30 mV/V and 60 mV/V and follows the trend of resistivity, increasing from top to bottom in the column (Figure 1b). The resistivity of a water sample collected from the column on the day of the measurements was 3.1 Ωm.

A chemical analysis (Table 2, line 3) was performed to better understand the origin of this significant drop in water resistivity. The analysis indicates that the decay in resistivity was mainly due to the dissolution of chemical elements in the interstitial fluid (water loaded with soluble ions). These elements are mainly calcium and sulphates. Then, tests were performed to measure hydraulic conductivity using deionised water which caused a significant leaching in the column. Once these tests were completed and after a rest period of about 5 days, a second series of electrical measurements were performed. Analysis of these measurements showed that the waste rock resistivity in the column had increased significantly (to about 400 Ω m), but still followed the same trend as before with an increase from top to bottom. Figure 1c shows a section of 3D resistivity of the column obtained by 3D inversion. The chargeability has also significantly increased to 140 mV/V-230 mV/V (Figure 1d) with the same trend (increasing from top to bottom). A water sample collected just after performing the electrical measurements on the column showed a resistivity of 73.5 Ωm. Chemical analysis of this sample (see Table 2, line 4) showed that the concentration of calcium and sulphates in the leachate had sharply decreased. This could be explained by the effect of leaching (during the permeability test) and of the relatively short residence time for the pore water in the material (5 days). It is assumed here that the majority of ions were released by dissolution and leaching.

Table 2: Ion concentrations measured in water for two residence times in the waste rock sample.

Sample/ Concentration	**Ni (mg/l)**	**Ca (mg/l)**	**Cu (mg/l)**	**Al (mg/l)**	**Ti (mg/l)**	**Fe (mg/l)**	**SO_4^{2-} (mg/l)**	**Mg (mg/l)**	**Na (mg/l)**
Deionised water	< 0.01	**0.22**	0.04	< 0.1	< 0.1	< 0.01	x	x	x
Pore water after installation, more than 20 days in the waste rock	0.29	**535**	0.16	< 0.1	< 1.0	0.04	1600	x	x
Pore water within 5 days after leaching (hydraulic conductivity test)	< 0.01	**26**	0.04	0.14	< 0.1	< 0.01	19.5	1.6	2.7

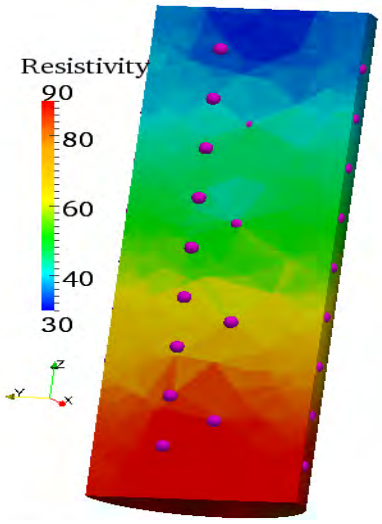

(a): Resistivity distribution in the column; resistivity of pore water is 3.1 Ω.m

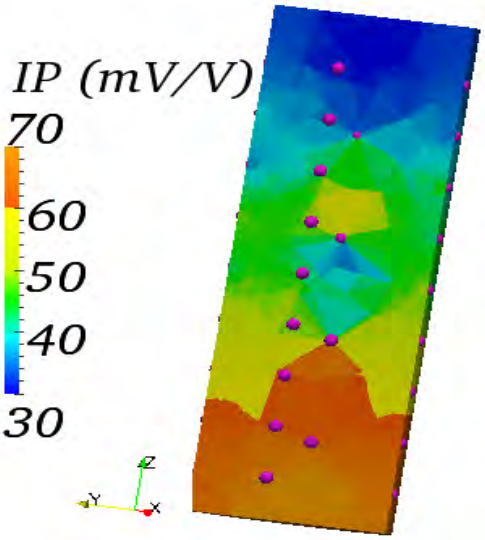

(b): Chargeability distribution in the column; resistivity of pore water is 3.1 Ω.m

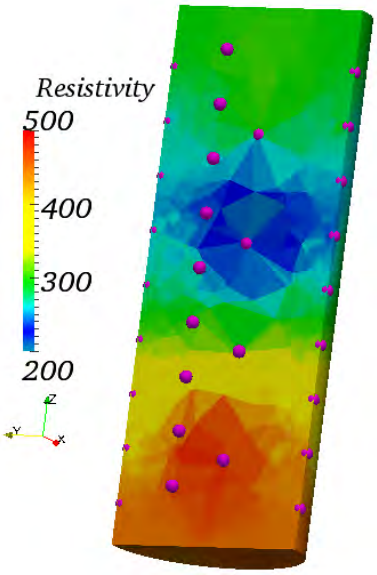

(c): Resistivity distribution in the column; resistivity of pore water is 73.5 Ω.m

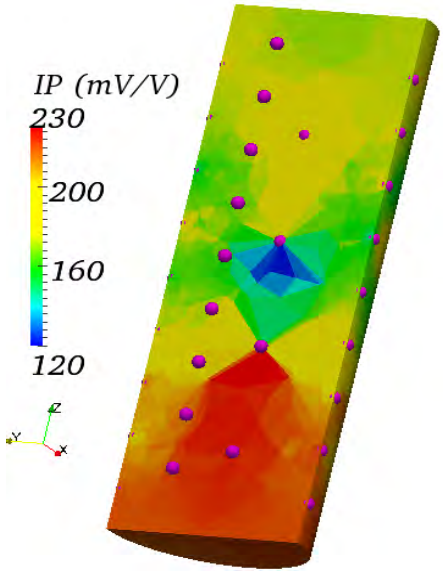

(d): Chargeability distribution in the column; resistivity of pore water is 73.5 Ω.m

Figure 1: Results of 3D inversion (using the BERT software) for data collected on waste rock in columns saturated with two fluids of different resistivity. Both measurements a degree of saturation close to 100%. The inversion was performed using the same processing sequence (with regularisation parameter λ=8). The fit between the calculated and observed responses is excellent (RMS < 3%). The pink spheres indicate position of electrodes on the column. Only half of the cylinder section is shown for convenience. The column is 1.0 m high with a diameter of 0.30 m.

Field electrical measurements

Petitpas is the largest pile at the mine site, with an area of 900 000 m^2 and a height between 80 m and 110 m (Figure 2). The waste rocks in the pile consist mainly of anorthosite (gangue) and hemo-ilmenite (ore). The cut-off grade for economic ore was set to 72% for many years (Pepin, 2009) and therefore the waste rock in the pile contains a high grade of metallic material. Resistivity measurements carried out on ore core samples in the laboratory showed values of 0.48 Ωm and 120 Ωm for 94.4% and 37% ilmenite respectively.

The measurements were made in the central part, on the top surface of the pile.

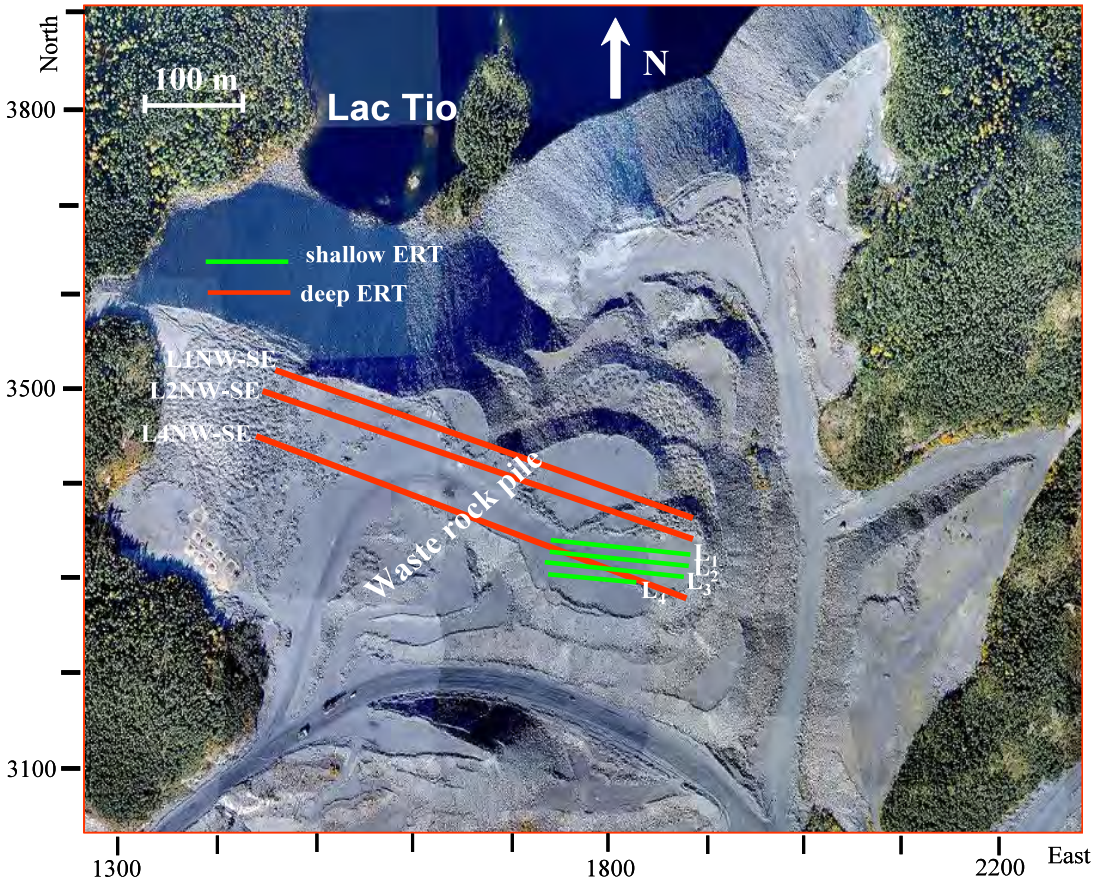

Figure 2: Map of the Petit Pas waste rock pile showing the short and long ERT lines for the measurements conducted in August 2008.

The pile structure near the surface is of great importance since it largely controls rain and snow melt infiltration and runoff. For this reason, electrical resistance tomography (ERT) measurements were conducted with a minimum electrode spacing of 2 m, giving a maximum investigation depth of about 8 m. The Syscal Pro 48 electrodes, with the dipole-dipole configuration and 16 levels were used to investigate the near surface. The location of four ERT lines (L1, L2, L3, and L4) is shown in Figure 2. The measurements were inverted using the software Res2Dinv (Loke and Barker, 1996). Figure 3 shows the results of inversion. The fit between the calculated and observed responses is excellent (RMS < 3%). Examination of the interpreted resistivity models shows that the resistivity of the waste rocks varies from 300 to 1500 Ωm in the near surface (Figure 3). To the west, resistive structures (ρ > 1000 Ωm) show that the material is dense with little moisture in these areas, except for profile L4.

These results probably reflect the presence of compacted waste rocks with a low metal content. In the eastern part, some horizontal layering is noted. It consists of a shallow layer with a thickness of about 2 or 3 m and a resistivity ranging from 500 Ωm to 1200 Ωm. It overlays a more conductive layer with resistivity ranging between 250 Ωm and 550 Ωm and thickness of about 5 m. The boundary between the two layers is not well defined, with undulations that are probably caused by natural heterogeneity in the near surface (Ritz et al, 1999). As is often the case on waste rock piles (Aubertin et al. 2002), the observed sub-horizontal stratification is probably caused, in part, by heavy equipment traffic on the surface. For line L4, the resistive surface layer (~ 2000 Ωm) is associated with the loose and dry condition of the waste. Lateral correlation from line to line is good. It indicates that cross-line variations of resistivity are low for this investigated area.

Resistivities estimated from the field survey are larger than those measured in the laboratory. This could be caused by the difference in grain size distribution. Laboratory measurements were carried out on material with a grain diameter < 10 mm, while the field grain-size distribution is very wide ranging, from very fine particles (clay-silt) to metric blocks. In addition, surface layers have undergone years of exposure with several cycles of leaching by water comparatively to the waste rock used in the laboratory tests.

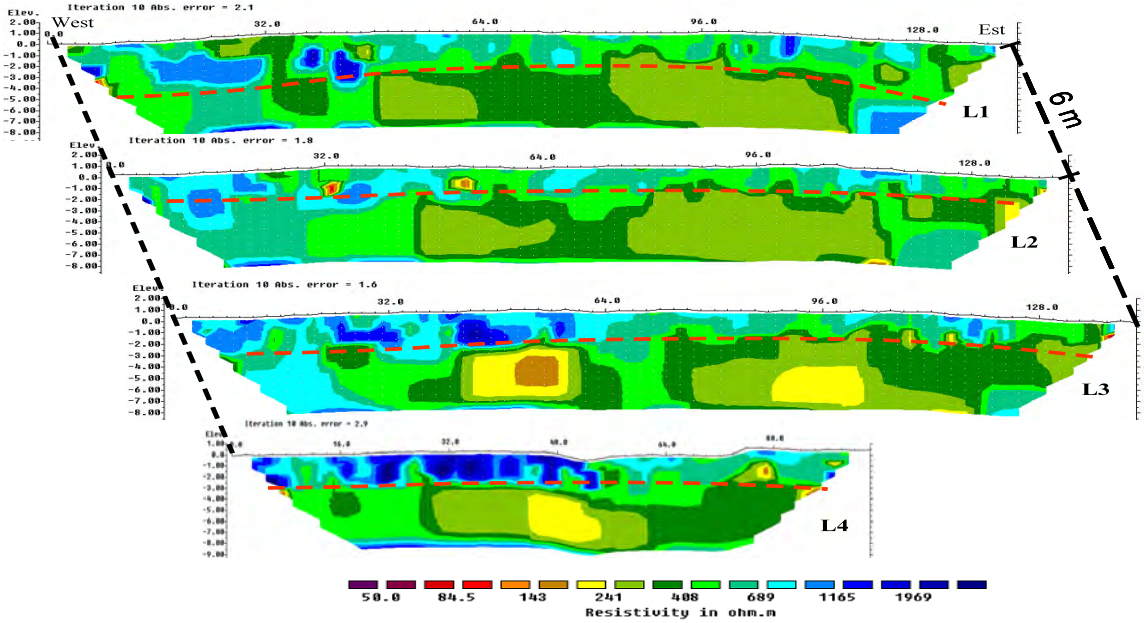

Figure 3: Resistivity models resulting from 2D inversion of ERT lines L1, L2, L3 and L4 separated by a distance of 6 m. The red dashed lines delineate two geoelectrical units with different resistivities.

For deeper imaging, dipole – dipole Induced Polarisation Tomography was used with a minimum spacing of 10 m and 25 levels. Profiles are 470 m long with a line separation of 20 m. (Figure 2, red lines) Figures 4 and 5 show the resistivity and chargeability models respectively for the parallel lines L1NW-SE, L2NW-SE, and L4NW-SE. Data fits are good (<6%) and fair (<16%) respectively for resistivity and chargeability.

Three major geoelectrical units are displayed over the maximum investigated depth of about 70 m. These consist of a shallow heterogeneous layer, with a thickness of about 30 m and relatively high resistivities and chargeabilities of 300 Ωm - 900 Ωm and 10 mV/V - 250 mV/V respectively. Within this surface layer, some anomalies, either resistive or conductive, are observed. Structures A, B, C, respectively indicated on survey lines L1NW-SE, L2NW-SE and L4NW-SE (Figure 4), are examples

of resistive anomalies (about 1500 Ωm). Areas of high chargeability (> 145 mV/V) could correspond to areas with partial water saturation and a strong dissemination of mineralization, while areas with lower chargeabilities could consist of waste containing more anorthosite than metallic ore. Some correlation between resistivity and chargeability exits in this layer, but it is not consistent.

The shallow layer is underlain by a conductive layer (80 - 250 Ωm) that is about 25m thick. The chargeabilities are relatively high (> 115 mV/V), in this layer, which may have formed as a result of the disposal conditions and origin of the waste rocks at the time of construction. This waste rock may contain more fine particles, and thus retain more moisture. Higher water content in this layer may also be the result of the natural motion of the wetting front that follows successive snow melts and large precipitations that occasionally occur on the mine site. The drop in resistivity for this layer can also be due to a more important waste rock mineralization. High chargeabilities are consistent with these interpretations. However, this layer could still contain resistive inclusions that are unresolved (undetectable) because the ERT resolution decreases with depth. For very large spacing between the transmitter and the receiver dipole relative to the size of resistive structures, the resistivity of the layers may appear homogeneous. This homogenization effect was discussed by Rey et al (2006).

The 3rd layer is highly resistive (> 1500 Ωm) and appears homogeneous. Chargeabilities show relatively lower values (<40 mV/V) compared to the two layers above. This layer may also include conductive structures which cannot be resolved because of the homogenization mentioned earlier. Sensitivity analyses (performed with Res2Dinv) show that sensitivity is weak for depths greater than 50 m. It is expected that the depth to the bedrock below the profiles is greater than 85 m (according to mine plans). Hence, this resistive layer does not correspond to the bedrock but to a particular type of waste rock. As this layer was placed at the beginning of the mine operation, it probably consists of very coarse waste rock extracted near the ground surface to reach the ore zone.

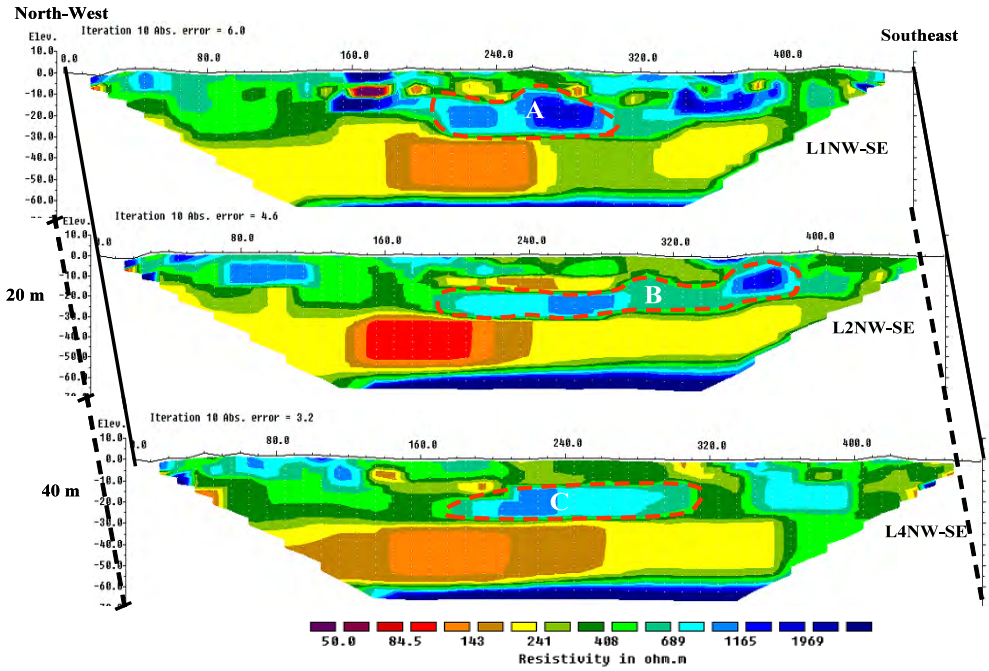

Figure 4: Resistivity models for the 3 parallel surveyed lines L1NW-SE, L2NW-SE, and L4NW-SE. [red color indicates conductive areas while blue color indicates resistive areas]. Zones A, B, and C, delineated by a red dotted boundary, are large resistive heterogeneities within the first layer. Maximum depth extent is approximately 70m.

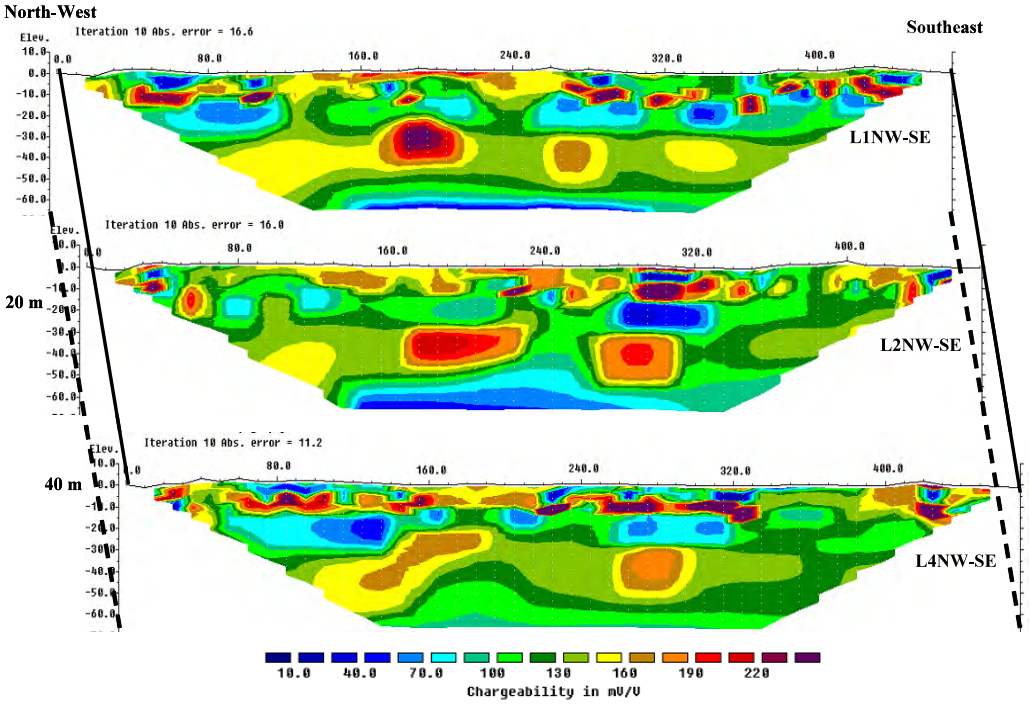

Figure 5: Chargeability models for the 3 parallel surveyed lines L1NW-SE, L2NW-SE and L4NW. [Red indicates highly chargeable areas while blue indicates low chargeability areas].

Discussion and conclusion

The strong heterogeneity of the waste rock together with the lack of information on the construction sequence and method complicate the interpretation of geophysical measurements carried out on the Petit-pas waste rock pile. Some drillings were made in the pile, but the recovery was very low and no geophysical well logging was conducted. Some trenches with a maximum depth of about 1.5 m were excavated at 3 different locations on the surface of the pile. In these trenches, the side walls showed dipping stratification at approximately 35 to 40^0, made of relatively thin layers with different physical properties (grain size and mineralogy). These differences, determined by visual inspection, can be related to the nature of the waste rock and deposition method along the crest of the pile.

The laboratory measurements can be used to constrain the interpretation of field measurements on the pile. Resistivity average is about 500 Ωm (as given by the shallow ERT survey). The laboratory measurements using dipole-dipole and horizontal equatorial dipole arrays on waste rock material with particles smaller than 10 mm showed similar resistivity values for a degree of saturation of about 37%. Measurements of water content w performed on samples from trenches showed values ranging from 1.3% to 2.4%. These values correspond to a degree of saturation ranging between 14% and 27% (for a porosity n = 0.25). These degrees of saturation appear to be lower than 37% for the laboratory test which led to an effective resistivity of 500 Ωm. Again, the difference in resistivity (between measurements in the laboratory and field) could be caused by the differing particle size of waste rock in the laboratory and in the trenches. It could also be due to the difference in resistivity of pore water that is not the same in the laboratory and the field. The highest resistivity measured in the laboratory is about 600 Ωm for a degree of saturation of 30 %. This indicates that zones within the pile that show a

resistivity higher than 600 Ωm could have a degree of saturation lower than about 30% (i.e. water content close to the residual value)

Chargeability measurements from the pile showed values ranging between 10 mV/V and 250 mV/V. These values are well correlated with laboratory measurements that showed chargeability values ranging between 30 mV/V and 200 mV/V. Both results are in agreement with the mineralogical analysis that indicates a high percentage of iron oxides (hemo-ilmenite, 30 to 72%).

Laboratory measurements also showed that chargeability significantly increases when resistivity of the interstitial fluid increases (i.e. Mg increases by a factor of 3 when fluid resistivity increases from 3.1 Ωm to 73.5 Ωm). The laboratory measurements also showed that chargeability decreases slightly with the degree of saturation. The observed decay could be explained by the tendency of electrical current to preferentially pass through the electrolyte rather than through the particles/electrolyte interface, which reduces the chargeability response. This indicates that the measured chargeability on the pile would be mostly related to mineralization rather than water content. Actually, it is sufficient that the waste rocks display high concentration in metallic mineralization to generate high chargeability responses (even at a low degree of saturation).

The low resistivity of the conductive layer (50 to 300 Ωm) identified at a depth below 30 m could be related to the disposal conditions prevailing during this phase of construction of the pile (particle size, ore concentration, method of construction). The measurements in the laboratory tend to indicate that these low resistivities could correspond to a degree of saturation higher than 30% with an interstitial fluid having a resistivity of about 30 Ωm. The last detected layer at depth is very resistive (about 2000 Ωm) and extending deeper than 70 m. This layer probably corresponds to coarse waste rocks (with low ore grade) dating back to the onset of pile construction. No laboratory measurements showed such large values, even those made with distilled water (ρ_w > 2000 Ωm) as interstitial fluid.

In general, it appears that resistivity provides information on moisture content and on the nature of solids, while chargeability yields information about concentration of mineralization. The results presented above gives a broad picture of what the internal structure of the pile might be over a depth range of 70 m. The conductive areas are essentially related to a finer grain size or compacted areas retaining more water. On the opposite, the resistive zones consist of relatively coarse grain size areas in shallow surface. Chargeable zones probably indicate fine grain waste displaying a large dissemination of mineralization. The geoelectrical model and the interpreted hydro-geotechnical model could be useful for modeling water flow and reactive transport through the waste rock pile.

Acknowledgements

Funding for this work was provided by the Industrial NSERC Polytechnique-UQAT Chair on Environment and Mine Wastes Management (http://www.enviro-geremi.polymtl.ca/). The authors would also like to thank Donald Laflamme and the personal of the Lac Tio mine (QIT – Rio Tinto) for their support. Anna Peregoedova helped with the laboratory tests.

References

Aubertin, M., Bussière, B., Bernier, L., 2002. Environment and mine wastes management. [in French].[Manual on CD-ROM]. Montreal: Presses internationales Polytechnique.

Anterrieu, O., Chouteau, M. and Aubertin, M., 2010: Geophysical characterization of the large-scale internal structure of a waste rock pile from a hard rock mine. Bulletin of Geological Engineering and The Environment, accepted February 10.

Bowles, J.E., 1984. Physical and Geotechnical Properties of Soils. McGraw-Hill.

Bussière, B., Benzaazoua, M., Plante, B., Pepin, G., Aubertin, M., et Laflamme, D. (2008). Evaluation of the geochemical behavior of the Lac Tio mine waste rocks, Havre-St- Pierre, Quebec Symposium 2008 Environment and Mines , Rouyn-Noranda, Québec (in French). Proc. On CD-ROM, CIM.

Günther, T., Rücker, Carsten., 2007. Boundless Electrical Resistivity Tomography (BERT), personal communication. http://dc3dinvres.resistivity.net.

Loke, M.H., Barker, R.D., 1996. Rapid least-square inversion of apparent resistivity pseudo-sections by a quasi-Newton method. Geophysical Prospecting, 44, 2, 131-152.

McCarthy, D.F., 2002. Essentials of Soil Mechanics and Foundations: Basic Geotechnics (6th ed.). N.J: Pearson Education Inc, Prentice Hall.

Nicholson, R.V., 2004. Overview of neutral pH drainage and its mitigation: results of a MEND study. Proceedings of the MEND Ontario workshop, Sudbury, 2003.

Pepin, G., 2009. Evaluation of the geochemical behaviour of waste rock,s potentially generating contaminated neutral drainage, using experimental test cells in situ. M.Sc.A, Thesis, Mineral Engineering, Ecole Polytechnique of Montreal (UQAT). December 2006, 136 pages (in French)

Plante, B., Benzaazoua, M., Bussière, B., Pepin, G., Laflamme, D., 2008. Geochemical behaviour of nickel contained in Tio mine waste rocks. 10 th International Mine Water Association Congress Mine Water and the Environment, Karlovy Vary, Republic Czech, pp.317-320.

Poisson, J., Chouteau, M., Aubertin, M., Campos, D., 2008. Geophysical experiments to image the shallow internal structure and moisture distribution of a mine waste rock pile. Journal of Applied Geophysics, 67 (2): 179-192.

Rey E., Jongmans D., Gotteland P., Garambois S., 2005. Characterisation of soils with stony inclusions using geoelectrical measurements. Journal of Applied Geophysics, 58 (3): 188-201.

Ritz, M., Robin, H., Pervago, E., Albouy Y., Camerlynck, Cristian., Descloitres, M., Mariko, A., 1999. Improvement to resistivity pseudosection modelling by removal of near-surface inhomogeneity effects: application to a soil system in south Cameroon. Geophysical Prospecting 47: 85-101.

MAPPING BEDROCK TOPOGRAPHY BENEATH GLACIAL OVERBURDEN NEAR CAPE HORN, SOUTH AMERICA

Melvyn E. Best, Bemex Consulting International, Victoria, BC Canada

Abstract

Placer gold mining operations were carried out on several of the small islands between Tierra del Fuego and Cape Horn in the late 1800's, just before the Klondike gold rush. As soon as the Klondike rush was announced to the world many of the miners and prospectors working in this isolated region went north. The area was quiet for nearly a hundred years before there was any renewed interest in it. This was due to the dispute between Chile and Argentina over ownership of these islands. Although the Chilean government was eventually granted ownership of these islands it is only recently that any exploration activity has occurred.

A placer gold exploration program that included surface sampling, geological mapping and bulk sampling was carried out in the early 1990's. The project looked promising but there was difficulty in unravelling the glacial history and obtaining estimates of gravel thickness for tonnage calculations. Bemex Consulting International was asked to set up a program to map the bedrock topography and estimate gravel thickness.

The project was carried out in two phases. The first phase was carried out during the summer season (December) to determine if time-domain EM soundings would provide the necessary accuracy to meet the above objectives. At the end of this phase the conclusion was the Geonics EM-47 system was capable of mapping the gravel thickness and bedrock topography. The second phase was conducted the following summer (January and February) and consisted of carrying out more than two hundred 40 m x 40 m loop soundings at the site. The results of this survey were verified with a series of manholes dug to depths varying from 15 m to more than 30 m. The depth to bedrock in these holes was consisted with the 1D interpretation provided from the Interpex software.

Location and geography

Figure 1 is an image of the southern part of South America showing the position of Punta Arenas and the location of the island where the EM-47 soundings were carried out. It is a very remote part of the earth and is difficult to get to, even within Chile. To reach the area where the work was performed required a flight from Santiago to Punta Arenas, a twin otter flight from Punta Arenas to Puerta Williams and then travel by fishing boat from Puerta Williams to the survey location.. The island still has a navel station on it consisting of two NCO's and their families. They stay from January 1 to December 31 and are there to provide a Chilean presence in the area.

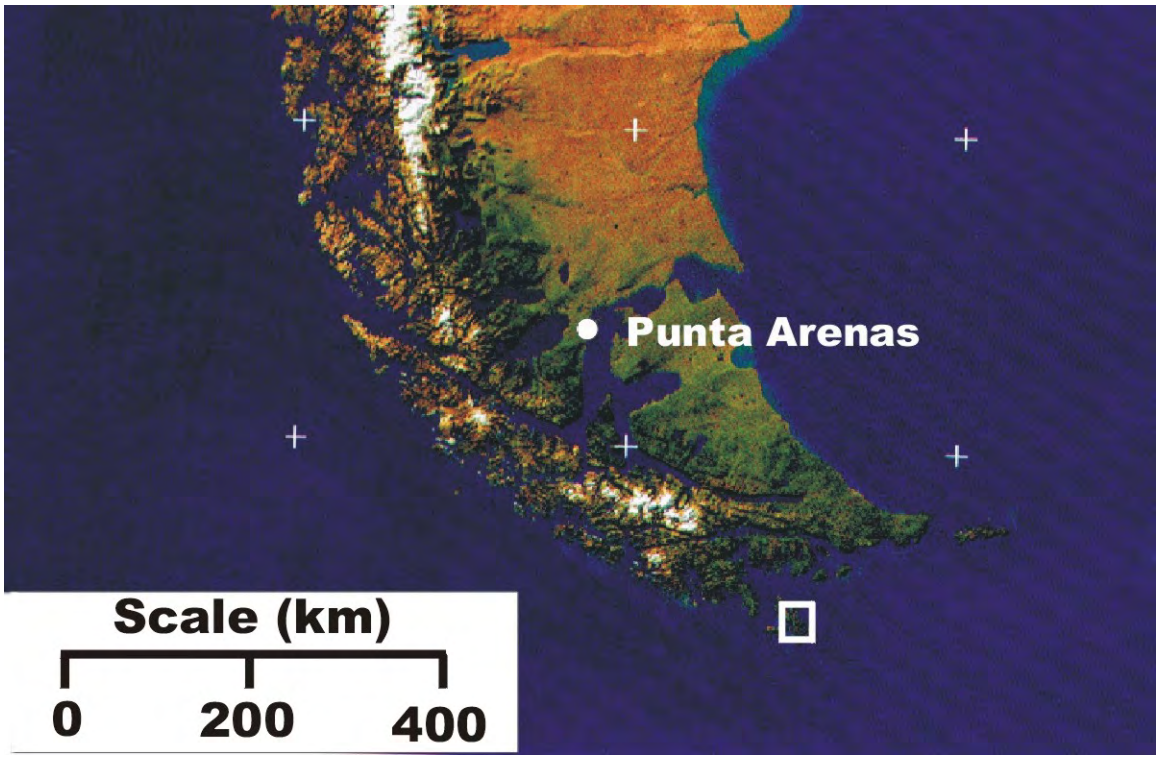

Figure 1 Location of Punta Arenas and the islands south of Tierra Del Fuego. Cape Horn is near the south edge of the white square.

The island has mountains on the west side but the east side is mostly undulating glacial overburden (Figure 2). There are several rivers crossing the region of the survey. The rivers cut into the glacial overburden forming steep sided cliffs along the rivers. Numerous small creeks feed into the major rivers in the area. Not many bedrock exposures have been observed in the area of the survey, although the bedrock geology has been mapped in the mountains. A few locations along the river valleys cut into a friable slate unit. The overburden consists of a mixture of tills and glacial fluvial sands and gravels. The gold is in the coarse sand and gravel horizons. The top few meters (up to 4 m in some places) consists of peat. Figure 2 also show the old sheep herders shack where the crew stayed. The area was populated by Welsh sheep herders who left this part of Patagonia for the Falkland Islands after the end of the first world war.

The weather is very unpredictable, even in the summer. The bad weather generally comes from the south off Antarctica which is only a few hundred miles south of Cape Horn. Most days during the survey there would be extremely high winds for part of the afternoon and heavy rain mixed with hail and snow. The Geonics 47 console had to be opened, drained of water and dried out every night with a hair dryer.

Figure 2 View from the fishing boat looking at the mountains to the west and the undulating glacial overburden near the camp. The building on the right was the original sheep herder's residence from the early 1900's that was fixed up for the project. This camp was approximately 5 km from the survey area.

Geophysical survey

The Geonics EM-47 (Geonics, Ltd., 1991) was used in the central sounding mode with a 40 m x 40 m square loop. Soundings were carried out along a number of lines (Figure 4) at 80 m centers. Se4veral hundred soundings were performed over approximately 6 weeks. GPS was used to locate the center of each sounding. The distance from the base camp to the survey area was approximately 5 kilometres so the wire for the transmitter loop was left in the field under plastic tarps each night. The receiver console, transmitter and ancillary cables had to be back-packed to and from the camp each day through the peat bogs. At each sounding receiver voltages were measured in 20 time windows for transmitter frequencies of 30, 75 and 285 Hz. Typically 3 data sets were collected for each of the 3 transmitter frequencies for statistical analysis. The data were downloaded each night and placed on a disk for storage. The data were also loaded onto a PC to check the quality of the soundings. A quick inversion using Interpex's TEMIX software (Interpex Limited, 1994) was performed on each of the soundings to see if there were any problems.

Interpretation

The sounding data were entered into Interpex's TEMIX software package for processing and interpretation. Bad data points were edited out using the editing option within the software package before carrying out further processing. The sounding data were subsequently parameterized into apparent resistivity as a function of time (Fitterman and Stewart, 1986) and inverted, assuming a multi-layered earth model (Interpex Limited, 1994). The best-fit model from the inversion

Figure 3 Transportation from Puerto Williams to the islands.

Figure 4 Coastal freighter used for transporting supplies around Patagonia.

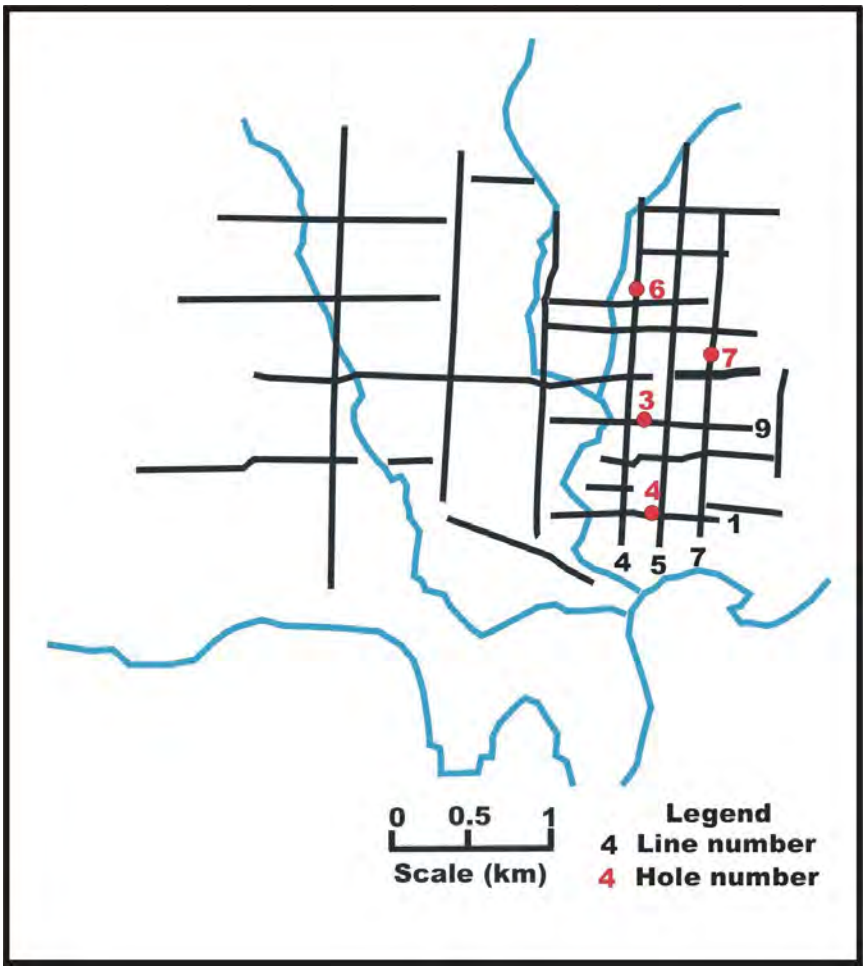

Figure 5 Location of EM-47 lines and main rivers in the area. Line numbers are shown for those lines near the manhole locations (red dots).

at each sounding was used to undertake an equivalence analysis, that is, to determine all models which fit the observed data to the same standard error of fit. This provided an estimate of the expected error of the overburden depth at each sounding.

During the geophysical survey several locations were selected for testing the gravel thickness. These locations are shown on Figure 4. The holes were dug by hand and were also used for bulk sampling the gravels for gold content. The holes were approximately 1 m in diameter and went straight down through the peat layer and into the glacial material. The holes varied in depth from 15 m to more than 30 m and were not shored up in any way. Luckily there were no collapses during the sampling program. Figure 5 shows two examples of the best-fit overburden depths from the EM soundings and their ground truth results for two of these manholes. Hole 6 was dug to a depth of 26 m before it encountered bedrock and hole 4 was dug to a depth of 16 m before encountering bedrock. The best-fit depths from the soundings at these hole locations were between 17 m and 22m at stations 1360 and 1440 respectively on Line 4 and 16 m at station 80 on Line 5. These results are very good and provide confidence that the overburden thickness and bedrock topography could be mapped reliably.

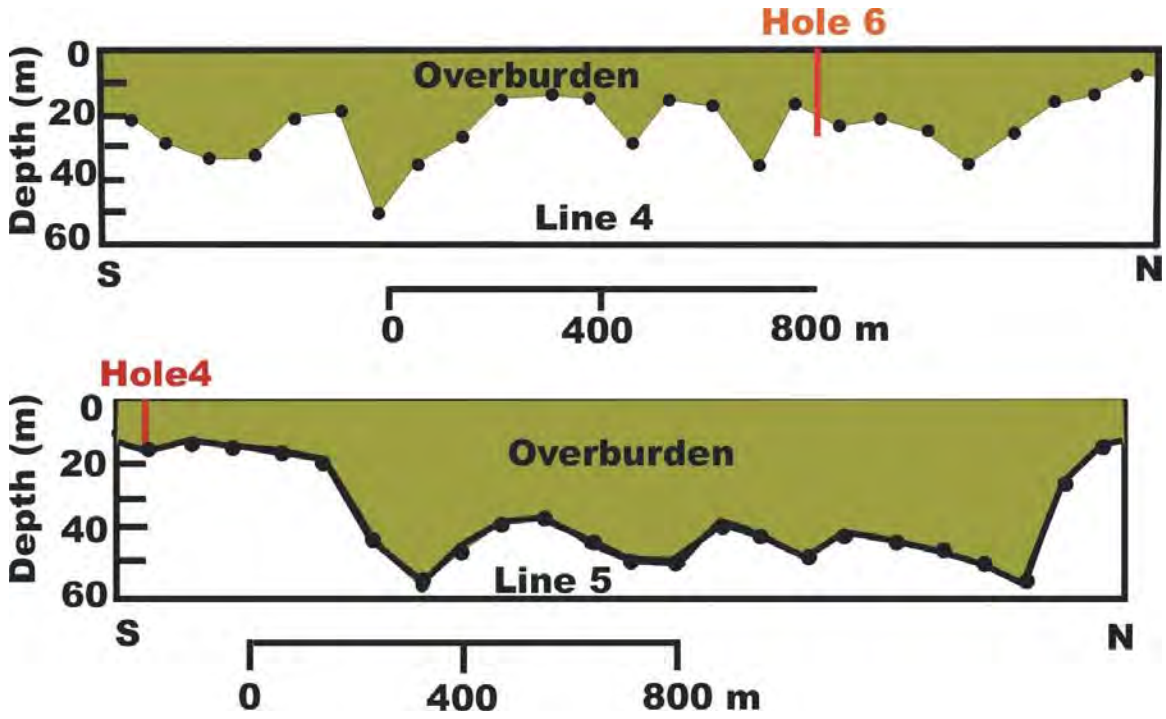

Figure 6 Best-fit overburden thickness from the Interpex software along lines 4 and 5 showing the depths to bedrock from holes 4 and 6.

Figure 7 Local inhabitant near Cape Horn

Conclusions

Tine-domain EM soundings were performed over the entire survey area as shown in Figure 4. The volume of combined gravel and till could be estimated with considerable accuracy from the EM results. The resistivity of the overburden (between 50 and 200 ohm-m but mostly around 100 ohm-m) and bedrock (slates – typically 700 to 1000 ohm-m and granitic rocks - typically several thousand or more ohm-m) were very different, thus providing a significant contrast that could easily be recognized from the EM data. Separation of the till from the sands and gravels was more problematic since these two units have nearly identical resistivity values. There were two main bedrock types in the survey area. There was a slate on the left side of Figure 4 which corresponds to a significant thickening of the overburden in that area due to its ease of weathering. There were more resistive granite rocks on the right side of Figure 4, both in resistivity and in weathering characteristics, so the thickness of the overburden in this area was not as great.

The EM-47 provided important information for developing a bulk sampling program over the property and also provided the first estimate of the volume of glacial overburden material. The results of this survey show that even in remote, hostile environments geophysical surveys can provide important information for exploration decision making.

References

Fitterman D.V., and Stewart M.T., 1986, Transient electromagnetic soundings for ground water: Geophysics, 15, 995-1005.

Geonics Ltd., 1991, Geonics Protem 47 Operating Manuel: Geonics Limited, 8-1745 Meyerside Drive, Mississauga, Ontario L5T 1C6, Canada

Interpex Limited, 1994, TEMIXGL User Manuel, transient electromagnetic data interpretation software: Interpex Limited, P.O. Box 839, Golden, Colorado 80402, USA.

EARTHQUAKE HAZARD MAPS OF THE CITY OF OTTAWA, CANADA, USING NEAR-SURFACE GEOPHYSICAL AND GEOLOGICAL METHODS

James A. Hunter, Geological Survey of Canada, Ottawa, Canada
Heather Crow, Geological Survey of Canada, Ottawa, Canada
Greg R. Brooks, Geological Survey of Canada, Ottawa, Canada
André J-M. Pugin, Geological Survey of Canada, Ottawa, Canada
Susan E. Pullan, Geological Survey of Canada, Ottawa, Canada
Dariush Motazedian, Carleton University, Ottawa, Canada
K. Kaheshi-Banab, Carleton University, Ottawa, Canada

Abstract

The city of Ottawa, Ontario, Canada, is in an area of elevated earthquake shaking hazard and is considered to be the Canadian city third-most at risk to damage (after Vancouver and Montreal). Maps showing regional variation of Vs30, fundamental site period, and an example map of the spectral accelerations at Sa=0.2s have been completed for the city at a reconnaissance scale. These have been developed from combined geological information from ~21,000 boreholes (water wells and geotechnical borings) within the city limits as well as ~700 surface and borehole shear wave seismic measurement sites. Borehole and surface shear wave measurement techniques developed for the operational area included: surface reversed refraction and reflection sites, MASW, downhole shear wave and horizontal-to-vertical spectral analyses of ambient noise. The surficial geology was subdivided into three basic units based on their geotechnical properties: (i) soft, fine-grained, post-glacial sediments, (ii) glacial till and coarse-grained, till-derived sediments, and (iii) firm Paleozoic and PreCambrian bedrock. A series of shear wave velocity-depth functions were assigned to each borehole based on interpolation from proximal geophysical sites. The resulting three-dimensional shear wave velocity database was then used to determine parameters such as Vs30 and fundamental site period. The Vs30 map of the city is subdivided in terms of the U.S. National Earthquake Hazard Reduction Program (NEHRP) zones which have been adopted by the 2005 National Building Code of Canada. Since the City of Ottawa has a large areal extent and is close to the West Quebec Seismic zone, the base accelerations for the 2% in 50 year earthquake event vary extensively within the city boundaries. Hence an example map of the spectral accelerations at Sa=0.2s has been developed to demonstrate regional variations and the effects of NEHRP zones.

Introduction - Effects of Near-Surface Sediments on Earthquake Shaking

The nature of earthquake seismic waves radiating through the earth is dependent on the source mechanism, the source location at depth, and the character of the rock types along the travel path to a particular surface site. The character of the shaking at the ground surface (amplitude, frequency and duration), however, is strongly affected by the materials through which the waves travel over the last few hundred meters (or less). It has long been known that damage from earthquake shaking tends to be concentrated at locations where soft soils are present (Anderson et al., 1986; Holzer., 1994, Choi and Stewart, 2003).

Substantial thicknesses of soft soil are widespread throughout the St. Lawrence Lowlands, resulting from the short-lived development of a post-glacial inland sea called the Champlain Sea. In the period 12000-9000 years before present, up to 130 m of fine material (clay, silt and fine sand) was deposited over a large area from Ottawa to Quebec City. These deposits, which have high water contents and low shear wave velocities (~150 m/s), overlie high velocity till and/or bedrock yielding seismic impedance contrasts commonly in the range of 12 to 45.

Over the last several decades, research on the response of soft soils to earthquake shaking has clearly established the link between ground motion amplification effects and large seismic impedance contrasts at shallow depths (Kramer, 1996). This can result in: i) velocity gradient amplification (Shearer and Orcutt, 1987), ii) resonance amplification (Kramer, 1996), iii) bedrock basin focusing / defocusing effects (Bard and Bouchon, 1985), as well as iv) bedrock basin edge effects which can generate constructively interfering surface waves (Lomnitz et al., 1999).

The key to unlocking the complexities of such ground motion effects lies with cost-effective detailed delineation of the fundamental geotechnical/geophysical properties of soils and the underlying bedrock.

Map Making

For our studies, we have chosen to follow the guidelines laid down by the 2005 National Building Code of Canada (NBCC; NRC, 2005); these are designed to address all aspects of seismic amplification of soils and rock including the above-mentioned soft soil phenomena. The provisions follow the system developed by NEHRP (National Earthquake Hazard Reduction Program) in the 1990s for the United States (BSSC, 1994; BSSC, 1995). Soils and rock have been divided into six site categories; five of the six categories (or classes) correspond approximately to hard rock (A), rock (B), soft rock or very dense soil (C), stiff soil (D), and soft soil (E). The classes are defined based on the travel-time-weighted average shear wave velocity of the upper 30 m of the ground, called Vs30. There is a sixth class (F), which is a special case defined on more site specific geotechnical characteristics (see Finn and Wightmann, 2003; Hunter and Motazedian, 2006).

Soil Classification Map

In the Ottawa area, the bedrock and surficial geology can be subdivided into three units which correlate with NEHRP soil and rock types: (i) soft, fine-grained, marine and fluvial post-glacial sediments (which comprises 65% of the surface area within the boundaries of the Ottawa Regional Municipality), (ii) glacial till and coarse-grained till-derived sediments (15% outcrop), and (iii) firm Paleozoic and Precambrian bedrock (20% outcrop) (Figure 1). In addition to these surface data, we have selected approximately 21,000 boreholes with interpreted geology from the Ottawa Urban Geology data bank (Belanger, 1998, 2008) which includes both water-wells and geotechnical borings. For every boring, we identified the three basic geological/geotechnical units for later assignment of velocity ranges by interpolation from proximal surface or borehole geophysical measurements. The glacial sediments commonly formed only a thin veneer beneath the marine sediments.

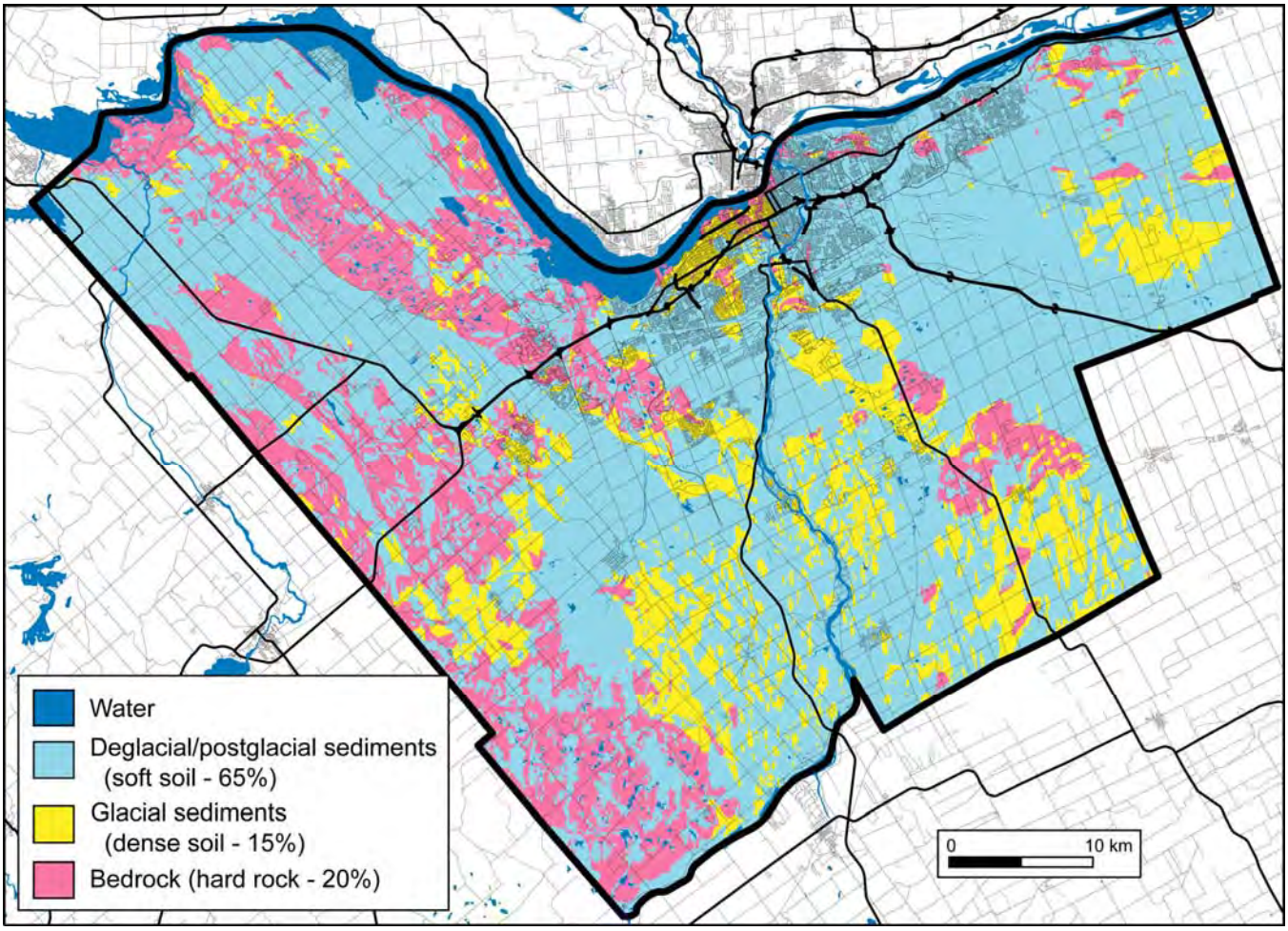

Figure 1: Major geotechnical/geophysical/geological units of the Ottawa area (2774 km^2). Within the bold outline (Regional Municipality of Ottawa-Carleton), 20% of the surface is bedrock outcrop, 15% is glacial sediment, and 65% is late/post-glacial sediments.

Shear Wave Velocity Measurements

Geophysical methods were adapted for this project area and consisted primarily of:

1) near-surface shear wave refraction-reflection site techniques (685 locations) designed to obtain refraction velocities and/or average reflection velocities to at least 30 m depth;
2) downhole shear wave seismic velocities (9 cased boreholes);
3) Multichannal Analysis of Surface Waves (MASW) in central Ottawa (37 sites);
4) 25 line-km of shear wave "Landstreamer" reflection profiling complete with Vs average velocity analyses (e.g. Pugin et al., 2007); and
5) horizontal-to-vertical-spectral ratios of ambient noise (HVSR) (~300 sites).

Hunter and Motazedian (2006) and Motazedian and Hunter (2008) discuss shear wave refraction-reflection techniques, while all are discussed in detail in Hunter et al. (2010).

The shear wave velocities determined from these geophysical surveys were used to determine shear wave functions or average values for our three basic units (bedrock, glacial and post-glacial sediments). For each site encountering substantial thicknesses of Champlain Sea sediments, average

shear-wave velocity-depth linear functions were derived for the post-glacial unit. Sufficient refraction velocity information was available from all geophysical sites to assign average velocities to rock types (limestone, shale, gneisses, etc). Although shear wave velocity measurements were sparse for glacial till, a single mean average velocity (500 m/s) was obtained. By combining these data with the three-dimensional stratigraphy obtained the borehole database, we have produced a three-dimensional, shear-wave velocity database for the region that can be used to calculate such parameters as Vs30 or site period estimates.

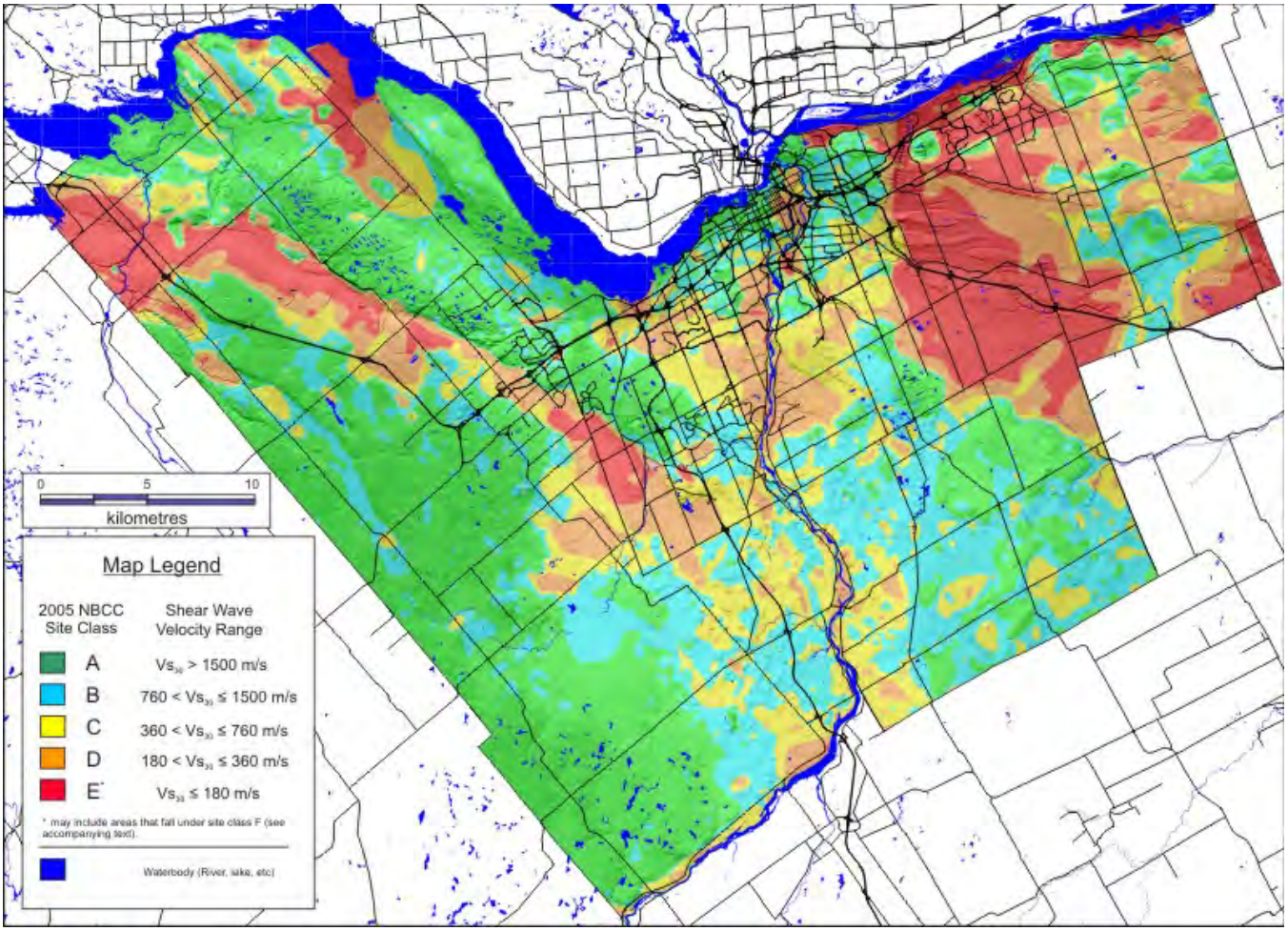

Figure 2: Map of the seismic site classes within the City of Ottawa based on Vs_{30}, as specified in the 2005 NBCC (after Hunter et al., 2009)

Vs30 Map

To produce the Vs30 map, Vs30 values were computed at all geophysical survey and borehole sites within the city. For each of the 21,000 boreholes, velocities were assigned to the bedrock and glacial units based on the borehole geological descriptions. For the post-glacial unit at any borehole, average velocity-depth linear functions were assigned using the "natural neighbor" contributions from the nearest geophysical sites. By applying such geostatistical approaches, unique velocity-depth

functions in the post-glacial soil were developed for borehole locations across the city. In areas where insufficient geophysical data were available to create a unique velocity-depth function, a single regional city-wide velocity-depth equation was derived using only data collected within the city limits. The city-wide average shear wave velocity as a function of depth Z is given as:

$$Vs_{av} = 123.86 + 0.88*Z \ +/- \ 20.3 \text{ m/s} \quad (1)$$

As a final stage in the mapping process, some editing of the contour lines was carried out to improve the presentation in the lower seismic categories (D & E) which had been smoothed by the gridding process. In this step, the surficial geology map (Belanger, 2008) was used as a guide to alter site boundaries in order to respect the known surficial geology. The final Vs30 map (Hunter et al., 2009) is shown in Figure 2. It should be noted that NEHRP zone F is defined on the basis of a number of special geotechnical considerations of poor ground conditions which cannot be determined from shear wave velocities only. However, such materials generally exhibit low shear wave velocities, and it is possible that NEHRP zones E and D (and less likely C) may contain areas of NEHRP F.

Fundamental Site Period Map

The motions experienced by a structure during an earthquake can be amplified significantly when the natural resonance period of the structure matches (or approaches) that of the underlying ground. This phenomenon of 'double resonance' can result in greater damage to the structure than might have been expected to occur based solely on the ground motion acceleration. Double resonance has been invoked to at least partially account for observed patterns of damaged buildings in the well-known case of the 1985 Mexico City earthquake, where buildings between 8 and 15 stories high were preferentially heavily damaged (see Anderson, 1985; Rosenblueth, 1986; Flores et al., 1987) Other examples related to more moderate earthquakes include the 1997 Mayville, Kentucky, event (Woolery et al., 2008), 1997-1998 Umbria-Marche seismic sequence, Italy (Nunziata and Natale, 2004), 1998 and 2004 events in the Bavec basin, Slovenia (Gosar, 2007), and 2002 Molise event, Italy (Mucciarelli et al., 2004).

The potential occurrence of double resonance can be reduced by mapping the fundamental site period of the ground and using it to regulate building designs so that the relative fundamental periods do not coincide (Elton and Martin, 1989). Use of such maps in conjunction with an inventory of the estimated fundamental period of buildings can help identify structures for more detailed study and therefore possible retrograding. Engineering options are available to mitigate or suppress building resonance (see Lomnitz, 1999).

Fundamental site periods have been computed within the City of Ottawa area from the depth and average shear wave velocity to the top of the firm glacial materials using T= 4H/Vs where H is the depth to the firm resonator and Vs is the average shear wave velocity of the soft soil (NBCC 2006; NRC, 2006, Commentary J, p. J-17). The contoured map, using natural neighbor interpolation followed by editing to recognize the known surficial geology is shown in Figure 3. A comparison of this map with the Vs30 map (Fig. 2) indicates that the longest periods are associated with NEHRP zone E, where the low-velocity post-glacial soil is thickest.

From ground-truth measurements of HVSR compared to seismic site (T= 4H/Vs) measurements, we have found that there is a systematic variation at longer fundamental periods. Figure 4 shows a comparison between HVSR measurements and those calculated from the velocity-depth functions for various thicknesses of post-glacial sediments. The origin of the variation between passive HVSR measurements and those computed from travel-time site methods is not yet understood. However the difference at longer periods can reach 30% or more.

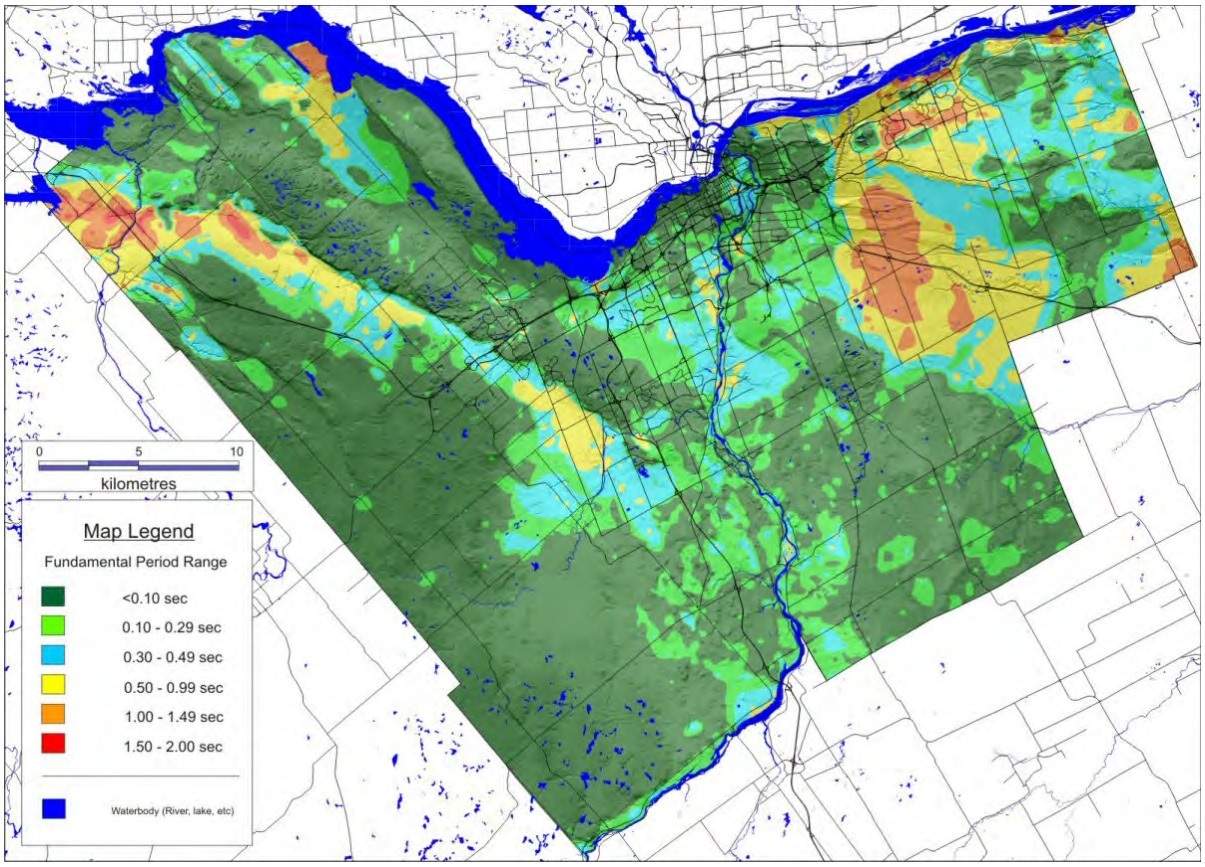

Figure 3: The fundamental site period map for the Ottawa area computed from overburden depth and average shear wave velocity measurements.

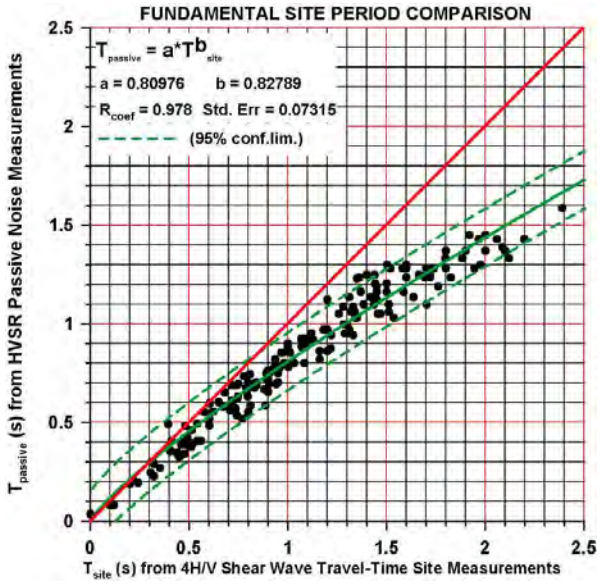

Figure 4: Comparison between fundamental site period measured by passive noise monitoring (Tromino) and calculated from the shear wave velocity, depth and travel time measurements at seismic site locations. The data was obtained from 185 independent measurement sites.

Example Ground Motion Map

The 2005 NBCC gives the design accelerations for NEHRP C site conditions. The City of Ottawa has a considerable areal extent, and since it is proximal to the West Quebec Seismic Zone, the "design" spectral accelerations vary considerably across the city (Halchuk and Adams, 2008). An example is given in Figure 5(a) showing the variation in accelerations at the period Sa = 0.2 across the city for the NEHRP site C (firm ground condition). Look-up tables in the 2005 NBCC give the multiplication factors associated with each NEHRP zone. The resultant "design" amplifications after consideration of the NERHP zones and the amplification factors are shown in Figure 5(b). The areas of largest amplifications shown in Figure 5(b) mirror the NEHRP zone map (Fig. 2) to a great extent. However, because of the proximity of the West Quebec Seismic Zone, somewhat higher ground surface accelerations would be expected in the north-eastern areas of the map because of the proximity of these areas to the West Quebec Seismic Zone.

Conclusions

Testing and application of various near-surface shear wave velocity measurement techniques has been conducted within the City of Ottawa. Data from approximately 685 surface sites, 9 boreholes and 25 km of shear wave "Landstreamer" seismic sections have provided sufficient shear wave velocity information to allow assignment of individual shear wave velocity-depth functions to geotechnical/ geophysical/geological units interpreted from 21,000 boreholes within the city. These data form the basis of both NEHRP zone maps (Vs30) and fundamental site period resonance maps. The results show considerable variation in the distribution of NEHRP zones or fundamental site periods throughout the city (Figs. 2, 3); these in turn suggest considerable variation in the shaking response to significant earthquake events (Fig. 5). It is recommended that these maps be used as a guide only for city planners and the geotechnical engineering community; hence, the following disclaimer should be applied to Figures 2, 3 and 5:

Disclaimer

Her Majesty the Queen, in right of Canada, as represented by the Minister of Natural Resources ("Canada"), does not warrant or guarantee the accuracy or completeness of the information ("Data") on these maps and does not assume any responsibility or liability with respect to any damage or loss arising from the use or interpretation of the Data.

The Data on these maps is intended to convey regional trends and should be used as a guide only. The Data should not be used for design or construction at any specific location, not is the Data to be used as a replacement for the types of site-specific geotechnical investigations recommended by the 2005 National Building Code of Canada, or Ontario's 2006 Building Code.

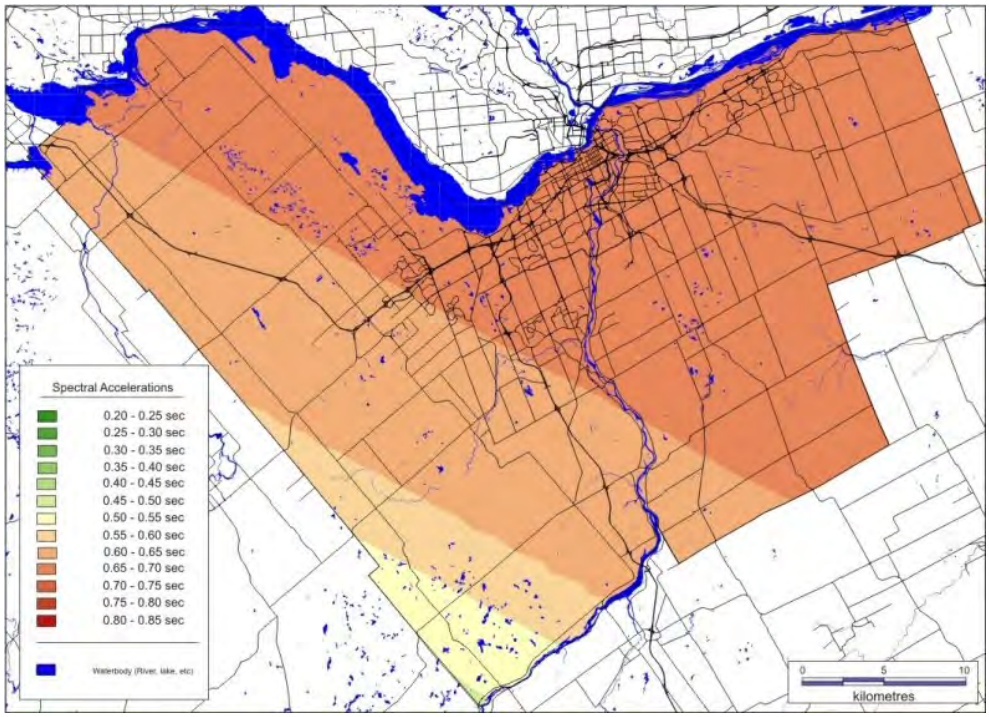

Figure 5: (a) Spectral values for Sa= 0.2 s (5 Hz) for NEHRP C (2%/50yr return). Gridded values provided by S. Halchuk, Geological Survey of Canada (pers.comm., 2009).

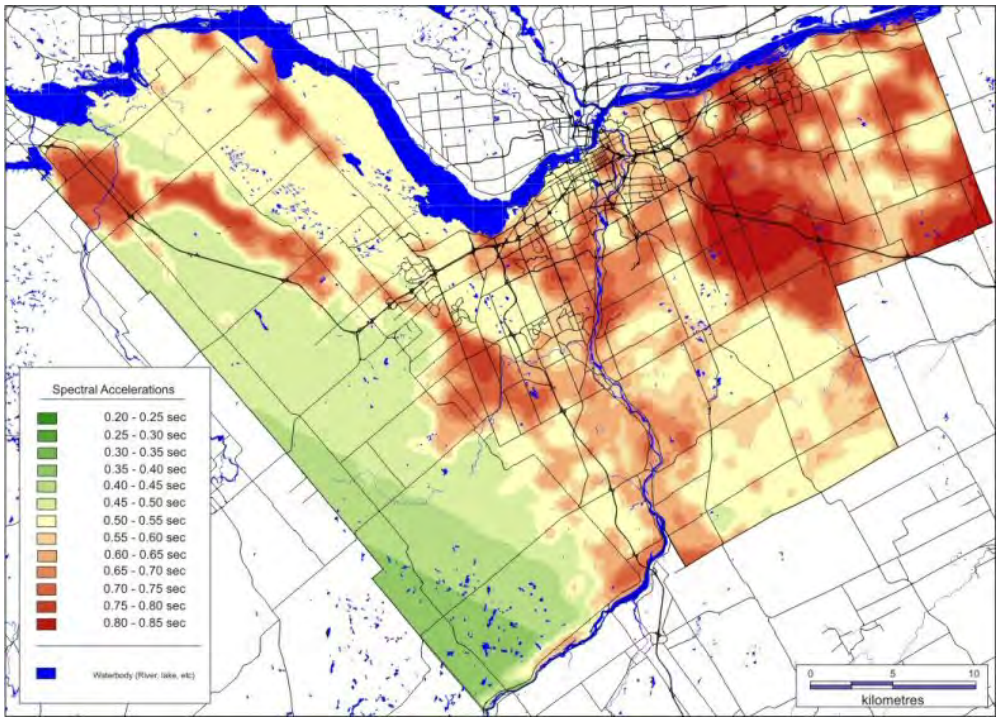

Figure 5: (b) Spectral acceleration values for Sa=0.2 s (5Hz) after correction for NERHP zone amplification factors.

References

Anderson, I. 1985. The harmony that caused disaster. New Scientist, 108 (1476), 32-33.

Anderson, J.G., Bodin, P., Brune, J.N., Prince, J., Singh, S. K., Quass, R., and ONate, M. 1986. Strong motion from the Michoacan, Mexico, earthquake. Science, 233, 1043-1049.

Bard, P-Y. and Bouchon, M. 1985. The two-dimensional resonance of sediment-filled valleys. Bulletin of the Seismological Society of America, 75, 519-541.

Belanger, J.R. 1998. Urban geology of Canada's National Capital Area. In Urban geology of Canadian cities. Karrow, P.F. and White, O.W., (eds.), Geological Association of Canada Special Paper 42: St. John's, Newfoundland, 365-384.

Bélanger, J. R. 2008. Urban geology of the national capital area/Géologie urbaine de la région de la capitale nationale. Geological Survey of Canada, Open File 5311, 1 DVD

Building Seismic Safety Council (BSSC). 1994. NEHRP recommended provisions for seismic regulations of new buildings: part 1, provisions. Publication FEMA 222A, Federal Emergency Management Agency, Washington, D.C.

Building Seismic Safety Council (BSSC). 1995. A non-technical explanation of the 1994 NEHRP recommended provisions. Publication FEMA 99, Federal Emergency Management Agency, Washington, D.C.

Choi, Y., and Stewart, J.P. 2003. Nonlinear site amplification as function of 30 m shear wave velocity. Earthquake Spectra, 21, 1-30.

Elton, D.J. and Martin II, J.R. 1989. Dynamic site periods in Charleston, S.C. Earthquake Spectra, 5, 703-734.

Finn, W.D.L., and Wightman, A. 2003. Ground motion amplification factors for the proposed 2005 edition of the National Building Code of Canada. Can. J. Civ. Eng., 30, 272-278.

Flores, J., Novaro, O. and Seligman, T. H. 1987. Possible resonance effect in the distribution of earthquake damage in Mexico City. Nature (London), 326 (6115), 783-785.

Gosar, A. 2007. Microtremor HVSR study for assessing site effects in the Bovec Basin (NW Slovenia) related to 1998 M (sub w) 5.6 and 2004 M (sub w) 5.2 earthquakes. Engineering Geology, 91, 178-193.

Halchuk, S. and Adams, J. 2008. Fourth generation seismic hazard maps of Canada: Maps and grid values to be used with the 2005 National Building Code of Canada. Geological Survey of Canada Open File 5813, 32 pages 1 CD-ROM.

Holzer, T.L. 1994. Loma Prieta damage largely attributed to enhanced ground shaking. EOS, Trans. Am. Geophys. Union, 75, 299-301.

Hunter, J.A. and Motazedian, D. 2006. Shear wave velocity measurements for soft soil earthquake response evaluation in the Eastern Ottawa Region, Ontario, Canada. In, Proceedings of Symposium on the Application of Geophysics to Environmental and Engineering Problems, Seattle, Washington, April 2-6, 2006, 1282-1295.

Hunter, J.A., Crow, H., Brooks, G.R., Pyne, M., Lamontagne, M., Pugin, A., Pullan, S.E., Cartwright, T., Douma, M., Burns, R.A., Good, R.L., Motazedian, D., Kaheshi-Banab, K., Caron, R., Kolej, M., Muir, D., Jones, A., Dixon, L., Plastow, G., Dion, K., Landriault, A., Ter-Emmanuil, V., Folahan, I. 2009. City of Ottawa seismic site classification map from combined geological/geophysical data. Geological Survey of Canada Open File 6191.

Hunter, J.A., Crow, H., Brooks, G.R., Pyne, M., Lamontagne, M., Pugin, A., Pullan, S.E., Cartwright, T., Douma, M., Burns, R.A., Good, R.L., Motazedian, D., Kaheshi-Banab, K., Caron, R., Kolaj, M., Folahan, I., Dixon, L., Dion, K., Duxbury, A., Landriault, A., Ter-Emmanuil, V., Jones, A.,

Plastow, G., and Muir, D. 2010. Seismic site classification and site period mapping in the Ottawa area using geophysical methods. Geological Survey of Canada Open File 6273.

Kramer, S.L. 1996. Geotechnical Earthquake Engineering, Prentice Hall, 653p

Lomnitz, C., Flores, J., Novaro, O., Seligman, T.H., and Esquivel, R. 1999. Seismic coupling of interface modes in sedimentary basins: a recipe for disaster. Bulletin of the Seismological Society of America, 89, 14-21.

Motazedian, D. and Hunter, J.A. 2008. Development of an NEHRP map for the Orleans suburb of Ottawa, Ontario. Canadian Geotechnical Journal, 45, 1180-1188.

Mucciarelli, M., Masi, A., Gallipoli, M.R., Harabaglia, P., Vona, M., Ponzo, F. and Dolce, M. 2004. Analysis of RC building dynamic response and soil-building resonance based on data recorded during a damaging earthquake (Molise, Italy, 2002). Bulletin of the Seismological Society of America, 9, 1943–1953.

National Research Council (NRC), 2005. National Building Code of Canada 2005, Volume 1, Division B, Part 4.

National Research Council (NRC). 2006. User's Guide – NBCC 2005 Structural Commentaries (Part 4 of Division B), Canadian Commission on Buildings and Fire Codes, National Research Council of Canada.

Nunziata, C. and Natale, M. 2004. Spectral amplification effects at Sellano, Central Italy, for the 1997-98 Umbria seismic sequence. Natural Hazards, 33, 365-378.

Pugin, A.J.-M., Hunter, J.A., Motazedian, D., Brooks, G.R., and Khaheshi-Banab, K. 2007. An application of shear wave reflection landstreamer technology to soil response of earthquake shaking in an urban area, Ottawa, Ontario. In, Proceedings of Symposium on the Application of Geophysics to Environmental and Engineering Problems, Denver, CO, April 1-5, 2007, 885-896.

Rosenblueth, E. 1986. The Mexican earthquake: a firsthand report. Civil Engineering ASCE, 56, 38-40.

Shearer, P.M. and Orcutt, J.A. 1987. Surface and near-surface effects on seismic waves - theory and borehole seismometer results. Bull. Seismol. Soc. Am., 77, 1168-1196.

Woolery, E.W., Lin, T.-L., Wang, Z. and Shi, B. 2008. The role of local soil-induced amplification in the 27 July 1980 northeastern Kentucky earthquake. Environmental & Engineering Geoscience. 14, 267-280.

FINDING FAULTS USING HIGH-RESOLUTION AEROMAGNETIC DATA IN GREAT SAND DUNES NATIONAL PARK AND VICINITY, SAN LUIS VALLEY, COLORADO

V.J.S. Grauch, U.S. Geological Survey, Denver, CO
David V. Fitterman, U.S. Geological Survey (retired), Denver, CO
Benjamin J. Drenth, U.S. Geological Survey, Denver, CO

Abstract

High-resolution aeromagnetic data reveal faults near the Great Sand Dunes National Park and Preserve (GRSA) and vicinity that offset both bedrock and sediments, even under the dunes themselves. Complicated fault patterns evident in the aeromagnetic data over the exposed range front may represent multiple-age events. The range-front and parallel faults to the west together suggest that basement steps down along high-angle faults. A prominent linear feature parallels the range front from the dunes southward ("the parallel fault"). Preliminary analysis suggests that the top of the parallel fault is about 50-70 m deep, with near-vertical dip, and offsets sediments with differing magnetic properties as well as basement rocks at greater depths. In places, it is paralleled by less prominent aeromagnetic features, which may also be faults. TEM soundings across the parallel fault indicate that sediments juxtaposed there contain abundant clay to the west and mostly sand to the east. The clay-rich sediments are underlain by eastward-shallowing sand at depth. This result suggests that the eastern limit of the confining clay in this area is fault-bounded at shallow depths and may be interfingered with sand at greater depths. These relations have implications for groundwater modeling, geologic studies, and seismic hazards.

Introduction

Great Sand Dunes National Park and Preserve (GRSA) is located at the eastern margin of the San Luis Valley in Colorado, nestled against an embayment in the Sangre de Cristo Mountains (Fig. 1). The valley is underlain by thick deposits (up to thousands of meters) of poorly consolidated sediments that serve as the main aquifer system for a thriving agricultural community. The sediments accumulated during the formation of the Rio Grande rift over the past 25-30 million years. Rifting continues today at the Sangre de Cristo mountain front along one of the most seismically active faults in Colorado. During most of the Pleistocene, a large lake occupied much of the valley floor and deposited great thicknesses (as much as several hundreds of meters) of massive clay to interbedded clay and sand (Machette et al, 2007). The clays now form a significant regional aquitard at depths of about 30-60 m throughout the central part of the valley (E. Harmon, written commun., 2004). The presence of this "confining clay" is an important consideration for water resource managers in the San Luis Valley because it separates an unconfined aquifer above and confined aquifer below.

GRSA is located over the deepest part of the Rio Grande rift basin in the valley, encompasses a segment of the seismically active range-front fault, and covers the inferred eastern limit of the confining clay deposited by the Pleistocene lake (Fig.1). It is a critical recharge area for the San Luis Valley. Recharge rates are elevated owing to the combination of unvegetated dunes, higher than average precipitation, and numerous streams. Yet, how the groundwater flows from the faulted mountain front through and below the dunes and interacts with the confining clay is poorly known, primarily because an extensive cover of sand and alluvium extends well beyond the dunes. Thus, important questions for

geophysics to investigate relate to the geometry of the clay, the nature of its lateral limits, and the configuration of range-front faulting.

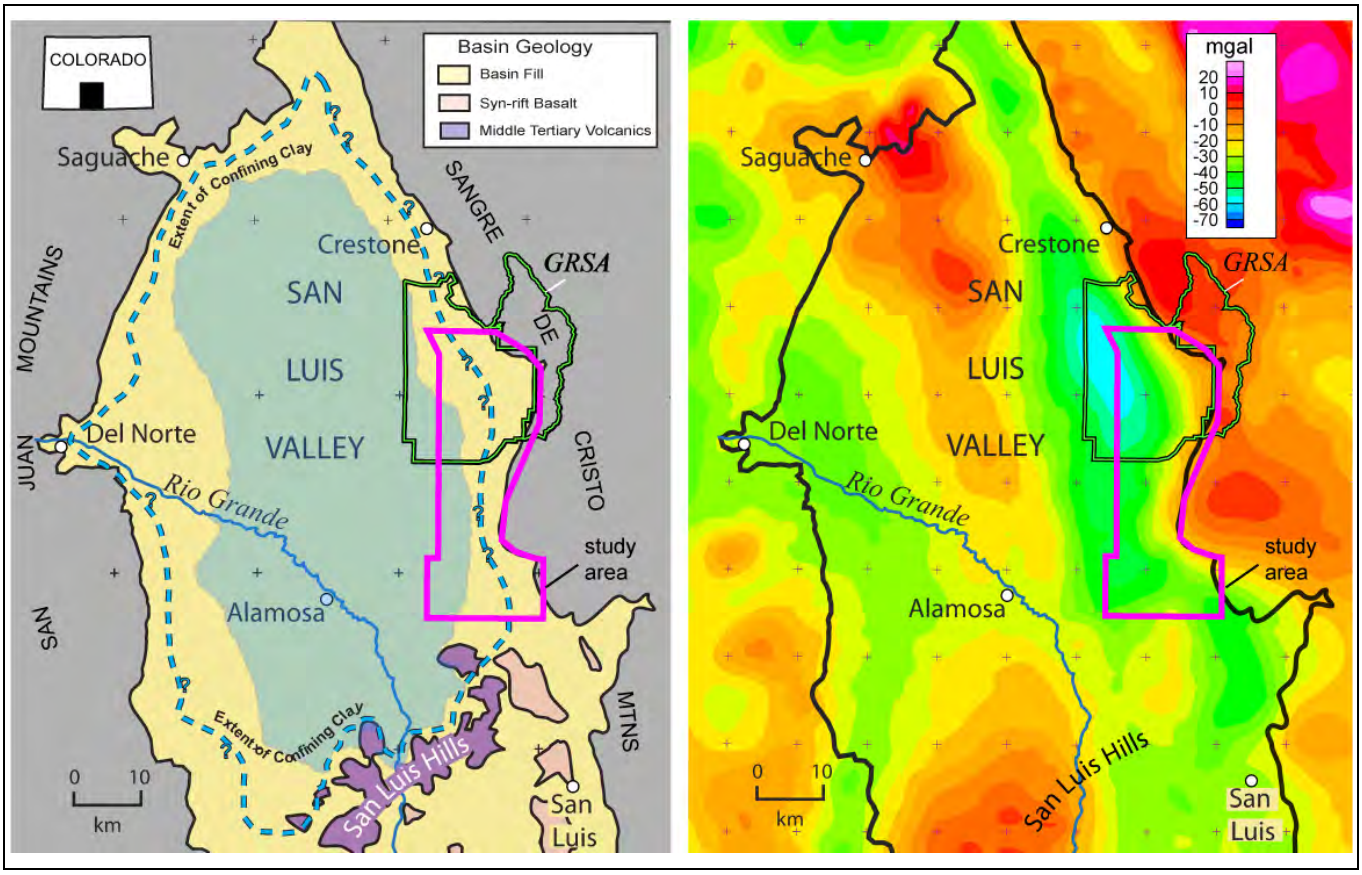

Figure 1: Location of the study area, Great Sand Dunes National Park and Preserve (GRSA), and San Luis Valley, Colorado (left). Also shown is generalized geology, the extent of the Pleistocene lake at its most recent high stand (blue-green shade) from Machette et al. (2007) and limit of the related confining clay at depth delineated by well data (blue dashed line; from E. Harmon, written communication, 2004). The isostatic residual gravity map (right) shows a low under the western part of the GRSA that corresponds to a deep basin of the Rio Grande rift. The range-front fault along the eastern side of the basin margin is seismically active.

We are using a combination of potential-field and electromagnetic geophysics to address these questions. We use high-resolution aeromagnetic data, the subject of this report, to focus on the questions related to finding and characterizing faults. We apply traditional and new approaches to find faults that offset bedrock as well as those that offset sediments.

Aeromagnetic Data

The U. S. Geological Survey has been systematically collecting high-resolution aeromagnetic data over basins of the Rio Grande rift since 1996 (http://crustal.cr.usgs.gov/projects/rgb/). Most of the study area (Fig. 2) is covered by the 2008 Great Sand Dunes survey (Drenth et al., 2009); the southern part (south and southwest of Mt. Blanca) is covered by the 2003 Blanca survey (Bankey et al., 2004). Both surveys were flown by helicopter along traverse lines oriented east-west. For the Great Sand Dunes survey, traverse lines were spaced 150 m (about 500 ft) apart and flown a nominal 100 m (300 ft)

above ground. Orthogonal lines were flown north-south at 1,500 m (4,920 ft) spacing. For the Blanca survey, traverse lines were spaced 200 m (about 650 ft) apart, and flown a nominal 150 m (500 ft) above ground. Orthogonal lines were flown north-south at 1,000-m (3,280-ft) spacing. Total-field magnetic data from the surveys were interpolated separately onto grids at 50-m intervals before analytical continuation to a consistent surface 100 m above ground. The data were then digitally merged and transformed to reduced-to-pole (RTP) data assuming a declination and inclination of the Earth's field of 10° and 64°, respectively. Based on considerations of rock type and age in the area, remanent magnetization is generally collinear with the Earth's magnetic field (Grauch and others, 2004), allowing use of the RTP transformation to correct for shifts of anomalies caused by the inclined Earth's magnetic field. The merged RTP data are shown as a color shaded-relief image alongside topography in Figure 2.

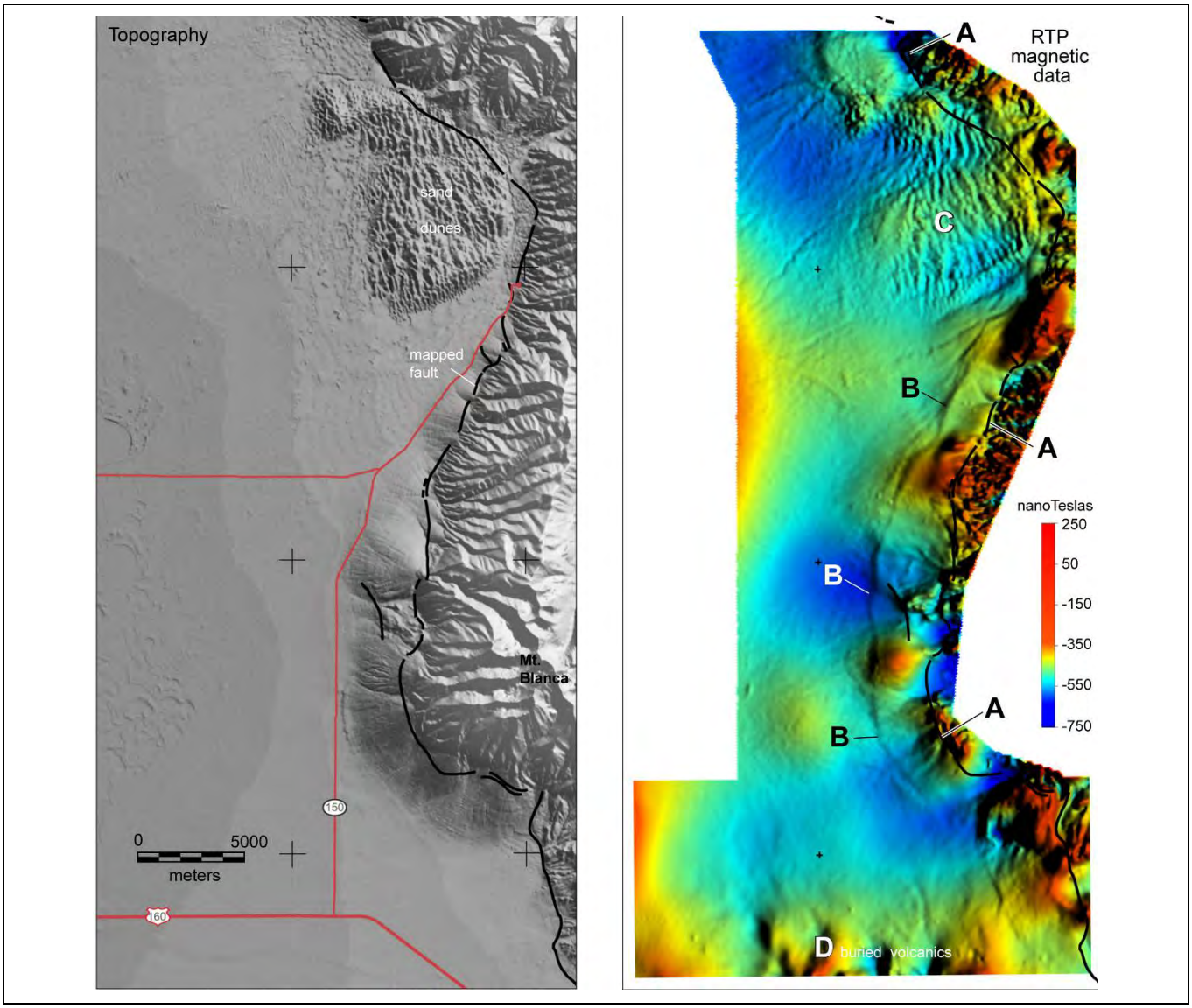

Figure 2: Digital elevation model (left) and reduced-to-pole aeromagnetic data draped 100 m above ground (right). Geologically mapped range-front fault (black line) is shown on both images (from U.S. Geological Survey and Colorado Geological Survey, 2006). Illumination is from the east in both images. Relief on the topography ranges from about 2300 m in the valley to 4372 m at the peak of Mt. Blanca in the southeastern part of the area.

Finding Faults

Faults are commonly recognized in aeromagnetic data by abrupt linear breaks in anomaly patterns or by low-amplitude, very narrow anomalies that look like linear features on shaded relief images. The linear features typically arise from sediments with differing magnetic properties that are juxtaposed at shallow depths (<100 m deep) by faults (Grauch and Hudson, 2007). Both representations of faults are evident in the RTP map for the GRSA and vicinity.

One of the most prominent fault representations is the break in anomaly pattern that generally coincides with the mapped range-front fault (A on Fig. 2). To the east of the fault, high-amplitude, "busy" aeromagnetic patterns correspond to exposed Precambrian basement rocks in the mountains. To the west, patterns of broader, lower amplitude anomalies likely correspond to the same types of rocks buried at greater depth. The abruptness of the pattern break is consistent with high-angle normal faults displacing the basement down into the basin.

Another prominent fault expression is both a break in anomaly patterns and a linear feature that parallels the mountain front from the dunes to south of Mount Blanca (B on Fig. 2). This previously unrecognized "parallel fault" is located generally about 2 km west of the range-front fault (Fig. 2). Because of its potential significance for the study area, we defer its discussion to the following section.

Two other features in the RTP data worth noting are the anomaly patterns that mimic the patterns of the sand dunes (C on Fig. 2) and the relatively high-amplitude, broad anomalies at the southern edge of the map (D on Fig. 2). The sources of the dune-like pattern are the dunes themselves, which are composed of relatively magnetic dune sand (on the order of 10^{-2} SI magnetic susceptibility from unpublished reconnaissance field measurements). The high-amplitude broad anomalies at the southern part of the study area extend even father south over exposed Middle Tertiary volcanic rocks (Fig. 1) that erupted prior to or early in rift history. The positive (red colors) and negative (blue colors) anomalies in this area correspond to volcanic rocks with known or inferred remanent magnetization that is normal and reversed, respectively.

Highpass and derivative-based digital filters were applied to the RTP data to enhance the detailed signatures of shallow faults so that their surface projections could be mapped. To get a better view of the deeper features, especially where the dune patterns mask the signal, we used matched filtering to do a regional/residual separation. The regional component is shown next to the first vertical derivative in Figure 3. Note that the dune-like pattern (C in Fig. 3) is almost entirely removed in the regional component. The pattern differences at the mapped range fault (A in fig. 3) are accentuated in the first vertical derivative. The parallel fault (B in Fig. 3) has signal in both components, suggesting that the fault affects both shallow sediments and deeper basement blocks.

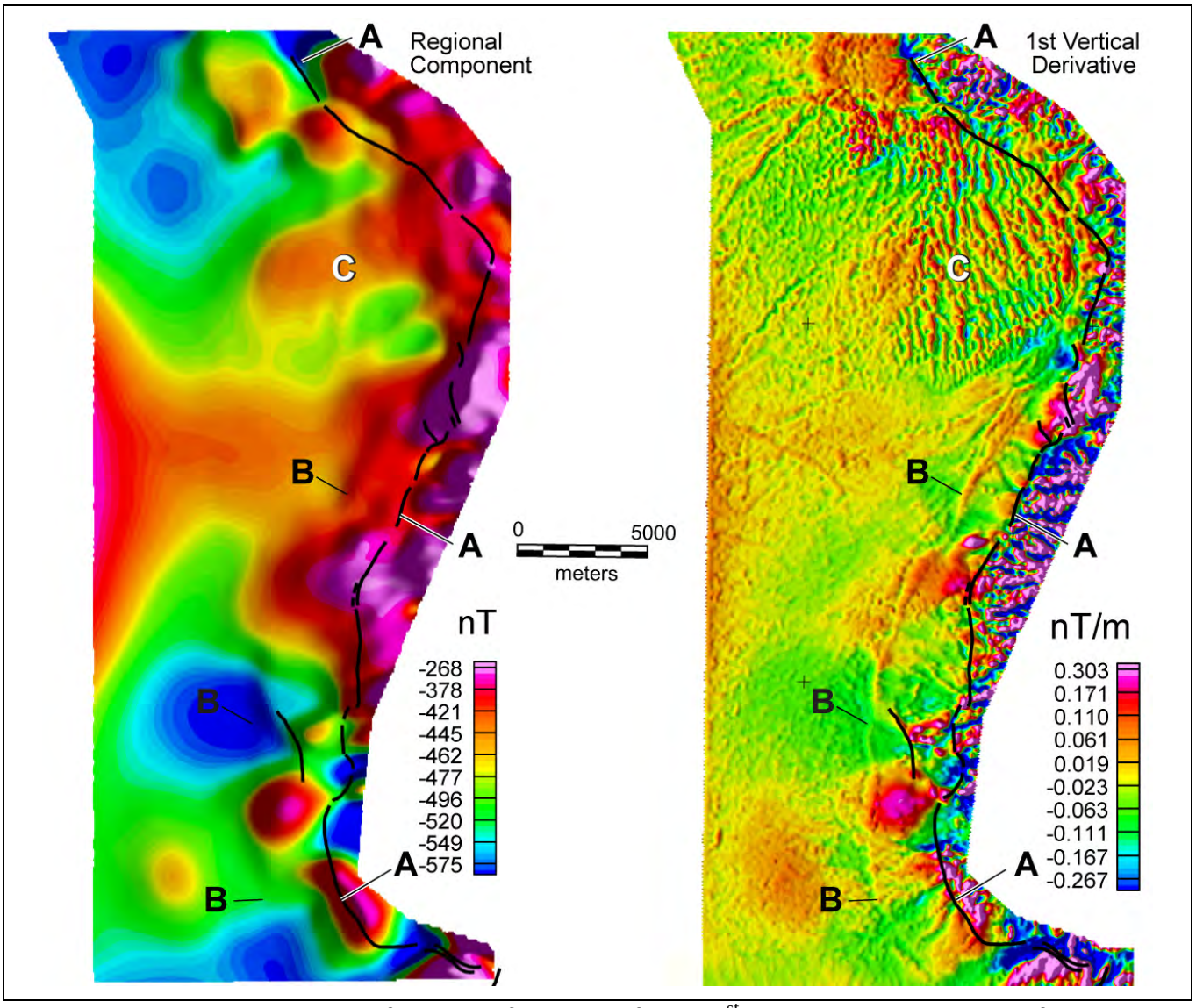

Figure 3: Regional component after match filtering (left) and 1st vertical derivative (right) for Great Sand Dunes survey area only. Note that the dune-like pattern in the 1st vertical derivative (C) has been almost completely removed in the regional component.

Faults were interpreted from the observed data, digitally filtered grids, and regional component following procedures discussed by Grauch and Hudson (2007) and are shown in Figure 4. Some linear features may not be fault-related; they may be present-day or past (buried) drainages, or drainages following faults. However, they follow trends of regional gradients, suggesting a relation to basement structure. Overall, the inferred deep faults show more easterly trends in the dunes area than expected. Complicated fault patterns are evident in the exposed range front, which may represent multiple-age events. The range-front and parallel faults together suggest a stepped-down basement along high-angle faults.

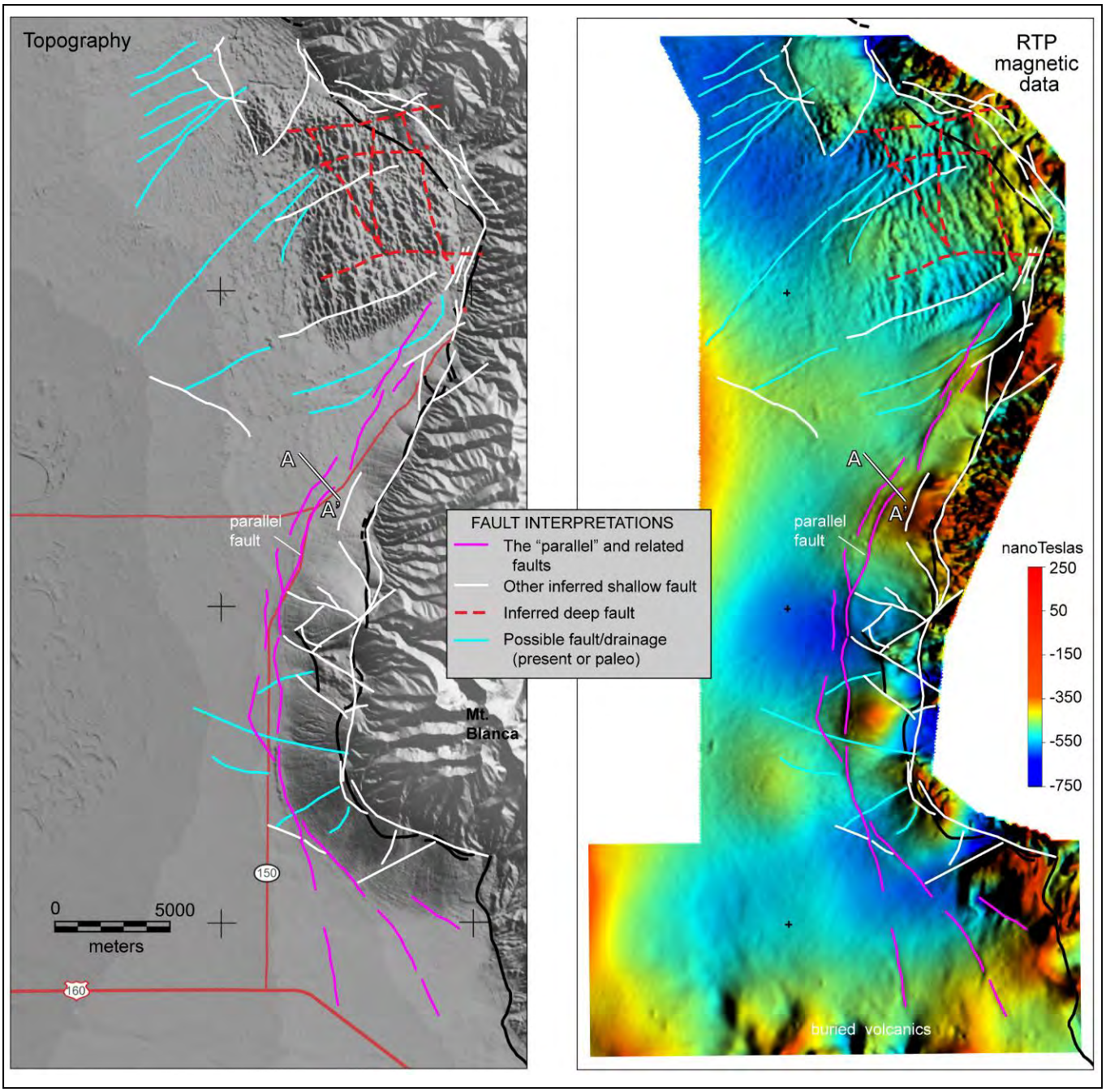

Figure 4: Interpreted faults overlain on topography (left) and reduced-to-pole aeromagnetic data (right). Geologically mapped range-front fault (black line) is shown on both images (from U.S. Geological Survey and Colorado Geological Survey, 2006). The section A-A' is shown in Figure 5.

Investigation of the Parallel Fault

In profile view, the linear feature defining the parallel fault is typically an abrupt 10-20 nT decrease in magnetic value to the west across a distance of about 400 m. The decrease appears as a "kink" on more regional gradients related to the broad anomalies along the mountain front (Fig. 4). Similar-shaped, but lower amplitude "kinks" occur west and parallel to the parallel fault, but these are much more discontinuous in extent, as shown by the interpreted lines on Figure 4. The anomaly signature at the parallel fault is typical of those originating from the juxtaposition of sediments of differing magnetic properties that is caused by vertical offset along a fault (Grauch and Hudson, 2007). Preliminary magnetic depth estimates of 50-70 m depth confirm that sources are within the sediments. The decrease in value on the west side indicates that the more magnetic material is on the east side of the fault.

Reconnaissance measurements and rock magnetic studies in the San Luis and neighboring basins indicate that magnetic susceptibilities of syn-rift sands range from 1-3.5 x 10^{-3} SI, whereas the thin veneer of overlying eolian sands are typically higher, on the order of 10 x 10^{-3} SI (Grauch and Hudson, 2007; Hudson et al., 2008). Spot measurements of clay beds encountered in a shallow borehole on the western boundary of GRSA showed variable, but typically lower, magnetic susceptibilities, on the order of 0.001 to 0.50 x 10^{-3} SI. Thus, initial hypotheses suggest that the parallel fault juxtaposes either sand of differing magnetic properties or sand against dominantly clay. The latter possibility has importance for understanding regional groundwater flow and geologic history.

To test these hypotheses, transient electromagnetic (TEM) soundings were collected along profiles across the inferred fault location using central induction sounding arrays with 40 m by 40 m transmitter loops. The TEM soundings are part of a larger study of the GRSA focused on defining the extent and depth of the confining clay. From comparisons between lithologic and resistivity logs and sounding results for a number of wells in the vicinity of GRSA, the TEM modeled resistivities appear to have a general relation to relative amounts of sand versus clay, which can be categorized by resistivity range (Fitterman and Grauch, 2010). This relation allows us to generally predict the dominant fraction of clay versus sand to depths as great as 200 m.

A cross section based on the interpreted resistivities from 1-D inversion of the TEM soundings is shown in Figure 5 (A-A', located on Fig. 4) along with the aeromagnetic data, derivative curves, and results of magnetic depth estimation. The parallel fault is located by the peak in the horizontal gradient magnitude, which indicates the steepest slope of the "kink" in the magnetic curve. At this location, magnetic depth solutions using several different methods cluster well at depths of 40-80 m. All the results suggest the source best matches a step-like shape (contact solution) with near-vertical dip, consistent with a normal fault (the slight dip to the southeast is perplexing, however).

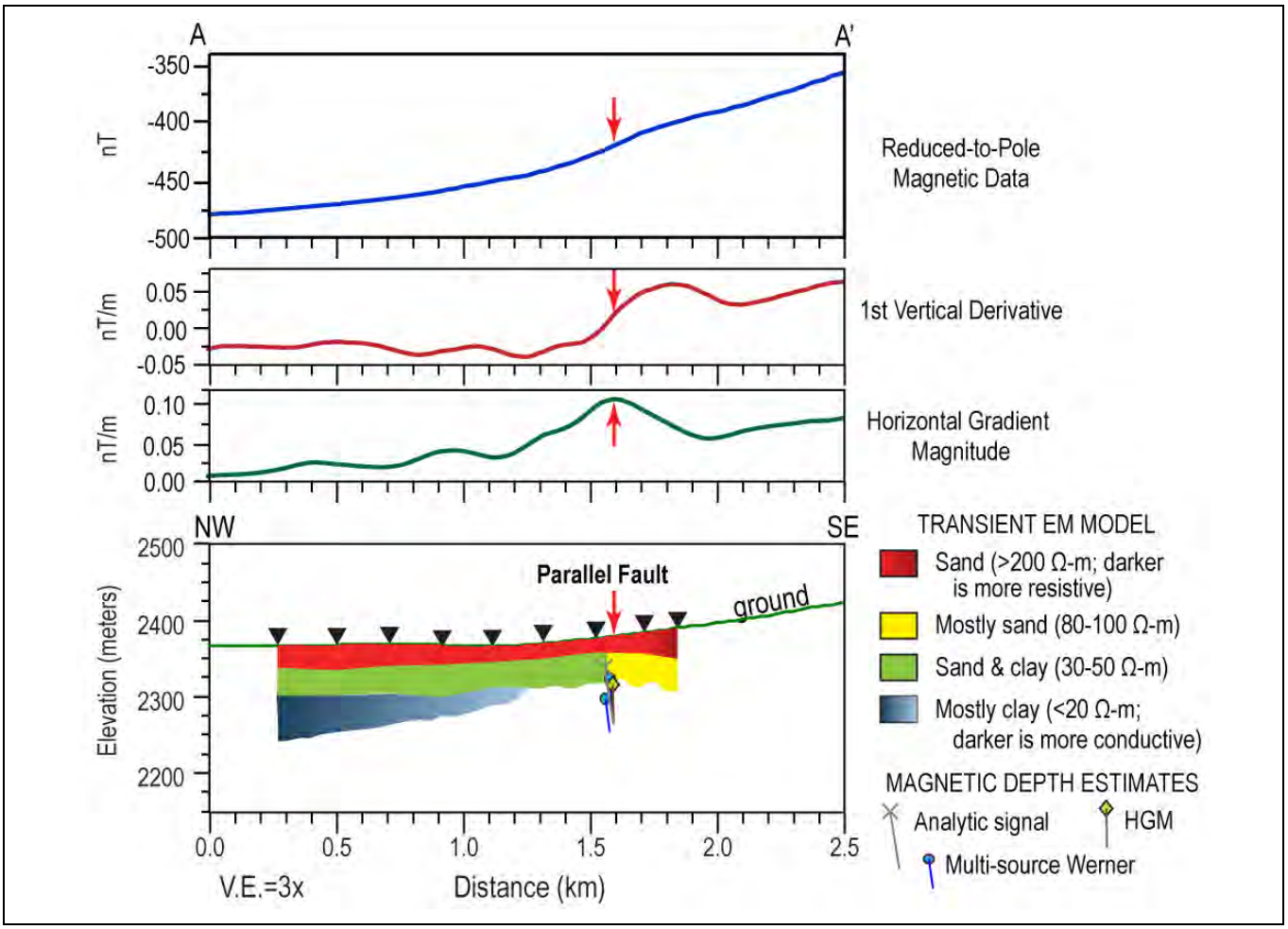

Figure 5: Magnetic profiles and TEM sounding profile across the parallel fault along A-A' (located on Fig. 4). The parallel fault, which has not been mapped at the ground surface, is located by the peak in the horizontal gradient magnitude. Magnetic depth estimates and dips used the analytic signal (Nabighian, 1972; 1974), horizontal-gradient magnitude (HGM) method (Phillips, 2000), and multi-source Werner methods (Hansen and Simmonds, 1993) as implemented by the computer program PDEPTH (Phillips, 1997).

The TEM results show an abrupt difference in resistivity between the two stations on either side of the parallel fault. The resistivity values suggest that a mixture of sand and clay on the west is juxtaposed against mostly sand on the east. A similar, abrupt resistivity difference is also observed in several of the other TEM profiles across the fault. The results suggest that clay is present on the west side of the fault and mostly absent on the east. From the A-A' model it is unclear how deep this boundary goes, nor how far the conductive layer on the west side of the profile extends underneath the east side of the profile. However, two other profiles identify a more resistive layer below the deepest conductive layer that appears to be increasing in depth to the west. This relation suggests that the clay progressively thins eastward toward the fault, terminates at the fault, and is underlain by sand.

Conclusions

High-resolution aeromagnetic data reveal fault patterns in and near the GRSA in bedrock and in sediments. Digital filtering of the aeromagnetic data reveals abundant linear features or gradients that we map as faults. Although some of the linear features appear related to present-day or past (buried) drainages, they follow trends of regional gradients, suggesting a relation to basement structure. The inferred faults related to basement below the dunes show more easterly trends than expected.

The mapped range-front fault corresponds well with an abrupt break in anomaly pattern that is consistent with a high-angle normal fault. This contrasts with other areas along the range front where low-angle faults have been reported. Complicated fault patterns evident in the aeromagnetic data over the exposed range front may represent multiple-age events. The range-front and parallel faults to the west of it suggest that basement steps down into the basin along high-angle faults.

A prominent linear feature that parallels the range front from the dunes to south of Mount Blanca is interpreted as a high-angle intrasedimentary fault (the "parallel fault"). Magnetic analysis suggests that the magnetic contrast at this fault is contained within sediments at about 50-70 m depth, but the fault also involves deeper basement rocks. TEM soundings collected in profiles across the fault show resistivity differences at the same depth range and locations as the magnetic analysis. The ranges of resistivities suggest that sediments containing abundant clay on the west thin progressively to the east before they are terminated at the parallel fault against mostly sand to the east. These relations suggest that the eastern limit of the confining clay in this area is sharp (faulted) at shallow depths but could be fuzzy (interfingered) at greater depths. Nevertheless, the location of the parallel fault can help focus future studies on where recharge may have the most interaction with the clay as it enters the basin. This result has geologic implications as well, suggesting that the Pleistocene lake may have had tectonic control on its eastern margins during at least part of its history. Evidence of more than one Quaternary-age fault related to the range front may also have implications for seismic hazards.

References

Bankey, Viki, Grauch, V. J. S., and Fugro Airborne Surveys Corp., 2004, Digital aeromagnetic data and derivative products from the Blanca airborne survey, covering areas in Costilla and Alamosa County, New Mexico: U. S. Geological Survey Open-file Report 2004-1229B, CD-ROM. http://pubs.usgs.gov/of/2004/1229/B/

Drenth, B.J., Grauch, V.J.S., Bankey, V., and New Sense Geophysics, L., 2009, Digital data from the Great Sand Dunes and Poncha Springs aeromagnetic surveys, south-central Colorado: U.S. Geological Survey Open-File Report 2009-1089, http://pubs.usgs.gov/of/2009/1089/.

Fitterman, D.V., and Grauch, V.J.S., 2010, Transient electromagnetic mapping of clay units in the San Luis Valley, Colorado: Proceedings of the Symposium on the Application of Geophysics to Engineering and Environmental Problems SAGEEP 2010, Keystone Colorado, Environmental and Engineering Geophysical Society.

Grauch, V.J.S., Bauer, P.W., and Kelson, K.I., 2004, Preliminary interpretation of high-resolution aeromagnetic data collected near Taos, New Mexico: New Mexico Geological Society Guidebook 55, p. 244-256.

Grauch, V.J.S., and Hudson, M.R., 2007, Guides to understanding the aeromagnetic expression of faults in sedimentary basins: Lessons learned from the central Rio Grande Rift, New Mexico: Geosphere, v. 3, no. 6, p. 596-623. DOI: 10.1130/GES00128.1.

Hansen, R.O., and Simmonds, M., 1993, Multiple-source Werner deconvolution: Geophysics, v. 58, p. 1792–1800.

Hudson, M.R., Grauch, V.J.S., and Minor, S.A., 2008, Rock magnetic characterization of faulted sediments with associated magnetic anomalies in the Albuquerque basin, Rio Grande rift, New Mexico: Geological Society of America Bulletin, v. 120, no. 5/6, p. 641-658.

Machette, M.N., Marchetti, D.W., and Thompson, R.A., 2007, Ancient Lake Alamosa and the Pliocene to Middle Pleistocene evolution of the Rio Grande, *in* Machette, M.N., Coates, M.-M., and Johnson, M.L., eds., 2007 Rocky Mountain Section Friends of the Pleistocene Field Trip-Quaternary geology of the San Luis Basin of Colorado and New Mexico, September 7-9, 2007: U.S. Geological Survey Open-File Report 2007-1193, available at http://pubs.usgs.gov/of/2007/1193/. p. 157-168.

Nabighian, M.N., 1972, The analytic signal of two-dimensional magnetic bodies with polygonal cross-section: Its properties and use for automated anomaly interpretation: Geophysics, v. 37, no. 3, p. 507-517.

Nabighian, M.N., 1974, Additional comments on the analytic signal of two-dimensional magnetic bodies with polygonal cross-section: Geophysics, v. 39, p. 85-92.

Phillips, J. D., 1997, Potential-field geophysical software for the PC, version 2.2: U. S. Geological Survey Open-File Report 97-725. Available from http://pubs.usgs.gov/of/1997/ofr-97-0725/

Phillips, J. D, 2000, Locating magnetic contacts: a comparison of the horizontal gradient, analytic signal, and local wavenumber methods: 70th Annual International Meeting, Society of Exploration Geophysicists, Expanded Abstracts, http://seg.org/publications/archive/exAbsHist/abs_pdf/2000/ea200004020405.pdf

U.S. Geological Survey and Colorado Geological Survey, 2006, Quaternary fault and fold database for the United States, accessed 29 March 2007, from USGS web site: http//earthquakes.usgs.gov/regional/qfaults/.

AIRBORNE FULL TENSOR GRAVITY

John H. Mims, Bell Geospace, Inc., Houston, TX
James Mataragio, Bell Geospace, Inc., Houston, TX

Abstract

The gravity tensor measures changes in the three dimensional gravity field along the three axes of motion, giving a nine component array of differentials. Because of symmetry and the Laplacian character of gravity, only five of the components are independent. Gravity has been used for resource exploration since the early 20th century. The first exploration gravity surveys used a ground based gradiometer that was eventually replaced with ground based gravimeters. In the late 20th century, a moving platform full tensor gradiometer was developed for use on submarines. Eventually the technology was declassified and applied to commercial resource exploration using marine and airborne acquisition. Since much of acceleration caused by the vessel motion is removed as the gradient is being measured, the gradiometer can provide a high resolution gravity image in a fraction of the time it takes for an equivalent ground gravity survey to be completed. A case study of alluvial diamond exploration provides one example of using airborne gravity gradiometry for resource exploration.

The Gravity Tensor

The earth's gravity generally is considered a constant force that causes bodies with mass to accelerate toward the center of a spherical planet of constant density. Of course, the earth is neither a perfect sphere nor constant density. Gravity exploration measures small changes in the gravity field associated with near surface changes in density. Surface gravity surveys measure the acceleration of gravity at a single point, which is a scalar measurement. Gravity, however, is a vector, having both a magnitude (scalar) and a direction (Figure 1). For the sake of gravity surveys, it typically is assumed that the direction of the acceleration is toward the center of the earth. If, however, a dense body (e.g., an ore body) is offset from the gravimeter position, a small component of the gravity vector points toward that body. Imagine moving in one direction (e.g., the x-direction) and continuously measuring how the gravity changes in the vertical direction (z-direction). This measurement [$\partial g(z)/\partial x$] would be one component of the gravity gradient. Moving in the x-direction two other components can likewise be determined [$\partial g(x)/\partial x$, $\partial g(y)/\partial x$]. Measuring each of the three components of gravity moving in the y-direction produces three other components, [$\partial g(x)/\partial y$, $\partial g(y)/\partial y$, $\partial g(z)/\partial y$], and measuring the three components moving in the z-direction produces three components, [$\partial g(x)/\partial z$, $\partial g(y)/\partial z$, $\partial g(z)/\partial z$], for a total of nine components that can be written in the array shown in Figure 1. Note that the differentials typically are abbreviated as [Txx, Txy, Txz, Txy, Tyy, Tyz, Tzx, Tzy, Tzz]. This array of differentials is the gravity tensor.

The gravity tensor has properties that reduce the number of independent components. First it is symmetric in that:

$$Txy = Tyx,\ Txz = Tzx, \text{ and } Tyz = Tzy.$$

Secondly, because gravity is Laplacian, the sum of the diagonal components is zero:

$$Txx + Tyy + Tzz = 0, \text{ or}$$
$$Txx + Tyy = - Tzz$$

Thus only five of the nine components need to be determined to define the entire array. Figure 2 shows the expected gradient response from a high density body. Even though it is not independent, since the vertical gradient component, Tzz, produces maps that best fits geologic structure, it is usually included with the tensor data.

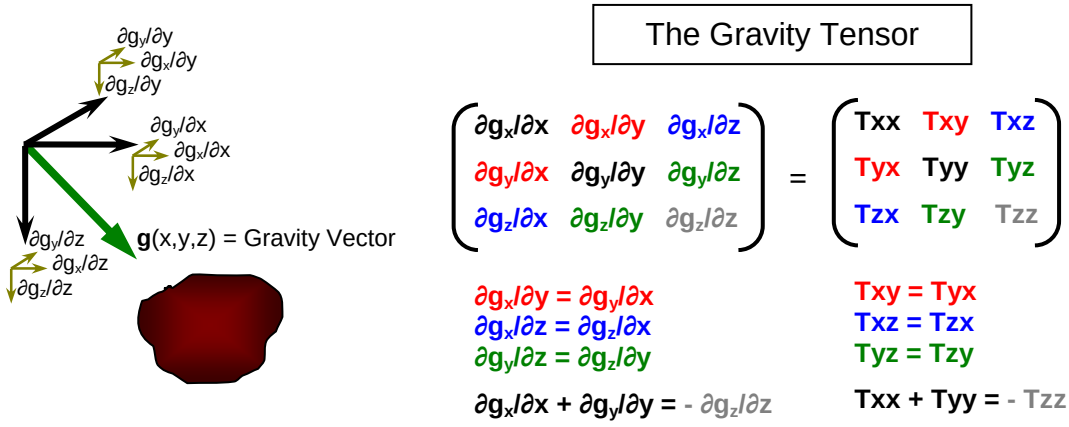

Figure 1: The gravity tensor.

A Brief History of Airborne FTG

Gravity has been used for resource exploration since the early 20th century. The Eötvös torsion balance gradiometer was the first gravity instrument used for geologic investigations for oil exploration in Czechoslovakia (now the Czech Republic). Gradiometry surveys began in the United States late 1923 and were common until 1936 when they were replaced by spring gravimeters, which provided faster acquisition and less sensitivity to near surface density variations (Eckhardt, 1940). The first airborne gravity surveys were acquired in the late 1950's. Because of induced noise from aircraft motion, airborne gravity was not widely accepted until the advent of GPS provided a dramatic improvement in positional accuracy (Nabighian, et al., 2005).

Although gravity instruments had been used for military purposes since 1929, the Cold War required more accurate gravity measurements on moving platforms. From this need, the U.S. Navy funded the development of the full tensor gradient system (FTG) by Bell Aerospace (now Lockheed Martin). In the mid-1980's the U.S. Air Force tested the system for land measurements in a large van, which was later driven onto a C-130 airplane for airborne measurements. In the mid-1990's

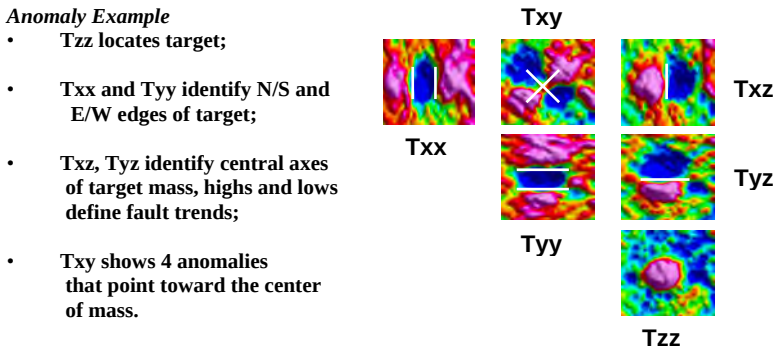

Figure 2: The response of each tensor component across a dense body.

FTG technology was declassified, and Bell Geospace acquired commercial rights to adopt marine acquisition of FTG data for oil and gas exploration. At about the same time, BHP Billiton funded Lockheed Martin to develop a partial tensor gradiometer based upon the concepts used in the FTG system for airborne surveys. In 2002, Bell Geospace installed the instrument into a Cessna Grand Caravan, a large single turboprop airplane, for airborne surveys using fixed wing aircraft. Since then the FTG system has acquired data using large twin-engine turboprop aircraft and a Zeppelin. Nagighian, et al. (2005) provides a brief history of gravity exploration, including the rotating disk gradiometers.

Gravity Gradiometry

On a moving platform, such as a ship or airplane, changes in motion produce accelerations. Since a gravimeter is measuring the acceleration of gravity, its measurement cannot distinguish acceleration from the platform from the acceleration of gravity. Thus, without some outside compensation, gravity measurements from a moving system contain a high level of noise. The gradiometer, however, is measuring the change in acceleration by subtracting signal recorded by two closely spaced accelerometers. Since both accelerometers are measuring nearly the same accelerations from the moving vehicle, most of the noise from the vehicle motion is removed when the signal from the two accelerometers are subtracted, leaving only accelerations from geologic sources. This process works as long as the response from each accelerometer is virtually identical. The FTG system therefore requires precise calibration and continuous feedback. The difference between the vertical gradients acquired on repeat surveys is less than 0.8 Eotvos (Mims, et al., 2009), and airborne vertical gradient (Tzz) data repeat to better than 3.5 Eotvos over 400 meter spacial wavelengths (Murphy et al., 2006).

Data Example: Paleochannel Detection

In 2004, airborne gravity gradiometry data was acquired for Etruscan Resources for alluvial diamond exploration in the Ventersdorp District of South Africa. The survey area was covered by Cretaceous and younger unconsolidated sediments such as gravels, laterites, etc., that lay over dolomite. The dolomite was deposited over a granitic basement. Paleochannels, referred to as “runs”, had cut through the dolomite and were buried beneath the overburden. The clay and gravel in the paleochannels had a density of approximately 2.0 g/cc, whereas the dolomite and granite had a density of approximately 2.7 g/cc. The objective for the survey was to map the runs and identify areas where the channels become wider, referred to as “potholes”. The potholes are believed to be related to karst (Marshall, 2008). Diamonds flowing down a channel would tend to drop out and accumulate in areas where the channel becomes wider, thereby slowing the current.

A forward model study based upon a cross section that was posted on the Etruscan web site (Figure 3) shows that a channel would produce a very large response of approximately 80 E, suggesting that airborne gravity gradiometry would be a good application for this objective. Figure 4 shows the data recorded over a test area. The dark outline indicates the expected position of the run prior to the survey. The survey indicates that the run continues toward the southeast rather than turning south. The survey detects the known pothole very well. Although the pothole appears to be wider than originally indicated, the low density toward the east turned out to be low density clay and was not prospective.

A simple forward model was calculated along the A-A’ profile in Figure 4. Note that the signal amplitude is 78 Eotvos, which agrees very well with the original forward model. Using a two layer model for the gravel and dolomite, a channel was constructed to fit the data. The model data fits the

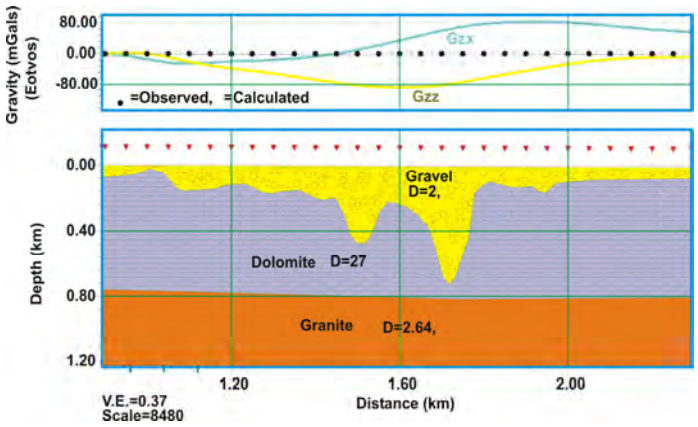

Figure 3: Model of alluvial diamond deposit shows an expected response of 80 Eotvos.

measured data well. The model indicates that the channel has a maximum thickness of 200 meters, which agrees well with nearby drilling results (e.g., Tirisano Mine, Blue Gum Project) (Marshall, 2008).

Conclusions

Gravity gradiometry measures the three dimensional change of the gravity acceleration in three coordinate directions. This nine component tensor can be simplified into five independent components due to the nature of the gravity field. For acquisition of gravity data from an airplane, changes in the aircraft motion create accelerations that would be recorded as noise in a gravimeter. For a gradiometer, much of this motion is removed during the measurement, allowing for collection of high resolution gravity data using a fixed wing airplane. Full tensor gravity gradiometry has been used for resource exploration since the late 1990's. Surveys have been acquired worldwide to explore for numerous resources including oil & gas, groundwater, nickel, copper, iron, gold, diamonds, and uranium. It is also an excellent tool for general regional and prospect level geologic mapping to identify geologic changes in density such as intrusives, structural interfaces, faults, and alteration.

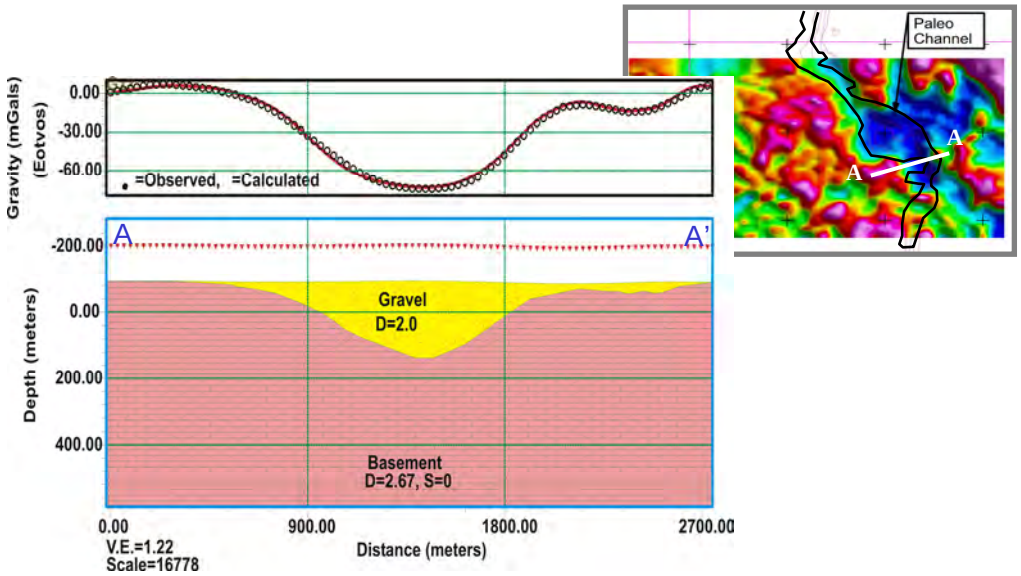

Figure 4: Calculating a model with a response that matches the measured data provides cross-section of paleochannel. FTG data shown with permission from Etruscan Resources, Halifax, Nova Scotia.

References

Eckhardt, E.A., 1940, A brief history of the gravity method of prospecting for oil, Geophysics, 5, 231-242.

Marshall, T.R., 2008, Technical report on the Bluegum Alluvial Diamond Project, Ventersdorp District Republic of South Africa for Etruscan Diamonds (Pty) Ltd., Etruscan Resources Inc., Etruscan Diamonds, and Mountain Lake Resources Inc.

Mims, John H., Selman, D., Dickinson, J., Murphy, C., Mataragio, J., Jorgensen G., 2009, Comparison study between airborne and ship-borne full tensor gravity gradiometry (FTG) data, Expanded Abstracts SEG Houston 2009 International Exposition and Annual Meeting, 942-946.

Murphy, C. A., J. Brewster, 2007, Evaluating Air-FTG survey data: Bringing value to the full picture, Presented at the Australian Society of Exploration Geophysics 18th Geophysical Conference.

Nabighian, M.N., Ander, M.E., Grauch, V.J.S., Hansen, R.O., LaFehr, T.R., Li, Y., Pearson, J.W., Phillips, J.D., Ruder, M.E., 2005, Historical development of the gravity method in exploration, Geophysics, 70, 63ND-89ND.

THE FALCON AIRBORNE GRAVITY GRADIOMETER FOR ENGINEERING APPLICATIONS

Greg Hodges, Fugro Airborne Surveys, Mississauga, Canada
Mark H. Dransfield, Fugro Airborne Surveys, Perth, Australia
Tai-chyi Shei, Fugro Airborne Surveys, Mississauga, Canada

Abstract

While airborne gravity has been available for decades, only with the advent of airborne gravity gradiometry (AGG), and specifically the FALCON AGG installed in a helicopter, has airborne gravity measurement reached a sensitivity and spatial resolution that can be effective for a wide range of engineering applications. Survey examples and gravity models comparing fixed-wing and helicopter AGG measurements demonstrate that voids as small as 10 m, or tunnels of 4 m width can be detected.

Introduction

Ground-based gravity measurements have been used in exploration and engineering geophysics for decades, to map geology and features defined by variations in density. For several decades airborne gravity measurements have been used to map geology and basin-scale structure for oil exploration, but generally lacked the sensitivity and resolution necessary for mineral exploration, and definitely were not suitable for most engineering applications. In the past 10 years airborne gravity gradiometry has become available on fixed-wing aircraft with resolution and sensitivity suitable for mapping geology and large mineral deposits at scales suitable for mineral exploration. More recently, the successful installation of the FALCON gravity gradiometer in a helicopter (Boggs et al., 2007) has improved the resolution of gravity measurements to the point where they are sensitive to many features of interest to engineering and environmental applications.

To be of use in engineering applications, gravity measurements need to be made to a sensitivity of one part-per-billion of the earth's gravitational pull. Einstein's General Relativity states, however, that acceleration of a body is locally indistinguishable from external gravity. The challenge of airborne gravity is to separate gravity from the acceleration of a fast-moving aircraft. This is done by minimizing the acceleration as much as possible, measuring the residual acceleration as accurately as possible, and using frequency characteristics to separate the accelerations from the gravity. The end result is measurement with a noise level as low as 0.5 mgal, but at wavelengths no shorter than 5-7km. This is much longer than the response of most geological features of interest in engineering.

Gravity gradiometry works by measuring the gradient (or change over distance) between two gravity sensors, on the principle that translational acceleration will be the same for both sensors, but the gravity field of an object in the earth will be very slightly different. Also, the gradient of the geologically smaller, near surface features of interest to engineering have proportionately higher gradient anomalies than gravity anomalies (relative to the regional field). This allows for much shorter wavelength measurements (in the order of 100m or less), with sensitivity requirements in the order of 1 part in 1000 of the average gradient.

Airborne Gradiometer Characteristics

All commercially available gravity gradiometers are based on the gravity gradient instrument (GGI) and inertial platforms developed by Bell Aerospace (now Lockheed Martin) since 1975. The sensor is comprised of pairs of accelerometers, arranged across a spinning disk to measure the gravity gradients tangential to the disk. This configuration rejects both common mode acceleration and rotations about the axis perpendicular to the plane of the complement (pairs). The FALCON's near-vertical axis GGI is a significant improvement from the original GGI instrument, both from an increase in the size of the disk (and spacing of the accelerometers) and the inclusion of a second full set of four accelerometers (bringing the total to 8) for two fully independent measurement of both horizontal gradients (Lee, 2001, Dransfield and Lee, 2004).

Rotation of the instrument about axes in the plane of the accelerometers results in an acceleration gradient which is indistinguishable from gravity gradients, so the instrument requires mounting in a high performance stabilized platform (Lee 2001).

Gravity gradiometers have a finite capability to reject translational accelerations and the largest amplitude aircraft accelerations on survey are in the vertical direction. By measuring horizontal gradients of the horizontal gravitational accelerations, the FALCON AGG is able to operate at low noise levels in conditions of high turbulence.

Survey Operations

Operations are not significantly different than other airborne geophysical surveys, like magnetic surveys. Flight lines are flown in a grid pattern with line spacing determined by the target size (and the budget). Run-in to the survey area is relatively short – less than a kilometre for fixed-wing surveys. Survey altitudes are 80m-120m for fixed wing, and could be as low as 2m for helicopter. Ancillary equipment includes differential GPS for navigation, but also a laser scanner for measurement of the terrain below the aircraft, to be used in calculation of the terrain correction.

Surveys can be flown concurrently with magnetic, electromagnetic, and/or radiometric surveys.

Only the digital FALCON AGG (named "Feynman") has been installed and successfully flown in a helicopter. This provides the advantage of low altitude and low survey speed to improve resolution. Surveys have been flown to simultaneously collect gravity gradiometry, frequency-domain electromagnetic data, and magnetic data (Rajagopalan, 2007).

An Air FTG full-tensor system was installed in a rigid, lighter-than-air airship. From a geophysical sense this was a nearly ideal platform: slow and stable. However, in practice it was not reliable, and in fact was incapacitated by a storm.

AGG Data

The FALCON AGG measures two components of the gradient, G_{NE} (the "north" gravity gradient measured along the "east" direction) and G_{UV} $\{=(G_{NN}-G_{EE})/2\}$. In some nomenclature G_{NE} is labelled G_{xy}. From these two measurements all components of the full gravity gradient tensor can be calculated, by integration techniques (in the wave-number domain) and by equivalent source techniques (Dransfield and Lee, 2004).

The noise in the G_{NE} and G_{UV} gradients is about 3.0 Eo for both fixed wing and helicopter. For fixed wing data the filtering frequency is about 0.18 Hz (at about 60m/s airspeed) resulting in a wavelength of about 330m, and sensitivity to anomalies as short as about 150 m. In helicopter the filtering is about 0.3 Hz, and the system is sensitive to anomalies as short as 50 m at "normal" airspeed of 30 m/s, and virtually unlimited at very low altitude where the helicopter can survey at very low

speeds – limited only by the need to get some coverage! The resolution provided by the low speed, coupled with the increased anomaly due to low altitude, make for a very significant sensitivity advantage.

Modelling AGG for Engineering Targets

In general, anomalies for engineering targets will be weaker and spatially smaller than mineral exploration targets. Detection of most targets will require a system flying at the low altitude and low speed of a helicopter.

Modeling Procedure

The gravity models were generated using Model Vision Pro, by Pitney Bowes. These provided ideal responses for all gravitational fields and gradients for each model. However, it is important to model the responses as they would be observed by the real systems, with their wavelength limitations. To accomplish this, each model was calculated at high resolution (0.5m) and then filtered with a Hanning filter of appropriate length for the airspeed and sampling wavelength of each system. For simplicity, the data were down-sampled to a spatial interval that would be appropriate for a 33 point Hanning to give the correct wavelength. Table 1 shows the system, the altitude, the airspeed, the sample interval, and the equivalent wavelength for each of the systems modeled. The survey parameters used were typical for: a helicopter flying a minimum altitude (2m); a helicopter with gravity gradiometer and magnetometer flying high resolution in clear country (altitude 20m); a helicopter flying gravity gradiometer with frequency-domain EM (helicopter altitude 60m); and a fixed wing aircraft at the normal altitude of 100m.

Table 1: System Model Parameters

	Heli-Low	Heli-std	Heli-EM	Fixed Wing
Altitudes(m)	2	20	60	100
Speed (m/s)	10	25	30	60
Sample spacing (m)	1	2.5	3	10
Filter (m) 0.3Hz	33	83	100	
Filter pts 0.3Hz	33	33	33	
Filter (m) 0.18Hz				333
Filter pts 0.18Hz				33

To test the gravity gradient responses, we used air-filled cavities, assuming a density contrast of -2.6 g/ml. Table 2 lists the cavities that were modeled, each at several depths below surface. All of the cavities were rectangular prisms. There are, of course many other types of subsurface features which could have been modeled.

Table 2: Cavity targets modeled.

	XYZ Dimension (m)	Depths (m)
Tunnel	1x100x2	2,5,10
Tunnel	4x100x4	2,5,10
Cavity	5x5x5	2,5,10,20
Cavity	10x10x5	2,5,10,20
Cavity	25x25x10	5,10,20,50
Cavity	100x100x25	50,100,200
Cavity	200x200x50	100,200,400

Figure 1 shows an example of the results for the 4m tunnel. In this case the G_{UV} measured response and G_{DD} calculated responses are shown for several depths of burial, with the nominal noise levels shown as a dotted line for each parameter. Since G_{NE} is zero when crossing exactly in the middle of a symmetrical

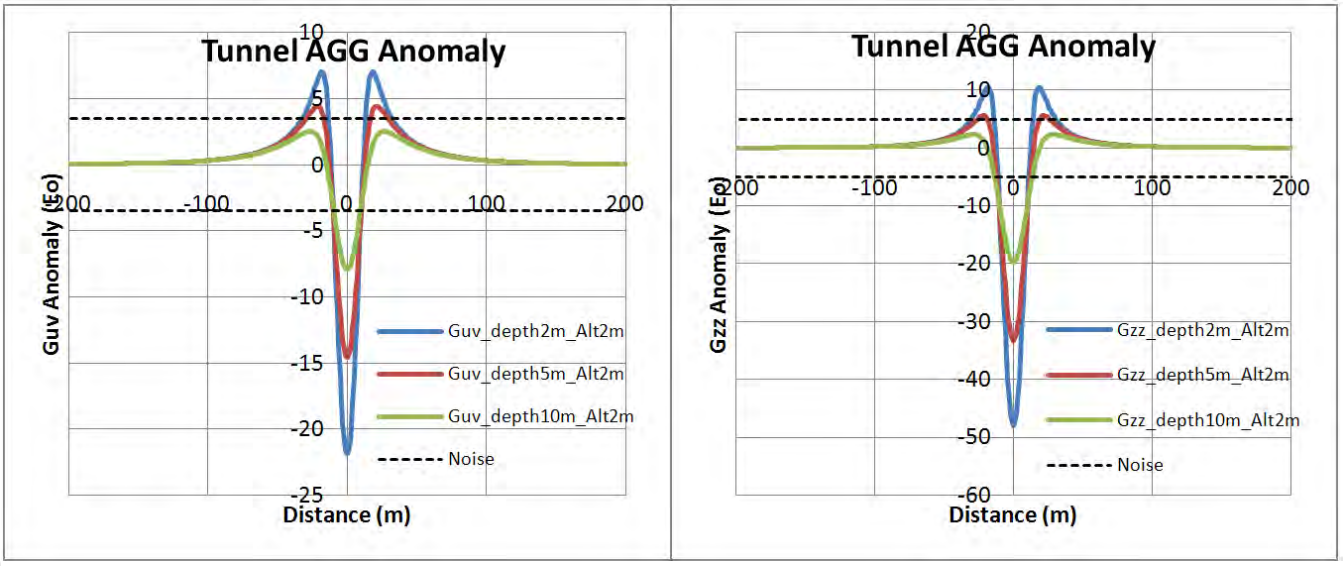

Figure 1. Gravity gradiometry model anomalies for 4m wide, 100m long, 4m high tunnel, buried at depths of 2m, 5m, and 10m, measured from FALCON on a helicopter at 2m altitude.

body, for the cavity models G_{NE} was modeled for a line over one edge of the cavity.

It can be seen in Figure 1 that the tunnel is definitely detectable from the helicopter system at 2m altitude when buried 2m deep and 5m deep, but detection is marginal at best when buried 10m. One can obviously infer that a helicopter flying at 20m or 30m above the ground would not detect this target.

Figure 2 shows helicopter FALCON data collected in a test for DARPA over the LEB ring of the Superconducting Super Collider, a circular tunnel of about 4m x 4m dimension, buried at a depth of about five metres. The correlation to the amplitude of the modeled data is excellent. Note that these data have a terrain correction applied – critical for detecting small targets from low altitude.

Table 3 gives a summary of the G_{UV} anomalies for the range of models, for those systems which detected the targets. The "ND" indicates that the target was not detectable (based on the noise threshold of 3.5 Eo). Blank spaces are models that were not tested, but are presumed detectable since they are shallower than detected targets.

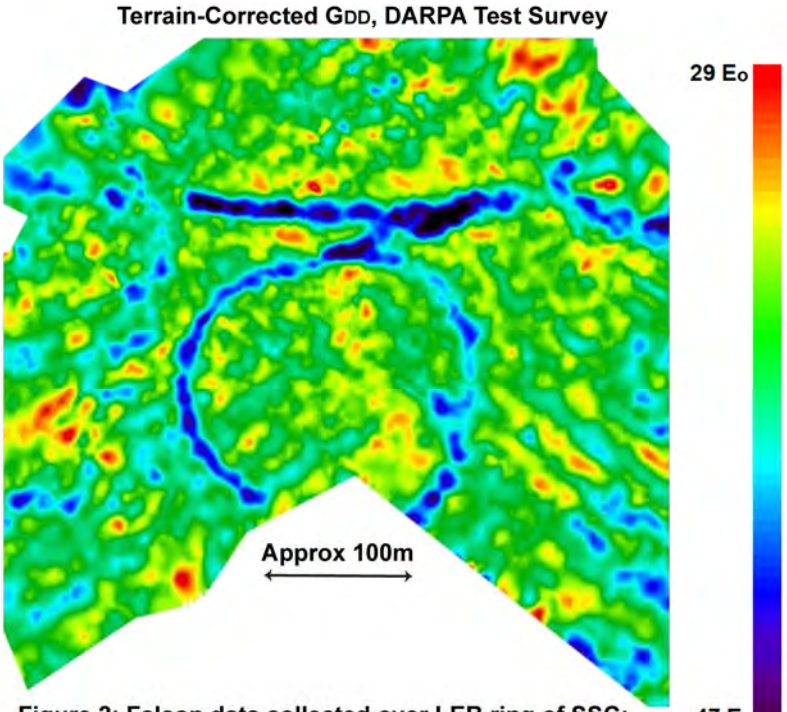

Figure 2: Falcon data collected over LEB ring of SSC: 4m tunnel at approx 5m depth.
Data from 090424_DARPA_GATE_Proposer_Day_Brief_v6.ppt

Detection limits will always depend on the accuracy of the terrain correction, and the complexity of the host geology. The accuracy required of the terrain corrections increases at lower altitude.

Table 3: Summary of G_{UV} peak anomalies (Eo) for all detectable targets.

		Depth (m)						
Cavity (m)	Alt.(m)	**2**	**5**	**10**	**20**	**50**	**100**	**200**
4x100x4	**Heli 2m**	21.9	14.6	7.9	ND	ND	ND	ND
5x5x5	**Heli 2m**	13.1	4.5	ND	ND	ND	ND	ND
10x10x5	**Heli 2m**	27.8	14.1	5.5	ND	ND	ND	ND
25x25x10	**Heli 2m**		53.3	29.9	11.0	ND	ND	ND
25x25x10	**Heli 20m**		6.7	4.7	ND	ND	ND	ND
100x100x25	**Heli 20m**					13.1	4.2	ND
200x200x50	**Heli 20m**						18.0	5.2
200x200x50	**Heli 60m**						10.4	3.5
200x200x50	**FW 100m**						5.9	ND

Conclusions

With the availability of gravity gradiometry on a helicopter platform, the gravity method now has the sensitivity and spatial resolution to detect many targets of interest in engineering and environmental applications. Cavities as small as 5m can be detected with very low altitude helicopter surveys. Cavities of a size of 100m or more can be detected from helicopter surveys at normal EM survey altitudes, and cavities larger than 200m could be detectable from fixed-wing surveys.

References

Boggs, D.B., Maddever, R.A.M., Lee, J.B., Turner, R.J., Downey, M.A., and Dransfield, M.H., 2007, First test survey results from the Falcon helicopter-borne airborne gravity gradiometer system: Preview, 126, 26-28.

Dransfield, M.H. and Lee, J. B., 2004, The FALCON® airborne gravity gradiometer systems, in R.J.L. Lane, editor, Airborne Gravity 2004 – Abstracts from the ASEG-PESA Airborne Gravity 2004 Workshop: Geoscience Australia Record 2004/18, 15-20.

Lee, J. B., 2001, FALCON gravity gradiometer technology: Exploration Geophysics, 32, 247-250.

Rajagopalan, S., Carlson, J., and Wituik, D., 2007, Kimberlite exploration using integrated airborne geophysics. Extended Abstracts of the ASEG, 2007 Perth WA, Preview, Australian Society of Exploration Geophysicists.

AIRBORNE EM DATA COMPLEMENT MAGNETICS IN AN UNEXPECTED WAY

Les P. Beard, William E. Doll, Jacob R. Sheehan, T. Jeffrey Gamey and Jeannemarie Norton
Battelle-Oak Ridge Operations, Oak Ridge, Tennessee

Monika Siwiak, Willy Van Vaerenbergh
AECOM Ltd., Brisbane, Australia

Abstract

In the fall of 2008, a low-altitude airborne geophysical survey was carried out at a military installation in Australia, the primary goal of which was detection and mapping of infrastructure, buried wastes, and other buried and surface metallic objects within a 1738 hectare area. The primary survey system was the Battelle VG-16 vertical magnetic gradient system. Because the base is active, the time frame for conducting the survey was limited to a few weeks. The short time frame and the added expense of an additional system were factors against adding on an electromagnetic survey. However, the Australian Department of Defence suggested that there might be non-ferrous targets of significance that the magnetic system would not detect. Moreover, the base was located some tens of kilometers from a field of extinct volcanoes, presenting the possibility of magnetic geology in the form of mafic igneous units. Therefore, it was determined that an airborne transient electromagnetic system should be included in the project.

The added electromagnetic system proved valuable, but not in the way that was expected. Concentrations of strong anomalies appeared in the magnetic data, the sources of which could be either buried debris or geological. The TEM-8 system was flown over some of the more dense concentrations of magnetic anomalies. In some of these areas the TEM data showed very few anomalies, indicating that either the VG-16 anomalies are associated with magnetic rock types, or that the metallic sources detected by the VG-16 system are too deeply buried to be detected with the TEM-8 system. A few carefully located excavations indicated that the sources of the magnetic anomaly concentrations without associated electromagnetic anomalies were localized concentrations of very magnetic iron-bearing rock.

Introduction

This report describes the results of a low-altitude helicopter geophysical survey carried out for the purpose of detecting and mapping infrastructure, buried wastes, and other buried and surface metallic objects within a 1738 hectare area at an Australian military installation. By low-altitude, we mean survey heights of one to three meters above ground level, where possible. To achieve such low survey altitudes, sensors are mounted on booms which are fixed to the frame of the helicopter, rather than being slung beneath the helicopter on tethers. Figure 1 shows the two Battelle boom-mounted systems used in the survey: the VG-16 (Doll et al, 2008), which measures the vertical magnetic gradient at eight evenly-spaced gradient pods, and the TEM-8, a transient electromagnetic system with two 3m x 4m transmitter loops (Doll et al, 2009). Each loop surrounds four receiver coils. Although these systems were originally designed for wide-area unexploded ordnance surveys, their exceptionally high resolution, effectively equivalent to that of a ground survey, has made the systems attractive for mineral exploration (Gamey et al, 2009) and engineering/infrastructure applications (Beard et al, 2009).

Figure 1: Battelle VG-16 vertical magnetic gradient system (left) and TEM-8 transient electromagnetic system (right) used for low-altitude (<2m) surveys.

The need for a geophysical survey arose from planned expansion of the base, which was used by Allied forces in World War II, and has been in continual use since that time. In the rapid de-mobilization of forces after the defeat of Japan, military supplies were sometimes disposed of hastily, and there was concern that undocumented items could be buried on or near the base, and could pose a hazard to construction workers. The choice of airborne methods for geophysical surveying of the base was driven by the size of the area to be surveyed—over 1700 hectares—and time constraints for getting the survey done because of ongoing military trainings, daily logistical operations, and current and planned base expansion activities.

Although the primary survey method was to be measured vertical magnetic gradient using the Battelle VG-16 system, it was ultimately decided that the Battelle TEM-8 electromagnetic system should also be included. The Australian Department of Defence argued that some of the buried items could be non-ferrous and therefore undetectable with the VG-16. It was also pointed out that extinct volcanoes exist in the near vicinity (within tens of km) of the base, and there was some possibility on that account of magnetic geology.

About 70 percent of the 1738 hectares were flown with the VG-16 system at low-altitudes. The mean altitude in these areas was 1.4 meters above ground level. A total of 9786 vertical gradient (VG) anomalies were identified above a 5 nT/m threshold. Of these, 1960 were classified as point-source anomalies of unknown origin. TEM-8 data were collected over 290 hectares, all in the low-altitude VG areas. A total of 1893 anomalies were detected above a 3 mV threshold. Of these, 458 were classified as point source anomalies of unknown origin. The overwhelming majority of TEM anomalies had an accompanying VG anomaly, indicative of metal.

Comparison of Anomalies

Figure 2 shows a map of the vertical gradient anomalies of the base and its immediate surroundings. Although the VG-16 survey produced about 9800 anomalies, two anomalous areas stood out as areas of concern. These areas are circled in blue in Figure 2. They were areas of multiple overlapping anomalies of relatively high amplitudes, and were in appearance similar to documented areas containing buried debris, shown circled in red in Figure 2.

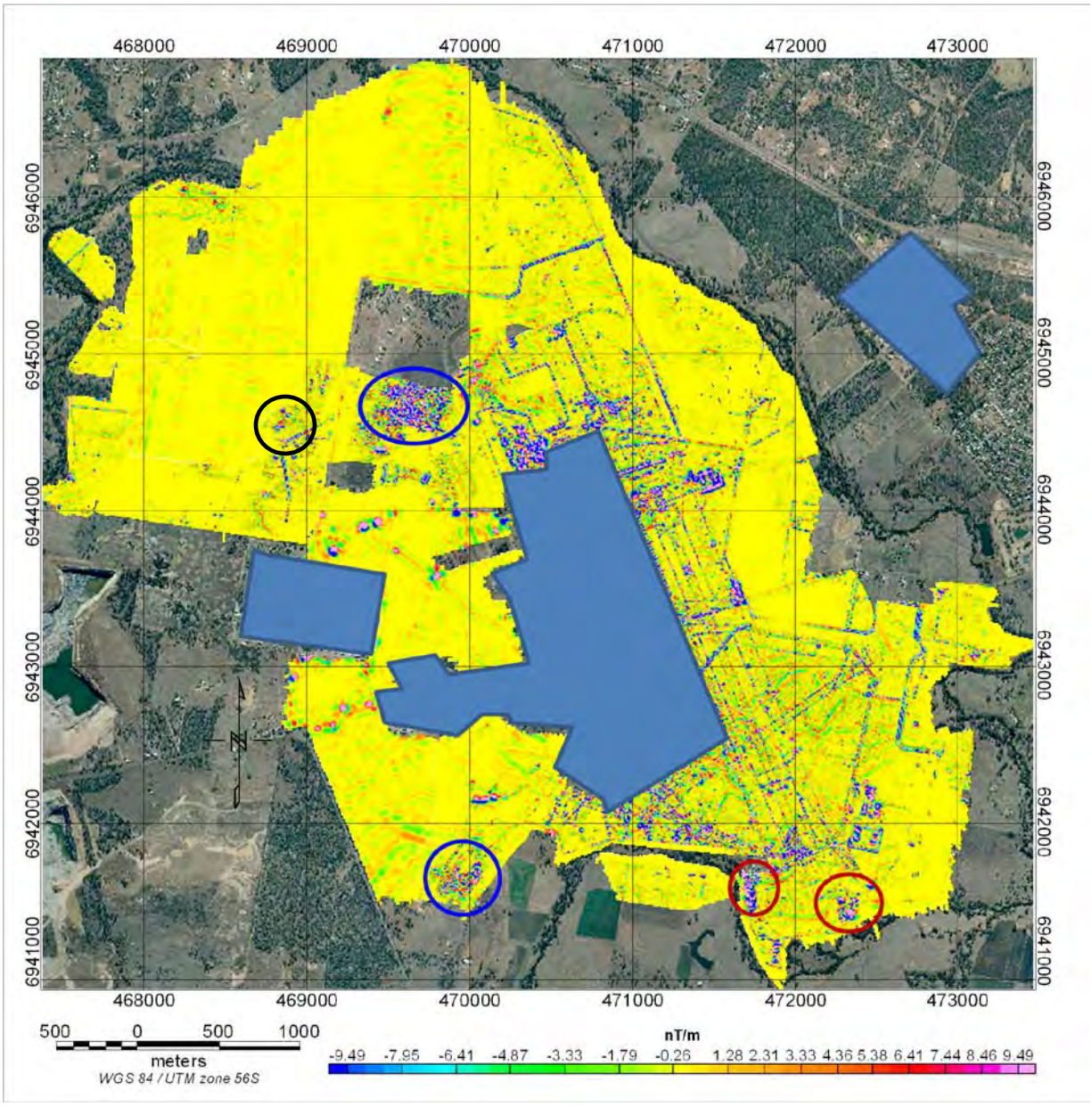

Figure 2: Vertical gradient anomaly map of base. Red circles indicate sites of known buried waste. Blue circles indicate areas with similar anomaly pattern as the known sites, but with unknown sources. Black circle is an area where exploratory excavations took place. Blue polygons represent collections of base buildings.

Upon completion of the VG-16 survey, it was determined, based partly on the presence of the two unknown areas in Figure 2, to use the TEM-8 system to survey portions of the base comprising in total about 290 hectares. These areas are shown in dark blue in Figure 3.

Figure 4 shows close up views of the two documented buried debris sites (in Figure 2, circled in red). Although superficially similar to the two unknown areas, in detail there were differences. The two known buried waste sites had visual cues in satellite imagery. They both had some degree of topographic expression visible in satellite photos. The texture of the ground was subtly different from

surrounding undisturbed earth, and one of the sites is encompassed by roads. In contrast, neither of the unknown sites showed evidence of disturbed earth. Both were in large open fields, one on the base proper, the second on farmland leased out by the base.

The magnetic anomalies of the known burial areas, although numerous and overlapping, appeared to have a measure of coherent magnetic "structure." In both areas, there are large positive magnetic anomalies alternating with negative in a more or less N-S pattern, as can be seen in Figure 4. In contrast to the known burial areas, the magnetic anomaly patterns of the two unknown areas have a more random appearance, with positive and negative magnetic lobes being smaller in area and adjoining one another in a variety of directions. This difference can be clearly seen in Figure 5, which shows the VG-16 anomalies of the more northerly unknown anomaly group.

The above-mentioned differences led us to suspect a geological origin for the unknowns, and the TEM-8 data, shown in Figure 6 for the northern unknown, supported that view. The TEM-8 data showed no large electromagnetic responses indicative of buried metal over the area of dense magnetic anomalies. The system detected known collections of metal near the site, and therefore the lack of response was not instrument insensitivity. Of note is a known area of waste soil deposited in rows at the ground surface, and shown in the lower right corner of Figure 5. The soil rows contain little metal, but nonetheless appear as small amplitude lineations in the vertical gradient data with a few small magnetic anomalies from metallic objects. The magnetic lineations show the sensitivity of the VG-16 to magnetic susceptibility changes in soil. The TEM-8 system covered only a portion of the site, but as can be seen in Figure 6, the buried metal appears as small TEM anomalies in the northwest corner of the soil rows, but otherwise there is no EM response in this area.

However, because the TEM-8 has limited depth detection ability, a remote possibility existed that metal debris was too deeply buried for the TEM-8 to detect. Two trenches, spaced about 70m apart and located near the center of the magnetic anomalies, were excavated to depths of over 2m. In both trenches, the field notes describe undisturbed silty clays to the bottom of the trenches. Magnetic susceptibility measurements on the silty clays at the trench sites yielded susceptibilities on the order of 10^{-3} SI, not particularly magnetic and typical of clays and sedimentary formations.

The source of the magnetic anomalies remained a mystery until examination of a second magnetic anomaly collection, labeled 17_a in Figure 7. As in the previous example, it also showed no TEM anomalies (Figure 8). In this instance, anthills in the area with magnetic anomalies were covered with bits of red rock excavated by the ants. The magnetic susceptibilities of the anthills measured approximately 0.03 SI, putting them somewhat above the average magnetic susceptibility for basic igneous rocks (Table 3.1, Telford et al, 1990).

At a third site, located about 500m west of the SW corner of the anomaly collection in Figure 5, and circled in black in Figure 2, two distinct types of magnetic anomalies appeared, as shown in Figure 9. One was a single, strong, very dipolar anomaly of several hundreds of nT/m in the north part of the area, and the second a collection of anomalies having magnitudes of tens of nT/m, and similar in pattern to those mentioned above. Based on prior excavations, we expected to find metal in the north area and magnetic geology in the south. Upon excavation, the predictions turned out to be accurate. A sizeable amount of buried metal debris was uncovered in the north (Figure 10, right panel), and in the south a red layer of sand and gravel having thickness of about 80 cm was uncovered at a depth of about 0.5 m (Figure 10, left panel). The gravelly soil had magnetic susceptibilities in excess of 100 SI, and a bright red piece (Figure 10, center panel) measured over 300 SI, which was effectively the same susceptibility as was measured on the steel frame of our field vehicle.

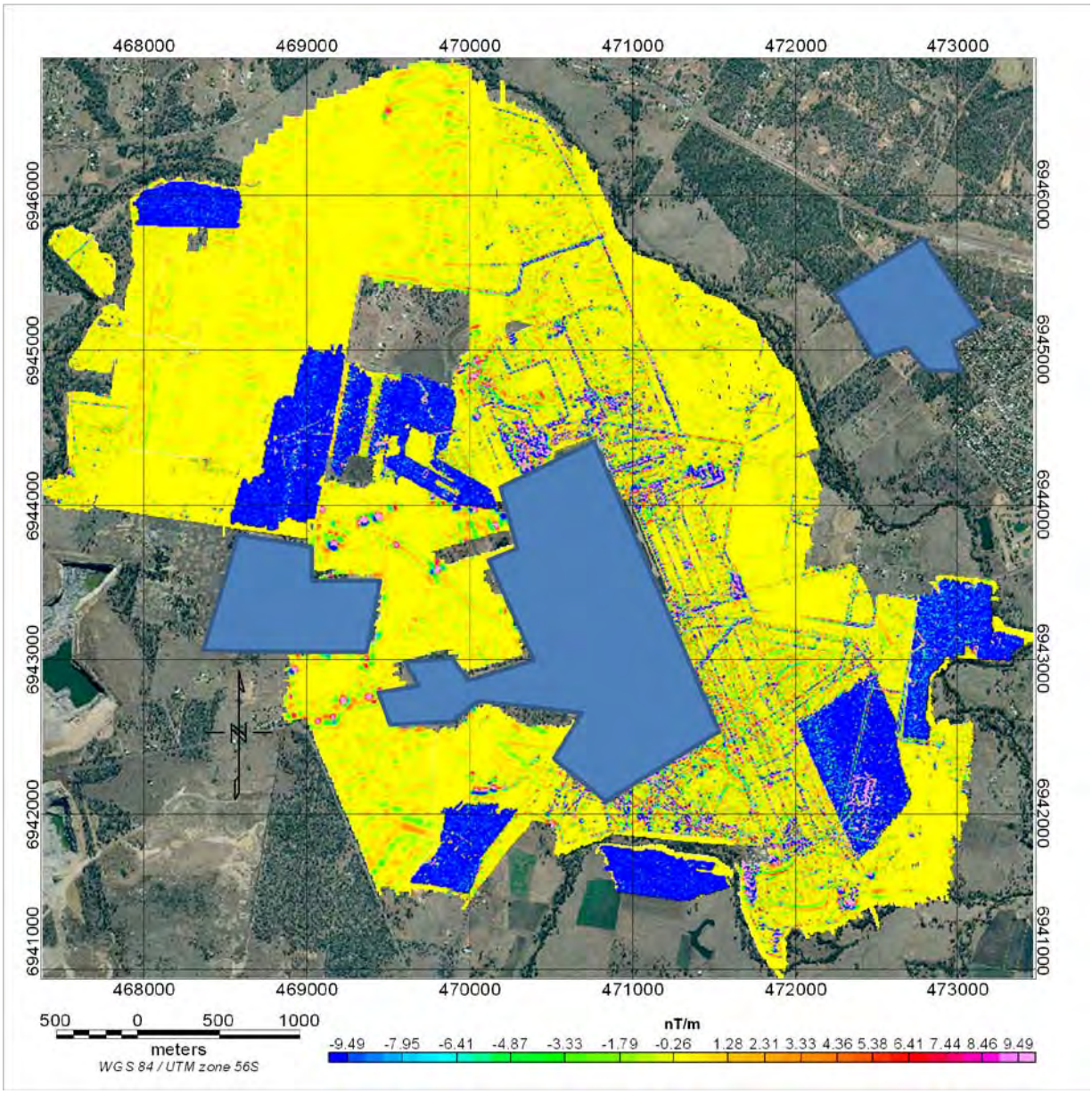

Figure 3: Areas (in blue) where TEM-8 was flown to complement the VG-16 survey. The areas included the anomalous areas circled in blue in Figure 2.

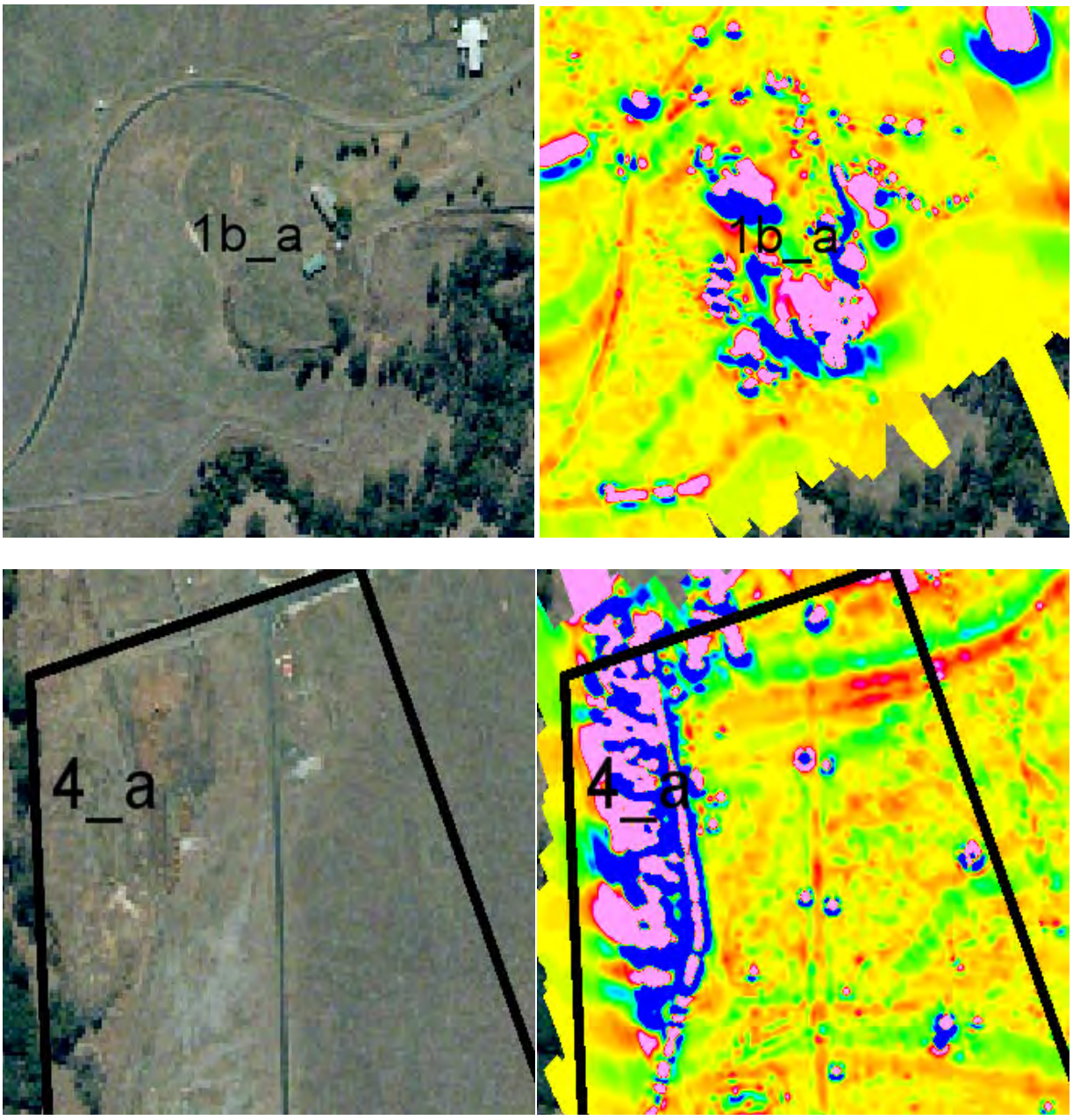

Figure 4: VG-16 anomalies over two documented buried debris sites, indicated by the red circles in Figure 2. Color scale is -10 nT/m to +10 nT/m (blue to red).

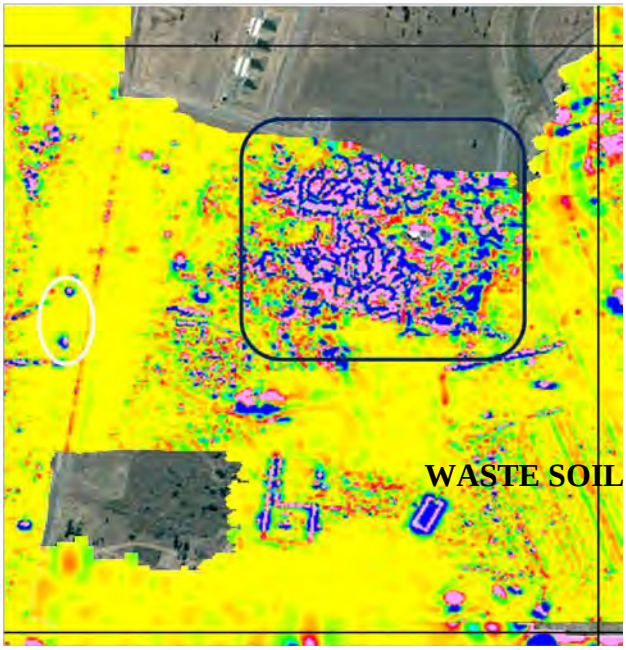

Figure 5: VG-16 anomalies of the more northerly of the two unknown areas circled in blue in Figure 2. Rows of waste soil with very little metal are shown by the magnetic lineations in the lower right. Color scale is -10 nT/m to +10 nT/m. Area shown is about 900m x 900m.

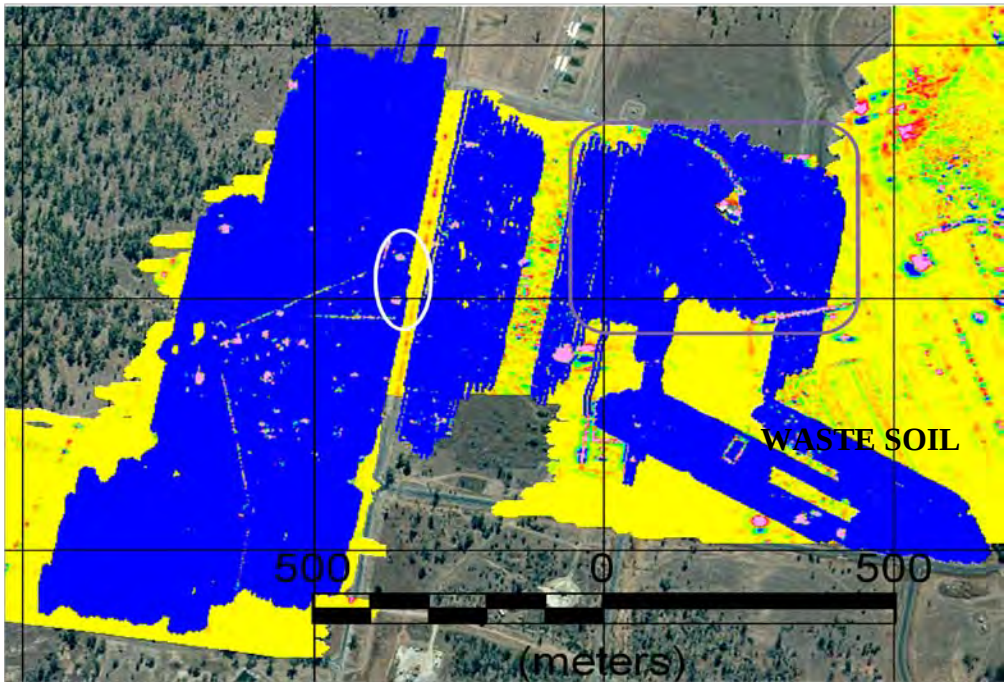

Figure 6: TEM-8 anomalies from time gate 2 (250 microseconds after turnoff) of the more northerly of the two unknown areas circled in grey. White oval encompasses two above ground collections of metal. The area of waste soil deposited along rows (shown in Figure 5) is indicated. EM color scale is -5 mV to +5 mV (blue to red).

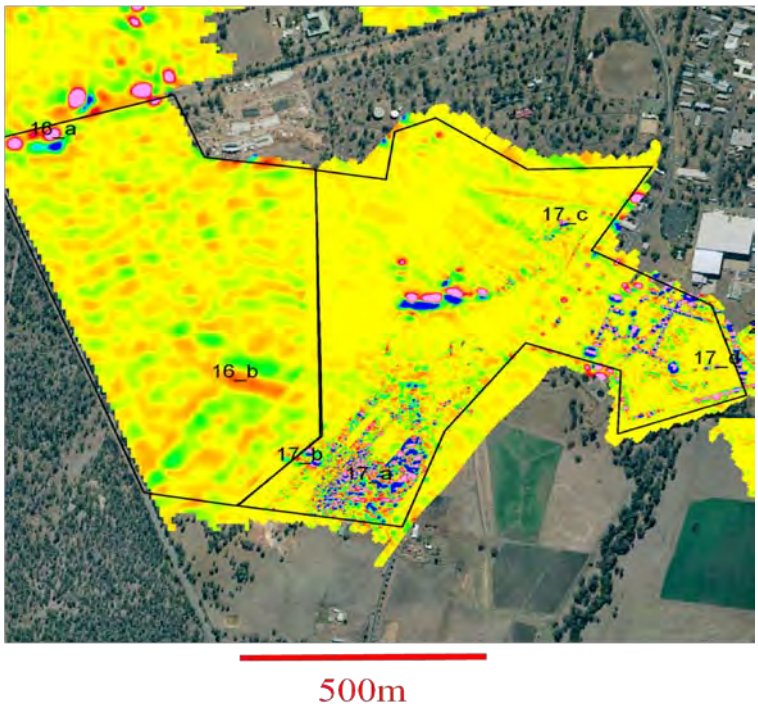

Figure 7: VG-16 anomalies of the southern unknown area, circled in blue in Figure 2. Color scale is -10 nT/m to +10 nT/m.

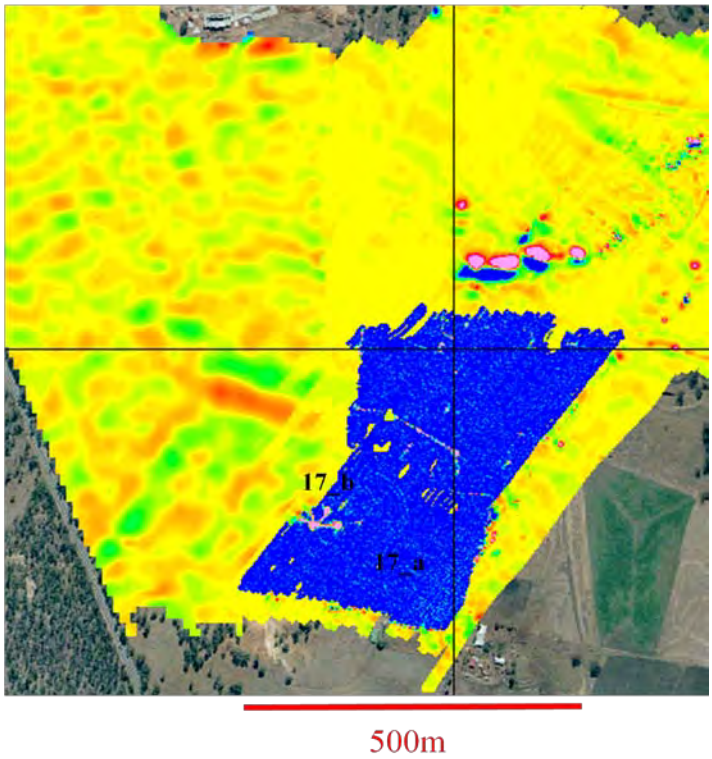

Figure 8: TEM-8 anomalies from time gate 2 (250 microseconds after turnoff) of the southern unknown area. EM color scale is -5 mV to +5 mV.

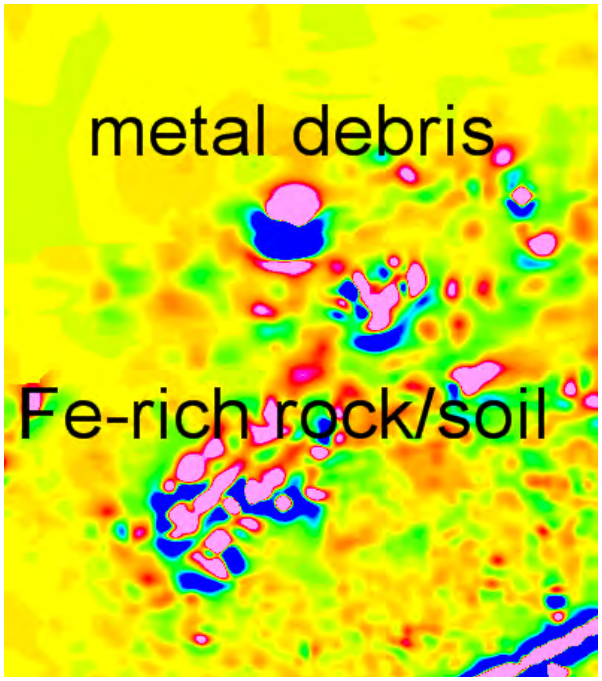

Figure 9: VG-16 anomalies of the exploratory excavation area, circled in black in Figure 2. Color scale is -10 nT/m to +10 nT/m.

Figure 10: VG-16 anomalies of the exploratory excavation area, circled in black in Figure 2. Color scale is -10 nT/m to +10 nT/m.

Conclusions

Although the Battelle airborne magnetic gradient system was the primary system used in a survey of an Australian military base, the Department of Defence requested that electromagnetic data be collected over some portion of the base in case some of the buried items of interest were metallic, but non-ferrous. However, the TEM-8 airborne EM system proved its worth not in detection of buried non-ferrous metal, but in helping the geophysical interpreters to determine whether the sources of sizeable concentrations of magnetic anomalies were metallic or geological. Prior to the survey, there were no strong indicators of magnetic geology in the area. However, subsequent follow-up excavations in areas that showed dense concentrations of magnetic anomalies with no electromagnetic anomalies found a shallow, highly magnetized gravel layer that was most likely responsible for the anomaly pattern. After a few exploratory excavations, we were able to more accurately predict which anomalies were caused by metal and which had geological sources.

Acknowledgments

The data used in this study were collected during a project funded through the Australian Department of Defence. Gold Coast Helicopters provided helicopter services for the project.

References

Beard, L.P., M. Siwiak, T.J. Gamey, W.E. Doll, J.R. Sheehan, and J. Norton, 2009, High-resolution helicopter survey for infrastructure and contamination sources: Extended abstract in 2009 SEG Annual International Meeting Proceedings, SEG International Meeting, Houston, Texas, October 2009.

Doll, W.E., J. Sheehan, T.J. Gamey, L.P. Beard, and J. Norton, 2008, Results of Airborne Vertical Magnetic Gradient Demonstration at Kirtland AFB: Journal of Environmental and Engineering Geophysics 13(3): 277-290.

Doll, W.E., T.J. Gamey, J.R. Sheehan, L.P. Beard, J. Norton, A.E. Hanson, R. Lahti, and N. Eklund, 2009, Demonstration of the Battelle TEM-8 airborne electromagnetic system for mapping and detection of UXO: Presentation at 2009 SERDP Symposium, Washington D.C., December, 2009.

Gamey, T.J., J. Norton, and G. Lockhart, 2009, A new high resolution magnetic gradient survey for kimberlites: Extended abstract in 2009 SAGEEP Proceedings, SAGEEP Symposium, Fort Worth, Texas, 409-423.

Telford, W.M., L.P. Geldart, and R.E. Sheriff, 1990, Chapter 3: Magnetic methods *in* Applied Geophysics, 2nd edition, Cambridge University press, 770 pp.

MAPPING EPIKARST IN THE ARBUCKLE-SIMPSON AQUIFER, SOUTH-CENTRAL OKLAHOMA, USING HELICOPTER ELECTROMAGNETIC SURVEY DATA

David V. Smith, U.S. Geological Survey, Denver, CO
Maryla Deszcz-Pan, U.S. Geological Survey, Denver, CO
Bruce D. Smith, U.S. Geological Survey, Denver, CO

Abstract

The U.S. Geological Survey has been actively using helicopter electromagnetic surveys over karstic aquifers as part of on-going research to aid in the creation of highly detailed three-dimensional geologic models. The geologic models are the basis for understanding the geohydrologic framework of the aquifers, and they provide essential information needed for groundwater models used to manage an increasingly important resource. As part of this research, the USGS has developed and applied methods for mapping epikarst, which plays an important role in groundwater recharge. A case study in the Arbuckle-Simpson aquifer in south-central Oklahoma is presented here.

Introduction

An airborne electromagnetic/magnetic survey was flown by the U.S. Geological Survey (USGS) in 2007 over four areas of interest (blocks A-D) located in the Arbuckle-Simpson aquifer area of the Hunton anticline in south-central Oklahoma (fig. 1). Survey coverage consisted of approximately 770.3 line-km, including 79.2 line-km of tie lines. The application of airborne electromagnetic surveys for ground-water mapping in karst environments has been described by Smith, Smith, and Blome (2008). This presentation summarizes the results of an interpretative of an report to the Oklahoma Water Resources Board by Smith and others, 2009.

The objective of this survey (as is the case for all airborne electromagnetic methods) was to provide a detailed, densely sampled distribution of electrical resistivity with depth from ground surface to depths of 100–150 m. The correlation of resistivity with lithostratigraphic units improves our understanding of subsurface geology in a more efficient way than would be possible with drillholes or ground-based surveys. Lateral changes in earth resistivity can be correlated with structural features (faults) and geologic contacts.

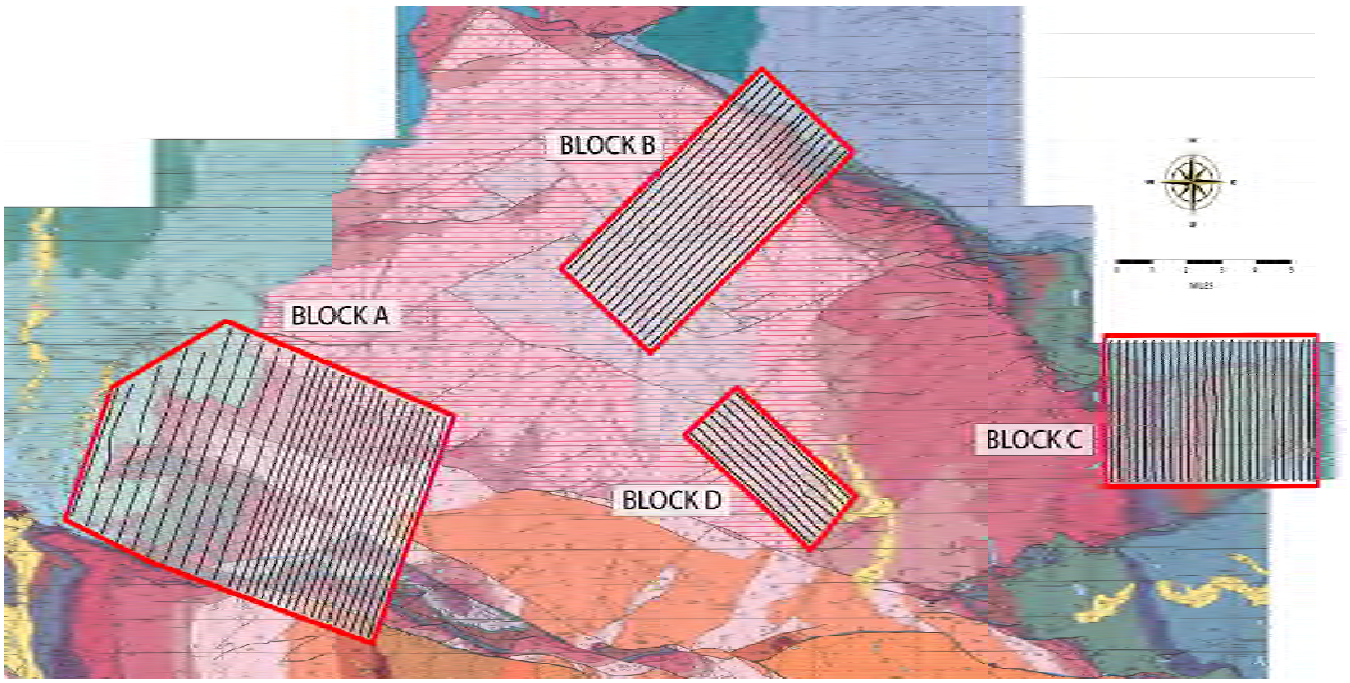

Figure 1: Index Map of Helicopter EM Survey Blocks (map adapted from Ham and others, 1990).

Discussion

Epikarst refers to a portion of the bedrock that extends from the base of the soil zone and is characterized by extreme fracturing and enhanced solution (Field, 1999). Soil developed in response to in-place weathering in karst terrains is frequently referred to as a residuum (Gamey and others, 2002). Epikarst is characterized by fractures and solution pockets that may or may not be filled with water. Epikarst in general is thought to be important in the near-surface hydrology of carbonate terrains (Klimchouk, 2004).

An airborne geophysical survey, similar to the one reported here, was carried out in Missouri over an area of epikarst and residuum (Gamey and others, 2002). The goal of that study was to map possible flow paths for contaminants in a well-developed, thick residuum. Epikarst, though recognized in the Hunton anticline, has not been consistently mapped. The Oklahoma Water Resources Board funded a study by Sample (2008) to characterize the geophysical, hydrologic, and geologic parameters of epikarst in the Hunton anticline in specific study areas. Smith and others (2007), Smith, Blome, and others (2008), and Smith, Smith, Blome, and Osborn (2008) have compared the results of the HEM resistivity-depth images (RDI) with ground electrical resistivity imaging (ERI) surveys, as have Riley (2004), Halihan and others (2009), and Sample (2008). The comparison between ground and airborne RDI is very good (fig. 2). In general the ground resistivity survey has greater detail, which is no surprise given that electrode spacings are much smaller than the airborne EM footprint. The resolution of high resistivities (above 2000 ohm-m) is better with a galvanic ground system than an induction system. In general the color scale used in the presentations of the HEM data and the RDI sections along flight lines does not have as high a resistivity as scales used for the ground surveys.

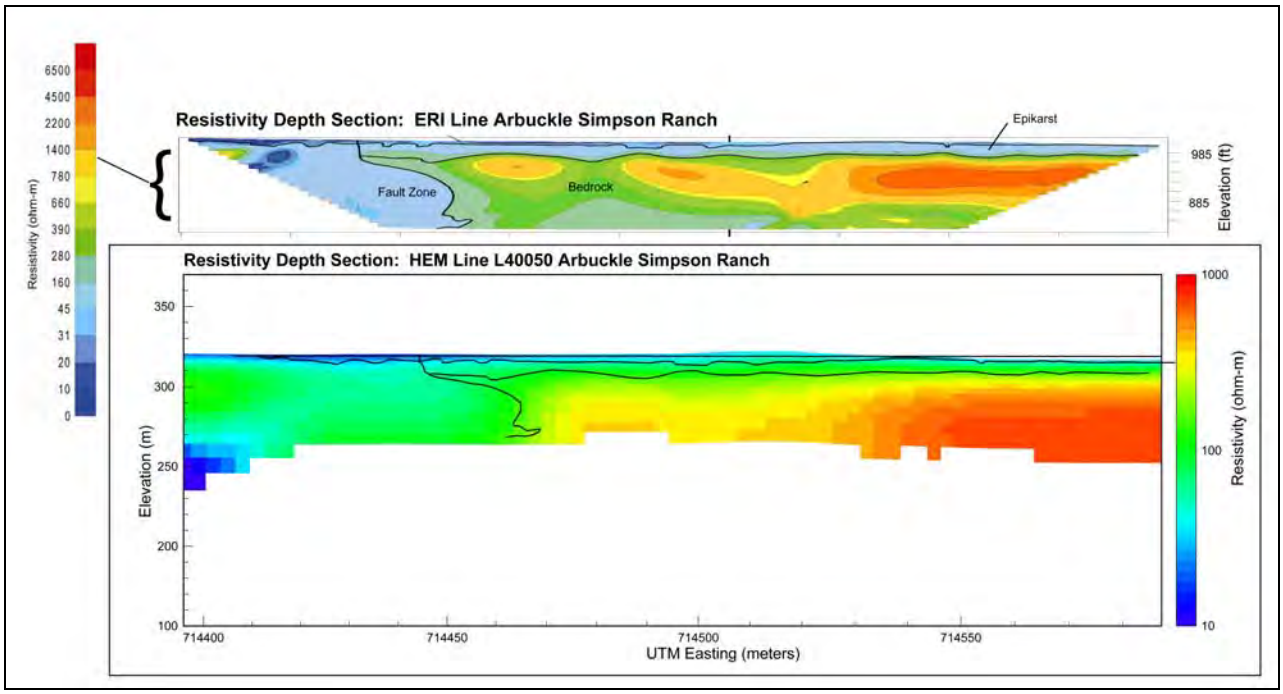

Figure 2: Ground electrical resistivity line at the Arbuckle Simpson Ranch site (top profile, Sample, 2008) is shown at the same vertical and horizontal scale as the airborne resistivity depth image along line L40050 (bottom profile). The interpreted units from the ground survey are shown superimposed on the airborne depth image. Note that the resistivity color scales for each depth section are different (see text for discussion).

The above studies have shown electrical resistivity of epikarst is typically lower than that of the source bedrock, due in part to higher concentrations of fine-grained residual material, such as clay. As a result, occurrences of epikarst are mapped as a low resistivity layer overlying higher resistivity country rock, in particular limestone and dolomite. Likewise, soils would exhibit a lower resistivity owing to relatively higher water or clay content. Thus, both epikarst and soil present similar HEM signatures with the major difference being the thickness. Soils appear as a veneer over bedrock or over epikarst.

The basic groundwater issue related to the soil, residuum, and epikarst is its significance for potential water storage and recharge to the bedrock. As in the study by Gamey and others (2002), the residuum also is a control on near-surface water flow paths. Sample (2008) concluded that the storage potential for these units was the same order of magnitude as the saturated thickness of the aquifer itself. The HEM survey offers critical data that can be used to map the extent of these units in the area of the Arbuckle-Simpson aquifers.

One of the sites that Sample (2008) studied with ERI, soil penetrometer, and other methods is near survey block D. Mapped structures and those interpreted from the HEM (fig. 3) described above would generally be expected to influence the depth and extent of epikarst development (Klimchouk, 2004). The two ground profiles are located near one HEM line (L40050). The RDI shown in figure 4B along the HEM flight line that is near both ground surveys indicates that the bedrock is more resistive in the northeast part of the survey area. Note that the color scale for the HEM in figure 4B has been chosen to match the color scale used by Sample (2008) for the ERI images. In general the major fault (fiducial 714490 Easting on fig. 4B) is associated with a zone of lower resistivity that extends to depth of at least

60 m that could indicate a thickening of the epikarst over a possible buried karstic feature. This is certainly an area where enhanced recharge or groundwater flow may occur.

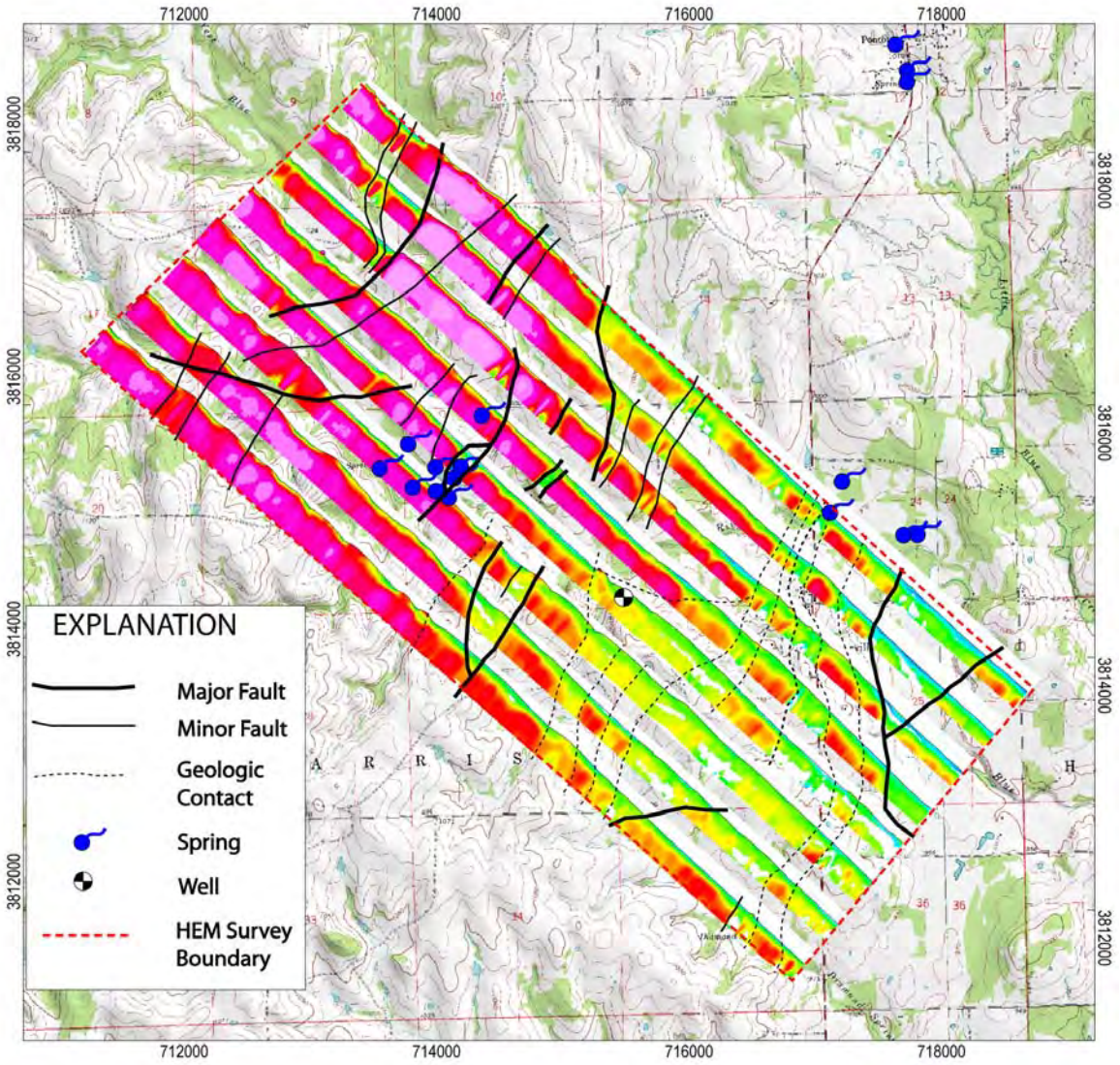

Figure 3: Block D fence diagram of RDIs with interpreted geologic structure with topographic features in the background. Hot colors (red/purple) are high resistivity, cool colors (green/blue) are low resistivity.

The ERI line at the SRW site shows that no high resistivity (greater than 500 ohm-m) bedrock is within the depth range of the survey (fig. 4C). However, the geologic map for this part of Block D does not show a change in basement geology (Arbuckle Group). The general comparison between the ERI depth section and the HEM depth section (fig. 4C and 4D) is good with both mapping lower resistivity in the SRW site. The ground profiles generally have a greater and higher range of resistivity than the airborne RDIs. Sample (2008) noted in general that direct-push electrical conductivity (EC) probe measurements were higher by at least a factor of two than the ground ERI survey values. Thus, part of the reason for the difference in resistivity range is a difference in the volume of ground sampled for the different techniques. The EC technique samples the smallest volume, the ERI senses a larger volume, and the airborne survey samples the largest.

Figures 4C and 4D show the airborne and ground RDI at the same general scale with the interpreted depth of the epikarst from Sample (2008). This particular ERI site is anomalous in that there is no resistive (more than 500 ohm-m) bedrock within the depth of investigation. If bedrock is within range of the geophysics, then it is not resistive limestones but a lower resistivity lithology such as silty sandstones or limestone. Since there is not a great electrical contrast between epikarst and bedrock, Sample (2008) relied heavily on penetrometer data. We have shown the HEM RDI with a different color scale in Figure 4D, which emphasizes the surface lower resistivity unit. This unit correlates generally well with the depth estimated by Sample (2008).

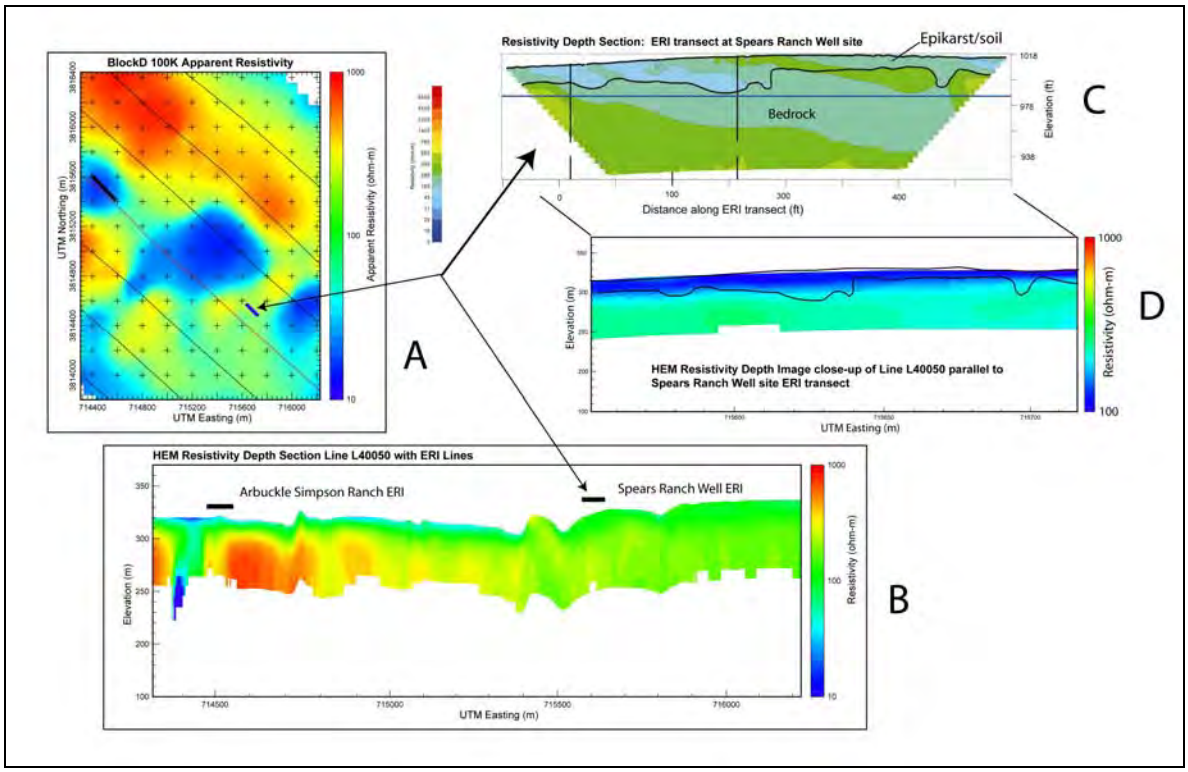

Figure 4: HEM resistivity depth image (RDI) along line L40050 showing the location of ERI transects at the Arbuckle Simpson Ranch site and the Spears Ranch well site. Map view (A) showing flight lines and ground profile lines on the 100-kHz apparent resistivity map. The HEM RDI for the entire line is shown in (B) with the locations of the ground profiles. The ERI profile for the Spears Ranch well site is shown in (C). An enlargement of the HEM profile (B) is shown in (D) at the same horizontal scale as the ERI line and with the interpreted depth of epikarst from direct-push penetrometer data. The HEM RDI is the projected length of the true ground RDI profile 200 m northeast of the HEM flight line (red line in A). Note that the resistivity color scales for apparent resistivity map and the depth section are different (see text for discussion).

In our treatment of soil/epikarst signatures, we analyzed shallow (less than 10 m) resistivity variations in the RDIs. Generally the epikarst has a markedly lower resistivity in comparison to the bedrock at the Arbuckle Spears Ranch in both the ground and airborne RDI. Thin, low resistivity layers overlying more resistive limestone were demarcated using white-filled rectangles, whose lengths equaled the lengths of the soil/epikarst signatures, as shown in figure 5. Areas devoid of the low resistivity layer were left blank. The set of these rectangles in a survey area were connected across

individual survey lines wherever adjacent lines had proximate rectangles. Maps were made showing the coverage of epikarst/soil in Block B (fig. 6) and in Block D (fig. 7). Areas with epikarst/soil are stippled, whereas thin soil/bedrock outcrops are blank.

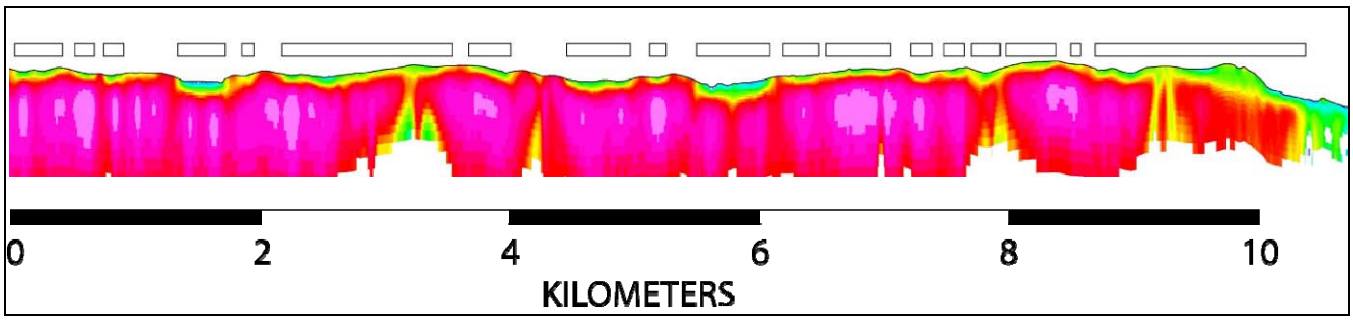

Figure 5: White boxes correspond to zones of epikarst or soil (green) overlying limestone (red) inferred from the underlying RDI.

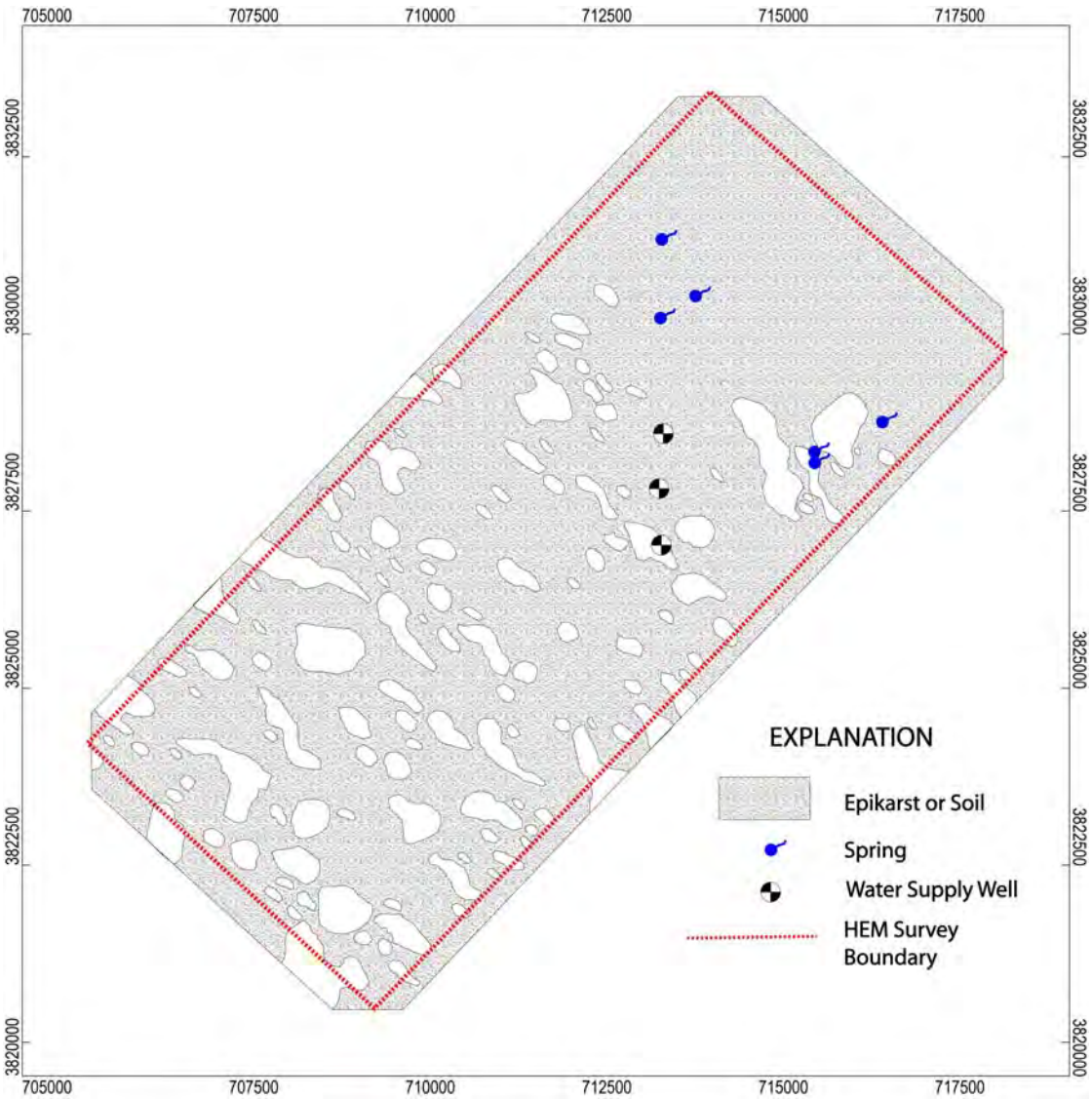

Figure 6: Map of epikarst or soil occurrence for Block B.

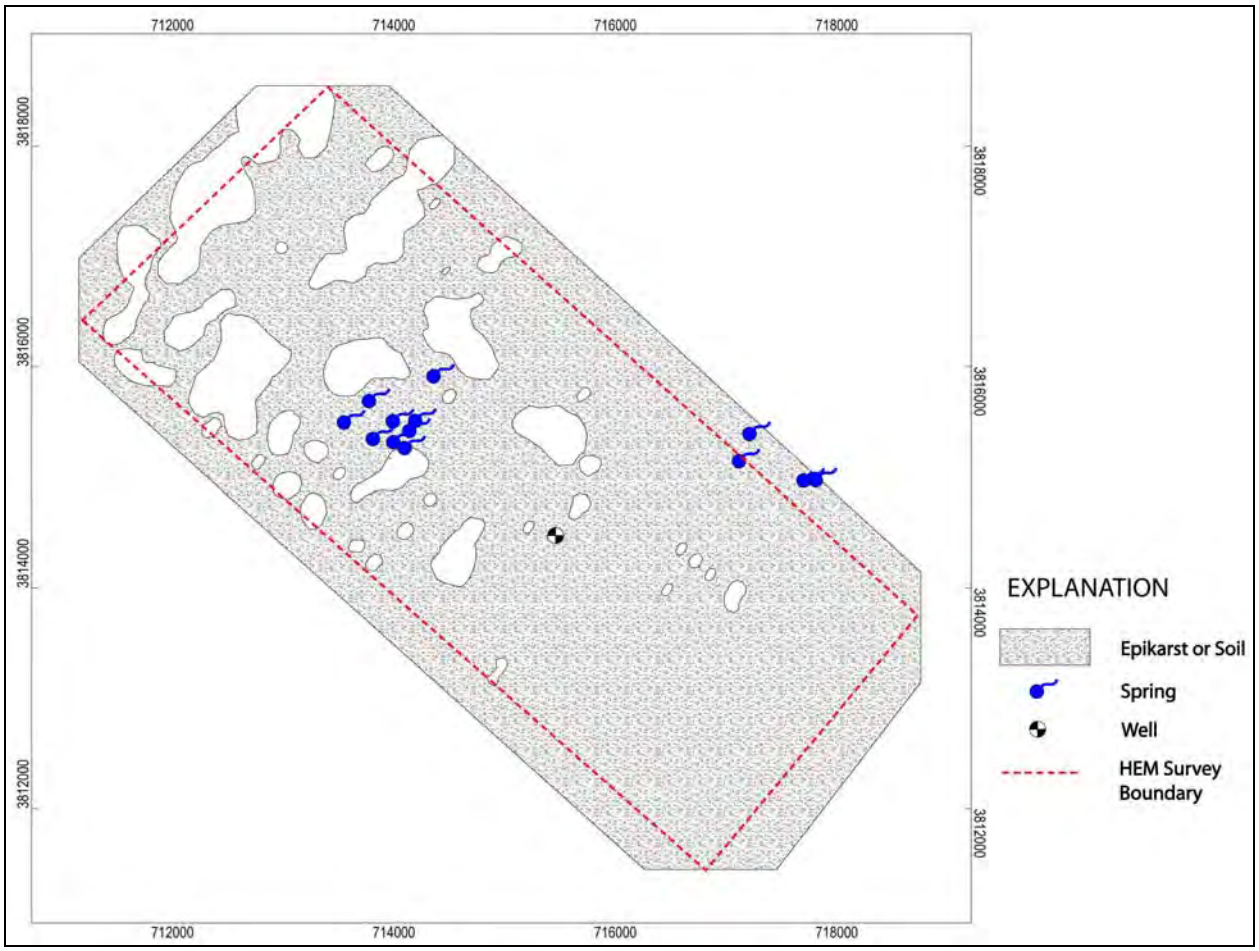

Figure 7: Block D map of interpreted epikarst/soil distribution.

Conclusions

HEM surveys over carbonate terrains effectively map the epikarst and geologic structure. Though the resolution of these features is less than the ground ERI surveys, they correlate well. Both surveys suggest that the epikarst is much more extensive than previously thought. The extent of the epikarst/soil has been interpreted for survey Blocks B and D of the present study. The occurrence of epikarst in these areas has not been previously mapped. Consequently, new geologic mapping should include epikarst since it appears to be a significant component of the hydrogeologic setting.

References

Field, M.S., 1999, A lexicon of cave and karst terminology with special reference to environmental karst hydrology: U.S. Environmental Protection Agency, National Center for Environmental Assessment, EPA/600/R-99/006, 201 p. Digital version by Karst Waters Institute.

Gamey, T.J., Thompson, M., Mandell, W., Frano, G., and Miller, S., 2002, Karst pathway delineation using combined spatial and geophysical analysis at Camp Crowder, Missouri: Proceedings for the 15th Symposium on the Application of Geophysics to Environmental and Engineering Problems, 12 p.

Halihan, T., Mouri, S., Puckette, J., 2009, Evaluation of Fracture Properties of the Arbuckle-Simpson Aquifer, Oklahoma State University School of Geology, report to the Oklahoma Water Resources Board.

Klimchouk, A., 2004, Towards defining and delimiting and classifying epikarst: Its origin, and variants of geomorphic evolution, *in* W.K. Jones, Culver, D.C., and Herman, J., eds., Karst Waters Institute Special Publication, v. 9, p. 13-35, republished (modified), 2004, in Speleogenesis and Evolution of Karst Waters, v. 2, no. 1, p. 1-13.

Riley, M.E., 2004, Investigation of fault properties using electrical resistivity imaging: Master of Science Thesis, Oklahoma State University, Norman, Oklahoma, 104 p.

Sample, M.S., 2008, Characterization of the epikarst over the Hunton anticline, Arbuckle-Simpson aquifer, Oklahoma: M.S. Thesis, Oklahoma State University, 220 p.

Smith, B.D., Blome, C.D., Smith, D.V., Scheirer, D.D., Deszcz-Pan, M., 2008, Geophysical surveys to characterize the hydrogeology of the Arbuckle uplift, south-central Oklahoma: Symposium on Environmental and Engineering Geophysics, Annual Meeting Proceedings, Philadelphia, Pennsylvania, p. 539-548.

Smith, D.V., Deszcz-Pan, M., and Smith, B.D., 2009, Depth section imaging for portions of an airborne geophysical survey of the Hunton anticline, south-central Oklahoma, Final administrative report to the Oklahoma Water Resources Board in fulfillment of the cooperative agreement #08C7OK002032407, released on the internet at: (http://www.owrb.ok.gov/studies/groundwater/arbuckle_simpson/pdf/2009_Reports/DepthSectionImagingAirborneGeophysicalSurveyHuntonAnticline_SmithDeszczPanSmith.pdf).

Smith, D.V., Smith, B.D., Blome, C.D., Halihan, T., Back, J., 2007, Preliminary results of airborne and ground resistivity surveys for subsurface mapping in the Hunton anticline, south-central Oklahoma: Geological Society of America Annual Meeting, Denver, Colorado, 1 p.

Smith, D.V., Smith, B.D., Blome, C.D., and Osborn, N., 2008, Airborne and ground electrical surveys for subsurface mapping of the Arbuckle aquifer, central Oklahoma: American Geophysical Union Annual Meeting, San Francisco, California, 1 p.

Acknowledgements

We wish to acknowledge the collaboration and support of the Oklahoma Water Resources Board for their funding of the epikarst interpretation effort.

HYDROGEOPHYSICAL SURVEYS OF THE TRINITY AND EDWARDS AQUIFERS AT CAMP BULLIS, NORTHERN BEXAR COUNTY, TEXAS, 2006

Jason D. Payne, U.S. Geological Survey, San Angelo, Texas
Bruce D. Smith, U.S Geological Survey, Denver, Colorado
Allan K. Clark, U.S. Geological Survey, San Antonio, Texas

Abstract

In 2002, the U.S. Geological Survey (USGS), in cooperation with the U.S. Army, began hydrogeologic studies of Camp Bullis in northern Bexar County, Texas, with mapping of hydrogeologic features and hydrostratigraphic units (Clark, 2003) at a scale of 1:24,000. In 2003, a USGS-contracted helicopter electromagnetic (HEM) resistivity and magnetic survey was flown over Camp Bullis and the adjacent Camp Stanley (Figure 1). This paper describes the integrated ground electrical and electromagnetic geophysical surveys that were conducted in 2006 in order to follow up on the previous studies and to map hydrogeologic features in more detail. The goal of the project is to better understand the hydrogeologic framework and structure of the Trinity and Edwards aquifers within the study area. The Edwards aquifer is classified as a sole-source water supply for the city of San Antonio.

Discussion

The aquifers within the Camp Bullis Training Site are considered karstic and consist of the older Trinity aquifer and the younger Edwards aquifer which are exposed in the southeastern part of the area. The Glen Rose Limestone of the Trinity Group is equivalent to the upper zone and the upper part of the middle zone of the Trinity aquifer (Ashworth, 1983). The Glen Rose Limestone crops out over all but the southeastern corner of the Camp Bullis Training Site (Clark, 2003). Underlying the Glen Rose Limestone is the Bexar Shale Member of the Pearsall Formation.fo The Trinity aquifer has been subdivided into hydrostratigraphic units A – E, which were mapped by Clark (2003) on Camp Bullis. The southeastern corner of the site lies within the recharge zone of the Edwards aquifer. Depending on the local porosity and associated permeability, the Glen Rose Limestone can provide avenues for recharge and groundwater flow to the down-gradient Edwards aquifer.

A helicopter electromagnetic (HEM) was flown of both Camps Bullis and Stanley to map and image subsurface features important in the understanding of the geologic framework and groundwater resources (Smith and others, 2005). The HEM system used five horizontal coplanar coils and one vertical coaxial coil for electromagnetic field measurements in a frequency range from 400 to over 100,000 kHz (Smith and others, 2005). The flight lines were flown at 100- and 200-m spacing, varying based on areas of interest (Figure 1). Results from the HEM survey helped refine the location of mapped faults and suggested unmapped faults in the area. In addition, the HEM survey provided more detailed mapping information on the hydrostratigraphy. In particular, thin limestone units of the upper Glen Rose not mapped in the previous geologic studies were mapped as thin, electrically resistive units in the high-frequency (115, 000 Hz) apparent resistivity maps. A geological and geophysical map for a small area in the junction of Salado and Lewis Creeks is shown in Figure 3. Hydrostratigraphic unit D is mapped in Salado Creek and is electrically resistive (red zones). Hydrostratigraphic unit C, exposed above the creek, is composed of yellow-to-white calcareous mud and vuggy mudstone and is characterized by moderate resistivities (greens in Figure 2). Higher resistivity zones (yellows) characterize hydrostratigraphic unit B.

.

The ground geophysical surveys consisted of time-domain electromagnetic (TDEM) soundings, capacitively-coupled (CC) resistivity profiling, and magnetic resonance soundings (MRS). The surveys were collected near the intersection of Salado and Lewis Creeks (Figure 1). Seven TDEM soundings were used to identify variations in the electrical resistivity of the subsurface (Figure 2). These TDEM soundings can be interpreted to map subsurface changes in the physical and chemical properties of soil, rock, and pore fluids. The soundings were done utilizing both 50-m and 100-m transmitter-loop sizes. The survey defines the thin, electrically resistive limestones that are within hydrostratigraphic unit B. Note that the resistivity expression of this unit is somewhat different on the east side of Salado Creek as suggested from the HEM survey. The CC resistivity data were acquired with an Ohm-mapper system[1] via a towed array pulled behind an all-terrain vehicle (ATV) (red line in Figure 1). The system was configured using 10-m dipole lengths and a rope length of 5 m and 15 m. The resultant towed array length is on the order of 50 m. The data was processed to give the resistivity depth section shown in Figure 4.

Two different magnetic resonance sounding (MRS) systems were used to collect ten soundings throughout the study area (Figure 1). The first set of soundings was done with a Numis[1] System (same location as TDEM soundings in Figure 1) in July of 2006. A second set of soundings was done in January of 2008 with a Clara Vista[1] system (black circles in Figure 1). Measures were taken to reduce effects of environmental noise, which is quite high in places on the military base. Figure 5 shows the pulse moment for both surveys, which shows scatter related to environmental and system noise. High-quality MRS data were acquired because of a favorable signal-to-noise ratio at the selected MRS sites. The maximum depth of exploration was determined to be approximately 50 m, which was limited by the size of the antenna loop used. Figure 3 shows the interpreted percent water estimated from soundings at site P1S1 from both magnetic resonance systems, each of which showed two water-bearing zones at different depths and with varying water content. In July of 2006 the water levels were extremely low due to an extended drought. The interpreted percentage of water content is below 5%. By January of 2008 after a very wet year, the water levels had increased to near normal. The second set of data has an interpreted percentage of water between 20 and 25%. Thus, the variations in both depth and amount of water might be the result of seasonal water-content variations.

Conclusions

Ground electrical geophysical surveys generally compare well with the HEM airborne survey resistivity-depth sections and map the hydrostratigraphic units in greater detail than the airborne survey. Both the HEM inversion and CC resistivity data show a near-surface resistive unit on either side of Salado Creek. The grid spacing of the airborne data is on the order of 50-m whereas the grid spacing for the CC data is about 1 m. Thus, resolution of the contacts between electrically resistive and conductive units can be mapped in greater detail to a depth of 5 to 10 m using the CC ground geophysical system. Additional CC survey lines in key areas would help to locate contacts for geologic or hydrologic models. The TDEM soundings map much deeper electrical variations than the HEM survey. Interpreted resistivity-depth soundings define electrically resistive reefal units of the lower Trinity aquifer at depths greater than 60 m below Salado and Lewis Creeks. Preliminary interpretation also suggests that the TDEM soundings may be able to map the contact between the Lower Trinity Aquifer and the Bexar Shale Member confining unit. The MRS surveys very generally map shallow water-bearing zones with variations in depth and the amount of water present. Variation in the MRS data taken at the same site in 2006 and 2008 is attributed to variations in the water levels.

.

==========

[1] Any use of trade, product, or firm names is for descriptive purposes only and does not imply endorsement by the U.S. Government.

References

Ashworth, J.B., 1983, Ground-water availability of the Lower Cretaceous Formations in the hill country of south-central Texas: Texas Department of Water Resources Report, 273 p.

Clark, A.K., 2003, Geologic framework and hydrogeologic characteristics of the Glen Rose Limestone, Camp Bullis Training Site, Bexar County, Texas: U.S. Geological Survey Water-Resources Investigations Report 03-4081, 9p., 1 pl.

Smith, B.D., Cain, M.J., Clark, A.K., Moore, D.W., Faith, J.R., Hill, P.L., 2005, Helicopter Electromagnetic and Magnetic Survey Data and Maps, Northern Bexar County, Texas, U.S. Geological Survey, Open-File Report 05-1158, 24p.

.

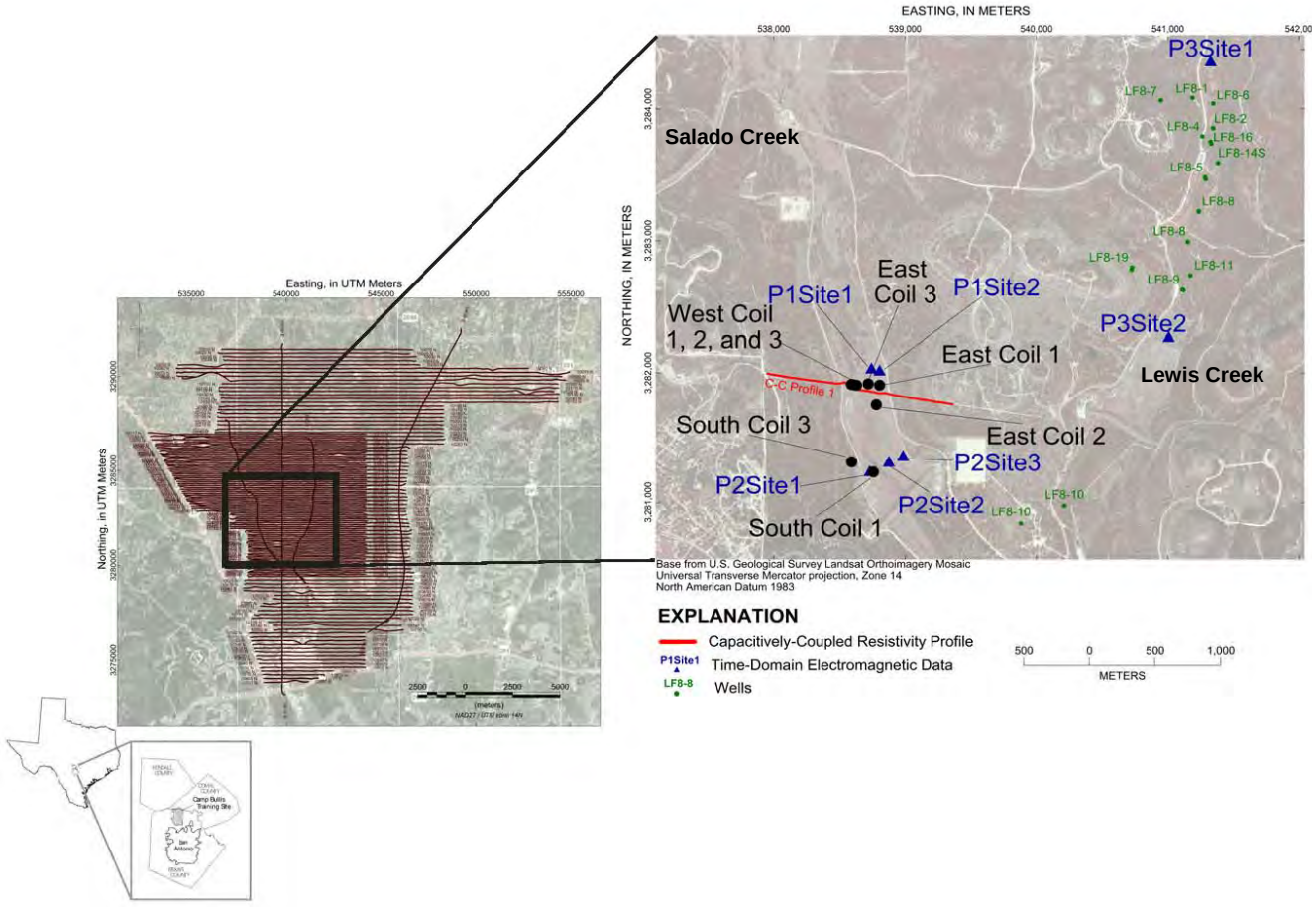

Figure 1. Index map showing flight lines (left) with 200 m and 100 m spaced lines. Detailed study area near Salado and Lewis Creeks shown on right. Red line is capacitively coupled resistivity survey line, black dots are locations of time-domain electromagnetic soundings, and blue triangles are locations of magnetic resonance soundings.

.

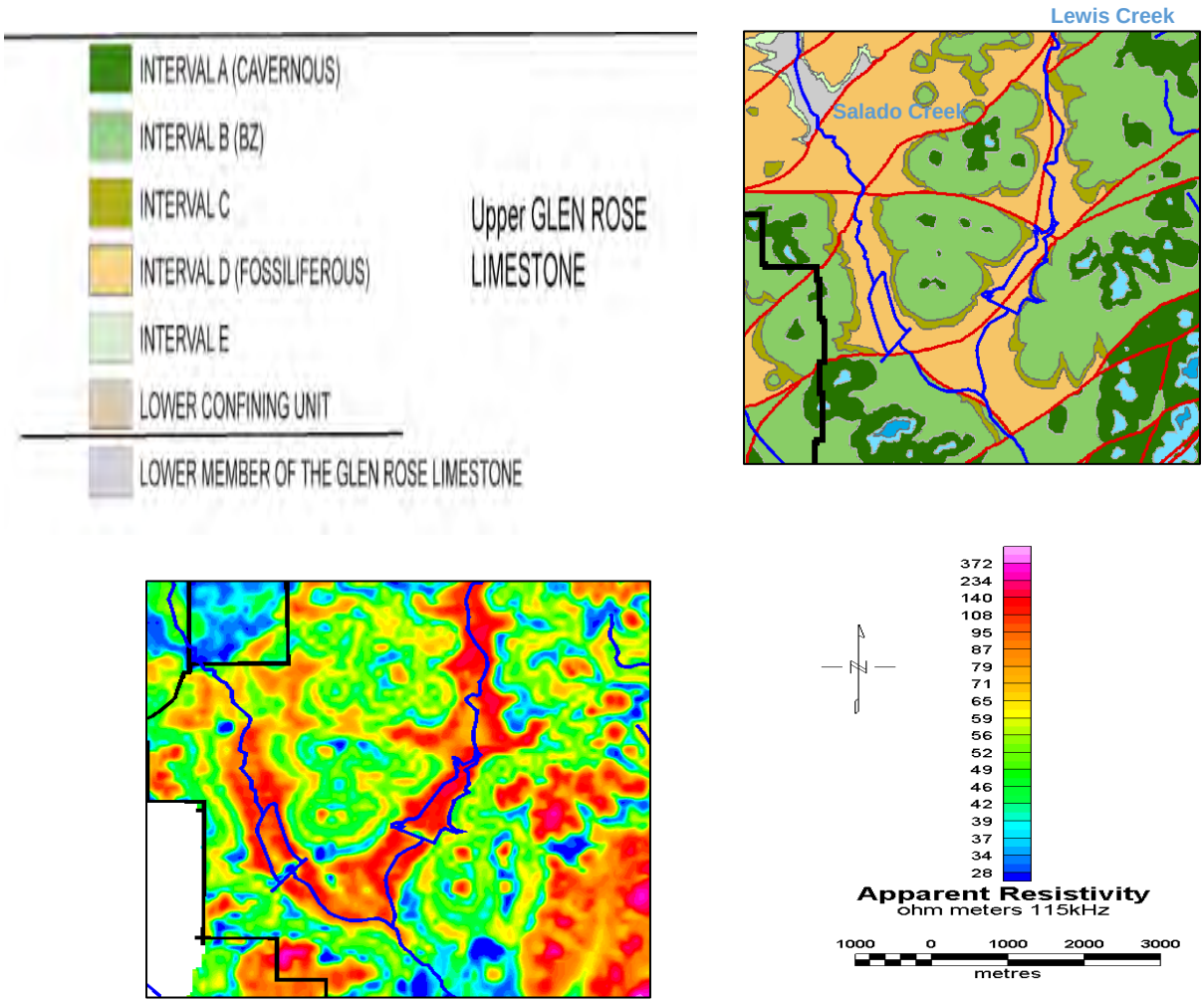

Figure 2. Hydrogeologic map (upper panel) of the ground geophysical survey study area near the junction of Lewis and Salado creeks (blue lines). The hydrogeologic map adapted from Clark (2003) shows different hydrostratigraphic units defined on the left. HEM apparent resistivity map for 115,000 Hz is shown in the bottom panel for the same area as the geologic map in the upper panel.

.

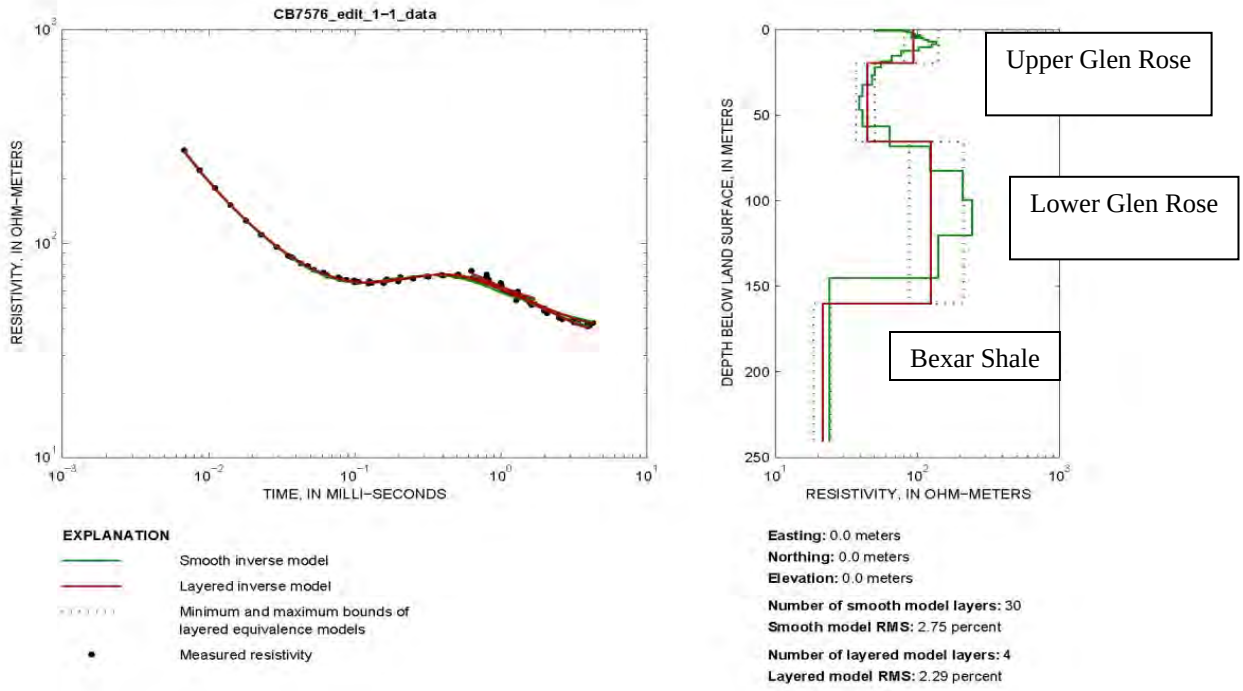

Figure 3. Time-domain EM sounding P1S1 collected in Lewis Creek. Sounding data is shown on the left. Inversion results for resistivity-depth models are shown on right for a multilayer model (green) and a simpler layered model (red). Interpreted geologic units are shown.

.

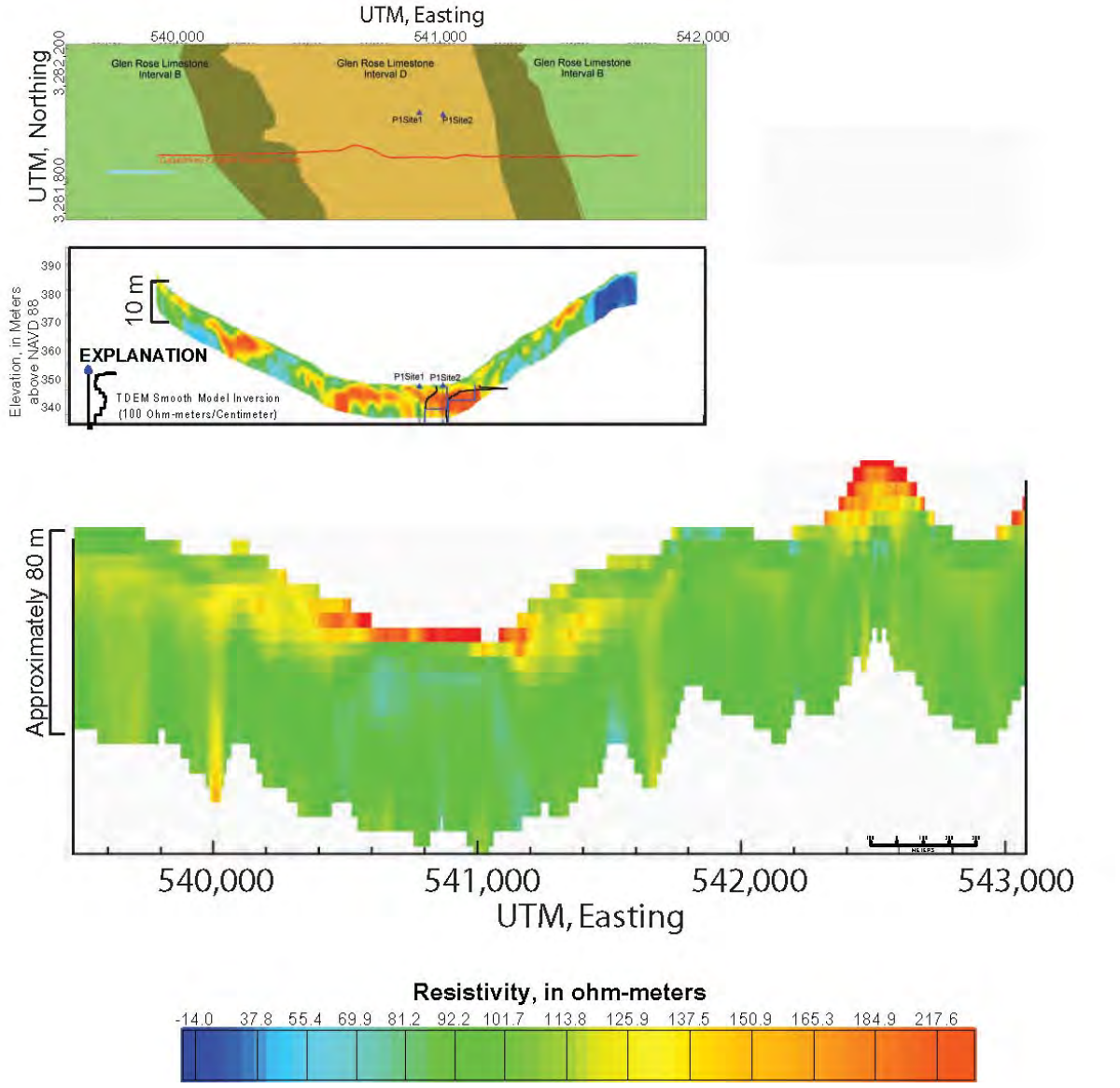

Figure 4. Top panel is location of capacitively coupled (CC) resistivity line shown on detailed geologic map (Figure 3). Middle panel shows details of CC resistivity depth section with time-domain sounding interpreted depth section. Bottom panel shows HEM flight line 10500 resistivity-depth section across Salado Creek.

.

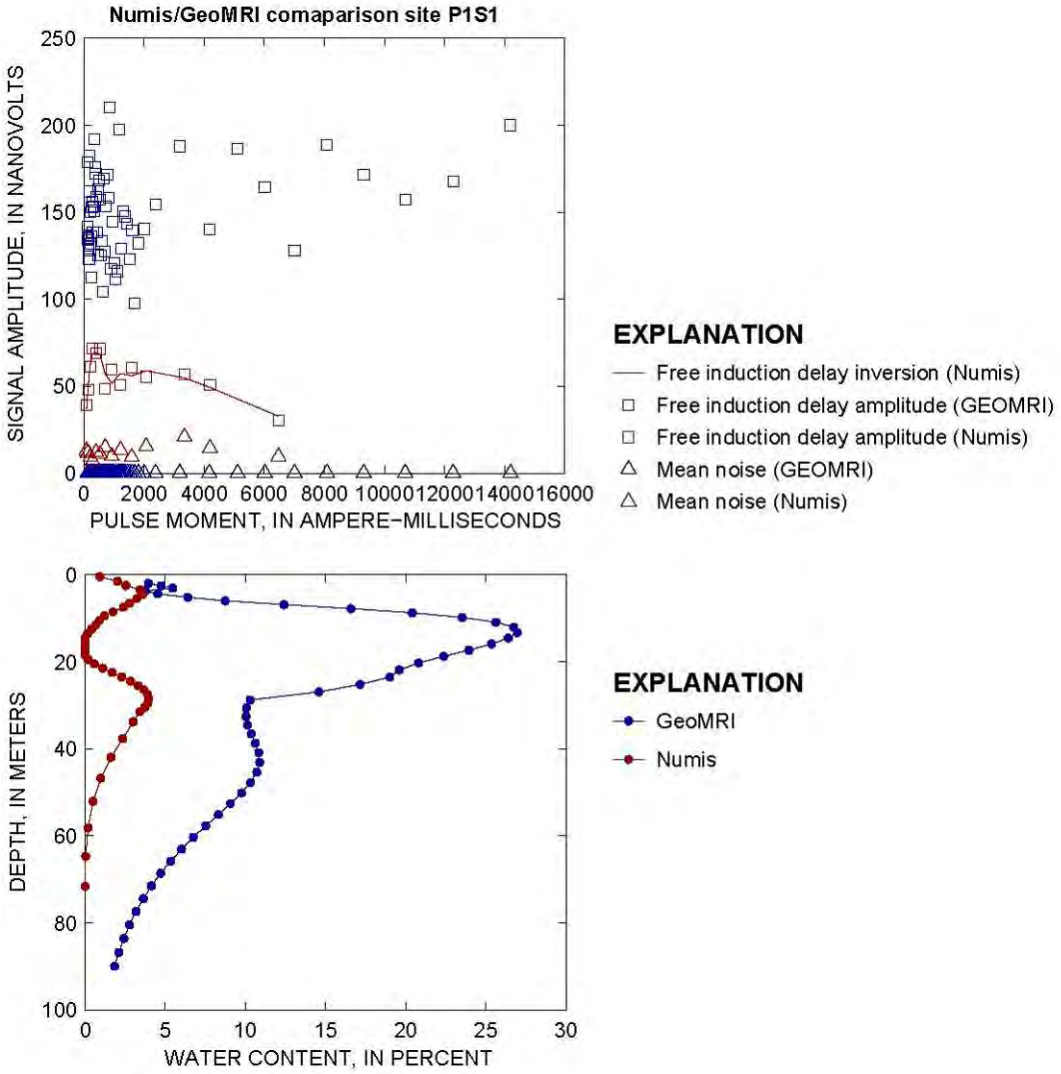

Figure 5. Magnetic resonance sounding (MRS) at site P1S1 located in Salado Creek. Top panel is the field MRS data pulse moment showing an increase in amplitude of the 2008 data (blue). Bottom panel are the inversion results for interpreted water content as a function of depth for the 2006 and 2008 MRS data.

.

SUBSURFACE IMAGING OF KARST GEOLOGY FOR ENERGY INFRASTRUCTURE EXPANSION

John A. Mundell, Mundell & Associates, Inc., Indianapolis, IN
Gabriel J. Hebert, Mundell & Associates, Inc., Indianapolis, IN

Abstract

The development of building infrastructure on top of karst geology always presents challenges and has the potential for catastrophic failure. Recently, an electrical substation located in southern Indiana known to sit atop potentially karstic limestone was scheduled to be expanded onto an adjacent 10-acre parcel. A standard preliminary geotechnical investigation consisting of 18 soil borings with three rock cores conducted across the parcel indicated that although the bedrock was slightly to moderately fractured, it was sufficiently competent to build upon. However, the presence of several active sinkholes across the parcel led the local electrical power company to request a more thorough, geophysical investigation of the bedrock. For this project, a preliminary terrain conductivity survey was performed to yield information regarding the thin residual soils and shallow bedrock, followed by two-dimensional resistivity profiling to detect any karst features deeper within the bedrock. The end result of the geophysical study gave the structural engineer and his client what they wanted - greater assurance that they had exercised diligence in their efforts to define site conditions and avoid hazards.

Introduction

It is commonly known by geotechnical and structural engineers that building on top of karst-prone limestone can prove disastrous if potentially hazardous features are not recognized prior to final design and construction, and dealt with appropriately. Given the recent interest and funding available to update and expand the nation's energy infrastructure, this preliminary due diligence is critical to the portions of the country affected by solution-prone limestone. As it is, southern Indiana is one of those areas. Recently, our company was contacted by a local electrical company in southern Indiana, to use geophysical methods to detect and map out karst features in the limestone bedrock beneath the proposed site of a power substation expansion. Prior to contacting us, another engineering consultant had recently performed a preliminary geotechnical investigation of the site consisting of advancing 18 random soil borings to bedrock, three of which were cored up to 10 feet into the bedrock. Although the rock cores indicated that the limestone in those areas were slightly to moderately fractured, the report concluded that soil and bedrock were sufficiently sound enough to build upon. However, an employee of the electrical company recalled that a cave had been detected during the construction of the original substation. Additionally, several active and developing sinkholes were present within the expansion area, just south of the proposed structure footings. For these reasons, the electrical company decided that a more in depth subsurface investigation was necessary.

Figure 1: Site Location Map. Ramsey is 20 miles west of Louisville, KY.

Site Description and Geology

The project site is located in Harrison County near the town of Ramsey, Indiana, approximately two hours due south of Indianapolis and thirty minutes west of Louisville, Kentucky (see Figure 1). At the time of the geophysical investigation, the site consisted of about 10 acres of agricultural land. There is approximately 20 feet of relief across the site, which slopes from west to east.

Ramsey, Indiana is located within the physiographic region known as the Mitchell Plateau. The soil in this part of the state is classified as the Baxter loam, and it is underlain by middle Mississippian limestone, specifically of the Sanders and Blue River Groups, which is highly susceptible to solutioning (Fenelon and Bobay, 1994). Karstification occurs when carbonic acid (H_2CO_3) from atmospheric carbon dioxide and rainwater, percolates downward into subsurface waters and dissolve carbonate bedrock. This process continues enlarging fractures into cavities that may collapse, causing a sinkhole. Karst, or karst geomorphology, is evidenced by numerous closed depressions, sink holes, karst windows or unroofed caves, springs, and cave openings, all of which are present in this portion of Indiana (Unterreiner, 2006). Within mature karst systems, surficial depressions are caused by the dissolving (or solutioning) of underlying carbonate rocks along existing joints and fracture systems that result in enlarged void spaces. Subsequently, the loss of shallow soils occurs as surface water infiltration is directed to these void spaces and the soil is swept into them through the resulting groundwater movement through fractures zones (see Figure 2).

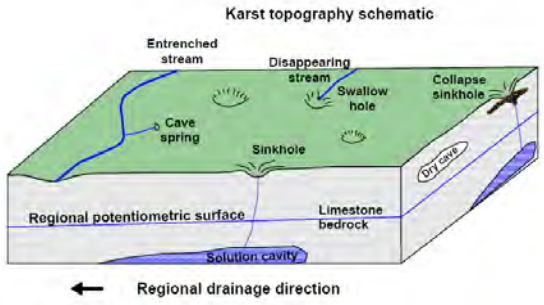

Figure 2. Karst Topography Features

Technical Approach

In cases such as this Site, where karst features are known to exist, geophysical mapping can provide insight into the locations of concealed features such as sinkholes, solution-enhanced fracture zones, and voids. In general, a variety of geophysical techniques can be applied to the mapping of subsurface karst features; however, certain methods, sensitive to a range of contrasting physical properties, can have attributes that make them more suitable than others depending on the site-specific conditions. Contrasting physical properties that typically are found to be useful for mapping soil and bedrock include electrical conductivity or resistivity, acoustic velocity, density, and magnetic susceptibility. Of these, electrical conductivity/resistivity has often been found to have the greatest range of contrast, and is often applicable to karst sites.

The technical approach used for the case history presented here is similar to the multi-step approach taken by Ahmed and Carpenter (2001) and Byer et al. (2002). It begins with reconnaissance mapping with terrain conductivity to form a basic understanding of the soil and bedrock relationships in terms of apparent conductivity or resistivity, preferably at a few depth levels. The interpretive emphasis is directed towards potential air or fluid filled voids and solution-enhanced features, which could contain underconsolidated soils (*i.e.*, materials with high moisture content and low shear strength). Interpretation of the terrain conductivity data is then supplemented with two-dimensional electrical resistivity imaging (2-D ERI) within the context of the interpreted terrain conductivity data. Finally, the terrain conductivity and 2-dimensional resistivity data are interpreted together and a final geologic model is developed. This approach, applied to the subject site, and other sites, has proven to be a useful tool in the investigation of karst limestone (Byer et al., 2002). It has been shown to be relatively rapid

and cost effective while still providing a reasonable degree of assurance to the geotechnical engineer that significant karst features have been addressed. A brief description of these two techniques is presented in the sections below.

Preliminary Terrain Conductivity Mapping

The approximate study area dimensions were 825 feet by 575 feet. Given the large area of the site (approximately 10 acres), it was determined that a preliminary conductivity survey would be conducted to delineate soil variations, yield insight into the upper most weathered bedrock layer, and guide the layout of the vertical resistivity profiles. For this investigation, a *Geonics EM-31* electromagnetic terrain conductivity meter was used. This instrument can gather apparent conductivity data at a relatively rapid pace without the need for direct (galvanic) ground contact, making it economical and efficient for covering large areas.

To assure that the *EM-31* was operating properly, five instrument checks were made at the start of the day. First, a battery check was made to ensure proper supply voltage over the duration of the survey. Second, a DC null adjustment was made to verify the zero position of the receiver circuitry. Third, a compensation check was made to verify the zero reading of the in-phase component. Fourth, a phase check was made to calibrate the conductivity reading. And finally, a sensitivity check was made to ensure that the instrument was reading as expected. No daily drift correction was necessary with this instrument.

Conductivity data was collected by securing the *EM-31* to a rigid plastic sledge and towing it behind an all terrain vehicle, collecting electrical conductivity data nearly continuously. *EM-31* data were collected along lines spaced approximately 1.5 to 3 meters (approximately 5 to 10 feet) apart with an in-line data point spacing of 0.3 to 1 meter (approximately 1 to 3 feet), depending on the speed of the instrument. Positioning data were provided by a *Trimble Ag114* global positioning system (GPS) receiver with real-time satellite based differential correction. GPS and conductivity data were simultaneously recorded in a handheld field data logger. The data stored in the data logger were in the form of apparent conductivity in milli-Siemens per meter (mS/m). However, this data was

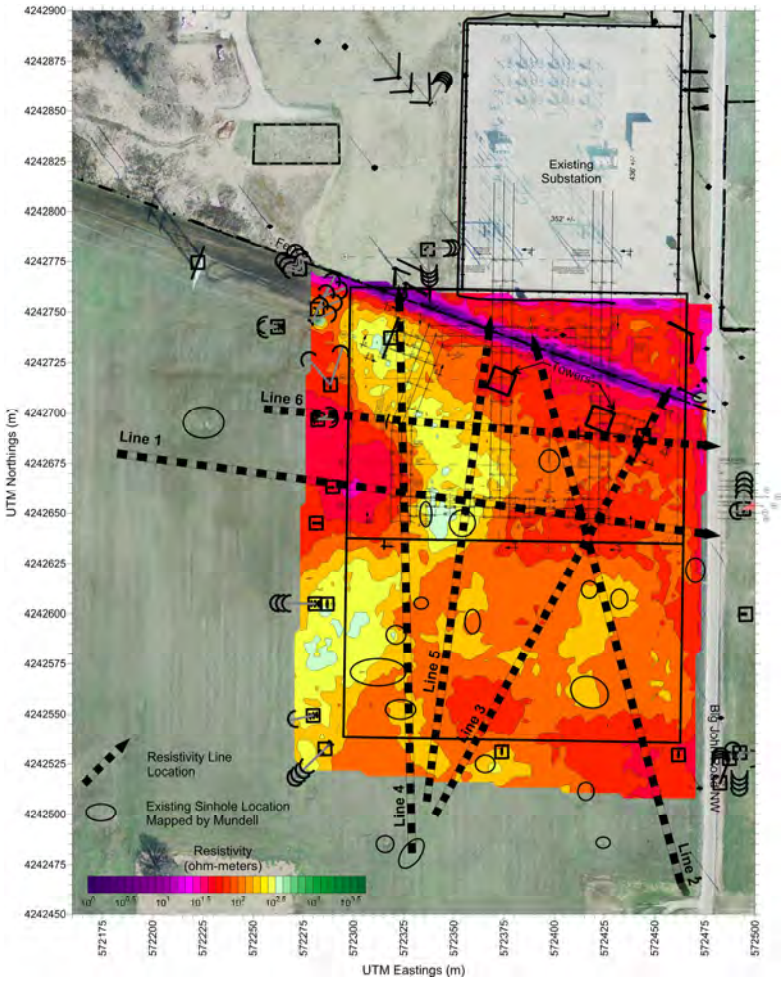

Figure 3: EM-31 Map. The data here are presented in ohm-meters, with a logarithmic color scale. The values detected range from 1 to 300 ohm-meters. A basemap of proposed substation features is overlying the EM-31 map.

later converted to apparent resistivity for mapping purposes and comparison to the 2-D ERI results by inverting the apparent conductivity data and multiplying by 1000. The resulting apparent resistivity data are in units of ohm-meters. Once the data were converted, they were imported into *Surfer* V*ersion 8.0* for contouring and plotting as a color-filled contour map of terrain resistivity (see Figure 3).

Two-Dimensional Electrical Resistivity Profiling

After the conductivity had been processed, revealing the variable, weathered-bedrock surface, the site was further investigated with 2-D ERI using a *Sting Resistivity Imaging System* from Advanced Geosciences, Inc. This method consists of recording direct measurements of the apparent electrical resistivity of subsurface materials *(i.e.*, resistivity of homogeneous isotropic ground that would give the same voltage-current relationship as that measured) in a profile-type data set known as an apparent resistivity pseudo-section. Once the apparent resistivity data were collected, they were downloaded to a computer and were subsequently inverse-modeled using the software *EarthImager 2D v1.9.9* to obtain a cross-section of the "actual" resistivities of subsurface materials. This is accomplished through the process of generating a model resistivity cross-section, calculating the theoretical apparent resistivity pseudo-section that would result from such a model, and comparing the theoretical pseudo-section to the one collected in the field. The model is then altered through a number of iterations until the theoretical and field-collected pseudo-sections closely match each other. At this point the model is considered to be a reasonable estimation of the "actual" resistivities of the subsurface materials.

Electrical resistivity (and its inverse, conductivity) is one of the most widely varying of the physical properties of natural materials. Certain minerals, such as native metals and graphite, conduct electricity via the passage of electrons; however, electronic conduction is generally very rare in the subsurface. Most minerals and rocks are insulators, and electrical current preferentially travels through the water-filled pores in soils and rocks by the passage of the free ions in pore waters (*i.e.*, ionic conduction). It thus follows that degree of saturation, interconnected porosity, and water chemistry (*i.e.*, totally dissolved solids) are the major controlling variables of the resistivity of soils and rocks. In general, electrical resistivity directly varies with changes in these parameters. Fine-grained sediments, particularly clay-rich sediments such as glacial till, are excellent conductors of electricity, often much better than fresh water found in the pores of sand and gravel. Carbonate rocks (*i.e.*, limestone and dolomite) are very electrically resistive when they are unfractured, but can have significantly lower resistivity values when fractured and/or solutioned.

For this geophysical investigation, a total of six (6) resistivity profiles were collected, utilizing both a 56 and a 60 electrode spread, and a dipole-dipole configuration to characterize the electrical properties of the upper 55 to 60 meters of the subsurface. It should be mentioned that resistivity cross sections are 2-dimensional representations of the general distribution of electrical resistivity in the 3-dimensional subsurface. Although there is no unique direct conversion from resistivity values to lithology, based on site knowledge, geometric shapes and relationships of various anomalies, and the observed ranges of resistivity values, reasonable geologic interpretations can be made. The interpretations of this survey are presented in the section below.

Interpretation

The *EM-31* results (Figure 3) show the apparent resistivity of the upper approximately 5 meters (approximately 16.5 feet) of the subsurface. The *EM-31* data is a reflection of the conditions in the relatively shallow subsurface materials (*e.g.*, generally overlying residual soils, or shallow upper competent/weathered bedrock). Resistivity variations on this map reflect variations in the depth to

bedrock as well as changes in porosity, moisture content, fracture density, clay content, and void space material. The lowest resistivity values, *i.e.*, approximately 45 ohm-meters and below, are interpreted as thicker soil layers that may also be higher in moisture content and/or clay and silt (presented as magenta to purple in color), except where metallic objects (fences and power line towers) have been noted. In upland areas these thicker soils are often moist, lower strength materials, which are not recommended for large structure foundations with high bearing pressures. The moderate resistivity values (45 to 130 ohm meters – red to orange in color) are interpreted to be thicker layers of coarser-grained clayey soils with an increased sand content. While this type of soil is typically preferable to build upon, it should be noted that these values occur in areas containing existing and developing sinkholes. This is likely because a large percentage of the fine-grained soils have been lost to the karst features. Finally, the moderate to high resistivity values, *i.e.* approximately 130 to 300 ohm meters (yellow to light green) are interpreted as the uppermost weathered bedrock layer. Essentially, these values show where the bedrock is shallowest across the site.

The six inverted and interpreted 2-D resistivity profiles collected are summarized on Figure 4. The resistivity values modeled, range from 1 (purple in color) to 4,500 Ohm-meters (dark green). In

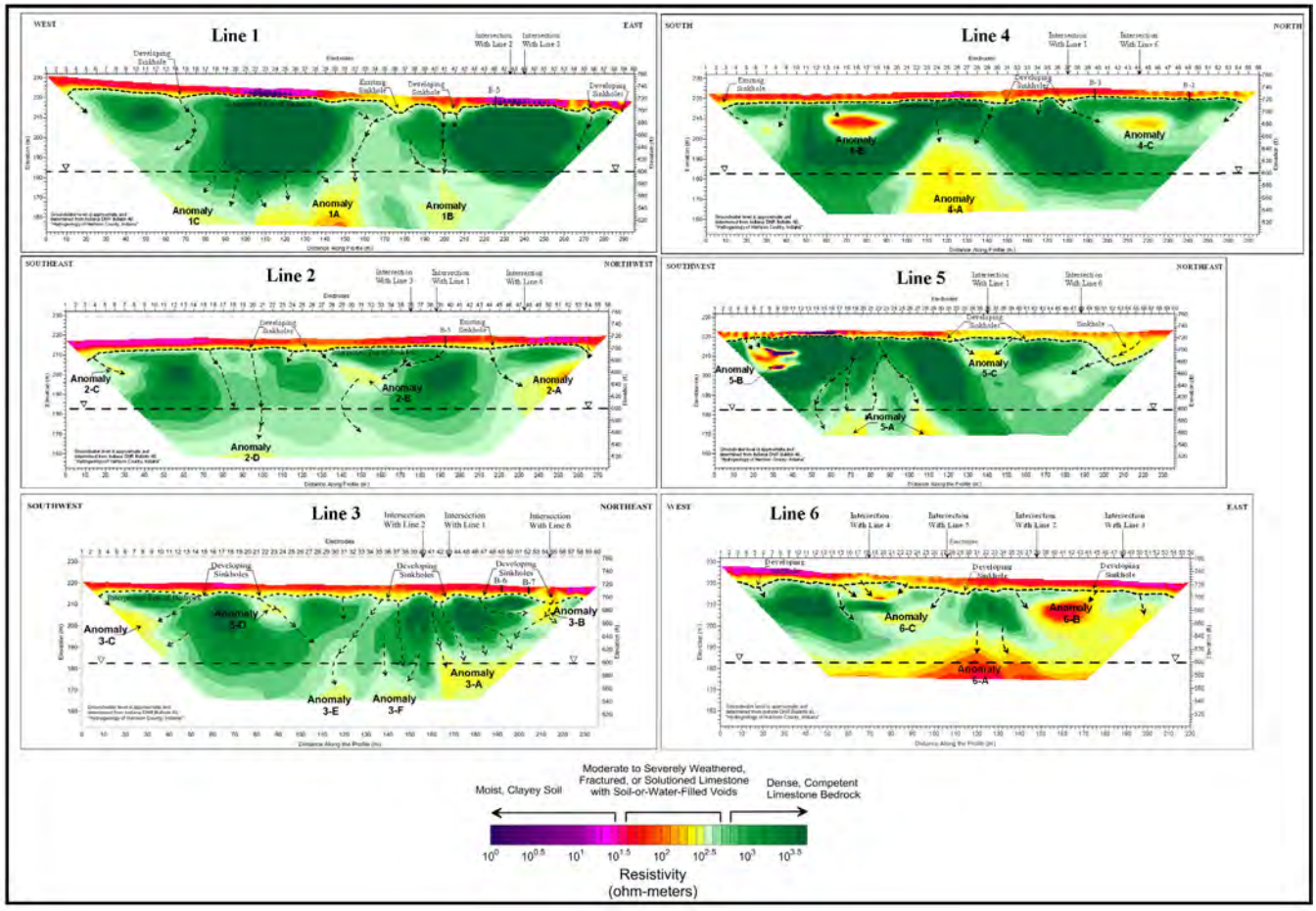

Figure 4: Vertical Resistivity Profiles. The data here are presented in ohm-meters, with a logarithmic color scale. The short dashed lines show the interpreted top of bedrock surface, whereas the longer dashed lines with arrows show possible flow pathways through the rock.

general, the cross-sections are quite similar: the upper 3 to 5 meters (10 to 16 feet) consists of an

inhomogeneous assortment of low (purple to pink) to moderately high (red to yellow) resistivity materials which are correspondingly interpreted as, from low to high, clay and silt to coarse sand and gravel. These unconsolidated materials lie directly on top of a moderate to high resistivity material, which is interpreted to be the Paleozoic bedrock. The highest resistivity bedrock is interpreted to be relatively competent, massive limestone or dolostone bedrock (dark green color), while the moderately high resistivity bedrock (red to light green color) is likely fractured carbonate bedrock, with the lower end values possibly indicating soil and/or water filled features. It should be noted that the lower resistivity soils appear to overlie the competent rock, while the higher resistivity soils generally overlie existing and developing sinkholes. This supports the theory implied by the conductivity data, that the finer-grained soils across the site are being lost to subsurface features, which suggests active karst development.

After the individual resistivity profiles were processed, they were compiled into a three-dimensional data set, and several lateral (*i.e.*, constant elevation) resistivity slice maps were generated in attempts to better understand the lateral and vertical location of active and developing karst features, and how they relate to the proposed building plans. Resistivity slices taken at elevations 700 feet, 680 feet, 660 feet, 640 feet, 620 feet, and 600 feet elevations are presented respectively as Figure 5. A comparison of these slices reveals that while the majority of the substation expansion appears to overlie mostly competent bedrock, approximately 20 to 30 percent of the proposed structures lie on top of highly weathered/fractured bedrock. In addition to the proposed structures, one of the existing power line towers (located in the northeast portion of the

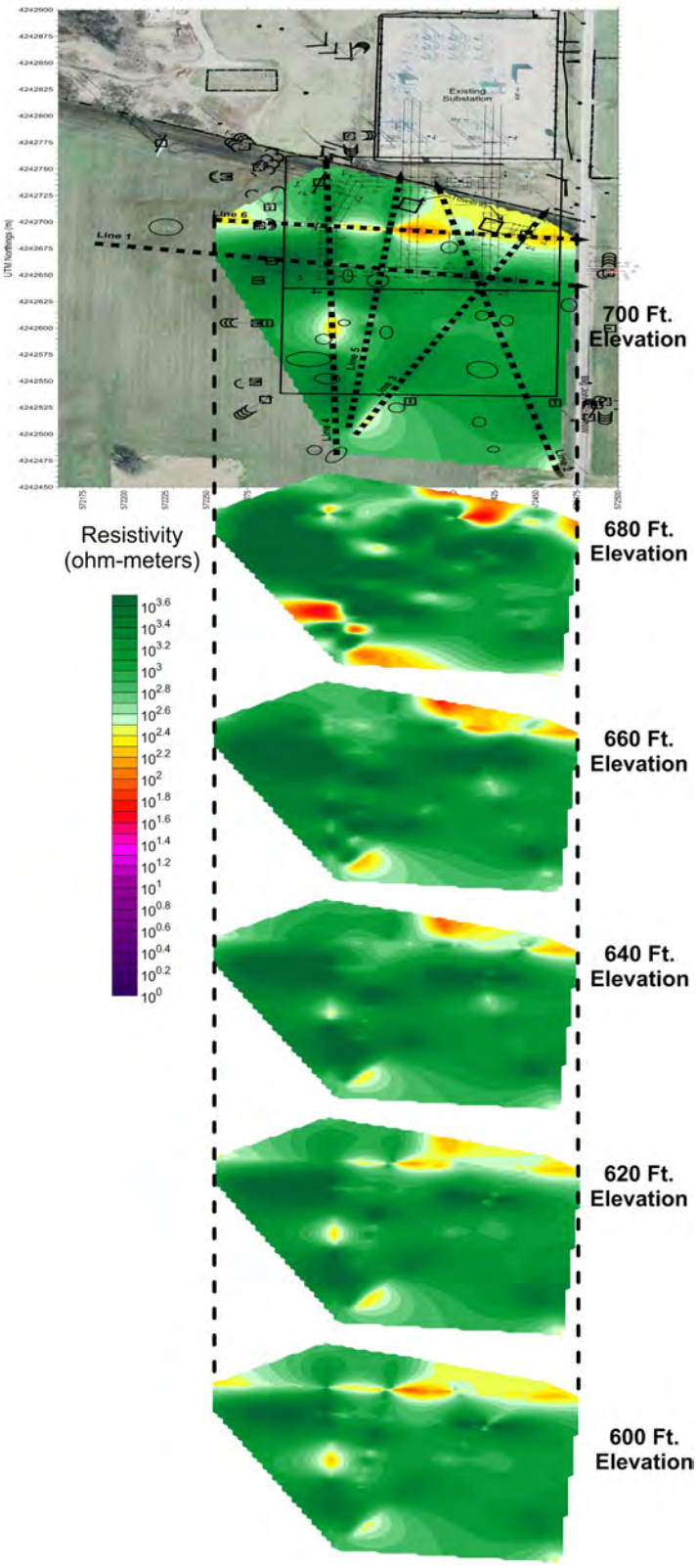

Figure 5: Constant Elevation Resistivity Slices. The data here are presented in ohm-meters, with a logarithmic color scale.

survey area) is located directly on top the most pronounced karst feature on the site.

Finally, in addition to the slice maps, all of the data gathered across the site was utilized to generate a map summarizing the degree of karst development across the site (Figure 6). As shown on the figure, the site has been segregated into the following classifications: low, shallow karst development (consists of dense, competent limestone likely present beneath residual clay soils at depths of less than 25 ft); moderate, shallow karst development (with weathered/ fractured/solutioned limestone beneath residual clayey/sandier soils at depths of less than 25 ft); and severe shallow karst development (characterized by severely weathered/fractured/solutioned limestone with clay soil in-fill and/or potential for small voids within the upper 25 ft). Essentially, this map showed the client which portions of the proposed expansion project were most susceptible to failure and required additional engineering measures to ensure the stability of the structures.

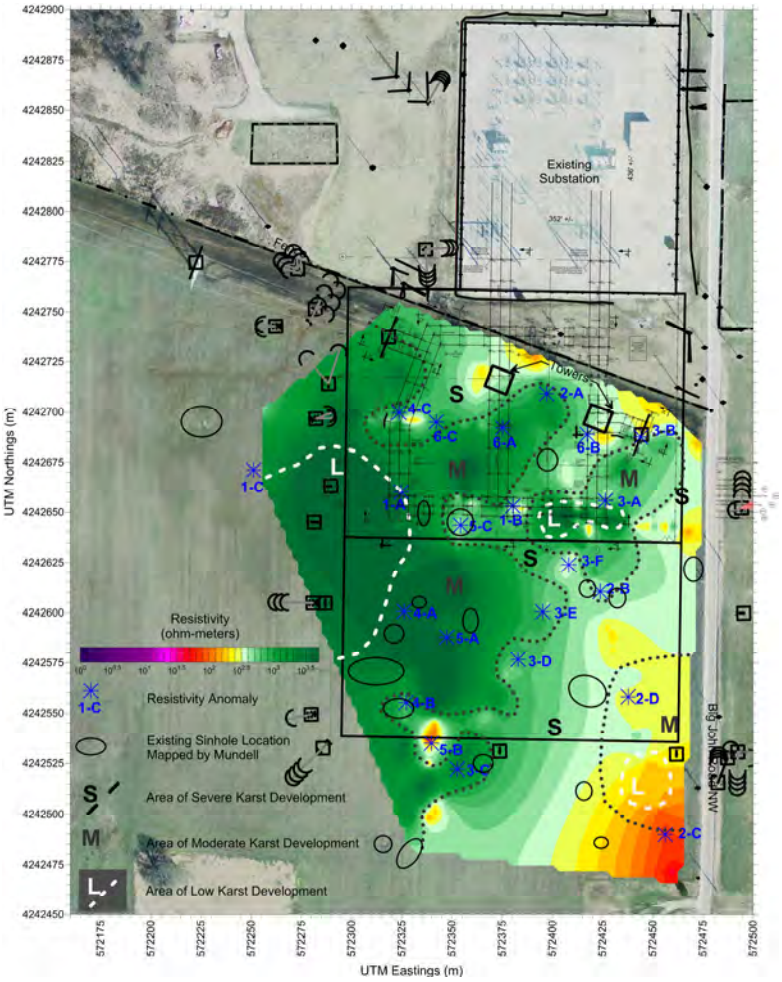

Figure 6: Karst Development Summary Map. This map summarizes the level of karst development across the site. As before, the data here are presented in ohm-meters, with a logarithmic color scale.

Summary and Conclusions

The geophysical consultant was confronted with the challenge of limited resources and a large, 10-acre project site. A solution was required which conformed to these restrictions while still providing the electrical power company with an acceptable level of assurance that a reasonable effort had been made to detect critical karst features.

To provide this assurance to the client, a combination of terrain conductivity mapping on a relatively tight spacing and 2D-ERI were implemented on this project. The resulting data were synthesized with regional data to develop a conceptual geologic model that was used as a tool to aid the company and the structural engineer responsible for the expansion project.

In conclusion, several key observations were provided to the client regarding the site in relation to the possibility of infrastructure expansion. First, the site is indicative of a typical highly-developed, karst terrain, with nineteen (19) sinkholes observed at the surface over the survey area. The position of the observed sinkholes correlated well with the conductivity and resistivity data. Also, these observed sinkholes appeared to be in active development, based on the detected weathered/solutioned zones emanating from them leading to deeper karst features, as well as the evidence of shallow fine-grained soil loss. While a substantial area of the proposed structural foundation features appeared to be

positioned on top of competent or moderately weathered bedrock, several areas needed to be further examined and redesigned for the possibility of loss of support or the need for substantial grouting measures. Had the client not realized these shortcomings in the foundation support from the benefit of a preliminary geophysical survey, expansion of the infrastructure without regard to these conditions could have lead to a catastrophic foundation failure.

References

Ahmed, Shawkat and Philip J. Carpenter, 2001, "Integrating Electrical Geophysical Surveys and Subsurface Probing to Locate Karst Aquifer Recharge Features, Northern Illinois" , *Proceedings of the Symposium on the Application of Geophysics to Engineering and Environmental Problems, Denver, Colorado, March 4-7, 2001, Paper ASP-1.*

Byer, G. B., Mundell, J. A. and Vanderlaan, J. H.M., 2002, A Geotechnical/Geophysical Evaluation of Karst Limestone Sites - A Case History, In Proceedings: SAGEEP 2002, Environmental and Engineering Geophysical Society, February, Los Vegas, Nevada, Paper 13CAV2.

Fenelon, J.M, and Bobay, K.E., 1994, Hydrogeologic Atlas of Aquifers in Indiana, USGS, Water Resources Investigations Report 92-4142, pp.6-9.

Unterreiner, G.A., 2006, Hydrogeology of Harrison County, Indiana, DNR, Bulletin 40, pp.5-8.

URBAN GEOPHYSICS: A MAPPING OF MOUNT BONNELL FAULT AND ITS KARSTIC FEATURES IN AUSTIN, TX

Mustafa Saribudak, Environmental Geophysics Associates, Austin, TX

Abstract

Although most karstic regions are characterized by caves, collapsed features, and sinkholes, such features often do not have surface expressions, and their presence may go unrecorded. Central Texas and the Greater Austin metropolitan area have been built on the karstic limestone (Lower Cretaceous of Glen Rose Formation and Edwards Aquifer) in the Balcones Fault Zone (BFZ), and their growth is expanding. Near-surface karst features in the Austin area have a profound effect upon geotechnical engineering studies, such as structural foundations (residential buildings, shopping malls), utility excavations, tunnels, pavements and cut slopes. Thus the practice of geotechnical engineering is and has been a challenging proposition in the Austin area.

Geophysical methods are sporadically used to estimate the locations and parameters of these karst features prior to any of these above-mentioned geotechnical studies. Opinions concerning the effectiveness of these geophysical surveys are mixed, and geophysical techniques are not generally recognized as primary tools in engineering-scale studies.

However, remarkable advances in the manufacturing of geophysical instruments over the last ten years have made geophysics a viable tool for geotechnical studies of these karstic features. Data quality has been increased by the advent of continuous data collection. The data are better processed and interpreted by new and improved software packages, which produce improved sub-surface imaging and mapping.

Thus integrated geophysical surveys can provide new insight into the near-surface karstic features in the Glen Rose Formation and Edwards Aquifer. I have conducted geophysical surveys (ground penetrating radar [GPR], resistivity imaging, magnetic [G-858], conductivity [EM-31] and natural potential [NP]) at three locations where the Mount Bonnell fault (MBF) is present, along the northern limiting boundary of the BFZ. Results indicate that all methods successfully imaged significant karst anomalies across the known fault locations. Integration of all these anomalies provides a much better understanding of near-surface geology defined by the caves, voids, collapsed materials, sinkholes and the fault itself.

Introduction

A study of the geologic map of Austin by Garner et., al., (1976) shows that normal faults along the BFZ are some of the main features, if not the primary features, that have shaped the geology and physiography of the city and its environs. At the regional scale, faults have positioned the geologic unit into a framework that juxtaposes contrasting rock, soil, and terrain, thereby establishing a major physiographic boundary: the Balcones Escarpment, which extends through west Austin, separates the Edwards Plateau to the west from the Blackland Prairies of the Gulf Coastal Plain to the east (Collins and Woodruff, 2001). The Balcones escarpment, with a topographic relief as great as 300 feet in Austin, is a fault-line scarp, and consists of normal faults, which dip toward the east and southeast. The BFZ's most prominent fault is the Mount Bonnell fault, which composes the northernmost part of the fault zone

with a throw of near 600 feet. The Lower Cretaceous Glen Rose Formation is at the surface to the west of the MBF, while east of the fault zone younger rocks of Edwards Aquifer are at the surface (Figure 1).

Geophysical methods have been an important component of effective hydrogeological investigations over the Edwards Aquifer. Geophysical surveys employing variety of electrical and electromagnetic methods have been used to successfully map stratigraphy, geologic structure, and depth to the water table in major aquifer systems (e.g., Fitterman and Stewart, 1985; Connor and Sandberg, 2001).

In this study, however, I demonstrate the utility of integrated surveys for the near-surface characterization of the MBF in the Austin area (Figure 2). To my knowledge, this is the first application of integrated geophysical techniques to the characterization of faults, fractures, caves, sinkholes and collapsed features in the metropolitan Austin area. The geophysical surveys were performed at the intersections of: 1) Height Drive and Highway 360; 2) West Park Drive and Highway 360; and 3) Bee Cave Road and Camp Craft Road (Figure 2). Conductivity, magnetic, GPR and NP methods were chosen for their ability to very rapidly map variations of their respective physical attributes (e.g., conductivity, magnetic susceptibility, dielectric contrast and ambient electrical current in miliVolts) within the surface. 2D resistivity imaging surveys were conducted to provide information about variation in electrical resistivity as a function of depth. Results of these surveys are described in the following.

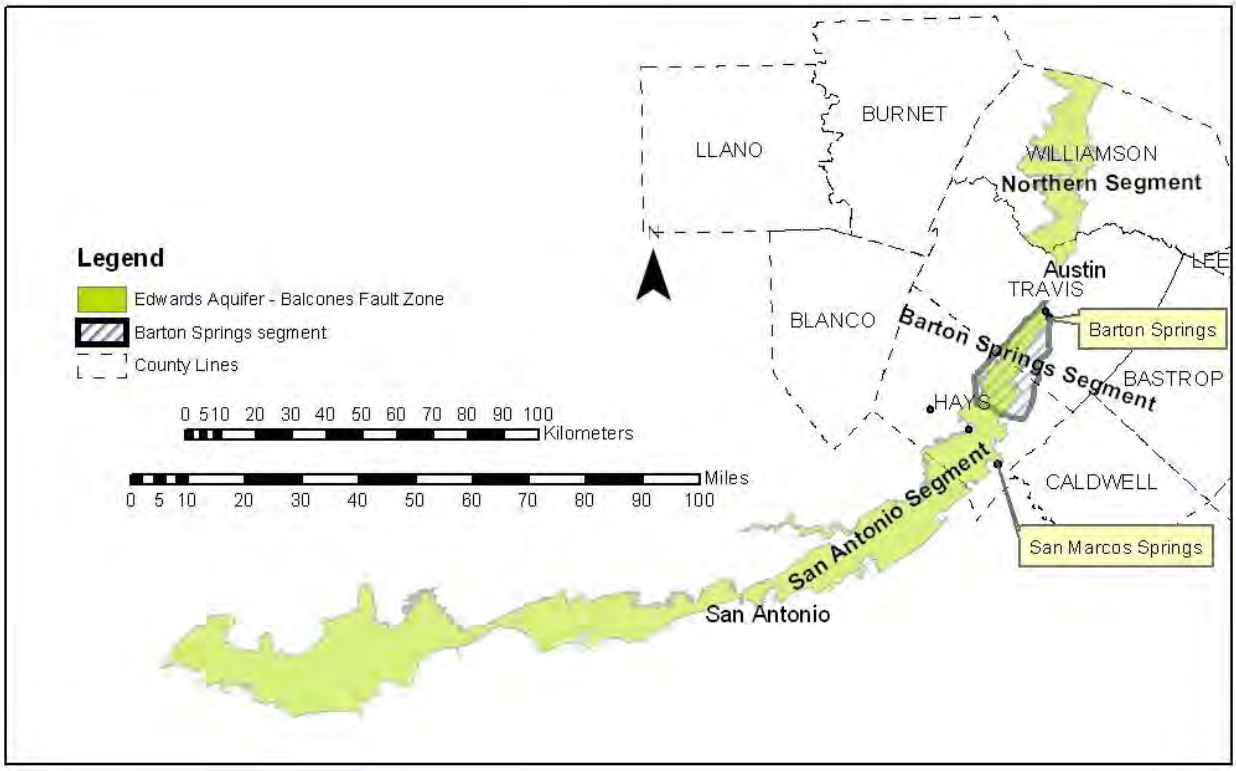

Figure 1: Balcones Fault Zone Portion of the Edwards Aquifer in Central Texas.

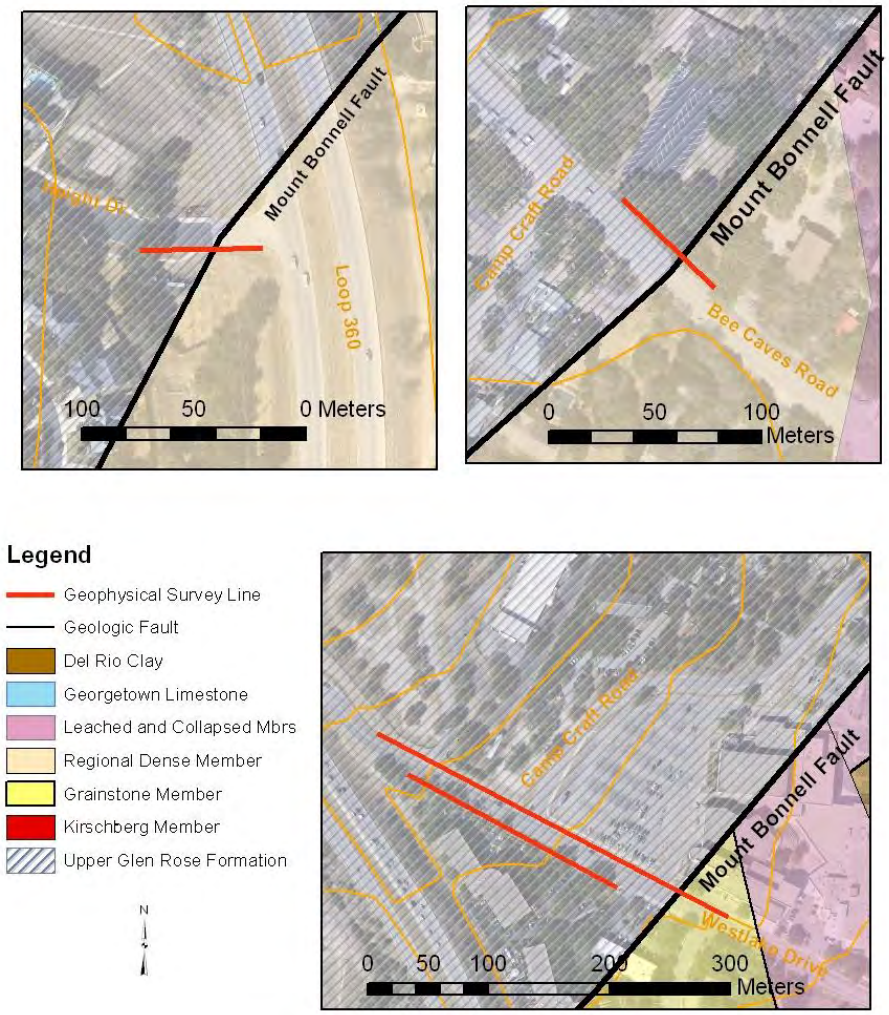

Figure 2: Surface geology of geophysical survey sites. Geologic interpretation modified from Hauwert, 2009 and Rodda et al. (1970) by Nico Hauwert.

Geophysical Results

Height Drive Site at Highway 360

A site map of the study area including the location of geophysical profiles and the MBF is shown in Figure 3. The magnetic and conductivity data are shown in Figure 4. Resistivity and NP data are shown in Figure 5. And 3-D GPR depth slices are given in Figure 6. The magnetic data indicate a high anomaly between the stations at 270 and 290 feet, whereas the conductivity data shows a high and low between the stations at 270 and 310 feet. These anomalies correspond to a very significant resistivity anomaly between stations 280 and 320 feet. The source of the anomaly appears to be the soil-filled material on top of a cave. The rest of the resistivity data between the stations at 320 and 418 feet shows significant resistivity anomalies: Low resistivity values shown in blue branch into higher resistivity values. This type of resistivity anomaly usually is an indicator of cave structures. The NP anomaly

shown in Figure 5, along with the resistivity data show a very significant "sine-wave" shaped anomaly where the MBF is located. In addition, the rest of the NP anomaly shows cave-like anomalies. The 3D GPR depth slices in Figure 6 indicate the trend of the MBF and three underground pipes.

In summary, NP and the GPR data indicate the location of the MBF, which is consistent with the geological data (Hauwert, 2009). The resistivity, NP, magnetic and conductivity data show cave-like anomalies. GPR, magnetic and conductivity data show location of subsurface pipes across the study area. Findings of geophysical surveys are given in Table 1. There is a patched asphalt area on Height Drive where the fault crosses, and the repair on the site may have been necessary because of the near-su

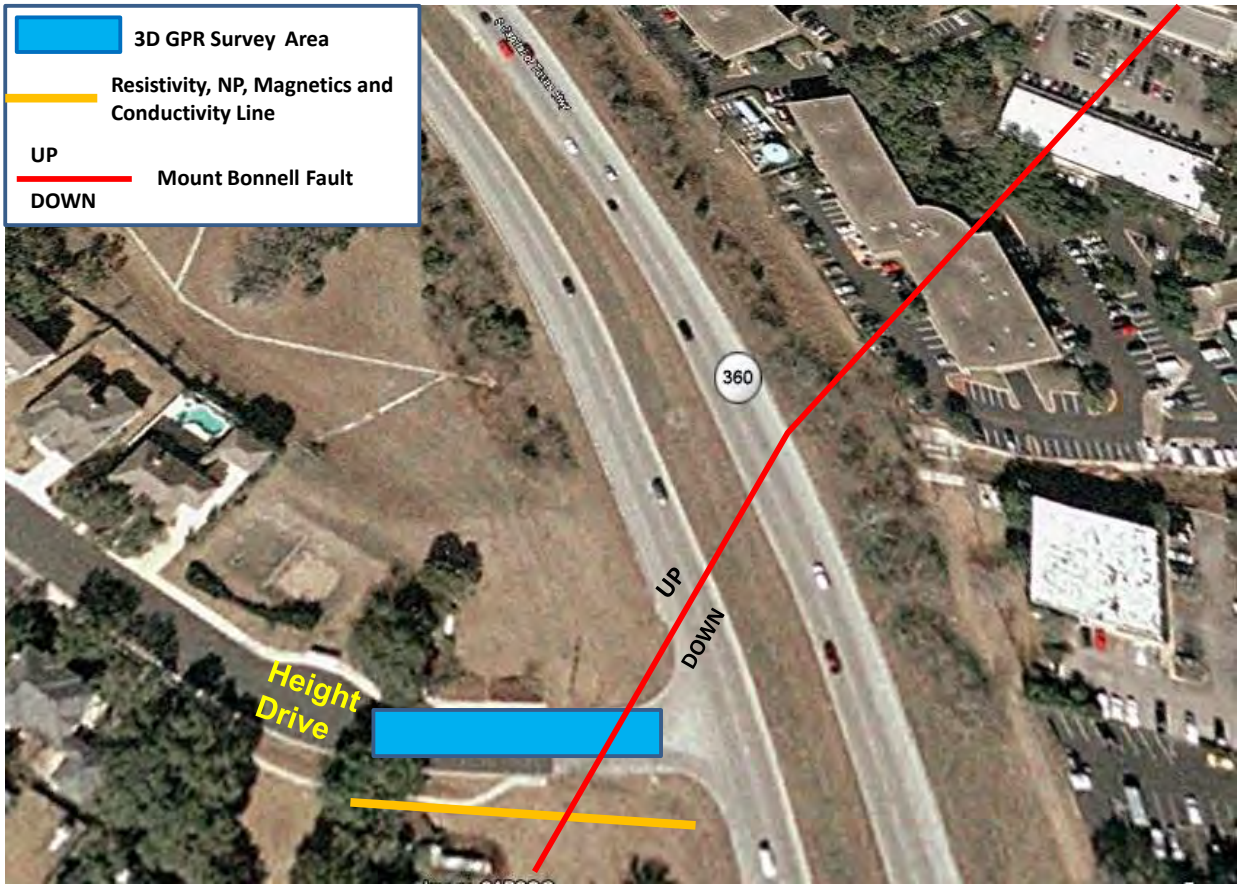

Fi
lo **Figure 3.** Site map showing the location of geophysical profiles and the Mount Bonnell fault. The fault location is taken from Hauwert, N., 2009.

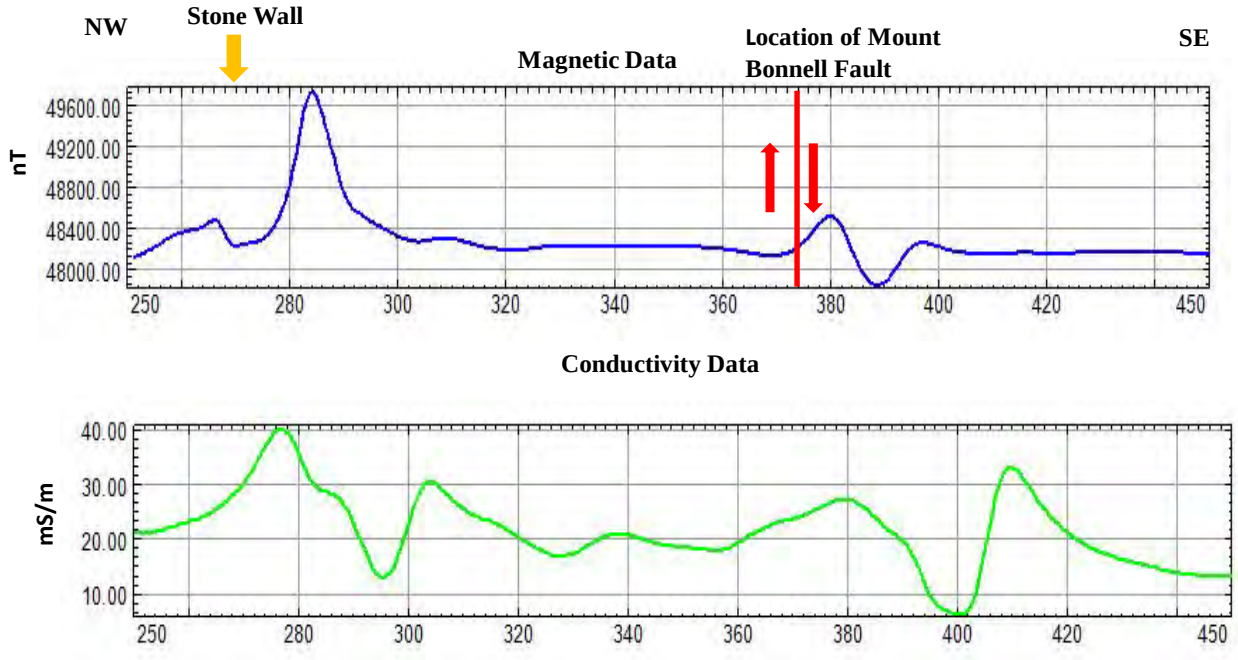

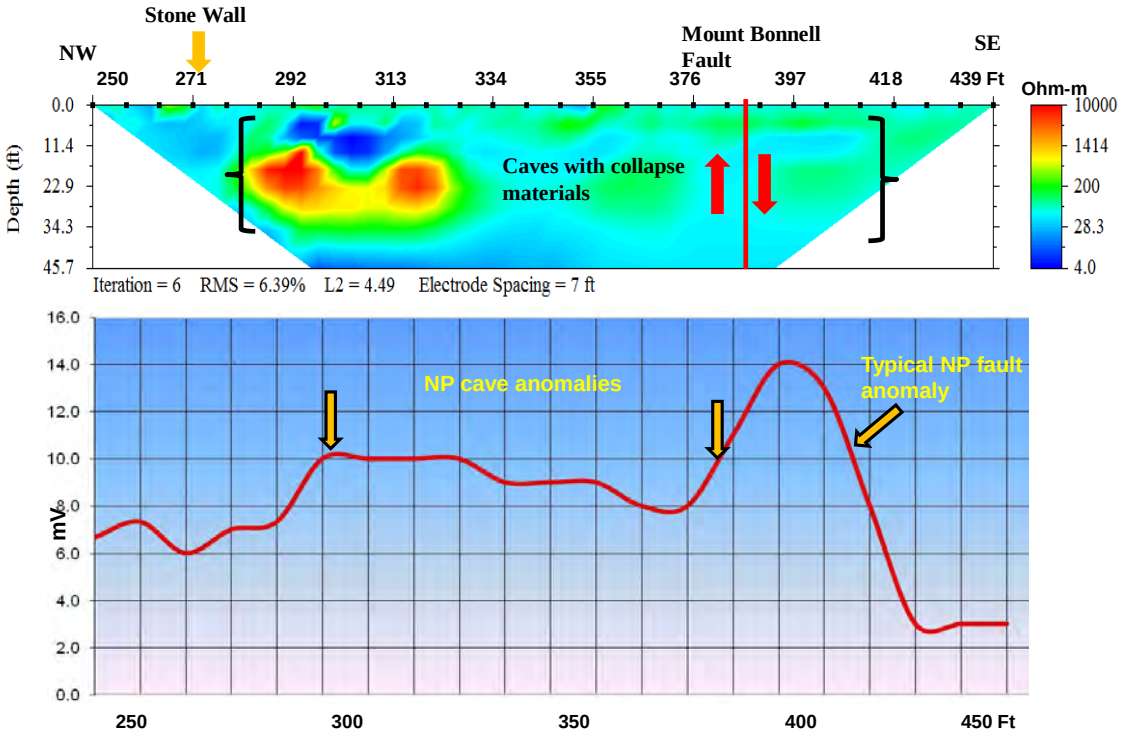

Figure e the correlat

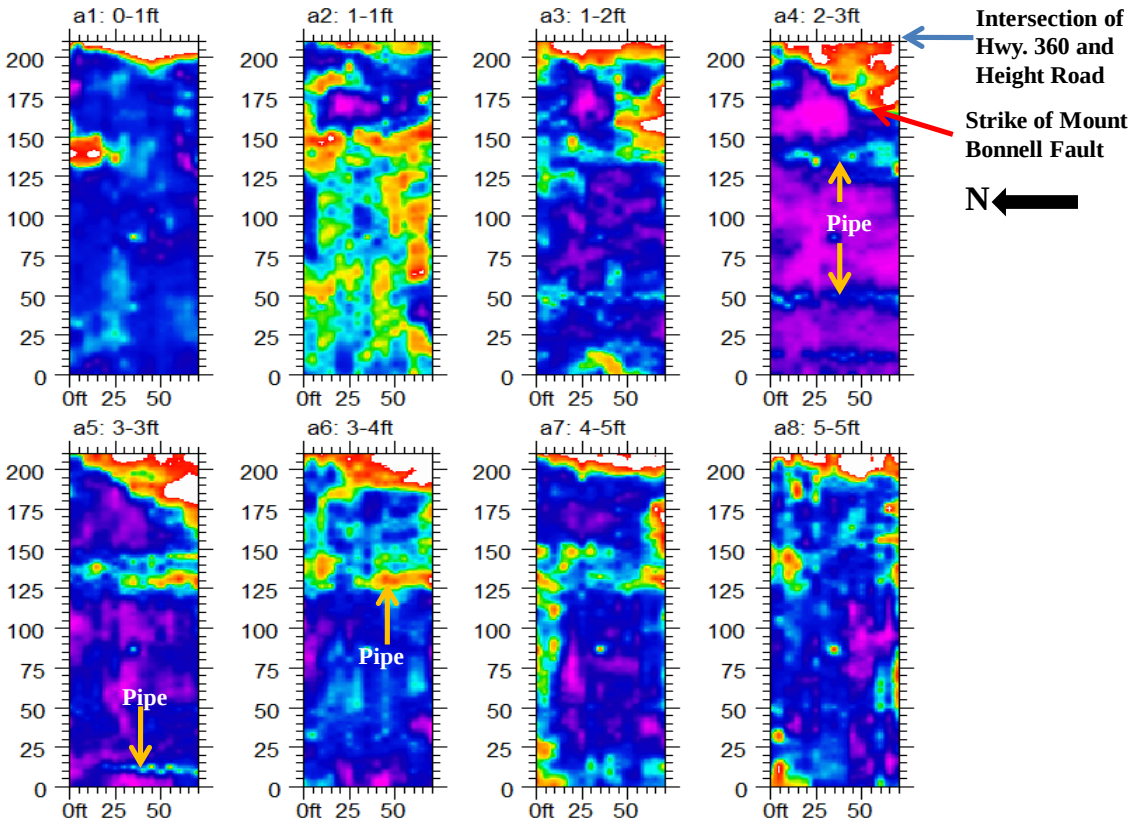

Fig

Table 1: Karstic features located by geophysical surveys at Height Drive.

Geophysical Methods	Karstic Features				
	Cave	Sinkhole	Collapse Materials	Faults and Fractures	Conduit
Magnetic	✓				
Conductivity	✓				
Resistivity	✓	✓	✓	✓	
NP	✓			✓	✓
GPR	✓	✓	✓	✓	
TOTAL	✓	✓	✓	✓	✓

West Park Drive at Highway 360

The site map of the study area is given in Figure 7. The geophysical fieldwork took two stages: I performed reconnaissance magnetic, conductivity and GPR surveys along the orange line; second, I focused on the observed anomalies from the above-mentioned methods, and collected additional resistivity and NP surveys. Thus, the locations of the surveys are based on the site conditions with respect to geophysical methods.

The magnetic and conductivity data are shown in Figure 8. The magnetic values vary between 48,200 and 47,200 nT between the start and end of the profile. The magnetic data indicate two significant changes between the stations at 400 and 520 feet and the stations at 700 and 800 feet, respectively (see Figure 8). The approximate location of the MBF (Hauwert, 2009) is shown on the magnetic data in Figure 8. The conductivity values also show anomalies at these locations. A first vertical derivative of the magnetic data indicates shallow anomalies, which may be caused by cultural features or shallow small-scale faults associated with the MBF (Figure 9). The power-spectrum of the magnetic data indicates that the deepest magnetic sources are within the range of 60 to 80 feet deep. Figure 10 shows the resistivity imaging and NP data. Note that the resistivity data was taken between the stations at 250 and 547 feet whereas the NP data is collected between stations at 0 (zero) and 740 feet. The reason for this was that the resistivity profile was limited by driveways. Both data sets show locations of significant karstic features and faults. In addition, the resistivity data show a fault anomaly at the station 420 feet. A section of the GPR data showing a significant collapsed feature is given in Figure 11. The GPR data also shows a shallow fault at about 425 feet, which correlates well with the resistivity data. The GPR data do not indicate any anomaly over a significant resistivity anomaly, which was observed at station 490 feet at a depth of 18 feet and below. This is probably due to the depth exploration of the GPR data, which is about 7 feet. There are other GPR anomalies (small sinkholes, small caves and collapsed areas) along the profile; but I will examine these in another paper or presentation.

In summary, the magnetic data showed several shallow faults and/or fracture zones, which correlate well with the resistivity and NP data. The resistivity data show two faults, which are located about 250 feet to the northwest of the MBF projected by the geological data (Hauwert, 2009). The conductivity data shows high anomalies the between stations at 200 and 450 feet, which is probably due to the shallow faults and fracture zones. The GPR data indicate a significant collapsed area, northwest side of which is controlled by a shallow fault. The location of this fault correlates well with the resistivity data. The NP data show fault and karstic anomalies along the entire length of the profile. There is also a significant gradient along the NP profile towards the southeast. This gradient is probably caused by the ground water movement within the conduits of the Edwards Aquifer. At the site, there is repaired, patched asphalt where the faults are located by the geophysical data. Findings of geophysical surveys are given in Table 2.

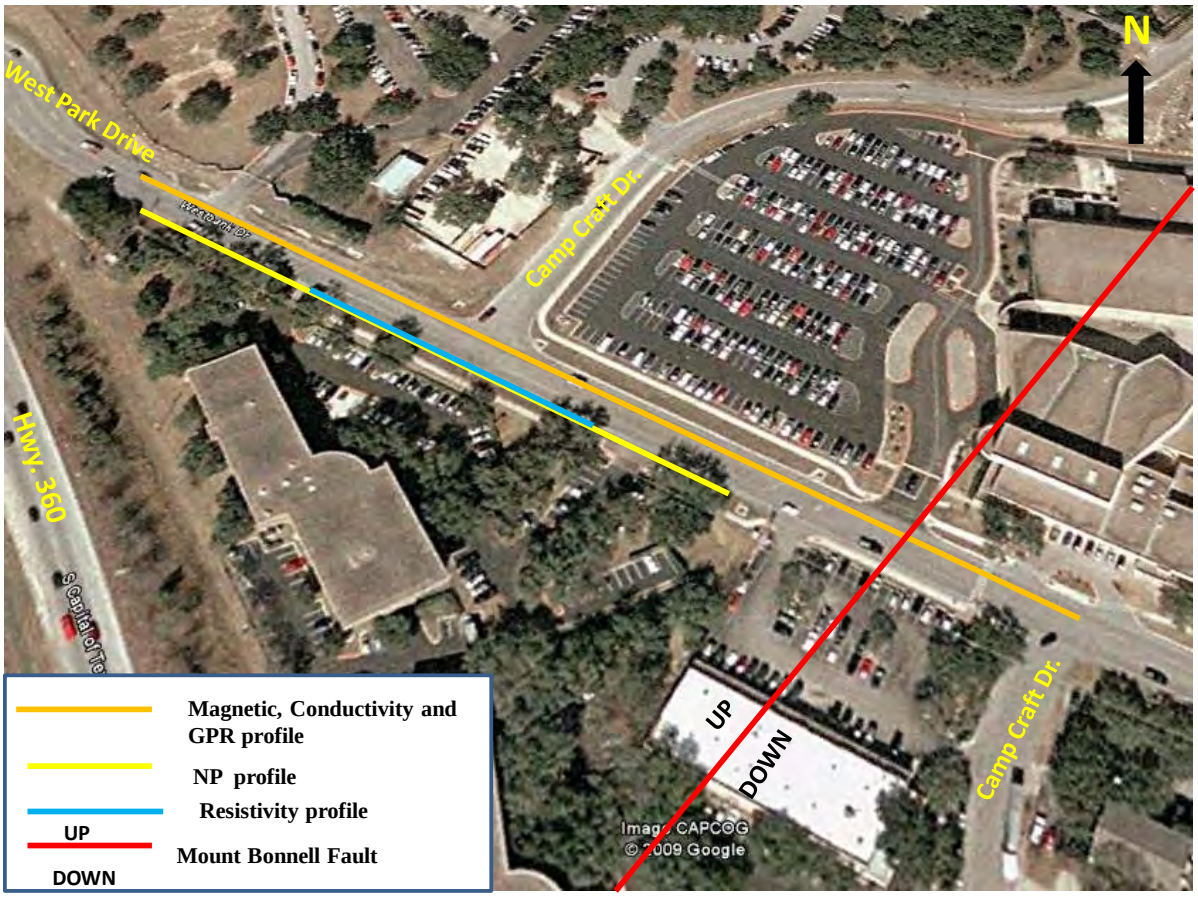

Fig
data (Hauwert, 2009).

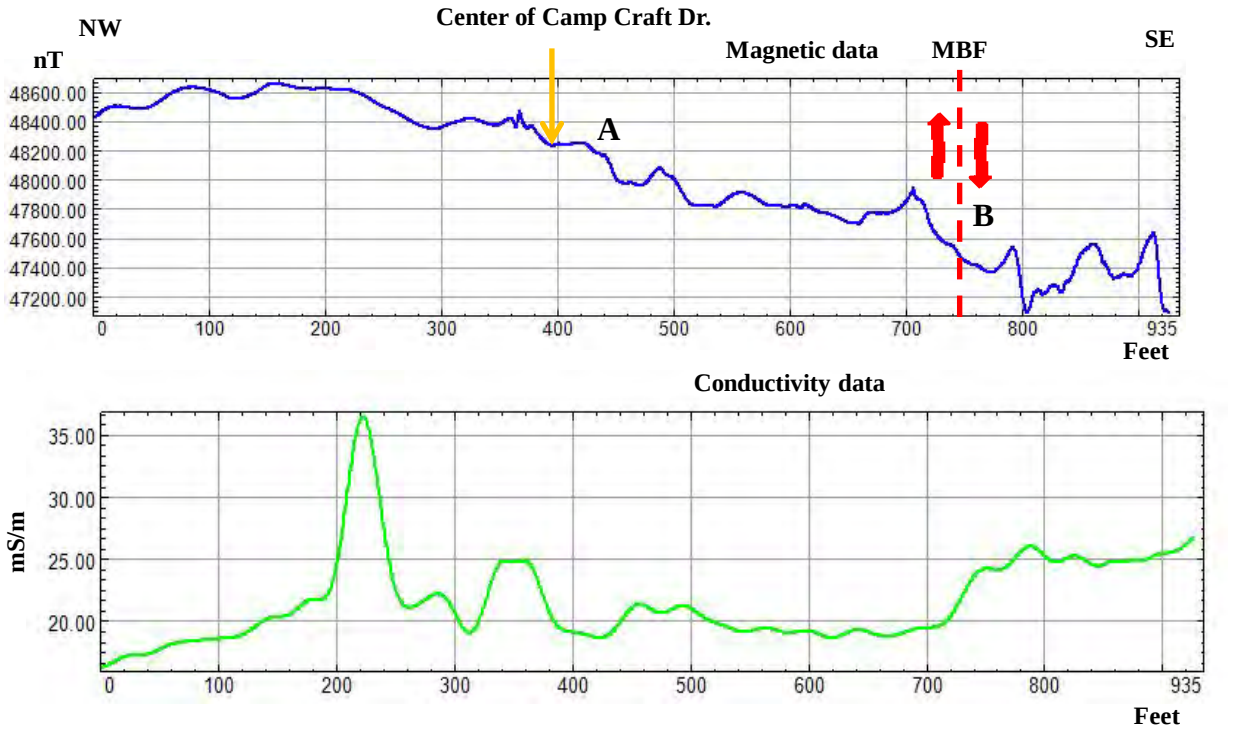
NW
Center of Camp Craft Dr.
SE
nT
Magnetic data
MBF
A
B
48600.00
48400.00
48200.00
48000.00
47800.00
47600.00
47400.00
47200.00
0
100
200
300
400
500
600
700
800
935
Feet
Conductivity data
mS/m
35.00
30.00
25.00
20.00
0
100
200
300
400
500
600
700
800
935
Feet

Figu
the
whe

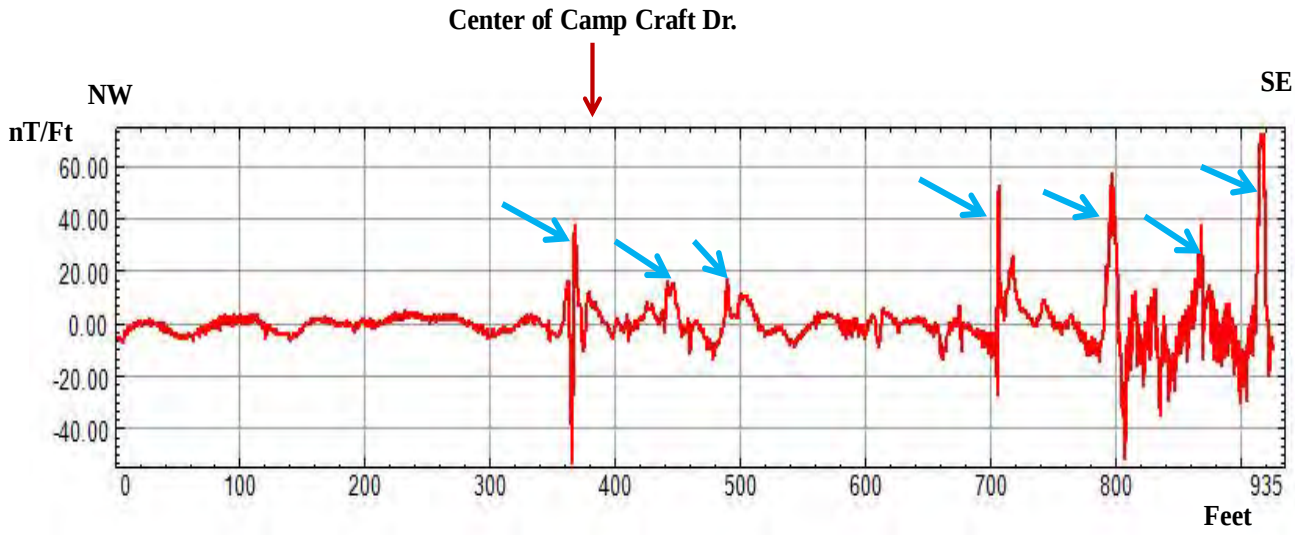
Center of Camp Craft Dr.
NW
SE
nT/Ft
60.00
40.00
20.00
0.00
-20.00
-40.00
0
100
200
300
400
500
600
700
800
935
Feet

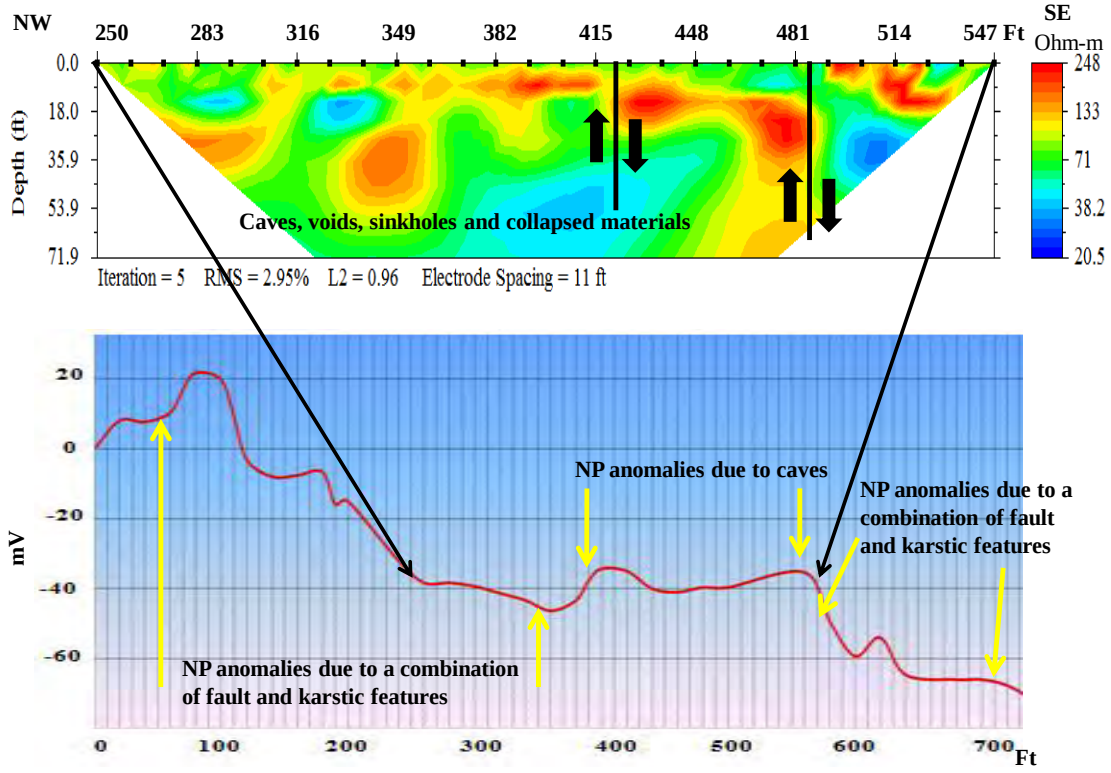

Figur
Horiz t.

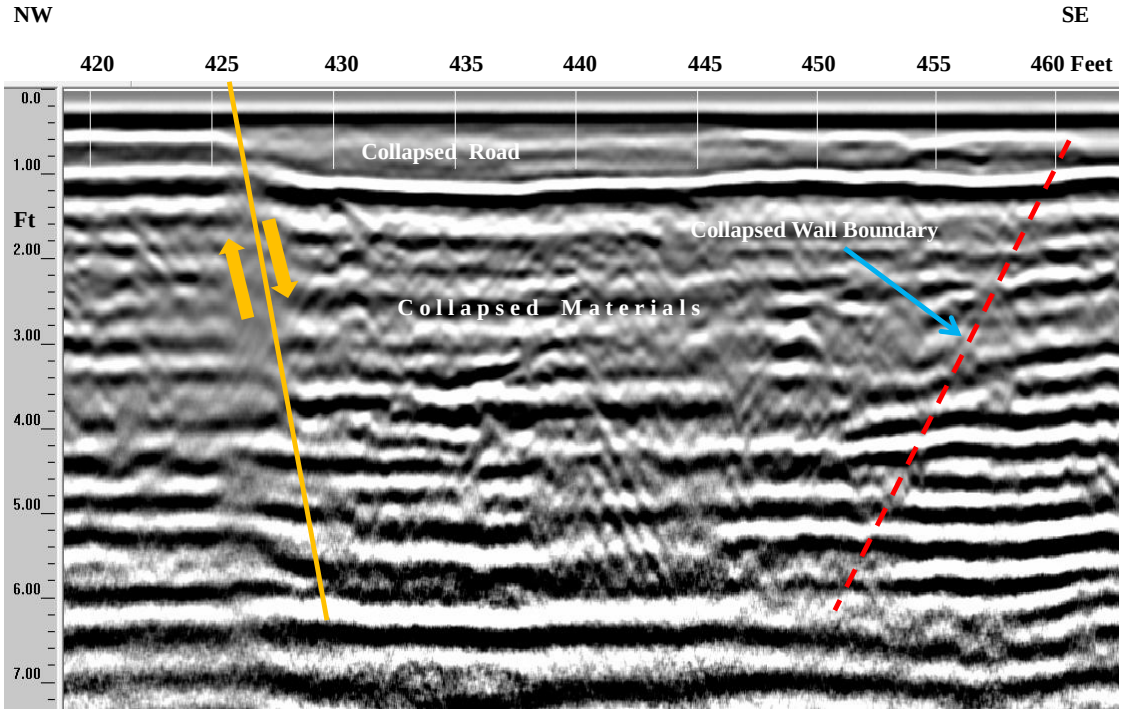

Figure
a
shallow
ıt 40
feet.

Table 2: Karstic features located by geophysical surveys at West Park Drive.

Geophysical Methods	Karstic Features				
	Cave	Sinkhole	Collapse Materials	Faults and Fractures	Conduit
Magnetic				✓	
Conductivity				✓	
Resistivity	✓		✓	✓	
NP	✓			✓	✓
GPR	✓		✓	✓	
TOTAL	✓		✓	✓	✓

Bee Cave Road Site at Camp Craft Road

A site map of the study area including the locations of geophysical profiles and the MBF are shown in Figure 12. The geophysical surveys, except the GPR, were all conducted along the grassy area between the two driveways of the West Lake Bible Church and West Lake Animal Hospital. The GPR data was collected along Bee Cave Road adjacent to other profiles (see Figure 12). There is an incipient sinkhole (recharge area) in the study area.

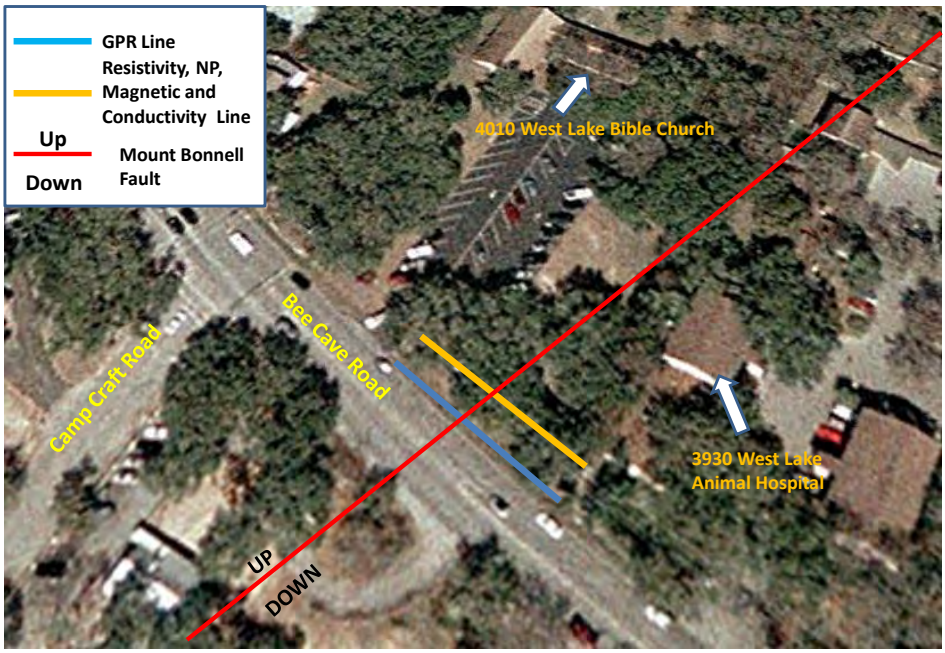

Figure 12: Site map showing locations of geophysical profiles and the MBF.

The magnetic and conductivity data are given in Figure 13 show high magnetic and conductivity anomalies between the stations 279 and 330 feet. The source of these anomalies appears to be subsurface. The incipient sinkhole is located at the station at 265 feet. The resistivity and NP data are given in Figure 14. The resistivity data show karstic anomalies (cave, sinkhole, collapsed materials, etc.) along entire length. The high magnetic and conductivity anomalies correlate well with the locations low

resistivity material (≤ 20 Ohm-m). Based on this correlation, the source of the magnetic and conductivity anomalies can be attributed to magnetic soils in the subsurface. The NP data shows a very unique "U" type anomaly along the profile. The NP values range between 10 and -38 mV. The NP anomaly appears to be caused by a conduit flow in the subsurface. Two sections of GPR are given in Figures 15 and 16. Both data sets indicate a sinkhole and a collapsed area, respectively. A change in elevation from high to low towards the southeast is observed on Bee Cave Road where the collapsed area starts.

In summary, the magnetic and conductivity data show high amplitude anomalies which correlate well with the low resistivity materials between the surface and 25 feet below. The NP data display a simple but strong amplitude anomaly between the stations at 215 and 350 feet, indicating a conduit flow in the subsurface. The GPR data show a sinkhole and a collapsed area along the profile taken on the road. None of the geophysical methods appears to detect the MBF's signature. This may be due to the

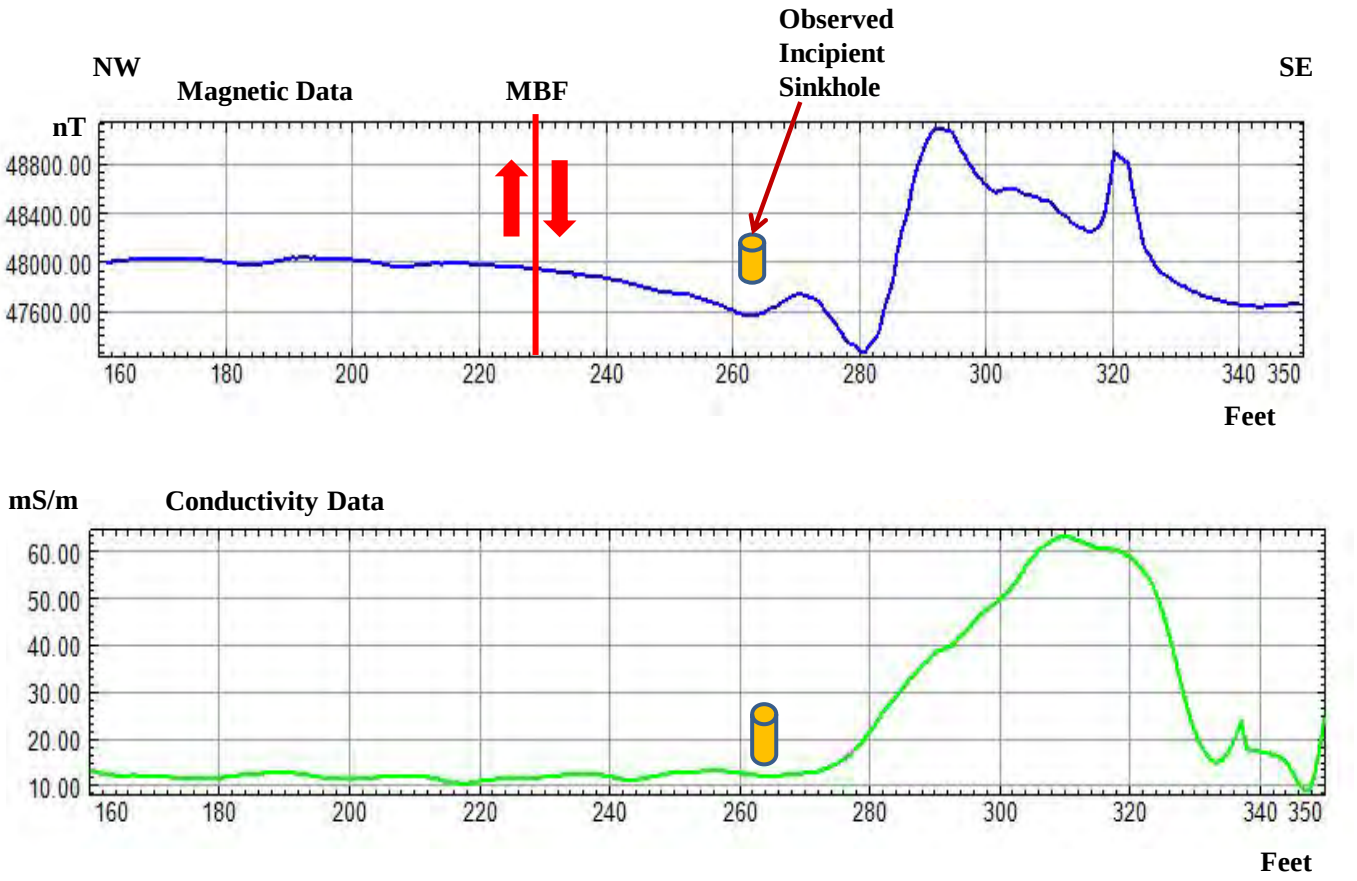

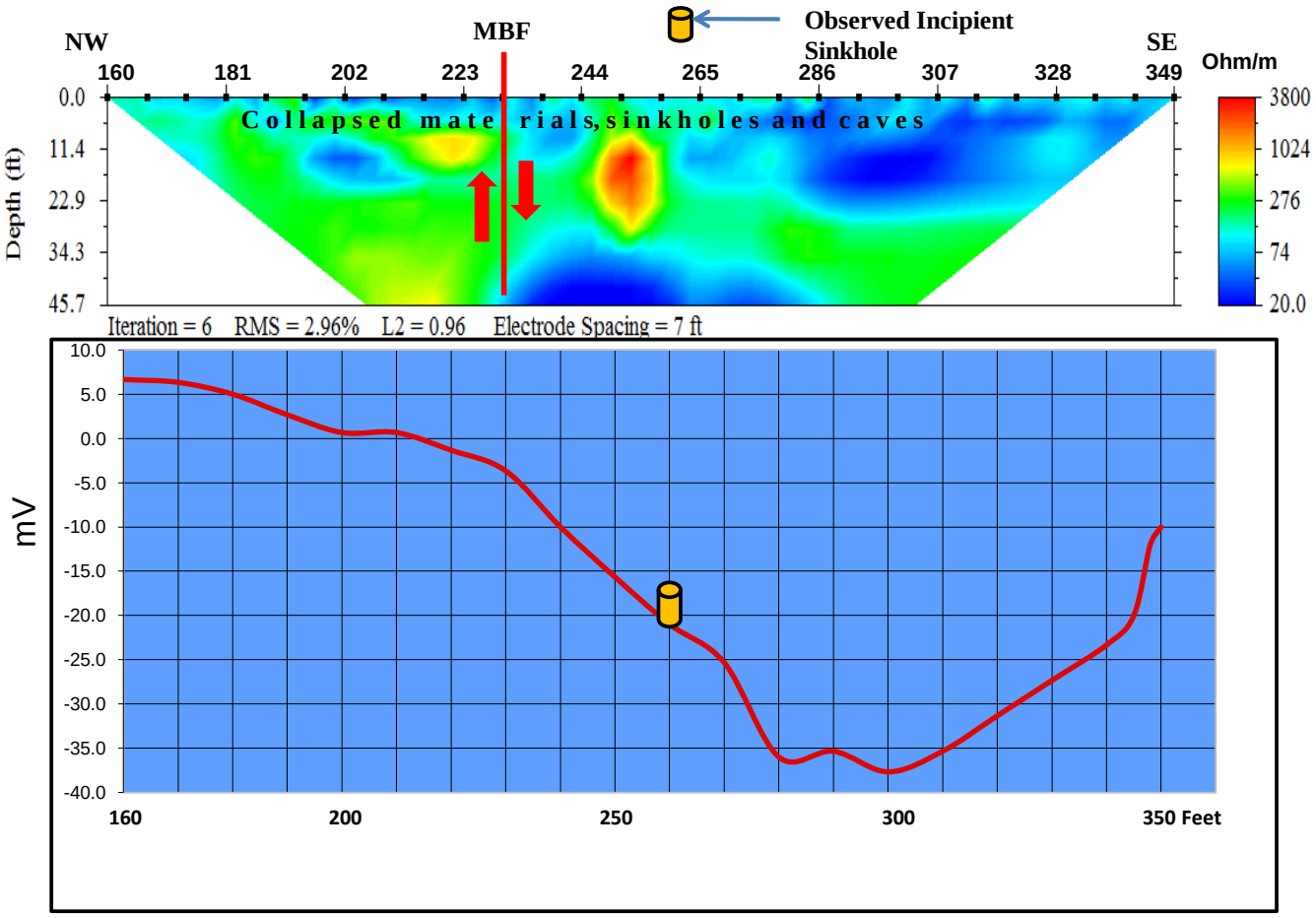

Figure 14. Resistivity (above) and NP (below) data across the MBF. Location of the MBF is given by Hauwert, Nico., 2009.

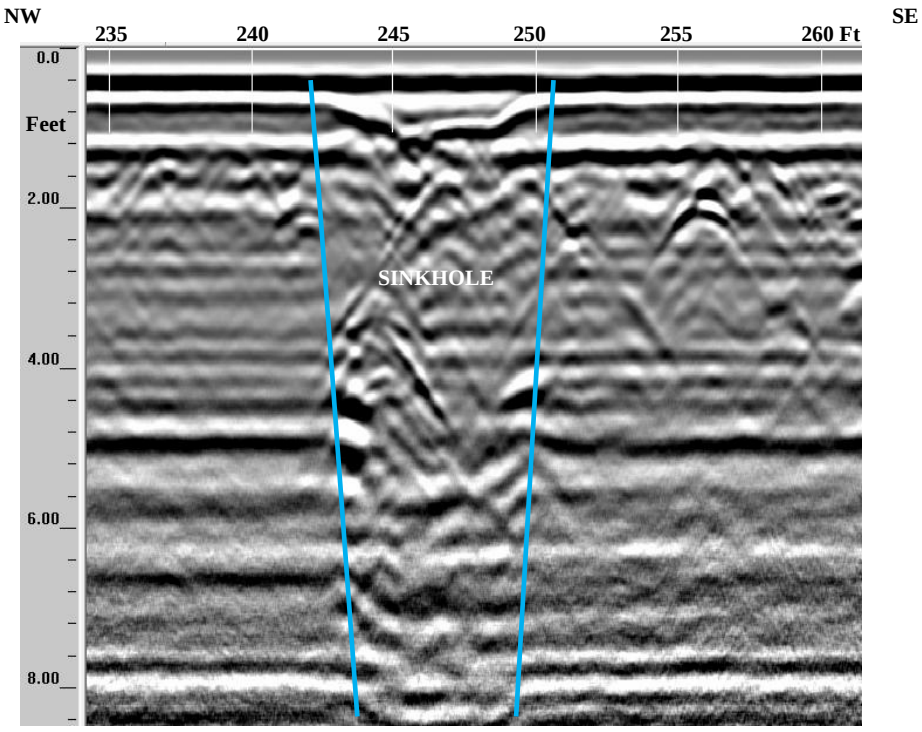

Figure 15 d 252
feet. Note hole
correlates well with the incipient sinkhole and the "sphere-like" high resistivity anomaly that are observed on the surface and the resistivity data, respectively.

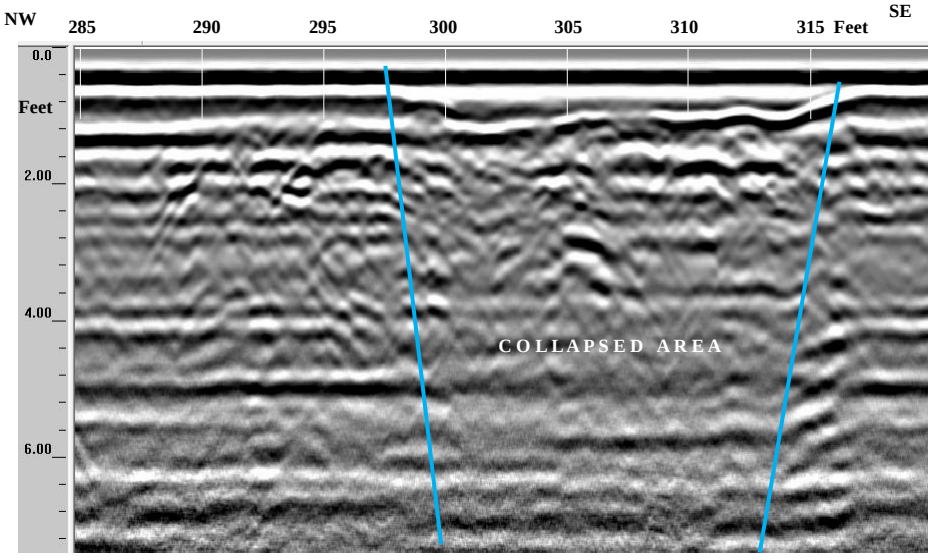

Figure 16. A ıe lines, is
observed bet ity anomalies
(see Figure 1

Table 3: Karstic features located by geophysical surveys at Bee Cave Road.

Geophysical Methods	Karstic Features				
	Cave	Sinkhole	Collapse Materials	Faults and Fractures	Conduit
Magnetic	✓				
Conductivity	✓				
Resistivity	✓	✓	✓	✓	
NP	✓				✓
GPR	✓	✓	✓	✓	
TOTAL	✓	✓	✓	✓	✓

Discussion of Results/Conclusions

All geophysical data obtained from the three sites across the MBF indicate significant subsurface anomalies. These anomalies appear to be due to caves, voids, collapsed materials, sinkholes, underground pipes, shallow faults and fracture zones. It should be noted that the magnitude of the NP anomalies are much stronger at the West Park Drive and Bee Cave Road than the Height Drive site. This observation may be related to the amount of the conduit flow within the Edwards Aquifer.

The GPR data taken along the roads indicate significant near-surface anomalies caused by collapsing soil, sinkholes and caves. It appears that these locations appear to be fixed periodically because of patched, repaired asphalt conditions observed on the roads.

In conclusion, data acquired and used to evaluate the effectiveness of geophysical methods in detecting karstic features and faults/fractures in the Austin area allowed correlation of unique and consistent anomalies with a known fault. It is clear from this study that integrated geophysical methods can be used to map Balcones faults and their associated karstic features quickly and inexpensively. Results of this study show the benefit of including as many as geophysical methods (five in this study) to both improve fault and karstic characterization of near-surface geology.

References

Collins, E.W., and Woodruff, C.M., 2001, Faults in the Austin, Texas, Area-Defining aspects of local structural grain, Austin Geological Society Guide Book 21, p.15-26.

Connor, C.B., and Sandberg, S.K., 2001, Application of Integrated Geophysical Techniques to Characterize the Edwards Aquifer, Texas, STGS Bulletin, March issue, p. 11-25.

Garner, L.E., Young, K.P., Rodda, P.U., Dawe, G.L., Rogers, M.A., 1976, Geologic map of the Austin area, Texas, in Garner, L.E., and Young, K.P., 1976, Environmental geology of the Austin area: an aid to urban planning: The University of Texas at Austin, Bureau of Economic Geology, scale 1:65,500.

Fitterman, D.V., and Stewart, M.T., 1986, Transient electromagnetic sounding for groundwater, Geophysics, v. 51, p. 995-1005.

Hauwert, N.M,. 2009, Groundwater flow and recharge within the Barton Springs Segments of the Edwards Aquifer, Southern Travis and Hay Counties, Doctor of Philosophy, The University of Texas at Austin.

Rodda, P.U., Garner, L.E., and Dawe, G.L., 1970, Austin West, Travis County, Texas: The University of Texas at Austin Bureau of Economic Geology, Geologic Quadrangle Map 38, p.11.

Acknowledgements

I thank Dr. Nico Hauwert for showing the Mount Bonnell fault in the field and for numerous discussions, and a number of friends and colleagues who helped in the data acquisition. I thank Vsevolod Egorov for his contribution on the interpretation of the magnetic data. And last but not least, I am thankful to Esin Saribudak for her contribution to the graphical improvement and edition of the paper. This research project was funded by Environmental Geophysics Associates.

3D MASW Characterization of Sinkhole: A Pilot Study at USF Geology Park, Tampa, FL

Choon B. Park, Park Seismic LLC, Shelton, Connecticut, USA
Chris Taylor, GeoView Inc., St. Petersburg, Florida, USA

ABSTRACT

By running three parallel and one crossing lines of conventional 2D MASW surveys followed by normal 1-D MASW inversions, a 3D characterization was attempted as a pilot study over an area of a known sinkhole 10-40 ft deep with lateral dimension smaller than 50 ft. Shear-velocity (Vs) data sets from each line were then used as constraints to calculate a cubic grid data in x (east-west), y (south-north), and z (depth) directions by using a 3D inverse-distance-weighted (IDW) interpolation scheme. When displayed in depth-stripping mode at 5-ft depth intervals, velocity anomalies of substantially lower values than those in the ambient are recognized in the surface and depth locations that correlate fairly well with those identified in a geologic cross section previously compiled from other methods of well drilling, CPT, and GPR surveys. Properly selecting offset range during data acquisition and subsequent dispersion analysis seems critically important for the successful detection of a sinkhole.

INTRODUCTION

Sinkhole development in cultural area always threatens human life and property integrity. Early detection and accurate characterization of its subsurface development, therefore, have become crucially important issues among relevant communities including geotechnical engineers. Its inherent nature of being localized and three-dimensional strongly calls for a 3D survey in order to make any subsequent remedial process, if necessary, become as effective as it can be. Recent introduction of simple and cost-effective 3D approach (Park and Carnevale, 2009) with the multichannel analysis of surface waves (MASW) method (Park et al., 1999) has shown that 3D seismic investigation—normally known as exceptionally expensive in field and data-processing efforts—can become an affordable option that implements multiple conventional 2D shear-velocity (Vs) surveys along several linear trajectories intersecting or paralleling each other on the surface.

The State of Florida may have possibly the most sinkhole areas developed within the cultural area of the world (Figure 1). Concern for sinkhole-related public safety is growing rapidly and the number of litigations in residential and commercial areas has grown exponentially in recent years. A variety of geophysical methods—including ground-penetrating-radar (GPR), resistivity, and MASW—have been applied to effectively characterize sinkhole-related subsurface features. Considering the most important subsurface property is usually the stiffness distribution in and around an existing or developing sinkhole area, the MASW method that generates shear-wave velocity (Vs), a direct indicator of stiffness, seems to be one of the most useful geophysical approaches.

Figure 1. The distribution of karst areas in the United States (from Davies, 1984)

GeoView Inc. and Park Seismic LLC conducted a pilot study with the 3D MASW approach over a sinkhole area with a mild surface depression (≤ 3ft) known to exist in Geology Park (GeoPark) at the University of Southern Florida (USF), Tampa, Florida (Figure 2), to evaluate the approach's potential effectiveness and future calibration. This area was intensively investigated previously by geologic (e.g., well drilling), geotechnical (e.g., CPT), and geophysical approaches (e.g., GPR) (see, for example, Parker, 1992). Figure 3 shows a geologic cross section of the area compiled from all previous survey results.

Figure 2. Location map of the studied sinkhole area.

PREVIOUS STUDIES

Sinkhole investigation has been one of the major issues in multidisciplinary fields including geophysics, geology, geotechnical engineering, geomorphology, remote sensing, etc., resulting in a vast number of publications in all these fields. Particularly, it has been the major purpose in geotechnical karst investigation sometimes considered analogous to the needle in the haystack problem (Yuhr et al., 2003). From the standpoint of geophysical investigation, it has been the detection of highly localized anomalies such as voids and cavities that often challenged resolution limits of such commonly used methods as GPR, resistivity, and seismic surveys. Although each of these geophysical approaches is continuously evolving in its own way in methodology and measuring instruments, none of them is exclusively superior in every aspect over others. We report our early-stage efforts to make the MASW approach further evolve and become better suited for future sinkhole and karst investigations.

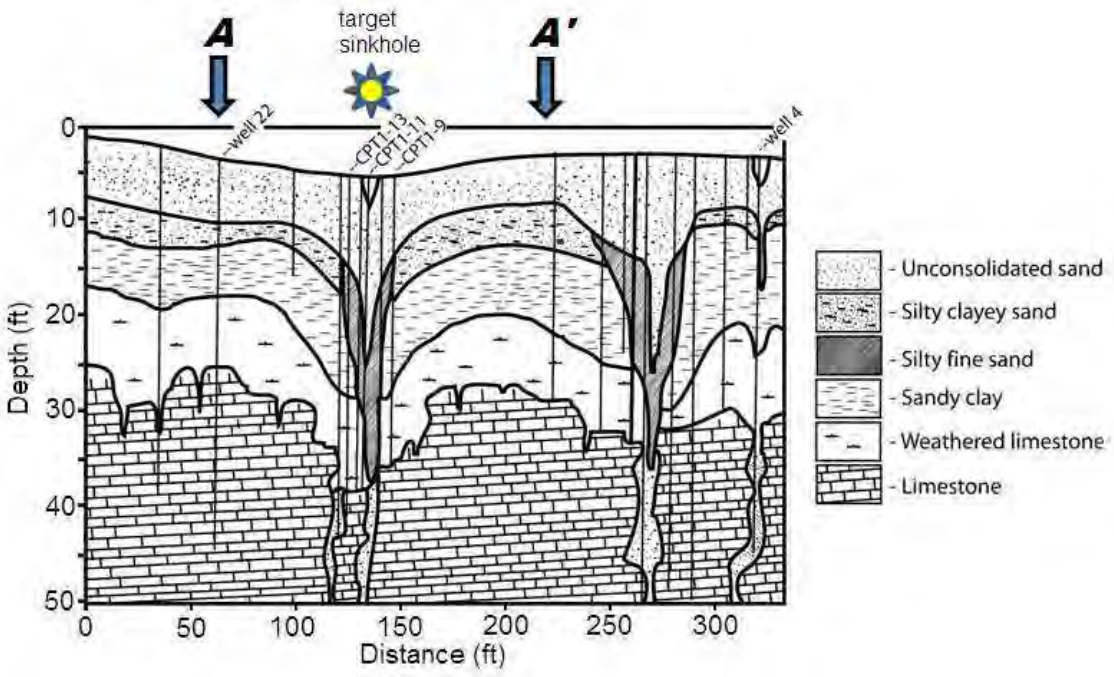

Figure 3. The geologic cross section of the sinkhole area compiled from results from the previous other surveys (from Parker, 1992).

Some of the most recent sinkhole- and karst-related studies include the investigation of large sinkholes (50 to 200 m in diameter) in Texas using satellite-based radar interferometry (Paine et al., 2009). De Kleine and Bakker (2009) used GPR to map and classify caves and cavities over a karst area in Bonaire, Netherlands Antilles. Campbell (2008) applied several different approaches of GPR, MASW, and resistivity surveys over karst limestone terrains in Australia. Xu et al. (2008) introduced a unique Rayleigh wave inversion approach to image subsurface cavities through a new dispersion analysis sensitive to existence of cavities, and Putnam et al. (2008) analyzed surface waves on several 24-channel field records acquired over a shallow ($\leq$ 2 m) spillway tunnel 1-m in diameter with focus on the surface wave scattering and corresponding attenuation phenomena. High-resolution seismic reflection approaches were also used to image subsurface boundaries related to sinkhole subsidence (Lambrecht and Miller, 2006; Dobecki and Upchurch, 2006; Miller, 2002). Kim et al. (2006) applied cross-hole resistivity tomography to detect an abandoned mine below a 25-story building in South Korea. Gelis et al. (2005) reported a numerical modeling study to delineate surface wave responses over shallow voids in association with their dispersion properties, and Nasseri-Moghaddam et al. (2005) performed similar numerical study over void zones with focus to surface wave scattering and attenuation properties. The first 2D application of MASW to a sinkhole investigation was done by Xia et al. (2001) during a feasibility study to define a sinkhole impact area at a nuclear power plant in Maryland. 3D MASW characterization of sinkhole and karst areas is unprecedented.

3D MASW METHOD

Park and Carnevale (2009) indicated that the conventional 2D MASW investigation focuses on the inline propagation of planar surface waves and therefore the resultant 2D shear-velocity (Vs) map best represents the cross sectional image of the subsurface stiffness distribution with a minimal influence from the offline features like side scattering. It showed that a 3D cubic data set of practical value can be constructed from multiple surveys (e.g., 4 or more) of conventional 2D mapping designed in a parallel or intersecting manner. It concluded that proper 3D interpolation and effective data presentation play key roles if the approach is to be of any practical value. It was suggested that the approach is more cost effective and possesses a greater practical value than the previous attempts of pseudo-3D MASW surveys by Miller et al. (2003) and Suto (2007).

For the pilot study to characterize the sinkhole feature in GeoPark at USF, we used proprietary software developed at Park Seismic LLC for 3-D interpolation and display purposes. To demonstrate its performance, we created a synthetic cubic grid data set of 100x100x100 size in x (east-west), y (south-north), and z (depth) directions that had only two different velocity values of 100 m/sec (blue) and 500 m/sec (yellow), with the latter value assigned to the hemispheric feature sitting on top of a half space of the same velocity value. Figure 4 shows this data set displayed in cubic, x-, y-, and z-layer stripping modes. Figure 5 shows results from a simulated 3D MASW survey that consisted of total six linear survey lines of 2D mapping indicated on top of the original cubic display. It was assumed that each 2D mapping along these six lines duplicated the exact cross sectional image of the original data. Then, the subsequent 3D interpolation process constructed a cubic grid data set of 100x100x100 size whose layer stripped images are shown in Figure 5. In comparison to the original data set displayed in Figure 4, the interpolated data set restored the original feature fairly well. The inverse-distance-weighted (IDW) scheme was used for the 3D interpolation.

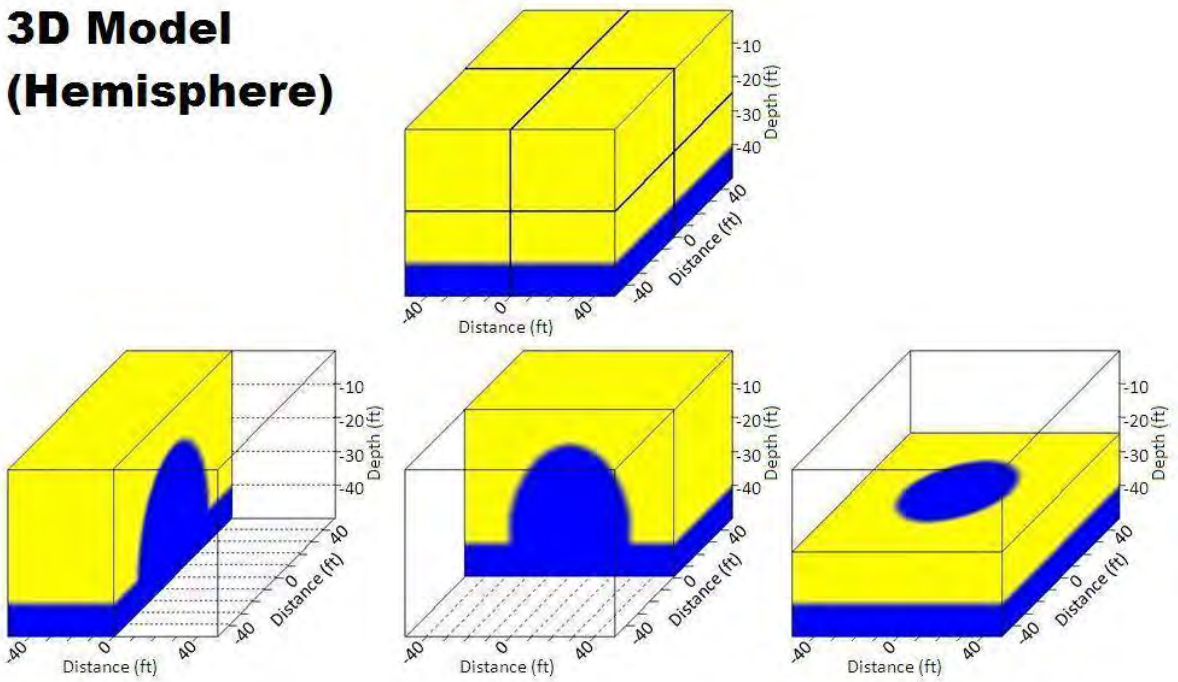

Figure 4. (Top) A synthetic 3D cubic grid data set with two velocity fields. (Bottom) 3D shape of the higher value field (blue) is illustrated by three layer-stripped displays along the x, y, and z axes.

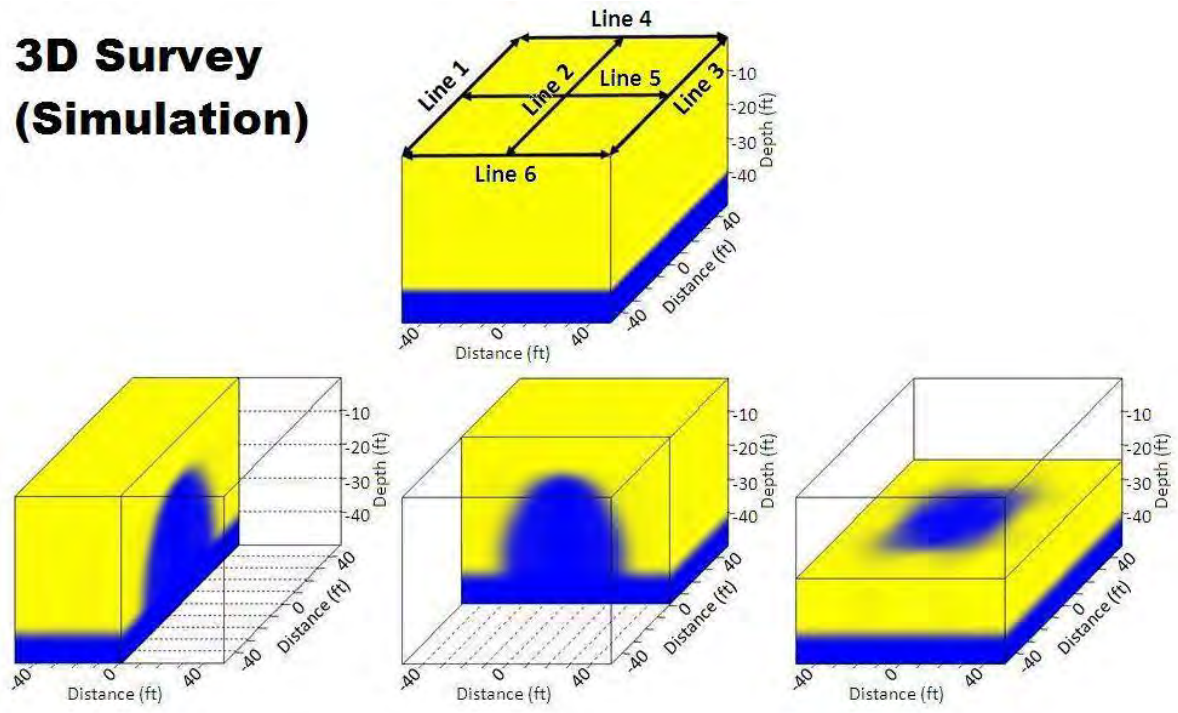

Figure 5. Simulation of 3D (MASW) survey on top of the synthetic cubic data displayed in Figure 4. Location of the six (6) lines used for the simulation (top), and results from the 3D interpolation (bottom).

3D MASW SURVEY AT USF GEOPARK

The GeoPark (Figure 2) in the campus of USF, Tampa, FL, was built in 2001 as a resource site for on-campus geological teaching and research, and nowadays continues to serve as a demonstration site for a variety of courses including hydrogeology, geophysics, and geomorphology (www.karst.usf.edu/USFGeoPark).

A 3D MASW survey was conducted in May 2009 over a sinkhole area located inside this park by running four (4) lines of a conventional 2D MASW survey, as indicated in Figure 6. The geologic cross section shown in Figure 3 compiled from results from other surveys previously performed over the same area indicates that there are approximately three sinkhole features. Although the MASW survey lines were laid to target the major sinkhole feature shown in the central part of the cross section (located at about 120 ft of surface distance), their actual locations were determined by those surface areas with the least surface obstacles such as trees and rocks. Their locations and surface transect of thecross section are indicated in Figure 6.

Using a 24-channel land streamer equipped with 4.5-Hz geophones spaced at 5-ft intervals, a total of twenty-four (24) field records were acquired per line by moving the streamer by 5 ft, while maintaining the source offset at 60 ft. A 20-lb sledge hammer was used as a seismic source and each saved field record was a stack of data from two hammer impacts. A sampling interval of 1-ms and total recording time of 1-sec were used throughout acquisition with a 24-channel Geometrics Geode.

Considering the maximum lateral dimension of the subsurface sinkhole feature was smaller than 60 ft, as indicated by the geologic cross section in Figure 3, it was speculated at the beginning stage of data processing that using all 24 traces of each field record spanning 115 ft of surface distance might smear off the target subsurface feature. Therefore, only the first twelve (12) traces of each record spanning 55 ft of surface distance were used for the subsequent dispersion imaging process performed with the method by Park et al. (1998). Then, one fundamental mode (M0) dispersion curve was extracted from the image. Most of the extracted curves had frequencies in the range of approximately 10-70 Hz, corresponding to approximately 5-100 ft in wavelength range. These curves were then inverted for the depth (1D) variation of shear velocity (Vs) by using the algorithm by Xia et al. (1999). Those 1D (depth) Vs profiles at different surface coordinates of x and y were then used to create a cubic grid data set of 100x100x100 data points in all three directions so that it covered the 120 ft x 120 ft surface area indicated in Figure 6 and 60 ft of depth. The IDW scheme previously tested was used for the 3D interpolation. Figure 7 shows this data set displayed in cubic modes of two different perspectives, whereas Figure 8 shows the data set displayed in depth-stripping mode at 5-ft intervals.

Interpretations have been made on some of the depth stripped displays in correlation with those sinkhole features identified in the geologic

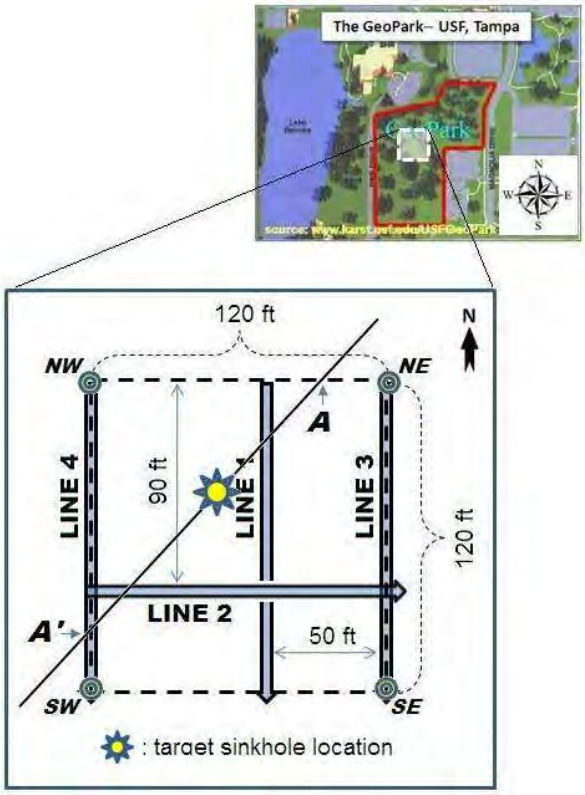

Figure 6. Location map of the four (4) MASW survey lines in the sinkhole area.

cross section. Localized velocities of noticeably lower values than those in the ambient area were interpreted as being possibly related to the sinkhole feature. This was based on the notion that shallower materials of lower stiffness would migrate down once influenced by the sinkhole activities below.

Prominent velocity anomalies marked on depth-strip displays in Figure 8 start to appear at a depth range of 10-40 ft that is in good accordance with the depth range of overburden soil most disturbed by the target sinkhole as shown in Figure 3. It seems that the sinkhole area on top of the weathered zone of limestone bedrock deeper than approximately 40 ft might not have a sufficient lateral dimension of disturbance to be resolved by the MASW method implemented with the particular acquisition parameters used during the survey. Surface (x and y) location of these interpreted anomalies correlates well with the location in the geologic cross section except for those appearing on the north-west corner of displays, which may indicate the possibility of another sinkhole area not yet identified.

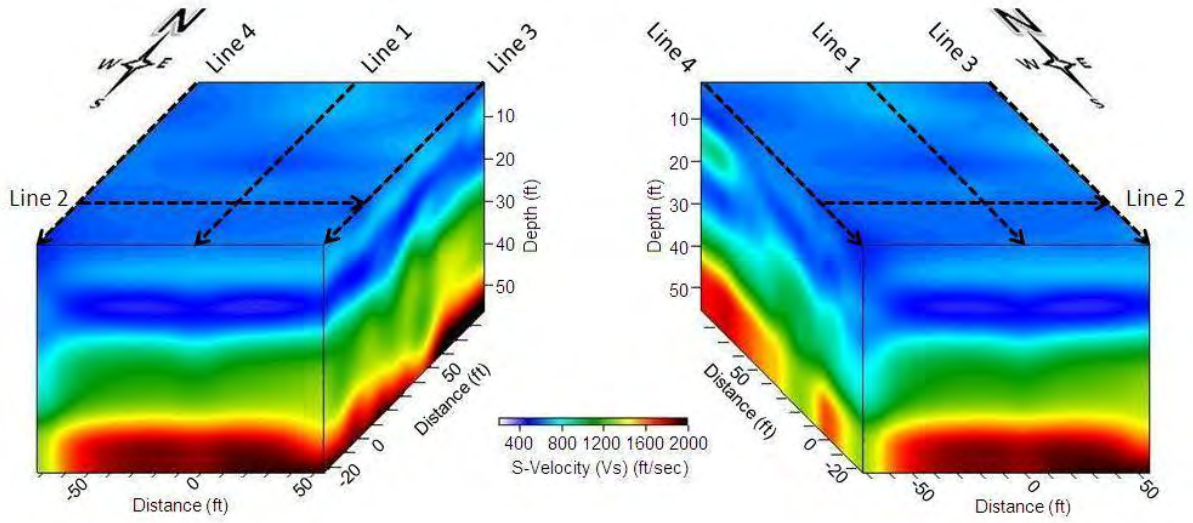

Figure 7. 3D cubic grid data set constructed by a 3D interpolation of shear-velocity (Vs) data obtained from the four (4) lines of MASW surveys marked on top of the cubic displays with two different perspectives.

DISCUSSIONS

The lateral resolution of a MASW survey is highly sensitive to the receiver spread length (L) because the subsurface model within the spread is considered to be a layered earth that has no lateral but vertical change in seismic velocities. This is an inherent premise in all surface wave methods currently in common use. In consequence, one multichannel field record is processed during the dispersion analysis by averaging out any lateral variation, if it exists, of surface wave propagation due to the plane-wave assumption used during the analysis, which results from the layered-earth assumption. Therefore, if the lateral dimension of the target anomaly (e.g., sinkhole) is excessively small in comparison to the spread length (e.g., $\leq 0.5L$), then the analysis may not detect any anomalous properties in the frequency-phase velocity relationship caused by the target anomaly. This can result in a Vs map (2D or 3D) that sometimes completely fails to detect the anomaly. Although we chose a spread length (115 ft) long enough to ensure a sufficient depth coverage, it was obviously too long to detect the target feature whose

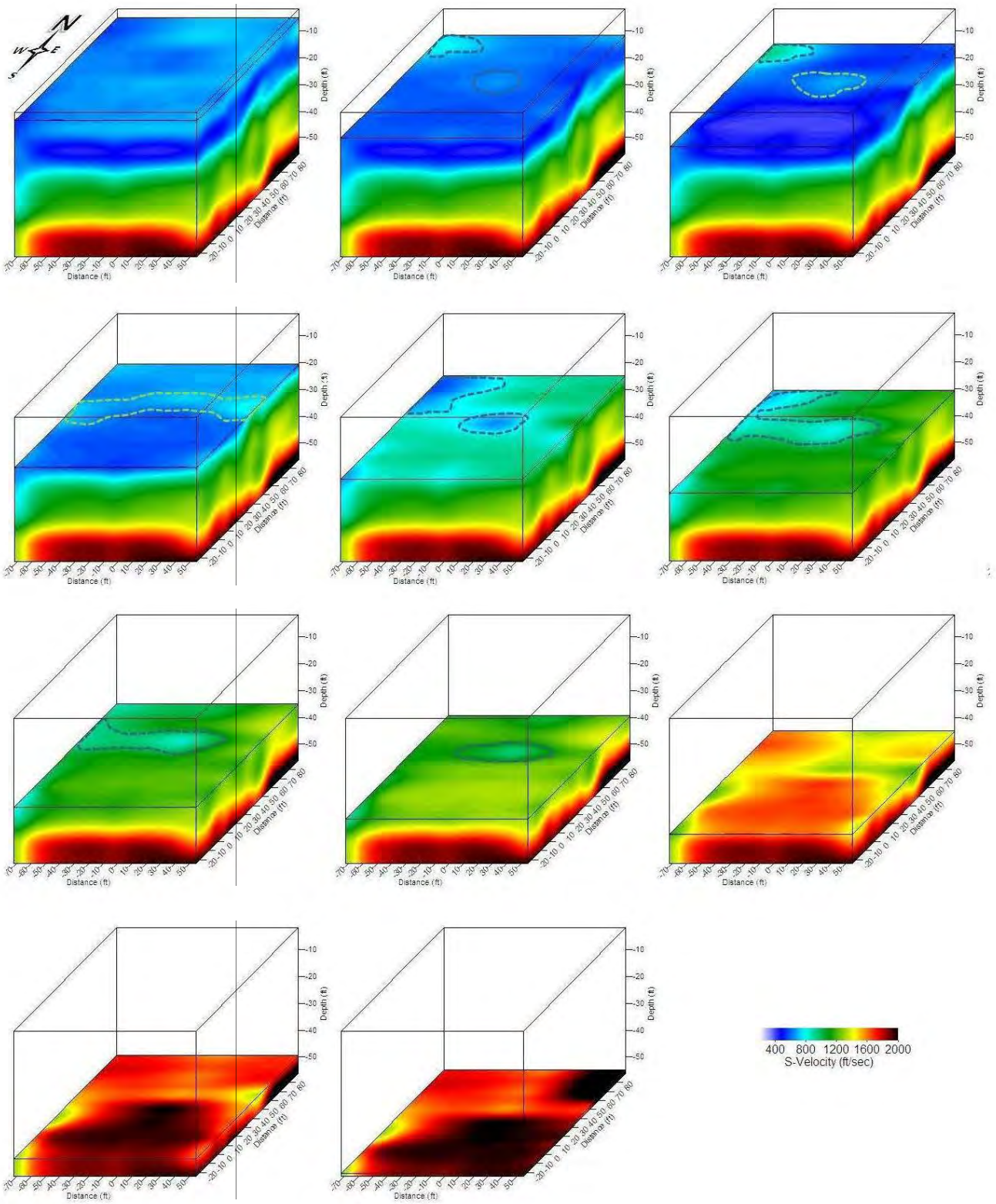

Figure 8. The 3D cubic grid data set of the sinkhole area in Figure 8 displayed in depth-stripping mode at 5-ft intervals. Suspected sinkhole features are indicated by dotted lines in certain displays.

maximum lateral dimension was smaller than 50 ft. This is illustrated in Figure 9. When the full 24

traces of each record were used, the 2D Vs map obtained from the analysis of the line 1 data set completely fails to detect the target feature (Figure 9a). On the other hand, the target becomes prominent when only the first twelve traces of the 55-ft spread length were used for the analysis (Figure 9b). Note that surface coordinates of these two maps are off by 30 ft due to the difference in midpoint of each field record used for the analysis.

Receiver spread length is usually selected to be long enough to ensure a sufficient depth coverage, which tends to be the issue of utmost importance during the early planning stage of a field survey. For example, it is usually set to be 200-300% of the maximum investigation depth (Zmax) (Park et al., 1999; 2002). However, considering the adverse influence on the lateral resolution with an excessively long spread, it is always recommended that the same data set be processed multiple times by choosing different offset ranges to evaluate the possible smearing effect.

CONCLUSIONS

Results from a 3D MASW survey over a known sinkhole area seem promising for a pilot study. Velocity anomalies suspected as sinkhole signatures are delineated at the surface and depth locations in a fairly good accordance with the geologic cross section compiled from previous results when different methods were used. Proper selection of offset ranges during data acquisition and processing stages seems critical in successful delineation of the subsurface feature related to the sinkhole existence. For

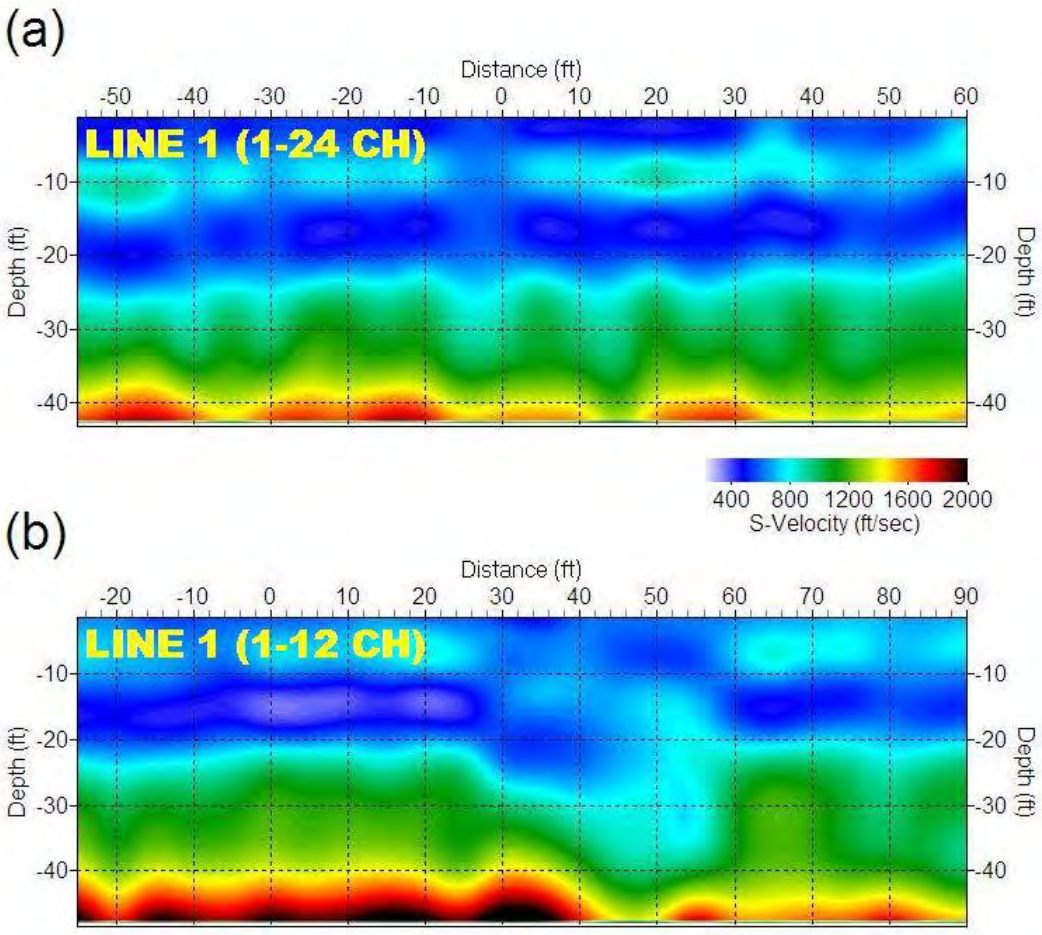

Figure 9. 2D shear-velocity (Vs) maps obtained by analyzing field records of line 1 using (a) full 24, and (b) only the near-offset 12 traces of each record.

the same area, it is recommended that another 3D MASW survey be conducted with lines more densely spaced (e.g., 10 or more parallel lines about 10 ft apart) in the future for the purpose of testing further improvement in overall resolution.

ACKNOWLEDGEMENTS

We would like to give our sincere appreciation to Professor Sarah E. Kruse at the Geology department of USF, Tampa, for her cooperation with classroom and site accessibility during the early stage of the project. We also thank Michael J. Wightman and Stephen R. Scruggs at GeoView Inc. for their help, especially during the field operation.

REFERENCES

Campbell, T. (2008). Multi-faceted geophysical characterization of limestone terrains: Proceedings of the Symposium on the Application of Geophysics to Engineering and Environmental Problems (SAGEEP 2008), Philadelphia, PA, April 6-10.

Davies, W.E., Simpson, J.H., Ohlmacher, G.C., Kirk, W.S., and Newton, E.G. (1984). Engineering aspects of karst: US Geological Survey, National Atlas.

de Kleine, M. and Bakker, M. (2009). Subsurface characterization in a karstified limestone area using ground-penetrating radar: Bonaire, Netherlands Antilles: Proceedings of the Symposium on the Application of Geophysics to Engineering and Environmental Problems (SAGEEP 2009), Fort Worth, TX, March 29-April 2.

Dobecki, T.L. and Upchurch, S.B. (2006). Geophysical applications to detect sinkholes and ground subsidence: *The Leading Edge* 25 (3): 336-341.

Gelis, C., Leparoux, D., Virieus, J., Bitri, A., Operto, S., and Grandjean, G. (2005). Numerical modeling of surface waves over shallow cavities: *Journal of Environmental & Engineering Geophysics* 10 (2): 111-121.

Kim, J.H., Yi, M.J., Cho, S.J., Son, J.S., and Song, W.K., 2006, Anisotropic crosshole resistivity tomography for ground safety analysis of a high-storied building over an abandoned mine: *Journal of Environmental & Engineering Geophysics* 11 (4): 225-235.

Lambrecht, L. and Miller, R.D. (2006). Catastrophic formation in Kansas: a case study: *The Leading Edge* 25: 342-347.

Miller, R.D., Anderson, T.S., Ivanov, J., Davis, J.C., Olea, R., Park, C.B., Steeples, D.W., Moran, M.L., and Xia, J. 2003, 3-D characterization of seismic properties at the Smart Weapons Test Range, YPG [Exp. Abs.]: Soc. Expl. Geophys., NSG 2.3.

Miller, R.D. (2002). High resolution seismic reflection investigation of the subsidence feature on U.S. Highway 50 at Victory Road near Hutchinson, Kansas: Kansas Geological Survey Open-File Report 2002-17.

Nasseri-Moghaddam, A., Cascante, G., and Hutchinson, J. (2005). A new quantitative procedure to determine the location and embedment depth of a void using surface waves: *Journal of Environmental & Engineering Geophysics*, 10 (1): 51-64.

Paine, J., Buckley, S., Collins, E., Wilson, C., and Kress, W. (2009). Assessing sinkhole potential at Wink and Daisetta using gravimetry and radar interferometry: Proceedings of the Symposium on the Application of Geophysics to Engineering and Environmental Problems (SAGEEP 2009), Fort Worth, TX, March 29-April 2.

Park, C.B., and Carnevale, M. (2009). 3D MASW: Proceedings of the Symposium on the Application of Geophysics to Engineering and Environmental Problems (SAGEEP 2009), Fort Worth, TX, March 29-April 2.

Park, C.B., Miller, R.D., and Miura, H. (2002). Optimum field parameters of an MASW survey [Exp. Abs.]: SEG-J, Tokyo, May 22-23, 2002.

Park, C.B., Miller, R.D., and Xia, J. (1999). Multi-channel analysis of surface waves (MASW): *Geophysics*, 64 (3): 800-808.

Park, C.B., Miller, R.D., and Xia, J. (1998). Imaging dispersion curves of surface waves on multi-channel record: [Exp. Abs.]: Soc. Explor. Geophys.: 1377-1380.

Parker, J.W. (1992). Surficial aquifer hydrogeology in a covered-karst terrain, Master's Thesis, University of South Florida, 228 pp.

Putnam, N., Nasseri-Moghaddam, A., Kovin, O., and Anderson, N. (2008). Preliminary analysis using surface wave method to detect shallow manmade tunnels: Proceedings of the Symposium on the Application of Geophysics to Engineering and Environmental Problems (SAGEEP 2008), Philadelphia, PA, April 6-10.

Suto, K. (2007). Multichannel analysis of surface waves (MASW) for investigation of ground competence: an introduction, in "Engineering Advances in Earthworks," Proceedings of the Sydney Chapter 2007 Symposium, Australian Geomechanics Society: 71-81.

Yuhr, L.; Benson, R.C.; Kaufmann, R.; Casto, D. and Jennings, J. (2003). A case history of a large karst investigation. 3rd International Conference on Applied Geophysics, Geophysics 2003, Orlando, Florida, December 8-12.

Xia, J., Miller, R.D., and Park, C.B. (2001). Feasibility of using the MASW method to define a sinkhole impact area at Calvert Cliffs nuclear power plant, Maryland: Kansas Geological Survey Open-File Report 2001-19.

Xia, J., Miller, R.D., and Park, C.B. (1999). Estimation of near-surface shear-wave velocity by inversion of Rayleigh waves: *Geophysics*, 64 (3): 691-700.

Xu, J.C.Q., Butt, S., and Ryall, R. (2008. Seismic Rayleigh wave method for localizing and imaging subsurface cavities in various and complicated districts: Proceedings of the Symposium on the Application of Geophysics to Engineering and Environmental Problems (SAGEEP 2008), Philadelphia, PA, April 6-10.

A MULTI-LEVEL APPROACH TO SITE CHARACTERIZATION C. W. BILL YOUNG REGIONAL RESERVOIR HILLSBOROUGH COUNTY, FLORIDA

Thomas L. Dobecki, SDII Global Corporation, Tampa, FL
Sam B. Upchurch, SDII Global Corporation, Tampa, FL

Abstract

The C.W. Bill Young Reservoir is located in southeastern Hillsborough County (Tampa Bay Area) of Florida and is a 15.5 billion gallon, above-ground reservoir designed for temporary storage of excess surface water flow during rainy periods with the intent of recovery during dry periods. The water is held by a continuous earthen embankment that is 300-ft wide at its base with a circumference of five miles along the top. During the site selection and reservoir planning stages of the project, it was recognized that several factors would have an impact on the reservoir's ability to retain water. Included among these are the risk of sinkholes and the presence of an abandoned phosphate strip mine underlying about one third of the 1,100 acre reservoir footprint. Each of these caused concern for both the ability of the reservoir to hold water (bottom leakage) and the ground stability beneath the embankment. The subsurface investigation included a multi-level approach to site characterization including:

- Photolinear analysis,
- Ground penetrating radar,
- Shear wave seismic refraction,
- High resolution seismic reflection, and
- Nearly 17,000 ft of soil borings

The intent of this program was to progress (going down this listing) from broad reconnaissance to successively more detailed investigations as important subsurface features became identified. The net result was identification and remediation of potential sinkhole and mining areas risks, which has resulted in a reservoir whose actual leakage volumes are less than the original design estimates.

Introduction

The C.W. Bill Young Reservoir is part of the Enhanced Surface Water System of Tampa Bay Water, the regional water supply authority. The reservoir is pump-storage facility that collects and stores surface water from local canals and river systems during periods of high discharge and supplies water for blending and treatment during drought conditions or periods of increased demand. The reservoir site is an above-ground, closed earthen embankment that has no inlet or outlet streams/rivers save for the pumping and pipeline networks that provide for water supply and withdrawal. The reservoir (Figure 1) covers over 1,100 acres and is specified to contain up to 15.5 billion gallons of water. The dimensions on Figure 1 are approximately 2 miles NS by 1 mile EW with a berm circumference of approximately 5 miles along the top.

Figure 1: Aerial photograph of the as-built C.W. Bill Young reservoir, SE Hillsborough County, Florida.

Geologic Setting

As part of its overall planning and design for the reservoir structure, Tampa Bay Water and its consultants realized that the geology of west-central Florida presented many challenges that would need to be addressed to ensure a successful project. The first step in development of the reservoir was site selection. A number of potential sites were considered, and the final selection was based, in part, on the presence of a relatively thick sequence of clay-rich strata of Miocene age. It was thought that this site would minimize risks associated with sinkhole activity and leakage. Even so, there were areas of concern that required extraordinary efforts for site characterization. For example, note the more-or-less circular features that surround the reservoir in Figure 1. Similar features also existed under the reservoir footprint, and there was concern that these might reflect relict sinkholes.

The study site is located within the Polk Upland Physiographic Province of Florida (Puri and Vernon, 1964). Land surface elevations range from approximately 70 to 100 feet above sea level. The land surface is flat to gently sloping.

Three major geologic units occur at or near the land surface. They are, in order of youngest to oldest, undifferentiated Plio-Pleistocene marine terrace deposits, the Miocene Peace River Formation and the Miocene Arcadia Formation (Scott, 1988; Scott et al., 2001).

The Plio-Pleistocene marine terrace deposits consist of 20 to 40 feet of fine to medium, well sorted sand. Scattered, small lenses of clay are present, and the sand mantle thickens to 60 – 70 feet in buried, relict sinkholes.

The Miocene Peace River Formation (Scott, 1988) includes an upper member, the Bone Valley Member, that generally consists of sand-sized and larger phosphorite grains set in a matrix of poorly consolidated sand, silt, and/or clay. The lithology of the unit is highly variable, and lateral and vertical

facies changes can be abrupt. The remainder of the underlying Peace River Formation is a mixed clastic-carbonate unit composed of interbedded quartz sand, clay and dolostone. The quartz sand is clayey, fine to medium grained, and poorly consolidated. The clay in the Peace River Formation may be sandy, silty, calcareous or dolomitic, and poorly to moderately consolidated. The dolostone is typically sandy, clayey, micro to fine crystalline (dolosilt), and poorly to moderately indurated. Peace River sediments range from 50 to 100 feet in thickness and overlie older Miocene deposits that are typically less than 100 feet thick.

The Arcadia Formation underlies the Peace River Formation throughout the region (Scott, 1988; Scott et al., 2001). The upper, undifferentiated Peace River Formation consists of interbedded sand, clay, and carbonate strata. In contrast to the Peace River Formation, the Arcadia is more carbonate rich, with widespread dolostone and limestone layers and lenses. The base of the Arcadia includes a sandy, sometimes phosphatic limestone known as the Tampa Member of the Arcadia Formation. The Tampa Member is typically limestone that is moderately sandy, clayey and locally may contain lenses of green and gray clayey sand, sandy clay and chert. Near the reservoir, the Tampa Member is found at depths greater than 200 feet below land surface.

After deposition of the Miocene strata, a major unconformity developed that is characterized by a well-developed paleo-soil locally known as the "leached zone." The leached zone is characterized by relict stream channels, in-filled sinkholes, and an irregular surface, all of which are at least partly masked by the overlying Plio-Pleistocene marine terrace deposits.

Because of its high phosphate content, the upper Peace River Formation, especially the Bone Valley Member, is mined throughout the area. About the southern third of the reservoir site was an abandoned phosphate strip mine that had been back filled with clay wastes and sand tailings, both of which typically have low soil strengths.

Multi-Level Investigation and Findings

Given the large areal footprint of the reservoir (see Figures 1 and 2), no single geophysical or invasive testing method would satisfy the dual requirements of covering expansive tracts of ground while being able to focus on potential geologic hazards that may only be a few tens of feet in diameter. We chose to stage our investigation by looking at the broadest of features (photolinears) and progressively focusing in on developing targets by relying on techniques that yielded increasing detail at the expense of slower (and more expensive) progress. The following sections describe the rationale for each technique and what subsurface features were ultimately defined at each stage of investigation.

Photolinear Analysis

Figure 2 is a pre-construction aerial photograph of the reservoir site with an overlay of interpreted photolinear features. Photolinears were tentatively identified on aerial photographs from six different years. Colors of lines on Figure 2 reflect confidence in the presence of the photolinear. Red lines represent highest confidence and yellow reflects lowest.

Areas for geophysical testing within the reservoir were selected based on the photolinear analysis. Photolinear intersections (Lattman, 1958; Lattman and Matzke, 1961; Lattman and Parizek, 1964; Littlefield et al., 1984), high and medium confidence photolinears, and apparent sinkhole features were subjected to geophysical testing. In addition, the proposed location of the berm surrounding the reservoir was subjected to extensive geophysical exploration.

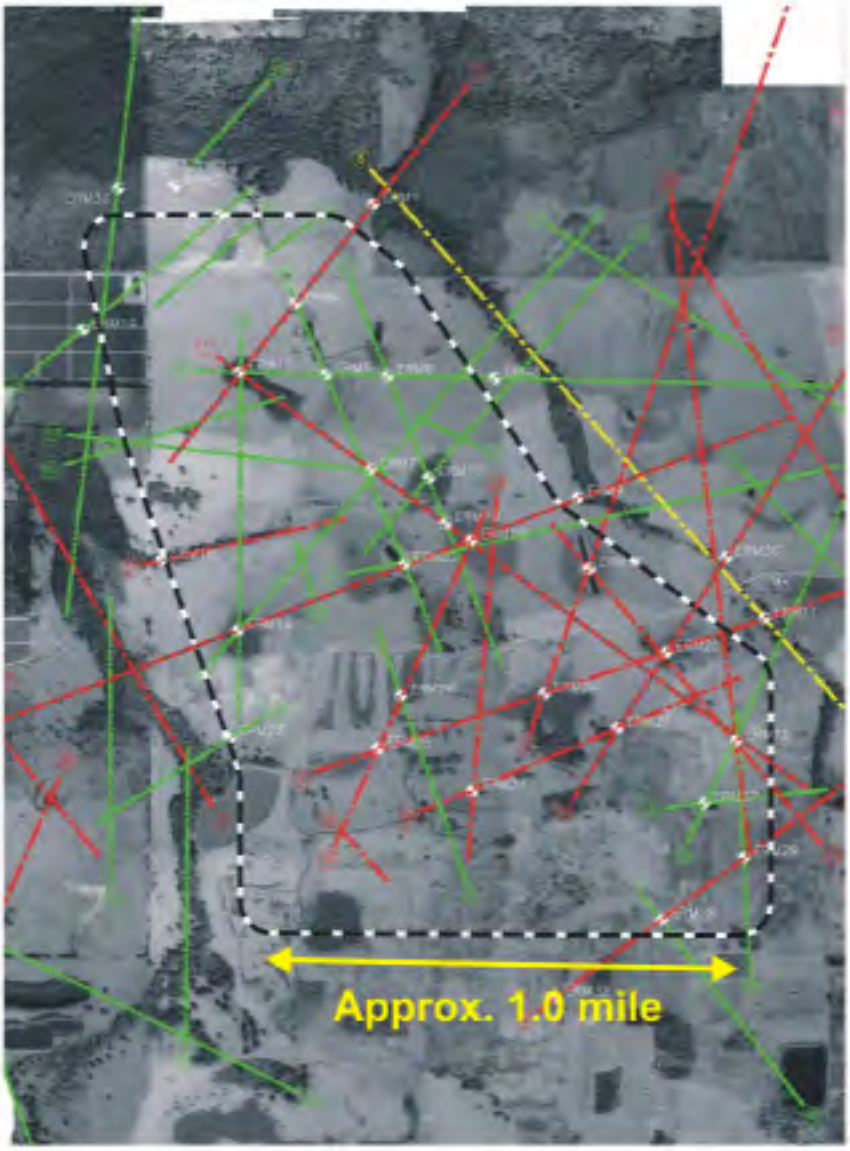

Figure 2: Pre-construction aerial photograph of reservoir site with superimposed photolinears and representative borehole locations.

Ground Penetrating Radar (GPR)

GPR has limited depth of penetration over much of the United States, but Florida is usually blessed with dry surficial sands that enable typical depths of penetration on the order of tens of feet. GPR is also one of the most rapid geophysical survey techniques, capable of being pulled behind a vehicle at a brisk walking speed. Even though the depth to limestone is on the order of 80-100 ft in this area, active and paleo-sinkhole features often are revealed by sagging or disruption of shallower soil horizons in response to past (or current) episodes of soil raveling (Dobecki and Upchurch, 2006). Given the speed with which GPR data are acquired, this enabled acquisition of data covering large areas of the reservoir project, including traverses along the centerline of the entire embankment plus parallel lines 100 ft to each side of the centerline. We also acquired gridded (areal) coverage over areas of interest

defined by the analysis of the photolinears. In total, approximately 156,000 lineal feet of GPR profiling was acquired across the property.

In general, the GPR had an approximate depth of penetration that ranged from 10 to 15 feet below land surface. This defined the basic surficial sand layer and occasionally would track the sand/clay (terrace sand/Peace River Formation) interface. Most of the detected anomalies were areas where we observed localized concentrations (vertical as well as lateral) of diffraction hyperbolae, which we interpreted as looser soil anomalies and potentially raveled soil zones. In the phosphate mined areas, the GPR signature was very complex showing both zones of minimal penetration (clay waste volumes) as well deep penetration over sand tailings piles.

Shear Wave Seismic Refraction

Regional geologic models had identified the presence of a cemented sand layer at a typical depth of approximately 30-40 feet below land surface, which is over twice as deep as the GPR data could reach. This layer, which is a hard layer within the leached zone and below the water table, offered the potential of providing a surface that could reflect potential raveling or sinkhole development. It was reasoned that areas where the layer was absent or depressed could reflect loss of underlying support.

Seismic refraction was selected as the test method to track this layer as it is an effective tool for mapping interfaces where a harder layer underlies a softer layer. Seismic shear (S) waves were selected over the compression (P) wave technique because of the level of contrast between the shallower/softer soils and the cemented layer. Preliminary testing of P versus S wave refraction showed that the P wave velocity of the cemented layer was approximately 15-20% higher than the loose soils above. The S wave velocity contrast however, was nearly 300% higher in the cemented layer than in the looser shallow soils. This is to be expected below the water table where the P wave velocity of all layers jumps due to water saturation. The shear wave velocity has almost no response to full water saturation, as it expresses contrast between the matrix of the soils and the degree of cementation. The high contrast using S waves led to more precise interpretations of the resulting refraction data. All major GPR anomalies were tested using refraction profiling. The entire berm length was also surveyed using S wave refraction because material strength and continuity beneath the berm is such an important factor. In total, approximately 71,800 lineal feet of shear wave seismic refraction profiling was acquired across the property.

Figure 3 is a plot of a raw shot record – 24 channels, SH geophones/SH hammer source with a 10-ft geophone spacing. The raw data show three clear velocity arrivals. Figure 4 shows an interpreted seismic refraction profile in an area where the deepest (cemented) layer exhibits an approximately 20 ft depression. The typical layer parameters are:

- Layer 1; Vs = 350 ft/sec; surficial (disturbed) soil
- Layer 2; Vs = 890 ft/sec; compacted sands and clays
- Layer 3; Vs = 2,415 ft/sec; cemented layer

Such anomalies were tracked and mapped and then they were scheduled for more detailed analysis using high-resolution seismic reflection, geotechnical borings, or both.

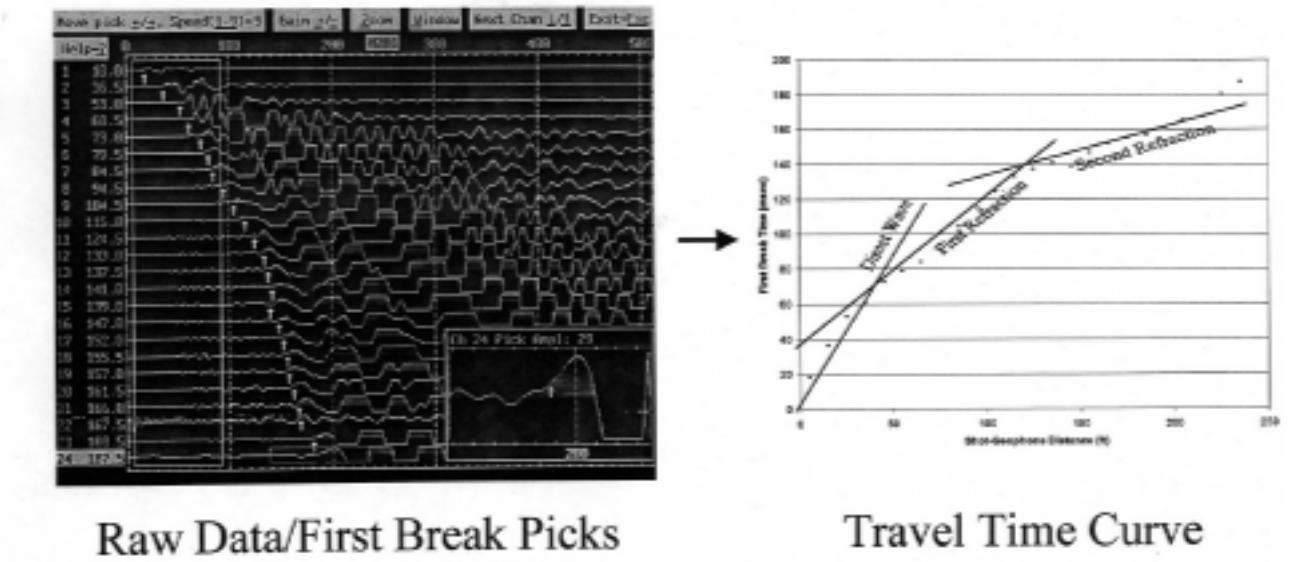

Figure 3: Raw shot record (left) and refraction travel time curve.

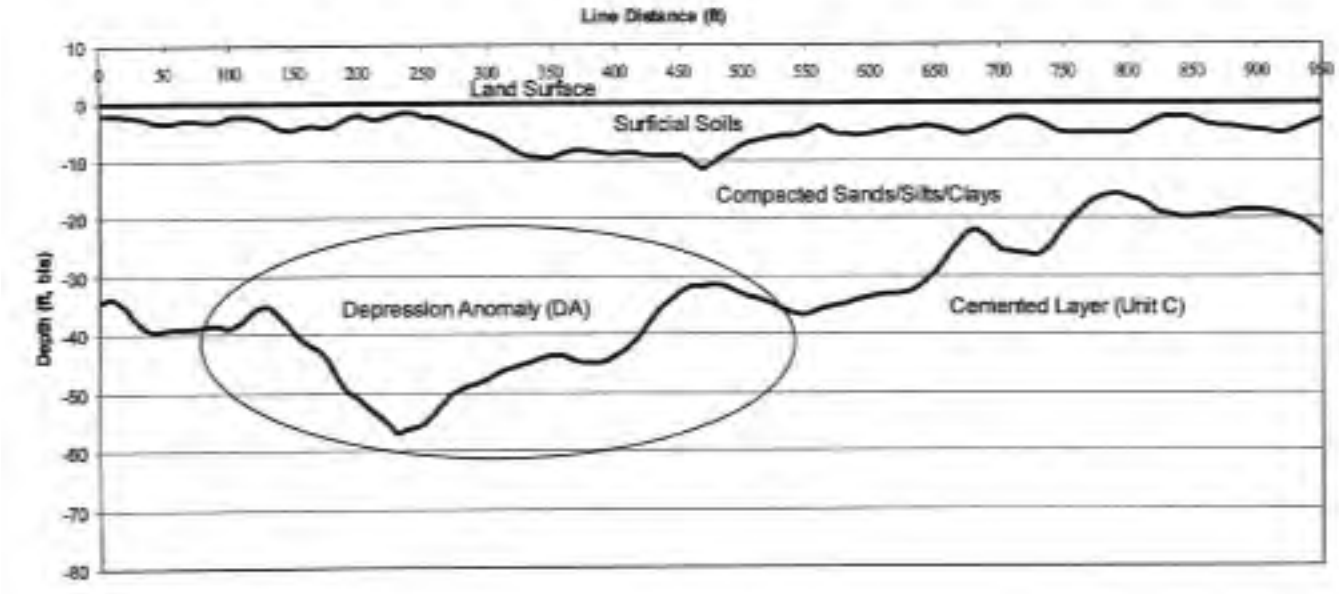

Figure 4: Interpreted S wave refraction cross section showing a depression anomaly.

High Resolution Seismic Reflection

Areas that were characterized by photolinears/intersections, GPR anomalies, and refraction depression anomalies were deemed to be potential sinkhole features that required deeper and more detailed investigation. These types of anomaly combinations were surveyed using high-resolution seismic reflection surveying. We utilized a 24-channel seismograph, 12-fold acquisition procedures with 5-ft shot and geophone spacing. The source was an 8 gauge Betsy Seisgun fired within a shallow

(2 ft) augered hole. In total, approximately 17,200 lineal feet of high resolution seismic reflection profiling was acquired across the property.

Figure 5 is a sample seismic reflection section that was acquired across shallow radar and refraction anomalies. The dashed line near 0.030 sec is the interpreted top of the dolostone layer. We have circled two anomalous areas where there is a loss of continuity of the dolostone reflection and where there is a depressed and down warped appearance of that reflection. We also show the location of two standard penetration test (SPT) borings (ERM-39A and ERM-40A) that were drilled at the locations of maximum disruption as seen on the reflection section. The results of these borings will be discussed in the following section.

Geotechnical (Invasive) Exploration

As stated initially, the objective of the combined geophysical surveys was to determine optimum locations for later drilling and other invasive testing. In all, more than 3 ½ miles of soil borings were drilled as part of the geotechnical investigation at the reservoir site. As an example of the results of drilling as compared with the geophysical interpretations, Figure 6 is a boring-derived subsurface cross section containing the same interval as defined by the seismic cross section in Figure 5. The two common borehole positions are ERM-39A and ERM-40A on both figures. The borehole results at ERM-40A clearly show increased depth (depth is nearly double the normal dolostone depth) to the dolostone layer because of what appears to be a sinkhole.

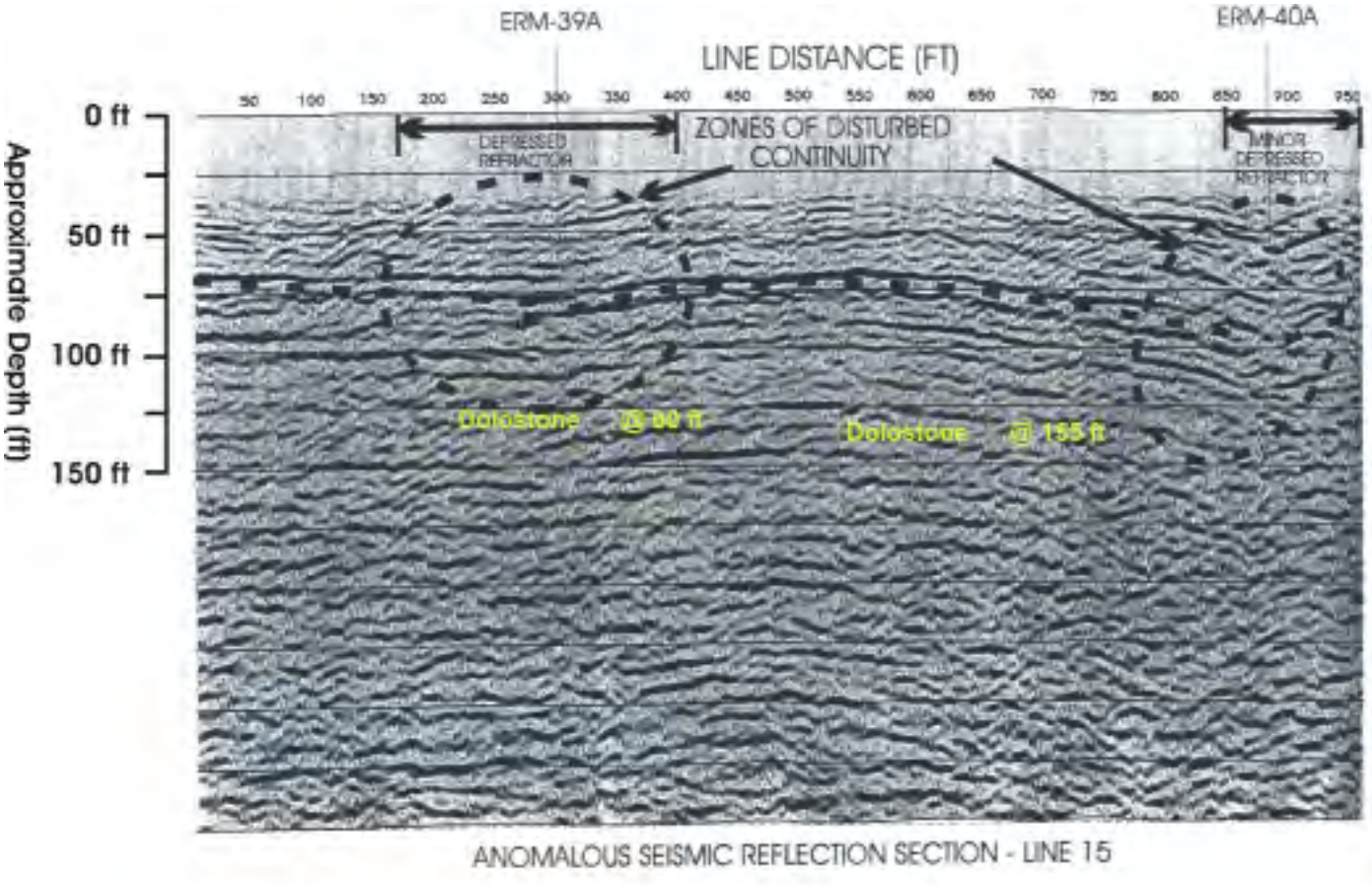

Figure 5: Interpreted P wave reflection section.

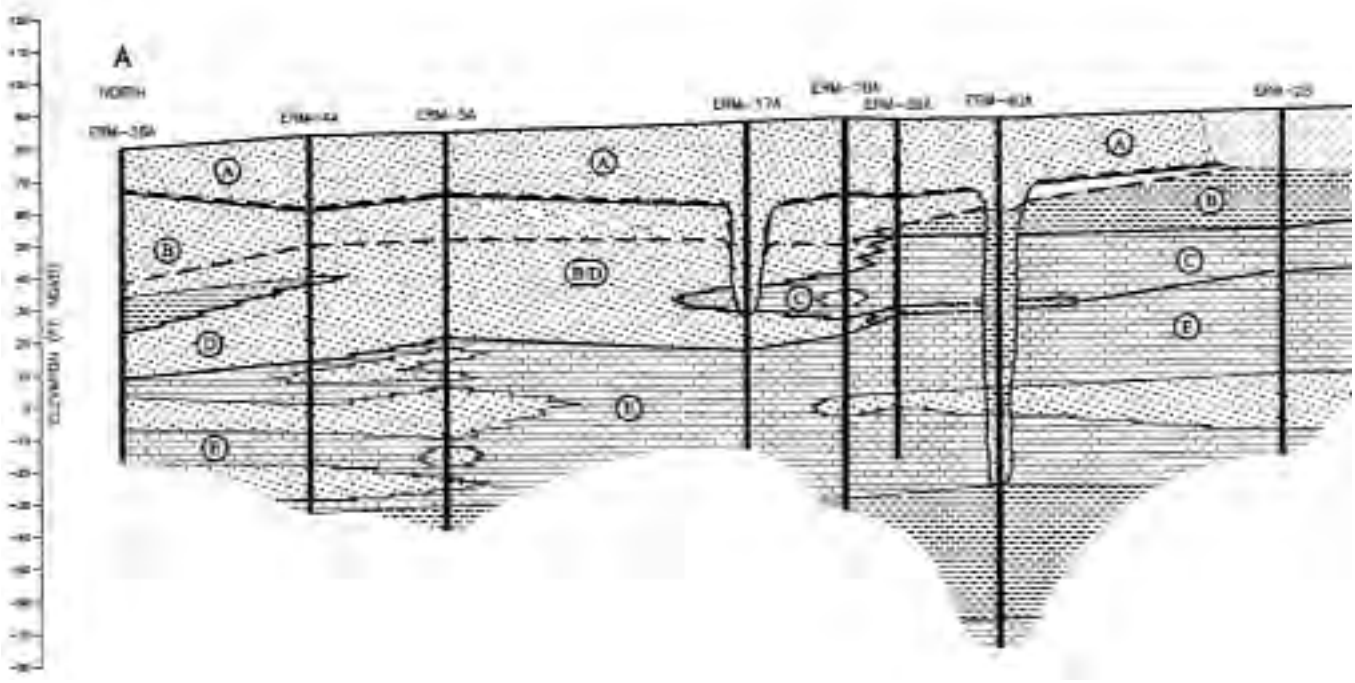

Figure 6: Interpreted subsurface cross section based on borehole data (includes boreholes ERM-39A and ERM-40A shown on seismic section of Figure 5). Dashed lines indicate the upper and lower surfaces of the paleo-soil known as the leached zone. Letters reflect different lithosomes.

Conclusions

The geophysical exploration program was successful. A number of karst features were identified and verified using standard penetration and/or cone penetrometer testing. It was also possible to detect buried relict stream channels and other topographic features developed on the paleo-soil known as the leached zone.

One apparent sinkhole feature within the original alignment of the berm was considered of sufficient importance that the berm was realigned to avoid it. Other karst features within the reservoir interior were dealt with through the use of impervious membranes and other measures. The reservoir has been in use for several years, and it is estimated that leakage from the reservoir is less than predicted. No sinkholes have developed.

References

Dobecki, Thomas L. and Upchurch, Sam B., 2006, Geophysical applications to detect sinkholes and ground subsidence, Geophysics The Leading Edge, v 25, pp336-341.

Lattman, L.H., 1958, Technique of mapping geologic fracture traces and lineaments on aerial photographs, Photogrammetric Engineering, v 24, pp 568-576.

Lattman, L.H., and R.H. Matzke, 1961, Geological significance of fracture traces. Photogrammetric Engineering, v 27, pp 435-438.

Lattman, L.H., and R.R. Parizek, 1964, Relationship between fracture traces and the occurrence of groundwater in carbonate rocks, Journal of Hydrology, v 2, pp 73-91.

Littlefield, J.R., M.A. Culbreth, S.B. Upchurch, and M.T. Stewart, 1984, Relationship of modern sinkhole development to large-scale photolinear features. In B.F. Beck (ed.), Sinkholes: Their Geology, Engineering & Environmental Impact. Rotterdam, B.A. Balkema, pp. 189-195.

Puri, H. S. and R. O. Vernon, 1964, Summary of the Geology of Florida and Guidebook to the Classic Exposures, Florida Geological Survey Special Publication no. 5 (revised), 312 p.

Scott, T. M. 1988, The Lithostratigraphy of the Hawthorn Group (Miocene) of Florida, Florida Geological Survey Bulletin No. 59, 148p.

Scott, T. M., K. M. Campbell, F. R. Rupert, J. D. Arthur, T. M. Missimer, J. M. Lloyd, J. W. Yon, and J. G. Duncan, 2001, Geologic Map of the State of Florida. Florida Bureau of Geology, Map Series No.114.

WAVE-ENERGY SOURCE FOR MASW?

Mario Carnevale, Hager GeoScience, Inc., Woburn, MA
Choon B. Park, Park Seismic LLC, Shelton, CT

Abstract

Since its inception as a subsurface imaging technique, the multichannel analysis of surface waves (MASW) seismic method has been used in a variety of environmental and geotechnical applications. One of the more interesting applications is performing subsurface imaging in a beach environment. Although the loose and dry ground surface appears to present a formidable obstruction to the application of MASW for deep imaging, there could be an anonymous unexploited source of energy to make it happen. We look at the possibility that low frequency energy from ocean wave fronts can be introduced into seismic recordings made during MASW surveys along a beach or shoreline. Seismic data from MASW beach and shoreline surveys in Massachusetts will be examined for possible evidence of constructive or destructive interference from energy produced by ocean waves. The possible relationships of MASW survey geometry and the geography of the project settings are also examined.

This study aims at evaluating the possible exploitation of ocean energy for deep MASW surveys in beach and shoreline environments.

Introduction

The MASW method introduced by the Kansas Geological Survey (KGS) (Park et al., 1999) was presented with suggested survey geometries intended to optimize imaging depths and object resolution. Table 1 (Park et al., 2002) illustrates the suggested survey parameters. These parameters are necessary because the 1D Vs depth profile generated by modeling one shot gather is assumed to be located at the midpoint of the geophone array. By moving the geophone array a set distance for another shot gather, a 2D Vs depth profile can be constructed by stitching together several 1D Vs depth profiles.

Although the parameter values in Table 1 reflect changes from initially proposed parameters, they are nonetheless based on theoretical considerations and modest field research analysis.

Figure 1: MASW site locations.

Table 1: Optimum Survey Parameters for active MASW (Park et al, 2002)

Receiver (Hz)	Max. Depth (m)	Minimum Offset (m)	Maximum Offset (m)	Receiver Spacing (m)
4.5	50	10	100	1
10	30	10	100	1
40	15	10	100	1

Since its inception, the active MASW method has been used in a variety of subsurface investigations, including soil characterization (Park and Miller, 2004), stratigraphy mapping (Miller, et al., 1999), anomaly detection (Xia et al., 2002 and Park and Carnevale, 2009), and structural analysis (Ivanov et al., 2006). In many commercial applications, site conditions are less than ideal and, in fact, can mandate significant deviation from an optimum suggested survey geometry.

The most common constraint experienced in the field is insufficient linear distance for accommodating shot offsets and geophone array lengths. The theoretical adverse impact of the survey geometry constraint (short geophone array length) is the inability to capture lower frequency surface waves generated by the active source, thereby limiting the depth of imaging and the number of 1D Vs profiles available for constructing 2D Vs profiles. However, in certain settings, low frequency surface waves are recorded during MASW surveys where the restricted survey geometry is not suitable for capturing low frequency surface waves generated by an active source (Carnevale and Hager, 2008). If the low frequency wave train is travelling from a source located in the opposite direction from that of the active source, it produces destructive interference. However, if it were traveling in the same direction, it could produce constructive interference.

This paper presents data from three project locations to illustrate the concept that the constructive interference of low frequency surface waves generated by active ocean mechanisms can supplement the active source energy and contribute to a coherent dispersion analysis.

Project Descriptions

The three project locations chosen for this study involved high resolution of relatively shallow targets and 2D subsurface profiles within constrained study areas. Their locations are in eastern Massachusetts (Figure 1). Two of the project areas (Areas 1 and 2) are located along mainland beaches in Hull and Rockport. The third (Area 3) is on Nantucket Island.

Area 1 on Nantasket Beach, Hull, MA

The project area is located along Nantasket Beach in Hull, Massachusetts. The objectives were to determine the angle of slope of a buried beach revetment surface defined by layered boulders and the depth to the bottom of the buried revetment. The MASW survey was used to image the base of the revetment. The survey was performed at low tide, with the seismic line oriented along the beach parallel to the revetment. Figure 2 shows the location of the beach section (left) at which the geophysical data were collected, and the setup for the MASW data collection (right).

Figure 2: Nantasket Beach (left) and MASW survey array (right).

Area 2 at Bearskin Neck, Rockport, MA

The project area is located in Rockport, Massachusetts. At this location the objective was to determine the depth to bedrock behind an existing seawall for a proposed seawall extension within the riprap area. The survey area lies at the west end of Rockport Harbor and is protected by a breakwater from direct impact by ocean waves (Figure 3 left). The seismic survey was restricted to a 20-meter length and by boulder rip-rap. These constraints affected the geophone array length and offset shots distances (Figure 3 right).

Figure 3: Rockport Harbor and site survey conditions.

Area 3 in Madaket, Nantucket Island, MA

The project area is located off the Massachusetts coast on the island of Nantucket. The site is at the west end of the island in a section known as Madaket (Figure 4 left). The objective of the investigation was to identify glacial outwash deposits, if present, beneath dune sand in an area identified as a possible barrier beach containing dune deposits.

MASW data were acquired along five lines along the main dirt access road to the site, parallel to the west shore and perpendicular to the north and south shores, and along two secondary dirt trails leading to the west shore (Figure 4 right).

Figure 4: Aerial views of Madaket Harbor (left) and MASW lines (shown in green on right).

Data Analysis

Area 1 on Nantasket Beach, Hull, MA

The MASW survey geometry was optimized for resolution of a shallow buried target (<6 m). Table 2 lists the survey parameters.

Table 2: Nantasket Survey Parameters

Receiver Array	Linear array over revetment
Line Orientation	N-S Orientation
Receivers	4.5 Hz Geophones
Number of Channels	15 Channels
Receiver Spacing	x = ~0.9m (3 ft)
Total Length of Receiver Array	Dx = ~12.8m (42 ft)
Source Offset	SO = ~2.7m (9 ft)
Survey Interval	Move = ~0.9m (3 ft)

Figure 5 shows the normalized spectral amplitude (left) for each trace of a 15-trace seismogram (right) from the Nantasket survey. The predominant frequency range for the spectra is approximately 35 to 60 Hz. However, all 15 traces also show a coherent frequency component centered at approximately 7 Hz.

Figure 6 shows an overtone image of a shot recorded from the survey. The dispersion trend ranges from ~ 7 Hz to ~37 Hz. Based on the survey geometry, the overtone image clearly illustrates a low frequency phenomenon, as reflected in the 2D Vs depth profile (Figure 7).

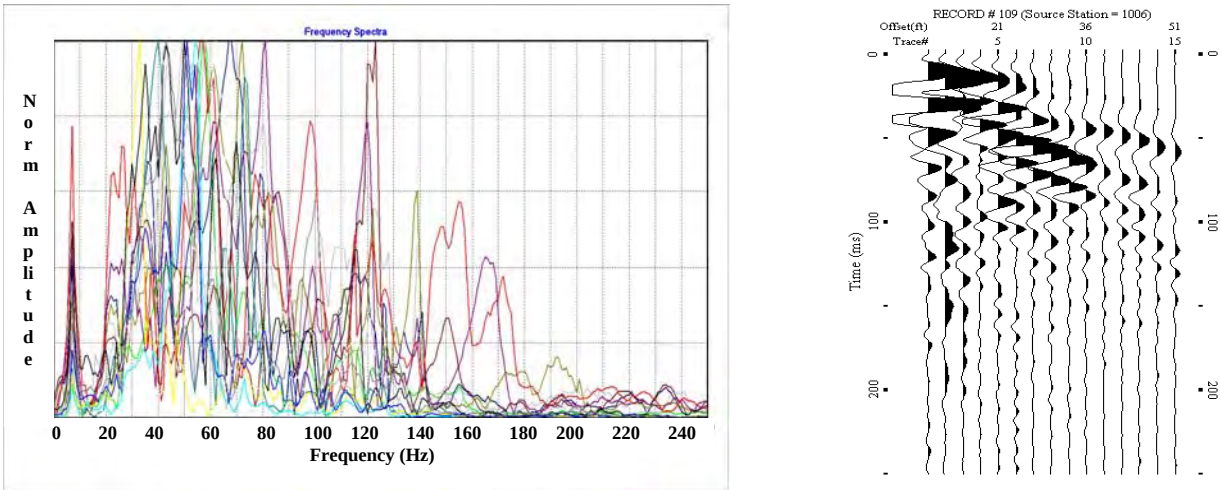

Figure 5: Normalized spectral amplitudes of 15 traces (left) of a Nantasket seismogram (right).

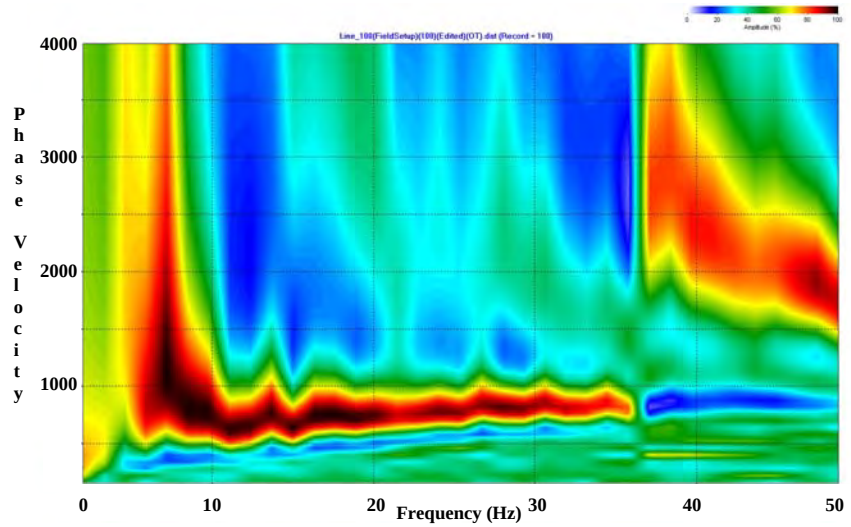

Figure 6: Overtone image from Hull survey.

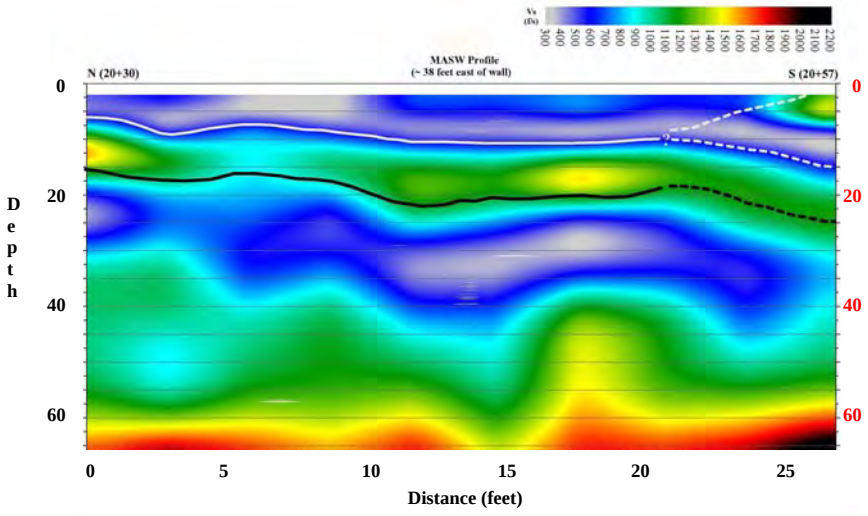

Figure 7: 2D Vs depth profile from Hull survey.

Area 2 at Bearskin Neck, Rockport, MA

This survey was performed to resolve the depth to shallow bedrock surface within a constrained distance of approximately 65 feet. Table 3 shows the survey parameters used for this survey.

Table 3: Rockport Survey Parameters

Receiver Array	Linear array over shallow bedrock
Line Orientation	N-S Orientation
Receivers	4.5 Hz Geophones
Number of Channels	16 Channels
Receiver Spacing	x = ~0.6m (2 ft)
Total Length of Receiver Array	Dx = ~9.15m (30 ft)
Source Offset	SO = ~3 & 6.1m (10 & 20 ft)
Survey Interval	Move = ~0.6m (2 ft)

Figure 8 shows the normalized spectral amplitude (left) for each trace of a 16-trace seismogram (right) from the Rockport survey. The predominant frequency range for the spectra is approximately 45 to 70 Hz. However, all 16 traces also show a coherent frequency component centered between approximately 10Hz and 12Hz. The low frequency content can also be seen in shot records shown in Figure 8 right.

Figure 9 shows an overtone image of a shot gathers from the survey. The dispersion trend ranges from ~ 7 Hz to ~37 Hz. Based on the survey geometry, the overtone image clearly illustrates an anomalous situation.

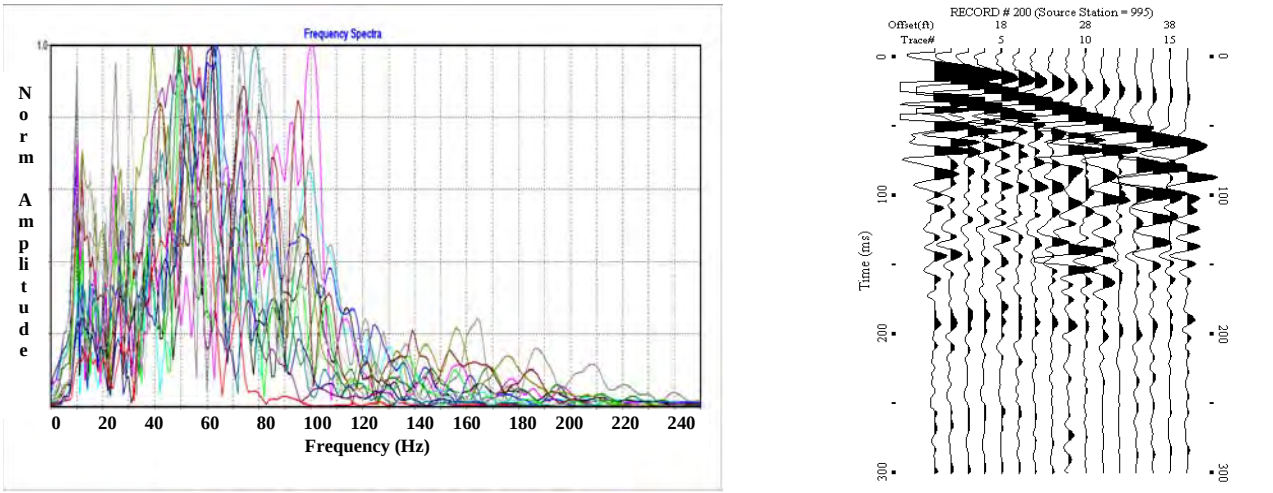

Figure 8: Normalized spectral amplitudes (left) of 16 traces of a Rockport seismogram (right).

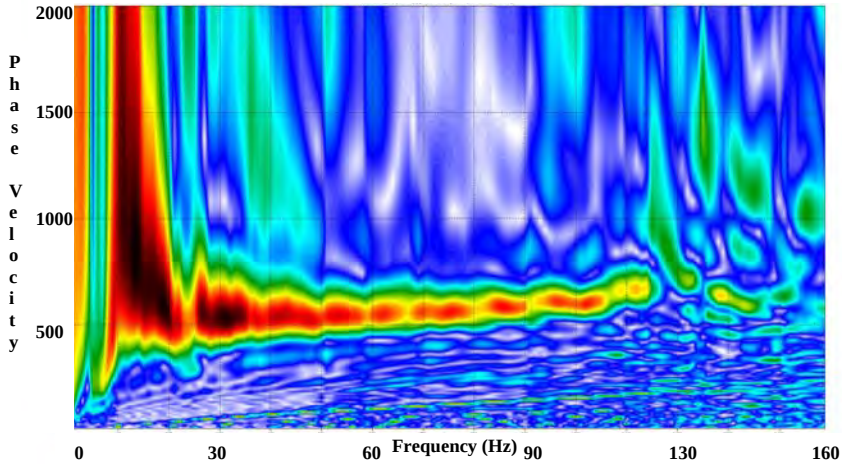

Figure 9: Overtone image from Rockport survey.

Area 3 in Madaket, Nantucket Island, MA

This survey was performed to resolve shallow soil stratigraphy in order to classify soils for land-use consideration. Table 4 shows the survey parameters used for this survey.

Table 4: Nantucket Survey Parameters

Receiver Array	Linear array over beach and glacial deposits	Linear array over beach and glacial deposits
Line Orientation	NE-SW Orientation	NW-SE Orientation
Receivers	4.5 Hz Geophones	4.5 Hz Geophones
Number of Channels	24 Channels	16 Channels
Receiver Spacing	x = ~1.2m (4 ft)	x = ~1.2m (4 ft)
Total Length of Receiver Array	Dx = ~28m (92 ft)	Dx = ~18.3m (60 ft)
Source Offset	SO = ~6.1m (20 ft)	SO = ~3.7m (12 ft)
Survey Interval	Move = ~6.1m (20 ft)	Move = ~1.2m (4 ft)

With the above survey geometry, we could expect an optimistic image depth of approximately 9 to 14 meters for the N-S lines and 6 to 9 meters for the NW-SE lines. We also expect a low fundamental mode frequency of approximately 15 Hz for the N-S lines and 25 Hz for the NE-SW lines.

Figure 10 and 11 show the normalized spectral amplitude (left) for each trace of 24-trace and 16-trace seismograms (right) from NE-SW and NW-SE arrays, respectively. In the NE-SW arrays, the predominant frequency range for the spectra is approximately 20 to 30 Hz. Relative to the predominant frequency, the lower frequency energy between 5 and 10 Hz is less, but, nonetheless, significant and coherent. In the NW-SE arrays, the spectral amplitude range is broader and less concentrated. The predominant frequency range for the spectra is approximately 45 to 65 Hz, with most of the energy concentrated between 25 and 70 Hz. However, significant energy is focused in the spectra at 15 Hz and 5 to 10 Hz. Seismograms in Figures 10 (right) and 11 (right) illustrate the surface wave characteristics.

Figures 12 and 13 show overtone images from NE-SW and NW-SE shot gathers, respectively. The fundamental mode low frequency component in both orientations is as low as 5 Hz, a value lower than that expected from the applied survey geometry. Based on overall data trends, the anomalous low

frequency energy contribution observed in data from the NE-SW surveys appear to be more coherent.

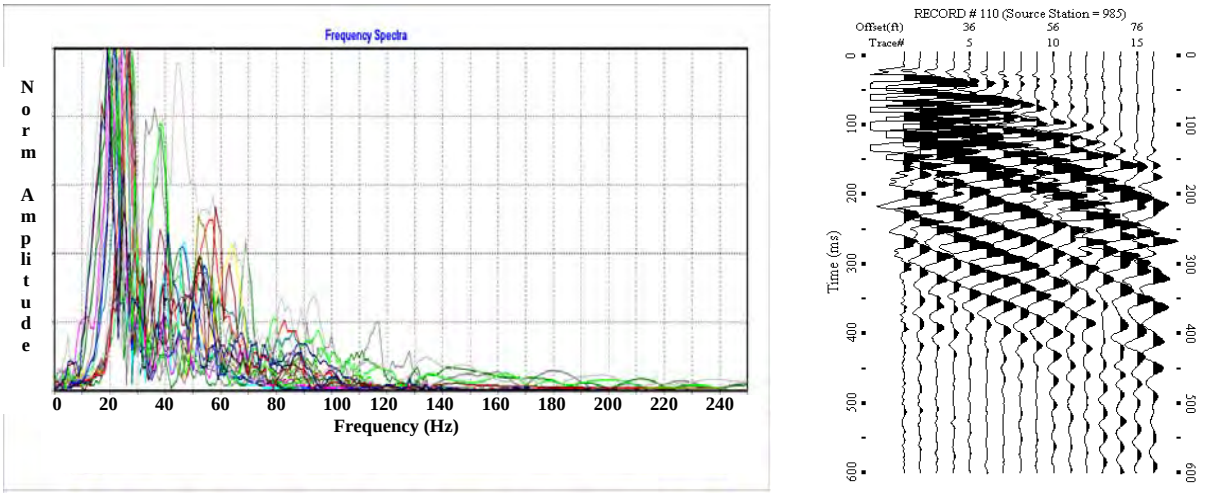

Figure 10: Normalized spectral amplitudes (24 traces) of a Madaket seismogram (right) from the NE-SW array.

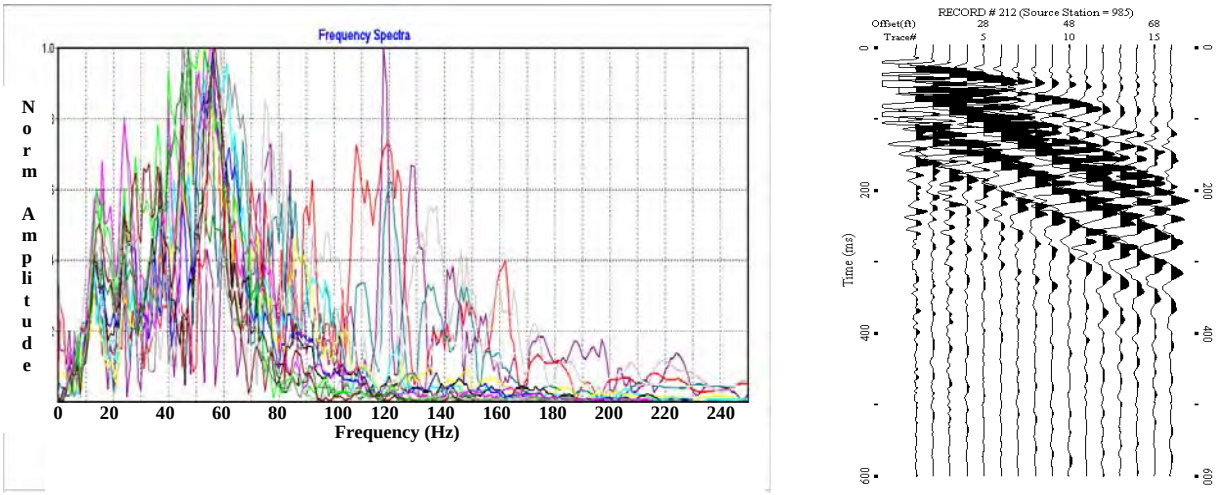

Figure 11: Normalized spectral amplitudes (16 traces) of a Madaket seismogram (right) from the NW-SE array.

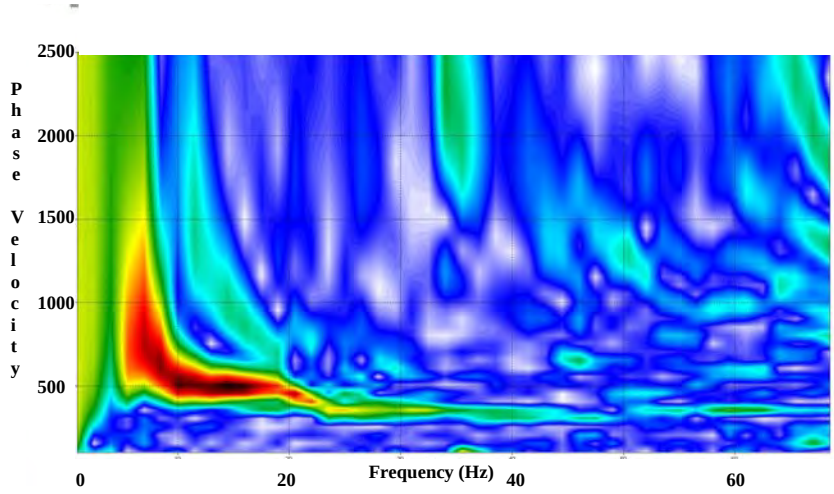

Figure 12: Overtone image from Nantucket N-S array.

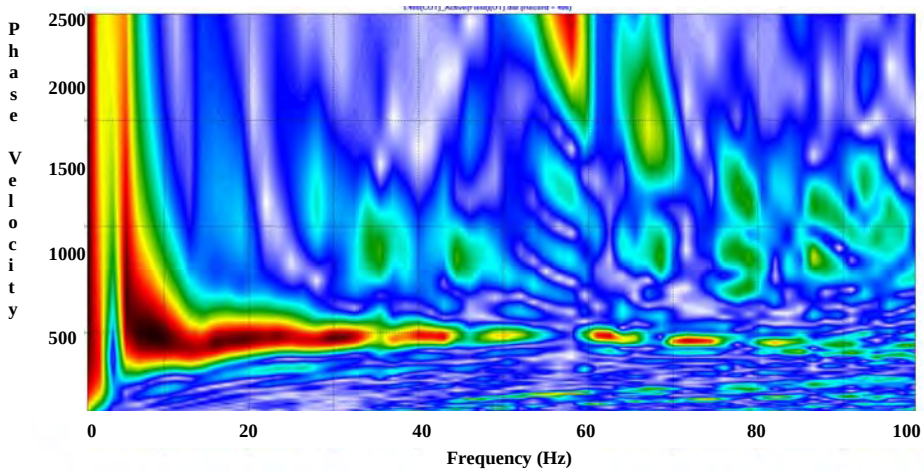

Figure 13: Overtone image from Nantucket E-W array.

Conclusions

The results of the three ocean-side projects show that the data collected using the active MASW survey method contain lower frequency content than those predictable from the survey geometry employed. This observation is most clearly demonstrated in the Hull (Area 1) and Rockport (Area 2) projects, where the survey lineal geometries were significantly constrained.

The direction of the source of low frequency energy is a subject of current discussion. Based on the survey geometries of the three projects, we can speculate that wave energy from an approximate in-line orientation contributes coherent low frequency signals. Figure 14 illustrates the regional pattern of wave energy (oceanwave.com). However, local variations occur in the regional pattern due to wave diffractions caused by the sea floor topography.

For the Hull (Area 1) survey, the MASW line orientation, the geographic alignment of Nantasket Beach, and the longshore drift directions are coincidental (Figure 1). At Rockport (Area 2), the MASW line orientation paralleled the shoreline of Rockport Harbor to the east. However, the N-S MASW line points toward the open ocean to the north, where constant wave trains pound the granite

bedrock along the open coast (Figure 15 left). The setting on Nantucket Island (Area 3), where potential wave energy is available from all directions, is more complex. However, Figure 4 illustrates the relationship of the island geometry to the open Atlantic Ocean. The shape of the island reflects the erosional history and, therefore, the direction of maximum wave energy, i.e. from the south (Figure 15 right). Additional study is needed to examine the effect of wave energy azimuth and MASW line geometry for active and passive surveys.

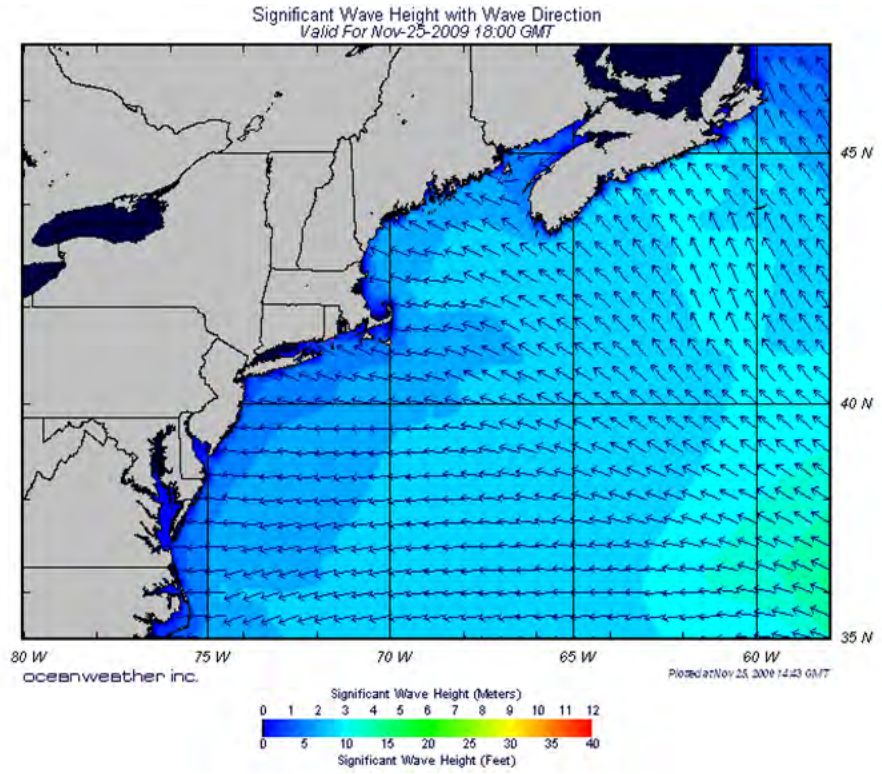

Figure 14: Regional wave energy pattern (oceanwave.com).

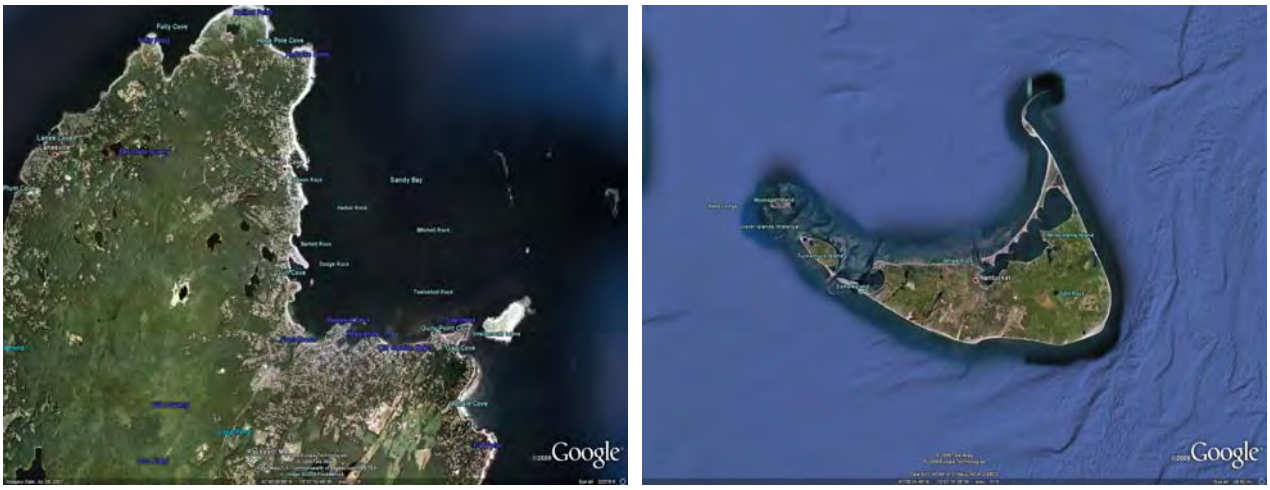

Figure 15: Cape Ann, MA. (left) and Nantucket Island (right).

References

Carnevale, M., and Hager, J. (2008). "Characterization of a beach revetment using ground penetrating radar and MASW", SAGEEP 2008, Philadelphia, PA, April 6-10, Proceedings on CD ROM.

Miller, R.D., Xia, J., Park, C.B., and Ivanov, J., (1999), "Using MASW to map bedrock in Olathe, Kansas" [Exp. Abs.], Soc. Explor. Geophys., p. 433-436.

Park, C.B., and Carnevale, M., (2009), "3D MASW survey," SAGEEP 2009, Fort Worth, TX, March 29-April 2, Proceedings on CD ROM.

Park, C.B., and R.D. Miller (2004), "MASW to map shear-wave velocity of soil", Kansas Geological Survey Open-file Report 2004-30.

Park, C.B., Miller, R.D., and Miura, H., (2002), "Optimum field parameters of an MASW survey", Proceed. SEG-Japan 2002, Tokyo, Japan.

Park, C.B., Miller, R.D., and Xia, J., 1999, "Multichannel analysis of surface waves", Geophysics, v. 64, n. 3, pp. 800-808.

Xia, J., Li, P.H., Lewis, M.J., Miller, R.D., and Park, C.B., (2002), "Using surface wave method to define a sinkhole impact area in a noisy environment", Proceedings of the SAGEEP 2002, Las Vegas, Nevada, 13CAV7.

Ivanov, J., R.D. Miller, N. Stimac, R.F. Ballard, J.B. Dunbar, and S. Smullen, (2006), "Time-lapse study of levees in southern New Mexico", *[Exp. Abs., Soc. of Expl. Geophys.*

Roadside Passive MASW Survey — Dynamic Detection of Source Location

Choon B. Park, Park Seismic, LLC, Shelton, Connecticut, USA

Abstract

In a roadside passive surface-wave survey under a typical urban setting with relatively heavy traffic and a complicated network of roads, a field record usually contains surface wave events generated from multiple source points scattered around the survey location. It is, however, those dominating energy events coming from one common surface point on the road that are used as signal in most advanced dispersion analysis methods based on the 2-D wavefield transformation. Events from other locations interfere adversely with signal events during the analysis if they take comparable energy or are largely ignored in the case of insignificant energy. A long record (e.g., 120 sec) is divided into many subsets of much shorter time of a proper length (e.g., 1 sec) and are treated as independent records of only one (or none) of a dominating event. By utilizing an advanced technique to detect fairly accurately the source location of the event, subsets are processed for their own dispersion images by using the scheme commonly used in the active MASW survey. Multiple data sets of the dispersion image are then stacked to result in an image of the highest signal-to-noise ratio (S/N) ever possible. This is demonstrated by using a field record acquired with a linear receiver array deployed along a busy street that contains events from complex source points and therefore could not be processed for any interpretable dispersion image using other methods currently available.

Introduction

The roadside MASW survey utilizes those surface wave events passively generated from ambient cultural activities, such as traffic. Under the typical urban setting, where a passive surface wave survey often takes place, one relatively long record (e.g., 120 sec) may contain dominating events generated from multiple source points scattered around the survey location due to the heavy traffic in a complicated network of roads. Park (2008; 2009), however, acknowledged it is usually those events of dominating energy originating from one common surface point that are used as signal in the subsequent step of dispersion analysis. The analysis method may be either a stochastic approach by Aki (1957) or a deterministic approach based on the 2-D wavefield transformation technique, which may include the conventional wavenumber method (Kx-Ky) (Claerbout, 1985) or an imaging method by Park et al. (2004). Although strong events from different locations may contribute positively in the process based on the wavefield transformation method if they are well apart in azimuth, they usually interfere adversely with each other due to the limited resolving power for a given recording aperture, which is usually below the degree necessary for any beneficial effects. All other events of relatively insignificant energy are then ignored (or averaged out) during the analysis. This potential harmful effect of multi-source (multi-azimuth) situation appears to exist even with a stochastic approach of the spatial autocorrelation (SPAC) method utilized in the microtremor survey method (MSM) (Aki, 1957; Okada, 2003). In this sense, all dispersion analysis methods of passive surface waves work on this unidirectional (single-azimuth) surface wave events of the most dominating energy as signal. This seems to be the main reason why an excessively long recording time (e.g., a few hundred seconds) has always been necessary to achieve the dominance.

It is, however, possible to utilize all events coming from different source locations if a long record (e.g., 120 sec) is divided into many subsets of much shorter time (e.g., 1 sec). If the length of

subset is properly chosen, then it becomes highly possible for each subset to contain only one event (or none). Then, each subset can be processed independently by using a method by Park (2008; 2009) that treats passive surface waves in a manner the same as would be used from an active survey with a known source location after detecting azimuth and distance of the source point most responsible for the recorded events. This approach is called the passive-with-active (PWA) scheme. An advanced technique (Park, 2010) to detect source location in subsets can show the time variation (e.g., every 1 sec) of azimuth and distance of detected events in a long record. Then, this information is used to apply the PWA method to each subset to produce one data set and dispersion image. Finally, multiple sets of dispersion images are stacked at the end to result in the final dispersion image of the highest signal-to-noise ratio (S/N).

Roadside Passive MASW — Dispersion Analysis

There are a few instances of dispersion imaging techniques recently developed specifically for use with passive surveys of multi-channel recording. Louie (2001) used the slant-stack approach by McMechan and Yedlin (1981) to treat most recorded events as inline propagation from both ends of the linear receiver array. It then claims the banded nature of dispersion image originates from the contribution of possible offline propagations and adopts an empirical scheme to pick the apparently correct phase velocities of inline propagation. This, however, lacks the knowledge of seismic signal processing that tells the banded image originates from the band-limited nature of seismic measurement in time and space (Yilmaz, 1987). Park et al. (2004) introduced a dispersion imaging technique based on the plane-wave propagation. This technique utilizes an azimuth-scanning technique accomplished by extending the conventional wavenumber (Kx-Ky) approach. It utilizes omnidirectional events through a stacking process after resolving azimuth of different events. Its effectiveness, however, is often limited due to the relatively low resolving power for a given size of receiver array. Then, Park and Miller (2008) acknowledged that those source points responsible for dominating events are usually within a finite distance from the receiver array and therefore the propagation should be treated as cylindrical instead of planar. This approach, however, can also produce dispersion images of low resolution and low signal-to-noise ratio (S/N) in the case of complex source points because of the same limitation in resolving power previously mentioned.

Park (2008; 2009) then improved this imaging technique simply by avoiding the azimuth stacking process and simply treating a recorded data set as one of an active survey (Park et al., 1998) after detecting azimuth (and approximate distance) of dominating events, which is in turn made through an improved azimuth-scanning technique introduced in Park et al. (2004). The new imaging technique, called the passive-with-active (PWA) scheme, showed detection of accurate azimuth is far more important than that of the distance and its azimuth detection technique is competent enough to achieve the necessary accuracy. Results from this approach were superb in comparison to those obtained by using other imaging methods by Park et al. (2004), Park and Miller (2008), and Louie (2001). As a consequence, this approach also works on those events of dominating energy generated from one common source point and treats other events as noise.

Dynamic Detection of Source Location (DDSL)

Although under typical urban setting there can be multiple source points scattered around the survey location generating events of comparably dominating energy, these events will very likely take place at different times. Therefore, if a long record is divided into many short (e.g., 1-sec) subsets of a proper length, each of them should contain only one (or none of) dominating event from one particular

source point. Then, each of these subsets can be processed for a dispersion image by using the PWA scheme by Park (2008; 2009). The resultant multiple data sets of dispersion image can then be stacked to improve the overall signal-to-noise ratio (S/N) of the dispersion image.

The original azimuth-scanning method by Park et al. (2004) based on the plane-wave propagation has been extended to account for cylindrical spreading of surface waves, and this improves the detection power of source location in azimuth and distance (Park, 2010). This technique can be applied to the aforementioned subsets to accurately detect source location of the event that may exist in the subset. Output from this new scanning approach consists of amplitude distribution in a 2-D space of azimuth and source distance. Then, the point where the maximum occurs represents the detected source location. By selecting data along the row and column directions at this detected point, respectively, two additional data sets are prepared. One shows amplitude variation along the azimuth axis and the other shows the variation along the source distance axis at different times. This will be illustrated in the next section by using a field data example. The former is called dynamic azimuth scan and the latter is called dynamic source-distance scan. These two output sets can be used for various purposes, including the evaluation of the stacked dispersion image obtained at the end as well as detecting source locations. For those subsets without any significant events, both scans show low amplitudes that can be used to judge whether any specific subset should be discarded from dispersion imaging or not. Once source location is determined from these two sets of scans, then each subset can be processed for its own dispersion image by using the PWA scheme.

Field Record

One field record selected for this study was acquired during the survey conducted on the sidewalk along Clinton Parkway in Lawrence, Kansas, using a 30-channel land streamer of 4.5-Hz geophones with 1.5-m spacing (Figure 1). Other passive MASW surveys were previously conducted near this area (Park and Miller, 2008; Park et al., 2004). The data acquisition was a combination of active and passive MASW surveys performed concurrently using a 20-lb sledge hammer source to apply impacts at 7.2-m inline off the 1st channel of the linear receiver spread that triggered a 120-sec recording with 4-ms sampling interval. The earliest 1-sec portion (Figure 2a) was then used for the active dispersion analysis (Figure 2b), and the remaining 119-sec portion was used for the passive dispersion analysis so that both results could be combined to produce a dispersion image of a wide frequency range that can lead to the final shear-velocity (Vs) profile of a large depth range (Park et al., 2005). The selected record was one of those with events of comparably dominating energy from different source locations and therefore could not lead to any interpretable dispersion image by using any other imaging methods currently available and outlined in the previous section. The 120-sec long record (Figure 3a) shows several prominent events, three of which are randomly selected and displayed in Figures 3b-3d at much a larger time scale. There are, however, many other events of relatively less dominating energy not noticeable in the display of this 120-sec record that exist almost at any instance in the record. Two of the selected events (A and B) show nonlinear arrival patterns indicating cylindrical wave propagation due to the proximity of a source point. The apex of each arrival pattern indicates a possible source point somewhere south of the first half part of the receiver array for event A, whereas it should be south of the second half (or near the end) of the receiver array for event B. The apparent linear arrival pattern of event C indicates a plane-wave propagation originating from a relatively remote source point west of the array.

The passive portion (1-120 sec) of this record was processed for a dispersion image using four different methods currently available: one by Louie (2001) based on the inline plane-wave propagation from both ends of the array (Figure 4a), one by Park et al. (2004) based on stacking of omnidirectional events of plane-wave propagation (Figure 4b), one by Park and Miller (2008) based on the stacking of

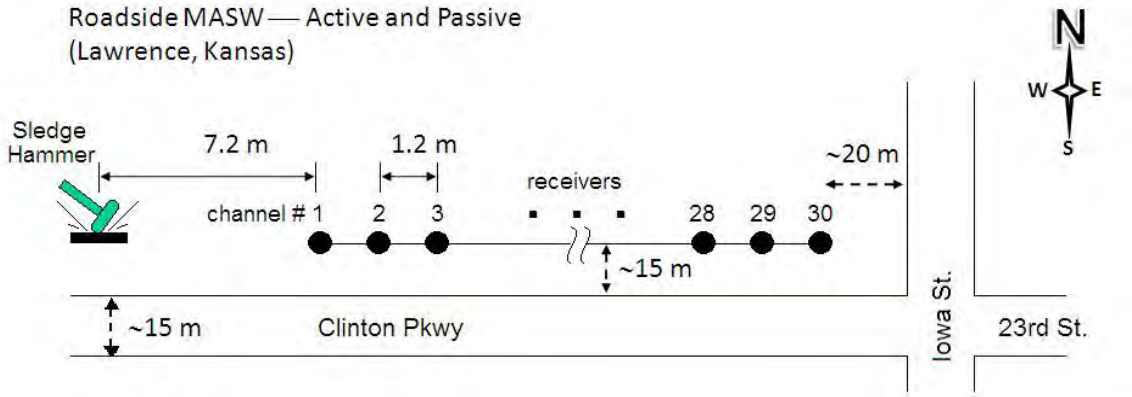

Figure 1. Field layout used in combined (active and passive) MASW survey.

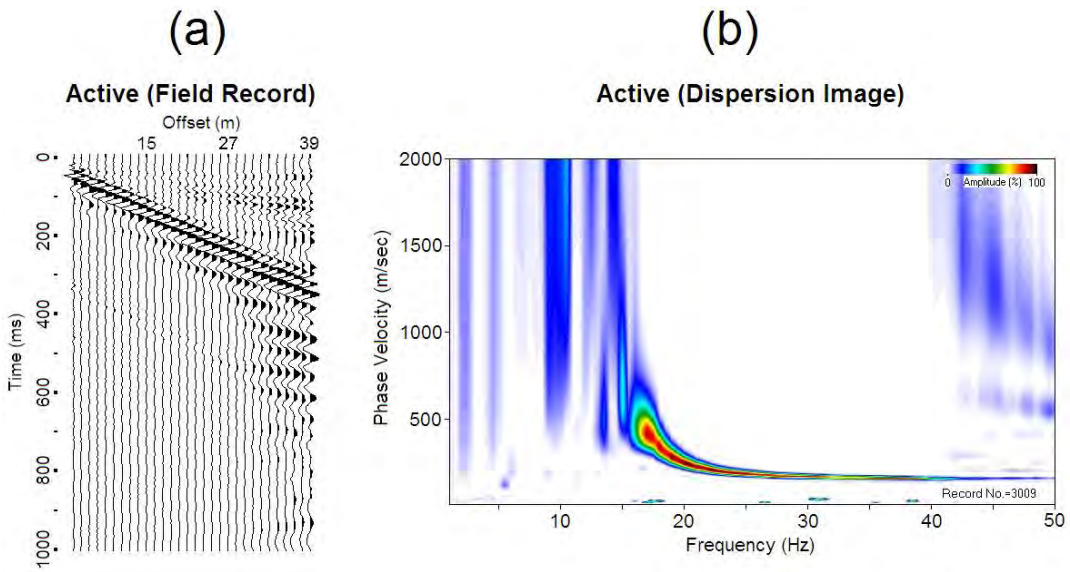

Figure 2. (a) Earliest 1-sec portion of the field record of 120-sec recording time, and (b) its dispersion image.

multi-directional events of cylindrical propagation (Figure 4c), and the PWA scheme by Park (2008; 2009) that treats the events as those of an active survey after detecting the source location responsible for the most dominating events (Figure 4d). The PWA scheme detected the source azimuth had a 300-degree and distance of 50 m, respectively. None of the results show any interpretable image of dispersion due to the events with complex source points.

The passive record is now subdivided into many (119) 1-sec subsets. Then, the source location scanning approach mentioned in previous section (Park, 2010) was applied to each subset in the azimuth range of 180-360 degrees (only two quadrants are necessary with a 1-D receiver array) with 10-degree increments, and in source distance range of 20-500 m with 20-m increments. Scanning results are displayed in Figure 5 in the form of dynamic variation of scanned amplitudes for the azimuth and the distance, respectively. The dynamic azimuth scan (Figure 5a) shows amplitude distribution better focused along the horizontal axis of the target variable (azimuth) than in the dynamic distance scan (Figure 5b), indicating the higher sensitivity achieved with the azimuth scan. For those subsets in

approximately 85-100 sec time intervals, both scans show relatively low amplitudes indicating relatively quiet time intervals without any events of significant energy.

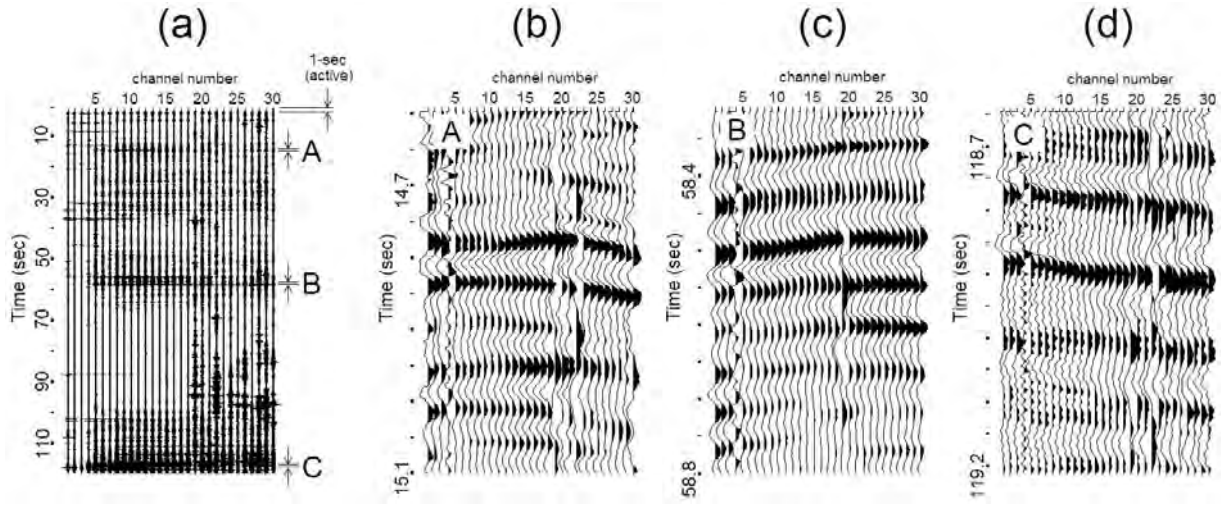

Figure 3. (a) Entire 120-sec part of the field record. Three selected prominent events (A, B, and C) marked in (a) are displayed with enlarged time scales in (b), (c), and (d), respectively.

Double circles marked on both scans indicate those points of azimuth and distance, respectively, picked from the amplitude maxima at each time of subdivisions. Many azimuth picks are shown aligned at around 300 degrees, which is the direction of the Clinton Parkway and Iowa Street intersection where a noticeably rugged road surface was previously identified (Park and Miller, 2008). Picks are also scattered around mostly in the 4th quadrant of south-east direction. Distance picks are clustered around low values around 50-m or less.

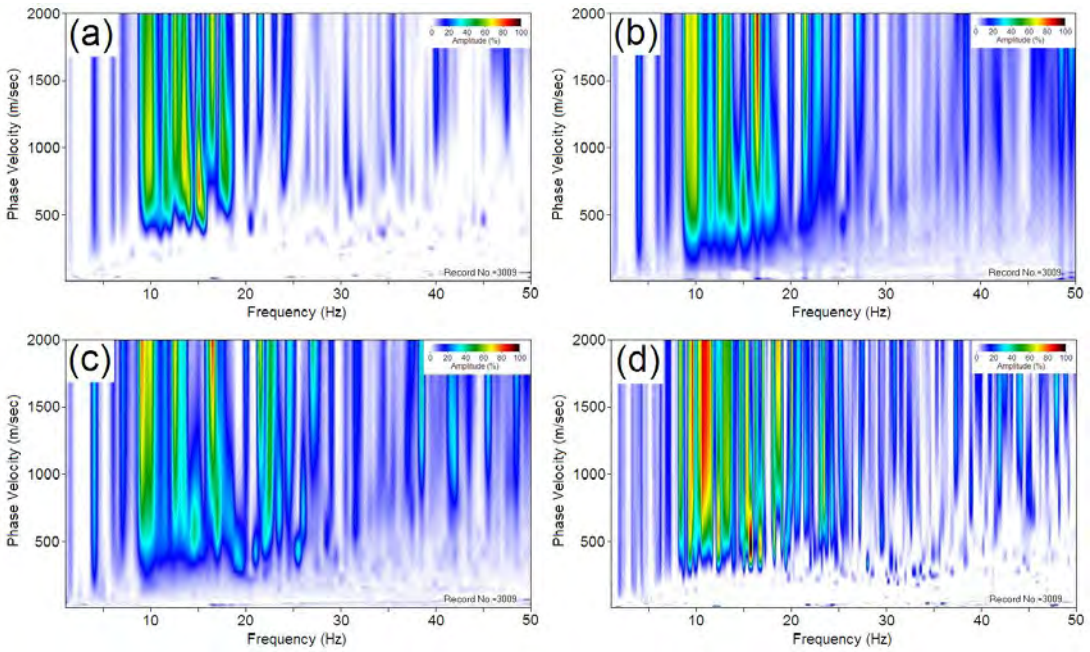

Figure 4. Dispersion images obtained from the passive portion (1-120 sec) of the field record in Figure 3a using four different schemes: (a) Louie (2001), (b) Park et al. (2004), (c) Park and Miller (2008), and (d) Park (2008; 2009).

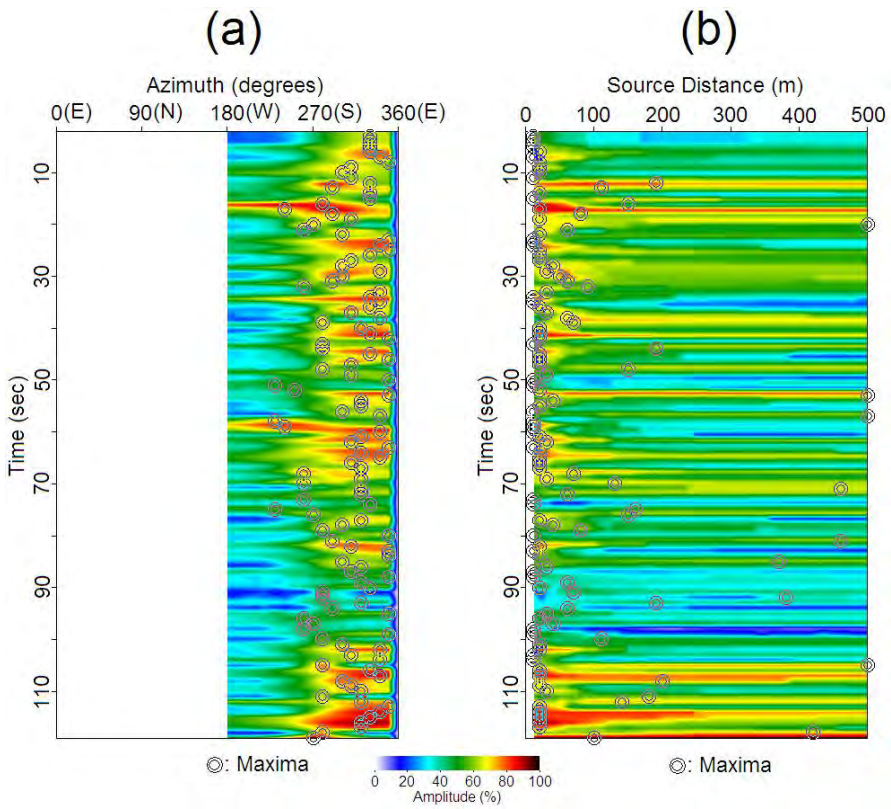

Figure 5. Dynamic (a) azimuth and (b) distance scans obtained from the passive portion (1-120 sec) of the field in Figure 3a by using the source location detection scheme (Park, 2010).

These picked pairs of azimuth and distance at times in the dynamic scans where the azimuth pick had amplitude greater than 50% were then used to apply the PWA scheme to the corresponding subsets. Approximately seventy (70) subsets were processed in this way and data sets of resultant dispersion image were stacked to produce the image shown in Figure 6a. This image clearly shows a dispersion trend at frequencies lower than 20 Hz that none of the previous attempts with other methods could achieve. Figure 6b shows this image combined with the active image previously shown in Figure 2b. A dispersion curve picked from the amplitude maxima at each frequency in this image is superimposed.

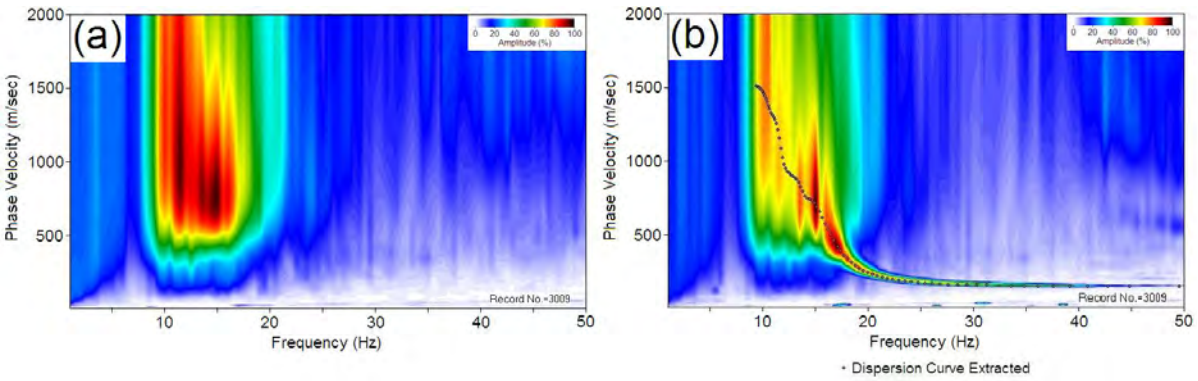

Figure 6. (a) Dispersion image obtained from the passive portion (1-120 sec) of the field record in Figure 3a using the scheme explained in this paper, and (b) its combined image with that from the active portion of the record shown in Figure 2b.

Discussion

There are several processing parameters that can play an important role for the successful outcome of the final stacked dispersion image. Length of the subsets, for example, should be long enough to encapsulate one surface wave event but short enough so they do not include multiple events of different origins. Applying proper tapering on both sides (begin and end) of a subset can also play a role for a smooth image with minimal inclusion of computational artifacts due to an abrupt truncation of wavefields. The advanced approach of source location detection (Park, 2010) could not be explained in any further detail than qualitatively and briefly explained in this paper due to space limitations.

Conclusions

Aided by a method that can detect azimuth and source distance of a surface wave event with a sufficient accuracy, a relatively long passive surface wave record can be divided into multiple subsets of much shorter time to be processed for independent dispersion images. Then, by stacking these dispersion images an image of the highest signal-to-noise ratio (S/N) can be obtained. This approach is especially effective under situations where multiple source points scattered around the survey generate events of relatively strong energy, which is a typical setting for an urban survey.

Acknowledgments

I would like to thank my former post, the Kansas Geological Survey (KGS), for the data used for this study.

References

Aki, K., 1957, Space and time spectra of stationary stochastic waves, with special reference to microtremors: Bull. Earthq. Res. Inst., v. 35, p. 415-456.

Claerbout, J.F., 1985, Fundamentals of geophysical data processing: Blackwell Scientific Publications, Palo Alto, California, 274 pp.

Louie, J.N., 2001, Faster, better: shear-wave velocity to 100 meters depth from refraction microtremor arrays; Bulletin of the Seismological Society of America, 2001, vol. 91, no. 2, p. 347-364.

McMechan, G. A., and Yedlin, M. J., 1981, Analysis of dispersive waves by wave field transformation: Geophysics, 46, 869-874.

Okada, H., 2003, The microtremor survey method; Geophysical Monograph Series, no. 12, published by Society of Exploration Geophysicists (SEG), Tulsa, OK.

Park, C.B., 2010, Detection of source locations in passive MASW surveys: in preparation for publication in Journal of Engineering and Environmental Geophysics (JEEG).

Park, C.B., 2009, Imaging dispersion of passive surface waves with active scheme: submitted for publication in Journal of Engineering and Environmental Geophysics (JEEG).

Park, C.B., 2008, Imaging dispersion of passive surface waves with active scheme: in Proceedings: Symposium on the Application of Geophysics to Engineering and Environmental Problems (SAGEEP 2008), Philadelphia, Pennsylvania, April 6-10, 2008.

Park, C.B., and Miller, R.D., 2008, Roadside passive multichannel analysis of surface waves (MASW): Journal of Engineering and Environmental Geophysics (JEEG), March, 2008, **13**, (1), 1-11.

Park, C.B., Miller, R.D., Ryden, N., Xia, J., and Ivanov, J., 2005, Combined use of active and passive surface waves: Journal of Engineering and Environmental Geophysics (JEEG), **10**, (3), 323-334.

Park, C.B., Miller, R.D., Xia, J., and Ivanov, J., 2004, Imaging dispersion curves of passive surface waves: SEG Expanded Abstracts: Soc. Explor. Geophys., (NSG 1.6), Proceedings in CD ROM.

Park, C.B., Xia, J., and Miller, R. D., 1998, Imaging dispersion curves of surface waves on multi-channel record; SEG Expanded Abstracts, 1377-1380.

Yilmaz, O., 1987, Seismic data processing: Soc. of Expl. Geophys. (SEG), Tulsa, Oklahoma, 526 pp.

COMPARISON OF FK AND SPAC METHODS IN DETERMINING DISPERSION CURVES FROM PASSIVE SURFACE WAVES

Don Zhao, Geogiga Technology Corp., Alberta, Canada
Vera Li, Geogiga Technology Corp., Alberta, Canada

Abstract

FK and SPAC are the two common approaches in determining dispersion curves from passive surface waves. To conduct a systematic comparison, we stimulate passive surface waves with randomly distributed sources and different types of arrays. A field data is also used in the comparison. The study shows that the SPAC method provides higher resolution on the dispersion image and is able to generate a dispersion curve with a larger frequency range. The FK method performs well within a limited frequency range. To reduce the uncertainty in determining dispersion curves, the combination of both methods is recommended.

Introduction

In recent years, the analysis of passive surface waves has gained considerable attention for retrieving the subsurface shear velocity structure. It utilizes background seismic noise typically generated by culture sources and natural sources to extract dispersion curves. Comparing with the active surface wave method, the major advantages of the passive surface wave technique are the low cost exploration and monitoring capabilities, the possibility to perform non-destructive measurement at every place of a densely populated city, and the relatively large penetration depth.

To provide the guidelines for using the passive surface wave technique in site effect studies, we compare two common methods in determining dispersion curves from a set of simulated passive surface waves and a field data: the frequency-wavenumber (FK) method (Capon, 1969; Louie, 2001; Park, 2005) and the spatial auto-correlation (SPAC) method (Aki, 1957; Ling, 1993; Bettig, 2001).

FK Method

The FK method assumes horizontal plane waves to travel across the array of geophones laid out at the surface. Considering a wave with a given frequency ω, a direction of propagation θ and a velocity v, the relative arrival times are calculated at all geophone locations and the phases are shifted according to the time delays. The array output is calculated by the summation of the shifted signals in the frequency domain.

$$E(\omega,v,\theta)=\left|\sum_{ix=1}^{NX} e^{-j\phi_{ix}} R_{ix}(\omega)\right|+\left|\sum_{iy=1}^{NY} e^{-j\phi_{iy}} R_{iy}(\omega)\right| \qquad (1)$$

Where, $E(\omega,v,\theta)$ is the semblance, $R_{ix}(\omega)$and $R_{iy}(\omega)$ are the Fourier transformation of i^{th} trace at the offset of x_{ix} and $y_{iy,}$ Φ_{ix} and Φ_{iy} are the relevant phase shifts.

If the waves effectively travel with the given direction and velocity, all contributions will stack constructively, resulting in the semblance peaks. A dispersion curve is picked by analyzing the semblance spectra.

SPAC Method

The SPAC method assumes that a stochastic wavefield is stationary both in time and space. Given this assumption, the correlation of the signals recorded at a pair of geophones separated by distance r can be written:

$$\overline{\rho(\omega,r)}=J_0\left(\frac{\omega r}{c(\omega)}\right) \qquad (2)$$

Where, $\overline{\rho(\omega,r)}$ is the spatially averaged coherency, J_o is the first order Bessel function, and $c(\omega)$ is the phase velocity at a give frequency ω. The formula shows that a dispersion curve can be generated from the observed coherencies.

Simulation of Passive Surface Waves

To compare the capability of the FK and SPAC methods in determining dispersion curves, we create several synthetic data by simulating passive surface waves. Here, only the fundamental mode is considered.

The velocity model as shown in figure 1 is chosen in the simulation. We use 200 sources randomly distributed within 12 km as shown in figure 2. The trigger and the magnitude of each source are randomly chosen, too. Four types of arrays are put in the center of the source distribution: Circular, Triangular, L-shape, and Linear array. Both the Circular and Triangular arrays have 10 geophones, while, the L-shape array has 12 geophones in X direction and 12 geophones in Y direction. The Linear array has 24 geophones. Figure 3 shows the example of simulated seismic data.

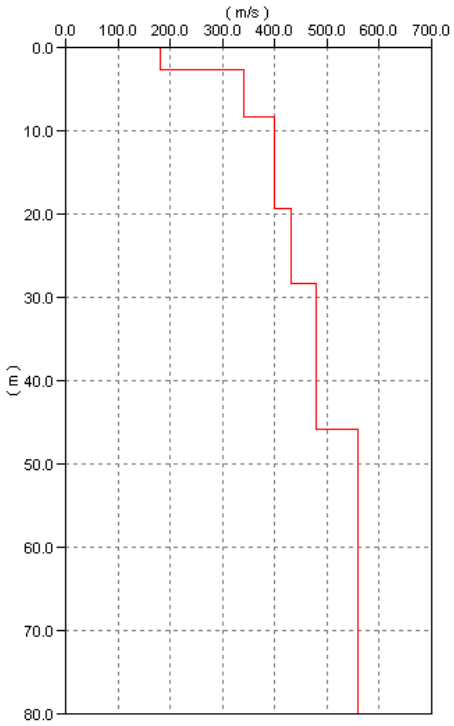

Figure 1: Velocity model used in the simulation

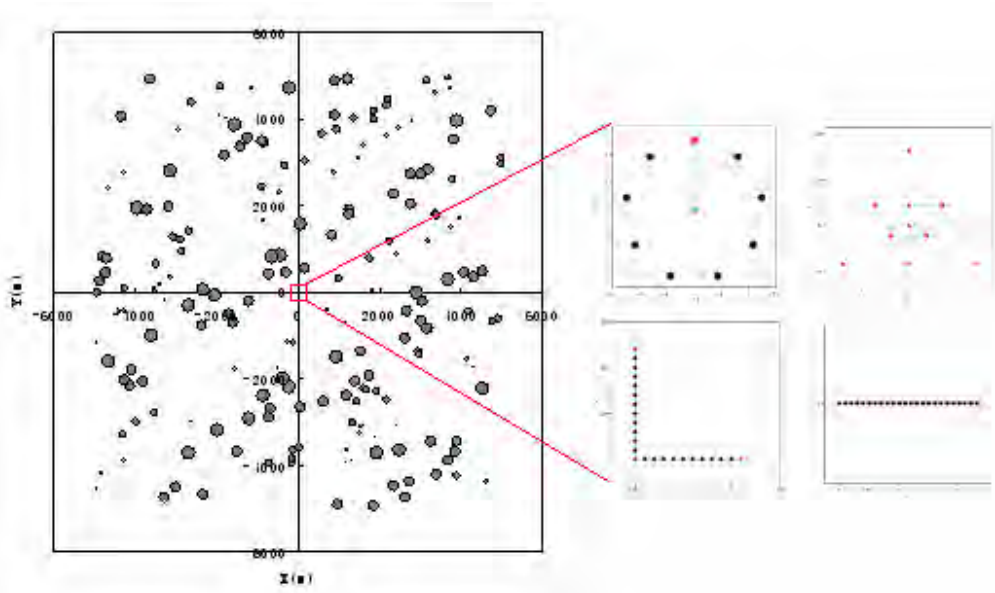

Figure 2: Spatial distribution of sources used to generate passive surface waves from the Circular, Triangular, L-shape and Linear arrays. The black dots represent the source magnitudes.

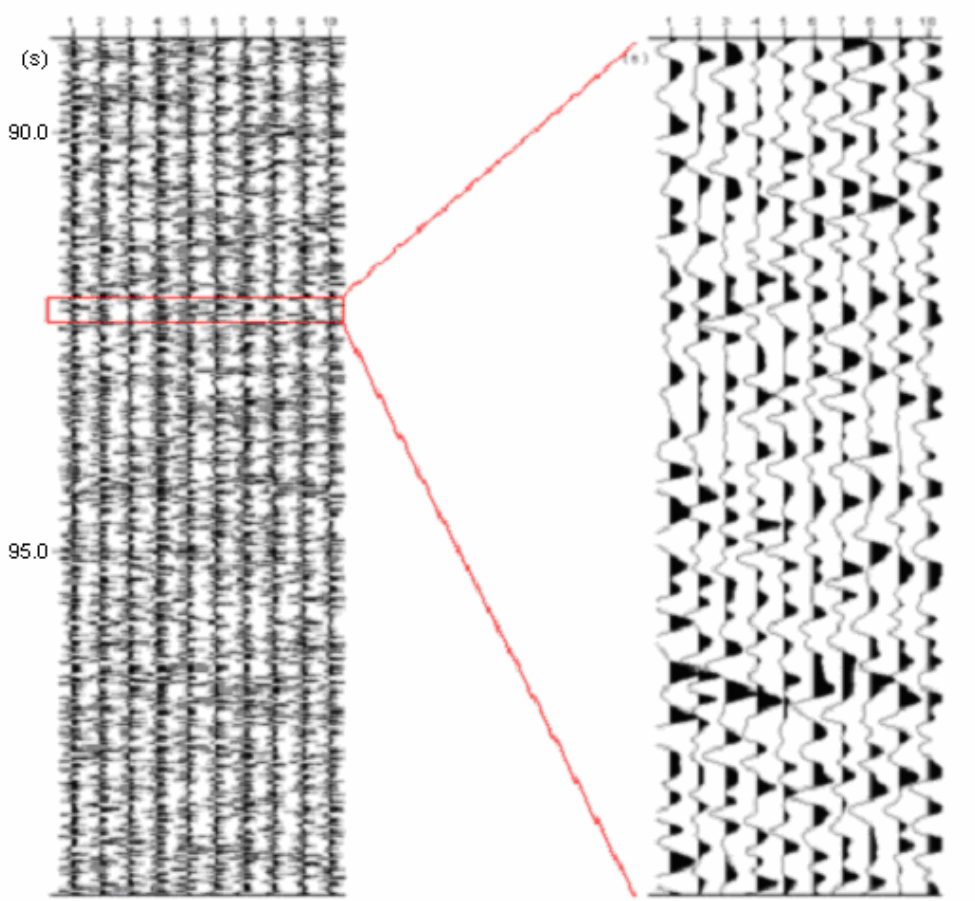

Figure 3: Example of simulated seismic data.

Comparison of FK and SPAC Methods

The comparison starts from the Linear array. The relative dispersion images are shown in figure 4. The image obtained by the SPAC method (Figure 4b) has higher resolution especially in lower frequencies compared with that by the FK method (Figure 4a). The dispersion curve can be clearly picked within the frequency range from 2Hz to 50Hz on the SPAC derived image, while the frequency range is limited to 4 ~42Hz on the image generated by the FK method.

In figure 5, all the dispersion curves generated by the SPAC method from 4 types of arrays perfectly follow the synthetic dispersion curves and nearly span the complete frequency range. A similar good fit between the synthetic and the FK determined dispersion curves is obtained from the L-Shape (Figure 5c) and Linear arrays (Figure 5d), but the frequency range is limited to 8 ~ 40 Hz for the L-Shape array, and 4~42Hz for the Linear array. For the Circular (Figure 5a) and Triangular (Figure 5b) arrays, dispersion curves agree very well within the frequency band from 30Hz to 40 Hz, however, a clear deviation is found from the synthetic and the FK generated dispersion curves below 30 Hz. The bias may be caused by the insufficient number of geophones.

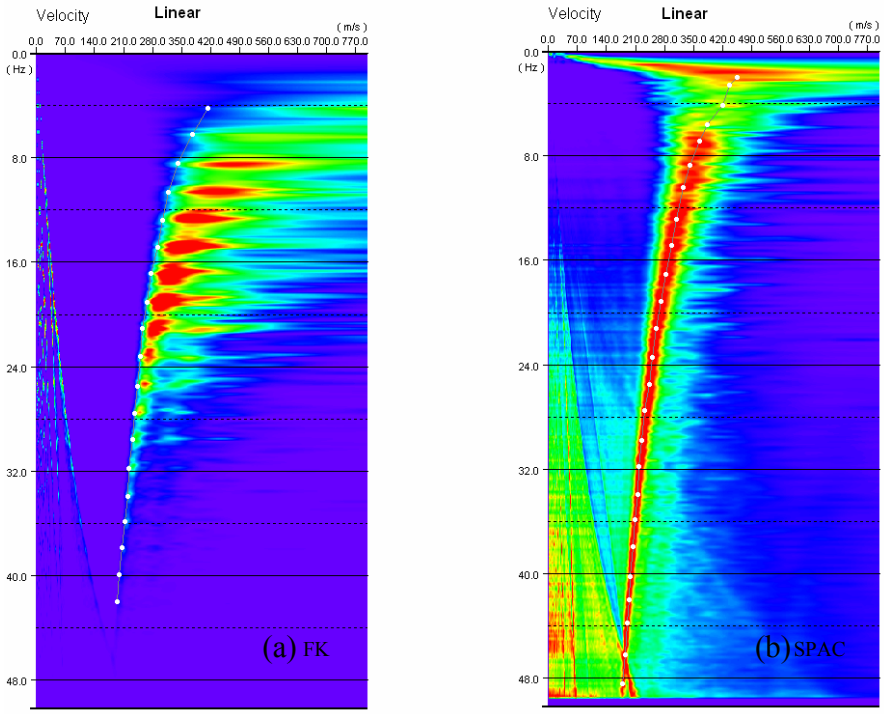

Figure 4: Dispersion images obtained by the FK (a) and SPAC (b) methods from Linear array.

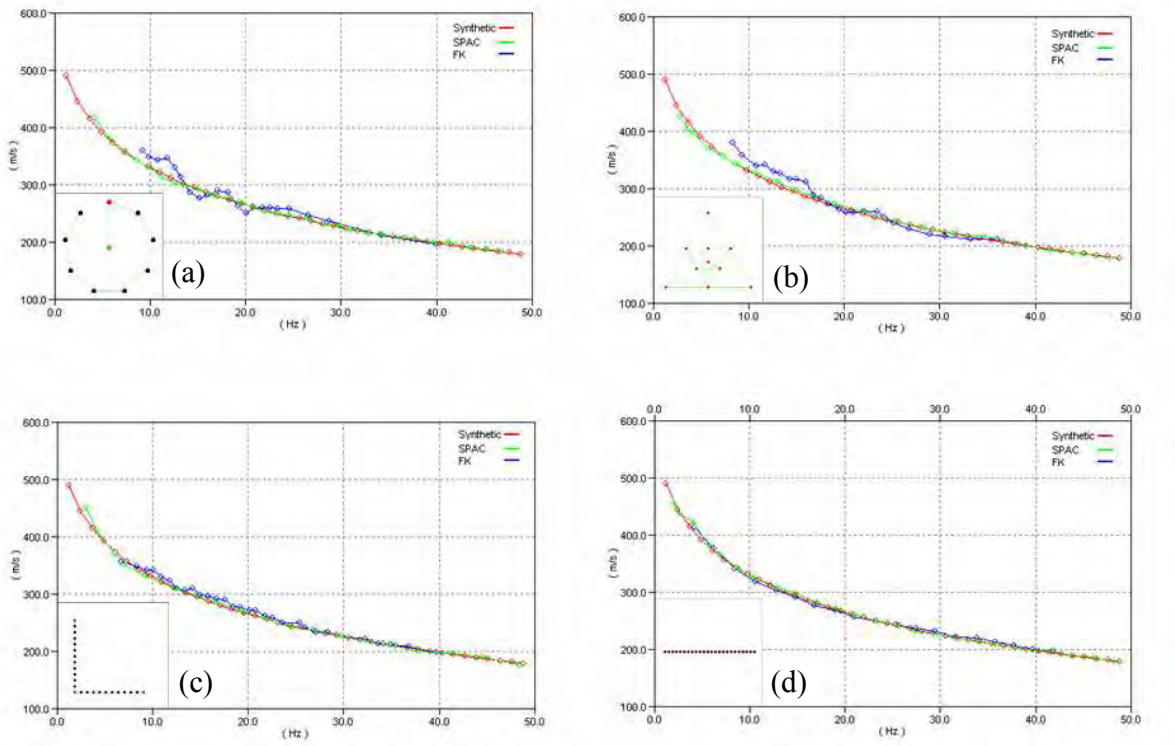

Figure 5: Comparison of synthetic dispersion curves and dispersion curves generated by the FK and SPAC methods from the Circular (a), Triangular (b), L-shape (c) and Linear (d) arrays.

Field Data

The field data was collected from a site in German. A circular array with the diameter of 25m and 10 4Hz geophones was used to acquire the field data with 400-second recording time.

Figure 6 shows the dispersion images generated by the FK and SPAC methods. The resolution of the dispersion image derived by the SPAC method is much higher than that by the FK method. The frequency range of the dispersion curve determined by the FK method is limited to 3~13Hz, while, the range expands to 2.5~15Hz for the SPAC method. Both dispersion curves agree well.

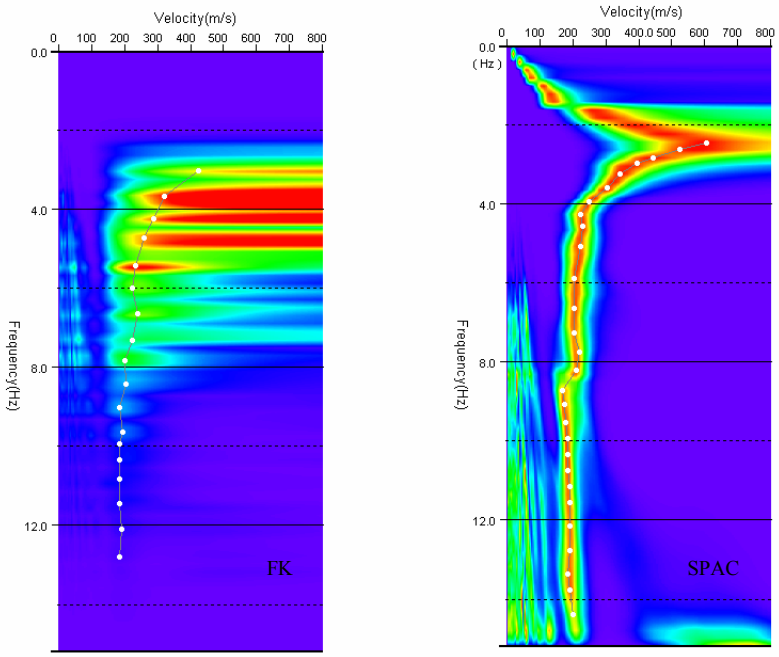

Figure 6: Dispersion images derived by the FK and SPAC methods from the field data.

Conclusion

We have compared the dispersion images and dispersion curves derived by the FK and SPAC methods from a set of simulated surface waves with the circular, triangular, L-shape and Linear arrays and a field data with the circular array. The results show that the SPAC method has higher resolution on the dispersion image especially in lower frequencies and can generate the dispersion curve with a larger frequency range. The FK method performs reasonably well with a limited frequency range. For the FK method, increasing the number of geophones may improve the image resolution and expand the frequency range of dispersion curves.

From the comparison, we recommend first using the SPAC method in the analysis of passive surface waves, and then checking the results with the same data by the FK method. The combination of both methods will reduce the uncertainty in determining dispersion curves.

References

Aki, K., 1957, Space and time spectra of stationary stochastic waves, with special reference to microtremors, Bulletin of Earthquake Research Institute, 35, 415-456.

Bettig B., P.Y. Bard, F. Scherbaum, J. Riepl, F. Cotton, C. Cornou, and D. Hatzfeld, 2001, Analysis of dense array noise measurements using the modified spatial auto-correlation method (SPAC) – Application to the Grenoble area, Bollettino di Geofisica Teorica ed Applicata, 42, 281-304.

Capon, J., 1969, High resolution frequency - wavenumber analysis, Proceedings of the IEEE, 57, 1408-1418.

Ling, S., and H.Okada, 1993, An extended use of the spatial autocorrelation method for the estimation of geological structure using microtremors, Proc. Conf. SEGJ, 89, 44-48.

Louie, J.N., 2001, Faster better shear-wave velocity to 100 meters depth from refraction Microtremor arrays, Bulletin of the Seismological Society of America, 91, 347-364.

Park, C.B., R.D. Miller, N. Ryden, J. Xia, and J. Ivanov, 2005, Combined use of active and passive surface waves: Journal of Environmental and Engineering Geophysics, 10, 323-334.

APPLICABILITY OF A SPATIAL AUTOCORRELATION METHOD (SPAC) USING A LINEAR ARRAY IN COMPARISON WITH TRIANGULAR AND L-SHAPED ARRAYS

Koichi Hayashi, OYO Corporation, Ibaraki, Japan
Takaho Kita, TK Ocean-Land Investigations Ltd., Hyogo, Japan

Abstract

We have examined the applicability of a spatial auto-correlation (SPAC) method using a linear array in comparison with triangular and L-shaped arrays. The SPAC requires two dimensional arrays, such as a circle, a triangle and a crossing for calculating the phase-velocity of the microtremor. Theoretically, isotropic arrays, such as a circle or an equilateral triangle, are preferable in the SPAC analysis. However, the isotropic arrays required wide space and it is difficult to obtain such wide space in urban area. Recently, several theoretical and experimental studies have shown the validity of irregular arrays. Results of these studies have also implied the validity of linear arrays in which receivers are placed only on a line. The use of linear arrays will enable us to apply passive methods in urban area much easily. In this paper, we are going to examine the applicability of the linear array in terms of numerical simulation and field experiments. The result of field experiment showed that the linear array provides almost identical dispersion curves as that of two dimensional arrays although numerical simulation showed clear disadvantage of the linear array. It implies that that the sources of the microtremor are distributed randomly in space and the microtremor does not have any specific propagation direction at most of sites.

Introduction

Microtremor consists of wide frequency range of surface waves from the period of 0.1 second to 10 seconds. Therefore, S-wave velocity models down to several kilometers can be obtained using the microtremor. A passive surface-wave method, so called microtremor array measurements (MAM), is a seismic exploration method in which the microtremor is observed by multi-receives and its phase-velocities are analyzed. The first researcher to give much attention to the microtremor is Aki. He investigated the microtremor as surface-waves and presented the theory of a Spatial Auto Correlation (Aki, 1957). Okada (2003) had developed large scale microtremor array measurements, using the long period microtremor. The penetration depth of the method is from 100m to several kilometers. We have employed the Okada's method and applied it to shallower problems, such as geo-technical, environmental, and earthquake engineering. Our depth of interests is from several ten meters to 100m and frequency range of microtremor is from 1 to 10Hz.

Unlike active surface wave methods, the MAM does not need any sources and needs two-dimensional arrays, such as triangles, circles or crosses. Because the sources of the microtremor are distributed randomly in space, the microtremor does not have any specific propagation directions. Therefore, two dimensional arrays are required for calculating the phase-velocity of the microtremor and a statistic analysis approach, so called the Spatial Auto Correlation (SPAC) is used in phase-velocity calculation. Theoretically, isotropic arrays, such as a circle or an equilateral triangle, are preferable in the SPAC analysis. However, the isotropic arrays required wide space and it is difficult to obtain such wide space in urban area.

Recently, several theoretical studies have been made on the applicability of irregular arrays (e.g. Yokoi et al., 2006, Hayashi, 2009). The results of these studies showed that the irregular arrays, such as

a L-shaped array, provides enough accurate phase-velocities in comparison with the isotropic arrays. Margaryan et al.(2009) applied the SPAC to the linear array (two-site SPAC) and showed validity of the linear array in comparison with a triangular array. On the other hand, the linear array using a tau-p method (REMI) is increasingly applied to near-surface investigations (Louie, 2001). The result of these experiments on the two-site SPAC and the REMI implies that the validity of a passive surface-wave method using the linear array. The use of linear arrays will enable us to apply the passive methods in urban area much easily. In this paper, we are going to examine the applicability of the linear array in terms of numerical simulation and field experiments.

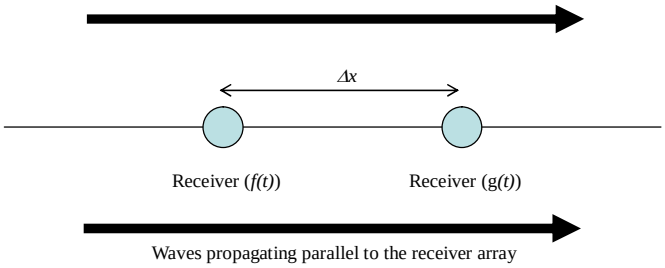

Figure 1: Two receives with separation Δx.

Numerical Simulation

SPAC for 1D and 2D arrays

Let us start with two traces *f(t)* and *g(t)* obtained at two receives with separation Δx (Figure 1). Microtremor propagates parallel to a receiver array. The spatial auto-correlation (SPAC) for this one dimensional array is defined as follows.

$$SPAC(\Delta x,\omega) = \mathrm{Re}\left(COH_{fg}(\omega)\right) = \cos\left(\frac{\omega \cdot \Delta x}{c(\omega)}\right). \quad (1)$$

where, $c(\omega)$ is phase-velocity at angular frequency ω. Complex coherence ($COH_{fg}(\omega)$) is defined as follows.

$$COH_{fg}(\omega) = \frac{CC_{fg}(\omega)}{A_f(\omega)A_g(\omega)}. \quad (2)$$

where, $CC_{fg}(\omega)$ is cross-correlation of two traces *f(t)* and *g(t)*. $A_f(\omega)$ and $A_g(\omega)$ are amplitude of *f(t)* and *g(t)* respectively. The equation (1) means the SPAC for one dimensional array is defined as real part of complex coherence and it goes to cosine function.

The spatial auto-correlation (SPAC) for two dimensional array is defined as the directional average of complex coherence as follows.

$$SPAC(r,\omega) = \frac{1}{2\pi}\int_{\varphi=0}^{\varphi=2\pi} \mathrm{Re}\left(COH(r,\varphi,\omega)\right)d\varphi. \quad (3)$$

where, r is separation of two receivers or radius of a circle, φ is direction of two sensors. Equation (3) means that calculating coherence for two sensors with separation r and direction φ, firstly and averaging complex coherence along a circle secondly (Figure 2).

The directional average of trigonometric functions goes to the Bessel function as,

$$J_0(kr) = \frac{1}{\pi}\int_{\varphi=0}^{\varphi=\pi} e^{ikr\cos\varphi}\,d\varphi \quad \text{or} \quad J_0(kr) = \frac{1}{2\pi}\int_{\varphi=0}^{\varphi=2\pi} e^{ikr\cos\varphi}\,d\varphi\,. \tag{4}$$

where, k is wave number. Using equation (4), directional average of right hand side of equation (3) can be written as,

$$J_0\left(\frac{\omega\cdot r}{c(\omega)}\right) = \frac{1}{2\pi}\int_{\varphi=0}^{\varphi=2\pi} \cos\left(\frac{\omega\cdot r}{c(\omega)},\varphi\right)d\varphi\,. \tag{5}$$

From the equation (3) and (5)

$$SPAC(r,\omega) = J_0\left(\frac{\omega}{c(\omega)}r\right). \tag{6}$$

The left term of equation (6) can be calculated from observed microtremor data. Phase-velocity is calculated by comparing the spatial autocorrelation in left term and Bessel function in right term of equation (6) changing the phase-velocity $c(\omega)$ in the right term of the equation. The velocity that minimize error in equation (6) can be considered as the phase-velocity at the angular frequency ω.

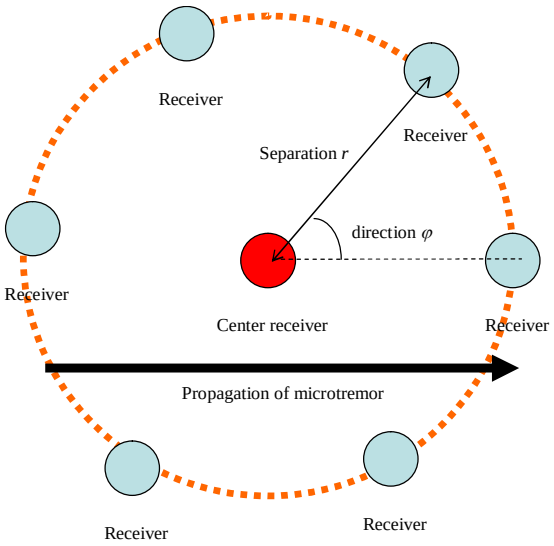

Figure 2: Receives on a circle.

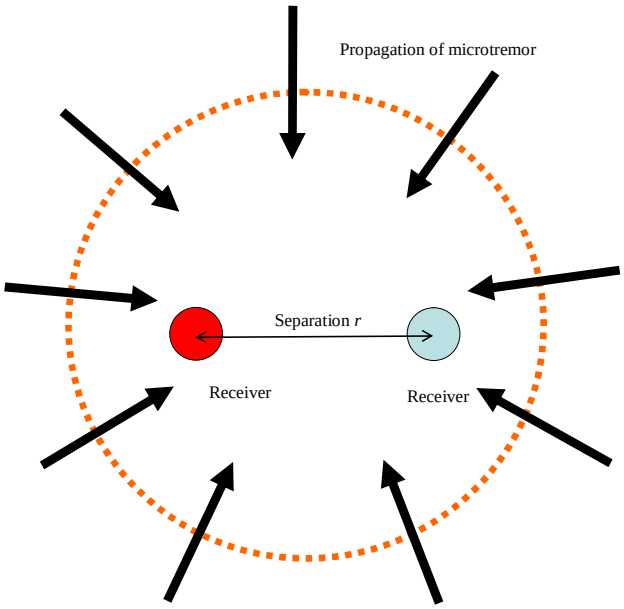

Figure 3: Microtremor does not have any specific propagation direction.

It should be noted that the equation (6) is valid for isotropic arrays, such as circle and triangle, handling microtremor propagating only single direction as shown in Figure 2. On the other hand, the equation (6) is also valid for linear array handling microtremor propagating all directions equally as shown in Figure 3. If sources of the microtremor are distributed randomly in space, the microtremor does not have any specific propagation direction and the condition of Figure 3 can be used. We are going to investigate the ability of Figure 3 in following discussion.

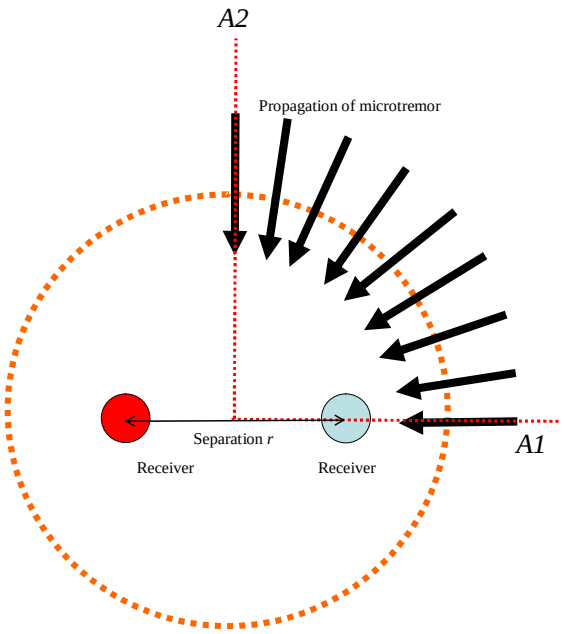

Figure 4: Directional average for limited propagation direction.

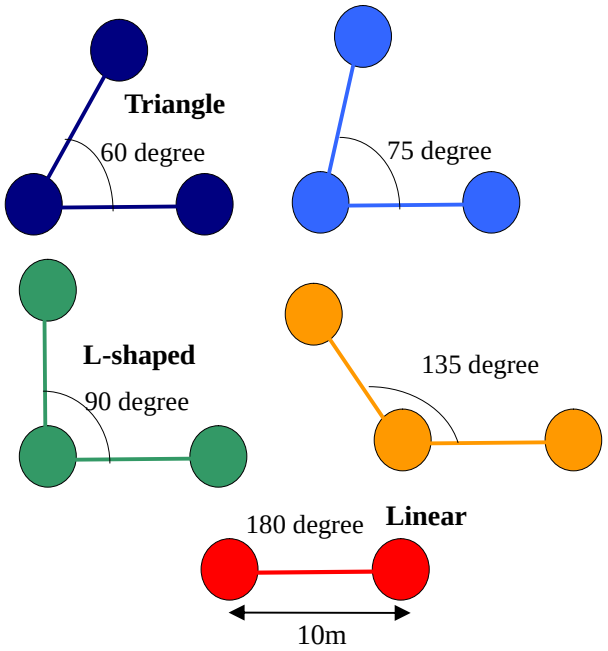

Figure 5: Calculated arrays

Directional average for limited propagation direction

Directional average in the linear array assumes that the microtremor propagates all directions equally as shown in Figure 3. If the microtremor propagates limited direction, the directional average using equation (3) has to include error. We are going to evaluate the error associated with the directional average as follows.

Let us assume the microtremor propagates limited direction as shown in Figure 4. The directional average is calculated by equation (7) using directions *A1* and *A2* in Figure 4.

$$DA(kr) = \frac{1}{A2 - A1}\int_{\varphi=A1}^{\varphi=A2} e^{ikr\cos\varphi}\, d\varphi \,. \qquad (7)$$

where, k is wave number associated with given phase-velocity c, r is separation of receivers. *DA(kr)* is the directional average and can be considers as the SPAC coefficient in the microtremor analysis. Phase-velocity (c) is calculated using the inverse of the Bessel function (J_0^{-1}) as follows.

$$c(\omega) = \frac{\omega \cdot r}{J_0^{-1}(DA(kr))}. \qquad (8)$$

Five different arrays are calculated (Figure 5). The 60 degrees array corresponds to a triangular array, the 90 degrees array corresponds to an L-shaped array and the 180 degrees array corresponds to a linear array respectively. Figure 6 shows the result of calculations. Four different directional ranges (*A2-A1*=30, 60, 90, 120 degrees respectively) are calculated. Propagation direction of the microtremor is also rotated. Frequency is fixed as 20Hz, phase-velocity is 100m/s and the separation of receivers is 10m. The result of calculation can be summarized as follows.

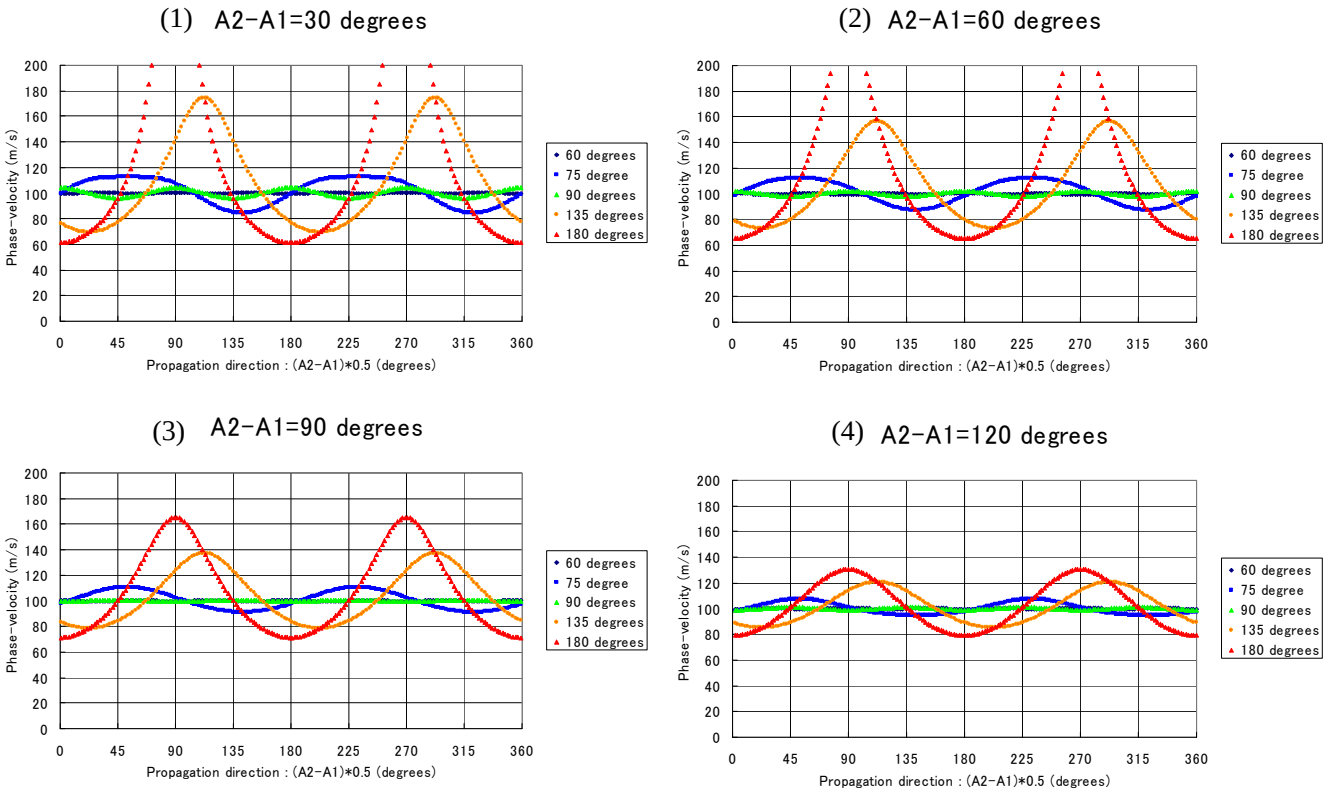

Figure 6: Error associated with limited propagation direction of microtremor.

Although range of propagation direction is limited (30 and 60 degrees), the 60 degrees array (triangle) and the 90 degrees array (L-shaped) provide almost correct phase-velocities. The 75 degrees array is little bit worse than the triangular and L-shaped arrays. The 135 degrees array and the 180 degrees array (linear array) generate large error when microtremor propagates perpendicular to the arrays. In the case of the range of propagation direction is 120 degrees, the 135 degrees array and the linear array provide phase-velocities with error less than 20% in the most of propagation direction. Figure 6 clearly shows the advantage of two-dimensional arrays in comparison with the linear array. It should be noted that L-shaped arrays in which angle is less than 90 degrees is much better than that angle is larger than 90 degrees. The linear array can provide usable phase-velocities when propagation direction of microtremor is distributed at least the range of 120 degrees.

Simulation of microtremor measurement

In order to evaluate the error associated with the linear array under the condition closer to actual data acquisition and analysis, synthetic microtremor data was generated and analyzed as follows. A linear array in which twenty-one receivers are placed on a line with 5m spacing is used in the simulation. Microtremor propagates 3 and 4 directions with the range of 90 and 120 degrees. Two propagation directions are examined as shown in Figure 7. Synthetic microtremor data was generated by putting delta functions having apparent velocity of propagating directions. Phase-velocity of propagation is 200m/s. Phase of the delta functions was randomly defined. Figure 8 shows the example of a synthetic waveform data set for the case C in Figure 7. Twenty waveform data sets were generated with different phase. The SPAC coefficients were calculated by averaging 20 waveform data sets and phase-velocity curves were obtained by equation (6). Obtained phase-velocity curves are shown in Figure 9.

Figure 9 shows that the 4 directions with the range of 120 degrees provides almost correct

phase-velocity although propagation direction is perpendicular to array. The result confirms that the SPAC method using the linear array is valid when propagation direction of microtremor is distributed at least 120 degrees as we already mentioned. The propagation direction of the case B, 3 directions with the range of 90 degrees, is also perpendicular to the array. The error in the case B, however, is about 30% and smaller than the error shown in Figure 6(3). It is likely that using many receivers increase the accuracy in the simulation.

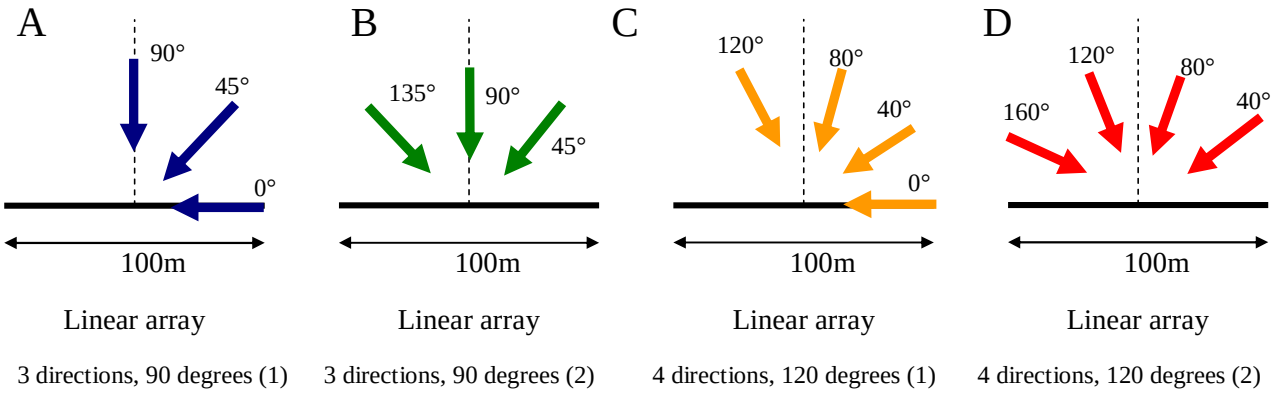

Figure 7: Error associated with limited propagation direction of microtremor.

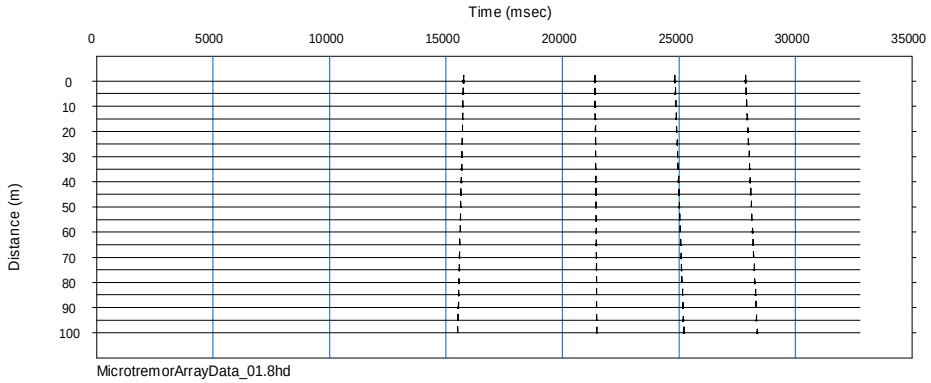

Figure 8: Example of synthetic waveform data.

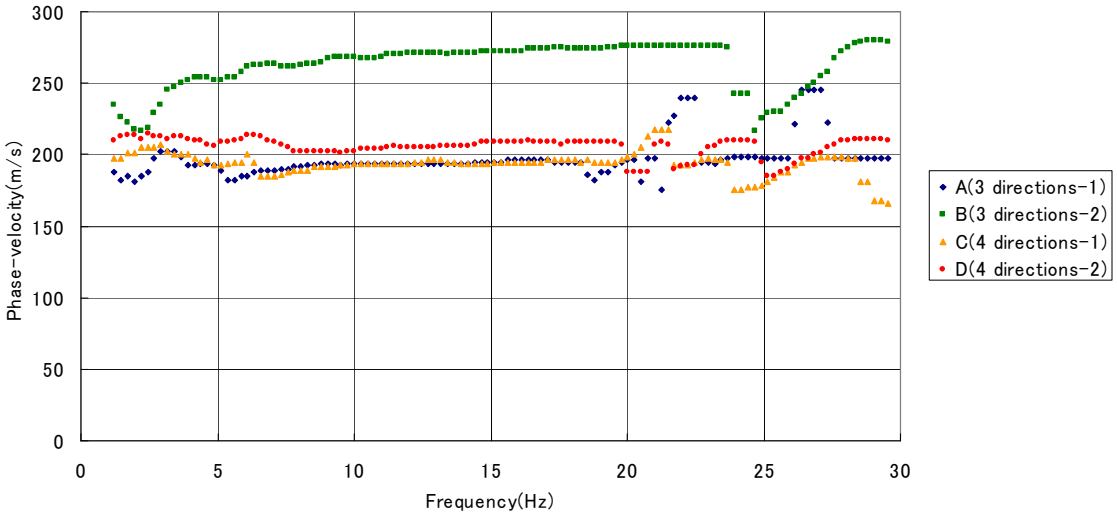

Figure 9: Comparison of phase-velocity curves.

Field Experiments

Data acquisition at the Dolphin Park in Los Angeles City, U.S.

Phase-velocity curves obtained through triangular and linear arrays were compared at the Dolphin Park in the downtown of Los Angeles city, U.S. Data length is about 10 minutes. The size of triangle array was 60m and the length of linear array was 110m. In the triangular array, two types of data acquisition were performed. In the first one, 4 geophones that have natural frequency of 1Hz were used. Next one, 10 geophones that have natural frequency of 4.5Hz were used (see Figure 10). The 4.5 Hz geophones were also used in the linear array. An OYO McSEIS-SXW was used for data acquisition. Figure 10 shows the phase-velocity curves obtained through the triangle and linear arrays. We can see that the triangle and linear array phase-velocity curves are almost identical. It must be noted that the dispersion curves obtained by 4.5Hz geophones is almost identical down to the frequency of 2Hz. More noteworthy is that the dispersion curve obtained by linear array agrees with that of triangular array down to the frequency of 2 Hz. It implies that the propagation direction of microtremor was widely distributed.

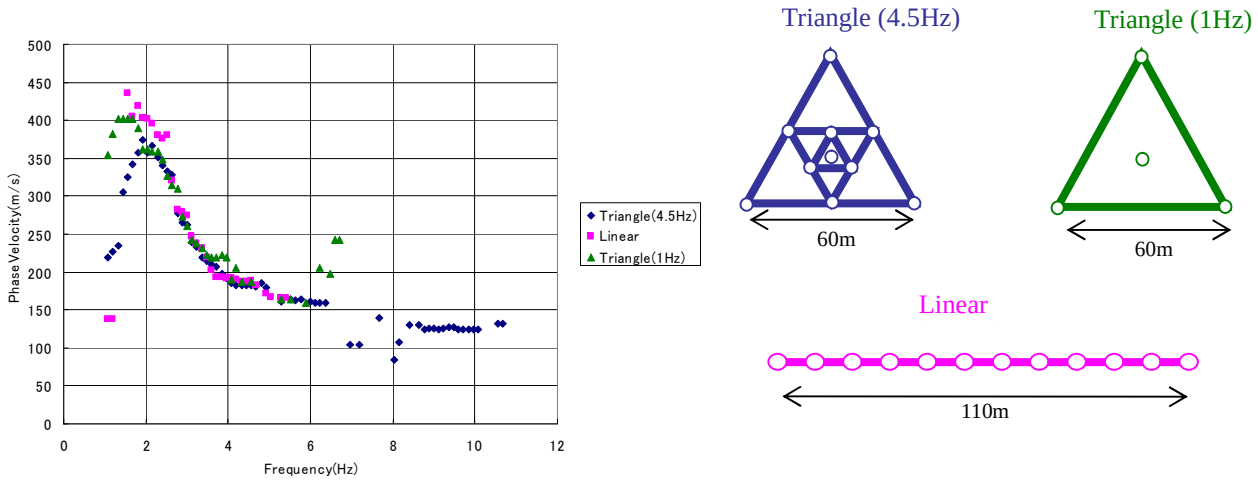

Figure 10: Comparison of phase-velocity curves in Los Angeles City, U.S.

Data acquisition in Istanbul City, Turkey

Linear arrays were compared with L-shaped arrays at 14 sites in Istanbul City, Turkey. One of these sites, a triangular array was also compared. Data length is about 10 minutes. The size of L-shaped and triangular arrays were 50 to 150m and 11 geophones that have natural frequency of 2Hz were used. The length of linear array was 115m and 24 geophones that have natural frequency of 4.5Hz were placed with 5m spacings. A Geometrics Geode was used for data acquisition. Figure 11 shows the example of dispersion curves. We can see that the dispersion curves obtained through linear arrays almost agreed with that of triangular and L-shaped arrays. It implies that the propagation direction of microtremor was widely distributed like the dolphin park's example.

Conclusions

Applicability of linear arrays was evaluated by numerical simulation and field experiments. The numerical simulation shows that the advantage of two-dimensional arrays in comparison with the

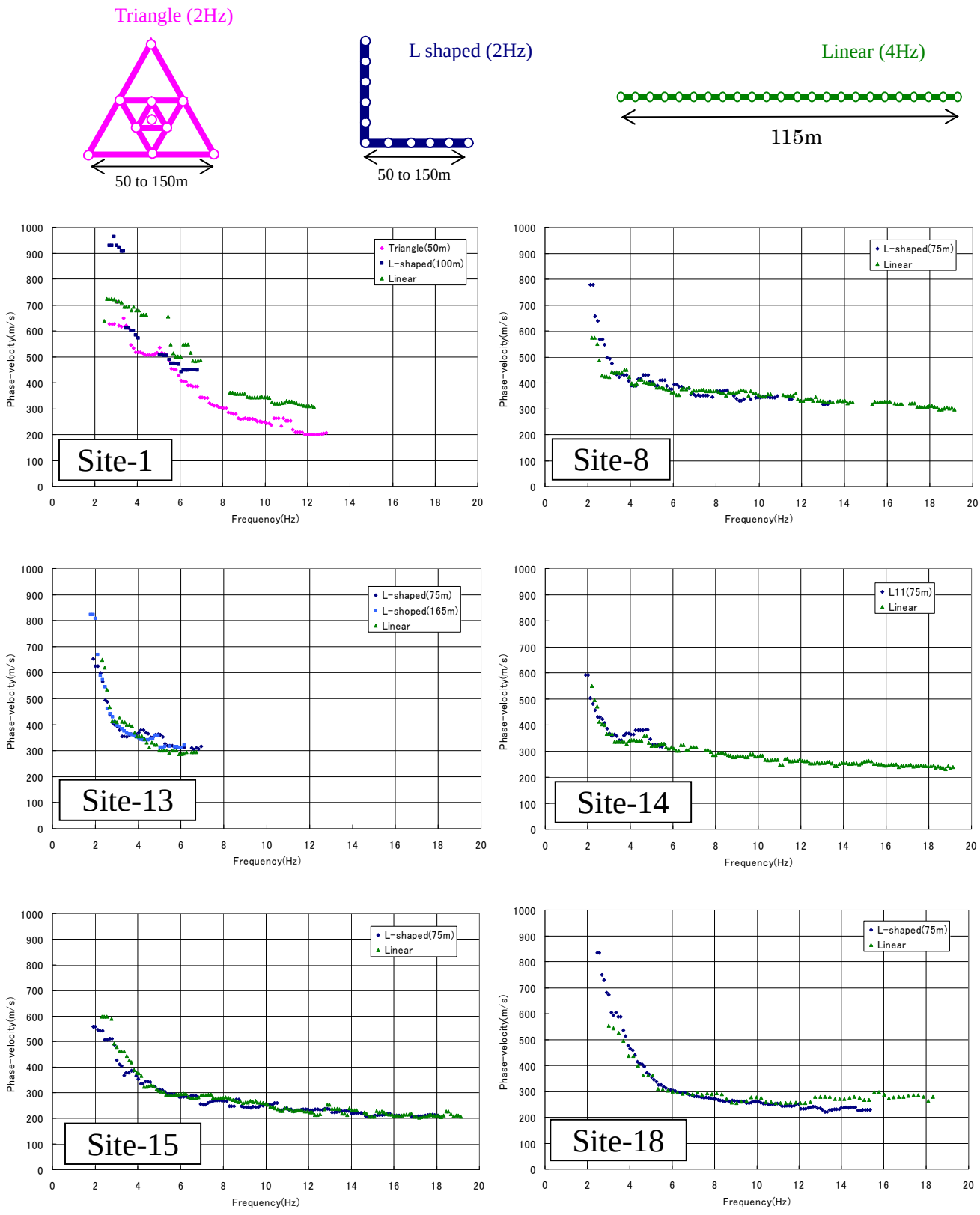

Figure 11: Comparison of phase-velocity curves in Istanbul City, Turkey

linear array. It should be noted that L-shaped arrays in which angle is less than 90 degrees is much better than that angle is larger than 90 degrees. The linear array can provide usable phase-velocities when propagation direction of the microtremor is distributed at least the range of 120 degrees. The result of field experiment showed that the linear arrays provided almost identical dispersion curves as that of two dimensional arrays although numerical simulation showed clear disadvantage of linear array. It implies that the sources of the microtremor are distributed randomly in space and the microtremor does not have any specific propagation direction at most of sites.

Acknowledgements

Author would like to thank Mr. Antony J. Martin of GEOVision, inc. for their support to field work.

References

Aki, K., 1957, Space and time spectra of stationary stochastic waves, with special reference to microtremors, Bull. Earthq. Res. Ins., 35, 415-456.

Hayashi, K., 2009, Effect of array shape on the spatial auto-correlation analysis of micro-tremor array measurements, Proceedings of the symposium on the application of geophysics to engineering and environmental problems 2009, 616-625.

Louie, J, N., 2001, Faster, Better: Shear-wave velocity to 100 meters depth from refraction microtremor arrays: Bulletin of the Seismological Society of America, 91, 347-364.

Okada, H., 2003, The microtremor survey method, Society of Exploration Geophysicist, Tulsa.

Yokoi, T., Hayashi, K. and Aoike, K., 2006, A case study on dependence of the complex coherence function on the azimuth SPAC method of microtremor array measurement, Proceedings of the 114th SEGJ Conference, 138-141, (in Japanese).

SUBSURFACE TUNNEL DETECTION USING ELECTRICAL RESISTIVITY TOMOGRAPHY AND SEISMIC REFRACTION TOMOGRAPHY: A CASE STUDY

Grey I. Riddle, Department of Physics, University of Alberta, Edmonton, AB, Canada
Craig J. Hickey, National Center for Physical Acoustics, University of Mississippi, Oxford, MS, USA
Douglas R. Schmitt, Department of Physics, University of Alberta, Edmonton, AB, Canada

Abstract

Seismic and electrical methods are two geophysical techniques commonly used to detect rock property changes in the subsurface. Surveys are usually carried out with sources and sensors placed at or near the earth's surface. Various levels of data processing are applied to construct a map of the subsurface distribution of a physical property. Seismic methods are sensitive to velocity and density changes of the rock, while the electrical response is dependent upon the electrical resistivity of the rock. In this paper, we present an evaluation of using both seismic refraction and electrical imaging to locate a tunnel. Although the contrast in seismic velocity and electrical resistivity between the tunnel and its surrounding material can be large, tunnels remain difficult to detect. The difficulty primarily arises because the spatial resolution of these methods is less than or on the order of the size of the tunnels. Detection is further complicated by heterogeneity of the near surface materials within which many tunnels are constructed. In this paper, we present a case study using ERT dipole-dipole data and seismic refraction data at a tunnel site. Both seismic and electrical surveys were acquired at the same time with a lateral offset of about 3m. The results from both techniques show anomalies at the location of the tunnel. The confidence in predicting the location of the tunnel is increased by using data from both techniques.

Introduction

Subsurface voids include any zone in the subsurface having physical properties that are significantly different than the surrounding earth material. Some examples of high-contrast voids are: tunnels, bunkers, cellars, tombs, pipes, tanks, culverts, caverns, and underground mines. In most cases these voids will contain water and/or air and the bulk properties of the void is equal to the properties of the occupying fluid. These voids may have exterior thin shells, as is the case for plastic or metal pipes and tanks, which may produce unique responses of the void. However, despite the large contrasts associated voids, they do not produce easily-detectable geophysical anomalies. The reasons include: (1) the size of the void with respect to the resolution of the geophysical technique, (2) the often irregular shape, and (3) the heterogeneity of the surrounding native material itself, which can produce a significant number of anomalies.

The problem of tunnel detection has been an issue for quite some time. Many meetings have been organized over the past 30 years to discuss possible detection methods (USARL, 2009; Daniels and Harmon, 2009; Simmons and Aldridge, 2008; Sabatier and Muir, 2006; Halihan and Nyquist, 2006; McKenna and Ketchum, 2006; Anon., 1988; Anon., 1981). Some of the techniques being considered for the detection and location of tunnels include: acoustic/seismic technologies, electro-magnetic and resistivity technologies, gravity technologies, optical sensing technologies, and radar technologies (Sabatier and Muir, 2006).

Geophysical techniques remain the only ways to remotely and non-destructively sense the earth's near subsurface and as such have the most promise for rapid and accurate detection of tunnels.

Detecting tunnels may be less difficult than studying and characterizing geologically important voids and structures because tunnels are usually somewhat cylindrical in shape and are constructed in otherwise competent media. Furthermore, the tunnel problem is concerned with detection only, whereas geological studies are concerned with characterization. For a successful characterization the geophysical attributes must have a clearly defined correlation to the physical/geological properties. The geophysical attributes used in detection schemes must be scientifically sound but the connection to physical properties does not have to be fully understood for the detection scheme to be successful. Although tunnel detection might be a simpler problem than say, studying karst environments, the tunnel detection problem still has the issues associated with the size of the tunnel with respect to the resolution of the geophysical technique and the heterogeneity of the surrounding native material.

Geophysicists performing site characterization for geotechnical applications, mining exploration, and oil exploration employ several techniques in order to alleviate the ambiquity in geophysical interpretation. The construction of a tunnel and the disruption of the material in its vicinity will change a group of physical properties which should manifest in a common set of geophysical signatures. For example, construction of a tunnel will produce a region of lower bulk density, lower seismic speeds, and, in many cases, lower water content. Since electrical resistivity is strongly dependent on water content, clay fraction, and the presence of soluble salts the tunnel should have a high electrical resistivity signature. The elasticity of soil is strongly dependent on the cohesion, degree of cementation, and water content and therefore a tunnel should have a low velocity signature. Crawford et al. (2006) suggested the use of microgravity and electrical resistivity techniques for the detection of caves and tunnels. They state that a low gravity anomaly and a colocated high resistivity anomaly indicates the presence of a cave.

In this paper we present some preliminary results on the simultaneous use of active seismic refraction tomography (SRT) and electrical resistivity tomography (ERT) for the purpose of tunnel detection. The SRT and ERT techniques were chosen because: (1) the ERT is sensitive to the electrical resistivity of the ground as opposed to the SRT which is sensitive to the elasticity of the ground; (2) the ability for both SRT and ERT surveys to be conducted simultaneously; and (3) the results are both displayed in terms of tomographic profile images, which facilitates joint interpretation of data.

ERT and SRT method

In near-surface refraction tomography, the travel times of seismic energy recorded at the surface by multiple source-receiver combinations are used to generate an optimized model of the distribution of seismic velocities in the subsurface (Baker, 2002). The "velocity image map" can be used to infer subsurface units/features having sufficient differences in elastic properties (Baker, 2002). This approach is commonly referred to as travel time tomography and uses the ray approximation to wave propagation. The limits of resolution for travel time tomography are often associated with the break-down of the ray approximation, i.e. when the scale of the perturbations is on the order of a wavelength. However, Williamson (1991) suggests that the smallest feature that can be accurately reconstructed using ray travel time tomography is given by

$$r_{min} \approx \sqrt{L\lambda} \quad (1)$$

which is the radius of the first Fresnel zone for propagation over a distance L. Resolution increases as the square root of the frequency and decreases as the square root of the path length.

Sheehan et al. (2005) performed a study using three different tomography codes. They showed that although the actual seismic velocity contrast may be abrupt, the resulting image smears the boundary into a gradient. This may be associated with the resolution of the actual seismic wave and/or with the regularization algorithms used for calculating the velocity distributions. The regularization algorithms are based on the assumption that the subsurface properties vary continuously; and, therefore, sharp physical boundaries are smeared into a gradient. Sheehan et al. (2005) also showed that none of the codes were able to "image" the cavity example using the velocity map. All three codes have artefacts located above the cavity, which is most likely associated with low ray coverage.

In this study we extend the work of Hickey et al. (2009) who studied sites containing buried pipes. This work showed that although the actual seismic velocity contrast between the pipe and the surrounding earth materials is large, the measured velocity contrast in the seismic refraction tomograms is diffuse. However, these field studies showed that spatial distribution or ray coverage within the subsurface is an attribute that can be used for detecting and locating pipes. The Rayfract^{TM} (Intelligent Resources Inc.) seismic tomography code was used to process the seismic data for locating the pipes. This code uses the Wavepath Eikonal Traveltime inversion (Schuster and Quintus-Bosz, 1993), which incorporates a Fresnel volume approach. This approach accounts for the finite wavelength of real waves and the influence of the model in the adjacent vicinity of the ray path. The Fresnel volume approach addresses this issue by taking into account ray paths that arrive within a half period of the fastest waveform.

Electrical resistivity methods utilize direct currents or low-frequency alternating currents to investigate the electrical properties of the subsurface. In the resistivity method, the source is artificially-generated electric current introduced into the ground using electrodes. The potential differences are measured at the surface and the pattern of potential differences provides information on the distribution of subsurface electrical resistivity. Factors that affect the resistivity of soil-water mixtures include ionic concentration, porosity, surface conduction, tortuosity, and connectivity of fluid or conductive solid phases. Tunnels constructed in the vadose zone will cause redistribution in soil moisture possibly causing a local reduction in electrical resistivity. Tunnels constructed in saturated soil will also cause a local reduction in soil resistivity associated with the pumping of water in order to keep the tunnel clear. Furthermore, if the tunnel alters the height of the water table, due to water entering the tunnel, this might be an indirect indicator when using the electrical resistivity method.

The development of multi-channel resistivity meters and electronic switches enables the use of many electrode configurations which has made data acquisition for tomographic reconstruction feasible (Griffiths and Barker, 1993). In ERT, the forward problem uses the finite-element method to compute the electric potential response of the earth due to a given input electric current. The inverse algorithm iteratively finds the best distribution of subsurface resistivity that best fits the observed data. Daily et al. (2004) presents a concise overview of ERT. ERT has been used for some time to detect caves and tunnels (Spiegel et al., 1980; Van Schoor, 2002; Burger, 1992). The Advance Geosciences, Inc. Website also has several examples of using ERT for finding various types of high contrast voids (http://www.agiusa.com/2Dvoids.shtml, accessed January 15, 2010).

In this study we use RES2D^{TM} inversion software from Geotomo to calculate the psuedosections for the resistivity data. There are many different types of resistivity arrays with

their respective advantages and disadvantages. For our situation we chose to use the dipole-dipole configuration due to its good lateral resolution. The results shown are given as an apparent resistivity and thus are interpreted as local changes within the subsurface and cannot be directly interpreted as true resistivity values. The final inverted model shows the resistivity distribution of the subsurface determined from the apparent resistivity pseudosection.

Field Experiment

Geophysical field surveys were performed at a site with a known tunnel and with good surface access for surveying. The tunnel is a ~1 mx1.6 m (3ftx5ft) concrete lined tunnel about 80m (250ft) long. In general the tunnel is approximately 13m below the ground surface. The tunnel has issues of flooding, indicating that the tunnel is below or near the water table at some time in the year. The data presented here was collected in a nearby drainage ditch where the tunnel is at a depth of about 6m. The site layout for both the ERT and the seismic survey is shown in Figure 1. Based on prior knowledge of the tunnel location the surveys are approximately perpendicular to the tunnel and were purposely centered on the approximate location of the tunnel in order maximize the geophysical sampling in the vicinity of the tunnel.

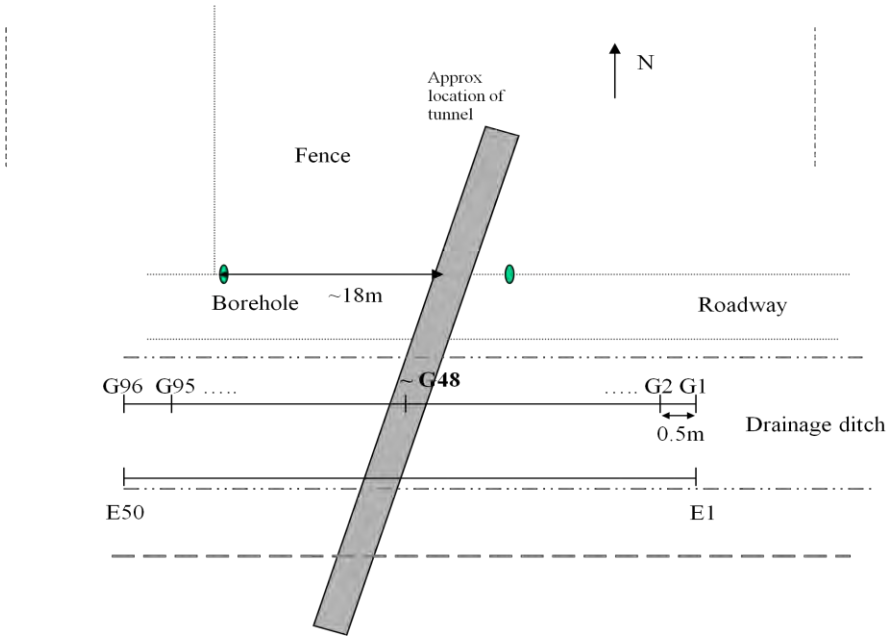

Figure 1: Site layout for the seismic refraction and ERT surveys conducted in a drainage ditch. The seismic line extends between geophone 1 (G1) and geophone 96 (G96). The ERT line is 3m south of seismic line and extends between electrode 1 (E1) and electrode 50 (E50). The location of the tunnel is approximate and intersects the surveys near the midpoint of the lines.

The seismic refraction survey was performed using 96 GS-20DM 14Hz OYO geophones with a Geometrics Geode^{TM} configuration and multichannel takeouts. The geophone layout was centered in the drainage ditch with the first channel at the east end of the line. A geophone spacing of 0.5m was used for a total spread length of 47.5m. The general rule for refraction tomography is that the depth of investigating is approximately 1/4th of the spread length, so a 47.5m spread length should give a depth of penetration of 10-12m. The tunnel is estimated to be about 5-6m deep. The source consisted of a 3.7 kg (8lb) sledgehammer impacting a 10cmx10cm aluminum plate. The shot locations were centered between the geophones at 1m intervals. This shot–receiver configuration results in 9312 seismic rays.

The ERT survey was acquired before the seismic acquisition; this was done by running the resistivity survey while setting up for seismic acquisition. The ERT system consisted of a Scintrex SARIS^{TM} automated imaging system, with two 25 takeout smart cables. The SARIS can produce up to 1A of current into the ground and 100W of power. The electrode layout consisted of 50 electrodes in a 1m dipole-dipole configuration for a total 49m spread length. The electrodes were one foot stainless steel rods and were planted near the edge of the ditch where the sand had slightly higher moisture promoting better coupling. The depth of investigation and the sensitivity of an ERT survey depend on the electrode spacing. The depth of investigation increases as the spacing between the potential and current dipoles increases. However, as the electrode dipole offset increases a higher current is needed to obtain a measureable voltage.

ERT Data

The data was edited to eliminate the improper lineations and large RMS data errors at the edge of the tomograms due to lack of current at larger offsets. The ERT results after three iterations are shown in Figure 2,. Figure 2a is the measured apparent resistivity at the site location; the results are then displayed in block format and seen in the pseudosection. Figure 2a is the final apparent resistivity pseudosection corresponding to the resistivity model shown in Figure 2c. The accuracy of the final model is evaluated by comparing the m Figure 2b to the measured apparent resistivity pseudosection shown in Figure 2a. For this case the forward modeled apparent resistivity was iteratively calculated until it the RMS error between it and the observed apparent resistivity differed by less than 2%. Figure 2c is the inverse model resistivity section representing the final distribution subsurface resistivity for this survey.

Due to the small size of our data set a finite element forward model with trapezoidal model blocks was acceptable. Smooth features near the edges of the measured apparent resistivity are created during the inversion and results near these sides must be ignored. In the final resistivity model (Figure 2c) , two high resistive anomalies with values reaching 60 Ωm are centered near at 20 m and 25.5 m. The two anomalies could represent a void buried within a fairly conductive weathered sands, in general, the resistivity of concrete ranges from 30-100Ωm and depends on a number of factors including porosity and grain composition.

The removed data points seen at 30m-40m was taken out due to being ten times larger than the standard deviation of surrounding material. Not all data was taken out since the anomaly of interest is at 25.5m, seen as E1 in (Figure 2C). This would skew the results and force the anomaly to fit if all bad data was removed. Another anomaly is seen at 3m depth and is shown as E2 in (Figure 2C). For this region we have an approximate water table depth of 5m, this is known due to prior information of the void filling full of water. Low resistivity region directly below and above the two anomalies are evidence for this water table. The resistivity deceases at

a depth of about 5-6m and is associated with the groundwater table. The resistive anomaly at E2 is unknown seen, while the anomaly at E1 corresponds with the approximate known location of the tunnel.

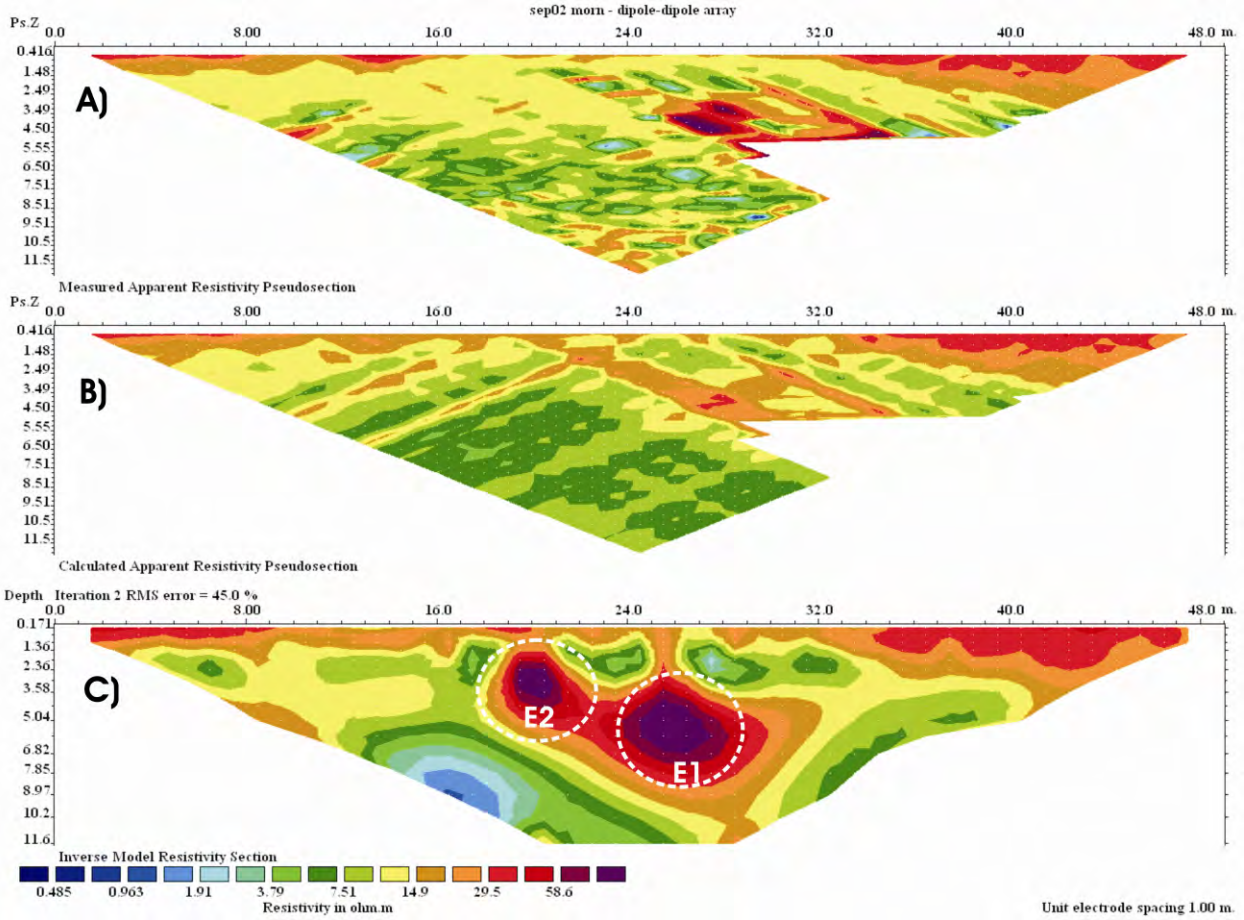

Figure 2: Resistivity tomography for the survey at a true tunnel site. A.): raw measured pseudosection of the apparent resistivity. B): calculated apparent resistivity from model resistivity, 3 iterations were used for the inversion. C): final model resistivity, this is the inverted model for the measured apparent resistivity section. Anomaly of interest is at E1, while E2 is not known.

Seismic Refraction

The sesimic field data was imported into Rayfract™ and 9312 first break arrival times were picked from the data. Starting with a simple 1-D gradient velocity model the program then determined the distribution of subsurface velocities that resulted in a best fit to the arrival times. The results were then displayed in a color scale cross-section referred to as a velocity tomogram and its corresponding ray coverage plot.

The velocity tomogram and its associated ray coverage map for the complete 96 geophone spread after 20 iterations are shown in Figure 3a and figure 3b, respectively. The majority of the rays (i.e. densest seismic sampling in red color) are concentrated above a depth of 12m. This is consistent with the usual assumption that the depth of investigation of a seismic refraction survey is about ¼ the spread length. The velocity tomogram exhibits a general

increase in velocity with depth that is typical for poorly consolidated materials. The saturated materials beneath the water table usually have seismic velocities of about 1500-1800m/s; and from Figure 3a this would infer that the water table is at a depth of about 10m from the bottom of the drainage ditch. The tunnel location is estimated to be near the center of the spread and at a depth of about 6m. The anomaly corresponding to the location of the tunnel is labeled S1. As expected, there velocity tomogram shows only a slight downward bend in the velocity contour; however, ray coverage plot shows a zone of low ray coverage at this location.

In order to focus in on shallower depths, a subset of the travel times using only geophones 24 through 72 was processed (Figure 4). The velocity tomogram shown in Figure 4a shows a slight lowering in the velocity contour in the general location of the tunnel (labelled S1), it does not have a strong anomaly associated with the tunnel. Figure 4b shows the ray coverage over the complete range; a region of low coverage encircled by high coverage is evident near the location of the tunnel. This type of signature was observed by Hickey et al. (2009) over various pipes. In the enhanced ray coverage mapping (Figure 4c), the local minimum in ray coverage is at a depth of 5.5m and at station location of 13.5. In terms of the complete survey this corresponds to the location of geophone 49. The center of this region of lower ray coverage is in excellent agreement with the known location of the tunnel.

With the correlation between low ray density and tunnel position in mind, and returning to the complete seismic spread of Figure 3, another region of low coverage and a slight dip in the velocity contour is seen at 44m (near geophone 88). This anomaly is labelled S2. This type of anomaly could possibly be associated with another tunnel. The anomaly is close to the end of the seismic line and additional data to west of the current spread is need to further investigate this anomaly.

ERT and Seismic Refraction

The tunnel produces visible anomalies in both the seismic refraction and the ERT data. In the ERT, the tunnel coincides with one of the high resistivity anomalies, but a second, shallower, resistive anomaly of unknown provenance appears just to the east. Based on the results of the seismic survey it would be difficult or impossible to interpret the existence of the tunnel on the basis of the velocity tomogram even with the slight dip in the velocity pattern near the known tunnel location. However, the location agrees well with a zone of low seismic ray density. There is no seismic anomaly corresponding to the shallower anomaly in the ERT data at location E2. In this instance the use of both methods would suggest that this second ERT anomaly is not a tunnel and illustrates how the use of both seismic refraction and ERT can be used to increase the reliability of detecting tunnels. A second anomaly is also present near the end of the seismic line seen at location S2. However, in this case neither the ERT nor the seismic surveys reached sufficiently far enough west to eliminate this anomaly as a possible tunnel.

-

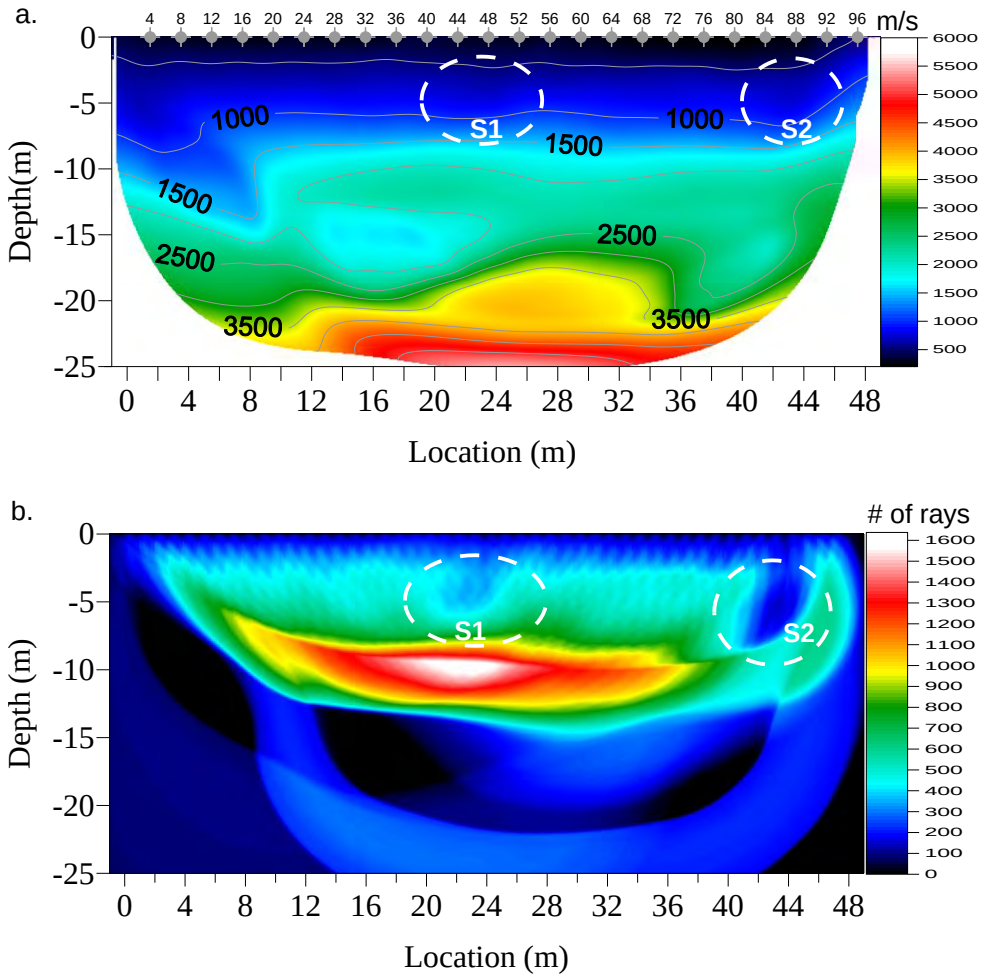

Figure 3: The measured a.): velocity tomogram and the corresponding,b.): ray coverage map* from the 96 geophone seismic line. The tunnel is located near the center of the spread and at a depth of about 6m. The anomaly S1 is associated with the tunnel. The anomaly S2 requires further investigation.

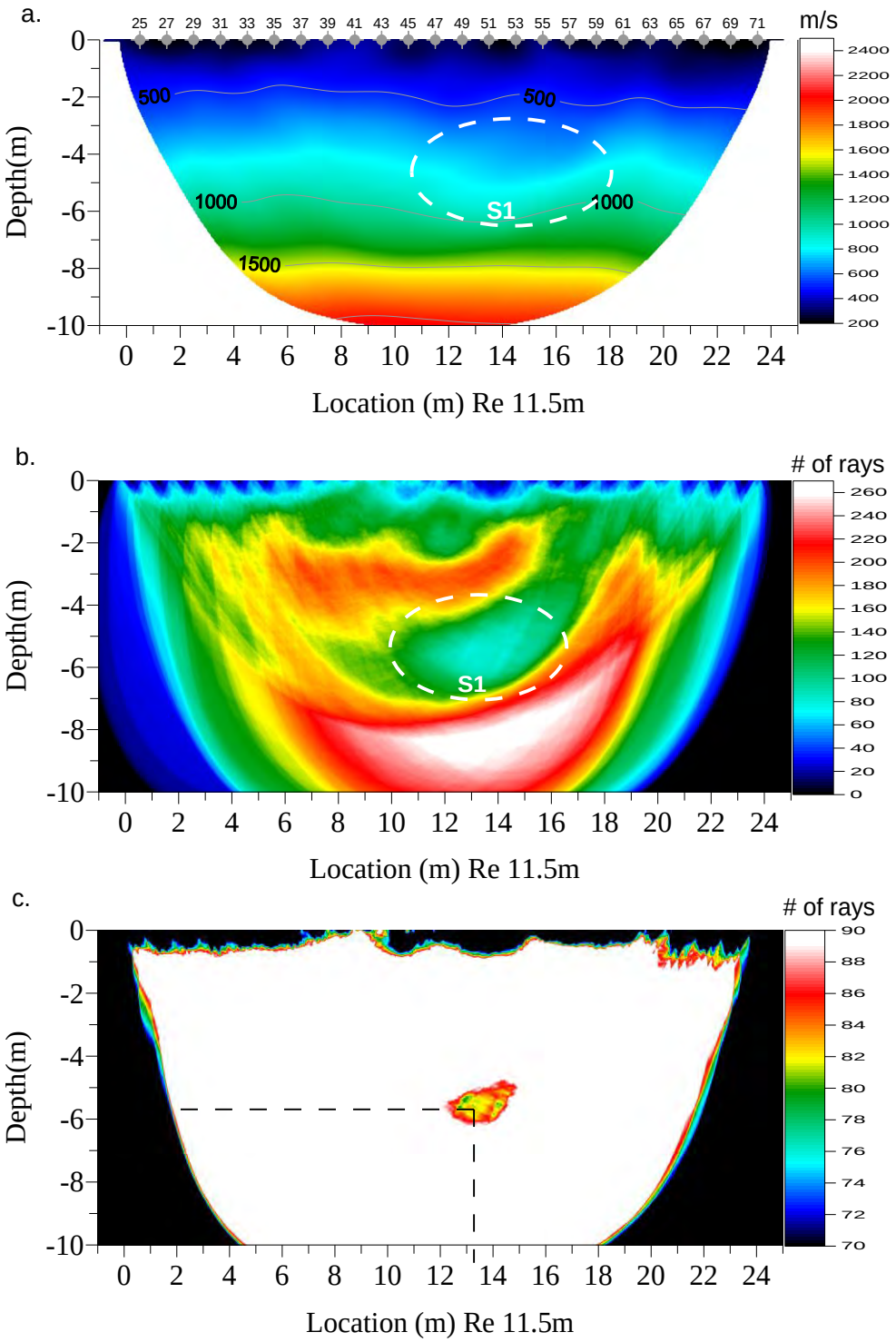

Figure 4: The data from the central part of the survey, from geophone 24 to geophone 72, processed using Rayfract. A.):the measured velocity tomogram, b.):the corresponding ray coverage map, and c.): the ray coverage map with a threshold.

Conclusion

The study shows how both seismic and electrical techniques can be used to detect tunnels and agrees with previous studies over buried pipes. Seismic and electrical properties are sensitive to different types of rock properties and anomalies are present in the data at corresponding to the tunnel location. Seismic tomography requires dense spatial sampling in order to obtain adequate ray coverage. The velocity tomographic image is inadequate for tunnel detection as the smoothing inherent to the tomographic calculations results in only slight changes in velocity near the tunnel location. Instead, the ray coverage density mapping associated with ray tracing displays small regions of low coverage associated with the tunnel. The tunnel should show up in the electrical imaging as regions of high resistivity since both the concrete and air of the tunnel are higher resistivity than the conductive weathered rock. In practice, the resistive anomaly of the tunnel gets smoothed out and is larger than the actual tunnel..

From this field study, the seismic data and the electrical both show an anomaly at the center of each spread that correlate with the location of the tunnel. The electrical data also shows another anomaly near the middle of the spread which is not present in the seismic data. Similarly near the edge of the seismic spread a drop in velocity is seen and a possible void site is suggested. Using results from both surveys together allows for a more confident detection of this tunnel.

References

Advanced Geosciences, Inc, 2007., Case and void detection, accessed January 15, 2010 from http://www.agiusa.com/2Dvoids.shtml.

Anon., Proceedings of the second technical symposium on tunnel detection, Colorado School of Mines, Golden, Colorado, July, 1981.

Anon., Proceedings of the third technical symposium on tunnel detection, Golden, Colorado, January, 1988.

Burger, H. R., 1992. Exploration Geophysics of Shallow Subsurface Prentice-Hall, Eaglewood Cliffs, NJ, 489pp

Daily, W., Ramirez, A., Binley, A., LaBrecque, D., 2005, Electrical Resistance Tomography-Theory and Practice. Investigations in Geophysics; no. 13, 525-550.

Daniels, J. and Harmon, R. "Special Session on Cavities and Tunnels", EEGS Annual Meeting, Forth Worth, TX, March 9-April2, 2009.

Griffiths, D.H., Barker, R. D., 1993. Two-dimensional resistivity imaging and modeling in areas of complex geology. J. Appl. Geophys. 29, 211-226

Halihan, T. and Nyquist, J.E. " Detection of voids, tunnels and collapse features," Session No. 218-T65, 2006 Philadelphia Annual Meeting of the Geological Society of America, Philadelphia, PA, October, 2006.

Hickey, C.J., Schmitt, D.J., Sabatier, J.M, and Riddle, G. " Seismic Measurements for Detecting Underground High-contrast Voids", Proceedings of Symposium on Applications of Geophysics to Environmental and Engineering Problems, Fort Worth, TX, May 30-April 3, p. 929-936, 2009b.

McKenna, J.R. and Ketchum, S.A. "Tunnel detection, monitoring, and modeling," Session NS21A, 2006 AGU, GS, MAS, MSA, SEG, UGM Joint Assembly, Baltimore, MD, May 2006.

Sabatier, J.M. and Muir, T.G. " Workshop on real-time detection of clandestine shallow tunnels," National Center for Physical Acoustics, Univ. Of Mississippi, NCPA report HB0306-01 for US Army Research Office, Grant No. W911NF-06-1-001, April, 2006.

Sheehan, J.R., Doll, W.E., Mandell, W., 2005, An evaluation of methods and available software for seismic refraction tomography analysis, JEEG, 10(1), 21-34, 2005.

Simmons, J. and Aldridge,D. "Special session on methods for tunnel detection," Sesimo. Soc. Am Annual Meeting, Santa Fe, Nm, April 16-18, 2008.Van Schoor, M., 2002, Detection of sinkholes using 2D electrical resistivity imaging., J. Appl. Geophys. 50,393-399.

US Army Research Lab, "Human, Light Vehicle, and Tunnel Detection Workshop" Beltsville, MD, June 16-17, 2009.

Williamson, P.R., 1991, A guide to the limits of resolution imposed by scattering in ray tomography, Geophysics, 56(2), 202-207.

Acknowledgements

This material is based upon work supported by the U.S. Department of Homeland Security under Grant Award Number 2007-ST-108-000003. The views and conclusions contained in this document are those of the authors and should not be interpreted as necessarily representing the official policies, either expressed or implied, of the U.S. Department of Homeland Security. Field data acquisition was assisted greatly by C.R. Schmitt, S. Taylor, J.D. Heffington, and G. Brasnett.

GEOSTATISTICAL ANALYSIS OF BOREHOLE AND SURFACE WAVE DATA A CASE STUDY

Marco de Kleine Deltares Netherlands
Rik Noorlandt, Netherlands

Abstract

A Surface wave study has been executed in the center of Surinam in order to determine the depth to bedrock. The site of investigated is located in the tropical rain forest of Surina so the overburden consists of tropical oils and lateritic soil. The topography at the site is very pronounced. The survey data was combined with other types of data, i.e. boreholes, spt's, cpt's. The additional information was used both during the inversion and during the interpretation of the data using an iteratively approach. By combining this data with geological and geostatistcal knowledge not only insight in the thickness of the overburden was obtained but also information about the limitations of the data and the reliability of the results was determined. This additional information is relevant for the construction company who can make better cost estimates based upon this type of information.

Introduction

For a construction project in the centre of Surinam information was needed about the depth to bedrock in an area with tropical soils underlain by gneiss and granulites (bedrock). This topsoil (overburden) has to be removed in order to create a flat construction site. The relief at the study area (1000x500 meter) is significant, the maximum difference in height in this area is 70 meters. The removal of the topsoil is relatively easy, but to create a big enough site it could be necessary that bedrock has to be removed also, which is expensive. To make a correct estimation of the costs for creating this construction site and optimize the plans, detailed information about the depth to bedrock is needed.

TNO Built Environment and Geosciences, Utrecht, The Netherlands/ Deltares, has applied the non-invasive and non-destructive technique ConsoliTest (Westerhoff et al, 2004) for the depth-to-bedrock mapping. This geophysical method, adapted from the MASW technique (Park et al, 1998), investigates the shear stiffness of the upper tens of meters of the subsurface using surface (Rayleigh) waves.

The investigated area is situated in the tropical rainforest of Surinam. In this area granulites and gneisses have undergone intensive (chemical) weathering resulting in a regolith. A regolith is an unconsolidated partially cemented cover that overlies coherent non weathered bedrock (granulites and gneisses). Significant variations over short distances in position of the top the bedrock can be expected. The regolith mainly consist of relatively soft, compressible layers however due to the lateritic character of the soil in this area stiff layers can also be present. These stiff layers tend to concentrate at the top and the base of the regolith.

SAGEEP 2010 Keystone, Colorado
http://www.eegs.orghttp://www.eegs.org/

Method

The ConsoliTest method was used to determine the position of the top of the bedrock in addition to a drilling campaign, which can be applied more cost-effectively by pointing out borehole locations based on 3D patterns imaged by ConsoliTest, compared to an unguided, random drilling campaign. Also, the chance of missing areas with significant variations in the depth to bedrock thickness is minimized when using continuous data. Additionally, the measurements are verified and calibrated by the borehole and cone penetration tests (CPT) information.

The ConsoliTest measurements in Suriname consisted of the following steps:

a. Acquiring Rayleigh wave data.
   - Using a hammer blow on a metal plate, recorded by a towed array of equidistant geophones with an interval of 1m.

b. Raw data QC and basic filtering:
   - checking the data quality in the space-time domain;
   - Blanking data parts not belonging to Rayleigh waves, below and above a maximum speed;
   - cutting or adding records to get the right amount of traces for the subsequent processing.

c. Extracting dispersion information:
   To extract the Rayleigh wave phase velocity dispersion, the raw data (x-t) is converted to velocity-frequency domain using the MASW method described in Park et al. (1998). The Rayleigh wave dispersion was then picked manually. This process is one of the most critical for eventually generating an accurate shear-wave profile. The method has been proved to yield a high-resolution dispersion curve without using an exceptionally large amount of geophones. Picking can now be done automatically, described by Westerhoff and Noorlandt (2008), although a critical check of the results is still needed.

d. Producing shear wave velocity models
   Inverting the dispersion information to 1D layered shear wave (Vs) models that fits the dispersion found in the data, a neighborhood algorithm (Sambridge, 1999) is used. The constraints of the inversion were determined from the drilling information available. The models consisted of one layer on top of a half space (representing the weathering layer on top of the bedrock) and two layers on top of a half space (representing the weathering layer with stiff inclusion on top of the bedrock). In both models the bedrock is depth is thought to be equal to the half space depth.

e. Interpretation of the depth to bedrock from each separate vertical shear wave velocity profile. Depths where large contrasts in shear wave velocity exist are identified as the top of bedrock. Because of the complex process of tropical weathering of bedrock, a large heterogeneity is expected.

f. Geostatistical modeling and data visualization in a 3D area. A Kriging method has been used to interpolate the depth of the bedrock between measurement locations. This modeling step was done in order to create a grid that covered the whole investigated area. Finally, we have plotted all borehole data and processed seismic data in a 3D volume.

SAGEEP 2010 Keystone, Colorado
http://www.eegs.orghttp://www.eegs.org/

This process, using different data types, (wells, CPTs and ConsoliTest measurements), together with geological knowledge and a geostatistical analysis of the data will result in an area-covering prediction of the position of the top of the bedrock and an indication of the accuracy of the results.

At the first rough processing only little was known about the subsurface (only four clustered wells were available) and the inversion results could hardly be validated on anything else than data misfit. Gridding was therefore done using only one model per record that fitted the data best. The result showed quite a large bedrock depth distribution/variation. In the second, more detailed, processing much more information was available (more wells and CPTs) on the subsurface, such that the inversion results could be validated in more detail and a better velocity model could be generated. The validation of the previous results showed the presence of non-uniqueness in the data; multiple models could equally well produce the dispersion curves within the frequency bandwidth of the data. The well data also showed that the models were biased to be overestimating the bedrock depth. Therefore the inversion was repeated with more weight on the dispersion picks at lower frequencies. Gridding was done using the distribution of the best 1%, 5% and 10% of the models produced during the inversion. The final inversion results are shown in figure 1.

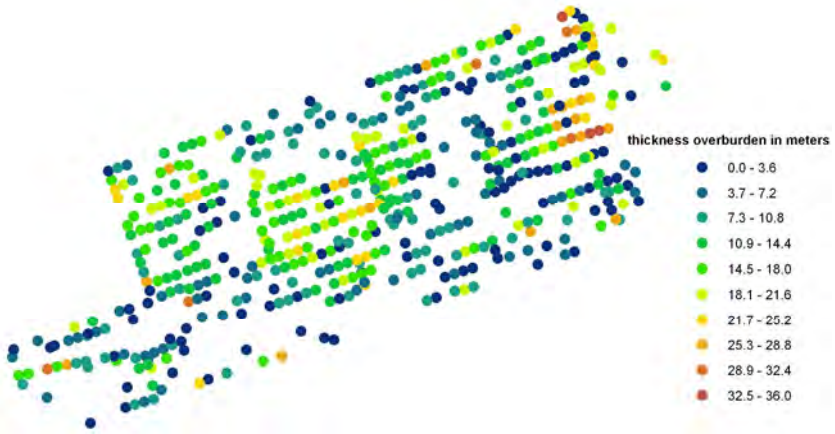

Figure 1: Results of the final inversion, depth to bedrock in meters. The investigated area is 1000m long and 500 meters wide.

SAGEEP 2010 Keystone, Colorado
http://www.eegs.orghttp://www.eegs.org/

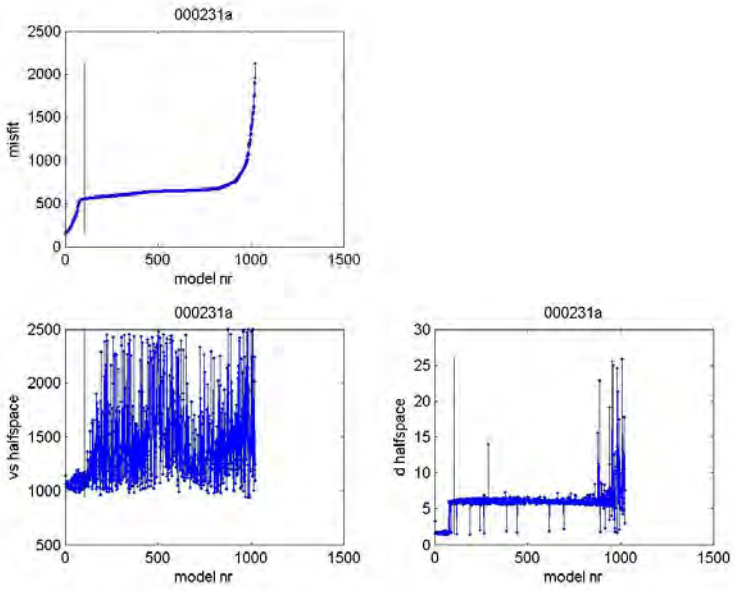

Figure 2 Convergence of the inversion of a record. On the top left the data misfit is shown, sorted on misfit. The two lower figures show misfit in the halfspace velocity and depth.

Figure 2 shows an example of the convergence, and misfits of a record. As can be seen, non-uniqueness at higher misfits is clearly visual. All models left of the vertical line were taken in to account in the gridding process (10% case). With this analysis we showed that, for the entire data set, it is better to use the median inversion values instead of the mean values. The use of the mean leads to an overestimation of the bedrock depth while the median value leads to more realistic values. Also, the consequences of the misfit between the field measurements and the inversion results on the final result are visualized, which gives insight in how well the inverse problem is constrained, converged, and how large the non-uniqueness is.

By comparing the inversion results and the gridded results with the borehole and CPT data an analysis is made of the accuracy of all the measured, inverted and gridded results. For this analysis also grids representing the standard deviation of the inverted data were made. This process has been repeated several times for different velocity models and has had a significant effect on the results and reliability of the inverted and gridded data. The final gridding result is shown in figure 3.

SAGEEP 2010 Keystone, Colorado
http://www.eegs.orghttp://www.eegs.org/

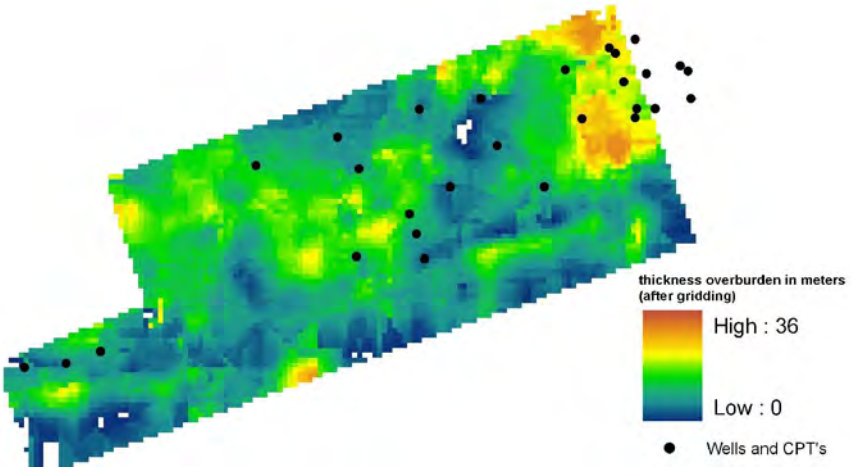

Figure 3: Results of the final gridding. Depth to bedrock is in meters. The black dots represent the available wells and CPTs. The investigated area is 1000m long and 500 meters wide.

The reliability of the calculated grid is shown in figure 4. At the position of data points the reliability is high, in the green areas between the data points depth to bedrock values have been calculated, the accuracy in this area is lower but acceptable. Outside these areas, shown in red, the reliability of the calculated grid is significantly less and the calculated values should be used with care.

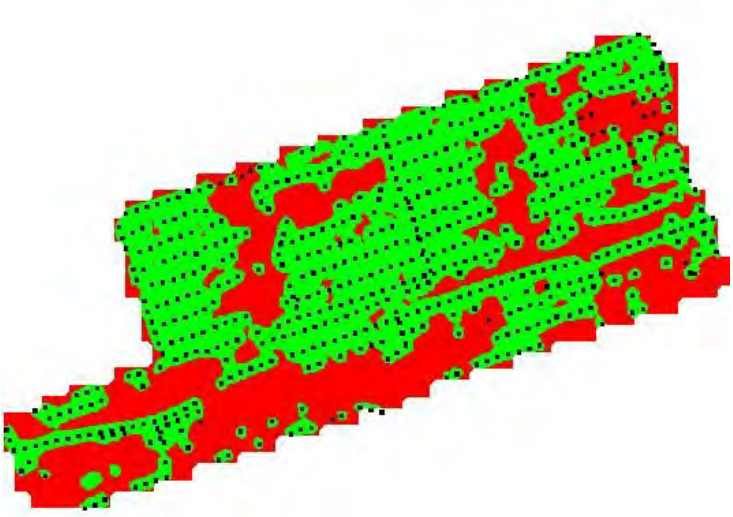

Figure 4 : Map of the relative reliability of the calculated grid. The investigated area is 1000m long and 500 meters wide.

SAGEEP 2010 Keystone, Colorado
http://www.eegs.orghttp://www.eegs.org/

Conclusion

By combining different sources of field data insight is gained in the value of adding additional validation points in the processing of ConsoliTest data and in the consequences of using a different approaches during the inversion and gridding. By combining geophysical measurements, well- and CPT information, geological and geostatistical knowledge significant steps can be made in the improvement of the potential use geophysical data for engineering applications, and more insight can be gathered about the limitations of the use of this data. This combination of data and knowledge types has to be made iteratively, because all steps are interacting and of influence in the final results.

References

Park, C., Miller, R., and Xia, J., 1998. Imaging dispersion curves of surface waves on multi-channel record. SEG Expanded Abstracts, 17:1377.

Sambridge, M., 1999. Geophysical inversion with a neighbourhood algorithm-I. Searching a parameter space. Geophysical Journal International, 138:479–494.

Westerhoff R.S., Hoegaerden V. van, Brouwer J.H. and Rijkers R., 2004. ConsoliTest - Using Surface Waves for Estimating Shear-Wave Velocities in the Dutch Subsurface. Lecture Notes in Earth Sciences 104, pp. 368-376

Westerhoff, R.S., Noorlandt, R.P., 2008. Automated Dispersion Mapping of Surface Waves. Near Surface 2008, EAGE, Krakow,15-17 september 2008.

REVISITING SH-WAVE DATA USING LOVE-WAVE ANALYSIS

Jianghai Xia, Kansas Geological Survey, The University of Kansas, Lawrence, Kansas
Richard D. Miller, Kansas Geological Survey, The University of Kansas, Lawrence, Kansas
Recep Cakir, Washington State Department of Natural Resources, Olympia, Washington
Yinhe Luo, China University of Geosciences, Wuhan, China
Yixian Xu, China University of Geosciences, Wuhan, China
Chong Zeng, Kansas Geological Survey, The University of Kansas, Lawrence, Kansas

Abstract

Although Love waves are widely analyzed in earthquake seismology, there is much less attention on utilizing Love waves than Rayleigh waves by the near-surface community. Unlike incident P and Sv waves, a plane SH wave for a series of horizontal layers refracts and reflects only SH waves, which makes the shallow SH-wave refraction method more popular to define shear (S)-wave velocity in near-surface geologic applications. For this reason, abundant SH-wave refraction data have been acquired and S-wave velocities have been determined using their first arrivals. If signals are recorded long enough, Love-wave energy can be clearly observed on SH-wave refraction data. Wave conversion may occur in an SH-wave refraction and Love-wave analysis only results in SH-wave velocities, which suggest that we may benefit from revisiting the existing SH-refraction data using multichannel analysis of Love waves (MALW). We used numerical modeling results and real-world examples to demonstrate three advantages of revisiting SH-wave data using the MALW method. Owing to a long geophone spread commonly used in SH-wave refraction survey, a sharp image of Love-wave energy can be generated, allowing better pickings for the phase velocities of Love waves. Because Love waves are independent of P-wave velocity, “mode crossing” in an image of Love-wave energy is less common than in Rayleigh-wave images. Fewer unknowns in the method MALW make dispersion curves of Love waves are simpler, which leads to more stable inversion of Love waves and reduces the degree of nonuniqueness.

Introduction

Surface-wave techniques have been given increasingly more attention by the near-surface community with applications to a variety of near-surface problems. Studies on high-frequency surface-wave techniques have been focused primarily on Rayleigh waves. Errors in shear (S)-wave velocities obtained by inversion of Rayleigh waves (Xia et al., 1999) using a multichannel recording system (e.g., Song et al., 1989) are 15% or less and random when compared with direct borehole measurements (Xia et al., 2002a). Examples of studies on Rayleigh-wave data analysis include: near-surface quality factors (Q) (Xia et al., 2002b); a pitfall using SH-wave refraction surveying (Xia et al., 2002c); joint inversion of refractions and Rayleigh waves (Ivanov et al., 2006a); estimation of S-wave velocities for a continuous earth model (Xia et al., 2006a); the nearest offset and cutoff frequencies (Xia et al., 2006b, Xu et al., 2006, 2009); discussion of Rayleigh-wave inversion with a high-velocity-layer intrusion model (Calderón-Macías and Luke, 2007); a low-velocity-layer intrusion model (Lu et al., 2007; Liang et al., 2008); dispersive images using slant stacking (Xia et al., 2007a) and high-resolution Radon transform (Luo et al., 2008); mode separation (Luo et al., 2009), numerical modeling (Xu et al., 2007); assessment of an inverted model (Xia et al., 2008, in press); inversion of multimode data (Xia et al., 2000, 2003; Beaty et al., 2002; Luo et al., 2007); and other applications of delineation of bedrock (Miller et al., 1999) and detection of voids (Xia et al., 2004, 2007b) and shallow fault zone (Ivanov et al., 2006b).

Although Love waves are widely analyzed in earthquake seismology (e.g., Aki and Richards, 1980), for example, a simultaneous inversion of phase velocities of Love and Rayleigh waves in the study of the earth structures (Lee and Solomon, 1979), there is much less attention on utilizing Love waves than Rayleigh waves by the near-surface community (Steeples, 2005). This may be because acquiring SH-wave data is not as easy as acquiring vertical-component P-wave and Rayleigh-wave data and/or the unavailability of software for Love-wave analysis. Recent improvements in data-acquisition techniques and developing of software make SH-wave data acquisition and processing easier. In addition, analyzing SH-wave data using Love-wave inversion for near-surface applications may become more useful because it provides SH-wave velocities that are critical for S-wave and anisotropy analysis.

Recent studies on high-frequency Love waves include sensitivity analysis (Zeng et al., 2007); improvement of S-wave velocity with Love-wave inversion (Safani et al., 2005), inversion of Love waves with a low-velocity layer (Safani et al., 2006), joint inversion of electric and Rayleigh- and Love-wave data (Misiek et al., 1997), and inversion of Love-wave data to measure the lateral variability of geo-acoustic properties of marine sediments (Winsborrow et al., 2003). High-frequency Love-wave modeling by Luo et al. (in review) could improve the inversion of Love waves in the time-space domain. Sharp dispersion images and stable inversion of Love-wave data with the weighted least-square method provided reliable S-wave velocities in several sites (Xia et al., 2009). Wave conversion may occur in an SH-wave refraction survey (Xia et al., 2002c) and Love-wave analysis only results in SH-wave velocities, which suggest that we may benefit from a revisit to existing SH-refraction data to use Love waves for determining S-wave velocities using multichannel analysis of Love waves (MALW).

Love waves are the result of total internal multiple reflections of SH waves at the free surface. Their particle motion is parallel to the surface but perpendicular to the direction of propagation. For a layered-earth model, the condition for existence of Love waves is the same as the condition for existence of refractions (e.g., Stoneley, 1950; Garland, 1979). Based on their field experiences, Eslick et al. (2008) concluded that a minimum thickness of 1 m of low-velocity material for the near-surface layer is needed to record usable Love-wave data in the frequency range of interest (5-50 Hz). Love-wave phase velocity of a layered-earth model is a function of frequency and three layer parameters: SH-wave velocity, density, and thickness of layer. The dispersion of Love waves is independent of P-wave velocity (Aki and Richards, 1980). This property is extremely useful in inversion of Love waves for S-wave velocities and reduces the degree of nonuniqueness of an inverted S-wave velocity model. In addition, Love waves in a layered-earth model also possess the unique properties that the asymptote of the phase and group velocities at high frequencies approaches the S-wave velocity of the top layer and the asymptote at low frequencies approaches the S-wave velocity of the half space. Xia et al. (2009) generally discussed an inversion algorithm of the MALW method and showed their dispersion analysis and inversion results of SH refraction data acquired at various sites in the US. Although the data were acquired for SH-refraction analysis focused on first breaks and recorded with a short time length (Love waves were not completely recorded), dispersion analysis of these data show that Love-wave energy can be sharply and clearly imaged and phase velocities then are easily determined. The inversion of these phase velocities was very stable and extremely fast.

In this paper, we will use numerical modeling results and real-world examples to demonstrate the three advantages of the MALW by revisiting SH-wave data with Love-wave analysis in defining S-wave velocity. Owing to a long geophone spread commonly used in SH-wave refraction survey, an image of Love-wave energy is cleaner and sharper than Rayleigh waves, which makes picking phase velocities of Love waves much easier and more accurate. Because it is independent of P-wave velocity, dispersion curves of Love waves are simpler than Rayleigh waves. “Mode crossing” is an annoying phenomenon in Rayleigh-wave analysis that causes mode misidentification and therefore produces S-wave velocities much higher than real ones (Zhang and Chan, 2003). “Mode crossing,” however, is less common in

dispersion images of Love-wave energy than Rayleigh waves. This simplicity of Love-wave dispersion curves leads to the inversion of Love waves much easier and more stable compared to Rayleigh waves.

Sharp Images of Dispersive Energy of Love Waves

Resolution (or sharpness of a trend of energy peaks) of a dispersive image is approximately proportional to a geophone spread, which is a distance between the first geophone to the last geophone (Forbriger, 2003; Xia et al., 2006b). SH-wave refraction surveying usually uses a long geophone spread. An image of dispersive energy generated from the SH-wave refraction data is normally sharp enough to ensure that the picked phase velocities are accurate in general, which provides a solid basis for reprocessing SH-wave refraction data using Love-wave analysis.

SH-wave refraction data of the first example was acquired in Wyoming during the fall of 1998 to determine shear-wave velocities in near-surface materials (upper 7 m). SH-wave refraction data were acquired using 48 28-Hz horizontal-component geophones oriented in a N-S direction. Geophones were deployed at a 0.9-m interval along a W-E line. A polarized seismic source was provided by a 6.3-kg hammer impacting the long dimension of a fixture (S-wave source plate) oriented perpendicular to the west-to-east geophone spread. Two records were generated for each source location, one with a blow from the south and the other from the north, with a phase difference of 180^o (Figure 1). Analysis of the SH-wave refraction data using first arrivals (direct and refracted waves) produced a velocity model that was very close to a P-wave velocity model except for the first layer (Xia et al., 2002c). Processing P-wave refraction data using Rayleigh-wave analysis showed the velocity model generated from SH-wave refraction data was converted P-wave velocities on a dipping interface, which was supported by the suspension logging data (Xia et al., 2002c).

We reprocessed the SH-wave refraction data using Love-wave analysis. Strong Love-wave energy can be observed in Figure 1. Sharp images (Figure 2) from both shots were generated using the high-resolution linear Radon transform (Luo et al., 2008). Phase velocities of the fundamental mode from 10 to 50 Hz and the first higher mode from 35 to 55 Hz can be easily picked out from either one of the images, which are visually identical. We will show the inversion results later in this paper.

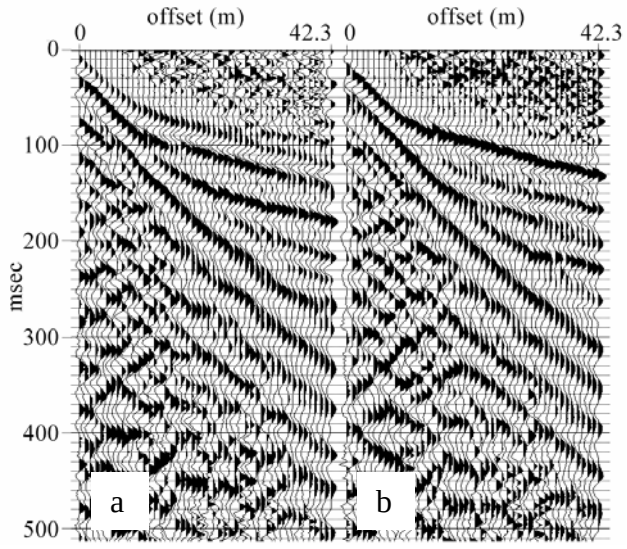

Figure 1. Forty-eight-channel SH-wave refraction data along a W-E line. N-S blows against both ends of the fixture generated data with the polarity revision of the first arrivals (a and b).

SH-wave data (Figure 3a) of the second example were acquired at the front grassy area of the Kansas Geological Survey building in the spring of 2009, where Rayleigh wave data were collected along the same line in 1995 (Xia et al., 1999). The data were acquired using 40 14-Hz horizontal component geophones oriented perpendicular to the line. Geophones were deployed at a 1-m interval, and the same hammer source and SH-wave generation procedure as described in the first example were used. Figure 3a shows the shot gather (three far offset traces were removed due to noises) with strong Love waves. A sharp image (Figure 3b) from the shot gather was generated. Phase velocities of the fundamental mode from 12 to 50 Hz and first higher mode from 38 to 55 Hz can be easily picked out from the image. We will show the inversion results later in this paper.

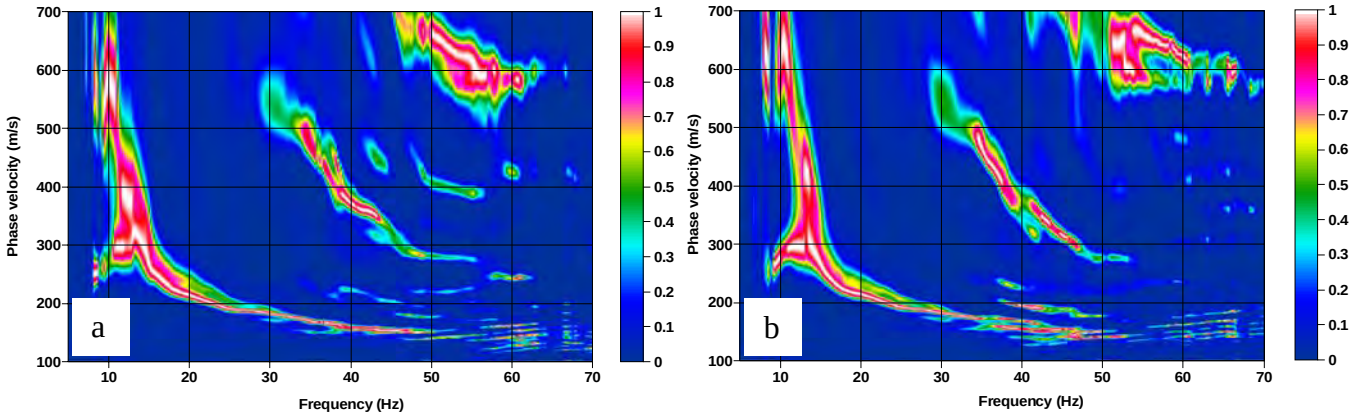

Figure 2. Images of Love-wave energy shown in Figure 1. (a) generated from the shot gather shown in Figure 1a from a blow from the south and (b) generated from the shot gather shown in Figure 1b from a blow from the north.

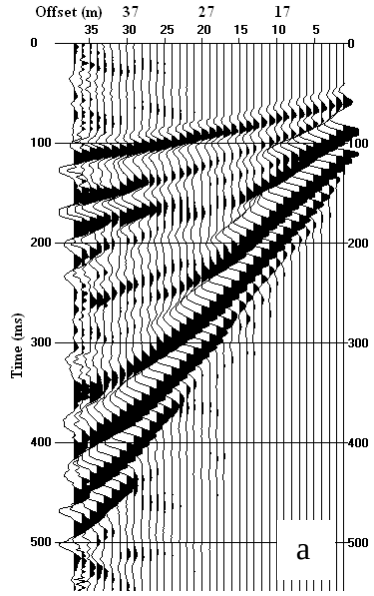

Figure 3. SH-wave data with well developed Love waves acquired in the front grassy area of the KGS building (a). An image (b) of Love-wave energy was generated using high-resolution linear Radon transform (Luo et al., 2008). The sharp Love-wave energy trend allows easy and accurate picking for phase velocities.

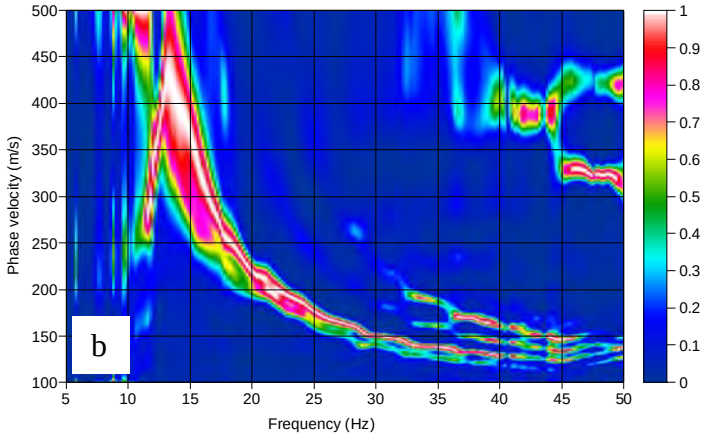

Finally, SH-wave data of the third example were acquired in Yuma, Arizona in the summer of 2009 to build a near-surface velocity model. A long-geophone-spread shot gather was used. The data were acquired using 240 14-Hz horizontal component geophones oriented perpendicular to the line. Geophones were deployed at a 1.2-m interval, and the same seismic source and procedure of SH-wave generation as described for the first example were used. Strong Love waves were present (Figure 4a). Just for a test, we kept all 240 traces for Love-wave processing. An image (Figure 4b) generated from the shot gather was sharp even though the signal-to-noise ratio was relatively low in the far offset traces (trace 170 and farther). Phase velocities of the fundamental mode from 5 to 95 Hz can be easily identified from the image, which are averaged values of the area covered by the geophone spread. To investigate the lateral velocity change, we also generated the dispersive image (Figure 4c) based on the first 50 traces. Comparing Figure 4b with Figure 4c, the phase velocities due to the shallower part of the subsurface (30 to 95 Hz) were identical but the velocities of the deeper part (5 to 30 Hz) were different, indicating lateral changes in S-wave velocity. We also noticed that longer wavelength components (> 40 m) were not well imaged in Figure 4c due to a short geophone spread.

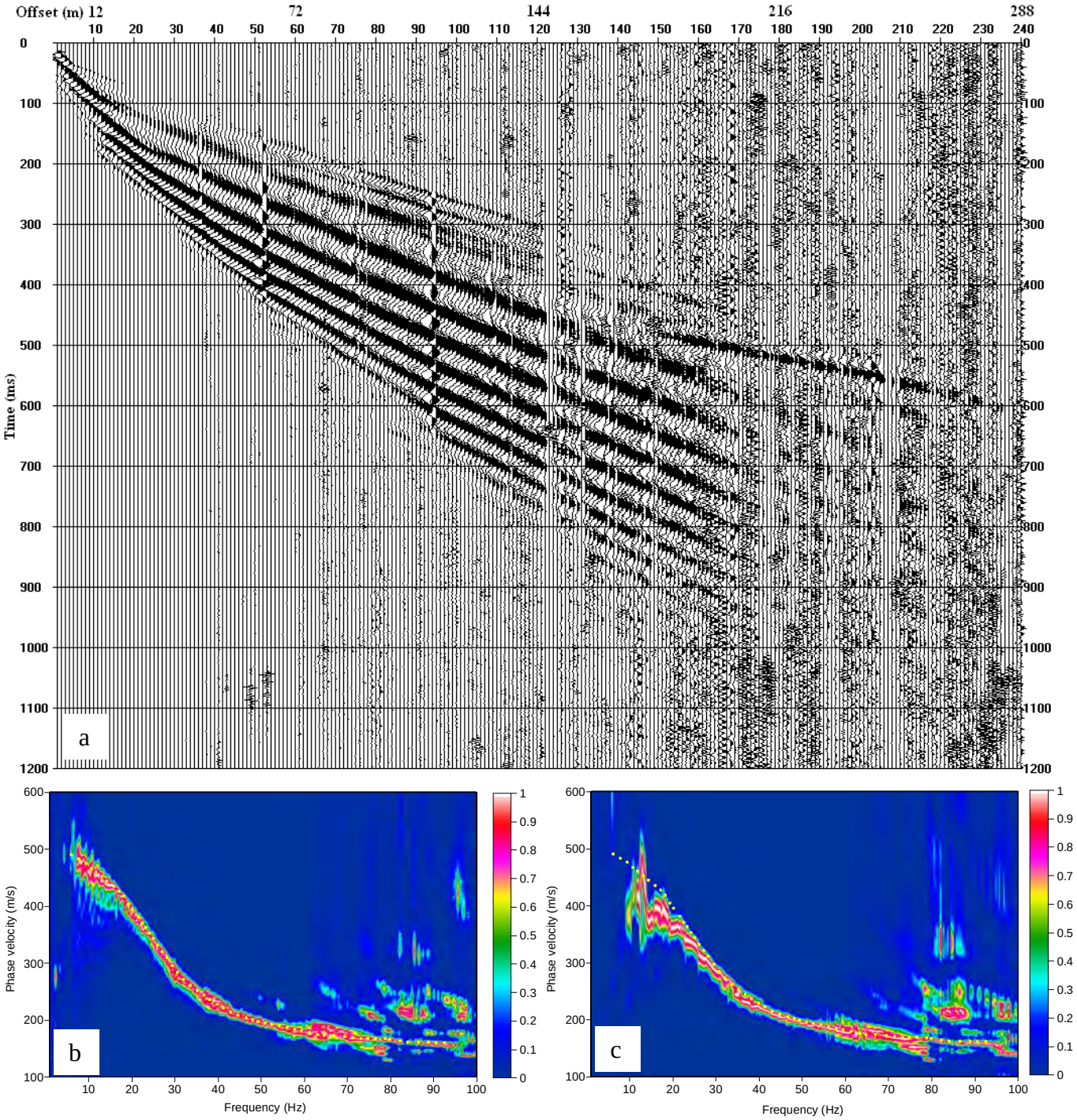

Figure 4. (a) SH-wave data with 240 traces acquired in Yuma, Arizona. Love-wave energy is dominant in the shot gather. (b) An image of Love-wave energy calculated from the 240-trace shot gather (a) containing noisy traces. The sharp Love-wave energy trend allows easy and accurate pickings of phase velocities (yellow dots). (c) An image of Love-wave energy was calculated from the first 50 traces of the shot gather (a) superposed with yellow dots that are phase velocities picked from (b). Note that phase velocities are the same from 30 Hz and up for both images, and phase velocities from 5 to 30 Hz are higher in (b) than in (c).

Simple Dispersion Curves of Love Waves

Unlike Rayleigh waves, the dispersion of Love waves is independent of P-wave velocity. Love-wave phase velocity of a layered-earth model is a function of frequency and three parameters: SH-wave velocity, density, and thickness of layers. A fewer parameters make the dispersion curves (or Love-wave energy trend) simpler.

We used a two-layer model, with the first layer Vs, Vp, density, and thickness as 150 m/s, 300 m/s, 1.5 g/cm^3, and 10 m, respectively, and the half space Vs, Vp, and density as 450 m/s, 900 m/s and 2.0 g/cm^3, respectively, to compare dispersion behaviors of Rayleigh and Love waves. This model simulates the case of a soft layer overlying bedrock. Figure 5a shows synthetic P-Sv data with 110 traces based on the two-layer model generated by Xu et al.'s algorithm (2007). Rayleigh waves are observed in the shot gather. Rayleigh-wave energy was mapped by the high-resolution linear Radon transform (Luo et al., 2008) in the frequency-velocity (f-v) domain (Figure 5b). It is interesting to point out that the fundamental mode may be picked from 4 to 50 Hz continuously and "confidently" if no other information is available on the subsurface, such as an S-wave velocity range. After we superposed the theoretical dispersion curves onto the image (Figure 5c), we found that at 6 Hz the fundamental mode is 313 m/s and the first higher mode 326 m/s. At current resolution of dispersive images, it is very difficult to tell that the modes have gone up at 6 Hz with this small difference, which we called "mode crossing." With some low-resolution techniques to generate an image of dispersive energy, the "mode crossing" between the second and third higher modes may also occur around 21 Hz. Previous studies (Figures 8 and 10, Xia et al., 2006b) showed that the "mode crossing" also occurs in multi-layer models in which Vs increases gradually with

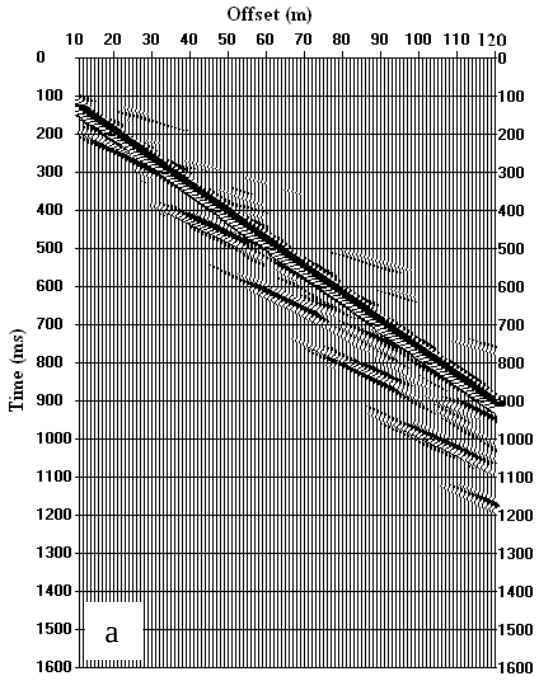

Figure 5. (a) A synthetic shot gather of P-Sv data used in Rayleigh-wave analysis.

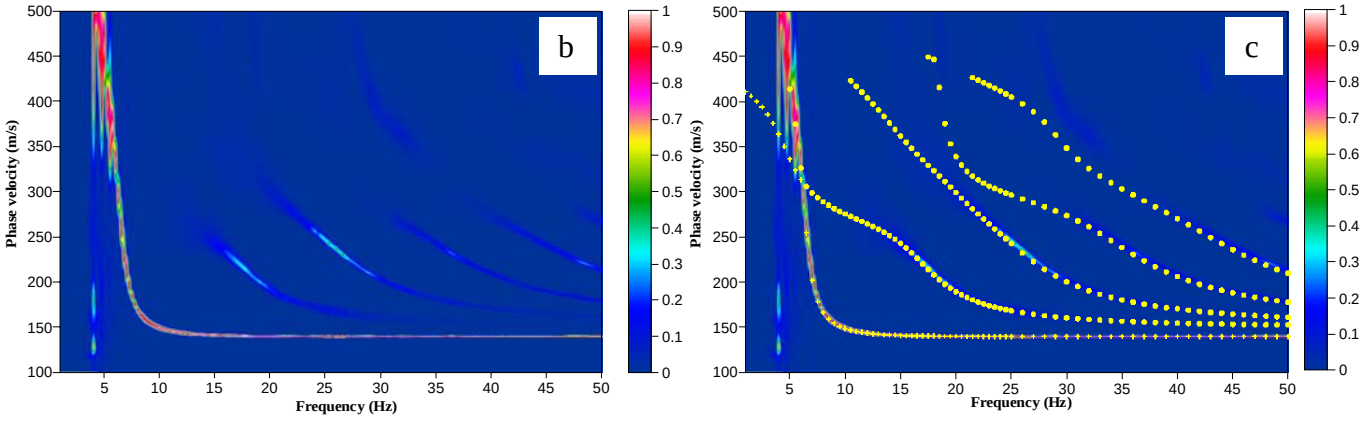

Figure 5. (b) An image of Rayleigh-wave energy calculated from the 110-trace shot gather (a). The energy of the fundamental mode appears continuously from 4 to 50 Hz. (c) Plus symbols and yellow dots, which are calculated by the Knopoff method (Schwab and Knopoff, 1972), are the fundamental and higher modes, respectively, and superposed onto (b). "Mode crossing" occurs at 6 Hz.

depth. The "mode crossing" causes mode misidentification (Zhang and Chan, 2003) that results in inverted S- wave velocities higher than true velocities.

We then modeled the SH-wave data (Figure 6a) based on the two-layer model described in the last paragraph (Luo et al., in review). The fundamental and higher modes are separated clearly (Figure 6b). The Love-wave energy trends accurately show phase velocities of different modes. The cutoff frequencies for this model can be calculated and are around n×8 Hz for the nth higher mode (Aki and Richards, 1980), where n is the order of higher modes. The asymptotes of all modes at the high-frequency end approach 150 m/s, which is the S-wave velocity of the first layer, and at the low-frequency end approach 450 m/s, which is the S-wave velocity of the half space. The "mode crossing" does not occur in the image of Love waves for this soft-layer model (Figure 6b) nor for the multi-layer models showed by Xia et al. (2006b). The "mode crossing" may occur between the second and third higher modes for a high-velocity layer model (Luo et al., in review). It is not common to observe the second and third higher modes in real data, so the "mode crossing" is rare in real Love-wave data.

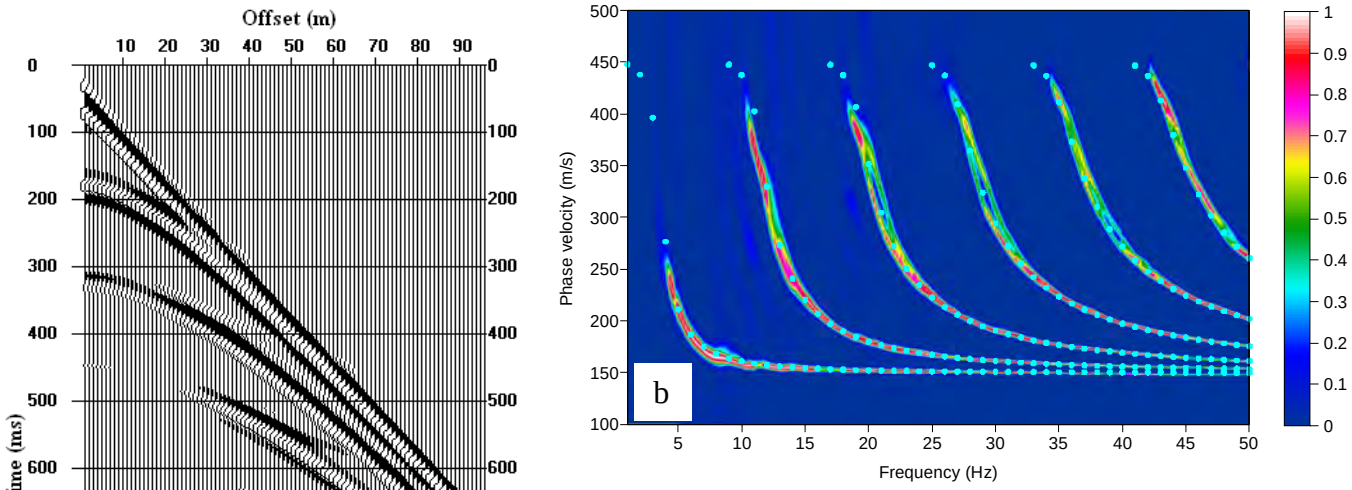

Figure 6. (a) Synthetic SH-wave data based on the two-layer model described in the text. (b) An image of Love-wave energy calculated from (a) with superposed cyan dots that are analytical results calculated by the Knopoff method (Schwab and Knopoff, 1972).

Stable Inversion of Love Waves

Inversion of phase velocities of Love waves was developed based on the algorithm discussed by Xia et al. (1999). Detailed description of the inversion algorithm can be found in Xia et al. (2009). As pointed out in the last section and based on the real-world examples demonstrated, fewer parameters make inversion of Love waves more stable.

We first inverted the data shown in Figures 1 and 2. Initial S-wave velocities were determined based on values of asymptotes at the high- and low-frequency ends for the S-wave velocities of the first layer and the half space and values of interpolations between the asymptotes for initial S-wave velocities of the layers between the first layer and the half space. We used the same thickness model as used in Rayleigh waves (Xia et al., 2002c). Two data sets of phase velocities shown by cyan dots (Figure 7a) were inverted. The first set, containing 39 fundamental phase velocities from 11 to 50 Hz, was picked by

following the energy trend in Figure 2a (the phase velocities picked from Figure 2b give the same values as those picked from Figure 2a). The second set contains the 39 fundamental phase velocities and 19 first higher mode phase velocities from 38 to 54 Hz that are also picked from Figure 2a. Inversion of either data set reached final S-wave velocity models went only in two iterations. Figure 7b shows phase velocities (Measured) picked from the image (cyan dots in Figure 7a), calculated from the initial model (Initial), and calculated from the final inverted S-wave velocity model (Final). Figure 7c shows the initial model, a final model by inversion of the fundamental data, and a final model by inversion of the fundamental and the first higher mode data simultaneously. The both inversion results are much closer to well-log results (Figure 7d), especially for the shallower part, than the SH-wave refraction results. The SH-wave refraction results, however, are converted P-wave velocities (Xia et al., 2002c).

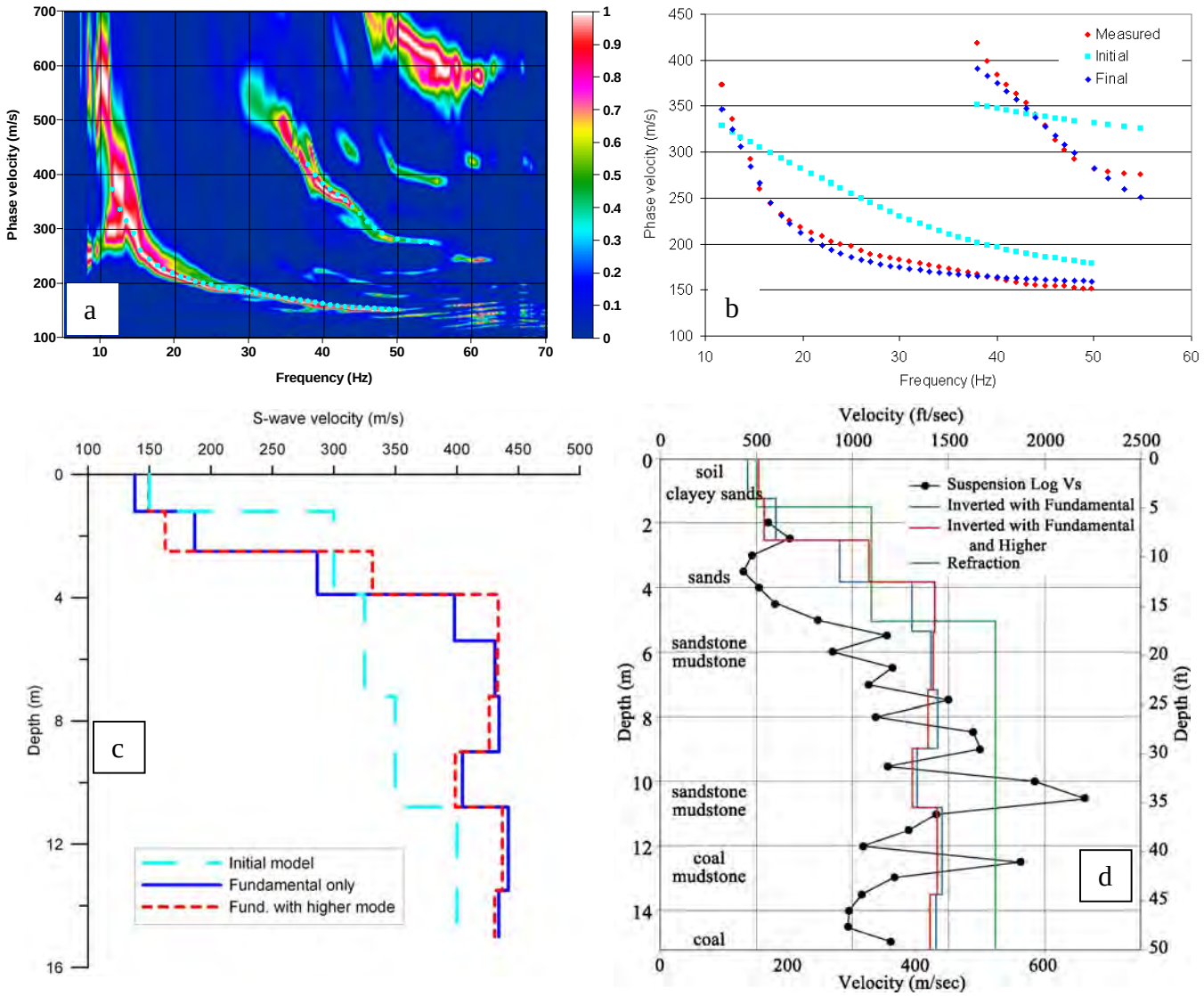

Figure 7. (a) The image of Love-wave energy (Figure 2a) superposed with picked phase velocities shown by cyan dots. (b) Phase velocities labeled “Measured” are picked from (a); those labeled “Initial” are calculated based on the initial S-wave velocity model; and those labeled “Final” are calculated based on the inverted S-wave velocity model. (c) S-wave velocity models: the initial model and inverted models from the fundamental data only and from the fundamental and the first higher mode data simultaneously. (d) Comparison among S-wave velocity models from inversion of Love waves, SH-wave refraction (a three-layer model), and the well log.

The S-wave velocity of the first layer of the final model by inversion of the fundamental and the first higher mode data simultaneously (Figure 7c) is almost the same as the asymptotic value of the fundamental phase velocities at the high frequencies (Figure 7a), while the S-wave velocity of the same layer by inversion of the fundamental data (Figure 7c) is 25% lower than the true value. This result showed that inversion of the fundamental and the higher mode data simultaneously could provide more accurate results than the fundamental data alone.

SH-wave data acquired at the front grassy area of the Kansas Geological Survey building were inverted and shown as our second example of inversion. We picked the phase velocities from the Love-wave image from 12 to 45 Hz (Figure 3b) as showed them in Figure 8a (cyan dots). We also selected a seven-layer model, the same one used in Xia et al. (1999), and arbitrarily constructed their initial S-wave velocity model. The phase velocities calculated from the initial model were far from the picked phase velocities (Figure 8b). After five iterations, the root-mean-squares error was reduced from 280 m/s to 5 m/s. The final inverted S-wave velocity model is shown in Figure 8c and compared to the borehole S-wave velocity measurements.

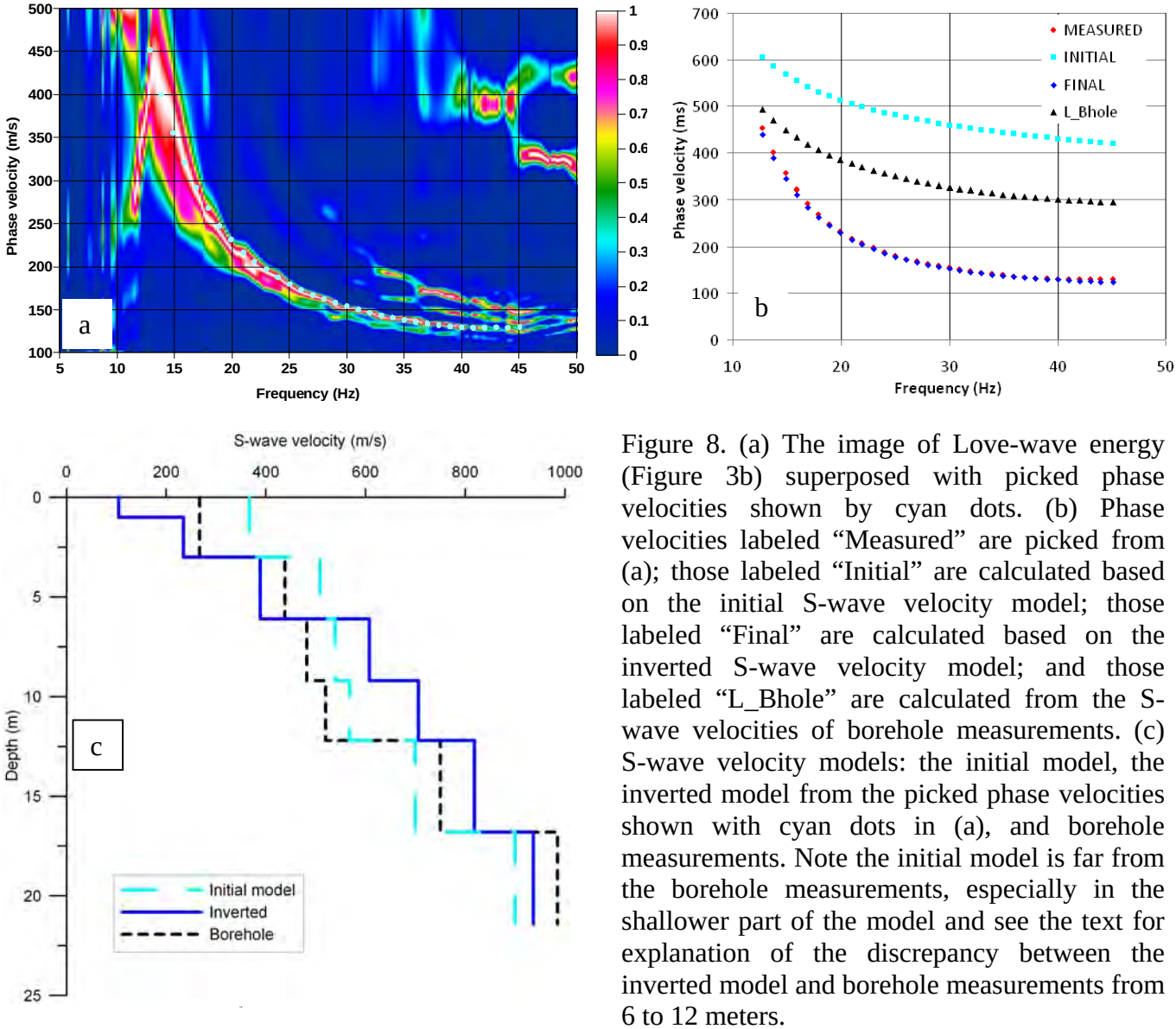

Figure 8. (a) The image of Love-wave energy (Figure 3b) superposed with picked phase velocities shown by cyan dots. (b) Phase velocities labeled “Measured” are picked from (a); those labeled “Initial” are calculated based on the initial S-wave velocity model; those labeled “Final” are calculated based on the inverted S-wave velocity model; and those labeled “L_Bhole” are calculated from the S-wave velocities of borehole measurements. (c) S-wave velocity models: the initial model, the inverted model from the picked phase velocities shown with cyan dots in (a), and borehole measurements. Note the initial model is far from the borehole measurements, especially in the shallower part of the model and see the text for explanation of the discrepancy between the inverted model and borehole measurements from 6 to 12 meters.

We noted that there are relative large differences between inverted results and borehole measurements from 6 to 12 meters (Figure 8c). To find causes of the difference, we calculated phase velocities due to borehole measurements. We found that the phase velocities due to the borehole measurements are in the middle of the phase velocities calculated from the initial model and the inverted model at each frequency (Figure 8b). This discrepancy indicates that borehole measurements provide a different S-wave velocity model and S-wave velocity anisotropy exists in this site.

Conclusions

We demonstrated and discussed three advantages of revisiting SH-wave data using the MALW method in defining S-wave velocity with synthetic and real-world data. 1) Owing to a long geophone spread commonly used in SH-wave refraction survey, images of Love-wave energy are usually cleaner and sharper than those generated from Rayleigh waves that are normally acquired using a relatively short geophone spread, which makes picking phase velocities of Love waves much easier and more accurate. 2) Because they are independent of P-wave velocity, dispersion curves of Love waves are simpler than Rayleigh waves. “Mode crossing” is an undesired phenomenon in Rayleigh-wave analysis that causes mode misidentification, which results in inverted S-wave velocities are much higher than real ones. Fortunately, this phenomenon is less common in images of Love-wave energy than Rayleigh waves. 3) Real-world examples showed that inversion of Love waves is much easier and more stable compared to Rayleigh waves, because of being independent of P-wave velocity and the simplicity of Love-wave dispersion curves. One real-world example also demonstrated that inversion of the fundamental and the first higher mode data simultaneously can provide more accurate results than the fundamental data alone. Abundant SH-wave refraction data containing non-utilized strong Love-wave energy have been acquired for various environmental and engineering applications. Our experimental study clearly shows that: 1) revisiting old SH-wave data containing Love waves can significantly contribute to detailed knowledge of existing S-wave velocity, and 2) considering Love-waves (by increasing the record length) during the future SH-wave refraction surveys can provide accurate near-surface S-wave velocities without additional cost in field.

Acknowledgments

The authors thank Marla Adkins-Heljeson of the Kansas Geological Survey for editing the manuscript.

References

Aki, K., and Richards, P.G., 1980, Quantitative seismology: W.H. Freeman and Company, San Francisco.

Beaty, K.S., Schmitt, D.R., and Sacchi, M., 2002, Simulated annealing inversion of multimode Rayleigh wave dispersion curves for geological structure: Geophys. J. Int., 151, 622–631.

Calderón-Macías, C., and Luke, B., 2007, Addressing nonuniqueness in inversion of Rayleigh-wave data for shallow profiles containing stiff layers: Geophysics, 72(1), U1-U10.

Eslick, R., Tsoflias, G., and Steeples, D.W., 2008, Field investigation of Love waves in near-surface seismology: Geophysics, 73(3), G1-G6.

Forbriger, T., 2003, Inversion of shallow-seismic wavefields: I. Wavefield transformation: Geophys. J. Int., 153, 720-734.

Garland, G.D., 1979, Introduction to geophysics: Mantle, core and crust (2nd ed.): Saunders, Toronto.

Ivanov, J., Miller, R.D., Xia, J., Steeples, D.W., and Park, C.B., 2006a, Joint analysis of refractions with surface waves: An inverse solution to the refraction-traveltime problem: Geophysics, 71(6), R131-R138.

Ivanov, J, Miller, R.D., Lacombe, P., Johnson, C.D., and Lane, J.W., Jr., 2006b, Delineating a shallow fault zone and dipping bedrock strata using multichannal analysis of surface waves with a land streamer: Geophysics, 71(5), A39-A42.

Lee, W.B., and Solomon, S.C., 1979, Simultaneous inversion of surface-wave phase velocity and attenuation: Rayleigh and Love waves over continental and oceanic paths: Bulletin of the Seismological Society of America, 69(1), 65-96.

Liang, Q., Chen, C., Zeng, C., Luo, Y., and Xu, Y., 2008, Inversion stability analysis of multimode Rayleigh-wave dispersion curves using low-velocity-layer models: Near Surface Geophysics, 6(3), 157–165.

Lu, L., Wang, C., and Zhang, B., 2007, Inversion of multimode Rayleigh waves in the presence of a low-velocity layer: Numerical and laboratory study: Geophys. J. Int., 168, 1235–1246.

Luo, Y., Xia, J., Liu, J., Liu, Q., and Xu, S., 2007, Joint inversion of high-frequency surface waves with fundamental and higher modes: Journal of Applied Geophysics, 62(4), 375-384.

Luo, Y., Xia, J., Miller, R.D., Xu, Y., Liu, J., and Liu, Q., 2008, Rayleigh-wave dispersive energy imaging by high-resolution linear Radon transform: Pure and Applied Geophysics, 165(5), 903-922.

Luo, Y., Xia, J., Miller, R.D., Xu, Y., Liu, J., and Liu, Q., 2009, Rayleigh-wave mode separation by high-resolution linear Radon transform: Geophys. J. Int., 179(1), 254-264.

Luo, Y., Xia, J., Xu, Y., Zeng, C., and Liu, J., in review, Finite-difference modeling and dispersion analysis of high-frequency Love waves for near-surface applications: Pure and Applied Geophysics.

Miller, R.D., Xia, J., Park, C.B., and Ivanov, J., 1999, Multichannel analysis of surface waves to map bedrock: The Leading Edge, 18, 1392-1396.

Misiek, R., Liebig, A., Gyulai, A., Ormos, T., Dobroka, M., and Dresen, L., 1997, A joint inversion algorithm to process geoelectric and surface wave seismic data, Part II: Application: Geophysical Prospecting, 45, 65-85.

Safani, J., O'Neill, A., Matsuoka, T., and Sanada, Y., 2005, Applications of Love wave dispersion for improved shear-wave velocity imaging: Journal of Environmental and Engineering Geophysics, 10(2), 135-150.

Safani, J., O'Neill, A., and Matsuoka, T., 2006, Love wave modelling and inversion for low velocity layer cases: Proceedings of the Symposium on the Application of Geophysics to Engineering and Environmental Problems (SAGEEP), Annual Meeting of the Environmental and Engineering Geophysical Society (EEGS), April 2-6, 2006, Seattle, WA, 1181-1190.

Schwab, F.A., and Knopoff, L., 1972, Fast surface wave and free mode computations; *in* Methods in Computational Physics, edited by B. A. Bolt: Academic Press, New York, 87-180.

Song, Y.Y., Castagna, J.P., Black, R.A., and Knapp, R.W., 1989, Sensitivity of near-surface shear-wave velocity determination from Rayleigh and Love waves: Technical Program with Biographies, SEG, 59th Annual Meeting, Dallas, Texas, 509-512.

Steeples, D.W., 2005, Near-surface geophysics: 75 years of progress: Supplement to The Leading Edge, 24 (s1), S82-S85.

Stoneley, R., 1950, The effect of a low-velocity internal stratum on surface elastic waves: Monthly Notices Royal Astronomical Society (Geophys. Suppl.), 6, 28-35.

Winsborrow, G., Huwsa, D.G., and Muyzert, E., 2003, Acquisition and inversion of Love wave data to measure the lateral variability of geo-acoustic properties of marine sediments: Journal of Applied Geophysics, 54, 71-84.

Xia, J., Miller, R.D., and Park, C.B., 1999, Estimation of near-surface shear-wave velocity by inversion of Rayleigh wave: Geophysics, 64(3), 691-700.

Xia, J., Miller, R.D., and Park, C.B., 2000, Advantage of calculating shear-wave velocity from surface waves with higher modes: Technical Program with Biographies, SEG, 70th Annual Meeting, Calgary, Canada, 1295-1298.

Xia, J., Miller, R.D., Park, C.B., Hunter, J.A., Harris, J.B., and Ivanov, J., 2002a, Comparing shear-wave velocity profiles from multichannel analysis of surface wave with borehole measurements: Soil Dynamics and Earthquake Engineering, 22(3), 181-190.

Xia, J., Miller, R.D., Park, C.B., and Tian, G., 2002b, Determining *Q* of near-surface materials from Rayleigh waves: Journal of Applied Geophysics, 51(2-4), 121-129.

Xia, J., Miller, R.D., Park, C.B., Wightman, E., and Nigbor, R., 2002c, A pitfall in shallow shear-wave refraction surveying: Journal of Applied Geophysics, 51(1), 1-9.

Xia, J., Miller, R.D., Park, C.B., and Tian, G., 2003, Inversion of high frequency surface waves with fundamental and higher modes: Journal of Applied Geophysics, 52(1), 45-57.

Xia, J., Chen, C., Li, P.H., and Lewis, M.J., 2004, Delineation of a collapse feature in a noisy environment using a multichannel surface wave technique: Geotechnique, 54(1), 17-27.

Xia, J., Xu, Y., Miller, R.D., and Chen, C., 2006a, Estimation of elastic moduli in a compressible Gibson half-space by inverting Rayleigh wave phase velocity: Surv. Geophys., 27(1), 1-17.

Xia, J., Xu, Y., Chen, C., Kaufmann, R.D., and Luo, Y., 2006b, Simple equations guide high-frequency surface-wave investigation techniques: Soil Dyn. Earthq. Eng., 26(5), 395-403.

Xia, J., Xu, Y., and Miller, R.D., 2007a, Generating image of dispersive energy by frequency decomposition and slant stacking: Pure and Applied Geophysics, 164(5), 941-956.

Xia, J., Nyquist, J.E., Xu, Y., Roth, M.J.S., and Miller, R.D., 2007b, Feasibility of detecting near-surface feature with Rayleigh-wave diffraction: Journal of Applied Geophysics, 62(3), 244-253.

Xia, J., Miller, R.D., and Xu, Y., 2008, Data-resolution matrix and model-resolution matrix for Rayleigh-wave inversion using a damped least-square method: Pure and Applied Geophysics, 165(7), 1227-1248.

Xia, J., Cakir, R., Miller, R.D., Zeng, C., and Luo, Y., 2009, Estimation of near-surface shear-wave velocity by inversion of Love waves: Technical Program with Biographies, SEG, 79th Annual Meeting, Houston, TX, 1390-1395.

Xia, J., Xu, Y., Miller, R.D., and Zeng, C., in press**,** A trade-off solution between model resolution and covariance in surface-wave inversion: Pure and Applied Geophysics.

Xu, Y., Xia, J., and Miller, R.D., 2006, Quantitative estimation of minimum offset for multichannel surface-wave survey with actively exciting source: J. Appl. Geophys., 59(2), 117-125.

Xu, Y., Xia, J., and Miller, R.D., 2007, Numerical investigation of implementation of air-earth boundary by acoustic-elastic boundary approach: Geophysics, 72(5), SM147-SM153.

Xu, Y., Xia, J., and Miller, R.D., 2009, Approximation to cutoffs of higher modes of Rayleigh waves for a layered earth model: Pure and Applied Geophysics, 166(3), 339-351.

Zeng, C., Xia, J., Liang, Q., and Chen, C., 2007, Comparative analysis on sensitivities of Love and Rayleigh waves: Technical Program with Biographies, SEG, 77th Annual Meeting, San Antonio, TX, 1138-1141.

Zhang, S., and Chan, L., 2003, Possible effects of misidentified mode number on Rayleigh wave inversion: Journal of Applied Geophysics, 53, 17-29.

SEISMIC REFRACTION SURVEYS— HOW MANY SHOTS DO I NEED?

Charles H Stoyer, Interpex Limited, Golden, CO

Abstract

Classical seismic refraction theory as discussed in most textbooks focuses on flat-lying or dipping layers and shows one or two shots. Most modern refraction surveys are shot with far more than two shots and use more sophisticated methods of interpretation and inversion. The use of only two shots, one on each end of a refraction spread, results in a critical lack of coverage, even for fairly simple velocity sections. This is in spite of the fact that the original section can sometimes be effectively recovered if some assumptions are made.

Inversions using geophysical inverse theory in two dimensions as well as the Generalized Reciprocal Method (GRM) are applied to synthetic data generated from 2-D models and to field data examples to illustrate the importance of additional shots taken away from the spread ends (far shots) and additional shots taken in the interior of the spread (interior shots). These additional shots allow the interpreter to determine the number of layers in the section, assist in the assignment of arrivals and further constrain the velocities and (time-) depths and the elevation section. This produces a better and more reliable interpretation.

Introduction

Typical seismic refraction surveys conducted for engineering, groundwater and Low Velocity Layer (LVL) studies contain from one to nine shots into each geophone spread of 12 to 96 geophones. Sometimes the goals of the survey are met and sometimes the results fall short of the survey objectives. One consideration in survey design is of course the number and spacing of the geophones, which must be sufficient to adequately respond to both the shallow and deep targets. A second and equally important consideration is the number and placement of the shots.

Most experienced practitioners of seismic refraction realize the importance of taking a sufficient number of shots so that the objectives of the survey can be realized. However, it is common for workers who lack this experience to take an insufficient number of shots and this is the problem this paper tries to address.

The number of shots required to meet the survey objectives depends on the geologic complexity of the survey area and the objective in terms of what is desired. Sometimes the refractor velocity is most important and depth and configuration are of less concern. Rippability studies might be an example of this. In other studies, the bedrock configuration might be important, while the velocity itself is of less concern. This might be the case in landfill studies. In other cases, the entire section of 2, 3 or more layers might be important, and lateral variations in velocity might even be of particular concern. Sometimes only the time-depth of the LVL is required.

Survey cost is always a factor. In many cases, the layout of the geophone spread might be the most costly while additional shots are relatively inexpensive. In other situations, particularly where shots must be placed in boreholes, the expense of an additional shot might be a limiting factor in survey design. Of course, taking too few shots can always be expensive if the survey goal is not met or if the site must be revisited to obtain more data.

In the following paper, we shall examine several geologic situations, consider survey objectives, and produce forward models of the seismic sections and then attempt to interpret them as we might do for real field data. We shall do this with varying numbers of shots to see what problems arise when too few shots are taken and what supplemental information is obtained by adding more shots. It is the hope that this paper might be useful for guiding survey design by refraction practitioners so they can get the best result for the least cost.

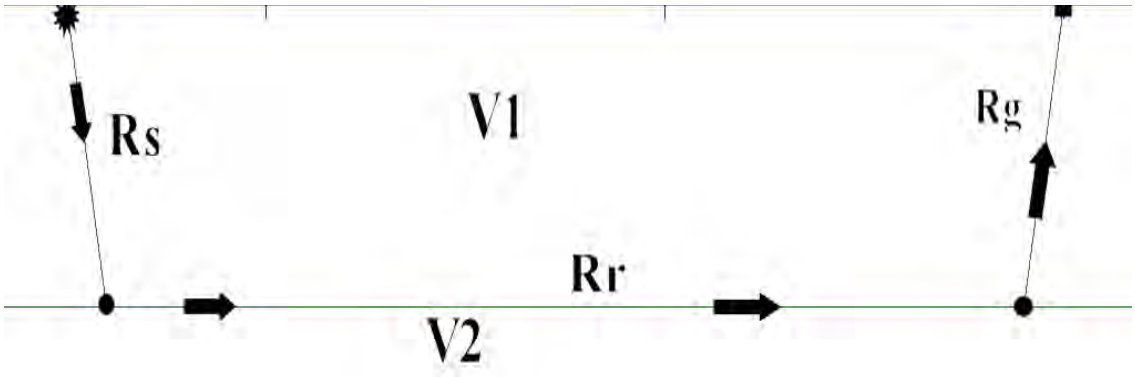

Figure 1. Illustration of the 3 travel paths which contribute to the travel time calculation for a simple refractor.

Forward Problem for Seismic Refraction

The forward problem used here is a simplified 2-D modeling method. The method makes the same assumptions as the Generalized Reciprocal Method (GRM) of Palmer (1980, 1981). The assumption is that the earth is locally flat and that the ray angles are controlled entirely by the velocity contrast between each interface that is crossed. According to Palmer, this is adequate provided the relative slopes of the seismic section are 20 degrees or less. Figure 1 shows the geometry, but keep in mind that the refractor may be undulating and/or sloping, but aside from the difference in the paths R_s and R_g, this fact is ignored as per our assumptions.

Direct arrivals are calculated by taking the distance between source and receiver and dividing by the surface velocity as follows:

$$tt_d = (x_s - x_g)/V_1 \quad (1)$$

Refracted arrivals are calculated by using the velocity contrasts to determine the angle of incidence on the (locally flat) refractor, and adding the time required to travel down to the refractor from the source, across the refractor to the point of leaving the refractor and the time required to travel up from the refractor to the receiver as follows:

$$tt_r = R_s/V_1 + R_r/V_2 + R_g/V_1 \quad (2)$$

The surface and the refractor can be undulating but the undulations are not used in the travel time calculations except to find the surface positions and the depth where the ray enters the refractor and where it leaves it. If the refractor is not the second layer, the time of travel through the overlying

layers is along the path determined from the contrast between the refractor and the layer being considered. These assumptions were designed to make the forward calculation as fast as possible without compromising too much accuracy as the goal was to use this in an inversion scheme where many forward models need to be calculated.

Inversion of Refraction Travel Time Data

The refraction data modelled in this paper as well as the field results shown near the end are interpreted by two inversion schemes. The first is an iterative forward/inverse scheme similar to that of Scott (1973) but using the forward modelling method described above; the second is a direct inversion scheme called the Generalized Reciprocal Method or GRM (Palmer, 1980, 1981).

The forward calculations shown above in eq. (1) and (2) are nonlinear in terms of the velocities and refractor structure and must be linearized in order to solve the inverse problem. Linearization is carried out by expanding the forward problem in terms of a Taylor series and retaining only the first two terms. In order to do this, we need a starting or seed model, $\boldsymbol{p}_0$. We then expand the forward solution around this seed model using a (small) incremental model, $\Delta\boldsymbol{p}$. The procedure is similar to that described by Inman (1975) except that the vertices describing the layers are constrained by roughness, rather than magnitude of the parameter change, while the velocities changes are constrained by magnitude. The use of roughness is known as Occam's Inversion and is described by Constable, et al, 1987.

The seed models used in the iterative inversion scheme are generated by specifying velocities and depths, one for each layer. The layer boundaries are either flat or follow the topography to a specified degree between 0 and 1. All synthetic models in this study will use flat topography, whereas the field data do contain topography.

The purpose of the iterative inversion in terms of layers with arbitrary undulations but constant

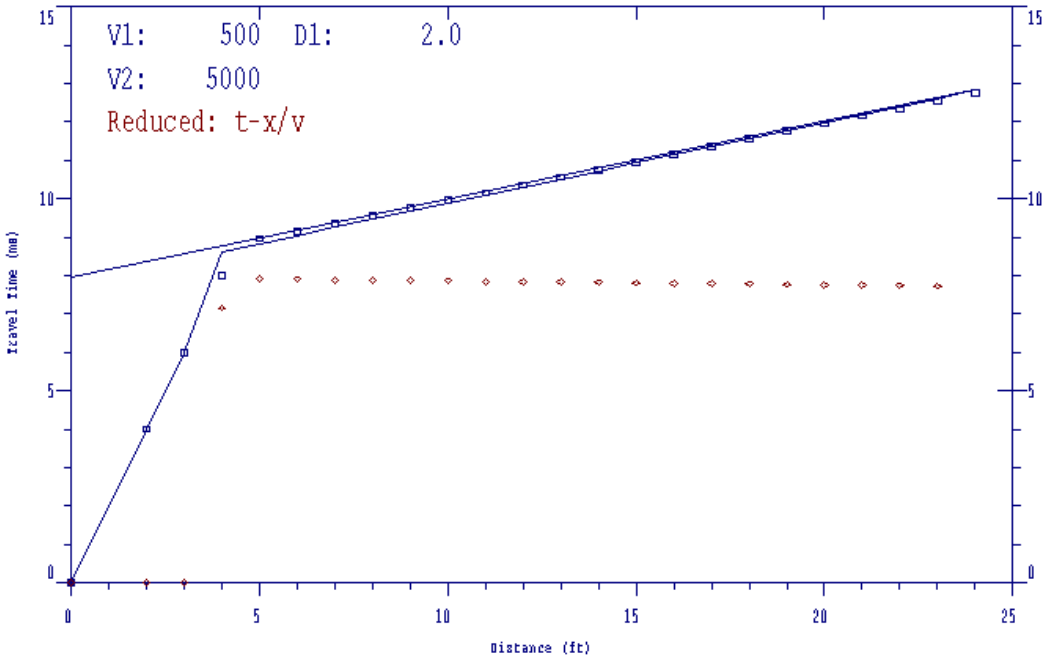

Figure 2. Travel time curve for a 1–D two-layer case with a single overburden and single refractor. Model derived from slope-intercept analysis is shown.

velocity is twofold: First, it creates an interpreted result. Second, it can be used to replace the labor-intensive assignment of arrivals to layers as well as to estimate reciprocal times in cases where they are not measured directly.

Simple Flat Layer Model

The modelling method described above accurately models a two-layer flat lying refractor under a flat earth surface. The inverse result for this situation is easily derived using the classic Slope-Intercept Method, described in most textbooks which discuss refraction (see, for example, Dobrin, 1960, p 71, Telford, et. Al., 1990, p 169).

For a two-layer earth having velocities of 500 m/sec and 5000 ft/sec and a first layer thickness of 2 ft, the travel time curve would appear as shown in Figure 2. In this case, the first 3 arrivals are direct arrivals and the rest are refracted. The slopes of these two segments of the travel time curve give the slowness of the respective layer and the point where the slopes intersect the vertical axis give the time depth of the layer. Velocities, of course, are the inverse of the slowness.

This method is so classic, in fact, that it is difficult for many people not steeped in refraction to see beyond it and this has hampered the proper and full use of the refraction method, especially with workers new to or not well experienced in the field. Although this method is quite useful for "quick and dirty" interpretation "back of an envelope" style, it is certainly not useful for determining much about the structure, including but not limited to the number of layers present. And it does not justify the use of too few shots in a refraction survey.

Although in the simple 1-D two-layer case the slope-intercept interpretation gives exactly the correct answer, it does not conclusively describe the earth in question. Looking at the travel time curve shown with ray paths in the seismic cross section as shown in Figure 3, we can see the limitations of

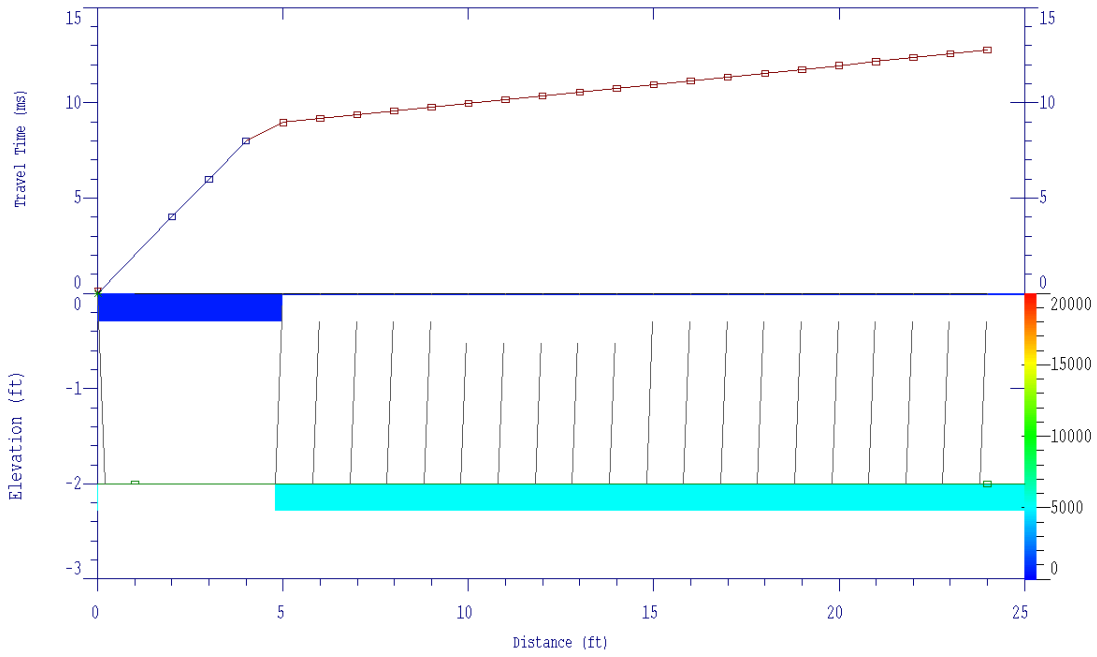

Figure 3. Travel time curve for a 1–D two-layer case with a single overburden and single refractor, showing ray paths and known velocities

this method if we assume that the case at hand may be more general than pure 1-D:

1. The first layer velocity is only defined from distance 0-5. Its value is not known from distance 5 to 25.
2. The second layer velocity is only defined from distance 5-25 and is not defined over the distance 0-5.
3. The depth to the refractor is only defined from distance 5-25.
4. There is no guarantee that the refractor is flat over distance 5-15. It could dip and have a different velocity such that the data appear to show the specified velocity. Only the time-depth is known.

With these things in mind, we will proceed to examine the behavior of travel time curves over additional models, interpret them and evaluate the interpretations.

Single Dipping Refractor

The next model to be considered has a refractor which dips from a depth of 2 on the left to 3 on the right, another classic "textbook" case. The model and travel time curves are shown in Figure 4. In this case, the slopes of the travel time curves give the apparent slowness (inverse of velocity), which is interpreted as a different velocity for the left and right shots. Having two shots for the dipping layer case is sufficient to resolve this dipping layer, provided that assumption can be made. However, we will take this opportunity to progress to more general interpretation methods, as promised earlier.

The depths interpreted from the slope intercept method are correct for the left and right sides as are the surface velocity. The apparent velocities are different, with one being greater and one being less than the true velocity of the dipping refractor. However, if we average the *slownesses* (not the velocities), we obtain the correct result for the refractor slowness and inverting that gives the correct velocity.

If we perform a 2-D inversion using the correct velocities and a constant 2-ft depth for the start-

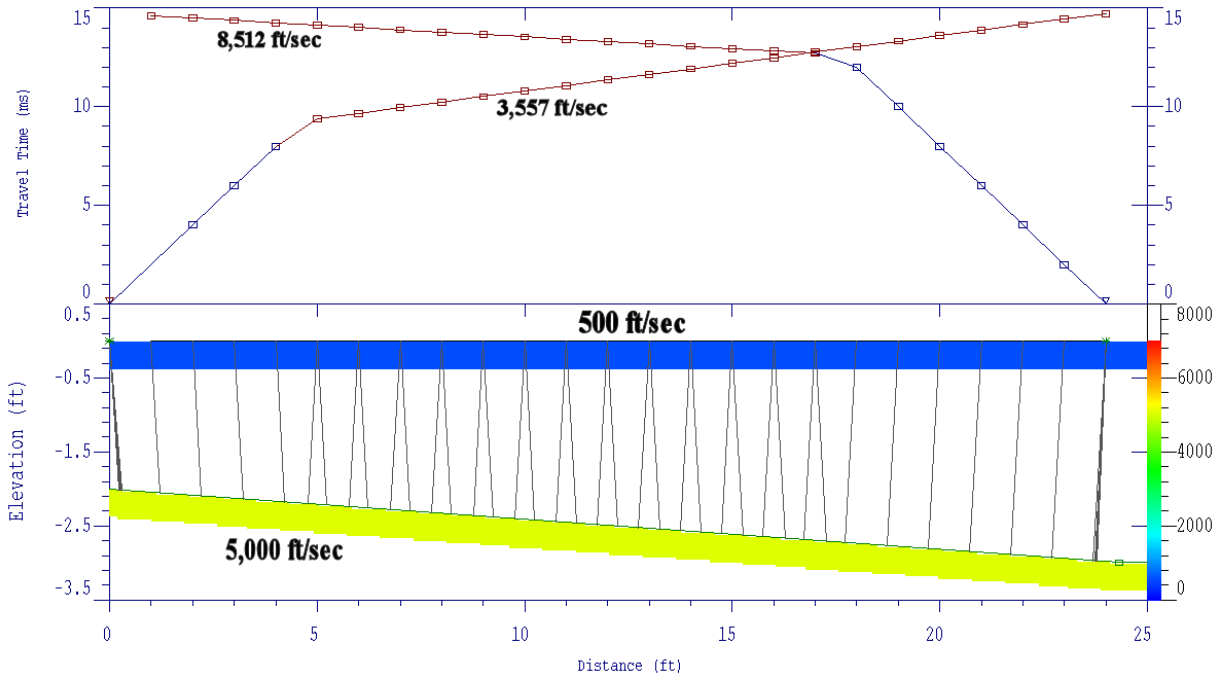

Figure 4. Travel time curve for a two-layer case with a single overburden and single dipping refractor, showing ray paths, apparent and specified velocities

ing model, we get the result shown in Figure 5, which is exactly correct and gives a perfect match. In the present circumstances, there is no reason to start with anything worse than this because the dipping refractor problem can be solved exactly. However, if we were instead start with the apparent velocities, we would get results different from this exact result and from each other.

Figure 6 shows the two results obtained from using the lower and higher apparent velocities.

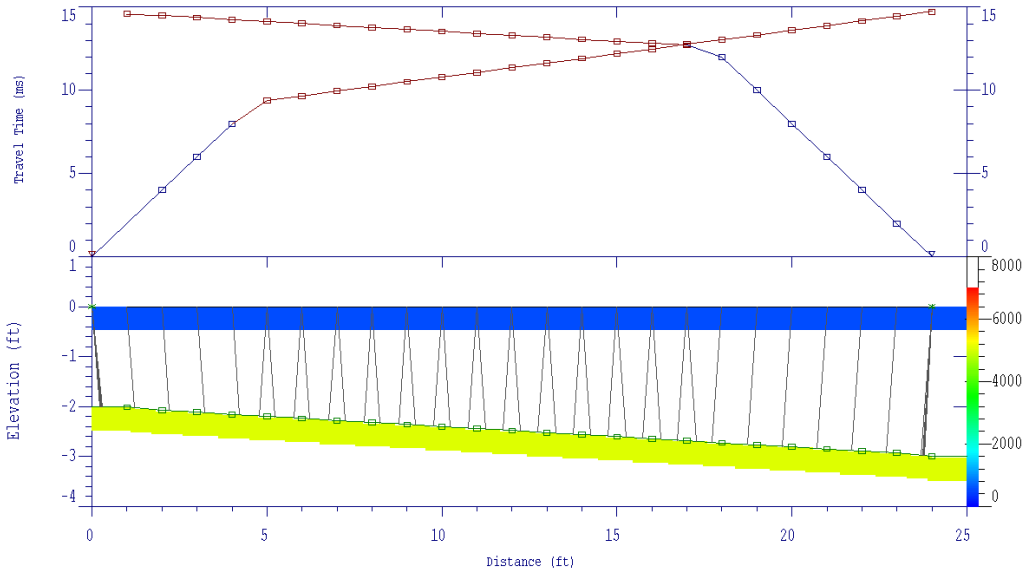

Figure 5. Travel time curve for a two-layer case with a single overburden and single dipping refractor, after inversion using a 2-D model starting with 2 ft depth and the correct velocities.

Note that the results are different from the correct refractor velocity and that the refractor depths from 0 to 5 ft and from 18 to 25 ft are incorrect. Again, we already know from the previous example that the surface velocity between 5 and 18 ft is not determined from the data but instead assumed to be the same in the center as on the ends.

Using the GRM method of inversion, arrivals from both forward and reverse shots are required. This limits the range over which the interpretation can be obtained to between 6 and 15 ft, leaving the refractor undefined from 0-6 ft and from 15-25 ft, which is more than half the section. This is not quite as good as the 2-D inversion which did not do well from 0-5 and 18-25 ft, although that method has its own limitations.

Figure 7 shows the resulting model from the GRM interpretation. Note that the result is correct, but remember that the surface velocity is still undefined between 5 and 18 ft. distance. This means the refractor position is defined in terms of time, but since the surface velocity is not really known, the actual depth is not determined.

Note also that using the GRM inversion on the flat 1-D model would produce a similar result with only two shots; the GRM inversion would at least require two additional far shots even for these simple models.

Deep V-Shaped Section

So far, we have examined simple and straightforward models. More complicated models than this can be tricky. We next consider a model with a V-shaped refractor, similar to models considered

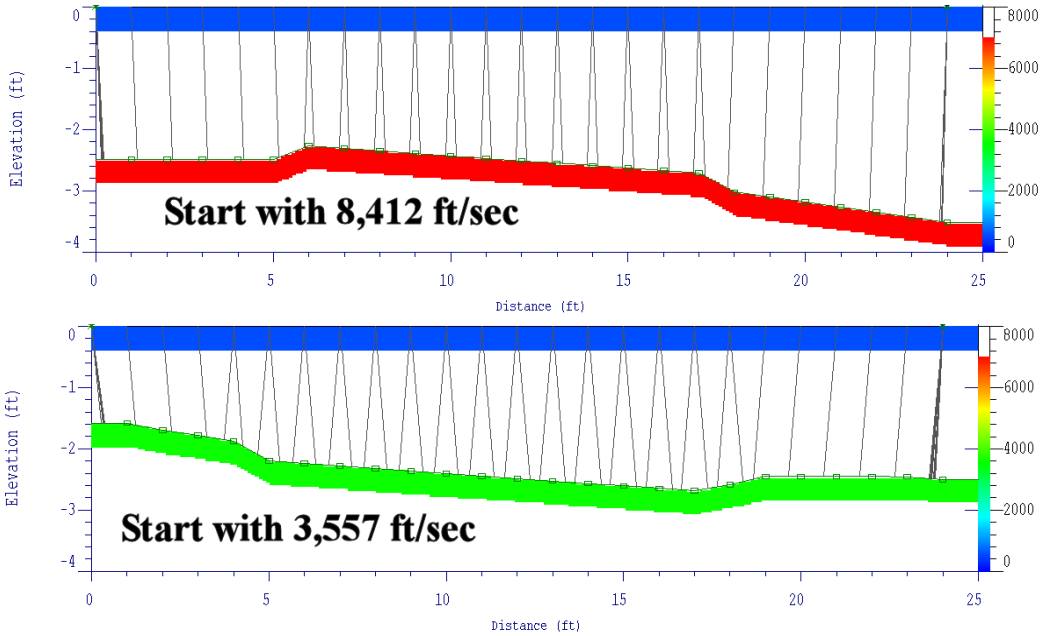

Figure 6. Models obtained for the data in Figure 5 starting with the apparent velocities as indicated on the figure. Note refractor velocities are incorrect and the sections from 0 to 5 ft and 18 to 25 ft are wrong**.**

so far. This model has the same structure as the first two models but the ends are still at 2 ft while the center is at 2.7 ft depth. The model and travel time curves are shown in Figure 8.

Slope-intercept analysis for these data show a 3-layer case as the change in refractor shape is being interpreted by the 1-D interpretation scheme as a third layer. The model given has velocities of 500, 2,945 and 11,751 ft/sec and depths of 2 and 4.5 ft. 2-D inversion using a starting model with 2 layers having the correct velocities and a depth of 1.8 ft gives the correct result as shown in Figure 8.

Interpreting these data using GRM gives the correct result for distances 7-17 ft and no result for the refractor outside of that (not shown but similar to Figure 7). 2-D inversion using wrong velocities (3,500 and 8,400 ft/sec) gives fairly close results for the depths in the distance range 6-19 ft but incorrect refractor velocity. In the range of 0-6 ft and 19-25 ft, the refractor surface is incorrect and different for the two starting velocities. The results (not shown) are similar to those shown in Figure 6.

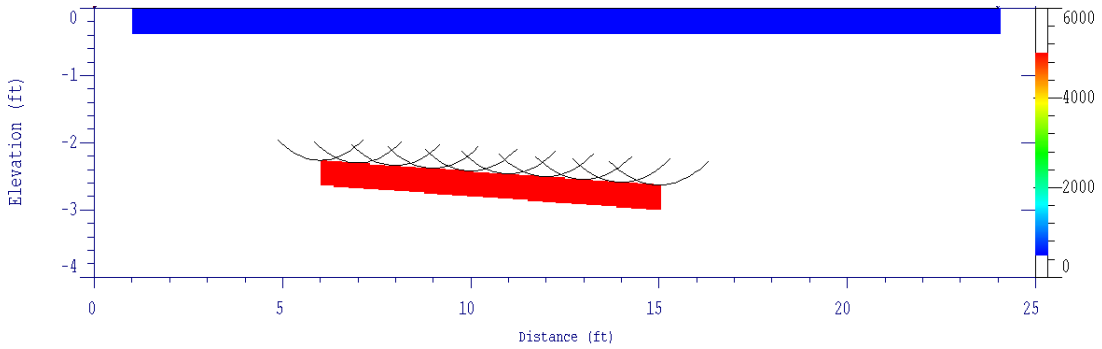

Figure 7. Model obtained for the data in Figure 5 using the GRM method of inversion. Note there is no result from 0-6 and from 18-25 ft because the required overlapping segments are not there.

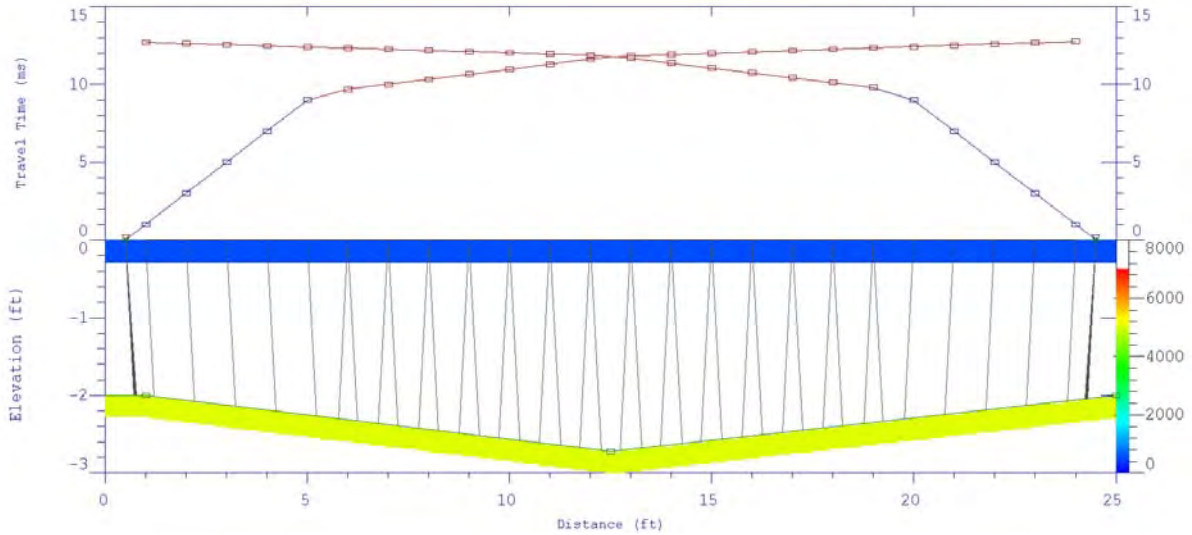

Figure 8. V-shaped model similar to the models considered so far. Velocities are 500 and 5,000 ft/sec and the edges are 2 ft deep while the center is 2.7 ft deep.

Shallow V-Shaped Section

If we move the V-shaped refractor higher in the section so that the ends are at a depth of 0.4 ft and the center is at a depth of 1.2 ft, we get a situation where the lion's share of the coverage moves to the refractor and the overburden dominates only one point on each travel time curve. The data curves shown in Figure 9 appear to be from a 3-layer case and in fact can be interpreted in terms of a 3-layer earth with flat refractors having a velocity profile of 659, 3,208 and 12,000 ft/sec and depths of 0.6 and 4.5 m. This works well for simple slope-intercept interpretation as well as 2-D forward/inverse modeling. Of course, we cannot interpret this 3-layer case using GRM because there is no overlap of the refracting segments. 2-D interpretation using either 2-D forward and inverse modeling or GRM in terms of 2 layers gives results similar to the previous models but there is a clear ambiguity here since the flat lying 3-layer case fits the data equally well.

More Information from Additional Shots

The examples shown so far indicate that the simple sections we have studied can be extracted from the data by 2-D forward/inverse modeling and to a lesser extent by GRM inversion. However, the sections are not well constrained in that the surface velocities are really unknown in the center of the section (in some cases a large part of the center section) and the refractor is constrained only in the center and not on the ends. In fact, since the surface velocities are constrained only on the ends of the spread, the refractor, the depth of which depends on the surface velocity, is really not constrained at all without the assumption that the surface velocity is constant. That is to say that the time-depth of the refractor is known but the actual depth itself is not. It is clear we need more shots in order to constrain the entire section.

Adding more interior shots will constrain the center section by increasing the coverage of direct arrivals and often provide some additional refractions. Both of these serve to constrain the position of the refractor in the center part of the section. Adding far shots - shots well away from the spread ends -

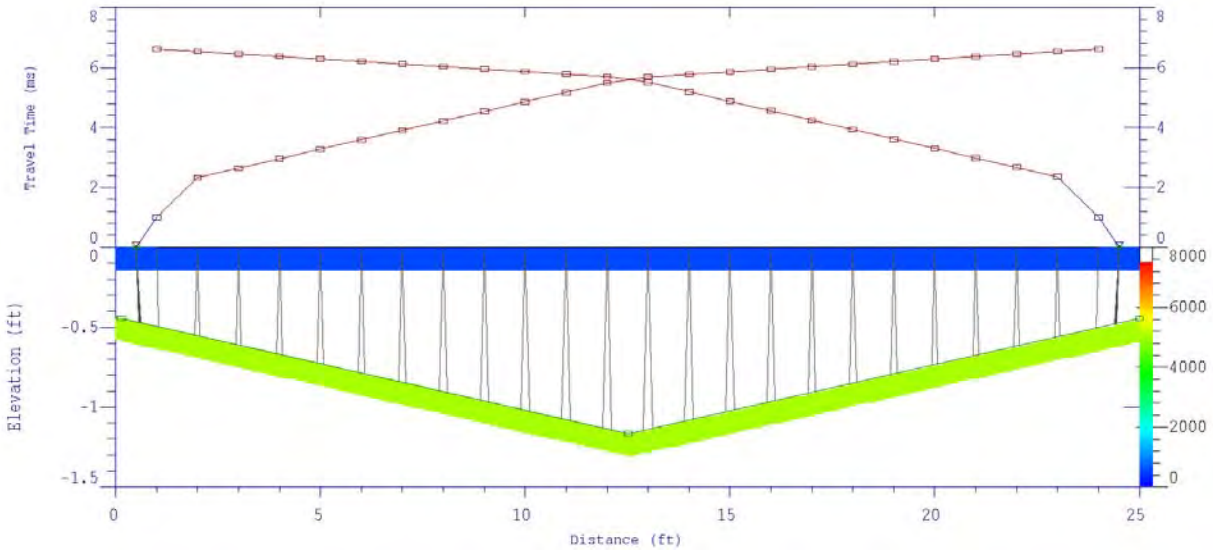

Figure 9. Shallow V-shaped model similar to the models considered so far. Velocities are 500 and 5,000 ft/sec and the edges are 0.4 ft deep while the center is 1.2 ft deep.

will provide the refracted arrivals necessary to define the refractor near the ends of the spread.

This is especially true of the shallow V-shaped example shown in Figure 9. These data appear to show a 3-layer earth and can in fact be interpreted that way. However, the addition of a single interior shot immediately resolves the ambiguity and shows that the second bend in the travel time curves (near distance 10 for the reverse shot and near distance 15 for the forward shot) is caused by refractor shape rather than a transition to a second refractor. The addition of one far shot off each end would resolve the ambiguity as well. Figure 10 shows the travel time data with the addition of a single interior

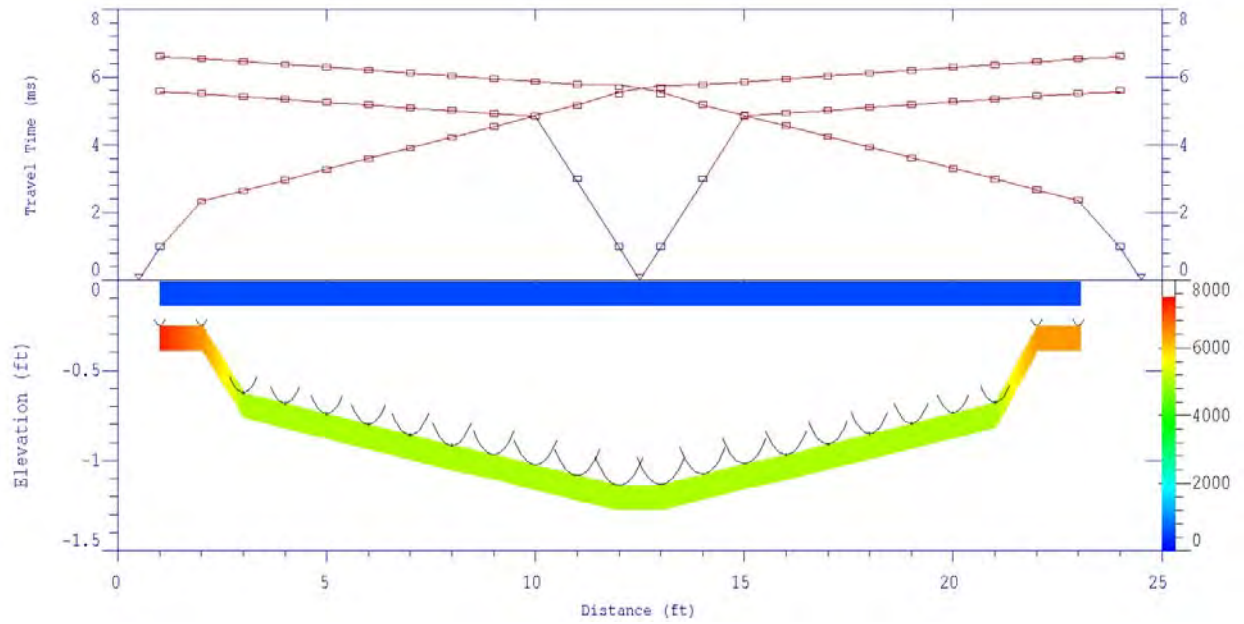

Figure 10. Shallow V-shaped model with a third shot in the interior and the GRM interpreted section below. Except for the very ends, the GRM result matches the original model.

shot and the GRM interpreted section. The results are correct except for the extreme ends and the surface velocity is constrained for an additional 5 ft. Adding two more interior shots would constrain the surface velocity over almost the entire spread and adding one far shot off each end (say, 6 feet away) would constrain the edges of the refractor.

Field Data Example

The field data example was taken in a two-layer situation and 7 shots were used. These included one pair of far shots, one pair of end shots and three interior shots. We begin by interpreting only the two end shots for comparison with the examples shown so far.

The section is shallow on the left and deep on the right as shown in Figure 11. The surface velocity is well constrained for a short section on the far left (2 geophones) and for a longer section on the far right (7 geophones). The refractor is defined in the center but not on the ends and it is less defined on the right than on the left. Figure 11 indicates that the surface velocity is defined across the section, but we can see this is not the case; it is defined only from 1500 to 1510 and from 1920 to 1980. The fact that the surface velocity is not defined in most of the center part of the section means that the refractor depth is known in terms of time but not in terms of actual depth.

Interpreting the data using all 7 shots resolves a lot of the unknowns about the section. Figure 12 shows that the refractor is well defined almost up to the edges of the spread. The surface velocity is defined on the right half of the spread but not on most of the left half where the surface layer becomes very thin (where the surface layer is very thin, the actual surface velocity is not so important). Here, the interior shots helped to define the surface velocity in the center of the spread while the far shots helped determine the refractor properties on the edges of the spread. Thus a section which looks correct but is fortuitously so because of the relatively constant surface velocity becomes quite well de-

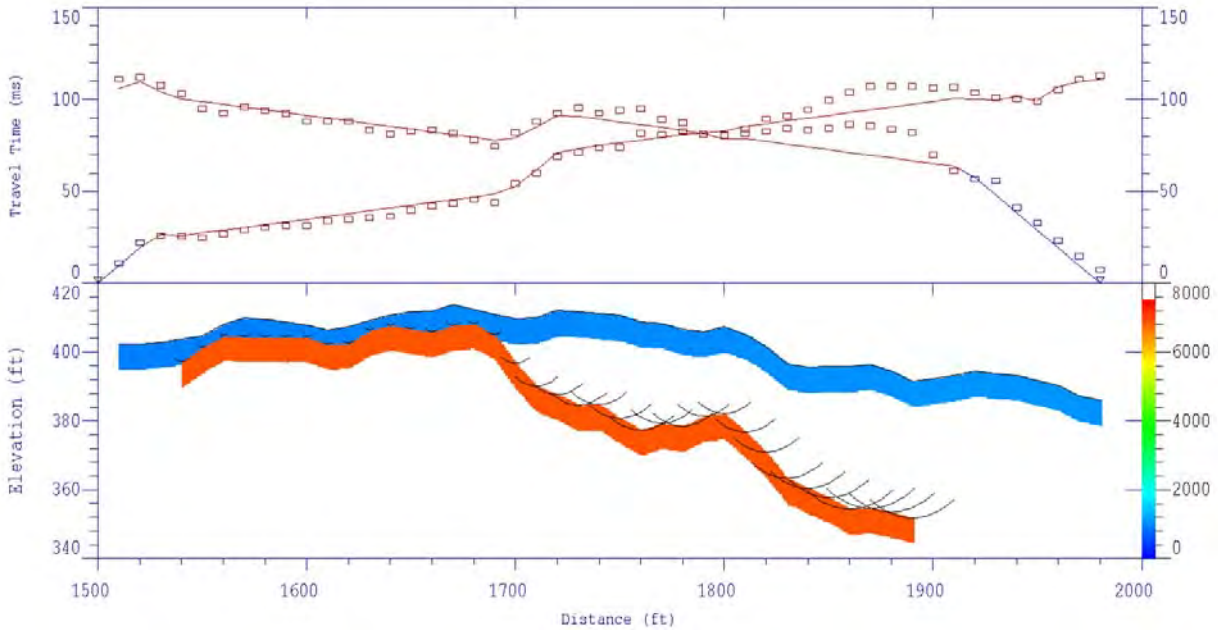

Figure 11. Two-layer field example interpreted with only two shots, one off each end. Note the refractor is not defined on the ends and the surface velocity is not defined in the center.

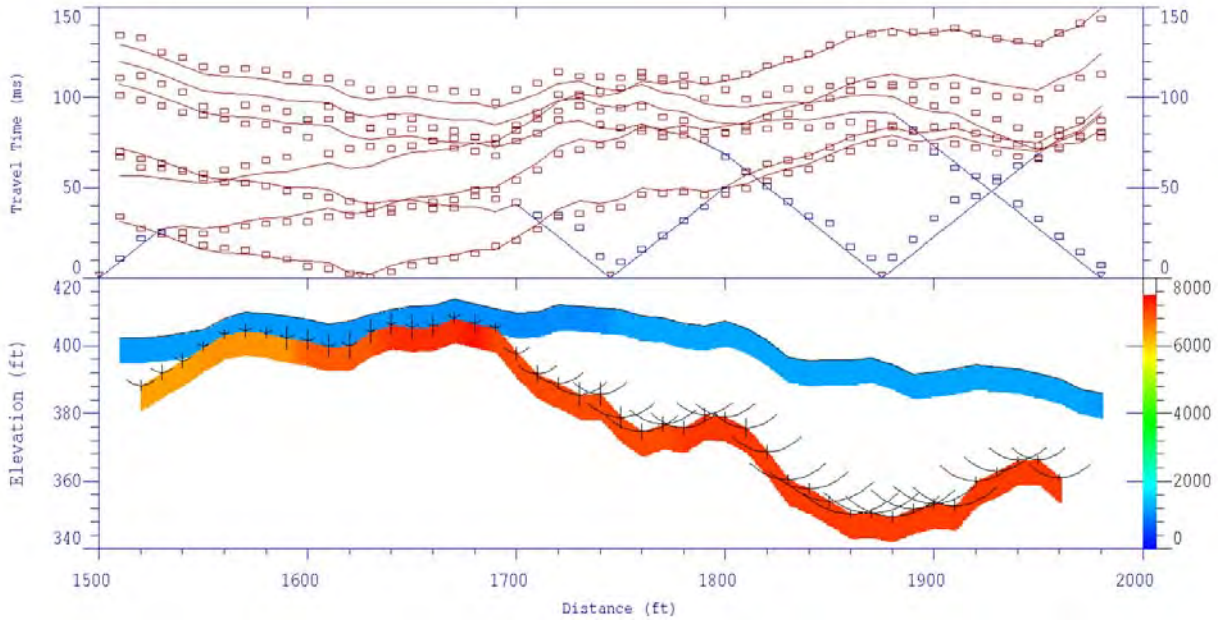

Figure 12. Two-layer field example interpreted with all seven shots. Now the refractor is defined across almost the entire width of the section and the surface velocity is defined except where the layer is very thin.

fined by the addition of 3 more shots to define surface velocity and two more to extend the definition of the refractor.

Conclusions

A single travel time curve taken with a shot on the spread end is sufficient to resolve a flat-lying layered structure and two shots, one from each end of the spread is sufficient to resolve a simple dipping refractor with constant velocities. Both require assumptions about the subsurface velocity structure which may or may not represent the truth. The use of only two shots leaves the surface velocity unconstrained over most of the central part of the section and leaves the refractor time-depth unconstrained on the ends. Although the refractor time-depth is resolved in the center of the section, the fact that the surface velocity is not resolved means that the actual depth or elevation section is not resolved because the refractor depths depend strongly on the velocity of the material above it. The coverage of a single shot depends on the depth of the refractor, with shallow depths favoring the refractor and deeper refractors favoring the shallow part of the section. In any case, it is necessary to take enough shots, placed at suitable locations, so that every geophone in the spread receives an arrival from both the surface layer and from each refractor in the section.

The addition of interior shots greatly increases the coverage for the surface velocity and thereby increases the constraints on the refractor depths. The addition of far shots increases the coverage of the refractor on the ends of the spread. Both assist in the definition of the layers from which the arrivals come and thereby increasing the confidence on the number of layers actually present in the section and on the interpretation itself.

References

Dobrin, Milton B.,1960, Introduction to geophysical prospecting, Second edition: McGraw-Hill, NY, 446 pp.

Inman, J. R., 1975, Resistivity inversion with ridge regression: Geophysics, **40**, pp. 798-817.

Constable, S.C., R.L. Parker, and C.G. Constable, 1987: Occam's Inversion: a practical algorithm for generating smooth models from EM sounding data, Geophysics, 52, pp. 289-300.

Palmer, D., 1980, The generalized reciprocal method of refraction interpretation (ed. Kenneth B. S. Burke): SEG, Tulsa, 104 pp.

Palmer, D., 1981, An introduction to the generalized reciprocal method of refraction interpretation: Geophysics, v. 46, pp 1508-1518.

Scott, James H., 1973, Seismic refraction modeling by computer: Geophysics, 38, pp271-284.

Telford, W. M., L. P. Geldart and R. E. Sheriff, 1009, Applied Geophysics Second Edition: Cambridge University Press, Cambridge, 770 p.

USING SYNTHETIC DATA TO GUIDE PROCESSING OF SHALLOW SEISMIC REFLECTION DATA COLLECTED ACROSS A HIGH SCARP IN SW MONTANA

Jose Pujol, University of Memphis, Memphis, TN
Mervin J. Bartholomew, University of Memphis, Memphis, TN
Andrew Michelson, University of Memphis, Memphis, TN
Michael Bone, Chesapeake Energy Corporation, Oklahoma City, OK

Abstract

We collected shallow reflection data in SW Montana across a 5.4 m high tectonic scarp. The goal of this survey was to try to image the fault associated with the scarp, which is visible in a trench close to the seismic line. However, processing the seismic data is challenging because the height of the scarp (about 5.4 m) is comparable to the depths of the reflectors of interest. The problem is most acute for the data from the scarp area, and to find out how to proceed we generated synthetic waveforms using the actual recording geometry and topography. To generate the synthetic data we assumed that the scarp was due to a normal fault and used velocity models based in part on parameters derived from the actual shot gathers. The analysis of the synthetic data shows that the velocity model could be recovered quite well by first determining interval velocities without consideration of the station elevations and then stacking the data after application of station corrections referred to a datum elevation equal to the height of the scarp. This procedure placed horizontal reflectors correctly in time in a relative sense, although those on the low side of the scarp were shifted to a later time. However, this shift is consistent with the velocity used to generate the corrections and the difference in elevation with respect to the datum. Moreover, away from the scarp the highest and lowest elevations can be chosen as datums, which places the horizontal reflectors correctly in time. Applying this procedure to the actual data shows a clear continuous horizontal reflector on the lower side of the scarp and more disrupted reflectors on the higher side with discontinuous reflectors under the scarp. The latter correlate with the main and secondary faults mapped in the trench, but because the early portion of the seismic data was muted, it is not possible to follow this correlation close to the surface.

Introduction

Southwestern Montana is within the northern Basin and Range and is characterized by high seismicity associated with clearly identified faults that ruptured during the late Quaternary. Furthermore, twelve Holocene faults are confined to the relatively narrow Centennial Tectonic Belt (CTB) that forms the northern flank of the Yellowstone hotspot track, which is marked by the Snake River Plain (e.g., Stickney and Bartholomew, 1987; Anders et al., 1989). The 1959, Ms=7.5, Hebgen Lake and the 1983, Ms=7.3, Borah Peak earthquakes occurred on the eastern and western ends of the CTB, respectively. To the east, the CTB abuts the Yellowstone caldera. Some of the known active faults in SW Montana are associated with large scarps, several meters high, and in an attempt to determine cumulative displacements across other equally large scarps that exist in the area, we collected shallow reflection data along some of them. One of the seismic lines is roughly parallel and adjacent to a trench that shows evidence of multiple surface ruptures along an active fault (Bartholomew et al., 2002), but processing the seismic data is a challenge because the height of the scarp (about 5.4 m) is comparable to the depths of the reflectors of interest. Clearly, away from the scarp standard processing techniques are directly applicable, but what is not obvious is how to handle

data from the scarp area. Handling this data correctly is essential to help correlate reflectors that may exist on both sides of the scarp at depth and thus establish the displacement across the fault at depths greater than can be reached by trenching. Thus, the pattern of reflections within the scarp represents a signature of the fault that can be correlated with other seismic lines across the same fault. To address this question we analyzed synthetic data generated using the actual recording geometry and topography, the latter shown in Fig.1. For the generation of synthetic data we assumed that the scarp was due to a normal dip-slip fault, which corresponds to the dominant style of faulting observed in trenches across this fault and across other faults in the area. Velocity models we used were based in part on parameters derived from actual shot gathers.

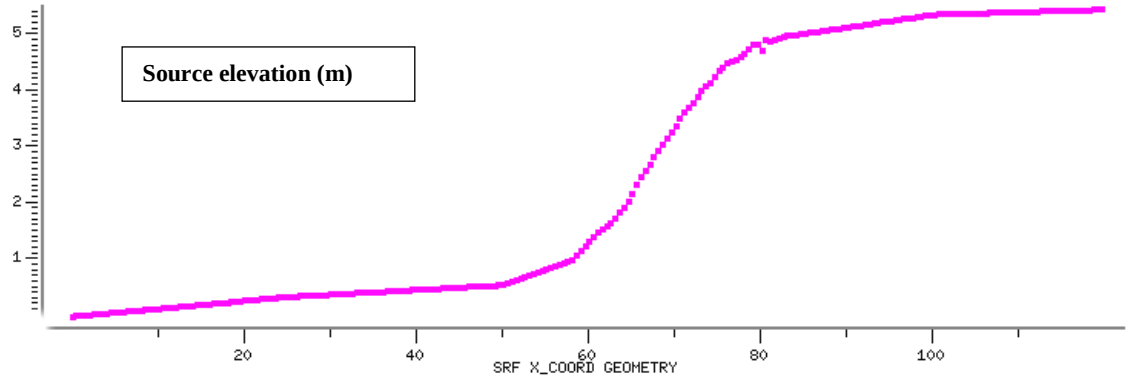

Figure 1: Surface elevation along the seismic line recorded in SW Montana. The horizontal axis shows the seismic source positions (in meters).

Data Acquisition and Examples

Reflection data were collected using a 72-channel recording system with 40-Hz vertical geophones 0.5 m apart. We used an end-on roll-along configuration and a hammer source, located adjacent to the first active channel. Each source hit was recorded by 48 channels, and to reduce the SNR the source was activated five times at the same position. The corresponding records were edited in the office and vertically stacked. Two typical shot gathers after vertical stacking are shown in Figs. 2 and 3. The surface waves are dominant in spite of the use of 40-Hz geophones, but some reflections are seen very clearly because of their higher frequencies, which allow us to infer the existence of strong impedance contrasts. For example, the reflection with a best-fitting velocity of 419 m/s in Fig. 2 has an intercept time of 60 ms, which corresponds to a 12.6-m thick layer.

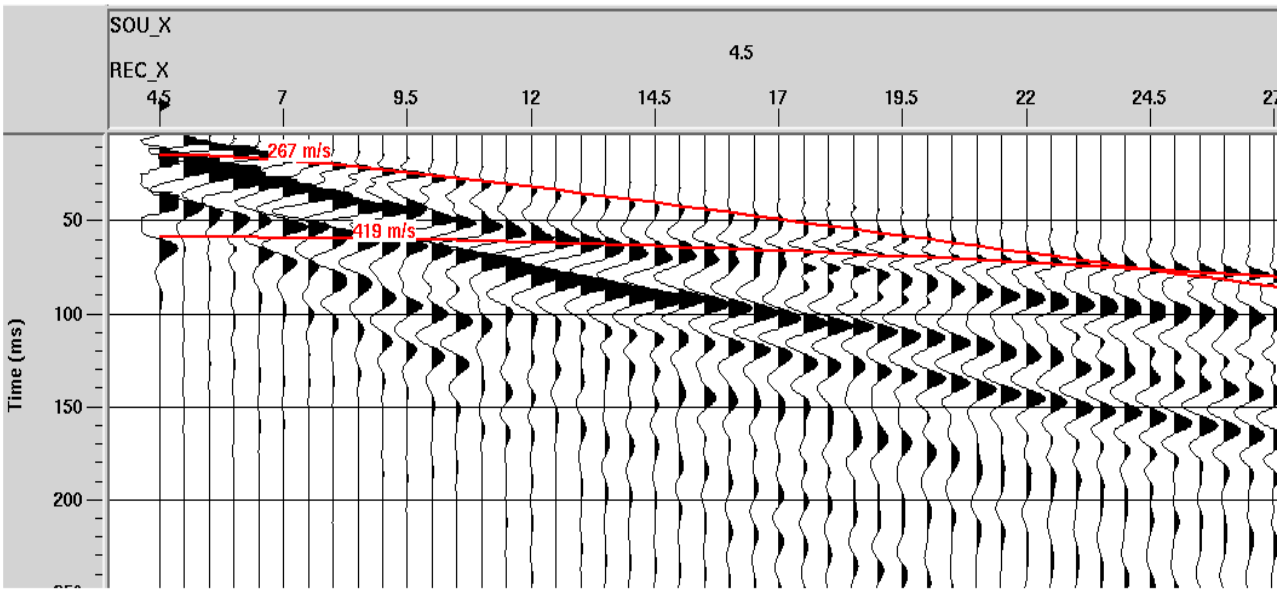

Figure 2: Actual shot gather. SOU_X and REC_X indicate source and receiver positions in meters. The scarp topography in Fig. 1 and the seismic line have the same origin. Note the presence of reflections, characterized by relatively high frequencies. The lower-frequency large amplitude waves correspond to surface waves. The red curves are best-fitting hyperbolas for a layer-over-a-halfspace model and the numbers in red indicate the corresponding best-fit velocities.

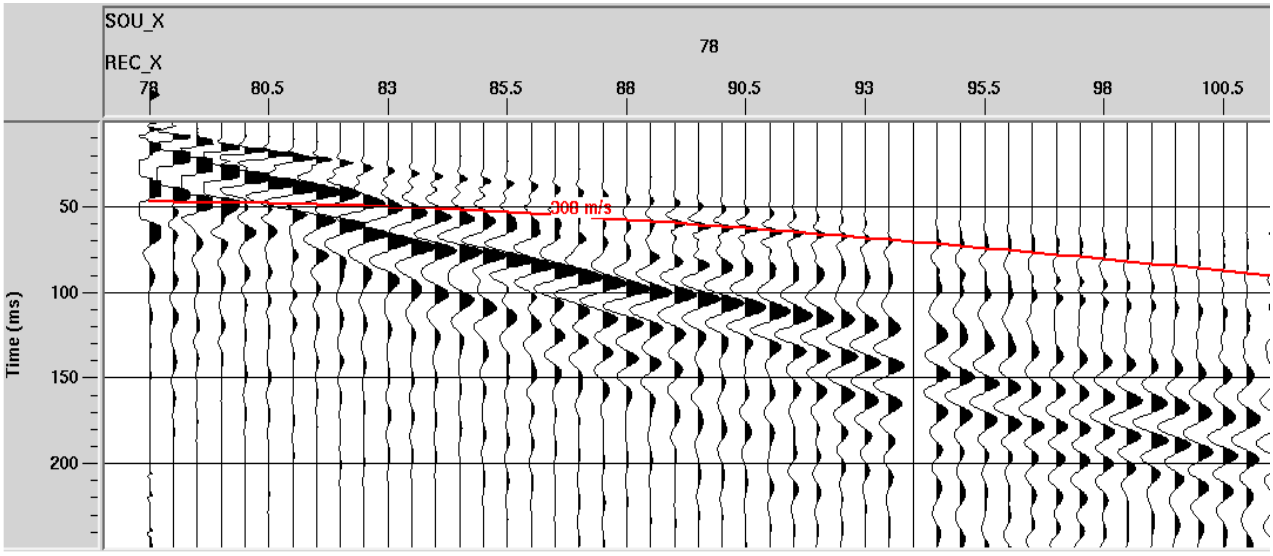

Figure 3: Similar to Fig. 2 for a different shot gather.

Processing of Synthetic Data

The synthetic velocity models used are variations of the model shown in Fig. 4. One of them has a constant velocity of 400 m/s between 0 and 12 m to the left of the fault and between 0 and 6.5 m to the right of the fault. Ray tracing was used to compute travel times from each source position to all corresponding actual receiver positions. The source time function was one cycle of a 100-Hz sine wave with an exponential time decay. The synthetic data set thus generated was processed using the Landmark Graphics Corporation ProMAX processing software. After some experimentation it was found that the following procedure produced a stacked section that gave an excellent representation of the velocity model used to generate the synthetics. The first step was the determination of stacking velocities, which were determined using the raw synthetic data. These velocities are shown in Fig. 5 after conversion to interval velocities using Dix equation. Not surprisingly, these velocities do not reproduce the input velocities because of the effect of the topography, for which no correction has been applied. This step was followed by (a) application of elevation statics computed using the true velocity (400 m/s) and referred to a datum of 5.4 m (corresponding to the highest point of the scarp), (b) normal moveout correction, and (c) cdp stacking using the stacking velocities determined in the previous step. The stacked data (Fig. 6) show two horizontal reflectors and the inclined reflector between them. The gap seen to the right of the latter is due to a shadow zone. The right reflector is placed correctly in time with respect to the datum, while the left reflector is placed correctly with respect to the right reflector but incorrectly with respect to the actual surface elevation. However, the time shift that affects the left reflector can be estimated using the computed interval velocity and the distance from the top of the model and the actual surface elevation. If a datum of 0 m is chosen, then the left reflector is placed correctly in time, with the right reflector shifted upwards.

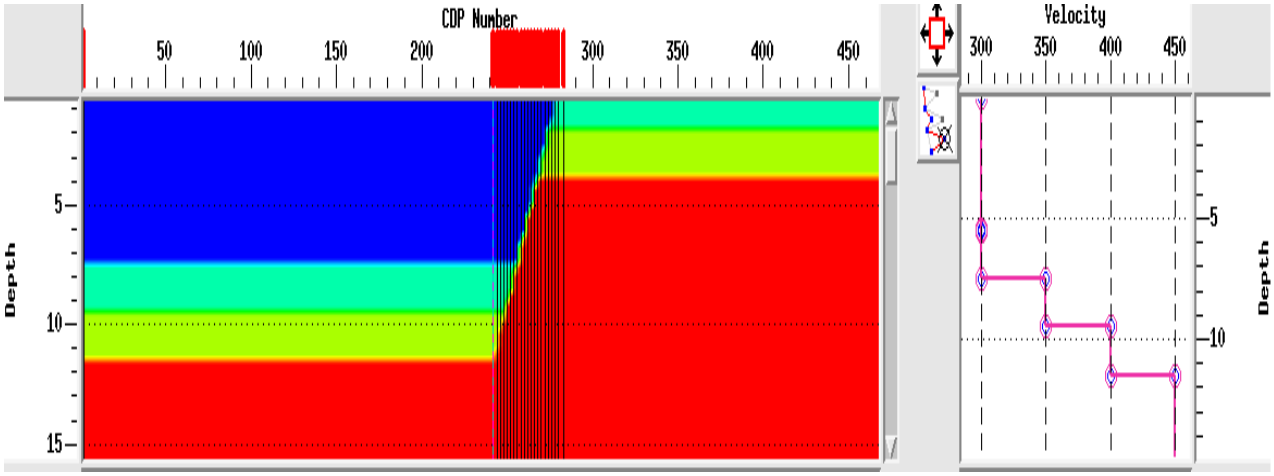

Figure 4: One of the velocity models used to generate synthetic data. The CDP numbers correspond to those of the actual reflection seismic line. The CDP spacing is 0.25 m. The vertical axis shows depth in m. The profile on the right corresponds to CDP 240. Velocities are given in m/s. For the generation of finite-difference synthetic data the zero depth of the model corresponds to the highest point of the scarp shown in Fig. 1.

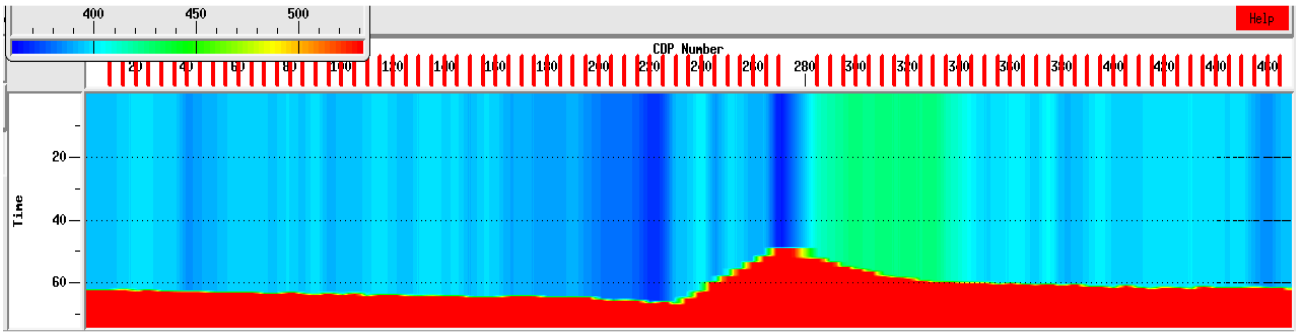

Figure 5: Interval velocities derived from the stacking velocities obtained using synthetic data generated for a velocity model with a constant velocity of 400 m/s between 0 and 12 m on the left of the inclined boundary shown in Fig. 4, and between 0 and 6.5 m to the right of the boundary. The scarp shown in Fig. 1 is above the zero depth of the model. The stacking velocities were converted to interval velocities using Dix equation. The scale on the top left corner corresponds to velocity in m/s. The vertical axis corresponds to two-way travel time in ms. The CDP spacing (0.25 m) is as in the actual data. Note that the effect of the scarp is to produce interval velocities different from the velocities used to generate the synthetic data, which give a two-way travel time of 60 ms where the reflectors are horizontal.

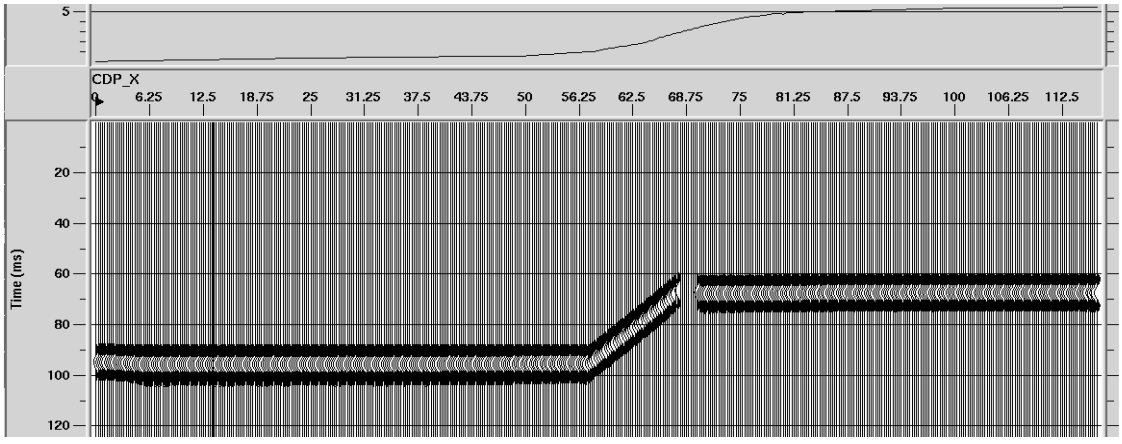

Figure 6: Synthetic data after CDP stacking using the stacking velocities corresponding to the interval velocities shown in Fig. 5. The reflector on the right of the inclined boundary is placed correctly in time. The reflector on the left is placed correctly only with respect to the right reflector.

The synthetic data just described are very useful because they only include reflections, and thus, they are not contaminated by any other type of wave, such as direct, refracted or surface waves. Therefore, we know exactly what the stacked section shows. On the other hand, the velocity model is too simple, which is a drawback. To address this problem we also generated synthetic data using the ProMAX 2-D acoustic finite-difference software, which allows 2-dimensional velocity variations as well as changes in the source and receiver elevations. To account for the latter, the zero elevation of the velocity model is the elevation of the highest receiver position. The sources and receivers are placed along the topography. One of the velocity models we used is that shown in Fig. 4. For the synthetics, the zero depth of the model was placed at an elevation of 5.5 m, close to the highest elevation of the scarp, which means that all of the source and receiver

locations are inside the model. Although the software has absorbing boundary conditions, spurious reflections from the top of the model can be seen. The direct waves are very strong and had to be muted. The software does not generate surface waves. The source wavelet was a minimum phase Ricker wavelet and the highest frequency 200 Hz. As in the previous case, the interval velocities corresponding to this data set, shown in Fig. 7, do not reproduce the input velocities. Similarly, the CDP stacking of the data, using the procedure described earlier, places the horizontal reflectors correctly in a relative sense (Fig. 8), but some of them will be placed incorrectly in time depending on the selection of the datum. Regarding the inclined reflector, its identification is hampered by strong diffractions. In this case, the frequencies below 50 Hz were filtered out before the data were stacked.

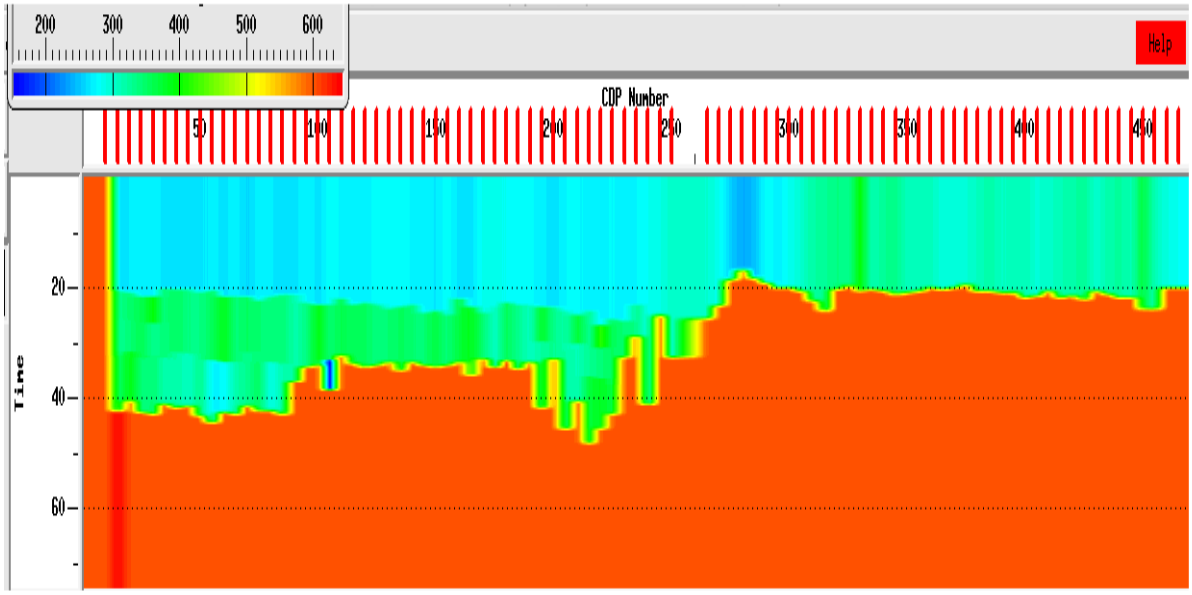

Figure 7: Similar to Fig. 5 determined using the finite-difference synthetic data generated using the velocity model shown in Fig. 4. To the left and right of the inclined boundary the actual velocity model has horizontal boundaries at about 35 ms and 21 ms, respectively.

Processing of the actual data

The actual data were also processed as described earlier. Although very shallow reflections are seen in the shot gathers (see Fig. 2), they are within the arrival of the surface waves, and for this reason the data were muted. The interval velocities (Fig 9) show the effect of the scarp. Before CDP stacking the frequencies below 45 Hz were filtered out and an f-k filter was used to remove the surface waves.

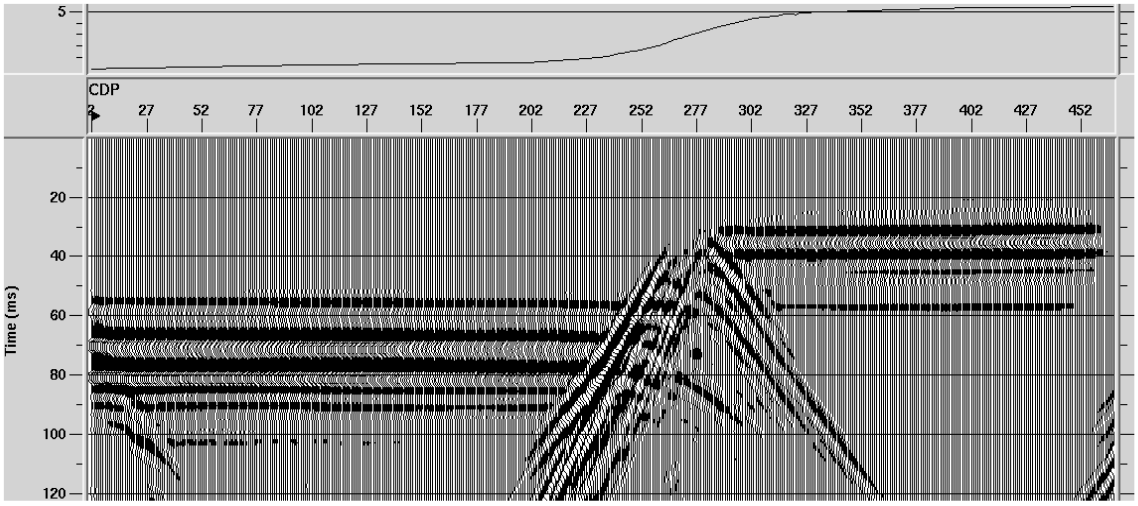

Figure 8: Synthetic data after CDP stacking using the stacking velocities corresponding to the interval velocities shown in Fig. 7. Because of strong direct waves, which were muted, the first arrivals of the top reflectors are not clearly seen. As in Fig. 6, the position of the reflections is correct on the right-hand side and correct in a relative sense on the left-hand side. The strong diffractions prevent identification of the inclined boundary. The profile on top gives the CDP elevation in meters.

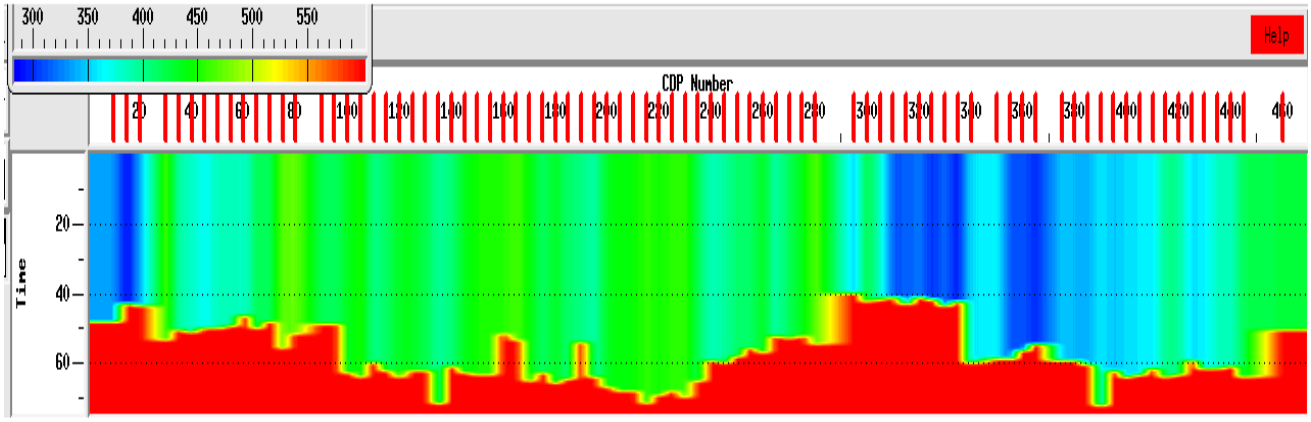

Figure 9: Interval velocities derived from the stacking velocities determined using the actual data.

The stacked data (Fig. 10) show clear and continuous reflections at about 90 ms to the left of the scarp, although the timing of the reflections is incorrect because the datum was chosen at 5.4 m. When the datum is 0 m, the 90 ms reflector is shifted to 60 ms, in agreement with the reflector seen in the shot gathers (e.g., Fig. 2). To the right of the scarp they are discontinuous reflectors between about 40 and 80 ms, which may be explained by the fractured nature of the near surface seen in the trench (Fig. 10) excavated earlier near the seismic line. Clearly, the character of the reflections near 60 ms seen to the right of the scarp is different from that of the reflections at 90 ms to the left of the scarp. As the latter actually correspond to 60 ms for a 0-m datum, we are confident that the two sets of reflections correspond to different impedance

boundaries. Regarding the reflections seen within the scarp, the analysis of the synthetic data shows that they are unlikely to be a processing artifact introduced by the topography. The question is whether the discontinuities seen in the scarp reflections between about 56 m and 69 m can be interpreted as an indication of faulting. We believe that this is the case because the discontinuities are roughly along the projections of the two faults seen in the trench MBMG1986-6 (Fig. 11), but a definitive answer will require modifications to the instrumentation used (i.e., 100 Hz geophones), to the recording geometry, and even to the type of waves recorded (SH- instead of P-waves). With these modifications it may be possible to reduce the amount of data muted and thus see what happens close to the surface.

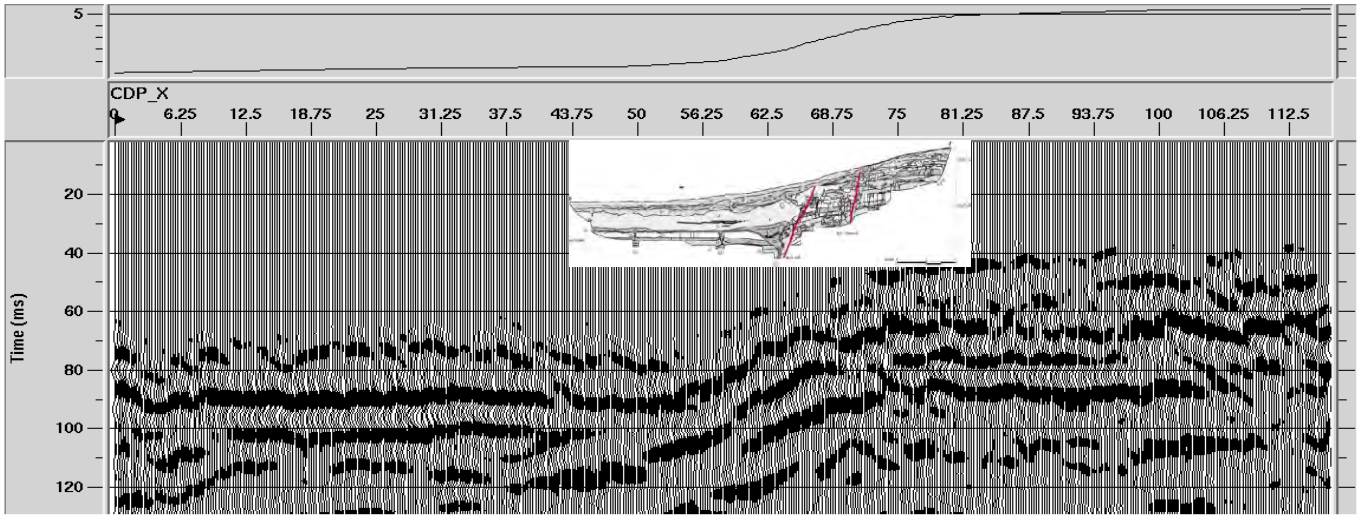

Figure 10: CDP stack of the actual data, processed with a datum elevation of 5.4 m. The inset shows the trench close to the seismic line. Red lines show the main and secondary faults (left and right, respectively). Clastic dikes associated with paleo-sandblows occur to left of the main fault. (From Bartholomew et al., 2002.)

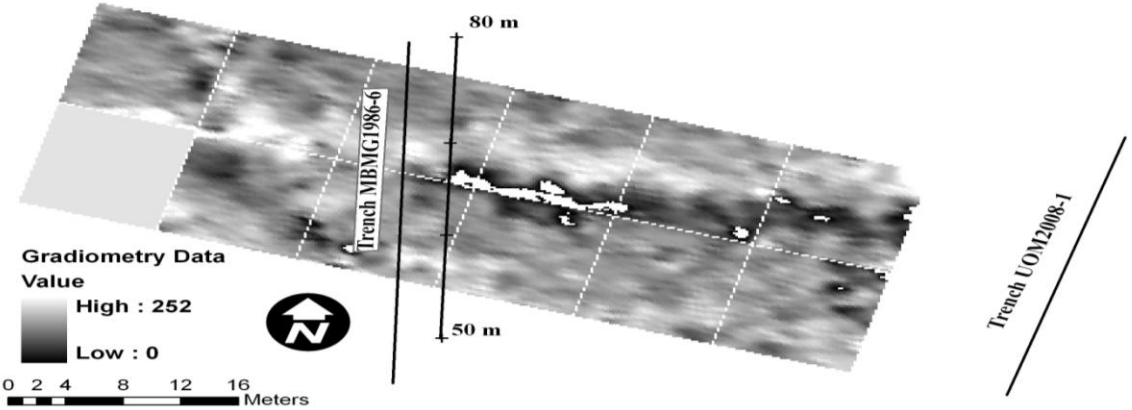

Figure 11: Magnetic gradiometer data. The N-S line indicates the position of the seismic line between 50 and 80 m where the fault trace in the gradiometer survey intersects the reclaimed trench BMG1986-6 (Bartholomew et al., 2002) west of the seismic line. To the east, the trench profile line marks trench UOM2008-1, which was opened at the time of the gradiometer survey.

Interestingly, magnetic gradiometer data (Fig. 11) show a clear positive anomaly around 65-67 m along the seismic line, thus correlating with the main fault seen in the scarp. The anomaly directly corresponds to buried A-horizons encountered during trenching. It appears that organic sediments were preserved or formed along the fault, although on the upper part of the scarp the thick A-horizon may not have formed or may have been stripped away.

Conclusions

The main conclusion of this work is that we have found a way to process shallow reflection data collected across a high scarp. Although the stacked data are not placed correctly in absolute time for reflectors on the lower side of the scarp, they are placed correctly in a relative sense with respect to the reflectors on the upper side of the scarp. The process was applied to data recorded across a high scarp in SW Montana close to a trench with evidence of Quaternary faulting. The stacked data show discontinuities in reflections within the scarp that appear to correlate with faults observed in an adjacent trench. However, because the early portions of data had to be muted, a definite conclusion will require modification to the data recording to reduce the amount of data that must muted.

Acknowledgments

Collection of the reflection data was supported by EPA Contract EM-96452106-0 to M. Bartholomew. The ProMAX 2-D processing package was provided by the Landmark Graphics Corporation through its University Software Grant Program. We gratefully acknowledge the outstanding support provided by Landmark's member D. Hackney.

References

Anders, M. H., Geissman, J. W., Piety, L. A., and Sullivan, J. T., 1989, Parabolic distribution of circumeastern Snake River Plain seismicity and latest Quaternary faulting: migratory pattern and association with the Yellowstone Hotspot, *Journal of Geophysical Research,* v. 94, B2, p. 1589-1621.

Bartholomew, M. J., Stickney, M. C., Wilde, E. M., and Dundas, R. G., 2002a, Late Quaternary paleoseismites: Syndepositional features and section restoration used to indicate paleoseismicity and stress-field orientations during faulting along the main Lima Reservoir fault, southwestern Montana, *in* Ettensohn, F.R., Rast, N., and Brett, C.E., eds., *Ancient Seismites, Geological Society of America, Special Paper* 359, p. 29-47.

Bartholomew, M. J., Bone, M. J., Rittenour, T. M., and Stickney, M. C., 2009, "Stress switching" along the Lima Reservoir fault in Yellowstone's wake, Geological Society of America, Abstracts with Programs, v. 41, no.7, p.55.

Stickney, M. C., and Bartholomew, M. J., 1987, Seismicity and late Quaternary faulting of the northern Basin and Range Province, Montana and Idaho, *Bulletin of the Seismological Society of America*, v. 77, p. 1602-1625.

APPLICATION OF WAVEFIELD TRANSFORMATION TO SPECTRAL ANALYSIS OF SURACE WAVE (SASW) DATA

Chun-Hung Lin, National Chiao Tung University, Hsinchu, Taiwan
Chih-Ping Lin, National Chiao Tung University, Hsinchu, Taiwan

Abstract

This paper introduces a source-to-receiver distance gather process to reconstruct the SASW data as MASW-imitating data, to which a wavefield transformation can be applied for dispersion curve analysis. Numerical simulations were performed to demonstrate its feasibility and advantages for analyzing SASW data. Furthermore, a new field testing procedure is suggested for better results when conducting surface wave testing with two or small number of recording channels. The results of this study advocate that multi-channel wavefield transformation can and should be used even though the field testing procedures may differ as restricted by the equipment capacity.

Introduction

Because of its non-invasive and non-destructive nature, surface wave method is widely applied to geotechnical site investigations. It provides a more effective and lower cost tool for in-situ shear wave velocity measurement. The data reduction method for dispersion relation in a surface wave testing is conventionally associated with certain method of data acquisition. At present, spectral analysis of surface wave (SASW, two-channel approach)(Stokoe et al., 1994) and multi-channel analysis of surface wave (MASW, multi-channel approach)(McMechan and Yedlin, 1981; Gabriels et al., 1987; Park et al., 1999; Lin and Chang, 2004) are the most popular methods used worldwide. Each method has its own favorers and the debate is still on going about their relative advantages and disadvantages.

Limited to the two channel data, conventional dispersion analysis of SASW suffers from possible phase un-wrapping errors, inefficient data filtering and synthesis, and inability to distinguish multiple modes. MASW, on the other hand, can overcome these problems by multi-channel wavefield transformation, such as f-k (frequency-wavenumber) and p-f (slowness-frequency) transforms. In this study, we show that, while the channel number of a seismograph may restrict the field testing procedure, it does not necessarily prescribe the method of dispersion analysis. A source-to-receiver distance gather process to reconstruct the SASW data as MASW-imitating data was proposed such that the wavefield transformation can be applied for dispersion curve analysis of SASW data. The feasibility and advantages of utilizing wavefield transformation even for SASW data were illustrated by numerical simulations.

Wavefield Transformation Analysis on two-channel data

To apply the wavefield transformation, such as f-k and p-f transforms, on two-channel SASW data, we propose a preprocess to rearrange and reconstruct the SASW data by the source-to-receiver distance gather to generate MASW-imitating data and then apply multi-channel wavefield transformation. Each pair of signals from different shots in a SASW testing was identified by the source-to-receiver distance. The SASW data were then rearranged in ascending order of source-to-receiver distance. Signals having the same source-to-receiver distance are averaged. The reconstructed data

mimics MASW data. The major difference between MASW data and MASW-imitating data is that MASW signals normally are equally spaced while MASW-imitating signals from SASW data are not. The wavefield transformation can be modified to accommodate spatially non-uniform data. Discrete Fourier transform (DFT) with respect to time is first applied to the reconstructed data $u(t_m, x_n)$, which is temporally uniform.

$$U(f_i, x_n) = \frac{1}{M}\sum_{m=0}^{M-1} u(t_m, x_n)\exp(-j2\pi f_i t_m) \quad [1]$$

where u is the velocity recorded by the receivers, U is real part of the DFT of u, $j=\sqrt{-1}$, $t_m = m\Delta t$, $f_i = i\Delta f = i/[(M-1)\Delta t]$, and $x_n = n\Delta x$. The subscripts i, n, and m in Eq. [1] are integer indices to represent respectively discrete points in the frequency, space, and time domain. For each frequency component, the wavefield $U(f_i,x)$ becomes a harmonic function of space. The wavenumber k (i.e. spatial frequency) can be determined from the wavenumber analysis (spectral analysis in space). The wavenumber analysis of the multi-station signals can be performed using the discrete-space Fourier Transform

$$Y(f_i, k) = \sum_{n=0}^{N-1} U(f_i, x_n)\exp(-j2\pi k x_n) \quad [2]$$

where $Y(f_i,k)$ represents the wavefield in the frequency-wavenumber domain. Equation [2] is actually not a rigorous discrete-space Fourier Transform in that x_n is not equlally spaced and the fast algorithm (FFT) cannot be used. The wavenumber (k) of the surface wave can be identified at the peaks of the amplitude spectrum of $Y(f_i,k)$. The phase velocity is then determined by the definition $v = 2\pi f/k$. Alternatively the f-v spectrum can be derived from Eq. [2] by simply changing the variable $k = 2*\pi f/v$ as

$$Y(f_i, v) = \sum_{n=0}^{N-1} U(f_i, x_n)\exp\left(-j\frac{2\pi f_i}{v}x_n\right) \quad [3]$$

where $Y(f_i,v)$ represents the wavefield in the frequency-velocity domain. The peaks of the amplitude of the frequency-velocity domain spectrum is the dispersion curve.

Numerical Verification

Two earth models were designed to verify the proposed method. Model 1 is dominated by the fundamental mode and the other has different dominant modes in different frequency ranges. The parameters of the earth models used are shown in Table 1. Surface wave testing data with 2-m receiver spacing were simulated by the modal summation method, which was programmed by Herrmann and Ammon(2002).

Table 1: parameters of earth models

Model	Layer	Vs(m/s)	Vp(m/s)	H(m)	Density(g/cm3)
1	1	300	600	10	1.8
	2	400	800	∞	1.8
2	1	300	600	4	1.8
	2	250	500	8	1.8
	3	400	800	∞	1.8

Figure 1 shows the results of the proposed dispersion analysis (Fig. 1a) for 6-shots SASW survey in earth model 1 (the common midpoint receiver spacings are respectively 2m, 4m, 8m, 16m, 32m, and 64m). Also shown in Fig. 1 for comparisons are the dispersion curves obtained from conventional

SASW (Fig. 1b) and the conventional equal-spacing MASW (Fig. 1c for short geophone spread L = 24 m and Fig. 1d for long geophone spread L = 128 m). In Model 1, SASW and the proposed method perform similarly and both can extract dispersion curves mostly identical to the analytic solution. The corresponding results for earth model 2 are shown in Fig. 2. It can be seen from Fig. 2a that the fundamental mode is separated from the higher modes and it agrees well with results from long MASW in Fig.2d. From the simulations, it can be concluded that the proposed method for SASW survey is an alternative way to analyze the dispersion curve more efficiently and correctly, taking advantages of the multi-channel wavefield transformation. However, there are some artificial patterns in the left part of the spectral image due to the non-uniform geophone spacing. Instead of common midpoint configuration conventionally adopted in SASW, a common receiver configuration survey is proposed to minimize this un-wanted effect. More equally-spaced source-to-receiver data may be recorded by walk-away shots.

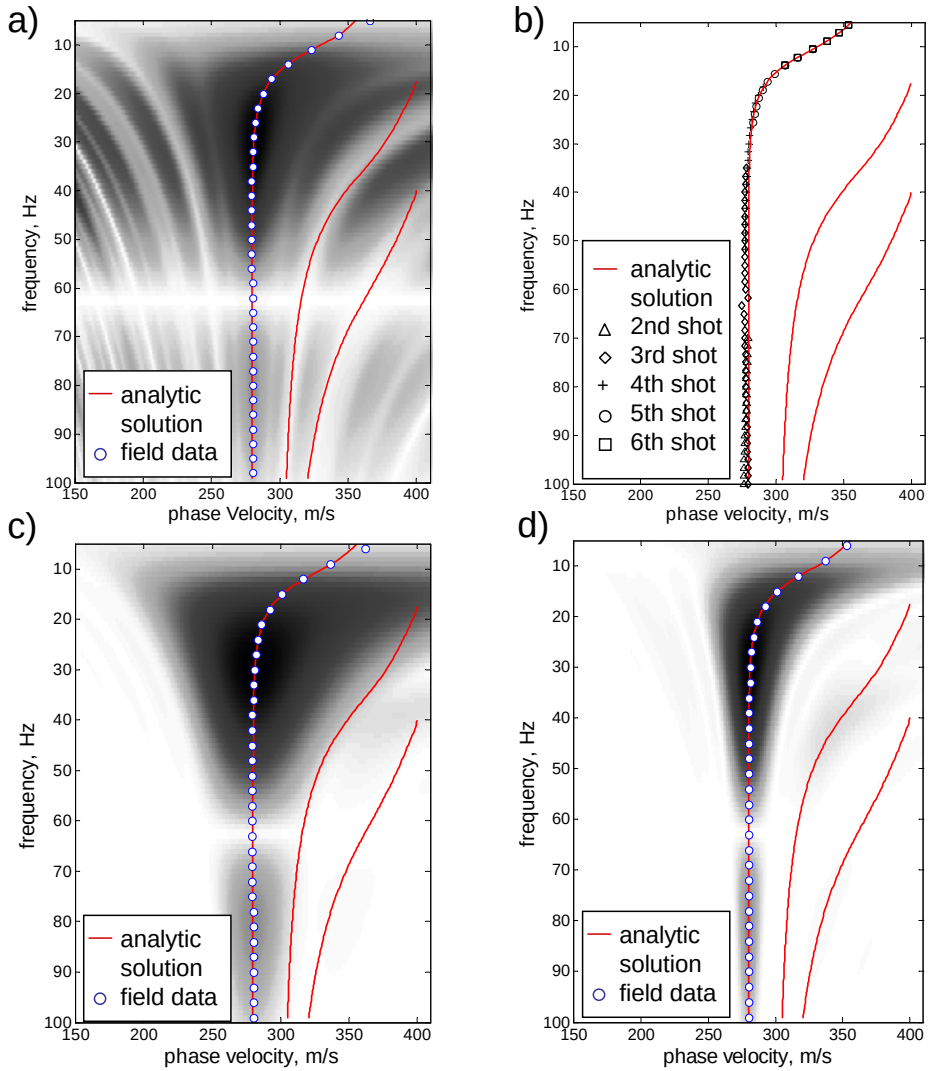

Figure 1: Dispersion curves for earth model 1. a) SASW data with MASW analysis, min. dx=2m, 6 shots; b) SASW, min. dx=2m, 6 shots ; c) MASW, dx = 2m, L = 24m; d) MASW, dx = 2m, L = 128m.

Conclusion

The data reduction method for dispersion relation in a surface wave testing is conventionally associated with certain method of data acquisition. Typical examples are phase angle analysis in the SASW method and wavefield transformation in the MASW method. This study advocated that multi-channel wavefield transformation can and should be used even though the field testing procedures may differ as restricted by the equipment capacity. A source-to-receiver distance gather process to reconstruct the SASW data as MASW-imitating data was proposed such that the wavefield transformation can be applied for dispersion curve analysis of SASW data. The proof-of-concept was given by numerical examples. The advantages of this new approach over conventional SASW analysis are (1) avoiding phase un-wrapping error, (2) easy automation of data reduction, and (3) ability to separate different modes when the geophone spread is long enough. While the channel number of a seismograph may restrict the field testing procedure, it does not necessarily prescribe the method of dispersion analysis. Mutil-channel wavefield transformation is more powerful and can be used even for the SASW method with two-channel recordings.

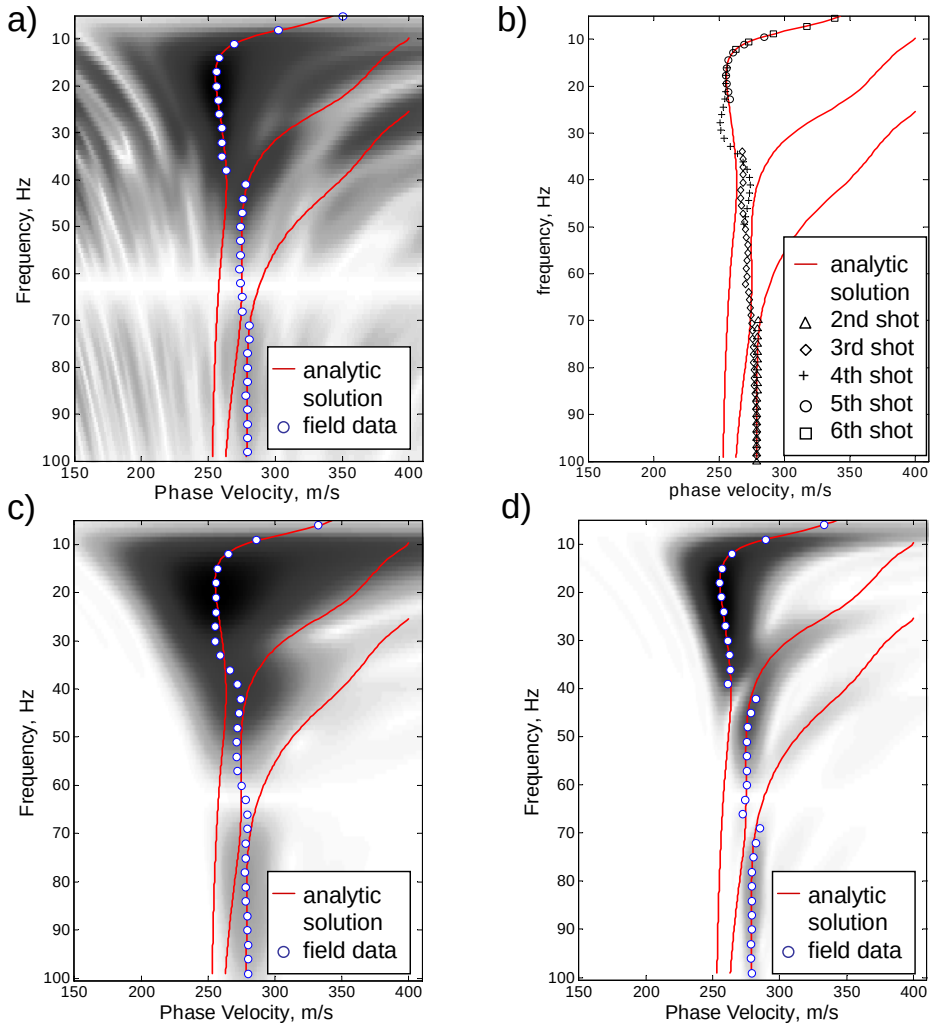

Figure 2: Dispersion curves for earth model 2. a) SASW data with MASW analysis, min. dx=2m, 6 shots; b) SASW, min. dx=2m, 6 shots ; c) MASW, dx = 2m, L = 24m; d) MASW, dx = 2m, L = 128m

Reference

Gabriels P, Snieder R, Nolet G. (1987) , “In situ measurements of shear-wave velocity in sediments with higher-mode Rayleigh waves.”, Geophys Prospect, vol..35, pp.187–96.

Herrmann, R. B., and C. J. Ammon, (2002), ”Computer Programs in Seismology – ver, 3.30”.

Lin C-P, Chang T-S. (2004) , “Multi-station analysis of surface wave dispersion.”, Soil dynamics and earthquake engineering, vol. 24, p. 877-86.

McMechan GA, Yedlin MJ. (1981), “Analysis of dispersive waves by wavefield transformation. Geophysics” , vol. 46, 869–74.

Park CB, Miller RD, Xia J. (1999), “Multichannel analysis of surface waves: Geophysics”, vol. 64, pp. 800-808.

Stokoe II KH, Wright GW, James AB, Jose MR. (1994) , “Characterization of geotechnical sites by SASW method.” In: Woods RD, editor. Geophysical characterization of sites. Rotterdam: A.A. Balkema, p. 15–25.

UPDATE ON RECENT OBSERVATIONS IN MULTI-COMPONENT SEISMIC REFLECTION PROFILING

André J-M. Pugin, Geological Survey of Canada, Ottawa, Canada
Susan E. Pullan, Geological Survey of Canada, Ottawa, Canada
James A. Hunter, Geological Survey of Canada, Ottawa, Canada

Abstract

Examples of multi-component shallow seismic reflection profiling from different environments in eastern Canada are presented to examine the benefits of shear wave reflection data and the latest developments in acquisition methodology, as well as our evolving understanding of the complex nature of seismic wave propagation. Examination of the wave motion through multi-component recording shows that, regardless of the source orientation, shear wave reflections may be polarized in varying directions. In "soft" soils characterized by low shear wave velocities, extremely high-resolution shear wave reflection sections can be obtained, with the highest-resolution data related to in-line or vertical components of motion. Data recorded in the transverse (SH) direction are generally somewhat lower in frequency but may be better able to penetrate into more compact (higher velocity) sediments. Multi-component recording provides the capacity to record all data, without having to know the main shear wave polarization direction prior to data acquisition.

Introduction

Shallow shear (S-) wave reflection methods potentially offer high resolution imaging of the near-surface because of the low shear wave velocities in unconsolidated sediments and have been of interest since the early 1980s (Helbig and Mesdag, 1982; Stumpel et al., 1984). Recent years have seen an increase in the use of shear wave reflection profiling in near-surface investigations, in part due to the development and increasing acceptance of landstreamers (Inazaki, 2004, Pugin et al., 2004, 2007). Landstreamers allow extremely efficient and cost-effective data acquisition especially for shear wave surveys when short geophone spacings are required to maintain the receiver array in the optimum window and to avoid aliasing of surface waves.

Most shallow seismic shear wave reflection work has considered only the SH-mode, using source and receivers which are oriented perpendicular to the survey line, though recent tests (Pugin et al, 2008) have highlighted the potential of recording and processing SV data. Pugin et al. (2008) showed that vertical sources and receivers can produce good shear wave reflection records, and that the optimum window for acquiring SV-reflections was farther from the source than the SH reflection window. More importantly, it was observed that SV reflections were higher in frequency than the corresponding SH data. In fact, SV sections using a vibrating source over thick soft soils characterized by a very low shear wave velocity, displayed the highest resolution the authors had yet observed in any land-based seismic reflection survey. Furthermore, the method allowed the acquisition of shear wave (S) and compressional wave (P) reflection data in a single vertical mode data set. With judicious choice of the number of receivers and receiver spacings, this presents an opportunity to image ultra shallow and deeper sedimentary units at the same time, as well as to better characterize the subsurface because both shear and compressional properties are observed.

Since the 2008 publication we have further experimented with multi-component recording and various source orientations. Pugin et al. (2009a) presented results from tests which involved the observation and analyses of P, SV and SH body waves from multi-component (2- or 3-component) records obtained with high frequency vibroseis equipment with an orientable source (vibrating in the vertical or horizontal direction). These data showed that the usual assumptions that SH data are produced using a cross-line source and acquired with cross-line receivers or that SV data require an in-line source and in-line receiver must be reassessed. In fact, it appears that any source direction produces all waves and in particular, both SH and SV energy.

In this paper, we look again at the differences between SH and SV and the benefits of multi-component recording. Using examples from several different areas in eastern Canada, we examine the results and present an update of our methodologies and our evolving understanding of the concept of shallow seismic reflection profiling.

Data acquisition system

The use of a vibrating seismic source coupled with a landstreamer offers a very efficient and adaptable seismic reflection data acquisition system (Figure 1). The Geological Survey of Canada's (GSC) landstreamer is designed for use along paved or gravel roads, and is built with 3 kg metal sleds connected using wire or low-stretch rope. The number of receivers and the receiver spacing can be varied depending on the near surface velocities and the targeted depths of observation. We typically use 24-72 receiver sleds at spacings ranging from 0.75 m to 3 m. Each sled can be equipped with a geophone or a number of geophones. We now use a 3-component (3-C) geophone unit constructed in-house using 30 Hz omni-directional geophone elements oriented in three directions, one vertical and two horizontal, in-line and cross-line.

Vibrating sources offer several advantages over the impulsive sources (e.g. sledge hammers, weight drops, shotgun sources, or explosives) that have traditionally been used for shallow seismic surveys. Vibrators are non-destructive, highly repeatable and the long recording times yield improved signal-to-noise ratios in many noisy environments (e.g. wind, traffic, etc.). Their disadvantages are that they are generally large and heavy (which affect portability), and relatively expensive, though there are ongoing efforts to design and build small and relatively inexpensive vibrators specifically for shallow seismic surveys (e.g. Ghose et al., 1998; Haines, 2006).

Figure 1: GSC Minivib/landstreamer system in operation in downtown Quebec City.

Our vibrating source is an IVI (Industrial Vehicles International, Inc) "Minivib" vibrator source mounted on a "minibuggy" (http://www.indvehicles.com/minivibminibu.pdf). This source vibrates a 140 kg mass in either vertical or horizontal mode, and allows the operator to program the sweep through a range of frequencies between 10 and 550 Hz. For these shallow applications we use it with very low "drive amplitudes" (i.e. 20-40% of the vibrator's possible motion). We have equipped it with a high-precision distance-measuring odometer linked to a small readout screen mounted in the cab, allowing the operator to move quickly and accurately to the next shotpoint while the seismograph is saving data. Data are recorded using Geometrics Geode engineering seismographs operated in the cab of the Minivib. We always record uncorrelated records to allow prewhitening of the data and careful choice of the correlating function as the first step in the data processing sequence.

Using the Minivib/landstreamer system described above, we typically collect 1000 to 1500 records a day at source spacings of 1.5-6 m.

Examples of shear wave seismic reflection profiling

We present here three examples of shear wave reflection profiling using the GSC Minivib/landstreamer system. These come from various areas in eastern Canada where we have been working on groundwater, geological mapping, and hazard projects. In all cases the data were acquired using a 48-channel landstreamer with 0.75 m spacing between sleds and a source spacing of 3 m. The Minivib was operated in horizontal mode (the orientation used in each survey is specified below) with a 7.5 second sweep from 20-300 Hz.

1) Quebec City – buried valley (urban environment) - H2

Shear wave reflection data were acquired in Quebec City using the GSC Minivib/landstreamer system to delineate a buried valley that underlies part of the downtown area (Figure 1). In just one and a half operational days, we acquired ~4 km of reflection data in a built-up and busy urban area (Fig. 1), recording both inline (H1) and transverse (H2) receivers. The Minivib was operated in horizontal mode oriented at 45 degrees (midway between in-line and transverse directions).

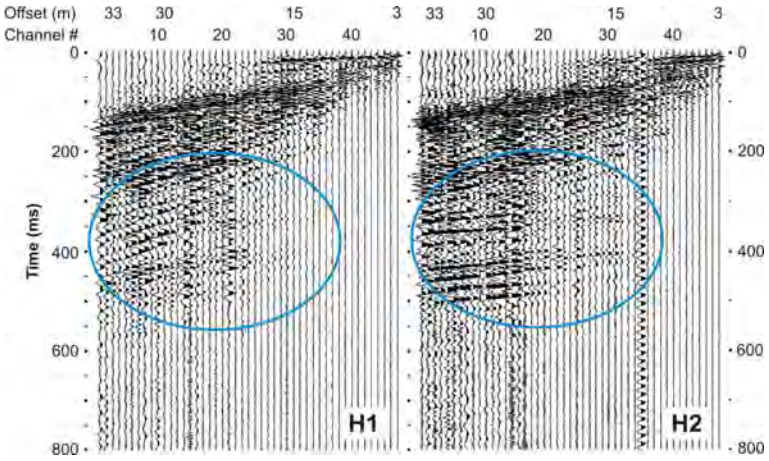

Figure 2: Raw field record (after correlation) from the Quebec City survey showing that the shear wave reflections from bedrock and the deeper parts of the valley (highlighted by the ellipse) are polarized in the SH (transverse or H2) direction (right panel).

An example field record is shown in Figure 2, separated into data acquired by the inline (H1) and transverse (H2) receivers. These results clearly show that energy reflected from the bedrock surface and from the lower part of the valley fill are polarized in the transverse (H2) direction. Very little energy from these reflections at 300-500 ms is visible on the H1 receivers, and there appears to be considerable interference with surface waves on these records.

Figure 3 shows a portion of the final processed shear wave reflection section over the buried valley using data acquired with the transverse (H2) receivers. The section clearly delineates the buried valley which reaches a depth of 80-90 m below ground surface. The average shear wave velocity (Fig. 3b) increases from ~180 m/s at very shallow depths to ~300-350 m/s in the bottom of the valley. These values are consistent with downhole velocity measurements acquired in a nearby borehole where interval velocities of 180-200 m/s were observed in shallow fine-grained marine deposits (Unit 1), and 300-400 m/s in the sands, gravels and diamictons found in the lower part of the section.

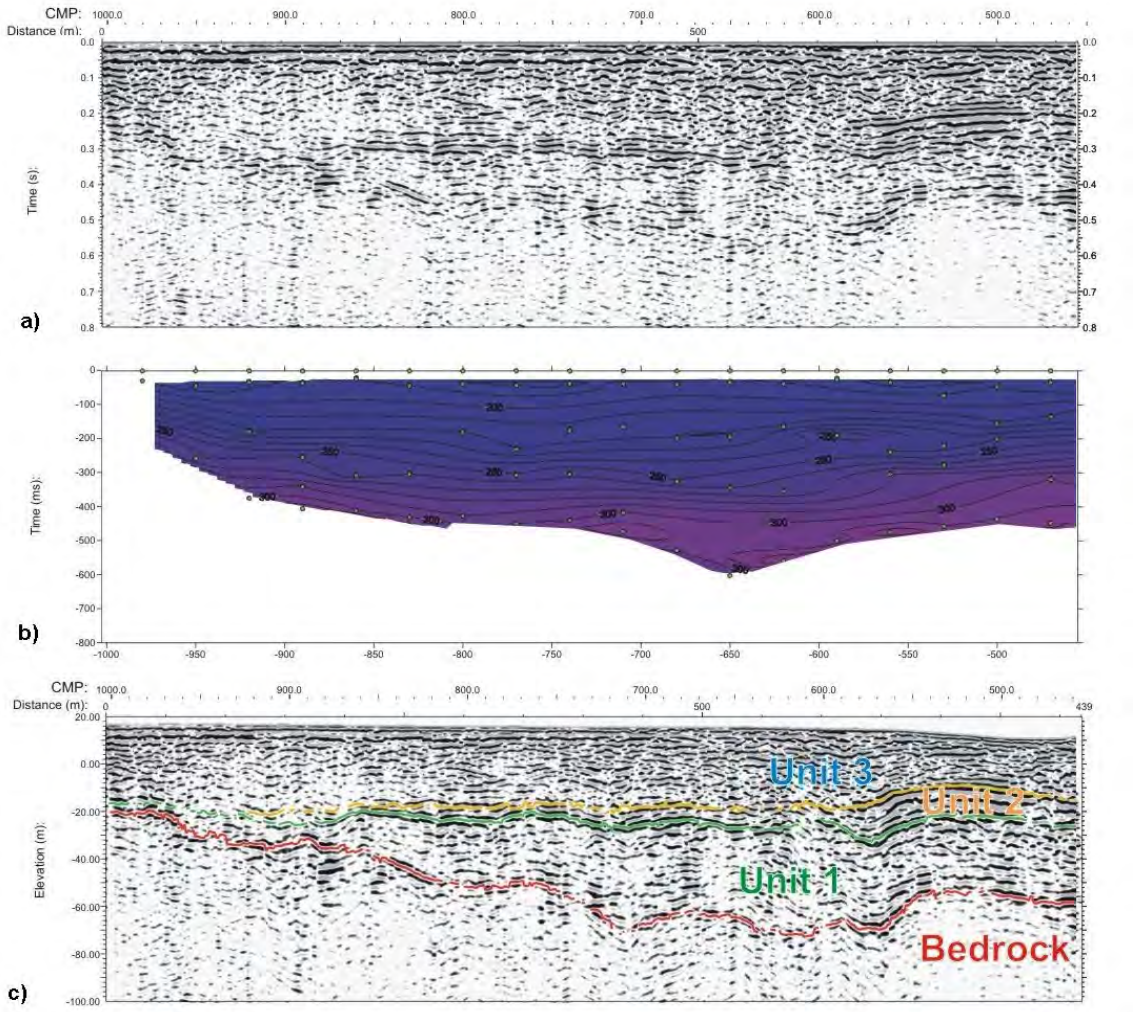

Figure 3: Example of ~800 m of a shear wave section acquired in downtown Quebec City, with the source vibrating horizontally at 45 degrees to the line direction and receivers oriented in the transverse direction (H2). a) processed time section; b) contoured NMO velocity function (green dots represent picked average velocity/time pairs); c) interpreted elevation section, corrected for surface topography.

2) Abitibi – shallow bedrock –H2

Shear wave reflection data were acquired in the Abitibi area in northwestern Quebec to delineate the bedrock surface and overburden stratigraphy as part of a surficial geology mapping program. Over much of the area, bedrock was within 20 m of the ground surface, too shallow to be observed in detail using compressional wave surveys. Here we recorded data from the vertical and transverse (H2) receivers, and again the Minivib was operated in horizontal mode oriented at 45 degrees (midway between in-line and transverse directions).

In this case, though the target depths were relatively shallow, shear wave velocities were found to be considerably higher than observed in the Quebec City survey. Despite being in what were interpreted to be "lacustrine" basin sediments, we observed velocities of 350 m/s near surface, increasing to ~450 m/s within the upper few tens of metres. These velocities suggest that the sediments are more compacted than would be expected in a simple lacustrine environment and there may be extensive fine-grained tills or over-compacted lacustrine sediments in the area. The best shear wave reflection energy was recorded on the transverse receivers (H2).

The seismic sections showed that there was considerable topography on the buried bedrock surface including some significant buried valleys. Figure 4 shows a portion of a final processed shear wave reflection section using data acquired with the transverse (H2) receivers. The section clearly delineates a buried valley which reaches a depth of 40 m below ground surface, and appears to have been eroded after the deposition of the sediments overlying bedrock on either side. The existence of such structures was not known prior to this survey, and such observations are critical in understanding the depositional history of an area and interpreting the surficial geology.

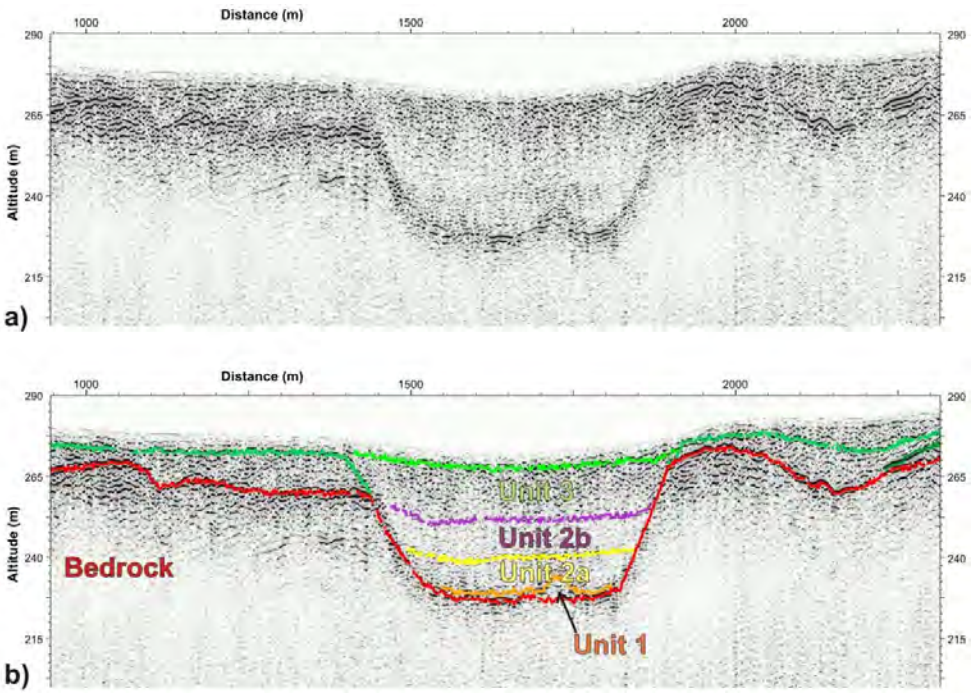

Figure 4: Example of ~1300 m of a shallow shear wave section acquired in the Abitibi area in northern Quebec with the source vibrating horizontally at 45 degrees to the line direction and receivers oriented in the transverse direction (H2). a) processed elevation section, corrected for surface topography; b) interpreted elevation section.

3) Alfred, Eastern Ontario – very high resolution – H1

Shear wave reflection profiles have been obtained in several areas around Ottawa and Eastern Ontario as part of a program aimed at evaluating earthquake hazards related to thick soft soils (e.g. Pugin et al., 2007). The example presented in this paper (Fig. 5) comes from the Alfred area, where earlier compressional wave surveys had identified a deep bedrock basin and disturbed soils (Benjumea et al., 2003). For this survey, we recorded data from the vertical and in-line horizontal (H1) receivers, while the Minivib was operated in horizontal mode oriented in the inline direction (H1).

Figure 5 shows data acquired along a 2.2 km line where Paleozoic bedrock is buried beneath ~30 m of Champlain Sea marine deposits. The upper two panels compare the processed sections from data acquired on the horizontal geophones (Fig. 5a) and the vertical geophones (Fig. 5b). Both sections provide an excellent high-resolution image of the subsurface, but on close inspection the reflections from within the Champlain Sea sequence are observed to be of better quality (higher signal-to-noise ratio and more coherent) when recorded on the vertical geophones (blue ellipses). Thus, despite the source being horizontal (H1), these reflections are more strongly polarized in the vertical direction. However, in the case of the bedrock reflection, the opposite is observed (red ellipses). Here the polarization of the reflected energy appears to be closely aligned with the horizontal. Figure 5c shows the final shear wave reflection section after correction for surface topography and identifies an area of disturbed sediments which are believed to have been caused by pre-historic earthquake shaking (Aylsworth et al., 2000).

Finally, as shown also in Pugin et al. (2009a, see Fig, 6), even though the data were acquired using a horizontal source, a P-wave section can also be obtained from the vertical component data. The P-wave section for this line is shown in Figure 5e, after correction for surface topography and near-surface statics (Fig. 5d). Even though the dominant frequency of the P-wave section is ~150-250 Hz, it is clearly much lower in resolution than the corresponding shear wave sections in this geological environment.

Conclusions

These data show once again that shear wave shallow seismic reflection profiling can produce very high resolution images of the subsurface in many geological environments. This is especially so where unconsolidated sediments consist of “soft soils”, that is sediments characterized by low shear wave velocities. The fine-grained Holocene marine sediments deposited in the St. Lawrence Lowlands by the Champlain Sea are an excellent example of this, with shear wave velocities on the order of 150 m/s. However, similar or comparable results might be expected in a variety of marine, lacustrine or fluvial environments. In such areas, SV profiling can produce extremely high-resolution sections.

We recommend that shear wave reflections are more routinely looked for in seismic data. This does not necessarily require different sources or receivers, but only that longer record lengths are recorded and examined through a broad band of frequencies. The source orientation is not a critical factor, and in fact we no longer routinely use a vertically-oriented source even when we anticipate that we may be depending on P-wave reflections to image the target. To date, we have found that P-waves may be needed to image deeper targets, or those buried beneath relatively thick high-velocity sediments such as coarse-grained deposits or glacial till (Pugin et al., 2009b).

The recording of multi-component data has completely changed our perception of what happens when seismic waves travel through the subsurface. It is now clear that all sources produce the complete spectrum of seismic waves which are then continually modified and reoriented as they travel through the ground. There is no rule about what source or recording orientation will result in the optimum record of

either shear or compressional wave reflections. Multi-component recording is required in order to be able to start to unravel the complexities of ground motion and to provide the best possible image of the subsurface.

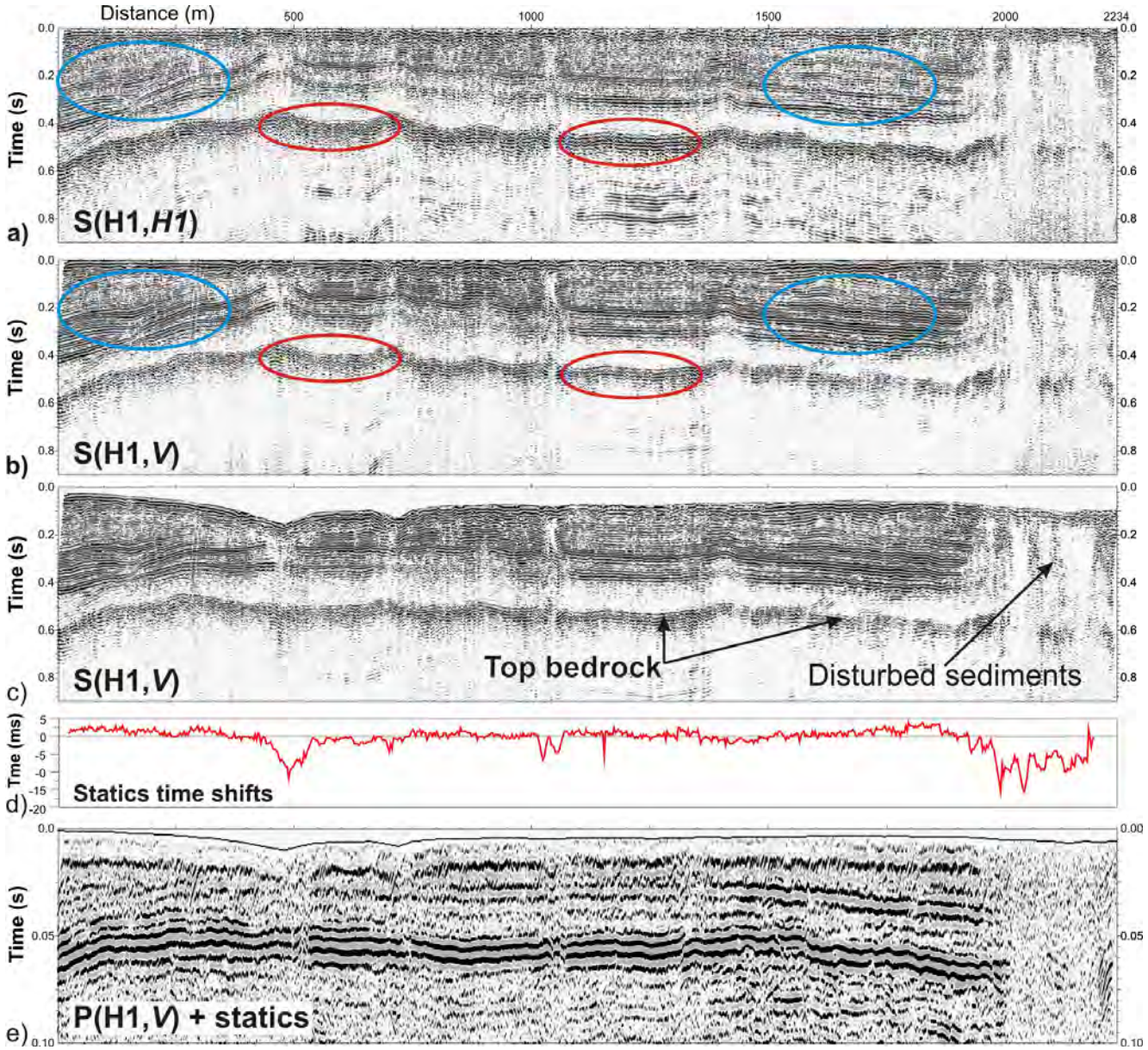

Figure 5: Example of ~2 km shallow seismic data acquired in the Alfred area in eastern Ontario with the source vibrating horizontally in the in-line direction (H1) and two sets of receivers; one vertical (*V*) and one horizontal (*H1*). a) processed shear wave reflection section using data acquired with the horizontal geophones (*H1*); b) same as a) but using data acquired with the vertical geophones (*V*); c) interpreted section b) after correction for surface topography; d) plot of near-surface static time shifts applied to the P-wave data; e) processed compressional (P-) wave reflection section, corrected for surface topography and near-surface statics.

Acknowledgments

The authors gratefully acknowledge the field assistance so capably provided by Robert Burns, Tim Cartwright and Marten Douma. Funding for this work has been provided through the Groundwater Mapping and Reducing Risk from Natural Hazards Programs.

Earth Sciences Sector (Natural Resources Canada) Contribution number 20090392.

References

Aylsworth, J.M., Lawrence, D.E., Guertin, J. 2000. Did two massive earthquakes in the Holocene induce widespread landsliding and near-surface deformation in part of the Ottawa Valley, Canada? Geology, **28**, 903–906.

Benjumea, B., Hunter, J.A., Aylsworth, J.M. and Pullan S.E. 2003. Application of high-resolution seismic techniques in the evaluation of earthquake site response, Ottawa Valley, Canada. Tectonophysics, **368**, 193-209.

Ghose, R., Nijhof, V., Brouwer, J., Matsubara, Y., Kaida, Y. and Takahashi, T. 1998. Shallow to very shallow, high-resolution reflection seismic using a portable vibrator system. Geophysics, **63**, 1295-1309.

Haines, S.S. 2006. Design and application of an electromagnetic vibrator seismic source. J. Environmental and Engineering Geophysics, **11**, 9-15.

Helbig K. and Mesdag C. S. 1982. The potential of shear-wave observations. Geophysical Prospecting, **30**, 413-431.

Inazaki, T. 2004. High resolution reflection surveying at paved areas using S-wave type land streamer. Exploration Geophysics, **35**, 1-6.

Pugin, A.J.M., Larson, T.H., Sargent, S.L., McBride, J.H. and Bexfield, C.E. 2004. Near-surface mapping using SH-wave and P-wave seismic land-streamer data acquisition in Illinois, U.S. Leading Edge (Tulsa, OK), 23(7), 677-682.

Pugin, A.J.-M., Hunter, J.A., Motazedian, D., Brooks, G.R. and Khaheshi-Banab, K. 2007. An application of shear wave reflection landstreamer technology to soil response of earthquake shaking in an urban area, Ottawa, Ontario. In Proceedings, SAGEEP'07 (Symposium on the Application of Geophysics to Engineering and Environmental Problems), Denver, CO, Environmental and Engineering Geophysical Society, 885-896.

Pugin, A. J.-M., Pullan, S.E., and Hunter, J.A. 2008. SV-wave and P-wave high resolution seismic reflection using vertical impacting and vibrating sources. In Proceedings, SAGEEP'08 (Symposium on the Application of Geophysics to Environmental and Engineering Problems) Philadelphia, PA, Environmental and Engineering Geophysical Society, 585-594.

Pugin, A.J.-M., Pullan, S.E. and Hunter, J.A. 2009a. Multicomponent high-resolution seismic reflection profiling. The Leading Edge, 28(10), 1248-1261.

Pugin, A.J.-M., Pullan, S.E., Hunter, J.A., and Oldenborger, G.A. 2009b. Hydrogeological prospecting using P- and S-wave landstreamer seismic reflection methods. Near Surface Geophysics, **7**, 315-327.

Stumpel H., Kahler S., Meissner R. and Milkereit B. 1984. The use of seismic shear waves and compressional waves for lithological problems of shallow sediments. Geophysical Prospecting, **32**, 662-675.

ULTRASONIC VELOCITIES IN LABORATORY-FORMED GAS HYDRATE-BEARING SEDIMENTS

Marisa B. Rydzy, Colorado School of Mines, Golden, CO
Michael L. Batzle, Colorado School of Mines, Golden, CO

Abstract

Gas Hydrates are widely distributed in the near surface at high latitudes and many ocean bottoms. Our laboratory measurements help calibrate the seismic and well log data that are used to ascertain the in situ distribution of hydrates. Ultrasonic velocities are measured in unconsolidated sand specimen under thermobaric conditions comparable to those found in shallow oceanic or permafrost regions, i.e. in the gas hydrate stability zone. Compressional-wave (p-wave) velocity data in *dry* Ottawa Sand samples subjected to a confining pressure that from 2 to 20 MPa range from about 700 to 1500 m/s. Gas hydrates were then formed a partially saturated Ottawa sand sample. As expected, this hydrate formation resulted in a dramatic increase in p-wave velocities from 700 m/s in the partially water saturated sample to 2100 m/s in the hydrate-bearing specimen. The hydrate effectively cements the sand such that nine hours after entering the hydrate stability region, the recorded waveforms remained constant even as the confining pressure was increased by more than 10 MPa.

Introduction

Gas hydrates are crystalline structures where a framework or 'cage' of water contains a guest molecule. In most natural hydrates, methane is contained within the water frame. These materials form and are stable under low temperatures and elevated pressures. The occurrence of natural hydrates is wide spread in arctic regions and in deep water sediments. Interest in hydrates is becoming more intense and they are perceived as a resource; a geohazard; and potential contributor to climate change. Estimates suggest that as a resource, the gas contained in natural hydrates match surpass that in conventional reservoirs. On the other hand, the occurrence of hydrates at or near the ocean floor can destabilize structures such as production platforms. In addition, another concern is that if widespread destabilization of hydrates occurs, substantial amounts of methane will be released, contributing to climate change.

The distribution and quantity of hydrates in place is usually made by a combination of seismic, well log information. However, estimates of the total available hydrates vary enormously depending on how one interprets the hydrate signature in seismic data. For example, Figure 1 shows a seismic section complicated by the presence of both hydrates and free gas. Well logs (Figure 2) pose a similar problem, since the measured response depends on the location and fabric of the hydrate within the sediment. As a result, laboratory measurements are required to calibrate the remote geophysical measurements. Natural gas hydrate-cores are rare, costly, heterogeneous, and almost always show some degree of damage. As an alternative, sediments containing laboratory-formed gas hydrates are often used to provide calibration data for well-logs and seismic. There are a number of different ways to form gas hydrate in sediment, and each

laboratory generally has its preferred technique. (Hyndman & Dallimore, 2001). Gas Hydrate occurrences are indicated by an increase in both sonic velocity and resistivity.

Previous work has shown that the method of hydrate formation tends to control the hydrate distribution within the sample, which impacts the physical properties of the sample. To date, however, no comprehensive testing has been conducted within a single experimental apparatus that would allow a quantitative comparison between the different hydrate formation techniques, and show the differences in the resulting hydrate distributions, as well as how those differences manifest themselves as bulk physical properties. The objective of this project was to construct an apparatus that allows us to investigate the effect on gas hydrate formation method on ultrasonic velocities.

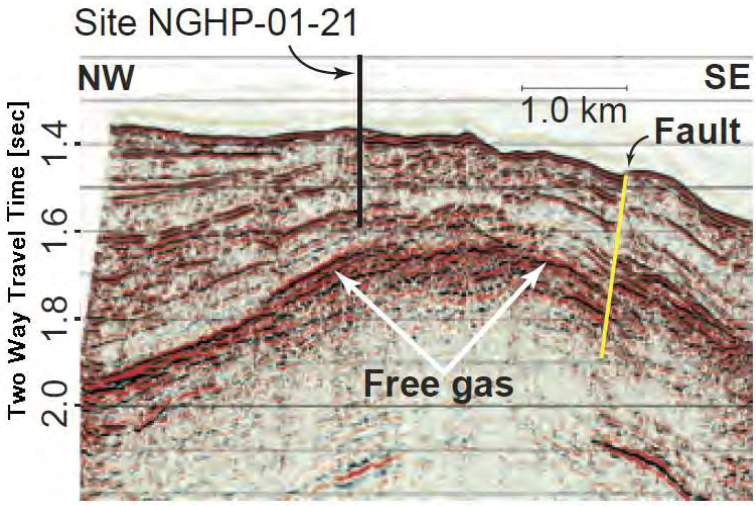

Figure 1: Seismic line crossing drill Site NGHP-01- 21 (*Collett et al.*, 2008). The reflection is complicated due both to the potential presence of hydrate as well as free gas.

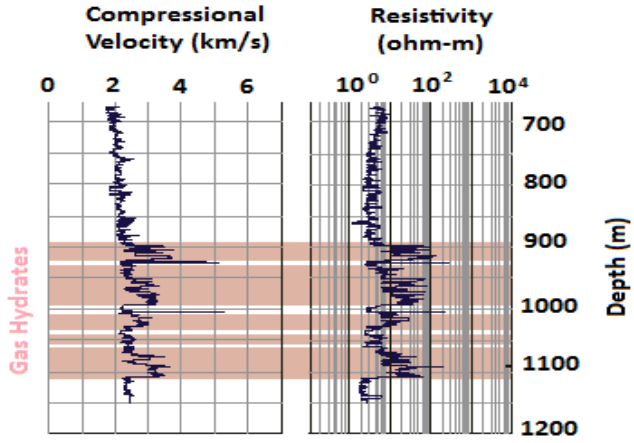

Figure 2: Sonic and Resistivity Log recorded at the JPEX/JNOC/GNC Mallik 2L-38 Gas Hydrate Research Well, Mackenzie Delta, Northwest Territories, Canada (Modified after Hyndman & Dallimore, 2001).

Experimental Configuration

We designed and built an experimental setup that would allow us to measure p-wave velocities in sediments during gas hydrate formation and dissociation under in situ conditions. The setup consists of a temperature-controlled pressure vessel filled with hydraulic oil which confines an instrumented sample holder. A maximum pressure of 20 MPa can be applied to the sample at temperatures between 25ºC and -5ºC. As can be seen in Figure 3, the sample is sandwiched between a pair of cylindrical end caps and is jacketed with flexible Tygon tubing. Ultrasonic transducers made of 100 kHz piezoelectric crystals are mounted on top of the end caps to generate and record the compression wave signal. The end caps have a diameter of (25.40±0.02) mm and are made of polyaryletheretherketone (PEEK). Often, metal end caps are used to hold the ultrasonic transducers. However, Zimmer et al. (2007) showed that the use of plastic transducer plates improves the impedance matching between transducer and sample when unconsolidated sand samples are measured. A high voltage pulse is utilized to excite one transducer and the velocity of the transmitted pulse is calculated by picking first arrivals from the recorded waveforms that are displayed on the oscilloscope. Both end caps also contain ports that enable fluid circulation through the sample and pore-pressure control. The end caps and sand sample are incased in a flexible jacket to isolate the sample from the confining fluid. Thermocouples are placed outside the sample holder to monitor the sample temperature with an accuracy of ±0.5ºC. Furthermore, linear potentiometers are attached to top and bottom end caps to measure changes in length (±0.2 mm) when the sample is subjected to pore and confining pressure. Pressure is controlled by an external ISCO pump with an accuracy of ±1.5 %.

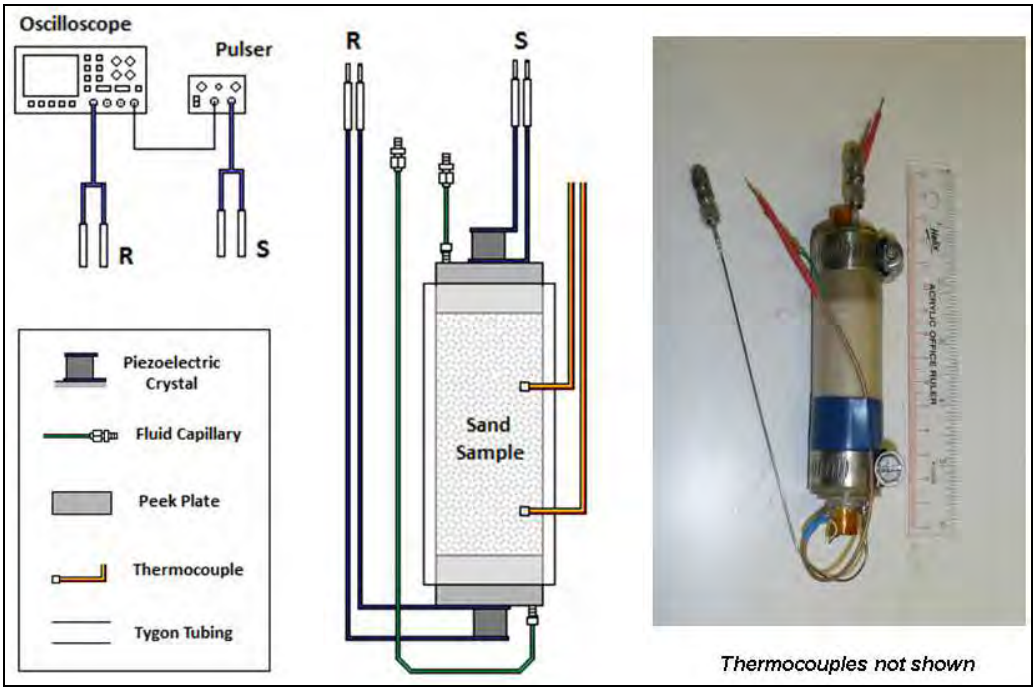

Figure 3: Instrumented Sample Holder Setup

In the current configuration (Figure 4), methane is injected into the sand sample to provide the desired pore pressure. Methane flow is controlled through a gas regulator and is monitored using a pressure transducer with an error of ±0.2%. The insulated vessel is cooled by circulating ethylene glycol from a cooling bath. Sample temperatures and pore pressures are digitized and stored in a computer as a function of time.

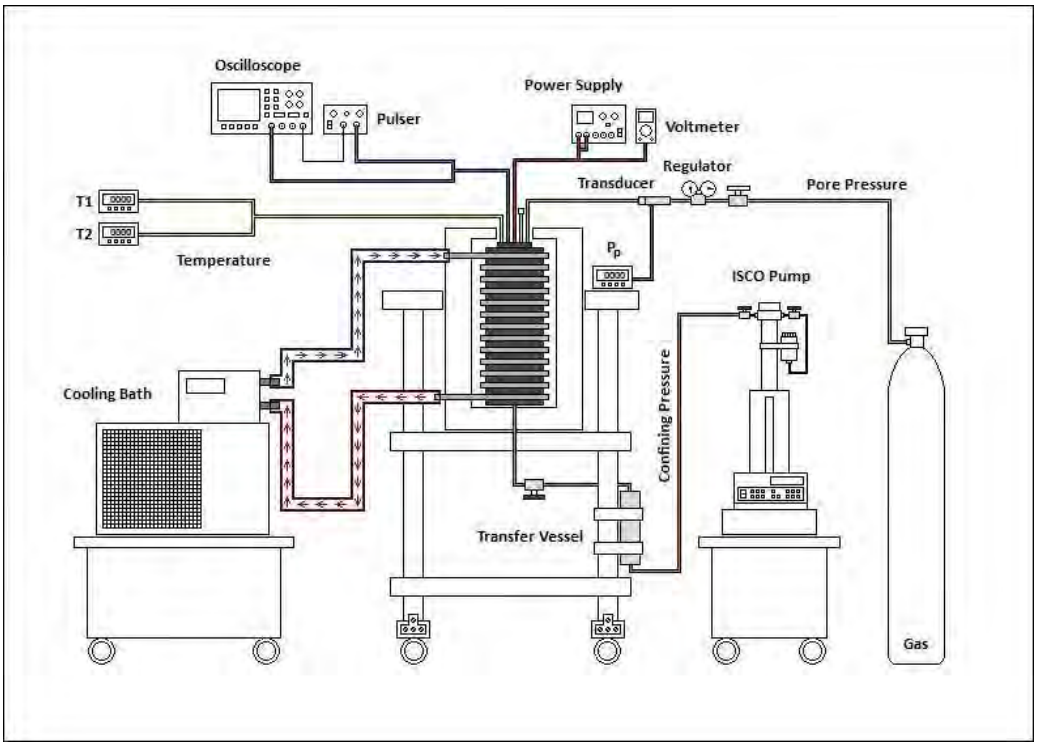

Figure 4: Experimental Setup for Ultrasonic Velocity Measurements on gas hydrate-bearing sediments.

Sample Preparation and Measurements

Dry Ottawa Sand

In an attempt to make measurements from different research facilities comparable, hydrate-researching institutes such as the USGS in Woods Hole, LBNL, GeorgiaTech as well as the CSM Center for Rock Abuse agreed on exclusively using Ottawa Sand Type F110 when forming gas hydrate-bearing specimen in the laboratory. This type of Ottawa Sand is mainly composed of quartz (>99%) and has a density of 2650 kg/m^3. Figure 5 shows micro-X-Ray CT images obtained of dry and partially water-saturated Ottawa Sand F110. Each prepared sand specimen sample is approximately (25.40±0.02) mm in diameter, but have variable length. The length of each specimen was measured with a digital caliper and is given in Table 1. An amount of Ottawa sand was filled into the sample holder, and compacted by hand using a Teflon tamping stick. The porosity of each specimen was calculated from dimensions of each sample, its mass and

the sand density. The prepared samples were placed inside the pressure vessel and subjected to the respective confining pressure while the pore pressure remained at atmospheric conditions. Sample 1 was tested under increasing confining pressure at 1, 2, 3, 4, 5, 10, 15, and 20 MPa, whereas Sample 2 and 4 were first subjected to an initial confining pressure of 20 MPa, which was then decreased incrementally.

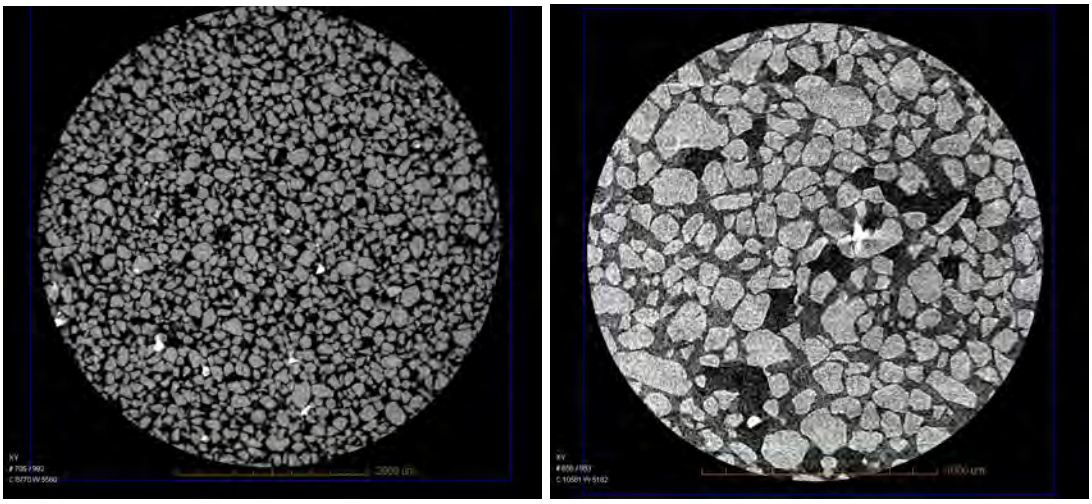

Figure 5: a) dry and b) partially water saturated Ottawa Sand (Micro X-Ray CT)

Table 1: Properties of Sample Preparation and Specimen

Sample	Length (mm)	Mass (g)	$\phi_{initial}$	Layers	Compaction
SMPL_1	69.6± 0.23	54.0± 0.1	0.42	8	60±1 s/layer
SMPL_2	36.3± 0.64	30.0± 0.1	0.39	10	90±1 s/layer
SMPL_4	37.2± 0.27	30.0± 0.1	0.40	10	90±1 s/layer

Methane-Hydrate-Bearing Ottawa Sand

To prepare the partially water-saturated sand sample, 93 wt% Ottawa Sand F110 and 7 wt% distilled water were mixed thoroughly in a plastic bag. The total mass of the sample and its length were measured as (35.74±0.10) g and (42.60±0.08) mm, respectively, which results in an initial porosity of 42% and an initial water saturation (fraction of pore space occupied with water) of about 27.5 %. After the sample assembly was placed inside the pressure vessel, the temperature of the system is lowered employing the external cooling system. It takes about 48 hours to cool the heavy, oil-filled steel vessel down to the designated temperatures of about 2.5- 3.0 ºC. After the temperature stabilized, a confining pressure of 3 MPa was applied to the sample. Afterward the methane was injected into the sample and the pore pressure is raised to 1 MPa below the confining pressure. Then, both confining and pore pressure were increased by 1 MPa and held constant for about an hour to allow injection of methane

gas. The pore pressure at that point was just below the methane hydrate equilibrium pressure, which at 2.5 ºC has a value of about 3.3 MPa (Figure 6). Once the sample temperature returned to its designated value, confining and pore pressure are further increased to 10 MPa and 7.5 MPa, respectively, and held constant. Ultrasonic waveforms are recorded every hour until the no more obvious changes in the waveforms occur. The confining pressure is then increased to about 20 MPa, after that incrementally decreased, and waveforms are recorded after every increment of 1 MPa.

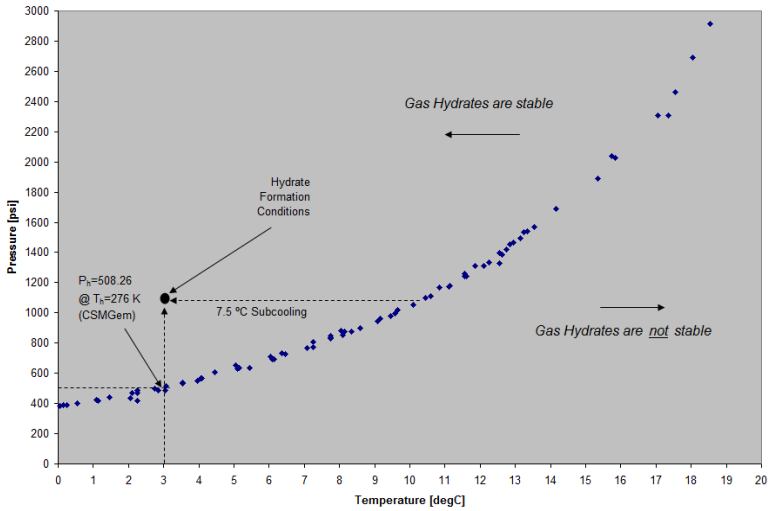

Figure 6: Phase diagram for methane hydrate (modified after Sloan & Koh, 2008)

Results

Dry Ottawa Sand

Figure 7 shows typical waveforms obtained for the dry Ottawa Sand samples measured under confining pressure. The p-wave velocities were calculated by picking first arrivals from the recorded pulse-transmission signals and are listed in Table 2. Figure 8 shows our measured p-wave velocities as a function of confining pressure alongside literature values. All data points depicted were collected for Ottawa Sand samples of similar initial porosities. Differences are small, and the variations among the results may be attributed to differences in sediment properties (grain size distribution, composition) or experimental settings (measurement frequency, etc.).

Methane-Hydrate-Bearing Ottawa Sand

Methane development is time-dependent, and waveforms change as a function of time. After about 25 minutes after the gas hydrate stability curve was surpassed noticeable changes occur in the waveform. Formation of hydrate results in a decrease in traveltime (increase in velocity) that is quite significant. Figure 9 shows the p-wave velocity increase with time and, most probably, with increasing gas hydrate saturation. The hydrate growth appears to stop after about 9 hours, which might indicate that either all the water was converted into hydrate or that the hydrate growth blocked all the pores near the gas inlet making the sample impermeable and, thus, preventing further hydrate

formation. The latter explanation seems more likely as hydrate-plugging in sediment cores is an often observed in other laboratories that produce hydrate-bearing sediments (Erik Spangenberg, Bill Waite, personal conversations). As can be seen in Figure 10, as an additional confining pressure of 10 MPa is applied to further compress the sample, no change can be observed in the waveforms. This behavior is also reflected in the minimal changes in sample length recorded as a function of pressure (Figure 11).

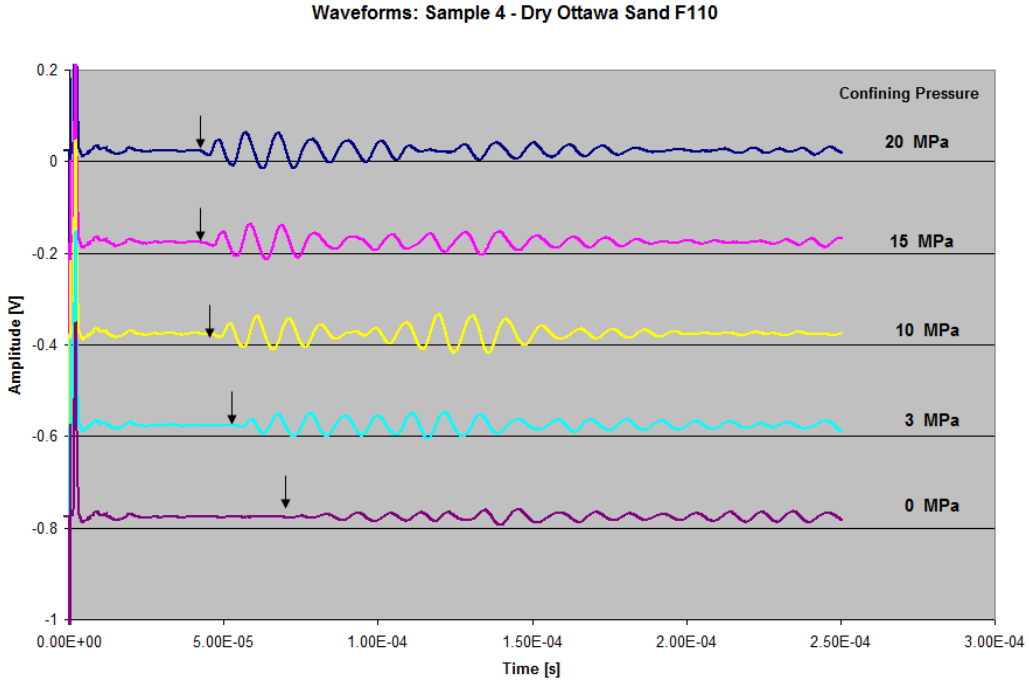

Figure 7: Typical waveforms recorded for Ottawa Sand under confining pressure

Table 2: Velocities calculated for Samples 1, 2, and 4

Sample 1		Sample 2		Sample 4			
P [MPa]	V_p [m/s]	P [MPa]	V_p [m/s]	P [MPa]	V_p [m/s]	P [MPa]	V_p [m/s]
2	729	20	1578	20	1532	10	1283
3	871	10	1417	19	1526	9	1248
4	871	15	1277	18	1514	8	1236
5	1016	4	1037	17	1483	7	1192
10	1241	3	989	14	1399	6	1181
15	1467	1	776	13	1343	3	978
20	1540	0	714	11	1305	1	724

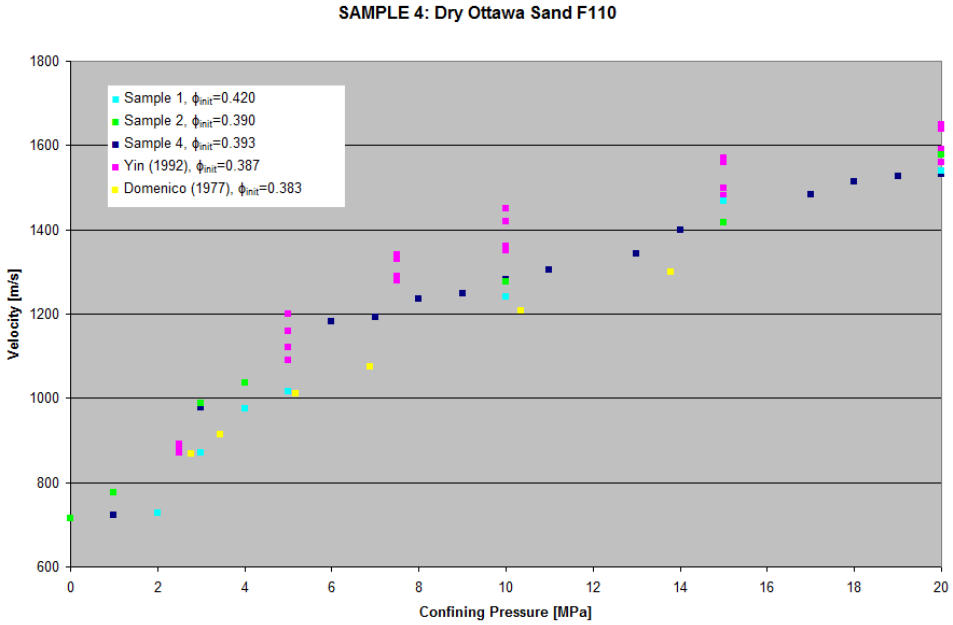

Figure 8: P-wave velocity in Ottawa sand versus confining pressure

This indicates that the sample might entirely be cemented with methane hydrate and can not undergo any further change in length under the confining pressures applied. After the measurements were completed, the sample was quickly recovered from the pressure vessel and sample holder. Because of the fine grain size gas hydrates could not be observed visually, but audible fizzing indicated the presence of dissociating gas hydrate in the sediment. Also, when part of the sand was submersed into water, gas bubbles emerged from the sand, which collapsed soon after as the hydrate fully decomposed.

Conclusions

Ultrasonic velocity measurements were performed on dry and hydrate-bearing sand using our newly constructed experimental setup. The results obtained for the dry Ottawa sand samples agree with data found in literature. Methane hydrate-bearing sediment was successfully generated by pressurizing partially water-saturated Ottawa sand. The data collected during the hydrate-formation process exhibits a logarithmic increase in p-wave velocity with time. Approximately nine hours after an increase in velocity was first observed, the waveforms remained unchanged indicating that hydrate formation stopped. Whether this behavior is due to full hydrate conversion or hydrate blocking gas pathways within the sand can not be answered with certainty. Planned Micro-CT measurements will help to interpret how gas hydrate content and distribution relate to p-wave velocities. In the next phase of the project, further ultrasonic compressional- and shear-wave measurement on gas hydrate-bearing sediments will be made. We will measure a series of hydrated Ottawa sand samples that will be formed using different hydrate formation techniques, e.g. bubbling gas through fully water-saturated samples, using tetrahydrofuran (THF).

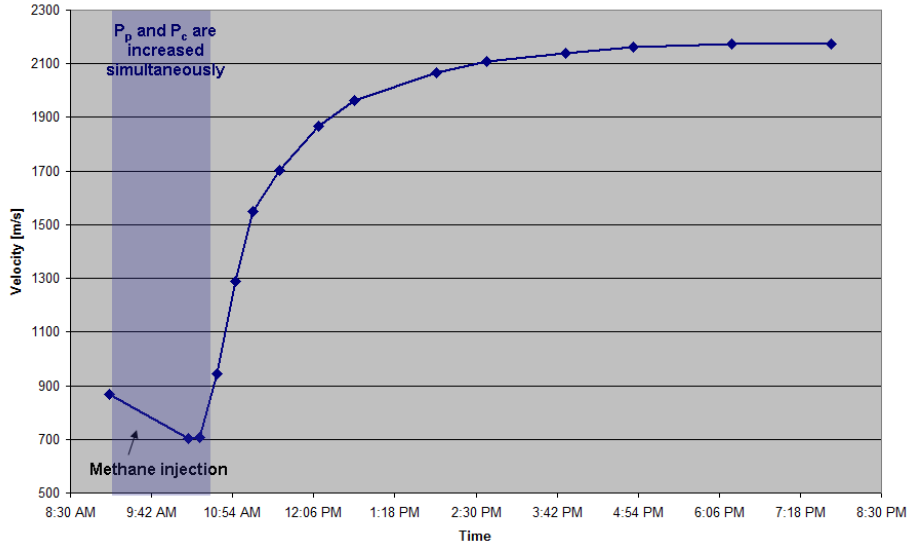

Figure 9: Gas hydrate formation: p-wave velocities versus time

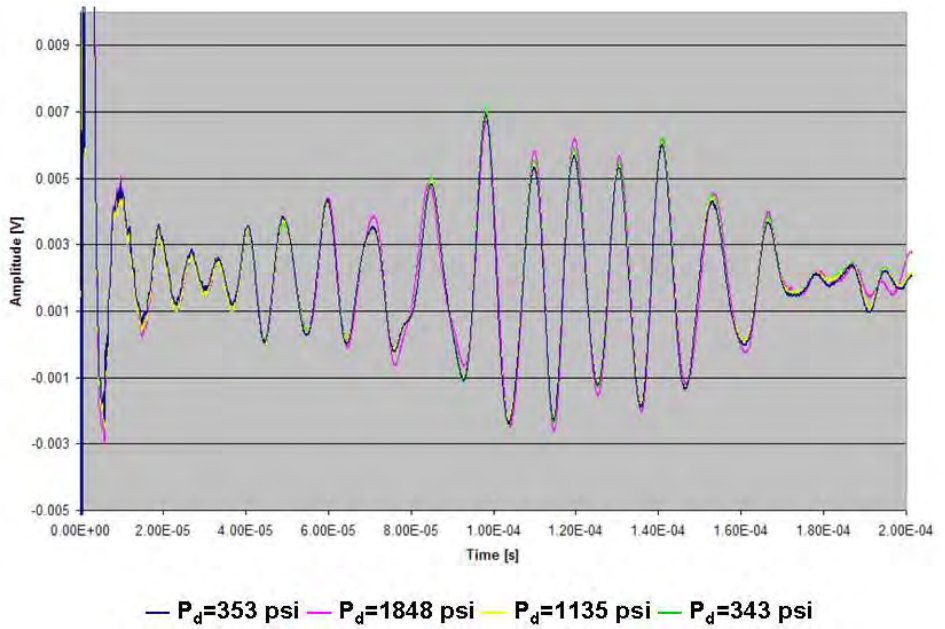

Figure 10: Pressure independence of p-wave velocities in hydrate-cemented sand

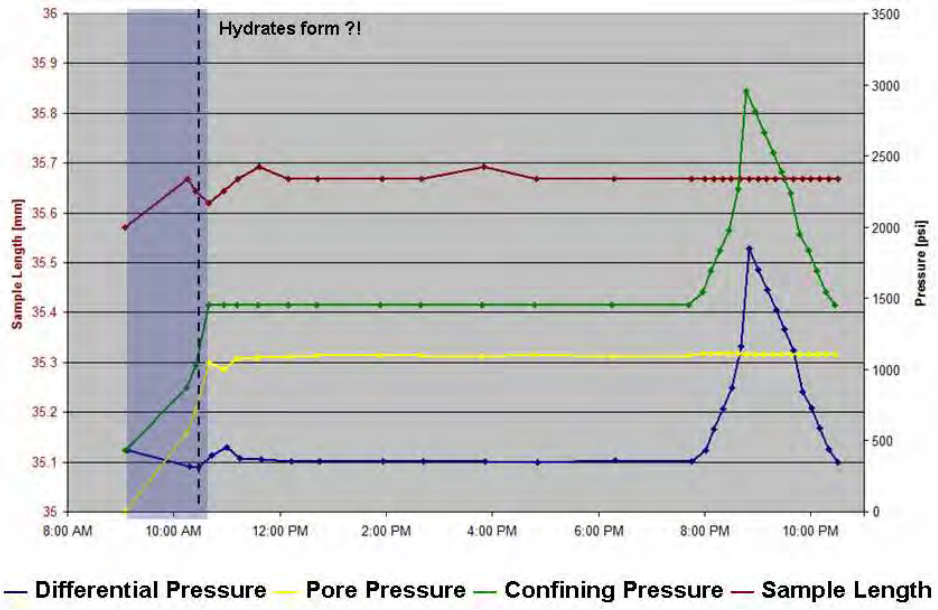

Figure 11: Sample length and pressures during the duration of the experiment

References

Collett, T., M. Reidel, J. Cochran, R. Boswell, J. Presley, P. Kumar, A. Sathe, A. Sethi, M. Lall, V. Sibal, and the NGHP Expedition 01 Scientists (2008), Indian national gas hydrate program expedition 01 initial reports: Expedition 01 of the Indian National Gas Hydrate Program from Mumbai, India to Chennai, India; Sites NGHP-01-01through NGHP-01-21, April 2006 - August 2006, Directorate General of Hydrocarbons, Ministry of Petroleum and Natural Gas (India), Noida, India.

Hyndman, R.D., and Dallimore, S.R. (2001), Natural Gas Hydrate Studies in Canada, the Recorder **26**, 11-20, Canadian Society of Exploration Geophysicists

Domenico, S.N., 1977, Elastic properties of unconsolidated porous sand reservoirs: Geophysics, **42**, 1339–1368

Yin, H., 1992, Acoustic velocity and attenuation of rocks: Isotropy, intrinsic anisotropy, and stress induced anisotropy: Ph.D. dissertation, Stanford University.

Zimmer, M.A., M. Prasad, G. Mavkov, and A. Nur (2007), Seismic velocities of unconsolidated sand: Part 1 – Pressure trends from 0.1 to 20 MPa, Geophysics **72**, 1-13

Sloan, E.D., and C.A. Koh (2008), Clathrate Hydrates of Natural Gases, 3rd Edition, CRC Press, Boca Raton

PHASE-SCANNING APPROACH TO CORRECT STATIC ERROR IN THE SURFACE WAVE WALK-AWAY METHOD

Edwin A. Obando, Department of Engineering Geology, Lund university, Sweden
Choon B. Park, Park Seismic LLC, Shelton, Connecticut, USA
Nils Ryden, Department of Engineering Geology, Lund university, Sweden
Peter Ulriksen, Department of Engineering Geology, Lund university, Sweden

Abstract

Synthesized surface wave records obtained from walk-away surveys normally suffer from time shift inaccuracies due to the abrupt variation in the soil stiffness characteristics which is regarded as static error effect. In this paper we present a method that uses a phase scanning procedure in frequency domain which applies the correction in a phase range from 0 to 2π aimed at alleviating the adverse effect of static error in the dispersion image. At each frequency the method searches for the optimum phase correction resulting in the highest maximum summed amplitude value along the offset range. The maximum summed amplitude-phase velocity curves are selected for all scanning frequencies and then used to construct a corrected dispersion image. Results show that the proposed phase scanning method reduces the distortions caused in the computed dispersion images efficiently and also account for the disturbances introduced by ambient noise.

Introduction

The Multichannel Analysis of Surface Waves (MASW) method is nowadays one of the most popular surface wave methods in a number of engineering problems. The wide number of applications of the MASW method (Park et al., 1999) includes, bedrock mapping (Miller et al., 1999), Poisson's ratio evaluation (Ivanov et al., 2000), pavement structures analysis (Ryden et al., 2004), soil liquefaction potential (Lin and Lin, 2004) and shear wave velocity profiling for site response evaluation (Foti, 2008; Anbazhagan et al., 2009; Mahajan, 2009). Particularly, in near-surface ground characterization, the conventional active MASW approach provides accurate information of the stiffness properties of the soil material in the site in terms of shear-wave velocity. Nonetheless its major drawback is the limited depth of penetration, normally less than 30 meters, which usually originates from low energy at low frequencies and the limited length of the receiver spread. An alternative to enhance longer wavelengths to increase the depth of penetration with high lateral resolution is by means of the walk-away scheme (Sheriff and Geldart, 1992). However, in sites where abrupt severe horizontal variation of soil stiffness occurs, synthesized records obtained from the walk-away method are sensibly affected by time shift inaccuracies, regarded as static error effect (Lin and Lin, 2007). The occurrence of static error manifests as a time shift which can be easily observed in the surface wave portion of the synthesized record illustrated in Figure 1a (two set of shot gathers of 21 traces and 24 traces, respectively). Thus, the time shift occurs between the last trace of the preceding shot gather (trace 21) and the first trace of the subsequent shot gather (trace 22) which adversely affects the dispersion image by introducing, for example, false higher modes or a poor definition of the prominent energy trend, misleading the correct interpretation of the dispersion curve. On the other hand, in the same record (Figure 1b) which has been band-pass filtered to enhance the body wave portion, the first arriving P-wave appears to be almost

unaffected by the static error. This result indicates that body-waves are less sensitive to the effect from static errors.

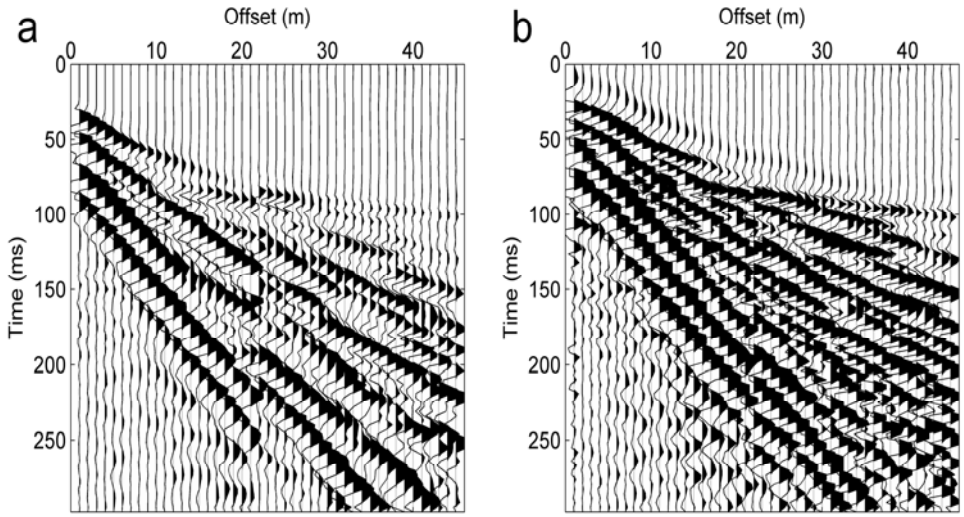

Figure 1: a) Ordinary walk-away record with static error in the surface wave portion, b) Filtered version of record in Figure 1a to enhance body-waves trend (P-waves).

In order to minimize the adverse effect of the static error in the dispersion image, in this paper, we propose a method that uses a phase scanning scheme correction in the frequency domain. The method is basically an improved version of the phase-seaming approach originally used for correcting the effect of heterogeneities of the soil material in the dispersion images (Lin and Lin 2007). The proposed method uses different possible phase shift values to minimize the amount of phase shift existing in the walk-away record in a phase range from 0 to 2π. This phase scanning procedure is performed with a very small interval to search for the optimum summed amplitude curve (Ryden et al., 2004). Then, the optimum summed amplitude curves are picked amongst the peak-values of all the summed amplitude curves calculated within the 0 to 2π range at each frequency. The final corrected dispersion image is constructed by using the optimum summed amplitude curves where the static error has been minimized.

Corrected vs. Uncorrected Dispersion Images

As previously discussed the occurrence of static error and the presence of ambient noise are the most adverse factors in the walk-away method. To test the effectiveness of the correction scheme proposed we use four sets of 24-trace shot gathers each with one trace overlapping with noticeable static error (Figure 2) occurring between traces 24-25, 47-48, and 70-71. Traces from dead geophones are also present. The correction of the dispersion images was carried out using a scanning interval of 4% of π within a phase range of [0 2π].

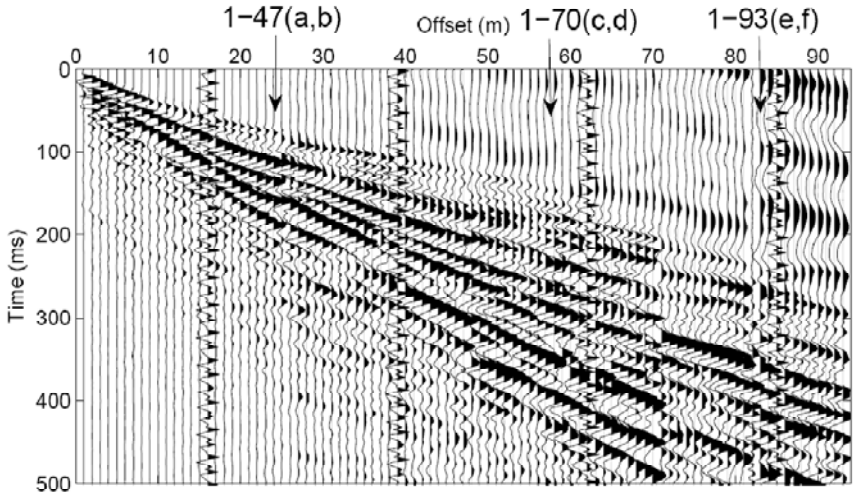

Figure 2: Collected field walk-away record using 4 sets of 24-traces (overlapping traces are omitted).

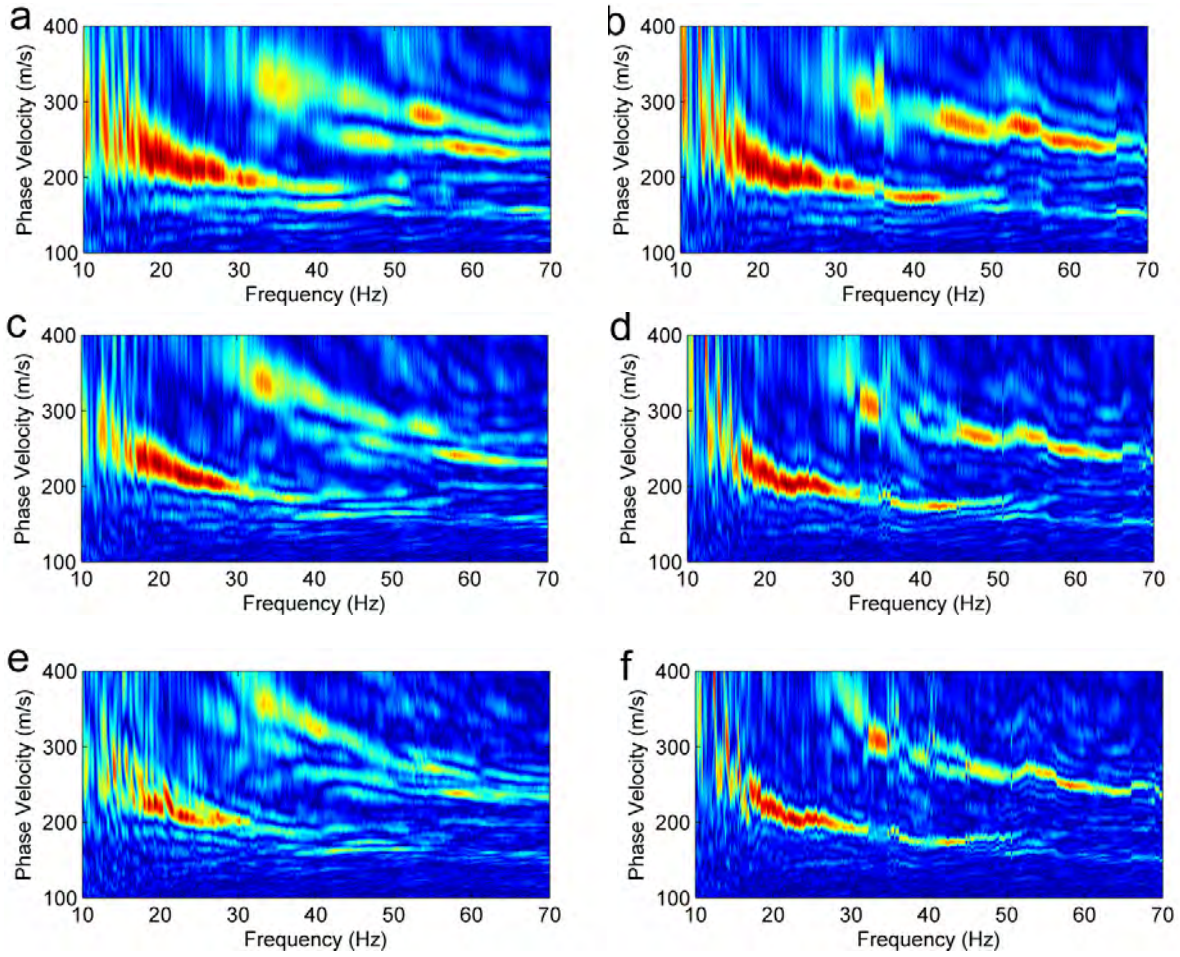

Figure 3: Uncorrected (a, c, and e) and corrected (b, d, and f) dispersion images.

As shown in Figure 3 the phase scanning method improves the distorted dispersion trends notably, even with traces at the farthest source-to-receiver distances where the effect of ambient noise is likely to occur. The correction is first made for the first 47 traces (1-47) where surface-wave energy generated by the sledgehammer prevails over ambient traffic noise. In Figure 3b, the corrected dispersion image depicts two well defined dispersion modes compared to the normal uncorrected image (Figure 3a). The same correction scheme was also applied to the dispersion images computed for 1-70 and 1-93 receivers where the ambient noise tends to introduce higher distortion compared to the case of 47 traces. Therefore, in Figures 3d and 3f the corrected images successfully restore both dispersion trends observed in Figures 3c and 3e that are obscured not only by the presence of the static error, but also due to the effect of ambient noise.

Conclusions

This study intends to provide an efficient alternative to compensate the deficiencies in the walk-away method from the data processing perspective. This method is somehow an improved version of the existing phase-seaming approach and its major advantage is that the effect of ambient noise is taken into account. The results presented in this paper using real world records show that after applying the phase-scanning scheme the most prominent energy trends are notably improved compared to the normal computed dispersion images. Therefore, this approach represents an opportunity for mapping the soil stiffness with high lateral resolution even in cases where there is a limited number of receivers available and in that way to increase the depth of exploration with a minimum risk of static error effect.

References

Anbazhagan, P, Sitharam, T.G, Vipin, K.S., 2009, Site classification and estimation of surface level seismic hazard using geophysical data and probabilistic approach: Journal of Applied Geophysics, 68, 219–230.

Foti, S., Comina, C., Boiero, D., and Socco, L.V., 2008, Consequences of solution non-uniqueness in surface wave tests for seismic response studies: Geotechnical Special Publication (181).

Ivanov, J., Park, C.B., Miller, R.D., and Xia, J., 2000, Mapping Poisson´s ratio of uncosolidated materials from a joint analysis of surface-wave and refraction events: Proceedings of the Symposium on the Application of Geophysics to Engineering and Environmental Problems (SAGEEP 2000), Arlington, Va., February 20-24, p. 11-19.

Lin, C.P. and Lin, C.H., 2007, Effect of lateral heterogeneity on surface wave testing: Numerical simulations and a countermeasure: Soil Dynamics and Earthquake Engineering, 27(6), 541-552.

Lin, C.P. and Lin, C.H., 2004, The use of MASW method in the assessment of soil liquefaction potential: Soil Dynamics and Earthquake Engineering, 24 (9-10), 689-698.

Mahajan, A.K., 2009, NEHRP soil classification and estimation of 1-D site effect of Dehradun fan deposits using shear wave velocity: Engineering Geology, 104, 232–240.

Miller, R.D., Xia, J., Park, C.B., and Ivanov, J., 1999, Multichannel analysis of surface waves to map bedrock: The Leading Edge (TLE), 18, 1392-1396.

Park, C.B., Miller, R.D. and Xia, J., 1999, Multichannel analysis of surface waves: Geophysics, 64, 800–808.

Ryden, N., Lowe, M.J. S., 2004, Guided wave propagation in three-layer pavement structures: Journal of the Acoustical Society of America, 116 (5), 2902-2913.

Ryden, N., Park, C. B., Ulriksen, P., and Miller, R. D., 2004, Multimodal approach to seismic pavement testing: Journal of Geotechnical and Geoenvironmental Engineering, 130 (6), 636-645.
Sheriff, R. E. and Geldart, L. P., 1982, Exploration seismology (vol 1); history, theory, and data acquisition, Cambridge University Press, 253 pp

SEISMIC INVESTIGATION OF UNDERGROUND COAL FIRES; A FEASIBILITY STUDY AT THE SOUTHERN UTE NATION COAL FIRE SITE, DURANGO, COLORADO

Sjoerd de Ridder, Department of Geophysics, Stanford University.
Nigel Crook, Department of Geophysics, Stanford University.
Seth S. Haines, U.S. Geological Survey.
S. Taku Ide, Department of Energy Resources Engineering, Stanford University.

Abstract

We conducted a near surface seismic test at a coal fire in the Southern Ute Nation near Durango, Colorado. The goal was to characterize and image the unburned coal and adjacent burned zone in order to determine the feasibility of any future seismic surveys. The field survey was preceded by a numerical study to optimize the survey design for the field test.

The numerical study suggested that field experiments would rely on creating energy with sufficiently high frequencies, ideally greater than 125 Hz. Reflections or refractions from the top of the coal layer might indicate its presence or absence. Separately imaging of both the top and bottom of the coal layer or burned zone likely would be beyond the resolution of a reflection survey.

Data from line 1, which overlies unburned coal at approximately 16 m depth, show useful frequency content above 100 Hz and a reflection that we interpret to originate at approximately 11 m depth. Data from line 2, which crosses the burn front and many fissures, are of lower quality with predominantly jumbled arrivals and some evidence of reflected energy at one or two shot points. It seems that neither the refraction nor reflection method is capable of imaging down to the coal layer; due in part to the presence of unexpected high-velocity layers overlying the coal.

We conclude that information about the coal is obscured by a reflection from shallower layers and by chaotic arrivals generated by fissures. Based on our data, we suggest that further seismic work at the site is unlikely to successfully characterize the coal fire zone of interest.

Introduction

In March 2009 personnel from Stanford University, the U.S. Geological Survey and the Southern Ute Department of Energy collected compression (P) wave near-surface seismic data along two transects at the site of a coal fire on Southern Ute Nation lands. The objective of this effort was to image and characterize the coal and ash layers of interest at the site, and to determine the feasibility of any future seismic surveys. The field survey was preceded by a numerical model in a simple geometry based on an estimate of the subsurface.

The field site, located near Durango in southwestern Colorado, is generally open terrain with a gently dipping (10°) ground surface. The shallowest geology consists of sandstone (highly fractured and fissured in many places). Throughout most of the site, the sandstone is overlain by a thin layer of soil, about .5 m. Well data shows the coal layer to be about 8 m thick and to be dipping in the same direction as the ground surface, at a slightly higher angle (20°). Figure 1 contains a log recorded in a well near the seismic survey locations. The top of the (partially burned) coal layer is approximately 5 m deep at the up-slope (up-dip) edge of the site (to the northwest) and up to 16 m deep in the down-slope part of the

site. Open fissures with visible red-hot rock .5 m below the ground surface and noxious gasses from vents, indicate the presence of a shallow fire.

Numerical seismic simulations, performed prior to the site visit, indicate that imaging the unburned coal would be possible using a high-frequency source, provided interference from fissures and shallow stratigraphy are minimal. A short site visit enabled the collection of a simple data set. We performed basic data processing to assess data quality and identify arrivals. For line 1, located above unburned coal, where no fissures where identified at the surface, data quality is good and reflections interpreted to be from the sandstone layer that overlies the coal are visible. For line 2, positioned across the burn front where numerous fissures were identified at the surface, data quality is lower. Simple velocity analysis indicates that neither refractions nor reflections image provide useful information from the depth of the coal layer. Previously unknown high-velocity layers and a strong reflector above the coal hinder characterization of the coal fire zone of interest.

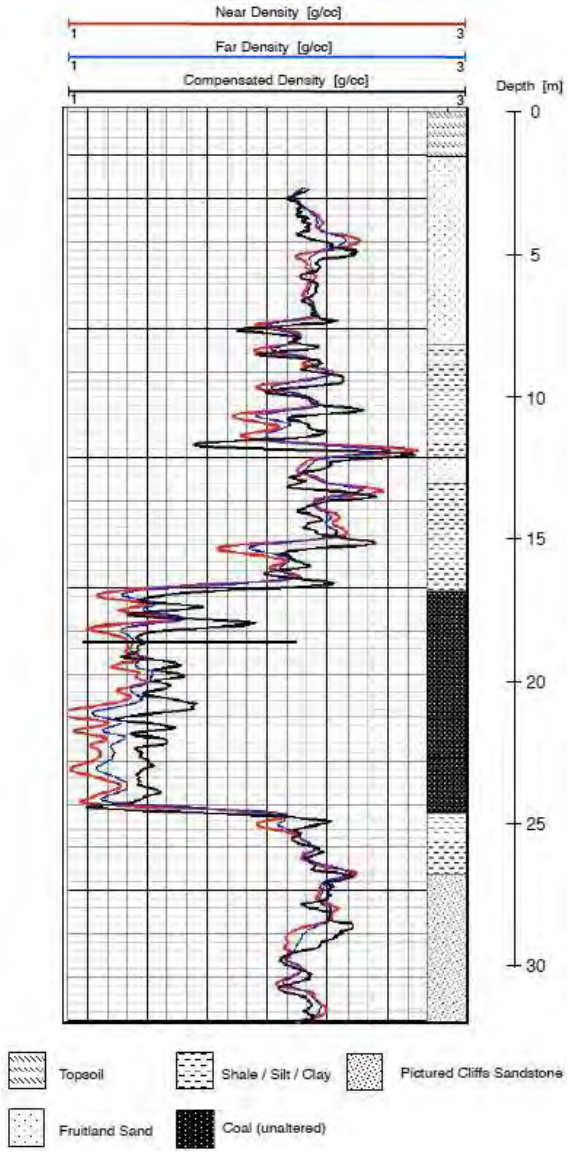

Figure 1: Well log and lithology at well #3. A 8-m-thick coal layer is situated at approximately 16 m depth.

Pre-Fieldwork Numerical Model

Synthetic Model

A model was designed prior to the site visit, based on a geological description of the site. The model consists of a homogeneous background with a gentle vertical velocity gradient overlain by a 10°-dipping structure that represents the coal layer (Figure 2). The burn front was estimated to be about 20 m deep. Sandstone velocity was estimated as 2000 m/s with a gentle vertical gradient of 0.154 s-1 (Table 1). Coal and ash velocities are rough estimates, as 1200 m/s and 300 m/s respectively. Ash velocity was set very low, but greater than zero to avoid numerical instability. Complicated geology such as fissures and voids in the ash layer were neglected; this is a major simplification of the real-life complexity expected in coal fire areas (e.g., Wolf, 2006) and that needs to be considered when interpreting the modeling results.

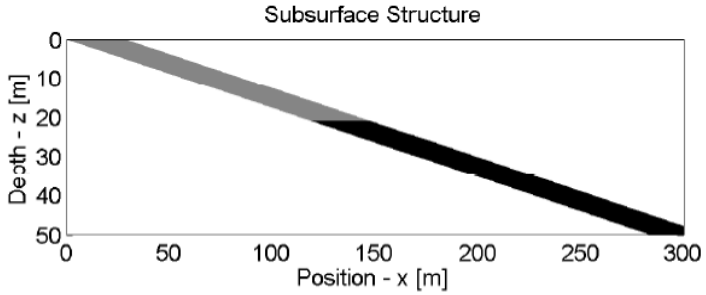

Figure 2: Velocity model for numerical simulation; a dipping, partially burned (grey) coal (black) layer in a sandstone (white) background. P and S wave velocities are given in Table 1.

Table 1: Seismic P and S wave velocities and velocity gradients.

Unit	V_p *(m/s)*	$\partial_z V_p$ (s^{-1})	V_s *(m/s)*	$\partial_z V_s$ (s^{-1})
Sandstone	2000	0.2	1200	0.154
Coal	1200	0.0	800	0.0
Ash	300	0.0	200	0.0

We synthesized a seismic survey across the model with shots and receivers at 1-m spacing, using the code e3d that is described by Larsen and Grieger (1998) and Martin (2006). The source was a vertical force with the waveform of a 125-Hz Ricker wavelet that is intended to simulate a better-than-average sledgehammer impact (e.g., Miller et al., 1992 and 1994). The receivers record both vertical, Vz, and horizontal, Vx, (in-plane) components of particle velocity.

Model Results

For interpretation we focused on the vertical (PP) component because we anticipated that compression (P) wave methods would perform better in a complex overburden than shear (S) waves. Figure 3 shows a pair of shot gathers for a shot at position 150 m, directly over the end of the burn front. The reflection arriving at 0.03 s at zero offset is the reflection from the top of the coal seam. There is no clear refraction observed in the vertical component; we know that even for our idealized velocity model it would be weak. From these models, we expected that in a field experiment we may be able to discern a reflection from the top of the coal bed. In addition, we expected changes across the burn front, such as diffractions, that could allow for delineating the burned zone. However any strong un-modeled heterogeneity would make imaging much more difficult. Separately imaging the top and bottom of the coal would require frequencies at least as high as those used in the model, preferably higher.

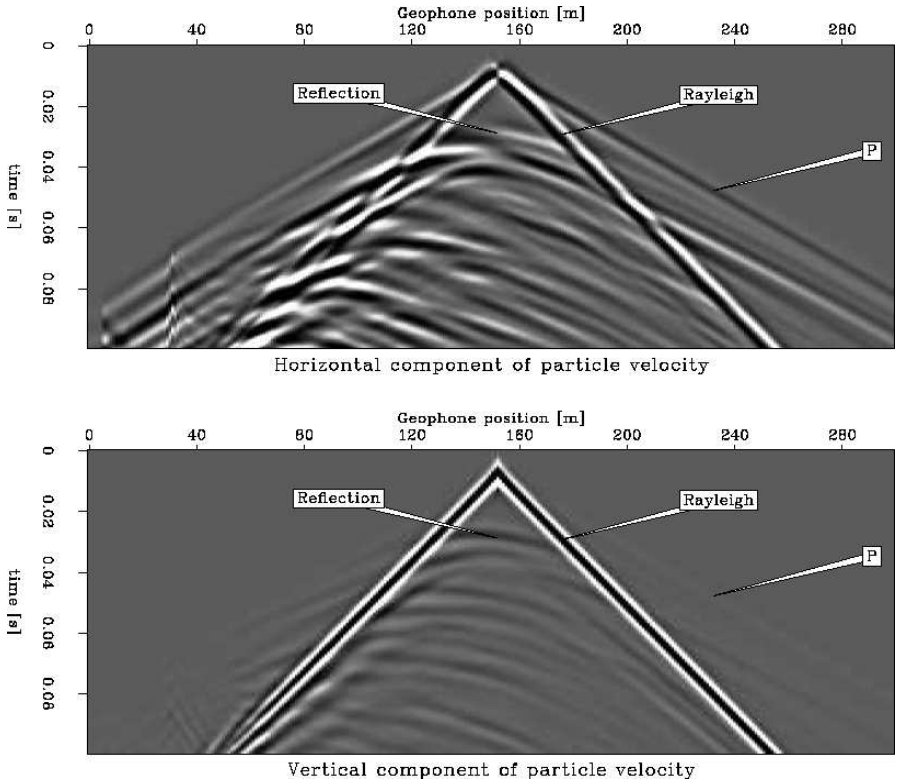

Figure 3: Shot gathers for a shot at 150 m. At t=0.03 s we see the reflection from the top of the coal layer.

Seismic Tests at the Southern Ute Nation Coal Fire Site

Data Collection

We collected P-wave seismic data along two transects using conventional hammer-plate seismic techniques. The recording arrays consisted of a Geometrics Geode with 24 live channels and 30 Hz vertical geophones at 3-m spacing. In order to create shot gathers with a greater number of traces at a narrower spacing, four shots were closely-spaced at each shot location. By placing these shots at a 0.75-m spacing, and then interleaving the resulting four 24-channel shot gathers, a 96-channel array was simulated, illustrated schematically in Figure 4 (left). This variation on normal "walk-away" testing is commonly used for acquiring data at a new field site; the interleaving technique assumes that geology does not vary too strongly along the transect.

Two survey lines were selected, one parallel with the geological dip and surface fissures, and one transverse to the geological dip and surface fissures, see Figure 4 (right). Only five to six shot locations were selected along each line, to reduce the acquisition time. The shot locations are evenly distributed along the line, with one shot point off the end of each line to observe longer-offset arrivals. Figures 5-7 show three gathers along lines 1 and 2. For each location a raw recording is shown together with a version that has been processed with automatic gain control (AGC, with a 37.5 ms window) and a band pass filter (80 Hz to 500 Hz). Each shown shot gather is the result of stacking approximately 5 hammer impacts, after manual data checking for trigger errors and other problems. For most data in this survey, the noise reduction benefits of stacking are minimal; repeatability for each individual hammer impact is very high.

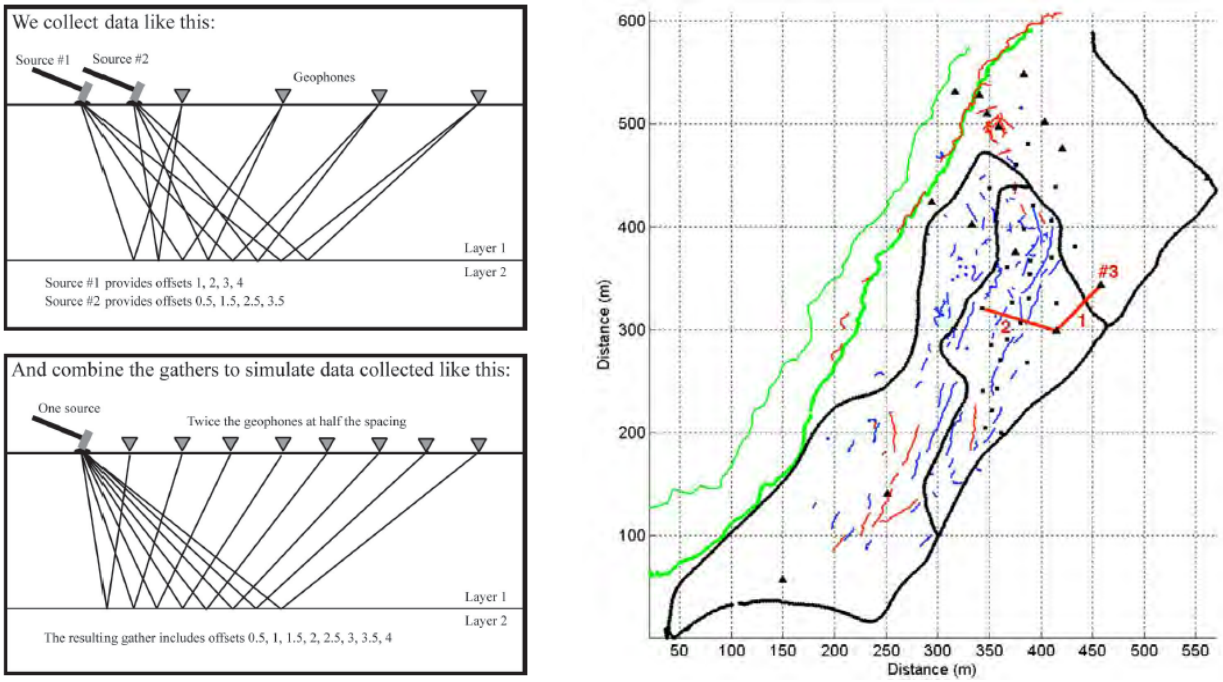

Figure 4: (left) Sketch of the interleaving approach. With Y geophones, at a spacing of X, and using N shots at a spacing of X/N, the interleave technique results in shot gathers with N x Y traces and a spacing of X/N. (right) Site map, showing mapped fissures as thin blue (cold fissures) and red (warm fissures) lines. The thick red lines show the seismic transects. Green lines denote the location of up-dip exposure of coal strata (edge of hill). Black triangles and squares denote well and probe locations, respectively. Thick black lines show road/path locations. Logs for well #3 are shown in Figure 1.

Spectral Analysis

Averaged, normalized frequency spectra of data recorded at lines 1 and 2 are shown in Figure 8 (left). The frequency content of our sledgehammer source is good, with energy above 100 Hz. The frequency wave-number spectrum in Figure 8 (right) shows significant high wave number noise. This is in part due to the interleaving technique. The energy associated with reflections, refractions and surface waves is concentrated below wave-numbers of 0.15 m-1 and frequencies below 25 Hz, leaving little opportunity to filter the refractions and surface waves from the reflection.

Velocity Analysis

In two of the better quality shot gathers (Figures 5 and 6) four different events can be distinguished: 2 refracted wave events, a direct P wave arrival, and a reflected wave arrival. These are annotated on the plot in Figure 9. At small offsets we see very slow and dispersive ground roll, annotated G. A weaker event (R_2) is barely visible in Figure 6 and Figure 9; it may be a second, deeper, reflection partially hidden behind the interpreted reflection R_1.

The slopes of the first arrivals indicate three velocities: v1 = 480 m/s, v2 = 1400 m/s and v3 = 3000 m/s. These are relatively consistent for both gathers. The intersection times in Figure 9 (left) indicate two layer thicknesses of h0 = 1.2 m and h1 = 5.8 m. The intersection times in Figure 9 (right) indicate two layer thicknesses of h0 = 0.9 m and h1 = 9.1 m.

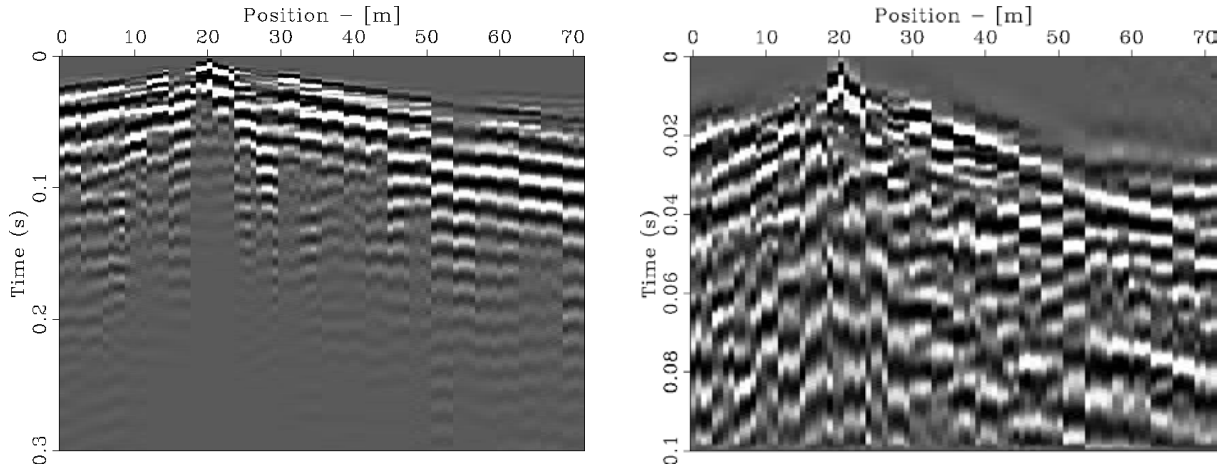

Figure 5: At left, a raw record for the shot at position 18 m along line 1, and at right the same data after AGC and band pass.

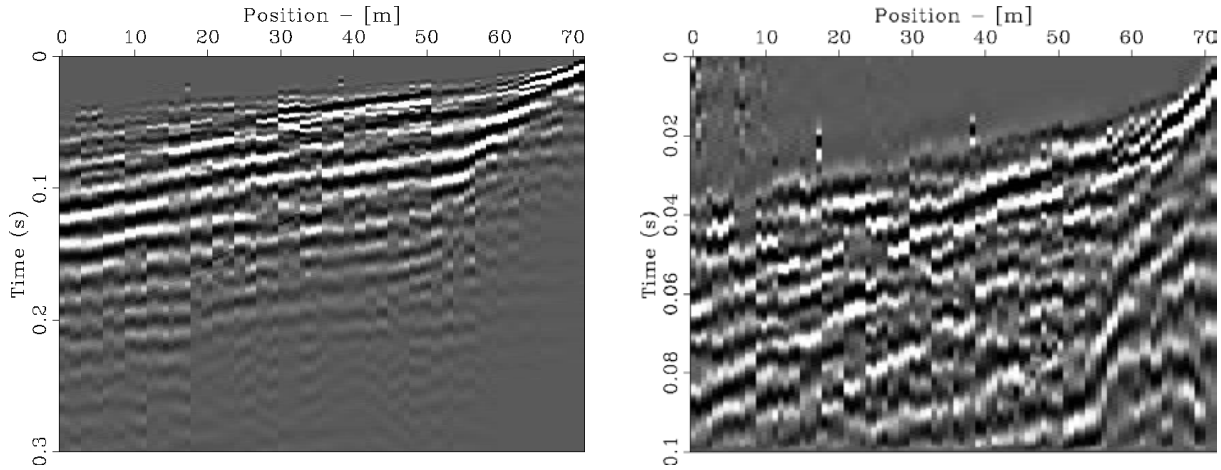

Figure 6: At left, a raw record for the shot at position 72 m along line 1 (southwest end of the line), and at right the same record after AGC and band pass filter.

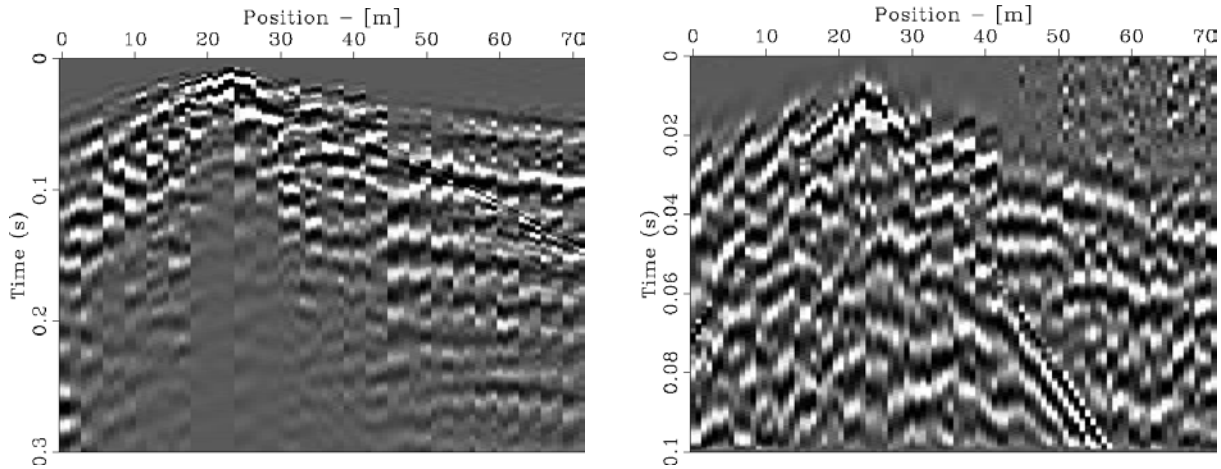

Figure 7: At left, a raw record for the shot at position 24 m along line 2 and at right the same data after AGC and band pass.

These differences are due both to estimation error and lateral variations of the geology and topography. However, they suggest two positive velocity discontinuities at approximately 1 m and 8 to 10 m. Comparing these depths to the log shown in Figure 1, suggests that these interfaces are not as deep as the coal and could be associated with the top of the thick sandstone bed. It is possible that the thin sandstone bed in the shale, or a sharp positive velocity gradient in the shale, is the reflector. The intersection time of the reflection is approximately 0.02 s. Using an estimated velocity of 1400 m/s, this would indicate a reflector at approximately 14 m depth.

Normal Move Out Analysis

In order to better constrain the velocities at the site and to gain certainty regarding the depth of the reflector, we analyzed the shot gather in Figure 6 to flatten the flank of the reflected event using normal move out (NMO), in Figure 10. Technically, NMO analysis is inappropriate for shot gathers; however we suggest that the approach is adequate because the seismic transect is a strike line and the reflector is not expected to dip strongly. Our goal is only to get an estimation of the velocity structure.

Seismic line 1 runs along the geologic strike, so the reflecting layer should appear flat in these seismic data. A NMO velocity of 1150 m/s seems optimal to flatten the flanks of the interpreted reflector. This NMO velocity was tested for consistency with the velocities coming from refraction analysis. Various stacking velocities and normal incidence travel times were tested for their equivalent interval velocity and layer thicknesses. Most combinations are fairly sensible, but pushing the lower velocity to 1400 m/s also pushes the slow top layer to 2 m thick. This result is unrealistic considering our data and field observations. It appears that the reflection originates at a depth of approximately 11 m. We did not perform NMO analysis on the possible second reflection (R2) because it is very weak and it is only seen on one of our shot gathers.

Table 2: Various combinations of NMO stacking velocities and normal incidence travel times and their equivalent interval velocity and layer thickness.

NMO stacking velocity (m/s)	Normal incidence travel times (s)	Interval velocity (m/s)	Layer thickness (h) (m)
480, 1150	0.0055, 0.020	480, 1317.86	1.320, 9.55446
450, 1150	0.0050, 0.020	450, 1302.24	1.125, 9.76681
500, 1150	0.0055, 0.018	500, 1339.55	1.375, 8.37220
480, 1150	0.0075, 0.020	480, 1406.33	1.800, 8.78955

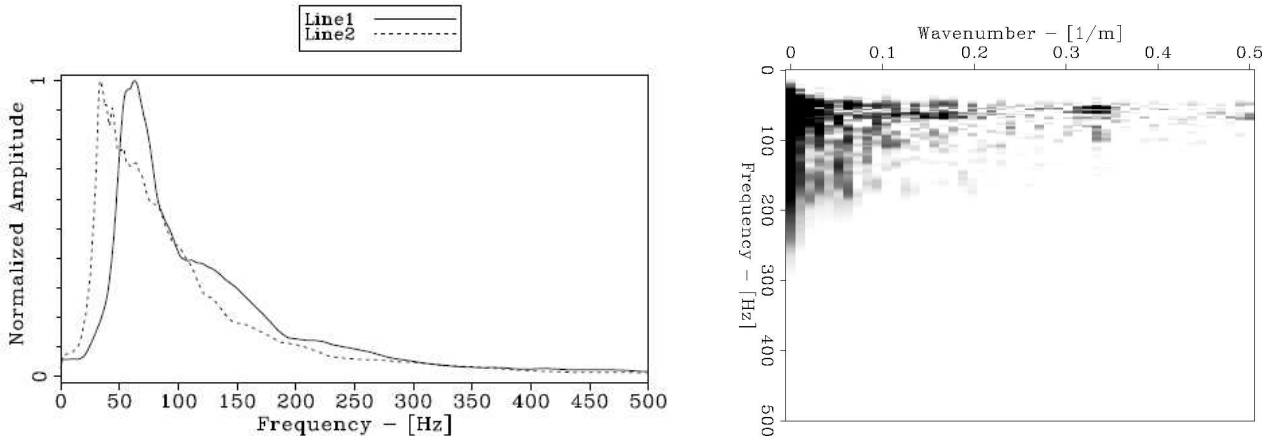

Figure 8: (left) Average normalized frequency spectra of surveys at lines 1 and 2, (right) Frequency wave number spectrum of the shot recorded at line 1, near position 72 m.

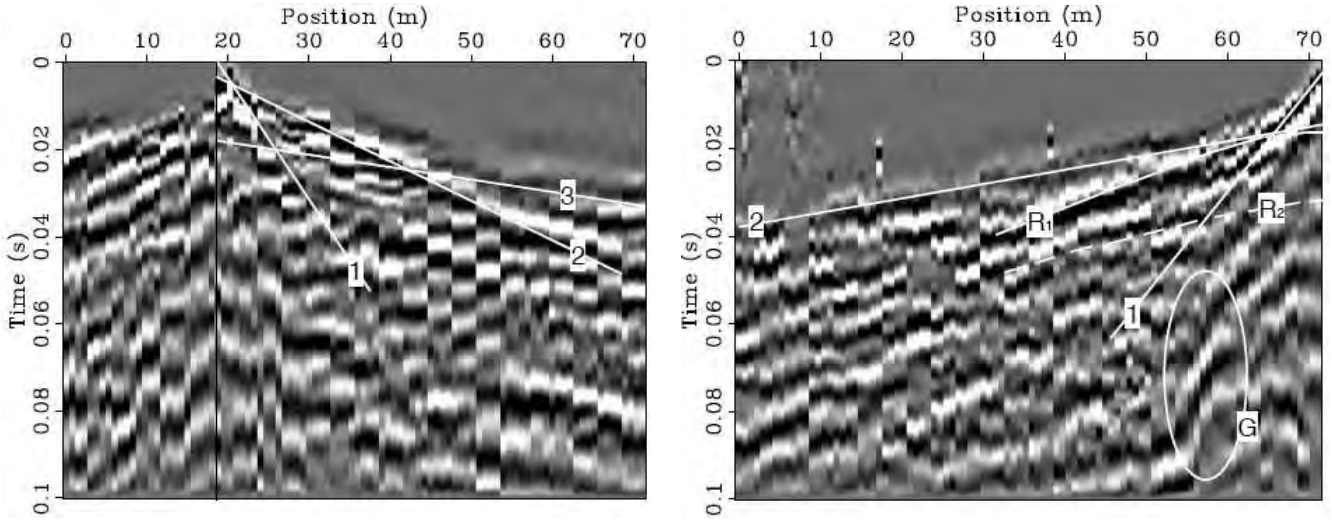

Figure 9: At left is the shot located at 18 m along line 1 (same data as Figure 5), with a direct P-wave event annotated "1", and two refracted events annotated "2" and "3". At right is the shot located at the southwestern end of line 1, with possible reflected events annotated "R_1" and "R_2", a direct P-wave event annotated "1", and two refracted events are annotated "2" and "3". Dispersive ground roll is annotated "G".

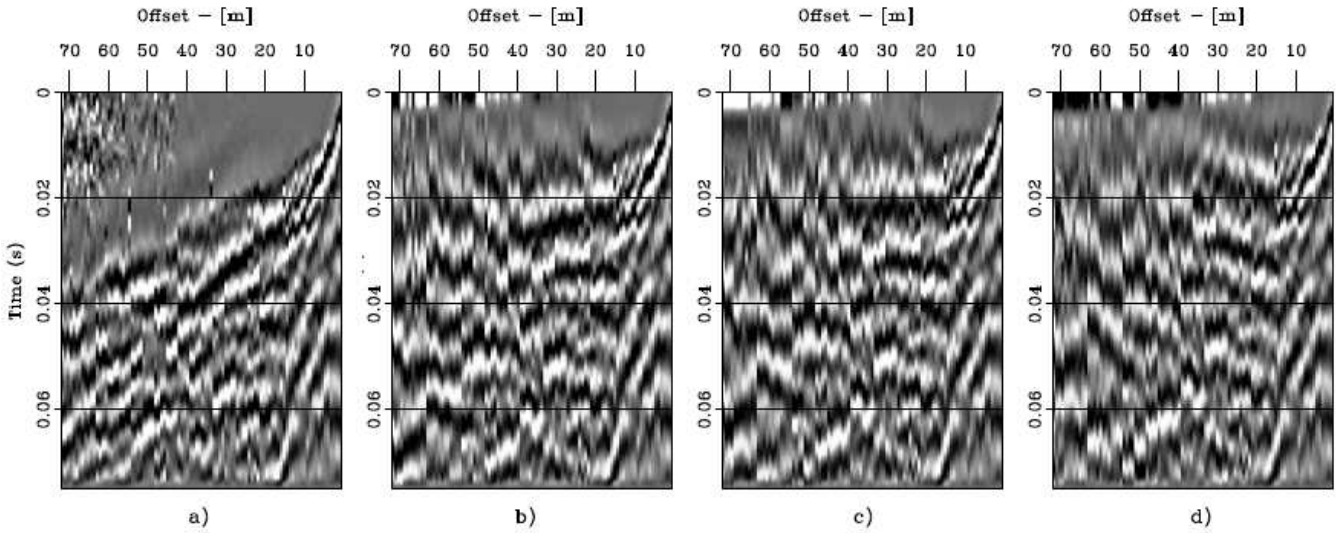

Figure 10: The shot at southwestern end of line 1 (same as Figure 6). a) Plotted with no NMO, b) with NMO stacking velocity 1300m/s, c) with NMO stacking velocity 1150m/s, d) with NMO velocity 1000 m/s.

Conclusions

We conducted a simple seismic test at the Southern Ute Nation coal fire site, after conducting synthetic modeling of the experiment. Field data quality is at the high end of what can be expected for sledgehammer-source data. The recorded frequency content is strong up to at least 100 Hz. The test shots were interpreted to contain several refracted events and a reflection event. Refraction and reflection analyses suggest a one-meter-thick layer with velocity of a little less than 500 m/s on top, and a layer of about 9-10 m and a velocity of about 1300 − 1400 m/s overlying a lowermost layer with a

velocity as high as 3000 m/s. The one prominent reflection event originates at a depth of approximately 11 m, which is well above the coal layer. It might hide possible reflections from the coal layer. The fast layers that are interpreted to overlie the coal pose a difficulty to any seismic surveying because they are an impediment to deeper wave propagation. As we expected, the fissures above the burned coal present a major impediment to wave propagation and substantially degrade data quality. In addition, the test shots indicate highly dispersive ground roll and strong statics in the area. There are no distinguishable events deep enough to adequately characterize the coal layer. Thus we must conclude that further surface seismic work at the site is unlikely to be successful at imaging the targeted coal or ash layer. Cross-well methods could find better success, though diffractions and other heterogeneity might also hinder these approaches.

Acknowledgements

We would like to acknowledge Lynn Orr from the Department of Energy Resources Engineering, Stanford University, for financial and aviation support of this project; Bill Flint, Kyle Siesser and Jonathan Begay from the Southern Ute Department of Energy for their financial support and expertise on the field site; Michael Krause from the Department of Energy Resources Engineering, Stanford University, for field support; the Southern Ute Indian Tribe Growth Fund for financial support and finally Jet West Geophysical Services for the log of Figure 1. We thank the sponsors of the Stanford Exploration Project for financial support of Sjoerd de Ridder. Bob Clapp and Biondo Biondi for helpful discussions on designing the numerical model. We are grateful to Shawn Larsen for providing and assisting with the e3d code. References to any specific commercial product, process, or service by trade name, trademark, manufacturer, or otherwise does not constitute or imply its endorsement, recommendation, or favoring by the United States Government or any agency thereof.

References

Larsen, S.C. and J.C. Grieger, 1998. Elastic modeling initiative, Part III: 3-D computational modeling: 68th Ann. Internat. Mtg., 1803-1806, Soc. of Expl. Geophys.

Martin, G.S., 2006. Marmoussi2: And upgrade for marmousi: The Leading Edge, 25, 156-166.

Miller, R.D., S.E. Pullan, D.W. Steeples, and J.A. Hunter, 1994. Field comparison of shallow P-wave seismic sources near Houston, Texas: Geophysics, 59, 1713-1728.

Miller, R.D., S.E. Pullan, D.W. Steeples, and J.A. Hunter, 1992. Field comparison of shallow seismic sources near Chino, California: Geophysics, 57, 693-709.

Wolf, K. H. A. A., 2006. The interaction between underground coal fires and their roof rocks: PhD thesis, Delft University of Technology.

MULTI GEOMETRY APPROACH FOR MASW SURVEY

Ali Nasseri-Moghaddam, Inspec-Sol Inc., Waterloo, ON
Choon B. Park, Park Seismic LLC., Shelton, CT.

Abstract

The effect of source offset distance and the geophone array length on the dispersion curves are discussed in this paper. The source offset distance was changed systematically at sites with various subsurface conditions to investigate its effect on quality of data and the corresponding dispersion curves. Further, tests were carried out at same locations with various geophone intervals to evaluate the effect of the array length on the quality of the data and dispersion curves. Active and passive data were collected and the dispersion images were combined for possible improvement in dispersion image with enhanced multimodal delineation over a broadened bandwidth.

It is observed that source offsets in the range of 25% to 45% of the array length provide dispersion curves with reasonable quality. Further, collecting data with different geophone intervals (same array mid station) improves the resolution of the obtained dispersion image. Multi geometry technique is suggested to obtain better quality field data. In this approach two (or more) different geophone intervals are used with same mid station. Passive and active data at two or more offset distances are collected for each of the array geometries. Stacking the obtained dispersion images can also result in a better quality dispersion curve.

Introduction

Multi channel analysis of surface waves (MASW) method is a seismic geophysical technique to estimate the soil shear wave velocity profile. MASW was developed in late 1990's as an advancement of other surface wave techniques, which were in use since early 1960's (Park et. al., 1999; Nazarian, 1984; Ballard Jr., 1964). This method has been used in various applications such as seismic site characterization according to building codes, dynamic soil parameter estimation, non-destructive evaluation of subsurface soil condition including hard-to-sample soil deposits, pre and post construction soil conditions, and detection of underground cavities (Xia, 2006; Nasseri- Moghaddam, 2006).

To carry out MASW test, several transducers (i.e. geophones) are deployed along a line at certain distances from an impact source (Figure 1). Commonly minimum 24 geophones are used. The length of the geophone array (D) determines the deepest investigation depth that can be obtained from the measurements. The distance between the source and first receiver (the source offset) determines the contamination level of the signals. The source should produce enough energy over the desired test frequency range to allow for detection of Rayleigh waves above background noise. A common source is a sledgehammer; though more complicated sources with better control over the generated frequency range are also available. The existing traffic noise can also be utilised as a source for investigating deep soil layers (Louie, 2001; Park, 2006). Generally, using a sledgehammer the maximum investigation depth is limited to about 15 m to 20 m below the existing ground surface (bgs). However, using traffic noise or heavier active sources the investigation depth can be increased to more than 30 m bgs. Successful application of MASW method to investigate depths of more than 100 m has also been

reported, though these types of applications are not common and are labour and resource intensive (Stokoe, 2008).

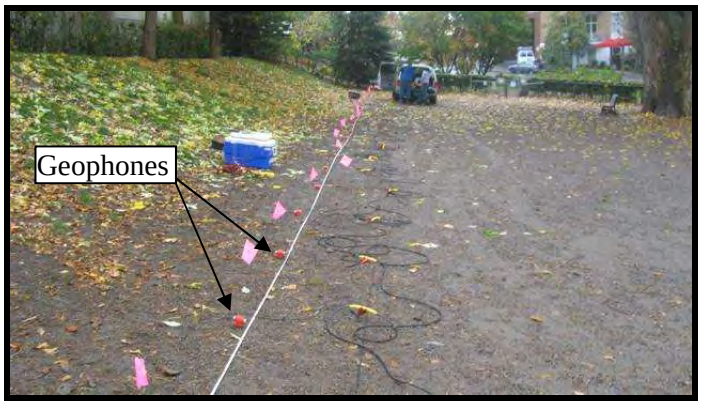

Figure 1: General set up of geophone array for MASW survey

Theoretically, MASW test is based on the dispersive behaviour of Rayleigh wave (R-wave) in a layered media (Park et al., 1999; Rix, 2005). Dispersion of R-wave arises because different frequencies traverse the medium with different velocities. The latter is due to the fact that the penetration depth of R-wave is inversely proportional to its frequency. Thus, higher frequencies travel through shallower strata, and lower frequencies propagate mostly in the deeper layers. For practical purposes, the maximum depth of penetration can be considered to be equal to one to one third of the wavelength (KGS, 2008; Stokoe, 2008). Therefore each frequency carries the information associated to a specific depth of the medium that it is traversing. The recorded signals in the field, which are in time domain, constitute the basis of the calculation of phase velocity profile (dispersion curve) of the site. Subsequently, inversion of the constructed dispersion curve leads to the estimation of the shear modulus profile of the medium.

In recent years significant advances were made in the theory and practice of MASW. However, still the choice of optimum field geometry for MASW investigations is under an active evolution (Ryden and Mooney, 2009; Park and Carnevale, 2010; Zhang et al., 2004; Yoon and Rix, 2009). The total array length determines the maximum depth of investigation. On the other hand the wider the geophones are spaced (i.e. longer array length) the lower will be the resolution for shallow layers because of the attenuation of high frequencies. The choice of active source to first geophone distance (source offset) is also a matter of dispute. Theoretically, the offset should be long enough for plane surface waves to develop (i.e. to avoid near field effect). Therefore, different wavelengths need different distances for full development, although the exact required distance for full development is not well understood. Also, long offsets and long arrays require stronger active sources to obtain good signal to noise ratios.

To overcome the above noted issues various techniques have been suggested and used. An evident approach is to use larger number of geophones, i.e. 48 geophones instead of 24. Another obvious and simple approach is the use of forward and reverse shots. Rix (2005) suggested the use of geophones with variable spacings. Park and Shawver (2009) investigated cases with multiple offset distances. Despite the efforts, further empirical and theoretical works are required to address the above noted issues. This paper presents two case studies designed and implemented to investigate the effect of source offset, geophone array geometry and passive data on the quality of measured dispersion curves. These tests and numerous other field works and corresponding interpretations (not presented) show that a multi

geometry (multi offset - multi station) approach for field data collection is warranted for specific applications. The approach is little more time consuming in the field, however it provides dispersion images with higher resolution and sometimes over a wider range of frequencies. The approach is specifically suitable for assessment of seismic site class according to building codes where generally one or two lines of investigation provide the required data for assessment.

Investigation Methodology

The results of two field studies are presented here. The first study (Case I) was designed and carried out to investigate the effect of source offset on the obtained active data and corresponding dispersion curves. The site was previously investigated by installing a borehole to a depth of about 16.5 m. The subsurface condition at this BH location consisted of about 2.0 m of fill and reworked earth overlying stiff to very stiff (SPT 'N' values from 10 to 30 blows per 0.3 m of penetration) clayey silt till/silty clay that was encountered to the termination depth of the borehole. The MASW investigation line was set up with geophone spacings of 2.0 m, i.e. total array length of 46.0 m. Using a fixed geophone array, the offset distances were systematically changed to cover a wide range of distances. Active shots were collected at fifteen (15) different locations, i.e. offsets started from 2.0 m (one geophone spacing) and increased to 30.0 m with an increment of 2.0 m. Thus the offsets covered a range from about 4% to 65% of the total array length (L). Figure 2A shows a schematic of the investigation line and offset locations. A 12 lb sledge hammer hitting a steel base plate was used as the active source. At each offset location 3 active shots were collected without stacking (total 45 data files).

Passive data were also collected in this case to generate low frequency energy. For this purpose a heavy track mounted excavator (20+ metric ton) was utilized to move along a path in the vicinity of the geophone array. The excavator path made an angle about 30 degrees with the geophone array alignment and its minimum distance with the middle of array was about 5.0 m. The excavator moved along the path as slow as feasible to increase the low frequency energy content. Figure 2B shows the schematic of the geophone array and the orientation of the excavator moving path.

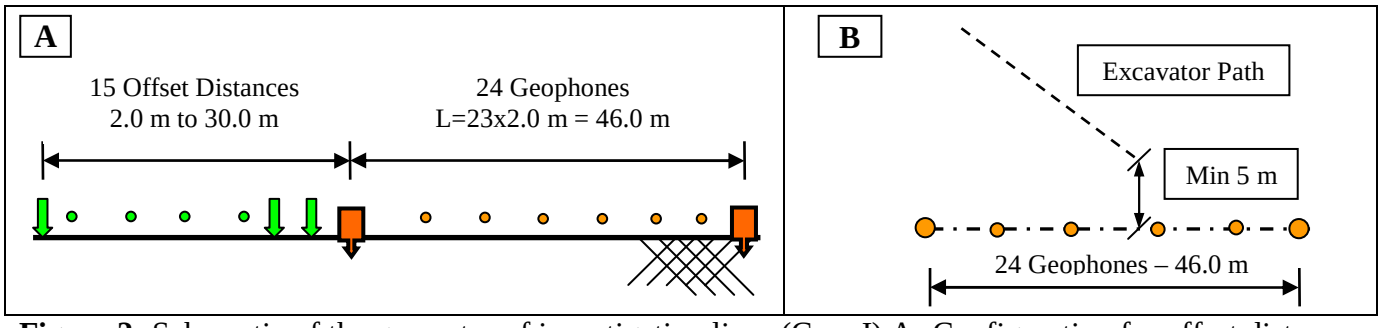

Figure 2: Schematic of the geometry of investigation lines (Case I) A- Configuration for offset distance effect investigation. The arrows show the hammer shot locations. B– Configuration for passive data collection.

The second study (Case II) was carried out to investigate the effect of geophone array geometry as well as the effect of offset distance on the measured dispersion curves. The site was previously investigated by boreholes which showed a thin layer of top soil overlying firm to stiff (SPT 'N' values

from 4 to 13 blows per 0.3 m of penetration) silty clay overlying bedrock which was generally found within the upper 5.0 m of the subsurface. This study consisted of acquiring data along a line with two different geophone spacings. The Long Array was set up with geophone spacing of 3.0 m and Short Array was set up with geophone spacing of 1.5 m. The arrays were aligned along one line and were set up in a way that their mid-stations coincide with each other. Hence, the obtained dispersion images could be stacked to obtain one dispersion curve. Active data were collected at three different offsets for each set up using a 20lb sledge hammer hitting a rubber base plate. In both set ups passive data were also collected. The obtained dispersion curves from the passive and active data were combined to obtain a final dispersion curves along the line. Figure 3 shows a schematic of the geometry used for Case II. Passive data were also collected in this case with similar set up as in Case I. Three data files at each offset location and four data files for each passive test were collected and the obtained images were stacked.

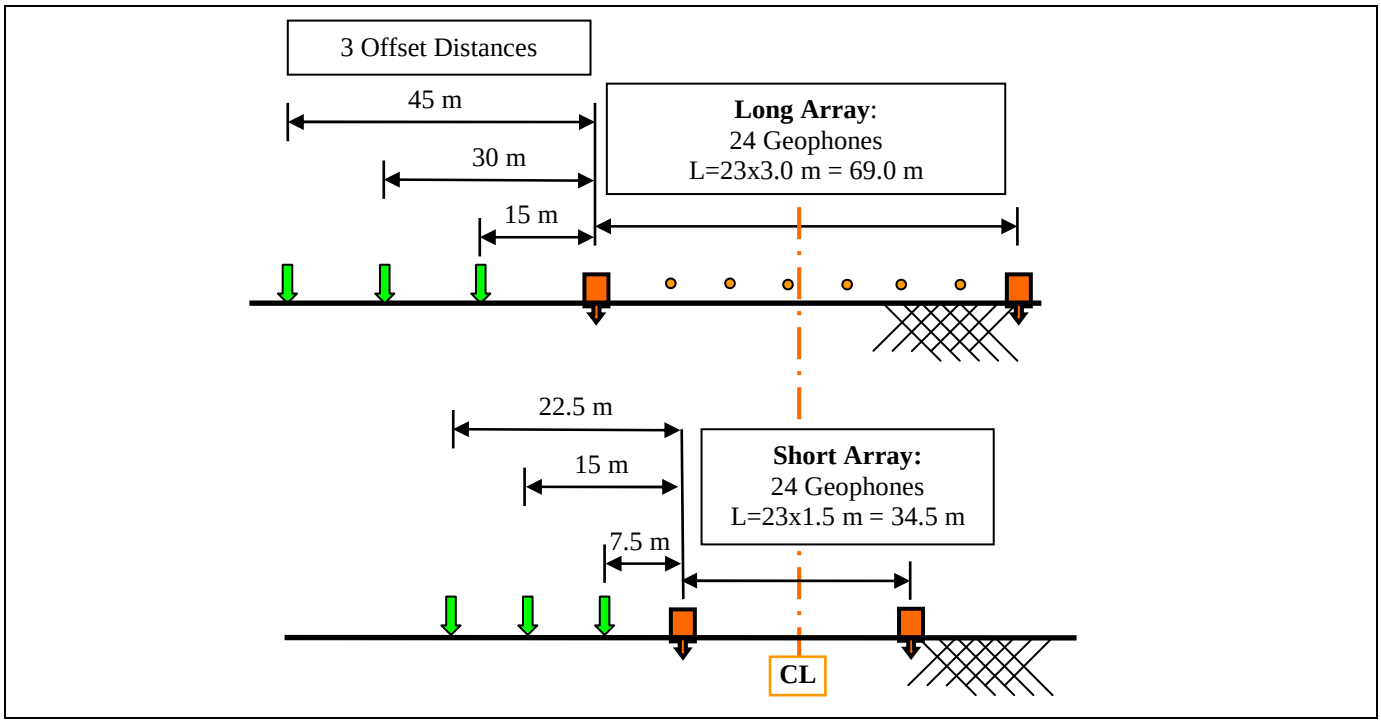

Figure 3: Schematic of the configuration used for offset distance effect investigation (Case II)

In both studies ground responses were recorded by 24-4.5 Hz Geophones connected to a 24 channel Geode® seismic recorder. All the data were analyzed using SurfSeis© version 2.05.

Offset Distance Effect

Figure 4 shows the dispersion curves obtained for Case I. For brevity, four representative active and the corresponding stacked active-passive dispersion images are depicted. Multiple propagation modes are observed in the active dispersion curves (Plots A to D). The fundamental mode is associated to the trends observed for frequencies from about 4 Hz to about 11 Hz corresponding to wavelengths of 77 m to 22 m. The trends at higher frequencies are associated to higher modes of propagation. It is

observed that in this case increasing the offset distance slightly increased the energy of the fundamental mode branch at low frequencies. Also, a better separation of higher modes are observed when the offset distance is more than about 25%L, with L being the total array length. Further comparing plots C and D it is observed that increasing the offset distance beyond 45%L does not add to the clarity of the dispersion curve.

Figure 5 shows the dispersion curves obtained for Case II-Long Array. Plots A to C show the curves for three different offsets and plot D shows the stacked dispersion curves. Plot A, corresponding to offset equal to 22%L, shows the fundamental mode trends from about 22 Hz to 56 Hz, corresponding to wavelengths from about 80 m to 21 m. Increasing the offset distances to 43%L and 65%L (plots B and C) does enhance the energy in the lower frequency (24 Hz to 32 Hz) ranges and provides a little more clarification up to frequencies of about 18 Hz. However this enhancement is obtained at the expense of loosing energy at higher frequencies. Plot D shows the stacked images of the three offsets. This plot clearly shows an improvement of the images over a wide range of frequencies from about 18 Hz to about 52 Hz.

Combining Active-Passive Dispersion Images

To investigate the effect of passive data on the quality of dispersion images the obtained passive images were stacked with the active data at different offsets. Figures 4 and 5 plots E to H show the dispersion images in plots A to D stacked with obtained passive image, respectively. It is observed that the energies in the low frequency ranges are enhanced in these plots. Specifically, the enhancement and better resolution in the image obtained from small offsets is conspicuous (compare plots A and B with E and F, respectively). In general in neither of the presented cases the resolution of the passive image (on its own) was good enough for extraction of a meaningful trend. However, when these passive images are combined with active images a better resolution in lower frequencies is obtained.

Array Geometry Effect

The dispersion images obtained along one line with two different geophone spacings are presented in Figure 6. The images from Long-Array (Geophone spacing of 3.0 m) are shown in plots A to C and the ones from Short-Array (Geophone spacing of 1.5 m) are shown in plots E to G. Plot D show the stacking of images A to C and plot H show the stacking of images E to G. The offset distances in active shots were selected such that the offset to total array length (L) ratio remains the same for both set ups, i.e. 22%, 43% and 65%.

A comparison between the plots reveals that both set ups show similar trends. The range of frequencies with meaningful dispersion image and range of the measured wavelengths are almost the same for both set ups. However, the images obtained from the Long-Array show a better resolution both in terms of frequency and wavelength. Similar observations are made when the stacked dispersion images (plots D and H) are compared.

Figure 7 shows the final dispersion images obtained from stacking the Long-Array and Short-Array dispersion images. Plot A shows the image from stacking all the active images and plot B shows the image obtained from stacking plot A with passive image. Both images show a good resolution in frequency and phase velocity over a relatively wide frequency range from about 16 Hz to about 48 Hz. A higher resolution is observed in phase velocity in the combined active-passive image.

Conclusions

The results of a series of investigations carried out to research the effect of offset distance and array length on the quality of obtained dispersion images from MASW data were presented. The effect of stacking dispersion images from active and passive data and multiple geometries were investigated. The multi-geometry technique for field data collection to improve the quality of the dispersion images was devised and tested. This approach improves the overall quality of the obtained results. However, comparing the obtained quality improvements in the images and the extra field time required its use may be warranted only for specific applications where limited number of investigation lines are required.

The main conclusions from the presented results are outlined below:

- The presented cases along with authors other experiments (not presented herein) show that choosing proper offset distances will provide dispersion images with better separation of higher modes. However, the investigation did not show a meaningful relation between the observed frequency ranges in the fundamental mode of dispersion images and the offset distance. Generally, the observed trends of this relation are complicated and vary with site conditions and array geometry. Therefore, providing a general comment about the optimum offset distance needs more experiments and theoretical works. The presented results show that in general offset distances within 0.25L to 0.45L (L is the total array length) provide reasonable results for practical purposes.

- The comparison between the dispersion images from long and short arrays show that the observed frequency ranges in the fundamental mode did not change significantly. However, a dispersion image with higher resolution was obtained from the longer array.

- In most of the cases the obtained passive data (using a heavy machine) did not provide meaningful dispersion images with distinct trends. However when these passive images are combined with the active images relatively better resolution in the lower frequency ranges is observed.

- Generally the combined dispersion images (multiple offset and geometries and passive data) resulted in a higher resolution dispersion image. The improvements in the results were not significant enough to warrant such approach as a standard practice. However, in applications such as seismic site class determination or dynamic soil property assessment where limited number of investigation lines are required the multi geometry approach is warranted. In these cases with little more field effort a better resolution dispersion curve is obtained.

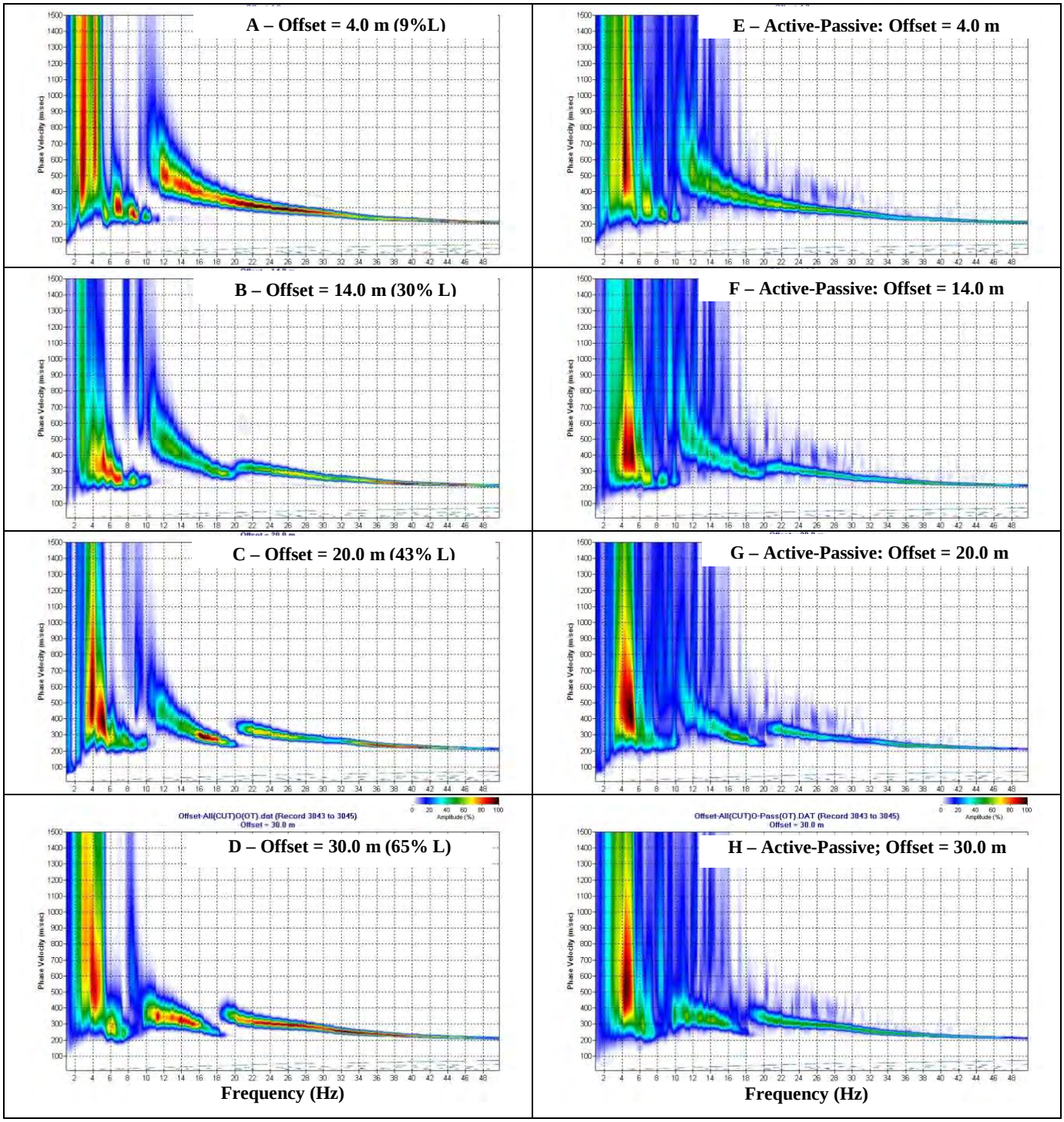

Figure 4: Effect of source offset and combination of active-passive data on dispersion images (Case I). Investigation line consisted of 24 geophones spaced at 2 m with total array length (L) of 46 m. Plots A, B, C and D show the dispersion images obtained from 4 m, 14 m, 20 m and 30 m offsets, respectively. Plots E, F, G and H show the same results stacked with the measured passive dispersion images.

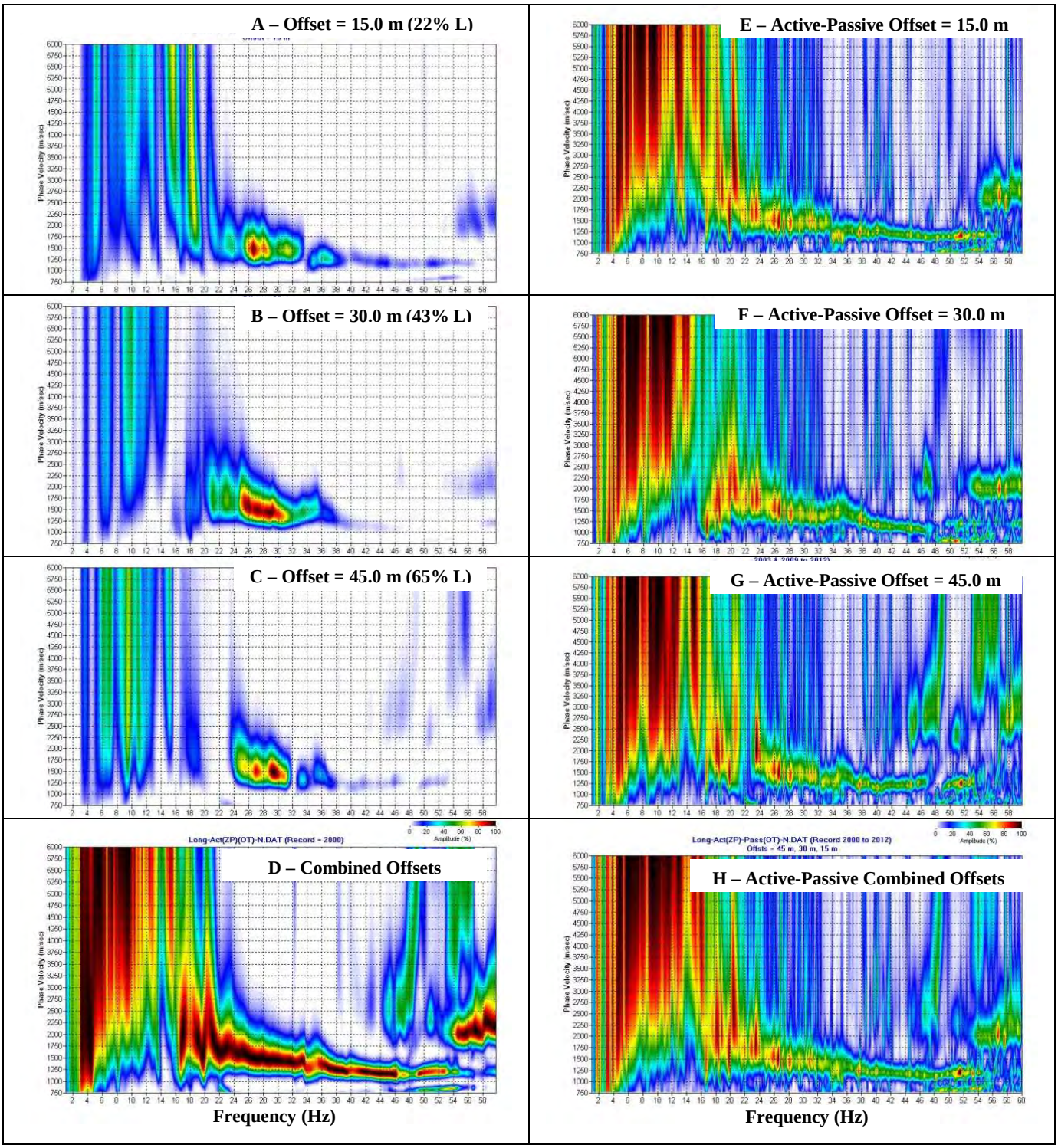

Figure 5: Effect of source offset and combination of active-passive data on dispersion images (Case II, Long-Array). Investigation line consisted of 24 geophones spaced at 3 m with total array length (L) of 69 m. Plots A, B and C show the dispersion images obtained from 4.0 m, 14.0 m, and 20.0 m offsets, respectively. Plots E, F and G show the same results stacked with the measured passive dispersion images. Plots D and H show the results obtained from stacking various offsets.

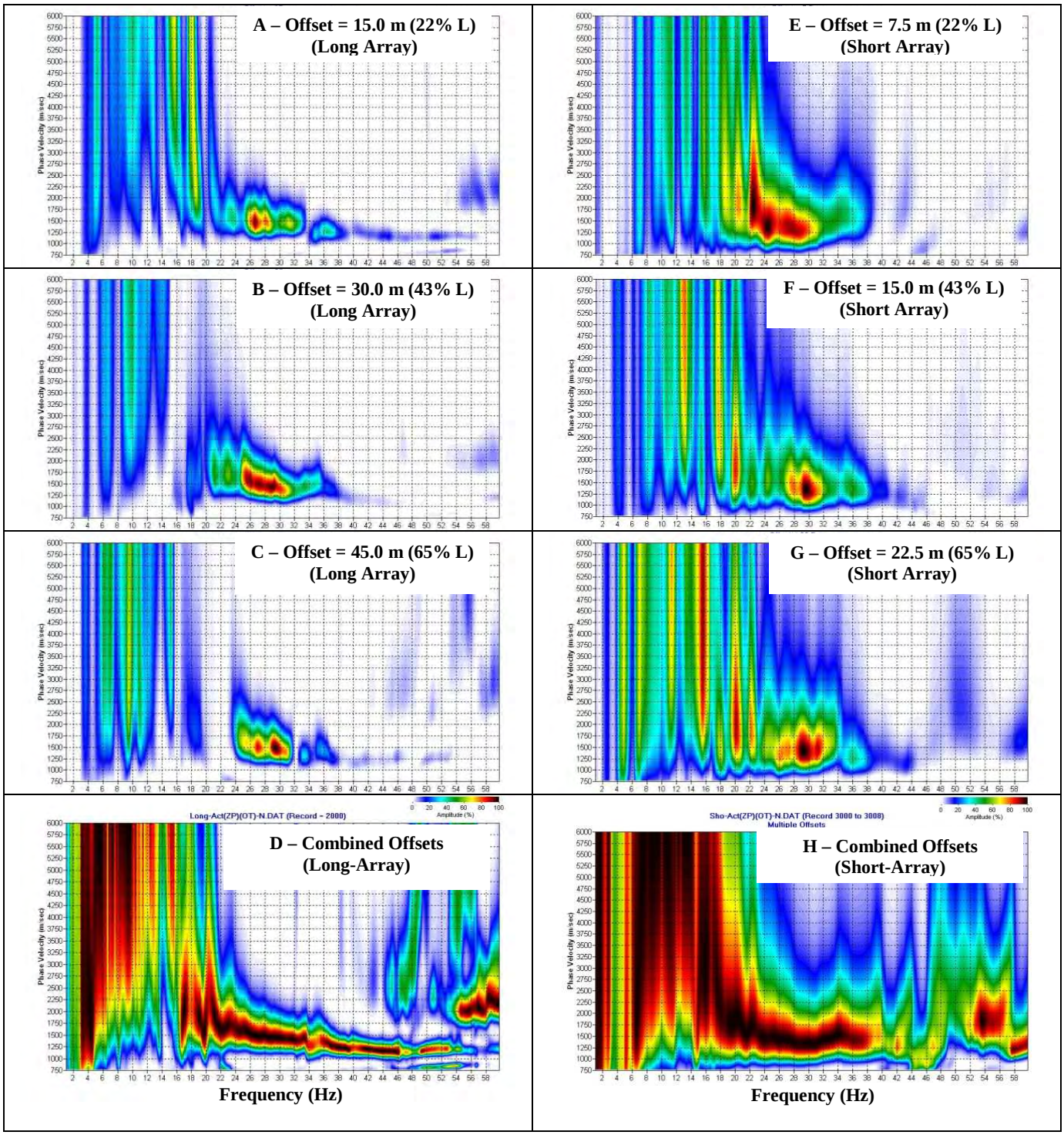

Figure 6: Effect of geophone array geometry on dispersion images. Plots A to C show the dispersion images at different offsets for Long-Array (Geophone spacing 3.0 m). Plots E to G show the dispersion images at different offsets for Short-Array (Geophone spacing 1.5 m). Plots D and H show the stacked images for Long and Short Arrays, respectively.

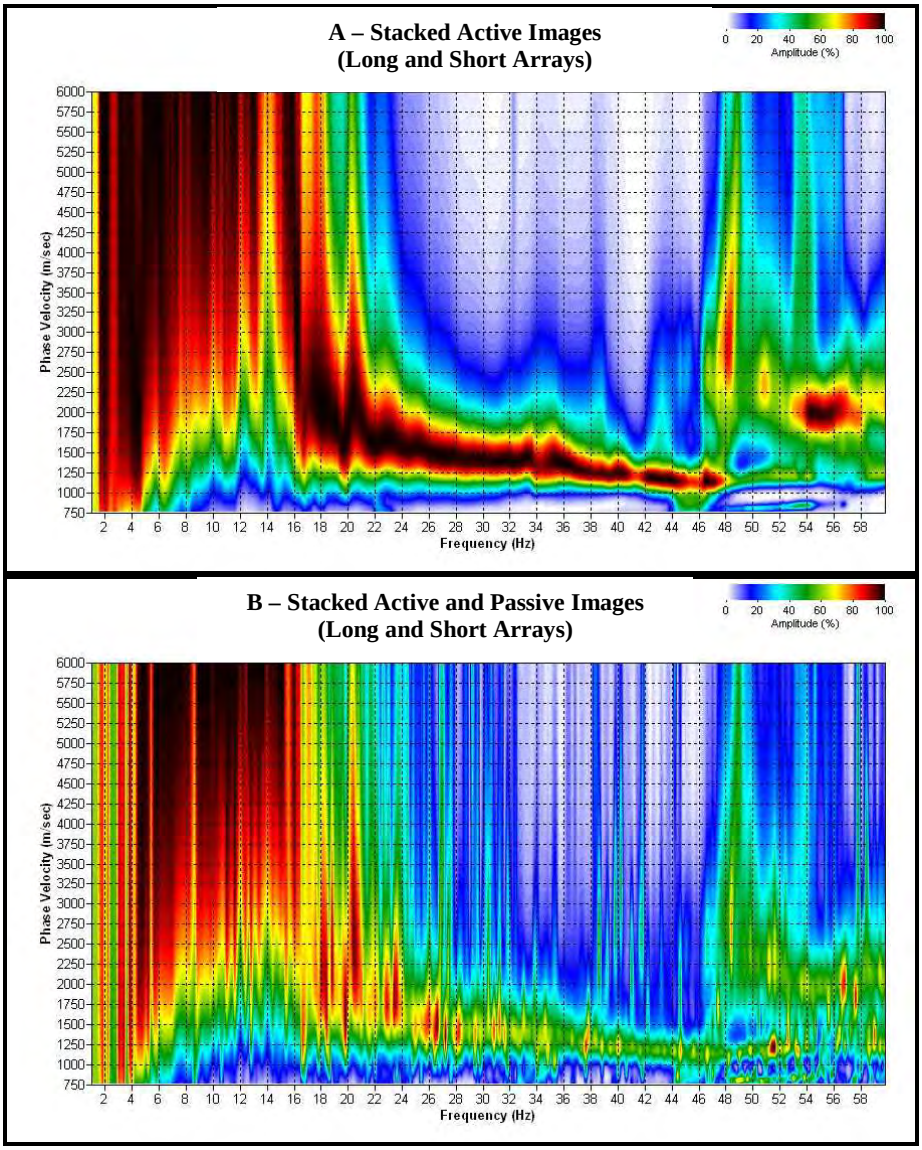

Figure 7: Final dispersion image obtained from multi offset-multi station approach. Plot A shows the active dispersion image and plot B shows the stacked active and passive dispersion images.

- Theoretical interpretations are required to fully explain the observed trends in the presented data. Specifically, the relative small sensitivity of the dispersion image to the source offset or the geophone array geometry needs further theoretical explanation.

References

KGS, 2008. MASW/Surfseis 2 workshop, Kansas Geological Survey, April 24-25, Lawrence, Kansas

Louie, J.N., 2001, Faster, better: shear-wave velocity to 100 meters depth from refraction microtremor arrays; Bulletin of the Seismological Society of America, v. 91, n. 2, p. 347-364.

Nasseri-Moghaddam, A., Cascante, G., Philips, C., Hutchinson, D.J., 2007. Effects of underground cavities on Rayleigh waves: field and numerical experiments. Soil Dynamics and Earthquake Engineering 27, 300-313

Nazarian, S., 1984. In situ determination of elastic moduli of soil deposits and pavement systems by spectral-analysis-of-surface-waves method, PhD dissertation, The university of Texas at Austin, Austin, Texas

Park, C.B., Miller, R.D., and Xia, J., 1999, Multichannel analysis of surface waves: Geophysics, v. 64, n. 3, pp. 800-808.

Park, C.B., Miller, R.D., 2006. Roadside passive MASW, Proceedings of SAGEEP, April 2-6, Seattle, Washington.

Park, C.B. and Shawver, J.B., 2009, MASW survey using multiple source offsets: Proceedings of the Symposium on the Application of Geophysics to Engineering and Environmental Problems (SAGEEP 2009), Fort Worth, Texas, March 29-April 2, 2009.

Park, C.B., and Carnevale, M., 2010, Optimum MASW survey–Revisit after a decade of use: Submitted for presentation in GeoFlorida 2010, West Palm Beach, February 20-24, 2010.

Rix, G. J., 2005. Near-Surface Site Characterization Using Surface Waves, in Surface Waves in geomechanics: direct and inverse modelling for soils and rocks, edited by Lai, Carlo G., and Wilmanski, Krzysztof, 2005, International Center for mechanical science, courses and lectures no. 481, SpringerWien, NewYork

Ryden, N. and Mooney, M., 2009, Analysis of surface waves from the light weight deflectometer: Soil Dynamics and Earthquake Engineering, v. 29, p. 1134-1142.

Stokoe II, K. H., 2008. The increasing role of seismic measurements in geotechnical engineering, The sixteenth Buchanan lecture, https://ceprofs.civil.tamu.edu/briaud/buchanan%20web/2008BuchananLecture.pdf

Xia, J., 2006, Delineating Subsurface Features with the MASW Method at Maxwell AFB in Montgomery, Alabama, KGS Open-File Report 2006-1, http://www.kgs.ku.edu/Geophysics/OFR/2006/OFR06_01/index.html

Yoon, S. and Rix, G.J., 2009, Near-field effects on array-based surface wave methods with active sources: J. Geotech. Geoenviron. Eng., 135 (3), p. 399-406.

Zhang, S.X., Chan, L.S., and Xia, J., 2004, The selection of field acquisition parameters for dispersion images from multichannel surface wave data: Pure and Applied Geophysics, 161, p. 1–17.

USING ULTRASONIC CODA WAVE INTERFEROMETRY FOR MONITORING STRESS-INDUCED CHANGES IN CONCRETE

Parisa Shokouhi, Ernst Niederleithinger, Andreas Zoëga, Andreas Barner, and Dieter Schöne
BAM – Federal Institute for Material Research and Testing, Berlin, Germany

Abstract

The velocity of ultrasonic coda waves, the diffusive tail of ultrasonic signals, was monitored in a concrete specimen under uniaxial compression. The ultrasonic measurements were taken in two directions: parallel and perpendicular to the loading. A geophysical correlation-based approach called coda wave interferometery (CWI) was used to calculate the incremental stress-induced changes in velocities. Ultrasonic pulse velocities were also calculated using the conventional time-of-flight (TOF) approach. A comparison of TOF and CWI velocities revealed that the CWI velocities are more sensitive to the level of stress and damage within concrete, especially in low stress levels. Also, the CWI velocities measured parallel to the loading showed greater sensitivity.

Introduction

The ultrasonic pulse velocity (UPV) method has long been used to estimate the strength properties of construction materials. The measurement setup consists of a pair of ultrasonic transducers (sender and receiver). The velocity is obtained by measuring the time-of-flight (TOF) of the transmitted pulse over a known distance within the material. Velocities measured lower than an expected threshold (delays in arrival times) indicate loss of strength in the test material. The stress-dependency of UPV in concrete has been investigated in a number of studies. A decrease in ultrasonic pulse velocities in concrete at stress levels higher than 70% of the strength has been by Raju [*1970*] and Shah & Chandra, [*1970*]. Suaris et al. [*1987*] showed that the amplitude of the ultrasonic waves begins to decrease when the stress reaches to about 40% of the strength, concluding that the amplitude is more sensitive to the state of stress than the velocity. This observation was later confirmed by Nogueira & Willam [*2001*].

Interesting results were obtained, when instead of analyzing the coherent field (i.e. the early part of the signal), the diffuse field (i.e. the later part or Coda waves) of ultrasonic signals was analyzed. Coda waves constitute the trail of strongly scattered waves in an ultrasonic signal. Coda waves are sensitive to changes in the medium because the scattering that generates these waves causes coda waves to repeatedly sample a limited portion of the material. CWI is a technique that exploits this sensitivity to estimate weak changes in the medium from a comparison of the coda waves before and after the perturbation [Snieder, 2006]. This method was developed by seismologists over 20 years ago, mainly to detect slight velocity changes in the earth crust due to seismic effects, mining influence or seasonal variations [Snieder et al. 2002; Sens-Shoenfelder & Wegler 2006; Grêt et al., 2006]. It was not until very recently that CWI was used to detect small changes in concrete microstructure (e.g. Stähler et al. 2009; Larose & Hall, 2009).

Experimental Study

The stress-dependency of coherent and diffuse ultrasonic wave velocities in concrete was investigated in an experimental study. Ultrasonic measurements were taken on a prismatic concrete

specimen subjected to uniaxial compression. The details of the test specimen, equipment, the measurement procedure, and some of the results are discussed in this paper.

Test Specimen

A prismatic 0.2 x 0.2 x 0.6 m^3 (7 7/8 x 7 7/8 x 23 5/8 $in.^3$) plain concrete specimen was tested in the experiment discussed in this paper. The characteristics of the concrete mixture together with some of its mechanical properties are provided in Table 1. The concrete mix was prepared according to the C30/C37 mix design given in the European (Eurocode2) or German guidelines (DIN 1045-1). Five identical specimens of the same batch were cast in wooden molds. The specimens were stripped of the molds after 5 days and then put in ambient conditions for 28 days before being tested.

Table 1: Mixture Proportions and Some Mechanical Properties of Concrete Mix

Sample Designation	**Mixture Proportions C:CA:FA (w/c)***	**Aggregate Proportions**						**Compressive Strength (MPa/ksi)**
		5/16" (8 mm)**	**No. 5 (4 mm)**	**No. 10 (2 mm)**	**No. 18 (1 mm)**	**No. 35 (0.5 mm)**	**No. 50 (0.3 mm)**	
		Coarse (CA)		**Fine (FA)**				
Test Specimen (C30/C37)	1:2.32:2.87 (0.55)	25%	20%	14%	10%	11%	21%	41.6/6.0

* Fractions in weight: C = Cement (Type I), CA = Coarse Aggregates, FA = Fine Aggregates, and (w/c) = water to cement ratio.
** The maximum aggregate size was 5/8" or 16 mm.

Testing Equipment

The test equipment consisted of a loading machine of the maximum capacity of 20 MN and the instrumentation necessary for ultrasonic and deformation measurements. As shown schematically in Figure 1, ultrasonic measurements were taken in transmission mode and along two perpendicular directions (i.e. parallel and perpendicular to the loading). A pair of 100-KHz longitudinal ultrasonic sensors from Acsys (Acoustic Control Systems Ltd.) was used for taking measurements in each direction. The ultrasonic sensors were all of dry point contact type and therefore, their application did not require the use of any coupling agents. Two of the sensors were built in the loading plates (for ultrasonic measurement parallel to the loading) while the other two were mounted on the surface of the specimen (for ultrasonic measurements perpendicular to the loading). An in-house built frame and two holders were used to attach the sensors to the surface of the specimen and to ensure that they remain in full contact over the entire duration of the test.

The deformation of the specimen under the load was recorded using linear variable displacement transducers (LVDTs) in both directions. As depicted in Figure 1(b), four LVDTs were installed in either direction. A number of strain gauges (not shown in Figure 1) attached along different directions on the surface of the specimen were also used for 'backup' deformation measurements.

Test Procedure

The specimen was instrumented and then placed in the loading machine, exactly in the middle of the loading plates. The specimen was gradually loaded along its length in prescribed load steps of approximately 50 KN (stress-controlled). In the experiment presented in this paper, the specimen was subjected to only one cycle of loading. The stepwise loading continued until the specimen broke.

The very first set of ultrasonic measurements was taken before the loading began, at the stress-free (or zero-load) state. At every subsequent load step, the stress was kept constant long enough to allow taking all the measurements. The measurements along each direction were repeated 10 times. Therefore, a total of 20 ultrasonic signals were recorded at every load step. Once the measurements were completed, the load was increased to the next prescribed level. This procedure continued until the specimen broke.

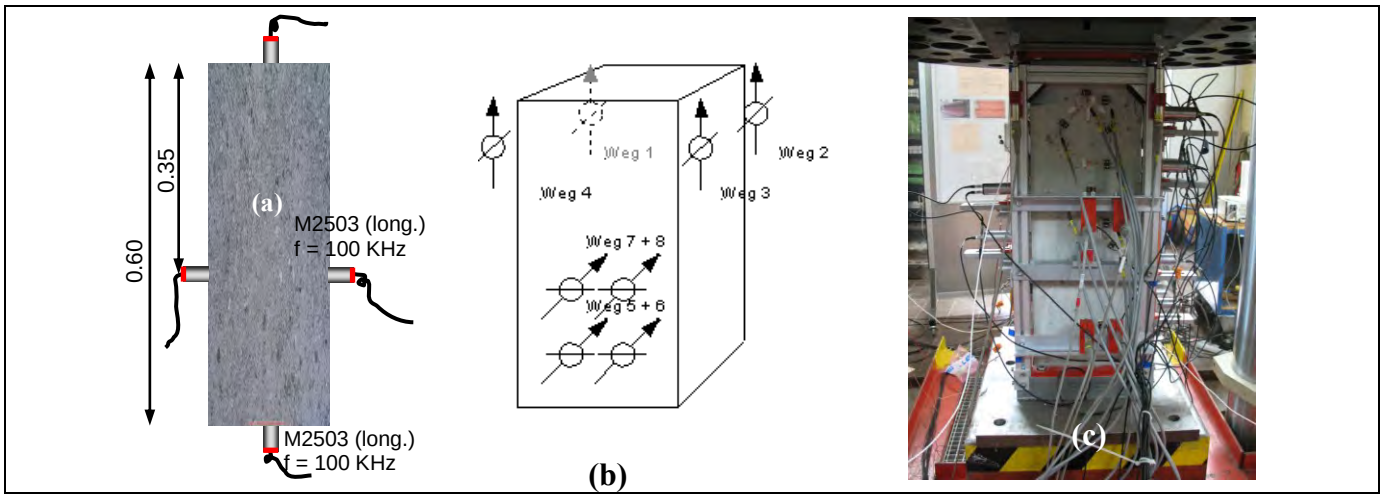

Figure 1: Schematics of the experimental setup for (a) ultrasonic and (b) deformation measurements. The instrumented specimen under load is shown on the far right (c).

Experimental Results

The examination of the records reveals that as the load increase, the arrival times of both set of records start to change. The relative changes in the corresponding TOF velocities vs. stress (normalized to the strength) were calculated and given in Figure 2. To calculate TOF velocities, a simple time-picking algorithm was employed. The velocities are corrected for the specimen longitudinal and lateral deformations (i.e. longitudinal contraction and lateral expansion). As seen in Figure 2, the TOF velocities do not show great sensitivity to the level of stress (and the corresponding damage) in concrete over the early load steps (low stress levels). It is not until reaching the critical levels that the changes in TOF velocities become notable. The trend of changes in velocities measured perpendicular to the loading agrees very well with those published previously by other researchers [Nogueira & Willam, 2001].

Coda Wave Interferometery (CWI)

The CWI algorithm utilized [Larose et al. 2009; Sens-Shoenfelder & Wegler 2006] is based on the assumption that, the perturbation causes the waveforms be stretched (or compressed) in time. To obtain the velocity change ($v = dV/V$), the perturbed signal S_2 should be first interpolated at times $t(1-v)$ with various velocity changes v. The desired velocity change v^* is the v that maximizes the cross-correlation coefficient between the perturbed signal $S_1(t(1-v))$ and the reference signal $S_1(t)$ calculated in the selected time window $[t_0\ T]$:

$$CC(v) = \int_{t_0}^{T} S_2(t(1-v))S_1(t)dt \Big/ \sqrt{\int_{t_0}^{T} S_2{}^2(t(1-v))dt \int_{t_0}^{T} S_1{}^2(t)dt}$$

The CWI velocities, superimposed on TOF velocities, are also shown in Figure 2. A slightly different approach has been taken in calculating the CWI velocities here. Since the load step size (1.25 MPa) was

considerably large in this experiment, the correlation coefficient *CC* calculated between the record at the stress-free state and the records obtained at later load steps, soon deviated from the ideal unity. After a few load steps, it was even hardly possible to detect a reliable peak in the *CC* vs. *v* curve and deduce the velocity change. Therefore, an alternative approach was used here. Instead of using the first record as

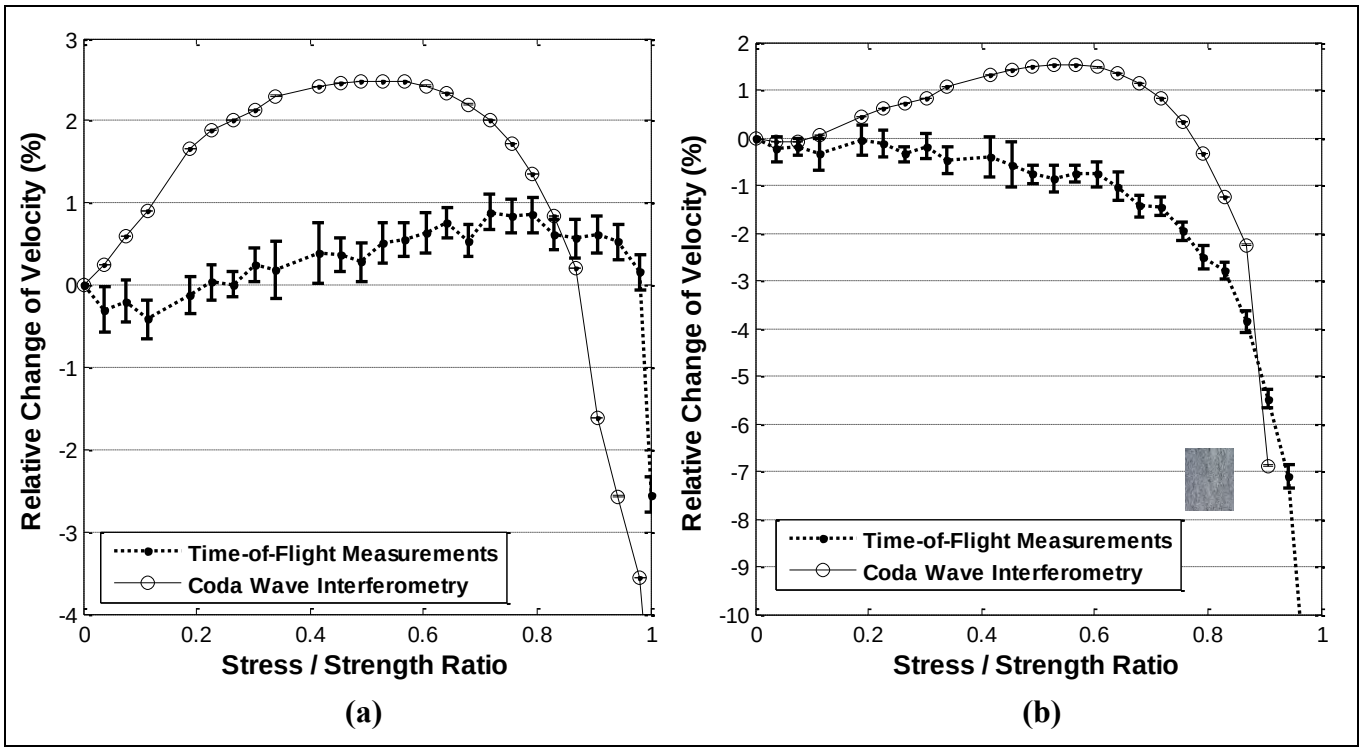

Figure 2: Relative stress-induced velocity changes obtained using TOF and CWI in two directions: (a) parallel and (b) perpendicular to the loading. The error bars correspond to one standard deviation in the calculated velocities from ten repeated measurements at every load step.

the reference signal, the correlation coefficient CC was calculated incrementally between the pair of signals recorded at two subsequent load steps. The accumulated errors were calculated and proved to be insignificant, as reflected in the very small size (hardly seen) of the error bars depicted in Figure 2.

Diffusive vs. Coherent Ultrasonic Velocities

The CWI velocities show a greater sensitivity to the level of stress and damage in the specimen. Not only are the velocity changes greater, but also show particular characteristics, which are useful in monitoring applications. The CWI velocities measured in both directions attain maxima at a stress-strength ratio of about 55%, well before the specimen reaches the critical levels of stress. Afterwards, the velocities start to gradually decrease. The velocities drop significantly after the stress/strength ratio goes beyond 80%. Therefore, such measurements can be used for monitoring in the warning mode. The CWI velocity-stress characteristics match very well those reported for sonic surface wave velocities [Zoëga et al, 2009]. Moreover, the velocity changes are direction dependent; the changes in velocities measured parallel to the loading are greater than those measured perpendicular.

Discussion

It should be noted that the CWI and TOF velocities are not immediately comparable. A diffuse field in a homogeneous solid medium partitions its energy between transverse and longitudinal waves in

a ratio $R = 2(V_P/V_s)^3$, where V_P and V_S denote the compression and shear wave velocities of the medium [Weaver, 1982]. Assuming a Poisson's ratio of 0.2, this ratio amounts to about 8.7 for concrete. Although the heterogeneity of concrete makes the diffusive energy partitioning even more complicated. Therefore, the CWI velocity is a weighted average of longitudinal and transverse velocities (as well as the surface waves travelling around the specimen), even though longitudinal transducers were used. The TOF velocities are on the other hand, the longitudinal ultrasonic velocities measured along two perpendicular directions. Nevertheless, the CWI velocities show much greater sensitivities to the subtle stress-induced changes in the microstructure of concrete.

Conclusions

The experimental results revealed that the velocity of coda waves is more sensitive to the subtle stress-induced changes in concrete than the conventional ultrasonic pulse velocity (obtained using conventional time-of-flight measurements). Coda wave interferometery (CWI), a geophysical technique, was used for the velocity calculations. This method may be used to monitor small changes in material properties due to other deterioration mechanisms, which go undetected if conventional approaches are taken.

References

A. Grêt, R. Snieder, R., and U. Özbay (2006), Monitoring in situ stress changes in a mining environment with coda wave interferometry, International Journal of Geophysics, 167, 504–508.

E. Larose and S. Hall (2009), Monitoring stress related velocity variation in concrete with a 2.10-5 relative resolution using diffuse ultrasound, Journal of Acoustical Society of America, 125, 4, 1853-1856.

C. L. Nogueira and K. J. Willam, (2001), Ultrasonic Testing of Damage in Concrete under Uniaxial Compression, ACI Materials Journal, 98, 3, 265-275.

N. K. Raju (1970), Small Concrete Specimens under Repeated Compressive Loads by Pulse Velocity Technique, Journal of Materials, Vol. 5, No. 2, pp. 262-273.

C. Sens-Schönfelder and U. Wegler (2006), Passive Image Interferometry and seasonal variations of seismic velocities at Merapi volcano, Indonesia, Geophysics Research Letters, 33, L21302.

S. P. Shah and S. Chandra (1970), Mechanical Behavior of Concrete Examined by Ultrasonic Measurements, Journal of Materials, Vol. 5, No. 3, pp. 550-563.

R. Snieder, A. Grêt, A., H. Douma, and J. Scales (2002), Coda Wave Interferometry for Estimating Nonlinear Behavior in Seismic Velocity, Science, 295, 253–2255.

S. Stähler, E., Niederleithinger, S., Pirskawetz, T.-R., Nowak, and F. Weise (2009), Detecting subtle changes in materials by coda wave interferometry. In Sens-Schönfelder, C., Ritter, J., Wegler, U.,and Große, C.,editors, Noise and Diffuse Wavefields – Extended Abstracts of the Neustadt Meeting, pages 59–62. Deutsche Geophysikalische Gesellschaft.

W. Suaris and V. Fernando (1987), Detection of Crack Growth in Concrete from Ultrasonic Intensity Measurements, Materials and Structures, Vol. 20, pp. 214-220.

R. L. Weaver (1982), On Diffuse Waves in Solid Media, Journal of the Acoustical Society of America, 71, 6, 1608-1609.

A. Zoëga, P. Shokouhi, and H. Wiggenhauser (2009), Propagation Time of Elastic Surface Waves on Concrete Specimens under Uniaxial Loads, Journal of Structural Engineering, 36, 1, 11-15.

COMBINED PARALLEL SEISMIC AND CONE PENETROMETER TESTING OF EXISTING BRIDGE FOUNDATIONS AND LEVEE SHEET PILES FOR LENGTH AND CAPACITY EVALUATIONS

Dennis A. Sack, Olson Engineering, Inc., Wheat Ridge, CO 80033
Larry D. Olson, Olson Engineering, Inc., Wheat Ridge, CO 80033

Abstract

The use of the Parallel Seismic (PS) test method has been well documented and has been shown to be effective for foundation length evaluation when used with a cased borehole adjacent to the foundation being evaluated. In addition, the use of the Cone Penetrometer Test (CPT) to evaluate soil properties without a borehole has also been well documented. Recent research, hardware development, and field testing have been conducted on a system which combines the two methods to allow fast and economical evaluation of both soil properties and foundation depth without requiring a drill rig. The combined system collects both PS and CPT data in one or two probe penetrations into the soil. The combined system can be used with a smaller, relatively low clearance CPT rig which is self-propelled and designed for use on rough site conditions. Thus, access is possible to bridge foundations that could not be tested with conventional means. The paper presents details of the principles and operations of the combined system, as well as field test data from driven pile bridge foundations as well as steel sheet piles under levee walls in New Orleans.

Introduction

Determining the true tip depth and foundation geometry for bridge foundations without documentation is becoming an increasingly important task for the nondestructive testing community. These unknown foundations are found under a wide variety of structures, ranging from bridges to antenna towers to buildings. For most of these foundations, the lack of any information is not a major concern if the structure has been performing adequately for a period of years. However, a variety of situations can arise which can suddenly make knowing the foundation depth and geometry be of prime importance. The most common situation that arises is a planned change in loading of the foundation element. For antenna towers, this situation occurs when new or heavier antenna elements must be added to the tower. For bridge foundations, this can be due to adding lanes to an existing bridge or reusing foundations for a totally new superstructure. The need for foundation information can also be driven by scour safety analyses for bridges, to verify that the predicted or historic scour depths will not undermine the foundations during a major flood event or high tides.

Regardless of the actual reason for needing information on foundation depth and type, there is a clear requirement for reliable, fast, and cost-effective test techniques to allow this determination. There are several methods that can be used for unknown foundation evaluation, with the specific utility of each method usually dependent on the actual foundation to be tested. These methods include electromagnetic methods such as surface and borehole based Ground Penetrating Radar and borehole based Induction Field, as well as various stress-wave based test methods such as surface Sonic Echo, Impulse Response, Ultraseismic (US) methods as well as the borehole-based Parallel Seismic method. Previous research

conducted for the National Highway Cooperative Research Program (NCHRP) by Olson Engineering (1,2) has shown that of the methods available, the Parallel Seismic (PS) test method is the most versatile and reliable. This method can be applied to a wide variety of foundation types and almost any foundation depth, and does not require direct physical access to the foundation being tested. The most significant limitation to wider application of the PS method is that it typically requires a cased borehole be placed in the ground next to the foundation in question using a truck-mounted drill rig.

As stated above, the biggest limitation to the wider application of the PS test method is the requirement for a cased borehole next to the foundation element. Recent research and development has resulted in a system that uses a cone probe system to simplify the borehole installation or eliminate it altogether. The newly developed system can be used to either install a small-diameter casing for PS testing, or can be used with an instrumented cone probe to allow collection of PS data without a borehole at all. For sites with stiffer soils, the cone probe rig can be used to install a cased borehole using hollow steel casing and a vibratory hammer. This casing can then be used to quickly perform a PS test using "conventional" methods, but still without requiring the use of a large truck-mounted drill rig. Sites with softer soil profiles can be tested with just an instrumented cone probe as the PS receiver. These two options are discussed below, after a brief summary of how the PS test method is used.

Parallel Seismic Test Method

The Parallel Seismic (PS) test is normally performed by impacting an exposed foundation top or side, or impacting a part of the structure above the foundation (such as a pile cap or column). The impacts can be either vertical or horizontal, and are typically done with an instrumented impulse hammer to generate compressional waves. Testing can also be done with a non-instrumented hammer, using an accelerometer mounted nearby for the trigger source. These waves travel down the foundation and couple into the surrounding soil as shown in Figure 1. The coupled compressional waves are then picked up in the soil by a nearby hydrophone or geophone receiver. This receiver is typically suspended in a water-filled cased borehole, but can also be near the tip of an instrumented cone probe pushed into the ground. The impact data is collected at a series of multiple receiver depths and stored. This data is then used to create a plot of receiver signal arrival time versus depth, from which the analysis is performed.

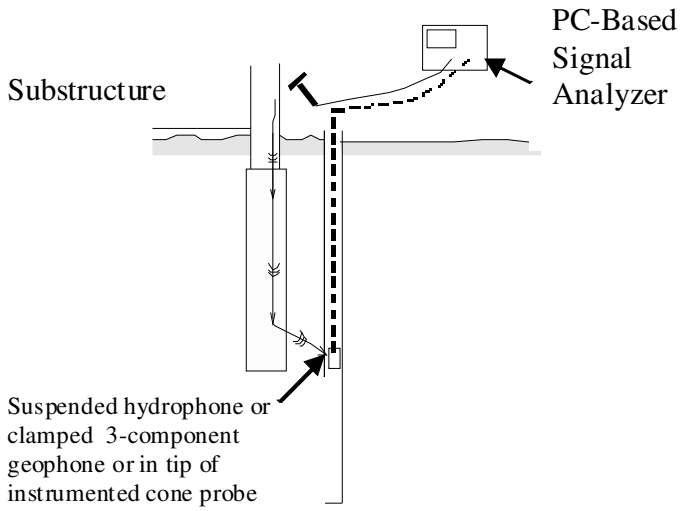

Figure 1: Parallel Seismic (PS) Test Method

Regardless of the type of equipment used to collect the PS data, the tip depth of a foundation is typically indicated by an inflection point in the arrival time versus depth curve, along with a sharp drop in signal amplitude. Diffraction of wave energy from the foundation bottom has also been found to be indicative of foundation tip depth in PS tests as well. Other research at Northwestern University National Geotechnical Site (NGS) has also indicated that the PS method is effective in measuring foundation lengths of inaccessible piles (piles with no access to the pile sides or tops), although this research also pointed out that some care must be taken when using the method under certain soil/rock interface depth versus pile length conditions (4).

Typical Parallel Seismic Test Equipment

The PS test method requires a relatively simple set of equipment to perform. A summary list is presented below:

1. PC based data acquisition system with a sampling rate of at least 100 kiloHertz (10 microseconds/12 bit digital data point) on at least 2 channels (4 channels needed for triaxial geophone) with at least 4096 data points per channel,
2. Signal amplifier(s) for receiver(s). Note: amplifiers can be built into the receivers in some cases.
3. Instrumented impulse hammer or non-instrumented hammer and an accelerometer. Hammers typically weigh 1.4 to 5.5 kg (3 to 12 lb) and must supply an accurate trigger time signal either through the built-in load cell or the nearby accelerometer.
4. Hydrophone or triaxial geophone receivers are required for borehole-based PS tests, while an instrumented cone probe is required for CPT-based tests.

Parallel Seismic Data Interpretation

The Parallel Seismic test is used primarily to determine the depth of unknown foundations, although information as to foundation type can usually be determined by an experienced testing firm based on the foundation velocity, inflection points, etc. The research done for NCHRP 21-5 and 21-5(2) (1,2) resulted in the establishment of several criteria for determining the foundation depths based on Parallel Seismic data as follows:

1. Breaks in the slope of the lines in a plot of depth versus recorded time,
2. Drop in energy amplitude below the bottom of the foundation, and
3. Diffraction of wave energy at the bottom of the foundation.

Example PS Test Data – Concrete Driven Pile Foundation

A PS test was performed on a 29 m (94 ft) deep foundation element supporting a bridge in Baton Rouge, Louisiana. The test was performed by using a CPT rig to install a hollow steel casing into the ground, into which a small diameter (2.5 cm, 1 inch ID) PVC pipe with a slotted bottom was inserted. After insertion of the PVC, the steel casing was removed, leaving the PVC pipe behind. A PS test was then conducted on the foundation, with the impacts being supplied by a 1.4 kg (3 lb) instrumented hammer hitting the side of the bridge column above grade. The signals were received by a small diameter hydrophone suspended in the water-filled PVC casing. A typical PS test result from this testing is presented in Fig. 2 for a test done with the hydrophone moved at 1 foot intervals for the entire length of the casing. As seen, the arrival time versus depth plot starts with a velocity versus depth slope of about 3,658 m/s (12,000 ft/s). This is typical of the compression wave velocity of concrete. At a depth of about 29 m (94.9 ft) below grade, the slope of the arrival time plot changes abruptly to about 2011 m/s (6,600 ft/s). This is the typical compression wave velocity of the saturated sands expected to

be at and below the tip of the foundation. The foundation bottom depth is at the intersection point of the two lines (at the inflection depth).

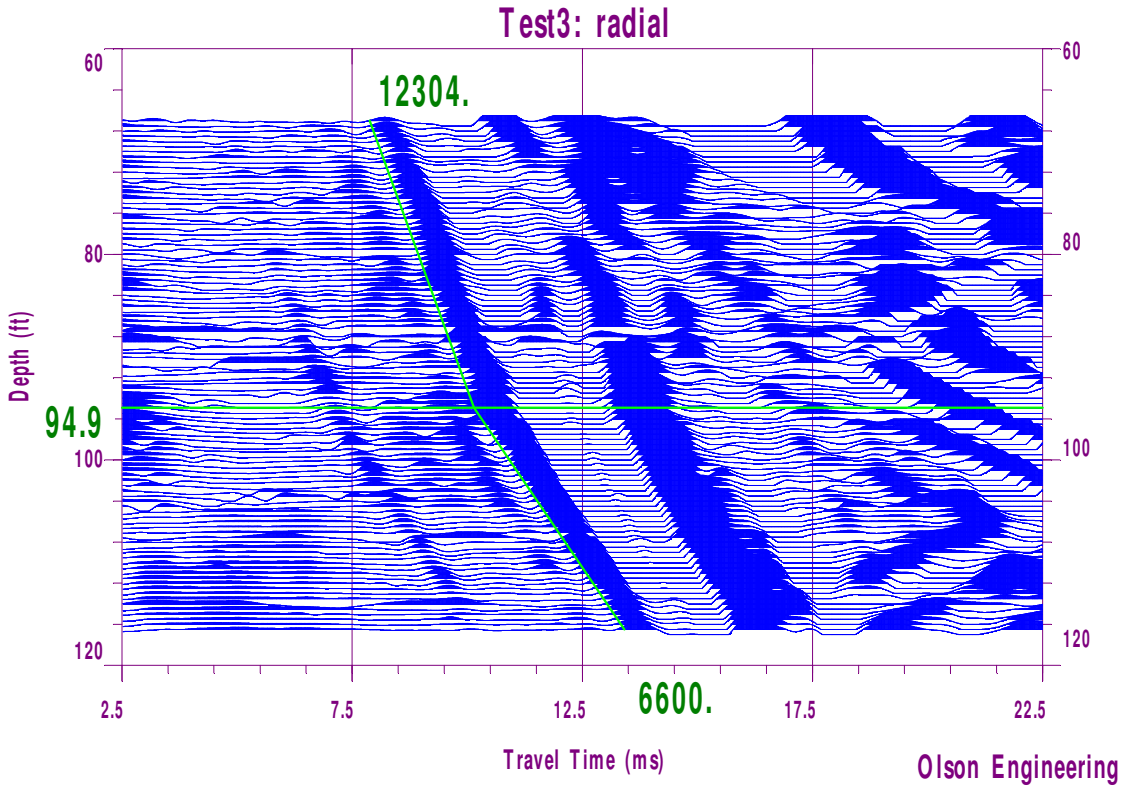

Figure 2: Sample PS Test Result for Concrete Bridge Pile – Tip at 29 m (94.9 ft)

Example PS Test Data – Steel Sheet Piles in New Orleans Levees

A series of tests were performed using the PS test method on sheet piles along the tops of levees in New Orleans, Louisiana in 2005 and 2006. The levee walls in the area of the testing consisted of steel sheet piles driven into the levee soil, topped by a concrete wall which extended several feet into the soil of the levee with the tops of the steel sheet piles embedded into it. The PS data sets were collected using both the PS/CPT and conventional PS testing using boreholes and by a Geoprobe CPT rig (see Figure 3) at selected locations near the levee walls.

The conventional PS data was collected for receiver depths from about 10 feet below the sheet pile tips up to just below grade. The impacts to the wall were done by impacting the concrete wall in both vertical and horizontal directions, as well as on the steel sheet pile itself at one location where a small excavation had been made to expose the top of the steel below the concrete.

An example of a PS test performed on a levee wall location is presented in Figure 4. This test was conducted using vertical impacts to the top of the concrete wall with a 1.4 kg (3 lb) instrumented impulse hammer, as shown in Figure 5. This location had a cased borehole installed using a CPT rig to install a small diameter PVC casing without a drill rig, as described in the previous section. Data was collected for receiver depths from 0.6 m (2 ft) to 9.1 m (30 ft) below grade using an Olson Instruments Freedom Data PC for both signal conditioning and digitization/storage as shown in Figure 6. It should

be noted that the borehole was located only about 0.76 m (2.5 ft) from the levee wall at this location, which provides for the best possible data. The data set showed clean data with a clear sheet pile tip depth. As seen in the figure, the steel sheet pile tip is apparent at a depth of 6.6 m (21.5 ft) below grade. The tip of the sheet pile acted as a point diffraction source, with much of the energy traveling in the pile coupling to the firmer sandy soil located only at or near the tip. Above the tip, the slope of the plot is negative, indicating that most of the energy picked up by the receivers at shallower depths was coming also from the pile tip and not from the sides of the pile. This unusual result is not uncommon with steel sheet piles, and still results in an easy to see pile tip depth indication.

Figure 3: Geoprobe CPT rig at Levee Concrete Wall on Sheet Pile

A seismic cone penetrometer probe for PS and seismic testing with three triaxial geophones and a hydrophone is shown in the photograph presented in Figure 7. The photo in Figure 8 presents both a small diameter hydrophone for 25.4 mm (1 inch) ID PVC casings installed with the Geoprobe rig and a larger hydrophone for 38 mm (1.5 inch) ID PVC and larger casings installed with a conventional borehole drilling rig which were used in the PS tests.

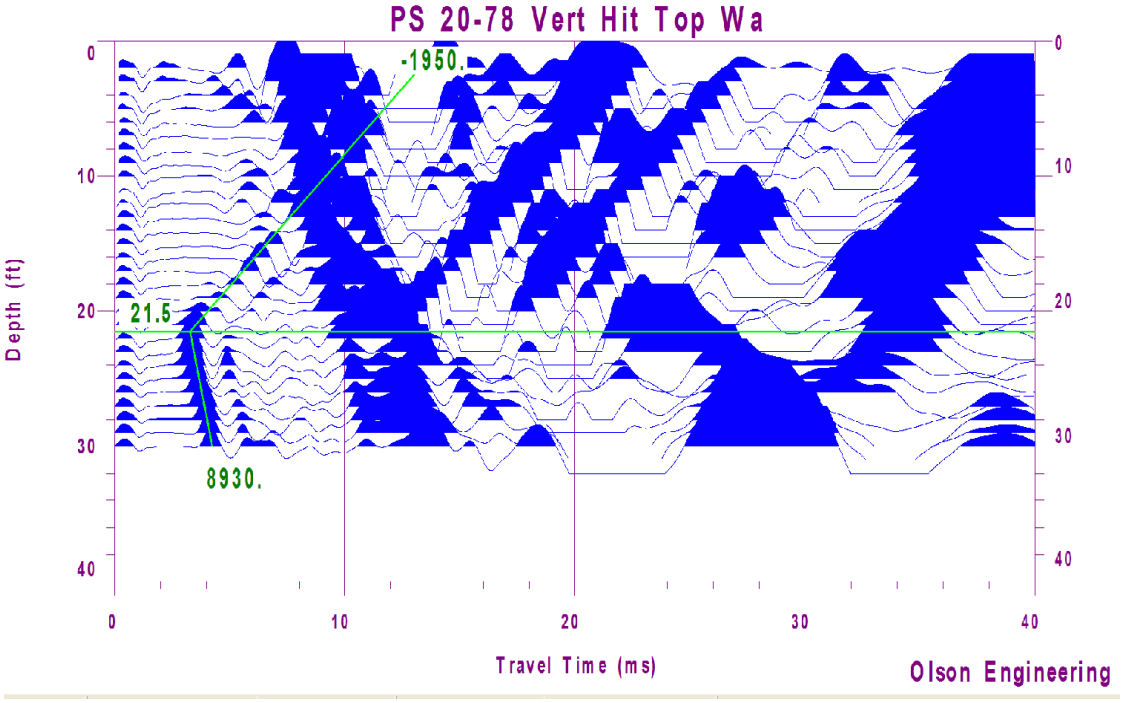

Figure 4: Sample PS Data on Levee Concrete Wall/Steel Sheet Pile – Note Sheet Pile Tip Depth is indicated by Diffraction Event at 6.6 m (21.5 ft)

Figure 5: Impacting the Top of the Levee Wall

Figure 6: Freedom Data PC for PS Borehole Test

Figure 7: Seismic Cone Probe with 3 Triaxial Geophones and 1 Hydrophone

Figure 8: Small and Large Hydrophones for PS Testing in Water-Filled PVC Casings

Parallel Seismic Test Recommendations

For successful use of the PS method, regardless of whether data is collected with a PS/CPT system or a standard PS test setup, there are several considerations which must be taken into account at each proposed testing site.

The most effective PS testing is done when the transducer is located as close as possible to the foundation under test. Typically, the borehole to foundation distance should be 3 m (10 feet) or less for the highest quality and greatest foundation tip depth accuracy. This requirement is to reduce the effects of the velocity and attenuation of the surrounding soil, particularly at sites with unsaturated soil conditions. Where saturated soil conditions exist, PS tests have been successfully performed with larger horizontal offsets from foundation edges. The CPT rig used for the new PS/CPT tests allows the probe to be pushed into the soil at locations as close as 1.5 to 2.1 m (5-7 feet) from the foundation edge, depending on access conditions

Ideally, the borehole (for traditional PS tests) or probe penetration depth (for PS/CPT tests) should extend at least 4.5 m (15 ft) below the minimum required foundation depth (from a capacity/scour perspective considering the subsurface geology) or suspected foundation depth, whichever is greater. This requirement is to ensure that data is collected to the depth of interest. If the borehole or probe is not at least somewhat deeper than the foundation bottom, one may only be able to determine that the foundation is at least as deep as the borehole or probe at the maximum depth (unless a foundation bottom diffraction event is recorded). We have seen a number of cases where the tip depth can be seen in the PS data at transducer depths above the tip depth based on diffractions from the pile tip. However, this type of analysis is not considered to be as reliable as collecting data to depths below the foundation tip and should only be used in cases where the borehole or probe is not or cannot be advanced to the required depth. It should be noted that when collecting data with a PS/CPT setup, it is possible to monitor the data from the PS tests as well as soil conditions from CPT data as the probe is gradually inserted deeper into the soil. Thus, the bottom depth of the foundation can be determined during the course of the testing along with the soil properties. This allows the early termination of testing if the foundation is found to be shallower than expected, or, conversely, allows the operator to continue testing until the bottom depth is seen if the foundation is deeper than expected.

For use of the PS/CPT system, site soil conditions must be suitable for testing with a CPT system. Thus, sites with shallow rock or boulders are not generally suited to this type of testing with a CPT rig. In addition, the testing cannot be extended into the bedrock for sites with shallow bedrock or sites where the piles bear into bedrock. Thus, this system is most suited for testing driven piles or other foundations placed into relatively soft to medium stiff clays or loose to medium dense sands and silts. Tests of sheet piles in a levee system are an ideal application for the PS/CPT system, since it can be driven along the levee top, and the soil conditions are ideal for pushing an instrumented cone probe to the depths required.

Based on experiences with PS testing of hundreds of unknown foundations as well as research tests conducted on known foundations, typical PS accuracies of 5% for bottom depth prediction are expected. If the data quality is poor, or the boreholes are located farther than 1.5 -2.1 m (5-7 ft) from the shaft being tested, accuracies of 10% may result. The accuracy of the method is greatest for sites with homogenous soil profiles, especially in the area around the foundation tip depth. Finally, the clearest

and most reliable results are produced by using a relatively high frequency source such as a steel sledge or instrumented hammer with a hard tip to impact the foundation top or column/pile cap.

Conclusions

The PS test method has been found in previous research to be the most accurate and versatile method for unknown foundation length determination. One major drawback to this method has been the requirement for drilling a cased borehole at each test location. The combined PS/CPT system allows the collection of both soil data and PS foundation length data with the ease of a simple CPT test in locations where the soil profile allows direct pushing of the cone probe to depths below the pile tip depth. For sites with stiffer soils, the same cone probe rig can be used to install a cased borehole using hollow steel casing and a vibratory hammer. This casing can then be used to quickly perform a PS test using "conventional" methods, but still without requiring the use of a large truck-mounted drill rig. The flexibility and mobility of the new system should allow for easier and more cost effective collection of PS data on a wider variety of sites than was previously possible. In addition, the ability to determine soil conditions in parallel with PS data collection results in a more "complete package" of information for engineers who ultimately need both sets of data to estimate the actual capacity of the foundation element being tested.

References

1. Olson, L.D., Jalinoos, F. and Aouad, M.F., Determination of Unknown Subsurface Bridge Foundations, NCHRP 21-5, Final Report, August, 1995.

2. Olson, L.D., and Aouad, M.F., Unknown Subsurface Bridge Foundation Testing, NCHRP 21-5 (2), Final Report, June, 2001.

3. Olson, L.D., Determination of Unknown Bridge Foundation Depths with NDE Methods, *Proceedings of 82nd Annual TRB Meeting* (CDROM), January 12-16, 2003, Paper No. 03-4039.

4. Finno, R.J, Gassman, S.L, and Osborn, P.W., Non-Destructive Testing of a Deep Foundation Test Section at the Northwestern University National Geotechnical Experimentation Site, A Report Submitted to the Federal Highway Administration, June 1997.

5. Schmertmann, J.H., "Guidelines for Cone Penetration Test Performance and Design", FHWA-TS-78-209, February, 1977.

Multiple Impact Surface Waves for Determination of Pavement System Moduli for Assessment and Design

Larry D. Olson P.E., Olson Engineering, Wheat Ridge CO
Christopher L. Barnes, P.E., Dalhousie University, Halifax, Nova Scotia, Canada
Matthew P. Hergert, Olson Engineering, Wheat Ridge CO
Patrick K. Miller, Olson Engineering, Wheat Ridge CO

ABSTRACT

The Multiple Impact Surface Wave (MISW) method involves the measurement and modeling of the propagation of surface waves in pavements. MISW can accurately determine not only the surface pavement thickness and low-strain elastic modulus of concrete and asphalt, but also the thicknesses and moduli of underlying base and subgrade layers. The MISW test method was used in a forensic concrete pavement investigation project and the thickness/moduli results for the concrete, base and subgrade layers are compared with Spectral Analysis of Surface Waves (SASW) results. The MISW method is able to accurately estimate the properties of base materials immediately below the much stiffer pavement layers by accounting for higher order wave modes during the inversion process in comparison to SASW results. Example results are presented of the use of MISW combined with Impact Echo (IE) data analyses to predict thickness/moduli of an asphalt pavement. Finally, a discussion is presented of the calculation of asphalt elastic moduli from MISW results for mechanistic-empirical design of asphalt pavements.

INTRODUCTION

As mechanistic-empirical design methods are increasingly used in pavement design, there is an increasing need to measure Young's elastic moduli in situ. In 2004, Ryden and Lowe (1) reported a study on guided waves in a layered half-space with large velocity contrasts where a decreasing velocity with depth is presented. They found by calculating multiple mode dispersion curves in the complex wave number domain and taking into consideration the attenuation caused by leakage into the underlying half-space, that they could better resolve the thicknesses and moduli of layered pavement systems with improved matching of the experimental and theoretical phase velocity vs. frequency dispersion curves. In particular, the lower moduli base and subgrade layers immediately below stiff pavement layers are resolved far better with the MISW approach than with other surface wave approaches. This method is called Multiple Impact Surface Waves (MISW) herein and is similar to Multi-Channel Analysis of Surface Waves (MASW) except multiple impacts are used rather than multiple receivers.

MULTIPLE IMPACT SURFACE WAVES DATA FOR CONCRETE PAVEMENT

The MISW method and process flow chart is illustrated in Figure 1. The source and receiver signals were recorded by an Olson Instruments Freedom Data PC and stored for further analysis. During MISW tests the generated surface waves were measured with a seismic accelerometer fixed at zero

offset. A series of multiple hammer impacts were generated from 0.20 to 5.00 m offset in 0.20 m increments. All recorded signals were then compiled to make an equivalent multi-channel record which can be transformed to a phase velocity spectrum similar to the MASW transformation technique (2).

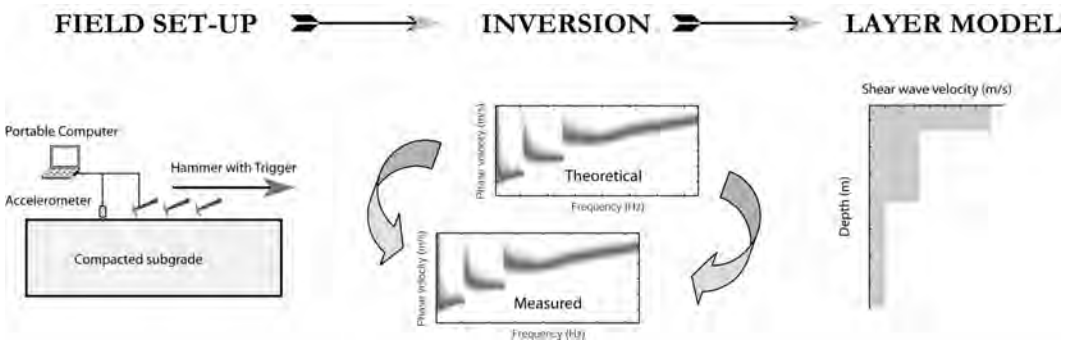

Figure 1: MISW process schematic showing data acquisition, processing and shear wave velocity profile output.

MISW Surface Wave Method

The MISW test method uses the dispersive characteristics of surface waves to determine the variation of the surface wave velocity (stiffness) of layered systems with depth. All surface (Rayleigh) wave velocity measurement methods are based on the fundamental relationship that Rayleigh wave velocity (V_R) is equal to the frequency (f) times the wavelength (λ) as given in Equation 1 below.

$$V_R = f * \lambda \qquad (1)$$

Accounting for the known impact to receiver spacing distances, the phase versus frequency information is used to develop an experimental dispersion curve which plots phase velocity versus wavelength. Figure 2 presents typical data from MISW testing on a single subgrade layer and the resulting dispersion image. All of the data taken during MISW testing is analyzed together to create a dispersion image or phase velocity spectrum. As seen in the phase velocity spectrum, the phase velocity increases as a function of frequency. This apparent increase in the dispersive trend at higher frequencies is built up by interference of higher modes of surface waves and it is believed that the data can be more accurately evaluated by taking this effect into account. This effect can be accounted for by modeling to match the dispersion image. Single layer systems can be adequately analyzed without performing a traditional inversion model but instead using the fundamental lamb wave mode curves to guide an experienced user to a direct fit of the phase velocity image. During this processing the impact echo displacement frequency spectrum of 1 or more summed traces is also used to determine the thickness of the concrete or asphalt.

MISW Theoretical Modeling Data Processing

In order to determine the shear wave velocity profile from the "apparent" velocities of the dispersion curve, analytical modeling is necessary. The analytical modeling used herein is a forward modeling process that is iterative and involves assuming a shear wave velocity profile and constructing a theoretical dispersion curve or dispersion image. The experimental (field) and theoretical curves are compared, and the assumed theoretical shear wave velocity profile is adjusted until the two curves or images match. For MISW modeling, SeisNDT, a program developed by Dr. Nils Ryden (1), was used

for data collection, analysis, and theoretical modeling. The modeling program iteratively adjusts multiple parameters in order to match the experimental dispersion velocity spectrum image. This technique and analysis algorithms have been shown to accurately determine the layer thicknesses and moduli of pavement and soil systems. A MISW result from a concrete pavement site (which was also tested with the SASW method (3)) is presented in Figure 2. The surface wave data is plotted in the right plots as (amplitude normalized and not normalized) impact points offset from the accelerometer receiver versus time while the phase velocity spectrum of the experimental data is plotted as amplitude normalized and not normalized in the two right hand plots.

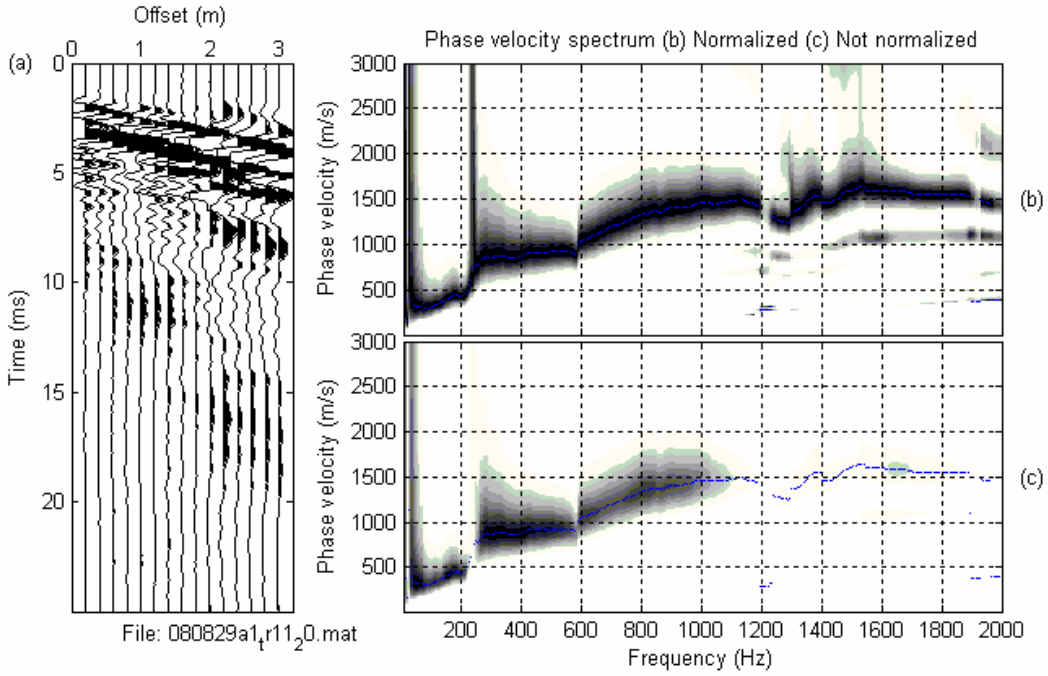

Figure 2: Example MISW results from Concrete Pavement Site with time domain data in left plot and Phase Velocity Spectrum in the 2 right plots (amplitude normalized by spectral frequency in plot (b))

The matching of the experimental phase velocity spectrum with the theoretical phase velocity spectrum is presented in Figure 3 with the top plot being the measured phase velocity spectrum, the second plot being the best fit theoretical velocity spectrum and the third plot comparing the mismatch between the experimental and theoretical results. The bottom plot on the left is the shear wave velocity profile versus depth while the layer data in terms of thicknesses, shear and compression wave velocities and Poisson's ratios are summarized in the lower right. Shear wave velocities of 2780, 135 and 229 m/s were measured for the concrete, cement treated clayey base and underlying natural clayey subgrade layers at the Figure 3 site. The cement treated clayey base layer had a much slower velocity than expected as it is important to note that shear wave velocities of cement treated soils are typically on the order of 500 to 1,500 m/sec which reflect the increased stiffness and moduli associated with the cement treatment. The ineffectiveness of the cement treatment was found at all of the sites tested with the MISW method. This was destructively confirmed by laboratory tests of boring samples as discussed below.

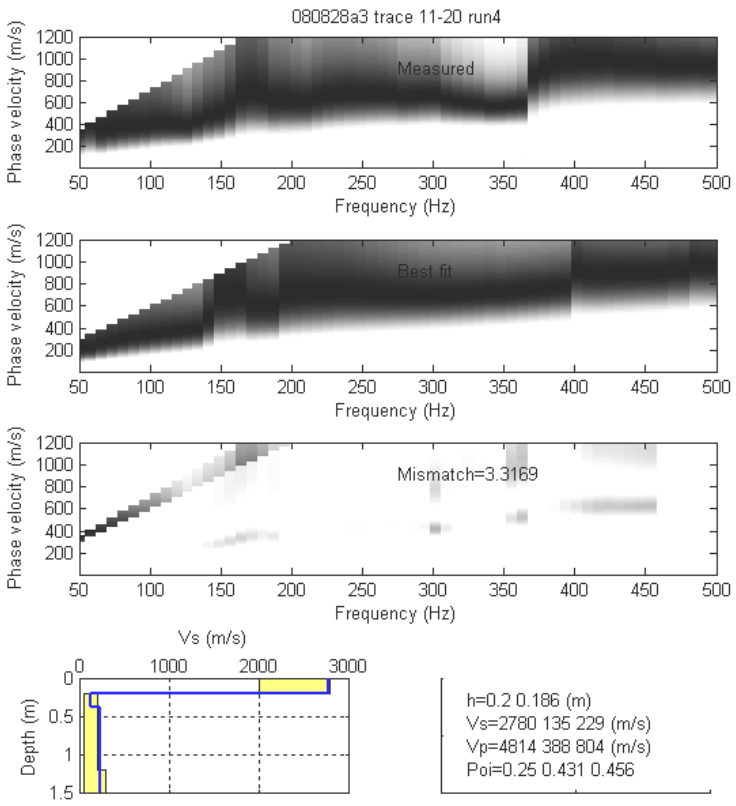

Figure 3: MISW Matching of Phase Velocity Spectrum for Experimental (top) and Theoretical Best-fit (2nd plot), and Mismatch (3rd plot) with MISW Theoretical Shear Wave Velocity Profile vs. Depth (left-bottom) and Layer Information (right-bottom).

Boring and Laboratory Test Results for Base and Subgrade at Concrete Pavement Sites

A total of 6 soil borings were performed at the concrete pavement test site corresponding to 6 of the 15 total locations tested with the MISW method. The borings provided physical samples with which to compare the nondestructive MISW and SASW test results. Generally, all six borings produced similar pavement layer system profiles. Four of the six borings consisted of a 200 – 225 mm thick pavement layer underlain by a 300 – 400 mm thick cement treated clayey base layer, followed by a 1.0 – 1.5 m thick stiff, sandy clay layer. One boring did not have a cement treated clayey base layer, while another boring had a 0.5 m thick clayey sand layer instead of the cement treated clayey base layer.

The cement treated clayey base would have been expected to be significantly faster in MISW and SASW tests with correspondingly higher moduli and stiffness values than the natural sandy clay subgrade layer directly beneath it. To check this, samples obtained from both of these layers in three borings were subject to unconfined compressive strength tests. In all three cases the sandy clay layer produced higher strengths than the cement treated clayey base layer. The unconfined compressive strengths ranged from 0.14 – 0.27 MPa for the cement treaded clayey base and ranged from 0.20 to 0.40 MPa for the sandy clay layer. The boring logs also show the same trend in data from a pocket penetration test that was performed in-situ in all borings. Thus, the laboratory strength test results agree with the MISW results that show the cement treated clayey base layer is weak and is actually less stiff with corresponding slower velocities and elastic moduli than the underlying natural sandy clay subgrade.

Comparison of SASW and MISW Results at Concrete Pavement Sites

A direct comparison from a typical test site of the theoretically best fit shear wave velocity profiles from the SASW and MISW testing is presented in Figure 4. Review of this figure indicates that the SASW method with the 3-D higher mode option selected in the WINSASW 2.4 software incorrectly predicted significantly higher shear wave velocity profiles for the cement treated clay base layer immediately below the concrete than the MISW method which utilized SeisNDT software in the data analysis (3). Generally, both methods predicted similar shear wave values for the pavement layer and tended to converge at depths greater than 1 meter when longer wavelengths dominated the results.

Further examination of Figure 4 indicates that the shear wave velocity of the cement-treated base was quite high below the concrete in the SASW results (700 - 1200 m/s). However, the MISW results predicted a much slower velocity (~100 to 200 m/s). As noted above, the unconfined compressive strength tests performed on samples of the cement-treated base revealed comparatively low strengths of the base layer at the concrete pavement site. This finding is in agreement with the MISW results as the cement-treated base was found to have similar or lesser strengths in comparison to the underlying natural sandy, clay subgrade soils that had not been treated with cement.

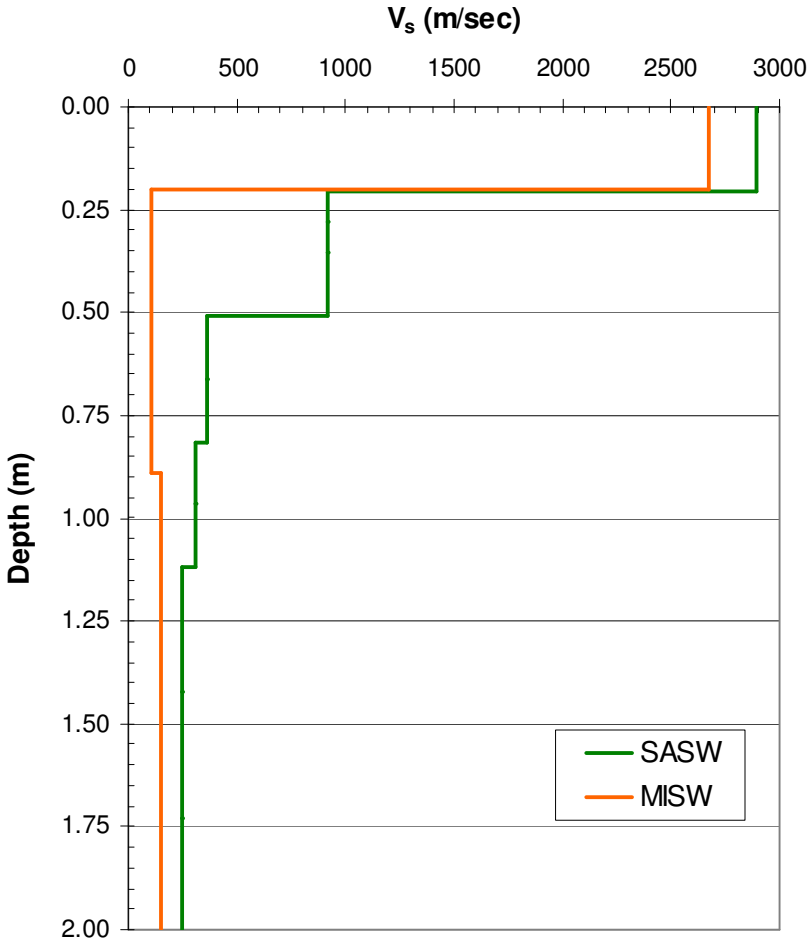

Figure 4: Comparison of SASW and MISW shear wave velocity profiles with depth. Example data from 1 of 9 similar concrete pavement sites.

The results from the MISW testing indicate that the cement treated clayey base layer had a shear wave velocity ranging from 100 – 200 m/sec. Based on experience this is considered a soft to average

stiffness subgrade layer. According to the modeling, the uppermost soil layer ranged in thickness from 4 inches to nearly 3 feet. The second soil layer beneath the concrete pavement has similar properties and typically shows a slight increase in shear wave velocity but is still considered a soft to average stiffness layer which was expected for the natural sandy clay subgrade layer. These results are well supported by the boring logs, pocket penetration tests performed in-situ at the time of the boring, as well as unconfined compression tests performed on soil samples of the base and subgrade as discussed above.

MULTIPLE IMPACT SURFACE WAVE TEST RESULTS FOR ASPHALT PAVEMENTS

In order to illustrate the use of MISW on asphalt pavement, the MISW test was performed at the National Center for Asphalt Technology test track at Auburn University in an area with a known asphalt pavement thickness of 229 mm. Each MISW test consisted of 5 impacts at 12 impact points at intervals of 50 mm for a shorter survey distance of 0.65 m for testing of only the asphalt layer (and not the base or subgrade layers which require surveys of 4-5 m in length) as shown in Fig. 5.

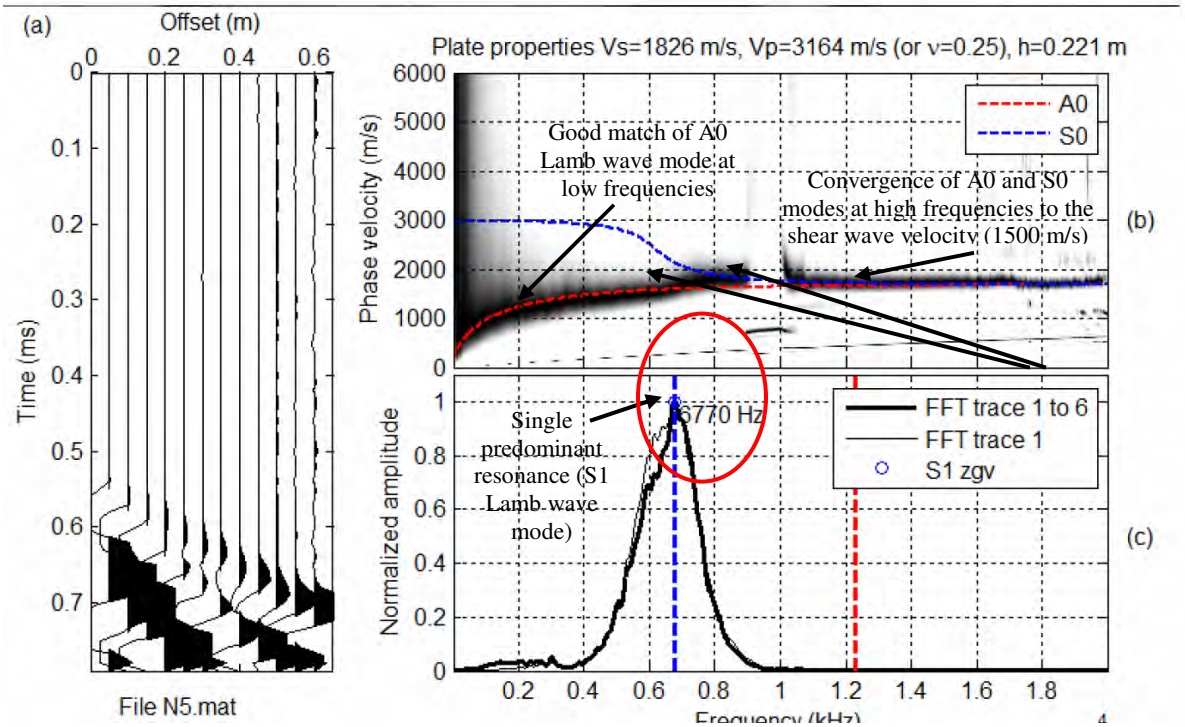

Figure 5: Test Point A1 MISW Results showing the A0 and S0 Lamb wave modes with a thickness of 218 mm (the full asphalt depth).

Review of Figure 5 indicates the asphalt was of sound condition and there are no apparent differences between the four placement lifts which totaled 229 mm in thickness. This compares to the predicted pavement thickness of 221 mm from the impact echo resonant frequency analyses of the first trace closest to the impact and the summed 6 traces closest to the impact. The thickness or height (h) is calculated per Equation 1 as a function of a shape factor ($\beta = 0.954$ for a flat slab and Poisson's ratio of

$\nu = 0.25$ (2)) multiplied times the compression wave velocity (V_p) and divided by twice the resonant frequency of the displacement spectrum of the receiver response on a slab as given in Equation 2.

$$D = \beta V_p/(2f) \quad (2)$$

The A0 wave mode generally fits the phase velocity image at frequencies less than 10,000 Hz. The frequency spectrum of a single trace (impact at 5 cm from the accelerometer) as well as the summed frequency spectrum of the 6 averaged traces (5 impacts averaged from the 6 closest impact points to the accelerometer) both show a single predominant resonance at approximately 6,770 Hz which, considering the shear wave velocity and Poisson's ratio, relate to an approximate asphalt thickness of 221 mm. This frequency domain resonance has been shown to be the S1 lamb wave mode resonance (see bottom right trace in Figure 5).

EVALUATION OF SURFACE WAVE MODULI

Barnes and Trottier (4) conducted recent research on surface waves with the MISW method on asphalt pavements and also have discussed in detail the calculation of moduli for asphalt from MISW results as is presented herein after their work. They, Dr. Ryden and others have used a simple visco-elastic frequency-dependent model for the stiffness behavior of asphalt concrete, which is characterized using a sigmoidal master curve (5) as shown in Equation 3.

$$\log(|E^*|) = \delta + \frac{\alpha}{1 + e^{\beta - \gamma \log(\xi)}} \quad (3)$$

where:
$|E^*|$ = dynamic complex modulus;
ξ = reduced frequency;
δ = minimum modulus value;
α = maximum - minimum modulus values; and,
β, γ = shape parameters.

Dynamic modulus tests are conducted at various temperatures and frequencies and are shifted to a reduced frequency, shown in Equation 4.

$$\log(\xi) = \log(f) + \log[a(T)] \quad (4)$$

where:
$a(T)$ = shift factor, $a(T_0) = 0$;
f = frequency; and,
ξ = reduced frequency.

The frequency shift factor is a function of temperature and has been approximated using a quadratic relationship as shown in Equation 5.

$$\log[a(T)] = aT^2 + bT + c \quad (5)$$

Barnes and Trottier (4) prepared six 100-mm diameter core samples which were drilled from each of three asphalt plate specimens for preparing dynamic (complex) modulus test specimens. These 100 x 210 mm specimens were produced by bonding three core samples together using a 3000 MPa compressive strength epoxy paste commonly used in repairing Portland cement concrete. The thin epoxy layers were not expected to influence the measured dynamic modulus. These samples were tested using a servo-controlled hydraulic test machine according to AASHTO TP62-03 to determine the dynamic modulus at frequencies of 0.1, 1, 5, 10 and 25-Hz at temperatures of -17.5, 0, 11.5, 18, and 40 ºC within a controlled environmental test chamber. Since all specimens contained 5.0-5.1% air voids, the dynamic modulus results for all six specimens were compiled to construct the master curve for the asphalt mixture, using a reference temperature of 18 ºC. Optimal solutions for all parameters of Equations 3 and 5 (δ, α, β, γ, a, b, and c) were obtained using the Microsoft Excel Solver function by minimizing the sum of the square of the errors between the fitted model and the experimental data. It is generally accepted that a frequency of 25-Hz provides a suitable approximation of traffic loading on highway pavements. The 18 ºC, 25-Hz design modulus was determined from the fitted master curve equation to be 3964 MPa.

Barnes and Trottier further presented a theoretical master curve (see Figure 6) fitted to the experimental dynamic modulus core data with their SASW and MISW-based high frequency moduli from the asphalt plate specimens they studied. MISW phase velocities at wavelengths occurring within the asphalt (or concrete pavements) were assumed to correspond to the fundamental Rayleigh wave velocity, V_R, from which the shear wave velocity, V_s, and modulus, E, were computed, assuming a Poisson's ratio, ν, of 0.35 and using the measured density of 2260 kg/m^3, according to Equations 6 and 7.

$$V_S = V_R(1.13 - 0.16\nu) \tag{6}$$

$$E = 2\rho V_S^2(1+\nu) \tag{7}$$

A good fit between the master curve and MISW results is visually apparent, with the position of the master curve occurring very close to the center of the MISW data. The SASW results appear to overestimate the dynamic modulus values and the fitted master curve. The master curve was used to shift the individual high frequency moduli from both the SASW and the MISW phase velocity curves down to a 25-Hz design value, using a ratio of the 25-Hz master curve modulus divided by the master curve modulus at the reduced frequency of interest, using Equations 3 and 4. The average value of all 25 Hz-shifted surface wave moduli was computed for comparison to the master curve.

It may also be seen from Figure 6 that the test frequencies for the surface wave moduli occur near the upper limit of an approximately linear portion of the sigmoidal master curve shape, while the design frequency of 25-Hz occurs near the lower limit of this range (note that the MASW results (6) were collected as an MISW data set with a single receiver also by Barnes and Trottier (4)). The linearity of this range has been approximated using a power function, of the form shown in Equation 8, to describe the frequency dependency of the shear wave velocity (7). This power function has also been used predicting the dynamic modulus at a design frequency, based on fitting the function to the shear wave velocity derived from each point of the surface wave phase velocity dispersion curve.

$$V_s = b_1 f^{b_2} \quad (8)$$

A power function of this form was fitted to each experimental MISW phase velocity dispersion curve, which tended to increase slightly with frequency as expected. The coefficients, b_1 and b_2 ranged from 530 to 1212 and 0.0178 to 0.0946, respectively, and appear to be similar to those reported elsewhere in the literature (7).

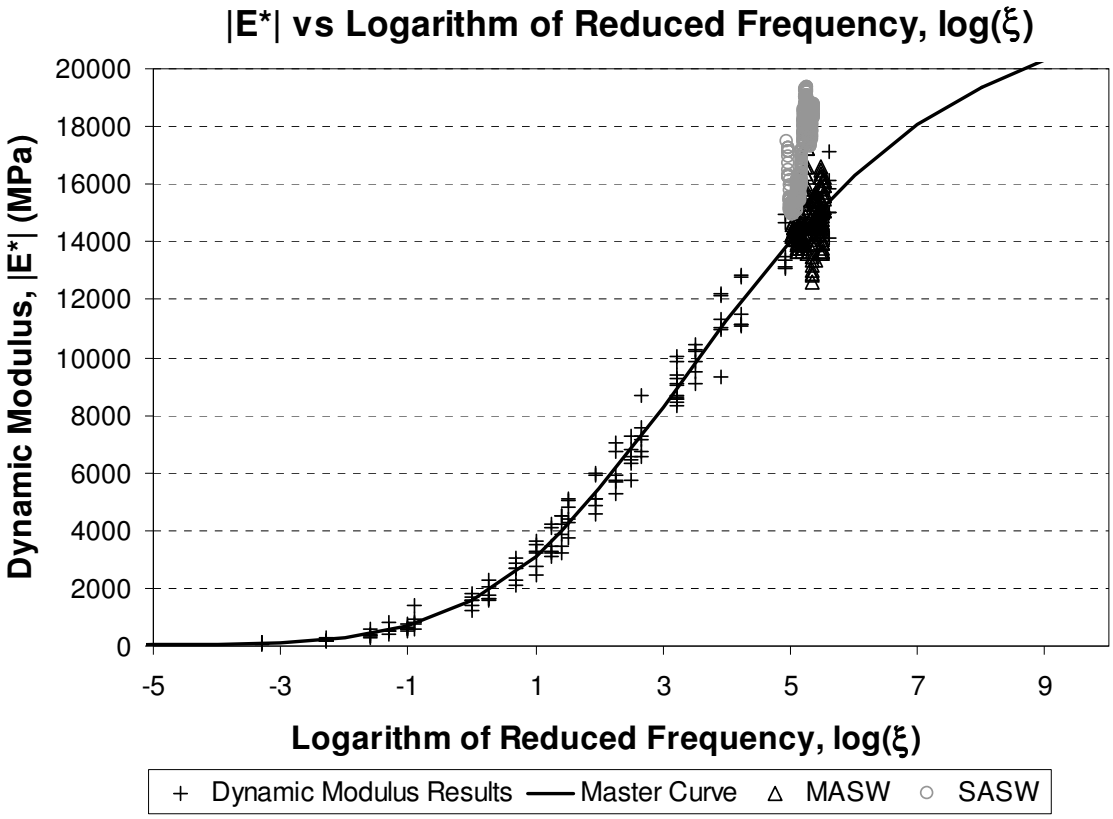

Figure 6: High frequency surface wave moduli superimposed onto shifted dynamic modulus data and master curve.

Barnes and Trottier found that the MISW analysis, which has the benefit of being able to identify and isolate the fundamental Lamb wave modes, indicates moduli which are almost identical to the standard dynamic modulus test results after applying the appropriate reduced frequency shift to the design frequency and temperature. The power function approximation tended to significantly overestimate the 25 Hz modulus value. Close inspection of Figure 6 reveals that the high frequency surface wave moduli from the MISW testing exist slightly beyond the linear region of the master curve where it begins to reduce in slope as it begins to approach the maximum theoretical modulus. As a result, the slope of the power function is flatter than that of the linear portion of the master curve, causing an overestimate of the design modulus. Based on Barnes and Trottier's results, it appears as though the most accurate method of shifting high frequency surface wave moduli to a design value can be achieved using the master curve. Unlike the power function approximation, other advantages of the master curve approach is that surface wave results obtained at any temperature within those used in its

construction can easily be shifted to a reference design value and the master curve is well established and accepted within the pavement engineering community.

CONCLUSIONS

The MISW method was shown to be more accurate than the SASW method at accurately measuring the velocity and moduli of base materials below rigid concrete pavements. The base materials immediately beneath the concrete pavement are described as cement treated clay in 4 of the 6 boring logs. The average shear wave velocity calculated for this layer was approximately 150 m/sec, however cement-treated soils typically have shear wave velocities at least 3 times greater than what was measured from the MISW method. It is also important to note that shear wave velocity squared is linearly related to elastic modulus, therefore the factor of 3 difference in shear wave velocity would correspond to a factor of 9 difference in modulus. If the soil base layer was indeed cement stabilized (as it appeared to be in 4 of the 6 boring logs), then the strength assumed in the design of the pavement is significantly greater than the current strength of the base. This reduced modulus and base strength will lead to the pavement system failing long before its intended design life. This case history illustrates the importance of the MISW measurements in a pavement rehabilitation project.

An example result of testing an asphalt pavement with MISW to determine the velocity and Poisson's ratio results to predict thickness using an impact echo resonance approach showed a predicted value of 221 mm versus an actual thickness of 229 mm. This is an accuracy of 3.5%. It is expected that asphalt thicknesses can be determined to within an accuracy of approximately 5% and this will be explored in future research. A discussion was presented about how to go from the high-frequency MISW moduli for asphalt to the low-frequency moduli needed for truck traffic for pavement design purposes (after Barnes and Trottier). They related the use of a master curve developed on laboratory test specimens and constructed from dynamic modulus tests in order to shift the high frequency MISW moduli to a 25-Hz reference truck traffic value for comparison. MISW results agreed well with the reference laboratory dynamic modulus, when shifted using the master curve equations, but overestimated the reference laboratory modulus when shifted using a power function approximation of the linear portion of the master curve.

The MISW method can thus be used to determine shear wave velocity profiles from which elastic Young's moduli and layer thicknesses can be accurately calculated for use in mechanistic-empirical (M-E) pavement design. Additionally, the MISW method can be applied for Quality Assurance/Quality Control (QA/QC) purposes during construction and in pavement monitoring and rehabilitation projects to provide accurate layer thickness and moduli data of layered pavement systems for both asphalt and concrete pavements. Finally, the MISW moduli can be used to predict the moduli for input in M-E pavement designs and analyses.

REFERENCES

(1) Ryden, N., and Lowe, M. (2004), "Guided wave propagation in three-layer pavement structures", *Journal of the Acoustical Society of America*, Vol. 116(5), pp. 2902-2913.

(2) Gibson, A. and Popovics, J. S., (2005), Lamb Wave Basis for Impact-Echo Method Analysis: *ASCE Journal of Engineering Mechanics*, 131, 438-443.

(3) Olson, L.D. and Miller, P.K., (2010), "Multiple Impact Surface Waves (MISW) – Improved Accuracy for Pavement System Thicknesses and Moduli vs. Spectral Analysis of Surface Waves (SASW), *GeoFlorida 2010 Proceedings*, GeoInstitute Annual Meeting, American Society of Civil Engineers, West Palm Beach, Florida.

(4) Barnes, Christopher L. and Trottier, Jean-François. (2009). "Evaluating High-Frequency Visco-Elastic Moduli in Asphalt Concrete", *Research in Nondestructive Evaluation*, 20: 2, pp. 116-130.

(5) Pellinen, T.K. and Witczak, M.W. (2002), "Stress Dependent Master Curve Construction for Dynamic (Complex) Modulus", *Assoc. of Asphalt Paving Technical Journal*, 71, 281-309.

(6) Park, C. B., Miller, R. D., and Xia, J. (1998), "Imaging dispersion curves of surface waves on multi-channel record", Kansas Geological Survey, *68th Annual International Meeting*, Society of Exploration Geophysicists., Expanded Abstracts, pp. 1377-1380.

(7) Ryden, N., and Park, C.B. (2006), "Fast simulated annealing inversion of surface waves on pavements using phase velocity spectra", *Geophysics*, Vol. 71, No. 4, R49-R58.

MEASUREMENT OF SHEET PILE LENGTH BY PILE INTEGRITY TESTING AND THE PARALLEL SEISMIC METHOD

Ernst Niederleithinger, BAM, Federal Institute for Materials Research and Testing, Berlin, Germany
Matthias Fritsche, Ingenieurbüro faust & fritsche, Berlin, Germany

Abstract

The non-destructive measurement of sheet pile lengths at existing constructions is a complex task. Low strain pile integrity testing is an easy and efficient method, but sometimes fails to give meaningful results. Statistical evaluation enhances the reliability and gives hints on length changes. Using the parallel seismic method, which has been developed for the assessment of drilled shafts and similar constructions, is an alternative possibility worth considering. Recently developed interpretation tools allow greater distances between piles and sensor boreholes compared to other methods. Two field examples show the use of both methods and some pitfalls, including ways to overcome them.

Introduction

Sheet piles have been used for more than one century in civil engineering. The protection of the edges of waterways is a major application area. Under favorable conditions they last for several decades without serious maintenance problems. But if load conditions change, a re-assessment has to be done. The most important parameter is the sheet pile length, which is not necessarily known after years. For example lots of files about construction projects in West-Berlin have been kept in Eastern Germany and could not be found after the reunion.

So far, the only way to determine sheet length exactly is to pull some of them. This is technically possible in many cases, but costly and by no means non-destructive. Thus an increasing demand for other methods arises. So far, only a few publications about alternatives are available (e. g. Jalinoos et al., 2006, Niederleithinger & Fritsche, 2009).

In the frame of re-assessment procedures and construction projects the authors were active at two sites in Berlin to investigate the possibilities of length measurement by a combination of low strain pile integrity testing and parallel seismic testing.

Methods

Several non-destructive foundation length measurement methods are established. Most of them have been developed for the inspection of new drilled shafts, but could also be applied to other foundation types. An overview is given e.g. by Turner (1997). In recent years the scope has also moved to existing foundations for re-assessment (Olson et al., 1998) or re-use (Butcher & Powell, 2006, Niederleithinger et al., 2007). The use of borehole geophysical methods at sheet piles is discussed by Jalinoos et al (2006).

Low Strain Pile Integrity Testing

Low strain pile integrity testing (PIT) is used since decades for the assessment of new piles. Standards exist in several countries (e. g. ASTM D5882, NF-P 94-160-2, DGGT, 2007). The top of the pile is hit by a hammer blow (Figure 1). The resulting stress wave travels downward and is reflected from the pile toe or major flaws. The resulting signal is measured by a geophone or accelerometer on the pile top. The shape of the reflected signals is influenced by concrete and soil parameters as well as shape and condition of the pile. The pile length L can be calculated from the measured travel time t and wave velocity c by

$$L = \frac{c \cdot t}{2} \qquad (1)$$

A major drawback is that the wave velocity is not exactly known in most cases. For concrete this leads to an error margin of up to 10% if local calibration values aren't available. For steel the error margin is somewhat smaller, but may still be significant. Typical values for c_{Steel} of sheet piles are 5100 to 5500 m/s.

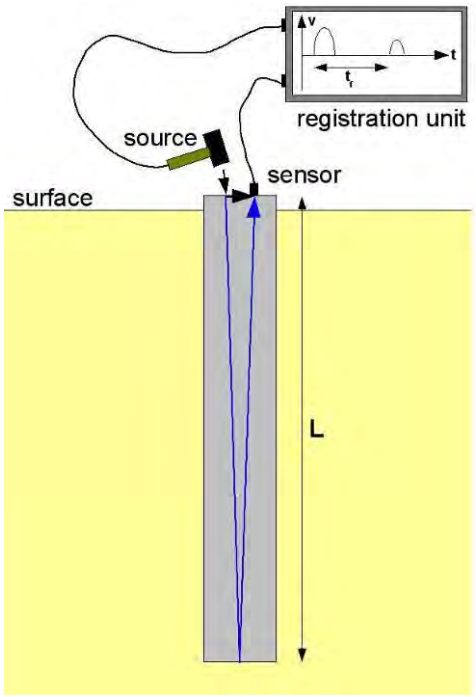

Figure 1: Principle of low strain pile integrity testing (left) and application on sheet piles (top).

If applied on wall type elements (sheet piles, secant pile walls) a significant part of the impulse energy may travel sideways to the adjacent elements. This leads to weaker toe (and flaw) reflections and possible additionally to lateral reflections. Thus the toe reflection may be hard to detect (Klingmüller & Kirsch, 2004). In addition, the optimum choice of hammer size, sensor position and other parameters is still researched. Some types of sheet piles seem to give better results than others, depending on welding scheme, anchoring and other factors.

Parallel Seismic Method

The Parallel Seismic Method (PS) uses the same source, but a different receiver geometry than PIT. Hydrophones or geophones are placed in a borehole near to the foundation (Figure 2). As simulations show (Niederleithinger, 2008) a guided wave is emitted into the soil while the stress wave

travels down the pile. The angle between pile and soil depends on the velocity contrast pile/soil. After the wave train reaches the pile toe, a diffracted, almost semicircular compressional and shear waves are travelling downward into the soil.

The first arrival time at each sensor is picked from the data and plotted in a time/depth plot. In most cases an inflection of the travel time curve near the depth of the pile toe is visible. The slope of the curve above and below this point reflects the wave velocities in pile and soil, respectively. The interpretation can be done by simply picking the inflection point, which neglects pile-borehole distance and tends to overestimate the length. It is better to use correction values (Liao et al., 2006) or curve fitting algorithms (Niederleithinger et al, 2005). The basic method was invented about 40 years ago in France, still the only country, which provides a standard (NF P94-160-3).

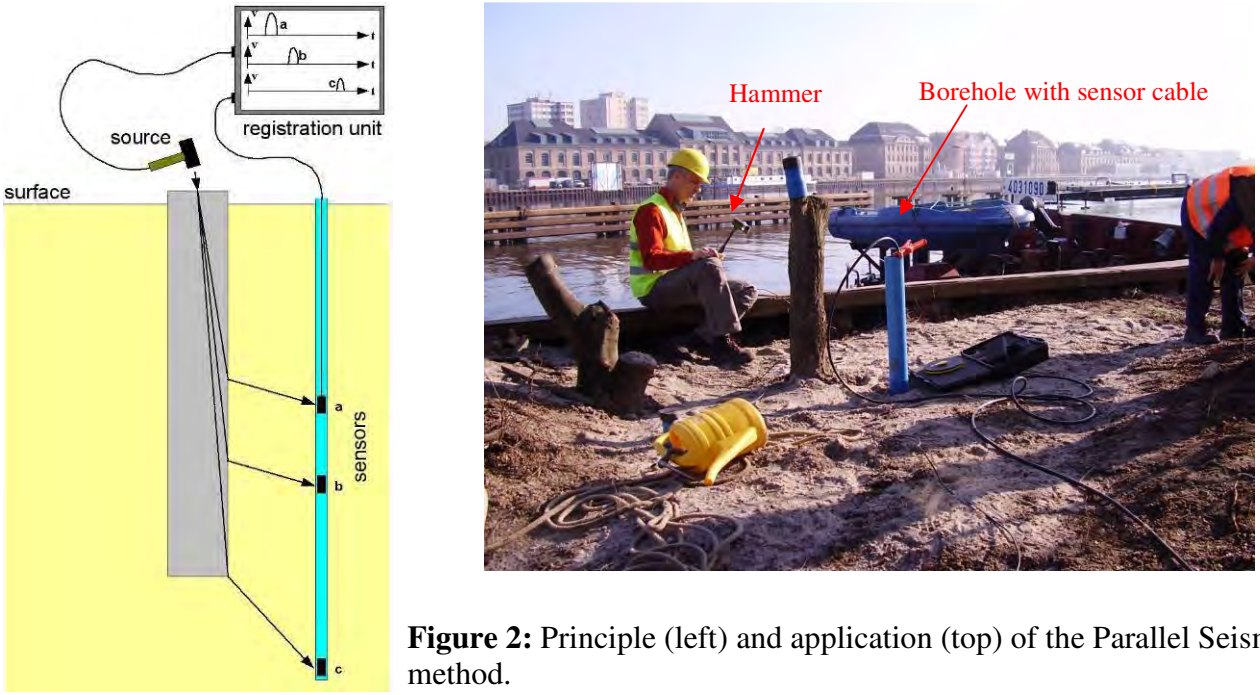

Figure 2: Principle (left) and application (top) of the Parallel Seismic method.

So far there have been no published applications on sheet piles except one from the authors themselves (Niederleithinger & Fritsche, 2009). As mentioned in the previous section one has to be aware that the impulse energy will travel from one sheet to the adjacent ones. This may lead to alternative ray paths providing the first arrival, particularly if the sheets have different lengths (Figure 4). This case is discussed in more detail in the Bootshandel example.

Field Examples

Napoleonkai

At the Napoleonkai in Berlin, a small pier mainly used for loading and unloading of sand and gravel, the authors had to investigate a sheet pile section of approximately 250 m width (Figure 5). The underground consists of 2.4 m backfill with fine to medium grade sands below.

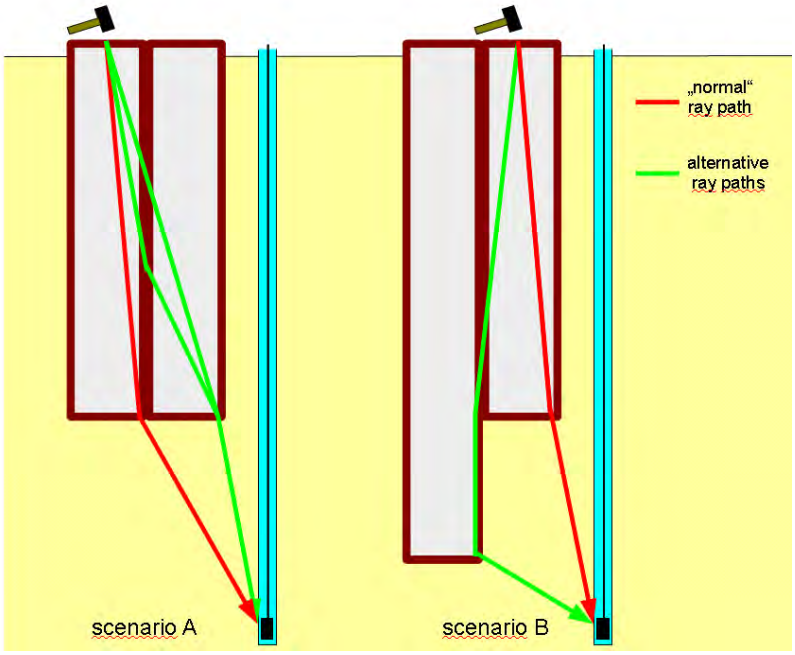

Figure 3: Alternative ray paths which may provide the first arrival in PS measurements at sheet pile walls

Figure 4: Sheet piles at Napoleonkai. Height above water level about 1.5 m.

The access for PIT measurements was limited as the top of the sheet piles was covered by a steel girder, which couldn't be removed. Only a couple of holes allowed impulse generation and sensor mounting directly on the sheet piles itself (Figure 1). Measurements on the top of the girder were not successful. The sheet piles were anchored in the backfill and had an expected length of about 8 m. Every second sheet was probably about 1 m shorter. Figure 5 shows the result of PIT measurements. While some of the records showed a significant toe echo (central record), it was difficult or even impossible to detect the sheet length (bottom and top record). The bottom record shows a significantly shorter pile length compared to the central one, supporting the assumption that the sheets are of different size. The overall average of the longer sheets was 7.78 +/- 0.23 m and 6.83 +/- 0.23 m of the shorter. The difference is 0.95 m, which is close to the typical value of 1.0 m for a construction with alternating length. According to standards the larger length can be used for load capacity calculations.

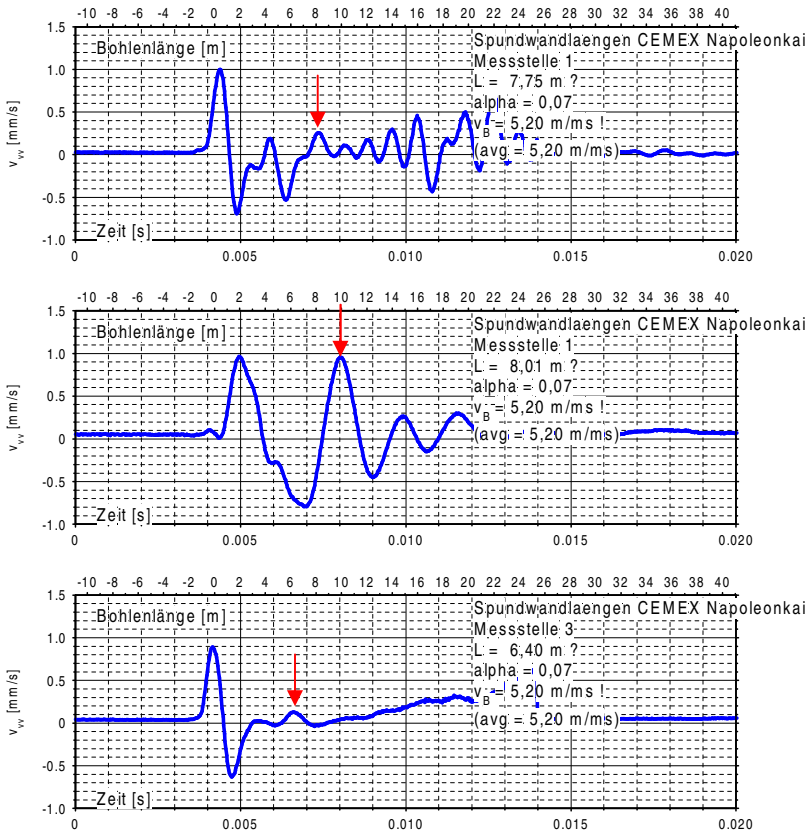

Figure 5: PIT records for the Napoleonkai sheet pile wall. Arrows: position of pile toe echo

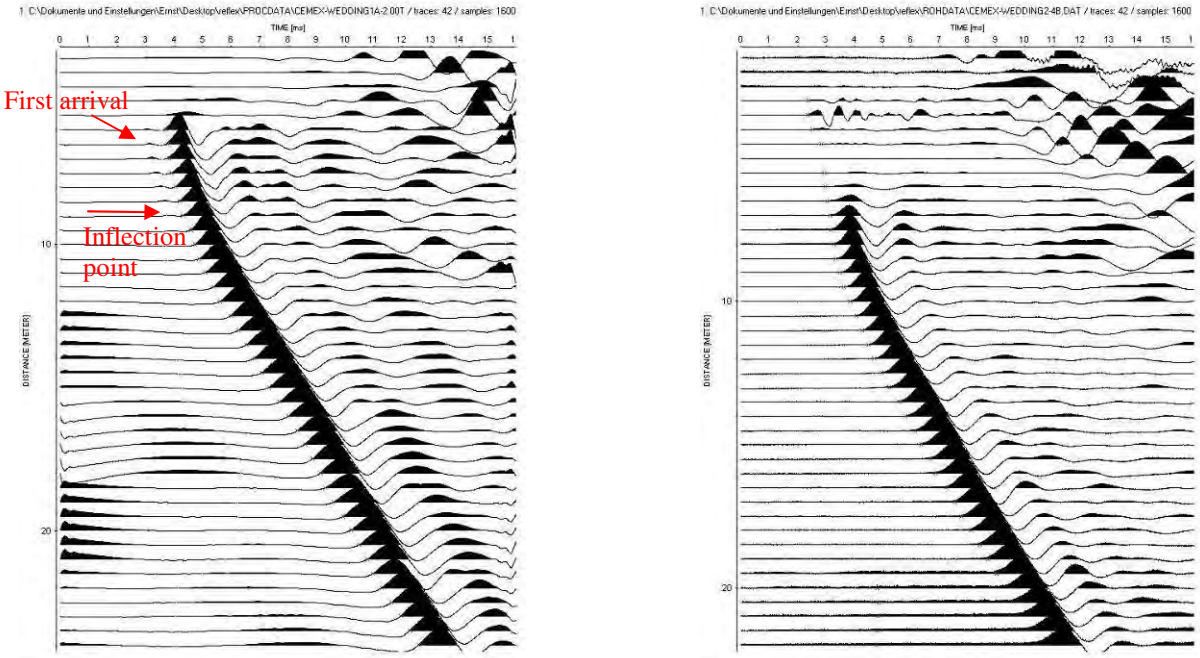

Figure 6: PS seismograms at the Napoleonkai sheet pile wall. Horizontal axis: time (ms), vertical axis: sensor depth (m). Left: Good contact borehole/soil. Right: Bad contact in top traces

Nine Parallel Seismic measurements were done using four boreholes, which are 1.0 – 1.6 m from the sheet piles. Two of the seismograms are displayed in Figure 6. The left one shows excellent data starting from 2.5 m depth (groundwater level). The inflection point is visible in about 8 m depth. The seismogram on the right misses near surface data, which is probably due to lack of acoustic contact between soil and borehole. Nevertheless the inflection point is visible and the dataset can be interpreted.

Figure 7 shows the picked first arrival times and curve fitting results acquired using the method described by Niederleithinger et al. (2005). Both examples show a calculated pile length of 7.8 m. Some other results showed somewhat shorter lengths (minimum 7.1 m, overall average 7.5 +/- 0.3 m). These lengths are significantly above the estimated values for the shorter sheets. This is not a surprise as the sensors will in most cases get signals from the longer sheets, even if the hammer blow is delivered to a shorter one (see Figure 3). As the waves are taking a "deviation", the calculated sheet lengths are somewhere in between the real values in this case.

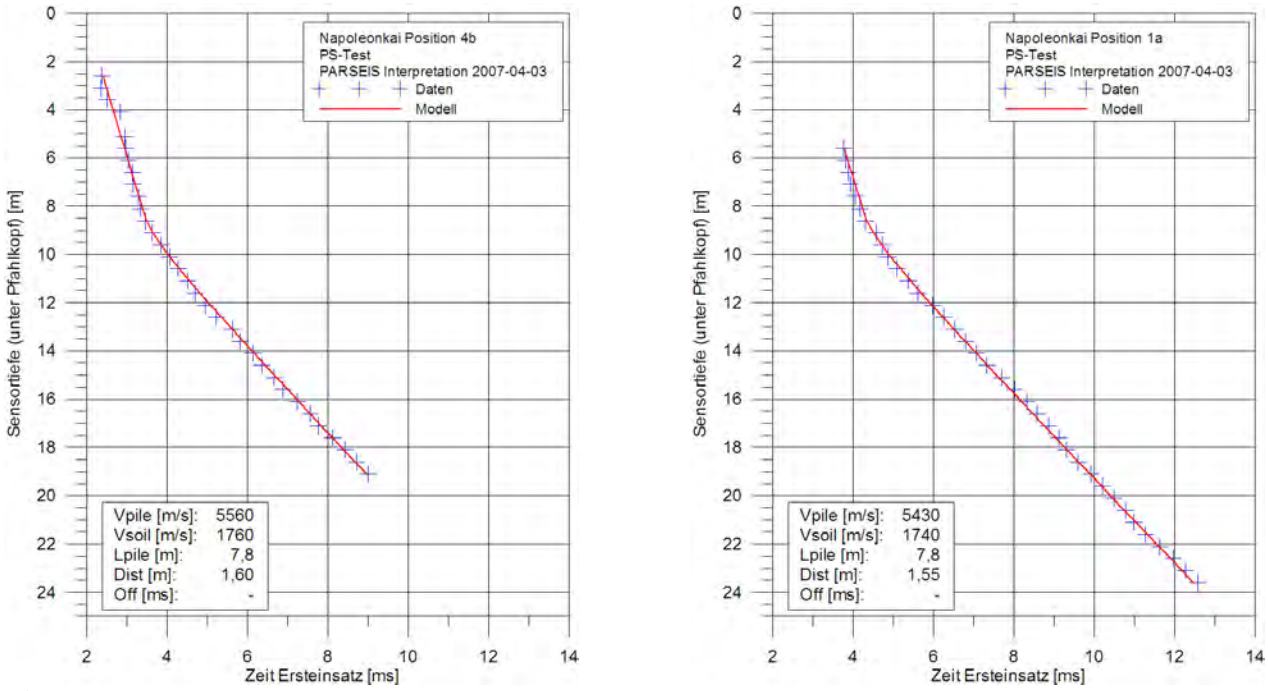

Figure 7: PS first arrival times and interpretation of the seismograms in Figure 6.

Bootshandel Hollandboot

A yacht trading and chartering company in Berlin wanted to extend its business by building a new 26 t crane near the waterline. The shore is protected by a sheet pile wall (Figure 9), but there were neither design or as built drawings nor files available. For the necessary load capacity calculations the determination of sheet pile length was demanded by the authorities.

At the eastern part of the construction (foreground of Figure 8) several records with clear toe echoes could be recorded (Figure 9), but some showed multiple reflections or erroneous results and have been rejected. Some others showed double peaks at the toe position (bottom record in Figure 9), which may be a sign of differing pile lengths but is still not fully understood.

Figure 8: Left: Sheet pile wall at Bootshandel Hollandboot. Top: PS borehole B2.

.

As in the Napoleonkai example, the results (about 50) can be divided in two groups. One showed an average length 8.59 ± 0.24m und 9.54 ± 0.22m. At the western part of the sheet pile wall a concrete slab had been cast with direct contact to the sheets (Figure 9 right). Here, we were not able to record any useful PIT measurements.

However, using the Parallel Seismic method the sheet pile length can be determined even in this case. Using the normal approach as described in the previous example, the final result was 9.5 ± 0.3 m. But as the first arrival travel time curves show irregularities and some of them even jumps, we undertook a more detailed investigation.

A sample record and its interpretation are shown in Figure 10. The first arrivals can clearly be identified in the seismogram. But the travel times in the upper part show a step at 7 m depth. If all values are used for interpretation (red curve), the calculated velocity for the steel is less than 4300 m/s, which is far too low even for low quality corroded material. Taking only travel times below the step into account, the velocity is reasonable (5200 m/s). Fortunately, this has minor influence on the calculated sheet length (9.8 compared to 10.0 m for this record).

There are several possible explanations, e. g. measurement and picking errors (which we tried to exclude by repetition of the entire procedure) or changing properties in layered soil (for which we had no evidence). Our interpretation is that these steps, which occurred in several records, are again due to signal travelling from one sheet to adjacent ones as described in Figure 3. This means that the pile-borehole distances, which are used in interpretation, are not necessarily correct. There is no reliable possibility to determine them from the surface. To overcome this uncertainty we repeated the calculations with different reasonable values for pile-borehole distance as well as with and without reducing the dataset as described above. At the same time we used not only the sheet next to the borehole for hammer impact but also adjacent ones (Figure 10).

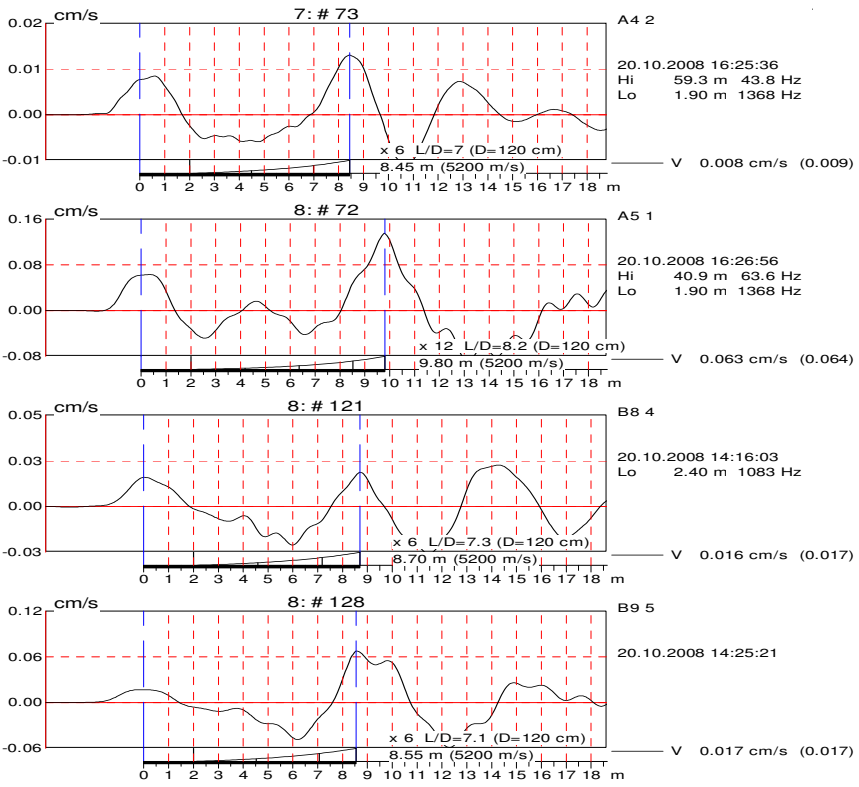

Figure 9: PIT records from the sheet pile wall at Bootshandel Hollandboot. Horizontal axis: Time converted to pile length by Vertical axis: Sensor vibration velocity

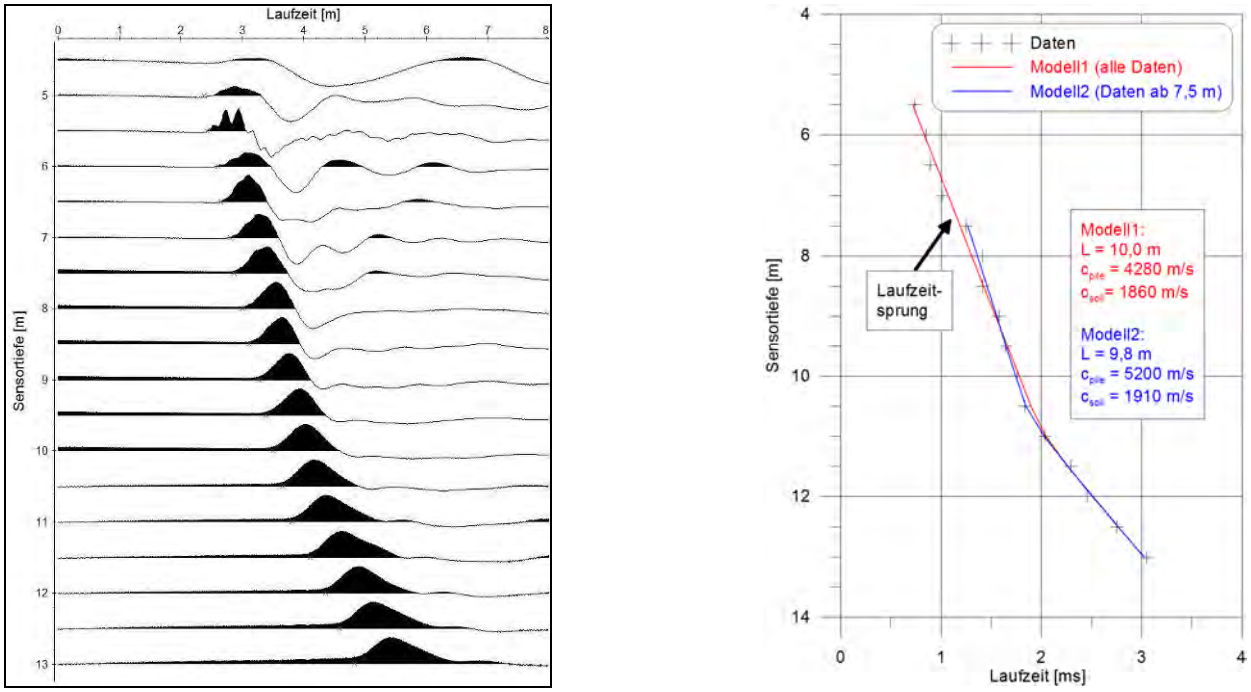

Figure 10: PS seismogram and interpretation at Bootshandel Hollandboot.

For borehole B2 (in the western part of the area, where no PIT results could be achieved) a total of eight configurations was used (2 impact points, 2 estimated distances, 2 dataset sizes). The pile lengths calculated are shown in Figure 11. They vary between 9.4 and 10 m, with an average of 9.65 +/- 0.3 m. To be on the safe side, the smallest length (9.4 m) was used for the following load capacity calculations. The sheet pile wall was proved to be strong enough to carry the lateral load generated by the new crane. Authorities and client were satisfied with the results. The crane came into operation in 2009.

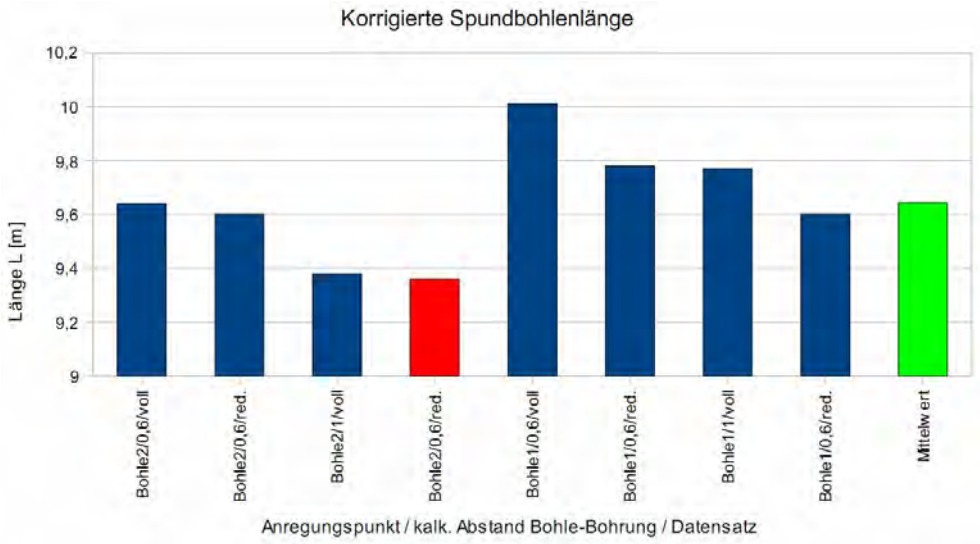

Figure 11: Sheet pile length calculated using different scenarios (impact point/distance/dataset). Smallest result in red, average in green.

Conclusions

Two measurement methods for the determination of sheet pile length have been introduced. Both have been originally developed for single drilled shafts, but can be applied to wall type elements with some restrictions.

In both of our field examples low strain pile integrity testing (PIT) was successfully used to determine sheet lengths. But in several cases the results suffer from signal energy traveling to and reflected from adjacent sheets, anchors or element welded to the sheets. In some cases we didn't get any useful information. A reliable prediction, whether a specific sheet can be tested or not isn't possible so far. Thus it is recommended to do measurements on as many sheets as possible to get the chance to reject erroneous records and to do statistical analysis of the accepted ones. Under favorable conditions it even seems to be possible to identify constructions with alternating lengths from sheet to sheet. The standard deviation of length measurement results was less than 0.3 m in our cases, which is fully sufficient. But as the velocity of the waves in the pile is not exactly known, calibration is required. Otherwise the error margin may be up to 10%.

Parallel Seismic (PS) testing requires (as all other methods introduced so far in the literature) a borehole near the piles. Using novel interpretation methods the distance to the sheets can be larger compared to other methods. In our examples we got good results for all situations and distances (up to 1.6 m in our cases). As for PIT tests, PS is affected by wave energy traveling from the hammer impact to adjacent sheets. The reliability of results can be checked by a scenario approach taking into account

reasonable ray paths. The standard deviation of measurement results is about the same as in PIT. But there is no need for calibration, as wave velocities can be determined from the data. In fact PS can be used to calibrate PIT interpretation. An optimized stepwise procedure combining both methods (and/or other borehole based tools) is recommended to achieve reliable and cost efficient results.

The length determination of a specific sheet is still a challenge. A sample sheet pile section is currently built at the BAM test site to allow validated development of new methods.

Acknowledgements

The authors wish to thank their clients and site owners CEMEX and Holland-Boot for the support and allowance to publish the results.

References

ASTM 5882-07: Standard Test Method for Low Strain Impact Integrity Testing of Deep Foundations.

Butcher, T., Powell, J., 2006, Re-use of foundations – a best practise handbook, BRE Press, Watford, UK

DGGT AK 2.1, 2007: Empfehlungen des Arbeitskreises „Pfähle“ (EA Pfähle), Ernst& Sohn, Berlin. (in German).

Jalinoos, F., Gibson, A., Diehl, J., Hadfield, P., Gordon, G., 2006, Determination of unknown length of sheet piles using three different geophysical logging tools, Proceedings of Highway Geophysics, St. Louis

Klingmüller, O., & Kirsch, F., 2004: A quality and safety issue for cast-in-place piles 25 years of experience with low-strain integrity testing in Germany: From scientific peculiarity to day-to-day practice. Current Practice and Future Trends in Deep Foundations, American Society of Civil Engineers, Geotechnical Special Publication No. 125, 2004, S. 202-22

Liao, S.-T., Tong, J.-H., Chen, C.-H., & Wu, T.-T., 2006: Numerical simulation and experimental study of Parallel Seismic test for piles. International Journal of Solids and Structures. 43, p.2279–2298

NF P94-160-2, 1993: Soil investigation and testing. Auscultation of buried work. Part 2 : method by reflection (French standard).

NF P94-160-3, 1993: Soil investigation and testing. Auscultation of buried work. Part 3 : parallel sonic method.

Niederleithinger, E., Taffe, A., Fechner, T., 2005, Improved Parallel Seismic Technique for Foundation Assessment, Proceedings of SAGEEP 2005, Atlanta, USA

Niederleithinger, E., 2007: Numerical simulation of low strain dynamic pile tests. Proceedings of the 8th conference on the Application of Stress wave theory to Piles, Lisbon, Portugal.

Niederleithinger, E., Fritsche, M., 2008, Nachträgliche Bestimmung der Länge von Spundbohlen mit dem Parallel-Seismik-Verfahren. Pfahlbau-Symposium 2009, Braunschweig, Germany (in German).

Niederleithinger, E., Taffe, A., Klingmüller, O., Katzenbach, R., 2007, Zerstörungsfreie Untersuchung von Gründungselementen im Rahmen von Wiedernutzungsprojekten. Geotechnik, Jg.: 29, Nr.3, p. 146-157 (in German).

Olson, L. D., Jalinoos, F., Aouad, M. F., 1998, Determination of Unknown Subsurface Bridge Foundations: NCHRP 21-5 Interim Report Summary, Federal Highway Administration, Geotechnical Engineering, Notebook Issuance GT-16

Turner, M. J., 1997, Integrity testing in piling practice, Ciria Report 144, London

CROSSHOLE SONIC LOGGING OF SECANT PILE WALLS A FEASIBILTY STUDY

Ernst Niederleithinger, BAM Federal Institute for Materials Research and Testing, Berlin, Germany
Joram M. Amir, Piletest Ltd., London, United Kingdom
Markus Hübner, GGU Gesellschaft für Geophysikalische Untersuchungen mbH, Karlsruhe, Germany

Abstract

Secant pile walls are used as permanent or temporary elements in foundations, excavations, slope stabilization, retaining walls or hydraulic barriers. In contrast to single piles, reliable non-destructive testing methods are not available so far. The reinforced secondary piles can be checked by standard crosshole sonic logging, but there is no access to the unreinforced primary piles. Experiments at construction sites using ray paths across several piles have shown encouraging results, but there have been several open questions. To evaluate the potential of cross-pile sonic logging, a real scale test model with built in flaws on two primary piles was constructed at the BAM test site. Measurements with two different instruments have been performed. In one primary pile relevant flaws could be detected. At the other one the signals showed anomalous damping, probably due to unintended delamination. The results can be used to interpret real site data.

Introduction

Secant pile walls are formed by a series of interlocking drilled shafts. Primary piles without reinforcement are built first. The gaps are filled by secondary reinforced piles, which overlap the primary ones (Figure 1). The concrete of the primary pile is often chosen to be weaker than for ordinary piles to facilitate drilling. Standard pile drilling rigs are used for construction (Figure 3).

Most secant pile walls are used as retaining walls or hydraulic barriers. Integrity of the piles and sound joints between them are thus of major importance and so is quality assurance. So far, there are no proven non-destructive testing methods for this purpose. The most common tool for single piles, low strain integrity testing, is in most cases not applicable to pile walls (Klingmüller & Kirsch, 2004, Niederleithinger et al, 2010). Crosshole Sonic Logging (CSL) was until now limited to be applied within the reinforcement cage of a single pile. Thus there is no possibility to check the integrity of the primary piles before excavation. Even if high standards are applied, the construction sometimes fails, e.g. at unexpected soil inhomogeneities (Figure 2).

Field trials to use crosshole sonic logging across several piles have shown encouraging results (Niederleithinger et al., 2010). Nevertheless, data showed significant anomalies, which could not be directly interpreted. This has led to the idea of evaluating this approach on a test model built under controlled conditions.

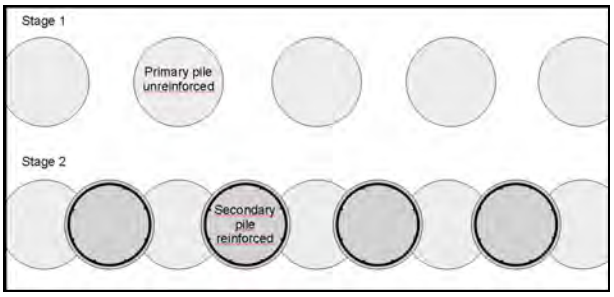

Figure 1: Construction of secant pile walls.

Figure 2: Secant pile wall with flaw at a power plant construction site in France.

Figure 3: Secant pile wall under construction at a river lock in northern Germany.

Crosshole Sonic Logging

Crosshole sonic logging is an established quality assurance method for drilled shafts. A transmitting and a receiving ultrasonic probes (40 - 80 kHz) are lowered into parallel access tubes, which have to be fixed to the reinforcement cage before casting the concrete (Figure 4). Measurements are taken each 1 to 5 cm with both probes at the same depth. First arrival time (which can be converted to apparent wave speed) and amplitude are recorded as well as the raw times series. The data are presented as log or waterfall diagrams, respectively (Figure 5). Application and interpretation are standardized in many countries (e. g. ASTM D6760 – 08, NF 094-160-1, DGGT EA Pfähle). In most cases the interpreter is mainly looking for local anomalies. The test is repeated for all available tube combinations.

The method can be extended by tomographic data processing, either by just combining all data from the same depth (giving horizontal slices) or by acquiring extra data with probes at different depths (giving vertical slices or 3D volumes). In theory the latter gives better coverage and resolution of inhomogeneities. But at the same time it means extra effort, which is currently seldom paid by clients.

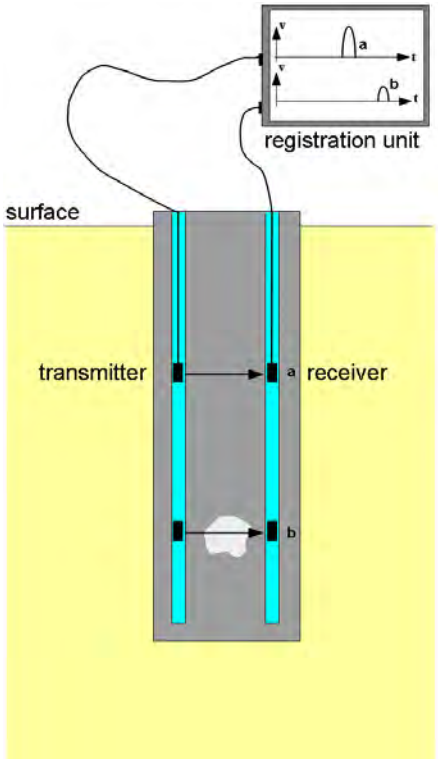

Figure 4: Principle of crosshole sonic logging

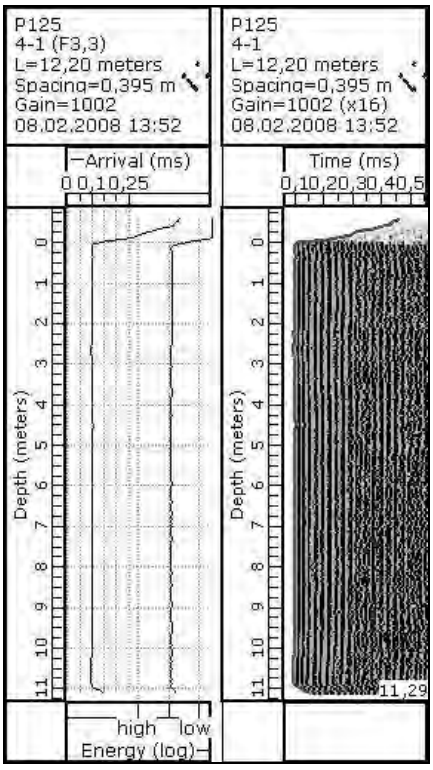

Figure 5: Crosshole sonic logging plot of a sound pile. Left: Amplitude and arrival time, Right: Stacked time series as waterfall diagram.

The Test Model

The BAM Test Site Technical Safety (BAM-TTS) is a former military training ground where (among many other facilities) a test and validation center for NDT in civil engineering is set up and maintained (Niederleithinger et al., 2009). The inventory of concrete test models and specimens includes drilled shafts, sheet piles, slabs, railway tracks and bridge girders. More objects are under construction.

As it is almost impossible to build a secant pile wall with artificial, well defined flaws and at the same time avoid unintended flaws, a test model with a somewhat different casting procedure was designed. Three secondary reinforced piles were built first as free standing columns (diameter 0.9 m, height 4 m) and equipped with CSL tubes. The primary unreinforced piles were cast in between after mounting pads of different materials (tape, textile, Styrofoam) and sizes on the inner surfaces (Figure 6). The pads were used to represent gaps and delaminated joints between piles, which may lead to hydraulic flow paths at real pile walls. The bottom of the model is 2 m below surface. The slope and plateau surrounding the model was made from the excavated material to stabilize the columns and to simplify measurements (Figure 7).

Four CSL access tubes (2” steel) in a square arrangement were fixed to the rebar cage of the secondary piles. The squares sides are aligned to the model geometry for two piles and rotated 45^0 for the last one. The available transmitter and receiver tube pairs are shown in Figure 8. The flaws discussed in this paper are as follows: between piles 4 and 5 - four textile patches covering 50% of the joint horizontally and heights of 5, 10, 20, and 40 cm, respectively. Between piles 2 and 3 - three patches of 40 cm height, covering the joint completely, made from tape, textile and Styrofoam, respectively. The artificial flaws at the joints between piles are marked in red in Figure 8.

Figure 6: Fixing the patches to the reinforced piles.

Figure 7: Secant pile wall test model ready to use.

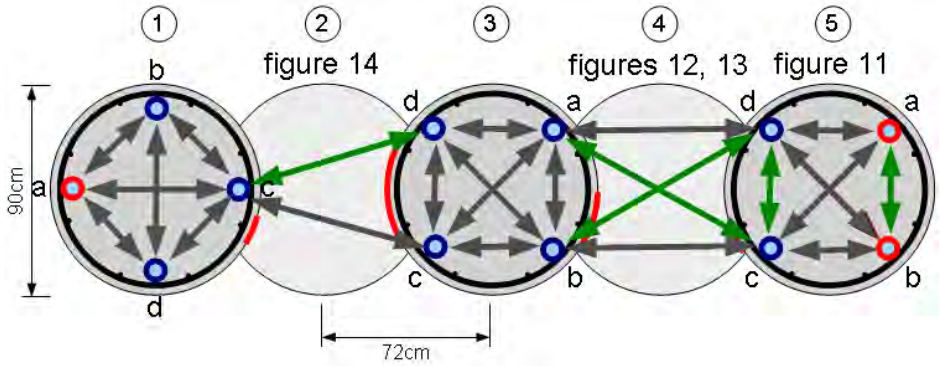

Figure 8: Tube layout (blue) and possible CSL transmitter and receiver tube pairs (gray arrows). Tube pairs dicussed in text in green. Approximate position of flaws in red.

Figure 9: Cross-pile CSL measurements with piletest CHUM at the BAM test model.

Figure 10: Single-pile CSL measurements of GGU with PDI CHAMP at the BAM test model.

Measurements And Results

Two sets of CSL measurements at the test model were carried out in June and September 2009 by independent operators with different instruments (Figures 9, 10). Data processing and display were done using the software supplied by the manufacturers according to manuals and standards.

Single Pile Logs

To check the integrity of the secondary piles (reinforced columns built first) logging was carried out on all pile internal tube pairs. Some of the tubes at the far ends of the model had intended delaminations (textiles wrapped around the tube) to prove the functionality of the instruments. The results of the measurements showed, that there were no flaws inside the secondary piles except for the intended ones mentioned above. Two logs from pile 5 are shown in Figure 11. The left part of these logs (and all other following logs) shows line plots of first arrival time and amplitude (or energy/attenuation, which is equivalent in this context). The waterfall presentation on the right of each log represents the recorded time series, with amplitudes converted to colors.

The log shown in Figure 11 was recorded between tubes 5c and 5d. There are no flaws to be detected. All graphs are almost flat. The right one was measured in the other tubes in pile 5. At three positions the tubes were separated from the concrete by textile patches. 5a2 is fully separated, 5a1 and 5b1 only partially (patches around 90° or 180° of perimeter, respectively). The approximate position of the patches can be seen clearly in the log. A small anomaly above 5b1 indicates an additional, unintended separation, according to other logs not shown here at tube 5a..

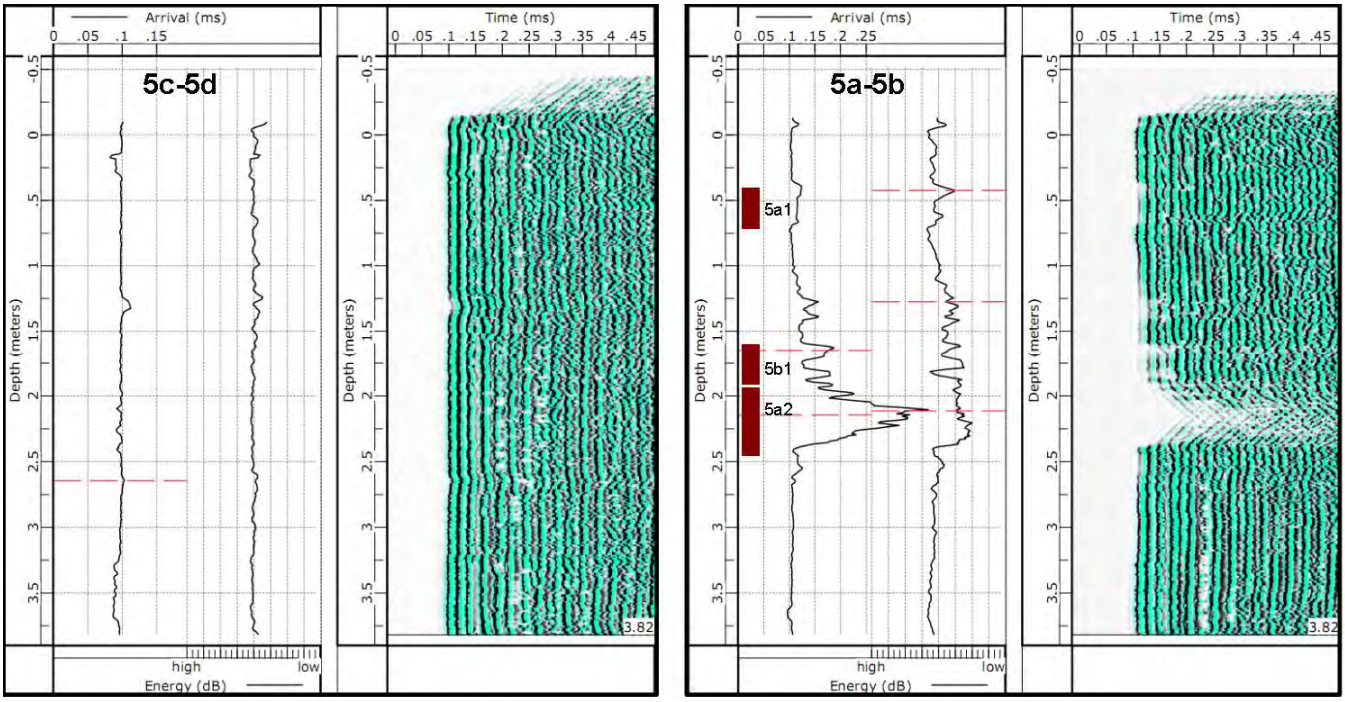

Figure 11: CSL logs from pile 5, Tube pairs 5c-5d (left) and 5a – 5b (right, with position of intended tube delaminations). PDI CHAMP.

Logs Across Pile 4

The joint between piles 3 and 4 is patched with 4 flaws of different heights, each covering half of the joint's width. Figure 12 shows logs measured from tubes in pile 3 to pile 5, crossing pile 4. The straight ray path between tubes 3b and 5d (left part of the figure) crosses the patches directly. The topmost flaw (height 40 cm) is clearly visible. The next one (height 20 cm) is still significant, but the smaller ones can hardly be identified and would not be labeled as flaws in standard CSL-measurements.. This result is in line with the observation by Amir & Amir (2009) that a flaw located half way between two access tubes is detectable if it's size exceeds about one third of the tube spacing. The reason is that there seems to be remaining acoustical contact across the patches. That means that travel times shouldn't be affected seriously, but the energy arriving at the receiver should (the larger the flaw size the larger the damping). Probably the same would happen at narrow real joints filled with drilling mud or soil. However, the first arrival log shows also increased travel times especially for the largest patch. This is due to the very weak amplitudes of the first arrival which can hardly be seen in the waterfall plots and are missed by the automatic detection algorithm. Detailed analysis has shown that there is still some signal at "normal" times. But lowering the detection threshold has lead to erroneous picking in other parts of the log.

The straight path of the tube pair used for the right log in Figure 12 isn't touching the patches. Nevertheless the two larger patches do have an influence on the measurements. Again, mainly the amplitude is affected. Our interpretation is that a large part of the CSL signal is not caused by direct waves but by refraction, diffraction and reflection at boundaries and interfaces. The patches are absorbing a part of the energy transported by these waves. This way flaws which are not directly in the wave path can be detected. This has to be taken into account in the interpretation.

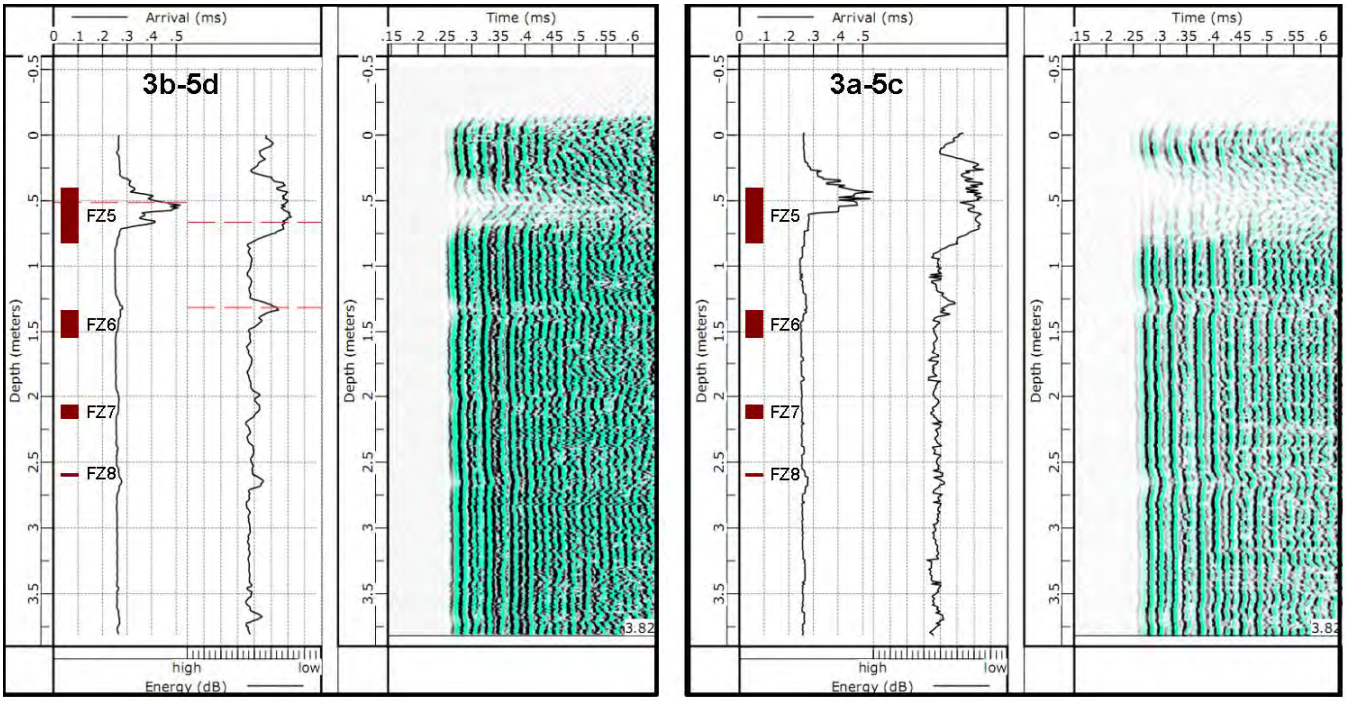

Figure 12: CSL Log across pile 4. Left: Tubes 3b-5d. Right: Tubes 3a-5c. Flaws at joint pile3/4 marked in red. PDI CHAMP.

To be sure that instruments effects are not influencing the results are compared to data previously collected with the CHUM device (Piletest Ltd.). Figure 13 shows the same log (tubes 3b-5d) as Figure 12 (left). The picture is almost identical. Again, mainly the amplitudes are influenced by the patches. Compared to Figure 12 the 10 cm patch (FZ7) is slightly better visible in the waterfall plot (which is of course depending on gain setting and color code), but still would not be recognized as serious flaw under real world conditions. The first arrival time detection seems to be more sensible to weak amplitudes (leading to an almost flat log). Reasons are a higher dynamic range and a different algorithm used. However, there is no obvious preference to one or the other instrument.

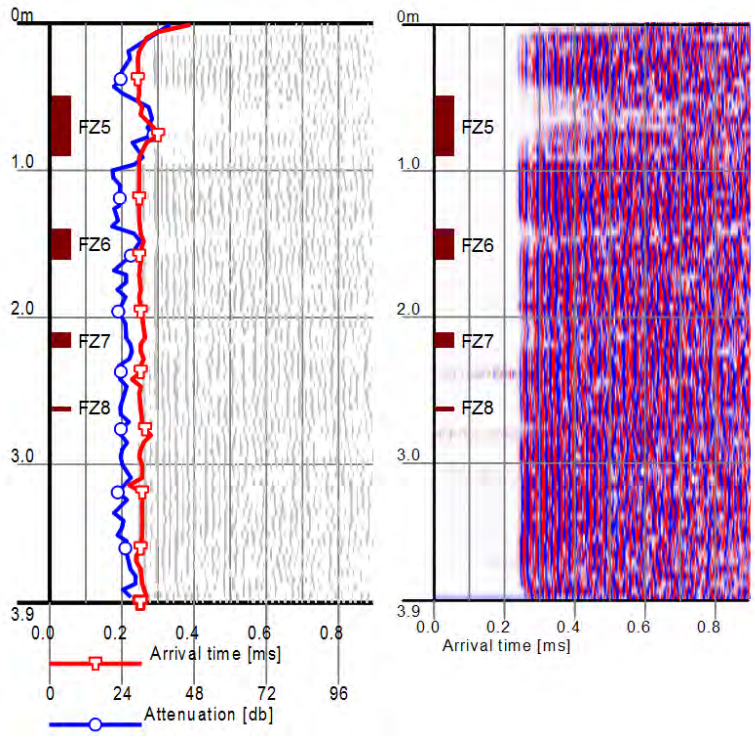

Figure 13: CSL result of tube pair 3b-5d (piletest CHUM).

Logs Across Pile 2

The joint between piles 2 and 3 was prepared in a different manner with the height of all three patches being 40 cm. They are covering the entire width of the joint and are made out of (from bottom) tape, textile and 1 cm Styrofoam to resemble different grades of delaminations. The reinforcement cage of pile 1 was rotated by 45°, so that we had only two different tube pairs to log across pile 2 (Figure 8).

The results of tubes 1c-3d, measured with both instruments mentioned above are shown in Figure 14. To get results the gain had to be increased by a factor of 20 to 100 compared to other logs shown in this paper. Even then, only at the very top and bottom of the log undisturbed signals are visible. In between (not only in the depth of the patches) the amplitudes are so low, that traveltime picking and energy calculations according to the standards have lead to erroneous results. The line plots shown have been generated using image processing (CHAMP) of filtering/smoothing algorithms (CHUM). The structures in the waterfall diagrams correlate only partially with the flaw positions. Measurements between tubes 1c and 3c showed the same.

There are two possible reasons for these results. One might be a delaminated access tube, but there was no sign of this in CSL logs done with tube pairs in pile 1 only and pile 3 only. The other one is an imperfect joint over almost the entire area between pile 1 and 2 and/or pile 2 and 3. Core drillings and endoscopy are planned for winter 2010 to check the state of the joints.

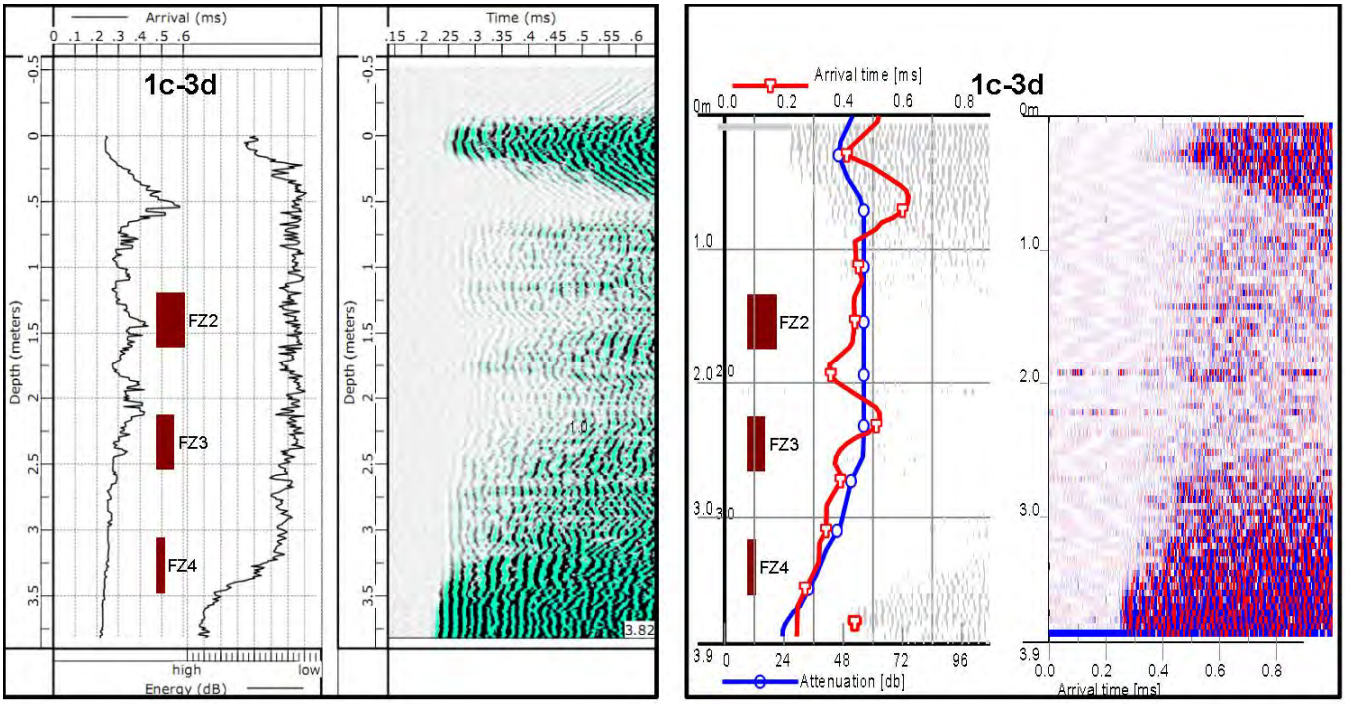

Figure 14: CSL log across pile 2, tube pair 1c-3d. Left: PDI CHAMP, Right: Piletest CHUM. Zero depth offset intended (due to different probe sizes).

Conclusions

The Crosshole Sonic Logging measurements on the BAM test model representing a secant pile wall shed some light on the applicability of checking for flaws on the joints between piles. It was shown that under favorable conditions, standard instruments are able to transmit and record signals, which travel across several joints and piles.

It was shown that flaws at joints can be detected, if their size exceeds certain values. The main influence is on signal amplitude. In the case presented here, a 20 by 40 cm flaw caused a significant anomaly. Any smaller flaws might not be detected. Signals are even influenced by large enough flaws outside the direct ray path. There is some evidence, albeit inconclusive, that thicker flaws produce larger signal attenuation.

Interpretation becomes difficult if the entire joint or the available access tubes are delaminated. So far, core drilling or visual inspection after excavation are the only available tools right then. Nevertheless, all these results are encouraging to continue the research on this method and to start with field applications. The use of tomographic measurements and interpretation will probably enhance the results. Due to the nature of the model, the results obtained should also be applicable to diaphragm walls.

Acknowledgements

The test model was built by at the BAM-TTS by Marco Lange, Sean Smith and Christoph Richter. A part of the measurements was funded by the BAW (German Federal Waterways Engineering and Research Institute). Tony Ballhause assisted during measurements.

References

Amir, J.M. & Amir, E.I., 2009: Capabilities and Limitations of Cross Hole Ultrasonic Testing of Piles, Proc. Conf. Contemporary Topics in Deep Foundation, ASCE GSP 185, Orlando.

ASTM D6760 - 08 Standard Test Method for Integrity Testing of Concrete Deep Foundations by Ultrasonic Crosshole Testing

DGGT AK 2.1: Empfehlungen des Arbeitskreises „Pfähle“ (EA Pfähle). Ernst& Sohn, Berlin, 2007.

Klingmüller, O., & Kirsch, F., 2004: A quality and safety issue for cast-in-place piles 25 years of experience with low-strain integrity testing in Germany: From scientific peculiarity to day-to-day practice. Current Practice and Future Trends in Deep Foundations, American Society of Civil Engineers, Geotechnical Special Publication No. 125, 2004, S. 202-221

Niederleithinger, E., Wiggenhauser, H., & Taffe, A., 2009: The NDT-CE test and validation center in Horstwalde. Proceedings of NDTCE’09, Nantes, France. (http://www.ndt.net/article/ndtce2009/papers/127.pdf)

Niederleithinger, E., Schallert, M., Klingmüller, O., & Bobbe, A., 2010: Quality assurance of a secant pile wall using three different non-destructive test methods. Accepted for proceedings of ISSMGE “Geotechnical Challenges in Megacities”, Moskau.

NF P94-160-1 Octobre 2000: Sols : reconnaissance et essais - Auscultation d'un élément de fondation - Partie 1 : méthode par transparence (French CSL standard).

Quantitative Integration of Multiple Near-Surface Geophysical Techniques for Improved Subsurface Imaging and Reduced Uncertainty in Discrete Anomaly Detection

Megan E Carr, University of Tennessee, Knoxville, TN
Gregory S Baker, University of Tennessee, Knoxville, TN

Abstract

The remote sensing community—in the traditionally-used connotation of satellite and airborne imagery—has been integrating multi-technique geophysical data extensively and successfully for nearly two decades to better discriminate targets, e.g., mineral deposits, specific types of vegetative land cover, etc. Currently, however, there is no quantitative methodology in place for the integration of two or more geophysical data sets collected using near-surface geophysical techniques such as Ground Penetrating Radar (GPR), Magnetic Gradiometry, and other Magnetic/EM methods. The primary objectives of this research are to investigate quantitative methodologies for integrating multi-tool surface geophysical data to improve subsurface imaging and reduce uncertainty in discrete anomaly detection. These objectives will be fulfilled by: (1) correlating multi-tool geophysical data with existing well characterized "targets"; (2) developing methods for quantitatively merging different geophysical data sets; and (3) testing these new methods at several different sites with varied targets (i.e., case studies). Three geophysical techniques primarily utilized in this research are: GPR, EM (ground conductivity) methods, and magnetic gradiometry. The two study sites (Cherokee Farm and the University of Tennessee Agricultural Extension Plot 4B) located within alluvial sediments along the Tennessee River will serve as case studies to verify methodologies in a terrestrial environment. A computer model will be developed that will simulate data that would be expected given various parameters such as heterogeneity of the subsurface, type of target, geophysical technique utilized, spatial sampling, etc. The simulated data sets will then be integrated together using the same methodologies as employed with data from Cherokee Farm and Plot B4 to further develop the necessary quantitative assessment scheme to determine if these merged data sets do in fact satisfy the objectives of the research.

Introduction

Motivation

Most subsurface data integration studies have involved one geophysical technique and with additional data such as boreholes (e.g., Hornby 2007, Ferré 2003) or general geological data such as soil surveys and other maps (e.g., Galicia 2001, Rahman et a. 2008, Allen et al. 2008). The research presented hre attempts to minimize these data integration problems by (1) setting up consistent parameters within geophysical technique utilized; (2) develop a comprehensive model for integration of data; and (3) utilize consistent visualization techniques to represent the processed data for a higher degree of confidence when interpreting the results of each individual case study within the scope of this research. Interpreting geophysical data commonly involves a qualitative correlation of different geophysical data sets. This research seeks a more refined, quantitative approach to combining data sets. The underlying concepts of this project are that one geophysical method cannot produce a breakthrough in the detection

of "targets", but that utilizing multiple techniques, and the integration of multiple technique data, can produce significant improvements in data quality and target detection.

Objectives and Hypothesis

Data sampling heterogeneities associated with geophysical databases have been identified as the main source of data integration problems (Stock and Pullar 1999). The primary objective for this component of the research project is to perform a statistical evaluation of various geophysical techniques in their individual capabilities to detect an assortment of targets. Additionally, there will be an assessment of different merging methodologies for reducing uncertainty in discrete anomaly detection. Understanding of this statistical and quantitative approach will aid in accomplishing the ultimate goal of the research, which is to have a quantitative assessment of data integration methodologies utilizing multiple near-surface geophysical techniques. This will aid in the interpretation of various geophysical surveys, possibly helping other scientists within multiple application scenarios (e.g. prospecting core sites for long sediment records, locating buried objects, mapping historical features). The objectives of this project will be fulfilled through the completion of the following:

- Correlation of geophysical data with known "targets" by utilizing multiple geophysical techniques on the East Tennessee Intensive Near-Surface Geophysics (TINGS) course site (Plot B4)
- Determine geophysical anomalies that may indicate locations of various targets
- Complete a statistical analysis to evaluate the effectiveness of the data integration methodology and applications

These objectives are designed to meet the following hypothesis:
I) Integration of two or more geophysical techniques will result in an improved subsurface image and reduce uncertainty in discrete anomaly detection.
II) Some targets will be detected with greater degree of certainty than others when a specified combination of processing and merging of data is implemented.

Study Site

Plot B4 allows the proposed methodology to be conducted in a controlled setting, located between Alcoa Highway 129 and the Tennessee River, approximately 2 miles south of the University of Tennessee campus in Knoxville, Tennessee, as shown in Figure 1. Soil conditions in the site vary from residual soils developed directly on sedimentary bedrock near the highway, to loamy soils developed on a series of alluvial terraces at different elevations above the river. Plot B4 contains known targets buried in 1999 with the locations given by latitude and longitude and depth within the subsurface. Additionally, information including size, shape, composition material, and orientation are given. It is assumed with this study that there has been enough time for the ground to settle and any disturbance to the subsurface (and resulting signal in the data) has been minimized.

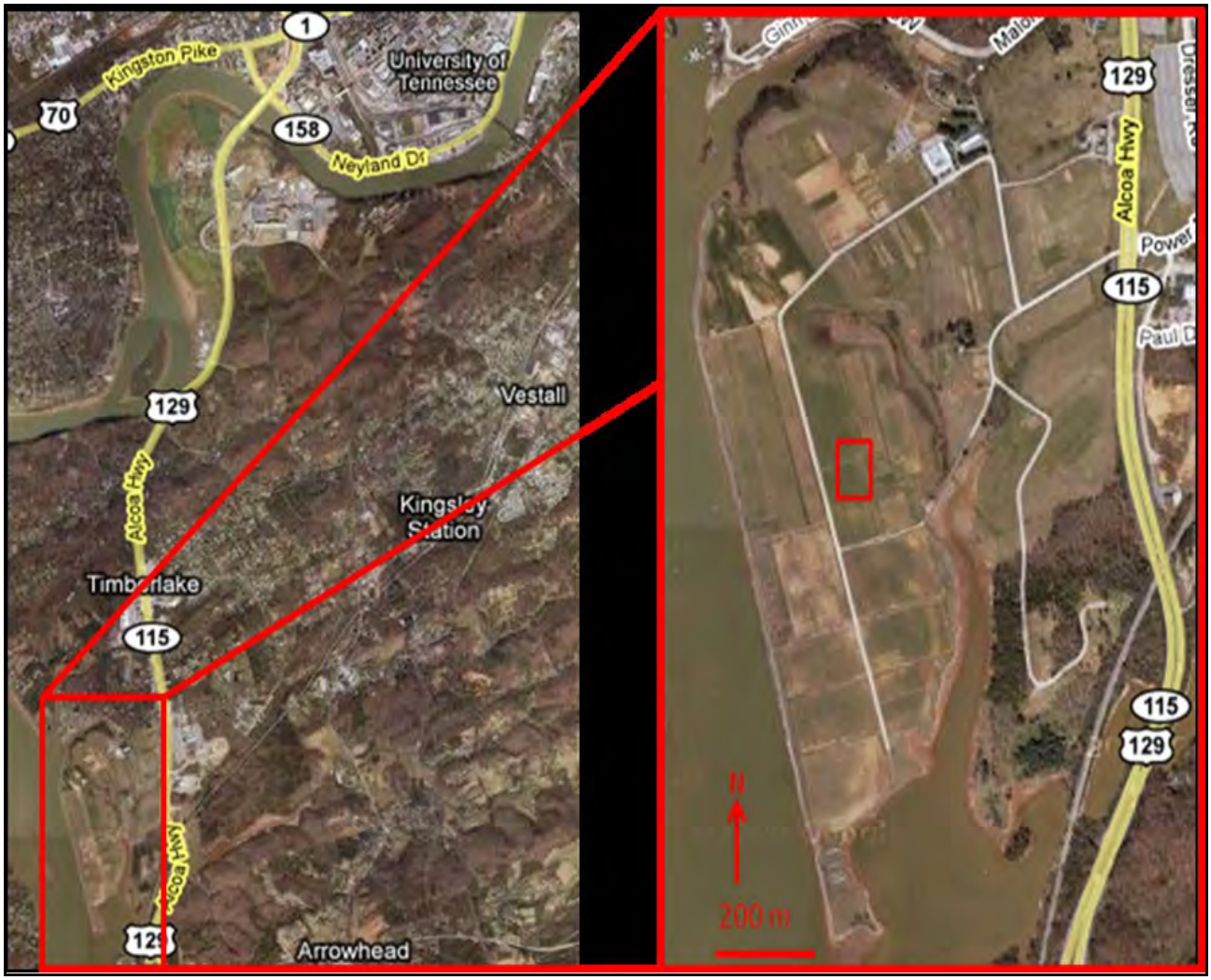

Figure 1: Location of Plot B4 study site. The University of Tennessee, as seen in the Northeast corner of the expanded map in located in Knoxville, Tennessee. The red square located in the zoomed in map shows the exact location of Plot B4.

The location of each of these targets is shown in Figure 2. The results for the known targets will be used to modify the integration methods to enhance uncertainty reduction and provide quality assurance in the manipulation of the data from areas of unknown target location. This will provide an improved interpretation of geophysical data in the study.

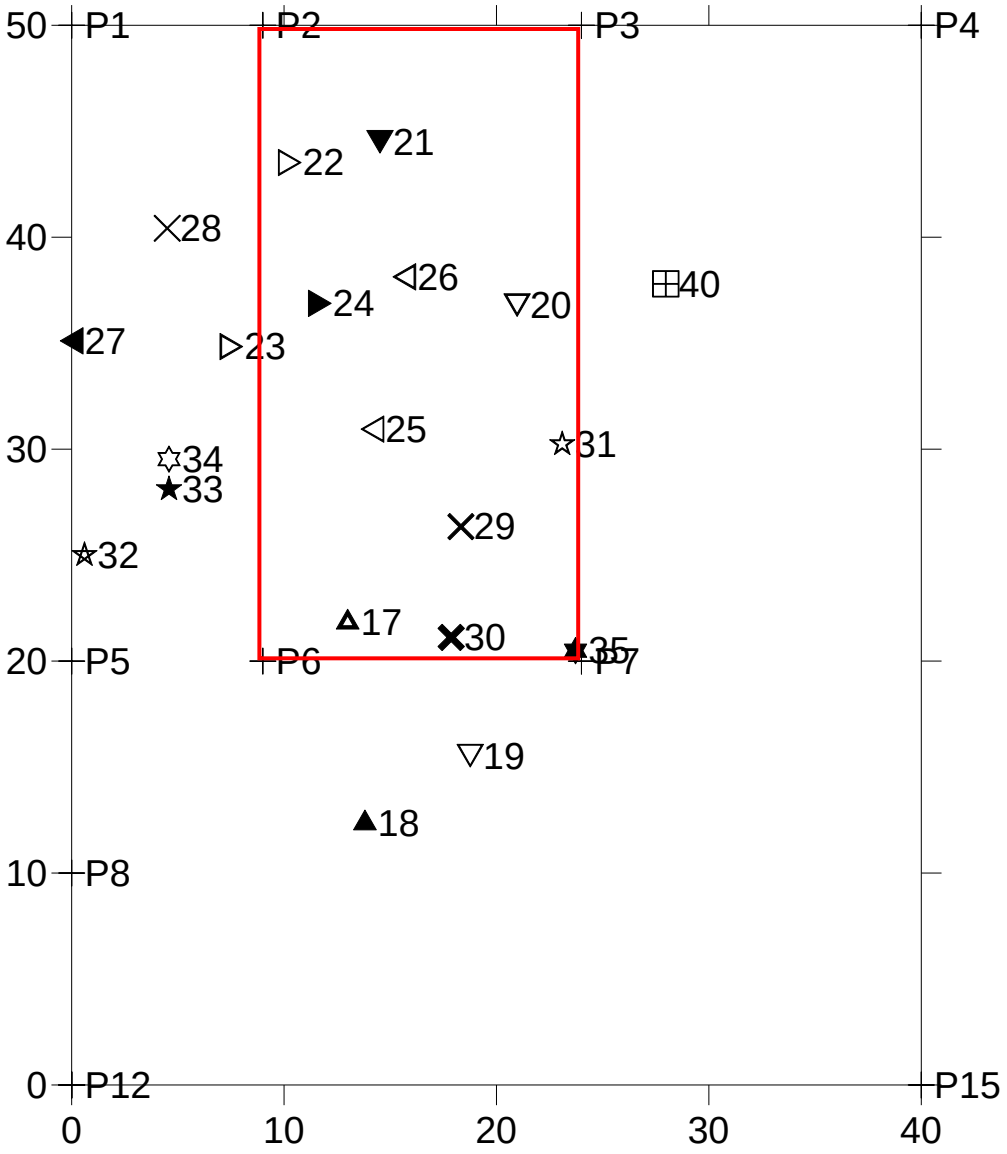

Figure 2: Map displaying locations of buried targets. Each number corresponds to a description of the target in regards to depth to top of objects, orientation, dimensions, and construction material (refer to Table 1). The boundaries of the GPR survey are also highlighted with a red box. Grid is measured in meters.

Table 1: Target locations for Plot B4. Depth is measured at the top of each buried object. For location of the targets in relationship to each other, refer to Figure 2.

Point ID	Longitude	Latitude	Description	Depth (m)
13	-83.960713057	35.899088420	Spider, within fenced area of hydrologic station	
14	-83.960670875	35.899066113	Control Panel, within fenced area of hydrologic station	
17	-83.960582282	35.899155434	Vertical 55 gal drum	0.635
18	-83.960545802	35.899074395	Horizontal 55 gal drum, N-S	0.6858
19	-83.960476764	35.899107315	Horizontal 55 gal drum, N-S	0.9906
20	-83.960499101	35.899298129	Horizontal 55 gal drum, E-W	0.6604
21	-83.960620057	35.899354722	Steel scrap, 3 pcs 3-4 ft long	0.635
22	-83.960681984	35.899341857	Vertical 55 gal drum	0.7747
23	-83.960700824	35.899261911	Plastic 55 gal drum, freshwater and gravel filled	0.6858
24	-83.960641925	35.899286029	Vertical 55 gal drum	1.1176
25	-83.960592642	35.899238017	Plastic 55 gal drum, saltwater and gravel filled	0.635
26	-83.960588449	35.899302733	Iron pipe, 3" diameter, 42" long	0.6096
27	-83.960829212	35.899252387	2 pcs styrofoam, 9'x2'x4", dipping N45E	0.91-1.1
28	-83.960764657	35.899306459	Cement blocks, 1.5 cu ft pea gravel	0.6858
29	-83.960513524	35.899203361	Aluminum gutter; 5 pcs, 6.5-8 ft long	0.3937
30	-83.960505952	35.899157725	Coil of 12/3 copper wire	0.3048
31	-83.960447594	35.899244504	Solid iron rod, ~41" long, 1" diameter	0.3302
32	-83.960783815	35.899165355	Iron Pipe, 4" diam, 80"? long	0.9144
33	-83.960730944	35.899199192	Two vertical drums, 33" center to center along N-S line	0.9906
34	-83.960734320	35.899210835		
35	-83.960412695	35.899159815	Iron Pipe, 4" diam, 64" long	0.5588
37	-83.960888227	35.899293243	Two horizontal drums, 19" separation end to end, N-S	0.9144
38	-83.960887295	35.899302785		
39	-83.960910127	35.899376011	Styrofoam block, 1 yd cube	0.3048
40			2 pcs galv pipe, 5.5 and 8 ft long	0.3-0.56

Methodology

Geophysical Techniques

There are three geophysical techniques that will be utilized in this research project. These techniques have been chosen because of their traditional use in detecting small, discrete targets with a relatively simple and easy acquisition of the data. Understanding of the science of each technique used is vital for the integration process.

Ground Penetrating Radar (GPR)

The GPR unit used is a Sensors and Software PulseEKKO Pro system. This technique utilizes propagating electromagnetic (EM) waves to detect changes in the EM properties of the shallow subsurface. The propagation velocity of EM waves (i.e., the controlling factor on the generation of reflections) is determined by the dielectric permittivity contrast between the background material and the target. Dielectric permittivity is defined as the ability of a material to store and then permit the passage of EM energy when a field is imposed on the material (Baker et al., 2007) and can be measured in the lab or in situ. A GPR unit consists of transmitting and receiving antenna, where the transmitting antenna generates an EM pulse in the subsurface that travels into the subsurface, reflects off an interface or scatters off point sources (both caused by contrasts in dielectric permittivity). This reflected/scattered energy then travels back to the surface where it is recorded by the receiving antenna.

EM-31 Ground Conductivity

A Geonics EM-31 terrain conductivity meter was used for this experiment. The EM-31 is a one-person device containing both transmitter and receiver coils on a 3.7-meter frame and uses an electromagnetic inductive technique that allows measurements without electrodes or ground contact. With this inductive method, surveys can be carried out under most geologic conditions including those of high surface resistivity such as sand, gravel, and asphalt. Effective exploration depth for this instrument is about 6 meters (Geonics 2007). The system is a non-intrusive conductivity measuring device, and data can be collected at the speed in which the operator can walk. Terrain conductivity (EM-31) measurements are made by inducing an electromagnetic current into the ground from a transmitter coil, and recording the resulting secondary electromagnetic field at a receiver coil a fixed distance away (Geonics 2007). Measurements are recorded in units of conductivity called milli-Siemens per meter (mS/m). Abrupt spikes in the inphase and conductivity measurements are indicative of locations of the desired targets within this study.

Magnetic Gradiometry

The instrument used during this phase of the project is a Geometrics G858 cesium vapor magnetometer. The device broadly consists of a photon emitter containing a cesium light emitter or lamp, an absorption chamber containing cesium vapor and a "buffer gas" through which the emitted photons pass, and a photon detector, arranged in that order (Geometrics 2001). For purposes of our study, we are interested in measuring how much the strength of a magnetic field changes between two specific points, or the "gradient" of the field. This instrument is a fluxgate gradiometer with data logger with two cylindrical sensor assemblies for use in geophysics and archaeology. Each sensor assembly contains two fluxgate magnetometers with a one meter vertical separation, together with electronics and non-volatile memory for calibration data. The system provides an enhanced depth response, exceptional stability and electronic adjustment.

Data Collection and Processing

Ground Penetrating Radar (GPR)

Data lines were collected in a grid type pattern, with 0.5 meter spacing and lines collected in both North/South and East/West directions. A differential GPS unit was integrated with the GPR data, allowing coordinates of any anomaly detected to be recorded, giving an exact XYZ location. The frequency utilized during this study was a 200 MHz antennae. The grid size for GPR is 15 meters by 24 meters, falling within the boundaries of the EM-31 and Magnetic Gradiometry grid.

Data was processed using EKKOView Deluxe and EKKOMapper 3 (Sensors and Software, Inc.). The EKKOView Deluxe software enables the GPR data to be manipulated using the processing

steps of dewow, migration, and autogain. The GPS data collected in succession with the GPR data was incorporated with the data during processing. The EKKOMapper 3 software was then used to plot the GPR data into one composite image, with the grid being divided into depth slices, which allowed easy identification of anomalies within the grid. Processed data was exported in a grid file to the program Surfer. The grid file was able to be displayed as various maps (contour, image, shaded relief, and surface maps) to allow for a 3D visualization of the data.

EM-31 Ground Conductivity

Survey design for this geophysical technique is different from the GPR data collection, with the 40 meter by 50 meter grid having data lines with 2 meter spacing. Data collection was obtained with lines alternating in an eastward/westward direction, with data points collected every tenth of a second along each traverse.

Grid data was downloaded directly from the instrument to the computer used for processing; the software used in processing was DAT31W (Geonics Limited, Inc.). Tools within DAT31W allowed data to be smoothed and lines to be corrected for linear drift. The terrain conductivity ASCII data was then converted into a Microsoft Excel spreadsheet and then processed and interpreted using Golden Software, Inc.'s Surfer software and used to construct plan views of EM data for the entire field survey area.

Magnetic Gradiometry

Plot B4 was surveyed with a 1 meter spacing and line data collected alternating in northward and southward directions, with 8 points of data recorded for each meter traversed. Data collection is set on a timer with the cesium vapor magnetometer instrument, with adjustments in the speed of collection allowed to be changed manually. The operator maintains the set pace set up within the parameters of the survey design ensures that all data points are evenly distributed amongst the grid. The following processes are performed to maximize the visualization of anomaly locations within the subsurface of the study area: Clip, Interpolate, Despike, Stretch, Destagger, and Deslope.

Organization of Data

In order to run any statistical analysis in SAS, the grid files created that contains the location of the buried targets must be at the same resolution as the data points collected with the various geophysical techniques. As discussed previously, each geophysical technique, and respective data set, is at a different resolution. To remedy this problem, individual files were created to match the locations of the buried targets to the corresponding grid locations with each geophysical technique. For example, the magnetic data was collected with a grid size of 1.0 m by 0.125 m. The target location was then identified with an X-Y coordinate according to the "southwest" corner of the grid space within the magnetic data. In the case of GPR, two separate grids were created for the two depths chosen to contain the greatest number of anomalies after processing of the data. It is also important to note that there has been no interpolation with the EM-31 and Magnetic Gradiometry data, but there is interpolation with the GPR data files. The location of the targets and descriptions can be found in Table 1.

Statistical Methods

A number of statistical methods were employed to aid in the quantitative assessment of target identification. These tests include variogram, logistic regression, proc freq, and univariate, of which were conducted using the prepared data; Kriging was utilized during the data processing stage. The variogram procedure computes empirical measures of spatial continuity for two-dimensional spatial data. These measures are a function of the distances between the sample data pairs. When the data are

free of nonrandom (or systematic) surface trends, the estimated continuity measures are the empirical semivariance and covariance. These measures can be used in subsequent analysis to perform spatial prediction.

Binary responses (for example, presence or absence of a target) set up logistic regression analysis to be the most appropriate means to investigate the relationship between these discrete responses and a set of explanatory variables. The logistic procedure fits a common slope cumulative model, which is a parallel line regression model based on the cumulative probabilities of the response categories rather than on their individual probabilities. The logistic procedure fits linear logistic regression models for discrete response data by the method of maximum likelihood.

Freq procedure produces one-way to *n*-way frequency and contingency (crosstabulation) tables. For one-way frequency tables, such as that used in this study, a goodness-of-fit tests is computed for equal proportions or specified null proportions. To estimate the strength of an association, Proc Freq computes measures of association that tend to be close to zero when there is no association and close to the maximum (or minimum) value when there is perfect association (SAS 2008). Proc Freq computes asymptotic standard errors, confidence intervals, and tests for measures of association and measures of agreement. Exact *p*-values and confidence intervals are available for many test statistics and measures.

The univariate procedure provides several important pieces of information to compute summary statistics. The most appropriate applications of this statistical test is that is provides (1) descriptive statistics based on moments (including skewness and kurtosis), quantiles or percentiles (such as the median), frequency tables, and extreme values, (2) histograms that optionally can be fitted with probability density curves for various distributions and with kernel density estimates, (3) cumulative distribution function plots (cdf plots). Optionally, these can be superimposed with probability distribution curves for various distributions, (4) quantile-quantile plots (Q-Q plots), probability plots, and probability-probability plots (P-P plots). These plots facilitate the comparison of a data distribution with various theoretical distributions, and (5) goodness-of-fit tests for a variety of distributions including the normal (SAS 2008).

Kriging is a group of geostatistical techniques to interpolate the value of a random field (e.g., the amplitude of the transmitting EM wave, *z*, of the subsurface as a function of the geographic location) at an unobserved location from observations of its value at nearby locations. Local kriging is performed by using only data points within a specified radius of each grid point. Contouring of the data is accomplished by defining the prediction grid point (node) locations. The prediction grid is rectangular, with the grid point population and spacing based on the available data in the GPR surveys.

Magnetic Model

In order to determine if the proposed statistical methods are appropriate in the assessment of various geophysical techniques being able to detect the targets in Plot B4, a model was created in SAS which generates random magnetic scores on a 100x100 grid and plants artifacts (targets) at random. The data was then analyzed with the Logistics procedure. The probability of a target being present is calculated from the logodds. The Wald Chi-squares in the table are tests of the hypothesis that intercept and slope are zero. For the slope parameter, it is shown that chi-square equals 1012.5876, with a p-value less than 0.0001 ($p<0.05$ indicates significance), so it is concluded that knowledge of magnetic data significantly affects the ability to predict the presence of an artifact.

There is also a table at the end of the output that summarizes the model predictions over the 100x100 grid. It is shown that 97.56% of the cells with no artifact were correctly predicted to not contain an artifact, and 86.47% of the cells which did contain an artifact were correctly predicted to contain an artifact. The program is set up so that it will generate a new set of data each time that is run,

with similar results each time. Based on the results of this model, it can be concluded that the statistical methods discussed previously are appropriate in the assessment of all three geophysical techniques detecting discrete targets.

Results

Ground Penetrating Radar

Sensors and Software's data processing software Ekko Mapper 3 allowed for depth slices to be taken of a pseudo 3D grid of the survey area. A qualitative assessment of the data was made by the author, concluding that a depth slice of 0.925 meters and 1.125 meters indicates the greatest number of anomalies (i.e., buried targets). At 1.125 meters, 3 anomalies are detected (targets 21, 22, and 31 in Figure 2) with an additional 3 anomalies not present in the target data. At 1.125 meters, 4 possible anomalies are identified (targets 17, 30, 31, and 35 in Figure 2) with an additional 2 anomalies not present in the target data. Together, GPR is able to detect 35 % of the targets present in the survey area. While this is a low percentage, there were only two arbitrary depths taken to evaluate detection for this project. A more comprehensive approach will be taken at a later date, with many more depth slices evaluated to determine location of targets. An example of contoured, normalized GPR data at 0.925 meter depth is given in Figure 3, with the yellow areas indicating possible locations of buried targets. Data maps similar to Figure 3 were created from each individual data set to aid in identification of anomaly location.

According to the SAS output from the model, there is some variation between the Upper and Lower levels of GPR data, but not to the point of being significant. For the Upper level, there were 1,797 data points designated as containing a target and 178,203 data points that do not. It is shown that 100% of the cells with no artifact were correctly predicted to not contain an artifact; conversely, 100% of the cells that did contain an artifact were predicted to not contain an artifact. From this, it can be concluded that it is not appropriate to normalize data using the formula: $T^* = (d_i - d_{min}) / (d_{max} - d_{min})$

Additionally, the Hasmer and Lemeshow goodness-of-fit test gives a chi-square of 98.3008 and $p<0.0001$ which confirms that the current model (of using the above formula for normalization of the data) is not sufficient enough to stand alone and emphasize the location of targets. Comparing the distribution of normalized values for target data points and non-target data points shows that a more sophisticated measure needs to be implemented to reduce uncertainty in discrete anomaly detection in a statistical manner. As shown in Figures 4, there is a strong correlation between the distribution of those grid points designated as not being over a target compared to grid points that are over a target.

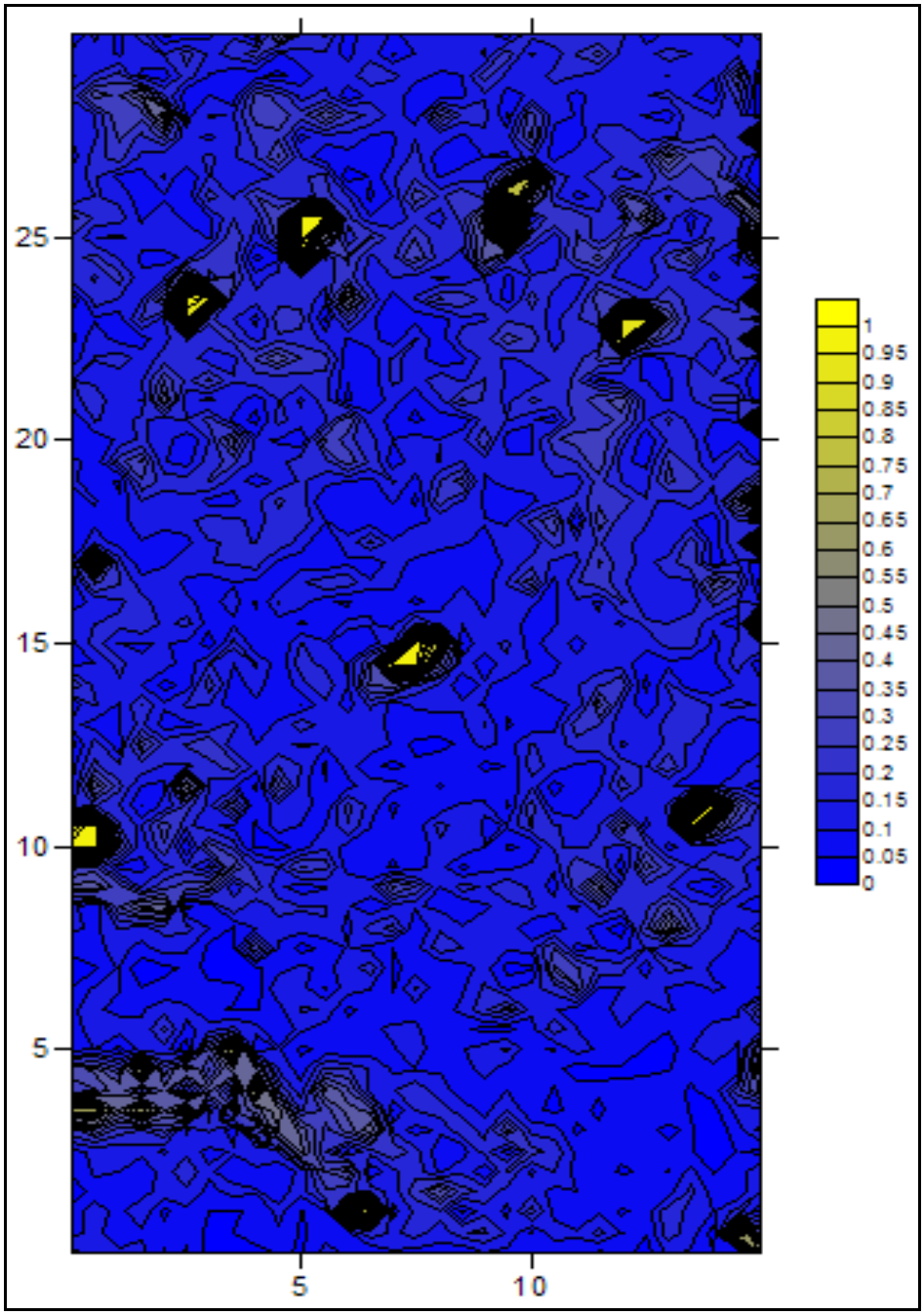

Figure 3: Ground Penetrating Radar Survey at 0.925 meters depth. Amplitudes of the EM wave data have been normalized, with a "1" (yellow) indicating possible locations of targets. Data has been plotted and contoured in Surfer. Grid is measured in meters.

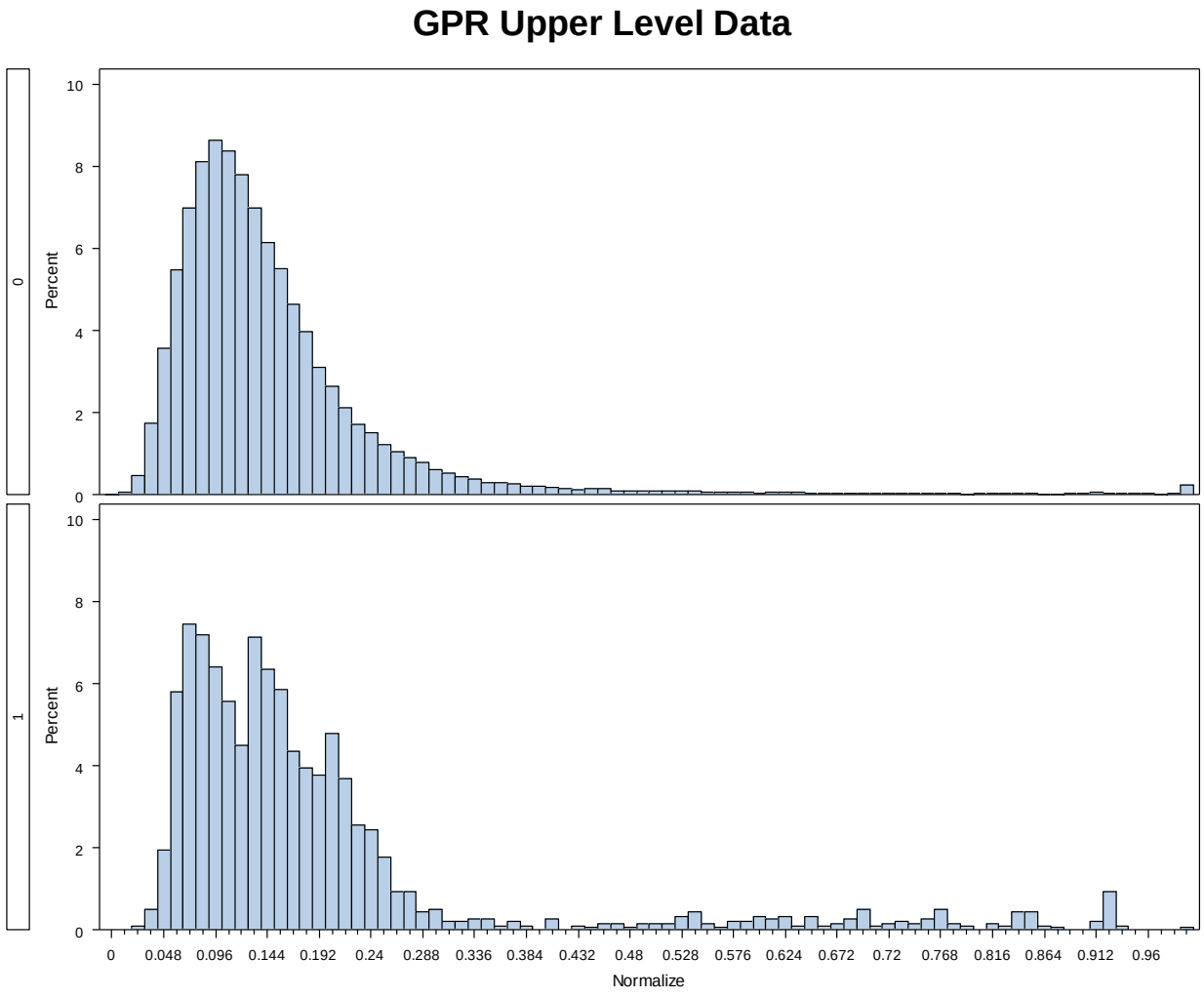

Figure 4: Histograms of the normalized GPR data points at 0.925 meter depth. There is a strong correlation between the distribution of those grid points designated as not being over a target (0) compared to grid points that are over a target (1). For the method in which the data was normalized to be considered appropriate, one would expect the histogram for (1) to be skewed to the right with a much larger number of data points having a value closer to 1.

For the GPR Lower level data, there is a similar pattern for the data points with targets and non-targets. The results of the Proc Freq procedure are the same as the Upper level, in that it is shown that 100% of the cells with no artifact were correctly predicted to not contain an artifact; conversely, 100% of the cells that did contain an artifact were predicted to not contain an artifact. For the Hosmer and Lemeshow goodness-of-fit test, there is a chi-square value of 90.6644, giving a p,0.0001 and confirming that knowledge of GPR data does not predict the location of targets effectively.

EM-31 Ground Conductivity

A contour map of the EM-31 data is not easily interpretable. The contrast between the signals is relatively small when compared to the other techniques used in this study, making contouring of the data

difficult to identify probable locations of the targets. Instead, a surface map was created in Surfer to show relative changes in conductivity measurements. Areas with large differences are shown as spikes and areas of small differences are seen as both "depressions" and small "bumps," depending on its' relative value to the average across the grid. Anomalies shown in the data map are associated with targets 18, 19, 23, 24, 26, 27, 28, 29, 31, 32, 33, 34, 35, and 40 (Figure 2). A total of 14 anomalies were detected; within the boundaries of the surveyed area, there are a total of 20 buried objects, resulting in 70% detection across the grid using the EM-31 technique.

Across the survey area, there are 789 grid spaces that do not contain targets and 42 that do contain targets. Results are similar to the GPR data results, in that using the normalized values do not accurately detect the location of targets; all grid points were predicted to not contain targets. The Hosmer and Lemeshow goodness-of-fit test gives a chi-square of 16.5651 and $p<0.0350$. Although this p-value is much higher than that of the GPR data, it is still within significance to reject the null hypothesis that the linear model fits the data. There is a very strong correlation between the distribution of those grid points designated as not being over a target compared to grid points that are over a target. The bars at the right of the graph for absence of target indicates that there are some grid points registering with the EM-31 instrument that do not have targets associated with them, possibly due to noise at the surface. There is no true distinction between data points that contain targets or not.

Magnetic Gradiometry

Using the maps produced in Surfer of the magnetic data, 14 anomalies were detected. These anomalies do not include the one detected at x=30, y=40 shown in Figure 5, as it is located next to metal fence post and considered to be noise. The anomalies have a nT reading ranging in gradients of about 180 nT to 1450 nT. As the targets are known to have varying size, shape, orientation, and construction material, this can be expected. Anomalies are associated with targets 17, 18, 19, 21, 22, 24, 26, 27, 31, 32, 33, 34, 35, and 40 (Figure 2), resulting in 70 percent of the targets were detected using the magnetic gradiometry technique.

For the magnetic data, there are 256 grid spaces that contain targets and 14,325 that do not contain targets. Again, results are similar to the other geophysical techniques, in that normalization of the data using the discussed method does not reduce uncertainty in anomaly detection. The magnetic data result in the highest value for the Hosmer and Lemeshow goodness-of-fit test with a 110.5393 and $p<0.0001$. Reviewing the distribution of the normalized values, there are no grids that contain a target with a value higher than 0.06, whereas the grids that do not contain targets have values up to 0.15.

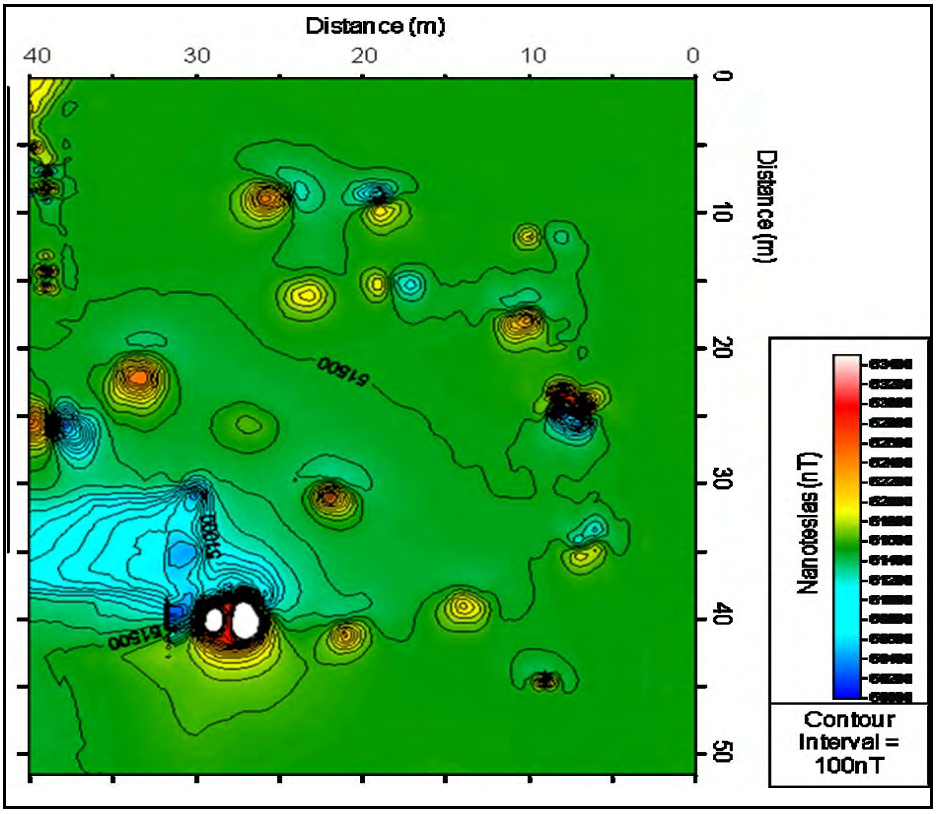

Figure 5: Magnetic Data Results. Anomalies, such as shown with the red circle, indicate targets that have remnant magnetism. Anomalies with a dipole effect, as shown with the blue circle, indicate targets that are metallic. Grid size is 40 meters by 50 meters, with north at the top of the grid.

Conclusions

Individual data sets by all geophysical techniques were able to produce maps showing anomalies of possible targets. These targets were then correlated with a data map showing the exact location of the targets, determining which targets were detected with which geophysical technique. The GPR was able to detect a total of 7 targets out of a possible 20, but this low percentage of detection may be in part to only choosing two depths to evaluate and not the entire pseudo 3D map. The EM-31 Ground Conductivity meter was able to detect 14 targets (70%) and the Magnetic Gradiometry detected 14 targets (70%). There were 3 targets in which only the EM-31 detected, 1 in which only the GPR detected, and none that were added to total detection capabilities by adding the magnetic gradiometer. In total, 90% of the targets in the survey field were detected. It is unclear what properties of the two remaining targets contributed to their not being detected, but will be further investigated.

Although a model to create synthetic magnetic data was able to accurately predict the presence or absence of a target, the same method was proven ineffective using real data. The data values from each geophysical technique were normalized with the assumption that the closer the grid data point was to 1, the more likely it would indicate the location of a target. According to the statistical output from SAS, this is not the case. However, this phase of the research project is viewed as a success, in that it

was able to meet its objectives and accurately perform a correlation of geophysical data with known "targets" by utilizing multiple geophysical techniques. Additionally, it was shown that certain types of targets are detected more clearly with a certain type of geophysical technique. Despite the third objective not being met (complete a statistical analysis to evaluate the effectiveness of the data integration methodology and applications), the methodology in which to explore the nearly countless ways of normalizing the data or manipulating the data to highlight targets is in place. These alternate methods will be explored in the next phase of this project.

Future Work

There are a number of projects conducted prior to this study that will be enhanced by the methodologies and results of this research. Primarily, geophysical data acquisition has been performed on an archaeological site south of Knoxville, TN, USA (Cherokee Farm). Geophysical surveys, compared to traditional archaeological surveys, can cover more extensive regions and with a tighter grid spacing for collecting data, helping to aid archaeologists in selecting excavation sites in a more strategic manner. The main objective of using geophysics at an archaeological setting is to give the archaeologists additional tools in their planning and choosing of locations and methods of excavations; this goal was accomplished throughout the course of this study as the original methodologies of the project evolved to include more geophysical techniques. The portion of the project discussed in this paper will be expanded to integrate multiple geophysical techniques and contribute towards meeting the project's main objectives. There have also been surveys conducted on an Eastern Tennessee church property, exploring possible locations of unmarked graves to help with the design of expanding the church sanctuary.

Cherokee Farm represents a site with unknown target features, and is an archaeological site on the Tennessee River floodplain. The area is divided into 437 (20 x 20 m) plots with 0.5 m spacing where magnetic gradiometry profiles were collected in a zig-zag pattern, resulting in over 350 km of line data. The magnetometer used in this phase of the project is a Bartington 601. Anomalies identified in the magnetic data indicate potential archeological features that will be further verified as areas of interest with the addition of GPR and EM-31 data. Data from the Cherokee Farm site will undergo similar statistics and merging methodologies as the data from Plot B4. This site will also serve as the baseline for running statistical analysis in regards to Type I and Type II errors in geophysical surveys with excavations from the Cherokee Farm site providing a ground-truth of the subsurface features. Statistics will also be calculated from the magnetic data map created of the Cherokee Farm area based on a set of parameters for the anomalies detected (size, shape, intensity) and the actual features excavated that match particular combination of parameters. Additionally, a historical land use map will be created for this part of the study.

The final product of this research will be an instructional flowchart outlining the combination of geophysical techniques used in data acquisition, various combinations in processing data, methodologies in merging data, and quantitative assessments of the data. Ultimately, a quantitative integration of multiple near-surface geophysical techniques will be developed for improving subsurface imaging and reducing uncertainty in discrete anomaly detection for multiple scenarios (i.e. subsurface characteristics, target type, and geographical settings).

References

Allen, D., Schuurman, N., Deshpande, A. and Scibek, J., 2008, *Data integration and standardization in cross-border hydrogeological studies: a novel approach to hydrostratigraphic model development*. Environmental Geology. Vol. 53, no. 7, pp. 1441-1453.

Baker, G.S., Jordan, T.E., and Talley, J., 2007, An introduction to ground penetrating radar (GPR), *in* Baker, G.S., and Jol, H.M., eds., Stratigraphic Analyses Using GPR: *Geological Society of America Special Paper 432*, p. 1–18

Ferré, T., von Glinski, G., and Ferré, L., 2003, *Monitoring the Maximum Depth of Drainage in Response to Pumping Using Borehole Ground Penetrating Radar* Vadose Zone J.,; 2: 511 - 518.

Galicia, Jose, 2001, *The offshore Golden Lane: New outline of opportunities from the integration of geologic and geophysical data.* The Leading Edge; 20: 763 - 782.

Geometrics, 2001, G-858 MagMapper Operator Manual. Retrieved on November 29, 2009 from ftp://geom.geometrics.com/pub/mag/Manuals/858Manual_D.pdf

Geonics Inc., 2007, Operation Manual for Geonics EM-31 Ground Conductivity Meter. Retrieved on December 1, 2009 from http://www.geonics.com/html/em31-mk2.html

Hornby, Brian and Herron, Don, 2007, *Introduction to this special section: Borehole geophysics/VSP* The Leading Edge; 26: 731.

Rahman, A., Frank, T., Tsai, C., White, C., Carlson, D. and Willson, C., 2008, *Geophysical data integration, stochastic simulation and significance analysis of groundwater responses using ANOVA in the Chicot Aquifer system, Louisiana, USA.* Hydrogeology Journal. Vol. 16, no. 4, pp. 749-764.

SAS Institute,2008, SAS 9.2 Help and Documentation: Your Complete Guide to Syntax, How To, Examples, Procedures, Concepts, What's New, and Tutorials. SAS Institute Inc., Cary, NC.

Stock, K. and Pullar, D. 1999. *Identifying semantically similar elements in heterogeneous spatial databases using predicate logic.* Interoperating geographic information systems, second international conference, INTEROP'99 Zurich, Switzerland, Springer, Heidelberg, pp 231–252

CORRELATIONS BETWEEN DIRECT CURRENT RESISTIVITY AND SEISMIC ATTRIBUTE TESTS ACROSS AN ACTIVE METHANE HYDRATE VENT IN MISSISSIPPI CANYON BLOCK 118, GULF OF MEXICO

Alan R. Gunnell, Baylor University, Waco, TX
John A. Dunbar, Baylor University, Waco, TX

Abstract

An active methane vent in Mississippi Canyon Block 118 (MC118), Gulf of Mexico, has been the focus of persistent research. This vent area contains both active and dormant vents as well as blocks of methane hydrate outcropping on the seafloor. It is proposed that methane hydrate blocks also form within the Hydrate Stability Zone (HSZ) beneath the vent. Through collaborative work done by the Gulf of Mexico-Hydrate Research Consortium (GOM-HRC), surficial characteristics and mound chemistry is understood, but quantifiable distributions of hydrate with the HSZ is unknown. High-frequency seismic imaging of the mound is hindered by the presence of free gas, hydrate, and biogenic carbonate blocks on the surface.

A direct current resistivity (DCR) land system is adapted to function on the sea floor and to locate the sub-seafloor distributions of hydrate. Continuous resistivity profiling (CRP), totaling 26.4 km in length, is able to resolve the distribution of hydrate whereas further distinguishing between disseminated gas and hydrate. This distribution of hydrate trends along faults and fractures while disseminated methane is found within sediment pores. Through combinations of resistivity profiles and seismic attribute tests, correlations between incoherent and coherent areas beneath the vent represent gas and hydrate respectively.

GEOTHERMAL INVESTIGATION OF WAUNITA HOT SPRINGS UTILIZING A VARIETY OF GEOPHYSICAL SURVEY METHODS AND TECHNIQUES

Joyce Hoopes, Colorado School of Mines, Golden, CO
Gordon Johnson, Colorado School of Mines, Golden, CO
Kristen Swaim, Colorado School of Mines, Golden, CO
Ariel Thomas, Colorado School of Mines, Golden, CO

Abstract

The results of a geothermal investigation will be presented. The project, part of the Colorado School of Mines Undergraduate Geophysics curriculum, is conducted throughout a student's senior year. The geothermal reservoir studied has surficial manifestations at Waunita Hot Springs, located in the southeastern corner of Gunnison County. The springs have been identified by the Colorado Geological Survey as a resource with potential for geothermal power generation, (Barrett and Pearl, 1978). The project goals are to better understand the geothermal reservoir and its geologic structure. To understand the fracturing system that defines and controls the reservoir, geophysical mapping of the subsurface conductivity will be presented. An image of the deeper conductivity distribution will be displayed as a result of a time domain electromagnetic survey. For imaging at shallower depths, with greater detail, the electrical methods, specifically SP and DC resistivity, were utilized. Detailed geologic maps of the area are limited; therefore, a geologic survey will be conducted along with the collection of hydrological data. A geochemical analysis of the water from the springs and temperature gradients calculated from borehole measurements will also be presented. The observations and data will be useful in assessing the geothermal potential of Waunita Hot Springs.

References

Barrett, J.K. and Pearl, R.H., 1978, An Appraisal of Colorado's Geothermal Resources: Colorado Geological Survey, Bulletin 39

STABLE PARAMETER ESTIMATION METHOD APPLIED TO CHARACTERIZATION OF PLUME TRANSPORT IN ENVIRONMENTAL INVERSE PROBLEMS

Hugo Bertete-Aguirre, Polytechnic Institute, RJ, Brazil.
Elena Cherkaev, University of Utah, Salt Lake City, UT

Abstract

The talk discusses a geophysical environmental inverse problem of characterization of water flow model from monitoring of plume transport. We present a stable method to calibrate transport models using measurements of concentration of a chemical over time. Such observations can be used as an input for geophysical environmental inverse problems. The ability to produce realistic characterization of plume transport relies on the calibration of the parameters of the flow, which in the presented case study is described by the two dimensional advection-diffusion equation. The inverse problem of transport model calibration from inaccurate observations of contaminant concentrations is ill-posed and requires regularization. In the current work, the regularized problem is solved by an adaptive gradient minimization. Stable prediction of plume transport parameters allows to describe the dynamics and transport of solutes or suspensions within the system.

Introduction

The preservation of existing water resources is one of most important current environmental problems. Stable characterization of transport flow model is required for monitoring of transport of contaminant solutes or suspensions within the system. This paper discusses the inverse problem of finding parameters of flow model from observations of concentration of a contaminant. Inverse problems in the monitoring of contaminant plume transport involve the ability to predict realistic models from noisy data. Joint inversion is usually preferred when possible (Berge et all, 2000, Bertete-Aguirre et all, 2002, 2003) in order to constrain solutions especially when working with noisy data.

In this paper we present a stable parameter estimation method using Tikhonov regularization technique. We construct solution using a proposed adaptive gradient minimization approach. To show effectiveness of the method we use numerically simulated example of synthetic data with noise level of 15% in a simulated experiment. The method allows to significantly reduce the uncertainties in the determination of the parameters of the plume transport models. The constructed solution can be used in the characterization of plume transport in environmental inverse problems.

Method

Numerous applications of numerical simulation of water quality in surface and underground reservoirs require a model of water flow. In this work we simulated the transport of constituents in solution and suspension described by the two dimensional equation of advection-diffusion for surface water. Several numerical solutions have been proposed to solve these equations (Fisher 1973, Telles 2009). They require that the geometry of the medium, initial conditions, and boundary are defined. Furthermore, the result of simulation is strongly affected by the values that are specified for the longitudinal and transverse dispersion parameters, whose values are not unique, but a cover band called acceptable. Thus, the best simulation depends crucially on the choice of such parameters, which are obtained from calibration of the model that best fit measured concentration.

The inverse problems for model calibration of contaminant transport are ill-posed, and regularization techniques are needed in order to estimate parameters from noisy observations. The main idea of regularization is to transform the ill-posed inverse problem into a sequence of well posed problems with the property that small variations in the data result in small changes in the solution.

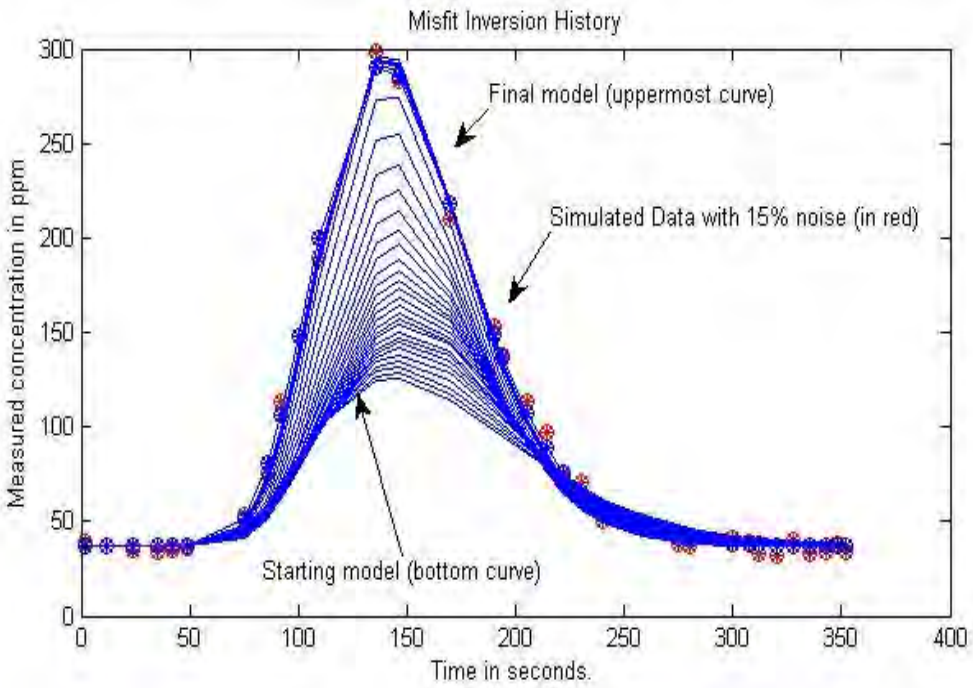

Figure 1: Sequence of runs showing the convergence of the concentration profiles in the inverse problem from a starting model (bottom curve) to the simulated (real) data with a level of noise of 15% (uppermost curve). Simulated data points are represented by filled circles.

The current work uses Tikhonov regularization in conjunction with adaptive gradient minimization to construct a stable parametric model. An adaptive gradient

minimization technique was shown to be efficient in the reconstruction of solution of the regularized problem (Bertete-Aguirrre, Cherkaev, and Oristaglio, 2002). This approach is used in the current work to recover stabilized reconstructions of model plume transport parameters from noisy observations. Figure 1 shows concentration profiles corresponding to sequential runs of the problem of estimation of flow parameters in a numerical simulation with data aggravated with 15% noise.

Conclusions

Stable predictions of plume transport can aid joint geophysical characterization of plume movements. This work shows that the proposed regularized method implemented with an adaptive gradient minimization can recover stabilized parameters of plume transport model from noisy measurements. The ability to obtain stable calibrated models of plume transport can be used to generate several scenarios to aid joint geophysical characterization. This work can be extended to other mathematical formulations of the problem, such as changing the forward problem to the surface or underground plume transport equations.

Acknowledgments

Computational resources and funds are thanks to the University of Utah and FAPERJ (Foundation for Scientific Research of RJ, Brazil).

References

Berge, P. A., Berryman J. G., Bertete-Aguirre, H., Bonner, B. P., Roberts J. J., Wildenschild, D., Joint Inversion of Data for Site Characterization and Restoration Monitoring, Lawrence Livermore National Laboratory Report UCRL-ID-128343, July 2000.

Bertete-Aguirre, H., Berge, P. A., and Jeffery J. Roberts, Using laboratory measurements of electrical and mechanical properties to assist interpretation of field data from shallow geophysical measurements, Journal of Environmental and Engineering Geophysics, Vol. 8, Issue 1, 23-29, 2003.

Bertete-Aguirre H., E. Cherkaev, and Michael Oristaglio, Non-Smooth Gravity Problem with Total Variation Penalization Functional, Geophysical Journal International, Vol. 149, p. 1-9, April 2002

Bertete-Aguirre, H., and Berge, P. A., 2002, Recovering soil distributions from seismic data using laboratory velocity measurements, Journal of Environmental and Engineering Geophysics, Vol. 7, 1-10.

Fischer, H. B., 1973, Longitudinal Dispersion and Turbulent Mixing in Open-Channel Flow Annual Review of Fluid Mechanics, vol. 5, pp.59-78.

Telles, W. R., 2009, Simulação do transporte bidimensional horizontal de substância conservativa, MSc. Thesis. Universidade do Estado do Rio de Janeiro - UERJ/IPRJ.

USING GROUND PENETRATING RADAR TO DETERMINE THE QUANTITY OF IMPOUNDED SEDIMENT BEHIND A DAM

David J. Santaniello, Boston College, Chestnut Hill, MA
Noah P. Snyder, Boston College, Chestnut Hill, MA
Allen M. Gontz, University of Massachusetts – Boston, Boston, MA

Abstract

We investigate the viability of ground penetrating radar (GPR) as a method to estimate the quantity of sediment stored behind the Merrimack Village Dam on the Souhegan River in southeastern New Hampshire. If the pre-dam riverbed can be imaged, the thickness and volume of the reservoir deposit can be calculated without sampling. We surveyed six cross sections with a Mala Geosciences ProEx 100 MHz GPR unit in May 2008. In a related study, topographic and bathymetric surveys were conducted in 2007, 2008, and 2009 to monitor the sediment flux associated with the removal. By 2009, these surveys measured the pre-dam riverbed in the uppermost cross sections from the dam. We compare these surveys to the interpreted GPR images to calculate a calibrated velocity through the impounded sand of 0.043 m/ns. Using this velocity, the average thickness of the sediment above the interpreted pre-dam riverbed calculated for each of the six cross sections varies between 0.81 m and 3.11 m. The estimate of the quantity of sediment stored behind the dam is ~67,000 m^3 compared to a 2004 estimate of ~62,000 m^3 based on probing the sediment with a steel rod to the point of refusal.

MAGNETIC PROSPECTION OF A TUMULUS IN THE ANCIENT HISTRIA NECROPOLIS

Dumitru IOANE[1], Sorin ANGHEL[2], Alexandra DUDU[2]

[1]*University of Bucharest, Faculty of Geology and Geophysics, Bucharest, Romania*
[2] *National Institute of Marine Geology and Geoecology – GeoEcoMar, Bucharest, Romania*

Abstract

Near surface geophysical investigations are employed in archaeology in order to estimate the location, depth, shape and physical properties of buried ancient structures. The geophysical study initiated in 2008 on tumuli located in the Histria necropolis was based on magnetics, the measurements being carried out with a proton precession magnetometer / gradientmeter. The networks where measurements of total magnetic field and magnetic vertical gradient were performed covered each tumulus and small adjacent areas. The magnetic measurement points situated at 2 m interval represented detailed rectangular networks.

The necropolis is situated at ca 2 km north-west of Histria ancient Greek city and includes a great number of tumuli of various dimensions and trends. Previous archaeological studies evidenced different rituals of burial for the ca 1300 years of continuous inhabitation during Greek colonization and Roman / Byzantine empires.

The magnetic data obtained for the tumulus analyzed in this paper, located toward the north-western limit of the Histria necropolis, suggest quite complex archaeological features, similar to those observed in the excavations. Generally, metallic artifacts, a clay layer affected by fire or active magnetic rocks employed in the buried infrastructures may represent sources of high magnetic anomalies.

The magnetic total field and vertical gradient anomalies are interpreted as being here mainly due to burnt materials and buried greenshist structure (high anomalies), or to an outer stone belt made of limestone boulders (low anomalies).

Key words: Histria, necropolis, tumulus, magnetic method, magnetic anomalies

Introduction

Non-destructive geophysical methods are used nowadays in archaeological studies to provide important information on the form, size, spatial arrangement and certain physical properties of the buried features in order to guide excavation works. Among these methods, high resolution magnetics was adopted in the last two decades in archaeological prospection being able to detect shallow archaeological targets at depths of a few meters. The effectiveness of the magnetic surveys, many times employing vertical gradient measurements, depends on the contrast between the magnetic properties of archaeological infrastructure and artifacts and those of the environment (soil and near-surface rocks).

The archaeological targets usually generate small magnetic anomalies in the range of a few tens of nT, for total field anomalies, or nT/m, for vertical gradient anomalies. Usually, magnetic archaeological remains are be represented by kilns, bricks, pottery and obviously, artifacts made from iron, all being characterized by high magnetic susceptibility and/or remanent magnetization.

Histria ancient necropolis

Histria is the oldest ancient Greek city in Romania, established on the Black Sea by Greek colonists from Milet during the seventh century B.C. The city was inhabited continuously about 1300 years, since ancient Greek times until Roman–Byzantine ones. During the Greek period (VIIth century B.C to Ist century B.C.), the city had two distinct parts, the acropolis and the civil settlement, following a widespread model of the ancient world.

Figure1 - Tumuli in Histria ancient necropolis

This structure was preserved until the city was abandoned during the VIIth century A.D., following probably the closure of the bay where the city port was constructed. Presently, the excavated remains of Histria are situated on the western shore of Sinoe Lake, separated by the sea by the Chituc sandy bank.

The necropolis is located outside the ancient city walls and includes a large number of tumuli displaying different sizes and trends (Fig. 1). Archaeological excavations carried out during the XXth century showed that often the encountered burial rite was incineration and the tumuli infrastructure consisted in a circular peripheral ditch, a funeral platform and a stone belt (Fig. 2 - Alexandrescu, 1982).

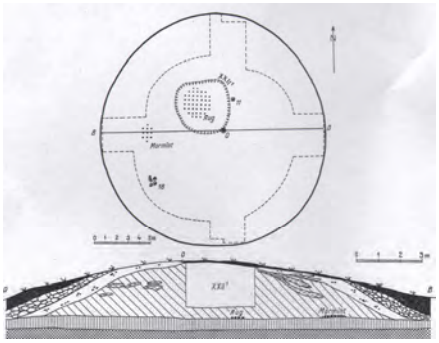

Figure 2 – Sketch of an excavated tumulus in Histria necropolis
(Alexandrescu, 1982)

Geophysical data

The magnetic measurements were carried out using a Geometrics G-856 proton magnetometer/gradiometer device in a 2m interval rectangular grid overlapping the investigated tumulus. The tumulus elliptical shape extends on 40m (N-S) and respectively 30m (E-W).

The readings of total magnetic field, taken with an accuracy of 0.1 nT, were subsequently corrected for diurnal variation effect in order to obtain the magnetic anomalies. The two magnetic sensors of the gradiometer system are positioned at the heights of 0.75m and 2.00m above the ground.

The magnetic data were processed using Oasis Montaj [TM] software, three maps being obtained for the investigated tumulus:

a) total field magnetic map at height 0.75m (Fig. 3);
b) total field magnetic map at height 2.00m (Fig. 4);
c) map of magnetic vertical gradient (Fig. 5).

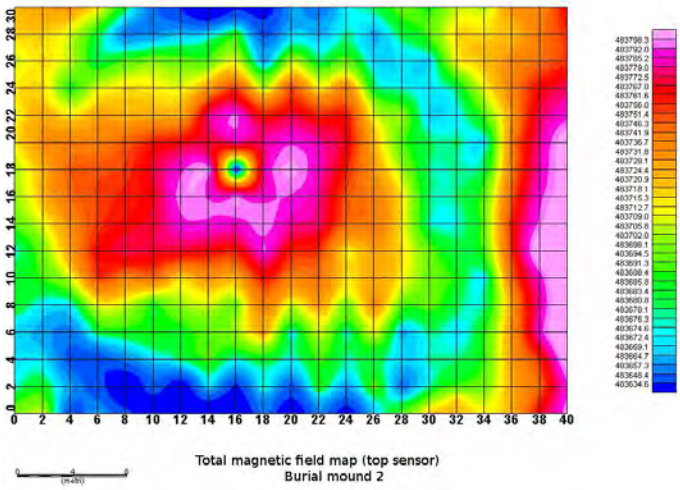

Figure. 3 – Map of total field magnetic map at height 0.75m

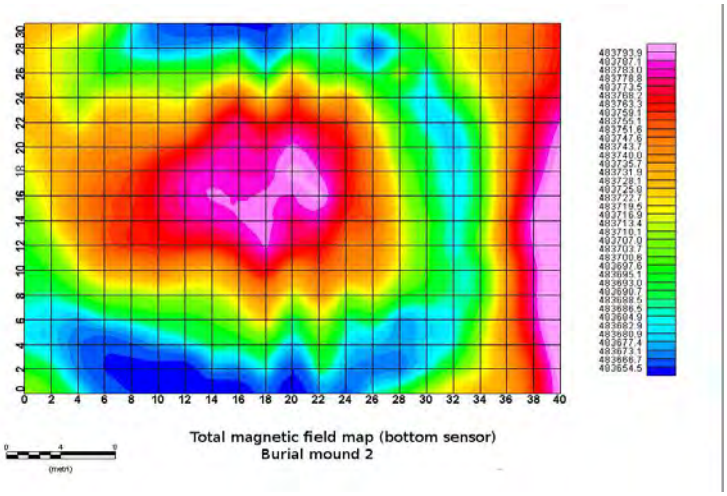

Figure. 4 – Map of total magnetic field at height 2.00m

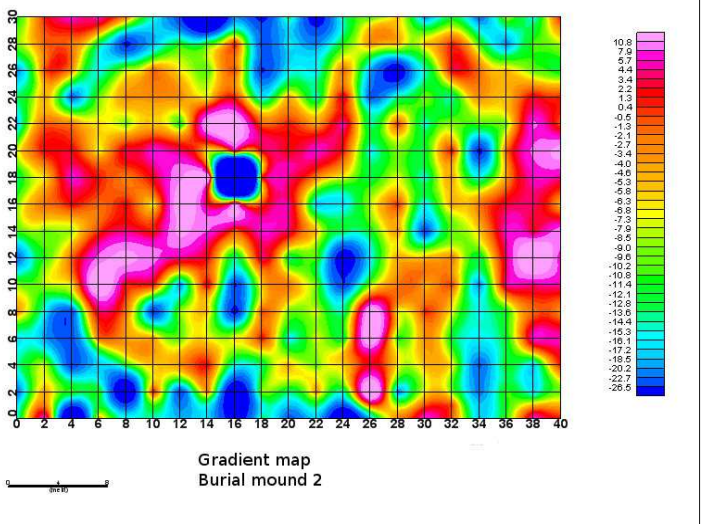

Figure. 5 – Map of magnetic vertical gradient

Magnetic data interpretation

The interpretation of the geophysical maps of magnetic total field and vertical gradient should be based on information of the magnetic properties of loess in the necropolis area, (since this is the material the tumulus was constructed) as well as other types of rocks that might be parts of the buried infrastructure.

Magnetic susceptibility measurements on rocks and soils in the Histria excavated city and inside the necropolis, taken during the geophysical observations using a KT-3 instrument, showed the following situation:

a) the lowest magnetic properties were observed on monuments exhibited in the Histria Museum that made of marble and limestone (lowest values on lumachellic limestone);
b) greenshists within the city inner walls are highly magnetic, but they may not be characteristic for this area, being possibly brought from remote areas during restoration;
c) greenshists that outcrop at the eastern limit of Histria city display higher magnetic properties than limestone and slightly higher than loess.

Considering these qualitative observations, due to weak magnetic contrasts between rocks and loess, low magnetic anomalies might detect buried structures made of limestone, while high magnetic anomalies might be associated with structures where greenshists are dominant. Locally, high magnetic anomalies should be related to burnt structures or pottery.

The analysis of total field anomalies measured at lower height above the tumulus (0.75m – Fig. 3) showed important magnetic variations on a quite small area, the difference between the highest and the lowest value being 163.7 nT. An elongated central high anomaly trending N-S (north is toward right in the figure) is contoured by a circular to ellipsoidal low anomaly. Considering the magnetic properties discussed above, the magnetic high may be determined by greenshist boulders utilized in the tumulus inner structure and possibly, by burnt materials in a central burial platform (as suggested in Fig. 2). The large low magnetic anomaly is considered to be related to the outer stone belt made of limestone boulders.

The map with total field anomalies measured at higher height above the tumulus (2.00m – Fig. 4) displays similar aspects as described above, the increased distance from the ground diminishing the difference between the highest and lowest value (139.4 nT). Another consequence that may be observed is the smoothing of the magnetic anomalies as compared to the previous map. The two local anomalies trending NE-SW situated at the high magnetic apex might reflect a more complex structure of the hypothetical burial platform.

The map of the magnetic vertical gradient (Fig. 5) presents large variations of this quantity, ranging between +10.8 and -26.6 nT/m. The vertical gradient anomalies are determined by shallower variations of magnetic properties as compared to the total field anomalies, and that is why they are so popular in archaeological prospection. From the main high total field magnetic anomaly is preserved here only a half, a feature that may be interpreted as a prolongation toward the tumulus upper part of the actively magnetic central structure. The other half, that is characterized by lower magnetic values, may represent an corridor toward the inner structure created by ancient “archeologists”, presently filled with loess. The outer main low magnetic anomaly is still seen in this map, but especially on the tumulus flanks, where measurements were taken at the topography height, closer to the buried stone belt.

Conclusions

A magnetic prospection carried out in August 2008 within the Histria ancient necropolis aimed at testing the capability of this geophysical method to investigate the tumuli infrastructure in this area.

Two magnetic total field maps were computed at heights above the tumulus (0.75m and 2.00m respectively), while the magnetic vertical gradient map was computed for half of the distance between sensors.

The interpretation of total field magnetic data correlated the central high magnetic anomaly with a complex buried burial platform, possibly including burnt materials and a structure made of greenschist boulders. The large circular low magnetic anomaly is interpreted as the effect of an outer stone belt made of limestone boulders.

The magnetic vertical gradient data suggest that half of the central buried structure is developed upward at depths where this magnetic quantity is able to bring useful information. For the other half of the high magnetic anomaly, the interpretation favors a partial destruction of the central buried structure performed by ancient "archeologists".

The authors consider that this geophysical test showed good possibilities for a future magnetic detailed prospection of the Histria necropolis.

Better results with clearer archaeological meaning may be obtained by a closer cooperation between geophysicists and archeologists before, during and after excavation works.

References

Alexandrescu P., 1982. Histria, Vol. II. Editura Academiei R.S.R., Bucuresti

Atanasiu, I,. 1981. Les tremblements de terre en Roumanie. *In*: Atanasiu I., Oeuvres choisies, , Ed. Acad. RSR, Bucureşti, p. 139-315

Butler, D. K., 2005. Near –surface geophysics, Society Of Exploration Geophysicists.

Chepalyga, A.L., 1985. Inland Sea Basins. *In*: Late Quaternary environments of the Soviet Union. A. A. Velichko. Minneapolis, Univ. Minnesota Press, p. 229-247.

Constantinescu, P, 1978. Geofizica Inginerească**,** Editura Tehnică, Bucureşti

Popescu, E., 1994. Constantinia, ville et évêché de la Scythie mineure. Un problème de géographie historique. *In*: Popescu Em., Christianitas Daco-Romana, Florilegium studiorum, , Editura Academiei Române, Bucureşti, p. 264-284

STUDIES OF ELECTRICAL CHARACTERISTICS OF HUKOU, HSINCHENG AND SANCHIAO ACTIVE FAULTS, NORTHERN TAIWAN

Hsing-Chang Liu and Chieh-Hou Yang
Ching Yun University , Taiwan

Abstract

Taoyuan, Hsinchu, and Taipei are three major metro areas in northern Taiwan. This study attempts to survey the resistivity structures and locations of the three active faults – Hukou Fault, Hsinchen Fault, and Sanchiao Fault – passing through the three metro areas and has thus provided resistivity imager profilings (RIP), vertical electrical soundings (VES), and audio-frequency magnetotellurics method (AMT) for this purpose.

This study has examined the relationships between faults and profilings in addition to the underground resistivity and has acquired following results accordingly:

1. Both Hukou Fault and Hsincchen Fault are thrust faults wherein the hanging walls are lowly resistivity and fault footwall are highly resistivity. Discontinuous geoelectrical or lateral rapid change resistivity is shown in electrical layers, especially in the fault trace or fault zone. Anomalous bands in a homogenous layer are one of the features shown in the Hsinchen fault. In addition to a large lateral resistivity contrast shown in the Sanchiao fault, the contacts surface is very rough.

2. The advantage of RIP result has a better stability, higher resolution and less time-consuming than other resistivity sounding methods. But in the study area, surface obstacles limited the spread of some survey lines, thus the targeted depth of investigation was unattained. AMT survey can be interfered by culture EM wave; the quality of its sounding results is always severely affected, especially in the Taipei area. However, combining the AMT sounding results with the gravity result, geologic data, and formal logging information, the Sanchiao fault and the boundary between the sediment and basement of Taipei Basin can be recognized.

3D LOOP-SOURCE EM INVERSION USING NON-LINEAR CONJUGATE GRADIENTS

Mark S. Hickey, Texas A&M University, College Station, TX
Mark E. Everett, Texas A&M University, College Station, TX

Abstract

Electromagnetic (EM) exploration on land has advanced a long way, but it still needs additional refinement. A 3D inversion would make the interpretation aspect simpler for a complicated subsurface, and make EM exploration easier to implement. We have formulated a 3D inverse solution for land-based loop-source EM exploration using a non-linear conjugate gradient method. This code was developed for exploration of complex subsurface structures like those of a meteorite impact crater or of a contamination plume. A finite element forward model is used to generate predicted data. The forward model uses a finite element mesh as well as coulomb-gauged potentials to solve the governing Maxwell equations and generate data for a single frequency. The finite element forward model code also permits discretization of the subsurface into an unstructured grid, allowing element edges to coincide with the boundaries of irregular subsurface inhomogeneities. The forward model can also take into account topography and its resultant effect on the response. A quasi adjoint Green's function approach is used to calculate the sensitivity matrix. For this presentation we will show our initial results from synthetic data as well as some preliminary results from actual field data.

MEASUREMENT OF SEISMIC LOCAL EFFECTS AND 1D NUMERICAL MODELING AT SELECTED SITES AFFECTED BY THE 2009 SEISMIC SEQUENCE OF L'AQUILA

Mario Luigi Rainone, CeRS-Geo, "G. d'Annunzio" University of Chieti-Pescara, Italy

Patrizio Torrese, Department of Earth Sciences, University of Pavia, Italy

Fabio Pizzica, CeRS-Geo, "G. d'Annunzio" University of Chieti-Pescara, Italy

Pasquale Greco, CeRS-Geo, "G. d'Annunzio" University of Chieti-Pescara, Italy

Patrizio Signanini, CeRS-Geo, "G. d'Annunzio" University of Chieti-Pescara, Italy

Abstract

Strong local effects occurred during the seismic sequence that affected the area of L'Aquila (Central Italy) in 2009, which culminated with a main shock of magnitude (M_w) 6.3 on the 6 April. Bearing in mind the magnitude, the vicinity of a regional capital to the epicentre, the presence of several historic centers and villages, which caused significant damage ($I_{MCS\ max}$=9.5) and approximately 300 victims, among the main characteristics of this earthquake, was the variability of the recorded damages within the scale of 100 m in spite of the near field conditions and a distinct source mechanism. These local effects were measured with an array of geophones at selected sites near the city of L'Aquila. In one of the sites, located at Onna village which experienced maximum damage levels, the 1D numerical modeling allowed verifying the influence that the frequencey of the input motion has in the determination of superficial seismic effects. The numerical modeling, which was undertaken on the basis of the results from geomechanical, seismic and geoelectrical surveys, also allowed verifying that underestimation of local seismic amplification can be introduced by the current regulatory framework (Italian seismic regulatory guidance "Norme Tecniche per le Costruzioni" – D.M. of 14 January 2008) in contexts similar to that of L'Aquila.

Introduction

Strong local effects were observed during the seismic sequence that affected the area of L'Aquila (Central Italy, Fig. 1) in 2009, which culminated with a main shock of magnitude (M_w) 6.3 (National Institute of Geophysics and Vulcanology "Istituto Nazionale di Geofisica e Vulcanologia - INGV, 2009) on the 6 April. Bearing in mind the magnitude, the vicinity of a regional capital (L'Aquila is the capital of the Abruzzo Region) to the epicentre, the presence of several historic centers and villages among the main characteristics of this earthquake, which caused significant damage ($I_{MCS\ max}$=9.5, Galli & Camassi,

Figure 1: Geographical setting of the test sites.

2009) and approximately 300 victims, was the variability of the recorded damages within the scale of 100 m in spite of the near field conditions and a distinct source mechanism (Chioccarelli & Iervolino, 2009; Walters et al., 2009). The seismological characteristics of the earthquake at L'Aquila are such that it can be considered without doubt to have been in a near field and near source context. The reconstructed macro-seismic context (Fig. 2) and the numerous velocity and accelerometric measurements have incontrovertibly shown significant different seismic actions within few tens of meters (Fig. 3). This is apparent from the measurements, shown within this work, undertaken with arrays of geophones at the selected sites of Onna, Monticchio, San Gregorio, Villa Sant'Angelo, Tussillo, Arischia and Poggio di Roio villages (Figg. 4-7), all located near the city of L'Aquila (Fig. 1). It should be noted that a significantly differentiated level of damage is in contrast with the generally accepted statement that the role of the local geological context of a site can be considered neglectable in near field context. The accelerometric records of the main shock of the 6 April, measured at different locations of the area from the seismic networks (max H PGA=0.68 g, Gruppo di Lavoro UNISANNIO – CIMA – DIGA, 2009), suggest that the amplification factors are difficult to justify applying current

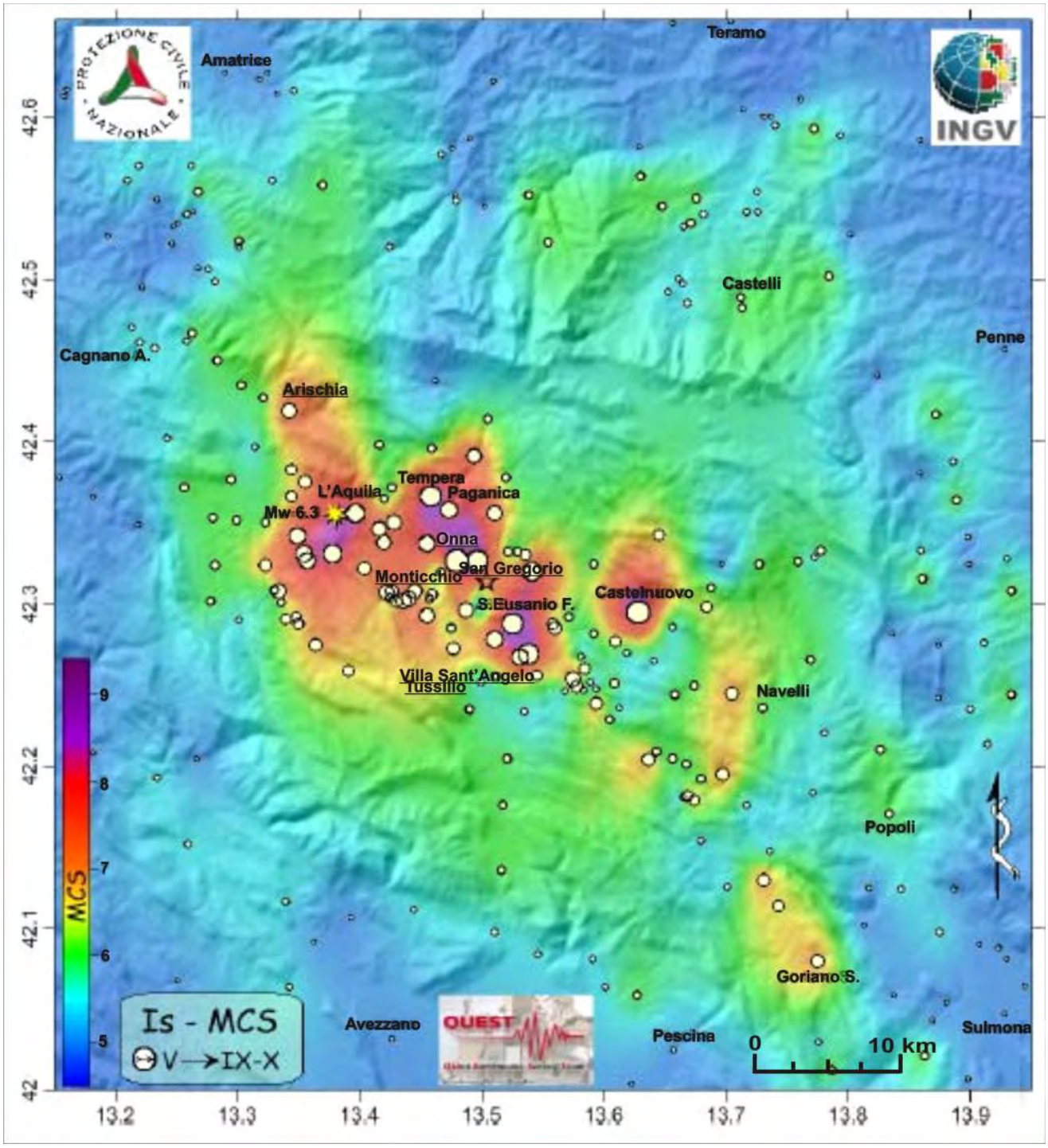

Figure 2: Distribution of damage intensity recorded after the L'Aquila earthquake of 6 April 2009 (main shock epicentre in yellow circle, local intensity (Is) proportional to the area of the circles (from Galli & Camassi, 2009).

regulation based on the Vs_{30} parameter (Italian seismic regulation contained in "Norme Tecniche per le Costruzioni" – D.M. of 14 January 2008 which conforms to European guidance Eurocode 8).

Figure 3: Damages caused at the village of Onna by the main shock of 6 April 2009, (I_{MCS}=9.5, Galli & Camassi, 2009).

On the other hand, Signanini et al. (2004) demonstrated that the application of the D.M of 14 January 2008 and the Eurocode 8 can causes underestimation of the local seismic amplification when compared to the results obtained from 1D numerical modeling. This is especially true with B soil category, when high Vs values for the drift deposits (>400 m/s) and strong seismic rigidity contrast between these drift deposits and the bedrock occur. Signanini et al. (2004) also showed that deep bedrocks (between 30 m and 100 m) and high velocities associated with the drift deposits, which can be considered ancient alluvial deposits, are associated with the recording of high amplifications, especially in the range of sensible frequencies.

In this context, 1D numerical modeling based on the results from geomechanical, seismic and geoelectrical surveys undertaken at the selected site of Onna village (Fig. 4), have allowed determining that local seismic amplification may have been more severe than the amplification predicted from applying the current regulatory provisions.

Seismic monitoring

Monitoring of the after shocks was undertaken at all the selected sites with arrays of SSU Micro-Seismograph (GeoSonics Inc.) seimometers and DAQLink III (Seismic Source Co.) seismometers with

arrays of HS-1–LT 3C (Geo Space Corporation) geophones. The monitoring was undertaken by programming the velocimeters with an activation threshold of 0.02 in/s, a pre-trigger of 1 s and a recording length of 15 s.

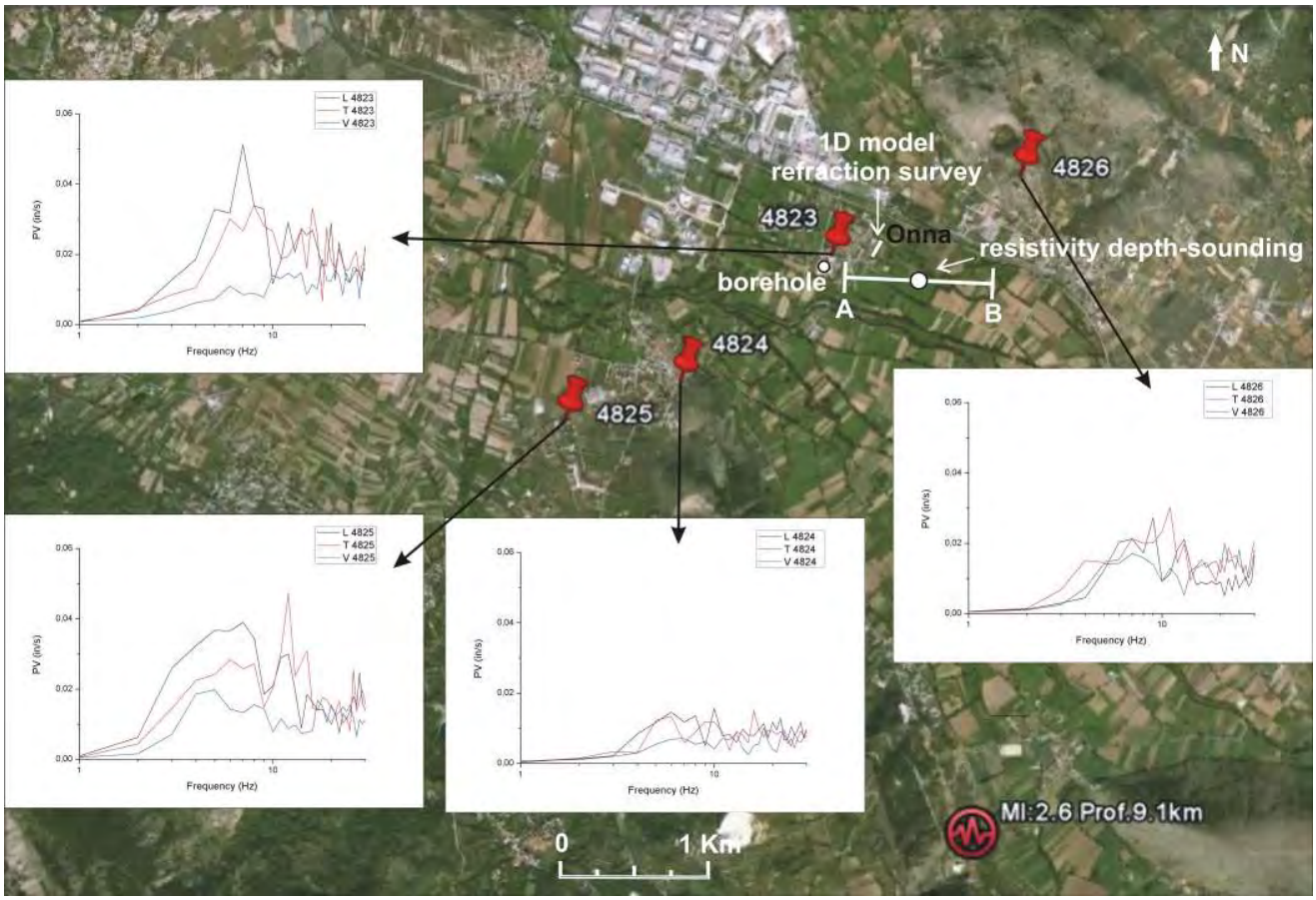

Figure 4: Onna (4823), Monticchio (4824 and 4825) and San Gregorio (4826) monitoring sites locations with signals spectra; geophysical surveys and borehole locations at the Onna site.

Onna, Monticchio and San Gregorio sites

Although these sites are within 3 km (Fig. 4), the values of PPV (Peak Pseudo Velocity) that were measured during the seismic event of 21/04/2009 at 23:35:13 (local time) with Ml=2.6 and depth of 9.1 km (INGV, 2009) are significantly different: the sensor that was installed on the silty-clayey and sandy-gravelly alluvial deposits at Onna measured a PPV of 0.05 in/s; the sensor installed on the mid-slope of calcareous-marly rocks at Monticchio measured a PPV of 0.03 in/s; the sensor installed at the top of the slope on calcareous-marly rocks at San Gregorio measured a PPV di 0.05 in/s. An additional sensor (4825) installed on incoherent deposits at the entrance of a narrow valley, approximately 1 km to the WSW of Monticchio, measured a PPV of 0.07 in/s. The signal at Onna shows a maximum at a frequency of 7 Hz while the other sites are around 10-15 Hz. It is apparent that the lithological amplificaton and the topographical and the wave focalization effects played an important role in causing different levels of damage, equal to a maximum of 3.5 units of the MCS scale between the sites during the main shock event (for Onna I_{MCS}=9.5, for Monticchio I_{MCS}=6, for San Gregorio I_{MCS}=9, Galli & Camassi, 2009, fig. 2).

Villa Sant'Angelo and Tussillo sites

Although the two sites are only 800 m apart (Fig. 5), the PPV values measured during the seismic event recorded on 07/07/2009 at 10:15 (local time) are quite different: a PPV value of 0.23 in/s was measured at Villa Sant'Angelo where the entire village rests on gravelly-sandy and sandy-silty alluvial deposits; a PPV value of 0.08 in/s was measured at Tussillo which is built on limestone and marly formations. The frequency content of both sites shows maximums of 15 Hz although a relative maximum of 10 Hz is present at Villa Sant'Angelo. It is apparent that the lithological amplification and probably the wave focalization effect played and important role in causing a difference in the levels of damage at the two locations equal to one unit of the MCS scale (for Villa Sant'Angelo I_{MCS}=9, for Tussillo I_{MCS}=8, Galli & Camassi, 2009, Fig. 2).

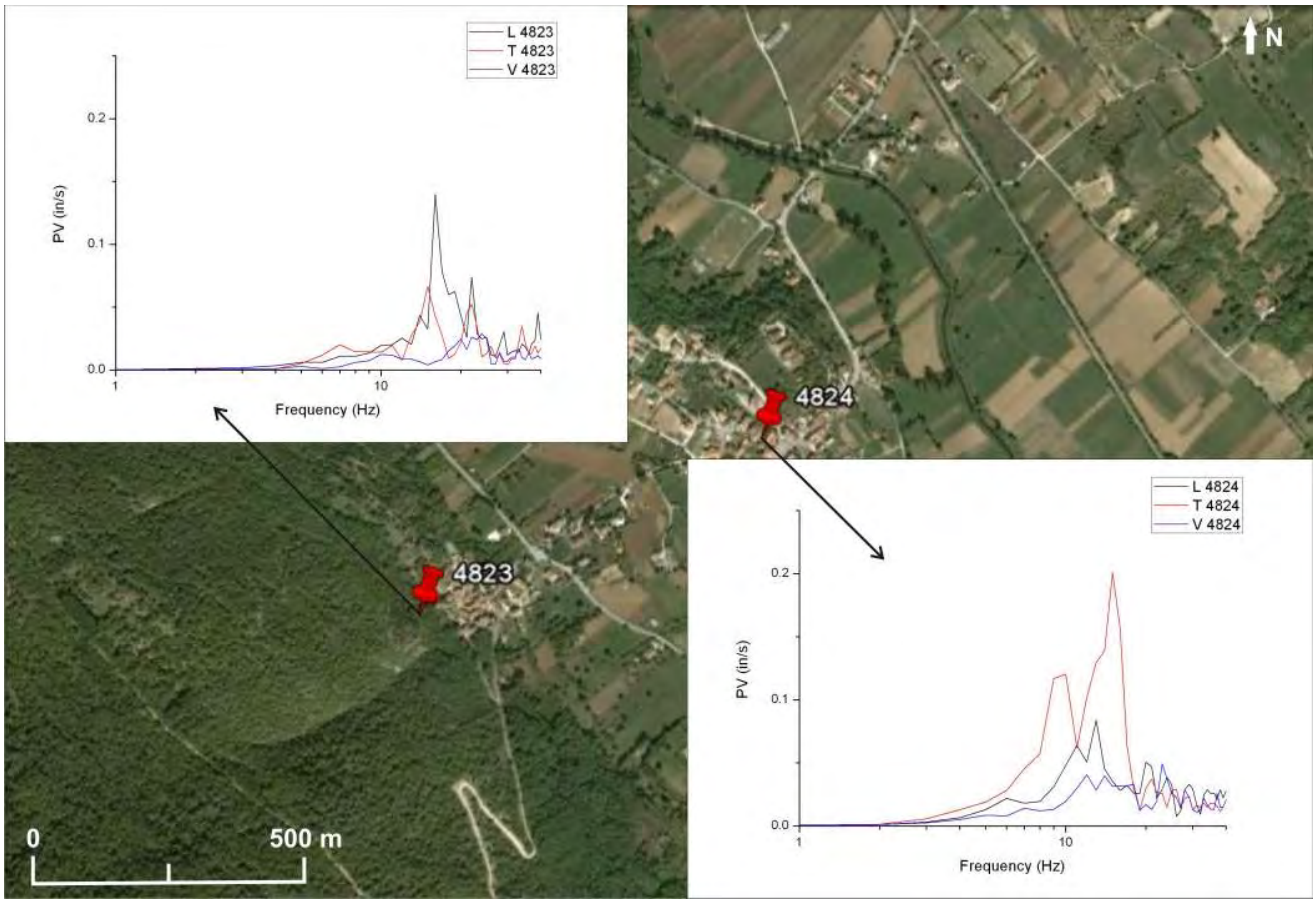

Figure 5: Villa Sant'Angelo (4824) and Tussillo (4823) monitoring site locations with signals spectra.

Arischia site

Alluvial plain deposits, constituted of sands, gravels and silts with clay lenses and metric to centrimetric blocks, which are overlying a marly bedrock, are cropping out at this location (Fig. 6). During the seismic event of 25/04/2009 at 13:13:04 (local time), with Ml=3 and depth of 9.1 km (INGV, 2009), PPV values that vary between 0.09 in/s (4823) and 0.25 in/s (4826) were measured at a distance of only 100 m. The spectral content is also quite different and rests on lower value (9-12 Hz) in the latter case. It is not clear why such different PPV values were recorded in the absence of targeted subsurface investigations.

Poggio di Roio site

The outcrops at this site (Fig. 7) are cobbly-sandy and sandy-silty deposits associated with lacustrine and marshland clayey-silty deposits with lenses of organic matter, all overlying a calcarenite bedrock. The four velocimeters installed at this site in different geological and topographical contexts measured significantly different PPV values during the seismic event of 18/04/2009 at 20:40 (local time). The PPV values are in ascending order: PPV=0.03 in/s with rocks cropping out at mid-slope (4824), PPV=0.04 in/s at the top of the slope (4825), PPV=0.07 in/s on alluvial plain deposits (4826), PPV=0.16 in/s on made ground at mid-slope (4823). PPV values differences show that the lithological amplification and the topographical effect occurred at these sites.

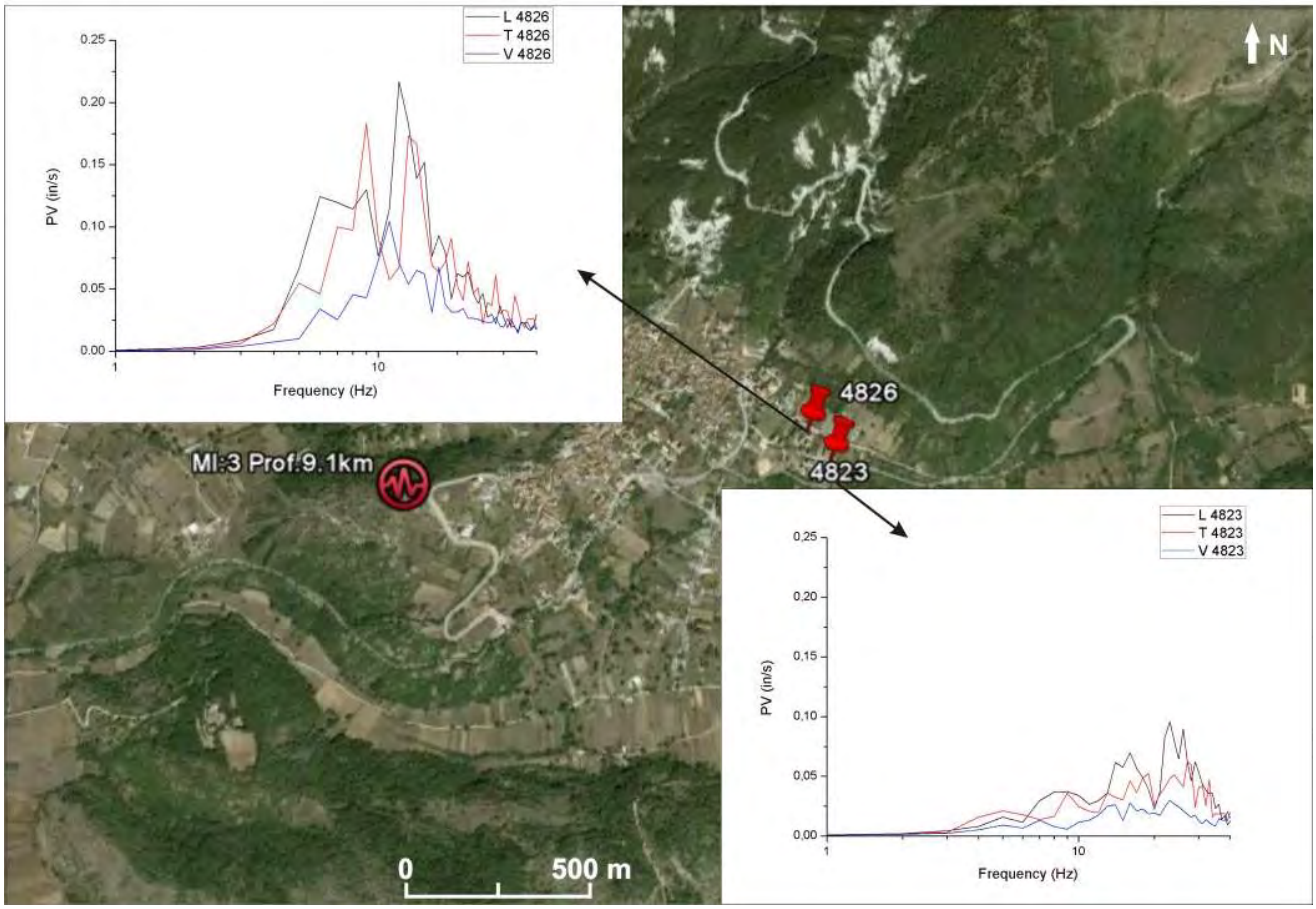

Figure 6: Arischia monitoring site locations with signals spectra.

1D numerical model of the Onna site

The hypothetical geological setting of the middle Aterno valley is shown in Fig. 9 (Cavinato et al., 2009). Given that the bedrock depth at Onna location was only supposed in this geological frame, in absence of deep drillings or geophysical surveys, a resistivity depth-sounding (Fig. 10) was carried out to identify the depth of the bedrock. Also a refraction seismic survey in P and SH waves processed with tomography techniques (Fig. 10) and a calibration continuously cored borehole were undertaken in order to get the geometric and physical-mechanical models used as input to the 1D numerical modeling.

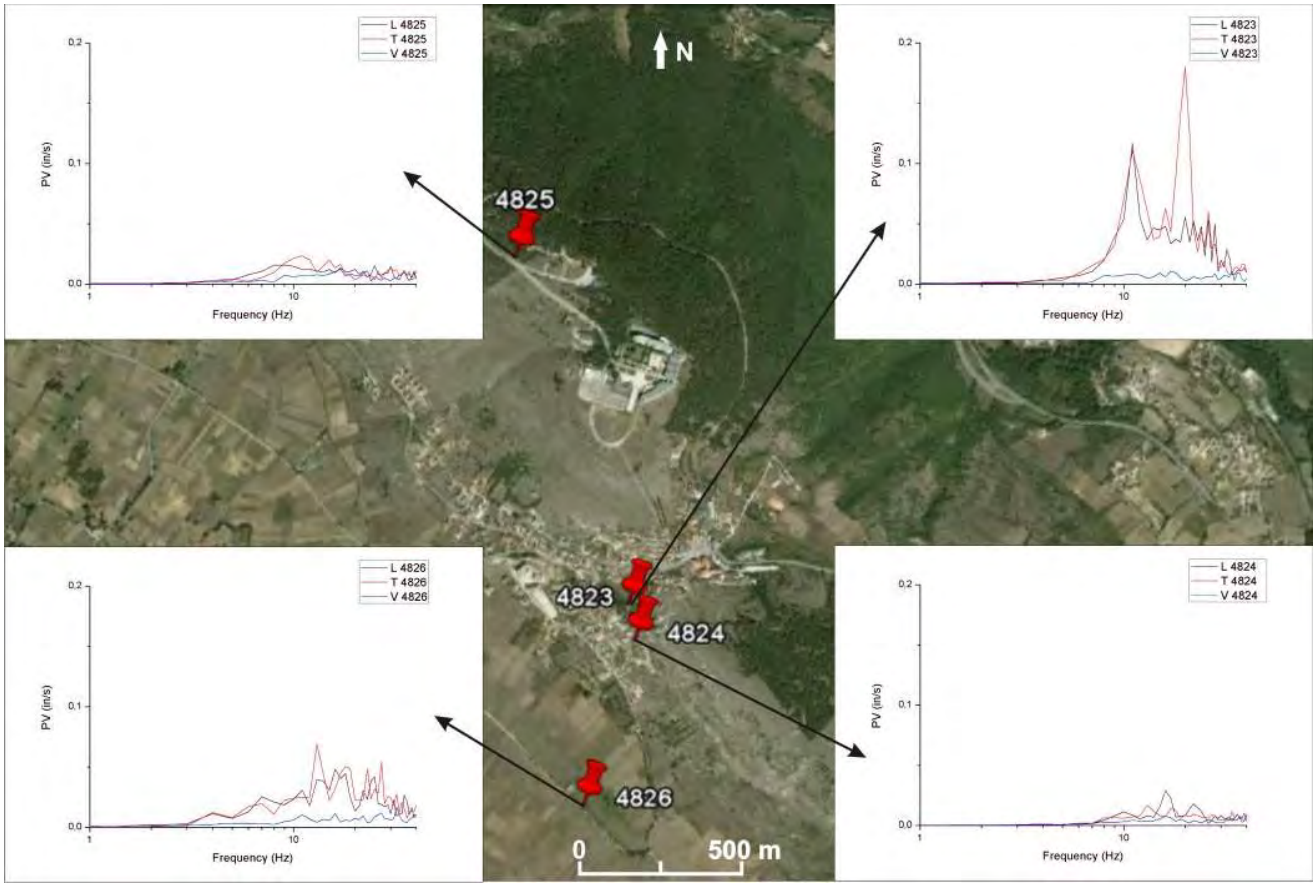

Figure 7: Locations of monitoring sites at Poggio di Roio with signals spectra.

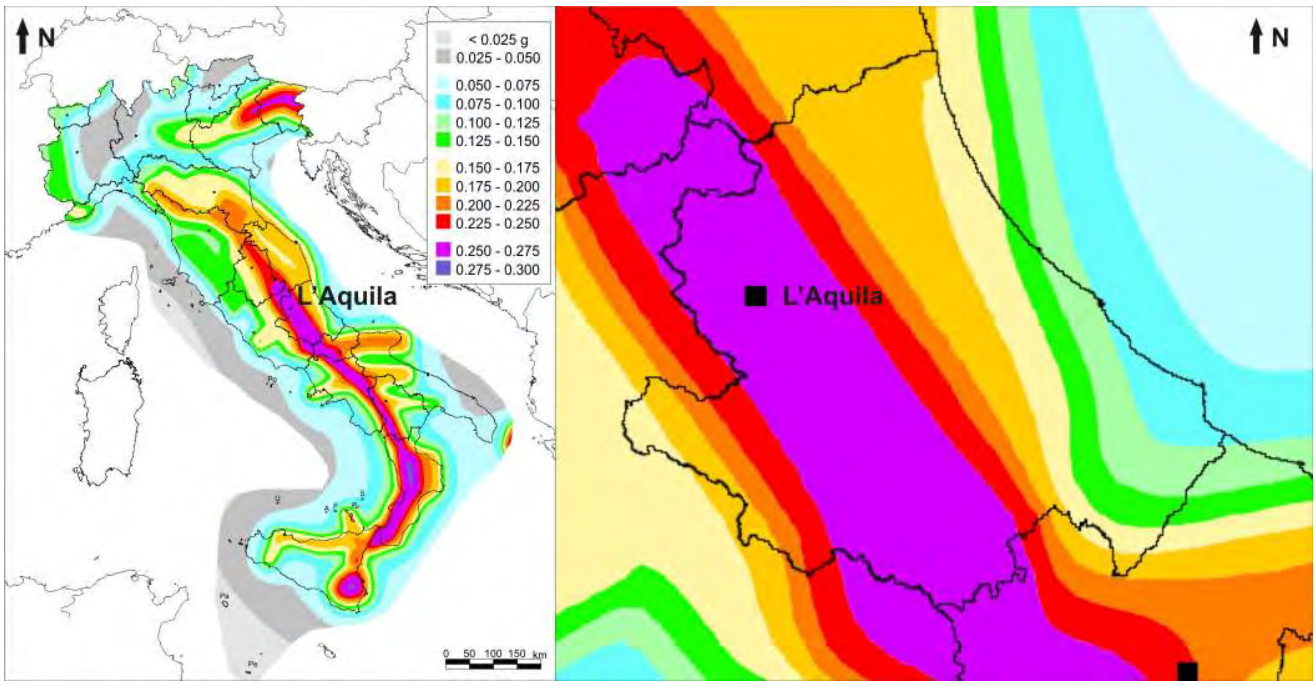

Figure 8: Seismic hazard map of the Italian territory (from Ordinance PCM 3519 of 28 april 2006).

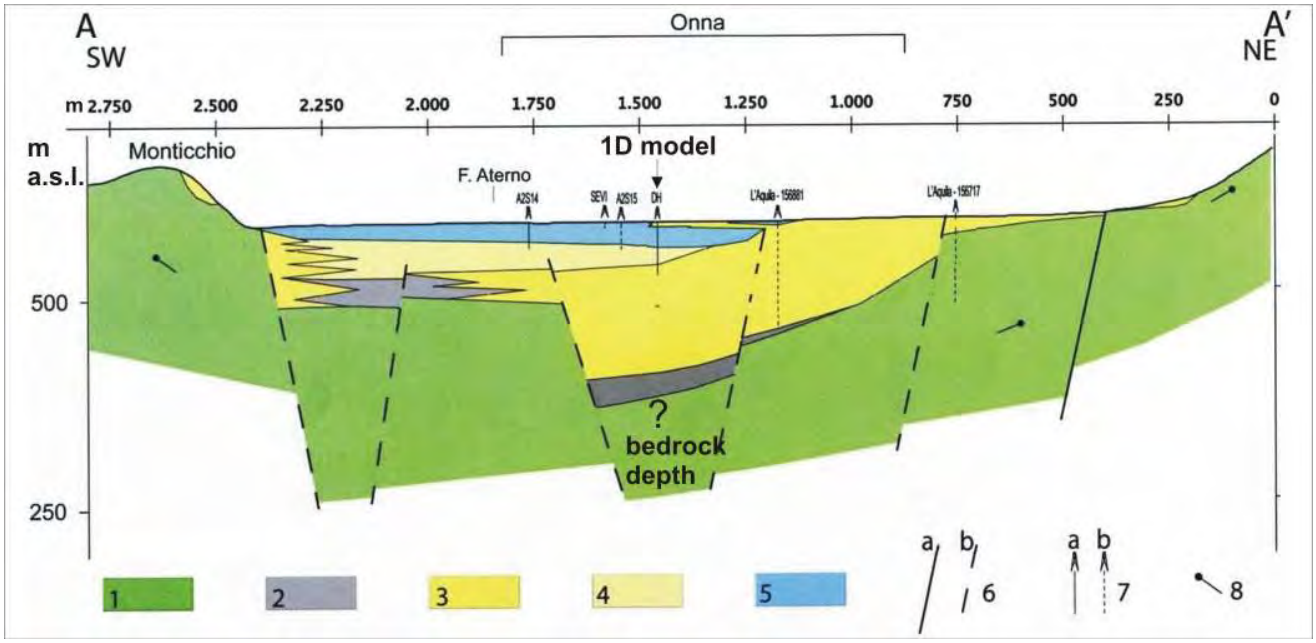

Figure 9: Hypothetical geological setting along a section crossing the middle Aterno valley (1: limestone or flysch bedrock; 2: silt and sandy silt; 3: conglomerates and gravel; 4: alternance of ancient gravel, sand and silt; 5: alternance of recent gravel, sand and silt; 6: fault (a) probable fault (b); 7: borehole or well (a), hatched if projected (b); 8: average dip of bedding; from Cavinato et al., 2009).

The bedrock which is constituted of limestone rocks (Vs=1500 m/s from other seismic surveys undertaken in the area) is 106 m deep (much less than that assumed in the geological cross-section of Fig. 9) in correspondence of the resistivity depth-sounding and underlies the alluvial and lacustrine deposits (B subsoil type classification on the basis of the refraction survey according to current regulation).

The 1D numerical modeling was undertaken with an equivalent linear analysis carried out in the frequency domain (Idriss & Sun, 1992; Schnabel et al., 1972) and applying as input motion two natural horizontal accelerograms that were scaled to a PGA=0.26 g value, which is required by the current regulation (Fig. 8). An accelerogram (L'Aquila main shock in Fig. 11B) was recorded by the GSG station of the RAN national network during the main shock. This station is located in the gallery of the INFN laboratories buried under the Gran Sasso massive. The other accelerogram (high frequency in Fig. 11C) was appropriately selected due to its high frequency spectrum; it was used to estimate the effects of the high frequencies which are few in the first accelerogram given the significant distance of the GSG station from the epicentre of the main shock (approximately 23 km).

The elastic response spectra (Fig. 11A) show that when using the first accelerogram the spectrum obtained from the application of the regulation is exceeded at the 0.28 s period with a maximum PGA=0.76 g. This indicates that the seismic regulation underestimates the PGA for a limited period but within the most sensible frequencies. The spectrum that is obtained from the second accelerogram actually estimates a PGA=1.31 g for the 0.16 s period which corresponds to the resonance frequency of the buildings that are most frequent in the historic centre of Onna (2 story buildings). These are the buildings that either collapsed or were severely damaged during the main shock. This result indicates that Onna may have been affected by accelerations that were significantly higher than those required by the regulation considering that the distance from the hypocentre (approximately 8 km) is such that the

high frequencies are maintained at the bedrock during the seismic action and the possible presence of 2D effects not contemplated by the numerical modeling.

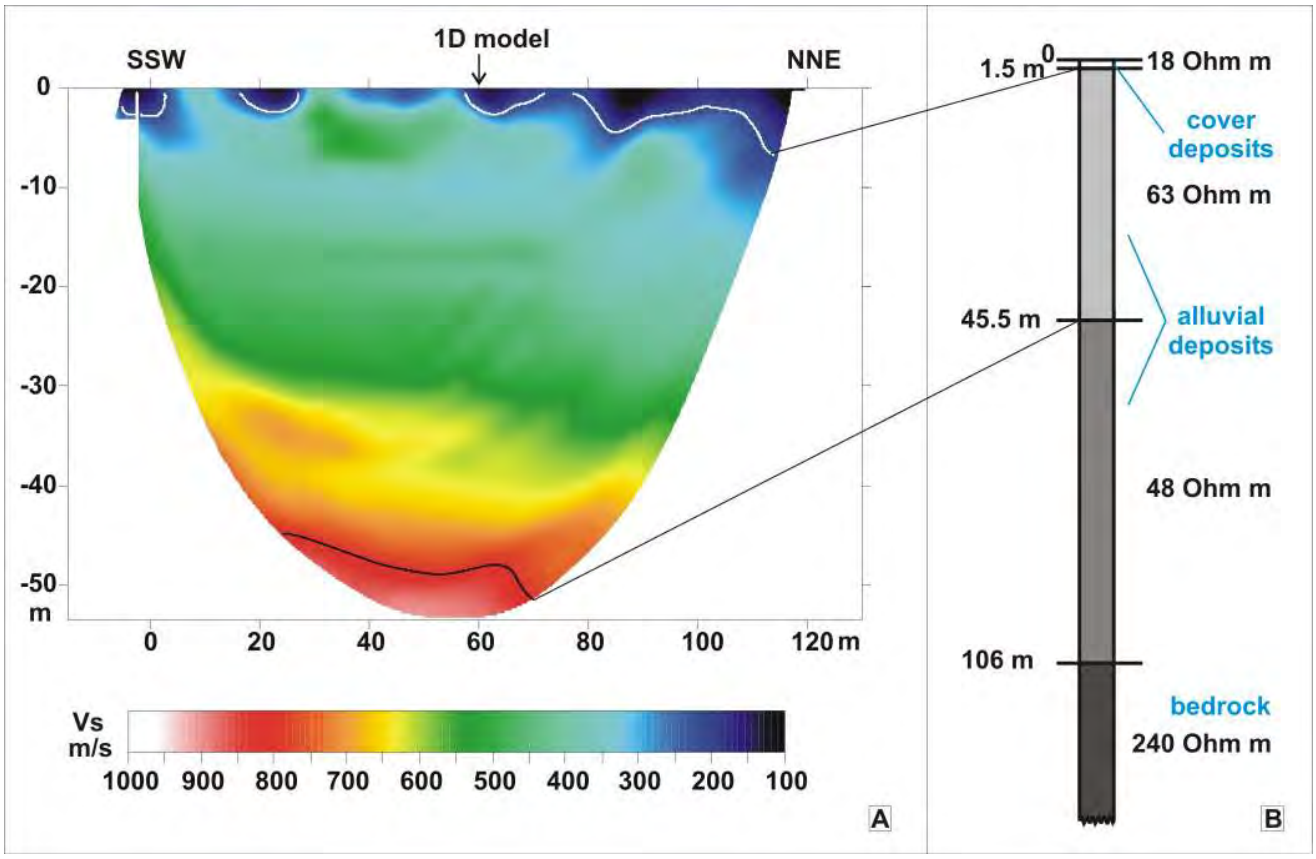

Figure 10: Shear waves tomographyc section carried out at the Onna site with 1D model location (A); resistivity depth-sounding carried out at the Onna site (B).

Conclusion

The monitoring undertaken with arrays of geophones on selected sites during the seismic sequence of L'Aquila in 2009 has shown that strong local responses are encountered. Differences of as much as 3 times were recorded for the PPV value over a distance of only 100 m (Arischia); differences of over 5 times were also encountered (Poggio di Roio). These local effects are attributable to lithological amplifications and topographical and wave focalization effects, that, in some cases, can have occurred simultaneously. 1D Numerical modeling undertaken for the Onna site, where the maximum macro-seismic intensity occurred (I_{MCS}=9.5), has shown that the spectrum dictated by the national regulation can locally underestimate the seismic action even though in a limited period range.

The frequency for which the numerical modeling estimated the maximum amplification corresponds to the resonance frequency of the buildings that are most frequent in the historical centre of Onna; this may be one of reasons that could explain the high macro-seismic intensity recorded at this location. The differences between the acceleration response spectra (sometimes of high entity) estimated by the modeling and those prescribed by the regulation can be attributed to: high velocities of the drift deposits (Vs>400 m/s); significant thicknesses of these drift deposits which are thicker than the 30 m considered by the seismic regulation; high velocities of the seismic bedrock (Vs≥1500 m/s) at depth

(between 30 m and 100 m). Other authors (Signanini et al., 2004) have highlighted the systematic underestimation of the seismic action dictated by the regulation under these conditions.

The modeling has also proven that the high frequency content of the input motion can strongly influence the seismic amplifications. In fact, considering the short distance between Onna and the epicentre of the main shock, the high seismic amplification that occurred at the historic centre could be partially justified by the presence of high frequencies in the bedrock seismic action.

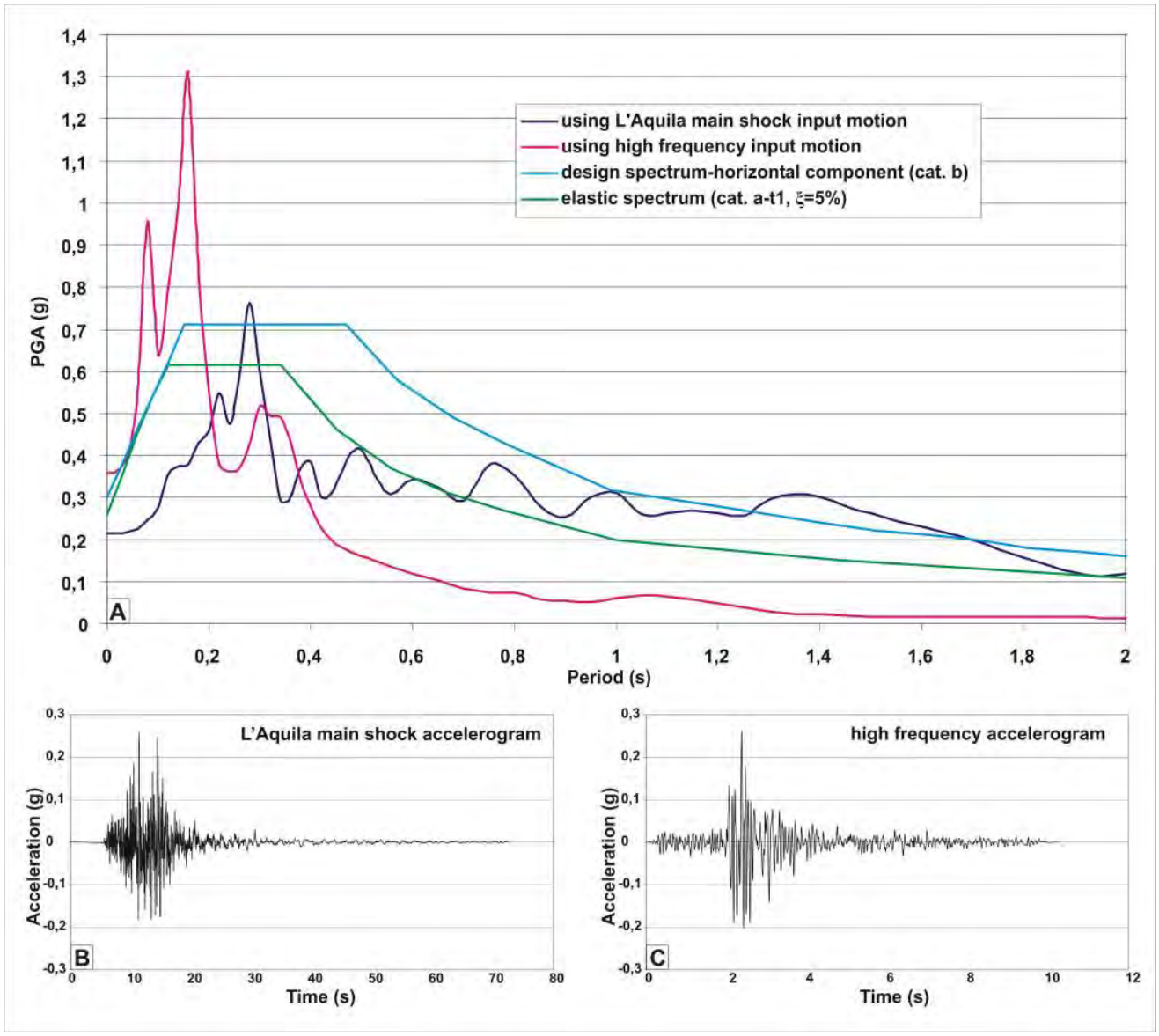

Figure 11: 1D model results compared with the elastic spectra provided by the Italian seismic regulation D.M. of 14 January 2008 (A), scaled L'Aquila main shock accelerogram (B) and high frequency natural accelerogram (C).

References

Cavinato G. P., Cavuoto G., Mancini M., Moscatelli M., Spadoni M. with the technical collaboration of Stigliano F., Marconi F., Pennica F., 2009, T2 – Modello geologico del sottosuolo dell'area di Onna, Progetto "Microzonazione sismica per la ricostruzione (terremoto 06/04/2009)", Consiglio Nazionale delle Ricerche, IGAG (Istituto di Geologia Ambientale e Geoingegneria).

Chioccarelli E. & Iervolino I., 2009, Direttività e azione sismica: discussione per l'evento de L'Aquila, http://www.reluis.it

Decreto 14/01/2008 del Ministero delle Infrastrutture, Norme Tecniche per le Costruzioni, GU n. 29 del 04/02/2008.

Eurocode 8 EN 1998, 2003, Design of structures for earthquake resistance, CEN European Committee for Standardization, Brusselles.

Galli P. & Camassi R. (eds.), 2009, Rapporto sugli effetti del terremoto aquilano del 6 aprile 2009, Rapporto congiunto DPC-INGV, 12 pp., http://www.mi.ingv.it/eq/090406/quest.html.

Gruppo di Lavoro UNISANNIO – CIMA – DIGA, 2009, Rapporto preliminare sugli Effetti indotti sull'ambiente fisico dalla sequenza sismica dell'aquilano, Ver.1.5, http:// www.reluis.it.

Idriss I.M. & Sun J.I., 1992, "SHAKE 91: A computer program for conducting equivalent linear seismic response analyses of horizontally layered soil deposits", User's Guide. University of California, Davis, California, 13 pp.

INGV, 2009, La sequenza sismica de L'Aquilano, Aprile 2009. Attività in corso e primi risultati. http://portale.ingv.it/primo-piano/archivio-primopiano/ notizie-2009/terremoto-6-aprile/copy_of_la-sequenza-sismica-dellaquilano-aprile-2009/.

Ordinance PCM 3519 of 28 april 2006, Criteri generali per l'individuazione delle zone sismiche e per la formazione e l'aggiornamento degli elenchi delle medesime zone (G.U. n.108 del 11/05/2006).

Schnabel P.B., Lysmer J., Seed H.B., 1972, SHAKE a computer program for earthquake response analysis of horizontally layered sites, User's Manual, Earthquake Engineering Research Center, University of California, Berkeley.

Signanini P., Rainone M.L., Dintinosante V., Ferrini M., 2004, Vs 30: Può essere sufficiente? Proceeding of 23° Convegno Nazionale G.N.G.T.S., Roma, 14 dicember 2004, Vol. Ext. Abs.

Walters R. J., Elliott J. R., D'Agostino N., England P. C., Hunstad I., Jackson J. A., Parsons B., Phillips R. J., Roberts G., 2009, The 2009 L'Aquila earthquake (central Italy): A source mechanism and implications for seismic hazard, Geophys. Res. Lett., 36, L17312, doi:10.1029/2009GL039337.

Acknowledgements

The authors wish to thank Sara Di Benedetto and Antonio Gennarini for the precious collaboration.

SOLID WASTES LANDFILL MONITORING BY MEANS OF DIFFERENTIAL HIGH-RESOLUTION INFRARED THERMOGRAPHY

Arcangelo Merla, ITAB and CeRS-GEO, University of Chieti-Pescara, Italy
Mario Luigi Rainone, CeRS-GEO, University of Chieti-Pescara, Italy
Patrizio Signanini, CeRS-GEO, University of Chieti-Pescara, Italy
Pasquale Greco, CeRS-GEO, University of Chieti-Pescara, Italy
Alfredo Ortolani, Corpo Forestale dello Stato, Italy
Patrizio Torrese, Dep. of Earth Sciences, University of Pavia, Italy

Abstract

Differential thermal imaging has been proposed to characterize the ground temperature distribution of two solid wastes landfills. The differential approach permitted to detect regions with thermal abnormalities potentially associated with either biogas leakage and migration or improper landfill settlement and management. Methods, results, limits, and potentialities of the proposed approach are discussed.

Introduction

The increased attention to the environmental protection demands innovative or improved technology for large-scale site monitoring. In particular, the monitoring and surveying of sanitary landfills for municipal solid wastes or the development of tools for the discover and/or the control of unauthorized landfills are gaining great attention, especially in our country. One of the major concerns regards the leakage or the migration of biogas outside sanitary landfills for municipal solid wastes. Biogas emission must be controlled for at least two main reasons:

1. Safety: biogas is a dangerous fluid, flammable, explosive and even toxic;
2. Environmental protection: sanitary landfills are an important source of methane emissions and offending odors into the atmosphere.

Uncontrolled biogas migration is a particularly relevant hazard, especially in presence of unauthorized or illegal situations.

Migrations may occur very often even in modern controlled sanitary landfills. The walls of the landfill are usually their weakest point both in terms of landfill design and monitoring. Wall linings ruptures occur frequently in landfills. Wall linings are weaker than the bottom liners and at the same time subject to much stronger strains, how it may occur because of the friction brought by the waste settling and its moving down on a fixed membrane lying on a slope of natural soil. Moreover, compacted landfills tend to stratify horizontally thus increasing the permeability to both gaseous and liquid fluids on the vertical boundaries. Many of the failures on the wall lining result in the migration of biogas outside the landfill when one or both the following conditions occur (Gandolla, 2002):

1. The natural soil outside the walls of the landfill offers a possible migration path due to unsaturated permeable layers;
2. The biogas extraction system operating inside the landfill is not sufficient to compensate for the pressure due to the biogas generation in the peripheral portion of the waste structure.

Biogas is essentially composed of a mixture of methane (from 45 to 65% in volume) and carbon dioxide (between 35 and 55%) plus other minor components. The biogas production is due to the fermentation of putrescible materials, with heat release as a side-product. For this reason, infrared thermography has been proposed as a possible tool for detecting biogas leakage from sanitary landfills (Raco, 2006). Infrared thermography relies on the thermal infrared emission by the surface layers of the soil. Modern thermal imagers provide adequate temperature resolution, frame rate sampling and spatial resolution for capturing minute temperature variation of soil surface. The approach generally followed in using infrared thermography in landfill management is based on the pure recording of the distribution of the soil temperature, searching for hyperthermic patterns or spots (thermal abnormalities) likely associated with biogas migration or leakage. More precisely, regions presenting thermal abnormalities should be considered those regions characterized by an average temperature value or pattern significantly different from those of surrounding regions with similar characteristics in terms of soil nature, vegetation, and antropic interventation. It has to be remarked that the information that can be obtained by using infrared thermography are limited to the first few centimeters of the soil and subsoil layers, for which the water content and the external heat production by biogas generation are the parameters that mostly influence the apparent temperature recorded by the thermal imager, under the same solar irradiation rate. On the other hand, the apparent temperature depends on the surface emissivity, which may vary locally thus determining apparent regional variations in the true soil temperature distribution. For these reasons, thermal imaging may provide false hyperthermic or hypothermic spots or patterns over the temperature distribution that could be erroneously interpreted in terms of biogas tracks. In order to bypass these limitations, the thermal response presented by the soil over time in front of thermal solicitations, deriving from environmental temperature variation, should be characterized. In other words, the regions that may worth attention are those presenting increased or decreased thermal inertia with respect to their surrounding rather than solely hyperthermic or hypothermic regions. In fact, the natural response might be influenced and altered by the presence of uncontrolled energetic endogen sources, like biogas accumulation or leakage. In order to measure the thermal response, we propose to use differential infrared thermography of the soil by performing two measurements of the same region at two different environment temperatures.

In this paper, we present the results of the application of differential high-resolution infrared thermography to individuate and characterize thermal abnormalities in two different landfills for municipal waste. In the first case, Santa Lucia Landfill (Atri, TE, Italy), given the specific position of the site, we used ground differential infrared thermography (Figure 1). Atri landfill insists on an area characterized by the presence of a plio-pleistocenic marly-clay sequence showing a mild monoclynal setting. In the second case, (Bellolampo Landfill, PA, Italy), the landfill insists over an area characterized by tectonic overlap of limestone and carbonate-silicoclastic deposits. Given the large size of the site and its orographyc characteristics, we developed an aerial differential infrared thermography (Figure 2), by installing the thermal equipment on helicopters provided by the Corpo Forestale dello Stato (Figure 2).

Example #1: Santa Lucia (Atri) Landfill – Ground Differential Infrared Thermography

Equipment

Thermal images were acquired by using the digital thermal camera AEG256 PtSi, equipped with a F50, f/1.5 lens. The camera is sensitive in the 3-5 μm range, with a 0.1 °C Noise Equivalent Temperature Difference (NETD) @ 30 °C in the 5-50 °C range. Each thermal image was obtained by averaging a series of 31 images, acquired at the maximum sampling rate (20 ms). This average

procedure permitted to achieve a post-processing temperature resolution as low as 0.04 °C. Each thermal image size is 256x256 pixels. Given the distance between the camera and the landfill (150 m) and the optics, the spatial resolution on the ground was established in 8 x 8 cm^2 per pixel. External black-body correction (NETD = 0.1 °C @ 30 °C) was performed before and at the end of each measurement sessions in order to perform drift/shift correction on the detectors' gain. Diurnal visible images of the landfill were acquired by means of 7.5 Mpx HP digital camera.

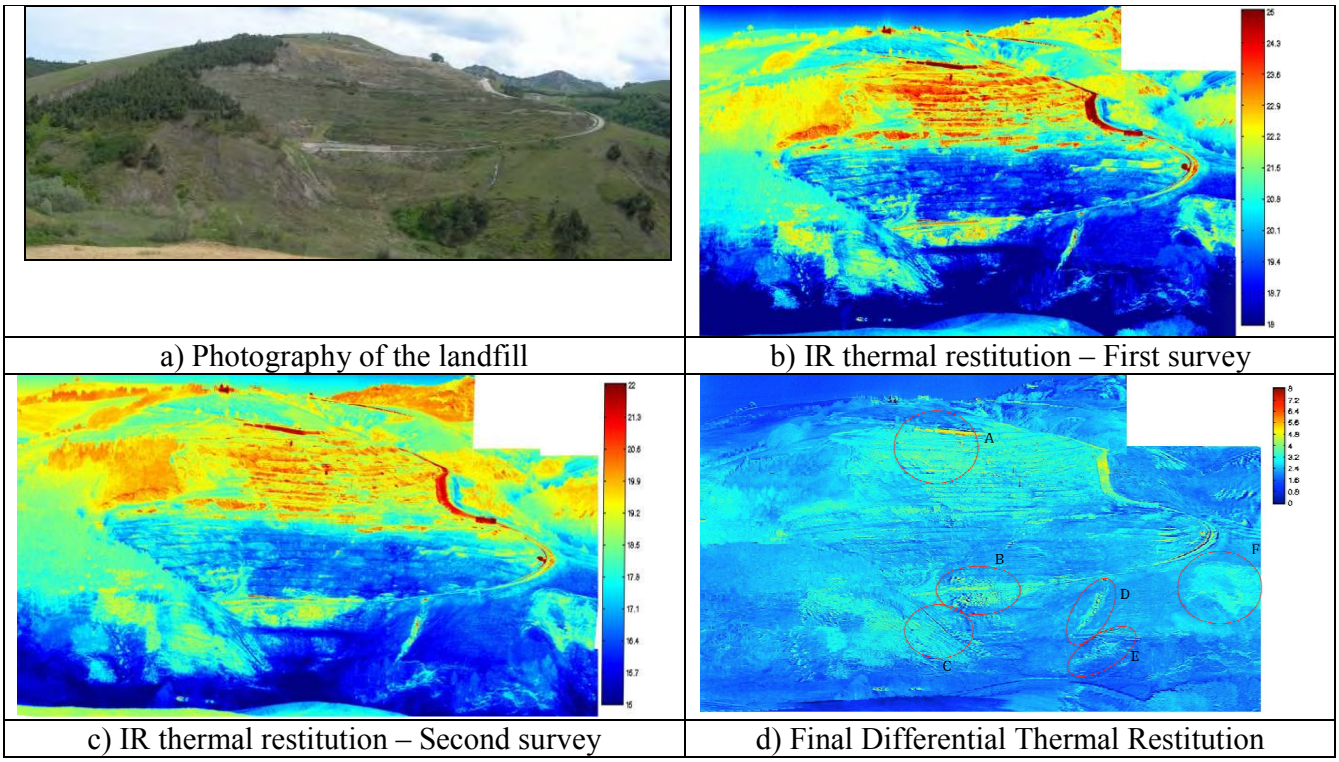

a) Photography of the landfill

b) IR thermal restitution – First survey

c) IR thermal restitution – Second survey

d) Final Differential Thermal Restitution

Figure 1: Santa Lucia Landfill (Atri, TE, Italy). The soil temperature distribution is reported on panel b and c, respectively for the first and the second survey. The temperature differences between the two surveys are shown on panel d, which highlights regions with increased temperature differences. The colorbar shows the false-color to temperature scheme. Temperature ranges from 15 to 22 °C for images in panel b and c, and from 0 to 8 °C for the image in panel d.

Measurements and Results

The differential thermography was based on 2 different measurements, as described in Table 1. In order to obtain the maximum advantage from the spatial resolution of the camera, a photogrammetric approach was used in both the measurement sessions, by acquiring a set of 30 photogrammetric images. The complete photogrammetric restitution for the two measurements is presented in Figures 1. An affine-transformation based method for image registration (Zitova, 2003) was then used to obtain an effective pixel-to-pixel difference image on which to highlight regions with increased thermal inertia and thermal abnormalities (Figure 1d). Both thermal imaging surveys on the landfill highlighted a soil temperature distribution that strictly describes the historical evolution of the landfill. In particular, the newest and active section on the top of the landfill showed a high soil temperature and a low thermal inertia (Figure 1d: A), with geometric patterns that follow the profile of the successive embankments. More compacted and impermeable embankments, like the flat grounds, showed a local high thermal

inertia, while the escarpments a lower one. Low thermal inertia values might be both related to lower humidity of the soil and biogas collection systems. The lower bottom section of the landfill, not longer operating, was characterized by lower soil temperature, greater thermal inertia and the presence of hyperthermic spots, oddly distributed (Figure 1d: B, C, D). Regions with increased thermal emission were found out of the perimeter of the landfill (Figure 1d: E, F). A more detailed on-site characterization of the suspected regions was not possible because the whole landfill area is under legal impound and therefore not accessible.

Table 1: Landfille #1 - Differential Thermography Measurements

	First Survey	Second Survey
Date	May, 25th, 2009	May, 26th, 2009
Time	09:30 PM – 10:10 PM	00.50 AM – 01.30 AM
Air Temperature Range	22.3 – 21.7 °C	19.4 - 19.0 °C
Relative Humidity	57%	55 %
Last Rain	8 days before	8 days before
Sun Luminosity	none	none

Example #2: Bellolampo Landfill – Helicopter-Ported Differential Infrared Thermography

Equipment

In this case, a multi-spectral thermal imaging approach was used. The equipment consisted of a set of thermal cameras operating within different infrared ranges, as specified in Table 2. The cameras were installed on an AB412 helicopter of the Corpo Forestale dello Stato by using a device specifically designed (Figure 1) and that allowed to obtain zenithal projections of the ground. All the cameras were enabled for atmospheric and optical automatic correction.

Table 2: Landfille #2 - Aerial Differential Thermography Measurements - Equipment

Camera	Spectral Range (μm)	Focal Plane Array	NETD (mk @ 30°C)	Spatial Resolution (mrad)
FLIR Cedip Titanium	MW: 3 – 5	320x256	18	1.1
FLIR SC3000 QWIP	LW: 8.9 -9.2	320x240	20	1.1
FLIR SC640	LW: 7 -14	640 x 480	30	1.1
XEVALN InGaAs	NIR: 0.9 – 1.7	320x256	//	2
SONY HDR SR12E	VIS: 0.4 – 0.8	1024x768	//	1.2

Sampling rate for all the cameras was set at 16 frames per sec. Such rate permitted an adequate forward covering for the aero-photogrammetric restitution.

Measurements and Results

The differential thermography was based on 2 different survey flights, as described in Table 3.

a) Aerial photography of the landfill

b) NIR restitution – morning survey flight

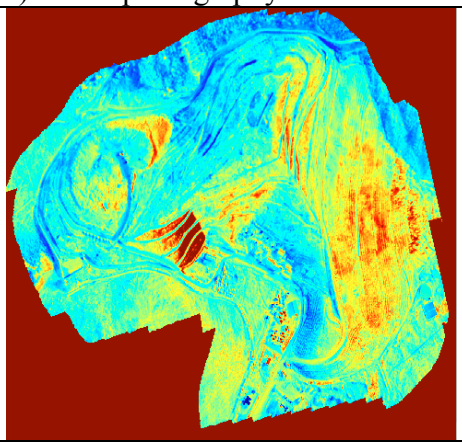

c) Thermal IR restitution – morning survey flight

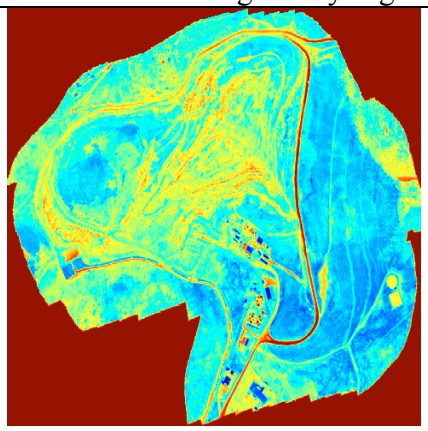

d) Thermal IR restitution – afternoon survey flight

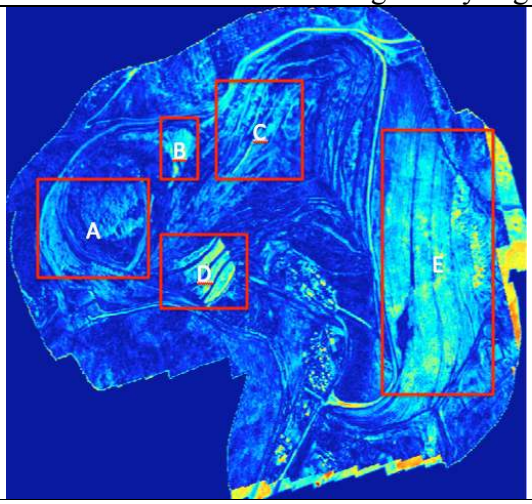

e) Final Differential Thermal Restitution (Temperature ranges from 0 to 12 °C)

f) The AB412 helicopter of the Corpo Forestale dello Stato used for the flight survey of Bellolampo landfill, and the thermal equipment setup.

Figure 2: Bellolampo Landfill (PA, Italy). The soil temperature distribution is reported on panel b and c, respectively for the first and the second survey. The temperature differences between the two surveys

are shown on panel d, which highlights regions with increased temperature differences. Temperature ranges from 10 to 30 °C.

Table 3: Landfill #2 - Aerial Differential Thermography - Measurements

	First Survey	**Second Survey**
Date	May, 21st, 2009	May, 21st, 2009
Take-Off/Landing Time	06:00 AM – 07:30 AM	06:30 PM – 08.00 PM
Flight Altitude (feet)	2500 GR	2500 GR
Flight speed (knots)	60	60
Flight Direction	East-West	East-West
Air Wind	Light- absent	Absent
Air Temperature Range	14 – 16 °C	19 - 21°C
Relative Humidity	57%	55 %
Last Rain	3 days before	3 days before
Sun Luminosity	Sunrise	Sunset

An aero-photogrammetric approach was used. The scanning path was controlled by a geo-referenced GPS.

The two surveys were performed at the sunrise and sunset, respectively, because of specific flight authorization and limitation. The complete photogrammetric restitution for the two measurements is presented in Figure 3. An affine-transformation based method for image registration (Zitova, 2003) was then used to obtain an effective pixel-to-pixel difference image on which to highlight regions with increased thermal inertia and thermal abnormalities (Figure 2).

The inspection of the infrared imaging surveys permitted to identify 5 regions with significant abnormal behavior, as reported in table 4.

Table 4: Landfill #2 – Figure 2e: Regions with thermal abnormalities

Region	**Feature**
A	Irregular scattered pattern, with low thermal inertia and moderate diurnal temperature variation
B	Hyperthermic triangular region, with low thermal inertia and moderate diurnal temperature variation
C	Elongated hyperthermic region, characterized by large temperature variation along the day.
D	Region with regular geometric shape, characterized by large temperature variation along the day and low thermal inertia.
E	Regularly shaped streaks, characterized by large temperature variation along the day and low thermal inertia.

The found regions were then characterized by visual inspection and analysis of the reflection properties within the NIR band, which provides indications about water content and vitality of the ground vegetation. To this analysis, it appeared that the thermal abnormalities of the A region should be attributed to the emerging surface rock, with extremely dry soil. Thermal abnormalities for B region

were determined by the ongoing activity of the landfill and the soil movement. Thermal abnormalities for region C were attributed to the irregular pattern of the ground vegetation over well-compacted ground layers. Thermal abnormalities for D region were caused by the presence of geo-membranes on the ground surface. The E region was characterized by terrace-settlement of the landfill slope, on which vegetation abnormalities insist. No specific track of biogas emission or leakage was found.

Conclusions

Differential thermal imaging may help to objectively detect and find landfill regions with thermal abnormalities. The method is extremely sensitive and therefore it has to be associated with on-site survey in order to characterize and increase the specificity of the found thermal signatures. In fact, the specific ground temperature may depend on several and concomitant factors, among which different soil thickness, different soil composition, vegetation, sun solar exposure, and landfill settlement. While simple direct thermal imaging could not distinguish among those factors, the differential thermal imaging may compensate some of them, making the survey more objective and the results more reproducible.

Acknowledgements

The authors wish to thank Luigino di Donato and Maurizio Stefanachi (ITAB – University of Chieti-Pescara), for their invaluable assistance with equipment setting-up, Peter A. Mattei (ITAB) and Micaela di Fazio (CeRS-GEO – University of Chieti-Pescara) for their contribute to the data processing; and Roberto Fantacci (Chief Pilot, Helicopters Nucleus, Corpo Forestale dello Stato) for his invaluable patience and assistance with flight operations.

References

Gandolla, M, 1997, Landfill gas migration in the subsoil: esperiences of control and remediation, International directory of solid waste management 1997/8, The ISWA yearbook, Kames & James Science Publisheres, Ltd, London, 237 – 245.

Raco, B, 2008, Monitoraggio del flusso di biogas diffuso dal suolo da discariche RSU: il caso di Legoli, Giornale di Geologia Applicata, 9(1), 49-59.

Zitova, 2003, Image registration methods: a survey, Image and Vision Computing, 21:977–1000.

RAYLEIGH-WAVE DISPERSION CURVES FOR LONG, LINEAR ARRAYS AT A PREDOMINANTLY-GRAVEL SITE

Barbara Luke, Applied Geophysics Center, University of Nevada Las Vegas (AGC, UNLV)
Helena Murvosh, AGC, UNLV and Stanley Consultants, Inc., Las Vegas, Nevada
Pinthep Kittipongdaja, AGC, UNLV
Andrew Karasa, AGC, UNLV
Prajwol Tamrakar, AGC, UNLV
Wanda Taylor, AGC, UNLV

Abstract

Experimental Rayleigh-type surface wave dispersion curves were developed for a gravel site over limestone bedrock. The work was performed as part of an earthquake site-response study. The SASW, MASW, and ReMi methods were applied in linear arrays that approached 1 km in length. For the SASW method, a Vibroseis source was used. The other methods used primarily ambient noise. Dispersion curves were resolved to a minimum frequency of 1 Hz, which corresponded to a maximum wavelength of well over 1 km. Dispersion curves from the three methods were in good agreement over a broad frequency band but differed at low and high extremes. The ambient noise at the site did not appear to introduce directional bias in the passive-source survey results.

Introduction

Seismic Rayleigh-type surface wave measurements were performed at an undeveloped site on the margin of the Las Vegas Valley, Nevada. The overarching research question driving the investigation is the nature of the earthquake response of the Las Vegas Basin's sediment fill (Luke et al., 2008). To this end, we are building a three-dimensional model of the shear-wave velocity (VS) of the Basin sediments. This work provides the opportunity to test different methods for developing one-dimensional VS profiles using Rayleigh waves.

Expanding upon work presented by Karasa et al. (2009), this paper presents Rayleigh wave dispersion curves generated for a single site using different processes. Sources used are a full-sized Vibroseis, ambient noise, and a sledgehammer. Approaches used to collect data and develop the dispersion curves are the SASW, MASW, and ReMi methods. The dispersion curves are compared to one another and in the context of known site conditions.

One goal of the tests is to determine the deepest possible resolution of VS using these methods. Site-response studies for the Las Vegas Valley indicate that it is beneficial to know the VS profile in alluvium to hundreds of meters depth (Luke and Liu, 2007). The deep surface-wave measurements performed here are intended to help bridge the gap between the shallow data (to approximately 30 m) that make up most of our velocity database and the deeper data that are derived from teleseisms, which resolve depths on the order of hundreds to thousands of meters (Snelson et al., 2004). The dataset may also provide an opportunity to continue studies of the influence of a high-velocity interface on VS profiling through inversion of surface waves (e.g., Casto et al., 2009).

Test site

The site is on the margin of the Valley, at the foot of the Spring Mountains, about 2 km from the nearest bedrock outcrop (Fig. 1). The Spring Mountains are the primary source of the alluvial basin-fill in this part of the Valley (Wyman et al., 1993), which unconformably overlies ~150 million years old and older bedrock. The contractional and extensional tectonic patterns for the region, since about 125 million years ago, are such that the bedrock surface is more shallowly inclined on the west side of the Valley than the east (Page et al., 2005), so the tests are expected to encounter bedrock.

Pertinent data collected by others and mapped as part of our research include lithologic logs and shallow VS measurements. Locations of these datasets are shown in Fig. 2.

Taylor et al. (2008) mapped sediment types from more than 1400 wells logged by the Nevada Division of Water Resources. Lithologic logs from several wells drilled near the site are identified in Fig. 2 and shown in Fig. 3. The non-lithified or partly lithified sediments are primarily gravel. The wells just to the west of the survey site intercept thick deposits recorded as limestone starting at about 120 m depth, and bedrock at about 200 m. The wells to the south of the survey location are about 240 and 270 m deep and do not encounter limestone or bedrock. A well to the northeast of the array encounters bedrock at 725 m.

Groundwater was encountered in only one of the surrounding wells, no. 1387, at 200 m depth.

Because the shallow sediments are primarily gravels, they are expected to have high velocity and low attenuation with respect to other sediments. We reviewed 30-m averaged shear wave velocities [VS(30)] determined by others from nine locations within 3 km of the test site (Fig. 2a). The VS(30) ranges from 900 to 1300 m/s. All nine tests yield site classifications for seismic design of “B, Rock” according to the International Building Code (International Code Council, 2009).

The site is an as-yet undeveloped parcel that is surrounded by developed land. Land use in the area is predominantly single-family residential and light commercial.

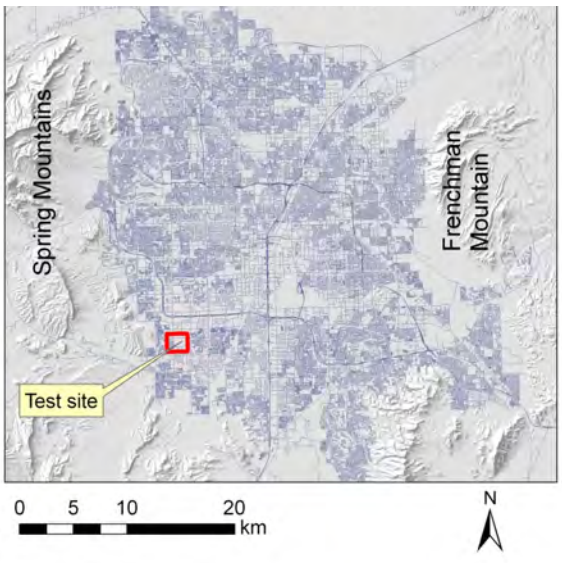

Figure 1: Test site location within the Las Vegas Valley, Nevada

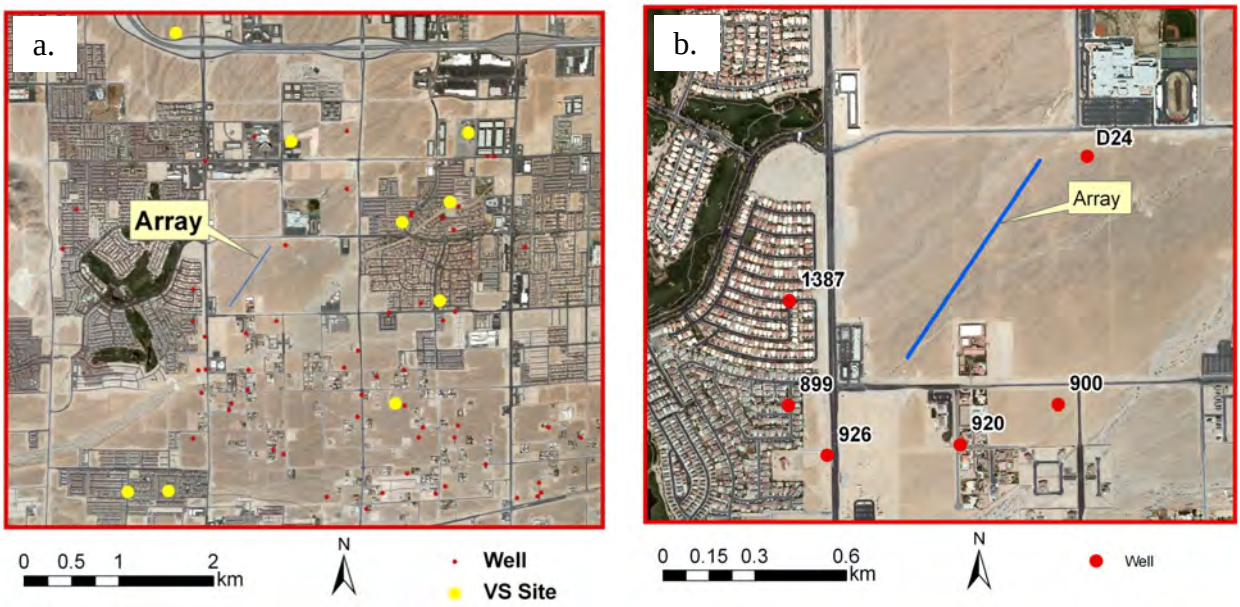

Figure 2: Site of test array and locations for supplemental data: (a) regional view; (b) closeup

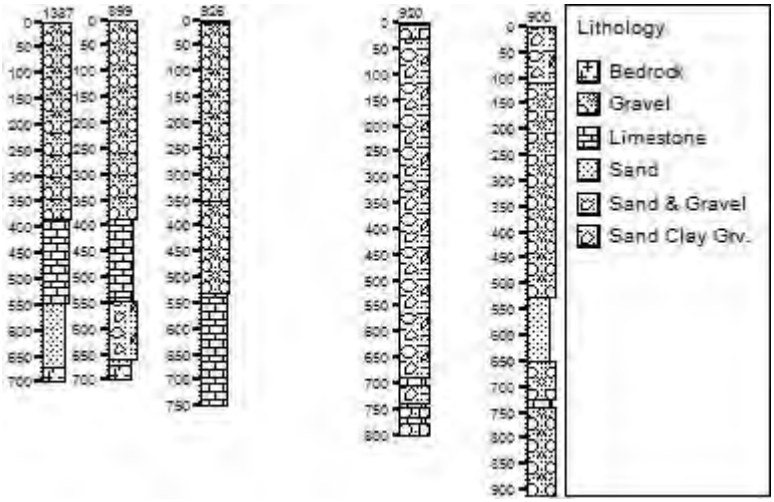

Figure 3: Lithologic logs for five boreholes close to test site. Depths are in feet from ground surface. Well D24 located northeast of the survey line (Fig. 2) was not logged above 725 m, but bedrock was logged at that depth.

Data collection

Most of the surface wave measurements that are conducted in the Las Vegas Valley use a 100-m long array to determine VS(30) for the purpose of assigning seismic site class. Our test arrays were longer, close to 900 m. We anticipated acquiring data to frequencies as low as 1 Hz, which would penetrate quite deep at this site.

SASW method

The SASW method is described by Stokoe et al. (1994). The dispersion curve is developed from a series of tests at different receiver spacings. A sledgehammer source was used for the shortest spacings. For larger spacings, we used the full-size Vibroseis source known as “Liquidator” from the National Science Foundation Network for Earthquake Engineering Simulation (Stokoe et al., 2006). The maximum array length tested, from source to farthest receiver, was 890 m.

Receivers were vertical geophones with 1 Hz resonant frequency. The geophones were positioned using survey equipment, shallowly buried and carefully leveled. The Vibroseis was placed at the north end of the array (Fig. 4). Data were acquired using a four-channel signal analyzer. Dispersion curves are derived from phase differences between the responses of geophone pairs from signals recorded as the source steps through a sine-wave sweep. An advantage of this stepwise approach to building the response spectrum is that data acquisition can be programmed to dwell at each frequency until some predetermined acceptance criterion is met. Acquisition proceeds rapidly for the high frequencies, but dwell times are extended for the longer wavelengths where, because of signal attenuation, it might be necessary to stack a large number of records.

The SASW dispersion curve is shown in Fig. 5. Figure 5a illustrates contributions from each receiver spacing. Figure 5b shows a condensed composite dispersion curve that was derived from the complete dataset.

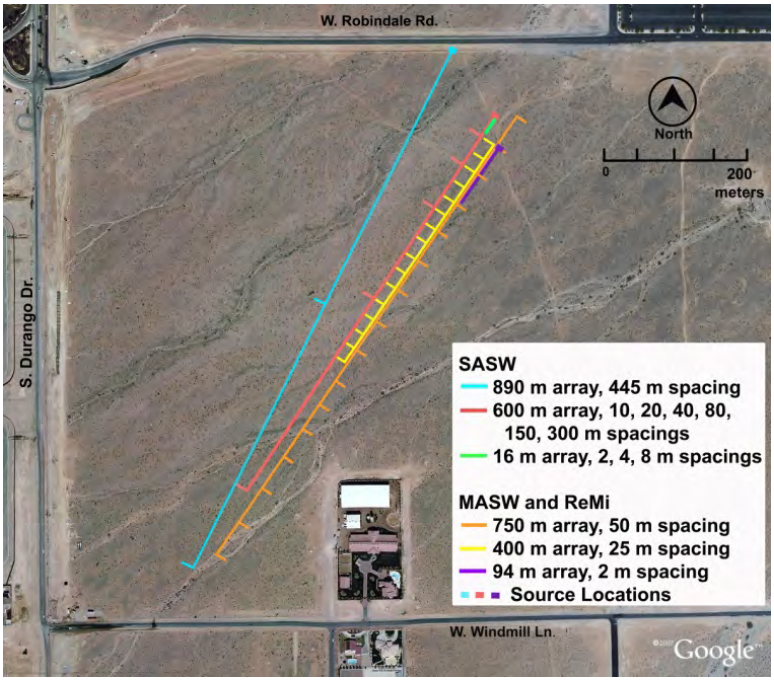

Figure 4: Test arrays

MASW method

The MASW method is described by Park et al. (1999). Application of the method for an ambient noise (passive) source is described by Park and Miller (2005). We acquired MASW data on three linear arrays (Fig. 4). The shortest, 94 m long, used 48, 4.5-Hz geophones at 2-m spacing. The geophones were coupled to the ground with spikes. Data were collected using a sledgehammer and also using strictly ambient noise. The two longer arrays recorded ambient noise only. For the longer arrays, sixteen, 1-Hz geophones were used. As with the SASW test, the geophones were positioned using survey equipment

and buried, level. The intermediate-length array used 25-m spacing for a total length of 375 m. The longest array used 50-m spacing for a total length of 750 m. The data were collected with a seismograph. Data collection parameters are summarized in Table 1.

The program SurfSeis, by the Kansas Geological Survey, was employed to develop dispersion curves. In Surfseis, a wavefield transformation is applied to convert the time histories to a contour plot of amplitude with respect to velocity and frequency ("overtone plot"). Following procedures recommended by Park and Miller (2005), we picked velocities with respect to frequency at the maximum amplitude of the energy band. Overtone plots with picks are shown in Fig. 6.

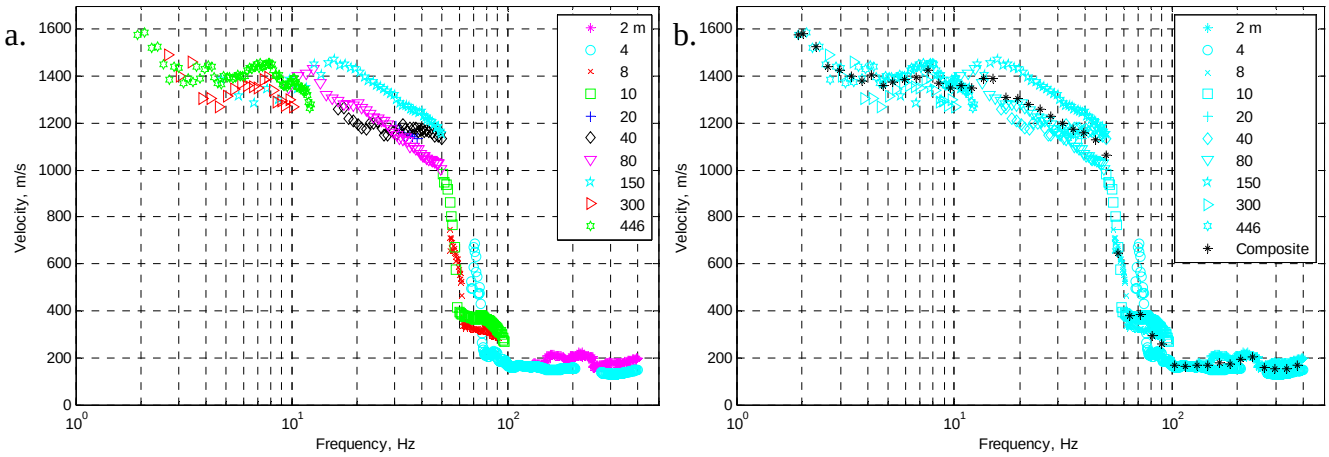

Figure 5: SASW dispersion curve (a) showing contributions from each receiver spacing; (b) representative composite

Table 1: Acquisition parameters for MASW and ReMi tests

Source	Array length (m)	Number of sensors	Sensor resonant frequency (Hz)	Spacing between sensors (m)	Sample interval (ms)	Record length (sec)	Number of records stacked
Hammer	94	48	4.5	2	0.125	1	5
Ambient noise	94	48	4.5	2	2	30	10
	375	16	1.0	25	8	240	10
	750	16	1.0	50	8	240	10

ReMi method

The ambient-noise data were also processed using the ReMi method. The ReMi method is described by Louie (2001). The acquisition parameters used for the 94-m long array are among those routinely recommended for ReMi surveys. The software package SeisOpt ReMi by Optim LLC was used to process data. The wavefield transformation in this software converts each set of time histories to a panel displaying spectral ratio with respect to slowness and frequency. Following recommended procedures, we picked a central value and two extreme values of slowness for each value of frequency. The central pick is made below the largest spectral ratio amplitude, the lower bound is at the first rise of spectral ratio over the background level, and the upper bound is at the peak. Panels with picks are shown in Fig. 7.

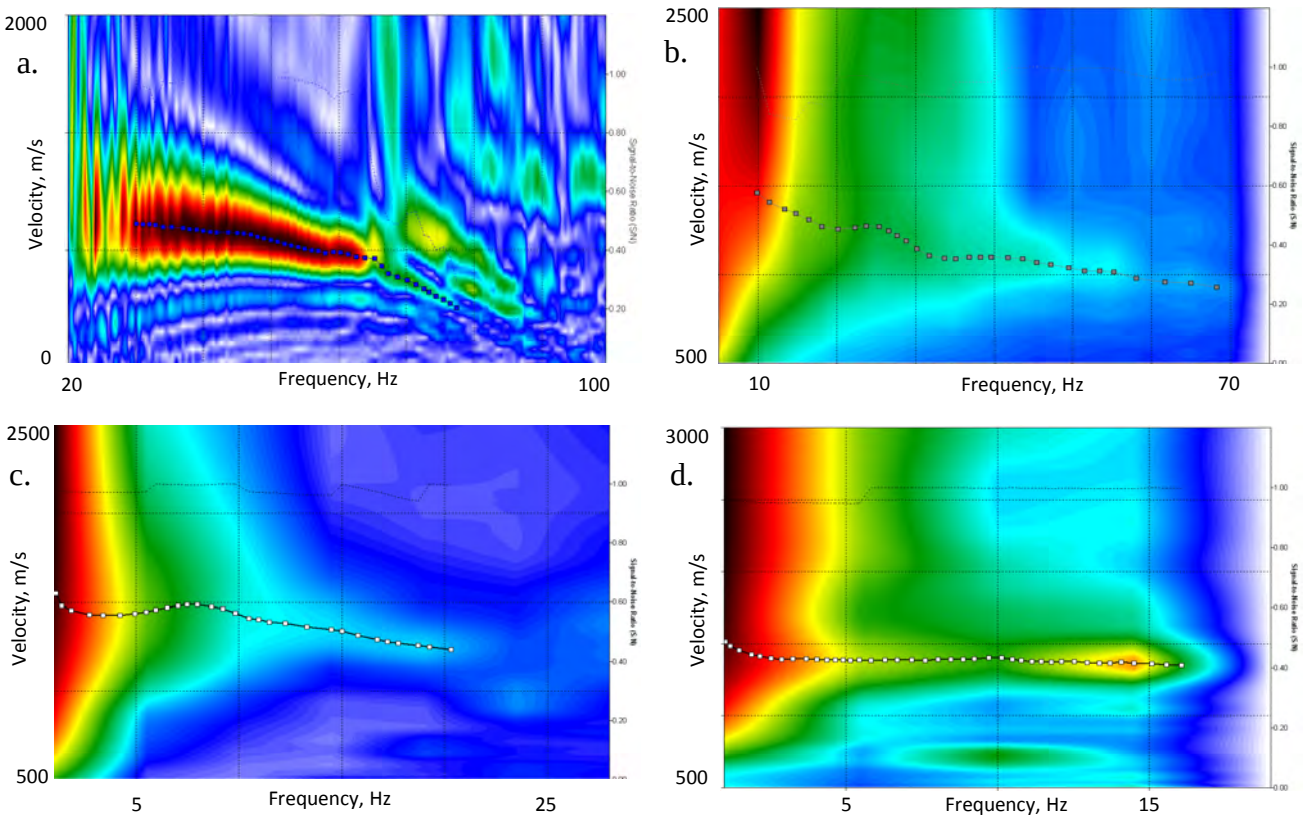

Figure 6: MASW method, overtone plots with dispersion curve picks: (a) 94-m array, hammer test; (b) 94-m array, passive source (c) 375-m array; (d) 750-m array

Discussion

The SASW test resolved frequencies from several hundred Hz to 1.9 Hz (Fig. 5). Velocities range from about 200 to 1600 m/s. Sharp bends appear in the curve at approximately 80, 50 and 3 Hz. Bends are indicative of distinct impedance contrasts at depth. We suspect that the bend at 3 Hz is related to the alluvium-bedrock interface.

Dispersion curves from the four MASW tests are superimposed in Fig. 8a, with the SASW dispersion curve also included for reference. The MASW dispersion curves demonstrate a consistent trend from 77 to 1.0 Hz. Over most of the range, results are virtually identical to those from the SASW measurement. Differences at high frequencies can be attributed to true differences in near-surface stiffness, which are to be expected because the tests were not precisely co-located (Fig. 4). The MASW method resolved a lower frequency than did the SASW method. In the frequency range 2 to 3 Hz, velocities are lower for MASW than for the SASW method, by as much as 10 percent.

The three ReMi dispersion curves are shown with the SASW curve for reference in Fig. 8b. At high frequencies, results are similar to those found from the MASW test (Fig. 8a). This is reasonable because the two processing methods were applied to the same data. Below 5 Hz, the velocities of the central picks are high with respect to the SASW results. The lowest frequency resolved is 1.6 Hz. The variability between the three ReMi dispersion curves increases with decreasing frequency.

Dispersion curves from all three methods are compared in Fig. 9. One disadvantage of a linear array for a passive-source survey is that when a predominant signal approaches the array at an oblique angle, the velocity picks would be erroneously high (e.g., Park and Miller, 2008). The MASW data do

not exhibit any tendency for elevated velocity with respect to the active-source SASW data; therefore, the hazard does not appear to be significant for this site. We plan to test this further using passive-source data acquired at the site using circular arrays. For the ReMi method, the central pick is plotted in Fig. 9a, and the lower-bound pick in 9b. The central pick (Fig. 9a) gives a better match to the others over most of the range, but the lower-bound pick has the better match below 4 Hz (Fig. 9b).

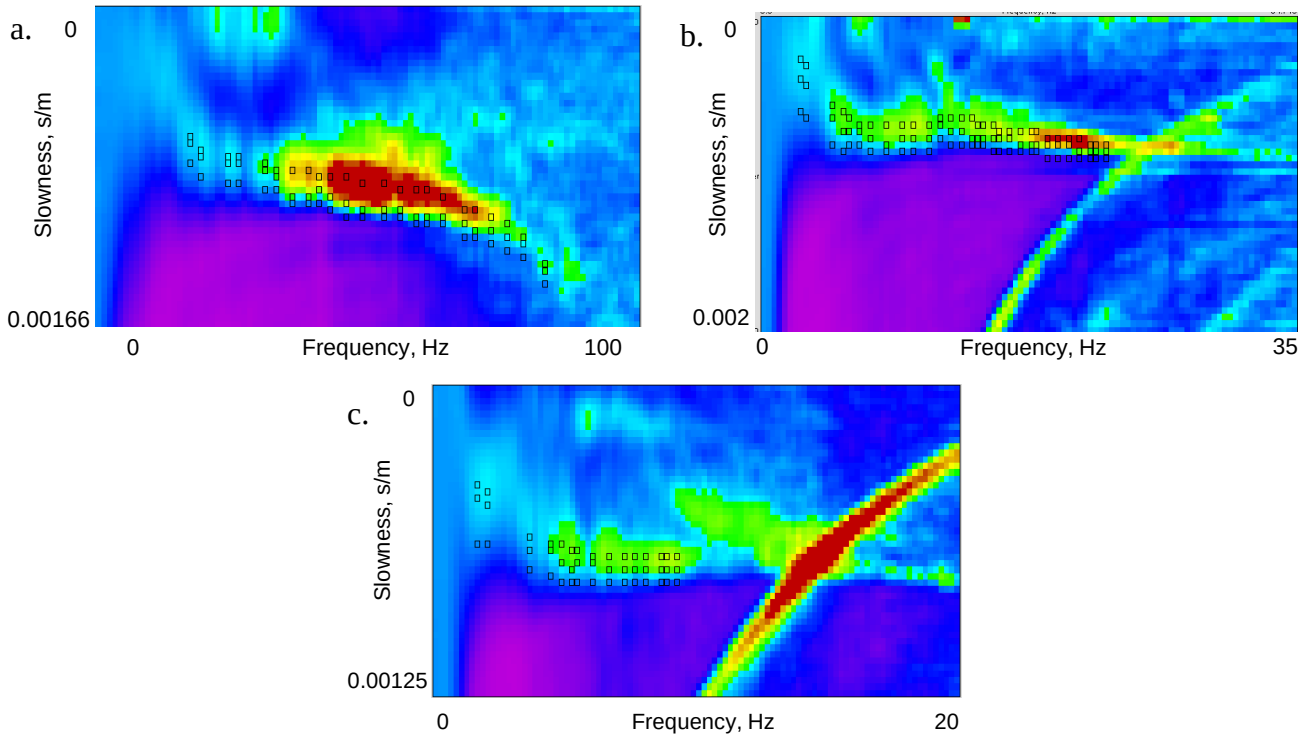

Figure 7: ReMi method, spectral ratio panels with dispersion curve picks: (a) 94-m array; (b) 350-m array; (c) 750-m array

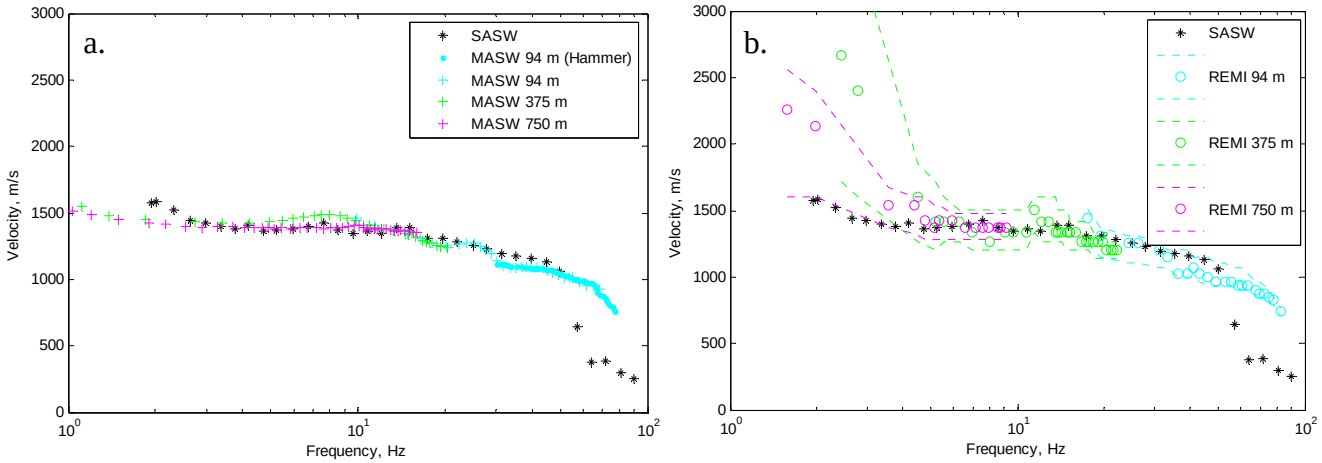

Figure 8: Dispersion curves from (a) four MASW tests and (b) three ReMi tests (upper and lower bound picks shown as dotted lines). Results from SASW test shown for comparison.

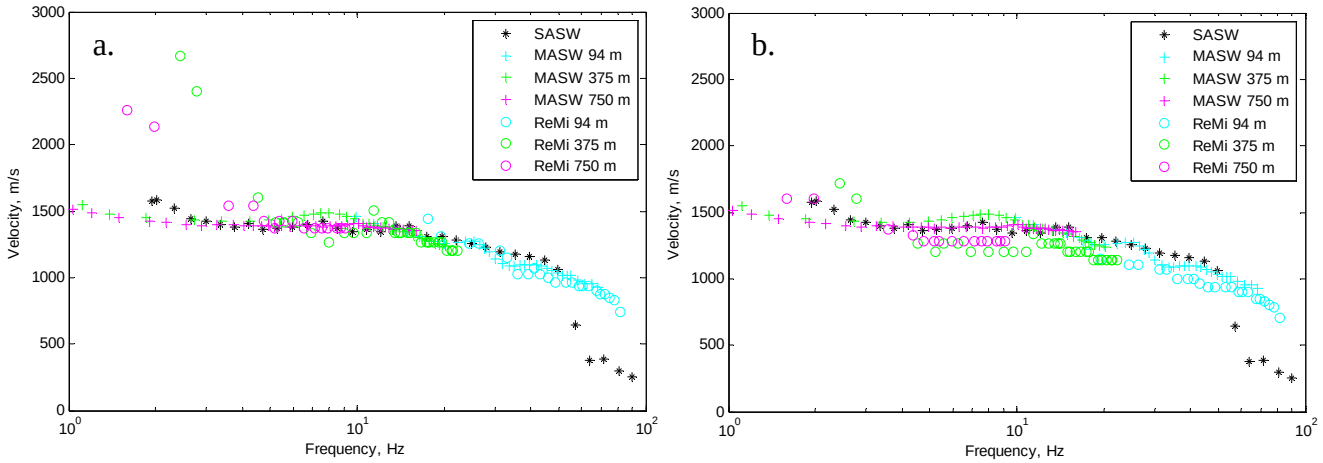

Figure 9: Comparing dispersion curves (a) using ReMi central pick; (b) using ReMi lower-bound pick

Conclusions

Surface-wave dispersion curves were resolved to 1.9 Hz using a Vibroseis (SASW method) and to 1.0 Hz using ambient noise (MASW method) at a high-velocity site. The low-frequency limit corresponds to wavelengths much longer than 1 km. For the two passive-source methods tested, MASW and ReMi, recommended methods were followed to process data and pick dispersion curves, although acquisition parameters were outside of normal bounds for the longer arrays. Dispersion curves from the three methods approximately coincided over the range 4 - 50 Hz. Differences at high frequencies are attributed to lateral variability of the shallow alluvium. Below 3 Hz, velocities from MASW and SASW tests differed by as much as 10%. Below 5 Hz, velocities from ReMi tests were much higher and more variable than the other methods; in this range the lower-bound dispersion picks tracked the others best. The data from the linear, passive-source arrays do not appear to be overly biased by any concentrated, off-line energy source.

References

Casto, D., Luke, B., Calderón-Macías, C., Kaufmann, R., 2009, "Interpreting surface wave data for a site with shallow bedrock," *Journal of Environmental and Engineering Geophysics*, 14(3), 115-127.

International Code Council, 2009, *International Building Code*, International Code Council, Country Club Hills, IL.

Karasa, A., Murvosh, H., Luke, B., 2009, "Seismic surface-wave dispersion curves for long, to 750-m, linear arrays," *Proceedings*, 42nd Symposium on Engineering Geology and Geotechnical Engineering, Idaho State University, Pocatello, 59.

Louie, J. N., 2001, "Faster, better: shear-wave velocity to 100 meters depth from refraction microtremor arrays," *Bulletin of the Seismological Society of America*, 91(2), 347-364.

Luke, B., Taylor, W., Calderón-Macías, C., Jin, X., Murvosh, H., Wagoner, J., 2008, "Characterizing anomalous ground for engineering applications using surface-based seismic methods," *The Leading Edge*, 1330–1334.

Luke, B., Liu, Y., 2007. "Effect of sediment column on weak-motion site response for a deep basin fill," *Journal of Geotechnical and Geoenvironmental Engineering*, 133(11), 1399-1413.

Page, W.R., Lundstrom, S.C., Harris, A.G., Langenheim, V.E., Workman, J.B., Mahan, S.A., Paces, J.B., Dixon, G.L., Rowley, P.D., Burchfiel, B.C., Bell, J.W., Smith, E.I., 2005, *Geologic and Geophysical maps of the Las Vegas 30' X 60' Quadrangle, Clark and Nye Counties, Nevada, and Inyo County, California*, U.S. Geological Survey Scientific Investigations Map 2814, scale 1:100,000, 55 pp.

Park, C. B., Miller, R. D., 2008, "Roadside Passive Multichannel Analysis of Surface Waves (MASW)," *Journal of Environmental & Engineering Geophysics*, 13(1): 1-11.

Park, C. B., Miller, R. D., 2005, "Roadside passive MASW," *Proceedings*, 19th Symposium on the Application of Geophysics to Engineering and Environmental Problems, Environmental and Engineering Geophysical Society, Denver, 1116-1127.

Park, C. B., Miller, R. D., Xia, J.,1999, "Multichannel analysis of surface waves," *Geophysics*, 64(3), 800-808.

Snelson C., McEwan, D., Hirsch, A., Zaragoza, S., 2004, "Imaging the Las Vegas basin: results from recent seismic refractions experiments" (Abstract S34A-07), *Eos Trans., AGU* 85**,** no. 47 (Fall Meet. Suppl.), S34A-07.

Stokoe, K.H., II, Wright, S. G., Bay, J.A., Roësset, J.M., 1994, "Characterization of geotechnical sites by SASW method," *Geophysical Characterization of Sites*, ed. Woods, R. D., Oxford and IBH Publishing Co., New Delhi, India, 15-25.

Stokoe, K., Cox, B., Lin, Y., Jung, M., Bay, J., Rosenblad, B., Wong, I., 2006, "Use of intermediate to large vibrators as surface wave sources to evaluate VS profiles for earthquake studies," *Proceedings*, 20th Symposium on the Application of Geophysics to Engineering and Environmental Problems, Environmental and Engineering Geophysical Society, Denver, 1241-1258.

Taylor, W. J., Carter, J., Luke, B., Snelson, C. M., Wagoner, J., 2008, "Development of Las Vegas Basin, Nevada with implications for seismic hazards," *Cordilleran Section (104th Annual) and Rocky Mountain Section (60th Annual) Joint Meeting (19–21 March 2008)*, The Geological Society of America (GSA), Boulder, CO,17-4.

Wyman, R. Karakouzian, M., Bax-Valentine, V., Slemmons, D.B., Peterson, L., Palmer, S., 1993, "Geology of Las Vegas, Nevada United States of America," *Bulletin of the Association of Engineering Geologists*, 30(1), 33-78.

Acknowledgments

This work was funded by the National Science Foundation under grant number CMMI-0749837 and the U.S. Department of Energy under contract number DE-FG52-03NA99204. Farn-Yuh Menq, Chris Cothrun, Lucas Gontijo, Eduardo Gonzalez, Dianna Feica, Jonathan Brown, P. K. Blaise Pfabe-Pisani, Suchan Lamichhane, M. Nihad Rajabdeen, Leah Irons, and Isaac Guzman helped with data collection or processing. Cathy Willey helped obtain site access. Julian Ivanov provided advice for processing MASW data.

STREAM VALLEY RESISTIVITY IN CENTRAL TEXAS: LAYING THE FOUNDATION FOR MULTI-DISCIPLINARY RESEARCH

Hallie E. Mintz, Baylor University, Waco, TX
John A. Dunbar, Baylor University, Waco, TX
Alan R. Gunnell, Baylor University, Waco, TX
Gary E. Stinchcomb, Baylor University, Waco, TX
Jason S. Mintz, Baylor University, Waco, TX
Steven G. Driese, Baylor University, Waco, TX

ABSTRACT

Increasing land-use and a changing climate can drastically modify floodplain habitats along low-order streams in central Texas. Investigating stream response to these factors on the site-scale can be costly. In an effort to streamline future site-specific investigations, a near-surface geophysical method was used along Williams Creek in Axtell, Texas.

A 2-D dipole-dipole resistivity reconnaissance study was employed to estimate depth to bedrock and locate buried channels in a partial-valley cross-section. Auger borings provided ground-truth along the resistivity profile, which confirmed depth to bedrock and the significance of varying resistivities.

The 276 meter resistivity profile was completed across a flowing Williams Creek and a portion of its floodplain, revealing a number of different fluvial landforms. Hand-augering confirmed the presence of a coarse-grained paleochannel fill that corresponds with a high-resistivity zone (50-100 ohm-m). At one location, auger refusal at bedrock occurred 3.15 meters below ground surface, consistent with the observed change to lower resistivity values. This decrease in resistivity at the bedrock contact is associated with groundwater flow along the fissile marl bedding planes. These data suggest that resistivity and ground-truthing combined, provide a cost-effective foundation to guide future research on the effects of climate and land-use on Williams Creek.

NEAR SURFACE BOREHOLE GEOPHYSICAL IMAGING IN A HIGHLY STRUCTURAL AREA, BEARTOOTH HILLS, MONTANA

Tania Mukherjee, Dr. R.R Stewart
University of Houston, Houston, TX -77204

Abstract

University of Houston conducted a student geophysical field camp at YBRA (Yellowstone Bighorn Research Association), Red Lodge Montana. The idea was to provide a detailed interpretation of the sub vertical Mississippian Madison lime stone bed beneath the YBRA camp using seismic and well logs. Several 2D seismic lines (E-W) were acquired and several logs were run in the two wells drilled in the camp.The depth of the wells are 30m and 60m , the wells were drilled then cemented and cased with PVC. SP, gamma, sonic, temperature, conductivity and sonic televiewer logs were run in the wells. Several multicomponent VSP (Vertical Seismic Profile) with different offset were also done. A shot offset of 3.5 m was selected for VSP. Both the wells were compared to see high frequency noise and shot signature. The limestone P wave velocity is about 2600 m and shale velocity is about 2800 m /s. The Vp/Vs is 2 for limestone and 1.7 for the shale unit. As there is very steep dipping reflectors, there is only little upgoing wave in the data .A VSP-NMO was also done and a corridor stack was then created. With the help of all dataset,composite plot and a quick look interpretation shows the limestone-Redbed encounter to be at 40 m and the probable dip of the bed looks to be 45° towards south.

GROUNDWATER INVESTIGATION IN GIGINYU, NASSARAWA LOCAL GOVERNMENT KANO STATE NIGERIA

Farouq A.U[1]. , Suru H.U[1]., Bello Maruff Akande[2] and Aminu U.A[3].

Abstract

DC Vertical Electrical Soundings were carried out in 10 stations in order to determine areas with groundwater potentials. Data collected were reduced and interpreted according to profiles (profile one and profile two). The interpretation yielded two geoelectric sections of (3) geoelectric layers for profile one and four (4) geoelectric layers for profile two. The topsoil thickness ranges between 0.8 and 2.6 m with resistivity values ranging between 103 Ohm-meter and 1031.2 Ohmï meter across the study area. The topsoil is lateritic clay, sandy clay and clayey sand. The thickness of the weathered layer ranges from 3.3 m to 20 m and resistivity ranges between 11.5 Ohm-meter to 294 Ohm-meter, this indicates the aquiferous formation. Depth to aquifer ranging between 1.6 m to 15.9 m. The partially weathered/fractured basement resistivity ranges between 98 Ohm-meter to 692.4 Ohm-meter, which indicate high degree of fracture and or water saturation with thickness range between 7.2 m and 52 m. Fresh bedrock is the last layer with resistivity values ranging between 1266 Ohm-meter to 100000 Ohm-meter at all the VES points in the study area at a depth ranging between 4.1 m to 70 m. Hence, VES9 and VES10 on profile two, having highest groundwater potentials.

Introduction

Giginyu is a densely populated town in Nassarawa Local Government Area of Kano State, Nigeria. It is situated about 3 km east of Kano City. It borders Hotoro in the east, Badawa in the north and Tarauni in the south.

The main sources of water are pipe borne from water board, hand dug wells and boreholes.

In most cases, groundwater can be free of pathogenic organism and need no purification before usage. Chemical and biological contamination of most groundwater is difficult compared to surface waters. Groundwater, which has been stored in the ground by nature through many years of recharge, is available and dependable than surface water, hence can readily be tapped (Todd, 1980)

The study is aimed at investigating the groundwater potential of this small area by using DC resistivity technique (Schlumberger array) for data collection in order to determine the areas of high groundwater potentials, depth to aquifer, aquifer thickness, depth to fractured basement, thickness of fractured basement and depth to fresh basement.

The theory of the resistivity method is that current is introduced into the ground by means of two current electrodes and the potential difference between a potential electrodes placed in line in between the pair of current electrodes is measured.

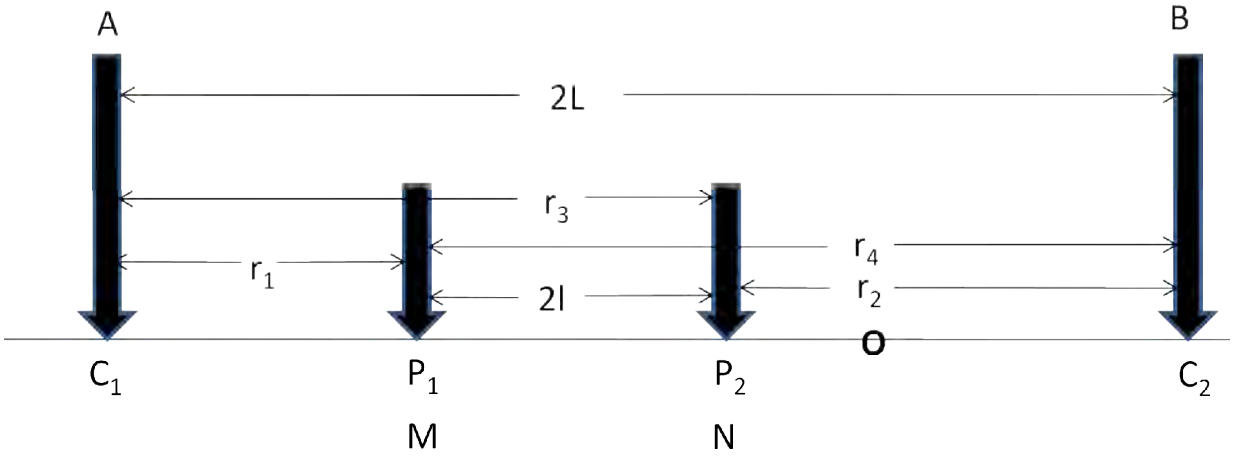

Figure1: Schlumberger Field Configuration

In the diagram above, C_1 and C_2 are current electrodes separated by a distance AB = 2L apart. P_1 and P_2 are potential electrodes separated by a distance MN = 2l apart.

Ohmôs law states that the current passing through a metallic conductor at a constant temperature is directly proportional to the potential difference applied between its ends.

$$I \propto V, \text{ which implies } V = IR \quad \text{---------- (1)}$$

Where R is resistance measured in Ohms. Also resistance R is proportional to length L of the conductor and inversely proportional to its cross sectional area A given by

$$R \propto \frac{L}{A}, \text{ which implies } R = \frac{\rho L}{A} \quad \text{---------- (2)}$$

where ɟ, is constant called resistivity of the material.

Using equations (1) in (2) yields,

$$V = \frac{I\rho L}{A} \quad \text{---------- (3)}$$

Consider A and B to point current electrodes located on a hemispherical equipotential surface downward into the ground at each electrode. The surface area is given by $2\acute{}L^2$, where L is the radius of the sphere. Equation (3) becomes,

$$V = \frac{I\rho L}{A} = \frac{I\rho}{2\pi L} \quad \text{---------- (4)}$$

Now, considering the individual potentials at M and N,

$$V_M = \frac{I\rho}{2\pi}\left[\frac{1}{r_1} - \frac{1}{r_2}\right] \quad \text{---------- (5)}$$

$$V_N = \frac{I\rho}{2\pi}\left[\frac{1}{r_3} - \frac{1}{r_4}\right] \quad \text{---------- (6)}$$

$$r_1 = (L - x) - l, \qquad r_2 = (L + x) + l, \qquad r_3 = (L - x) + l, \qquad r_4 = (L + x) - l$$

The potential difference, ΔU across MN is given by V_M-V_N i.e.,

$$\Delta U = \frac{I\rho}{2\pi}\left[\left(\frac{1}{r_1} - \frac{1}{r_2}\right) - \left(\frac{1}{r_3} - \frac{1}{r_4}\right)\right] \quad \text{---------- (7)}$$

Substituting the values of r_1, r_2, r_3 and r_4 in equation (7), yields,

$$\frac{2\pi\Delta U}{I\rho_a} = \left[\left(\frac{1}{(L-x)-l} - \frac{1}{(L+x)+l}\right) - \left(\frac{1}{(L-x)+l} - \frac{1}{(L+x)-l}\right)\right] \quad \text{------- (8)}$$

where ρ_a is the apparent resistivity.

The smallest current-potential electrode distance is always much greater than the distance between the two potential electrodes (at least a factor of 10). Equation (8) becomes,

$$\rho_a = \frac{\pi\Delta U}{2Il}\frac{[L^2 - x^2]^2}{[L^2 + x^2]} \quad \text{---------- (9)}$$

But the array is symmetrical, as a result, equation (9) becomes;

$$\rho_a = \frac{\pi\Delta U L^2}{2IlL^2} = \frac{\pi L^2 \Delta U}{2Il} = \frac{\Delta U}{I}K \quad \text{---------- (10)}$$

$$Where\ K = \frac{\pi L^2}{2l}\ is\ called\ geometric\ factor.$$

Depth of investigation is a function of the electrode spacing. The greater the spacing between the outer current electrodes, the deeper the electrical currents will flow in the earth, hence the greater the depth of exploration. The depth of investigation is generally 20 to 40% of the outer electrode spacing, depending on the earth resistivity structure.

Climate, Vegetation and Geomorphology

The climate of Kano State is seasonally arid. In the south, the rainy season averages 150 days from May to October, and the mean annual rainfall is 1000 mm; north of Kano city this decreases to 635 mm. the vegetation is derived from Sudan savannah, and has been greatly disturbed by cultivation

Geology and Regional Setting

Crystalline rocks of the Basement Complex are widespread in Africa (Jones, 1985). In Kano state, the Basement complex consists of a variety of metamorphic and igneous rocks ranging in age from Precambrian to Jurassic.

The metamorphic rocks are migmatite, gneiss, schist, and some quartzite, which have been deformed structurally into antiforms, synforms and down faulted blocks. Foliations and fold axes trend approximately north ï south, and lithological variations are common.

The older granite is composed of coarse-grained granite, granodiorite, diorite, and aplite. Lithological variations are less common than in the metamorphic suite but are often found within one village. A distinctive rock type is very coarse-grained microcline-rich ñpink granite,ò with less than 10 percent each of white feldspar and mafic minerals; this is an important aquifer.

The younger granite occurs as ring complexes of coarse-grained riebeckite or biotite granite associated with some rhyolite and basalt.

The region underlain by the Basement Complex can be subdivided into three geomorphological areas as follows;

1. West ï This area is drained by the headwaters of major rivers, and valleys tend to be narrow and incised. Inselbergs, tors and rock pavements are common, and fresh bedrock is found near the surface. The weathering profile is commonly truncated by erosion so that thick weathered zones are rare and narrow.
2. Center and North ï The terrain is generally flat and rock outcrops are rare. The few valleys are broad and well developed. The weathering profile is mature, and laterite duricrusts are widespread. Weathered zones are of wide lateral extent and the depth to fresh bedrock is usually greater than 40 m.
3. Southeast ï This is an intermediate area; the weathering profile is usually not truncated by erosion, but fresh bedrock is commonly only a few meters below static water level.

Groundwater Occurrence

Groundwater occurs either within the weathered zone above the crystalline bedrock, or in fractures within the bedrock itself.

About 75 percent of the boreholes completed in the Basement Complex obtain water from the weathered zone. In most cases, the aquifer is the well-stained, unstable, clay-free material immediately above fresh bedrock. The permeability of this material is quite variable, and largely unpredictable. Within the three geomorphological areas, the character of the weathered zone is influenced by bedrock lithology and structure so that:

- In area (1) thick weathered zone are less common over granite than over metamorphic rock, where foliation, folds, faults and lithological variations facilitate deep weathering, so that in some places clay has been encountered at depths exceeding 70 m.

- The ñpink graniteò found in area (2) has a distinctive weathering profile; a clay-rich mantle between 20 and 40 m thick overlies discolored rock containing water which is probably stored in hairline fractures within the feldspar.
- In places underlain by other granites, thicker weathered zones may occur where the lithology, grain size, or structure is slightly different. The location of these tends to be randomly distributed, not visible on aerial photographs, and not related to topography.

The remaining 25 percent of the boreholes obtain water from fracture porosity, which is important whether the weathered zone is unsaturated. Fracture zones as narrow as 5 m have been successful. The fractures appear to be associated with specific rock types, such as pegmatite, or places where mineral proportions are locally different. This applies to granite as well as to metamorphic rock and is important because the analysis of fracture pattern at the surface proved largely irrelevant to the location of fractures at depth in granite, whereas over the metamorphic rock, lithological variations and associated fractures derive from the regional north-south trend (Beeson and Jones 1988).

Adepelumi *et al* (2006) applied electrical imaging and very low frequency (VLF) to investigate and delineate basement fracture zones within a basement rock. They carried out experiments to evaluate the efficacy of the methods in detecting low-resistivity fracture zones in a typical crystalline basement rock that is favorable for groundwater accumulation. They found out that most wells drilled in such an environment usually have low yields. Results of the numerical experiment generally indicate that fractures covered by moderate overburden, and having considerable depth, extent, and thickness compared to the depth of fracture burial, produce good responses resulting in high-resolution resistivity images. Lower resolution resistivity images were obtained as the thickness of the overburden increased.

Mohammed *et al* (2007) carried out regional geoelectric investigation for groundwater exploration in Minna area North West Nigeria, which is a basement complex terrain. Their results indicated a surface

layer, which is the first layer made up of low resistivity and consists of clayey soil in some sections and high resistive fresh laterites mixed with loose sands and gravels in others. The average resistivity value of this layer varies between 10 - 900 Ohm-m. The average resistivity value of the second layer underlying the area is in the range of about 28 - 400 Ohm-m. This layer is the aquiferous formation in their study area, and has an average thickness that varied between 5-20m. Its maximum thickness of about 45 m is found where it is deeply seated. This layer together with the overlaying layer forms the basic aquifer formation of their study area.

Material and Method

Schlumberger array was chosen for this work due to its convenience and advantage over other arrays. The data collected in 10 VES point using ABEM Terrameter SAS1000 were reduced and interpreted using software by Vander Velpen B.P.A (ITC MSc Research Project 1988).

Two profiles were taken based on five VES point each, with profile one with VES1, VES2, VES3, VES5 and VES8, while profile two has VES4, VES6, VES7, VES9 and VES10.

Result and Discussion

The data collected using Schlumberger array (Figure 1) was interpreted using partial curve matching and the results were iterated using computer iterative (winresist) software by Vander Velpen B.P.A (ITC MSc Research Project 1988)

A typical plot and interpretation of VES1 and VES4 are given in figure 2 and figure3 respectively.

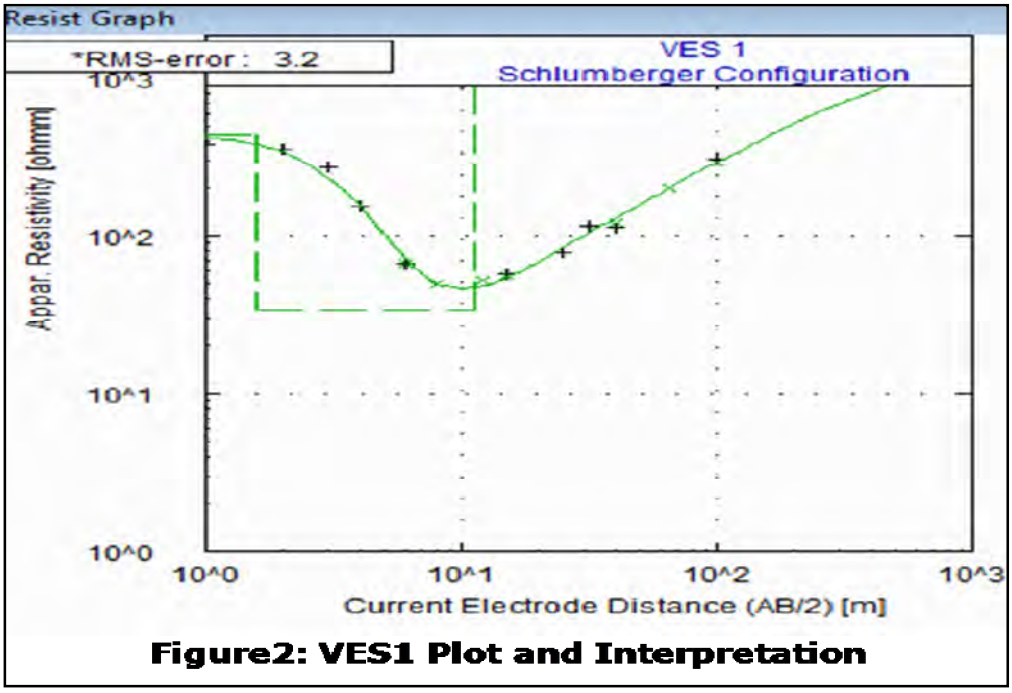

Figure2: VES1 Plot and Interpretation

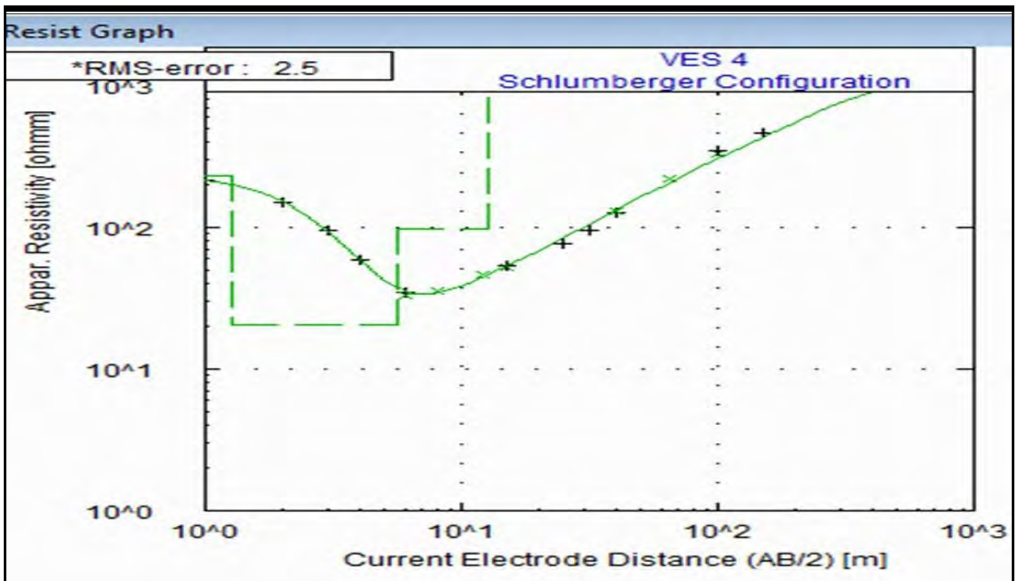

Figure 3: A Plot and Interpretation of VES 4

Analysis of all the 10 VES plots and their interpretations revealed 3-geoelectric layers for profile one (fig.4).

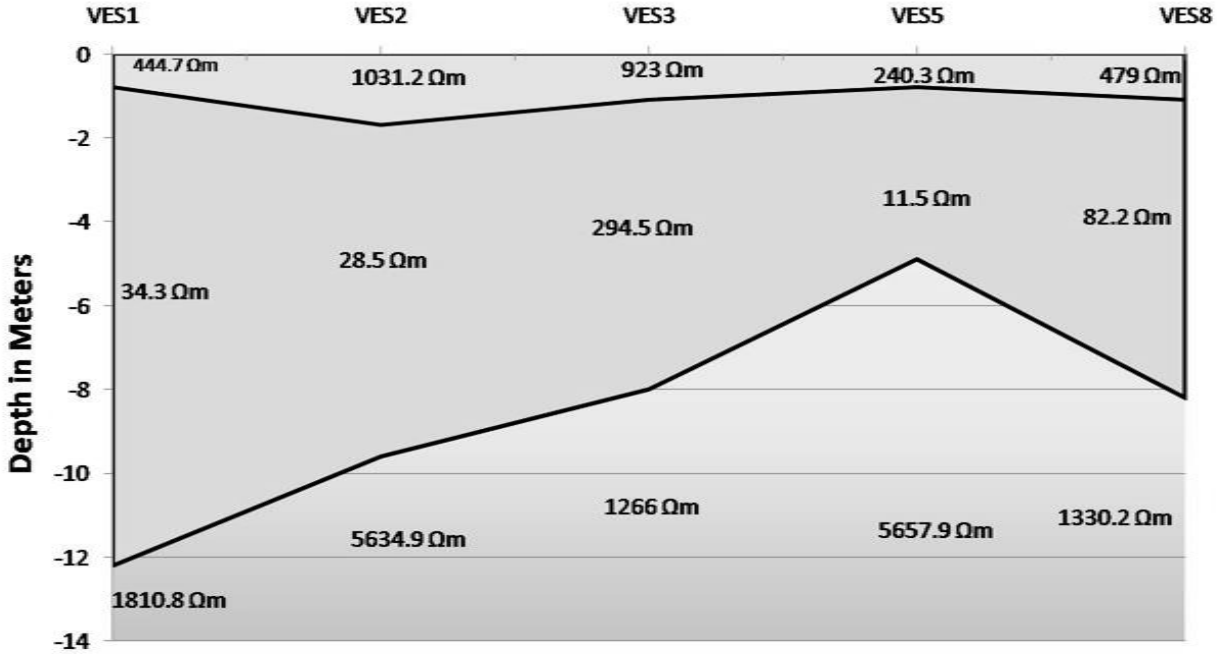

Figure 4: Geoelectric Section of Profile One

The first layer has resistivity ranges of about 240.3 Ohm ï meter to 1031.2 Ohm-meter with thickness varying from 0.8 to 1.6 m, second layer has resistivity ranges of about 11.5 Ohm ï meter to 294.5 Ohm-meter with thickness varying from 3.3 to 9.8 m, while the third layer has resistivity ranges of about 1266 Ohm ï meter to about 5657.9 Ohm-meter with an infinite thickness.

Whereas the geoeletric section of profile two revealed 4-geoelectric layers throughout (fig.5).

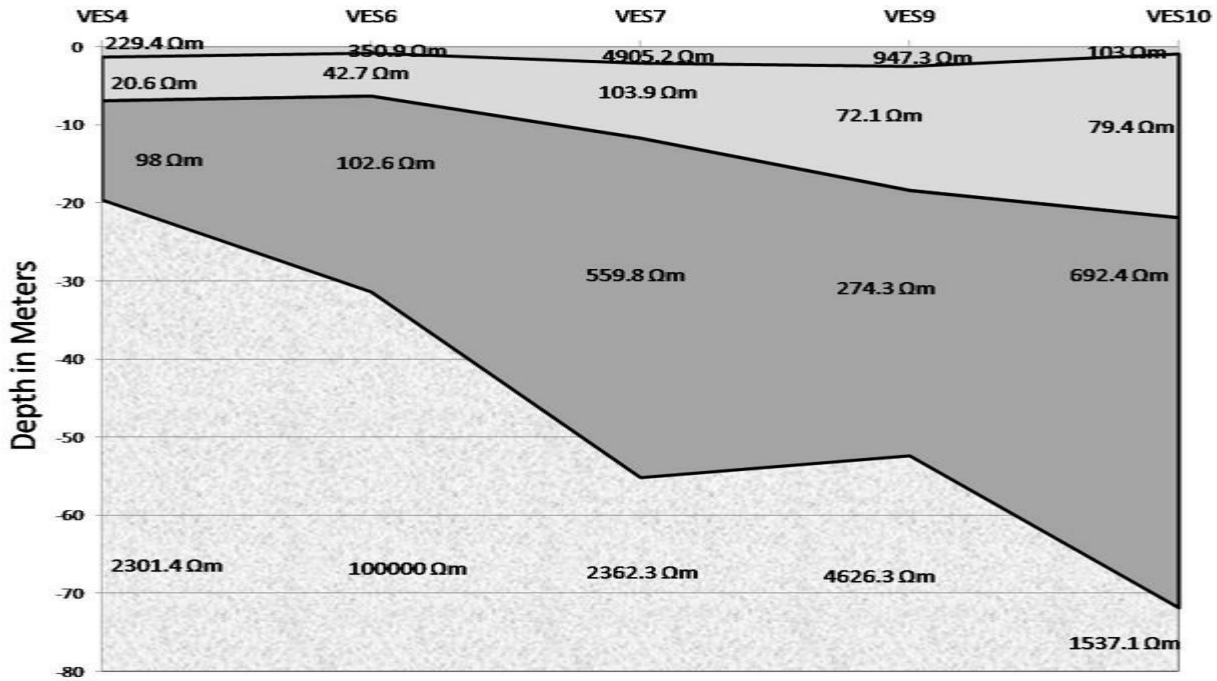

Figure 5: Geoelectric Section of Profile Two

The first layer has resistivity ranges of about 103 Ohm-meter to 947 Ohm meter with thickness varying from 0.8 m to 2.5 m, second layer has resistivity ranging from about 20.6 Ohm-meter to 103 Ohm-meter with thickness varying from 4.3 m to 20 m, the third layer has resistivity ranging from about 98 Ohm - meter to 692.4 Ohm ï meter with layer thickness varying from about 7.2 m to 52 m, while the fourth layer has a resistivity ranging from about 1537.1 Ohm-meter to 100000 Ohm ï meter with infinite thickness.

Interpretation

The Topsoil

The topsoil thickness is relatively thin along the two profiles and ranges between 0.8 and 2.6 m with resistivity values range between 103 Ohm-meter and 1031.2 Ohmï meter across the study area. The

predominant composition of the topsoil is lateritic clay, sandy clay and clayey sand. The high resistivity around VES2 could be due to sandy soil.

The Weathered Layer

The thickness of the weathered layer in the entire study area ranges from 3.3 m to 20 m and resistivity ranges of 11.5 Ohm-meter to 294 Ohm-meter, this indicates the aquiferous formation in the study area. Depth to aquifer ranging between 1.6 m to 15.9 m

Fractured Layer

The partially weathered/fractured basement resistivity values range between 98 Ohm-meter to 692.4 Ohm-meter, which indicate high degree of fracture and or water saturation. The thickness of this layer ranges between 7.2 m and 52 m, evident in profile two.

The Fresh Bedrock

The fresh bedrock is the last layer and has resistivity values that range between 1266 Ohm-meter to 100000 Ohm-meter. It is evident at all the VES points in the study area at a depth ranging between 4.1 m to 70 m.

The observed thickness and nature of the weathered layer are important parameters in the groundwater potential evaluation of a basement complex terrain (Clerk, 1985; Bala and Ike, 2001).

Discussion of Result

The results obtained above correlated well with the results obtained by Shemang (1990), Olatunji (1999), Dogara, and Ajayi (2001) as tabulated below:

Table1: Resistivity Values Obtained in Basement Complex

Rock Type	Resistivity Range(Ohm-meter)
Fadama loam	20 ï 90
Clay, silt and sand	70 ï 300
Weathered basement	100 ï 500
Fractured basement	501-1,000
Fresh basement	Greater than 1000

Source: *Shemang (1990), Olatunji (1999) Dogara and Ajayi (2001)*

A recent work on the Basement Complex was that of Jatau and Bajeh (2007) where they obtained the following results; first layer resistivity of 60 ï 100 Ohm-meter as top soil (laterite). The second layer resistivity of about 30 ï 500 Ohm ï meters of sandy ï clay with laterite in some places, third layer resistivity ranged between 40 ï 200 Ohm ï meter of weathered regolith transition zone (Jones, 1985) and the fourth layer of fresh basement resistivity ranged between 300 and above.

Conclusion

Depth to aquifer ranges between 1.6 m to 15.9 m and aquifer thickness ranges between 3.3 m to 20 m. Depth to fractured basement ranges between 5.6 m to 18 m and thickness of between 7.2 m and 52 m and depth to fresh basement ranging between 4.1 m to 70 m.

The thickest portion of the aquifer coincided with the thickest portion of the fractured basement at VES9 and VES10 on profile two, hence, areas of high groundwater potentials.

References

Adepelumi A. A. , Yi M. J. , Kim J. H., Ako B. D. and Son J. S., 2006, Integration of surface geophysical methods for fracture detection in crystalline bedrocks of southwestern Nigeria. Hydrogeology Journal, **14**, 1431-2174

Bala A.E. and Ike E.C., 2001, The aquifer of the crystalline basement rocks In Gusau area, Northwestern Nigeria. J. Min. Geology, **37**, 177-184.

Beeson S. and Jones R.C., 1988, The Combined EMT/VES Geophysical Method For Siting Boreholes. Ground Water, **26**, 54 ï 63.

Clark, L.M., 1985, Groundwater Abstraction from the Basement Complex Areas of Arica. Quarterly Journal of Engineering Geology, London, **18**, 25 ï 34.

Dogara, M.D. and Ajayi C.O., 2001, Unexposed Younger Granites Series of Central Nigeria. Deduction from Geological Investigation. Nigeria Journal of Physics, **13**, 11-15.

Jatau B.S and Bajeh I. 2007, Hydrogeological Appraisal of Parts of Jemaâa Local Government Area North-Central Kaduna State, Nigeria. Research Journal of Applied Science **2**, 1174 ï 1181.

Jones, M. 1985, The Weathered Zone Aquifers of the Basement Complex Areas of Africa. Quarterly Journal of Engineering Geology, **18**, 35-46.

Mohammed L.N., Aboh H..., and Emenike E.A., 2007, A Regional Geoelectric Investigation for Groundwater Exploration in Minna Area North West Nigeria. Science World Journal (SWJ), **2**, 15 - 19

Olatunji, S. 1999, Geophysical Site Investigation of the Federal College of Education, Zaria, Nigeria: M.Sc. Thesis. A.B.U., Zaria, Nigeria.

Shemang, E.M. 1990, Electrical Depth Sounding at Selected Well Sites within Kubani River Basin; Zaria: M.Sc. Thesis. A.B.U. Zaria, Nigeria.

Todd, D.K. 1980, Groundwater Hydrology, Second Edition, John Wiley and Sons, New York, 450 pp.

Velpen, V., 1988. Resist: A Computer Processing Package For DC Resistivity Interpretation for the IBM PC and Compatibles: MSc Thesis, ITC-Delft, the Netherlands.

GEOPHYSICAL INVESTIGATIONS AT THE CHIMNEY ROCK GREAT HOUSE, COLORADO

Sarah Devriese, Colorado School of Mines, Golden, CO
Michael A. Mitchell, Colorado School of Mines, Golden, CO
Roxanna Frary, Colorado School of Mines, Golden, CO

Abstract

In conjunction with the National Forest Service, a number of different geophysical datasets were collected over the region adjoining the southwest end of the Great House at Chimney Rock, Colorado. The investigations aim to determine if the foundations for more rooms exist in this region, as early archeological sketches indicate. The following types of datasets were collected: magnetic, frequency-domain electromagnetic (FEM), DC resistivity (middle gradient and 2D dipole-dipole), and microgravity. This multipronged approach was used to provide a diverse range of data types, all of which have different physical property sensitivities. Since the expected physical property contrast between the wall foundations and possible room infill has yet to be characterized, it is difficult to determine which of the utilized methods will produce the best results. A thorough analysis of our geophysical field data along with the results gleamed from processing and inversion, will allow us to develop a meaningful interpretation, upon which recommendations for future investigations can be based.

By determining whether or not the additional rooms exist, this study will help archeologists and the National Forest Service characterize the extent of the Chimney Rock Great House, plan future archeological studies, and set a basis for future geophysical investigations at the site.

Acknowledgements

Thanks to archeologists Dr. Wendy Sutton, (Archaeologist, Pagosa District, San Juan National Forest) Brenda Todd (PhD candidate, CU Boulder), and Dr. Steve Lekson (Professor, CU Boulder), our faculty advisor Dr. Rich Krahenbuhl, (Professor, Colorado School of Mines), and other professors at the Colorado School of Mines including Dr. Misac Nabighian and Dr. Yaoguo Li, for helping us make this project possible.

MEC CLASSIFICATION PARAMETER SELECTION BASED ON SITE-SPECIFIC MUNITIONS CHARACTERISTICS

Steve Saville, Parsons, Denver, Colorado
Nathan Harrison, Parsons, Denver, Colorado
Craig Murray, Parsons, Denver, Colorado

Abstract

Parsons has participated in the Environmental Security Technology Certification Program (ESTCP) unexploded ordnance (UXO) Discrimination Study at Camp Sibert, Alabama, and most recently at Camp San Luis Obispo (SLO), California. In 2008, ground truth results from Camp Sibert were used to identify commonly used target parameters from EM61-MK2 data that would improve the classification of munitions and clutter. UXA-Size (size), a parameter based on instrument response across the three major axes of an object, and a decay constant were identified as having the greatest potential for classifying the 4.2-inch mortar seed items found at Camp Sibert. A simple rule-based classification was developed based on size and decay, and the resulting receiver operating characteristic (ROC) curve showed improvement over a previous rule-based classification of the Camp Sibert ground truth results.

In 2009, Parsons participated in a similar target classification study for the SLO site. Unlike Camp Sibert, which included only the 4.2-inch mortar, the SLO site included a range of munitions types: 2.36-inch rockets, 4.2-inch mortars, 60-millimeter (mm) projectiles, and 81mm projectiles. This range of munition types made application of the size and decay based classification of anomalies detected using the EM61-MK2 at Camp Sibert more challenging for the SLO site. Because of the variety of munitions types at SLO, a single size parameter could not be identified for effective classification of all munitions types from clutter. Attempts to define unique rules involving size per munitions type were not as diagnostic for the SLO data set due the wider range of size values observed for munitions and clutter at this site. The most effective rule-based classification at the SLO site was to use two sets of decay values from the EM61-MK2 data to classify the munitions and clutter.

Introduction

This paper provides a brief narrative on the ESTCP UXO Discrimination Study, a background on the geophysical parameters used, why they were chosen to classify targets at each site, and the results of target classification at each site. We will discuss the reasons behind the success of the size parameter at Camp Sibert and the reasons for its limited value at the SLO site. Finally, we will discuss possible solutions for using size at sites with a variety of munitions types, and the anticipated constraints of these solutions.

Parsons participated in the ESTCP UXO Discrimination Study at Camp Sibert and at the SLO site. The goal for both studies was to evaluate effective classification techniques of geophysical anomalies as either munitions or clutter. Each study has challenged demonstrators to develop instruments or data processing solutions that will improve the industry's ability to accurately classify munitions (potential UXO) and clutter (non-UXO), thereby reducing project costs related to excavating anomalies associated with non-hazardous clutter anomalies.

At the Camp Sibert and SLO sites, Parsons relied upon advanced processing of EM61-MK2 data and the identification of parameters that may be useful in classifying munitions and clutter. For the Camp Sibert study, approximately 300 ground truth dig results were available for development of a rule-based classification. At the SLO site, Parsons received a list of 249 ground truth targets for the purpose of developing a rule-based classification. In each of these instances, commonly used parameters available from industry-standard Geosoft were reviewed for useful relationships to classify munitions and clutter.

Geophysical Parameters

UXA-Size

Size is a parameter related to instrument response across the three major axes. Its use in UXO investigations is limited, but the size parameter is increasing in popularity as a result of recent developments within processing software (industry-standard Oasis montaj by Geosoft). Size is a function of instrument response to an item's aspect ratio. In this way, size may be used to quantify the physical contrast between munitions (e.g., cylindrical items) from clutter (e.g., disks or tablet-shaped items). The use of the size parameter requires high-quality geophysical data. Size values are qualified by a fit coherence parameter describing the agreement of the data to an ideal model of the data. Therefore, a size value with low fit coherence may not be accurate enough for target classification.

Figure 1 presents a sample target with low fit coherence, with the target's actual data (top left), its modeled results (top right), and the difference, or residual, between the actual and modeled data (bottom left). It is clear from visual inspection that the modeled data (top right) does not accurately represent the actual data (top left). Because of this and the resultant low fit coherence, the size parameter for this target would be of limited use in target classification. In contrast, Figure 2 presents a target with high fit coherence. This target's size parameter would be acceptable for target classification due to the high fidelity between the actual and modeled data.

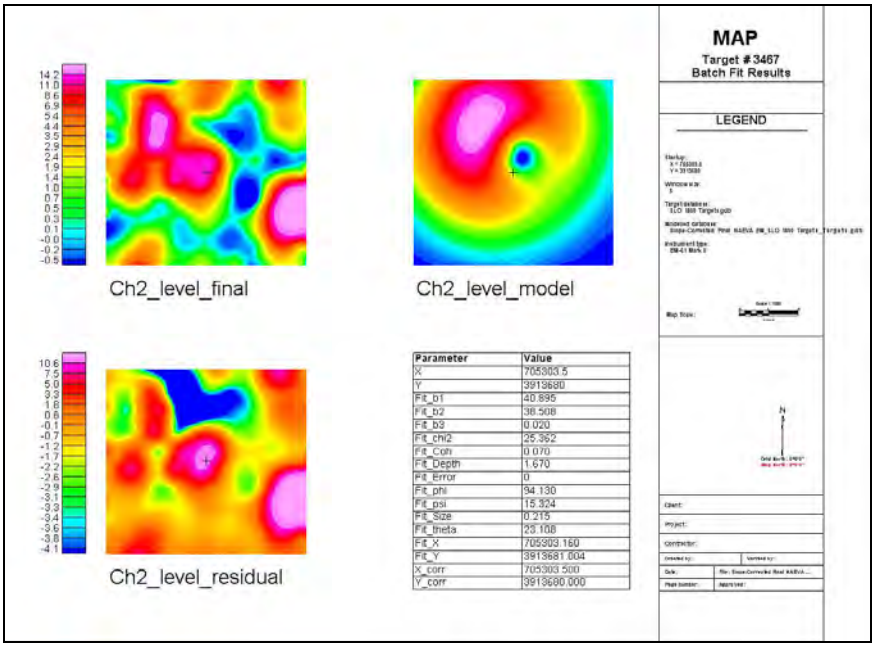

Figure 1. Target with low fit coherence

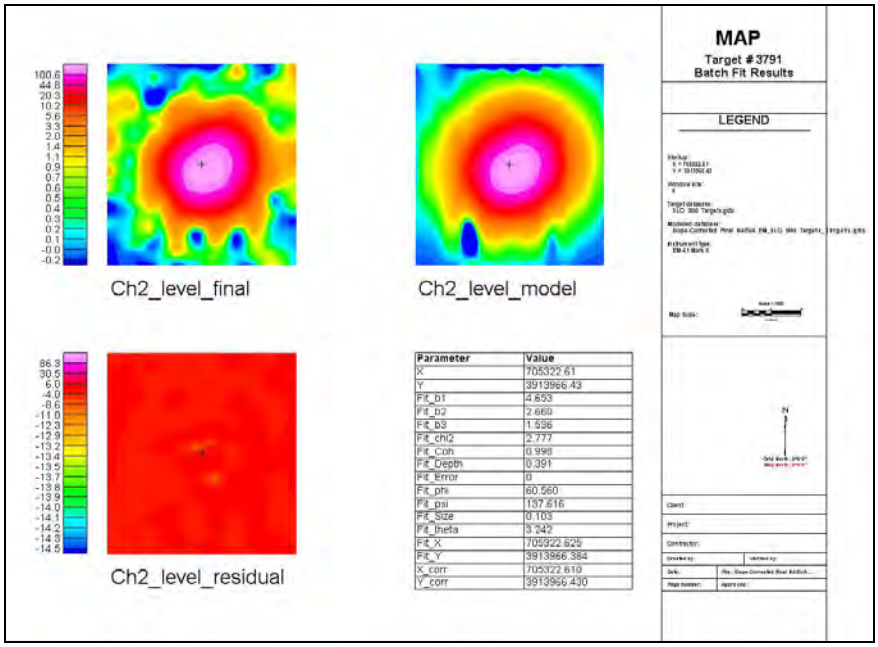

Figure 2. Target with high fit coherence.

Decay Constants

Decay constants are an increasingly popular parameter for target classification. Decay constants are a function of an object's material thickness, and can be used to exploit the contrasts between thin-walled scrap metal and thicker-walled items such as grenades or mortars. Thin-walled items, such as sheet metal, typically have smaller decay constants as instrument response from the item decays quickly. A variety of decay constants may be calculated, depending upon the geophysical instrument used. The ubiquitous EM61-MK2 with its four time gates allows for the calculation of six decay constants (i.e., Ch1-Ch2, Ch1-Ch3, etc.); however, within an investigation, as few as one may serve the needs of target classification.

Rule-Based Classifications

As part of the UXO Discrimination Study, ESTCP has challenged Parsons and other firms with classifying targets at two sites (ESTCP, 2009). The initial study at Camp Sibert, Alabama, was chosen for its benign geology, flat terrain, and one munitions type (4.2-inch mortars). The SLO site was chosen for its more difficult conditions: the SLO site has rolling terrain and a range of munitions types (each munitions type requiring consideration during target classification).

Parsons' approach to the rule-based classification at Camp Sibert began by reviewing ground truth dig results and identifying useful relationships among parameters available within Geosoft. Figure 3 is a scatter plot of dig results at Camp Sibert, with the recovered items' size and decay on the X and Y axis, respectively. This scatter plot illustrates the useful relationship between size and decay for the classification of munitions from clutter, which provided the basis for the rule-based classification of targets at Camp Sibert. Targets with larger size and decay values were classified as more munitions-like, and those targets with smaller size and decay values were classified as less munitions-like.

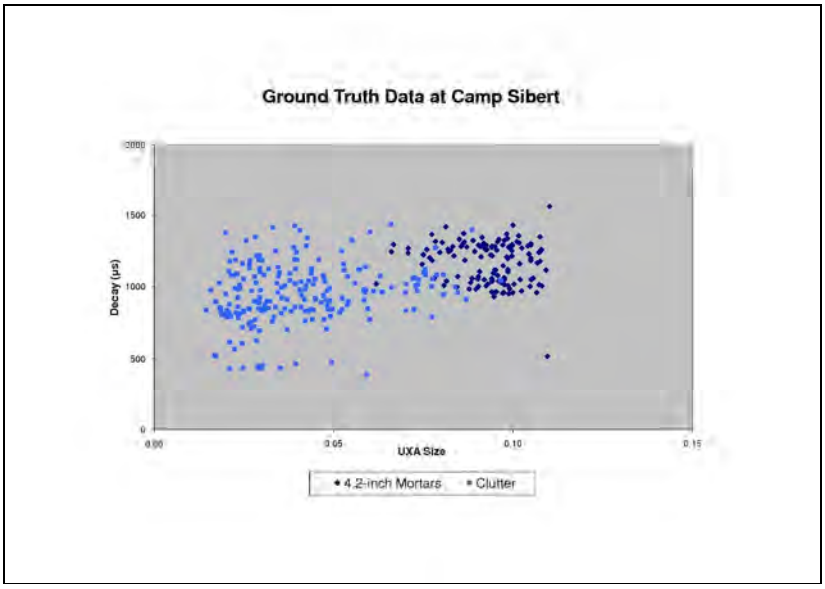

Figure 3. The difference in size and decay between munitions and clutter at Camp Sibert is evident in scatter plot.

Camp Sibert

As part of a Huntsville Innovative Technology-funded project in 2008, Parsons used the ground truth results from Camp Sibert to identify commonly used target parameters that improve the classification of munitions and clutter (Parsons, 2009). The size and decay constant parameters were identified as having the greatest potential for classifying the 4.2-inch mortar seed items found at Camp Sibert. A simple rule-based classification was developed based on size and decay, and the resulting ROC curve (Figure 4) showed improvement over a previous rule-based classification of the Camp Sibert ground truth results.

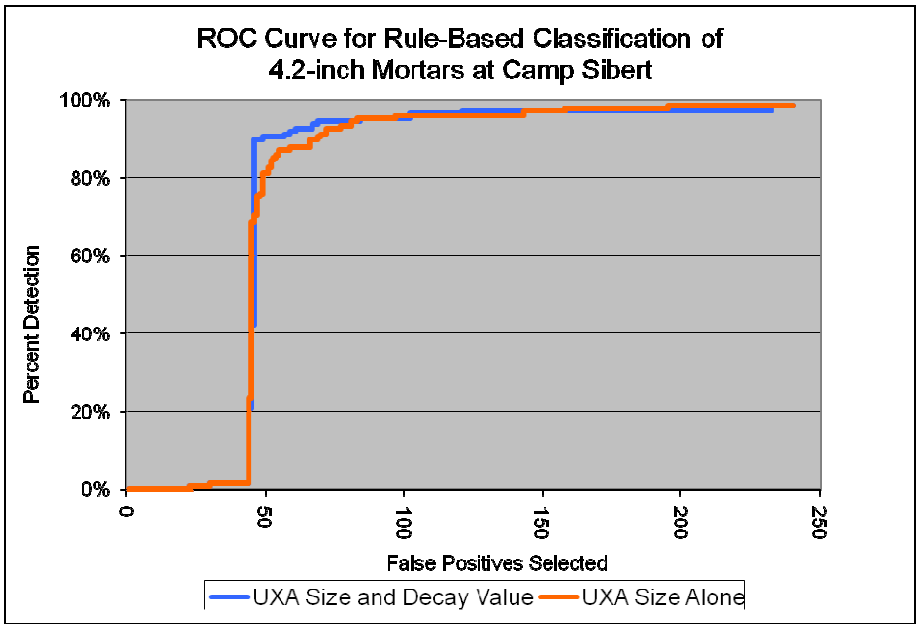

Figure 4. Size and decay are effective parameters when used to classify one unique munitions type.

Camp San Luis Obispo

In 2009, ESTCP invited demonstrators to participate in a study at Camp San Luis Obispo similar to the Camp Sibert study. The SLO site was selected for this second study due to its more difficult conditions: the terrain at SLO is not flat as at Camp Sibert, and the SLO site contains a range of munitions types to characterize from clutter. Each of the munitions types (2.36-inch rockets, 4.2-inch mortars, 60mm projectiles, and 81mm projectiles) has a unique size parameter.

This difference in site conditions made application of the size- and decay-based classification at Camp Sibert less appropriate for the SLO site. Because of the variety of munitions types at the SLO site, a single size parameter could not be identified for the classification of munitions from clutter. Figure 5 presents a scatter plot of size versus decay for the SLO site's ground truth targets. The targets of interest show a wide range of values, which overlap cultural debris and munitions debris size values. This is not surprising because the multiple types of munitions seeded at the SLO site have unique sizes. Attempts to define unique rules involving size per munitions type were unsuccessful at the SLO site due the range of size values observed per munitions type.

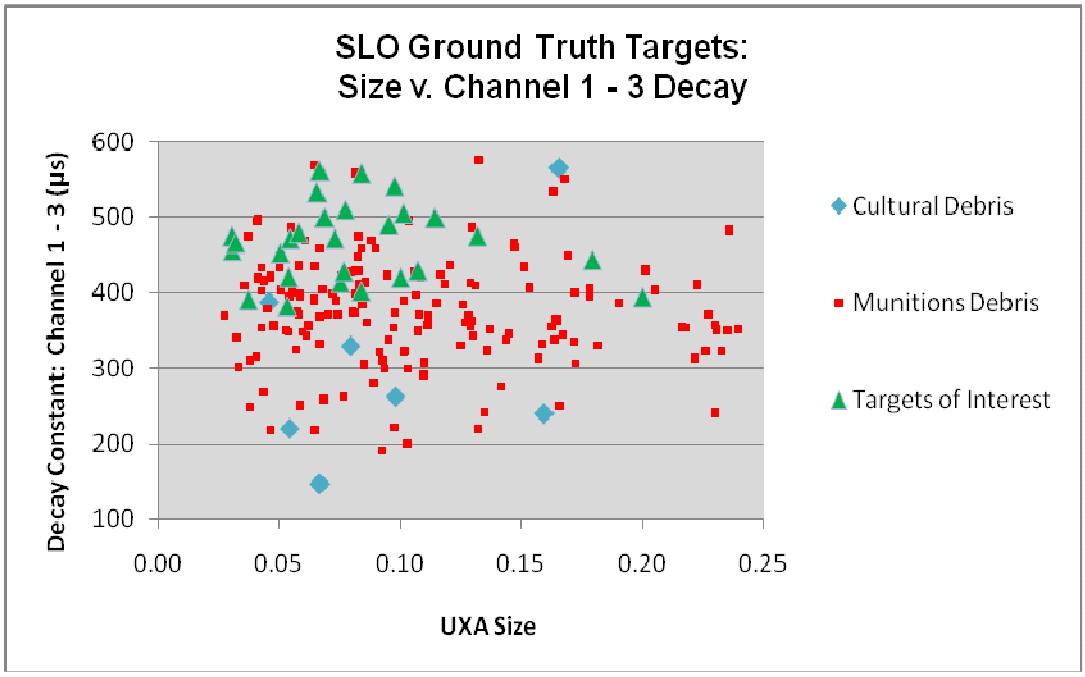

Figure 5. The range of size values for targets of interest overlaps those for clutter.

Figure 6 is a scatter plot of the same SLO ground truth targets using Channel 3 – 4 Decay versus Channel 1 – 2 Decay. This combination of target parameters showed the greatest partitioning of targets of interest from clutter. This is likely because two decay values used together are better than one in contrasting a target of interest (e.g., munitions) from clutter. Similar to the Camp Sibert study, a simple rule-based classification was developed based on these two decay constants.

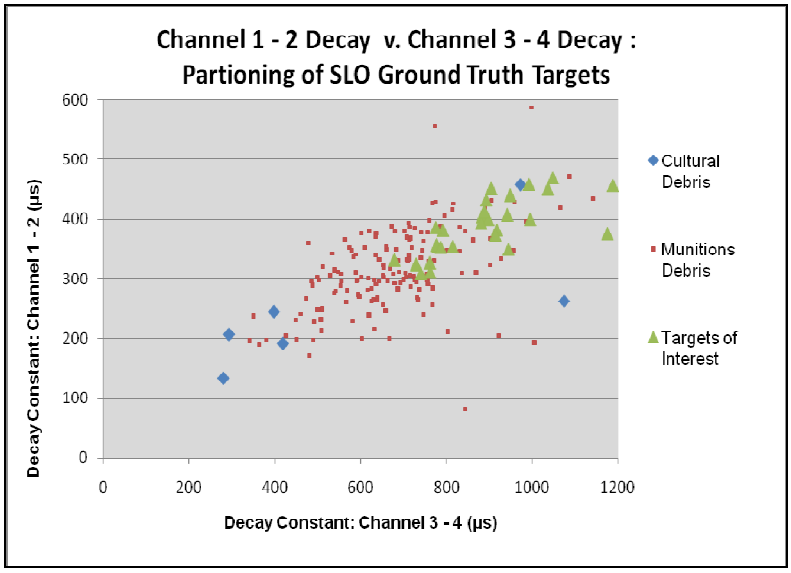

Figure 6. Two decay constants partitioned targets of interest from clutter.

Figure 7 presents ROC curves for the Camp Sibert and SLO sites for each site's ground truth data. Each ROC curve was made using the Camp Sibert rule-based classification of size and decay. These ROC curves illustrate the success of the size and decay rule-based classification for Camp Sibert with its singular munitions type, and how it is inappropriate to classify targets using a single size value at sites containing a variety of munitions types.

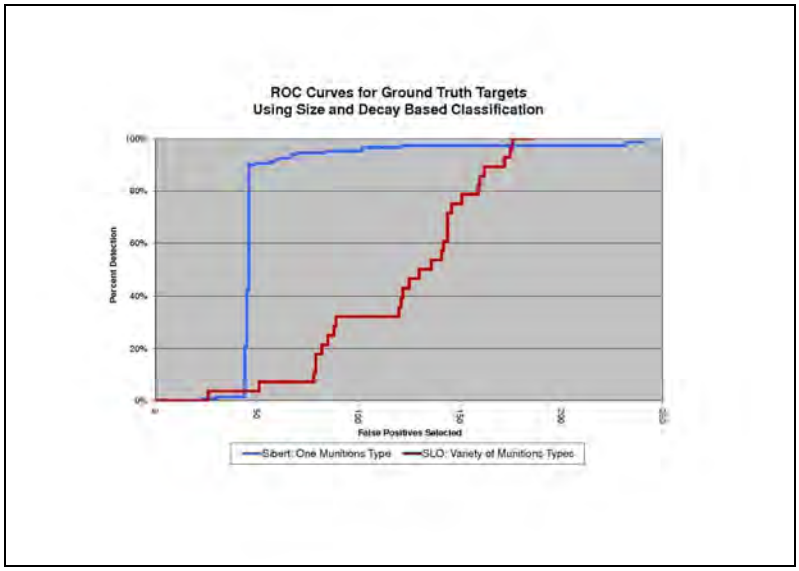

Figure 7: Efficacy of the size and decay rule-based classification at Camp Sibert and the SLO site.

Conclusions

The differences in the rule-based classifications between the Camp Sibert and the SLO sites serve as a case study in selecting parameters for target classification. The use of a single size parameter was successful at Camp Sibert due the single munitions type at this site. In reviewing the SLO site ground truth data, it was evident early that if size were to be used, unique values would be required per munitions type. In practice, this was not feasible due to the widely ranging sizes across munitions types. Future investigations will benefit from a thorough study of expected size values per munitions types, similar to the frequently used instrument response curves per munitions types. Additionally, use of size at any site will require adequate preparation for quality geophysical data, with due attention paid to positional data and data density. Significant improvements have been demonstrated by advanced electromagnetic induction techniques and instruments. However, size currently is of limited applicability for EM61-MK2 target classification at sites with clutter and munitions of similar size.

References

Environmental Security Technology Certification Program, April 2009, 2009 ESTCP UXO Classification Study, San Luis Obispo, CA.

Parsons, August 2009, Final Report of Environmental Security Technology Certification Program (ESTCP) UXO Discrimination Support Activities.

SELF-GUIDING ROBOTIC GEOPHYSICAL SURVEYING FOR SHALLOW OBJECTS IN COMPARISON TO TRADITIONAL SURVEY METHODS

Nathan Harrison, Parsons, Denver, CO
Bob Selfridge, U.S. Army Engineering and Support Center, Huntsville
Craig Murray, Parsons, Denver, CO
David Hodo, Auburn University, Auburn, AL

Abstract

The quality of geophysical data is a critical aspect of the digital geophysical mapping process. Human factors in geophysical mapping can affect navigation, background noise, and speed control, impacting data quality. An important issue facing MEC geophysicists is to find ways to limit these factors as a first step towards successful consistent reproducible geophysical surveying.

Human data acquisition errors can be significantly improved with self-guidance/robotic technology. ESTCP and the Huntsville Innovative Technology Program funded Auburn University to develop a path-following robotic vehicle to address those problems. Parsons worked with the Innovative Technology Program to perform the first technology transfer to a contractor of the government's semi-autonomous robotic Segway geophysical platform to a Remedial Investigation/Feasibility Study RI/FS MEC project at the former Great Salt Plains Bombing Range (GSPBR) in Alfalfa County, Oklahoma and a removal action at a former firing range within Camp Sibert, Alabama. To characterize two munitions response site's (MRS) during the RI/FS at the Great Salt Plains, a total of 16.5 acres of transect data and 12.1 acres of grid-based data were collected between 12/1/08 and 1/12/09 using time-domain electromagnetics (TDEM). Three methods of data collection included towing either two Geonics EM61-MKII coils with a self-guiding robotic system or a small utility vehicle, or one coil operated by a person. Two of these three methods, including the self-guiding robotic system and the one coil operated by a person, were also used to geophysically map the 20 acre range at Camp Sibert. This study compares the three methods based on overall performance, including geophysical prove-outs, data quality and productivity.

Site conditions and equipment problems inhibited productivity of the robotic system, however future improvements or careful site selection could make the self-guiding technology useful to UXO projects. The Great Salt Plains field tests identified system weaknesses and solutions, which were applied to the Camp Sibert project allowing for high production rates with the Segway System. The results of these projects indicate that the robotic system is a viable option for DGM on many future UXO projects.

Introduction

Robotic technology has been used in electromagnetic and other types of surveying. A robotic towing system and self-guidance software was developed by David Hodo at Auburn University with funding from ESTCP and the Huntsville Innovative Technology Program. Parsons used the robotic system at two sites, both of which involved investigating possible buried MEC and MD in the shallow subsurface. The first was the Great Salt Plains in Oklahoma where three collection methods were used to collect transect and grid data to characterize bombing targets. The second was a small site within Camp Sibert, Alabama, where two collection methods were used to collect data over a former range.

One of the reasons that all three methods were used at the Great Salt Plains was for the purpose of comparing data quality and productivity of the robotic system to traditional survey methods.

The team at Auburn University modified the Segway Robotic Mobility Platform (RMP) 400 to carry EM61-MK2's and real time kinematic (RTK) global positioning system (GPS) equipment and to develop control software that allows the RMP 400 to follow a preprogrammed path while towing one or multiple geophysical sensors. The Segway sensors, geophysical electronics, onboard computer, and batteries are mounted within a weather-resistant chassis. A Novatel Synchronous Position, Altitude, and Navigation (SPAN) integrated RTK GPS and inertial navigation system was mounted on top of the Segway chassis to provide positional data. Geophysicists from the USAESCH designed and constructed a trailer for two EM61-MK2 bottom coils to be towed behind the RMP 400. The trailer was constructed of fiberglass framing rods and bolts, and nylon nuts (Figure 1).

The team at Auburn University also developed the Segway Client software to interface with the Segway. The software can be used for mission planning (Figure 2), configuring, and monitoring the status of the Segway, controlling autonomous operations, and manual control of the Segway robot. Mission planning can be performed without a connection to the Segway onboard computer. A copy of the software must be running on the onboard computer to control the Segway.

Figure 1: Segway-towed geophysical system at the Auburn, Alabama, test area

The software is designed so that the operator can remotely upload, download and monitor information on the Segway from a field office computer as well as control the Segway manually using a remote interface. Communication with the Segway's onboard computer/sensors was accomplished with a pair of FreeWave HTPlus 900-megaHerz (MHz) radio modems. The video and differential GPS signals each used separate radio modems and antennae. All three signals (computer, video, and GPS) were received and/or sent via 3 decibels referenced to isotropic gain (dBi) antennas mounted on the center section of the robot chassis. The computer and GPS signals were received/sent on the remote interface end by directional Yagi antennas. The video signal was received by the remote display through a VFM ANTP1209 1.2-gigaHerz (GHz) directional panel antenna.

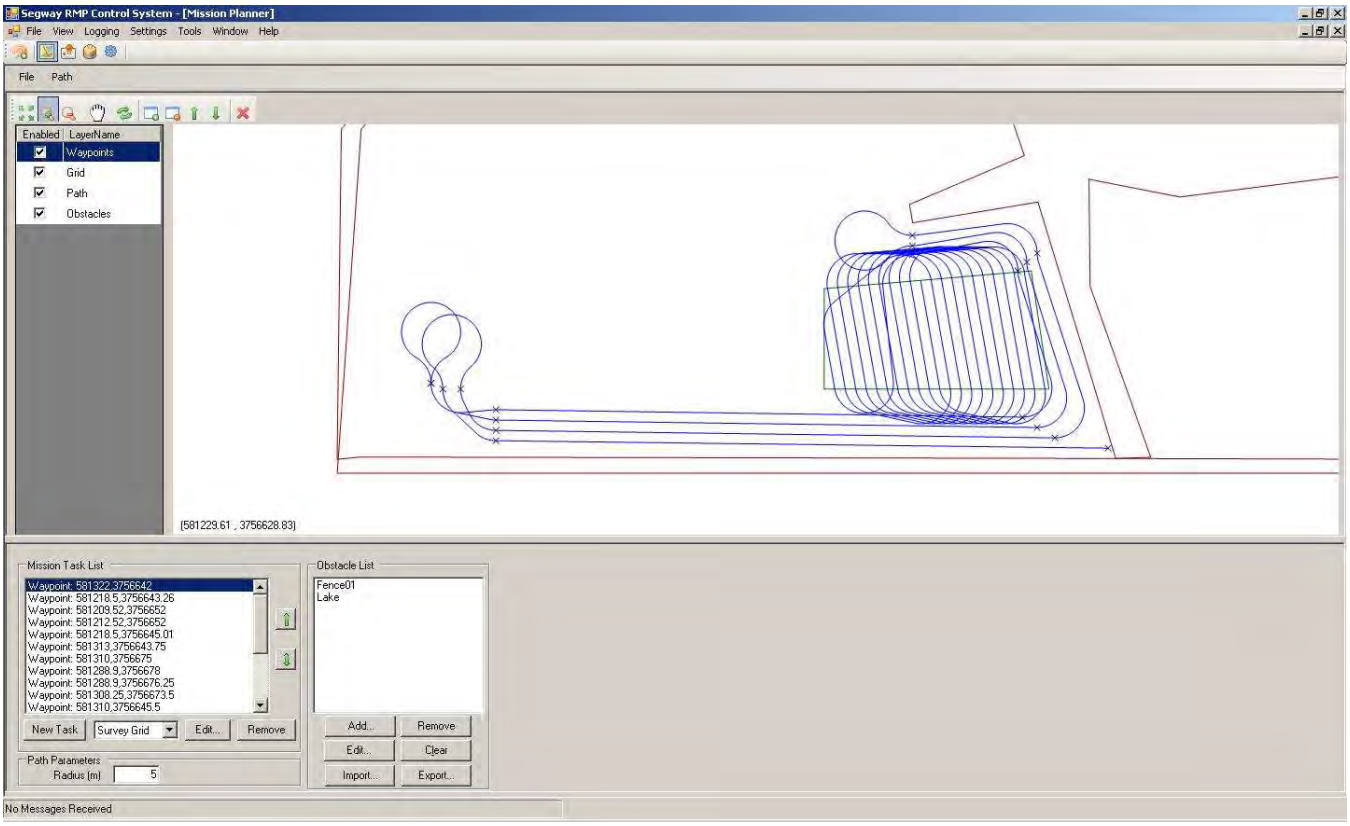

Figure 2: A screen capture of the mission planning software developed by the team at Auburn University for designing commands used to control the Segway Robot. Waypoints (marked by an "X") or Grids (outlined in green) are input by the user and the line path (blue) is calculated by the software.

The RI/FS at the Great Salt Plains called for collecting geophysical data across two former bombing ranges in the salt flats of northwestern Oklahoma, and included 15 acres of transects and 10 acres of grids. The data collection was split up between the man-portable, vehicle-towed, and robotic systems. Camp Sibert Site 20 contained many cultural obstacles (fences, ponds, etc.) which separated several open pastures. The removal action called for collection of geophysical data across the entire 20 acre site. The robotic system and to a lesser degree, a man-portable system, were used to collect approximately 20 acres of electromagnetic data with tightly spaced lines. The robotic system was used in the open pastures, and the man-portable system was used in areas with cultural features or other obstacles.

Performance Comparisons of the Segway Robotic System

Geophysical Prove-Outs

Data collected at the GPO with the Segway showed comparable results to hand-towed data. As shown in Table 1, the values from the total channel were very similar for the AN-MK23 3-pound practice bomb seed items buried at the Great Salt Plains GPO. The larger, deeper M38A2 100-lb practice bomb seed items produced higher-amplitude responses in the Segway and Vehicle-towed data. The width and time decay values did not show any significant difference between the two methods.

Table 1: GSP GPO Target Selections for Segway-towed, Hand-towed and Vehicle-towed Surveys

			Segway			Hand-towed			Vehicle-towed		
Item	Descri-ption	Depth (m)	Total (mV)	Time Decay (ns)	Width (µm)	Total (mV)	Time Decay (ns)	Width (µm)	Total (mV)	Time Decay (ns)	Width (µm)
GPO-1	AN-MK23	0.16	337.8	744.3	1.0	314.3	725.2	0.8	663.2	747.6	0.7
GPO-2	AN-MK23	0.20	152.1	661.5	1.2	112.4	669.4	1.3	211.8	686.5	1.2
GPO-3	AN-MK23	0.36	76.0	489.7	1.0	70.0	492.7	0.8	119.4	504.3	0.7
GPO-4	AN-MK23	0.38	49.7	606.5	0.8	40.1	525.6	0.6	110.8	555.8	0.6
GPO-5	M38A2	0.83	2579.3	554.5	1.6	1147.6	524.8	1.4	2885.2	564.9	1.4
GPO-6	M38A2	0.47	1494.4	873.6	1.1	775.4	801.4	1.2	1516.0	817.5	1.2
GPO-7	M38A2	1.19	284.0	686.5	1.7	144.3	656.7	1.7	391.3	666.0	1.5
GPO-8	M38A2	1.04	452.2	911.2	1.3	247.6	831.9	1.3	670.3	904.9	1.2

Table 2 shows the results for the Camp Sibert GPO. The values from the average channel were commonly between 1 and 3 orders of magnitude greater for the Segway-towed data than the Hand-pulled. The increased response from the Segway-towed data is probably because the Segway system used a two-coil array resulting in a higher transmit moment, and because the coils in the towed array rest about 19cm closer to the ground.

Table 2: Camp Sibert GPO Target Selections for Segway-towed and Hand-towed Surveys

			Peak Response, Average Channel (mV)	
ID	Item Description	Depth (in)	Segway-Towed Array	Man-Portable
1	Hand Grenade (Simulated)	6.13	20.8	8.0
2	Hand Grenade (Simulated)	5.94	22.1	9.9
3	Hand Grenade (Simulated)	8.99	7.1	5.5
4	Hand Grenade (Simulated)	9.80	15.2	4.9
5	Hand Grenade (Simulated)	13.55	7.5	2.8
6	Hand Grenade (Simulated)	11.11	10.2	2.9
7	4.2-inch mortar fuze	6	*	*
8	4.2-inch mortar fuze	9	*	*
9	4.2-inch mortar (Practice)	14.05	634.7	213.3
10	4.2-inch mortar (Simulated)	5.78	897.9	254.4
11	4.2-inch mortar (Simulated)	24.86	102.0	38.6
12	4.2-inch mortar (Practice)	20.34	87.9	39.2
13	4.2-inch mortar (Simulated)	42.94	5.7	2.7

ID	Item Description	Depth (in)	Peak Response, Average Channel (mV)	
			Segway-Towed Array	Man-Portable
14	4.2-inch mortar (Simulated)	44.00	8.5	2.8
15	Rifle Grenade (Practice)	8.62	2.5	10.4
16	Rifle Grenade (Practice)	9.36	47.9	15.6
17	Rifle Grenade (Simulated)	10.02	58.3	23.8
18	Rifle Grenade (Simulated)	10.45	55.5	23.3
19	Rifle Grenade (Simulated)	15.11	13.4	10.3
20	Rifle Grenade (Simulated)	16.13	10.0	7.3
21	2.36-inch rocket (Practice)	8.74	61.1	24.6
22	2.36-inch rocket (Practice)	14.17	51.9	13.0
23	2.36-inch rocket (Practice)	14.36	41.8	16.0
24	2.36-inch rocket (Practice)	11.64	39.9	17.3
25	2.36-inch rocket (Simulated)	20.81	29.6	10.0
26	2.36-inch rocket (Simulated)	23.24	21.8	7.5
27	Mustard Mine (Simulated)	11.84	7.1	2.9
28	Mustard Mine (Simulated)	12.07	*	*
29	One 30-gallon drum	37.94	411.0	126.0
30	Three 30-gallon drums	37.04	515.4	194.1
31	4.2-inch mortar half-shell	11.86	106.0	72.3
32	4.2-inch mortar half-shell	8.93	214.2	95.3
33	4.2-inch mortar half-shell	5.88	226.0	165.0
34	4.2-inch mortar half-shell	7.67	384.7	265.1
35	4.2-inch mortar half-shell	12.53	170.8	72.6
36	4.2-inch mortar half-shell	16.84	140.8	48.7
37	4.2-inch mortar half-shell	21.16	33.0	19.1
38	4.2-inch mortar half-shell	19.56	23.6	17.2
39	4.2-inch mortar half-shell	8.06	198.6	139.6
40	4.2-inch mortar half-shell	10.18	115.8	83.5
41	4.2-inch mortar half-shell	22.92	37.1	17.3
42	4.2-inch mortar half-shell	21.91	37.7	19.9

Data Quality

Several methods were used to check the quality of the data for both projects. The background geophysical noise levels were calculated from the standard deviation of total (Great Salt Plains) or average channel (Camp Sibert) measurements over a background region with no anomalies. The noise levels measured from the Segway-towed system were consistently low at the Great Salt Plains (i.e., > 2 millivolts [mV]), while the other two systems showed at least one or two days of elevated noise levels (Figure 3). The person-towed data showed some of the highest noise levels of the three methods at the Great Salt Plains. The vehicle-towed system showed its lowest noise levels on the days in the GPO grid (day 1) and the practice target area (days 5, 6, and 7), which were the flattest parts of the GSPBR.

The effects of terrain were also evident from the noise levels calculated at Camp Sibert (Figure 4). Noise levels from the Segway data were consistently higher than the hand-towed datasets, a reverse of the results from the Great Salt Plains. The hand-towed data was predominantly collected around

cultural features or in front and back yards (save for days 1 and 5 in which data was collected in the open fields), whereas the Segway data was collected in open fields used for cattle grazing. As a result of the grazing, the open pastures have a much rougher terrain, combined with the increased speed of the Segway system would account for the increased noise. However, the noise levels from both methods proved adequate for the project.

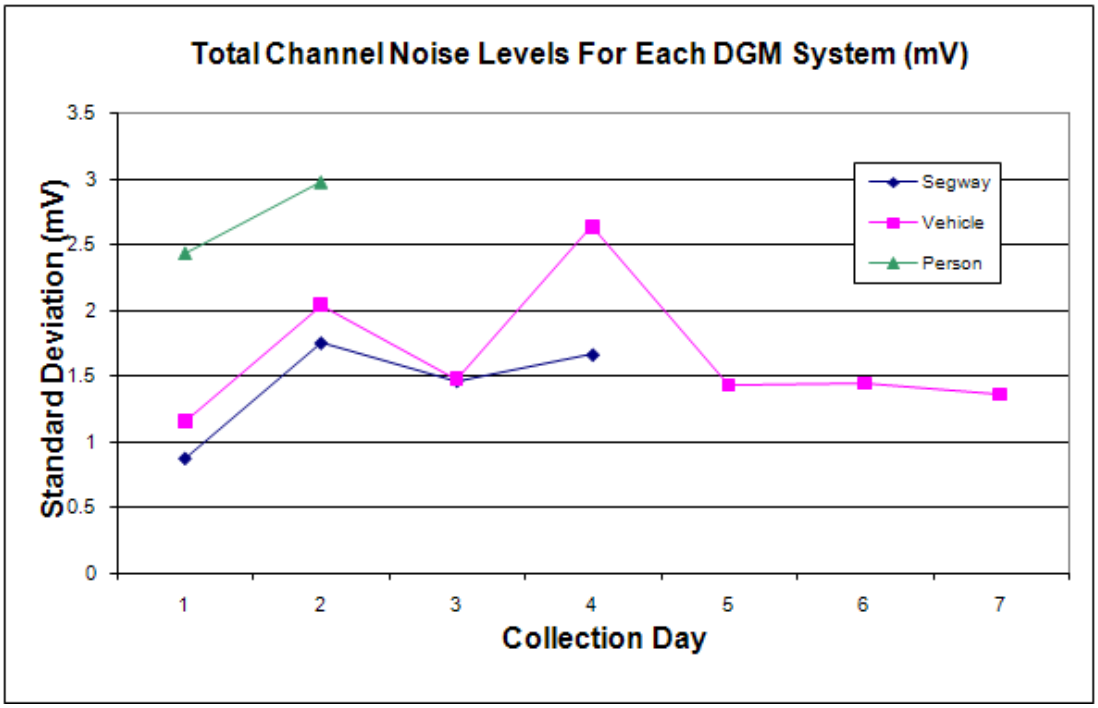

Figure 3: Noise level comparison by collction day from three methods of data collection at the GSP.

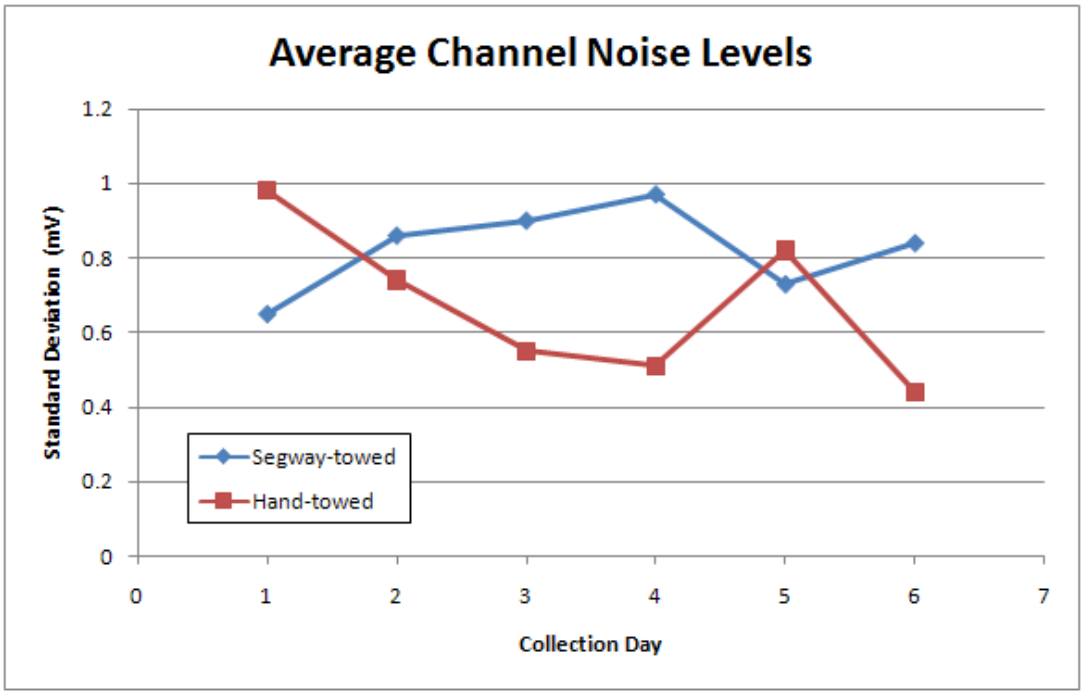

Figure 4: Noise comparison by collction day from two methods of data collection used at Camp Sibert.

Data quality was also assessed through GPS position tests for the three data collection systems used at the Great Salt Plains (hand-towed, vehicle-towed, and Segway-towed). The Segway GPS position test results were more consistent than the other systems (Figure 5). As shown in Table 6, the first GPS position tests with the vehicle- and hand-towed systems resulted in higher offset results than the systems were later shown capable of achieving. After the initial problems, the operators guided the sensors more accurately, resulting in consistent GPS position tests, whereas the Segway data had removed this human error from the start.

One of the GPS position tests was significantly higher than the others, however, due to a mechanical issue with the towing mechanism. There is a back-and-forth, or wiggle, in the positional line path of the Segway data that is caused by the movement of the hitch while the Segway is moving forward in a straight line. Although the wiggle of the hitch causes little movement of the coils at the back of the trailer, it is recorded by the hitch-angle sensor at the top of the Segway chassis used to calculate the position of the coils. The hitch wiggle caused the positional offset observed on the fourth day of data collection (Figure 5). The hitch wiggle could be removed by applying a low-pass filter to the x and y position channels during processing. Although this correction was not applied at the Great Salt Plains, there was some success in its use at Camp Sibert.

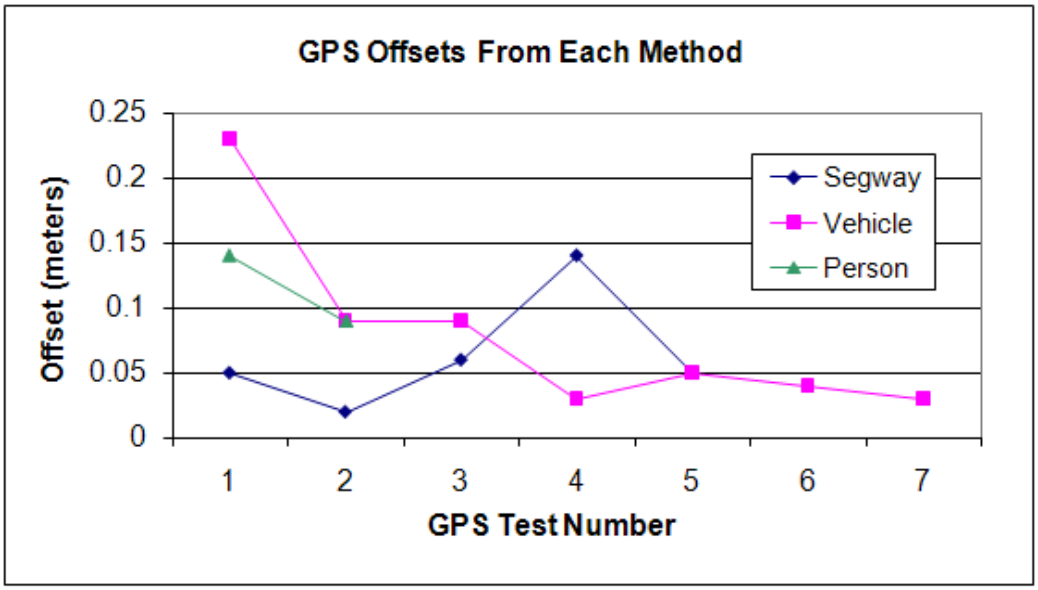

Figure 5: Comparison of GPS offsets from the GPS QC check at the GSP for three collection methods.

Remapping

Some of the data at the Great Salt Plains was mapped with both the Segway-towed and man-portable systems for a side by side comparison. A 50-foot by 50-foot grid of data for both systems is shown in Figure 6. All of the remapped data indicated lower noise levels in the Segway-towed data than for the hand-towed method. There are also fewer negative spikes in the Segway-towed data, which may be a result of the sturdier trailer and more consistent towing force of the Segway which would help to decrease noise caused by rough terrain. Many of the negative spikes were caused by topographic changes (e.g., dry creek channels), which seem to affect the hand-towed method more than the Segway system. Furthermore, one anomaly only shows up in the Segway-towed data (about 25 mV in the total channel) to the west of the larger anomalies in Figure 6.

A comparison of the time required to collect data over the three remapped grids was based on the data file time stamps (including transit time between grids). The Segway-towed system took 1.5 hours to collect three 100-foot by 200-foot grids, approximately 1.4 acres, resulting in a 0.93 acre per hour rate. The hand-towed system collected three 100-foot by 100-foot grids (0.7 acres) in 3.75 hours, resulting in a 0.19 acre per hour rate.

One would expect higher data acquisition efficiency when collecting data over larger areas (100-foot by 200-foot grid vs 100-foot by 100-foot grid), but this does not explain the nearly five-fold increase in production rate. The large difference between the production rates demonstrates how much more efficient the Segway-towed system could be if problem-related downtime could be eliminated. Parsons attributes increased production rate of the Segway system to the following factors:

- The Segway-towed system used two EM61-MK2 sensors, effectively covering twice as much area with each pass.
- The Segway-towed system followed a preprogrammed path to cover all three grids, while the hand-towed system operator took longer to transfer from one grid to another.
- The Segway-towed system travelled at 1.5 meters per second (m/s) compared to 0.85 m/s for the hand-pulled system.
- The Segway-towed system used GPS positions to navigate the grid, while the hand-pulled operators took time to lay out tape measures and traffic cones to guide data acquisition.

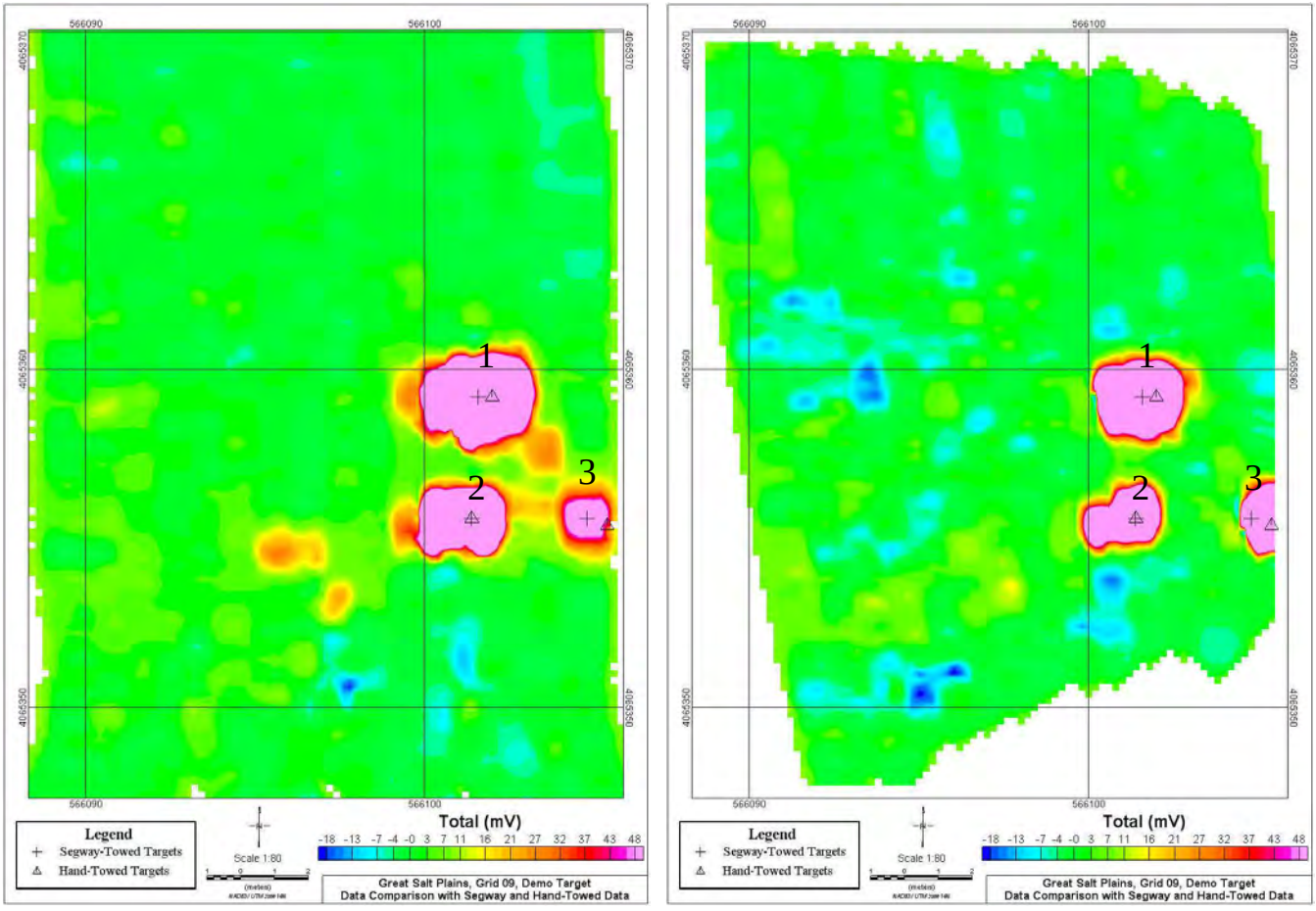

Figure 6: A side-by-side comparison of Segway Robot-towed data (left) and hand-pulled data (right) from the same grid at the GSP.

Production

The production by acre of each collection method was measured by day at each of the project sites and for each collection method for comparison. The production was calculated by acre of the instrument line path and the width of the instrument added. The production comparison results are shown in Figures 7 and 8.

The average Segway production at the Great Salt Plains of 2.2 acres per day was lower than the vehicle-towed average of 3.5 acres per day. The main reasons for the lower production by the Segway-towed system were problems with insufficient radio communication range and negative effects of the cold weather on the Segway batteries. The clearest and flattest areas were on the northern end of the field area at the practice bombing target, and only the vehicle-towed system was used in this area. The vehicle-towed system attained the highest production days on the project (days six and seven) while in this area. The one day of hand-pulled data showed significantly lower production due to speed, setup time, and the single sensor vs. dual sensor design.

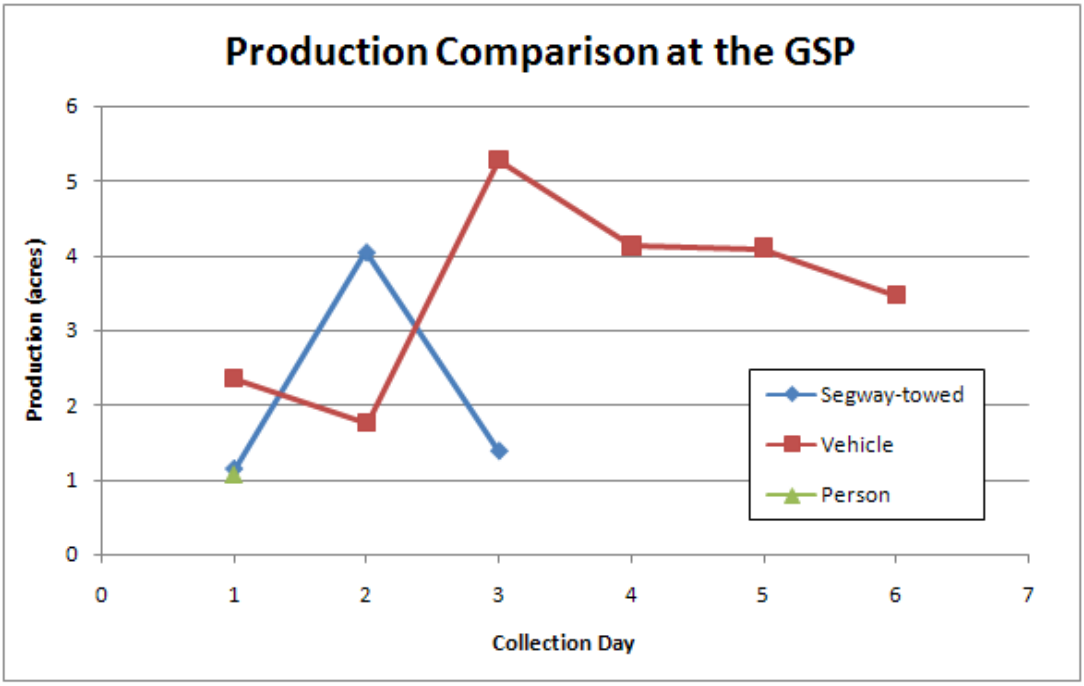

Figure 7: Production data from the GSP for three methods of data collection.

The average Segway production at Camp Sibert of 2.5 acres per day was much higher than the hand-towed average of 0.7 acres per day. As previously stated, the main reasons for the higher production of the Segway-towed system are the two coil systems superiority, path following software, and acquisition speed. There were, however, some days of low production from the Segway system due to equipment problems, most of which could be attributed to mechanical issues rather than software problems. The results of the production analysis at Camp Sibert indicate that the Segway is capable of achieving values comparable to what the vehicle-towed system achieved at the Great Salt Plains.

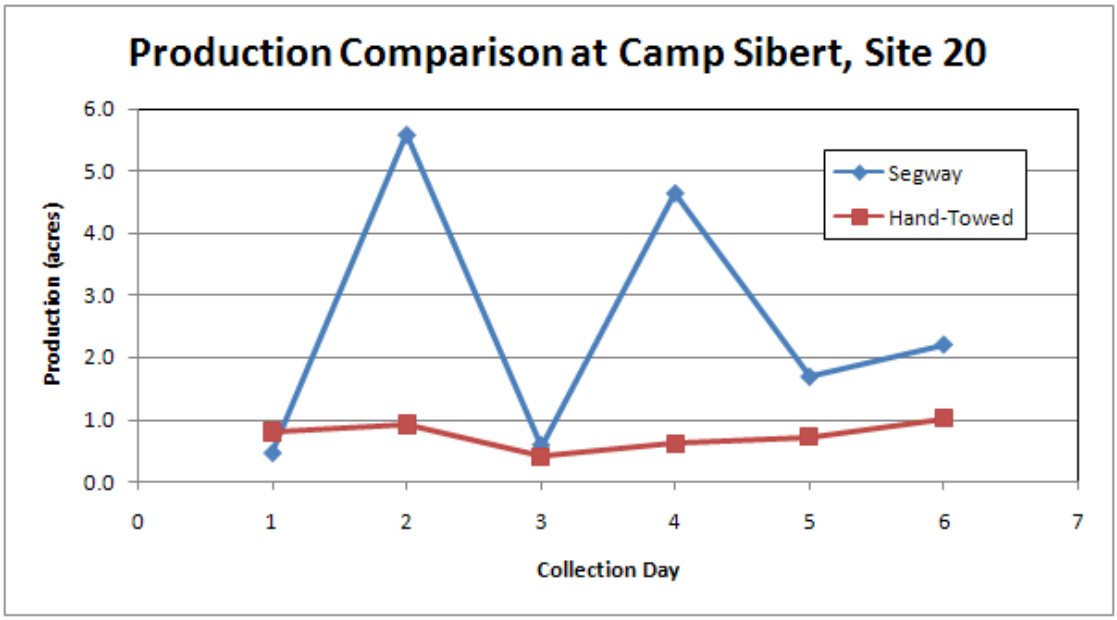

Figure 8: Production data from the GSP for two methoeds of data collection.

Conclusions

Additional testing may be required for using the Segway in certain conditions. Because the current antenna setup has not been tested for maximum range, additional tests should be run if the remote interface location is to be placed more than 1.5 miles from the survey area. Because of the low clearance of the Segway, further tests should be run to test the weather-resistant chassis if the Segway is to be used in areas with significant water. Furthermore, the Segway is not recommended for use at temperatures below 20 degrees Fahrenheit.

Production and cost of the Segway-towed system show potential for its use as a viable option for digital geophysical mapping on MEC projects. For the Great Salt Plains project, there was no significant cost difference between the vehicle and Segway systems in field personnel, so most of the value of the Segway was in its potential to increase production. Higher production values are possible because the self-navigating software would eliminate field/grid setup time. Also, one less person may be necessary for future Segway operations if less troubleshooting is required or the survey area is closer to the base station. These and other lessons learned from the Great Salt Plains were applied at Camp Sibert to attain the highest production rates yet with the Segway-system, and indicate that it is able to match or surpass a vehicle-towed production value.

MULTI-CHANNEL ANALYSIS OF SURFACE WAVES: AN APPLICATION TO MONTANA FIELD DATA

Soumya Roy, Graduate Student, University of Houston, Houston, TX
Dr. Robert R. Stewart, Professor, University of Houston, Houston, TX

Abstract

The multi-component (3C or 4C) seismic method is being used to more fully capture the seismic wavefield and to generate complementary P-wave and S-wave (PS) images of the subsurface. One of the complicating issues in processing PS data is the effect of receiver statics. The S-wave receiver static can be quite large due to low S-wave near-surface velocities. We are thus interested in techniques to estimate the shallow S-wave velocity (Vs) structure. The analysis of surface waves (especially Rayleigh waves) has been useful to delineate Vs in near-surface. Multi-Channel Analysis of Surface Waves (MASW) uses the dispersion properties of Rayleigh waves to create a dispersion curve (Park et al., 1998), then S-wave near-surface velocity profile (Xia et al., et al., 1999). We have applied the MASW method to seismic datasets from Elk Basin Oilfield in Bighorn Basin, Montana/Wyoming acquired by students of University of Houston. Vertical and horizontal component seismic lines are analyzed. Preliminary results show extracted S-wave velocities for vertical and horizontal component lines varying between 400-1000 m/sec.

GROUND PENETRATING RADAR INVESTIGATION OF DINOSAUR QUARRIES IN MORRISON, COLORADO

Renee Francese, Colorado School of Mines, Golden, CO
Orion Sandoval, Colorado School of Mines, Golden, CO

Abstract

Students conducting the investigation are doing so through the Colorado School of Mines Undergraduate Geophysics curriculum as a senior project. Investigation has been done in Morrison, Colorado for similar purposes, however little geophysical data has been collected in the area of interest. The goal of this project is to image the dinosaur bones and model the sandstone to mudstone boundary, where the extent of dinosaur bones has been found. A quarry about 100 feet to the north of the site has been previously excavated to find large dinosaur artifacts. The director at the Morrison Museum of Natural History, Matt Mossbrucker, has reason to believe that Quarry XYZ will contain dinosaur artifacts based on geology trends, bone fragments found at the surface, and notes by Arthur Lakes (A. Hunt, M. Lockley, S.White, 2002). By experimenting with different antennas and other GPR equipment, the students will find the optimal setup to better model the geology boundaries and find large targets beneath the surface up to depths of 10-15 feet. The data collected will be useful in further understanding the geology and ability to locate dinosaur artifacts in the Morrison area.

References

A. Hunt, M. Lockley, S. White, *Historic Dinosaur Quarries of the Dinosaur Ridge Area.* A publication of the Friends of Dinosaur Ridge and the University of Colorado at Denver Trackers Research Group, 2002

FRACTURE IMAGING IN THE UPPER KAMA POTASH MINE USING 3-D GPR DATA

Oleg N. Kovin, Missouri University of Science and Technology, Rolla, MO

Abstract

Fracture detection and delineation is very important for salt mines operation because fracturing significantly increases the probability of failure of supporting pillars and overlaying water protective beds.

Results of forward modeling studies confirmed the feasibility of georadar with a 400 MHz antenna to reliably detect the millimetric scale fracture.

3-D GPR data were acquired in the potash mine near the city of Solikamsk, Russia to evaluate the effectiveness of imaging technology to detect and delineate the fractures in heterogeneous salt rock. Continuous common-offset data were obtained at seven parallel profiles across the fracture exposed in the wall of a mine pillar. The pillar was 4.5 m thick and comprised of interbedded layers of salt rock and clay. The open millimetric scale subvertical fracture crosscuts the pillar at angle of 25°.

Data were collected using commercial OKO georadar system (Logis, Russia) with a 400 MHz shielded antenna. ReflexW and OpendTect software were used for processing and interpretation of the 2-D radargrams and combined 3-D data set.

The 3-D migration allowed generating a true image of subsurface structures and creating a spatial model of fractures. Using the image of known fracture as interpretation template, fracture having no surface evidence was detected.

Introduction

The stability of the rock mass is a function of the distribution of discontinuities and their spatial parameters, such as surface geometry, opening and orientation. Sudden failure of supporting pillars and fracturing in impermeable overlaying rocks pose a danger of flooding or even gradual to catastrophic collapse at the ground surface at the salt mines (Jeremic, 1994; Whyatt, 2008).

Mining engineers need the information about the bulk properties of relevant rock mass to successfully mitigate potential structure damage. More specifically, they need to know the spatial distribution, shape, size, opening and orientation of fracture discontinuities in order to develop appropriate remediation strategies.

Geophysical methods, particularly GPR, are increasingly being used to determine bulk rock properties, because these tools are non-invasive, less expensive and safer than conventional direct methods such as drilling. They are also more effective when large areas require high-resolution assessment.

The successful application of 2-D GPR technologies for fracture detection and characterization is reported in numerous publications. Annan et al. (1988) used GPR to map fractures in Canadian potash mines. Buursink and Lane (1999) mapped vertical and dipping fractures in road cuts, and Grandjean and Gourry (1996), and Grasmueck et al. (2004) investigated fracture zones within a quarry.

A number of geological, engineering and archeological publications (Czerbiak et al., 2001; McMechan et al., 1997; Nuzzo et al., 2002; van der Kruk et al., 2003) show improving of the fracture characterization using a three-dimensional imaging technique.

This study presents the use of 3-D GPR imaging technology for fracture investigation within rock pillar in a potash mine. The experimental 3-D GPR data were acquired in the Solikamsk mine 3 of the Joint Stock Company (JSC) "Silvinit", located near the city of Solikamsk, Russia. Common-offset GPR data were collected at seven parallel profiles across the fracture (Figure 1) exposed during the mine operations within a 4.5 m wide pillar.

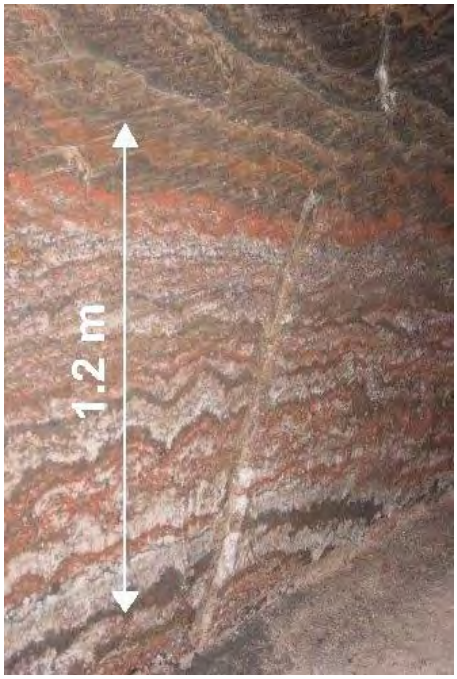

Figure 1: Fracture used for testing intersects the mine pillar comprised of folded salt rock and clay layers at angle of approximately 25°. Seven lines spaced 0.2 m apart were set up parallel to the floor of mine opening.

The heterogeneous pillar body consists of interbedded strongly folded potash salt, rock salt and parting clay layers. The millimetric scale fracture crosscuts the pillar at angle of approximately 25°. Opening of the fracture gradually decreases in upward direction and upper visible part of fracture is closed that provide an opportunity to examine the sensitivity and resolution of the method.

This fracture is a part of a system of natural fractures exposed also in adjacent mine workings. Natural millimetric to centimeter scaled fractures are distributed over an area of approximately 400x100 m, and are spaced-apart at distance of a few to tens meters (Kudryashov et al., 2004).

In order to test the ability of detection of the upper edge of fracture, the observation area was expanded beyond its visible portion.

Data acquisition

The GPR data were acquired using the commercial georadar system OKO manufactured by the Logis (http://www.geotechru.com/file/oko2manual_en_2009.pdf). A 400 MHz shielded antenna was used providing both the necessary resolution and penetrating depth of investigation (Figure 2).

The 400 MHz antenna was chosen experimentally in order to demonstrate clear reflection from opposite side of pillar at 5 m distance and capability to detect the millimetric scale fracture.

The 3-D GPR data were acquired along seven horizontal parallel profiles of 8 m in length and spaced at 0.2 m intervals, oriented across the fracture exposed in the wall of pillar. Constant-offset continuous profiling mode with 0.05 m trace spacing was used. The routine of the GPR data acquisition in potash mine is shown in Figure 3.

Figure 2: Assembling the 400 MHz georadar antenna for mine measurements.

Figure 3: Ground penetrating radar operation in the potash mine.

The site with the smooth surface was chosen for the measurements. The total study area was 8 x 1.2 m of size. The topography corrections were not applied to the GPR data because of the flat surface of the test site.

Data processing

The recorded data were processed and interpreted using the ReflexW and OpendTect software.

Before 3-D migration, the raw 2-D GPR data were processed to reduce the noise affecting the quality of migration procedure. Then three-dimensional Kirchhoff migration algorithm was used for construction of the 3-D data volume.

Because of good quality of raw data the processing flow included only most common steps:

- correction of time delay at the beginning of each trace (zero-time correction);
- "*dewow*" filtering to suppress the very low-frequency noise;
- subtracting the average amplitudes over a sliding window in the time interval of first arrivals to remove the air and ground direct waves;
- exponential gain correction to improve weak signals preserving a true amplitude contrast.

After 2-D processing with ReflexW software, the georadar data were converted to the SEG-Y format and loaded to OpendTect seismic post-processing and interpretation system.

An image of subsurface structures was produced using 3-D Kirchhoff migration program of the Madagascar data processing plugin available in the Linux version of the OpendTect system.

The raw data show that the direct air wave, direct ground wave and the reflections from the fracture and wall of adjacent mine working are the most regular events on a radargram (Figure 4). The random and semi-random noise is presented by the scattered waves from the irregular surface of folded layers and small-size heterogeneities in salt rock.

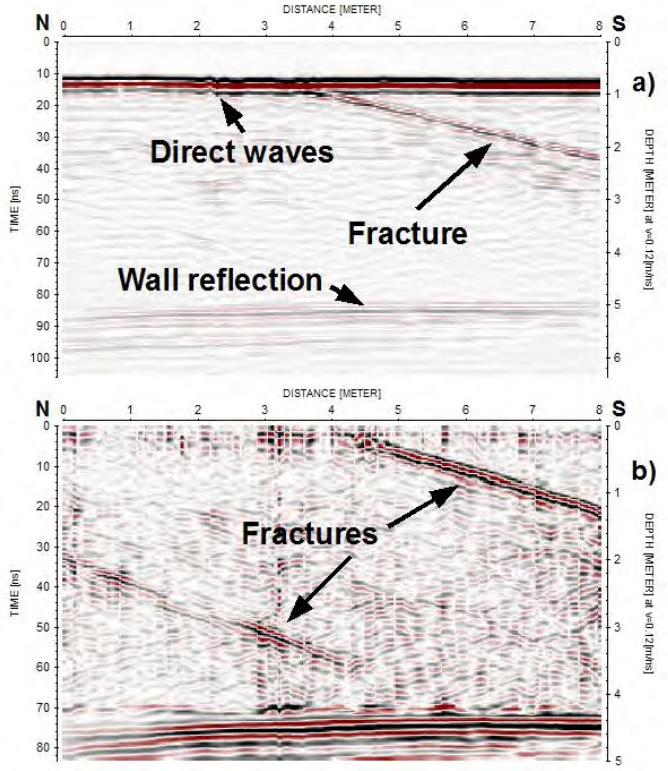

Figure 4: Example of 2-D data obtained at Line 5: (a) raw record, (b) processed data. Note that after processing a prominent reflection from second fracture is clearly identified.

The constant propagation velocity of 0.12 m/ns was used for data processing and depth calculation. The value of propagation velocity was based on the results of previous walk-away sounding and the known distance to the opposite wall of pillar. The salt rocks are having the uniform properties over the deposit so usage of constant velocity is assumed reasonable.

The migration procedures are very sensitive to signal-to-noise ratio. Noisy data often lead to generation of numerous artifacts, which make the georadar data difficult to interpret. Hence corresponding efforts were made to reduce noise level first.

Subtracting the average amplitude defined over sliding window was used to suppress the direct wave. Conventional background removal procedure proved less effective because of considerable variation of parameters of direct wave along the radargram. The window of 10 traces length in the time interval of direct wave was implemented.

After loading to OpendTect system, the data were migrated using a 3D Kirchhoff migration algorithm. Constant velocity 0.12 m/ns was used for migration. The 3-D volume (Figure 5) was constructed and analyzed.

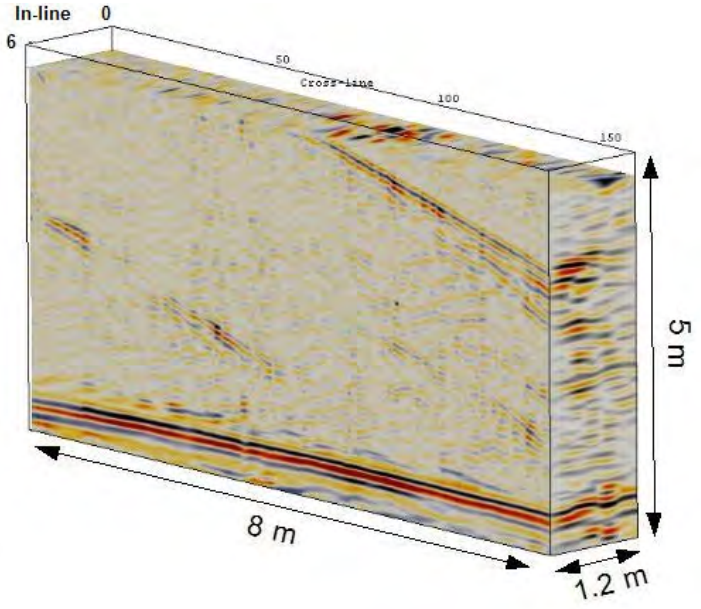

Figure 5: Three-dimensional data volume calculated using 2-D GPR profiling data. The reflections from visible and suspected fractures are clearly identified.

Using calculated three-dimensional volume, the time/depth slices and X, Y, Z cuts were built and the structures of interest were picked through the data volume to create a digital spatial model of subsurface.

Interpretation and results

The FDTD modeling study of the response of fracture was performed. The model of air filled fracture of 1 mm opening and having the dipping angle of 25° was used. Modeling results have confirmed that 400 MHz electromagnetic signals are capable to produce a prominent reflection from the millimetric scale fracture (Figure 6).

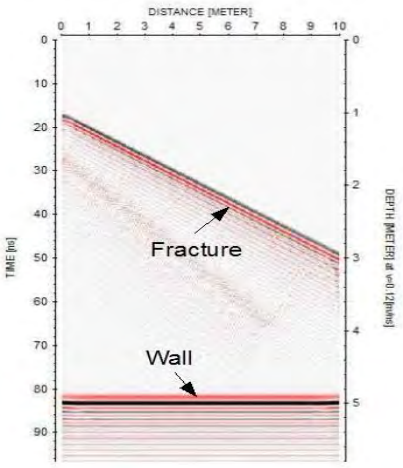

Figure 6: FD modeling of air filled fracture of 1 mm opening embedded in material having properties of salt rock. The opposite wall of pillar was included in model for comparison.

Despite poor binning caused by the limited number of parallel profiles, the 3D processing significantly improved the interpretability of the GPR data. The random noise was also effectively suppressed. Three-dimensional migration increased the reliability of fracture detection and delineation. The panels of in-line images shown in Figure 7 give evidence of gradual decay of amplitude of reflection at the edge of fracture. At in-line 0 the amplitude from the fracture is compared to the noise level. It suggests the fracture is closed at this area, which is consistent with visual observation.

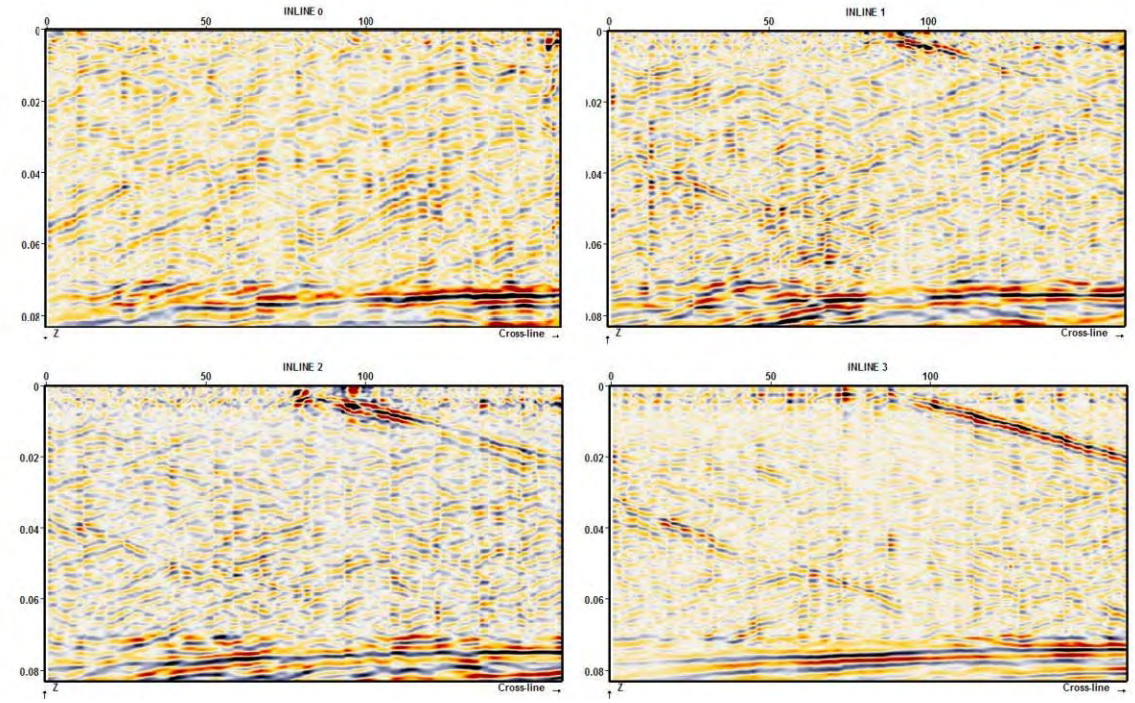

Figure 7: Panels of inline (0-3) images show the gradual decay of amplitude of reflection from the fracture that suggests decreasing of its opening. The fracture is closed at the Line 0.

Using orientation, amplitude, and continuous signature of the exposed fracture as an interpretation template, the reflector between 2 and 4 m depth was interpreted as fracture. This feature is not exposed on the wall; however the orientation, continuity and geometry of this reflector are consistent with those characterizing the known fracture. Significant amplitude variation along this reflection is interpreted as a variation in the fracture opening.

Finally a spatial model of subsurface structures was created using semi-automatic picking of the events through the volume (Figure 8).

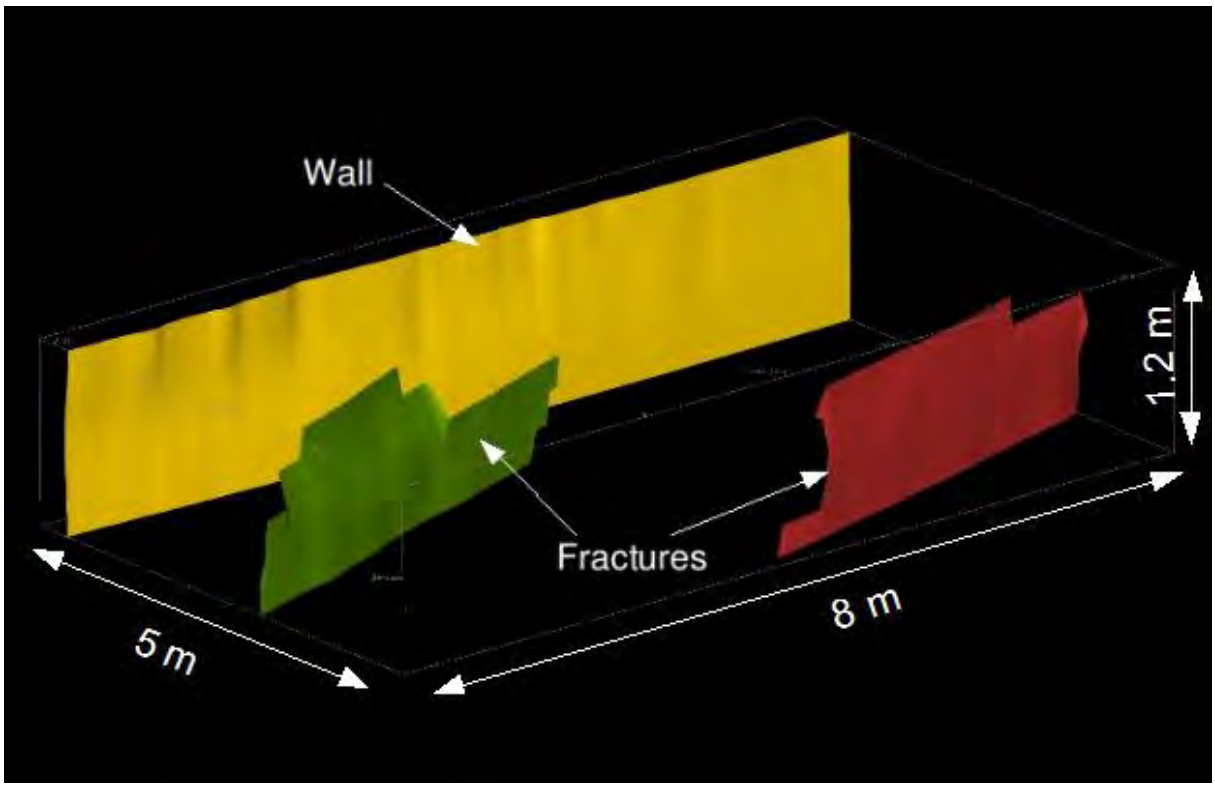

Figure 8: Spatial model of subsurface structures derived from the 3-D GPR image. Orientation of data volume is changed with respect to the original orientation of the observation plane at the wall of pillar.

Conclusions

The experimental study was conducted in the Solikamsk Potash Mine 3 to evaluate the effectiveness of 3-D GPR data for fracture detection and delineation in heterogeneous salt rock mass. Data were acquired across the millimetric scale subvertical fracture that intersects a 4.5 m wide pillar.

The processing flow applied to GPR data allowed effective reducing noise levels, enhancing weak reflections, and creating 3-D true geometry image of subsurface. The 3-D data processing considerably improves the fracture detection and delineation. The fracture, not evident on the surface, was detected using the characteristics of known fracture as the interpretation template.

The spatial models of the subsurface structures were created in the form suitable for easy import to engineering software for further geomechanical calculations.

The results of study show that the 3D imaging technique has proven to be an effective tool for mapping of the millimetric scale fracture in heterogeneous media.

References

Annan A.P., Davis J.L., Gendzwill D., 1988, Radar sounding in potash mines, Saskatchewan, Canada: Geophysics, Vol. 53, No. 12, 1556-1564.

Czerbiak, R.B., McMechan, G.A., Corbeanu, R., Forster, C., Snelgrove, S.H., 2001, 3-D characterization of a clastic reservoir analog: From 3-D GPR data to a 3-D fluid permeability model: Geophysics, Vol. 66, No. 4, 1026-1037.

Buursink, M., Lane, J., 1999, Characterizing fractures in a bedrock outcrop using ground-penetrating radar at Mirror Lake, Grafton County, New Hampshire: *in* Morganwalp, D.W. and Buxton, H.T., eds., U.S. Geological Survey Toxic Substances Hydrology Program: Proceedings of the Technical Meeting, March 8-12, 1999, Charleston, South Carolina: USGS Water-Resources Investigations Report 99-4018C, v. 3, pp. 769-776.

Grandjean, G., Gourry, J.C., 1996, GPR Data processing for 3D fracture mapping in a marble quarry (Thassos, Greece): Journal of Applied Geophysics, 36, 19-30.

Grasmueck, M., Weger, R., Horstmeyer, H., 2004, Three-dimensional ground-penetrating radar imaging of sedimentary structures, fractures, and archeological features at submeter resolution: Geology, Vol. 32, No. 11, 933-936.

Jeremic, M.L., 1994, Rock mechanics in salt mining. A. A. Balkema, Rotterdam.

Kudryashov, A.I., Vasyukov, V.E., Von-der-Flaass, G.S., Ikonnikov, E.A., Gershanok, V.A., Gershanok, L.A., Glebov, S.V., 2004. Rupture tectonics of the Upper Kama (Verkhnekamskoye) rock salt deposite. Mining Institute of Ural Branch of the Russian Academy of Sciences & Perm State University, Perm (in Russian).

McMechan, G.A., Gaynor, G.C., Czerbiak, R.B., 1997, Use of ground-penetrating radar for 3-D sedimentological characterization of clastic reservoir analogs: Geophysics, Vol. 62, No. 3, 786-796.

Nuzzo, L., Leucci, G., Negri, S., Carrozzo, M. T., and Quarta, T., 2002, Application of 3D visualization techniques in the analysis of GPR data for archeology: Annals of Geophysics, Vol. 45, No. 2, 321-337.

Van der Kruk, J., Wapenaar, C., Fokkema, J., van der Berg, P., 2003, Three-dimensional imaging of multicomponent ground-penetrating radar data: Geophysics, Vol. 68, No. 4, 1241-1254.

Whyatt, J.K., Varley, F.D., 2008, Catastrophic failures of underground evaporite mines: *in* Peng, S.S., Mark, C., Finfinger, G.L., Tadolini, S.C., Khair, A.W., Heasley, K.A., Luo-Y, eds., Proceedings of the 27th International Conference on Ground Control in Mining, July 29-31, 2008, Morgantown, West Virginia: West Virginia University, 2008, pp. 113-122.

Acknowledgements

The author thanks the Department of Geological Sciences & Engineering at the Missouri University of Science and Technology for financial support of this research project. I especially appreciate the Geological Survey of JSC “Silvinit” for the kindly permission and assistance to georadar survey in their potash mine. I am also very grateful to the company “Orgtechstroy” for allowing GPR equipment and Sergey Baluyev for assistance in conducting the field work.

LABORATORY ASSESSMENT OF NANO-SILVER TRANSPORT IN SAND COLUMNS USING COMPLEX CONDUCTIVITY MEASUREMENTS

Dalton Hawkins[1], Matt McGuire[1], Gamal Z. Abdel Aal[2], Estella A. Atekwana[1], and Dale D. Werkema[3]
[1]Boone Pickens School of Geology, Oklahoma State University, Stillwater, OK, 74078
[2]Geology Department, Faculty of Science, Assiut University, Assiut 71516, Egypt
[3]U.S. Environmental Protection Agency, 944 East Harmon, Las Vegas, NV 89119

Abstract

Nano-materials are emerging into the global marketplace. Nanoparticles, and other throwaway nano-devices may constitute a whole new class of non-biodegradable pollutants that scientists have very little understanding of. Therefore, the production of significant quantities of nano-materials will inevitably result in the introduction of these materials to the environment with important implications for both environmental and human health. Currently there are many unanswered questions related to the release of nano-materials, their fate, transport, and transformation in the environment, and their potential toxic effects. Due to their desirable chemical–physical, electronic, and optical properties, metal nanoparticles have attracted much attention and demonstrated a wide range of applications (Kamat, 2002; Oliveira et al., 2005). Among metal nanoparticles, silver nanoparticles possess many superior properties, such as increased electrical conductivity, antimicrobial activity, catalytic effect, etc. (Kabashin et al., 2003).

In the present study, a flow through experiment was conducted to investigate the sensitivity of complex conductivity measurements (e.g., imaginary conductivity component) to the mobility and transport of three different concentrations (100, 500, 1000 mg/l) of nano-silver (90-210 nm) in laboratory sand columns. Stabilized aqueous suspensions of the different concentrations of the nano-silver particles were prepared following the procedure of Bihari et al. (2008), with fluid conductivity (0.08 S/m) and pH (7.2) values kept constant. Three identical columns constructed from polyvinyl chloride (PVC) pipe and dry filled with clean quartz sands were prepared (Figure 1). Each of the stabilized nano-silver dispersions was further kept homogenized by using a magnetic stirrer and a Teflon-coated stir bar.

Current (Ag) and potential (non-polarizable Ag-AgCl) electrodes were installed along the side of the sand columns and a two channel dynamic signal analyzer (DSA) based around a National Instruments (NI) 4551 was used to perform the complex conductivity measurements between 1 to 1000 Hz at 30 equal logarithmic intervals (Slater and Lesmes, 2002). The impedance magnitude $|\sigma|$ and the phase shift φ (between a measured voltage sinusoid and an impressed current sinusoid) of the sample were measured relative to a high-quality resistor. The real ($\sigma' = |\sigma| \cos \varphi$) and imaginary ($\sigma'' = |\sigma| \sin \varphi$) parts of the sample complex conductivity were then calculated. The real conductivity is an energy loss term that contains an electrolytic (σ_{el}) and interfacial (σ'_{surf}) component (e.g., Lesmes and Frye, 2001). The σ'_{surf} results from surface conduction via the formation of an electrical double layer (EDL) at the grain-fluid interface (Revil and Glover, 1998). The σ'' is an energy storage or polarization term, which at low frequencies (<1000 Hz) results primarily from the polarization of ions in the EDL at the mineral-fluid interface (Lesmes and Frye, 2001).

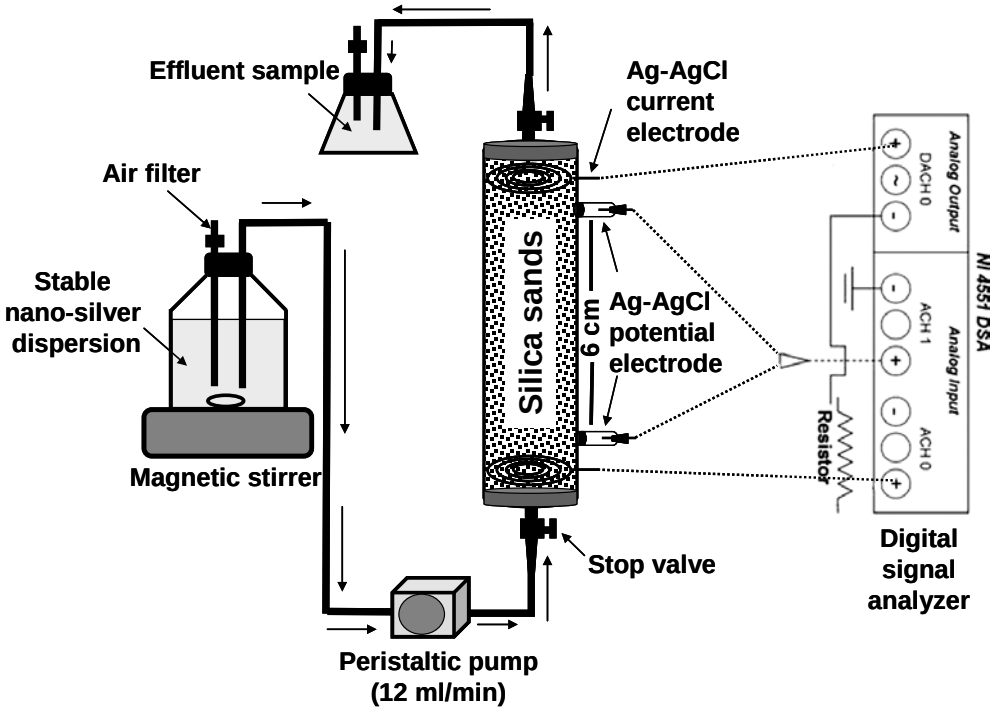

Figure 1: Schematic diagram of the experimental setup.

Prior to the start of the experiment, the three sand packed columns were flushed with 100 pore volumes of background solution similar to that used to prepare the stabilized nano-silver dispersions until the fluid conductivity and pH of the inlet and outlet fluids were the same. Thereafter, experimental columns were calibrated by performing low frequency electrical measurements to make sure that all columns have the same geophysical response as background. In addition, a tracer test was conducted to check the transport properties of the three sand columns prior to the start of the experiment. The tracer test was conducted using phenol red (Fisher Scientific) in which the absorbance at 3 minutes time interval (A) to the initial absorbance at time zero (A_o) using 600 nm wave length were plotted as a function of time and breakthrough curves (BTC) were obtained. The break through curves obtained from the dye tracer test using phenol red exhibit identical trend and shape (Figure 2) which indicate a great similarity in transport properties between the three packed sand columns used in this experiment.

A peristaltic pump was used to introduce the stabilized suspensions of nano-silver into the sand columns with flow rate of 12 ml/minute. Effluent samples of the nano-silver suspensions from the sand columns and complex conductivity measurements were collected every one minute. The optical density of the nano-silver in the effluent samples were determined at 600 nm wavelength using spectrophotometer and then converted into concentrations using the following equation (concentration (mg/l) = 1109 × optical density) which was previously determined from the linear correlation between different concentrations of nano-silver suspensions and their measured optical densities. During the course of the experiment, the concentration of the nano-silver introduced to the column, C_0, and the concentrations exiting the column, C, were monitored to obtain a breakthrough curve of C/C_0 as a function of the number of pore volumes passing through the porous medium. Similarly the imaginary conductivity component (σ'') obtained from the complex conductivity measurements every one minute were normalized to initial imaginary conductivity value σ''_o and plotted as a function of pore volume.

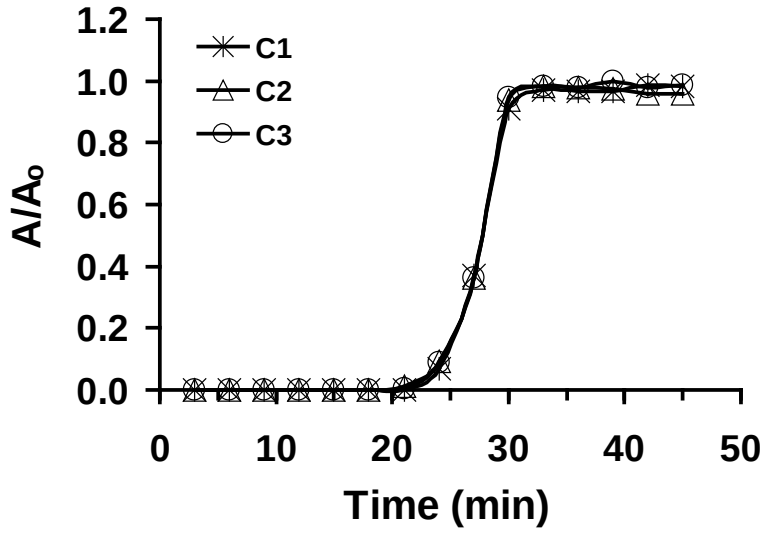

Figure 2: Break through curves (BTC's) from tracer tests using phenol red conducted prior to the start of the experiment for the three sand packed columns used in the experiment.

The break through curves (BTC's) obtained from the three normalized concentrations (100, 500, and 1000 mg/l) of the nano-silver effluent reached a plateau after two pore volumes (Figure 3). The three BTC's were also separated after two pore volumes upward towards the lower concentration of nano-silver suspension (100 mg/l). This indicates that the lower concentration of the nano-silver suspension has more mobility compared to the other two higher concentrations (500 and 1000 mg/l). In addition, previous studies show that at higher concentrations and pH values, nano particles tend to aggregate (Baalousha, 2009). Therefore, the possible aggregation of the nano-silver dispersion at higher concentrations (> 100 mg/l) may result in lowering the mobility of nano-silver and surface area as well as resulting in greater retention as shown in figure 3.

Similar observations were obtained from the BTC's of the normalized imaginary conductivity values. The BTC's reached a plateau after two pore volumes and exhibit a separation upward towards the lower concentration of nano-silver suspension (Figure 4). Surface conductivity (e.g., imaginary conductivity) is primarily controlled by the product of surface area, surface charge density and surface ionic mobility (Lesmes and Frye, 2001; Slater and Lesmes, 2002; Slater and Galser, 2003). Nanoparticles have a large surface area relative to their mass. However, the possible aggregation of the nano-silver at higher concentrations will result in reduction of the surface area. This explains the shift upward in the normalized imaginary conductivity component towards the lower concentration of nano-silver dispersion. However, scanning electron microscopy images are needed to examine the surfaces of the sand grains and possible aggregation of the nano-silver particularly at higher concentrations.

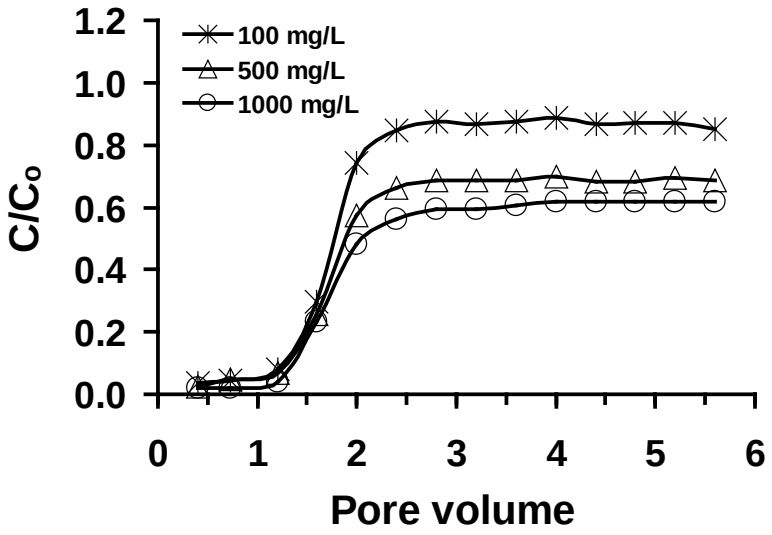

Figure 3: Breakthrough curves of nano-silver dispersions, showing the change in normalized effluent nanoparticle concentration (C/C_o) as a function of pore volume.

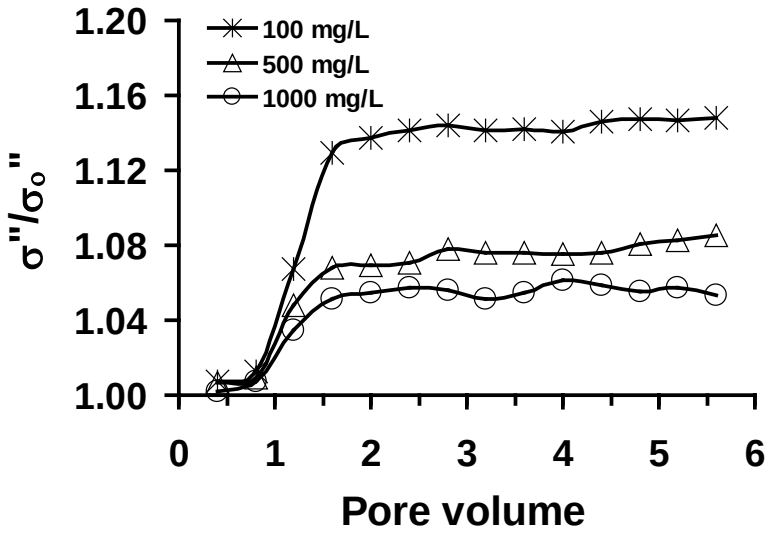

Figure 4: Breakthrough curves of nano-silver dispersions, showing the change in normalized imaginary conductivity values at 10 Hz (σ''/σ_o'') as a function of pore volume.

Conclusion

The results from this study demonstrated the sensitivity of complex conductivity measurements specifically the imaginary conductivity (σ") component to the fate and transport of different concentrations of nano-silver in porous media. Breakthrough curves obtained from normalized imaginary conductivity component showed a similar trend and shape to those obtained from normalized concentrations of nano-silver dispersions. This suggests that geophysical measurements can be used to monitor the presence and transport of nanoparticles in the subsurface. However, further studies are

needed to investigate the effect of pH, ionic strength, and surface chemistry of nanoparticles and porous media on the transport of nanoparticles in the subsurface environment and their associated geophysical signatures.

Acknowledgments

This material is based in part on work supported by the National Science Foundation under Grant No. OCE-0729642 and the DOE- BER- Grant # DE543 FG02-07ER64413. This work was partially funded through the U.S. Environmental Protection Agency through the student services contracts, EP09D000547 and EP09D000553. Although this work was reviewed by EPA and approved for presentation, it may not necessarily reflect official Agency policy. Mention of trade names or commercial products does not constitute endorsement or recommendation by EPA for use.

References

Baalousha, M., 2009, Aggregation and disaggregation of iron oxide nanoparticles: Influence of particle concentration, pH and natural organic matter, Science of the Total Environment, 407, 2093-2101.

Bihari, P., M. Vippola, S. Schultes, M. Praetner, A.G. Khandoga, C.A. Reichel, C. Coester, T. Tuomi, M. Rehberg and F. Krombach, 2008, Optimized dispersion of nanoparticles for biological in vitro and in vivo studies, Particle and Fibre Toxicology, doi:10.1186/1743-8977-5-14.

Kabashin, A., Meunier, V.M., Kingston, C.J., Luong, H.T., 2003, Fabrication and characterization of gold nanoparticles by femtosecond laser ablation in an aqueous solution of cyclodextrins. Journal of Physical Chemistry B, 1074, 527–4531.

Kamat, P.V., 2002, Photophysical, photochemical and photocatalytic aspects of metal nanoparticles. Journal of Physical Chemistry B, 106, 7729–7744.

Lesmes, D. P., and K. M. Frye, 2001, Influence of pore fluid chemistry on the complex conductivity and induced polarization responses of Berea sandstone, J. Geophys. Res., 106 (B3), 4079-4090.

Oliveira, M.M., Ugarte, D., Zanchet, D., Zarbin, J.G., 2005, Influence of synthetic parameters on the size, structure, and stability of dodecanethiol- stabilized silver nanoparticles. Journal of Colloid and Interface Science, 292, 429–435.

Revil, A., and P. W. J. Glover, 1998, Nature of surface electrical conductivity in natural sands, sandstones, and clays, J. Geophys. Res., 103(B10), 23925-23936.

Slater, L., and D. Glaser, 2003, Controls on induced-polarization in sandy unconsolidated sediments and application to aquifer characterization: Geophysics, 68, 1547–1558.

Slater, L., and D. P. Lesmes, 2002, Electrical-hydraulic relationships observed for unconsolidated sediments, Water Resour. Res., 38, 1213, doi: .1029/2001WR001075.

AQUIFER CHARACTERISTICS NEAR CUESTAS AND THEIR RELATION TO ROCK TENSILE STRENGTH

Roger H. Morin, U.S. Geological Survey, Denver, CO
William H. Schulz, U.S. Geological Survey, Golden, CO

Abstract

Along the northeast coast of North America, extensional tectonic processes have generated lithologic and topographic features that are common to several rift basins. A cap of igneous rock overlies sedimentary rock to form a cuesta with both rock types exposed along a steep ridge flank. Field studies investigating the near-surface hydrogeologic properties of the caprocks at several of these sites have reported a narrow range of results; some fractured rocks form modest aquifers whereas others do not. To examine this behavior in terms of geomechanical responses to gravitational stresses imposed near ridges, a finite-element model is presented that incorporates the geometry of a ridge-valley configuration and its major structural elements. Model simulations reflect the effects of a lack of buttressing along free faces and a contrast in Poisson's ratios between the superposed igneous and sedimentary rocks. Three-dimensional Mohr's circles are constructed from principal stress magnitudes and directions to evaluate the response of individual fracture planes to this stress state. Results depict a predominantly tensional stress environment where numerous pre-existing fractures may be favorably aligned for opening and enhanced caprock permeability. However, the lack of conclusive field evidence to support this hypothesis suggests that the *in situ* tensile strength of the fractured rock mass is substantial enough to resist failure by shear or dilation, and that critically-stressed fracture planes do not convey large volumes of groundwater in ridge-valley settings.

Introduction

The state of stress to which a rock mass is subjected can affect the hydraulic conductivities of pre-existing fractures interspersed within it (e.g., Brown and Bruhn, 1998). Numerous theoretical and experimental studies of hydromechanical coupling have been reported that investigate links between hydrologic properties and mechanical deformation over a wide range of scales (Stephansson, 2003). In this report, we investigate the relation between stress and hydrology near cuestas associated with the formation of rift basins. A finite-element stress model of a valley-ridge setting is devised that incorporates structural elements and typical rock elastic properties. Results are examined within the context of shallow groundwater investigations undertaken at two rift basins located in Nova Scotia and in New York. By interpreting direct field observations from the perspective of mechanical responses derived from numerical stress models, the *in situ* tensile strength of the caprock is shown to be an important factor in determining aquifer properties and accounting for poor water yields.

Finite-Element Stress Model

In an effort to design a two-dimensional model that adequately represents typical structural elements found along ridges formed by extensional tectonic processes, we refer to Froelich and Robinson (1988) and their descriptions of the numerous rift basins along the eastern seaboard of North America. Characteristic lithologic and topographic features appear at several stages of basin

development whereby a layer of igneous rock, either intrusive or extrusive, overlies sedimentary rocks that are exposed along a steep ridge flank. The two field sites to which the results of this model are applied share these same features and the model's specifications were chosen to produce a generalized representation of their geomorphological characteristics.

Although analytical solutions have been previously derived that predict gravity-induced stresses near a cliff (e.g., Savage, 1993), a finite-element model is proposed for this case because of the contrast in superposed materials (and hence elastic properties) that form the cuesta. The finite-element code PLAXIS© was used to automatically generate an unstructured mesh of 4th order, 15-node triangular elements; finer discretization was applied for the caprock and near the bluff face. The resulting finite-element mesh (**Figure 1)** incorporates topography and lithology into the two-dimensional cross-section. The materials consist of a layer of igneous caprock gently dipping away from the valley floor at 5° that is underlain by sedimentary rock that comprises the valley floor. By convention, the greatest principal stress is designated as σ_1 and $\sigma_1 > \sigma_2 > \sigma_3$. The model also assumes plane strain conditions.

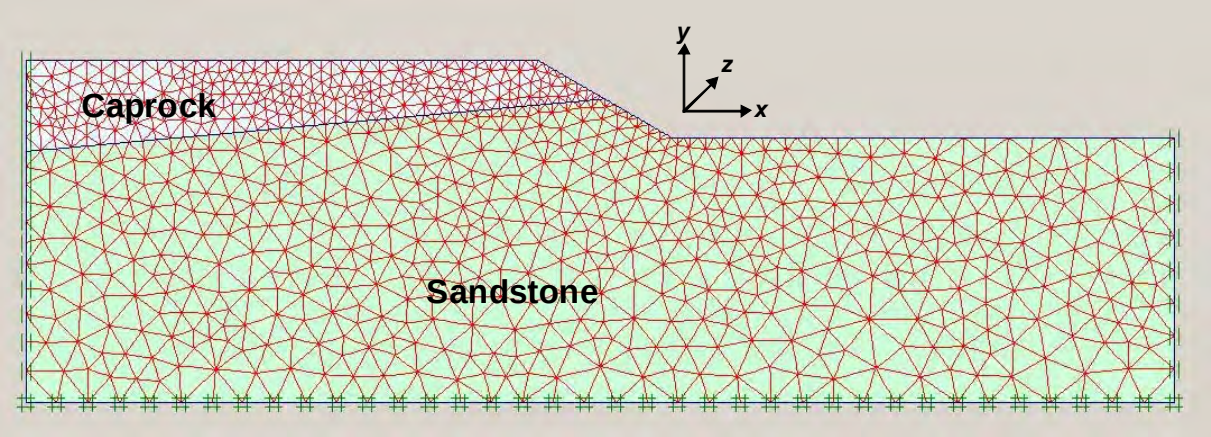

Figure 1. Two-dimensional finite-element mesh of valley-ridge configuration with structural elements and reference coordinates. Direction *z* is parallel to valley axis. Poisson's ratios for caprock and sandstone are 0.30 and 0.35, respectively.

The effective stresses σ_x, σ_y, and σ_z are determined from these initial boundary conditions. The vertical stress σ_y increases systematically with depth and is compressional everywhere. However, σ_x and σ_z may be compressional or tensional, and their relative magnitudes may interchange such that $\sigma_x > \sigma_z$ or $\sigma_z > \sigma_x$ depending upon location. In order to visualize where these relative magnitudes reverse order, a plot of the stress difference ($\sigma_z - \sigma_x$) is presented in **Figure 2**. The tan colors depict areas in the model where $\sigma_x > \sigma_z$; i.e., the stress perpendicular to the valley axis is greater than that parallel to it. The areas in blue identify zones where $\sigma_z > \sigma_x$. This reversal is produced by a counterclockwise rotation at the ridge flank due to differential spreading between the superposed rocks and a lack of buttressing at the free face.

Three-dimensional Mohr's circles (Jaeger and Cook, 1976) can be utilized to represent any particular state of stress acting upon a fracture plane and to recognize failure criteria. The coefficient of friction μ defines the slope of the straight-line portion of the normal/shear (σ/τ) stress relation, known as the Coulomb failure line, and its value is assumed to be 0.6 (Byerlee, 1978). Direction cosines are used to convert values of σ_x, σ_y, and σ_z to stress magnitudes acting upon pre-existing fracture planes.

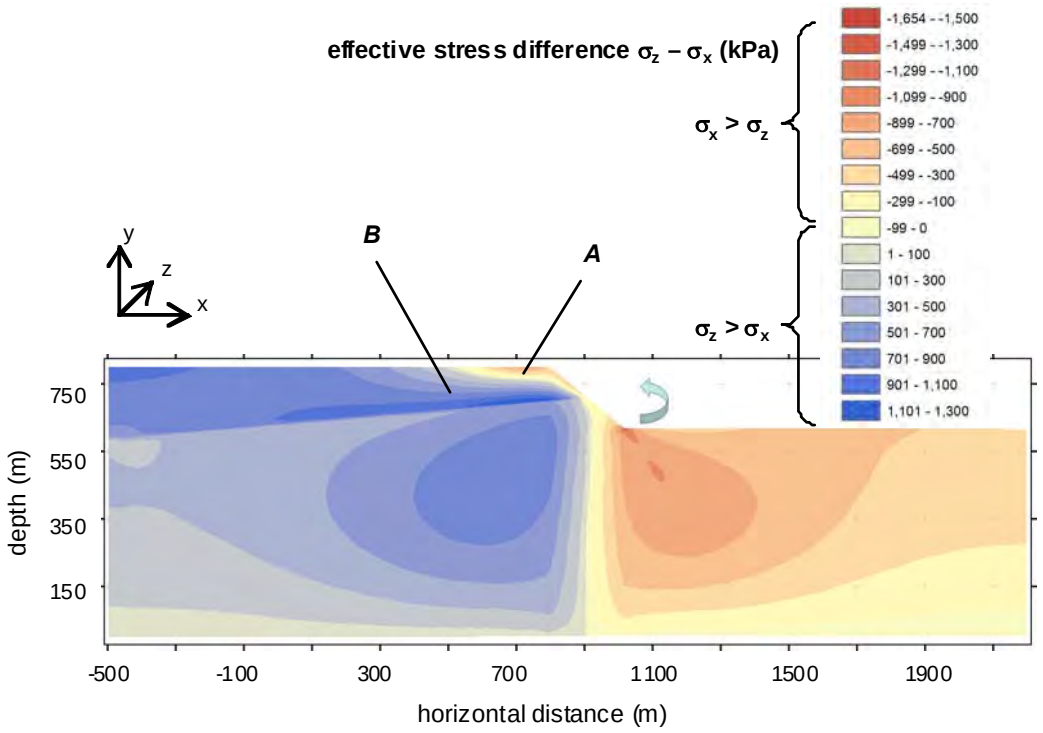

Figure 2. Distribution of differences in stress between σ_z and σ_x. Blue colors identify areas where $\sigma_z > \sigma_x$ and tan colors where $\sigma_x > \sigma_z$. Points A and B refer to locations where 3-D Mohr's circles are utilized to interpret stress conditions at hydrogeologic study sites.

The caprocks considered in this analysis are basalt and diabase. These rocks are classified as having very high strength and bearing capacity (Hatheway and Kiersch, 1982), with tensile strengths T_o of roughly 21 and 38 MPa, respectively. These values represent the properties of intact rocks sampled under controlled laboratory conditions. In characterizing a rock mass, numerous geologic factors must be considered in evaluating its overall toughness (e.g., Suorineni et al., 2009); most of these factors, such as chemical dissolution and stress history, tend to weaken the rock. Consequently, a value of T_o derived from a laboratory specimen may not be realistic when describing the physical properties of a large rock mass, and *in situ* tensile strength is often assumed in engineering practice to be a small fraction of the intact value or even zero.

Hydrogeologic Field Studies

Fundy Basin, Nova Scotia

The Fundy Basin is the largest of the twenty early Mesozoic rift basins exposed along the northeast coast of North American (Froelich and Robinson, 1988). Bordering its southern boundary is the Annapolis-Cornwallis Valley. It is flanked to the north by Jurassic basalt that caps North Mountain and the valley floor is underlain by Triassic sedimentary rocks consisting of sequences of sandstone, siltstone, and mudstone (Hamblin, 2004). A multidisciplinary study has recently been completed to characterize the hydrogeologic properties of this valley and its surroundings (Rivard et al., in press), as roughly 90 percent of residents rely on groundwater from private or municipal wells. This stress analysis focuses on downhole measurements obtained in one well located on North Mountain

approximately 70 m from the ridge flank that penetrated through the basalt cap and into the underlying sedimentary rocks. The basalt unit dips gently (~ 5°-10°) to the northwest and forms the cuesta with the valley where slopes reach a maximum angle of about 40°. A variety of geophysical logs recorded in this well help to locate the contact between the massive basalt flow unit and the sedimentary rocks. Borehole flowmeter measurements (Molz et al., 1989) identify several permeable zones in the caprock and transmissivity is determined to be about 6 m^2/day. An acoustic televiewer log shows the basalt unit to be extensively fractured and a total of 117 planes were identified, corresponding to a fracture frequency of about 2 per meter. The basalt is mostly intersected by steeply dipping (~ 56°) conjugate fracture sets that strike subparallel to the valley axis, and it is within this fracture population that the subset of permeable fractures is found.

Very near the surface and the ridge crest, stresses are such that $\sigma_x > \sigma_z$ (**Figure 2**) and, consequently, fracture planes in the basalt are not favorably aligned for failure; i.e., their strike is not perpendicular to σ_3. The well on North Mountain is drilled deeper into the caprock and slightly further away from the ridge crest; its location is identified by Point A in **Figure 2**. Here, the corresponding Mohr diagram (**Figure 3a**) shows the magnitudes of the normal and shear stresses acting on each individual fracture plane (depicted as a circle) and located within the largest semi-circle whose diameter is bounded by σ_1 and σ_3. Many pre-existing fracture planes are favorably oriented for failure, particularly if the rock mass has no tensile strength, and the transmissivity is expected to be high. However, if the *in situ* tensile strength is only a small fraction of its intact, laboratory-determined value of about 21 MPa, then a relatively few fractures may still meet the failure criteria. The Coulomb failure line corresponding to $T_o > 0$ was arbitrarily estimated to represent potential strength parameters consistent with these hydrologic observations. Consequently, the transmissivity of this well is low but not insignificant, and the caprock on North Mountain constitutes part of a weak local aquifer.

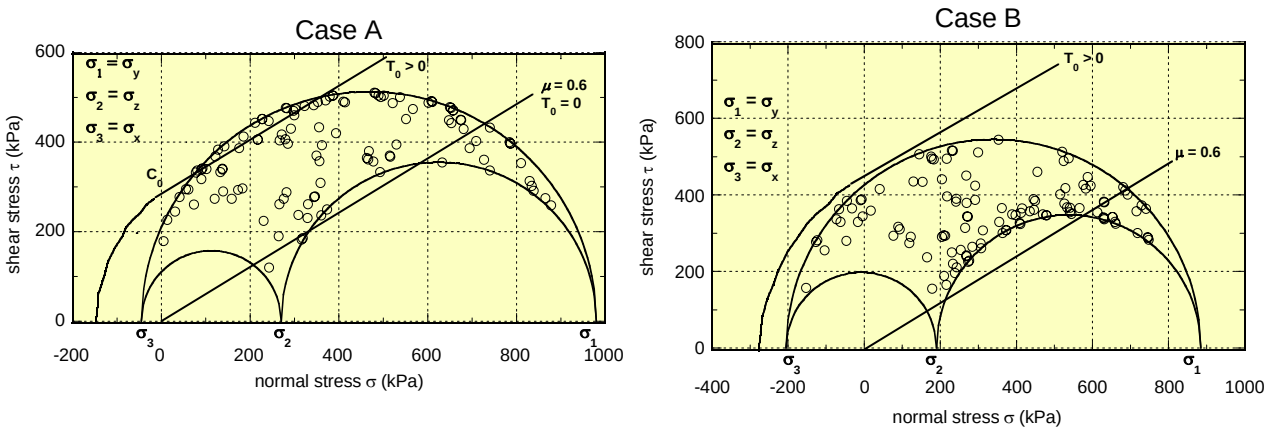

Figure 3. Three-dimensional Mohr diagrams depicting stresses acting on population of pre-existing fractures located in Figure 2 at (a) Point A and (b) Point B.

Newark Basin, New York

The Newark Basin is another of the eastern seaboard rift basins. It is a northeast-southwest elongated fault trough filled with mostly late Triassic and early Jurassic fluvial and lacustrine sediments (Olsen, 1980); these are overlain by igneous rocks that include intrusives (Palisades diabase sill) and extrusives (Watchung flows). The basin is bounded by the Hudson River valley along the northeast and southwest (Schlische, 1992), where the Palisades sill is exposed at the top of the ridge and forms the structural caprock.

Matter et al. (2006) characterized the hydrogeologic properties of this intrusive unit and underlying sedimentary rocks through the analysis of geophysical logs obtained in two wells. The sill dips gently to the northwest (~ 5°-10°) and forms a cuesta with slopes reaching almost 50°. In this stress analysis, we refer to downhole measurements recorded in a well located at an elevation of about 120 m above the Hudson River valley floor and roughly 300 m from the ridge crest. Several of the geophysical logs recorded in this well are qualitatively similar to those obtained in Nova Scotia. One property that is not similar is the complete lack of transmissivity in the caprock. Although a flowmeter/injection test performed in this well identified a prominent flow interval at the lithologic contact, no permeable zones were detected in the overlying sill.

The acoustic televiewer log recorded in the well revealed 337 fracture planes in the diabase unit, corresponding again to a fracture frequency of about 2 per meter. The directional data show that the majority of the overall fracture population consists of conjugate sets of steeply dipping (~ 58°) fractures. Rather than being subparallel to the ridge, as was the case for the Nova Scotia basalt, their strike direction is almost perpendicular to the ridge axis. Consequently, we apply the fracture data once more, but rotate the orientations 90° and again reference them to the model coordinates shown in **Figure 1**.

Point B shown in the stress model (**Figure 2**) identifies this well within the valley-ridge setting. A Mohr diagram representing stresses acting on fracture planes at this location (**Figure 3b**) illustrates that almost all pre-existing fractures are above and clustered near the Coulomb failure line for a rock mass with little or no tensile strength ($T_o \approx 0$). Uniformly high tensile stresses are generated in this area and our arbitrary choice of a Coulomb failure line corresponding to a substantial tensile strength ($T_o >> 0$) dictates that failure by either shear or dilation is prevented.

Conclusions

The primary objective of this study was to develop a generalized finite-element model that considered gravitational stresses near cuestas in order to evaluate their hydrologic consequences when viewed in the context of fracture response to imposed forces. The model was applied to two sites chosen for their locations within rift basins and because their hydrogeologic properties had previously been characterized through extensive field programs. At both sites, fracture populations within the caprock were similar, with steeply dipping (~ 57°) conjugate fracture sets appearing at a frequency of roughly 2 per meter. Results show that caprock that forms a cuesta in a valley-ridge setting is almost uniformly exposed to a tensile stress environment, except for a shallow area near the ridge crest.

In the case of the Fundy Basin, most fracture planes were aligned such that the principal stress acting normal to them was also σ_3; i.e., favorably oriented for opening. A low but not negligible tensile strength would permit several fractures to be critically stressed, thereby modestly improving hydraulic communication through the rock mass. Consequently, the basalt formed a weak local aquifer. Conversely, in the Newark Basin, only a few pre-existing fracture planes were optimally oriented to the stress field and the diabase was found to have a very low transmissivity. This indicates that the rock mass has a substantial enough *in situ* tensile strength to prevent opening of those few fractures through either shear or dilation. Thus, fracture orientation and tensile strength combine to become important factors in determining the aquifer productivity of caprocks that form cuestas.

Acknowledgments

The authors would like to thank Juerg Matter and David Goldberg (New York), and Christine Rivard and Daniel Paradis (Nova Scotia) for logistical support during field operations and informative scientific discussions.

References

Brown, S.R. and Bruhn, R.L., 1998. Fluid permeability of deformable fracture networks, *J. Geophysical Research*, v. 103, no B2, 2489-2500.

Byerlee, J., 1978. Friction of rocks, *Pageoph*., v. 116, 615-626.

Froelich, A.J. and Robinson, G.R. Jr. (eds.), 1988. Studies of the early Mesozoic basins of the eastern United States, U.S. Geological Survey Bulletin 1776, 423 pp.

Hamblin, T., 2004. Regional geology of the Triassic/Jurassic Fundy Group of Annapolis Valley, Geological Survey of Canada Open-File Report 4678, 17 pp.

Hatheway, A.W. and Kiersch, G.A., 1982. Engineering Properties of Rock, Chapt. 3 *in* Handbook of Physical Properties of Rocks, Vol. II, R.S. Carmichael (ed.), CRC Press, Boca Raton, Florida, 289-331.

Jaeger, J.C. and Cook, N.G.W., 1976. Fundamentals of Rock Mechanics, 2nd edition, 585 pp., Chapman and Hall, London.

Matter, J.M., Goldberg, D.S., Morin, R.H. and Stute, M., 2006. Contact zone permeability at intrusion boundaries: New results from hydraulic testing and geophysical logging in the Newark Rift Basin, New York, USA, *Hydrogeology J*., v. 14, 689-699.

Molz, F.J., Morin, R.H., Hess, A.E., Melville, J.G. and Güven, O., 1989. The impeller meter for measuring aquifer permeability variations: evaluation and comparison with other tests, *Water Resources Research*, v. 25, no. 7, 1677-1683.

Olsen, P.E., 1980. The latest Triassic and early Jurassic formations of the Newark Basin (eastern North America, Newark Supergroup): Stratigraphy, structure, and correlation, New Jersey Academy of Science Bulletin, v. 25, 25-51.

Rivard, C., Paradis, D., Paradis, S., Bolduc, A., Morin, R., Liao, S., Pullan, S., Gauthier, M.-J., Trépanier, S., Blackmore, A., Spooner, A., Deblonde, C., Fernandes, R., Castonguay, S., Michaud, Y., Drage, J. and Paniconi, C., in press. Canadian Groundwater Inventory : Regional hydrogeological characterization of the Annapolis-Cornwallis Valley aquifers, Geological Survey of Canada Bulletin 598, 114 pp.

Savage, W.Z., 1993. Gravity-induced stresses near a vertical cliff, *Int. J. Rock Mechanics, Mining Sciences & Geomechanics Abstr*., v. 30, no. 4, 325-330.

Schlische, R.W., 1992. Structural and stratigraphic development of the Newark extensional basin, eastern North America: evidence for the growth of the basin and its bounding structures, *Geological Society of America Bulletin*, v. 104, 1246-1263.

Stephansson, O., 2003. Theme issue on hydromechanics in geology and geotechnics, *Hydrogeology J*., v. 11, 3-6.

Suorineni, F.T., Chinnasane, D.R. and Kaiser, P.K., 2009. A procedure for determining rock-type specific Hoek-Brown brittle parameter *s*, *Rock Mech. Rock Eng*., v. 42, 849-881.

ELECTRICAL RESISTIVITY IMAGING TO EXPLORE SOLUTE TRANSPORT IN A STREAM SYSTEM

Julianne Hagarty, The Pennsylvania State University, University Park, PA
Adam S. Ward, The Pennsylvania State University, University Park, PA
Kamini Singha, The Pennsylvania State University, University Park, PA
Michael N. Gooseff, The Pennsylvania State University, University Park, PA

Abstract

Time-lapse electrical resistivity imaging (ERI) was used to map the movement of a conservative salt tracer through a stream system at the Leading Ridge Experimental Watershed in central Pennsylvania. A transect of 12 electrodes was established perpendicular to the direction of stream flow to allow for imaging of the stream, streambed, and surrounding aquifer. ERI measurements were taken at regular intervals during the 21-hour tracer test and for 23 hours after the injection ended. The purposes of this test were 1) to identify the movement of a saline tracer through subsurface preferential pathways and the extent of the hyporheic zone, or subsurface actively connected to the stream, and 2) to determine the behavior of saline tracer in the subsurface as based on spatial moments. At early time, the tomograms show a drop in resistivity of up to 10 percent in the immediate area of the stream relative to background measurements taken before the start of the salt injection; later, a region of low resistivity develops in a hypothesized abandoned streambed on the inside of a meander bend. Transport of the tracer through the subsurface occurs at a slower rate than its movement in the stream. Spatial moments indicate that a substantial quantity of solute is entrained in the subsurface and persists in the hyporheic zone well after the end of tracer injection. ERI effectively images the movement of a saline tracer through hyporheic pathways, providing a higher resolution image of transport behavior in the subsurface.

Introduction

The hyporheic zone is a region of the subsurface of a streambed in which water is actively exchanged between the near subsurface and the stream channel (e.g., Brosten *et al.*, 2009). The movement of water into and within the hyporheic zone is, as yet, very poorly understood. This has serious implications for geologists and engineers seeking to characterize solute transport in streams as interactions with the hyporheic zone contribute greatly to divergence from idealized stream behavior. Hyporheic flowpaths are unlike groundwater flowpaths in that water is exchanged between stream channel and hyporheic zone multiple times within a typical study reach, whereas groundwater-surface water exchange typically happens only once (Harvey and Wagner, 2000). Hyporheic zones have profound impacts on stream transport, as water flows more slowly in the hyporheic zone than through the stream channel; this may contribute to the non-ideal transport of solutes in a stream system. Understanding solute transport through the hyporheic zone is crucial to effective modeling of solute transport in stream systems.

Traditional tests for quantifying stream-aquifer interaction involve the injection of tracer at a point source and monitoring for the concentration of that tracer downstream (Stream Solute Workshop, 1990). Theoretically, a pulse of tracer will move by advection and dispersion, appearing downstream as a quasi-Gaussian concentration history—nearly symmetrically approaching and decreasing from a peak concentration. In reality, the appearance of the tracer is far less uniform: a plot of concentration versus time may show a delayed peak, multiple peaks, a long tail, a lower-than-anticipated peak concentration, or any combination of these patterns. These divergences from the

ideal case are typically attributed to exchange between surface and ground water in the hyporheic zone (Bencala and Walters, 1983), or other less mobile zones in the stream channel (e.g., dead zones, Gooseff *et al.*,2008).

Traditional methods for detecting a saline tracer in the subsurface require wells, but limitations on the number of wells that can reasonably be placed in a stream system result in low resolution and high degrees of uncertainty regarding tracer behavior. Electrical resistivity imaging (ERI) is a promising method for monitoring and modeling solute transport in a stream system, particularly the near-stream aquifer. Electrical resistivity surveying has typically been employed for determining the depth to bedrock, mapping karst, and monitoring contamination of soil and groundwater (Dogwiler and Gernes, 2008; Martinez-Pagan *et al.*, 2009). ERI has also been effective for mapping the hyporheic zone architecture, imaging subsurface architecture near streams, and determining the contribution of groundwater to a stream (Acworth and Dasey, 2003; Crook *et al.*, 2008; Nyquist *et al.*, 2008). Singha *et al.* (2008) suggest ERI as a promising method for the modeling of solute exchange between stream and hyporheic zone, and Ward *et al.* (in revision) show that ERI is capable of illustrating both spatial and temporal exchange characteristics. This work expands on the recent research of Ward *et al.* by exploring the use of spatial moments to quantify stream behavior in central Pennsylvania.

Background

The Leading Ridge Experimental Watershed

This study took place at Leading Ridge #1, an experimental watershed managed by the Pennsylvania State University and U.S. Forest Service. The 0.43 km^2 catchment is forested mainly by oak, maple, and hickory; the stream and lower slope of the watershed consist of well-drained silts and cobbly loams and are underlain by Rose Hill shale (Dann *et al.*, 1986). The stream has a gradient of approximately 5%; through the study reach, the stream is approximately 1.5-2 m wide and 0.1-0.2 m deep.

Electrical Resistivity Imaging (ERI)

Electrical resistivity is the reciprocal of electrical conductivity. Because ERI is sensitive to changes in fluid electrical conductivity (i.e., the presence of an electrically conductive tracer), it is likely that ERI can be applied to successfully identify preferential flowpaths (e.g., buried streambeds) as well as the salt tracer's exchange between the near-stream aquifer and stream channel in the hyporheic zone. As electrical resistivity methods allow for surveying of the stream system at multiple points, ERI can create a more detailed view of the exchange of water between surface and subsurface water systems in the hyporheic zone as the solute tracer moves laterally through the study reach.

After determining the study reach, electrodes are installed in a transect across the study area. The electrodes are connected to a control unit that delivers a known current across one pair of electrodes and measures the voltage across one or more pairs of other electrodes. The resistance of the region between these pairs of electrodes is then calculated by Ohm's Law (R=V/I). Resistance is related to apparent resistivity by a geometric constant, K, calculated by the equation:

$$K = \frac{2\pi}{\left(\frac{1}{AM} - \frac{1}{AN} - \frac{1}{BM} + \frac{1}{BN}\right)} \quad (1)$$

where AM, AN, BM, BN are distances between electrodes A, B, M, and N.

Apparent resistivity is, however, not equivalent to the "true" subsurface resistivity, which does not assume a homogeneous half space as shown in Equation 1. To get these values, ERI data must be inverted. Inversion is the process of using numerical models to find the best-fit model resistivity, in some sense, that fits the measured resistance or apparent resistivity data from the field. When the measured and calculated resistivities compare well, the resistivity model used to produce the calculated resistivities is assumed to be representative of the true surface conditions. This model can be incorrect for a number of reasons including poor parameterization or poor data sensitivity (e.g., Day-Lewis *et al.*, 2005).

In this work we use AGI's EarthImager2D (Advanced Geosciences, 2008) for data inversion. Using a pre-injection dataset as a baseline, EarthImager performs a time-lapse inversion, wherein each subsequent dataset is inverted using the baseline as the a-priori information. The result of this series of inversions is the percent change in resistivity at each time from the baseline case.

Data Collection

Data were collected at Leading Ridge #1 over a three-day period in October 2008 using a 10-channel SYSCAL Pro by IRIS Instruments. A transect of 12 electrodes with 2-m spacing was installed at the site, with the first electrode located at x = 0 m and the last electrode at x = 22 m. The stream is located from x = 10 to 12 m. Each transect was composed of 166 quadripole measurements, which took approximately 20 minutes to collect. Four background datasets were collected immediately before the start of tracer injection. Data collection began 5.5 hours before the start of salt injection and continued throughout the injection and for 23 hours after the injection had stopped.

The stream's flow rate was measured as 0.6 L/s at a weir approximately 70 meters above the observation locations at the start of the sampling event. The average background fluid electrical conductivity at Leading Ridge 1 is 0.12 mS/cm. A NaCl tracer with a fluid electrical conductivity of 61.9 mS/cm was injected at a constant rate (~1 mL/s) at the weir to allow for thorough mixing prior to arriving at the sensors. The tracer's electrical conductivity and injection rate were set such that the tracer would produce a measurable signal without causing undue stress on the stream ecosystem.

Data Analysis

Thirty-six timesteps were analyzed using time-lapse inversion to produce models displaying the percent change in resistivity of the subsurface with respect to initial conditions over time. The differenced resistivity data from each timestep were interpolated to a uniform grid (Figure 1).

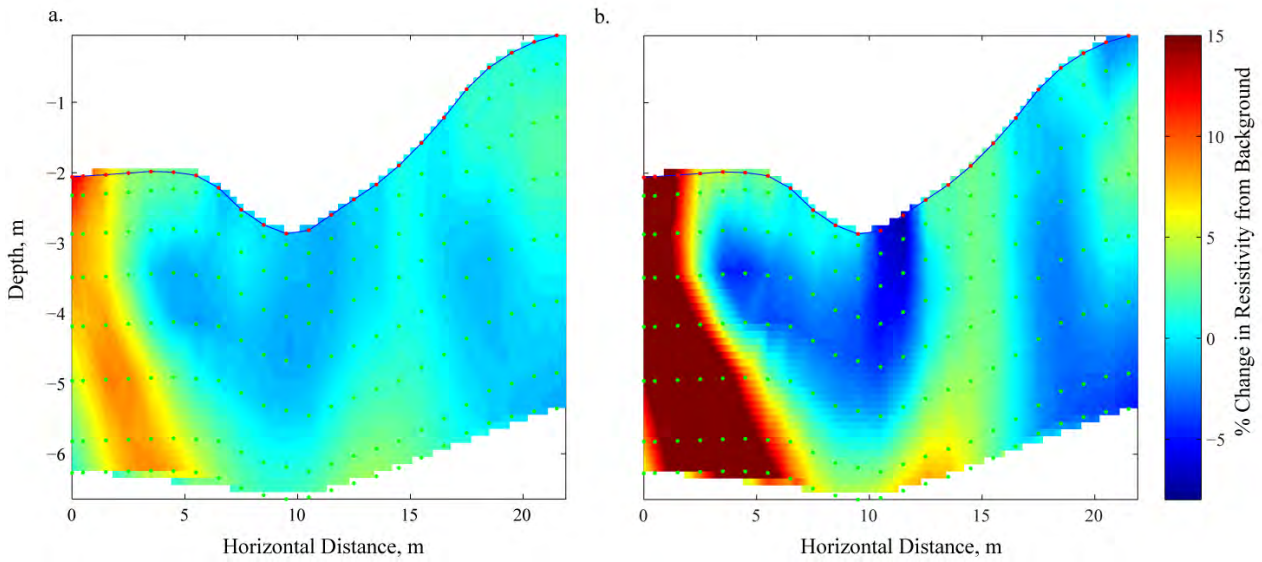

Figure 1: Differenced resistivity inversions in percent change, where negative values represent a decrease in resistivity with respect to background a) before injection (hour 1.5) and b) at end of injection (hour 27). Before the start of salt injection, the system shows little change. By the end of the injection, the tracer has created an 8% drop in resistivity both in the stream and on the inside of the meander bend.

To quantify the behavior of the tracer through time, spatial moments are utilized. Spatial moments are commonly used by hydrogeologists to describe the movement of solutes through the aquifers. Here, we use them to analyze the movement and behavior of a solute tracer in the stream system through time. Spatial moments at each timestep were calculated by the equation:

$$M_{i,j}(t) = n \iint_{\Gamma} \Delta C * x^i z^j dx dz$$

where

$M_{i,j}$	the spatial moment of interest;
i,j	exponents with values 0 to 2 depending on the moment of interest;
n	effective porosity;
Γ	test domain;
ΔC	change in concentration;
x,z	Cartesian coordinates; and
dx,dz	pixel dimensions in x and z directions.

The change in concentration used in this equation for spatial moments is calculated by the equation:

$$\Delta C = 2 * F * \Delta \sigma_b$$

where the F is the formation factor, a unitless value assumed to be equal to 5 based on a porosity of 0.3 and a cementation exponent of 1.3 (Archie, 1942), and $\Delta\sigma_b$ represents the change in bulk electrical conductivity relative to background in mS/m. The value 2 converts the fluid conductivity in uS/cm to concentration in mg/L as described in Keller and Frischknecht (1966).

Using the labeling convention shown above, $M_{0,0}$ represents the total solute mass in the test domain at time t after the start of the study. We note that this is a two-dimensional "mass", so will impacted by out-of-plane effects as has been described in other studies (e.g., Bentley and Gharibi, 2004).

Results and Discussion

Once tracer injection began, the solute was consistently present in the test area, even after the injection was stopped 26.5 hours after the start of the study. The fact that the total solute mass continues to increase after the conclusion of the tracer test suggests that a substantial amount of tracer was entrained in the hyporheic zone. Figure 2 indicates that increased conductivity in the subsurface persisted well after the injection had stopped. The total amount of salt in the system as determined by spatial moments correlate well with the findings of Ward *et al.* (in revision) with respect to the amount of subsurface showing increased conductivity over time. The second increase of tracer presence in the subsurface (Figure 2, 35-51 hours) suggests that tracer mass is still moving past the transect—or due to 3-D effects, within the support volume of the measurements slightly up or down stream—even well after the stream has flushed. This is confirmed by tomography presented by Ward *et al*. indicating areas of increased conductivity beneath the streambed and on the inside of the meander bend until the end of the study, approximately 23 hours after injection had ceased.

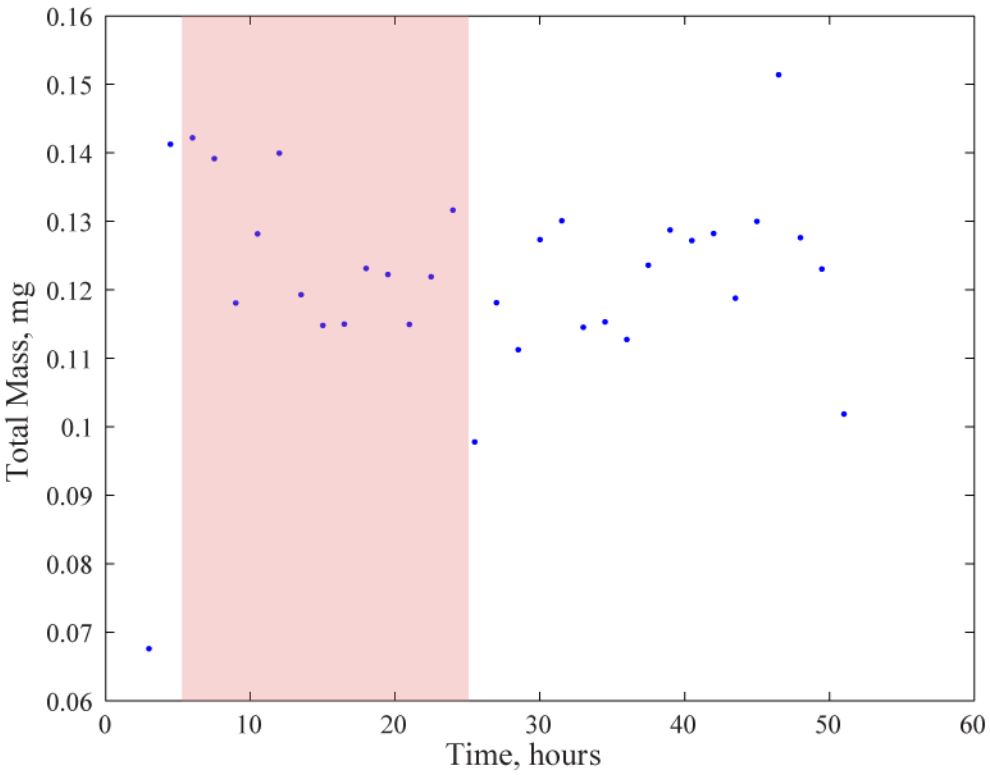

Figure 2: Total solute mass in the 2-D plane perpendicular to flow as calculated from moments differenced electrical resistivity vs. time after start of study. Shading represents period of tracer injection.

The center of mass of the tracer in the x-direction (perpendicular to flow) vs. time shows a gradual shift from the inside of the stream meander (x=4 m) toward the stream (x=10 m) and back to the stream meander (Figure 3a). The center of mass in the z-direction (depth into the subsurface) shifts about 0.5 m over the test period and with some pull up in tracer location around 26.5 hours into the study (Figure 3b). Plots of spatial variance in the x and z directions (Figure 3c and d) demonstrate a similar trend, showing decreasing variance at early and late times with a maximum variance between 23.5 and 26.5 hours into the study. The decrease in spatial variance at early time is likely due to the arrival of low concentrations of solute in the transect, decreasing the natural

variance associated with the background condition as the current focuses in the areas with tracer. The variance increases as high concentrations of tracer appear in the transect, and decreases again as the tracer leaves the transect area. This trend suggests that salt concentration spreads through the subsurface throughout the injection and slowly flushes out of the subsurface after the injection had stopped, confirming the findings of Ward *et al*. (in revision).

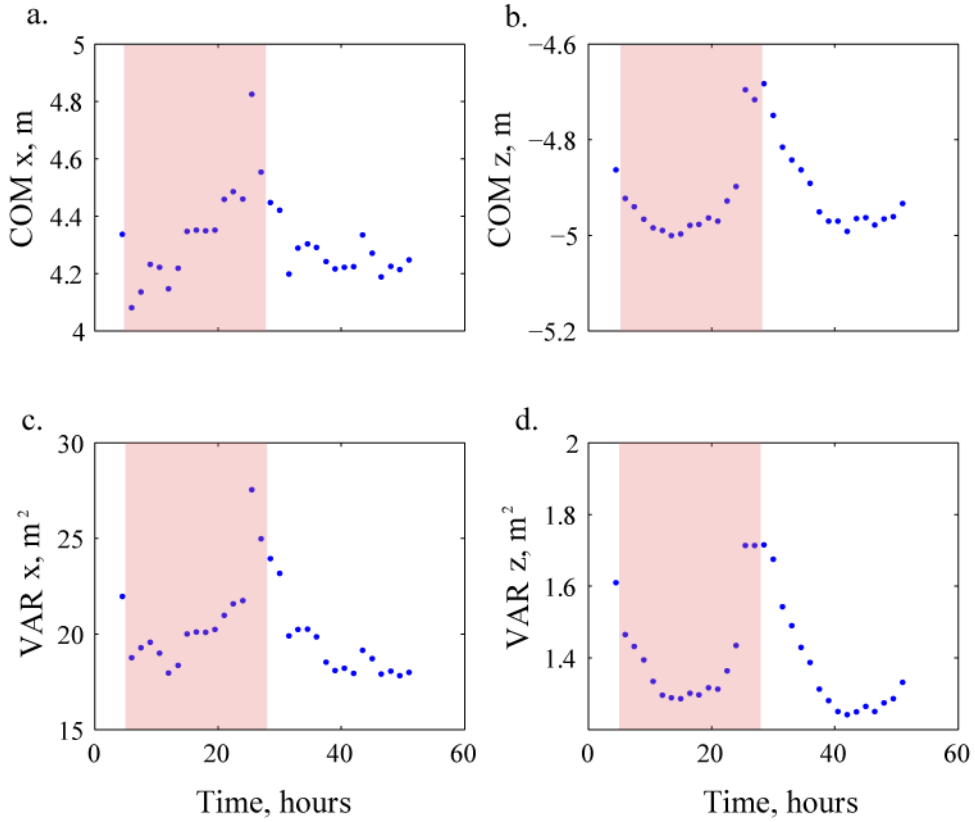

Figure 3: Moments calculated from the 2-D plane perpendicular to flow based on differenced electrical resistivity tomograms, including a) center of mass in x direction vs. time; b) center of mass in z direction vs. time; c) variance of center of mass in x direction vs. time; and d) variance of center of mass in z direction vs. time. Shading indicates period of tracer injection. As the tracer mass passes the transect, we see the shift from background condition to a center of mass which is located near the stream centerline (a) and in the shallow subsurface (b). (c) and (d) suggest spreading of tracer through the subsurface during the tracer test and flushing from the subsurface after the end of injection.

The change in variance is not a function of variable fitting of the field data through time to the model prediction, which could lead to variable smoothing. The root mean square error (RMSE) of these inversions is approximately 1.5 percent at all time; this value is slightly higher than the amount of noise in the system (approximately 0.4 percent).

Conclusions

In this work, we find spatial moments to be a viable method for analyzing ERI data from a stream system in central Pennsylvania. Using a transect of electrodes installed across a small stream in Huntingdon County, we were able to collect data before, during, and after tracer injection. This data, analyzed using time-lapse inversion available in EarthImager 2D, produced tomograms illustrating the change in resistivity of the subsurface over time. When further analyzed using spatial

moments, we estimated the change in mass of solute present in the study area, in a 2D sense, as well as the center of mass and variance of this tracer in the subsurface. Our findings agree with the findings of Ward *et al.* (in revision).

Spatial moments show that solute was present near the transect even well after the injection had ceased, fitting previous data that made similar conclusions based on qualitative inference from geophysical tomograms. This suggests that a substantial quantity of tracer left the stream and traveled through the less mobile hyporheic zone. Additionally, we use these moments to quantify solute transport within the system; the center of mass of the solute moves from its initial position near the stream toward the inside of the meander bend during and shortly after the injection, then slowly back its original position. The fact that the mass remains high through time suggests that a significant quantity of solute is present in the hyporheic zone. The increase in variance and movement of center of mass over the injection period represent the arrival and spreading of solute through the study area. The subsequent decrease in variance suggests that the hyporheic zone is slowly flushed of this tracer after injection was stopped.

Acknowledgments

This material is based upon work supported by the National Science Foundation (NSF) under Grant Nos. EAR-0747629 and EAR-0911355. Any opinions, findings and conclusions or recomendations expressed in this material are those of the author and do not necessarily reflect the views of the NSF.

References

Acworth, R.I. and Dasey, G.R. (2003). "Mapping of the hyporheic zone around a tidal creek using a combination of borehole logging, borehole electrical tomography and cross-creek imaging, New South Wales, Australia." *Hydrogeology Journal*, **11**, 368-377.

Advanced Geosciences, Inc. (2008). Instruction Manual for EarthImager 2D v2.3.0.

Archie, G.E. (1942). "The electrical resistivity log as an aid in determining some reservoir characteristics." *Transactions of the American Institute of Mining and Metallurgical Engineers*, **146**, 54-61.

Bencala, K.E. and Walters, R.A. (1983). "Simulations of solute transport in a mountain pool-and-riffle stream: a transient storage model." *Water Resources Research*, **19**, 718-724.

Bentley, L.R. and Gharibi, M. (2004). "Two- and three-dimensional electrical resistivity imaging at a heterogeneous remediation site." *Geophysics*, **69**, 674-680.

Brosten, T.R., Bradford, J.H., McNamara, J.P., Gooseff, M.N., Zarnetske, J.P., Bowden, W.B., and Johnston, M.E. (2009). "Estimating 3D variation in active-layer thickness beneath arctic streams using ground-penetrating radar." *Journal of Hydrology*, **373**, 479-486.

Crook, N., Binley, A., Knight, R., Robinson, D.A., Zarnetske, J., and Haggerty, R. (2008). "Electrical resistivity imaging of the architecture of substream sediments." *Water Resources Research*, **44**, W00D13, doi: 10.1029/2008WR006968.

Dann, M.S., Lynch, J.A., and Corbett, E.S. (1986). "Comparison of methods for estimating sulfate export from a forested watershed." *Journal of Environmental Quality*, **15**, 140-145.

Day-Lewis, F.D., Singha, K., and Binley, A. (2005). "The application of petrophysical models to radar and electrical resistivity tomograms: resolution dependent limitations." *Journal of Geophysical Research*, **110**, B08206, doi: 10.1029/2004JB003569, 17 p.

Dogwiler, T. and Gernes, M. (2008). "Using electrical resistivity imaging to evaluate karst hazards in agricultural land planning decisions." *Abstracts with Programs-Geological Society of America*, **40**, 357.

Gooseff, M.N., Payn, R.A., Zarnetske, J.P., Bowden, W.B., McNamara, J.P., and Bradford, J.H. (2008). "Comparison of in-channel mobile-immobile zone exchange during instantaneous and constant rate tracer additions: Implications for design and interpretation of non-conservative tracer experiments. *Journal of Hydrology*, **357**, 112-124.

Harvey, J.W. and Wagner, B.J. (2000). "Quantifying hydrologic interactions between streams and their subsurface hyporheic zones." In Jones, J.B. and Mulholland, P.J., ed. *Streams and Ground Waters*. Academic Press, New York.

Keller, G.V. and Frischknecht, F.C. (1966). *Electrical Methods in Geophysical Prospecting*, Elsevier, New York.

Martinez-Pagan, P., Cano, A.F., Aracil, E., and Arocena, J.M. (2009). "Electrical resistivity imaging revealed the spatial properties of mine tailing ponds in the Sierra Minera of southeast Spain." *Journal of Environmental and Engineering Geophysics*, **14**, 63-76.

Nyquist, J.E., Freyer, P.A., and Toran, L. (2008). "Stream bottom resistivity tomography to map ground water discharge." *Ground Water*, **46**, 561-569.

Singha, K., Pidlisecky, A., Day-Lewis, F.D., and Gooseff, M.N. (2008). "Electrical characterization of non-Fickian transport in groundwater and hyporheic systems." *Water Resources Research*, **44**, W00D07, doi: 10.1029/2008WR007048.

Stream Solute Workshop (1990). "Concepts and methods for assessing solute dynamics in stream ecosystems." *Journal of North American Benthological Society*, **9**, 95-119.

Ward, A.S., Gooseff, M.N., and Singha, K. (in revision). "Imaging hyporheic zone solute transport using electrical resistivity." Submitted to *Hydrological Processes*.

ANALYTICAL AND GEOPHYSICAL ASSESSMENTS OF HEAVY METALS DISPERSION FROM AN AUTOMOBILE MECHANIC VILLAGE AND ITS POLLUTION PREVENTION.

Michael A. Nwachukwu
Montclair State University New Jersey, U.S.A
Huan Feng
Montclair State University New Jersey, U.S.A
Jude Alinnor
Federal University of Technology Owerri, Nigeria

Abstract

This paper assesses metal dispersion from Nekede mechanic village (MV) in the lower Imo River basin Nigeria, to introduce the concept of environmentally friendly MV. Analysis of composite soil samples derived from three replicates collected at each measurement point using atomic absorption spectrophotometer was carried out. Mean values (mg kg^{-1}) above the background, 0-200m from the MV are Pb, 853±572; Mn, 604±531; Cu, 137.3±202; Fe, 17713±4770; Cd, 3.4±12.8; Zn, 444±190, and Ni, 29.4±35.2 measured in the direction of drainage. The dispersion rates (mgkg-1/m) are Fe, 197; Pb, 12.9; Mn, 6.7; Zn, 4.9; Cu, 1.5; Ni, 0.3; and Cd, 0.04. Concentration and dispersion rates were confirmed by metal depth ratio (MDR), and metal distance ratio (MDsR). Electrical resistivity profiling showed metal dispersion to 350 m from the MV, representing a safe distance for farming in the direction of drainage. Both uphole refraction seismic and vertical electric sounding (VES) showed a weathered base (WB) average 18m, consisting of sand and gravel bed (GB). Water table (WT) at 16-21m fluctuates below and above the WB, showing that shallow wells located in areas where WT is above WB, and overlain by GB may easily be polluted by heavy metals. As a result, safe depth of shallow wells is: WT+48m were WB is above WT, and WT+66m were WB is below WT. Relatively higher elevation and slope (1:20) of the MV indicates greater metal dispersion dynamics. Pollution prevention model designs of infiltration basin and shallow water well are presented.

Introduction

An automobile mechanic village (MV) is an area of open land allocated to automobile repair workers within an urban area. A typical city may have one to three MVs, in proportion to its population and activities, whereas some cities have more. The Imo River basin is situated in the tropical rain forest belt of West Africa, where annual rainfall range from about 1700mm to 2500mm, annual temperature varies from 27 to 36^{o} C, and static water level fluctuates between 15.8 and 20.5m, (Onyeagocha 1980). It has a relatively limited land area (about 11,420 km^2) with high population growth rate and density (about 230 – 1400 person km^{-2}), and home of about eleven million people based on the 2005 Nigeria census. Geographically, the basin is a 140 km N-S trending sedimentary syncline located at the mid south-eastern part of Nigeria (Figure 1a). The most important rivers in the basin are the tributaries of the Imo River; Njaba, Otamiri, Oramiriukwa, Orashi, Awgu, Qua Ibo and the Aba Rivers Figure 1b). Mechanic villages are among the largest contaminated sites of serious ecological and public health concerns. The establishment of automobile MVs or the concept is on the increase, in response to the increasing demands by developing countries and supplies by the industrialized nations of used motor vehicles. Ajayi and Dosunmu (2002) estimated an increase in the importation of used motor vehicles from less than 500 in 1988 to about 30,000 in 2000, yet there is no commensurate increase in infrastructure to take care

of the excess in recent time. Abdulahi (2008) in analysing budgetary allocations and selected sectors' contributions to economic development in Nigeria, highlighted transport sector as central to economic activities and therefore paramount that this sector be given more attention than the government is currently doing.

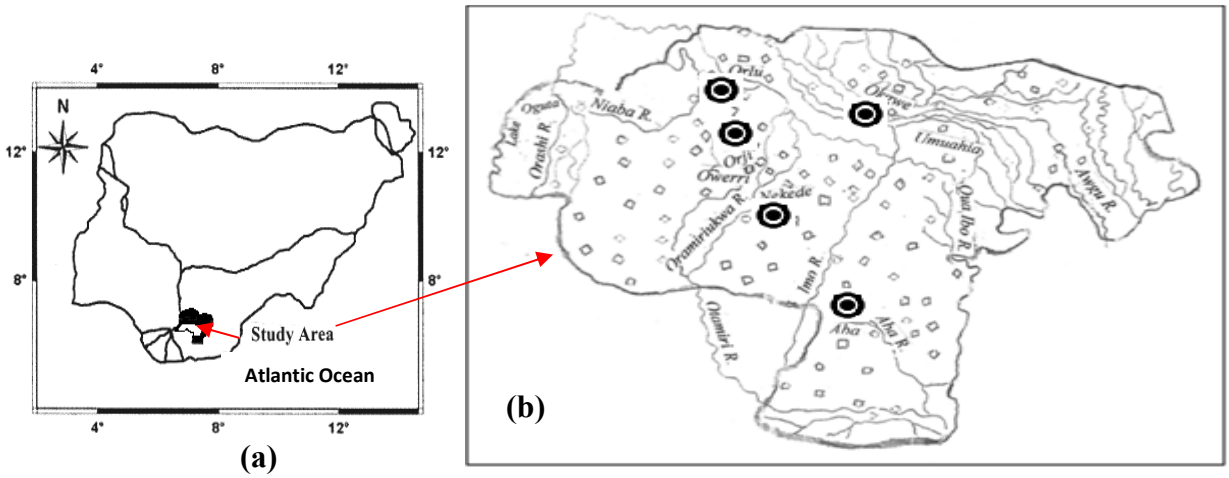

Figure 1: a. Map of Nigeria showing the Imo River basin, **b.** Drainage map of the Imo River basin

MVs have numerous advantages over a city wide spread of mechanic workshops. They save automobile owners the trouble of searching for mechanic specialists; to prevent motorists from falling into the hands of incompetent mechanics and to create opportunities for knowledge sharing among mechanics. They also serve as large scale skill acquisition centers for auto mechanics, auto-electricians, spray-painters, panel beaters and welders, spare parts fabricating and machine operators, spare parts dealers (old and new), particularly since the late 1980's when the import of used cars from Western Europe and the USA increased dramatically. MVs also improved urban aesthetics by removing a large number of degraded makeshift workshops scattered throughout the cities, and removing poorly dressed workers from the public eyes. In addition they provide accommodation for some of the trainees, space for spare parts shops, and restaurants, as well as yards for junk cars and unserviceable vehicles that would have otherwise constituted environmental nuisance in homes and public places. Despite the numerous advantages, MVs are poorly developed by the government proprietors, and thus lack occupational waste management. The Nekede MV is located in the sandy Benin Formation (Coastal plain sand), in the southwest flank of the lower Imo River basin (Figure 1a). While an automobile engine is running, the motor oil collects particles of heavy metals such as Pb, Cd, Cr, Fe, Mn, Zn and Cu. Used engine oil or transmission oil poured on the ground therefore enriches the soil with heavy metals, which can drain into both surface waterways and groundwater. Spilling waste automobile fluids on the ground, and the processes of metal corrosion thus enriches the soil with heavy metals.

Perhaps the most serious occupational hazard of mechanics is spraying and painting, as mechanics performing this task gets exposed to paint dust and fumes that may cause respiratory and pulmonary diseases. Fine particles of metals and paint become aerosol, eventually returning to the soil through rain or as settling dust. Figure 2 illustrates the expected interactions among pollutants, topsoil, surface water and groundwater within and around a mechanic village. These interactions constitute a cyclic process which is described as the mechanic village soil pollution cycle. High

environmental moisture due to extensive rain enhances corrosion of automobile body and the scrap metals that litter over years in Nekede MV, thus increasing the pollution of soil.

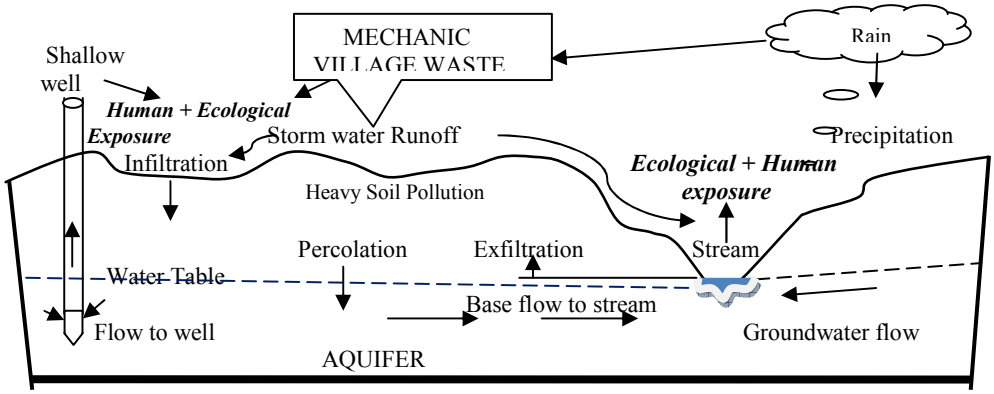

Figure 2: Conceptual soil pollution cycle within and around mechanic villages

Storm water from a mechanic village travels with the collected trace metals to surface and groundwater simultaneously. This is enhanced by the soil and the hydraulic characteristics of coastal plain sand of the study area. In the groundwater zone, a hydraulic conductivity of 20-26.41m/day, and Transmissivity of 500-1370m^2/day were obtainable in the area (Ekwe, *et al.* 2006). In Nigeria recently, soil pollution problems associated with automobile wastes has been reported (Onianwa *et al.,* 2001; Ipeaiyeda et al., 2007; Iwegbue 2007, Adie and Osibanjo 2009). However none of these papers contain a detail study of trace metal enrichment of soil in MVs, the trace metal dispersion dynamics from a mechanic village or specific control and remediation strategies.

The Nekede MV is used as a case study due to its large size 136 acres, its high workshop density of 3/acre approximately for 1000 mechanics, and its nearness to the city centre and poorly situated at the bank of the Otamiri river. In this paper, the distance and depth dispersion of trace metal from the Nekede MV are assessed. It is essential to establish a safe distance from a MV for farming, so that citizens may be prevented from untold exposure to toxic farm products and water supply. Nwachukwu (2008) stated that poor living environment in many developing countries are connected with lack of awareness and environmental education. Significant ecological impacts can be observed depending on the degree, depth and distance of dispersion of the metal contaminants.

Typical gully type in the Imo River basin 3a

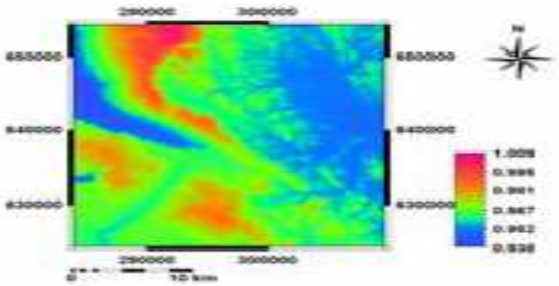

Soil loss due to gullies in the study area 3b

Figure 3: a. V-shape gully erosion site, **b.** Soil loss map from satellite imagery (Igbokwe *et al.* 2008).

Liu *et al.* (2007) observed that heavy metal concentration in soils is usually high near the sources, and decline with both distance and depth due to physical dilution and increasing restrictions in mobility. Depth of dispersion accounts for the bioavailability of contaminants, and the tendency for groundwater pollution. Though the threat posed by trace elements to human health and the environment is thought to be dependent on their speciation in the soil solution rather than the total concentration **(**Murray and Hendershot 2000). Metal speciation is expected to be enhanced in a sandy soil such as the coastal plain sand environment of the Nekede MV.

In a tropical rain forest belt of the study area consisting of coastal plain sandy soil, gully erosion becomes a common phenomenon as shown in figure 3a, and enhances the mobility of trace metals in soil profiles. Gullies are steep-sided ravines cut into susceptible, frequently shallow slope materials by the surface water from heavy rain falls. Once initiated, they offer avenues for easy down slope movement of water and particles (including metallic ions) from later storms, causing short resident time of trace metals in the affected soil profile (Figure 3a). Igbokwe *et al* (2008) estimated soil loss due to gully erosion in the study area as 9.23-9.93 Tons/Ha/yr based on the analysis of satellite imagery (Figure 3b). Local dredging and sand excavation in the Otamiri River channel directly behind the Nekede MV aggravates erosion which enhances metal dispersion around the MV. This study tested three mathematical relations: metal to depth ratio (MDR), metal to distance ratio (MDsR), and dispersion rate (DR) as composite parameters to explain heavy metal dispersion and pollution processes within and around a mechanic village located on sandy soil, in a tropical rain forest belt. It presented model designs to minimize pollution of soil and shallow wells in the area. Our secondary objective is to introducing the concept of environmentally friendly mechanic villages.

Materials and Methods of Assessments

Samples were collected at 0-15cm depth for the top layer, 15-30cm depth for the second layer, 30-45cm depth for the third layer, and longitudinal distances of 10, 50, 100 and 200m started from the edge of the MV site. Standard sampling procedure (Figure 4) was adopted for replicates and composite samples in the absence of a national guideline for soil pollution studies, but with cognizance to the remarks made by Okunade and Okunade (2007).

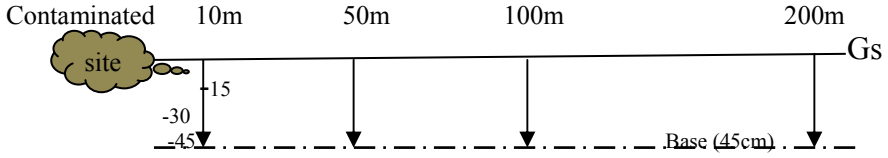

Figure 4: Soil sampling field procedure

The composite samples, each derived from three replicate samples were digested following the EPA method 3050B, and analyzed on a SOLAAR UNICAM 969 Atomic Absorption Spectrometer (AAS), at precision and accuracy better than 10% (Barabara *et al.* 2002). Metal dispersion and enrichment in soil profiles can be assessed by various methods, based on the available data, and interest of the study. Generally, factors such as concentration of the respective trace metals, infiltration rate or convective flux, moisture content, pH, and time are usually considered. According to Solaka (2007) a calculated rainfall intensity value of 25 mm/hr is considerable for the Imo River basin, and rate of soil detachment (F) in kg/m^2 to depend on detachability index. In this study we

have used metal depth ratio (MDR) eqn.1, and metal distance ratio (MDsR) eqn. 2, to assess the rate of metal dispersion, and used dispersion rate eqn. 3, to assess metal enrichment as a composite parameter to measure soil pollution. The relationships are mathematically represented as follow:

$$\text{Metal-Depth Ratio (MDR)} = \frac{Mi}{Depth} \quad \text{mgkg}^{-1}\text{cm}^{-1} \qquad (1)$$

$$\text{Metal-Distance Ratio (MDs)} = \frac{Mi}{Distance} \quad \text{mgkg}^{-1}\text{m}^{-1} \qquad (2)$$

$$\text{Dispersion rate (DR)} = \frac{\frac{\sum(Mi)}{n} - B}{D(ave)} \quad \text{mgkg-1/m} \qquad (3)$$

Where *Mi* represents the concentration of the i^{th} metal pollutant in the numbered tests, *B* is the background value of the ith pollutant; *D (ave)* is the average of measurement distance and *n* is number of tests.

A good number of people between twenty and thirty were interviewed in the MV during the field work about their occupational waste management, health and safety. These were the union executives (invited), mechanics and the associated workers who came to witness our field measurements or to understand what was going on. These mechanics reported occurrences of reddish coating over water collected from nearby shallow wells, if left in a container for some hours. The mechanics proved this by presenting their several water cans originally colorless or whitish but now having rust-brownish color and stains. To understand the dispersion mechanism and extent, with respect to distance and depth, including configuration of the subsurface, geophysical methods became necessary. Applicable geophysical methods however were based on data and instrument availability. Uphole seismic refraction data generated by Chevron Nigeria across the study area was obtained from Nwachukwu (2003), and both vertical electric sounding (VES) and electrical profiling techniques were conducted. For literature demonstrating the field techniques of electrical resistivity and uphole refraction seismic, the readers are referred to Dobrin and Savit (1988) and Telford *et al.* (1990). The apparent resistivity (Ω-m) at each measurement point was computed by multiplying the field resistance with a geometric factor eqns (4 and 5). In the VES, **L** is the current electrode spread (m), and ***l*** is the potential electrode spread (m). The apparent resistivity values were then applied in an automated Schlumberger analysis to obtain the VES curves, with number of layers constrained to the model curve. VES traversers were run east to west in the direction of regional strike.

Apparent resistivity $\rho_a = K \times R$ (Ω-m), where K = geometric factor; R = field resistance (4)

$$\rho_a = \frac{\pi[(L/2)^2 - (l/2)^2]}{l} R \quad \text{for VES, and } 2\pi aR \text{ for the profiling} \qquad (5)$$

A total of ten VES, were conducted within and around the MV 1 km from the span ends of the MV. All necessary precautions for VES measurement were duly considered for perfect selection of VES stations. Uphole velocity (V) eqn (6), and intercept time (Ti) eqn (7) were both important in the data processing. The two parameters can be obtained as follows:

$$V = \frac{(D+Z)}{T} \quad (6)$$

$$T_i = \frac{2D_w (V_B^2 - V_w^2)^{1/2}}{V_B V_w} \quad (7)$$

where Vw is the weathered layer velocity, Dw; the depth of weathered layer (low velocity layer), VB is the bedrock velocity (Enikanselu (2008), Z is travel distance inclined to the receiver (m), D+Z is total distance, and T is the arrival time milliseconds (m-sec).

The weathered depth or the low velocity layer can be used to estimate porosity, as a factor of contaminant transport in a suspected environment. Porosity is an important factor for determining rock velocity, and relationships have been developed between the porosity of a rock and its seismic velocity. In order to understand the characteristics of the topsoil regarding dispersion of heavy metals from surface to the groundwater zone, we collected replicate soil samples at the VES stations upstream and at the drainage collection zones downstream to obtain two composite samples. Clay-silt content, pH, moisture content, and bulk density based on the two composite samples were determined. In the field, we measured infiltration rate by applying the ASTM (D3385 – 2009) standard test methods for infiltration rate of soils in the field with a double-ring infiltrometer. Particle size distribution were determined through wet and dry sieving, and then classified according to the scheme described by Falk and Ward (1957), used by Nwachukwu (2004).

Results and Discussions

Analytical Result

Analytical results of Nekede MV (Table 1) soil shows spatial dispersion, which according to the order of relative abundance for seven metals is as follows: Fe > Pb> Mn> Zn> Cu> Ni> Cd (Figure 5). This order of abundance is accordingly supported by the values of MDR and MDsR. Both MDR and MDsR reveal that metal dispersion in soil from a point source may decrease or increase with both distance and depth in a discontinuous manner before the background level is reached.

Table 1: shows metal dispersion in soil (mg/kg) within the Nekede mechanic village.

Distance (m)	Depth (cm)	Pb	Mn	Cu	Fe	Cd	Zn	Ni
10	0-15	250	607.15	323.35	50000	11.16	445.7	10.5
10	15-30	1108.35	1996.45	255.1	47500	22.5	967.15	16.86
10	30-45	516.65	412.5	583.5	47875	51.5	424.3	60.5
50	0-15	1550	694.65	236.65	56250	20.11	915.0	19.45
50	15-30	1433.35	410.7	326.65	60000	10.6	795.7	98.78
50	30-45	1341.64	505.35	373.35	46250	14.45	852.15	12.41
100	0-15	1933.35	1026.8	418.35	52500	39.6	981.45	36.0
100	15-30	1908.35	669.65	228.35	47500	21.0	877.15	14.625
100	30-45	1666.65	753.55	945.0	48675	10.43	944.3	84.125
200	0-15	641.65	708.95	368.35	46250	12.4	836.45	12.3
200	15-30	1066.65	1891	240.0	45000	20.0	962.85	14.6
200	30-45	525	692.85	325.0	43750	11.0	889.3	96.4
Computations based on mean values								
Mean 90	30	1162±572	864±531	385±202	49295±4770	20±12.8	824±190	40±35.2
Mean MDR ($mgkg^{-1}$/ cm)		39	29	13	1643	0.7	27.5	1.3
Mean MDsR (mgkg-1/m)		13	10	4.3	547	0.23	9.2	0.4

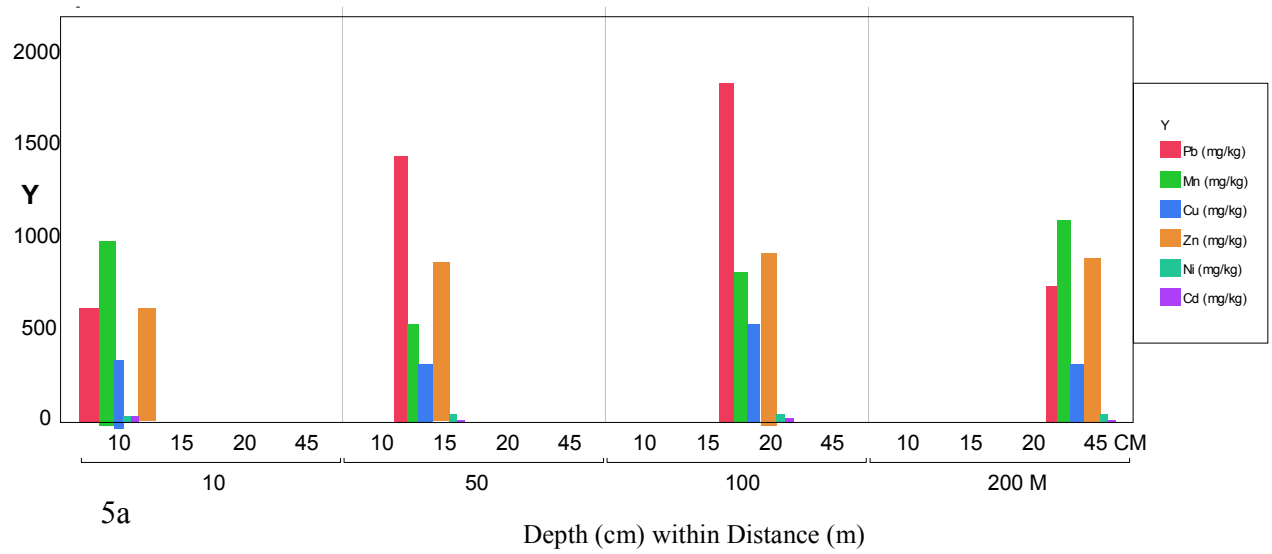

5a

Depth (cm) within Distance (m)

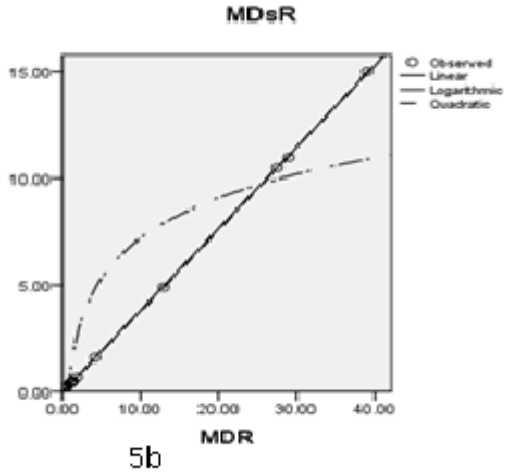

Figure 5: a Chart showing trace metal dispersion from the Nekede MV; **b.** Correlation analysis of MDR and MDsR of the Nekede MV.

Figure 5 explains that the spatial dispersion of trace metals follow a similar trend with respect to depth and distance. There is less significant decrease in metal accumulation within the 200m distance and the 45cm depth investigated, indicating that metal dispersion exceeds 200m. This implies that metal enrichment of soil does not immediately decrease with depth and distance from a point source, in a coastal plain sand environments of a tropical rain forest belt. The point of significant decrease in dispersion and storage to the background levels varies with metals over a number of factors such as rainfall intensity, drainage and slope, soil erodibility, infiltration rate and local terrain features. Zn and Mn have the widest dispersion, while Pb has greater accumulation between 15-20cm depth and 50-100 m distance from the Nekede MV.

Table 2: Dispersion rate of trace metals from Nekede MV based on mean values

Metal	Background (mgkg-1) B	Nekede MV (mgkg-1) M	Pollution (mgkg-1) M-B	Std Dev	Dispersion Rate (DR) (mgkg-1/m)
Pb	309	1162	853	572	12.9
Mn	260	864	604	531	6.7
Cu	248	385.3	137.3	202	1.5
Zn	380	824	444	190	4.9
Fe	31582	49295	17713	4770	197
Cd	17	20.4	3.4	12.8	0.04
Ni	10.3	39.7	29.4	35.2	0.3

On the other hand, in a silty-clay soil environment with poor rate of infiltration, terrain features and slope supportive of drainage, metal enrichment may tend to the order of distance. Fe being the second most abundant crustal metal after Al is expected to be of excessive abundance in the mechanic village. Based on mean values of the metals investigated, dispersion rates (Table 2) is in the order of: Fe > Pb > Mn > Zn > Cu > Ni > Cd.

Geophysical Results

Similar data were obtained from the ten upholes as presented in table 3. In the sample uphole curve (Figures 6a), the first break of seismic signal showed depth of 0.55-1.5m, representing the top soil. This was followed by an inflection point at depths 1.4-8.14m, representing a layer of silty-sand. A final break approximately at an average of 18.5m represented the weathered base, consisting of sand, or sand/gravel bed. This layer was not terminated, but the WB provided a seismic break that differentiated it from the rest of the layer (Figure 6 a and b).

Table 3: Uphole refraction data across the study area

Uphole	D1 (m)	D2 (m)	D3 (m)	Z1 (m)	Z2 (m)	Z3 (m)	T1 (m-sec)	T2 (m-sec)	T3 (m-sec)	V1(m/s)	V2(m/s)	V3(m/s)
1	1.2	5.4	18.3	5.7	11.6	16.5	26.4	25.3	18.4	260.9	670.89	1888.8
2	1	4.7	18.3	5.9	13	16.6	20.0	27.0	18.8	347.3	657.6	1856.4
3	0.76	5.8	18.3	5	12	17.1	18.1	27.0	18.1	318.2	658.9	1956.9
4	0.83	5.46	18.3	4.85	12.8	17	14.1	28.0	20.3	402	654	1739.7
5	0.76	6.7	18.3	5.9	14.2	20.34	20	32.0	19.8	328.6	654.5	1948.7
6	0.83	7.2	18.3	5.7	13	19.33	19.4	28.6	19.5	335.4	705.1	1928.7
7	1.2	6.3	18.3	5.8	11.13	16.25	15.6	26.0	17.8	449.4	670.7	1945.5
8	1.5	6.13	18.3	5.9	15	19.63	18	30.0	21.2	500	705.5	1789.2
9	1.2	4.9	18.3	4.7	12	19	12.6	25.1	20.3	469.1	674	1833.3
10	1.46	7.4	18.3	5.6	13	19.33	14.6	30.3	19.3	484.9	673.6	1945.6

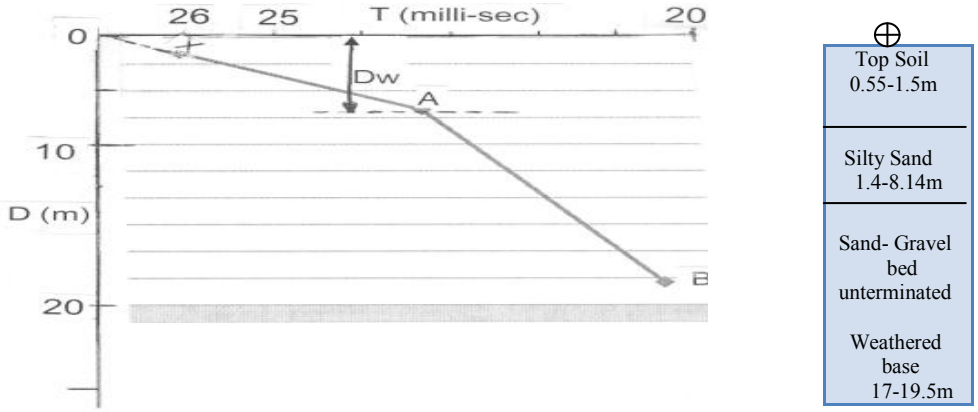

Figure 6: a Time-depth curves, b. 3-layer model of the weathered profile.

The six VES conducted around the area presented three characteristic type curves: K-type ($\rho1<\rho2>\rho3$), H-type ($\rho1>\rho2<\rho3$), and a combination of K and H (HK or KH) type curves (Figure 7). VES results similarly indicating that the near surface aquifer is unconfined, and followed by a sequence of highly saturated sand unit.

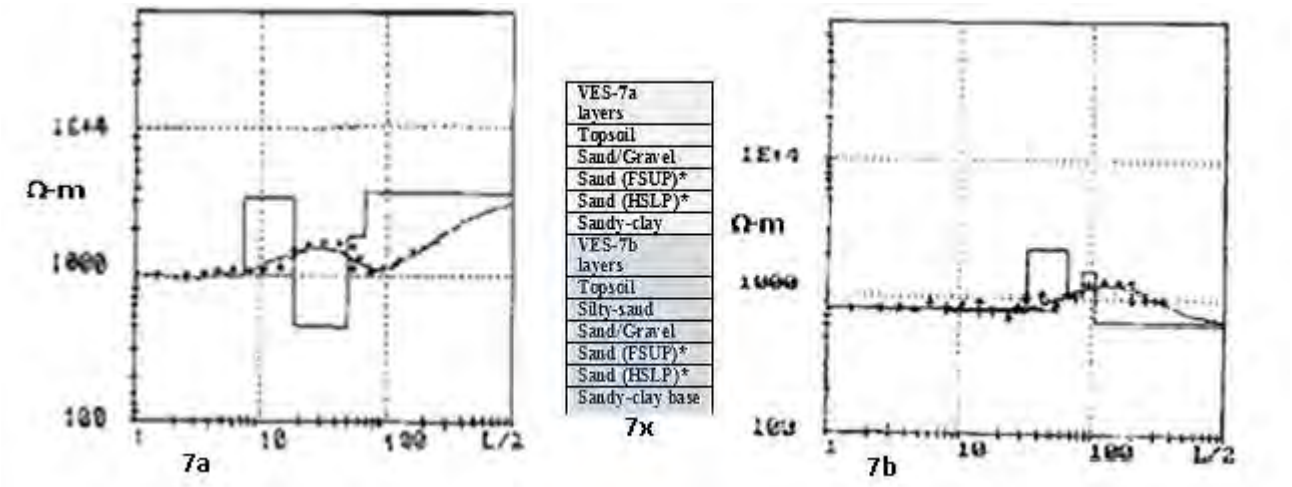

Figure 7: Sampled VES curves; a. polluted well site (GB in layer 2), b. unpolluted well site (GB in layer 3), 7x. Explanation of VES layers for the sample curves 7a and 7b. *FSUP (fairly saturated upper prospect) *HSLP (highly saturated lower prospect)

VES Curve (Figure 7a) has GB occurred in the 2nd layer within the weathered profile, which coincides with the water table, which may enhanced transport of heavy metals in the shallow aquifer that recharge the shallow wells. VES Curve 7b, has GB occurred in the 3rd layer, below the weathered base and water table, and shallow wells may not be polluted. VES results confirm depth of the shallow aquifer as varying between 76m to 86 m around the area, and our investigations confirm the existing shallow wells are of depth ranges 36.6m (120ft) to 55m (180 ft).

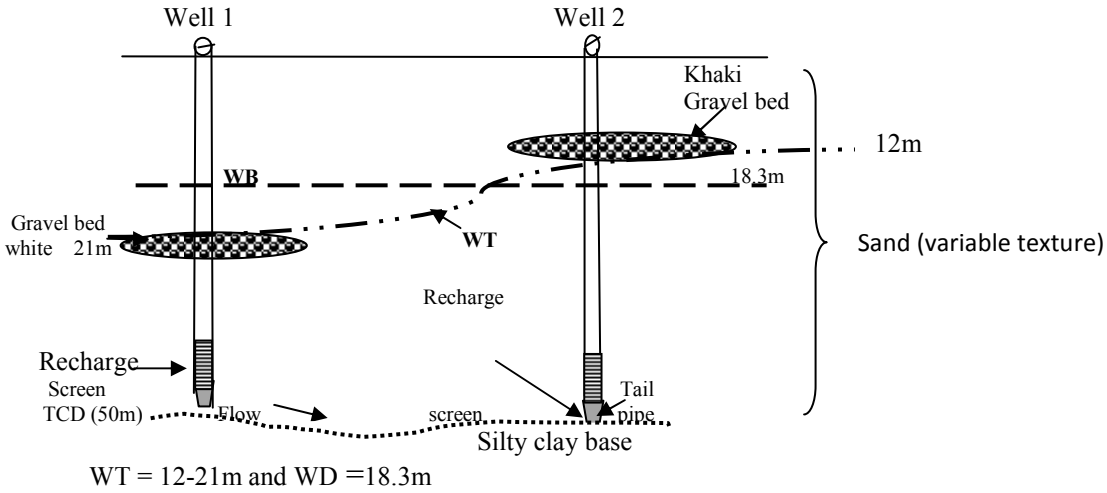

Figure 8: Subsurface model conditions for water quality variation among shallow wells due to heavy metal dispersion in the study area.

An explanation of a subsurface scenario for the selective pollution of shallow wells around Nekede MVs is shown in figure 8 based on the geophysics result. The gravel beds enhance vertical transport of heavy metals by increasing percolation into the recharge area of nearby wells. Water table (WT) may be higher or lower than WB, but frequently coincides with the base of gravel bed. This fluctuation controls the pollution of shallow wells by heavy metals in the Sandy lower Imo

River basin. Electrical resistivity and elevation profiles (Figure 9a and 9b) show the dispersion extent of heavy metals from Nekede MV. The area marked A in the resistivity profile is the active zone of the mechanic village in the direction of drainage (about 600m). The zone marked C is part of the active zone of the MV opposite the direction of drainage. The area marked B is the drainage collection zone characterized by lower resistivity and lower elevation (Figure 9b). This implies zone of higher conductivity which is attributed to the accumulation of trace metals transported by storm water. This suggests that trace metals from the Nekede MV is dispersed to a distance of B, approximately 350m from the edge of the MV in the direction of natural drainage over a slope of approximately 1: 20. The trace metal contaminants loaded storm water finally discharges into the Otamiri River (Figure 1b) without treatment.

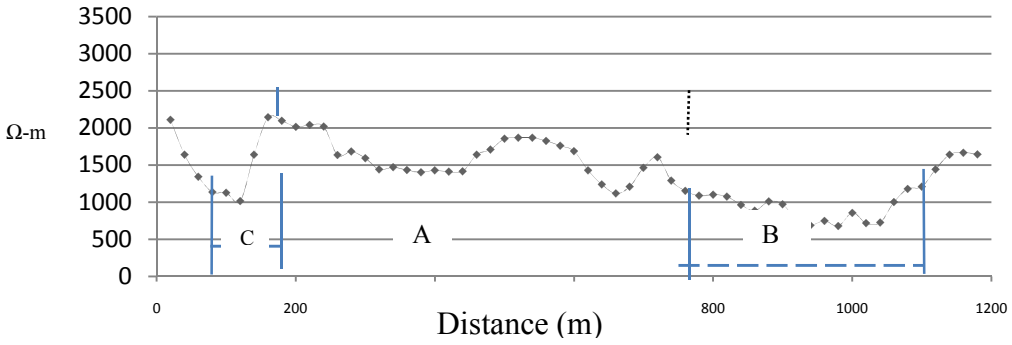

Figure 9a: Nekede mechanic village electrical resistivity profile. Traverse in the direction of drainage (west-east); Coordinates: 5° 31′ 15″ S, 7° 02′ 22″ W. Three impacted zones are shown: the active area (A), and zone (B) along the drainage, and a small zone (C) against the drainage. Mean Resistivity = 1513 ± 519.

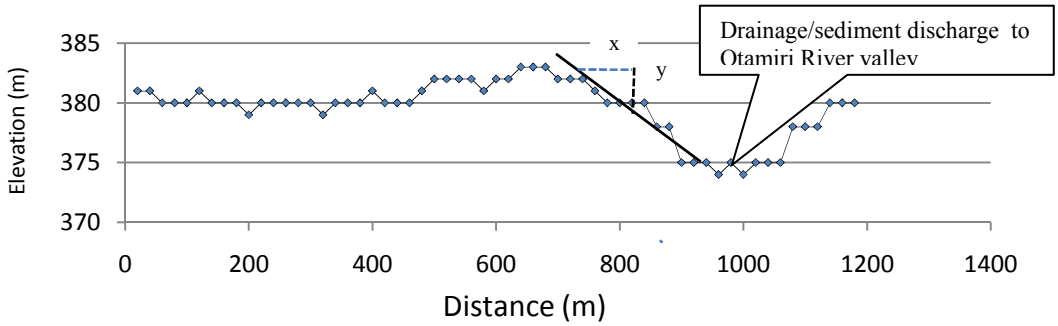

Figure 9b: Elevation profiles from Nekede Mechanic village in the direction of electrical resistivity profile.

Particle size analysis show grain size ranging from 0.0625 mm – 2.0 mm, most predominant in the range of 0.425 mm - 0.6 mm, with median 0.425mm size up to 27% of sample weight for depth 0-20 cm, and 17% of sample weight for depth 90-100 cm layer. Bulk density of the soil averaged 1.85 of soil layer 0-20cm, and 1.81 for soil layer 90-100cm. An average clay-silt content of 20% was obtained of the soil, indicating greater potentials for high infiltration rates (18-23cm/h). Generally, the topsoil has a mean pH of 4.3 and a moisture range of 20% - 70%, while ionic metal loading of the environment remained continuous. Values of the above measured parameters are supportive of rapid dispersion of heavy metals in soil profiles, capable of direct pollution of shallow wells.

Pollution Prevention

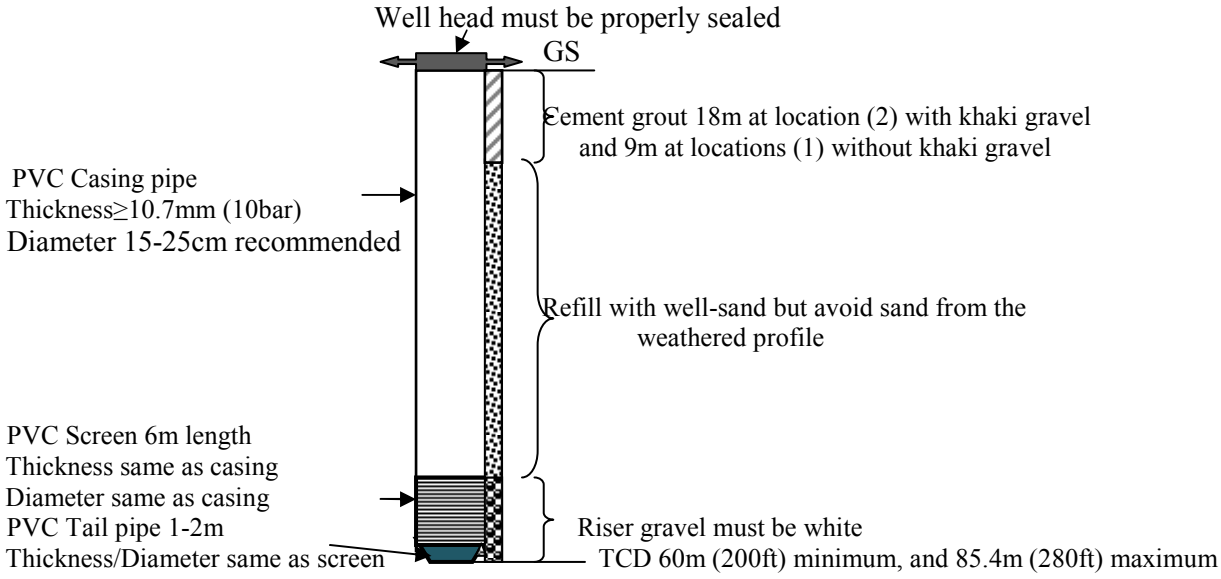

Figure 10: Model casing tally for shallow wells (pollution prevention model design) in the study area

A model design to control heavy metal pollution of shallow wells based on the scenario illustrated in figure 8 is presented in figure 10. In the areas where WT occurs below WB and no presence of gravel bed in the weathered layer shallow wells are not likely to be easily contaminated, whereas the reverse is the case at locations where WT is above WB. The most important aspects of the model for pollution control are the TCD, the annulus, depth of cement grout, size and nature of riser gravel, and well head protection.

For successful control of well pollution, casing to well annulus may not be less than 2 inches or approximately 5 cm. This implies that a shallow well planned to be constructed with a 6 inch (about 15 cm) diameter casing pipe requires a drill hole of not less than 10 inches (about 25 cm) diameter. This will provide allowance for proper filling, sorting and settling of gravel and sand packs during backwashing, thereby providing adequate filter column to the well recharge area. Depth of cement grout is very essential, but often this is neglected during completion. Drillers, irrespective of their level and their drilling tools are required to own a set of special riser pipes of not more than 1 inch or 2.5 cm diameter specifically reserved for measuring depths manually during their well completion operation, to ensure that the required depth of grouting is reached. Matching well head must be used, and based on the original casing diameter. Crossover from narrow to wider diameter casings, or from casing of poor quality to that of good quality are often practiced as a deceit by the drillers, probably to claim compliance with the contract specifications. Such practice may cause well pollution, because most contaminated wells are usually the shallow hand-dug rather than drilled, and have poor casing material (Comely, 1987). Rusting of a well head should not be allowed; the interior and exterior should be coated with anti rust material, and properly inspected during well servicing. Well head and the well platform may project to about 3ft (approximately 1meter) above the surrounding ground level to avoid being submerged by flood. Gonzales (2008) classified well head protection into poor, fair, and good, and observed that 71% of wells classified as having poor and fair wellhead protection were more vulnerable to pollution.

Figure 11 is a model of storm water treatment facility considered to be appropriate for the removal of heavy metals from MV storm water. The main treatment chamber (B) should be an infiltration basin if the topsoil and underlying material are sandy or a detention basin if they are shaly. The decision should not be based solely on the infiltration rate of the topsoil. Galli (1992), Pitt and Clark (2008), Obrompta and Kados (2007), and others have discussed the use of storm water management facilities to improve urban environmental quality. In mechanic villages, the natural processes of soil filtration, gravity, and phyto-extraction can be adapted to remove pollutants in storm water runoff before it follows the drainage system.

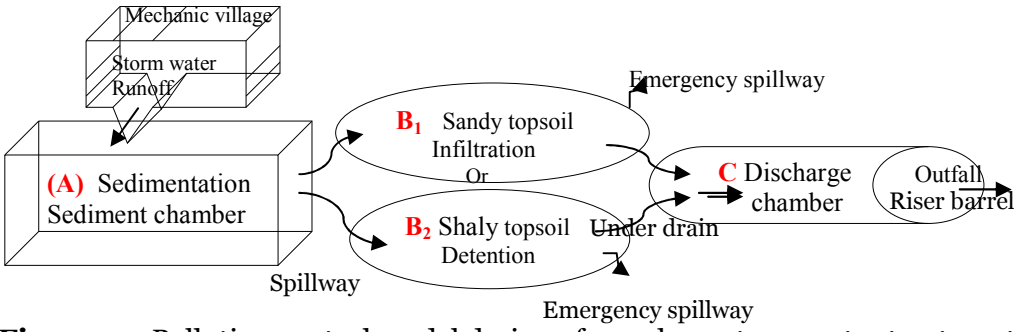

Figure 11: Pollution control model design of a 3-phase storm water treatment process applicable to mechanic villages

Two or more small shallow treatment basins should be adequate for most mechanic villages, depending on their size, and considered based on the local soil type, infiltration rate, and nature of the underlying material. Infiltration basins are not feasible if the infiltration rate is below 0.5 in/hr (Galli, 1992), but are useful at sites with infiltration rates between 0.5 - 3.0 in/hr or more. At Nekede MV infiltration rates of 4 - 6.0 in/hr were recorded indicating accelerated depth transport of heavy metals. Figure 11 is a model of a 3-phase storm water treatment process that may be applicable in mechanic villages with sandy topsoil, followed by sandy underlying rock. 'A' is a sediment chamber, 'B' is the central chamber (an infiltration or detention basin) and 'C' is a discharge chamber. Considerable depths of the treatment units are: (A) = 4 ft for an infiltration basin or 3 ft for detention basin; (B) = 2 ft for an infiltration basin or 3 ft for a detention basin; and C = 3 ft for either basin. The lengths of the treatment units depend on the size conceived for the treatment facility but the proportions of A, B and C by size recommended is approximately 1:3:2/3 respectively. The treatment chambers and pathways would require phyto-extraction of heavy metals using local plants. For MVs sited on shaly or silty-clay soil, detention basin (B2) is recommended, while a combination of infiltration and detention basins becomes appropriate in transition areas.

Conclusions and Recommendations

This study has successfully tested the mathematical relations of MDR, MDsR, and DR, as composite parameters in the analysis of heavy metals dispersion and storage from a continuous point source such as a MV. The paper has shown the application of electrical resistivity and uphole seismic refraction surveys in understanding possible subsurface lithology and complexity that could enhance dispersion of heavy metals to pollution of shallow wells in the vicinity of Nekede MV, which may be similar to other polluting sites. This study has shown that dispersion of heavy metals varies per metal, and distance of metal dispersion from Nekede MV is estimated at 350m in the

direction of drainage. This depends on elevation, slope, rainfall intensity, erodibility, characteristics of topsoil, nature of underlying materials and terrain features. Environmental impacts of metals dispersion from MVs are enormous, and require that MVs be environmentally friendly. The absence of storm water management facilities in MVs is regrettable, because heavy metals should be removed from storm water before it joins the city waterways. The already polluted soil within and around the MVs requires restoration, and local phytoremediation plants sensitive to Pb, Mn, Zn and Cu extractions are recommended. The difficulty in obtaining water samples from the predominant private shallow wells for research objectives and the suspected pollution of shallow wells around MVs demands the installation of groundwater monitoring wells within 500m from MVs in the direction of groundwater flow. The actual distance may depend on the proximity of human residence and shallow domestic wells to a mechanic village.

We recommend extended producer responsibility (EPR) for recycling or otherwise disposing of used engine and transmission oil rather than spilling on the ground. The EPR require that major petroleum marketers or their gas stations representing the producers are to decide on how best to manage the used motor oil. They may collect the used oil from mechanics on regular bases, whereas the mechanics may be required by law to preserve all used or waste motor oil for collection. Our goal is to introduce the concept of environmentally friendly mechanic villages that have concrete floor workshops, tarred roads with good drainage system linked to the storm water facility. They must have toilet facilities, because the absence of toilet facilities presently in mechanic villages having over 1000 human population daily is lamentable. The result is that the surrounding environments are littered with human wastes. High counts of coliform bacteria in shallow well water in different parts of Nigeria is a known issue (Adekunle et al. 2007, Olabisi et al. 2008, and Ejechi and Ejechi, 2007), etc. However none of these researchers have focused on tracing and evaluating the major source areas of the coliform bacteria. Environmentally friendly MVs require to be equipped with emission testing facilities, and to be supported by strong local and global CO2 emission control regulations. The emission testing facilities will provide a base for developing countries to participate in the efforts to reduce the rising global temperature. The plan should include a public health center, recreational facilities, and continued education program for mechanics, emphasizing on their occupational waste management and safety.

References

Abdulahi IB (2008). Budgetary allocations and selected sectors' contribution to economic development in Nigeria; *Pakistan Journal of Social Sciences* 5 (9) 894-898

Adekunle IM, Adetunji MT, Gbadebo AM, Banjoko O B (2007) Assessment of Groundwater Quality in a Typical Rural Settlement in Southwest Nigeria; *Int. J. Environ. Res. Pub Health*, *4(4)*, 307-318

Ajayi AB, Dosunmu OO (2002). Environmental hazards of importing used vehicles into Nigeria; Procedings of int. symposium on environ pollution control and waste management *Tunis EPCOWM* P 521-532

Barabara F, Stephen K, William W (2002) Speciation and characterization of heavy metals contaminated soil using computer-controlled scanning electron microscope; *Environ forensic 3: 131-143*

Comely HH (1987) Cyanosis in Infants Caused by Nitrates in Well Water, Journal of the *American Medical Association, v. 257, p. 2788-2792.*

Dobrin MB, Savit CH (1988) Introduction to geophysical prospecting 4th Ed McGraw-Hills New York

Ejechi EO, Ejechi BO (2007) Sociological dimensions in the handling habit and sanitary quality of hand-dug well water from oil-producing area of Nigeria; J. of Environ monitoring and assess 134: 255-261

Ekwe AC, Onu NN, Onuoha KM (2006) Estimation of aquifer hydraulic characteristics from electric sounding data: the case of middle Imo River basin aquifers, south-eastern Nigeria. *Journal of Spatial*

Hydrology; vol.6 No 2.

Enikanselu P (2008) Geophysical Seismic Refraction and Uphole Survey Analysis of Weathered Layer Characteristics in the "Mono" Field, North Western Niger Delta,Nigeria. *The Pacific Journal of Science and Technology* 539 Vol. 9 No. 2

Galli J (1992) Analysis of Urban BMP Performance and Longevity in Prince George's County Maryland: Metropolitan Washington Council of Governments, Washington, DC

Gonzales TR (2008) The effects that well depth and wellhead Protection have on bacterial contamination of Private Water Wells Estes Park Valley, Colorado *Jnl. of Env. Health, Vol*. 71

Igbokwe JI, Akinyede JO, Dang B, Alaga T, Ono MN, Nnodu VC, and Anike L (2008) Mapping and monitoring of the impact of gully erosion in SE Nigeria with satellite remote sensing and GIS *Remote Sensing and Spatial Infor Sc Vol. XXXVII B8 Beijing*

Ipeaiyeda AR, Dawodu M. (2008) Heavy metals contamination of topsoil and dispersion in the vicinities of reclaimed auto-repair workshops in Iwo Nigeria: *Bull of the Chem Soc. of Ethiopia 22(3), 339-348.*

Iwegbue CM (2007) Metal fractionation in soil profiles at automobile mechanic waste dumps around Port-Harcourt; *Waste Management & Research, Vol. 25, No. 6, 585-593.*

Liu C, Zhang Y, Zhang F, Zhang S, Yin M, Ye H, Hou H, Dong H, Zhang M, Jiang J, Pei L (2007) Assessing pollutions of soil and plant by municipal waste dump, *Environ Geol Vol. 52 (4), p641-651*

Murray VG, Hendershot WH (2000) Trace metal speciation and bioavailability in urban soils; *Environmental Pollution: Volume 107, Issue 1, P137-144*

Nwachukwu MA (2004) Determination of weathered layer by Up-hole shooting technique within Owerri, NE Nigeria: *Global journal of Geological Sciences* Vol.2 # 1

Nwachukwu M A (2008) Environmental sanitation enforcement and compliance best management strategies for Nigeria; Proc. *INECE 8th Int Conf.* ~ 5-11 April 2008 ~ Cape Town, S. Africa~ Track A

Obrompta C, Kardos J (2007) Review of Urban Stormwater Quality Models: Deterministic, Stochastic, and Hybrid approaches1 *J. of the American Water Res Assoc*, Vol 43, No 6 (2007), pp. 1508-1523.

Okunade JO, Okunade KA (2007) Towards Standardization of Sampling Methodology for Evaluation of Soil Pollution in Nigeria *J. Appl. Sci. Environ. Manage. Vol. 11(3) 81 - 85*

Olabisi OE, Awonusi1AJ Adebayo OJ (2008) Assessment of bacteria pollution of shallow well water in Abeokuta, Southwestern Nigeria; *Life Science Journal, Vol 5, No 1, 2008*

Onyeagocha AC (1980) 'Petrography and depositional environ. of the Benin Formation; Nig. *Jnl of Min. and Geol.* 17, 147-11

Onianwa PC, Jaiyeola OM, Egekenze RN (2001) Heavy metal contamination of topsoil in the vicinities of auto-repair workshops, gas stations, motor parks, Nigerian city: *Toxicol Environ. Chem., 84;33-39*

Pitt R, Clark SE (2008) Integrated Storm-Water Management for Watershed *Sustainability Journal, Vol. 134, No. 5, September/October 2008, pp. 548-555,*

Salako F (2008) Rainfall variability and kinetic energy in Southern Nigeria; Climatic Change Springer Netherlands; 1573-1480 (Online)

Telford WM, Geldart LP, Sheriff RE (1990) Applied geophysics; *Cambridge Univ. Press*

U.S Department of Transport (U.S DOT 2004); Federal highway administration: Application of geophysical methods to highway related problems. *Pub. No FHWA-IF-04-021 (2004)*

IS IT TIME FOR THE NEXT GENERATION RESISTIVITY INVERSION PROGRAMS?

William A. Sauck; Western Michigan University, Kalamazoo, MI

Abstract

The program RES2DINV and its variants have been widely used and have become the standard for electrical resistivity inversion software for nearly a whole generation of geophysicists, geologists, engineers and environmental technicians. It has been an extremely useful package, and for many geological environments it produces satisfactory depth results. However, there are many geological situations where the depth scale of the inverted (interpreted) section is quite exaggerated, giving the casual user the mistaken impression that detection depths are always a simple linear function of electrode spacing. This paper reviews the theory and points out some cases in which the depth of exploration is really much less than that implied by the vertical scale. It must be emphasized that the vertical scale of the output of this inversion program is always pseudo-depth, which does not equate to true depth in all situations. Suggestions are made for improving this shortcoming by compressing the model mesh upward by a factor proportional to the cumulative longitudinal conductance (S).

Introduction

Since its development by Loke (1994) and subsequent commercial release (Loke & Barker, 1996) the RES2DINV software for the inversion of 2-D electrical resistivity multi-spacing profile data has become very popular with both geophysicists and with non-geophysicist users. Various upgrades have been issued, extending it to 3-D cases, adding adjustments for topography, cross-borehole surveys, adding joint inversion with Induced Polarization data, forward modeling, etc. Because it is rather robust software, contains many options, and produces very striking and colorful output sections, it has been embraced by users from across the entire spectrum; from geophysicists to archaeologists, soils scientists, engineers, and environmental technicians. However, regardless of the appearance or not of a shallow conductive layer or layers along the measured profile, the program output always shows a constant depth along the inverted section (flat-bottomed solution). Unfortunately, today the majority of users does not have formal training in electrical resistivity theory and thus generally accepts these “flat-bottomed” solutions as valid. The solution should in fact be shallower, or “pulled up” below those parts of the section containing the conductive layers. This paper shows examples in the next two sections of how current lines can be “deflected” toward the horizontal, thus diminishing depth of penetration. Finally, a suggestion is made for progressively compressing the finite difference model mesh upward in the case of conductive layer(s) in the geoelectric section.

Conductive Surface Layer

The presence of a conductive layer at or near the surface is relatively common. In glaciated environments, a clay-rich till may overlie more resistive units such as outwash sands or gravels. In deltaic environments the fine-grained surface sediments may be highly conductive for a number of reasons – one of which is windblown salt aerosols from the coast. In semi-arid environments with restricted seasonal rainfall regimes, a conductive layer often develops near the surface as rising soil

moisture evaporates and leaves behind its ionic load. Targets for resistivity surveying in such areas might be a fresh-water aquifer or a conductive contaminant plume in groundwater underlying two or more other geoelectric units (such as soil, unsaturated zone, or clay lenses). The conductive layer at or near the surface tends to gather the current lines and limits their depth penetration. Additional conductive layers at greater depths tend to compound this tendency and limit depth penetration even further.

Anisotropy and Macro-anisotropy

Another common situation in which the penetration of current lines is much less than that expected or predicted for a homogeneous and isotropic medium is that where the soils are anisotropic such that resistivity is minimum in the horizontal plane (usually the plane of deposition of sediments). This can be at the microscopic or mineral grain scale as in shales, or at the scale of laminations of finely alternating material. On a larger scale, alternating layers of high and low resistivity units, each internally isotropic, cause an effect known as macro-anisotropy. This has the same effect of gathering the current lines into the uppermost low-resistivity layers, thus reducing the depth of penetration of the applied current lines, relative to the depth attained in a homogeneous medium.

Transverse Resistance and Longitudinal Conductance

Transverse unit resistance (T) of a layer is defined as the product of thickness and resistivity of that layer, or also as the summation of the h*? products of all the layers in a geoelectric section (Maillet, 1947). This is defined in the direction perpendicular to the bedding planes. The same layer has a longitudinal unit conductance (S), defined as the ratio of thickness divided by resistivity for that layer, or as the summation of the h/? ratios of all the layers in a geoelectric section under consideration. This parameter, S, is defined in the direction parallel to the bedding or lamination planes.

These two fundamental parameters are known as the Dar Zarrouk parameters, and are extremely important for anyone using electrical resistivity methods to understand. In fact, any vertical electrical sounding, or multi-spacing electrical profiling can only determine the approximate T-value for a high resistivity target layer, or the S-value of a low-resistivity layer. In other words, the h*? product is relatively well-determined for a high-resistivity layer, but the individual h and ? values can have an infinite number of values, within a reasonable range, (T-equivalence). Similarly, for a conductive layer, S, or h/?, is well-determined, but many different h and ? values can be used to match the sounding curve (S-equivalence). Interestingly, in EM induction surveying, it is the conductivity*thickness product that is really measured for a conductive target, which is the same as h/?.

Depth of Investigation

There have been numerous studies on the investigation depths of various electrode arrays and geometries. Roy & Apparao (1971) defined the depth of investigation as that depth at which a thin horizontal layer contributes the maximum amount to the total measured signal at the ground surface. In other words, this was the maximum point of the “depth of investigation characteristic”, or DIC curve. They examined only the homogeneous earth (single layer), and a 2-layer case. The need to account for the entire array geometry (not just the current electrode separation) was emphasized. By their criteria, the Schlumberger Array has a DOI of 0.125 L, where L is the current electrode separation (AB). Barker

(1989) also used the normalized DIC, or NDIC, and pointed out that it may be more appropriate to use the median point (rather than the maximum) on the NDIC curve to define the depth of investigation of a given array. By that criterion, the Schlumberger Array has a more favorable DOI of 0.191 L. He applied his analysis to the uniform half-space model, but also showed results for 3-layer maximum and minimum type curves. Oldenburg & Li (1999) extended the DOI discussion to the inversion of 2-D data sets, involving discrete block models embedded in a uniform half-space. They emphasized that any resistivity inversion is not unique, *ie*, that there are an infinity of possible solutions. Bhattacharya and Sen (1981) were among the first to examine the depth of investigation for the case of an anisotropic subsurface.

In summary, these methods for examining depths of investigation should not be used for more than they were intended. They are in fact primarily for comparing the theoretical performance of the many different possible electrode arrangements, and usually based on a uniform half-space. None of them can predict *a priori* the depth that a given array can detect a layer or discrete body at a field area where the overlying electrical resistivity distribution is unknown. Unfortunately, this has been overlooked by some users, to the extent that 3 fixed Wenner Array spacings are prescribed for measuring to 3 fixed depths for pipeline corrosion studies (ASTM G57-78). The presence of a shallow conductive layer can greatly reduce the DOI.

Example

In SW Michigan the geologic section (resulting from the last glacial advance) in areas of groundwater investigations commonly involves a shallow or surficial layer of clayey till overlying a thick outwash unit of clay-free sand and/or gravel. If the water table is relatively deep, this constitutes a section with less than 100 Ohm-m at the surface, 2000-3000 Ohm-m for the vadose zone sand, and 20-50 Ohm-m for the saturated sand. At some locations the surface till is absent, leaving a simpler 2-layer case with high-resistivity sand at the surface.

These two cases are represented for comparison by the 1-D forward models of Vertical Electrical Soundings (VES) using the Schlumberger Array shown in Fig. 1. Where present, the surficial till is about 1 m thick, and the depth to water table is about 6.5 m. As can be seen, the falling portion of the VES curve, which defines the aquifer unit, has a very significant displacement to the right for Case B. One can use various criteria to define the AB/2 or the half current electrode spacing at which the aquifer unit is detected. If we choose the value at 75% of the peak value on the curve, this occurs at AB/2 of 8 m for Case A, and at AB/2 of 44 m for Case B. The ratio of these current electrode spacings with and without the conductive layer is then 5.5. If we choose the value for detection of the lower layer at the point where resistivity falls to 50% of its peak value, the two current electrode spacings are 12 and 55 m, or a ratio of 4.6. Another criterion for detection of the lower (aquifer) unit might be the spacing at which the descending curve has a maximum slope. At this point the resistivity of the lower or target layer is better defined. In this case, the necessary electrode half-spacings are 25 and 85 m, or a ratio of 3.4. Thus, in this simple exercise it can be seen that with a relatively thin surface layer that is moderately conductive, the current-electrode spacing must be in the range of 3.4 to 5.5 times greater than where the surface layer is absent, in order to detect the aquifer unit.

This example is not an extreme model, as the conductive layer resistivity can be much less in some environments such as saline soil, making the ratios even greater. However, the added effort in extending the array that is required to detect the target layer in Case B, relative to Case A, is already very large for the cases shown. The common rules of thumb for choosing the spacing necessary to reach

the aquifer depth all fail when the surface conductive layer is present. When a multi-spacing resistivity profile is done across the boundary where Case A is at one end and Case B at the other end, and the data inverted using RES2DINV, a "flat-bottomed" solution is always presented, implying that the depth of exploration is the same along the entire profile. The inverted solution depth for such a profile should conform to the far smaller depth of investigation at the right end of the profile (Case B), as defined in the above paragraph. It is the constant-depth solution that I feel should be modified in future versions of such inversion software. It has given the false impression to a whole generation of students and users of RES2DINV that depth of exploration is a constant for a given electrode array and separation.

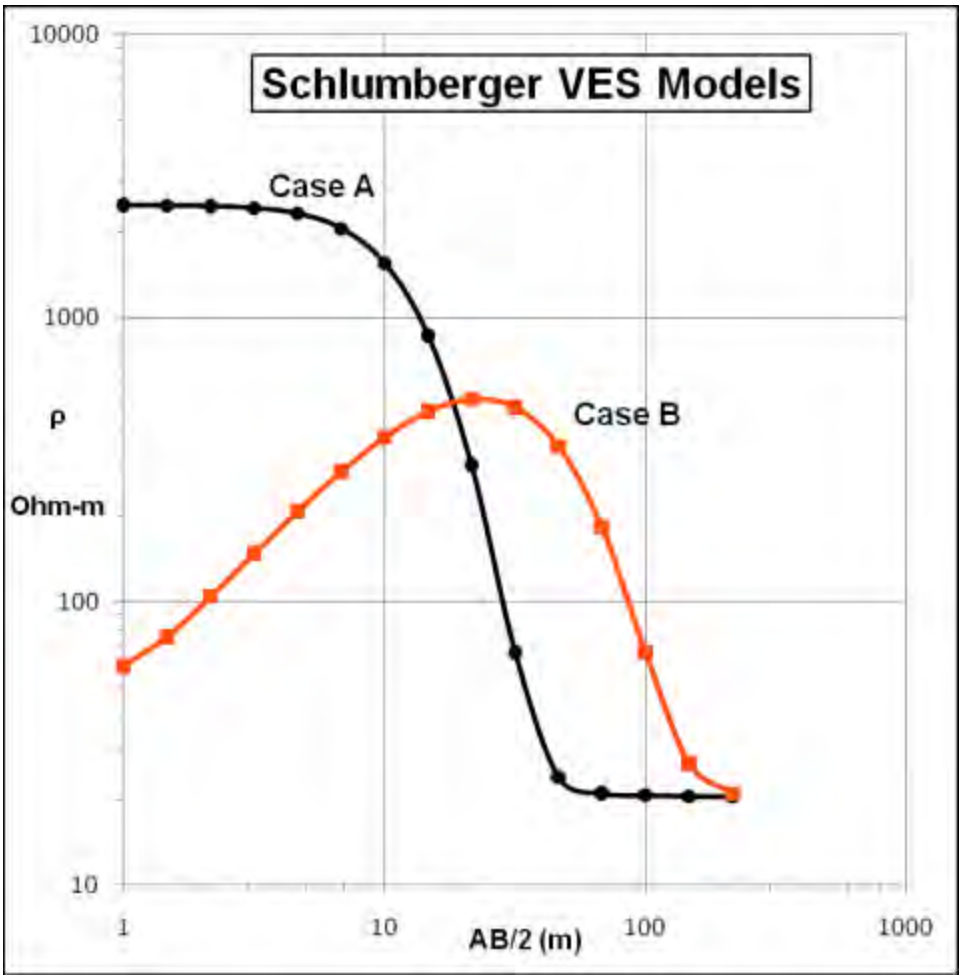

Figure 1: Forward model VES curves for the Schlumberger Array. Case A is for a 6.5m vadose zone of resistivity 2500 Ohm-m overlying a 20 Ohm-m aquifer. Case B has the same depth to the aquifer, but contains a 1m-thick surface layer of 50 Ohm-m.

Discussion

The RES2DINV program has been a powerful and important routine used world-wide for nearly a generation by geophysicists and by many more who are not geophysicists. For many resistivity

profiles the above shallow conductive layer conditions do not apply. But, there are published inversion sections that clearly contain shallow low-resistivity layers and lenses that show the "flat-bottomed" solution. Experienced geophysicists know that the inversion result can not have constant depth below a profile having variable surficial resistivity. However, many and perhaps the majority of users do not have this insight and thus are being led to believe that the resistivity method explores to a depth that can simply be predicted by knowing the maximum electrode spacing, for a given array. Or, they take it at face value as being correct because it was produced by a computer. In any case, I think it is time to work on improving the software to account for variable depths of investigation along a resistivity transect. This would probably require more iterations, early ones to look at the approximate layering structure by assembling equivalent VES's at various locations along the transect (analogous to velocity determinations along a reflection seismic profile), and later ones to modify the model mesh accordingly. Presumably, the model mesh would have to be compressed upward progressively below each conductive layer or significant lens. The amount of compression could be determined by resistivity contrasts (ratios) at the base of the conductive layer(s), or by an amount related to the cumulative "S" value to that depth at the various locations where an equivalent VES was produced. In the end, the base of the inverted section would not be flat.

References

Barker, R.D., 1989, Depth of investigation of collinear symmetrical four electrode arrays. Geophysics, Vol. 54, pp. 1031-1037.

Battacharya, B.B. and Sen, M.K., 1981, Depth of investigation of collinear electrode arrays over homogeneous anisotropic half-space in direct current methods. Geophysics, Vol. 46, pp. 768-780.

Loke, M.H., 1994, The inversion of two-dimensional resistivity data. Unpubl. PhD thesis, Univ. of Birmingham.

Loke, M.H. and Barker, R.D., 1996, Rapid least-squares inversion of apparent resistivity pseudosections using a quasi-Newton method. Geophysical Prospecting, Vol. 44, pp. 131-152.

Maillet, R., 1947, The fundamental equations of electrical prospecting. Geophysics, Vol. 12, pp. 529-556.

Oldenburg, D.W., and Li, Y., 1999, Estimating depth of investigation in dc resistivity and IP surveys. Geophysics, Vol. 64, pp. 403-416.

Roy, A. and Apparao, A., 1971, Depth of investigation in direct current methods. Geophysics, Vol. 36, pp. 943-959.

SEAFLOOR RESISITIVTY INVESTIGATION OF METHANE HYDRATE DISTRIBUTION IN MISSISSIPPI CANYON, BLOCK 118, GULF OF MEXICO

John Dunbar, Baylor University, Waco, TX
Alan Gunnell, Baylor University, Waco, TX
Paul Higley, Specialty Devices, Inc., Wylie, TX
Markus Lagmanson, Advanced Geosciences, Inc. Austin, TX

Abstract

We test the applicability of the direct current resistivity method for marine methane hydrate investigations. Methane hydrate is an ice-like compound found in near-bottom sediments in deep-marine environments. Hydrate-bearing sediments have resistivities ranging from 1 to 100 Ωm for saturation increasing from zero to 100%. The seafloor resistivity system used in the study is based on an existing engineering-scale land system. It consists of electronic components mounted in a pressure housing and a 1.1 km long, 56-electrode array constructed using graphite electrodes and high-pressure cable and connectors. For continuous resistivity profiling, the system is attached to a remotely operated underwater vehicle, which provides power, remote control functions, and navigational data. In June 2009, the system was towed along the seafloor across a known hydrate mound in 1 km water in Mississippi Canyon, Block 118. Seven profiles, totaling 26 km in length were collected. Inversions of the resistivity profiles were performed using a fixed seawater resistivity. Areas within the mound are underlain by resistivity anomalies ranging from 3 to 100 Ωm, in contrast to resistivities between 0.6 and 1.0 Ωm in areas adjacent to the mound. The 100 Ωm resistivity anomalies, likely associated with massive hydrate, occur where deep-seated normal faults intersect the seafloor.

Introduction

Methane hydrate is an ice-like compound that forms from methane and water beneath permafrost in the Arctic and in near-bottom sediments on continental slopes (Sloan, 1998). Interest in geophysical methods for identifying and mapping hydrate deposits stems from its potential as a drilling hazard, future energy resource, and possible contributor to climate change. Marine deposits are commonly associated with bottom simulating seismic reflectors (BSR) (Markl et al., 1970; Shipley et al, 1979). BSR are essentially bright spots that occur at the base of the hydrate stability zone (HSZ), where hydrate-saturated sediments form a seal, trapping free gas below the stability zone. Within the stability zone, hydrate-bearing sediment can be recognized in borehole and remote geophysical data by association with increased seismic velocity and electrical resistivity. Seismic velocity more than doubles and resistivity increases from less than 1 Ωm to more than 100 Ωm as hydrate saturation increases from zero to 100 %. In the marine environment the base of the hydrate stability zone (BHSZ) ranges from less hundred meters to over a kilometer beneath the seafloor, depending on water depth, bottom temperature, and the local geothermal gradient. This places marine hydrate investigations on the cusp between the normal depth ranges of near-surface and petroleum-scale geophysical methods, albeit on the deep seafloor. To date, most investigations have been done with petroleum-scale, multi-channel seismic and/or controlled source electromagnetic methods. These methods have the penetration needed to reach objectives at the deep end of the BHSZ depth range, but lack the resolution achievable with near-surface methods, which could be applicable at the shallow end of the range.

In this study, we use the DC resistivity method to conduct a reconnaissance survey of Woolsey Mound, Mississippi Canyon, Block 118 (MC118) (Figure 1). This is a particularly well studied example of a hydrate deposit in relatively shallow water (< 1 km) and with a relatively shallow BHSZ (~100 m). The idea is to use high-resolution geophysical methods to study shallow hydrate deposits, as a guide to the morphology and workings of marine hydrate systems in general. At Woolsey Mound, methane vents at the seafloor occur where deep-seated faults that flank a salt dome provide a path for thermally-derived gas to migrate up from depth. The BHSZ is particularly shallow at this site because of an elevated geothermal gradient caused by focused heat flow above the salt dome and the vertical movement of water from depth. An additional complicating feature is that microbes feeding on the methane and higher-order organisms feeding on the microbes have produced carbonate mud, which has consolidated to form a carbonate mound on the seafloor.

Figure 1: Location map of Woolsey Mound in Mississippi Canyon Block, 118, Gulf of Mexico.

For the past ten years, the mound has been studied by the Gulf of Mexico-Hydrate Research Consortium (GOM-HRC), which is a group of universities, private companies, and State and Federal agencies, headed by the University of Mississippi. To date GOM-HRC has investigated Woolsey Mound using a manned submersible and a remotely operated vehicle (ROV). The site has been photographed and probed by gravity coring, near-bottom multi-beam bathymetric profiling, acoustic sub-bottom profiling, and single channel seismic profiling. The group has also interpreted an industry 3D seismic data set over the site. This work has established that there are active gas vents at the site, with irregular of blocks of carbonate and massive hydrate exposed on the seafloor near the vents. The hydrate blocks are not stable on the seafloor and dissolve over a period of a few months to a year. Hence, the hydrate must form below the bottom, prior to its exposure on the seafloor. A possible BSR at a depth of about 100 m beneath the mound has also been identified on the 3D seismic data. However, because of the combination of scattering from irregular carbonate blocks and signal attenuation due to disseminated free gas, the mound is a no record area for both the sub-bottom acoustic and single channel seismic data. Hence, the distribution of hydrate within the stability zone remains unknown. The reconnaissance survey conducted in this study was done to test the extent to which the sub-bottom hydrate distribution at Woolsey Mound can be determined using the DC resistivity method.

Seafloor Resistivity Profiling for Hydrate Exploration

Instrumentation

To test the applicability of the electrical resistivity method to shallow hydrate investigations, we adapted an existing engineering-scale land resistivity system for use on the deep seafloor. The electronic components of an eight-channel resistivity instrument with a 2 A maximum output current are installed in a pressure housing with a 1 km maximum working depth. The electrode array is 1,100 m long, with 56 graphite electrodes spaced 20 m apart. The array is constructed from high-pressure, multi-conductor cable with internal water-blocking material added to prevent seawater intrusion. The link to the resistivity instrument is made though a high-pressure underwater connector that penetrates the housing. Graphite electrodes are used to prevent corrosion damage during long deployments. This array is intended to serve as a general-purpose seafloor array for conducting a variety of experiments, including continuously towed resistivity profiling (CRP) and long-term, fix deployments.

For continuous profiling, the instrument and array are attached to a ROV (Figure 2). The ROV provides power to the system from its onboard battery and remote control communication with the surface ship via a fiber optic connection through its tow cable. The ROV is also equipped with an ultra-short-baseline acoustic tracking system. An acoustic beacon mounted on the ROV communicates with an acoustic array mounted on the surface ship, which when combined with the GPS ship navigation provides the geographic position of the ROV. An independent acoustic altimeter continuously measures elevation of the ROV above the seafloor. Surveys are conducted by lowering the ROV and electrode array to the bottom and towing the ROV 10 to 20 m above the seafloor, with the array trailing behind on the seafloor (Figure 2 b). Tow speeds are kept between 0.5 and 1.0 knot to limit streaming potential noise on the electrodes and to keep the active segment of the array on the seafloor.

Field parameters

In addition logistical challenges, there are geophysical challenges as well as benefits to collecting resistivity data in the deep marine environment. The main challenge is low signal level. With seawater resistivities of about 0.33 Ωm and near-bottom sediment resistivities averaging about 1.0 Ωm, voltages measured between potential electrodes are an order of magnitude lower than those measured on land at comparable offsets. On the positive side, achieving good electrical contact with the medium, which is the bane of land resistivity work, is never a problem in seawater. The deep seafloor is also electrically quiet at frequencies of 1 Hz and higher. Instrument and electrode noise are normally the limiting sources of noise. To minimize electrode noise when using multiple array configurations, A and B electrodes are not reused as potential electrodes in the other arrays. This results in small deviations from the uniform electrode spacing in standard array geometries.

At the engineering scale, the deep marine environment acts approximately like the interface between two half spaces, with an upper half space with the resistivity of seawater, ρ_w and a lower half space with the resistivity of shallow marine sediments, ρ_s. The solution of this problem for a general four-electrode resistivity measurement on the seafloor can be found using the method of images, as is done for the conventional half-space problem (Roy, 2008)

$$\Delta V = \frac{\rho_w \rho_s I}{2\pi(\rho_w + \rho_s)}\left(\frac{1}{AM} - \frac{1}{AN} - \frac{1}{BM} + \frac{1}{BN}\right), \quad (1)$$

where ΔV is the potential difference between the M and N electrodes, I is the injected current, and AM, AN, BM, and BN are the respective distances between the A, B source electrodes and the M, N potential electrodes.

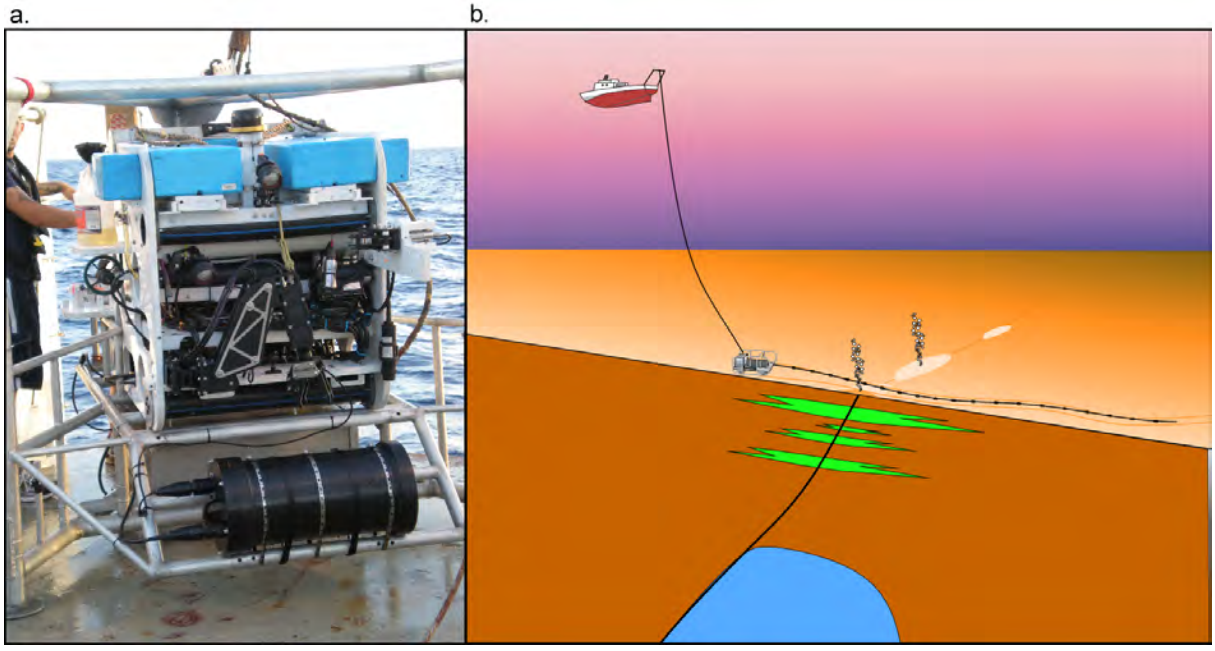

Figure 2: Seafloor resistivity profiling system. (a) Electronic components of the resistivity instrument are contained in the black, cylindrical pressuring housing mounted to the front of an ROV. There are two high-pressure connections to the housing. One connection provides power and remote control functions from the ROV and the other is attached to the 1.1 km long electrode array. (b) To conduct a survey, the ROV, with the instrument and array attached, are towed continuously at an elevation of 10 to 20 m above the bottom.

Voltage levels versus offset for different array types and lengths can be predicted from Equation 1, combined with knowledge of the falloff in injected current versus A-B offset. When continuously towing the array, it is necessary to collect data rapidly. For this reason, array configurations, such as the dipole-dipole and gradient arrays, that allow full use of the eight-channel capability of the system are preferred. The predicted system performance in the typical hydrate-free, deep seafloor setting indicates that offsets achievable with gradient arrays are significantly greater than for dipole-dipole arrays (Figure 3). Hence, for cases in which depth of penetration is desired over resolution, the gradient array is the best choice. For the current system with offsets up to 400 m, signal-to-noise ratios are expected to range from 10 to over 100, and result in average noise levels of approximately 5%. Because the gradient array is a generalization of the Wenner array, maximum depths of investigation are expected to be approximately one-third of the array length, or 133 m. Higher received voltage levels, allowing larger offsets and greater penetration, would occur in areas with higher sub-bottom resistivities, such as expect for hydrate deposits.

The field procedures for collecting seafloor resistivity data using the CRP method are essentially the same as those used for collecting CRP data in shallow water (Dunbar et al., 2008). In the shallow-water case, the array is towed on the surface of the water directly from the survey boat. The profile heading is maintained until the array is straight behind the boat and then recording is begun. The GPS

track of the boat is then used to reconstruct the locations of the electrodes during the survey, assuming that the array follows the track of the boat. In the seafloor case, the acoustically measured track of the ROV is used in place of the GPS track of the survey boat of the shallow-water case. The main difference is that the orientation of the array cannot be check visually. Instead, we reach and maintain the desired profile heading for at least one array length before the start of recording. Experience from shallow-water profiling indicates that this is sufficient to insure a straight array. Because the array is pulled along the bottom, its path is not expected to be influenced by cross currents in the water column.

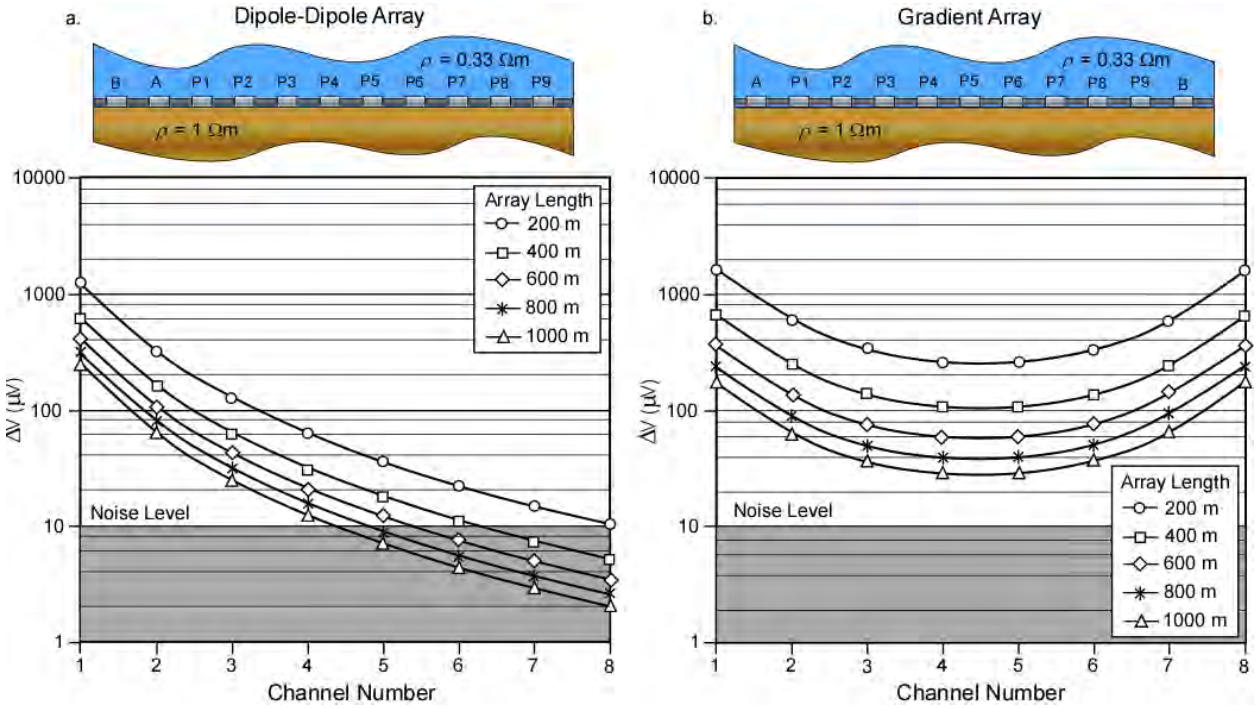

Figure 3: Predicted performance of the seafloor resistivity system. (a) Dipole-Dipole array. (b) Gradient array. The total noise level on the seafloor was estimated by computing the root-mean-square voltage in the last of six 200 ms IP windows, after a 2 s charge cycle. This noise estimate includes system noise, electrode noise, residual IP effects from the previous reading, as well as any ambient noise present on the seafloor.

Data processing

Processing seafloor resistivity data collected using the CRP method is also similar to the processing of CRP data collected in shallow water (Dunbar et al., 2008). The geographic coordinates of the track of the ROV are merged with the resistivity data, using time-of-day recorded with each entry in both data sets. In the shallow water case, the electrode elevations are assigned a constant elevation, referenced from the water surface. In the seafloor case, seafloor topography influences the results, just as topography influences a land survey. In principle, the z-coordinate of the electrode locations could be computed by summing the readings from the ROV's depth gauge and acoustic altimeter for each time point. However, the depth gauge is intended for navigational purposes and is not sufficiently accurate to produce a usable bathymetric profile. Instead, we estimate the z-coordinates for each x, y electrode location from independently collected, near-bottom, multi-beam bathymetric map of the survey area.

The electrode locations are then projected onto a best-fit straight line through the profile and exported in terms of positions along the line of the straight profile.

As is the case for most shallow water CRP data sets, the seafloor profiles are normally too long to be efficiently inverted all at once. Instead, the long lines are divided into multiple, overlapping segments. The segments are inverted independently and then merged to reconstruct the long inverted profile. In the seafloor case, water depth information along the profile is used to construct a variable-thickness water layer above the model seafloor in the finite element model region. During the inversion, the resistivity of the water column is fixed to a constant value, consistent with the average water column resistivity within 300 m of the bottom, measured on the day of the survey.

Results

In June 2009 we used the seafloor resistivity system to collect seven CRP profiles totaling 26 km in length over Woolsey Mound and the surrounding area of MC118 (Figure 4). The CRP data were collected using consecutive reads of five gradient arrays of expanding lengths of 220, 380, 600, 800, and 1100 m, continuously repeated along the profiles. At the end of the survey, we collected a vertical electrical conductivity profile from the surface to the seafloor with an independent instrument. This profile indicated an average seawater resistivity of 0.36 Ωm within 300 m of the seafloor. As expected, not all of the array offsets provided useful information. We evaluated the quality of the measurements by comparing the average and standard deviation of the full-space apparent resistivity by channel for each array length over the entire survey. For this environment, average apparent resistivities in the 0.4 to 0.5 Ωm range are reasonable. In addition, standard deviations of the apparent resistivity are expected to be less than the average. For all array lengths, channels 1 and 2 produced unreasonably low and high apparent resistivities, respectively. Both criteria were met by the remaining six channels for the 220 m array, channels 3, 6, 7, and 8 of the 380 m array, and channels 3 and 8 of the 600 m array. None of the measurements collected with the 800 and 1100 m arrays provided useful information. As a first step in processing the CRP data from the June 2009 survey, all channels and array lengths that did not meet the average apparent resistivity and standard deviation criteria were removed. The remaining measurements were processed as described in the previous section. Example inverted profiles are shown in Figures 5, 6, and 7.

Line 1 starts on the north central flank of Woolsey Mound, crosses the central part of the mound, and extends down the its southern flank, a distance of 2,730 m (Figure 5). The segment from the start of the profile to a profile distance of 1000 m, crosses center of the mound. The middle 500 m of the mound is underlain by resistivities in the 3 to 100 Ωm range from the seafloor to depths of 40 to 50 m. This region is near where massive blocks of hydrate have been observed protruding from the seafloor. The maximum anomaly occurs in a 50 m wide, 100 Ωm plug, which is located at a point (marked “A”) where the profile crosses the seafloor trace of a known fault (Figure 4). The fault is known to be a deep-seated, north-dipping normal fault from the 3D seismic data. In contrast, the segment crossing the southern flank of the mound, from 1000 m to the end of the profile, shows a 40 to 50 m thick upper layer that averages about 1 Ωm, underlain by a layer averaging about 0.6 Ωm to the base of the section.

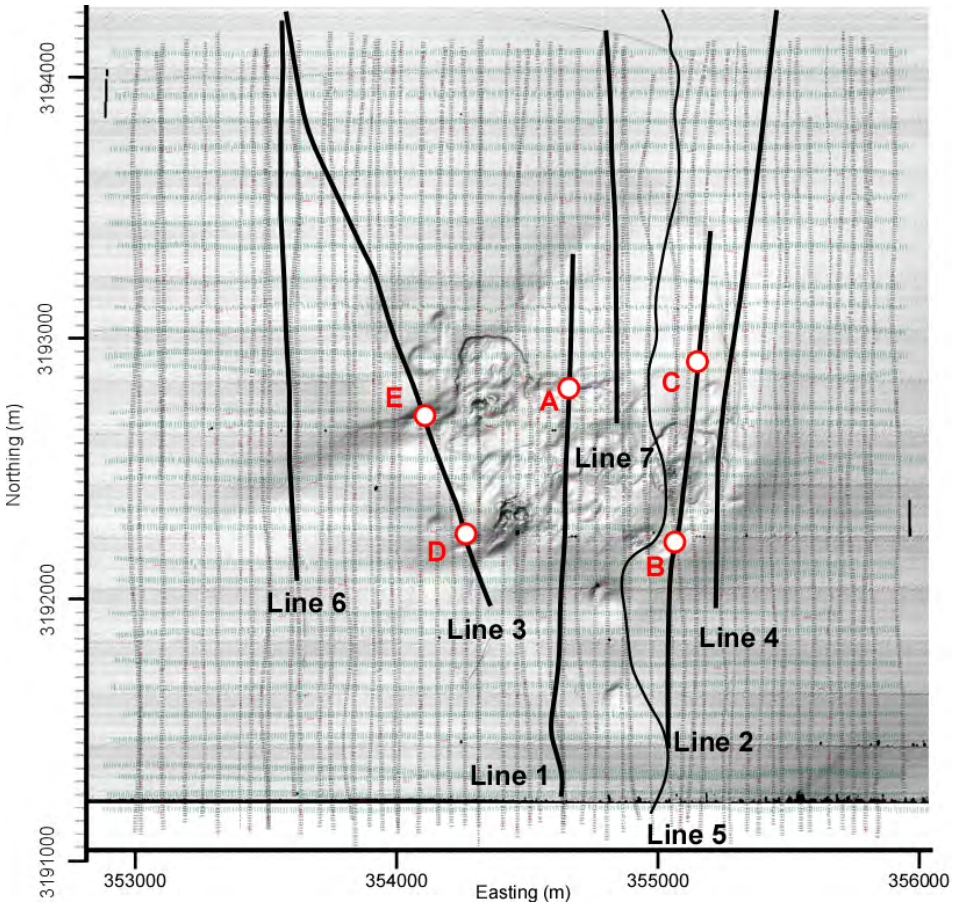

Figure 4: Seafloor resistivity profiles collected in MC118, Gulf of Mexico. Black curves are the track of the seven CRP lines. Grey curves indicate track lines of single-channel seismic profiles. Red circles indicate the locations of features on resistivity profiles shown in Figures 5, 6, and 7. Geographic coordinates are UTM North, Zone 16 meters.

Line 2 starts on the southern flank of the mound, 150 m east of Line 1, and crosses the eastern part of the mound (Figure 6). On this line, the mound and much of its southern flank is underlain by irregularly shaped resistivity anomalies in the 1 to 3 Ωm range, which extend to depths of 40 to 50 m. The two exceptions are at points marked "B" and "C". At point B there is a 120 m wide region of 100 Ωm, which extends to a depth of about 30 m. At point C there is a similar width region of 3 Ωm, which extends to a depth of 100 m. Point B occurs where Line 2 crosses the trace of a second north-dipping, deep-seated fault and point C occurs where the profile crosses the eastward extension of the fault at point A on Line 1 (Figure 4).

Line 3 crosses the western part of the mound, from the northwest to the southeast (Figure 7). On the segment approaching the mound from the northwest, between distances 1000 m to 1750 m, there is 1 Ωm layer to a depth of 50 m, underlain by 0.6 Ωm to the base of the section. The southeastern segment that crosses the mound contains a 20 m wide anomaly (marked "D") of 3 Ωm that extends from the seafloor to the base of the section, with an apparent northwest dip. Southeast of this anomaly there is a shallower anomaly of 20 Ωm. These anomalies occur at the point where Line 3 crosses the trace of a third north-dipping normal fault (Figure 4). In contrast, the point marked "E" occurs where the line crosses a steep scarp visible on the seafloor, but is not associated with a significant resistivity anomaly.

This seafloor feature is not associated with any fault recognized in the 3D seismic data and appears to be associated with a shallow slump.

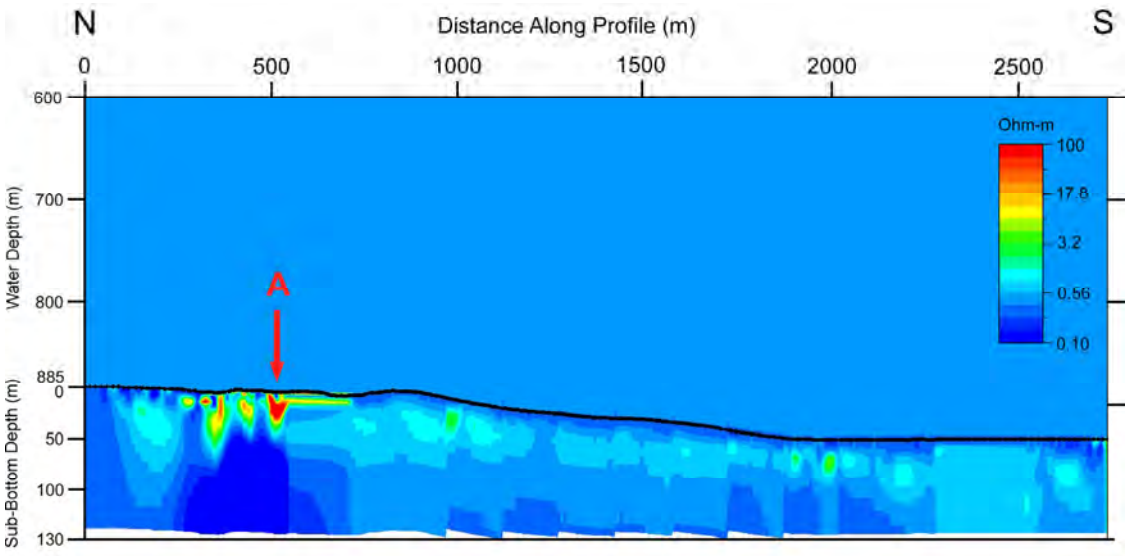

Figure 5: Resistivity Line 1. The track of Line 1 and the location of anomaly A are shown in Figure 4.

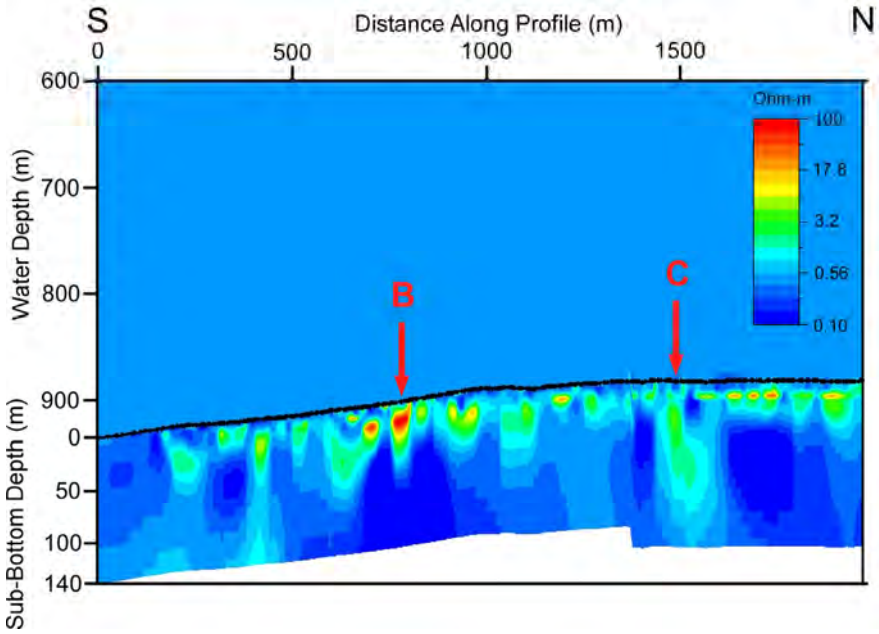

Figure 6: Resistivity Line 2. The track of Line 2 and the locations of anomalies B and C are shown in Figure 4.

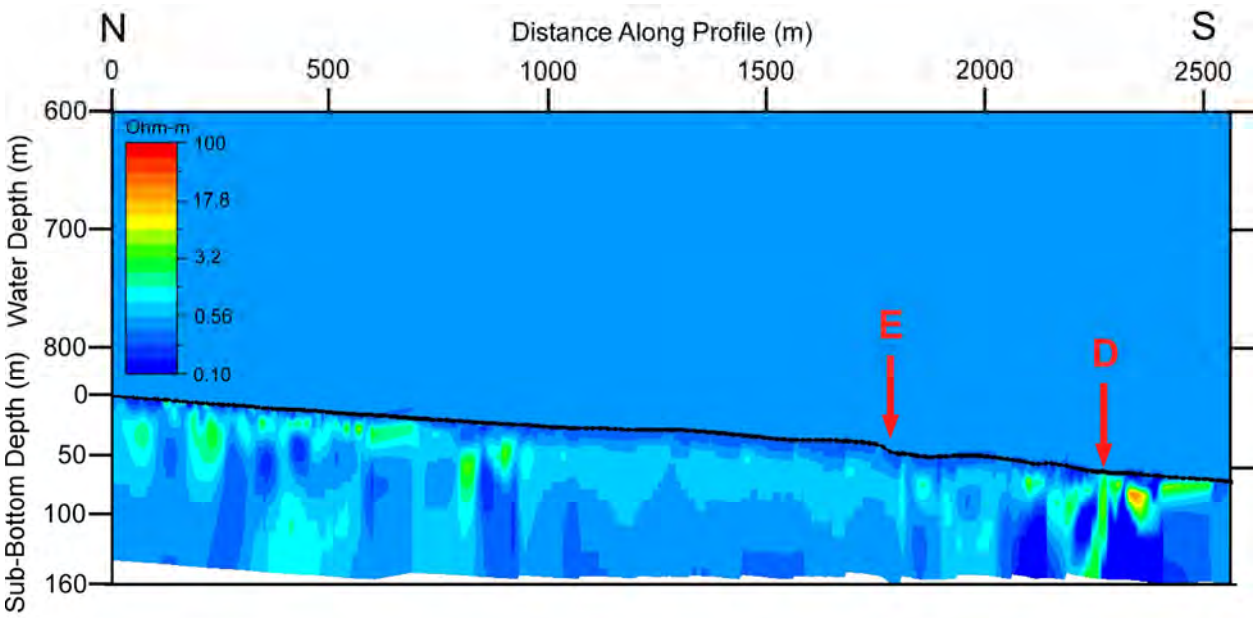

Figure 7: Resistivity Line 3. The track of Line 3 and the locations of anomaly D and point E are shown in Figure 4.

Conclusions

The reconnaissance resistivity survey of Woolsey Mound demonstrates that it is possible to collect valid resistivity data on the deep seafloor using relatively conventional near surface methods. Originally, there was concern about damaging the array by dragging it along the bottom. However, after towing the system for 32 hours, the array was recovered with no detectable damage. There was also concern that the signal levels would be too small relative to noise on the graphite electrodes to produce useful data. The results indicate performance levels consistent with those predicted by Equation 1 and that penetration depths of 100 to 130 m were achieved. It is likely that substantially greater penetration depths could be reached by using non-polarizing electrodes and an electrically isolated, low noise pre-amplification unit to condition the signals prior to their entry into the resistivity instrument.

The results suggest that the resistivity method can be used to detect and map shallow hydrate deposits beneath the seafloor. High resistivity anomalies, consist with high saturations of either hydrate or free gas, occur where profiles cross the traces of deep-seated faults previously known from the 3D seismic data. At the point Line 3 crosses a pronounced scarp not associated with a deep-seated fault, no anomaly is indicated. Hence, the anomalies on the fault traces are not likely to be due to residual effects of the seafloor topography, but instead reflect high resistive bodies beneath the seafloor. It is not possible to discriminate between hydrate and free gas within sediment based on resistivity data alone and it is clear that there is some free gas present, as is indicated by the gas seeps. However, it is difficult to see how the near 100% saturations needed to explain 100 Ωm anomalies could be maintained directly beneath the seafloor within fault zones. Given the occurrence of non-stable massive blocks of hydrate on the seafloor and high resistivity anomalies directly beneath the seafloor in fault zones, it is reasonable to conclude that the upper 40 to 50 m of the deep-seated faults are infused with hydrate.

The ultimate goal of this work is to not only detect hydrate, but map its concentration beneath Woolsey Mound. Comparison between resistivity anomalies at different crossing points along the same fault, such as at point A on Line 1 and point C on Line 2, indicate significant lateral variation in the amplitude and character of the anomalies. This means, not surprisingly, that hydrate is not distributed in

a 2D manner beneath Woolsey Mound. Therefore, 3D data will be required to make reasonable estimates of the sub-bottom resistivity distribution. Also, the size and depth of the observed anomalies are smaller than can be optimally imaged with 20 m electrode spacing. Work is now underway to modify the system for higher resolution 3D data acquisition. To infer hydrate saturation, it will be necessary to independently determine the small-scale morphology of the hydrate. The transfer function between resistivity hydrate saturation differs, depending on whether the hydrate is disseminated through the host sediment as pore fill or grain cement or as vein fill (Spangenberg and Kulenkampff, 2006). The results of the reconnaissance survey provide targets for shallow coring, which can be tested to confirm the presences of hydrate and to determine the morphology of the hydrate.

References

Dunbar, J. A., S. A. Amidu, and P. M. Allen, 2008, A study of seasonal salinity variation in Lake Whitney Texas using continuous resisitivty profiling, 21st Symposium on the Application of Geophysics to Environmental and Engineering Problems (SAGEEP), Philadelphia Pa, April 6-10.

Shipley, T. H. M. H. Houston, R. T. Buffler, F. J. Shaub, K. J. McCillen, J. W. Ladd, and J. L. Worzel, 1979, Seismic evidence of widespread possible gas hydrate horizons on continental slopes and rises, American Association of Petroleum Geologists Bulletin, 63, 2204-2213.

Sloan, E. D., 1998, Clathrate Hydrates of Natural Gas, Marcel Dekker, New York, 705 p.

Spangenberg, E. and J. Kulenkampff, 2006, Influence of methane hydrate content on electrical sediment properties, Geophysical Research Letters, 33, L24315, doi:10.1029/2006GL028188.

Roy, K. K., 2008, Potential Theory in Applied Geophysics, Springer New York, 651 p.

Acknowledgement

This work was supported by U.S. Department of Energy grant DE-FC26-06NT142959. We are grateful for technical and logistical help from University of Mississippi and the crew the RV Pelican.

GEOPHYSICAL IMAGING TO ENHANCE ANALYSIS, DESIGN AND DRILLING OF LARGE-SCALE GEOTHERMAL SYSTEMS

John A. Mundell, Mundell & Associates, Inc., Indianapolis, Indiana
Gabriel Hebert, Mundell & Associates, Inc., Indianapolis, Indiana

Abstract

Improvements in alternative energy sources in the United States have received much attention over these last few years as petroleum-based fuel availability and prices have been tied to concerns about national security and the need to control global warming through reductions in greenhouse gas emissions. Consideration has increased for alternative energy sources, notably wind and solar. Geothermal energy, while considered a 'mature' industry, is again being reviewed as a potential alternative for new, large-scale, multi-structure, high-occupancy energy systems. New efforts are now being made to improve the design and installation techniques so that enhanced system efficiency and reduced 'first costs' are achieved. This has led to the desire to better understand the impact that the subsurface geologic environment within large geothermal wellfields can have on the thermal conductivity distribution that has been assumed to be present using limited boring information. Geophysical surveys using 2-D Electrical Resistivity Imaging (2-D ERI) and downhole logging, supplementing standard site drilling information, have recently been applied to the largest geothermal heat pump project in the United States. The technique has been shown to yield detailed subsurface characteristics that can be used to improve the analysis, design, and drilling of these large-scale geothermal systems.

Introduction

Geothermal heat pump (GHP) systems have been in use for decades and are a recognized alternative energy system for residential and small commercial facilities. Also known as geoexchange, earth-coupled, earth energy or ground-source heat pumps, they act as central heating and/or coolling systems that pump heat to or from the ground using a system of tubing containing heat-exchange fluids. The U.S. Environmental Protection Agency (EPA) has called GHPs the most energy-efficient, environmentally clean, and operationally cost-effective space conditioning systems available (U.S. EPA, 1993). However, because they are characterized by high initial capital costs, their expansion for use in large-scale systems involving multiple structures and larger populations has been limited.

The high initial costs for GHPs include the material costs for geothermal well installation, as well as the actual drilling of borings for the placement of the supply line tubing loops. Currently, geothermal borehole fields are "laid out" based on the thermal conductivity distribution of the ground in the area under consideration. In order to determine the thermal conductivity, the owner of the system must engage the services of a well driller and diagnostics firm to drill a "test" hole and to run a multi-day test to determine the degree to which that ground will conduct heat. The higher the thermal conductivity the better, since GHPs are most efficient when the surrounding ground more readily defuses heat from (in the cooling season) or transfers heat to (in the heating season) the fluid that is running through the pipe.

The problem with today's practice is that the limited pre-design and installation test borehole process (*i.e.*, the drilling of only 1 or 2 pre-construction holes) that has commonly been used for small scale systems (less than 50 geothermal wells), is likely not a scalable process for large geothermal systems that require much larger areas and more than a 1000 wells. Subsurface conditions in many geologic areas vary considerably over short distances, and the likelihood that the system will be designed with inappropriate assumptions is very high. As a result, the system's costs may be higher than required to achieve the thermal performance that is necessary, or may operate in an inefficient manner for the selected wellfield area. As such, in order to obtain a better picture of the thermal conductivity, the owner must bear the rather significant costs of additional test boreholes.

The use of geophysics coupled with selected drilling has the capability to dramatically reduce the need for extensive pre-installation test boreholes. In addition, the ability to rapidly map entire green spaces for their thermal conductivity capabilities at various depths, can permit a designer to more precisely lay out the field using the fewest number of production boreholes, resulting in more efficiency for a given area. In addition, knowing the distribution of geologic materials using geophysics will allow improved determination of the spacing and depth of the installation boreholes ahead of time, as well as improved drilling installation bids. It will be important to determine at what depths the various piping systems will be more efficient, due to a higher a thermal conductivity of the surrounding strata. When paired with a clear understanding of the surrounding geologic formations, new knowledge about the "sweetest spots" (and depths) will prove of immense value to system designers.

Project Background

Ball State University, located on a 660-acre campus in Muncie, Indiana, plans to convert its central heating and cooling system consisting of coal-fired boilers and electric chillers, to one employing geothermal fields and energy centers, which will service more than 45 buildings on campus. This conversion process will occur over a 10-year transition period. The proposed system, which would be the largest of its kind in the United States, will require more than 4,100 boreholes in two geothermal well fields located near "energy stations" that contain several heat pump chillers (see **Figure 1**). A closed-loop piping system, with water as the exchange fluid, will draw and replace heat from the boreholes that each extend 400 ft into the earth. A heat pump chiller will cycle the water into a campus wide network of pipes, entering into cold or hot water loops and passing through campus buildings' exchanges to cool or heat the interior. The university expects that heating and cooling via geothermal will realize more than $ 2 million in annual energy savings and cut BSU's on-campus carbon footprint in half, or by approximately 80,000 tons per year. The price of the project is estimated at $65 million to $70 million.

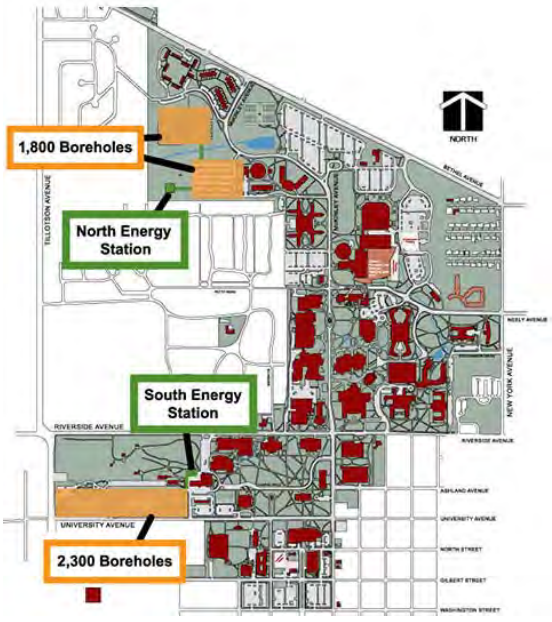

Figure 1: Geothermal Wellfield Map for Ball State University

As a typical initial characterization program for their North Wellfield, the university drilled two test boreholes to determine the subsurface conditions there. Test Boring #1 was located in the extreme northwest corner of the wellfield, and Test Boring #2 was located along the southern border of the wellfield. The interpreted linear-sloping top of bedrock map produced from these two borings is shown in **Figure 2a**. Later drilling of three additional boreholes completed in the northern portion of the wellfield resulted in the 'improved' top of bedrock map shown in **Figure 2b**, which conservatively covered only the western one-half of the proposed wellfield.

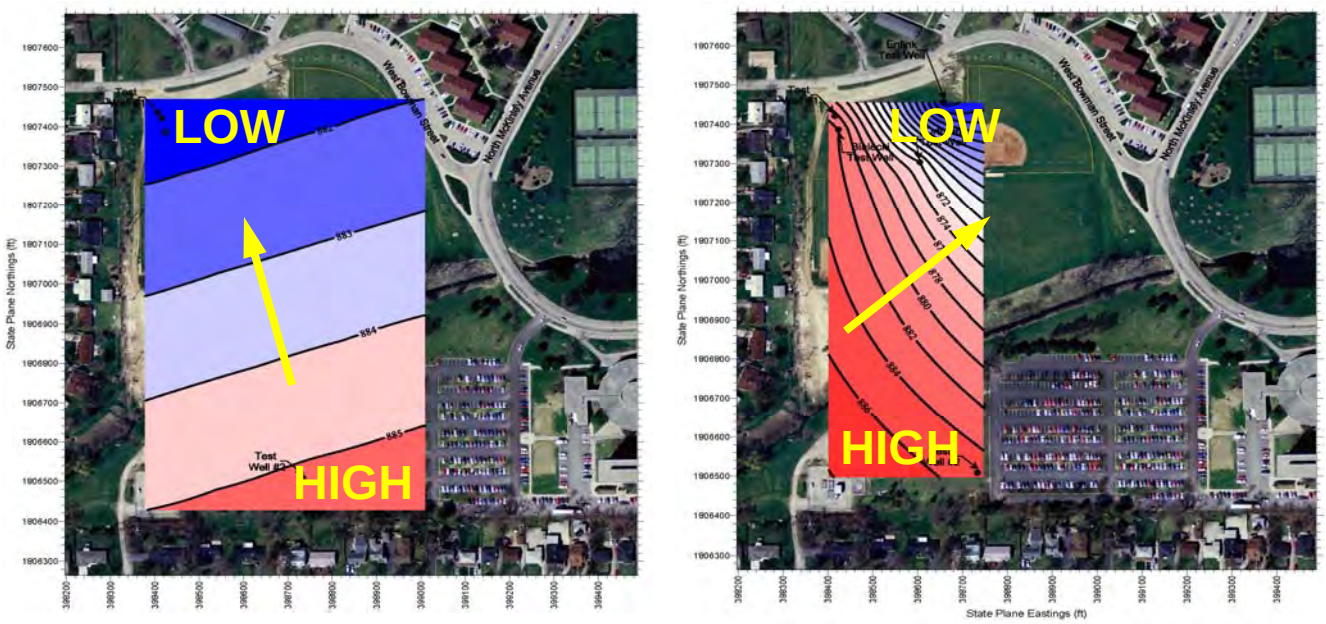

Figure 2: Top of Bedrock Map based on a) a 2-point constant slope model and b) a 5-point interpolated borehole model.

The Ball State campus lies within the Indiana Tipton Till physiographic plain. In this part of the state, the thickness of the unconsolidated material above bedrock (which consists predominantly of fine-grained glacial till with lesser amounts of interbedded coarse-grained sediments) ranges from approximately 20 to 140 feet. The underlying bedrock is composed of Silurian limestone and dolomite, which is prone to weathering and solutioning. Concerns regarding the accuracy of the interpreted subsurface conditions based on the limited boring program led BSU to consider the use of geophysics as a supplemental methodology for characterizing the wellfield. Based on the expected subsurface soil and bedrock conditions at the site, and the type of information desired by the geothermal designers and well drillers, two-dimensional electrical resistivity imaging (2-D ERI) supplemented with downhole logging was selected as the technique that could provide the best results within a limited budget.

Field Techniques

The area of investigation for this project consists of the North Wellfield, which contains two softball diamonds, a soccer field, and a southern parking lot that is separated by Cardinal Creek. An electric substation and radio towers were located in the southwest quadrant. This area is approximately 20 acres in size, and is located south and west of the intersection of West Bowman Street and North McKinley

Avenue in Muncie, Indiana (see **Figures 1** and **3**). At the time of the field work, approximately 1,700 geothermal wells were to be installed at this site, each to a depth of 400 feet. Thus, the goal of this geophysical survey was to provide Ball State with detailed non-intrusive data that provides insight into the geologic conditions beneath the site.

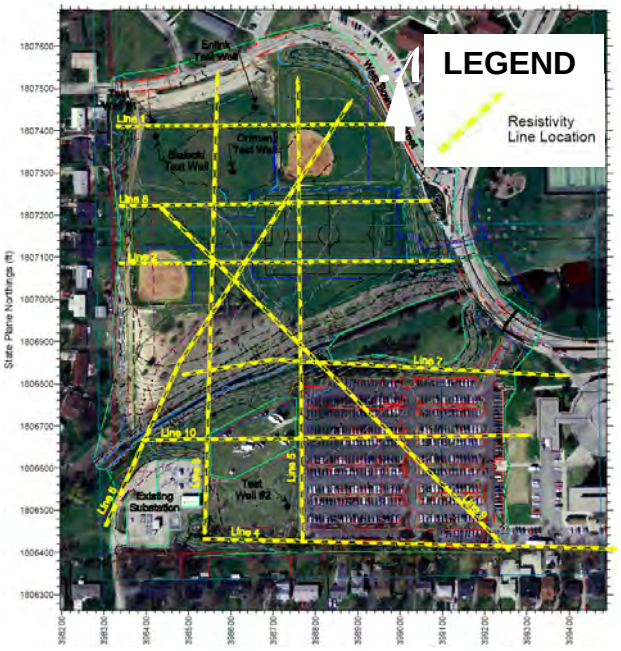

Figure 3: North Wellfield and 2D Resistivity Profile Line Orientations

Ten (10) 2-D ERI lines were collected in north-south, east-west, southwest-northeast, and northwest-southeast orientations (see **Figure 3**). For this project, resistivity data were collected with an *AGI SuperSting R8* earth resistivity meter using a dipole-dipole array of 60 electrodes along profile *Lines 2, 4, 6,* and *9*; and a dipole-dipole array of 56 electrodes along profile *Lines 1, 3, 5, 7, 8,* and *10*. The electrode spacing of each of the resistivity lines was dependent on the orientations of the lines and the amount of area available for data collection. Thus, *Line 1* has an electrode spacing of 3.5 meters (approximately 11.5 feet), *Lines 2* and *8* have a spacing of 4 meters (approximately 13 feet), *Lines 4, 7,* and *10* have a spacing of 5 meters (approximately 16.5 feet), and *Lines 3, 5, 6,* and *9* have a spacing of 6 meters (approximately 20 feet). Once the data were collected, they were downloaded to a computer and subsequently inverse-modeled using the software *EarthImager 2D v1.8.1* to obtain an "actual", true resistivity cross-section of the subsurface.

Downhole conductivity and caliper logging were completed in two of the boreholes to a depth of 400 ft in order to directly evaluate the variation in the subsurface soils and bedrock encountered, and to aid in the calibration of the 2-D ERI results.

Results of Analysis

Four (4) selected east-west 2-D ERI are presented in **Figure 4**. Based on the survey results, it is apparent that the subsurface soil and bedrock conditions underlying the site are much more complex than would have been anticipated by the drilling companies (based on the few test borings that were completed for the area), with rapidly changing conditions observed over distances of less than a hundred feet. However, while there is variability over all of the resistivity profiles, there are general patterns that are common among them. High resistivity values, *i.e.*, approximately 750 to 3000 ohm-meters, are generally interpreted to reflect the presence of dense, competent limestone rock (presented as a pink color). Moderately high values (300 to 750 ohm-meters) reflect areas where the bedrock is weathered, fractured or solutioned. Mid-range values (80 to 300 ohm-meters) are interpreted to be coarser-grained soils (sand and gravel) in the shallow subsurface, and possible severely weathered/fractured rock or soil/water-filled voids in the lower subsurface. The lowest range of values, *i.e.*, less than 80 ohm-meters, is interpreted to be fine-grained glacial till soils with a high clay content (purple to green). A resistivity of 0 ohm-meters (dark purple) is indicative of buried metallic utilities and interference from buried electrical lines and the electrical substation in the southwestern corner of the Site.

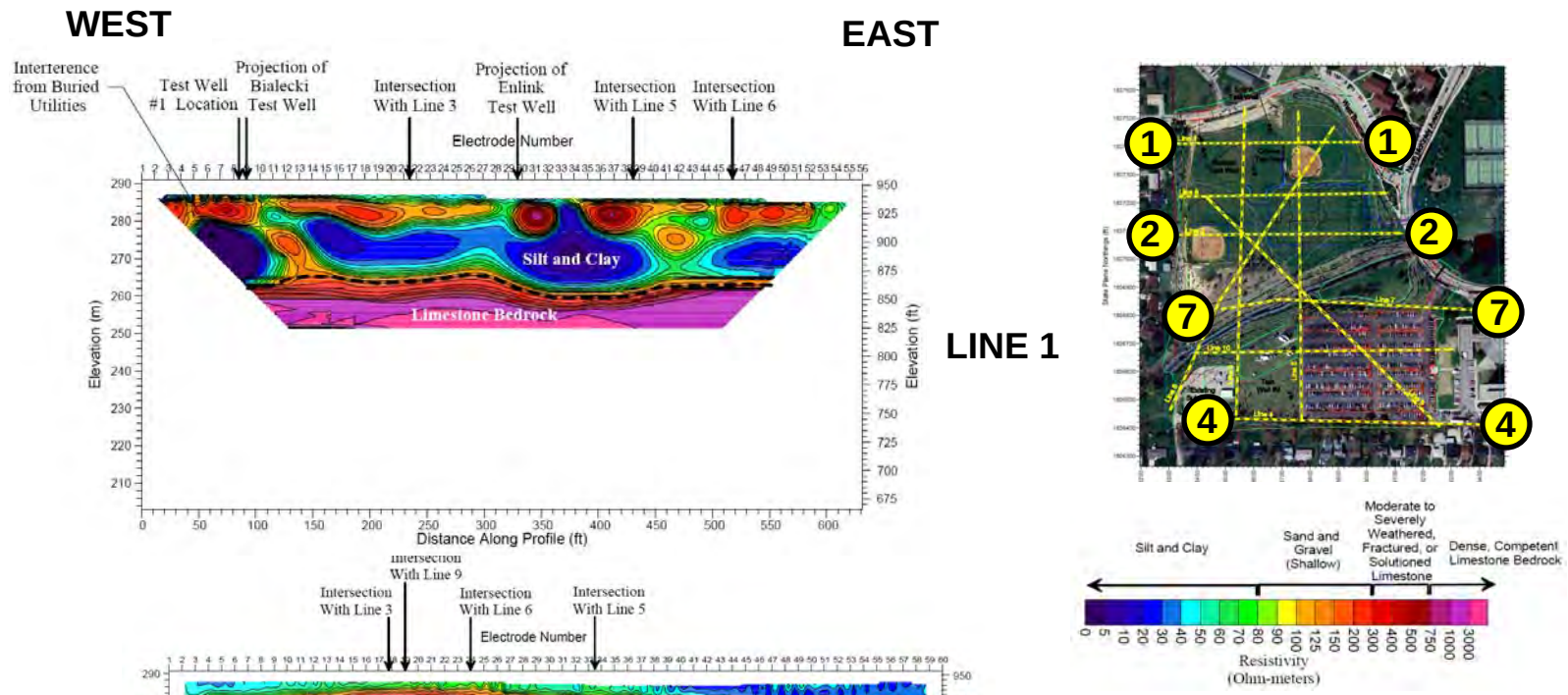

Figure 4: Selected East-West 2-D ERI Profile Lines

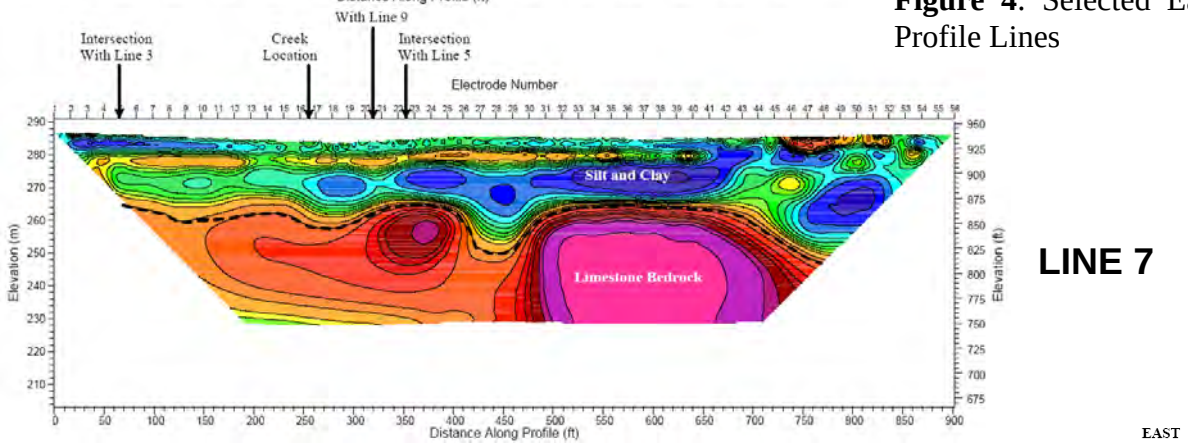

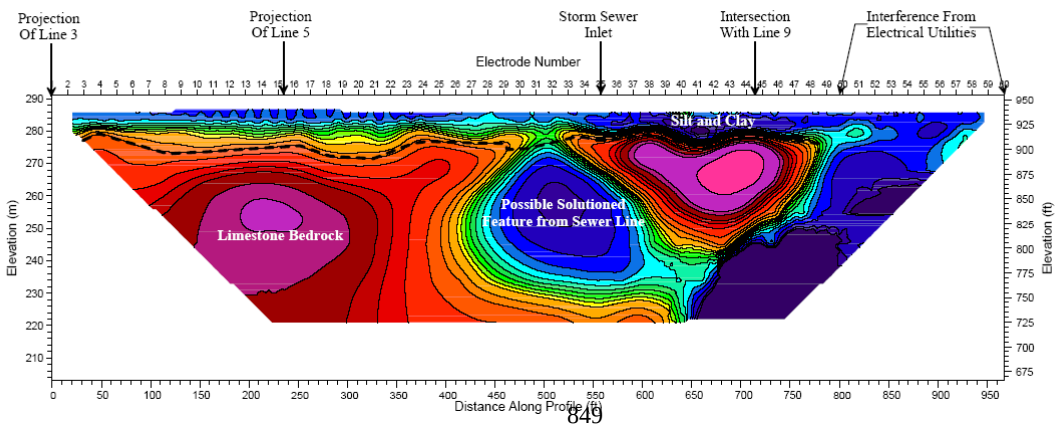

In general, the majority of the profiles show a thin (10 to 20 feet) layer of silt and clay overlying a thicker (20 to 30 feet) body of sand and gravel, under which lies a clayey layer of variable thickness (30 to 70 feet). The estimated bedrock surface shown on these profiles is denoted by a black dashed line, and one can see that it is quite variable and undulating, ranging in depth from just over 20 feet on *Line 4* to 140 feet on *Line 3*. Some of this variability is likely due to solutioning of the calcareous

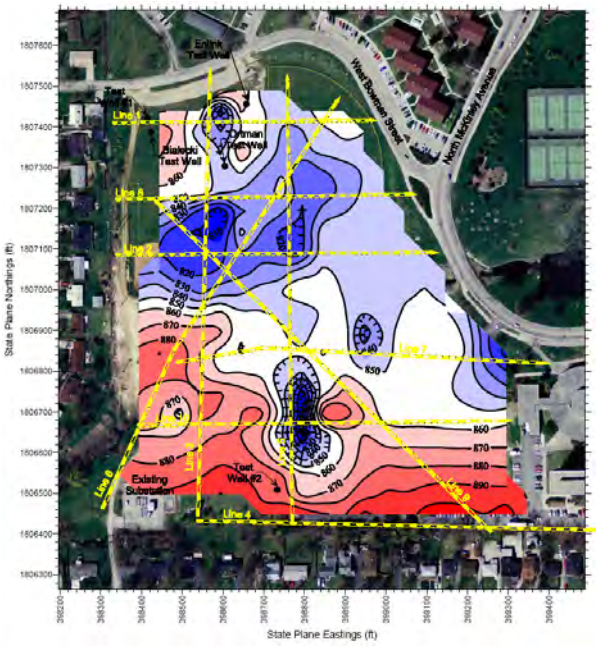

Figure 5: Top of Bedrock Topographic Map.

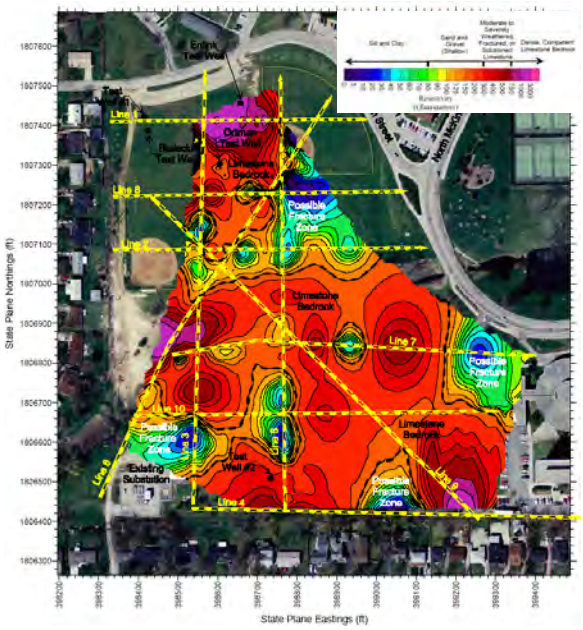

Figure 6: Resistivity Slice Map at Elevation 840.

limestone bedrock, and several solution prone features can be seen on the resistivity profiles, the most notable of which is located on *Line 4*, just west of a storm sewer inlet.

After the individual resistivity cross-sections had been generated, the interpreted bedrock surface from the individual profiles was digitized and uses to generate a top of bedrock topography map, which is presented as **Figure 5**. In addition to this map, several lateral (*i.e.*, constant elevation) resistivity slice maps were generated as well, by combining the individual cross-sections into a three-dimensional data set and taking slices at various constant elevations. The resistivity slice taken at elevation 840 feet is presented in **Figure 6**. While the shallower slice maps show the lateral extent of the shallower fine- and coarse-grained layers, the deeper maps detail where the bedrock is competent and where it is more fractured and solutioned. It should be noted that electrical interference from utility lines, the existing substation, and the foundations of the radio antennas are likely to have caused decreases in measured resistivity values in some areas that may not be indicative of actual subsurface conditions. In these areas, only direct inspection through drilling will determine actual conditions.

Further evidence of bedrock solutioning is found in the conductivity and caliper logs of the two test well locations (see **Figure 7**). These logs show the presence of several fractured/solutioned zones, the most severe of which is located from approximately 360 feet to 400 feet below ground surface. This zone of severely weathered limestone and clay is very soft and was confirmed by the drilling logs.

The results of this mapping were included in the drilling bid packages, and resulted in extremely positive comments from the dozens of well drillers around the country who reviewed them. The drillers were fascinated to "see" what they would encounter at various depth strata. The geophysical mapping occurred at the ground surface, but produced a multi-colored 3D image down to an excess of 250 feet.

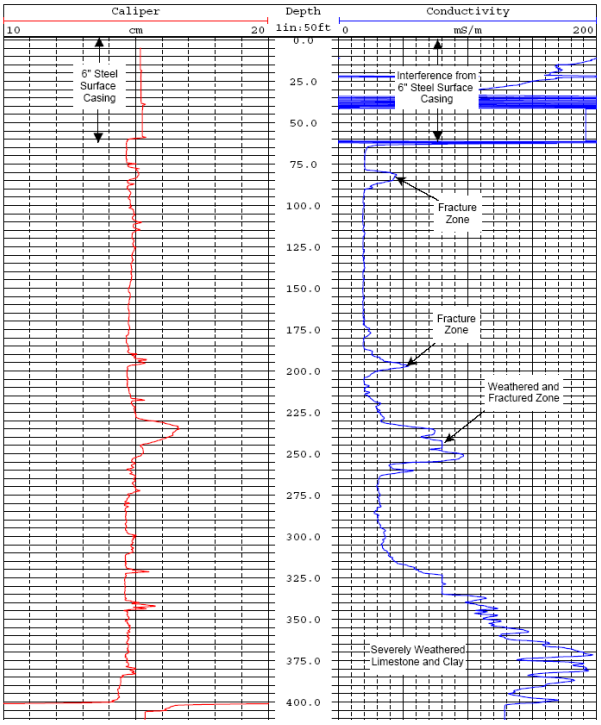

Figure 7: Downhole Log of North Wellfield Boring.

Conclusions

The use of geophysical surveys of the location of proposed geothermal wellfields provides enhanced characterization for final design and development of drilling specifications for the geothermal system. In this case history, the combination of a few selected drill holes with 2-D resistivity imaging and downhole logging over a period of a few days, allowed for detailed subsurface information that would have taken more than one year of continuous drilling to accomplish. This added information has the potential for allowing a more detailed design and drilling analysis of these large-scale systems prior to their installation, which could lead to more efficient systems and reduced 'first costs', making the systems a more competitive alternative to existing energy systems. As the understanding of the performance of large-scale (1000 plus wells) geothermal systems are better understood with their installation and operation, an enhanced understanding of how the system performance is impacted by the underlying geologic strata will be allowed by the greater knowledge gained through geophysical surveys.

References

Environmental Protection Agency (1993). *Space Conditioning: The Next Frontier - Report 430-R-93-004*. EPA.

GEOPHYSICAL MAPPING OF HOCKLEY GROWTH FAULT IN NW HOUSTON, TEXAS: A FEW SURPRISING RESULTS

Mustafa Saribudak, Environmental Geophysics Associates, Austin, TX

Abstract

Active growth faults cutting the land surface in the Gulf Coast area represent a serious geo-hazard. Considering the average movement of these faults is a few inches per decade, the potential is high for structural damage to highways, industrial buildings, residential houses and railroads that cross these features.

Common methods used to identify these faults include analysis of aerial photographs and field mapping; borehole data on both the down and up-thrown sides of the faults; core data; and familiar geophysical methods such as resistivity, gravity, magnetic, conductivity and ground penetrating radar and gravity. A pioneering resistivity work was done over some of the Houston faults by Kreitler and McKalips, 1978. Field mapping and analysis of aerial photographs are the most frequently used methods for locating faults in the Gulf Coast area. Geophysical methods are sporadically used to estimate the locations and parameters of these faults. Opinions concerning the effectiveness of these geophysical surveys are mixed, and geophysical techniques are not generally recognized as primary tools in engineering-scale fault studies.

However, remarkable advances in the manufacturing of geophysical instruments over the last ten years have made geophysics a viable tool for engineering studies of these faults. Data quality has been increased by the advent of continuous data collection. The data are better processed and interpreted by new and improved software packages, which results in improved sub-surface imaging and mapping. We have conducted an integrated geophysical survey using ground penetrating radar (GPR) and resistivity imaging methods over the Hockley Fault located in the northwest part of Houston, Texas. Results indicate that both methods successfully imaged significant anomalies across the known fault location.

Introduction

The coastal plain of the Gulf of Mexico is underlain by a thick sequence of largely unconsolidated, lenticular deposits of clays and sands. Growth faults are common throughout these unconsolidated sediments. Based on a study of borehole logs and seismic reflection data, faults have been delineated to depths of 12,000 feet below surface (Kasmarek, M. & Strom, E., 2002). Most of these faults are associated with natural geologic processes such as differential compaction and salt movement and have been active since the Cretaceous. Some of these faults are currently active and disturb the surface in areas throughout the coastal plain of the Gulf of Mexico (Clanton and Verbeek, 1981). The Houston area has a very active shallow fault system as evidenced by active surface movement and measurable localized subsidence (Verbeek and Clanton, 1981).

Evidence of faulting is visible from structural damage such as fractures and/or displacement. Fault movement is predominantly normal, dip-slip down to the south, and listric; but some growth faults are antithetic and down to the north. Some active faults are clearly indicated by surface damage such as scarps that cut across lots, fields and streets. The dip on the near-surface faults is generally between 60° and 75° (Figure 1a), with vertical exceeding horizontal displacement (Figure 1b).

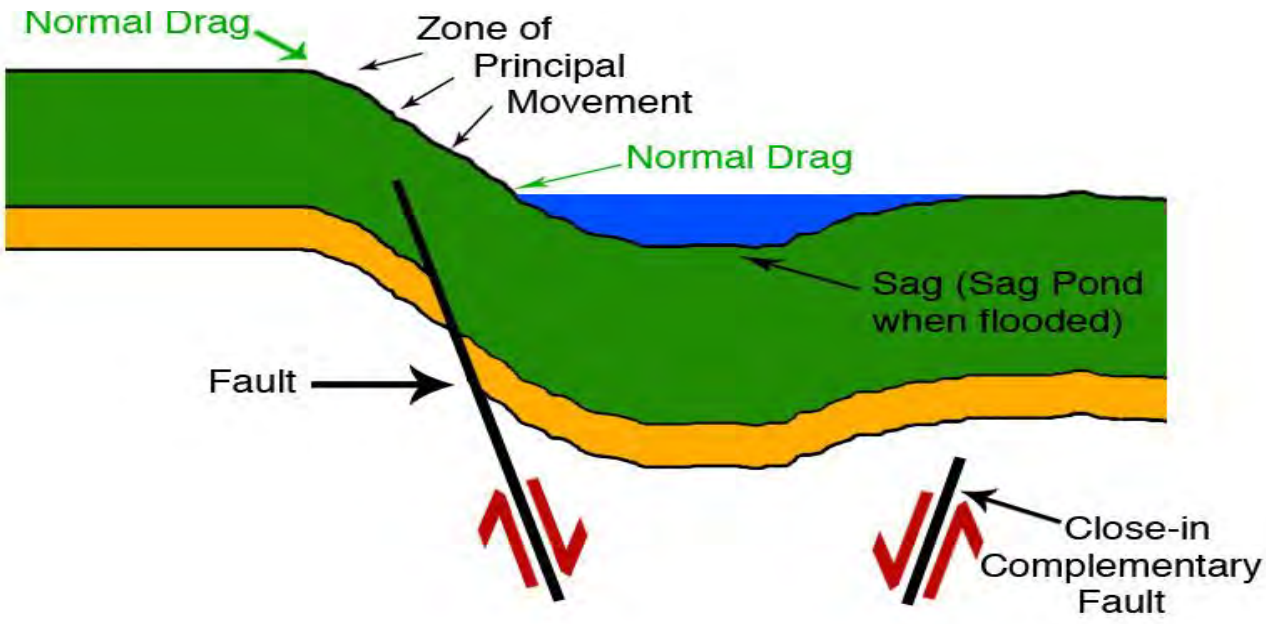

Figure 1a: Typical deformation features of a growth fault. The fault scarp may be flattened by erosion and deposition or by man's activities (modified from Elsbury et al. 1980).

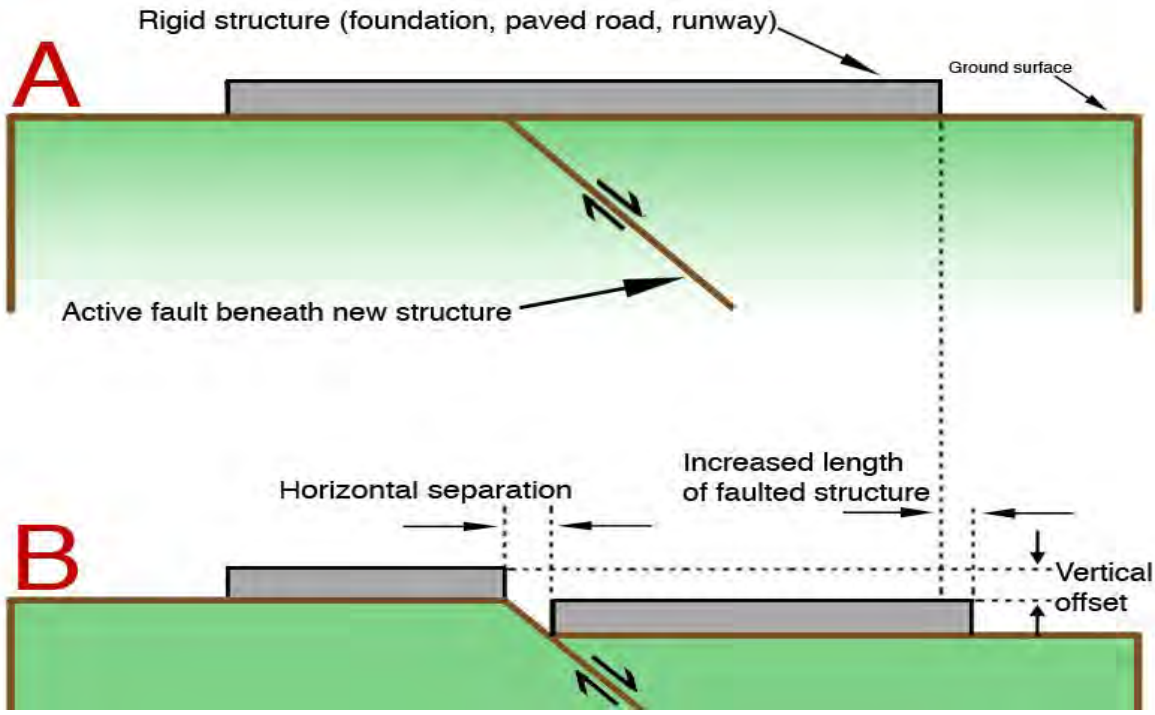

Figure 1b: Effect of fault movement on a rigid structure built on an active fault. A, original construction; B, structure damaged by fault movement. Both vertical offset and horizontal separation are necessary consequences of displacement. Rigid structures may literally be pulled apart as faulting proceeds (modified from Elsbury et al. 1980).

Today, active faults can be the source of considerable damage to pavements, utilities, homes businesses, and other man-made structures in the Gulf Coast region. In the Houston area alone (Harris County), there are more than 300 active or potentially active faults totaling over 300 miles in length. These active faults are usually not discrete ruptures, but zones of sheared ground tens of meters wide (Clanton and Verbeek, 1981).

The NE-SW Hockley Fault is over five miles long, extends from the Hockley Salt dome, across Highway 290 to its terminus in Fairfield Village (Figure 2). Hockley fault is downthrown toward the coast, and is considered to be the near-surface expression of very slow gravity creep of more ductile materials (rock salt and shale) at greater depths toward the Sigsbee Deep of the Gulf of Mexico (Elsbury et al., 1981).

The study area was evaluated by Turner et al. (1991) in a report for the construction of Fairfield Village that describes the Hockley fault passing through the site with a fault scarp of 40 feet in height.

This paper presents and evaluates the use of two non-invasive geophysical methods for investigating the Hockley growth fault across the Highway 290 (Figure 2).

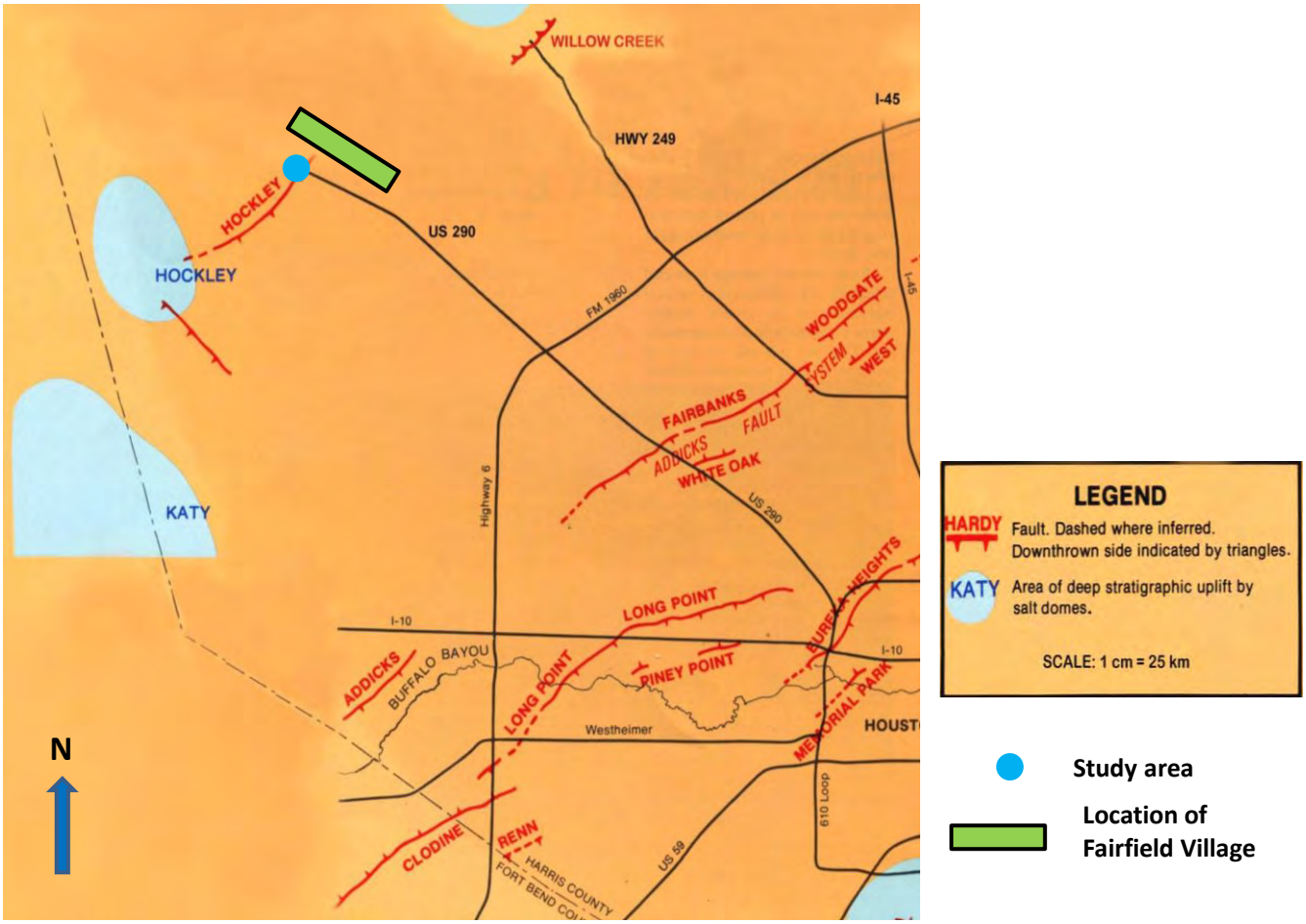

Geophysical Instruments

Resistivity imaging is a survey technique that aims to map of the electrical properties of the subsurface by passing an electrical current between electrodes and measuring the associated voltages. This technique has been widely used in mapping contaminant plumes, karst features (voids), and subsurface structures, such as faults and fractures. In this study, Advanced Geosciences, Inc. (AGI) Super R1 Sting/Swift resistivity meter with the dipole-dipole resistivity technique is used. This technique is more sensitive to horizontal changes in the subsurface, and provides a 2-D electrical image of the near-surface geology. Electrode spacing was held to 6 m along all profiles. The depth of the investigation was about 135 feet (~41 meters).

The 400 MHz antenna was used with a cart system to collect GPR data. GPR is the general term applied to techniques that employ radio waves in the 1 to 1000 megaHertz (MHz) frequency range to map near-surface structures and man-made features. Depth penetration of the radio waves is limited by the antenna chosen and the conductivity of the soil. The ability of a GPR system to work successfully depends upon two electrical properties of the subsurface, electrical conductivity and relative dielectric permittivity (i.e. dielectric constant). The value of dielectric constant ranges between 1 (for air) and 81 (for water). The dielectric constant for sandy clayey soils varies between 10 and 15. A dielectric constant of 12 was chosen for the study area, and the depth exploration with the GPR unit was about 8 feet. Thus, differences in dielectric constant of subsurface soils along distinct boundaries, such as fractures and faults, can cause highly significant reflections in the radar signal, which are recorded and displayed by the system. In summary, GPR radar reflections occur when GPR waves encounter a change in velocity due to dielectric contrast. The bigger the change the more signal is reflected (Geophysical Survey System, Inc. GPR SIR-2000 Manual, 2000).

Field Survey Design and Data Processing

In 2004 and 2005 I performed GPR and resistivity surveys along Line 1 on the east-bound side of Highway 290 (Figure 3). I also obtained resistivity profiles on both sides of Highway 290, and along a line located between Fairfield Village and Highway 290. In November 2009, I recollected GPR data along the east-bound and west-bound profiles (Figure 3). A total of seven resistivity and one GPR profiles were surveyed.

During the field surveys in 2004, I sketched the locations of the cracks and patched pavement locations on both sides of the highway and mapped a discrete fault scarp on the south side of the highway (Figure 3). Another fault scarp was also mapped along one of the resistivity profiles, in an open field between the highway and Fairfield Village (Figure 3). In addition, a major crack is observed crossing the highway on the north side (Figure 3 and 4). Resistivity profiles L4, L5 and L6 crossed over this significant crack.

Resistivity data was processed and inverted using AGI Earth Imager software. The resistivity values obtained in this study varied between 24 and 400 Ohm-m. Resistivity values, in general, of 30 Ohm-m and greater correspond to sand units; whereas resistivity values less than 30 Ohm-m corresponds to clayey sand, sandy clay and silty sand.

The 400 MHz GPR data is displayed in a color-amplitude format, and a color is assigned to a specific positive or negative value of the recorded signal. In this study, white and pink colors on the profiles correspond to the highest positive amplitude pulses, strong reflections due to a high dielectric contrasts. Therefore, when it appears on the radar record, it means that there is a strong reflection where colors are observed due to a high dielectric contrast. Gray and purple colors could also represent a

"strong" negative reflection and similar high dielectric contrast. Background values are represented by red and brown colors.

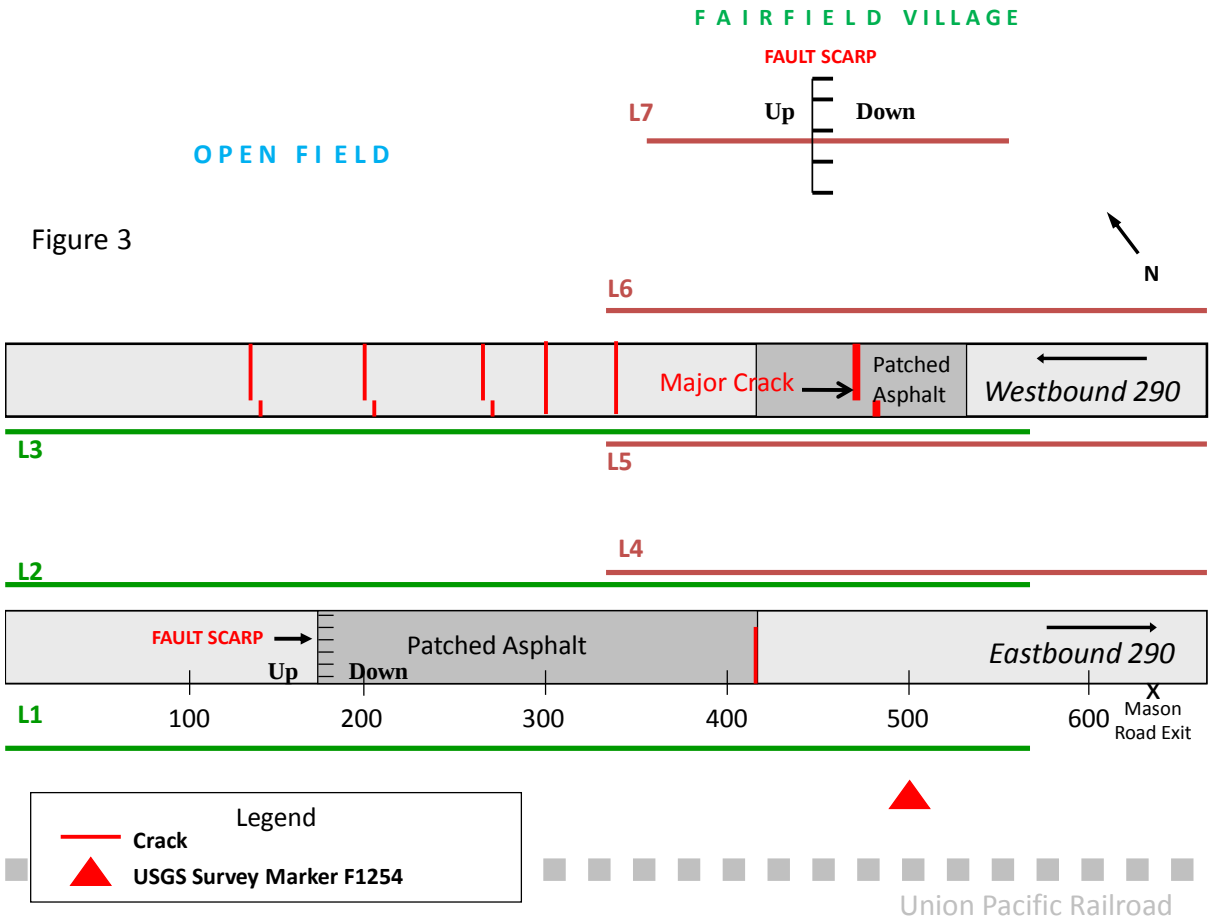

Figure 3: Schematic map of Hockley fault at Highway 290 and Fairfield Village. The thinner red lines show fracture locations. Resistivity data were collected along Lines L1, L2, L3, L4, L5, L6 and L7. GPR data were collected only along Line 1 (L1). Not to scale.

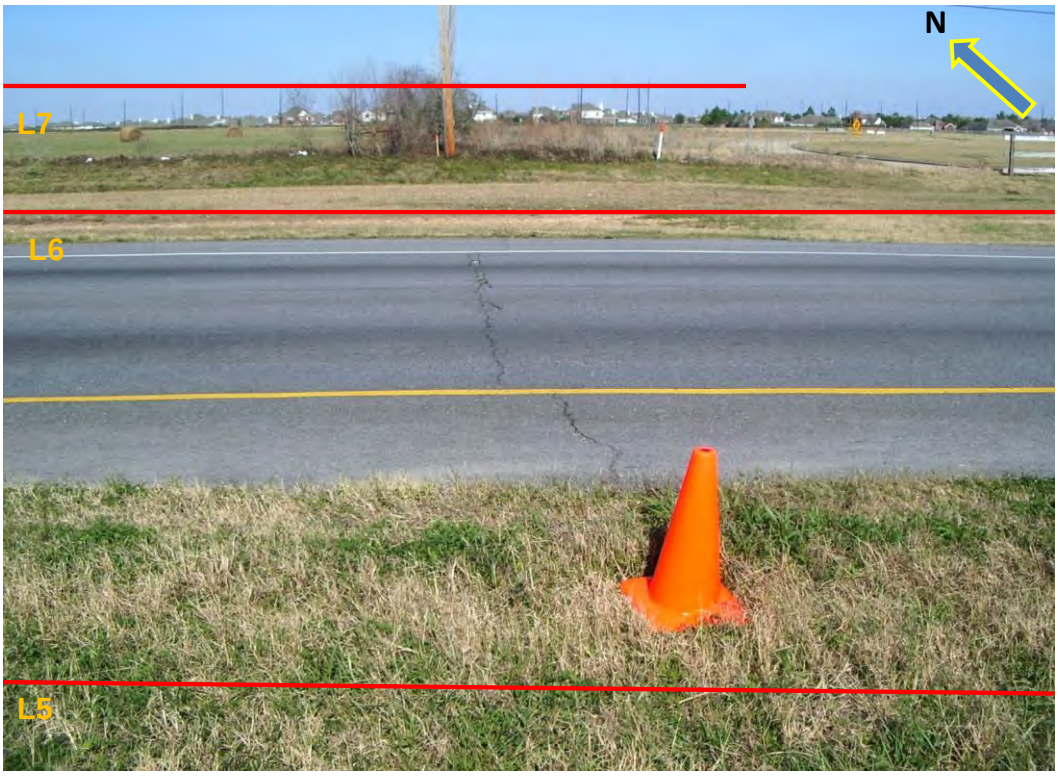

Fig
totl
resi

Geophysical Results

The resistivity profiles in Figures 5 through 7 indicate sandy clay and sand units. Spacing of resistivity profiles L1, L2, and L3 (Figure 5) is from 75 to 100 feet. Profile L1 does not indicate any fault offset visible in the soil layers over the fault scarp, which was several inches in height. Instead, a fault-like anomaly is observed at about 300 feet towards the southeast. Resistivity profiles L2 and L3 do not indicate any fault offset along their entire lengths. However, there is an apparent resistivity contrast towards the end of the profiles between the sand and clay layers; although the resistivity data loses its reliability towards the edges.

In order to map the resistivity contrast, three more resistivity profiles (L4, L5 and L6) were surveyed (see Figure 3 for locations of profiles). Figure 6 shows the resistivity data along profiles L4, L5 and L6. A fault-like anomaly is present from 240 to 280 feet on all three resistivity data sets.

Figure 7 shows the resistivity profile L7. This profile is taken in an open field between the west-bound of Highway 290 and Fairfield Village (see Figure 3). This area was covered with high plants and vegetations during the resistivity survey. . For reference purposes, the SE end of the profile was next to the asphalt pavement. A distinctive fault scarp (several inches in height) was observed at this location, and profile L7 displays the resistivity data over the fault. The fault scarp was located at a station 360 feet on the resistivity profile; and a fault-like anomaly is observed at the same station of 360 feet.

GPR data along the resistivity profile L1 indicates significant anomalies between the fault scarp and the USGS survey marker F1254. The deformation may consist of small faults and fractures in the

fill materials beneath the pavement and sandy soil underlying the fill materials of the highway road. Location of GPR anomalies are selected with their respective station coordinates, and are shown in Figures 8 through 10. It should be noted that the horizontal scale for the GPR profile is exactly the same as for the resistivity profile L1.

Figure 7a indicates a vertical offset over the fault scarp observed at about 160 feet. This offset covers the fill materials and the underlying soil layers. Figure 7b shows several small-scale faults between stations 215 and 240 feet. Figures 8a and 8b show small faults between stations 250 and 415 feet. Figure 10 displays small faults between stations 430 and 470 feet. There are two micro-graben-like structures formed by the small-scale faulting. Dimension of each graben block is about 14 feet long.

I resurveyed Line 1 on the south side and Line 6 on the north side of the highway. The repeated GPR survey data on Line 1 and Line 6 did not show any of the anomalies (including the fault scarp) that we discussed above. The reason for this may be the removal of the soil and the reconstruction of the highway roads. It should be noted that since the first phase of the geophysical surveys, Highway 290 was rebuilt and a Houston Primary Outlet Shopping Mall was constructed in the vicinity of the Hockley fault. Thus the original east and west bounds of the Highway 290 have been rebuilt and have become feeder roads.

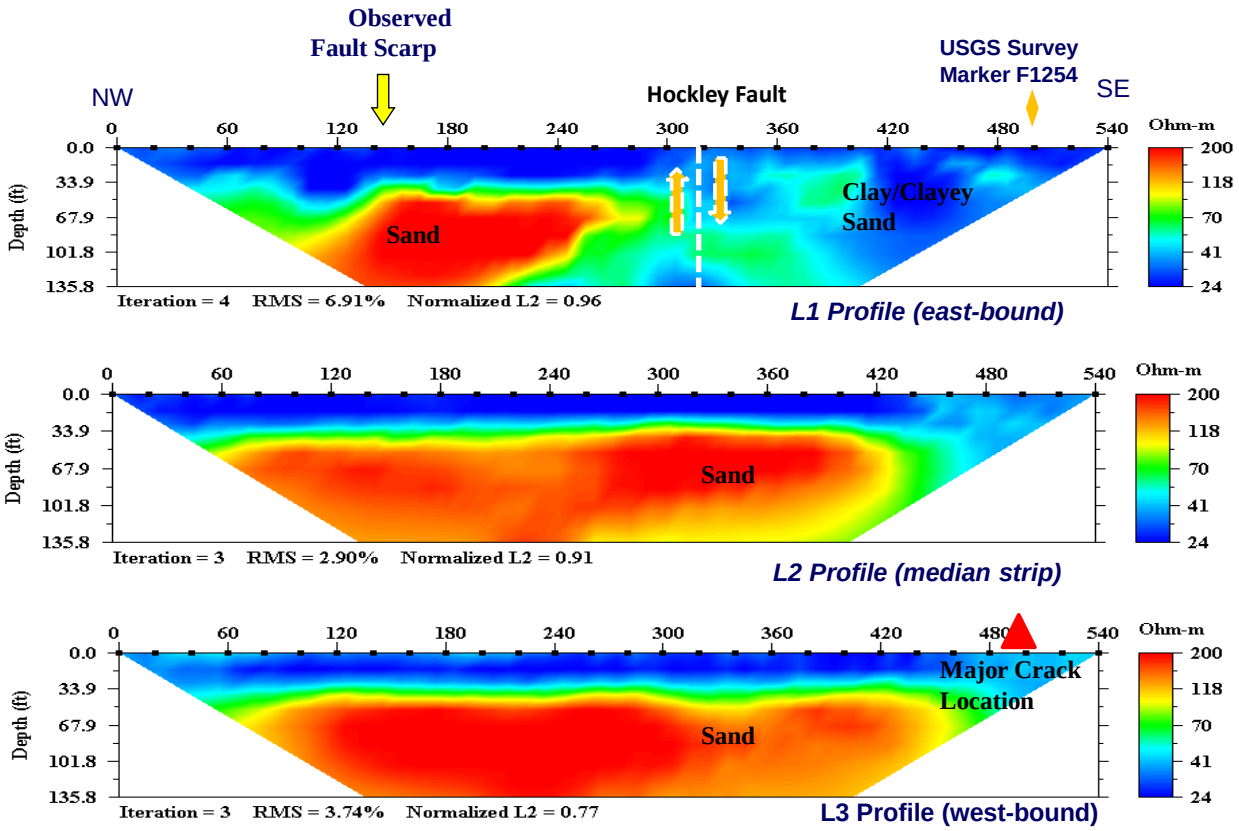

Figure 5: Resistivity imaging data along profiles L1, L2 and L3 (see Figure 3 for location).

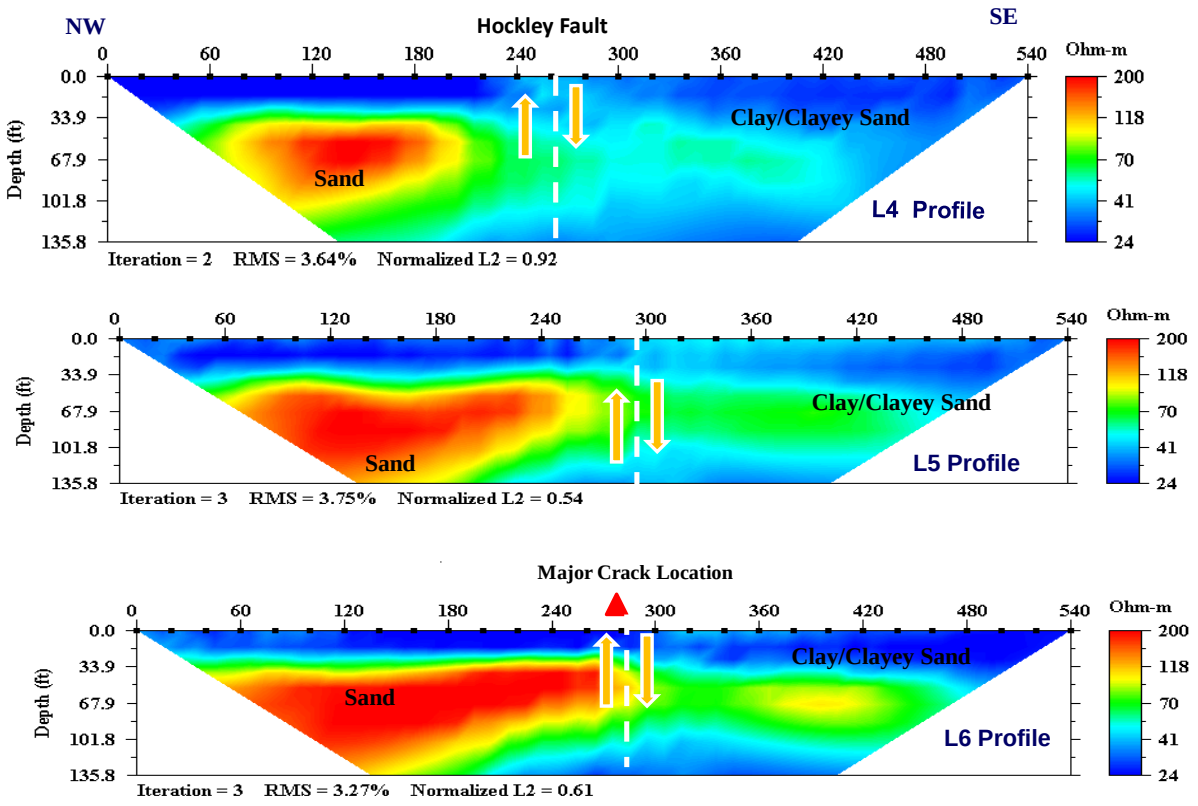

Figure 8. Resistivity imaging data along profiles L4, L5 and L6 (see Figure 5 for location).

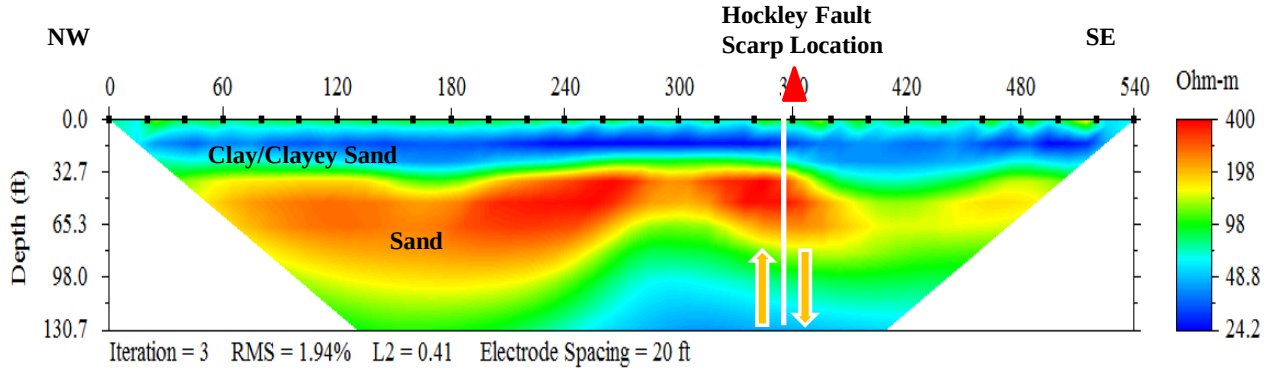

F
ol in
th

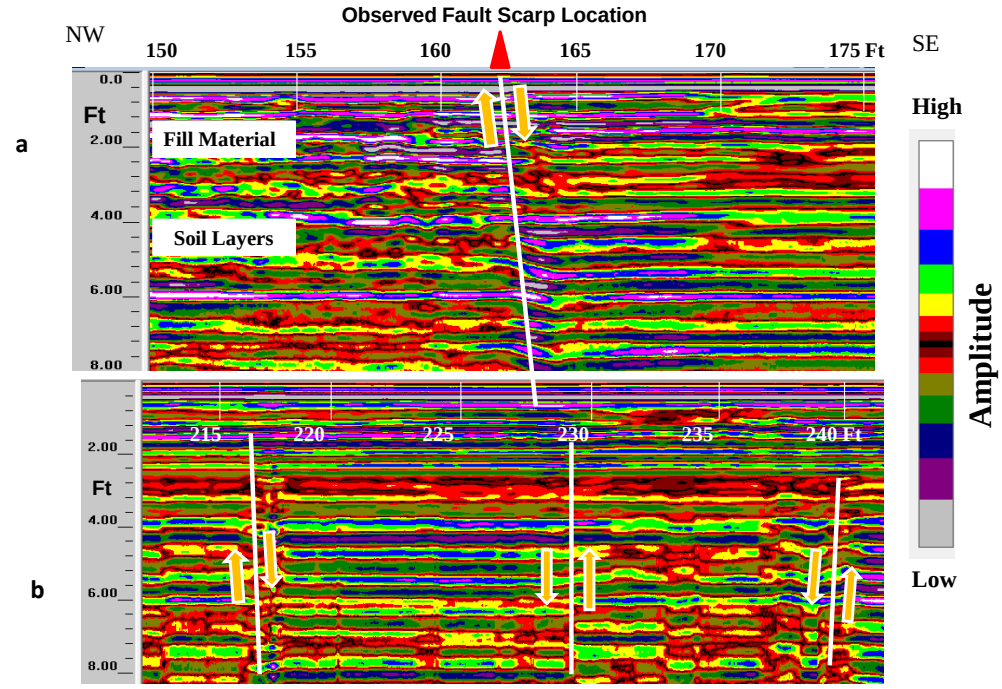

Figure 5 and 240 feet
(b). No s downthrown
to the s

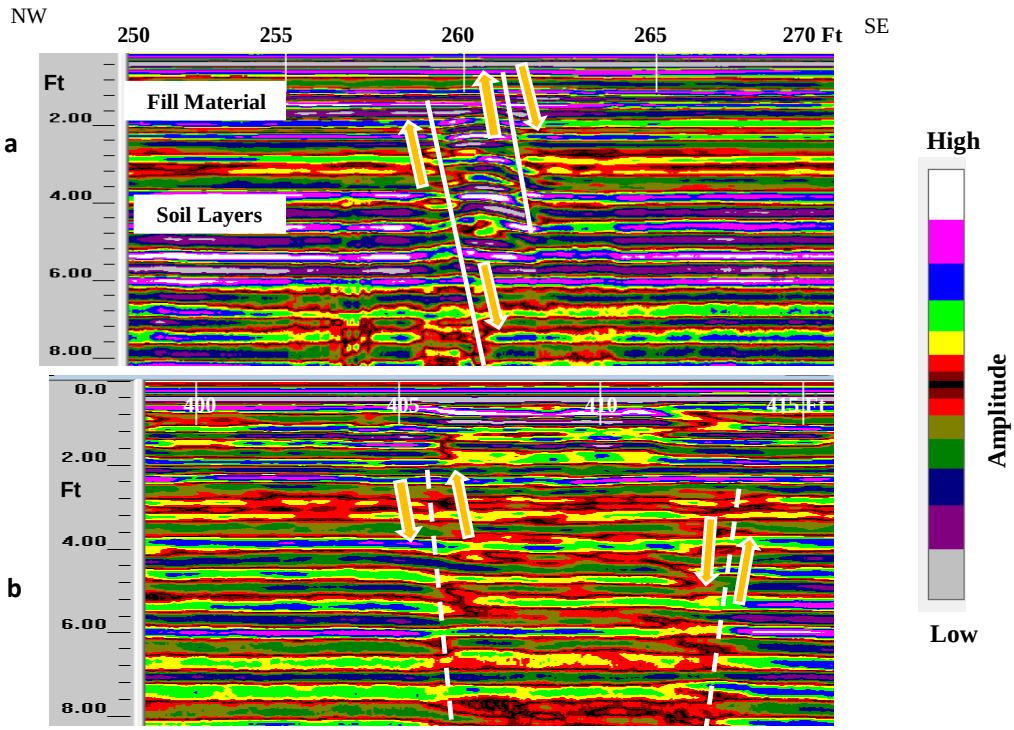

Figure l 240 feet
(b). There are small-scale faults downthrown to the southeast as well as to NW.

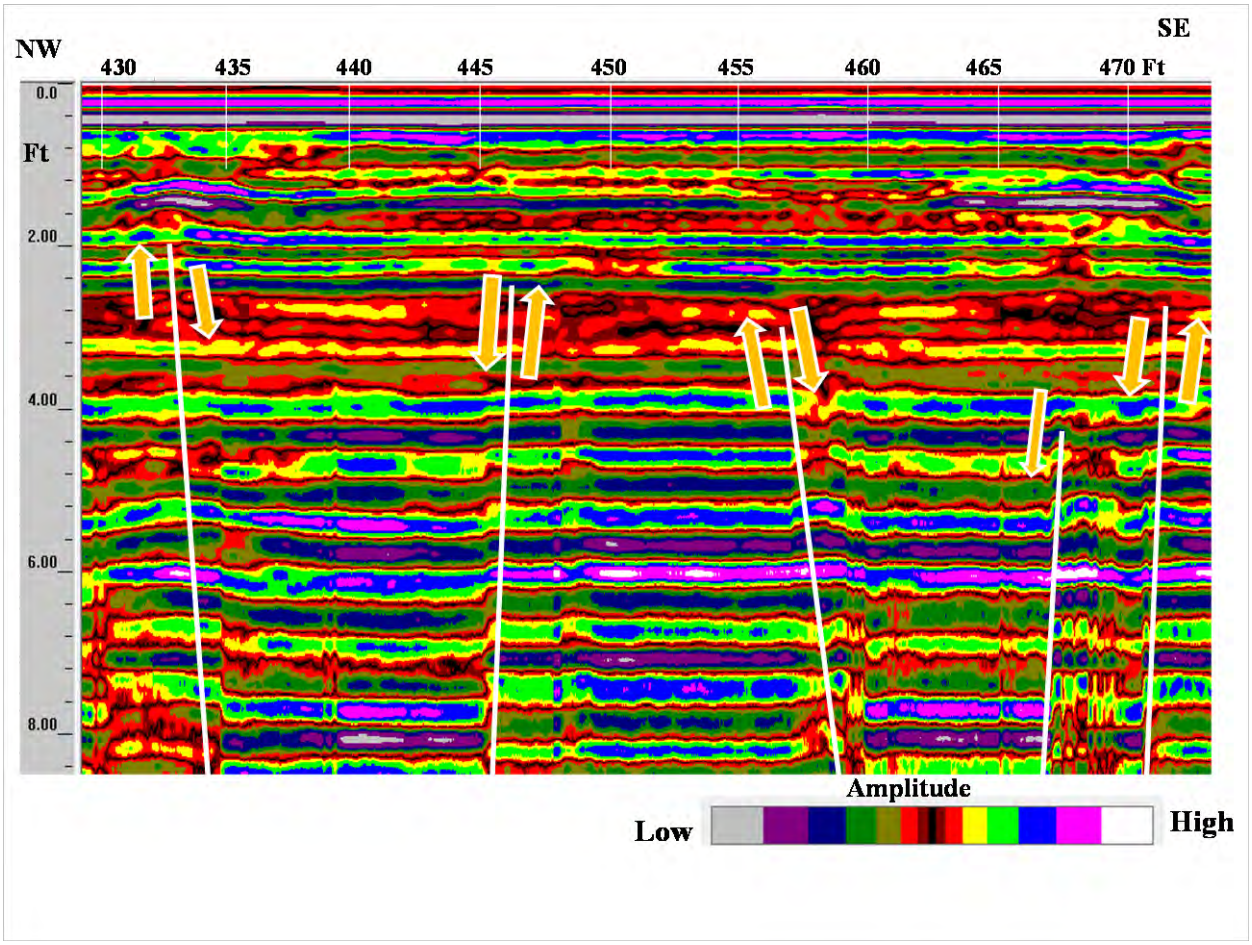

Figure 10: GPR data along Line 1 between stations 430 and 470 feet.). There are small-scale faults downthrown to the southeast as well as to NW. Note the graben-like structure between stations 430 to 445 feet and 455 to 470 feet.

Discussion of Results/Conclusions

The resistivity data from four profiles (L4, L5, L6 and L7) indicate normal fault offset down-thrown to the southeast. Location of the observed fault scarp in the field correlates very well with the resistivity Line 7. The combination of clayey sand with 24 Ohm-m resistivity (shown with blue color), and sand layers with 70 Ohm-m resistivity (shown by green colors) indicates a dipping and curved fault plane. The resistivity data on L2 and L3 do not indicate any fault anomaly (no offset between the soil layers). Resistivity profile L1 shows an anomaly at the approximate location of the fault but does not display the fault offset as well as the other profiles. The reason for this may be the presence of more clayey soil where the fault plane crosses the east-bound lane. Unpublished magnetic, gravity and conductivity data on Line 1 also indicate a fault anomaly where the resistivity data shows the fault (Saribudak and Van Nieuwenhuise, 2005). Locations of the fault determined by the resistivity data shift to the northwest from L7 through L1 (Figure 11). Resistivity profile Line 1 does not show the anomaly over the fault scarp that is observed in the field. The reason for the lack of resistivity anomaly over the fault scarp is not known.

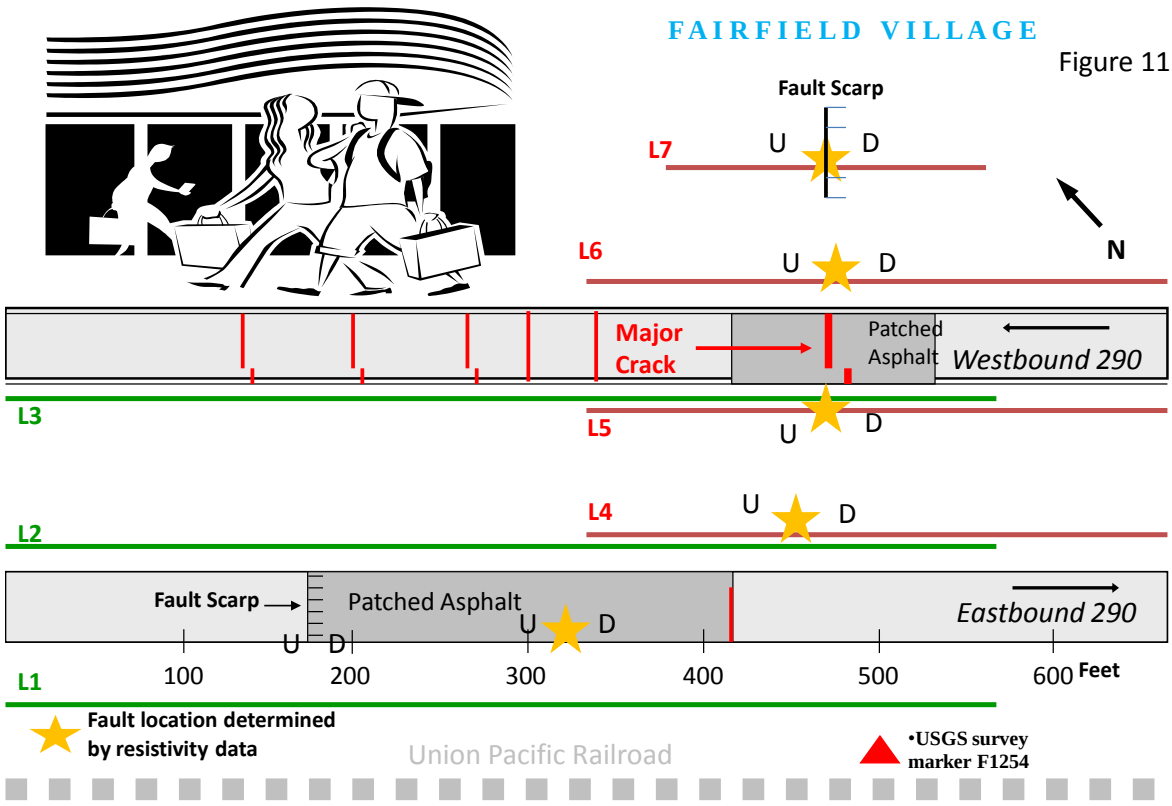

Figure 11: Approximate locations of Hockley fault determined by the geophysical data. A sketch figure of shopping mall is shown in the NW section of the study area.

The GPR data along profile L1 indicate significant anomalies that are believed caused by small faults in the near-surface. These small faults are likely normal faults downthrown to the south-east, like the movement of the Hockley fault.

The resistivity and GPR data indicate a wide zone of deformation across the Hockley fault. Geophysical data presented here combined with the field observations indicate a deformation zone of about 400 feet including the east and west-bound lanes of highway 290 (now the feeder roads). The principal fault plane and its associated shallow zone of deformation are located in the vicinity of newly-built shopping mall. The fault deformation zone projects under the eastern part of the parking lot and the major entrance road to the Outlet mall (Figure 12).

Figure 12: Site map showing approximate extension of the Hockley fault zone in the vicinity of Houston Premium Outlet Shopping Mall.

In conclusion, data acquired and used to evaluate the effectiveness of geophysical methods in detecting growth faults in the NW Houston area allowed correlation of unique and consistent anomalies with a known fault zone. It is clear that, as this study and a study of the Willow Creek Fault (Saribudak and Van Nieuwenhuise, 2007) suggest, these geophysical methods can be used to map Gulf Coast faults quickly and inexpensively. Further geophysical surveys of these faults will better define their geophysical signatures. Confidence to independently describe growth faults in the Houston metropolitan area in the future should increase as successful detection of fault-based anomalies becomes more routine. Depending on site conditions, future fault studies should include as many of the geophysical techniques described here as possible to both improve fault characterization and correlate surface features with the sub-surface. Results of this study show the benefit of including geophysical methods in addition to borehole logging, the most common method for mapping faults today.

References

Clanton, S. U., and Verbeek, R.E., 1981, Photographic portraits of active faults in the Houston metropolitan area, Texas, Houston area environmental geology: Surface faulting, ground subsidence, hazard liability, edited by Etter, M.E., Houston Geological Society, p. 70-113.

Elsbury, B.R., Van Siclen, D.C., and Marshall, B.P., 1980, Engineering aspects of the Houston fault problem, September ASCE Fall Meeting, El Paso, Texas.

Elsbury, B.R., Van Siclen, D.C., and Marshall, B.P., 1981, Living with faults in Houston. Soundings, Spring.

Geophysical Survey Systems, Inc., 2000, GPR SIR-2000 Manual.

Kasmarek, C. M., and Strom, W.E., 2002, Hydrogeology and simulation of ground-water flow and land surface subsidence in the Chicot and Evangeline aquifers, Houston, Texas, U.S. Geological Survey, Water-Resources Investigations Report 02-4022.

Kreitler, W.Charles and McKalips, 1978, Dawn., Identification of surface faults by horizontal resistivity profiles, Texas coastal zone, Bureau of Economic Geology, Geological Circular 78-6.

Saribudak, M., Van Nieuwenhuise, Bob., 2005**,** Integrated geophysical studies over growth faults in NW Houston, Texas, GSA-AEG South-Central Section 39th Meeting, San Antonio, Texas.

Saribudak, M., Van Nieuwenhuise, Bob., 2007, Integrated geophysical studies over an active growth fault in Houston, Leading Edge, v. 25; no. 3; p. 332-334.

Turner, Collie & Braden, Inc., 1991, Feasibility study for the implementation of a water reuse project in Fairfield Village, Final report.

Verbeek R.E., and Clanton, S.U., 1981, Historically active faults in the Houston metropolitan area, Texas, Houston area environmental geology: Surface faulting, ground subsidence, hazard liability, edited by Etter, M.E., Houston Geological Society, p. 28-69.

Acknowledgements

I thank Dr. Carl Norman for showing the Hockley fault in the field and for numerous discussions, and a number of friends and colleagues who helped in the data acquisition. I am thankful to Bill Rizer for his instructive and critical editing of the manuscript. I also thank Esin Saribudak for her graphical contribution to this paper. This research project was funded by Environmental Geophysics Associates.

FAULT DETECTION USING ELECTRICAL RESISTIVITY TOMOGRAPHY

Evgeniy V. Torgashov, Missouri University of Science & Technology, Rolla, MO
Neil L. Anderson, Missouri University of Science & Technology, Rolla, MO
Oleg Kovin, Missouri University of Science & Technology, Rolla, MO

Abstract

Electrical Resistivity Tomography (ERT) data were acquired on the ground surface across an underground limestone mine access tunnel in an effort to characterize the roof rock. This investigation was conducted because simultaneous localized failure occurred on the ceiling of the access tunnel and elsewhere in the mine along a previously unknown northwest trending lineament.

The interpretation of the ERT data indicates the limestone roof rock above the tunnel is dissected by several prominent clay-bearing near-vertical solution-widened fractures (joints or faults) that are not visually exposed on the ceiling of the tunnel. Roof rock failure in the mine access tunnel occurred at the intersection of projected lineament and one of the more prominent interpreted solution-widened fractures.

Introduction

In 2007, simultaneous localized roof rock failure occurred in a mine access tunnel and several rooms elsewhere in a limestone aggregate mine. A plot of incident locations indicated the failures occurred along a previously unknown northwest trending lineament. The approximate location and orientation of the lineament is shown in Figure 1. The lineament, as shown in Figure 1, extends across public roadway and intersects the access tunnel immediately to the west of the DOT right-of-way (ROW).

The rock fall debris in the access tunnel was uniformly comprised of limestone. However, in other areas of the mine, significant quantities of clay was intermixed with the fallen rock, suggesting failure occurred along a pre-existing solution-widened fracture (joint or fault). The linear and vertical nature of the more extensive roof failures indicated collapse probably occurred along a previously unknown near-vertical solution-widened fracture (joint or fault).

To prevent further rock fall, anchor bolts were installed immediately in the ceiling of the access tunnel (Figure 2). During the installation of the 10 ft long anchor bolts, workers encountered uniform Burlington-Keokuk limestone; there was no evidence of prominent solution-widened fractures (Figures 2 and 3). However, water with entrained sediment flowed freely through several narrow fractures (estimated widths of less than 0.25 in) in the collapse zone (Figure 4). It was noted that the fractures through which water flowed were oriented east-northeast, rather than northwest (parallel to the projected lineament).

In an effort to determine the cause of the rock fall and to elucidate the geologic nature of the lineament, electrical resistivity tomography (ERT) data were acquired along four parallel traverses located on the shoulders of the north and south bound lanes and in the median (Figure 1) (Ultimately, to ensure the safety of mine workers and the overlying roadway, the access tunnel was abandoned and back-filled).

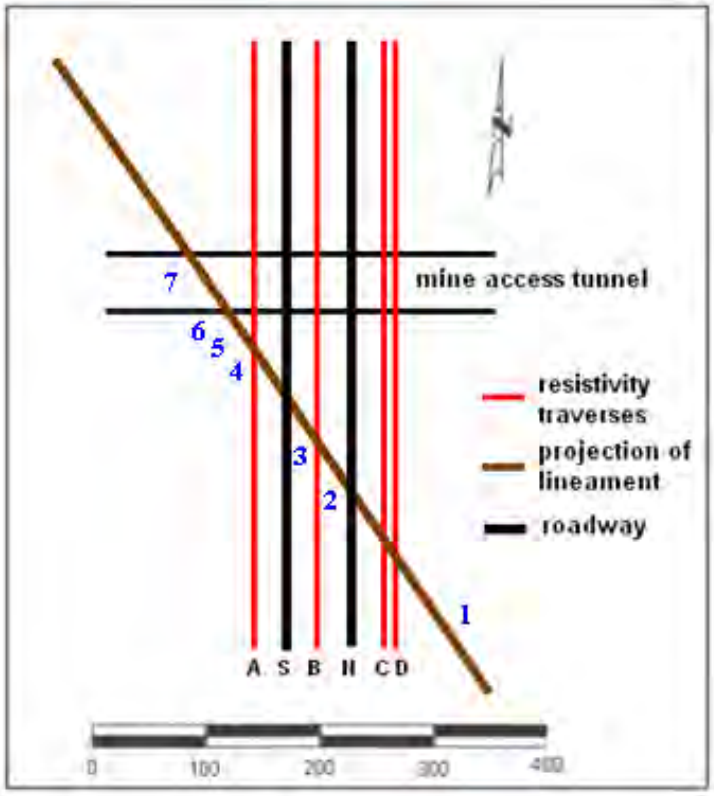

Figure 1: Map of study site showing locations of four north-south surface electrical resistivity tomography profiles (A, B, C and D). The centerlines of the northbound (N) and southbound (S) roadways, the mine access tunnel, the projected lineament and the approximate locations of seven boreholes are shown. **(**Profile D extends farther to south, not shown on the map**).**

Figure 2: Photograph of ceiling of access tunnel several tens of feet to the west of the zone of failure. Newly installed rock bolts are observed. The crew is acquiring GPR data using a 200 MHz GSSI antenna in an effort to locate clay-filled solution-widened fractures.

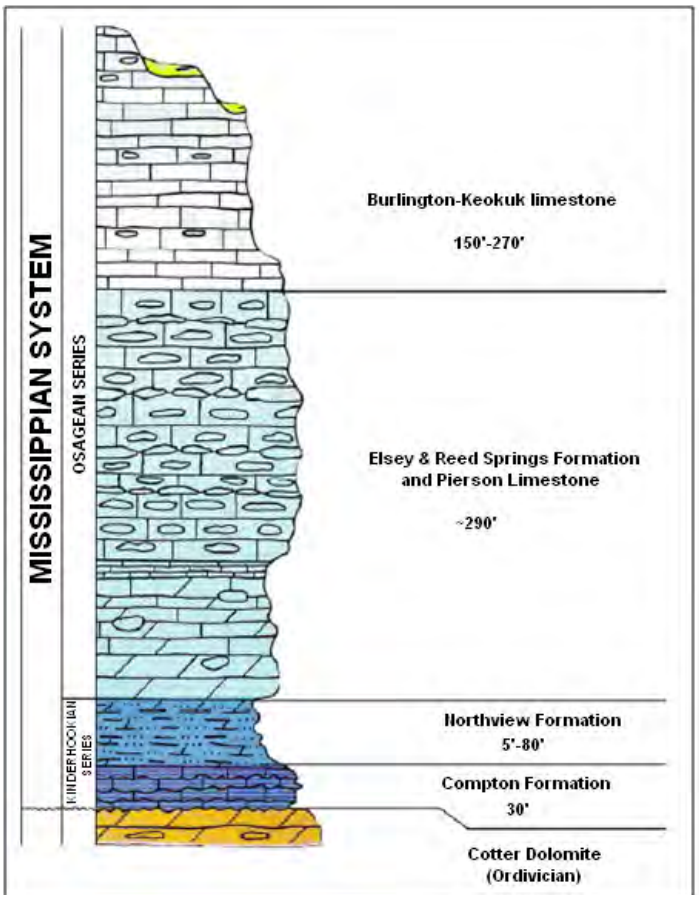

Figure 3: Stratigraphic column for the study site (after Fellows, 1970).

Figure 4: Water, with entrained sediment, flowed freely from several newly-exposed linear fractures (estimated widths of less than 0.25 in) in the collapse zone. Water influx increased dramatically after the rock fall.

Geology and Mining

The shallow subsurface in the study area is comprised of a thin veneer of residuum (0-20 ft) overlying Mississippian Burlington-Keokuk limestone (Figure 2). The limestone, where it outcrops, is intensively jointed and faulted (Figure 5). Faults and lineaments in the Greene County tend to strike approximately northwest or northeast (Figure 6).

The Burlington limestone is "room and pillar" mined in the study area. The ceiling of the access tunnel (connecting mined areas on either side of the roadway; Figure 1) is at a depth of about 80 ft relative to the ground surface (elevated embankment). The ceiling of the access tunnel is not characterized by prominent solution-widened fractures. However, water, with entrained sediment, flowed freely from several newly-exposed linear fractures (estimated widths of less than 0.25 in) in the collapse zone.

The apparent relative uniformity of the roof rock immediately above the ceiling of the access tunnel is consistent with anchor bolt information and acquired ground penetrating radar (GPR) control. The workers who placed the anchor bolts reported relatively solid rock to depths of 10 ft at all anchor bolt locations. The interpretation of acquired GPR control also suggests the roof rock within 10 ft of the ceiling is not intensely karsted. On the GPR profile of Figure 7, a relatively uniform near-horizontal reflector (parallel to mine ceiling) is imaged at an estimated depth of about 10 ft (dielectric permittivity of 15 for moist limestone). Two less prominent vertical anomalies are observed centered at stations 39 and 46 (collapse zone). These anomalies appear to originate several feet from the mine ceiling and may be images of near-vertical fracture zones that are not prominently exposed on the mine ceiling.

Borehole data

Seven exploratory boreholes were acquired in the study area in immediate proximity to the surface projection of the failure lineament (Figure 1 and Table 1). Overburden was not sampled in any of the borings, but is described as red, high plasticity residual clay with chert and limestone rock fragments. Its thickness is highly variable, ranging from 8.6 feet in Boring 1 to 24.8 feet in Boring 4.

The deepest borehole (Borehole 1) was drilled to 122.6 feet. Boreholes 2 through 7 were terminated at depths of between 39.3 feet to 90.0 feet. Burlington Limestone only was encountered in boreholes 2-7. This unit is generally described as gray to light gray, alternating from fine- to coarse-grained with occasional stylolites and fossils. At a depth of 94.5 feet in Boring 1 (off embankment), the Reeds Spring Formation was encountered. This unit is generally described as a brown to gray, fine grained limestone with chert nodules.

The Rock Quality Designation (RQD) for the Burlington-Keokuk limestone was generally in the Good to Excellent range, with some isolated core runs having RQDs in the Fair range. The lower RQD values are generally associated with broken zones near the overburden contact, healed vertical fractures, weathered seams, and/or fractures. Near-vertical clay-filled solution-widened fractures were not encountered in any of the boreholes. However, multiple fractures were encountered. Borehole 4 (Figure 1) which is on-line with the projected lineament (Profile A; Station 320) encountered open seams or fractures with and without flow at multiple depths (26.7 ft, 29.2 ft, 30.5 ft, 30.8 ft, 32.4 ft, 41.3 ft, 41.7 ft, 42.0 ft, 48.8 ft, 49.4 ft) and standing water at 47.9'.

Figure 5: Outcropping Burlington-Keokuk limestone is typically dissected by solution-widened joints or faults. The ceiling of the access tunnel in underground limestone (~100 ft below the ground surface) is not characterized by prominent fractures (Figure 2).

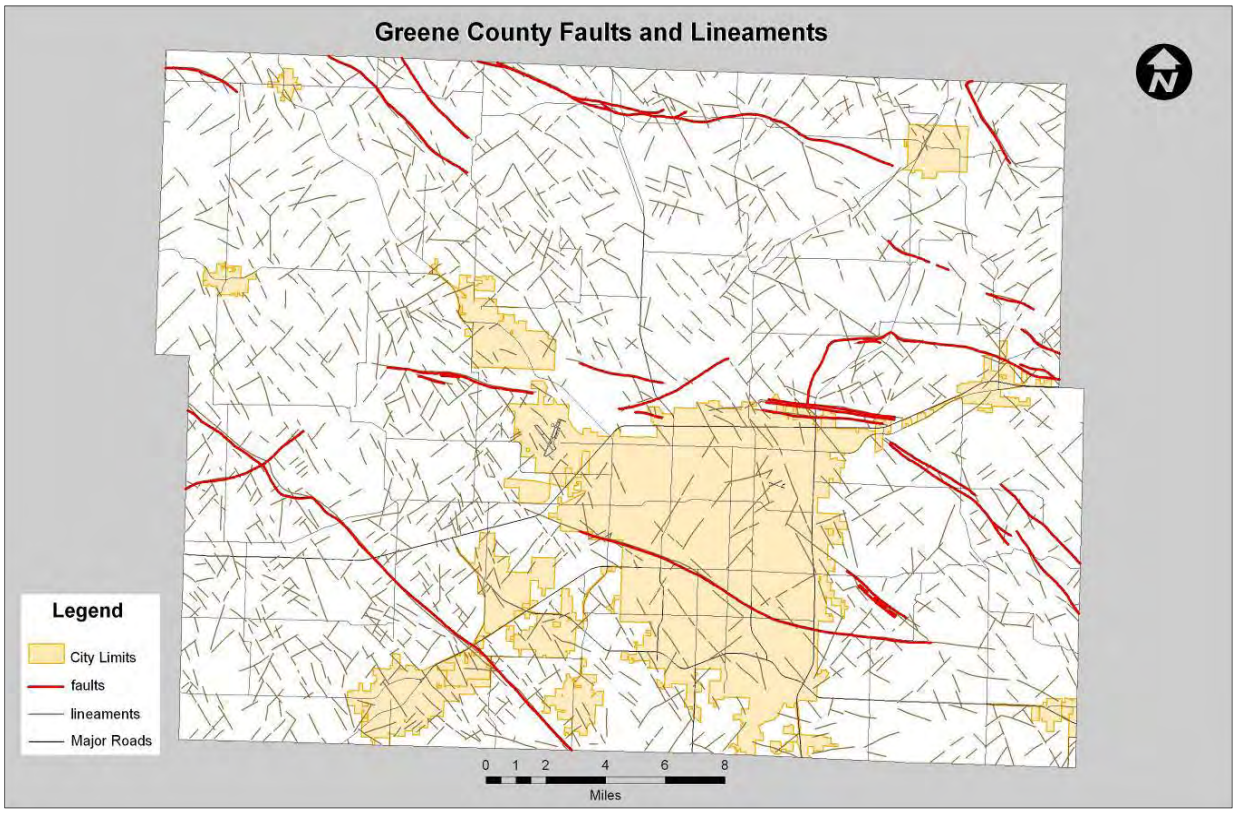

Figure 6: Locations and orientations of mapped faults and lineaments in Greene County (Coots, 2007). Faults and lineaments in the region tend to strike approximately northwest or northeast.

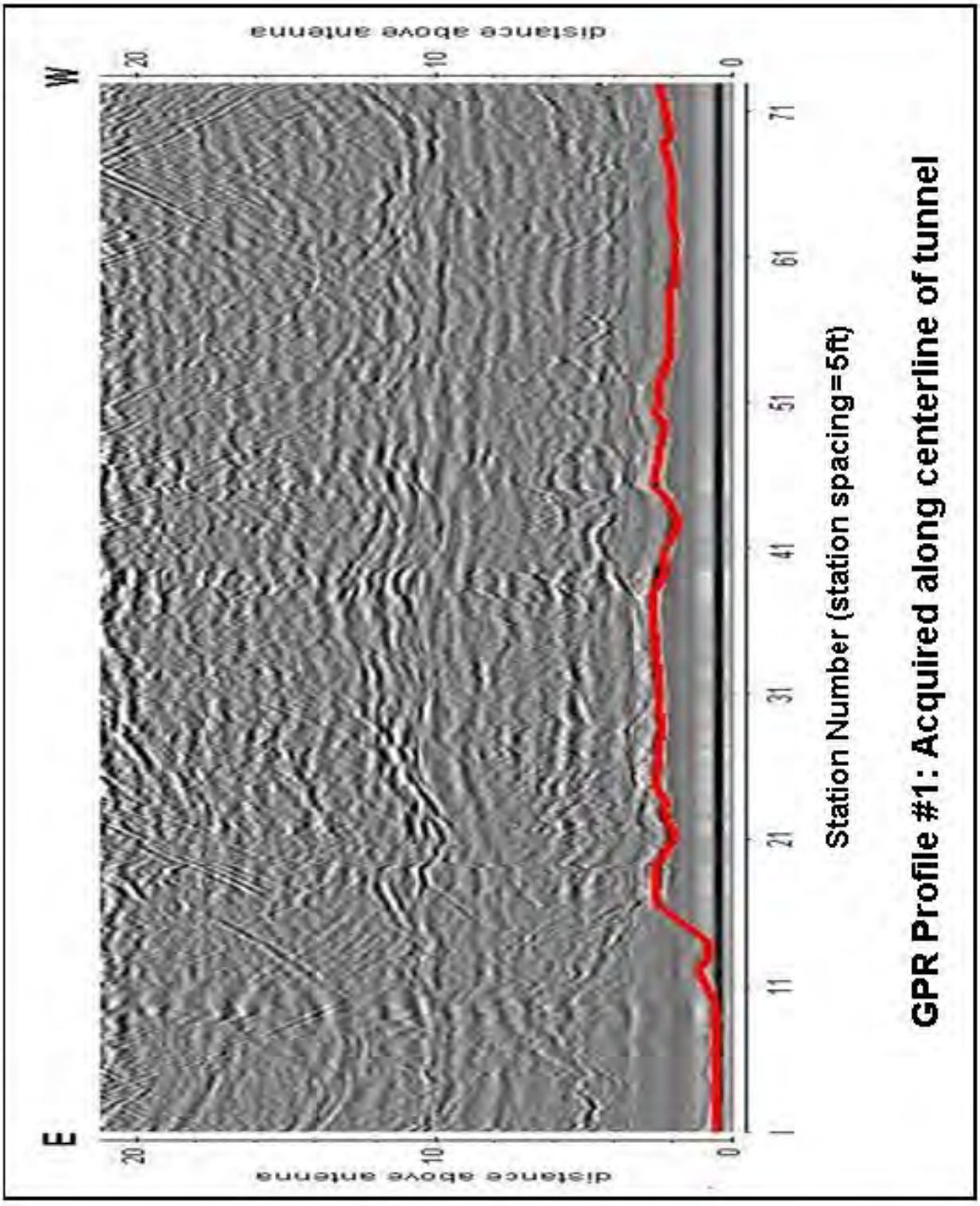

Figure 7: Example GPR profile (length ~370 ft) acquired along centerline of access tunnel ceiling using a GSSI 200 MHz antenna. The vertical axis is in feet; the lower continuous red line represents the surface of the ceiling. The apparent effective depth of investigation (highest prominent continuous reflector) is at least 10 ft.

Acquisition of Electrical Resistivity Tomography Data

Four parallel north-south ERT profiles (A, B, C and D) were acquired on the ground surface above the mine access tunnel in an effort to characterize the roof rock from the top down (Figures 1 and 8). The ERT data were acquired using a GSSI SuperSting R8 resistivity unit equipped with a dipole-dipole array consisting of 72 electrodes spaced at 5-ft intervals. The acquired field data were good quality with the exception of the northernmost segment of Profile C (Stations 0 to 300). This segment of Profile C is immediately adjacent to a metal guard rail. Poorer quality data was obtained along this segment of roadway, probably because some of the induced current flowed through the guard rail, rather than into the subsurface. The acquired resistivity data were processed using RES2DINV.

Interpretation of ERT Data

Uninterpreted versions of the ERT profiles are presented as Figure 8; interpreted versions of the four profiles acquired are displayed as Figure 9. The interpreted top of bedrock has been superposed on the ERT profiles. As indicated in Table 1 the interpreted top of rock correlates reasonably well with boring control (In addition to the boreholes listed in Table 1, the authors had access to 18 shallow borings placed in the roadway right of way that terminated at top of rock. These data were also used to constrain the interpretation of the ERT data). The locations of several interpreted near-vertical solution-widened fractures (joints or faults) have been highlighted on the ERT profiles.

To the south of Station 600, bedrock does not appear to have been extensively dissected by solution-widened fractures. The top of limestone bedrock, as per borehole control, correlates reasonably well with the 50 ohm-m contour interval (except where interpreted fractures are present). Soil to the south of Station 600 is characterized by resistivities less than 50 ohm-m. (The roadway embankment south of station 600 is elevated by only a few feet. The eastern right of way south of station 600 was largely covered by up to 1 ft or more of ponded water).

As noted, the resistivity of bedrock to the south of Station 600 is less than 50 ohm-m only where interpreted solution-widened fractures are present. Presumably, bedrock in proximity to the fractures is more extensively fractured and weathered, and contains some clay. This interpretation is supported by boring data. As noted previously, Borehole 4 (Figure 1; Table 1) encountered open seams or fractures with and without flow at multiple depths. Similarly, Boring 2 which is immediately adjacent to an interpreted solution-widened fracture (Profile B; Station 398) encountered open seams or fractures with/without flow at multiple depths (24.0 ft, 26.2 ft, 27.0 ft, 28.0 ft, 29.3 ft, 33.5-35.0 ft, 37.4 ft, 38.0 ft, 39.2 ft, 40.1 ft, 44.0 ft, 48.5 ft) and standing water at 60.0 ft.

The authors' experience has been that limestone bedrock in Greene County is more typically characterized by resistivities higher than 200 ohm-m, rather than resistivities higher than 50 ohm-m (Anderson et. al., 2006; Muchaidze, 2009; Myat et. al., 2008A, 2008B; Robison and Anderson, 2008). The low bedrock resistivities observed at the mine access tunnel study site are attributed mostly to the relatively high moisture content (as evidenced by the presence of ponded water on the ground surface in the right of way, boring reports and flow from the mine ceiling).

Bedrock to the north of Station 600 is interpreted to be more intensely dissected by solution-widened fractures, so the top of rock, in many places, does not coincide with the 50 ohm-m contour interval (Figure 9). The identification/mapping of top of rock is further complicated because the resistivities of the shallower soils to the north of Station 600 are greatly in excess of 50 ohm-m in places.

Table 1. Borehole and electrical resistivity data comparison.

Borehole	Elevation of Bedrock in Borehole (ft)	Tie Point: ERT Profile (Figures 1, 4 and 5)	Elevation of Bedrock on ERT Profile at tie point (ft)
1	1379	Profile D; Sta. 543	1373
2	1375	Profile B; Sta. 410	1375
3	1376	Profile B; Sta. 398	1374
4	1374	Profile A; Sta. 320	1376
5	1374	Profile A; Sta. 305	1372
6	1375	Profile A; Sta. 290	1370
7	1373	Profile A, Sta. 266	1374

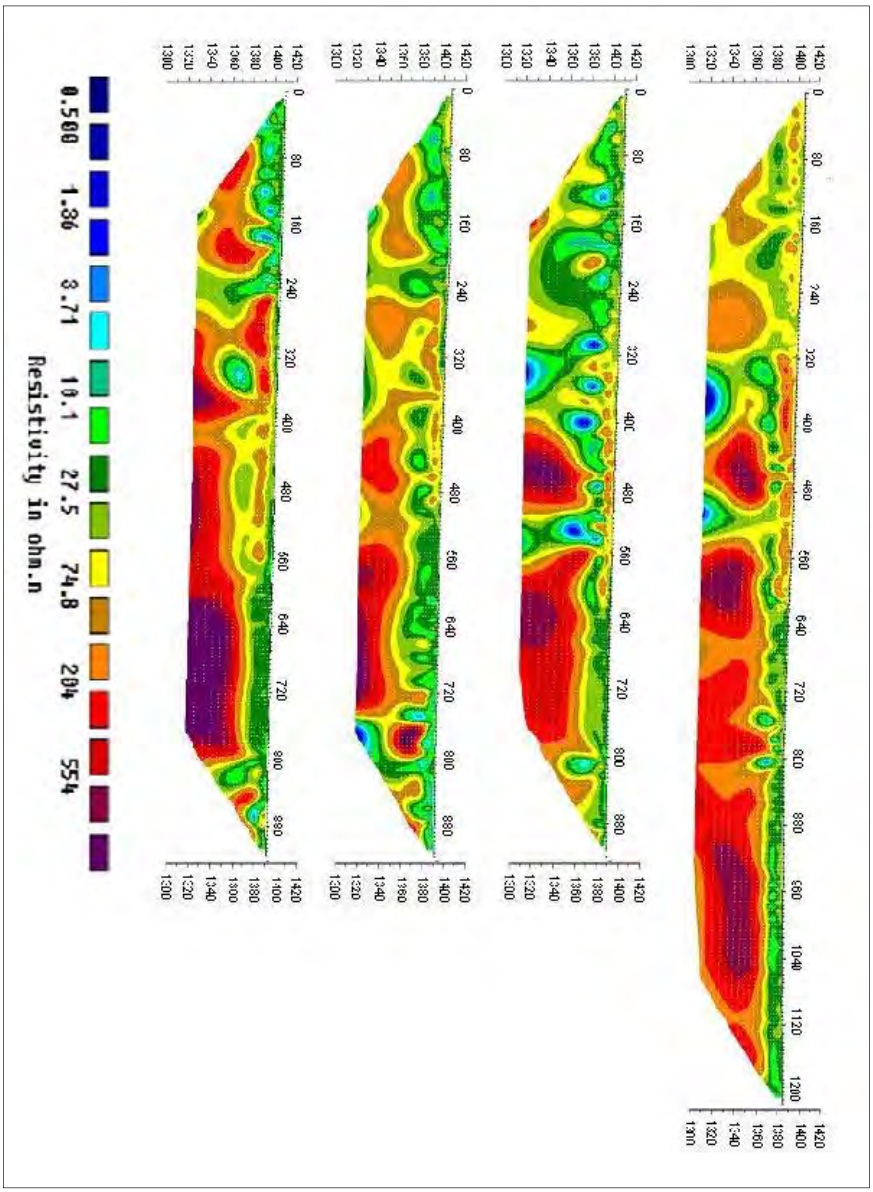

Figure 8: Uninterpreted ERT profiles (A-D; left to right; Figure 1). Distances and depths are in feet. Station 270 overlies the center of the mine access tunnel on all profiles. The top of the mine access tunnel is about 10 feet below the base of the zone imaged on the ERT profiles.

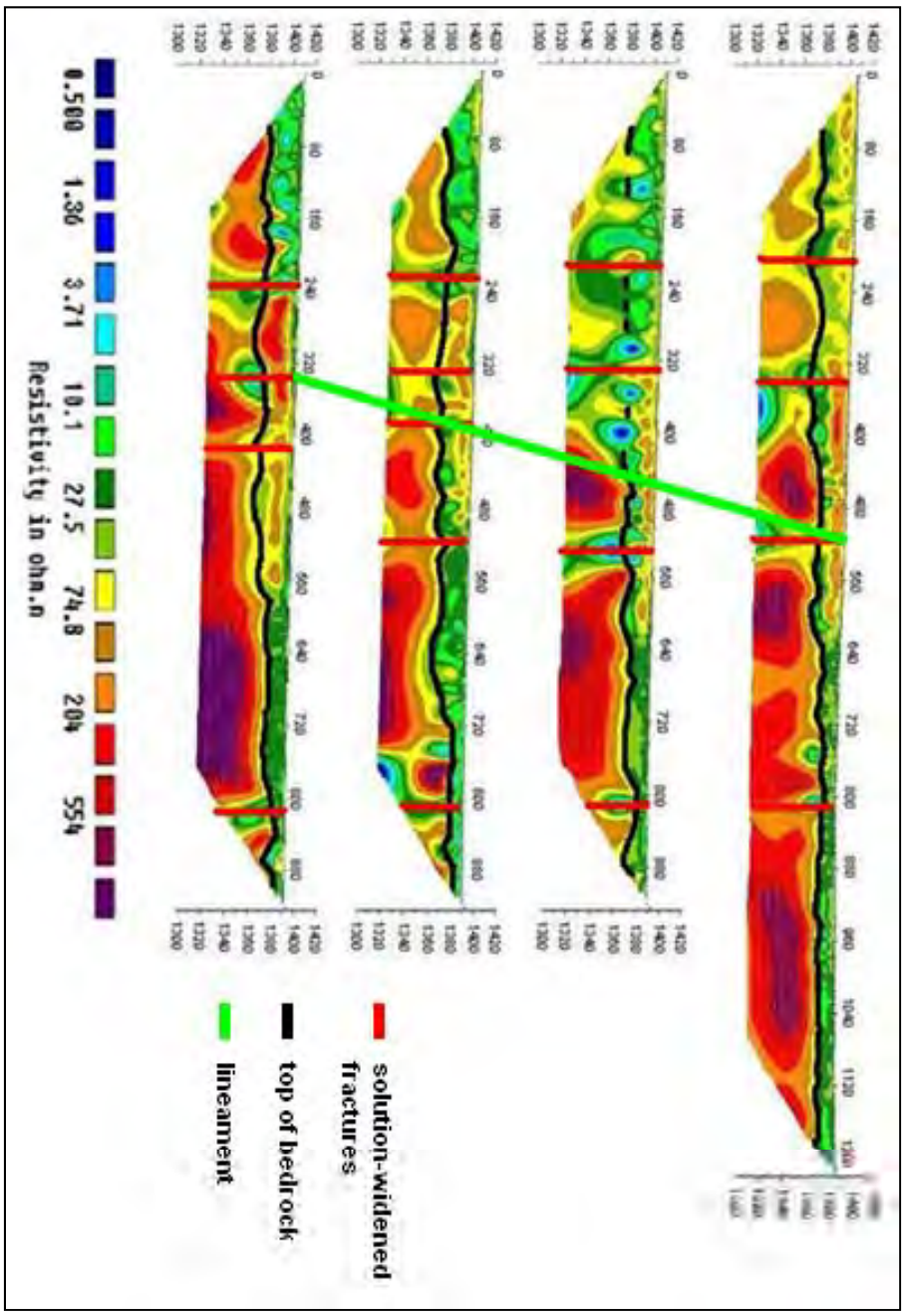

Figure 9: Interpreted ERT profiles (A-D; left to right; Figure 1). Several prominent interpreted solution-widened fractures and the projected lineament have been superposed on the ERT profiles. Distances and depths are in feet (the horizontal scale is exaggerated so the northwest-trending lineament does not appear to be properly oriented). The top of rock correlates well with borehole control. Station 270 overlies the center of the mine access tunnel on all profiles.

These higher soil resistivities north of station 600 are attributed to the presence of thicker and drier embankment fill along this elevated section of roadway (the embankment to the north of Station 600 becomes increasingly elevated with respect to the waters ponded in eastern right of way).

In Figure 9, the northwest lineament along which roof failure occurred has also been superposed. (This lineament does not appear to be oriented northwest because the horizontal and vertical axes use

different scales). We note that the projected lineament correlates reasonably well with the locations of interpreted solution-widened fractures and conclude that roof rock failure in the mine access tunnel (and elsewhere) probably occurred along a prominent northwest-trending solution-widened fracture.

Several other prominent interpreted solution-widened fractures have been highlighted on Figure 9. These solution-widened fractures are characterized are characterized on the ERT profiles as near-vertical zones of low electrical resistivity (relative to adjacent more intact limestone). The lowered relative resistivity of the fractured rock is attributed to some combination of enhanced porosity and permeability, increased water saturation, and increased clay content. Our inclination is to correlate these features as shown in Figure 10.

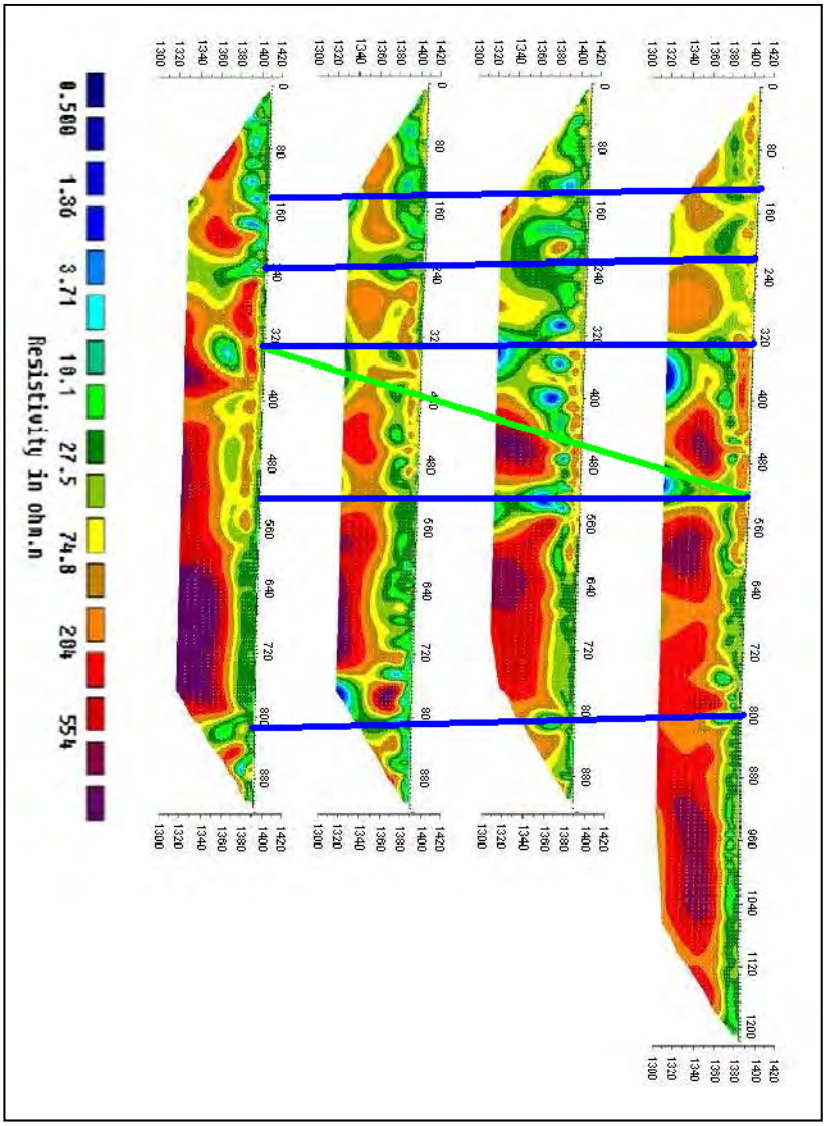

Figure 10: Interpreted ERT profiles (A-D; left to right; Figure 1). Several prominent interpreted solution-widened fractures (blue) and the projected lineament (green) have been superposed on the ERT profiles. Station 270 overlies the center of the mine access tunnel on all profiles.

This interpretation appears to be reasonable based on the ERT images and the observation that waters flowed primarily from east-northeast trending fractures on the ceiling of the access tunnel where

failure occurred. This interpretation is also supported by the literature. As shown in Figure 6, the dominant near-orthogonal faults and lineaments in Greene County trend approximately north-northwest and east-northeast, respectively

It is interesting to note that roof rock failure in the mine access tunnel occurred at the intersection of projected lineament and one of the more prominent interpreted solution-widened fractures (Figure 11), and speculate this zone was especially susceptible to failure. Similar observations have been reported by Robison and Anderson (2008).

It is also interesting to note that the resistivity anomalies associated with both interpreted fractures diminishes with depth on ERT profile A. This may indicate why the postulated fractured zone is not readily identified on the ceiling of the access tunnel or on the GPR data. Unfortunately, the ERT data do not image the top of the tunnel, so more specific conclusions cannot be drawn.

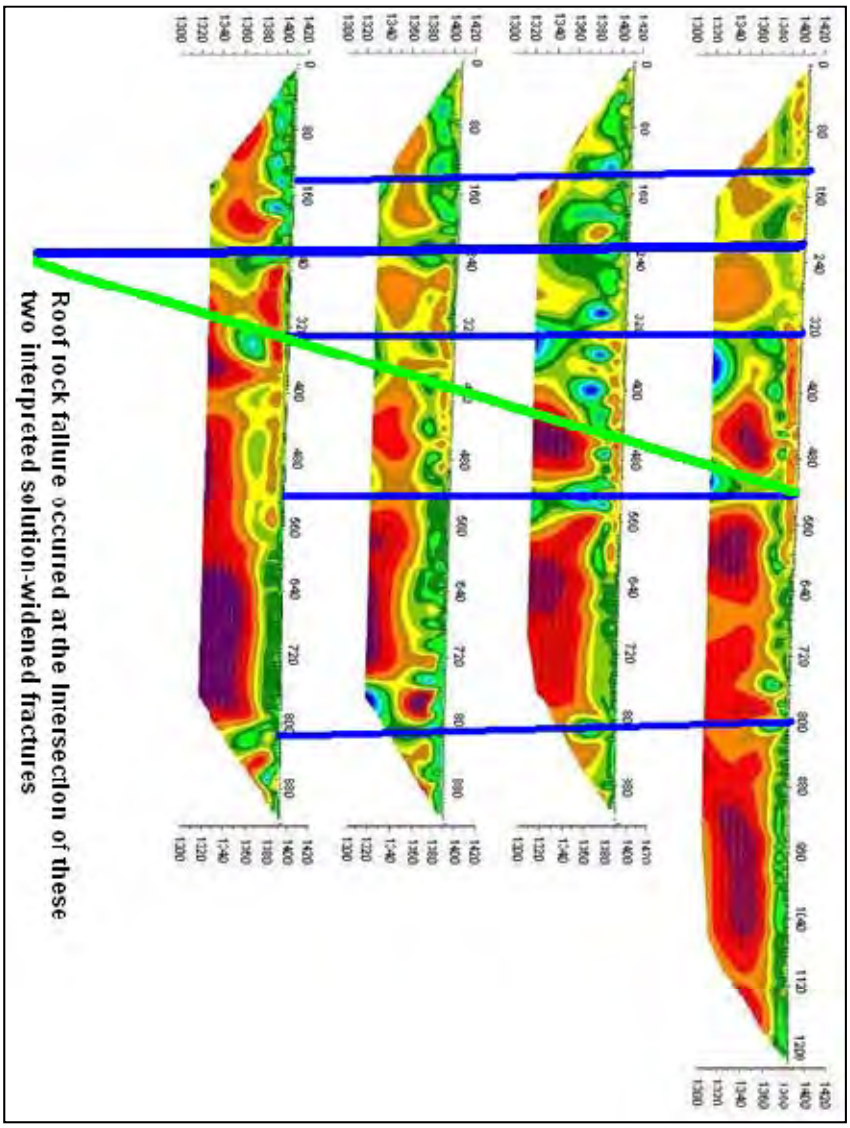

Figure 11: Interpreted ERT profiles (A-D; bottom to top; Figure 1). Station 270 overlies the center of the mine access tunnel on all profiles. Roof rock failure in the mine access tunnel occurred at the intersection of the projected lineament (green) and one of the more prominent interpreted solution-widened fractures (blue).

Conclusion

Bedrock in proximity to the mine access tunnel is interpreted to be dissected by a suite of near-orthogonal near-vertical solution-widened fractures, trending predominantly northwest or east-northeast. The solution-widened fractures are characterized on the ERT profiles as near-vertical zones of low electrical resistivity (relative to adjacent more intact limestone). The lowered relative resistivity of the fractured rock is attributed to some combination of enhanced porosity and permeability, increased water saturation, and increased clay content.

Roof rock failure on the ceiling of the mine access tunnel appears to have occurred at the intersection of a two prominent solution-widened fractures: one trending northwest; one trending east-northeast. This intersection zone was probably most susceptible to failure.

References

Anderson, N.L., Ismail, A. and Apel, D., 2006, Assessment of Karst Activity at Highway Construction Sites in Greene and Jefferson Counties, Missouri, using the Electrical Resistivity Method: Highway Geophysics-NDE Conference proceedings, 497-513

Coots, T. 2007, Greene County Comprehensive Plan, http://www.greenecountymo.org/web/Public_Information/files/Comp.pdf: Greene County Planning and Zoning, 82 p.

Fellow, L. D., 1970, "Geology of Galloway Quadrangle Greene County Missouri," Missouri Geological Survey and Water Resources.

Muchaidze, I., 2009, Imaging in Karst Terrain Using Electrical Resistivity Tomography. Masters Thesis, Missouri Science and Technology University, 2009.

Myat, M., Wamweya, A., Kovin, O., Anderson, N., and Robison, J., 2008a, Application of Electrical Resistivity Method in Steeply Dipping Karst Terrain: 11th Multidisciplinary Conference on Sinkholes and the Engineering and Environmental Impacts of Karst: Integrating Science and Engineering to Solve Karst Problems, September 22-26, 2008, Ramada Conference Center Tallahassee, Tallahassee, FL.

Myat, M., Muchaidze, Y., Wamweya, A., Anderson, N., and Robison, J., 2008b, Assessment of Karst Activity at Springfield Route 60 Study Site: 11th Multidisciplinary Conference on Sinkholes and the Engineering and Environmental Impacts of Karst: Integrating Science and Engineering to Solve Karst Problems, September 22-26, 2008, Ramada Conference Center Tallahassee, Tallahassee, FL.

Robison, J. and Anderson, N., 2008, Geophysical Investigation of the Delaware Avenue Sinkhole, Nixa, Missouri: 11th Multidisciplinary Conference on Sinkholes and the Engineering and Environmental Impacts of Karst: Integrating Science and Engineering to Solve Karst Problems, September 22-26, 2008, Ramada Conference Center Tallahassee, Tallahassee, FL.

CONSTRAINING CAUSES OF STRUCTURAL FAILURE USING ELECTRICAL RESISTIVTY TOMOGRAPHY (ERT): A CASE STUDY OF LAGOS, SOUTHWESTERN, NIGERIA

Elijah A. AYOLABI; Adetayo F. FOLORUNSO and Moroof O. OLORUNTOLA
Department of Geosciences, University of Lagos, Lagos, Nigeria

Abstract

The phenomenon of building collapse in recent times has become a source of national concern. Particularly alarming is the situation in Lagos, the commercial nerve center of Nigeria. Several attempts made to proffer solution to this excluded geophysical investigations, as general opinion did not support subsurface geology as being responsible. However, 2-D and 3-D electrical resistivity surveys were carried out using wenner electrode configuration with 64 electrodes connected to a multi-core cable, along three (3) profiles of 260 m length at an inter-electrode spacing of 4m. Resistivity measurements were taken alongside with Induced Polarization measurements using the same electrode configuration. The survey was conducted round to cover all the areas where distress in building structures is noticeable. The 2-D and 3-D electrical resistivity and IP images for the three profiles revealed that the main cause of structural defect in buildings around the area is the subsurface geology, contrary to general opinion which favours insufficiency and/or lack of genuine of building materials. From the results, it is quite obvious that the entire land mass of the study area is underlain by materials of very low resistivity values below 30 Ωm at the near-surface depth of 5 m down to above 30 m. Local high resistivity in the near surface material is due to either the effect of sand-filling for road network and/or the presence of exotic highly resistive concrete materials used to reclaim land. The IP inversion models help to delineate clay formation from sandy formation filled with saline water. The high IP signals in the subsurface mainly confirm the presence of clayey formation.

INTRODUCTION

The present work is aimed at showing the efficiency of 2-D and 3-D Electrical Resistivity Tomography (ERT) in probing the subsurface soil for foundation investigation. Many works have been done to establish a relationship between soil engineering test and ERT data (Israil and Pachauri, 2003; Cosenza et al., 2006; Gay et al., 2006). Also it has been discovered that 2-D ERT method is cost effective, efficient and less time consuming in geotechnical investigation than most geotechnic tests (Sudha *et al.*, 2009). Another important advantage of ERT is that it produces continuous information of the subsurface and probes into several meters below the surface whereas, engineering soil test is a point investigation and does not go beyond a few meters below the surface. Interpretation of electrical measurement can give an understanding of the subsurface composition (geology), depth to competent layer (soil) and help to proffer safe measure for construction of different categories of buildings. The length of the pipe that must be sunk to hold the foundation of a building could be determined from electrical resistivity survey. Lack of such approach led to partial collapse of big building structure as previously reported by Folorunso (2009) and Ayolabi *et al*., (2009a).

The parameters commonly studied in geotechnical tests are the grain size, soil strength and the number of blows (N-values). Though literature reported that the relationship between electrical parameters such as chargeability, resistivity and N-values is poor (Giao, *et al.*, 2003; Sudha *et al*., 2009), we know this cannot be so between electrical properties on one side and grain size distribution, degree of saturation, porosity and cementation, on the other. Thus, in the present work, ERT data were complemented with Induced Polarization data to evaluate the cause of distress in buildings around the study area.

The theory of electrical resistivity suggests that electric current flows in the subsurface soil by electrolytic rather than electronic processes (Kearey *et al*, 2002). Hence, porosity is the major control of resistivity of rocks, and that resistivity generally increases as porosity decreases. Porosity and cementation, on the other hand, are related. It then means that electrical resistivity could be used to determine the degree of cementation to better characterize the subsurface soil for engineering foundation. Another important factor in knowing soil strength is the amount of fine (clay) present. Many authors have equally reported the relationship between the duos such that clay content in soil affects both soil strength as well as its resistivity (Sudha *et al*., 2009). Clay has very low electrical resistivity (Zhdanov and Keller, 1994); therefore, its contents in the soil may change the relationship between electrical parameter and soil strength (Sudha *et al*., 2009).

The present paper reports recent 2-D and 3-D Electrical Resistivity and IP surveys in a popular area within the Lagos metropolis where there are large-scale distress in buildings and even complete collapse of some. The only challenge the present study would have faced is differentiating between clay formation and saline water. This was taken care of by the IP measurements which differentiate moist clay formation and saline sandy formation from the IP response (Sastry and Tesfakiros, 2006, Ayolabi *et al*., (2009b).

Geomorphology and Geology of the Area

The area lies on latitudes 726350 to 727000 N and longitudes 874300 to 875350 E (UTM coordinate unit). The total area cover is approximately 46.8 square kilometers (Fig 1). The topography is undulating and generally looks like a subsidence relative to Lagos landmass. Incidentally, buildings structures in the area are also subsiding, thereby typifying the area as an active region of mass subsidence. Surface water flow is highly impaired by the poor drainage channels that characterize the whole area since water from the neighbouring area flows in to Gbagada, being a valley. This leads to flooding, most during the rainy season.

The geology of Lagos was extensively studied alongside the geology of the Nigerian portion of Dahomey basin by many researchers (Jones and Hockey, 1964; Omatshola and Adegoke, 1981; Agagu, 1985; Enu, 1990; and Nton, 2001). The oldest formation identified in Dahomey basin is the Abeokuta formation (Jones and Hockey, 1964). This was upgraded to a group status with three formations by (Omatshola and Adegoke, 1981), comprising Ise formation having a conglomeratic and grity base overlain by coarse to medium grained sandstone with interbeded kaolinite; followed by a coarse to medium grained sandstone with interbeded shale, siltstone and claystone, having a sandy facies that is tar-bearing while the shale is organic-rich, called Afowo formation (Enu, 1990); overlain by Araromi formation, which is the youngest in the group: a Cretaceous sediment made of fine to medium grained sandstone at the base, overlied by shale, siltstone with interbeded limestone, marl and lignite. Abeokuta group is overlain by Ewekoro formation. This formation is made of a shaly limestone unit (Adekoge, 1977) reported to be highly fossiliforous (Jones and Hockey, 1964) assigned with the age of Paleocene. The formation is Akinbo which is composed of shale and clay sequence (Ogbe, 1972) belonging to Eocene age. Oshoshun is the next formation comprising pale greenish grey laminated phosphate and glauconitic shale of Eocene age. This is overlain by massive yellowish and poorly consolidated cross-bedded sandstone called Ilaro formation. The youngest formation in the basin is the Benin formation, also known as the coastal plain sands (Jones and Hockey, 1964). It comprises poorly sorted sands with lenses of clays belonging to Oligocene to Recent.

Lagos belongs to the coastal plain sand formation which is made up of loose sediment ranging from silt, clay and fine to coarse grained sand (Fig 2). The exposed rock unit in the area consists of poorly sorted sands with lenses of clays. The sands are in part cross bedded and show transitional to continental characteristics according to Jones and Hockey (1964), Omatshola and Adegoke (1981), Agagu (1985), Enu (1990) and Nton (2001). The age Oligocene to Recent was assigned to this formation on the basis of fauna contents.

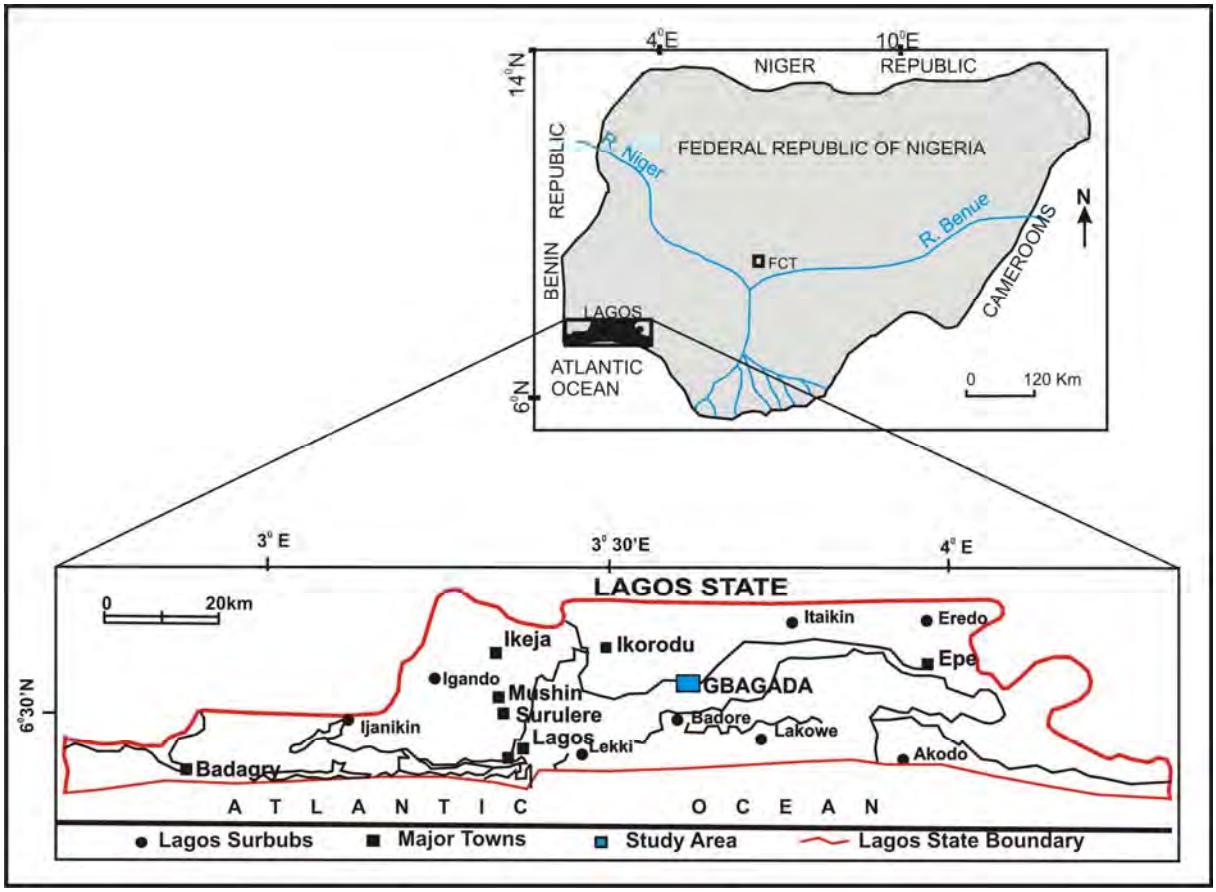

Fig 1: Location Map Showing Gbagada with Nigeria Map Inset

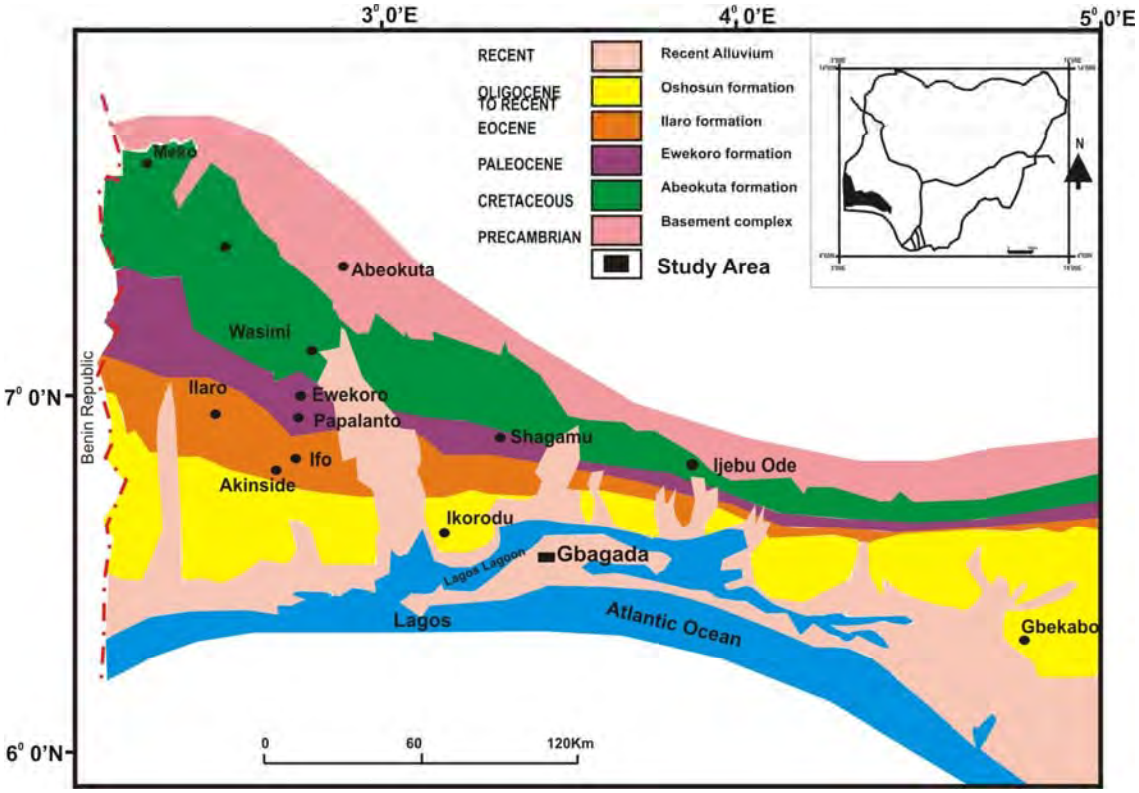

Fig 2: Geological Map of Eastern Dahomey Basin (Modify After Billman, 1992)

The Problem

The major challenge building structures in Lagos are facing is the subsurface geology of the city being a loose unconsolidated sediment. During deposition of sediment, plant and debris are equally deposited. Another regime of sedimentation where other materials are deposited on top of previously deposited ones occurs. In such cases, the plant and debris become a peat. This problem is prominent in some part of Lagos such as the study area – Gbagada.

Gbagada is a popular area in the Lagos metropolitan city that host residential, industrial, institutional and religious buildings. It accommodates a sizeable number of people among the over 15 millions dwellers in Lagos. The incessant building collapse in Lagos has assumed an alarming dimension in recent years. Properties worth millions of naira and lives of people have been lost to building collapse in various parts of the city (Fig 3), hence the necessity to find a more dependable technique of characterizing the subsurface soil prior to building construction works. A reconnaissance survey conducted recently in the study area shows that almost all the houses are structurally defective. Some buildings are completely submerged in the sand; some are tilted, while storey buildings have their down-stairs completely sunken into the subsurface, leading to total evacuation (Fig 4).

Many a time, when building collapses, an outpour of blames is directed at the building engineers for using inappropriate, inadequate or inferior materials. However, recent scientific study has proven this wrong as magnificent building complexes are found constructed on faults and buried river channel (Folorunso, 2009). Most engineering soil tests carried out prior to building construction are inadequate in that they are point investigations rather than continuous imaging of the subsurface. A similar problem is exhibited by the use of vertical electrical sounding (VES) in engineering survey (Ayolabi *et al*., 2009a). Thus, engineering soil tests must be carried along with 2-D and 3-D electrical resistivity measurements for better characterization of the subsurface soil prior to any kinds of construction work.

Fig 3: A Scene of Collapsed Building in Lagos (Source: The Nation, 27 March, 2009)

Fig 4: Different Degrees of Structural Instability Observed on Buildings in the Area

Investigative Methods

The methods adopted in the field investigation are electrical resistivity tomography (ERT) technique for the 2-D and 3-D and IP tomography. The ERT and IP investigations were carried out in three locations within the area, including a site being developed as a housing estate (profile 3). The synoptic view of data acquisition and profile lane and direction at Gbagada is shown in Fig 5.

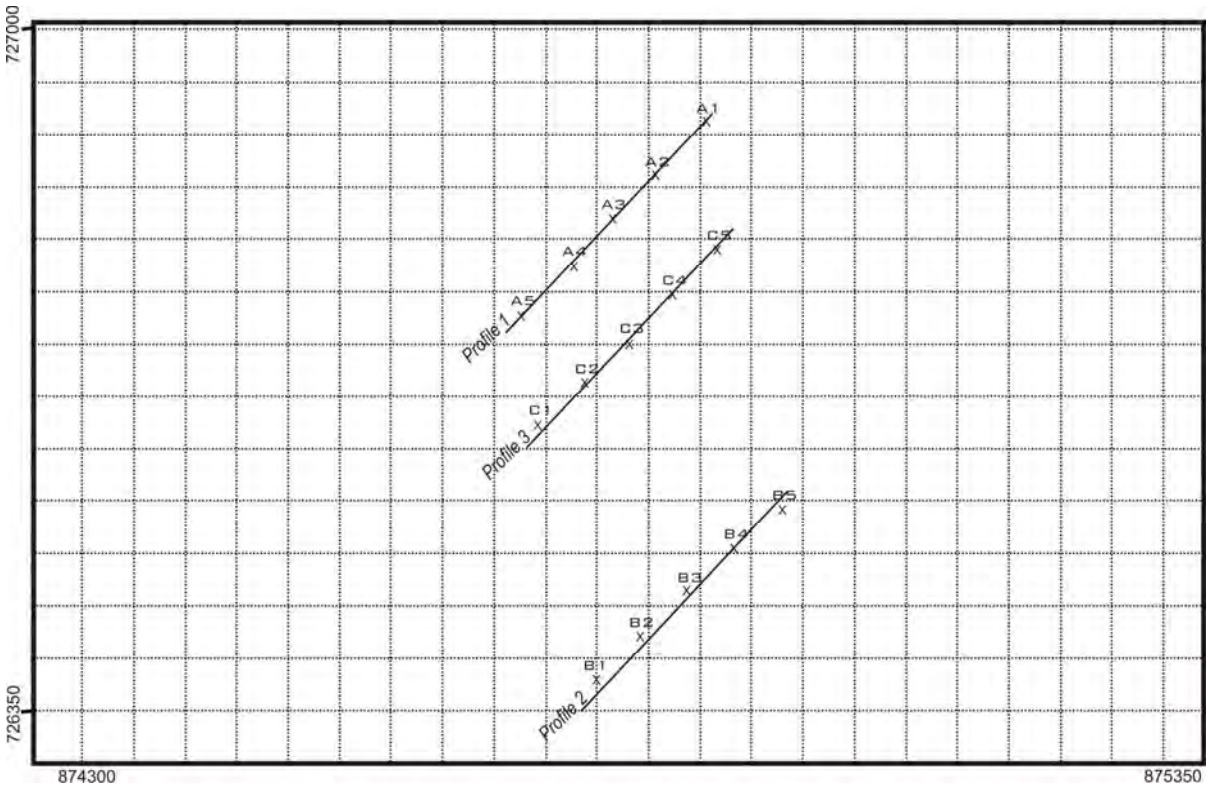

Fig 5: The synoptic view of data acquisition and profile lane

Geoelectrical Investigations

Electrical Resistivity Tomography Method

ERT survey data were acquired using ABEM SAS-1000 Lund Imaging System with 64 electrodes connected to a multi-core cable (Griffiths and Baker, 1993). With this equipment, consecutive readings were taken automatically and the results averaged continuously. SAS results are more reliable than those obtained using manually operated single-shot systems (ABEM, 2008), because the latest equipment is an automated machine connected with a laptop with an electronic switching unit that automatically selects the relevant four electrodes for each measurement (Loke, 2000, 2004). Wenner electrode configuration was chosen for its high resolution and depth of penetration (Loke, 2004). The array was popularized by the pioneering work of the University of Birmingham research group (Griffiths and Turnbull, 1985 and Griffiths *et al.*, 1990). The total length of each prolife was 260 m at an inter-electrode spacing of 4m. The data was processed and inverted using Earth Imager inversion software. The program generates the inverted resistivity-depth image for each profile line. The software was used for both 2-D and 3-D ERT

and their corresponding IP (Figs 6 and 7). Global Positioning System (GPS) was used to obtain the coordinates at survey stations.

IP Survey Method

Induced Polarization data were also acquired using the same SAS-1000 ABEM Terrameter with the same electrode configuration in the multi-electrode resistivity meter system. Murali and Patangay (2006) observed that it is a common practice to measure the IP sounding along with resistivity for correct interpretation of field data. Measuring IP with ERT enables us to interpret the data in 2-D and 3-D as well as using the Earth Imager software. This robust attempt is one of the more recent developments in the instrumentation of electrical imaging surveys (Loke, 2004). The Earth Imager software developed by AGI Austin was also used.

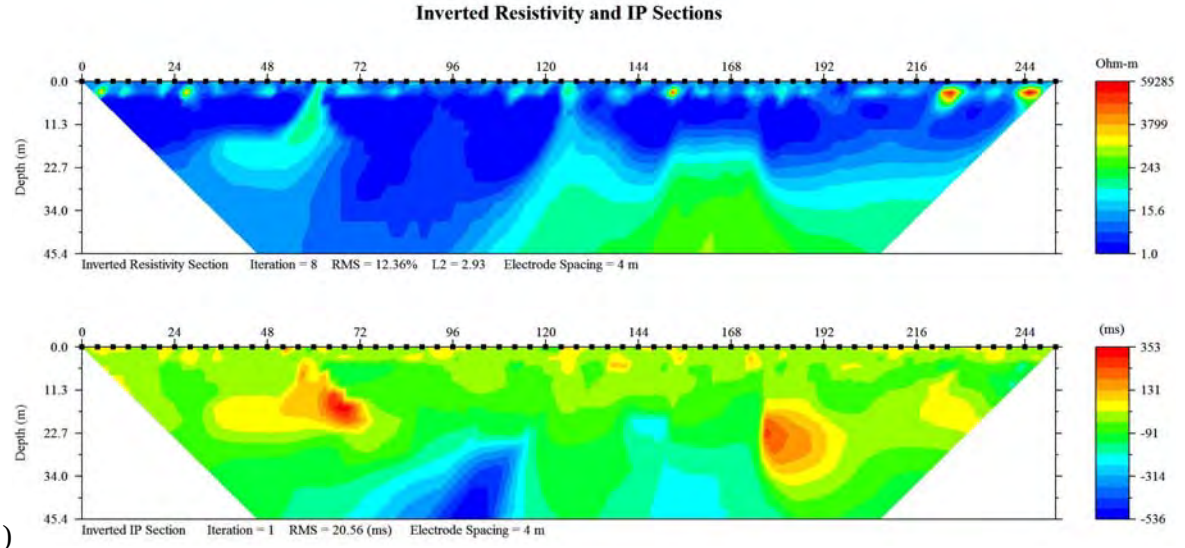

(a)

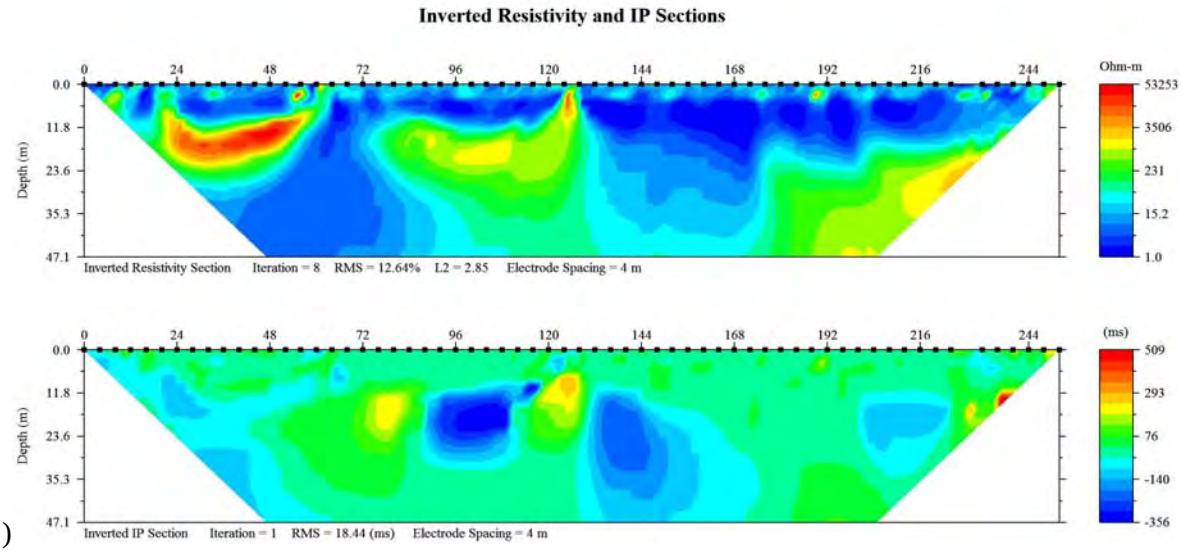

(b)

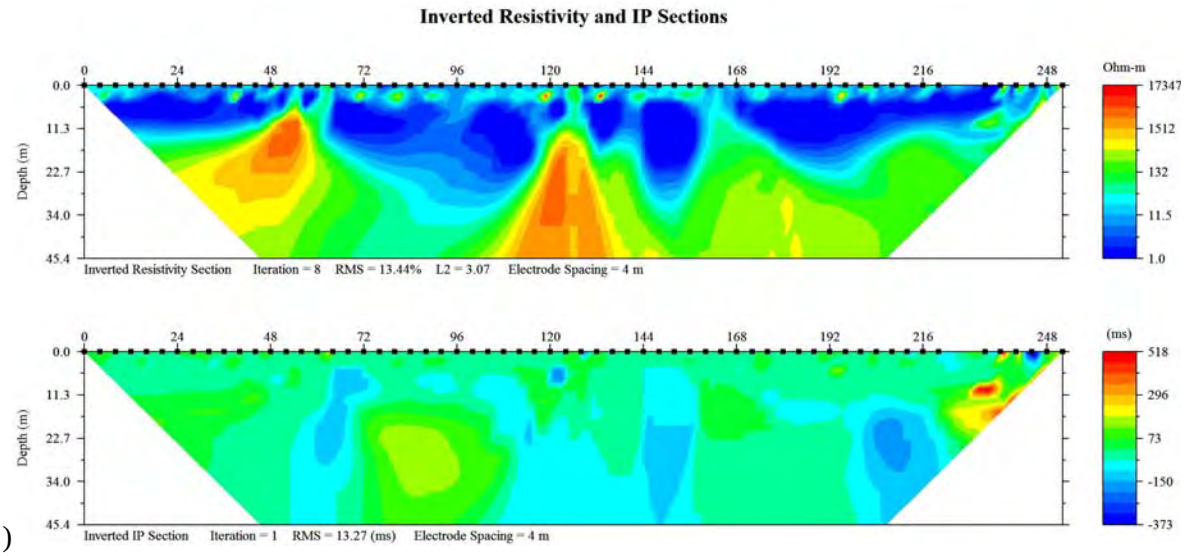

(c)

Fig 6: The inverted resistivity and IP sections along ERT lines (a) Profile 1; (b) Profile 3; and (c) Profile 2.

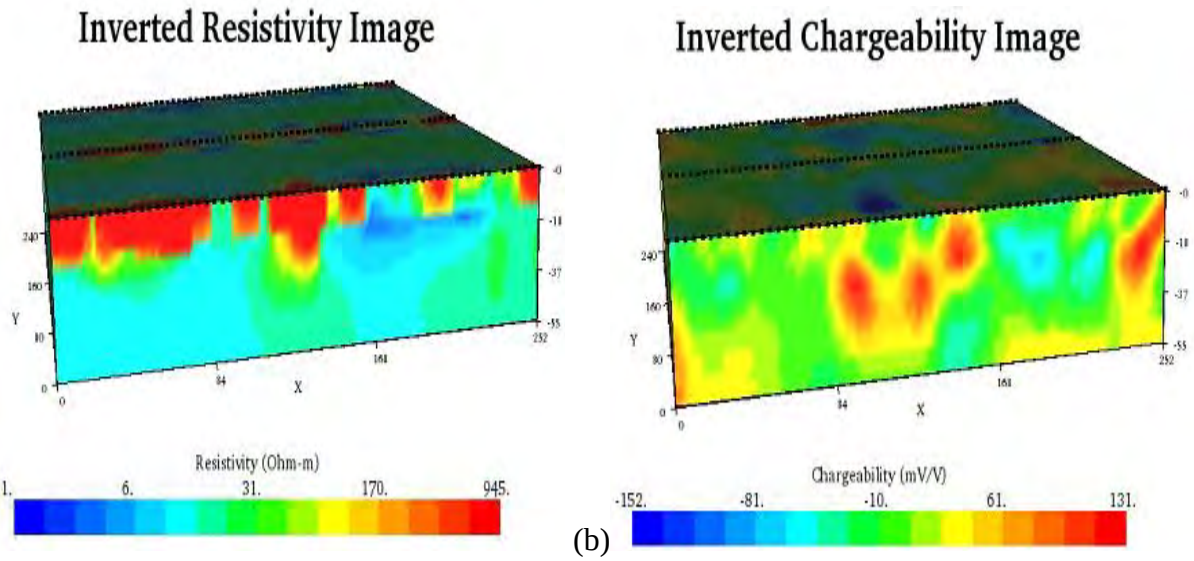

(a) (b)

Fig 7: 3-D resistivity and IP block measured in the study area

Result and Interpretation

2-D ERT Result

The problems of non-uniqueness, equivalence and suppression are well known in 1-D sounding. Similar problems, in different forms, also occur in 2-D and 3-D modeling. (Loke, 2004). These result in two different targets giving the same signal, as in the case of clay and groundwater (Kearey *et al.*, 2002; Ayolabi *et al.*, 2009b). The best way to reduce such ambiguity is to use additional data/information from other sources (Sudha *et al*., 2009). We use IP data to constrain and identify clay from sandy formation holding saline water. The IP signal from clay horizon is relatively high (Ayolabi *et al*., 2009b), while signal from groundwater in a sandy layer is nearly zero (Murali and Patangay, 2006). In addition, the RMS values below 14% obtained in the three profiles indicate that the data are fitted with the computed response and the average error floors is less than 14% in all the data. The inverted resistivity and IP sections for the three profiles are shown in Fig 8 (a to c).

The distribution of resistivity in the subsurface soil of the study site shows a wide variation of resistivity of soil at different depths along each profile line, starting from a low value of 1Ωm to a higher value of 59285 Ωm. In profile 1, the top layer is characterized by relatively high resistivity of a very thin thickness less than 4m. This could probably be due to sand-filling along the profile line while pockets of high resistivity materials near the surface could be as a result of concrete boulder materials used during land reclamation process, which are now buried in the sediment (e.g. electrode positions 224 and 244 m), (Fig 8a). The decrease in resistivity at depth below the top soil indicates the presence of saturated soil interpreted as peat material – fine grained silty soil with decomposed organic matters (less than 10 Ωm). The peat (blue colour) (Fig 8a) is encountered at almost all level below the topsoil to a depth of 45m. The subsurface soil under the profile is grossly incompetent to hold any building unless a competent layer is struck definitely far below the current depth of penetration. However, a fine sand formation (100 to 400 Ωm) was encountered at 20 m depth below the surface at surface positions 112 – 220 m which could have good engineering properties for building construction. The IP inversion result equally buttresses the presence of water-saturated clayey formation dominating the subsurface soil of the study area.

Resistivity-depth model obtained in profile 2 (Fig 8b) is similar at near surface with that of profile 1 as the top soil reveals sand-filling effect at a depth less than 4m with resistivity of <100 Ωm. However, there is a ‘lens’ of very high resistivity (between 250 to 2500 Ωm) materials encountered at about 10m below the surface between electrode positions 20 and 60 m. The very high resistivity structure could likely be an earlier concrete bridge put in place during construction work in this area, which has now sunken deep into the soil, confirming the weak nature of the subsurface soil materials in the area. At electrode positions 74 to128 m, a sandy formation was encountered with high resistivity value between 230 and 1300 Ωm. In fact, the IP section with very low chargeability (-350 to -140 mV/V) further confirms the sandy formation. Subsurface soil toward the end of the profile at a depth of 24 m

downward exhibits another stable soil of high resistivity value similar to the one just described above, which is interpreted as a sandy formation. All other areas are marked by relatively low resistivity (> 30 Ωm), indicating the presence of fine soil material – clay/peat (Fig 8b).

Fig 8c indicates the similar inverted resistivity and IP sections obtained as resistivity-depth model in the previous profiles, especially in the topsoil with high resistivity (> 130 Ωm) that reflects exotic materials used for road construction; the road serves as the platform for this survey. Similarly, 'spots' of high resistivity (e.g., electrode positions 40, 80, 120, 132, and 196 m) in the near surface come from exotic concrete materials used in reclaiming land in the area. However, peat and clay formation underlay the top resistive layer. The very low resistivity value (> 20 Ωm) of these materials indicates the presence of fine soil material and increase in the percentage of clay in soil matrix. These are silt and clay in full saturation condition (marked by high IP values above 70 mV/V). Such high IP value has been attributed to clay formation by Ayolabi *et al*., (2009b). Below the clay horizon are highly resistive reef-like structure materials with resistivity ranging between 500 and 2000 Ωm at electrode positions 24 to 64 m and 108 to 144 m (Fig 8c). These are interpreted to be the concrete and materials from collapsed buildings that were previously used to reclaim land in the area. These exotic materials have sunken due to density and formed a wavy topography as displayed by resistivity section along the profile. It is known that bridge surroundings are sand filled after construction to enhance accessibility. This was also revealed by a drop in the resistivity values (< 300 Ωm) around the suspected bridge (electrode positions 56 to 108 m and 144 to 236 m).

From the resistivity and IP inverted sections, it was noted that areas of high resistivity values correspond with areas of low IP value and vice versa as depicted by Figs. 8a - c. This was the general trend in the three inverted sections. This observation helps to confirm the consistency and that the process of data acquisition is error-free. It could also be used as reference to the inverse relationship between resistivity and IP values.

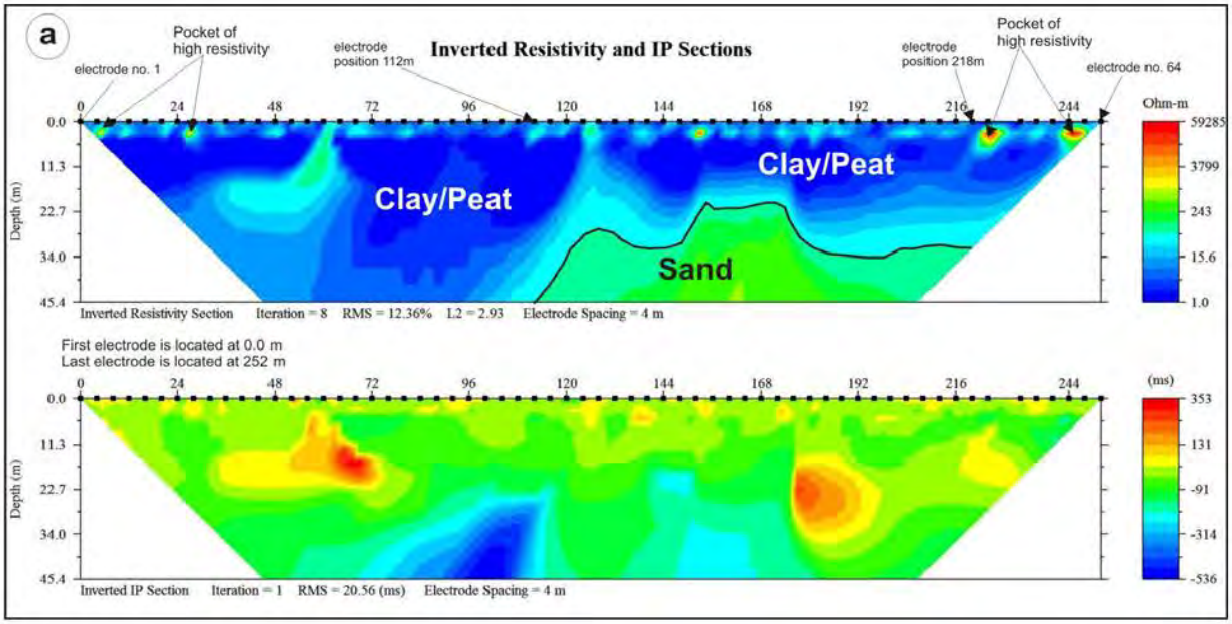
a
Inverted Resistivity and IP Sections
Pocket of high resistivity
electrode no. 1
electrode position 112m
electrode position 218m
Pocket of high resistivity
electrode no. 64
Clay/Peat
Clay/Peat
Sand
Depth (m)
Ohm-m
Inverted Resistivity Section Iteration = 8 RMS = 12.36% L2 = 2.93 Electrode Spacing = 4 m
First electrode is located at 0.0 m
Last electrode is located at 252 m
(ms)
Inverted IP Section Iteration = 1 RMS = 20.56 (ms) Electrode Spacing = 4 m

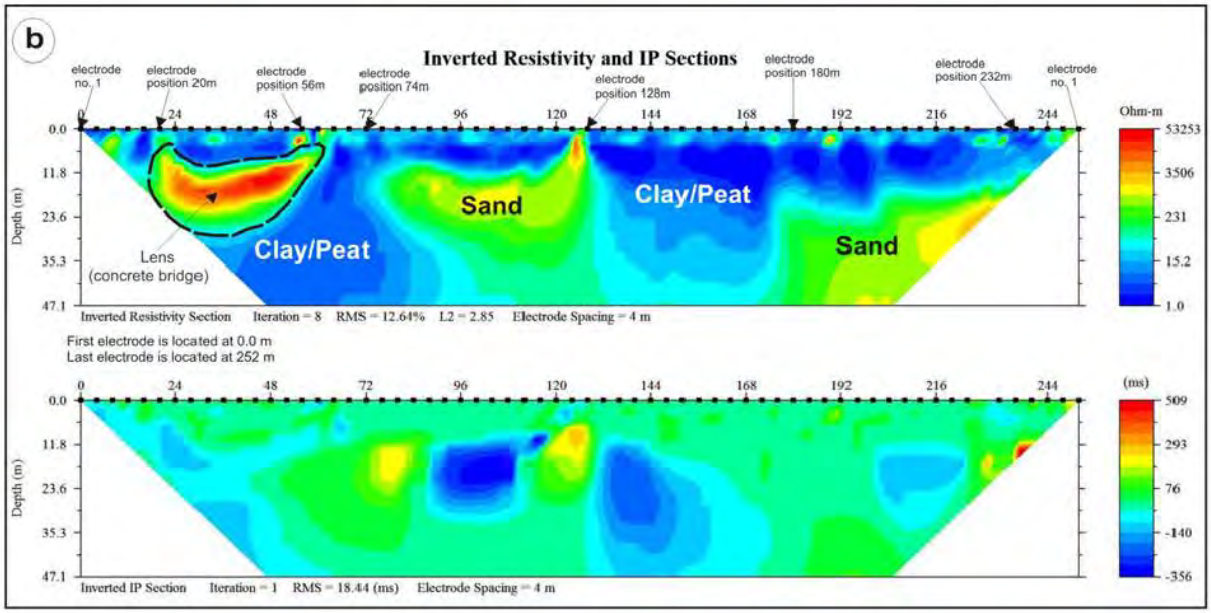
b
Inverted Resistivity and IP Sections
electrode no. 1
electrode position 20m
electrode position 56m
electrode position 74m
electrode position 128m
electrode position 180m
electrode position 232m
electrode no. 1
Lens (concrete bridge)
Clay/Peat
Sand
Clay/Peat
Sand
Depth (m)
Ohm-m
Inverted Resistivity Section Iteration = 8 RMS = 12.64% L2 = 2.85 Electrode Spacing = 4 m
First electrode is located at 0.0 m
Last electrode is located at 252 m
(ms)
Inverted IP Section Iteration = 1 RMS = 18.44 (ms) Electrode Spacing = 4 m

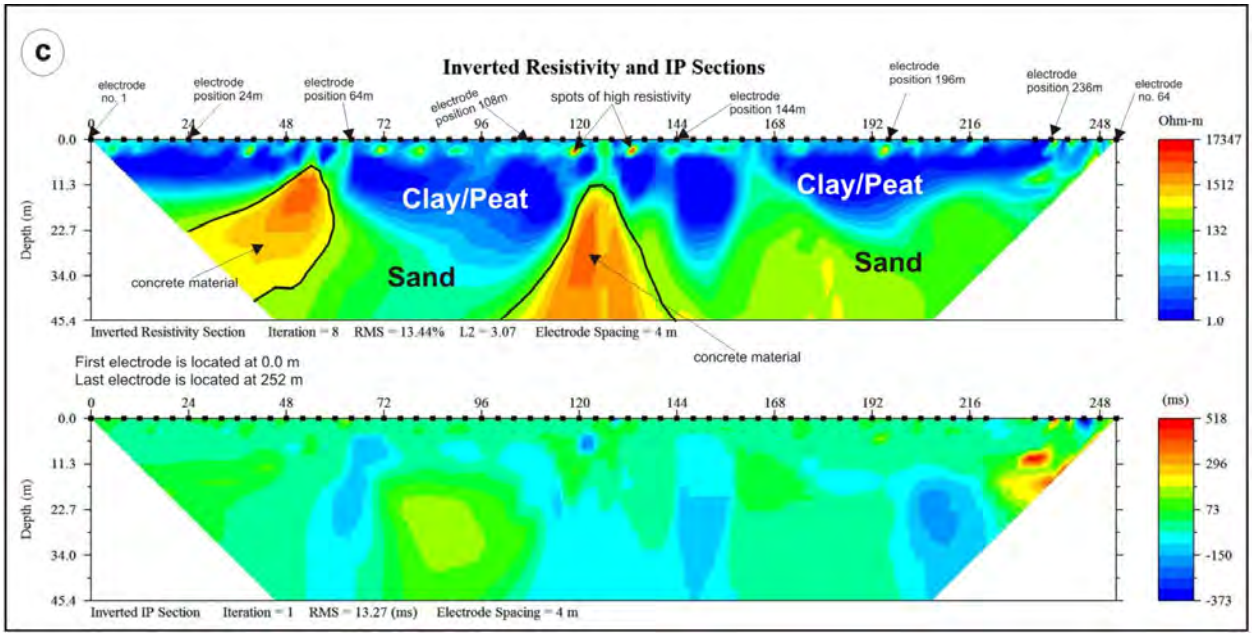

Fig 8: The Resistivity-Depth Model and IP Sections along the ERT Lines (a) Profile 1; (b) Profile 2 and (c) Profile 3

3-D ERT and IP Results

From the 3-D tomography image for the three profiles (Fig 9a and b), it was quite obvious that the entire land mass of the study area is underlain by materials of very low resistivity values below 30 Ωm from the depth of less than 7 m (Fig 9a). Local high resistivity in the near surface materials is due to either the effect of sand-filling for road network and/or the presence of exotic highly resistive materials. The IP inversion model (Fig 9b) shows high signal values in the subsurface. This is mainly an indication of clayey formation, thereby differentiating it from saline water.

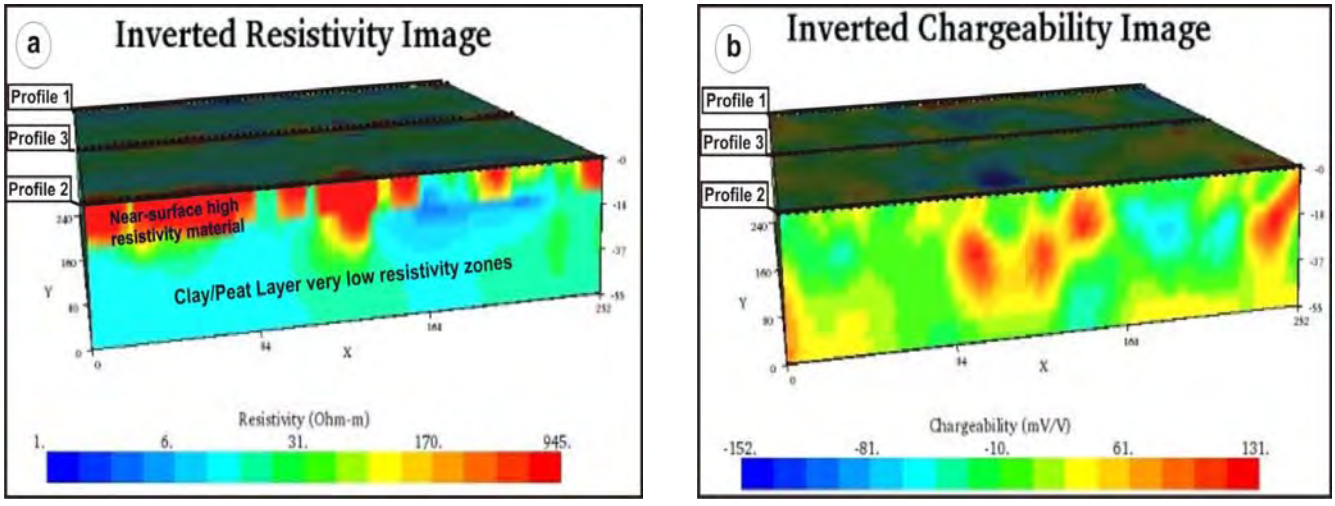

Fig 9: 3-D IP Section for the three Profiles

Conclusions

Our study has demonstrated the practical application of both 2-D and 3-D ERT and IP tomography in characterizing the subsurface soil for engineering investigation. Interpretation of both ERT images has revealed that the subsurface soil at the study site is mainly fine/clayey soil in oversaturation condition with a low resistivity of less than 30 Ωm. The low resistivity indicates the conductive capacity of the associated water. Maximum depth of penetration in all the 2-D profiles is put at 47 m while the 3-D interpretation gives a deeper depth of 55 m. Local high resistivity in the near surface material is due to either the effect of sand-filling for road network and/or the presence of exotic highly resistive materials used during land reclamation process. To separate saline formation from clayey formation, IP 2-D and 3-D tomography images were acquired which confirm the low resistivity regions to be saturated clayey formation. All the profiles represent the geologic conditions of the entire Gbagada area as a region of intense subsidence covered by oversaturated clay/peat formation. Thus, building failure in this area results from the incompetent nature of the subsurface soil.

References

ABEM (2008): Instruction Manual for Terrameter SAS 1000/4000. *ABEM Instrument AB, Sundbyberg, Sweden.* 135p.

Adegoke, O.S. (1977): Stratigraphy and Paleontology of the Ewekoro Formation (Paleocene) of Southwestern Nigeria. *Bulls. A Paleontol*., Vol. 71, No. 295, 275pp.

Agagu, O.K. (1985): A Geological Guide to Bituminous Sediments in Southwestern Nigeria, *(Unpubl Monograph). Dept of Geology, University of Ibadan.*

Ayolabi E.A., Folorunso A. F., Adeoti L., Matthew S. and Atakpo E: (2009a): 2-D and 3- D Electrical Resistivity Tomography and Its Implications. *A paper presented at the 4th Annual Research Conference and Fair held @ the University of Lagos, Akoka*, 8th Jan, 2009. p189.

Ayolabi, E.A., Atakpo, E.A., Adeoti, L., Otobor, E.C. and Arerin, T. (2009b): Groundwater Quality Assessment Using Predrilling Electrical Measurements. *Journal of Environmental Hydrology*, Vol, 17, pp. 1-12.

Billman, H.G., (1992**):** Offshore Stratigraphy and Palaeontology of the Dahomey Embayment, West Africa: *Nigerian Association of Petroleum Explorationists Bulletin,* v. 72, p. 121- 130.

Cosenza, P., Marmet, E., Rejiba, ., Cui, Y.J., Tabbagh, A., Charlery, Y. (2006): Correlations between geotechnical and electrical data: A Case Study of Garchy in France. *Journal of Applied Geophysics*, **60**, 165-178.

Enu, E.I. (1990): Aspect of Rock Evaluation Studies of the Maastrichtian – Eocene Sediments. *Jour. Min and Geol*., Vol 40(1), pp 29 – 40.

Folorunso, A.F. (2009): Integrated Geological and Resistivity Imaging Survey of Olabisi Onabanjo University Main Campus, Ago-Iwoye, Southwestern Nigeria. *An Unpld MSc dissertation, Fac. Of Sci., Dept of Earth Sci, Olabisi Onabanjo University, Ago-Iwoye, Nigeria*. P 136.

Gay, D. A., Morgan, F. D., Vichabian Y., Sogade, J. A., Reppert, P. and Wharton, A. E. (2006): Investigations of andesitic volcanic debris terrains: Part 2 – Geotechnical. *Geophysics 71, B9–B15*

Giao, P.H., Chung, S.G., Kim, D.Y., Tanaka, H. (2003): Electrical imaging and laboratory resistivity testing for geotechnical investigation of Pusan clay deposits. Journal of Applied Geophysics 52, 157-175.

Griffiths, D.H. and Turnbull, J., 1985. A multi-electrode array for resistivity surveying. *First Break **3*** (No. 7), 16-20.

Griffiths D.H., Turnbull J. and Olayinka A.I. 1990, Two-dimensional resistivity mapping with a computer- controlled array. *First Break **8***, 121-129.

Israil, M., Pachauri, A.K., 2003. Geophysical characterization of a land slide site in the Himalayan foothill region. *Journal of Asian Earth Sciences* 22, 253-263.

Jones, M.A. and Hockey, R.O., 1964: The Geology of Part of Southwestern Nigeria. *Nig. Geol. Surv, Bull.* No. 31, 101p.

Kearey, P. Brooks, M. and Hill, I. (2002): An Introduction to Geophysical Exploration. *Blackwell Pub.3rd Ed*. P.262

Loke, M.H. (2000): Electrical Imaging Surveys for Environmental and Engineering Studies: A Practical Guide to 2D and 3D Surveys. *www.terrajp.co.Jp/lokenote.pdf,2004*. P.59

Loke M.H. (2004): Tutorial: 2-D and 3-D Electrical Imaging Surveys.2004 Revised Edition. *www.geometrics.com* P.136

Murali, S. and Patangay, N. S. (2006): Principles of Application of Groundwater Geophysics. *Association of Geophysicists, Hyderabad, India*, 3rd Ed. 371p

Nton, M.E. (2001): Sedimentological and Geochemical Studies of Rock Units in the Eastern Dahomey Basin, Southwester Nigeria. Upbli *Ph.D Thesis University of Ibadan*, 315pp.

Ogbe, F.G.A. (1972): Stratigraphy of Strata Exposed in the Ewekoro Quarry, Southwestern Nigeria. *In: T.F.J. Dessauvagie and Whiteman (Eds) African Geology, University Press, Nigeria*, pp305

Omatsola, M.E., and Adegoke O.S. (1981): Tectonic and Cretaceous stratigraphy of Dahomey Basin. *Journal of Min. Geol*. Vol. 54 pp. 65-87.

Sastry, R.G. and Tesfakiros, H.G. (2006): Neutral based interpretation for combined induced polarization and vertical electrical soundings of coastal zones. Journal of Environmental and Engineering Geophysics 11, 197-211.

Sudha, K., Israil, M., Mittal, S. and Rai, J. (2009): Soil characterization using electrical resistivity tomography and geotechnical investigations. *Journal of Applied Geophysics,Elsevier* **67**: 74-79

The Nation, (2009): Building Collapse: Anguish, Tears as Relative still hope for Survivors. *The Nation daily Newspaper,* Friday March 27, 2009, p.12

Zhdanov, M.S. and Keller, G.V.(1994): The geoelectrical method in geophysics exploration. Elsevier, Amsterdam.

RESISTIVITY IMAGING AT MN/DOT: 'BUILDING BRIDGES' IN DULUTH

Jason L. Richter, Minnesota Department of Transportation, Maplewood, MN

Abstract

Electrical resistivity imaging (ERI) has become an effective supplement to the subsurface investigation process at the Minnesota Department of Transportation (Mn/DOT). Mn/DOT has employed ERI on a variety of projects related to scoping, preliminary design and post-construction failures. ERI profiles were the only source of subsurface information utilized in the foundation design of Bridge #69656 (Kohl's Bridge) over Miller Creek in Duluth, MN. Mn/DOT's conventional methods of acquiring soil and rock data such as standard penetration testing, cone penetration testing, and rock coring could not be performed due to the sensitive nature of the project site. Consequently, Mn/DOT bridge, foundation and district engineers elected to incorporate deep foundations into the design of the bridge with no design option for shallow foundations. ERI was performed and revealed shallow bedrock depths (<10 feet) on the east side of Miller Creek suggesting that spread footings on bedrock could be utilized for at least a portion of the project area. Footing excavations prior to construction ultimately revealed that shallow foundations on bedrock could be incorporated for all project structures (roadway retaining walls and bridge) resulting in construction of the proper foundation design for the site conditions and modest savings in terms of cost. The Kohl's Bridge Project marked the first time a Mn/DOT bridge design had ever been based solely on geophysical data. Because of these accomplishments, the Duluth District was recently awarded an American General Contractors Bridge Construction Award for the structural design and investigative approach. The effectiveness of ERI instilled a sense of confidence at Mn/DOT towards the use of geophysics and opened up opportunities for geophysical applications on subsequent projects in the Duluth District and throughout the state.

Introduction

The acquisition and use of electrical resistivity imaging (ERI) technology at the Minnesota Department of Transportation (Mn/DOT) was initiated by the need for an adequate means of assessing sinkholes and other forms of subsidence. Within a four-year period between 2001 and 2005, Mn/DOT Geology Unit and Foundation Unit staff investigated subsidence within Mn/DOT right of way near Hastings, Red Wing, Pilot Mound, Sandstone, Chisholm and Fountain. In each instance drilling (auger, soil sampling, rock coring) and, in most cases, ground penetrating radar (GPR) were performed to acquire subsurface information around or within the collapse areas. Though drilling was performed at each site the boreholes were guided mostly by 'wildcatting' since an accepted drilling process could not be established in unique and complex situations created by karst and karst-like conditions. The borehole data, essentially point-source information, acquired from these environments could not account for any undisclosed inhomogeneities which likely existed between boreholes. Consequently, the information obtained from soil and rock borings often could not provide a clear understanding of the source or mechanism of the subsidences to minimize doubts about the proposed solutions. In addition, the urgent need for information was hampered by the typically slow drilling process which consists of clearing utilities, mobilizing drilling equipment, collecting samples, occasionally addressing equipment malfunctions, classifying samples and completing the boring log. Though easy to deploy and user-friendly, GPR analyses were unreliable due to attenuation of the electromagnetic signal by moisture laden and cohesive soil. A means of acquiring information in a timely fashion which could give a

seamless subsurface view of an investigation area and provide guidance for soil and rock sampling was needed and pursued.

In the spring of 2006, the Mn/DOT Geology Unit purchased a SuperSting R8/IP earth resistivity and induced polarization meter with associated cables and accessories from Advanced Geosciences, Inc. Since acquiring the ERI system, the Geology Unit has performed approximately 80 ERI/IP surveys (2D and 3D) on 32 different projects. Though initially purchased for investigating bedrock-related cavity/void and subsidence issues, the equipment has also been used to acquire general soil-rock stratigraphy and bedrock conditions, constrain dimensions and/or locations of organic deposits, ascertain groundwater elevations and locate buried structures and underground mine workings. In one instance, 3D ERI methods were used on a bituminous roadway to assess the failure mechanism in an embankment constructed with Geofoam. These applications have collectively encompassed the scoping, pre-construction and post-construction phases of Mn/DOT projects. The usefulness of ERI has prompted plans to incorporate the method into the new Mn/DOT Scoping Initiative to help curb unwanted, construction phase cost overruns from unplanned organic excavations. ERI, along with other newly-acquired geophysical methods, is now a fully integrated supplement to the subsurface investigation process at Mn/DOT.

Bridge #69656 Over Miller Creek- Duluth, MN

One of the earliest applications of ERI at Mn/DOT took place in the summer of 2006 during the subsurface investigation for a new bridge, roadway and associated retaining walls located in the Miller Hill shopping area on the west side of Duluth, MN. The new structures would provide frontage road and shopping area access via newly proposed Maple Grove Road (referred to as Burning Tree Drive in Fig. 1). The improvements were proposed in response to reconstruction of nearby TH53 (a four-lane divided highway), necessitating the modifications to the TH53/mall entrance intersection. A single span bridge over Miller Creek was proposed near the southeast end of the adjacent Kohl's Department Store parking lot and intersection of Sundby Road and Page Street (orange portion on Fig. 1). The proposed bridge would be roughly 70 feet long, 54 feet wide, and constructed with pre-stressed concrete beams. Cast in place cantilever walls with multi-colored architectural features would support approximately 400 feet of roadway west of the bridge. The roadway alignment would not only curve through the approach areas but through the bridge as well.

Figure 1: Portion of TH53 construction layout. Bold orange area denotes proposed bridge location.

Subsurface Investigation

A request to the Mn/DOT Geotechnical Engineering Section for investigation and assistance was received from the Duluth District. For most new structures, a typical request consists initially of a site-specific drilling regiment. Soil/rock samples are collected, classified and subjected to various forms of testing to acquire engineering properties. All information acquired from the investigation is subsequently used to formulate a foundation recommendation which is incorporated, in this case, into a bridge design by the Mn/DOT Bridge Office. For this project, depth to bedrock determinations were important since either a deep or shallow foundation or hybrid combination could be anticipated based on knowledge of the area geology; rock depths tend to be within twenty feet of the surface in the Duluth area. However, historical borings obtained for a nearby culvert (approximately 500 feet southwest of bridge site) directing Miller Creek under TH 53 showed bedrock about 40 feet below surface.

Figure 2: Photo of proposed bridge site looking west. Geologist is standing in vicinity of southeast corner of bridge footing. Overhead power lines can be seen paralleling the future bridge alignment. Large gabbro boulder (one of many) visible in lower left foreground of photo. Kohl's Department store and parking lot visible in background. Miller Creek is visible for a short distance in center of photo.

A site reconnaissance was performed and revealed a heavily wooded and mostly boulder laden terrain (Fig. 2). Some large knobs of Duluth Gabbro, the predominant rock type in the area, are present and either represent glacial erratics or inplace bedrock. A steep rock fill embankment was present along the south side of the Kohl's parking lot where the location of the frontage road, retaining walls and west bridge approach were proposed. An overhead power line ran directly across the future bridge alignment limiting any potential drilling and earth moving operations in the immediate area of the proposed bridge.

Miller Creek runs roughly north-south through the area and is a designated trout stream; proximity restrictions would limit the amount of allowable work near the stream. Additionally, access to the site was denied by Kohl's management (on the west side of the stream) who were interested in minimizing property disturbance and was discouraged by nearby property owners (on the east side of the stream) who were concerned about impacts to the woods. It was determined that traditional methods of obtaining subsurface information, soil/rock borings and/or CPT soundings, could not be utilized at this site. Therefore, a method which could acquire subsurface information, overcome the site access and safety issues, and preserve the natural integrity of the site was needed.

The Mn/DOT Geology Unit was contacted to assist in finding an investigative alternative. Geophysical methods were suggested as a possible solution, particularly seismic methods, since bedrock depth estimates were being pursued. However, this capability was not available at the time at Mn/DOT nor was a consultant contract for geophysical investigation a palatable option to district personnel. A Ground penetrating radar system (GPR) is maintained and utilized by Mn/DOT's Research Section for pavement thickness studies and was broached as a potential investigative tool. It was believed that the soil conditions in addition to the expected high water table would render the method ineffective. There was certainty that the Geology Unit's newly-acquired electrical resistivity imaging system was at least capable of achieving the access, safety and preservation goals. It was communicated that the terrain and surficial soil characteristics could present some obstacles for both setting up the surveys and obtaining good quality data. Nonetheless, it was decided that ERI should at least be attempted to acquire subsurface information since all other available options were exhausted.

ERI Setup, Data Acquisition and Data Quality

A second site reconnaissance was performed to identify locations for ERI and revealed that surveys could only be set up within the area of the proposed bridge site. Soils west of the bridge site and within the new roadway alignment were extremely boulder laden and/or covered by rock fill used to construct the nearby store parking lot. Soil conditions within the bridge area were also difficult with many boulders present coupled with variably saturated silty, sandy and gravelly organic soil. The presence of gabbro 'knobs', which were either very large boulders or outcrops, would also limit the location and length of ERI surveys within the bridge area. Both 2D and 3D ERI options were considered but given the difficult nature of the site soils only 2D ERI surveying could be achieved at two specific locations. Acquired data sets would be processed via EarthImager 2D.

The first ERI survey was oriented roughly north-south through the middle of the proposed east bridge abutment (Fig. 3). Conveniently, a nearly straight, flat, compacted and unobstructed deer path was present at this location reducing the need for brush cutting and soil remediation. A 56 electrode dipole-dipole array with 1-meter electrode spacing was initially chosen but due to complications with one of the resistivity cables a 28 electrode survey was performed. Good quality data was acquired and, following inversion, yielded a resistivity distribution with minimal misfit (Fig. 4).

Repairs to the cable were made and a second survey was undertaken roughly orthogonal to the first survey, transecting both Miller Creek as well as both abutments of the proposed bridge (Fig. 3). Extensive brush cutting with some boulder removal was carried out to allow for a 56 electrode dipole-dipole array with 1-meter electrode spacing. Three of the 56 electrodes were implanted into the bed of Miller Creek. Two electrodes were eventually removed and the take-outs deactivated during data acquisition since either large boulders or possible bedrock were encountered at their locations. Data quality varied but mostly good quality data was obtained from the eastern two-thirds of the line. A mix of noisy data and good quality data was obtained from the western third of the survey line and was thought to have been due to poor contact resistance created by loose, rocky and less saturated conditions at localized points near surface.

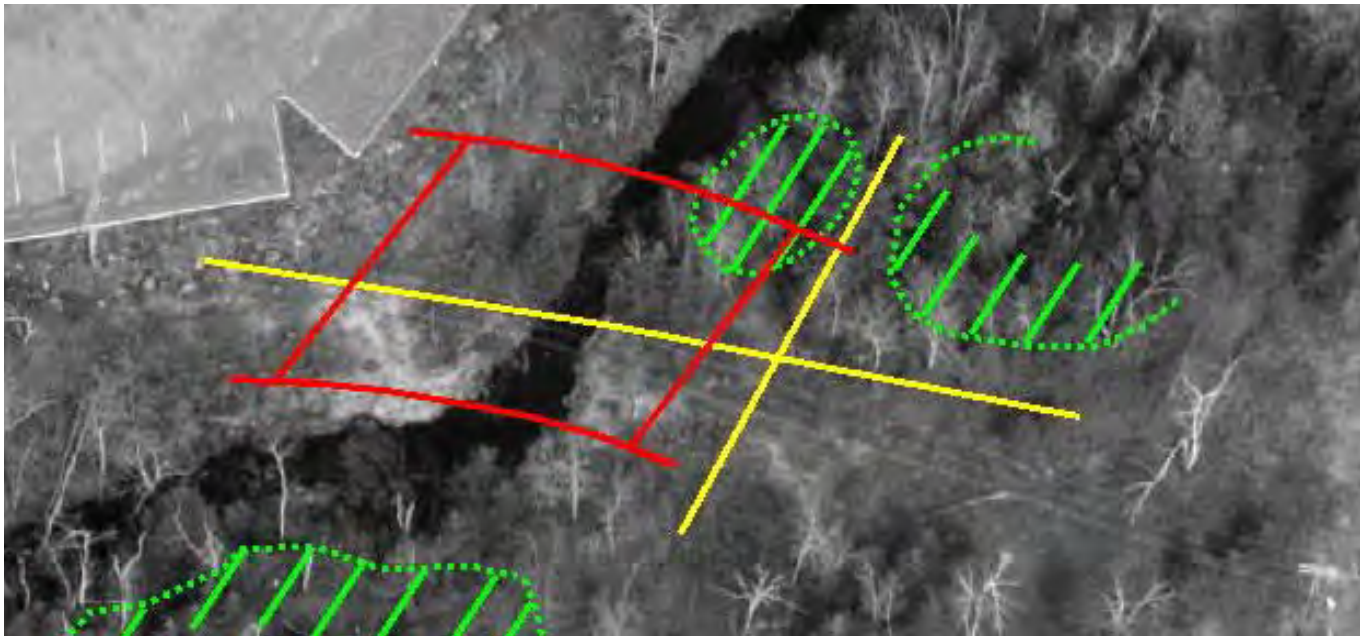

Figure 3: Aerial photo of bridge site. Bridge outline (red) spans Miller Creek. Kohls parking lot in northwest corner. 'North-south' resistivity survey (yellow) is oriented through east abutment. 'East-west' resistivity survey (yellow) oriented through both abutments. Green square dot and stippled areas represent possible gabbro outcrops or large erratics (later determined to be bedrock).

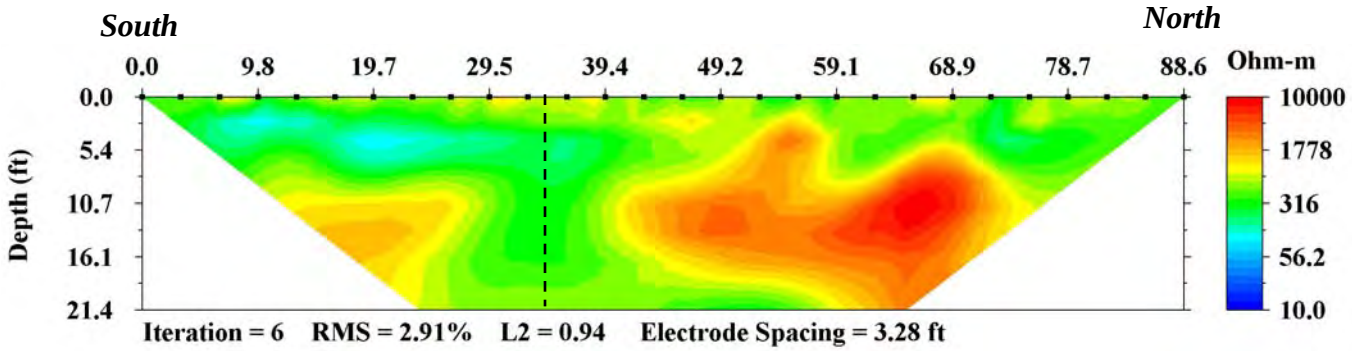

Figure 4: Resistivity distribution of north-south line. Intersection of east-west profile denoted by vertical dash marks.

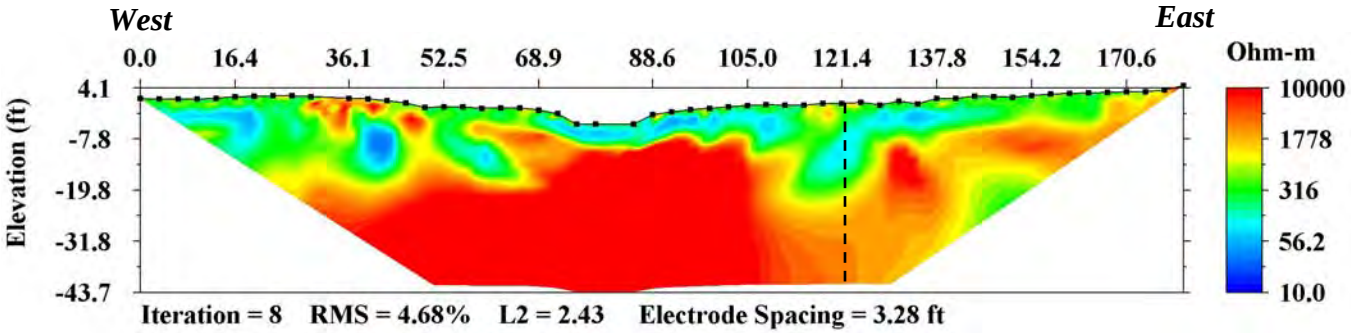

Figure 5: Resistivity distribution of east-west line. Intersection of north-south profile denoted by vertical hash marks.

Subsurface Interpretation

Though drilling information was not available to corroborate the resistivity profiles, information from site observations assisted in the interpretation. As mentioned previously, boulders and boulder rich zones comprised of Duluth Gabbro, the predominant bedrock unit in the area, are present at surface and suspended in a matrix of silty to sandy (and often gravelly) organic soil. Soil saturation varies in the near surface but given the proximity of the creek the water table is likely within 5 feet. The large 'knobs' illustrated in Figure 3 are composed of Duluth Gabbro and appeared to be bedrock manifestations. However, distinguishing potential outcroppings such as these from large boulders can be difficult since car to bus sized glacial erratics are not uncommon in this region of Minnesota. Regardless, the identification of localized outcroppings at surface does not imply that adjacent and buried bedrock surfaces are shallow since bedrock depths in the Duluth area can fluctuate dramatically over short distances.

Generally speaking, both the north-south and east-west profiles show a marked contrast in electrical properties starting at about 10 feet below surface. Resistivities in the upper 10 feet tended to range between 100 to 300 ohm-m while underlying material was typically one to two orders of magnitude higher (Figures 4 and 5). It seemed likely that the strong contrast in resistivity was due to a sharp transition from the more conductive, saturated, silty/sandy matrix of the near surface soils to the underlying gabbro bedrock. Some noisy data generated in the western third of the east-west profile (Figure 5) produced conductive-looking artifacts which complicated the interpretation. Two interpretations were assumed for this noisy area: one, bedrock is within 5 feet from surface or, two, bedrock is about 20 feet below surface. Data redundancy is present at the intersection of the two resistivity lines where a conductive 'hole' is present within interpreted bedrock. It was believed that this feature could either be a glacial pothole or a zone of highly weathered and/or fractured gabbro bedrock. A denser collection of boulders was also encountered at this location and is represented on both profiles by higher resistivity near surface. Additionally, the buried, highly-resistant knob-shaped features visible in the northern half of the north-south profile were believed to be submerged extensions of the two gabbro 'knobs' which flanked the survey line at surface (Figures 3 and 4).

Recommendations

The findings of the resistivity surveys were communicated to Mn/DOT's Foundations Unit and personnel from the Bridge Office and Duluth District. Prior to the surveys, it was assumed that deep foundations, specifically drilled piles, would be needed to support the bridge structures at this site. Deep foundations were the defaulted option by both the Bridge Office and Duluth District since little to no information was available prior to the resistivity surveys to suggest that other foundational options, such as spread footings, would be feasible (traditional driven piling and drilled shafts were also considered unsuitable due to the boulder-laden nature of the site soils).

Results from the resisitivity surveys suggested that shallow foundations could at least be constructed on the east side of the creek for all retaining walls and bridge abutment. Some structural modifications to the east bridge abutment footing would be made if indeed a glacial pothole were encountered during excavation. For structures west of Miller Creek, recommendations were complicated by the questionable resistivity data quality in the area of the west abutment in addition to the lack of subsurface information for the roadway retaining walls. Regardless, since shallow bedrock appeared to be present on the east side of Miller Creek some flexibility could be incorporated into the design to allow for spread footings if shallow rock was encountered west of the creek. A spread footing had been suggested for the northern portion of the west abutment since it appeared that bedrock was extending through the creek from the newly-defined bedrock outcrop (formerly a potential glacial erratic) found on the northern half and west side of the north-south resistivity line. The spread footing

would transition toward the south into a drilled pile-supported grade beam/pile cap for the south side of the abutment. Since the elevation of the footing base could fluctuate considerably (possibly as much as 20 feet, based on knowledge of area geology and ERI) the plans accommodated any shifting of the transition area encountered during construction. In regards to remaining structures, the need for drilled piles with a pile cap/grade beam was also anticipated for a 300 foot length of retaining walls adjacent and west of the bridge site and in close proximity to the stream. It was believed that this design would help retain embankment backfill in the event of erosion and undermining at the face of both the west abutment and wall area. The remaining 100 feet of retaining walls to the west were designed to be supported on spread footings on bedrock or soil.

Excavations would begin on the east side of Miller Creek where shallow foundations were proposed. The excavation would be undertaken at least 3 weeks prior to footing construction to allow time for potential excavation/construction difficulties or to redesign structures as a result of any deviations from the geophysical investigation. Excavations would progress to the west side of Miller Creek where further assessments and necessary design adjustments could be made, if needed. The need for drilled pile elements would, particularly, be assessed since it was possible that excavations would reveal that shallow foundations could also accommodate this portion of the project area.

Excavation and Construction

Excavations for the east bridge footing began in August of 2008. As recognized by the geophysical survey, bedrock was encountered within 10 feet from surface, specifically between 2 to 8 feet from surface (groundwater infiltration eventually filled much of the subcut to within 2 to 3 feet from surface). In addition to correctly estimating bedrock depth, three subsurface features visible on the north-south resistivity profile became apparent during the excavation. Two bedrock knobs were identifiable in the subcut and correlate to two high-resistivity protrusions visible between the 50 foot and 70 foot surface distances on the resistivity profile (Fig. 6; locations ‘A’ and ‘B’). Additionally, the conductive ‘hole’ referenced in the subsurface interpretation manifested as a pocket of weathered and highly fractured bedrock (Fig. 6; location ‘C’). Though most gabbro bedrock uncovered in the area is competent with widely spaced fractures, rock within this localized pocket formed small cubes or slabs which were easily excavated. Since bearing strength of the weathered and highly fractured zone appeared to be adequate for placement of a bridge footing, the excavator was told to cease with further excavating. Shaping of the bedrock surface via blasting methods was not necessary during footing construction; lean mix concrete was formed directly on the bedrock surface with some re-bar bored into rock.

Excavations for the west bridge footing immediately revealed bedrock surfaces within 1 to 8 feet from surface with most bedrock encountered within 1 to 3 feet. A large protruding gabbro block with about 6 feet of vertical relief was encountered where a portion of the east-west resistivity survey was performed (Fig. 7). The shallow bedrock characteristics coupled with some locally poor contact resistances in soil during surveying likely explain the data quality issues identified during processing of portions of the east-west survey data set. Nonetheless, further excavations adjacent and west of the abutment also revealed shallow bedrock thereby precluding the need for any deep foundational elements originally designed for the west bridge abutment and 300 feet of roadway retaining walls. Shaping of the bedrock surface was not necessary during footing construction for both walls and abutment; lean mix concrete was formed directly on the bedrock surface with some rebar bored into rock (Fig. 8).

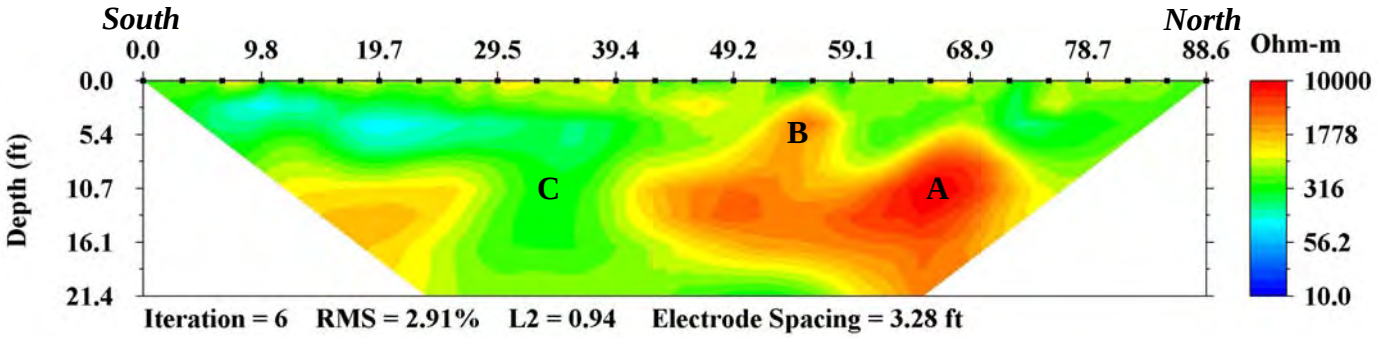

Figure 6: Photo of east footing excavation (above) looking south and associated resistivity distribution of north-south ERI line (below). Letters 'A,B,C' denote locations of subsurface features identified by resistivity survey.

Figure 7: Photo of west footing excavation area looking south.

Figure 8: Photo showing portion of west bridge abutment footing transitioning to retaining wall footing.

Figure 9: Photo of completed bridge looking west from east bridge approach.

Figure 10: Photo of roadway and completed retaining walls looking west from bridge deck.

Conclusion

The Kohl's Bridge Project reached completion in June of 2009 (Figures 9 and 10). All bridge and retaining wall structures were founded on shallow foundations (spread footings) as opposed to mostly deep foundations (drilled piles) which were specified prior to the geophysical investigation. Electrical resistivity imaging (ERI) was the only investigative tool readily available to characterize the subsurface in the project area. ERI profiles showed that shallow bedrock (<10 feet) was present on the east side of Miller Creek and suggested to foundation, bridge and district engineers that spread footings would be a viable option for at least a portion of the project area. Footing excavations eventually revealed shallow bedrock throughout the project area thereby completely modifying the original plan. Drilled piles could have been a functional foundational option at this site but are not the preferred, nor standard, Mn/DOT approach when encountering the above mentioned subsurface characteristics. A modest cost savings (estimated around $50,000 to $100,000) was realized by constructing shallow foundations and was due mostly to differences related to material and equipment needs. To quote a foundations engineer, "a price tag cannot be placed on the reduction of uncertainty that was gained from information acquired from the ERI survey."

The Kohl's Bridge Project marked the first time a Mn/DOT bridge design had ever been based solely on geophysical data. Because of the investigative approach and structural design, the Duluth District was recently awarded an American General Contractors Bridge Construction Award for the Kohl's Bridge Project. The effectiveness of ERI instilled a sense of confidence at Mn/DOT towards the use of geophysics and opened up opportunities for geophysical application on subsequent projects throughout the whole state, but particularly in the Duluth District. Since the Kohl's project, the Mn/DOT Geology Unit has responded to several Duluth District requests to utilize geophysical capabilities on projects related to retaining wall design, underground abandoned mine investigation and remediation, roadway design, rock slope design and building design.

PRELIMINARY ER AND EM GEOPHYSICAL INVESTIGATIONS OF A WASTE LANDFILL NEAR THE CITY OF FORTALEZA – NE OF BRAZIL

R.Mariano G. Castelo Branco, Ailton Amorim, Jackson Alves Martins, Nilo Costa Pedrosa Junior, Nilton Cesar Vieira, Luiz Ricardo Cunha Braga
Geophysical Laboratory – Federal University of Ceará - Fortaleza, Brazil

Abstract

We have performed a geophysical investigation on a site used for disposal waste of several types and sources. The site is located near the city of Fortaleza, state of Ceará, in the NE part of Brazil. The area is characterized by a flat surface without significant relief, unless the elevations of compacted landfill. The geology is composed by recent sediments of Barreiras Formation (TQ), mainly clays, sands and residual soils. The objective of the geophysical surface investigation was to use a multi-electrode dipole-dipole array with an AGI instrument and an electromagnetic 3 frequency method with a Geonics instrument to delineate possible buried zones through 2D interpreted sections. The information collected in this investigation may be useful to delineate possible contaminated plumes and its influences in the shallow aquifer system. This research began in December 2009 and it will still continue along the year of 2010 with other complementary geophysical and geochemical studies. The results shown that the geophysical techniques are able to map contaminated areas and that the ER method has a higher resolution. Direct investigations prove their efficiency.

Introduction

The landfill site of Aquiraz, located in the region of Machuca, dates back to the 1980's and is located in the metropolitan region of the city of Fortaleza, a city with about 3 million inhabitants. The site is just 27 km SE away from Fortaleza downtown. The access is by the state highway CE040 (figure

Figure 1: Localization of Aquiraz Landfill 27km SE away from the city of Fortaleza in the NE part of Brazil. The figure also shows the ER, EM and ER+EM geophysical sections over the site (Google images). EM+ER in green captions are the sections presented here.

1). This figure also shows the position of geophysical sections. The landfill receives a total of approximately 7.5 tons of solid waste per month (personal information manager). The solid waste is buried without being incinerated.

There is no environmental management, control or separation of waste on the site. Figure 2 shows some general photos of the site focusing on some cells and compressed waste landfill with leachate that springs up in all sides.

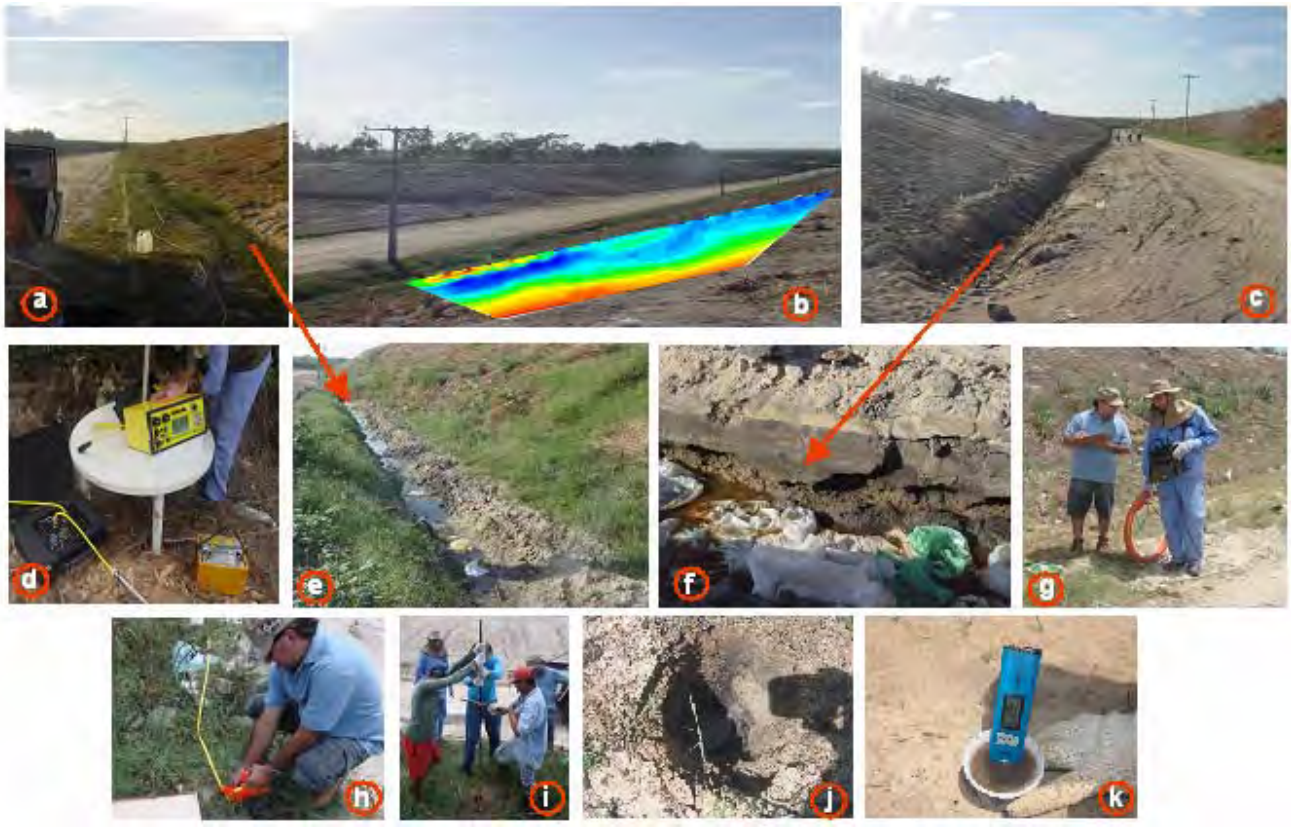

Figure 2: Some photos of Aquiraz landfill. (a) cable for dipole-dipole array parallel to one of the compacted waste landfill, (a,b) the position of AT_2 dipole-dipole resistivity section and the EM section (c,e) trench with leachate bordering a compacted waste landfill, (d) SuperSting R8 (f) detail of the leachate and claystones materials, (g) EM-34 collecting data, (h) positioning a 185m anomaly over the ER section, (i) beginning of the perforation, (j) a view of the well with 57cm and the emergence of the leachate, (k) measuring the conductivity.

General Geological and hydrogeological informations

The region of Aquiraz Landfill is known as Pre-coastal Trays of Cretaceous/Tertiary age and are characterized by a flat zone near the coast and is geologically composed by the lithologies of the Barreiras Formation that covers the entire coastal area of Brazilian Platform. These sedimentary deposits have a terrestrial origin but sediments of marine origins can occur. These lithologies are essentially composed of sandstones, claystones and conglomerates covering, stratigraphically, a gneiss-migmatite

crystalline basement. Near the landfill the claystones dominate at the shallow levels. Based on information from wells for groundwater, it was possible to estimate the depth of the crystalline basement around 25-35m below the surface. The aquifer system in the region is shallow, with a static level ranging from 2,5 to 5m, and the discharge rate of the wells are low which means that groundwater is extracted mainly from very shallow wells (Castelo Branco, 2006).

Geophysical characterization

The geophysical ER research was conducted using a dipole-dipole array, 84 electrode 10m spaced, four 210m cables, and 8 depth levels investigations with a SuperSting R8 multichannel equipment made by AGI Instruments. An EM-34 electromagnetic equipment made by Geonics with 6 HD-VD arrays was also used. Eight sections were performed strategically in the landfill and positioned only in locations where it was possible to measure. One ER section was positioned 600m away from the landfill to collect data about the background resistivity responses. The same strategy was used with several EM soundings. Only one ER and one EM section will be presented here. The apparent resistivity data were processed with the software Earthimager where models were generated by inversions that are presented through geoelectric 2D sections with distance between electrodes *versus* investigation depth. Figure 1 shows the positions of ER, EM and ER+EM sections in the area and the general situations near the AT_2 ER section are presented in figure 3.

Figure 3 also shows one of the ER dipole-dipole section (AT_2) with 210m that was placed laterally to a compacted waste, in one of the few places where it is possible to work on. The figure shows the inverted resistivity section where we can observe the good RMS and L2 results for 8 iterations and the same section with the anomalous zone interpretation.

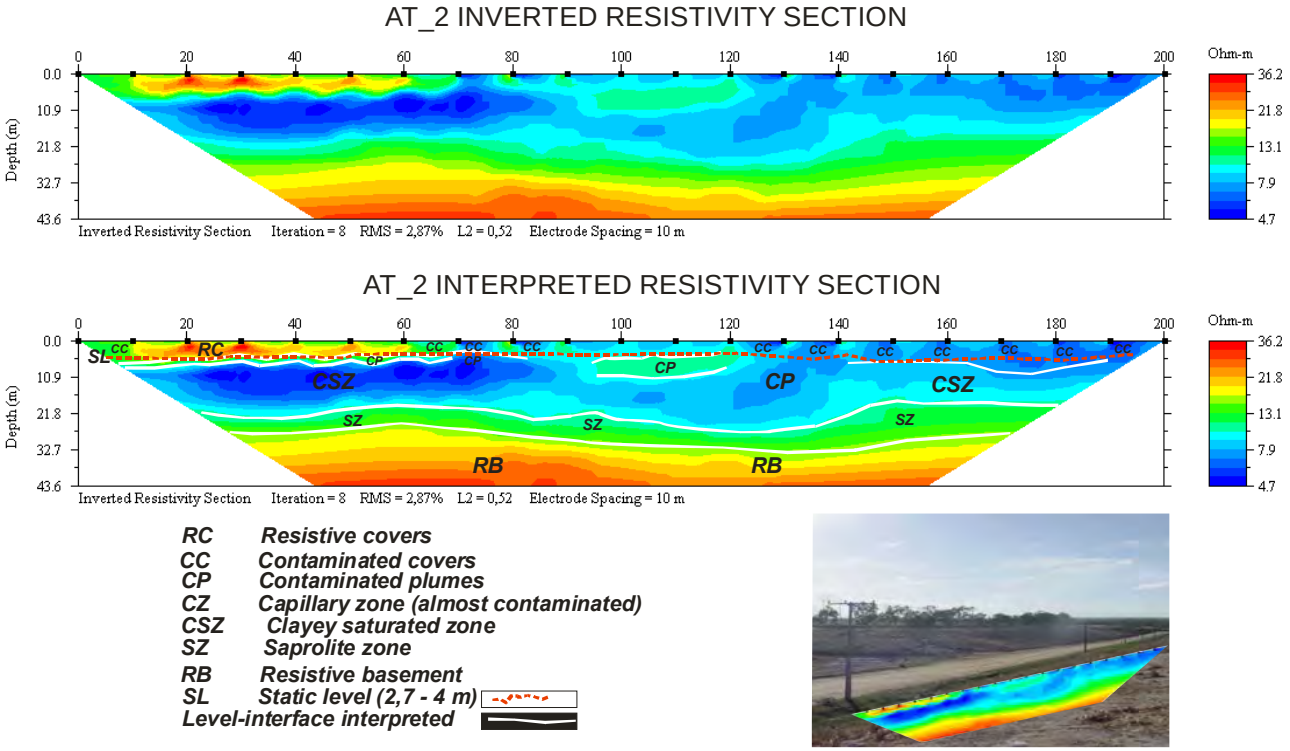

Figure 3: AT_2 inverted resistivity section and its interpretation.

It is possible to observe that some strongly conductive zones (<5Ω.m) occur inside the clayey saturated zone. Although the regional resistivity of the shallow part of the area corresponds to clayey and conductive materials, it is observed that there are still material concentrations in the AT_2 section more conductive than adjacent zones. It is possible that there is a high amount of dissolved salts indicating an electrolytic composition making the conductivity high in certain parts of the shallow aquifer system. As mentioned before, the electric conductivity usually increases due to the ion chloride which is an indicator of the waste presence in landfill sites (Mondelli, 2008).

In this AT_2 interpreted section (figure 3) it is observed that some shallow resistive covers (RC) are placed in the beginning of the section between the surface and 5m depth (>20 Ω.m). From electrode 60 to 210, it is observed that the resistivity fall substantially and that are several others conductive zones, interpreted as contaminated covers (CC), inside it. This 5-6m depth level has a strong coincidence with the static level of the shallow aquifer system as noted in the figure. Looking down of the section its follows the zone of clayey saturated part follows, ranging from around 8 to 10m depth (CSZ), almost conductive, but with some more conductive interfaces, that we can interpret as contaminated plumes (CP) inside the CSZ. Note that some of these conductive interfaces are interconnected with shallow contaminated covers. From this CSZ to an interpreted saprolite zone (SZ) there is a 22-25m range. The interpreted section ends with a relative increment in resistivity that can correspond to a resistive basement (RB) near 27-32m.

Figure 4 shows an EM-34 section in the same position of the ER AT_2 section, with all possible arrays for its 3 frequencies HD (horizontal dipole) and VD (vertical dipole) with 10, 20 and 40m cables spacing them. The section shows the variation of conductivity and its theoretical investigation depth. All the same conductive zones can be noticed in shallow levels (>80mS⁄m) and that the same interface occurs in a more resistive zone, near 25m depth (<50mS⁄m), occurs. Shallow conductive zones (>50 mS⁄m) also can be found in the end part of the section. It is possible to suppose that the clayey saturated zone is also visible. On the other hand, exact comparisons between EM conductivity and ER resistivity are not possible. It is extremely reasonable to consider that these data are of good quality due to the proximity of the observed values between the two different techniques. The EM data have not been inverted as the ER data have. It is possible to observe that the resolution of the EM method is smaller than that of the ER method one.

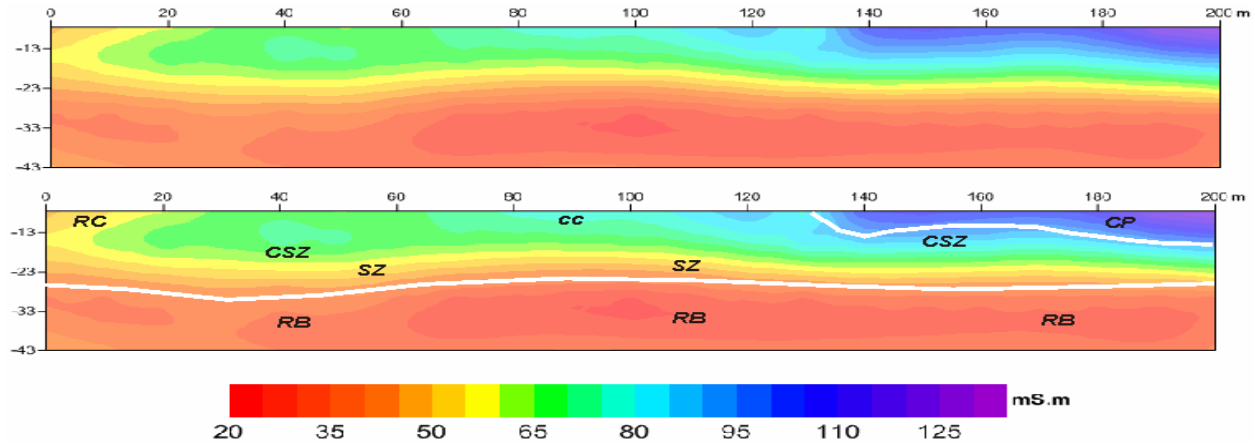

Figure 4: EM HD VD, 10, 20, 40m section and its interpretation. Subtitle is the same of figure 3.

We have performed a shallow well with 78cm depth over the 185m position (high conductivity anomaly) of the AT_2 ER section, which is shown in figure 2 (h,i,j). The leachate begins to emerge in 57cm depth (figure 2j) and has a measured conductivity (figure 2k) of 2.94mS⁄cm (≈3.4Ω.m) at room temperature, around 25-28°C in the well. As it can be noted, that means a strong correlation with the geophysical ER data in the high conductivity portion at the end of the ER section.

Main Conclusions

The objective of this preliminary geophysical investigation on Aquiraz waste landfill near Fortaleza City was to use an ER+EM technologies to test their applicability and resolution to delineate possible buried contaminated zones. This landfill has a complex problem because the clay sediments from regional geology are conductive. The ER dipole-dipole array shows a good inverted section presenting a high resolution image with excellent details of the investigated subsurface. Several important zones were detected as resistive covers, contaminated covers and plumes, a saturated zone, a possible saprolite zone and the resistive basement. Thus, several important interfaces were mapped, as the static level and probably, the capillary zone. One of the geophysical anomaly (high conductive) was examined directly through a shallow well and the sample of contaminated fluid has proven its very conductive character. The EM VD and HD (10,20,40m) section, collected in the same ER place, was also able to map some general characterization of the site. It was possible to observe a good correlation between the two techniques but with important differences in resolution. The ER dipole-dipole section shows a better resolution than the EM section. As can be seen, this combination of geophysical tools can be used in the region of the site to delineate some important pieces of information in the fields of the geology, environment and contamination of the shallow aquifer system. Direct information for geochemical analysis is being collected to complement these geophysical interpretations. Other geophysical techniques like GPR with very high frequencies and VLF, TDEM will also be used.

References

Castelo Branco, R.M.G. *et al.* – 2006 – Zoneamento ecológico-econômico da zona costeira do estado do Ceará. Parte Geologia e Geofísica. Relatório Semace. FCPC/UFC/LGPSR.

Mondelli, G. – 2008 – Integração de diferentes técnicas de investigação para avaliação da poluição e contaminação de uma área de disposição de resíduos sólidos urbanos. Tese de Doutorado, Universidade de São Carlos, 392p.

Acknowledgements

This work was supported in part by the CNPq/Proc.N.479283/2008-7 and FINEP/PETROBRAS/CNPq/UFC/FCPC/LGPSR. We are grateful for technical support from MARQUISE (Carlos).

MARINE AND LAND ELECTRICAL RESISTIVITY SURVEY FOR ASSESSING WATER QUALITY ISSUES IN CARTER LAKE, IOWA & NEBRASKA

Douglas E. Laymon, Tetra Tech, Austin, TX
Jeremy Gunter, Tetra Tech, Austin, TX
Sara Hanson, Tetra Tech, Omaha, NE

Abstract

A geophysical site characterization was completed by and consisted of a land and water borne resistivity survey. Carter Lake (the Site), is located adjacent to the Omaha International Airport, and is bisected by the Nebraska-Iowa state line. The geophysical survey was designed to assist in the characterization of the local hydrogeologic framework which affects the water quality of Carter Lake. The objective of the geophysical survey was to assist in identifying lithologic units with high hydraulic conductivities (sands and gravels), aquitards (silts and clays) peripheral and within Carter Lake. Differentiation and delineation of site lithology, with respect to, electrical resistivity data provided additional information for understanding potential water seepage in delineated site areas. The data presented herein in conjunction with known hydrogeologic parameters was used to contribute to the development of a preliminary design for the watershed and in-lake treatment alternatives identified in the area Management Plan to assist in improving the overall water quality of Carter Lake. This paper presents a summary of the collection methodology, interpretation, and findings of the resistivity data collected for this study. The resistivity data was collected from two Site areas: land data collected from, the southern perimeter areas; and water borne resistivity data collected from the in-lake areas.

Site Description

Carter Lake lies in both Pottawattamie County, Iowa and Douglas County, Nebraska, and is west of and adjacent to the Omaha International Airport. The lake consists of three legs in a horseshoe shape and is approximately 315 acres in size and three-miles long. Two canal areas feed into the residential area from the southern side of the central leg of the lake. A golf course is located along the southern and eastern shore of the western leg of the lake. The lake is bordered by residential and park lands. Vegetative cover in the lake perimeter consists of low lying and/or managed cut grasses and tree covered areas. The lake is used for active and passive recreational activities.

The near-surface geology consists of Quaternary glacial, fluvial, and lacustrine deposits which consist of interbedded clays, silts, sands, and gravels. Review of seven historical soil boring logs from the Army Corp of Engineers indicate that approximately three to 20 feet of clay which overlies a sand, is present at these boring locations in Carter Lake. The seven borings are located in the center of the lake and evenly spaced along its length. These unconsolidated materials are approximately 100 feet thick in this area and overly lower to Middle Pennsylvanian shale and limestone bedrock of the Bronson Group and Marmodon Group, respectively. The resistivity data was used to provide a more comprehensive mapping of these unconsolidated deposits within upper 50 feet of the subsurface.

Data Acquisition

The land electrical resistivity survey was performed using Advance Geophysical Systems Inc. (AGI) Super Sting R8 56-channel resistivity imaging system. The survey equipment consisted of a transmitter/receiver, four 14-takeout electrode cables, each with evenly spaced takeouts. Each array consisted of 56 evenly spaced stainless steel electrodes placed in the ground at 20 foot intervals, creating a single array length of approximately 1,100 feet. The electrodes were attached to a cable take-out and connected to the Sting R8 positioned at electrode number one at the start of an array. Data was collected from six single spread resistivity Wenner arrays for a total survey covering 6,600 linear feet.

In addition to the land resistivity data water borne resistivity data, Continuous Resistivity Profiling (CRP), was collected in Carter Lake. CRP is a variation of traditional stationary electrical resistivity profiling and is employed in either fresh or marine water bodies. CRP employs a streamer of electrodes that is pulled behind a boat or ship. The 11 electrode streamer employed for this investigation consisted of nine potential electrodes and two current electrodes spaced 20 feet apart, for a total array length of 200 feet. The end of the streamer was attached to an anchor, or similar, to provide sufficient drag to keep the array straight with the boats forward progression.

The array employed was a Dipole-Dipole array. Investigation depth is determined by array length, signal strength, and subsurface material composition, and is approximately 25% of the total array length or 50 feet. Measurement cycle time was three seconds using AGI's Marine Log Manager firmware. AGI's Super Sting R8/IP was used to collect the CRP data. Additionally, water temperature, depth, and GPS data were simultaneously input into the Super Sting R8/IP and recorded with measured resistivity values. The water borne data consists of 18 separate profiles of varying lengths. Total data coverage is greater than 10.5 miles, consisting of approximately 2.3 million data points.

Data Interpretation and Findings

The land and water borne resistivity data was processed used EarthImager software package for profile inversion, using a smooth inversion scheme, and constrained inverted values (1 to 100 ohm-m). Quality control was performed on the inversions by looking at the Root Mean Square (RMS) and L2-Norm values, measured versus predicted resistivity values crossplots, and inversion convergence curves. These quality control tools help produce the best inversion model, while minimizing error and not over-fitting the data. The data was then checked for resistivity distributions and contour color levels (10 to 100 ohm-meters) were chosen accordingly. These distributions were then cross checked with accepted geologic resistivity values (Telford, et. al.), and then interpretative geologic profiles and plan view material maps were created.

The interpretation process involved the review of data to determine the nature of subsurface lithology and related hydrogeologic framework which included but is not limited to:

- Presence, lateral extent, depth and thickness of weak hydraulically conductive units, such as silts and clays; and
- Presence, lateral extent, depth and thickness of moderate to strong hydraulically conductive units such as silty sands, sands, and gravels.

The inverted profiles reveal three distinct subsurface layers within and around Carter Lake; sand; gradational silty-sand to silty-clay; and clay. The sand layer areas were assigned resistivity values

greater than 44 ohm-m. The gradational silty-sand to silty-clay layer is assigned resistivity values between 44 ohm-m and 25 ohm-m. The higher values within this gradational zone represent increasing fractionations of sand in the material matrix and the lower values represent increasing fractionations of fine grained silts and clays in the material matrix. The third distinct layer is clay with resistivity values less than 25 ohm-m. Additionally, the water, was assigned a constant resistivity value of 20 ohm-m, and is thought to be a reasonable estimation of the water resistivity of Carter Lake. The location of the near surface sand layers were plotted on the Site map used to assist in constructing Site seepage model.

The resistivity survey was successful in assessing local lithology and respective hydrogeologic framework with respect to hydraulically conductive subsurface areas and confining lithology. Three main soil types where interpreted in the resistivity data and include sand, a gradational silty-sands to silty-clays, and clays. The sands and silty-sands located near the lake water-bottom interface are identified as being more hydraulically conductive and having a higher potential for seepage of water from the lake. Detailed soil borings would assist in further interpreting these resistivity values with the Site hydrogeology.

REFERENCES

Advanced Geosciences, Inc., 2008 Instruction Manual for EarthImager 2D Version 2.2.8 Resistivity IP Inversion Software. Advanced Geosciences, Inc., Austin, TX. April 4, 2008.

Telford, W.M.; Geldart, L.P.; Sheriff, R.E.; Keys, D.A., 1982 Applied Geophysics. Cambridge University Press. Cambridge, London. 1982 (Reprint).

Witzke, Brian J., Anderson, Raymond R., Bunker, Bill J., Ludvigson, Greg A., 2003 Bedrock Geologic Map of Southwest Iowa. Iowa Department of Natural Resources and Iowa Geological Survey. Iowa City, IA. September 2003.

BRINE DELINEATION AND MONITORING WITH ELECTRICAL RESISTIVITY TOMOGRAPHY AND ELECTROMAGNETIC BOREHOLE LOGGING AT THE FORT KNOX WELL FIELD NEAR WEST POINT, KENTUCKY

Rory D. Henderson, U.S. Geological Survey, Storrs, CT, and Univ. of Connecticut, Storrs, CT
Michael D. Unthank, U.S. Geological Survey, Louisville, KY
Doug D. Zettwoch, U.S. Geological Survey, Louisville, KY
John W. Lane, Jr., U.S. Geological Survey, Storrs, CT

Abstract

The potable water system at Fort Knox is threatened by brine contamination from improperly abandoned natural gas exploration wells. The Fort Knox well field is located near the town of West Point, Kentucky, in the flood plain of the Ohio River. At the site, unconsolidated sediments approximately 30 – 40 m thick, overlie shale and porous limestone. Brine is believed to flow vertically from the underlying formations to the unconsolidated aquifer through damaged or leaky well casings under a high hydraulic gradient from the artificially pressurized porous limestone, which is utilized for natural gas storage by a regional energy company. Upon reaching the unconsolidated aquifer, brine-contaminated groundwater enters water supply production wells under the pumping-induced gradient. As part of the Fort Knox remediation strategy to reduce the impact of brine contamination, electrical resistivity tomography (ERT) and borehole electromagnetic (EM) logs are being collected annually to detect gross changes in subsurface conductivity.

The 2009 ERT data show areas of high conductivity on the western (contaminated) side of the site with conductivities more than an order of magnitude higher than on the eastern (uncontaminated) side of the site. The areas of high conductivity are interpreted as brine contamination, consistent with known regions of brine contamination. Conductivities from the EM logs are consistent with the results from the ERT inversions. The EM logs show little change between 2008 and 2009, except for some small changes in the brine distribution in well PZ1. Yearly ERT surveys will be continued to detect new areas of brine contamination and monitor the remediation effort.

Background

The alluvial aquifer near West Point, Kentucky, supplies potable water to 50,000 people in the town of West Point, the U.S. Army Installation Fort Knox, and the Hardin County Water District 1 (Lyverse and Unthank, 1988). Several public wells in the vicinity of West Point have been abandoned as a result of high chloride levels. Increasing chloride concentrations spurred an initial investigation of the aquifer in the West Point area in 1987. The aquifer is situated in the flood plain of the Ohio River (Figure 1). Approximately 30-40 m of sediment overlies bedrock. The sediments consist of clay and silt to approximately 10-m depth. Sand and gravel outwash deposits are found between approximately 10- and 40-m depth. Bedrock, consisting of shale and porous limestone, is found beneath the sediments (Lyverse and Unthank, 1988).

Several natural-gas exploration wells were completed in the limestone formation. An inventory of these wells and local knowledge revealed that "sulfur water" was observed flowing at the ground

surface from the wells (Lyverse and Unthank, 1988). The 1988 study also included a Geonics EM-34[1] survey, which indicated the presence of two high-conductivity targets in the immediate vicinity of the well field. Test drilling confirmed the presence of high chloride concentrations at depths of 30.5 and 31.7 m in these locations. Brine contamination is believed to flow from improperly abandoned natural-gas exploration wells (Lyverse and Unthank, 1988). In addition, the porous limestone formation is pressurized by a regional energy company that uses the formation to store natural gas during times of low demand.

A follow-up study was performed from 1996 to 1999 consisting of groundwater level measurements, aquifer tests, and a seismic reflection survey in the Ohio River (Unthank and Nelson, Jr., 1999). A groundwater flow model was constructed and calibrated using these data. Because the bedrock layer was not simulated as a no-flow boundary, the model was able to simulate groundwater exchange. The model indicated that groundwater generally flows from south to north, toward the Ohio River. The model simulation also indicated that 50 percent of recharge occurs through infiltration of precipitation, 49 percent from the bedrock valley walls of the surrounding area, and 1 percent from infiltration from the Ohio River. No measurable recharge occurs from the underlying bedrock. Discharge from the aquifer consists of 29 percent from pumping wells, 68 percent as flow to the Ohio River, and 3 percent as flow to the underlying bedrock (Unthank and Nelson, Jr., 1999). A working conceptual model is shown in Figure 2.

Fort Knox is considering connecting to public water utilities provided by the Louisville Water Company. The well field, however, will be maintained as a secondary source of water. The U.S. Geological Survey assisted the Directorate of Public Works at Fort Knox and the U.S. Army Corps of Engineers, Louisville District in devising a remediation strategy to control further impacts imposed by brine migration. Contaminated wells will be used to manipulate the hydraulic gradient of the unconfined aquifer at the site, drawing the brine-contaminated water away from potable drinking-water wells. Pumped brine water will be discharged to the Ohio River. Prior to the remedial action, a groundwater-level survey was completed in July 2009 to map the hydraulic gradient at the site (Figure 3). Groundwater level measurements will continue to be used to ensure that pumping and subsequent discharge is steering the brine away from the potable wells.

In August 2007, a pilot study was conducted to evaluate the use of ERT for mapping the extent of brine contamination. Initial field efforts focused on known areas of contamination, and high conductivity anomalies were detected in several areas. Based on these preliminary results, a periodic geophysical monitoring program was initiated at the site. Yearly ERT surveys will be used to detect new areas of brine contamination and monitor the remediation effort. In June 2008, in addition to two-dimensional (2D) ERT surveys, EM borehole logs were collected in four newly installed monitoring wells (Henderson et al., 2009). Results from the EM logs have aided in interpretation of the ERT tomograms. Here, we present results from the latest round of geophysical monitoring at the site that occurred in July 2009.

Methods

ERT was used at the site to delineate the spatial extent of brine contamination in the unconsolidated aquifer. Electrical current flow in earth materials is sensitive to the bulk resistivity of the material, which is a function of material saturation, porosity, fluid conductivity, and pore connectivity (Archie, 1942). Assuming that intrinsic material properties do not change over time (i.e.,

[1] Any use of trade, product, or firm names is for descriptive purposes only and does not imply endorsement by the U.S. Government.

porosity, cementation/pore connectivity), ERT is used to monitor changes in pore-water conductivity or percent saturation. In this case, we are interested in monitoring areas well below the water table, which by definition is always 100 percent saturated. Thus, ERT is used here to view changes in conductivity due to changes in water quality (e.g. brine contamination).

To optimize the tradeoff between spatial coverage, depth of investigation, and imaging resolution, we used a 56-electrode, dipole-dipole array with 8-m electrode spacing. The total length of each survey line was 440 m, ensuring an adequate depth of investigation (approximately 1/3 to 1/5 the total length of the survey) because brine was assumed to lie near the sediment/bedrock interface, 30-40 m below the land surface. ERT surveys were performed with an 8-channel SuperSting resistivity meter, manufactured by Advanced Geosciences, Inc. We performed ERT surveys perpendicular to groundwater flow to measure the distribution of brine in the subsurface, and to monitor the migration of the brine plume resulting from ongoing and future pumping. Reciprocal measurements were collected to incorporate data weighting in the inversion, and reciprocal errors did not exceed 3 percent. We inverted the ERT data using RES2DINV (Loke, 2004). The inversion process was stopped once the data misfit achieved an RMS error between 3 and 5 percent. Where appropriate for long survey lines (e.g., Figure 2, PARW2), ERT datasets were concatenated and inverted to provide spatially-continuous subsurface resistivity models across the known areas of brine contamination and in the vicinity of the brine-mitigation pumping wells.

In addition to ERT surveys, EM induction logs were collected in two PVC-cased onsite wells using a Mount Sopris[1] EM-39 logging tool. The tool was calibrated with a 4EMD-1000 induction probe calibration coil supplied by Mount Sopris during the July 2008 fieldwork. The July 2009 EM logs were post-calibrated to match features that were not expected to change in the previous year's logs.

Results and Discussion

In general, the ERT tomograms (Figure 4) indicate a layered geologic setting. The tomograms show a low resistivity layer, overlying a high resistivity layer, which overlies a lower resistivity layer. This configuration is consistent with the working conceptual model of the site: silt and clay overlies sand and gravel, which overlies brine-saturated sand on the western portion of the site and freshwater-saturated sand on the eastern portion of the site. It is important to note that ERT tomograms represent a blurry, blunted version of reality because of the diffuse nature of the measurement physics and the regularization in the inversion procedure. Thus, depth of anomalies may not represent true depth in the subsurface. Interpretation with respect to EM logs and previous site knowledge is essential to extrapolate useful information from the results.

Areas of low resistivity at depths greater than 25-30 m on the tomograms (Figure 4) are interpreted as regions of brine contamination, with highest brine concentrations adjacent to the contaminated wells (north) and a previously identified area of contamination (west) (Lyverse and Unthank, 1988), as noted in survey lines PARW2-PARW5 (Figure 4) by low resistivity values between 3-6 ohm-m (dark blue to blue) below 25 m. Resistivity values for brine-contaminated areas are on the order of 3-6 ohm-m. Assuming sediment porosity between 20 and 30 percent, cementation exponent of 1.3, and fully saturated conditions, a bulk resistivity of 3-6 ohm-m corresponds to a pore-water conductivity of at least 10 mS/cm. The lower resistivity range (~3 ohm-m), corresponds with a pore-water conductivity of 10-20 mS/cm (Figure 5), which is consistent with values measured in the EM borehole logs (Figure 6). Based on low resistivity values in the deeper portions of the tomograms, brine concentration is highest just south of the contaminated wells (PARW2) and in the middle of the previously identified area of contamination (PARW4). Brine is unlikely to be discharging to the river

on the northern portion of the site as indicated by resistivity values of 25-30 ohm-m in the deeper portions of the PARW1 tomogram, which is located between the pumping wells and the river.

On the eastern portion of the site, the lowest resistivity values were approximately 25-30 ohm-m (PARE1 and PARE2) in the lower portion of the tomograms, corresponding to a pore-conductivity of ~3 mS/cm (Figure 5). While this value is high for drinking water standards, it is an order of magnitude lower than found in the western portion of the site. Because potable wells are likely pumping a mix of site water and water from riverbed infiltration due to the wells' proximity to the Ohio River, the quality of the pumped water remains high and meets applicable drinking water standards of 250 mg/L for chloride.

EM borehole logs are presented from monitoring wells PZ1 and PZ2 (location shown in Figure 4, logs presented in Figure 6) from the 2008 and 2009 field campaigns. Electrical conductivity in PZ1 appears to vary smoothly with depth, with the exception of a high conductivity anomaly near 8-m depth and near the bottom, starting at approximately 28 m and continuing to the bottom of the well. In July 2008, the deep high conductivity anomaly was sharp and elevated off the bedrock basement. In July 2009, the anomaly appears to be sinking. Diffusive processes and density effects may be influencing the apparent spreading of the anomaly. Groundwater flow and transport on the northern portion of the site is modulated by river stage and pumping conditions, which also may influence the brine distribution in the lower portion of the aquifer. A driller's log was provided for PZ1 (M. Nickter, written commun., September 21, 2007). In general, the driller's log indicates that fine-grained materials (silt and clay) overlie fine to coarse grained sand, with trace gravel, which is consistent with the ERT results.

In PZ2 (Figure 6), electrical conductivity appears to vary smoothly with depth. At approximately 30-m depth, a high conductivity anomaly is present. The driller's log (M. Nickter, written commun., September 21, 2007) is similar to that of PZ1, showing a layered geology where fine materials (silt and clay) overlie coarser materials (fine sand with fine gravel). The high conductivity values in the two EM logs approach 200 mS/m, which translates to a resistivity value of ~5 ohm-m. This finding is consistent with the ERT results. Between July 2008 and July 2009, the electrical conductivity associated with the brine contamination remained relatively unchanged. While river stage and pumping conditions may influence hydraulic conditions near this well, the lack of change in the electrical conductivity indicates that these effects are substantially damped in this location. Additionally, groundwater-level contours are more widely spaced, indicating the hydraulic gradient is lower than at the northern portion of the site (Figure 3).

Conclusions and Future Work

This study showed that ERT was effective for identifying regions of brine at the Fort Knox site in Kentucky. Subsurface conductivities on the western side of the site were more than an order of magnitude higher than on the uncontaminated eastern side of the site. In general, EM borehole logs were consistent with the tomograms from the west side of the site (contaminated with brine). In contaminated portions of the aquifer, the subsurface geology consists of a conductive layer overlying a resistive layer, which overlies brine-contaminated fine sands and gravel. The driller's logs showed a general coarsening of materials with depth, indicating that silt and clay overlie fine sand and fine gravel. Silts and clays are generally more conductive than sands, as can be seen in the tomograms and borehole EM logs. With respect to the high conductivity features near the sediment/bedrock interface, the material does not change, so the transition from resistive to conductive is interpreted as a change in water quality. This is consistent with the conceptual model at the site. Brine is denser than fresh groundwater, so it tends to stay close to the bedrock/sediment interface.

As part of the site remediation strategy, ERT and borehole EM logs will be collected annually to detect gross changes in subsurface conductivity. The ERT data will be collected on the same lines each year; the tomograms, however, cannot be used for quantitative time-lapse estimation of spatially and temporally variable salinity values because electrodes will not be placed in exactly the same locations from year to year. The ERT method will continue to be useful for determining areas of new brine contamination and detecting gross changes in groundwater quality. If used in conjunction with EM borehole logs, groundwater-quality sampling, and groundwater-level monitoring, ERT will be useful to monitor the effectiveness of the remedial pumping effort.

References

Archie, G.E., 1942, The electrical resistivity log as an aid on determining some reservoirs characteristics, Journal of Petroleum Technology, 5, p 1-8.

Henderson, R.D., Unthank, M.D., Zettwoch, D.D., and Lane, J.W., Jr., 2009, Subsurface brine detection and monitoring in West Point, Kentucky, with 2D electrical resistivity tomography [abs.]: *in* Symposium on the Application of Geophysics to Engineering and Environmental Problems, March 29 - April 2, 2009, Fort Worth, Texas, Proceedings: Denver, Colorado, Environmental and Engineering Geophysical Society.

Loke, M.H., 2004, Tutorial: 2-D and 3-D electrical imaging surveys, www.geoelectrical.com, (Accessed 9 January 2010).

Lyverse, M.A. and Unthank, M.D., 1988, Assessment of ground-water contamination in the alluvial aquifer near West Point, Kentucky, U.S. Geological Survey Water Resources Investigations Report 88-4166.

Unthank, M.D. and Nelson Jr., H.L., 1999, Hydrogeology and simulation of ground-water flow in the Ohio River alluvial aquifer near West Point, Kentucky, U.S. Geological Survey Water Resources Investigation Report 99-4265.

Acknowledgments

The authors acknowledge funding provided by the Directorate of Public Works at Fort Knox. Additional funding was provided by the U.S. Geological Survey Groundwater Resources and Toxic Substances Hydrology Programs. Project management was provided by the U.S. Army Corp of Engineers, Louisville District.

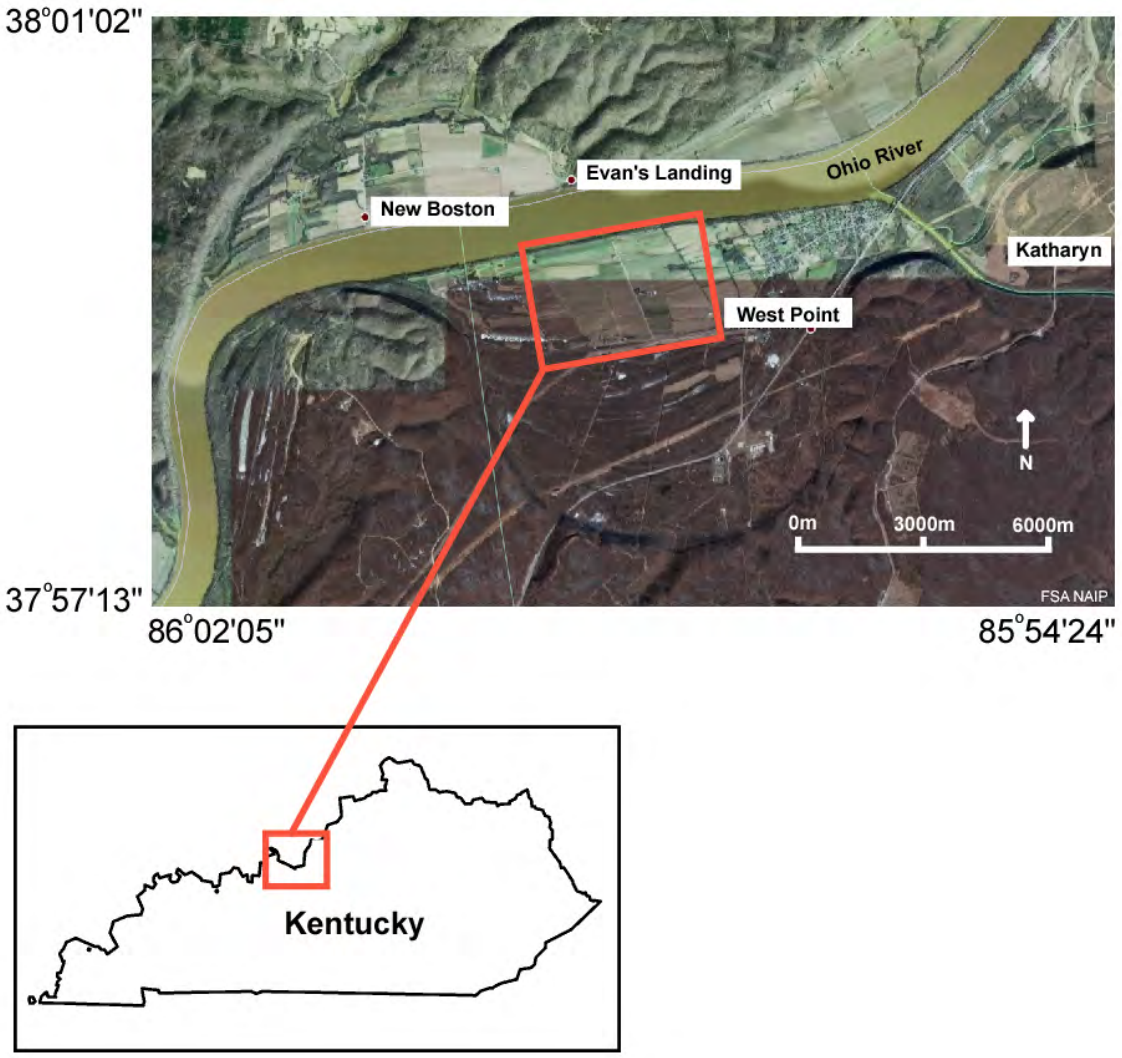

Figure 1: Site map. The site, outlined in red, is located near the town of West Point, Kentucky, bordered to the north by the Ohio River.

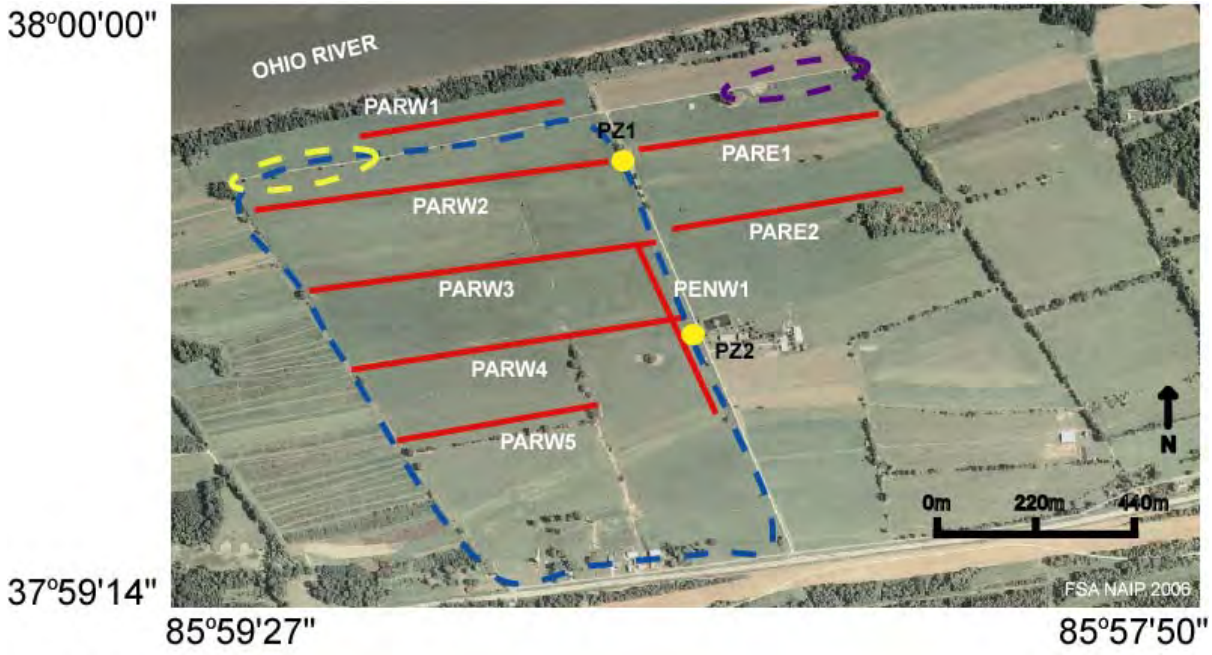

Figure 2: Conceptual model and survey layout. Previously identified area of brine contamination is located on the western portion of the site, (blue dashed line). Brine pumping wells are located on the northwest side of the site (yellow dashed line). Potable wells are located on the northeast side of the site (purple dashed line). ERT survey lines (red lines) were laid perpendicular to the dominant direction of groundwater flow. EM logging was performed in two boreholes (yellow dots).

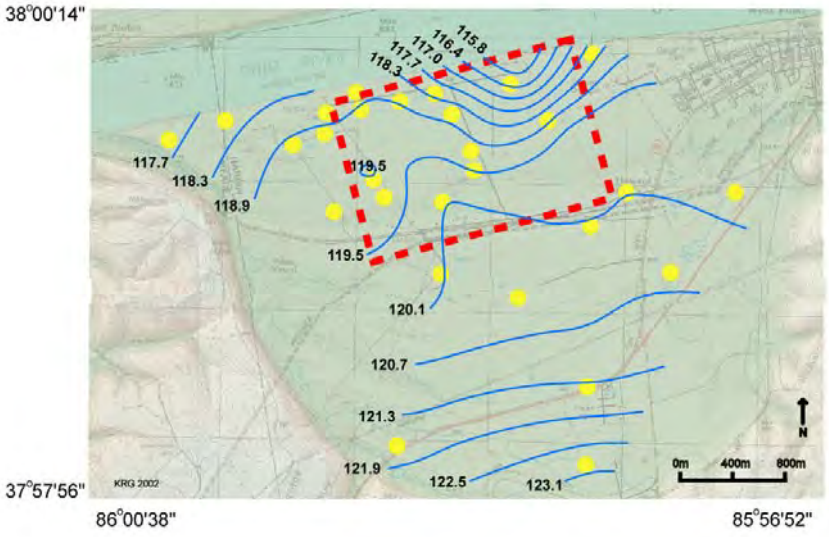

Figure 3: Groundwater-level contour map. Groundwater levels were measured during July 2009 prior to performing the ERT and EM borehole log surveys. Well locations are shown in yellow. Contours represent groundwater elevation in meters above mean sea level. Red dashed area outlines the site.

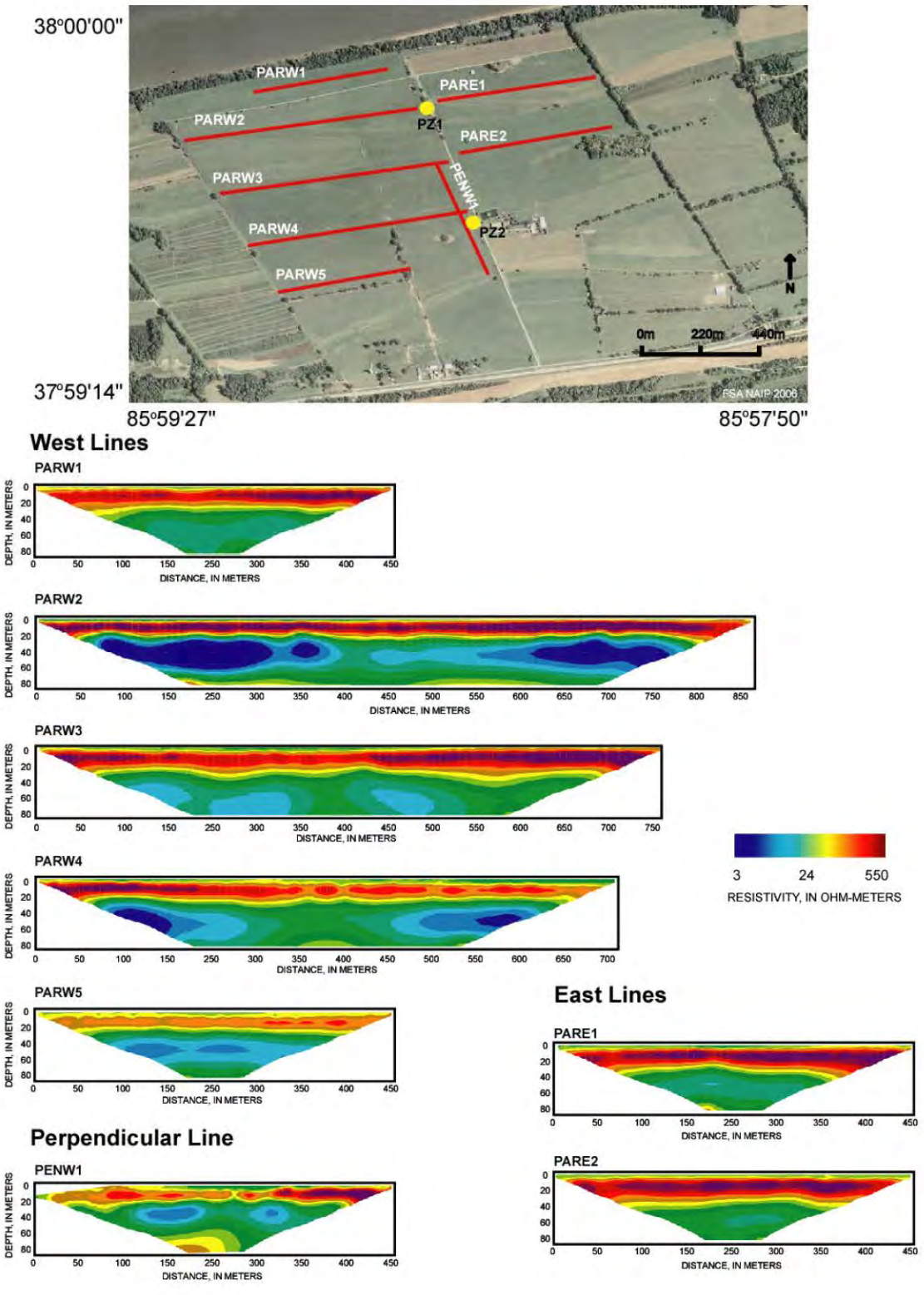

Figure 4: ERT inversions for data collected July 2009. The site map indicates the location of the tomograms in red. Yellow circles are the locations of the monitoring wells that were logged. Tomograms are aligned such that left is west, right is east. For PENW1, the tomogram is aligned such that left is south, right is north.

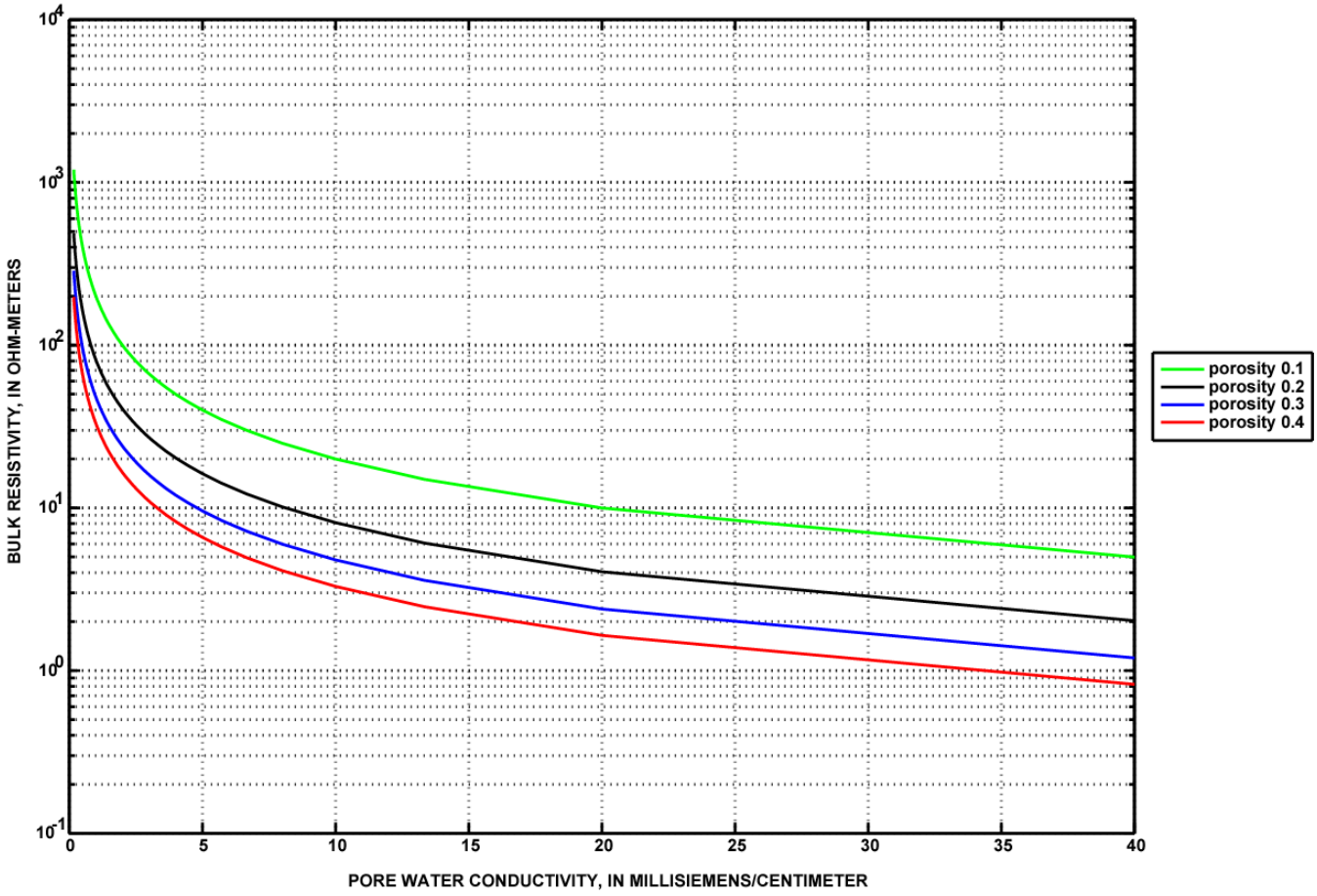

Figure 5: Archie's relation between bulk resistivity and pore-water conductivity for varying porosities under fully saturated conditions. A cementation exponent of 1.3 was used for unconsolidated materials.

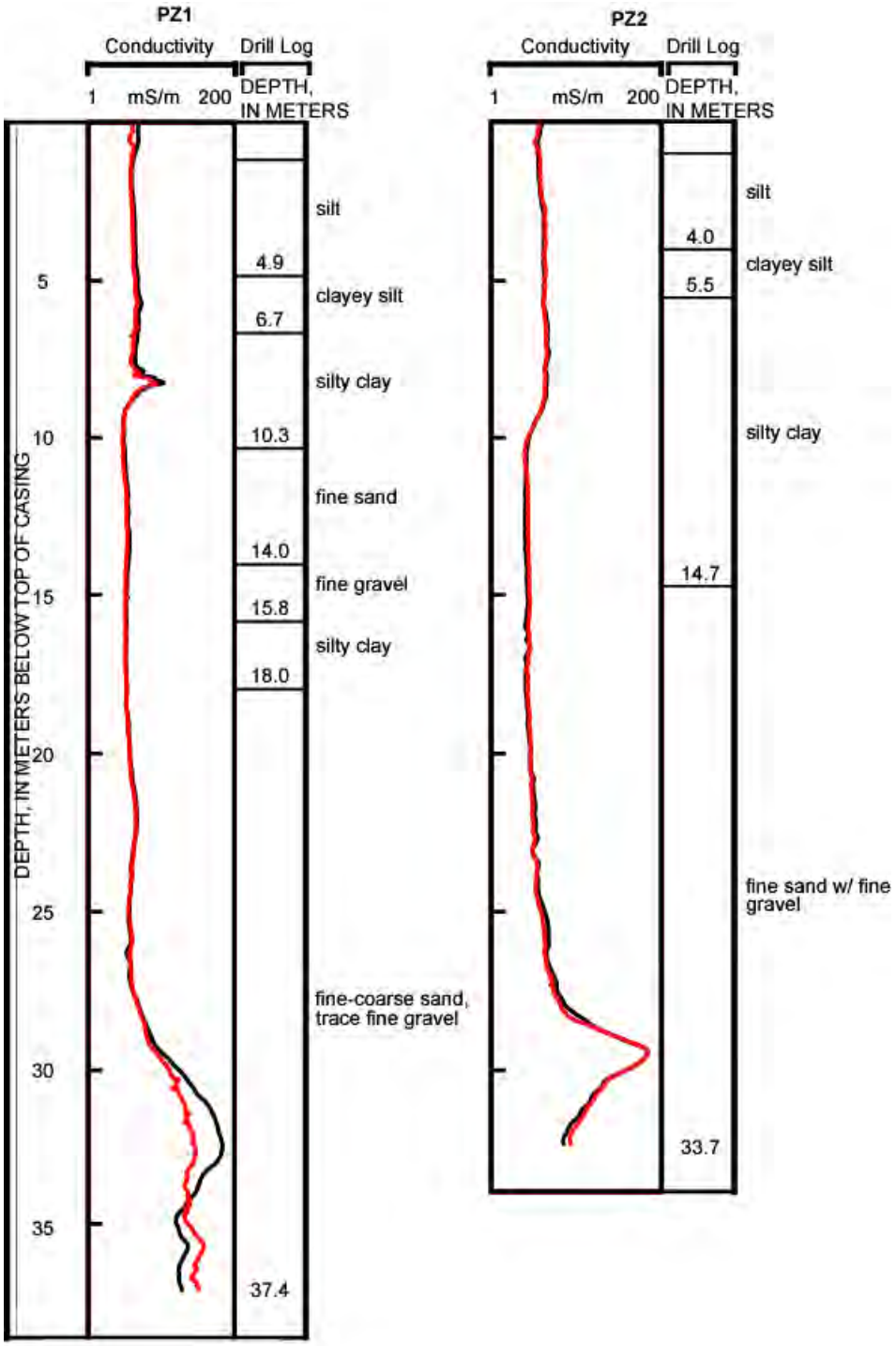

Figure 6: Borehole logs from monitoring wells PZ1 and PZ2. Red lines are data from July 2009; black lines are data from July 2008.

TRACKING TRACER BREAKTHROUGH IN THE HYPORHEIC ZONE USING TIME-LAPSE DC RESISTIVITY, CRABBY CREEK, PENNSYLVANIA

Jonathan E. Nyquist, Temple University, Philadelphia, PA
Laura Toran, Temple University, Philadelphia, PA
Allison C. Fang, Temple University, Philadelphia, PA
Robert J. Ryan, Temple University, Philadelphia, PA
Donald O. Rosenberry, United States Geological Survey, Denver, CO

Abstract

Characterization of the hyporheic zone is of critical importance for understanding stream ecology, contaminant transport, and groundwater-surface water interaction. A salt water tracer test was used to probe the hyporheic zone of a recently re-engineered portion of Crabby Creek, a stream located near Philadelphia, PA. The tracer solution was tracked through a 13.5 meter segment of the stream using both a network of 25 wells sampled every 5-15 minutes and time-lapse electrical resistivity tomographs collected every 11 minutes for six hours, with additional tomographs collected every 100 minutes for an additional 16 hours. The comparison of tracer monitoring methods is of keen interest because tracer tests are one of the few techniques available for characterizing this dynamic zone, and logistically it is far easier to collect resistivity tomographs than to install and monitor a dense network of wells. Our results show that resistivity monitoring captured the essential shape of the breakthrough curve and may indicate portions of the stream where the tracer lingered in the hyporheic zone. Time-lapse resistivity measurements, however, represent time averages over the period required to collect a tomographic data set, and spatial averages over a volume larger than captured by a well sample. Smoothing by the resistivity data inversion algorithm further blurs the resulting tomograph; consequently resistivity monitoring underestimates the degree of fine-scale heterogeneity in the hyporheic zone.

Introduction

The hyporheic zone is the region directly beneath the streambed where shallow groundwater and surface water mix. There is both vertical exchange between the two flow systems and lateral flow paralleling flow in the stream (Jones and Mulholland, 2000). Characterization of the hyporheic zone has important implications for stream management because the configuration of this zone affects aquatic habitat by influencing the migration of nutrients and contaminants (Dahm et al., 1998; Hancock et al., 2005). Characterization of fluxes between surface and groundwater is difficult in practice because stream sediments are invariably heterogeneous, their distribution evolving continually with storms, seasons and disturbances by man (Sophocleous, 2002). A key parameter of interest is transient storage, the temporary lingering of stream water in pools, eddies or sediments. Tracer tests are one of the few proven methods for characterizing transient storage in the hyporheic zone (Jones and Mulholland, 2000; Kalbus et al., 2006). Tracer introduced into a stream flows quickly in the surface waters, but also enters the hyporheic zone where it travels more slowly, advecting, dispersing and either entering the groundwater system or gradually reemerging into the stream waters. The logistics of a tracer test are invariably challenging because the flow is quick and numerous wells must be sampled rapidly to capture the solute breakthrough.

In this study we compare the breakthrough of a saline tracer determined by analyzing water samples collected using a network of shallow wells with tomographs constructed using time-lapse resistivity. Resistivity data can be collected more efficiently and analyzed more rapidly than water samples, but first it must be established that the breakthrough curves generated from resistivity data yield comparable results. The site selected for this study was Crabby Creek, a small stream located near Valley Forge in southeastern Pennsylvania, outside Philadelphia. This stream is of particular interest because migration and down-cutting of the streambed threatened one of the community's sanitary sewer lines, prompting excavation of a new course for the offending section of stream. In the design of this new streambed, the planners installed a series of cascades and J-hooks to control erosion and to create fish habitat. Our study involved two tracer tests on two separate but nearby reaches of Crabby Creek with different streambed characteristics. In this paper we discuss preliminary results, and focus only on comparing geophysical and well data for the Upper Reach. A more lengthy and detailed presentation of the entire study is in preparation.

Methods

Experimental Layout

The geophysical monitoring was conducted using an 8-channel AGI Superstring® resistivity system with a 28-electrode underwater cable having a 0.5 m electrode spacing for a total length of 13.5m. The cable was deployed down the center of Crabby Creek parallel to the direction of flow, centered on one of the J-hooks (Figure 1). Seven rows of 3-4 shallow wells (25 total) were installed in the hyporheic zone along transects perpendicular to the electrode cable at the 3, 4, 5.5, 8.0, 9.5, and

Figure 1: Photograph of Crabby Creek showing the underwater resistivity cable, monitoring wells, and sampling setup. A resistivity survey was completed every 11 minutes and well samples collected every 5-15 minutes for over six hours. Note the stone J-hook (solid white line) crossing the center of the resistivity line.

11.0-m marks from the downstream end. These wells were constructed from 1.25 m sections of 1.27 cm (0.5 in) diameter polyethylene tubing. The bottom 10 cm of tubing was perforated every centimeter and a mesh was glued over the openings to screen out sediments. Most of the wells were installed 20-cm beneath the streambed, with a few installed down to 40 cm. In addition to the wells, we monitored the stream water conductivity using a Global Water GL 400 meter set to log a reading every 10 seconds. We surveyed the locations of the stream bank water line, all electrodes, and the wells using a total station.

Tracer Release

The tracer solution was prepared by dissolving 54.5 kg (120 lbs) of salt (NaCl) in a 379 L (100 gallon) tub filled with stream water. The tracer was mixed the day before the release to allow time for the salt to dissolve. The tracer solution had an average concentration of 88,000 mg/L of Cl and was added to the stream using a drip line over a period of two hours at a rate that ranged between 2.39 and 2.50 L/min, which is roughly 0.1% of the flow rate of Crabby Creek measured to be 2,300 L/min at a location 1-m upstream of the injection site. The tracer release point was 31 m above the upstream end of resistivity cable.

Well Sampling

For sampling, a 0.63 cm (0.25 in) diameter polyethylene tube was inserted into each well and cut to a length that reached the creek bank to allow samples to be extracted without entering the creek. Considerable care was taken once the tracer test was started as not to disturb the streambed or electrodes. Samples were withdrawn using a syringe attached to a shut-off valve dedicated to each well (Figure 1). For each measurement 20 mL was drawn and purged, and then a second 20 mL was drawn and stored in a plastic canister to be analyzed in the laboratory. Laboratory conductivity measurements were converted to specific conductivity at 25^{o}C using a standard temperature correction.

Geophysical Monitoring

We used a dipole-dipole array to emphasize resolution of along-line changes in resistivity, and because this array speeds data acquisition by taking optimal advantage of the eight recording channels provided by the Supersting. A full dipole-dipole survey comprising 216 measurements can be performed in roughly 10 minutes. Automated resistivity soundings were collected one after the other with one minute intervals between soundings, thus the temporal resolution of the geophysical data was 11 minutes.

The data were inverted using the EarthImager2D time-lapse inversion module, which inverts directly on the resistivity differences using an Occam's Inversion algorithm (Constable et al., 1987; DeGroot-Hedlin and Constable, 1990). We used water depths measured at each electrode to constrain the electrode geometry (Figure 2a) for the inversion, but the resistivity of the water was not included a priori because it changed over the course of the experiment. To facilitate interpretation of the geophysical data we measured depth to bedrock along each of the well transects with a tile probe – a metal rod pushed into the ground until refusal. To distinguish between bedrock and cobbles each location was probed repeatedly over an area in the case of sudden shallowing.

Results and Discussion

The background resistivity survey (Figure 2a) clearly shows the depth to bedrock (about 0.5 to 0.75 m below the streambed), but the section was also affected by the J-hook in the center of the line, which shows as a shallow resistive feature. The time-lapse resistivity data clearly show that the tracer

lingered in the hyporheic zone above and below the J-hook after the injection was stopped (Figure 2b). The more intense region of tracer upstream is consistent with studies that have shown that an obstruction such as a J-hook tends to drive upstream water into hyporheic zone (Crispell and Endreny, 2009). However, well samples showed tracer remained in sediments at the J-hook as well, so the structure may have masked the resistivity signal near the center of the line. Note also that the smoothing tendency of the inversion algorithm makes it appear in Figure 2a that the tracer penetrated bedrock and reached depths of over a meter. However, breakthrough curve modeling suggests that the tracer stayed in the sediments, penetrating 50-60 cm.

Although we stopped intensive well sampling about 4 hrs after ending the tracer injection (one sample was collected the following morning), we continued the resistivity data collection through the night. The final data set (Figure 2c) still shows slightly decreased subsurface resistivities. However, is

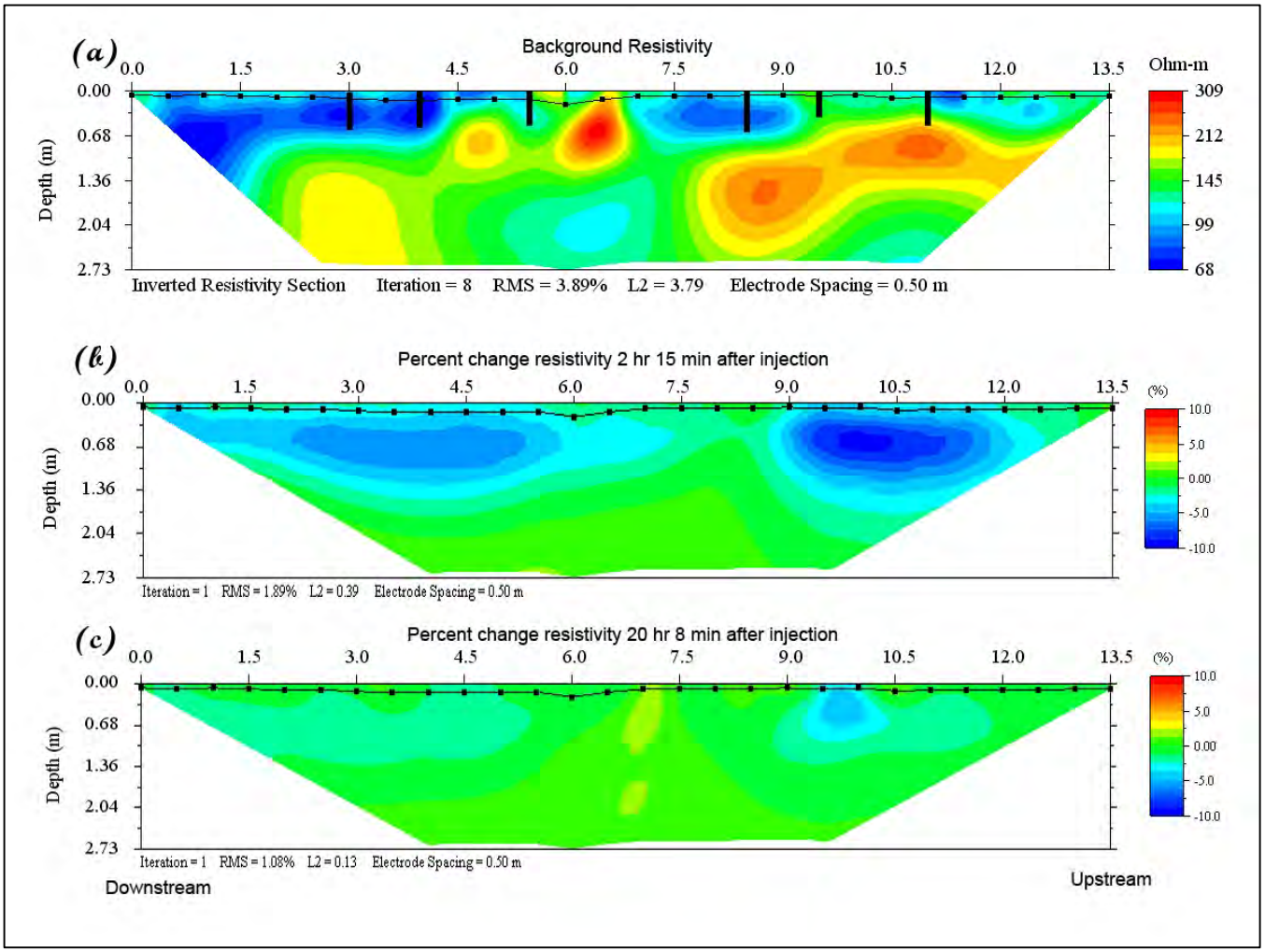

Figure 2: (a) Longitudinal cross sections of the background resistivity collected before the tracer release. The spacing of the electrodes (black dots) was 0.5 m and the water depth averaged 10 cm. Vertical black lines show depth to bedrock determined by tile probe. (b) Percent change in resistivity 2 hr 15 min after the start of the tracer injection, 15 min after it ended. (c) Percent change in resistivity 20 hr 8 min after the start of the injection, 18 hr 8 min after it ended. Well transects 2, 3, 4, 5, 6, and 7 crossed the resistivity line at the 11, 9.5, 8.0, 5.5, 4.0, and 3.0 m marks, respectively. Upstream is to the right for all sections.

it is not clear whether or not this represents lingering tracer. The doubt arises because the stream water conductivity gradually increased about 4% (comparable to the magnitude of the lingering resistivity anomaly) over the 6 hr period of intensive monitoring as the stream recovered from dilution created by a rainstorm a few days earlier, whereas the time-lapse inversions were developed using the background survey collected just before the start of the test. However, the source of this anomaly is likely to have been greater in magnitude than 4% because the inversion process blurs resistivity contrasts by spreading the region of signal. Furthermore, if this lingering decrease in resistivity were solely a consequence of drift in stream water conductivity we would expect the distribution to be laterally uniform and not concentrated in the same locations as immediately after the tracer injection (Figure 2b).

We also used the resistivity data to look at tracer breakthrough curves. Figure 3 shows well conductivity data for Line 3 located at the 9.5 m mark on Figure 2. Three of the wells were screened from 10-20 cm, and one from 30-40 cm. The center well was adjacent (0.09 m away) to the resistivity line running down the middle of the stream. The left and right wells are designated from a perspective of someone looking downstream, and were 1.26 m and 0.77 m from the resistivity line, respectively, but still in the stream. To put the well and resistivity data on the same scale we expressed the hyporheic zone conductivity as a percent change normalized to the equilibrium value measured after the tracer pulse had passed through. For comparison of well samples with the resistivity data it might have been

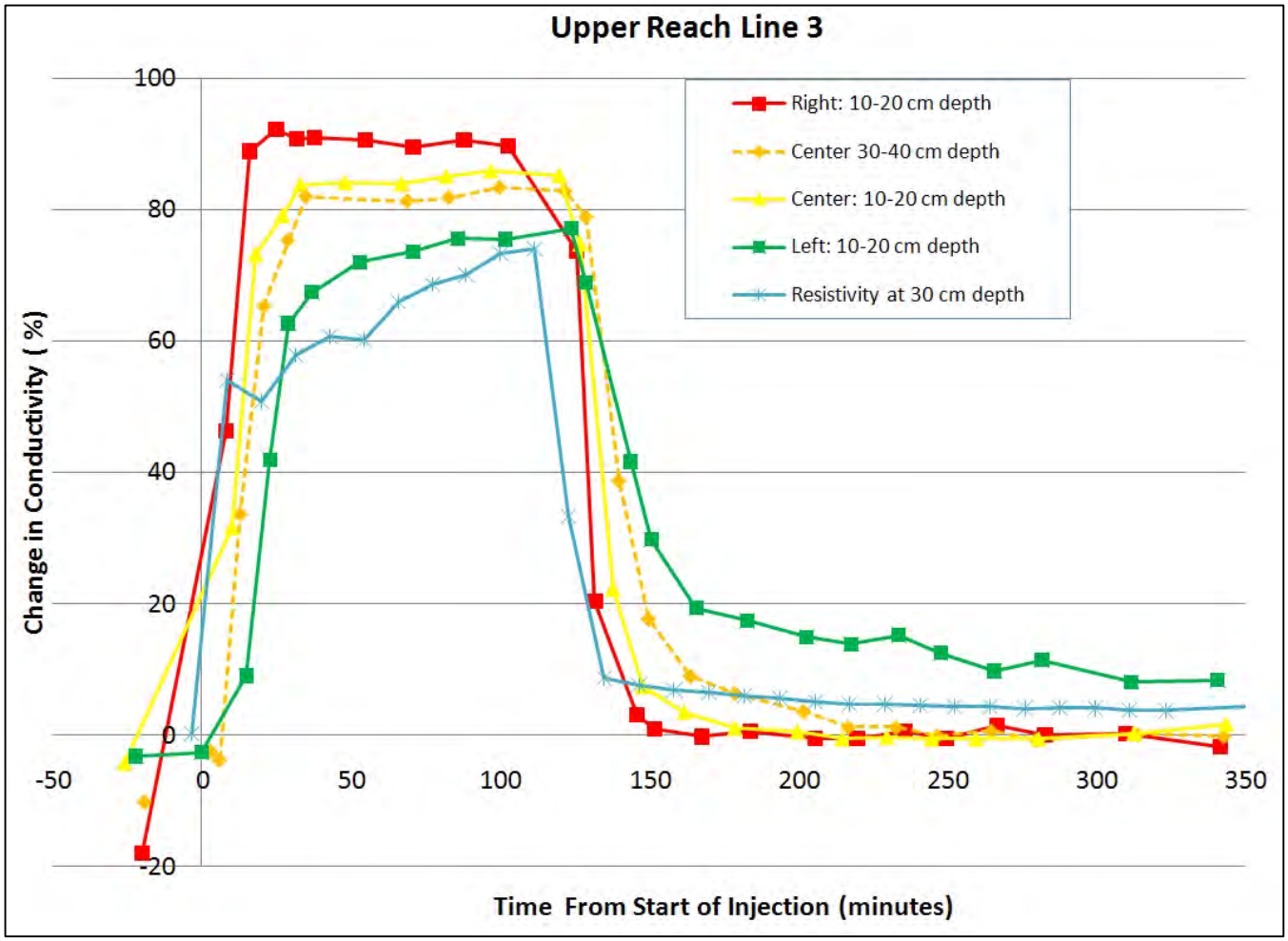

Figure 3: Comparison of breakthrough curves from well data and time-lapse resistivity monitoring.

preferable to use the stream water value at the time of the background resistivity survey. We did not for two reasons. First, for an unknown reason there is more scatter in the background conductivity values measured in the wells before the tracer test than in the asymptotic values afterward. Second, determining the fall-off rate back to zero tracer is critical for hydrologic modeling; the asymptotic value is more accurate for this purpose. The resistivity values at roughly the depth-center of the plume (30 cm) were extracted from all of the time-lapse inversions to develop a time series.

The wells show a rapid rise in conductivity after the tracer tests start. Note that the abrupt rising limb of the tracer pulse in the resistivity data (Figure 3) mainly reflects the rapid increase in the conductivity of the stream water and should not be used for modeling transient storage. The resistivity data took longer to plateau after the concentration in the stream stabilized than the adjacent center wells. This may reflect either the larger zone influencing the resistivity measurement (decrease in conductivity at depth can change the inversion result at 30 cm), or a gradual diffusion of salt into lower porosity materials not sampled by the wells and consequent decrease in bulk resistivity. The right well in Line 3 recovered the most rapidly after the end of the injection at 120 min, the shallow center well was second, the deeper center well third, and the left well (furthest from the cable) was the last to build up tracer and the last to recover. The left well, which was furthest from the center line, also exhibited a more gradual conductivity rise. A gradual rise in tracer concentration heralded a gradual decrease after the injection. Both the resistivity data and the left well exhibited a longer tail than the right or center well, but unfortunately the question remains whether the elevated tail in the resistivity data (expressed as percent change in conductivity) is a consequence of lingering tracer, or an artifact of the aforementioned increasing stream water conductivity.

One factor complicating the comparison between geophysical data and well data is the difference in measurement support volumes. Each well sample collected by syringe was only 20 mL, drawing from a correspondingly small volume of sediments; conversely the geophysical measurements reflect a volume with dimensions at least as large as the electrode spacing (0.5 m). The smaller sample volume of the wells leads to variations in response if the sediments are heterogeneous; such heterogeneity was observed in the well breakthrough curves but would not be apparent from the single resistivity line. Another complicating factor is the differences in sampling created by dual or multiple permeabilities within a sampling volume. A well will preferentially draw from the larger pores, biasing the sample. Once these zones have flushed the apparent solute concentration will drop, even though solute that diffused into low-permeability zones may remain. (This is one reason pump-and-treat remediation of aquifers can take decades.) Conversely, resistivity soundings respond to the average salinity of the pore fluids without regard to permeability (Singha et al., 2008). Thus, the wells and the geophysical resistivity sample heterogeneity and dual permeability differently.

Conclusions

The data presented here represent only a small portion of an extensive data set, but they suffice to illustrate both the promise and the challenges of using time-lapse resistivity to monitor tracer tests in the hyporheic zone. Resistivity captures the breakthrough of the tracer, but averages over a larger volume than a well sample. Even with background subtraction of the geologic heterogeneity the sensitivity of the method may be affected by large features such as the J-hook at the center of our array. Resistivity has the potential to be used to monitor large segments of a stream with much less effort than an intensive campaign of well sampling, but the smoothing inherent in data inversion also makes it difficult to characterize the degree of small-scale heterogeneity. There also is no easy way to ascertain the precise time a particular measurement was made within the acquisition period for one complete sounding as

multiple measurements are incorporated in the data inversion for each grid cell. Software advances are needed to reduce the vertical smoothing of the tracer imaging. This could be accomplished by constraining the time-lapse resistivity to change only the model blocks located within the zone of interest,while still subtracting the effects of the full background resistivity. Time-lapse monitoring of hyporheic tracer appears promising, but the technique clearly needs to be developed further before it can be used reliably to calculate parameters for modeling hyporheic flow.

Acknowledgements

This work was supported by the National Science Foundation Hydrologic Sciences Program under Award No. 0609827. Thanks to the Rich Bauer of Trout Unlimited and a team of Temple University students for providing logistical support during the tracer test. Any use of trade, firm, or product names is for descriptive purposes only and does not imply endorsement by the U.S. Government.

References

Constable, S., Parker, R.L., and Constable C.G., 1987. Occam's inversion: a practical algorithm for generating smooth models from electromagnetic sounding data, Geophysics, 52, 298–300.

Crispell, J.K. and Endreny, T.A., 2009. Hyporheic exchange flow around constructed in-channel structures and implications for restoration design. Hydrol. Process. 23, 1158–1168.

Dahm C.N., Grimm N.B., Marmonier P., Valett M.H., Vervier P., 1998. Nutrient dynamics at the interface between surface waters and groundwaters. Freshw. Biol. 40, 427–451.

DeGroot-Hedlin, D., and Constable, S., 1990. Occam's inversion to generate smooth, two-dimensional models from magnetotelluric data, Geophysics, 55, 1613–1624.

Hancock, P.J., Boulton, A.J., and Humphreys, W.F., 2005. Aquifers and hyporheic zones: Towards an ecological understanding of groundwater. Hydrogeol. J. 13, 98–111.

Jones, B.J., Mulholland, P.J., editors, 2000. Streams and Groundwater. Academic, San Diego, California.

Kalbus, E., Reinstrof, F., and Schimer, M., 2006. Measuring methods for groundwater-surface water interactions: a review, Hydro. Earth Syst. Sci., 10, 873–887.

Singha, K., Pidlisecky, A., Day-Lewis, F.D., Gooseff, M.N., 2008, Electrical characterization of non-Fickian transport in groundwater and hyporheic systems, Water Resources Research, 44(3), 14pp.

Sophocleous, M.: Interactions between groundwater and surface water: the state of the science, Hydrogeol. J., 10, 52–67, 2002.

INVESTIGATING THE EFFECT OF BIOCLOGGING ON ELECTRICAL AND FLOW AND TRANSPORT PROPERTIES OF POROUS MEDIA.

Estella A. Atekwana[1], Gamal Z. Abdel Aal[2], and Eliot A. Atekwana[1]
[1]Boone Pickens School of Geology, Oklahoma State University, Stillwater, OK 74078, USA
[2]Geology Department, Faculty of Science, Assiut University, Assiut 71516, Egypt

Abstract

In many natural and engineered contaminant remediation systems, microbial growth and biomass accumulation can lead to pore clogging and cause significant changes in the flow and transport properties of the porous media (Seifert and Engesgaard, 2007; Brovelli et al., 2009). Bioclogging in porous media may result from accumulation of bacterial cells in the pore space, from biofilm development, or from excretion of extra-cellular polymers (Vandevivere and Baveye, 1992; Rinck-Pfeiffer, 2000). Recent advances in biogeophysical investigations have demonstrated the potential of geophysical techniques to elucidate microbial processes both in the laboratory and in the field (*Atekwana and Slater, 2009*). In the present study, flow through sand columns inoculated with *Pseudomonas aeruginosa* wild type (PAO1 Gfp), which is a model biofilm forming microorganism were used to investigate the effect of bioclogging on the complex conductivity and flow and transport properties. Our main objective is to determine how bioclogging manifests in the electrical properties of sands. Our secondary objective is to determine how complex conductivity relates to changes in hydraulic conductivity, which is a key parameter needed to model flow and transport in porous media. Our results suggest that bioclogging resulting from increases in microbial cell concentration and the production of exopolymeric substances (EPS) had a large impact on the imaginary conductivity, hydraulic conductivity, and porosity.

Methods

A schematic representation of the sand column and complex conductivity setup used in this study is shown in Figure 1. Four identical columns constructed of polyvinyl chloride (PVC) were used; two experimental (sand, growth media, and bacteria innocula) and two control (sand, growth media, and no bacteria innocula). Pressure transducers were implanted on the opposite side of the columns, and connected to a data logger to record variation in pressure resulting from flow variations. Growth media (25% Bushnell Hass broth + 30 mM Glucose) was pumped through each sand column to equilibrate the sand pack until the pH (7.01 ± 0.01) and fluid electrical conductivity (0.098 ± 0.003 s/m) of the inlet and outlet solutions were the same. A multichannel peristaltic pump was used to continuously feed the growth media through the control and experimental sand columns at a constant flow rate of 0.25 ml/min.

Complex conductivity measurements (0.1-1000 Hz) were obtained using a two channel dynamic signal analyzer (DSA) based around a National Instruments (NI) (Slater and Lesmes, 2002). The impedance magnitude $|\sigma|$ and the phase shift φ (between a measured voltage sinusoid and an impressed current sinusoid) of the sample were measured relative to a high-quality resistor. The real ($\sigma' = |\sigma| \cos \varphi$) and imaginary ($\sigma'' = |\sigma| \sin \varphi$) parts of the sample complex conductivity were then calculated. The real conductivity is an energy loss term that contains an electrolytic (σ_{el}) and interfacial (σ'_{surf}) component (e.g., Lesmes and Frye, 2001). The σ'_{surf} results from surface conduction via the formation of an electrical double layer (EDL) at the grain-fluid interface (Revil and Glover, 1998). The σ'' is an energy

storage or polarization term, which at low frequencies (<1000 Hz) results primarily from the polarization of ions in the EDL at the mineral-fluid interface (Lesmes and Frye, 2001).

Measurements of complex conductivity (0.1-1000 Hz), flow rate, and pressure head were made and fluid samples were taken from the column outlets every day for the first 14 days and every two to three days thereafter. The hydraulic conductivity values were calculated from the flow rate and hydraulic head measurements using the very well known Darcy law. Aliquots of fluid samples collected periodically from the column outlet were analyzed for optical density (OD_{600}) and converted into microbial cell counts (CFU/ml). The fluid electrical conductivity, pH, and temperature were determined immediately after sampling using microelectrodes. Afterward, the sand columns were dismantled and triplicate sediment samples were collected near the inlet, in the mid-section, and near the outlet. The sediments were fixed with 2.5% glutaraldehyde for later observation using an environmental scanning electron microscope. Images of the sand surface characteristics and attached microbial cells and biofilms were obtained using a FEI Quanta 600 FEG integrated with electron backscattering diffraction (EBSD) System.

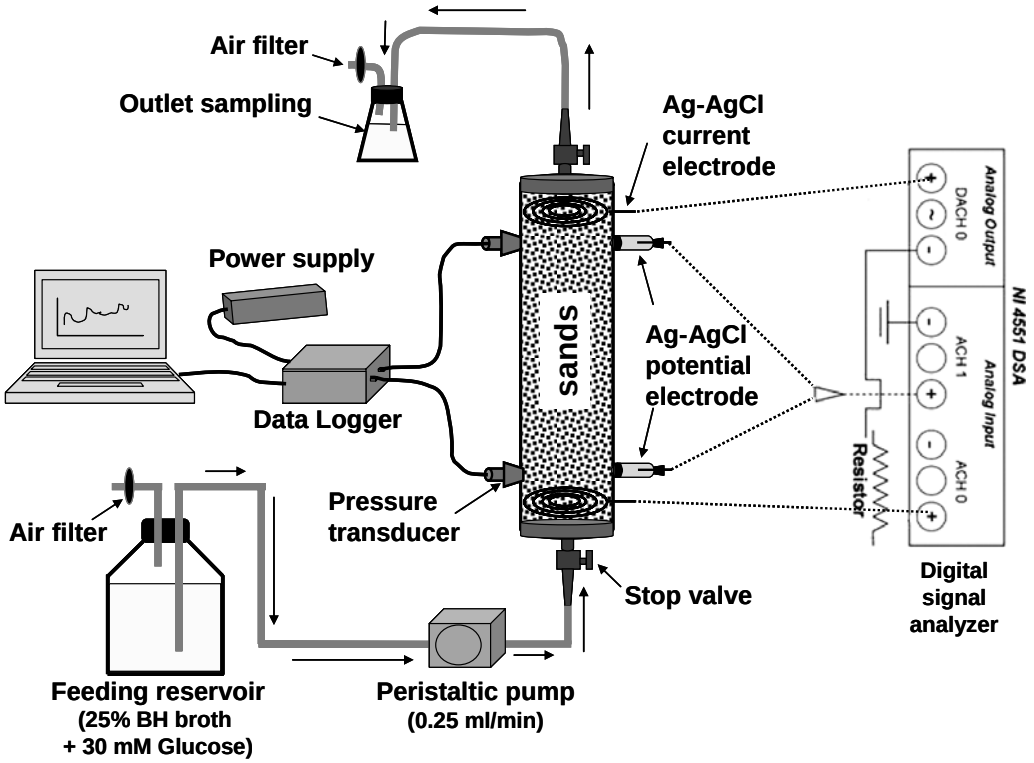

Figure 1. Schematic diagram showing the experimental setup. A digital signal analyzer (DSA) was used to collect the low frequency complex conductivity measurements. Pressure transducers along the side of the column were used to measure changes in hydraulic head.

Results and Discussion

The results except for the microbial cell count are evaluated as percent change from the measured initial values. Figure 2 shows the percent changes in complex conductivity measurements (real σ' and imaginary σ'' conductivities) at 1 Hz. The control columns showed no significant changes in σ'

and σ'' over the duration of the experiment (Figure 2a). However the σ'' of the experimental columns exhibited a sigmoidal shaped curve. Minimal changes (3.13×10^{-5} S/m) were observed in σ'' of the experimental columns for the first 8 days. After Day 8, σ'' increased slowly, reaching ~ 20 % by day 16. There after, σ'' increased rapidly, reaching a maximum of 127 % by day 24. After Day 24, σ'' remained steady to the end of the experiment (Figure 2b). The experimental columns show relatively minor changes in σ' between days 1 and 8. After Day 8, σ' gradually decreased to -37% by day 16. After Day 16, σ' increased to near background values by day 24, and thereafter, remained constant to the end of the experiment (Figure 2b).

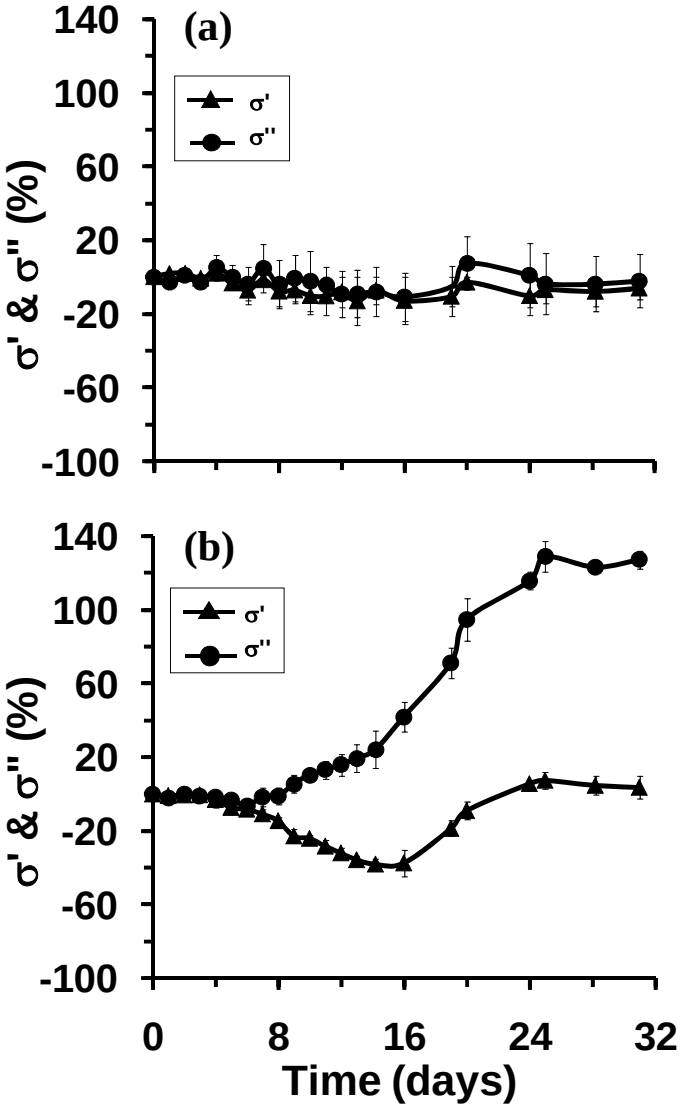

Figure 2. Temporal percent change in σ' and σ'' of (a) the control columns and (b) the experimental columns. Error bars represent measurement uncertainty reported as standard deviation of the average of duplicate measurements.

Figure 3 shows the temporal change in microbial cell counts. The control columns showed negligible changes in the microbial cell counts. However, similar to the σ'', the microbial cell counts in the experimental column exhibit a sigmoidal shaped curve. The curve was characterized by minimal changes in cell counts for the first 8 days (~ 0.77 x 10^9 CFU/ml). This was followed by a rapid increase in microbial cell counts (maximum growth rate) reaching ~ 2.99 x 10^9 CFU/ml by Day 16, after which the microbial cell counts increased more slowly to Day 24. After Day 24, the microbial cell counts remained nearly constant to the end of the experiment.

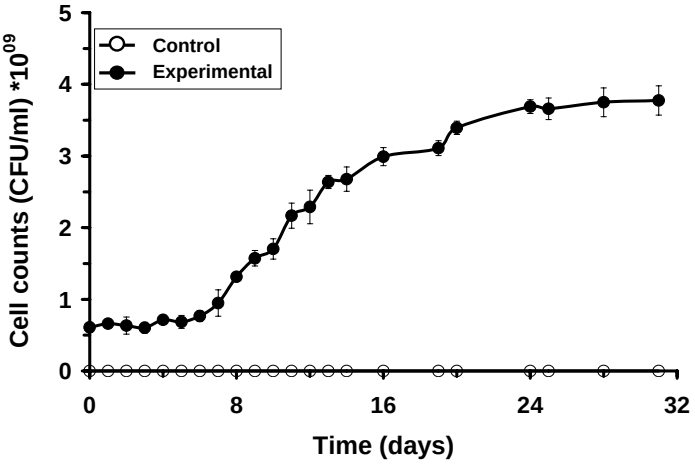

Figure 3. Temporal change in microbial cell of control (open symbols) and experimental (filled symbols) columns. Error bars represent measurement uncertainty reported as standard deviation of average of duplicate measurements.

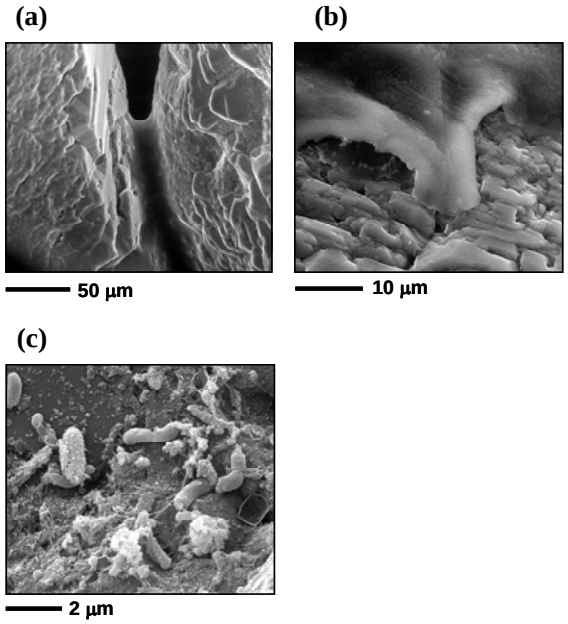

Figure 4. Environmental scanning electron microscope images of sand from experimental columns at the end of the experiment (a) Exopolymeric substance (EPS) connecting two sand grains together, (b) thick gelatinous layer of EPS, and (c) cluster of cells that have colonized a sand grain.

Figure 4 shows representative ESEM images of sands collected from the experimental columns. Figure 4a shows two sand grains connected by a gelatinous material believed to be an exopolymeric substance (EPS). The extracellular polymer produced by *P. aeruginosa* help the bacterial cells to adhere to the sand grains. Figure 4b shows a thick gelatinous material covering the surface of a sand grain. Figure 4c shows a sand grain colonized by cells of *P. aeruginosa*.

Temporal percent change in hydraulic conductivity (K) estimated from pressure head measurements and Darcy's Law is shown in Figure 5. No significant changes were observed in K for the control column. The experimental columns show minimal changes in K for the first 8 days. The K decreased rapidly to ~ 58% by day 16 and very slowly to Day 24, after which it remained nearly constant to the end of the experiment.

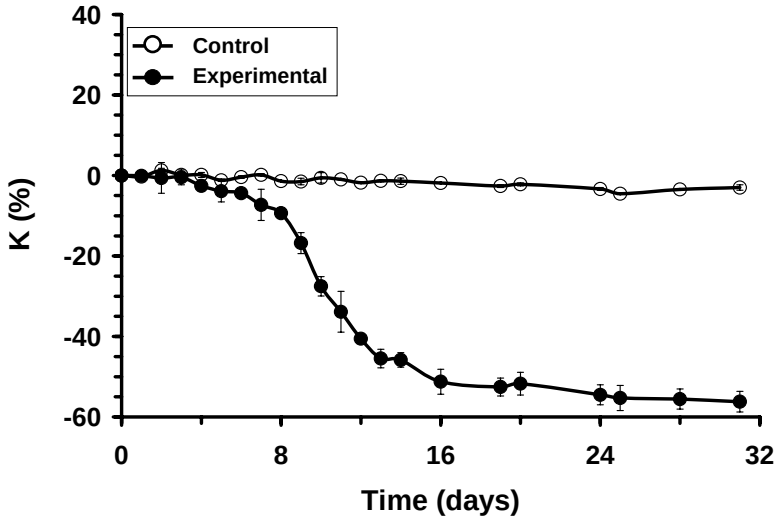

Figure 5. Temporal percent changes in hydraulic conductivity estimated from flow and Darcy's Law (K) of control (open symbols) and experimental (filled symbols) columns.

The results of this study show that in sand columns inoculated with *P. aeruginosa*, microbial growth and bioclogging also has a significant effect on the electrical properties. The temporal microbial cell counts and σ'' both follow a sigmoidal curve, suggesting that increase in σ'' is directly related to microbial growth and the associated changes in the petrophysical properties of the sands. The ESEM images show biomass on the sands and confirm that biofilms developed in the inoculated sand columns. Plugs of biomass and biofilm as demonstrated in the ESEM images will constrict pores and cause a reduction in the pore space, leading to the observed decreases in K (~58%). The observed increase in σ'' (~120%) represents a bulk signal recording the effects of microbial abundance, pore constriction, and biofilms, whereas, K only reflects the alteration of flow paths resulting from the biomass distribution in the pore structure (i.e., effective bioclogging).

Our results demonstrate that changes in electrical and transport properties developed in three stages: an initial stage (1) with no significant changes in all measured parameters (Days 1-8), which we attribute to the reversible and irreversible attachment of microbial cells to the sand. In stage 2a (Days 9-16), bioclogging caused by the rapid growth of biomass either as micro-colonies filling pore throats and/or as uniform covering on the sand surfaces resulted in maximum decrease in K, but with only moderate increases in σ''. In stage 2b (Days 17-24), significant production of EPS substances and

increase in biofilm thickness resulted in higher rate of increase in σ'' compared to stage 2a. In stage 3 (Days 25-32), biofilm growth reached a quasi-steady state and insignificant changes are observed in all measured parameters. The results of this study suggest that σ'' can be used in assessing bioclogging of porous media.

Conclusion

Complex conductivity measurements were employed to investigate the effects of microbial growth and bioclogging in laboratory sand columns inoculated with *P. aeruginosa* wild type (PAO1 Gfp). The growth of bacteria and the alteration of the flow and transport properties of sands due to bioclogging manifest in the σ'' component. Our results suggest that the changes in σ'' due to changes in the transport properties in the sands develop in three stages: an initial stage with insignificant changes in σ'', microbial cell counts, and transport properties; stage 2 with two different stages of biofilm development: stage 2a with maximum rate of bioclogging due to biomass growth in pores as microcolonies which result in rapid decrease in K but moderate increase in σ''; stage 2b with biofilm development and production of EPS that causes rapid increase in σ'' but modest decrease in the K; and stage 3 with biofilm fully developed in which the σ'' and K reach a steady-state condition. The results of this study suggest that σ'' can be potentially used to assess bioclogging of porous media.

Acknowledgments

This material is based in part on work supported by the National Science Foundation under Grant No. OCE-0729642 and the DOE- BER- Grant # DE-FG02-07ER64413 and Oklahoma State University EPScOR Program. The ESEM used for imaging was obtained through NSF-MRI grant # EAR 0722410. We thank C. Ownby for help with ESEM imaging. We thank Drs. S. Pamp and T. Tolker-Nielsen for providing the *Pseudomonas* strain and S. Rossbach for help with the culturing. R. Joyce and H. Ezzeldin provided laboratory assistance.

References

Atekwana, E., and D. Slater, 2009, Biogeophysics: A New Frontier in Earth Science Research, Rev. Geophys., in press.

Brovelli, A., F. Malaguerra, and D. A. Barry, 2009, Bioclogging in porous media: Model development and sensitivity to initial conditions, Environ. Modell. Softw., 24, 611-626.

Lesmes, D. P., and K. M. Frye, 2001, Influence of pore fluid chemistry on the complex conductivity and induced polarization responses of Berea sandstone, J. Geophys. Res., 106 (B3), 4079-4090.

Revil, A., and P. W. J. Glover, 1998, Nature of surface electrical conductivity in natural sands, sandstones, and clays, J. Geophys. Res., 103(B10), 23925-23936.

Rinck-Pfeiffer, S., 2000, Physical and Biochemical Clogging Processes arising from Aquifer Storage and Recovery (ASR) with Treated Wastewater. Ph.D.-thesis. School of Chemistry, Physics & Earth Sciences. Flinders University of South Australia.

Seifert, D. and P. Engesgaard, 2007, Use of tracer tests to investigate changes in flow and transport properties due to bioclogging of porous media, J. Contam. Hydrol., 93, 58–71.

Slater, L., and D. P. Lesmes, 2002, Electrical-hydraulic relationships observed for unconsolidated sediments, Water Resour. Res., 38, 1213, doi: .1029/2001WR001075.

Vandevivere, P., and P. Baveye, 1992, Effect of Bacterial Extracellular Polymers on the Saturated Hydraulic Conductivity of Sand Columns, Appl. Environ. Microbiol., 58, 1690–1698.

HOW USEFUL IS SPECTRAL INDUCED POLARIZATION?

André Revil Colorado School of Mines, Golden, CO

Abstract

Induced polarization represents the accumulation of charge carriers (electrons and ions) in a porous material and their back-diffusion in their concentration fields. This geophysical method can be carried out either in the time domain or in the frequency domain. In principle frequency domain induced polarization (SIP) may offer a powerful geophysical method to solve a number of hydrogeochemical problems including imaging permeability distribution and a reconnaissance tool for contaminant plumes. In practice, this method is limited by a number of issues including electromagnetic coupling above 100 Hz, the mutiplicity of polarization contributions that make the interpretation delicate, flat spectra that are poorly informative in systems characterized by a broad distribution of relaxation times, the long duration needed to take a snap-shot and so on. Therefore it is legitimate to wonder under what conditions spectral induced polarization is a powerful method, ... or not.

Relation to permeability

In a granular material, the phase shift between the current and the voltage can be related to the specific surface area of a porous material or to the grain size distribution. In addition, electrical conductivity is related to the electrical formation. Permeability is related to both the specific surface area and to the formation factor. Therefore a quest has been lauched the past three decades to connect induced polarization to permeability, the dream being to use SIP as a non-intrusive permeability imaing tool (e.g., Börner et al., 1996; Slater and Lesmes, 2002a, b; Scott and Barker, 2003; Hörd et al., 2007). However, even in a simple material like a sand, a complete theory relating permeability to SIP is still missing. One of the reason seems that SIP shows a very broad distribution of relaxation times that seems to be much broader than just associated with the grain size distribution (Vinegar and Waxman, 1984). Leroy et al. (2008) observed for instance that the roughness of the grains provides small additional heneterogenities. These heterogenities express themselves in the frequency domain by increasing he phase between the low frequency relaxation processes associated with the grains and the so-called Maxwell-Wagner polarization associated with the discontnuity in the current displacement at higher frequencies. Figure 1 shows that a reasonable estimate of permeability can be however obtained with sandstones. One main problem is that in the case of a broad grain size distribution, the permeability is strongly controlled by the smaller grains but the polarization of these small grains is occurring at relatively high frequencies (several kHz) and can be masked by Maxwell Wagner polarization or can be difficult to see in the field because of electromagnetic coupling at these frequencies.

Relationship between SIP and aqueous contaminants

The presence of contaminants in the aqueous phase can be unnoticed through DC resistivity measurements alone but these contaminants can have a very strong signature on the phase shift between the current and the voltage. If one wants to bridge the gap between SIP and numerical codes for reactive

transport modeling, one has to understand the role of chemical speciation on SIP. At low frequencies, SIP is mainly controlled by electrical double layer processes at the mineral water interface. It is clear that in a polyphasic porous material with a diversity of contaminants, SIP can only be used to provide some constraints on the presence of contaminants but cannot be used to invert all the chemistry. In this context, sensitivity analysis still needs to be carried out to see the SIP signature to a variety of contaminants and their mixtures.

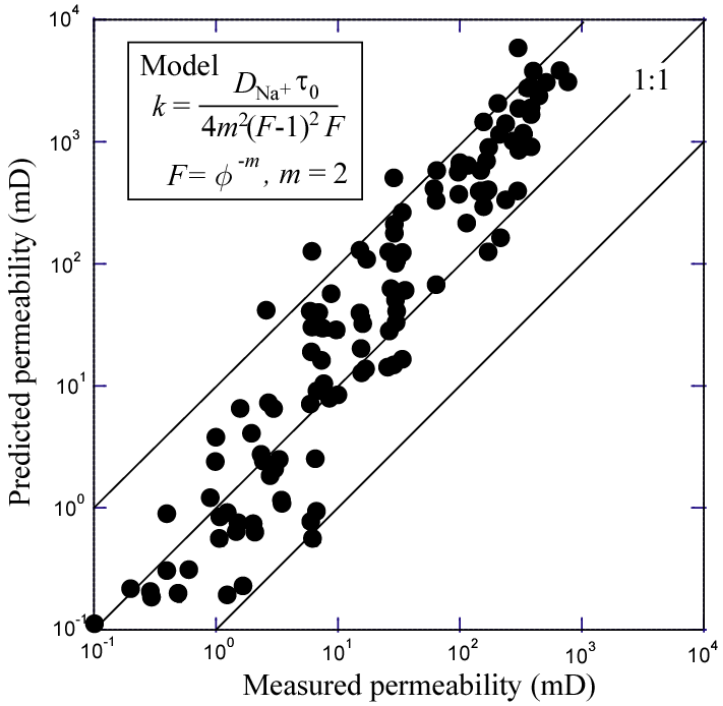

Figure 1: Comparison between a simplified model to connect permeability k and the main relaxation time τ_0 of SIP and the data from Tong et al. (2006, their Table 1), D_{Na+} represents the diffusion coefficient of sodium in the stern layer coating the mineral surface, m is thecementation exponent, and F is the formation factor. We see that the predictions are accurate inside one order of magnitude over four decades without the need for free-parameters. The two lines parallel to the 1:1 line correspond to a variation of plus or minus one order of magnitude with respect to the predicted trend.

Relationship between SIP and non-aqueous contaminants

The presence of non-aqueous contaminants has also a strong influence on SIP depending on their saturation and wettability. While this problem has been tacked by a number of researchers (Vinegar and Waxman, 1984; Olhoeft 1986; Vanhala et al. 1992; Börner et al. 1993; Vanhala, 1997; Cassiani et al., 2009), the effect of wettability has not been quantatively analyzed as far as we know. We carried out several experiments to see the influence of wetting and non-wetting oils on SIP. Figures 2 and 3 show that the responses, both in terms of the magnitude of the resistivity and the phase shift between the current and the voltage, to the saturation and oil wettability. These data show that the phase is very sensitive to the wettability of oil, a new result. We are presently analysis how complex resistivity tomography can be used to image non-aqueous contaminant plumes.

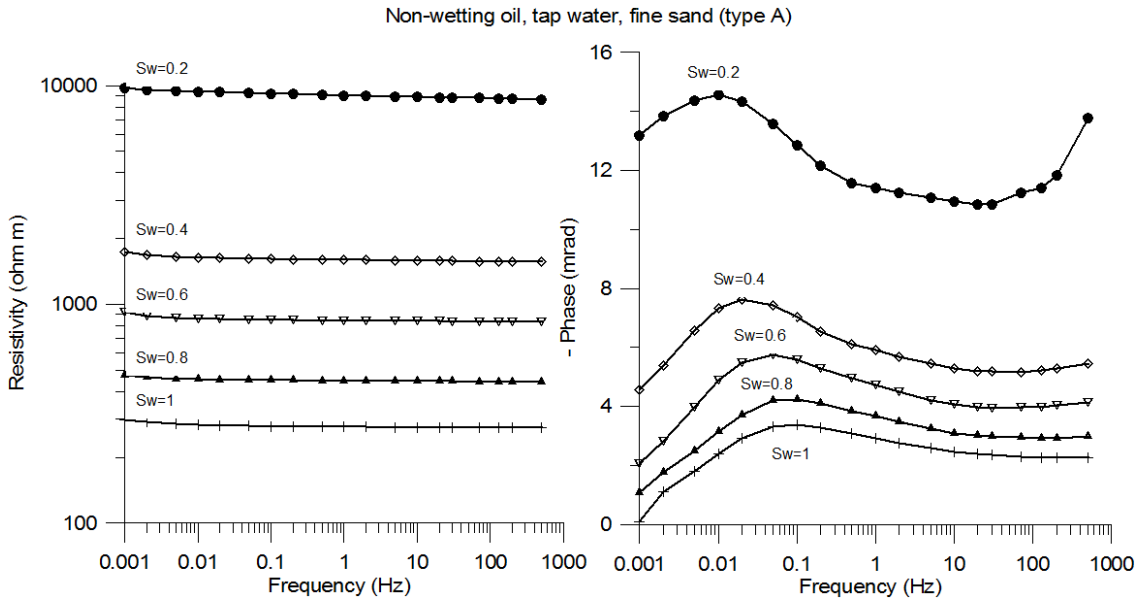

Figure 2: Modulus and phase of the complex resistivity for a non-wetting (NW) oil for different values of the water saturations in the range 1.0 to 0.2 (the case corresponding to the fully oil saturated sand could be measured). Sand: Type A (fine sand).

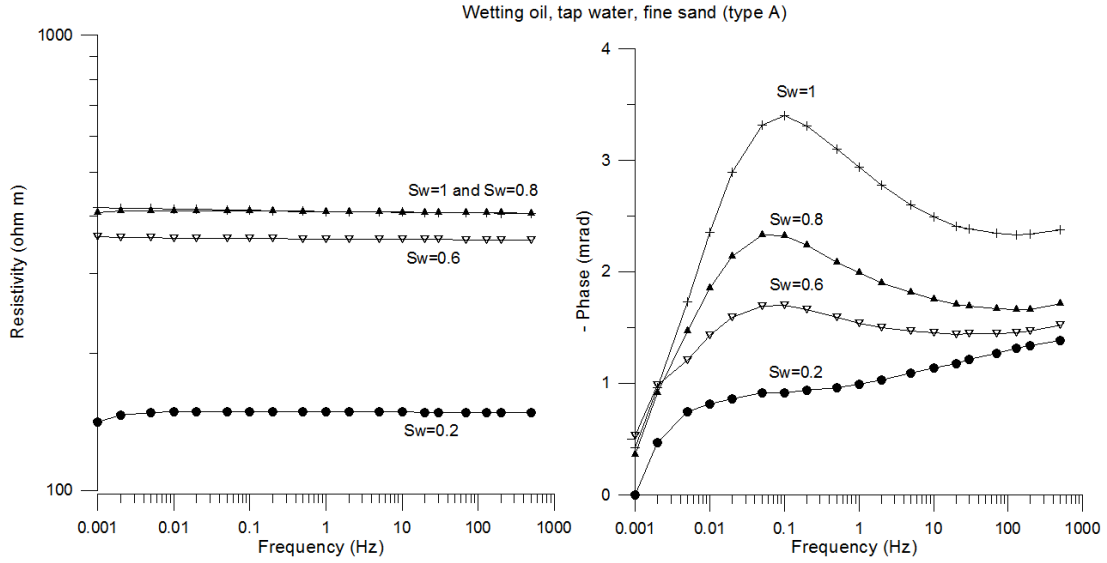

Figure 3: Modulus and phase of the complex resistivity for a wetting (W) oil for different values of the water saturations in the range 1.0 to 0.2 (the case corresponding to the fully oil saturated sand could be measured). Sand: Type A (fine sand).

Conclusions

Spectral induced polarization is a very exciting geophysical method and because it is performed with an additional dimension (given by the frequency domain), it is more powerful than DC resistivity in solving various hydrogeophysical problems. However, SIP should not be oversold. In addition to require

a complex physics, this method suffers from inherent drawbacks (EM coupling, long duration of the measurements requested to investigate low frequencies etc.). All these drawbacks can be however adressed. SIP systems with a high number of channels have already been developed to speed up data acquisition and EM coupling problems can be modeled using the information on the properties of the ground and the geometry of the recording system. A complete understanding of all the contributions of SIP is still a goal in itself. Once this goal will be reached, a sensitivity of this method to various envronmental conditions would be very useful to assess the limits of SIP to solve hydrogeophysical problems in conjonction with other geophysical methods, like self-potential and GPR, and in situ sources of data, in a Bayesian framework.

References

Binley, A., Slater, L.D., Fukes, M. & Cassiani, G. 2005. Relationship between spectral induced polarization and hydraulic properties of saturated and unsaturated sandstone: Water Resources Research, 41, W12417.

Börner, F., Gruhne M., and Schön J., 1993. Contamination indications derived from electrical properties in the low frequency range, Geophysical Prospecting, 41, 83-98.

Börner, F.D., Schopper, W. and Weller, A., 1996. Evaluation of transport and storage properties in the soils and groundwater zone from induced polarization measurements, Geophys. Prospect., 44, 583 - 601, doi:10.1111/j.1365-2478.1996.tb00167.x.

Cassiani, G, Kemna, A. Villa, A., et al., 2009, Spectral induced polarization for the characterization of free-phase hydrocarbon contamination of sediments, Near Surface Geophysics, 7, 5-6, 547-562.

Hördt, A., Blaschek, R., Kemna, A. & Zisser, N., 2007. Hydraulic conductivity estimation from induced polarisation data at the field scale-the Krauthausen case history, J. Appl. Geophys., 62, 33–46.

Leroy P., Revil A., Kemna A., Cosenza P., and Gorbani A., 2008. Spectral induced polarization of water-saturated packs of glass beads, Journal of Colloid and Interface Science, 321 (1), 103-117.

Olhoeft, G. R., 1986, Direct detection of hydrocarbon and organic chemicals with ground-penetrating radar and complex resistivity: Petroleum, hydrocarbons and organic chemicals in ground water-Prevention, Detection, and Restoration, NWWA/API, Proceedings, 284–305.

Scott, J. and Barker, R., 2003, Determining pore-throat size in Permo-Triassic sandstones from low-frequency electrical spectroscopy, Geophysical Research Letters, 30 (9), 1450.

Slater, L., and Lesmes, D., 2002a, IP interpretation in environmental investigations, Geophysics, 67(1), 77-88.

Slater, L., and Lesmes, D., 2002b. Electrical-hydraulic relationships observed for unconsolidated sediments, Water Resources Research, 38 (10), 1213.

Tong, M., Li, L., Wang, W. et Jiang, Y., 2006b. A time-domain induced-polarization method for estimating permeability in a shaly sand reservoir, Geophysical Prospecting, 54, 623–631.

Vanhala, H., Soininen H., and Kukkonen I., 1992. Detecting organic chemical contaminants by spectral-induced polarization method in glacial till environment, Geophysics, 57, 1014–1017.

Vanhala, H., 1997. Mapping oil-contaminated sand and till with the spectral induced polarization (SIP) method, Geophys. Prospect., 45, 303–326.

Vinegar, H.J., and Waxman M.H., 1984. Induced polarization of shaly sands, Geophysics, 49, 1267-1287.

Joint Modeling of EM Coupling and Spectral IP Data

Douglas LaBrecque
Daniel Casale
Paula Adkins
Multi-Phase Technologies, LLC
Sparks, Nevada

Abstract

Recent research into the induced polarization (IP) method and in particular the spectral induced polarization (SIP) method has shown that the method may well be able to provide detailed petrophysical data including estimates of grain-size distributions and/or distributions of hydraulic conductivity. However, this approach will likely require a broad range of spectral data. At high frequencies this will require an effective method to deal with electromagnetic coupling. The approach of this research is to jointly model SIP and electromagnetic data using a scalar-vector approach. This approach will allow accurate estimates of SIP data from .001 to 1000 Hz. This forward model will be used in an innovative inversion strategy that tries to find a model that has the smoothest spectra as well as the smoothest spatial extent.

Introduction

Recent research into the induced polarization (IP) method and in particular the spectral induced polarization (SIP) method has shown that the method may well be able to provide detailed petrophysical data including estimates of grain-size distributions and/or distributions of hydraulic conductivity (Slater and Lesmes, 2002a,b; Lesmes and Friedman, 2005; Binley et al., 2005; Scott and Barker, 2005; Tong et al., 2006; Slater, 2007). Even qualitative estimates of grain-size distributions or hydraulic conductivity will allow the delineation of aquifers and the determination of the integrity of aquitards.

Making these estimates for a range of sediments usually requires spectral measurements over a fairly broad frequency range. For medium to coarse sands, IP time constants are of the order of seconds or tens of seconds (Kemna et al., 2005). For clays, IP time constants are very short, typically fractions of milliseconds (see for example Slater et al, 2006). For this reason, laboratory studies of SIP commonly use frequencies from .001 Hz to 1 kHz or higher (see for example Klein and Sill, 1982; Slater and Lesmes, 2002a,b; Lesmes and Friedman, 2005; Slater et al, 2006). In the field, the lowest frequency collected is primarily dictated by economics as the lower the frequency the longer it takes to acquire data and thus the higher the cost.

At present, the primary constraint on the highest frequency used for spectral IP data is our ability to interpret spectral IP data in the presence of phase and amplitude shifts caused by electromagnetic (EM) coupling. EM coupling results from magnetic fields induced by the source current flowing both in the wires connecting the measurement system to the electrodes and the flow current within the earth itself (Pelton et al., 1978; Wait, 1982; Kemna et al., 1999). The magnitude of these fields is dependent on the conductivity structure of the earth and the physical layout of the measurement system. These magnetic fields induce phase and amplitude shifts in received data that generally increase with increased frequency, increased distance, and increased conductivity. For moderate survey scales (tens of meters) and high frequencies (tens or hundreds of Hertz) EM coupling effects overwhelm SIP measurements.

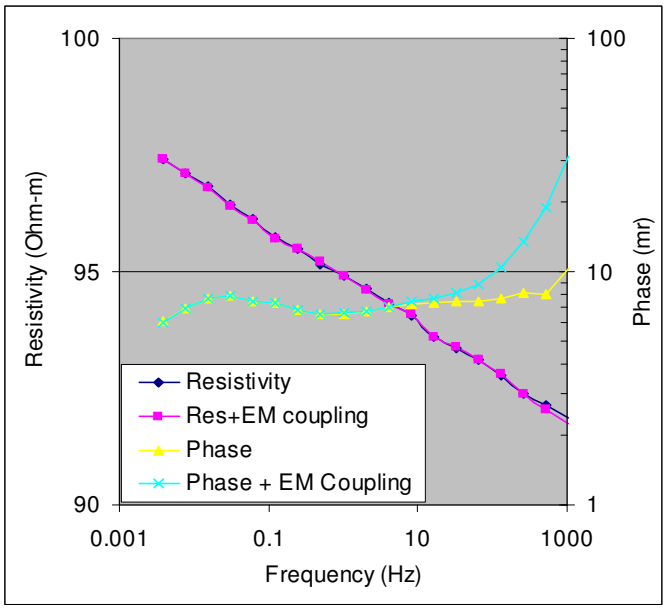

Figure 1. Comparison of Dipole-Dipole data with and without EM coupling for SIP response of a homogeneous half space.

An example of EM coupling effects on SIP measurements is shown in Figure 1 for a standard dipole-dipole array with 10 m dipoles, and receiver and transmitter dipole separation of 30 m (i.e. n= 3) . The earth below the system is a homogeneous half-space with resistivity and IP values equal to those given by laboratory results measured by Groenewold (1988). At frequencies over 10 Hz, EM coupling leads to substantially increased phase values.

Methodology

There are a number of ad-hoc schemes to subtract coupling effects from SIP data. For example, the scheme used by Pelton et al. (1978) fits a Cole-Cole model with a very short time constant to the highest frequency IP data. Built into this method is the assumption that phase response due to EM coupling increases roughly linearly with increasing frequency whereas the true SIP response decreases with increasing frequency. For sediments dominated by clay responses that tend to increase rapidly with frequency, the method is almost certain to fail and will overestimate EM coupling and underestimate the SIP response. Further, there is substantial information about the subsurface structure contained in the electromagnetic coupling data. Using the coupling data will improve the resolution of both the resistivity and IP structure. Our approach is to incorporate the modeling of electromagnetic coupling into the forward and inverse modeling routines.

Forward model

EM modeling by nature is numerically intensive, therefore we are developing a 2-D/3-D of the three-dimensional (3-D) solution routine described by LaBrecque (1999). In this method,

the electromagnetic response of a 3-D earth is represented by coupled vector and scalar potential equations given by:

$$\nabla^2 \mathbf{A} - \hat{z}\hat{y}\mathbf{A} = \mu_0 \hat{y} \nabla V - \mu_0 \mathbf{J} \tag{1}$$

and

$$\nabla \cdot \hat{y} \nabla V = I - i\omega \mathbf{A} \cdot \nabla \hat{y} \tag{2}$$

Where the variables $\hat{z}$ and $\hat{y}$ are given by:

$$\hat{z} = -i\omega\mu_0 \tag{3}$$

and

$$\hat{y} = \sigma + i\omega\varepsilon \tag{4}$$

and where

A is the divergence free magnetic vector potential,
V is the scalar electric potential,
μ_0 is the magnetic permeability of free-space,
$\mathbf{J}_e$ is the distribution of electric source currents (in other words the current in the wires connecting the transmitter to the electrodes),
I is the distribution of current sources in the ground (in other words the current entering or leaving the ground at the electrodes),
i is the square root of -1,
ω is radian frequency,
σ is the electrical conductivity, and
ε is the dielectric constant.

To model IP, we allow electrical conductivity to be a complex number and therefore we can write:

$$\hat{y} = \sigma' + i\sigma'' \tag{5}$$

where σ' and σ'' are the real and imaginary parts of conductivity respectively. We have left out the dielectric constant term $+ i\omega\varepsilon$ in Equation (5) as it can be considered as part of σ'' without any loss of generality. Therefore, in so-called "non-polarizable media", for example water, we would have $\sigma'' = i\omega\varepsilon$. Thus even pure water is not truly non-polarizable; the complex part is just very small at low frequencies.

This formulation (Equations (1) through (4)) provides a stable, accurate solution for calculating 3-D electromagnetic fields from finite electric sources such as the grounded dipoles used for resistivity and induced polarization measurements. If we set $\omega = 0$ then Equation (2) becomes the direct-current (DC) approximation routinely used for IP and resistivity. Equation

(1) represents the effects of electromagnetic coupling which are ignored in the DC approximations.

If we assume that the anomalous regions are 2-D in nature, we can reduce the 3-D problem to a series of 2-D problems by Fourier Transforming Equations (1) and (2) along the strike direction which we assume is the Y-Cartesian direction. The Fourier Transformed equations become:

$$\frac{\partial^2}{\partial x^2} A_x + \frac{\partial^2}{\partial z^2} A_x - k_y^2 A_x = \mu_0 \hat{y} \frac{\partial}{\partial x} V - \mu_0 J_x, \tag{6}$$

$$\frac{\partial^2}{\partial x^2} A_y + \frac{\partial^2}{\partial z^2} A_y - k_y^2 A_y = i\mu_0 \hat{y} k_y V - \mu_0 J_y, \tag{7}$$

$$\frac{\partial^2}{\partial x^2} A_z + \frac{\partial^2}{\partial z^2} A_z - k_y^2 A_z = \mu_0 \hat{y} \frac{\partial}{\partial z} V - \mu_0 J_z, \tag{8}$$

and

$$\frac{\partial}{\partial x} \hat{y} \frac{\partial}{\partial x} \mathrm{V} + \frac{\partial}{\partial z} \hat{y} \frac{\partial}{\partial z} \mathrm{V} - \hat{y} k_y^2 \mathrm{V} = \mathrm{I} - i\omega A_x \frac{\partial}{\partial x} \hat{y} - i\omega A_z \frac{\partial}{\partial z} \hat{y}, \tag{9}$$

where

A_x, A_y, and A_z are the individual components of magnetic vector potential in Fourier Transform domain,

V and I are the scalar potential and current divergence terms, also in the Fourier Transform domain, and

k_y is the Fourier Transform variable in the Y direction (also referred to as the wavenumber).

Note that Equation (9), the scalar potential equation, does not have any terms related to A_y. For the present algorithm we assume that the receiver wires are run perpendicular to Y, and therefore can neglect A_y. The resulting 2-D systems of equations are solved for the three unknown potentials using the finite-element (FE) method.

Inversion Algorithm

A stable, efficient inversion algorithm is a critical part of the integrated acquisition and interpretation system. Many IP inversion algorithms invert at each frequency or time window one at a time. Generally this is done as a two-step process; first, the resistivity data are inverted and second, the phase or chargeability data are inverted using a local, linear approximation found by taking the first order terms of a Taylor's series about the final resistivity solutions (see LaBrecque, 1991; Ramirez et al., 1999). Since the IP response is usually (though not always) much smaller than the resistivity response, we should be able to accurately approximate the IP response using this linear approximation assuming that we have the correct resistivity model.

Unfortunately, when the subsurface contains large contrasts in resistivity, the resistivity model tends to be smoothed substantially and the linear approximation is rather poor. In fact, we have noticed that for a small, highly conductive, strongly polarizable body, the inverted IP response tends to appear on the edges of the body rather than the center (not shown). Inverting resistivity and IP data simultaneously should reduce this problem. Several existing codes accomplish this by inverting on resistivity and phase as a single complex variable (Ramirez et al., 1999; Kemna et al., 2000; LaBrecque and Yang, 2001).

For SIP data, a number of researchers have taken this approach one step further and jointly invert several frequencies to directly determine for parameters for a Cole-Cole model. The Cole-Cole model (Pelton et al., 1978) is given by:

$$H(\omega) = \rho_0 \left[1 - m \left(1 - \frac{1}{1 + (i\omega\tau)^c} \right) \right], \tag{10}$$

where

$H(\omega)$ is the approximate spectral response of the sample,
ω is the radian frequency of the sinusoid,
ρ_0 is the steady-state resistivity of the sample,
m is called the intrinsic chargeability,
τ is the time constant, and
c is the Cole-Cole exponent.

Thus the spectral response can be characterized by the four parameters: ρ_0, m, τ, and c. The Cole-Cole model has been used extensively to model the IP responses of laboratory samples. It is generally accepted that the chargeability, m, is strongly correlated to the volume fraction of polarizable minerals, and the time constant, τ, to the grain size of conductive mineral grains (Pelton et al., 1978) or the pore size of sedimentary rocks (Klein and Sill, 1982; Lesmes and Friedman, 2005; Slater, 2007).

Although direct inversion for Cole-Cole parameters makes very efficient use of IP data, we chose an alternative approach for a number of reasons. First, in many cases, the spectral responses of clay bearing rocks do not closely follow a single simple Cole-Cole response curve. Figure 2 shows a representative SIP response of fine-to-medium grained sandstone (Groenewold, 1988) which was used for the model shown in Figure 1. We have fit the low-frequency data to a single Cole-Cole response. It is not possible to accurately fit this curve using a single Cole-Cole response. In fact, many of the published studies (see for example, Klein and Sill, 1982; Vanhala et al., 1992; Aal et al., 2006) show somewhat similar, non Cole-Cole behavior. It is possible to apply multiple Cole-Cole models. This particular curve would likely require three Cole-Cole models. Second, the parameters of the Cole-Cole equation are highly nonlinear and thus it is fairly important to have a good starting model to fit the data. This is of concern for the general 2-D case where the subsurface may have several thousand elements where each element is allowed to have different Cole-Cole parameters. Finally, because the Cole-Cole parameters represent different physical quantities with different units of measure, there is an issue with the proper scaling of regularization factors.

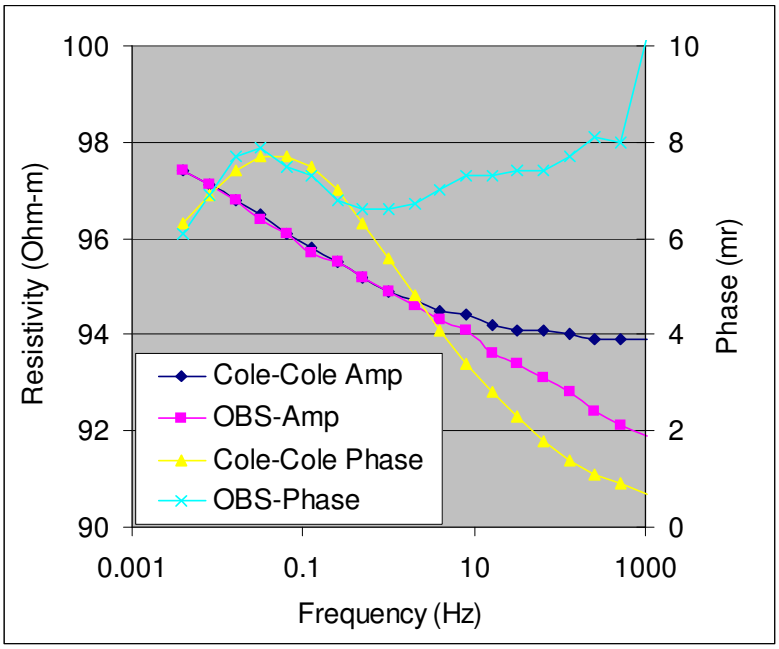

Figure 2. Comparison of Cole-Cole model fit to low frequency IP data to complete spectrum measured by Groenewold, 1988.

We and other researchers have had a great deal of success with Occam's-like inversion methods and they are the obvious candidate here. So how do we apply our regularization such that both chargeability, which is dimensionless, varies between 0 and 1, and time constant, which is in units of seconds and varies from milliseconds to tens of seconds, are both appropriately controlled by the regularization function? Finally, we do not want to tie ourselves to a single model. Our goal is a spectrally estimated method that can be adapted to a number of uses and a number of petrophysical models. Therefore, we have chosen a more straightforward approach which is to invert for a separate value of complex conductivity for each of the frequencies included in the original data set. The solutions will be regularized in the frequency dimension using essentially the same operator as in the spatial dimensions.

The objective minimized using Occam's inversion is given by

$$\mathbf{S}(\mathbf{m}) = (\mathbf{d}_{obs} - g(\mathbf{m}))^{*}\mathbf{W}_{D}(\mathbf{d}_{obs} - g(\mathbf{m})) + \alpha\,\mathbf{m}^{*}\mathbf{R}\mathbf{m}\,, \qquad (11)$$

where **d** is the vector of data values,
m is the vector of parameters,
g(m) is the complex forward solution found by solving Equations (6), (7) and (9) using the FEM,
$\mathbf{W}_D$ is the diagonal data weight matrix,
R is the regularization operator which is discussed in detail below,
$\mathbf{d}_{obs}$ is the vector of observed data,
the superscript * indicates the Hermitian of a given matrix, and
α is an empirical factor that controls the amount of regularization versus the fit of the forward model to the data.

Minimizing the objective function for large values of α results in a smooth solution but a poor data fit. The optimal solution corresponds to the largest possible value of α which still fits the data to some a-priori value. In the new algorithm, the parameters, **m**, are the complex conductivity of an element of the finite-element method (FEM) mesh at each of a series of frequencies.

The nonlinear iterations can be expressed as $\mathbf{m}_{n+1} = \mathbf{m}_n + \Delta\mathbf{m}_n$. The parameter change vector at n^{th} iteration, $\Delta\mathbf{m}_n$, is obtained by solving the linear system

$$\left(\mathbf{G}_n^* \mathbf{W}_D \mathbf{G}_n + \alpha \mathbf{R}\right) \Delta\mathbf{m}_n = \mathbf{G}_n^* \mathbf{W}_D \left(\mathbf{d}_{obs} - g(\mathbf{m}_n)\right) - \alpha \mathbf{R}\mathbf{m}_n , \qquad (12)$$

where the elements of the sensitivity matrix, **G**, are given by:

$$\mathrm{G}_{\mathrm{n}}^{\mathrm{ij}} = \left.\frac{\partial \mathbf{g}^{\mathrm{i}}(\mathbf{m})}{\partial \mathrm{m}^{\mathrm{j}}}\right|_{m_n} . \qquad (13)$$

The system of equations given by Equation (12) is solved using the conjugate-gradient method with a diagonal preconditioner (LaBrecque et al., 1999). A data-error reweighting scheme is implemented to suppress the effects of data outliers (Morelli and LaBrecque, 1996).

Conclusions/Discussion

In order to use spectral induced polarization data to estimate grain-size distributions and related hydrological properties, it will likely require measurements at broad range of frequencies. In particular, measurement of high frequency IP data will require us to deal with electromagnetic coupling. Although ad-hoc schemes have been applied to EM coupling in the past, with the advent of modern computers, we can jointly model IP and EM coupling. This approach may well improve the resolution of resistivity models as well as more accurately determine phase responses.

References

Aal, Gamal, Z. Abdel, Lee D. Slater, and Estella A. Atekwana, 2006, Induced-polarization measurements on unconsolidated sediments from a site of active hydrocarbon biodegradation: Geophysics, **71**, H13–H24.

Binley, A, L. Slater, M. Fukes, and G. Cassiani, 2005, The relationship between frequency dependent electrical conductivity and hydraulic properties of saturated and unsaturated sandstone: Water Resources Research, **41**, W12417.

Groenewold, J. C., 1988, Electrical properties of clay-bearing sandstones: Master of Science Thesis, University of Utah, 86 p.

Kemna A, H.M. Munch, K. Titov, E Zimmermann, H. Vereecken, 2005, Relation of SIP relaxation time of sands to salinity, grain size and hydraulic conductivity. Extended Abstracts: Near Surface 2005 - 11th European Meeting of Environmental and Engineering Geophysics P054:4.

Kemna, A., A. Binley, A. Ramirez and W. Daily, 2000, Complex resistivity tomography for environmental applications: Chemical Engineering Journal, **77**, 11-18.

Kemna, Andreas, Eiko Räkers and Lothar Dresen, 1999, Field Applications of complex resistivity tomography: Society of Exploration Geophysicists Technical Program Expanded Abstracts, 331-334.

Klein, J. D. and W.R. Sill, 1982, Electrical properties of artificial clay-bearing sandstones: Geophysics **47**, 1593– 1605.

LaBrecque, D. J. and X. Yang, 2001, Difference inversion of ERT data: A fast inversion method for 3-D in situ monitoring: Journal of Environmental and Engineering Geophysics, **6**, 83-90.

LaBrecque, D., G. Morelli, W. Daily, A. Ramirez, and P. Lundegard, 1999, Occam's inversion of 3D electrical resistance tomography: in Orstaglio, M., and Spies, B., Three Dimensional Electromagnetics, Society of Exploration Geophysicists, Tulsa, Oklahoma, 146-160.

LaBrecque, D. J., 1999, A scalar-vector potential solution for 3D EM finite-difference modeling: in: Spies, B., (Ed.), Three-Dimensional Electromagnetics, Society of Exploration Geophysicists, Tulsa, 146-160.

LaBrecque, D. J., 1991, IP tomography: Society of Exploration Geophysicists Technical Program Expanded Abstracts, 413-416.

Lesmes, D. P. and S. P. Friedman, 2005, Relationships between the electrical and hydrogeological properties of rocks and soils: In Rubin, Y. and S. S. Hubbard, eds, HydroGeophysics, Chapter 4. Springer, Dordrecht, The Netherlands, 87–128.

Morelli, G., and D. J. LaBrecque, 1996, Robust scheme for ERT inverse modeling: European Journal of Environmental and Engineering Geophysics, **2**, 1-14.

Pelton, W. H., S. H. Ward, P. G. Hallof, W. R. Sill, and P. H. Nelson, 1978, Mineral discrimination and removal of inductive coupling with multifrequency IP: Geophysics, **43**, 588–609.

Ramirez, A., W. Daily, A. Binley and D. LaBrecque, 1999, Electrical impedance tomography of known targets: Journal of Environmental and Engineering Geophysics, **4**, 11-26.

Scott, J. B. T. and R. D. Barker, 2005, Characterization of sandstone by electrical spectroscopy for stratigraphical and hydrogeological investigations: Quarterly Journal of Engineering Geology and Hydrogeology, **38**; 143-154.

Slater, L., 2007, Near surface electrical characterization of hydraulic conductivity: from petrophysical properties to aquifer geometries—a review: Surveys of Geophysics, **28**, 169–197.

Slater, L., D. Ntarlagiannis, and D.B. Wishart, 2006, On the relationship between induced polarization and surface area in metal-sand and clay-sand mixtures: Geophysics 71, A1.

Slater, L. and D. P. Lesmes, 2002a, Electrical-hydraulic relationships observed for unconsolidated sediments: Water Resources Research, **38**, 1213.

Slater, L., and D. P. Lesmes, 2002b, IP interpretation in environmental investigations: Geophysics, **67**, 77–88.

Tong, Maosong, Li Li, Weinan Wang, and Yizhong Jiang, 2006, Determining capillary-pressure curve, pore-size distribution and permeability from induced polarization of shaley sand: Geophysics, **71**, N33-N40.

Vanhala, Heikki, Heikki Soininen, and Limo Kukkonen, 1992, Detecting organic chemical contaminants by spectral-induced polarization method in glacial till environment: Geophysics, **57**, 1014-1017.

Wait, J. R., 1982, Geo-electromagnetism: Academic Press, 268 p.

ELECTRICAL IMPEDANCE TOMOGRAPHY FOR GEOPHYSICAL APPLICATIONS

Nick Polydorides[*], *MIT, Cambridge, MA.*

Andrea Borsic, Dartmouth, Hanover, NH.

Abstract

We report on the development of a new software package for image reconstruction in three-dimensional Electrical Impedance Tomography (EIT). Designed for large-scale computations, the software includes mesh generation utilities, a simulator of the quasi-static electrical potential fields based on finite elements and regularized inversion algorithms. We describe in brief some of its main functions and characteristics to demonstrate its utility and efficiency in handling high dimensional geophysical models.

Introduction

We present a software framework for the electrical impedance tomography problem in three axial dimensions. In this overview we consider the forward problem for the underlying electromagnetic model, the sensitivity of the measurements to the electrical properties of the medium of interest, the computation of the nonlinear solution using regularization methods and the visualization of the results. The motivation for developing this software is to exploit the recent advances in inverse problem theory and state of the art models for surface and borehole electrodes while implementing computationally efficient algorithms aimed to reduce the complexity introduced by the dimensionality of the resulting models. Incorporating meshing and visualization utilities this Matlab [4] based software is suitable for processing data from any EIT or resistivity survey acquisition instrument on a personal computer. The software relates to the releases of RES3DINV [3], R3 by Binley et al. [1], and EIDORS 3D by Polydorides et al. [6], but it differs in various ways as it is designed to handle models with realistic large-scale complexity.

Forward Modeling and Simulation

We consider the complete electrode model for 3D electrical impedance tomography, although simpler electrode models are also implemented, see for example the review [5]. The model was introduced and analyzed by Somersalo et al. [8] and subsequently implemented via numerical approximation by Vauhkonen et al. [11], Borsic [2] and Polydorides et al. [6]. Assume a domain Ω with boundary $\partial\Omega$, and electrical admittivity $\gamma = \sigma + \imath\omega\varepsilon$, where σ is the electrical conductivity, ε the dielectric permittivity, ω the angular frequency of the applied excitation and $\imath = \sqrt{-1}$. Electrically isotropic or anisotropic domains can be considered, in the later case the electrical properties admit tensor definitions (with respect to the Cartesian frame), but here we address the simple isotropic case with $|\gamma| > 0$. When a number L of borehole and surface electrodes are attached at $\partial\Omega_E \subset \partial\Omega$ and excited in a pair drive mode, the resulting electric potential field u satisfies

$$\nabla \cdot \gamma \nabla u = 0 \quad \text{in } \Omega \tag{1}$$

For the two excited electrodes, the impressed currents of magnitude I_l satisfy the Neumann conditions

$$\int ds \; \gamma \nabla u \cdot \hat{\mathrm{n}} = I_l \tag{2}$$

[*] Now at the Energy Environment and Water Research Center, The Cyprus Institute, Cyprus.

where the integral is taken on the surface of the electrode and $\hat{n}$ the outward init normal there. For the remaining electrodes we impose

$$\gamma \nabla u \cdot \hat{n} = 0 \quad (3)$$

The voltage measurement recorded by the k'th electrode with contact impedance z_k is given by

$$V_k = u + z_k \gamma \nabla u \cdot \hat{n} \quad (4)$$

At the model termination boundaries $t_1, t_2, \ldots$ we assume absorbing boundary conditions

$$u + z_{t_i} \gamma \nabla u \cdot \hat{n} = 0 \quad (5)$$

Enforcing the required charge conservation principle $\sum_{k=1}^{L} I_k = 0$, the model admits a unique solution when a choice of ground is made, i.e. for a point $g \in \Omega$, we enforce $u(g) = 0$. The finite element approximation of this model relies on discretizing the domain of interest in linear tetrahedral elements. Compatible with various mesh generators, this package includes its own high level meshing utilities aimed to ease the manipulation of the boundary for electrode assignment and borehole allocation. Moreover, the mesh's outer surfaces and electrode-domain interfaces are automatically labeled for efficient application of boundary and mesh termination conditions. For a given tessellation the domain's electrical properties, are defined using constant or linear basis functions having local support on elements.

In the adopted finite element method the forward model is approximated by a system of linear equations involving a sparse, symmetric and positive definite (SSPD) coefficients matrix. Under some mild continuity assumptions on the electrical properties, the matrix is well-conditioned, however its dimension scales to that of the nodes (vertices) in the finite element model. As such, the computation of the forward solution may become computationally expensive or even prohibitive for moderate architectures and algorithms relying on inverting the coefficients matrix. To overcome this limitation, the software incorporates an iterative solver customized for multithread processing of SSPD systems called Pardiso [7]. To provide an indication of the computational benefits we present in table 1 some timing information from a benchmark test on a model with about 98000 nodes and 540000 elements. The results are based on an 8-core, shared memory PC architecture based on two quad core Xeon 5355 CPUs, with an internal clock of 2.66 GHz and a front side bus speed of 1.33 GHz, operating Ubuntu Linux 7.05 64-bit, running Matlab 2009a 64-bit.

Solver/Problem	**1 thread**	**2 threads**	**4 threads**	**8 threads**
Matlab default /Real	138.74	102.24	85.43	83.74
Pardiso / Real	18.46	11.19	7.66	6.91
Matlab default /Complex	418.84	277.22	207.75	190.18
Pardiso / Complex	58.60	34.21	21.05	19.56

Table 1. CPU times in seconds for 30 forward solutions corresponding to different current patterns. Note the substantial improvement in speed provided by the Pardiso solver.

Moreover, to treat the situations where the forward problem has to be solved for a large number of current patterns, i.e. greater than L; the number of the system's electrodes, we propose the use of canonical patterns introduced by Borsic in [2], and this bounds the number of right hand side vectors to a maximum of L. In the conventional four electrode data acquisition protocol which implements pair drive current patterns, one typically considers right hand side vectors for the fem problem that have zero entries apart from the two excited electrodes which are typically assigned values $+I_l$ and

$-I_l$. In order the reduce the number of forward problems that need be solved, we remark that all possible forward solutions can be synthesized by linear operations from a total of L solutions that correspond to the canonic patterns defined by the vectors $\{1-1/L\,,-1/L,\cdots,-1/L\}\in\Re^L$, $\{-1/L\,,1-1/L,\cdots,-1/L\}\in\Re^L$ and so on**.** To exploit further the recent advances in multithread computing, a future release of this software will facilitate GPU processing, thereby maximizing the utilization of the available resources on a single machine.

As it is well known, forward solutions are also needed in the computation of the sensitivity of the system, a linear operator mapping perturbations in the electrical properties in the interior of the domain to the boundary; surface of borehole, potential measurements. Details on the derivation and computation of this *m* by *n* matrix, where *m* the number of boundary data and *n* the dimension of the electrical parameter space can be found in [6]. As it well known the computation of the linearized sensitivity map (matrix) requires the forward solutions for all direct and adjoint current patterns. In three-dimensional models, *n* can be very large; whereas *m* may be smaller by comparison, and this may introduce limitations in regards to the storage and thereafter processing of this matrix in the inverse solver. To alleviate this difficulty, we propose an automatic change of basis for the electrical properties, where the new basis, used exclusively for the inverse fitting problem, has a lower dimension. This change is achieved by projecting the elements of the sensitivity into regions of interest according to their topology in the mesh. This yields a projected sensitivity matrix of manageable dimensions, which we subsequently use to formulate the (linearized) inverse problem.

Inverse Problem

The nonlinear inverse problem is addressed in the context of Newton-Raphson iterative algorithm with Tikhonov type regularization. Beginning with an initial feasible estimate on the solution, our software implements a "linearization – regularization" strategy where the sensitivity matrix is dynamically updated and the next solution estimate is obtained using a linear least squares fitting and some a priori information that is available on the solution. The generalized form of the inverse problem considered is given by

$$\gamma^* = \text{argmin}\left\{\|F(\gamma)-d\|^2_{\Sigma_\epsilon^{-1}} + \|D(\gamma-\gamma_0)\|^2_{\Sigma_\gamma^{-1}}\right\} \tag{6}$$

where $F(\gamma)$ the data corresponding to a forward model with admittivity γ, d is the measurements, D is the regularization matrix that represents the prior information assumptions, γ_0 is a initial guess on the solution and $\Sigma_\epsilon\,,\Sigma_\gamma$ are the noise and prior information uncertainty covariance matrices respectively. To ensure convergence, a line search algorithm is used to optimize the size of the regularized step solution. Alternative regularization options include smoothness or sparsity imposing priors, where the norms in the minimization become ℓ_2 or ℓ_1 and total variation respectively. The nonlinear regression problem (6) is solved iteratively, after linearizing the argument at feasible estimates γ_i, where F is approximated by its first-order Taylor expansion at these points. Effectively this requires the computation of the Jacobian matrix $J=\nabla_\gamma F$ whose elements indicate how the measurements will change for small perturbations in the admittivity of the elements. In a high-dimensional model the computation of this matrix becomes cumbersome in terms of storage and speed. Moreover, forming and inverting the normal equations coefficient matrix $J'J$, (prime denotes transposition), required in solving the linearized problem becomes prohibitive even in cases with heavily underdetermined models. To cope with this bottleneck, the code implements an element grouping-weighting strategy that yields a projection operator $\mathcal{P}$ that maps the elements of the fine grid to a new coarser mesh of manageable dimension. Effectively, the data term $J\delta\gamma$ encountered in the calculations (of dimension *m*) is approximated by $J\delta\gamma\approx J\mathcal{P}\widetilde{\delta\gamma}=\tilde{J}\widetilde{\delta\gamma}$, where the tilded quantities are defined on the coarse grid.

Visualization of Results

Reconstructed images of the conductivity and or permittivity of the domain are exported along with the inverse problem mesh in vtk format. This allows their three-dimensional manipulation for diagnosis and visualization in a timely and memory efficient manner. The exported files are readily available to be imported in various visualization packages such as Paraview [9] and Mayavi [10], which allow the application of various graphical filters such as extraction of planar solutions, isosurfaces, gradients, etc. Apart from the electrical parameter the software is suitable for visualizing the induced electrical potential and current density fields.

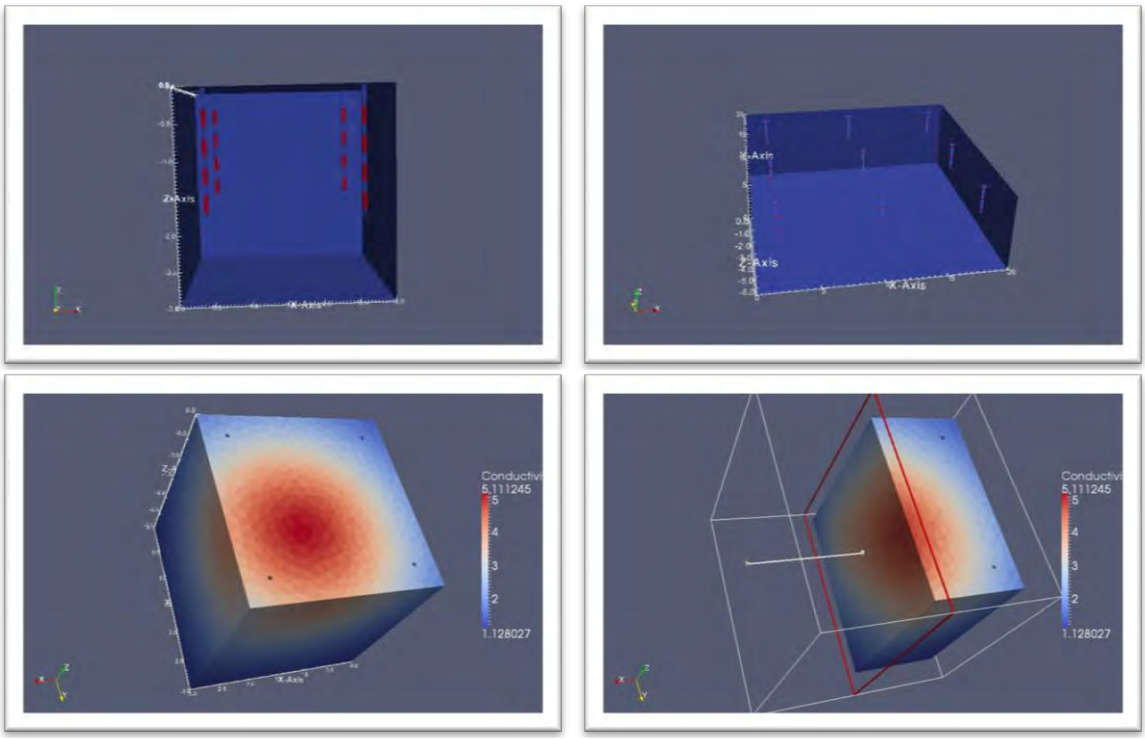

Figure 1: Visualization of borehole electrode arrangements and admittivity models with Paraview.

Conclusions

In this paper we have presented the main features of a new software for three-dimensional Electrical Impedance Tomography. We have outlined its main utility functions in solving the forward problem, and gave indicative figures of its computational performance in handling high-dimensional models. The code implements a nonlinear inverse solver based on a Newton-Raphson algorithm with a Tikhonov regularization formulating at the linearized step solutions. Some simulated results from borehole electrical resistivity tomography are also presented.

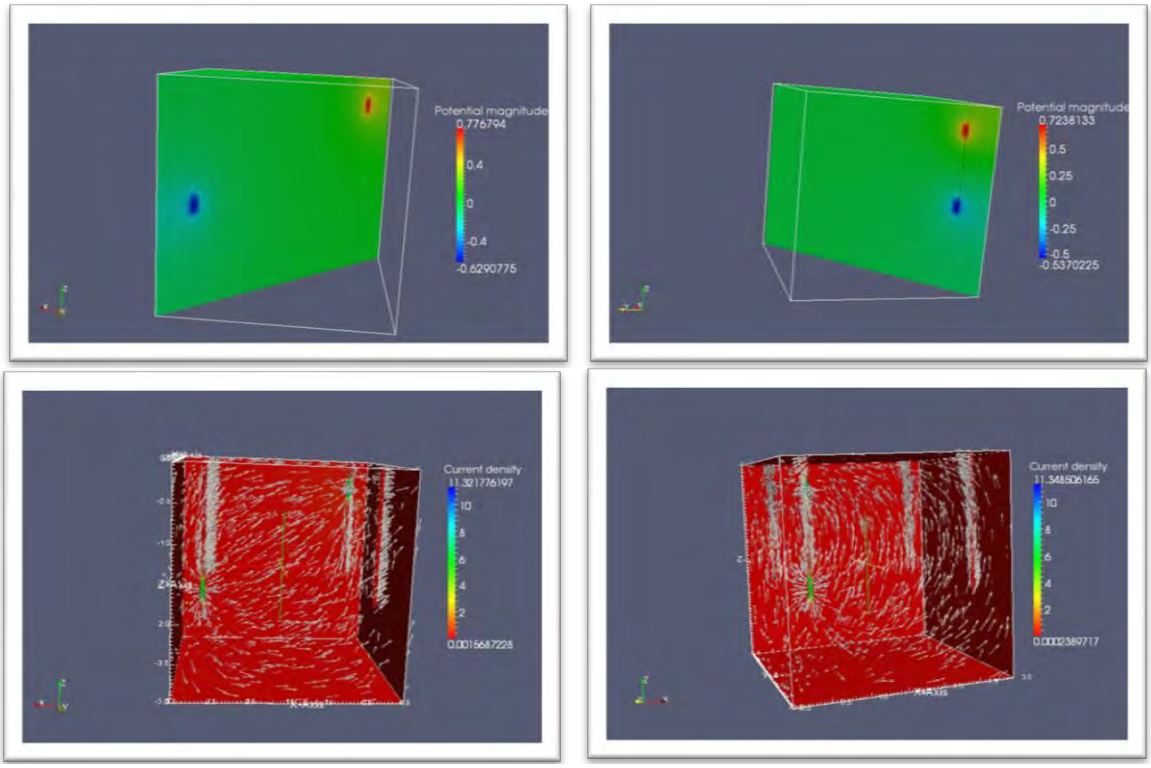

Figure 2: Visualization of borehole electrical potential and current density fields with Paraview.

References

[1] Binley, A. and Kemna, A., 2005, Electrical Methods, In: Hydrogeophysics by Rubin and Hubbard (Eds.), 129-156, Springer.

[2] Borsic, A. Regularization methods for imaging from electrical measurements, 2002, PhD Thesis, Oxford Brookes University.

[3] Geoelectrical Ltd, RES3DINV - 3D resistivity and IP inversion software for Windows 98/2000/NT/XP/Vista.

[4] Mathworks Ltd, Matlab: The language of technical computing.

[5] Paulson, K. S., Breckon, W. R., Pidcock, M. K., 1992, Electrode modeling in Electrical Impedance Tomography', SIAM Journal of Applied Mathematics, 52:1012-1022.

[6] Polydorides, N. and Lionheart W.R.B., 2002, A Matlab toolkit for three-dimensional electrical impedance tomography: a contribution to the Electrical Impedance and Diffuse Optical Reconstruction Software project, Measurement Science and Technology, 13:(12), 1871-1883.

[7] Schenk O., and Gärtner, K. 2004, Solving un-symmetric sparse systems of linear equations with PARDISO, Journal of Future Generation Computer Systems, 20(3): 475-487.

[8] Somersalo, E., Cheney, M., and Isaacson, D., 1992, Existence and uniqueness for electrode models for electric current computed tomography. SIAM J Appl. Math, 52:1023–1040.

[9] ULR source, 2009, http://www.paraview.org

[10] URL source, 2009, http://mayavi.sourceforge.net

[11] Vauhkonen, P.J., Vauhkonen, M., Savolainen, T. and Kaipio, J.P., 2002, Three-dimensional electrical impedance tomography based on the complete electrode model, IEEE Trans. On Biomedical Eng., 56:1150-1160.

USE OF INDUCED POLARIZATION TO CHARACTERIZE THE HYDROGEOLOGIC FRAMEWORK OF THE ZONE OF SURFACE-WATER/GROUNDWATER EXCHANGE AT THE HANFORD 300 AREA, WA

Lee D. Slater, Rutgers-Newark, Newark, NJ
Dimitrios Ntarlagiannis, Rutgers-Newark, Newark, NJ
Frederick D. Day-Lewis, U. S. Geological Survey, Storrs, CT
Kisa Mwakanyamale, Rutgers-Newark, Newark, NJ
John W. Lane, Jr., U. S. Geological Survey, Storrs, CT
Andy Ward, Pacific Northwest National Laboratory, Richland, WA
Roelof J. Versteeg, Idaho National Laboratory, Idaho Falls, ID

Abstract

An extensive continuous waterborne electrical imaging (CWEI) survey was conducted along the Columbia River corridor adjacent to the U.S. Department of Energy (DOE) Hanford 300 Area, WA, in order to improve the conceptual model for exchange between surface water and U-contaminated groundwater. The primary objective was to determine spatial variability in the depth to the Hanford-Ringold (H-R) contact, an important lithologic boundary that limits vertical transport of groundwater along the river corridor. Resistivity and induced polarization (IP) measurements were performed along six survey lines parallel to the shore (each greater than 2.5 km in length), with a measurement recorded every 0.5-3.0 m depending on survey speed, resulting in approximately 65,000 measurements. The H-R contact was clearly resolved in images of the normalized chargeability along the river corridor due to the large contrast in surface area (hence polarizability) of the granular material between the two lithologic units. Cross sections of the lithologic structure along the river corridor reveal a large variation in the thickness of the overlying Hanford unit (the aquifer through which contaminated groundwater discharges to the river) and clearly identify locations along the river corridor where the underlying Ringold unit is exposed to the riverbed. Knowing the distribution of the Hanford and Ringold units along the river corridor substantially improves the conceptual model for the hydrogeologic framework regulating U exchange between groundwater and Columbia River water relative to current models based on projections of data from boreholes on land into the river.

Introduction

Electrical geophysical methods are based on the injection of current and measurement of the resulting electrical potentials in the earth using many combinations of electrodes. Continuous waterborne electrical imaging (CWEI) is a recent advancement in electrical geophysical methods whereby a string of electrodes is pulled along the water surface whilst electrical measurements are continuously recorded (e.g. Day-Lewis et al., 2006; Mansoor and Slater, 2007). This approach results in spatially rich datasets that can be inverted for the subsurface distribution of electrical resistivity and induced polarization (IP) parameters.

The objective of this study was to explore the use of high-resolution CWEI to improve the conceptual model for how surface-water/groundwater interaction at the U.S. Department of Energy (DOE) Hanford 300 Area, WA, regulates Uranium (U) transport from the contaminated aquifer into the river. The study was motivated by the hypothesis that lithologic heterogeneity, widely believed to

regulate exchange between surface water and groundwater, could be imaged at an unprecedented spatial scale and resolution using CWEI relative to direct investigation methods performed within the river corridor of this important site. We describe the use of CWEI to resolve lithologic variability from the spatial variation in the electrochemical polarizability, a property closely related to lithology, obtained from IP measurements, in addition to the electrical resistivity as more routinely captured in CWEI studies. Most importantly, we estimate variations in the thickness of the aquifer contributing U to the river along the corridor.

Hydrogeology at the Hanford 300 Area

Hydrogeology at the Hanford 300 Area is in large part determined by two formations. The uppermost unit is the Hanford Formation, containing pebble- to boulder-size gravels and interbedded sands resulting in high horizontal hydraulic conductivity (K) of ~100 m/day (Williams et al., 2007). The underlying unit is the Ringold Formation, a highly heterogeneous unit of granule- to cobble-size gravels intebedded with fine sand and silt resulting in a lower K of ~0.2 m/day (Williams et al., 2007). The Hanford-Ringold (H-R) contact is interpreted represents an important contact limiting vertical migration of contaminants. Paleochannels incised beneath the H-R contact may provide preferential flowpaths for rapid contaminant transport to the river. Identifying the location of the H-R contact is likely a critical factor in determining the U distribution along the river corridor as the shape of the confining layer is assumed to regulate contaminant discharge along the shoreline (Fritz et al., 2007).

The current hydrogeological framework for the river corridor at the Hanford 300 Area is largely based on direct probing techniques aimed at determining the elevation of the H-R contact, and projections of the H-R contact identified in boreholes drilled inland onto the riverbed (Fritz et al., 2007). This work supports the presence of a hydraulically resistive layer (the Ringold Formation) underlying the uppermost hydrologic unit (Hanford Formation) through which surface-water/groundwater exchange and connectivity between the aquifer and surface water is concentrated. Figure 1 includes an estimate of the area of the riverbed (170,000 m^2) that has the potential to discharge U to the Columbia River based on direct sampling and boreholes (Fritz et al., 2007).

Figure 1: Boat track for CWEI (white). Yellow line indicates the suggested U contributing area to the Columbia River (Fritz et al., 2007); Orange contour lines are for U concentration (ug/L) (after Williams et al., 2007).

Continuous Waterborne Electrical Imaging (CWEI)

Field Survey

Our study focused on the river corridor adjacent to the Hanford 300 Area, although the CWEI was extended to the south in an effort to fully characterize lithologic variability close to the Hanford 300 Area. Figure 1 shows the location of ~30 km of CWEI survey lines. Water depths varied substantially across the surveyed area from a minimum of 2 m close to shore to a maximum of 18 m when crossing the channel thalweg. Data were collected in July 2008 when relatively high water levels facilitated surveying close to the western bank of the river. All datasets were acquired from a 7 m aluminum hull jet boat, with water depth continuously measured using a 200/50-kHz – 10/40-degree depth finder (estimated accuracy of ~25 cm based on field tests) and all measurements were geo-referenced using a differential GPS (Garmin GPSmap 420s[1]) unit with ±0.5-m horizontal accuracy. CWEI surveys were conducted using a 10-channel time-domain resistivity/IP instrument (Syscal Pro, Iris Instruments, France). This time-domain instrument records the polarization as an apparent chargeability (M_a) determined from the decay curve after current shutoff. All data were acquired using a 13-electrode cable with graphite electrodes spaced at 5-m intervals. The configuration of the 10 measurement channels was chosen so as to (1) provide a high signal-to-noise ratio for all 10 channels (critical to collecting reliable IP data), (2) result in a desirable sensitivity pattern relative to other common configurations (Mansoor and Slater, 2007), and (3) optimize the 10-channel capabilities of the instrument used here. Measurements were recorded every 0.5-3.0 m depending on survey speed (in part dictated by strong currents on the Columbia River), resulting in ~65,000 measurements conducted on ~30 km of survey line.

Data Processing

CWEI surveys (i.e., with the boat and cable in motion) do not permit application of standard methods for assessing measurement error (e.g., repeatability/stacking tests and/or reciprocity). Bad measurements were therefore identified by examining histograms of the CWEI data and locating obvious outliers, assuming that the subsurface geology will generate a smooth distribution of apparent resistivity (ρ_a) and M_a. Confidence in the mapped variability of ρ_a and M_a along a two-dimensional (2D) line was also established by comparison with ρ_a and M_a structure observed on adjacent parallel lines. Data quality was very good with only 1.2 percent of the datapoints removed before further processing. The shore-perpendicular variability is strongly affected by the substantial increase in water depth towards the channel center (exerting a strong control on M_a in particular). However, it is the shore-parallel variability that is of most interest here as this describes the variability of the hydrogeologic framework along the river corridor at the Hanford 300 Area.

The CWEI dataset was inverted for an estimated subsurface distribution of resistivity (ρ) and chargeability (M) using the RES2DINV package (Loke et al., 2003) as it efficiently handles large datasets and permits a variable-thickness water layer of uniform resistivity and zero chargeability to be incorporated as an inversion constraint. Given the significant discrepancy between the sample density shore-parallel (1 measurement every few meters) and shore-perpendicular (1 measurement every ~20 m), the dataset was treated as a series of near-parallel 2D lines. True electrode locations (calculated from the boat location and the azimuth of the electrode cable behind the boat) were first projected onto a best-fit 2D line. Each line was then inverted for a 2D electrical structure along the river corridor using the

[1] Any use of trade, product, or firm names is for descriptive purposes only and does not imply endorsement by the U.S. Government.

common smooth regularization constraint whereby model structure is minimized subject to fitting the data to some acceptable tolerance (deGroot-Hedlin and Constable, 1990). These 2D inversion results were then also represented in terms of normalized chargeability ($M_n = M/\rho$) (Slater and Lesmes, 2002).

We primarily focus here on M_n as a lithologic indicator because interfacial polarization largely is controlled by grain surface area (e.g., Weller et al., 2010). Furthermore, although lithology exerts a strong control on ρ due to variations in porosity and clay content, ρ also is dependent on fluid conductivity (σ_w). Given that σ_w in the river corridor varies spatially and temporally as a result of surface-water/groundwater exchange, ρ is thus not considered a robust indicator of lithologic variability at this site.

Results and Discussion

Figure 2 shows the inversion result along the river corridor from a 2D dataset for Line 20 located approximately 20 m from the western bank. The normalized chargeability is plotted in Figure 2a and the ρ model is shown for reference in Figure 2b. The electrical structure shown in Figure 2 largely is reproduced in the other shore-parallel transects. Image resolution below the riverbed is reduced due to greater water depths further offshore.

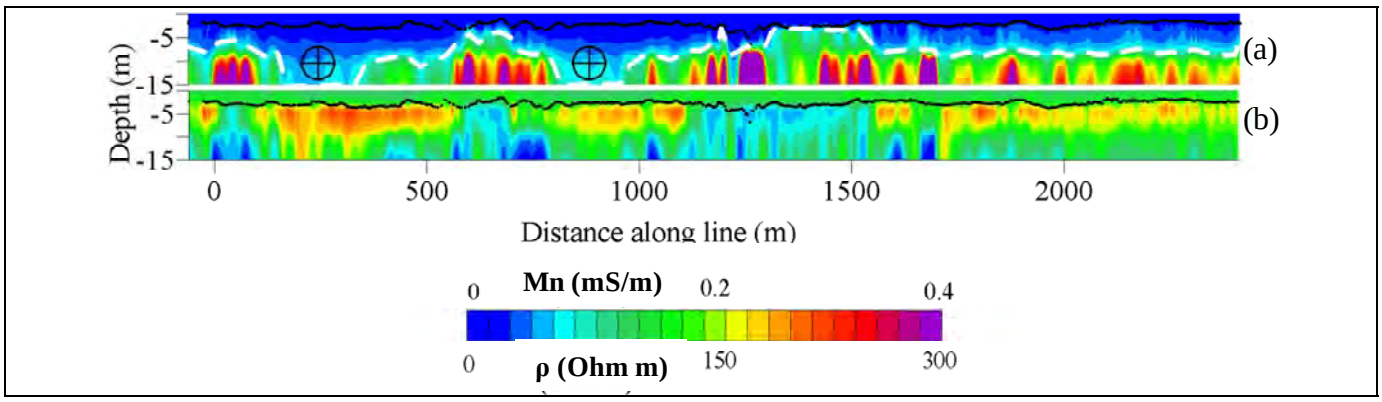

Figure 2: Inverted (a) normalized chargeability (*Mn*), and (b) resistivity (ρ) of CWEI Line 20 (approximately 20 m from shore); solid black line shows the river bed and white dashed line shows the interpeted Hanford–Ringold contact. Two locations showing apparently less polarizable deposits eroded beneath the H-R contact (possible paleochannels) are also marked (⊕).

Figure 2 generally shows a 2-layer model comprised of a low M_n (high ρ) layer overlying a high M_n (low ρ) layer. The upper layer includes the water layer, the river bed being shown as a black line in Figure 2. We attribute the lower part of this upper layer to the Hanford Formation, where the very low M_n is consistent with a coarse-grained aquifer devoid of silt and clay. The lower layer is interpreted as the Ringold Formation, where the much higher M_n is consistent with the substantial silt fraction in this unit.

The white dashed line in Figure 2a represents our interpretation of the H-R contact based on the 2-layer electrical structure of the site. As noted previously, the H-R contact is a critical boundary in any

hydrogeologic model of the Hanford 300 Area as it limits vertical movement of contaminants in the overlying permeable Hanford unit. The CWEI provides an unprecedented characterization of the hydrogeologic setting along this 2.5-km reach of the river corridor at the 300 Area, revealing substantial variability in the depth to the H-R contact. In some places, the Ringold appears to be in contact with the riverbed, e.g. between ~1,300-1,550 m (Figure 2), which is consistent with estimates of the Ringold exposure on the riverbed based on projection of the H-R contact from inland boreholes combined with point probe tests performed on the riverbed (yellow outline in Figure 1). However, CWEI captures many details in the lithologic variability along the river corridor that are not resolved using projections based on boreholes and direct probing techniques. For example, the H-R contact is imaged at 5-10 m below the river bed in some places. Furthermore, the imaging identifies a second location where the Ringold is in contact with the riverbed between 600-700 m that was not resolved from the borehole projections.

Figure 3 shows a revised estimate of variations in the U-contributing area along the river corridor based on the CWEI survey. Whereas the contributing area defined by Fritz et al., (2007) was based on predicted locations where the Hanford Formation is likely exposed on the riverbed, we utilize the CWEI data to determine variations in the thickness of the Hanford Formation along the river corridor (Figure 3). This CWEI estimate clearly contains much along-corridor structure that is not captured in the original estimate (Fritz et al., 2007 and Figure 1) based on projections of the H-R contact recorded in boreholes.

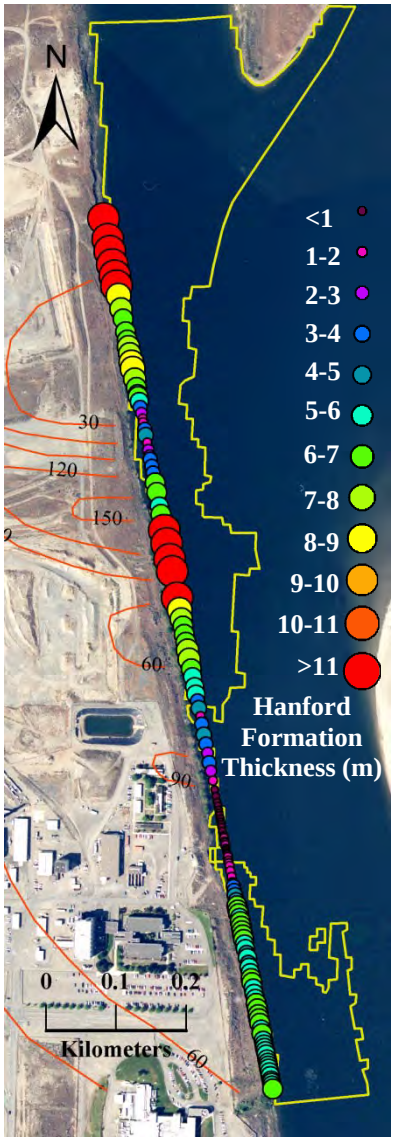

Figure 3: Hanford Formation thickness along the river corridor at the Hanford 300 Area estimated from CWEI measurements. Yellow line indicates the suggested U contributing area to the Columbia River (Fritz et al., 2007). Orange contour lines are for U concentration (ug/L) (after Williams et al., 2007).

Conclusions

Our study illustrates the unique, spatially-rich information on the hydrogeologic framework at the Hanford 300 Area obtained from this large-scale CWEI survey. Most importantly, CWEI defines the variable elevation of the H-R contact along 2500 m of river corridor centered on the Hanford 300 Area. The picture that emerges is distinctly different from that obtained from previous studies that were based on point observations at boreholes drilled at the 300 Area, along with probing and sampling on the riverbed. Fritz et al. (2007) noted that their predicted U-contributing area was likely overestimated from these previous studies. This study shows that there is indeed much spatial variability in elevation of the H-R contact that was not captured in previous estimates of the U-contributing area. Our CWEI investigations of hydraulic connectivity between the Hanford aquifer and Columbia River provides a

revised conceptual model in which to interpret the complex spatial pattern of U concentration contours developed in past work at the Hanford 300 Area.

References

Day-Lewis, F.D., White, E.A., Johnson, C.D., and Lane Jr., J.W., 2006, Continuous resistivity profiling to delineate submarine groundwater discharge—Examples and limitations, The Leading Edge, 724-728.

Degroot-Hedlin, C., and Constable, S., 1990, Occam inversion to generate smooth, 2-dimensional models from magnetotelluric data, Geophysics, 55, 1613-1624.

Fritz, B.G., Kohn, N.P., Gilmore, T.J., McFarland, D., Arntzen, E.V., Mackley, R.D., Patton, G.W., Mendoza, D.P., and Bunn, A.L., 2007, Investigation of the hyporheic zone at the 300 Area, Hanford Site, Report # PNNL-16805, Pacific Northwest National Laboratory, Richland, WA, 90 pp.

Loke, M.H., Acworth, R.I., and Dahlin, T., 2003, A comparison of smooth and blocky inversion methods in 2D electrical imaging surveys, Exploration Geophysics, 34, 182-187.

Mansoor, N., and Slater, L., 2007, Aquatic electrical resistivity imaging of shallow-water wetlands, Geophysics, 72(5), F211-F221

Slater, L. and Lesmes, D., 2002, IP interpretation in environmental investigations, Geophysics, 67, 77-88.

Weller, A., Slater, L., Nordsiek, S., and Ntarlagiannis, D., *in press*, On the estimation of specific surface per unit pore volume from induced polarization: A robust empirical relation fits multiple datasets, Geophysics.

Williams, B.A., Brown, C.F., Um, W., Nimmons, M.J., Peterson, R.E., Bjornstad, B.N., Lanigan, D.C., Serne, R.J., Spane, F.A., and Rockhold, M.L., 2007, Limited field investigation report for U contamination in the 300 Area, 300 FF-5 Operable Unit, Hanford Site, Washington, PNNL-16435, Pacific Northwest National Laboratory, Richland, WA., 137 pp

Acknowledgments

This research was supported by the Office of Science (BER), U.S. Department of Energy under the Environmental Remediation Sciences Program grant DE-AI02-08ER64565. We thank Carole Johnson (USGS), Eric White (USGS), Chris Curran (USGS), Christopher Strickland (PNNL) and Jay Nolan (Rutgers-Newark) for valuable assistance in the collection of field datasets. We are also grateful to Brad Fritz, Bob Peterson and John Zachara (all at Pacific Northwest National Laboratory) for their insights into the hydrogeologic framework of the Hanford 300 Area. Rory Henderson (USGS), Burke Minsley (USGS) and Alison Waxman (USGS) provided valuable review comments that improved the quality of this abstract.

GEOPHYSICAL EXPLORATION OF THE FORMER EXTERMINATION CENTER AT SOBIBÓR, POLAND

Paul Bauman, WorleyParsons, Calgary, Alberta, Canada
Brad Hansen, WorleyParsons, Calgary, Alberta, Canada
Yoram Haimi and Isaac Gilead, Ben Gurion University of the Negev, Israel and Yad VaShem
Richard Freund, University of Hartford, Hartford, CT
Philip Reeder, The University of South Florida
Marek Bem and Wojciech Mazurek , Sobibór Museum, Poland

Abstract

Background

The Sobibór Extermination Center was one of three such secret death centers constructed during World War II in eastern Poland by the Nazis. Unlike such well known camps as Auschwitz-Birkenau and Majdanek that were concentration camps, labour camps, internment camps, etc., the three extermination centers of Treblinka, Belzec, and Sobibór were constructed in1942 for the sole purpose of exterminating the Jewish population of Europe. After disembarking from the rail platform in Sobibór, the life expectancy of a person was then measured in hours. At Treblinka, 850,000 Jews were killed, with only about 40 surviving until the end of the war. At Belzec, 600,000 Jews were killed, with only two survivors.

At Sobibór, 250,000 Jews were killed. At Sobibór, on October 14, 1943, about 600 Jews carried out a planned revolt. Of those, approximately 300 broke through the fences, trenches, and mine fields surrounding the center. And of those 300, only 52 survived until the end of the war. Following the breakout, and given the secret nature of the inhumanity prosecuted at Sobibór, the Nazis then proceeded to remove all physical evidence and traces of the center. Remaining prisoners were used to destroy the camp. The gas chamber was dynamited. Foundation piles were pulled from the ground. Other buildings, fences, and remaining structures were razed. Debris was burned and buried. A dense pine forest was planted where the camp once stood. Jewish labour used to destroy the camp was exterminated. Nazi staff were sent to the Italian front where many were killed. Most of the known air photos of Sobibór taken before 1944 were destroyed. Today, besides a small museum and monuments, there is little about the site to suggest that it is anything other than a bucolic destination for cyclists looking for a gentle ride in the countryside.

From July 18 through July 23, 2008, geophysical surveys and aerial photographic investigations were carried out over portions of the site of the Nazi World War II Sobibór Extermination Center. The goal of the investigations was to provide subsurface reconnaissance information that would assist archaeologists in focusing their intrusive excavations. Specific tentative objectives of the surveys included delineating the boundaries of the extermination area of the Camp (Camp III), locating the gas chambers, delineating possible mass burials, locating individual subsurface features that may be precisely targeted by future intrusive investigations, and providing map coordinates for surface features that are known to be present in American aerial photographs taken in 1944 immediately after the destruction of the Camp.

Two areas were investigated by the geophysical surveys. These included the several hectare open field around the prominent existing circular monument known as “the hill of ashes”, and eight 20 m X 20 m chained survey squares placed immediately south and east of the 2007 archaeological

excavations. The open field was known to contain mass burials. The 400 m^2 gridded area was suspected to be over, or in proximity to the gas chambers. Aerial photography was carried out over most of the original footprint of the camp. GPS data were collected at various locations on the original camp footprint, as specified by the archaeologists on site.

FIELD METHODS

Geophysical Surveys

Metal detection surveys (EM61, magnetic gradiometer, EM38) were carried out with the objective of locating objects associated with the gas chamber or gas chambers, and the subsequent cremation process. Such objects or targets could include rebar, railroad rail, narrow gauge rail or spikes, personal possessions, barbed wire, shovels, baked soil, etc. Other surveys were carried out that had the potential to locate disturbed soil that may be associated with trenches or footings. These surveys included EM38 terrain conductivity mapping and ground penetrating radar (GPR).

EM61 data were collected both in the open field and in the eight 20 m X 20 m gridded squares. In the open field, EM61 data were positionally coupled to a Global Positional System (GPS). Data were collected every 10 cm along the travel path of the handheld sensor. Lines in the field were spaced approximately 5 m apart. The Trimble GeoXH GPS with an external Zephyr antenna, with sub-meter positional accuracy, was used in the field survey. In the eight 400 m^2 grids, EM61 data were collected every 10 cm along 20 m lines spaced one meter apart.

Magnetic gradiometer data were collected over the entire open field in the vicinity of the large circular monument. In this area, data were collected in the "GPS Walking Mode". In this mode of operation, data are collected continuously (approximately every meter) as the operator continually walks through the field. Lines were spaced approximately 5 m to 10 m apart. GPS positions were updated with the integrated GPS system and an external antenna. Both magnetometer sensors were mounted on a backpack, with the lower sensor being at approximately shoulder height, and the upper sensor being 56 cm above the lower sensor.

Over the four 20 X 20 m grids, magnetic gradiometer data were collected every meter along lines spaced one meter apart. The sensors were mounted on a staff, with data being collected at stationary locations in what is termed as the "Mobile Mode." The lower sensor was approximately 30 cm above the ground, with the upper sensor being 56 cm above the lower sensor.

EM38 data coupled to a GeoXH GPS were collected in the open field area around the circular monument. Data were collected approximately every meter on lines spaced approximately 5 to 10 m apart.

GPR data were collected in the eight grids in the wooded areas, and along four lines across areas of interpreted mass burials. In the eight grids, GPR data were collected every 10 cm along lines spaced 1 m apart. In this survey, a PulseEkko Noggin system with a 250 MHz antenna and an odometer were used. The depth of investigation was 2 m and greater.

Low Altitude, High Resolution Aerial Photography

The objectives of the aerial photography were to: 1. Provide photographs for the construction of photographic base maps of the surveyed areas, 2. To identify areas of ground disturbance based on tree height, vegetation height, vegetation stress, etc., and 3. To identify landscape or anthropogenic features that could be related to features identified in the 1944 American aerial photograph of the site. Approximately 350 aerial photographs were taken from cameras mounted on the tether of helium filled balloons. About 280 digital photographs were shot using a 12.1 megapixel Canon PowerShot A650 IS.

Two rolls of Fujichrome Sensia 400 slide film were shot from a Rollei with a 28 mm lens. Photographs were taken from elevations varying from 20 m to approximately 400 m above ground surface (mags). The vast majority of the photographs were taken with the camera lens looking directly downward, though some shots were taken at oblique angles.

GPS Mapping

With the exception of the magnetic gradiometer, all external GPS data were collected with a Trimble GeoXH coupled to an external Zephyr antenna. The Zephyr antenna is designed to provide improved coverage in wooded areas, or in the vicinity of buildings and other sources of interference with the GPS signal. GPS data were corrected to a Polish base station. Base station corrected data accuracy in the X-Y plane is estimated at being sub-0.3 m.

Outside of the geophysical surveys, GPS data were collected for three reasons. First, present day site features were mapped so as to provide a physical context to the geophysical data sets. Second, specific points were targeted to serve as targets for georeferencing the aerial photographs. Finally, and perhaps most importantly, a number of site features were mapped that exist today, but also existed at the time of the 1944 American aerial photograph, and also existed when the extermination center was in full operation. Such features included the rail siding, the rail stop, the house of the center commander, the railway station, a moat surrounding the barracks of the inmates, a forestry tower, and the foundation of one of the barracks of the Nazi SS soldiers.

Results and Preliminary Conclusions

The EM61 high resolution metal detector has identified hundreds of small to medium sized metal objects scattered in the 400 m^2 area of grids 1 through 8. Some of this buried metal debris appears to form distinct geometric patterns which may be related to former buildings, blast patterns, camp infrastructure (narrow gauge rail, fences, etc.), or other unknown sources. Random shovel tests of 10 anomalies indicated all anomalies are related to artifacts from the period of activity of the extermination center.

GPR depth slices (map view images) from a depth of about 0.5 m beneath the area of grids 1 though 8 suggest the presence or previous presence of a foundation beneath a portion of the gridded area. In another portion of the gridded area, GPR depth slices from a depth of about 1.75 m suggest the presence of additional debris.

Magnetic gradient data in the open field has identified a number of buried metal anomalies. One anomaly particularly large in magnitude and in area was identified at the junction of two tentatively identified mass burials. It has been hypothesized that this anomaly may indicate the locations of steel rails used in cremating human remains.

Discrete and evenly spaced magnetic anomalies beneath the gridded area are suggestive of evenly spaced post holes. It is known that only the gas chamber or gas chambers was built on a proper foundation of posts raised above the ground surface.

Low altitude aerial photography from weather balloons appears to have delineated areas of possible mass burials in the open field, as defined by deeper green hues in the vegetation. This conclusion is supported by coring activities by previous archaeologists in 2001. Also, the aerial photographs appear to distinguish areas of the Sobibór camp from surrounding forest by the subtle but clear change in tree canopy height and homogeneity of tree canopy height.

GPS mapping of existing ground features that also existed in 1944, and before the destruction of the camp in 1943, allowed more precise georeferencing of a 1944 American aerial photograph of the camp. Improved georeferencing of this photograph, combined with the geophysical information, allowed archaeologists to concentrate their efforts on a very specific area.

A second season of excavation on behalf of Ben-Gurion University of the Negev, Yad Vashem Institute and the Sobibór Museum was carried out in Sobibór for 12 days in late October of 2009. The location of the 2009 excavation probes was chosen in wake of the results of the GPR survey and GPS mapping carried out in July 2008. The preliminary results of the excavation probes include the identification of 17 post-holes, and artifacts similar to those known from other extermination and concentration centers. Although the post-holes are indicative of a structure, further excavations are required in order to determine its function

USING GEOPHYSICAL METHODS FOR ARCHAEOLOGICAL EXCAVATION IN 2008 SEASON FOR URARTIAN SITES LOCATED IN VAN, YONCATEPE

Nihan HOSKAN[1], Fethi Ahmet YUKSEL[1], Oktay BELLI[2]
[1]Istanbul University, Engineering Faculty, Department of Geophysical Engineering, Istanbul, TURKEY
[2]Istanbul University, Faculty of Letters, Department of Archaeology, Istanbul, TURKEY

Abstract

This Paper presents the results of the archeological excavation carried out for Urartian settlement located in Yoncatepe (Van-Turkey) in 2008. The Yoncatepe Palace is located 9 km away from the city of Van, to the west of Varak and Erek Mountains, 1.5 km to the southwest of Yukarı Bakraçlı (Yedikilise) village. The Yoncatepe Palace acropol and necropol kept its strategical position from 1000 B.C. until the Urartian kingdom.

The archeological excavation carried out at a flat elevated hillside since 1998 positioned the locations of an acropol at the summit of Yoncatepe Palace, a settlement site to the northeast of it, and the necropol site to the north of the hillside. An acropol study carried out at an area of 900 square meters at the summit of the settlement identified an architectural structure complex distributed all over the study area. The wall of the structures usually expanded East-West is constructed using slab-stone's mud mixture. As in the other castle and settlement centers belonging to early iron age the necropol and the settlement site in Yoncatepe are overlapped.

The southern part of Acropol ends in a deep and steep valley. The Doni stream flowing from southeast to west has wide and deeply excavated bed. Although the northern side of Acropol is steep, the northeast and northwest sides are gentle.

During the conventional archeological well-drillings aiming to determine the distribution of the Acropol settlement, we determined an architectural complex that is a likely settlement located to the north of Yoncatepe Palace and to the east of necropol. In 2008 excavation season we used geophysical exploration techniques to locate the sites.

6 tombs belonging to iron age are identified during the excavation studies to determine the necropol site at northern hillside of Yoncatepe Palace during the 1997-2008 period. Important knowledge on architecture is inferred owing to the fact that the cover of the tombs is not collapsed. In addition to these 6 tombs another tomb is identified using geophysical exploration methods.

Results and Conclusions

In archaeological prospecting, several geophysical techniques based on magnetic, gravimetric, seismic, electrical, or GPR methods have been used (Aitken, 1961). One of the most potent geophysical methods is magnetic surveys. The proton precession magnetometer has made possible a large area in a short time.

For Urartian site had located in Yoncatepe, Littlemore SCI. ENG CO. Oxford UK. Protonmagnetometer type 820 was used to take magnetic measurements. After collecting the data, it is identified that 6 tombs belonging to iron age during the excavation studies have done to determine the necropol site at northern hillside of Yoncatepe Palace during the 1997-2008 period. Important knowledge on architecture is inferred owing to the fact that the cover of the tombs is not collapsed. Some tombs located at 70-100 cm. depths are of front entrance (dromos) type and are made up from walls constructed within holes excavated in the soil layer (Belli, 2006). All the tombs that we have identified are East-West oriented. The entrance to the tombs is through a hole at the western wall or through a dromos. The tombs are covered with large slab-stone blocks.

We applied Ground Penetrating Radar (GPR) method to help for the archeological excavation carried out in Yoncatepe Palace (Van-Turkey) in 2008 excavation season. GPR is an electromagnetic method that employs the principle of propagation of electromagnetic waves in the ground using high frequency radio waves (usually 1-1000 MHz) to map structures and features buried in the ground (Annan, 1992). It is commonly used in archaeological studies (Bevan and Kenyon, 1975; Imai et al., 1987, Bevan, 1991). In addition to these 6 tombs, using GPR method we located another tomb.

We have determined new sites around the Yoncatepe Palace using the geophysical tools (Figure 1). We used magnetic data to identify the front entrances, the extension of the walls located beneath the ruins of the Yoncatepe Palace (Figure 2).

Figure 1. The new sites around the Yoncatepe Palace discovered by the magnetic methods.

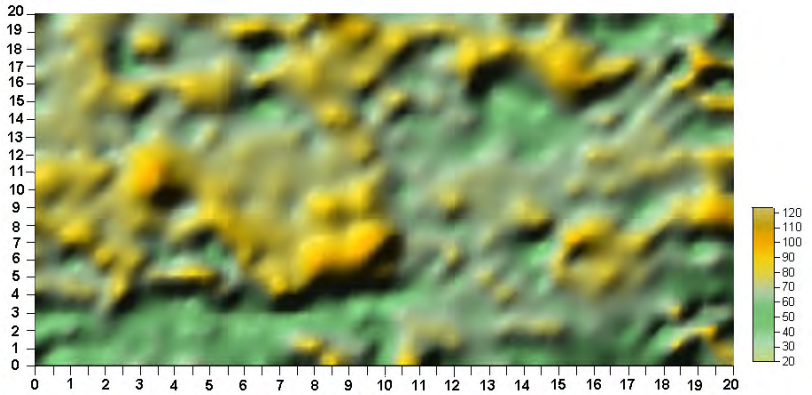

Figure 2. Counter map of the magnetic data from the new sites around the Yoncatepe Palace.

A necropol distributed over a large area is located to the north of the acropol. A M8 tomb was discovered using GPR (500 MHz antenna) methods in these areas (Figure 3). The architecture of M8 tombs differs from the features of the other tombs that can be seen in F14c. The tomb is located 40 cm beneath the surface, expanding of east-west, the size is 1.00 x 1.05 cm, excavated within stiff soil having east-west elongation with dimensions of 1.85x2.45 cm.

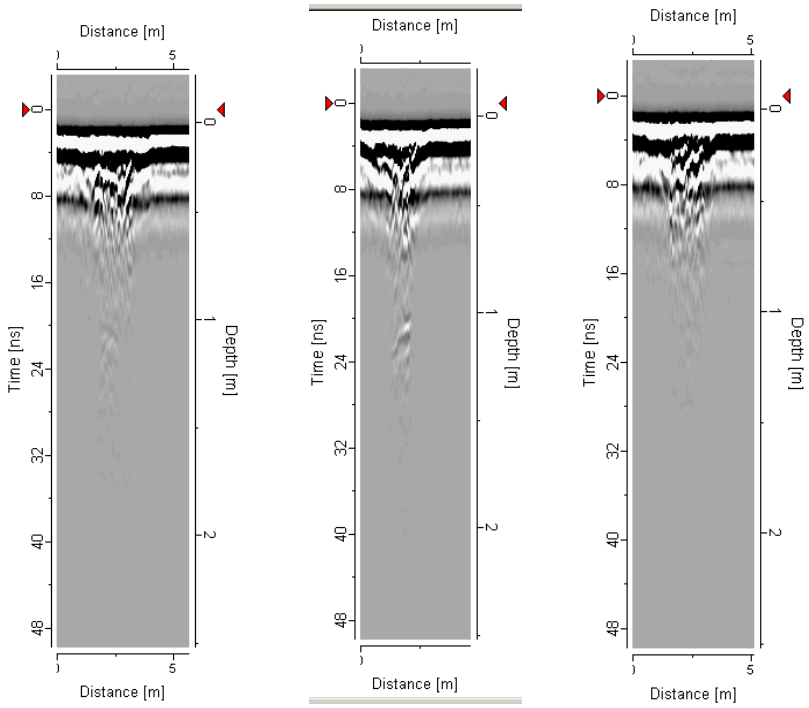

Figure 3. GPR profiles acquired with 500-MHz antenna and obtained from the new sites around the Yoncatepe Palace. Using these radargram profiles, a new tomb (M8) was found in the ground.

Moreover, we detected archeological remnants of new settlements through geophysical surveys achieved at lower elevation sites to the east of Yoncatepe Palace.

References

Aitken, M. J., 1961. Physics and Archaeology. London. Interscience, p.2.
Annan, A. P.,1992. Ground Penetrating Radar Workshop Notes. San Diego, CA.
Belli, O., 2006. Van and Urartian Kingdom (ed. O. Belli) I. Van Gölü Havzası Sempozyumu, 8-10 Sept. 2004, Van, Turkey, Van Valiliği Kültür Yayınları Güzel Sanatlar Matbaası, pp. 15-29, Istanbul, Turkey.
Bevan, B., and J. Kenyon (1975). Ground-penetrating Radar for Historical Archaeology. MASCA Newsletter 11(2):2-7.
Bevan, B.W., 1991. The Search for Graves. Geophysics 56 (9), 1310-1319.
Imai, T., Sakayama, T., Kanemori, T., 1987. Use of ground probing radar and resistivity surveys for archaeological investigation. Geophysics 52 (2), 137-150.

APPLICATION OF GEOPHYSICAL METHODS FOR ARCHAEOLOGICAL EXCAVATION (2009) IN AMASYA-OLUZ HOYUK (YASSI HOYUK)

Fethi Ahmet YUKSEL[1] Nihan HOSKAN[1], Sevket DONMEZ[2]
[1]Istanbul University, Engineering Faculty, Department of Geophysical Engineering, Istanbul, TURKEY
[2]Istanbul Üniversity, Faculty of Letters, Department of Archaeology, Istanbul, TURKEY

Abstract

Oluz Höyük, in the Amasya Province, situated in the Land Zone of the Central Black Sea Region, resides at the 27th km of the Corum Mainroad, in the territory of the Gökhöyük Agriculture Operation Management. Oluz Höyük, which has dimensions of 280 x 260 m, is 15 m higher than the plate level and has a field of 45.000 m² and one of the biggest hoyuks of the region.

A total of 6 architectural layers were discovered resulting from the excavations of Oluz Höyük 2007 (first season) carried out in two trenchs. In this context The 0 Layer of the Oluz Höyük could be dated to Middle Age; The 1st Architectural Layer to Hellenistic Period (The end of 2nd century BC and the beginning of the 1st century BC); The 2nd Architectural Layer to the Late Phase of the Late Iron Age (4th and 3rd centuries BC). The 3rd and 4th Architectural layers could be dated to the Early Phase of the Late Iron Age (6th and 5th centuries BC), 5th Architectural Layer to the Middle Iron Age (7th century BC) and 6th Architectural Later to possibly either Early Iron Age or Late Bronze Age in other words, to the Age of Hittite Empire Period.

Geophysical tecniques were applied for archaeological excavation in Amasya, Oluz Hoyuk. Geophysical studies were shown some anomalies that can be interpreted as walls and tombs. Location of anomalies were excavated in 2008 season.

Results and Conclusions

Previously some Hittite artifacts were found at Doğantepe so it is naturally Hittite settlements were expected in the area. Because a bronze Hittite Storm God (Teşup) figurine found at Doğantepe that settlement considered as a religious center; so it is conceivable that Oluz Höyük is a civil center related to Doğantepe (Donmez and Donmez, 2007).

Before the excavations begin at Oluz Höyük geophysical (magnetic, geoelectric and GPR) and underground visualization studies were conducted. Geophysical studies conducted before the excavation saves time and manpower. Geophysics studies showed some anomalies. When locations of those anomalies excavated, archaeologists revealed some so important ruins and building complexes. Some locations fixed during 2008 excavation season were excavated. Those are form highest portion of the Oluz Höyük and thought to belong to either a monumental or Hittite place building (Figure1).

We applied Ground Penetrating Radar (GPR) method to help for the archeological excavation carried out in Amasya, Oluz Hoyuk (Turkey) in 2009 excavation season. GPR is an electromagnetic method that employs the principle of propagation of electromagnetic waves in the ground using high frequency radio waves (usually 1-1000 MHz) to map structures and features buried in the ground

(Annan, 1992). It is commonly used in archaeological studies (Bevan and Kenyon, 1975; Imai et al., 1987, Bevan, 1991). Figure 2 shows the radargram obtain from A-Spreading in Oluz Hoyuk. It is seen in Figure 3 that 3-D cubic model of GPR measurement in south of the adobe wall in Oluz Höyük (Yuksel and Bal-Tarhan, 2008).

Figure 1. The excavation site in Amasya- Oluz Hoyuk.

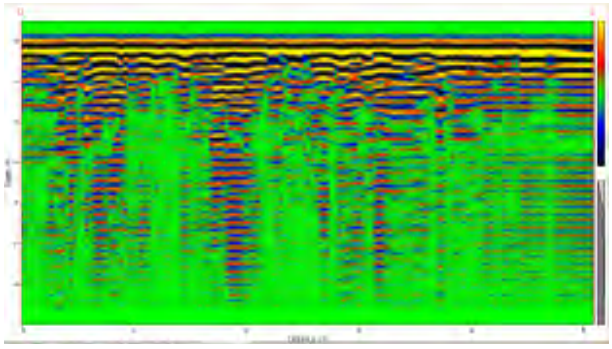

Figure 2. Radargram profil obtained from A Spreading.

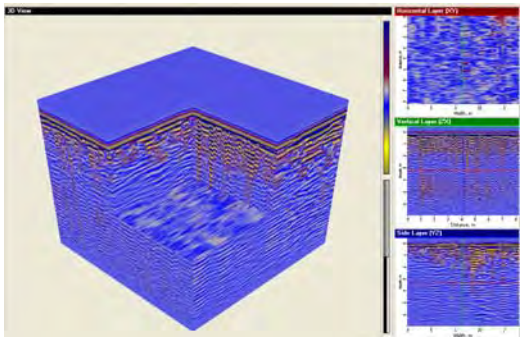

Figure 3. 3-D cubic model of GPR measurement in the plansquares (south of the adobe wall) 0.5m level in Oluz Höyük.

Amasya is one of the least searched provinces as archaeologically until today. But we believe that it must be as Hittite as Çorum. It is thought that Amasya is northern boundary of Hittite empire and not necessarily has developed cities as Çorum. But since at the north of Amasya by the Black Sea Shore (namely Samsun, Ordu, Sinop) Kashkaeas were living which no archeological evidence found yet but well known from Hittite texts. Since it is a border area it is conceivable that Oluz Höyük had a defensive role. It is also possible that it has defensive walls.

Studies conducted at 10x10m 20 units at Oluz Höyük. Magnetic measurement taken at 0,50x0,50 grid corners. Those measurement units lay at East-West direction and covered highest point of the höyük. Besides the magnetic studies units were covered by GRP and Geoelectric (Dipol-Dipol Elektrod sequence). Geophysical studies had shown some anomalies that can be interpreted as walls and tombs.

References

Annan, A. P.,1992. Ground Penetrating Radar Workshop Notes. San Diego, CA.
Bevan, B., and J. Kenyon (1975). Ground-penetrating Radar for Historical Archaeology. MASCA Newsletter 11(2):2-7.
Bevan, B.W., 1991. The Search for Graves. Geophysics 56 (9), 1310-1319.
Dönmez, Ş., , and Dönmez, E., 2007. Amasya-Oluz Höyük Kazısı 2007 Dönemi Çalışmaları: İlk Sonuçlar, Colloquium Anatolicum VI pp. 49-74, İstanbul, Turkey.
Imai, T., Sakayama, T., Kanemori, T., 1987. Use of ground probing radar and resistivity surveys for archaeological investigation. Geophysics 52 (2), 137-150.
Yuksel, F. A., Bal-Tarhan, O., 2008. Amasya-Oluz Höyük 2007 Yılı Jeofizik Uygulamaları, T.C. Kültür ve Turizm Bakanlığı Kültür Varlıkları ve Müzeler Genel Müdürlüğü, 24. Arkeometri Sonuçları Toplantısı, 26-30 Mayıs 2008, pp. 1-12, Ankara, Turkey

.

WHERE HAVE ALL THE ABOITEAUX GONE? MAPPING BURRIED HISTORIC DRAINAGE SYSTEMS IN NEW BRUNSWICK, CANADA

Justin Rogers, AMEC, Minneapolis, MN
Darcy J Dignam, AMEC, Fredericton, New Brunswick, CA
Raye Lahti, AMEC, Minneapolis, MN
William Webb, AMEC, Fredericton, New Brunswick, CA
Elissa Atkinson, AMEC, Fredericton, New Brunswick, CA
Andri Hanson, AMEC, Minneapolis, MN

Abstract

The provincial government of New Brunswick Canada has undertaken the task of rehabilitating historic agricultural marsh lands along the shores of the Petitcodiac River. Since this proposed undertaking will negatively impact shoreline indigenous soils, provincial regulations triggered an archaeological resources assessment. One component of the archaeological program conducted by AMEC was an EM31-SH survey of the proposed shoreline impact areas. Spatial reference was recorded using a Trimble AG114 Global Positioning System (GPS). The principal archaeological objective of the EM31-SH survey was to identify potential subsurface prehistoric and historic archaeological resources. Historically, since the 17th century, the shoreline marshes of the Petitcodiac River have been utilized for agricultural purposes; using a system of dykes (berms) and aboiteaux (drainage structures including one-way valves) that allow water to drain from the marsh while preventing river tidal waters from flooding the marsh. The construction of dykes and aboiteaux in the 1950s "eliminated" any preexisting historical structures. Thus, while there remains physical remnants of the mid-19th century drainage system, there is little surficial evidence of the preexisting historical systems, Identifying the locations of the both potential prehistoric and historic archaeological features using traditional archaeological testing methods would have been both expensive and time consuming given the large area. The use of the EM31-SH and with GIS data analysis, in addition to geotechnical testing and excavation monitoring (ground truthing) was proposed as an alternative. Four parallel transects were walked with the EM31-SH along the Petitcodiac River, covering the project impact area. The data were interpolated to produce raster data coverage's using Geosoft. In addition, two test areas with known subsurface historical structural features were surveyed to serve as a baseline. Spatial analysis utilizing GIS was performed to pick possible targets for further archaeological investigation. Various high pass filters were employed in an effort to sharpen possible features. In addition, various stretches were employed for better visualization of the data. The most effective for visualization was three standard deviations with a bilinear or cubic convolution resampling (for continuous data). The statistics used for display, stretch and resampling, were derived from the present display scale to provide better visualization at varying scales. This enabled the identification of localized anomalies at large scales that were not identifiable using the entirety of the data for representation. The initial ground truthing of a single segment with 12 targets resulted in the identification of two pre 19th century aboiteaux features (106-119 millisiemens per meter [mS/M] and 185-204 mS/M) and a 1950s era aboiteau feature (23-30 mS/M). The 1950s era aboiteau accounted for two adjacent targets. Each of the three features is distinguished by different EM signatures both in their range of return values and in their shape size and pattern of response.

Introduction

The Petitcodiac River causeway is a gated dam structure with an installed vertical slot fishway that was built across the Petitcodiac River between the City of Moncton and the Town of Riverview in New Brunswick Canada (Figures 1). Construction of the Petitcodiac River causeway between 1966 and 1968 resulted in a number of challenges with respect to fish passage. Even though a fishway was included in the control structure as part of the authorization to construct the causeway, the fishway proved ineffective and subsequent modifications to the fishway and gate management failed to provide a solution to the fish passage issues for all fish species requiring passage upstream and downstream of the causeway. Following a variety of reports and actions, and based on the Niles Report recommendations (Niles, 2001), it was resolved that an environmental impact assessment (EIA) was necessary to evaluate potential project options to address the fish passage and other ecosystem issues. A modelling workshop was organized by Environment Canada (EC) and the Department of Fisheries and Oceans Canada (DFO) in March 2002 to address the issues associated with modelling of the Petitcodiac River in order to facilitate an EIA. The New Brunswick Department of Supply and Services (NBDSS) was appointed as the Proponent and a harmonized federal-provincial EIA was established with the issuance of joint guidelines. The AMEC (AMEC Earth and Environmental Inc.) study team was retained in November 2002 to conduct the EIA completed in 2005 (AMEC 2005a).

One of the conditions of approval of the EIA was to "ensure that the dykes and aboiteaux in the headpond area are repaired/upgraded prior to the permanent opening of the causeway gates" (condition of approval 13). In order to meet this condition, a rehabilitation plan for marshes upstream of causeway (AMEC 2009) and new aboiteaux design considerations were developed and proposed to the project Technical Review Committee (TRC) in February 2009. Since this proposed undertaking will negatively impact shoreline indigenous soils, provincial regulations triggered an archaeological resources assessment. The current archaeological field program for the Petitcodiac River Causeway Project is one component of the revised Follow-up Program Plans and covers approximately 25 kilometers (km) of dyke construction along both sides of the Petitcodiac River (Figure 1). One component of the archaeological program conducted by AMEC was an EM31-SH survey of the proposed shoreline impact areas.

The goal of the EM survey was to collect data for both archaeological and construction purposes. The principal archaeological objective of the EM31-SH survey was to identify potential subsurface prehistoric and historic archaeological resources. Of main concern was the identification of buried historic aboiteaux structures, that will either be avoided (pre-WWII structures) or plugged (post-WWII structures). Any aboiteaux suspected to be 100 years old or older are considered to be heritage resources (Archaeological Services Unit (ASU) 2009). An archaeological research and field program was required in order to identify both potential and known heritage resources within the proposed upstream study area and to protect them from being negatively impacted as a result of this project. The shorelines of the Petitcodiac River, upstream of the causeway, are considered to have an elevated potential for historic and prehistoric archaeological resources.

Historical Significance

The Petitcodiac River is a substantial New Brunswick waterway and has in the past been an area used for habitation, food procurement, and transportation for the Natives (First Nations), the Acadians, the Planters, and the Loyalists of New Brunswick.

Native Heritage Resources

The First Nations used the Petitcodiac River for transportation during Pre-contact times (pre-1604). There are no documented Native sites within the project study area. However, in 2004, a Pre-contact Native site (BlDf-2) was identified along Turtle Creek (AMEC 2005b, AMEC 2006), a tributary of the Petitcodiac River. This well documented Native site is situated approximately 12 km south of the Petitcodiac River, at the confluence of the east and west arms of Turtle Creek. This Native site has been interpreted as an Early Maritime Woodland seasonal occupation site (2800-2400 years before present) (AMEC 2006). While not located within the project impact area it is physical evidence of pre-historic habitation in this general area.

Historic Heritage Resources

As early as 1633, the first wave of Acadian immigrants began to settle New Brunswick, which at that time was part of Acadia (Burley 1976). This area was inhabited by the Acadians until the 1755 expulsion (Ganong 1899, Bourque 1971, Surette 1996, Surette 1985). Following the 1755 Acadian expulsion, English, Irish, and German immigrants re-settled the areas previously inhabited by the Acadians (Burley 1976). In the present day, much of the population living along south bank of the Petitcodiac River is descended from these later settlers (Ibid.). However, Ganong (1899) notes that many Acadians in the Petitcodiac area escaped to the woods and that in 1761 the British allowed them to resume their original livelihoods.

In 1974, David Burley conducted an historical survey of the Petitcodiac River for heritage resources (Burley 1976). The survey resulted in the identification of 12 pre and post-expulsion historic sites along the Petitcodiac River, west of Moncton. The identification of these sites in the field confirmed the validity of the historical documentation on Acadian occupation by Ganong (1899) and Bourque (1971). Including seven of the sites identified by Burley, there are a total of nine documented historic archaeological sites along the shoreline of the Petitcodiac River within the present project study area (see AMEC 2009b, Burley 1976, Ferguson 1998). These historic sites include Acadian and post-Acadian habitation sites, a shipbuilding dry-dock, and Acadian aboiteaux structures.

In 1998 Ferguson reported a few dykes that were supported by limited surficial evidence at the river's edge (Ferguson, 1998). In 2008, AMEC identified an archaeological site (CaDf-10) along the shore of the Petitcodiac River (near Boundary Creek) that included one surficial dyke feature and four subsurface features (AMEC 2009b). While all of the features at this site are likely associated with the historic dyking of the salt marshes along the shore of the Petitcodiac River, one wooden trough feature has a calibrated radiocarbon date of 1650 AD. The use of these dyke systems is well documented in both New Brunswick and Nova Scotia (Fowler 2006, Bleakney 2004, Ross 2002, Leonard 1991, Cormier 1990). Initially, these dyke systems were used by the Acadians as a primary means of preparing the land for agriculture by draining the salt marshes (Burley 1976). Variations of these dyke

drainage systems were used by the Acadians in the 17th−18th centuries, the Planters in the 18th−19th centuries, the Loyalists in the 19th century, and their descendants in the 20th century.

The 20th Century

By the 1950's, many of the dykes and aboiteaux were in disrepair and required upgrading beyond routine maintenance. In the 1950's, the *Marshland Reclamation Act* (*MRA*) was implemented to facilitate the renovation including maintenance of the dykes and aboiteaux and provide ongoing maintenance on many of the marshes. The *MRA* required an agreement between the federal and provincial governments as well as the owners of the land on which each marsh was situated. In instances where the owners could not fulfill their responsibilities, as defined by the agreement, no agreement was reached. The land owner responsibilities included formalizing their association as a marsh executive and signing off on the terms of the agreement that included the stipulation of a permanent easement to the dyked land for ease of repair and maintenance. Marshes 15, 46, 41, 28, 42, 33, 4, 43, 54 and 36, arranged from east to west as indicated on the attached Figure 3, were formed as part of the *MRA*. Some of the marshes are subdivided into A, B and C partly because the entire marsh area is not contiguous. Intervening portions of the land were not considered farmable in the 1950's *MRA* redevelopment or, in the case of Marsh 41, the subdivision is based on the presence of Turtle Creek and Route 112. The associated dykes and aboiteaux structures were reconstructed in the early 1950's in conjunction with this process. Over 25 km of dykes were reconstructed bordering these ten numbered marshes upstream of the causeway along the Petitcodiac River.

Objectives of Proposed Investigations

The proposed field program includes multiple components including a visual survey, a geotechnical survey, a remote sensing geophysical survey, archaeological evaluation testing, and monitoring. The construction of new dykes and aboiteaux will primarily impact soils from deep stratified silt deposits. The depth of the excavations from the borrow trench is estimated to be between 0.3 and 3.0 meters (m). The areas of concern for prehistoric resources are the subsurface soil layers on which aboriginal peoples may have resided or journeyed. These elevated potential layers include both the surface of the glacial till layer (below the silt) and any podzol layers within the silt. Therefore, the proposed archaeological program focuses on identifying any existing heritage resources within the proposed impact area and either avoid these resources or propose mitigation measures.

Methods

The following is a brief step-by-step outline of the archaeological assessment, evaluation, and monitoring program for the proposed upstream impact area of the Petitcodiac River Causeway Project.

1. Background research was conducted for the impacted area (heritage resources and geological background) to identify known heritage resources (sites) and additional high potential areas. This included geo-referencing historical mapping (1792, 1862, and 1950s dyke design survey) and aerial photographs (1945 & 1953) to 2008 aerial photographs.
2. Contact was made with local informants (stakeholders) for input regarding heritage resources in the proposed upstream impact area (the closest First Nation, historical societies, landowners, etc.).

3. A visual survey was conducted of the proposed impact area, paying particular attention to existing dykes and aboiteaux (identified during desktop review) to potentially date these features. Dendrochronological analysis will be conducted on selected wood samples collected from field identified structural remnants to assist in dating them.
4. A geotechnical survey[1] of impact areas was conducted to identify when till and bedrock are reached, and where podzol layers exist above the till. A vibracore drill was used for this testing, which resulted in the collection a four inch diameter soil sample from every test hole along the centerline of the impact area. The geotechnical survey will also identify where organic podzol layers are encountered within the silt layers and where proposed excavations could impact till layers (elevated potential areas for Woodland, Archaic, and Palaeo archaeological resources).
5. A geophysical survey (remote sensing) was conducted for the impact areas for the proposed dyke construction trenching. The goal of the geophysical survey for these areas was to identify potential archaeological cultural features as "anomalies" within the soil matrix. The electromagnetic (EM) survey was conducted using the Geonics Ltd. EM31-SH. The EM31-SH measures apparent ground conductivity (quadrature phase) and was operated in vertical dipole mode, providing an effective exploration depth of up to four meters. Changes in apparent conductivity, or "anomalies", may be associated with natural gradation of soils or may also represent a transition from soils impacted by excavation areas (such as dykes, or aboiteaux) to non-disturbed soils. The survey involved walking four parallel lines (covering a survey width of 20 metres plus) for the entire length of the proposed impact area. Initial field testing was conducted at two locations along the shore of the Petitcodiac River where known (previously discovered) subsurface archaeological features were present. These features were both almost 100 cm below the surface. One is a linear stone feature, while the other is a wooden platform feature. While portions of these features were excavated the previous season, the area surveyed with the EM31-SH extended beyond the excavated areas. In both cases, the features were clearly identified both inside and outside of the excavated portions using apparent conductivity measurements with the EM31-SH.
6. All excavation activities associated with the construction of dykes and new aboiteaux are presently being monitored by licensed archaeologists. Mechanical excavation activities have been observed by the monitoring archaeologist to ensure that heritage resources are not negatively impacted during construction, with particular attention being paid to locations where anomalies were identified during the EM survey.

Results

The EM31-SH survey of the two previously identified archaeological features resulted in the identification of both features as defined anomalies (Figure 4 and 5). Feature 1 is an angled linear stone feature (Photograph 1) at 75-82cm below ground surface and is estimated at 10 m long and 1 m wide (AMEC 2009b). The apparent conductivity measured over the anomaly is between 15 and 18.25 milliSiemens per meter (mS/M). The linear orientation and of the feature is clearly visible. Feature 2 is

[1] The geotechnical survey will be collecting data required for both the archaeological program and the construction program.

a large 4 x 6 meters wooded platform buried 74 to 90 cm below the ground surface (Photograph 2). The apparent conductivity measured over the anomaly is between 22 and 26 mS/M (Figure 4 and 5).

Photograph 1. Feature 1.

Photograph 2. Feature 2.

While a total of thirteen separate areas have been surveyed by the EM31 only one grid area, Grid 28, currently has preliminary results from the archaeological investigations. Grid area 28 is located along the south bank of the Petitcodiac River and stretches for a total of 1.25 kilometers. The apparent conductivity data ranges from -17.49 to 209.86 mS/m with a mean of 57.11 and standard deviation of 53.41. A total of 12 anomalies were identified from the EM31 data. (Table 1, Figure 4).

Table 1. Table of Anomalies EM values and ranges for each of the 12 anomalies

Anomaly Number	Grid	Map Sheet	mE UTM Zone 20N	mN UTM Zone 20N	Results	EM minimum (mS/m)	EM maximum (mS/m)
1	28	28-2	353012.873	5101183.379		100	116
2	28	28-2	353014.4545	5101161.436		100	110
3	28	28-2	352803.8636	5101150.069		53	59
4	28	28-2	352873.5353	5101166.878	Feature 28-2	106	119
5	28	28-3	353071.2562	5101189.888		185	209
6	28	28-3	353199.1558	5101156.107	Feature 28-3	100	183
7	28	28-4	353520.4834	5101146.133	Feature 28-1	24	34
8	28	28-4	353504.9888	5101130.001		27	32
9	28	28-5	353666.1269	5101194.316		12	20
10	28	28-5	353768.7118	5101282.669		12	15
11	28	28-4	353383.9187	5101146.012		83	134
12	28	28-5	353720.1768	5101216.089		1	4

A total of three features were identified on Marsh 28, two archaeological features identified as Feature 28-1, located at anomaly # 7 and Feature 28-2 located at anomaly # 4. In addition the remnants of a previously eliminated "eliminated aboiteau" Feature 28-3, was identified at Anomaly # 6.

Feature 28-1

This feature includes dyke/aboiteau construction elements that appear to be associated with the 1950s aboiteau (Photograph 3). There were 1950s artifacts identified at 60 cm dbs (depth below surface) and brush and stone features at 90 cm dbs. This appears to be a part of the 1950s aboiteau. Excavations were stopped on the east side of the proposed aboiteau location to investigate.

Photograph 3. Feature 28-1 Linear Excavated Stone component.

Feature 28-2

This is dyke/aboiteau construction elements that do not appear on any historic mapping however, a local resident, Mr. Lahiti, mentioned that he remembered an "old" aboiteau at this location. The wooden feature uncovered has one exposed portion within the excavation trench and one out into the Petitcodiac River (Photograph 4). This is an aboiteau, and it appears to be neither Acadian (17th-18th century) nor 20th century. Therefore, it seems to be 19th century.

Photograph 4. Feature 28-2 wooden matting.

Feature 28-3

This feature is the remnants of an aboiteau structure located at Anomaly # 6. The 1950s dyke construction mapping clearly indicates that there was an "eliminated aboiteau" at this location during the 1950s construction of the “new” dykes and aboiteaux. The feature is the wooden remnants of this structure.

Conclusion

Preliminary results from archaeological investigations indicate three out of the twelve anomalies were subsurface features. Because differing features, including the test features, have differing apparent conductivity signatures, the selection of anomalies based purely on signature values is difficult to impossible. Selection of target anomalies was through the morphology and signature values in comparison to those apparent conductivity values surrounding of the surrounding areas. This was accomplished utilizing dynamic resampling and display of the raster data at varying scales. In addition, various stretches were employed for better visualization of the data. The most effective for visualization was three standard deviations with a bilinear or cubic convolution resampling (for continuous data). The statistics used for display, stretch and resampling, were derived from the present display scale to provide better visualization at varying scales. This enabled the identification of localized anomalies at large scales that were not identifiable using the entirety of the data for representation.

Figure 1: Project Location and Test Grid Locations

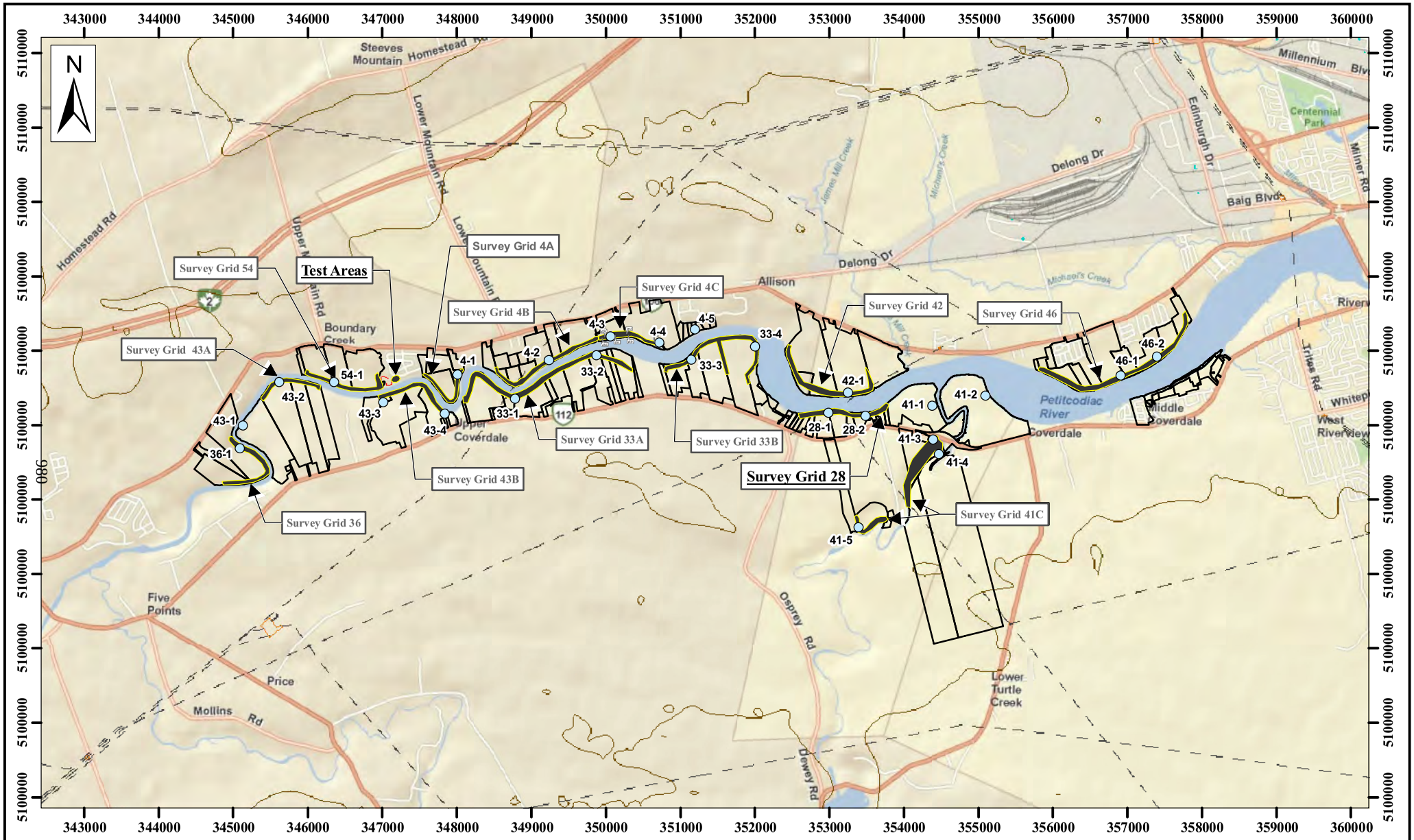

LEGEND

- Sewage settling pond
- Electrical, Transformer substation
- Tank (vertical outline)
- Electrical, Transmission line
- Pipeline
- Arboiteaux Location
- EM31 Survey Areas
- PID Areas Affected by Dykes

SCALE: 1 centimeter = 697 meters

0 1,000 2,000 Meters

amec AMEC Earth and Environmental
A Division of AMEC Americas Ltd.

DATE: 09/03/09
DRAWN BY: JNR
PROJECT NO.:
FILE NAME: Figure_1_Project_Area_overview.mxd
DATUM: NAD 83
PROJECTION: UTM Zone 20N
DATA SOURCE(S): EM31 data

Petitcodiac EM31 Geophysical Achaeological Survey
Project Area Overview

FIGURE 1

Map Document: (E:\Projects\2009\Petitcodiac_River\MXD\Letter Report\Figure_1_Project_Area_Overview.mxd) 2/2/2010 -- 9:08:10 AM

Figure 2: Test Grids and Cross Sections

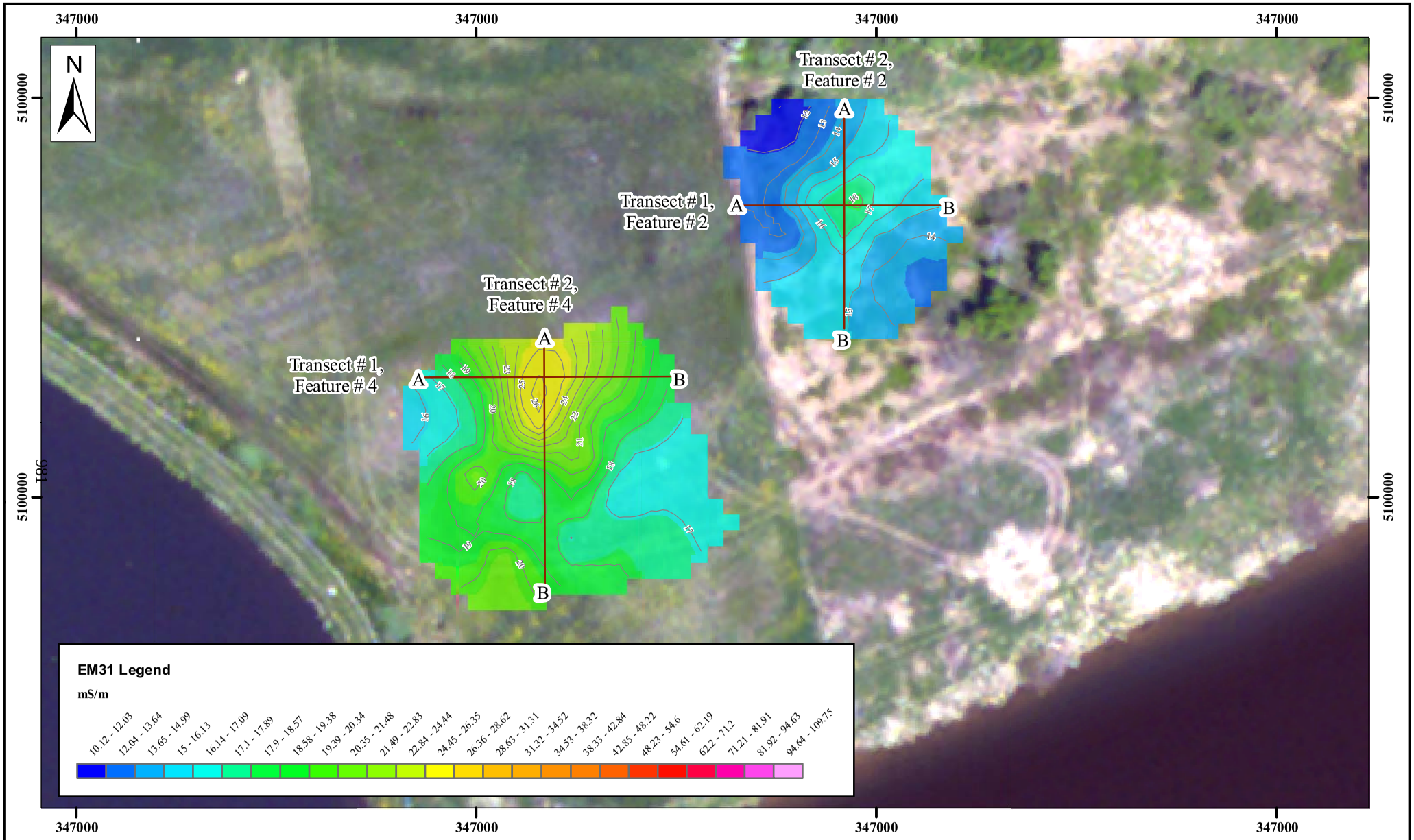

LEGEND

Cross Section Transect

Contous (1 mS/m interval)

SCALE: 1 centimeter = 6 meters

0 5 10 15 20

Meters

AMEC Earth and Environmental
A Division of AMEC Americas Ltd.

DATE: 09/03/09
DRAWN BY: JNR
PROJECT NO.:
FILE NAME: Figure_4_EM31_data_testgrds_results_aireal.mxd
DATUM: NAD 83
PROJECTION: UTM Zone 20N
DATA SOURCE(S): EM31 data

Petitcodiac EM31 Geophysical Achaeological Survey Test Grids, Geosoft Results

FIGURE 2
Test Grids

Map Document: (C:\Documents and Settings\justin.rogers\My Documents\Petiticodiac_River\MXD\sageep\Figure_4_EM31_data_testgrds_results_aireal.mxd) 2/10/2010 -- 7:01:13 AM

Figure 3. Test Grid Profiles of Features 2 and 4

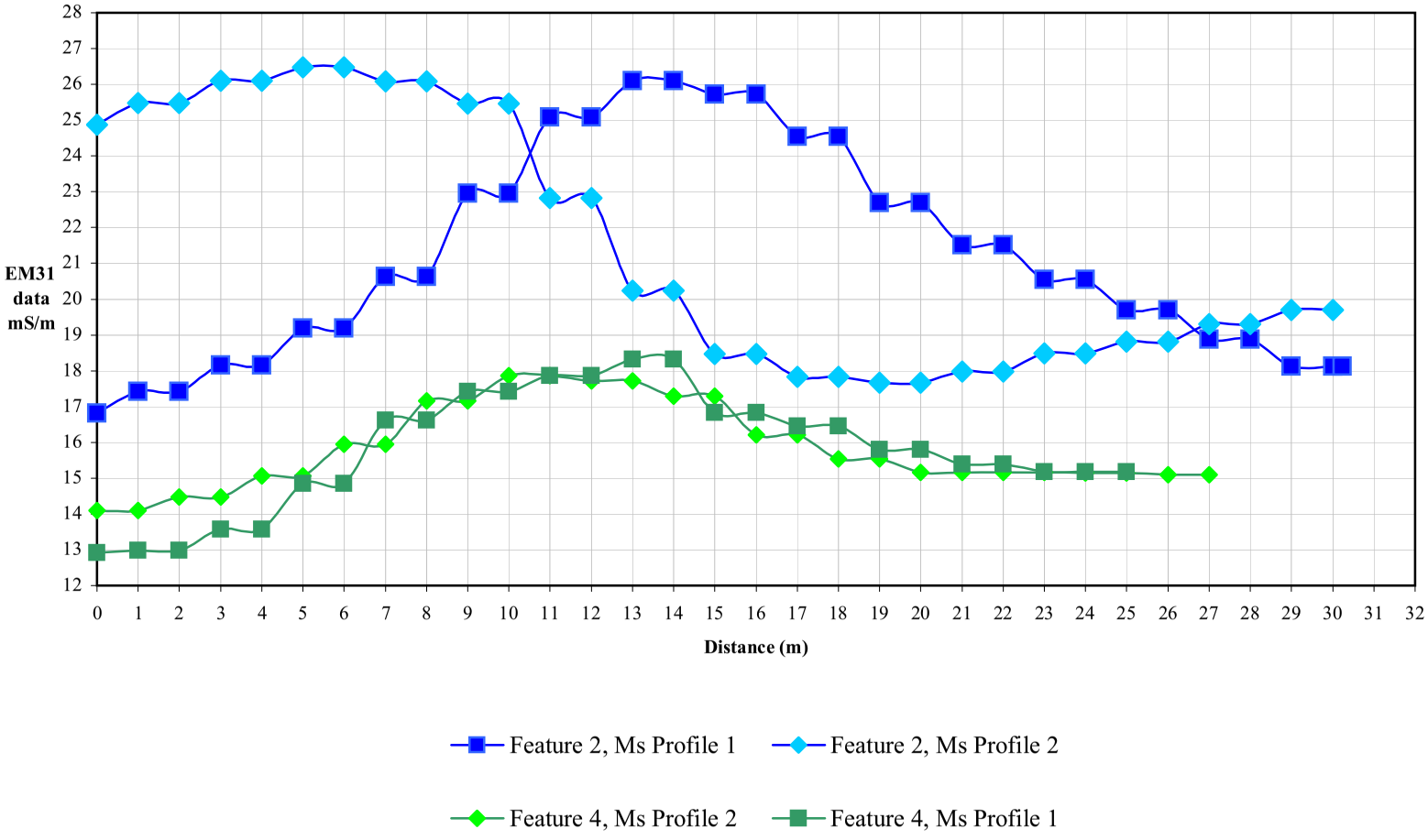

Figure 4. Grid 28 with anomalies

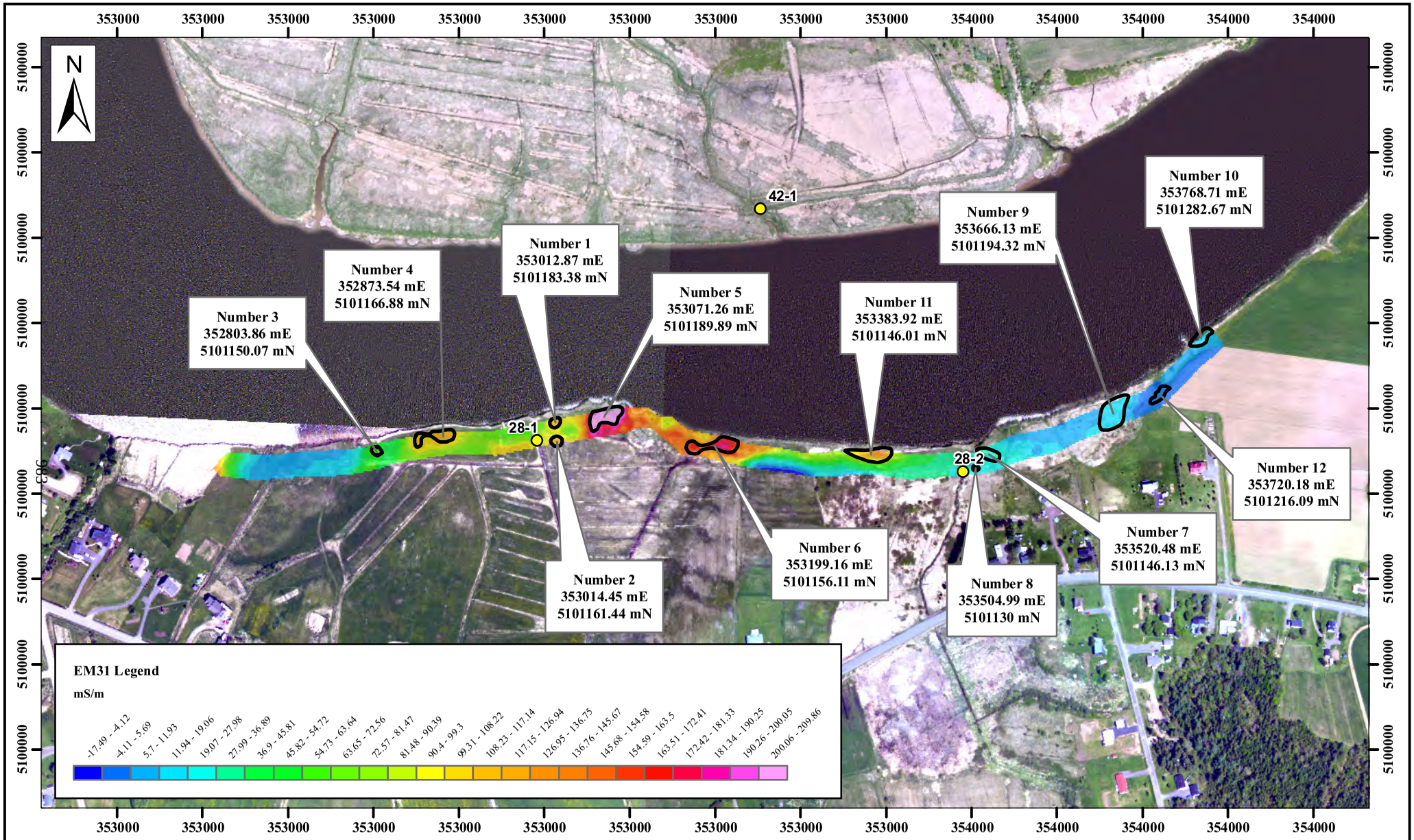

LEGEND

- Aboiteau Location
- Anomalies

SCALE: 1 centimeter = 61 meters

0 50 100 150 200 Meters

AMEC Earth and Environmental
A Division of AMEC Americas Ltd.

DATE: 09/03/09
DRAWN BY: JNR
PROJECT NO.:
FILE NAME: Figure_XX_EM31_data_28-Map__Series_results_aireal.mxd
DATUM: NAD 83
PROJECTION: UTM Zone 20N
DATA SOURCE(S): EM31 data

Petitcodiac EM31 Geophysical Achaeological Survey
28 Geosoft Results

FIGURE 4
28 - Map Series

Map Document: (H:\Projects\2009\Petiticodiac_River\MXD\Figure_XX_EM31_data_28_4_results_aireal.mxd) 9/17/2009 -- 3:54:51 PM

Figures 5 Anomaly 4

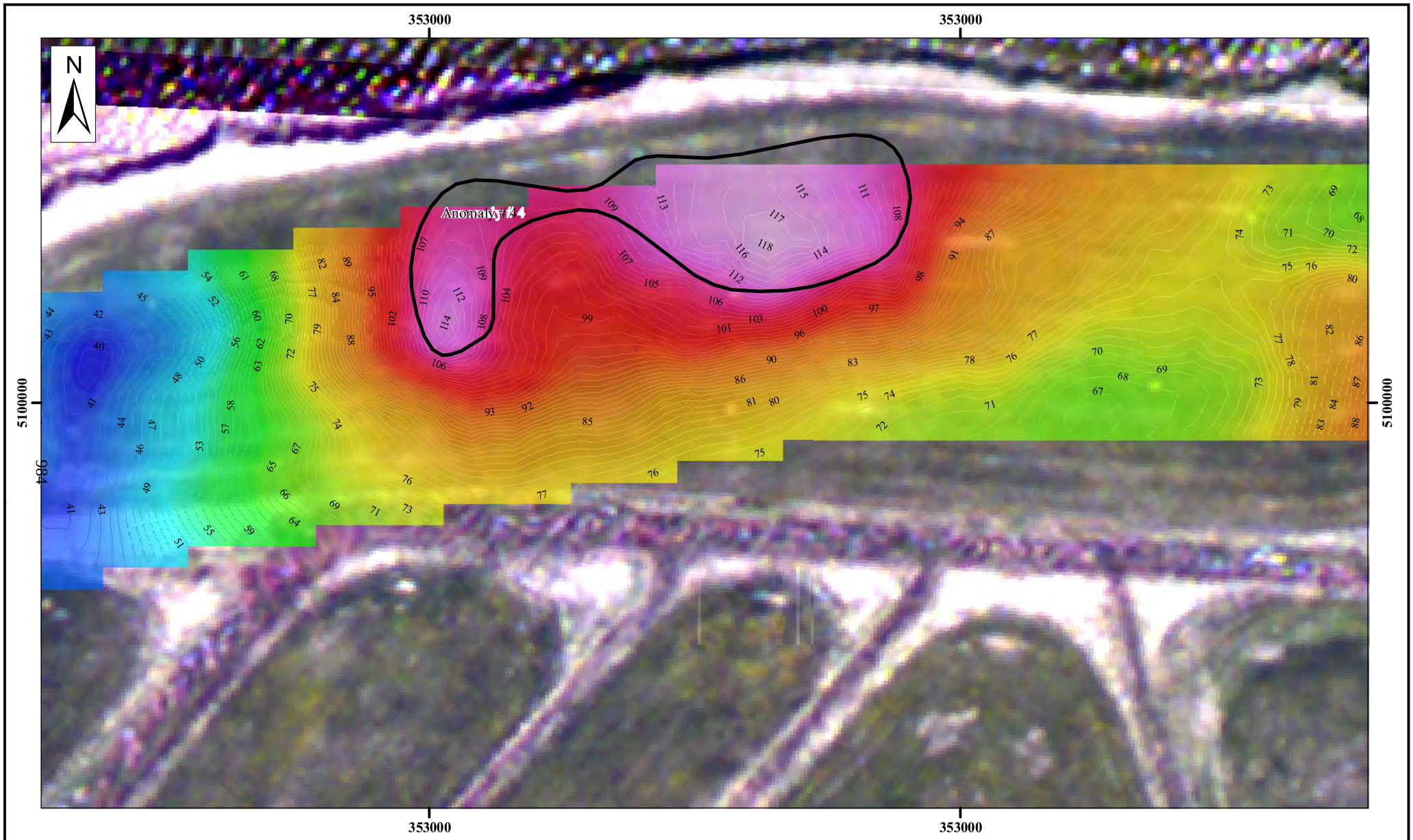

LEGEND

- Aboiteau Location
- Contours 1 mS/m
- Anomalies
- High : 117.853
- Low : 39.6146

SCALE: 1 centimeter = 5 meters

0 5 10 15 20 Meters

AMEC Earth and Environmental
A Division of AMEC Americas Ltd.

DATE: 09/03/09
DRAWN BY: JNR
PROJECT NO.:
FILE NAME: Figure 8 Anomalies 4.mxd
DATUM: NAD 83
PROJECTION: UTM Zone 20N
DATA SOURCE(S): EM31 data

Petitcodiac EM31 Geophysical Achaeological Survey
28 Geosoft Results

FIGURE 5
Anomaly 4

Map Document: (C:\Documents and Settings\justin.rogers\My Documents\Petiticodiac_River\MXD\sageep\Figure 8 Annomalies 4.mxd) 2/9/2010 -- 4:55:54 PM

Figures 5. Annomaly 6

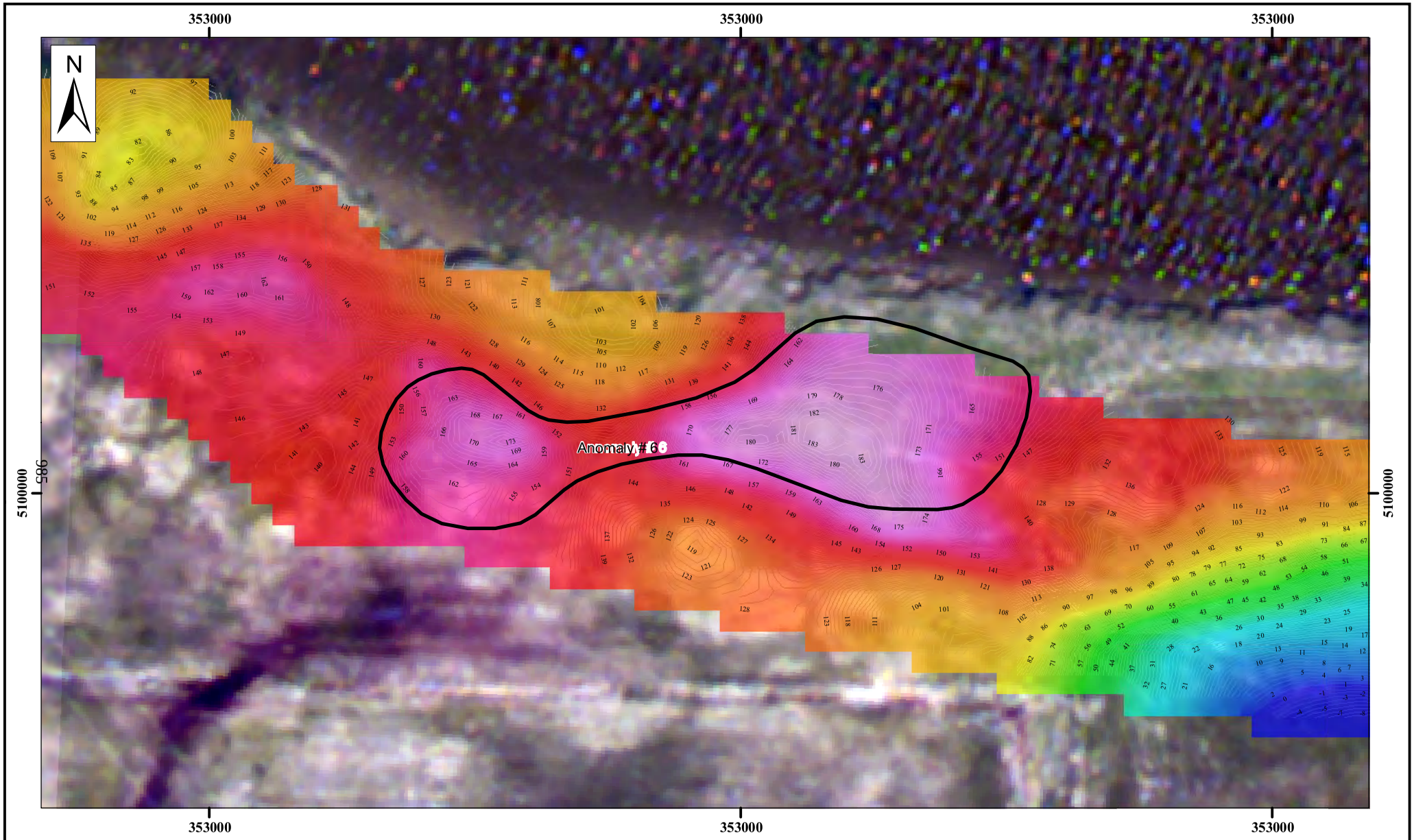

LEGEND

Contours 1 mS/m

Anomalies

High : 183.458

Low : -8.99519

SCALE: 1 centimeter = 5 meters

0 5 10 15 20 Meters

AMEC Earth and Environmental
A Division of AMEC Americas Ltd.

DATE: 09/03/09
DRAWN BY: JNR
PROJECT NO.:
FILE NAME: Figure 9 Anomalies 6.mxd
DATUM: NAD 83
PROJECTION: UTM Zone 20N
DATA SOURCE(S): EM31 data

Petitcodiac EM31 Geophysical Achaeological Survey 28 Geosoft Results

FIGURE 6
Anomaly 6

Map Document: (C:\Documents and Settings\justin.rogers\My Documents\Petiticodiac_River\MXD\sageep\Figure 9 Annomalies 6.mxd) 2/9/2010 -- 4:47:52 PM

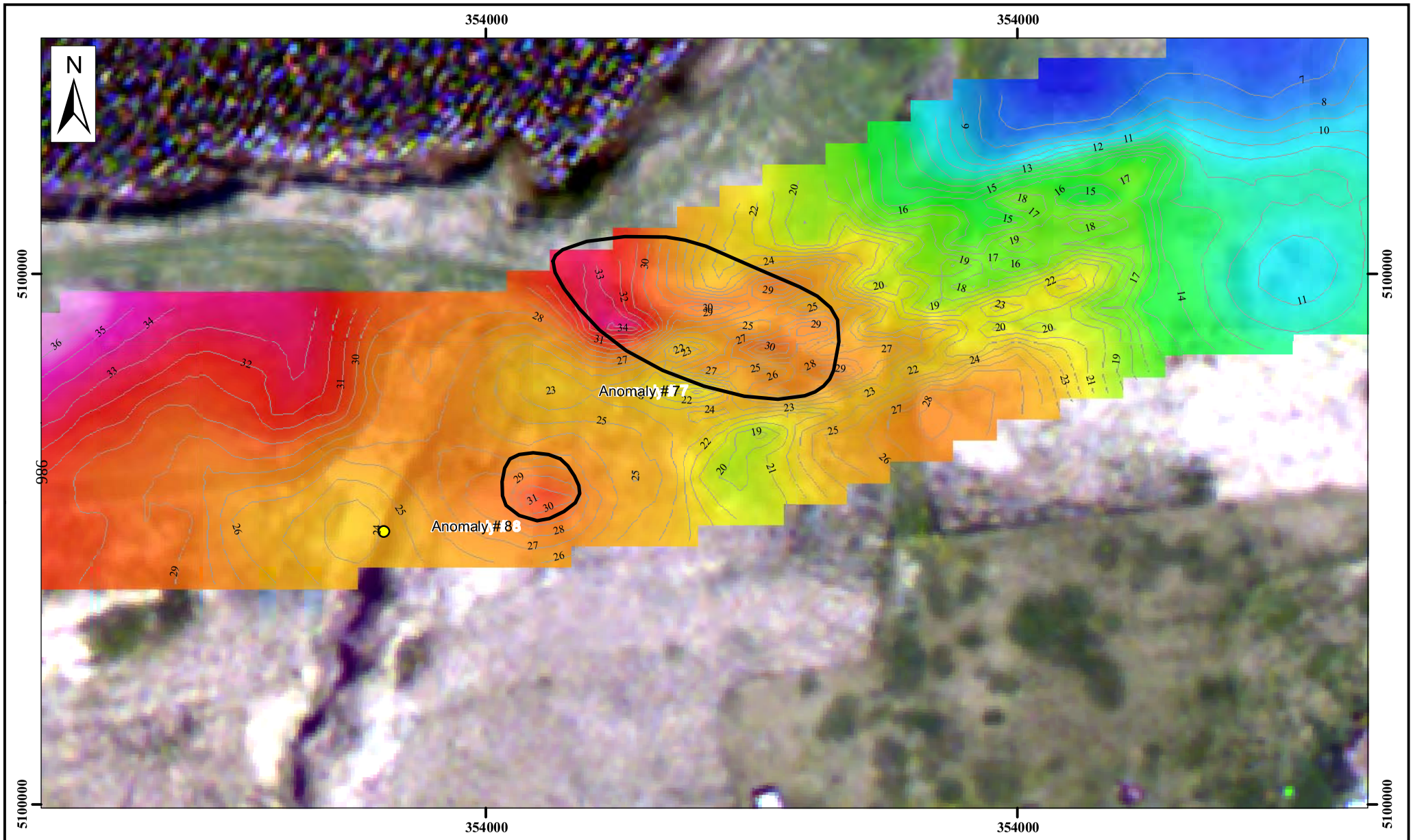

LEGEND

Anomalies

Aboiteau Location

Contours 1 mS/m

High : 36.7819

Low : 6.00972

SCALE: 1 centimeter = 5 meters

0 5 10 15 20 Meters

AMEC Earth and Environmental
A Division of AMEC Americas Ltd.

DATE: 09/03/09
DRAWN BY: JNR
PROJECT NO.:
FILE NAME: Figure 10 Anomalies 7.mxd
DATUM: NAD 83
PROJECTION: UTM Zone 20N
DATA SOURCE(S): EM31 data

Petitcodiac EM31 Geophysical Achaeological Survey
28 Geosoft Results

FIGURE 7
Anomalies 7 and 8

Map Document: (C:\Documents and Settings\justin.rogers\My Documents\Petiticodiac_River\MXD\sageep\Figure 10 Annomalies 7.mxd) 2/9/2010 -- 4:58:13 PM

References

AMEC 2009a. Rehabilitation Plan for Marshes Upstream of Causeway (Dykes And Aboiteaux) for Conditions of Approval 13, Modifications to the Petitcodiac River Causeway. NBDSS Project No. 257-B03 YB299A. Submitted to New Brunswick Department of Supply and Services. Fredericton, New Brunswick.

AMEC 2009b. Preliminary Report: Heritage Resource Impact Assessment Spring Garden Lagoon Project, Boundary Creek, Westmorland County, NB. Prepared for the NB Department of Supply and Services and Archaeological Services Unit, Heritage Branch, Culture and Sport Secretariat, Government of New Brunswick: Canada.

AMEC 2006. Final Report: Continuing Evaluation of Identified Heritage Resource (Bldf-2), Turtle Creek Moncton, New Brunswick. Prepared for the City of Moncton, NB and Archaeological Services Unit, Heritage Branch, Culture and Sport Secretariat, Government of New Brunswick: Canada.

AMEC. 2005a. Environmental Impact Assessment Report for the Modifications to the Petitcodiac River Causeway. AMEC Earth & Environmental, a Division of AMEC Americas Limited Fredericton, New Brunswick.

AMEC 2005b. Heritage Resources Assessment for the Proposed Turtle Creek, Tower Road Dam Project. Prepared for the City of Moncton, NB and Archaeological Services Unit, Heritage Branch, Culture and Sport Secretariat, Government of New Brunswick: Canada.

Archaeological Services NB. 2009. Guidelines for Conducting Heritage Resource Impact Assessments in New Brunswick. Archaeological Services Unit, Heritage Branch, Department of Wellness, Culture and Sport, New Brunswick. April 21, 2009.

Bleakney, S. 2004. Sods, Soil, and Spades: The Acadians of Grand-Pré and their Dykeland Legacy. Montreal: McGill-Queens University Press, Montreal.

Bourque, J. Rudolph, 1971. "Social and Architectural Aspects of the Acadians in New Brunswick" New Brunswick: Research and Development Branch, Historical Resources Administration, Government of New Brunswick.

Burley, David V., 1974. "An Historic Site Survey within Pre-expulsion Acadian New Brunswick". Fredericton, New Brunswick: Archaeological Services Unit of the Heritage Branch, Culture and Sport Secretariat.

Cormier, Y. 1990. Les aboiteaux en Acadie: Heir et aujourd' hui. Moncton: Université de Moncton.

Ferguson, A.M. 1998. Maritime Archaeological Resource Inventory Form for Site CaDf-9 ("The Cox Site"). Archaeological Services Unit, Heritage Branch, Culture and Sport Secretariat, Government of New Brunswick: Canada.

Fowler, Jonathan. 2006. Archaeological Salvage Excavation of a 17th-Century Acadian Sluice from the Grand-Pré Marsh. Archaeological Research Report: Heritage Research Permit A2006NS53.

Ganong, W.F. 1899. Proceedings and Transactions of the Royal Society of Canada. Second Series, Vol. V, 626. Meeting of May, 1899. Ottawa: James Hope & Son.

Leonard, Kevin. 1991. The Origin and Dispersal of Dykeland Technology. Les Cahiers de la Société Historique Acadienne, Vol. 22, No. 1. Pp. 31-59.

Niles, E. 2001. Review of the Petitcodiac River Causeway and Fish Passage Issues. Prepared by Eugene Niles, Special Advisor to the Minister of Fisheries and Oceans, for the Minister of Fisheries and Oceans.

Ross, S. 2002. Les digues et les aboibeaux: Les Acadiens transforment les marais sales en prés ferties / Dykes and Aboiteaux: The Acadians Turned Salt Marshes into Fertile Meadows. Grand Pré, NS: Société Promotoin Grand-Pré.

Surette, Paul, 1996. "Atlas de l'établissement des Acadians aux trois rivières du Chignectou 1660-1755". Moncton: Les Éditions d'Acadie.

Surette, Paul, 1985. Le Grand Petcoudiac, dans "Histoire des Trois-Rivières, Volume III 1763 à 1832". Dieppe: la ville de Dieppe.

APPLICATION OF POTENTIAL GEOPHYSICAL FIELDS AT ARCHAEOLOGICAL SITES IN ISRAEL: AN INTRODUCTION

Lev V. Eppelbaum, Dept. of Geophysics, Tel Aviv University, Ramat Aviv, Tel Aviv, Israel

Abstract

In Israel occur a giant number of archaeological objects of various age, origin and size. Geodynamical active, multi-layered, and geologically variable surrounding media in many cases damages ancient objects and disturbs their physical properties. This calls to application different geophysical methods armed by the modern interpretation technology. Potential geophysical fields (magnetic, gravity, resistivity, self-potential and thermal) are non-expensive, rapid and effective tools for investigation of the most part of archaeological remains. One of the main advantages is that quantitative analysis of these fields may be realized by the use of similar interpretation methodology. Several examples illustrate effective application of potential geophysical methods over some typical archaeological remains in Israel.

Introduction

The territory of Israel, in spite of its comparatively small dimensions (about of 22,000 km^2), contains extremely large number of archaeological remains due to its rich ancient and Biblical history. Many authors (e.g., Kenyon, 1979; Kempinski and Reich, 1992; Meyers, 1996) note that density location of archaeological sites on Israeli territory is the highest in the world. Potential geophysical fields (magnetic, gravity, resistivity, self-potential and thermal) are applied for the revealing and localization of archaeological remains as rapid, effective and non-invasive tools for the study of a broad range of various targets in Israel (e.g., Ginzburg and Levanon, 1977; Eppelbaum, 2000, 2009a; Eppelbaum et al., 2000c, 2001b, 2003, 2004a, 2006b, 2008, 2010; Eppelbaum and Itkis, 2003; Itkis, 2003; Itkis et al., 2003; Boyce et al., 2004, 2009; Weiss et al., 2007). One of the most important advantages is the proved possibility to apply similar methodologies for the analysis of the all mentioned fields (Alexeyev et al., 1996; Khesin et al., 1996; Eppelbaum, 1999; Eppelbaum et al., 2001a; Eppelbaum, 2009b). It permits to apply the advanced interpretation methods developed in magnetic prospecting for complex environments (Khesin et al., 1996) to other potential geophysical fields (with necessary modifications).

Employment of potential geophysical fields has significant preferences due to their different physical principles and varied scales of survey, various locations of measuring sensors and different possible combinations of methods. Geophysical surveys provide a ground plan of cultural remains before excavations or may be even used instead of excavations. Road and plant construction, selection of areas for various engineering and agricultural aims are usually accompanied by detailed geophysical investigations. Rapid and reliable interpretation of geophysical data should provide protection of archaeological remains from unpremeditated destruction. Besides this, non-invasive potential geophysical fields are the most significant tools by the studying of the world recognized religious and cultural artifacts (Eppelbaum, 2010).

Among the variety of ancient objects in Israel, the most typical sites of different ages and origins (taking into account also a frequency of geophysical methods application) are presented in this paper.

Potential Geophysical Fields Application

Magnetic field

The detailed magnetic survey is the most widely used geophysical tool in studying archaeological remains in Israel (e.g., Itkis and Eppelbaum, 1998; Eppelbaum, 2000; Eppelbaum et al., 2000b, 2001b, 2003a, 2008; 2009a; Eppelbaum and Itkis, 2000, 2003; Itkis et al., 2003). Therefore, conditions of this survey will be considered in detail.

Interpretation of magnetic surveys in Israel is complicated by the strong inclination of the Earth's magnetic field (about 42-46^{o}). In addition, the multi-layered and variable structure of the upper part of the geological sequence (Horowitz, 1979; Dan, 1988) presents difficulties in the determination of the level of the normal magnetic field within the sites studied. Sometimes ancient seismological activity found essential reflection in the observed magnetic pattern. Industrial iron and iron-containing objects sometimes produce an intensive noise effect. Uneven terrain relief also disturbs the effect of buried objects and complicates examination of magnetic anomalies. A significant number of the archaeological studied targets are situated in the vicinity of various industrial-agricultural objects that also disturb the archaeogeophysical measurements. The complex conditions of the survey require application of sophisticated geophysical equipment and advanced methods of qualitative and quantitative interpretation (Khesin et al., 1996; Eppelbaum et al., 2001b). Detailed magnetic survey was successfully analyzed in the sites of Banias, Beit-Gouvrin, Beit Shemesh, Emmaus, Eynan, Evora, Halutza, Kissufim Road, Megiddo, Munhata, Nahal-Zehora, Nahal Nagit, Sha'ar Ha-Golan, Tel Kara Hadid, Yodefat, etc. (Eppelbaum et al., 2000a, 2001b; 2003a; Itkis, 2003; Eppelbaum et al., 2004a, 2006b, 2007, 2010; Itkis and Eppelbaum, 2009). Studying of magnetic susceptibility of ancient remains and surrounding media was performed practically at all archaeological sites where magnetic survey was performed (Eppelbaum and Itkis, 2001; Itkis, 2003; Itkis and Eppelbaum, 2009).

Some qualitative conclusions about the ancient targets might be obtained from the analysis of low-intensive temporary magnetic variations observed over the desired archaeological targets (Finkelstein and Eppelbaum, 1997). A new laser magnetic field detector permits to observe picoTesla anomalies over ancient targets with a very low magnetic contrast (Finkelstein and Eppelbaum, 1998).

The complex and multi-layered structure of many archaeological sites and their remains, and known ambiguity of interpretation of results from single geophysical methods, calls for an integration of different geophysical methods. Methods of potential fields integrated analysis are presented in detail in Khesin et al. (1996) and Khesin and Eppelbaum (1997).

The generalized scheme of magnetic data examination at archaeological sites is presented in Fig. 1. As it follows from analysis of this figure, the final aim of magnetic (and any geophysical method employment) is development of the Physical-Archaeological Model (*PAM*).

The constructed *PAM*s of different hierarchical complexity (the simplest *PAM*s reflect recognition of the desired target while complete *PAM*s represent 3D models of archaeological remains) are used for substantiation of direct excavations in the recognized areas (as well as for prohibition of industrial activity) and for generating further strategies for archaeological investigations at sites where ancient remains have been discovered.

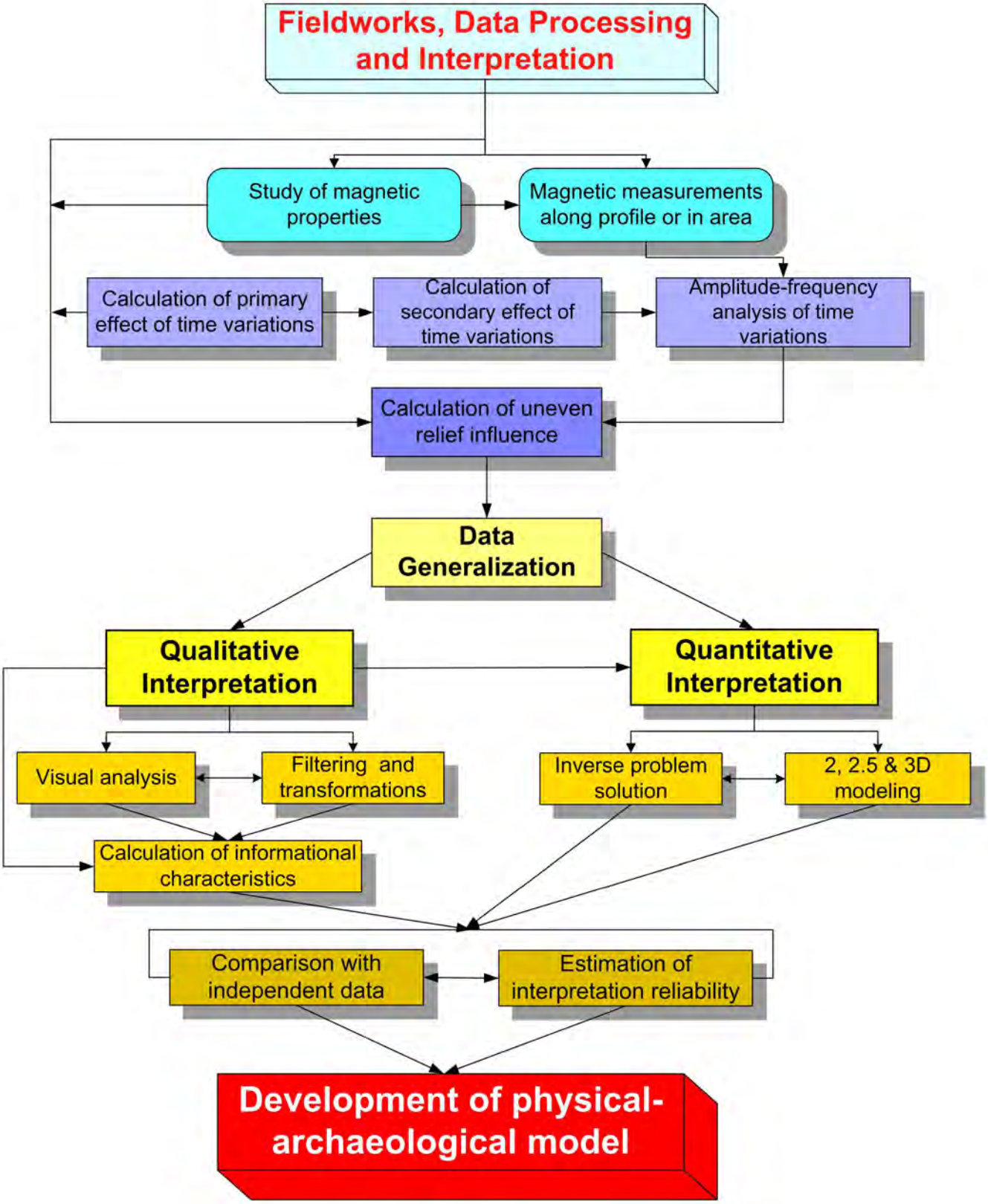

Figure 1: High-precision magnetic prospecting: A generalized block-scheme

Sometimes, for removing the noise of different origin, distributed as quasi-white noise, it is useful to transform observed geophysical fields to some informational features. Khesin (1974) and later – Khesin et al. (1996) suggested to apply for this aim the following informational parameters:

$$J_i = -\log P_j, \quad \text{or} \quad J_i \approx \log\left|\frac{U_i}{\Delta U_i}\right|, \tag{1}$$

where J_i is the informational parameter, P_j is the relative frequency of the j-th interval of the i-th indicator on the histogram of its distribution, U_i and ΔU_i are the amplitude and the error of this indicator determination, respectively.

Eppelbaum (2001) and Eppelbaum et al. (2003a) proposed to use the following expression:

$$J_i = U_i\left(\sum_i^n U_i\right)^{-1} \log\left[U_i\left(\sum_i^n U_i\right)^{-1}\right]K, \tag{2}$$

where U_i is the geophysical observation at i^{th} point ($U_i > 0$) at the area under study and n is the total number of observations, K is the some coefficient.

An experimental testing indicates that application of expression (2) is more effective, especially in the complex media.

Let us consider converting of magnetic survey data, observed at the site of Munhata, to the informational parameter J_i. The site of Munhata is located on a terrace at the outlet of Nahal Tabor to the Jordan Valley, some 11 km south of Lake Kinneret (northern Israel), 215 m below sea level. The depth of archaeological remains at the Munhata site is between 2 and 3 meters. The magnetic survey at this site was expected to be successful taking into account the considerable contrast between features of interest (built mainly of different kinds of basalts) and dark brown surrounding soil. The magnetic survey was carried out to the north of the excavation area.

In the compiled magnetic map (Fig. 2A) it is difficult to reveal the anomalous objects, but map processed by the use of Eq. (2) (Fig. 2B) clearly displays the desired objects (they outlined by white rectangular and circular frames). The known archaeological objects excavated to the south of the surveyed area are presented in Fig. 2C. Obviously, that archaeological targets shown in Fig. 2C (discovered objects) and informational images presented in Fig. 2B (proposed objects) have a good agreement. Thus, Fig. 2B represents the simplest qualitative *PAM*.

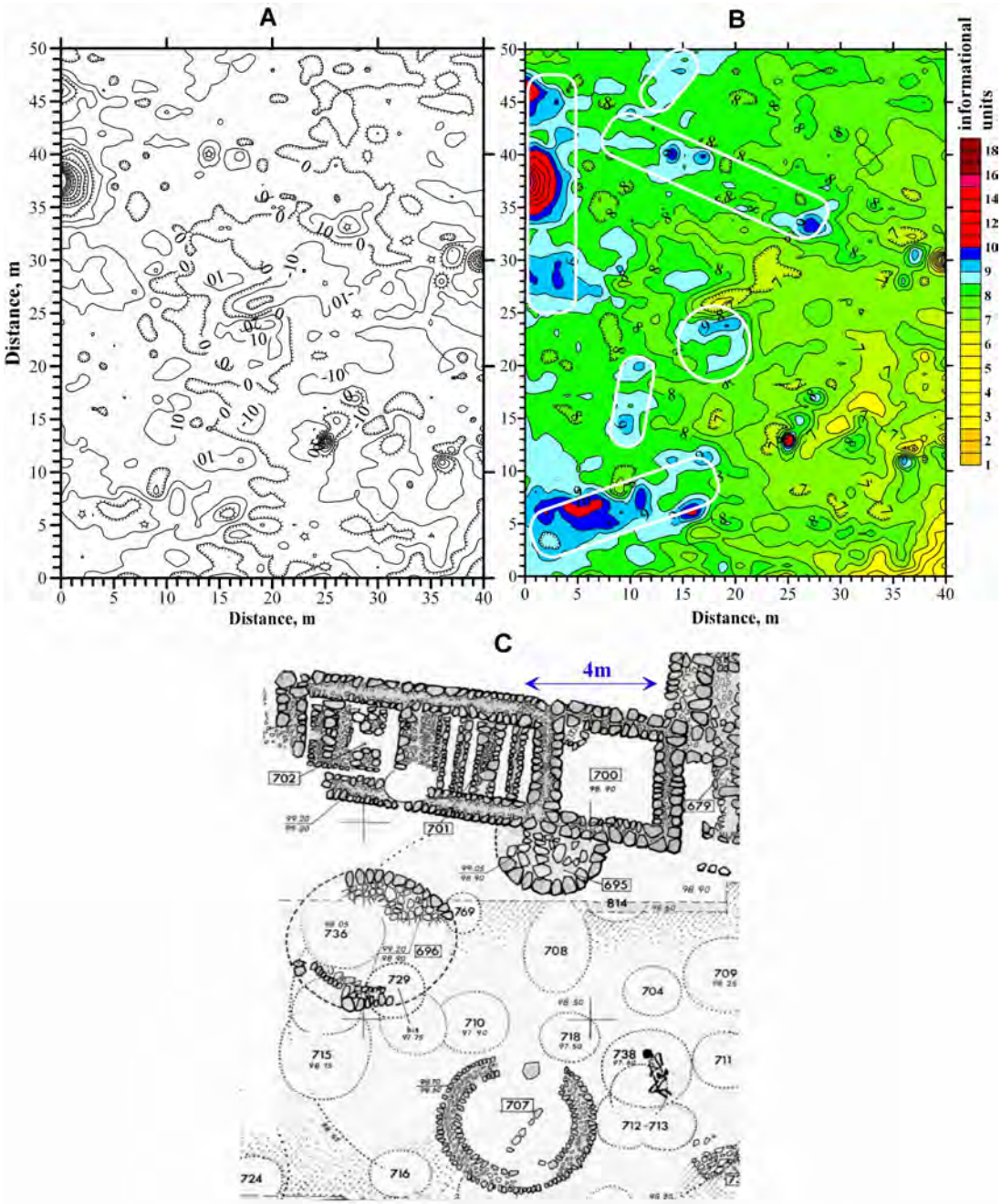

Figure 2: Magnetic maps of the northern part of Munhata site: (**A**) observed magnetic map (after Eppelbaum et al., 2000b), (**B**) the same magnetic map after transformation by the use of Eq. (2), (**C**) excavated part of the Munhata site, some 10 m south of the studied site (after Commenge, 1996)

Inverse problem solution occupies a very important place in the magnetic anomalies analysis. A simple example of inverse problem solution for the model of buried archaeological cavity (J = 0) occurring in the magnetized medium (J = 300 mA/m) with underlying layer of J = 150 mA/m is displayed in Fig. 3. Strong oblique magnetization (44^o, typical for Israeli archaeological sites) and inclined surface relief complicate quantitative analysis of this anomaly. Simple visual analysis of the magnetic curve indicates that minimal amplitude of this anomaly might not coincide (see vertical green dash line) with the

projection of hidden ancient object to the earth' surface. Application of the developed methodology of inverse problem solution (improved versions of tangents and characteristic points method) (Khesin et al., 1996) permitted to determine the position of sphere center (a model of horizontal circular cylinder was applied) with high accuracy (Fig. 3). Hence, a trouble-free quantitative *PAM* has been constructed.

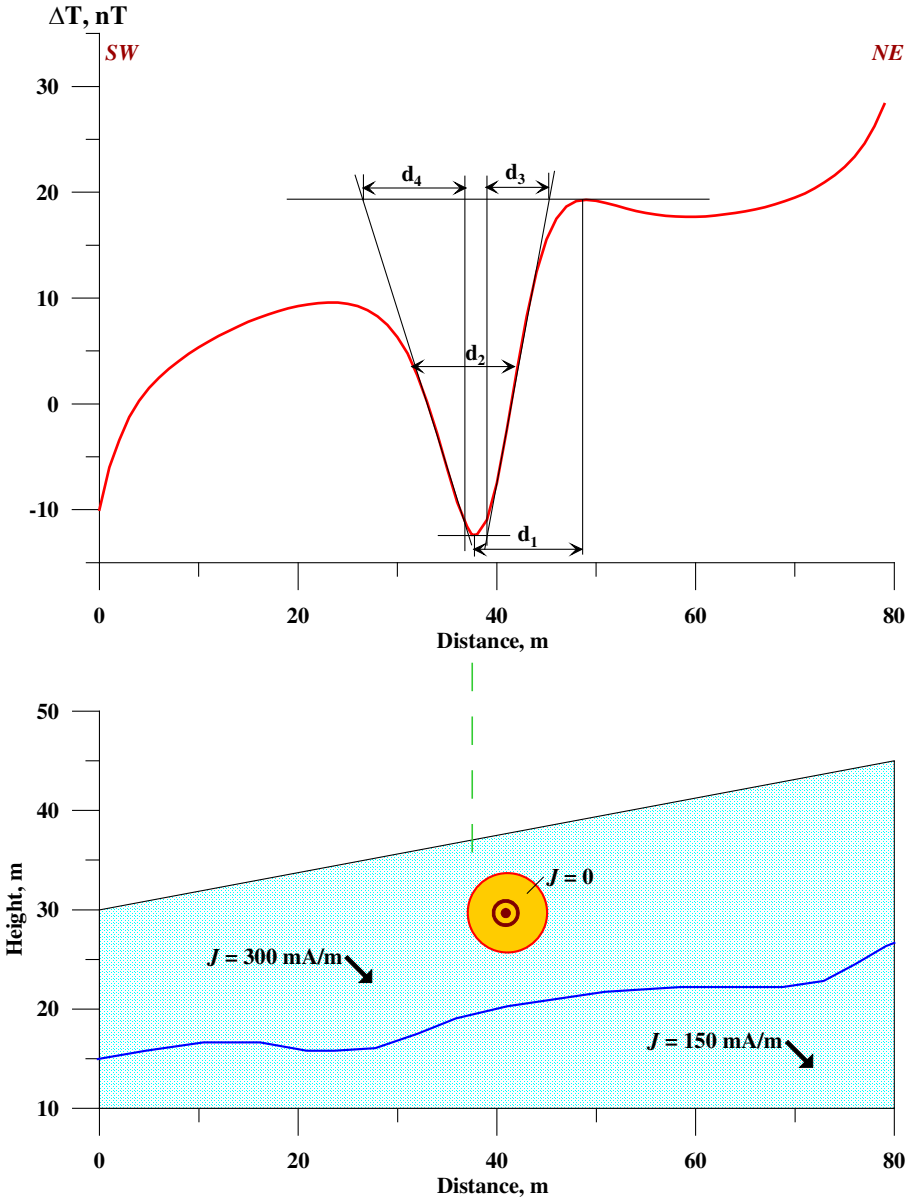

Figure 3: Model example of magnetic field quantitative analysis under complicated environments. Symbol ⊙ designates location of the sphere center and arrows show the position of the total magnetic field vector

Magnetic anomalies analysis at Ashqelon-Marina (southern Israel) had the aim to examine this area prior to large-scale commercial development. Within this area over 90 pits were identified and most of them were revealed using detailed magnetic prospecting (field works were performed by S. Itkis). The overlying layer of dark brown sandy soil was found to be over 0.5 m in thickness. The pits were all full of refuse (pottery, flints, bones, and stone vessel fragments, some botanical remains and shells). These features were displayed in the magnetic map as ring (radius of 1.5-2 m) positive anomalies (12–20 nT).

Fig. 4 shows an example of magnetic anomaly interpretation over one such ancient garbage pit (the disturbing body was approximated here by the model of a thick bed) (after Eppelbaum et al., 2000b). This is a *PAM* of more high level comparing with Figs. 2 & 3.

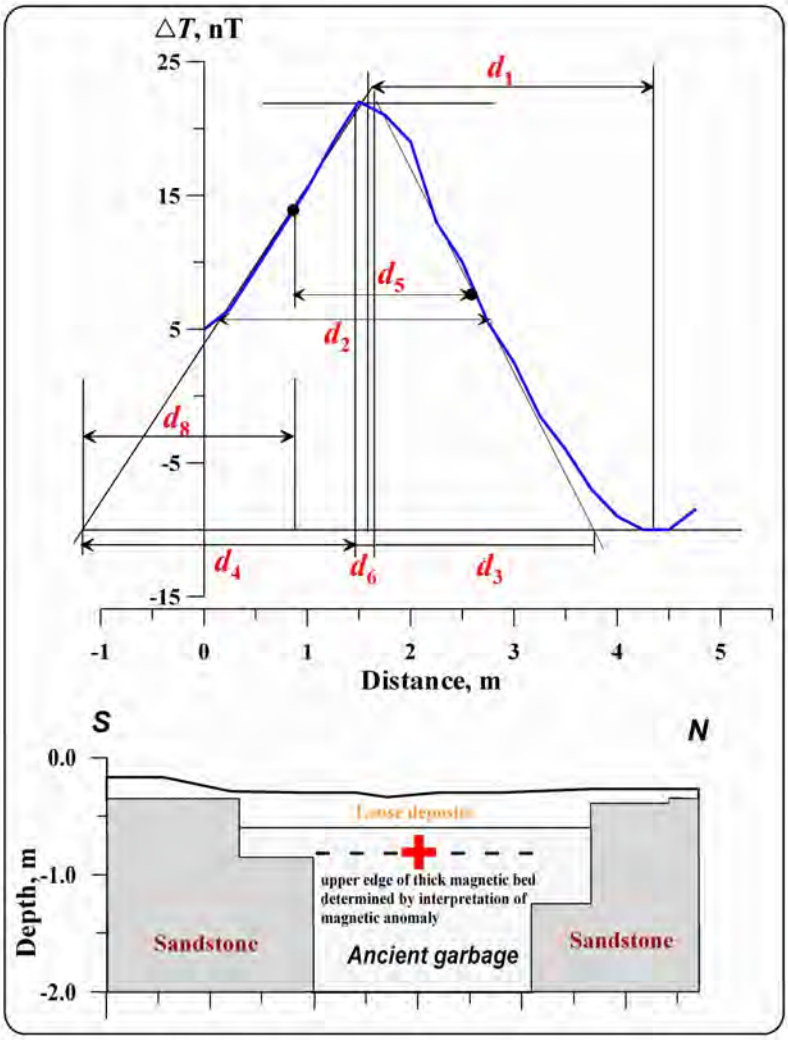

Figure 4: Interpretation of magnetic anomaly due to ancient garbage at the site of Ashqelon-Marina

Next example illustrates efficient application of magnetic survey at the ancient metallurgical site of Tel Kara Hadid. This site (Early Islamic period, 7^{th}–11^{th} centuries A.D.) is located on the western side of the southern Arava Valley, several km north of Eilat in southern Israel. The site contains to a series of copper mines and smelting camps of that period. The same type of slag, reflecting a uniform technology, characterizes all these smelting sites. On the magnetic map two anomalies are clearly detected (Fig. 5A), which were recognized as furnaces used in ancient metallurgy. Positions of the upper edges of the anomalous bodies (approximation model of thick (Anomaly 1) and thin (Anomaly 2) beds were used) and their magnetization were determined (Fig. 5B). A 3D modeling of the magnetic field was applied to develop the final *PAM* (Fig. 5C) (after Eppelbaum et al. (2001b), with modifications).

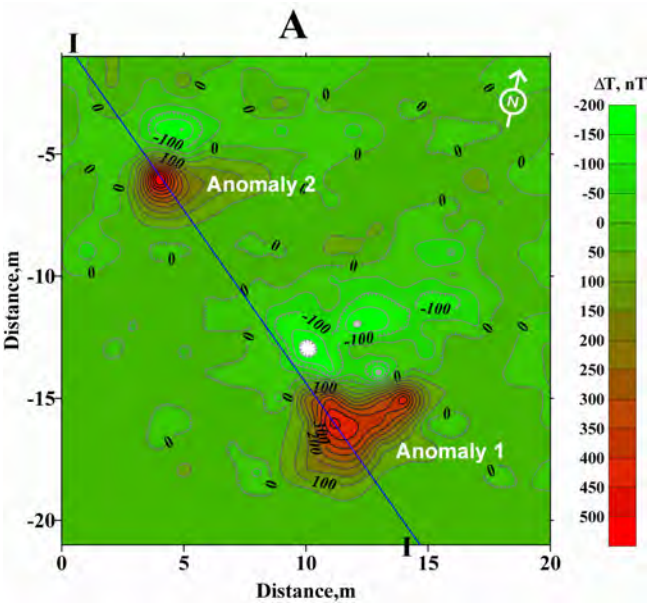

Figure 5: Solving inverse problem and 3-D modeling of magnetic field in the Tel Kara Hadid site (southern Israel).
(**A**) Magnetic map of the studied site

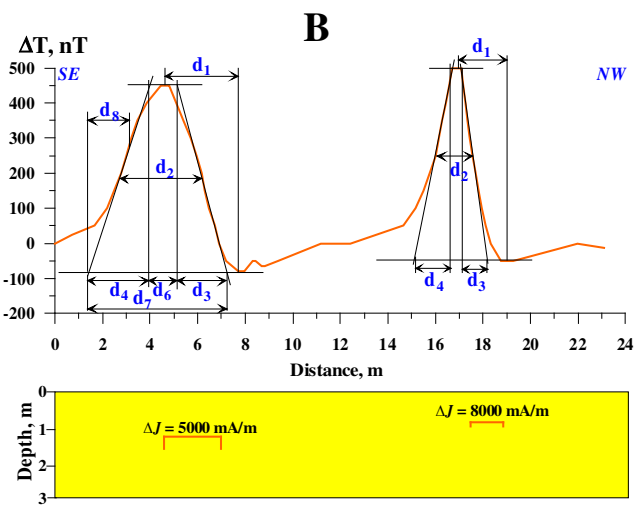

Figure 5B: Rapid interpretation of magnetic anomalies using developed procedures along profile I – I

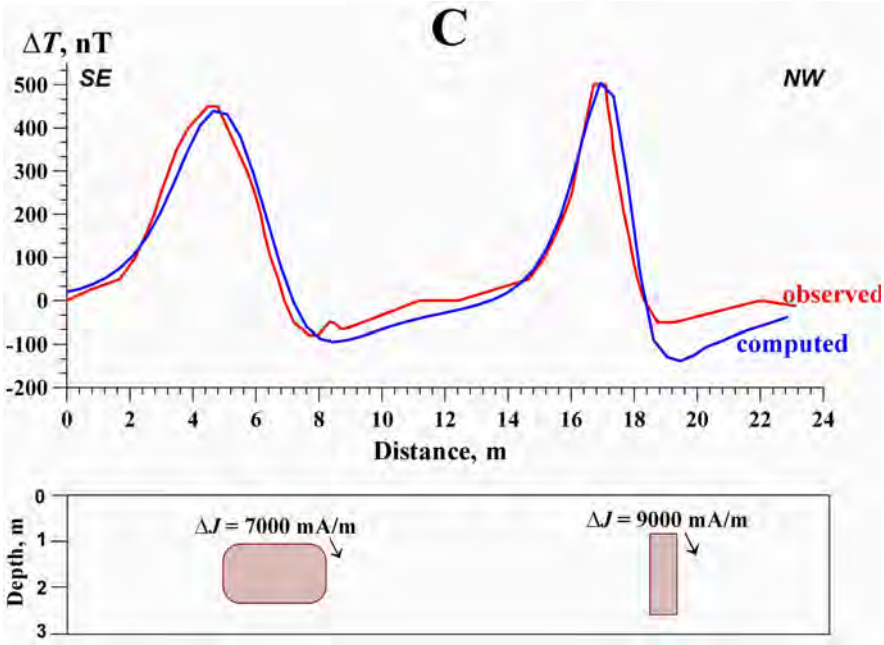

Figure 5C: Results of 3-D modeling along profile I – I. Δ*J* is the defined effective magnetization of the studied furnaces, and arrows show the determined position of the total magnetic field vector

Among other successful magnetic field analysis at archaeological sites in Israel the following published results are distinguished. Weiss et al. (2007) fruitfully employed a system developed for detection and accurate mapping of ferro-metallic objects buried below the seabed in the vicinity of Atlit (northern Mediterranean coast of Israel). A paper of Boyce et al. (2004) suggesting to magnetic marine studying of submerged Roman Harbour (Caesarea Maritima, central Israel) is of a great interest. The

magnetic survey identified the presence of an extensive hydraulic concrete foundation below the ruined harbour moles. The magnetic anomaly patterns indicate that the concrete foundation was laid out in a header fashion. Magnetic lows within the structure have localized the baffles that were composed by sand to stabilize the concrete foundation walls. A continuation of this investigation (Boyce et al., 2009) has demonstrated that ancient ship ballast (basalts) could be reliably detected and mapped on the seabed using precise magnetic survey.

Paleomagnetic data analysis in many cases assists to recognize an intricate magnetic pattern at archaeological sites. Paleomagnetic investigations were effectively applied at Abu Matar, Ashqelon, Tel Miqne and Megadim (Sternberg et al., 1999), Bizat Ruhama (Laukhin et al., 2001), Evron Quarry (Ron et al., 2003), Kebara Cave (Sternberg and Lass, 2007), Timna, Yotvata, Mitzpe Evrona, Givat Yocheved, Beer Ora Hill, Tel Kara Hadid (Ben Yosef et al., 2008; Shaar et al., 2010), etc. Segal et al. (2003) carried out paleomagnetic tests on two archaeological structures as an oven and a limekiln in the Crusader fortress Vadum Iacob (northern Israel). These fireplaces enable determination of the local direction and intensity of the geomagnetic field on 24 August 1179, when its construction was terminated by the Arab conquest. Borradaile and Almqvist (2006) analyzed young viscous remagnetization directions at Armageddon (Megiddo), northern Israel.

Self-Potential field

Apparently, firstly SP measurements at archaeological sites in Israel were performed at the sites of Banias, Shaar-Ha-Golan and Halutza (Eppelbaum et al., 2001a, 2003b, 2004b). Later SP survey was performed at the site of Emmaus-Nikopolis (Eppelbaum et al., 2007), where small SP anomalies were registered over little caves of an artificial origin.

Let us consider combined SP/magnetic investigations at the site of Halutza. Halutza is located 20 km southwest of Be'er-Sheva town, in southern Israel. It was the central city of southern Palestine in the Roman and Byzantine periods and was occupied from the Nabatean (7th-2nd centuries BC) through the Byzantine period (4th-7th centuries AD). Halutza was founded as a way station for Nabatean traders traveling between Petra (Jordan) and Gaza. Combined geophysical investigations consisting of magnetic and SP measurements were performed in an area of 200 m^2 using a 1 x 1 m grid (Figs. 6A,B). According to *a priori* information, limestone structures had been excavated in the area of the site. It was expected that limestone (nonmagnetic) remains occur in the medium with magnetization of 70-100 mA/m that could produce the appearance of small negative magnetic anomalies; SP anomaly arising is based on the difference of the electric properties of the target/medium and the generation of the oxidation-reduction processes. The magnetic sensor level was located at 30 cm above the earth's surface. SP measurements were performed using a microVoltmeter with high input impedance and special non-polarized electrodes (*Cu* in $CuSo_4$ solution) (Eppelbaum et al., 2001a). The potential-array scheme (with a base point electrode) was applied; the depth of electrode grounding was 10-15 cm. Visual analysis of the maps (Figs. 6A,B) indicates that the SP and magnetic fields have different trends, but the recognized negative anomalies in the southern part of this site are placed 2 m apart. Quantitative interpretation of SP and magnetic anomalies gave similar depths: 90 and 70 cm, respectively. The corresponding *PAM*s for the performed examination are displayed in Figs. 6C and 6D. The ancient walls excavated in direct proximity to the surveyed area occur at a depth of about 80 cm. It allows us to suggest that the similar objects are the sources of anomalies in the area covered by the integrated geophysical survey.

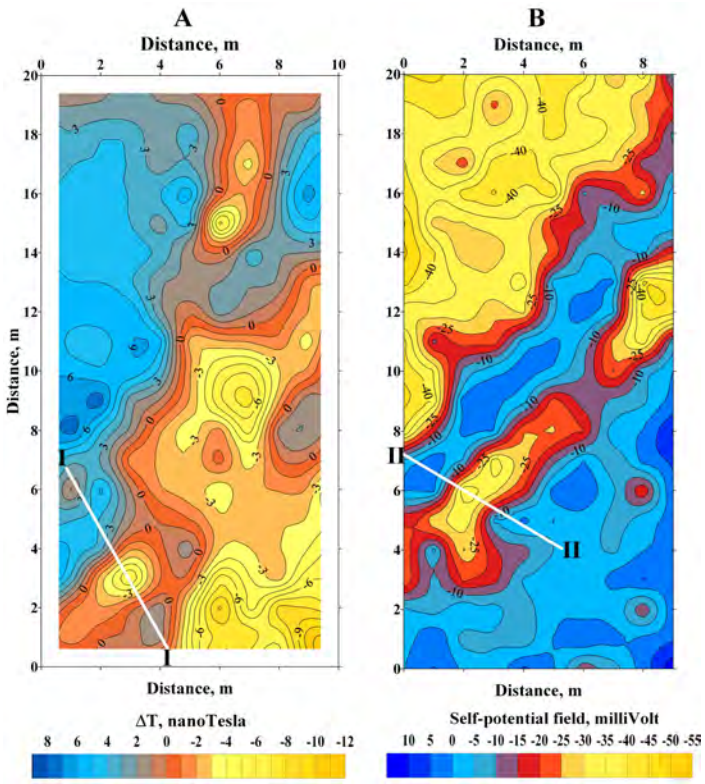

Figure 6A&B: Maps of magnetic (**A**) and self-potential (**B**) fields in the Halutza site (Negev desert, southern Israel)

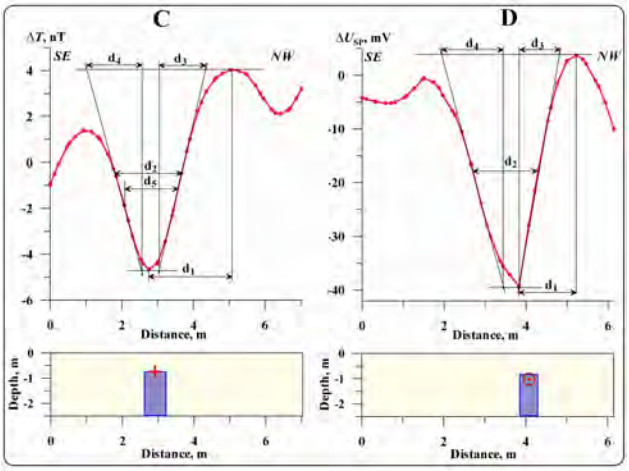

Figure 6C&D: results of the quantitative interpretation for profile I - I (**C**) and II - II (**D**). A cross indicates the position of the middle of upper edge of anomalous body for magnetic anomaly (Fig. 6C), and a small circle is inscribed in the upper edge of anomalous body for the SP anomaly

Direct current

Resistivity (direct current) survey has been successfully carried out at several archaeological sites in Israel (Tanzi et al., 1983). This method was profitably applied at the site of Nahal-Tut for identification of remains of Roman fortress in northern Israel in 1997 (personal communications with Drs. Yu. Gurevich and S. Itkis). Electric resistivity tomography (ERT) has been productively explored in Tel Yavne for identifying the thickness of cultural debris, the plan view extent of cultural debris, and the underlying bedrock contact (Bauman, 2005). Nahas et al. (2006) displayed effective application of electrical resistivity tomography at the coastal sites of Yavne, Yavne Yam and Tel Nami on the Israeli Mediterranean and Bethsaida at the Lake Kinneret. Ginzburg and Levanon (1977) very successfully applied resistivity method in Jerusalem for studying the thickness of the wall of the Mount of the Temple and determination of the underground location of pre-Herodian city walls in the City of David, as well as at the site of Tel-Afek.

DC mapping of the site of Tel-Afek is the classic example of this method application. The archaeological site of Tel Afek, dating to the Late Bronze Age (1550-1200 BC), is situated about 10 km east of Tel-Aviv. One of the main geophysical-archaeological problems at this site consisted in mapping walls of ancient structures, almost completely covered by sediments. Ginzburg and Levanon (1977)

previously applied at this site the resisitivity method (altogether 8 profiles were observed) based on the essential differences in geoelectric characteristics between the ancient objects and sediments, and effectively localized several buried wall foundations in the studied area. One of the electric resistivity anomalies was examined (Fig. 7) with applying the advance interpretative methods developed in magnetic prospecting (Eppelbaum, 1999). For developing a *PAM*, the *HCC* model was applied. As evident from Fig. 7, the interpretation is in good agreement with the archaeological data.

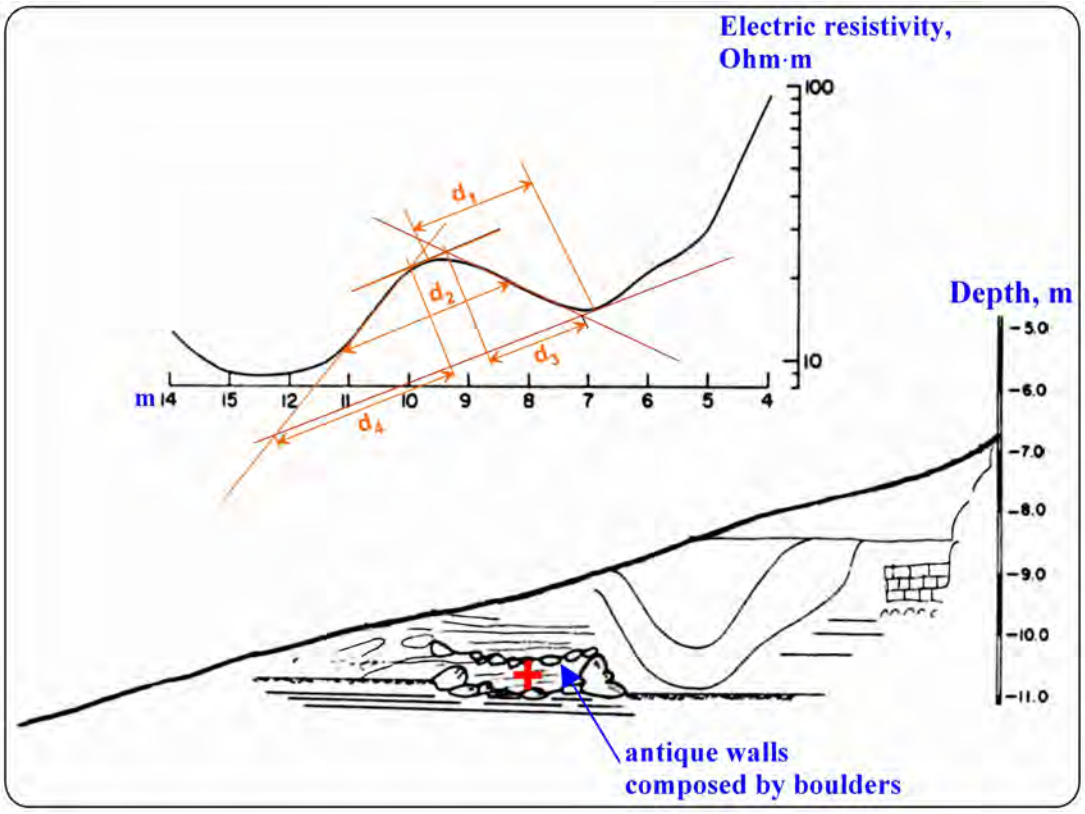

Figure 7: Inverse problem solution for resistivity anomaly in the archaeological site of Tel Afek, central Israel (initial data from Ginzburg and Levanon, 1978). A cross in the section designates the location of the center of anomalous body

Temperature field (*near-surface*)

Paparo (1991) applied near-surface thermal prospecting to qualitative delineation of the remains of a Crusader fortress in the city of Netanya (central Israeli Mediterranean coast). In his investigation, limestone and kurkar (silicious limestone) ancient remains were identified in the clay and loam surrounding. This investigation demonstrated more high effectiveness comparing with the previous thermal studying in the site of Gamla, northern Israel (Paparo, 1991). Obviously, it was caused by complex geological-archaeological sequence of the Gamla area and insufficient calculation of some disturbing factors. A complete methodology of the near-surface temperature investigations at archaeological sites was presented in Eppelbaum (2009b).

Temperature field (*boreholes*)

Eppelbaum et al. (2006c) assessed the possibility of archaeo-temperatures determination by the measurements of modern temperature values observed in shallow boreholes. It should be noted that

obtained values of ancient temperatures would help estimate the present physical-chemical conditions of materials utilized for building of antique constructions.

Gravity Field

Analysis of the numerous archaeological and geological publications as well as the author's investigation (e.g., Eppelbaum, 2000) indicates that the ancient objects supposed for examination by the use of microgravity survey in Israel may be classified (in the decreasing order) by the following way: (1) underground ancient cavities and galleries, (2) walls, remains of temples, churches and various massive constructions, (3) pavements and tombs, (4) Roman aqueducts [under favorable physical-geological environments], (5) areas of ancient primitive metallurgical activity (including furnaces) [under favorable physical-geological environments]. Examining the different archaeological targets in Israel, it was supposed that microgravity method might be effectively applied at least on 20-25% of ancient sites (Eppelbaum, 2009a).

It is necessary to underline that physical measurement of vertical gravity derivatives cannot be replaced by computing of this parameter obtained by any transformation procedures: the second vertical derivative of gravity potential W_{zz} values computed from the field Δg_B, as rule, show decreasing values comparing with the W_{zz} obtained from physical measurements. A few model examples showing buried ancient targets delineation (e.g., pavement and caves) on the basis of detailed gravity analysis are presented in Eppelbaum (2009a). A simplified model example of buried pavement (this model has been developed on the basis of excavations at the Megiddo site, northern Israel) delineation is shown in Fig. 8. A buried pavement having the positive density contrast of 400 kg/m^3 and occurring at a depth of 1.8 m in uniform medium could be easily recognized by microgravity survey (Fig. 8A, integrated anomalous effect from two bodies). Let us assume a low-density layer (2100 kg/m^3) over the pavement. It makes the delineation of the pavement practically impossible in field conditions (registered anomaly is oscillating about 1 microGal) (Fig. 8A, integrated anomalous effect from three bodies). At the same time values of the second vertical derivative of gravity potential W_{zz} (computed for the levels of 0.3 and 1.5 m) with a measurable accuracy testify to a presence of disturbing body (Fig. 8B). The similar graphs were developed for the models of buried ancient caves of various radius, ancient iron furnaces, Roman aqueducts, etc.

Development of multi-dimensional physical-archaeological database

The constant increase in geophysical-archaeological data and their revision has necessitated the development of an Integrated Archaeological-Geophysical Data Base (IAGDB). Obviously, it must be multi-componental and dynamic in character (Eppelbaum and Ben-Avraham, 2002). Besides spatial topographic coordinates (*x, y, z*) of archaeological sites, the IAGDB should include all values of the potential (and not only) geophysical fields (s) observations *over* or *under* the earth's surface, results of the repeated measurements of the geophysical fields (s) repeated measurements over different periods of time, as well as during archaeological excavations. It is also necessary to digitize the geophysical survey results of previous years and to distinguish their relation to other databases (geological, geochemical, paeleostructural, paleosedimentation, paleobotanical, paleobiogeographical, etc.) (Eppelbaum et al., 2010).

As a basis for the IAGDB development one could use *Access* (obviously, with utilization of all necessary graphic archaeological-geological data sets). Development of such a constantly growing database will increase effectiveness of geophysical examination of archaeological targets by simplifying and speeding up the planning, implementation and analysis of archaeogeophysical investigations. From a regional point of view, the Israeli IAGDB could be connected with similar databases from neighboring

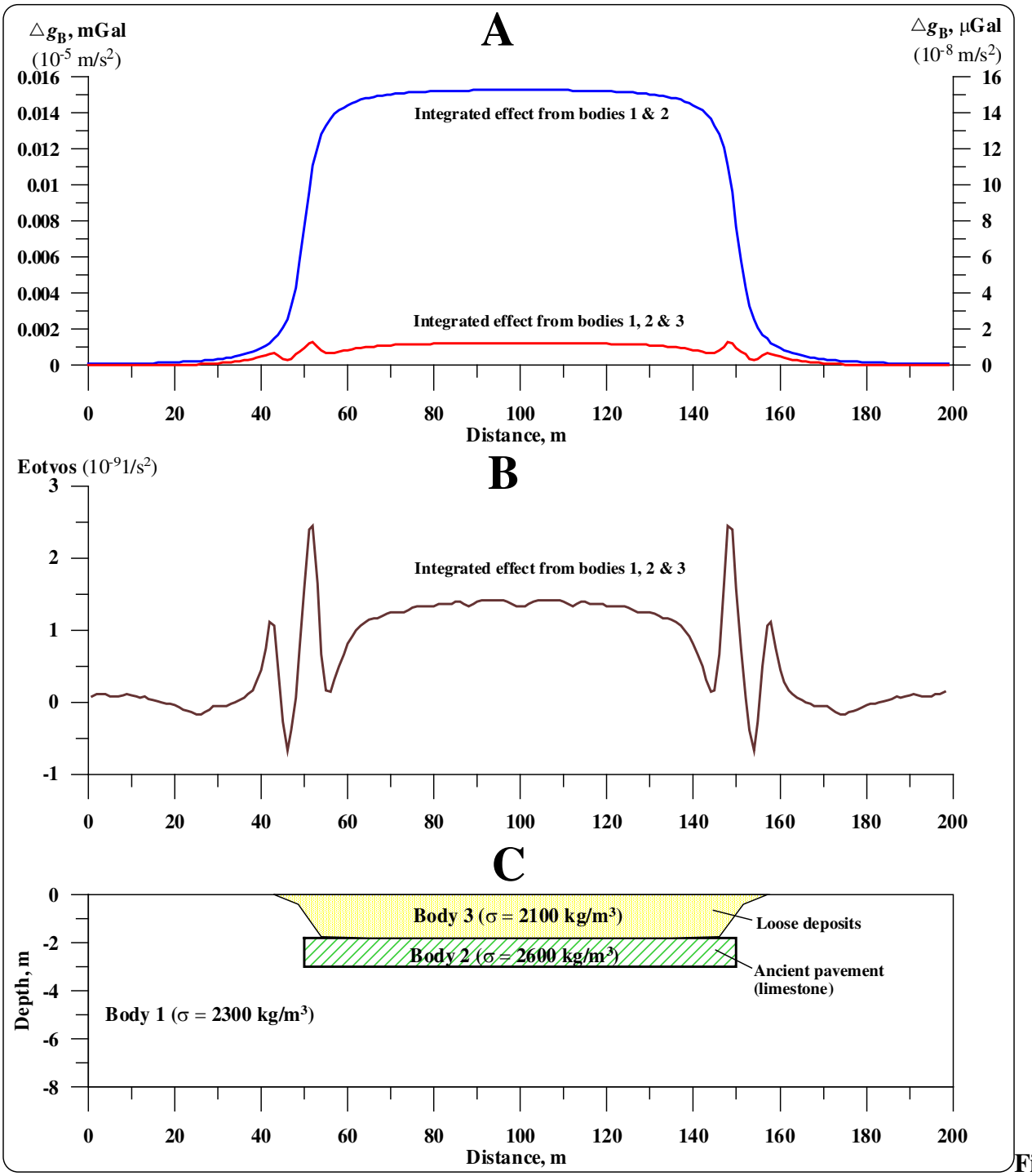

Figure 8: Comparison of Bouguer gravity and vertical gradient anomalies. (**A**) Bouguer gravity, (**B**) vertical gradient g_z (W_{zz}) computed for the base of 1.2 m, (**C**) archaeological sequence

countries in the Mediterranean, the Near and Middle East. The next step, apparently, will include creation of Virtual Archaeology models (Pelfer et al., 2004; Jeffery, 2007) on the basis of combined

simultaneous analysis of all possible geophysical, physical, chemical, environmental and other indicators.

Future perspectives: remote operative vehicle multilevel survey

Among the natural stationary disturbances such factors as swampy soil, dense vegetation, loose ground and uneven terrain relief often complicate performing land archaeogeophysical survey. The new Remote Operated Vehicles (ROV) generation – small and maneuvering vehicles – can fly at levels of few (and even one) meters over the earth's surface (flowing the relief forms) and carry out combined geophysical measurements. The ROV geophysical investigations may be performed during short time period and will have a low exploitation cost. Measurements of geophysical fields at different observation levels could provide new unique archaeological-geophysical information (for instance, see Eppelbaum (2005), besides this, the most effective application of characteristic point method for inverse problem solution (Khesin et al., 1996) demands knowledge of geophysical field behavior at two levels). In addition, multilevel areal observations might be utilized for the procedure of downward continuation on the basis of Gauss' theorem. The ROV archaeogeophysical surveys at the areas of world recognized religious and cultural artifacts (where excavations practically always are suppressed and surface survey is hampered) might have a great importance (Eppelbaum, 2010).

It is proposed that the most prospective geophysical integration for ROV should include measurements of magnetic and *VLF* (electromagnetic very low frequency) and gravity fields (Eppelbaum et al., 2000a; Eppelbaum, 2008a). GPS (with utilization of the improved wide-band Kalman filtering (Eppelbaum, 2008a)) will assure an exact topogeodetic relation for the proposed observations. Integration of land and ROV geophysical data will provide a distinctive success in the archeological sites examination (Eppelbaum, 2008a).

Conclusions

Many thousands of archaeological sites occur in complex geological media in Israel. Potential geophysical fields (first of all, precise magnetic prospecting) at present are the most employed and efficient geophysical methods at archaeological sites in Israel. For their analysis a powerful interpretation methodology applicable under complex geological-archaeological environments has been developed. The final aim of different processing methods application, employment of various algorithms and interpretations, is creation of the Physical-Archaeological Models (*PAM*s) of the ancient buried remains. *PAM*s of different types may be used to undertake excavations in recognized areas and for planning upcoming archaeological investigations at sites where ancient remains have been discovered. Development of the multi-dimensional dynamic physical-archaeological database will help effectively join different branches of geophysical, archaeological and related sciences. It is anticipated that employments of a new generation of remote operated vehicles for geophysical field multi-altitude observations might cardinal improve observation and examination in archaeogeophysics.

References

Alexeyev, V.V., Khesin, B.E., Eppelbaum, L.V., 1996, Geophysical fields observed at different heights: A common interpretation technique, *Proceed. of the Meeting of Soc. of Explor. Geophys*., Jakarta, pp. 104-108.

Bauman, P., Parker, D., Coren, A., Freund, R., Reeder, P., 2005, Archaeological Reconnaissance at Tel Yavne, Israel: 2-D Electrical Imaging and Low Altitude Aerial Photography, *CSEG Recorder*, No. 6, pp. 28-33.

Ben-Yosef, E., Tauxe, L., Ron, H., Agnon, A., Avner, U., Najjar, M., Levy, T.E., 2008, A new approach for geomagnetic archaeointensity research: insights on ancient metallurgy in the Southern Levant, *Journal of Archaeological Science*, **25**, pp. 2863-2879.

Borradaile, G.J., Almqvist, B.S., 2006, Installation age of limestone masonry determined from its viscous remagnetization, *Geoarchaeology,* **21**, No. 1, pp. 29-60.

Boyce, J.I., Reinhardt, E.G., Raban, A., Pozza, M.R., 2004, The utility of marine magnetic surveying for mapping buried hydraulic concrete harbour structures: Marine Magnetic Survey of a Submerged Roman Harbour, Caesarea Maritima, Israel**,** *The International Journal of Nautical Archaeology*, **33** (1), pp. 122-136.

Boyce, J.I., Reinhardt, E.G., Goodman, B.M., 2009, Magnetic detection of ship ballast deposits and anchorage sites in King Herod's Roman harbour, Caesarea Maritima, Israel, *Journal of Archaeological Science*, **36**, pp. 1516-1526.

Commenge, C., 1996, Horvat Minha (el-Munhata), *Excavations and Survey in Israel*, **15**, p.43.

Dan, J., 1988, The soils of the land of Israel, In: Yom-Tov Y. and Tchernov E. (Eds), *The Zoogeography of Israel*, W. Junk Publishers, Dordrecht, pp. 95-128.

Eppelbaum, L.V., 1999, Quantitative interpretation of resistivity anomalies using advanced methods developed in magnetic prospecting, *Trans. of the XXIV General Assembly of the Europ. Geoph. Soc*., Strasburg **1** (1), p.166.

Eppelbaum, L.V., 2000, Applicability of geophysical methods for localization of archaeological targets: An introduction, *Geoinformatics*, **11**, No.1, pp. 19-28.

Eppelbaum, L.V., 2001, *Introduction to Potential Geophysical Fields*, Handmanual for students, Tel Aviv University.

Eppelbaum, L.V., 2005, Multilevel observations of magnetic field at archaeological sites as additional interpreting tool, *Proceed. of the 6th Conference of Archaeological Prospection*, Roma, Italy, 4 pp.

Eppelbaum, L.V., 2009a, Application of microgravity at archaeological sites in Israel: some estimation derived from 3D modeling and quantitative analysis of gravity field, *Proceed. of the 22nd SAGEEP Conference*, **22**, No. 1, pp. 434-446.

Eppelbaum, L.V., 2009b, Near-surface temperature survey: An independent tool for buried archaeological targets delineation, *Journal of Cultural Heritage*, **12**, Suppl.1, pp. e93-e103.

Eppelbaum, L.V., 2010, Methodology of Detailed Geophysical Examination of the Areas of World Recognized Religious and Cultural Artifacts, *Trans. of the 6th EUG Meet.*, Geophysical Research Abstracts, Vol. **12**, EGU2010-5859, Vienna, Austria, 3 pp.

Eppelbaum, L., Ben-Avraham, Z., 2002, On the development of 4D geophysical Data Base of archaeological sites in Israel, *Trans. of the Conf. of the Israel Geol. Soc. Ann. Meet*., MaHagan - Lake Kinneret, Israel, p.21.

Eppelbaum, L., Ben-Avraham, Z., Itkis, S., Kouznetsov, S., 2001a, First results of self-potential method application at archaeological sites in Israel, *Trans. of the EUG **XI** Intern. Symp*., Strasbourg, France, p. 657.

Eppelbaum, L., Ben-Avraham, Z., Itkis, S., 2003a, Ancient Roman Remains in Israel provide a challenge for physical-archaeological modeling techniques, *First Break*, **21** (2), pp. 51-61.

Eppelbaum, L.V., Ben-Avraham, Z., Itkis, S.E., 2003b, Integrated geophysical investigations at the Halutza archaeological site, *Proceed. of the **64** EAGE Conf.*, Florence, Italy, P151, 4 pp.

Eppelbaum, L.V., Itkis, S.E., 2000, Magnetic investigations in the Proto-Historic site to the east of Tel Megiddo, *In*: (Eds. I. Finkelstein, D. Ussishkin and B. Halpern), *Monograph Series of the Inst. of Archaeology,* Tel Aviv University, "Megiddo III", Monogr. Ser. No. 18, pp. 504-514.

Eppelbaum, L.V., Itkis, S.E., 2001, Detailed magnetic investigations at the ancient Roman site Banias II (northern Israel), *Proceed. of the 1st Intern Symp. on Soil and Archaeology*, Szazhalombatta, Hungary, pp. 13-16.

Eppelbaum, L.V., Itkis, S.E., 2003, Geophysical examination of the Christian archaeological site Emmaus-Nicopolis (central Israel), *Collection of Papers of the **XIX** CIPA Conf. "New Perspectives to Save the Cultural Heritage"*, Antalya, Turkey, pp. 395-400.

Eppelbaum, L.V., Itkis, S.E., Fleckenstein, K.-H., Fleckenstein, L., 2007, Latest results of geophysical-archaeological investigations at the Christian archaeological site Emmaus-Nicopolis (central Israel), *Proceed. of the 69th EAGE Conference*, P118, London, Great Britain, 5 pp.

Eppelbaum, L.V., Itkis, S.E., Khesin, B.E., 2000b, Optimization of magnetic investigations in the archaeological sites in Israel, In: *Filtering, Modeling and Interpretation of Geophysical Fields at Archaeological Objects*, Special Issue of *Prospezioni Archeologiche*, pp. 65-92.

Eppelbaum, L.V., Itkis, S.E., Khesin, B.E., 2004a, Initial visualization of magnetic survey results at the Prehistoric archaeological sites in Israel, *Proceed. of the 5th Intern. Symp. on Eastern Mediterranean Geology*. Thessaloniki, Greece, Vol. **2**, pp. 747-750.

Eppelbaum, L.V., Itkis S.E., Petrov, A.V., 2000c, Physics and archaeology: magnetic field as a reliable tool for searching ancient remains in Israel, *Scientific Israel*, **2**, pp. 68-78.

Eppelbaum, L.V., Khesin, B.E., Itkis, S.E., 2001b, Prompt magnetic investigations of archaeological remains in areas of infrastructure development: Israeli experience, *Archaeological Prospection*, **8** (3), pp. 163-185.

Eppelbaum, L.V., Khesin, B.E., Itkis, S.E., 2006b, Some peculiarities of geophysical investigations at archaeological sites in Israel, *Russian Archaeology*, **1**, pp. 59-70.

Eppelbaum, L.V., Khesin, B.E., Itkis, S.E., 2010, Archaeological geophysics in arid environments: Examples from Israel, *Journal of Arid Environments*, **74**, No. 5.

Eppelbaum, L.V., Khesin, B.E., Itkis, S.E., Ben-Avraham, Z., 2004b, Advanced analysis of self-potential data in ore deposits and archaeological sites, *Proceed. of the 10th European Meeting of Environmental and Engineering Geophysics*, Utrecht, The Netherlands, 4 pp.

Eppelbaum, L.V., Kutasov, I.M., Barak, G., 2006c, Ground surface temperature histories inferred from 15 boreholes temperature profiles: Comparison of two approaches, *Earth Sciences Research Journal* **10** (1), pp. 25-34.

Finkelstein, M., Eppelbaum, L., 1997, Classification of the disturbing objects using interpretation of low-intensive temporary magnetic variations, *Trans. of the Conference the Geological Society of America*, Salt Lake City **29** (6), p. 326.

Finkelstein, M., Eppelbaum, L., 1998, A new laser magnetic field detector and its application in geophysics, *Trans. of the Conference of Israel Geological Society*, *Annual Meeting*, Mizpe-Ramon, Israel, p.30.

Ginzburg, A., Levanon, A., 1977, Direct current resistivity measurements in archaeology, *Geoexploration*, **15**, pp. 47-56.

Horowitz, A., 1979, *The Quaternary of Israel*, Academic Press, NY.

Itkis, S.E., 2003, Magnetic susceptibility measurements of soil: A diagnostic tool for location of human activity areas, *In*: (H. Khalaily and O. Marder, Eds.) *The Neolithic Site of Abu Ghosh*: *The 1995 Excavations*, Chapter 14, (IAA Reports 19), Jerusalem, pp. 129-131.

Itkis, S.E., Eppelbaum, L.V., 2009, Magnetic survey in the vicinity of the Paneas, *In*: (Ed. M. Hartal) *Paneas: The Survey, the Aqueduct*, *the northern cemeteries and excavations in the northwestern Suburb*, The Israel Antique Authority, Jerusalem, 143-151.

Itkis, S., Khesin, B., Eppelbaum, L., Khalaily, H., 2003, The Natufian site of Eynan (Hula valley, northern Israel): Magnetic prospecting reveals new features, *Israel Journal of Earth Sciences*, **52** (3-4), pp. 209-219.

Jeffery, K.G., 2007, New generation grid for environmental science, *Environmental Modelling & Software*, **22**, pp. 281-287.

Kempinski, A., Reich, R. (Eds.), 1992, *The Architecture of Ancient Israel*, Israel Exploration Society, Jerusalem.

Kenyon, K.M., 1979, *Archaeology in the Holy Land*, Norton, NY.

Khesin, B.E., 1974, Informational technique for prognosis of geological objects in the absence of standards in the area under investigation, *Methods of Exploration Geophysics*, **24**, pp. 98-102 (in Russian).

Khesin, B.E., Alexeyev, V.V., Eppelbaum, L.V., 1996, *Interpretation of Geophysical Fields in Complicated Environments*, Kluwer Academic Publishers, Ser.: Modern Approaches in Geophysics, Boston – Dordrecht – London.

Khesin, B.E., Eppelbaum, L.V., 1997, The number of geophysical methods required for target classification: quantitative estimation, *Geoinformatics*, **8** (1), pp. 31-39.

Laukhin, S.S., Ronen, A., Pospelova, G.A., Sharonova, Z.V., Ranov, V.A., Burdukiewicz, J.M., Volgina, V.A., Tsatskin, A., 2001, New data on the geology and geochronology of the Lower Palaeolithic site Bizat Ruhama in the Southern Levant, *Paleorient*, **27** (1), pp. 69-80.

Meyers, E.M. (Ed.), 1996, *The Oxford Encyclopedia of Archaeology in the Near East*. 5 Vols., Oxford University Press, Oxford.

Nahas, C., Bauman, P., Jol, H., Reeder, P., Freund, R., 2006, Geophysical investigations at coastal archaeological sites in Israel, *Proceed.* of the *SAGEEP Confer.*, Seattle, Washington, pp. 1397-1406.

Paparo, H., 1991, Temperature study of the archaeological site Crusades Fortress Um Haled (Netanya), *Trans. of the Conf. of Israel Geol. Soc., Annual Meeting*, Akko, Israel, p. 77.

Pelfer, P.G., Barcelo, J.A., McDonaill, C., Pelfer, G., 2004, ArchaeoGRID, a GRID for archaeology, *Proceed. of the IEEE Nuclear Science Symp. Conf.*, **4**, pp. 2095-2099.

Ron, H., Porat, N., Ronen, A., Tchernov, E., Horwitz, L., 2003, Magnetostratigraphy of the Evron Member – implications for the age of the Middle Acheulian site of Evron Quarry, *Journal of Human Evolution*, **44**, pp. 633-639.

Segal, Y., Marco, S., Ellenblum, R., 2003, Intensity and direction of the geomagnetic field in 24 August, 1179 measured in Vadum Iacob (Ateret) Crusader Fortress, northern Israel, *Israel Jour. Earth Sci.*, **52**, pp. 203-208.

Shaar, R., Ron, H., Tauxe, L., Kessel, R., Agnon, A., Ben-Yosef, E., Feinberg, J.M., 2010, Testing the accuracy of absolute intensity estimates of the ancient geomagnetic field using copper slag material, *Earth and Planetary Science Letters*, **290**, pp. 201-213.

Sternberg, R., Lass, E.H.E., 2007, An archaeomagnetic study of two hearths from Kebara Cave, Israel, In: (O. Bar-Yosef and L. Meignen, eds.) Kebara Cave, Mt. Carmel, Israel: The Middle and Upper Paleolithic Archaeology, Part I, *American School of Prehistoric Research*, Bull. **49**, Peabody Museum of Archaeology and Ethnology, Harvard University, Cambridge, pp. 123-130.

Sternberg, R., Lass, E., Marion, E., Katari, K., Holbrook, M., 1999, Anomalous archaeomagnetic directions and site formation processes at archaeological sites in Israel, *Geoarchaeology*, **14** (5), pp. 415-439.

Tanzi, J.D., Vickers, R.S., Burns, P.L., 1983, Application of electrical resistivity techniques to archaeological surveys, *Proceed. of the Intern. Geoscience and Remote Sensing Symp.*, pp. 1-3.

Weiss, E., Ginzburg, B., Cohen, T.R., Zafrir, H., Alimi, R., Salomonski, N., Shatvit, J., 2007, High resolution marine magnetic survey of shallow water littoral area, *Sensors*, **7**, pp. 1697-1712.

PERFORMANCE ASSESSMENT OF A NEW BOOM-MOUNTED AIRBORNE TIME-DOMAIN ELECTROMAGNETIC SYSTEM

William E. Doll[1], *T. Jeffrey Gamey*[1], *Les P. Beard*[1], *Jacob R. Sheehan*[1], *Jeannemarie Norton*[1], *J. Scott Holladay*[2], *Andri E. Hanson*[3], *and Raye M. Lahti*[3]
[1.] *Battelle-Oak Ridge Operations, Oak Ridge, TN*
[2.] *Geosensors, Toronto, Ontario, Canada*
[3.] *AMEC Earth and Environmental, Minneapolis, MN*

Abstract

In 2008, design and construction was completed on a new boom-mounted airborne time-domain electromagnetic system, the Battelle TEM-8 system. Review of survey results led to secondary hardware and software modifications throughout following year. The system was designed primarily for wide-area assessment of sites contaminated with unexploded ordnance (UXO), but has already found broader application. To date it has seen use in five deployments: 1) Battelle's UXO airborne technology test grid in Ohio, 2) an Australian air base where infrastructure mapping was needed in advance of new construction, 3) Twentynine Palms, a Marine base in California, 4) Camp LeJeune, a Marine base in North Carolina, and 5) a pair of proximal sites in New Mexico which were used for bomber training.

Results of these surveys are compiled to provide insight into the capabilities of airborne metal-detecting systems in general, and the TEM-8 system in particular. Sensitivity is assessed as a function of the ability to detect ordnance of different sizes. Positional accuracy is also derived from the UXO surveys. Comparison of airborne magnetometer and TEM-8 results provide a basis for assessing the strengths of each. Likewise, the advantages of joint analysis of magnetometer and electromagnetic data sets can be assessed at sites where both were acquired. Finally, the benefits of TEM data for mapping infrastructure and distinguishing spurious geologic response from metallic waste can be demonstrated.

Background

Boom-mounted airborne geophysical systems have been used for mapping and detection of unexploded ordnance for over ten years (Doll et al., 1999). Most of the systems developed during this time period have been magnetometer systems, which have shown steady improvements in sensitivity and positional accuracy through several generations of development. Current state-of-the art magnetometer systems have been shown to be effective for detection of ordnance as small as 40mm with mean miss distances of 30 cm or less (Doll et al., 2008).

Airborne electromagnetic (EM) systems for UXO mapping and detection, similarly mounted in booms that attach directly to the helicopter, have been in development since 2000 (Doll et al., 2005). Improvements in EM systems have required more iterations and more effort at each iteration, so that it has been more costly and time-consuming to develop an effective EM system than a similarly sensitive magnetometer system. The primary motives for developing these systems have been to 1) improve sensitivity to smaller and smaller ordnance, and 2) to develop a capability for airborne mapping of ordnance at sites where geologic conditions are problematic for magnetometer systems. More specifically, mafic geologic units, including basalts, frequently produce magnetic anomalies that approach or exceed those from ordnance, generating so many false positives that the data can have little practical value. Ground-based EM systems have demonstrated less sensitivity to such conditions, and demonstrate the benefits of EM over magnetometer systems in basaltic environments. Airborne EM

systems can also be used to detect non-ferrous metals (including UXO) and can provide additional attribute information that can be used to better prioritize anomalies.

The first prototype of a boom-mounted airborne EM system employed a modified Geonics EM61 mounted to a boom structure that was usually used a for magnetometer system (Doll et al., 2005). This experimental system was called the Oak Ridge Airborne Geophysical System – EM Prototype, or ORAGS-EMP. Although the results were noisy, the ORAGS-EMP demonstration showed that a level of sensitivity to ordnance could be achieved with a boom-mounted EM sensor, and provided impetus for a more thorough examination of such systems for UXO mapping and detection. The ensuing study resulted in the development of the ORAGS-TEM system (Beard et al., 2004), which was a two-channel time-domain system mounted on a 12m X 3m boom structure that attached directly to the helicopter. The ORAGS-TEM systems showed sensitivity that was similar to that of the contemporaneous magnetometer systems, such as the ORAGS-Arrowhead system (Doll et al., 2002), but had a lower spatial accuracy of about 3m (Beard et al., 2008). More importantly, because it had only two receiver channels, it was not well-suited for cost-effective high-density production surveys.

Battelle TEM-8 System

In 2007, Battelle initiated development of a new airborne time-domain system based on the results from the earlier development of the ORAGS-TEM system. The TEM-8 system is an eight-channel system mounted on a 12m X 3m boom structure (Figure 1) with 3m X 4m transmitter loops on each side of the helicopter. There are four receivers on each side of the aircraft, located within 4 m tube segments that are oriented parallel to the long axis of the boom structure (Figure 2). As with most transient EM systems, a current is established in the transmitter loop, then rapidly switched off, inducing a secondary magnetic field in the earth, the decay of which is measured in the receiver coils. Because there are no receivers located within about 3m of the center of the boom structure, it is necessary to interleave flight lines in order to achieve full coverage of the area of interest.

Figure 1. Battelle TEM-8 system.

The TEM-8 transmitter produces an alternating "castle" type waveform. Alternating positive and negative "on-time" current pulses with linear on- and off-ramps are separated by "off-time" periods during which the transient measurements are made. During the waveform's on-time, the transmitted magnetic field interacts with nearby conductive objects, initially inducing eddy currents. As the on-time magnetic field stabilizes, these eddy currents decay exponentially, and are at or near zero toward the end of the on-time. Then when the transmitted field is rapidly turned off, "early time" eddy currents are again generated at the surface of the conductive object, and these currents migrate into the object and attenuate in amplitude as the off-time progresses. At "late time", the eddy current density becomes constant throughout the conductor and the secondary field due to the eddy currents decays with a single time constant.

The selection of base frequency is site-specific to some extent. Regardless of the base frequency used, the time gate structure remains the same. Samples are taken at 0.09 ms intervals. Gate 1 is one sample long, Gate 2 is two samples long, Gate 3 is four samples long, Gate 4 is eight samples long, etc to the end of the available off-time. A 270 Hz base frequency would compress the castle waveform into 1/3 the time for a 90 Hz base, and the first downward pulse would therefore occur shortly after the end of Gate 3.

Sensitivity and Positional Accuracy

In January and February of 2009, the authors conducted a demonstration of the TEM-8 system for the Environmental Security Technology Certification Program (ESTCP) near Albuquerque, New Mexico. The demonstration had two components: 1) a “blind test” over a 100-acre portion of a 617-acre survey area where ESTCP had buried 110 ordnance items and where moderate interference from basalt was known to occur, and 2) a 444-acre portion of a bombing target on a basalt flow where a previous airborne magnetometer survey showed high-amplitude geologic noise that exceeded the signal from ordnance known to occur at the site. The results from these sites, known as the Former Kirtland Precision Bombing Range (FKPBR) and Precision Bombing Range S-12 (PBR-S12), respectively, provide insight into the sensitivity of the system to ordnance and enable calculation of the positional accuracy of the system.

Figure 2 shows the TEM-8 data acquired at FKPBR, and Table 1 shows the numbers and types of ordnance emplaced in the blind test area at FKPBR. Table 1 also lists the number of seeded items that were detected within a 1.50m search radius of the positions reported to ESTCP by AMEC and Battelle on a 1292 anomaly prioritized “dig list”. These results were compiled by the Institute for Defense Analyses (IDA) before actual locations were disclosed to AMEC and Battelle. Only one of the

Table 1. List of emplaced ordnance items, the number detected, and miss distance statistics for the FKPBR Blind Test Site

.

UXO Type	Total # Seeds	# Seeds Detected	P_d	Mean Miss Distance (m)	Standard Deviation of Miss Distance (m)
All UXO	110	109	0.99	0.34	0.23
105mmP	8	8	1.00	0.42	0.37
4.2"	52	51	0.98	0.37	0.23
155mmP	24	24	1.00	0.25	0.15
81mmM	12	12	1.00	0.38	0.24
105H	14	14	1.00	0.30	0.22

seed items was not detected, and it was missed because its actual position was 0.01m beyond the limit of the search radius.

In Table 1, the UXO types are specified as “P”, “M”, or “H”, for projectile, mortar, and high-explosive anti-tank rounds respectively. P_d is used to represent the probability of detection. Figure 2 shows a map view of the 617-acre FKPBR area with the 100-acre Blind Seed Area highlighted with a red box. The 109 seed items were all among the first 565 anomalies on the prioritized list. Because the blind seed area was located in proximity to an old bombing target (visible in the northwest and west-central portions of Figure 2), it is probable that many of the unidentified anomalies are associated with ordnance or fragments of ordnance from that target. This target, known as the N-3 target, was used for post-World War II bomber training. Nearly all of the ordnance at the site are M38 practice bombs, which are sheet metal encased, sand-filled practice bombs that have a “spotting charge” but no high explosives. They have a nominal weight of 100-lb. when filled with sand. No validation was conducted at the site to assess the origin of anomalies that were not associated with seed items.

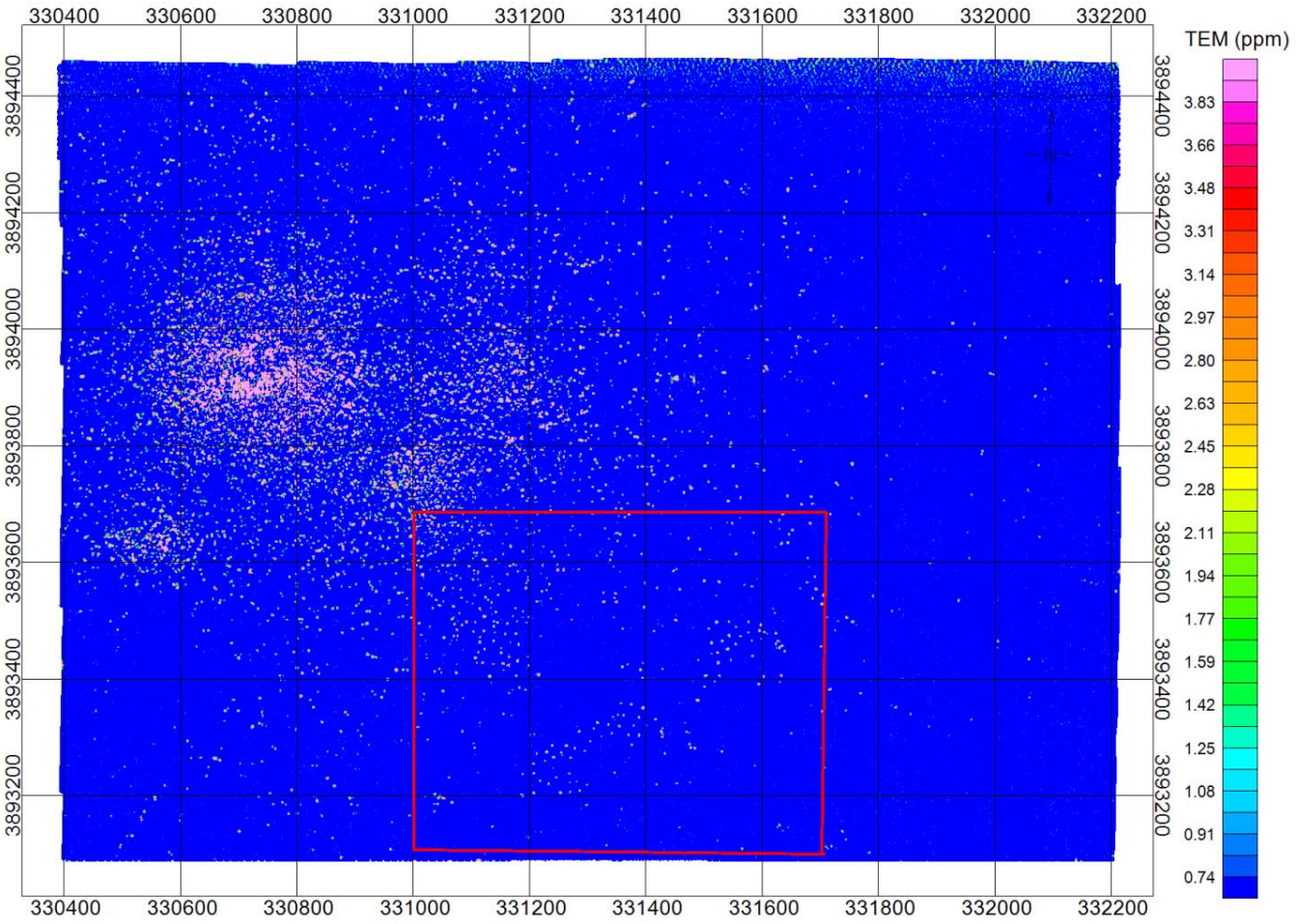

Figure 2. TEM-8 map of the FKPBR survey area. The location of the 100-acre Blind Seed Area is highlighted in red.

The PBR-S12 target is located about 45km northwest of FKPBR on land belonging to the Pueblo of Laguna nation. It was used for bomber training with M38 test bombs, as at FKPBR. It was known from a previous airborne magnetometer survey (Figure 3a) that the geologic anomalies from the basalt flow at the site were large enough to overwhelm any anomalies associated with ordnance or ordnance fragments at the site. However, M38 bombs and fragments can be seen at the surface and in a scrap pile near the center of the target. The TEM-8 map for PBR-S12 is shown in Figure 3b.

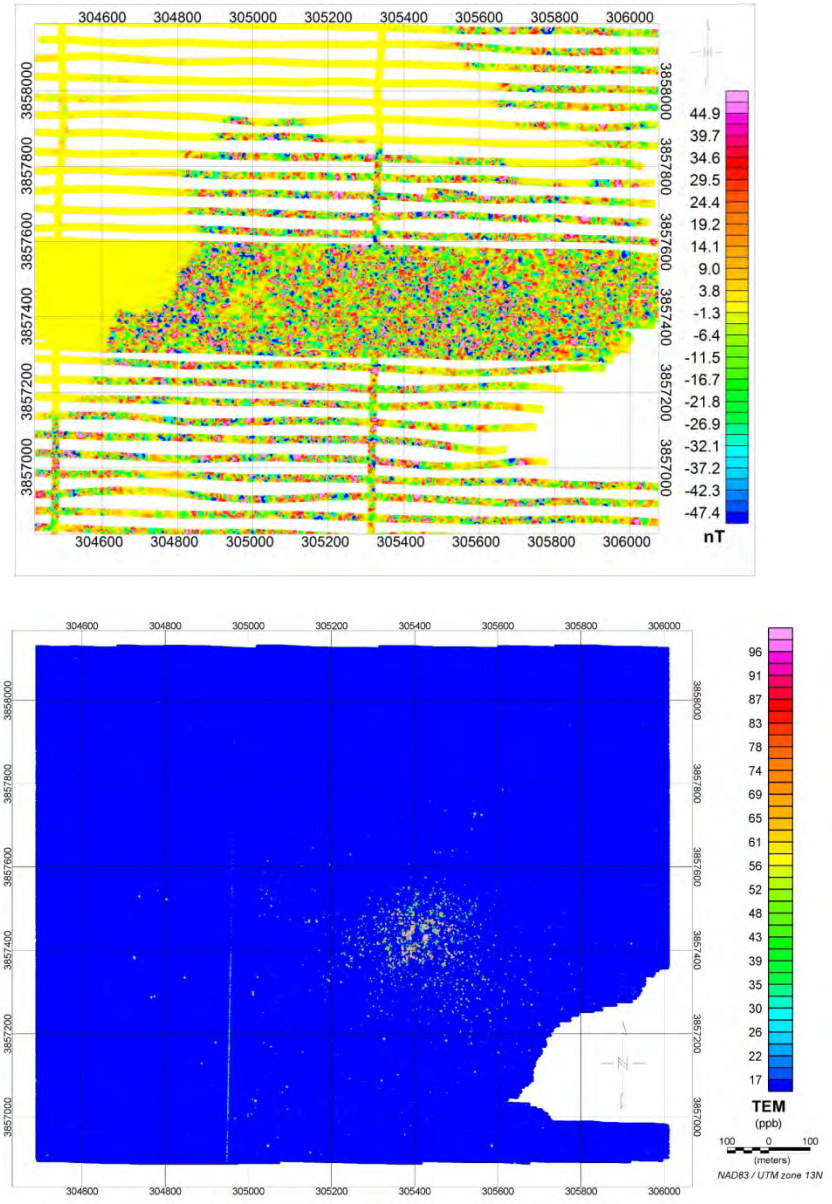

Figure 3. Airborne geophysical maps of the PBR-S12 site in New Mexico. a) total field magnetic anomaly map acquired with the ORAGS-Arrowhead system in 2002; b) TEM-8 map from data acquired in 2009.

To validate the TEM-8 results at PBR-S12, anomalies were picked within two 100m X 100m blocks (Area 1 and Area 4) in proximity to the target center. Data were also acquired in each block with a Geonics EM61, and anomalies were picked from those data using a threshold that corresponded to the threshold used for the TEM-8. Both anomaly lists (TEM-8 and EM61), were prioritized, primarily as a

function of anomaly amplitude. From the two lists, anomalies were selected for excavation, and the results of each excavation were documented. These are summarized in Tables 2 and 3 and Figure 4. In Table 2, "Picks" are the number of anomalies that were selected above the threshold from the EM61 and TEM-8 data sets. Three categories of TEM-8 anomalies are shown, indicated as "A", "B", and "C". "Digs" are the number of anomalies that were selected for excavation from each portion of the data set, and "Detects" are the number of anomalies in the category that successfully encountered ordnance, frag, or similar scrap metal. "Overlap" refers to anomalies that were on both EM61 and TEM-8 dig lists. The total number of digs was 168 in Area 1 and 157 in Area 4 (total = EM61 digs + TEM-8 digs – overlap).

Table 2. Validation results for Area 1 (left) and Area 4 (right) at PBR-S12.

Source	Picks	Digs	Detects
EM61	222	143	143
TEM-8	136	100	86
TEM-8 A	41	41	39
TEM-8 B	33	28	24
TEM-8 C	62	31	23
Overlap	77	75	75

Source	Picks	Digs	Detects
EM61	180	130	129
TEM-8	126	93	71
TEM-8 A	34	34	34
TEM-8 B	40	29	24
TEM-8 C	52	30	13
Overlap	69	66	66

Table 3. Summary of Validation results at PBR-S12 by item type.

	Excavated	Detected by EM61	Detected by TEM-8
Mostly Intact M38	56	53	54
Nose cone	45	44	33
Initiator	42	41	6
2" band	22	21	4
Wire	7	6	1

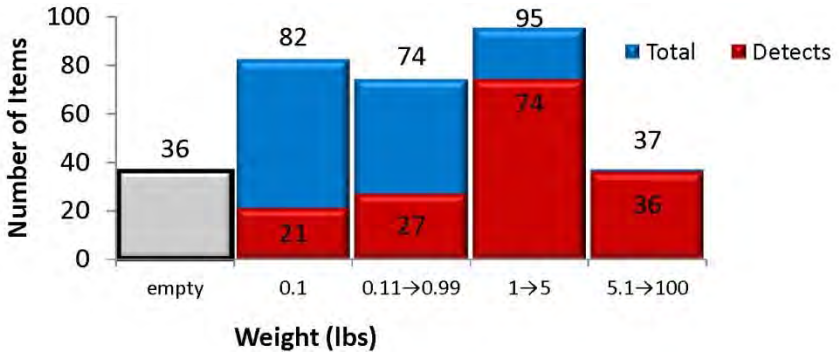

Figure 4. TEM-8 detections at PBR-S12 as a function of their weight.

As shown in Table 2, all but one of the EM61 excavations yielded detections. There were more non-detects in the TEM-8 digs, but as shown in Table 2, most of these were in the "C" or low priority category. The "C" category was deliberately chosen to straddle the preconceived noise threshold for the system in order to enable better understanding of the system sensitivity. Nearly all of the large pieces and more than 75% of the pieces weighing more than one pound were detected with TEM-8 (Figure 4). Most of the missed items were initiators, two-inch bands, and pieces of barbed wire (Table 3). These are all very small targets, and present no explosive hazard.

Positional accuracy for PBR-S12 was assessed by comparing the positions of the recovered items with the reported anomaly locations. This yielded a mean miss distance of 0.58m with a standard deviation of 0.31m for the successful TEM-8 excavations. The positional accuracy at PBR-S12 is poorer than that at FKPBR. This is likely due in part to the proximity to the GPS base station (which was within a few km of FKPBR, but about 45km from PBR-S12), and the accuracy with which the locations of excavated items could be measured at PBR-S12, compared to the positioning of seeded items at FKPBR. At both sites, the positioning accuracy is well within that which is required for follow-on investigations where the standard policy is to sweep a metal detector in a 1.5m radius about the reported location.

Data that were acquired at Battelle's Ohio UXO Test Site for airborne systems provided additional insight into detection of small ordnance items and altitude effects. The Ohio site was established in 2007 as a fixed site for monitoring improvements and defining limits of new systems as they become available. It was previously used to assess the VG-16 and VG-22 magnetometer systems. Test items at the site include some which are larger and some which are smaller than those emplaced at FKPBR. Analysis of data from this site show similar sensitivity to 81mm 105mm and 155mm projectiles. There are no 4.2-in mortars or 105 HEAT rounds emplaced at the Ohio Test Grid. There are nineteen 60mm mortars emplaced at the Ohio Test Site, with three primary orientations and three representative depths. TEM-8 was successful in detecting 53% of these during the 2008 test.

Altitude effects on sensitivity

Data were acquired over a range of altitudes at Battelle's Ohio UXO Test Site and at a calibration site at FKPBR. These tests provide into the rate of decay of response as a function of altitude. Figure 5 shows measured peak response for 8 representative items emplaced at the FKPBR

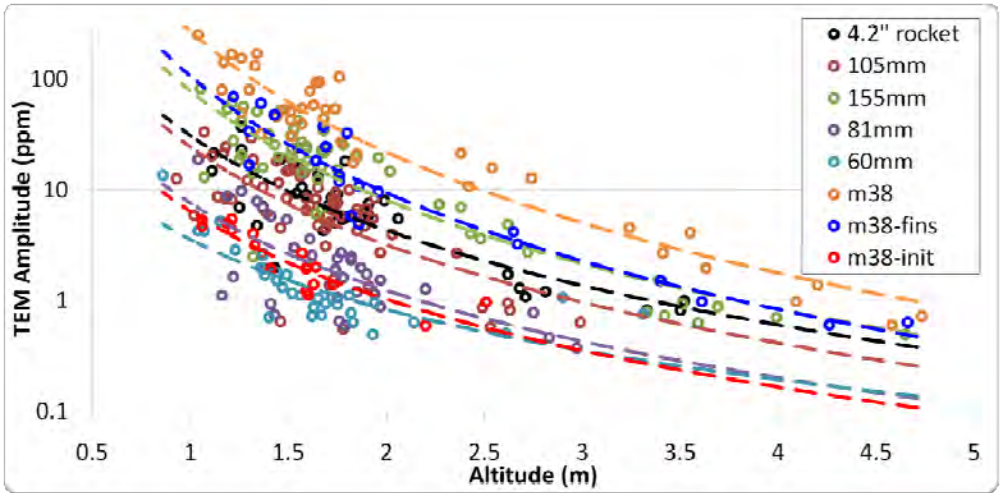

Figure 5. Measured amplitude as a function of altitude from the FKPBR calibration site.

calibration lines. The lines were flown each day of the survey for quality control, and over a suite of altitudes early in the project to assess performance as a function of altitude. In general, observed decay rates are roughly inversely proportional to the fourth power of altitude.

Joint analysis of TEM-8 and vertical magnetic gradient data

Data from a pair of test lines at Twentynine Palms, California (Figure 6), acquired in early 2008, reinforce the previous discussion (based on Figure 2) regarding the differences between magnetic and electromagnetic data sets at sites where basalts are known to occur. The geologic interference is much more prominent in the VG-22 magnetometer data set than in the TEM-8 data set from the same site. Review of these data sets also revealed differences in the items that each system detected and benefits from jointly analyzing the magnetic and EM anomalies (Sheehan et al., 2008).

A total of thirty emplaced and one extant bomb were located in the test area, ranging in size from fragments to 155mm artillery rounds. Both the VG-22 magnetometer system and the TEM-8 system were used to acquire data at the site, and both data sets were independently analyzed. Anomalies were automatically picked from each data set, including all false positive (or unknown) responses, and stored as two separate anomaly lists, prioritized by amplitude. Neither system was able to detect all of the targets (Figure 7). The VG-22 system detected 22 of the 31 items with 51 false positives. TEM-8 detected 26 of the 31 items with 77 false positives, or if a higher detection threshold were used, could detect 24 of the 31 items with 19 false positives.

An improved result was obtained by using a combined analysis of the two data sets (Figure 7). Using a scheme that gave priority to high amplitude anomalies in either data set (Sheehan et al., 2008), the combined analysis enabled detection of 30 of the 31 anomalies with 33 false positives.

Applications of TEM-8 for site characterization

There is growing need for technologies that can be used to examine large areas at industrial sites and defense installations for existing infrastructure and buried waste in preparation for land reuse such as construction of new buildings, roads, waste areas or other facilities. Historic activities were often undocumented or poorly documented, and can cause costly redesign and lost time if encountered midstream in a new construction project. In October and November 2008, the TEM-8 and VG-16 were deployed at an Australian air base to support planning for new construction. TEM-8 was used for follow-on investigation of portions of the site where the magnetometer data had encountered interesting anomalies. Both TEM-8 and VG-16 responded to buried utilities at the site. VG-16 was more sensitive to geologic anomalies at the site, including some associated with previous stream channels, and large anomalous areas that were apparently caused by outcrops of mafic rocks (Beard et al., this volume).

To date, little effort has been made to calibrate the TEM-8 system for measurement of ground conductivity. This is another possible use for the system, and could be beneficial for various environmental and engineering applications.

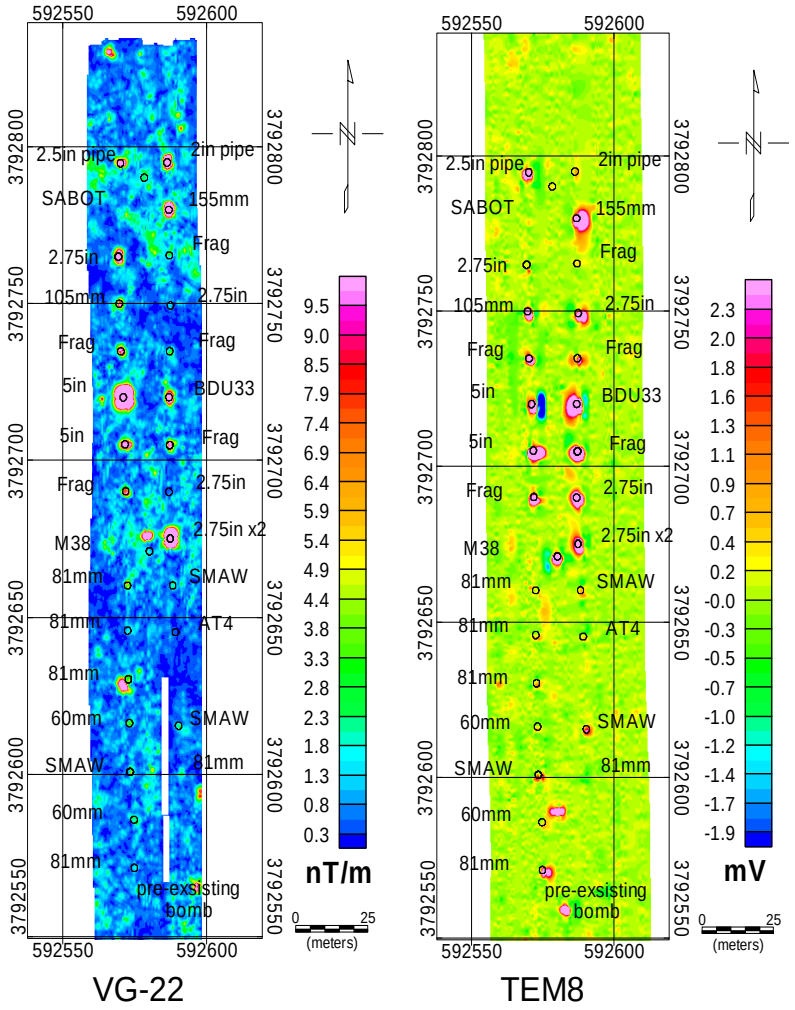

Figure 6. Vertical magnetic gradient (left) and TEM-8 (right) data from a test grid at Twentynine Palms, California.

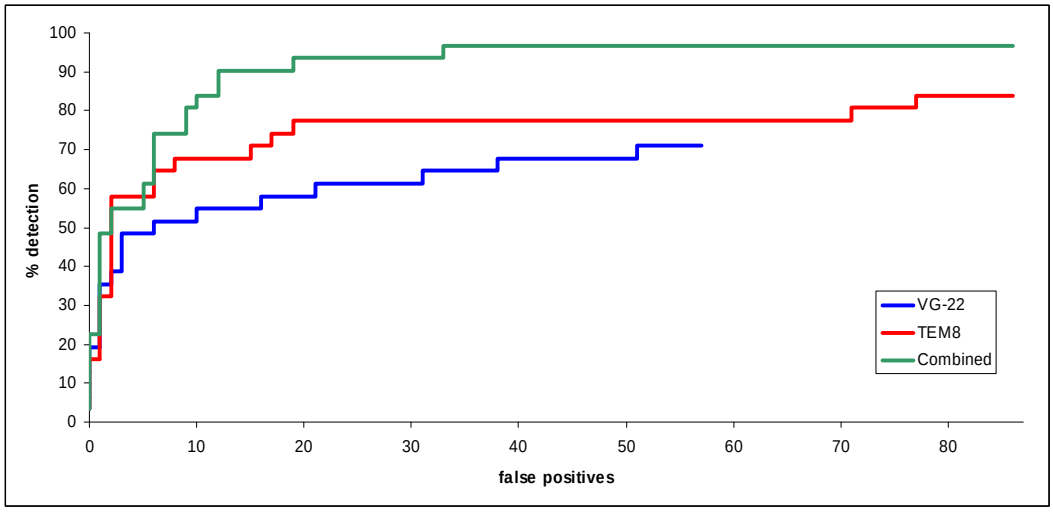

Figure 7. Receiver-Operator Characteristic curve for the test lines at Twentynine Palms.

Conclusions

In surveys conducted to date, the TEM-8 system has proven to be a very effective tool for detecting UXO in the presence of moderate to high geologic noise, with few false positives and excellent positional accuracy. The system has a higher rate of amplitude decay with altitude than boom-mounted magnetometer systems. As a result, it is best suited for detection of moderate to large ordnance at sites which can be safely flown at altitudes of 2m or less. Results from Twentynine Palms and an Australian air base show that the TEM-8 system can complement magnetometer systems to provide an improved assessment of anomalies that can reduce the number of false positives and/or the extent of follow-on work.

Acknowledgements

We thank Dr. Herb Nelson, Dr. Jeff Marqusee, and the ESTCP Program Office staff for their support of this research. National Helicopters and our pilot, Doug Christie, contributed to the success of this project. We also thank Sky Research for providing the 2005 magnetometer data from FKPBR.

References

Beard, L. P., W. E. Doll, J. S. Holladay, T. J. Gamey, J. L.C. Lee, and D. T. Bell, 2004, Field Tests of an Experimental Helicopter Time-Domain Electromagnetic System For Unexploded Ordnance Detection, *Geophysics*, v. 69, n. 3, p. 664-673.

Beard, L. P., W. E. Doll, T. J. Gamey, J.S. Holladay, J.L.C. Lee, N.W. Eklund, J. R. Sheehan and J. Norton, 2008 Comparison of performance of airborne magnetic and transient electromagnetic systems for ordnance detection and mapping, , Jour. Env. and Eng. Geophysics, v. 13. n. 2, p. 291-305, 2008.

Beard, L. P., W. E. Doll, J. R. Sheehan, T. J. Gamey, and J. Norton, This Volume, Airborne EM Data Complement Magnetics in an Unexpected Way, *Proceedings of the 2010 Symposium on the Application of Geophysics to Environmental and Engineering Problems*, 10 pp.

Doll, W. E., P. Hamlett, J. Smyre, J. E. Nyquist, T. J. Gamey, and J. S. Holladay, 1999, A field evaluation of airborne techniques for detection of unexploded ordnance, abstract, *Proceedings of the 1999 Symposium on the Application of Geophysics to Environmental and Engineering Problems*, p. 773-782.

Doll, W. E., L. P. Beard, and T. J. Gamey, 2002, An advanced airborne magnetic system for high-resolution mapping, *Expanded Abstracts, Society of Exploration Geophysicists Annual Meeting, Salt Lake City, Utah, October 6-11, 2002*, 4 pp., available on CD-ROM.

Doll, W. E., J. R. Sheehan, T. J. Gamey, L. P. Beard and J. Norton, 2008, Results of an Airborne Vertical Magnetic Gradient Demonstration, New Mexico, Jour. Env. and Eng. Geophysics, v. 13. n. 3, p. 277-290.

Sheehan, J., L., Beard, J. Gamey, W. Doll, and J. Norton, 2008, UXO Detection and Prioritization Using Combined Airborne Vertical Magnetic Gradient and Time-Domain Electromagnetic Methods, *Expanded Abstracts, 2008 Society of Exploration Geophysicists Annual Meeting,* , 4 pp., available on CD-ROM.

A PSEUDO-TIME CONSTANT APPROACH TO TARGET DISCRIMINATION IN AIRBORNE TIME-DOMAIN ELECTROMAGNETIC UXO SURVEYS

Jacob R. Sheehan, Battelle—Oak Ridge Operations, Oak Ridge, TN
William E. Doll, Battelle—Oak Ridge Operations, Oak Ridge, TN

Abstract

A simple combination of data from three time-domain electromagnetic time gates is used to drastically reduce the total number of picks required to detect a set number of known seed items. This approach takes advantage of the physics of time-domain electromagnetic geophysical systems and signal decay properties in a way that does not require as much data as that needed to calculate the actual delay constant.

Introduction

Battelle completed development of a new airborne 8-channel boom-mounted time-domain electromagnetic (TEM-8) system (Figure 1) in September 2008 (Doll et al., this volume).

Figure 1: Battelle TEM-8 airborne UXO detection system.

The TEM-8 system is contained within a 12 m by 3 m rectangular boom structure with a two-lobed transmitter loop composed of two 3m by 4 m rectangles. There are four receivers on each side of the aircraft, located within 4 m tube segments that are oriented parallel to the long axis of the boom structure. As with most time-domain electromagnetic (EM) systems, a current is established in the transmitter loop, then rapidly switched off, inducing a secondary magnetic field in the earth, the decay of which is measured in the receiver coils. Data were acquired at a 225 MHz base frequency, with the response recorded for three time geometrically spaced gates at approximately 0.1ms, 0.2ms and 0.4ms.

Two sites near Albuquerque, New Mexico were selected for a February 2009 demonstration for the Environmental Security Technology Certification Program (ESTCP). The first was a 617-acre portion of the Former Kirtland Precision Bombing Range (FKPBR) in New Mexico, and the second was a 444-acre portion of the Kirtland Precision Bombing Range (PBR)-S-12 Target (S-12). A 100 acre area within the FKPBR area (Figure 2) was specified for emplacement of seed items ("blind" seed). This area is known to contain some pre-existing M-38 ("100-pound bombs") ordnance associated with the nearby N-3 target area. The seed items were emplaced under the direction of the ESTCP Program Office without involvement from Battelle. Performance of the system for this area was assessed by the Institute for Defense Analyses (IDA) by comparing dig lists to the master list of seeded items. A total of 110 seed items were emplaced, including 81 mm and 4.2-in mortars, 105 mm projectiles and high explosive anti-tank (HEAT) rounds, and 155 mm projectiles. IDA determined that TEM-8 detected 109 of the 110 seed items for a probability of detection (Pd) of 99.1%. One 4.2-in mortar was classified as missed because it was 1 centimeter (cm) outside of the 1.5 m detection halo. The mean miss distance was 0.34 m with a standard deviation of 0.23 m.

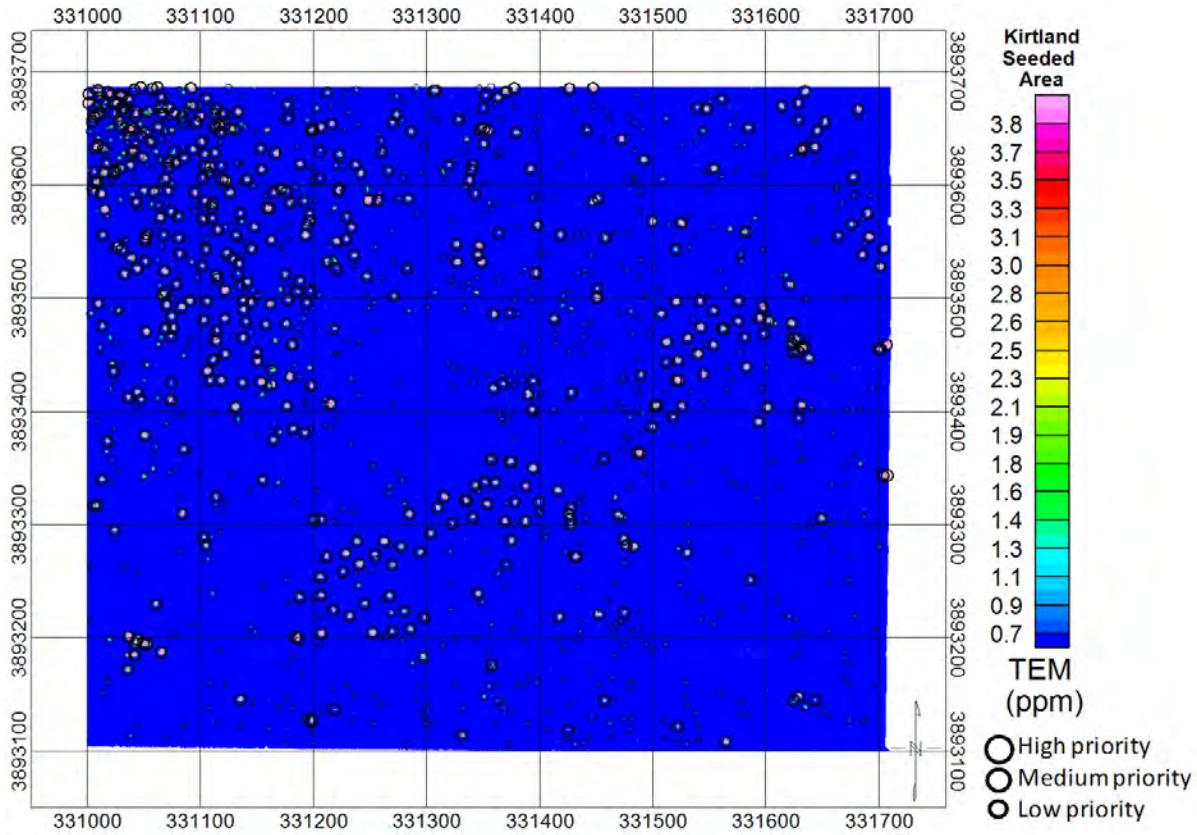

Figure 2: TEM-8 first time gate response map of the seeded test area at the Former Kirtland Precision Bombing Range (FKPBR).

Performance of any geophysical detection system is only partially characterized by the detection metrics described above. The number of picks required to obtain a given detection rate is also important. In actual ordnance clearance, this metric constrains the cost of remediation because it can lead to many unnecessary excavations. In order to detect 109/110 seeds, a total of 1,292 picks were made. It is important to note that there are pre-existing (non-seeded) ordnance items at the site which account for some of the anomalies categorized as "false positives". The "false positives" were not investigated to differentiate between pre-existing ordnance items and those associated with geology or system noise. After receiving the detection assessment results from IDA, we were given the locations of all the seed items, enabling us to investigate methods of reducing the total number of picks without compromising detection performance.

Methodology

Every pick list is prioritized in some way. One very simple prioritization method is to sort the list by anomaly amplitude. The 1,292 picks for the seeded area sorted by the second time gate amplitude (shown in blue) are illustrated in Figure 3. Also illustrated in this figure are all picks associated with a seeded item (shown in orange). Once complete, it is clear that all the seed items could have been detected with less than 565 picks rather than the 1,292 picks that were submitted. However, there is no obvious feature in the data to indicate the appropriate cut-off threshold.

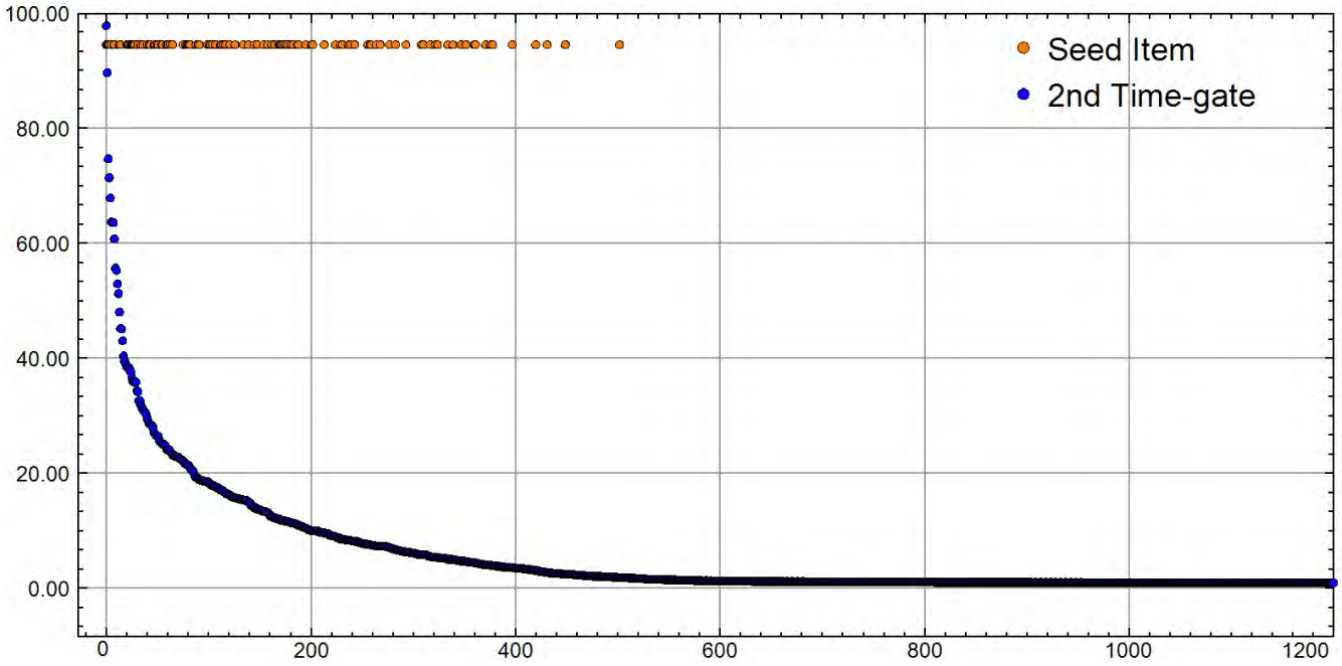

Figure 3: All picks sorted by the second time gate amplitude. All the seed items are located in the top 600 picks, but there is no obvious way to predict this *a priori* based on the data values.

However, if the amplitude for all three time gates are plotted, a pattern emerges. In Figure 4 the three time gates are shown for a small section of the picks, along with symbols showing which picks correspond to a seed item.

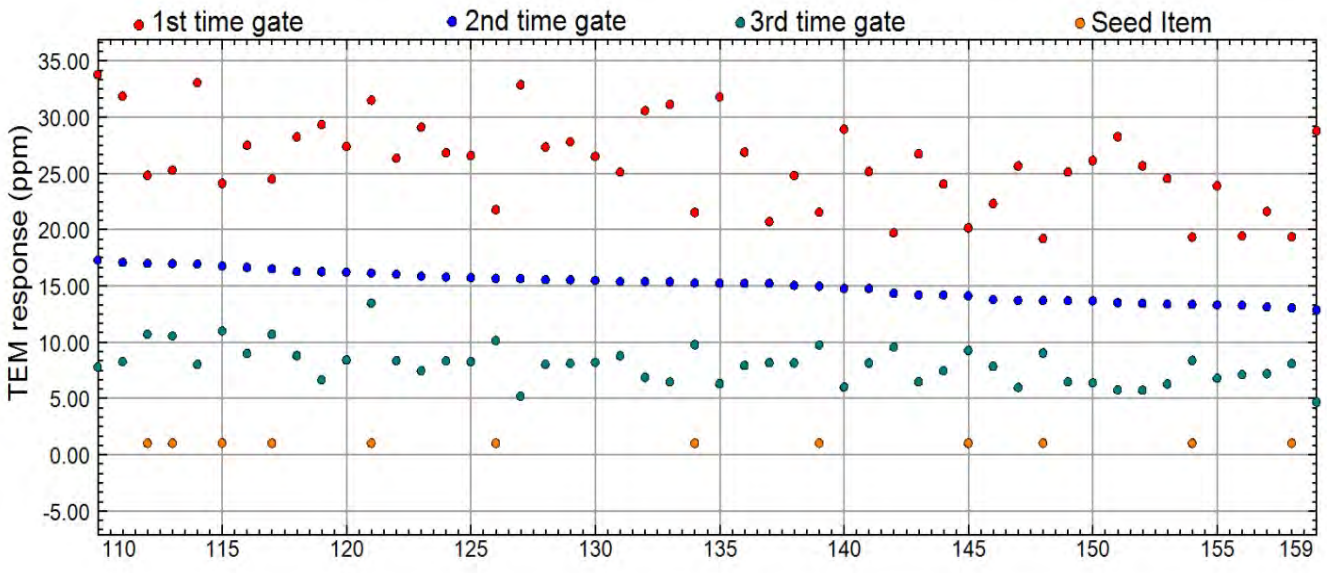

Figure 4: First three time gates, sorted by gate number 2. The picks that represent seed items are also displayed. Note that for every seed item the spread between the three time gates decreases.

For every pick that represents a seed item the spread between the three time gates is smaller than the picks that do not represent a seed item. This corresponds to a slower decay in the induced current for the seed items than for small scrap or other minor conductors. Any response that does not decay with time is most likely not caused by a metallic object but is likely associated with a high noise peak. In order to quantify this relationship we used the following simple equation:

$$TV = \frac{(b1 - b3)}{b2}$$

Where b1, b2 and b3 are the three time gates and TV is the test value that will be used to eliminate many of the non-seed items. In order to demonstrate the relationship between TV and the seeded picks, we sort the data by the second time gate value (Figure 5), and plot the seed picks along with all picks that have a TV value between empirically derived values of 0.5 and 1.25.

Unlike the result shown in Figure 3, there is a very obvious shift in the TV value that corresponds to the last of the seed items. This shift occurs where the third time-gate approaches zero response. Using this shift point as a cutoff would reduce the number of picks from 1,292 to 528 picks. Furthermore, if only picks with a TV between 0.5 and 1.25 are retained, the number of picks required to capture all of the seeded items is reduced by more than another factor of two to about 227 picks.

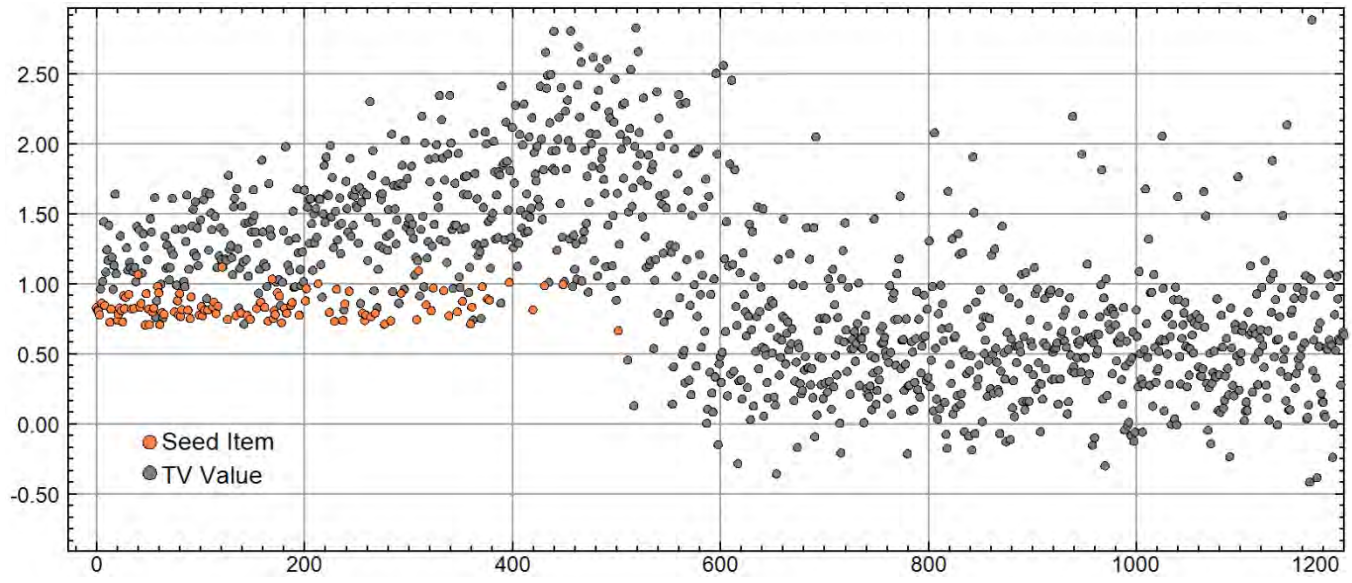

Figure 5: The vertical scale of this plot represents the TV values. Note the obvious change in values located around x=500. This is also the end of picks that produce seeded hits (orange symbols). This plot is sorted by descending second time gate values.

S-12 Bombing Target

In addition to the seeded test grid, data were also acquired at the S-12 bombing target, located approximately 45 km southwest of the FKPBR site. Using the same methodology at the S-12 bombing target shows a similar break in the TV values (Figure 6). The reduction in anomalies that lie above the threshold is similar to FKPBR results, eliminating 597 of the top 1,139 picks. Validation was conducted in two 100 m x 100 m areas where:

- A total of 262 anomalies were selected from the airborne data.
- Of these, 170 were chosen for excavation (130 others excavations were based on EM61 ground study).
- Of the 170, 142 were M38 ordnance or fragments, or other metallic debris.
- The remaining 28 were empty holes.
- Using the TV method described above, the resultant dig list would have only 41 anomalies, with no empty holes.

In this case the TV method is too restrictive, eliminating more anomalies from the dig list than would be desired. It would still be a useful tool for ranking anomalies, as the 42 anomalies picked using the method all represented metallic targets.

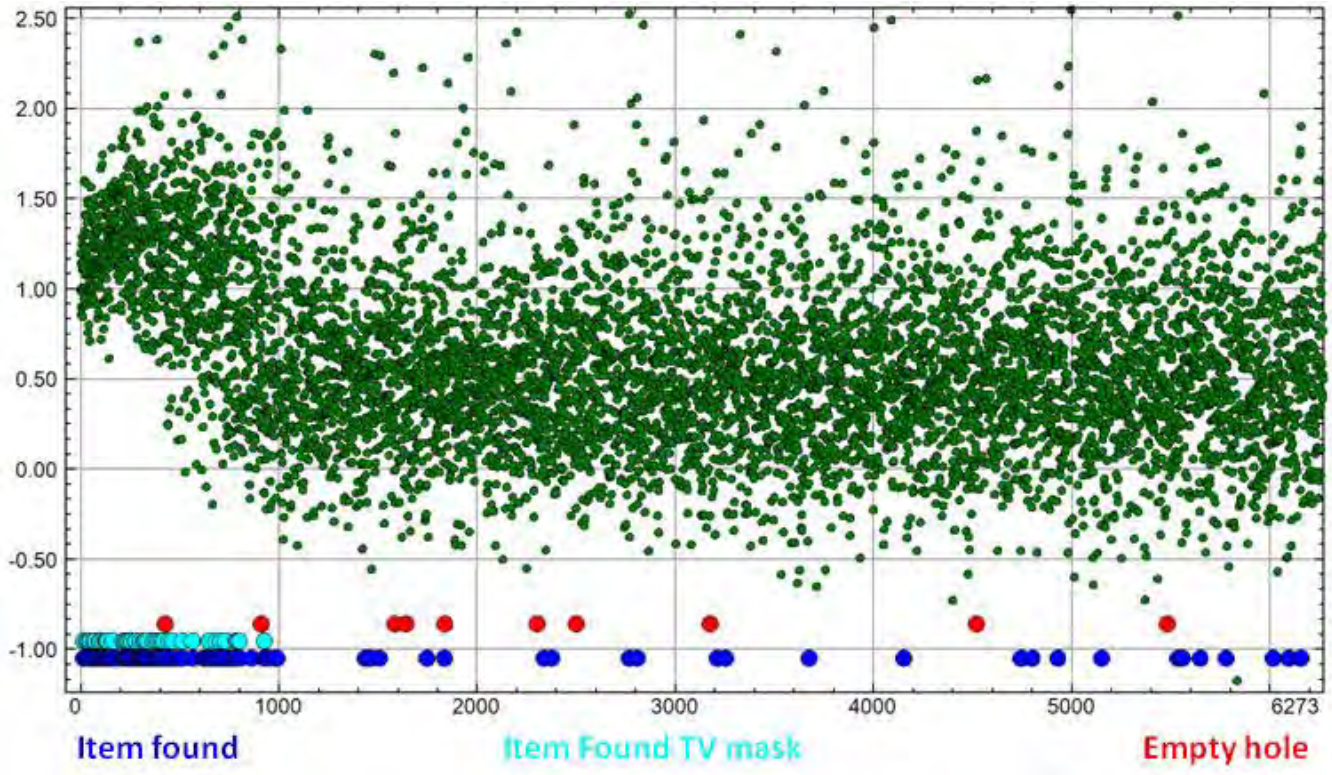

Figure 6: TV value for S-12 bombing target. Note a similar inflection point in the TV values as seen in Figure 5, located at a level of 1,000 picks.

Discussion

It is interesting that the TV method is considerably more effective at FKPBR than at S-12. At FKPBR, all of the seeded ordnance items were "thick-walled" or had solid projectile components. Most of the pre-existing ordnance at FKPBR is associated with "thin-walled" components of M38 or "100-pound" bombs. Seeded items emplaced at the site were all thick-walled. Holladay et al (2006) demonstrated that a similar airborne TEM system could discriminate between thin-walled and thick-walled ordnance items. At S-12, detected ordnance consisted exclusively of M38s or M38 fragments. The fact that most of the M38 related ordnance was rejected by applying this method demonstrates that it may be discriminating between thick- and thin-walled items, as previously indicated.

Conclusions

Any reduction in the number of picks that can be provided to a sponsor by way of a "dig list" without rejecting anomalies associated with the items of interest may significantly increase the value of the geophysical survey and save money in follow-up activities based on the data set. The simple methods demonstrated here have the potential to reduce by one-half the number of digs resulting from the picked anomalies. In addition, it has the potential to aid in defining the lower threshold for picking, further reducing the total number of anomalies on a dig list. For the example shown here for FKPBR, the final number of picks that would be chosen under this methodology would be about 230, compared to 1,292 that were chosen based on anomaly amplitude alone. Approximately one-half of the eliminated anomalies result from the method defining a higher amplitude threshold for the anomaly list. A second

reduction is accomplished by using a decay-rate based prioritization. The picks retained after the decay-rate prioritization are spread throughout the amplitude range. If the amplitude based prioritization were used exclusively, excavation field crews might decide to abort excavations once they reach a threshold beyond where the amplitude at which no more targets would be encountered. Because the decay-rate based picks are dispersed among the full range of amplitudes, a prioritization based on the decay rate would eliminate many more unnecessary excavations and would undoubtedly reduce the effort and cost of any follow-up actions that are based on the survey results.

Apart from the obvious effectiveness, the principle benefit of this method is its simplicity. The method is fairly generic and can be applied to almost any time-domain electromagnetic system. For example, the time-gates used here are very similar to those of the standard EM61-mk2. The technique should therefore be directly applicable to ground-based surveys with little modification and without the more onerous requirements of a full polarizability inversion (β) routine or decay constant calculation.

References

Doll, W. E., T. J. Gamey, L.P. Beard, J. R. Sheehan, J. Norton, J. S. Holladay, A. E. Hanson, and R.M. Lahti, 2010 (this volume), Performance Assessment of a New Boom-Mounted Airborne Time-Domain Electromagnetic System, Extended abstract, 2010 Symposium on the Application of Geophysics to Environmental and Engineering Problems, 10 pp.

Holladay, J. S., W. E. Doll, L. P. Beard, J. L. C. Lee, and D. T. Bell, 2006, UXO time-constant estimation from helicopter-borne TEM data, *Jour. Env. and Eng. Geophysics*, v. 11, n. 1, p. 43-52, 2006.

Acknowledgements

We thank Dr. Herb Nelson, Dr. Jeff Marqusee, and the ESTCP Program Office staff for their support of this research. National Helicopters and our flight crew, Mr. Doug Christie (pilot) and Mr. Marcus Watson (system operator), contributed to the success of this project. We would also like to thank Mr. Raye Lahti and Ms. Andri Hanson of AMEC for project management.

ALLTEM UXO CLASSIFICATION AND DISCRMINATION RESULTS FROM THE YUMA PROVING GROUND STANDARDIZED TEST SITE

Theodore H. Asch, U.S. Geological Survey, Denver, CO
David L. Wright, U.S. Geological Survey, Denver, CO
Craig W. Moulton, U.S. Geological Survey, Denver, CO
Trevor P. Irons, U.S. Geological Survey, Denver, CO
David V. Smith, U.S. Geological Survey, Denver, CO

Abstract

An advanced multi-axis electromagnetic induction system, ALLTEM, has been specifically designed for detection and discrimination of unexploded ordnance (UXO). This work has been funded by ESTCP (Project MM-0809). ALLTEM uses a continuous triangle-wave excitation that measures the target step response rather than the more common impulse response. Ferrous and non-ferrous metal objects have opposite polarities. The system multiplexes through all three orthogonal (H_x, H_y, and H_z axes) transmitting loops and records a total of 19 different transmitting (Tx) and receiving (Rx) loop combinations with a spatial data sampling interval of 15 cm to 20 cm. 2008 saw improvements to the ALLTEM with a new, lighter cart made of NOMEX honeycomb with fiberglass facing and new electronics with approximately 40% higher current output. An Attitude Heading and Reference System has also been integrated into the acquisition stream and is used to generate more precise locations of sensor locations. Software improvements include development and integration of ALLTEM analyses onto the Oasis Montaj platform. This includes importing survey data, gridding, noise analysis for threshold determination, automatic selection of targets, batch inversion of selected targets using PEST (a forward model independent non-linear inversion), and automatic classification of inverted targets into clutter and targets of interest. This paper presents some of the results of a demonstration and validation survey at the Yuma Proving Ground in February 2009. The U.S. Geological Survey operated ALLTEM with a Leica 1200 GPS over the Army's UXO Calibration and Blind Test Grids and a portion of the Open Field Area. Ongoing data analyses indicate that this new and improved version of the ALLTEM is able to detect anomalous features and to automatically classify targets as being items of interest or not and then to discriminate the munitions' types.

The ALLTEM System and Triangle Wave Excitation

ALLTEM is one of several multi-axis electromagnetic and magnetic prototype systems being developed for UXO applications (Barrowes et al., 2006; Snyder and George, 2006; Smith, J.T., et al., 2004; Smith and Bracken, 2004; Wright et al., 2006). The motivation for using multi-axis excitation and observation of target response is that the additional information aids in going beyond detection of metal objects in the ground to the critical task of discriminating between probable UXO and harmless scrap metal that can be safely left in the ground. The system was described in Wright et al., 2006, and Wright et al., 2007. The ALLTEM prototype is shown in figure 1. System control and data acquisition software, written in National Instruments LabVIEW®, provides the flexibility of selecting a single Tx polarization or multiplexing through all three polarizations. Table 1 presents the naming conventions used for the different receiver configurations.

Table 1: Receiver configurations naming scheme.

Type	Hz Tx	Hx Tx	Hy Tx
1 m Receiver	ZZM	XZM	YZM
Sub-Vertical Diagonal Gradient Receivers	ZZE	XZE	YZE
	ZZF	XZF	YZF
	ZZG	XZF	YZF
	ZZH	XZF	YZF
Horizontal Gradient Receivers	ZX1	XX1	YY1
	ZY1		

In Wright et al., 2006 we discussed advantages of using a triangle-wave excitation as was pioneered by the UTEM system (West et al., 1984). One advantage for UXO applications is that the responses of ferrous and non-ferrous metal objects have opposite polarities.

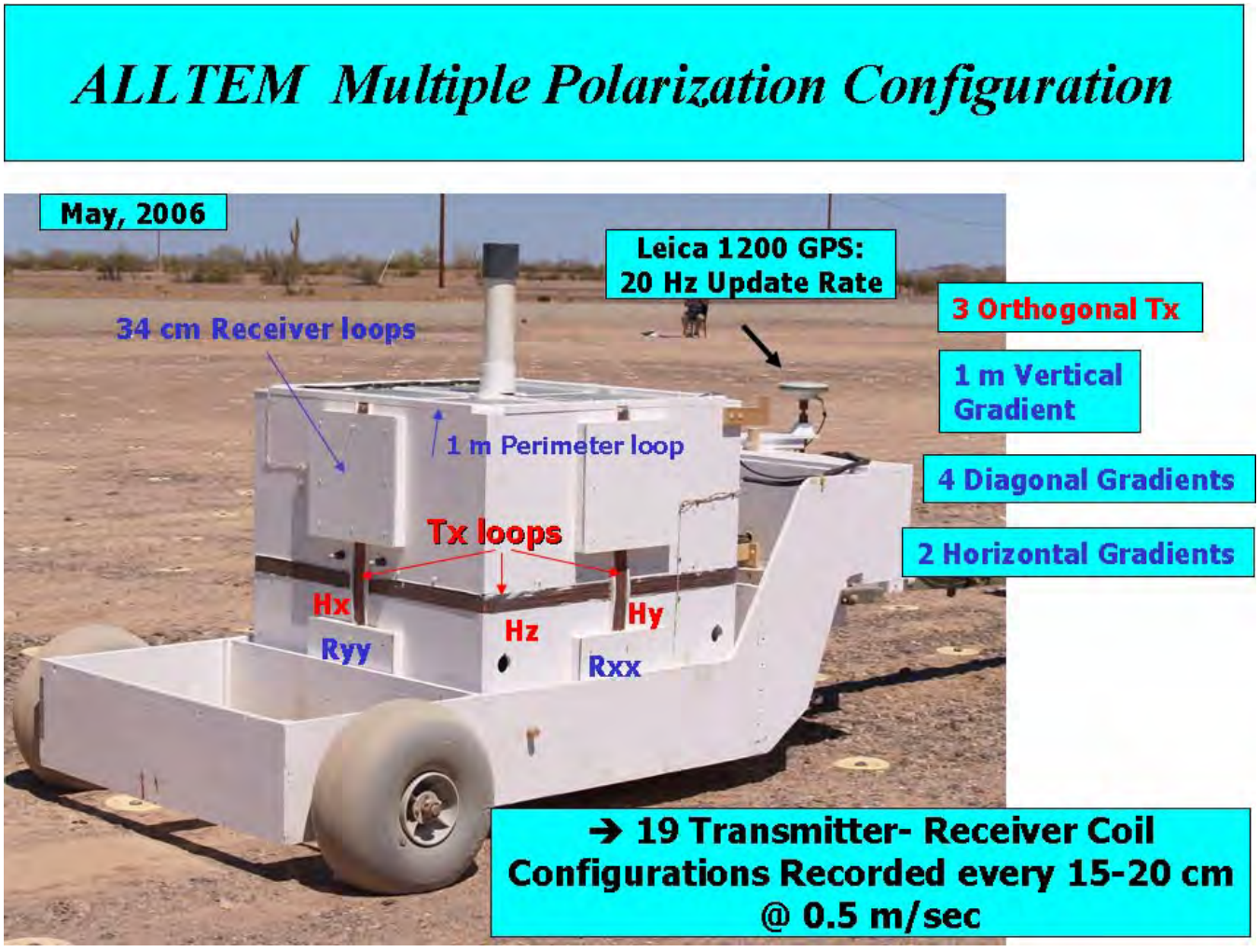

Figure 1: This annotated photograph of the ALLTEM system shows the three orthogonal square Tx loops and the square Rx loops of 1 m and 34 cm size.

This provides an immediate distinguishing visual cue. The response of a ferrous target has a non-zero late time value which may provide an improvement in late-time SNR. Both of these characteristics are consequences of the fact that the secondary magnetic flux density, **B**, from a target is produced by two competing physical phenomena. First, by Lenz's Law, currents induced on a conducting body oppose the change in magnetic flux density that produced them. For non-ferrous metal objects these induced currents are the only source for the secondary magnetic flux density. For ferrous metal objects, however, magnetic domains in the metal are aligned by the primary magnetic field intensity, **H**, and this alignment causes a secondary magnetic flux density that enhances the primary field through the familiar relationship $\mathbf{B}=\mu\mathbf{H}$ where μ is the magnetic permeability of the metal. These two competing physical processes explain the opposite polarity responses of ferrous and non-ferrous targets shown in Figure 2.

The Leica 1200 real-time kinematic global positioning system (RTK-GPS) has a 20 Hz position update rate that is fast enough to greatly reduce or perhaps even eliminate the need to interpolate position data. Dynamic tests indicate that positions for the rover GPS antenna are accurate to within +/- 2 cm when the solutions are in "fixed" mode. Although there are additional position errors due to cart roll, pitch, and yaw, these errors, at YPG, were typically small enough that the inversions provided good estimates of target position, depth, and orientation, and reasonable and reproducible values for dipole moments of these targets, even though the system was moving. The impact of position errors on our inversions is considered in a later section of this paper.

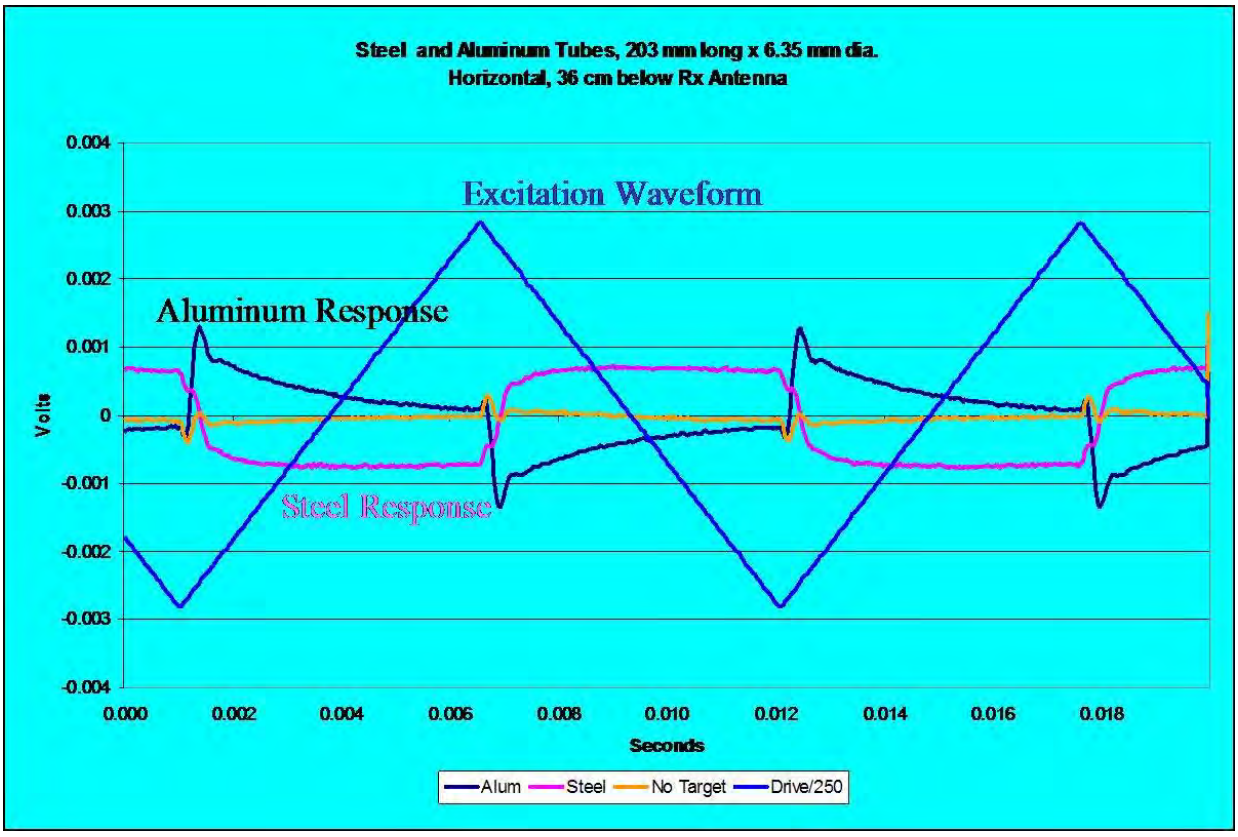

Figure 2: This figure shows a scaled current excitation in blue. The peak amplitude of this current waveform is +/- 8 amperes. The initial slopes of the aluminum and steel responses after each inflection point of the excitation waveform are opposite and the later time response of the steel object approaches a non-zero value.

Making measurements of small secondary responses in the presence of a large primary signal requires that leakage of the primary signal into the received signal be suppressed by some means. We suppress primary signal leakage in four ways. The first reduction is geometrical; the receiving loops are symmetrically placed and recorded as opposite gradient pairs. Second, because it is very difficult to position coils with enough precision to completely eliminate primary imbalances and almost impossible to maintain complete balance as temperature changes, we also use programmable differential gains on the gradiometer loop outputs to null unwanted residual primary signal leakage. Third, in processing we apply a "rolling background subtraction" algorithm in which the patterns of waveforms along each line are examined and, where we know there are no targets, a moving background average value is determined and subtracted from each of the other records along the line until a new background average is determined (Figure 3).

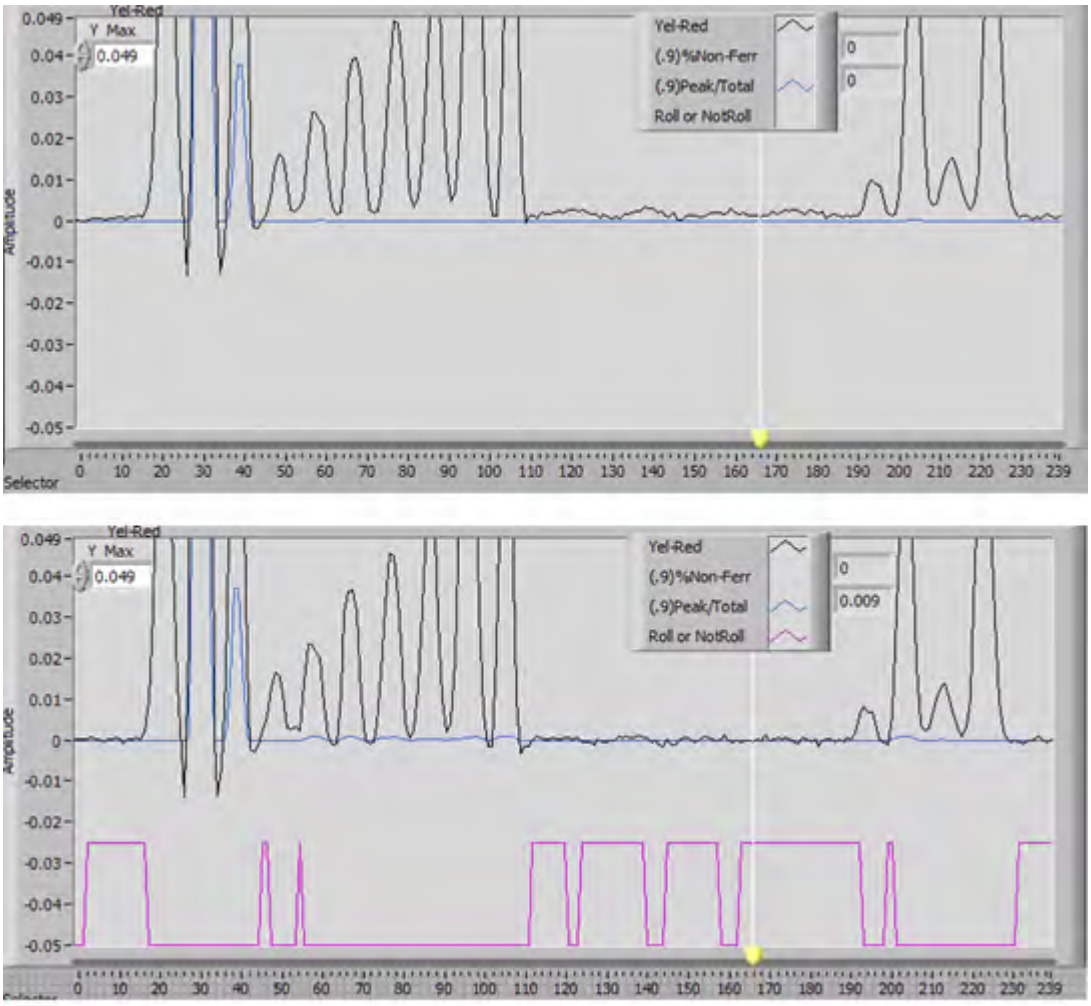

Figure 3: Illustration of the application of rolling background subtraction and the improvement in drift reduction. Top – No rolling background subtraction. Bottom – Rolling background subtraction applied.

Finally, we process amplitude differences along waveforms rather than the amplitudes themselves. ALLTEM responds to the conductivity and magnetic susceptibility of the ground. The ground conductivity response dies much faster than the responses from metal objects buried in the ground. After the ground conductivity transient, the response to the ground is a square wave whose amplitude depends on the ground susceptibility and on the cart height and attitude. Because ground

response varies, we do not use simple signal amplitude for target detection, but rather a difference between the waveform amplitude at a relatively early time and at a later time as illustrated in Figure 4.

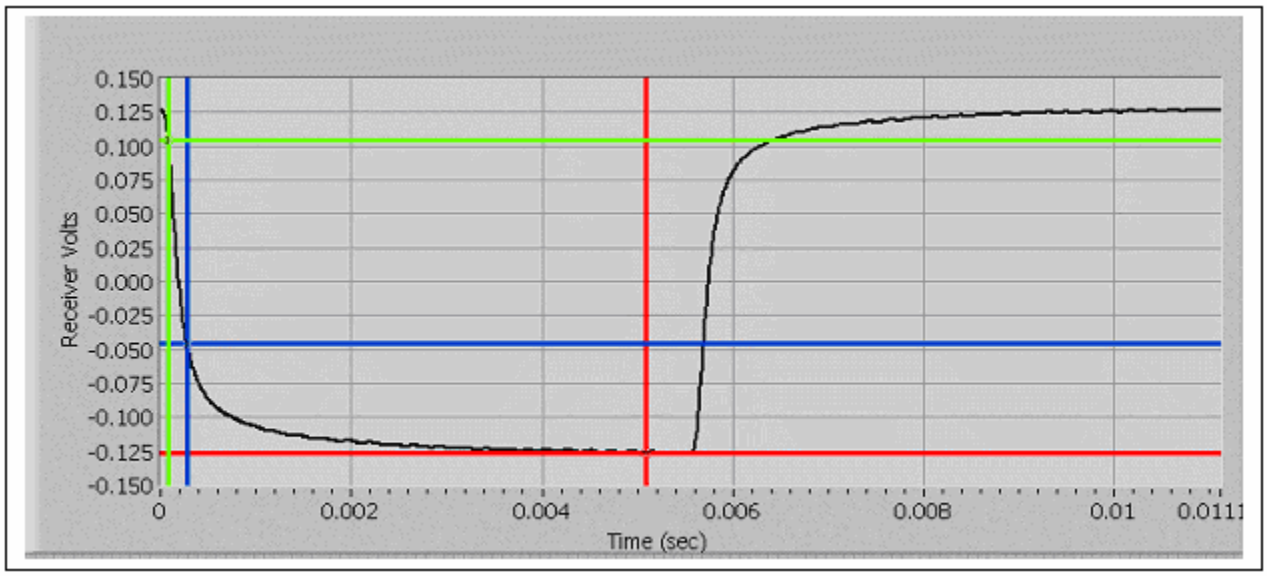

Figure 4: This figure shows a waveform (black curve), a late-time cursor (red) and two early-time cursors (green and blue). Amplitude difference maps are produced from differences between voltages at the red cursor and the blue cursor.

Mechanical and Electrical Upgrades

Beginning in 2008 and continuing into 2009 mechanical and electronic upgrades to the ALLTEM were initiated. This included a new survey transport platform for the ALLTEM using a honey-comb material made of NOMEX with fiberglass face plates. In addition, in order to reduce the likelihood of flat tires which reduce the in-field survey time, new racing slick-style tires have replaced the Rolleze balloon-style tires. These tires are set at the ambient air pressure. That is, they have no internal air pressure and so cannot go flat. In order for the tires to maintain their shape 3-inch thick ENSOLITE foam has been inserted into the tires between the bead-locks and the tire face.

All the electronic acquisition boards were redesigned, repopulated, and underwent thorough testing that is ongoing. The CROWN amplifier that was the current driving force of the previous prototypes has been replaced by a Class D amplifier. When the CROWN amplifier gets too hot, it automatically, and unexpectedly, shuts down. In the field this can severely interfere with the survey schedule. The new Class D amplifier outputs 38% more current than the CROWN amplifier (11 Amperes versus 8 Amperes) and remains cool even on a hot day. Another bonus of the Class D amplifier is that it needs less power and so the large 4.5 kW generator that has been used in the past has been replaced by a 2 kW generator. This results in a lighter and quieter system.

Yuma Proving Ground 2009

In 2006 the analysis of the Yuma Proving Ground Blind Test Grid data took approximately three months to process, analyze, interpret, classify, and finally discriminate individual UXO from clutter and blank holes. In 2008 and 2009 much emphasis has been placed on decreasing the processing and analysis time used to analyze the ALLTEM data. The entire ALLTEM analysis process has now been migrated to GEOSOFT Oasis Montaj. Within Oasis the user can load the survey data, grid the data,

statistically determine significant data levels, automatically select targets, and invert and classify the data. The statistics are performed using R (also known as "GNU S") which is a language and environment for statistical computing and graphics (Bates, 2008).

The inversion analysis has been migrated from manually conducting individual inversions for each time gate for each target to batch processing all time gates for all targets. This is has been accomplished using the parameter estimation algorithms (PEST) developed by Doherty (2004). PEST takes an independent forward model, adds a complete non-linear regularized inversion, and outputs an inverted model with parameter sensitivities.

Classification of the targets of interest and non-targets of interest is being accomplished using the active learning process developed by Zhang et. al. (2004) and applied to unexploded ordnance type targets.

Yuma Proving Ground 2009

In February 2009 the USGS conducted surveys of the UXO Standardized Test site at the Yuma Proving Ground (Figure 1). Surveys of the Calibration and Blind Test grids were conducted first and then approximately 5 acres of the Open Field Area were investigated.

Yuma Proving Ground Standardized UXO Test Site

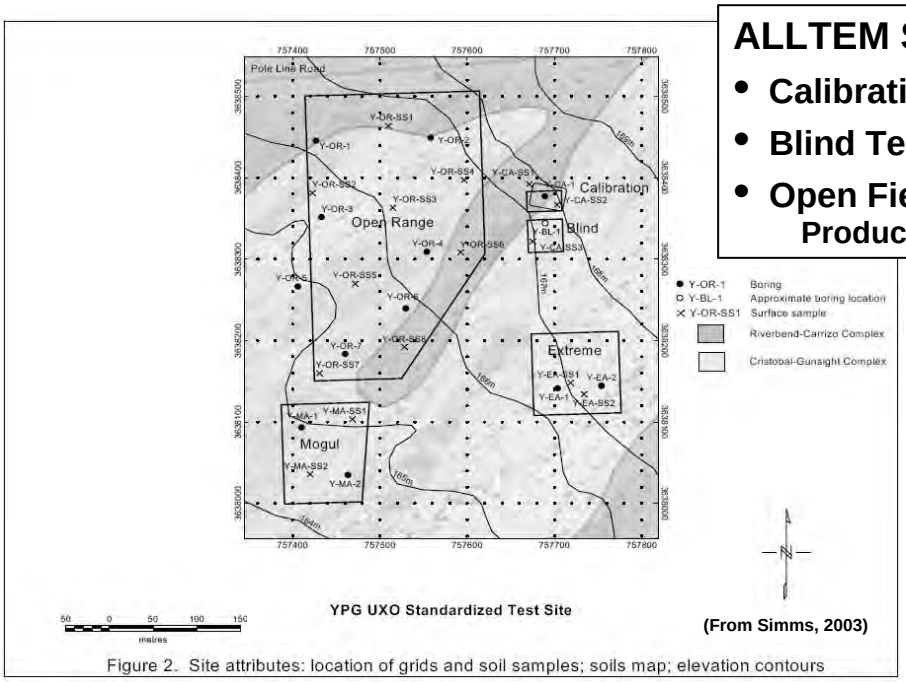

ALLTEM Surveyed:

- **Calibration Grid (0.27 acres)**
- **Blind Test Grid (0.43 acres)**
- **Open Field Area (5.1 acres)**
  Production ~ 1 – 1.25 acres/day

Figure 5: Yuma Proving Ground .

A few photos of the investigation are presented in figures 6 and 7. The ALLTEM system in the field is displayed in figure 6. The ALLTEM is pulled by a Kubota tractor with the generator positioned in the front and the electronics just behind the driver. The survey in progress of the Open Field Area is shown in Figure 7. Surveys were conducted at about 0.5 m/second and the traverses were separated by 0.5 m.

Figure 6: The ALLTEM at YPG.

Figure 7: Close up view of the racing slick tires set at ambient air pressure.

Survey results are presented in figures 8, 9, 10 and 11. Figure 8 shows the results for the Calibration grid with numbered patch polygons, Figure 9 the results for the Blind Test Grid with numbered patch polygons, and Figures 10 and 11 the results for the 5 acres surveyed of the Open Field Area.

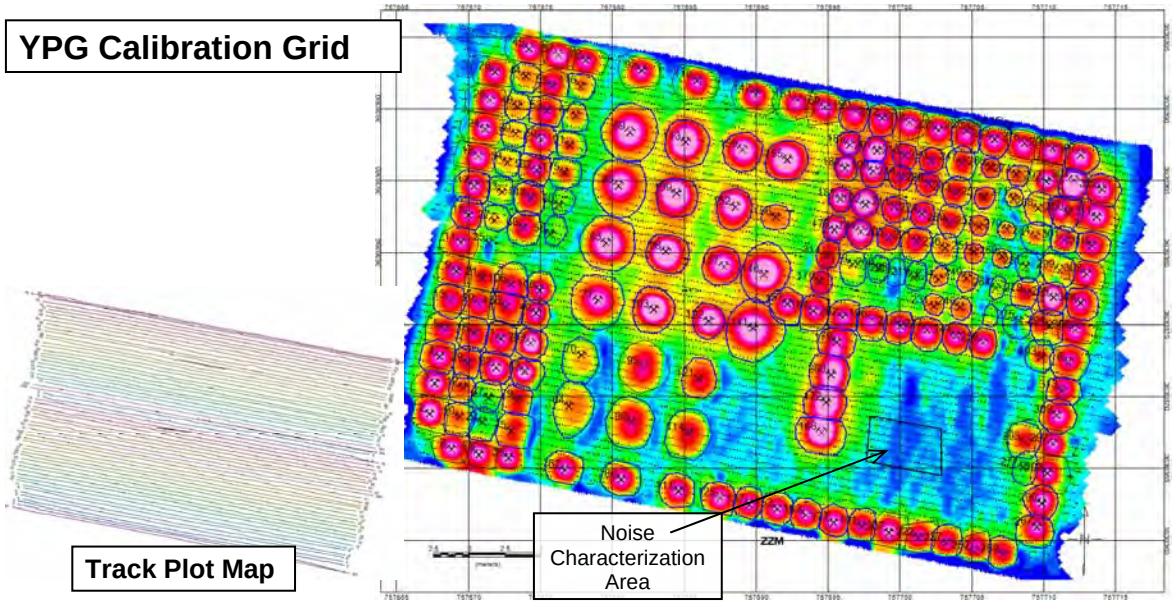

Figure 8: ALLTEM survey results with numbered patch polygons for the YPG Calibration Grid.

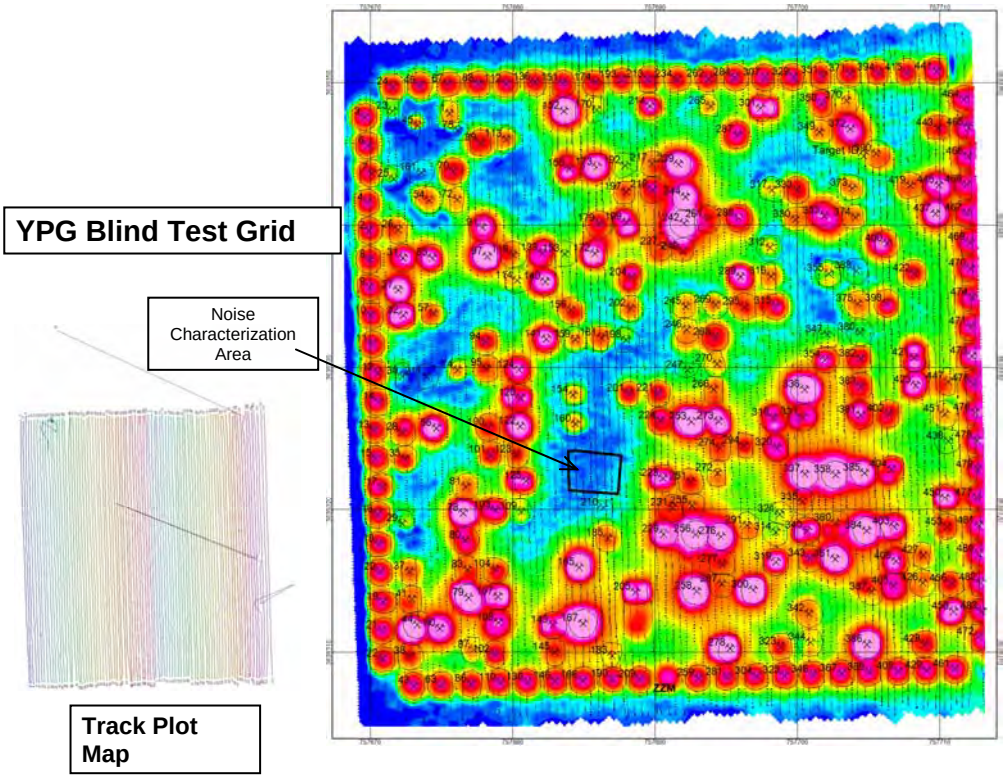

Figure 9: ALLTEM survey results with numbered patch polygons for the YPG Blind Test Grid.

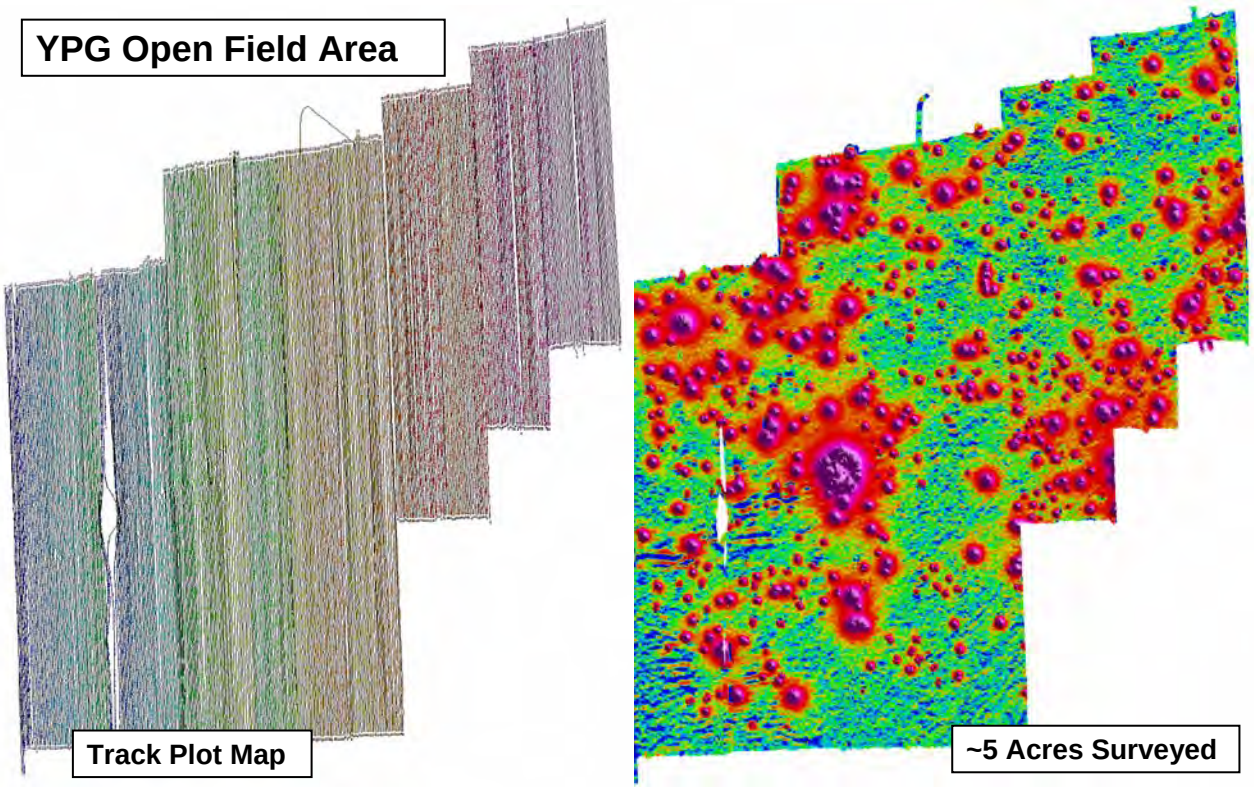

Figure 10: ALLTEM survey results for the YPG Open Field Area.

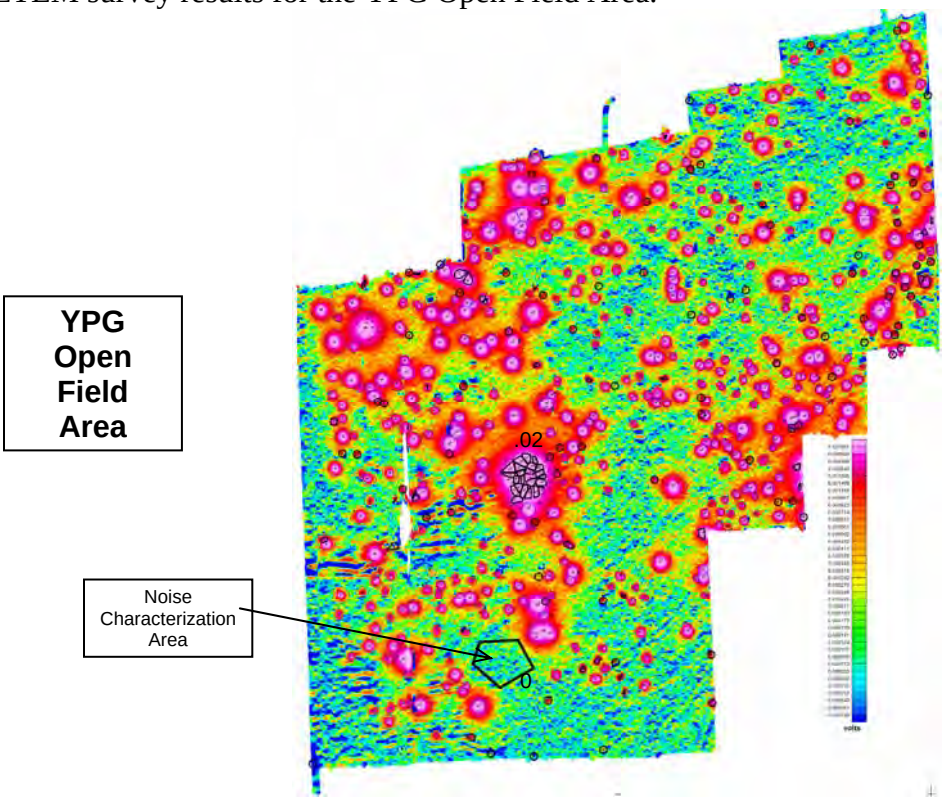

Figure 11: ALLTEM survey results with numbered patch polygons for the YPG Open Field Area.

Figure 12 presents an example of the inversion results for cell F10 in the Calibration Grid. The target of interest in that cell is a 60 mm mortar oriented in a north-south direction. The blue line is the measured data and the magenta line is the inversion result.

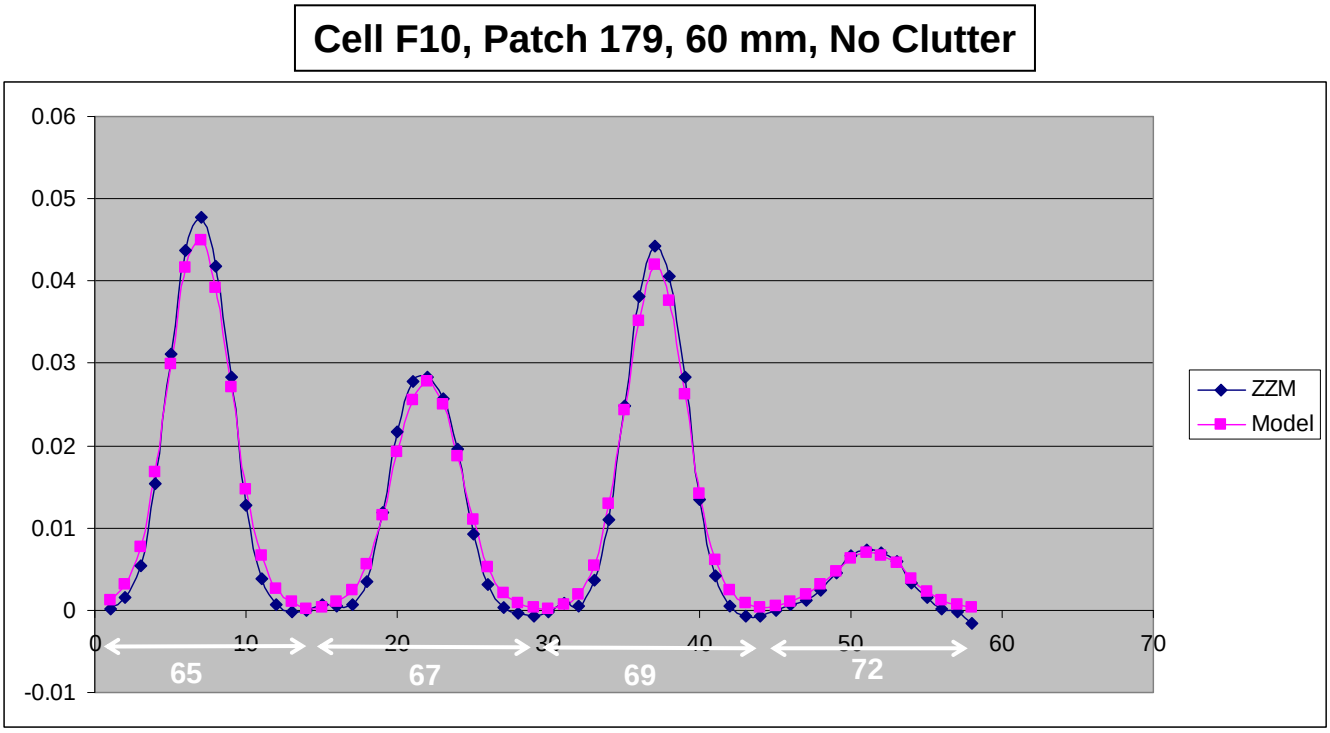

Figure 12: PEST inversion result for cell F10 of the YPG Calibration Grid.

The classification process is based on a statistical comparison between known feature parameters of various ordnance types and the inversion results for each polygon patch of data. Figure 13 presents the known data from the Calibration Grid that is used in analyses of the Blind Test Grid and the Open Field Area data. Examples of the results of the classification process are presented in figures 14 through 18.

The results in Figure 18 show the effects of varying amounts of clutter on the accuracy of the classification algorithm. As more clutter is added to the single 60 mm mortar in those cells the classification determines that a larger and larger object is present at those locations.

YPG Data Analysis – Calibration Grid Classification Comparators

8 lb. Shot			
mu_1	mu_2	mu_3	NF
0.402	0.332	0.335	0.023
0.802	0.706	0.681	0.0669
0.753	0.361	0.654	0.0706
0.817	0.614	0.71	0.081
0.488	0.409	0.425	0.188
0.655	0.458	0.562	0.0835

105mm_M60			
mu_1	mu_2	mu_3	NF
10.488	2.828	2.783	0.3238
10.514	2.802	2.793	0.3238
11.214	2.808	3.034	0.3238
11.29	3.016	3.038	0.9935

BDU28			
mu_1	mu_2	mu_3	NF
0.353	0.331	0.323	0.3115
0.212	0.17	0.194	0.4929
0.354	0.316	0.288	0.3115
0.317	0.273	0.234	0.2805
0.362	0.32	0.273	0.4386
0.337	0.306	0.26	0.5981
0.409	0.375	0.286	0.5981

40mm MK2 Projectile			
mu_1	mu_2	mu_3	NF
1.093	0.11	0.175	0.4622
0.849	0.416	0.114	0.1268
0.888	0.412	0.147	0.475
1.007	0.172	0.154	0.7172

BLU-26			
mu_1	mu_2	mu_3	NF
0.25	0.208	0.203	0.4596
0.272	0.249	0.236	0.4596
0.267	0.21	0.242	0.3369
0.205	0.178	0.178	0.8236
0.227	0.155	0.226	0.6332

81mm			
mu_1	mu_2	mu_3	NF
8.611	2.507	2.389	0.1696
9.172	2.547	2.617	0.1032
5.114	2.758	2.649	0.0827

155mm			
mu_1	mu_2	mu_3	NF
33.196	14.747	15.062	0.3353
25.752	18.271	17.431	0.3353
30	18.36	17.895	0.1984

M42			
mu_1	mu_2	mu_3	NF
0.117	0.037	0.021	0.1831
0.182	0.127	0.124	0.1831
0.126	0.094	0.056	0.2512
0.1	0.05	0.075	0.1831

2.75 Inch			
mu_1	mu_2	mu_3	NF
12.25	5.217	2.993	0.0512
6.839	3.347	4.482	0.1406
9.949	2.783	1.622	0.0376
9.097	3.781	1.449	0.0134

Figure 13: Known feature parameters of various ordnance used in the classification process.

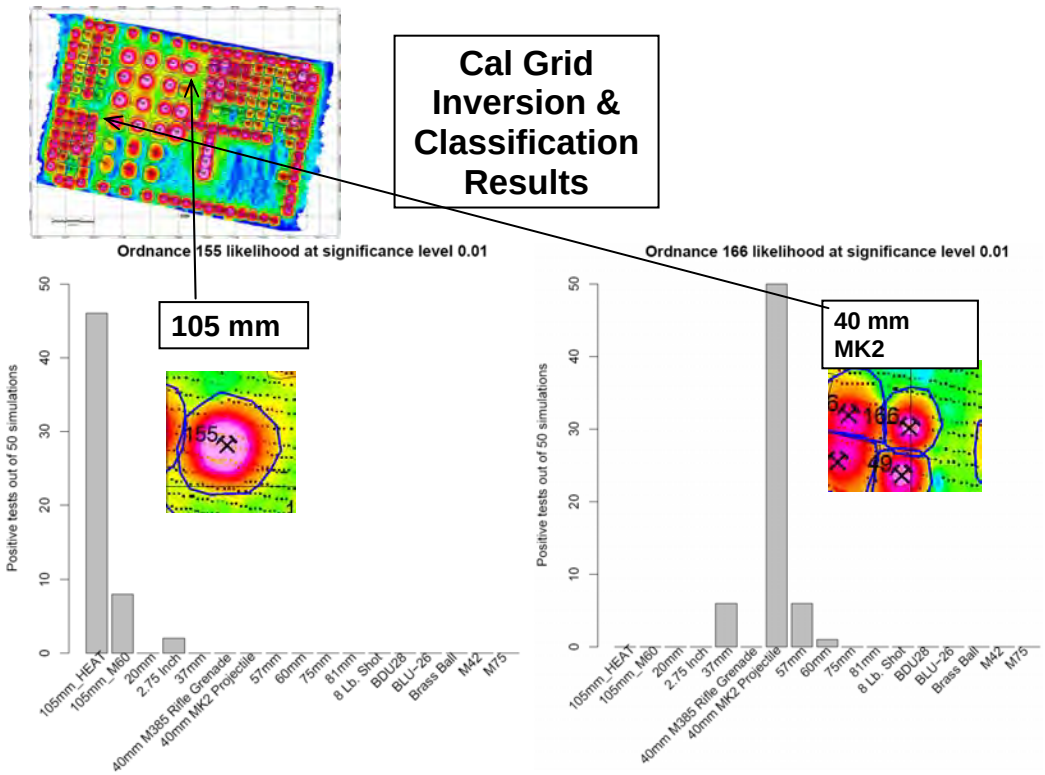

Figure 14: Example of the classification process for data in the Calibration Grid.

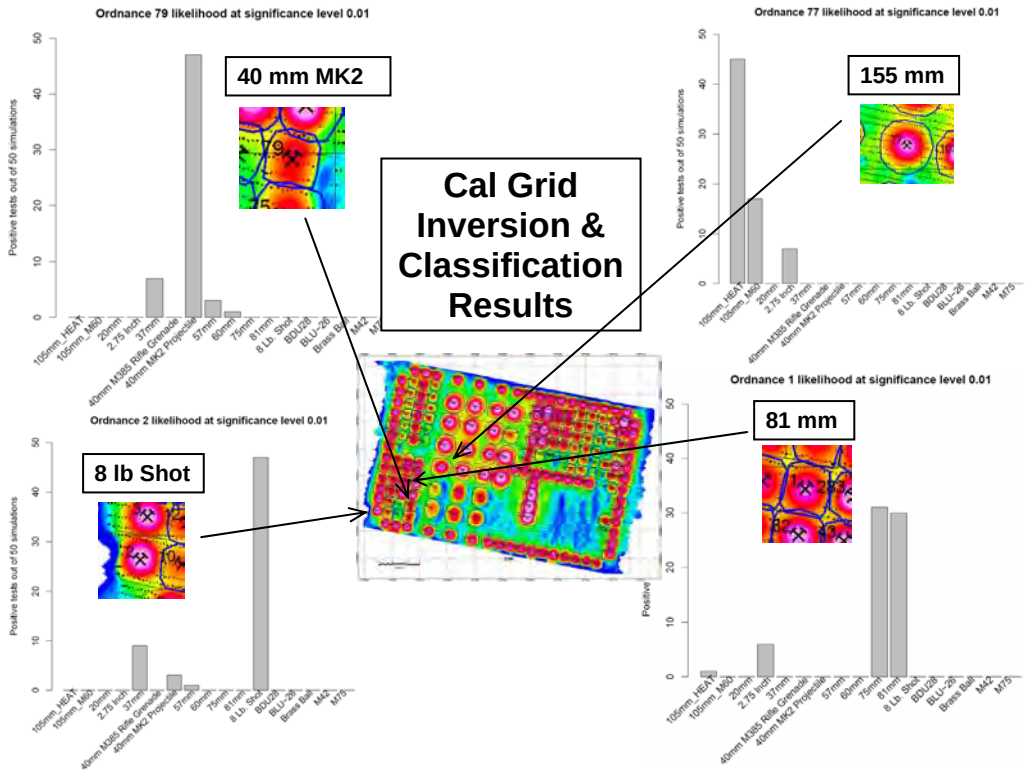

Figure 15: Example of the classification process for data in the Calibration Grid.

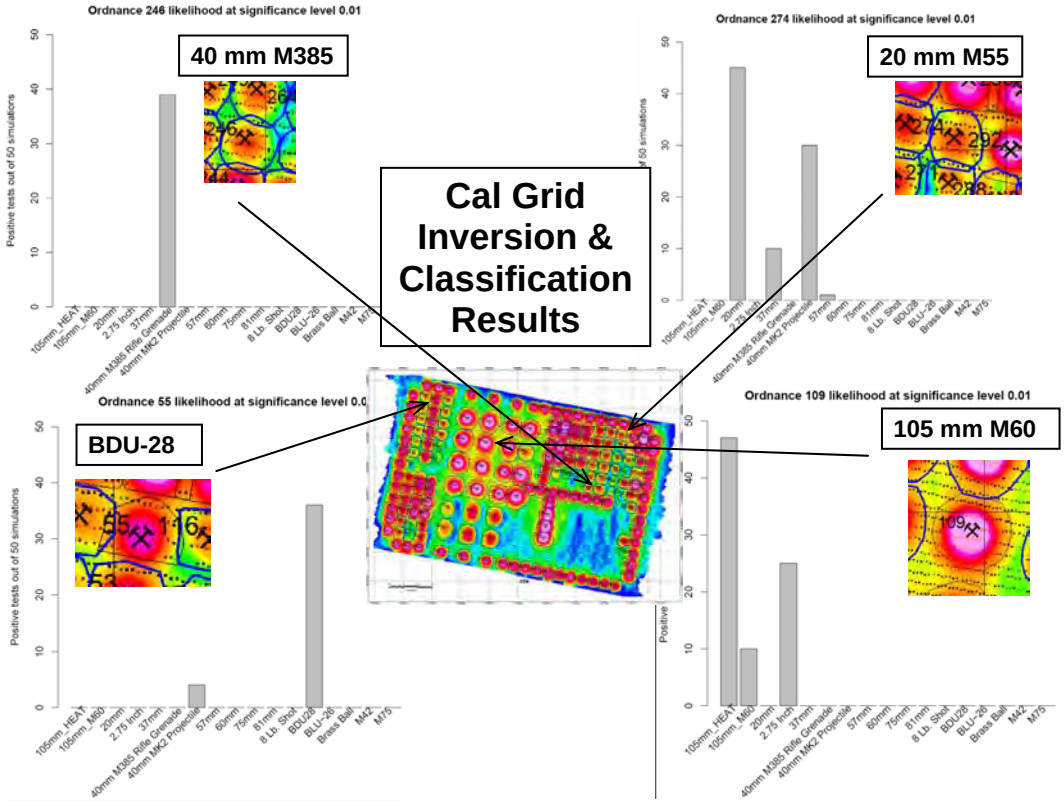

Figure 16: Example of the classification process for data in the Calibration Grid.

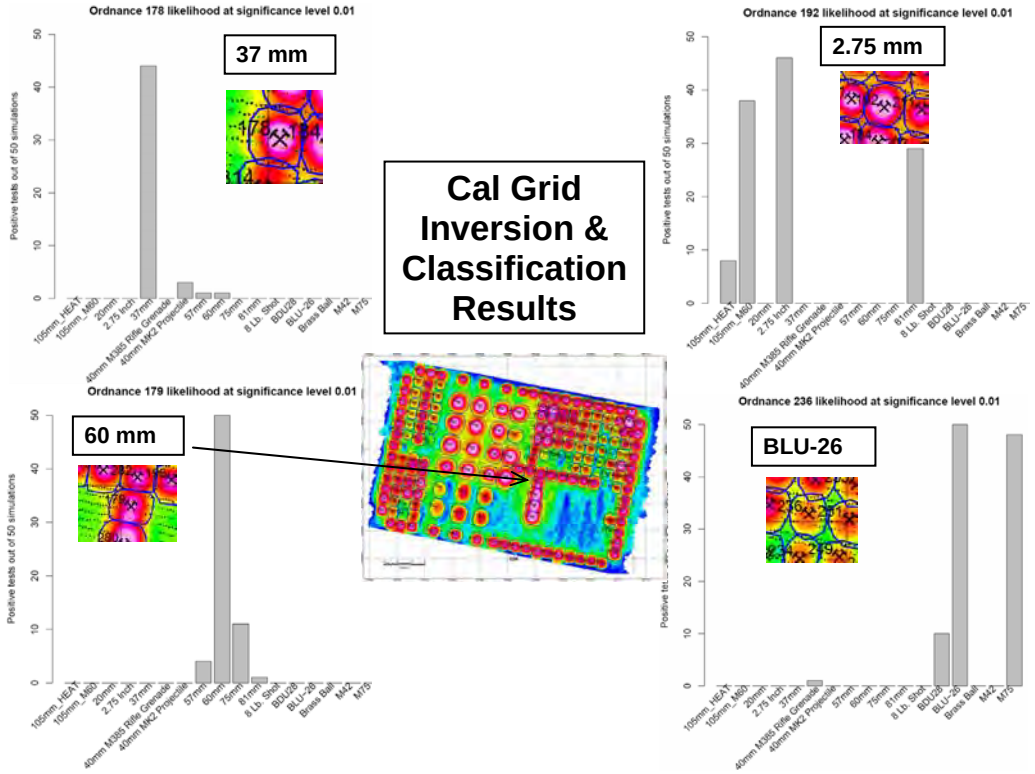

Figure 17: Example of the classification process for data in the Calibration Grid.

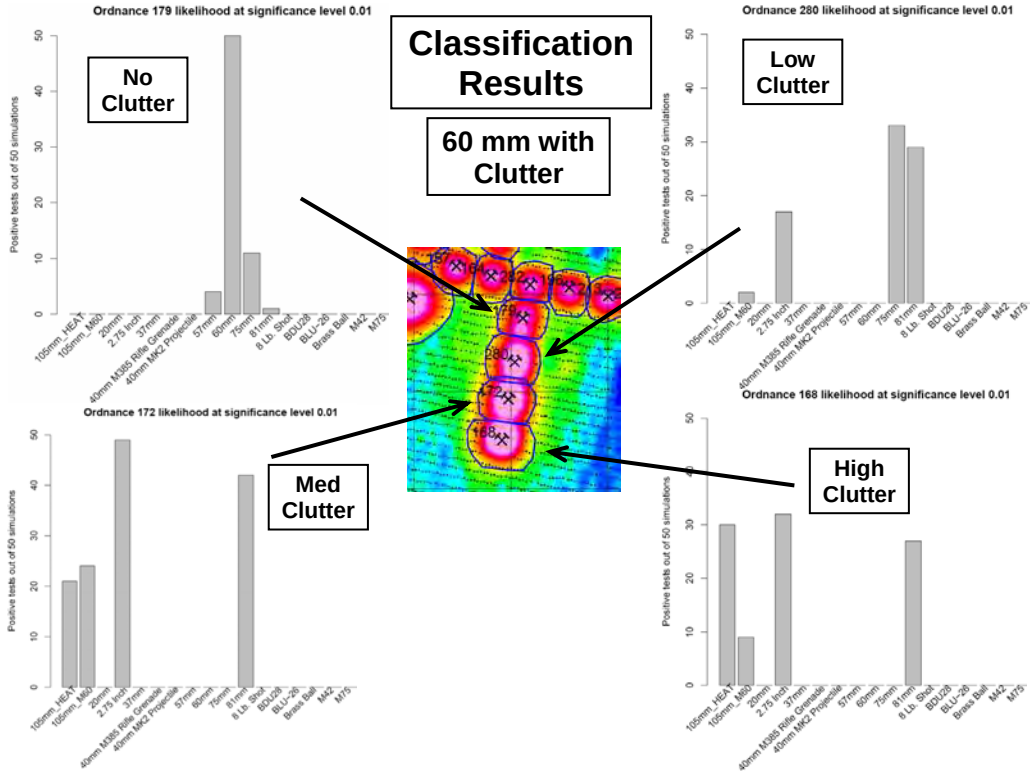

Figure 18: Example of the classification process for data in the Calibration Grid.

Conclusions

The ALLTEM has acquired data and demonstrated an ability to detect, discriminate, and classify different types of munitions. The presence of clutter and possibly more than one target of interest at a location are still challenges that need to be resolved.

References

Barrowes, B., O'Neill, K., Snyder, D.D., George, D.C., Shubitidze, F., 2006, New man-portable vector time domain EMI sensor and discrimination processing, *in* Proc. of the UXO-Countermine-Range Forum, July 10-13, 2006, Las Vegas, NV, (Power Point presentation, 18 slides).

Bates, D., 2008, R: a language and environment for statistical computing: R Foundation for Statistical computing, Vienna, Austria, http://www.R-project.org.

Doherty, J., 2004, PEST: model-independent parameter estimation, user manual: 5th edition: Watermark Numerical Computing.

Smith, D.V., and Bracken, R.E., 2004, Field experiments with the tensor magnetic gradiometer system at Yuma Proving Ground, Arizona, *in* Proc. of the Symp. on the Application of Geophysics to Engineering and Environmental Problems (SAGEEP), February 2004, pp. 1675-1690.

Smith, J.T., Morrison, F.H., and Becker, A., 2004, Resolution depths for some transmitter-receiver configurations: IEEE Transactions on Geoscience and Remote Sensing., vol. 42, no. 6, pp. 1215-1221.

Snyder, D.D., and George, D.C., 2006, Qualitative and quantitative UXO detection with EMI using arrays of multi-component receivers, *in* Proc. of the Symp. on the Application of Geophysics to Engineering and Environmental Problems, April 2-6, 2006, pp. 1749-1760.

West, G.F., Macnae, J.C., and Lamontagne, Y., 1984, A time-domain electromagnetic system measuring the step response of the ground: Geophysics, vol. 49, pp. 1010-1026.

Wright, D.L., Moulton, C.W., Asch, T.H., Brown, P.J., Hutton, S.R., Nabighian, M.N., and Li, Y., 2006, ALLTEM for UXO applications – first field tests, *in* Proc. of the Symp. on the Application of Geophysics to Engineering and Environmental Problems, April 2-6, 2006, pp. 1761-1775.

Wright, D.L., Moulton, C.W., Asch, T.H., Brown, P.J. II, Nabighian, M.N., Li, Y., and Oden, C.P., 2007, ALLTEM UXO detection sensitivity and inversions for target parameters from Yuma Proving Ground Test Data, *in* Proc. of the Symp. on the Application of Geophysics to Engineering and Environmental Problems, April 1-5, 2007, pp. 1422-1435.

Zhang, Y., Liao, X., and Carin, L., 2004, Detection of buried targets via active selection of labeled data: application to sensing subsurface UXO: IEEE Transactions on Geoscience and Remote Sensing, 42, no. 11, pp. 2535-2543.

Acknowledgments and Disclaimer

This research was supported by the U.S. Department of Defense, through the Environmental Security Technology Certification Program (ESTCP) Project MM-0809.

Any use of trade, product, or firm names in this paper is for descriptive purposes only and does not imply endorsement by the U.S. Government.

ESTCP SAN LUIS OBISPO CLASSIFICATION DEMONSTRATION

H. H. Nelson, SERDP/ESTCP, Arlington VA
K. Kaye, HGL, Inc. Reston VA
A.M. Andrews, SERDP/ESTCP, Arlington VA

Abstract

The second demonstration in the Environmental Security Technology Certification Program's Classification Pilot Program was conducted in the summer of 2009 at a range on former Camp San Luis Obispo, CA that contained a mix of munitions. The objective of the demonstration was to correctly classify as many of the detected buried objects as possible as non-hazardous and thus safe to leave in the ground. A number of commercial and developmental magnetometer and electromagnetic induction sensor systems were used to map the site. The detected anomalies in each sensor data set were analyzed by a number of groups to extract target parameters. After training on roughly 200 excavated targets, each analyst constructed a prioritized list of the roughly 1300 remaining anomalies indicating which were non-hazardous, which were hazardous, and which could not be successfully analyzed. Substantial classification performance was achieved in the analysis of carefully collected commercial EMI sensor data and even better performance was achieved by the developmental, cued sensors that were demonstrated. Example results are presented as receiver operating characteristic curves.

Background

When a munitions-contaminated site is cleaned up, it is typically mapped with a geophysical system, based on either a magnetometer or electromagnetic (EM) induction sensor, and the locations of all detectable signals are excavated. Many of these detections do not correspond to munitions, but rather to other harmless metallic objects or geology; often in excess of 90% of objects excavated during the course of a munitions response are found to be non-hazardous items.

Current technology, as it is commonly implemented, does not provide a physics-based, quantitative, validated means to discriminate between hazardous munitions and non-hazardous items. Thus, all anomalies must be treated as though they are intact munitions when they are dug. They are carefully excavated by certified unexploded ordnance (UXO) technicians using a process that often requires expensive safety measures, such as barriers or exclusion zones. As a result, most of the costs to remediate a munitions-contaminated site are currently spent on excavating targets that pose no threat. If these items could be determined with high confidence to be non-hazardous, some of these expensive measures could be eliminated or the items could be left unexcavated entirely.

Classification is the process by which buried targets are divided into those targets that are hazardous and those that are not. This is most often accomplished by interpreting high-quality geophysical data collected over the target with physics-based models to estimate target parameters. The parameters in these models are related to the physical attributes of the object that resulted in the signal and the values of these parameters may be used to estimate the likelihood that the signal arose from a target of interest (TOI), that is, a munition or something sufficiently like a munition that it must be removed from the site.

Electromagnetic Induction (EM) data are typically inverted using a three-axis polarizability model that can yield a set of parameters that relate to the physical size of the object, its aspect ratio, the wall thickness, and the material properties [Smith 2004, Snyder 2008, Walker 2007]. Munitions are

typically long, narrow cylindrical shapes that are made of heavy-walled steel. Common clutter objects can derive from military uses and include munitions fragments, fins, base plates, nose cones and other munitions parts or be man-made nonmilitary items such as barbed wire, horseshoes, nails, hand tools, and rebar. These objects and geology give rise to signals that will differ from munitions in the parameter values that are estimated from geophysics data.

ESTCP Classification Pilot Program

Significant progress has been made in the research program on technologies needed to accomplish classification. To date, emerging technologies have primarily been tested at constructed test sites, with only limited application at live sites. The routine implementation of classification technologies requires demonstrations at real munitions response sites under real-world conditions. To accomplish this, the Environmental Security Technology Certification Program (ESTCP) initiated a Classification Pilot Program to validate the application of a number of recently developed technologies in a comprehensive approach to munitions response. The goal of the pilot program is to demonstrate that classification decisions can be made explicitly, based on principled physics-based analysis that is transparent and reproducible.

The first demonstration in this program was conducted at former Camp Sibert, AL. This site presented a single munitions type (the 4.2-inch mortar) and benign conditions where high-quality data could be collected. The motivation of this selection was to demonstrate a process under conditions where the technologies were expected to perform well, so that a meaningful discussion regarding the application of successful classification could be initiated with all stakeholders.

The pilot program demonstrated successful classification on this simple site. With carefully collected survey data from either magnetometers or EM sensors and transitioning physics-based analysis techniques, well over half the detected clutter items were routinely eliminated with high confidence, while retaining all the munitions [Nelson, 2008].

ESTCP sponsored a second demonstration in 2009 at a site with more challenging topography and a wider mix of targets-of-interest. A hillside range at the former Camp San Luis Obispo, CA was selected for this demonstration. At this site, there were at least four known targets-of-interest including 60-mm, 81-mm, and 4.2-in mortars and 2.36-in rockets.

In this paper we begin with a brief description of the site and overview of the program design. We then summarize the major results and draw a number of conclusions regarding the implementation of classification on munitions response projects.

Site Description

Camp San Luis Obispo was established in 1928 by California as a National Guard Camp consisting of 5,800 acres. Additional lands were added in the early 1940s until the acreage totaled 14,959. During World War II, Camp San Luis Obispo was used by the U.S. Army for infantry division training including artillery, small arms ranges, and mortar, rocket, and grenade ranges. Following the Korean War, the camp was maintained in inactive status until it was relinquished by the Army in the 1960s and 1970s. Approximately 4,685 acres was relinquished to the General Services Administration in 1965 who then transferred most of the property to Cal Poly San Luis Obispo and Cuesta College.

The site for this demonstration was a mortar target on a hilltop in Munitions Response Site (MRS) 05 (within former Rifle Range #12). It is situated along Highway 1, approximately five miles northwest of the city of San Luis Obispo. The majority of the area consists of mountains and canyons.

A 10-acre area on the hillside, divided into 45 30m x 30m grids was established as the demonstration site. An additional 1.8 acre area was designated to be surveyed by vehicular systems only. An overview map of the hillside with the demonstration area outlined is shown in Figure 1.

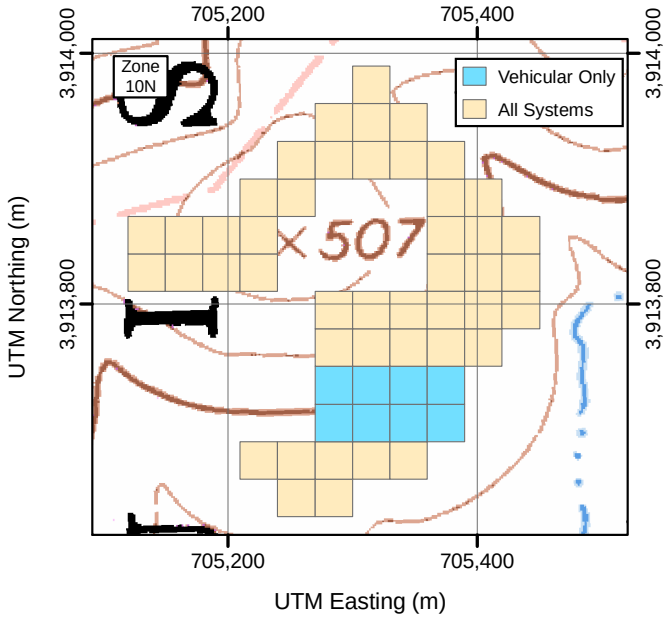

Figure 1: Layout of the demonstration site showing the 45 grids surveyed by the cart systems (10 acres) and the additional 8 grids (1.8 acres) surveyed by vehicular systems.

Program Design

Geophysical data were collected by a variety of survey and cued sensors on the demonstration site, Table 1. Detections from the EM61 MK2 array were used to cue the Naval Research Lab (NRL) and Berkeley (LBNL) static sensors; the MetalMapper system was deployed in both survey and cued mode and so was self-cued. Each individual data set and its associated detections were then processed by data analysis demonstrators to extract target parameters. These parameters were passed to the classification routines which, after training on a limited amount of site-specific ground truth, were used to produce prioritized anomaly lists.

Table 1: Geophysical systems demonstrated at SLO and the data analysis demonstrators.

Survey Data Systems	Cued Data Systems	Data Analysis Demonstrators
EM61 MK2 Cart	MetalMapper	SAIC
EM61 MK2 Towed Array	NRL TEMTADS	LBNL
Magnetometer Array	LBNL BUD	SIG, Inc
SAIC MSEMS		Sky Research
MetalMapper		Geometrics
		RML Technologies
		NAEVA Geophysics

Figure 2 shows an example of the anomaly list format requested from the demonstration participants. The focus of the program is identifying items that can be safely left in the ground. Thus, the first item on the anomaly list is that item that the analyst is most confident is not hazardous. The dig threshold is drawn below the targets that fall into the "confident not TOI" class. Continuing down the anomaly list there are those targets for which a decision could not be made with the available data, those targets that the analyst is confident are targets of interest, and finally, any targets for which the data quality is so poor that reliable features could not be estimated. The anomalies would then be excavated from the bottom to the top of the list. The rationale for these categories is that anomalies with insufficient S/N to extract reliable parameters must be treated as hazardous but further training as the digs proceed may allow decisions to be made on the items in the "can't decide" class.

Rank	Anomaly ID	$P_{clutter}$	Comment
1	247	.97	
2	1114	.96	High confidence NOT TOI
3	69	…	
…	…	…	
…	…	…	
…	…	…	Can't make a decision
…	…	…	
…	…	…	
…	…	…	
…	…	…	High confidence TOI
…	…	.03	
…	…	.02	
	…		
	…		Can't extract reliable features
	…		

Threshold

Figure 2: Example of the prioritized anomaly list submitted by the analysts in this demonstration. All targets below the threshold must be dug.

At the conclusion of the data analysis stage, all identified anomalies were excavated and ground truth labels assigned. With this truth data, the performance of each data set/analyst combination was scored.

Demonstration Data

Examples of the data collected in this demonstration are shown in Figure 3. The left panel shows an anomaly image map of the data collected by the NRL EM61 MK2 array. The right panel shows an anomaly image map of the magnetometer data. Although preliminary magnetometer transects collected a year before the demonstration did not reveal this, it is immediately obvious that the magnetometer is not the sensor of choice for this site. In fact, only one analysis demonstrator even submitted an anomaly list based on the magnetometer data. Data are presented for the entire site; due to funding limitations, only those data in the "All Systems" grids in Figure 1 were analyzed and excavated.

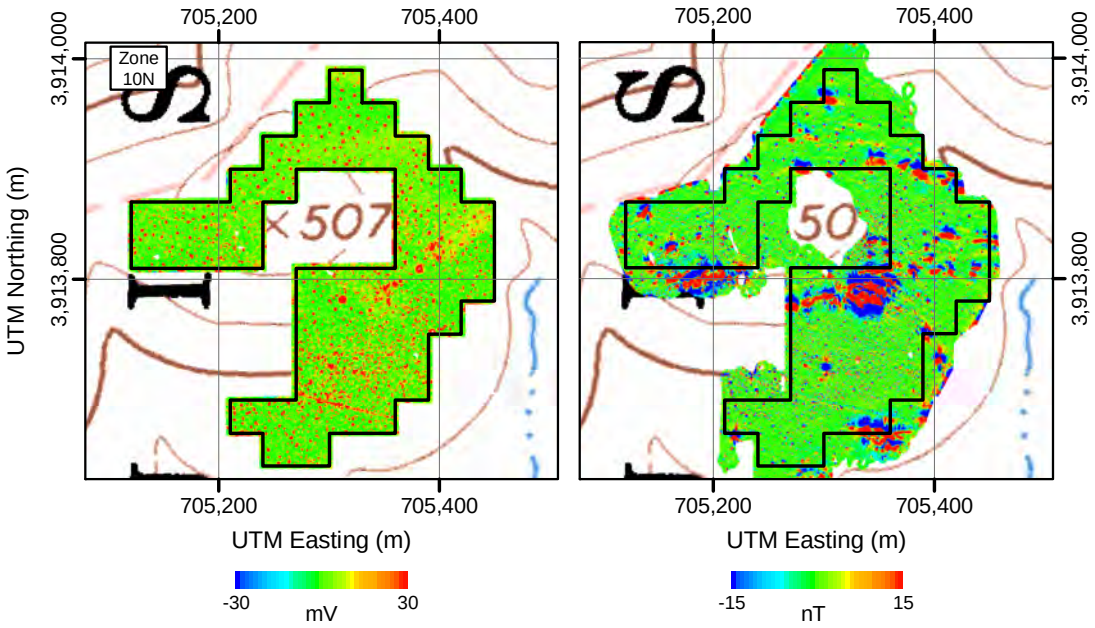

Figure 3: EM61 MK2 array data (left panel) and magnetometer data (right panel) collected over the demonstration site.

For each sensor data set, an anomaly selection threshold was chosen based on the minimum response predicted for the smallest munition expected to be on the site at a depth of 45 cm. Preliminary excavation of two 50′ x 50′ grids near the target center had shown that there were no targets deeper than 30 cm. The 45-cm depth of interest was chosen in conjunction with the Pilot Program Advisory Board to give a sufficient margin of safety. Using this threshold, 1464 above-threshold anomalies were identified in the EM61 MK2 array data in the 45 grids analyzed. For comparison, 5511 anomalies were above the magnetometer threshold. These 1464 anomalies constituted the cued target list given to the static sensor operators.

Classification Results

We present here a brief overview of the classification performance of the various analysts. A fuller discussion of the demonstration and results will be available in a summary report being prepared by the ESTCP Program Office and a complete listing of all results will be contained in a report being prepared by the Institute for Defense Analyses. Both these reports will be available on the ESTCP web site (www.estcp.org) when they are complete.

Three demonstrators analyzed the EM61 MK2 cart data using the freely available UX-Analyze module. These data were collected using standard commercial procedures with the exception of the lane spacing which was 0.5-m for this demonstration. An example result is shown in Figure 4 as a modified receiver operating characteristic (ROC) in which the first point on the ranked dig list is plotted offset from the origin to reflect the 200 (seventeen of which happened to be targets of interest) targets dug for training. The data plotted represent very good performance using a commercial sensor; almost half of the non-hazardous items were correctly identified by this demonstrator before the first target of interest was encountered (orange dot). The demonstrator was slightly too aggressive in determining their

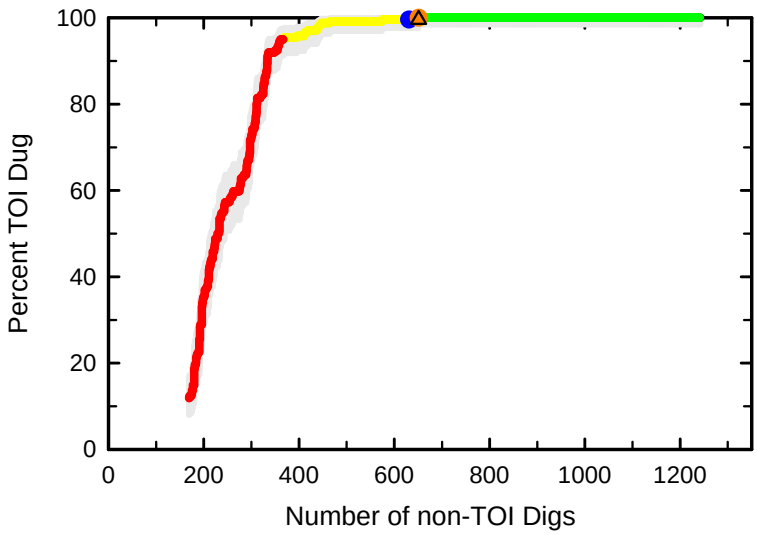

Figure 4: ROC curve resulting from analysis of the EM61 MK2 cart data using UX-Analyze with the points color-coded according to their assignment by the demonstrator. Also plotted are the demonstrator threshold (dark blue dot), the point corresponding to $P_D = 1.0$ (orange dot), and the missed target of interest above the demonstrator threshold (triangle).

threshold (dark blue dot); one target of interest (triangle) was just below the demonstrator-specified threshold. In contrast to the results from the first Classification demonstration, this analyst was able to extract reliable parameters for all but two of the 1500 identified anomalies.

As shown in Figure 3, data were also collected with a vehicular-towed EM61 MK2 array outfitted with three GPS antennae to give a continuous measure of platform pitch and roll. A comparison of the results for the cart and array data analyzed using UX Analyze is shown in Figure 5. Although there appear to be slight differences in the number of targets assigned to the three classes, the ROC curves are virtually indistinguishable. For this site, the choice between cart-based and array-based deployment should be made on survey costs grounds; their classification performance does not differ.

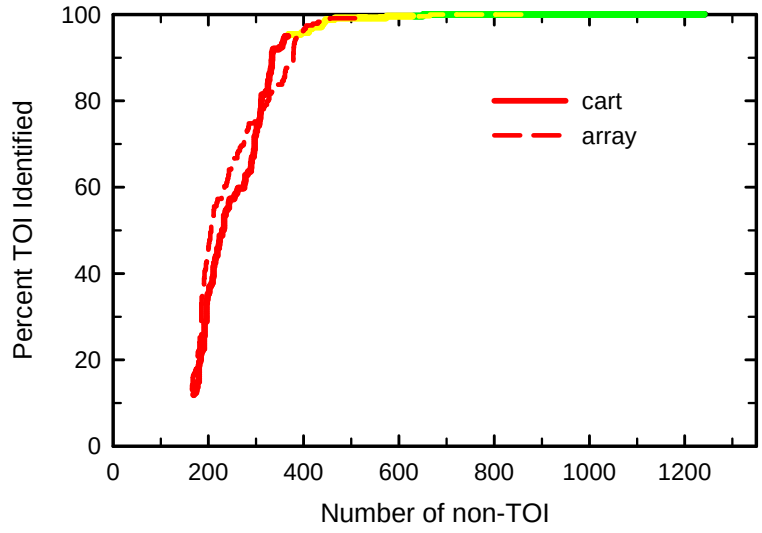

Figure 5: Comparison of the results obtained from analysis of the EM61 MK2 cart (solid line) and EM61 MK2 array (dashed line) using UX Analyze.

As was mentioned above, several developmental EMI sensors were demonstrated at San Luis Obispo. Results from one of these, the MetalMapper system [Snyder 2009], are shown in Figure 6. The MetalMapper consists of three mutually orthogonal transmitter loops and a spatial array of seven 3-axis receiver antennas (21 independent measurements of the transient secondary magnetic field). When operating in survey mode, only the Z (horizontal) transmitter loop is fired and decay data are collected for a short time. After mapping the field, the MetalMapper visits each anomaly in cued mode in which each of the three transmitter loops are fired in turn and data collected out to 8 ms. Results based on cued, single point data are plotted in Figure 6.

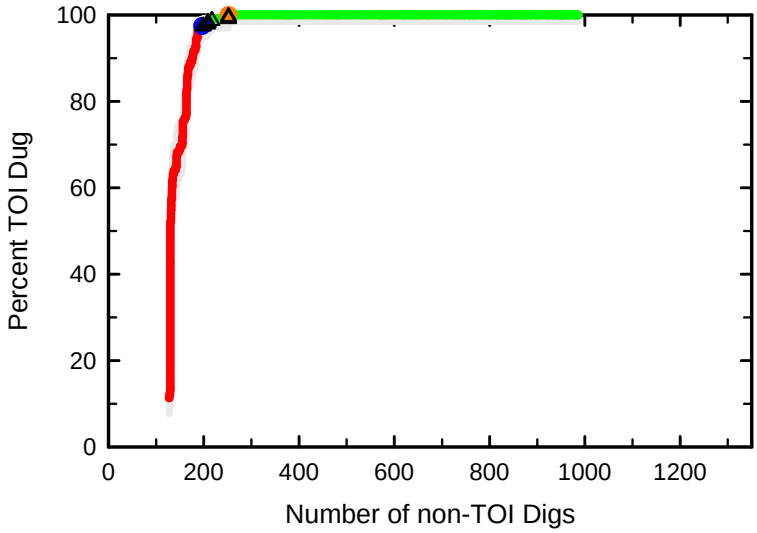

Figure 6: ROC curve resulting from analysis of the MetalMapper cued data with the points color-coded according to their assignment by the demonstrator. Also plotted are the demonstrator threshold (dark blue dot), the point corresponding to $P_D = 1.0$ (orange dot), and the missed targets of interest above the demonstrator threshold (triangle).

The MetalMapper classification results shown in Figure 6 are quite good. This analyst was too aggressive in setting their threshold (there are four TOI after the threshold) but it only required a little over 100 "wasted" digs to recover over 200 targets of interest.

Summary

The second demonstration of the ESTCP Classification Pilot Program was conducted in the summer of 2009 on a range at former Camp San Luis Obispo, CA. Compared to the first demonstration in the series, this site featured a wider variety of munitions types and more challenging topography and geology. Nonetheless, substantial classification performance was achieved in the analysis of carefully collected commercial EMI sensor data using freely available software. Even better performance was achieved by the developmental, cued sensors that were demonstrated. The few targets that caused classification problems to these new sensors were more the result of data quality and management issues than classifier failures.

Several more demonstrations are planned as part of this program, including sites contaminated with 37mm projectiles and sites with sufficient vegetation to require the use of man-portable sensors. As we continue through this program, we continue to involve all stakeholders in the design and analysis of the demonstrations in an effort to facilitate acceptance of these technologies.

References

Nelson, H. H., Kaye, K. and Andrews, A. M., November 2008, "ESTCP Pilot Program Classification Approaches in Munitions Response," http://www.estcp.org/Technology/upload/MM-WAA-08-ESTCP-FR.pdf.

Parsons, Inc., "Final Site Inspection Report, Former Camp San Luis Obispo, San Luis Obispo, California," Contract W912DY-04-D-0005, 2007.

Smith, J.T. and Morrison, H.F., 2004, "Estimating equivalent dipole polarizabilities for the inductive response of isolated conductive bodies, IEEE Trans. Geoscience and Remote Sensing, 42, 1208-1214.

Snyder, D.D., George, D.C., MacInnes, S.C. and Smith, J.T., 2008, "An assessment of three dipole-based programs for estimating UXO target parameters with induction EM, SEG Expanded Abstracts 27, 2902-2906.

Snyder, D.D., George, D.C., Prouty, M., and King, T., 2009, "Testing of the MetalMapper™, an Advanced EMI Ordnance Detector," UXO/Countermine Forum, Orlando, FL August 2009

Walker, S.E., Pasion, L.R., Oldenburg, D.W. and Billings, S.D., 2007, Investigating the effect of data quality on time domain electromagnetic discrimination, J. Applied Geophysics, 61, 254-278.

CLASSIFICATION OF BURIED OBJECTS USING MULTI-AXIS ELECTROMAGNETIC INDUCTION SURVEY DATA

Thomas H. Bell, SAIC, Arlington, VA
Bruce J. Barrow, SAIC, Arlington, VA
Daniel A. Steinhurst, Nova Research, Alexandria, VA

Abstract

Multi-axis electromagnetic induction (EMI) sensors are capable of reliably classifying buried objects. To date, they have been used in a static cued interrogation mode. Here, we demonstrate that a single survey line of multi-axis data over a target can be inverted to determine the object parameters used for classification. Two processing approaches are considered: conventional dipole inversion and a new, simpler approach that exploits rotationally invariant properties of the EMI response.

Introduction

Recent demonstrations conducted under the auspices of the Environmental Security Technology Certification Program (ESTCP) have shown that the new generation of multi-axis transient EMI sensors can reliably distinguish between munitions items and metallic clutter in the ground such as munitions fragments, scraps of exploded metal objects, cultural or agricultural artifacts, *etc*. (Gasperikova et al., 2008, Snyder *et al*., 2008, Bell *et al*., 2008). These sensors classify targets using a cued interrogation approach. In cued interrogation, the sensor is parked over an anomaly of interest, the transmit coils are excited sequentially, and the response from the target at the various receive coils is recorded while the sensor remains stationary. These data are inverted using a dipole response model to estimate object parameters (Pasion and Oldenburg, 2001, Bell *et al*., 2001). The object parameters are then supplied to classification engines that decide whether they are more likely associated with munitions or clutter.

The cued interrogation process has to be preceded by a geophysical survey to locate the anomalies, and re-visiting anomalies for cued interrogation costs time and money. Here, we use the Geonics EM63-3D MkII (EM633D) to demonstrate that a single line of multi-axis data collected while the sensor moves over a target can be inverted to determine the object parameters used for classification. Conventional dipole inversion was originally developed to meet the demands of single axis EMI data. The new multi-axis sensors provide much more information about a target's EMI response, which can be exploited using inherently simpler processing schemes. We describe an alternative processing approach for multi-axis survey data that exploits rotationally invariant aspects of the EMI response and should be more noise-tolerant than standard dipole inversion.

Dipole Response Model

Munitions/clutter classification centers on the intrinsic EMI response represented by the magnetic polarizability $\mathbf{B}(t)$ of the target. The polarizability describes the decaying dipole moment induced in the target by a primary field pulse. It has elements β_{ij} corresponding to the dipole moment component in the *i* coordinate direction induced by excitation in the *j* coordinate direction. Using the standard dipole response representation the EMI signal S measured by a transmit/receive coil pair is given by

$$S = \mathbf{R}^T\mathbf{B}\mathbf{T} \quad (1)$$

where $\mathbf{T} = (T_x, T_y, T_z)^T$ and $\mathbf{R} = (R_x, R_y, R_z)^T$ are field vectors at the target from the transmit and the receive coils, respectively. The convention here is that **T** and **R** are column vectors, and the transpose operator $()^T$ carries row vectors into column vectors and *vice versa*. **T** and **R** depend on details of the sensor and on the location of the target relative to the sensor. **B** is a second rank tensor that depends on the orientation, shape, size and composition of the target. Its eigenvalues are the principal axis polarizabilities of the target. They are intrinsic to the target and are the basic object parameters used for classification.

Provided that all of the elements of the polarizability tensor are interrogated by a suitably distributed set of transmit/receive coil pair measurements, the dipole response model can be used to invert EMI data collected over a target and determine the target's principal axis polarizabilities. This can be accomplished using a spatial distribution of single axis coil measurements (Pasion and Oldenburg, 2001, Bell *et al*., 2001) or a suitable set of multi-axis coil data (Snyder *et al*., 2004, Smith and Morrison, 2004). The basic idea of the dipole inversion is to search out the combination of target location and principal axis orientations and polarizabilities which minimizes the difference between the measured response and the response predicted by the dipole model. This process is extremely sensitive to positioning errors when applied to spatially distributed single axis coil measurements (Walker *et al.*, 2007). The multi-axis sensors used in the ESTCP demonstrations avoid this problem by using multiple transmit/receive coil pairs in fixed arrays that are positioned over a target of interest and held stationary while the data are collected.

Multi-axis coil data collected along a line passing over the target should also support dipole inversion. Figure 1 shows the basic multi-axis coil geometry. For simplicity only two coils are shown in the diagram. In practice, the sensor would have three mutually perpendicular transmit coils and a corresponding set of receive coils. The blue and green lines show the field lines from a pair of orthogonal coils A and B. If the sensor is moving to the right, then P_1, P_2 and P_3 correspond to successive target locations relative to the sensor. The pairs of arrows at each point show the directions of the field vectors **A** and **B** from the two coils, and serve to illustrate how the target is excited from different directions as the sensor passes by. Multi-axis coil sensors normally interleave pulses from the different transmit coils rather than transmitting from all coils simultaneously, so that in Figure 1 only field vector **A** would be present at point P_1, **B** at P_2, *etc*. Signals from all of the receive coils are measured for each transmit pulse. For a simple three axis system, this produces a sequence of three sets (different transmitters) of three readings (different receivers) each. If the cycle is repeated several times as the sensor passes over an object, then the data can be inverted using the dipole model to determine the object's location, orientation, and intrinsic EMI response parameters. There will be a right/left cross track ambiguity in the target location if the sensor is symmetric. This can be easily resolved by examining adjacent survey lines.

Multi-Axis Survey Data Example

The Geonics EM63-3D MKII (EM633D), pictured in Figure 2, is a simple three axis transient EMI sensor. It has three large transmit coils arranged in orthogonal directions (orange loops) and three smaller orthogonal receive coils (inside the box suspended within the transmitter cube). The axis of the Z coil is vertical, the X coil axis points along track in the direction of travel, and the Y coil axis points cross track to the left. There is also an upper receive coil that is used to suppress noise in the vertical

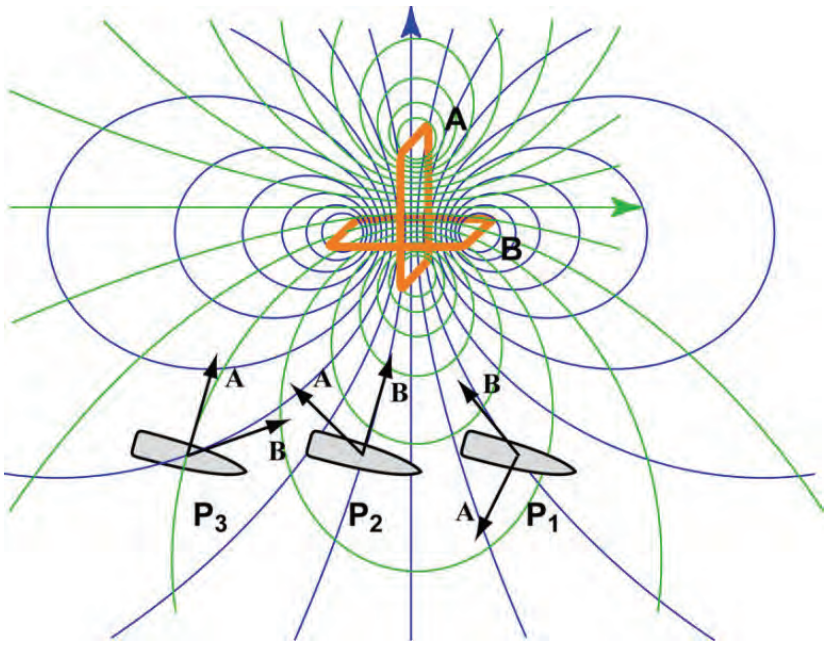

Figure 1: Diagram illustrating fields from a multi-axis coil sensor. Green and blue lines show field lines for orthogonal coils A and B, respectively. Arrows at points P_1, P_2 and P_3 show directions of the corresponding field vectors.

receive channel. The EM633D can operate at three different base frequencies: 7.5 Hz, 30 Hz and 75 Hz. At 7.5 Hz it samples the secondary field decay at 26 time gates ranging from 0.39 to 25.3 msec after the primary field cutoff. The response is truncated at the higher base frequencies, sampling the first 20 gates (to 7.3 msec) at 30 Hz and the first 16 (to 3.0 msec) at 75 Hz. It can be paired with a GPS unit to record the positions of the sensor readings, or use an integral wheel tick counter to locate the data along a survey line.

Figure 3 is an example of EM633D data collected along a line over a 2" diameter by 8" long piece of steel pipe aligned perpendicular to the track. The base frequency was 30 Hz, and along track positions of the sensor readings were dead reckoned using the wheel tick counter. The walking speed during the data collection was ~0.4 m/sec, which produced a sample spacing of ~8 cm for each transmitter. Each plot shows the signals at the three receive coils for one of the transmitters: Z at the top, X in the middle and Y at the bottom. Symbols show the measured signals, and the corresponding lines show the dipole model fit to the measured signals using parameters determined by conventional dipole inversion of the data from all transmit/receive pairs.

The principal axis polarizabilities determined from dipole inversion of these data for the first 16 gates are shown as functions of decay time by the circle symbols in the left hand plot in Figure 4. There are three sets of circle symbols in the plot, corresponding to the three principal axis polarizabilities. Two are approximately equal. These correspond to transverse excitation of the pipe. The third is larger, and corresponds to axial excitation. The triangle symbols show polarizabilities calculated from data collected with the pipe oriented parallel to the survey line, and are basically the same as those for the cross track pipe. The plot on the right shows the corresponding principal axis polarizabilities for a 4" diameter steel ball. As expected for a spherical target, the polarizabilities are all basically equal.

Figure 2: The Geonics EM63-3D MkII used to collect multi-axis EMI data over various test objects. The large orange loops are the transmit coils. The receive coils are in the box suspended inside the transmit coils.

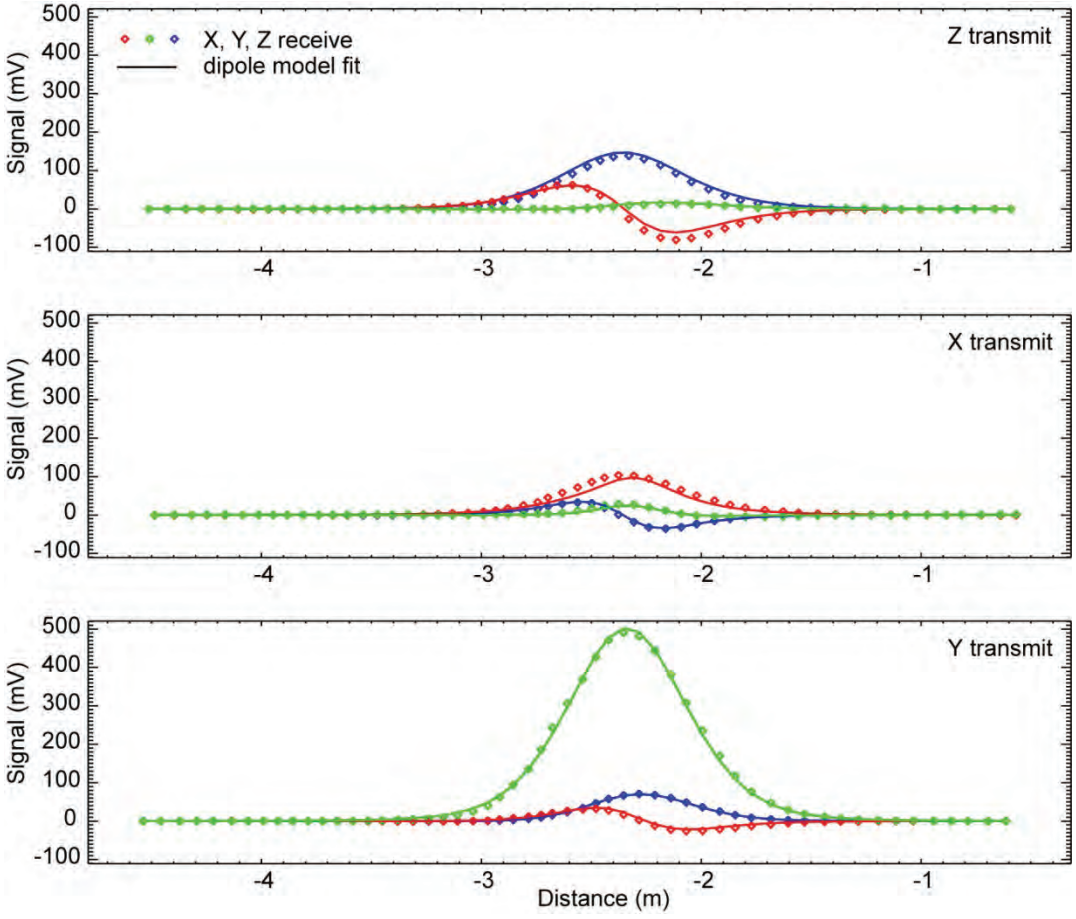

Figure 3: EM633D data collected along a line over a 2" diameter by 8" long piece of steel pipe. Symbols show individual measurements for the various transmit/receive coil pairs, and lines show dipole model fits to the data.

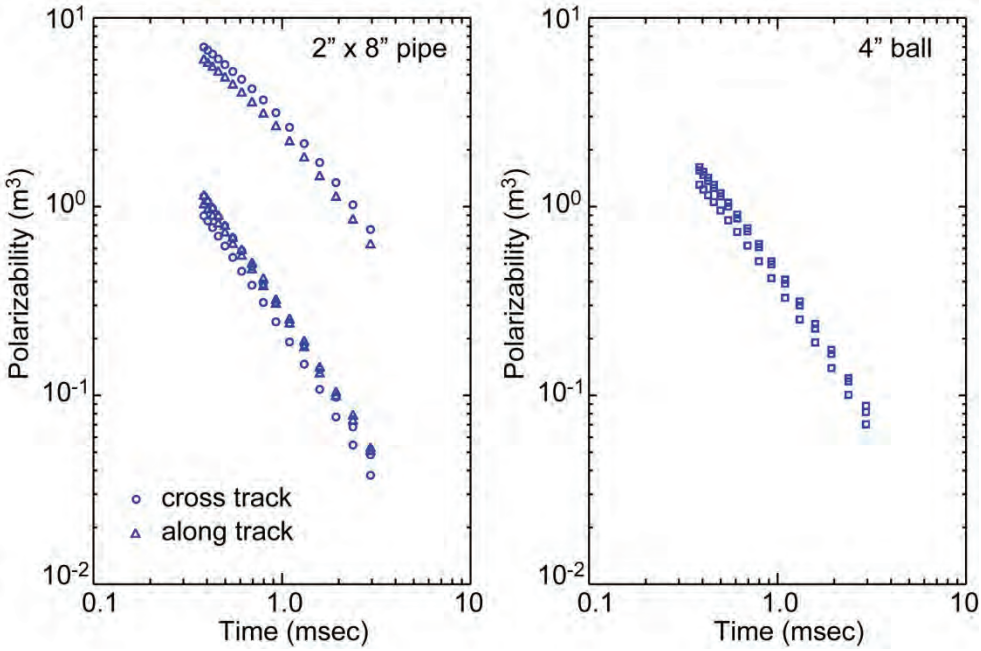

Figure 4: Principal axis polarizabilities determined by inverting EM633D data collected over a 2" diameter by 8" long steel pipe (left) and a 4" diameter steel ball (right).

Rotational Invariant Processing

Conventional dipole inversion processing was developed with data collected using single axis sensors in mind. Multi-axis sensors collect much more information about the target's EMI response. Enough more, as it turns out, to allow the polarizabilities to be calculated more directly. The polarizability **B** is a second rank tensor, which has three associated factors which are invariant to rotation of the target. The trace Tr(**B**) is the sum of the diagonal elements. Because it is rotationally invariant, the trace is equal to the sum of the eigenvalues of **B**. The other two invariants are the determinant of **B** and the sum of the determinants of the 2x2 diagonal sub-matrices of **B**, equal respectively to the product of the eigenvalues and the sum of products of the eigenvalues taken pairwise. The invariants are the coefficients of the characteristic polynomial of **B**, so the principal axis polarizabilities can be directly calculated from them (e.g. Korevaar, 1968, §10.2, or any similar reference on linear algebra).

Calculating Tr(**B**) from multi-axis EMI data collected over a target is a simple matter if the (x, y, z) location of the target relative to the sensor is known. As noted previously, **B** has elements β_{ij} corresponding to the dipole moment component in the *i* coordinate direction induced by excitation in the *j* coordinate direction. If the transmit and receive field vectors **T** and **R** are directed along the x-axis (so that $T_y = T_z = 0$ and $R_y = R_z = 0$), then equation (1) becomes $S = \beta_{xx} T_x R_x$ and β_{xx} is simply equal to the measured signal divided by the transmit and receive field strengths. Analogous results pertain to the other diagonal elements β_{yy} and β_{zz}. The basic idea, then, is to combine outputs of a multi-axis sensor so as to effectively synthesize transmit and receive fields in the x, y, and z directions, so that each of the diagonal elements of **B** can be measured in turn. Summing the results yields $\text{Tr}(\mathbf{B}) = \beta_{xx} + \beta_{yy} + \beta_{zz}$.

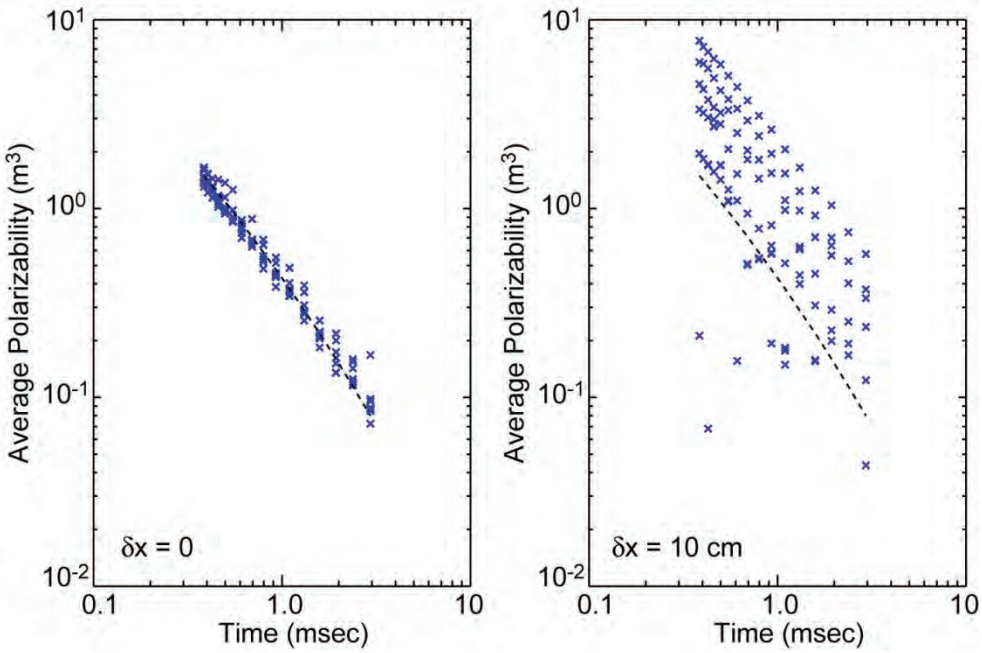

Figure 5: Average polarizability of the 4" steel ball determined by tensor invariant processing when the correct target location is used (left) and when the assumed location is off by 10 cm. Dashed lines show the average polarizability determined from dipole inversion (Figure 4, right).

Referring back to Figure 1, unit strength fields in the x and z directions can be synthesized from the pair of coil fields using coefficients a_x, b_x, a_z and b_z obtained by solving the pair of linear vector equations

$$a_x \mathbf{A} + b_x \mathbf{B} = \mathbf{n}_x \qquad \text{and} \qquad a_z \mathbf{A} + b_z \mathbf{B} = \mathbf{n}_z \tag{2}$$

in which $\mathbf{n}_x$ and $\mathbf{n}_z$ represent unit vectors in the x and z directions. Including the third dimension is trivial, and accommodating pulse interleaving is a simple bookkeeping matter. Signals corresponding to β_{xx}, β_{yy} and β_{zz} (or for that matter any other elements of **B**) can then be synthesized using appropriate combinations of the coefficients for the transmit and the receive coils, and Tr(**B**) can be calculated directly.

Of course, we get Tr(**B**) wrong if we use the wrong target location. More importantly, if we apply the procedure to a series of multi-axis measurements as the sensor passes over the target, then it turns out that we get *different* wrong answers along the way. However, because the real Tr(**B**) is rotationally invariant, with the right target location we get the same (correct) value for Tr(**B**) from each of the measurements. The basic idea, then, is to search out the target location for which we get the *same* value of Tr(**B**) for all of the measurements along a line. Figure 5 is an example using a line of EM633D data over the 4" steel ball. The plot on the left shows values for the average polarizability $\langle\beta\rangle = \frac{1}{3}\mathrm{Tr}(\mathbf{B})$ for the first 16 time gates calculated at each measurement point using this procedure with the correct target location, while the plot on the right shows the same thing with the assumed target location off by 10 cm. The dashed lines show the average polarizability determined by dipole inversion (Figure 4, right). The calculated values of $\langle\beta\rangle$ from successive measurements as the sensor passes over the target cluster about the correct value when the correct target location is chosen, but spread out as the assumed target location shifts away from the true location.

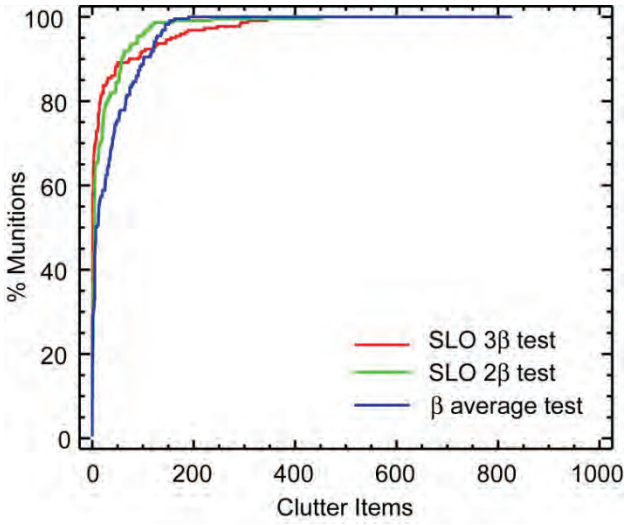

Figure 6: ROC curves comparing the classification performance of three different test criteria applied to in-air EMI measurements of 827 clutter items from former Camp San Luis Obispo (SLO) and 221 measurements of seed munitions used at the site.

This procedure is quite different from, and much simpler than conventional dipole inversion. Inversion of data to estimate target parameters is all about minimizing objective functions. In conventional dipole inversion the objective is to find the combination of target location and principal axis orientations and polarizabilities which minimizes the difference between the measured response and the response predicted by the dipole model. Here, the objective is to find the target location which minimizes the dispersion of the sum of orthogonal response coefficients calculated directly from the measurements. In the conventional approach we must estimate nine quantities (x, y, z location, θ, ϕ ψ principal axis orientations, and three principal axis polarizabilities). In the tensor invariant approach we only estimate three quantities (x, y, z location) while directly calculating the average polarizability, or equivalently Tr(**B**). Since we are not wasting signal-to-noise estimating extraneous quantities, tensor invariant processing should be more noise tolerant than conventional dipole inversion processing. Once the target location has been determined we can go on to calculate the other invariants or the principal axis polarizabilities as desired.

That said, the average polarizability is interesting in its own right. It is a rotationally invariant scalar function that expresses the average EMI response of the target (Douglas and Garboczi, 1995). It also seems to capture much of the information about the EMI response that is useful for target classification. Figure 6 is a set of Receiver Operating Characteristic or ROC curves (Fawcett, 2006) which compare the classification performance of three different test criteria applied to in-air EMI measurements of clutter and munitions items from former Camp San Luis Obispo (SLO) in California. The former Camp SLO was the site of a recent large scale ESTCP classification demonstration. The SLO 3β and 2β tests correspond to the library matching procedures (Pasion *et al*., 2007) that we used in the study. The 3β test uses all three principal axis polarizabilities, while the 2β test uses only the first two. The β average test uses a comparable library matching procedure with the average polarizability. Perhaps surprisingly, there is little difference in classification performance among the three tests. The β average test climbs a bit more slowly at the outset than the others, but correctly identifies all of the munitions after fewer clutter items than either of the other tests.

Conclusions

Provided that there is adequate signal compared to the sensor and geophysical noise, multi-axis EMI sensors should be able to classify buried targets in a dynamic survey mode. Specifically, a single survey line over, but not necessarily directly over, a target should suffice. We have shown that single lines of data collected with the Geonics EM63-3D MkII can be inverted using the standard dipole response model to determine the target's location and the object parameters (principal axis polarizabilities) typically used for classification. Because the multi-axis sensors collect a complete picture of the target's EMI response, a simpler processing approach that exploits tensor invariant properties of the polarizability can also be used to extract the object parameters for classification.

Acknowledgements

This research was supported by the Strategic Environmental Research and Development Program under project MM-1658.

References

Bell, T.H., Barrow, B.J. and Miller, J.T., 2001, Subsurface discrimination using electromagnetic induction sensors, IEEE Trans. Geoscience and Remote Sensing, 39, 1286-1293.

Bell, T., Nelson, H., George, D., Kingdon, J. and Keiswetter, D., 2008, EMI array for cued UXO discrimination, SEG Expanded Abstracts, 27, 2907-2911.

Douglas, J.F. and Garboczi, B.E., 1995, Intrinsic viscosity and the polarizability of particles having a wide range of shapes, Adv. Chem. Phys., 91, 85-153.

Fawcett, T., 2006, An introduction to ROC analysis, Pattern Recognition Letters, 27, 861–874.

Korevaar, J., 1968, Mathematical Methods, vol. 1, Academic Press.

Gasperikova, E., Smith, J.T., Morrison, H.F., Becker, A. and Kappler, K., 2008, UXO discrimination using a multiple-component AEM system, SEG Expanded Abstracts, 27, 2897-2901.

Pasion, L.R. and Oldenburg, D.W., 2001, A discrimination algorithm for UXO using time domain electromagnetics, J. Environmental and Engineering Geophysics, 6, 91-102.

Pasion, L.R., Billings, S.D., Oldenburg, D.W. and Walker, S.E., 2007, Application of a library based method to time domain electromagnetic data for the identification of unexploded ordnance, J. Applied Geophysics, 61, 279-291.

Smith, J.T. and Morrison, H.F., 2004, Estimating equivalent dipole polarizabilities for the inductive response of isolated conductive bodies, IEEE Trans. Geoscience and Remote Sensing, 42, 1208-1214.

Snyder, D.D., MacInnes, S.C., Hare, J.L., Grimm, R.E., Poulton, M. and Szidarovsky, A., 2004, The value of multi-component TEM data for the estimation of UXO target parameters, Proc. SAGEEP, 17, 1641-1653.

Snyder, D.D., George, D.C., MacInnes, S.C. and Smith, J.T., 2008, An assessment of three dipole-based programs for estimating UXO target parameters with induction EM, SEG Expanded Abstracts 27, 2902-2906.

Walker, S.E., Pasion, L.R., Oldenburg, D.W. and Billings, S.D., 2007, Investigating the effect of data quality on time domain electromagnetic discrimination, J. Applied Geophysics, 61, 254-278.

UXO DISCRIMINATION AT CAMP SAN LUIS OBISPO WITH THE METALMAPPER

Donald D. Snyder, Snyder Geoscience Inc, Grand Junction, CO
Mark Prouty, Geometrics, Inc, San Jose, CA
David C. George, G&G Sciences, Inc, Grand Junction, CO
Tom King, Zapata Blackhawk, Golden, CO
Mary Poulton, University of Arizona, Tucson, AZ
Anna Szidarovszky, Zonge Engineering, Tucson, AZ

Abstract

The MetalMapper is an electromagnetic metal detector that is being commercialized by Geometrics, Inc with support from the Environmental Security Technology Certification Program (ESTCP). Together with several other systems, the MetalMapper participated in an ESTCP-sponsored classification study at the former Camp San Luis Obispo (SLO) located a few miles northwest of San Luis Obispo, CA. Operating independently, the MetalMapper conducted two surveys: a dynamic mapping survey for target detection; a precision ("Cued ID") static measurement over detected targets for use in discrimination. The SLO study involved a number of different organizations deploying both commercially available EM and magnetic sensors and advanced EM systems such as the MetalMapper. Following the completion of the field work by these organizations, nearly 2000 targets identified from the detection surveys were then dug. Using a common set of targets, demonstrators prepared a dig list prioritized according to the probability that a particular target was a target of interest (TOI). The dig lists were scored by the Institute for Defense Analyses (IDA).

The primary objective of this paper is to describe MetalMapper system, the data processing, and the methodology employed for assembling the prioritized dig list. We also present the scoring results for the MetalMapper as provided to us by the IDA.

Figure 1: Location map, Camp SLO discrimination study.

Introduction

Over a period of 10 years or more, the UXO community has relied on so-called "seeded" sites to test and validate commercially available technology as well as new technology for the detection and classification of UXO. Two such sites are the Standardized UXO Technology Demonstration Sites (USAEC 2009) located at Aberdeen Proving Ground (APG) and Yuma Proving Ground (YPG). Demonstrators who access these sites submit prioritized dig lists and are scored by the Aberdeen Test Center (ATC) for performance as detectors and for discrimination. Constructed at considerable expense, the ground truth for the sites at APG and YPG is not provided to demonstrators and hence there is no opportunity for retrospective study. The ESTCP discrimination studies are designed to provide

the opportunity to demonstrate technology on live sites that have been carefully selected to provide tractable operational and discrimination challenges. The site at Camp SLO is the second site to be selected by ESTCP. It was selected to be more challenging from both the operational and interpretational viewpoint than the first such demonstration area, which was located at the former Camp Siebert in Alabama. The SLO site is located approximately 7 mi NW of the town of San Luis Obispo, CA (Figure 1). Covering an area of approximately 12 acres (4.77 ha), the site was formerly used as a mortar (4.2 in, 81mm, and 60mm) and rocket (2.36 in anti-tank) range.

The MetalMapper: An Advanced EMI System

With support from ESTCP, Geometrics, Inc (San Jose, CA) is commercializing an advanced time-domain electromagnetic induction (EMI) sensor for the detection and classification of UXO. The MetalMapper system is based on concepts and technology for an Advanced Ordnance Locator (AOL) developed and implemented to the proof-of-concept stage with support from the Naval Explosive Ordnance Demolition Technology Division (NAVEODTECHDIV, Indian Head, MD)(Snyder 2005; George 2006; George 2007).

Figure 2 shows the MetalMapper being deployed at SLO. The antenna array is mounted to a wooden skid attached to the front-loader of a Kabota tractor. The antenna array consists of 3 mutually orthogonal 1m x 1m transmitter loops (red/green/blue squares in Figure 2) and an array of 7 triaxial receiver cubes with side dimension 10cm. Each cube has 3 identical and mutually orthogonal induction coils. The receiver therefore approximates a point measurement of the time rate of change of the vector secondary magnetic field $\partial \mathbf{B}/dt$. A battery-powered man-portable instrument package weighing approximately 45 lbs operates the system in the time-domain mode.

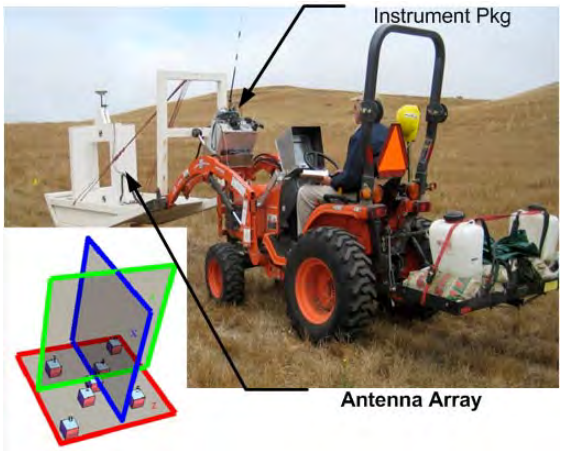

Figure 2: Photograph of the MetalMapper as it was deployed at SLO. The inset (lower left) shows the antenna configuration. The transmitter loops are each 1x1m.

Modes of Operation

The instrument package contains a transmitter and a 24-ch 16-bit data acquisition system. The base frequency of operation is under operator control. There are two acquisition modes: a) Continuous Mode; b) Static Mode.

Continuous Mode Acquisition: The continuous operating mode is used for mapping. In this mode, only the Z (horizontal) transmitter loop is activated, and after activation the data sampling continues until the operator halts data acquisition. All data samples are stored in a single binary data file. Typically, data from a single survey profile are stored in the same data file. The operator selects a base frequency (f_0), and a sample period (T). Sampling at a rate of 250 KHz (4 μs), the DAQ acquires data for each of the 22 channels over the prescribed sample period T, and rectifies and stacks the transient (off-time) intervals Then, each of the transients are decimated into a sequence of logarithmically spaced time gates controlled by a decimation factor set by the operator. The parameters for both continuous and static mode acquisition used at SLO are shown in Table 1.

Table 1: Acquisition parameters for continuous (Cont) and static mode MetalMapper data acquisition at SLO.

Mode	Tx	f_0 (Hz)	T (s)	N_1	N_2	Δt (s)	tmin	tmax	Ngates
Cont.	Z	270	0.1	27	1	0.1	114	900	44
Static	Z/Y/X	30	0.9	27	10	27	106	7912	42

Tx	Z' = Z transmitter only; 'Z/Y/X' = All 3 Tx loops (sequential)
f0 (Hz)	Base frequency of Tx waveform
T (s)	Sample Period
N1	Tx period per sample period (T)
N2	Number of sample periods to stack
Δt (s)	Effective sample period
tmin	delay time at minimum time gate (μs)
tmax	Delay time at maximum time gate (μs)
Ngates	Number of time gates per transient

Static Mode Acquisition: The static operating mode is used for acquiring precision data while the system is not moving (static). In this mode, the three transmitters are activated sequentially during which time 22 transients (21 receiver coil plus a current sensor) for each transmitter polarization are acquired. These data are assembled into a single data sample, decimated as explained above, and stored to a binary data file. Only a single data sample is stored in each data file. Similar to continuous-mode acquisition, the operator can control the base frequency, and the acquisition sample time. In addition, he can set a **stack count** that permits stacking successive acquisition cycles. Acquisition is halted at the end of the stack count, and the average data sample is stored into a binary file. The acquisition parameters for static acquisition (Table 1) were set so that we acquired 8 ms time-bandwidth transients sampled over 42 logarithmically spaced time gates.

MetalMapper Surveys at SLO

Of the three advanced EMI systems demonstrated at SLO, the MetalMapper was the only system that was operated in the mapping mode as well as in the static mode. We surveyed the entire study area in the mapping (continuous) mode with a lane spacing of 0.75m. Using a detection map compiled from the continuous-mode detection survey, we picked targets that we used in a static-mode (Cued ID) survey.

The Detection Survey

The target map (Figure 3) is a base map for the SLO study area. The area consists of 53 30x30m blocks. We have over-plotted as green or blue dots the locations of 1561 MetalMapper targets that were

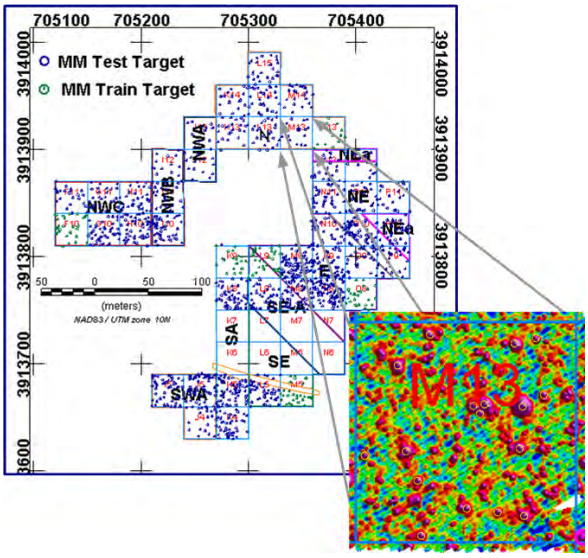

Figure 3: Base map showing the 53-block study area at Camp SLO. The survey blocks are 30x30m.

dug after geophysical field work was completed at the site. The dig results for the 154 targets marked with green symbols were supplied to demonstrators to use as training data. The remaining 1407 targets marked with blue symbols represent the test set that was used for scoring. The ground truth for those targets was withheld from the demonstrators until after the target list was scored by the Institute for Defense Analyses (IDA). Although the detection map covered all 53 blocks, targets falling within the 8-block area (K6-N7) and the narrow NW-SE trending strip immediately below it were excluded from the test set for budgetary reasons. The inset in Figure 3 is a segment of the target detection map covering survey block M13. Targets are marked with yellow circles. The map also shows the survey line coverage for block M13. It took approximately 10 field days to acquire the data for the detection map giving us an average production rate of 1.2 acre/day.

The Static-Mode Survey

During the static-mode survey, the MetalMapper returned to the site of the target anomaly and acquired a static-mode data point using the acquisition parameters listed in Table 1. In many cases, two or more data sets were acquired for a single target. In some cases, this was due to the fact that both peaks from a double-peak anomaly were picked. In other cases, the target was one we selected for a second reacquisition during our repeat static survey. We picked a total of 2179 targets for the static survey. At the end of the survey, we selected 314 targets to repeat based on the horizontal offset between the estimated target positions from the antenna platform. Targets with good signal-to-noise (SNR) and other data quality measures (e.g., model fit) that had a horizontal offset of 40cm or more from the antenna platform were measured again at the estimated site of the target rather than the original target pick. Over a period 7 field days, we acquired a total of 2492 static data points for an average production rate of 360 pts/day (40 pts/hr). On our best day, we measured 494 data points.

Static Data Processing and Discrimination

Static Data Processing

Static data sets are processed by approximating the observed secondary fields with a single point dipole as a model. The dipole-model has been widely used for interpretation of EM data from UXO surveys (MacInnes 2002; Grimm 2003; Smith 2004; Pasion 2007; Snyder 2008). We refer the interested reader to our reference citations for details on the theory for the modeling. A flow diagram for the processing is shown in Figure 4. A static data point from SLO consists of a set of 21 transients from each of 3 transmitter polarizations (Z,Y, and X). After subtracting a background transient, these transient data are input into a modeling program (MM/RMP). The modeling program estimates the target position and its three attitude angles and, from knowledge of those values, it estimates a set of 3 principal polarizability rate transients.

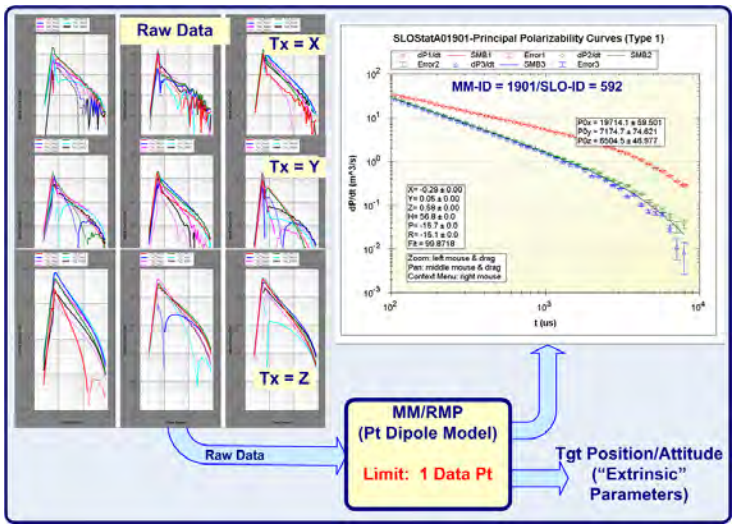

Figure 4: Flow diagram illustrating target parameter extraction with a dipole model. Observed transient data are reduced to a set of 3 principal polarizability rate transients.

The input data and the resulting polarizability transients for a 60mm target are illustrated in Figure 4. Principal polarizability transients such as those in Figure 4 are the electromagnetic characterization of the target. For the purpose of discrimination, we reduce the polarizability transients to a set of scalar "features" by computing the 0th and 1st order moments of each of the three principal polarizability curves as illustrated in Figure 5 (Smith 2002). Using ratios of the moments, we obtain a parameter τ with units of time that is indicative of the persistence of a particular principal transient in time. We also compute parameters relating to shape. For discrimination with neural nets, we selected 9 of the scalar parameters listed in Figure 5 as the feature vector to use as the input to our neural networks.[1]

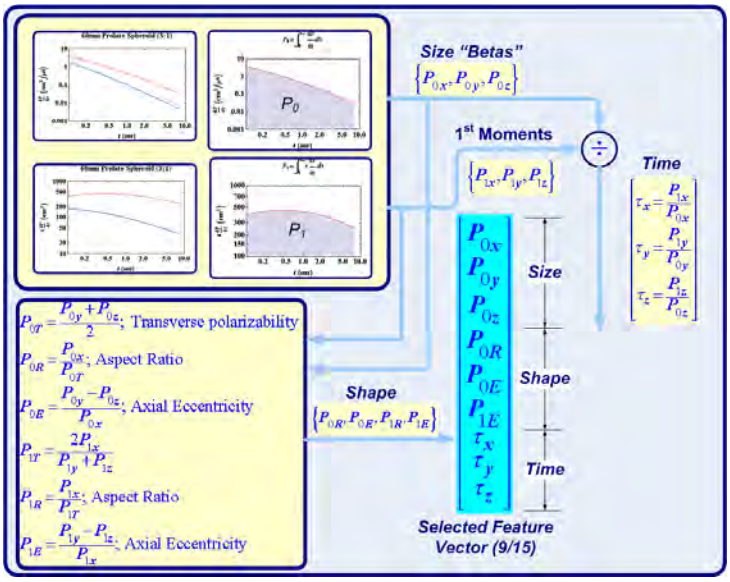

Figure 5: Definitions for 9 scalar "features" derived from the polarizability transients. These features are used as inputs to a neural network for discrimination.

Discrimination with an Automated Neural Network

Our training set consisted of MetalMapper static data sets acquired in proximity to the 154 targets for which ground truth was provided to demonstrators plus 58 additional data sets acquired from targets seeded in a test strip and a test pit located at SLO. Altogether there were 269 static data sets with ground truth that could be used as training. Graphical analysis with these data shows that the targets of interest separate and cluster together in distinct regions. Typical of such scatter plots is the "beta" plot shown in Figure 6. The plot indicates that the targets of interest separate into clusters and that much of the clutter can be discriminated simply on the basis of a feature such as P_{0x} that indicates relative target size.

Using the scalar features (Figure 5) extracted from training data, we trained a multi-layer perceptron neural network (ANN) with a single output value p in the range $0 \le p \le 1$ (Figure 7 - inset). Targets with ANN output values $p > 0.5$ are more likely to be UXO and conversely those with values

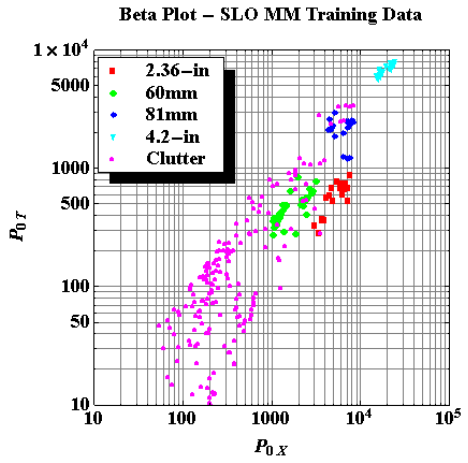

Figure 6: Categorized "beta" plot for the training dig at SLO.

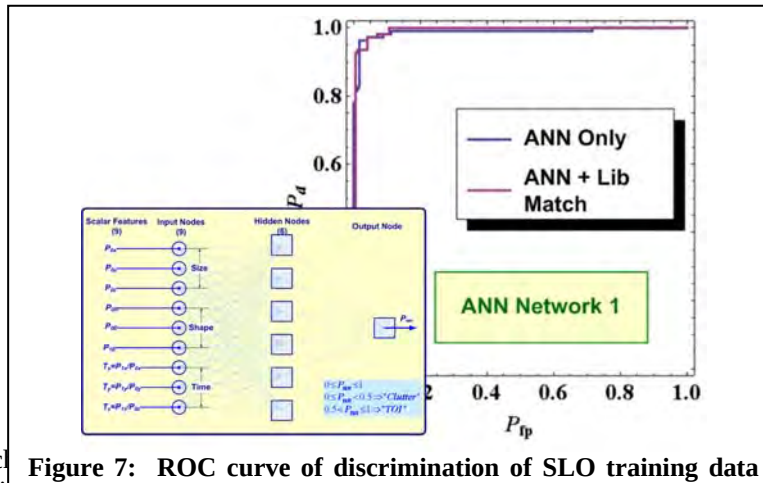

Figure 7: ROC curve of discrimination of SLO training data with an ANN.

$p<0.5$ are more likely to be non-UXO.

The performance of the ANN when applied to the whole training set[2] is shown by the ROC curve in Figure 7. These results show the ANN is able to correctly discriminate 95% of the UXO with a false positive rate (clutter targets incorrectly identified as UXO) of less than 5%. However, there is one outlying target that would require us to dig approximately 80% of the clutter before we finally dig the target.

Target ID Using Library Matching

As we indicated earlier, historical records and limited reconnaissance digging indicated that there were only 4 munitions targets of primary interest (TOI): mortars (4.2 in, 81mm, and 60mm), and 2.36 in "bazooka" rockets. Each of these target types are easily distinguished by visually examining the shape of their principal polarizability curves. Average polarizability curves for the 4 TOI at SLO are shown in Figure 8. The averaged curves (red/green/blue lines) are derived from 12-15 static measurements of the targets placed at different depths and orientations. Using a library of 5 "type" curves[3], we ran a mathematical curve matching algorithm on the unknown polarizability curve sets resulting from the processing of the target data sets. It is beyond the scope of this paper to explain in detail the matching algorithm. Suffice it to say here that we matched the major (largest) polarizability (P_x) curve for amplitude and shape to each of the library curves. Secondly, we matched the ratio of the average of the two minor curves ($P_T = \sqrt{P_y P_z} / P_x$) for shape only. We combined the 3 matching scores (major curve-size and shape, aspect ratio-shape) to provide a final matching score. For each target, we reported the best (maximum) of the 5 possible scores together with target type that produced it.

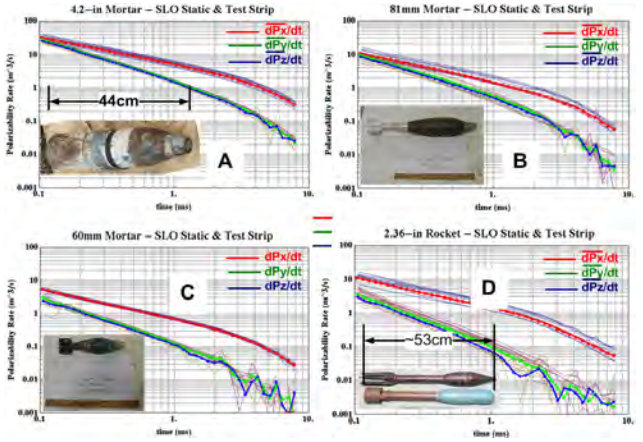

Figure 8: Principal polarizability transients for the 4 TOI at SLO.

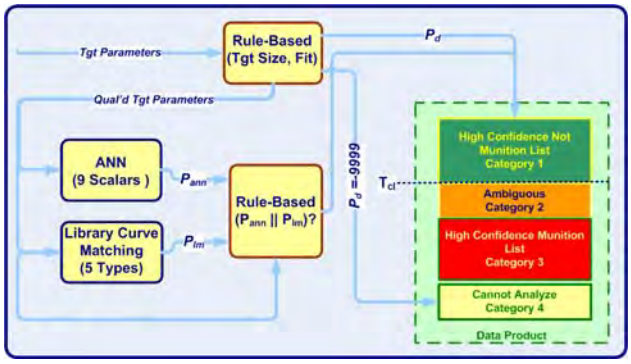

Figure 9: A simplified flow diagram showing the assembly of the "Dig List", which is the final output of the discrimination process.

Assembling the Dig List

The final product of any effort to discriminate is a "dig list" that establishes the priority for digging each target. A flow diagram of the process we used to assemble the dig list is shown in Figure 9. The dig list is divided into 4 target categories as follows:

[2] During training, the training set is randomly divided into 3 groups: a training group (~50%), a selection group (25%), and a test group(25%).

[3] There were in fact 2 variations of 60mm mortars encountered at SLO. One variation was an intact mortar round complete with fins and a fuse. The other type consisted of the mortar body alone. The 60mm mortar body has a distinctly different electromagnetic size and its largest polarizabity transient decays more rapidly than its full-bodied counterpart. As such, we found it necessary to add a 5th type (60mm body) to our library for matching.

1. Category 1: High confidence not munitions targets. These targets can be safely left in the ground.
2. Category 2: Targets for which the discrimination decision is ambivalent. **Dig!**
3. Category 3: High confidence munitions targets. **Dig!**
4. Category 4: Targets wherein the data are either too poor or too confusing to analyze. **Dig!**

An important element of the dig list is the boundary or threshold (marked $\mathbf{T_{cl}}$ in Figure 9) established by the interpreter between category 1 and category 2 targets. Ideally, all target lying above $\mathbf{T_{cl}}$ are clutter that can be safely left in the ground. Figure 9 also suggests how we integrated 2 different discrimination methods (ANN and Library Curve Matching) together with a set of rules to generate the target list. Briefly the rules go as follows:

1. **Data Quality** – If data quality (represented by the model Fit statistic) falls below an established threshold (75%), the target is designated as Category 4.
2. **Target Size** – Small targets (P0x < 500 cm3) are designated as Category 1 targets and ranked in that category according to their Fit statistic. Thus, small targets with a poor fit statistic will fall closer to Tcl than a similar target with a better fit statistic.
3. **ANN vs. Library Match** – This is basically a "winner-take-all" decision where we accept the result that gives the highest dig priority. If, for example, the ANN decision suggests "clutter" but the library match suggests "TOI", then we accept the library matching.

The effect of the rule-based decisions, primarily the ANN vs. Library Match decision, can be seen in the training ROC curve (Figure 7 – Red curve). The library matching tends to catch some TOI targets that are erroneously classified as clutter. In particular, note on the red curve that the hard false negative seen at $P_{fp} = 0.8$ is now gone. As a result, the modified ROC curve rises to $P_d = 1.0$ at the point where $P_{fp} = 0.1$. That means that 90% of the clutter objects can be safely left in the ground (i.e., there are no more TOI targets in the remaining items to dig).

An alternative way of viewing the results of the rule-based decision is to overlay a contour plot of the decision surface (i.e., a contour plot of the decision statistic $0 \le p_d \le 1$) over a scatter plot of 2 scalar features. In Figure 10, we show such a plot using the ($Log_{10}\tau_x$, $Log_{10}P_{0x}$,) plane of the 9-dimensional feature space. The underlying scatter plot is based on the ground-truth for all the targets in the test dig at SLO. The ground truth was provided by IDA to those involved in interpretation only after the target lists had been scored. By comparing the 2 panels in Figure 10 (left to right), one can see that the effect of the decision rules is to slightly modify the position of the 0.5 contour (T_{cl}) in order to capture some of the false negative points on the left hand panel (i.e., magenta colored symbols falling on the dark side of the red contour) so that in the right-hand they are correctly classified as TOI.

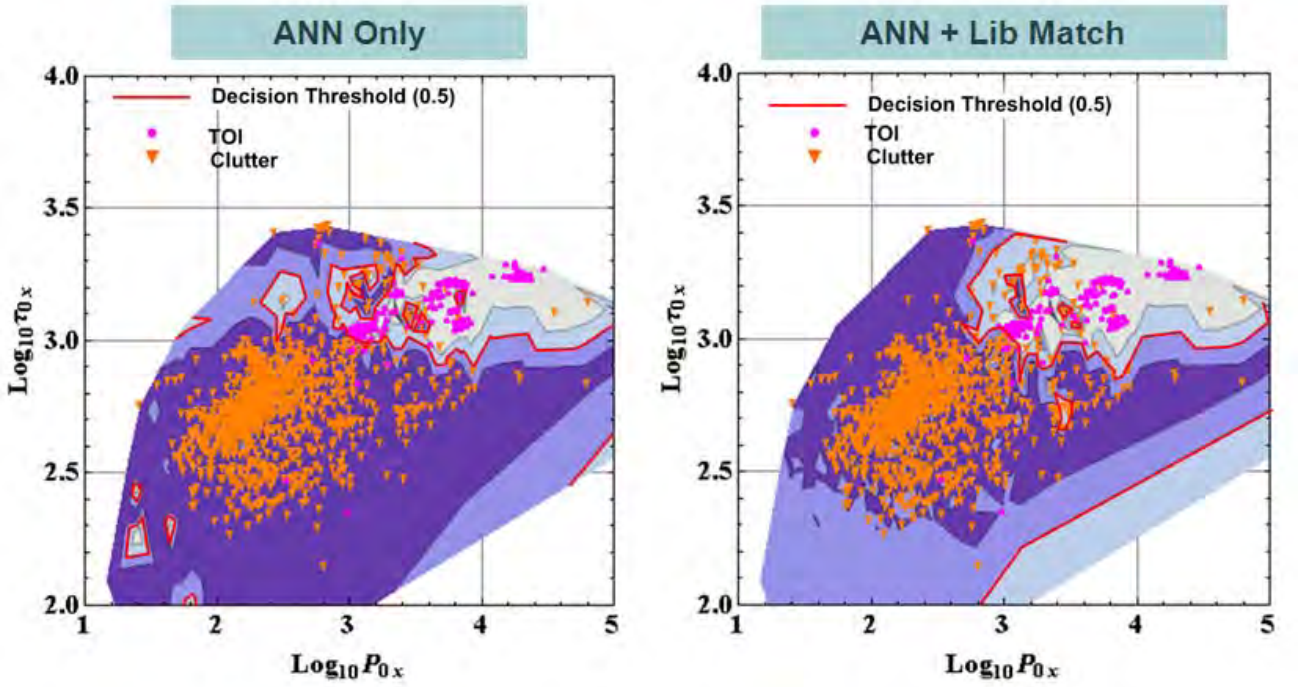

Figure 10: Figures showing the overlay of a contour plot of the discrimination statistic onto a categorized scatter-plot of target features from the SLO test dig. The target category ("TOI"/"Clutter") have been tagged according to ground truth supplied by IDA. The contour interval is 0.25 and the 0.5 contour has been highlighted in red. Lighter colors correspond to higher values of the statistic. Targets with a decision statistic p_d >0.5 are classified as TOI.

Scoring Results

We were scored by IDA on a target set consisting of 1063 targets blind targets (all MetalMapper targets that were not training targets where a priori ground truth was provided). Of those targets, there were 206 that were designated TOI. The remaining 857 targets (clutter) mostly consisted of munitions debris (MD). Figure 11 shows the MetalMapper performance in the form of the ROC curve provided to us by the IDA. We have enhanced the graphics in order to highlight various important details.

The abscissa on the graph is labeled (Number of) "Unnecessary Digs". Another term for this is number of false positives (targets designated as TOI but found to be clutter). Note that the ROC curve starts at 15 digs, corresponding to the number of targets we placed in the "Cannot Analyze" category (4). Three points on the curve are marked with colored dots. The dark blue dot indicates the designated threshold point (Tcl) defining the boundary between category 1 and category 2 on the dig list. The line colors match the color scheme shown for the dig list in Figure 9. The cyan dot marks the point in the list at which the last TOI would have been dug. On our list, this point occurs at 310 unnecessary digs.

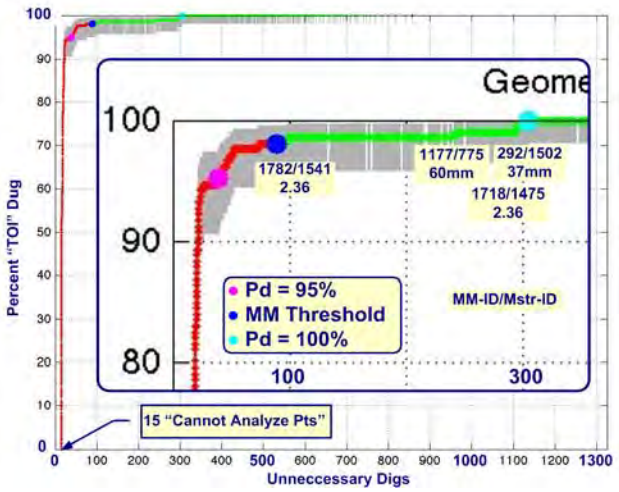

Figure 11: The ROC curve indicating the performance of the MetalMapper for 1063 blind targets at SLO.

On the expanded inset to the plot, we have labeled the 4 TOI that were improperly classified. It is beyond the scope of this paper to elaborate in detail on each of these "misses". Suffice it to say here that with regard to the 2 targets labeled "2.36" there are persuasive reasons for suggesting that the ground-truth for those 2 targets (1782/1541 and 1718/1475) were incorrectly labeled. But the 37mm (292/1502) and the 60mm (1177/775) represent real misclassifications. In retrospect analyses, we have established that we would definitely identify the 37mm as a TOI had we known that it was among the munitions of interest. The 60mm target (1177/775) on the other hand represents a deep 60mm that was overlain by two much smaller 60mm tail booms (Figure 12C). In this case, the magnitude of the 2 shallow 60mm tail booms shown on the white board (Figure 12C) overpowered a weaker field arising from the deep 60mm TOI. Our modeling program is based on a single point dipole. That program estimated the principal polarizability curve set shown in Figure 12A. More advanced modeling software is currently under development that permits modeling a target with 2 or more dipoles (Song 2009; Song 2010). Using a multiple dipole model on this particular target (again in retrospect), Song has successfully modeled the data from the 1177/775 target to show that there is a deeper target with a polarizability characteristics much like a 60mm

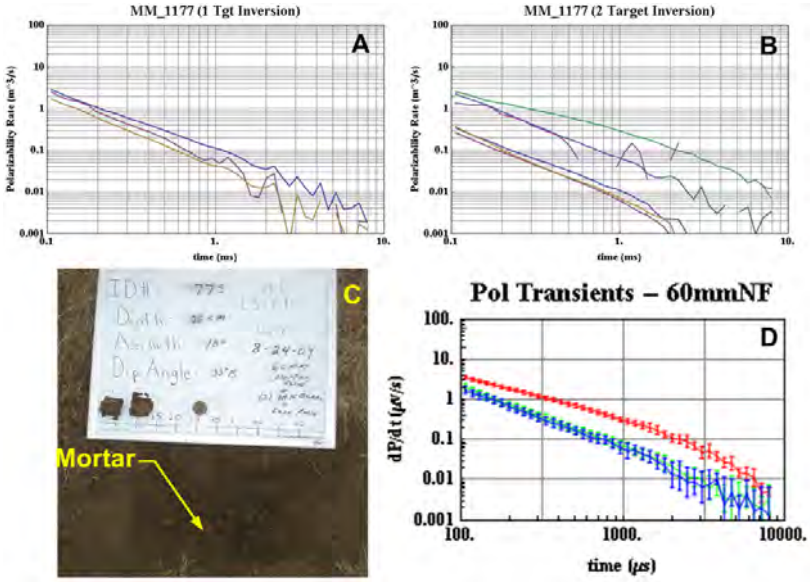

Figure 12: Figure showing how a multiple dipole inversion program (Song 2009; Song 2010) helps interpretation in the case of multiple interfering targets. The TOI is a deep 60mm mortar overlain by shallow 60mm tail booms. Panel A shows the polarizability curves for 1-tgt inversion. Panel B shows the resulting 2 sets of curves when analyzed with Song's program. Panel D shows the geometric mean curves for static measurements over 10-15 60mm mortar bodies.

mortar. For comparison, Figure 12D shows the average polarizability curves for a 60mm body from an ensemble of MetalMapper static data sets for 60mm targets at different depths, and attitudes.

Summary and Conclusions

At the former Camp San Luis Obispo we demonstrated the MetalMapper, one of the advanced EMI systems for UXO detection and classification. The MetalMapper was operated in its dynamic acquisition mode to generate a detection map over the 12 acre site. When used in this mode, our average production was approximately 1.2 acres/day with a profile spacing of 0.75m. Using targets picked from the detection map, the MetalMapper was deployed in its static "cued ID" acquisition mode. Each target site was reacquired using GPS navigation to position the MetalMapper antenna over the target. A single static measurement consisting of 21 8ms receiver transients for each of 3 transmitter loops is acquired. When operating in the static mode, the average production rate was approximately 40pts/hr. The performance of the system during field operations met or exceeded our expectations.

Target parameters were extracted from each of the static data sets and used to compile a prioritized dig list. Targets were classified and prioritized for digging based on a combination of classification with a neural network, target identification using a library matching method based on target library consisting of 5 types, and rule-based decisions that helped to integrate everything into a final list. The neural network was trained with parameters derived from free-air static measurements from target specimens provided at the site together with ground-truth from 154 targets from a "training dig". All other dig results were withheld from the demonstrators until the dig lists were submitted and scored by the IDA. The MetalMapper scoring was based on a total of 1063 targets comprising all targets that had been dug excluding targets used for training. The discrimination scores were excellent. They show that using simple scalar features we were able to achieve a 95% probability of detection (Pd) with a very low rate of false positives (Pfp~5%). Our specified operating point was at Pd (98%). At that point our false positive rate doubles to 10%. At our operating point, we ended up leaving misclassifying 4 targets of interest. After retrospective target analyses, two of the misclassification are explainable and should probably be removed. The other two misclassifications were due to 1) a new target type (37mm projectile) that we did not train for, and 2) a deep mortar that was screened by overlying clutter.

The performance of the MetalMapper at SLO demonstrates that this new generation of advanced EMI sensors can be deployed at live sites having significant operational challenges. Discrimination performance using target parameters extracted from static-mode MetalMapper data was excellent. The performance we have shown here in this paper is confirmed and reinforced by similar performance scores returned by the IDA for three other (data processing only) demonstrators using the same MetalMapper data set. The performance scores suggest that advanced EMI systems like the MetalMapper can be used to generate dig lists that can significantly reduce the number of unnecessary digs.

Our retrospective analyses show that there is room for incremental improvement in discrimination performance. On the operational level, feed-back into the interpretation process in which new UXO types such as the 37mm projectiles are made known as soon as they are identified during digging can eliminate one source of miss-classification. Improvements in modeling software that automatically tag a target anomaly as possibly resulting from 2 or more interfering targets will also help to reduce false negatives. It is likely, however, that there will always be a few miss-classified targets no matter how sophisticated our modeling and classification methods become.

Acknowledgement

We would like to acknowledge help from Dr. Lin-Ping Song (University of British Columbia/Sky Research, Inc) for providing us with the polarizability curve estimates shown in Figure 12B. These estimates are based on his multiple target inversion program. The case history of the MM-1177 target is discussed in more detail in (Song 2010).

References

George, D. C., and D.D. "Skip" Snyder (2006). The AOL Dual-Mode (MAG/EM) System for UXO Detection and Classification. Proceedings of the UXO/Countermine Forum 2006, Las Vegas, NV.

George, D. C., and D.D. "Skip" Snyder (2007). The AOL2 Dual-Mode (MAG/EM) System for UXO Detection and Classification. Proceedings of the UXO/Countermine Forum 2007, Orlando, FL.

Grimm, R. E. (2003). "Triaxial Modeling and Target Classification of Multichannel, Multicomponent EM Data for UXO Discrimination." Jour. Envir. & Eng. Geophys **8**(4): 239-250.

MacInnes, S. C., D.D. Snyder, D.C. George, and Kenneth L. Zonge (2002). Model-Based UXO Classification Based on Static 3-Component TEM Measurements. SAGEEP Las Vegas, NV, Environ. & Eng. Geophys. Soc.

Pasion, L. R. (2007). Inversion of Time Domain Electromagnetic Data for the Detection of Unexploded Ordnance. Department of Earth and Ocean Sciences. Vancouver, B.C., University of British Columbia. **Ph.D.:** 289.

Smith, J. T., H. Frank Morrison (2004). "Estimating Equivalent Dipole Polarizabilities for the Inductive Response of Isolated Conductive Bodies." IEEE Trans. Geosci. & Rem. Sens. **42**(6): 1208-1214.

Smith, R. S., and Terry J. Jones (2002). "The moments of the impulse response: A new paradigm for the interpretation of transient electromagnetic data." Geophysics **67**(2): 1095-1103.

Snyder, D. D., and David C. George (2005). The Advanced Ordnance Locator (AOL): A Dual-Mode TEM and Magnetics System for Detection and Classification of UXO. SAGEEP 2005, Atlanta, GA, Envir. & Eng. Geophys. Soc.

Snyder, D. D., D.C. George, Scott C. MacInnes, J. Torquil Smith (2008). An assessment of three dipole-based programs for estimating UXO target parameters with induction EM. SEG 2008, Las Vegas, NV, Society of Exploration Geophysicists.

Song, L. P., Douglas W. Oldenburg, Leonard R. Pasion, and Stephen D. Billings (2009). Transient electromagnetic inversion of multiple targets. SPIE **7303**: 73030R-73030R-12.

Song, L. P., Leonard R. Pasion, and Stephen D. Billings,Douglas W. Oldenburg (2010). "Non-Linear Inversion for Multiple Objects in Transient Electromagnetic Induction Sensing of Unexploded Ordnance: Technique and Application." IEEE Trans. on Geosc. & Rem. Sens (Submitted).

USAEC. (2009, 28 Sep 2009). "Standardized UXO Technology Demonstration Site Program." Retrieved 12 Oct 2009, 2009, from http://aec.army.mil/usaec/technology/uxo01.html.

TECHNICAL OVERVIEW OF THE SEISMIC ACOUSTIC IMPACT MONITORING ASSESSMENT (SAIMA) SYSTEM

Thomas F. VanDeMark, Quantum Technology Sciences, Inc., Cocoa Beach, FL
Ray Conner, Quantum Technology Sciences, Inc., Cocoa Beach, FL
Lars B. Johnson, Quantum Technology Sciences, Inc., Cocoa Beach, FL
Jay Bennett, U.S. Army Engineer Research and Development Center, Vicksburg, MS
Janet E. Simms, U.S. Army Engineer Research and Development Center, Vicksburg, MS
Don E. Yule, U.S. Army Engineer Research and Development Center, Vicksburg, MS

Introduction

The Department of Defense (DoD) uses over two million high-explosive (HE) munitions per year at live-fire training and testing ranges, which generates unexploded ordnance (UXO) at a substantial rate. The DoD is responsible for environmental restoration of all properties (*i.e.*, BRAC, FUDS) affected from these firing range activities. Current remediation approaches that require UXO location by geophysical methods, (*e.g.*, magnetometry and electromagnetic induction) are costly because of high false alarm rates caused by the presence of scrap metal (Report of the Defense Science Task Board on UXO, 2003). The focus of this research is not to remediate ranges through the removal of UXO that has accumulated through years of firing, but to sustain present and future ranges at a zero UXO net gain status through the development of a complementary technology that will alleviate false alarm rate and reduce the UXO search area by detecting, locating, and classifying UXO in real time as a munition impacts the range. The objective is to determine the status of ordnance impacts (high order explosion, low order explosion, or dud (UXO)), and to determine the location of impacts within two meters.

Research using seismic-acoustic sensors began in 2005 to determine if it is feasible to detect, classify, and locate UXO rounds in real time as they impact the range. Initial work at Yuma Proving Ground (YPG), Arizona showed that acoustic and seismic phases propagated from HE artillery impacts and could both be observed on a seismic sensor and positively identified (Anderson and Weale, 2006; Anderson and Tinker, 2006). Follow on research at Ft. Ethan Allen, Vermont and Eagle River Flats, Alaska proved the capability to seismically discriminate between inert training rounds and high explosive impacts and to calculate seismic location solutions of explosive sources to within 10 m of actual impact location (QTSI, 2007a; QTSI, 2007b). Finally, seismic/acoustic data generated from mortar and artillery impacts at the U.S. Army Aberdeen Proving Ground (APG) in late May and early June of 2008 (VanDeMark *et al.*, 2009) and August of 2009 were analyzed to develop and validate hardware, procedures, and algorithms for an automated range monitoring system known as the Seismic Acoustic Impact Monitoring Assessment (SAIMA) system.

This paper presents an overview of the resulting prototype SAIMA system and each of its components. The system is composed of a buried seismic array, which encircles a calibrated mortar or artillery impact area, and employs a set of algorithms to detect, locate, and classify impacts. Actionable information can be presented graphically on a user interface, or within a generated event report suitable for range administration.

System Overview

Hardware Configuration

The SAIMA prototype system is composed of twelve (12), coherent, individually buried seismic-acoustic sensors (known as Q-sensors) to cover a roughly circular impact area with a radius of up to 600 meters. The sensors are evenly spaced around the impact area with respect to azimuth and are connected via fiber optic and Ethernet cable, which provides connectivity for the system. The current coverage area of the system is appropriate for monitoring of smaller munitions (*e.g.*, 60 mm, 81 mm), however the system can be scaled to cover larger areas for larger munitions (*e.g.*, 105 mm, 155 mm). In addition to the arrays of Q-sensors, a Q-sensor located near each firing point is used to detect the trigger time of the weapon firing. A UXO Monitoring Station receives input data from the sensors. Each Q-sensor converts raw sensed signals to a continuous data stream (CD1.1) format and forwards the data to the UXO Monitoring Station. The UXO Monitoring Station receives data from all sensors, processes the data, displays results, and generates an event report to system operators via a set of software subsystems (Figure 1).

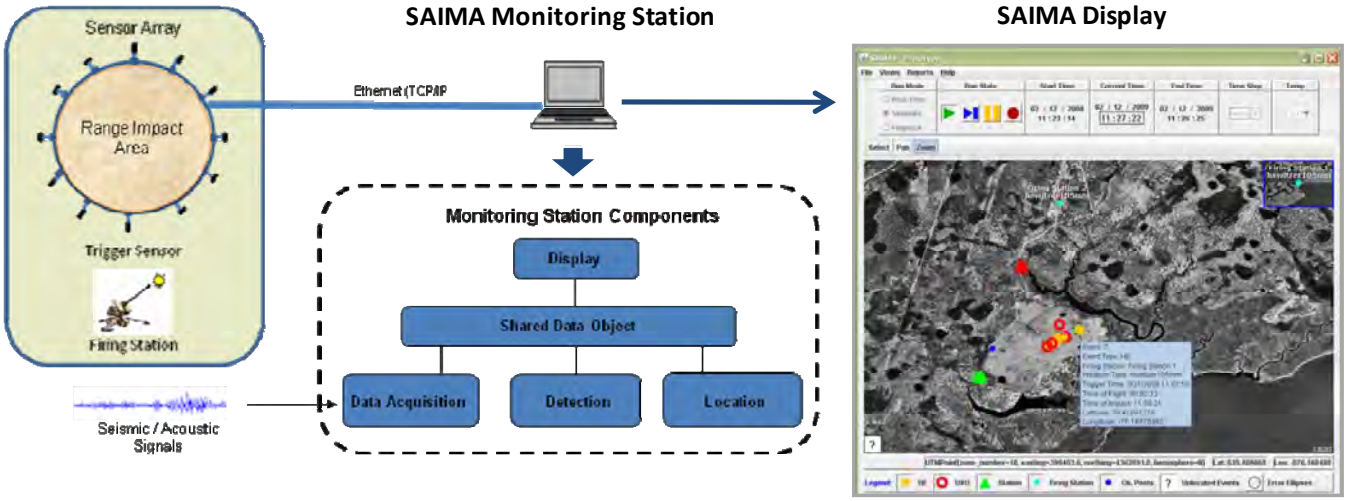

Figure 1: Layout overview of the current SAIMA system.

Software and Data Flow

The SAIMA prototype system is written in the Java programming language and based on a flexible software architecture that can be expanded with future capabilities. The program is capable of running in a Windows or Linux environment and is configurable using the standard XML format. The SAIMA flexible software architecture also provides the means to dynamically select a family of algorithms during runtime to accomplish the task of impact detection, location, and classification. An overview of the SAIMA software components is illustrated below (Figure 2).

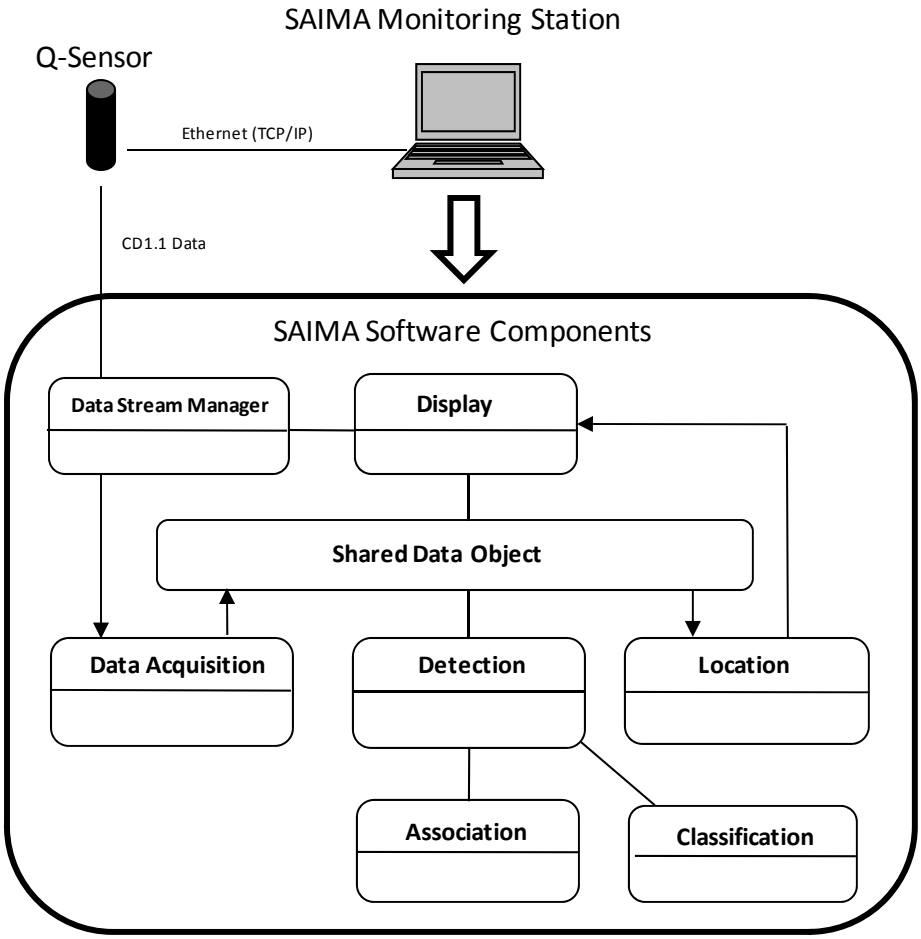

Figure 2: An overview of data flow through SAIMA software components. Data are acquired from Q-sensors which perform onboard signal processing and sensor health checks. CD1.1 data from the Q-sensors are transmitted over a TCP/IP network to the UXO Monitor Station for data processing, report generation, and display.

Graphic User Interface (GUI)

The SAIMA GUI comprises five components:

1) The **control panel** provides an interface to control the run mode and state of the SAIMA system. *Run Mode* operates in either real-time, simulate, or playback mode. The *Run State* controls the start and stop of the system in all modes. *Start* and *End Times* specify a time range for both simulate and playback modes. *Current Time* displays GPS time from the sensors in real-time. The *Temp* displays the range temperature entered by the range operator and is used for variations in the velocity model.

2) The **range map viewer** gives the user the ability to zoom and pan over the range areas as well as view events on a map in real-time, simulate, and playback mode. Symbols are used to display events and objects on a map with detailed information (*i.e.*, event type, name, and location) available when hovering over the symbol on the map. Events displayed on range map viewer can be sent to the event waveform viewer for analysis by right-clicking on an event and selecting "*Send Event to the Waveform Viewer.*"

3) The **message output window** displays information on user actions and SAIMA processing. Messages are automatically cleared when the system is stopped (Figure 3).

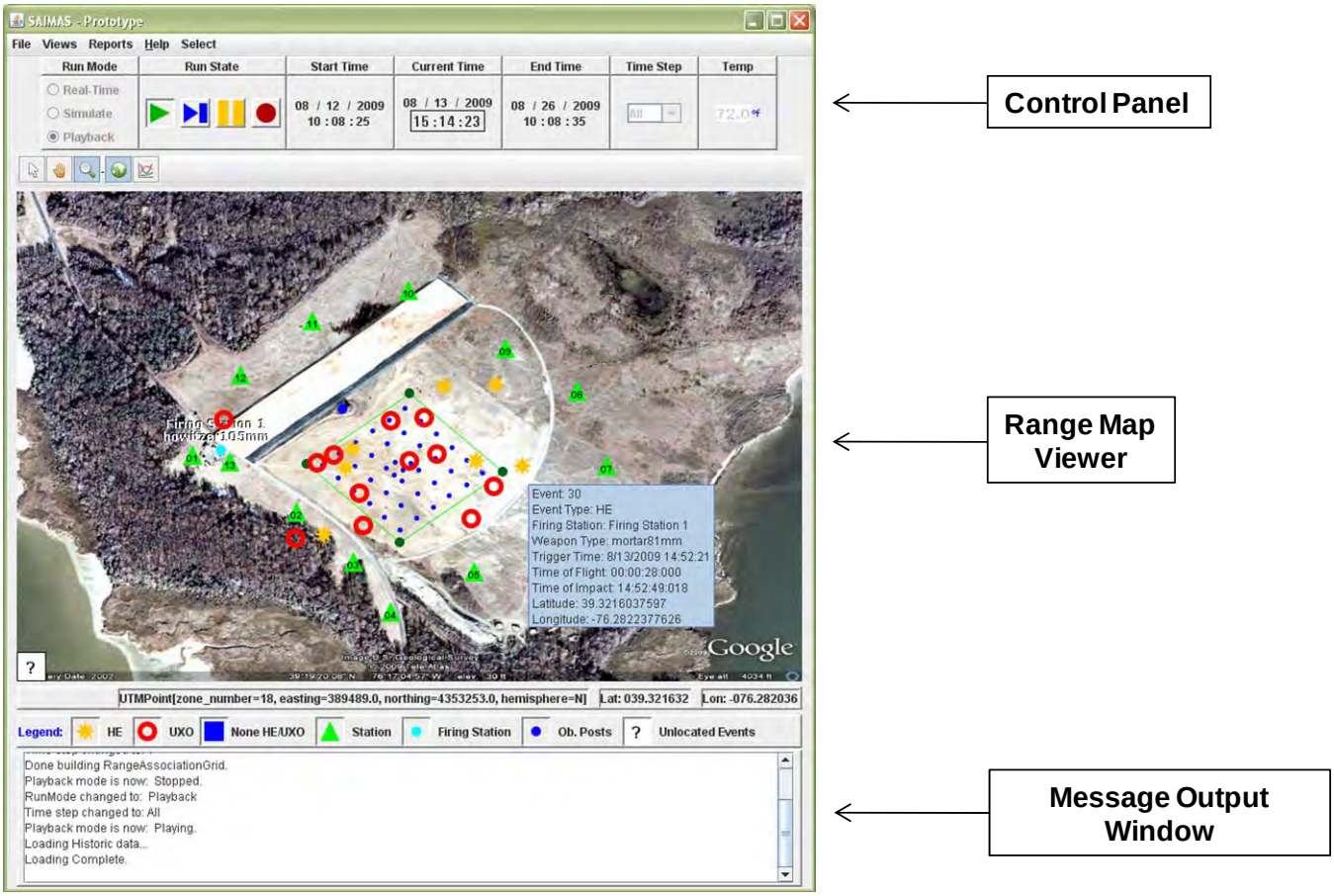

Figure 3: SAIMA GUI display of a real-time live-fire exercise at "I" Field, Aberdeen Proving Ground, Maryland. The panel above contains the control panel, range map viewer, and the message output window.

4) The **event waveform viewer** has the capability to zoom, pan, and view event waveforms in real-time, simulate, and playback mode. Detailed information on auto-detections and associations of event waveforms are displayed for analysis. The ability to ignore auto-detections and specify user arrivals is also available for analyst to analyze and improve location results (Figure 4).

5) The **event report** is generated for all detected events in real-time, simulate, and playback mode. In simulate and playback modes, reports are generated for events in the specified time range. The output report includes the event number, event type, firing station, weapon type, trigger time, time of flight, time of impact, latitude and longitude of impact, and bearing of the direction of impact (Figure 5).

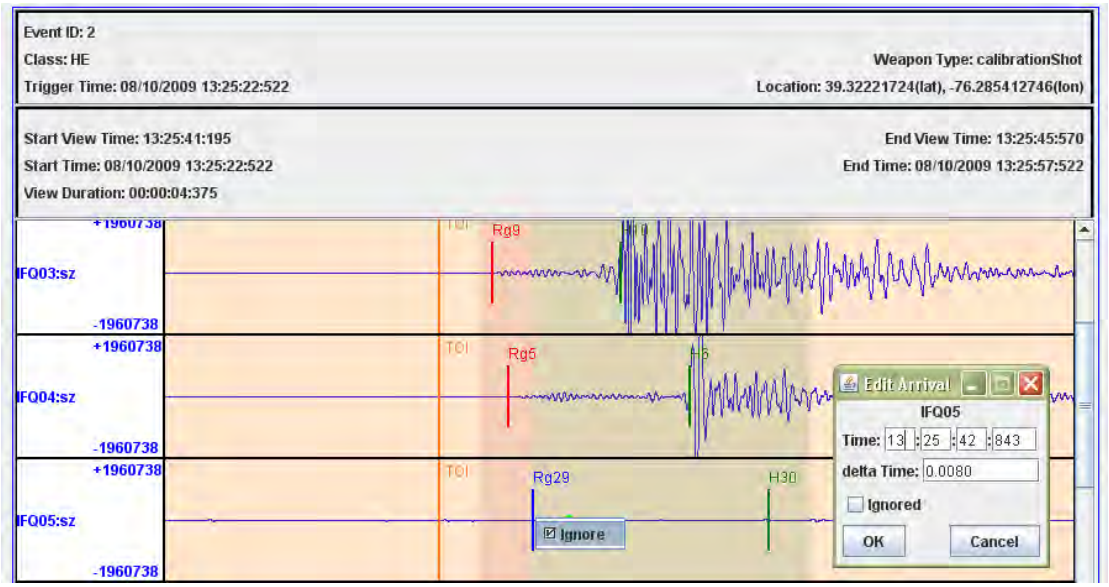

Figure 4: Event waveform viewer display of a HE event showing the system's ability to edit arrival data for a specific event.

Event	Event Type	Firing Station	Weapon Type	Trigger Time	Time of Flight	Time of Imp...	Latitude	Longitude	Bearing
1	UXO	Firing Statio...	mortar81mm	08/13/2009 13:16:47:671	00:00:28:0...	13:17:15:671	39.3218656101	-76.2837924113	90.9929...
2	UXO	Firing Statio...	mortar81mm	08/13/2009 13:20:07:604	00:00:28:0...	13:20:35:604	39.3218692325	-76.2848222795	91.1962...
3	UXO	Firing Statio...	mortar81mm	08/13/2009 13:22:37:464	00:00:28:0...	13:23:05:464	39.3221002916	-76.2843824859	86.9608...
4	UXO	Firing Statio...	mortar81mm	08/13/2009 13:26:25:778	00:00:28:0...	13:26:53:778	39.3218628872	-76.2842947476	91.1580...
5	UXO	Firing Statio...	mortar81mm	08/13/2009 13:31:20:202	00:00:28:0...	13:31:48:202	39.3224659383	-76.2852444938	78.1302...

Figure 5: An example of an event report from the SAIMA system. This report can provide range officials a tool to mitigate UXO threats.

Algorithms

Impulsive Transient Detection (ITD)

The impulsive transient detection (ITD) algorithm is similar to other auto-pickers in seismic data processing (*e.g.*, Diehl *et al.*, 2009), and is used for the detection of seismic and acoustic phases from UXO and HE events for the SAIMA system. The ITD runs only during periods when an impact event is expected to occur. This is accomplished through a synchronized trigger sensor, which upon detecting a muzzle blast at the firing point alerts the ITD to the impending event and creates a detection window for ITD to work within based on a theoretical time of impact (TOI). The ITD employs a short term averaging/long term averaging (STA/LTA) signal-to-noise ratio (SNR) technique to identify statistical changes that indicate the detection of an impulsive signal. The STA is sensitive to a rapid increase in amplitude in the time series, whereas the LTA measures the noise, interference, and clutter background in the time series. The ratio of the two becomes an estimate of the local SNR. If the ratio is higher than a threshold $\boldsymbol{T}$, a detection object is declared. The STA/LTA ratio detector operates optimally on the variance of the time series for this application; however, it also works with other derived statistical time-series (*e.g.*, absolute value, kurtosis). The ITD delineates the area of the time series that contains an

impulse by creating a detection object that is passed to the Cluster/Feature Extractor algorithm for further processing (Figure 6).

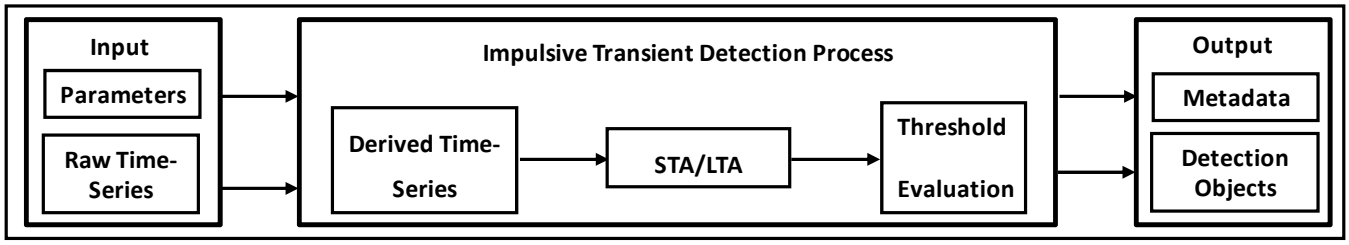

Figure 6: Flowchart of the ITD process.

Impulsive Transient Cluster Feature Extractor

The impulsive transient cluster/feature extractor (IT-CFE) takes in raw continuous data and derived information in the form of detection objects and outputs discrete cluster objects that contain the associated cluster time-series as well as cluster metadata in the form of derived statistical features. The output is in the form of discrete cluster objects that contain features derived from the entire detected time span (Figure 7). The IT-CFE performs three tasks:

1) **Cluster agglomeration** measures the temporal proximity between detection objects and applies a simple rule to determine when detection objects should be linked to form a single discrete cluster. Cluster agglomeration is designed to ensure that detection objects originating from a single impulsive source are linked into one discrete cluster object.

2) **Time segment retrieval** isolates the segment from the original, pre-discretized time series corresponding to the entire time spanned by a discrete cluster object. Using the retrieved time segment, this function applies an Akaike Information Criteria (AIC) (Akaike, 1973) method to refine the start time and duration of the discrete cluster object, and the resulting time-series segment is made available to the feature extraction function.

3) **Feature extraction** derives statistical measurements from the entire time-series segment that spans the discrete cluster object as set by the time segment retrieval function. Typically this includes such measurements as root-mean-square (RMS) and power-spectral-density (PSD); however, other measurements can be included as needed.

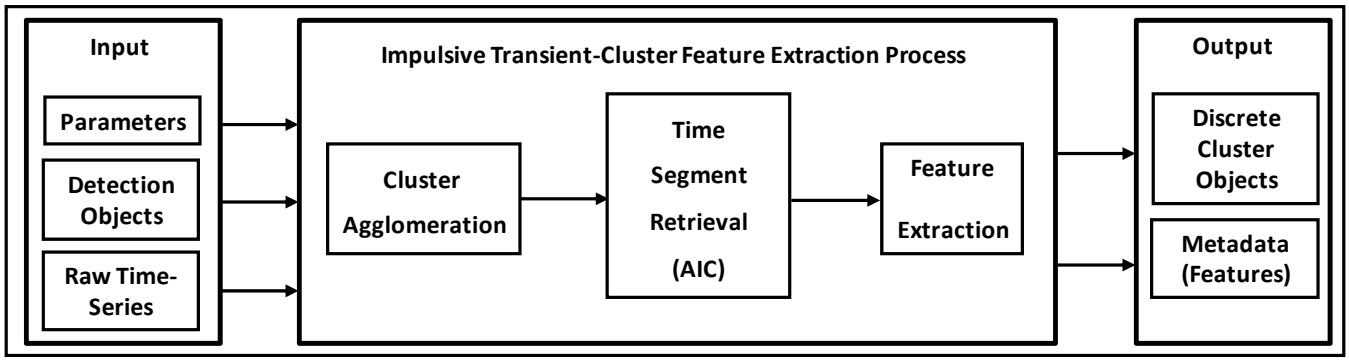

Figure 7: Flowchart of the IT-CFE process.

Impulsive Transient Phase Associator

The task of the impulsive transient phase associator (IT-PA) is to identify temporally coherent sets of discrete cluster objects from all stations and validate them as a signal of interest (*i.e.*, seismic or

acoustic) for an impact event. The IT-PA accomplishes this with the use of pre-defined seismic and acoustic phase association windows. The temporal lengths of these windows are set through a priori knowledge of station geometry and phase velocities. The IT-PA looks for a set of incoming clusters from all stations that fit within the phase association windows given the assumption that the origin of the signal is somewhere within the impact area. Once this is accomplished the clusters are validated as seismic or acoustic and labeled with the appropriate phase. The derived features from these phases are then forwarded to the location and classification algorithms for further processing (Figure 8).

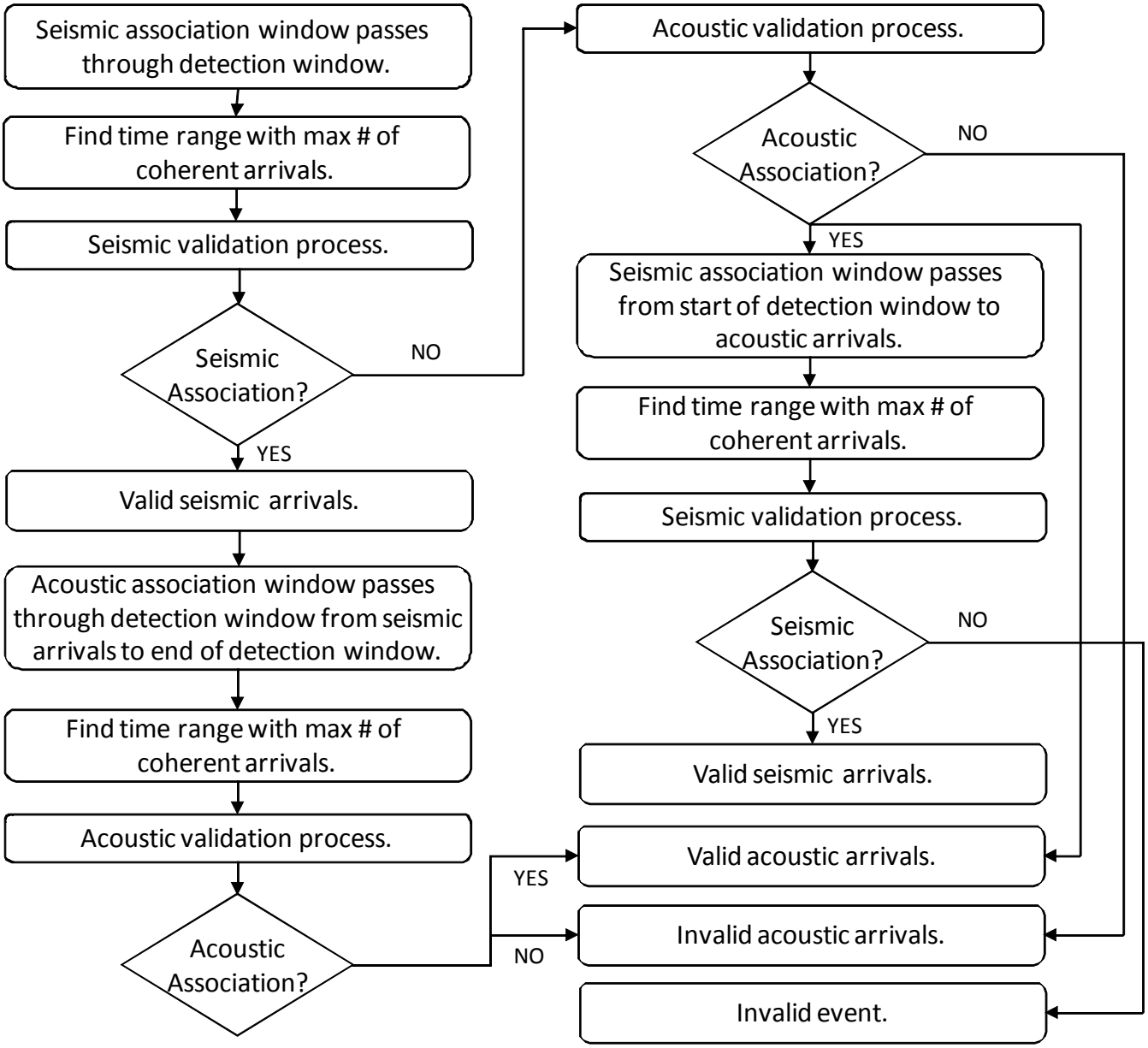

Figure 8: Flowchart of the association process.

An example of SAIMA auto-detected arrivals is shown below (Figure 9).

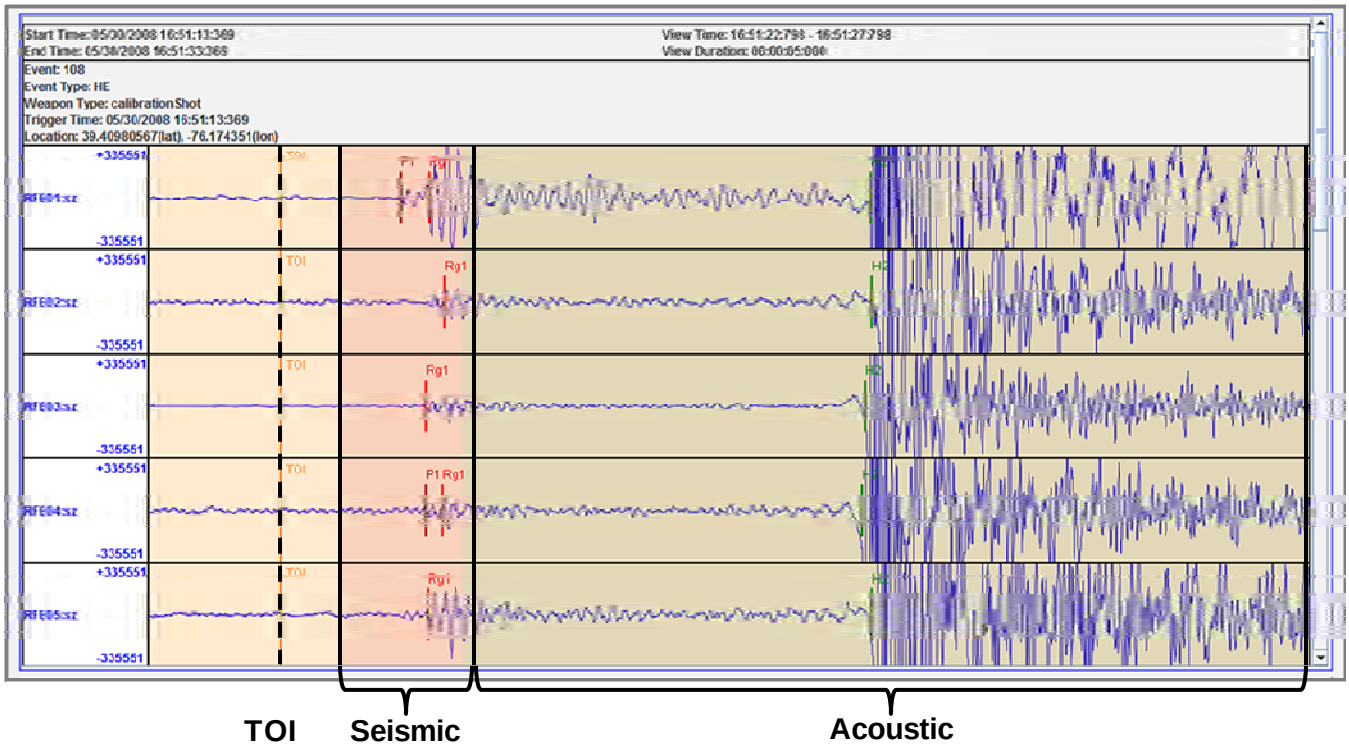

Figure 9: The SAIMA waveform viewer displaying auto-detected arrivals from a HE event within the detection window with the use of the ITD, IT-CFE, and IT-PA. Seismic body- (*P*) and surface-wave (*Rg*) arrivals (red) and acoustic-wave (*H*) arrivals (green) are present. The dashed line denotes the theoretical time of impact initiated from the trigger sensor. The seismic and acoustic time association windows are bracketed respectively.

Event Location

SAIMA utilizes the Joint Hypocenter Determination, Slowness, Azimuth, Time (JHDSAT) application to calculate location solutions for all mortar and artillery impacts. The first step is to calculate a "coarse" location solution of each impact using a single event location (SEL) algorithm (Lay and Wallace, 1995). This is followed by relocation of the event using a master event location (MEL) algorithm (Erickson *et al.*, 2003).

Specifically, the SEL algorithm uses arrival time data to determine the cartesian coordinates of the true hypocenter and the origin time, which involves relating the N arrival data (number of observations) to M hypocentral (M=4) parameters via a velocity model in a set of non-linear equations:

$$t_p = \tau_p + T_{model}(x_k,x_j), \tag{1}$$

where t_p is the predicted arrival time, τ_p is the predicted origin time of the event, and $T_{model}(x_k,x_j)$ is the travel time from the source located at x_j to the receiver located at x_k through the velocity model. Since all Earth models are approximations, the calculated travel time, T_{model}, will always differ from the true travel time T_{true} , resulting in a discrepancy between the observed and predicted arrival times:

$$r = t_o - t_p = \tau_o + T_{true}(x_k,x_j) - \tau_p - T_{model}(x_k,x_j), \tag{2}$$

where r is the travel time residual, t_o is the observed arrival time, and τ_o is the true origin time.

The goal of seismic location is to determine the hypocenter and the origin time that minimize this residual vector. Since the calculated travel time is nonlinearly related to the hypocenter location, the

above system of equations must first be linearized before standard inversion techniques can be applied. The predicted arrival times can be linearized using a Taylor-series expansion around the current hypocenter locations and dropping the second order and higher terms. Equation (2) then becomes approximately equal to

$$t_p = \tau_p + T_{model}(x_k,x_j) + \delta\tau_p + \delta T/\delta x_1|_{x_k,x_j}\ \delta x_1 + \delta T/\delta x_2|_{x_k,x_j}\ \delta x_2 + \delta T/\delta x_3|_{x_k,x_j}\ \delta x_3 + \varepsilon\,, \qquad (3)$$

where ε accounts for the error. The residual for each observation can be expressed as:

$$r = \delta\tau_p + \delta T/\delta x_1|_{x_k,x_j}\ \delta x_1 + \delta T/\delta x_2|_{x_k,x_j}\ \delta x_2 + \delta T/\delta x_3|_{x_k,x_j}\ \delta x_3\,. \qquad (4)$$

A MEL uses station corrections generated from a single, pre-determined event. For SAIMA these events are in the form of calibration shots, which are small explosive shots that are precisely placed and detonated within the impact area. The location and origin time of the event should be known exactly, otherwise the resulting station corrections will be arbitrary. The residuals for each station are calculated from the fixed location of the master event, and these residuals become the station corrections for subsequent locations of other events. For subsequent events, Eq. (2) becomes:

$$t_p = \tau_p + T_{model}(x_k,x_j) + S_n\,, \qquad (5)$$

where S_n is the correction for station n.

For all the previously mentioned location methods, a seed origin is generated for each impact, composed of latitude, longitude, depth and origin time. A seed latitude/longitude is assigned for all impacts, which is approximately the center of the impact area, and the origin depth is constrained to zero. We specify a seed origin time of 0.2 s before the first arrival at the closest array to impact. This default seed origin yields repeatable results throughout the analysis and will be configured into the future automated SAIMA system. We use the single layer over a half-space velocity model developed from the cal-shot data to make the predicted arrival times within the location algorithm.

Using the above methodology, location solutions within 2 m of impact ground truth locations have been calculated. Ongoing work is being conducted to increase the consistency of this level of accuracy (Figure 10).

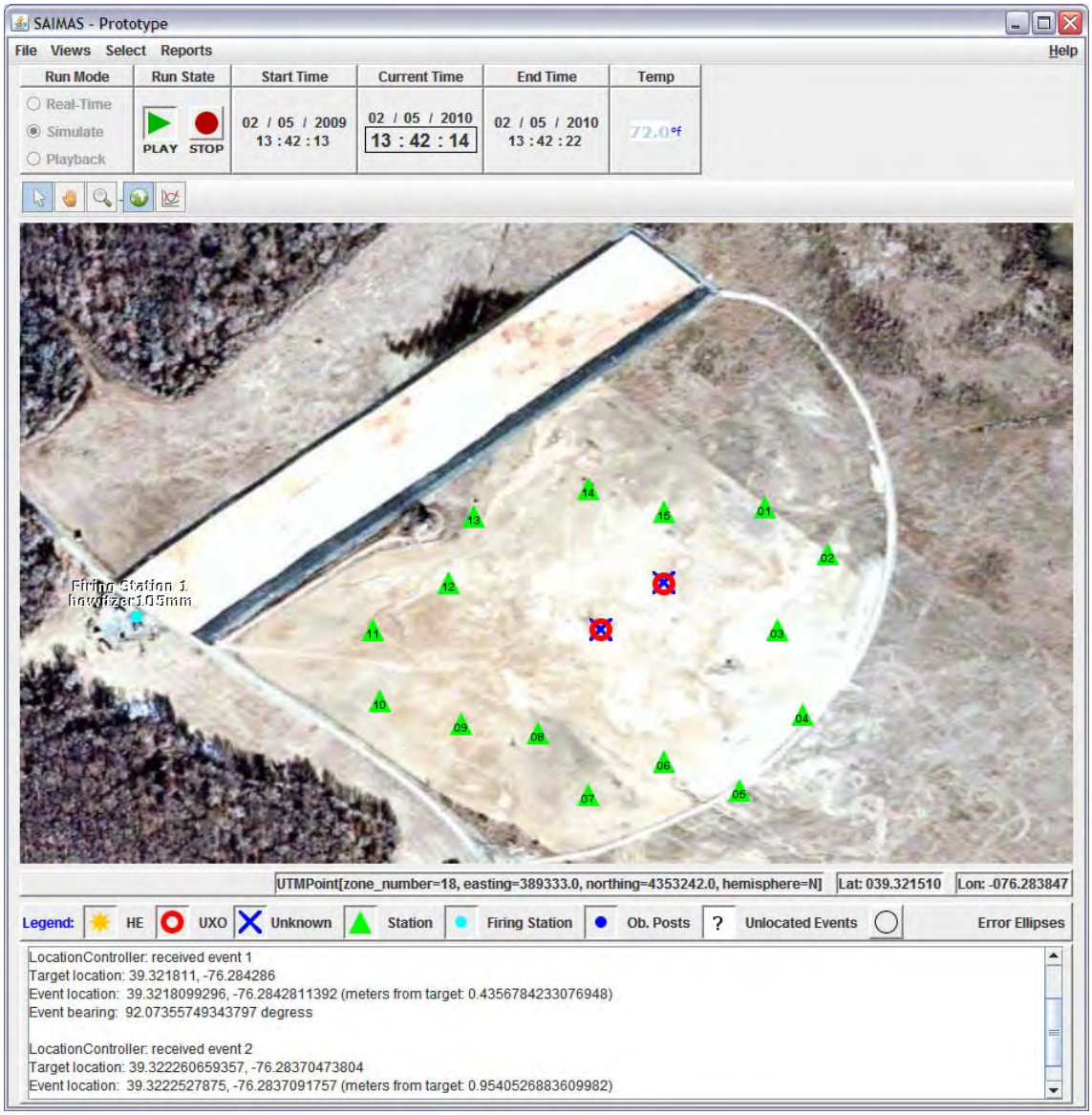

Figure 10: A screenshot of the SAIMA GUI. Location solutions (red circles) of two simulated UXO events at I-Field, Aberdeen Proving Ground, Maryland located by the system. The blue crosses closest to each solution represent the event ground truth locations. Green triangles denote active seismic-acoustic sensors, and the blue dot denotes location of the firing point. Accuracy of the locations is annotated in the message output window (bottom).

Event Classification

SAIMA utilizes a linear discrimination analysis (LDA) (Fisher, 1936; Hastie *et al.*, 2009) classification architecture to determine if an unknown event type is either HE or UXO. This is accomplished by first defining a set of classification features that are individually capable of discriminating between the two event types. The classification features used for SAIMA are mean signal energy of the seismic phase, phase ratio between the seismic and acoustic phases, and spectral ratio (VanDeMark *et al.*, 2009) (Figure 11). A training set of known event types is then defined and classification feature measurements are taken from this set. From this set of measurements a parameter estimate is created for each event type. Subsequently, as each unknown event enters into the SAIMA

system the probability of the subsequent unknown event being a member of either of the two known event types is calculated and the classification decision is made. The probability is calculated as:

$$P(x \mid type) = (x - \mu_{type})^T C_P^{-1} (x - \mu_{type}) \quad (6)$$

where x is the unknown event, μ_{type} is the mean of the training data by type, and C_P^{-1} is the inverse of the pooled covariance matrix of the training data. An initial test of the LDA on a known data set has yielded 100% accuracy discriminating between HE and UXO event types using the leave-one-out-cross-validation (LOOCV) method.

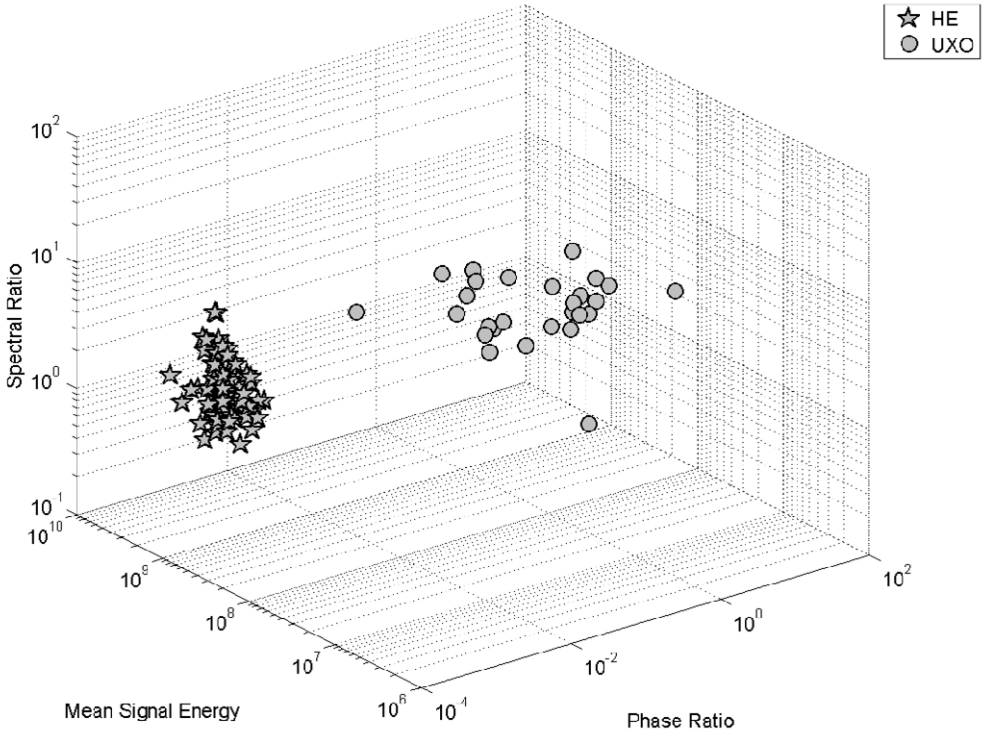

Figure 11: Multivariate plot of classification features used for SAIMA's LDA classifier. Note the clean separation between the HE and UXO event types. The data was collected at I-Field, Aberdeen Proving Ground, Maryland.

Conclusions and Discussion

The benefit of the SAIMA system is that it will drastically reduce the false alarm rate for future range cleanup operations by providing an accurate location (within 2 m) of ordnance impacts (including UXO) in real time. For a new (pristine) range area, it is conceivable that the only cost factors would be locating the UXO given the location information provided by the SAIMA system and digging and disposing of the UXO. Current ranges would still have the problem of legacy UXO, but the SAIMA system would transfer the range to a "zero UXO net gain status." This would reduce future DoD liability and contribute to long-term sustainability of the range.

An alternative application of the SAIMA system would be to serve as a training tool for mortar and artillery units by providing real-time locations of mortar and/or artillery impacts during gunnery exercises. This would give the unit real-time feedback to the accuracy of their fires, as well as the ability to play back engagements in an after-action review scenario.

References

Akaike, H., 1973, Information theory and an extension of the maximum likelihood principle, Proceedings of the 2nd International Symposium on Information Theory, Budapest, Hungary.

Anderson, T.S. and Weale, J.C., 2006, Seismic-acoustic active range monitoring for characterizing low-order ordnance detonation, Hanover: Engineer Research and Development Center/Cold Regions Research Engineering Laboratory.

Anderson, T.S., and Tinker, M.A., 2006, Seismic and acoustic location and characterization of ordnance upon emplacement: Proceedings of the UXO/Countermine/Range Forum, Las Vegas, Nevada.

Defense Science Board Task Force, 2003, Report of the Defense Science Board Task Force on unexploded ordnance: Office of the Under Secretary of Defense for Acquisition, Technology, and Logistics, Washington, D.C.

Diehl, T., Deichmann, N., Kissling, E., and Husen, S., Automatic S-wave picker for local earthquake tomography, BSSA, 99, 1906-1920.

Erickson, J., Ortiz, A., Tinker, M., Owiensy, L., Hutchenson, K., and Kraft, G., 2003, Seismic location methods and capabilities, QTSI_03/0001.

Fisher, R.A., 1936, The use of multiple measurements in taxonomic problems, Eugen., 7, 179-188.

Hastie, T., Tibshirani, R., Friedman, J., 2009, The elements of statistical learning (data mining, inference, and prediction), 2nd Edition, New York, Springer.

Lay, T., and Wallace, T.C., 1995, Modern global seismology, San Diego, Academic Press.

Quantum Technology Sciences, Inc. (QTSI), 2007a, Seismic-acoustic analysis of the Eagle River Flats data collection, Eagle River Flats, AK, U.S.A. Cocoa Beach: QTSI.

Quantum Technology Sciences, Inc. (QTSI), 2007b, Seismic-acoustic analysis of the Ft. Ethan Allen data collection, Ft. Ethan Allen, VT, U.S.A. Cocoa Beach: QTSI.

VanDeMark, T.F.,Johnson, L.B., Bennett, J., Simms, J.E., and Yule, D.E., 2009, Evaluation of seismic-acoustic analysis methods for a real-time UXO monitoring system, Proceeding of the 22nd Symposium on the Application of Geophysics to Engineering and Environmental Problems, Ft. Worth, Texas.